AusIMM

BRISBANE, AUSTRALIA
17–19 JUNE 2024

MOLTEN 2024

SUPPORTING THE TRANSITION TO SUSTAINABLE TECHNOLOGIES

Conference Proceedings

EDITED BY: P. HAYES AND E. JAK



12TH INTERNATIONAL CONFERENCE ON MOLTEN SLAGS, FLUXES AND SALTS

Supporting the Transition to Sustainable Technologies

17–19 June 2024
BRISBANE, AUSTRALIA

Edited by:
P Hayes and E Jak

The Australasian Institute of Mining and Metallurgy
Publication Series No 3/2024



Published by:
The Australasian Institute of Mining and Metallurgy
Ground Floor, 204 Lygon Street, Carlton Victoria 3053, Australia

© The Australasian Institute of Mining and Metallurgy 2024

No part of this publication may be reproduced, stored in a retrieval system or transmitted in any form by any means without permission in writing from the publisher.

All papers published in this volume were peer reviewed before publication.

The AusIMM is not responsible as a body for the facts and opinions advanced in any of its publications.

ISBN 978-1-922395-28-3

ADVISORY COMMITTEE

Emer Prof Peter Hayes
FAusIMM(CP)
University of Queensland – Conference Chair

Prof Evgueni Jak
University of Queensland – Conference Chair

Dr Denis Shishin
AAusIMM
University of Queensland – Conference Co-Chair

Dr Maksym Shevchenko
University of Queensland – Conference Co-Chair

Prof Akbar Rhamdhani
Swinburne University of Technology

Prof Brian Monaghan
University of Wollongong

Dr Chunlin Chen
CSIRO

Prof Geoff Brooks
Swinburne University of Technology

Dr Jeff Chen
University of Queensland

Dr John Rankin
Swinburne University of Technology

Prof Oleg Ostrovski
UNSW

Dr Sharif Jahanshahi
Metalogical Solutions

Dr Stuart Nicol
MAusIMM
Glencore Technology

Dr Svetlana Sineva
University of Queensland

INTERNATIONAL ADVISORY COMMITTEE

AFRICA

Buhle Xakalashe, Mintek, South Africa

ASIA AND PACIFIC

Adj Prof Gerardo Alvear, University of Queensland, Australia

Prof Chenguang Bai, Chongqing University, China

Prof Jung Wook Cho, POSTECH, Korea

Prof Yongsug Chung, Korea Polytechnic University, Korea

Prof Xiaohui Fan, Central South University, China

Dr Taufiq Hidayat, Institut Teknologi Bandung, Indonesia

Prof Shuqiang Jiao, University of Science and Technology Beijing, China

Prof In-Ho Jung, Seoul National University, Korea

Prof Youn-Bae Kang, POSTECH, Korea

Prof Jong Hyeon Le, Chungnam National University, Korea

Prof Joonho Lee, Korea University, Korea

Prof Chenjun Liu, Northeaster University, China

Assoc Prof Hiroyuki Matsuura, Tokyo University, Japan

Prof Kazuki Morita, University of Tokyo, Japan

Prof Toru Okabe, University of Tokyo, Japan

Prof Joo Hyun Park, Hanyang University, Korea

Prof Hiroyuki Shibata, Tohoku University, Japan

Prof Il Sohn, Yonsei University, Korea

Prof Toshihiro Tanaka, Osaka University, Japan

Prof Jilai Xue, University of Science and Technology Beijing, China

Prof Baijun Yan, University of Science and Technology Beijing, China

EUROPE

Dr Moritz to Baben, GTT Technologies, Germany

Prof Bo Bjorkman, Luleå University of Technology, Sweden

Prof Bart Blanpain, KU Leuven, Belgium

Prof Timo Fabritus, University of Oulu, Finland

Prof Bernd Friedrich, RWTH Aachen University, Germany

Dr Muxing Guo, Katholieke Universiteit Leuven, Belgium

Prof Miroslaw Karbowniczek, AGH University of Science and Technology, Poland

Prof Zushu Li, University of Warwick, United Kingdom

Dr Alexander Pisch, French National Centre for Scientific Research, France

Prof Markus Reuter, SMS Group GmbH, Germany

Prof Johannes Schenk, Montanuniversitaet Leoben, Austria

Prof Merete Tangstad, NTNU, Norway

Prof Emer Pekka Taskinen, Aalto University, Finland

NORTH AMERICA

Prof Antoine Allanore, Massachusetts Institute of Technology, United States of America

Prof Mansoor Barati, University of Toronto, Canada

Prof Patrice Chartrand, Polytechnique Montréal, Canada

Dr Sina Mostachel, SNC-Lavalin, Canada

Prof Chris Pistorius, Carnegie Mellon University, United States of America

Prof Ramana Reddy, University of Alabama, United States of America

Assoc Prof Leili Tafagodhi, McMaster University, Canada

SOUTH AMERICA

Prof Roberto Parra, University of Concepción, Chile

AUSIMM

Julie Allen
Head of Events

Kathryn Laslett
Conference Program Manager

REVIEWERS

We would like to thank the following people for their contribution towards enhancing the quality of the papers included in this volume:

Dr Alejandro Abadias Llamas
Dr Hamed Abdeyazdan
Adj Prof Gerardo Alvear
Prof Antoine Allanore
Dr Anton Andersson
Prof Chenguang Bai
Prof Mansoor Barati
Prof Bo Bjorkman
Prof Geoff Brooks
Dr Chunlin Chen
Dr Jiang (Jeff) Chen
Prof Jung Wook Cho
Prof Yongsug Chung
Prof Timo Fabritius
Prof Xiaohui Fan
Dr Jonah Gamutan
Dr Muxing Guo
Dr Joseph Hamuyuni
Dr Taufiq Hidayat
Dr Sharif Jahanshahi
Prof In-Ho Jung
Prof Youn-Bae Kang
Prof Miroslaw Karbowniczek
Georgii Khartcyzov
Dr Anna Klemettinen
Dr Lassi Klemettinen
Dr Alex Kondratiev
Prof Jong Hyeon Lee
Prof Joonho Lee
Prof Zushu Li
Prof Chengjun Liu
Assoc Prof Hiroyuki Matsuura
Prof Brian Monaghan
Dr Sina Mostaghel
Dr Evgenii Nekhoroshev
Dr Stuart Nicol
Prof Oleg Ostrovski
Prof Joohyun Park
Dr Alexander Pisch
Dr Chris Pistorius
Dr John Rankin
Prof Ramana Reddy
Prof Markus Reuter
Prof Akbar Rhamdhani
Prof Johannes Schenk
Dr Maksym Shevchenko
Prof Hiroyuki Shibata
Dr Denis Shishin
Dr Svetlana Sineva
Prof Il Sohn
Prof Emeritus Pekka Taskinen
Dr Moritz to Baben
Xi Rui (Jason) Wen
Prof Jilai Xue
Prof Baijun Yan
Dr Johan Zietsman

FOREWORD

On behalf of the organising committee, welcome to the 12th International Conference on Slags, Molten Salts and Fluxes (MOLTEN2024). This important series of MOLTEN conferences brings together the leading researchers and engineers from around the world to exchange information and discuss the latest ideas, developments and concepts in the field. For those interested in developing and optimising high temperature processing systems, this conference, held once every four years, is our version of the Olympics!

Our society faces major and immediate challenges in the form of the sustainability of our natural ecosystems and environment. This has resulted in commitments to transition globally to circular economy and corresponding recycling, to renewable energy, electrical power storage, the use of electricity in transportation and reduction in the use of fossil fuels. The new technologies required to achieve these objectives all rely on the use of metals and metal compounds.

The majority of metals undergo some form of high temperature processing in the molten state whether in production, refining or recycling. Critical for the design, development and optimisation of efficient, environmentally benign processes is the availability of fundamental scientific information on the physical and chemical properties of these multi-phase systems. It is the aim of this conference to make a positive contribution to the exchange and dissemination of knowledge on this important class of processing systems, and thereby enhance the rate of progress to more sustainable industrial processes.

The conference proceedings contains both peer reviewed articles, based on the oral presentations made at the conference, and summaries of poster presentations. These articles cover topics in the following themes.

1. Experimental measurements:
    - Thermodynamic properties, multi-phase equilibria, minor element distributions.
    - Physico-chemical properties (viscosity, surface tension, conductivity…).
    - Reaction / Process kinetics.
2. Mathematical descriptions:
    - Thermodynamic databases and models.
    - Physico-chemical property models.
    - Process simulations.
3. Research:
    - Industrial slag / flux / molten salt design and optimisation.
    - Refractory-melt interactions.
    - New energy and metal production technologies.
    - Recycling and environment sustainability.
4. Implementation of research outcomes by industry:
    - Application of fundamental research to industrial practice.

We trust you will find this record of discussions at MOLTEN2024 useful and stimulating.

Yours faithfully,

Peter Hayes and Evgueni Jak

on behalf of the Advisory Committee of MOLTEN2024

SPONSORS

Gold Sponsor

HATCH

Conference Dinner Sponsor

GLENCORE TECHNOLOGY

Host City Partner

brisbane australia

Supporting Partners

MET SOC
Metallurgy & Materials Society
Société de la métallurgie et des matériaux

中國金屬學會

GDMB
Gesellschaft der Metallurgen und Bergleute e.V.

PROMETHADO
ASOSIASI PROFESI METALURGI INDONESIA

I·M3 Institute of Materials, Minerals & Mining

JIMM

KIM
THE KOREAN INSTITUTE OF METALS AND MATERIALS

中国 JSOC 有色金属学会

SME
Society for Mining, Metallurgy & Exploration

SAIMM
THE SOUTHERN AFRICAN INSTITUTE OF MINING AND METALLURGY

CONTENTS

Volume 1

History of MOLTEN

The MOLTEN Conference series and research trends in slags, fluxes and salts 1980–2023 3
P Hayes and D Fadhlurrahman

Experimental measurements of – Physico-chemical properties (viscosity, surface tension, conductivity…)

Electrical conductivity measurement of CaO-Al_2O_3-CaF_2 slags by van der Pauw-Ohta Method 17
K Aya, T Sumita, N Saito and K Nakashima

Methodology development of electrical conductivity measurements for non-ferrous slags 27
P-J Boeykens, R Starykh, M Shevchenko, L Scheunis, A Van den Bulck, E Jak, I Bellemans and K Verbeken

Calcium based ternary nitrate salts for concentrating solar power applications 39
P Gandhre, V Shrotri and L Muhmood

Analysis of the melting behaviour of CaF_2-free welding fluxes using hot thermocouple technique 57
S L A Gowravaram and S Basu

Assessment of phase evolution in CaO–MgO–Al_2O_3–SiO_2 system with varied Al_2O_3/SiO_2 ratio using *in situ* high-temperature Raman spectroscopy and X-ray scattering 73
F Gyakwaa, S Wang, H Singh, G King, Q Shu, W Cao, M Huttula and T Fabritius

Effects of FeO/SiO_2 ratio and optical basicity on viscosity and melt structure of FeO–SiO_2–Al_2O_3–CaO–MgO–Cr_2O_3 melts 81
J Isaksson, A Andersson, A Lennartsson, F Gyakwaa, Q Shu and C Samuelsson

Viscosity measurement of FeO-SiO_2 based slags under controlled oxygen partial pressures 91
H-R Lee, H Shin, S-C Shim and Y Kang

Study on change in mould slag characteristics during casting Ti containing steel grades 101
P P Sahoo, M Ranjan, P Palai and C R Borra

Ionic structure analysis of relaxed surface of molten oxide slags for surface tension modelling 107
M Suzuki

In situ analysis of steelmaking slags and mold fluxes at elevated temperatures using a remote fibre-optic Raman probe 117
H Tekle, B Zhang, T Sander, J D Smith, R E Gerald II, J Huang and R J O'Malley

Viscosity of foaming fluid measured by falling-ball method 133
S Ueda, T Iwama, Y Mita and R Inoue

Monitoring Sb in lead refining using advanced techniques in Industry 4.0 141
A Van den Bulck, T De Staercke, S Zummar and T Van Rompaey

Effect of solid particle size on the viscosity of a secondary copper smelting slag 149
O Vergote, I Bellemans, K Verbeken and A Van den Bulck

Relationship between thermal conductivity and structure of alkaline earth (Ca, Mg) aluminoborosilicate melts 159
S Yamada, H Aoki, A Nakayama and K Morita

Quantitative studies on the microstructures of ternary CaO-Al_2O_3-SiO_2 glasses, melts and correlation with their high-temperature viscosities 165
J You, X Tang, F Zhang, A Canizarès, C Bessada, L Lu, K Tang, Q Zhang and S Wan

Viscosity evaluation of hot metal containing vanadium and titanium via a novel measurement technology and the thermodynamic analysis method 181
W Yu, J Wen, Z Jiang, P Hou, M Hu and C Bai

Viscosity of CaO-aluminosilicate slags 189
Z Zhang and R G Reddy

Experimental measurements of – Reaction/Process kinetics

Effect of carbon on the sintering kinetics of a single hematite pellet 201
R A Anand, N N Viswanathan and M M Pande

Synthesis of actinide chlorides for molten salt preparation 211
P Chevreux, S Serp and M Duchateau

Dissolution of quartz in Mn-slags during production of SiMn alloy 219
S Jayakumari, V Canaguier and E Ringdalen

Carburisation and melting of hot compacted iron in a coke bed 231
J Park, M Kim, I-K Suh, E Kim and J Lee

Theoretical and experimental approaches to determine the mass transfer coefficient in the steel/slag/refractory system 239
M Schickbichler, E Karimi-Sibaki, A Kharicha and S K Michelic

Sulfur loss from the slag during desulfurisation of liquid steel 251
A Sharma, M Jain, S Kumar, S Karosiya, M M Pande, N N Viswanathan and D Kumar

Deoxidation of Ti-Ni alloy by the calcium and CaF_2-$MgCl_2$ flux 261
Y Su, K S Park, J K Kim and J H Park

Comparative dissolution behaviours of recycled cement paste and lime in EAF slag under static conditions 267
M Yang, Z Yan and Z Li

Experimental measurements of – Thermodynamic properties, multi-phase equilibria, minor element distributions

Experimental study and thermodynamic modelling of phase equilibria in the FeO-$FeO_{1.5}$-$SbO_{1.5}$-SiO_2 system in equilibrium with metal 279
H Abdeyazdan, M Shevchenko, J Grogan, D Graf and E Jak

Overview of the experimental phase equilibria studies of the Ni-Sn-S, Cu-Sb-S, Cu-Sn-S, Fe-Sb-As and Fe-Sn-As systems 287
M Akhtar, M Shevchenko and E Jak

Distribution behaviour of B and P in Si-slag system at 1500°C 301
K Avarmaa, A Putera, J Chen, G Brooks and M A Rhamdhani

Phase diagram study and thermodynamic modelling of the $CaO-TiO_2-CaF_2$ system 313
J Bang and I-H Jung

Chemical- and micro-analytical techniques for molten slags, mattes, speisses and alloys 321
J Chen, P Hayes and E Jak

Coupled phase diagram experiments and thermodynamic modelling of the $CaO-SiO_2-Ga_2O_3$ system for Ga recycling 335
W O Choe and I H Jung

Increasing the deportment of titanium species to, and the stability field of pseudobrookite phase for valourisation of titaniferous slags 343
X C Goso, J Petersen and J Nell

Effect of MgO concentration on phase evolution during steelmaking slag cooling process 353
W F Gu, J Diao, H Qin, H F Yu, Y Sasaki and S Ueda

Studying the smelting behaviour of bauxite residue pellets reduced by hydrogen using high temperature thermal analysis 361
D Hariswijaya and J Safarian

The effect of iron oxide on sulfide capacities of CaO-based molten slags 375
M Hasegawa and K Saito

Effect of alumina on microstructures of iron ore sinters from the perspective of the phase equilibria of the $CaO-SiO_2-Fe_2O_3-Al_2O_3$ system 389
M Hayashi, A Takahashi, Y Uchisawa, T Watanabe and M Susa

The possibility of using an autogenous Hydrogen-DRI slag as a raw material for vanadium extraction 401
J Huss, A Vickerfält and N Kojola

Solubility of nitrogen and inclusion characteristics in high aluminium steels 413
M Ishfaq and M M Pande

Carbon distribution behaviour between molten iron and $CaO-Al_2O_3-FeO-SiO_2-MgO$ slag at 1873 K 423
Y J Jun, G H Park and J H Park

Thermodynamic behaviour of TiO_2 in $CaO-Al_2O_3-MgO-TiO_2$ slag at high temperatures 427
D Y Jung, Y J Jun, M J Lee, S J Park, S C Kang, Y-B Kang and J H Park

Equilibrium distribution of Pb between copper metal and slags 433
T Kan and C Chen

Distribution of Pb, Zn, Fe, As, Sn, Sb, Bi and Ni between oxide liquid and metal in the '$CuO_{0.5}$'-$CaO-AlO_{1.5}$ system in equilibrium with Cu metal at 1400°C 447
G Khartcyzov, M Shevchenko and E Jak

In situ observation of phase transition of silico-ferrite of calcium and aluminium 459
H Kim, J Park and J Lee

Phase equilibrium study in the sodium metasilicate primary phase field of $PbO-Na_2O-SiO_2$ system between 800 and 1000°C 471
X Ling, E Moosavi-Khoonsari and M Barati

Fusion of molten phase R&D into the metallurgical industry to drive circularity 477
S Nikolic, A Burrows, S L Nicol, O J Mendoza and B J Hogg

Phase equilibria of Al_2TiO_5–Ti_3O_5 pseudobrookite solid solution in the Al_2O_3–TiO_x system under various oxygen partial pressures 487
Y-J Park, W-Y Kim and Y-B Kang

Boron removal through multistage refining treatment using $CaO-SiO_2-Al_2O_3$ slag 495
A D P Putera, K L Avarmaa, H T B M Petrus, G A Brooks and M A Rhamdhani

Activities of components in Ca_2SiO_4-$Ca_3P_2O_8$ solid solution at 1573 K 505
K Saito and M Hasegawa

Thermal analysis of molten salts and their mixtures with metals 517
D Sergeev, J Qi, S Gezgin, D Rapp, A Lichtinger, F Beckstein and M Müller

Advancement in experimental methodologies to produce phase equilibria and thermodynamic data in multicomponent systems 531
M Shevchenko, D Shishin and E Jak

Experimental and thermodynamic study of the phase equilibria in the $NiO-CaO-FeO-Fe_2O_3$ system in air and in equilibrium with metal (Fe-Ni) alloy 559
S Sineva, M Shevchenko, D Shishin and E Jak

Slag chemistry on the Moon 569
S P Singh, G A Brooks, M G Shaw, B Eisenbart, A R Duffy, M A Rhamdhani and A K Shukla

Phase relationship of quaternary system $FeO-Al_2O_3-SiO_2$-‘V_2O_3’ at 1873 K and its impact during melting of H-DRI for possible vanadium extraction 581
A Vickerfält, J Huss and J Martinsson

Phase diagram of $V_2O_3-Fe_tO-SiO_2-CaO$(15 mass%) system at 1623 K 585
B Yan, D Wang, T Deng, B Song and Q Shu

Implementation of research outcomes by industry – Application of fundamental research to industrial practice

Understanding the side-blown furnace slag system at Glencore Nordenham’s lead plant – from theory to industrial application 599
A Abadias Llamas, A Kandalam and C Zschiesche

Improving industrial copper processing operations through the application of thermodynamic fundamentals and advanced predictive tools 611
G R F Alvear Flores

Visualisation of calculated thermodynamic properties by integration of FactSage™ with SEM-EDS element maps 625
N Barrett, S Mitra, E Copland, D O’Dea and T Honeyands

Transient slag behaviour in the Direct Reduced Iron (DRI) and scrap-based Electric Arc Furnace (EAF) process – case study for high and low-grade DRI input 635
S Chatterjee, S K Panda and M A Van Ende

Practicalities of the use of fayalite slags for recovery of metals from urban wastes 647
J Chen, S Nicol, B Hogg, E Jak and S Nikolic

Research on *in situ* recovery technology of hot-dip galvanized dross 651
R Chu, X Deng and X Li

Direct observation of the fayalite slag formation behaviour from large SiO_2 grains 653
Y Goto, S Kawanishi, S Natsui, J Takahashi and H Nogami

Combining the power of computational thermochemistry with the convenience of Python within the digital platforms of SMS group GmbH 663
S Khadhraoui, M Reuter, A Akouch, C Kirmse, T Yusuf, R Degel, N Borowski and E Hecker

Hy^3 (Hy-cube) project – Hyundai Steel's carbon neutral strategy 671
H Kim and M J Sun

Characterising bubble size distribution and generation position in iron oxide-containing slag smelting reduction 675
K Ohno and T Kon

A study of heat and material balances in direct reduction plant with various conditions 685
M J Sun and H Kim

Reducing CO_2 emissions from the ferro-alloy and silicon production 691
M Tangstad and G M Tranell

Thermal phosphorus – it's a hot commodity with a hot process 705
E Wingate, Y Liu, R Prasad, R Atmuri and W Liang

Mathematical descriptions of – Physico-chemical property models

Combined molecular dynamics – experimental investigation of oxidic slag properties 715
I Bellemans, A Maslov, D Seveno and K Verbeken

Molecular dynamics simulation of viscosity of selected pure oxide melts 725
A E Moiseev and A Kondratiev

Evaluation of thermal conductivities of molten SiO_2-Al_2O_3-CaO slags 735
K Tang, M Zhu, J You, X Ma and G Tranell

On the development of a viscosity model for molten multicomponent slag systems with several glass-forming, amphoteric and modifier oxides 743
G M Zhomin, A S Arkhipin and A Kondratiev

Determining the properties of CaO-Al_2O_3-SiO_2 slags from molecular dynamics simulation 759
M Zhu and J Safarian

Mathematical descriptions of – Process simulations

Process modelling and high-throughput thermochemical calculations using ChemApp for Python 771
Ö K Büyükuslu, F Tang, M Baben and S Petersen

An investigation of potential wear occurring on refractory lining and coating formation – a remedy of wear in a basic oxygen steelmaking furnace using CFD modelling 781
R Chowdhury, S Mitra, G Evans, T Honeyands, B J Monaghan and D Scimone

Modelling of gas-slag flow behaviour in the ironmaking blast furnace – a review 795
X F Dong, B J Monaghan and P Zulli

Molten slag flow in an ironmaking blast furnace – a mesoscopic level investigation 807
X F Dong, A Jayasekara, D Sert, R Ferreira, P Gardin, S J Chew, D Pinson, B J Monaghan and P Zulli

A phenomena-based model to investigate the possibility of scrap melting in an Open Slag Bath Furnace (OSBF) for green ironmaking 821
A Emami, S van der Sluijs, M van Ende and Y Tang

Modelling of liquid/liquid interface movement during spindle rotation of refractory – slag corrosion test 831
H Lee, B Choi and Y Chung

CFD modelling of slag fuming, with focus on freeze-lining formation 839
C M G Rodrigues, M Wu, M Chintinne, A Ishmurzin, G Hackl, N Voller, A Ludwig and A Kharicha

Integrated process modelling for the Kalgoorlie Nickel Smelter 847
G Sartor, A Rich, D Grimsey, M White and R Forzatti

Pyrometallurgical process simulations using CALPHAD thermodynamic databases 857
M-A Van Ende, N Kumar and I-H Jung

Development of a nitrogen prediction model for 320 tonne converter 871
C M Yoon, C-H Eom, Y D Jeon and K S Kim

Efficient material descriptions for modelling high-temperature processes 877
J H Zietsman

Volume 2

Mathematical descriptions of – Thermodynamic databases and models

Thermodynamic modelling of species distribution in $AlCl_3$:BMIC salts 895
M K Nahian and R G Reddy

Continuous method of thermodynamic optimisation using first-derivative matrices for large multicomponent systems 901
E Nekhoroshev, D Shishin, M Shevchenko and E Jak

Thermodynamic modelling of the Fe-Al-Ti-O system and evolution of Al-Ti complex inclusions during Ti-added ultra-low carbon steel production 915
Y-J Park and Y-B Kang

Sulfur distribution ratio in iron and steelmaking slags 923
R G Reddy and A Yahya

Challenges and limitations in development of large thermodynamic databases for multiple molten phases using the Modified Quasichemical Formalism 931
D Shishin, M Shevchenko, E Nekhoroshev and E Jak

Prognostic models for electroslag remelting process and slag engineering 949
G Stovpchenko, L Medovar, L Lisova, D Stepanenko and D Togobitskaya

Research on – Industrial slag/flux/molten salt design and optimisation

Recent advances in understanding phosphorus in oxygen steelmaking 965
G Brooks

Reoxidation of Al-killed ultra-low C steel by Fe_tO in $CaO-Al_2O_3-MgO_{sat.}-Fe_tO$ slag representing RH slag by experiment and kinetic modelling 971
Y-M Cho, W-Y Cha and Y-B Kang

Effect of liquefaction controlling components in carbon-free mould powder for the continuous casting of ultra-low carbon steels 979
N Gruber

Fluxing options and slag operating window for Metso's DRI smelting furnace 997
J Hamuyuni, K Vallo, T Haimi, F Tesfaye, J Pihlasalo and M Lindgren

Mixed alkali effect on structure of Al_2O_3-based slags 1007
S H Hyun and J W Cho

Effect of solid-solved FeO and MnO on hydration of free MgO in steelmaking slag 1013
R Inoue, N Kado, T Iwama and S Ueda

University research on molten slags, matte, speiss and metal systems for high temperature processing – challenges, opportunities and solutions 1029
E Jak, M Shevchenko, D Shishin, E Nekhoroshev, J Chen and P Hayes

Genetic design of personalised slag for manufacturing die steel via electroslag remelting method and an industrial application case 1061
Z H Jiang, Y M Li, J L Tian and J W Dong

Flux smelting behaviour of pre-reduced Mn ore by hydrogen at elevated temperatures 1077
P Kumar and J Safarian

Machine learning for predicting chemical system behaviour of $CaO-MgO-SiO_2-Al_2O_3$ steelmaking slags case study 1087
B Laidens, W Bielefeldt and D Souza

Perspectives of chemical metallurgy fundamentals in slag innovation 1109
S Lee and I Sohn

Effect of slag composition on titanium distribution ratio between ferrosilicon melt and $CaO-SiO_2-Al_2O_3$ slag at 1773 K 1117
M J Lee and J H Park

Using novel methods to characterise slag films for continuously casting challenging and innovative steel grades 1123
Z Li, T Zhang, S Qin, X Yang, Z Yan, P Wilson and M A Williams

The recovery of pig iron from the Zimbabwean limonite-coal composite pellet 1135
S Maritsa, S M Masuka and E K Chiwandika

Effect of SiO_2 on the structure and crystallisation of CaF_2-CaO-Al_2O_3 slag used in electroslag remelting 1149
P M Midhun and S Basu

A machine learning model to predict non-metallic inclusion dissolution in the metallurgical slag 1169
W Mu, C Shen, C Xuan, D Kumar, Q Wang and J H Park

Effect of C/A ratio on the crystallisation behaviour and structure of calcium-aluminate based alternative mold fluxes for casting medium and high Mn/Al steels 1177
A Nigam, K Biswas and R Sarkar

Improving cobalt extraction through oxidative blowing of copper-nickel matte 1187
R A Pakhomov, P V Malakhov, L V Krupnov and I M Dymov

Comparative study of oxide dissolution modelling in secondary steelmaking slags 1195
N Preisser and S K Michelic

Impurity capacities of non-ferrous slags 1205
R G Reddy

Flow investigation of multiphase manganese slags 1217
V Rimal and M Tangstad

Improvement of the copper flash smelting furnace (FSF) and the slag cleaning furnace (SCF) process by advice-based control of silica and coke addition 1231
A Schmidt, S Winkler, E Klaffenbach, A Müller, V Montenegro and A Specht

Characterisation and assessment of B_2O_3 added LF slag 1235
S Soumya Varanasi, K Sripushpa, M Bhaskara Venkata Rao, S Mahboob Basha and A Kamaraj

Slag-steel reactions in the refining of advanced high-strength steel 1249
P Su, P C Pistorius and B A Webler

Crystallisation control of CaO-SiO_2-Al_2O_3-MgO system inclusion 1259
Y Wang, S Sukenaga, W Z Mu, H Zhang, H W Ni and H Shibata

Effect of Al_2O_3/SiO_2 ratio on structure and properties of mould flux for high-Al steel continuous casting 1267
Q Wang, J Zhang, O Ostrovski, C Zhang and D Cai

Pushing the boundaries of slag operability – processing of high-MgO nickel concentrates with the Ausmelt TSL process 1281
J Wood, J Coveney, S Creedy, D Grimsey and A Rich

A fundamental investigation on welding flux tunability geared towards high heat input submerged arc welding for shipbuilding applications 1297
H Yuan, H Tian, Y Zhang, Z Wang and C Wang

Electrodeposition and electrochemical behaviour of molybdenum ions in $ZnCl_2$-NaCl-KCl molten salt 1305
H Zhang, S Li, Z Lv and J Song

Development of solid waste-based flux and its application in out-of-furnace dephosphorisation of low-silicon hot metal 1315
Z Zhao and Y Zhang

Analysis on composition and physical-chemical property change of PbO-bearing slag in Pb smelting 1325
J X Zhao, Y R Cui, G Cao, G H Wang, B Li, M M Ren, Z M Wang and H P Gui

Slag volume effects on direct-reduced iron (DRI)-based electric furnace steelmaking 1337
Q Zhuo, P C Pistorius and M N Al-Harbi

Research on – New energy and metal production technologies

An attempt towards ferrochromium production using molten oxide electrolysis 1349
J Biswas, L Klemettinen, D Sukhomlinov, W Malan and D Lindberg

Ferroalloy extraction from a Zimbabwean chrome ore using a closed DC furnace 1361
S Dandi, M J Masamvu, S M Masuka, S B Chinosengwa and E K Chiwandika

Production of molybdenum disilicide using a silicon-containing molten bath via the hot dipping method 1375
J Gamutan, H Fukaya and T Miki

Reduction and melting behaviours of carbon – iron oxide composite using iron carbides and free carbon obtained by vapour deposition 1387
R Higashi, D Maruoka, Y Iwami and T Murakami

Electrolytic reduction of metal sulfides/oxides in molten salts for sustainable metal production 1395
X Hu, L Sundqvist Ökvist and J Björkvall

Aluminothermic production of silicon using different raw materials 1401
K Jakovljevic, N Simkhada, M Zhu, M Wallin and G Tranell

Manufacturing of FeSiB high-temperature phase change material by silicothermic reduction 1413
J Jiao, M Wallin, W Polkowski and M Tangstad

Physical properties optimisation of the Zimbabwean limonite ore-carbon composite pellets as a sustainable feed for pig iron production 1423
S M Masuka, D Simbi, S Maritsa and E K Chiwandika

State-of-the-art of electroslag refining and challenges in the control of ingot cleanness 1429
L Medovar, G Stovpchenko and G Jianjun

Hydrogen plasma in extractive metallurgy application 1445
B Satritama, D Fellicia, M I Pownceby, S Palanisamy, A Ang, G A Brooks and M A Rhamdhani

Challenges facing non-ferrous metal production 1455
P Taskinen and D Lindberg

The extraction of white phosphorus in molten salt 1465
X Yang

Research on – Recycling and environment sustainability

The effect of FeO/SiO_2 ratio on the feasibility of utilising iron silicate slags as supplementary cementitious materials 1471
A Andersson, J Isaksson, L Brander, A Lennartsson, Å Roos and F Engström

Pyrometallurgical treatment of nickel smelting slag with biochar 1481
D Attah-Kyei, D Sukhomlinov, M Tiljander, L Klemettinen, P Taskinen, A Jokilaakso and D Lindberg

An investigative study on the interfacial behaviour of waste graphite resource with liquid iron 1495
S Biswal, S Udayakumar, F Pahlevani, N Sarmadi and V Sahajwalla

Distribution of impurity elements in oxygen-enriched top-blowing nickel smelting with Fe extraction-oriented slag adjustment 1501
G Cao, J Zhao, J Wang, S Yue, B Li, J Zheng, Y Cui and H Zong

Lessons learned from attempts at minimising CO_2 emissions in process metallurgy – pyrolysed secondary raw materials, bio-coke, and hydrogen as alternative reducing agents 1519
F Diaz, M Sommerfeld, G Hovestadt, D Latacz and B Friedrich

A short review – hydrogen reduction of copper-containing resources 1533
D M Fellicia, M I Pownceby, S Palanisamy, R Z Mukhlis and M A Rhamdhani

Smelting of different hydrogen-reduced bauxite residue-calcite pellets for iron and alumina recovery 1543
M K Kar and J Safarian

Effect of mill-scale and calcined dolomite on high Al_2O_3 sinter and its reduction behaviour 1553
S J Kim, L Tomas da Rocha, S W Kim and S Jung

Slag-metal interfacial reactions in pyrometallurgical processing of industrial wastes for recovery of valuable metals 1565
H J Kim, R R Kim, H S Park and J H Park

Towards integration of pyro- and hydrometallurgical unit operations for efficient recovery of battery metals from waste lithium-ion batteries 1571
L Klemettinen, J Biswas, A Klemettinen, J Zhang, H O'Brien, J Partinen and A Jokilaakso

Physicochemical properties of steelmaking slags for the mitigation of CO_2 emissions in steel sector 1585
M J Lee, J H Heo and J H Park

Understanding zinc-containing species in basic oxygen steelmaking dust 1591
R J Longbottom, D J Pinson, S J Chew and B J Monaghan

Effect of oxygen on the interfacial phenomena and metal recovery rate in recycling process 1603
J Park, Y-B Kang and J H Park

Measuring circular economy through life cycle assessment – challenges and recommendations based on a study on recycling of Al dross, bottom ash and shavings 1609
E Pastor-Vallés, A Vallejo-Olivares, G Tranell and J B Pettersen

A thermodynamic and sustainability assessment of PCB recycling through the secondary Cu smelting process 1621
P Tikare, M Mohanasundaram, R Kumar and A Kamaraj

Melting behaviour investigation of municipal solid waste incineration fly ash samples from different incineration technologies for metal recovery – an integrated experimental and thermodynamic modelling approach 1631
E Soylu and G Tranell

Conversion of hard-to-use wastes to new raw materials for low-energy glass/mineral-wool manufacturing 1643
Z Yan, T Htet, S Zhang and Z Li

Research on – Refractory-melt interactions

Radical involved reaction and weak magnetic effect between alumina refractory and high alumina slags 1655
A Huang, S H Li and H Z Gu

On the stability of CaS in liquid steel containing alumina or spinel inclusions 1665
S Kumar, N N Viswanathan and D Kumar

Corrosion behaviour of ferrite and aluminate refractories in cryolite-aluminium melts 1675
R Z Mukhlis and M A Rhamdhani

The interaction between slag and MgO refractory at conditions relevant to nickel laterite ore smelting 1693
Y H Putra, Z Zulhan, A D Pradana, D R Pradana and T Hidayat

Author Index 1709

History of MOLTEN

The MOLTEN Conference series and research trends in slags, fluxes and salts 1980–2023

DOI: 10.62053/HZBP9541
P Hayes[1] and D Fadhlurrahman[2]

1. Emeritus Professor, PYROSEARCH, University of Queensland, Brisbane Qld 4072. Email: p.hayes@uq.edu.au
2. PhD student, PYROSEARCH, University of Queensland, Brisbane Qld 4072. Email: d.fadhlurrahman@uq.edu.au

ABSTRACT

Molten slags, fluxes and salts play key roles in a wide range of the high temperature industrial process applications, including metals production, refining and recycling, metal manufacturing processes, electrochemical metal production cells, batteries, and efficient heat transfer media. Recognising the importance and significance of fundamental scientific knowledge of these systems, the International MOLTEN Conference series was established to provide a forum to bring together leading academic researchers and industrial engineers to present and discuss the latest scientific ideas and findings, and their application in their respective fields. This article presents an analysis of the research carried out in this field over time in terms of the number of journal articles, fields and slag systems studied and geographical origin of the research.

INTRODUCTION

Brief history of the MOLTEN Conference series

The MOLTEN Conferences, a series of international conferences on molten slags, fluxes and salts, provide a platform for presenting and discussing the latest scientific findings and advances in this field of research with particular focus on applications to metallurgical processing.

The conference series started in 1980 with the International Symposium on Metallurgical Slags, held in Halifax (Nova Scotia), Canada. The conference was initiated by Charles Masson, National Research Council of Canada at the Atlantic Research Laboratory, and Jim Toguri, University of Toronto. The success of this first slag symposium led to the establishment of the MOLTEN Conferences, which have been held every four years since then in different parts of the world (see Table 1). The conferences are led by academic researchers supported by advisory committees made up of leading researchers from around the world. The MOLTEN Conference is now fondly regarded as the ‘Slag Olympics’. The conference attracts leading academic researchers focusing on fundamental scientific issues and engineers working on industrial research and development in this field.

TABLE 1

History of the MOLTEN Conference series.

MOLTEN Conference #	Year	Country, Venue	Chairs
1	1980	Canada, Halifax	Masson, Toguri
2	1984	USA, Lake Tahoe	Gaskell
3	1988	Scotland, Glasgow	Bell
4	1992	Japan, Sendai	Banya
5	1996	Australia, Sydney	Belton
6	2000	Sweden, Stockholm; Finland, Helsinki	Seetharaman, Holappa
7	2004	South Africa, Cape Town	Pistorius, Geldenhuis
8	2008	Chilie, Santiago	Sanchez
9	2012	China, Beijing	Chou
10	2016	USA, Seattle	Reddy
11	2020/21	Korea, Seoul	Min, Choi
12	2024	Australia, Brisbane	Hayes, Jak

Our particular thanks go out to the hosts of the 11th MOLTEN Conference held in Korea – Conference Chairs Min and Choi, Conference Secretary Prof Joohyun Park, and the many volunteers and industry sponsors who made this possible. This conference was due to be held in 2020 at the height of the COVID pandemic. It was postponed and held as a virtual online conference in 2021. This involved not only organising the conference twice but also ensuring the smooth delivery over a relatively new computer platform across time zones around the world. Our gratitude goes out for these efforts and for ensuring that the MOLTEN Conference series goes on without interruption. A truly great effort!

PROFILE OF RESEARCH PUBLICATIONS IN THE FIELD

As part of the proceedings of MOLTEN 1996 Conference, Boom and Mills (1996) initiated a series of surveys on the changing trends in research on slags. This series continued for each MOLTEN Conference until 2012, Boom and Mills (1997, 2000); Boom, Riaz and Mills (2000, 2004, 2005, 2009, 2010) and Boom *et al*, (2012). The surveys contain information on the total number of research papers published each year and the breakdown of research topics including slags, mould fluxes, casting powders and mattes. The surveys covered the period 1980 to 2011, that is starting from the year of the first MOLTEN Conference. These previous reviews were carried out using the METADEX database, which is no longer available. Where direct comparison is possible these previous data have been used to assess the overall trends with time.

In the following pages we provide the findings of a review aimed at continuing the analysis of research trends using the currently available ‘Scopus database’. Since it has not been possible to repeat exactly the metadata and methodology used in the previous reviews the current review covers the data available from 2011 onwards. Following as closely as possible to the previous reviews, the current methodology has involved firstly selecting the search Keywords ‘slag(s)’, ‘matte(s)’ and ‘speiss’. As was the case for the previous reviews ‘salts’ were not used as a keyword in the search since this was not found to be sufficiently selective as to be able to give an accurate indicator of relevant activities. Metallurgical Engineering is not listed as a discipline area in the Scopus database. To retain the focus on metallurgical practice, the search was limited to only those papers under ‘Material Science’ and ‘Chemical Engineering’ subject areas. Only journal articles were included but contributions from all language groups were examined. Paper titles and abstracts were examined to

refine the sorting of the articles into appropriate categories in terms of the subject matter studied to ensure the papers included in the survey related to metallurgical processes. The country of origin of an article was selected based on the address of the corresponding author. The searches did not include articles that principally provided descriptions of metallurgical processing operations and industrial practices rather the focus was on fundamental research reported in peer-reviewed scientific literature.

Annual number of published research articles

The numbers of papers published annually in all topic areas obtained using METADEX searches by Boom and colleagues for the years 1980 to 2010 (Boom and Mills, 1996; Boom and Mills, 1997, 2000; Boom, Riaz and Mills, 2000, 2004, 2005, 2009, 2010) are given in Figure 1 and Table 2, and data for the current SCOPUS searches for the period 2011–2023 are given in Figure 2 and Table 3. The total numbers of articles published in 2011 obtained using the METADEX and SCOPUS searches data differ; the SCOPUS data being approximately half that in the previous survey set. There may be several reasons for the differences, for example the origin and content of the data sets used compiled by the respective databases and the methodologies and criteria used in selecting the data. For these reasons direct comparison is not appropriate other than to demonstrate overall trends, and the analyses of these sets have been kept separate.

As noted by the research, the reported overall level of research activity was relatively constant between 1980 and 2000, then there was a rapid increase in the number of articles published, almost doubling in volume, by 2008. This was followed by a dramatic reduction to back down to the 1980 level of activity by 2010. This downward trend appears to closely correspond to the impacts of the global financial crisis (GFC) between mid–2007 and early 2009, a period of extreme stress in global financial markets and in the banking systems.

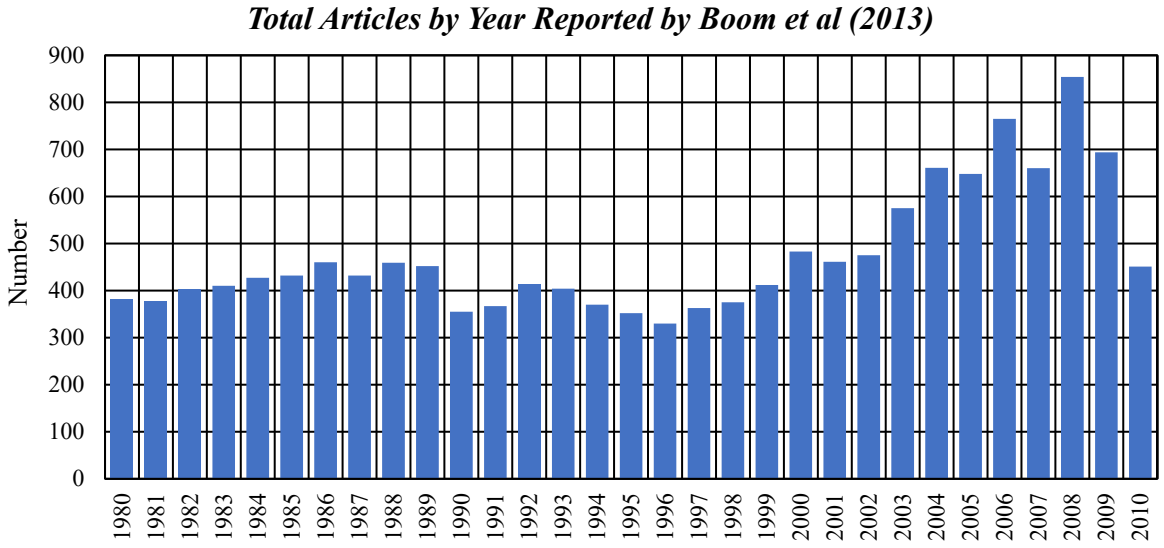

FIG 1 – Number of research articles on molten slag and fluxes reported by Boom *et al* (2012) for the period 1980–2010 retrieved from METADEX.

TABLE 2

Number of research articles on molten slag and fluxes by year in the period 1980–2010 reported by Boom *et al* (2012).

Year	Articles	Year	Articles	Year	Articles	Year	Articles
1980	382	1988	459	1996	330	2004	661
1981	378	1989	452	1997	363	2005	648
1982	403	1990	355	1998	375	2006	765
1983	410	1991	367	1999	412	2007	660
1984	427	1992	413	2000	483	2008	854
1985	432	1993	404	2001	461	2009	694
1986	460	1994	370	2002	475	2010	451
1987	432	1995	352	2003	575		
					Total articles		**14 703**

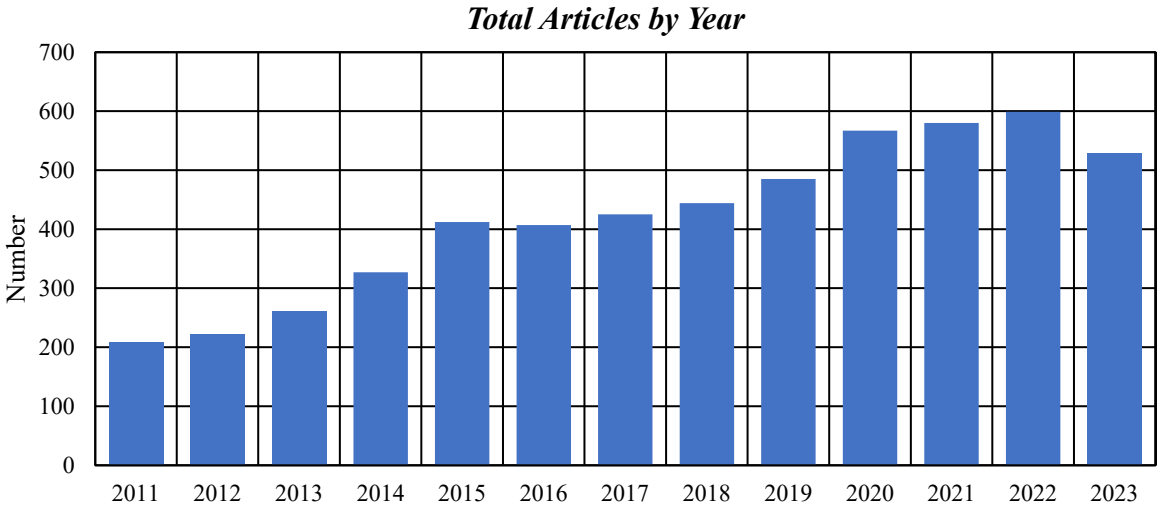

FIG 2 – Representation of the number of research articles on molten slag and fluxes by year for the period 2011–2023 retrieved from Scopus.

TABLE 3

Number of research papers on molten slag and fluxes by year 2011–2023 retrieved from Scopus.

Year	Articles	Year	Articles	Year	Articles
2011	209	2016	407	2021	580
2012	222	2017	425	2022	599
2013	261	2018	444	2023	529
2014	327	2019	485		
2015	412	2020	567		
			Total articles		**5467**

The data given in Figure 2 and Table 3 shows a steady increase in research activity from 2011 to 2023, the annual number of articles doubling over this period of time.

Fields of research

The data has been further analysed to differentiate the fields of research within the data sets. The fields selected for the 2011–2023 data correspond closely to those used in previous reviews by Boom and Mills (1996), Boom and Mills (1997, 2000), Boom, Riaz and Mills (2000, 2004, 2005, 2009, 2010):

The data show that:

- The total number of studies in each field has progressively increased and almost doubled for most categories for the period 2011–2023 (see Figure 3 and Table 4). The annual number of publications on thermodynamics and kinetics have remained approximately unchanged over the same period. The largest increase is seen in the amount of research focused on recycling and environmental issues. The proportions of publications in the various fields are given in Figure 4 and Table 5.
- Phase equilibria/mineralogical studies consist principally of experimental determination or optimisation phase diagrams, particularly focused on liquidus and solid/liquid equilibria. Mineralogical investigations included the phases present in partially crystallised slags.
- Thermodynamics studies include mathematical model development, thermodynamic modelling of phase diagrams, chemical activities of components in slag systems, and the development of thermodynamic databases that can be used to predict complex high temperature equilibria.
- Kinetics studies encompass crystallisation of slags, kinetic studies of desulfurisation or dephosphorisation of slags, kinetics dissolution of elements or compounds in slags, reaction mechanisms/sequences involving molten slags.
- Physical properties include the measurement and prediction of physico-chemical properties of slags, eg rheological behaviour, fluidity, density, surface tension, thermal conductivity, and electrical conductivity of slags.
- Research under recycling and environmental includes valourising slags produced from primary and secondary processes, for example, extracting valuable metals from slags, assessing and preparing slags for use in structural materials, aggregates, concrete or cement, and the synthesis of products, such as glass, catalysts, ceramics. Environmental issues generated by pyrometallurgical slags are also discussed.

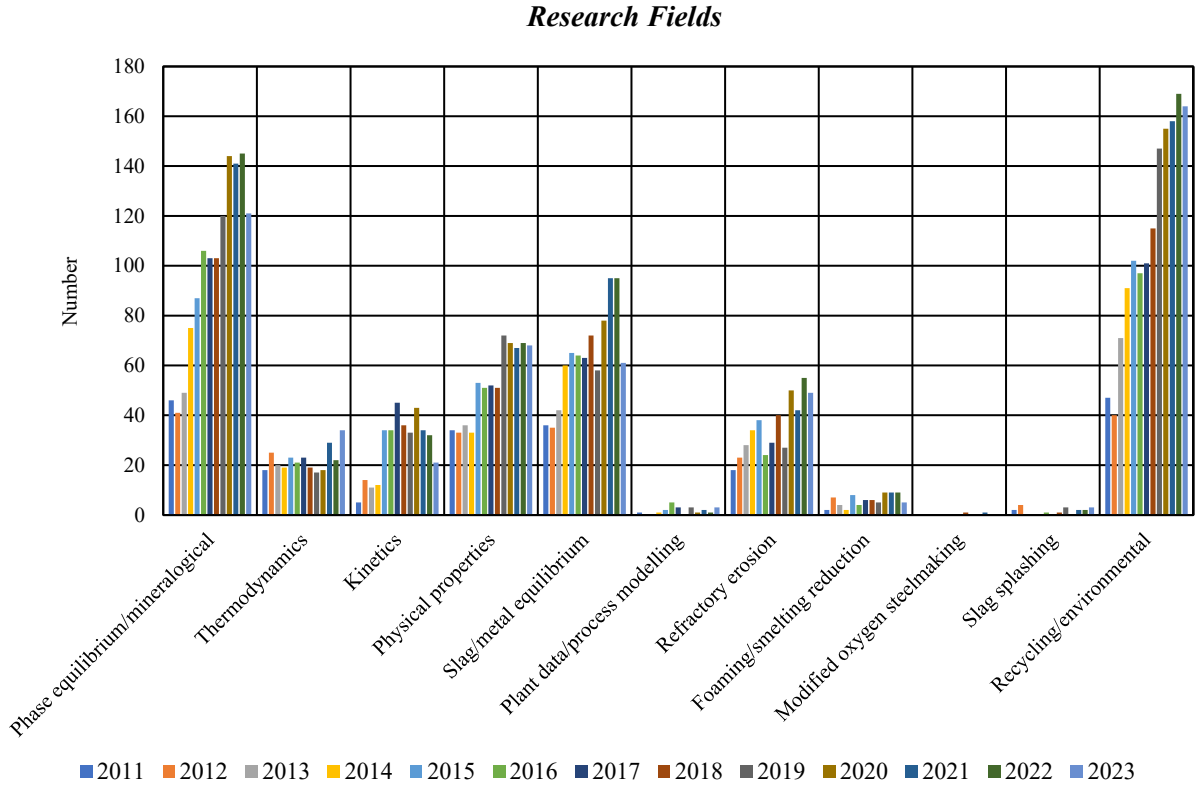

FIG 3 – Representation of the number of articles involving molten slag and fluxes in selected fields of research between 2011–2023 retrieved from Scopus.

TABLE 4

Number of articles involving molten slag and fluxes in selected fields of research between 2011–2023 retrieved from Scopus.

Field	2011	2012	2013	2014	2015	2016	2017	2018	2019	2020	2021	2022	2023
Phase equilibria/ mineralogical	46	41	49	75	87	106	103	103	120	144	141	145	121
Thermodynamics	18	25	20	19	23	21	23	19	17	18	29	22	34
Kinetics	5	14	11	12	34	34	45	36	33	43	34	32	21
Physical properties	34	33	36	33	53	51	52	51	72	69	67	69	68
Slag/metal equilibrium	36	35	42	60	65	64	63	72	58	78	95	95	61
Plant data/process modelling	1	0	0	1	2	5	3	0	3	1	2	1	3
Refractory erosion	18	23	28	34	38	24	29	40	27	50	42	55	49
Foaming/smelting reduction	2	7	4	2	8	4	6	6	5	9	9	9	5
Modified oxygen steelmaking	0	0	0	0	0	0	0	1	0	0	1	0	0
Slag splashing	2	4	0	0	0	1	0	1	3	0	2	2	3
Recycling/ environmental	47	40	71	91	102	97	101	115	147	155	158	169	164
Total	**209**	**222**	**261**	**327**	**412**	**407**	**425**	**444**	**485**	**567**	**580**	**599**	**529**

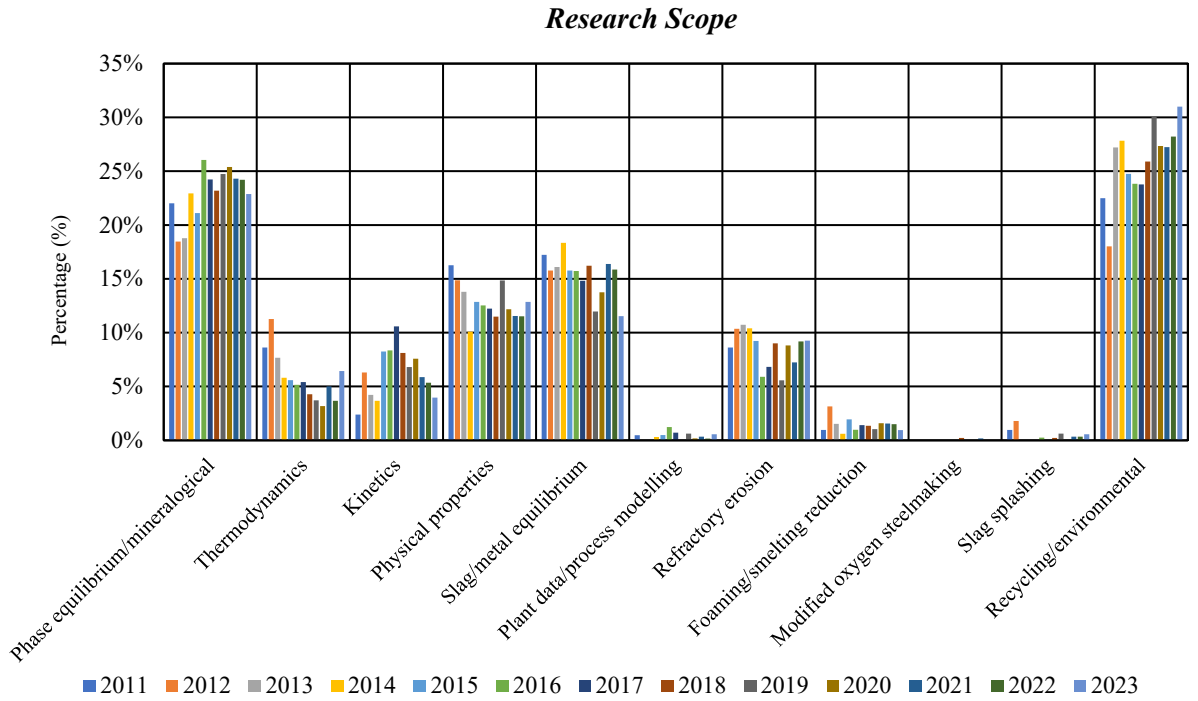

FIG 4 – Representation of the distribution of research articles between fields of research for articles involving molten slag and fluxes between 2011–2023 retrieved from Scopus.

TABLE 5

Distribution (%) of research scope on articles involving molten slag and fluxes between 2011–2023 retrieved from Scopus.

Field	2011	2012	2013	2014	2015	2016	2017	2018	2019	2020	2021	2022	2023
Phase equilibria/ mineralogical	22	18	19	23	21	26	24	23	25	25	24	24	23
Thermodynamics	9	11	8	6	6	5	5	4	4	3	5	4	6
Kinetics	2	6	4	4	8	8	11	8	7	8	6	5	4
Physical properties	16	15	14	10	13	13	12	11	15	12	12	12	13
Slag/metal equilibrium	17	16	16	18	16	16	15	16	12	14	16	16	12
Plant data/process modelling	0	0	0	0	0	1	1	0	1	0	0	0	1
Refractory erosion	9	10	11	10	9	6	7	9	6	9	7	9	9
Foaming/smelting reduction	1	3	2	1	2	1	1	1	1	2	2	2	1
Oxygen steelmaking	0	0	0	0	0	0	0	0	0	0	0	0	0
Slag splashing	1	2	0	0	0	0	0	0	1	0	0	0	1
Recycling/ environmental	22	18	27	28	25	24	24	26	30	27	27	28	31

Slag systems

Slags are used in a variety of metallurgical applications. The data has been further analysed to differentiate between these applications.

The data show that:

- The total number of studies in each application has progressively increased and almost doubled for most categories for the period 2011–2023 (see Figure 5 and Table 6). The annual number of publications on mould fluxes, welding fluxes, ferroalloy slags and coal ash slags have remained approximately unchanged over the same period. The largest increase is seen in the amount of research focused on recycling and environmental issues.
- The data given in Figure 6 and Table 7 show that the proportions of articles in each of these categories have not significantly changed over this time frame.

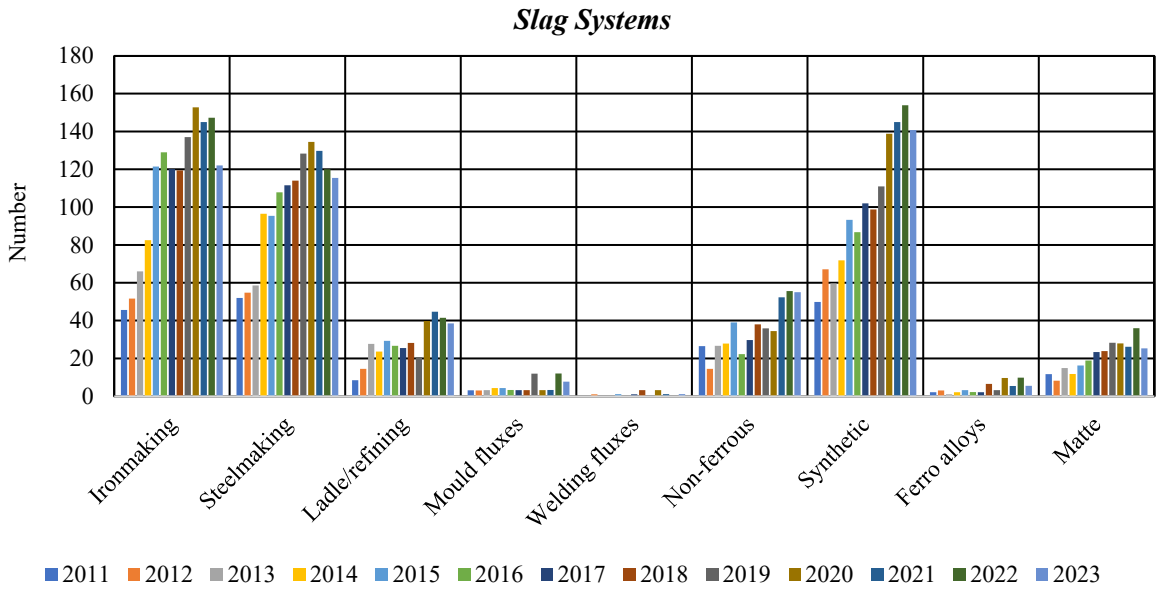

FIG 5 – Representation of number of articles based on slag systems under study between 2011–2023 retrieved from Scopus.

TABLE 6

Number of articles based on slag systems under study between 2011–2023 retrieved from Scopus.

Slags	2011	2012	2013	2014	2015	2016	2017	2018	2019	2020	2021	2022	2023
Ironmaking	46	52	66	83	121	129	120	119	137	153	146	147	122
Steelmaking	52	55	59	96	96	108	112	114	128	134	130	120	115
Ladle/refining	7	14	28	24	29	27	26	28	21	40	45	41	38
Mould fluxes	3	3	3	4	4	3	3	3	12	3	3	12	8
Welding fluxes	0	1	0	0	1	0	1	3	0	3	1	0	1
Non-ferrous	27	14	27	28	40	22	30	38	36	34	52	56	55
Synthetic	50	68	59	72	93	87	102	99	111	139	145	154	141
Ferro alloys	2	3	1	2	3	2	2	7	3	10	5	10	5
Coal	10	4	3	6	9	10	6	9	9	23	27	23	19
Matte	12	8	15	12	16	19	23	24	28	28	26	36	25
Total	**209**	**222**	**261**	**327**	**412**	**407**	**425**	**444**	**485**	**567**	**580**	**599**	**529**

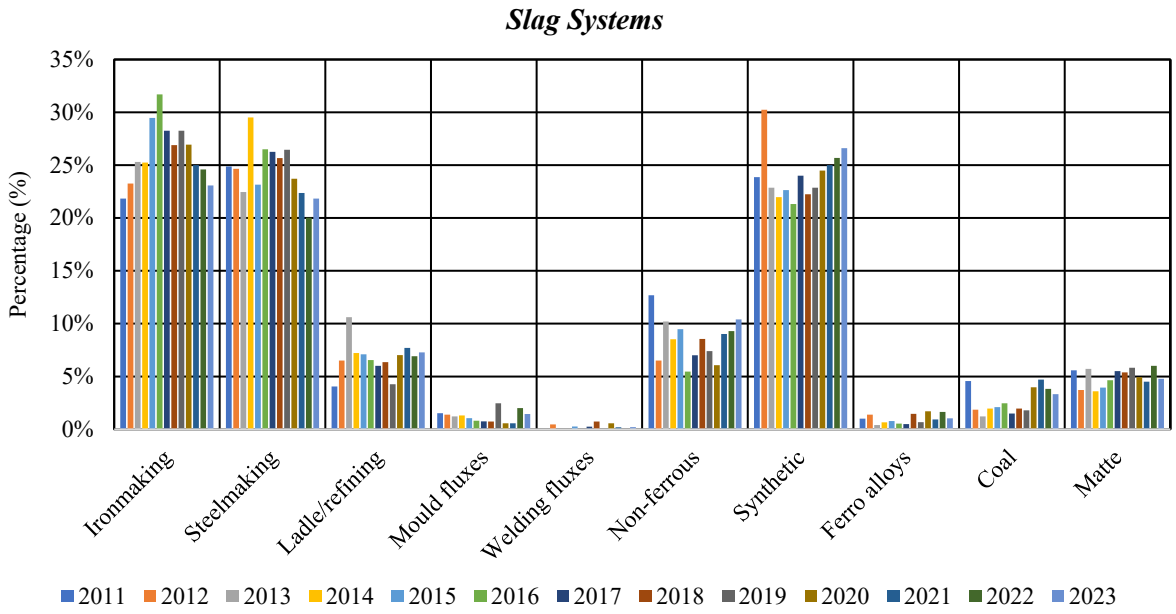

FIG 6 – Representation of distribution of articles based on slag systems under study between 2011–2023 retrieved from Scopus.

TABLE 7

Distribution (%) of articles based on slag systems under study between 2011–2023 retrieved from Scopus.

Slags	2011	2012	2013	2014	2015	2016	2017	2018	2019	2020	2021	2022	2023
Ironmaking	22	23	25	25	29	32	28	27	28	27	25	25	23
Steelmaking	25	25	22	30	23	27	26	26	26	24	22	20	22
Ladle/refining	4	7	11	7	7	7	6	6	4	7	8	7	7
Mould fluxes	2	1	1	1	1	1	1	1	2	1	1	2	1
Welding fluxes	0	0	0	0	0	0	0	1	0	1	0	0	0
Non-ferrous	13	7	10	9	9	5	7	9	7	6	9	9	10
Synthetic	24	30	23	22	23	21	24	22	23	24	25	26	27
Ferro alloys	1	1	0	1	1	1	1	1	1	2	1	2	1
Coal	5	2	1	2	2	2	2	2	2	4	5	4	3
Matte	6	4	6	4	4	5	6	5	6	5	5	6	5

Geographical origin

The geographical origins of research articles are based on the location/country of the corresponding author of the articles. Figure 7 and Table 8 provide information on the total annual numbers given by country. Figure 8 and Table 9 show the proportion (%) of research by continent/country of origin. Most of the articles under the ‘Oceania’ category are from Australia. Most articles under the ‘Africa’ category are published from South Africa. The majority of articles under the ‘Korea’ category are published from South Korea.

The standout feature is the 400 per cent increase in the number of papers published in China since 2011. In contrast, the number of papers published elsewhere are low and are either unchanged or in decline over this period. These data reflect not only the significant increase in metal production and refining in China but also the major investment that has taken place in research and development capabilities in that country.

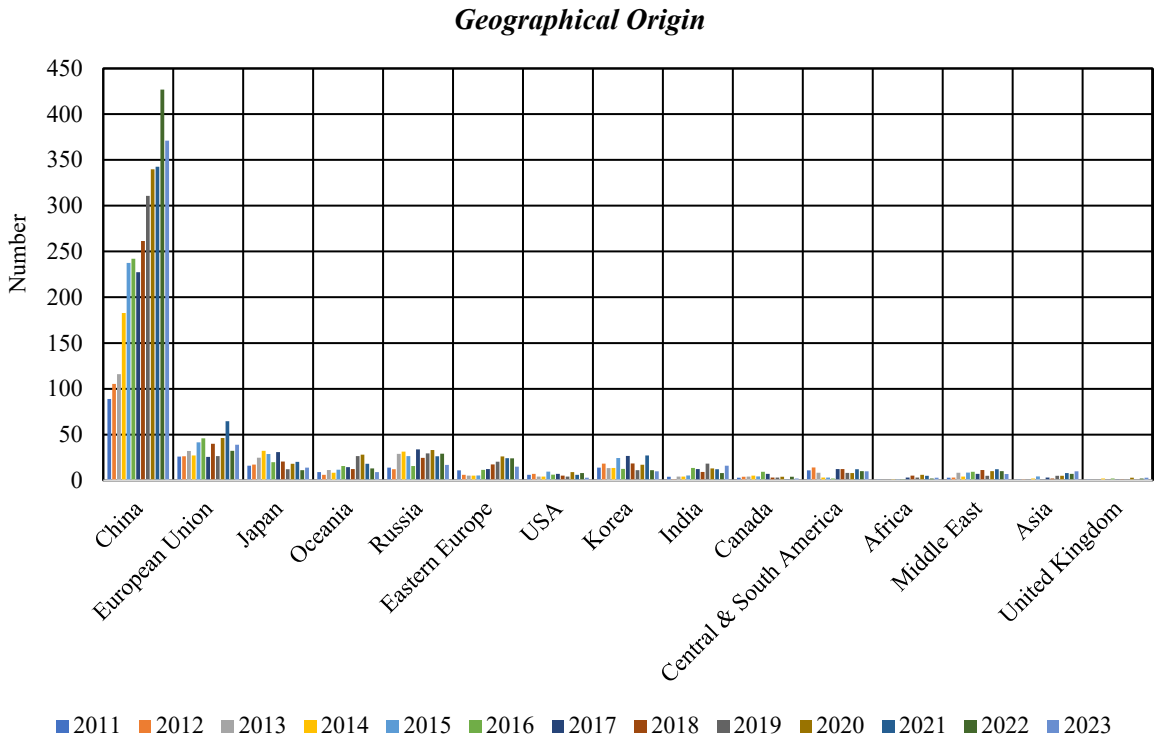

FIG 7 – Representation of number of articles on slag systems by continent/country of origin published in between 2011–2023 retrieved from Scopus.

TABLE 8

Number of articles based on continent/country of origin published in between 2011–2023 retrieved from Scopus.

Continent/ country	2011	2012	2013	2014	2015	2016	2017	2018	2019	2020	2021	2022	2023
China	89	107	118	183	237	242	228	261	312	341	344	428	371
European Union	26	26	32	28	42	46	26	41	26	46	65	32	39
Japan	16	17	25	33	29	20	31	21	12	18	20	11	14
Oceania	9	6	11	8	12	16	15	13	27	28	18	13	9
Russia	14	12	29	31	27	16	34	25	30	33	26	29	17
Eastern Europe	11	6	5	5	5	11	12	17	20	26	24	24	15
USA	6	7	4	4	10	6	7	5	4	9	6	8	3
Korea	14	18	13	14	24	13	27	18	11	17	27	11	10
India	4	1	4	4	5	14	12	9	18	13	12	8	16
Canada	3	4	4	5	4	9	7	3	3	4	1	4	2
Central and South America	11	14	8	3	3	2	12	12	8	8	12	10	10
Africa	1	0	0	1	1	1	3	5	3	6	5	2	3
Middle East	3	3	8	4	9	9	7	11	5	10	12	10	7
Asia	1	1	0	2	4	0	3	2	5	5	8	7	10
United Kingdom	1	0	0	2	0	2	1	1	1	3	0	2	3
Total	**209**	**222**	**261**	**327**	**412**	**407**	**425**	**444**	**485**	**567**	**580**	**599**	**529**

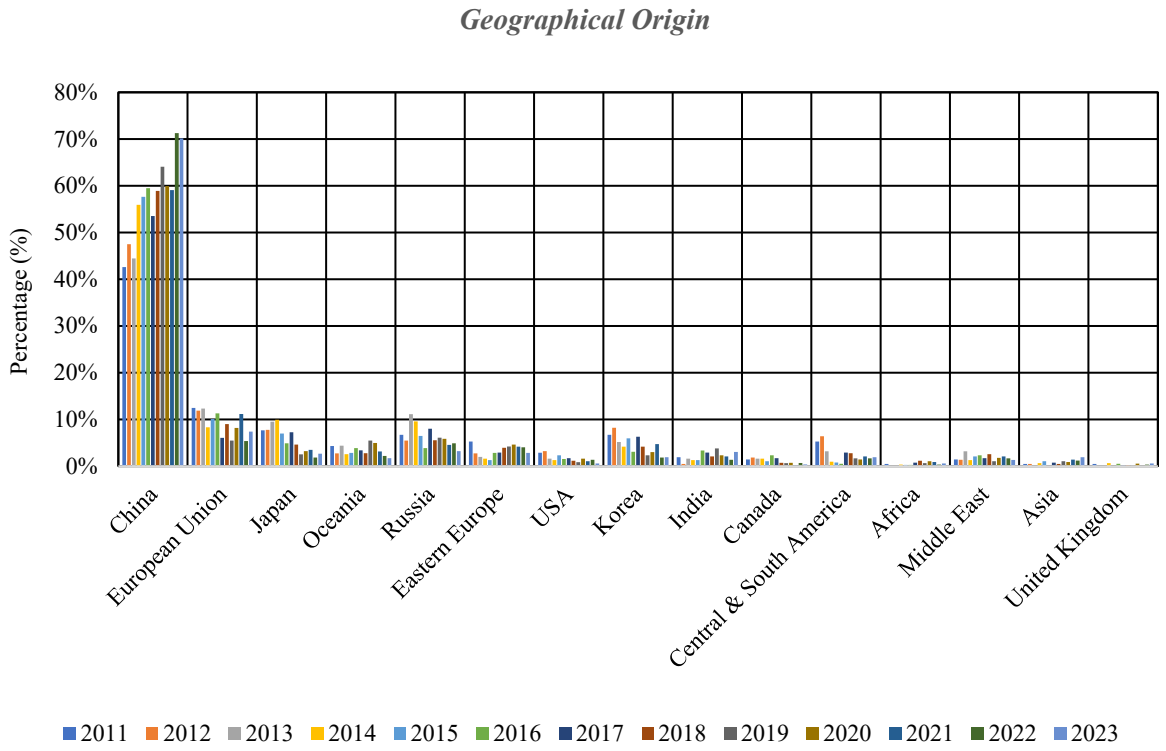

FIG 8 – Trends in research on molten slag and flux by continent/country of origin published in between 2011–2023 retrieved from Scopus.

TABLE 9

Distribution (%) in research on molten slag and flux by continent/country of origin published in between 2011–2023 retrieved from Scopus.

Continent/ country	2011	2012	2013	2014	2015	2016	2017	2018	2019	2020	2021	2022	2023
China	43	47	44	56	58	59	54	59	64	60	59	71	70
European Union	12	12	12	8	10	11	6	9	5	8	11	5	7
Japan	8	8	10	10	7	5	7	5	3	3	3	2	3
Oceania	4	3	4	3	3	4	3	3	5	5	3	2	2
Russia	7	5	11	10	6	4	8	6	6	6	5	5	3
Eastern Europe	5	3	2	2	1	3	3	4	4	5	4	4	3
USA	3	3	2	1	2	2	2	1	1	2	1	1	1
Korea	7	8	5	4	6	3	6	4	2	3	5	2	2
India	2	0	2	1	1	3	3	2	4	2	2	1	3
Canada	1	2	2	2	1	2	2	1	1	1	0	1	0
Central and South America	5	6	3	1	1	1	3	3	2	1	2	2	2
Africa	0	0	0	0	0	0	1	1	1	1	1	0	1
Middle East	1	1	3	1	2	2	2	3	1	2	2	2	1
Asia	0	0	0	1	1	0	1	0	1	1	1	1	2
United Kingdom	0	0	0	1	0	1	0	0	0	1	0	0	1

WHAT IS DIFFERENT ABOUT MOLTEN 2024?

To date the individual MOLTEN Conferences have been principally supported by professional societies in the countries in which they were held. The world has changed, and we are now more

interconnected than ever. It is appropriate then that at MOLTEN 2024 we have been able to bring together the following supporting partners:

- Australasian Institute of Mining and Metallurgy (AusIMM)
- Chinese Society for Metals (CSM)
- GDMB Society for Metallurgists and Mining (GDMB)
- Indonesian Metallurgy Professional Association (Prometindo)
- Institute of Materials, Minerals and Mining (IOM3)
- Korean Institute of Metals and Materials (KIM)
- Society for Mining Metallurgy and Exploration (SME)
- Southern African Institute of Mining and Metallurgy (SAIMM)
- The Japan Institute of Metals and Materials (JIMM)
- The Iron and Steel Institute of Japan (ISIJ)
- The Non-Ferrous Society of China (NFSOC)

We welcome this collaboration and efforts to assist with the promotion of the MOLTEN Conference series by professional societies from across the globe. This collaboration also provides appropriate recognition of the ongoing importance and significance of this field of research to our respective countries.

The collaboration also brings benefits to members of these societies in the form of:

- Access online to the entire MOLTEN 2024 Conference Proceedings through the OneMine platform.
- Reduced conference registration fees for these members.

For the first time DOI numbers have been assigned to all MOLTEN 2024 oral presentations published in the proceedings, this has enabled these publications to be readily identified and retrieved by computer search engines, and officially recognised in researcher publication profiles. The conference proceedings will be available in both electronic form and hardcopy. The print edition will be available through print on demand Amazon publishers.

REFERENCES

Boom, R and Mills, K C, 1996. The Changing Trend in Research on Slags, in *Proceedings of the 5th International Conference on Molten Slags, Fluxes and Salts '97* (ed: G Belton), pp 3–9 (Iron and Steel Society AIME, Warrendale).

Boom, R and Mills, K C, 2000. Recent trends in research on slags, in *Proceedings of the 6th International Conference on Molten Slags, Fluxes and Salts*, 13 p.

Boom, R, Riaz, S and Mills, K C, 2000. Recent trends in research on slags, *Ironmaking and Steelmaking*, 27(2):99–102.

Boom, R, Riaz, S and Mills, K C, 2004. Slags and fluxes entering the new millennium: an analysis of recent trends in research and development, in *Proceedings of the 7th International Conference on Molten Slags, Fluxes and Glasses,* 9 p (South African Institute of Mining and Metallurgy: Johannesburg).

Boom, R, Riaz, S and Mills, K C, 2005. Slags and fluxes entering the new millennium: an analysis of recent trends in research and development, *Ironmaking and Steelmaking*, 32(1):21–25.

Boom, R, Riaz, S and Mills, K C, 2009. A boost in the research on slags: a doubling in publications since 2003, in *Proceedings of the VIII Conference on Molten Slags, Fluxes and Glasses MOLTEN2009* (eds: M Sánchez, R Parra, G Riveros and C Díaz), pp 3–11 (Gecamin: Santiago).

Boom, R, Riaz, S and Mills, K C, 2010. A boost in the research on slags: a doubling in publications since 2003. *Ironmaking and Steelmaking,* 37:476–481.

Boom, R, Riaz, S, Xiao, Y and Mills, K C, 2012. Evolution of published research on molten slags and fluxes in the second Millennium, in *Proceedings of the 9th Conference on Molten Slags, Fluxes and Glasses MOLTEN2012*, paper W040 (Scopus, Elsevier).

Experimental measurements of – Physico-chemical properties (viscosity, surface tension, conductivity…)

Electrical conductivity measurement of CaO-Al_2O_3-CaF_2 slags by van der Pauw-Ohta Method

DOI: 10.62053/CTYP4513

K Aya[1], T Sumita[2], N Saito[3] and K Nakashima[4]

1. Graduate Student, Department of Materials, Kyushu University, 744, Motooka, Nishi-ku, Fukuoka 819-0395, Japan. Email: kenta.aya.874@s.kyushu-u.ac.jp
2. Assistant Professor, Department of Materials, Kyushu University, 744, Motooka, Nishi-ku, Fukuoka 819-0395, Japan. Email: sumita.takehiro.799@m.kyushu-u.ac.jp
3. Associate Professor, Department of Materials, Kyushu University, 744, Motooka, Nishi-ku, Fukuoka 819-0395, Japan. Email: saito.noritaka.655@m.kyushu-u.ac.jp
4. Professor, Department of Materials, Kyushu University, 744, Motooka, Nishi-ku, Fukuoka 819-0395, Japan. Email: nakasima@zaiko.kyushu-u.ac.jp

ABSTRACT

Electro slag remelting (ESR) is one of the methods used to produce high-cleanliness steel. In the ESR method, the product steel electrode is immersed in flux, and the electrode is melted by the Joule heat of the flux generated by high current. CaF_2-based melts are mainly used as fluxes, but the electrical conductivity of CaF_2-based melts varies widely among researchers and measurement methods. Therefore, this experiment aims to measure the electrical conductivity of CaF_2-based melts based on the van der Pauw-Ohta method, which does not require the cell constant that is a fundamental error factor in electrical conductivity measurement at high temperatures. The measurement temperature was set at 1450–1600°C, and dehydrated Ar flowed through the furnace at 200 mL/min. Electrodes were fabricated by Pt-30mass per cent Rh alloy, and the electrodes were connected to an impedance analyser using a four-terminal probe. The electrodes were immersed in the melt, and the impedance and phase angle were measured by AC frequency sweep (50 Hz to 200 kHz). The electrical conductivity was then calculated by utilising the impedance's real part values when the impedance's imaginary component was zero. The electrical conductivity showed a positive temperature dependence. The electrical conductivity of $60(CaO{\cdot}Al_2O_3)$-$40CaF_2$ melt increased with increasing temperature but was found to be roughly one-third of those of the previous studies. In the conductivity measurement of $60(CaO{\cdot}Al_2O_3)$-$40CaF_2$ melt, the AC frequency with a phase angle of 0° was found to be different depending on the temperature and immersion depth. By sweeping the frequency, the impedance at the phase angle of 0° can be obtained, which enables us to measure the electrical conductivity more accurately.

INTRODUCTION

Various technologies have been developed in the field of high-grade steel production, such as vacuum technology (Koshiba, 1958; Asakuma, 1973) (vacuum melting, vacuum treatment, vacuum arc remelting etc), technology using new heat sources (Kato, 1984; Ono, 1993) (plasma, electron beam etc), and technology using the physical and chemical properties of slag (Ogino, 1979) (electroslag remelting etc).

The ESR (Electro Slag Remelting) method is a remelting process that effectively utilises the electrical properties of slag. In the ESR method, the electrode metal is remelted by the resistive heat of the molten slag, and the molten metal absorbs inclusions and impurities as it falls through the slag. During this process, slag flows between the ingot and the mold, forming a slag skin that covers the surface of the ingot, resulting in ingots with excellent surface properties. Thus, in the ESR process, slag plays an extremely important role in each process of metal melting, refining, and solidification. Therefore, a thorough understanding and knowledge of the characteristics of slag is required for effective operation. The electrical conductivity of the slag is one of the most important factors controlling the operating conditions. It is known that the temperature of the slag bath, the depth of the electrodes in the slag, and the shape of the metal pool vary depending on the choice of the electrical conductivity of the slag, which in turn has a significant effect on the properties of the ingot and the power consumption (Ogino and Hara, 1979).

In addition, ESR slags are often made from systems containing fluorides such as CaF_2. Therefore, many researchers have measured the electrical conductivity of fluoride slag, but there is a large difference in the reported data. As an example, Figure 1 shows the electrical conductivity of the CaO-CaF_2 system. Winterhager, Kammel and Gad (1970), Mitchell and Cameron (1971), and Hajduk and El Gammal (1979) reported that the electrical conductivity of the CaO-CaF_2 system decreased with the addition of CaO, while Ogino, Hara and Hashimoto (1978) and Zmoidin (1970) reported that the conductivity increases when the CaO content is low and decreases when the CaO content is high. The electrical conductivity data of the fluoride slag varies widely among the reported data. The reason for these differences may be due to the influence of the imaginary component of impedance caused by the measurement temperature and the cell constant of the electrode. As for the effect of the imaginary component of the impedance, in the past experiments, the frequency was kept constant and the measurement was made without considering the imaginary component of the impedance.

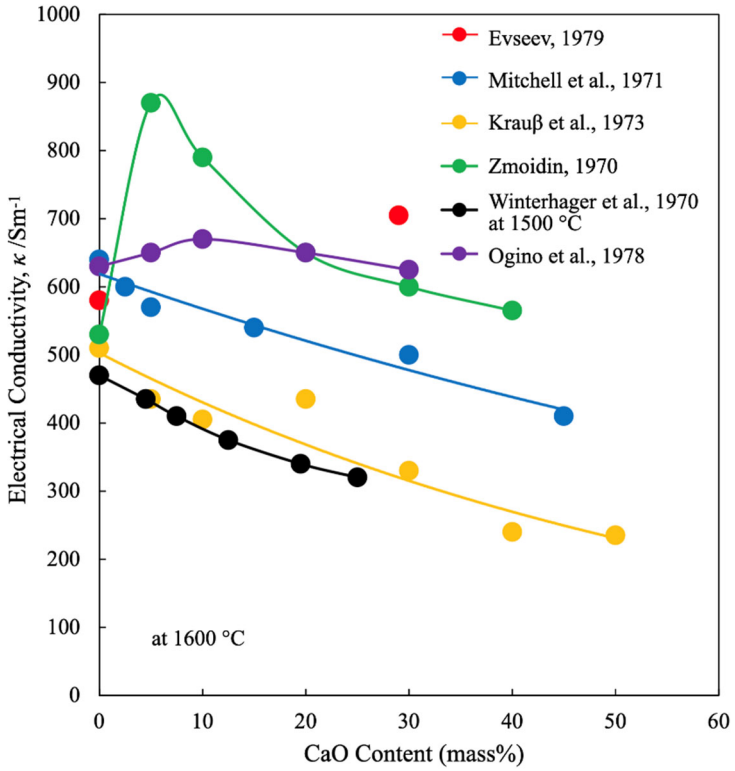

FIG 1 – Electrical conductivity of CaF_2-CaO melt at 1600°C as a function of CaO content.

However, since the frequency at which the imaginary component of the impedance becomes zero depends on the temperature and immersion depth, it is possible that the imaginary component of the impedance is not eliminated. Therefore, the imaginary component of the impedance can be eliminated by using the value of the real component of the impedance as the resistance value when the imaginary component of the impedance becomes zero by performing a frequency sweep. Since the cell constant of the electrode differs between room temperature and high temperature, it is thought that the electrical resistance of the electrode differs. We focused on the van der Pauw method as a measurement method that does not use the cell constant, because the distance between electrodes does not affect the conductivity measurement using the van der Pauw method, and the electrodes can be regarded as points. Since the cell constant can be calculated from the distance between electrodes and the electrode area, the van der Pauw method can be applied to calculate the electrical conductivity without considering the cell constant. Therefore, the purpose of this study is to measure the electrical conductivity of fluoride slag using the van der Pauw-Ohta method.

EXPERIMENTAL

Principle of the van der Pauw method

The two-pole and four-terminal methods (Kato and Minowa, 1965; Ogino, Hara and Hashimoto, 1978) have been mainly used to measure the electrical conductivity of melts. In the four-terminal method, on the other hand, the voltage and current measurement terminals are independent, so the internal resistance of the probe is less affected. However, both methods use cell constants for measurement, which can cause large errors at high temperatures when the electrode is easily deformed. In addition, when the resistivity of the electrode metal shows a temperature dependence, it is very difficult to exclude the effect. In this study, we applied the van der Pauw method (van der Pauw, 1958) to the measurement of the electrical conductivity of melts at high temperatures, and tried to measure the electrical conductivity without using the cell constant.

As shown in Figure 2, we placed four electrodes around a sample of thickness W, applied a voltage between two terminals to measure the current, and measured the voltage between the remaining two terminals:

$$\rho = \frac{\pi W}{ln2} \cdot \frac{R_1 + R_2}{2} \cdot f\left(\frac{R_1}{R_2}\right) \tag{1}$$

where $R_1=V_{cd}/I_{ab}$, $R_2=V_{da}/I_{bc}$, and ρ is the electrical resistivity of the sample. Expressing Equation 1 in terms of ρ, we get:

$$\exp\left(-\frac{\pi R_1 W}{\rho}\right) + \exp\left(-\frac{\pi R_2 W}{\rho}\right) = 1 \tag{2}$$

$$f\left(\frac{R_1}{R_2}\right) = 1 - \left(\frac{R_1 - R_2}{R_1 + R_2}\right)^2 \cdot \frac{ln2}{2} - \left(\frac{R_1 - R_2}{R_1 + R_2}\right)^4 \left\{\frac{(ln2)^2}{4} - \frac{(ln2)^3}{13}\right\} \tag{3}$$

If the values of R_1 and R_2 are close, f (R_1/R_2) = 1 can be regarded, and the reciprocal of the electrical resistivity calculated by Equation 2 becomes the electrical conductivity. In this way, the electrical conductivity can be measured by the difference between W_1 and W_2 without the need for cell constants.

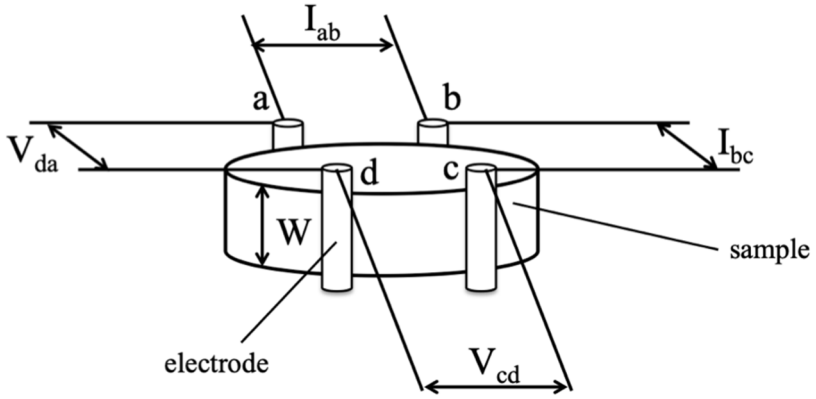

FIG 2 – Principle schematic for electric conductivity measurement based on the van der Pauw method.

Principle of the van der Pauw-Ohta method

As shown in Figure 3, when the van der Pauw method is applied to the melt, the measured resistance R_M is considered to be the parallel composite resistance of the resistance R_A (the immersed part of the electrode) and the spreading resistance R_B (the non-immersed part) (Ohta *et al*, 1981). This makes it necessary to remove the spreading resistance R_B, but since R_A and R_B cannot be separated from a single immersion depth, they cannot be removed. Therefore, the electrical conductivity is

calculated using the measured resistances of two points with different immersion depths. First, for the immersed part of the electrode, the depth of immersion is W. From Equation 2, the following equation is obtained:

$$\rho = \frac{2\pi W}{ln2} \cdot R_A \tag{4}$$

If $R_M = (R_1 + R_2)/2$ and the R_Ms at W_1 and W_2 are R_{M1} and R_{M2}, respectively, then the spreading resistance R_B becomes:

$$R_B = \frac{R_{M1}R_{M2}(W_1 - W_2)}{R_{M1}W_1 - R_{M2}W_2} \tag{5}$$

Since R_M is the parallel composite resistance of R_A and R_B:

$$R_A = \frac{-R_M R_B}{R_M - R_B} \tag{6}$$

Organising Equations 4, 5 and 6, we obtain:

$$\rho = \frac{2\pi W}{ln2} \cdot \frac{R_M R_{M1} R_{M2}(W_2 - W_1)}{R_{M1}W_1(R_M - R_{M2}) - R_{M2}W_2(R_M - R_{M1})} \tag{7}$$

Where W is W_1 or W_2, Equation 7 is expressed as Equation 8:

$$\rho = \frac{2\pi}{ln2} \cdot \frac{R_{M1}R_{M2}(W_2 - W_1)}{R_{M1} - R_{M2}} \tag{8}$$

Therefore, the electrical resistivity ρ can be obtained by determining R_{M1} and R_{M2} for W_1 and W_2, and its reciprocal is the electrical conductivity.

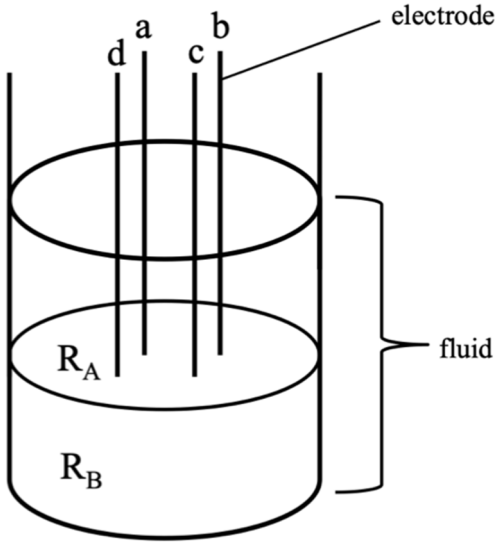

FIG 3 – Schematic of electrical conductivity measurement of liquid sample based on van der Pauw-Ohta method.

Electrical Conductivity Measurement of $15Na_2O$-15CaO-$70SiO_2$ Melt

The applicability of Equation 8 was confirmed by measuring the electrical conductivity of $15Na_2O$-15CaO-$70SiO_2$ oxide melt. A square electrode was immersed in a Pt crucible filled with the sample. Four electrodes are a, b, c, and d in a clockwise direction (Figure 3), and each electrode is connected to an impedance analyser using a four-terminal probe. The impedance was measured by frequency sweeping at 50 mV (open circuit voltage) and 50 Hz to 200 kHz. After that, the connection terminal was rotated counterclockwise, and the impedance was measured in the same way. From the

obtained data, an approximate curve was drawn with the imaginary part of the impedance near zero, and the impedance was defined as the value of the real part when the imaginary part of the approximate curve was zero. In this experiment, (W_1, W_2)=(5,10), (10,15), and (15, 20)/mm, and the electrical conductivity was calculated from Equation 8 by obtaining the impedance at each immersion depth, and the average of the impedance was used as the electrical conductivity. The electrodes were immersed in the samples by raising and lowering the crucible with a lifting motor under the furnace. The samples were melted in a Pt crucible and placed in the furnace. After that, the electrical conductivity was measured by the above procedure, and then the temperature was set at 100°C intervals and held for 30 mins.

Electrical conductivity measurement of 21.3CaO-38.7Al_2O_3-40.0CaF_2 melt

The electrical conductivity of the 21.3CaO-38.7Al_2O_3-40.0CaF_2 melt was measured. $CaCO_3$ was calcined at 1200°C for 1 hr in a muffle furnace to obtain CaO. Then, various special-grade reagents were weighed and mixed to obtain the specified composition. The weighted and mixed powder samples were melted in a Pt crucible at 1550°C in an Ar atmosphere. The experimental procedure was the same as that for the measurement of the electrical conductivity of oxide melts in the previous section. When CaF_2 is heated in air, it reacts with moisture in the air, and the reaction:

$$CaF_2+H_2O \rightarrow CaO+2HF\uparrow \quad (9)$$

occurs, which may cause a change in the composition of the sample and the generation of hydrogen fluoride. Therefore, the measurement was carried out in a dehydrated Ar gas atmosphere. The sample prepared in the previous section was placed in the furnace. The sample in the Pt crucible was melted in the furnace at 1600°C and held for 1 hr. After that, the conductivity measurement was carried out according to the procedure described above, and then the conductivity measurement was carried out in the same way after holding the sample at each set temperature for 30 mins at 50°C intervals during the temperature decrease process.

RESULTS AND DISCUSSION

Figure 4 shows the results of electrical conductivity measurements of 15Na_2O-15CaO-70SiO_2 melt. As shown in Figure 4, the electrical conductivity of the 15Na_2O-15CaO-70SiO_2 melt is close to that of the previous measurement. The reason for the lower values is that Mazurina (1967) measured the melt at a constant frequency (10 kHz) and did not consider the imaginary component of the impedance, which may have caused the error in the measured values. Therefore, we were able to measure the electrical conductivity of the oxide melt with good accuracy.

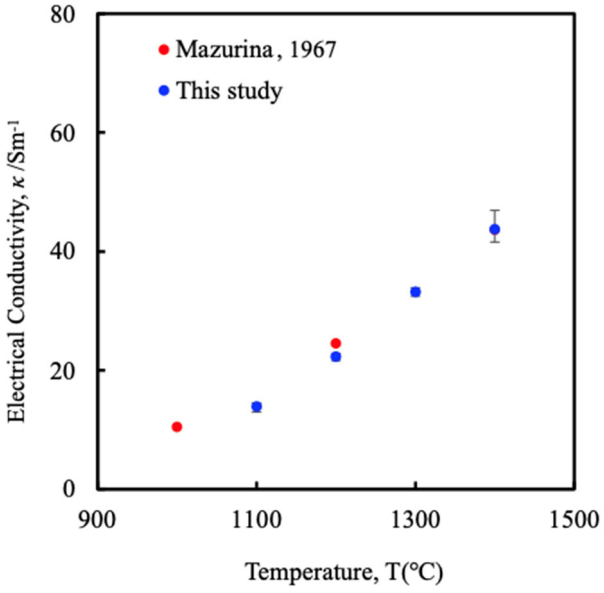

FIG 4 – Temperature dependence of electrical conductivity of 15Na_2O-15CaO-70SiO_2 melt.

The electrical conductivity of the $15Na_2O$-$15CaO$-$70SiO_2$ melt showed a positive temperature dependence. This is because ionic conductivity plays a major role in electrical conduction in $15Na_2O$-$15CaO$-$70SiO_2$ melt, and the conductivity of the melt is determined by the ease of diffusion of ions. In the $15Na_2O$-$15CaO$-$70SiO_2$ melt, the Na^+ and Ca^{2+} cations modify the glass (melt) network, but the network deformation is caused by the Na^+ and Ca^{2+} cations. In the $15Na_2O$-$15CaO$-$70SiO_2$ melt, Na^+ and Ca^{2+} ions modify the glass network, but this requires activation energy for the network deformation. Therefore, as the temperature increases, more new diffusion paths can be created, and it is predicted that the electrical conductivity increases due to the easier diffusion of ions (Matsuoka, 2017).

Figure 5 shows the results of the electrical conductivity measurements of the $21.3CaO$-$38.7Al_2O_3$-$40.0CaF_2$ melt. As shown in Figure 5, the electrical conductivity of the $21.3CaO$-$38.7Al_2O_3$-$40.0CaF_2$ melt showed a positive temperature dependence. Comparing the present measurements with those of Ohta *et al* (1981), it was found that the electrical conductivity of the present measurements was about one-third of that of Ohta *et al* (1981). The reason for the positive temperature dependence of the electrical conductivity is thought to be that the mobility of ions in the $21.3CaO$-$38.7Al_2O_3$-$40.0CaF_2$ melt has become larger since ionic conduction plays a major role in the electrical conduction of the $21.3CaO$-$38.7Al_2O_3$-$40.0CaF_2$ melt. Therefore, it is considered that the thermal motion of the ions (Ca^{2+}, Al^{3+}, F^-, and O^{2-}) in this system increases due to the increase in temperature, which facilitates the diffusion of the ions and increases the electrical conductivity.

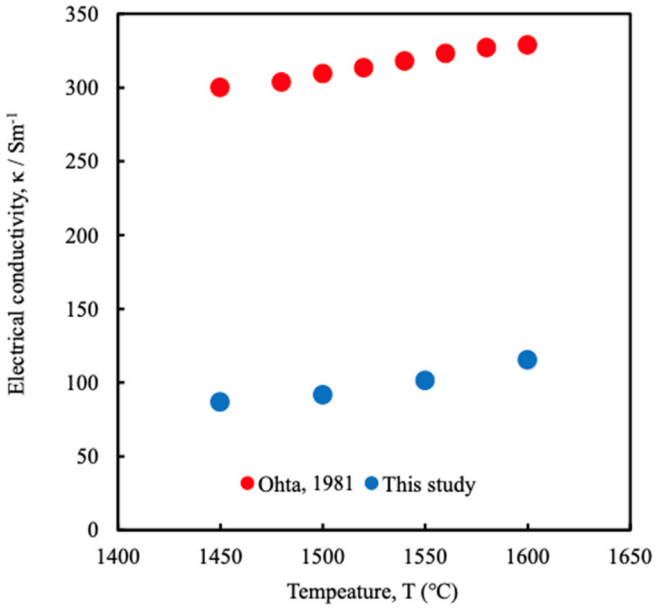

FIG 5 – Temperature dependence of electrical conductivity measurement results of $21.3CaO$-$38.7Al_2O_3$-$40.0CaF_2$ melt.

Table 1 summarises the measurement methods used for the past conductivity measurements of the same melts. In the present study, we used the four-terminal method, in which the current and voltage measurement terminals are independent, and we measured the electrical conductivity without using the cell constant, which is a source of error in the measurement of electrical conductivity at high temperatures. As shown in Figures 6 and 7, the AC frequency at which the phase angle reaches 0° varies greatly with temperature and immersion depth. These indicate that the frequency at which the phase angle is 0° was not properly selected because the frequency was kept constant regardless of the temperature and immersion depth in previous studies. Therefore, it is thought that the frequency with a phase angle of 0° was not properly selected, resulting in errors due to imaginary impedance components. In this study, on the other hand, we performed a frequency sweep to ensure the removal of the imaginary impedance component, which enabled us to measure the electrical conductivity with higher accuracy.

TABLE 1

Experimental methods and conditions for electrical conductivity measurement in the previous studies.

Researchers	Methods	Cell constants	AC frequency
Mitchell and Cameron (1971)	Two-terminals	o	1 kHz
Winterhager, Kammel and Gad (1970)	Two-terminals	o	multiple Hz
Ogino, Hara and Hashimoto (1978)	Four-terminals	o	1 kHz
Ohta *et al* (1981)	Four-terminals	x	2 kHz
present study	Four-terminals	x	50 Hz ~ 200 kHz

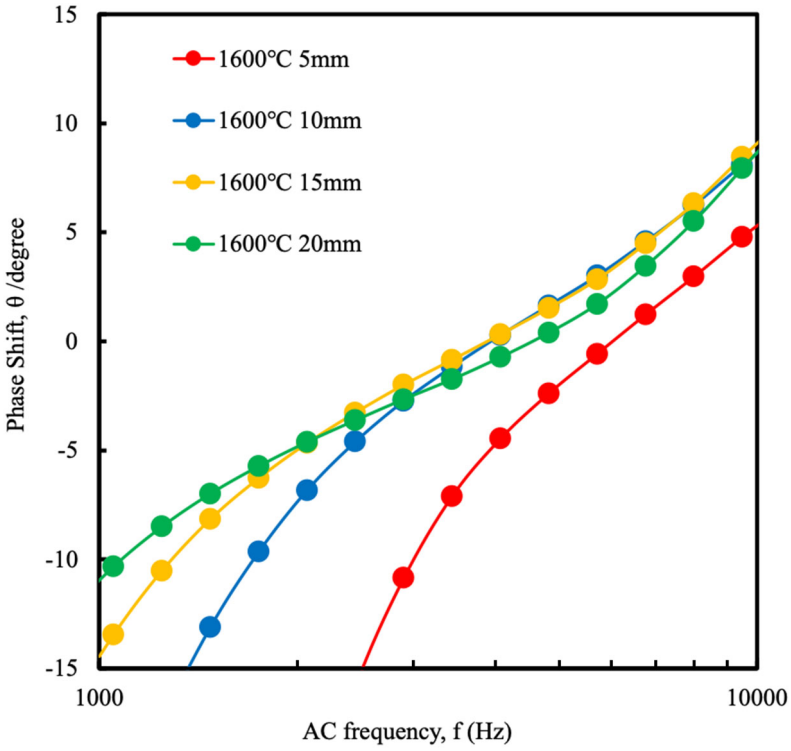

FIG 6 – Phase shifts of $CaO-Al_2O_3-CaF_2$ melts at 1600°C as a function of AC frequency and immersion depth of electrodes.

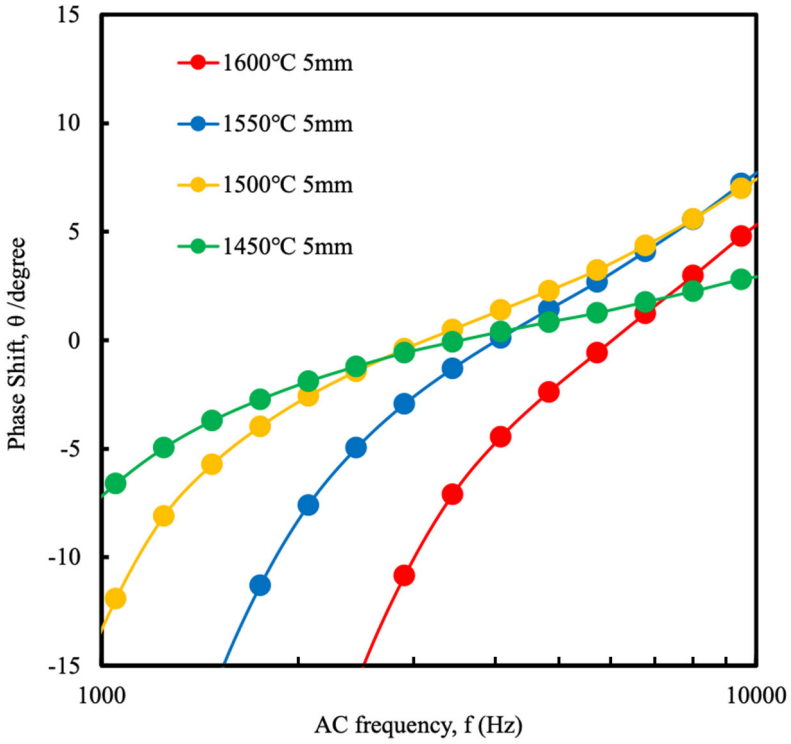

FIG 7 – Phase shifts of $CaO\text{-}Al_2O_3\text{-}CaF_2$ melts as a function of AC frequency and temperature.

CONCLUSIONS

In the present study, we quantitatively measured the high-temperature electrical conductivity of ESR flux by the van der Pauw-Ohta method and obtained the following findings.

- A method for measuring the electrical conductivity of melts at high temperatures using a four-terminal method based on the van der Pauw method has been established.
- The electrical conductivity of the $15Na_2O\text{-}15CaO\text{-}70SiO_2$ melt was close to that of previous measurements.
- The electrical conductivity of $15Na_2O\text{-}15CaO\text{-}70SiO_2$ melt increased with increasing temperature.
- The electrical conductivity of $60(CaO{\cdot}Al_2O_3)\text{-}40CaF_2$ melt increased with increasing temperature but was found to be roughly one-third of those of the previous studies.
- In the conductivity measurement of $60(CaO{\cdot}Al_2O_3)\text{-}40CaF_2$ melt, the AC frequency with a phase angle of 0° was found to be different depending on the temperature and immersion depth.
- By sweeping the frequency, the impedance at the phase angle of 0° can be obtained, which enables us to measure the electrical conductivity more accurately.

REFERENCES

Asakuma, T, 1973. Recent Development of Consumable Vacuum Arc Remelting, *Tetsu-to-Hagané*, 59(3):508–531.

Hajduk, M and El Gammal, T, 1979. Schrifttumszusammenstellung von Leitfähigkeitsmessungen an CaF2-haltigen Schlackenschmelzen, *Stahl und Eisen*, 99(1979):113–116.

Kato, M and Minowa, S, 1965. Determination of Cell Constant at High Temperature for the Electrical Conductivity Measurement of Molten Slags, *Tetsu-to-Hagané*, 51(10):1844–1846.

Kato, T, 1984. Metal Melting by Using Plazma Arc, *Bull Jpn Inst Met*, 23(11):934–940.

Koshiba, S, 1958. Vacuum Meling of Special Steels, *Zairyo-Shiken*, 7(61):500–506.

Matsuoka, J, 2017. Properties of Glass Melt, *New Glass*, 32(120):4–9.

Mazurina, E K, 1967. Influence of two-valence metal oxides on electrical conductivity of alkali silicate glasses in the temperature range 200–1400°C (in Russian), Thesis, Lensoviet Technological Institute, Leningrad.

Mitchell, A and Cameron, J, 1971. The electrical conductivity of some liquids in the system CaF_2+CaO+Al_2O_3, *Met Trans*, 2:3361–3366.

Ogino, K and Hara, S, 1979. Special Refining Subcommittee, Report of the 4th subcommittee, The Iron and Steel Institute of Japan, 8:63.

Ogino, K, 1979. Electro Slag Remelting, *Bull Jpn Inst Met*, 18(10):684–693.

Ogino, K, Hara, S and Hashimoto, H, 1978. Study of the Conduction Mechanism of Molten Fluxes for Electroslag Remelting, *Tetsu-to-Hagané*, 64(2):232–239.

Ohta, Y, Miyanaga, A, Morinaga, K and Yanagase, T, 1981. Study on the Measuring Method of the Electrical Conductivity of Ionic Solutions and Melts, *J Jpn Inst Metals*, 45(10):1036–1043.

Ono, K, 1993. Electron Beam Melting and Refining of Metals and Alloys, *Shiegen-to-Sozai*, 109(5):313–318.

van der Pauw, L J, 1958. A Method of Measuring Specific Resistivity and Hall Effect of Discs of Arbitrary Shape, *Philips Research Reports*, 13:1–9.

Winterhager, H, Kammel, R and Gad, A, 1970. Electrical conductivity, density and surface tension of fluoride-containing slags for the electroslag remelting process, Kon u Opladen, Forschungsbericht des Landes Norderhein_Westfalen Nr. 2115.

Zmoidin, G I, 1970. Electroconductivity of fluoride containing melts, *Izvestiya Akademii Nauk SSSR, Metally*, 3:69.

Methodology development of electrical conductivity measurements for non-ferrous slags

DOI: 10.62053/SLAU5977

P-J Boeykens[1], R Starykh[2], M Shevchenko[3], L Scheunis[4], A Van den Bulck[5], E Jak[6], I Bellemans[7] and K Verbeken[8]

1. PhD Candidate, Ghent University, Ghent Oost-Vlaanderen Belgium. Email: pieterjan.boeykens@ugent.be
2. Research Fellow, University of Queensland, Brisbane Qld 4000. Email: r.starykh@uq.edu.au
3. Research Fellow, University of Queensland, Brisbane Qld 4000. Email: m.shevchenko@uq.edu.au
4. Senior Scientist, Umicore N.V., Olen Antwerpen Belgium. Email: lennart.scheunis@eu.umicore.com
5. Scientist, Umicore N.V., Olen Antwerpen Belgium. Email: amy.vandenbulck@eu.umicore.com
6. Full Professor, University of Queensland, Brisbane Qld 4000. Email: e.jak@uq.edu.au
7. Assistant Professor, Ghent University, Ghent Oost-Vlaanderen Belgium. Email: inge.bellemans@ugent.be
8. Full Professor, Ghent University, Ghent Oost-Vlaanderen Belgium. Email: kim.verbeken@ugent.be

ABSTRACT

As a result of the globally increasing consumer use of electronic devices, it is expected that pressure will increase on the supply chain of precious metals. Hence, recycling of these electronics becomes increasingly important, as well as optimising the current processes. One major issue in metallurgical processes is the amount of metal that is lost into the slag. This metal loss is inherent to the production process and therefore, additional processing steps such as slag cleaning may be required. Slag cleaning can be done in electrical resistance furnaces where heat is produced using the Joule effect, making the slag's electrical conductivity an important operating parameter. Since slags are ionic liquids, the electrical conduction happens via the movement of ions which is called ionic conductivity. However, within the presence of transition metal oxides, a second mechanism of conductivity occurs as electrons are able to hop from one transition state to another, which is known as electronic conductivity. As 'FeO' is a common slag component in the non-ferrous pyrometallurgical industry, both mechanisms are present, but their proportions vary with the respective amounts of the two forms of the multi-valent ions and hence, with the oxygen partial pressure. The goal of the present study is to develop an experimental set-up and methodology for measuring the electrical conductivity of synthetic SiO_2 – CaO – $AlO_{1.5}$ – 'FeO' slags at various oxygen partial pressures.

INTRODUCTION

One of the major current challenges within the metallurgical industry is the reduction of CO_2 emissions or so called decarbonisation. To achieve decarbonisation, the typical paths being explored are the use of green hydrogen as alternative for fossil based reductants and/or the electrification of production processes (Dalvi, 2023). In addition to decarbonisation, reduction of metal losses during primary production and recycling should also be taken into account to optimise resource efficiency. During pyrometallurgical processing, metal is frequently lost to the slag (metal oxide) phase as either a dissolved oxide or entrained droplets (Bellemans *et al*, 2018). One way to target both challenges is the use of submerged electric arc furnaces which operate as a decantation furnace to allow metal droplets from the slag to settle and be recovered while heat is generated via the conversion of electricity using the slag's resistance (Joule heating) (Friedrich *et al*, 2018). As a result, the modelling, dimensioning and operating of these furnaces require knowledge on the electrical conductivity of the used slag (Karalis *et al*, 2016).

The present study focuses on silicate slags containing CaO, $AlO_{1.5}$ and 'FeO' and thus current will be carried via both ionic and electronic conduction (NB: The authors prefer the use of $AlO_{1.5}$ over Al_2O_3 for the alumina content in the slag system as this gives an easier visualisation of the amount of cations in the slag, which are the main contributors to the ionic conductivity; 'FeO' is used throughout the text as a representation of iron oxide regardless of the iron oxidation state.) The ionic

mechanism involves the movement of cations (Ca^{2+}, Fe^{2+}) throughout the (alumino)silicate network (Mills *et al*, 2013). The main factors affecting the ionic conductivity are the amount of network forming oxides (SiO_2, $AlO_{1.5}$), the size of the mobile/network breaking cations and their valence (NB: $AlO_{1.5}$ is technically an amphoteric oxide, meaning that it can both have a network forming and network breaking role in the slag). Electronic conduction within slags requires the presence of transition metal oxides in different oxidation states which allows electrons to hop from one oxidation state to the other (Barati and Coley, 2006a). As this second mechanism is highly dependent on the iron oxidation state, the electrical conductivity of 'FeO'-containing slags is rather sensitive to the applied gas atmosphere, ie the oxygen partial pressure (Hundermark, 2003; Barati and Coley, 2006a).

In order to obtain more insight in both mechanisms and to construct a predictive model, a lot of accurate data on both contributions is required. This in turn demands experimental techniques to distinguish between both contributions. One such experimental method is stepped potential chronoamperometry which was proposed by Fried, Rhoads and Sadoway (2001) for BaO-'TiO_2' slags. This technique was applied by Barati and Coley (2006a) for SiO_2 – CaO – 'FeO' slags and recently on the SiO_2 – CaO – $AlO_{1.5}$ – 'FeO' system (Liu, Zhang and Chou, 2015; Liu *et al*, 2016, 2018). In each study, the oxygen partial pressure (pO_2) was varied to study its effect on the slag's electrical conductivity.

However, neither study verified the slag's chemical composition or microstructure after the experiment. In addition, the influence of the crucible was also not reported in any studies. For the study of Barati and Coley (2006a), zirconia (ZrO_2) crucibles were used and thus there could be an influence of zirconia dissolution within the slag. Liu *et al* (2015, 2016b, 2018) used Pt crucibles of which is known that they can react with FeO at sufficiently low pO_2 values which results in the uptake of Fe in the Pt crucible (Schupsky *et al*, 2020). Also, it is unclear for both studies whether they targeted a similar bath volume/bath height for each experiment and between the high temperature experiments and room temperature calibrations. Thus, in order to further improve the methodology of high temperature conductivity experiments, an experimental set-up was developed that allows quenching of the slag and crucible after each experiment for microstructural analysis. The aim of the present paper is, on the one hand, to verify that our electrical conductivity apparatus provides reliable experimental data and, on the other hand, to further contribute to the experimental methodology within the field.

METHODOLOGY

Electrical conductivity measurements

A detailed overview of general electrical conductivity measurements by the present authors was already published before (Boeykens *et al*, 2023a) and as such a summary of the measurement technique is given. The electrical conductivity of a material is derived from the resistance according to Equation 1 in which σ_{tot} is the total conductivity ($S \cdot cm^{-1}$), R is the measured resistance (Ω), l is the length of the current path (cm) and A is the cross-section of the current path (cm^2). The length l and the area A are typically grouped together in a geometric constant G which is known as the cell constant (cm^{-1}). For a solid material, the geometry of the sample can be measured and thus, the cell constant is easily determined. However, as a slag is a liquid/suspension, it needs to be put in a container and electrodes have to be submerged into the liquid. As a result, the current can travel throughout the entire volume of the container and therefore, a calibration is necessary to take into account the geometry of the current path. Typically, calibration procedures are carried out with aqueous solutions of which the conductivity is well known. During the calibration, the temperature is also carefully recorded, as the electrical conductivity has an Arrhenian temperature dependency as shown in Equation 2 in which E_a is the activation energy ($J \cdot mol^{-1}$), R the universal gas constant ($J \cdot mol^{-1} \cdot K^{-1}$), T the temperature (K) and σ_0 a pre-exponential factor ($S \cdot cm^{-1}$).

$$\sigma_{tot} = \frac{l}{A} * \frac{1}{R} = \frac{G}{R} \quad (1)$$

$$\sigma(T) = \sigma_0 exp\left(\frac{-E_a}{RT}\right) \quad (2)$$

Second, a slag is an ionic liquid and therefore, the current is (partially) carried via the movement of ions. As such, direct current (DC) resistance measurements are impossible due to polarisation of

the ions at the electrodes which blocks the current (Fried, Rhoads and Sadoway, 2001). Therefore, an alternating current (AC) needs to be applied and the slag's resistance/conductivity needs to be derived from the impedance Z (Ω). As the current is applied as a sine wave with a certain frequency f (Hz), capacitive and inductive responses of the melt/measurement set-up are measured as well and thus, the impedance is divided in a real Z_{real} (Ω) and imaginary part Z_{im} (Ω), as shown in Equation 3, which are both frequency dependent (Bard and Faulkner, 2001).

$$Z_{tot}(f) = Z_{real}(f) + j * Z_{im}(f) \quad (3)$$

To isolate the resistance corresponding to the slag's electrical conductivity, a frequency sweep is carried out to locate a frequency f_0 for which $Z_{im} = 0$. Typically though, a region of frequencies is found where the impedance is frequency independent and $Z_{real}(f) = Z_{real}(f_0)$.

Third, the aim of the current work is to measure the conductivity of 'FeO'-containing slags for which it is known that they exhibit both ionic and electronic conduction (Hundermark, 2003; Barati and Coley, 2006a, 2006b; Liu, Zhang and Chou, 2015; Liu *et al*, 2016b, 2018). From AC impedance measurements, the total conductivity of the slag can be derived which includes the contribution of both ions and electrons as charge carriers. To measure the contribution of each charge carrier, Fried, Rhoads and Sadoway (2001) proposed a method to determine the electronic transference number t_e (-) from stepped potential chronoamperometry (SPC) measurements. In their work, they laid the theoretical foundations of this technique applied for a binary BaO – 'TiO_2' system. The SPC technique has since been used in several slags containing transition metals such as Fe, Mn and Ti (Barati and Coley, 2006a; Pomeroy *et al*, 2012; Liu, Zhang and Chou, 2015; Liu *et al*, 2016a, 2016b, 2018; Liu, Zhang and Wang, 2017; Martin-Treceno *et al*, 2022; Boeykens *et al*, 2023a).

The basic idea of SPC is that a small DC voltage is applied to the slag and that the responsive current is recorded as a function of time. If the applied voltage is sufficiently low so that no faradaic reactions occur, then polarisation of the ions occurs and as a result ionic conduction will cease to happen at a certain time. On the contrary, electrons will continue to hop from one oxidation state to the other. The resulting current as a function of time will therefore have a current peak at the start and will decay to a stable, lower value. An example of such a voltage step and corresponding decaying current is provided in Figure 1. Assuming a homogeneous spread of the cations within the slag before the voltage step, the initial current response or the current peak I_{peak} corresponds to both ions and electrons moving within the slag. Due to the current decay, after a sufficiently long time, only electrons will continue to pass on current and this corresponds to I_∞.

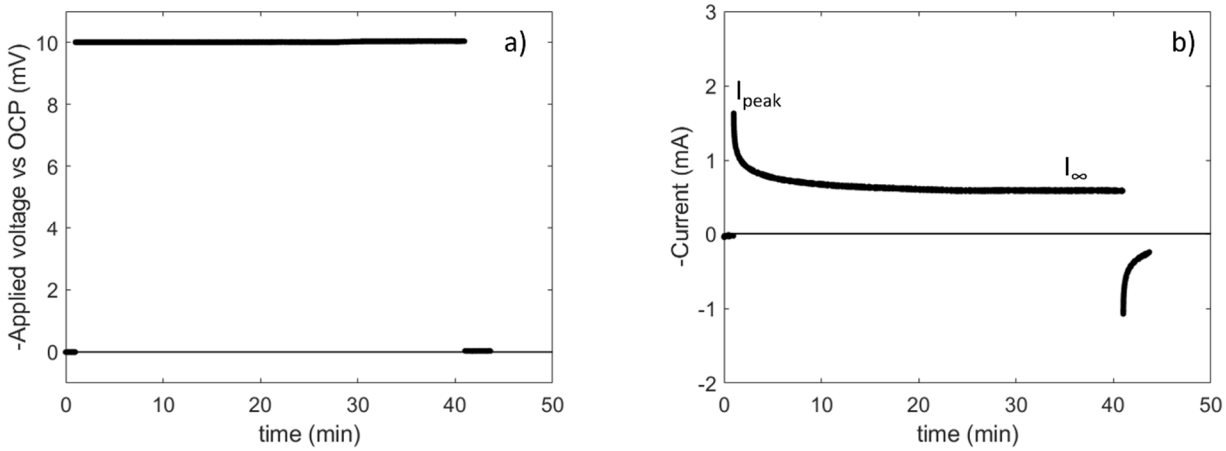

FIG 1 – (a) Example of the applied voltage step versus open circuit potential (OCP); and (b) example of the current response for stepped potential chronoamperometry (SPC).

The relative contribution of each charge carrier to the total current is denoted as the transference number. Thus, from the SPC measurement, the electronic transference number is equal to the ratio of the stable current over time, I_∞, over the initial peak current, I_{peak} as shown in Equation 4. Correspondingly, the ionic transference number t_i can be derived from t_e as the sum of both equals unity by definition (Equation 5).

$$t_e = \frac{I_\infty}{I_{peak}} \quad (4)$$

$$t_i + t_e = 1 \quad (5)$$

The transference numbers can then be utilised to determine the ionic σ_i and electronic conductivity σ_e of the slag via multiplying the respective transference number with the total conductivity obtained from AC impedance measurements as given in Equations 6 and 7. This is, however, on the assumption that the charge carriers are homogeneously distributed within the melt and that each charge carrier is similarly affected by the applied potential.

$$\sigma_i = t_i * \sigma_{tot} \quad (6)$$

$$\sigma_e = t_e * \sigma_{tot} \quad (7)$$

Electrical conductivity apparatus

Electrical conductivity measurements were performed in a high-temperature set-up similar to the one developed and described in an earlier article (Zhao *et al*, 2009). A schematic drawing of the apparatus is shown in Figure 2. The set-up can be divided into three parts:

1. A Pyrox vertical tube furnace (resistive heating up to 1650°C) with a temperature controller.
2. A steel chamber at the top which houses three vertically moving platforms and the electrode holder.
3. A stainless steel guiding tube at the bottom of the furnace which is placed in a bucket containing water.

Optionally, a stainless steel tip can be placed inside the bucket as well. The furnace was made gas-tight via sealing of the top steel chamber with a plastic window and via submerging the quench-guiding tube in the quenching water.

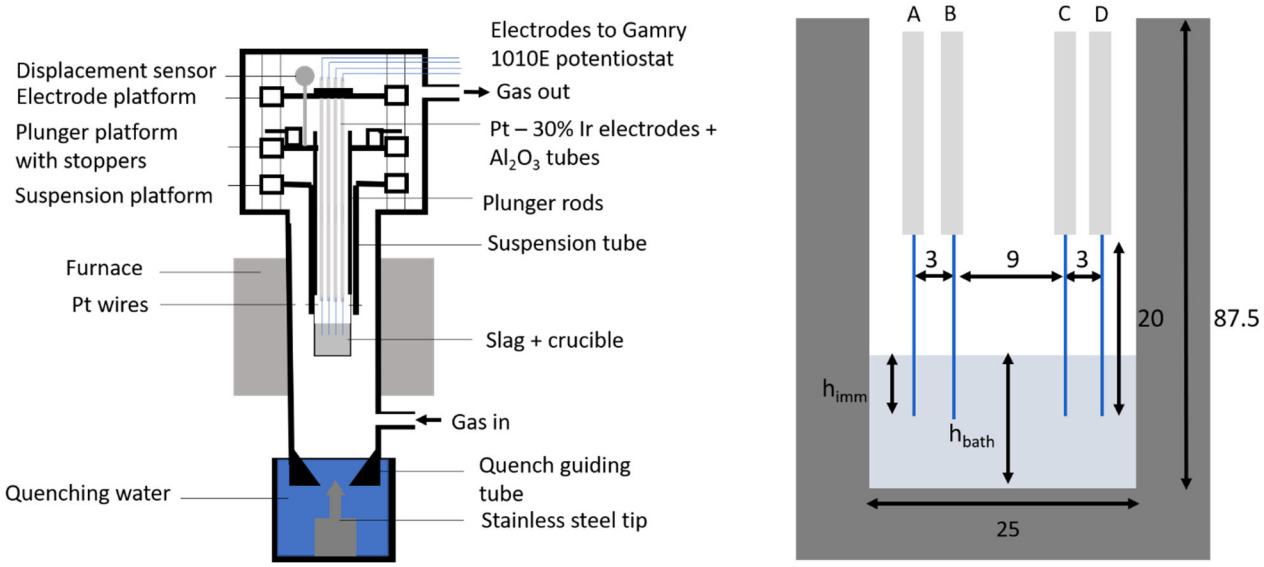

FIG 2 – Schematic overview of the high temperature electrical conductivity set-up and detailed close-up of the electrode and crucible geometry. Dimensions are in mm.

An alumina crucible was used to contain the slag and this crucible was positioned within the isothermal zone of the furnace via an alumina suspension tube which is connected to the suspension platform. To ensure the connection between the crucible and the suspension tube, both the crucible and the tube have four holes through which Pt – 13 per cent Rh wires were inserted. The electrodes were placed within an electrode holder on the electrode platform. A digital displacement sensor with a 90 mm stroke and 0.01 mm precision was placed on the movable electrode platform to monitor the movement of the electrodes. To quench the crucible from the furnace, two alumina plunger rods were positioned on the plunger platform inside the suspension tube so that they touch the top of the

crucible. Via lifting up the suspension platform and keeping the plunger platform stationary, the plunger tubes push on the crucible which shears/breaks the Pt wires allowing the crucible to fall into the quenching water. When the stainless steel tip is placed inside the quenching water, the alumina crucible will shatter on impact. This causes direct contact between the hot slag (1310°C) and the water (25°C) to ensure fast quenching. This quenching procedure allows to freeze the sample microstructure at high temperature which subsequently can be analysed via microscopic techniques to verify the slag composition, the presence of any solids, etc. However, the quenching procedure with the stainless steel tip cannot provide information on the location and distribution of eventual solids within the slag. Therefore, some experiments were also carried out without the steel tip which allows the crucible to be quenched as a whole. A microscopic analysis was then carried out on the crucible cross-section instead.

The temperature of the furnace in the hot zone was calibrated using a type B thermocouple at different heights, while the oxygen partial pressure (pO_2) was controlled via controlling the ratio of (CO + Ar)/CO_2 gas inside the furnace. The ratio of both gas mixtures was adjusted to meet the desired target pO_2 using a similar procedure as the small scale equilibrium experiments. A total flow rate of 1 L/min was used. To verify the current set-up, three pO_2 values were chosen: air (0.21 atm), 10^{-5} atm and $10^{-7.92}$ atm which correspond to Fe^{3+}/Fe_{tot} ratios of 0.89, 0.51 and 0.20, respectively, as predicted by FactSage™ (Bale *et al*, 2016) (UQPY database (Jak *et al*, 2022)).

Given the high conductivity of 'FeO'-containing slags, a four-electrode set-up was utilised to measure the electrical conductivity as this method omits the need for cable corrections and the potential errors associated with two-electrode set-ups (Boeykens *et al*, 2023b). The electrodes were made of 25 mm long 1 mm diameter Pt – 30 per cent Ir tips which were welded to a long thin (0.3 mm diameter) Pt – 30 per cent Ir wire. The electrodes were sheathed into a single bore alumina tube (inner diameter = 1 mm). The tips were positioned 5 mm inside the alumina tube to fix their position. In addition, the position of the tubes with respect to each other was fixed via three ceramic spacers along the length of the alumina tubes. A detailed schematic of the electrode positions with respect to each other and the crucible is provided in Figure 2. The thin wires were connected via electrical connectors to electrically isolated steel bolts which protrude the top steel chamber. As a result, alligator clips were clipped to these bolts to make the electrical connection between the Gamry 1010E Interface potentiostat and the electrodes. A potentiostat was utilised as both AC and DC measurements are needed to fully describe the electrical conductivity of 'FeO'-containing slags.

Measurement procedure

Cell calibration

As mentioned earlier, the geometry of the current path or the cell constant G needs to be determined in order to convert resistances to electrical conductivities. As the cell constant is (strongly) dependent on the cell construction in terms of electrode geometry, electrode immersion depth, crucible material, solution etc (Gruener *et al*, 1998; Schiefelbein *et al*, 1998; Boeykens *et al*, 2023b), the calibration was done as a function of the electrode immersion depth h_{imm} (3–15 mm) for different bath heights h_{bath} (21 mm, 23 mm, 25 mm and 27 mm). An aqueous 1D (demal) KCl conductivity standard (111.3 mS/cm at 25°C, Radiometer analytical) was chosen as the calibration liquid.

The bath surface was located via lowering the electrodes and simultaneously measuring the impedance. In air, the impedance was of the order kΩ/MΩ and strongly fluctuated, whereas when it touched the conductive liquid, the impedance dropped to an order of Ω and was stable. This process was done via a two-electrode configuration using multiple electrode combinations (A-B, A-C and A-D). The bath surface was set to be the displacement sensor reading for which all electrodes touched the bath surface. The electrodes were subsequently lowered to an immersion depth of 10 mm for calibration impedance measurements.

These measurements were done galvanostatically using an excitation current of 100 µA. For each experiment, a frequency sweep was first carried out at a 10 mm immersion depth to determine the frequency at which the solution's resistance can be extracted. The real impedance was found to be frequency independent between 10 kHz and 100 kHz at 10 mm insertion for different bath heights and calibration solutions. Thus, single frequency measurements were done at 20 kHz for 3 mins.

After the single frequency measurement, the electrode's position was changed to vary the immersion depth and the single frequency measurement at 20 kHz was repeated. During each measurement, the temperature was recorded using a type-K thermocouple next to the crucible. The temperature dependency of the conductivity standards was fitted to Equation 2 from data provided by the suppliers. From this fit, the electrical conductivity at the measured temperature was determined and multiplied by the measured real impedance at 20 kHz to obtain the cell constant G. The measured cell constant as a function of the immersion depth and bath is shown in Figure 3.

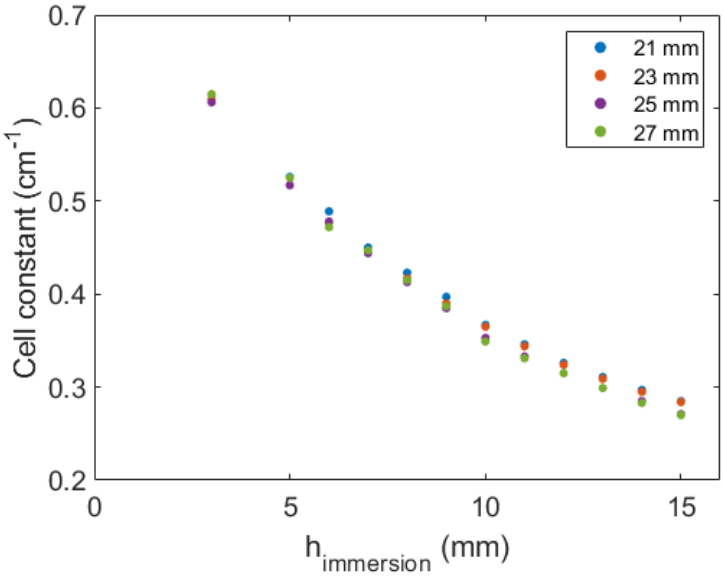

FIG 3 – Cell constant G (cm^{-1}) as a function of the electrode immersion depth h_{imm} (mm) for different bath heights.

High temperature measurements

For the high-temperature conductivity measurements, a bath height of 25 mm was desired. The amount of slag needed was calculated based on the density/molar volume model of Thibodeau, Gheribi and Jung, 2016a, 2016c, 2016b). The slag mixture was prepared in two steps. First, a sinter of CaO – $AlO_{1.5}$ – SiO_2 (CAS) was prepared via mixing high-purity powders of $CaCO_3$ (99.9 per cent), Al_2O_3 (99.7 per cent) and crushed SiO_2 glass (99.999 per cent) together to match the compositions in Table 1. Fe and Fe_2O_3 were added to create the predicted amount of FeO according to calculated via FactSage 7.3 (database UQPY 2023) (Bale *et al*, 2016) in the slag assuming a stoichiometric reaction as shown in Equation 8.

$$Fe_2O_3 + Fe \rightarrow 3\,FeO \tag{8}$$

TABLE 1

Starting composition of the slag for electrical conductivity measurements (in mol per cent).

	CaO	**SiO_2**	**$AlO_{1.5}$**	**'FeO'**
Mol%	33.55	29.75	16.00	20.70

This mixture was put in an alumina crucible inside a muffle furnace at 1240°C overnight. This CAS sinter was then added to Fe_2O_3 powder (99.8 per cent) and Fe powder (99.9 per cent). All powders were thoroughly mixed in a pestle and mortar before being pelletised. This powder mixture was then brought into the alumina crucible and put inside the furnace. The advantage of using the CAS sinter compared to the pure powders was that it aided the pelletising procedure and that it prevented powder ejection/slag foaming due to a release of CO_2 gas at elevated temperatures. After the furnace was completely sealed off from the surrounding atmosphere, it was flushed with the desired gas composition at a flow rate of 1 L/min for 9 hrs. The temperature was subsequently increased to

1310°C at a rate of 5°C/min and kept for 6 hrs to allow melting of the powder and homogenisation of the bath.

The bath surface was then determined in a similar way as for the calibration. However, it was found that the slag wetted the crucible significantly which resulted in the formation of a meniscus as illustrated in Figure 4. To take into account this difference in bath geometry between high temperature experiment and low temperature calibration, a correction procedure for the slag meniscus was adopted which is schematically illustrated in the right side of Figure 4. The idea is that the displacement sensor readings h_{sensor} upon touching the slag surface for each electrode combination are recorded. Plotting the sensor reading as a function of the electrode positions allowed then to estimate the slag meniscus via a parabolic function to extract the bath surface which was defined as the minimum of the meniscus. The authors are aware that this method is only an approximation of the reality and that this fitting is influenced by the electrode spacing and deviations of the meniscus from a parabolic profile. However, since differences of 1–2 mm were found between positions $h_{A,D}$ and $h_{A,B}/h_{A,C}$ it was deemed necessary to estimate the meniscus profile and to correct for the geometry difference at high temperature and calibration.

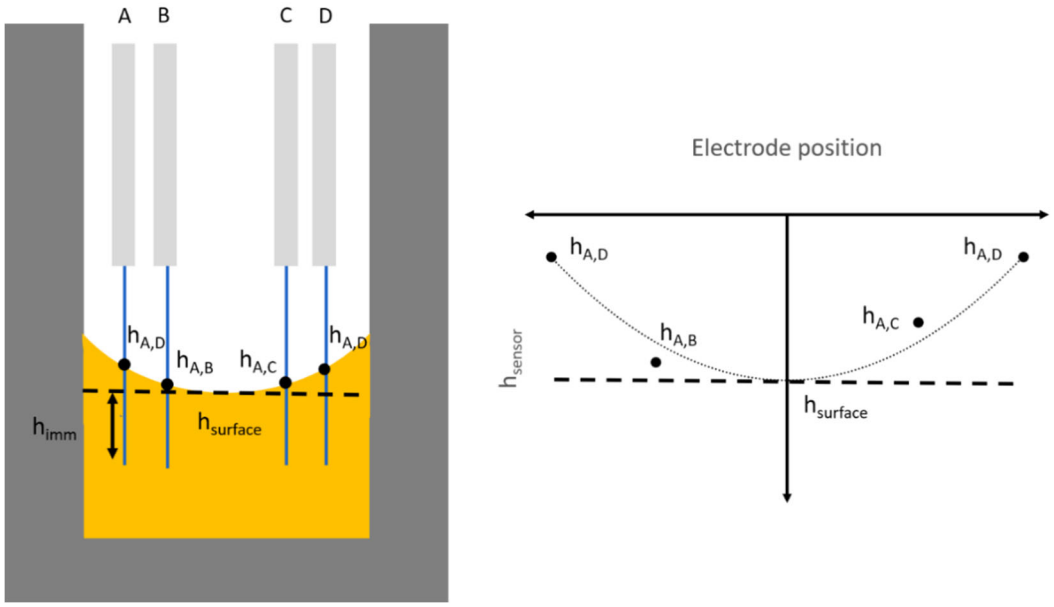

FIG 4 – Schematic illustration of the fitting procedure for determining the bath surface at high temperature experiments.

After determination of the bath surface, the electrodes were lowered to an immersion depth of 10 mm. Similar to the calibration, a frequency sweep was carried out. For the high temperature experiments, the real impedance was frequency-independent over a broad range from 100 Hz to 50 kHz. Single frequency measurements were carried out at 10 kHz at immersion depths of 8, 9, 10, 11 and 12 mm starting with the one at 10 mm. After the single frequency measurements, the electrode configuration was changed to a three-electrode configuration using electrode positions B, C and D for the counter, reference and working electrode, respectively, and the immersion depth was again placed at 10 mm. The open circuit potential of the system was then recorded for 10 mins after which stepped potential chronoamperometry was executed. The system was held at OCP for 1 min prior to a voltage step of -10 mV (versus OCP) for 40 mins during which the current was measured at a scan rate of 100 Hz. Preliminary experiments indicated that positive voltages, applied between working and reference electrode, would result in electrode plating at the counter electrode for low oxygen partial pressures. In addition, a long time for the voltage step was needed as the system progressed slowly to a stable current I_{∞}. After stepped potential chronoamperometry, the configuration was switched back to the earlier four-electrode set-up and single frequency measurements were done at the same immersion depths as before. Comparison of these values allowed to quantify any changes in the electrical conductivity as a result of crucible dissolution into the slag, which could have taken place during the stepped potential chronoamperometry. After this final measurement, the electrodes were lifted outside the slag and the crucible was quenched. The

slag was then mounted in epoxy resin for electron probe X-ray microanalysis (EPMA) with wavelength dispersive detectors (JEOL 8200L EPMA, Japan Electron Optics Ltd, Tokyo, Japan). All elements were measured using the conventional EPMA technique. The conventional EPMA measurement was performed with an acceleration voltage of 15 keV, a beam current of 20 nA and a probe diameter ranging from 5 to 30 μm depending on the specific phase being analysed. The following detectors and spectral lines were employed for elemental measurement: Al K_α – TAP, Fe K_α – LIF, Si K_α – PET J, Ca K_α – PET J. For the measurement of Al, Fe, Si and Ca cations, pure (synthetic) $AlO_{1.5}$, Fe_2O_3, SiO_2 and $CaSiO_3$ standards were used, respectively, provided by Charles Taylor. Raw measured data underwent standard ZAF correction using the Armstrong/Love Scott approach.

Results

The measured compositions of the slag samples using EPMA for different conditions are provided in Table 2. Both CaO and SiO_2 match the desired target composition, whereas for $AlO_{1.5}$ and 'FeO', there seems to be respectively a 1 per cent increase and decrease. The increase in $AlO_{1.5}$ stems from a continuous dissolution of the crucible into the liquid slag. The decrease in 'FeO' on the other hand might stem from reactions going on between the crucible and the slag at the slag-crucible interface, such as dissolution of hematite ($FeO_{1.5}$) into the alumina crucible and/or the formation of Fe/Al-containing spinels. For pO_2 values of 10^{-5} atm and $10^{-7.92}$ atm, a spinel layer covering the crucible was indeed observed. For the sample at 10^{-5} atm, an additional loose spinel layer was found up to about 1.57 mm above the crucible bottom where spinels are suspended in the liquid slag. However, it is expected for this layer to have a limited effect on the measurements as there always is around 9–14 mm of fully liquid slag between the lowest points of the electrodes and the loose layer. Due to this relatively large distance, it is expected that only a minor fraction of the total current reaches this loose spinel layer.

TABLE 2

Measured slag compositions (mol per cent) after quenching for different oxygen partial pressures (pO_2, log(atm)).

pO_2	Fe^{3+}/Fe_{tot}	SiO_2	CaO	$AlO_{1.5}$	'FeO'
-0.67	0.89	29.78 ± 0.18	33.27 ± 0.14	17.46 ± 0.16	19.50 ± 0.11
-5.00	0.51	29.95 ± 0.33	33.24 ± 0.31	17.02 ± 0.48	19.79 ± 0.20
-7.92	0.20	30.02 ± 0.22	33.43 ± 0.18	16.69 ± 0.19	19.80 ± 0.12

The total, electronic and ionic conductivity and the electronic transference number as a function of the predicted Fe^{3+}/Fe_{tot} ratio is given in Figures 5 and 6. The experimental reproducibility lies between 3 per cent and 20 per cent for the total electrical conductivity and below 3 per cent on electronic transference numbers. The uncertainty due to crucible dissolution before and after stepped potential chronoamperometry was below 5 per cent on the total electrical conductivity. This mild effect of crucible dissolution is likely the result of working at near saturation conditions of the slag which was the target of the initial small scale experiments as well as the formation of this protective spinel layer at the slag-crucible boundary (Vergote *et al*, 2021).

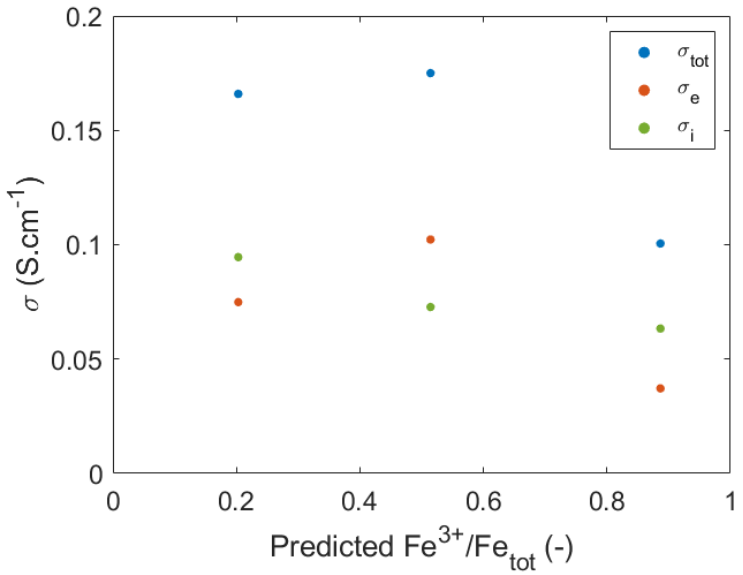

FIG 5 – Total, electronic and ionic conductivity (S/cm) as a function of the predicted Fe^{3+}/Fe_{tot} ratio for the slag.

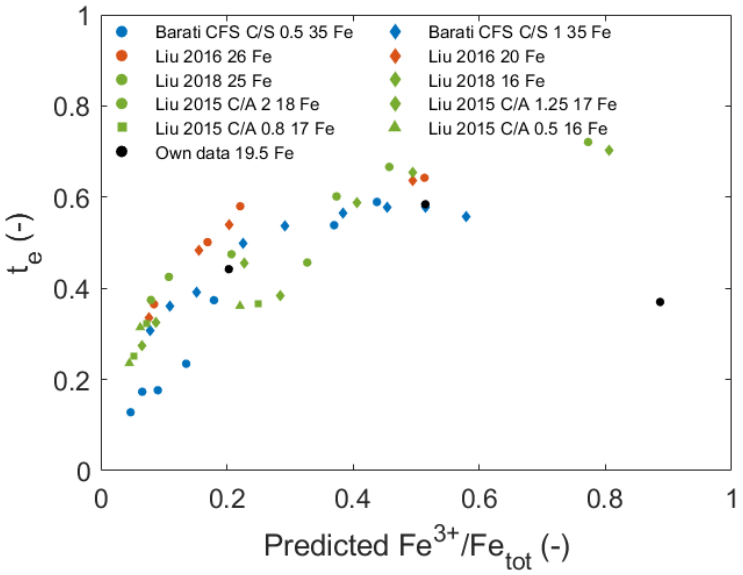

FIG 6 – Electronic transference number as a function of the Fe^{3+}/Fe_{tot} ratio predicted via FactSage UQPY 2023 for our experimental data and data obtained from literature. The amount of Fe cations per 100 mol slag for each study is also included in the figure's legend.

Even from a limited number of experimental conditions, some trends can already be confirmed. First of all, both the total and electronic conductivity seem to exhibit a maximum between the two extremes of a pO_2 of $10^{-0.67}$ atm and 10^{-8} atm or Fe^{3+}/Fe_{tot} values of 0.89 and 0.20, respectively. This is expected as an equal number of Fe^{2+} and Fe^{3+} provides optimal conditions for electron hopping (Barati and Coley, 2006a, 2006b). Second, the ionic conductivity increases with decreasing Fe^{3+}/Fe_{tot} ratio as the less mobile Fe^{3+} cations are replaced by more mobile Fe^{2+} cations.

Finally, the obtained electronic transference number is compared with several reported literature values (Barati and Coley, 2006a; Liu, Zhang and Chou, 2015; Liu *et al*, 2016b; Liu *et al*, 2018). The Fe^{3+}/Fe_{tot} ratios of these other studies are estimated via FactSage UQPY 2023 from the reported slag composition and conditions (gas flow rate, temperature). Since electronic transference numbers are independent of temperature, this value can provide a better means for comparing electrical conductivity set-ups/measurements. Moreover, comparison of electronic transference numbers between different slag compositions is roughly possible on the condition that the concentration of the two Fe cations between both slags is of a similar magnitude. From Equation 5, the electronic

transference number is the ratio of the electronic conductivity over the sum of the electronic and ionic conductivity. The electronic conductivity, Equation 9, is assumed to depend on the Fe^{2+} diffusion coefficient DF_{e2+} (cm^2/s), the concentration of Fe cations [Fe] (mol/cm^3) and the Fe^{3+}/Fe_{tot} ratio y (-) (Engell and Vygen, 1968; Barati and Coley, 2006b). The ionic conductivity is typically described via the Nernst-Einstein equation (Thibodeau and Jung, 2016) which assumes that the total ionic conductivity is the sum of the contribution of each cation in the melt as shown in Equation 10 in which z_i is the charge of cation i, F is the Faraday constant, R is the universal gas constant, T is the temperature (K), [i] is the concentration of cation i (mol/cm^3) and D_i its diffusion coefficient (cm^2/s). Therefore, the electronic transference number can be described according to Equation 11. This equation shows that the electronic transference for slags with a similar Fe concentration has a more or less parabolic shape as a function of the Fe^{3+}/Fe_{tot} ratio (y) with the maximum value being shifted according to the ionic conductivity of the other cations in the slag. Figure 6 shows that the electronic transference number of the current study lies within the expected order of magnitude for slags with a similar 'FeO' content.

$$\sigma_e = C_1 D_{Fe2+}[Fe]^2 y(1-y) \tag{9}$$

$$\sigma_{ion} = \sum_i \frac{{z_i}^2 F^2}{RT}[i]D_i \tag{10}$$

$$t_e = \frac{\sigma_e}{\sigma_e+\sigma_i} = \frac{C_1 D_{Fe2+}[Fe]^2 y(1-y)}{C_1 D_{Fe2+}[Fe]^2 y(1-y)+\frac{4F^2}{RT}D_{Fe2+}(1-y)[Fe]+\sum_{i,i\neq Fe2+}\frac{{z_i}^2F^2}{RT}[i]D_i} \tag{11}$$

CONCLUSION

The aim of the present study was to validate and obtain a methodology for electrical conductivity measurements on CaO – $AlO_{1.5}$ – SiO_2 – 'FeO' slags for varying oxygen partial pressures in a newly built set-up which allows quenching and post-experimental verification of the composition and microstructure. Experiments were carried out in three different atmospheres: air (pO_2 = 0.21 atm) and two CO_2/CO/Ar gas mixtures with an oxygen partial pressure of 10^{-5} atm and $10^{-7.92}$ atm. The electrical conductivity was found to be stable throughout the experiment due to saturation of the slag with $AlO_{1.5}$ and the formation of protective layer at the slag-crucible interface for some conditions. In addition, microstructural analysis of the samples showed that an unexpected loose spinel layer formed during the experiment at $pO_2 = 10^{-5}$ atm. Although the effect of this layer was assumed to be negligible, it nonetheless shows the need for post-experimental microstructural analysis to confirm which phases were present during the effective measurement. Overall, the experimental reproducibility of the set-up varied between 3 per cent and 20 per cent. From a limited set of conditions, the expected trends were confirmed: an increase in the ionic conductivity from more oxidising (Fe^{3+} rich) to more reducing (Fe^{2+} rich) conditions. Also, a maximum in the electronic conduction is expected based on the observed peak at the predicted Fe^{3+}/Fe_{tot} ratio of 0.5 within the other two conditions. Finally, it was proven that electronic transference numbers of the current study have a similar order of magnitude as those from earlier studies in literature.

ACKNOWLEDGEMENTS

Author P J Boeykens holds a grant [HBC.2020.2248] which is supported by VLAIO, the Flanders Innovation and Entrepreneurship Agency, in co-operation with Umicore. Author I Bellemans holds a grant from the Research Foundation Flanders [1239024N]. The authors would like to express their thanks to R Starykh for aiding in the construction of the electrical conductivity set-up and for EPMA measurements.

REFERENCES

Bale, C W, Belisle, E, Chartrand, P, Decterov, S A, Eriksson, G, Gheribi, A E, Hack, K, Jung, I H, Kang, Y B, Melancon, J, Pelton, A D, Petersen, S, Robelin, C, Sangster, J, Spencer, P and Van Ende, M A, 2016. FactSage thermochemical software and databases, 2010–2016. *CALPHAD*: *Computer Coupling of Phase Diagrams and Thermochemistry*, 54:35–53. https://doi.org/10.1016/j.calphad.2016.05.002

Barati, M and Coley, K S, 2006a. Electrical and electronic conductivity of CaO-SiO_2-FeO x slags at various oxygen potentials: Part, I, Experimental results, *Metallurgical and Materials Transactions B*: *Process Metallurgy and Materials Processing Science*, 37(1):41–49. https://doi.org/10.1007/s11663-006-0084-x

Barati, M and Coley, K S, 2006b. Electrical and electronic conductivity of CaO-SiO_2-FeO_x slags at various oxygen potentials: Part II, Mechanism and a Model of Electronic Conduction, *Metallurgical and Materials Transactions B*: *Process Metallurgy and Materials Processing Science*, 37(1):51–60. https://doi.org/10.1007/s11663-006-0085-9

Bard, A J and Faulkner, L R, 2001. Electrochemical Methods Fundamentals and Applications, *Annual Review of Materials Science*, second edition (John Wiley and Sons Inc).

Bellemans, I, De Wilde, E, Moelans, N and Verbeken, K, 2018. Metal losses in pyrometallurgical operations - A review, *Advances in Colloid and Interface Science*, 255:47–63. https://doi.org/10.1016/j.cis.2017.08.001

Boeykens, P-J, Bellemans, I, Scheunis, L and Verbeken, K, 2023a. Electrical conductivity measurements in PbO-SiO_2-FeOx slags, in European Metallurgical Conference (EMC 2023), pp 951–963.

Boeykens, P-J, Bellemans, I, Scheunis, L and Verbeken, K, 2023b. Parameter investigation of the experimental methodology of electrical conductivity measurements for PbO containing slags, *Electrochimica Acta*, 464:142846. https://doi.org/10.1016/J.ELECTACTA.2023.142846

Dalvi, A D, 2023. Decarbonization of Mining and Metals Industry, A Critical Overview, in *Proceedings of the 61st Conference of Metallurgists, COM 2022*, pp 917–937. https://doi.org/10.1007/978-3-031-17425-4_103

Engell, H-J and Vygen, P, 1968. Ionen- und Elektronenleitung in CaO-FeO-Fe_2O_3-SiO_2-Schmelzen, *Berichte der Bunsengesellschaft für physikalische Chemie*, 72(1):5–12. https://doi.org/10.1002/bbpc.19680720104

Fried, N A, Rhoads, K G and Sadoway, D R, 2001. Transference number measurements of TiO_2-BaO melts by stepped-potential chronoamperometry, *Electrochimica Acta*, 46(22):3351–3358. https://doi.org/10.1016/S0013-4686(01)00531-X

Friedrich, B, Kalisch, M, Friedmann, D, Degel, R, Kaußen, F and Böhlke, J, 2018. The Submerged Arc Furnace (SAF): State-of-the-Art Metal Recovery from Nonferrous Slags, *Journal of Sustainable Metallurgy*, 4(1):77–94. https://doi.org/10.1007/s40831-017-0153-1

Gruener, G, Dembinski, K, Bouvier, A, Loup, J P and Odier, P, 1998. Measurements of conductivity in liquids, Application to $2CaOAl_2O_3SiO_2$, *EPJ Applied Physics*, 4(1):101–106. https://doi.org/10.1051/epjap:1998248

Hundermark, R, 2003. The electrical conductivity of melter type slags, University of Cape Town.

Jak, E, Shishin, D, Shevchenko, M and Hayes, P C, 2022. Integrated Experimental Phase Equilibria and Thermodynamic Modelling Research and Implementation in Support of Pyrometallurgical Copper Processing, in *Proceedings of the 11th International Conference on Copper,* pp 608–634.

Karalis, K T, Karkalos, N, Cheimarios, N, Antipas, G S E, Xenidis, A and Boudouvis, A G, 2016. A CFD analysis of slag properties, electrode shape and immersion depth effects on electric submerged arc furnace heating in ferronickel processing, *Applied Mathematical Modelling*, 40(21):9052–9066. https://doi.org/10.1016/j.apm.2016.05.045

Liu, J H, Zhang, G H, Wu, Y D and Chou, K C, 2016a. Electrical Conductivity and Electronic/Ionic Properties of TiOx-CaO-SiO_2 Slags at Various Oxygen Potentials and Temperatures, *Metallurgical and Materials Transactions B*: *Process Metallurgy and Materials Processing Science*, 47(1):798–803. https://doi.org/10.1007/s11663-015-0499-3

Liu, J H, Zhang, G H, Wu, Y D and Chou, K C, 2016b. Study on electrical conductivity of FexO–CaO–SiO_2–Al_2O_3 slags, *Canadian Metallurgical Quarterly*, 55(2):221–225. https://doi.org/10.1080/00084433.2016.1150545

Liu, J H, Zhang, G H and Chou, K C, 2015a. Electronic/ionic properties of FexO-SiO_2-CaO-Al_2O_3 slags at various oxygen potentials and temperatures, *ISIJ International*, 55(11):2325–2331. https://doi.org/10.2355/isijinternational.ISIJINT-2015-325

Liu, J H, Zhang, G H and Chou, K C, 2015b. Study on electrical conductivities of CaO-SiO2-Al2O3 slags, *Canadian Metallurgical Quarterly,* 54:170–176. https://doi.org/10.1179/1879139514Y.0000000174

Liu, J H, Zhang, G H and Wang, Z, 2017. Experimental Study on Electrical Conductivity of MnO-CaO-SiO_2 Slags at 1723 K to 1823 K (1450°C to 1550°C) and Various Oxygen Potentials, *Metallurgical and Materials Transactions B*: *Process Metallurgy and Materials Processing Science*, 48(6):3359–3363. https://doi.org/10.1007/s11663-017-1072-z

Liu, Y X, Liu, J H, Zhang, G H, Zhang, J L and Chou, K C, 2018. Experimental Study on Electrical Conductivity of FexO-CaO-SiO_2-Al_2O_3 System at Various Oxygen Potentials, *High Temperature Materials and Processes*, 37(2):121–125. https://doi.org/10.1515/htmp-2016-0102

Martin-Treceno, S, Allanore, A, Bishop, C M, Watson, M J and Marshall, A T, 2022. Determination of the Partial Contributions to the Electrical Conductivity of TiO_2-SiO_2-Al_2O_3-MgO-CaO Slags: Role of the Experimental Processing Conditions, *Metallurgical and Materials Transactions B*: *Process Metallurgy and Materials Processing Science*, 53(2):798–806. https://doi.org/10.1007/s11663-022-02433-5

Mills, K C, Hayashi, M, Wang, L and Watanabe, T, 2013. The Structure and Properties of Silicate Slags, in *Treatise on Process Metallurgy* (Elsevier Ltd), chapter 2, pp 149–286. https://doi.org/10.1016/B978-0-08-096986-2.00008-4

Pomeroy, M, Brown, G, Barati, M and Coley, K S, 2012. Comparison of the electronic conduction mechanism in MnO x-CaO-SiO 2 and FeO x-CaO-SiO 2 slag systems, *High Temperature Materials and Processes*, 31(3):231–236. https://doi.org/10.1515/htmp-2012-0042

Schiefelbein, S L, Fried, N A, Rhoads, K G and Sadoway, D R, 1998. A high-accuracy, calibration-free technique for measuring the electrical conductivity of liquids, *Review of Scientific Instruments*, 69(9):3308–3313. https://doi.org/10.1063/1.1149095

Schupsky, J P, Guo, M, Blanpain, B and Müller, M, 2020. The Impact of Sample Homogeneity, Crucible Material and Oxygen Partial Pressure on the Crystallization of Fe-Rich Oxidic Slag in CLSM Experiments, *Journal of Sustainable Metallurgy*, 6(2):216–226. https://doi.org/10.1007/S40831-020-00262-X

Thibodeau, E and Jung, I H, 2016. A Structural Electrical Conductivity Model for Oxide Melts, *Metallurgical and Materials Transactions B*: *Process Metallurgy and Materials Processing Science*, 47(1):355–383. https://doi.org/10.1007/s11663-015-0458-z

Thibodeau, E, Gheribi, A E and Jung, I H, 2016a. A Structural Molar Volume Model for Oxide Melts Part I: Li2O-Na2O-K2O-MgO-CaO-MnO-PbO-Al_2O_3-SiO_2 Melts—Binary Systems, *Metallurgical and Materials Transactions B*: *Process Metallurgy and Materials Processing Science*, 47(2):1147–1164. https://doi.org/10.1007/s11663-015-0548-y

Thibodeau, E, Gheribi, A E and Jung, I H, 2016b. A Structural Molar Volume Model for Oxide Melts Part II: Li2O-Na2O-K2O-MgO-CaO-MnO-PbO-Al_2O_3-SiO_2 Melts—Ternary and Multicomponent Systems, *Metallurgical and Materials Transactions B*: *Process Metallurgy and Materials Processing Science*, 47(2):1165–1186. https://doi.org/10.1007/s11663-015-0543-3

Thibodeau, E, Gheribi, A E and Jung, I H, 2016c. A Structural Molar Volume Model for Oxide Melts Part III: Fe Oxide-Containing Melts, *Metallurgical and Materials Transactions B*: *Process Metallurgy and Materials Processing Science*, 47(2):1187–1202. https://doi.org/10.1007/s11663-015-0549-x

Vergote, O, Bellemans, I, Van den Bulck, A and Verbeken, K, 2021. Towards More Reliable {PbO}-{SiO}$_2$ Based Slag Viscosity Measurements in Alumina via a Dense Intermediate Spinel Layer, *Metallurgical and Materials Transactions B,* 52(6):3646–3659. https://doi.org/10.1007/s11663-021-02328-x

Zhao, B, Jak, E, Hayes, P C, Font, J and Moyano, A, 2009. Viscosity and electrical conductivity of copper slag at controlled oxygen potential, in *Molten* 2009: *Proceedings of the VIII International Conference on Molten Slags, Fluxes and Salt*, pp 225–235.

Calcium based ternary nitrate salts for concentrating solar power applications

DOI: 10.62053/VGHV1884

P Gandhre[1], V Shrotri[2] and L Muhmood[3]

1. Research Scholar, K J Somaiya College of Engineering, Somaiya Vidyavihar University, Mumbai Maharashtra 400077, India. Email: pranjal.gandhre@somaiya.edu
2. Project Engineer, C-DAC, Kolkata, West Bengal 700091, India. Email: varunshrotri59@gmail.com
3. Professor, K J Somaiya College of Engineering, Somaiya Vidyavihar University, Mumbai Maharashtra 400077, India. Email: luckman@somaiya.edu

ABSTRACT

The current work deals with the measurement of some thermophysical properties of $Ca(NO_3)_2$ based ternary nitrate molten salts as HTF (heat transfer fluid) / TES (Thermal Energy Storage) material for CSP (Concentrating solar power) plants. The density and viscosity of different compositions of the ternary salt mixture containing $Ca(NO_3)_2$, $NaNO_3$ and KNO_3 close to the liquidus has been experimentally measured. An attempt has also been made to measure the melting point of the salt using the cooling curve technique as well as Differential Scanning Calorimetry (DSC). Thermogravimetric analysis has also been performed to estimate the peak operating temperature of the salt. Compatibility of suitable pipe material (SS304) with molten salt has also been discussed. The salt mixture proves to be a viable alternative to the already existing HTFs like Therminol VP-1 (organic oil) or Solar Salt® in regards to its lower melting point, wider operating range, low cost, non-toxicity, sufficiently high density and comparable viscosity.

INTRODUCTION

With the increasing interest in sustainable power production and the need to reduce CO_2 emissions, renewable energy sources are becoming an important element of today's world energy balance. Among the current options of renewable energy, the Concentrating Solar Power (CSP) technologies *viz*: parabolic trough, linear fresnel reflector, parabolic dish and central tower, are gaining importance. In solar concentrator plants, the heat from the solar irradiance is transferred to a heat transfer fluid. A more popular method of transferring heat to the water is to transfer it to a fluid with higher thermal conductivity and heat storage capacity than water. This allows for more heat to be transferred to the working fluid.

Molten salts, namely fluoride salts, have been widely used in nuclear powerplants for heat transfer decades earlier than their use in CSP (Vignarooban *et al*, 2015; Rosenthal, 2010). It is only in the past four decades that molten salts have been used as heat transfer fluids in CSP to improve their effectiveness. Molten salts stand apart as a unique class of fluids that provide various advantages over their organic counterparts. Many of the salt mixtures developed and/or proposed for CSP applications are based on molten alkali nitrates. These mixtures make excellent HTFs (Heat Transfer Fluids) due to their lower viscosity, high volumetric heat capacity, and compatibility with the environment, high operating and decomposition temperature. Another important advantage of using molten salts is that they can also be used as a thermal energy storage medium. However, few thermophysical property data exist for promising ternary and quaternary salt mixtures as compared to simple binary mixture like 'Solar Salt®' containing 60 per cent $NaNO_3$ and 40 per cent KNO_3.

A poising problem with Solar Salt® is their high freezing point. This is not an issue during the diurnal operation, but when the temperature drops at night, special care must be taken to keep the salt from freezing. Auxiliary heaters are provided to keep this from happening, but the problem remains nonetheless. Hence, for solar thermal power to be cost-effective as a base load generation plant, the cost and efficiency of the plant must be improved. One possibility is by reducing the melting point of the heat transfer fluid, hence increasing the plant operation time. Currently, the most widely used molten salt HTF, the Solar Salt®, melts at 223°C (Vignarooban *et al*, 2015).

Classification of HTFs

HTF is one of the most important components for overall performance and efficiency of CSP systems. Since HTF is required in large quantities to operate a CSP plant, it is necessary to minimise the cost of HTF while maximising its performance. Besides transferring heat from the receiver to steam generator, hot HTF can also be stored in an insulated tank for power generation during periods of low solar insolation and at off-peak hours. Desired characteristics of an HTF include: low melting point, high boiling point and thermal stability, low vapour pressure (<1 atm) at high temperature, low corrosion with metal alloys used to contain the HTF, low viscosity, high thermal conductivity, high heat capacity for energy storage and low cost (Vignarooban *et al*, 2015; Srivastva, Malhotra and Kaushik, 2017).

Thermal oils can be either of petroleum origin or artificially synthesised in laboratories. These oils have a low freezing point. Most of these oils can be operated within a temperature range from 120°C to 280°C. Some of the thermal oils like Slytherm^{TM} 800 have a peak temperature of 400°C, but costs more than other HTFs like air, steam and molten salts (Ouagued, Khellaf and Loukarfi, 2013). Using air as HTF, an extensive temperature range can be obtained as there are no temperature limits for its use under practical applications. A major disadvantage of using air is the low thermal capacity and heat transfer rate between the fluid and the surfaces of the pipelines, so high pressure and high fluid velocities must be maintained. Liquid metals have only been tested for their use in CSP plants but have not been used for commercial CSP applications even though they have promising properties as HTF like excellent heat conductivity, low viscosity and a wide operating range (Boerema *et al*, 2012). Their practical applications in CSP have been limited as liquid metals like Sodium are highly reactive when in contact with air or moisture, while the lead-bismuth eutectic mixture is toxic in nature and prohibitively expensive even though it has the highest peak temperature of 1500°C (Pacio *et al*, 2013). Table 1 lists the key characteristics of some of the HTFs used in the industry.

Molten salts are regarded as the ideal materials for use in solar powerplants because of their excellent thermal stability under high temperatures, low vapour pressure, low viscosity, non-flammability and non-toxicity (Tian and Zhao, 2013). The increasing use of Solar Salt® as HTF and thermal energy storage medium even with its obvious limitations like high melting point and low operating range potentially creates the possibility to research for modified/new molten salts which could possibly replace the existing salt. Adding a third alkali nitrate to a binary salt mixture like Solar Salt® could have a positive effect on the thermophysical properties of the salt like, reducing its melting point, reducing its viscosity, increase in density and specific heat capacity and or improving the thermal stability of the salt at higher temperatures (Chen and Zhao, 2017). The properties of a ternary salt can in some cases be further improved by adding a fourth alkali nitrate; although at this point cost considerations comes into the picture.

Thermophysical properties have a huge impact on systems like heat exchangers and collector design in a powerplant. Viscosity is an important transport property having major implications on the economics and design of plant equipment's like pumps and heat exchangers. Density is needed for system sizing calculations as well as being a constituent of many dimensionless groups used for heat transfer and fluid flow calculations. Specific heat capacity is a very important heat transport property of an HTF having a major impact on selection of heat transfer components such as pipelines, heat exchangers and solar receiver lengths of a solar CSP plant. By using molten salts, the solar field output temperature can be increased to 450–500°C, thereby increasing the Rankine cycle efficiency of the power block steam turbine in the 40 per cent range as compared to 37.5 per cent for oil HTFs (Kearney *et al*, 2004). In addition to the thermal properties, other properties such as corrosivity have to be considered. Low or no corrosivity is desired to ensure safe and efficient usage and storage of the heat transfer fluid to the maximum lifetime possible of the system.

Table 2 compares the physical and thermal properties of the molten salt HTFs being used or under study. The binary eutectic salts like Solar Salt® has the highest melting point, at 223°C, compared to the group of eutectic salts mentioned in the table. A higher melting point would naturally reduce the operating range and working time and will also increase the start-up time. Reducing the melting point of the fluid has been one of the motivations of this study.

TABLE 1

Thermophysical properties of some heat transfer fluids in use.

	Therminol VP-I (@ 400°C) [a]	Dow-Corning 550® (@ 100°C) [b]	Xceltherm® 600 (@ 200°C) [c]	Air (@ 600°C) [d]	Water/steam (@ 600°C) [d]	Solar Salt® (@ 400°C) [e]	HITEC® (@ 400°C) [f]	HITEC XL® (300–400°C) [e,g]	Liquid Na (@ 550°C) [d,e]	Pb-Bi (@ 450°C) [h]
Density (g/cm^3)	0.649	1.098	0.53	0.0004565	0.000211	1.84	1.87	1.455	0.82	10.13
Viscosity (cP)	0.146	18.21	2.73	0.0025	0.028	1.7	2.8	12	0.23	1.44
Specific heat (kJ/kg-K)	2.62	1.615	2.24	1.023	2.42	2.66	1.32	1.15	1.25	0.143
Thermal conductivity (W/m-K)	0.0756	0.13	0.13	0.03779	0.08	0.55	0.57	0.52	62	13.7
Freezing point (°C)	12	-50	N/A	-	0	232	142	120	97	125
Decomposition temperature (°C)	400	315	315	-	-	600	535	550	883	1670
Remarks	These oils have a low freezing point. Most operate safely within a temperature range of 120°C to 280°C.			It does not freeze under practical application temperatures, does not boil and is inert by nature. It has poor heat transport properties, very low heat capacity and has containment issues	Preferred fluid for low temperature solar collectors' applications. It has high specific heat and is easy to pump due to having very low viscosity. Although, high pressure and high velocity must be maintained for steam.	They have a high freezing point and can be used up to 500°C. Molten salts also have low vapour pressure and are economical. They can also be used as a thermal energy storage medium.			Liquid metals have excellent heat transfer properties and a very high operating temperature range. However, liquid metals and their alloys can be volatile, toxic, corrosive and very expensive.	

NB: [a] – Eastman Chemical Company (2019); [b] – Dow Chemical Company (2017); [c] – Radco Industries (2024); [d] – Vignarooban *et al* (2015); [e] – Sohal *et al* (2010); [f] – Coastal Chemical Co. LLC (2024); [g] – Fernández *et al* (2014); [h] – Pacio *et al* (2013).

TABLE 2

Thermophysical properties of some existing alkali nitrate salt mixtures.

	Solar Salt® (KNO_3-$NaNO_3$) [a,b]	Hitec® (KNO_3-$NaNO_3$-$NaNO_2$) [b,c]	Hitec XL® (KNO_3-$NaNO_3$-$Ca(NO_3)_2$) [d,e]	$NaNO_3$-KNO_3-$LiNO_3$ [f,g,h,i]	KNO_3-$LiNO_3$-$Ca(NO_3)_2$ [e,j]	$NaNO_3$-KNO_3-$CsNO_3$ [k]	$NaNO_3$-KNO_3-$LiNO_3$-$Ca(NO_3)_2$ [l]	$NaNO_3$-KNO_3-$LiNO_3$-$CsNO_3$-$Ca(NO_3)_2$ [m]
Composition (wt%)	60/40	50/7/43	48/16/36	28/52/20	65/10/25	20/24/56	12/40/21/27	7/21/7/41/25
Density (g/cm^3)	1.83 @ 300°C	1.86 @ 300°C	1.93 @ 300°C	1.97 @ 140°C	N/A	2.4 @ 200°C	N/A	N/A
Viscosity (cP)	3.26 @ 300°C	3.16 @ 300°C	6.3 @ 300°C	3 @ 300°C	2 @ 300°C	9.5 @ 200°C	5 @ 300°C	N/A
Specific heat (kJ/kg-K)	1.1 @ 400°C	1.56 @ 300°C	1.45 @ 300°C	N/A	1.395 @ 390°C	1.18 @ 300°C	N/A	1.22 @ 150°C
Thermal conductivity (W/m-K)	0.55	0.605	3.25	N/A	0.1	N/A	N/A	N/A
Melting point (°C)	232	142	120	121	~100	152	95	65
Decomposition temperature (°C)	600	535	550	540	500-567	525	520	>500

NB: [a] – Sohal *et al* (2010); [b] – Serrano-López, Fradera and Cuesta-López (2013); [c] – Coastal Chemical Co. LLC (2024); [d] – Dow Chemical Company (2017); [e] – Fernández *et al* (2014); [f] – Olivares and Edwards (2013); [g] – Bradshaw (2009); [h] – Bradshaw (2010); [i] – Roget, Favotto and Rogez (2013); [j] – Zhao and Wu (2011); [k] – Zhang *et al* (2018a); [l] – Bradshaw and Siegel (2008); [m] – Jonemann (1979).

Table 3 lists the positive and negative effects of adding different cations to the existing binary mixture Solar Salt®. Adding suitable salts to a binary mixture can reduce the melting/freezing point of the mixture. Adding sodium nitrite to the Solar Salt® reduces the melting point to 142°C, while adding calcium nitrate or lithium nitrate will reduce the melting point to ~120°C. The addition of calcium nitrate to $NaNO_3$ and KNO_3 decreases the mixture freezing point to about 110°C, but also increases the viscosity of the mixture. A quaternary mixture such as the 'Sandia Mix' (Bradshaw and Siegel, 2008), containing sodium, potassium, calcium and lithium nitrate brings down the melting point to 95°C while adding caesium nitrate to the same forms a mixture of five salts, which has a melting point of 65°C (Jonemann, 1979). Although, the low melting point of a four or five component salt mixture appears appealing, the addition of lithium nitrate and or caesium nitrate increases the cost of the final product making it not economical.

TABLE 3

Effect of adding different cation(s) to $NaNO_3$-KNO_3 mixture on different properties of the heat transfer fluid.

	Ca^{2+}	Li^+	Cs^+	Li^+-Ca^{2+}	Li^+-Ca^{2+}-Cs^+
Melting point	+	+	+	+	+ +
Decomposition temperature	–	–	–	–	–
Density	+	–	+	0	0
Viscosity	–	0	0	0	0
Specific heat	0	0	+	0	0
Cost	+	–	–	–	– –

NB: '+' stands for a positive impact on the property, '–' means a negative impact while '0' means no significant change in property. '++'means the best and '- -'means the worst of various combinations.

The Solar Salt® and the ternary salt with calcium and lithium nitrate have a viscosity of 3–5 cP at around 300°C, while the Hitec® is at 3.6 cP at 300°C. The mixtures containing $Ca(NO_3)_2$ present viscosity values relatively high at 6 cP @ 300°C depending on the composition. The Sandia Mix quaternary salt has a viscosity of 2–3 cP at 400°C. The addition of calcium nitrate always results in a higher density and a glassy state at the melting point which increases its viscosity at lower temperatures (Chen and Zhao, 2017). However, calcium nitrate has the lowest cost among the alkali nitrates and adding it to the binary mix reduces the melting point of the HTF which increases the operating range and reduces the cost in freeze protection of the salt during off-peak hours (Kearney *et al*, 2003).

The thermophysical data of molten salts are not easily obtained due to the inherent difficulty in conducting experiments at elevated temperatures and the thermophysical data of other promising ternary salt mixtures such as the current composition in focus has not been reported to a similar extent. Any uncertainty in the thermophysical data of a fluid can have implications wherein the equipment design depending on those properties will be either under or over-designed. Therefore, it becomes imperative to choose the right HTF and equally important to have accurate data on the properties of the same to help in the design of a new HTF. The authors have thus attempted to measure the density, viscosity, melting point, corrosivity and thermal decomposition of one such salt mixture containing $Ca(NO_3)_2$, $NaNO_3$ and KNO_3.

MATERIALS AND METHODOLOGY

The salt mixtures (Composition 1 and 2 – see Table 4) were prepared using $Ca(NO_3)_2$, $NaNO_3$ and KNO_3, purchased from AB Enterprises, Mumbai, with a known purity of 99 per cent, while for Composition 3, the raw materials were purchased from Sigma Aldrich. The salts were pre-heated in a Muffle furnace at 220°C for at least six hours. To compare the results, Composition 3 was heated to 250°C under vacuum. Post-treatment of the salts: the weights of the individual salts were measured before and after heating them to measure the mass loss due to the evaporation of

moisture and chemically bound water in the salts. The salts were mixed according to the desired compositions after being finely grounded. Suitable weights of the salt mixtures were taken for density and viscosity measurements. The same quantity of salt was used for the cooling curve measurement (Composition 1) while 1 g of salt was used for the thermogravimetric analysis (TGA) experiment.

TABLE 4

Composition of the salt mixtures being tested.

	$Ca(NO_3)_2$ (wt%)	$NaNO_3$ (wt%)	KNO_3 (wt%)	Melting point (°C)
Composition 1	32	24	44	130 [a]
Composition 2	36	16	48	132 [b]
Composition 3	39	15	46	150

NB: [a] – Chen and Zhao (2017); [b] – Calvet *et al* (2013).

Melting point determination

A cooling curve provides a complete picture of the heat dissipation and cooling of a substance as a function of temperature. This test has been performed on the HITEC® salt (Figure 1), to determine the melting point of the salt for the purpose of process calibration. For the experiment, the salt was initially heated in a crucible to 300°C in a muffle furnace and allowed to melt completely. Once in liquid form, the molten salt is removed from the furnace and allowed to cool naturally while a thermocouple connected to a data logger logs the temperature readings continuously. The reduction in temperature of the salt is then graphically represented as a cooling curve. The nature of the curve – as the temperature reduces with time – is exponential, except for a certain portion where the temperature remains seemingly constant. This suggests that there is a change of state going on from liquid to solid.

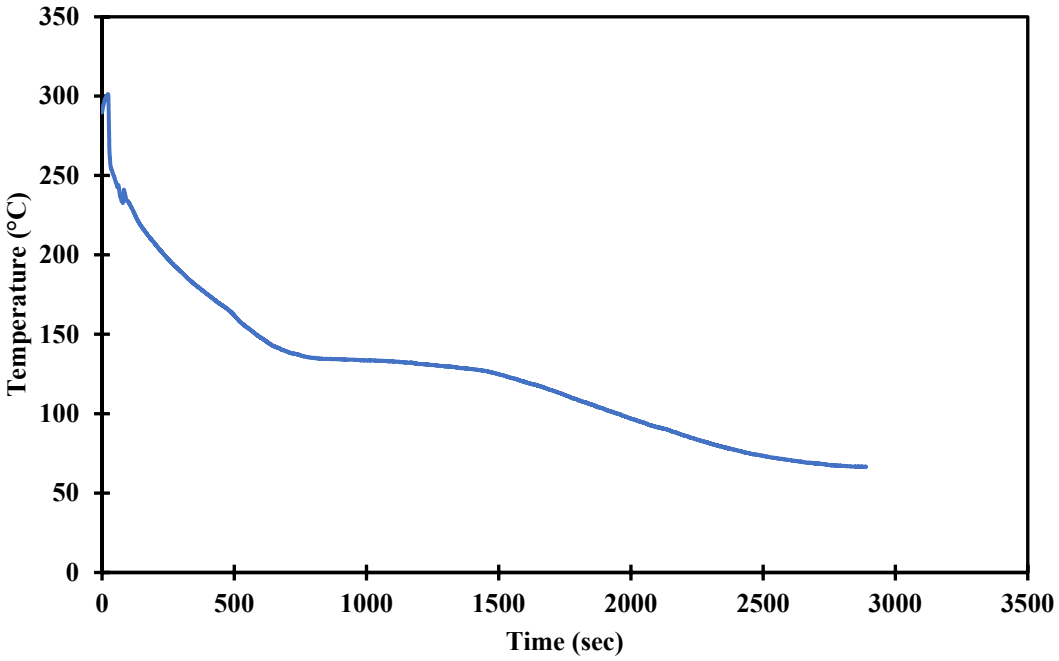

FIG 1 – Cooling curve test results for HITEC® salt.

The same technique was used to estimate the melting point of the ternary salt mixture. Differential Scanning Calorimetry (DSC) of the salt mixture was also used to confirm the same.

Density and viscosity measurement

The salt mixtures were melted on a hot plate to check for the presence of solids. It was observed that the liquid was clear and uniform at temperatures above the melting point. Measurements of both density as well as viscosity were performed after the sample attained its liquidus temperature. Brookfield DV-II viscometer and a bottom loaded Mettler-Toledo precision balance was used to measure the viscosity and density of the molten salts respectively. The rotating element used for viscosity measurement and the sinker for the density measurement is an SS304 bob and an SS304 crucible. SS304 was used for both the sinker and the crucible since it has been shown to have good corrosion resistance in the presence of nitrates at high temperatures under various atmospheric conditions and time periods (Zhai *et al*, 2017).

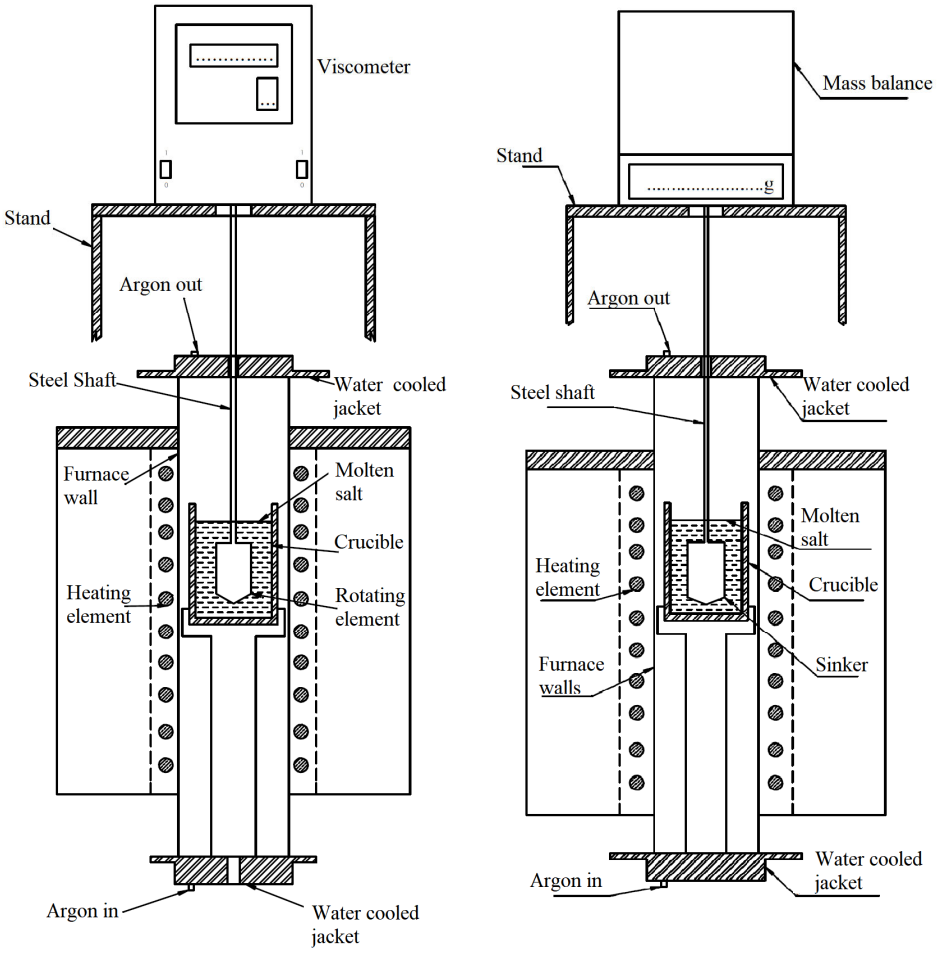

FIG 2 – Set-up for viscosity (left) and density (right) measurement.

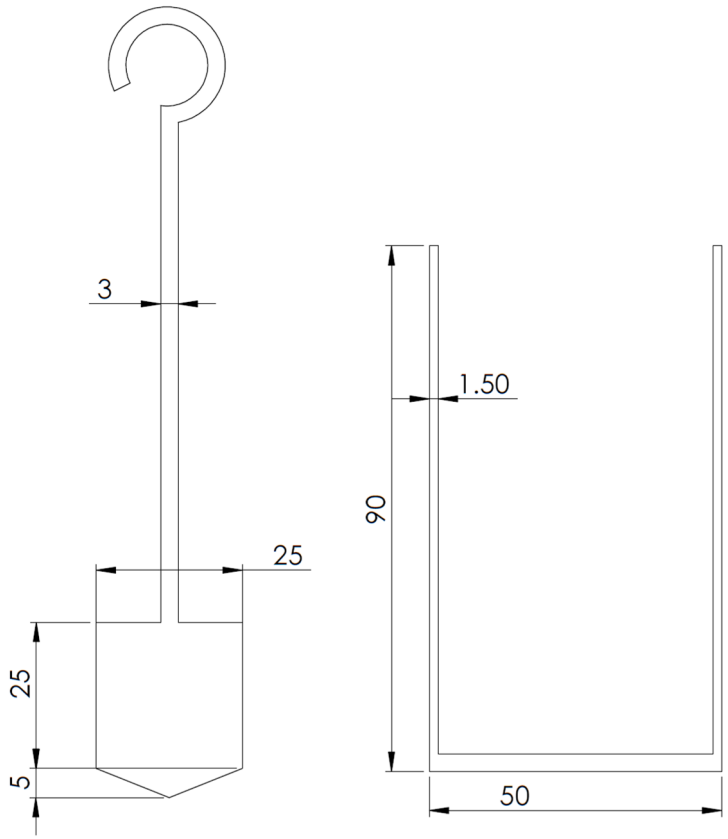

FIG 3 – (a) Rotating element/sinker; (b) Crucible used for density and viscosity measurement. All dimensions are in mm.

The viscosity measurements were performed using Brookfield DV-II (Figure 2), which measures the viscosity of a fluid by a rotational method in which the bob rotates in a crucible filled with the desired liquid. It measures the torque applied on the rotating element by the fluid due to the resistance to its rotation in the fluid (Zhang *et al,* 2018b). In order to obtain the necessary sensitivity to measure the low viscosity liquids the clearance between the stationary and rotating parts has to be made very small. The viscometer reading is first set to zero by using the 'auto zero' function on the front panel. The spindle is attached to the viscometer at this point and the motor is run at 12 rev/min. The display blinks ten times and the reading will settle to zero, indicating that the set-up is complete. The SS304 bob is attached to the spindle. The bob at this point is completely immersed in the liquid in the crucible. The motor is run, starting from the lowest rev/min reading for the % torque to be measured, which is shown on the display. Only % torque values between 10 and 90 per cent are considered as recommended by the viscometer manufacturer. The rev/min of the motor is progressively increased using the dial on the side of the viscometer and % torque for each rev/min is noted. The viscosity of the salt mixture is calculated using Equation 1 which is provided in the system manual of the viscometer.

$$\eta = \frac{100 \times \mathrm{TK} \times \mathrm{SMC} \times \mathrm{Y}}{\mathrm{rev/min}} \tag{1}$$

where:

TK is a system constant equal to 0.09373

SMC is a constant of the rotating element, measured using standard fluids of known viscosity

Y is the % torque read by the viscometer for a particular rotation speed

The density of the salt mixture is measured by using the Archimedean method (Figure 2), where a sinker is weighed before and after being immersed in the liquid. The reduced weight of the sinker after being immersed in the liquid is the consequence of the sinker being provided an upward force

on it due to the buoyancy of the fluid. The weight is measured using a bottom loaded Mettler-Toledo precision balance ME 204 with 0.0001 g accuracy.

The density of the salt mixture was measured between the temperatures of 190 and 462°C. The sinker was weighed before and after immersing it in the salt mixture, once beyond its melting point. The density of the salt mixture was then calculated using Equation 2 which accounts for the increase in volume of the steel sinker at elevated temperatures. Temperature was measured after allowing the system to attain equilibrium for 20 mins and then measuring the temperature using a K–type thermocouple.

$$\rho = \frac{\Delta m}{V \times [1+3 \times (\alpha \times (T - T_0))]} \quad (2)$$

where:

- ρ is the density of the salt sample
- Δm is the difference in the mass readings before and after being immersed in the molten salt
- V is the volume of the sinker that is immersed in the salt
- α is the thermal expansion coefficient of the sinker material
- T is the temperature of the salt in °C
- T_o is the ambient temperature in °C

Corrosion

Goods and Bradshaw (2004) reported corrosion rates of around 6–10 µm per annum for two different stainless-steel alloys (SS304 and SS316) immersed in HITEC XL® for 7008 hrs at 570°C. This suggests that the SS alloys could be acceptable candidates for use with HITEC XL® molten salt at temperatures up to 500°C.

For this experiment, the corrosion testing has been performed on SS304 by the salt with Composition 1. The specimens obtained as 26 × 28 × 2 mm SS304 strips, were cleaned thoroughly and dried before being immersed in the salt. The test was conducted as static immersion test, to obtain the data on corrosion. Each of the SS strips was weighed before the test in order to monitor the weight change. The exposure test was performed at 400°C in a muffle furnace with five samples immersed in five crucibles. Each sample was removed every 120 hours to measure the weight change. Microscopy can be employed to check the micro-structural changes in the metal due to its interaction with the salt. The following formula is used to calculate the corrosion rate (Trent, Goods and Bradshaw, 2016):

$$A = \frac{m_0 - m_1}{S} \quad (3)$$

where:

- A is the corrosion amount of metal (mg/mm^2)
- m_o is specimen quality before test (mg)
- m_1 is specimen quality after test (mg)
- S is the total surface area of the specimens (mm^2)

Thermogravimetric analysis

Cordaro, Rubin and Bradshaw (2011) had observed that the nitrate salt decomposed to nitrite at high temperatures in a reversible manner. This is followed by the nitrite decomposing to metal oxides, nitrogen oxide and other gases (Mohammad, Brooks and Rhamdhani, 2017). Thermogravimetric analysis was performed on the salt (Composition 1) to evaluate the thermal stability of the material at high temperatures. The mass of the sample is measured over time as the temperature increases. This provides the data about the changes in the mass of the sample due to phase changes, absorption, desorption and thermal decomposition. For a particular temperature range, there will be no observable mass change in the sample. Loss of moisture from the sample

usually corresponds to a negligible mass loss, while beyond a certain temperature will gradually increase to drastic proportions as the material begins to degrade. This will indicate the upper temperature limit for the material.

Initially, the TGA test was carried out using an empty SS304 crucible to determine the change in mass occurring for the crucible alone. This will help in accounting for the mass loss from the crucible occurring during the actual experiment. The crucible was connected to a bottom loaded Mettler-Toledo precision balance mounted above a vertical furnace using a SS304 wire. The mass balance was connected to a computer which logged the readings to an Excel sheet at a specific rate. The temperature was recorded using a thermocouple connected to a data logger to record the readings.

After the experiment was performed on the blank, it was repeated for the salt sample. The crucible was loaded with 1 g of salt (Composition 1) and the crucible was underneath the balance using a SS304 wire. The heating rate of the furnace was kept low, at 3°C/min and an inert atmosphere of argon was maintained inside the furnace. The mass readings were recorded up to a temperature of 600°C.

RESULTS AND DISCUSSION

Density and viscosity

Density and viscosity variations with temperature for both compositions were measured and are shown in Figures 4 and 5 respectively.

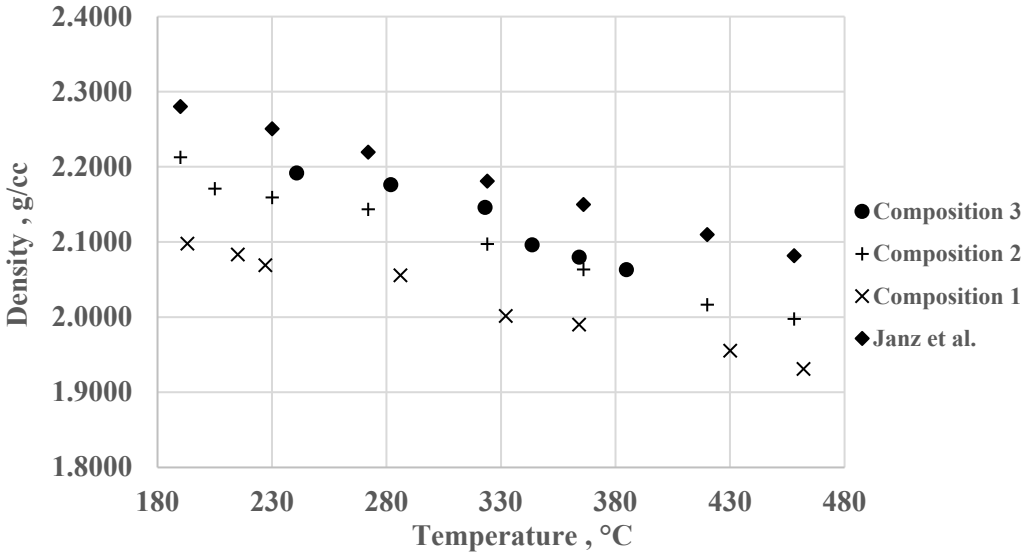

FIG 4 – Density temperature relations for Compositions 1, 2 and 3. The density of Composition 2 was also compared with (Janz, 1998).

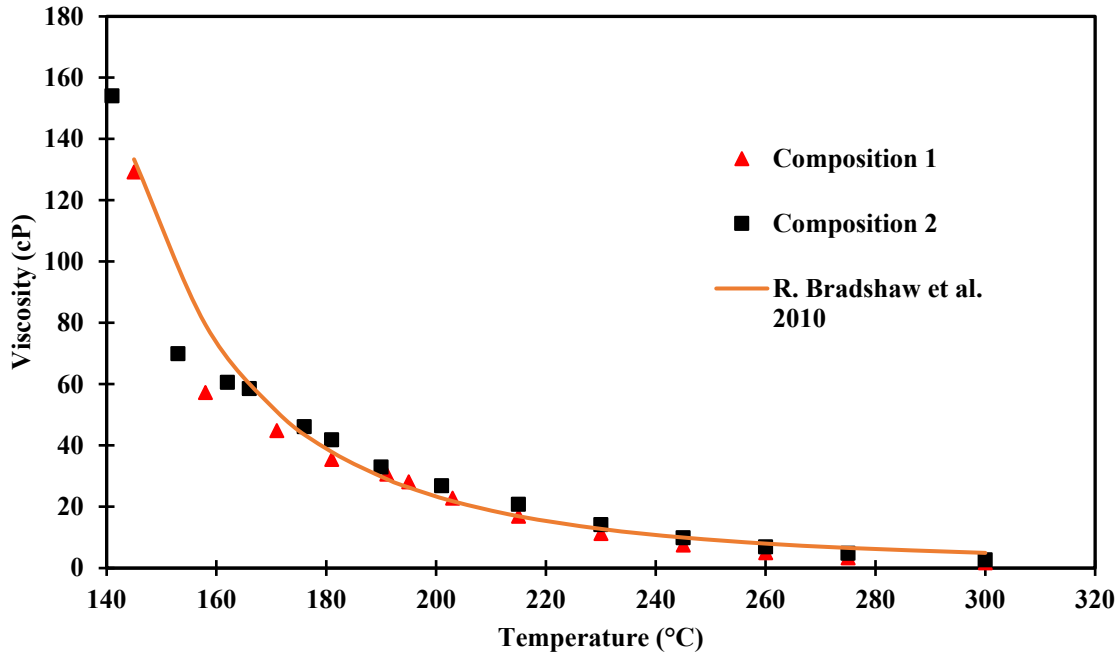

FIG 5 – Viscosity temperature relations for Compositions 1 and 2.

The density of the compositions was measured between 190°C and 462°C and is reported in Figure 4. The density of both the compositions is found to decrease linearly with temperature, with Composition 2 showing a slightly higher density. Composition 2 has 4 per cent more calcium nitrate which results in higher density and is consistent with the literature data reported by Bradshaw (2009) and Zhang *et al* (2018b) for other calcium nitrate-based salt systems. Upon repeating the measurements for the same composition an average error of ±2 per cent was obtained. The densities measured of the compositions are correlated to the density of the similar salt mixtures obtained from the volumetric additive rule using the Equation 5:

$$\rho = \frac{\sum X_i \times MW_i}{\sum V_i} \tag{4}$$

$$and\ V_i = A_v + B_v \times T \tag{5}$$

The constants A_v and B_v were referred from Bradshaw (2009). The deviation in the measured and estimated values (additive rule) was very close with an error less than 5 per cent for the measured temperature range.

The viscosity of the salt mixture Compositions 1 and 2 was observed to be decreasing exponentially. The results of the experiment are plotted in Figure 5. The viscosity of the compositions beyond 203°C is extrapolated from the previous values as the temperature of the crucible could not be raised any further due to extremely low viscosity which could be measured by the viscometer. The viscosity of the compositions varied from 154 cP at 141°C to less than 11 cP beyond 230°C. The high viscosity of the compositions near the melting point is known to be due to the presence of calcium nitrate in the mixture as has been observed by Bradshaw and Siegel (2008). This trend can also be observed in the experimental data as Composition 2 having more viscosity than Composition 1. This would mean that the temperature of the collector loop in a CSP plant to be near or above 200°C in order to reduce the pumping power required. The viscosity of Composition 2 has been correlated with the viscosity-temperature relation obtained by fitting a curve in the experimental data reported by Bradshaw (2010) whose ternary salt system has the same composition. An average error of 17 per cent was obtained and on repeating the experiments, a deviation of less than ±2 per cent was obtained. The viscosity data for Composition 1 could not be found in the literature implying that it may not have been measured yet. It has been successfully applied by the authors to predict the density and viscosity of $LiNO_3$ and $CsNO_3$ based ternary alkali nitrate salt systems (Shrotri and Muhmood, 2020) and further details of the model and its correlation to the current salt composition can be referred to elsewhere.

Melting point

A sharp cooling could not be replicated to obtain the melting point (Figure 6). However, a change in slope can be observed at two points *viz*, 145°C and 115°C which suggests that the liquid freezes within this temperature range. This is likely due to the melting point of the pure salts in the mixture being dissimilar. The melting points of sodium nitrate, potassium nitrate and calcium nitrate are 308°C, 334°C and 561°C respectively and hence the mixture freezes at a uniform rate as the pure components solidify at different time.

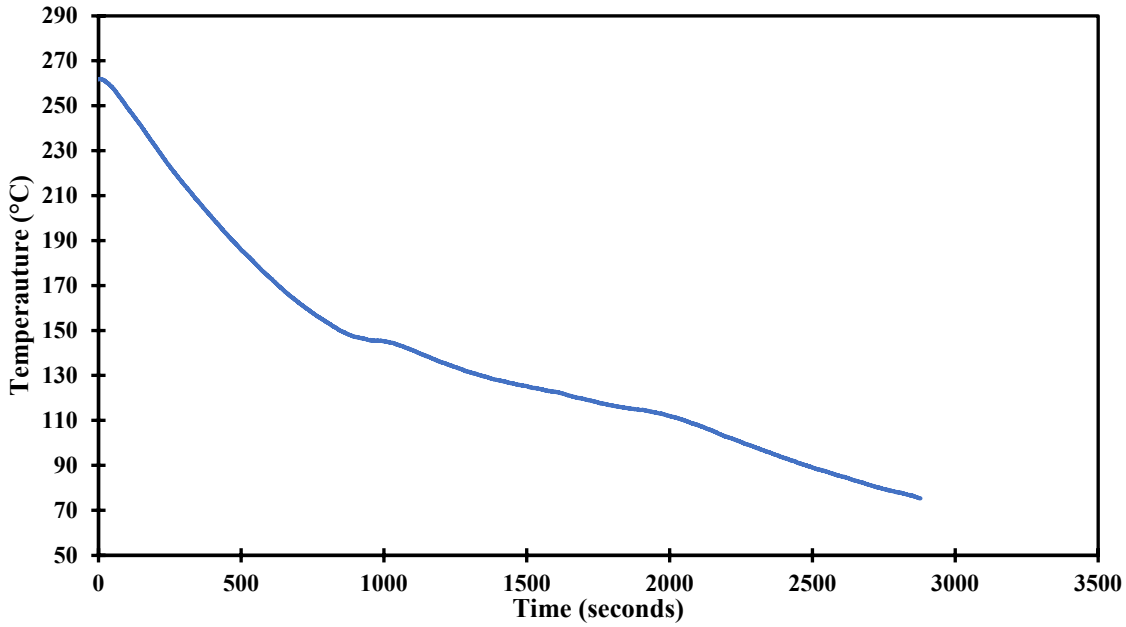

FIG 6 – Cooling curve test results for Composition 2.

Differential Scanning Calorimetry (DSC) was carried out for Compositions 2 and 3 (Figures 7 and 8) in order to obtain a better understanding of the melting range. It can be seen that in both these samples, there is a range of temperature where the melting starts and ends. For Composition 2, it is between 108°C and 180°C and for Composition 3 showed melting between 112°C and 155°C.

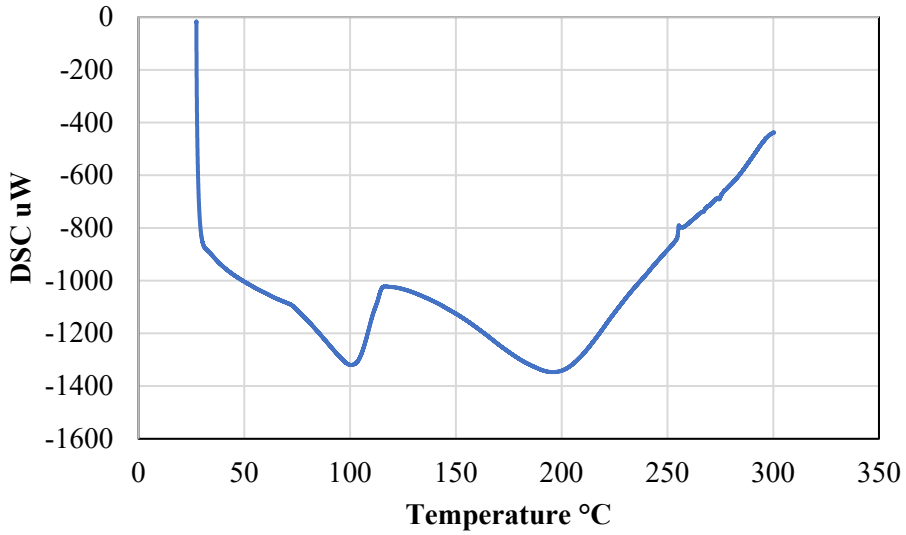

FIG 7 – Differential Scanning Calorimetry (DSC) of Composition 2.

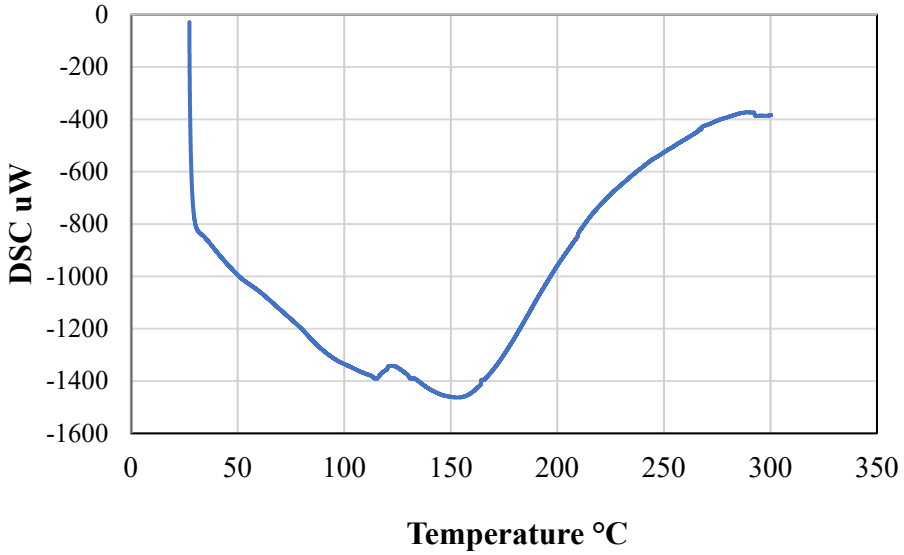

FIG 8 – Differential Scanning Calorimetry (DSC) of Composition 3.

Corrosion

Coupons of 26 × 28 × 2 mm dimensions were machined from SS304 to ensure complete immersion in the salt mixture as per the standard guidelines for evaluating corrosion (ASTM G1–03; ANSI, 2003). After the experiment, descaling is required to remove the corrosion products and the weight loss of the coupon was measured. The following methodology was used to estimate the corrosion rate.

The increase in weight of the sample was assumed to be due to the oxidation of Fe to Fe_2O_3 and could be calculated by finding the weight gained after through washing the coupon with warm water. The amount of Fe corroded can be calculated as follows:

$$\mathrm{m_{Fe}/time} = \frac{\mathrm{m_1 - m_0}}{wt.of\ Fe\ in\ the\ oxidation\ product} \tag{6}$$

$$\mathrm{m_{loss}/area/time} = \frac{\mathrm{m_{Fe}}}{\mathrm{A_s}} \tag{7}$$

$$\mathrm{t_{loss}/time} = \frac{\mathrm{m_{loss}/time}}{\rho} \tag{8}$$

where:

- mF_e is the weight loss due to oxidation
- A_s is the surface area of the sample
- t_{loss} is the thickness loss due to the oxidation of iron on the surface
- ρ is the density of the oxidation product (5.24 g/cc)

The experimental data is provided in Table 5 and Figure 9. Extrapolating the results based on the data yields a total corrosion rate of 2.58 µm/a for the current salt mixture (Composition 1).

TABLE 5

Corrosion in the SS304 sample in ternary molten salt (Composition 1).

Time (hrs)	Initial weight, m_0 (gm)	Final weight, m_1 (gm)	Net weight increase (m_1-m_0) (mg)	A_s (cm^2)	mF_e (mg/a)	wt loss/ area ($g/cm^2/a$)	t_{loss}/time (µm/a)
120	9.5678	9.5678	0	1.482	0.0000	0.0000	0.0000
240	9.6185	9.6187	0.2	1.482	0.0009	0.0006	0.0758
360	9.6285	9.6291	0.6	1.456	0.0027	0.0018	0.2273
504	9.6514	9.6525	1.1	1.508	0.0049	0.0033	0.4168
624	9.5502	9.5519	1.7	1.456	0.0076	0.0052	0.6441

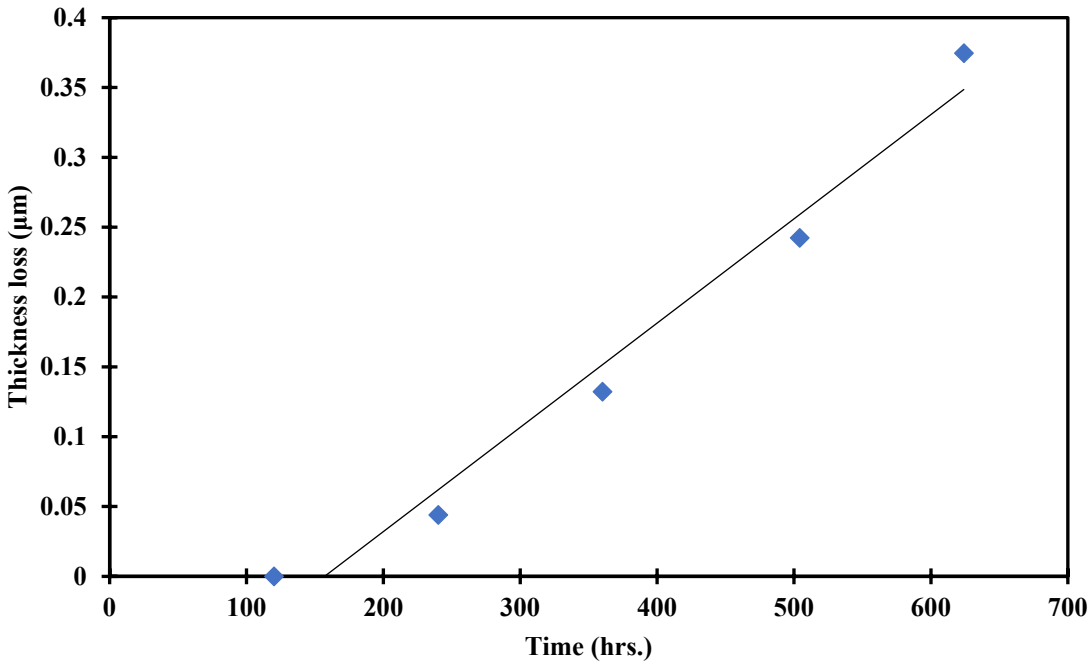

FIG 9 – Corrosion rate for SS304 at 400°C.

Thermogravimetric analysis

The TGA was performed on the salt sample (Composition 1) as well as the blank crucible in order to account for any mass change in the crucible. Both the tests were performed up to 600°C with a heating rate of 10°C/min in an inert atmosphere of argon.

The result is shown in Figure 8 and it is observed that apart from a slight weight loss (1 per cent) due to chemically bound water release, the salt showed no significant change up to 600°C. Beyond this point the weight loss of the salt reduced below 98 per cent of the initial weight. However, the weight loss increased drastically after 600°C. This consistent with the findings in the literature, where the maximum temperature of the ternary salt system of a similar composition was reported to be 550°C.

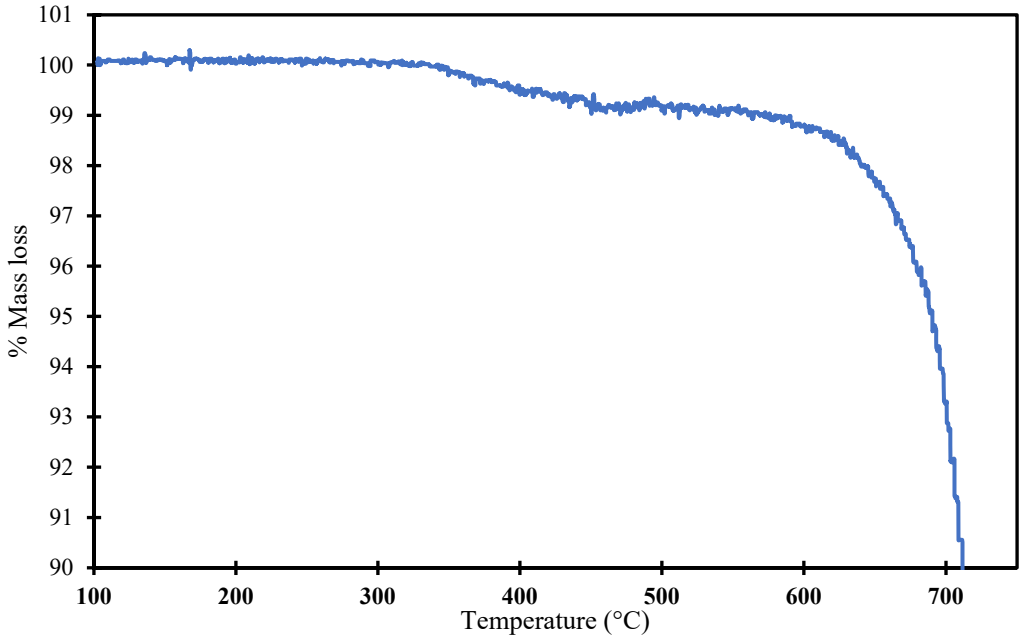

FIG 10 – TGA curve for the ternary salt sample.

Comparison to existing molten salt HTFs

The binary eutectic salts like Solar Salt® has the highest melting point, at 223°C (Table 6), compared to the group of eutectic salts mentioned in Table 2. A higher melting point would naturally reduce the operating range and working time and will also increase the start-up time. Adding another salt to a binary mixture has the effect of reducing the melting point of the mixture, like adding calcium nitrate reduced the melting point to around 130°C and the ternary salt mixture Hitec® which has a melting point of 142°C. The peak operating temperature limit of the salt.

TABLE 6

Thermophysical properties of Solar Salt® compared with the new ternary salt.

	Solar Salt®	**$Ca(NO_3)_2$–$NaNO_3$–KNO_3**	**Hitec®**
Density (g/cc)	1.84 @ 400°C	1.93 @ 400°C	1.87 @ 400°C
Viscosity (cP)	3.2 @ 300°C	4.9 @ 300°C	3.16 @ 300°C
Corrosivity on SS304 (µm/a)	6–10 @ 570°C [a]	2.58 @ 400°C	N/A
Melting point (°C)	223	~130	142
Decomposition temperature (°C)	600	~ 600	535

NB: [a] – Goods and Bradshaw (2004).

Due to the presence of calcium nitrate in the salt system, the density of the salt has increased by 5 per cent. A higher density and specific heat would imply that the heat transfer fluid has a higher volumetric heat storage capacity. The viscosity of molten salts as this property strongly affects pumping costs, among other aspects of system performance. It is an important transport property having major implications on the economics and design of plant equipment's like pumps and heat exchangers. The mixtures containing $Ca(NO_3)_2$ exhibit relatively high viscosity. However, the viscosity of the salt reduces to a comparable value to the Solar Salt® at higher temperatures.

Stainless steel alloys have been suggested to an acceptable candidate for use with nitrate salts. The corrosion test was performed of SS304 specimens for 620 hours at 400°C. The experimental data was extrapolated to yield a total corrosion rate of 2.58 µm/a. This corrosion is compared to the

corrosion rate of 6–10 μm/a. of the Solar Salt® (Goods and Bradshaw, 2004) however at a higher temperature.

The maximum temperature of the salt was found to be at 600°C using TGA, which is comparable to the Solar Salt® which has a maximum temperature of 565°C. Coupled with a lower melting point the operating temperature range for this salt is increased leading to a lower cost of freeze protection of the salt. It should also be noted that adding calcium nitrate also reduces the materials cost as it is the cheapest of the alkali nitrates used for the mixtures mentioned in this study (Kearney *et al*, 2003).

CONCLUSION

It was observed from experiments that the addition of calcium nitrate to the binary nitrate salt mixture resulted in a lowering of the melting point of the system from 223°C to 130°C. A commonality between Compositions 1, 2 and 3 is their relatively high density and viscosity, which is mainly attributed to the presence of calcium nitrate. Moreover, both the properties were observed to increase proportionally with the increase in the amount of calcium nitrate present in the ternary system. This is supported by the data observed in the literature. Although calcium nitrate causes a relative increase in the viscosity of the salt system, the viscosity eventually decreases beyond the temperature of 200°C to pose no hindrance in its use as HTF. This ternary salt mixture has a relatively high density of around 2 g/cc and is cheaper than the organic oils being used currently. It would therefore offset any increase in the cost of the system resulting from upgrading the heat transfer loop.

Static immersion tests performed on SS304 suggest stainless steel alloys to be a potential metal for use with nitrate salts as they appear to be more resistant to corrosion due to nitrates. The peak operating temperature of the salt was found to be comparable to the Solar Salt® which has a maximum temperature of 600°C. Since the minimum operating temperature is also reduced, the cost in freeze protection of the salt also gets reduced while maintaining high temperature efficiency. The properties measured in this study can further be modified by changing the composition and or the components of the system to obtain the optimum balance between cost and efficiency. The result of such projects would imply a possible alternative to the already existing molten salt HTF Solar Salt® and would open doors to assess its long-term performance for its application in concentrating solar powerplants.

ACKNOWLEDGEMENT

The authors would like to acknowledge the Department of Science and Technology (SERB/EMR/2016/002784) and (SERB/CRG/2022/001796) for funding the project.

REFERENCES

American National Standards (ANSI), 2003. ASTM G1–03 – Standard Practice for Preparing, Cleaning, and Evaluating Corrosion Test Specimens, December 2003.

Boerema, N, Morrison, G, Taylor, R and Rosengarten, G, 2012. Liquid sodium versus Hitec as a heat transfer fluid in solar thermal central receiver systems, *Solar Energy*, 86:2293–2305. https://doi.org/10.1016/j.solener.2012.05.001

Bradshaw, R W, 2009. Sandia report effect of composition on the density of multi-component molten nitrate salts, Sandia National Laboratories Report SAND2009-8221. https://doi.org/10.2172/983681

Bradshaw, R W, 2010. Sandia report viscosity of multi-component molten nitrate salts-liquidus to 200°C, Sandia National Laboratories Report SAND2010-1129. https://doi.org/10.2172/983680

Bradshaw, R W and Siegel, N P, 2008. Molten nitrate salt development for thermal energy storage in parabolic trough solar power systems, in *Proceedings of the Second International Conference on Energy Sustainability 2008, ES 2008*. https://doi.org/10.1115/ES2008-54174

Calvet, N, Gomez, J C, Faik, A, Roddatis, V V, Meffre, A, Glatzmaier, G C, Doppiu, S and Py, X, 2013. Compatibility of a post-industrial ceramic with nitrate molten salts for use as filler material in a thermocline storage system, *Applied Energy*, 109:387–393. https://doi.org/10.1016/j.apenergy.2012.12.078

Chen, Y Y and Zhao, C Y, 2017. Thermophysical properties of Ca(NO3)2-NaNO3-KNO3 mixtures for heat transfer and thermal storage, *Solar Energy*, 146:172–179. https://doi.org/10.1016/j.solener.2017.02.033

Coastal Chemical Co. LLC, 2024. HITEC heat transfer salt [online]. Available from: https://coastalchem.com/products/heat-transfer-fluids/hitec-heat-transfer-salt/ (Accessed: 20 January 2024).

Cordaro, J G, Rubin, N C and Bradshaw, R W, 2011. Multicomponent molten salt mixtures based on nitrate/nitrite anions, *Journal of Solar Energy Engineering, Transactions of the ASME*, 133. https://doi.org/10.1115/1.4003418

Dow Chemical Company, 2017. DOWSIL TM 550 Fluid features and benefits. Available from: <www.dow.com/en-us/document-viewer.html?docPath=/content/dam/dcc/documents/22/22-0071-01-dowsil-550-fluid.pdf>

Eastman Chemical Company, 2019. Therminol® VP-1 Technical Bulletin Report. Available from: <https://productcatalog.eastman.com/tds/ProdDatasheet.aspx?product=71093459&pn=Therminol+VP-1+Heat+Transfer+Fluid#_ga=2.100194838.961084841.1716276248-1262082965.1716276248>

Fernández, A G, Ushak, S, Galleguillos, H and Pérez, F J, 2014. Development of new molten salts with LiNO3 and Ca(NO3)2 for energy storage in CSP plants, *Appl Energy*, 119:131–140. https://doi.org/10.1016/j.apenergy.2013.12.061

Goods, S H and Bradshaw, R W, 2004. Corrosion of stainless steels and carbon steel by molten mixtures of commercial nitrate salts, *J Mater Eng Perform*, 13:78–87. https://doi.org/10.1361/10599490417542

Janz, G, 1988. Thermodynamic and transport properties for molten salts: Correlation equations for critically evaluated density, surface tension, electrical conductance and viscosity data, *J Phys Chem Ref Data*, 17.

Jonemann, M, 1979. Advanced Thermal Storage System with Novel Molten Salt, NREL/SR-5200–58595.

Kearney, D, Herrmann, U, Nava, P, Kelly, B, Mahoney, R, Pacheco, J, Cable, R, Potrovitza, N, Blake, D and Price, H, 2003. Assessment of a molten salt heat transfer fluid in a parabolic trough solar field, *Journal of Solar Energy Engineering, Transactions of the ASME*, 125:170–176. https://doi.org/10.1115/1.1565087

Kearney, D, Kelly, B, Herrmann, U, Cable, R, Pacheco, J, Mahoney, R, Price, H, Blake, D, Nava, P and Potrovitza, N, 2004. Engineering aspects of a molten salt heat transfer fluid in a trough solar field, *Energy*, 29:861–870. https://doi.org/10.1016/S0360-5442(03)00191-9

Mohammad, M, Bin, Brooks, G A and Rhamdhani, M A, 2017. Thermal analysis of molten ternary lithium-sodium-potassium nitrates, *Renew Energy*, 104:76–87. https://doi.org/10.1016/j.renene.2016.12.015

Olivares, R I and Edwards, W, 2013. LiNO3–NaNO3–KNO3 salt for thermal energy storage: Thermal stability evaluation in different atmospheres, *Thermochim Acta*, 560:34–42. https://doi.org/10.1016/j.tca.2013.02.029

Ouagued, M, Khellaf, A and Loukarfi, L, 2013. Estimation of the temperature, heat gain and heat loss by solar parabolic trough collector under Algerian climate using different thermal oils, *Energy Convers Manag*, 75:191–201. https://doi.org/10.1016/j.enconman.2013.06.011

Pacio, J, Singer, C, Wetzel, T and Uhlig, R, 2013. Thermodynamic evaluation of liquid metals as heat transfer fluids in concentrated solar power plants, *Appl Therm Eng*, 60:295–302. https://doi.org/10.1016/j.applthermaleng.2013.07.010

Radco Industries, 2018. XCELTHERM® 600 – Engineering Properties. Available from: https://www.radcoind.com/fluid/xceltherm-600/ [Accessed 20 January 2023].

Roget, F, Favotto, C and Rogez, J, 2013. Study of the KNO3–LiNO3 and KNO3–NaNO3–LiNO3 eutectics as phase change materials for thermal storage in a low-temperature solar power plant, *Solar Energy*, 95:155–169. https://doi.org/10.1016/j.solener.2013.06.008

Rosenthal, M W, 2010. An Account of Oak Ridge National Laboratory's Thirteen Nuclear Reactors. Oak Ridge National Lab Report ORNL/TM-2009/181. Available from: <https://info.ornl.gov/sites/publications/Files/Pub20808.pdf>

Serrano-López, R, Fradera, J and Cuesta-López, S, 2013. Molten salts database for energy applications, *Chemical Engineering and Processing: Process Intensification*, 73:87–102. https://doi.org/10.1016/j.cep.2013.07.008

Shrotri, V and Muhmood, L, 2020. Application of geometric models for calculation of viscosity and density of LiNO3 and CsNO3 based ternary nitrate salt systems, *CALPHAD*, 68:101749. https://doi.org/10.1016/j.calphad.2020.101749

Sohal, M S, Ebner, M A, Sabharwall, P and Sharpe, P, 2010. Engineering Database of Liquid Salt Thermophysical and Thermochemical Properties. https://doi.org/10.2172/980801

Srivastva, U, Malhotra, R K and Kaushik, S C, 2017. Review of heat transport properties of solar heat transfer fluids, *J Therm Anal Calorim*. https://doi.org/10.1007/s10973-017-6441-y

Tian, Y and Zhao, C Y, 2013. A review of solar collectors and thermal energy storage in solar thermal applications, *Appl Energy*, 104:538–553. https://doi.org/10.1016/j.apenergy.2012.11.051

Trent, M C, Goods, S H and Bradshaw, R W, 2016. Comparison of corrosion performance of grade 316 and grade 347H stainless steels in molten nitrate salt, in *Proceedings of the AIP Conference* (American Institute of Physics Inc). https://doi.org/10.1063/1.4949258

Vignarooban, K, Xu, X, Arvay, A, Hsu, K and Kannan, A M, 2015. Heat transfer fluids for concentrating solar power systems – A review, *Appl Energy*, 146:383–396. https://doi.org/10.1016/j.apenergy.2015.01.125

Zhai, W, Yang, B, Li, M, Li, S, Xin, M, Zhang, S and Huang, G, 2017. Study on corrosion of metal materials in nitrate molten salts, in *Proceedings of the AIP Conference* (American Institute of Physics Inc). https://doi.org/10.1063/1.4971898

Zhang, P, Cheng, J, Jin, Y and An, X, 2018a. Evaluation of thermal physical properties of molten nitrate salts with low melting temperature, *Solar Energy Materials and Solar Cells*, 176:36–41. https://doi.org/10.1016/j.solmat.2017.11.011

Zhang, Y, Huang, M, Kan, Y, Liu, L, Dai, X, Zheng, G and Zhang, Z, 2018b. Influencing factors of viscosity measurement by rotational method, *Polym Test*, 70:144–150. https://doi.org/10.1016/j.polymertesting.2018.06.034

Zhao, C Y and Wu, Z G, 2011. Thermal property characterization of a low melting-temperature ternary nitrate salt mixture for thermal energy storage systems, *Solar Energy Materials and Solar Cells*, 95:3341–3346. https://doi.org/10.1016/j.solmat.2011.07.029

Analysis of the melting behaviour of CaF_2-free welding fluxes using hot thermocouple technique

DOI: 10.62053/EXIZ4418

S L A Gowravaram[1] and S Basu[2]

1. Graduate student, Indian Institute of Technology Bombay, Powai, Mumbai 400076, India. Email: gsla10@iitb.ac.in
2. Professor, Indian Institute of Technology Bombay, Powai, Mumbai 400076, India. Email: somnathbasu@iitb.ac.in

ABSTRACT

CaF_2 has been a common constituent in a wide variety of welding fluxes, including those used for submerged arc welding (SAW). The widespread use of CaF_2 stems from its role in lowering the liquidus temperature as well as the viscosity of the molten slag that covers the weld pool. However, the harmful effect of fluoride evaporation from molten flux, on the environment as well as the health of the users is becoming increasingly evident over the years. This has led to increasing attention towards reducing the CaF_2 concentration in the fluxes. The fluoride-free formulations face the challenging requirement to maintain the thermo-physical properties (viscosity, liquidus temperature etc) like those observed in fluoride-containing fluxes.

In the present work, three fluxes with compositions in the CaO-MnO-SiO_2-Al_2O_3 system have been identified as promising alternatives to the CaF_2-rich fluxes. However, the thermo-physical properties of any such flux need to be comparable to CaF_2-based commercial SAW fluxes before it can be adopted for regular use. The single hot thermocouple technique (SHTT) has been used by several researchers in the past as a tool for observing the melting and solidification characteristics of fluxes. This device has been developed in the present work and is used to characterise the melting behaviour of the fluxes. The measured solidus and liquidus temperatures from SHTT were compared with the results from differential thermal analysis (DTA) and simulations using the FactSage™ software for a comprehensive understanding. In spite of having a slight deviation in the measured values from the multiple techniques, the results obtained from these multiple methods show that the selected compositions could be potential CaF_2 free alternative welding fluxes.

INTRODUCTION

The role of flux in fusion welding processes has been the subject of extensive research due to its ability to protect the weld pool and welding electrode tip from atmospheric contamination (Kou, 2003). Apart from this, flux also aids in element transfer between the weld metal and slag. Among the many types of fusion welding processes, the current work is focused on the fluxes used for the submerged arc welding (SAW) of low carbon steel plates. In this process, the welding flux and electrode wire are fed continuously throughout the welding duration. The arc remains fully covered by the flux, which allows better control over the rate of heat transfer, and aids chemical reactions that improve the properties of the final weld (Coetsee *et al*, 2021). Optimal combination of viscosity and interfacial tension of the molten slag enables a uniform protective layer to form over the melt pool, thus minimising chances of oxygen pickup from the atmosphere (Singh, Khan and Siddiquee, 2013). Even when the weld pool is fully covered, the flux plays a crucial role in determining the final composition of the weld metal due to its influence over the dissolved oxygen potential of the weld pool (Mitra and Eagar, 1991a; Chai, 1980). The liquidus temperature of the flux also needs to be at least 50°C lower than the solidus of the base metal (Mitra and Eagar, 1991b) so that the slag remains melted until the solidification of the weld metal.

CaF_2 is a major component in most of the commercial SAW fluxes. It helps to lower the liquidus of the flux, and acts like a network breaker for SiO_2 bonds reducing the viscosity of fluxes and minimising the hydrogen entrapment in the weld due to the formation of hydrogen fluoride (Plessis, Toit and Pistorius, 2007). There are also studies that indicate that the fluoride content affects the arc length due to the change in the ratio of fluoride to oxygen content and helps to control the oxygen content of the weld (Eagar, 1979). However, due to the large volume of the flux used in the

SAW process, the evaporation and eventual leaching of fluorides from the discarded slag has been a major concern over the years (Mills and Fox, 2003). Despite all these concerns, extensive research is yet to be done in the direction of making a fluoride-free flux due to the complex role of fluoride in flux. Based on the understanding of the work done over the years, the current research focuses on the development of a sustainable and environmentally friendly flux formulation which is the welding industry's hour of need. The first step in this direction was to find a flux and to work with the chemistry, without changing the properties required from a welding flux. Not many researchers have worked in this direction, but a lot of work has been done in the context of Mold fluxes, where a similar fluoride problem is present and successful fluoride-free fluxes have been developed without any compromise in flux properties, a similar approach has been taken in the current context as well (Mills and Fox, 2003).

The welding flux system proposed to be used in the current work is the CaO-MnO-SiO_2-Al_2O_3 system. This system was chosen based on consideration of the melting behaviour properties and possible inclusion formations (Ren and Zhang, 2019; Li *et al*, 2018). Apart from its effect on inclusion control and the subsequent evolution of weld metal microstructure, the welding flux also needs to satisfy other requirements for successful welding, including arc stability. Ferrera and Olson (1975) and Zhang *et al* (2020), have reported that the presence of CaO in the flux is more effective in maintaining both arc stability and depth of arc penetration, in comparison with constituents like SiO_2 or MnO. At the same time, CaO concentration within the range of 30–50 mass per cent in the flux is helpful in maintaining the liquidus temperature under 1400°C, in CaO-MnO-SiO_2 as well as CaO-Al_2O_3-SiO_2 ternary oxide systems. Ferrera and Olson (1975) have also reported that optimising the concentrations of the chemical species in flux is essential in optimising its ability to break the silicate network and enhance the slag fluidity. Based on these factors, it is recommended to maintain CaO concentration in the flux around 40 ± 5 mass per cent when used in combination with SiO_2 and MnO, in welding fluxes (Ferrera and Olson, 1975). While SiO_2 is generally considered a viscosity-enhancer, it can also enable the formation of low-liquidus eutectics with CaO, MnO and Al_2O_3, which is beneficial for lowering the liquidus temperature of the welding slag (Allibert, 1995), Addition of a small amount of MnO helps to broaden the range of compositions with low-liquidus temperatures composition range (Ferrera and Olson, 1975).

Three different fluxes with compositions in the CaO-MnO-SiO_2-Al_2O_3 system were identified as potential alternates for CaF_2-containing fluxes after analysing many fluxes in the same system. The melting behaviour of the flux needs to be established before recommending its use. The technique of single hot thermocouple (SHTT) has been used by several researchers in the past as a tool for observing the melting and solidification characteristics of fluxes. Most of the thermal analysis techniques used have been reliable only for the measurement of either solidus or liquidus temperatures of the samples under study. For a better understanding of the melting behaviour and to obtain both the solidus and the liquidus of the samples the hot thermocouple technique has been developed (Kashiwaya *et al*, 1998a). This technique was first developed to overcome the limitations of the DTA technique and to understand the solidification phenomenon seen in mould fluxes *in situ* (Kolbl, Marschall and Harmuth, 2011). However, over the years it was understood that this technique is also useful in understanding the melting behaviour of fluxes and slags. In this method, the sample is placed on the thermocouple tip and is melted by passing a current through the thermocouple, allowing it to simultaneously heat and measure the temperature at which the samples melted. There are two variations of the hot thermocouple method, the single hot thermocouple technique (SHTT) and the double hot thermocouple technique (DHTT). However, the first reported usage of the SHTT device was by Ordway (2012), who used the device to study the formation and growth of single crystals from refractory materials. Several other studies that have used the SHTT device for slag-metal interactions, liquidus temperature predictions of slags and glass formation mechanisms (Sarkar and Li, 2021). In the current work, the device was built based on the work by Kashiwaya, Cicutti and Cramb (1998b), where the SHTT device was used to understand the isothermal crystallisation process in Na_2O-containing mould flux.

The device has been calibrated and tested to characterise the melting behaviour of the fluxes identified. Further, the measured values of solidus and liquidus temperatures were compared with the results from differential thermal analysis (DTA) and simulations using the FactSage™ software for a comprehensive understanding. Also to understand if the current fluxes are good alternatives

to Industry fluoride fluxes, a commercially available flux has been used as a benchmark against which the developed fluxes were compared.

EXPERIMENTAL METHODOLOGY

Materials used

The synthetic fluxes were prepared using laboratory reagent grade CaO, SiO_2, Al_2O_3 and MnO powders; Table 1 lists the respective sources. CaO, SiO_2 and Al_2O_3 powders were first pre-heated to remove any adsorbed moisture and then calcined at 1000°C. As-received MnO was preheated to 400°C to remove any adsorbed moisture. Requisite quantities of CaO, SiO_2 and Al_2O_3 were mixed well and then pre-melted in a graphite crucible using an induction furnace at 1700°C. The slag formed was quenched, crushed and mixed with the requisite quantity of MnO. This mixture was ground to a fine powder using a ball mill. This process allowed the preparation of the Al_2O_3-CaO-MnO-SiO_2 synthetic flux without the risk of MnO reacting with the graphite crucible during pre-melting. These prepared fluxes were pre-melted in interstitial-free (IF) steel crucible at 1500°C and these pre-melted samples were used for the melting behaviour analysis and viscosity analysis. The samples for the chemical composition analysis were taken after air cooling the samples with maximum effort to avoid any contamination from the IF steel crucible.

TABLE 1

Raw materials used in the current study.

Material	Description
CaO	Calcium oxide Powder, Extra pure (90%), Loba Chemie
SiO_2	Quartz fine Granular (AR), Loba Chemie
Al_2O_3	Aluminium oxide G (Neutral), Loba Chemie
MnO	Manganese (II) oxide, pure (99%), Sigma Aldrich

Separately, the CaF_2 containing Commercial flux, Flux O, was crushed and mixed thoroughly to obtain a fine powder. Post that the samples were crushed in a slag crusher to a very fine powder and passed through a sieve of 50 µm for a uniform particle size. Table 2 and Table 3 present the chemical compositions of the three CaF_2- free fluxes and commercially available flux, estimated using the ICP-AES technique. Although the samples for the composition analysis were taken with precaution, there is a significant Fe dissolution in the flux post the melting in the IF steel crucible, as seen in Table 3. This fraction of Fe content has affected the liquidus estimation of the CaF_2 free fluxes. Fluoride ion-selective electrode (FISE) method was used to detect the fluoride content in the commercially available Flux O. The presence of CaF_2 was detected in the XRD analysis of the Flux O. Hence the Fluoride content of the flux is taken to be in present as CaF_2. Post the melting of the Flux O, the CaF_2 content decreased significantly, indicating the vaporisation of the fluoride in the flux. A proportionate increase in the calcium oxide component was observed post melting, indicating that indeed the fluoride was present as CaF_2.

TABLE 2

Composition of CaF_2 free fluxes estimated using ICP-AES techniques.

Wt%		CaO	SiO_2	Al_2O_3	MnO	Fe_2O_3
CM1	Planned	39.5	39.5	6	15	-
	Pre mixed	36.2	39.7	8.46	15.5	-
	Pre melted	24.0	25.6	7.1	13.1	30.2
CM2	Planned	37	37	6	20	-
	Pre mixed	36.5	36.3	9.19	18	-
	Pre melted	31.2	33.1	10.6	22.5	2.54
CM3	Planned	34.5	34.5	6	25	-
	Pre mixed	27.6	34.8	7.5	29.9	-
	Pre melted	26.7	28.2	10.6	23.2	11.3

TABLE 3

Composition of the Commercial flux estimated using ICP-AES and FISE techniques.

Wt%		Fe_2O_3	K_2O	MnO	TiO_2	Al_2O_3	CaO	CaF_2	SiO_2	MgO
Flux O	As received	0.96	ND	3.77	1.51	22.65	19.13	7.11	15.10	29.75
	Pre melted	1.80	1.59	3.26	0.06	23.89	27.51	0.22	10.22	31.36

Construction and working of the Single Hot Thermocouple (SHTT)

The set-up as shown in Figure 1, found to work best contained an Arduino-relay-based set-up to switch between the heating and measuring modes based on a program. A B-type thermocouple was placed in a quartz tube, with an opening in the quartz tube at the tip of the thermocouple to place the sample and for observation of the sample during the process. A model LD3210 regulated Dual DC power supply (made by Aplab company) was connected to the thermocouple through a relay circuit which was controlled by a programmable Arduino-Uno R3 module. The time interval at which the thermocouple needs to switch was controlled by the program. The signals obtained during the heating and switching cycles were processed to obtain the temperature at which the sample was being heated. A camera was used to take images of the sample during the process of the experiment.

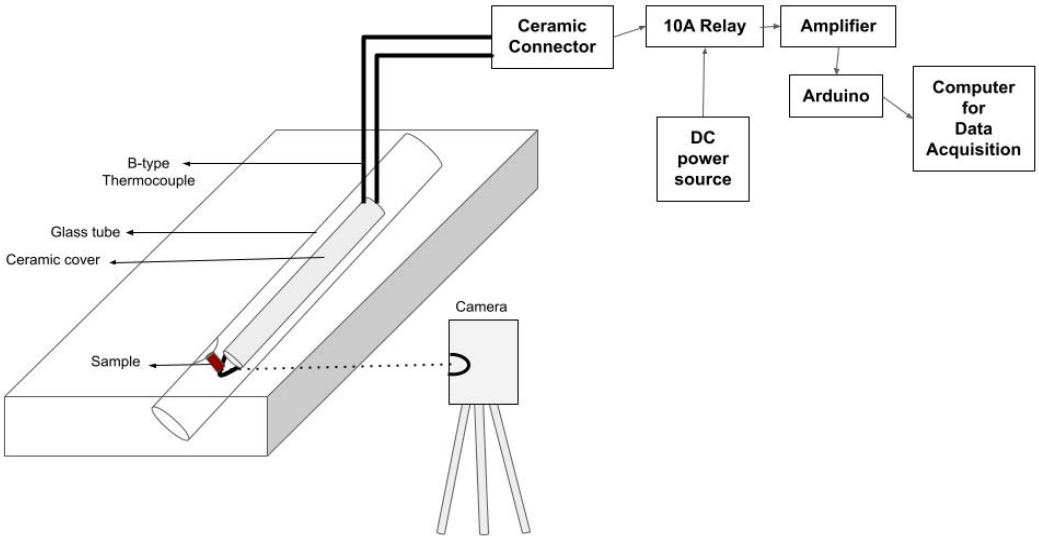

FIG 1 – Schematic of the SHTT set-up.

The samples for the device were prepared by finely grinding the flux/slag powders and mixing them with a few drops of 99.9 per cent pure Ethyl alcohol. This mixture was applied onto the tip of the thermocouple or made into small pellets of 2 mm height, depending on the type of the sample as shown in Figure 2. Initial calibrations of the device were performed using Zn, Al, Cu and fayalite slag. From the calibration process, it was understood that a temperature difference of ±30–40°C could be possible between the actual and measured temperatures. This was reduced to ±10°C by using insulation and shorter switching times. Images of the sample were obtained continuously throughout the experiment and analysed to understand the melting behaviour. In the Single hot thermocouple device, the samples as shown in Figure 2 were applied to the tip of the thermocouple. The programmable Arduino code for the test is then loaded into the Arduino and relay set-up. After that the thermocouple was slowly heated with a gradual increase in current and voltage. The thermocouple switched between heating and cooling mode based on the time interval set for the switching. The switching time was 1000 ms between room temperature and 1000°C, after which the switching time was decreased to 200 ms due to observe the changed sample behaviour.

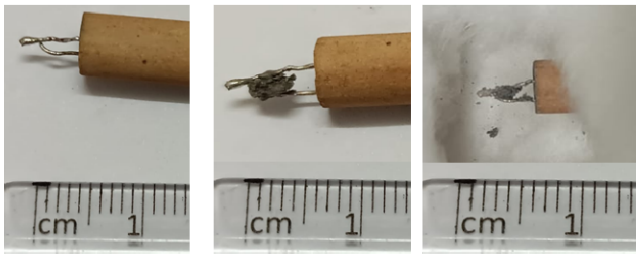

(a) (b) (c)

FIG 2 – Thermocouple tip: (a) before sample loading; (b) after sample loading; (c) placed in insulating material in the device during heating.

Differential thermal analysis (DTA)

Two of the most used techniques for analysing melting behaviour are DTA and differential scanning calorimetry (DSC). In the DTA technique, the reference and the sample are heated to the same temperature by a controlled program. Any changes seen in the sample due to its nature appear as a temperature difference. Hence this technique is well suited to understanding the melting behaviour studies due to its qualitative temperature characterisation process (Sarkar and Li, 2021; Ray and Ray, 2018). In the current work, the DTA of the flux samples were completed out using a Netzsch™ STA 449 Jupiter unit, maintaining an ambient Argon (Ar) atmosphere around the samples, in an Alumina crucible. Post the experiment it was observed that the samples were glassy and did not react with the Alumina crucible. Hence the effect of Alumina crucible dissolution in samples is neglected. The temperature profile used for DTA is shown in Figure 3.

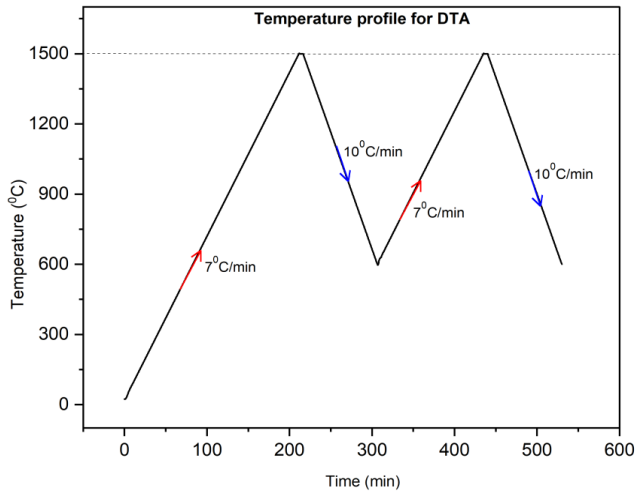

FIG 3 – Temperature profile for DTA.

Simulations using FactSage™

The thermodynamic software FactSage 8.1 is an excellent tool to predict the liquidus, solidus and transition temperatures of the samples under study. The 'Equilib' module in the software provides a function to understand the changes in the phases and composition of the sample at a defined temperature range. FactPS and FToxid were the databases chosen. In the current work the compositions of the samples post the pre-melting were taken and equilibrated at a range of temperatures to understand the changes in the sample composition. These obtained values were then compared with SHTT and DTA experimental data to obtain better confidence in estimating the melting behaviours.

RESULTS AND DISCUSSIONS

Observations from SHTT analysis

All the fluxes used in the current study were not transparent so a clear solid/liquid formation could not be visually observed to accurately determine the solidus temperature However, during the cooling process, the temperature at which the first significant shrinkage in the sample was observed, it was taken as the solidus. The liquidus temperature was estimated when the sample expands and flows on the tip of the thermocouple with ease. This ease to flow is obtained only when the entire flux is in a liquid form. The ease to flow/melt is dependent on several factors like the viscosity of flux, sample selection and quantity of sample. To be sure of the estimations, the experiments were repeated five times for each sample and an average of the same has been reported in Table 4. There was no significant weight loss of the CaF_2 free flux samples post the SHTT measurement. However, a weight loss of ~10 per cent was observed for the commercially available Fux O. This was essentially due to the Fluoride vaporisation from the flux.

TABLE 4

Solidus and Liquidus predictions using the SHTT technique.

Sample	Estimated values from SHTT experimental data	
	Solidus (°C)	Liquidus (°C)
CM1	1200 ± 20	1340 ± 40
CM2	1190 ± 39	1330 ± 14
CM3	1160 ± 42	1350 ± 43
Flux O	1185 ± 46	1290 ± 34

From the results obtained, the solidus temperature estimations were very similar in all three CaF_2 free fluxes and the commercially available flux. However, the liquidus temperature of the CM fluxes was significantly higher than the commercially available flux. Based on FactSage™ estimations and phase diagram analysis, it was expected that the liquidus temperatures of the CaF_2-free fluxes decrease with increasing MnO content, which means that the CM3 flux was supposed to have the least liquidus temperatures. However, the liquidus temperature of the CM2 flux is the least and the deviation is also minor in this case. This could be because of the local inhomogeneity in the sample despite proper crushing and sample selection. On further analysis, from the XRD data as shown in Figure 4a, it could be inferred that the Ca-Fe-Mn-Si Oxide complex commonly referred to as Ilvaite (Ilvaite Mineralogy data, 2001), has a broad range of melting temperatures from 1300 to 1400°C. The quantity of this phase in the sample taken could affect the liquidus temperature estimate. The presence of Fe in the CaF_2-free samples was due to the use of the IF steel crucible for melting the samples and is clearly seen in the ICP-AES analysis. But when the values were compared with the commercially available flux, the solidus and liquidus of the CaF_2-free fluxes were very much in similar ranges. Also, it should be noted that the liquidus of the fluxes is less than 1400°C, which is a good indication as these fluxes are meant to be used for welding of Low carbon steels whose solidus temperatures are generally around 1400°C.

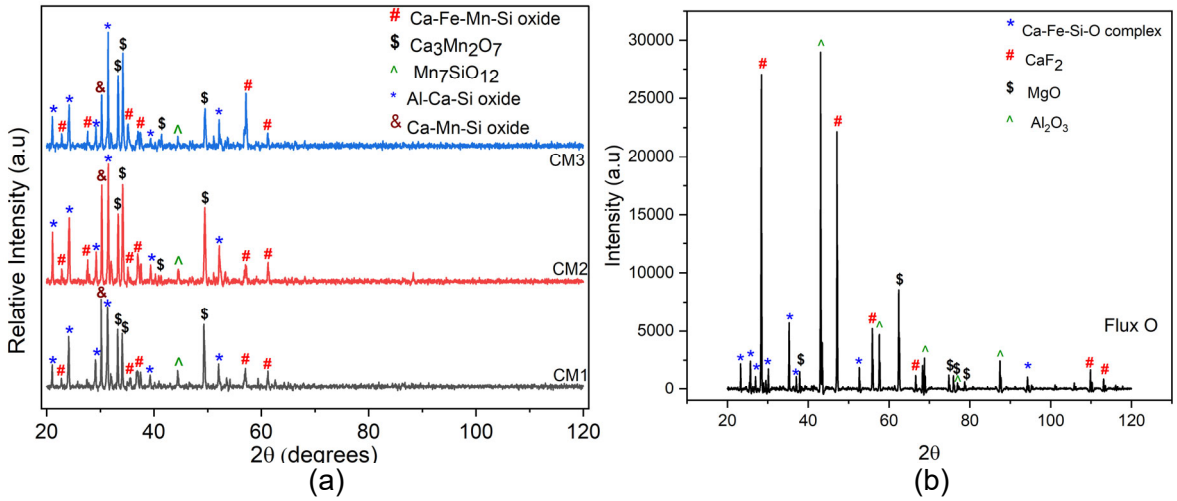

FIG 4 – XRD plots: (a) CaF_2 free fluxes CM series; (b) Commercially available flux – Flux O.

Observations from DTA

Differential thermal analysis was carried out on all four flux samples, using the thermal profile illustrated in Figure 3. Since the simultaneous thermal analyzer (STA) equipment was configured to run in TG-DTA mode (thermogravimetry – differential thermal analysis), continuous weight measurement could also be carried out on the samples. The TG-DTA values are analysed and reported post the data subtraction from the blank experiment (with two empty crucible) made at completely the same experimental conditions. Figures 5–8 show the output from TG-DTA studies on the samples CM1, CM2, CM3 and Commercially available Flux-Flux O respectively. In the current program setting, the upward peaks account for exothermic reactions and the downward peaks to the endothermic peaks. As seen in Figure 4a. XRD plots, of the CaF_2 free fluxes, a phase containing Fe was observed. This particular phase, Ca-Fe-Mn-Si Oxide, seems to have affected the estimated liquidus temperatures to some extent.

In the TG plots of the CM series fluxes, there was a slight increase in the weight around (~0.5 per cent), during the entire two cycle duration of heating and cooling. This is due to the volume expansion of the Ar gas during heating cycle. This slight increase in the weight is observed in all the three TG plots of CaF_2 free fluxes. However, the increase in weight was not significant when the run was completed. Apart from this, there seems to be no significant weight loss in the samples indicating that the pre-melting process was effective.

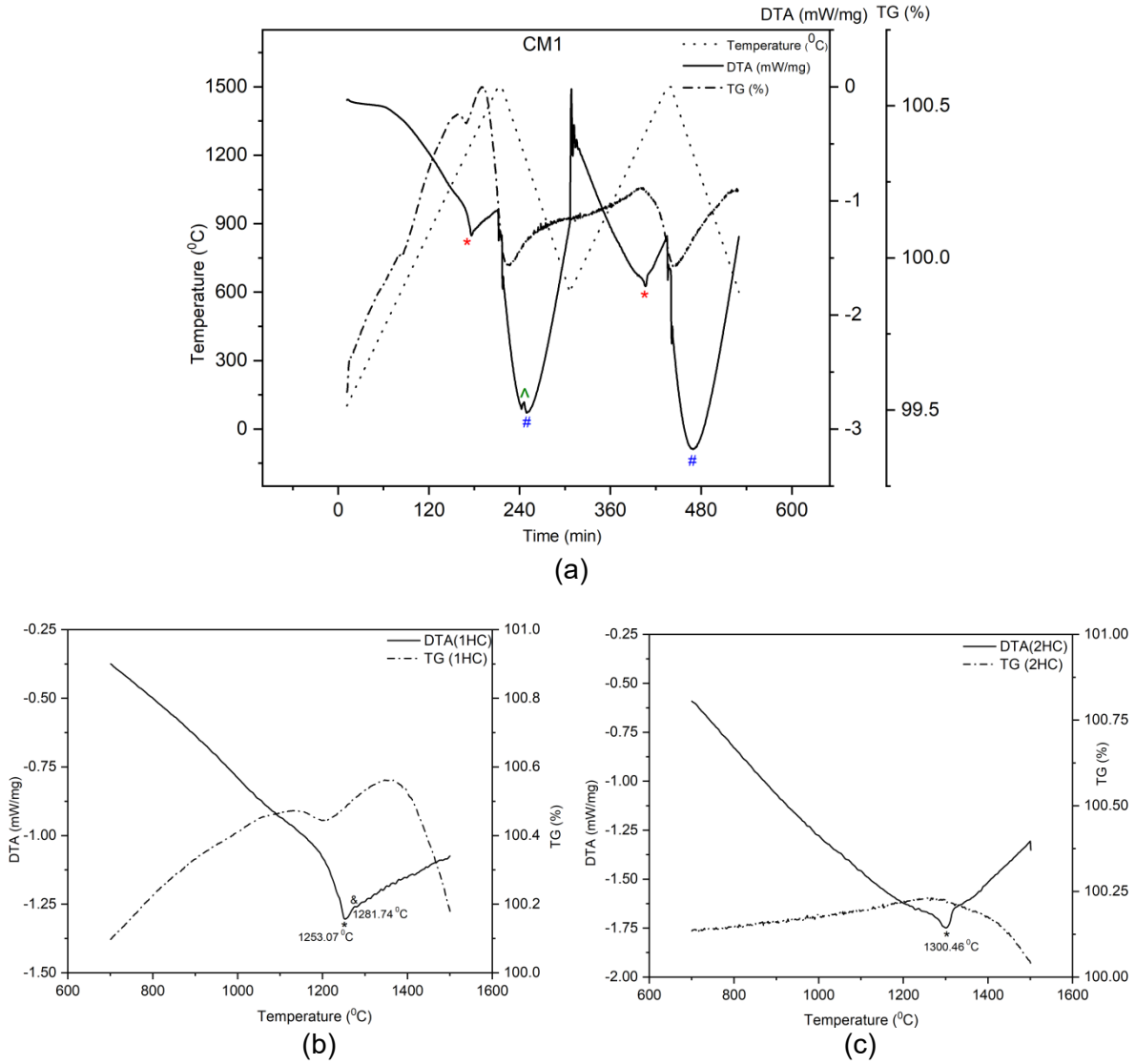

FIG 5 – DTA plot of CM1 flux: (a) All plots; (b) DTA and TG plot in 1st heating cycle; (c) DTA and TG plot in the 2nd heating cycle.

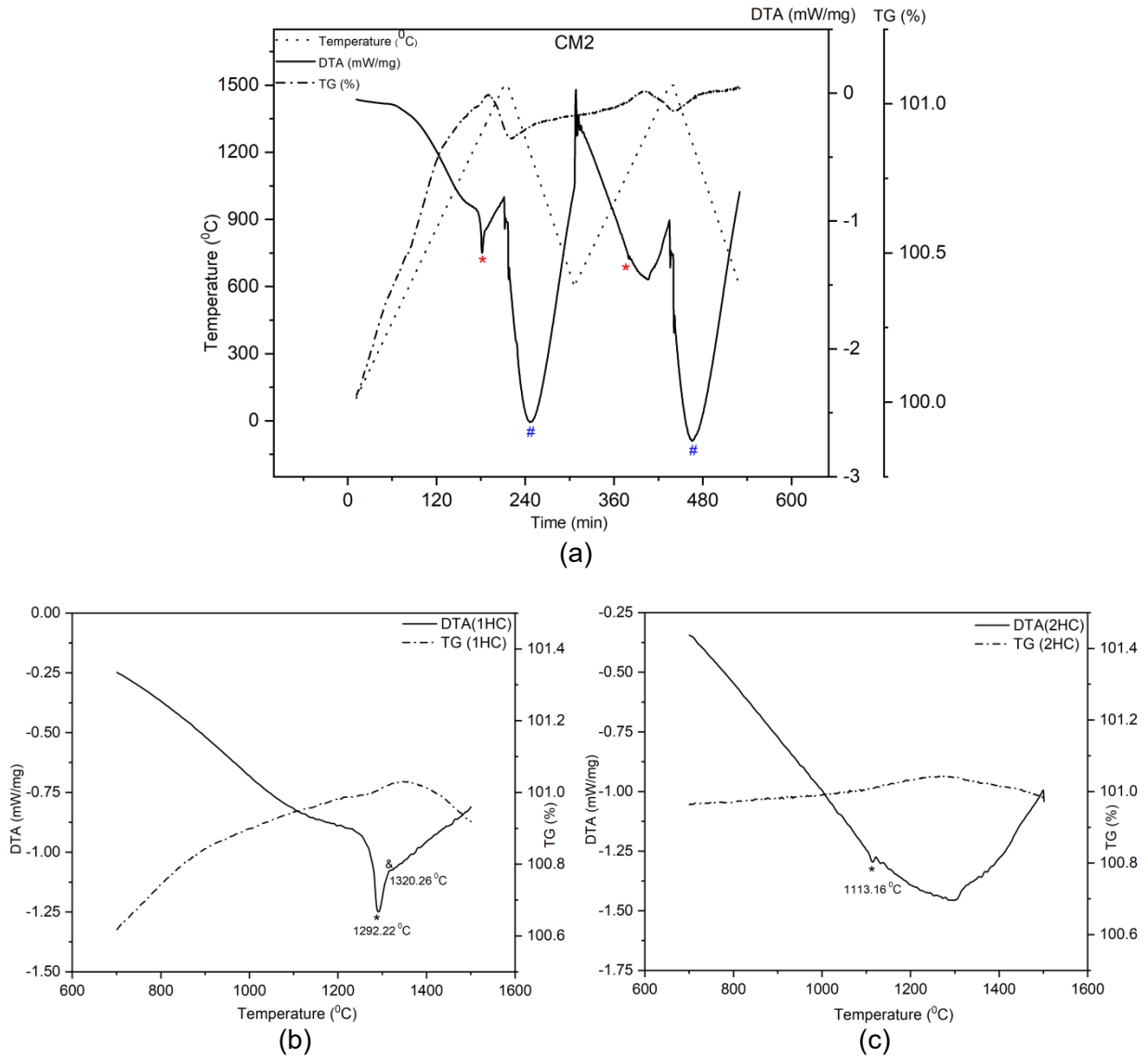

FIG 6 – DTA plot of CM2 flux: (a) All plots; (b) DTA and TG plot in 1st heating cycle; (c) DTA and TG plot in the 2nd heating cycle.

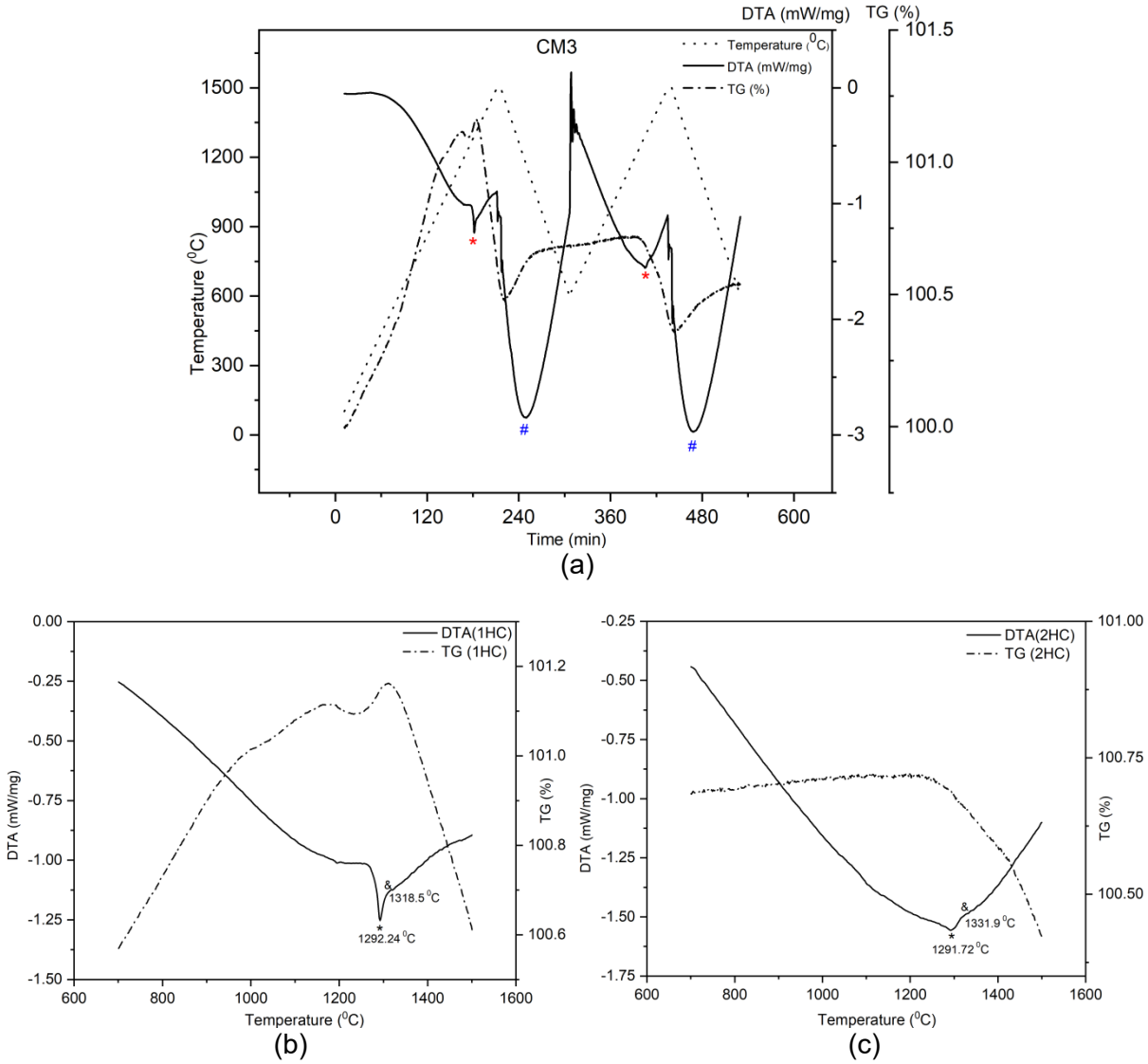

FIG 7 – DTA plot of CM3 flux: (a) All plots; (b) DTA and TG plot in 1st heating cycle; (c) DTA and TG plot in the 2nd heating cycle.

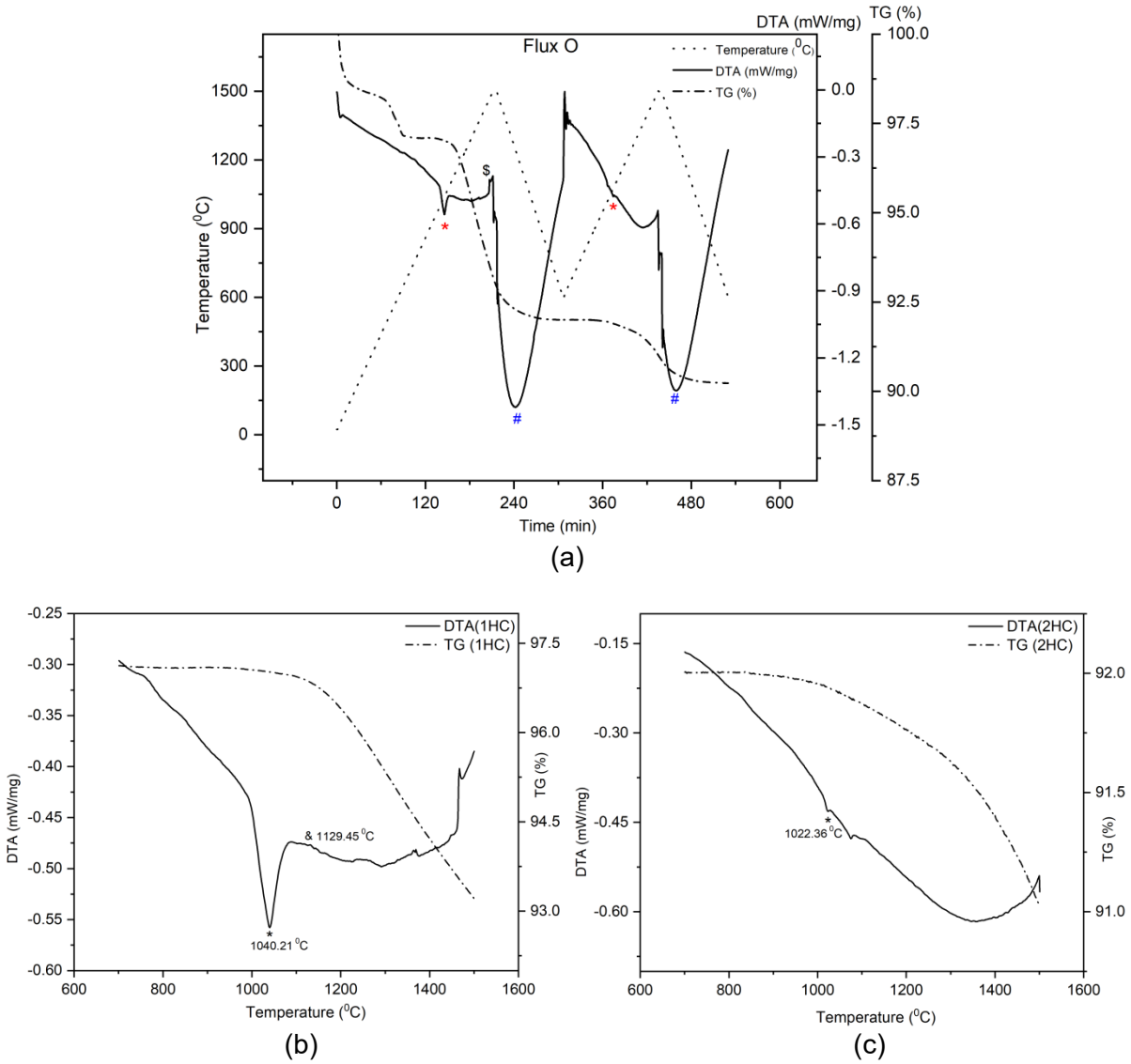

FIG 8 – DTA plot of Commercially available Flux O: (a) All plots; (b) DTA and TG plot in 1st heating cycle; (c) DTA and TG plot in the 2nd heating cycle.

In the TG plots of the commercially used flux containing 8 per cent CaF_2, a weight loss of ~10 per cent was observed in the process. Most of the weight loss was observed in the first cycle, where the process of pre-melting was done. Significant decomposition started around 600°C, which was due to the presence of CaF_2 and small fractions of $CaCO_3$ present in the flux. CaF_2-$CaCO_3$ complex decompose between 600–850°C. A significant weight loss was seen between 1200–1400°C, this accounts for phase changes in the sample, which is also reflected in the DTA plot, which will be explained further.

In the DTA plot, of the CaF_2 free fluxes and the commercially available flux, the point indicated by '*' corresponds to the solidus temperatures, which is the first endothermic peak. The point where the DTA signal line is almost flat and starts to deviate from the flat line, corresponds to the liquidus and is marked by the '&' sign. In the three CaF_2 free fluxes, the solidus temperatures were from 1250 to 1290°C. This could be attributed to the decomposition of the Bustamite (Ca-Mn-Si Oxide) (Bustamite Mineralogy data, 2001), which seems to aid in decreasing the liquidus of the CaF_2 fluxes as well. It cannot be clearly inferred from the current studies that the increase in MnO is helping in the reduction of liquidus temperatures. The presence of Fe_2O_3 in the CaF_2 free fluxes also effected the liquidus predictions. CM2 flux post the pre melting had the least amount of Fe_2O_3 and it shows the least liquidus temperatures. For an accurate demonstration of the effect of MnO on the flux, the sample selection for the analysis needs to be done with more precision to avoid the contamination from the IF steel crucible. The observations from the DTA plots are shown in

Table 5. It can be seen in the Table 5 that the liquidus temperature estimations for CM1, CM2 and Flux O could not be made from the second Heat cycle (HC) as the DTA signal was not clearly flat. A slight increase was observed in the solidus and liquidus values from the first and second heating cycle. This is analysed to be due to the chemical homogeneity attained in the sample post the first Heating cycle, which results in requirement of higher energy/heat to melt the sample. An average temperature from the first and second heating cycle was taken to be the estimated solidus and liquidus of the samples respectively and is reported in Table 6.

TABLE 5

Observations from DTA plots.

Sample		Estimated solidus (°C)	Estimated liquidus (°C)
CM1	1HC	1253.1	1281.7
	2HC	1300.5	_
CM2	1HC	1292.2	1320.3
	2HC	1113.2	_
CM3	1HC	1292.2	1318.5
	2HC	1291.7	1331.9
Flux O	1HC	1040.2	1129.5
	2HC	1022.4	-

TABLE 6

Summary of observations.

Sample	Experimental measurement				Estimations using FactSage™
	SHTT		DTA		
	Solidus temperature (°C)	Liquidus temperature (°C)	Solidus temperature (°C)	Liquidus temperature (°C)	Liquidus temperature (°C)
CM1	1200 ± 20	1340 ± 40	1276.8	1281.7	1434.2
CM2	1190 ± 39	1330 ± 14	1202.7	1320.3	1317.7
CM3	1160 ± 42	1350 ± 43	1292.0	1325.2	1381.3
Flux O	1185 ± 46	1290 ± 34	1031.3	1129.5	-

Observations from FactSage™ simulations

The ‘Equilib’ module of FactSage™ (version 8.1) was used to simulate the expected solidus and liquidus temperatures based on the chemical composition and a given range of temperatures. The predicted values are shown in Table 6 along with the other values estimated from SHTT and DTA measurements. Figure 9 shows the FactSage™ simulations for the compositions of the flux post premelting. As seen in Figure 9, the solidus of the three CaF_2 free fluxes seem to be very similar. Hence, FactSage™ was not used for solidus estimations in the current work as the accuracy of the estimations were very doubtful at lower temperatures as irrespective of the composition the solidus temperature for the CaF_2 free fluxes were converging at ~920°C. Apart from this the estimations for multi component fluxes, like Flux O, having more than four components system, seem to not give accurate results due to mathematical approximations made in this composition range. Also, the fluoride solubility in the flux also may not be modelled accurately with the current available database. Because as per the DTA tests the commercially available Flux O showed a liquidus at around 1130°C. If the flux had a liquidus as seen in Figure 10 from FactSage™ simulation, the

sample should not have melted in the DTA test as the maximum temperature was 1500°C. Hence the Liquidus temperature estimation value is not reported for the commercially available Flux O in the Table 6. The Fe content in CM2 flux was lower than CM1 and CM3 flux, hence the lowest liquidus is predicted for this flux and the effect of increasing the MnO content is not significantly seen.

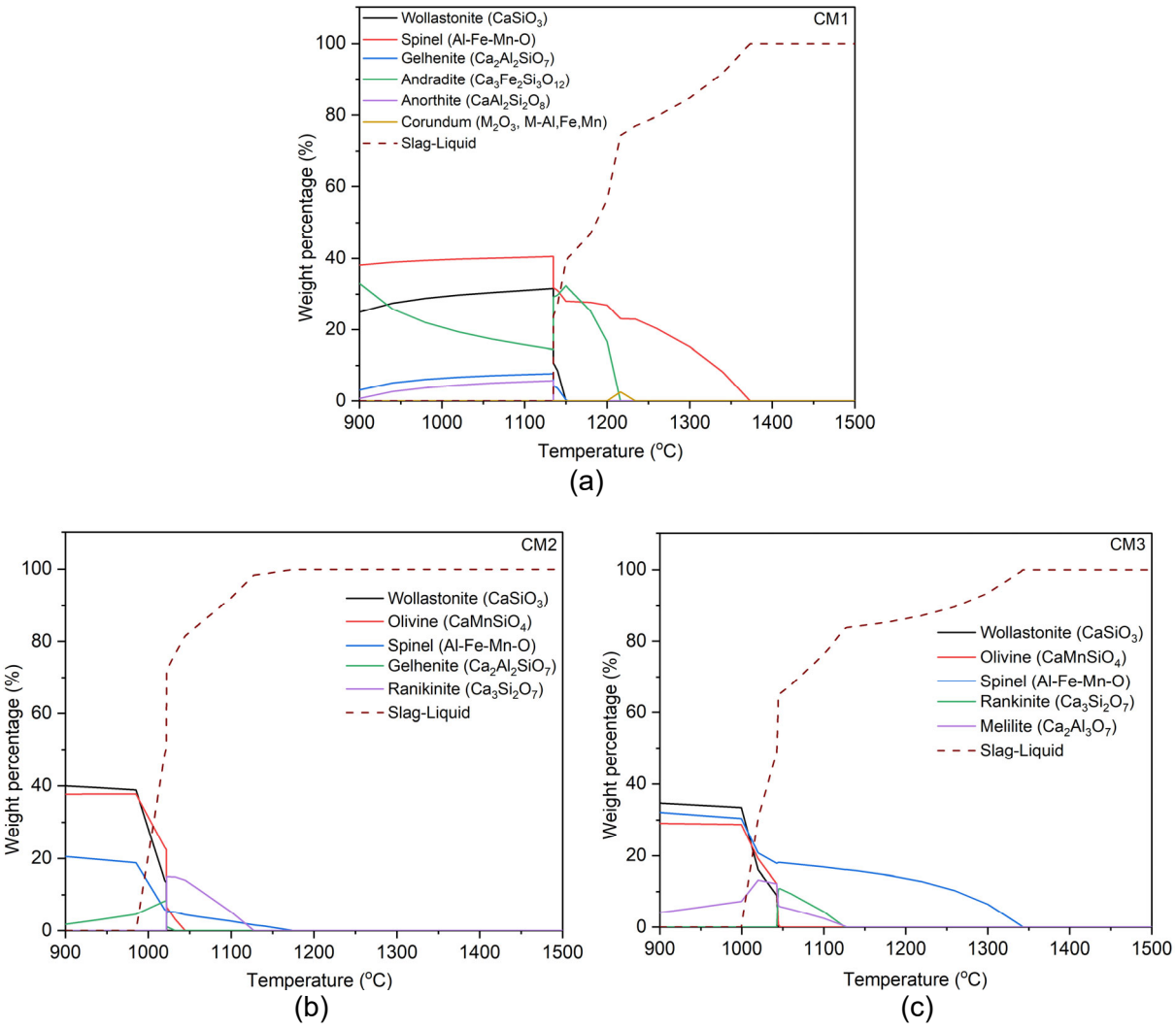

FIG 9 – FactSage™ simulations of CaF2 free fluxes: (a) CM1; (b) CM2; (c) CM3.

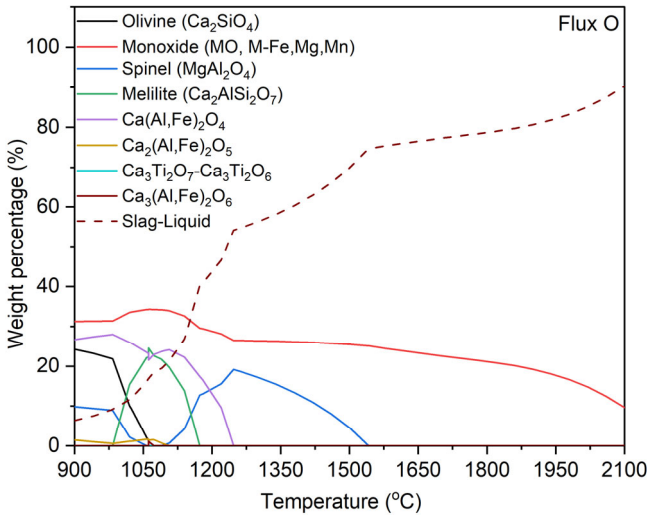

FIG 10 – FactSage™ simulation of commercially available Flux O.

CONCLUSIONS

Three fluoride-free compositions were identified as potential fluxes suitable for use in SAW. The melting behaviour properties of these fluxes were compared with a commercially available flux, to understand if the fluxes are suitable for industry. A hot thermocouple device was developed to understand the melting behaviour properties and to overcome the limitations of Thermal analysis techniques. The melting behaviour properties which are the liquidus and solidus temperatures were estimated using the single hot thermocouple technique (SHTT) and thermal analysis and simulated using FactSage™. A comparison of the experimentally measured values with the simulation results was also done for better estimation of the melting behaviour. The apparent deviations in the identification of liquidus temperature from thermal analysis might have resulted, at least in part, from issues with the DTA data acquisition practice. Since the working of the SHTT depends on the image captured of the sample, the liquid phase might start to form even before any visible deformation can be observed. This is particularly true for these MnO-containing fluxes as they are not transparent. Apart from these, local inhomogeneity in the samples and the presence of Fe_2O_3 in the samples post premelting also have contributed to the difference between the values obtained through different techniques. The positive effect of increasing MnO concentration on lowering of liquidus temperature was not observed explicitly. MnO in the flux along with Fe and Al form a spinel, which has a high melting point. Hence, the sample selection for the tests post premelting need to be taken with more precision. Interesting thing to be noted is that inspite of having Fe in the CaF_2 free flux, the liquidus of the flux is around 1400°C which is less than the solidus of low-carbon steel. Another significant observation that was made was that the Melting behaviour properties of the CaF_2-free fluxes and the commercially available flux are very similar, indicating that these fluxes are promising alternatives to CaF_2-free fluxes.

ACKNOWLEDGEMENTS

Remuneration towards one of the authors (GLSA) was provided by the generous financial support from the PMR Fellowship. The authors wish to thank the staff members at the Ferrous Process Laboratory, IIT Bombay, for their support towards the design and conduct of the experiments. The authors also wish to acknowledge the cooperation from the Research and Development Division, Tata Steel Ltd, towards carrying out making a pre-melting for some of the samples. The authors also wish to acknowledge the support from Dr Niyanth Sridharan and Mr Manikandan, Lincoln Electric Pvt Ltd, for providing the commercially used fluxes. The authors also wish to acknowledge the help from Mr Aakash Devgan and Mr Ablilash, PhD students, Department of Mechanical Engineering, IIT Bombay, for their support in making the SHTT device.

REFERENCES

Allibert, M, 1995. *Slag Atlas*, 2nd edition (Verlag Stahleisen GmbH, Düsseldorf).

Anthony, J W, Bideaux, R A, Bladh, K W and Nichols, M C (eds), 2001. Bustamite Mineralogy data, *Handbook of Mineralogy* (Mineralogical Society of America). Available from: <http://www.handbookofmineralogy.org/>

Chai, C, 1980. Slag-Metal Reactions During Flux Shielded Arc Welding, Doctoral Thesis, Massachusetts Institute of Technology, Cambridge, MA.

Coetsee, T, Mostert, R J, Pistorius, P G H and Pistorius, P C, 2021. The effect of flux chemistry on element transfer in Submerged Arc Welding: application of thermochemical modelling, *Journal of Materials Research and Technology*, 11:2021–2036.

Eagar, T, 1979. Sources of Weld Metal Oxygen Contamination during Submerged Arc Welding, *Welding Journal,* 57:76–80.

Ferrera, K P and Olson, D I, 1975. Performance of the MnO-SiO_2-CaO System as a Welding Flux, *Welding Research Supplement,* 211-s.

Anthony, J W, Bideaux, R A, Bladh, K W and Nichols, M C (eds), 2001. Ilvaite Mineralogy data, *Handbook of Mineralogy* (Mineralogical Society of America). Available from: <http://www.handbookofmineralogy.org/>

Kashiwaya, Y, Cicutti, C E and Cramb, A W, 1998b. An Investigation Mold Slag Using of the Crystallization of a Continuous Single Hot Thermocouple Technique, *ISIJ International*, 38(4):357–365.

Kashiwaya, Y, Cicutti, C E, Cramb, A W and Ishll, K, 1998a. Development of Double and for in Situ Observation and Single Hot Thermocouple Technique Measurement of Mold Slag Crystallization, *ISIJ International,* 38(4):348–356.

Kolbl, N, Marschall, I and Harmuth, H, 2011. Single hot thermocouple technique for the characterization of the crystallization behaviour of transparent or translucent liquids, *J Mater Sci,* 46:6248–6254.

Kou, S, 2003. *Welding Metallurgy*, 2nd edition, pp 223–225 (John Wiley and Sons, Inc: New Jersey).

Li, F, Li, H, Huang, D, Zheng, S and You, J, 2018. Mechanism of MnS Precipitation on $Al2O_3$–SiO_2 Inclusions in Non-oriented Silicon Steel, *Metals and Materials International,* 24:1394–1402.

Mills, K C and Fox, A B, 2003. The Role of Mould Fluxes in Continuous Casting—So Simple yet So Complex, *ISIJ International,* 43(10):1479–1486.

Mitra, U and Eagar, T W, 1991a. Slag-Metal Reactions during Welding: Part II, Theory, *Metallurgical Transactions B,* 22B:73–81.

Mitra, U and Eagar, T W, 1991b. Slag-Metal Reactions during Welding: Part I, Verification of the Theory, *Metallurgical Transactions B,* 22B:83–100.

Ordway, F, 2012. Techniques for growing and mounting small single crystals of refractory compounds, *J Res Natl Bur Stand,* 48(2):152.

Plessis, J D, Toit, M D and Pistorius, P C, 2007. Control of Diffusible Weld Metal Hydrogen through Flux Chemistry Modification, *Welding Research*, pp 273s–280s.

Ray, H S and Ray, S K, 2018. Kinetics of Metallurgical processes, *Indian Institute of Metals series* (Springer Nature Singapore Pty Ltd).

Ren, Y and Zhang, L, 2019. Effect of Al_2O_3–SiO_2–MnO inclusions on precipitation of MnS in Si–Mn-killed 304 stainless steels, *Ironmaking and Steelmaking*, 46:6:558–563.

Sarkar, R and Li, Z, 2021. Isothermal and Non-isothermal Crystallization Kinetics of Mold Fluxes used in Continuous Casting of Steel: A Review, *Metallurgical and Materials Transactions B,* 52B:1357–1378.

Singh, B, Khan, Z A and Siddiquee, A N, 2013. Effect of flux composition on element transfer during Submerged Arc Welding (SAW): A literature review, *Int J Curr Res*, 5:4181–4186.

Zhang, J, Coetsee, T, Dong, H and Wang, C, 2020. Fine-Tuned Element Transfer Strategies for Ternary CaF_2-SiO_2-CaO Fluxes in Submerged Arc Welding: An Environmentally Friendly Approach, *Metallurgical and Materials Transactions B,* 51B:16–21.

Assessment of phase evolution in $CaO–MgO–Al_2O_3–SiO_2$ system with varied Al_2O_3/SiO_2 ratio using *in situ* high-temperature Raman spectroscopy and X-ray scattering

DOI: 10.62053/WAHA9886

F Gyakwaa[1], S Wang[2], H Singh[3], G King[4], Q Shu[5], W Cao[6], M Huttula[7] and T Fabritius[8]

1. Postdoc, Process Metallurgy Research Unit, University of Oulu, FI-90014 Oulu, Finland. Email: francis.gyakwaa@oulu.fi
2. Postdoc, Nano and Molecular Systems Research Unit, University of Oulu, FI-90014 Oulu, Finland. Email shubo.wang@oulu.fi
3. Adjunct Professor, Nano and Molecular Systems Research Unit, University of Oulu, FI-90014 Oulu, Finland. Email: harishchandra.singh@oulu.fi
4. Scientist, Canadian Light Source, Saskatoon, Saskatchewan S7N 2V3, Canada. Email: graham.king@lightsource.ca
5. Professor, Process Metallurgy Research Unit, University of Oulu, FI-90014 Oulu, Finland. Email: qifeng.shu@oulu.fi
6. Professor, Nano and Molecular Systems Research Unit, University of Oulu, FI-90014 Oulu, Finland. Email: wei.cao@oulu.fi
7. Professor, Nano and Molecular Systems Research Unit, University of Oulu, FI-90014 Oulu, Finland. Email: marko.huttula@oulu.fi
8. Professor, Process Metallurgy Research Unit, University of Oulu, FI-90014 Oulu, Finland. Email: timo.fabritius@oulu.fi

ABSTRACT

Metallurgical slag, such as refining slag, is essential to enhance or promote steel cleanliness. The $CaO–MgO–Al_2O_3–SiO_2$ system is the primary source of oxides-based inclusions. It plays a vital role in applications in various pyrometallurgical processes. Numerous thermodynamic databases and physicochemical properties of slag studies mainly focus on quenched samples and measurements at room temperature. Consequently, the present study explored the physicochemical, structural properties and crystallisation evolution for $CaO–MgO–Al_2O_3–SiO_2$ glassy slags via *in situ* high-temperature Raman spectroscopy and synchrotron X-ray diffraction. The study was carried out by synthesising $CaO–MgO–Al_2O_3–SiO_2$ slag with varying Al_2O_3/SiO_2 ratios. The results from the *in situ* high-temperature measurement demonstrated a pattern showing a transformation of a broad peak from the glassy matrix to crystalline peaks. The study showed crystallisation of dominant phases such as Ca_2SiO_4, $Ca_2Al_2SiO_7$ and $CaAl_2O_4$ that correspond and are attributable to changes of structural units during *in situ* high-temperature measurements. The results further showed a correlation between an increase and transformation in crystalline phases observed from the spectra obtained from non-isothermal heating of the samples.

INTRODUCTION

Metallurgical slag, such as refining slag, is essential to enhance steel cleanliness (Lia and Dua, 2022; Sniegoň *et al*, 2021; Yoon *et al*, 2002; Yu *et al*, 2021). Promoting steel cleanliness includes optimising inclusion composition in ladle furnace refining, such as using the deoxidation process. Refining slag main components such as SiO_2, CaO, MgO and Al_2O_3 can form the $CaO–MgO–Al_2O_3–SiO_2$ system. The $CaO–MgO–Al_2O_3–SiO_2$ system is the primary source of oxides-based inclusions predominantly for Al-deoxidised treated with calcium steels. This makes the optimisation of quaternary slag systems such as $CaO–MgO–Al_2O_3–SiO_2$ systems have an important role for secondary refining, such as for improving absorption of non-metallic inclusions and for refractory protection (Bielefeldt, Vilela and Heck, 2014; Jiang, Wang and Wang, 2012; Kim *et al*, 2013; Ma *et al*, 2014; Xu *et al*, 2014, 2015). Researchers have shown that the crystallisation behaviour of the $CaO–MgO–Al_2O_3–SiO_2$ slag system is essential in optimising its applications for various processes (Bielefeldt, Vilela and Heck 2013; Lin *et al*, 2023; Yao, Ma and Lyu, 2021). The work carried out by Jung and Sohn (2012) suggests this can be achieved by controlling the formation volume ratio of the crystalline phase to that of the amorphous phase in the slag. Also, detailed studies have been covered concerning thermodynamic and viscosities analysis of this slag system to enhance

inclusions control and performance of mould fluxes mechanism (Gan, Xin and Zhou, 2017; Jiao *et al*, 2007; Shankar *et al*, 2007; Song, Shu and Sichen, 2011; Li *et al*, 2017; Lin *et al*, 2023). Considering the essential role of metallurgical slag constituting components such as SiO_2, CaO, MgO and Al_2O_3, various detailed studies have aimed to examine the physicochemical and structural properties such as crystallisation behaviour (Pereira *et al*, 2023; Zhang *et al*, 2010).

To further explore CaO–MgO–Al_2O_3–SiO_2 quaternary slag for process optimisation, various studies have been conducted to examine the role of varying some components such as Al_2O_3/SiO_2 ratios (Kim *et al*, 2013; Liao *et al*, 2012; Wang and Sohn, 2018; Zhang *et al*, 2008). Various analytical techniques, such as hot thermocouple technique (Kashiwaya *et al*, 2007), confocal laser scanning microscopy (Wang and Sohn, 2018) and single hot thermocouple technique (Kashiwaya *et al*, 2007; Esfahani and Barati, 2018) had been utilised to characterise this slag system. Raman spectroscopy has been demonstrated as a potential analytical technique for studying the constituents such as metallurgical slag for structural analysis, especially from recent studies under *in situ* high-temperature conditions (Wang *et al*, 2022; Zhang *et al*, 2023). However, to the present authors' knowledge, the *in situ* and high-temperature crystallisation transformation mechanism of CaO–MgO–Al_2O_3–SiO_2 slags with Al_2O_3/SiO_2 ratios is yet to be explored using Raman spectroscopy. Such a study will further contribute to understanding the role of SiO_2 as a network former and Al_2O_3 as a network intermediate for the crystallisation mechanism of CaO–MgO–Al_2O_3–SiO_2 based slags.

This work will explore the crystalline phase evolution of CaO–MgO–Al_2O_3–SiO_2 glassy slags with varying Al_2O_3/SiO_2 ratios using *in situ* high-temperature Raman spectroscopy. Raman spectroscopy will be used to analyse the network microstructure of the slag and the structural formation of the crystalline phase of the samples during the non-isothermal melt process. The *in situ* high-temperature crystalline phases formation mechanism of CaO–MgO–Al_2O_3–SiO_2 glass slags with varying Al_2O_3/SiO_2 will also be investigated using high energy synchrotron X-ray diffraction (HE-SXRD). The glassy slag's transformation temperatures and crystallisation behaviours will be examined using a differential scanning calorimeter (DSC) thermogram. Furthermore, X-ray diffraction (XRD) analysis of *in situ* samples was also used to identify the final phases formed at room temperature (RT). These analytical techniques provide comprehensive structural information about the glassy sample and its melt.

EXPERIMENTAL

Sample preparation

Reagent-grade chemicals of aluminium oxide (α-Al_2O_3), calcium oxide (CaO), silicon dioxide (SiO_2) and magnesium oxide (MgO), a purity that ranged from 99.7 per cent to 99.9 per cent and supplied by Alfa Aesar were used to synthesise the experimental slag samples. A thorough moisture removal and mixing were carried out and pressed into pellets. The pellets were subsequently placed in a Pt crucible, sintered at a high temperature of 1450°C in a chamber furnace and quenched to obtain the desired CaO–MgO–Al_2O_3–SiO_2 quaternary glassy slag. The elemental composition of the prepared samples was estimated using X-ray fluorescence (XRF), an Axios Max model from Panalytical. The XRF operates using SuperQ's analysis software with an X-ray generator Rh-tube. It has a maximum power of 4 kW. The glassy slag was also measured using XRD to determine how amorphous the samples prepared were, as shown in Figure 1. Details features concerning the XRD used for this work can be found in previous studies (Gyakwaa *et al*, 2019). The CaO–MgO–Al_2O_3–SiO_2 quaternary slag composition used for this study is shown in Table 1.

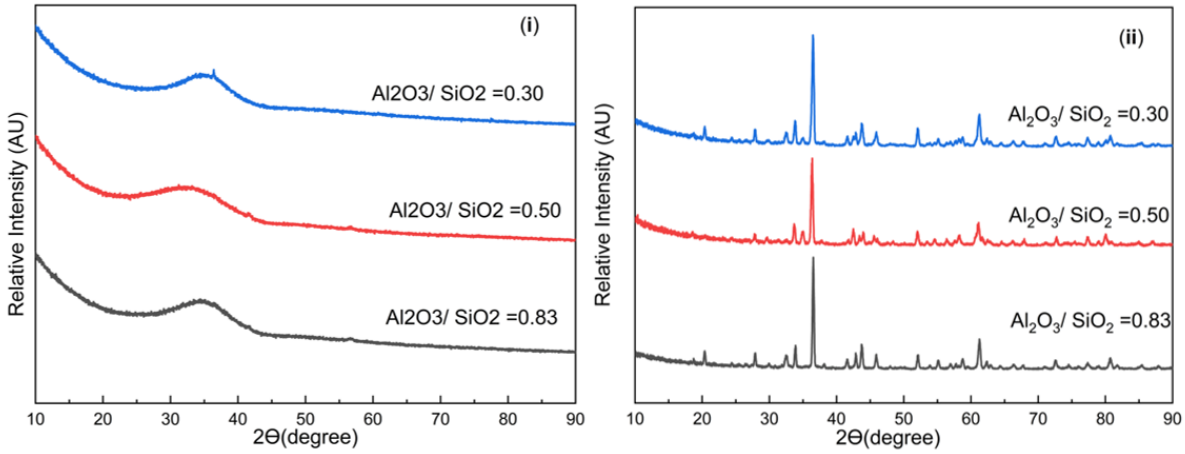

FIG 1 – X-ray diffraction (XRD) patterns of the (i) glassy slag samples and (ii) crystalline phase samples.

TABLE 1

The experimental compositions (weight percentage, wt%) used to prepare the glassy slag samples and X-ray fluorescence (XRF) analysis (wt%).

Sample number	Al_2O_3/SiO_2	Pre-experimental composition							
		Chemical composition (wt%)				XRF (wt%)			
		MgO	Al_2O_3	SiO_2	CaO	MgO	Al_2O_3	SiO_2	CaO
S1	0.30	5.00	15.00	50.00	30.00	5.62	14.45	50.2	29.73
S2	0.50	5.00	20.00	40.00	35.00	4.83	20.41	39.39	35.37
S3	0.83	5.00	25.00	30.00	40.00	5.61	24.73	29.88	39.78

In situ high-temperature Raman spectroscopic measurements

The *in situ* high-temperature Raman spectroscopy measurements of the glassy samples were performed using a reformative laser confocal micro-Raman spectrometer. The confocal micro-Raman spectrometer from B&W Tek (Plainsboro, US) utilises He-Cd laser with an excitation wavelength of 532 nm and is equipped with a rotatable stage. The *in situ* Raman spectra from the sample were collected at RT and desired temperatures with a heating rate of 20 K/min and a Raman spectral frequency range of 200–1200 cm^{-1} was used for this study. The desired temperatures selected for this study were RT, 760, 800, 850, 900, 1000, 1100 and 1200°C. To achieve reproducibility for the acquired *in situ* Raman spectra, measurements were carried out by measuring the samples at least three times. The glassy samples were analysed using Raman spectroscopy at RT and subsequently *in situ* high temperature was carried to determine the melt structure and the influence of Al_2O_3/SiO_2 for sample matrix of $CaO–MgO–Al_2O_3–SiO_2$. The Raman Spectra obtained from the measurements were deconvolved using Gaussian line shapes (Mysen *et al*, 1982) for fitting the peaks that correspond to the vibrations of various structural units in the samples.

HE-SXRD and DSC measurements

Experimental diffraction patterns were collected at every 100°C from RT to 1000°C and then again one pattern after cooling to RT, following the heating. The data collection went well, with 30 keV photons for the proposed XRD measurements. A 2D Perkin Elmer area detector (200 × 200 μm^2 pixel size, 40 × 40 cm^2 in area) was placed behind the sample, allowing data acquisition in a Debye-Scherrer or transmission geometry. The refined wavelength was 0.4087 Å and the sample to detector distance was 481.3 mm. Here, the exposure time was 0.5 sec and 120 snapshots were acquired to optimise the data collection and to ensure a reasonable statistic.

The crystallisation behaviours and transformation temperatures for glassy powder samples were determined by DSC measurements using a thermal analyser (model: STA 449 F3, Netzsch-

Gerätebau Germany) with the purge gas as Ar. Temperature, balance and sensitivity calibrations were performed prior to DSC measurements using metals with high purity and known melting points as reference materials. The platinum crucible without samples was used as reference material in obtaining the baseline. The glass powder samples were placed in the platinum crucible and heated to 1350°C (a heating rate of 20°C/min) to obtain the DSC signals and subsequently cooled to RT. The peak crystallisation temperatures, glass transition temperatures and DSC continuous heating transformation (CHT) curves of crystalline phases from the measured samples were obtained from the DSC measurements.

RESULTS AND DISCUSSION

Raman spectra analysis

The relationship between the composition and structure of the prepared glassy slag samples is explored using Raman spectroscopy. The Raman spectra of the glassy CaO–MgO–Al_2O_3–SiO_2 quaternary samples obtained at RT with varying Al_2O_3/SiO_2 ratios of 0.30, 0.50 and 0.83 are presented in Figure 2. The Raman spectra could be divided into three frequency regions to contain dominant vibration bands. Between 420–600 cm^{-1} is a low-frequency region; between 600–800 cm^{-1} is a medium region and the high-frequency region is between 850–1000 cm^{-1}. It can be observed from Figure 2 that an increment in the Al_2O_3/SiO_2 ratio in the samples had a corresponding increase in the intensity of the Raman shift at a lower frequency region of 420–600 cm^{-1}. A corresponding decrease in the Raman shift in the region between 600–800 cm^{-1} was noticed when the ratio for Al_2O_3/SiO_2 increased for the samples.

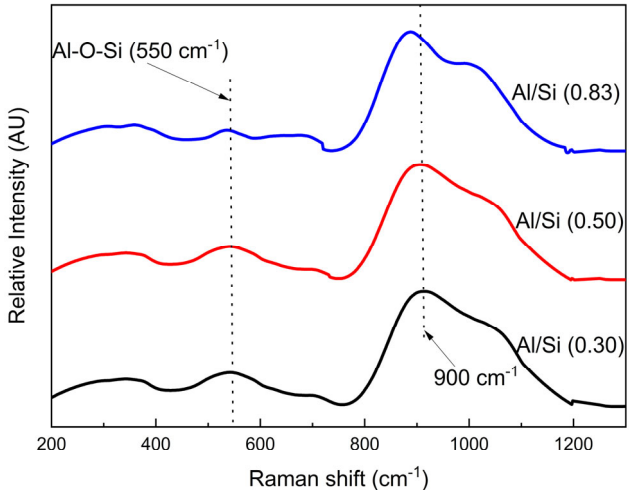

FIG 2 – Raman spectra for glassy samples with different Al_2O_3/SiO_2 ratios.

Researchers have shown (Matson, Sharma and Philpotts, 1983; Han *et al*, 2016) that a Raman shift region between 420–600 cm^{-1} is associated with the activities of mixed stretching and bending vibration from the Al–O–Si bridge oxygen linkage and a Raman frequency region between 600–800 cm^{-1} corresponds to mixed bending and stretching vibration occurring at of the Si–O–Si bridge oxygen linkage. Consequently, it can be estimated that the Al_2O_3/SiO_2 ratio influences the bridge oxygen linkage of Al–O–Si and Al–O–Si, where a rise in Al_2O_3/SiO_2 has a corresponding gradual increase for the bridge oxygen linkage of Al–O–Si and a decrease for the bridge oxygen linkage of Si–O–Si.

The present study corresponds to the findings by (Mysen *et al* 1982; Matson, Sharma and Philpotts, 1983; Mysen, 2003; Han *et al*, 2016), suggesting that the existence of the Al–O–Si linkage is more possible compared to the combinations of Si–O–Si and Al–O–Al and attribution of the formation of the Al–O–Si linkage mostly in aluminosilicate glasses. With increasing Al_2O_3/SiO_2 ratios, it can also be noticed that within the higher frequency range 800–1100 cm^{-1}, the Raman peaks linked with the vibrations of depolymerised aluminosilicate and silicate units became more pronounced toward lower frequency. According to the studies conducted by Loewenstein (1954), which have a similar

slag system as in this work, the tetrahedral $[AlO_4]^{5-}$ unit and tetrahedral $[SiO_4]^{4-}$ units structural can serve as the network formers.

The Raman spectra obtained at RT were deconvoluted using the Gaussian-fitting method adopted by Mysen *et al* (1982). It can be observed from the deconvoluted results obtained from the glassy samples before the *in situ* high temperature. Four main structural units of the symmetric stretching band of (SiO_4^{4-}) tetrahedra are represented as Q^n and n, denoted as a number of bridging oxygen in the tetrahedra for estimating the structural properties of the samples. Characteristic Raman bands at approximately 850 cm^{-1} are associated with silicate structure as monomer silicate units (Q^0) (Mysen *et al*, 1982) at approximately 900 for dimer silicate units (Q^1), at 950 cm^{-1} for chain-like silicate structures, Q^2 and 1030 cm^{-1} attributable to sheet-like silicate structures, Q^3, with corresponding BO/Al = 0, 1, 2, 3, as according to studies conducted by researchers (Li, Shu and Chou, 2014; Mysen *et al*, 1982; Wang, Shu and Chou, 2011) on silicate glasses. From the deconvolution results, the fitted Raman spectra full width at half maximum values were observed to reduce with a corresponding gradually raised Al_2O_3/SiO_2 ratio, which could be attributed to enhanced crystallisation ability compared with glass formation ability.

Figure 3 shows the Raman spectra for the slags with different Al_2O_3/SiO_2 ratios for estimating the sample's crystalline phases generated during heating and cooling. Figure 3 is an illustrative example using sample 2 (Al_2O_3/SiO_2 = 0.50). *In situ* high-temperature Raman spectroscopy measurements were used to predict the crystalline phase formation from an amorphous phase in the slag system. It was noticed from the study that Raman spectra obtained from the glassy sample at RT did not significantly change until 500°C. As the temperature increased from 500°C, it was observed that the relative intensity of the Raman shift became sharper, indicating the formation of crystalline phases. It was evident when the sample was cooled to RT. Based on the Raman shift positions, prominent crystalline phases such as Ca_2SiO_4, $CaAl_2O_4$ and $Ca_2Al_2SiO_7$ can be predicted when compared with reference Raman spectra (Allu *et al*, 2017; Bouhifd *et al*, 2002; Fujimori *et al*, 2002; Gyakwaa *et al*, 2019; Pešková, Machovič and Procházka, 2011; Remy, Reynard and Madon, 1997).

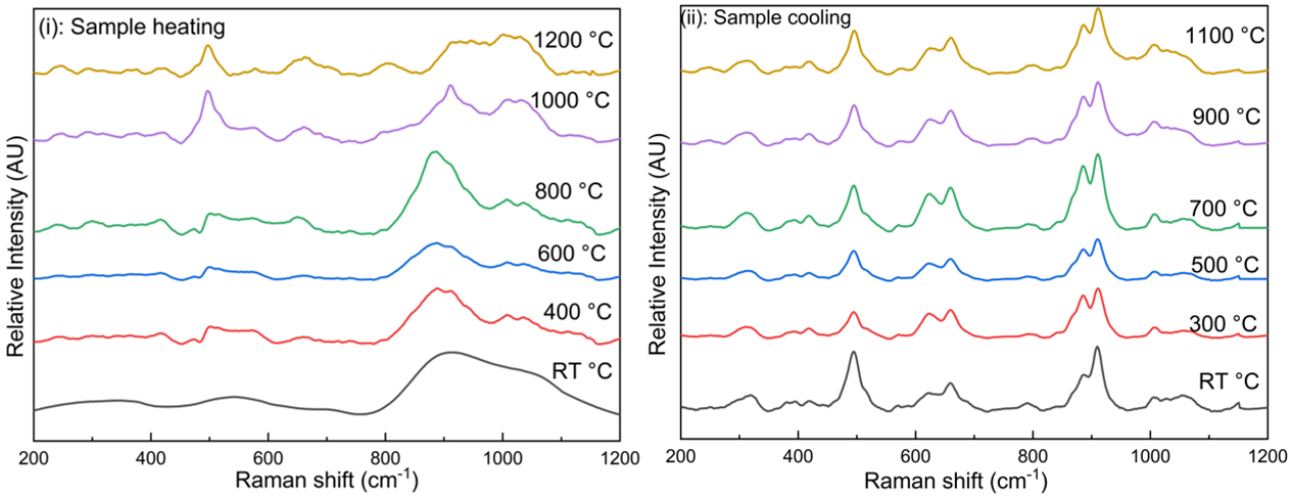

FIG 3 – Example to illustrate *in situ* high-temperature Raman spectra for the glassy samples (Al_2O_3/SiO_2 =0.50) during heat and cooling.

Qualitative Raman spectra from *in situ* high-temperature measurements obtained from 700–1200°C and cooling to RT show Raman bands (shifts) located at approximately 308, 440, 540, 600, 614, 634, 660, 724, 796 cm^{-1}, which are characteristic of various phase attributable with this glassy samples (Allu *et al*, 2017; Bouhifd *et al*, 2002; Fujimori *et al*, 2002; Gyakwaa *et al*, 2019; Pešková, Machovič and Procházka, 2011; Remy, Reynard and Madon, 1997). These Raman bands could be associated with the evolution of the glassy or amorphous phase and the formation of a crystalline phase since the crystallisation process is enhanced by increasing temperature. It was also observed that the Raman analysis from 600°C to RT when cooling the samples during the *in situ* measurements showed no noticeable variation in the Raman spectra obtained, suggesting no significant crystalline phases were formed.

DSC and identification of the crystalline phases using XRD

The thermogravimetric DSC curve of the glassy powder sample slag ($CaO–MgO–Al_2O_3–SiO_2$) with varied Al_2O_3/SiO_2 ratios using a heating rate of 20°C/min is shown in Figure 4. It is observed from the DSC curve that the sample remained in a glassy state until approximately 600°C. The exothermic peak noticed from the three samples had some variation corresponding to the Al_2O_3/SiO_2 mass percent ratio. The number of observed exothermic peaks gradually increases with a rise in the Al_2O_3/SiO_2 ratio. For instance, samples 2 and 3 increased with shoulder exothermic peaks appearing at 813°C for sample 2 (A/S = 0.30); at 848°C for sample 3 (A/S = 0.50), compared with sample 1(A/S = 0.30) at 801°C. This feature can be attributable to the formation of more crystalline phases for samples 2 and 3. Therefore, it can be predicted that the crystallisation temperatures shift to higher temperatures with an increase in the Al_2O_3/SiO_2 ratio in the glassy samples. Sample 1's onset of crystallisation temperature is estimated at 780°C and samples 2 and 3 range from 750–780°C. Therefore, the DSC analysis indicates that increasing the Al_2O_3/SiO_2 ratio tends to raise the crystallisation temperature and form more crystallisation ability Al_2O_3/SiO_2 ratios.

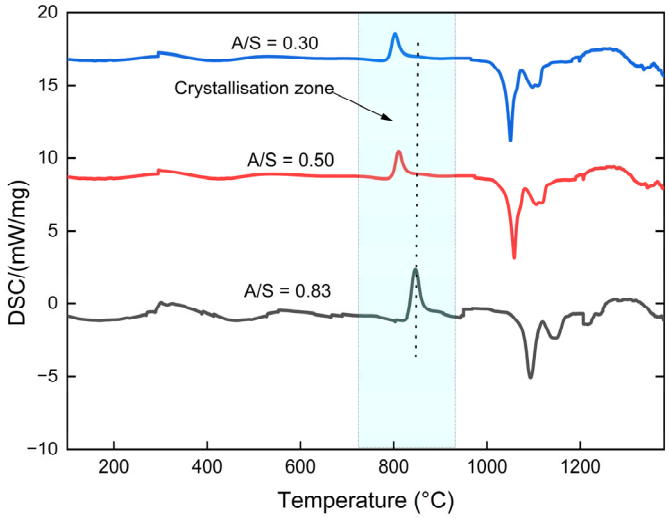

FIG 4 – Differential scanning calorimeter (DSC) curve of the glassy slag samples with different Al_2O_3/SiO_2 ratios analysis.

XRD was used to analyse the crystalline phases formed to identify further the various specific crystallisation products generated from the samples based on their varying Al_2O_3/SiO_2 ratios. In the *in situ* high-temperature Raman spectroscopy analysis, samples gradually cooled to RT, showing a predominantly mixture of crystalline phases from the study. These identified crystalline phases correspond and are consistent with qualitatively estimated phases based on their Raman band. Additionally, the samples obtained after DSC analysis were analysed using XRD and crystalline phases formed during the cooling of the glassy slag were obtained. XRD analysis of the precipitated crystalline phases shows some variation in the slag analysis based on the characteristic peaks of XRD. Crystalline phases of calcium silicate (Ca_2SiO_4) and calcium aluminosilicate ($Ca_2Al_2SiO_7$) showing for samples 1, 2 and 3 and additional crystalline phase of $CaAl_2O_4$ for sample 3. The additional phase of $CaAl_2O_4$ could be attributed to the transformation mechanism of Ca_2SiO_4 with increasing Al_2O_3 content in the $CaO–MgO–Al_2O_3–SiO_2$, as also previously shown by Yao, Ma and Lyu, (2021).

Subsequently, *in situ* high-temperature studies using high-energy synchrotron X-ray diffraction (HE-SXRD) were used to crystallise phases for the glassy samples. At RT, it can be easily observed that the diffraction pattern consists of a broad peak from the glassy matrix and three crystalline diffraction peaks. These crystalline peaks disappear until 700°C, while new peaks show up. No significant change has been observed when heating onward to 900°C. At 1000°C, significant crystallisation is observed. A preliminary peak indexing from the HE-SXRD measurements suggests the crystalline phases heating to 1000°C consist of mainly $Ca_2Al_2SiO_7$ and $CaAl_2O_4$ for the samples.

CONCLUSIONS

The present work examined the evolution of multicomponent crystalline phase products and the structural characterisation of glassy glassy Al_2O_3–CaO–SiO_2–MgO system. The effect with different Al_2O_3/SiO_2 ratios was explored by the DSC, XRF, XRD, *in situ* high-temperature Raman spectroscopy and high energy synchrotron X-ray diffraction (HE-SXRD) techniques. Based on the increase of the Al_2O_3/SiO_2 ratio in glassy slag. The findings from this study were concluded as follows:

- *In situ* heating experiment using Raman spectroscopy and HE-SXRD, X-ray diffraction (XRD) analysis estimated primary crystalline phases of Ca_2SiO_4, $Ca_2Al_2SiO_7$ and with $CaAl_2O_4$ phases predicted at higher for Al_2O_3/SiO_2 ratio samples.
- Differential scanning calorimeter (DSC) thermogram crystallisation temperature increased with increasing Al_2O_3/SiO_2 ratio in the *in situ* heating experiment.
- The glassy slag shows types of bridge oxygen linkages and predicted the existence of a higher ratio of tetrahedral $[AlO_4]^{5-}$ structural units with an increase in the Al_2O_3/SiO_2 ratio where enhanced the polymerisation of tetrahedral $[SiO_4]^{4-}$ and $[AlO_4]^{5-}$ structural units improved from the Raman spectra analysis.

REFERENCES

Allu, A R, Balaji, S, Tulyaganov, D U, Mather, G C, Margit, F, Pascual, M J, Siegel, R, Milius, W, Senker, J, Agarkov, D A, Kharton, V V and Ferreira, J M F, 2017. Understanding the Formation of $CaAl_2Si_2O_8$ in Melilite-Based Glass-Ceramics: Combined Diffraction and Spectroscopic Studies, *ACS Omega*, 2:6233−6243.

Bielefeldt, W V, Vilela, A C F and Heck, N C, 2014. Thermodynamic evaluation of the slag system CaO–MgO–SiO_2–Al_2O_3, in *Proceedings of the Iron Steel Technology Conference*, 2:1433–1445 (AISTech).

Bielefeldt, W V, Vilela, C A F and Heck, N C, 2013. Evaluation of the slag system CaO-MgO-Al_2O_3-SiO_2, presented to the 44th Steelmaking Seminar, Brazil.

Bouhifd, M A, Gruener, G, Mysen, B O and Richet, P, 2002. Premelting and calcium mobility in gehlenite ($Ca_2Al_2SiO_7$) and pseudowollastonite ($CaSiO_3$), *Phys Chem Minerals*, 29:655–662.

Esfahani, S and Barati, M, 2018. Effect of slag composition on the crystallisation kinetics of synthetic CaO-SiO_2-Al_2O_3-MgO slags, *Metallurgical and Materials Transactions B*, 49:590–601.

Fujimori, H, Komatsu, H, Ioku, K and Goto, S, 2002. Anharmonic lattice mode of Ca_2SiO_4: Ultraviolet laser Raman spectroscopy at high temperatures, *Physical Review B*, 66:064306.

Gan, L, Xin, J and Zhou, Y, 2017. Accurate viscosity calculation for melts in SiO_2–Al_2O_3–CaO–MgO systems, *ISIJ International*, 57:1303–1312.

Gyakwaa, F, Aula, M, Alatarvas, T, Vuolio, T, Huttula, M and Fabritius, T, 2019. Applicability of Time-Gated Raman Spectroscopy in the Characterisation of Calcium-Aluminate Inclusions, *ISIJ International*, 59(10):1846–1852.

Han, C, Chen, M, Rasch, R, Yu, Y and Zhao, B, 2016. Structure Studies of Silicate Glasses by Raman Spectroscopy, in *Proceedings of the 10th International Conference on Molten Slags, Fluxes and Salts: Advances in Molten Slags, Fluxes and Salts*, pp 175–182.

Jiang, M, Wang, X H and Wang, W J, 2012. Study on refining slags targeting high cleanliness and lower melting temperature inclusions in Al killed steel, *Ironmaking and Steelmaking*, 39:20.

Jiao, K, Chang, Z, Chen, C and Zhang, J L, 2007. Thermodynamic properties and viscosities of CaO–SiO_2–MgO–Al_2O_3 slags, *Metall Mater Trans B*, 50:1012–1022.

Jung, S S and Sohn, I, 2012. Crystallisation behavior of the CaO-Al_2O_3-MgO system studied with a confocal laser scanning microscope, *Metallurgical and Materials Transactions B*, 43:1530–1539.

Kashiwaya, Y, Nakauchi, T, Pham, K S, Akiyama, S and Ishii, K, 2007. Crystallisation behaviors concerned with TTT and CCT diagrams of blast furnace slag using hot thermocouple technique, *ISIJ International*, 47:44–52.

Kim, H, Matsuura, H, Tsukihashi, F, Wang, W, Min, D J and Sohn, I, 2013. Effect of Al_2O_3 and CaO/SiO_2 on the viscosity of calcium silicate-based slags containing 10 mass Pct MgO, *Metallurgical and Materials Transactions B*, 44:5–12.

Li, J, Shu, Q and Chou, K, 2014. Structural study of glassy CaO-SiO_2-CaF_2-TiO_2 slags by Raman spectroscopy and MAS-NMR, *ISIJ International,* 54:721–727.

Li, S-J, Cheng, G-G, Yang, L, Chen, L, Yan, Q-Z and Li, C-W, 2017. A Thermodynamic Model to Design the Equilibrium Slag Compositions during Electroslag Remelting Process: Description and Verification 17, *ISIJ International*, 57(4):713–722.

Lia, S and Dua, X, 2022. Effect of Al_2O_3 in Refining Slag on the Cleanliness and Fatigue Property of Ultra-low-carbon Automotive, *Steel Materials Research*, 25(9). https://doi.org/10.1590/1980-5373-MR-2021-0556

Liao, J, Zhang, Y, Sridhar, S, Wang, X and Zhang, Z, 2012. Effect of Al_2O_3/SiO_2 ratio on the viscosity and structure of slags, *ISIJ International*, 52:753–758.

Lin, Y, Yi, Y, Fang, M, Ma, W and Liu, W, 2023. Prediction Model for SiO_2 Activity in the CaO-Al_2O_3-SiO_2-MgO Quaternary Slag System, *Minerals*, 13:509.

Loewenstein, W, 1954. The distribution of aluminium in the tetrahedra of silicates and aluminates, *Am Mineral*, 39:92–97.

Ma, W J, Bao, Y P, Wang, M and Zhao, D W, 2014. Influence of slag composition on bearing steel cleanness, *Ironmaking and Steelmaking*, 41(1):26–30.

Matson, D W, Sharma, S K and Philpotts, J A, 1983. The structure of high-silica alkali-silicate glasses, A Raman spectroscopic investigation, *Journal of Non-Crystalline Solids*, 58:323–352.

Mysen, B O, Finger, L W, Virgo, D and Seifert, F A, 1982. Curve-fitting of Raman spectra of silicate glasses, *American Mineralogist*, 67:686–695.

Mysen, B, 2003. Physics and chemistry of silicate glasses and melts, *European Journal of Mineralogy*, pp 781–802.

Pereira, A L, Pereira, J A M, Bielefeldt, W V and Vilela, A C F, 2023. Thermodynamic evaluation of viscosity behavior for CaO–SiO_2–Al_2O_3–MgO slag systems examined at the temperatures range from 1500 to 1700°C, *Scientific Reports*, 13:16274.

Pešková, Š, Machovič, V and Procházka, P, 2011. Raman spectroscopy structural study of fired concrete, Ceramics – Silikáty, 55(4):410–417.

Remy, C, Reynard, B and Madon, M, 1997. Raman Spectroscopic Investigations of Dicalcium Silicate: Polymorphs and High-Temperature Phase Transformations, *Journal of the American Ceramic Society*, 80(2):413–423.

Shankar, A, Gornerup, M, Lahiri, A K and Seetharaman, S, 2007. Experimental investigation of the viscosities in CaO–SiO_2–MgO–Al_2O_3 and CaO–SiO_2–MgO–Al_2O_3–TiO_2 slags, *Metallurgical and Materials Transactions B*, 38:911–915.

Sniegoň, M, Tkadlečková, T, Huczala, K, Michalek, Chudobová, L, Strouhalová, M, Walek, J and Pieprzyca, J, 2021. Thermodynamic analysis of CaO–SiO_2–Al_2O_3–MgO slag system, in *Proceedings of the 30th Anniversary International Conference on Metallurgy and Materials*, 46–52.

Song, M, Shu, Q and Sichen, D, 2011. Viscosities of the quaternary Al_2O_3–CaO–MgO–SiO_2 slags, *Steel Research International*, 82:260–268.

Wang, S, Rani, E, Gyakwaa, F, Singh, H, King, G, Shu, Q, Cao, W, Huttula, M and Fabritius, T, 2022. Unveiling Non-isothermal Crystallization of CaO–Al_2O_3–B_2O_3–Na_2O–Li_2O–SiO_2 Glass via In Situ X-ray Scattering and Raman Spectroscopy, *Inorg Chem*, 61(18):7017–7025.

Wang, Z and Sohn, I, 2018. Effect of the Al_2O_3/SiO_2 mass ratio on the crystallisation behavior of CaO-SiO_2-MgO-Al_2O_3 slags using confocal laser scanning microscopy, *Ceramic International*, 44(16):19268–19277.

Wang, Z, Shu, Q and Chou, K, 2011. Structure of CaO-B_2O_3-SiO_2-TiO_2 Glasses: a Raman Spectral Study, *ISIJ International*, 51(7):1021–1027.

Xu, J, Su, L, Chen, D, Zhang, J and Chen, Y, 2015. Experimental investigation on the viscosity of CaO–MgO(–Al_2O_3)–SiO_2 slags and solid–liquid mixtures, *Journal of Iron and Steel Research International*, 22(12):1091–1097.

Xu, J-F, Zeng, T, Sheng, M-Q, Jie, C, Wan, K and Zhang, J-Y, 2014. Viscosity of low silica CaO–5MgO–Al_2O_3–SiO_2 slags, *Ironmaking and Steelmaking*, 41(7):486–492.

Yao, Z, Ma, X and Lyu, S, 2021. Phase equilibria of the Al_2O_3–CaO–SiO_2-(0%, 5%, 10%) MgO slag system for non-metallic inclusions control, *CALPHAD: Computer Coupling of Phase Diagrams and Thermochemistry*, 72:102227.

Yoon, B-H, Heo, K-H, Kim, J-S and Sohn, H-S, 2002. Improvement of steel cleanliness by controlling slag composition, *Ironmaking and Steelmaking*, 29:215.

Yu, H, Qiu, G, Zhang, J and Wang, X, 2021. Effect of Medium Basicity Refining Slag on the Cleanliness of Al-killed Steel, *ISIJ International*, 61(12):2882–2888.

Zhang, B, Tekle, H, O'Malley, R J, Sander, T, Smith, J D, Gerald, R E and Huang, J, 2023. In Situ and Real-Time Mold Flux Analysis using a High-Temperature Fiber-Optic Raman Sensor for Steel Manufacturing Applications, *Journal of Lightwave Technology*, 41:4419–4429.

Zhang, Z, Wen, G, Liao, J and Sridhar, S, 2010. Observations of crystallisation in mold slags with varying Al_2O_3/SiO_2 ratio, *Steel Research International*, 81:516–528.

Zhang, Z, Wen, G, Tang, P and Sridhar, S, 2008. The influence of Al_2O_3/SiO_2 ratio on the viscosity of mold fluxes, *ISIJ International*, 48:739–746.

Effects of FeO/SiO_2 ratio and optical basicity on viscosity and melt structure of $FeO–SiO_2–Al_2O_3–CaO–MgO–Cr_2O_3$ melts

DOI: 10.62053/MHJC2933

J Isaksson[1], A Andersson[2], A Lennartsson[3], F Gyakwaa[4], Q Shu[5] and C Samuelsson[6]

1. Associate Senior Lecturer, Luleå University of Technology, Luleå Sweden 971 87. Email: jenny.isaksson@ltu.se
2. Associate Senior Lecturer, Luleå University of Technology, Luleå Sweden 971 87. Email: anton.andersson@ltu.se
3. Senior Lecturer, Luleå University of Technology, Luleå Sweden 971 87. Email: andreas.lennartsson@ltu.se
4. Postdoc, University of Oulu, Oulu Finland FI-90014. Email: francis.gyakwaa@oulu.fi
5. Professor, University of Oulu, Oulu Finland FI-90014. Email: qifeng.shu@oulu.fi
6. Professor, Luleå University of Technology, Luleå Sweden 971 87. Email: caisa.samuelsson@ltu.se

ABSTRACT

The physico-chemical property, viscosity, is essential for pyrometallurgical processes and influences the settling rate of valuable metal droplets in slag, affecting the metal recovery. The copper slag from smelting furnaces typically contains between 1 and 2 wt per cent Cu, which equals to or is higher than in most sulfidic copper ores mined today, meaning the slag is a valuable resource for copper extraction. A low viscosity is desirable for slag-cleaning through a settling furnace where entrained droplets settle under gravity. One approach to control the viscosity is through the slag composition. The literature has limited data on the correlation between viscosity, slag structure, and optical basicity of iron silicate slag with FeO/SiO_2, CaO, and Al_2O_3 as factors. Therefore, the present study evaluated the influence of these factors on viscosity and correlations with slag structure and optical basicity. The FeO/SiO_2 ratio (at%/at%) and the CaO and Al_2O_3 content were altered in two levels, resulting in a two-level full factorial design with three factors. The study was done by synthesising $FeO–SiO_2–Al_2O_3–CaO–MgO–Cr_2O_3$ melts, followed by water granulation. The melt structure of the samples was analysed with the help of Raman Spectroscopy. The viscosity was then estimated with a high-temperature rheometer using a Mo spindle and crucible. The results showed a correlation between the optical basicity, FeO/SiO_2 ratio, and viscosity, where a high optical basicity and FeO/SiO_2 ratio were beneficial for achieving a low melt viscosity.

INTRODUCTION

The slag viscosity in pyrometallurgical processes is crucial for determining the efficiency of metal extraction. It impacts various aspects of the extraction process, including tapping and handling of the slag (Bellemans *et al*, 2018) to mass and heat transfer (Kucharski, Stubina and Toguri, 1989), refractory life, freeze lining on a water-cooled reactor (Bellemans, Zietsman and Verbeken, 2022; Nagraj *et al*, 2022), the kinetics of slag-metal reactions (Viswanathan *et al*, 2001), and the settling rate of metal-containing droplets in slag (Isaksson *et al*, 2023b; Stokes, 1850). The increasing global demand for copper highlights the significance of raw material efficiency. Copper losses to slag represent a limiting factor, making it crucial to understand and control slag viscosity for optimising pyrometallurgical extraction of metals.

In the context of pyrometallurgical copper extraction, copper is distributed as entrained droplets and dissolved copper in the slag matrix. The entrained droplets can be recovered through slag cleaning operations, including a settling furnace where droplets settle under gravity. Slag from copper smelting furnaces usually contains the oxides FeO and SiO_2, along with smaller amounts of Al_2O_3, CaO, MgO, and minor elements such as Cu, As, Sb, Sn, and Pb. Al_2O_3, CaO, and MgO are introduced to the process through the concentrate feeds, flux materials, other additives, or through the dissolution of the refractory material. Additionally, Al_2O_3 is introduced to the processes via recycling of, eg waste electrical and electronic equipment (Mostaghel *et al*, 2013). The presence of these components affects the phase equilibria and the distribution of components between the gas, slag, matte, and solid oxide phases. This is particularly important in a slag cleaning process, including settling, as the copper distributed as dissolved copper in the slag matrix limits the recovery.

Sineva *et al* (2020) showed through an equilibrium study that Al_2O_3, CaO, and MgO reduced the copper concentrations in the slag in a Cu-Fe-O-S-Si-Al-Ca-Mg system. This means that modifications of the slag can decrease the dissolved copper content, which enhances the recovery as part of the dissolved copper becomes entrained. Isaksson *et al* (2023b) showed that the industrial CaO modification of slag increased the copper recovery in a settling process. The improvement was attributed to decreased viscosity, increased copper droplet sizes, and decreased copper solubility. The viscosity influences the settling rate of entrained copper in slag, where a lower viscosity benefits a high settling rate. The impact of FeO/SiO_2, Al_2O_3, and CaO on viscosity in copper smelting slag is thus of interest for pyrometallurgical processes associated with copper extraction. Reduced copper losses enhance raw material efficiency, leading to a more sustainable extraction.

Moreover, the slag viscosity depends on the temperature, atmosphere, composition, and melt structure. The structure of silicate-based melts is affected by: (i) the degree of polymerisation of the silicate network, (ii) the fitting of certain cations, eg Al^{3+}, and (iii) the nature of network-breaking cations, eg Ca^{2+} and Mg^{2+} (Mills, 1993). In addition, the melt structure can be described with a basicity index, taking the relevant oxides in a smelting slag from copper extraction into account, namely the optical basicity. The optical basicity is calculated with Equations 1 and 2.

$$\Lambda = \sum_{i=1}^{n} \Lambda_i N_i \quad (1)$$

$$\mathrm{N_i} = \frac{x_i n_i}{\sum_{i=1}^{n} x_i n_i} \quad (2)$$

where:

Λ is the optical basicity of the melt

Λ_i is the optical basicity of the component i

N_i the equivalent fraction of oxide i in the melt

x_i the mole fraction of component i in the melt

n_i is the number of oxygen atoms in oxide i

Duffy (1989) introduced the measure of optical basicity to metallurgical slags and showed that the optical basicity of various oxides could be calculated from Pauling electronegativities. Duffy and Ingram (1992) presented values of the optical basicity, and the relevant values for this paper are presented in Table 1.

TABLE 1

Optical basicities of individual oxides (Duffy and Ingram, 1992).

Oxide	Optical basicity
CaO	1
FeO	1
MgO	0.78
Al_2O_3	0.60
SiO_2	0.48
Cr_2O_3	0.8

Building on this idea, the present study investigated the influence of optical basicity on the slag viscosity and structure of melts related to pyrometallurgical copper extraction. It involved measuring the high-temperature viscosity of the synthetic $FeO\text{-}SiO_2\text{-}Al_2O_3\text{-}CaO\text{-}MgO\text{-}Cr_2O_3$ melts and analysing the structure of granulated samples with varying FeO/SiO_2 ratios, Al_2O_3 content and CaO content. The study contributes insight into the correlation between optical basicity, viscosity and melt structure. The obtained information can be used industrially to obtain smooth pyrometallurgical operations focusing on slag handling and improving slag cleaning, including a settling process. A decreased copper content in the slag will increase the efficiency of raw materials.

EXPERIMENTAL

The influence of composition and optical basicity on viscosity and melt structure was estimated in a two-level full-factorial design of experiments with the factors Al_2O_3 and CaO content and the FeO/SiO_2 ratio. The targeted sample compositions, FeO/SiO_2 ratio and the calculated optical basicity are shown in Table 2. The valence state of iron was not analysed and assumed to be present as FeO. Chromium(III) oxide was included in the system as it is present in the slag related to the pyrometallurgical extraction of copper. Chromium comes into the process with, eg electronic scrap and refractories and is a nucleation agent in the slag, forming chromium-rich spinels (Isaksson *et al*, 2021; Lennartsson *et al*, 2015). Solid phases in a melt increase the viscosity (Wright *et al*, 2000; Zhen, Zhang and Chou 2015), and thus, chromium was determined to be an essential component to include for a more accurate reflection of the industrial slag viscosity.

TABLE 2

FeO/SiO_2 ratio, optical basicity and sample compositions.

Sample no	FeO/SiO_2 (at%/at%)	Optical basicity	FeO (at%)	SiO_2 (at%)	CaO (at%)	Al_2O_3 (at%)	MgO (at%)	Cr_2O_3 (at%)
1L	1.08	0.665	49.83	45.99	1.2	1.4	1.5	0.08
2L	1.08	0.660	47.95	44.27	1.2	5	1.5	0.08
3L	1.08	0.689	44.21	40.81	12	1.4	1.5	0.08
4L	1.08	0.684	42.34	39.08	12	5	1.5	0.08
1H	1.25	0.682	53.25	42.59	1.2	1.4	1.5	0.08
2H	1.25	0.676	51.23	40.99	1.2	5	1.5	0.08
3H	1.25	0.706	47.23	37.79	12	1.4	1.5	0.08
4H	1.25	0.699	45.23	36.19	12	5	1.5	0.08

Sample preparation

The slag samples of the experimental matrix were synthesised using the reagent-grade chemicals Fe, Fe_2O_3, SiO_2, $CaCO_3$, MgO, and Cr_2O_3. The dry chemicals were mixed, packed in Fe crucibles (>99.82 per cent Fe), and melted in a Ruhstrat resistance furnace in an inert atmosphere using N_2 (99.996 per cent) and Ar (99.999 per cent) with a flow rate of 12 L/hr and 3 L/hr respectively. Fe was used as a crucible material during the synthesis to provide an oxygen buffer to the system that would approach Fe-FeO conditions (Mysen and Richet, 2018). The Fe crucible thus ensures that a partial pressure of oxygen relevant to iron silicate slags undergoing a zinc-fuming process is attained during the synthesis (Andersson *et al*, 2023a).

The material was heated at 10 K/min until the temperature reached 100 K above the calculated liquidus temperature using the Equilib module of FactSage 8.2 (Bale *et al*, 2016) and the database GTOx. The melt was held at the temperature for one hr, removed manually from the furnace, and granulated in water jets with cold tap water at a flow rate of 1.1 L/s. Andersson *et al* (2023b) have published additional information about the granulation procedure.

Rheological measurements

The rheological measurements were performed using the rotating cylinder technique and a Mo spindle and crucible (tzm molybdenum 364). The rheometer system was an Anton Paar High Temperature Viscometer and Furnace Rheometer System (FRS 1800). More details about the rheometer can be found in a previous study (Isaksson *et al*, 2023a). The temperature registered during the viscosity measurements was measured with a B-type thermocouple positioned in a hollow Al_2O_3 shaft holding the crucible, approximately 5 mm from the bottom of the melt. Ar (99.999 per cent) was introduced into the furnace via the crucible shaft, using a constant flow rate of 2.5 L/min. Figure 1 illustrates the rheometer employed in the experiments.

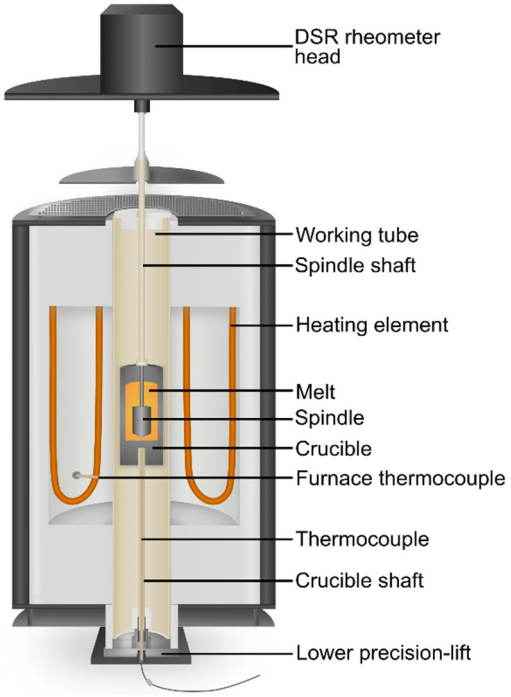

FIG 1 – Schematic overview of the rheometer set-up.

The spindle was lowered when the heating started and descended continuously as the material melted until it reached the measuring position, 9 mm above the crucible bottom. The viscosity was measured during the cooling cycle every 50 K starting at 1723 K. Before viscosity measurement at a specific temperature started, the furnace was held at the target temperature for at least 45 min while rotating the spindle (shear rate of 4 1/s). This was done to reach a homogeneous temperature in the melt. A constant viscosity at a fixed shear rate indicated that the melt had homogenised. An automated program measured the viscosity with different constant shear rates of 1, 2, 4, 8, and 16 1/s. When the measurements were finalised, the samples were cooled with the natural cooling of the furnace while maintaining the Ar atmosphere.

Raman spectroscopy

A representative sample of the granulated materials was ground using a ring mill. X-ray diffraction (XRD) was used to estimate if the samples were amorphous. The scans were performed with a Malvern Panalytical Empyrean X-ray diffractometer (Malvern Panalytical, Malvern, UK) operating on copper K_α generated at 45 kV and 40 mA. The scans were performed between 10 and 90 °2θ. The refinement was performed using HighScore+ and the FIZ Karlsruhe inorganic crystal structure database.

The ground samples were also analysed using Raman spectroscopy to determine the melt structure and the influence of FeO/SiO_2 ratio, Al_2O_3 and CaO. The Raman spectra of samples were collected in the 100–2000 cm^{-1} spectral range by a confocal micro-Raman spectrometer from B&W Tek (Plainsboro, US) with an excitation wavelength of 532 nm. Spectra were deconvolved by fitting the peaks corresponding to vibrations of various structural units using Gaussian line shapes (Mysen *et al*, 1982). The full widths of half maximum (FWHM) of various peaks were fixed to reduce the uncertainty of deconvolution.

RESULTS AND DISCUSSION

Viscosity measurements

The viscosity measured at 1723 K and 1673 K are presented in Table 3 and plotted against the optical basicity in Figure 2. Overall, the viscosity for each composition increased with decreasing temperature. An increased temperature means increased kinetic energy in the melt, which increases

the random motions of atoms and molecules, facilitating the migration of particles, and decreasing the internal friction in the fluid and, thus, the viscosity.

TABLE 3

Viscosity data obtained at 1723 K and 1673 K.

Sample no	Viscosity (Pa·S)	
	1723 K	1673 K
1L	0.132	0.16
2L	0.160	0.204
3L	0.074	0.091
4L	0.089	0.111
1H	0.089	0.111
2H	0.108	0.134
3H	0.055	0.067
4H	0.073	0.089

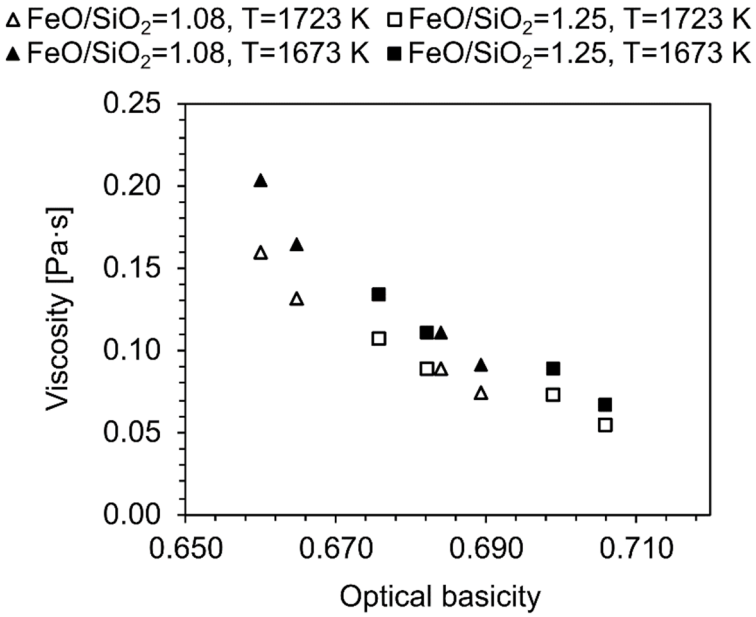

FIG 2 – Viscosity at 1723 K and 1673 K plotted against optical basicity.

The melt contains mainly iron and silica, where silica forms a silicate network. Molten silicate oxide systems consist of three-dimensional networks of SiO_4^{4-} tetrahedra where there are three types of oxygen: (1) bridging, (2) non-bridging, and (3) free oxygen (Mysen, 2003). The covalent bond between the silicon and oxygen atoms in the silicate network is resistant to motion, meaning a high silicate content has higher internal friction and, thus, higher viscosity. Adding basic oxides to the melt decreases the viscosity as the cat ion breaks the covalent bond between the silicon and oxygen atom, resulting in non-bridging oxygen or free oxygen in the structure and a more depolymerised slag. Optical basicity is an index of the amount of basic and acidic components within a system. The results showed that the viscosity decreased when increasing the optical basicity of the melt. At lower temperatures (1623–1423 K), the effect of optical basicity on viscosity remained but became more pronounced.

Evaluating the effect of the factors individually, it was concluded that CaO had the most significant effect on the viscosity, followed by the FeO/SiO_2 ratio. The effect of CaO addition on the viscosity has been examined with similar results, where the viscosity decreased with the CaO addition (Ducret

and Rankin, 2002; Kaiura, Toguri and Marchant, 1977; Selivanov *et al*, 2015; Shen *et al*, 2019; Yan *et al*, 2019; Zhang *et al*, 2019), which supports the effect of CaO on viscosity in this study.

The melt with a high FeO/SiO_2 ratio and a high CaO and Al_2O_3 content has the second-highest optical basicity. However, it can be seen that the viscosity is deviating from the trend, with a higher viscosity than expected. The explanation is that Al_2O_3 can act as a network-forming oxide in the melt structure, meaning the increased Al_2O_3 content increases the melt viscosity. When Al_2O_3 acts as a network-forming oxide, it connects to free oxygen in the melt, forming the tetrahedra (AlO_4^{-5}). These findings align with the study by Mostaghel *et al* (2013), which investigated the impact of Al_2O_3 additions on viscosity in an industrial iron silicate slag. Their results showed an increase in viscosity corresponding to higher Al_2O_3 content. Park, Park and Sohn (2011) demonstrated the amphoteric behaviour of Al_2O_3 while examining the influence of Fe/SiO_2 ratio and Al_2O_3 content on viscosity in a FeO_t-Al_2O_3-SiO_2 system. The results indicated an initial increase in viscosity with the addition of Al_2O_3, reaching a minimum before rising at higher Al_2O_3 concentrations. This behaviour was attributed to the amphoteric behaviour of Al_2O_3, wherein it initially acts as a basic oxide and shifts to an acidic oxide with the changes in slag composition (Park, Park and Sohn, 2011).

The lowest viscosity was obtained when the FeO/SiO_2 ratio and CaO content were high and the Al_2O_3 content was low. From an industrial perspective aiming for a slag with low viscosity, it is beneficial to operate with lower SiO_2 additions to obtain a higher FeO/SiO_2 ratio and to modify the slag with CaO, contributing to a higher optical basicity of the slag.

Raman spectroscopy

The XRD analysis confirmed that the slags were predominantly amorphous. However, in samples 1L and 2H, a peak corresponding to cristobalite was detected, and a peak corresponding to spinel was detected in samples 3H and 4H. The Raman spectra were analysed to characterise the water-granulated slag structure. The collected Raman spectra had envelopes in the medium frequency range (400–800 1/cm) and high frequency (800–1200 1/cm). The Raman bands within medium frequency correspond to the bending vibration of the oxygen bridge Si(Fe)-O-Si(Fe). The high-frequency envelopes were deconvoluted into individual bands by assuming a Gaussian line shape. This study adopts Q^n to represent the structural unit of the symmetric stretching band of (SiO_4^{4-}) tetrahedra, where n represents the number of bridging oxygen in the tetrahedra. Q^n is generally available in the silicate structure as monomer silicate units (Q^0), dimer silicate units (Q^1), chain-like silicate structures (Q^2) and sheet-like silicate structures (Q^3).

The high-frequency envelope can be deconvolved by the bands from stretching vibrations of Q^0 with a Raman shift of 810–830 1/cm (Baert *et al*, 2011; Mysen, Seifert and Virgo, 1980; Mysen *et al*, 1982; Nayak and Desa, 2018), Q^1 with a Raman shift 880–910 1/cm, Q^2 with a Raman Shift 970–990 1/cm and Q^3 with a Raman shift 1030–1060 1/cm (Baert *et al*, 2011; Kashio *et al*, 1979; Li, Shu and Chou, 2014; Mysen, Seifert and Virgo, 1980; Mysen, Virgo and Scarfe, 1980; Mysen *et al*, 1982; Nayak and Desa, 2018; Park, 2012; Wang, Shu and Chou, 2011).

An example of the deconvolution results (sample 1L) is shown in Figure 3. The areas of individual peaks were calculated, and the relative percentages of Q^0, Q^1, Q^2 and Q^3 in various samples were calculated from areas of corresponding peaks and shown in Table 4. It can be seen that Q^0 and Q^1 are the most abundant structural units in the samples, which means that the silicate network in the melt structure of the samples was largely depolymerised.

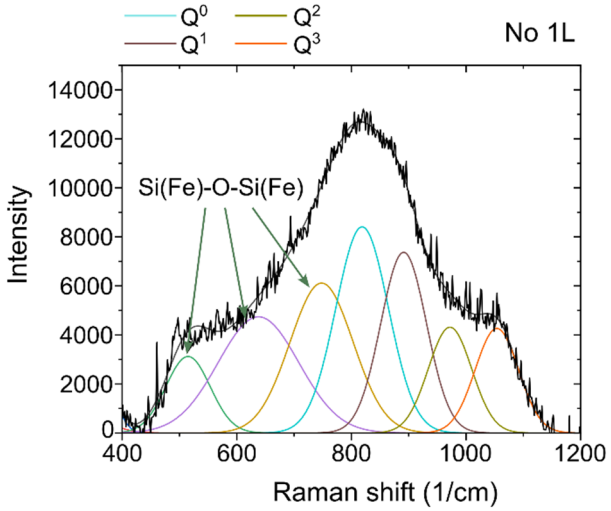

FIG 3 – The deconvolution results of sample 1L.

TABLE 4

Relative percentages of Q^0, Q^1, Q^2, Q^3.

Sample no	Relative percentages				Q^0/Q^1
	Q^0	Q^1	Q^2	Q^3	
1L	0.42	0.29	0.13	0.16	1.44
2L	0.42	0.28	0.14	0.16	1.48
3L	0.46	0.23	0.12	0.18	1.97
4L	0.49	0.23	0.08	0.19	2.11
1H	0.43	0.27	0.13	0.17	1.61
2H	0.43	0.26	0.15	0.16	1.64
3H	0.51	0.24	0.09	0.16	2.08
4H	0.50	0.23	0.10	0.18	2.19

Q^0/Q^1 ratios for various samples illustrate the variation of depolymerisation in the structure of slags with composition and are also listed in Table 4. The effects of FeO/SiO_2 ratios and additions of Al_2O_3 and CaO on structures of slags were investigated through calculated Q^0/Q^1 ratios. The samples with the same number but different letters can be compared to determine the effect of the FeO/SiO_2 ratio on the Q^0/Q^1 ratios, showing that a higher FeO/SiO_2 ratio leads to higher Q^0/Q^1 ratios, and thus a more depolymerised slag. For example, the Q^0/Q^1 ratios increased from 1.44 in 1L (low FeO/SiO_2 ratio) to 1.61 in 1H (high FeO/SiO_2 ratio), indicating that the 1H was more depolymerised. The effect of the FeO/SiO_2 ratio on the depolymerisation of the melt was in accordance with the study by Wang *et al* (2022).

The same data can be correlated to the viscosity measurements, where the samples with a higher FeO/SiO_2 had a significantly lower viscosity. These correlations confirm that a higher FeO/SiO_2 ratio leads to more depolymerised slag, decreasing the viscosity of the melt. The bond between silicon and oxygen is covalent, which is relatively resistant to motions; breaking this bond means that the internal friction in the material decreases, leading to lower viscosity.

Samples 3 and 4 (both L and H) have higher CaO contents than samples 1 and 2 (L and H). As seen in Table 4, the Q^0/Q^1 ratios for samples with a high CaO content are significantly higher than those with low CaO content. For example, 1L and 3L have the same composition besides the CaO content, which is higher in 3L. The Q^0/Q^1 ratio increases from 1.44 in 1L to 1.97 in 3L, indicating that the slag was more depolymerised in 3L. This indicates that CaO behaves as a network modifying oxide to

depolymerise network structure. The depolymerisation effect on the viscosity was also confirmed, where the sample with higher CaO content had a lower viscosity.

For Al_2O_3, the content is higher in the even samples (2 and 4); when comparing the Q^0/Q^1 ratios, it indicates that Al_2O_3 (up to 5 at%) has a minor effect on the structure of the slag. However, the Q^0/Q^1 ratios were consistently higher when the Al_2O_3 content was higher, indicating that the melt structure became depolymerised when the Al_2O_3 content increased. The opposite trend was observed when comparing this data with the viscosity measurements. The viscosity was higher when the Al_2O_3 content was higher, indicating that Al_2O_3 acts as a network-forming oxide in the melt. One explanation for the decreased Q^0/Q^1 ratios may be because the increased content of Al_2O_3 reduces the absolute amount of SiO_2 in the samples, thus decreasing the relative amount of SiO_4^{4-} in the melt.

CONCLUSIONS

The present study investigated the correlation between optical basicity, viscosity, and the melt structure in a FeO-SiO_2-Al_2O_3-CaO-MgO-Cr_2O_3 system. The influence of the basicity was estimated in a two-level full-factorial design of experiments with the factors Al_2O_3 and CaO content and the FeO/SiO_2 ratio. Based on the experimental results, the following was concluded:

- The viscosity was lower in the melts with a higher optical basicity. A high FeO/SiO_2 ratio of 1.25 (at%/at%) and a high content of CaO was beneficial for obtaining a low viscosity. A higher content of Al_2O_3 (5 at%) increased the viscosity.
- The samples with a higher FeO/SiO_2 ratio resulted in a more depolymerised slag than those with a lower ratio (1.08 at%/at%). The samples with a higher CaO and Al_2O_3 content also resulted in a more depolymerised slag (higher Q^0/Q^1), according to the results from the Raman spectra. This indicates that the current analysis does not fully explain the melt structure when the Al_2O_3 content is higher.

The results from this study support the correlation between optical basicity, where samples with a higher optical basicity resulted in a more depolymerised slag with a lower viscosity. Indicating that optical basicity can be used as an index for the melt viscosity of FeO-SiO_2-Al_2O_3-CaO-MgO-Cr_2O_3 melts.

ACKNOWLEDGEMENTS

The present work was conducted in collaboration with Boliden through Bolidenpaketet and within the Center of Advanced Mining and Metallurgy (CAMM) at Luleå University of Technology, Sweden.

REFERENCES

Andersson, A, Brander, L, Lennartsson, A, Roos, Å and Engström, F, 2023a. A Method for Synthesizing Iron Silicate Slags to Evaluate Their Performance as Supplementary Cementitious Materials, *Applied Sciences*, 13(14):8357.

Andersson, A, Isaksson, J, Lennartsson, A and Engström, F, 2023b. Insights into the Valorization of Electric Arc Furnace Slags as Supplementary Cementitious Materials, *Journal of Sustainable Metallurgy*, pp 1–14.

Baert, K, Meulebroeck, W, Wouters, H, Cosyns, P, Nys, K, Thienpont, H and Terryn, H, 2011. Using Raman spectroscopy as a tool for the detection of iron in glass, *Journal of Raman Spectroscopy*, 42:1789–1795.

Bale, C W, Bélisle, E, Chartrand, P, Decterov, S A, Eriksson, G, Gheribi, A E, Hack, K, Jung, I H, Kang, Y B, Melançon, J, Pelton, A D, Petersen, S, Robelin, C, Sangster, J, Spencer, P and Van Ende, A D, 2016. FactSage Thermochemical Software and Databases, 2010–2016, *CALPHAD*, 54:35–53.

Bellemans, I, Cnockaert, V, De Wilde, E, Moelans, N and Verbeken, K, 2018. Metal Droplet Entrainment by Solid Particles in Slags: An Experimental Approach, *Journal of Sustainable Metallurgy*, 4:15–32.

Bellemans, I, Zietsman, J and Verbeken, K, 2022. Fundamental and Formation Aspects of Slag Freeze Linings: A Review, *Journal of Sustainable Metallurgy*, 8:64–90.

Ducret, A C and Rankin, W J, 2002. Liquidus temperatures and viscosities of FeO-Fe_2O_3-SiO_2-CaO-MgO slags at compositions relevant to nickel matte smelting, *Scandinavian Journal of Metallurgy*, 31:59–67.

Duffy, J A and Ingram, M D, 1992. Comments on the application of optical basicity to glass, *Journal of Non-Crystalline Solids*,144:76–80.

Duffy, J A, 1989. A common optical basicity scale for oxide and fluoride glasses, *Journal of Non-Crystalline Solids*, 109:35–39.

Isaksson, J, Andersson, A, Lennartsson, A and Samuelsson, C, 2023a. Interactions of Crucible Materials With an FeO_x–SiO_2–Al_2O_3 Melt and Their Influence on Viscosity Measurements, *Metallurgical and Materials Transactions B,* 54:3526–3541.

Isaksson, J, Andersson, A, Vikström, T, Lennartsson, A and Samuelsson, C, 2023b. Improved Settling Mechanisms of an Industrial Copper Smelting Slag by CaO Modification, *Journal of Sustainable Metallurgy*, 9:1378–1389.

Isaksson, J, Vikström, T, Lennartsson, A and Samuelsson, C, 2021. Influence of Process Parameters on Copper Content in Reduced Iron Silicate Slag in a Settling Furnace, *Metals*, 11:1–15.

Kaiura, G H, Toguri, J M and Marchant, G, 1977. Viscosity of Fayalite-Based Slags, *Canadian Metallurgical Quarterly* 16:156–160.

Kashio, S, Iguchi, Y, Goto, T, Nishina, Y and Fuwa, T, 1979. Raman Spectroscopic Study on the Structure of Silicate Slag, *Transactions ISIJ,* 20:251–253.

Kucharski, M, Stubina, N M and Toguri, J M, 1989. Viscosity measurements of molten Fe-O-SiO_2, Fe-O-CaO-SiO_2 and Fe-O-MgO-SiO_2 slags, *Canadian Metallurgical Quarterly*, 28:7–11.

Lennartsson, A, Engström, F, Björkman, B and Samuelsson, C, 2015. Characterisation of buildup in an electric furnace for smelting copper concentrate, *Canadian Metallurgical Quarterly*, 54:477–484.

Li, J, Shu, Q and Chou, K, 2014. Structural Study of Glassy CaO-SiO_2-CaF_2-TiO_2 Slags by Raman Spectroscopy and MAS-NMR, *ISIJ International*, 54:721–727.

Mills, K C, 1993. The Influence of Structure on the Physico-chemical Properties of Slags, *ISIJ International*, 33:148–155.

Mostaghel, S, Matsushita, T, Samuelsson, C, Björkman, B and Seetharaman, S, 2013. Influence of alumina on physical properties of an industrial zinc-copper smelting slag: Part 1 - viscosity, *Mineral Processing and Extractive Metallurgy*, 122:42–48.

Mysen, B and Richet, P, 2018. *Silicate Glasses and Melts*, 2nd ed, Elsevier.

Mysen, B, 2003. Physics and chemistry of silicate glasses and melts, *European Journal of Mineralogy*, 15:781–802.

Mysen, B, Finger, L, Virgo, D and Seifert, F, 1982. Curve-fitting of Raman spectra of silicate glasses, *American Mineralogist*, 67:686–695.

Mysen, B, Seifert, F and Virgo, D, 1980a. Structure and redox equilibria of iron-bearing silicate melts, *American Mineralogist*, 65:867–884.

Mysen, B, Virgo, D and Scarfe, C, 1980b. Relations between the anionic structure and viscosity of silicate melts - a Raman spectroscopic study, *American Mineralogist*, 65:690–710.

Nagraj, S, Chintinne, M, Guo, M and Blanpain, B, 2022. Investigation of Bath/Freeze Lining Interface Temperature Based on the Rheology of the Slag, *JOM,* 74:274–282.

Nayak, M T and Desa, J A E, 2018. Roles of iron and lithium in silicate glasses by Raman spectroscopy, *Journal of Raman Spectroscopy*, 49:1507–1513.

Park, H-S, Park, S S and Sohn, I, 2011. The Viscous Behavior of FeO_t-Al_2O_3-SiO_2 Copper Smelting Slags, *Metallurgical and Materials Transactions B,* 42:692–699.

Park, J H, 2012. Structure-property correlations of CaO-SiO_2-MnO slag derived from Raman spectroscopy, *ISIJ International*, 52:1627–1636.

Selivanov, E, Gulyaeva, R, Istomin, S, Belyaev, V, Tyushnyakov, S and Bykov, A, 2015. Viscosity and thermal properties of slag in the process of autogenous smelting of copper-zinc concentrates, *Mineral Processing and Extractive Metallurgy*, 124:88–95.

Shen, Y, Chong, J, Huang, Z, Tian, J, Zhang, W, Tang, X, Ding, W and Du, X, 2019. Viscosity and structure of a CaO-SiO_2-FeO-MgO system during a modified process from nickel slag by CaO, *Materials* 12:1–16.

Sineva, S, Fallah-Mehrjardi, A, Hidayat, T, Hayes, P C and Jak, E, 2020. Experimental Study of the Individual Effects of Al_2O_3, CaO and MgO on Gas/Slag/Matte/Spinel Equilibria in Cu-Fe-O-S-Si-Al-Ca-Mg System at 1473 K (1200 °C) and p(SO_2) = 0.25 atm, *Journal of Phase Equilibria and Diffusion*, 41:859–869.

Stokes, G G, 1850. On the Effects of the Internal Friction of Fluids on the Motion of Pendulums, *Transactions of the Cambridge Philosophical Society*, 9:75–129.

Viswanathan, N N, Ji, F Z, Sichen, D and Seetharaman, S, 2001. Viscosity measurements on some fayalite slags, *ISIJ International*, 41:722–727.

Wang, B, Yang, H, Jin, Z, Liu, Z and Zou, M, 2022. Effect of Fe/SiO_2 Ratio and Fe_2O_3 on the Viscosity and Slag Structure of Copper-Smelting Slags, *Metals*, 12:1–18.

Wang, Z, Shu, Q and Chou, K, 2011. Structure of $CaO-B_2O_3-SiO_2-TiO_2$ Glasses: a Raman Spectral Study, *ISIJ International*, 51:1021–1027.

Wright, S, Zhang, L, Sun, S and Jahanshahi, S, 2000. Viscosity of a $CaO-MgO-Al_2O_3-SiO_2$ Melt Containing Spinel Particles at 1646 K, *Metallurgical and Materials Transactions B,* 31:97–104.

Yan, Z, Reddy, R G, Lv, X, Pang, Z and Bai, C, 2019. Viscosity of Iron Oxide Aluminosilicate Melts, *Metallurgical and Materials Transactions B,* 50:251–261.

Zhang, H, Fu, L, Qi, J and Xuan, W, 2019. Physicochemical Properties of the Molten Iron-Rich Slags Related to the Copper Recovery, *Metallurgical and Materials Transactions B,* 50:1852–1861.

Zhen, Y L, Zhang, G H and Chou, K C, 2015. Viscosity of $CaO-MgO-Al_2O_3-SiO_2-TiO_2$ Melts Containing TiC Particles, *Metallurgical and Materials Transactions B,* 46:155–161.

Viscosity measurement of $FeO\text{-}SiO_2$ based slags under controlled oxygen partial pressures

DOI: 10.62053/LYVJ9833

H-R Lee[1], H Shin[2], S-C Shim[3] and Y Kang[4]

1. Research Engineer, YoungPoong Corp., Ansan-si Gyeonggi-do 15904, South Korea. Email: hyeran9322@ypzinc.co.kr
2. Graduate student, Dong-A University, Saha-gu Busan 49315, South Korea. Email: tlsgusdn001109@gmail.com
3. Research Professor, Dong-A University, Saha-gu Busan 49315, South Korea. Email: skjihu@dau.ac.kr
4. Professor, Dong-A University, Saha-gu Busan 49315, South Korea. Email: youngjok@dau.ac.kr

ABSTRACT

Since iron oxide and silicon oxide are major gangue components in various types of ore, $FeO\text{-}SiO_2$ base slag, ie fayalite slag, has been often encountered in pyrometallurgical processes of non-ferrous metals. During most matte production processes such as the smelting of Cu, Pb, and Ni, the $FeO\text{-}SiO_2$ based slag is inevitably formed and plays an important role in refining crude metal as well as engineering aspects. Recently, similar pyrometallurgical approaches have been attempted in the recovery of valuable metals (Ni, Co, Cr) from wasted secondary batteries. Thus, the viscosity of the $FeO\text{-}SiO_2$ based slag has great significance in properly controlling smelting processes. However, when molten metal or matte does not coexist with the slag during the measurement, there has been a serious difficulty in maintaining Fe valance and consequently, the slag composition.

In the present research, the viscosity of molten $FeO\text{-}SiO_2$ slag was measured in 1573~1673 K using a rotational viscometer. In order to keep the state of iron oxides, the oxygen partial pressure was controlled using CO/CO_2 gas mixture. The optimised ratio of CO/CO_2 could be calculated using Fe/Fe^{2+} and Fe^{2+}/Fe^{3+} equilibria at each temperature. The composition of the slag, particularly Fe valance, after the measurement was analysed with the aid of an inductively coupled plasma – optical emission spectroscopy (ICP-OES) and an automatic potentiometric titrator. The measurement showed that the $FeO\text{-}SiO_2$ slag has considerably low viscosity values in the molten state, and it sharply increases as the temperature decreases. In spite of the careful oxygen partial pressure control, a part of Fe^{2+} was found to be oxidised to Fe^{3+}, with a maximal case reaching about 20 per cent. The increase in viscosity of $FeO\text{-}SiO_2$ at low temperatures can be attributed to the composition change due to an unavoidable Fe^{2+} oxidation. In addition, the relationship between the change in the viscosity and the liquidus temperature of $FeO\text{-}SiO_2$ based slag was discussed to understand the composition dependence of viscosity.

INTRODUCTION

$FeO\text{-}SiO_2$ based slag, ie fayalite slag, plays an important role in many non-ferrous metallurgical processes because most types of ores contain a considerable amount of iron oxide and silicon oxide. While the molten matte phase is formed in the smelting process of non-ferrous metals such as Cu, Pb, and Ni, gangue components and the oxidation of Fe in ore cause the formation of $FeO\text{-}SiO_2$ based slag. Not only to the smelting ores, similar pyrometallurgical approaches can be applied but also to the recovery of valuable metals (Ni, Co, Cr) from wasted secondary batteries. Moreover, the Ni-based compounds attract great interest as one of the most important raw materials for cathode active material in secondary batteries, as the demand for electric vehicles abruptly increases. In fact, there are commercialised smelting production processes of Ni-based compounds, an example of which is shown in Figure 1 (Sohn, 2021).

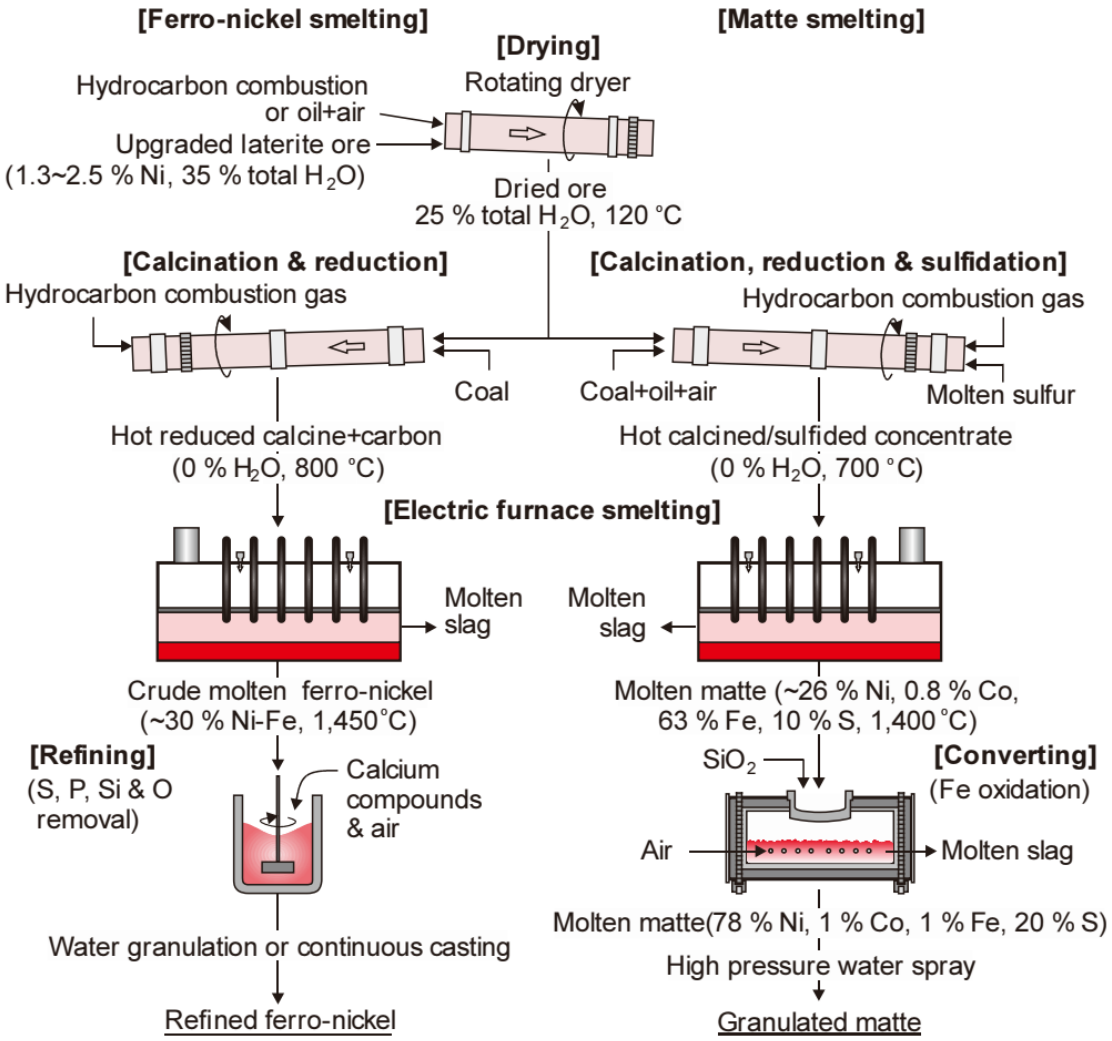

FIG 1 – Process flow chart of FeNi and Ni matte production from Ni ore.

In the existing manufacturing process, Ni matte is manufactured through Fe removal and Ni sulfurisation in the combination of a rotary kiln and an electric arc furnace. And further refining is carried out in the Pierce-Smith, PS converter. During the process, a large amount of FeO-SiO_2 based slag is generated and its composition can be dynamically varied with the operational conditions. For successful smelting processes, the physical properties of the FeO-SiO_2 based slag should be carefully controlled. Among them, the viscosity of molten slag has the most important impact on the performance of smelting processes. However, when molten metal or matte does not coexist with the FeO-SiO_2 based slag during the measurement, there has been serious difficulty in maintaining Fe valance and the slag composition. Thus, in the present study, the viscosity measurement of FeO-SiO_2 based slag was carried out using a rotational viscometer. Throughout the measurement, the oxygen partial pressure was controlled using CO/CO_2 gas mixture.

EXPERIMENTAL

Sample preparation and viscosity measurement

The composition for the measurement was chosen considering the liquid region at the temperature range for the measurement. Liquidus temperatures at each composition are presented as coloured circles shown in the FeO-SiO_2 binary phase diagram in Figure 2. Their detailed compositions in which the ratio of FeO/SiO_2 varies from 1.6 to 3.2 are also tabulated along with the phase diagram. Though the premelting of the slag was omitted to minimise undesirable oxidation of Fe, the synthetic FeO was separately prepared by sintering Fe powder and reagent grade Fe_2O_3 powder. They were

well mixed so that the molar ratio of Fe:O is 1:1 and the mixture in an iron crucible was held at 1373 K in Ar atmosphere for at least 7 hrs.

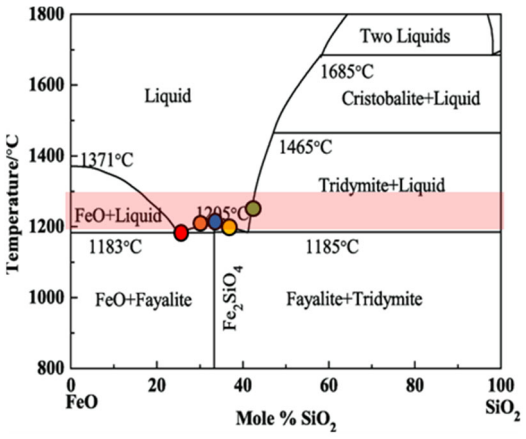

No.	FeO	SiO_2	FeO/SiO_2
1	77.3	22.7	3.4
2	72.2	27.8	2.6
3	**69.7**	**30.3**	**2.3**
4	66.7	33.3	2.0
5	61.5	38.5	1.6

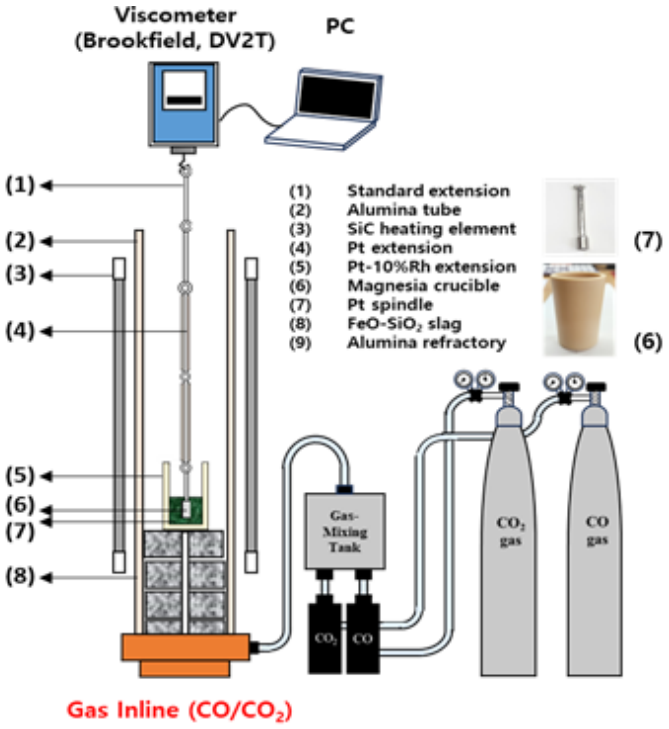

FIG 2 – Slag compositions and schematic apparatus for the viscosity measurement.

The prepared FeO was inserted in a MgO crucible along with reagent-grade SiO_2 to be predetermined compositions, and the sample was heated in a furnace equipped SiC heating elements. After the slag sample in was completely melted over 1573 K, a platinum spindle was carefully inserted at the centre of the sample. And the spindle was connected using Pt-Rh rods to a rotational viscometer (DV-2T, Brookfield, MA, USA) on the top of the furnace. While rotating the spindle at a certain rev/min, the torque level was continuously measured, and the viscosity value could be estimated by the inter-relationship, which had been determined in advance using the viscosity standard solutions. Throughout the entire measurement procedure, well-controlled CO/CO_2 mixture gas flow was used to maintain the state of Fe in molten slag. The apparatus for the measurement is schematically presented in Figure 2.

Control of oxygen partial pressure

Due to the nature of the viscosity measurement method, it is difficult to completely avoid the influence of oxygen in the atmosphere. Thus, an optimised reducing atmosphere condition is required to inhibit the oxidation of FeO. At the same time, however, it is also necessary to take care of excessive reduction of FeO, which may damage the platinum spindle. For precise control of oxygen partial pressure, the CO/CO_2 gas mixture was utilised. An appropriate ratio range of CO/CO_2 could be determined by considering FeO/Fe_2O_3 as well as Fe/FeO equilibrium. Using the reactions and the equilibrium constants for those equilibria shown below, the acceptable range of oxygen partial pressure in the temperature range in the present measurement could be obtained as shown in Figure 3. According to the desirable oxygen partial pressure, the ratio of CO/CO_2 mixing ratio was controlled in the range of about 0.5~1.9.

$$Fe + \frac{1}{2}O_2 = FeO \qquad 2FeO + \frac{1}{2}O_2 = Fe_2O_3$$

$$\Delta G^\circ = \Delta H^\circ - T\Delta S^\circ = -RT\ln K \qquad \Delta G^\circ = \Delta H^\circ - T\Delta S^\circ = -RT\ln K$$

$$K = \frac{a_{FeO}}{a_{Fe} \cdot P_{O_2}^{1/2}} \qquad K = \frac{a_{Fe_2O_3}}{a_{FeO}^2 \times P_{O_2}^{1/2}}$$

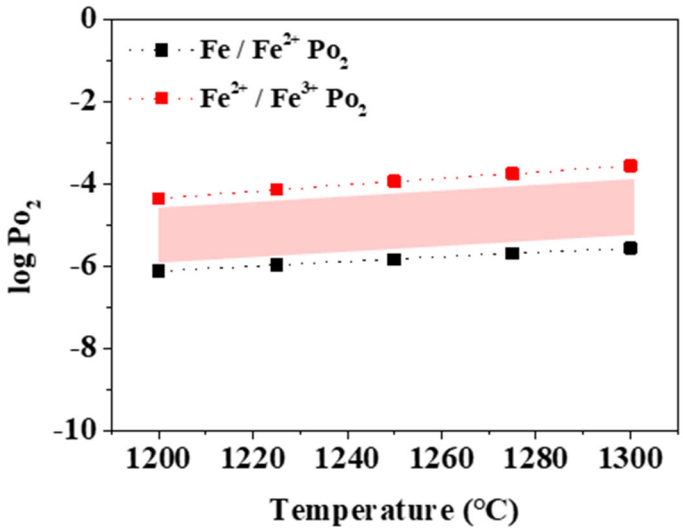

FIG 3 – Range of oxygen partial pressure for maintaining the state of Fe in molten slag.

RESULTS AND DISCUSSION

Viscosity of molten FeO-SiO_2 slag

The results of the viscosity measurement of molten FeO-SiO_2 slag are shown as a function of temperature in Figure 4 with the previous studies (Kaiura, Toguri and Marchant, 1977; Shiraishi *et al*, 1978; Viswanathan *et al*, 2001; Shi *et al*, 2016; M-S Seo, personal communications, 2022; unpublished results) The viscosity measurements at 1573 K were possible in all compositions, and the viscosity values in the present study showed good agreement with the other results. As the temperature further lowered, the viscosity showed a sudden increase, which sometimes caused the measurement failure due to the sudden increase in torque at a lower temperature. Compared with the previous studies, the viscosity value in the present study starts to increase at a rather higher temperature, which may be caused by crystallisation in molten slag.

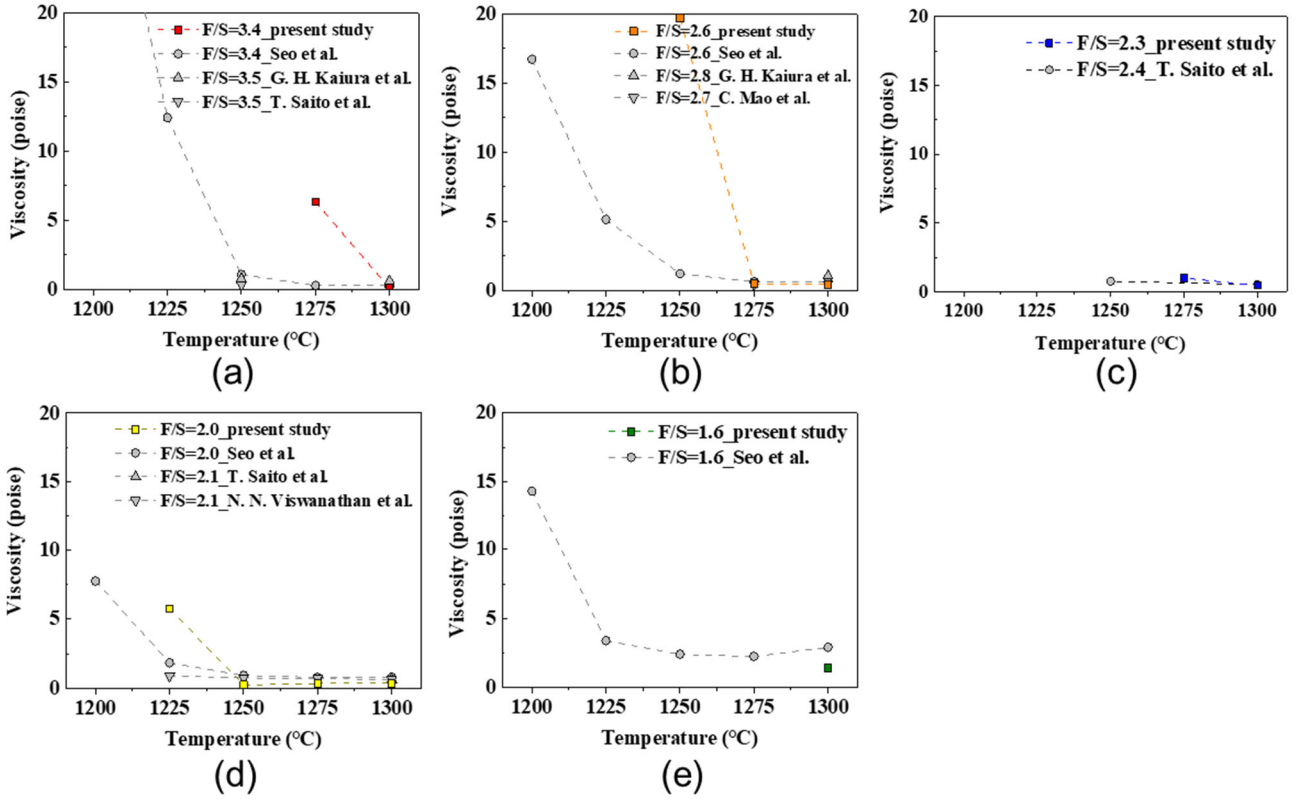

FIG 4 – Viscosity of FeO-SiO_2 slag as a function of temperature with various FeO/SiO_2 ratio (a) 3.4, (b) 2.6, (c) 2.3, (d) 2.0, (e) 1.6.

For the verification of the viscosity measurement in the present study, it was attempted to calculate the viscosity of FeO-SiO_2 based slag using thermodynamic calculation software, FactSage™ ver 8.1 (by Thermfact Ltd.), which is based on the Quasi-Chemical model. It was found that the estimated viscosity value is much lower than the measured values not only in the present study but also in the previous studies. According to the estimation, the viscosity is no more than 2.0 poise even at the lowest temperature, 1473 K. Regarding the disagreement, additional discussion may be needed.

At a constant temperature, the viscosity initially has shown a decreasing tendency as the FeO/SiO_2 ratio decreases, and it increases again when the FeO/SiO_2 ratio is lower than 2.0, which may infer that there are a local minimum and a local maximum value within the present composition range. In order to clarify the effect of composition on the viscosity of molten slag, the results of viscosity measurements at 1573 K are shown in Figure 5 as a function of the SiO_2 concentration. The viscosity of molten FeO-SiO_2 based slag showed a local maximum when the FeO/SiO_2 ratio is 2.3 and the corresponding SiO_2 concentration is about 30 per cent. After a slight decrease at 2.0 of FeO/SiO_2 ratio, the viscosity tends to increase rapidly when the SiO_2 concentration is larger than 34 per cent with a smaller FeO/SiO_2 ratio. A similar tendency of viscosity with the local minimum and the local maximum can be confirmed as shown in Figure 6. This composition dependence may be attributed to the change in liquidus temperature in the corresponding composition range of the FeO-SiO_2 binary system.

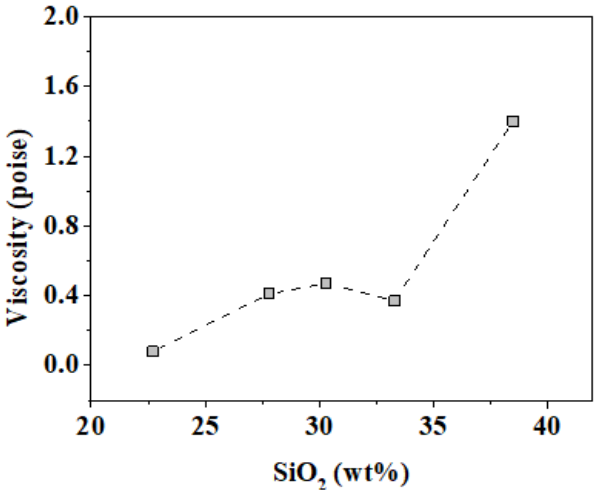

FIG 5 – Viscosity of FeO-SiO_2 slag as a function of SiO_2 concentration at 1573 K.

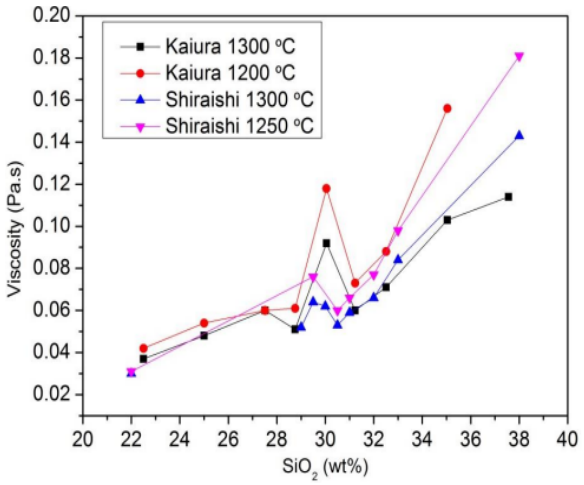

FIG 6 – Viscosity of FeO-SiO_2 slag as a function of SiO_2 concentration (Shi *et al*, 2016).

Change in the composition of slag during the measurement

In order to examine the reason why the viscosity in the present study was relatively high compared to the previously reported viscosity measurement results, the change in the composition of the molten slag during viscosity measurement was examined. Due to the nature of the measurement method, the inside of the furnace is maintained in a relatively reducing atmosphere, but the slight opening for the spindle to rotate may allow oxygen in the atmosphere to penetrate so that some amount of Fe_2O_3 can be generated. In addition, there is a possibility that the concentration of MgO in the slag will increase under the circumstance of melting in MgO crucibles.

To confirm the degree of composition change after measurement, the slag in the molten state was suctioned with a quartz tube and quantitatively analysed. The composition changes of FeO-SiO_2 molten slag are summarised in Table 1 and presented in Figure 7. As shown in the table, the oxidation of FeO to a certain extent was confirmed. When the ratio of FeO/SiO_2 is sufficiently high, the oxidation of FeO could reach up to 20 per cent. On the other hand, the oxidation of FeO gradually decreased with the decrease in the FeO/SiO_2 ratio, and it was estimated that it exists in about 10 per cent based on the amount of formed Fe_3O_4. After the viscosity measurement, the concentration of MgO in the slags also increased to about 4~5 per cent level on average and up to close to 7 per cent level after the viscosity measurement, which is judged to be due to dissolution from the MgO crucible, and it was confirmed that the dissolution tendency of MgO did not heavily change depending on the slag composition. Therefore, in considering the viscosity of FeO-SiO_2 binary molten slag, it is necessary to consider changes in composition during measurement.

TABLE 1

Comparison of the compositions before and after the viscosity measurement.

FeO/SiO_2		FeO (wt%)	SiO_2 (wt%)	Fe_2O_3/Fe_3O_4 (wt%)	MgO (wt%)	FeO/SiO_2
3.4	aimed	77.30	22.70	-	-	3.4
	measured	59.83	18.46	17.25/25.01	4.47	3.2
2.6	aimed	72.20	27.80	-	-	2.6
	measured	54.58	26.34	16.55/24.00	2.53	2.1
2.3	aimed	69.70	30.30	-	-	2.3
	measured	54.39	28.76	10.02/14.53	6.82	1.9
2.0	aimed	66.70	33.30	-	-	2.0
	measured	57.78	30.49	6.81/9.86	4.94	1.9
1.6	aimed	61.50	38.50	-	-	1.6
	measured	52.73	36.56	7.59/11.0	3.12	1.4

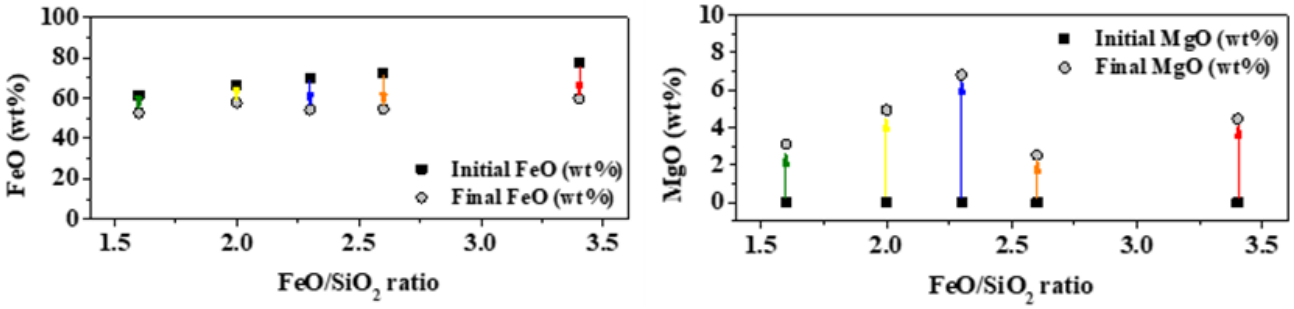

FIG 7 – Changes in FeO and MgO concentration during the viscosity measurement.

Viscosity critical temperature of $FeO\text{-}SiO_2$ based slag

The temperature dependence of the viscosity measured in the present study was found to be somewhat different from the previous measurement results, and in particular, the tendency for the viscosity to rise sharply was confirmed at higher temperatures. Since the melting point (1870 K) of Fe_2O_3 (1838 K) or Fe_3O_4 as a pure material is higher than the melting point (1650 K) of FeO, it can be predicted that the melting point of the slag will increase when Fe_2O_3 is generated in the molten slag. Although the addition of MgO in molten slag usually decreases the liquidus temperature, the SiO_2 (tridymite) saturated liquidus line may shift to the lower SiO_2 side, resulting in an increase in the liquidus point in the present composition range for the viscosity measurement.

The effect of the composition on the liquidus temperature was examined using thermodynamic calculation software, FactSage™ ver 8.1, Thermfact Ltd. to determine how the liquid phase line would change. For the iron oxide phase, when a certain amount of MgO coexists under the condition of mixing FeO and Fe_3O_4, it was confirmed how much the liquidus line can rise compared to the $FeO\text{-}SiO_2$ binary with the initial composition. In Table 2, these liquidus temperatures were also compared to the 'viscosity critical temperature', which can be defined as the temperature at which the viscosity of the molten slag suddenly increases during cooling. The change in the critical temperature and liquidus temperature with various compositions is presented in Figure 8.

TABLE 2

Viscosity critical temperature and liquidus temperature based on the analysed slag composition.

FeO/SiO_2	Viscosity critical temperature	Calculated liquidus temperature
3.4	1573 K	1603 K
2.6	1548 K	1576 K
2.3	1573 K	1623 K
2.0	1523 K	1573 K
1.6	1573 K	1503 K

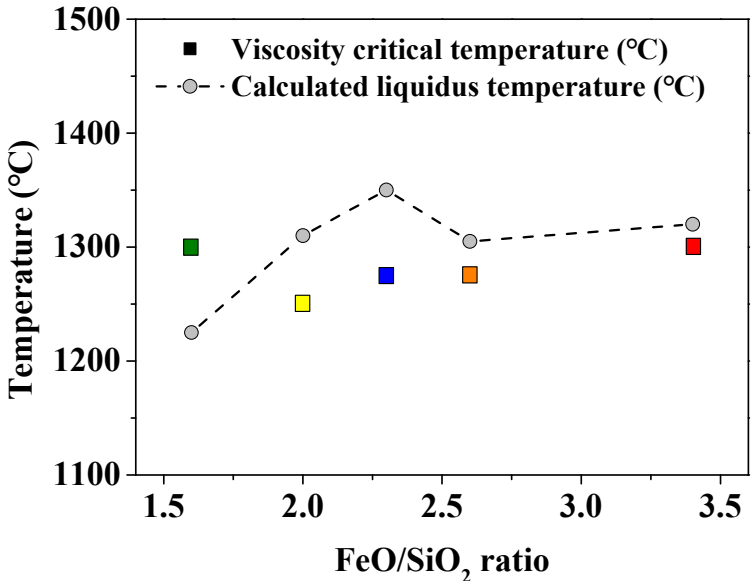

FIG 8 – Change in viscosity critical temperature and liquidus temperature with various FeO/SiO_2 ratio.

CONCLUSIONS

In the present research, the viscosity of molten $FeO\text{-}SiO_2$ slag was measured in 1573~1673 K using a rotational viscometer. In order to keep the state of iron oxides, the oxygen partial pressure was controlled using CO/CO_2 gas mixture. The optimised ratio of CO/CO_2 could be calculated using Fe/Fe^{2+} and Fe^{2+}/Fe^{3+} equilibria at each temperature. The composition of the slag, particularly Fe valance, after the measurement was analysed with the aid of an ICP-OES and an automatic potentiometric titrator. The measurement showed that the $FeO\text{-}SiO_2$ slag has considerably low viscosity values in the molten state, and it sharply increases as the temperature decreases. In spite of the careful oxygen partial pressure control, a part of Fe^{2+} was found to be oxidised to Fe^{3+}, with a maximal case reaching about 20 per cent. The increase in viscosity of $FeO\text{-}SiO_2$ at low temperatures can be attributed to the composition change due to an unavoidable Fe^{2+} oxidation and MgO dissolution from a crucible. In addition, the compositional dependence could be understood using the relationship between the liquidus temperature of $FeO\text{-}SiO_2$ based slag and the viscosity critical temperature, directly related to the change in the viscosity.

ACKNOWLEDGEMENTS

The present work was financially supported by the Research Institute of Industrial Science and Technology, Pohang, Korea. The authors are grateful for valuable advice in the determination of the slag compositions for the viscosity measurement.

REFERENCES

Kaiura, G H, Toguri, J M and Marchant, G, 1977. Viscosity of Fayalite-Based Slags, *Can Metall, Q,* 16(1):156–160.

Shi, H, Chen, L, Malfliet, A, Jones, T P, Blanpain, B and Guo, M, 2016. Rheological Behavior of Fayalite Based Secondary Copper Smelter Slag in Iron Saturation, in *Proceedings of the 10th International Conference on Molten Slags, Fluxes and Salts* 2016. pp 1301–1308 (TMS: Pittsburgh).

Shiraishi, Y, Ikeda, K, Tamura, A and Saito, T, 1978. On the Viscosity and Density of the Molten $FeO–SiO_2$ System, *Trans Jpn Inst Met*, 19(5):264–274.

Sohn, H-S, 2021. Current Status of Nickel Smelting Technology, *Resources Recycling*, 30(2):3–13.

Viswanathan, N N, Ji, F Z, Du, S and Seetharaman, S, 2001. Viscosity Measurements on Some Fayalite Slags, *ISIJ Int*, 41(7):722–727.

Study on change in mould slag characteristics during casting Ti containing steel grades

DOI: 10.62053/HFQB7016

P P Sahoo[1], M Ranjan[2], P Palai[3] and C R Borra[4]

1. Principal Scientist, R&D, Tata Steel Ltd, Jamshedpur 831001, India. Email: p.sahoo@tatasteel.com
2. Researcher, R&D, Tata Steel Ltd, Jamshedpur 831001, India. Email: mani.ranjan@tatasteel.com
3. Head QA, Tata Steel Ltd, Jamshedpur 831001, India. Email: pabitra.palai@tatasteel.com
4. Assistant Professor, IIT Kharagpur 721302, India. Email: chenna.borra@metal.iitkgp.ac.in

ABSTRACT

Change in mould slag composition during casting of medium alloy steel is caused by the redox reaction between molten steel and mould flux. Mould flux generally contains a certain amount of SiO_2, but elements such as Al, Mn and Ti in high/medium alloy steels reduce SiO_2 in the mould flux, causing remarkable changes in the composition of the mould slag. As a result, the properties of the mould slag change greatly as continuous casting proceeds. This causes casting instability, process abnormality and casting defects. Effect of Ti as an alloying element in steel on mould slag is studied extensively through high temperature laboratory measurements and plant measurements. TiO_2 gets picked up by the mould slag up to 3 per cent during casting a steel grade containing 0.1 per cent Ti. This changes the mould slag composition and results in decreasing the slag viscosity by up to 10 per cent and decreases slag break temperature by 30–40°C.

INTRODUCTION

Mould flux plays many important roles in the continuous casting of steel, including:

- providing insulation to molten steel
- prevents reoxidation of the molten steel
- helps in adsorption of inclusions
- controls mould heat transfer
- ensures lubrication between the mould and solidified shell as described by Mills and Fox (2003) and Mills (2016a).

In order to produce high-quality slabs and realise stable production, it is extremely important to design and use the optimum mould flux that can fulfill these roles based on the molten steel composition and casting conditions. Even if mould fluxes are designed and used, their properties change during casting. For example, as described by Mills (2016b), Rudnizki *et al* (2014) and Wang, Lu and Xiao (2017), the composition change that occurs in the mould flux during casting of high alloy steels such as high Al, high Mn and Ti steel.

Cho *et al* (2017), Kim *et al* (2018) and He *et al* (2019) showed that, composition change of mould flux during casting of high alloy steel is reportedly caused by the reduction reaction between molten steel and mould flux. Mould flux generally contains a certain amount of SiO_2, but elements such as Al and Ti in high alloy steels reduce SiO_2 in the mould flux, causing remarkable changes in the composition of the mould flux. As a result, the properties of the mould flux change greatly as continuous casting proceeds and casting becomes unstable, causing various types of problems and defects. This can be attributed to the mould flux and liquid steel interaction and the reactions are mentioned below:

$$3SiO_2 + 4Al \rightarrow 2Al_2O_3 + 3Si \quad (1)$$

$$3MnO + 2Al \rightarrow Al_2O_3 + 3Mn \quad (2)$$

$$SiO_2 + Ti \rightarrow Si + TiO_2 \quad (3)$$

SiO_2 in the mould flux is continuously reduced by Al and Ti and form Al_2O_3 and TiO_2. In the following study, effect of Ti on mould flux behaviour is reported.

EXPERIMENTATION

Steel grade containing Ti and another steel grade without Ti are chosen for experimentation during continuous casting of steel. The compositions of both steel grades are presented in Table 1.

TABLE 1

Composition of steel used for plant trials.

Steel grade	C	Mn	Al	Si	Ti
Grade 1	0.04	1.2	0.02	0.09	0.1
Grade 2	0.05	0.45	0.02	0.07	0.01

It is ensured that the same mould flux is used during casting of both these steel grades to study the effect of Ti on mould slag properties. Slag samples are collected at the middle of each heat from a casting sequence for both steel grades. Sampling is done carefully by removing the top dry powder layer and sinter layer, so that only liquid slag is collected using a stainless-steel spatula. The collected slag samples are sent for the following analysis after grinding them in a ring mill:

- Chemical analysis using X-ray fluorescence (XRF).
- Hemisphere and flow temperature measurement using a heating microscopy.
- Viscosity and crystallisation temperature measurement using high temperature viscometer.
- Measurement of fluidity using inclined plane test.
- scanning electron microscope - energy dispersive x-ray spectroscopy (SEM-EDS) analysis of mould slag.

RESULTS AND DISCUSSIONS

Change in chemical composition

After collecting mould powder and mould slag, the slag was sent for chemical analysis using XRF. The chemical analysis of mould powder and mould slag are reported in Table 2. We can observe that, in the case of steel grade containing Ti, there is an increase of ~3 per cent of TiO_2 in the mould slag. This increase in TiO_2 can be attributed to Equation 3. Similarly, the MnO pick up in the Ti containing steel grade is higher due to higher Mn in steel.

TABLE 2

Chemical composition of mould slag with only the affected components: (A) Mould Powder, (B) Steel grade without Ti, (C) Steel grade with Ti.

(A)

Composition (wt%)	Fe(T)	CaO	SiO_2	MgO	MnO	Al_2O_3	TiO_2
Mould powder	1.3	32.3	36.4	0.93	0.83	5.1	0.08

(B)

Heat no / (wt%)	Fe(T)	CaO	SiO_2	MgO	MnO	Al_2O_3	TiO_2
Heat 1	1.27	34.6	38.53	0.89	1.65	9.9	0.26
Heat 2	0.92	34.97	38.73	0.97	1.29	9.74	0.27
Heat 3	0.9	37.65	37.78	0.84	1.62	9.43	0.24

(C)

Heat no / (wt%)	Fe(T)	CaO	SiO_2	MgO	MnO	Al_2O_3	TiO_2
Heat 1	1.29	43.68	32.72	1.31	4.03	8.47	**2.74**
Heat 2	1.07	45.22	31.49	1.37	5.17	8.65	**2.34**
Heat 3	1.25	43.08	33.9	1.23	4	7.9	**2.89**

Change in melting characteristics of slag

The melting characteristics of slag are determined using a heating microscope (Model: EM201–15, Hesse instruments). A cylindrical pellet of size 3 mm height and 3 mm diameter is made with pellet making hand press using the fine slag powders. This pellet is then put inside the furnace of the equipment to see the continuous change in its shape and other characteristics while heating the furnace. The images are captured continuously using a CCD camera. A sample image showing the hemisphere temperature and flow temperature of slag is shown in Figure 1. Hemisphere temperature is the melting start temperature which is defined when the pellet start to melting and the height of pellet becomes half of the base width. Flow temperature is defined when the height of the sample shrinks to under a third of the base, it is assumed that the sample has completely liquified and has reached the melting point.

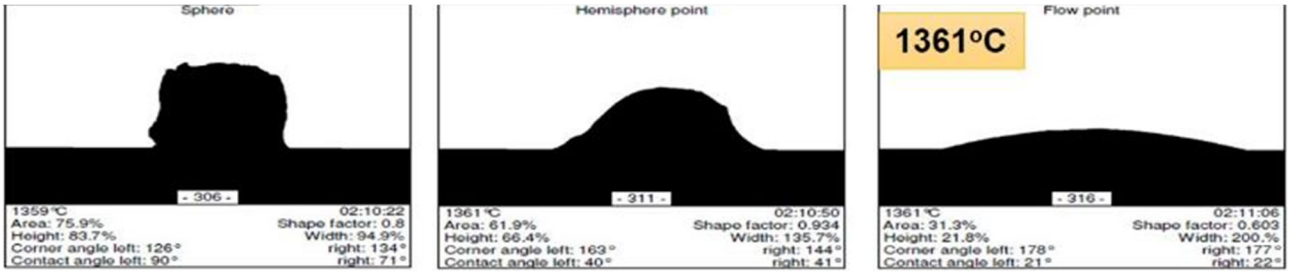

FIG 1 – Determination of hemisphere and flow temperature using heating microscope.

The results of measurement of all slag samples are reported in Table 3. We can observe that the melting/flow temperature of the slag increased by 50–60ºC with increase in TiO_2 content in the slag.

TABLE 3

Change in melting characteristics.

	Hemisphere temp	Flow temp (ºC)
Grades without Ti		
Heat 1	1108.7	1115
Heat 2	1101.6	1112
Heat 3	1109.2	1120
Grades with Ti		
Heat 1	1140	1161
Heat 2	1146	1169
Heat 3	1133	1160

Change in viscosity and crystallisation of the slag

Two the slag samples, one with TiO_2 and one without TiO_2, are subjected to measurement of high temperature viscosity using a high temperature viscometer. The results of viscosity measurement are reported in Figure 2. As we can see, the viscosity of the mould slag decreased by 10 per cent at 1300°C when there is a TiO_2 pick up of about 3 per cent. At the same time the break temperature

falls drastically by 50°C making the slag more glassy. This will increase the heat flux through the mould wall.

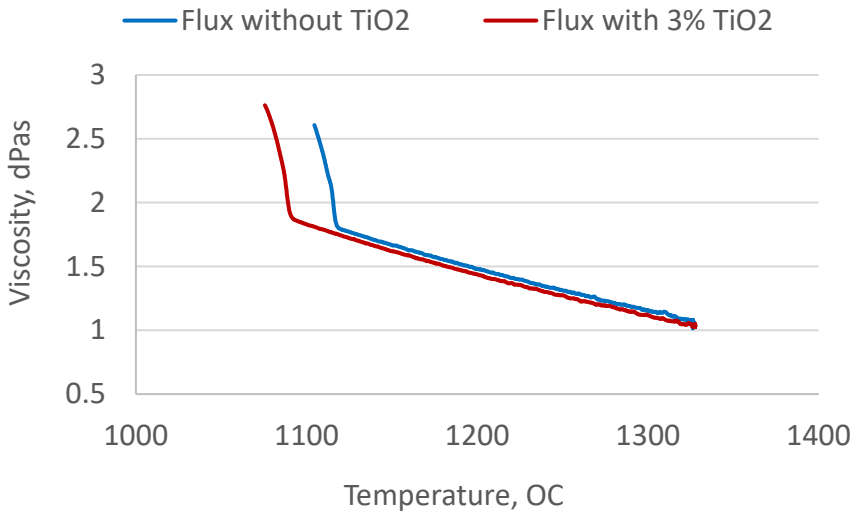

FIG 2 – Viscosity and break temperature of mould slag with and without TiO_2.

Slag microstructure using SEM and EDS

Further analysis of mould slag from the Ti containing steel grade under scanning electron microscope (SEM) proved the formation of secondary phase of Perovskite ($CaTiO_3$) along with Cuspidine ($3CaO.2SiO_2.CaF2$) as shown in Figure 3.

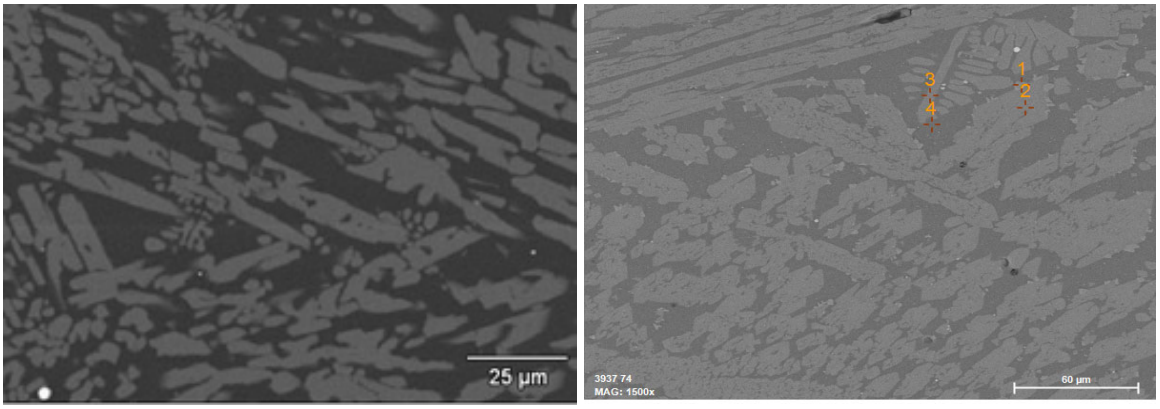

(a) (b)

FIG 3 – Scanning electron microscope - energy dispersive x-ray spectroscopy (SEM-EDS) analysis of Mould slag: (a) showing only cuspidine in non-TiO_2 containing slag, (b) showing Perovskite formation (Point 1), Cuspidine (Point 3 and 4) for Mould slag containing 3 per cent TiO_2.

Change in fluidity of slag

The fluidity of slag is measured using an inclined plane test, where a measured quantity of slag is melted at 1350ºC in a furnace and poured over inclined plane to solidify. The ribbon length is measured which is a measure of its comparative fluidity. The results are reported in Figure 4. As can be seen clearly, the slag with TiO_2 had more ribbon length compared to the slag without TiO_2. This also corroborate the lower viscosity value as shown above for the TiO_2 containing slag.

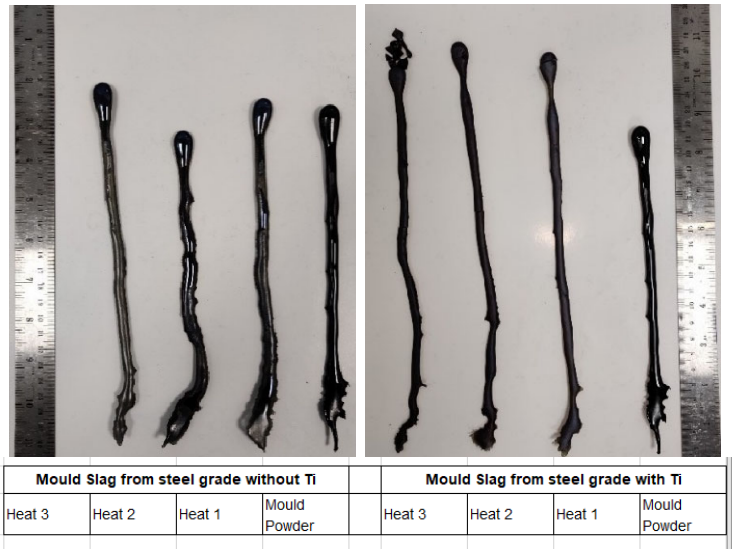

FIG 4 – Fluidity of slag measured using inclined plane test method.

CONCLUSIONS

The following points can be concluded from the above study:

- TiO_2 gets picked up by the mould slag while casting of Ti containing steel grade up to an extent of about 3 per cent when the steel contained 0.1 per cent Ti.
- The melting temperature of mould slag with TiO_2 increases by ~50°C when there is TiO_2 pick up in the slag by 3 per cent.
- TiO_2 in mould slag decreased the slag viscosity by up to 10 per cent and decreased slag break temperature by ~40°C.
- Perovskite phase formation is observed in case of TiO_2 pick up in mould slag.
- This reduces the slag pool depth, hence due to thin glassy slag layer between the mould and the solidifying strand, the heat transfer is high and reflected in the Breakout Detection System.

REFERENCES

Cho, J W, Yoo, S, Park, M S, Park, J K and Moon, K H, 2017. Improvement of castability and surface quality of continuously cast TWIP slabs by molten mould flux feeding technology, *Metallurgical and Materials Transactions B*, 48:187–196.

He, S, Li, Z, Chen, Z, Wu, T and Wang, Q, 2019. Review of Mould Fluxes for Continuous Casting of High-Alloy (Al, Mn, Ti) Steels, *Steel Research International*, 90(1):1800424.

Kim, M S, Park, M S, Kang, S E, Park, J K and Kang, Y B, 2018. A reaction between high Mn–high Al steel and CaO–SiO_2-type molten mould flux: reaction mechanism change by high Al content ([pct Al] 0= 5.2) in the steel and accumulation of reaction product at the reaction interface, *ISIJ International*, 58(4):686–695.

Mills, K C and Fox, A B, 2003. The role of mould fluxes in continuous casting-so simple yet so complex, *ISIJ International*, 43(10):1479–1486.

Mills, K C, 2016a. Structure and properties of slags used in the continuous casting of steel: Part 1 conventional mould powders, *ISIJ International*, 56(1):1–13.

Mills, K C, 2016b. Structure and properties of slags used in the continuous casting of steel: Part 2 specialist mould powders, *ISIJ International*, 56(1):14–23.

Rudnizki, J, Shepherd, R, Balichev, E, Karrasch, S and Krüger, F, 2014. Investigation of Al2O3 pick-up in mould slag during continuous casting of al containing steels, in *Proceedings of the 8th European Continuous Casting Conference (ECCC)*, 23:26.

Wang, W, Lu, B and Xiao, D, 2016. A review of mould flux development for the casting of high-Al steels, *Metallurgical and Materials Transactions B*, 47:384–389.

Ionic structure analysis of relaxed surface of molten oxide slags for surface tension modelling

DOI: 10.62053/KYRU9379
M Suzuki[1]

1. Associate Professor, Osaka University, Suita, Osaka 565-0871, Japan.
   Email: suzuki@mat.eng.osaka-u.ac.jp

ABSTRACT

Although several models for the surface tension of molten oxide slag have been proposed, suitably accurate predictions of this property are not yet possible. The surface tension, or surface excess free energy, of molten oxides is largely determined by the ionic coordination induced by surface relaxation. However, the associated mechanism of surface structural relaxation for molten oxide mixtures such as slag is complex and not yet fully understood. To allow a better evaluation of surface relaxation characteristics, the present work analysed the ionic coordination associated with the surface-relaxed states of several oxide mixtures. This work especially focused on calcium aluminate slags because these materials exhibit complex relationships between composition and surface tension. The effects of incorporating low concentrations of SiO_2 as a surface active component on the surface ionic coordination were also examined. X-ray absorption techniques were used to assess oxygen and cationic elements in glassy samples after surface relaxation treatments, and molecular dynamics simulations based on a polarisable ion model of molten slag with vacuum/melt interfaces were also performed. The X-ray absorption techniques provided data related to electron yields (which are primarily associated with surface features) and fluorescence yields (which evaluate the bulk material). Thus, the ionic coordination characteristics of both regions were investigated. The results of molecular dynamics calculations allowed statistical analysis of the distributions of Al- or Si-centred polymorphs as well as the bond angles between cations and oxygen anions in the vacuum-exposed and bulk regions in the equilibrated melt. The results indicated that bridging oxygen ions were preferentially distributed in the relaxed surface region rather than non-bridging oxygens. These bridging oxygen ions represented vertex connections between AlO_4 or SiO_4 tetrahedra. In the case of the calcium aluminate slags, the addition of one Ca^{2+} ion as charge compensation for two Al^{3+} ions was found to be necessary to form two AlO_4 tetrahedra. This specific feature of surface ionic coordination could be responsible for the complex trends observed in surface tension data. The incorporation of low concentrations of SiO_2 reduced the proportion of tetrahedrally-coordinated Al ions such that higher coordination states become dominant in the bulk of the material, whereas AlO_4 tetrahedra were preferentially distributed in the surface region. SiO_4 tetrahedra were the preferred Si-centred polymorph and were likely connected to one another to form bridging oxygen ions at the surface. On the basis of these results, a model to predict slag surface tension was proposed, and the energy of the formation of the ionic clusters resulting from surface relaxation was taken into account.

INTRODUCTION

Surface tension is one of the most important physical properties of molten slag and can affect interfacial phenomena during the processing of various materials at high temperatures. As an example, the Marangoni flow of slag, which is driven by localised changes in surface tension, can result in the local loss of furnace wall refractory materials by dissolution (Mukai, 1998). The slag-forming behaviour during refining processes is also significantly affected by the surface tension of the molten slag (Luz *et al*, 2018). Hence, it is vital to control surface tension so as to maximise productivity and quality as well as to reduce the cost of maintaining furnace wall materials. This control will, in turn, require an understanding of surface properties, particularly the effect of the slag composition on such parameters.

The surface tension of a liquid is related to the surface free energy per unit area, which can be considered equivalent to the excess energy generated by the incomplete bonding of surface atoms (Tanaka *et al*, 1996). Consequently, surface tension typically increases as the bonding energy between atoms increases. However, this rule cannot be applied to the surface tension properties of molten oxides. As an example, the relationship between the surface tension of a pure molten oxide

at its melting point and the cationic potential ($U = Z/r$; where Z is the valence of the cation and r is the ionic radius of the cation) (King, 1951) does not show a simple trend. MnO, which has a moderate cationic potential, exhibits the highest surface tension among pure molten oxides, whereas SiO_2, with a high cationic potential, shows a low surface tension.

The surface tension of molten oxides strongly depends on the ionic coordination in the surface region induced by surface structural relaxation. In the case of unary oxides, oxygen ions are thought to occupy the surface region because these are larger than the corresponding cations. As such, the coordination between oxygen ions and cations can be modified to decrease the surface excess energy caused by incomplete bonding (Livey and Murray, 1956). However, in molten oxide mixtures such as slags, the surface structural relaxation mechanism is much more complex and is not yet fully understood. Although several models that partially account for surface modification have been proposed for the prediction of the surface tension of ionic melts or molten slag (Tanaka *et al*, 1998; Choi and Lee, 2002), the relationship between surface relaxation and the surface tension of molten slag has not been explored in detail. Hence, the effect of composition on the surface tension of certain oxide systems remains unpredictable. Thus, the precise prediction of surface tension will require more data concerning the surface structural relaxation mechanism in molten oxide slags.

The present work analysed the ionic coordination structures within the surface regions of molten oxide slags, taking into account surface structural relaxation. This work examined two specific cases. First, the surface ionic structure of an Al_2O_3−CaO slag, for which surface tension is minimised at an intermediate composition, was examined. Second, the effect of incorporating a low concentration of SiO_2, a surface active agent, on the surface ionic structure of the Al_2O_3−CaO slag was assessed. Two novel approaches were employed, consisting of soft X-ray absorption spectroscopy to assess oxygen and cationic elements in glassy materials with relaxed surfaces, and molecular dynamics (MD) simulations of oxide mixture melts with vacuum/melt interfaces.

EXPERIMENTAL

X-ray absorption spectroscopy

X-ray absorption near edge structure (XANES) spectroscopy was used to determine the chemical valence values and coordination states of the target elements. In the case of this technique, the surface electrons generate an electrical current that reflects the number of such electrons and is also surface-dependent (providing information to depths of several to tens of nm from the sample surface). In contrast, monitoring the X-ray fluorescence intensity provides information concerning the bulk of the specimen (to depths of more than several tens of μm). Thus, it is possible to separately analyse the coordination states of ions in the surface and bulk regions using these two techniques. Such analyses are normally conducted at room temperature and under a high vacuum to minimise X-ray scattering by gaseous species.

The work reported herein employed oxide glasses instead of high-temperature melts based on the assumption that the surface ionic structure of the glass following structural relaxation would be similar to that of the corresponding melt. During the annealing of a crushed oxide glass sample, relaxation of the surface ionic structure takes place so as to reduce the surface excess energy caused by partially incomplete ionic bonding, similar to the mechanism proposed for the surface relaxation of an ionic melt (Tanaka *et al*, 1998). Table 1 summarises the chemical compositions of the glass samples. Each specimen was prepared by first calcining a special grade chemical of $CaCO_3$ at 1223 K in air overnight to form CaO. Following this, special grades of Al_2O_3 and SiO_2 were combined with this CaO (with all materials in the powdered state), and the mixture was pressed into a pellet by applying a pressure of 10 MPa for 15 min. The resulting pellet was cut into pieces with diameters in the range of 1–2 mm, after which each piece was melted by laser irradiation. This irradiation was performed in conjunction with aerodynamic levitation to enable effective melting of the oxide samples without contamination from the container. The melting step was followed by quenching into a glassy state via rapid cooling. During this process, each slag sample was levitated and melted at 2073–2273 K, subsequently held at 1873–1973 K for 10 min, and then quenched by turning the laser power off. The cooling rate was greater than -500 K/s during the latter stage. The resulting glass samples were annealed at 873 K for 24 hrs to adjust any structural distortion, after which each specimen was crushed into a powder to produce a large surface area with incomplete

surface relaxation. Each glass sample was subsequently annealed again at 873 K for 48 hr to promote surface structural relaxation. The annealing temperature during this step was lower than the glass transition temperature of the material to avoid crystallisation of the sample during the annealing.

TABLE 1

Chemical compositions of the glass samples assessed in the present study.

Sample name	Composition [mol%]		
	Al_2O_3	CaO	SiO_2
A1	30	70	0
A2	36.8	63.2	0
A3	50	50	0
B1	35	60	5
B2	33.2	56.8	10
B3	29.5	50.5	20

The soft X-ray absorption analyses were performed at the Ritsumeikan University SR Centre (Shiga, Japan). The powdered glass samples and the reference materials, including SiO_2 glass, α-Al_2O_3, and Mayenite ($Ca_{12}Al_{14}O_{33}$) crystals, were each separately attached to a pure indium plate on the sample holder to support electrical conduction, after which the holder was placed in a sealed chamber. These preparations were performed in a glovebox under Ar to avoid the absorption of moisture by the specimens. The sample chamber was subsequently attached to the soft X-ray absorption spectroscopy instrumentation, and the analyses were performed under a high vacuum of less than 10^{-6} Pa. The O K-edge XANES spectra were obtained in both the partial electron yield and partial fluorescence yield (PFY) modes using a diffraction grating with 1200 lines/mm. The Al and Si K-edge XANES spectra were obtained in the total electron yield and PFY modes using $KTiOPO_4$ (011) and InSb (111) dispersive crystals. The latest version of the Athena program was employed to draw the background lines using a spline function and to normalise the spectra.

Molecular dynamics simulations

Classical MD calculations based on a polarisable ion model (PIM) were performed to simulate the ionic distributions in the oxide melts, including vacuum/melt interfaces. This PIM evaluated the dipole moment between each ion, $\boldsymbol{\mu_i}$, based on the polarisation parameter α_i and the electric field $\boldsymbol{E_i}$ formed at the position of the focused ion by the charges and dipoles ($\boldsymbol{\mu}_i = \alpha_i \cdot \boldsymbol{E}_i$) (Ishii *et al*, 2016). The potential energy function was decomposed into four parts, comprising the charge, dispersion, repulsion, and polarisation terms, expressed as:

$$\phi_{\mathrm{Total}} = \left(\frac{q_i q_j}{r_{ij}}\right) + \left(-\sum_{i<j}\left[f_6^{ij}\frac{C_6^{ij}}{(r_{ij})^6} + f_8^{ij}\frac{C_8^{ij}}{(r_{ij})^8}\right]\right) + \left(\sum_{i<j} A_{ij}e^{-B_{ij}r_{ij}}\right) + \left(\sum_{i<j}\left[\frac{q_i \boldsymbol{r_{ij}}\cdot\boldsymbol{\mu_j}}{r_{ij}^3}f_4^{ij} - \frac{\boldsymbol{\mu_i}\cdot q_j \boldsymbol{r_{ij}}}{r_{ij}^3}f_4^{ij} + \frac{\boldsymbol{\mu_i}\cdot\boldsymbol{\mu_j}}{r_{ij}^3} - \frac{3(\boldsymbol{r_{ij}}\cdot\boldsymbol{\mu_i})\cdot(\boldsymbol{r_{ij}}\cdot\boldsymbol{\mu_j})}{r_{ij}^5}\right] + \frac{|\boldsymbol{\mu_i}|^2}{2\alpha_i}\right). \quad (1)$$

The polarisation term consists of charge–dipole, and dipole–dipole interactions as well as the energy required to deform the electric fields of ions. The parameters for the PIM force field were determined to reproduce the force and dipole moment acting on each ion, which was calculated using first-principles MD calculations for identical oxide systems in the glassy and molten states.

The computation methodology employed in this work is illustrated in Figure 1. Initially, a cubic cell containing approximately 3000 atoms was held at 2273 K for 30 000 steps (where 1 step = 1 fs) and then equilibrated at 2073 K for 30 000 steps, using a rigid-ion model (RIM) that neglected the polarisation term in the potential energy function. The cell was subsequently equilibrated for 100 000 steps using the PIM so as to achieve a steady value for the total cell energy. Next, the ionic

configuration was extended by a factor of from three to six in one direction, and the system was again equilibrated at 2073 K in the same manner as described above. Following this, vacuum spaces were inserted in the upper and lower sides of the rectangular cell to form vacuum/melt interfaces, and the cell was equilibrated using a RIM and PIM. All these calculations were performed in the *NVT* ensemble and using the program code made by the PIM developer (Ishii *et al*, 2016). Note that, in the present MD simulations, the effects of gas molecules on the surface structure of the oxide melt were regarded as negligible.

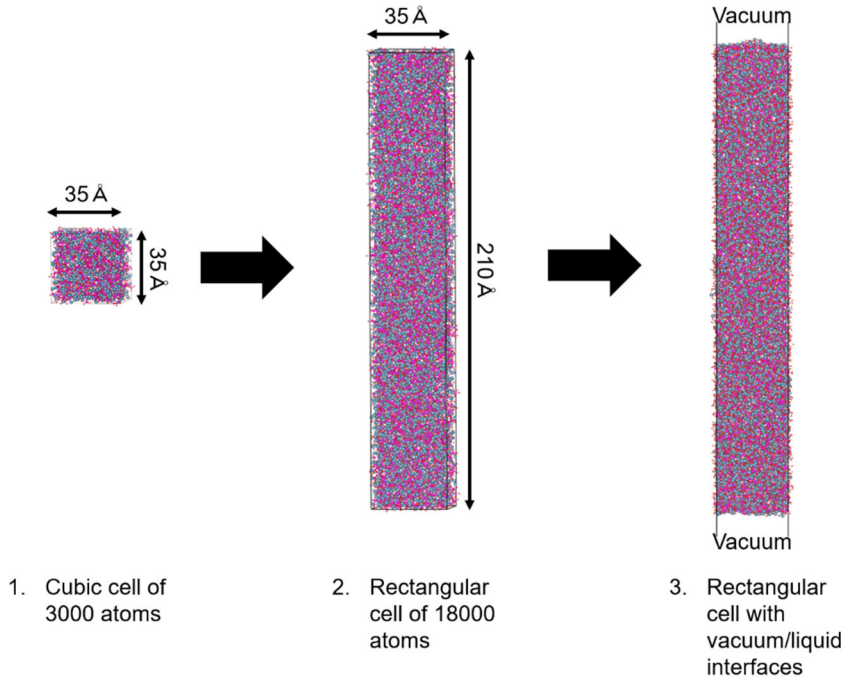

FIG 1 – Schematic diagram summarising the MD simulation procedure.

The ionic coordination between oxygen ions and cations in the equilibrated cell was analysed using the tetrahedral order parameter *q* (Errington and Debenedetti, 2001), calculated according to:

$$q = 1 - \frac{3}{8}\sum_{j=1}^{n-1}\sum_{k=j+1}^{n}\left(\cos\theta_{ijk} + \frac{1}{3}\right)^2 \quad (2)$$

where θ_{ijk} is the angle formed between the central cationic atom, denoted by *j*, and its neighbouring oxygen atoms, denoted by *i* and *k*. The equilibrated rectangular cell with vacuum/liquid interfaces was divided into several layers, each approximately 2 nm in thickness, and the distributions of Si- or Al-centred polymorphs were analysed for the upper and lower layers exposed to the vacuum spaces (corresponding to the surface region) and middle layers (corresponding to the bulk region).

RESULTS AND DISCUSSION

Local structure analyses

Al_2O_3-CaO system

Figure 2a presents the O K-edge XANES spectra obtained from the Al_2O_3–CaO glass samples (A1–A3 in Table 1) after annealing to promote surface structural relaxation. Each of these spectra exhibits two broad absorption peaks (labelled a or a' and b). According to Henderson, Neuville and Cormier (2007), peaks a and a' correspond to Al–O–Ca non-bridging oxygen (Al–NBO), whereas peak b corresponds to Al–O–Al bridging oxygen (Al–BO). Al^{3+} ions in these glasses are thought to have primarily had tetrahedral coordination states. In the case of the surface spectrum, the intensity of the Al–BO peak (that is, peak b) is higher than that of the Al–NBO peak (a'). In the range of 30–50 mol per cent Al_2O_3, this trend becomes more pronounced with increases in the Al_2O_3 content. In contrast, the intensities of these two peaks are comparable in the bulk spectra, and there is no

significant effect of composition. These results indicate that Al–BO was preferentially situated at the surface rather than in the bulk of the glass. For glasses A1 and A2, the positions of the Al–NBO peaks (a') in the surface spectra are negatively shifted relative to those in the bulk spectra (a). This change may have resulted from the differences in oxygen coordination to Ca^{2+} ions between the surface and bulk regions, which in turn was related to the energy required for core electron transitions (Jiang, 2006).

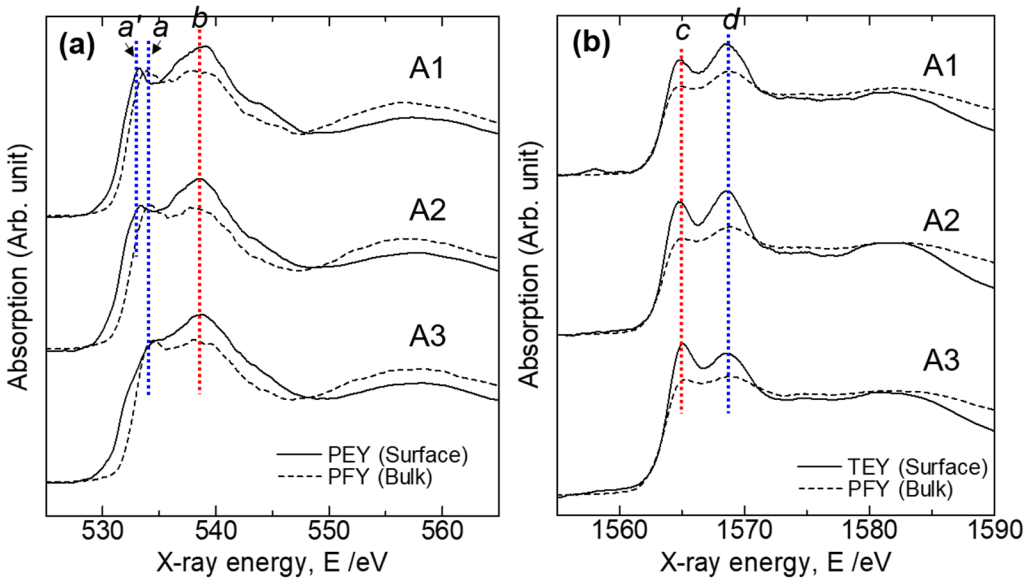

FIG 2 – (a) O K-edge and (b) Al K-edge XANES spectra of Al_2O_3–CaO glass (samples A1–A3) after annealing for surface structural relaxation.

Figure 2b shows the Al K-edge XANES spectra of the Al_2O_3–CaO glass samples after surface structural relaxation. Two absorption peaks (c at 1565 eV and d at 1568 eV) can be seen, corresponding to Al^{3+} cations that are tetrahedrally and octahedrally coordinated with oxygen anions, respectively (Kato *et al*, 2001). In the surface spectra, the intensity of peak c is obviously increased compared with that of peak d as the Al_2O_3 content increases, while the ratio of the c and d peak intensities in the bulk spectra varies only minimally. From these data, it appears that tetrahedral coordination was preferred for Al^{3+} ions in the surface region, particularly with increasing Al_2O_3 content. In this case, BO ions could be formed by the connection of two AlO_4 tetrahedra. However, it should be noted that one Ca^{2+} cation had to be supplied in conjunction with the formation of every two AlO_4 tetrahedra for charge compensation. Therefore, the connection of dual AlO_4 tetrahedra was possible only at intermediate compositions within the Al_2O_3–CaO system.

Al_2O_3-CaO-SiO_2 system

Figure 3a shows the O K-edge XANES spectra of the Al_2O_3–CaO–SiO_2 glass samples (B1–B3) after annealing for surface relaxation. Similar to the results obtained from the Al_2O_3-CaO glass specimens, a negative shift in the NBO absorption peak position in the surface region (e') compared with that in the bulk region (f) is apparent. In the case of the surface spectra, the intensity of the BO absorption peak (f) is higher than that of the NBO peak (e'), regardless of the SiO_2 content. With increases in the SiO_2 content, the location of the BO peak in the surface spectra (f') shifts negatively and approaches the peak corresponding to (Si–O–Si) BO (f'') in the spectrum of the silica glass. This finding demonstrates that Si cations partially contributed to the formation of BO ions in the surface region.

Figure 3b presents the Al K-edge XANES spectra obtained from the Al_2O_3–CaO–SiO_2 glasses after surface structural relaxation. These spectra contain two absorption peaks corresponding to AlO_4 (c) and AlO_6 (d) coordination states. With increases in the SiO_2 content, the intensity of the AlO_4 peak in the surface spectra can be seen to greatly increase and eventually exceed those of the AlO_6 peaks. Thus, it appears that the AlO_4 coordination state was selectively distributed throughout the

surface region when increasing the SiO_2 content. Conversely, the bulk spectra show no change in the intensity ratio of these two peaks.

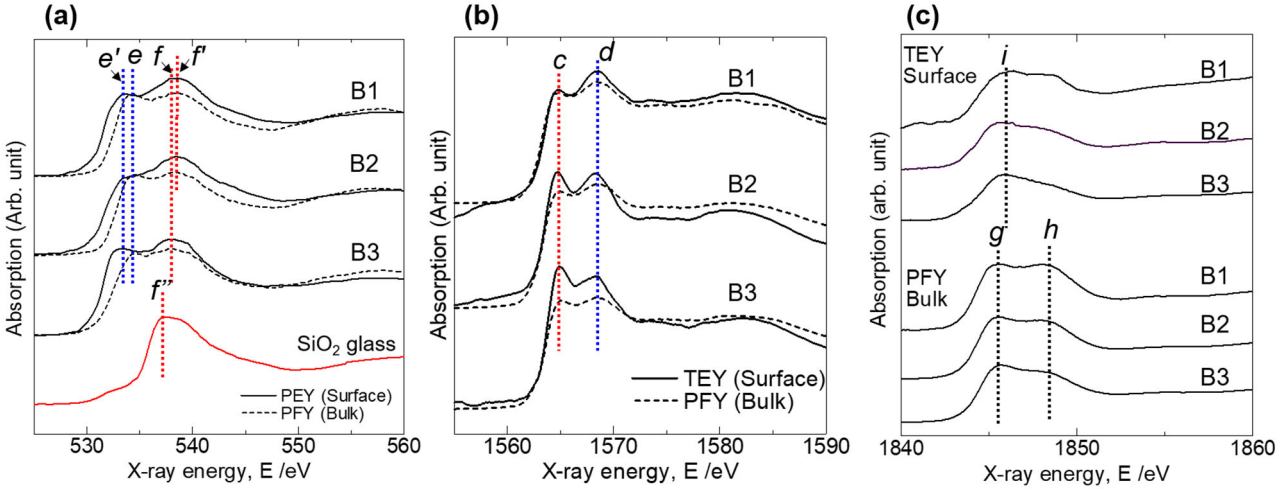

FIG 3 – (a) O K-edge, (b) Al K-edge and (c) Si K-edge XANES spectra obtained from Al_2O_3–CaO–SiO_2 glass specimens (B1–B3) after annealing for surface structural relaxation.

Figure 3c shows the Si K-edge XANES spectra acquired from the Al_2O_3–CaO–SiO_2 glasses after surface structural relaxation. The bulk spectra clearly exhibit two absorption peaks (g and h). The peak g corresponds to that observed for grossular ($Ca_3Al_2[SiO_4]_3$) crystals in which SiO_4 tetrahedra are surrounded by AlO_6 octahedra through NBO (Si^{IV}–O–Al^{VI}). The other peak (h) indicates the presence of octahedrally coordinated Si cations in silicon phosphate (SiP_2O_7). Thus, while SiO_2 was a minor component in these glasses, Si cations evidently had both tetrahedral and octahedral coordination states in the bulk region. In contrast, the surface spectrum shows only one broad absorption peak. As the SiO_2 content was increased, the central peak can be seen to approach the peak (i) associated with anorthite ($CaAl_2Si_2O_8$) crystals, in which SiO_4 tetrahedra are connected to AlO_4 tetrahedra through BO (Si^{IV}–O–Al^{IV}). These results confirm that the dominant coordination state in the surface region changed from Al^{IV}–O–Al^{IV} to Si^{IV}–O–Al^{IV} following the addition of a small amount of SiO_2, although both states involved BO.

MD simulations of ionic configurations

Al_2O_3-CaO system

This study examined melts having the compositions $25Al_2O_3$–75CaO and $50Al_2O_3$–50CaO (mol per cent). Figure 4a shows the distribution of Al-centred polymorphs in different layers throughout an equilibrated cell having vacuum/melt interfaces for the former in the molten state, based on the *q* parameter as expressed in Equation 2. Three different Al–O coordination states (AlO_4, AlO_5, and AlO_6) were identified in this material. The proportion of the AlO_4 coordination state was slightly higher than average in the surface layers, whereas those of the AlO_5 and AlO_6 states were lower. In contrast, the bulk region exhibited a lower proportion of AlO_4 but higher proportions of AlO_5 and AlO_6 than average. These data indicate that tetrahedral coordination was preferred in the surface layer.

Figure 4b summarises the distribution of Al-centred polymorphs in the equilibrated $50Al_2O_3$–50CaO (mol per cent) melt cell with vacuum/melt interfaces. As the Al_2O_3 content was increased, AlO_5 became the dominant coordination state in the bulk layer rather than AlO_4. However, these results clearly demonstrate that AlO_4 was preferentially distributed in the surface layers.

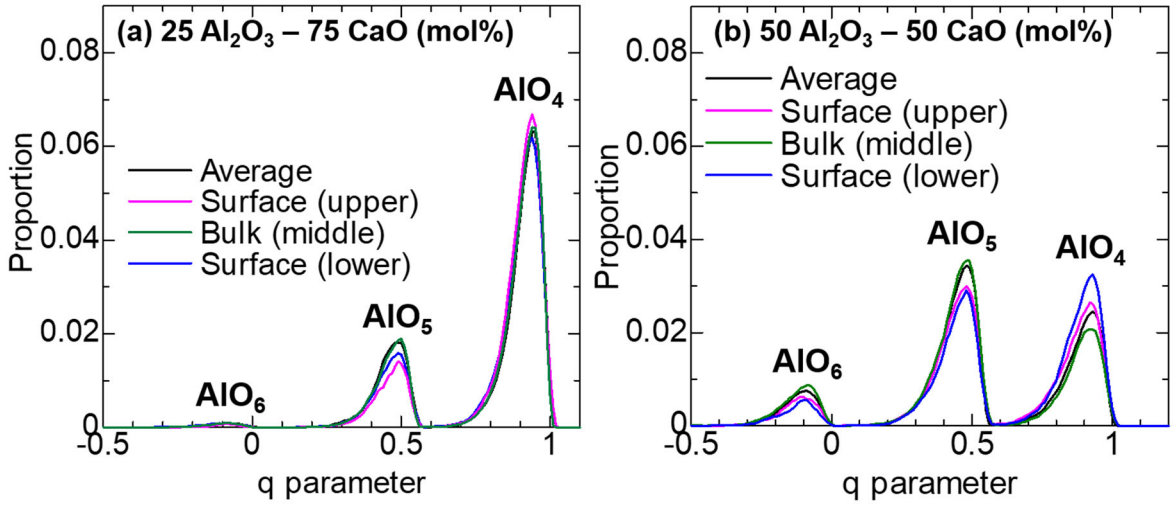

FIG 4 – Distributions of Al-centred polymorphs in the cells of Al_2O_3-CaO melts with vacuum/melt interfaces equilibrated at 2073 K. (a) $25Al_2O_3$–75CaO (mol per cent) and (b) $50Al_2O_3$–50CaO (mol per cent).

Connections among the Al-centred polymorphs were examined by analysing the distributions of Al–O–Al bond angles. Figure 5a shows the result for the $25Al_2O_3$–75CaO (mol per cent) melt, while Figure 5b presents the data for the $50Al_2O_3$–50CaO (mol per cent) melt. In both cases, two broad peaks can be seen. The first, θ_1, is located at approximately 100° and corresponds to the edge connections between pairs of polymorphs via two oxygen anions. The other, θ_2, is situated at approximately 125° and corresponds to vertex connections between pairs of tetrahedra through single BO ions. The surface layers produced a more intense θ_2 peak but a less intense θ_1 peak compared with the averages and the peak intensities obtained from the bulk layer. These data indicate that vertex connections between AlO_4 tetrahedra via single BO ions (Al^{IV}–O–Al^{IV}) were preferentially formed in the surface region.

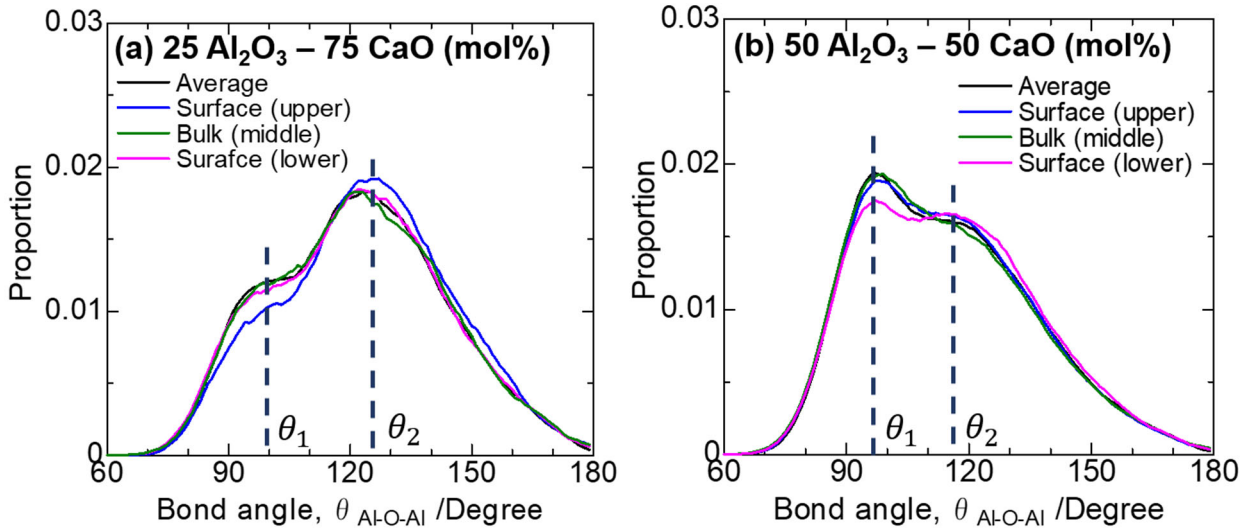

FIG 5 – Distributions of Al–O–Al bond angles in the cells of Al_2O_3-CaO melts with vacuum/melt interfaces equilibrated at 2073 K. (a) $25Al_2O_3$–75CaO (mol per cent) and (b) $50Al_2O_3$–50CaO (mol per cent).

Al_2O_3-CaO-SiO_2 system

Figure 6 summarise the distributions of SiO_n polymorphs in different layers for the trials in which 5 and 20 mol per cent SiO_2 were added to the $37Al_2O_3$–63CaO (mol per cent) melt, respectively. A SiO_2 content of 5 mol per cent generated various types of Si–O coordination, although the octahedral state was dominant. The proportion of SiO_4 tetrahedra was slightly higher in the surface layers,

whereas the amounts of other polymorphs were lower compared with the bulk layer. At a SiO_2 concentration of 20 mol per cent, the SiO_4 tetrahedra became dominant, and no specific differences were observed between the surface and bulk layers.

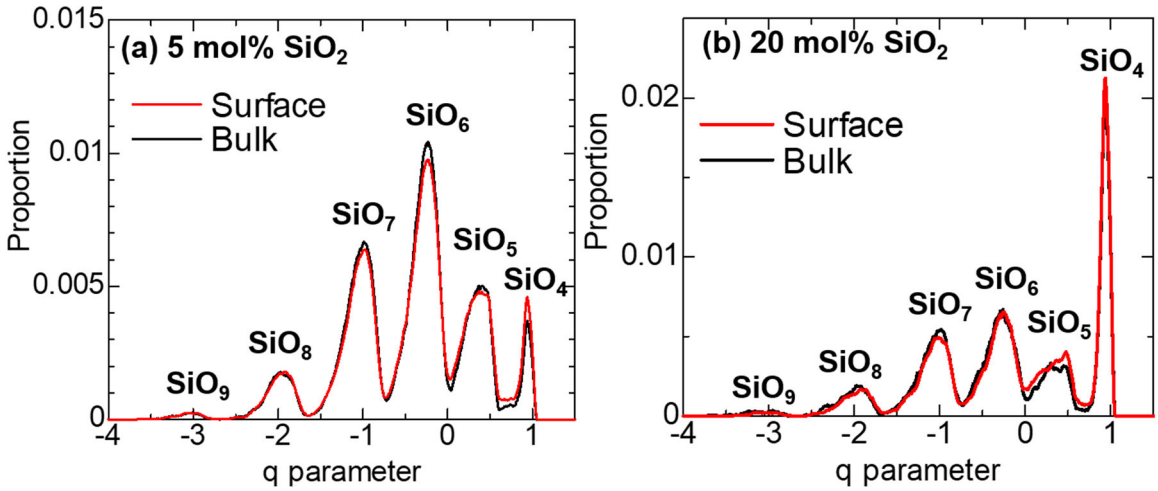

FIG 6 – Distributions of Si-centred polymorphs in the cells of Al_2O_3–CaO–SiO_2 melts with vacuum/melt interfaces equilibrated at 2073 K. (a) 5 mol per cent SiO_2 and (b) 20 mol per cent SiO_2.

The distributions of AlO_n polymorphs in the surface and bulk layers are shown in Figure 7. At a SiO_2 content of 5 mol per cent, the AlO_n distributions in the surface and bulk layers were comparable. However, after the SiO_2 concentration was adjusted to 20 mol per cent, AlO_4 tetrahedra were preferentially located in the surface layer rather than AlO_5 or AlO_6.

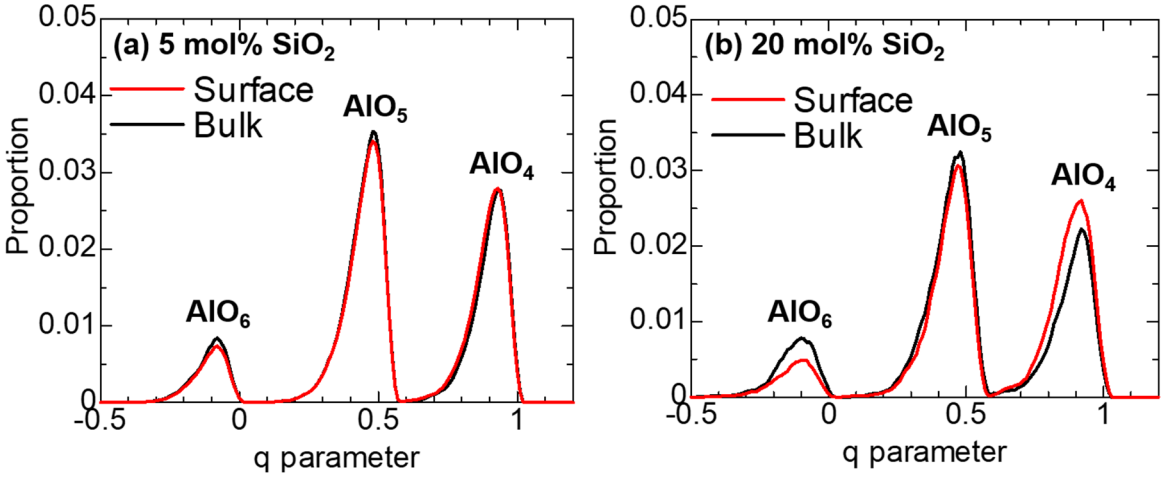

FIG 7 – Distributions of Al-centred polymorphs in the cells of Al_2O_3–CaO–SiO_2 melts with vacuum/melt interfaces equilibrated at 2073 K. (a) 5 mol per cent SiO_2 and (b) 20 mol per cent SiO_2.

Analyses of the connections between Si- and Al-centred polymorphs based on bond angle distributions established that vertex connections between AlO_4 and SiO_4 tetrahedra to form Si^{IV}–O–Al^{IV} units via BO ions were preferentially situated in the surface region in conjunction with SiO_2 concentration of 5 mol per cent. This effect is demonstrated by the greater intensity of the θ_2 peak but lower intensity of the θ_1 peak in the surface region compared with the bulk (see Figure 8a). The above results clearly indicate that the incorporation of a small amount of SiO_2 significantly affected the distribution of AlO_n in the melt. In particular, AlO_4 and SiO_4 tetrahedra were preferentially distributed in the surface region, some of which contributed to the formation of BO ions such as Si^{IV}–O–Si^{IV}, Al^{IV}–O–Si^{IV} and Al^{IV}–O–Al^{IV}. This trend is consistent with the results obtained using XANES spectroscopy to assess the quenched Al_2O_3–CaO–SiO_2 glasses with surface structural relaxation.

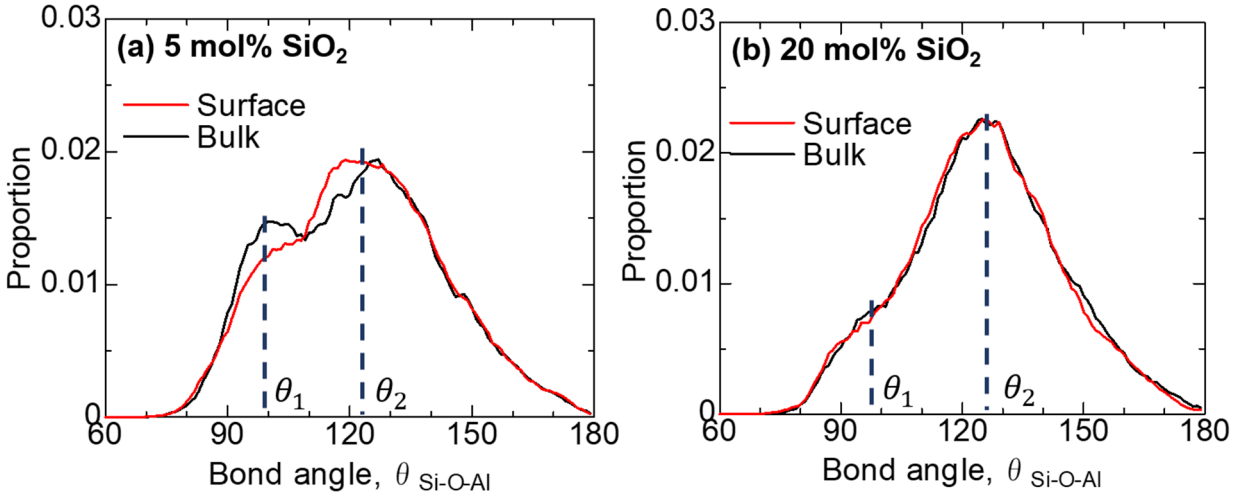

FIG 8 – Distributions of Si–O–Al bond angles in the cells of Al_2O_3-CaO-SiO_2 melts with vacuum/melt interfaces equilibrated at 2073 K. (a) 5 mol per cent SiO_2 and (b) 20 mol per cent SiO_2.

Modelling the surface tension of molten slag

The results obtained from XANES spectroscopy of the glass specimens after surface structural relaxation and the MD simulations of the melt structures with vacuum/melt interfaces both indicated that BO ions were preferentially formed in the surface region. This phenomenon was associated with the selective distribution of AlO_4 or SiO_4 tetrahedra with vertex connections. Because these tetrahedra formed strong covalent bonds with the nearest cations, the distribution of BO ions significantly decreased the surface excess energy, which in turn was related to the surface tension. This trend is believed to explain the surface structural relaxation of molten aluminosilicate slags.

On the basis of the analyses of surface structural relaxation described above, a novel model for predicting the surface tension of molten slag can be proposed. Based on the fundamental equation (Butler, 1932) used to predict the surface tension of a liquid solution, the surface tension of a slag in which oxygen ions are bonded to two different cations *i* and *j* (*i*-O-*j*, described as *ij*) to form structural units can be calculated as:

$$\sigma = \sigma_{ij} + \frac{RT}{A_{ij}} \ln \frac{X_{ij}^{\text{Surface}}}{X_{ij}^{\text{Bulk}}} + \frac{1}{A_{ij}} \left\{ \begin{bmatrix} \text{Difference in energy of formation} \\ \text{of ionic clusters between} \\ \text{surface and bulk regions} \end{bmatrix} + \begin{bmatrix} \text{Difference in energy of energy} \\ \text{of connected chain structures} \\ \text{between surface and bulk} \end{bmatrix} \right\} \quad (3)$$

In the above equation, σ_{ij} is the surface tension of pure component, A_{ij} is the molar area of the melt comprising *i*-O-*j* structural units, and X_{ij}^{Surface} and X_{ij}^{Bulk} are the mole fractions in the surface and bulk regions, respectively. Thus, the surface tension of an oxide melt can vary with the relative proportions of the structural units (such as Si^{IV}–O–Si^{IV} or Al^{IV}–O–Al^{IV}) in the surface and bulk regions. Surface tension can also be affected by differences in the partial interaction energies of these structural units (that are, in turn, related to their connecting states in the short and middle-order ranges) between the surface and bulk regions. The partial interaction energies of the structural species in the surface region are being evaluated, and modelling of the effect of structural relaxation on the surface tension of oxide slag will be studied in the future by the author.

CONCLUSIONS

Structural analyses of the relaxed surfaces of molten calcium aluminosilicate slags were conducted based on soft X-ray absorption spectroscopy of quenched glass samples after surface structural relaxation and MD simulations of ionic configurations of oxide melts with vacuum/melt interfaces. The results obtained from these two techniques were consistent with one another and established that BO ions were preferentially formed in the surface region by vertex connections between Al- or Si-centred polymorphs. In the case of the Al_2O_3–CaO system, Al^{3+} ions tetrahedrally-coordinated with oxygen ions (AlO_4 or Al^{IV}) were preferentially distributed in the surface region, and some such units were connected through BO ions (Al^{IV}–O–Al^{IV}). However, it should be noted that Ca^{2+} ions were

required for the purpose of charge compensation for Al^{3+} ions when generating the AlO_4 tetrahedra. Hence, this ionic configuration occurred at the intermediate composition. The incorporation of a minor amount of SiO_2 in the calcium aluminate slag greatly changed the ionic coordination states in the surface region. Tetrahedral coordination states with oxygen ions (SiO_4 or Si^{IV}) were preferentially situated in the surface region. Additionally, the incorporation of SiO_2 resulted in the segregation of AlO_4 in the surface region while the proportions of AlO_5 and AlO_6 in the bulk were increased. These structures partially combined with one another at their vertexes to form BO ions (that is, Al^{IV}–O–Si^{IV}). Based on these findings, a new model was constructed that allows the surface tension of molten slags to be predicted.

ACKNOWLEDGEMENTS

This work was financially supported by the Japan Society for the Promotion of Science through a KAKENHI Grant-in-Aid for Scientific Research (no. JP21H01683). The soft X-ray absorption analyses were performed under projects nos. S19010, S20003 and S22016 with the support of the Ritsumeikan University SR Center (Shiga, Japan). Molecular dynamics simulations were conducted at the Research Center for Computational Science, Okazaki, Japan, under project nos. 21-IMS-C097, 22-IMS-C097 and 23-IMS-C084. The author is grateful to Dr Norimasa Umesaki (previously at Osaka University, Japan) for suggestions regarding both the X-ray absorption analyses and molecular dynamics simulations. In addition, the author wishes to thank Associate Professor Yoshiki Ishii (Kitasato University, Japan) and Mr Yusuke Asano (Osaka University, Japan) for supporting the computational and experimental studies.

REFERENCES

Butler, J A V, 1932. The thermodynamics of the surfaces of solutions, *Proc R Soc Lond A*, 135:348–375.

Choi, J Y and Lee, H-G, 2002. Thermodynamic Evaluation of the Surface Tension of Molten CaO–SiO_2–Al_2O_3 Ternary Slag, *ISIJ Int*, 42(3):221–228.

Errington, J R and Debenedetti, P G, 2001. Relationship between structural order and the anomalies of liquid water, *Nature*, 409:318–321.

Henderson, G S, Neuville, D R and Cormier, L, 2007. An O K-edge XANES study of calcium aluminates, *Canad J Chem*, 85:801–805.

Ishii, Y, Salanne, M, Charpentier, T, Shiraki, K, Kasahara, K and Ohtori, N, 2016. A DFT-Based Aspherical Ion Model for Sodium Aluminosilicate Glasses and Melts, *J Phys Chem C*, 120:24370–24381.

Jiang, N, 2006. Structure and composition dependence of oxygen K edge in CaAl2O4, *J Appl Phys*, 100:013703.

Kato, Y, Shimizu, K, Matsushita, N, Yoshida, T, Yoshida, H, Satsuma, A and Hattori, T, 2001. Quantification of aluminium coordinations in alumina and silica-alumina by Al K-edge XANES, *Phys Chem Chem Phys*, 3:1925–1929.

King, T B, 1951. The surface tension and structure of silicate slags, *J Soc Glass Technol*, 35:241–259.

Livey, D T and Murray, P, 1956. Surface Energies of Solid Oxides and Carbides, *J Am Ceram Soc*, 39(11):363–372.

Luz, A P, Tomba Martinez, A G, López, F, Bonadia, P and Pandolfelli, V C, 2018. Slag foaming practice in the steelmaking process, *Ceram Int*, 44(8):8727–8741.

Mukai, K, 1998. Marangoni Flows and Corrosion of Refractory Walls, *Phil Trans: Math Phys Eng Sci*, 356(1739):1015–1026.

Tanaka, T, Hack, K, Iida, T and Hara, S, 1996. Application of Thermodynamic Databases to the Evaluation of Surface Tensions of Molten Alloys, Salt Mixtures and Oxide Mixtures, *Z Metallkd*, 87(5):380–389.

Tanaka, T, Hara, S, Ogawa, M and Ueda, T, 1998. Thermodynamic Evaluation of the Surface Tension of Molten Salt Mixtures in Common Ion Alkali–Halide Systems, *Z Metallkd*, 89(5):368–374.

In situ analysis of steelmaking slags and mold fluxes at elevated temperatures using a remote fibre-optic Raman probe

DOI: 10.62053/OWKO6204

H Tekle[1], B Zhang[2], T Sander[3], J D Smith[4], R E Gerald II[5], J Huang[6] and R J O'Malley[7]

1. Graduate Student, Missouri University of Science and Technology, Rolla MO 65409, USA. Email: hwtr29@mst.edu
2. Assistant Research Professor, Missouri University of Science and Technology, Rolla MO 65409, USA. Email: bzdtx@mst.edu
3. Lab Specialist, Missouri University of Science and Technology, Rolla MO 65409, USA. Email: tpsand@mst.edu
4. Professor, Missouri University of Science and Technology, Rolla MO 65409, USA. Email: jsmith@mst.edu
5. Research Professor, Missouri University of Science and Technology, Rolla MO 65409, USA. Email: geraldr@mst.edu
6. Associate Professor, Missouri University of Science and Technology, Rolla MO 65409, USA. Email: jieh@mst.edu
7. Professor, Missouri University of Science and Technology, Rolla MO 65409, USA. Email: omalleyr@mst.edu

ABSTRACT

In the steelmaking process, mold fluxes are essential for ensuring thermal insulation, refining, and the efficiency of continuous casting. Real-time understanding of the in-service composition of slags and fluxes are crucial for optimising the steel production process and improving the quality of the final product. An *in situ* fibre-optic Raman probe that enables the study of the structure, composition, and viscosity of molten slags and fluxes at steelmaking temperatures has been developed and demonstrated both in the lab and in foundry scale experiments. The focus of this study is on the structural, compositional, and property analysis of molten fluxes in a laboratory setting, with the aim of applying this technology for *in situ* monitoring during industrial production. Raman spectra were successfully collected at various temperatures from 1000°C to 1400°C in real-time and analysed using a deconvolution algorithm to isolate and quantify peaks in the spectra associated with the specific structures of molecular components in molten and solidifying flux. The research successfully combines *in situ* Raman spectroscopy with high-temperature viscosity data, specifically targeting CaO-CaF-SiO_2-Al_2O_3 based mould flux systems. Specified ratios of the deconvoluted Raman peaks, such as Al-O-Al/Si-O-Si ratio, shows good correlation with the flux chemistry, while the Q^3/Q^0 peak ratio shows good correlation with viscosity. A ruggedised Raman probe system was also developed and demonstrated in an 80 kg induction furnace. Ultimately, the goal of this work is to demonstrate *in situ* slag and mould flux analysis in industrial processes, such as in the continuous caster or electric arc furnace (EAF).

INTRODUCTION

In steelmaking, the significance of slags and fluxes cannot be overstated. They are an integral component of the steelmaking process that are required to ensure product quality and process efficiency. As elucidated in studies by Mills (2016) and Pretorius (2020), fluxes and slags serve many roles in the production of steel. In the continuous casting process, mold fluxes create a protective slag film that prevents the molten steel from adhering to the mold and plays a pivotal role in thermal insulation, surface lubrication, inclusion absorption, and in managing the growth of the solidifying steel shell. In the electric arc furnace (EAF), slag composition is managed to maintain a target basicity and MgO supersaturation level to protect the refractory and promote slag foaming and phosphorous removal. Control of the slag composition during oxygen blowing and FeO generation is essential for sustaining a foamy slag practice conducive to efficient high-power EAF operations. Similarly, in continuous casting, mold flux must be designed to account for inclusion absorption and exchange reactions with the steel when reactive elements in the steel are present. These changes in composition affect the properties of the flux during the casting process, often degrading the functionality of the flux over time. Min and Jung (2016) underscore the importance of slag

composition and viscosity in metallurgical processes. Slags can undergo substantial compositional shifts due to the addition of various constituents throughout the steelmaking process. These additions affect the physicochemical properties of the slag, thereby influencing their behaviour and efficacy in steelmaking. In each of these scenarios, whether in the EAF or during continuous casting, *in situ* determination of the in-service composition of the slag or flux would be invaluable. Such knowledge would provide insights into the current state of the process and opens the possibility for dynamic composition adjustments during operation. This real-time monitoring and adjustment capability could significantly enhance process control, leading to better quality steel production with optimised efficiency.

Raman spectroscopy has been demonstrated to provide useful information about the composition and structure of slags, glasses, and fluxes used in metallurgical processes. Most investigations have focused on Raman spectra measurements on quenched materials at room temperature. A recent study investigated the structure and viscosity of quenched $CaO\text{-}SiO_2\text{-}Fe_XO$ slags during the early stages of basic oxygen steelmaking by Zhang *et al* (2020). Their research showed that Raman spectroscopy can effectively analyse the glassy samples of different slag systems, shedding light on the proportion of various silicate and iron structures. By tracking the coordination of Fe^{3+} transformations from octahedron to tetrahedron, the provided O^{2-} was shown to contribute to the depolymerisation of the silicate network. The information found on bridging and nonbridging oxides was incorporated into a viscosity estimation equation that showed a 20 per cent error when comparing estimations to actual measurements. Gyakwaa *et al* (2019, 2020a, 2020d) demonstrated the applicability of time-gated Raman spectroscopy in characterising calcium-aluminate inclusions in steel. In separate studies, from Gyakwaa *et al* (2020b, 2020c), showcased how Raman spectroscopy can be used to estimate phase fractions for duplex oxide-sulfide inclusions, providing valuable information about their composition and structure. In addition, the use of the relative Raman peak intensities produced good correlations with phase fractions of CaS phases. Gao *et al* (2016a, 2016b) highlighted the use of Raman spectroscopy in understanding the structure and crystallisation behaviour of various alumina and silica mold fluxes and slags. They found that increased Al-O-Al and Si-O-Al peaks were indicative of depolymerising behaviour of the silica network. Han *et al* (2016) leveraged Raman spectroscopy to analyse the structure of mold flux by indexing the degree of polymerisation and correlating that to basicity and activation energy of the silicate melt. As such, by understanding relative quantities of molecular bonds, inferences can be made about the structure and properties of the material. Raman spectroscopy provides insights into the degree of polymerisation and the distribution of various polymerised silicate and aluminosilicate structures within the slag, which are key determinants of structure.

McMillan *et al* (1994), Daniel *et al* (1995), Malfait, Zakaznova-Herzog and Halter (2007) and Malfait and Halter (2008) have performed Raman measurements at elevated temperatures using hot wire or hot stages systems demonstrating the viability of performing high-temperature Raman analysis. The works show the temperature sensitivity of Raman. McMillan *et al* (1994) showed that the silica melts relaxed due to the breakage of Si-O-Si bonds and was consistent with viscosity. In addition, they attribute Raman peak shifts to the decreasing Si-O-Si bond angle as temperature was increased. The primary barrier to implementation of high temperature *in situ* Raman spectroscopy in the production environment stems from the limitations of the existing benchtop systems. To address this, an enhanced configuration has been developed by Zhang *et al* (2023a). This fibre-optic Raman system boasts significant advantages, such as its portability due to a smaller form factor compared to traditional tabletop systems, its adaptability to a range of high-temperature conditions including those in steelmaking environments, and its remote sensing capability. Unlike previous methods such as hotwire thermocouple set-ups, this system allows for the observation of larger samples, yielding more industrially relevant data. Additionally, background signal filtering of radiant heat has shown improvements in signal-to-noise ratio (SNR). This approach enables the application of Raman analysis in an industrial environment.

This paper investigates the use of an *in situ* Raman probe for on-line monitoring for molten mould flux at steelmaking temperatures and correlates these measurements with high-temperature viscosity data and chemistry to investigate the underlying structure of these compositions. The findings show that polymeric structures measured using Raman analysis of $CaO\text{-}CaF\text{-}SiO_2\text{-}Al_2O_3$ fluxes are well correlated with viscosity measurements. Additionally, various Raman relative ratios

trend with chemistry and basicity. Evidence of the amphoteric nature of alumina can be observed in the measurement of high temperature Raman spectra, particularly in the Al-O-Al bond peak. A ruggedised remote Raman immersion probe has also been developed and demonstrated in an 80 kg foundry induction furnace to showcase suitability for larger industrial environments.

EXPERIMENTAL PROCEDURE

Materials preparation

The chemical compositions of the fluxes examined in this study are presented in Table 1. The flux compositions incorporate CaO/SiO_2 basicity ratios from 0.84 to 1.31 at specific alumina contents of 4.7 wt per cent (S-series), 7.5 wt per cent (SB-series), 10.0 wt per cent (SA-series). To minimise their impact, Na_2O and F contributions to the system were held constant across the samples. Basicity in this study is defined as the ratio of CaO/SiO_2, although other components can be incorporated in the basicity value. The preparation process of the samples was carried out employing laboratory reagent-grade chemicals. Key to achieving the desired chemical accuracy, calcium carbonate and sodium carbonate were carefully measured and added to furnish the necessary CaO and Na_2O contributions. The calcination of these samples was conducted in a controlled vented furnace at 700°C for a duration of 5 hrs. This process was crucial for ensuring chemical stability and consistency in the samples. After this calcination, the powdered samples were transferred to an electric furnace and melted at 1300°C. The melting process, lasting between 8–10 mins, was monitored to effectively minimise the loss of volatile components. Upon reaching a molten state, a rapid quenching process was implemented using a large copper block. The quenched glassy samples were catalogued and preserved for the subsequent testing.

TABLE 1

Chemical composition of synthetic $CaO-SiO_2-Al_2O_3$ based mold powder flux.

Sample ID	CaO	SiO_2	Al_2O_3	Na_2O	F	CaO/SiO_2
S-1	35.9	42.9	4.7	7.5	9.1	0.84
S-2	39.2	39.5	4.7	7.5	9.1	0.99
S-3	42.2	36.6	4.7	7.5	9.1	1.15
S-4	44.6	34.1	4.7	7.5	9.1	1.31
SA-1	33.5	40.0	10.0	7.5	9.1	0.84
SA-2	36.6	36.8	10.0	7.5	9.1	0.99
SA-3	39.3	34.1	10.0	7.5	9.1	1.15
SA-4	41.6	31.8	10.0	7.5	9.1	1.31
SB-1	34.6	41.3	7.5	7.5	9.1	0.84
SB-2	37.8	38.1	7.5	7.5	9.1	0.99
SB-3	40.6	35.3	7.5	7.5	9.1	1.15
SB-4	43.0	32.9	7.5	7.5	9.1	1.31

In situ fibre-optic raman system

A significant advancement in this study was the development of a custom-built remote Raman probe, developed and demonstrated by Zhang *et al* (2023a). This device was engineered specifically to capture Raman spectra from slags and fluxes in the high-temperature environments typical of steelmaking. The probe's design and functionality were evaluated using two distinct experimental set-ups. In the first set-up, as illustrated in Figure 1, a compact induction heating system equipped with a graphite susceptor, and crucible was employed. This system facilitated the controlled thermal treatment of flux samples, each weighing 2–3 g. The process commenced with the preheating of the

graphite crucible to a target temperature of 1400°C. Following this, the remote Raman probe was deployed to acquire a baseline signal of the radiant heat at this temperature. This baseline acquisition was critical in enhancing the SNR for the subsequent collection of Raman spectra from the flux samples. The procedure for capturing background signals was repeated at various testing temperatures, spanning from 1400°C to 1000°C, at intervals of 50°C. For each temperature setting, quenched glass samples were melted in the crucible, and Raman signals were systematically captured under these controlled conditions. The working distance of the probe head to the molten flux was set to 8 mm to collect the high-temperature Raman spectra. Each sample was rapidly cooled, typically within 2–3 mins, due to the small sample size. The time allocated for Raman spectra collection at each temperature was 1–2 mins to minimise the loss of volatile flux components throughout the testing process. The second experimental set-up included an immersible probe tip to allow direct immersion into molten flux, which will be discussed later.

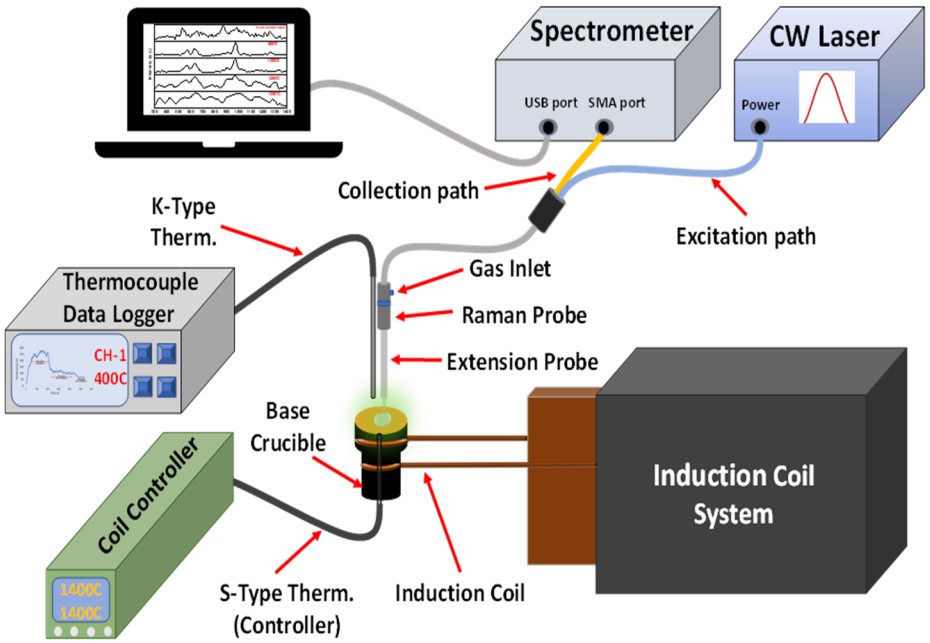

FIG 1 – Schematic of the fibre-optic Raman system combined with an induction coil system for *in situ* high-temperature experimentation. Induction coil was controlled by an imbedded S-type thermocouple and furnace controller. Ambient probe temperatures were monitored by an external thermocouple. The Raman system is comprised of a remote probe, a continuous-wave (CW) laser, spectrometer, and computer for data collection.

High-temperature viscometry

High-temperature viscosity measurements of synthetic mold flux compositions were undertaken. The system utilised a platinum rotational viscometer set-up, as delineated in Figure 2. The apparatus consisted of a platinum spindle head designed in accordance with Brookfield® SC4-14 specifications and a custom platinum crucible. The crucible and spindle were placed within a high-temperature molybdenum disilicide furnace. The initial phase of the experiment involved heating the furnace to a temperature of 1400°C. Subsequently, the platinum crucible, loaded with the quenched glass samples, was introduced into the furnace. Upon reaching the molten state, the spindle was carefully lowered into the sample to ensure precise alignment and complete spindle submersion. The rotation speed was set at 50 rev/min to satisfy the minimum 10 per cent shear torque requirement of the Brookfield® LV viscometer at the anticipated starting viscosity, thereby ensuring the accuracy of the viscosity measurements. For each viscosity measurement, the temperature was held for approximately 15 mins at the target temperature for the measurement and reduced in 50°C increments. This procedure was repeated for a temperature range of from 1400°C to 1000°C for all samples, unless flux freezing occurred. The total measurement time for each sample was approximately 2–2.5 hrs.

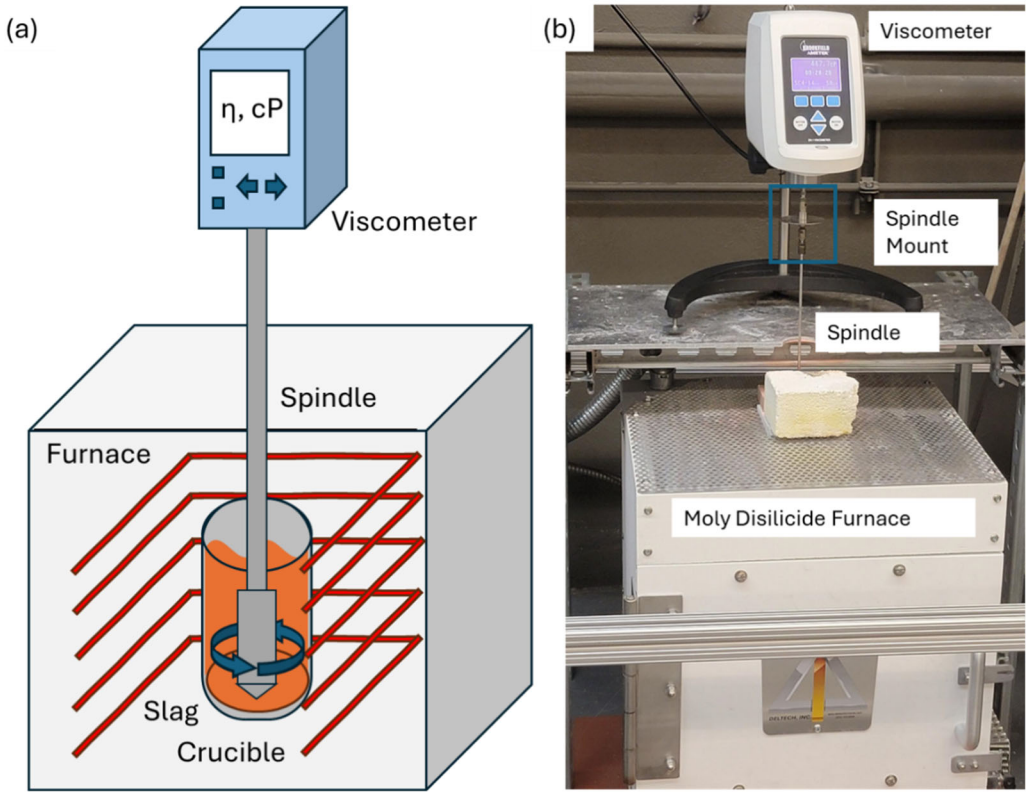

FIG 2 – High-temperature viscometry set-up utilising a platinum spindle and crucible in a moly-disilicide furnace. (a) Diagram of the platinum spindle operating in a furnace. (b) Photograph of a viscometry test of one of four samples presented.

RESULTS AND DISCUSSION

Raman chemistry analysis – alumina and silica

High-temperature Raman spectroscopy is influenced by thermal radiation, a phenomenon highlighted in the works of Mysen, and Frantz (1992), and McMillan *et al* (1994). Thermal radiation at high temperatures can interfere with the Raman signal, but if remained constant would allow for its impact to be mitigated in analyses. Zhang *et al* (2023a) proposed a background subtraction technique to address this issue. In the experimental set-up, an empty furnace heated to 1400°C provided a baseline for background signal collection. The Raman probe, positioned post-heating, captured this background before introducing the sample for melting. Enhancing signal clarity, the integration time for signal acquisition was set between 1 to 5 secs, with an averaging of ten sets of spectra per temperature to reduce noise and uncertainty.

The study analysed Raman spectra from 12 melted sample compositions to explore the link between alumina content in mold flux and Raman spectra at high temperatures. Preliminary results of S-series samples at 1400°C are shown in Figure 3, with indicated distinct Raman peaks corresponding to Al-O-Al and Si-O-Si bending vibrations within the 480–560 cm^{-1} and 590–740 cm^{-1} range respectively. Additionally, the Q-region is annotated in the figure. It comprises of four distinct Q^n peaks described in the table as Q^0, Q^1, Q^2, and Q^3. The quantities of nonbridging oxides over number of tetrahedron and the polymeric structure of each is found in the table in Figure 3.

(a)

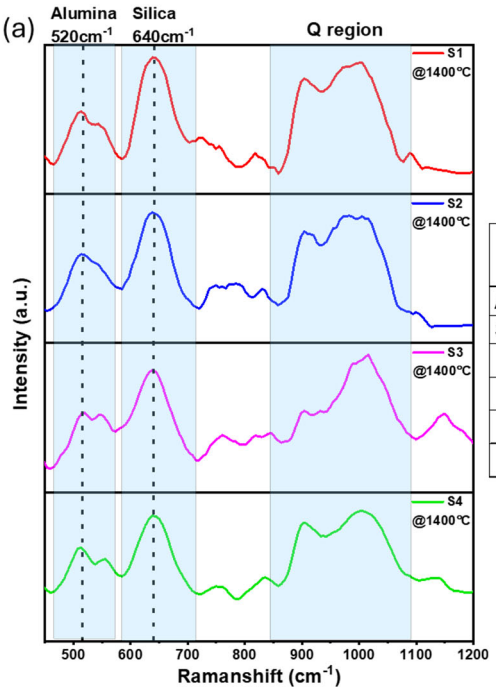

(b)

Name	Peak Raman Shift (cm^{-1})	NBO/T	Polymer Theory
Al-O-Al	480-560	N/A	4-fold ring
Si-O-Si	590-740	N/A	3-fold ring
Q^0	850-880	NBO/T=4	SiO_4 with zero bridging oxygen
Q^1	900-930	NBO/T=3	Si_2O_7 with one bridging oxygen
Q^2	950-980	NBO/T=2	Si_2O_6 with 2 bridging oxygen
Q^3	1040-1060	NBO/T=1	Si_2O_5 with one bridging oxygen

FIG 3 – Original Raman spectra of S-series samples from 400 to 1200 cm^{-1} (a). Regions for alumina, silica, and polymerised Q-region are highlighted. A table (b) containing known peaks, regions of Raman shift, nonbridging oxides/tetrahedron (NBO/T), polymeric structure. Peak positions are sourced from the works of Gao *et al* (2016a), Wang *et al* (2020), and Yan, Zhang, Li (2020).

The complex role of Al_2O_3, fluctuating between a network former and modifier, makes it a unique behaviour in these systems, therefore Al_2O_3 and CaO/SiO_2 basicity were the primary independent variables selected for this study. Original spectra measurements are plotted along cumulative, alumina, silica Gaussian fits for each plot in Figure 4. The R^2 values are provided for each profile for the cumulative fit to address uncertainty in peak measurements. The minimum R^2 value for all 12 plots was 0.921. Initial observations showed a dual peak behaviour of alumina at low basicity and only resolves when alumina content is sufficient higher. Additionally, at low alumina contents the dual peaking behaviour is prominent with increased twinning at higher basicity. This is believed to be due to the amphoteric nature of alumina as it transitions from network modifier to repolymeriser as the system basicity increases.

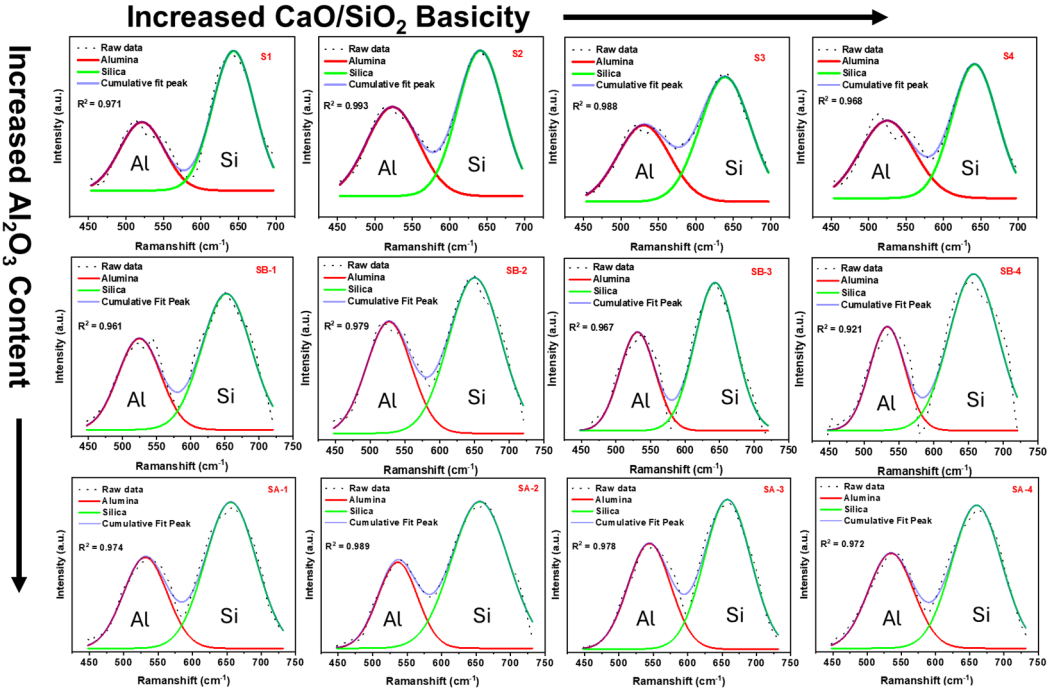

FIG 4 – Raman deconvoluted peak areas of Al-O-Al and Si-O-Si bonds for all 12 samples including S-series (4.7 wt per cent), SB-series (7.5 wt per cent), and SA-series (10.0 wt per cent). All samples were captured at 1350°C.

The general role of alkali oxides such as CaO and Na_2O as network modifiers in silicate structures is well-established. In steelmaking slags, Min, and Jung (2016) and Han *et al* (2016), note that the addition of basic oxides like CaO and Na_2O to a silicate matrix results in the breakdown of Si-O-Si linkages, leading to a more depolymerised and fluid slag. In the CaO-SiO_2-Na_2O system, both CaO and Na_2O act as network modifiers, breaking Si-O-Si bridges in the silica network and creating non-bridging oxygen (NBO). This process reduces the viscosity of the slag and alters its melting behaviour. Al_2O_3 in a CaO-SiO_2-Al_2O_3 slags can behave both as a network former and a network modifier, depending on the overall composition and the basicity of the slag. When Al_2O_3 is added to a silicate melt, it can participate in the network by substituting for Si^{4+} in the silicate structure, often forming Al-O-Si bridges. However, this substitution requires the presence of a charge-compensating cation, such as Ca^{2+} or Na^{+}, because Al^{3+} has a lower charge than Si^{4+}. In environments with sufficient basic oxides, Al_2O_3 acts more like a network former. The behaviour of Al_2O_3 is significantly influenced by the slag's basicity because of this charge compensation as further discussed in detail by Moretti (2009). Min, and Jung (2016) highlights that understanding the slag composition, including the role of components like Al_2O_3, is crucial for predicting the slag's properties, including viscosity.

To investigate the dual peaks caused by varied alumina content, deconvolution results for samples S-1, SB-1, and SA-1 were adjusted to identify the peak area and positions of alumina-1 and alumina-2 in Figure 5. The results show a convergence of peak position as alumina content increases from 4.7 wt per cent to 10 wt per cent, ultimately resulting in dual peaks fully blending. At a relatively low basicity of 4.7 wt per cent, alumina-1 peak centre was measured at 512 cm^{-1} and alumina-2 peak centre was measured at 552 cm^{-1}. As Al_2O_3 content increased to 7.5 wt per cent, the bimodal peaks converged were alumina-1 centre shifted about 4 cm^{-1} and alumina-2 centre shifted 3 cm^{-1}. Lastly, as Al_2O_3 content increased to 10 wt per cent the alumina peaks were indifferentiable from one another with a cumulative peak centra around 530 cm^{-1}. All samples maintained a consistent basicity value of 0.84 CaO/SiO_2 ratio. Additional work on this subject can be found by Zhang *et al* (2023b).

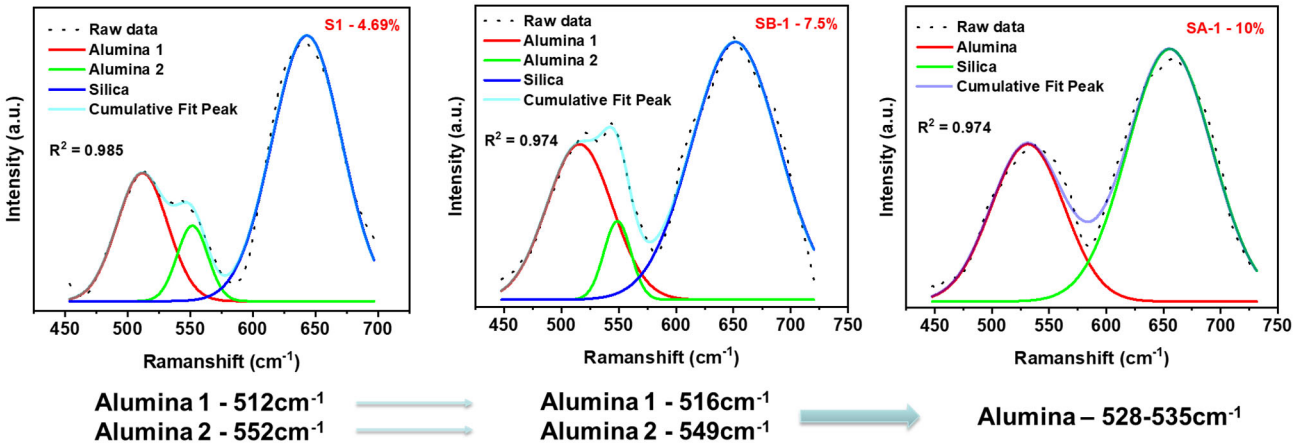

FIG 5 – Raman deconvoluted peak areas of Al-O-Al and Si-O-Si bonds of varied alumina chemistry at a constant CaO/SiO_2 basicity of 0.84. All data was captured at 1350°C.

A NBO is an oxygen atom in a silicate structure that is bound to only one silicon atom, rather than bridging between two silicon atoms. In a typical silicate structure, oxygen atoms usually bridge between two silicon atoms, forming a network. However, when modifiers such as alkaline earth oxides are added, they can break these Si-O-Si bridges, creating non-bridging oxygen. This process results in a more open, less polymerised structure. NBOs are crucial in understanding the properties of silicate glasses and melts, as their presence influences the physical and chemical characteristics of these materials, including viscosity, melting behaviour, and chemical reactivity. In the study by Kim and Sohn (2012), detailed analysis revealed significant structural changes in calcium silicate-based melts when Al_2O_3 was substituted for SiO_2. The research showed that the introduction of Al_2O_3 led to the formation of more complex aluminosilicate networks, altering the fundamental structure of the melt. As Al_2O_3 content increased, it replaced some of the SiO_2 in the melt structure. This substitution caused a reduction in the number of NBOs due to the formation of Al-O-Si bonds. Al_2O_3 acts differently from SiO_2 in the melt as Al^{3+} ions prefer to be surrounded by four oxygen ions, compared to Si^{4+} ions which are surrounded by four oxygens in a tetrahedral structure in silica. This difference in coordination leads to an increase in the degree of polymerisation within the melt.

A valuable aspect of mold flux and slag systems is knowing the basicity. Given that the basicity can vary based on interactions with steel it would be valuable to monitor changes in-line at high temperature. To demonstrate the value of high temperature Raman spectroscopy an inquiry into the correlations of Raman peaks to chemical composition was conducted. Q-region peak height ratios are plotted against compositions of CaO (a), SiO_2 (b), and CaO/SiO_2 basicity (c) in Figure 6. The Q^3/Q^0 ratio relationship to chemistry shows a stronger correlation than Q^3/Q^2 ratio. This comparison of sheet to monomers of polymerised silica are more closely tied to the overall composition. Since CaO is a depolymeriser, the Q^3/Q^0 ratio decreases as CaO increases. Contrary, SiO_2 polymerising behaviour is captured by the increasing Q^3/Q^0 ratio as SiO_2 content increases. Overall, this relationship is consistent for CaO/SiO_2 basicity. This provides one method for correlation of Q-region to chemistry. In addition to these first three plots, all 12 samples, S-series, SB-series, and SA-series with increasing contents of Al_2O_3, were investigated to show the relationship of Al-O-Al and Si-O-Si relative peak ratios. Using peak height measurements of the Al-O-Al and Si-O-Si peaks centred in the regions of 535 cm^{-1} and 655 cm^{-1} respectively, a relationship was found correlating relative peak height ratios to compositional ratios that can be found in Figure 6d–6f). Across a range of CaO/SiO_2 basicity of 0.84 to 1.31, the SiO_2 content correlates with the Al-O-Al and Si-O-Si relative ratios. As SiO_2 content increases the measured Raman peak ratio decreases, providing a means to predict SiO_2 content across a wide range of basicity. Additionally, as CaO/SiO_2 basicity increases, the Al-O-Al/Si-O-Si peak ratio increases. Overall, the trend shows a consistent structural change that occurs due to basicity changes. The increase in basicity means there are more Ca^{2+} and potentially Al^{3+} cations to depolymerise the silicate network resulting in breakage of more Si-O-Si bonds resulting in reduced peaks in Raman spectra. The deviations across groups of S, SB, and SA samples are attributed to the amphoteric nature of Al_2O_3 as basicity transitions from an acidic to a basic mold flux. This trend with Al-O-Al/Si-O-Si ratio holds true to the overall basicity of the composition as the ratio

of peaks increase alongside the overall basicity in a linear trend. It is believed that the combined relationships of the Al-O-Al, Si-O-Si, and Q-region peaks could yield an indiscriminate method to detect *in situ* chemistry.

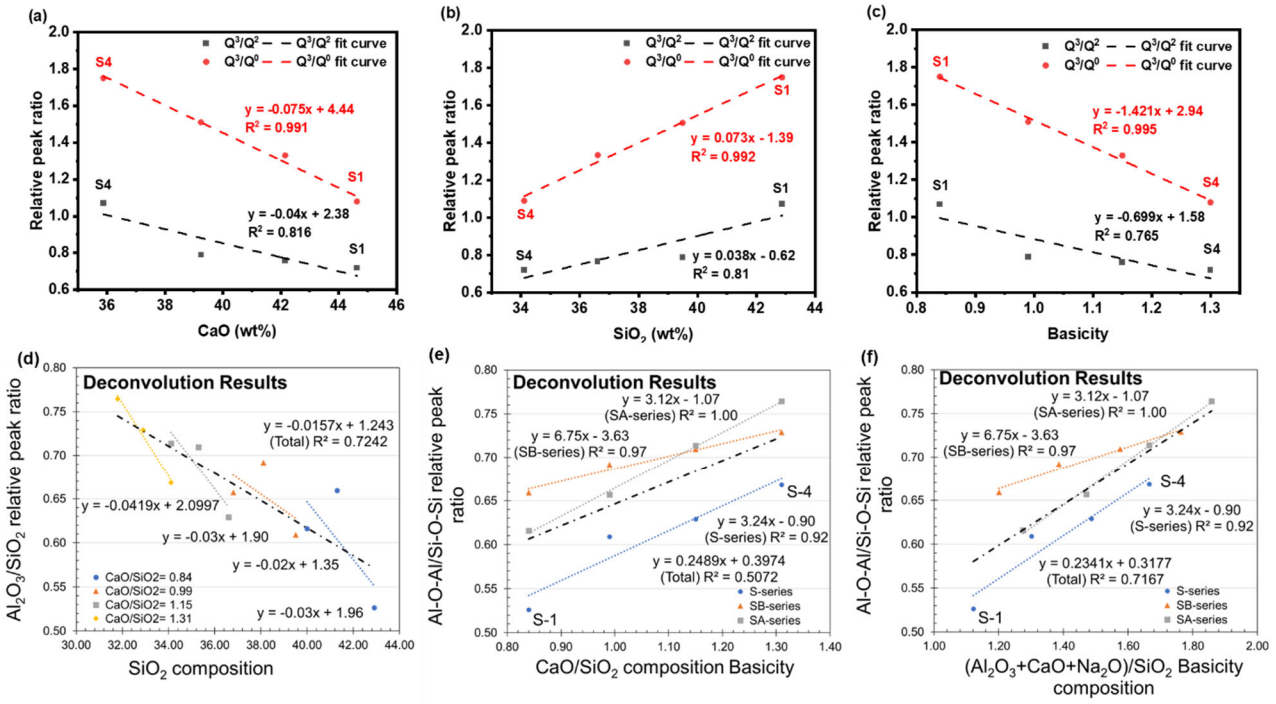

FIG 6 – Raman deconvoluted relative peak height ratios of Al-O-Al, Si-O-Si, and Q-region correlated with stochiometric chemical composition. This includes Q-region to CaO (a), SiO_2 (b), and CaO/SiO_2 basicity (c). Additionally, Al-O-Al and Si-O-Si peak height relative ratios are correlated to SiO_2 (d), CaO/SiO_2 basicity ratio (e), and $(Al_2O_3+CaO+Na_2O)/SiO_2$ basicity ratio (f).

The peak intensities are tied to bond vibrations and increase in frequency and intensity based on the chemical composition. The peaks correspond to specific bond types and arrangements, such as Si-O-Si in silicates or Al-O-Al in aluminates. As greater quantities of chemical bonds exist in the mixture, a greater intensity of generated Raman signal from these bonds is produced. As a result, the relative peak intensities provide valuable information as to the overall composition. In order to normalise the arbitrary units per individual samples, relative ratios must be used. Since each peak in the same spectra is signal processed under the same conditions it is appropriate to compare and ratio peaks within the sample. To compare spectra from different samples relative ratios must be used to identify changes in intensities.

Raman analysis of viscosity temperature dependance

The primary focus in this study is investigating the *in situ* high-temp Raman spectra for sample SA-1. Nine Raman spectra from nine temperature conditions are performed, as shown in Figures 7 and 8. The temperature dependence of viscosity has been well documented in literature notably in McMillan *et al* (1994), Daniel *et al* (1995) and Zhang *et al* (2023b). To compare the range of viscosity measurements to Raman, a comprehensive analysis of Raman spectra across the range of temperatures was performed. Deconvolution of Raman spectra is a sophisticated analytical technique used to resolve complex Raman signals into individual components that are tied to specific molecular linkages. Through deconvolution overlapping peaks can be separated and quantified. Previously described bonds such as Al-O-Al (530 cm^{-1}) and Si-O-Si (650 cm^{-1}) have well known positions that provide conditions for measurement. In addition to these individual peaks, a large overlapping region of peaks can be identified from 850 to 1100 cm^{-1} typically described as the Q-region. The Q-region contain peaks generated from various polymerised stated of silica. It is these peaks that provide the most value when interpreting the structure of liquid slags and mold fluxes and their viscosity behaviour. For this reason, the Raman spectra of the Q-region was focused and underwent baselining and deconvolution techniques to identify area peaks by Gaussian

approximation. Peak feature positions are defined within a tight range based on consensus in documented literature findings. Known peak positions were identified and supported by reference literature found in the works of Gao *et al* (2016a), Wang *et al* (2020), and Yan, Zhang and Li (2020). Resulting figures can be found in Figure 8.

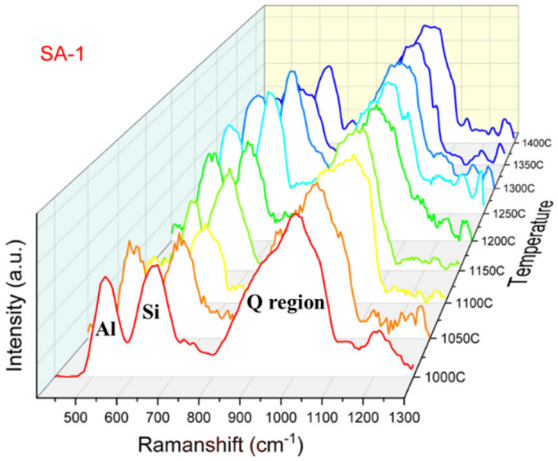

FIG 7 – Waterfall plot of original captured Raman signal SA-1 ranging from temperature 1400°C (back) to 1000°C (front). Significant regions include spectral peaks for Al-O-Al 530 cm^{-1}, Si-O-Si around 650 cm^{-1}, and the Q region spanning from 850 to 1100 cm^{-1}.

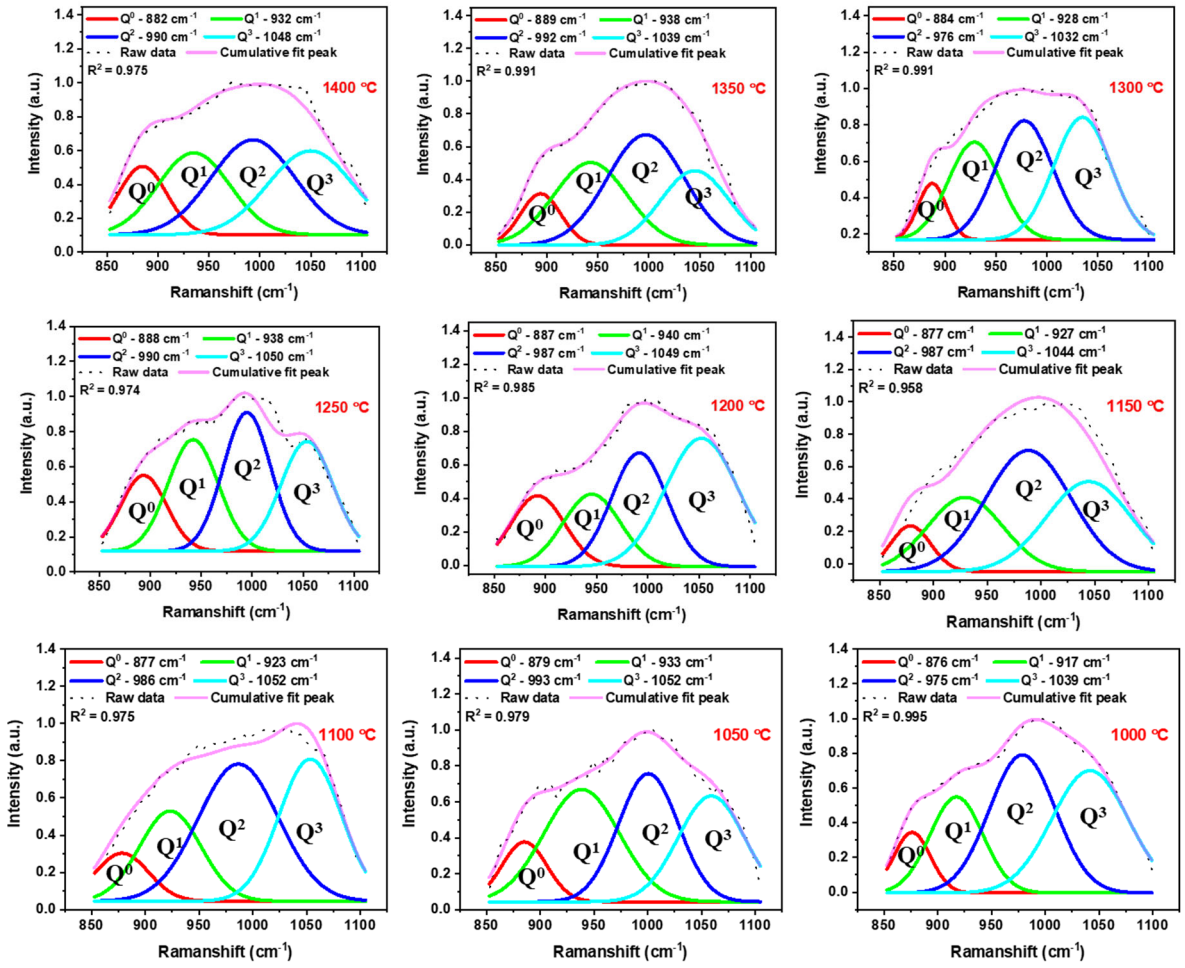

FIG 8 – Deconvoluted Raman spectra of SA-1 samples at nine testing temperature conditions from top left (1400°C) to bottom right (1000°C). A range of 800 to 1150 cm^{-1} is shown to illustrate the deconvolution results of Q-region.

The Q-region comprises of a multitude of various peaks depending on the composition in question. In this sample case there are believed to be four polymerised silica states. All nine samples have successfully deconvoluted for four individual peaks, as shown in Figure 8. Each peak was represented by Q^0- SiO_4 – Monomer; Q^1- Si_2O_7 – dimer; Q^2- SiO_3 – chain; Q^3- Si_2O_5 – sheet. In Raman spectroscopy applied to silicate systems, the Q-region is a vital part of the spectrum. This region represents the polymerised silica (SiO_4) tetrahedron. This region is key to understanding silicate material structures, revealing the degree of polymerisation of the silica network through distinct peaks associated with different silica structures, known as Q^n species, where 'n' indicates the number of bridging oxygen atoms. For instance, the Q^0 species, or monomer, represents isolated SiO_4 tetrahedra with no bridging oxygens, or all being non-bridging. The Q^0 species is typically measured from 850 to 880 cm^{-1}. The Q^1, or the dimer form, consists of two SiO_4 tetrahedra connected by a single bridging oxygen, with its presence in the range of 900 to 930 cm^{-1}. The Q^2, or chain structure, where each SiO_4 tetrahedron shares two bridging oxygens with its neighbours, forming chain-like configurations, also shows distinct peaks in the range of 950 to 980 cm^{-1}. The Q^3, or sheet structure, involves each SiO_4 tetrahedron linking to three others via bridging oxygens, forming sheet-like structures, and is detectable in the Raman spectra from 1040 to 1060 cm^{-1}. Overall, a strong fit was established for all spectra with R^2 values greater than 0.958 for the combined Gaussian fit. Transitions between relative peak sizes can be observed when temperature is varied, specifically Q^2 and Q^3 peaks were predominant to Q^0 and Q^1 at lower temperatures.

The viscosity data compiled for the SA-1 to SA-4 samples show consistency, evident in the repeatability of measurements under both cooling and heating conditions seen in Figure 9. Viscosity measurements were plotted linearly as the inverse of temperature versus the natural log of viscosity measured. This is due to the typical Arrhenius behaviour of viscosity and temperature. Similar works have illustrated this behaviour in detail including Han (2017), and Wan *et al* (2024). The Arrhenius equation profiles well as temperature increases in slag and mold flux systems the viscosity, measured in centipoise, decreases at an exponential rate. For this reason, linear regression lines were used to support this and to measure an activation energy for the profile. Furnace temperature uniformity had minimal impact on measurement accuracy is shown by the high R^2 results being equal to or greater than 0.986 for all four samples. Instead, the precision of measurements was more significantly influenced by the alignment of the spindle, as observed during the early testing of sample SA-1 where realignment of the viscometer set-up was necessary. The overall profiles of viscosity data align well with the exponential Arrhenius behaviour observed in other studies, suggesting a commonality in the rheological properties of such slag materials.

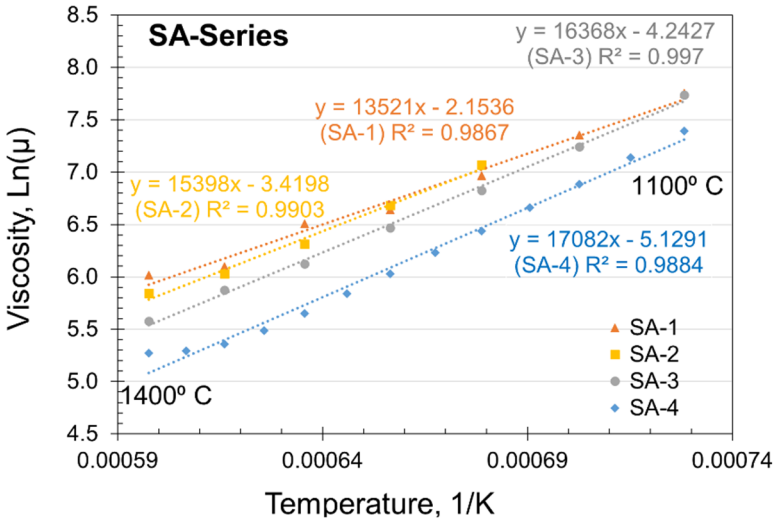

FIG 9 – High-temperature viscometer data collected for samples SA-1, SA-2, SA-3, and SA-4 from 1400°C to 1100°C.

In similar works by Kim and Sohn (2012), increased polymerisation and structural complexity of the melt, resulting from higher Al_2O_3 content, had a direct impact on the physical properties of the melt, notably its viscosity. The melt became more viscous with increasing Al_2O_3, attributed to the enhanced

polymerisation and the formation of a more interconnected network structure. This observation was also consistent with Figure 9, samples behaved more viscous-like increasing as the Al_2O_3/SiO_2 ratio increased across the samples SA-1 to SA-4. It is important to address that this was observed at high temperatures where precent solids are at relatively low quantities. As temperatures are reduced, overlap of the viscosity versus temperature trend can be seen were the influence of solid fractions play a more prominent role. Further analysis of these forming crystallite is needed to address their impact on viscosity.

To further analyse the relationship between Raman spectra and viscosity of mold flux samples, the peak area measurement is investigated for a correlation. According to the nature of the polymerised network, higher order Q^n provides the silicate structure with larger sized linkages which are less prone to mobility, leading to a more viscous mixture. To index the total polymerised silica structure measured from the Raman spectra, an equation, Equation 1 was constructed:

$$[(X_1*Q^1) + (X_2*Q^2) + (X_3*Q^3)]/(X_0*Q^0) \quad (1)$$

In the proposed model expressed by Equation 1, each observable Q^n nomenclature is assigned a coefficient. The assignment is based on the relative molecule sizes of each polymerised state, with a basic increasing geometric ratio designated for each X_n. Then, based on the model discussed above, the results of Equation 1 was used to correlate with the measured viscosity, as shown in Figure 10. Since Q^0 represents a monomer, X_0 is assigned a value of 1. For subsequent X_n values, an increase by factors of two or more is applied as a baseline for optimisation. Optimising the X_1, X_2, and X_3 values involves utilising an adjusted R^2 value as a response, with adjustments made through a sequential quadratic programming (SQP) script in MATLAB®. The optimised values of X_1, X_2, and X_3 are then used to construct Figure 10, adhering to predefined bound constraints of $X_0 = 1$, $1 < X_1 < X_2 < X_3$. This was later modified to $X_1 = 1.5$, $X_2 = 2$, and $X_3 = 12$ to retain the geometric progression which better fits the sizes of Q^n. The most significant impact on the response was observed when minimising X_1 and X_2 while maximising X_3. This implies that the Q^3 (sheet) has a greater impact to viscosity compared to Q^1 (dimmer), and Q^2 (chain) structures based on the weighted sum of Q^n. A linear regression fit is plotted using the natural logarithm of measured viscosity as a response variable. An R^2 of 0.89 was achieved using the methods previously described. The Q^3/Q^0 relationship still holds the strongest correlation to viscosity, suggesting the dominant contribution to viscous properties of molten mold flux systems is the Q^3 sheet of SiO_4 tetrahedron. However, further work is required to enhance the robustness and accuracy of Equation 1 and its X_n values, ensuring a more reliable and comprehensive understanding of the contributions of the various Q^n to the overall structure of the composition. Particularly, expanding the data set to incorporate SA-2, SA-3, SA-4 and additionally a S-series of samples containing a lower Al_2O_3 content of 4.7 wt per cent. The existence of Al-O-Si bonds near the Q-region have been reported in aforementioned works, but no evidence of their presence has been found in the proposed samples in this study. Using this proposed model, a method for predicting viscosity based on the measured *in situ* high temperature Raman spectra is proposed. This provides a valuable tool for process control for industrial steelmaking environments.

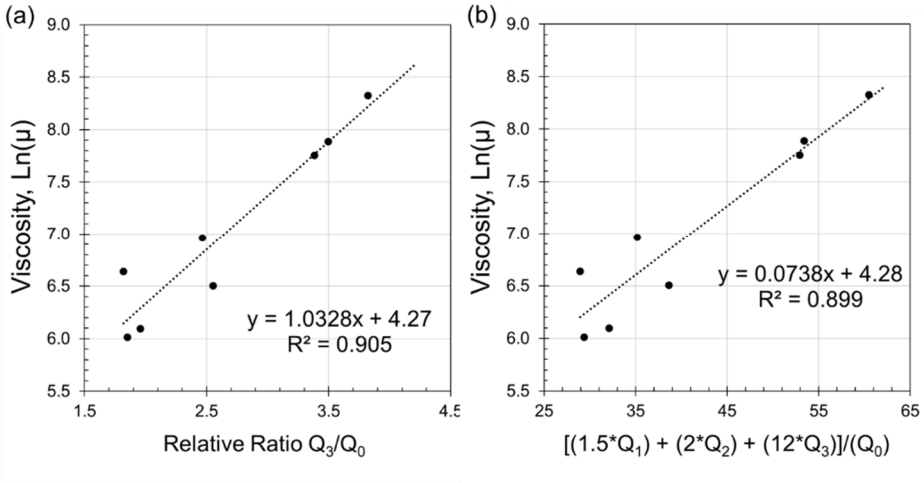

FIG 10 – Quantified Q-region formula for predicting viscosity using data from SA-1 going from 1400°C to 1100°C. A comparison of Q^3/Q^0 ratio (a) and Equation 1 (b) can be seen in the figure above.

The interplay between depolymerisation and viscometry in silicate melts is a complex but critical aspect of understanding the behaviour of these materials under molten conditions. Raman spectroscopy serves as a powerful tool in deciphering the molecular dynamics that underlie these changes. The insights gained from these studies are valuable in numerous scenarios in metallurgical processes, where control over melt properties is essential.

Raman immersion dip test

To enhance the methodology presented, a ruggedised Raman probe was developed and demonstrated for larger-scale dip testing. This probe, capable of short-duration dips of 30 sec or more in steelmaking environments, features improvements like a telescopic extension lens and air-cooling channels in its copper housing This ensures an effective working distance and improves probe protection. An apparatus for dip testing has been created to enable highly precise position control, adjustable within 1–3 mm. Complementing this, a molybdenum viscometry set-up is in development to address complex industrial mold flux compositions, which are not suitable for the existing platinum viscometry set-up due to platinum-iron embrittlement. A large-scale experimental set-up, illustrated in Figure 11, simulates an industrial-scale environment. This includes a 90 kg steel induction melting furnace, designed to handle large quantities of steel and mold powder flux samples. The centrepiece of the set-up is the enhanced version of the remote Raman probe, encased in a custom-designed copper block with air-cooling channels. This design is critical for protecting the probe from the furnace's extreme temperatures and harsh conditions. The telescopic lens, extending the working distance to 3 cm reducing contact and proximity to the molten flux/slag. Additionally, the cooling system's exhaust gas is used to create a positive pressure environment at the probe tip, effectively preventing slag or steel from entering the probe body and thus reducing damage risk.

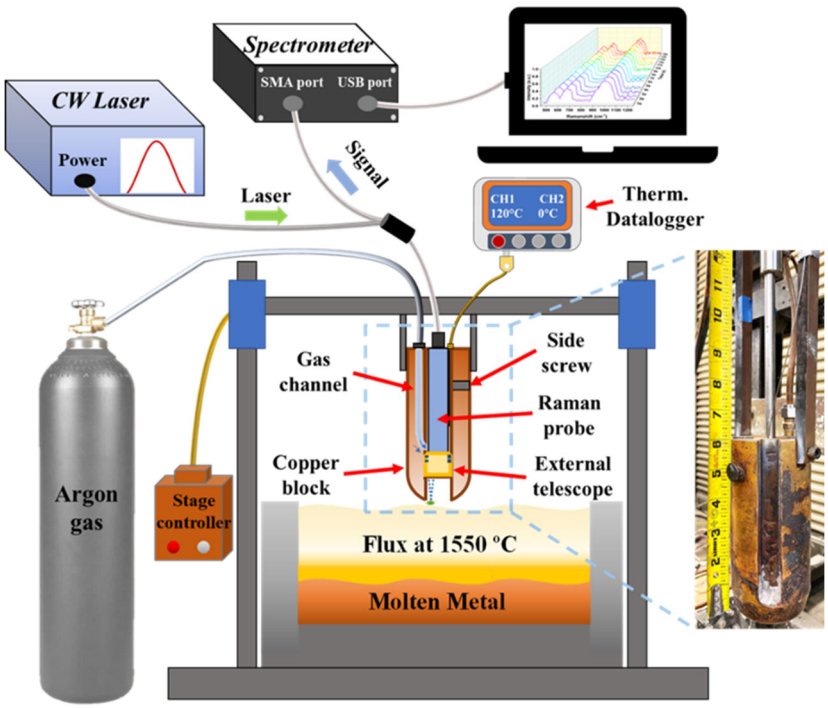

FIG 11 – Industrial foundry mold flux dip testing set-up with ruggedised Raman probe. Raman system includes continuous wave (CW) laser, spectrometer, computer, and probe. Ruggedised Raman probe housing including argon gas cooling is mounted to a motorised dipping stage.

The housing is attached to an automated dip tester, managed by a programmable logic controller (PLC), which offers meticulous control over the dipping depths. The melting process in the induction furnace highlighted challenges like natural convection, leading to the liquid mold powder flux accumulating around the furnace's perimeter and forming thinner layers of suspended flux. In conclusion, the development of a suitable high-temperature viscometry set-up for FeO-bearing slags and fluxes, alongside the larger scale dip tests, aims to provide comprehensive viscosity and Raman data. This data will assist in proving the scalability of the proposed methodology. Moving forward, a model for various mold flux compositions is being prepared for an industrial caster dip test, aiming to fully demonstrate the Raman probe's suitability in practical steelmaking applications. Future work is planned to enhance and further evaluate the ruggedised Raman probe dip testing set-up, aiming to facilitate longer duration dips and potentially yield more comprehensive data of exchange reactions between steel and molten mold flux. This improvement is expected to provide a deeper insight into the flux's behaviour under varied operational conditions.

CONCLUSIONS

In this study, the development and application of a remote fibre-optic Raman probe for real-time analysis of steelmaking slag and mold flux compositions at elevated temperatures has been demonstrated. The research combined *in situ* Raman spectroscopy with high-temperature viscosity data to elucidate the underlying structural behaviours in CaO-CaF-SiO_2-Al_2O_3 based systems. Experimental procedure for high-temperature viscometry and Raman spectra collection was demonstrated. The deconvolution of overlapping peaks in the alumina, silica, and Q-region of the Raman spectra enabled a clearer understanding of the high-temperature structural features. This deconvolution was key in correlating Raman spectral features to chemical composition, particularly ($Al2O_3/SiO_2$) ratio to SiO_2 content and ($Al2O_3$+CaO+Na_2O)/SiO_2 basicity. Furthermore, viscosity measurements were explained by Raman deconvoluted Q-region as the degree of polymerisation in the silicate network dictated structure. The results underscored the reliability of Raman spectroscopy in predicting synthetic mold flux viscosity, particularly with Q^3/Q^0 ratio as other more comprehensive Qn calculations could not achieve a better fit. This illustrates how Q^3 is the predominant feature in the Raman Q-region tied to the underlining structure including viscosity. This observation aligns with the understanding that larger polymeric linkages, such as Q^3 (sheet), have a more substantial impact on viscosity compared to smaller linkages like Q^1 (dimmer), and Q^2 (chain). The research concluded

that the Raman spectra of CaO-CaF-SiO_2-Al_2O_3 based mold flux systems exhibit fundamental behaviours closely related to the structure of these compositions, influencing both the Raman spectra and viscosity measurements. This study not only contributes to the field of metallurgy by providing a deeper understanding of the structural dynamics of mold fluxes and slags but also offers a practical approach for real-time monitoring and control of these materials in various industrial settings. The integration of Raman spectroscopy with viscometry presents a powerful tool for advancing our understanding of material properties under extreme conditions, with significant implications for improving industrial processes and material design.

ACKNOWLEDGEMENTS

This research was funded by the U.S. Department of Energy's Office of Energy Efficiency and Renewable Energy (EERE) under the Advanced Manufacturing Office (AMO) Awards DE-EE0009392 and DE-EE0009119. The views and opinions of authors expressed herein do not necessarily state or reflect those of the United States Government or any agency thereof. Additional support was provided by the Peaslee Steel Manufacturing Research Center (PSMRC) at Missouri University of Science and Technology.

REFERENCES

Daniel, I, Gillet, P, Poe, B T and McMillan, P F, 1995. In-situ high-temperature Raman spectroscopic studies of aluminosilicate liquids, *Physics and Chemistry of Minerals*, 22:74–86. https://doi.org/10.1007/bf00202467

Gao, J, Wen, G, Huang, T and Tang, P, 2016a. Effects of the composition on the structure and viscosity of the CaO–SiO2-based mold flux, *Journal of Non-Crystalline Solids*, 435:33–39. https://doi.org/10.1016/j.jnoncrysol.2016.01.001

Gao, J, Wen, G, Huang, T and Tang, P, 2016b. The structure and the crystallization behaviour of the CAO-SIO2-AL2O3-Based mold flux for High-Al Steels casting, in *Proceedings of the 10th International Conference on Molten Slags, Fluxes and Salts (MOLTEN16)* (ed: R G Reddy, P Chaubal, P C Pistorius and U Pal), pp 291–298 (The Minerals, Metals and Materials Society). https://doi.org/10.1007/978-3-319-48769-4_31

Gyakwaa, F, Aula, M, Alatarvas, T, Shu, Q, Huttula, M and Fabritius, T, 2020b. Quantification of Synthetic Nonmetallic Inclusion Multiphase Mixtures from a CaO–Al2O3–MgO–CaS System Using Raman Spectroscopy, *Steel Research International*, 92(1). https://doi.org/10.1002/srin.202000322

Gyakwaa, F, Aula, M, Alatarvas, T, Vuolio, T, Huttula, M and Fabritius, T, 2019. Applicability of Time-Gated Raman Spectroscopy in the characterisation of Calcium-Aluminate inclusions, *ISIJ International*, 59(10):1846–1852. https://doi.org/10.2355/isijinternational.isijint-2019-122

Gyakwaa, F, Aula, M, Alatarvas, T, Vuolio, T, Shu, Q, Huttula, M and Fabritius, T, 2020c. Application of Raman spectroscopy for characterizing synthetic Non-Metallic inclusions consisting of calcium sulphide and oxides, *Applied Sciences*, 10(6):2113. https://doi.org/10.3390/app10062113

Gyakwaa, F, Aula, M, Alatarvas, T, Vuolio, T, Shu, Q, Huttula, M and Fabritius, T, 2020d. Characterisation of binary phase mixtures of Magnesium-Aluminate spinel and Calcium-Aluminates using Time-Gated Raman spectroscopy, *ISIJ International*, 60(5):988–997. https://doi.org/10.2355/isijinternational.isijint-2019-576

Gyakwaa, F, Aula, M, Vuolio, T, Alatarvas, T, Shu, Q, Huttula, M and Fabritius, T, 2020a. Characterization of multiphase mixtures of calcium aluminates and magnesium aluminate spinel using Time-Gated RAMAN spectroscopy, *Steel Research International*, 91(8). https://doi.org/10.1002/srin.202000084

Han, C, 2017. Viscosity studies of High-Temperature metallurgical slags relevant to ironmaking process, PhD thesis, University of Queensland, Brisbane. https://doi.org/10.14264/uql.2017.995

Han, C, Chen, M, Rasch, R, Yu, Y and Zhao, B, 2016. Structure studies of silicate glasses by Raman Spectroscopy, in *Proceedings of the 10th International Conference on Molten Slags, Fluxes and Salts (MOLTEN16)* (ed: R G Reddy, P Chaubal, P C Pistorius and U Pal), pp 175–182 (The Minerals, Metals and Materials Society). https://doi.org/10.1007/978-3-319-48769-4_18

Kim, G and Sohn, I, 2012. Effect of Al2O3 on the viscosity and structure of calcium silicate-based melts containing Na_2O and CaF_2, *Jrnl of Non-Crystalline Solids*, 358(12–13):1530–1537. https://doi.org/10.1016/j.jnoncrysol.2012.04.009

Malfait, W J and Halter, W E, 2008. Structural relaxation in silicate glasses and melts: High-temperature Raman spectroscopy, *Physical Review B*, 77(1). https://doi.org/10.1103/physrevb.77.014201

Malfait, W J, Zakaznova-Herzog, V P and Halter, W E, 2007. Quantitative Raman spectroscopy: High-temperature speciation of potassium silicate melts, *Journal of Non-Crystalline Solids*, 353(44–46):4029–4042. https://doi.org/10.1016/j.jnoncrysol.2007.06.031

McMillan, P F, Poe, B T, Gillet, P and Reynard, B, 1994. A study of SiO2 glass and supercooled liquid to 1950 K via high-temperature Raman spectroscopy, *Geochimica Et Cosmochimica Acta*, 58(17):3653–3664. https://doi.org/10.1016/0016-7037(94)90156-2

Mills, K C, 2016. Structure and properties of SLAGS used in the continuous casting of steel: Part 1 Conventional mould powders, *ISIJ International*, 56(1):1–13. https://doi.org/10.2355/isijinternational.isijint-2015-231

Min, D J and Jung, S M, 2016. Current status of slag design in metallurgical processes, in *Proceedings of the 10th International Conference on Molten Slags, Fluxes and Salts (MOLTEN16)* (ed: R G Reddy, P Chaubal, P C Pistorius and U Pal), pp 17–28 (The Minerals, Metals and Materials Society). https://doi.org/10.1007/978-3-319-48769-4_2

Moretti, R, 2009. Polymerisation, basicity, oxidation state and their role in ionic modelling of silicate melts, *Annals of Geophysics*, 48(4–5). https://doi.org/10.4401/ag-3221

Mysen, B O and Frantz, J D, 1992. Raman spectroscopy of silicate melts at magmatic temperatures: Na2O-SiO2, K2O-SiO2 and Li2O-SiO2 binary compositions in the temperature range 25–1475°C, *Chemical Geology*, 96(3–4):321–332. https://doi.org/10.1016/0009-2541(92)90062-a

Pretorius, E B, 2020. The role of transient slags in steelmaking, AISTech2020 Proceedings of the Iron and Steel Technology Conference [Preprint]. https://doi.org/10.33313/380/066

Wan, X, Wang, Z, Yang, J and Shi, C, 2024. Insight into compositional dependence of thermophysical properties and structure of Al2O3-SiO2-CaF2-CaO-Li2O melts, *Journal of Non-Crystalline Solids*, 626:122807. https://doi.org/10.1016/j.jnoncrysol.2023.122807

Wang, W, Dai, S, Zhou, L, Zhang, J, Tian, W and Xu, J, 2020. Viscosity and structure of MgO–SiO2-based slag melt with varying B2O3 content, *Ceramics International*, 46(3):3631–3636. https://doi.org/10.1016/j.ceramint.2019.10.082

Yan, W, Zhang, G and Li, J, 2020. Viscosity and structure evolution of CaO–SiO2-based mold fluxes with involvement of CaO–Al2O3-based tundish fluxes, *Ceramics International*, 46(9):14078–14089. https://doi.org/10.1016/j.ceramint.2020.02.208

Zhang, B, Tekle, H, O'Malley, R J, Sander, T P, Smith, J D, Gerald II, R E and Huang, J, 2023b. In situ and Real-Time mold flux analysis using a High-Temperature Fiber-Optic Raman sensor for steel manufacturing applications, *Journal of Lightwave Technology*, 41(13):4419–4429. https://doi.org/10.1109/jlt.2023.3239428

Zhang, B, Tekle, H, O'Malley, R J, Smith, J D, Gerald II, R E and Huang, J, 2023a. In situ High-Temperature raman spectroscopy via a remote Fiber-Optic raman probe, *IEEE Transactions on Instrumentation and Measurement*, 72:1–8. https://doi.org/10.1109/tim.2023.3244238

Zhang, R, Wang, Y, Zhao, X, Jia, J, Liu, C and Min, Y, 2020. Structure and viscosity of molten CAO-SIO2-FEXO slag during the early period of basic oxygen steelmaking, *Metallurgical and Materials Transactions B: Process Metallurgy and Materials Processing Science*, 51(5):2021–2029. https://doi.org/10.1007/s11663-020-01888-8

Viscosity of foaming fluid measured by falling-ball method

DOI: 10.62053/MAZA8264

S Ueda[1], T Iwama[2], Y Mita[3] and R Inoue[4]

1. Professor, Tohoku University, Sendai Miyagi 980-8577, Japan. Email: tie@tohoku.ac.jp
2. Assistant Professor, Tohoku University, Sendai Miyagi 980-8577, Japan. Email: takayuki.iwama.a6@tohoku.ac.jp
3. Graduate student, Tohoku University, Sendai Miyagi 980-8577, Japan. Email: yusaku.mita.p1@alumni.tohoku.ac.jp
4. Researcher, Tohoku University, Sendai Miyagi 980-8577, Japan. Email: ryo.inoue.e2@tohoku.ac.jp

ABSTRACT

In the iron and steel manufacturing industries, efforts are being made to achieve carbon neutrality by 2050, and the transition from a coal-based steelmaking process to that utilising renewable energy is being pursued. An alternative process in which directly hydrogen-reduced iron is melted in an electric furnace is being investigated. It is known that foaming slag reduces heat loss from the steel bath in electric arc furnace, but iron loss due to the suspension of steel particles in the slag is indispensable. To improve the separation of steel particles from the slag, the control of the slag viscosity is important.

Although the slag viscosity has been extensively studied, in those studies the slag was considered to be a simple liquid. However, in actual operations, slag is a multiphase fluid consisting of solid, gas and liquid phases. Therefore, in this study, by measuring the sedimentation velocity of titanium, stainless steel and glass spheres in an aqueous glycerin solution containing bubbles generated by the reaction between $NaHCO_3$ and $C_2H_2O_4$, the apparent viscosity of the gas-liquid fluid was evaluated based on Stoke's law. It was found that the apparent viscosity of the gas-liquid fluid is larger than the viscosity of liquid phase and depends on both the bubble volume ratio in solution and the density of the falling solid sphere, and the apparent viscosity was different from that previously obtained by the rotation method. The apparent viscosity derived from the sedimentation velocity of solid spheres changed depending on the specific gravity of the ball. This is because the apparent viscosity is derived from the velocity of a ball falling in a static bubble in this method, whereas that is derived from the force applied by a stationary flow in the rotational method.

INTRODUCTION

Currently, carbon neutrality in steel production is required to combat global warming. Since the conventional blast furnace/converter process mainly uses coke as a reductant, even when some of the coke is replaced with hydrogen-based reductants, CO_2 reductions are limited. On the other hand, the electric arc furnace (EAF) steelmaking method, which usually uses scrap as raw material, requires less energy for steel production, resulting in lower CO_2 emissions. For this reason, it is predicted that the proportion of steel produced by electric furnace could increase in the future.

When EAF steelmaking becomes the mainstream, steel scrap is smelted repeatedly, causing a cycle of elements contained in the scrap. In particular, the concentration of elements called trump elements such as Cu and Sn, which cannot be removed by oxidation refining, is a serious concern. To control the concentration of such circulating elements, it is necessary to use pig iron and reduced iron sources. Direct reduced iron (DRI), reduced by hydrogen etc, is expected to be a raw material free of circulating elements. However, DRI contains gangue components (oxides), which are the source of slag. Therefore, more slag is produced in DRI melting than conventional scrap melting.

At the end of the EAF smelting process, the slag is foamed by CO gas generated by the coal material blown into the furnace. This foaming slag functions as a heat insulator for molten steel, improving heat transfer efficiency from the arc and contributing to reducing CO_2 emissions. On the other hand, iron particles are easily entrapped in the foaming slag phase. When those particles do not fall down and remain in the slag, it causes iron loss, ie lower iron yield. Although iron particles fall into the slag after long static holding, which improves the iron yield, it must be balanced against the productivity of the process. Since slag viscosity is an important property in predicting the sedimentation velocity

of iron particles, it has been measured for many slag systems. However, most measurements were performed on single-phase liquids.

For solid-gas-liquid multiphase fluids such as EAF slag, the viscosities reported for single slag melts are not applicable. The properties of slag-based multiphase fluids had been measured within limited experimental conditions. Saito *et al* (2020) measured the viscosity of silicone oil, in which polyethylene beads were suspended, by a fluid-rotation method. They derived an empirical formula based on the following Einstein-Roscoe's equation proposed by Roscoe (1952).

$$\frac{\eta_{SL}}{\eta_L} = \left(1 - \varphi_s\right)^{-2.5} \quad (1)$$

Where:

η_{SL} [mPa·s] viscosity of solid-liquid fluid

η_L[mPa·s] viscosity of liquid phase

ϕ_S volume fraction of dispersed solid phase in solid-liquid fluid

Li *et al* (2021) also measured the viscosity of the same mixture by a falling-ball method. However, the viscosity obtained was lower than that measured by the rotational method. In their study, the mixture exhibited dilatant fluid behaviour with properties different from those obtained by the rotational method.

The viscosity of gas-liquid fluids simulating foaming slag has been studied only by Martinsson (2018) and Hatano *et al* (2021). Hereafter, this viscosity is called 'apparent viscosity' to distinguish it from that of a single liquid. In the present study, the apparent viscosity of gas-liquid fluid was measured by the falling-ball method based on Stokes' equation to confirm the difference from that obtained by the rotation method. For the evaluation of the sedimentation velocity of iron particle in the gas-liquid fluid, it is necessary to consider not only the macroscopic viewpoint of the sedimentation velocity of dispersed particles in the foaming fluid but also the microscopic viewpoint of the morphology of foams around the particle, so the sedimentation behaviour of solid particle was observed simultaneously with the measurement of apparent viscosity.

EXPERIMENT

Sample preparation

To create a gas-liquid fluid simulating foaming slag at room temperature, the method proposed by Saito *et al* (2020), in which CO_2 gas is generated by mixing and reacting a $C_2H_2O_4$-saturated aqueous solution with a glycerin aqueous solution containing $NaHCO_3$, was employed. The glycerin concentrations $X_{Glycerin}$ in weight fraction after mixing were 0.20, 0.35, 0.50, 0.65 and 0.80, whose viscosities η_L are 1.76, 3.06, 6.01, 15.2 and 60.1 mPa·s, respectively (Glycerine Producer's Association, 1969). To increase the generation rate and stability of bubbles, 0.1 g of polyoxyethylene-laurylether, a surfactant, was added to the $NaHCO_3$ solution.

In the viscosity measurements, three types of spheres with different densities were used as sedimentation particles: stainless steel sphere (density ρ_p = 7.93 g/cm^3), titanium sphere (ρ_p = 4.51 g/cm^3) and glass beads (ρ_p = 2.50 g/cm^3). The diameter of these spheres was chosen to be 2.0 mm because it is close to the maximum size of iron particles observed in the slag and easy to observe during measurement. These particles were pre-wetted with glycerin solution to smooth the initial sedimentation.

Experimental apparatus

Figure 1 presents an overview of the experimental set-up. The bath is a rectangular made of acrylic plate with a thickness of 3 mm, whose internal dimensions are 25 mm × 44 mm in horizontal cross-section (cross-sectional area A = 0.0011 m^2) and 326 mm in height. By installing a glass filter (6 mm thickness, open pore size = 100–120 μm) at a height of 20 mm from the inner bottom of the bath, it is possible to separate the $NaHCO_3$ -glycerine solution above the filter from the $C_2H_2O_4$ solution injected from the bottom.

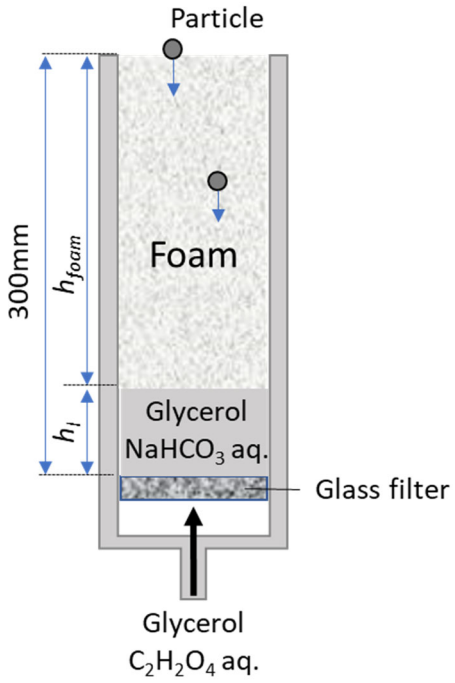

FIG 1 – Experimental apparatus of the falling-ball method for creating gas-liquid fluid.

Experimental procedure

In this study, the gas-phase volume fraction ϕ_g of the obtained gas-liquid fluid is defined as follows:

$$\varphi_g = \frac{h_0 - h_L}{h_0} \left(= \frac{h_{foam}}{h_0} \right) \quad (2)$$

where

h_0 [m]	maximum height of gas-liquid fluid (0.30 m)
h_L [m]	height in single liquid phase
h_{foam} [m]	height in gas-liquid phase

Gas-liquid fluids with ϕ_g = 0.5 and 0.7 were created by adjusting the $NaHCO_3$ concentration and mixing ratio of two solutions. The total amount of $NaHCO_3$ solution and $C_2H_2O_4$ solution charged in the apparatus was determined to fill the volume above the glass filter, which is $A \times h_0$ [m^3], with the gas-liquid fluid. When these two solutions are mixed, the volume of the liquid phase without foaming is $A \times h_0 \times (1-\phi_g)$ [m^3]. On top of the generated gas-liquid fluid, several stainless steel, titanium and glass spheres were gently placed. The falling behaviour of these particles was photographed continuously with a video camera. The sedimentation velocity of the spheres was derived from the video image by measuring the transit time every 5 mm in a 150 mm section from the bath depth of 50 mm to 200 mm while watching.

Derivation of apparent viscosity of gas-liquid fluids

In the falling-ball method, the viscosity of a single liquid η_L can be derived from the sedimentation velocity of a sphere using the following Stokes equation (Stokes, 1845):

$$\eta_L = \frac{D_P{}^2(\rho_P - \rho_L)}{18U} g \quad (3)$$

where

DP [m]	diameter of a sedimentation particle
ρP [kg/m^3]	density of a sedimentation particle
ρ_L [kg/m^3]	density of a fluid
U [m/s]	sedimentation velocity of a particle

g [m/s^2] gravitational acceleration

Although this Equation 3 is applicable only to Newtonian fluids, it is assumed that the equation can be applied to a gas-liquid fluid in the analysis of this study.

When the density of a gas-liquid fluid can be expressed as $(1-\phi_g)\,\rho_L$, the apparent viscosity of gas-liquid fluid η derived from Equations 2 and 3 will be as follows:

$$\eta = \frac{{D_P}^2\left(\rho_P-\left(1-\varphi_g\right)\rho_L\right)}{18U} g \tag{4}$$

RESULTS AND DISCUSSION

The apparent viscosity of gas-liquid fluid at $\phi_g = 0.7$ was measured by the falling-ball method while changing the viscosity of liquid, which composes foams.

Figure 2a shows the relationship between the elapsed time and the position of stainless steel and titanium spheres sedimented in the foaming glycerin solution with $\eta_L = 60.1$ mPa·s.

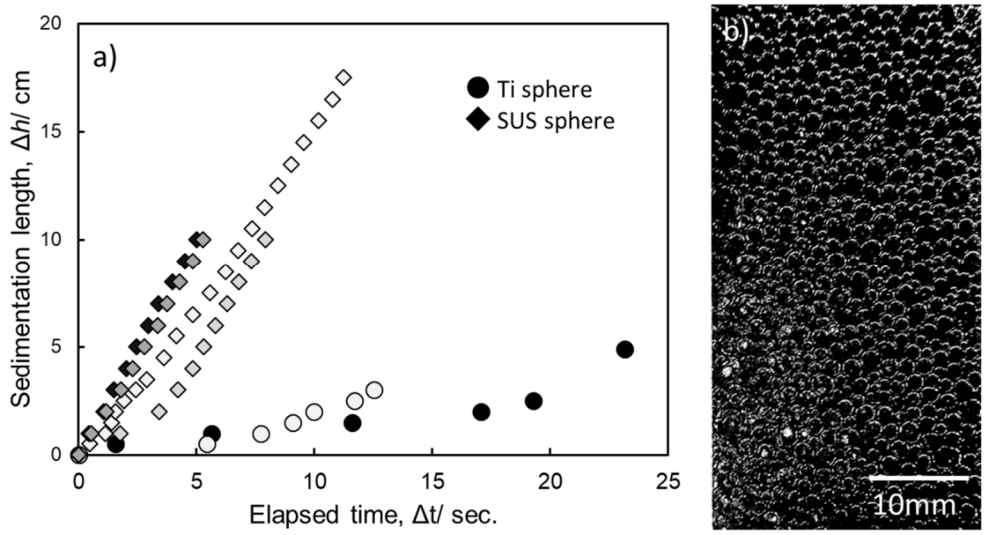

FIG 2 – Particle descent behaviour: (a) and foam morphology, (b) in glycerin solution with $\eta_L = 60.1$ mPa·s.

The experimental points marked ● and ♦ in this figure represent the results for stainless steel sphere and titanium sphere, respectively. The different colours of the symbols indicate the different trajectories of stainless steel and Ti spheres. It can be seen that in the gas-liquid fluid under this condition, both the stainless steel and titanium spheres descend while pushing away the bubbles, and that the sedimentation velocity of stainless steel spheres with high density is higher than that of titanium spheres with low density.

The apparent viscosity η derived from the sedimentation velocity of stainless steel and titanium spheres using Equation 4 is 419 and 671 mPa·s, respectively. The latter is particularly large. These values are large compared to the viscosity of single liquid phase, $\eta_L = 60.1$ mPa·s. The apparent viscosity could not be determined from the sedimentation velocity of the glass beads because they were trapped between bubbles and did not sediment.

Figure 2b shows a binarised image of a gas-liquid fluid with $\phi_g = 0.7$ immediately after foaming. Large bubbles with diameters of 1.0 to 1.5 mm are found to be homogeneously distributed. Since it is expected that in this glycerine aqueous solution, the high viscosity of liquid decreases the liquid drainage rate in the bubble film, slowing down the generation of bubbles, it took about 2 mins to reach the desired gas phase fraction. Meanwhile, the bubbles have grown.

Figure 3a shows the time dependence of the falling length of stainless steel, titanium, and glass spheres in a gas-liquid fluid of glycerine solution with $\eta_L = 6.01$ mPa·s. The spheres made of stainless steel, titanium, and glass all descended, pushing away the bubbles and reaching the terminal velocity. The apparent viscosity η derived from the terminal velocity of each sphere was 340,

415 and 439 mPa·s, respectively. Although these values were larger than that of the liquid phase, there were no significant differences depending on the type of falling sphere. As shown in Figure 3b, foams were generated quickly, and the packing of fine bubbles was maintained until the drainage in the liquid film progressed. No bubbles with a diameter larger than 1 mm were observed during this period.

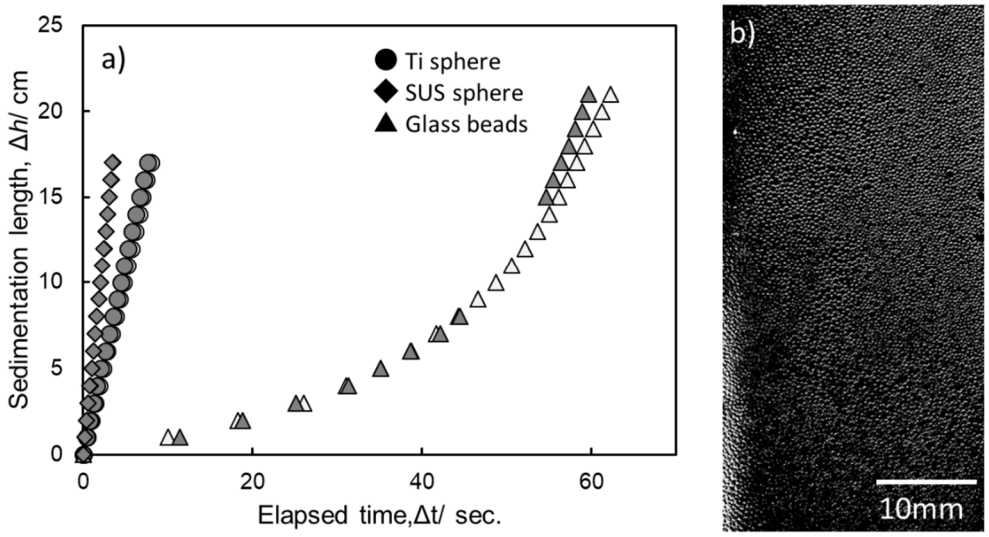

FIG 3 – Particle descent behaviour: (a) and foam morphology; (b) in glycerin solution with η_L = 6.01 mPa·s.

The sedimentation of stainless steel and titanium spheres in a gas-liquid fluid in a glycerin solution with η_L = 1.76 mPa·s is shown in Figure 4a. As is seen in Figure 4b, the foams are not homogeneous in size, and the forming region is divided into two parts: a region with coarsened bubbles in the upper part and that with dense bubbles in the lower part. The stainless steel spheres descended while breaking the coarsened bubbles and its terminal velocity was reached at 0.6 sec after falling. In the case of the titanium sphere, the sedimentation velocity is slow in the upper region and increases in the lower region. The titanium sphere did not break the bubbles and was repeatedly accelerated and decelerated due to the movement by pushing the bubbles away and stopping by the bubbles. The glass sphere was suspended at the top of the fluid and did not fall down. Therefore, it was considered difficult to derive the apparent viscosity of the gas-liquid fluid from the sedimentation velocity of the titanium spheres and glass beads. From the terminal velocity of the stainless steel spheres, η = 50 mPa·s was derived, approximately 28 times larger than the viscosity of the single liquid phase.

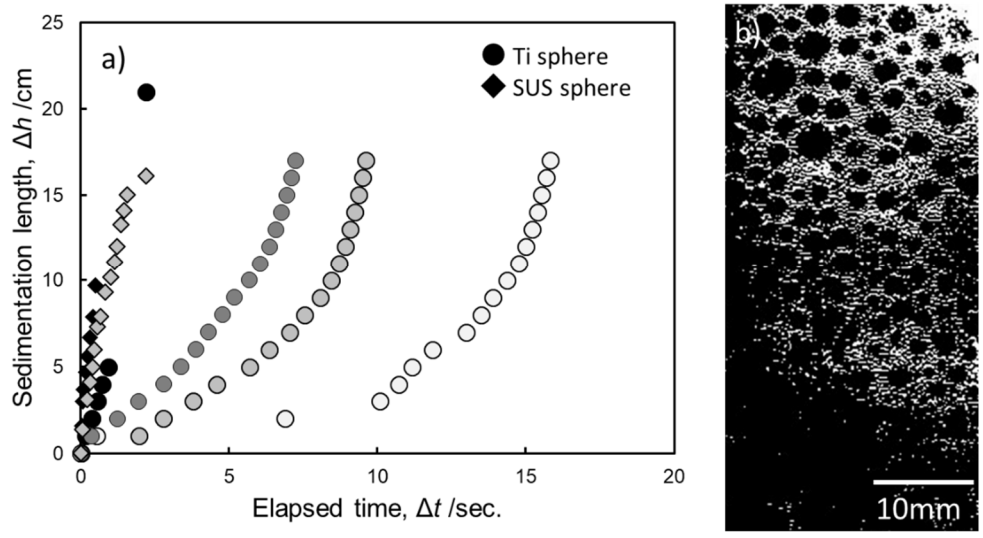

FIG 4 – Particle descent behaviour: (a) and foam morphology, (b) in glycerin solution with η_L = 1.76 mPa·s.

RELATIONSHIP BETWEEN LIQUID VISCOSITY AND APPARENT VISCOSITY OF FOAM

The apparent viscosities of the gas-glycerin solution systems at $\phi_g = 0.7$ obtained in this study are compared with those determined by Hatano *et al* (2021) using the rotational method.

Figure 5 shows the relationship between the viscosity of liquid-phase and the apparent viscosity of the foaming gas-liquid fluid. The apparent viscosity measured by the falling-ball method using stainless steel and Ti balls is shown by a solid line and a broken line, respectively, and that measured by Hatano *et al* (2021) using the rotation method at 50 and 100 rev/min is shown by a grey dotted line and a grey dash-dotted line, respectively. Regardless of the measurement method, the apparent viscosity shows an increasing behaviour as a logarithmic function of the viscosity of single liquid phase. In the falling-ball method, the apparent viscosity estimated using stainless steel spheres is lower than that using titanium spheres because the sedimentation velocity U in Equation 4 of the stainless steel sphere is higher. The apparent viscosity measured by the rotation method tends to decrease with increasing rotational velocity. Therefore, it can be concluded that both measurement methods show similar results regarding the decrease in apparent viscosity with an increase in the velocity of the moving object. Under the present experimental condition, the apparent viscosities derived from the sedimentation velocity of stainless steel and titanium spheres with a diameter of 2 mm are in good agreement with those obtained at rotational velocity of 50 and 100 rev/min in rotation method, respectively.

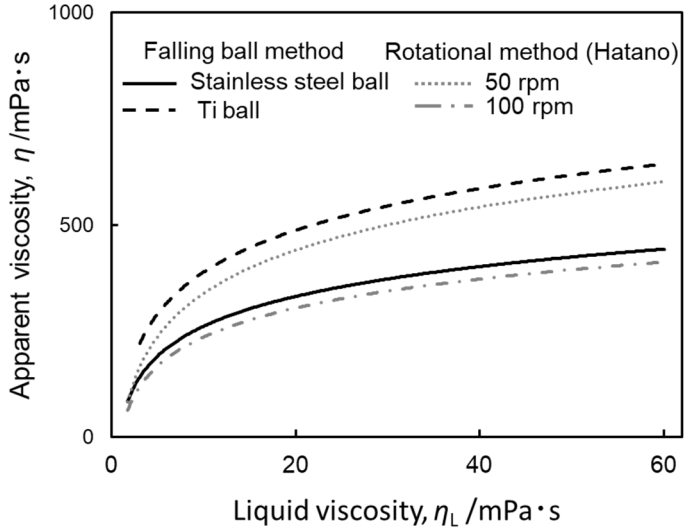

FIG 5 – Comparison of apparent viscosity of gas-liquid fluid estimated by the falling-ball method and rotation method.

The falling-ball method utilises particle sedimentation and the rotation method uses constant rotation of a cylinder. Since the motion of the moving object is different in those two methods, it is not necessary that the values for apparent viscosity obtained by each method be equal to each other. However, it was found in this study that the apparent viscosity of gas-liquid fluid obtained by falling-ball method is comparable to that by the rotation method. Further accumulation of experimental data in the future may lead to derive a quantitative relationship between rotation rate and sedimentation velocity.

CONCLUSIONS

To understand the sedimentation behaviour of iron particles suspended in foaming slag, the apparent viscosity of a gas-liquid fluid with glycerin solution was estimated by the falling-ball method.

The apparent viscosity obtained was larger than the viscosity of a single liquid phase. When the viscosity of the liquid phase is large, the particles fall while pushing away the bubbles and sewing the liquid part of the foam film since the progress of liquid drainage is slow and wet foam can be easily maintained. However, under the present experimental condition, particles with low density,

such as glass beads, could not push bubbles away and did not fall. The higher the density of particles, the smaller the apparent viscosity of the gas-liquid fluid derived by the Stokes law.

REFERENCES

Glycerine Producer's Association, 1969. Physical Properties of Glycerine and Its Solutions., New York.

Hatano, S, Hayashi, S, Saito, N and Nakashima, K, 2021. Viscosity Evaluation of Simulated Foaming Slag via Interfacial Reaction at Room Temperature, *ISIJ Int*, 61:2904–2914.

Li, W, Iwama, T, Yu, H, Ueda, S, Saito, N and Inoue, R, 2021. Apparent Viscosity Measurement of Solid-liquid Coexisting Fluid by Falling Ball Method for Evaluation Iron Particle Sedimentation Velocity in Slag, *ISIJ Int*, 61:2915–2922.

Martinsson, J, 2018. *A Study of the Behavior of Foaming Slag in Steelmaking* (Stockholm).

Roscoe, R, 1952. The Viscosity of Suspensions of Rigid Spheres, *Br J Appl Phys*, 3:267–269.

Saito, N, Hara, D, Teruya, S and Nakashima, K, 2020. Viscosity of Slag Suspensions with a Polar Liquid Matrix, *ISIJ Int*, 60:2807–2818.

Stokes, G G, 1845. On the Theories of the Internal Fricsion of Fluids in Motion, and of the Equilibrium and Motion of Elastic Solids, *Trans Camb Philos Soc*, 8:287–319.

Monitoring Sb in lead refining using advanced techniques in Industry 4.0

DOI: 10.62053/LGCJ9629

A Van den Bulck[1], T De Staercke[2], S Zummar[3] and T Van Rompaey[4]

1. Scientist, Corporate R&D Umicore, 2250 Olen, Belgium.
   Email: amy.vandenbulck@eu.umicore.com
2. R&D Project Chemist Adviser, Umicore, 2250 Olen, Belgium.
   Email: tinne.destaercke@eu.umicore.com
3. Process Engineering Manager, Umicore, 2660 Hoboken, Belgium:
   Email: shady.zummar@eu.umicore.com
4. Head of Research Operations and Technology, Umicore, 2250 Olen, Belgium.
   Email: tim.vanrompaey@eu.umicore.com

ABSTRACT

An increase of 22 per cent in lead usage is expected in the European Union by 2050. During lead refining, the Harris process is a critical step in which a salt melt is used to remove arsenic, tin and antimony. During this process, the caustic salt melt absorbs these impurities, requiring regular evacuation before saturation. Current metallurgical practices for: 1) determining the end point of the lead alloy involve time-consuming sampling and offline analysis, and 2) determining the end point of the caustic salt melt are based on subjective visual observations by the operator. In the context of Industry 4.0 concept, automating these processes becomes desirable, as smart sensors systematically collect real-time data in an unbiased manner. This research focuses on monitoring the Harris refining process using objective methodologies. Two different methodologies are investigated. The first methodology focuses on electrical conductivity changes of the caustic salt melt as function of Sb content. For this study, synthetic and industrial samples are used. A lab-scale electrical conductivity set-up was built to accommodate the aggressiveness of the salt melt. Initial findings suggest a promising relationship between electrical conductivity and Sb content in the caustic salt melt. Although the results are preliminary, the study provides valuable insights by enabling real-time measurements. The second methodology focuses on measuring the electromotive force (EMF) in lead doped with Sb at pilot-scale. Multiple probes are reevaluated for their effectiveness in Sb measurement. Ultimately, a partially stabilised MgO probe with Ni as a reference, without cardboard and copper protection caps, yields promising results. A correlation between EMF and Sb content is observed. However, repeatability issues arise due to possible wire interference at low temperatures. The results underscore the potential of advanced measurement techniques in optimising lead alloy production within the context of Industry 4.0.

INTRODUCTION

Lead (Pb) recycling has witnessed significant growth, rising from approximately 50 per cent of total production output in 1990 to around 75 per cent of current production (Roberts, 2020). The vital role of lead in the circular economy has been a point of discussion (Blanpain, Reuter and Malfliet, 2019). As a ‘carrier metal,’ lead can dissolve or transport diverse materials—either directly or as compounds—into other processing pathways for subsequent recovery. Extensive studies have explored the thermodynamic relationships and limitations associated with lead, underscoring its critical importance within the metallurgical ecosystem. Despite efforts to reduce lead usage, such measures may adversely affect the recyclability of other materials, including Ag, Cu, Sb, Sn, Te and Zn (Blanpain, Reuter and Malfliet, 2019). Notably, if the European Union aims to achieve climate neutrality, it is projected that lead utilisation will increase by 22 per cent by 2050 (Gregoir, 2022). For these reasons, it is important to continue to improve lead operations by making them safer and more efficient. At Umicore’s lead refinery, the Harris process is employed to extract arsenic (As), tin (Sn) and antimony (Sb). In this process, sodium hydroxide and sodium nitrate serve as sources of oxygen for the oxidation reaction, operating at temperatures exceeding 450°C (Sinclair, 2009; Lauterbach, 1931). The chemical reactions are as follows:

$$2[\mathrm{As}] + 2\mathrm{NaNO_3(s)} + 4\mathrm{NaOH(l)} \rightarrow 2\mathrm{Na_3AsO_4(s)} + \mathrm{N_2(g)} + 2\mathrm{H_2O(g)} \quad (1)$$

$$5[\mathrm{Sn}] + 4\mathrm{NaNO_3(s)} + 6\mathrm{NaOH(l)} \rightarrow 5\mathrm{Na_2SnO_3(s)} + 2\mathrm{N_2(g)} + 3\mathrm{H_2O(g)} \quad (2)$$

$$2[\mathrm{Sb}] + 2\mathrm{NaNO_3(s)} + 4\mathrm{NaOH(l)} \rightarrow 2\mathrm{Na_3SbO_4(s)} + \mathrm{N_2(g)} + 2\mathrm{H_2O(g)} \quad (3)$$

$$5[\mathrm{Pb}] + 2\mathrm{NaNO_3(s)} \rightarrow 4\mathrm{PbO} + 4\mathrm{Na_3PbO_2(s)} + \mathrm{N_2(g)} \quad (4)$$

The targeted elements are removed as sodium arsenate, sodium stannate and sodium antimonate. Within the Harris cylinder, a layer of molten sodium hydroxide (NaOH) and sodium chloride (NaCl) floats atop the molten lead, called the caustic salt melt. The above compounds are present as a solid suspension in this molten caustic salt melt. However, a single Harris caustic salt melt is insufficient to eliminate all contaminants. As impurity concentrations rise in the caustic melt, its viscosity changes. When the melt reaches saturation and approaches excessive viscosity, it is evacuated from the cylinder. The melts can hold up to 20 wt per cent of arsenic or tin and 30 wt per cent of antimony. Exceeding these limits results in overly viscous melts that cannot be evacuated from the cylinder (Lauterbach, 1931; Davey, 1980; Leroy, Lenoir and Escoyez, 1970). While the Harris process recognises viscosity as a limiting factor, the melt saturation level is currently assessed subjectively by the operator's visual judgment. Unfortunately, there are no recorded efforts to precisely measure the viscosity of the caustic salt melt; existing literature only provides information on saturation limits. In contrast to monitoring the Harris slag melt, attempts to monitor the lead melt have been done to determine when the impurities have been lowered to a desirable level. Traditionally, the end point refining of lead alloys involves time-consuming sampling and offline analysis. However, the use of electromotive force (EMF) of the oxygen potential has been demonstrated (Grange and Heerman, 1974; Kapusta, Meadowcroft and Richards, 2002). In the first experiment (Grange and Heerman, 1974), a cell configuration involving Pt, Fe, Pb(l), PbO(s) | NaOH | Cu_2O(s), Cu(s), Pt is used to measure oxygen potential. The addition of different impurities to lead shows a clear effect on measured EMF. Industrial efforts were made where the tin concentration throughout the Harris process was compared to EMF measurements. A clear end point of the refining process emerged when the EMF measure decreased by 215–220 mV and stabilised. These findings highlight the feasibility of using EMF measurements to monitor impurity levels during lead refining via the Harris process. However, challenges related to probe reliability exists, as specialised probes were required and only 65–70 per cent of them yielded successful measurements. In another attempt (Kapusta, Meadowcroft and Richards, 2002), an oxygen probe is employed using a copper-copper oxide electrode within a cell configuration represented as: Fe (Stainless steel), Pb(l), PbO(s) | ZrO_2 doped Y_2O_3 | Cu_2O(s), Cu(s), Fe(stainless steel). The experimental approach mirrored the previous one, starting with laboratory tests to validate the probe's performance and followed by industrial monitoring of lead melts. The results show that utilising oxygen activity EMF measurements to monitor the impurity content during lead softening is a viable approach. However, similar to the previous authors, probe construction challenges, particularly related to the thermal shock resistance of zirconia tubes, remains a major obstacle. The aim of the current study is two-fold. The first goal is to examine the electrical conductivity of the caustic salt melt as it relates to antimony (Sb) content. The hypothesis is that as Sb content increases, the presence of solid particles will alter the electrical conductivity path, resulting in changes to the overall electrical conductivity of the melt. The second part of the study focuses on testing new probes to address the existing construction challenges associated with the current probes. These new probes aim to enhance reliability and performance in measuring relevant parameters. By accomplishing these dual objectives, the way for automating the refining of the Harris process through the utilisation of intelligent sensors is a possibility.

MATERIALS AND METHODS

Materials

Industrial samples

The industrial caustic salt melt samples are directly obtained from the Umicore-Hoboken Sb-Harris cylinder at various points during the Sb removal process. The process operates within a 4-hour interval, commencing with a single pour of sodium hydroxide. This ensures a consistent rise in sodium antimonate content and prevents any dilution of the melt due to additional sodium hydroxide pours. Samples are collected at the 2-, 3- and 4-hour marks, with the final sample taken just before cylinder evacuation. The samples are cast into round shapes with a diameter of 5 cm.

Synthetic samples

Pure anhydrous sodium antimonate is obtained from the Harris process wet plant at Umicore Hoboken and is used to create synthetic samples. These synthetic samples are prepared by mixing sodium antimonate with sodium hydroxide and sodium chloride, see the compositions outlined in Table 1. The quantities are calculated based on stoichiometry, assuming that the initial Harris salt melt has a 4:1 mass ratio of sodium hydroxide to sodium chloride, with only the former being consumed in the reaction to form sodium antimonate. Each sample weighs 250 g. To prevent exposure to ambient moisture, given the high hygroscopic nature of sodium hydroxide pellets, the preparation is conducted inside a glove box flushed with argon.

TABLE 1

Synthetic caustic melt compositions for electrical conductivity measurements.

No.	Na_3SbO_4 (wt.%)	NaOH (wt.%)	NaCl (wt.%)	NaOH:NaCl ratio
1	0	80	20	4
2	32.5	52	15.5	3.4
3	44.0	42	14	3
4	53.0	34	13	2.6
5	31.0	27	12	2.3
6	73.0	17	10	1.7
7	0	60	40	1.5

Synthetic lead alloy samples are made by mixing pure lead (99.999 wt per cent) coming from the end-product of Umicore's Hoboken lead refinery and fluxing with a Pb-65 wt per cent/Sb-35 wt per cent alloy during the EMF process. During the process samples are taken and sent for ICP-OES analysis.

Methods

Electrical conductivity measurements

A two-wire configuration is used to measure the electrical conductivity of both industrial and synthetic caustic melt samples. The set-up includes 316 L stainless steel crucibles with a volume of approximately 40 mL. For corrosion resistance, 1 mm diameter nickel wires are used as electrodes. These wires are enclosed in alumina tubes to enhance protection and rigidity, ensuring consistent cell geometry throughout the experiment. The electrodes protrude about 20 mm from the alumina tubes, maintaining a 6.2 mm distance between them. The electrodes are connected to a Keysight E4980A/AL Precision LCR Meter, which supplies an alternating current. The settings are set to 1 V and 100 kHz. A schematic of the set-up can be found in Figure 1.

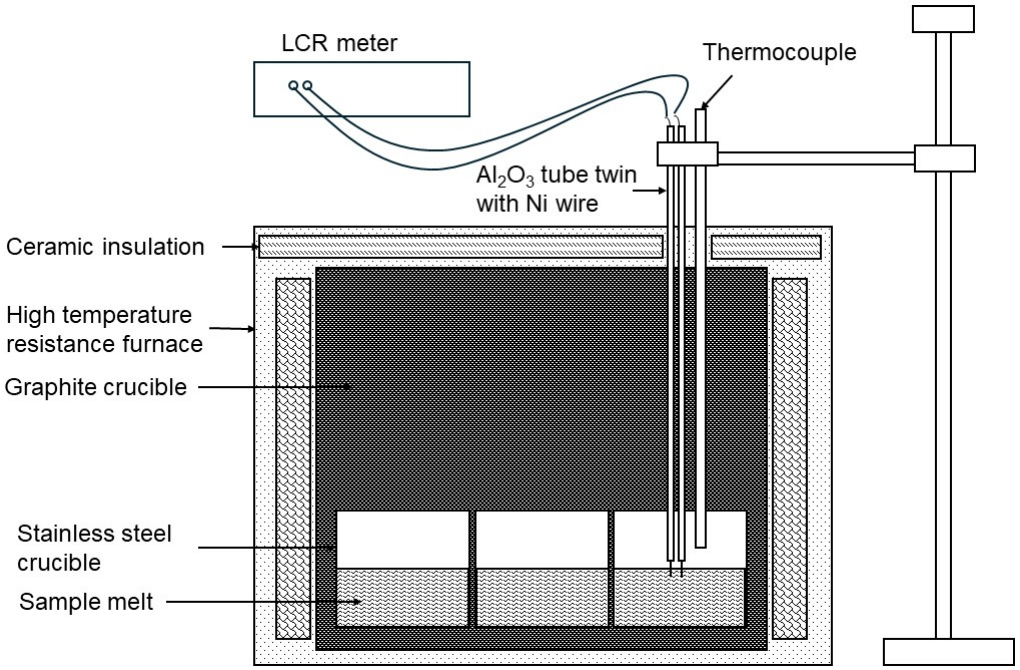

FIG 1 – Schematic of set-up for electrical conductivity measurement.

To maintain precise control, the set-up is positioned atop a resistance furnace. Before conducting experiments, the cell constant is determined using 20 mL solutions of 0.01 M and 0.1 M potassium chloride. The electrodes are immersed to a depth of 4.5 mm and the temperature-resistance data are used to derive the cell constant which is determined to be 1.41 cm^{-1}. Once the cell constant is established, crucibles containing the samples are placed in the furnace, raising the temperature to 485°C. The estimated mass equivalent to 20 mL is carefully loaded into the crucible, avoiding direct exposure to ambient air. A nearby thermocouple ensures precise temperature control. Refractory bricks cover the furnace top, minimising thermal fluctuations, while a continuous flow of argon prevents sample reactions with air. After reaching the target temperature, the samples are allowed to equilibrate for approximately an hour. A crucible containing material is positioned directly under the electrodes and the electrodes are lowered into the bath. As the electrodes lowered, a sudden decrease in resistance indicates contact with the melt's surface. At this point, the electrodes are further lowered by 4.5 mm and the resistance is recorded. Afterward, the electrodes are raised and the crucible is replaced with the next sample. This process is repeated for each sample. Post-experiment, the distance between the electrodes is remeasured and no significant changes are observed, ensuring the cell's integrity.

Electromotive force measurements

The Pb-65 wt per cent/Sb-35 wt per cent alloy is created by melting pure lead with 99.999 wt per cent pure Sb in a lab-scale resistance furnace using a graphite crucible at 650°C under a nitrogen environment. The EMF experiments are performed on a pilot-scale resistance furnace. Pure lead of 439 kg is loaded into the furnace and melted to a temperature of 450°C in an air environment. Throughout the experiments, the Pb-65 wt per cent/Sb-35 wt per cent alloy is added every 30 minutes. To ensure mixing, nitrogen is bubbled through the melt. Before conducting the EMF measurements, a sample is taken for chemical inductively coupled plasma – optical emission spectroscopy (ICP-OES) analysis. The details of the added material and the targeted Sb content in the lead alloy are provided in Table 2.

TABLE 2

Added material to pure lead and target Sb content for electromotive force (EMF) measurements.

No.	Pb/Sb alloy (kg)	Sb (wt.%)
1	0	0
2	311	0.02
3	313	0.05
4	1249	0.20
5	4370	0.75

Several EMF probes are tested. At low temperatures, probes with protective cardboard and/or copper caps did not dissolve, so it was decided to avoid using any protective caps. Furthermore, the sensitivity to thermal shock prevents the use of yttria-stabilised probes. Ultimately, a partially stabilised MgO cell with a Ni reference and a celox insert is used. The analysis of the EMF measurements is performed by the supplier.

RESULTS AND DISCUSSION

Electrical conductivity measurements

After reaching the target temperature of 485°C, the samples are allowed to equilibrate for approximately one hour. Upon visual inspection, it is evident that the synthetic samples containing sodium antimonate did not fully melt; instead, they form a paste-like consistency. These synthetic samples differ significantly from the industrial samples, as confirmed by probing the melts with a stainless-steel rod. The material exhibits extreme stickiness and adhered tightly to the rod. To maintain the electrode integrity, measurements are excluded for the synthetic samples. Only the pure salt synthetic sample and the fully melted industrial samples undergo the measurement. The sample composed of a pure salt mixture exhibits an electrical conductivity of 2.3 S/cm—significantly lower than the theoretical value for pure sodium hydroxide (17.3 S/cm) (Marcus, 2016). However, this measurement aligns more closely with findings from a study on the electroconductivity of sodium and potassium hydroxide eutectics, which reported a value of 1.7 S/m at 450°C (Dauby, Glibert and Claes, 1979). The discrepancy likely arises from variations in melt compositions and higher temperatures. Subsequent measurements for the industrial samples reveal a notable increase in resistance and a corresponding decrease in conductivity with each additional hour of processing. Additionally, the magnitude of measured reactance increases over time. The detailed results of the conductivity measurements are shown in Figure 2.

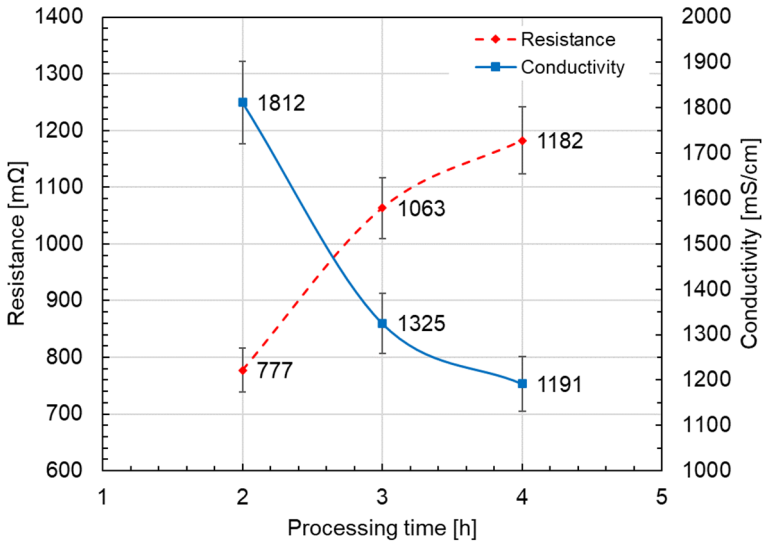

FIG 2 – Measured resistance and conductivity of industrial Harris caustic salt melt at 485°C. The error bars indicate a 5 per cent error.

During the measurement, it is observed that resistance values exhibit continuous increase. However, after a few minutes, the resistance partially stabilises. Although the rate of resistance increase becomes negligible, it never completely ceases. This fluctuation is likely attributed to the initial rapid corrosion of the electrodes, followed by a slower degradation. The degradation of the electrodes is visible notable. To assess the impact of corrosion uncertainty, the initially measured samples are retested, revealing an uncertainty of no more than 5 per cent. Nonetheless, the electrical conductivity changes significantly as function of process time. The change in conductivity is likely attributed to: 1) the presence of antimonate solids, and 2) the NaOH-NaCl ratio within the matrix. The overall outcome of this study is positive, but further optimisation of the cell design is necessary. Nickel has been selected due to its high corrosion resistance in sodium hydroxide melts. However, it still experiences some attack during the measurements. The question remains whether the material will eventually form a passivating layer after initial exposure or continue to corrode.

Electromotive force measurements

Prior to conducting the EMF measurements, a representative sample for Sb content measurement in the lead alloy is taken. Subsequently, two EMF measurements are carried out for each fixed Sb content within the alloy. The resulting data is presented in Figure 3.

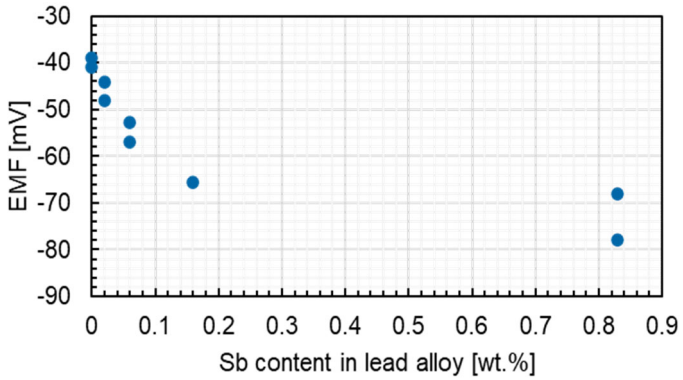

FIG 3 – Electromotive force (EMF) measurement as function of Sb content in lead alloy at 450°C for one run. A second run could not yield the same results.

While the initial results indicate a positive outcome, a subsequent test repetition fails to reproduce the same findings. Specifically, these repeated tests reveal incomplete stabilisation, which was attributed to the elevated resistance encountered due to the low temperatures of 450°C. The increased resistance may trigger other factors, including cable resistance, lance quality and the

overall measurement system. To address this challenge, ongoing efforts are focused on designing a specialised cell by the supplier. The primary goal is to minimise resistance during the measurement process.

CONCLUSIONS

Lead production volumes are projected to consistently increase and lead's integral role within the circular economy is firmly established. Consequently, it remains critical to enhance lead operations by boosting efficiency and ensuring safety. In the context of Industry 4.0, it can be envisioned that the utilisation of objective sensors and data-driven analyses can be made to draw informed conclusions. The objective of this study is to explore techniques for automating the Harris lead refinery process by incorporating real-time sensors in place of time-consuming analyses and subjective visual inspections of the Harris caustic salt melt saturation. In the first technique, the electrical conductivity changes as function of Sb content in the caustic salt melt that is investigated. This approach capitalises on the interplay between chemical composition changes and the accumulation of particles within the molten material as the antimony concentration in the melt increases. The experiments focus on industrial caustic medium samples, exclusively containing antimony coming from Umicore's lead refinery, alongside to synthetic slags composed of pure materials to mimic the industrial composition. Interestingly, the behaviour of synthetic and industrial slags diverges significantly. While the former exhibits a thicker, paste-like consistency, the latter fully melts at operational temperatures. Unfortunately, a definitive explanation for this discrepancy could not be provided. Nevertheless, the insights primarily stem from the analysis of industrial samples. Given the plausibility of electrical conductivity as a reliable method, it is recommended to further refine this technique. Additional measurements using industrial samples can provide deeper insights into the relationship between electrical conductivity and antimony content. Additionally, the cell design must be investigated, as the nickel electrodes employed in the study suffer corrosive attack upon immersion in the melts. Aside its application in determining antimony saturation, it is suggested to investigate the impact of arsenic and tin on the electroconductivity of Harris slags as well. In the second technique, electromotive force measurements are reinvestigated. Unfortunately, akin to prior investigations, issues related to probe sensitivity hinders the attainment of satisfactory results. This challenge was attributed to the elevated resistance induced by the low operating temperature of 450°C. To address this limitation, designing a specialised cell that can reduce resistance during measurements is proposed, thereby minimising the impact of other artefacts.

ACKNOWLEDGEMENTS

The authors extend their gratitude to J Peeters for coordinating the acquisition of samples from the Umicore Hoboken lead refinery. Additionally, we appreciate the cooperation of the operational team at the Umicore Hoboken lead refinery, which facilitated CRD's sampling from their kettles.

REFERENCES

Blanpain, B, Reuter, M and Malfliet, A, 2019. Lead metallurgy is fundamental to the circular economy, Socrates Policy Brief EU MSCA-ETN.

Dauby, C, Glibert, J and Claes, P, 1979. Electrical conductivity and specific mass of the molten NaOH-KOH eutectic mixture, *Electrochimica Acta*, 24(1):35–39.

Davey, T, 1980. The Physical Chemistry of Lead Refining, in *Lead-Zinc-Tin '80 – Proceedings of a World Symposium on Metallurgy and Environmental Control* (eds: J M Cigan, T S Mackey and T J O'Keefe), pp 477–507 (The Metallurgical Society of AIME).

Grange, C and Heerman, L, 1974. Monitoring of impurities in molten lead by e.m.f. measurements, Application to the Harris process of lead refining, *Journal of Applied Electrochemistry*, 4:279–288. https://doi.org/10.1007/BF00608969

Gregoir, L, 2022. Metals for Clean Energy: Pathways to solving Europe's raw materials, report for KU Leuven.

Kapusta, J P, Meadowcroft, T R and Richards, G G, 2002. Oxygen Softening of Lead: On-Line Measurement of Bullion Quality, *Canadian Metallurgical Quarterly*, 41(4):451–464. https://doi.org/10.1179/cmq.2002.41.4.451

Lauterbach, H, 1931. Beitrage zur Bleiraffination nach dem Harris-Verfahren (Contributions to lead refining using the Harris process), *Metall und Erz (Metal and Ore)*, 27(13):317–326.

Leroy, J L, Lenoir, P J and Escoyez, L E, 1970. Lead Smelter Operation at N V Metallurgie Hoboken SA, in *AIME World Symposium on Mining and Metallurgy of Lead and Zinc: vol II – Extractive Metallurgy of Lead and Zinc* (ed: C H Cotterill), pp 824–852 (New York).

Marcus, Y, 2016. Ionic Liquid Properties: From Molten Salts to RTILs, in *Ionic Liquid Properties*, first edn (Springer Cham). https://doi.org/10.1007/978–3-319–30313–0

Roberts, H, 2020. Evolution of Global Secondary Lead Production, in *Proceedings of the 9th International Symposium on Lead and Zinc Processing*, pp 3–15 (Springer International Publishing).

Sinclair, R J (ed), 2009. *The Extractive Metallurgy of Lead*, Spectrum Series (The Australasian Institute of Mining and Metallurgy: Melbourne).

Effect of solid particle size on the viscosity of a secondary copper smelting slag

DOI: 10.62053/ZIGO4105

O Vergote[1], I Bellemans[2], K Verbeken[3] and A Van den Bulck[4]

1. Postdoctoral Researcher, Ghent University, Department of Materials, Textiles and Chemical Engineering, Gent 9052, Belgium. Email: olivier.vergote@ugent.be
2. Assistant Professor, Ghent University, Department of Materials, Textiles and Chemical Engineering, Gent 9052, Belgium. Email: inge.bellemans@ugent.be
3. Associate Professor, Ghent University, Department of Materials, Textiles and Chemical Engineering, Gent 9052, Belgium. Email: kim.verbeken@ugent.be
4. R&D Competence Manager, Umicore NV, Umicore Research and Development, Olen 2250, Belgium. Email: amy.vandenbulck@eu.umicore.com

ABSTRACT

Viscosity is one of the most important physicochemical properties during pyrometallurgical operations. In the sub-liquidus regime, an important factor is the presence of suspended solid particles, yet its influence is not well-described in earlier literature, despite the significance of this factor. This project aims to determine the influence of spinel particles ($Zn(Al,Fe)_2O_4$) on the rheology of a multiphase synthetic PbO-SiO_2-ZnO-Fe_2O_3-CaO-Al_2O_3 slag system. Three data sets with a well-controlled methodology and three different spinel sizes (small (13 μm), medium (34 μm) and large particles (76 μm)) were published previously, using a custom-built high-temperature rheometer. This study presents an additional data set of slag viscosity measurements, performed using a different apparatus, the Anton Paar FRS 1800, to verify the consistency of the earlier determined viscosity behaviour. Within this data set, no consistent trend could be found between the predicted wt per cent spinel and the relative viscosity. Therefore, additional quenching experiments were conducted to identify the morphology and experimentally determined volume fraction of the spinel particles in the slag. These measurements revealed a difference in spinel size across the samples and corresponding viscosity behaviour, emphasizing the importance of spinel particle size on slag viscosity. Once the spinel size was taken into account, consistent viscosity results (relative apparent viscosity and flow index) were observed across the two devices. This study confirms that, once all parameters affecting slag viscosity are considered, the viscosity behaviour of a heterogeneous slag can be uniquely determined. The resulting optimised slag viscosity models can be used to predict viscosity before processing, addressing relevant phenomena such as slag tapping, slag foaming and copper droplet settlement.

INTRODUCTION

Viscosity is one of the key physicochemical parameters to control during pyrometallurgical processes. Nowadays, a large amount of viscosity models are available to predict the viscosity of the liquid slag phase. However, the rheology of partially crystallised slags (a suspension, ie a liquid slag matrix with small solid particles suspended in the melt) remains insufficiently understood and a large discrepancy exists across various published works (Sichen *et al*, 2022). Rheological aspects such as the non-Newtonian behaviour of slags containing suspended solid particles are poorly understood, resulting in a low reproducibility of the viscosity data across various studies. A key reason for the scatter on the obtained viscosity data is the lack of control/description of all parameters affecting the final viscosity of a heterogeneous slag. Liu *et al* (2018) reviewed a large number of viscosity studies regarding heterogeneous silicate melts and reported the following parameters of interest: solid particle volume fraction, particle shape and the shear rate. For the particle shape, both the aspect ratio, ie the ratio of the longest axis of the particle to the shortest perpendicular axis and the size were reported. In pyrometallurgical literature, the focus has mainly been on the aspect ratio of the particle as the main morphological parameter (Liu *et al*, 2018). Consequently, the main mode of shear thinning, ie the preferential re-orientation of the particles in the melt with respect to the flow direction, caused by a variation in the shear rate, was described in literature as individual particle orientation. This type of shear thinning has been visualised in Figure 1a. Initially, the particles are randomly oriented. Upon shearing the suspension with an increasing flow rate, the hydrodynamic

force acting on the particles increases, which causes the rotation of the particles around their axis perpendicular to the flow direction. Consequently, the flow lines of the melt are less disturbed, which causes a reduction in the apparent viscosity at large shear rates. Particles with a large aspect ratio can exhibit more of this type of shear thinning compared to equiaxed, symmetrical particles (Mueller, Llewellin and Mader, 2009).

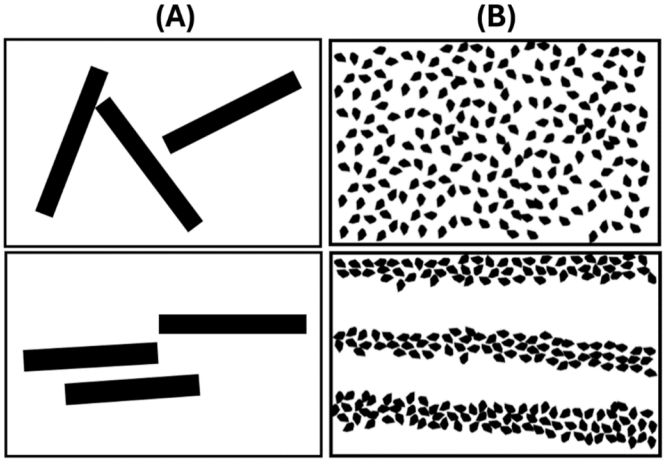

FIG 1 – Illustration of shear thinning, ie the re-orientation of the particles with respect to the flow direction. Top: random orientation, Bottom: preferential orientation with respect to the flow direction. (a): Individual particle orientation (b): Particle-particle orientation.

A second type of shear thinning is the particle-particle orientation, ie the re-orientation of the particles with respect to their closest neighbours. In Figure 1b, at low shear rates and the associated random orientation of the particles, the path of the melt flow lines is largely disturbed. Upon shearing, the particles may group in more closely packed clusters to decrease the disturbance of the melt flow lines (Caricchi *et al*, 2007). The elongated clusters have been observed experimentally by Lyon *et al* (2001) for cold suspensions. Suspensions for which the suspended particles have a larger number of closest neighbours can exhibit this type of shear thinning to a larger extent. Consequently, the particle size will influence the degree of shear thinning associated with particle-particle orientation. Moreover, this mode of shear thinning also explains the observed shear thinning for suspensions containing spherical/equiaxed particles, which cannot show individual particle orientation (Mueller, Llewellin and Mader, 2009; Saito *et al*, 2020).

For slag suspensions, literature commonly does not focus on the particle size. The work of Wright *et al* (2000) is one of the few studies which examined the effect of the spinel size on the viscosity of a CaO-MgO-Al_2O_3-SiO_2 slag. Suspensions with three different spinel sizes were examined: 100–210 μm, 210–440 μm and 440–990 μm. They noted that the quality of their data was insufficient to make conclusions on the effect of particle size on the viscosity.

In our previous work (Vergote *et al*, 2023), the effect of the spinel size was examined for three different spinel sizes: small (13 μm), medium (34 μm) and large particles (76 μm). By employing a custom-built rheometer with quenching possibilities, accurate microscopical examination of the slag as it was during high-temperature viscosity measurement was possible. As a result, three accurate data sets were obtained from which the following conclusions were obtained:

1. The viscosity increases for decreasing spinel size at similar solid phase fractions.
2. Fully liquid samples at the spinel saturation composition showed Newtonian behaviour. Therefore, it is confirmed that no additional spinel particles located at the interface of the crucible and spindle (Vergote *et al*, 2021) affected the bulk slag viscosity measurement.
3. All examined samples containing spinel particles, even at low vol per cent of 1.8 per cent, showed shear thinning behaviour. The amount of shear thinning increases for decreasing spinel size.

These conclusions were similar to the ones obtained from experiments with magmas containing solid particles (Del Gaudio, Guido and Taddeucci, 2013). Yet, additional viscosity data for slags relevant

for the copper recycling industry are required to further establish the accuracy of our previous study. Therefore, this work examines the viscosity for slags with a relevant composition, while employing a different slag preparation and viscosity apparatus. This cross-check is required due to the low availability of accurate relevant viscosity data in literature, for which all parameters are well-described.

METHODOLOGY

Slag selection and preparation

An earlier work by Vergote *et al* (2021) identified the interaction between the slag and the alumina labware as the main experimental error for slag viscosity measurements. In this work, liquid lead-silicate based slag compositions were reported which were compatible with alumina, ie resulted in a low degree of interaction with crucible and spindle. One such composition (Slag 1, Table 1) was used in this work as the liquid slag matrix to prepare the heterogeneous slag-spinel samples. For this slag composition, it was confirmed that the interaction of the alumina spindle and crucible during the viscosity measurement is negligible. This slag is predicted by FactSage™ 8.3 (Private database UQPY 2020) to be in equilibrium with spinel (with composition 'Spinel' in Table 1) at 1200°C (Bale *et al*, 2016). A similar tie line approach as described in Vergote *et al* (2023) was employed in this work. This approach includes a constant liquid viscosity of the slag matrix, with a composition fixed at the slag-spinel equilibrium, while uniquely varying the amount of spinel particles in the system across the various samples in the data set. Therefore, the influence of the solid particles on the overall slag viscosity can be determined more accurately.

TABLE 1

Bulk slag and predicted spinel composition (wt%) for the considered samples for the slag-spinel suspensions. Slag liquidus temperature (T_{liq}) and the corresponding amount equilibrium weight fraction spinel (Sp) particles at 1200°C were both calculated using FactSage (Private database UQPY 2020).

Sample	PbO	SiO_2	CaO	Al_2O_3	ZnO	Fe_2O_3	T_{liq} (°C)	wt% Sp
Slag 1	47.8	19.3	9.6	5.0	11.1	7.1	1200	0.0
Slag 2	46.8	18.9	9.4	4.9	11.6	8.2	1230	2.0
Slag 3	45.9	18.5	9.2	4.9	11.9	9.3	1258	3.8
Slag 4	44.8	18.1	9.0	4.8	12.5	10.7	1279	6.2
Slag 5	43.8	17.5	8.7	4.7	13.1	12.6	1321	9.4
Slag 6	40.5	16.3	8.1	4.5	14.4	16.0	1371	15.2
Spinel	0	0	0	1.5	32.5	66.0	/	100.0

The five other bulk slag compositions (Slag 2–6, Table 1) were determined by adding the desired wt per cent equilibrium spinel composition to the liquid slag composition. All viscosity experiments were performed at 1200°C in order to maintain slag-spinel equilibrium and a constant liquid slag viscosity across the various samples.

All samples were pre-melted using an induction furnace (Hüttinger TIG 20/100) using the methodology described earlier in (Vergote *et al*, 2021). First, at 1200°C, the slag subsystem (PbO-SiO_2-CaO-Al_2O_3-ZnO) was pre-melted for one hour. FactSage predictions indicated that for all samples, these slag subsystems were fully liquid at this temperature. As a result, low viscosity samples were obtained which enhanced mixing and melting of all powder chemicals. After the pre-melting, the required amount of Fe_2O_3 powder was added to the crucible. This resulted for slag samples 2–6 in the precipitation of spinel particles in the slag, where the Fe_2O_3 acted as a nucleating agent for these particles. The slag was further homogenised and mixed by blowing air in the bath through an alumina blowing tube for one hour to ensure homogeneity of the sample. Afterwards, the slag was quenched in water. Microscopical analysis indicated proper dissolution of all chemicals and

formation of spinel particles, ie no large Fe_2O_3 powder particles but all well-formed crystalline spinel particles. The obtained slag particles were used as starting material for the viscosity measurements.

Viscosity measurements

Viscosity measurements were performed using a Searle concentric cylinder set-up in an Anton Paar FRS 1800 rheometer, consisting of an alumina spindle and crucible. The details of this apparatus were described previously in Vergote *et al* (2021). The necessary amount of slag (±150 g) was determined based on the slag density to yield a 9 mm slag layer above and below the spindle, in order to minimise the effect of the spindle height on the obtained viscosity values (Chen and Zhao, 2013). The quenched slag particles from the pre-melting were directly heated to 1200°C at a heating rate of 5°C/min. Subsequently, the slag was homogenised for one hour in order to obtain thermal and chemical equilibrium. Afterwards, the spindle was inserted into the slag bath and the measurement sequency as described before (Vergote *et al*, 2021) was executed. Fully liquid slag samples behave Newtonian, ie the viscosity is independent of the shear rate, whereas slag samples containing solid particles show shear thinning behaviour, ie a decreasing viscosity with increasing shear rate. Therefore, it is necessary for slag samples containing solid particles to examine the viscosity at various shear rates ($\dot{\gamma}$ = 0.245–24.5 s^{-1}) to get a comprehensive understanding of the rheological behaviour of the sample. Once the measurements were finished, the slag was slowly cooled (5°C/min) to room temperature.

Several repetition viscosity experiments were performed in order to verify the consistency of the obtained results. For each experiment, a unique slag batch was prepared using the methodology described above.

To enable the comparison of the obtained viscosity data set with the previous viscosity data, the apparent viscosity data, ie measured at a specific shear rate, is converted to the apparent relative viscosity (η_{rel}):

$$\eta_{rel} = \frac{\eta_{app}}{\eta_{liq}}$$

With η_{app} the apparent viscosity and η_{liq} the viscosity of the liquid slag matrix. As a result, the effect of solid particles in suspensions on the overall viscosity can be examined across heterogeneous slag samples with a different liquid slag viscosity.

Quenching experiments and microscopical analysis

In contrast to custom-built rheometer from the previous work (Vergote *et al*, 2023), it is not possible to quench samples directly after viscosity measurement in the FRS 1800. Quenching experiments were performed using the slowly cooled slag from the viscosity measurement. Slag particles in between the spindle and crucible (ie the measurement gap) were removed from the sample. These particles were used as the material for the quenching experiment to examine the microstructure of the sample as it was at high-temperature. Only 20 g of slag was added to an alumina crucible which was suspended in the hot zone of a resistance tube furnace (Carbolite HTRV 1800). The sample was heated from room temperature at a heating rate of 5°C/min and held for one hour at 1200°C. Afterwards, the wire suspending the crucible was cut from above and the sample was rapidly quenched in a water bucket. The quenched crucible was cross-sectioned, cold embedded in Epofix resin and prepared for microscopical analysis.

The microstructure of the samples was examined using a scanning electron microscope (SEM, JEOL, JSM-7600, FEG-SEM). The SEM was operated in backscattered electron (BSE) mode to increase the contrast between the amorphous slag phase and the spinel particles. The volume fraction, size and aspect ratio of the spinel particles was determined using ImageJ. These parameters were determined using at least 20 SEM-BSE images randomly selected in the bulk of the quenched sample. For the size of the particles, the Sauter average diameter is reported, since this parameter was found to be more suitable to describe the rheology of slag suspensions (Vergote *et al*, 2023). It is defined as:

$$D_{sauter} = \frac{\sum_{i=1}^{n} D_i^3}{\sum_{i=1}^{n} D_i^2}$$

With D_{sauter} the Sauter average diameter, D_i the diameter of the spinel particles of a certain particle '*i*' and *n* the amount of considered spinel particles.

RESULTS AND DISCUSSION

This study

Slag 1 showed a Newtonian flow behaviour with a constant viscosity of 0.45 Pa.s over the entire shear rate range ($\dot{\gamma}$ = 0.245–24.5 s^{-1}). This viscosity was used to determine the relative viscosity for the other samples within this data set. All other samples showed shear thinning behaviour, therefore it is required to define the shear rate to report the apparent viscosity. Figure 2a shows the relative viscosity increase for the calculated spinel weight fractions (Table 1) for the various samples at $\dot{\gamma}$ = 24.5 s^{-1}. First of all, a large scatter on the relative viscosity can be seen for the repetition experiments of slags 3, 4, 5, eg both η_{rel} = 1.8 and 7.1 were measured for the similar intended slag composition slag 5.

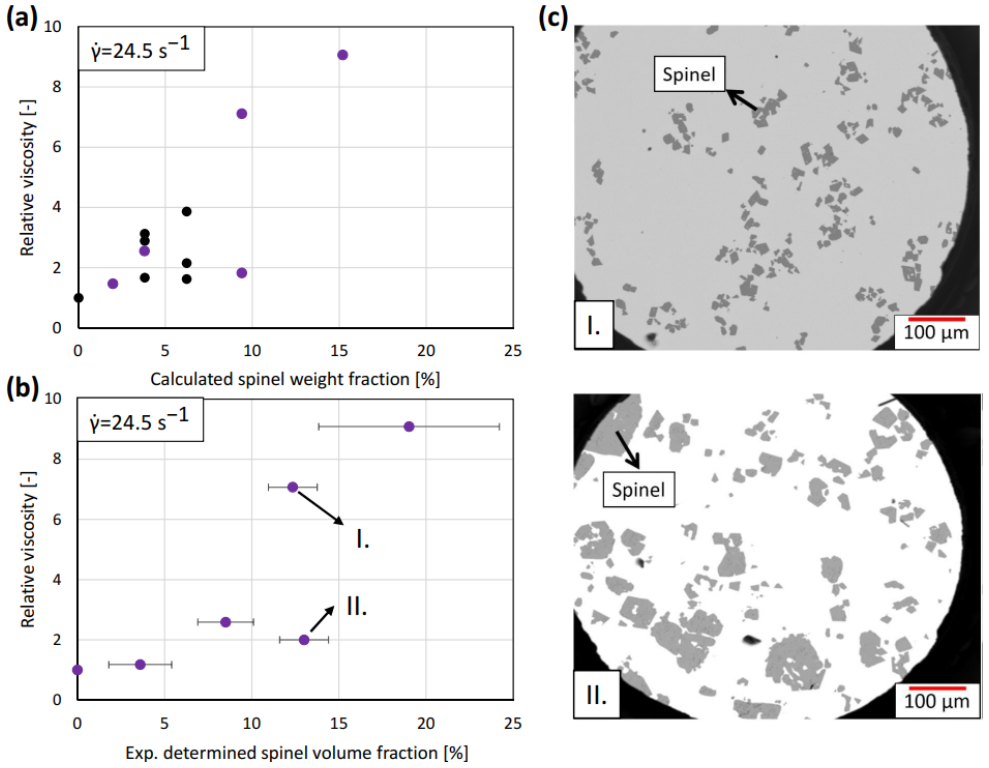

FIG 2 – (a): Relative viscosity (η_{liq}= 0.45 Pa.s, 1200°C) at $\dot{\gamma}$ = 24.5 s^{-1} for all samples in this data set, as a function of the calculated spinel weight fraction (Table 1). The purple markers indicate the samples for which additional quenching experiments were performed, (b): Relative viscosity at $\dot{\gamma}$ = 24.5 s^{-1} of the selected samples from (a), for which the volume fraction was experimentally determined, (c): scanning electron microscope – backscattered electron (SEM-BSE) images of samples I and II from (b).

As discussed in the introduction, there is a large number of parameters which affect the overall viscosity of a heterogeneous slag. Since every experiment in Figure 2a originates from an individual pre-melt, the consistency of the morphology of the spinel particles is not guaranteed. Therefore, additional quenching experiments were performed on selected samples (purple markers in Figure 2a) in order to determine the volume fraction of the spinel particles and their morphology.

Figure 2b shows the relative viscosity as a function of the experimentally determined spinel volume fraction for a selected number of samples. A first conclusion is that the volume fraction is higher for each sample compared to the predicted weight fraction, caused by the density difference between

the slag and spinel particles (Vergote *et al*, 2023). This observation highlights the importance of experimentally determined parameters instead of thermodynamic predictions to examine the rheological behaviour of slag samples. Moreover, quenching experiments were performed on the two repetition experiments of slag 5 (9.4 wt per cent spinel). For the two samples, a similar volume percentage of spinel particles was present in the slag, ie 12.4 and 13.0 vol per cent spinel. Therefore it can be concluded that the reproducibility of the pre-melting step is high. Yet, despite their similar volume percentage, a significantly different relative viscosity was obtained at $\dot{\gamma}$ = 24.5 s^{-1}. The microstructures of both repetition experiments of slag 5 (I and II) are shown in Figure 1c. First, the aspect ratio of all spinel particles was constant (±1.5) for all observed quenched samples. Second, the spinel particles for sample II are significantly larger (D_{sauter} = 78 µm) compared to the spinel particles of sample I (D_{sauter} = 30.2 µm). It was concluded before that large spinel particles cause a lower viscosity increase compared to small particles (Vergote *et al*, 2023). Lastly, the microstructures of the other samples which were microscopically studied (Slags 2, 3, 6) showed spinel particles with a size similar to sample I.

In the previous study, the size of the spinel particles was controlled by pre-sintering the spinel particles before adding them to the liquid melt. In this work, Fe_2O_3 powder was added to the liquid PbO-SiO_2-CaO-Al_2O_3-ZnO slag subsystem at 1200°C. This powder acted as a heterogeneous nucleating site for spinel particles. Using this methodology, the spinel size is largely affected by the Fe_2O_3 powder size and possible agglomeration of powder upon adding it to the liquid slag. Therefore, using this methodology, there is no control over the spinel size. The lack of control over this parameter, which is known to largely affect the slag viscosity, results in the observed scatter in Figure 2a and 2b for a constant intended amount of spinel particles.

Comparison to the previously obtained data sets

From the previous discussion, it is clear that for the samples for which the volume fraction was experimentally determined, all samples except repetition experiment II from slag 5 had an equal spinel size. Therefore, the data set in this work is divided in two sub data sets, the samples with a medium spinel size (Medium FRS 1800) and the one sample of slag 5 with the large spinel particles (Large FRS 1800). These two data sets can be compared with the three previously obtained data sets from (Vergote *et al*, 2023), where the spinel particle size was well-controlled. Figure 3b shows the distribution of the spinel particle size for the five data sets, the small, medium and large data set from the previous work (Vergote *et al*, 2023) and the medium and large FRS 1800 data set from this work. It is important to note that not only the number average spinel diameter should be considered (x-markers on Figure 3b) to define the size of the particles in a data set, but the entire distribution. The boxplots of the two medium data sets agree well and therefore their viscosity results can be compared against each other. The number average of the large FRS 1800 data set (36 µm) is significantly smaller compared to the previously obtained data set with large spinel particles (62 µm). Yet, based on their Sauter-average diameter, 61 and 78 µm for the FRS and the previous data set, respectively, the difference between both data sets is smaller, due to several large spinel particles in the FRS data set, seen by the large upper limit of the boxplot.

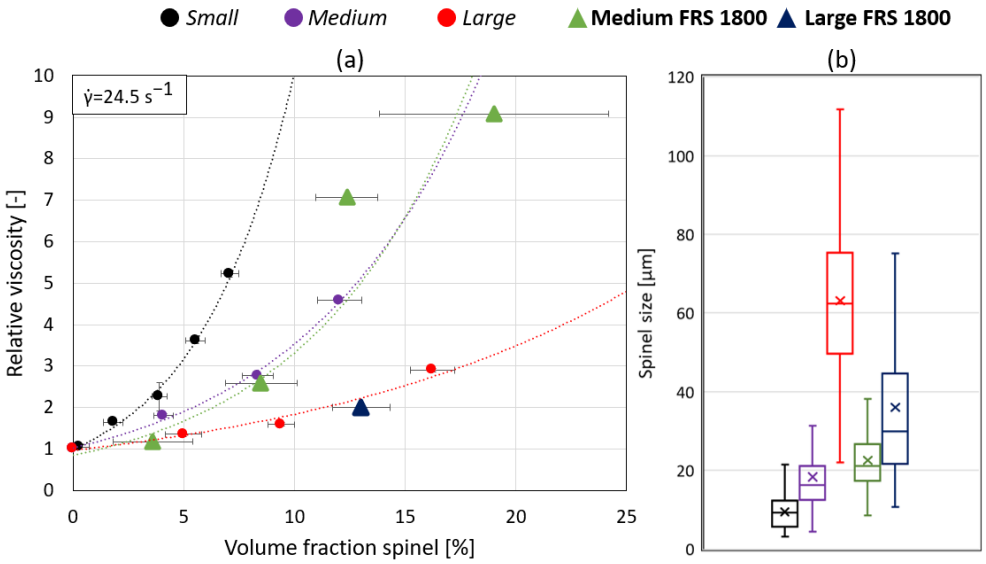

FIG 3 – (a): Comparison of the relative viscosity at $\dot{\gamma}$ = 24.5 s^{-1} for the samples in this work (triangles, medium and large FRS 1800) and the ones from the previous work (circles, small, medium and large, Vergote *et al*, 2023). The dotted lines represent optimisations of the Krieger-Dougherty equation for each data set, (b): Spinel particle size boxplots for all considered data sets, the number-average diameter is indicated with a x-marker on each boxplot.

The spinel volume fraction – relative viscosity trend at $\dot{\gamma}$ = 24.5 s^{-1}, reported in Figure 3a, agrees well for both medium data sets. In the previous data set, the maximal volume fraction was limited to 12.0 vol per cent whereas in the FRS 1800 this is extended to 19.2 vol per cent. To all data sets, Krieger-Dougherty equations were fitted to correlate the relative viscosity with the solid volume fraction (Krieger and Dougherty, 1959). The trend from the medium FRS 1800 data sets agrees well with the extrapolated trend from the previous data set. The one datapoint from the large FRS 1800 data set corresponds with the trend of the large data set from the previous study, despite the slightly smaller spinel particles in the FRS 1800 data set.

A second parameter to be able to compare the rheological behaviour across various data sets is the flow index. This parameter is fitted to the flow curves and reflects the degree of shear thinning (n = 1 reflects Newtonian behaviour, n < 1 reflects shear thinning behaviour). An Ostwald-de Waele equation is fitted to the flow curves:

$$\eta_{app} = K * \dot{\gamma}^{n-1}$$

Where K is a parameter which equals the viscosity at $\dot{\gamma}$ = 1 s^{-1} and n is the flow index, respectively. Similar to the previous work, the shear rate range 2.4–10 s^{-1} was considered in order to avoid the second Newtonian regime at large shear rates (Vergote *et al*, 2023). The resulting flow indices for various volume fractions are shown in Figure 4. First of all, all data sets show a decreasing flow index, ie more shear thinning, with increasing volume fraction of spinel particles. This observation can be explained by the increased number of particles with increasing volume fraction. As a result, the particles have more close neighbours in the melt to be influenced by (particle-particle orientation) and consequently the internal structure can be more affected by the shear rate (Vergote *et al*, 2023). Secondly, the large FRS 1800 data set show less shear thinning compared to the medium data set. This observation can be explained in a similar way: a decrease in particle size, for a constant volume fraction, result in a larger number of particles, hence more particle-particle orientation. Both rheological observations, a smaller relative viscosity (Figure 3a) and the lower degree of shear thinning, can be explained by the microstructural observation of the larger spinel particles.

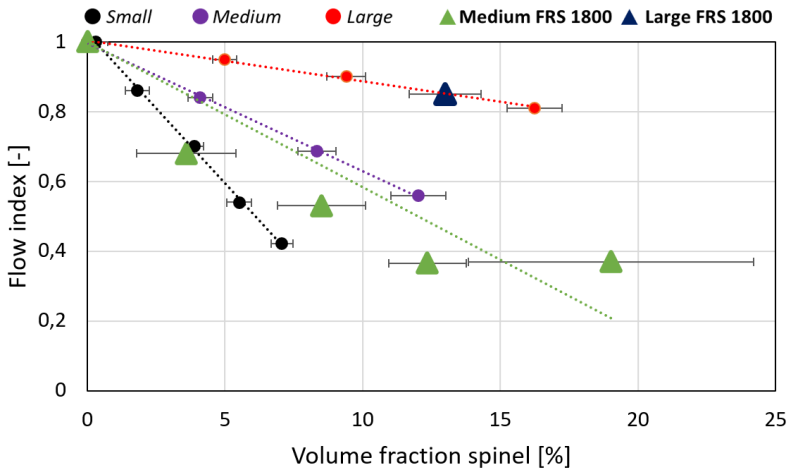

FIG 4 – Flow index as a function of the experimentally determined spinel volume fraction for all considered data sets. Linear trendlines (dotted lines) were fitted to all data sets.

Moreover, the flow indices of the medium FRS data set from this work are slightly smaller compared to previously obtained flow indices for the medium data set. Furthermore, it is observed that the flow index does not further decrease at larger spinel volume fractions. This flow index plateau is also commonly reported in literature (Mueller, Llewellin and Mader, 2009). Therefore, the applicability of the linear trendline may be limited at large volume fractions. For the large FRS data set, the flow index aligns with the previously determined trendline for the large spinel particles, despite the small difference in size between both data sets (Figure 3b).

CONCLUSION

The previous study largely focused on providing reliable data sets with a strong control overall parameters affecting the rheology of heterogeneous slag containing spinel particles. The methodology involved control over the spinel particle size via pre-sintering the spinel particles before adding them to the liquid melt. This study was performed to verify the consistency of the previously obtained insights in the viscosity behaviour of a slag containing spinel particles.

In this study's methodology, the size of the spinel particles was not well-controlled, which was reflected in the scatter on the relative viscosity for a constant intended amount of spinel particles. Microstructural analysis of quenched samples showed that the spinel size differed across various samples. Therefore, the samples were divided into two data sets, with medium and large spinel particles. Similar to the conclusions from the previous study, it was observed that the relative viscosity increase was larger for smaller spinel particles. Moreover, the samples with smaller spinel particles also showed stronger shear thinning behaviour, which was also previously concluded. The numerical values for the relative viscosity and the flow index were in the similar range as the one determined earlier.

This study further supports the importance of considering the particle size for viscosity studies and models regarding heterogeneous silicate melts. As a result, particle-particle orientation as a mode of shear thinning should also be considered. The initially obtained conclusions are further supported by this study, using an independent slag preparation and different high-temperature rheometer.

ACKNOWLEDGEMENTS

The principal author, O Vergote, holds a grant (No. HBC.2023.0671) which is supported by VLAIO, the Flanders Innovation and Entrepreneurship Agency, in co-operation with Umicore. The author I Bellemans, holds a grant from the Research Foundation Flanders (No. 1239024N).

REFERENCES

Bale, C W, Bélisle, E, Chartrand, P, Decterov, S A, Eriksson, G, Gheribi, A E, Hack, K, Jung, I H, Kang, Y B, Melançon, J, Pelton, A D, Petersen, S, Robelin, C, Sangster, J, Spencer, P and Van Ende, M-A, 2016. FactSage Thermochemical Software and Databases – 2010–2016, *CALPHAD*, 54:35–53.

Caricchi, L, Burlini, L, Ulmer, P, Gerya, T, Vassalli, M and Papale, P, 2007. Non-Newtonian rheology of crystal-bearing magmas and implications for magma ascent dynamics, *Earth and Planetary Science Letters*, 264:402–419.

Chen, M and Zhao, B, 2013. Viscosity Measurements of SiO_2-'FeO'-CaO System in Equilibrium with Metallic Fe, *Metallurgical and Materials Transactions B*, 46:577–584.

Del Gaudio, P, Guido, V and Taddeucci, J, 2013. The effect of particle size on the rheology of liquid-solid mixtures with application to lava flows: Results from analogue experiments: Rheology of Liquid-Solid Mixtures, *Geochemistry Geophysics Geosystems*, 14(8):2661–2669.

Krieger, I M and Dougherty, T J, 1959. A mechanism for non-Newtonian flow in suspensions of rigid spheres, *Transactions of the Society of Rheology*, 3:137–152.

Lyon, M K, Mead, D W, Elliott, R E and Lea, L G, 2001. Structure formation in moderately concentrated viscoelastic suspensions in simple shear flow, J Rheol*,* 45(4):881–890.

Liu, Z, Pandelaers, L, Blanpain, B and Guo, M, 2017. Viscosity of Heterogeneous Silicate Melts: Assessment of the Measured Data and Modelling, *ISIJ International,* 57:1895–1901.

Mueller, S, Llewellin, E and Mader, H, 2009. The rheology of suspensions of solid particles, *Proc R Soc A*, 466:1201–1228.

Saito, N, Hara, D, Teruya, S and Nakashima, K, 2020. Viscosity of Slag Suspensions with a Polar Liquid Matrix, *ISIJ International*, 60:2807–2818.

Sichen, D, Huss, J, Vickerfält, A, Berg, M, Martinsson, J, Allertz, C and Kojola, N, 2022. The Laboratory Study of Metallurgical Slags and the Reality, *Steel Research Int*, 93:2100132.

Vergote, O, Bellemans, I, Van den Bulck, A and Verbeken, K, 2021. Towards More Reliable PbO-SiO_2 Based Slag Viscosity Measurements in Alumina via a Dense Intermediate Spinel Layer, *Metallurgical and Materials Transactions B*, 52(6):3646–3659.

Vergote, O, Bellemans, I, Van den Bulck, A, Shevchenko, M, Starykh, R, Jak, E and Verbeken, K, 2023. Viscosity experiments of slag-spinel suspensions: The effect of volume fraction, particle size and shear rate, *J Rheol,* 67(6):1159–1174.

Wright, S, Zhang, L, Sun, S and Jahanshahi, S, 2000. Viscosity of a CaO-MgO-Al_2O_3-SiO_2 melt containing spinel particles at 1646K, *Metallurgical and Materials Transactions B*, 31:97–104.

Relationship between thermal conductivity and structure of alkaline earth (Ca, Mg) aluminoborosilicate melts

DOI: 10.62053/FVBR3402

S Yamada[1], H Aoki[2], A Nakayama[3] and K Morita[4]

1. The University of Tokyo, Bunkyo-ku, Tokyo 113-8656, Japan.
   Email: yamada@wood3.t.u-tokyo.ac.jp
2. JFE Steel Corporation, Chiyoda-ku, Tokyo, Japan.
3. Nippon Steel Corporation, Tokai city, Aichi, Japan.
4. The University of Tokyo, Bunkyo-ku, Tokyo 113-8656, Japan.

ABSTRACT

The thermal conductivity of mold flux is crucial for optimising the productivity and quality of steels. This study investigates the thermal conductivity of molten oxides, including CaO-$BO_{1.5}$-$AlO_{1.5}$ (CBA), CaO-$BO_{1.5}$-$AlO_{1.5}$-SiO_2 (CBAS), and CaO-MgO-$BO_{1.5}$-$AlO_{1.5}$ (CMBA) melts, using a hot wire method. Additionally, their structure is examined using Raman spectrometry and magic angle spinning nuclear magnetic resonance (MAS-NMR) to explore their relationship. Furthermore, first-principles calculations are employed to assess the covalency of each bond in the melts for a more quantitative analysis of their relationship. The study confirms that an increase in the CaO concentration of the CaO-$BO_{1.5}$-$AlO_{1.5}$ melts reduces the amount of bridging oxygen and consequently decreases thermal conductivity. The covalency of the B[4]-O bond is highest, especially when the second-nearest-neighbour Al atoms transition from Al[6] to Al[4], forming the AlB_3O_7 structure with B[4]. The relationship between thermal conductivity and the structure of CaO-$BO_{1.5}$-$AlO_{1.5}$-SiO_2 melts can be quantitatively assessed using the degree of polymerisation of the network structure and the variation of covalency as indicators.

Furthermore, replacing CaO with MgO in the CaO-MgO-$BO_{1.5}$-$AlO_{1.5}$ melts reveals a mixed alkaline earth effect on thermal conductivity.

INTRODUCTION

During the continuous casting process, mold flux is applied to the surface of the molten steel. Serving as a lubricant, mold flux regulates the cooling rate of the molten steel's surface to prevent cracking, thus enhancing the quality of steel products. The thermal conductivity of mold flux is crucial in achieving this objective. A typical mold flux comprises CaO, SiO_2, and $BO_{1.5}$. In a SiO_2-based mold flux, CaO serves as a network modifier, whereas $BO_{1.5}$ and SiO_2 function as network formers. The role of $AlO_{1.5}$ depends on the coordination number. Regarding the modifier effect, the molar volume of the crystal containing CaO and MgO is not independent of the proportion of Ca to the alkaline earth metal.

Measuring the thermal conductivity of molten oxides accurately presents a challenge due to the effect of convection and radiation at high temperatures (Shirayama *et al*, 2012; Kang and Morita, 2006; Mills, 1993). The hot wire method, which is known for its effectiveness in reducing these effects, was adopted for measuring the thermal conductivity of molten oxides (Nagata *et al*, 1983).

The effects of composition on the thermal conductivities of fluxes containing $BO_{1.5}$ and $AlO_{1.5}$ were not thoroughly understood due to their complex structures. The coordination number of B and Al in the flux drastically depends on changes in composition.

In the previous study, the thermal conductivity of molten oxides was measured using the hot wire method, and structural analyses were conducted using Raman spectrometry and magic angle spinning nuclear magnetic resonance (MAS-NMR) to verify the CBA system (Shirayama *et al*, 2012) The correlation between thermal conductivity and structure was evaluated quantitatively.

Furthermore, the covalency of bonds in the molten oxides was evaluated using first-principle calculations to assess their impact on thermal conductivity.

EXPERIMENTAL PROCEDURES

The thermal conductivity of the molten oxides was measured using the hot wire method in the homogeneous liquid state. Figure 1 shows a schematic of the experimental setup for thermal conductivity measurement. Samples were held in a Pt-10 per cent Rh crucible. After the samples were melted at 1773 K in a SiC furnace, a thin Pt-13 per cent Rh wire was inserted into the molten samples. A current of 1.0 A was applied to the wire, and the change in voltage was measured using a digital multimeter. Thermal conductivity was estimated from the variation in voltage over time. The measurement temperature was lowered from 1773 K to 1473 K in increments of 50 K.

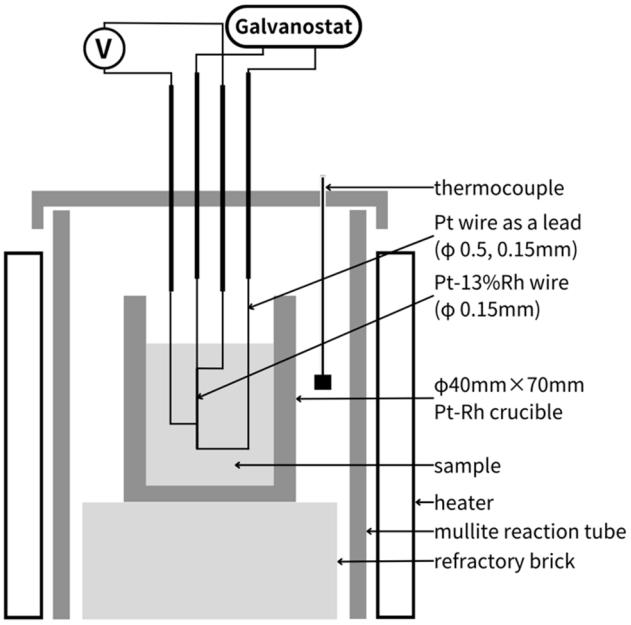

FIG 1 – Schematic of the experimental set-up for thermal conductivity measurement.

Structure analysis was conducted on the crystal sample melted at 1773 K and quenched. Raman spectrometry and MAS-NMR were performed on each sample. The Raman signal was collected in the range of 400 to 1600 cm^{-1}, and nuclear magnetic resonance (NMR) spectra for ^{11}B, ^{27}Al and ^{29}Si of each sample were recorded. The detailed measurement conditions for each nucleus are listed in Table 1.

TABLE 1

Detailed measurement conditions for MAS-NMR spectroscopy.

Nuclear property	^{11}B	^{27}Al	^{29}Si
Nuclear spin	3/2	5/2	1/2
Larmor frequency [MHz]	160.4	130.3	202.4
Repetition times	256	4096	2000
Flip angle [°]	30	30	30
Delay time [sec]	1.25	0.17	10
Spinning rate [kHz]	15	15	15

First-principle calculations were performed to determine the electron density distribution, and the centre of the maximum localised Wannier functions was calculated. The covalency of each bond was evaluated based on the distance between the centre of the chemical bond and the centre of the maximum localised Wannier functions. The GPAW/ASE was utilised for the calculations.

RESULTS AND DISCUSSION

Thermal conductivity and structure

The results revealed a negative correlation between temperature and thermal conductivity in all the CBA, CBAS, and CMBA systems. Figure 2 shows the thermal conductivity of the CBA system at 1673 K. In the CBA system, when the $CaO/AlO_{1.5}$ ratio was 1.38, the thermal conductivity exhibited a local maximum with an increase in the concentration of $BO_{1.5}$. The relative fraction of the B[3]-O-Al[4] bond, which comprises a B atom with three coordinations (B[3]) and an Al atom with four coordinations (Al[4]), showed a similar trend based on the concentration of $BO_{1.5}$.

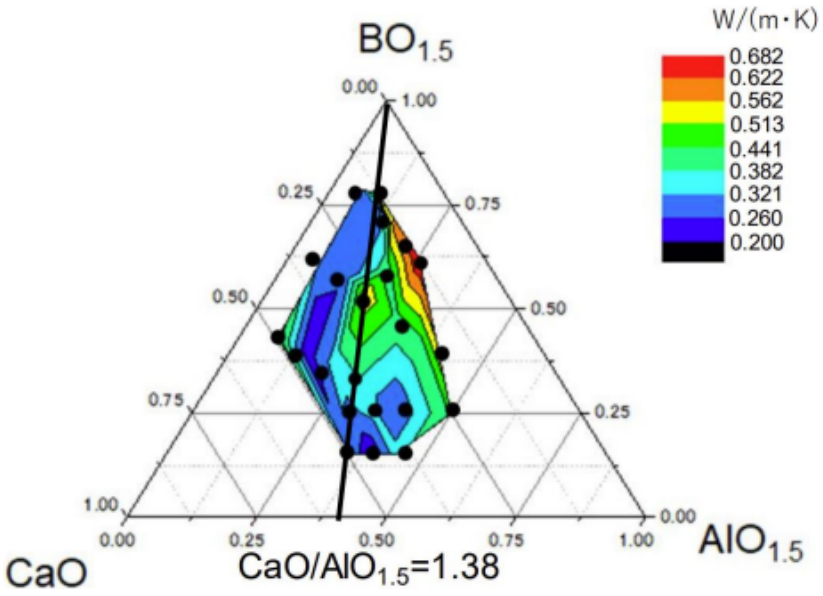

FIG 2 – Thermal conductivity of the CBA system at 1673 K (Shirayama *et al*, 2012).

MAS-NMR measurements revealed a correlation between thermal conductivity and the relative fractions of B[4] and Al[4]. Figure 3 shows the thermal conductivity at 1673 K and relative fraction of Al[4] and B[4] for the CBA system. It indicates that in the low $BO_{1.5}$ range, Al[4] acts as the network former, while in the high $BO_{1.5}$ range, it shifts to B[4]. These findings suggest the AlB_3O_7 structure contributes to heat conduction in the CBA system. Figure 4 shows the AlB_3O_7 structure unit. The AlB_3O_7 structure comprises one B[4], a Al[4], and more than two B[3] per unit.

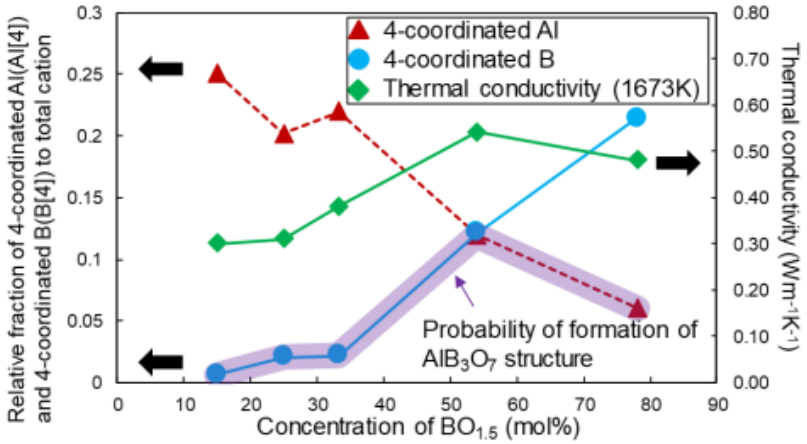

FIG 3 – Thermal conductivity at 1673 K and relative fractions of Al[4] and B[4] for the CBA system ($CaO/AlO_{1.5}$=1.38) (Shirayama *et al*, 2012).

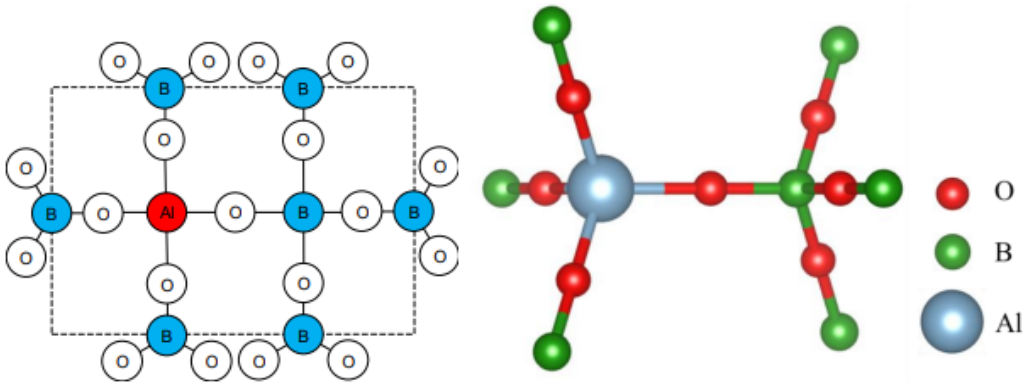

FIG 4 – AlB_3O_7 unit structure.

Thermal conductivity and covalency of bonds

To assess the covalency of each bond, calculations were performed using Wannier functions, which indicate the centre of the electron distribution of the bond. The distance between the centre of the Wannier functions and the chemical bond centre, denoted as D (Å), serves as a negative indicator of covalency. Table 2 shows the D of X-O bond in X-O-Y bond and Figure 5 shows the Wannier function centre and D of B[4]-O-Al[4] bond. The B[4]-O bond exhibits the highest covalency, while the Al[6]-O bond displays the least covalency. The order of covalency was determined to be Al-[6]-O < Al[4]-O < B[4]-O. Notably, the B[4]-O bond in the B[4]-O-Al[4] configuration exhibited the highest covalency, suggesting its significant contribution to heat conduction in the CBA system.

TABLE 2

D of X-O bond in X-O-Y (Å).

X \ Y	B[4]	Al[4]	Al[6]
B[4]	0.317	0.299	0.417
Al[4]	0.548	0.532	0.705
Al[6]	0.604	0.600	0.571

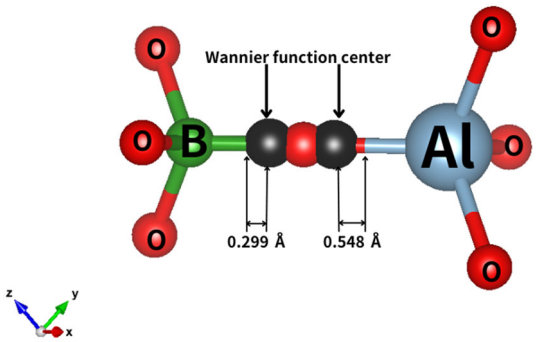

FIG 5 – Wannier function centre and D of B[4]-O-Al[4].

From D, S, which is the standard deviation of D in the network formed by B[3], B[4], Al[4], and Si of the CBSA and CBA systems, was calculated using Equation 1 (Matuoka, 2012):

$$S = \sqrt{\frac{\Sigma_{M[n]}(D_{M[n]} - D_{ave})^2 \times n \times X_{M[n]}}{\Sigma_{M[n]}(n \times X_{M[n]})}}. \quad (1)$$

BO%/S is the ratio of S to the proportion of bridged oxygen in the system (Equations 2 and 3).

$$BO\% = \frac{O_{total} - NBO}{O_{total}}, \quad (2)$$

$$NBO = 2X_{CaO} + 2X_{MgO} + 3X_{Al[5]} + 3X_{Al[6]} - X_{Al[4]} - X_{B[4]}. \quad (3)$$

Thermal conductivity of CBSA system and CBA system is increased with the increasing of BO%/S.

Mixed alkaline earth effect

Figure 6 shows the thermal conductivity and proportion of Mg to all alkali earth metal of CaO-MgO-$BO_{1.5}$-$AlO_{1.5}$ system. In the CaO-MgO-$BO_{1.5}$-$AlO_{1.5}$ thermal conductivity exhibited a local minimum with the increase in MgO concentration replacing CaO. This phenomenon is akin to the alkaline earth effect observed in the molar volume and density of glasses containing both Ca and Mg (Calahoo and Zwanziger, 2017).

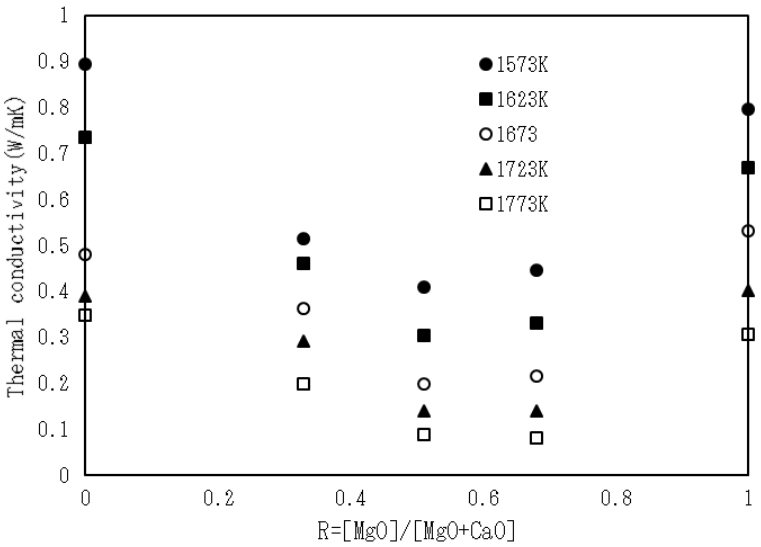

FIG 6 – Thermal conductivity and proportion of Mg to all alkali earth metal.

CONCLUSION

Thermal conductivity measurements were conducted on the CBA, CBAS, and CaO-MgO-$BO_{1.5}$-$AlO_{1.5}$ system. The correlation between thermal conductivity and structure was investigated using Raman spectrometry, MAS-NMR, and first principle calculations. The AlB_3O_7 structure contributed to an increase in thermal conductivity. The relationship between thermal conductivity and structure could be quantitatively evaluated using BO%/S, a combination of the variation in the degree of polymerisation BO% and its covalency in the network structure S. A mixed modifier effect is observed on the thermal conductivity of molten oxides containing CaO and MgO. Relation between the covalency and the mixed modifier effect on thermal conductivity of CaO-MgO-$BO_{1.5}$-$AlO_{1.5}$ system will be investigated.

ACKNOWLEDGEMENT

I would like to express my gratitude to Mr Kimura and Mr Yanaba for their assistance with the thermal conductivity and NMR measurements.

REFERENCES

Calahoo, C and Zwanziger, J W, 2017. The mixed modifier effect in ionic conductivity and mechanical properties for xMgO-(50-x)CaO-50SiO_2 glasses, *J Non-Cryst Solids*, 460:6.

Kang, Y and Morita, K, 2006. Thermal Conductivity of the CaO-Al_2O_3-SiO2 System, *ISIJ Int,* 46:420.

Matuoka, J, 2012. Composition Dependence of the Thermal Conductivity of Glass, *New Glass*, 27:20.

Mills, K C, 1993. The Influence of Structure on the Physico-chemical Properties of Slags, *ISIJ Int*, 33:148.

Shirayama, S, Aoki, H, Yanaba, Y and Morita, K, 2012. Relation between Thermal Conductivity and Structure of the CaO-$BO_{1.5}$-$AlO_{1.5}$ System, *Metall Mater Trans B*, 43B:1420.

Quantitative studies on the microstructures of ternary CaO-Al_2O_3-SiO_2 glasses, melts and correlation with their high-temperature viscosities

DOI: 10.62053/LNVG1782

J You[1], X Tang[2], F Zhang[3], A Canizarès[4], C Bessada[5], L Lu[6], K Tang[7], Q Zhang[8] and S Wan[9]

1. Professor, SKLASS, Shanghai University, Shanghai 200444, China. Email: jlyou@staff.shu.edu.cn
2. Doctor, SKLASS, Shanghai University, Shanghai 200444, China.
3. Doctor, SKLASS, Shanghai University, Shanghai 200444, China.
4. Senior Scientist, CNRS, CEMHTI UPR3079, Université d'Orléans, Orléans, France.
5. Professor, CNRS, CEMHTI UPR3079, Université d'Orléans, Orléans, France.
6. Senior Scientist, Queensland Centre for Advanced Technologies, CSIRO Mineral Resources, Pullenvale Qld 4069.
7. Senior Scientist, SINTEF AS, 7034 Trondheim, Norway. Email: kai.tang@sintef.no
8. Researcher, Anhui Key Laboratory for Photonic Devices and Materials, Anhui Institute of Optics and Fine Mechanics, Chinese Academy of Sciences, Hefei 230031, China.
9. Researcher, Anhui Key Laboratory for Photonic Devices and Materials, Anhui Institute of Optics and Fine Mechanics, Chinese Academy of Sciences, Hefei 230031, China.

ABSTRACT

Microstructure of CaO-SiO_2-based glassy samples with various Al_2O_3 contents were examined quantitatively by Raman spectroscopy and ^{27}Al MAS NMR (magic-angle spinning nuclear magnetic resonance). Sequence of multiple cluster models of aluminosilicate system modified with Ca^{2+} and Na^+ cations have been designed, and Raman spectra simulation were carried out after geometric optimisation by quantum chemistry (QC) *ab initio* calculation. The functional relationship between Raman scattering cross-section (*RSCS*) and stress index of silicon-oxygen tetrahedron (*SIT*) for aluminosilicates was established, which was applied to the calibration of experimental Raman spectra. Some five-fold coordinated aluminium (Al^V, around 5 per cent) and less than 2 per cent six-fold coordinated aluminium (Al^{VI}) were detected by ^{27}Al MAS NMR, while most of aluminium remained in tetrahedral sites (Al^{IV}). The hyperfine quantitative results of Raman spectroscopy and NMR showed a gradually production of Al^{IV} with addition of Al_2O_3, along with the significant adjustment of Q_i species distribution, in which Q_1, Q_2 reduced and fully polymerised Q_4 increased while Q_3 showed a non-monotonic variation and obtained the maximum at Al_2O_3 = 18 mol per cent. Furthermore, the effects of aluminium to bridging oxygen bond types (T-O_b, T = Si, Al) and the degree of polymerisation were also discussed in detail. The evolution of microstructure and its correlation with the viscosity of CaO-SiO_2 based melts, incorporating various Al_2O_3 additives, have been investigated by employing *in situ* high temperature Raman spectroscopy at 1823 K and viscosity model. These structural features related to composition are essential theoretic foundation to understand their properties. The average Q_i evolution culminates in an overall enhancement of the degree of polymerisation. Viscosity was determined utilising a rigorously selected viscosity model, elucidating a consistent upward trajectory as Al_2O_3 content is incrementally added. Furthermore, a quantitative analysis of the relationship between viscosity and structure was conducted based on the average number of non-bridging oxygen per network-forming tetrahedron (NBO/T). It provides valuable insights for examining and predicting viscosity behaviour of aluminosilicate systems.

INTRODUCTION

CaO-Al_2O_3-SiO_2 (CAS) glasses and melts are of special interest for their technological significance and structural peculiarities and have a wide range of industrial applications (Sharma and Chhibber, 2020; Sokol'skii *et al,* 2018; Li, Shu and Chou, 2014). For instance, the CAS system is a major component of blast furnace (BF) slags and mold fluxes extensively used in metallurgical processes (Takahashi, Neuville and Takebe, 2015). A comprehensive understanding of the physical properties of aluminosilicate molten slags, encompassing thermal conductivity, density, and viscosity, is indispensable for unravelling the intricate mass, momentum, and energy transfer phenomena. This knowledge is crucial for optimising slag compositions, enhancing fuel usage efficiency, and achieving superior performance in diverse industrial processes (Wang *et al,* 2020; Siafakas *et al,* 2018;

Rajavaram *et al,* 2017). Among these properties, viscosity hold critical significance in metallurgical melts, in view of its direct effect on the kinetic and thermodynamical conditions of the processes. Therefore, the comprehensive investigation of viscous behaviour of molten slags carries imperative theoretical and practical implications for comprehending the fluid dynamic and slag-metal reaction kinetics during the metallurgical processes.

In the ternary CAS system, the network former SiO_2 constructs various structural units through diverse connections of silicon-oxygen tetrahedrons (SiOTs), such as monomer (SiO_4), dimer (Si_2O_7), chain (SiO_3), layered (Si_2O_5) and three-dimensional network structures (SiO_2). These structural units can also be indicated by primary structural species Q_i (i = 0–4, denotes the number of bridging oxygen (BO, O_b) in each tetrahedron) (Sano *et al,* 1997). Moreover, You *et al* (2005) stated that the complex connections among SiOTs cannot be described by primary structure species alone and hyperfine secondary structures adopted the shorthand symbol $Q^{jklm}_{i\ (n_1h,\ n_2q,\ n_3t)}$ must be adopted, where: subscript *i* refers to the number of BO of the central SiOT; superscript *j*, *k*, *l* and *m* correspond to the numbers of BO of the adjacent tetrahedra Q_j, Q_k, Q_l and Q_m of the central Q_i, respectively; n_1, n_2 and n_3 are the number of various rings involved in the central SiOT, respectively, while *h*, *q* and *t* represent six-, four- and three- membered rings, respectively.

Aluminium, as a representative amphoteric oxide, may exhibit different coordination roles, in which the four-fold coordinated aluminium-oxygen tetrahedra (AlOT) is commonly observed as the network former, facilitating polymerisation of the network by consuming alkali metal or alkaline-earth metal cations for charge compensation. Additionally, the existence of five- and/or six-fold coordinated aluminium has been detected in aluminosilicate, although their definitive structural characteristics and formation mechanisms remain elusive, thereby adding complexity to the overall structure and viscosity behaviour (Mysen, 2021). Extensive research has been undertaken to elucidate the amphoteric behaviour of Al_2O_3 in aluminosilicate and establish the correlation between structure and viscosity (Zhang and Chou, 2013; Chen *et al,* 2019, Gu *et al,* 2020; Atila *et al,* 2019; Le Losq *et al,* 2014). Park, Kim and Min (2008) conducted an assessment on the viscosity of CaO-Al_2O_3-SiO_2 slag, revealing an initial increase in viscosity upon the addition of Al_2O_3, followed by a subsequent decrements at higher Al_2O_3 concentrations. However, their analysis of viscous flow behaviour was predominantly based on a qualitative examination of the structural aspects. The majority of studies thus far have focused on the impact of the CaO/Al_2O_3 ratio on viscosity (Shao *et al,* 2019; Zhen *et al,* 2014), leaving the investigation of the effect of Al_2O_3 with a fixed CaO/SiO_2 ratio relatively understudied. Therefore, to clearly get insight into the influence of Al_2O_3 on viscosity, it is essential to quantitatively explore the dependence of viscosity on the structural characteristics of molten slags.

In previous studies, amorphous glasses have been commonly employed as surrogate models for investigating the structural properties of melts, primarily due to the obstacles of high temperature experimental techniques in studying the structural characteristics of molten systems (Chen *et al,* 2019; Veit *et al,* 2016). However, numerous investigations have highlighted that the microstructure of silicate and aluminosilicate glasses may not be entirely representative of their corresponding melts, potentially stemming from divergent thermal histories influencing the glass microstructure (Richet *et al,* 2022; Mysen, Lucier and Cody, 2003). The rapid advancement of high-temperature measurement techniques has underscored the pressing need to directly investigate the microstructural characteristics of molten systems. Among them, *in situ* high temperature Raman spectroscopy stands out for its exceptional capability to probe the microstructure of molten substance because of its remarkable sensitivity to the network microstructure, including short-range environment and network connectivity. Some researchers have conducted deep quantitatively analysis of melt structure evolution using *in situ* high temperature Raman spectroscopy in binary CaO-SiO_2, ternary MgO-CaO-SiO_2 and Na_2O-Al_2O_3-SiO_2 system (Mysen, Lucier and Cody, 2003; Gong *et al,* 2022; Ma *et al,* 2020). For ternary CAS system, because of the high melt point and complex amphoteric behaviour of Al_2O_3, the information of melt microstructure is absent. As such, it is significant to examine the microstructure of CAS melts by using *in situ* high temperature Raman spectroscopy, and further construct the relationship between structure and properties, which is essential in understanding the fundamental mechanisms of various compositional effect on the macroscopic physical properties.

In the Raman spectra of aluminosilicate, the characteristic Raman-active band in the high wavenumber range (>800 cm^{-1}) can be assigned to the symmetric stretching vibration of the non-bridging oxygen (NBO) of SiOT (Si-O_{nb}). This band, is approximately monotonically related to the type of central SiOT, ie delicate $Q^{jklm}_{i\ (n_1h,\ n_2q,\ n_3t)}$ or primary Q_i species with different connections between central SiOT and adjacent tetrahedra and is the object of Raman spectra quantification. Nonetheless, quantitative analysis by Raman spectroscopy is still being developed, You *et al* (2005) proposed a concept involving the stress index of silicon-oxygen tetrahedra (*SIT*) to reflect the complex connectivities among SiOTs. This was performed to establish a relationship between the Raman scattering cross-section (*RSCS*) and *SIT* and further quantitatively analyse the microstructures of binary sodium silicate.

Therefore, in the present work, *SIT* and *RSCS* values were employed to help quantitatively investigate the evolution of delicate $Q^{jklm}_{i\ (n_1h,\ n_2q,\ n_3t)}$ and primary Q_i species by Raman spectroscopy and simulate calcium aluminosilicate glasses and melts that exhibit various Al_2O_3 contents with a fixed CaO/SiO_2 ratio of 1. Additionally, viscosity predictions were carried out through the Urban model and then to bridge of the correlation between melt microstructure and viscosity.

EXPERIMENTAL METHODS

Material synthesis

Six calcium aluminosilicate glassy samples were prepared by melting mixtures of CaO, Al_2O_3 and SiO_2. The compositions of the samples, ranging from 0 to 30 mol percentage of Al_2O_3 with a constant CaO/SiO_2 ratio of 1, are presented in Table 1. The starting materials with stoichiometric amounts of CaO, Al_2O_3 and SiO_2 (analytical reagent-grade, Sinopharm Chemical Reagent Co., Ltd) were accurately weighed and thoroughly mixed in an agate mortar with ethyl alcohol for 2 hrs. Subsequently, the mixtures were premelted, placed in a muffle furnace at a rate of 10 K/min until 1873 K (above the liquidus temperature of the samples) was reached and held for 1 hr to obtain a homogeneous and bubble-free melt. The resulting liquids were cooled, ground into powder and then pressed into thin sheets with a diameter of 10 mm and a height of 1 mm. An aerodynamic levitation (ADL) furnace equipped with two beams of CO_2 lasers approximately 80 W and capable of achieving an extremely high cooling rate of 300 K/s was applied to prepare the glassy samples. CASx (x = 0, 6, 12, 18, 24, 30) was adopted as a shorthand notation for the glassy samples with compositions of $(100\text{-}x)/2CaO{\cdot}xAl_2O_3{\cdot}(100\text{-}x)/2SiO_2$.

TABLE 1

Chemical compositions of calcium aluminosilicate glassy samples.

Sample number	CaO/mol%	Al_2O_3/mol%	SiO_2/mol%
CAS0	50	0	50
CAS6	47	6	47
CAS12	44	12	44
CAS18	41	18	41
CAS24	38	24	38
CAS30	35	30	35

Experimental details

Raman spectra of the vitrified and molten samples were recorded in the range of 50–1600 cm^{-1} by using Horiba Jobin Y'von (LabRam HR) micro-Raman spectrometer equipped with pulse laser with a wavelength of 532 nm and ICCD (intensified charge coupled device). Six vitrified powders of CASx (x = 0, 6, 12, 18, 24, 30) were placed in a platinum crucible and then heated at a rate of 300 K/min from room temperature (RT) to 1273 K by using a high temperature observational system (IRF-DP, Japan), followed by a subsequent ramp-up from 1273 K to 1823 K at a rate of 100 K/min. After melting, the Raman spectra were recorded at 1823 K.

^{27}Al MAS NMR (magic-angle spinning nuclear magnetic resonance) spectra of glassy samples were collected using a Bruker Advance III WB 400 MHz spectrometer at a Larmor frequency of 104.25 MHz (9.4 T). The samples were spun in cylindrical aluminium free zirconia rotors with a diameter of 4 mm at a spinning rate of 12 kHz. One-pulse acquisition was used while the cycle delay time was 0.5 sec and the cumulative times were 600.

Computational details

The model clusters of ternary CaO-Al_2O_3-SiO_2 aluminosilicate with different aluminium introduction and various Q_i connections were constructed on the basis of CaO-SiO_2 binary silicates, which were optimised and calculated by QC *ab initio* calculations by using Gaussian 09W software. The Restricted Hartree-Fock (RHF) self-consistent field and 6–31G(d) basis set were employed to optimise clusters and Raman spectra were then simulated for those clusters after being optimised on the same computational methodology (Nowak *et al,* 1994; Lee and Jayatilaka, 1993).

Notably, the 'Loewenstein Al avoidance' rule (Loewenstein, 1954) was preferentially considered for the introduction position and amount of Al of model cluster construction. Considering the charge balance of AlOTs, a cluster structure with n(Al) requires 1/2n(Ca) for charge compensation, which greatly increases the difficulty of cluster structure construction to maintain higher symmetry and reduces computational success. Therefore, the Na^+ cation was selected to partially displace the Ca^{2+} cation as a charge compensated ion to simulate more reliable structures. Previous studies showed that the influence of different alkali metal and alkaline earth metal cations on the symmetric stretching vibration frequency of Si-O_{nb} in silica tetrahedral structure units can be negligible (Piriou and McMillan, 1983; Brawer and White, 1977).

RESULTS AND DISCUSSIONS

Quantification of microstructure of CaO-Al_2O_3-SiO_2 glasses and melts

In this work, a series of model clusters were designed with connections of AlOTs and SiOTs as network formers, Ca^{2+} cations acted as network modifiers, and Na^+ cations were used, as they are needed to balance the charge of AlOTs. The optimised model clusters by QC *ab initio* calculations with different connections are illustrated in Figure 1. The calculated Raman-active wavenumbers of the symmetric stretching vibrations of Si-O_{nb} and its *RSCS* are shown in Table 2 The calculation results indicate that the characteristic peaks with notable intensity in 800–1200 cm^{-1} are mainly the symmetric stretching vibrations of Si-O_{nb}. The wavenumbers of identical Q_i species in this range decreased with increasing aluminium introduction, which is consistent with the results obtained for kyanite, sillimanite and andalusite by Feng *et al* (2006). Compared to the Si-O bond, the Al-O bond has a smaller force constant, and the coupling of the Al-O and Si-O bonds leads to a decrease in the wavenumber of the Si-O_{nb} symmetrical stretching vibration.

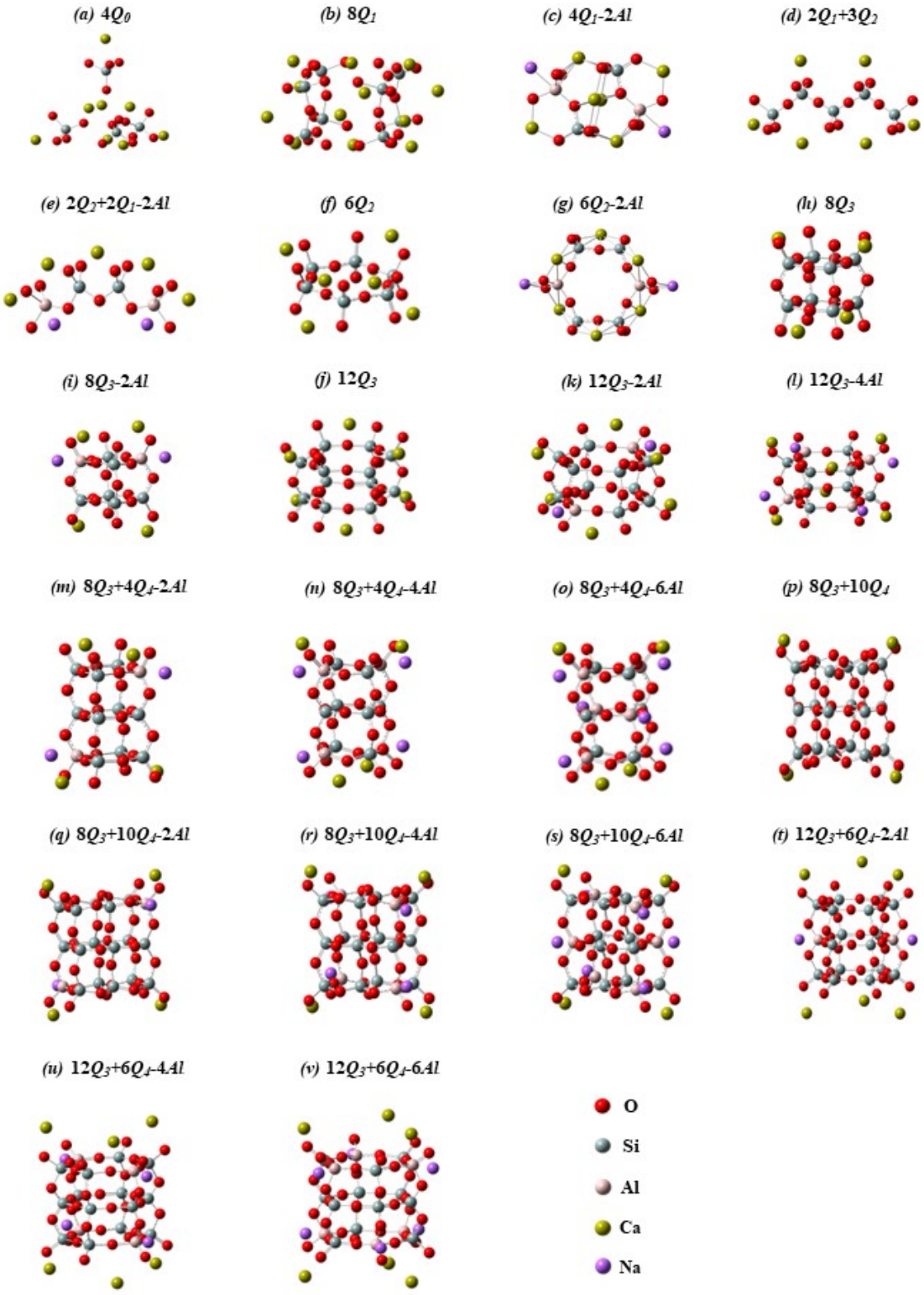

FIG 1 – Diagrams of model clusters with different connections between the central silicon-oxygen tetrahedron (SiOT) and adjacent SiOT or aluminium-oxygen tetrahedra (AlOT), forming a network framework. Additionally, Ca^{2+} cations act as network modifiers, and Na^{+} cations act as charge compensators of AlOTs, partially replacing Ca^{2+}:
(a) $Ca_8Si_4O_{16}$; (b) $Ca_{12}Si_8O_{28}$; (c) $Ca_6Na_2Si_2Al_2O_{14}$; (d) $Ca_6Si_5O_{16}$; (e) $Ca_5Si_4O_{13}$; (f) $Ca_6Si_6O_{18}$; (g) $Ca_6Na_2Si_4Al_2O_{18}$; (h) $Ca_4Si_8O_{20}$; (i) $Ca_4Na_2Si_6Al_2O_{20}$; (j) $Ca_6Si_{12}O_{30}$; (k) $Ca_6Na_2Si_{10}Al_2O_{30}$; (l) $Ca_6Na_4Si_8Al_4O_{30}$; (m) $Ca_4Na_2Si_{10}Al_2O_{28}$; (n) $Ca_4Na_4Si_8Al_4O_{28}$; (o) $Ca_4Na_4Si_6Al_6O_{28}$; (p) $Ca_6Na_2Si_{16}Al_2O_{42}$; (q) $Ca_6Na_4Si_{14}Al_4O_{42}$; (r) $Ca_6Na_6Si_{12}Al_6O_{42}$; (s) $Ca_4Si_{18}O_{40}$; (t) $Ca_4Na_2Si_{16}Al_2O_{40}$; (u) $Ca_4Na_4Si_{14}Al_4O_{40}$; (v) $Ca_4Na_4Si_{14}Al_4O_{40}$.

TABLE 2

The stress index of silicon-oxygen tetrahedron (SIT), Raman scattering cross-section (RSCS), and the wavenumber of symmetric stretching vibration of Si-O_{nb} by quantum chemistry *ab initio* calculation of designed model clusters probably existed in ternary CaO-Al_2O_3-SiO_2 glasses and melts.

Chemical formula	Q_i species	*SIT*	*RSCS*	Si-O_{nb} stretching/cm^{-1}
(a) $Ca_8Si_4O_{16}$	$4Q_0$	0.00	11.39	902
(b) $Ca_{12}Si_8O_{28}$	$8Q_1$	1.00	5.87	949
(c) $Ca_6Na_2Si_2Al_2O_{14}$	$4Q_1$	0.50	9.29	936
(d) $Ca_6Si_5O_{16}$	$2Q_1+3Q_2$	1.71	5.46	1013
(e) $Ca_5Na_2Si_2Al_2O_{13}$	$2Q_1+2Q_2$	1.35	7.58	993
(f) $Ca_6Si_6O_{18}$	$6Q_2$	2.25	5.40	1024
(g) $Ca_6Na_2Si_4Al_2O_{18}$	$6Q_2$	1.71	6.20	983
(h) $Ca_4Si_8O_{20}$	$8Q_3$	4.50	3.47	1149
(i) $Ca_4Na_2Si_6Al_2O_{20}$	$8Q_3$	3.83	1.56	1099
(j) $Ca_6Si_{12}O_{30}$	$12Q_3$	4.25	3.29	1142
(k) $Ca_6Na_2Si_{10}Al_2O_{30}$	$12Q_3$	3.85	1.56	1105
(l) $Ca_6Na_4Si_8Al_4O_{30}$	$12Q_3$	3.30	2.15	1068
(m) $Ca_4Na_2Si_{10}Al_2O_{28}$	$8Q_3+4Q_4$	4.22	2.95	1127
(n) $Ca_4Na_4Si_8Al_4O_{28}$	$8Q_3+4Q_4$	3.41	2.71	1071
(o) $Ca_4Na_4Si_6Al_6O_{28}$	$8Q_3+4Q_4$	2.70	4.24	1021
(p) $Ca_6Na_2Si_{16}Al_2O_{42}$	$12Q_3+6Q_4$	4.13	2.34	1147
(q) $Ca_6Na_4Si_{14}Al_4O_{42}$	$12Q_3+6Q_4$	3.80	1.65	1101
(r) $Ca_6Na_6Si_{12}Al_6O_{42}$	$12Q_3+6Q_4$	3.22	2.07	1064
(s) $Ca_4Si_{18}O_{40}$	$8Q_3+10Q_4$	4.81	4.05	1173
(t) $Ca_4Na_2Si_{16}Al_2O_{40}$	$8Q_3+10Q_4$	4.60	3.33	1154
(u) $Ca_4Na_4Si_{14}Al_4O_{40}$	$8Q_3+10Q_4$	4.18	3.01	1131
(v) $Ca_4Na_4Si_{14}Al_4O_{40}$	$8Q_3+10Q_4$	3.48	1.40	1108

In order to explain the microscopic stress functioning mechanism and establish the relationship between wavenumbers and microstructures, the *SIT* of SiOT was empirically defined by You *et al* (2005). As mentioned, the introduction of aluminium heavily affects the symmetrical stretching vibration of Si-O_{nb}. Therefore, to establish the relationship between microstructural stress and characteristic Raman vibration wavenumbers in the ternary CaO-Al_2O_3-SiO_2 system, the influence of aluminium on the microscopic stress environment must be considered. The developing calculation formula of *SIT* is as follows:

$$SIT = {}^1X_i + \alpha R \tag{1}$$

$${}^1X_i = \frac{1}{i}\left(\sum_{j=1}^{k} \sqrt{Q_i Q_{(j)}} + \beta \sum_{j=k+1}^{i} \sqrt{Q_i Q_{(j)}} \right) \tag{2}$$

$$R = \sum_{1}^{m} \frac{n_{Si} + \beta n_{Al}}{n_i \left(n_i - 2 \right)} \tag{3}$$

where:

${}^1X_i$	is the first-order molecular connectivity index of SiOT
R and α	are the contribution of the ring and proportionality coefficient (α = 1 in nonalumina silicate), respectively
Q_i	is the number of BO in the ith SiOT
Q_j	is the BO number of SiOT or AlOT adjacent to the ith SiOT
n_i	is the number of rings Q_i participates in
n_{Si} and n_{Al}	are the number of rings SiOT and AlOT participate in, respectively
β	is a constant (β = 0.5)

The *SIT* values in the clusters are presented in Table 2.

The linear relationship between the *SIT* of Q_i and the calculated wavenumber of the Si-O_{nb} symmetric stretching vibration is established, as shown in Figure 2a, which is consistent with that of binary sodium silicates and calcium silicate in previous studies (You *et al,* 2005; Ma *et al,* 2020). The process used to determine this relationship is well proven, specifically, the concept of *SIT* can be extended to ternary calcium aluminosilicate glasses. On the other hand, Q_i with different *SITs* should have a specific *RSCS* value, and the relationship between *SIT* and *RSCS* is shown in Figure 2b, which was fitted by polynomial regression. This polynomial function can be applied to correct the experimental Raman spectra of glasses, and then the relative concentrations of Q_i in calcium aluminosilicate glasses can be obtained from the areas of the corrected Raman spectra.

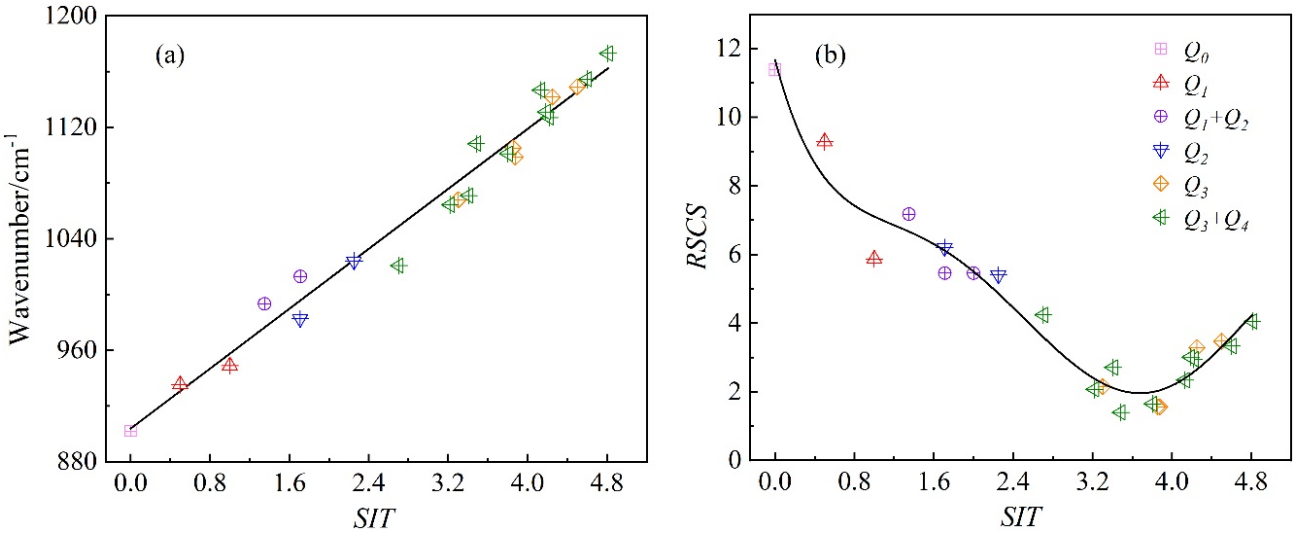

FIG 2 – (a) Fitted linear relationship (y(x) = 903.91+53.74x, R^2 = 0.91) between stress index of silicon-oxygen tetrahedron (*SIT*) and Wavenumber of Si-O_{nb} symmetric stretching vibration; (b) Fitted relationship between *SIT* and Raman scattering cross-section (*RSCS*) by polynomial regression (y(x) = 11.68–11.00x+10.57x^2–5.11x^3+1.06x^4–0.076x^5, R^2 = 0.9554), in which the icons with different shapes and colours refer to the original fitting data (ie the calculated Q_i by quantum chemistry *ab initio* calculation based on the designed probable cluster microstructures in calcium aluminosilicate).

^{27}Al MAS NMR spectra

^{27}Al MAS NMR spectra can effectively probe subtle variations in the local environment of aluminium. Consequently, to identify the roles of aluminium in the aluminosilicate network, ^{27}Al MAS NMR spectra of the prepared glassy samples were obtained, as shown in Figure 3. The ^{27}Al MAS NMR

spectra for the five glasses exhibit a dominant asymmetric peak (approximately 60 ppm) with a shoulder (approximately -20–40 ppm), which denote the chemical shifts of Al^{IV}, Al^{V} and Al^{VI} respectively. Significantly, the ^{27}Al MAS NMR spectra in this study were recorded at a relatively moderate magnetic field intensity (9.4 T), resulting in a long intensity tail at lower frequency due to the strong second-order quadrupolar coupling effect of aluminium; this occurs because quadrupolar coupling constants (C_Q) are widely distributed at low field strength, which will cover and obscure the possible peaks of Al^{V} and Al^{VI}.

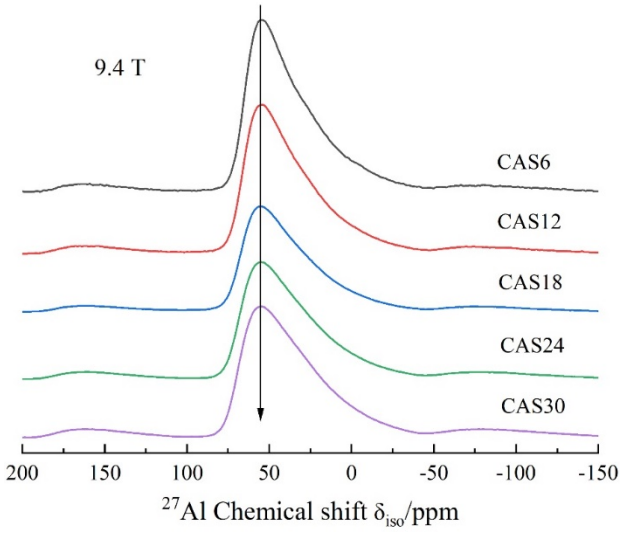

FIG 3 – Experimental ^{27}Al MAS NMR spectra of CAS6, CAS12, CAS18, CAS24, and CAS30 glassy samples recorded at a magnetic field of 9.4 T.

In addition, it can be observed that the NMR spectra show almost an undifferentiated chemical shift and subtle change in full width at half maximum (FWHM). This phenomenon implies that the local environments of aluminium with different constituents did not change significantly, ie the presence of aluminium in fourfold coordination predominantly acts as a network former.

To consider the effect of second-order quadrupolar interaction, the spectra were fitted in DMFit (Massiot *et al,* 2002) software by using Czjzek line shapes, through which the experimental spectra can be fitted with average isotropic chemical shift value (δ_{iso}), distribution, and mean C_Q, to simulate the second-order quadrupolar broadened peaks from aluminium in different coordination environments. The fitting results of the obtained ^{27}Al MAS NMR spectra are shown in Table 3.

For all investigated glasses, most aluminium atoms are in fourfold coordinated Al^{IV} sites (more than 90 per cent, Table 3). Furthermore, a substantial fraction of fivefold coordinated Al^{V} sites are detected (approximately 5 per cent, Table 3) while a minor amount (less than 2 per cent, Table 3) of sixfold coordinated Al^{VI} sites are present. Theoretically, in the peralkaline(-earth) field, aluminium atoms are stabilised in the tetrahedral position without forming higher coordinated species due to having enough Ca^{2+} ions for charge compensation of AlOTs. However, previous studies on ^{27}Al MQ-MAS NMR confirmed that (Stebbins *et al,* 2000; Neuville *et al,* 2007; Neuville, Cormier and Massiot, 2004), less than 10 per cent of highly coordinated Al^{V} and Al^{VI} were observed even for percalcic CAS glasses. This counterintuitive conclusion is further indicated by the ^{27}Al MAS NMR results for the present samples.

TABLE 3

The fitting parameters of relative intensity (I), average isotropic chemical shift (δ_{iso}), full width at half maximum (FWHM) of the Czjzek distribution and average quadrupolar coupling constant (C_Q) using Czjzek line shapes to the ^{27}Al MAS NMR spectra of glassy samples.

Sample	Coordination environment	I/%	δ_{iso}/ppm	FWHM/ppm	C_Q/MHz
CAS6	Al^{IV}	93.41	65.45	12.86	6.26
	Al^{V}	5.15	33.20	12.76	5.54
	Al^{VI}	1.44	7.97	13.75	5.26
CAS12	Al^{IV}	93.80	66.62	13..36	6.50
	Al^{V}	4.60	35.17	14.39	5.41
	Al^{VI}	1.60	6.57	12.70	5.26
CAS18	Al^{IV}	97.19	67.83	13.89	6.74
	Al^{V}	2.81	34.57	14.39	5.55
	Al^{VI}	-	-	-	-
CAS24	Al^{IV}	96.98	68.76	13.86	7.08
	Al^{V}	3.02	37.84	14.39	5.55
	Al^{VI}	-	-	-	-
CAS30	Al^{IV}	93.11	65.58	12.26	6.33
	Al^{V}	5.25	34.16	14.39	5.73
	Al^{VI}	1.64	7.14	12.70	5.26

Raman spectra of calcium aluminosilicate glasses and melts

The glasses and their molten state Raman spectra of all the six samples recorded at 1823 K are respectively illustrated in Figure 4. For the room temperature Raman spectra of glasses, alumina-free CAS0 glass can be roughly distinguished into three regions. For the low-frequency range between 200–400 cm^{-1}, the vibration caused by modifier cations (Ca-O), which can mainly be associated with the lattice vibrations of the skeleton or framework with a broad band centred near 350 cm^{-1}, reflects the long-distance order of the structure. Its relative intensity decreases significantly with the addition of Al_2O_3 until it vanishes completely at x ≥ 18, which indicates that the disorder degree of the silicate network increased violently, and the remaining ordered region of the glassy structure disappeared completely at x ≥ 18. The intermediate frequency range of 400–800 cm^{-1} corresponds to the symmetric bending vibration of the Si-O_b-Si linkages in silicate. For the CAS0 glass, a strong band at 622 cm^{-1} appears, which is assigned to the bending vibrations of Si-O_b-Si linkages. With increasing Al_2O_3 content, the relative intensity decreases sharply and disappears at x > 18. Correspondingly, a new large band grows at 570 cm^{-1} with a shoulder near 508 cm^{-1}, which reflects the motions of bridging oxygen in T-O_b-T linkages (T = Si or Al).

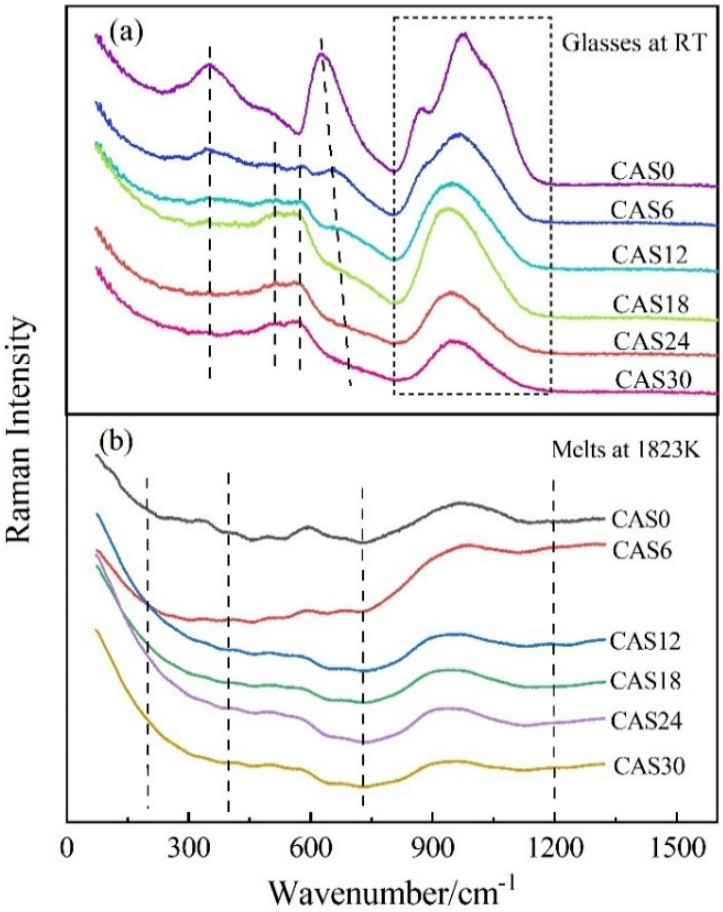

FIG 4 – Original Raman spectra of CASx (x = 0, 6, 12, 18, 24, 30): (a) Glasses, and (b) Melts recorded at 1823 K.

The high-frequency range 800–1200 cm^{-1} is the most informative Raman characteristic band with the strongest relative intensity. Mysen and Virgo (1994) testified that the band in this region belongs to the symmetric stretching vibration of Si-O_{nb}, which is the sum of various Q_i species centred on SiOTs with diverse connections, reflecting the significant microstructural characteristics of aluminosilicates.

Compared with the Raman spectra of glasses, the vibrational bands of Raman spectra of melt exhibit pronounced flattening, along with the broadening of linewidth, due to the introduction of anharmonicity and dynamic disorder resulting from the elevated temperature. Additionally, three major spectral ranges can be distinguished: a low wavenumber range spanning 200–400 cm^{-1} associated with external vibrations involving modifier cations and certain (coupled) deformation modes; an intermediate wavenumber range spanning 400–700 cm^{-1}, indicative of bending vibrations of T-O-T. In the high wavenumber range from 700 to 1200 cm^{-1}, corresponding to the symmetric stretching vibrations of T-O_{nb} bonds, it is noteworthy that the vibrational intensity of Al-O_{nb} within the 700–800 cm^{-1} range can be disregarded due to their significantly lower intensity compared to Si-O_{nb} vibrations.

Quantitative analysis of calcium aluminosilicate glasses and melts

Regarding the deconvolution in the high-frequency range (800–1200 cm^{-1}), it should be noted that the original experimental spectra must be calibrated while applying the results of the QC *ab initio* calculation in the experimental quantitative analysis of aluminosilicate microstructure units, including the temperature correction by the Bose-Einstein factor and frequency correction by the excitation sources (You *et al,* 2005; Gong *et al,* 2022; Ma *et al,* 2020).

As mentioned above, *RSCS* is a significant correction coefficient that concatenates the ratio of Raman peak intensity and the concentration of microstructure species. Therefore, to obtain the

microstructure contents of calcium aluminosilicates, Equation 4 was used to correct the frequency in the original Raman spectra.

$$I(x) = \frac{f(x)}{g(x)} \tag{4}$$

where:

I(x) is the corrected Raman intensity

f(x) is the original Raman intensity

g(x) is the functional relationship between the *RSCS* and wavenumber

The functional relationship between the *RSCS* and wavenumber was obtained by considering the relationships between wavenumber-*SIT* (Figure 2a) and *RSCS*-*SIT* (Figure 2b) relationships.

Figure 5a and 5d shows the calibration procedure of the original Raman spectra for CASx (x = 0, 6, 12, 18, 24, 30) glass and melt by taking CAS18 sample as a case, in which a significant distinction is uncovered both in shape and peak positions. This is the result of $Q^{jklm}_{i\ (n_1h,\ n_2q,\ n_3t)}$ with different optical sensitivities, and the corrected curve can reflect the authentic $Q^{jklm}_{i\ (n_1h,\ n_2q,\ n_3t)}$ species contents. The delicate structures of glasses and melts are obtained by deconvolution of the corrected Raman spectra, as illustrated by the CAS18 sample in Figure 5b and 5e. In addition, the area percentage of Raman bands for Q_i species was determined by summing up all $Q^{jklm}_{i(n_1h,n_2q,n_3t)}$ units with the same BO number i together, and it has been shown in Figure 5c and 5f. The area percentage of the calibrated Raman bands assigned to Q_i species from 800 to 1200 cm^{-1} was proportional to the abundance of different Q_i species. In summary, the aforementioned processing techniques for Raman spectra of glasses and melts, encompassing the calibration of original spectra and the meticulous deconvolution of microstructural constituents, facilitate a more rigorous assessment of the distribution of Q_i species within the aluminosilicate system.

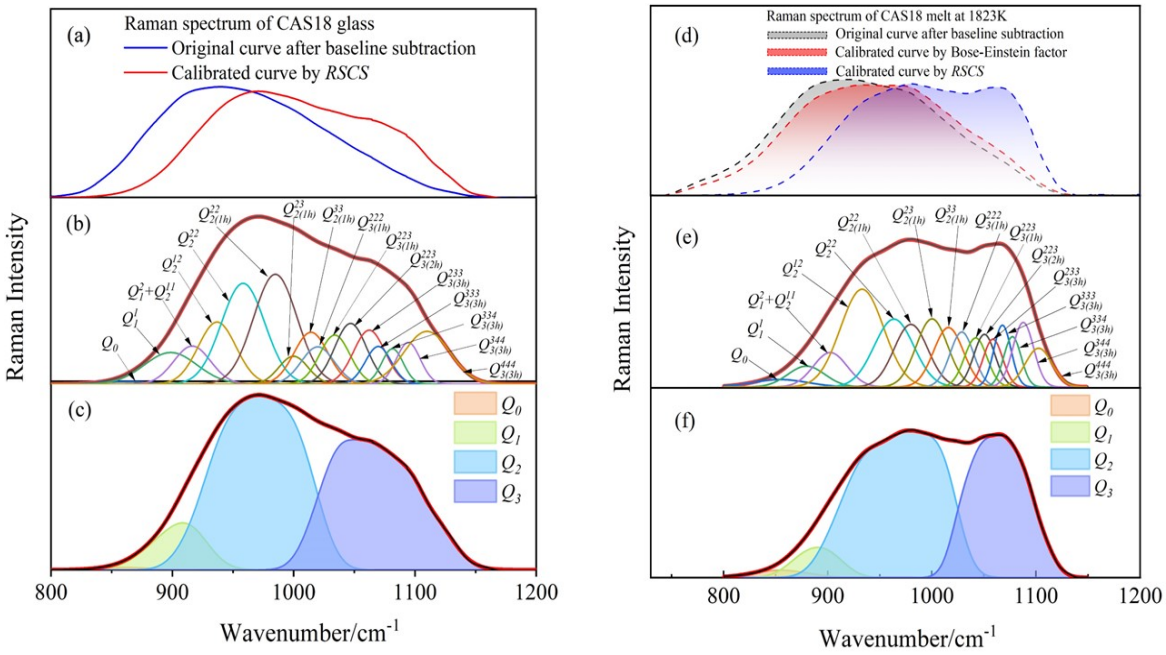

FIG 5 – Quantification process of Raman spectra for CAS18 glass (a)-(c) and their corresponding melts (d)-(f). Specifically, (a) and (d): Calibration of the original Raman spectra, (b) and (e): Deconvolution of the calibrated spectrum with delicate $Q^{jklm}_{i(n_1h,n_2q,n_3t)}$ species, (c) and (f): Distribution of primary Q_i species obtained by summing up all the area of delicate $Q^{jklm}_{i(n_1h,n_2q,n_3t)}$ units with the same BO number i.

The quantitative distribution of primary structures Q_i (i = 0, 1, 2, 3, 4) of glasses and melts as a function of Al_2O_3 concentrations is depicted in Figure 6. It shows that the distribution trend of Q_i species in melts is similar to that in glasses, albeit with differences in relative abundances and the continuity of variation. In detail of evolution, both Q_1 and Q_2 decrease with increasing alumina content, while fully polymerised Q_4 exhibits a sustained and drastic augmentation across the entire compositions range. Meanwhile, Q_3 demonstrates a downward convex trend, increasing initially with alumina content up to 12–18 mol per cent and decreasing with further alumina additions. Besides, a minimal amount of Q_0 is detected in all vitreous and melting samples. The fluctuation in Q_i distribution, corresponding to varying Al_2O_3 content, attests to the introduction of aluminium, resulting in increased network complexity and connectivity. This outcome is attributed to the preferential consumption of Ca^{2+} ions by AlOTs to achieve charge equilibrium. On the other hand, it displays the richer abundance of Q_2 and Q_4 species in melts than that in glasses, while less Q_3 species was observed in melts. This intriguing phenomenon suggests a potential reaction of $Q_2 + Q_4 \rightarrow Q_3$, taking place during the transformation of the samples from a molten to a vitreous state. It elucidates the propensity for phase separation within the molten state, while the glassification process leans towards the amalgamation of microstructure species.

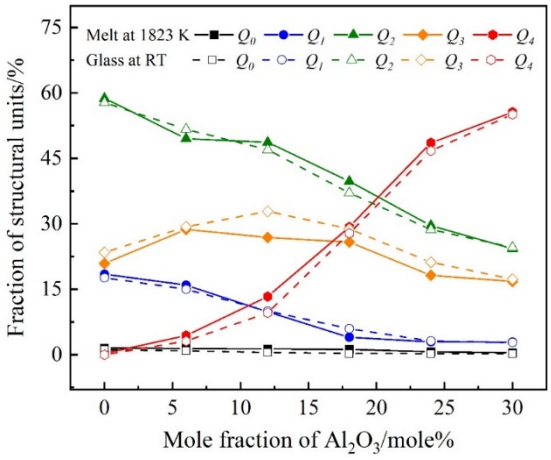

FIG 6 – The quantitative distribution of primary Q_i (i = 0–4) species with the increase of Al_2O_3 content determined by Raman spectroscopy in calcium aluminosilicate melts (solid line) and glasses (dashed line).

The distribution of Q_i species in both the glasses and melts highlights a significant convergence in their microstructures, indicating that the melts effectively retain partial microstructure characteristics during the rapid quenching process. Obviously, this is primarily attributed to the utilisation of the ADL furnace for sample preparation in this study, which enables the attainment of sufficiently rapid cooling rates. However, it should be emphasised that noticeable disparities in microstructures are anticipated between glasses obtained through slower cooling rates and their corresponding melts. In such cases, conducting *in situ* high temperature Raman spectroscopy directly on the molten state becomes of paramount significance.

Relationship between microstructural features and viscosity in calcium aluminosilicate melts

In order to obtain reliable viscosity data, the Urbain model was selected for viscosity prediction of CAS samples. The Urbain model, a widely used slag viscosity models in ternary CAS system, relies on WF (Weymann-Frenkel) equation to establish the relationship between compositionally dependent parameters A and B. These parameters are categorised based on the constituents into glass former, modifiers and amphoterics (Urbain, 1987; Urbain, Bottinga and Richet, 1982).

Figure 7 depicts the predicted viscosity values of six calcium aluminosilicate melts at 1823 K by the Urbain model. Meanwhile, six experimental data are given, which have different alumina contents with fixed ratio CaO/SiO_2 of 1, measured by Zhang and Chou (2013), Kou, Mizoguchi and Suginohara (1978) and Danek, Licko and Panek (1985) at 1823 K. The graph illustrates a notable

agreement between the estimated viscosities and the experimental viscosities, performing a highly consistent trend with increase of alumina. A nearly linear increment is exposed when adding alumina from 0 to 18 mol per cent, followed by a gradual deceleration in viscosity growth with further increases in alumina content.

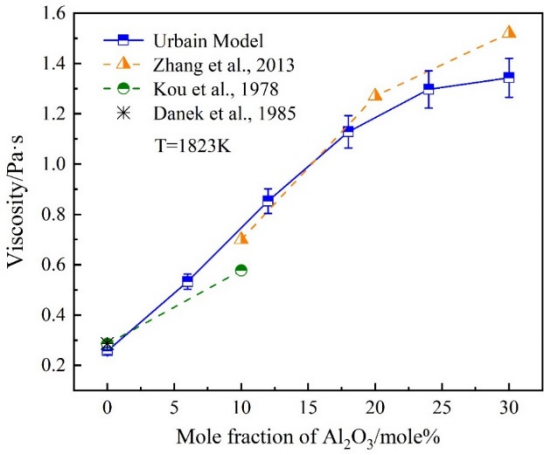

FIG 7 – Viscosity values as a function of Al_2O_3 content in calcium aluminosilicate melts at 1823 K. The blue half-solid line presents viscosity values estimated by employing Urbain model, which lacks corresponding experimental viscosity data with the identical composition and temperature. The green and orange dashed dotted line and black icon are experimental values collected from the reference (Zhang and Chou, 2013; Kou, Mizoguchi and Suginohara, 1978; Danek, Licko and Panek, 1985).

In order to gain insight into the viscosity change mechanism, it is significant to correlate the structure evolution with composition variations. Previous studies have manifested that diverse Q_i species exert individual influence on viscosity (Gong *et al,* 2022; Park, 2013). Therefore, it is conceivable to assume that the viscosity variations accompanying the increase in Al_2O_3 content are intricately related to the distribution of Q_i species. As delineated in Figure 5, for the alumina content is below 12–18 mol per cent, a monotonic reduction in the concentrations of Q_1 and Q_2 species is observed, concurrent with a continuous ascent in more highly connected species, such as Q_3 and Q_4. This shift in distribution precipitates a linear escalation in viscosity. Conversely, upon exceeding the 12–18 mol per cent for alumina content, Q_3 begins to diminish, while the monotonic trends of Q_1, Q_2 and Q_4 remain unabated. Moreover, it's noteworthy that when x ≥ 18 mol per cent, the alumina avoidance parameter (AAP) exceeds 1, signifying the emergence of weaker Al^{IV}-O_b-Al^{IV} bond, which supplants Si-Q_b bonds (Zhang and Chou, 2013). These two interplaying factors collectively contribute to a gradual deceleration in the increase of viscosity.

To further ascertain the structural effects on viscosity and establish the quantitative correlation between them, the degree of polymerisation (DOP) of network was evaluated which has been borne out a higher DOP tended to induce a higher viscosity in silicate. The DOP is typically quantified by assessing the average number of NBO per coordinated network-forming atom, denoted as NBO/T (T represents the total number of SiOT and AlOT units in the aluminosilicate system). In detail, the value of NBO/T can be obtained by Equation 5:

$$NBO/T = \frac{n_{SiO_2}\sum_{i=0}^{4}(4-i)X_{Q_i}}{n_{SiO_2}+2n_{Al_2O_3}X_{Al^{IV}}} \quad (5)$$

Figure 8 shows the calculation results of NBO/T of melts by using Raman deconvolution results, as a function of alumina content. For contrastive analysis, the values of NBO/T of glasses is presented in Figure 8. As anticipated, both NBO/T types exhibit a gradual decline with the addition of alumina, evidencing a strengthening of network connectivity. Notably, even though the Q_i distribution between the glass and corresponding melt exhibits noticeable disparities, the DOP between the two remains virtually identical, with no discernible differences. This can be attributed to the collective effect of various Q_i species.

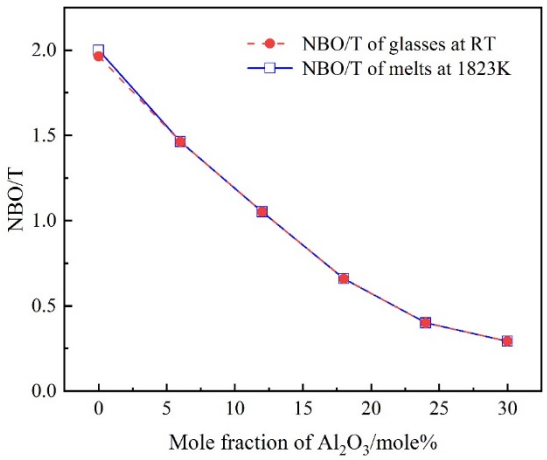

FIG 8 – The variation of NBO/T of melts and glasses with adding of alumina.

Figure 9 shows the linear fitting results of the logarithm of viscosity and NBO/T of melts at 1823 K. As can be seen, with increasing NBO/T which means that the DOP of melts decreases, the logarithm of viscosity progressively decreases, which is in accordance with the above analyses. The negative functional relationship between them can be expressed mathematically as Equation 6:

$$\log \eta(Pa \cdot s) = -0.43\left(NBO/T\right) + 0.31 \tag{6}$$

With the coefficient of determination R^2 of 0.98. In previous studies, Wu *et al* (2015) established a robust correlation between the logarithm of viscosity and NBO/T of CaO-SiO_2 system by Molecular dynamics simulation method. But for CaO-Al_2O_3 system, the fitting result was deemed inadequate due to the amphoteric nature of alumina, resulting in the more complicated structure. In our present work, an overall remarkable linear correlation is exhibited between the logarithm of viscosity and the experimentally determined NBO/T of melts, which clearly demonstrates the quantitative relationship of them.

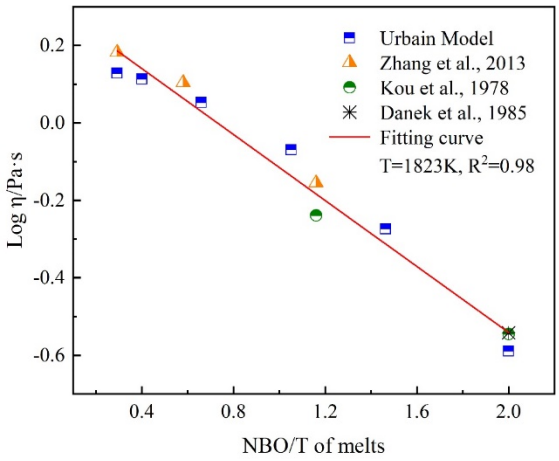

FIG 9 – The quantitative linear relationship between the logarithm of viscosities and NBO/T of melts. The blue icon presents viscosity values obtained by Urbain model at 1823 K and red line is the corresponding fitting curve with the function of $\log \eta(Pa \cdot s) = -0.43\left(NBO/T\right) + 0.31$.

CONCLUSIONS

The microstructure characteristics and viscosity behaviour of CaO-SiO_2-based melts at 1823 K were investigated by incorporating varying Al_2O_3 contents from 0 to 30 mol per cent. By considering the influence of aluminium, alongside calibrations for temperature and *RSCS*, a refined deconvolution of Raman spectra for CAS glasses and melts have been achieved. Comparative analysis reveals a congruence in Q_i distribution trends between rapidly quenched glass and corresponding melts, implying that a higher cooling rate during glass formation may effectively conserve the *in situ*

structural characteristics of the melts, and the evolution of Q_i conveyed a monotonic augmentation in the DOP across the entire compositional range. Yet, notable discrepancies are also observed, especially for Q_2, Q_3 and Q_4 species, with a potential $Q_2 + Q_4 \rightarrow Q_3$ reaction seems to transpire during the shift from a molten to a vitreous state.

Further exploration of the relationship between composition, microstructure and viscosity was conducted within the defined compositional range of CAS melts. The results revealed a gradual increase in viscosity with the addition of alumina, displaying a progressively leveling off non-linear trend. However, a robust linear relationship was observed between the logarithm of viscosity and the DOP quantified by NBO/T.

ACKNOWLEDGEMENTS

This work was supported by National Natural Science Foundation of China (21773152), National 111 project (D17002, the Program of Introducing Talents of Discipline to Universities), the Key Basic Research Projects of the Basic Strengthening Plan of the Commission of Science and Technology (2021-JCJQ-ZD-051-00-02), the Shanghai Committee of Science and Technology Fund, China (12520709200), the Open Project Program of the State Key Laboratory of Advanced Special Steel, Shanghai University, China (SKLASS2020-06) and Special Fund Project of Shanghai Municipality for Science and Technology Development (YDZX20173100001316), the China Scholarship Council under the Grant CSC No. 202006890136.

REFERENCES

Atila, A, Ghardi, E M, Hasnaoui, A and Ouaskit, S, 2019. Alumina effect on the structure and properties of calcium aluminosilicate in the percalcic region: A molecular dynamics investigation, *Journal of Non-Crystalline Solids*, 525:119470.

Brawer, S A and White, W B, 1977. Raman spectroscopic investigation of the structure of silicate glasses (II), Soda-alkaline earth-alumina ternary and quaternary glasses, *Journal of Non-Crystalline Solids*, 23:261–278.

Chen, Z, Wang, H, Sun, Y, Liu, L and Wang, X, 2019. Insight into the Relationship Between Viscosity and Structure of CaO-SiO_2-MgO-Al_2O_3 Molten Slags, *Metallurgical and Materials Transactions B*, 50:2930–2941.

Danek, V, Licko, T and Panek, Z, 1985. Viscosity of melts in the system CaO-FeO-Fe_2O_3-SiO_2, *Silikaty*, 29:291–299.

Feng, P, Xuehui, Y, Xuanxue, M, Jinglin, Y, Chen, W, Hui, C and Guochang, J, 2006. Raman Active Vibrations of Aluminosilicates, *Spectroscopy and Spectral Analysis*, 26:1871–1875.

Gong, X, Wang, J, You, J, Wang, M, Tang, X, Zhang, F, Tang, K, Lu, L, Wan, S and Zhang, Q, 2022. Room temperature Raman spectroscopy and ^{29}Si MAS NMR combined with high temperature Raman spectroscopy and DFT calculation of $xMgO$-$(1-x)CaO$-SiO_2 glasses and melts, *Ceramics International*, 48:4911–4920.

Gu, S, Wen, G, Guo, J, Wang, Z, Tang, P and Hou, Z, 2020. Effect of Al_2O_3 on non-Newtonian property and its relation to structure of mold fluxes during shear stress field at 1573 K, Journal of Non-Crystalline Solids, 547:120312.

Kou, T, Mizoguchi, K and Suginohara, Y, 1978. The Effect of Al_2O_3 on the Viscosity of Silicate Melt, *Journal of the Japan Institute of Metals and Materials*, 42:775–781.

Le Losq, C, Neuville, D R, Florian, P, Henderson, G S and Massiot, D, 2014. The role of Al^{3+} on rheology and structural changes in sodium silicate and aluminosilicate glasses and melts, *Geochimica et Cosmochimica Acta*, 126:495–517.

Lee, T J and Jayatilaka, D, 1993. An open-shell restricted Hartree-Fock perturbation theory based on symmetric spin orbitals, *Chemical Physics Letters*, 201:1–10.

Li, J L, Shu, Q F and Chou, K, 2014. Effect of Al_2O_3/SiO_2 mass ratio on viscosity of CaO-Al_2O_3-SiO_2-CaF_2 slag, *Ironmaking and Steelmaking*, 42:154–160.

Loewenstein, W, 1954. The distribution of aluminium in the tetrahedra of silicates and aluminates, *American Mineralogist: Journal of Earth and Planetary Materials*, 39:92–96.

Ma, J, Wang, M, You, J, Tang, K, Lu, L, Wan, S, Wang, J, Gong, X and Wang, Y, 2020. Quantitative studies on the structure of $xCaO\cdot(1-x)SiO_2$ glasses and melts by *in-situ* Raman spectroscopy, ^{29}Si MASNMR and quantum chemistry *ab initio* calculation, *Journal of Non-Crystalline Solids*, 546:120252.

Massiot, D, Fayon, F, Capron, M, King, I, Le Calvé, S, Alonso, B, Durand, J-O, Bujoli, B, Gan, Z and Hoatson, G, 2002. Modelling one- and two-dimensional solid-state NMR spectra, *Magnetic Resonance in Chemistry*, 40:70–76.

Mysen, B and Virgo, D, 1994. *Structure and Properties of Silicate Glasses and Melts; Theories and Experiment, Advanced Mineralogy*, pp 238–254 (Springer).

Mysen, B O, Lucier, A and Cody, G D, 2003. The structural behavior of Al^{3+} in the system Na_2O-Al_2O_3-SiO_2 in peralkaline melts and glasses, *American Mineralogist*, 88:1668–1678.

Mysen, B, 2021. Structure of Aluminosilicate Melts, *ISIJ International*, 61:2866–2881.

Neuville, D R, Cormier, L and Massiot, D, 2004. Al environment in tectosilicate and peraluminous glasses: A, ^{27}Al MQ-MASNMR, Raman and XANES investigation, *Geochimica et Cosmochimica Acta*, 68:5071–5079.

Neuville, D, Cormier, L, Montouillout, V and Massiot, D, 2007. Local Al site distribution in aluminosilicate glasses by ^{27}Al MQMASNMR, *Journal of Non-Crystalline Solids*, 353:180–184.

Nowak, M, Rostkowska, H, Lapinski, L, Kwiatkowski, J and Leszczynski, J, 1994. Experimental matrix isolation and theoretical ab initio HF/6–31G (d, p) studies of infrared spectra of purine, adenine and 2-chloroadenine, *Spectrochimica Acta Part A: Molecular Spectroscopy*, 50:1081–1094.

Park, J H, 2013. Structure-Property Relationship of CaO-MgO-SiO_2 Slag: Quantitative Analysis of Raman Spectra, *Metallurgical and Materials Transactions B*, 44:938–947.

Park, J H, Kim, H and Min, D J, 2008. Novel Approach to Link between Viscosity and Structure of Silicate Melts via Darken's Excess Stability Function: Focus on the Amphoteric Behavior of Alumina, *Metallurgical and Materials Transactions B*, 39:150–153.

Piriou, B and McMillan, P, 1983. The high-frequency vibrational spectra of vitreous and crystalline orthosilicates, *American Mineralogist*, 68:426–443.

Rajavaram, R, Kim, H, Lee, C-H, Cho, W-S, Lee, C-H and Lee, J, 2017. Effect of Al_2O_3 Concentration on Density and Structure of (CaO-SiO_2)-xAl_2O_3 Slag, *Metallurgical and Materials Transactions B*, 48:1595–1601.

Richet, P, Polian, A, Vo-Thanh, D and Bottinga, Y, 2022. Brillouin scattering in aluminosilicate glasses and melts up to 2550 K, Temperature and composition effects, *Journal of Non-Crystalline Solids: X*, 14:100086.

Sano, N, Lu, W-K, Riboud, P V and Maeda, M, 1997. *Advanced physical chemistry for process metallurgy* (Academic Press).

Shao, H, Gao, E, Wang, W and Zhang, L, 2019. Effect of fluorine and CaO/Al_2O_3 mass ratio on the viscosity and structure of CaO-Al_2O_3-based mold fluxes, *Journal of the American Ceramic Society*, 102:4440–4449.

Sharma, L and Chhibber, R, 2020. Design and development of SAW fluxes using CaO-SiO_2-CaF_2 and CaO-SiO_2-Al_2O_3 flux systems, *Ceramics International*, 46:1419–1432.

Siafakas, D, Matsushita, T, Jarfors, A E W, Hakamada, S and Watanabe, M, 2018. Viscosity of SiO_2-CaO-Al_2O_3 Slag with Low Silica – Influence of CaO/Al_2O_3, SiO_2/Al_2O_3 Ratio, *ISIJ International*, 58:2180–2185.

Sokol'skii, V E, Pruttskov, D, Busko, V, Kazimirov, V, Roik, O, Chyrkin, A, Galinich, V and Goncharov, I, 2018. Investigation of structure of CaO-Al_2O_3-SiO_2 melts as a basis for the development of new agglomerated welding fluxes and industrial refractories, *Journal of Mining and Metallurgy, Section B: Metallurgy*, 54:133–141.

Stebbins, J F, Kroeker, S, Lee, S K and Kiczenski, T, 2000. Quantification of five-and six-coordinated aluminium ions in aluminosilicate and fluoride-containing glasses by high-field, high-resolution ^{27}Al NMR, *Journal of Non-Crystalline Solids*, 275:1–6.

Takahashi, S, Neuville, D R and Takebe, H, 2015. Thermal properties, density and structure of percalcic and peraluminus CaO-Al_2O_3-SiO_2 glasses, *Journal of Non-Crystalline Solids*, 411:5–12.

Urbain, G, 1987. Viscosity estimation of slags, *Steel Research*, 58:111–116.

Urbain, G, Bottinga, Y and Richet, P, 1982. Viscosity of liquid silica, silicates and alumino-silicates, *Geochimica et Cosmochimica Acta*, 46:1061–1072.

Veit, U, Rüssel, C, Houet, Y and Laurent, D, 2016. Viscosity and Liquidus Temperature of Ternary Glasses Close to the Eutectic Composition in the CaO-Al_2O_3-SiO_2 System, *International Journal of Applied Glass Science*, 7:295–309.

Wang, Z, Huang, S, Wen, G, Jiang, W, Chen, F and Tang, P, 2020. Effects of temperature on the thermal conductivity of amorphous CaO-SiO_2-Al_2O_3 slags: a computational insight, *Phys Chem Chem Phys*, 22:8808–8816.

Wu, T, He, S, Liang, Y and Wang, Q, 2015. Molecular dynamics simulation of the structure and properties for the CaO-SiO_2 and CaO-Al_2O_3 systems, *Journal of Non-Crystalline Solids*, 411:145–151.

You, J L, Jiang, G C, Hou, H Y, Chen, H, Wu, Y Q and Xu, K D, 2005. Quantum chemistry study on superstructure and Raman spectra of binary sodium silicates, *Journal of Raman Spectroscopy*, 36:237–249.

Zhang, G-H and Chou, K-C, 2013. Influence of Al_2O_3/SiO_2 Ratio on Viscosities of CaO-Al_2O_3-SiO_2 Melt, *ISIJ International*, 53:177–180.

Zhen, Y-L, Zhang, G-H, Tang, X-L and Chou, K-C, 2014. Influences of Al_2O_3/CaO and Na_2O/CaO Ratios on Viscosities of CaO-Al_2O_3-SiO_2-Na_2O Melts, *Metallurgical and Materials Transactions B*, 45:123–130.

Viscosity evaluation of hot metal containing vanadium and titanium via a novel measurement technology and the thermodynamic analysis method

DOI: 10.62053/TFNW6977

W Yu[1], J Wen[2], Z Jiang[3], P Hou[4], M Hu[5] and C Bai[6]

1. Associate Professor, Chongqing University, Chongqing 400044, China. Email: yuwenzhoucd@cqu.edu.cn
2. Student, Chongqing University, Chongqing 400044, China. Email: 202209131296@stu.cqu.edu.cn
3. Student, Chongqing University, Chongqing 400044, China. Email: 202109131267@cqu.edu.cn
4. Student, Chongqing University, Chongqing 400044, China. Email: houpiaocqu@163.com
5. Professor, Chongqing University, Chongqing 400044, China. Email: hml@cqu.edu.cn
6. Professor, Chongqing University, Chongqing 400044, China. Email: bguang@cqu.edu.cn

ABSTRACT

Vanadium titano-magnetite (VTM) is one of the important iron ore resources in the world. High viscosity and low fluidity are the basic characteristics of hot metal containing vanadium and titanium during the ironmaking process. Clarifying the influencing mechanism of the melt viscosity would be a significant issue for the high efficiency smelting of VTM. In this paper, a self-developed melt viscometer based on the principle of torsional vibration theory was employed to measure the viscosity of hot metal accurately. Simultaneously, the thermodynamic calculations and some modern detection methods were also used to investigate the precipitation behaviour of high-melting-point phases in hot metal containing vanadium and titanium. The measuring results show that the viscosity of molten iron gradually increases with the increase of titanium content when the mass fraction of titanium is between 0.09 wt per cent – 0.50 wt per cent. Meanwhile, the viscosity of the hot metal was affected significantly by the vanadium content. When the vanadium mass fraction was higher than 0.30 wt per cent, the viscosity of hot metal increased sharply, which will have a serious impact on the fluidity of the hot metal. Furthermore, it was revealed by thermodynamic calculations that an increase in titanium and vanadium content would result in the precipitation of high melting point phases such as TiC, TiN, VC, and VN in the molten iron, ultimately resulting in a decrease in its fluidity. Meanwhile, it was confirmed by Scanning Electron Microscope (SEM) observation that the precipitates in the hot metal were compounds consisting of V, Ti, C, and N elements, which agrees well with the thermodynamic analysis results.

INTRODUCTION

Vanadium titano-magnetite (VTM) is a crucial mineral in the world, which contains valuable elements such as iron, vanadium and titanium, and has significant comprehensive utilisation value in metallurgical industry (Chen, 2015; Tan *et al*, 2011). VTM is mainly located in South Africa, Russia, China, and Canada, etc. In China, the VTM is primarily distributed in Panzhihua and Chengde regions. Generally, the hot metal produced by the VTM exhibits lower fluidity than that produced by the conventional iron minerals, due to the high content of vanadium and titanium in VTM (Zhang *et al*, 2013; Lü *et al*, 2016; Gou, 2012). Poor fluidity of hot metal in ironmaking could result in various issues such as operational difficulties and low productivity. Additionally, the steelmaking process can be also impeded by the reduced fluidity of hot metal, thereby exerting a detrimental impact on industrial production efficiency (He *et al*, 2010; Zhao and Miao, 2015; Zhang *et al*, 2015b).

Normally, viscosity is defined as the shear stress needed to generate a unit shear rate and is expressed as the ratio of shear stress to shear rate (Gu, 2018). In the 17th century, Newton's proposal of the concept of viscosity provided a theoretical basis for viscosity measurement. However, a unified standard for the measurement of viscosity has not been developed, due to the complexity of fluid research (Qu, 2015). Although there are a lot of mature devices for measuring the viscosity of fluids at room temperature or low temperature, there has been less development of equipment for measuring high-temperature melt viscosity, especially for low viscosity melt at high temperature. The primary reason for this is that the measurement of high-temperature melt viscosity is often accompanied by complex physical and chemical changes and irregular thermal disturbance, which

further complicates the measurement process and reduces the accuracy (Qu, 2015; Zhang *et al*, 2015a; Jia *et al*, 2010; Liu, 2015; Gancarz and Gasior, 2016; Wen *et al*, 1996).

In this study, a self-developed viscosity equipment was employed to measure the viscosity of hot metal containing vanadium and titanium. The objective is to clarify the impact of vanadium and titanium content on the fluidity of hot metal. Additionally, thermodynamic analysis and characterisation methods were employed to investigate the underlying mechanisms. This study not only has important exploration value for the accurate measurement of low viscosity in molten metal, but also has important practical guidance for the improvement of industrial production efficiency.

EXPERIMENTAL

Materials

The pig iron used in the study was taken from an iron and steel plant in China and the vanadium and titanium contents of the samples were adjusted by blending in some amounts of ferrovanadium and high purity titanium (99.99 per cent). The compositions of the pig iron and alloys are in Table 1.

TABLE 1

Composition of pig iron and alloy (wt%).

Elements	Pig iron	Ferrovanadium
C	4.325	0.032
Si	0.145	0.860
Mn	0.240	0.046
P	0.079	0.036
S	0.065	0.014
Ti	0.090	-
V	0.040	80.900

Methods

Before the measurement of viscosity, the sample was pre-melted using an induction furnace until the composition is uniform. Thereafter, the sample was placed in a self-developed equipment to carry out the viscosity measurement. Figure 1 shows the schematic diagram of the viscosity measurement equipment, which contains the heating system, the torsion pendulum vibration system, the photoelectric sensing system and a real-time computer recording system. After the sample was melted at 1450°C, the viscosity measurement began through applying an external twisting force to the rotor, by which the rotor will rotate in the testing melt to do the damping motion until it stop. During this period, the damping motion of the rotor can be detected by the photoelectric sensing system and recorded by the real-time computer recording system. The viscosity value of the molten material could be obtained by analysing the curve of the damping motion.

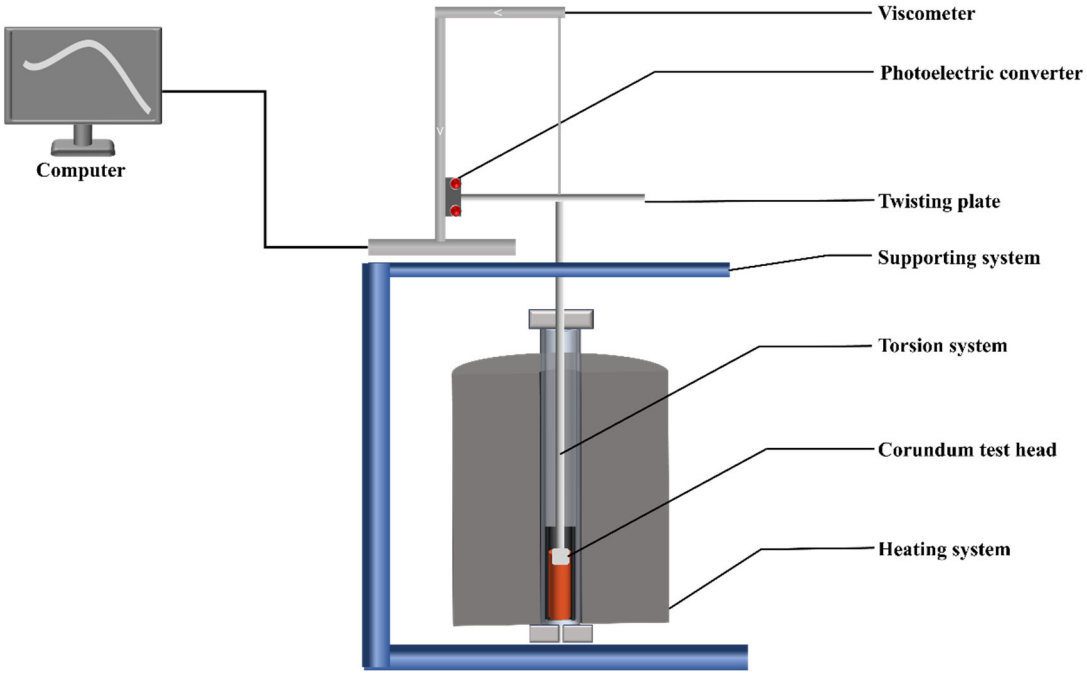

FIG 1 – Schematic diagram of the self-developed viscometer.

For the internal column torsional vibration theory, the viscosity of the liquid to be measured is positively correlated with the logarithmic decay rate (λ) of the torsional vibration system, and the relationship can be expressed by Equation 1.

$$\eta = \frac{(\mathrm{DI})^{1/2}}{K}\lambda \tag{1}$$

where:

η	is the viscosity of the liquid
I	is the moment of inertia in the system
D	is the torque per unit of twist
K	is a constant

For a definite viscosity measurement system, the D, I, and K are regarded as the fixed values.

For damped vibrations with attenuated damping, the logarithmic decay rate is defined as Equation 2.

$$\lambda = \frac{lnA_n - lnA_{n+m}}{m} \tag{2}$$

Where A_n and A_{n+m} are the amplitudes of the nth and n+mth vibrations, respectively, and m is the difference between the corresponding number of vibrations when the amplitudes are A_n and A_{n+m}.

The functional relationship between the viscosity of the tested liquid and the vibration amplitude and frequency could be obtained by combining Equations 1 and 2, as shown in Equation 3.

$$\eta = \frac{(DI)^{\frac{1}{2}}(lnA_n - lnA_{n+m})}{Km} \tag{3}$$

For a definite measurement system, the D, I and K are fixed values, so the variables in the above equation include the logarithmic difference of the two amplitudes and the number of vibrations. When the amplitude difference is fixed within a specific range, the viscosity of the liquid could be inferred from the number of vibrations in that amplitude range. This relationship is expressed in Equation 4, where a is a constant.

$$\eta = \frac{a}{m} \tag{4}$$

From Equation 4, the viscosity (η) of the liquid is inversely proportional to the number of vibrations (m) within the fixed amplitude interval. To eliminate the effect of systematic error on the viscosity of the liquid, it is necessary to introduce another constant b, as shown in Equation 5.

$$\eta = \frac{a}{m} + b \tag{5}$$

Based on the above equation, the determination of the constants a and b is the only requirement to calculate the viscosity of the liquid to be measured by using Equation 5.

The values of parameters a and b can be calibrated using a standard liquid with a known viscosity. In this experiment, three standard liquids with viscosities of 1, 5 and 10 mPa·s were used to calibrate the values of a and b, respectively. The damping curve of a known viscosity standard solution was measured by using the self-developed viscosity measurement equipment at room temperature and the results are shown in Figure 2. The viscosities (η) and 1/m measured by the standard liquids with known viscosities are plotted as scatter plots and the values of a and b can be obtained by analysing the curves.

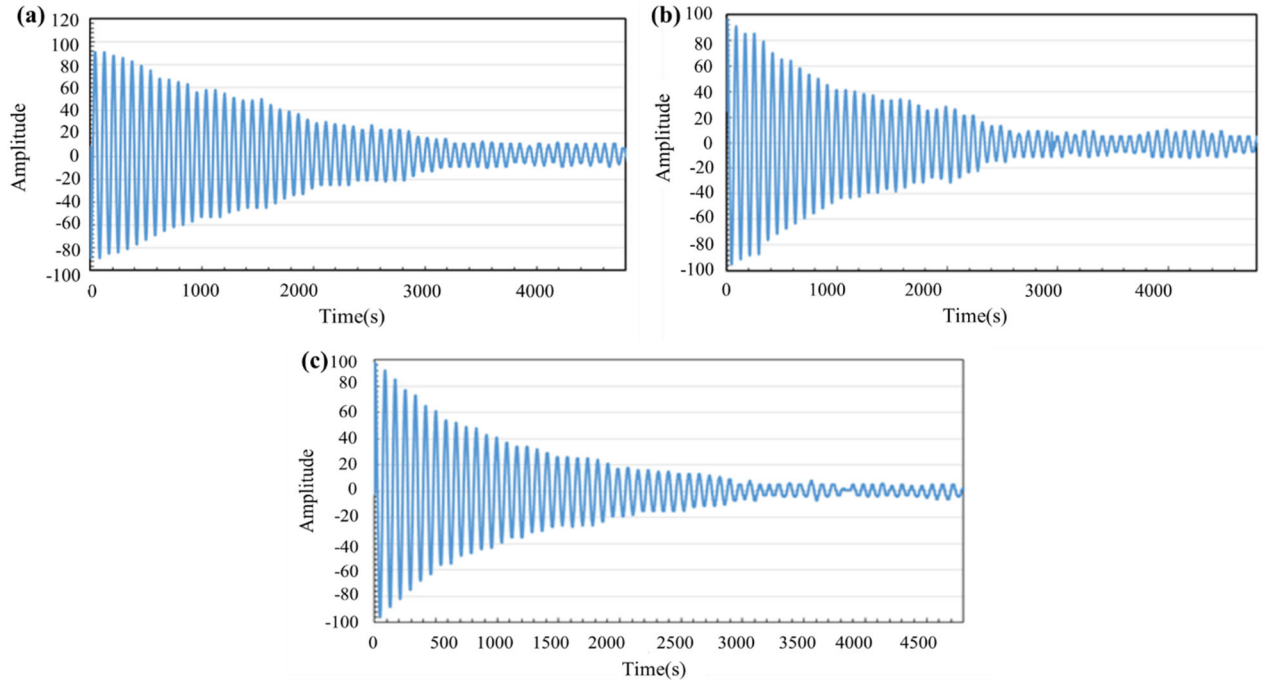

FIG 2 – Damping curves for standard fluids: (a) viscosity of 1 mPa·s; (b) viscosity of 5 mPa·s; (c) viscosity of 10 mPa·s.

Characterisation

The morphology of the high melting point phase and its composition were confirmed by a scanning electron microscope equipped by the energy dispersive X-ray spectroscopy (SEM-EDS, TESCAN VEGA 3 LMH, Czech Republic).

Thermodynamic analysis

Thermodynamic calculations of the precipitation of VC, VN, TiC, and TiN compounds were performed by using FactSage 8.0 software. The database used was 'F-Steel'.

RESULTS AND DISCUSSION

Effect of vanadium and titanium content on the hot metal viscosity

Figure 3 illustrates the results of the viscosity experiment. The viscosity of the hot metal shows a strong correlation with both temperature and composition. In Figure 3a, it can be seen that the viscosity of the hot metal gradually increases with the increasing of the titanium content. The viscosity of the hot metal at 1300°C is 24.6 mPa·s with a titanium content of 0.09 wt per cent.

However, the viscosity increases to 124.5 mPa·s at the same temperature when the titanium content is increased to 0.40 wt per cent. In addition, the melting temperature of the hot metal gradually increases.

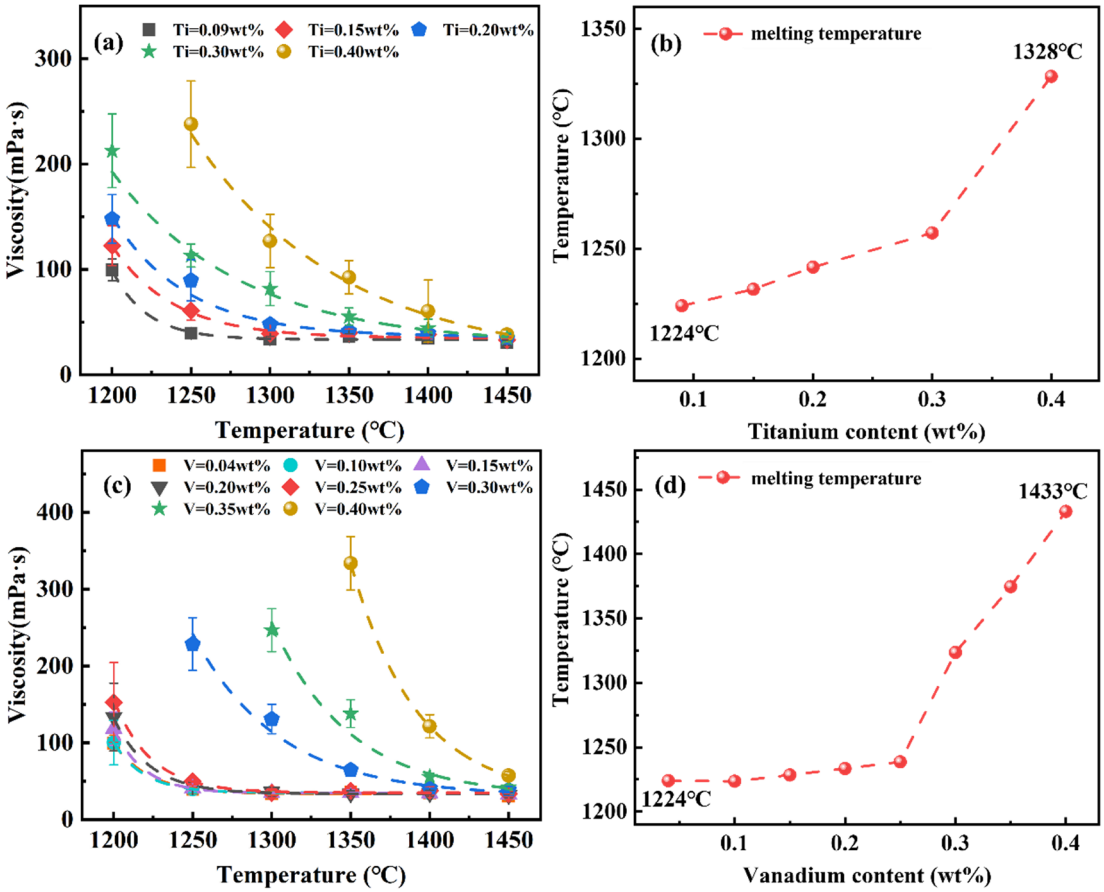

FIG 3 – Viscosity-temperature curve and melting temperature curve (Hou, 2022).

From Figure 3c, it can be seen that the viscosity of the hot metal is also closely related to the vanadium content. As the temperature decreases, the viscosity of the hot metal gradually increases. When the vanadium content is less than 0.30 wt per cent, its effect on viscosity is not significant. However, when the vanadium content exceeds 0.30 wt per cent, the viscosity of hot metal sharply increases with the increasing of the vanadium content and the melting temperature of the hot metal increases significantly (Figure 3d). Furthermore, the viscosity of the hot metal increases with vanadium content at the same temperature. Based on the above experimental results, theoretical calculations and microscopic observations will be used to further explore the mechanism of the influence of titanium and vanadium content on the viscosity of molten iron.

Thermodynamic calculation

Figure 4 displays the results of thermodynamic calculations concerning the precipitation temperature and the mass of the compounds (VC, VN, TiC, and TiN) at varying titanium and vanadium contents in hot metal. Note that the content of [N] in hot metal was set as 0.05 per cent according to our previous study (Hou, 2022; Hou *et al*, 2022). As depicted in Figure 4a and 4b, the precipitation temperatures of both TiC and TiN exhibit a gradual rise as the titanium content increases. Specifically, when the titanium content is 0.10 wt per cent, the precipitation temperatures for TiC and TiN are 1249°C and 1435°C, respectively. As the titanium content increases to 0.50 wt per cent, these precipitation temperatures also increase to 1392°C and 1628°C, respectively. In the previous study, Gao *et al* (2019) proved that as the temperature decreases, the supersaturated titanium reacts with carbon and nitrogen to produce high-melting-point phases such as TiC, TiN and Ti (C, N). The precipitation of these high-melting-point phases leads to reduced fluidity and increased viscosity in the hot metal. This conclusion consists with the viscosity experiment results mentioned above.

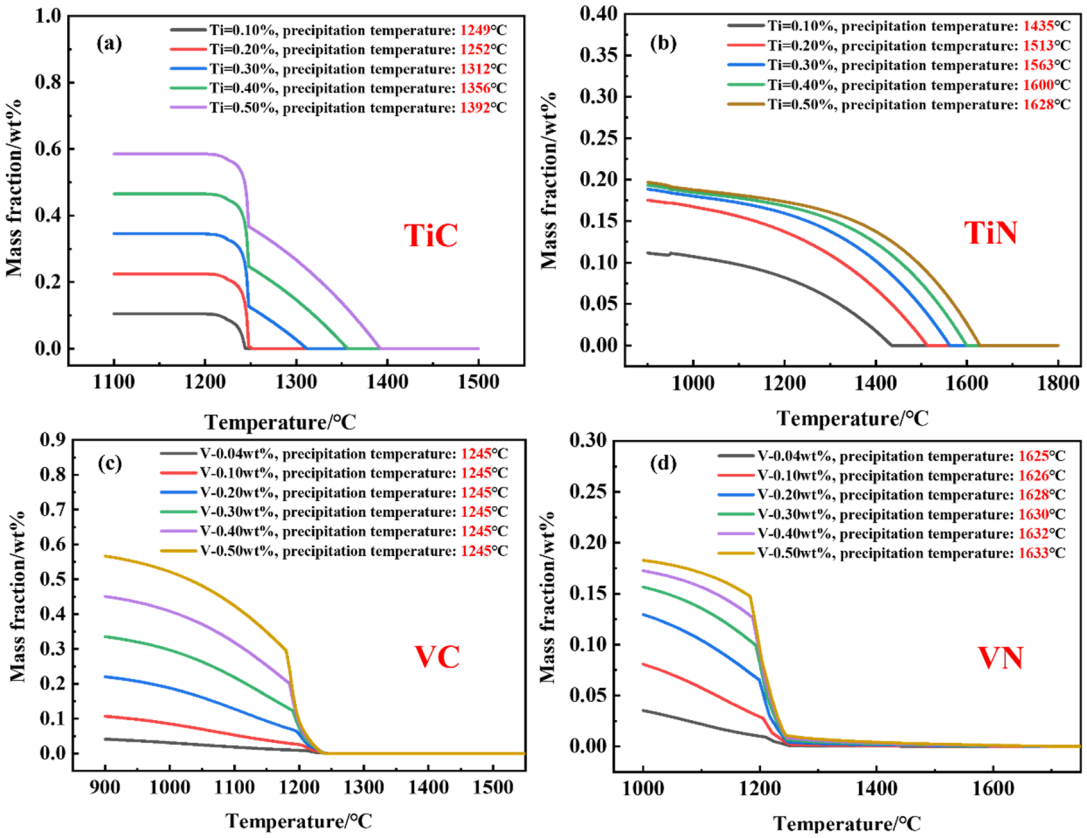

FIG 4 – Thermodynamic calculation results of precipitation for hot metal with different titanium and vanadium contents (Hou *et al*, 2022).

Figure 4c and 4d reveal that the precipitation temperature of VC remains constant at 1245°C regardless of the vanadium content, while the precipitation temperature of VN gradually increases as the vanadium content increases. Specifically, when the vanadium content is 0.04 wt per cent, the precipitation temperature of VN is 1625°C. Increasing the vanadium content to 0.50 wt per cent, the precipitation temperature of VN remains at 1633°C. This suggests that the precipitation temperature of the VN phase exceeds that of the VC phase, indicating the impact of the VN phase on viscosity in hot metal is greater than that of the VC phase. Simultaneously, the precipitation mass of VC and VN phases in the hot metal rises with increasing vanadium content, which is consistent with the viscosity results mentioned above. When the vanadium content is less than 0.30 wt per cent, the vanadium in the hot metal has not reached saturation due to the high solubility of vanadium in hot metal and the precipitation amount is low. However, when the vanadium content exceeds 0.30 wt per cent, the vanadium in hot metal reaches supersaturation as the vanadium content increases, and a large amount of VN and VC begin to precipitate, resulting in the sharp increasing of the viscosity. In addition, the VC and VN phases continue to aggregate and grow as the temperature decreases, which will further worsen the fluidity of the melt.

Precipitation behaviour of compounds in the hot metal

The composition of the high melting point phase was analysed by Scanning Electron Microscope (SEM) and the results are shown in Figure 5. It shows that the precipitated phases in the hot metal predominantly consist of elongated and irregularly shaped crystals, possibly due to different cooling conditions across different parts of the sample. Furthermore, the EDS analyses of points 1, 2, and 4 in Figure 5a and 5b demonstrate that the primary elements at these locations are C, Ti, and V, indicating that the precipitated phases at these points are primarily TiC and VC. In addition, the EDS analysis of point 3 shows that the major elements at this location are C, N, Ti, V, and Fe, indicating that Fe_3C precipitated during solidification. From Fe-C phase diagram, it was found that the precipitation temperature of Fe_3C was lower than 1150°C when the carbon mass fraction was 4.3 per cent. Therefore, the precipitation of Fe_3C has small effect on the viscosity of the hot metal.

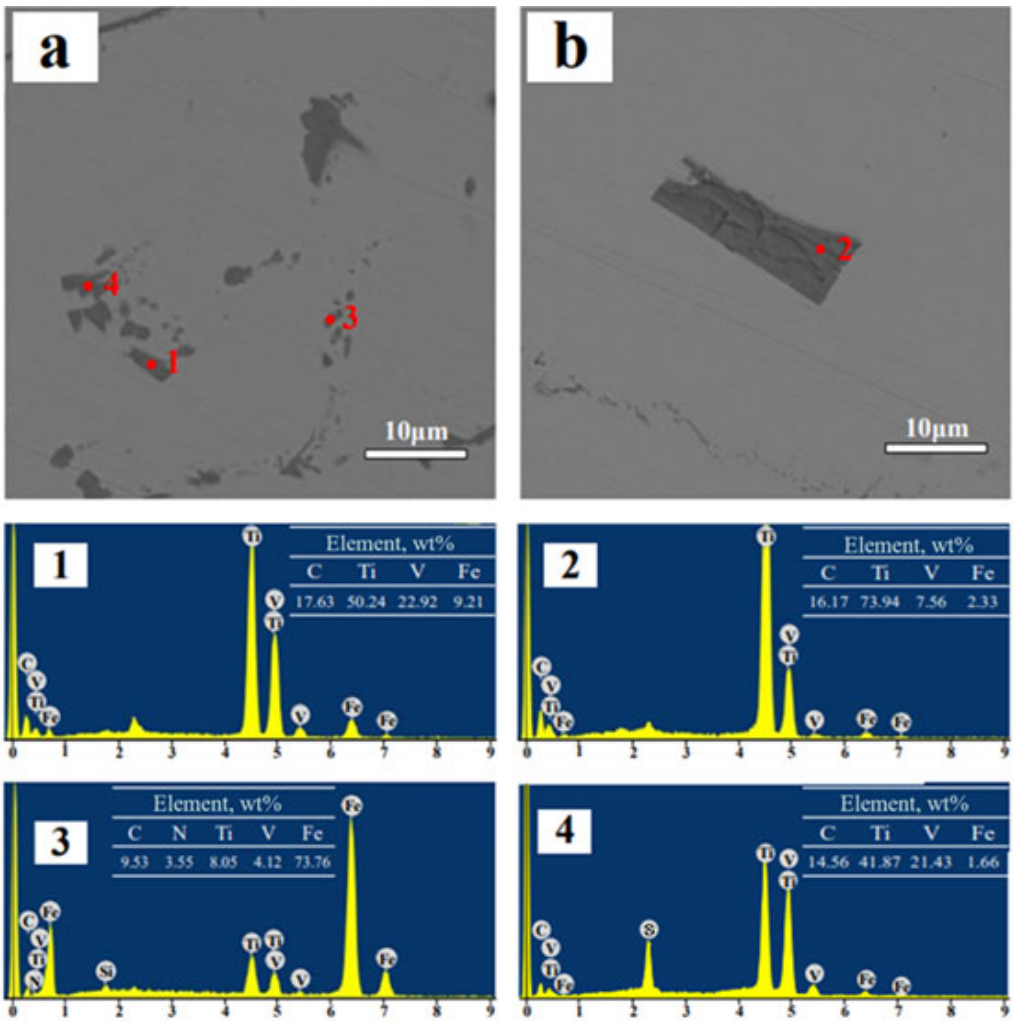

FIG 5 – Scanning Electron Microscope (SEM) and Energy Dispersive X-ray Spectroscopy (EDS) images of molten iron samples (Hou, 2022).

In summary, high melting point phase precipitated and existed in the form of either large particles or dispersed particles within the hot metal as hot metal cooled. With the particles continued to grow, the fluidity of the hot metal gradually decreased and its viscosity increased.

CONCLUSIONS

The viscosity of hot metal containing titanium and vanadium was measured accurately by using a self-developed viscosity measurement equipment and the basic conclusions were summarised as follows:

- With the increasing of vanadium and titanium content, the viscosity of hot metal increased gradually. When the titanium content increased from 0.09 wt per cent to 0.5 wt per cent, the viscosity of the hot metal changed from 24.6 mPa·s to 124.5 mPa·s. When the vanadium content is less than 0.30 wt per cent, its effect on viscosity was not significant. However, when the vanadium content exceeded 0.30 wt per cent, the viscosity of hot metal increased sharply.
- Thermodynamic calculation shows that when the titanium content in the hot metal is 0.5 wt per cent, the precipitation temperature of TiC is 1392°C and that of TiN is 1628°C; when the vanadium content in the hot metal is 0.5 wt per cent, the precipitation temperature of VC is 1245°C and that of VN is 1633°C. The high melting point phases precipitated from vanadium and titanium-containing hot metal are mainly TiN, TiC, VN, and VC, and with the decrease of temperature, the precipitation phase gradually increased, resulting in the elevation of the viscosity of the hot metal.

ACKNOWLEDGEMENTS

This research is supported financially by the National Natural Science Foundation of China (No. U2003215).

REFERENCES

Chen, L L, 2015. Current situation of vanadium-titanium magnetite resource utilization, *China Resources Comprehensive Utilization*, 33(10): 31–33.

Gancarz, T and Gasior, W, 2016. The effects of Na addition on the density, surface tension and viscosity of liquid Sn-Zn alloys, *Fluid Phase Equilibria*, 418:57–61.

Gao, L Z, Ma, T X, Hu, M J, Yan, Z M, Lü, X W and Hu, M L, 2019. Effect of titanium content on the precipitation behavior of carbon-saturated molten pig iron, *International Journal of Minerals Metallurgy and Materials*, 26(4):483–492.

Gou, X F, 2012. 1# blast furnace protection vanadium shallow discussion, *Sichuan Metallurgy*, (3):5–9.

Gu, P, 2018. Investigation on viscosity and melting temperature of V-Cr containing hot metal, Master's thesis, Chongqing University, Chongqing.

He, Y Y, Liu, Q C, Yang, J, Chen, Q X and Ao, W Z, 2010. Experimental investigation on fluidity of hot metal bearing titanium, *Iron Steel Vanadium Titanium*, 31(2):10–14.

Hou, P, 2022. Precipitation behavior of high melting point phases in vanadium-titanium-containing molten iron and its influence on the viscosity of molten iron, Master's thesis, Chongqing University, Chongqing.

Hou, P, Yu, W Z, Bai, C G, Pan, C, Yuan, W N and Li, T, 2022. Viscous flow properties and influencing factors of vanadium-titanium magnetite smelting iron, *Iron and Steel*, 57:57–65.

Jia, R, Bian, X F, Lü, X Q, Song, K K and Li, X L, 2010. The relationship between viscosity and glass forming ability of Al-(Ni)-Yb alloy systems, *Science China Physics, Mechanics and Astronomy*, 53(3):390–393.

Liu, Y H, Lü, X W, Bai, C G, Lai, P S and Wang, J S, 2015. Viscosity evaluation of Fe-Ni-Co ternary alloy from the measured binary systems, *Journal of industrial and Engineering Chemistry*, 30:106–111.

Lü, Q, Tang, Q, Sun, Y Q, Liu, X J and Qie, Y N, 2016. The relationship between the properties of vanadium-titanium magnetite smelting blast furnace slag and vanadium oxide reduction, *Iron Steel Vanadium Titanium*, 37(6):1–4+12.

Qu, D Y, 2015. The new method and instrument for measuring viscosity of the alloy metal liquid, Master's thesis, Harbin University of Science and Technology, Harbin.

Tan, Q Y, Chen, B, Zhang, Y S, Long, Y B and Yang, Y H, 2011. Characteristics and current situation of comprehensive utilization of vanadium titano-magnetite resources in Panxi Region, *Mineral Resources*, (6):6–10.

Wen, G Y, Yan, Y Z, Zhao, S J, Huang, J J, Jiang, G H and Yang, X M, 1996. Properties of liquid iron containing vanadium and titanium, *Iron and Steel*, 31(2):6.

Zhang, F, Du, Y, Liu, S H and Jie, W Q, 2015a. Modeling of the viscosity in the Al-Cu-Mg-Si system: Database construction, *CALPHAD*, 49:79–86.

Zhang, J L, Wei, M F, Guo, H W, Mao, R, Hu, Z W and Zhao, Y B, 2013. Effect of Ti and Si on the viscosity and solidification properties of molten iron, *Journal of University of Science and Technology Beijing*, 35(8):994–999.

Zhang, Y P, Zhang, Z W, Mao, X M and Du, H J, 2015b. Discussion on sticking of Cr-containing hot metal in torpedo ladle, *Baosteel Technology*, (1):50–54.

Zhao, X L and Miao, G Z, 2015. Analysis about hot metal adhesion in ladle, *Hebei Metallurgy*, (10):33–36.

Viscosity of CaO-aluminosilicate slags

DOI: 10.62053/WEYV5175

Z Zhang[1] and R G Reddy[2]

1. Graduate student, The University of Alabama, Tuscaloosa, Alabama 35487, USA. Email: zzhang@crimson.ua.edu
2. Professor, The University of Alabama, Tuscaloosa, Alabama 35487, USA. Email: rreddy@eng.ua.edu

ABSTRACT

Viscosities of CaO-aluminosilicate ternary melts were estimated using a structure-based model. The model considers depolymerisation effects and related breakdown of the silicate network structure on the addition of metal oxides to the melts. The predicted values are in good agreement with the experimental values over the whole temperature and composition range.

INTRODUCTION

An understanding of the mechanism of the metallurgical process phenomena and an optimisation of the processes require access to accurate data of the physical properties of the systems involved. Among them, the most important property in the case of molten systems is viscosity, in view of its direct effect on the kinetic conditions of the processes. Although, the viscosity measurements that have been conducted in the case of slag systems are numerous, the data available in literature are still too few to meet the technological demands. This is particularly true in case of complex slag systems, for which, experimental data are very often found to be available only for a few temperature and composition ranges. With the help of a suitable theoretical model, carefully assessed viscosity data can be stored as model parameters so that the values for relevant conditions can be calculated and even be retrieved online.

Quite a few models have been developed to evaluate viscosities of pure liquids as well as solutions. These models could be classified into two categories, that is, models based on fundamental molecular approach and those that employ semi-theoretical procedure. The former type of theories is still under development and hardly meet the technological requirements of today. On the other hand, the semi-theoretical or empirical procedures give satisfactory results. Among such models for high temperature slag systems, the structure-based model proposed by (Bockris and Reddy, 1977) considers depolymerisation effects and related breakdown of the glass network structure, on the addition of metal oxides to the melts. The specific expressions of this model were developed and used to calculate the viscosities of various binary silicate systems (Hu and Reddy, 1988, 1990; Reddy and Hebbar, 1991, 2001), binary borate systems (Shrivastava and Reddy, 1992; Reddy, Yen and Shrivastava, 1992), and ternary borosilicate systems (Reddy, Yen and Zhang, 1997; Zhang and Reddy, 1998, 1999, 2004), lead silicate slags (Zhang and Reddy, 2002; Mantha and Reddy, 2005; Yen *et al*, 2006), spent pot liner (Hu and Reddy, 1989), fluidity of slags from waste incinerators (Zhang, Arenas and Reddy, 2002), solid particle effect on viscosity of slags (Reddy and Yen, 1993), semisolid aluminium alloys and composites (Zhang, Reddy and Viswanathan, 1999, 2001), structure based viscosity model for borate melts (Zhang and Reddy, 2001, 2005), titania aluminosilicate slags (Yan *et al*, 2018), iron oxide aluminosilicate melts, (Yan *et al*, 2019), and structure based model for the aluminosilicate slags (Yan, Reddy and Lv, 2019), as a function of temperature and compositions. Excellent agreement was obtained between the calculated and experimentally determined viscosities. In this paper the viscosity model for SiO_2-Al_2O_3-CaO glass melts and calculated results are presented.

THEORETICAL CONSIDERATIONS

According to Flood's theory (Flood and Grjotheim, 1952), the mole fraction of cation is equal to 'electrically equivalent fraction'. Thus N_{Si4+}, and N_{Al3+} imply:

$$N_{Si^{4+}} = \frac{4n_{Si^{4+}}}{4n_{Si^{4+}} + 3n_{Al^{3+}}} \quad (1)$$

$$N_{Al^{3+}} = \frac{3n_{Al^{3+}}}{4n_{Si^{4+}} + 3n_{Al^{3+}}} \quad (2)$$

where $3nAl^{3+}$, $4nSi^{4+}$, are the number of equivalents of cations Al^{3+}, Si^{4+}. If expressing nAl^{3+}, and nSi^{4+} in term of $X_{Al2}O_3$, and $X_{S}iO_2$, then, one mole of Al_2O_3 consists of 2 mole Al^{3+} and one mole of SiO_2 consists of one mole Si^{4+}. Thus, $nAl^{3+}=2X_{Al2}O_3$ and $nSi^{4+}=X_{S}iO_2$. Then, Equations 1 and 2 can be expressed as:

$$N_{Si}4+ = \frac{4X_{SiO_2}}{4X_{SiO_2} + 3(2X_{Al_2O_3})} = \frac{2X_{SiO_2}}{2X_{SiO_2} + 3X_{Al_2O_3}} \quad (3)$$

$$N_{Al}3+ = \frac{3(2X_{Al_2O_3})}{4X_{SiO_2} + 3(2X_{Al_2O_3})} = \frac{3X_{Al_2O_3}}{2X_{SiO_2} + 3X_{Al_2O_3}} \quad (4)$$

The mole fraction of cation used to estimate several quantities of present model. For the ionic liquids containing holes, Bockris and Reddy (1977) presented the following expression for the viscosity:

$$\eta = \frac{2}{3}N_hR_h(6.28mkT)\frac{1}{2}\exp(\frac{E}{RT}) \quad (5)$$

where:

η	the viscosity (Ns/m^2)
N_h	the number of holes per unit volume (m^{-3})
R_h	the average radius of the holes (m)
m	the mass of the ionic unit (kg)
k	Boltzmann constant, 1.38×10^{-23} (Joules/moles)
T	the absolute temperature (Kelvin)
E	the energy of ionic unit for viscous flow (Joules/moles)
R	Gas constant, 8.3144 (J/mol.K)

Equation 5 is a general expression, and its application requires calculation of N_h, R_h, m and E. A brief description of the calculation method for these quantities is given further.

Calculation of $(6.28mkT)^{1/2}$

The term $(6.28mkT)^{1/2}$ was rearranged as follows:

$$(6.28mkT)\frac{1}{2} = (6.28\frac{m\,Av}{Av\,k\,T})\frac{1}{2}\,kT = (6.28\frac{W}{R})\frac{1}{2}kT\frac{1}{2} \quad (6)$$

where W is the molecular weight of an ionic unit and Av is the Avogadro constant (6.023 × 1023).

For CaO-Al_2O_3 melts, the molecular weight considered as the weight of AlO_6 unit. For CaO-SiO_2 melts, the molecular weight considered as the weight of SiO_4 unit. The combined molecular weight is obtained as:

$$W = N_{Si}4+W_{SiO_4} + N_{Al}3+W_{AlO_6} \quad (7)$$

where $W_{Si}O_4$ = 0.092 (kg/mol), and $W_{Al}O_6$ = 0.123 (kg/mol). Thus, Equation 6 can be rewritten as:

$$(6.28W/R)\frac{1}{2}k\,T\frac{1}{2} = (6.28/R)\frac{1}{2}[N_{Si}4+(0.092) + N_{Al}3+(0.123)]\frac{1}{2}k\,T\frac{1}{2} \quad (8)$$

Calculation of R_h

Fürth (1941) has shown that the size of a typical hole in a liquid is the same as the ionic unit and the hole can accommodate an ionic unit. The basic building units are SiO_4 tetrahedra and AlO_6 octahedra for silicate and aluminate melts, respectively.

For SiO_4 tetrahedra, the minimum radii of holes should be equal to the radii of SiO_4 tetrahedra. The ionic radius of oxygen is 1.38Å and the radius of silicon is 0.26Å. According to this structure, the radius of SiO_4 tetrahedra can be deduced as 3.07Å. For AlO_6 octahedra, the minimum radii of holes should be equal to the radii of AlO_6 octahedra. The ionic radius of oxygen is 1.40Å and the radius of aluminium is 0.38Å. Therefore, the radius of AlO_6 octahedra can be calculated as 3.38Å.The radius of an ionic unit in the system containing SiO_2 and Al_2O_3 can be expressed by Equation 9:

$$R_h = N_{Si^{4+}} R_{h,SiO_4} + N_{Al^{3+}} R_{h,AlO_6} \tag{9}$$

Calculation of N_h

The number of holes per unit volume was expressed in terms of NO^0, where NO^0 is mole fraction of bridging oxygen in melts. This calculation involves that the number of holes is equal to SiO_4 and AlO_6 ionic units present in the melts and that all the holes are occupied by the ionic species. Thus,

$$N_h = NO^0 \cdot A_V = 6.023 \times 10^{23} \cdot NO^0 \tag{10}$$

Substituting $(6.28mKT)^{1/2}$, Rh and Nh in Equation 5, the following viscosity expression in Ns/m^2 for the system containing SiO_2 and Al_2O_3 as network formers can be obtained:

$$\eta = 4.8184 \times 10^{-10}(6.14X_{SiO_2} + 10.14X_{Al_2O_3}) \cdot (0.184X_{SiO_2} + 0.369X_{Al_2O_3})^{\frac{1}{2}} \cdot (2X_{SiO_2} + 3X_{Al_2O_3})^{-\frac{3}{2}} \cdot NO^0 \cdot T^{\frac{1}{2}} \cdot \exp\left(\frac{E}{RT}\right) \tag{11}$$

Estimate viscosity by Equation 11, NO^0 and E need to be calculated. The calculation of NO^0 and E are described further.

Calculation of NO^0

If B mole of Al_2O_3 is mixing with S mole of SiO_2 and M mole of CaO, the charge and mass balance considerations, respectively, require that:

$$nO^0 = 3B + 2S - \frac{1}{2}nO^- \tag{12}$$

$$nO^{2-} = M - \frac{1}{2}nO^- \tag{13}$$

where:

- nO^0 the number of bridging oxygen bonded to two silicon or aluminium atoms
- nO^- the number of non-bridging oxygen bonded to only one silicon or aluminium atom
- nO^{2-} the number of free oxygen ions

The total number of anions can be calculated as:

$$nO^0 + nO^- + nO^{2-} = 3B + 2S + M \tag{14}$$

The mole fraction of bridging oxygen of total anions can be calculated by using Yokokawa's model (Yokokawa and Niwa, 1969) and expressed as Equation 15:

$$NO^0 = \frac{nO^0}{\textit{total number of oxygen anions}} = \frac{3B + 2S - \frac{1}{2}nO^-}{3B + 2S + M} \tag{15}$$

Considering the mole fraction in liquid melts, then:

$$NO^0 = \frac{3X_{Al_2O_3} + 2X_{SiO_2} - \frac{1}{2}nO^-}{3X_{Al_2O_3} + 2X_{SiO_2} + X_{CaO}} = \frac{3X_{Al_2O_3} + 2X_{SiO_2} - \frac{1}{2}nO^-}{2X_{Al_2O_3} + X_{SiO_2} + 1} \quad (16)$$

The nO^- further can be calculated by Equation 17:

$$[1 - \exp(\frac{\Delta G^0}{RT})](nO^-)^2 - 2(X_{SiO_2} + 2X_{Al_2O_3} + 1)(nO^-) + 4(2X_{SiO_2} + 3X_{Al_2O_3})(1 - X_{SiO_2} - X_{Al_2O_3}) = 0 \quad (17)$$

ΔG^0 is the standard Gibbs energy of depolymerisation reaction (Joules/mole). For SiO_2-CaO, and Al_2O_3-CaO melts, the depolymerisation reactions can be described as Reactions 18 and 19 respectively:

$$SiO_2(l) + 2CaO(l) = 2CaO \cdot SiO_2(l) \quad (18)$$

$$Al_2O_3(l) + CaO(l) = CaO \cdot Al_2O_3(l) \quad (19)$$

ΔG^0 can be expressed as:

$$\Delta G^o = N_{Al}3 + \Delta G^o_{Al} + N_{Si}4 + \Delta G^o_{Si} \quad (20)$$

where ΔG^0_{Al} and ΔG^0_{Si} are the Gibbs energy for Reactions 18 and 19 respectively.

Calculation of E

The energy of ionic unit for viscous flow is the function of composition and temperature. In the case of silicate melts the energy term is considered to be composed of energy required to break the silicate bonds in SiO_4^{4-} tetrahedral units and move the tetrahedral unit into the adjacent hole. Energy required for the jump is small. This has been determined to be equal to $3.3RT_m$, where R is the gas constant and T_m is the melting temperature of the slag system. Hence, E is dependent on the number of Si-O-Si bonds to be broken.

The value of E was calculated based on the experimental viscosity data choosing from literature (Urbain, Bottinga and Richet, 1982; Kozakevitch, 1960; Machin and Yee, 1948) by using Equation 11. A correlation of these E values as a function of temperature was made. As observed, the energy term can be expressed as Equation 21:

$$E = f_0 + f_1 T + f_2 T^2 \quad (21)$$

where f_i are constants and function of composition. The constants f_i are correlated with mole fraction of CaO and expressed by polynomial expression which are given by Equation 22:

$$f_i = a_i + b_i X_{CaO} + c_i X^2_{CaO} \quad (22)$$

where a_i, b_i and c_i are function of r, the ratio between the molar fraction of SiO_2 and the sum of the molar fractions of SiO_2 and of Al_2O_3, and:

$$a_0 = 3050672.55 + 33225477.52r - 100908358.79r^2 + 67346588.18r^3$$

$$b_0 = -7755748.01 - 210431186.31r + 579249233.04r^2 - 369704483.2074r^3$$

$$c_0 = 6172363.82 + 282764773.05r - 741066602.32r^2 + 459301295.09r^3$$

$$a_1 = -2791.73 - 38511.50r + 114603.27r^2 - 75668.14r^3$$

$$b_1 = 7737.08 + 245431.66r - 668916.39r^2 + 423976.96r^3$$

$$c_1 = -6245.89 - 331028.64r + 863749.57r^2 - 533355.28r^3$$

$$a_2 = 0.696 + 10.914r - 31.981r^2 + 20.987r^3$$

$$b_2 = -1.916 - 70.170r + 189.968r^2 - 119.997r^3$$

$$c_2 = 1.571 + 95.057r - 247.522r^2 + 152.695r^3$$

The calculated E value along with the NO^0 value were substituted into Equation 11 to give the viscosity of the melt at a particular temperature and composition. The viscosity for multi component silicate melts was calculated using Weymann-Frenkel Equation with empirical parameters (Kondratiev and Jak, 2001). In this paper, the calculated viscosities of several melts are given in the following results and discussion section.

RESULTS AND DISCUSSION

Al_2O_3-CaO binary melts

When r [SiO_2 / (SiO_2 + Al_2O_3)] = 0, the present model predicts viscosity values of the Al_2O_3-CaO binary melts. The experimental viscosity data and calculated results for r = 0 are shown in Figure 1. The calculated results are in good agreement with the experimental data. The viscosities decrease with the increase in temperature of the melts for all compositions. As can be seen from the figure, the viscosities decrease with increase in X_{CaO}.

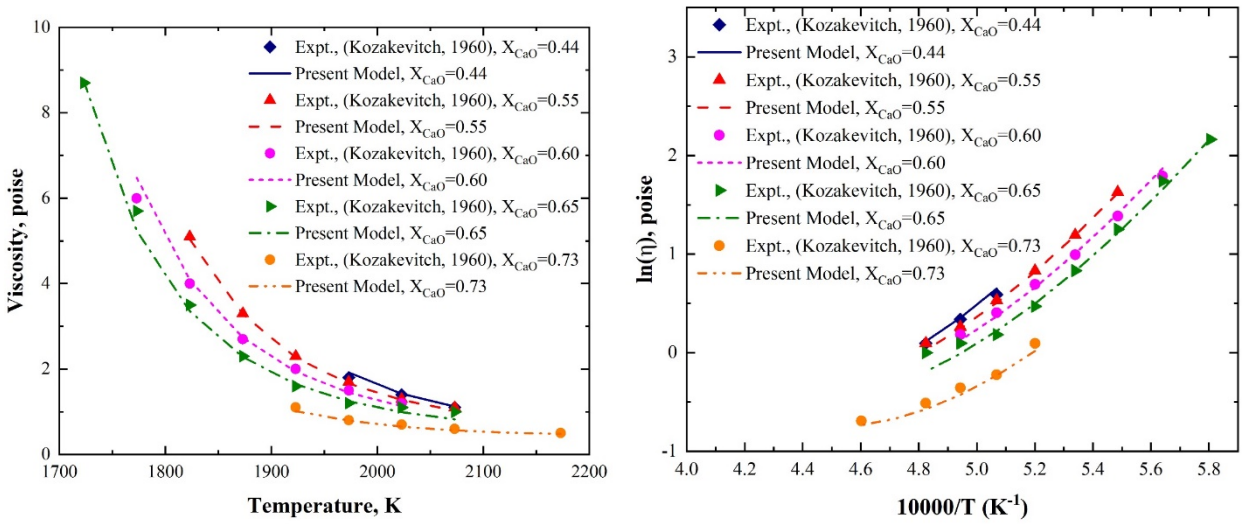

(a) (b)

FIG 1 – (a) Viscosity (η) versus temperature (T), and (b) ln(η) versus temperature (1/T) for CaO-Al_2O_3 melts, at r = [SiO_2 / (SiO_2 + Al_2O_3)] = 0.

SiO_2-CaO binary melts

When r [SiO_2 / (SiO_2 + Al_2O_3)] = 1, the present model predicts viscosity values of the SiO_2-CaO binary melts. The experimental viscosity data and calculated results for r = 1 are shown in Figure 2. Again, the viscosities decrease with the increase in X_{CaO} and temperature of the melts for all compositions. The calculated results are in good agreement with the experimental data.

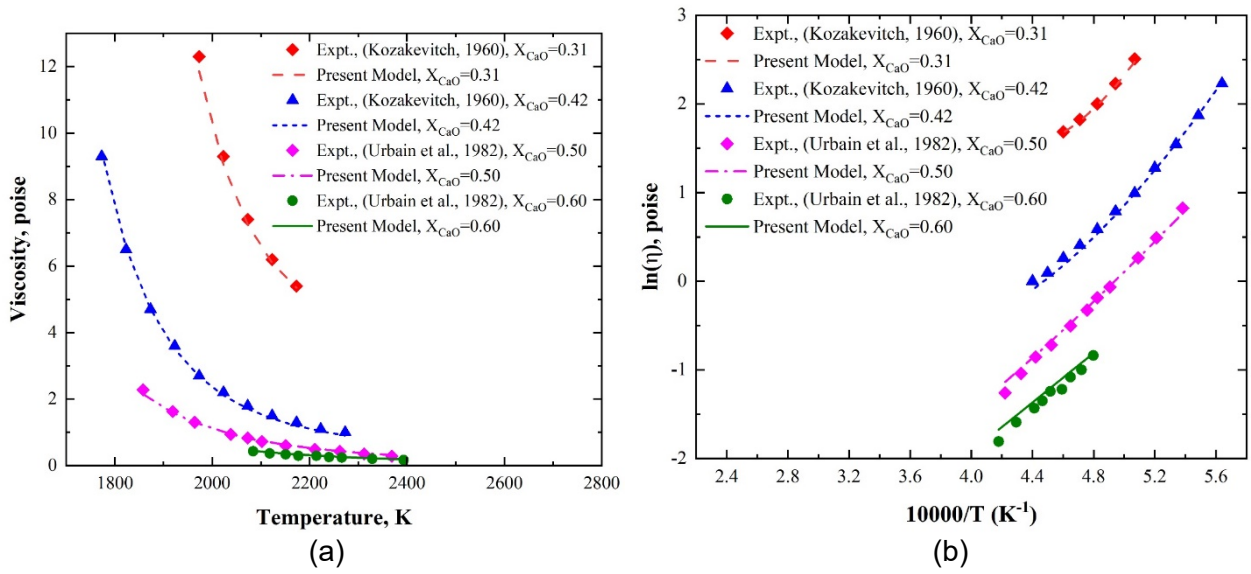

FIG 2 – (a) Viscosity (η) versus temperature (T), and (b) ln(η) versus temperature (1/T) for CaO-SiO_2 melts, at r = [SiO_2 / (SiO_2 + Al_2O_3)] =1.

The viscosities of SiO_2-CaO and Al_2O_3-CaO binary melts as function of X_{CaO} at 2073 K is shown in Figure 3. As can be seen at constant temperature, the viscosities of SiO_2-CaO melts decrease much significantly with increase X_{CaO} compared with that of Al_2O_3-CaO melts.

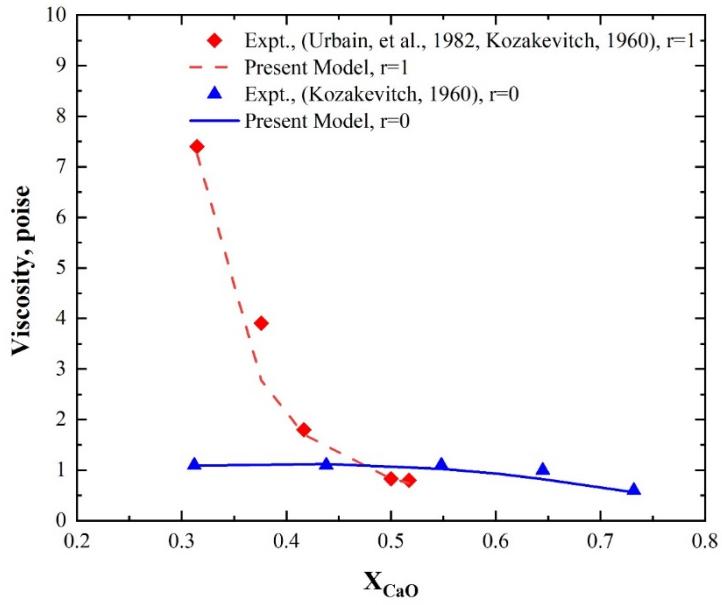

FIG 3 – Viscosity (η) versus CaO mole fraction (X_{CaO}) for CaO-Al_2O_3 and CaO-SiO_2 melts at 2073 K at r = [SiO_2 / (SiO_2 + Al_2O_3)] = 0, and at r = [SiO_2 / (SiO_2 + Al_2O_3)] = 1.

SiO_2-Al_2O_3-CaO ternary melts

Figures 4 and 5 show the experimental viscosity data and calculated data for r = 0.75 and 0.82, respectively. As can be seen, viscosities decrease significantly with the increase in temperature for all compositions. Viscosities decrease with increase in X_{CaO}. Good agreement between calculated and experimental data can be seen in the temperature and composition range of experimental data.

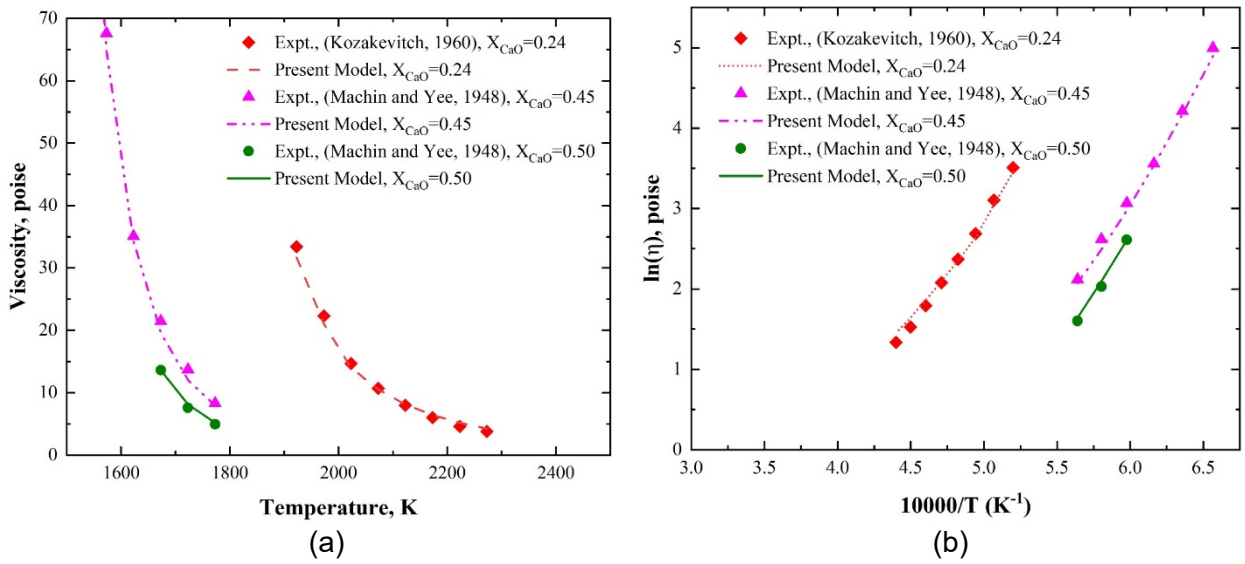

FIG 4 – (a) Viscosity (η) as a function of temperature (T), and (b) ln(η) as a function of 1/T at r = 0.75 for SiO_2-Al_2O_3-CaO ternary melts r = [SiO_2 / (SiO_2 + Al_2O_3)].

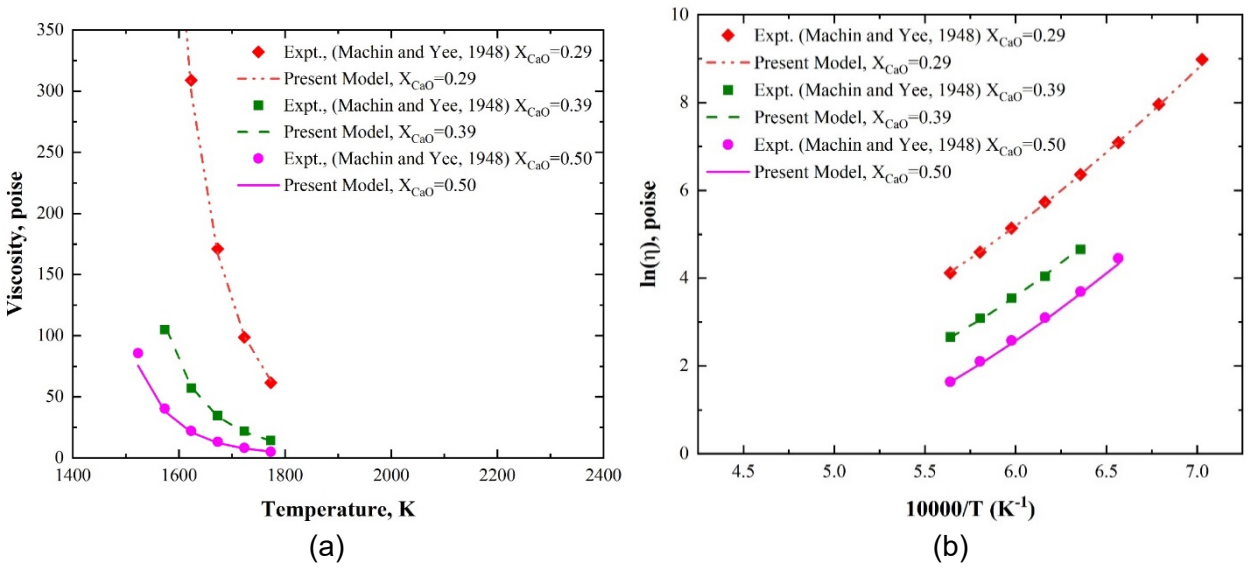

FIG 5 – (a) Viscosity (η) as a function of temperature (T), and (b) ln(η) as a function of 1/T at r = 0.82 for SiO_2-Al_2O_3-CaO ternary melts r = [SiO_2 / (SiO_2 + Al_2O_3)].

The viscosities of SiO_2-Al_2O_3-CaO melts as function of (X_{Al2O3}/X_{CaO}) ratio at 1773 K and X_{SiO2} = 0.58 are shown in Figure 6. As expected, it can be seen that at constant temperature and mole fraction of SiO_2, the viscosities of ternary melts increase significantly with increases in (X_{Al2O3}/X_{CaO}) ratio.

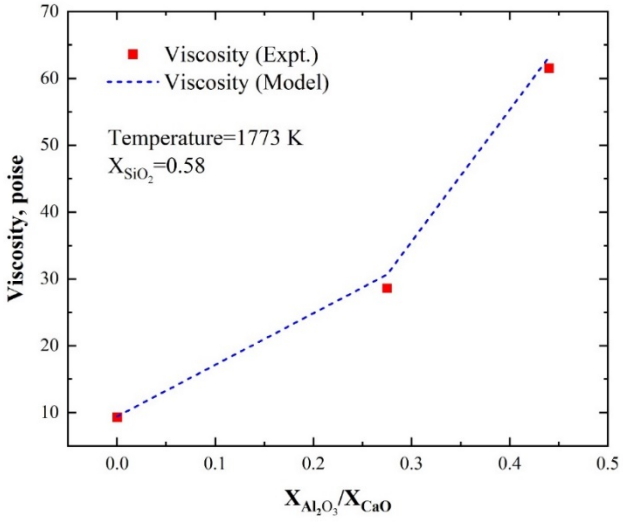

FIG 6 – Viscosity versus ($X_{Al2}O_3/X_{Ca}O$) ratio for SiO_2-Al_2O_3-CaO ternary melts at 1773 K and $X_{Si}O_2$ = 0.58.

Performance of present model

The model calculated viscosity values are compared with the experimental values in the SiO_2-Al_2O_3-CaO system and its subsystems over a wide composition and temperature ranges summarised in Figure 7. The present model reproduces most of the experimental data within experimental uncertainties, the average of relative value for this model was found to be 18.2 per cent. The model calculated data are in good agreement with the experimental data over a large temperature and composition range.

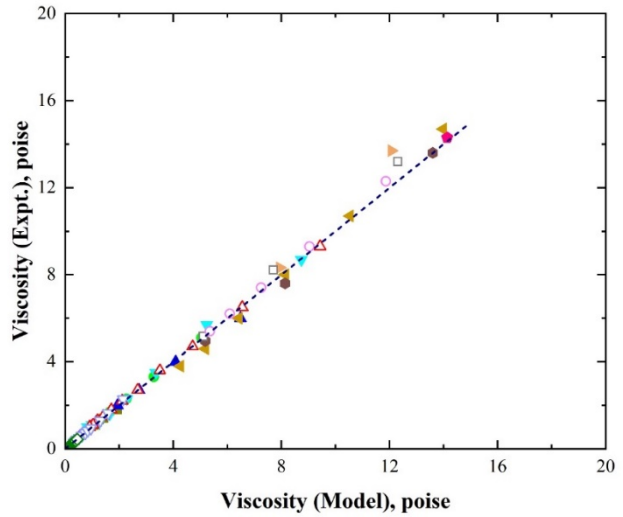

FIG 7 – Comparison of experimental data and model calculated data for viscosities for SiO_2-Al_2O_3-CaO ternary melts for different ratios r = [SiO_2 / (SiO_2 + Al_2O_3)] and temperatures.

(! Expt., (Kozakevitch, 1960), X_{CaO}=0.44, r=0; , Expt., (Kozakevitch, 1960), X_{CaO}=0.55, r=0; 7 Expt., (Kozakevitch, 1960), X_{CaO}=0.60, r=0; B Expt., (Kozakevitch, 1960), X_{CaO}=0.65, r=0; Λ Expt., (Kozakevitch, 1960), X_{CaO}=0.73, r=0; Ω Expt., (Kozakevitch, 1960), X_{CaO}=0.24, r=0.75; β Expt., (Machin and Yee, 1948), X_{CaO}=0.45, r=0.75; μ Expt., (Machin and Yee, 1948), X_{CaO}=0.50, r=0.75; ξ Expt., (Machin and Yee, 1948) X_{CaO}=0.29, r=0.82; ϒ Expt., (Machin and Yee, 1948) X_{CaO}=0.39, r=0.82; ∀ Expt., (Machin and Yee, 1948) X_{CaO}=0.50, r=0.82; – Expt., (Kozakevitch, 1960), X_{CaO}=0.31, r=1; 8 Expt., (Kozakevitch, 1960), X_{CaO}=0.42, r=1; X Expt., (Urbain et al., 1982), X_{CaO}=0.50, r=1; M Expt., (Urbain et al., 1982), X_{CaO}=0.60, r=1; - - - - y=x)

CONCLUSIONS

A structure-based viscosity model was developed for CaO-aluminosilicate ternary melts, which can predict not only viscosities of SiO_2-Al_2O_3-CaO ternary glass melts. The experimental viscosity data and calculated results show that viscosities of SiO_2-Al_2O_3-CaO glass melts decrease with the increase in $X_{Ca}O$ and temperature of the melts. The model calculated data are in good agreement with the experimental data over a large temperature and composition range.

ACKNOWLEDGEMENTS

The authors acknowledge the financial support from the Department of Energy and ACIPCO for this research project. Authors also thank the Department of Metallurgical and Materials Engineering, the University of Alabama for providing the experimental and analytical facilities.

REFERENCES

Bockris, J O'M and Reddy, A K N, 1977. Ionic liquids, *Modern Electrochemistry*, 1:513–622.

Flood, H and Grjotheim, K, 1952. Thermodynamic Calculation of Slag Equilibria, *JISI*, 171:64–70.

Fürth, R, 1941. The statistical treatment of the thermodynamics of liquids by the theory of holes, *Mathematical Proceedings of the Cambridge Phil Soc*, 37(3):252–275.

Hu, H and Reddy, R G, 1988. Viscosity of Binary Silicate Melts, in *International Symposium on Casting of Near Net Shape Products*, pp 705–722 (The Minerals, Metals and Materials Society).

Hu, H and Reddy, R G, 1989. Viscosity of Spent Potliner, *Light Metals*, pp 801–803 (The Minerals, Metals and Materials Society).

Hu, H and Reddy, R G, 1990. Modeling of Viscosities of Binary Alkaline Earth Metal Oxide and Silicate Melts, *High Temperature Science*, 28:195–202.

Kondratiev, A and Jak, E, 2001. Review of Experimental Data and Modeling of the Viscosities of Fully Liquid Slags in the Al_2O_3-CaO-'FeO'-SiO_2 System, *Metall Met Trans B*, 32B:1015–1025.

Kozakevitch, P, 1960. Viscosité et éléments struturaux des aluminosilicates fondus: Laitiers CaO-Al_2O_3-SiO_2 entre 1600 et 2100°C, Revue de Métallurgie, Février, pp 149–160.

Machin, J S and Yee, T B, 1948. Viscosity studies of system CaO-MgO-Al_2O_3-SiO_2: CaO-Al_2O_3-SiO_2, *Journal of The American Ceramic Society*, 31(7):200–204.

Mantha, D and Reddy, R G, 2005. Viscosities of Industrial Lead Blast Furnace Slags, *High Temperature Materials and Processes*, 24(1):73–78.

Reddy, R G and Hebbar, K, 1991. Prediction of Viscosities of Binary Silicate Melts, in *EPD Congress '91*, pp 523–540 (The Minerals, Metals and Materials Society).

Reddy, R G and Hebbar, K, 2001. Viscosity of FeO-SiO_2 Slags, *Minerals & Metallurgical Processing,* 18(4):195–199.

Reddy, R G and Yen, J Y, 1993. Solid Particles Effect on Viscosity of Slags, The *P E Queneau International Symposium on Extractive Metallurgy of Copper, Nickel and Cobalt – Volume I: Fundamental Aspects*, (eds: R G Reddy and R N Weizenbich), pp 309–324 (The Minerals, Metals and Materials Society).

Reddy, R G, Yen, J Y and Shrivastava, S, 1992. Viscosity of Na_2O-B_2O_3 Melts, *ISIJ International*, pp 450–455.

Reddy, R G, Yen, J Y and Zhang, Z, 1997. Viscosities of Na_2O-SiO_2-B_2O_3 melts, in *Proceedings of the 5th International Conference on Molten Slag, Fluxes and Salts '97*, pp 203–213.

Shrivastava, S and Reddy, R G, 1992. Viscosity of K_2O-B_2O_3 Melts, in *EPD Congress '92,* pp 989–1004 (The Minerals, Metals and Materials Society).

Urbain, G, Bottinga, Y and Richet, P, 1982. Viscosity of liquid silica, silicates and aluminosilicates, *Geochimicaet Cosmochimica Acta*, 46:1061–1072.

Yan, Z, Reddy, R G and Lv, X, 2019. Structure Based Viscosity Model for Aluminosilicate Slag, *ISIJ International*, 59(6):1018–1026.

Yan, Z, Reddy, R G, Lv, X, Pang, Z and Bai, C, 2019. Viscosity of Iron Oxide Aluminosilicate Melts, *Metallurgical and Materials Transactions B*, 50(1):251–261.

Yan, Z, Reddy, R G, Lv, X, Pang, Z and He, W, 2018. Structure-based Viscosity model development for Titania Aluminosilicate Slags, *Ironmaking and Steelmaking*, pp 1–7.

Yen, J Y, Divakar, M, Evrard, L, Van Camp, M and Reddy, R G, 2006. Effect of Composition and Temperature on Viscosities of Lead Blast Furnace Slags, *Minerals and Metallurgical Processing*, 22(3):165–170.

Yokokawa, T and Niwa, K, 1969. Free energy of solution in binary silicate melts, *Trans JIM*, 10(1):3–7.

Zhang, Z and Reddy, R G, 2001. Distribution of Various Structural Species in alkali Borate Melts, in *EPD Congress 2001*, pp 353–367 (The Minerals, Metals and Materials Society).

Zhang, Z and Reddy, R G, 2002. Viscosity of Lead Silicate Slags, *Minerals and Metallurgical Processing*, 19(1):37–42.

Zhang, Z and Reddy, R G, 2004. Experimental Determination and Modeling of Viscosities in the Na_2O-SiO_2-B_2O_3 system, *High Temperature Materials and Processes*, 24(4):247–259.

Zhang, Z and Reddy, R G, 2005. Structure Model and Properties of Alkali Borate Melts, *Trans Inst Min Metall C*, 114:C192–C199.

Zhang, Z, and Reddy, R G, 1998. Viscosity of Na_2O-SiO_2-B_2O_3 Ternary Melts, in *EPD Congress '98*, pp 957–970 (The Minerals, Metals and Materials Society).

Zhang, Z, and Reddy, R G, 1999. Viscosity Measurement and Modeling of Borate and Borosilicate Melts, *Fluid Flow Phenomena in Metals Processing*, pp 253–260 (The Minerals, Metals and Materials Society).

Zhang, Z, Arenas, M and Reddy, R G, 2002. Fluidity of Slags from Waste Incinerators, in *EPD Congress 2002,* pp 801–809 (The Minerals, Metals and Materials Society).

Zhang, Z, Reddy, R G and Viswanathan, S, 1999. Viscosity Measurement of Aluminum Alloy Containing SiC Particulates, *Fluid Flow Phenomena in Metals Processing*, pp 543–550 (The Minerals, Metals and Materials Society).

Zhang, Z, Reddy, R G and Viswanathan, S, 2001. Viscosities of Semisolid Aluminum Alloys and Composites, in *Proceedings of MC Flemings Symposium on Solidification and Materials Processing*, pp 267 – 271 (The Minerals, Metals and Materials Society).

Experimental measurements of – Reaction / Process kinetics

Effect of carbon on the sintering kinetics of a single hematite pellet

DOI: 10.62053/JQUI5091

R A Anand[1], N N Viswanathan[2] and M M Pande[3]

1. PhD Research scholar, Department of Metallurgical Engineering and Materials Science, Indian Institute of Technology Bombay, 400076, India. Email: ankit_anand@iitb.ac.in
2. Sajjan Jindal Steel Chair Professor, Centre of Excellence in Steel Technology (CoEST), Department of Metallurgical Engineering and Materials Science, Indian Institute of Technology Bombay, 400076, India. Email: vichu@iitb.ac.in
3. Assistant Professor, Department of Metallurgical Engineering and Materials Science, Indian Institute of Technology Bombay, 400076, India. Email: manish.pande@iitb.ac.in

ABSTRACT

The pellet qualities primarily depend upon the thermal profile and gaseous environment during induration. During the induration of the pellet, it undergoes physical as well as chemical changes. Physical changes are mostly due to sintering and chemical changes are due to carbon burning inside the pellet. The effect of carbon on sintering is investigated on a single pellet scale using an optical dilatometer. Sintering is a complex process that involves transportation through various mechanisms. Sintering is quantified in terms of sintering ratio and the kinetic parameter, exponent 'n', under isothermal conditions is deduced using the power law equation. The value of n can be used to estimate the sintering mechanism at different isothermal temperatures. Also, the activation energy is calculated using the empirical Arrhenius equation. The activation energy of 0 per cent coke and 1 per cent coke-containing pellets are 531.0 kJ/mole and 552.6 kJ/mole respectively. The order of magnitude of activation energy suggests the same mechanism in both cases. Although the mechanism of sintering is the same, 1 per cent coke-containing pellet sinters more at any isothermal temperature.

INTRODUCTION

Pelletisation is an agglomeration technique for effective utilisation of raw material and to address the environmental concern arising due to fine (particles <150 μm) generation in the iron and steel industry. The pelletisation process involves three main steps:

1. Feed preparation – where the chemistry of the pellet is decided.
2. Balling process – where the size of the green pellets and their fraction can be manipulated.
3. Induration Process – where the pellet mechanical property is enhanced through heat hardening process in the air to a temperature of up to 1350°C, termed as induration (Ball *et al*, 1973; Umadevi *et al*, 2013; Zhu *et al*, 2015).

During induration pellets undergo sintering which gives the strength needed during the reduction process. Hematite and Magnetite ore are the primary sources of raw materials for iron production. The sintering behaviour of hematite and magnetite during the induration is quite different. Typically, the magnetite sinters more easily than the hematite. The main reason for this could be attributed to the non-stoichiometric nature of magnetite at sintering temperature which aids in faster diffusion (Sandeep Kumar *et al*, 2016). The non-stoichiometric behaviour of magnetite can be seen in Fe-O_2 phase diagram as shown in Figure 1 with the spinel region that is shaded area in green. Magnetite also forms diffusion bonds at a lower temperature due to oxidation during induration (Sandeep Kumar *et al*, 2019; Ayyandurai and Pal, 2022). Oxidation leads to a lot of internal heat generation since it is an exothermic reaction. In the hematite pellets, no internal heat generation takes place, and the diffusion bonds are also limited at a lower temperature. Thereby, the external fuel requirement is high. The pellet quality thus produced will depend upon the raw material mix and the induration the pellet undergoes. Researchers have explored the idea of using a part of the energy requirement as an alternate heat source so that the fuel consumption and maintenance of the furnace would be easier. The addition of carbon up to 1.5 per cent as an *in situ* heat source showed improved pellet properties, such as better cold crushing strength and lowered reduction degradation index. Also, improved productivity, fuel saving and reduced greenhouse gas generation have been reported with the addition of carbon in hematite ore pellet (Hamidi and Payab, 2003; Sadrnezhaad,

Ferdowsi and Payab, 2008; Umadevi *et al*, 2013; Pal and Venugopalan, 2015). No study has been done to understand the effect of carbon on the sintering of hematite pellets during induration.

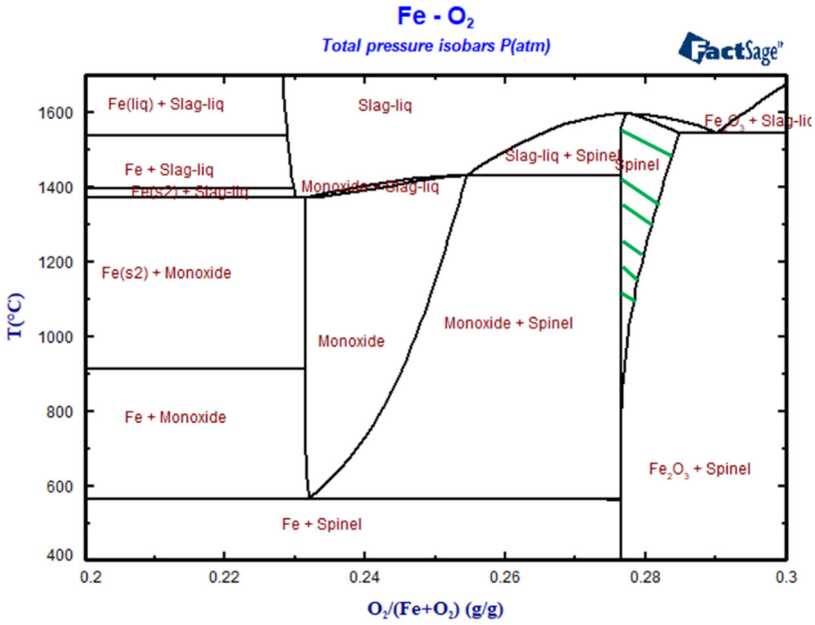

FIG 1 – Fe-O_2 phase diagram with O_2 capacities calculated using FactSage.

Unlike conventional powder processing where the objective is to achieve 100 per cent densification, only the initial stages of the sintering are important for the induration of iron ore pellet. For most of the materials, the sintering temperature lies between 0.5–0.8 times their melting point. The presence of excess free energy due to irregularity in particle shape is the driving force of sintering. Sintering is a complex process involving the transportation of species through various mass transport mechanisms, such as surface diffusion, bulk diffusion, viscous flow, gaseous diffusion, etc. Depending on the temperature, extent of sintering and particle size, the dominant mechanism will vary. Surface transport mechanisms like evaporation-condensation and surface diffusion produce neck formation and growth without densification when the particles come close to each other. Bulk transport mechanisms like volume diffusion, grain boundary diffusion and viscous flow produce neck growth with densification (Kuczynski, 1949a; Coble, 1958; German, 1996).

Sintering kinetics for pure hematite reagent powder and commercial magnetite concentrate in the form of briquettes under isothermal conditions was studied by Wynnyckyj and Fahidy in 1974. They observed a power law relation with time for isothermal sintering where the sintering has been quantified in terms of sintering ratio. The same model is going to be used in the present study. Interestingly, the sintering behaviour study of hematite is very scarce in literature. No study has been done by using optical dilatometer for hematite ore pellet. The model and the instrument details are discussed in more details in later section.

MATERIAL AND METHOD

Raw materials

Pellet preparation has been done at Electrotherm, Ahmedabad (India). First, the green mix was prepared using Muller cum mixer having a diameter of 60 cm at 26 rev/min. In the mixer, Iron ore fines and bentonite are mixed properly. In our present study bentonite is kept constant (0.7 per cent) in all pellet compositions. After properly getting mixed, coke was added to them in pre-defined ratios. Water addition was kept constant at 8.6 per cent in all pellets during balling. Green pellets were prepared using a laboratory balling disc of 18 inches (~46 cm) in diameter with a tilt angle of 45° at 27 rev/min. Raw material properties are listed in Tables 1 to 3.

TABLE 1

Chemical composition of hematite ore particles.

Wet chemical analysis						XRF			
Fe(T)	SiO_2	Al_2O_3	CaO	FeO	P_2O_5	MgO	MnO	TiO_2	LOI
63.11	4.5	2.17	0.11	0.98	0.04	0.15	0.07	0.10	1.26

TABLE 2

Chemical composition of bentonite using wet chemical analysis.

Fe_2O_3	SiO_2	Al_2O_3	CaO	MgO	Na_2O	Moisture
15.75	48.70	17.90	1.56	2.60	2.02	11.00

TABLE 3

Proximate analysis of coke.

Fixed C	Ash	Volatile matter	Inherent moisture
85.42	12.9	1.3	0.38

Ture density of the raw material was calculated using Helium pycnometer. The obtained result is in Table 4.

TABLE 4

True density of raw materials.

Raw material	Iron ore	Bentonite	Coke
True density (g/cm^3)	5.0428	2.7528	2.1369

Sintering experiments

In order to investigate the effect of carbon on sintering kinetics, pellets having no coke and 1 per cent coke was chosen. The sintering studies was performed on a single pellet scale in a very narrow size range (≈ 9 mm diameter) in the optical dilatometer. Narrow size is chosen because of the instrument limitation where the sample size requirement is < 10 mm. Also sintering is a function of porosity, so pellets having porosity in a similar range was chosen and all the experiments were performed in the still air. The experimental details are listed in the Table 5.

TABLE 5

Experimental details with thermal cycle and the pellet porosities used at different temperatures.

Pellet	Sintering temperature	Porosity		Heating rate	Isothermal hold time
	K (°C)	0% coke	1% coke	K/min (°C/min)	min
HP0 (0% coke)	1423 (1150)	28.63	30.74	10	20
	1473 (1200)	31.59	31.21		
HP1 (1% coke)	1523 (1250)	29.56	29.07		
	1573 (1300)	31.05	30.54		
	1623 (1350)	29.07	29.41		

Sintering studies were performed using contactless optical dilatometer of TA instruments HM 867. It has three units:

1. A horizontal tube furnace with a sample stage (maximum temperature 1600°C).
2. An illuminated 478 nm LED light source.
3. A continuous image capturing microscope with a recording facility.

The pellet sample is loaded on an alumina plate placed on a thermocouple inside the tube furnace. The microscope transfers the image of the spherical pellet sample from the furnace at 5X magnification onto the recording camera. The entire set-up is accessed by a computer system facilitated with specific Misura Thermal Analysis software to acquire and store the images of the pellet subjected to a thermal profile. These images were processed to determine for change in area as a function of time during the experiment.

Results and discussion

The area change plot for 0 per cent coke pellet and 1 per cent coke pellet with respect to temperature and time obtained from optical dilatometer as shown in Figures 2 and 3 respectively. As shown in Figures 2 and 3 in a thermal profile, the pellets expand initially due to thermal expansion. But once the temperature reached around 1000°C, sintering starts to occur and due to sintering, shrinkage in the area pellet was observed. During cooling as well, pellet continue to shrink due to thermal contraction. From the obtained thermal profile, area change only due to sintering need to be calculated which is obtained by fitting a line till 1000°C during thermal expansion and subtracting it. The area change only due to sintering with temperature for 0 and 1 per cent coke pellet are shown in Figure 4.

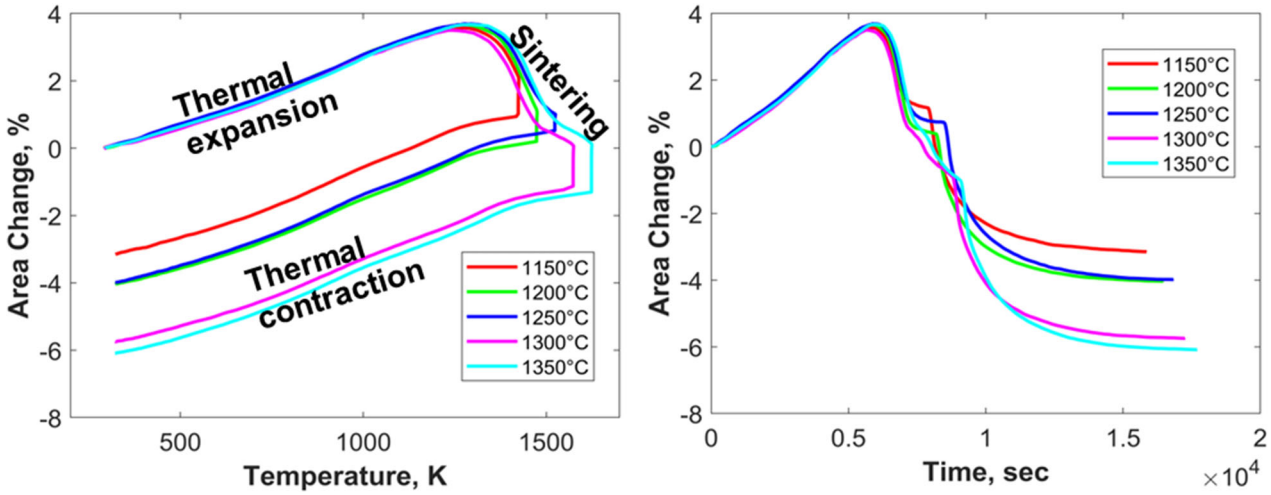

FIG 2 – Change in area with temperature (left), with time (right) for zero carbon pellet at different isothermal temperatures.

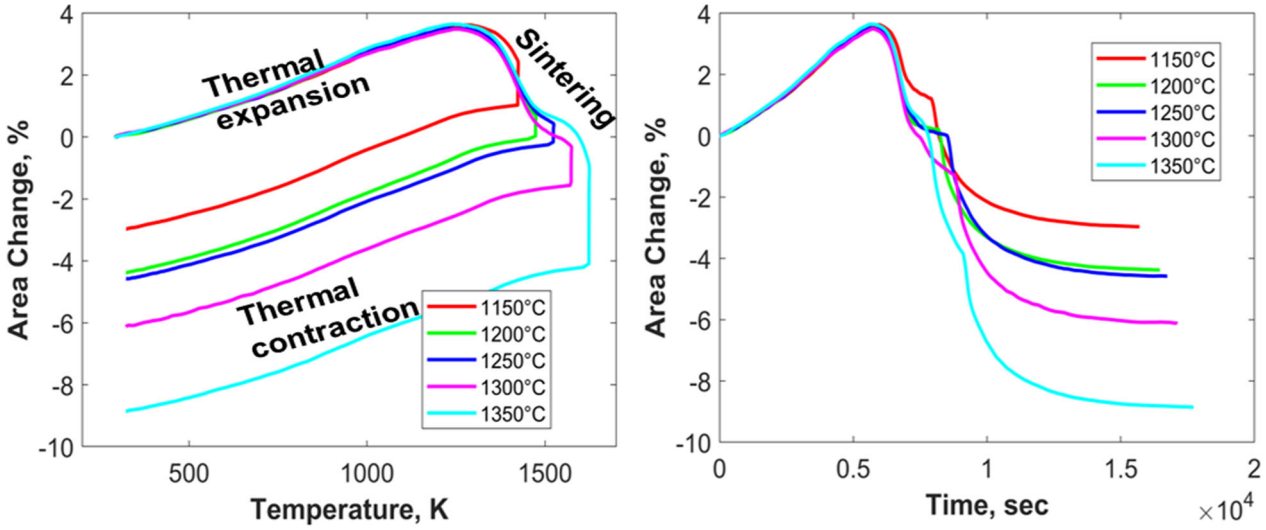

FIG 3 – Change in area with temperature (left), with time (right) for 1 per cent coke pellet at different isothermal temperatures.

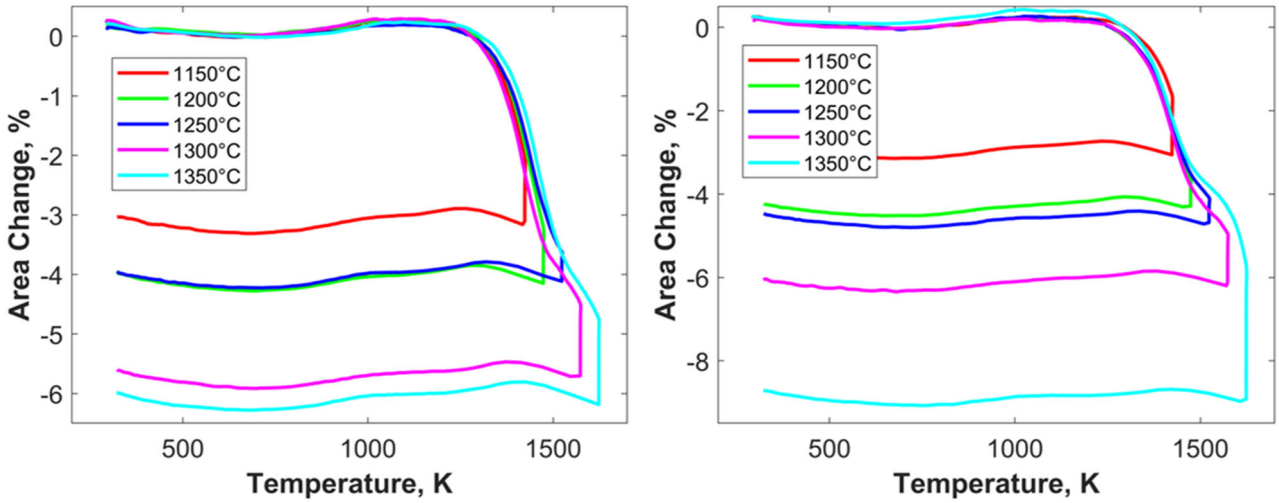

FIG 4 – Area-change only due to sintering for 0 per cent coke (left), for 1 per cent coke (right) pellet at different temperatures.

A term sintering ratio (sintering extent) is proposed by Wynnyckyj and Fahidy (1974) to quantify sintering. The sintering ratio can be defined as the ratio of sintering already achieved to the sintering yet to be achieved.

$$\gamma = \frac{Sintering\ already\ achieved}{Sintering\ yet\ to\ be\ achieved} = \frac{V_\circ - V}{V - V_{true}}$$

Where V_{true} is the volume of the pellet if it would have undergone complete sintering with no pores. The percentage change in area due to sintering, δ_A, can be defined in terms of bulk density of a pellet at any time, ρ, as:

$$\delta_A = \frac{2}{3}\left(\frac{\rho_o - \rho}{\rho}\right) * 100 \text{ and } \delta_{A,true} = \frac{2}{3}\left(\frac{\rho_o - \rho_{true}}{\rho_{true}}\right) * 100$$

The true density, ρ_{true}, of the solid constituents of the pellet is measured using a helium pycnometer. From the above two equations:

$$\gamma = \left(\frac{-\delta_{A,sintering}}{\delta_{A,true} - \delta_{A,sintering}}\right)$$

The above equation relates the sintering ratio to the percentage area change measured (Wynnyckyj and Fahidy, 1974; Sandeep Kumar *et al*, 2016). The calculation of $\delta_{A,true}$ requires an initial bulk

density (ρ_o) and a final true density (ρ_{true}). Since the same pellet is treated repeatedly, a non-destructive density measurement technique in needed. The true density measurement of raw materials was performed using helium gas pycnometer and the obtained values are listed in Table 4. These obtained values were used to calculate the true density of pellet. To measure the bulk density, the stereomicroscope is used where 15 photographs of a pellet at different orientations were captured. From the photographs, the area of the pellet is calculated to statistically acceptable average value. The sintering ratio (Gamma), thus calculated, and plotted with time on X-axis as shown in Figure 5. It is observed that the area change due to sintering is more in the case of 1 per cent coke containing pellet.

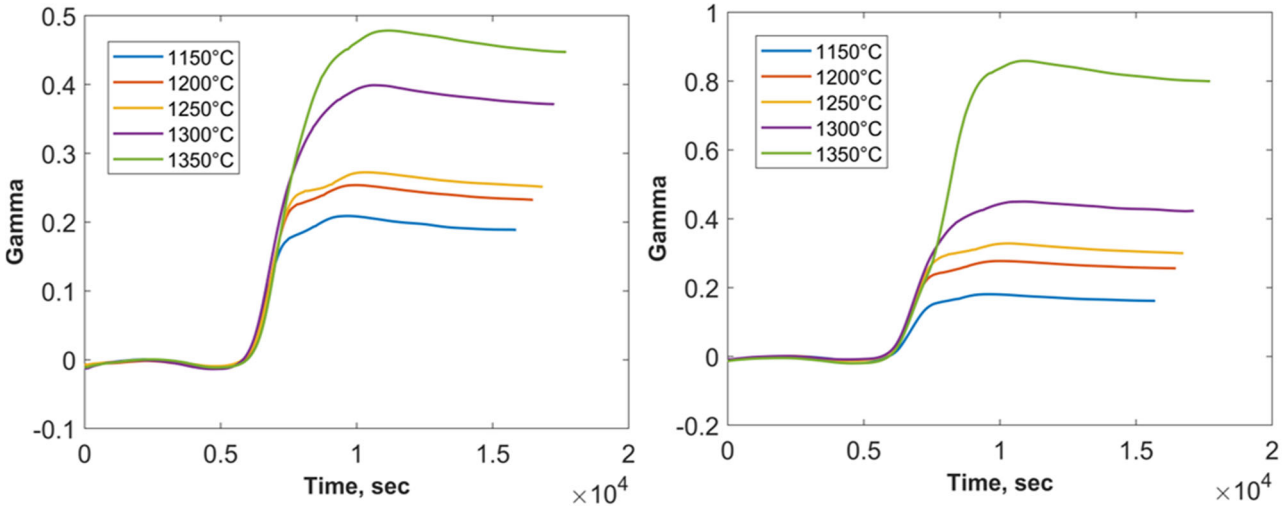

FIG 5 – Sintering ratio with time for 0 per cent coke (left), for 1 per cent coke (right) pellet at different temperatures.

Estimation of sintering kinetic

It has been proposed that the isothermal sintering kinetics can be expressed as:

$$\gamma = kt^n$$

where, *t* is the isothermal time, *n* is the time exponent and *k* is the reaction constant. The pellet cannot be inserted directly into the isothermal segment due to an instrumentation limitation. Due to this, even before the start of the isothermal section, the pellet achieves some sintering. However, in order to estimate sintering kinetic parameters, only the isothermal segment of the curve is used. An alternate methodology can be used to obtain the kinetic parameters. Let us assume γ^* as the sintering ratio at the start of the isothermal section, above equation was written as:

$$\gamma^* = \mathrm{k}\,(t^*)^n$$

where t^*corresponds to the time if the pellet had attained a sintering ratio of γ^* from the start under isothermal condition. Beyond t^*:

$$\gamma = k(t^* + t_m)^n$$

where t_m is the time measured from the start of isothermal section. From the above two equations:

$$\ln\left(\frac{\gamma}{\gamma^*}\right) = nln(\frac{t^* + t_m}{t^*})$$

Using the data of sintering ratio on the isothermal section and above equation, the parameters *n* and t^* were estimated using least square fit as shown in Figure 6. A straight-line fit indicate that the above equation is excellent in capturing the sintering kinetics. Also depending upon the value of exponent '*n*', the sintering mechanism can be predicted. The numerous studies have been reported which shows different sintering mechanism depending on different exponent values (Kuczynski, 1949a; German, 1996; Sandeep Kumar *et al*, 2016, 2019). The reported values of '*n*' along with their mechanisms and the calculated value of '*n*' for 0 per cent coke and 1 per cent coke pellet is listed in Table 6.

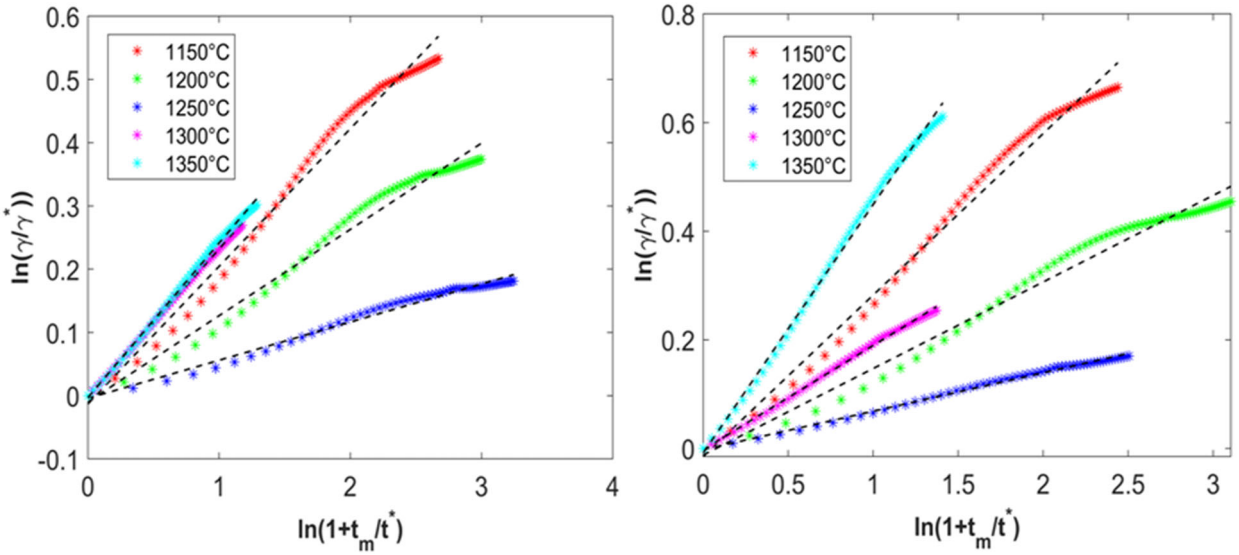

FIG 6 – Exponent 'n' for 0 per cent coke (left), for 1 per cent coke (right) at different temperatures.

TABLE 6

Exponent value and the respective mechanism from literature along with the calculated values at different temperatures.

Literature	Sintering mechanism	Temperature	0% coke pellet	1% coke pellet
1/7 (0.14)	Surface diffusion	1150°C	0.148	0.165
1/6 (0.17)	Grain boundary diffusion	1200°C	0.1634	0.200
1/5 (0.20)	Volume diffusion	1250°C	0.1785	0.234
1/2 (0.5)	Viscous flow	1300°C	0.1935	0.271
		1350°C	0.2086	0.306

Many investigators have proposed '*n*' increasing with the increase in temperature which is also in line with the current findings (Kuczynski, 1949a, 1949b; German and Munir, 1976; German, 1996; Xuebin *et al*, 2010).

Further the value of *k* is estimated for the isothermal sintering temperature. The temperature dependence of the rate constants is expressed by the empirical Arrhenius equation:

$$k = (\frac{k'}{T})^n exp^{\frac{-nQ}{RT}}$$

Where Q is the activation energy. Taking logarithms and re-arranging:

$$\ln\left(Tk^{\frac{1}{n}}\right) = lnk' - \frac{Q}{RT}$$

The activation energy was obtained from the slope of the plot between $\ln\left(TK^{\frac{1}{n}}\right)$ versus 1/T as shown in Figure 7. Here the least square fit has done for four points only.

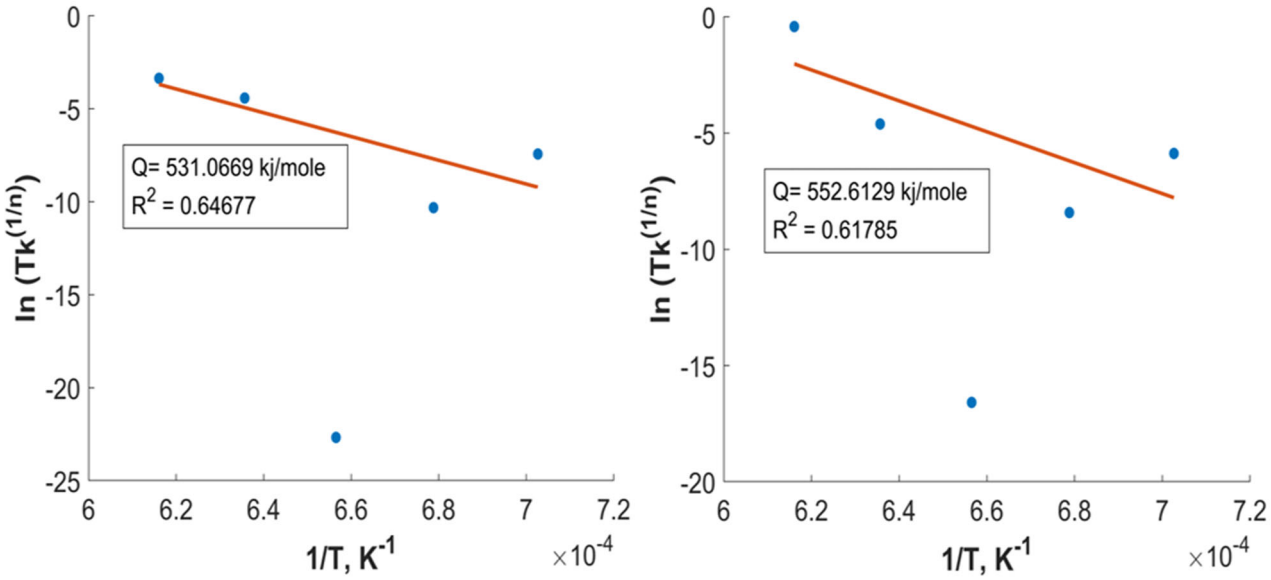

FIG 7 – Activation energies for the 0 per cent coke(left), for 1 per cent coke (right).

An activation energy of 531.1 kJ/mole and 552.6 kJ/mole is calculated for 0 per cent coke and 1 per cent coke containing pellet respectively. An activation energy for magnetite ore pellet was reported 451 kJ/mole (Sandeep Kumar *et al*, 2016). A high activation energy is attributed to the possibility of initial neck formation at bentonite/gangue minerals through reaction or solid- state diffusion. A high activation energy of 1000 kJ/mole order of magnitude is reported for tetragonal zirconia polycrystals (Bernard-Granger and Guizard, 2007). They have suggested that due to high porosity and low amount of grain boundaries, the creation of point defect is too hard and it controls the sintering. Further investigations are required to confirm these speculated reasons for high activation energy.

CONCLUSIONS

Effect of carbon on sintering kinetics of a single hematite pellet has been estimated using optical dilatometer. Sintering is quantified as sintering ratio which is related to time using power law equation at any isothermal temperature. Sintering mechanism is related to different kinetic parameters, namely, activation energy and exponent ‘n’. Although the order of the magnitude of activation energy is similar, the amount of sintering achieve is more in case of carbon containing pellet (see Figures 4 and 5).

ACKNOWLEDGEMENTS

I would like to acknowledge the efforts made by Electrotherm, India for providing the raw materials and facility for making green pellet. I would also like to acknowledge the financial support provided by the Centre of Excellence in Steel Technology, IIT Bombay towards this project.

REFERENCES

Ayyandurai, A and Pal, J, 2022. Reaction Mechanism of In-situ Carbon in Hematite Ore Pellet during Induration, *Mineral Processing and Extractive Metallurgy Review,* 43(1):40–54.

Ball, D F, Darntell, J, Davision, J, Grieve, A and Wild, R, 1973. *Agglomeration of Iron Ores*, 1st edition (Elsevier: New York).

Bernard-Granger, G and Guizard, C, 2007. Apparent activation energy for the densification of a commercially available granulated zirconia powder, *Journal of the American Ceramic Society,* 90(4):1246–1250.

Coble, R, 1958. Initial Sintering of Alumina and Hematite, *Journal of American Ceramic Society,* 41(2):55–62.

German, R M, 1996. *Sintering Theory and Practice* (Wiley Interscience: New York).

German, R M and Munir, Z A, 1976. Surface Area Reduction During Isothermal Sintering, *Journal of The American Ceramic Society,* 59:379–383.

Hamidi, A A and Payab, H, 2003. Mathematical Model for energy saving in induration of Iron ore pellets containing solid fuel, *IJE Transactions B*: *Applications,* 16(3):265–278.

Kuczynski, G C, 1949a. Self-Diffusion in Sintering of Metallic Particles, *Transaction of the AIME,* 85:169–178.

Kuczynski, G C, 1949b. Study of the sintering of glass, *Journal of Applied Physics,* 20(12):1160–1163.

Pal, J and Venugopalan, T, 2015. Carbon as in situ energy source in induration of hematite pellets and its effect on pellet properties, *Ironmaking and Steelmaking,* 42(2):139–147.

Sadrnezhaad, S K, Ferdowsi, A and Payab, H, 2008. Mathematical model for a straight grate iron ore pellet induration process of industrial scale, *Computational Materials Science,* 44(2):296–302.

Sandeep Kumar, T K, Viswanathan, N N, Ahmed, H, Dahlin, A, Andersson, C and Bjorkman, B, 2019. Developing the Oxidation Kinetic Model for Magnetite Pellet, *Metallurgical and Materials Transactions B*: *Process Metallurgy and Materials Processing Science,* 50(1):162–172.

Sandeep Kumar, T K, Viswanathan, N N, Ahmed, H M, Andersson, C and Björkman, B, 2016. Estimation of Sintering Kinetics of Magnetite Pellet Using Optical Dilatometer, *Metallurgical and Materials Transactions B*: *Process Metallurgy and Materials Processing Science,* 47(1):309–319.

Umadevi, T, Lobo, N F, Desai, S, Mahapatra, P C, Sah, R and Prabhu, M, 2013. Optimization of firing temperature for hematite pellets, *ISIJ International,* 53(9):1673–1682.

Wynnyckyj, J R and Fahidy, T Z, 1974. Solid State Sintering in the Induration of Iron Ore Pellets, *Metallurgical Transaction,* 5(5):991–1000.

Xuebin, Z, Yunfei, D, Songlin, W, Jie, X U and Yi, F, 2010. sintering behaviour and kinetic evaluation of hydroxyapatite bio-ceramics from bovine bone, *Ceramics-Silikáty,* 54(3):248–252.

Zhu, D, Pan, J, Lu, L and Holmes, R J, 2015. Iron ore pelletisation, In: *Iron Ore*: *Mineralogy, Processing and Environmental Sustainability*, pp 435–473.

Synthesis of actinide chlorides for molten salt preparation

DOI: 10.62053/ICCA8834

P Chevreux[1], S Serp[2] and M Duchateau[3]

1. CEA, DES, ISEC, DMRC, Univ Montpellier, 30207 Bagnols-sur-Ceze, Marcoule, France. Email: pierrick.chevreux@cea.fr
2. CEA, DES, ISEC, DMRC, Univ Montpellier, 30207 Bagnols-sur-Ceze, Marcoule, France. Email: jerome.serp@cea.fr
3. CEA, DES, ISEC, DMRC, Univ Montpellier, 30207 Bagnols-sur-Ceze, Marcoule, France. Email: maxime.duchateau@cea.fr

NB: CEA: Commissariat à l'énergie atomique et aux énergies alternatives; DES: Direction des énergies; ISEC: Institut des Sciences et technologie pour une Economie Circulaire des énergies bas carbone; DMRC: Département de recherche sur les procédés pour la mine et le recyclage du combustible.

ABSTRACT

Molten salt reactor (MSR) is a promising advanced reactor system aiming to the transmutation of minor actinides such as americium in order to reduce the inventory of ultimate nuclear waste. The fuel is a molten salt in which actinides are homogeneously dissolved in the liquid phase. A chloride salt may be retained for this concept, as it provides low melting point, high solubility of actinides, harder neutron spectrum. To avoid corrosion and precipitation issues, molten salt composition has to be carefully controlled with impurity content as low as possible. Obtaining pure actinide chlorides without contaminants such as oxide, oxychloride, hydroxide and water is still a challenge. To prepare actinide-bearing salt, the chlorination of actinides oxides was investigated in an unstirred reactor under flowing gas as solid-gas reaction. The carbochlorination of PuO_2 were performed in the temperature range of 600 to 800°C with chlorine gas as a chlorinating agent and the presence of solid carbon. $PuCl_3$ was successfully synthesised by this method and characterised by X-ray diffraction measurements but some impurities such as oxide phase remain inside the formed product. Refinements of anhydrous and hydrated $PuCl_3$ phases by Le Bail method were also performed for crystalline materials definition. Conversion mainly depends on the chlorinating temperature and the contact between the oxide and the chlorinating agent. A conversion value of 70–80 per cent was achieved at 700°C from PuO_2 with quite high specific surface area. The conversion rate was not improved with increasing the chlorination time. The volatilisation of Pu was observed during the carbochlorination experiments. To avoid a loss of Pu caused by sublimation, the chlorination temperature should be limited to 650°C despite that the conversion of PuO_2 to $PuCl_3$ was enhanced by increasing temperature. Both carbochlorination and hydrochlorination of AmO_2 were also carried out leading to the formation of $AmCl_3$. These first results suggest that americium oxide was chlorinated more readily than plutonium oxide. The purity of produced $PuCl_3$ and $AmCl_3$ still deserves further investigations.

INTRODUCTION

Molten Salt Reactors (MSR) represent a potential new answer to the question of transmutation of minor actinides in order to reduce the footprint of nuclear waste storage. Producing low-carbon electricity and heat, MSR allow reducing the generated radioactive waste and the closure of the fuel cycle. A fast-neutron reactor used as actinides converter, especially for americium, is currently investigated in France. The fuel is a molten salt in which actinides are homogeneously dissolved in the liquid phase. A chloride salt is selected for this concept, as it provides high solubility of actinides, low melting point, harder neutron spectrum than fluoride salts and is consistent with French nuclear waste management using hydrometallurgical processes. To avoid corrosion and precipitation issues, molten salt composition has to be carefully controlled with oxygen impurity content as low as possible. Obtaining pure actinide chlorides without contaminants such as oxide, oxychloride hydroxide and water is still a challenge and mandatory to produce an actinide bearing salt suitable for its use in a reactor.

Data on the synthesis of plutonium and americium trichloride ($PuCl_3$ and $AmCl_3$) are reported in the literature. Anhydrous $PuCl_3$ was usually prepared using a carbochlorination technique, a solid gas

reaction between a metal oxide and a chlorinating gas with the addition of carbon. Different chlorinating agents such as gas mixture of argon and tetrachloride Ar-CCl_4 (Tolley, 1953), of tetrachloride and chlorine CCl_4-Cl_2 (Ferran and West, 1993), of carbon monoxide and chlorine CO-Cl_2 (Ferran and West, 1993) and phosgene $COCl_2$ (Ferran and West, 1993; Rasmussen and Hopkins, 1961; Tolley, 1953) are used for the carbochlorination of plutonium oxide (PuO_2). According to these studies, $COCl_2$ seems to be the most efficient gas at 500°C and yields 98 per cent of conversion to the plutonium chloride on a large scale in batch (around 500 g). Due to the use of hazardous $COCl_2$ gas, a mixture of oxide and carbon powder with Cl_2 gas were also performed to produce many other chlorides such as rare-earth elements (Anderson and Mishra, 2015; Esquivel, Bohé and Pasquevich, 2003a, 2003b; Gaviría and Bohé, 2010; Pomiro *et al*, 2015; Wang *et al*, 2019). Chloride salts containing $PuCl_3$ were prepared thanks to bubbling of Cl_2 in the molten salt in which solid PuO_2 and graphite rod were present (Caravaca *et al*, 2008; Vigier *et al*, 2018). Few data in the literature are available on the synthesis of americium trichloride by a solid-gas reaction. The carbochloration of americium oxide (AmO_2) with CCl_4 vapor between 800 and 900°C yielded a sublimed product, namely an anhydrous and pure $AmCl_3$ (Fried, 1951). $AmCl_3$ was also synthesised in LiCl-KCl melt by carbochlorination using chlorine gas bubbling and a mixture of carbon and AmO_2 as starting material (Lambertin *et al*, 2000). Contrary to PuO_2 (West, Ferran and Fife, 1988), AmO_2 can react with hydrogen chloride gas (HCl) at 500–600°C to form anhydrous $AmCl_3$ by hydrochlorination process (Burns and Peterson, 1970; Fuger, 1966).

This study focused on evaluating the conversion of plutonium and americium oxides to their respective chlorides, main compounds of the molten salt fuel used for transmutation purposes. $PuCl_3$ and $AmCl_3$ were synthesised based on a solid gas reaction between an oxide precursor and a chlorinating agent. Chlorination experiments were carried out in a static bed reactor and several reaction parameters were investigated such as the reactivity of solid precursor, the nature of chlorinating gas and temperature.

MATERIAL AND METHODS

All experiments took place in a glove-box under air atmosphere. The chlorination experiments were conducted in a fixed-bed reactor allowing a gas-solid reaction at high temperature between an actinide oxide, PuO_2 or AmO_2 powder, and a chlorinating agent in a flow-through mode. PuO_2 with different specific surface area (0.4, 2.9 and 14.0 m^2g^{-1}) are used. For carbochlorination experiments, actinide oxides and carbon powder were mechanically mixed into a carbon crucible, inserted into the quartz reactor vessel. Carbon used as a reducing agent was introduced in excess (molar ratio Pu/C <0.5) to ensure a favourable carbochloration reaction based on thermodynamic calculations. The sample (<0.5 g) was homogeneously heated up to the desired temperature (600–800°C) inside a furnace in an argon gas flow (2 L/h). The flow of argon was then shut off and chlorine gas was introduced in a large excess (from 1 to 6 L/h) during the chlorination step. The exit gas were bubbled through 4 M NaOH or KOH which completely trapped excess of chlorinating agent. After the chlorination step during 1–4 hrs, the furnace was turned off and argon gas was introduced into the system instead of chlorine during the cooling process. The cooled sample was removed from the reactor and analysed (X-ray diffraction (XRD) and Pu and Cl content). For hydrochlorination experiments, the same experimental procedure was followed, except that chorine gas was replaced by hydrogen chloride gas without carbon. Reactions that occurred could be written as follows:

$$PuO_{2\,(s)} + {}^{3}/_{2}\ C_{(s)} + {}^{3}/_{2}\ Cl_{2\,(g)} \rightarrow PuCl_{3\,(s)} + CO_{(g)} + {}^{1}/_{2}\,CO_{2\,(g)}$$

$$AmO_{2\,(s)} + {}^{3}/_{2}\ C_{(s)} + {}^{3}/_{2}\ Cl_{2\,(g)} \rightarrow AmCl_{3\,(s)} + CO_{(g)} + {}^{1}/_{2}\,CO_{2\,(g)}$$

$$AmO_{2\,(s)} + 4\,HCl_{(g)} \rightarrow AmCl_{3\,(s)} + 2\,H_2O_{(g)} + {}^{1}/_{2}\,Cl_{2\,(g)}$$

The conversion was determined using the solubility of the formed product in an aqueous solution, assuming $PuCl_3$ to be 100 per cent soluble contrary to PuO_2 and to a lesser extent other plausible impurities such as PuOCl. The product was thus dissolved in aqueous solution with nitric acid (0.3 M HNO_3) to give a blue or purple solution, subsequently filtered to remove insoluble impurities and finally the solution was analysed for Pu and Cl content. Plutonium was measured by alpha counting and spectrometry and chloride by ionic chromatography. The conversion rate R was expressed by:

$$R = \frac{n_{Pu\ from\ dissolved\ Pu}}{n_{Pu\ from\ starting\ PuO2}}$$

Considering the small amount of matter used and the possible loss of matter, R is probably underestimated. To ensure that the synthesised product was primarily $PuCl_3$, the molar ratio Pu/Cl was checked to be close to 3 for all chemical analyses and XRD analyses were also performed. Before analysing, powder samples were stored in a desiccator. XRD measurements were carried out on powders by a Bruker D8 Advance diffractometer (Bragg-Bretano geometry using the Cu Kα radiation, solid detector Lynexe XE-T) and crystalline phases were identified using the DIFFRAC.EVA software from Bruker company. The data acquisition was performed in the step scan mode (10–140° 2θ, step size 0.01 ° 2θ, total counting 4h or 18h). Gold was introduced into the XRD samples as an internal standard. Lattice parameters were determined by refinement using the Le Bail method (Le Bail, 2012) and the Fullproof software (Carvajal, 1990).

RESULTS AND DISCUSSION

Carbochlorination of PuO_2

Carbochlorination experiments from plutonium oxide were performed at several temperatures. The chlorination with Cl_2 gas at 600°C was not really efficient. After synthesis, the C7 sample was a brownish-coloured powder similar to the starting material. Although some low intensity peaks belonging to the anhydrous and probably hydrated phases were detected, the main phases observed in the product by XRD analysis were PuO_2 and carbon as shown in Figure 1. Carbochlorination reaction was more effective between 650–700°C as a green-blue fine powder, feature of $PuCl_3$ compound (Rasmussen, Stiffler and Hopkins, 1961), was obtained as shown in Figure 2. The conversion of PuO_2 to $PuCl_3$ was confirmed by XRD analysis but chlorination was incomplete since some residual PuO_2 was still present in the chlorinated C5 sample (Figure 1).

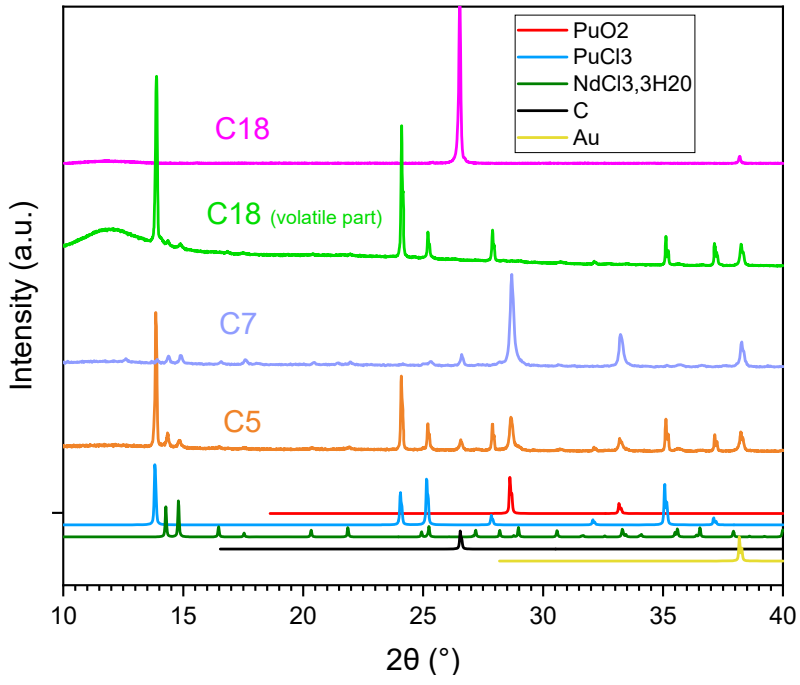

FIG 1 – XRD patterns of C5, C7 and C18 samples synthesised by carbochloration of PuO_2 at 700°C, 600°C and 800°C, respectively.

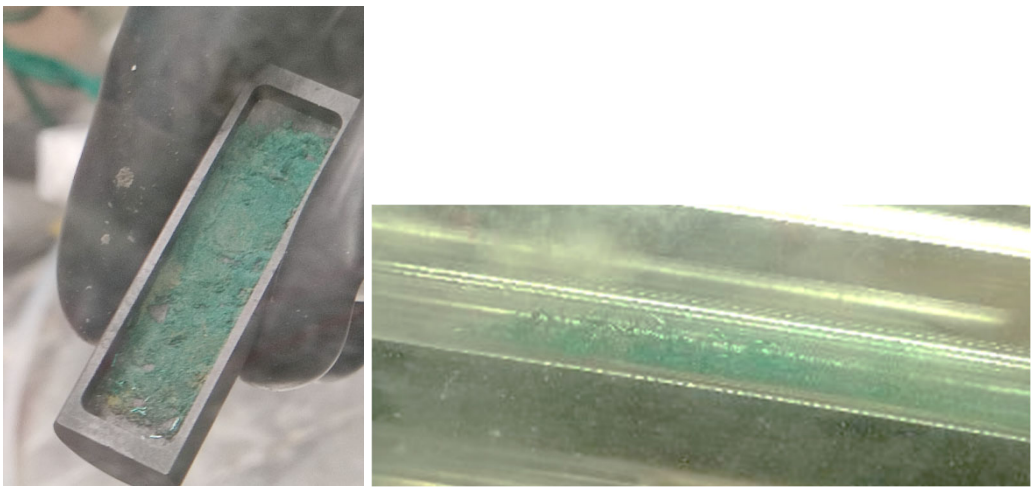

(a) (b)

FIG 2 – Pictures of (a) C5 sample in the carbon crucible and (b) a part of C23 sample located in the quartz off-gas line the after carbochlorination reaction at 700°C.

The average conversion values achieved for carbochlorination experiments are given in Table 1. The conversion rate for carbochlorination at 700°C was evaluated at 70–80 per cent. When the chlorination temperature increased up to 800°C, above the melting point of $PuCl_3$, the conversion might be almost complete because there was no evidence of PuO_2 in the C18 sample. However, an important volatilisation rate of the product was observed in good agreement with thermodynamics (Figure 2b). Blue-green needle-shaped crystals corresponding to $PuCl_3$ without PuO_2 contamination as shown in Figure 1 (C18 sample) were collected on the surface of the colder area of the quartz tube in the off-gas line (<550°C). The volatilisation process is explained by the formation of $PuCl_4$ gas by the following equilibrium (Gruen and Dekock, 1967):

$$PuCl_{3\,(s)} + {}^{1}/_{2}\,Cl_{2\,(g)} \leftrightarrow PuCl_{4\,(g)}$$

TABLE 1

Synthesis parameters, conversion and volatilisation values for carbochlorination and hydrochlorination of actinide oxides (Pu and Am). SSA means surface specific area and L, M and H represent respectively, low, medium and high surface specific area used for PuO_2. (*) denotes conversion and volatilisation values were probably under-evaluated because the whole volatile fraction might be not totally trapped and collected.

Name	Oxide	Oxide mass	SSA	Gas	Temperature	Cl_2: Pu or Am (molar ratio)	Time	Conversion R	Volatilisation
C5	PuO_2	302 mg	M	Cl_2	700°C	30	45 min	Not complete	Weak
C7	PuO_2	303 mg	M	Cl_2	600°C	60	75 min	Low	None
C15	PuO_2	151 mg	M	Cl_2	650°C	100	75 min	72%	5%
C18	PuO_2	154 mg	M	Cl_2	800°C	100	75 min	62% (*)	62% (*)
C19	PuO_2	151 mg	L	Cl_2	700°C	100	75 min	41%	15%
C21	PuO_2	156 mg	H	Cl_2	700°C	100	75 min	80%	18%
C22	PuO_2	154 mg	M	Cl_2	700°C	100	75 min	73%	14%
C23	PuO_2	151 mg	M	Cl_2	700°C	393	300 min	70%	34%
A1	AmO_2	34 mg	/	Cl_2	500°C 680°C	236	360 min	/	None
A2	AmO_2	31 mg	/	HCl	600°C	173	240 min	/	None

According to the literature, condensed $PuCl_4$ turns into solid $PuCl_3$ and gaseous Cl_2 as Cl_2 gas feed stops. When the chlorination temperature was reduced to 650°C, the conversion rate remained similar to run at 700°C in the same experimental conditions (C15 and C22 samples) but the volatilisation process was limited. To minimise sublimation of plutonium tetrachloride which could be an issue for an industrial process, the chlorination temperature must be limited to 650°C with chlorine gas without any impact on the conversion rate. However, the sublimation of Pu chloride is a good way of purifying $PuCl_3$ and leads to a complete conversion.

The conversion rate was not affected by increasing the chlorination time up to 300 min (C22 and C23 samples). This result suggested that the carbochlorination reaction was kinetically limited, a $PuCl_3$ layer might prevent the chlorinating gas getting to the unreacted oxide. In addition, the conversion rate was enhanced by using PuO_2 with high specific surface area (C19, C21, C22 samples). This leads to the conclusion that the conversion of PuO_2 to $PuCl_3$ was strongly impacted by the contact between the solid oxide, carbon powder and the gaseous chlorinating agent. Conversion might be improved by adding an agitation system for carbochlorination reaction (Soine, 1965).

The refinement by Le Bail method of the anhydrous and hydrated $PuCl_3$ phases obtained by carbochlorination reaction were successfully performed allowing to confirm the crystalline phase identification previously done. The cell parameters, extracted from the refinement, were summarised in Table 2. The $PuCl_3$ phase structure was in good agreement with data reported in literature (Zachariasen, 1948). Since the $PuCl_3,3H_2O$ phase were not referenced in the database, the structure of hydrated $PuCl_3$ were determined by X-ray diffraction and refined by the Le Bail method. The $PuCl_3,3H_2O$ phase is isotructural with $NdCl_3,3H_2O$ phase (Reuter, Fink and Seifert, 1994). The obtained cell parameters of $PuCl_3,3H_2O$ were consistent with the cell parameters of $NdCl_3,3H_2O$ given in the literature. $PuCl_3$ is hydroscopic (Rasmussen, Stiffler and Hopkins, 1961) and can be readily hydrated by moisture from the atmosphere. To avoid hydration, $PuCl_3$ must be kept in a controlled and dehumidified atmosphere.

TABLE 2

Cell parameters and angles obtained after refinement by Le Bail method for synthesised anhydrous and hydrated $PuCl_3$ phases compared to data from literature.

Compound	Crystal system	Space group	a(Å)	b(Å)	c (Å)	α, β (°)	γ (°)	Reference
$PuCl_3$	Hexagonal	$P6_3/M$ (n°176)	7.3978 (4)	7.3978 (4)	4.2458 (4)	90	120	This study
$PuCl_3$	Hexagonal	$P6_3/M$ (n°176)	7.3800 (1)	7.3800 (1)	4.2380 (4)	90	120	Zachariasen (1948)
$PuCl_3$, 3 H_2O	Orthothombic	Pnma (n°62)	12.3663 (1)	8.7381 (2)	6.8566 (3)	90	90	This study
$NdCl_3$, 3 H_2O	Orthothombic	Pnma (n°62)	12.408	8.735	6.832	90	90	Reuter, Fink and Seifert (1994)

Carbochlorination and hydrochlorination of AmO_2

Carbochlorination and hydrochlorination experiments of americium oxide were performed with chlorine and hydrogen chloride gas (Table 1). The carbochlorination of AmO_2 at 680°C yielded a black powder. XRD analysis revealed the presence of $AmCl_3$ phase and an hydrated $AmCl_3$ phase, being very likely $AmCl_3,3H_2O$, and carbon (Figure 3). No americium oxide was really found in the product. The hydrochlorination of AmO_2 at 600°C produced a pale green-yellow powder. Some authors (Burns and Peterson, 1970) found that the colour of $AmCl_3$ was pale yellow-pink. The main phase present in the product was $AmCl_3,6H_2O$. Some small unidentified peaks at 2θ 31.7° and 52.9° were detected by XRD indicating that some impurities may be present inside the synthesised product. For both syntheses, the conversion of AmO_2 to $AmCl_3$ seemed to be complete and no volatilisation of americium chloride was observed. The strong hydration of $AmCl_3$ might be explained by the XRD measurements were not performed under an inert atmosphere with a low water content.

These results suggest that Am was chlorinated more readily than Pu. The chlorination parameters were not optimised for $AmCl_3$ synthesis and the evaluation of actinide chloride purity is the subject of ongoing studies.

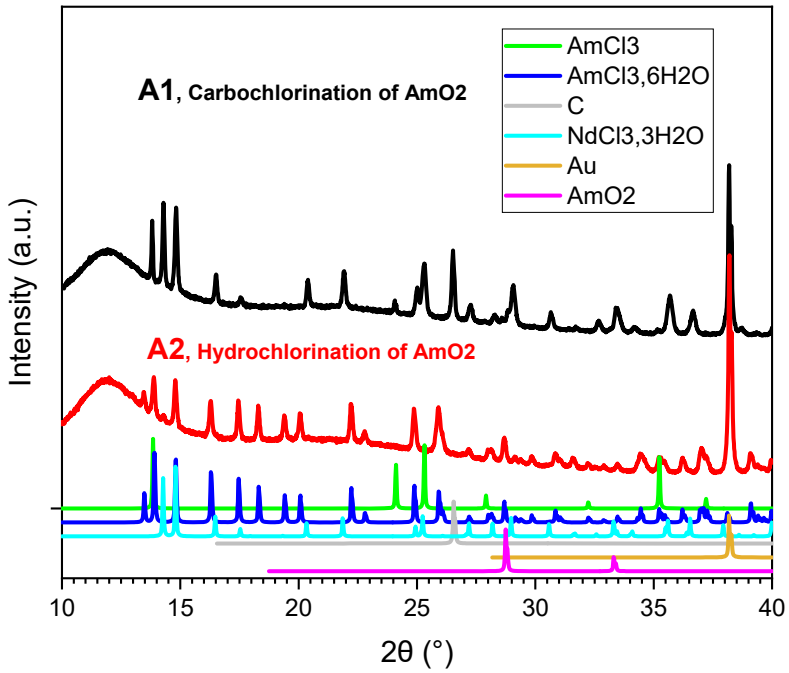

FIG 3 – XRD patterns of A1 and A2 samples synthesised by carbochloration and hydrochlorination of AmO_2, respectively.

CONCLUSION

The main results obtained on the synthesis of $PuCl_3$ and $AmCl_3$ from actinide oxides by carbochlorination or hydrochlorination technique may be summarised as follow:

- $PuCl_3$ and $AmCl_3$ were successfully synthesised by a solid-gas reaction using chlorine or hydrogen chloride gas.
- The conversion by carbochlorination reaction mainly depends on the chlorinating temperature and the contact between the oxide and the chlorinating agent. The conversion rate was not improved with increasing the chlorination time.
- The conversion rate of PuO_2 to $PuCl_3$ was improved by increasing the temperature. However, volatilisation of Pu was observed beyond 700°C. To minimise it, the optimal temperature was adjusted around 650°C for carbochlorination reaction with Cl_2 gas and carbon powder.
- The sublimation of Pu chloride is a good way of obtaining pure $PuCl_3$.
- Am was chlorinated more readily than Pu, since AmO_2 could directly react with HCl at 600°C to form $AmCl_3$.

ACKNOWLEDGEMENTS

The authors gratefully acknowledge G. Serve and A. Soler for the setting up the chlorination experiments and M Pons for performing XRD analyses. They would also like to thank F Chaussepied for the supply of americium oxide. This research was funded by CEA, Orano and within the investments for France 2030 by the French Government through the ISAC project.

REFERENCES

Anderson, A and Mishra, B, 2015. Investigation of the Carbochlorination Process for Conversion of Cerium and Neodymium Oxides into Their Chlorides, *Journal of Sustainable Metallurgy,* 1:189–198.

Burns, J H and Peterson, J R, 1970. Refinement of the crystal structure of AmCl3, *Acta Crystallographica,* B26:1885–1887.

Caravaca, C, Laplace, A, Vermeulen, J and Lacquement, J, 2008. Determination of the E-pO2− stability diagram of plutonium in the molten LiCl–KCl eutectic at 450°C, *Journal of Nuclear Materials,* 377:340–347.

Carvajal, J R, 1990. Fullprof: A Program for Rietveld Refinement and Pattern Matching Analysis, Satellite Meeting on Powder Diffraction of the XV Congress of the IUCr.

Esquivel, M R, Bohé, A E and Pasquevich, D M, 2003a. Carbochlorination of samarium sesquioxide, *Thermochimica Acta,* 403:207–218.

Esquivel, M R, Bohé, A E and Pasquevich, D M, 2003b. Chlorination of cerium dioxide, *Thermochimica Acta,* 398:81–91.

Ferran, M D and West, M H, 1993. The Synthesis of Plutonium Trichloride by Chlorination of Plutonium Dioxide with Phosgene, Los Alamos National Laboratory.

Fried, S, 1951. The Preparation of Anhydrous Americium Compounds, *Journal of the American Chemical Society,* 73:416–418.

Fuger, J, 1966. Thermal expansion coefficients of the anhydrous trichlorides of cerium, plutonium and americium, *Journal of Inorganic and Nuclear Chemistry,* 28:3066–3069.

Gaviría, J P and Bohé, A E, 2010. Carbochlorination of yttrium oxide, *Thermochimica Acta,* 509:100–110.

Gruen, D M and Dekock, C W, 1967. Electronic absorption spectra of gaseous PuCl3, PuBr3 and PuCl4: The thermodynamics of PuCl4, *Journal of Inorganic and Nuclear Chemistry,* 29:2569–2575.

Lambertin, D, Lacquement, J, Sanchez, S and Picard, G S, 2000. Americium chemical properties in molten LiCl–KCl eutectic at 743 K, *Plasmas and Ions,* 3:65–72.

Le Bail, A, 2012. Whole powder pattern decomposition methods and applications: A retrospection, *Powder Diffraction,* 20:316–326.

Pomiro, F, Fouga, G, Gaviria, J and Bohé, A, 2015. Study of the Reaction Stages and Kinetics of the Europium Oxide Carbochlorination, *Metallurgical and Materials Transactions B,* 46.

Rasmussen, M J and Hopkins, H H, 1961. Preparing Plutonium Metal- Via The Chloride Process, *Industrial and Engineering Chemistry,* 53:453–457.

Rasmussen, M J, Stiffler, G L and Hopkins, J H H, 1961. Parameters In The Conversion Of Plutonium Nitrate To Plutonium Trichloride By A Direct Calcination-Fluid Bed Chlorination Process, General Electric Co, Hanford Atomic Products Operation, Richland, Wash.

Reuter, G, Fink, H and Seifert, H J, 1994. Hydrate des Cer(III)-chlorids, *Zeitschrift für anorganische und allgemeine Chemie,* 620:665–671.

Soine, T S, 1965. *Stirred-bed gas-solids reactor for preparing plutonium trichloride*, United States.

Tolley, W B, 1953. Plutonium Trichloride: Preparation By Reaction With Phosgene Or Carbon Tetrachloride, And Bomb Reduction To Metal, General Electric Co, Hanford Atomic Products Operation, Richland, Wash.

Vigier, J F, Laplace, A, Renard, C, Miguirditchian, M and Abraham, F, 2018. Uranium (III)-Plutonium (III) co-precipitation in molten chloride, *Journal of Nuclear Materials,* 499:394–400.

Wang, L, Zhang, T-A, Lv, G-Z, Dou, Z-H, Zhang, W-G, Zhang, J-Z, Niu, L-P and Liu, Y, 2019. Carbochlorination of alumina and silica from high-alumina fly ash, *Minerals Engineering,* 130:85–91.

West, M H, Ferran, M D and Fife, K W, 1988. The chlorination of plutonium dioxide, Los Alamos National Laboratory.

Zachariasen, W H, 1948. Crystal chemical studies of the 5f-series of elements, I, New structure types, *Acta Crystallographica,* 1:265–268.

Dissolution of quartz in Mn-slags during production of SiMn alloy

DOI: 10.62053/EEHA7202

S Jayakumari[1], V Canaguier[2] and E Ringdalen[3]

1. Research Scientist, SINTEF, Trondheim 7034, Norway.
   Email: sethulakshmy.jayakumari@sintef.no
2. Research Scientist, SINTEF, Trondheim 7034, Norway. Email: vincent.canaguier@sintef.no
3. Senior Research Scientist, SINTEF, Trondheim 7034, Norway. Email: eli.ringdalen@sintef.no

ABSTRACT

Silicomanganese (SiMn), containing approximately 16–30 per cent Si, is produced in submerged arc furnaces using various Mn sources and quartz as the primary raw materials, along with fluxes and reductants. In the high-temperature zone known as the coke bed, a silica-rich slag is formed. SiMn is produced through the reduction of SiO_2 from the slag. Dissolution of quartz into slags with different compositions, the primary slag formed from the Mn sources and flux before any MnO reduction occurred, representing conditions at the top of the coke bed, and dissolution of quartz into a partially reduced slag to simulate conditions inside the coke bed has been investigated. Experimental investigations were carried out to study the dissolution of quartz particles of varying sizes, 5 mm and 25 mm in synthetic slags with different compositions at temperatures between 1400°C and 1600°C, with varying holding times. Observed results are compared with liquidus compositions and equilibrium phases for original and formed slags. Particle size has been shown to be of little importance for the dissolution. Quartz dissolved more easily in slag at top of the coke bed than slag in the coke bed. Complete dissolution was observed after 30 mins at 1600°C in all cases, but not after 0 mins.

INTRODUCTION

Manganese ferroalloys are essential functional additives in steel production, they are produced in two main qualities: High Carbon Ferromanganese (HCFeMn) and Silicomanganese (SiMn), with the main difference being the higher Si-content in SiMn. Globally, around 4 million tonnes (Mt) of High Carbon Ferromanganese (HCFeMn) and around 16.6 Mt of Silicomanganese (SiMn) were produced in 2022. Several different grades are produced. For standard SiMn the analyses are in the range 65–68 per cent Mn, 1.5–3 per cent C and 12.5–21 per cent Si.

The major part of SiMn is produced by carbothermic reduction of oxides in large electric Submerged Arc Furnaces (SAF) of 10–45 MW as illustrated in Figure 1.

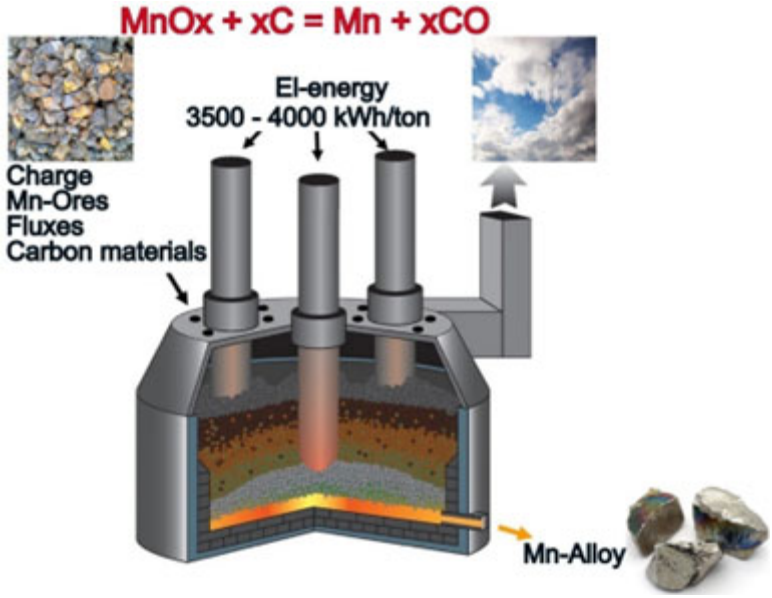

FIG 1 – Overview of Mn-alloy production (Olsen, Tangstad and Lindstad, 2007).

Manganese ores and HCFeMn slags are the main Mn sources and quartz the main Si source. Fluxes as dolomite and limestone are added to adjust the properties of the final slag. Several carbon sources are used as reductant, coke is most common. Raw materials are fed at room temperature to the top of the furnace. Slag and alloy are tapped out at the furnace bottom, at around 1500°C. Reduction of Mn-oxides produces a CO/CO_2 gas mixture that leaves at the top of the charge mixture. The process and reactions were extensively studied and described by Olsen, Tangstad and Lindstad (2007).

During the production of silicomanganese alloys, the submerged arc furnace can be divided into two main reaction zones (Olsen, Tangstad and Lindstad, 2007). Their existences have been confirmed by excavation of industrial furnaces of Mn-alloys (Ringdalen and Ksiazek, 2018; Olsen, Tangstad and Lindstad, 2004; Norbø, Øvrelid and Gridset, 2021). In the upper part of the furnace, the prereduction zone, the raw materials are solid, and reductions take place by gas-solid reactions. In the lower part of the furnace, the coke bed, slag, and metal are liquid. Here heat is generated by ohmic resistance in solid coke. Most of the supplied energy is consumed here, and the final reduction of MnO to Mn and of SiO_2 to Si takes place in this zone by the following main reactions.

$$(MnO) + C = \underline{Mn} + CO_{(g)} \quad (1)$$

$$(SiO_2) + 2C = \underline{Si} + 2CO_{(g)} \quad (2)$$

$$2(MnO) + \underline{Si} = 2\underline{Mn} + (SiO_2) \quad (3)$$

At the top of the coke bed, the initial slag is formed by melting and reduction of the Mn sources and dissolution of the fluxes. When the viscosity of the slag is low enough, it will drain into the coke bed. The temperature where this is achieved defines the temperature at the top of the coke bed and influences the temperature in the coke bed (Olsen, Tangstad and Lindstad, 2007). The type of Mn sources and their composition as well type of fluxes and reductants affects melting and reduction at the top of the coke bed (Ringdalen, Tangstad and Brynjulfsen, 2015).

In SiMn-production, quartz is added to obtain high enough SiO_2 content in the slag, typically 38–44 per cent, to have high enough SiO_2 activity in the slag to obtain the required Si-content in the alloy. Composition of the charge mixture vary with the Mn source used and targeted product composition. Its MnO content is normally so high that during melting it will first form a MnO containing liquid slag in equilibrium with solid MnO, or MnO-containing phase (Ringdalen *et al*, 2010). This will be present until MnO in the solid-liquid mixture have been reduced to a MnO content where there are no solid equilibrium phase present at the given temperature. Slag with around 10 per cent MnO is tapped out at around 1600°C at the bottom of the furnace. Quartz transforms during heating to other SiO_2 polymorphs and is at the top of the coke bed, where the temperature is 1200–1600°C, present as cristobalite or amorphous silica or a mixture of these (Ringdalen, 2015; Ringdalen and Tangstad, 2016). SiO_2 will here dissolve in the primary slag formed from MnO sources and fluxes with a MnO-SiO_2 content of the primary slag as illustrated in Figure 2.

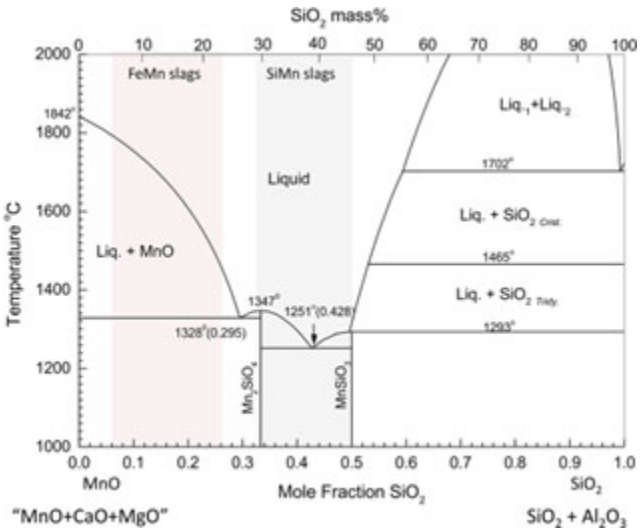

FIG 2 – MnO-SiO_2 phase diagram indicating the primary slag in FeMn and SiMn production (Tangstad *et al*, 2021).

Dissolution rate of SiO_2 into the slag will, as described by Tangstad *et al* (2021), affect the reduction to SiMn-alloy according to two main scenarios: if SiO_2 dissolves fast and simultaneously with solid MnO, the reduction will be from the average charge composition. If dissolution of SiO_2 is slower, this will determine the composition of the liquid slag and reduction of SiO_2 to Si is determined by SiO_2 dissolution in the primary Mn-slag. In small-scale experiments where Mn sources and quartz particles up to 2 cm were mixed, SiO_2 was found to dissolve in the slag from Mn sources at temperatures below 1400°C (Tangstad *et al*, 2021; Kim, 2018). In contrast, Maroufi *et al* (2014) found that the dissolution rate of SiO_2 in Mn slags was determined by mass transfer of silica in the slag. The experiments were conducted at 1400–1500°C, using an industrial tap slag with 15 per cent MnO and 45 per cent SiO_2. The SiO_2 source was fused silica, either as a crucible in static experiments with 1 g of slag or as a rotating rod in dynamic experiments with 130 grams of slag. Undissolved quartz has, as shown in Figure 3, been found in the coke bed in industrial excavations (Ringdalen and Ksiazek, 2018) while no quartz was observed in the coke bed in other (Ringdalen and Ksiazek, 2018; Norbø, Øvrelid and Gridset, 2021). Similarly, quartz has been observed in the coke bed in some pilot experiments with SiMn-production, while not seen in most (Ringdalen and Tangstad, 2013; Ringdalen and Solheim, 2018). If large amounts are present, it will strongly affect the electrical current paths and coke bed temperature.

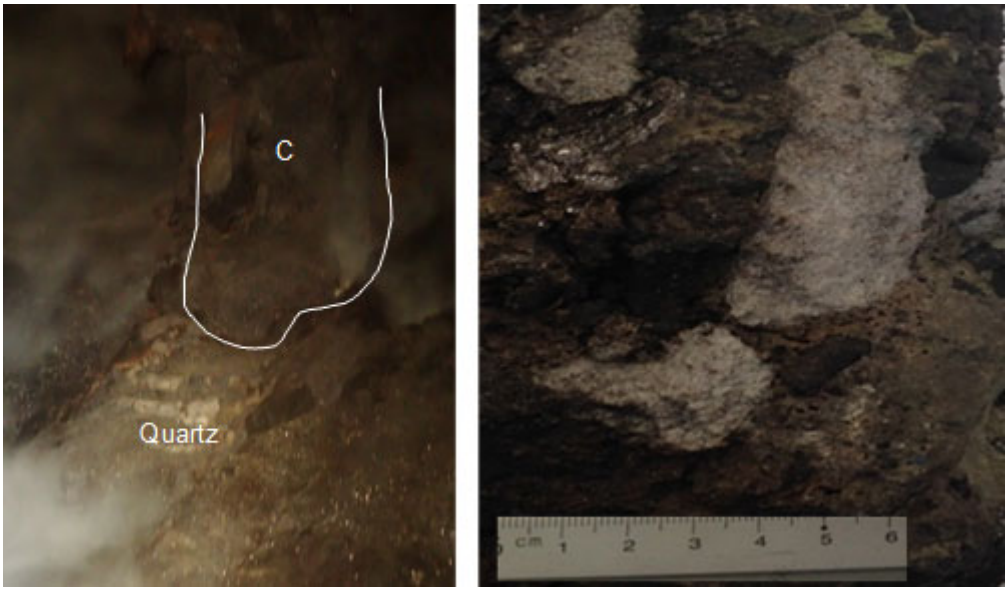

FIG 3 – Quartz in coke bed from excavation of SiMn furnace at Glencore (Ringdalen and Ksiazek, 2018). Position of layers of quartz in coke bed below electrode C to the left and quartz pieces in the coke bed to the right.

Effect of different parameters on dissolution of quartz in Mn-slag under various conditions as well as its effect on industrial furnace operation seems from this not to be clear and requires further investigations.

In the current study, dissolution of quartz in primary slag at the top of the coke bed and partly reduced slag in the coke bed has been compared for two different particle sizes of quartz. The basis was a slag from a charge mixture with Comilog ore, quartz and limestone earlier used in small scale reduction experiments (Larssen, 2017; Canaguier and Tangstad, 2020). Based on this slag, two different slag compositions were investigated. In both slags %SiO_2 was around 75 per cent of target, simulating the situation when not all SiO_2 had been dissolved into the slag. One of the slags had the original MnO content simulating the situation at the top of the coke bed with simultaneous melting of Mn-ore and dissolution of quartz. The other slag contained around 15 per cent MnO, simulating the situation in the coke bed when MnO is partly reduced and when there still is undissolved quartz present. The value 15 per cent is taken from measurements of %MnO in slag in pilot scale experiments (Ringdalen and Solheim, 2018). In industrial furnaces the slag content is expected to be lower. To allow investigations of near industrial particle sizes of quartz, the experiments were run in a graphite crucible with diameter of 11.8 cm heated in an induction furnace.

EXPERIMENTAL

In the dissolution experiments, quartz in two different size fractions were dropped into preheated synthetic slags with two different compositions, one simulating quartz dissolution at the top of the coke bed, and the other simulating quartz dissolution in the coke bed during SiMn production. Compositions of the two slags used in the experiments were based on a charge mixture of Comilog, ore, quartz and limestone used in earlier experiments (Larssen, 2017; Canaguier and Tangstad, 2020) and with a composition given in Table 1.

TABLE 1

Composition of charge mixture of Comilog ore, quartz and limestone used as basis for calculations of slag compositions (Canaguier and Tangstad, 2020).

MnO [wt%]	SiO_2 [wt%]	CaO [wt%]	MgO [wt%]	Al_2O_3 [wt%]
49.81	31.36	13.58	0.3	4.95

This composition was used to simulate the slag at the top of the coke bed. To simulate the slag in the coke bed, MnO content was adjusted to 15 per cent, maintaining the same ratio between the other oxides. Additionally, for both slags, the percentage of SiO_2 was adjusted to 75 per cent of the calculated value to simulate the dissolution of remaining SiO_2, with the MgO content excluded. The composition was then normalised to 100 per cent. The calculated slag compositions are given in Table 2. Synthetic slags with these compositions were prepared from powders of pure oxides MnO, SiO_2, CaO, and Al_2O_3 from VWR chemicals. These powders were mixed, melted in a graphite crucible heated to 1700°C in an induction furnace, cooled down and crushed to 20–25 mm pieces. electron probe micro-analyser (EPMA) analysis of the synthetic slag showed that it was homogenous, only phases formed during solidification, and no undissolved particles were observed. The composition of the synthetic slag was determined by XRF at an independent laboratory (Nemko Norlab). As shown in Table 2, the synthetic slag has a composition close to the planned one. This also confirms that slags with high MnO content can be produced in a graphite crucible without reduction of MnO.

TABLE 2

Composition of the planned and the produced slags for the dissolution of quartz experiments.

Slag	MnO [wt%]	SiO_2 [wt%]	CaO [wt%]	Al_2O_3 [wt%]
Slag 1 planned	54.22	25.60	14.78	5.39
Slag 1 produced	54.05	26.58	15.12	5.54
Slag 2 planned	15.00	47.54	27.45	10.01
Slag 2 produced	15.12	48.71	25.84	10.04

Quartz pieces for the dissolution experiments were Snekkevik quartz provided by Eramet Norway with typical composition given in Table 3. The quartz particles had, as seen in the EPMA picture in Figure 4, small inclusions of minerals containing either Fe or Mg, K rich silicates, mainly along the grain boundaries.

TABLE 3

Typical composition of Snekkevik quartz used in the dissolution experiments (Larssen, 2017).

MnO [wt%]	SiO_2 [wt%]	CaO [wt%]	MgO [wt%]	Al_2O_3 [wt%]	K_2O [wt%]
0.36	94.13	3.4	0.06	0.61	0.14

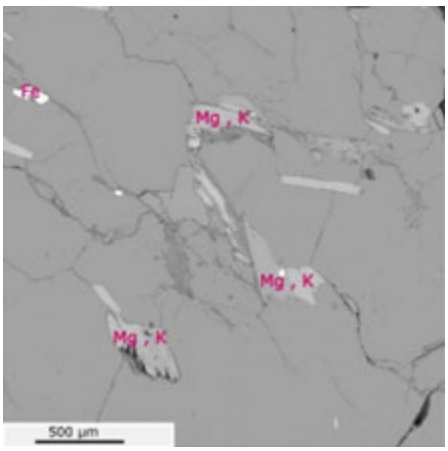

FIG 4 – The untreated quartz used for dissolution experiments contained inclusions of minerals such as Mg, K and Fe along grain boundaries as observed in the EPMA image.

The quartz was crushed and screened to make two different particle sizes: 5 mm and 25 mm, which were used to investigate effect of particle size in the dissolution experiments. 5 mm particles were made by screening at 5 mm and 6.5 mm, and 25 mm particles by screening at 20 mm and 30 mm.

The experiments were conducted in a 75-kW induction furnace produced by Inductotherm with a frequency of 2500 kHz. The materials were placed in an inner graphite crucible, 11.5 cm in diameter and 40 cm high with a closed bottom, open top and no gas purging. Temperatures were measured with a type C thermocouple placed at the crucible bottom. This was also used to control the heating of the furnace. Temperature at the top of the molten slag was assumed to be the same as the measured temperatures at the bottom of the crucible. Stirring of the liquid slag due to induction was assumed to cancel out the large temperature gradient normally found in this apparatus. Experimental temperatures have due to this some uncertainties. The same furnace and crucible were used both for production of synthetic slag and for dissolution experiments. Set-up for dissolution experiments is shown in Figure 5.

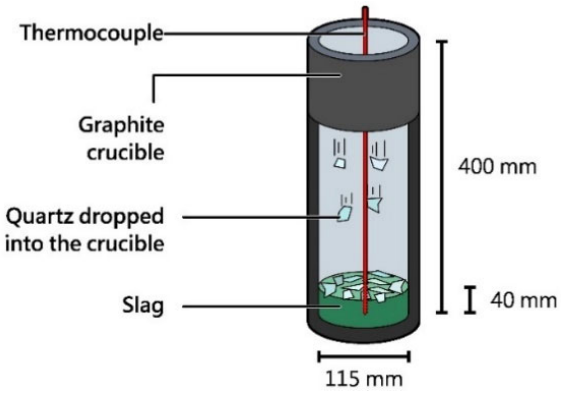

FIG 5 – Crucible used for production of synthetic slag and for dissolution experiments, here illustrating set-up for dissolution experiments.

In the dissolution experiments, the crucible was initially filled with either 1000 or 1500 grams of synthetic slag which, when melted, would reach a level of around 40 mm from the crucible bottom. The temperature was then heated at a rate of 40°C/min until the desired temperature of 1400°C, 1500°C or 1600°C was reached. Once the temperature stabilised, 50–150 grams of either 5 mm or 25 mm quartz particles were dropped into the molten slag, as shown in Figure 5. Behaviour of the quartz during dissolution was recorded using a DJI Osmo video camera for experiments at 1500°C and 1600°C. The crucible was held at the designated temperature for either 0 min or 30 mins, after which it was removed from the furnace for rapid cooling. The cooled crucible was then vertically cut into two halves. Samples were taken from the lower part of the crucible and their compositions determined by chemical analysis by XRF at a commercial laboratory, Nemko Norlab. Samples from the upper part of the crucible with partly dissolved quartz were drilled out and investigated using a

back-scattered electron probe micro-analyser (EPMA), type JEOL JXA-8500, The investigations included qualitative elemental mapping as well as quantitative phase composition analysis from various positions. Composition of the various slags were calculated from composition of the solidified phases determined by EPMA, and their relative amounts determined by Adobe Photoshop CC. Liquidus temperatures and equilibrium solid phase below this, was calculated by FactSage 8.3 with the Equilib module using the FToxid and FactPS databases.

In total, 24 dissolution experiments were conducted, with the experimental parameters detailed in the results section.

RESULTS

The main effects of the investigated parameters can be seen in Table 4 where conditions for the different experiments are provided and the experiments where undissolved quartz particles were found, by EPMA, in the slag after the experiment are marked with grey.

TABLE 4

Overview over conditions in the conducted experiments with experiments with undissolved quartz particles marked in grey.

	Slag 1	Slag 2	Quartz size		Temperature			Holding time		Amount, gram	
Exp	26% SiO_2	48% SiO_2	5mm	25 mm	1400 °C	1500 °C	1600 °C	0 min	30 min	Slag	Quartz
1	x		x				x	x		1500	100
2	x		x				x		x	1500	100
3	x			x			x	x		1000	153
4	x			x			x		x	1000	156
5	x		x			x		x		1000	50
6	x		x			x			x	1000	50
7	x			x		x		x		1000	107
8	x			x		x			x	1000	104
9	x		x		x			x		1000	50
10	x		x		x				x	1000	50
11	x			x	x			x		1000	104
12	x			x	x				x	1000	102
13		x	x				x	x		1000	100
14		x	x				x		x	1000	100
15		x		x			x	x		1000	100
16		x		x			x		x	1000	100
17		x	x			x		x		1000	50
18		x	x			x			x	1000	50
19		x		x		x		x		1000	102
20		x		x		x			x	1000	113
21		x	x		x			x		1000	50
22		x	x		x				x	1000	50
23		x		x	x			x		1000	104
24		x		x	x				x	1000	108

No clear effect of quartz particle size could be observed in these experiments Slag composition had, as expected, a major influence on quartz dissolution: in Slag 2 with high SiO_2 content, quartz was only completely dissolved only when it had been held for 30 mins at 1600°C, while in Slag 1 with

lower SiO_2 content quartz was completely dissolved after 0 mins at 1600°C and 30 mins at 1500°C. The temperatures will also affect the dissolution, and quartz was not dissolved in any of the slags after 30 mins at 1400°C, while all quartz was dissolved in both slags after 30 mins at 1600°C. Similarly, the holding time was of importance and in Slag 1 quartz had not dissolved after 0 mins at 1500°C but was completely dissolved after 30 mins at this temperature. The same was observed at 1600°C in Slag 2.

Introduction of the quartz to the slag bath lowered the temperature of the slag by around 50°C for a short time. Together with the assumption of uniform temperature in the slag bath, this introduced uncertainties in the experimental temperature. This is not expected to have a major influence on the qualitative effects described above.

Videos from dropping of quartz into the slag revealed, as illustrated in Figure 6, that the large 25 mm quartz particles formed cracks and disintegrated to smaller pieces in the initial stages of the dissolution when quartz met and reacted with the slag bath. Occurrence of slag filled cracks in the partly dissolved 25 mm particles, as seen in Figure 7, was confirmed by EPMA investigations of particles from experiments stopped immediately after the quartz was introduced. In Figure 6 quartz seem to have been completely dissolved in the last pictures, after 2 mins. This is not the case: the quartz has just disintegrated and been immersed in the slag to a degree where it cannot be observed. Slag 2 contained undissolved quartz particles after 30 mins at 1500°C.

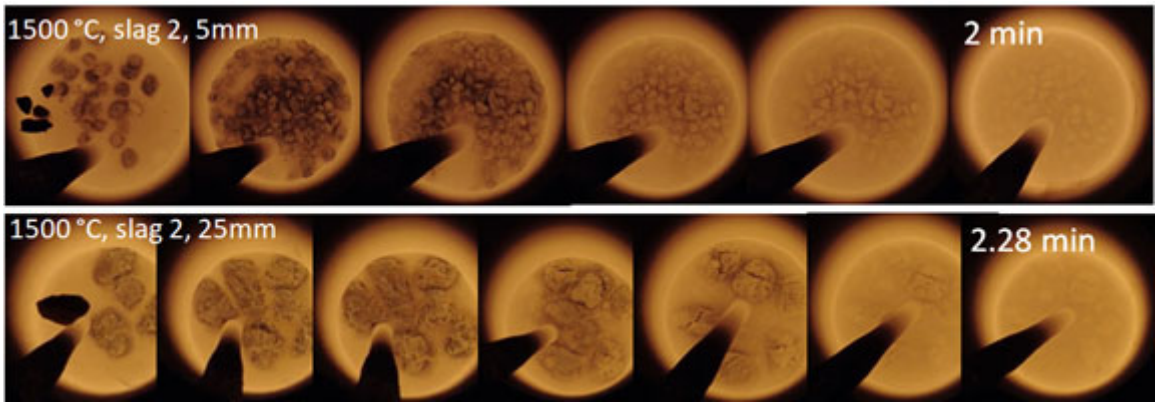

FIG 6 – Details from dissolution of 5 mm and 25 mm quartz particles into slag 2 at 1500°C, Pictures taken from videos from the first 2 mins of dissolution.

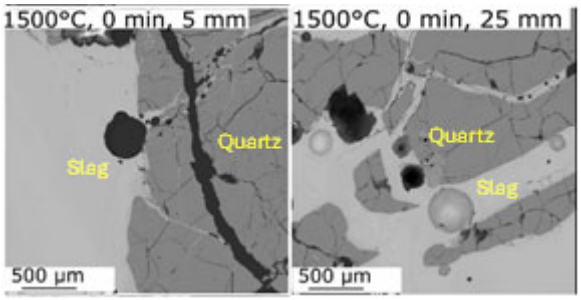

FIG 7 – Quartz, 5 mm and 25 mm particles, partly dissolved in slag 2 with 48 per cent SiO_2 after 0 mins.

Cracking and disintegration of quartz particles that meet the warm slag can explain why particle size will not affect the observed dissolution of quartz after 0 mins and 30 mins.

Detailed studies of the first minutes of dissolution indicates, as seen in Figure 8, that the larger, 25 mm particles in spite of the cracking kept their shape longer and needed longer time than the smaller particles to be immersed in the slag. These observations are only indicative. More quantitative data regarding reactions the first 2 mins will require a clearly defined zero point and high accuracy for the temperature measurements at the top of the slag. This phenomenon and its effect were thus not further investigated in the current work.

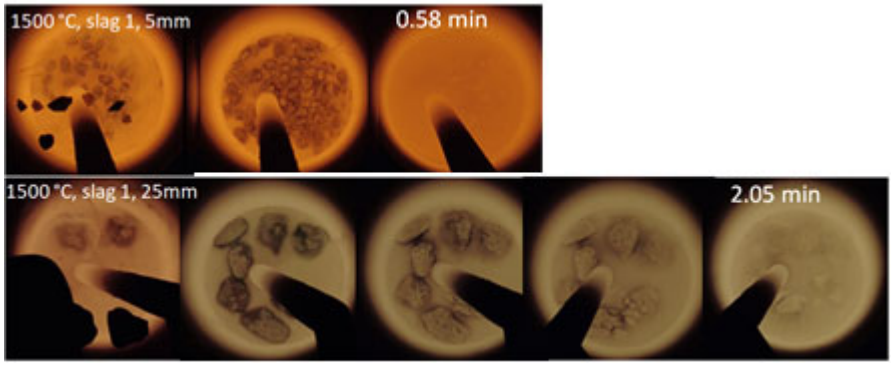

FIG 8 – Difference between 5 mm and 25 mm quartz during first 2 min of dissolution in Slag 1 at 1500°C. Pictures taken from videos.

Slag 2, simulating the slag in the coke bed, has a higher SiO_2 content (48 per cent SiO_2) than Slag 1 with (26 per cent SiO_2) simulating slag at the top of the coke bed, formed from the charge mixture without any MnO reduction. Both slags are, at all the experimental temperatures, at or above their liquidus temperature and SiO_2 will not be the first phase formed in any of the two slags. This liquidus temperature and the first solid phase formed during solidification of the two investigated slags are detailed in Table 5.

TABLE 5

Liquidus temperature and first solid phase formed during solidification of the two investigated slags. Calculated by FactSage 8.3 with the Equilib module using the FToxid and FactPS databases.

	MnO [wt%]	**SiO_2 [wt%]**	**Liquidus [°C]**	**First solid phase**
Slag 1	54.05	26.58	1401	MnO
Slag 2	15.12	48.71	1255	$(Mn,Ca)SiO_3$

Quartz, SiO_2 particles, dissolved easiest in the slag with the lowest SiO_2 content and was completely dissolved at lower temperatures and after shorter time in Slag 1 than in Slag 2. Quartz was, for example, dissolved at 1500°C after 30 mins in Slag 1, but not after 30 mins in Slag 2. At 0 mins, quartz was not dissolved in Slag 1 at 1500°C, and completely dissolved at 1600°C in Slag 1, but not dissolved in Slag 2 at 1600°C. This difference is also indicated when the first minutes of dissolution of quartz at 1500°C in Slag 1 and Slag 2 are compared in Figure 9. Quartz particles were completely immersed in Slag 1 after around 1 min while around 2 mins were needed for the quartz to be immersed in Slag 2.

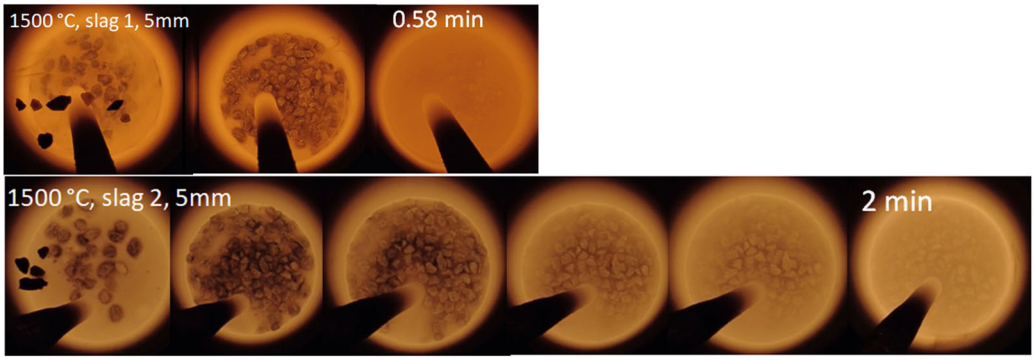

FIG 9 – Comparison of first minutes of dissolution of quartz in Slag 1 and Slag 2 at 1500°C. Pictures taken from videos.

The difference between dissolution in the two slags were investigated more in detail by studying partly dissolved quartz particles and the slag surrounding them with backscatter pictures and analysis by EPMA. This showed a major difference between the dissolution in the two slags as illustrated in Figure 10.

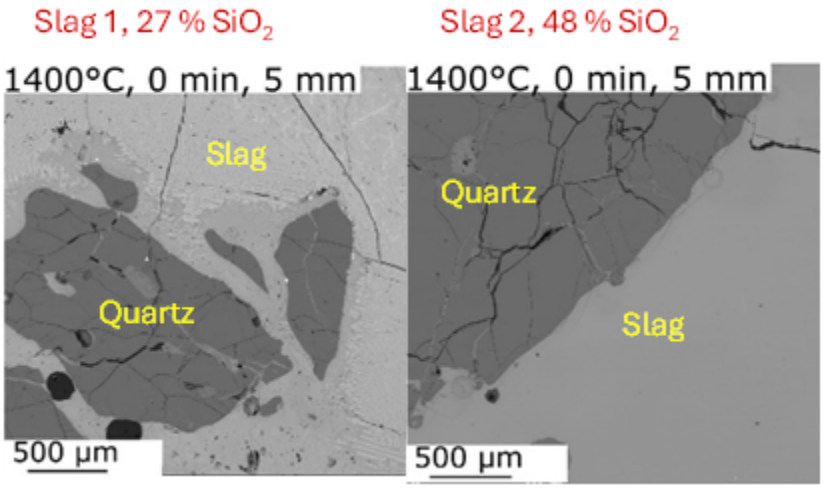

FIG 10 – Quartz, partly dissolved in Slag 1 left and slag 2 to right. 5 mm particles after 0 mins at 1400°C.

Slag surrounding quartz particles dissolved in Slag 2, with highest SiO_2 content, was homogenous and had approximately the same composition as the original slag. This was seen in all cases with undissolved quartz in Slag 2 for all temperatures, holding times and particle sizes. There were no indications of concentration gradients of elements due to slow mass transfer in the slag phase. This could indicate that dissolution mechanism of quartz in Slag 2, is controlled by the chemical reaction at the quartz/slag interface.

In contrast quartz partly dissolved in Slag 1 was, as shown in Figure 11, surrounded with layers of slag with different compositions. $\%SiO_2$ was highest in slag closest to the quartz particles and decreased outwards. Around 500–1000 µm away from the quartz particle, the slag had the same composition as the original slag. Solid MnO, the first solid phase to form in Slag 1, was not found in any of the slags. The slag must then have been above liquidus also at 1400°C. Composition of the slag layers varied with temperature and at 1500°C the layers closest to the quartz had higher SiO_2 content than corresponding layers at 1400°C. At 1600°C all quartz was dissolved. Similar layering was seen for dissolution of 25 mm quartz particles.

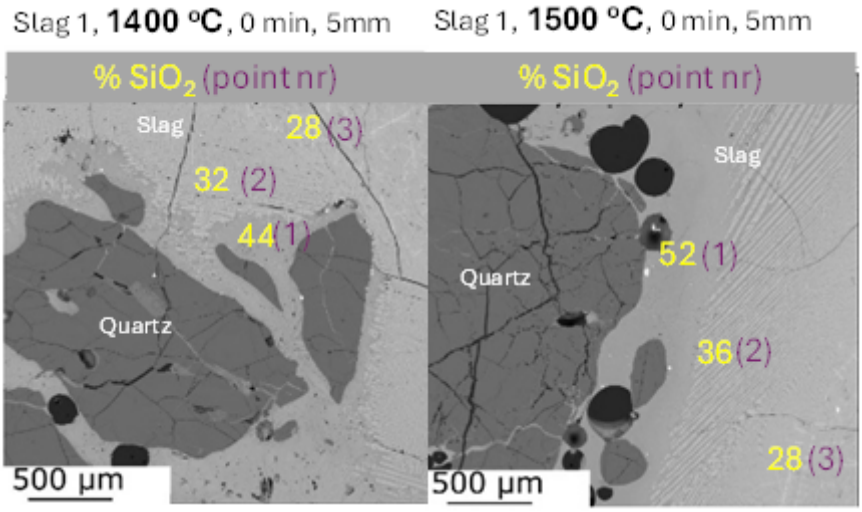

FIG 11 – Layers of slag surrounding quartz partly dissolved in Slag 1 at 1400°C to left and at 1500°C to the right, $\%SiO_2$ and point nr for the different slag layers are marked. Backscatter images with analysis from EPMA.

Content of the other elements in the slag vary with distance from the quartz particles and is given in Table 6 for the points marked in Figure 11.

TABLE 6

Content of selected elements in slag around 5 mm quartz partly dissolved in Slag 1 after 0 mins at 1400°C and 1500°C, given for points marked in Figure 11. Liquidus and first solid phase calculated by FactSage 8.3 with the Equilib module using the FToxid and FactPS databases.

	SiO_2		MnO		CaO		Al_2O_3		K_2O		Liquidus °C		First solid phase	
T °C	1400	1500	1400	1500	1400	1500	1400	1500	1400	1500	1400	1500	1400	1500
(1)	44	52	36	33	14	10	6	5	0.20	0.23	1355	1310	$(Mn,Ca)SiO_3$	SiO_2
(2)	32	36	41	48	15	13	12*	5	0.18	0.23	1112	1234	Olivine	Olivine
(3)	28	28	53	53	16	16	5	5	0.01	0.01	1355	1338	MnO	MnO

* This Al_2O_3 value is assumed to be an outlier

All the slags were, during the experiments, above their liquidus temperature and thus completely molten. K_2O content is not included in these calculations but is expected to reduce the liquidus temperature. In the experiments at 1400°C, liquidus temperature for the slag in contact with quartz was less than 50°C below the experimental temperature. This is within the range of temperature reduction that can be caused by quartz introduction in the slag bath. A solid phase could have been present in this slag, but no indications of this were observed. Since the equilibrium solid phase just below liquidus for this slag is $(Mn,Ca)SiO_3$, and not SiO_2, existence of the solid phase would not have stopped the dissolution of SiO_2. K_2O had accumulated around the quartz was with 0.20–0.23 per cent higher here than in the quartz where it is 0.14 per cent and in the bulk slag where it is 0.01 per cent. Quartz was the source of K_2O while there was no K_2O in the synthetic slag. The accumulation of K_2O around the quartz particles can be a factor affecting the dissolution. Since K_2O in the original quartz occur mainly in cracks and along grain boundaries, its concentration is not expected to have a major impact on the dissolution of the SiO_2 grains. K_2O content affects the slag properties such as viscosities and diffusivities and may through this affect both the dissolution of SiO_2 at the grain boundaries and the mass transfer in the slag.

Formation of slag in or intrusion of slag along grain boundaries or into cracks was observed in many of the experiments as illustrated in Figure 12. In the case shown here, there was a thin zone with slag around the quartz particle, with small SiO_2 grains partly connected to the quartz. This phenomenon can provide more information about the mechanism for quartz dissolution but was not systematically studied in the current investigation and will not be further discussed.

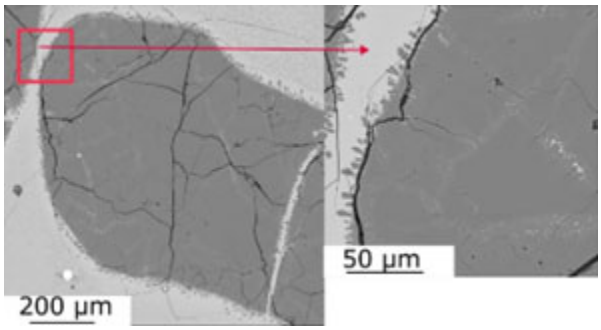

FIG 12 – Details of dissolution of 25 mm quartz particles in Slag 1 after 30 mins at 1400°C.

DISCUSSION

The main objective of the current investigations was to study the effect of quartz particle size on the dissolution in slags relevant for SiMn-production, eg slag at top of coke bed (Slag 1) and slag in coke bed (Slag 2). Slag composition was based on a case with Comilog ore as Mn source.

Particle size of quartz, 5 mm versus 25 mm, seems to have very little effect on the time or the temperature needed for quartz to dissolve in any of the slags. The larger quartz particles

disintegrated to smaller particles when meeting the slag, cancelling out the original size difference. The quartz particles were immersed in the slag during the first 1 to 2 mins, and larger particles seemed to need longer time, around 1 min more than the smaller particles to be completely immersed. Disintegration of the particles and intrusion of slag into the cracks are assumed to have taken place during this period. In industrial SiMn-production, quartz is heated together with the other materials, and will have the same temperature as the slag it is dissolved in. The quartz will then not experience the same thermal shock as in these experiments. In industrial SiMn production it could thus be possible that the particles keep their original size down to the coke bed and size effects could be seen. Investigations for Si and FeSi production on cracking and fines formation from quartz during continuous heating for 1 hr by the TSI method, show that quartz will disintegrate during heating, but the extent varies considerably with quartz source (Ringdalen, 2015). Based on this some disintegration of quartz that will cancel out effect of original size differences is expected.

Time and temperature needed for dissolution of quartz in slag depend on slag composition. Quartz was completely dissolved in Slag 1, simulating slag at the top of the quartz bed, after 30 mins at 1500°C, while it was not dissolved under the same conditions in Slag 2 simulating the slag in the coke bed. A main difference between the two slags is the lower SiO_2 content in the slag at the top of the coke bed where quartz dissolved at lowest temperatures.

When quartz dissolved in Slag 1, simulating the slag at the top of the coke bed, layers with different slag composition were formed around the quartz particles. SiO_2 and K_2O contents were highest close to the quartz-slag interface. The slags were above liquidus, not saturated with SiO_2. But the high SiO_2 content in slag, in immediate contact with quartz, will give a lower driving force for the dissolution. Both mass transfer and quartz-slag reaction at the interface can thus be of importance. A higher SiO_2 content in the boundary layer at 1500°C versus 1400°C indicates that rate of the chemical reaction increases more with temperature than the mass transfer in the slag. The boundary slag layer also had a higher K_2O content than the slag further away from the quartz particles indicating slow mass transfer of this compound from its source, quartz. In studies with continuous heating of similar charge mixtures, slag was formed at lower temperatures than the liquidus temperature for the charge mixture (Tangstad *et al*, 2021; Larssen, 2017; Kim, 2018). In these cases, longer heating times were used. A major difference is that in these cases the slag was formed from ores that contained minor elements that are expected to affect slag properties and wetting between solid phases and slag, with K_2O being one of those. The studies of continuous heating of a charge mixture are more a simulation of the conditions in an industrial production, while the current studies give more detailed information about the dissolution of quartz and effect of parameters related to this.

When quartz was dissolved in a slag simulating the conditions in the coke bed, higher temperatures or longer time were needed for complete dissolution compared with the slag with lower SiO_2 content at the top of the coke bed. The difference was seen both in the cooled down samples and in the videos of the first minutes of dissolution. Slag close to the interface of quartz partly dissolved in Slag 2 had the same composition as the bulk slag. Based on the characterisation methods used in these investigations, it was not observed any. layers of slag with higher concentration of SiO_2 close the quartz particles. Dissolution of quartz in the coke bed is thus assumed not to be governed by mass transfer in the slag. Reaction between quartz and slag is believed to determine rate of dissolution. The high SiO_2 content in this slag compared with Slag 1 will give a lower driving force for dissolution that can be a main reason for this. Other investigations have, in contrast, found mass transfer in the slag to be rate determining (Maroufi *et al*, 2014). The investigation this was based on used a slag with a slightly lower SiO_2 content than in the present work. The raw materials were an industrial SiMn slag and fused silica, in contrast to the synthetic slag and industrial SiO_2 sources used in the current investigations. In the current investigations K_2O, which is 0.14 per cent in the quartz, was dissolved into a slag without K_2O, while in the other case pure SiO_2 was dissolved in a slag with 2.7 per cent K_2O (Maroufi *et al*, 2014). Behaviour of K_2O or other minor elements may affect the dissolution and is a potential reason for the observed differences. Such phenomena were not investigated in the current work.

CONCLUSIONS

Dissolution of 5 mm and 25 mm quartz particles at 1400°C, 1500°C and 1600°C in two different slags have been investigated, one simulating conditions at the top of the coke bed and one simulating conditions in the coke bed during SiMn production. With the investigation methods used here, it was not observed any effect of particle size on time or temperature needed for complete dissolution. The coarser particles disintegrated to smaller particles when they met the slag. Dissolution of quartz in slag at the top of the coke bed required shorter time and lower temperature to be completed than dissolution of slag in the coke bed. When quartz dissolves in slag at the top of the coke bed it is surrounded by layers with different slag composition with decreasing SiO_2 content outwards from quartz. When quartz dissolves in the coke bed, it was surrounded by bulk slag without any layering. In both cases, all slags were above liquidus. Mass transfer seems to play a role in dissolution of quartz at the top of the coke bed but was in the current case not of importance for dissolution of quartz in the coke bed. This can be changed by minor elements that occur in industrial slags.

ACKNOWLEDGEMENTS

This work is done as a part of Recursive project funded by Research council of Norway, grant number 326581, and the industrial ferroalloy producers Eramet, Elkem, Wacker, Finnfjord. Inspiring discussions with Professor Merete Tangstad at NTNU have contributed to the work. They are all acknowledged.

REFERENCES

Canaguier, V and Tangstad, M, 2020. Kinetics of Slag Reduction in Silicomanganese Production, *Metallurgical and Materials Transactions B*, 51(3):953–962.

Kim, P P, 2018. The reduction rates of SiMn Slags from various raw materials, PhD thesis, NTNU, Trondheim.

Larssen, T A, 2017. Reduction of MnO and SiO_2 from Assmang and Comilog based slags, MSc thesis, NTNU, Trondheim.

Maroufi, S, Ciezki, G, Jahanshahi, S, Sun, S and Ostrovski, O, 2014. Dissolution Rate and Diffusivity of Silica in SiMn Slag, *Metallurgical and Materials Transactions B*, 46:101–108.

Norbø, E A, Øvrelid, S and Gridset, E, 2021. Excavation and Analysis of a 31MW SiMn furnace at Eramet Kvinesdal in *Proceedings of the 16th International Ferro-Alloys Congress (INFACON XVI) 2021*.

Olsen, S, Tangstad, M and Lindstad, T, 2004. 2018. Silicomanganese production, Process Understanding in *Proceedings INFACON X,* pp 231–238 (Southern African Institute of Mining and Metallurgy: Johannesburg)

Olsen, S, Tangstad, M and Lindstad, T, 2007. *Production of Manganese Ferroalloys* (Tapir Forlag: Trondheim).

Ringdalen, E and Ksiazek, K, 2018. Excavation of a SiMn furnace: Furnace Tapping, in *Proceedings Furnace Tapping 2018*, pp 167–178 (Southern African Institute of Mining and Metallurgy: Johannesburg).

Ringdalen, E and Solheim, I, 2018. Study of SiMn process in a pilot furnace, in *Proceedings of Infacon XV: International Ferro-Alloys Congress* (Southern African Institute of Mining and Metallurgy: Johannesburg)

Ringdalen, E and Tangstad, M, 2013. Study of SiMn production in Pilot Scale experiments – Comparing Carajas sinter and Assmang ore, in *Proceedings of the 13th International Ferroalloys Congress INFACON XIII*.

Ringdalen, E and Tangstad, M, 2016. Softening and Melting of SiO_2, an Important Parameter for Reactions with Quartz in Si Production, in *Proceedings of the 10th International Conference on Molten Slags, Fluxes and Salts 2016*, pp 43–51 (Springer International Publishing: Cham).

Ringdalen, E, 2015. Changes in Quartz During Heating and the Possible Effects on Si Production, *JOM*, 67(2):484–492.

Ringdalen, E, Gaal, S, Tangstad, M and Ostrovski, O, 2010. Ore Melting and Reduction in Silicomanganese Production, *Metallurgical and Materials Transactions B*, 41(6):1220–1229.

Ringdalen, E, Tangstad, M and Brynjulfsen T, 2015. Melting Behaviour of Mn sources- effect on furnace performance, in *Proceedings of the 14th International Ferroalloys Congress INFACON XIV*.

Tangstad, M, Bublik, S, Haghdani, S, Einarsrud, K E and Tang, K, 2021. Slag Properties in the Primary Production Process of Mn-Ferroalloys, *Metallurgical and Materials Transactions B*, 52(6):3688–3707.

Carburisation and melting of hot compacted iron in a coke bed

DOI: 10.62053/GLXC9456

J Park[1], M Kim[2], I-K Suh[3], E Kim[4] and J Lee[5]

1. Researcher, POSCO, Gwangyang 57807, South Korea. Email: j_park@posco.com
2. Research Engineer, Hyundai Steel, Dangjin 31719, South Korea. Email: mkkim26@hyundai-steel.com
3. Industry-Co Professor, Korea University, Seoul 02841, South Korea. Email: iksuh@korea.ac.kr
4. PhD Candidate, Korea University, Seoul 02841, South Korea. Email: kukuridie@korea.ac.kr
5. Professor, Korea University, Seoul 02841, South Korea. Email: joonholee@korea.ac.kr

ABSTRACT

One of the key technologies in developing hydrogen-enriched ironmaking operations is the control of the carburisation, melting, and dripping behaviour of the iron ore burden materials. When a hot compacted iron (HCI) is charged in the blast furnace or the FINEX Melter-Gasifier, iron oxide reduction, the reduced iron's carburisation, and the melting of iron and slag occur successively. This study investigated the reduction, carburisation, melting and dripping behaviour of HCI under a CO-H_2 gas mixture using the high-temperature X-ray radiographic technique. Under 100 per cent CO gas atmosphere, the dripping temperature was 1410°C. When 5 per cent H_2 was introduced, the dripping temperature slightly decreased to 1400°C. Furthermore, the dripping temperature gradually increased as the H_2 gas composition increased. As 30 per cent H_2 was introduced, the dripping temperature reached 1414°C. The carbon concentration in the drained metal samples gradually increased with increasing H_2 composition. It is considered that H_2 decreased FeO content in the slag, yielding the increased melting temperature and viscosity of the slag. On the other hand, H_2 accelerated the carburisation of the reduced iron by CO gas, enabling the homogenisation of the oxide materials to form a liquid phase. Therefore, it is considered that introducing H_2 in the reactor is helpful to increase productivity and energy efficiency by accelerating the liquid phase's formation.

INTRODUCTION

Steel is recognised as an essential material for sustainable development (IEA, 2020). Steel is used as an essential core material in renewable energy production, such as solar and wind power generation and nuclear power generation. Steel is also used as the core material of energy-efficient transportation: automobiles, ships, and trains. For example, steel is used for electric vehicle bodies, battery packs, and electric motors. The adoption of steel is also increasing for zero-energy building construction. At the same time, however, the demand for the reduction of greenhouse gas emissions from the iron- and steel-making processes cannot be ignored; the steel industry emits about 7 per cent of global greenhouse gas emissions (IEA, 2020), so the development of new zero-carbon processes is required.

Technology that utilises hydrogen in the blast furnace process and FINEX process is considered the most realistic alternative to reduce greenhouse gas emissions (Yi, 2019). New iron ore burdens have been developed to be used in the H_2-enriched ironmaking process (Park, 2023b, 2022, 2020; Rajavaram, 2016). Here, low-reduced iron (LRI) is charged in the blast furnace or in the Melter-Gasifier as a form of hot compacted iron (HCI) (Yi, 2021). As the hydrogen is introduced in the reactor, the reduction of iron oxide is accelerated, and the liquid slag formation temperature increases (Lan, 2020; Long, 2016). Accordingly, the melting and dripping temperature of burden materials would be delayed, when compared to the conventional blast furnace operation (Dereje, 2018). Then, a stable gas permeability in the coke bed becomes complex to establish, and the efficient heat transfer from the gas to the burden materials would not be guaranteed. Consequently, controlling the holdup of liquid phases in the coke bed will be difficult.

In the coke bed, the carburisation of the reduced iron generally takes place in advance, yielding successive liquid slag formation by homogenising the oxide phases (Park, 2021). Therefore, much attention is paid to the acceleration of the carburisation of the reduced iron. Fruehan reported that the carburisation of solid iron was enhanced by introducing H_2 gas (Fruehan, 1973). Shin *et al* carried out a series of experiments and revealed that the carburisation was affected mainly by the ash content in the coke (Shin, 2014, 2012; Jang, 2012b). Shin *et al* also reported that FeO content

lowered the carburisation and melting behaviour of the reduced iron (Shin, 2015). Kim *et al* suggested that the reaction was accelerated due to Marangoni flow (Kim, 2001). Despite much research on this matter, no report has been published for *in situ* observation of the carburisation, melting, and dripping behaviour of the HCI sample under the CO-H_2 gas atmosphere.

Recently, the high-temperature X-ray radiographic technique has been utilised to investigate liquid phases' melting and dripping behaviour through the coke bed (Shin, 2010; Park, 2021). In the present study, the carburisation, melting, and dripping behaviour of HCI in the coke bed is investigated by using the high-temperature X-ray radiographic method. Here, the effect of the composition of the CO-H_2 gas mixture is investigated.

EXPERIMENTAL

The experimental apparatus comprised a $MoSi_2$ resistance furnace and a high-temperature X-ray radiographic inspector system. A schematic illustration is shown in Figure 1. An alumina reaction tube (inner diameter of 90 mm and length of 1000 mm) was placed vertically in the furnace. Coke particles of 8~9 mm diameter were charged in a graphite crucible (inner diameter of 55 mm and height of 75 mm) with 33 holes of 5 mm diameter drilled in the bottom. There were four layers of coke particles in the crucible. An ellipsoidal-type HCI sample (longer-axis length of 3.8~4.7 mm, shorter-axis length of 3.1~3.3 mm, and height of 1.5~2 mm) was then placed on the top of the coke layer. The samples used in this study were provided by POSCO. The chemical compositions of the HCI are given in Table 1. The reduction degree of HCI is 57.2 per cent. The chemical composition of the coke and its ash contents are given in Tables 2 and 3, respectively. The sample assembly was covered by a graphite lid, and it was heated to 1000°C at a heating rate of +5°C/min under an N_2 gas atmosphere. From 1000°C, the reaction gas was changed into a CO or CO-H_2 gas mixture with a predetermined mixing ratio. The reaction gas was blown on the surface of the HCI sample with a flow rate of 1 L/min STP through an alumina lance (inner diameter of 6 mm) with a distance of 10 mm. The melting and dripping behaviour of metal and slag was investigated with the high-temperature X-ray radiographic system with a tungsten target X-ray tube. The experiment finished at 1500°C, and the sample was cooled to room temperature in the furnace. After experiments, the carbon and sulfur compositions of the drained metal samples were analysed with LECO-C/S analyser.

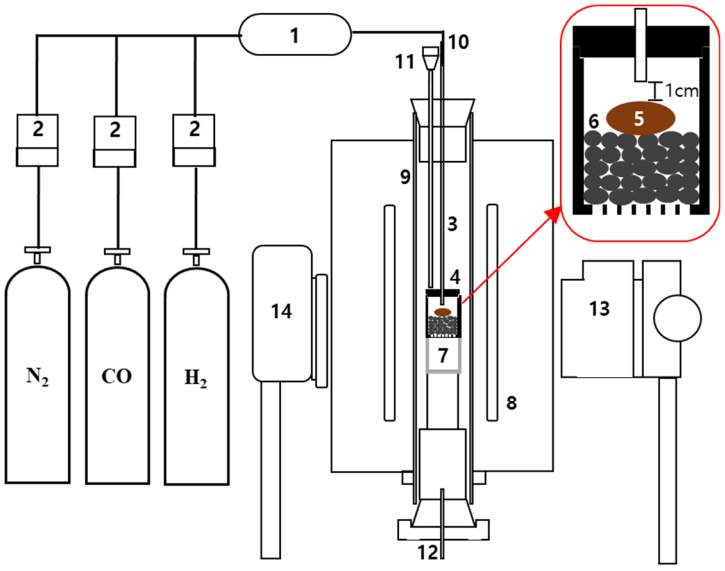

1. Gas Mixer
2. Mass Flow Controller
3. Alumina Lance
4. Graphite Crucible
5. HCI sample
6. Coke Particles (d=8~9mm)
7. Alumina Crucible
8. Heating Element
9. Alumina Reaction Tube
10. Gas Inlet
11. Thermocouple
12. Gas Outlet
13. X-ray Source
14. CCD

FIG 1 – Experimental apparatus for *in situ* observation of carburisation and melting.

TABLE 1

Chemical composition of the HCI sample.

Element	Total Fe	Metallic Fe	FeO	CaO	SiO_2	Al_2O_3	MgO
wt%	72.2	32	36	3.7	4.2	2.1	1.2

TABLE 2

Chemical composition of the coke particle.

Element	Fixed C	Ash	Volatile matter	Moisture
wt%	86.36	11.66	1.76	0.22

TABLE 3

Chemical composition of the ash contents in the coke.

Element	SiO_2	Al_2O_3	Fe_2O_3	CaO	K_2O	P_2O_5	MgO
wt%	54.55	27.40	6.08	2.78	1.28	1.09	0.87

RESULTS AND DISCUSSION

Ex situ observation

Figure 2 shows the top view and the cross-section view of the sample assembly. It is considered that the amount of metal holdup decreased while the slag holdup increased. The colour of the slag was changed from grey-green to white, indicating that the FeO content in the slag gradually decreased. Figure 3 shows the carbon and sulfur contents of the drained metal samples. The carbon concentration gradually increased, whereas the sulfur concentration monotonically decreased. Since the contact between the reduced iron and the coke particles was not controlled precisely, it is more reasonable to investigate the general trend of the chemical composition change with increasing the H_2 concentration in the gas mixture. Here, the decrease in the sulfur content supported the idea that the carburisation reaction by the CO-H_2 gas mixture was more pronounced than that by direct contact with coke particles because the sulfur source was the coke (Lee, 2007). Accordingly, it is speculated that the increased H_2 concentration accelerated the reduction of iron oxide, which might increase the melting point of the slag, while increasing the slag viscosity (Nakamoto, 2004).



FIG 2 – Top and cross-section views of the sample assembly after experiments. The gas composition was varied (a)100 per cent CO, (b) 95 per cent CO – 5 per cent H_2, (b) 80 per centCO – 20 per cent H_2, (c) 75 per centCO – 25 per cent H_2, and (d) 70 per centCO – 30 per cent H_2. The drained metal and slag samples are shown separately.

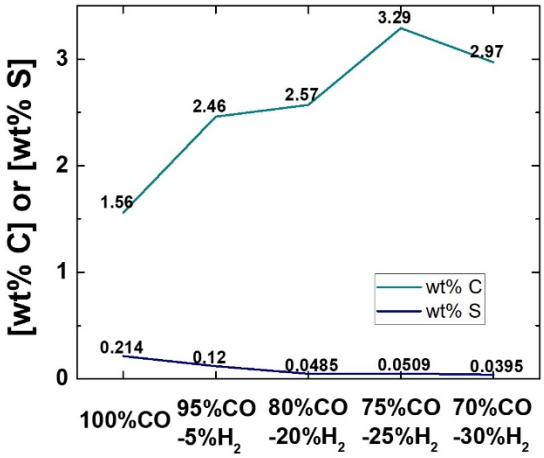

FIG 3 – Top and cross-section views of the sample assembly after experiments. The gas composition was varied (a) 100 per cent CO, (b) 95 per cent CO – 5 per cent H_2, (b) 80 per cent CO – 20 per cent H_2, (c) 75 per cent CO – 25 per cent H_2, and (d) 70 per cent CO – 30 per cent H_2. The drained metal and slag samples are shown separately.

Consequently, the slag holdup increased with increasing H_2 concentration. This observation shows a similar trend as the experimental results of Shin *et al* (Shin, 2015) with designed model experiments. In this study, the ash content would prevent carburisation by solid coke. Park *et al* reported that solid ash or high-viscosity liquid ash slag might prevent the carburisation reaction by direct contact with coke particles (Park, 2023a). Therefore, there were more chances for the CO-H_2 gas mixture to provide the carbon source for the reduced iron.

In situ observation

Figure 4 shows the *in situ* observation results of the sample assembly under a CO gas atmosphere. At 1280°C, liquid slag first appeared. Liquid metal formation was first investigated from 1380°C. This carburisation and melting might be accelerated by the involvement of the FeO-containing slag (Kim, 2001). The liquid metal suddenly started to drain at 1409°C, while liquid slag remained in the coke bed. The drain of liquid slag occurred when the liquid metal pulled the liquid slag together. The liquid slag flew over the surface of liquid metal. A similar observation was reported by Jeong *et al* (Jeong, 2013). However, in the present experiment, some part of the liquid metal eventually remained in the coke bed.

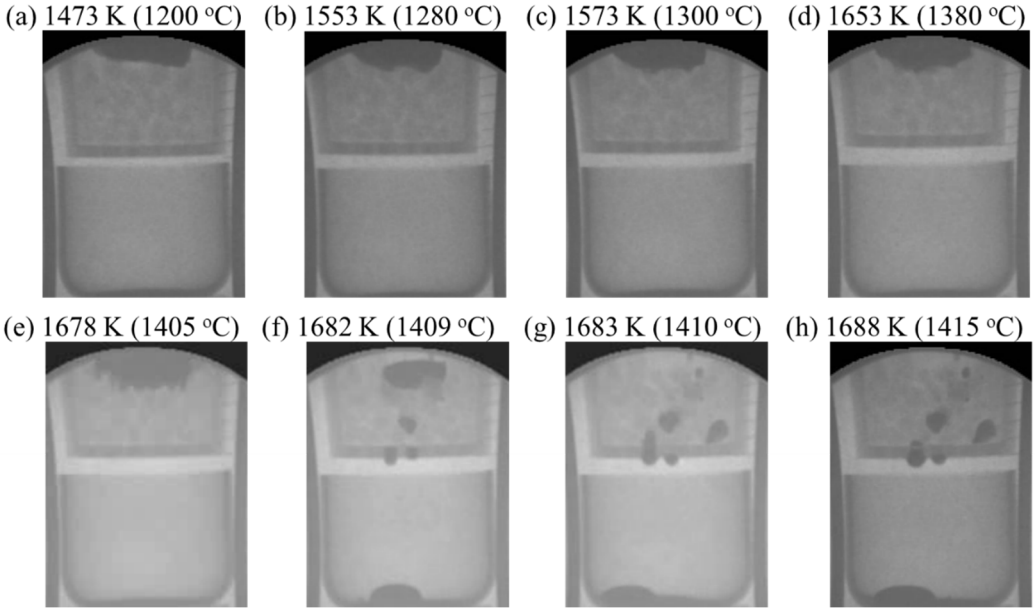

FIG 4 – *In situ* observation of liquid metal and liquid slag formation from HCI on a coke bed under CO gas atmosphere.

Figure 5 shows the *in situ* observation results when the CO-20 per cent H_2 gas mixture was introduced. In this experiment, the first liquid slag formation was investigated at 1280°C, which is the same as the experiment with 100 per cent CO gas. The liquid metal formation appeared at 1403°C. Due to the rapid reduction of iron oxide by H_2 gas, the carburisation would not be enhanced by the existence of liquid slag. At 1405°C, the drain of liquid slag was investigated, followed by the drain of liquid metal. It is considered that the introduction of H_2 gas enhanced the carburisation by CO gas.

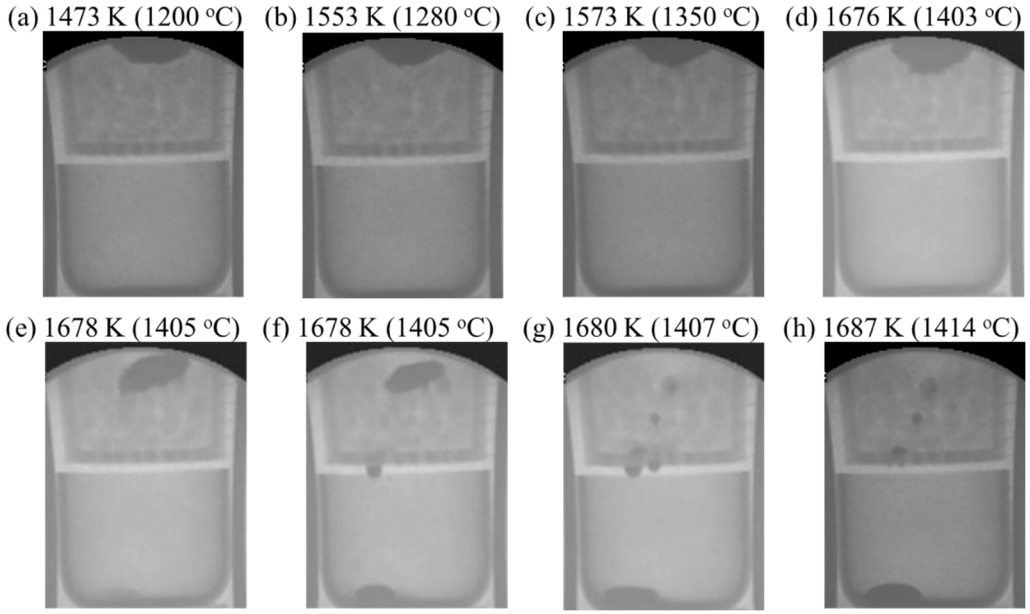

FIG 5 – *In situ* observation of liquid metal and liquid slag formation from HCI on a coke bed under CO-20 per cent H_2 gas atmosphere.

It is considered that the introduction of H_2 gas decreased FeO content in the slag, yielding the increased melting temperature of the slag as well as the slag viscosity (Park, 2023a). On the other hand, H_2 gas accelerated the carburisation of the reduced iron, enabling the homogenisation of the oxide materials to form a liquid phase (Oh, 2017). Therefore, it is considered that a reasonable introduction of H_2 in the blast furnace of the FINEX melter-gasifier is helpful to increase productivity and energy efficiency by accelerating the liquid phase's formation.

The slag holdup is affected by the particle size of the coke and thermophysical properties of liquid slag, such as density, surface tension, viscosity, and wettability (Jang, 2012a; Dereje, 2021, 2020). In the practical blast furnace or FINEX melter-gasifier operations, the formation of the SiC layer would reduce the slag holdup by drastically modifying wettability (Kim, 2023; Oh, 2016). Therefore, the increased slag holdup investigated in this study would be reduced by the introduction of H_2 gas. Hence, the H_2-injecting ironmaking process would be more favourable for the establishment of an energy-efficient ironmaking process (Park, 2023a).

In this study, however, detailed critical analysis, such as microstructure analysis of the sample and phase identification, was not carried out because the slag composition was changed by the reaction with the crucible. More sophistical experimental design is anticipated in future work.

CONCLUSIONS

The reduction, carburisation, melting, and dripping behaviour of HCI was investigated under a CO-H_2 gas mixture with the high-temperature X-ray radiographic technique. Figure 6 shows the summary of the experimental results. Under 100 per cent CO gas atmosphere, the dripping temperature was 1410°C. When 5 per cent H_2 was introduced, the dripping temperature slightly decreased to 1400°C. As the H_2 gas composition increased further, the dripping temperature gradually increased. The carbon concentration in the drained metal samples gradually increased with increasing H_2 composition. It is considered that H_2 decreased FeO content in the slag, yielding the increased melting temperature of the slag, while it also accelerated the carburisation of the reduced iron by CO gas, enabling the homogenisation of the oxide materials to form a liquid phase. It is considered that

a reasonable introduction of H_2 in the reactor is helpful in increasing productivity and energy efficiency by accelerating the liquid phase's formation.

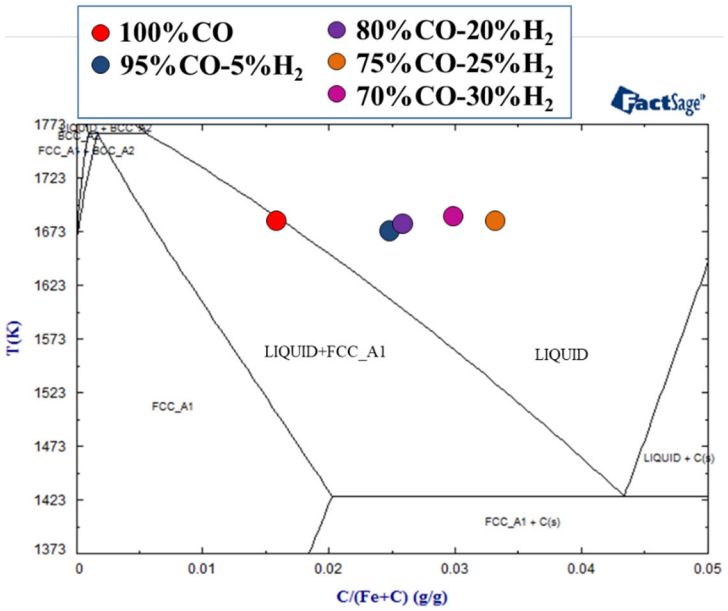

FIG 6 – Dripping temperature with respect to the carbon concentration of the dripped metal under various gas atmosphere.

ACKNOWLEDGEMENTS

This work was supported by the Industrial Strategic Technology Development Program (RS-2023-00262421, Development of basic design technology for hydrogen based ironmaking), funded by the Ministry of Trade, Industry and Energy in the Republic of Korea.

REFERENCES

Dereje, D G and Lee, J, 2018. Effects of Particle Diameter and Coke Layer Thickness on Solid Flow and Stress Distribution in BF by 3D Discrete Element Method, *Metall Mater Trans B*, 49:3594–3602. https://doi.org/10.1007/s11663-018-1368-7

Dereje, D G and Lee, J, 2021. Analysis of the wettability effect on slag holdup in a fixed bed of carbonaceous particles using CFD–DEM simulations, *Metallurgical and Materials Transactions B*, 52:2883–2891. https://doi.org/10.1007/s11663-021-02249-9

Dereje, D G, Siddiqui, M I H and Lee, J, 2020. Characterization of Slag Flow in Fixed Packed Bed of Coke Particles, *Metallurgical and Materials Transactions B: Process Metallurgy and Materials Processing Science*, 51(1):102–113. https://doi.org/10.1007/s11663-019-01750-6

Fruehan, R J, 1973. *Metall Trans*, 4:2123. https://doi.org/10.1007/BF02643276

International Energy Agency, 2020. Iron and Steel Technology Roadmap, IEA Publications. Available from: <https://www.iea.org/reports/iron-and-steel-technologyroadmap> [Accessed: 29 Sept 2023].

Jang, D, Kim, Y, Shin, M and Lee, J, 2012b. Kinetics of carbon dissolution of coke in molten iron, *Met Mater Trans B*, 43:1308–1314.

Jang, D, Shin, M, Seok Oh, J, Kim, H-S, Yi, S H and Lee, J, 2012a. Static Holdup of Liquid Slag in Carbonaceous Beds, *ISIJ Int*, 54:1251–1255.

Jeong, I-H, Kim, H-S and Sasaki, Y, 2013. Trickle Flow Behaviors of Liquid Iron and Molten Slag in the Lower Part of Blast Furnace, *ISIJ Int*, 53:2090–2098. https://doi.org/10.2355/isijinternational.53.2090

Kim, H S, Lee, S H and Sasaki, Y, 2001. *ISIJ Int,* 50:71 https://doi.org/10.2355/isijinternational.50.71

Kim, M, Jeon, S, Park, J, Park, J, Choi, M-E and Lee, J, 2023. Investigation of SiC formation on the graphite surface by CO-H2-SiO gas, *J Mat Res Tech*, 26:5373–5382. https://doi.org/10.1016/j.jmrt.2023.08.238

Lan, C, Zhang, S, Liu, X, Lyu, Q and Jiang, M, 2020. *Int J Hydrog Energy*, 45:14255. https://doi.org/10.1016/j.ijhydene.2020.03.143

Lee, J, Tazuke, A, Tanaka, T, Park, J-H, 2009. Estimation of sulfur segregation at the interface between molten iron and graphite substrate from wetting experiments, *Metals and Materials International*, 15(3):501–505.

Long, H M, Wang, H T, Zhao, W, Li, J X, Liu, Z G and Wang, P, 2016. *Ironmak Steelmak,* 43:450. https://doi.org/10.1080/03019233.2015.1108480

Nakamoto, M, Tanaka, T, Lee, J and Usui, T, 2004. Evaluation of Viscosity of Molten SiO_2-CaO-MgO-Al_2O_3 Slags in Blast Furnace Operation, *ISIJ Int*, 44(12):2125–2129.

Oh, J S and Lee, J, 2016. Composition-dependent reactive wetting of molten slag on coke substrates, *J Mater Sci*, 51:1813–1819. https://doi.org/10.1007/s10853-015-9588-6

Oh, J S, Lee, J and Lee, J, 2017. Effect of Additive Size on Softening and Melting Behavior of Slag, *Korean J Met Mater*, 55,(8):566–571. https://doi.org/10.3365/KJMM.2017.55.8.566

Park, J, Kim, E, Suh, I-K and Lee, J, 2022. A Short Review of the Effect of Iron Ore Selection on Mineral Phases of Iron Ore Sinter, *Minerals*, 12:35. https://doi.org/10.3390/min12010035

Park, J, Kim, E, Suh, I-K and Lee, J, 2023b. Effects of basicity and Al_2O_3 content on the crystal structure of silico-ferrite of calcium and aluminum, *ISIJ Intl*, 63(2):235–243. https://doi.org/10.2355/isijinternational.ISIJINT-2022-375

Park, J, Kim, M, Suh, I-K, Kim, E and Lee, J, 2023a. Investigation of carburization and melting behavior of fully reduced LRI and IOS on coke substrates, *Metals and Materials International*. https://doi.org/10.1007/s12540-023-01551-2

Park, J, Park, H, Dereje, D G, Kim, W H and Lee, J, 2021. In-Situ Observation of Slag Holdup in a Fixed Bed of SiC Particles Using High-Temperature X-ray Radiographic Technique, *Metall Mater Trans B*, 52:3561–3563. https://doi.org/10.1007/s11663-021-02295-3

Park, J, Rajavaram, R, Suh, I-K, Jeon, J, Son, S and Lee, J, 2020. Effects of basicity and Al_2O_3 content on the chemistry of phases in iron ore sinter containing ZnO, *Metallurgical and Materials Transactions B: Process Metallurgy and Materials Processing Science*, 51(6):3016–3027. https://doi.org/10.1007/s11663-020-01940-7

Rajavaram, R, Lee, J, Oh, J S, Kim, H G and Lee, J, 2016. Microwave Heating Characteristics of Magnetite Ore, *Met Mater Int*, 22(6):1116–1120. https://doi.org/10.1007/s12540-016-6045-2

Shin, M, Cho, S, Lee, J and Park, J-H, 2010. *In situ* observation of dynamic interfacial phenomena between CaO(-SiO_2 or Al_2O_3) slag and Fe-11%Cr alloy near the MgO-6%C refractory at 1823K, *Met Mater Int*, 16(3):495–499.

Shin, M, Min, S, Lee, J, Park, J G and Min, D J, 2012. In-Situ Observation of the Carburization of Solid Iron by Graphite, *Met Mater Int*, 18(6):1041–1047.

Shin, M, Oh, J S and Lee, J, 2015. Carburization, Melting and Dripping of Iron through Coke Bed, *ISIJ Int*, 55(10):2056–2063. https://doi.org/10.2355/isijinternational.ISIJINT-2015-115

Shin, M, Oh, J S, Lee, J, Jung, S and Lee, J, 2014. Dissolution Rate of Solid Iron by Liquid Fe-C Alloy, *Met Mater Int*, 20(6):1139–1143. https://doi.org/10.1007/s12540-014-6018-2

Yi, S H, Choi, M E, Kim, D H, Ko, C K, Park, W-I and Kim, S Y, 2019. FINEX(R) as an environmentally sustainable ironmaking process, *Ironmak Steelmak*, 46:625e31. https://doi.org/10.1080/03019233.2019.1641682

Yi, S H, Lee, W J, Lee, Y S and Kim, W H, 2021. *Korean J Met Mater,* 59:41 https://doi.org/10.3365/KJMM.2021.59.1.41

Theoretical and experimental approaches to determine the mass transfer coefficient in the steel/slag/refractory system

DOI: 10.62053/KESL5090

M Schickbichler[1], E Karimi-Sibaki[2], A Kharicha[3] and S K Michelic[4]

1. PhD student, Christian Doppler Laboratory for Inclusion Metallurgy in Advanced Steelmaking, Leoben Styria 8700; Chair of Ferrous Metallurgy, Leoben Styria 8700. Email: manuel.schickbichler@unileoben.ac.at
2. Privatdozent, Christian Doppler Laboratory for Metallurgical Applications of Magnetohydrodynamics, Leoben Styria 8700; Chair of Simulation and Modeling Metallurgical Processes, Leoben Styria 8700. Email: ebrahim.karimi-sibaki@unileoben.ac.at
3. Full Professor, Christian Doppler Laboratory for Metallurgical Applications of Magnetohydrodynamics, Leoben Styria 8700; Chair of Simulation and Modeling Metallurgical Processes, Leoben Styria 8700. Email: abdellah.kharicha@unileoben.ac.at
4. Full Professor, Christian Doppler Laboratory for Inclusion Metallurgy in Advanced Steelmaking, Leoben Styria 8700; Chair of Ferrous Metallurgy, Leoben Styria 8700. Email: susanne.michelic@unileoben.ac.at

ABSTRACT

The requirements for the controllability of metallurgical processes are increasingly becoming the focus of both industry and research. Advances in this field of research not only impact the stability of processes but often also influence the quality of the final product. One important way to examine processes in-depth, and thus show potential for improvement, is to describe them using physics-driven models. In metallurgy, thermodynamic and kinetic descriptions of interactions between individual components of a system are often used to describe and analyse important metallurgical phenomena across the entire process. However, for the creation of physics-based models, boundary conditions and process variables must be implemented to enable a description that is as realistic as possible. The collection and generalisation of boundary conditions and process variables is, therefore, an important step towards functional models.

The focus of this study is the determination of mass transfer coefficients between all components in a steel/slag/refractory system. For this purpose, experimental and theoretical methods are applied. Laboratory scale experiments are carried out in an induction furnace, and the mass transfer coefficients of the defined steel/slag/refractory system are calculated from changes in the chemical composition of the various components. Additionally, a calculation of the mass transfer coefficients based on dimensionless quantities is carried out. By comparing the values of the mass transfer coefficients determined theoretically and those determined experimentally in the trials, the suitability of the calculation is examined. The collection of mass transfer coefficients provides essential findings for future kinetic descriptions of inclusion modification based on the effective equilibrium reaction zone (EERZ) approach.

INTRODUCTION

The modelling of metallurgical processes is becoming increasingly important due to the ever-increasing demands on materials and process control. Two different approaches for developing models have become the main focus of current research. Data-driven models, such as those described by Boto *et al* (2022), are based on the computer-aided processing and analysis of historical data in order to establish relationships between process inputs and process outputs. In contrast, in physics-based models, as shown in the work of Scheller and Shu (2014), relationships between process inputs and process outputs are defined by physical laws. As Johansen *et al* (2023) have described, the advantage of physics-based models, despite the required in-depth knowledge of the process itself, is that no large amounts of historical data are required to develop the model, as is the case with the data-driven model. Kouraytem *et al* (2021) note that physics-based models are, therefore, more suitable, especially for production processes with many different end products.

One way of describing metallurgical processes, such as the modification of inclusions or the interaction of phases using physics-based models, is with the effective equilibrium reaction zone

(EERZ) model developed by Hsieh *et al* (1983). Ding *et al* (2000) describe this as a thermodynamic and kinetic model of the interaction between individual system components based on the consideration that a local thermodynamic equilibrium is reached at the interfaces of these system components. Using the EERZ model, several researchers (van Ende *et al*, 2011; You, Michelic and Bernhard, 2020; Goulart, Castro and Costa e Silva, 2023) have already investigated the processes in various metallurgical aggregates.

To describe the kinetics in the EERZ model, the mass transfer coefficients of the individual system components must be determined. One way to achieve this in the steel/slag/refractory system is to use the method described by Shin, Chung and Park (2017) to empirically determine these coefficients based on the change in the composition of the individual systems over time. Another method for determining mass transfer coefficients is to calculate them from dimensionless parameters of the respective interfaces, as described by Zhang and Xu (2003). Since complex flow conditions are often found in metallurgical processes, the method of computational fluid dynamics (CFD) is often used to determine the dimensionless coefficients, as in the work of Vollmann and Harmuth (2010).

To simulate the processes in the experimental system (induction furnace) used in this work, the interactions between the liquid phases and electromagnetic fields must be considered. This field of research, known as magnetohydrodynamics (MHD), has already been explored in detail by other researchers (eg. Al-Nasser *et al*, 2021; Kharicha *et al*, 2021; Zhang *et al*, 2022). Furthermore, Perminov and Nikulin (2016) specifically investigated flow conditions in induction furnac including MHD.

The present work focuses on the determination of mass transfer coefficients at laboratory scale, using the methods described in the same system. The associated comparison of the procedures is intended to demonstrate their equivalence. The aim is to enable a target-oriented selection of a determination method for mass transfer coefficients, even for processes for which one of the methods is not applicable. For future process descriptions based on the EERZ model, this represents a possibility for standardising the model creation in the future.

MATERIALS AND METHODS

To investigate the kinetic parameters in the present work, laboratory experiments were carried out in an Inductotherm 150 kg A/F-type induction furnace. An isostatically pressed magnesium/ aluminium spinel crucible with low values of silicon was used as a melting vessel. The respective charge materials (steel and steel/slag) were placed in the furnace for the test and inductively heated to a predetermined temperature. The temperature was controlled by adjusting the power applied and regularly measuring the temperature using immersion thermocouples. To prevent possible reactions between liquid phases and the atmosphere, the bath surface was flushed with argon throughout the experiment. The described test set-up is shown schematically in Figure 1. The set-up features a crucible with a diameter of 14 cm and a height of 27 cm. Additionally, the steel pool has a height of 10 cm, and the slag layer is 3 cm thick.

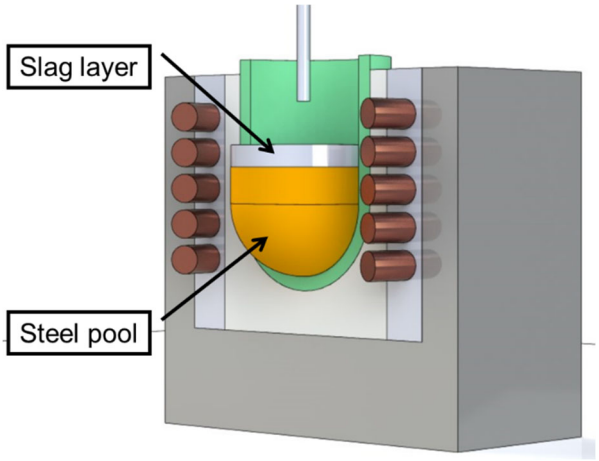

FIG 1 – Schematic representation of the experimental set-up.

The reactions of different phases and the associated changes in their compositions are described in this paper using the EERZ model. In considering the metallurgical processes, reaction zones are identified between all relevant phases. According to the model, a local thermodynamic equilibrium is established in the reaction zones at the interfaces of two phases in a defined time step. The quantities of phases that react with each other in the reaction zones are taken from a bulk zone that is not involved in the reaction at each reaction step. After the time step, in which a thermodynamic equilibrium is reached between the phases and the quantities of phases involved in the reaction zones change in their composition, these are reintegrated into the bulk zone of the respective phase and, thus, change the chemical composition of this for the next time step. The procedure described above makes it possible to investigate processes thermodynamically and kinetically, which in turn enables us to predict changes in concentration during the process. The sample crucible used, with the phases involved, the respective bulk zones and the reaction zones identified as relevant for this work, are shown schematically in Figure 2.

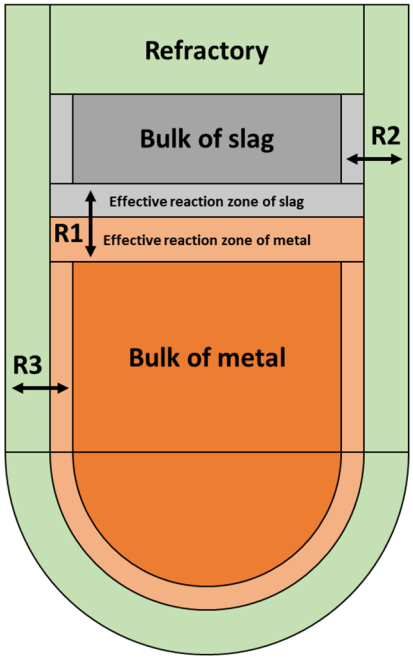

FIG 2 – Schematic representation of the reaction zones in the experimental set-up.

The following reactions between the two phases are examined within this work:

- R1: Reaction between liquid steel and slag.
- R2: Reaction between liquid slag and refractory material.
- R3: Reaction between liquid steel and refractory material.

Two different experiments were conducted in the induction furnace to investigate the described reactions. The specifications of those experiments are summarised in Table 1.

TABLE 1

Specifications of the conducted experiments.

Trial	Temp (°C)	Phases involved	Investigated reactions	Determined concentration curves
T1	1500	Steel (10 kg), refractory material	R3	Mg content
T2	1500	Steel (10 kg), Slag (2 kg), Refractory material	R1	Cr content
			R2	Mg content

High-speed steel was used for the tests. The chemical composition of the selected material with the DIN/EN designation HS6-5-3C is listed in Table 2.

TABLE 2

Chemical composition of the steel used in experiments T1 and T2.

C (wt%)	Si (wt%)	Mn (wt%)	Cr (wt%)	Mo (wt%)	V (wt%)	W (wt%)	S (wt%)	O (wt%)	Fe (wt%)
1.29	0.60	0.30	4.20	5.00	3.00	6.30	0.012	0.004	balance

The slag composition used in the tests is shown in Table 3. The slag for these tests was selected to present as a liquid phase at a planned test temperature of 1500°C. By performing a thermodynamic calculation using FactSage, the liquidus temperature of the slag was calculated to be 1404°C.

TABLE 3

Chemical composition of the slag used in experiment T2.

MgO (wt%)	SiO_2 (wt%)	CaO (wt%)
25	55	20

The tests aimed to produce concentration profiles of the different compounds over time. In order to determine these in defined time steps, steel samples were taken using unkilled lollipop samplers and slag samples via immersion sampling. The first sampling, performed shortly after the phases had completely melted, also marked the starting point of the subsequent analysis. The steel and slag samples were analysed using spark spectroscopy (SPECTROMAXx) and X-ray fluorescence analysis (ARL Fisons Instruments 8410), respectively.

Concept of calculation

To describe the phase reactions using the EERZ model, it is necessary to obtain the mass transfer coefficients (k_i) as determining kinetic parameters. So the zone thicknesses of the corresponding effective reaction zone can be calculated.

As shown by Shin, Chung and Park (2017), the mass transfer coefficients of the phases can be derived from the concentration curves of the bulk zones over time. The relations proposed by Jönsson and Jonsson (2001) for increasing and decreasing concentration curves, respectively, can be used for this purpose:

$$\frac{dMe_{BZ}[wt\%]}{dt} = k_i * \frac{\rho_i * A}{W_i} * (Me_{RZ}[wt\%] - Me_{BZ}[wt\%]) \quad (1)$$

$$\frac{dMe_{BZ}[wt\%]}{dt} = k_i * \frac{\rho_i * A}{W_i} * (Me_{BZ}[wt\%] - Me_{RZ}[wt\%]) \quad (2)$$

The values Me_{BZ} and Me_{RZ} represent the concentrations of the analysed metals in the bulk zone and the reaction zone, respectively. Furthermore, the variables ρ_i, W_i and A are the density, the total mass of the investigated phase and the contact surface on which the reaction takes place, respectively. Shin, Chung and Park (2017) showed that by including considerations of the equilibrium distributions of the investigated metals in the phases, a conversion of Equation 1 and Equation 2 is possible as follows:

$$-\left(\frac{Me_{eq}[wt\%]}{Me_0[wt\%]}\right) * \frac{W_i}{\rho_i * A} * \ln\left(\frac{Me_{BZ}[wt\%] - Me_{eq}[wt\%]}{Me_0[wt\%] - Me_{eq}[wt\%]}\right) = k_i * t \quad (3)$$

$$-\left(\frac{Me_0[wt\%] - Me_{eq}[wt\%]}{Me_0[wt\%]}\right) * \frac{W_i}{\rho_i * A} * \ln\left(\frac{Me_{BZ}[wt\%] - Me_{eq}[wt\%]}{Me_0[wt\%] - Me_{eq}[wt\%]}\right) = k_i * t \quad (4)$$

Here, the values Me_0 and Me_{eq} represent the concentration of the metal in the phase at time t=0 and the concentration of the metal in thermodynamic equilibrium, respectively.

By plotting the left part of Equation 3 or Equation 4 on the ordinate and the time on the abscissa of a diagram, the corresponding mass transfer coefficient can be obtained from the slope of a regression line placed on the curve. The values Me_{BZ} for the respective times and Me_0 are determined from the concentration curves resulting from the induction furnace experiments. The values for W_i, ρ_i and A are defined by the specifications of the respective test (shown in Table 1). To obtain Me_{eq}, thermodynamic calculations were also carried out using FactSage for the respective systems.

Concept of simulation

A CFD simulation of the system, shown in Figure 1, was conducted as a further method of determining the effective mass transfer coefficients. Considering the symmetrical aspects of geometry, a 2D axisymmetric computational domain is assumed for the calculation. Also, it is considered that slag and steel are isothermal, with the temperature specified in the system. The analysis involves solving the electromagnetic and flow fields in the molten slag and steel under the assumption that the interface between slag and steel remains stationary. The finite volume method (FVM) is employed for solving the governing equations of the flow and magnetic field. These equations, along with the boundary conditions, are implemented in ANSYS Fluent v.15.0 using user-defined functions (UDF), as referenced in the work of Karimi-Sibaki *et al* (2018). The calculated time-averaged Lorentz force is incorporated as a source term in the momentum equation, following guidelines described by Karimi-Sibaki *et al* (2018). Since the system is considered isothermal, thermal buoyancy effects are neglected, leading to flow driven solely by the Lorentz force. This results in the generation of the well-known electro-vortex flow within the slag and steel.

The outcomes of the simulation yielded the velocity field within the distinct phases involved. Also, simulation results provided the distribution of velocity magnitude along the interfaces. To compute the mass transfer coefficients at these interfaces, it is necessary to calculate the mean Reynolds number (Re) and the mean Schmidt number (Sc) as follows:

$$Re = \frac{\bar{u} * L}{\nu} \tag{5}$$

$$Sc = \frac{\nu}{D} \tag{6}$$

The variables $\bar{u}$, L, v and D are the mean values of the characteristic velocity over the length of the respective interface, the characteristic length, the kinematic viscosity, and the diffusion coefficient of the investigated species, respectively.

The Sherwood number (Sh) can subsequently be calculated from the resulting values for Re and Sc for each of the interfaces between phases as a further dimensionless parameter. For this purpose, the empirical relationship developed by Vollmann and Harmuth (2010) for rotational disks is applied.

$$Sh = 1.468 * Re^{0.526} * Sc^{0.199} \tag{7}$$

Finally, the described relationship (Equation 7) can be equated with the generally valid definition of Sh which is shown in Equation 8, and the mass transfer coefficient at the respective interface can be calculated. In this context, Sh is generally formulated as follows:

$$Sh = \frac{k_i * L}{D} \tag{8}$$

RESULTS

The course of the Mg content in the steel over time for test T1 is shown together with the evaluation of the measuring points according to Equation 2 in Figure 3. Only the interaction between liquid steel and refractory material was investigated in this experiment. The slope of the regression line in Figure 3 indicates that the mass transfer of the steel at the interface of the system d has a value of $k_{st\text{-}ref} = 6 \times 10^{-7}$ m/s.

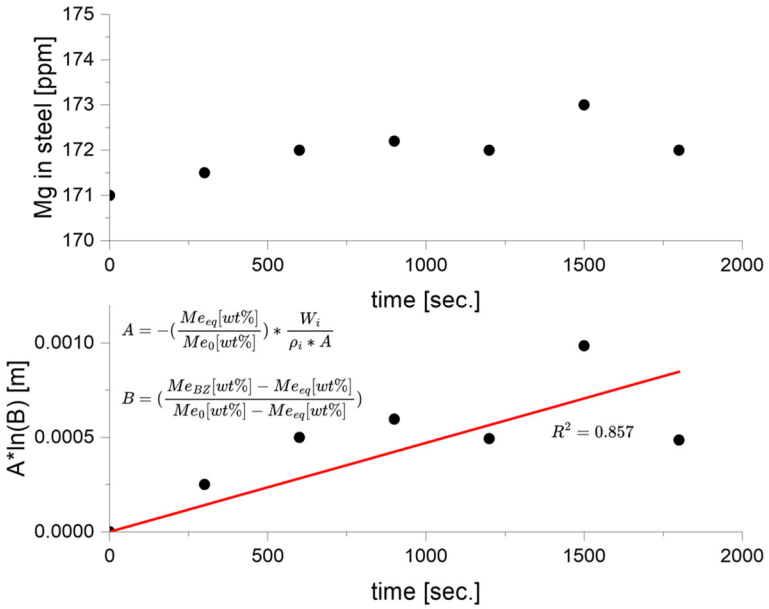

FIG 3 – Development of the Mg content in steel over time in experiment T1, together with the corresponding evaluation.

In experiment T2, the slag phase was included in addition to the steel phase, as described in Table 2. The interaction between liquid slag and refractory material described in Figure 2 was investigated via the Mg content curve in the slag (see Figure 4). In the set-up of test T2, in addition to the interaction investigated, Mg intake in the slag can also occur due to interaction between steel and refractory material and subsequent interaction between steel and slag. In experiment T1, however, it could be shown that the Mg uptake into the steel phase already assumes such a low value (see Figure 3) that it is acceptable to attribute the increase in the Mg content in the slag to the interaction between slag and refractory material. With this consideration, the slope of the regression line shown in Figure 4 of the measurement point evaluation according to Equation 2 results in a mass transfer coefficient of the slag at the corresponding interface of $k_{sl\text{-}ref}$ = 1 × 10^{-5} m/s.

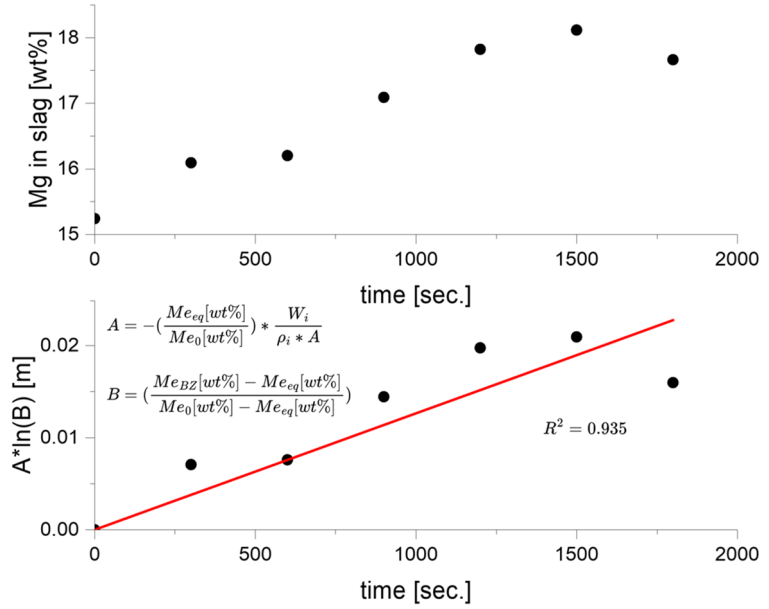

FIG 4 – Development of the Mg content in slag over time in experiment T2, together with t he corresponding evaluation.

In order to investigate the interaction between liquid steel and slag, the mass transfer coefficients of both the steel and the slag in the described reaction zone were determined in experiment T2. For this purpose, the course of the Cr content in both phases was investigated. The Cr curve in the steel

phase is plotted in Figure 5. Since this curve shows a negative trend, the measuring points in Figure 5 were evaluated according to Equation 4. The slope of the regression line introduced in Figure 5 shows that the steel at the interface between steel and slag has a mass transfer coefficient of $k_{st\text{-}sl}$ = 2 × 10^{-5} m/s.

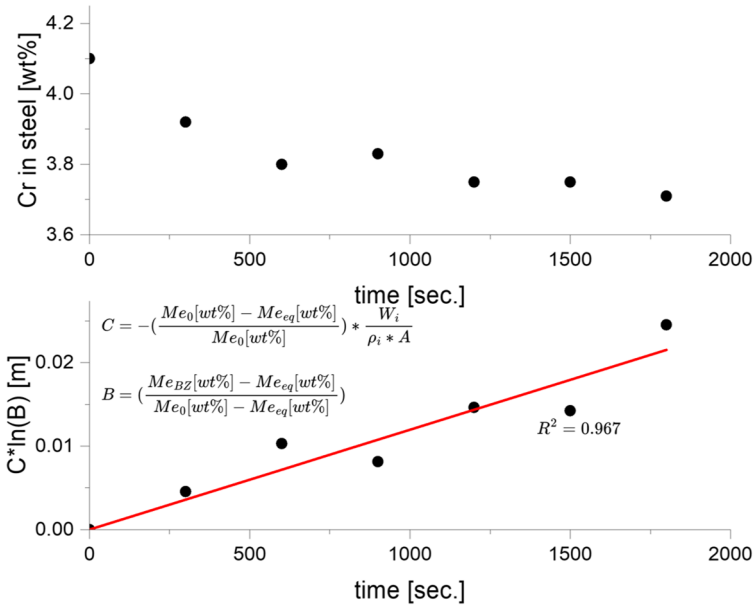

FIG 5 – Development of the Cr content in steel over time in experiment T2, together with the corresponding evaluation.

To determine the mass transfer coefficient of the slag at the steel/slag interface, the Cr curve in the slag, shown in Figure 6, was analysed. For this purpose, the measuring points were also evaluated according to Equation 3, and these are shown in Figure 6. The slope of the introduced regression curve shows that the mass transfer coefficient of the slag in this system holds a value of $k_{sl\text{-}st}$ = 5 × 10^{-6} m/s.

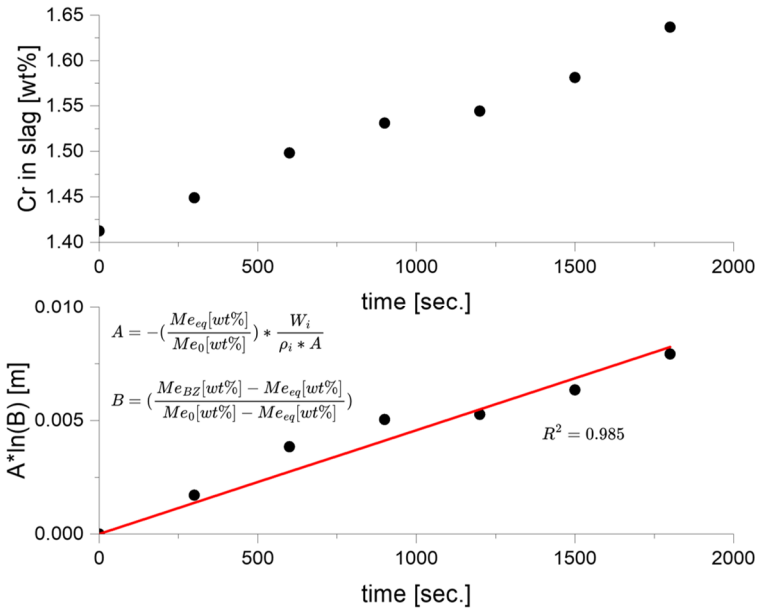

FIG 6 – Development of the Cr content in steel over time in experiment T2, together with the corresponding evaluation.

Figure 7 displays the results from the CFD simulation of the induction furnace, focusing on the velocity field in the slag and steel phases. The simulation reveals distinct flow characteristics in the phase domains, including the formation of vortices in both the slag and steel phases. Also, the

computed velocity distributions at the interfaces, capturing the specific flow characteristics at the phase boundaries, are the necessary data for additional calculations to determine the mass transfer coefficients.

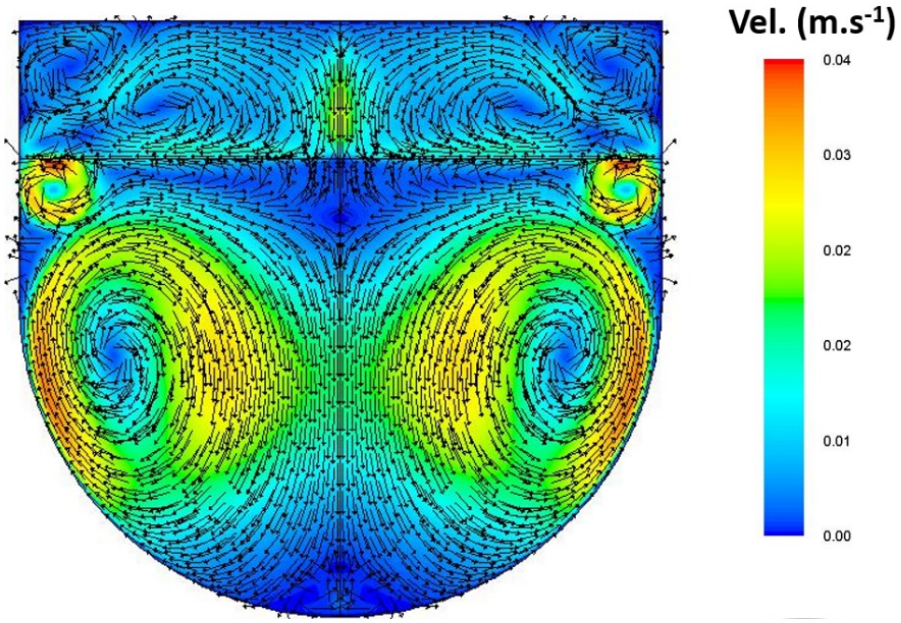

FIG 7 – Velocity field obtained from CFD simulation.

To calculate the mass transfer coefficients from the velocity profiles obtained along the phase interfaces, the previously described method of calculation using the dimensionless numbers was applied for each phase. The diffusion coefficients required for the calculation were taken from the literature for similar systems and are summarised in Table 4.

TABLE 4

Diffusion coefficients used for the calculation of the mass transfer coefficients (based on the simulation).

System	Diffusion coefficient (m^2/s)	Source
MgO in steel	2.7×10^{-10}	Lei and He (2012)
MgO in slag	1×10^{-8}	Amini *et al* (2006)
Cr in steel	3.04×10^{-9}	Ono *et al* (1975)
Cr in slag	4.16×10^{-10}	Park, Song and Min (2004)

The kinematic viscosity of the steel required for the calculation was determined by measurements using high-temperature viscometry. Meanwhile, the kinematic viscosity of the slag was estimated with FactSage Viscosity 8.3 using the Melts database.

The mass transfer coefficients for the different interfaces calculated in the described manner are summarised in Table 5.

TABLE 5

Results of the calculation of the mass transfer coefficients based on the simulation.

Phase interface	Simulated mass transfer coefficients (m/s)
Steel/Refractory	1.7×10^{-6}
Slag/Refractory	8.5×10^{-6}
Steel/Slag	2.2×10^{-5}
Slag/Steel	1.6×10^{-6}

DISCUSSION

To compare both methods for determining the mass transfer coefficients at the respective interfaces, the resulting values for each method are listed in Table 6. The values of both methods are in the same order of magnitude but show a different degree of deviation in each case.

TABLE 6

Comparison of the values obtained for the mass transfer coefficients.

Phase interface	Mass transfer coefficients (experiments) (m/s)	Mass transfer coefficients (simulation) (m/s)
Steel/Refractory	6.6×10^{-7}	1.7×10^{-6}
Slag/Refractory	1.1×10^{-5}	8.5×10^{-6}
Steel/Slag	1.4×10^{-5}	2.2×10^{-5}
Slag/Steel	5.2×10^{-6}	1.6×10^{-6}

The deviations between the experimental method and the simulation can be explained by the assumptions made in the simulation itself and in the subsequent calculation based on it. At those phase interfaces where steel is the investigated phase (Steel/Refractory and Steel/Slag) there is an overestimation of the simulation results compared to the experimentally determined values for the mass transfer coefficients. In contrast, an underestimation can be seen at those phase interfaces where slag is the investigated phase (Slag/Refractory and Slag/Steel). Those findings could be connected to the fact that the kinematic viscosities of steel and slag were determined in different ways. A more realistic representation and an alignment of the experimental and simulation results may be possible if the electrical and rheological parameters of the slag were determined by actual measurements and not, as is the case in this work, based on empirical values. The estimates of the diffusion coefficients obtained from the literature should also be mentioned as a possible source of error, as they are partly based on systems that slightly differ from the actual test set-up.

With regard to the usability of the collected mass transfer coefficients in the described physics-based models for determining the metallurgical processes during the test, initial calculations already show promising results. Both the mass transfer coefficients determined experimentally, and those calculated on the basis of the simulation were used to analyse the process using the EERZ model. The results, thus, obtained show good agreement with the compositional curves of steel and slag experimentally determined over the process duration. The details of the modelling will be referred to in future work.

CONCLUSIONS

Due to the increasing demands on steel materials in terms of sustainability, applicability in increasingly critical areas of use and challenging economic conditions, the controllability of manufacturing processes is increasingly becoming the focus of both research and industry. The physics-based modelling of individual processes and process chains presents an opportunity to solve the challenges mentioned in a targeted manner. In the field of metallurgy, thermodynamic and

kinetic modelling, which are based on the EERZ model, are widely used. This type of model makes it possible to understand metallurgical phenomena during the production cycle over time and, thus, gain in-depth knowledge about the processes themselves. The focus of the present work is to determine the mass transfer coefficients, an important kinetic parameter for the modelling of processes using EERZ models, using different methods and, thus, comparing the suitability of the methods. For this purpose, experiments were performed under controlled conditions and a simulation was conducted, with subsequent calculations of those tests including the conditions.

The values for the mass transfer coefficients at the respective interfaces obtained using the two methods show that both approaches lead to applicable results. This can be concluded based on the respective results having the same order of magnitude and the characteristics corresponding well with the results from the literature for similar systems. Furthermore, the first experimental use of the results based on the different methods in EERZ models of the experiment shows, in both cases, a good agreement with the experimentally determined concentration curves of the phases over time.

While the values for the mass transfer coefficients at the respective interfaces determined using different methods agree well with each other and with the literature for similar systems, it is important to determine the sources for the deviations that can be found between the experimental method and the simulation. These deviations may primarily result from the assumptions made in the simulation and the subsequent calculations. The use of empirical estimates instead of actual measurements, especially when determining the parameters of the slag, leads to potential inaccuracies. The next step would be to measure these parameters specifically for the test systems and models used. This, and a repeated verification of the mass transfer coefficients obtained by means of experiments, will be the subject of further research.

ACKNOWLEDGEMENTS

The financial support by the Austrian Federal Ministry for Labour and Economy, the National Foundation for Research, Technology and Development, and the Christian Doppler Research Association is gratefully acknowledged.

REFERENCES

Al-Nasser, M, Kharicha, A, Barati, H, Pichler, C, Hackl, G, Gruber, M, Ishmurzin, A, Redl, C, Wu, M and Ludwig, A, 2021. Toward a simplified arc impingement model in a direct-current electric arc furnace, *Metals*, 11(9):1482.

Amini, S, Brungs, M, Jahanshahi, S and Ostrovski, O, 2006. Effects of additives and temperature on the dissolution rate and diffusivity of MgO in CaO–Al_2O_3 slags under forced convection, *ISIJ International*, 46(11):1554–1559.

Boto, F, Murua, M, Gutierrez, T, Casado, S, Carrillo, A and Arteaga, A, 2022. Data driven performance prediction in steel making, *Metals*, 12(2):172.

Ding, R, Blanpain, B, Jones, P T and Wollants, P, 2000. Modeling of the vacuum oxygen decarburization refining process, *Metallurgical and Materials Transactions B,* 31(1):197–206.

Goulart, L L d O, Castro, J A de and Costa e Silva, A, 2023. Development of a computational thermodynamics EERZ model for the improvement of hot rolled light steel profiles steel refining, *CALPHAD*, 81:102550.

Hsieh, Y, Watanabe, Y, Asai, S and Muchi, I, 1983. Effect of recirculating flow rate of molten steel in refining processes, *Tetsu-to-Hagane*, 69(6):596–603.

Johansen, S T, Løvfall, B T, Duran, T R and Zoric, J, 2023. Pragmatism in industrial modelling, applied to 'ladle lifetime in the steel industry, Prepared for JSAIMM special edition on Computational Modelling. Available from: <https://arxiv.org/pdf/2302.14650.pdf>

Jönsson, P G and Jonsson, L T I, 2001. The use of fundamental process models in studying ladle refining operations, *ISIJ International*, 41(11):1289–1302.

Karimi-Sibaki, E, Kharicha, A, Wu, M, Ludwig, A, Bohacek, J, Holzgruber, H, Ofner, B, Scheriau, A and Kubin, M, 2018. A multiphysics model of the electroslag rapid remelting (ESRR) process, *Applied Thermal Engineering*, 130:1062–1069.

Kharicha, A, Karimi-Sibaki, E, Vakhrushev, A, Wu, M, Ludwig, A and Bohacek, J, 2021. Hydrodynamically enhanced electrochemical mass transfer on the surface of an electrically conductive droplet, *Heat and Mass Transfer*, 57(10):1697–1705.

Kouraytem, N, Li, X, Tan, W, Kappes, B and Spear, A D, 2021. Modeling process–structure–property relationships in metal additive manufacturing: a review on physics-driven versus data-driven approaches, *Journal of Physics*: *Materials*, 4(3):32002.

Lei, H and He, J, 2012. Nucleation and growth kinetics of MgO in molten steel, *Journal of Materials Science and Technology*, 28(7):642–646.

Ono, Y and Matsumoto, S, 1975. Diffusion of chromium, manganese and nickel in molten iron, *Transactions of the Japan Institute of Metals*, 16(7):415–422.

Park, J H, Song, H S and Min, D J, 2004. Reduction behavior of EAF slags containing Cr_2O_3 using aluminum at 1793 K, *ISIJ International*, 44(5):790–794.

Perminov, A V and Nikulin, I L, 2016. Mathematical model of the processes of heat and mass transfer and diffusion of the magnetic field in an induction furnace, *Journal of Engineering Physics and Thermophysics*, 89(2):397–409.

Scheller, P R and Shu, Q, 2014. Inclusion development in steel during ladle metallurgical treatment - a process simulation model – part: industrial validation, *Steel Research International*, 85(8):1310–1316.

Shin, J H, Chung, Y and Park, J H, 2017. Refractory–slag–metal–inclusion multiphase reactions modeling using computational thermodynamics: kinetic model for prediction of inclusion evolution in molten steel, *Metallurgical and Materials Transactions B,* 48(1):46–59.

van Ende, M-A, Kim, Y-M, Cho, M-K, Choi, J and Jung, I-H, 2011. A kinetic model for the Ruhrstahl Heraeus (RH) degassing process, *Metallurgical and Materials Transactions B,* 42(3):477–489.

Vollmann, S and Harmuth, H, 2010. Investigation of refractory corrosion of a gas-stirred steel ladle by simulation, in *12th International Ceramics Congress Part I*, *Advances in Science and Technology, Refractories: Recent Developments in Materials, Production and Use*, pp 199–204 (Trans Tech Publications Ltd: Switzerland).

You, D, Michelic, S K and Bernhard, C, 2020. Modeling of ladle refining process considering mixing and chemical reaction, *Steel Research International*, 91(11).

Zhang, H, Wu, M, Zhang, Z, Ludwig, A, Kharicha, A, Rónaföldi, A, Roósz, A, Veres, Z and Svéda, M, 2022. Experimental evaluation of MHD modeling of EMS during continuous casting, *Metallurgical and Materials Transactions B,* 53(4):2166–2181.

Zhang, Y and Xu, Z, 2003. Kinetics of convective crystal dissolution and melting, with applications to methane hydrate dissolution and dissociation in seawater, *Earth and Planetary Science Letters*, 213(1–2):133–148.

Sulfur loss from the slag during desulfurisation of liquid steel

DOI: 10.62053/WYIP1331

A Sharma[1], M Jain[2], S Kumar[3], S Karosiya[4], M M Pande[5], N N Viswanathan[6] and D Kumar[7]

1. Deputy Manager, JSW Steel, Dolvi, Mumbai 402107, India. Email: anurag.sharma1@jsw.in
2. Manager, JSW Steel, Dolvi, Mumbai 402107, India. Email: manish.jain@jsw.in
3. Graduate student, Metallurgical Engineering and Materials Science, Indian Institute of Technology Bombay, Mumbai 400076, India. Email: sandeep_kumar@iitb.ac.in
4. Graduate student, Metallurgical Engineering and Materials Science, Indian Institute of Technology Bombay, Mumbai 400076, India. Email: 22m1879@iitb.ac.in
5. Assistant Professor, Metallurgical Engineering and Materials Science, Indian Institute of Technology Bombay, Mumbai 400076, India. Email: manish.pande@iitb.ac.in
6. Sajjan Jindal Steel Chair Professor, Metallurgical Engineering and Materials Science, Indian Institute of Technology Bombay, Mumbai 400076, India. Email: vichu@iitb.ac.in
7. Assistant Professor, Metallurgical Engineering and Materials Science, Indian Institute of Technology Bombay, Mumbai 400076, India. Email: deepook@iitb.ac.in

ABSTRACT

Desulfurisation of steel during ladle refining is governed by both thermodynamics and kinetics. For effective desulfurisation, thermodynamically, a low partial pressure of oxygen at the steel-slag interface and highly basic slag which possess a large sulfide capacity are desired. Kinetically, the mass transfer coefficient of sulfur in the liquid steel and in the slag determines the rate of desulfurisation. A fast desulfurisation rate is achieved by maintaining sufficiently strong argon stirring of the melt.

In the present work, sulfur mass balance for steel and slag was performed after the desulfurisation treatment for several industrial heats. The decrease in the sulfur quantity of the liquid steel was more than the increase in the sulfur quantity of the slag. The discrepancy in the sulfur mass balance suggests that the sulfur could be transferred to: (a) the gas (via slag) phase; or to (b) the refractory (crucible) phase. The preliminary investigation of the refractory samples taken at slag-refractory and steel-refractory interface showed no interaction of sulfur with the refractory. Therefore, the possibility of sulfur transfer to the gas phase was verified by carrying out melting experiments of sulfur containing slag in an argon/air atmosphere. Sulfur containing slag was initially melted in an MgO-C crucible under an argon atmosphere followed by creating the air atmosphere just above the melt. Careful sampling and analysis from the cold spots of the crucible, much above the melt surface, revealed formation of a fibrous structure. Scanning electron microscopy energy dispersive X-ray spectroscopy (SEM-EDS) analysis of these fibrous deposits confirmed the presence of oxides and sulfides. Oxidation of sulfur containing slag under air atmosphere was also performed using a thermogravimetric analysis (TGA) set-up. It showed a constant sulfur loss in the range of 1300–1500°C. Thermodynamic calculations carried out using FactSage™ ver 8.3 for these experimental conditions are in good agreement with the observed results.

INTRODUCTION

Delsulfurisation is one of the main tasks performed at the ladle refining steel for many steel grades. The mechanism of desulfurisation is well established. The sulfur removal from steel is typically described using the following chemical reaction: $[S] + (O^{2-}) = [O] + (S^{2-})$, where [] and () represent species in the liquid steel and slag respectively. It is understood that low dissolved oxygen in steel and availability of free oxide ion in the slag favour the desulfurisation process. These can be considered equivalent to higher aluminium level in steel and CaO level in slag. Hence, steel-slag desulfurisation reaction is also written as: $[S] + (CaO) + 2/3[Al] = (CaS) + 1/3(Al_2O_3)$. It is important to mind lime saturation level in the slag. Bannenberg, Bergmann and Gaye (1992) showed that there exists an optimum level of lime addition that is beneficial for desulfurisation. Any addition beyond that point can bring down desulfurisation as mass transfer in the slag slows down in the presence of solids. Roy, Pistorius and Fruehan (2013) highlighted the role of parasitic reactions such as reduction of SiO_2, FeO and MnO leading to depletion of aluminium and its effect on retardation of

desulfurisation reaction. Kinetically, the desulfurisation reaction is considered to be controlled by mass transfer in both steel and slag phase.

The interaction of the melt with the atmosphere is also of great importance. For example, the reoxidation of liquid steel at the slag eye can significantly impact the extent of steel-slag reaction and aluminium consumption during the ladle refining process. However, there are not many studies focused on the impact of slag-gas reaction on desulfurisation reaction. Fincham and Richardson (1954) reported that slag stores sulfur as sulfide ions for the partial pressure of oxygen below 10^{-5} atm and the storage capacity is presented as sulfide capacity of the slag. This range of partial pressure is relevant at the steel-slag interface. However, at slag-gas interface, pO_2 may be higher and there could be formation of sulfate ions in the slag. The interaction of the molten slag with air is also important from the perspective of utilisation of spent ladle slag which is often limited by its sulfur content. Pelton, See and Elliott (1974) performed kinetic studies on evolution of SO_2 during oxidation of slag at varied pO_2. They reported that the SO_2 evolution is rapid at low oxygen partial pressure (less than 0.1 atm) but becomes chemical kinetics limited at higher pO_2 level probably due to surface poisoning. Allertz and Sichen (2015) reported a similar study. However, in their work, the effect of the partial pressure of oxygen was not significant. The reaction rate, albeit slower, was found to be limited by the surface area at the slag-gas atmosphere. Wu *et al* (2021) reported the utilisation of a mixture of $CaSO_4$ and $CaSO_3$ to remove sulfur present as CaS in the slag. The kinetics of sulfur removal using this method was much slower than that reported by previous studies. Zhao, Lin and Wu (2016) reported oxidation of sulfur from the slag at high temperatures by flowing air. It was shown that up to 90 per cent of the sulfur could be removed within one hour. The method can be potential useful for utilisation of spent ladle refining slag.

In this work, the slag-air interaction is studied at different scales – industrial, laboratory scale induction furnace and using thermogravimetric techniques. Several steel and slag samples were collected during four industrial heats and sulfur balance was performed. It revealed the possibility of sulfur loss from slag potentially due to oxidation of sulfur in the slag by air. This was studied in a very carefully designed experiments using induction furnace. The slag was melted in an MgO-C crucible prepared from ladle bricks. Slag oxidation was carried out by passing air over molten slag. Similar experiments were carried out at a smaller scale using thermogravimetric technique. The rate of weight loss was recorded during the experiment.

PLANT OBSERVATION

Preliminary sulfur analysis of steel and slag analysis showed significant sulfur loss from the system during ladle refining of low carbon Al-killed steels. Four heats were closely tracked to understand the behaviour of sulfur. Steel and slag samples were periodically taken for sulfur analysis. Typical aluminium concentration in these heats were in the range of 0.03–0.05 per cent. A basic slag was used; typical composition: 55 per cent CaO, 32 per cent Al_2O_3, 8 per cent MgO, 3 per cent SiO_2, 1 per cent FeO, 1 per cent S. the steel and slag weight towards end of the refining process were about 200 t and 3.5 t respectively. The slag mass was estimated by considering about 0.7 t of the carryover slag from ConArc furnace and additions made at the ladle refining station. Initial and final concentration of sulfur in steel and slag, as measured using LECO, are shown in Table 1. The final sulfur concentration in the product was in the range of 50–70 ppm. It can be clearly seen that the increase in the sulfur concentration in the slag is much less than that expected from the sulfur loss from the steel. For example, for 220 ppm of sulfur loss from the steel (Heat-B), there should be 1.05 per cent sulfur gain in the slag. Hence, significant amount of sulfur seems to be escaping the system.

TABLE 1

Sulfur analysis results for four heats.

Heat	Sample	[S] ppm	(%S)
A	Initial	330	0.39
	Final (108 min)	70	0.82
B	Initial	280	0.49
	Final (55 min)	60	0.76
C	Initial	200	0.57
	Final (45 min)	60	0.80
D	Initial	180	0.66
	Final (48 min)	50	0.82

Sulfur analysis of steel and slag samples collected during these four heats were used to calculate the percentage of sulfur not accounted in the steel + slag system. The percentage was calculated with respect to combined initial sulfur amounts in steel and slag. Figure 1 shows the increase in sulfur loss percentage with time during the ladle refining process. The rate of sulfur loss is almost similar for Heats-A, B and D. Overall, the sulfur loss varies from ~20–40 per cent.

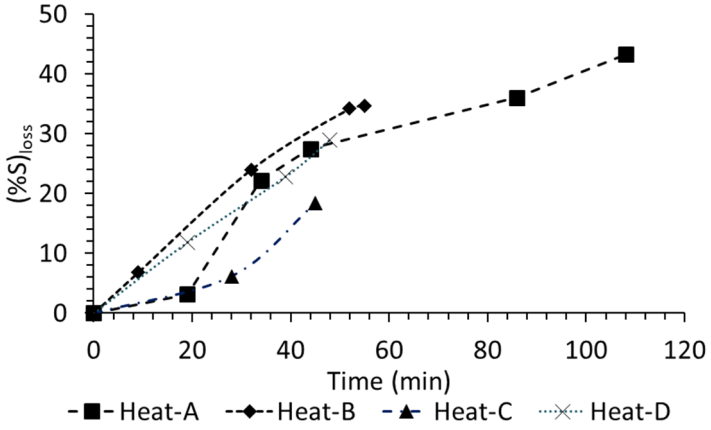

FIG 1 – Sulfur loss with time for four heats.

The refractory samples taken from the slag and steel region and analysed for sulfur using LECO. The sulfur amount at both locations were similar and relatively low (0.1–0.3 per cent) at the end of the refractory life. Such small sulfur concentration is likely due to sulfide ions present in the slag and in the glaze layer. There was no clear evidence of sulfur removal through refractory based on this analysis. The likely reason for the sulfur loss is the oxidation of the slag in contact with air. The extent and rate of sulfur loss through this mechanism is expected to depend on: 1) the partial pressure of SO_2 at the slag-air interface; 2) the rate of desulfurisation of liquid steel; and 3) the rate of mixing of slag due to argon stirring of the melt. The mass transport in the gas phase and oxidation reaction of sulfur are not expected to be rate limiting due to continuous supply of argon gas and high temperature of the process.

In order to test the feasibility of sulfur loss due to oxidation of slag, laboratory scale experiments were designed using induction furnace and thermogravimetric analysis (TGA) set-up.

LABORATORY EXPERIMENTS

Induction furnace experiments

Oxidation of sulfur from the slag in the presence of air was studied by passing air over molten slag. Slag composition was selected based on expected slag composition during ladle refining process. Two slag compositions were prepared, see Table 2. Appropriate amounts of oxides were premelted in a graphite crucible at 1550°C. The premleted slag was crushed and decarburised before performing slag oxidation experiments. Slag oxidation experiments were performed at 1550°C in a MgO-C crucible of internal diameter 5.5 cm, wall thickness 1 cm and height 17 cm. The crucibles were prepared by machining MgO-C refractory bricks used for the steel refining ladle. Figure 2 shows a schematic of the induction furnace and related set-up for conducting slag oxidation experiments. The induction furnace set-up was placed in a stainless steel chamber. The chamber was first evacuated to 10^3 Pa using a rotary pump. Subsequently the chamber was filled with gettered argon. The argon was passed through a moisture trap followed by passing it over tubes containing copper and magnesium chips at 400°C to remove residual oxygen. The slag was re-melted under argon atmosphere at 1550°C. After 10 mins of homogenisation, melting was confirmed by dipping a mild steel rod. The stainless steel chamber has a port directly above the melt to making additions. 10 g of FeS was added in the form of chunk by dropping it from the feeding tube inserted through the port. The port is normally closed with a silicon stopper. After melting of the slag, the port was opened and a 12.7 mm diameter mild steel tube was inserted to flow air at 500 sccm over the molten slag. Two experiments were conducted to ensure repeatability of the observation. Table 3 describes three experiments conducted using induction furnace. It should be noted that the experiment I-1 is essentially a slag premelting work for a similar slag composition. It serves as a blank experiment for the purpose of study of evaporation from molten slag under these experimental conditions. Three slag samples were collected during I-2 experiment by dipping a mild steel rod in the molten slag. The frozen slag layer over the mild steel rod was broken out, crushed and analysed for sulfur concentration using LECO. These three samples were taken as: after remelting (I2S1), after FeS addition (I2S2) and after completion of air blowing (I2S3).

TABLE 2

Composition of premelted slag.

	%CaO	%MgO	$\%SiO_2$	$\%Al_2O_3$	%FeO	%MnO	Tm*
Slag-1	47	7	4.5	40	1.5	0	1350°C
Slag-2	46.6	6.8	4.5	40.1	1.5	0.71	1340°C

*T_m estimated from FactSage™ (Bale *et al,* 2016) corresponds to 95 per cent liquid.

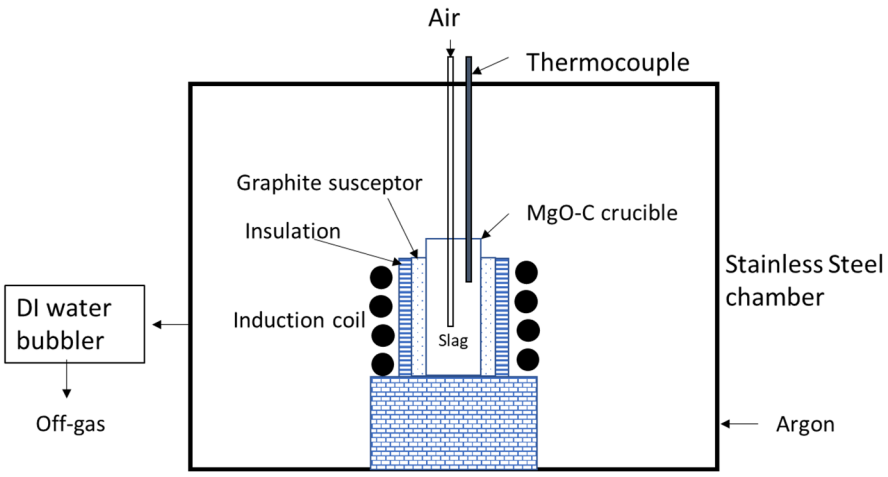

FIG 2 – Schematic of induction furnace set-up.

TABLE 3

Description of induction furnace experiments.

Exp.#	Slag composition and amount	Crucible	FeS added in molten slag	Air flow over molten slag
I-1	Slag-1, 600 g	Graphite	No	No
I-2	Slag-2, 200 g	MgO-C	Yes, 10 g	Yes, 500 sccm for 20 mins
I-3	Slag-2, 120 g	MgO-C	Yes, 10 g	

TGA experiment

Thermogravitmetric analysis (TGA) experiments were performed to accurately estimate the sulfur removal from the ladle refining slag. About 90 g of the premelted slag-1 (see Table 1 for slag composition) was pulverised in a vibrating cup mill for 4 mins to ensure chemical homogeneity of the slag. The powdered slag was decarburised by placing it in a muffle furnace 950°C for 3 hrs. Two experiments (T1 and No.2) for the TGA of the slag were performed using Netzsch STA 449 F1 instrument. In these experiments, slag was placed in a platinum crucible and exposed to air (60 sccm) at a high temperature: 1300–1500°C. The samples were heated under argon atmosphere at the rate of 20°C/min. The heating rate was reduced to 5°C/min to allow the reaction between slag and air, if any.

TABLE 4

TGA experiment conditions.

Exp.#	Slag amount	FeS amount	Air flow condition
T-1	7 mg	0	60 sccm, 1300–1500°C, heating rate: 5°C/min
T-2	4.4 mg	0.6 mg	

In Experiment T-1, 7 mg of the powdered slag sample is taken in platinum crucible. The sample is heated to 1300°C at 20°C/min in the argon atmosphere and then to 1500°C at 5°C/min in the air atmosphere. Further, the sample is cooled to room temperature in argon atmosphere. In Experiment T-2, 5 mg of the sample is taken from a mixture of slag-1 and powdered FeS (8.8 g of slag with 1.2 g of FeS). Thermal profile as well as gas atmosphere were maintained in a manner similar to experiment T-1.

RESULTS AND DISCUSSION

The primary interest for conducting induction furnace experiment was to observe interaction between molten slag and gas phase. Based on the work of Kumar and Pistorius (2017), further reaction in the gas phase followed by deposition of the solid products at colder regions were expected. Hence, crucible walls above the induction coil was carefully observed for all experiments. Figure 3 shows the scanning electron microscopy energy dispersive X-ray spectroscopy (SEM-EDS) analysis of the fibrous deposits found on top of the graphite crucible wall. The deposit includes fibrous structure and micro-aggregates of MgO. High resolution image in Figure 3a shows that fibre thickness is about a micrometre or less. Many globular tips are observed in the fibrous structure, see bright regions of Figure 3b. The EDS analysis show presence of iron at those bright tips. Since FeO-MgO forms a liquid phase at this temperature, the likely growth mechanism is vapor-liquid-solid. The Mg and iron vapor forms due to reaction between slag and graphite crucible. FeO condenses at the top wall of the crucible (colder region). MgO dissolves in FeO and the supersaturation leads to the formation of MgO fibre. The presence of MgO micro-aggregates is likely through vapor-solid growth mechanism ie Mg and O in the gas phase reacts and deposits on MgO crucible wall. It is not clear whether graphite crucible acts as a substrate or pre-existing MgO fibre.

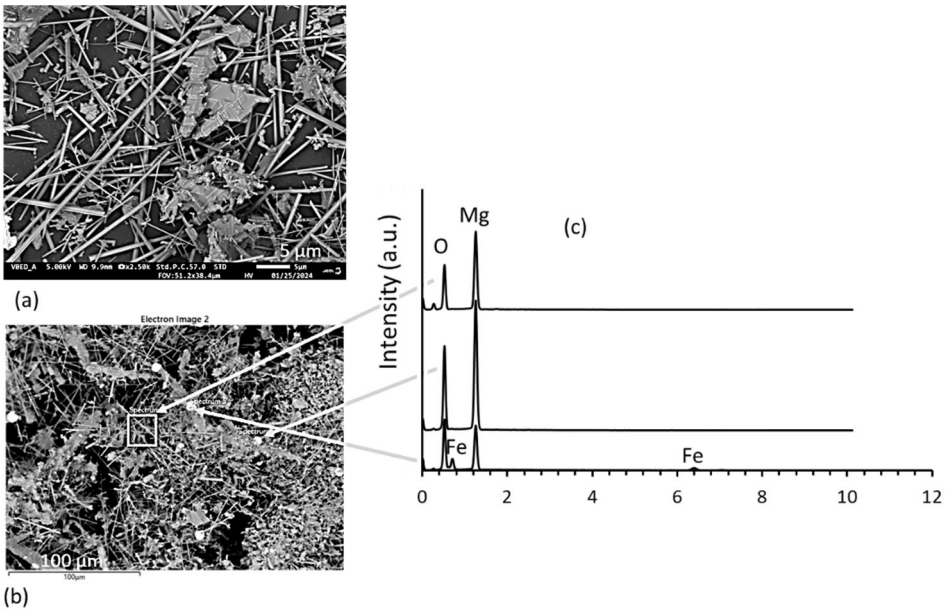

FIG 3 – SEM analysis of fibrous deposit on top of the crucible wall for experiment I-1: (a) high resolution image of deposit; (b) showing spots for EDS analysis; and (c) EDS spectra of various locations.

Experiments I-2 and I-3 are very similar. Table 5 shows the Sulfur analysis of slag samples taken during experiment I-2. 5 per cent FeS was added in the slag which corresponds to 1.8 per cent of sulfur in the slag. Sulfur concentration in the slag after FeS addition was found to be 1.4 per cent. The Sulfur addition looks reasonable. The sample taken after air purging show a remarkable decrease in sulfur concentration in the slag indicating oxidation of Sulfur from the slag during air blowing. Fibrous deposits were observed on top of the MgO-C crucible wall after both experiments I-2 and I-3. Figure 4 shows SEM-EDS analysis of the fibrous structure observed after experiment I-3. The EDS analysis of the fibre shows that these are primarily MgO. MgO formation is likely due to reduction of MgO from slag or MgO-C bricks by carbon. Sulfur is present in the structure in three forms as illustrated in the EDS spectra: a) Fe-S; b) Mn-S; and c) small amount of Ca-S. It is not clear whether these are sulfides or sulfates of iron, manganese and calcium. The removal of Sulfur from the slag during the oxidation experiment is clearly evident. The presence of almost iron free $MnS/MnSO_4$ further confirms that the source of Sulfur is not just reaction between FeS added and air.

TABLE 5

Sulfur analysis of slag samples taken during experiment I-2.

Sample#	Condition	$S_{LE}CO$
I2S1	Molten slag-2	0.06%
I2S2	After FeS addition	1.4%
I2S3	After completion of air blowing	0.04%

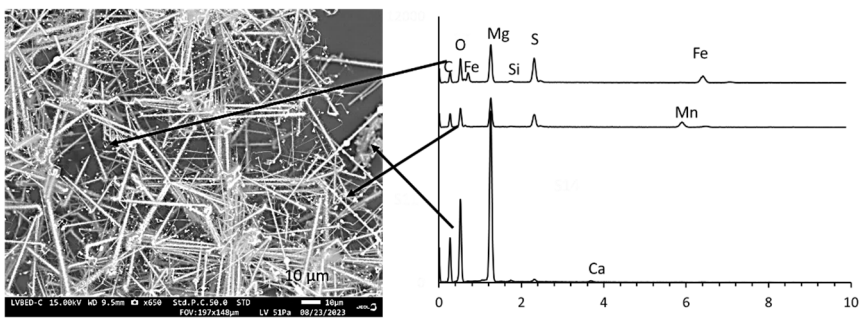

FIG 4 – SEM-EDS analysis of fibrous deposit on top of MgO-C crucible wall for experiment I-3.

Induction furnace experiment shows that about 20 mins of air purging at 200 sccm can reduce sulfur concentration to 0.04 per cent. TGA experiments were conducted to demonstrate the same through weight loss measurements. TGA experiment can also be used to calculate the rate of sulfur removal as well. Figure 5 shows weight change during TGA experiments. It should be noted that the heating (up to 1300°C) and cooling was conducted under argon atmosphere. The gas atmosphere was switched to air at 1300°C and maintained so until 1500°C. Further the heating rate was only 5°C/min. It should be noted that slag is expected to be 40 per cent liquid at 1300°C, 93 per cent liquid at 1330°C and 99 per cent at 1450°C as calculated using FactSage™ 8.3 (Bale *et al*, 2016). The overall weight loss for T-1 and T-2 was 1.28 per cent and 4.72 per cent respectively. It should be noted that 4.4 per cent S equivalent FeS was added in the slag for experiment T-2. The additional weight loss was 3.44 per cent in exp.# T-2 compared to T-1. Further the weight loss rate almost becomes zero at the onset of cooling ie as soon as the gas atmosphere is switched from air to argon. These results clearly demonstrate the sulfur loss from the slag due to oxidation by air. The rate of weight loss during the air oxidation appears to be constant at 0.18 per cent/min. It is interesting to note a constant sulfur removal rate with temperature and sulfur concentration in the molten slag. Allertz and Sichen (2015) also reported that there was no significant effect of temperature on the rate of sulfur removal from the liquid slag. Hence, these results indicate that the sulfur removal is limited by gas phase mass transfer. Pelton, See and Elliot (1974) reported that the sulfur removal is limited by gas phase mass transfer control for pO_2<0.1 atm. In the current work, sulfur removal is found to be linear at a higher oxygen partial pressure (0.21). The likely reason is the presence of iron in the system. In their work, it was reported that the presence of transient metal ions can enhance the rate of reaction. The effect was found to be stronger for iron than manganese. Hence, it appears that in the presence of about 7.5 per cent Fe in slag, the rate of sulfur removal remains controlled by gas phase mass transfer even for higher pO_2 level. Coombs and Munir (1989) reported weight gain due to oxidation of FeS at low temperatures (425–525°C) but the weight gain in the current experiments is much larger considering lower amount of FeS in the system. The reason for initial weight gain is not clear.

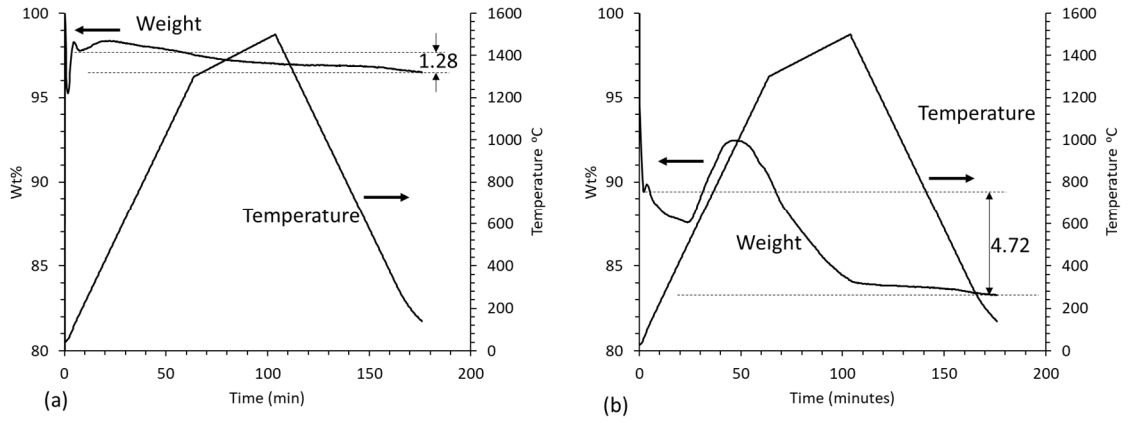

FIG 5 – Weight change during TGA experiments; the gas atmosphere was switched from argon to air in the temperature between 1300–1500°C: (a) the slag without sulfur; and (b) slag with sulfur.

Figure 6 shows calculate partial pressure of SO_2 for the equilibrium between slag and inert/air atmosphere. The calculation was performed using FactSage™ 8.3. FToxid and FactPS databases were selected for these calculations. The equilibrium between slag and air was calculated by fixing pO_2 = 0.21. The partial pressure of SO_2 is significant in presence of air, the atmosphere becomes SO_2 saturated after 1480°C. The sulfur removal is also possible at a lower temperature as the chamber is continuously purged with fresh air. The partial pressure of SO_2 is negligible in inert atmosphere, it is unlikely to observe significant sulfur removal in the absence of air. As expected, FactSage™ (Bale *et al*, 2016) calculations show that sulfur is present in the slag as sulfate and sulfide in presence of air and inert atmosphere respectively. The activity of $CaSO_4$ and CaS in equilibrium with air is 1 and ~0 respectively at all calculated temperatures. These activities are ~0 and 0.6–0.85 in the inert atmosphere.

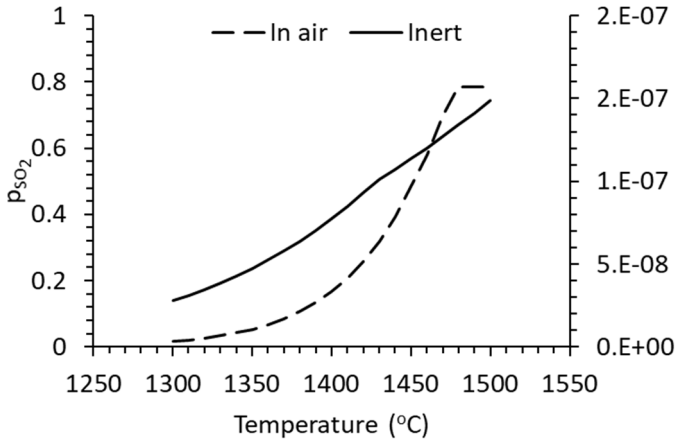

FIG 6 – Partial pressure of SO_2 with and without air calculated using FactSage™ (Bale *et al*, 2016).

The current work highlights the role of ambient air on the potential sulfur removal from steel refining slag. Certainly, more work is needed under laboratory conditions to clarify the effect of atmospheric condition on desulfurisation of liquid steel. The steel-slag reaction needs to be studied in more detail using MgO-C crucible. Another potential implication of this study is to desulfurise steel refining slag using air at high temperature.

CONCLUSIONS

Following conclusions can be made based on the current work:

- Plant observation show that sulfur may be oxidising from the slag during ladle refining.
- There is a significant evaporation for molten slag in the presence of source of carbon (graphite crucible or C in MgO-C crucible). Magnesium consistently evaporate and form MgO. Fibrous deposits are consistently seen in the colder region.
- Sulfur is also observed to be removed through gas phase during oxidation of slag experiment conducted using induction furnace. In this case, the fibrous structure showed presence of sulfur in association with Fe, Mn and Ca.
- Oxidation of slag with and without sulfur was also studied using a TGA set-up. A constant weight loss rate was observed for sulfur containing slag indicating the slag desulfurisation to controlled by gas phase mass transport for such set-up.

ACKNOWLEDGEMENTS

The support from Science and Engineering Research Board (SRG/2020/001495) and internal funding from the Industrial Research and Consultancy Centre, Centre of Excellence in Steel Technology and the Department of Metallurgical Engineering and Materials Science, IIT Bombay are acknowledged.

REFERENCES

Allertz, C and Sichen, D, 2015. Possibility of Sulfur Removal from Ladle Slag by Oxidation in the Temperature Range 1373–1673 K, *Journal of Sustainable Metallurgy*, 1(3):229–239. https://doi.org/10.1007/s40831-015-0018-4

Bale, C W, Bélisle, E, Chartrand, P, Decterov, S A, Eriksson, G, Gheribi, A E, Hack, K, Jung, I H, Kang, Y B, Melançon, J, Pelton, A D, Petersen, S, Robelin, C, Sangster, J, Spencer, P and Van Ende, M A, 2016. FactSage thermochemical software and databases, 2010–2016. *CALPHAD*: *Computer Coupling of Phase Diagrams and Thermochemistry*, 54:35–53. https://doi.org/10.1016/j.calphad.2016.05.002

Bannenberg, N, Bergmann, B and Gaye, H, 1992. Combined decrease of sulfur, nitrogen, hydrogen and total oxygen in only one secondary steelmaking operation, *Steel Research International*, 63(10):431–437.

Coombs, P G and Munir, Z A, 1989. The mechanism of oxidation of ferrous sulfide (FeS) powders in the range of 648 to 923 K, *Metallurgical Transactions B,* 20(5):661–670. https://doi.org/10.1007/BF02655922

Fincham, C J B and Richardson, F D, 1954. The behaviour of sulphur in silicate and aluminate melts, *Proceedings of the Royal Society of London A,* 223(1152):40–62. https://doi.org/10.1098/rspa.1954.0099

Kumar, D and Pistorius, P C, 2017. Use of slag (CaO-Al2O3-SiO2-MgO) droplet as a catalyst to grow MgO whiskers through VLS mechanism, *Ceramics Intnl*, 43(17):15478–15485. https://doi.org/10.1016/j.ceramint.2017.08.095

Pelton, A D, See, J B and Elliott, J F, 1974. Kinetics of Evolution of So2 From Hot Metallurgical Slags, *Metall Trans*, 5(5):1163–1171. https://doi.org/10.1007/BF02644328

Roy, D, Pistorius, P C and Fruehan, R J, 2013. Effect of silicon on the desulfurization of Al-killed steels: Part II, Experimental results and plant trials, *Metallurgical and Materials Transactions B*: *Process Metallurgy and Materials Processing Science*, 44(5):1095–1104. https://doi.org/10.1007/s11663-013-9888-7

Wu, L, Liu, K, Xu, W, Wang, J, Wang, H and Dong, Y, 2021. Sulfur Removal from Spent Ladle Refining Furnace Slag at High Temperature, *Metallurgical and Materials Transactions B*: *Process Metallurgy and Materials Processing Science*, 52(2):590–593. https://doi.org/10.1007/s11663-021-02098-6

Zhao, L H, Lin, L and Wu, Q F, 2016. Experimental study on sulfur removal from ladle furnace refining slag in hot state by blowing air, *Int Journal of Minerals, Metallurgy and Materials*, 23(1):33–39. https://doi.org/10.1007/s12613-016-1208-1

Deoxidation of Ti-Ni alloy by the calcium and CaF_2-$MgCl_2$ flux

DOI: 10.62053/EUHB4983

Y Su[1], K S Park[2], J K Kim[3] and J H Park[4]

1. Department of Materials Science and Chemical Engineering, Hanyang University, Ansan 15588, Korea. Email: s2022251432@hanyang.ac.kr
2. Korea Institute of Industrial Technology (KITECH), Gangneung 25440, Korea. Email: kpark63@kitech.re.kr
3. Department of Materials Science and Chemical Engineering, Hanyang University, Ansan 15588, Korea. Email: jinkyungkim@hanyang.ac.kr
4. Department of Materials Science and Chemical Engineering, Hanyang University, Ansan 15588, Korea. Email: basicity@hanyang.ac.kr

ABSTRACT

The present study investigates the possibility of the direct removal of oxygen from the Ti-30Ni (wt per cent) alloy melt through the thermodynamic equilibrium reactions at 1623 K in the vertical tube furnace. The deoxidation efficiency of Ti-Ni alloy melt by adding different contents of metallic calcium (Ca) as a deoxidant was evaluated with the binary CaF_2-$MgCl_2$ flux.

The thermodynamic equilibrium experiments showed that the total oxygen content in the alloy decreased from about 650 ppm to 350 ppm when 3.5 wt per cent Ca was added to the Ti-30Ni (wt per cent) alloy.

Alternatively, the effect of flux composition in the CaF_2-$MgCl_2$ flux on the oxygen content was also investigated at 1623 K. Therefore, the effect of binary flux systems on the deoxidation ability was compared at 1623 K. According to the results, the flux system with 80 per centCaF_2–20 per cent$MgCl_2$ exhibited the best deoxidation capability, ie total oxygen content in the alloy reduced from 1450 to 550 ppm.

INTRODUCTION

The escalating global energy crisis and the urgent need to address climate change have compelled the industrial sector to prioritise sustainability and responsible energy consumption (Hossain et al, 2024). Titanium alloy is one of the most crucial structural materials for advanced lightweight applications, especially in aerospace and automotive areas, due to its low mass density of 4.5 g/cm^3 and high strength, coupled with excellent corrosion and high-temperature creep resistance (Raabe, 2023). However, it cannot be ignored that the cost of manufacturing titanium alloys and their low utilisation is a major limiting factor in their development. For example, machining produces titanium chips, and up to 90 per cent of the material is lost and turned into scrap in the manufacturing step in aerospace sector. The main impurity elements are oxygen (from corrosion and oxidation during machining) and iron (from abrasion of machining tools) (Lu et al, 2012; Takeda and Okabe, 2019). Therefore, the most urgent problem is research direction and the vital challenge for the entire Ti industry to develop a sustainable and circular economical route for Ti scraps to produce high-clean Ti alloys (Jiao et al, 2020).

Several researchers have discussed different methods to remove the impurity element oxygen from Ti alloys and scrap, such as powder metallurgy (Kim et al, 2016), electrochemical deoxidation (Chen et al, 2000), remelting methods (Okabe et al, 1992) and utilisation of hydrogen (Zhang et al, 2022). However, few fundamental studies have been conducted to systematically investigate the deoxidation behaviour of TiNi alloy by high-temperature thermodynamic equilibrium reactions. To address this gap in the literature, the present study investigates the effect of metallic Ca with the CaF_2-$MgCl_2$ binary flux on the equilibrium content of oxygen in Ti-30Ni (wt per cent) alloy at 1623 K. In addition, the effect of flux composition in the CaF_2-$MgCl_2$ flux on the oxygen content was also investigated.

EXPERIMENT

Titanium scrap produced from machining, Ca granule (99.99 per cent, Alfa-Aesar), and Ni pellet (99.99 per cent, Rnd-Korea) were used as raw materials. Ti scraps were pickled in 1 mol oxalic acid

solution at 70°C for 40 min, after that, the pickled Ti scraps were ultrasonically cleaned in distilled water and ethanol in sequence and then dried 12 hrs at 40°C to remove any remaining moisture. Meanwhile, reagent-grade powders of CaF_2 (>98 per cent, Junsei-Chemical) and $MgCl_2$ (>98 per cent, Sigma-Aldrich) were used as flux materials. The Ti-Ni master alloy was manufactured in a vacuum arc remelting (VAR) furnace under the pressure of 1.6×10^{-4} Torr.

Examination of the chemical reactions between the CaF_2-$MgCl_2$ flux and Ti-30 per cent Ni alloy was conducted in a super Kanthal electric resistance furnace with a $MoSi_2$ heating element, as shown in Figure 1. The temperature of the furnace was controlled by a PID controller connected to an R-type reference thermocouple. The temperature was calibrated to 1623 K using another R-type thermocouple before the experiment. The Ti-Ni master alloy (10 g), nickel capsule (with different Ca content), and flux powder mixture (4 g) were loaded into a graphite crucible (15×12×50 mm) and placed in a graphite holder (50×40×65 mm), which were linked with a molybdenum wire. When the furnace temperature reached 1623 K, the graphite holder was then positioned in the constant hot zone of the furnace. The reaction chamber was flushed with highly purified Ar gas at a constant rate to avoid oxidation of the alloy. After 60 min of equilibration time, the samples were quickly extracted from the furnace and quenched by dipping the crucible into brine.

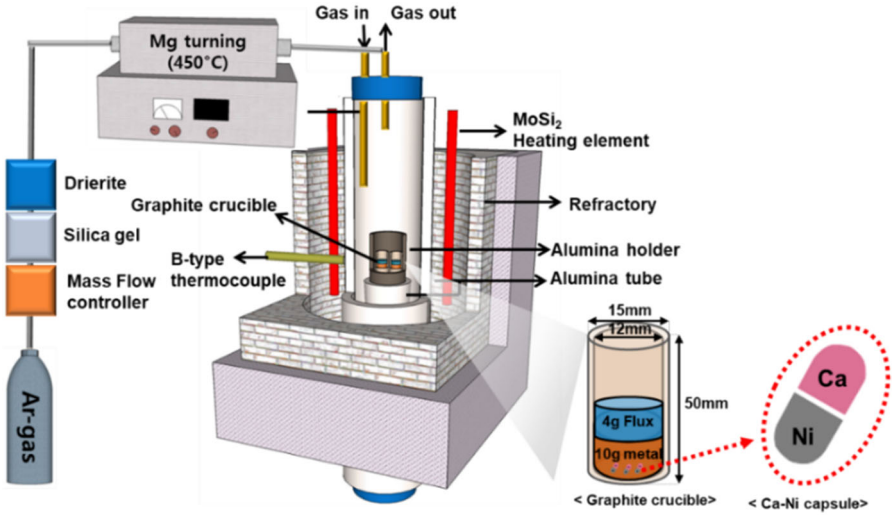

FIG 1 – Schematic diagram of the experimental apparatus.

After quenching, alloy samples were polished using a grinder to remove the surface layer, which can affect the analysis results, and then cut to a constant weight to reduce analytical error. The total oxygen and nitrogen content in the alloy samples was analysed using a combustion analyser (TC-300, LECO). The carbon content in the alloy samples was measured using a combustion analyser (CS 800, ELTRA).

RESULT AND DISCUSSION

Oxygen removal by different remelting methods

To investigate the effect of the melting methods and halide flux on the Ti-30Ni (wt per cent) alloy, the changes in the total oxygen and nitrogen contents in the alloy under various melting conditions are displayed in Figure 2. According to Figure 2, there is no significant change in the oxygen content of the alloy remelted in a graphite crucible without flux compared to the master alloy. However, the total oxygen content in the alloy reacted with the $80CaF_2$–$20MgCl_2$ flux exhibits a sharply increasing tendency in Figure 2. To understand this problem, the source of oxygen contamination needs to be found. Therefore, the CaF_2 and $MgCl_2$ powder as raw materials were checked by an X-ray diffraction (XRD) analysis, and the result is shown in Figure 3. It was found that the $MgCl_2(H_2O)_6$ phase was confirmed in the reagent $MgCl_2$ powder.

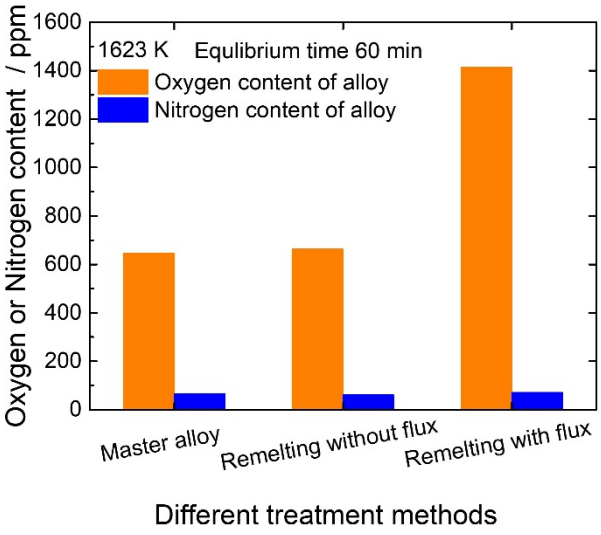

FIG 2 – Change of total oxygen and nitrogen content in Ti-30Ni alloy with different melting method.

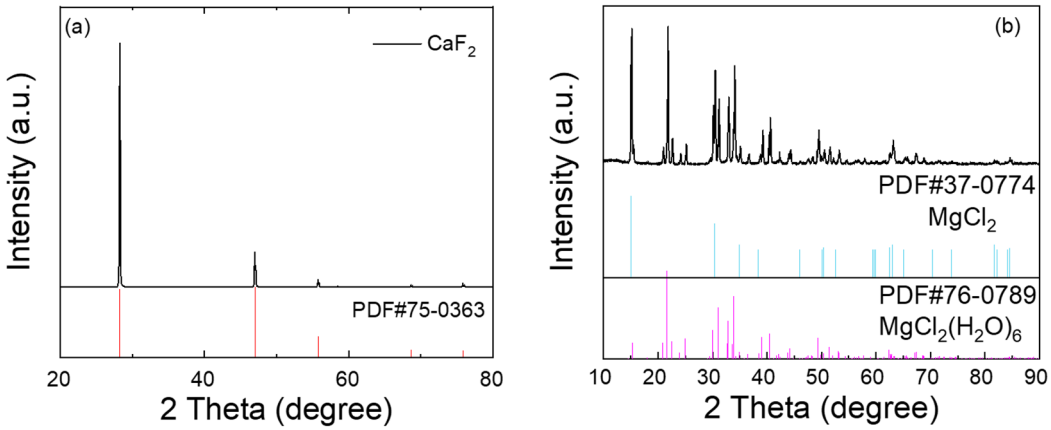

FIG 3 – XRD (scan rate of 1°/min) results of raw materials; (a) CaF_2, (b) $MgCl_2$.

Huang et al (2011) reported that the magnesium chloride hexahydrate, $MgCl_2(H_2O)_6$, could be decomposed to form MgO and H_2O at a temperature higher than 633 K. Therefore, it is indicated that when only adding the CaF_2-$MgCl_2$ flux, the oxygen content in the alloy sample sharply increased almost double compared with VaR and remelted sample without flux.

To investigate the deoxidation efficiency of the metallic Ca in the Ti-30Ni (wt per cent) alloy, the amount of Ca was increased from 0.17 wt per cent to 3.5 wt per cent in conjunction with flux system, $80CaF_2$–$20MgCl_2$. Changes in the total oxygen and nitrogen content in the alloy with different Ca additions are illustrated in Figure 4. The total oxygen content of the Ti-30Ni alloy initially increases up to about 0.5 wt per cent Ca, followed by a dramatic decrease and reaching about 350 ppm when 3.5 wt per cent Ca is added. The initial increase is possibly due to the effect of the binary halide flux, which might have $MgCl_2(H_2O)_6$ compound as mentioned above. However, a significant decrease in oxygen content is found as the calcium content increases further because Ca is the most effective deoxidation agent which is enough to compensate the reoxidation due to hydrate formation at high temperature (Okabe et al, 1992).

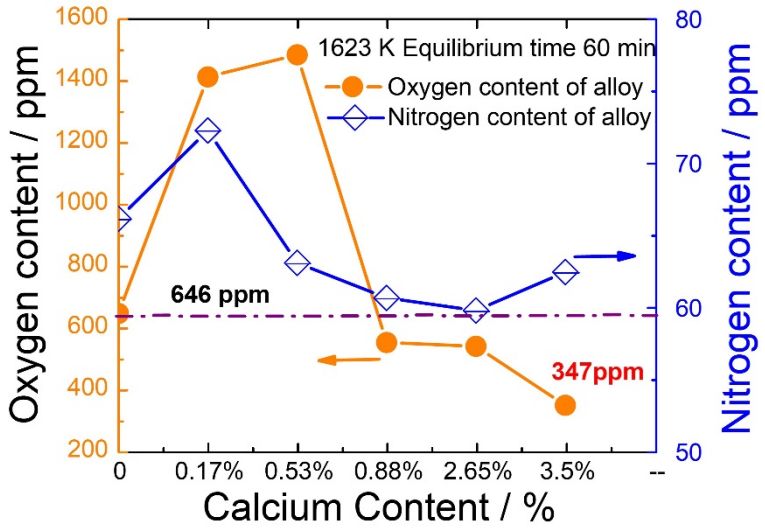

FIG 4 – Change of total O and N content in the Ti-30Ni alloy by adding metallic calcium at 1623 K.

Alternatively, the effect of different flux composition in the CaF_2-$MgCl_2$ binary flux in conjunction with about 0.9 per cent Ca on the oxygen content in the Ti-30Ni alloy was also investigated at 1623 K and the results are shown in Figure 5. As the content of $MgCl_2$ increases from 10 per cent to 25 per cent, the total oxygen content of the alloy maintains nearly constant but slightly decreases to about 550 ppm even with slight fluctuation up to 20 per cent $MgCl_2$, after which it sharply increases by adding more $MgCl_2$. The FactSage™ calculation shows that CaF_2 activity (a_{CaF_2}) in the CaF_2-$MgCl_2$ system sharply decreases from 1.0 to ca. 0.1 up to about 20 per cent $MgCl_2$ (ie strong negative deviation from an ideality), after which a_{CaF_2} smoothly decreases. A sharp decrease in a_{CaF_2} indicates the lower volatilisation and the higher stability of CaF_2 in the flux, which potentially promotes the absorption capability of deoxidation product, ie CaO. However, when the content of $MgCl_2$ is greater than 20 per cent, the reoxidation rate due to $MgCl_2$ would be much higher than the deoxidation rate due to combination of CaF_2 and Ca. Consequently, the flux system with $20MgCl_2$–$80CaF_2$ exhibited good deoxidation efficiency in the present study.

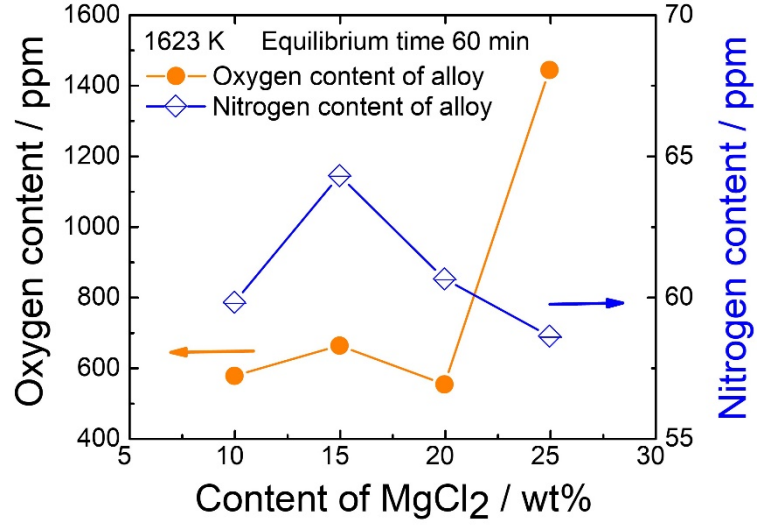

FIG 5 – Change of total oxygen and nitrogen content in the Ti-30Ni alloy with different $MgCl_2$ content in the CaF_2-$MgCl_2$ binary flux at 1623 K.

CONCLUSIONS

To establish an efficient recycling process for Ti scrap, a novel method relying on the deoxidation of Ti-Ni alloys by Ca and CaF_2-$MgCl_2$ flux was proposed. Equilibrium reactions between the Ti-30Ni (wt per cent) alloy and metallic Ca and CaF_2-$MgCl_2$ flux were investigated in a vertical tube furnace

with a high-density graphite crucible at 1623 K. The principal findings of the present study are summarised as follows:

- The amount of Ca added to the molten Ti-30Ni (wt per cent) alloy was varied from 0.17 wt per cent to 3.5 wt per cent in conjunction with the $80CaF_2$–$20MgCl_2$ flux system. When 3.5 wt per cent Ca was added, the total oxygen content in the alloy decreased from about 1500 ppm to 350 ppm.
- The flux system with $20MgCl_2$–$80CaF_2$ in conjunction with about 0.9 per cent Ca exhibited good deoxidation efficiency. The total oxygen content in the alloy reaches about 550 ppm at 1623 K.

REFERENCES

Chen, G Z *et al,* 2000. Direct electrochemical reduction of titanium dioxide to titanium in molten calcium chloride, *Nature*, 407:361–364.

Hossain, M E *et al,* 2024. A novel direct reduction and alloying process for making additive manufacturing of titanium alloys greener, *J Clean Prod*, 37:140723.

Huang, Q *et al,* 2011. Thermal decomposition mechanisms of MgCl2·6H2O and MgCl2·H2O, *J Anal Appl Pyrolysis*, 91:159–164.

Jiao, H *et al,* 2020. Sustainable recycling of titanium scraps and purity titanium production via molten salt electrolysis, *J Clean Prod*, 261:121314.

Kim, S J *et al,* 2016. Thermodynamic evaluation of oxygen behavior in Ti powder deoxidized by Ca reductant, *Met Mater Int*, 22:658–662.

Lu, X *et al,* 2012. Thermodynamic analysis of separation of alloying elements in recycling of end-of-life titanium products, *Sep Purif Technol*, 89:135–141.

Okabe, T *et al,* 1992. Preparation and characterization of extra-low-oxygen titanium, *J Alloys Compd*, 184:43–56.

Raabe, D, 2023. The materials science behind sustainable metals and alloys, *Chem Rev*, 123:2436–2608.

Takeda, O and Okabe, T H, 2019. Current status of titanium recycling and related technologies, *JOM*, 71:1981–1990.

Zhang, Y *et al,* 2022. Determination of the oxygen removal limits from Ti and Ti-6Al-4V by the hydrogen-assisted Mg deoxygenation method, *J Alloys Compd*, 927:167121.

Comparative dissolution behaviours of recycled cement paste and lime in EAF slag under static conditions

DOI: 10.62053/FVAX8267

M Yang[1], Z Yan[2] and Z Li[3]

1. Research Fellow, Advanced Steel Research Centre WMG, University of Warwick, Coventry CV4 7AL, UK. Email: mingrui.yang@warwick.ac.uk
2. Research Fellow, Advanced Steel Research Centre WMG, University of Warwick, Coventry CV4 7AL, UK. Email: zhiming.yan@warwick.ac.uk
3. Professor, Advanced Steel Research Centre WMG, University of Warwick, Coventry CV4 7AL, UK. Email: z.li.19@warwick.ac.uk

ABSTRACT

Recycled cement paste (RCP) is a kind of CaO-rich recourse, which is separated and recycled from waste concrete. Due to its chemical composition, RCP could partially replace lime as a flux and be loaded into electric arc furnace (EAF) steelmaking process. Rapid RCP assimilation and liquid slag formation have significant effects on EAF steelmaking process. In this study, the dissolution behaviours of RCP and lime at temperatures of 1400°C to 1500°C were investigated using static dissolution experiment. The dissolution rate, interfacial microstructure, as well as dissolution mechanisms were discussed. It was found that the dissolution rate of RCP was much higher than that of lime. RCP could be completely dissolved into slag in 60 secs at 1500°C. The dissolution rate of lime was in range of 3.9×10^{-4} g/(cm^2·s) to 2.6×10^{-3} g/(cm^2·s), while that for RCP was in range of 1.5×10^{-3} g/(cm^2·s) to 4.9×10^{-3} g/(cm^2·s). As for lime dissolution, a dense layer of dicalcium silicate (C_2S) generated at the dissolution interface, and the diffusion of Ca^{2+} in C_2S layer was the limited step for lime dissolution. Some of calcium ferrite could be observed at the interface between lime and C_2S layer. As for the RCP dissolution, there is no obvious product layer of C_2S formed at the dissolution interface, Fe^{2+} continuously diffused into RCP layer during the dissolution, and small amount of FeO·MgO solid solution generated and gathered at the dissolution interface. The dissolution rate of RCP in EAF slag was quite higher than that of lime, partially add RCP as flux in EAF could accelerate the slag formation process.

INTRODUCTION

Recycled cement paste (RCP), a CaO-rich resource obtained through the separation and recycling from waste concrete and cement (Silva *et al*, 2022; Bordya *et al*, 2017), could partially replace lime as a flux in the electric arc furnace (EAF) steelmaking process for resource utilisation (Wang, Mu and Liu, 2018; Zhutovsky and Shishkin, 2021). In the EAF steelmaking process, rapid slag formation plays a crucial role in refining reactions, resulting in a shortened refining duration and energy savings, and the slag formation is heavily influenced by the dissolution of flux into the slag (Wang, Mu and Liu, 2018; Zhutovsky and Shishkin, 2021).

In the last few decades, many experiments (Lesiak *et al*, 2022; Amini, Brungs and Ostrovski, 2007; Martinsson, Glaser and Du, 2018; Deng and Du, 2012; Li *et al*, 2014; Fruehan, Li and Brabie, 2013; Kitamura, 2017) have been carried out to investigate the dissolution behaviours of solid oxides in steel slag. Lesiak *et al* (2022) investigated the effects of calcination condition of dolomite-based materials dissolution in EAF slag, found that the dissolution amount decreases with deceasing of porosity. Fruehan, Li and Brabie (2013) studied the dissolution of magnesite and dolomite in EAF slag using both the dipping test and rotating cylinder test, found that during the dissolution of dolomite, CaO dissolved away first, and then the MgO particles entered the solution. The dissolution of lime in steel slag is a very common topic for steelmaking. The influence factors for dissolution could be listed as:

- chemical composition of solid and liquid
- temperature
- particle size
- forced convection.

Based on the experimental techniques and influencing factor, these dissolution experiments could be divided into five types which were briefly reviewed by Li *et al* (2022):

1. Under static conditions.
2. Rotating rod/disc method.
3. Under forced convection
4. Direct observation
5. Sampling from industry.

Based on the dissolution mechanism, the dissolution could be divided into: a) direct dissolution; and b) indirect dissolution. Direct dissolution, where only physical diffusion occurs without involving chemical reactions, is exemplified in processes such as the dissolution of Al_2O_3 (Yu *et al*, 2016) and SiO_2 (Xiang *et al*, 2014) into CaO-Fe_2O_3-based slag, dissolution of Al_2O_3 into CaO-Al_2O_3-SiO_2 slag (Cho and Fan, 2004). Dissolution of solid oxide into slag may involve the formation of an intermediate reaction product, and this type of dissolution is called as indirect dissolution. Sandhage and Yurek (1988) observed that spinal ($MgAl_2O_4$) formed at the Al_2O_3/CaO-SiO_2-MgO-Al_2O_3 interface. Yu *et al* (2015a) and Yang *et al* (2018a) found the $MgFe_2O_4$ and $CaTiO_3$ produced at the MgO/CaO-Fe_2O_3 and TiO_2/CaO-Fe_2O_3 interface, respectively. While product layer of $CaAl_4O_7$ could be found near the sapphire/CaO-SiO_2-Al_2O_3 interface, reported by Oishi, Cooper Jr and Kingery (1965). As for the lime dissolution into CaO-SiO_2-FeO based slag (generally basic oxygen steelmaking (BOS) slag and EAF slag), it has been confirmed that the formation of C_2S phase during the dissolution process, and the C_2S crystal distribution depends on the experimental conditions. The reaction of CaO and SiO_2 to produce C_2S is considered inevitable in these conditions. Typically, the C_2S phase demonstrates high thermodynamic stability in CaO-SiO_2-MgO-Al_2O_3-FeOx slag systems, particularly under basicity ranging from 1.5 to 3.0 at high temperatures.

RCP is a CaO-rich resource that can fully or partially replace lime as a flux in EAF steelmaking. The dissolution process, dissolution mechanism and dissolution rate of RCP also play a crucial role in EAF slag formation, but these have not been fully understood or reported yet. This study aims to explore the dissolution behaviours of RCP and lime (for comparison) in simulated EAF slag at 1400°C and 1500°C under static conditions. The dissolution process, dissolution interfacial microstructure, and dissolution mechanisms were thoroughly discussed.

EXPERIMENTAL

Materials preparation

The RCP is made by commercial Portland cement with water at a water to cement mass ratio of 0.6. It was then cured at room temperature for one month in sealed condition to avoid evaporation. After curing, these cement paste bricks were heated up around 450°C to 500°C in a muffle furnace to produce RCP. The chemical and phase compositions of RCP were examined by X-ray fluorescence (XRF) (PANalytical Epsilon 3) and X-ray diffraction (XRD) (Panalytical Empyrean, Co target). The RCP was of the following composition: 68.093 per cent CaO, 19.455 per cent SiO_2, 4.864 per cent Al_2O_3, 0.737 per cent MgO, 3.613 per cent Fe_2O_3, 0.486 per cent K_2O, 0.120 per cent Na_2O and 0.250 per cent TiO_2. The XRD result of RCP is shown in Figure 1. It can be seen that the phase composition of RCP was mainly composed of dicalcium silicate (C_2S), CaO, and small amount of C_3S, SiO_2 and $Ca(OH)_2$. During the heating process, there were dehydration reactions for calcium silicate hydrate (C-S-H) phase to produce C_3S (tricalcium silicate) and C_2S. Then the C_3S phase would decompose into C_2S and CaO because C_3S is not thermodynamic stable at the roasting temperature. Some of $Ca(OH)_2$ were detected due to the moisture absorb of CaO.

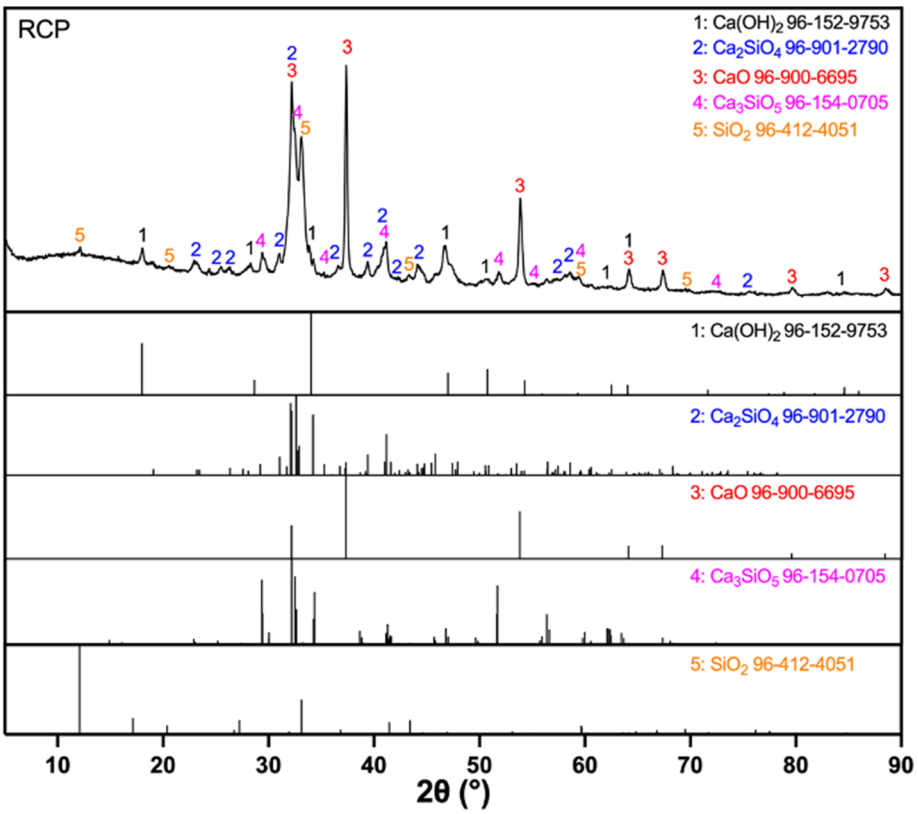

FIG 1 – XRD patterns of recycled cement paste and standard components.

The slag used was synthesised to simulate the initial liquid EAF slag before steel refining. The investigation of RCP and lime dissolution in slag has been carried out with a synthesised EAF steelmaking slag of the following chemical composition: 40 per cent of CaO, 30 per cent of SiO_2, 20 per cent of FeO, 6 per cent of MgO and 4 per cent of Al_2O_3. The chemical reagents of CaO, SiO_2, MgO, Al_2O_3 and FeO in purity of 99.5 wt per cent (Alfa Aesar) were used to prepare the slag samples and CaO tablet. Homogeneously mixed the chemical regents powder using a ball milling at ratio of grinding ball mass to material mass of 5:1 for 30 mins. Then used a cylinder mold to press them into tablets and pre-melted the slag tablet in a sealed furnace at 1500°C in Argon atmosphere for 30 min. To minimise the influence of solid porosity on dissolution behaviours, the sintered dense solid tablets of CaO and RCP were prepared for dissolution experiments. The CaO and RCP powders were load into a cylinder mold with diameter of 5 mm under 1 ton pressure for 1 min, then roasted the solid sample of CaO and RCP in a muffle furnace in air for 10 hrs at 1400°C and 1000°C, respectively.

Dissolution experiment

The dissolution experiments were carried out in a confocal laser scanning microscope furnace at 1400°C and 1500°C in Argon, the schematic diagram for device is shown in Figure 2. The chamber is ellipsoid in shape, with the heating element and sample holder positioned at the upper and lower focal points of the ellipsoid. The heating principle involves the reflection and focusing of thermal radiation through the gold coating on the chamber. The dissolution times were 30 sec, 60 sec, 90 sec, and 120 sec. The heating and cooling rates were set as quickly as possible at 400 K/min and 1200 K/min, respectively, to minimise dissolution time errors. Zero dissolution time was defined as the moment when samples reached the desired temperature. The experimental conditions, geometry size of solid samples etc, are summarised in Table 1. The samples labelled from L1 to L8 represent lime dissolution samples, while those labelled from R1 to R8 represent RCP dissolution samples. After dissolution, the samples with crucibles were embedded in resin, subsequently cut, and polished along the cross-section. The thickness of solid parts after dissolution was measured using a digital optical microscope (OM, Keyence VHX7000), while the microstructure and element distribution of the dissolution interface were examined using a scanning electron microscope (SEM, Zeiss, Sigma) equipped with energy dispersive X-ray spectroscopy (EDS, Oxford, Ultim Extreme).

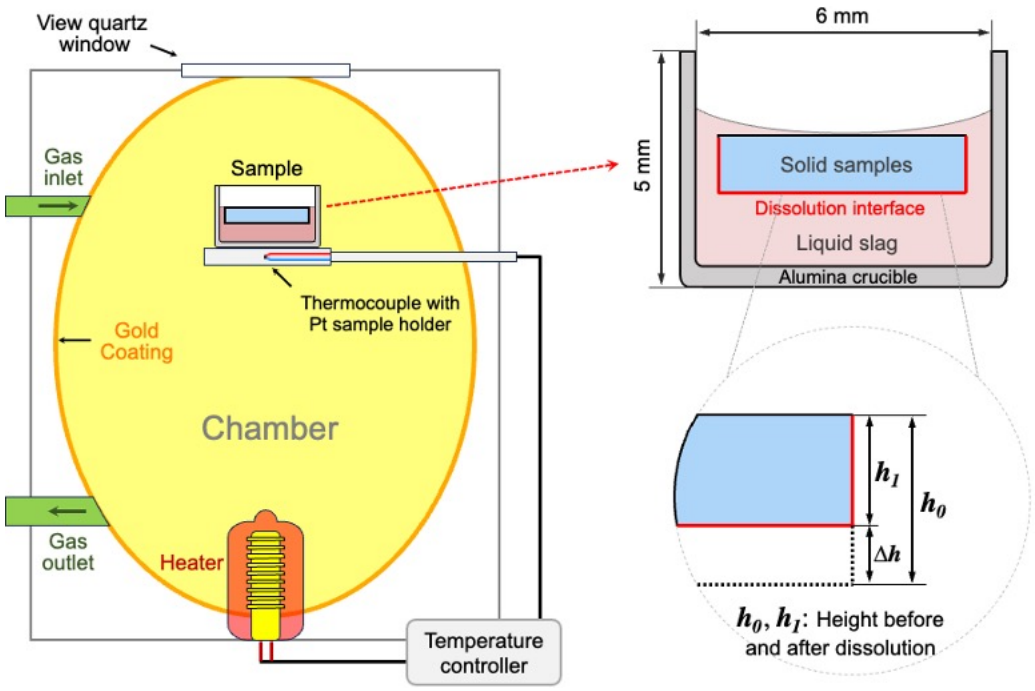

FIG 2 – Schematic of confocal laser furnace and present dissolution experiments.

TABLE 1

Dissolution conditions and measured parameters of samples.

Samples	Temperature (°C)	Dissolution Time (sec)	Weight loss fraction
L1	1400	30	0.1067
L2	1400	60	0.1673
L3	1400	90	0.1967
L4	1400	120	0.2285
L5	1500	30	0.2647
L6	1500	60	0.3917
L7	1500	90	0.4409
L8	1500	120	0.4784
R1	1400	30	0.3536
R2	1400	60	0.5460
R3	1400	90	0.6244
R4	1400	120	0.6800
R5	1500	30	0.7421
R6	1500	60	1
R7	1500	90	1
R8	1500	120	1

RESULTS AND DISCUSSIONS

Dissolution behaviours

The density of RCP ranges from 2.43 g/cm^3 to 2.51 g/cm^3, while that of lime ranges from 2.63 g/m^3 to 2.66 g/m^3. The density of liquid slag is 2.83 g/cm^3. During the dissolution process, the solid samples of RCP and lime tend to float in the liquid slag due to their lower densities compared to that of the liquid slag. The liquid slag exhibits good wettability on both the solid samples and the Al_2O_3 crucible. It can be observed in Figure 3 that the solid samples are continuously and gradually wetted by the liquid slag. Assuming that the shape of the solid parts in slag after dissolution still remains cylindrical, the height of the solid sample after dissolution was measured using an optical microscope. The dissolution of the solid sample in the liquid slag primarily occurred through the bottom and sides of the cylinder. Consequently, the decrease in sample height (Δh) and the decrease in sample radius (Δr) can be considered as the same value, $\Delta h = \Delta r$. The volume, weight, weight loss, and weight loss fraction after dissolution can also be calculated, and the weight loss fraction for solid samples after dissolution are summarised in Table 1 and in Figure 4. The experimental results indicate that the dissolution of RCP at 1500°C slowed down and eventually stopped at 60 sec. In samples R6, R7, and R8, no original solid RCP parts could be observed, indicating that RCP had completely dissolved into the slag in these samples. Based on the weight loss of samples, the dissolution rate of RCP could be calculated as 13.73×10^{-5} m/s and 29.05×10^{-5} m/s at 1400°C and 1500°C, while that of lime are 3.12×10^{-5} m/s and 8.42×10^{-5} m/s at 1400°C and 1500°C.

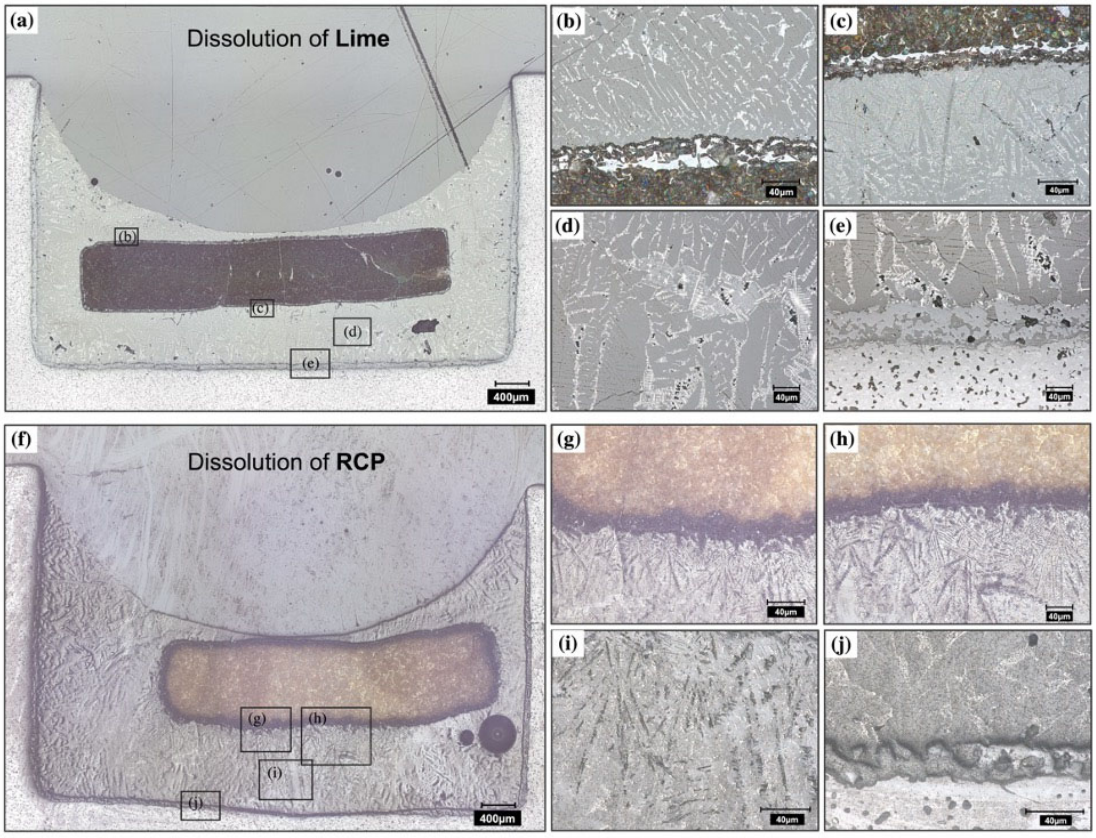

FIG 3 – Optical images for cross-section of samples, (a) to (e): L2 (lime, 1400°C, 60 sec); (f) to (j) R2 (RCP, 1400°C, 60 sec).

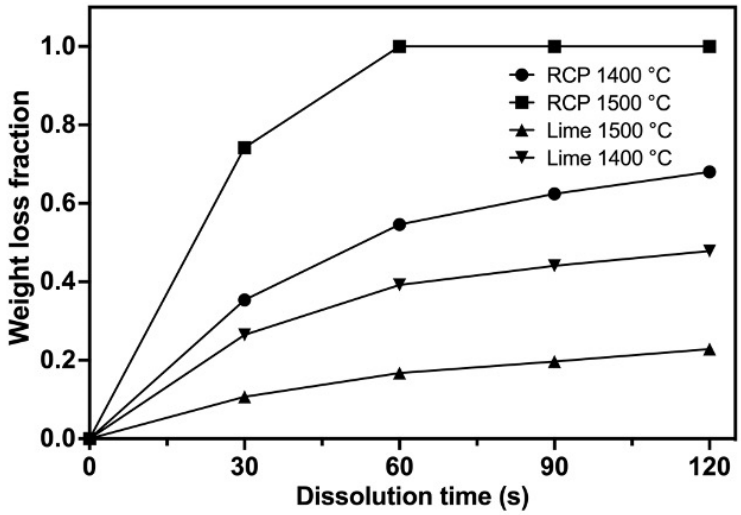

FIG 4 – Dissolution weight loss fraction of RCP and lime in different temperature and dissolution time.

Interfacial microstructure

Figure 5 displays the scanning electron microscope (SEM) image and energy-dispersive X-ray spectroscopy (EDS) results illustrating the interfacial microstructure of lime dissolution in slag. The presence of the Fe element was detected in the lime layer, indicating that a small amount of slag had penetrated into the lime layer during the dissolution process. Results reveals that the bright area is primarily composed of Ca, Fe, and O, suggesting that this phase corresponds to a calcium ferrite-based slag phase. From the EDS mapping results of Ca and Si, it can be seen that a significant dense product layer of C_2S, with a thickness of approximately 20 μm, is clearly visible at the forefront of the dissolution interface layer. The observed interfacial microstructure during the dissolution of lime into EAF slag aligns with previously reported findings (Lesiak *et al*, 2022; Amini, Brungs and Ostrovski, 2007; Martinsson, Glaser and Du, 2018; Deng and Du, 2012; Li *et al*, 2014). Those studies also noted the accumulation of a C_2S product layer at the dissolution interface of lime into steel slag (CaO-SiO_2-FeO based slag). Deng and Du (2012) investigated the dissolution of lime in steel slag (CaO-SiO_2-FeO) under forced convection and concluded that the removal of the C_2S dense product layer by liquid forced mobility could accelerate the lime dissolution process. They also identified some tricalcium silicate (C_3S) crystals generated at the dissolution interface and within the lime layer. The dissolution of lime into slag at high temperatures depends on dissolution of dense C_2S layer into liquid slag. In the liquid slag layer, massive crystals of C_2S and a small amount of fine iron oxide crystals precipitated along with the C_2S crystals. No tricalcium silicate (C_3S) phases were found at the dissolution interface. The main reaction for C_3S formation is $C_2S+CaO=C_3S$. The formation of C_3S requires certain conditions, such as a specific temperature (>1300°C) and sufficient reaction time. However, the maximum dissolution duration in the present experiments is 120 secs, and the reaction time is insufficient for the formation of C_3S.

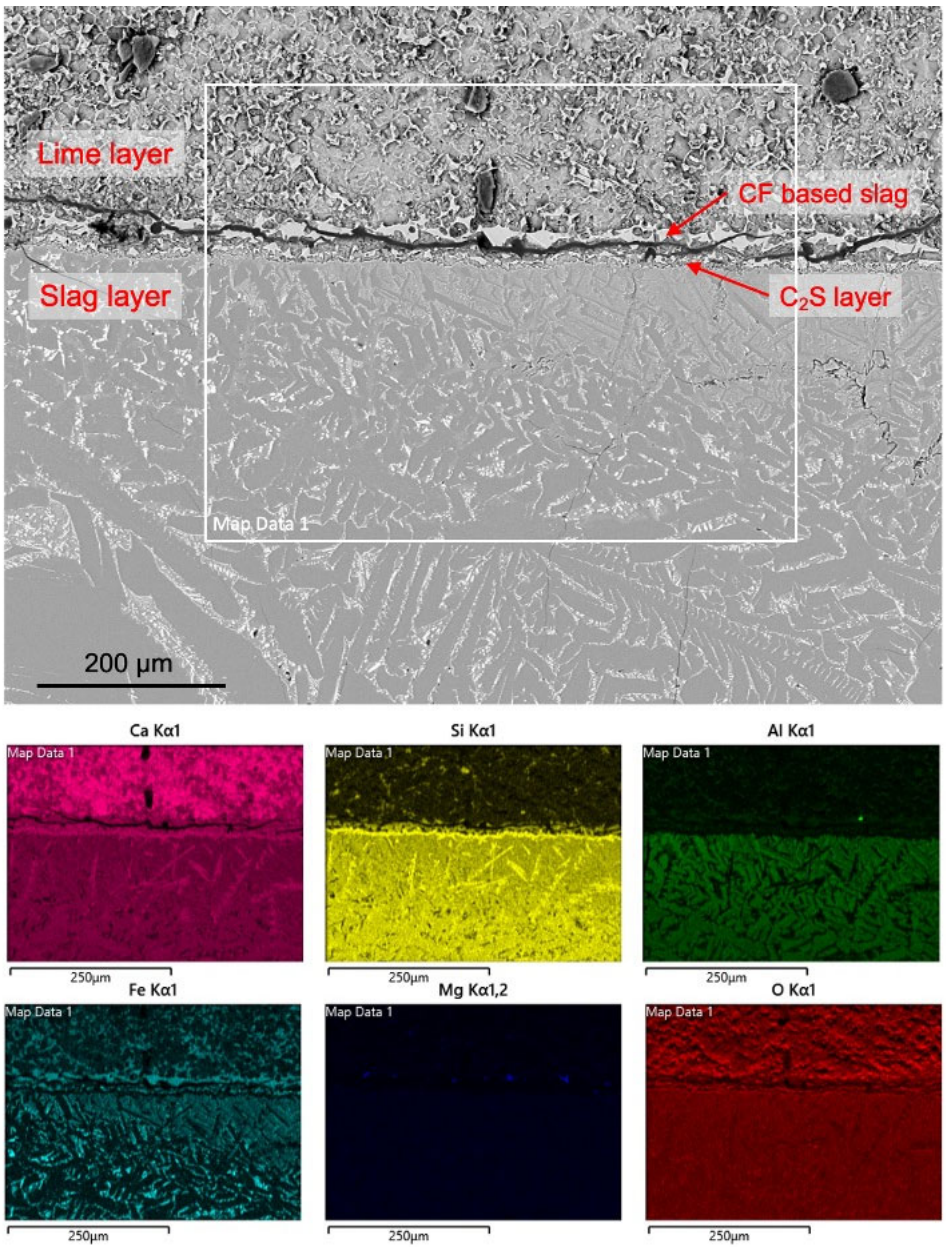

FIG 5 – SEM image and EDS results for dissolution interface of sample L2 (Lime, 1400°C, 60 sec).

The SEM images and EDS results depicting the interfacial microstructure of RCP dissolution are shown in Figure 6. In comparison with the dissolution of lime, no dense product layer of C_2S could be observed in the samples, and some dendritic C_2S crystals can be found in the slag. EDS results show that some of FeO_x could be detected in RCP layer, indicating that some of Fe ions diffused into the solid RCP layer during dissolution process. The thickness of the sample-slag interlayer is approximately 100 µm. The Al_2O_3 content in the sample-slag interlayer is higher than that in the slag bulk, indicating that AlO_4^{5-} diffuses in the slag bulk and accumulates in the interlayer. Some of massive C_2S crystals and fine FeO_x could be detected in residual slag. As mentioned before, the phase in RCP is mainly composed of C_3S, C_2S, CaO and SiO_2, these phases could directly dissolve into EAF slag. The content of CaO in RCP is too low to produce a dense layer of C_2S. But in dissolution of lime, C_2S would be produced, and it is hard to remove under static conditions. The dissolution process of C_2S is the limiting step in lime dissolution; this is the main reason for the dissolution of RCP is faster than that of lime.

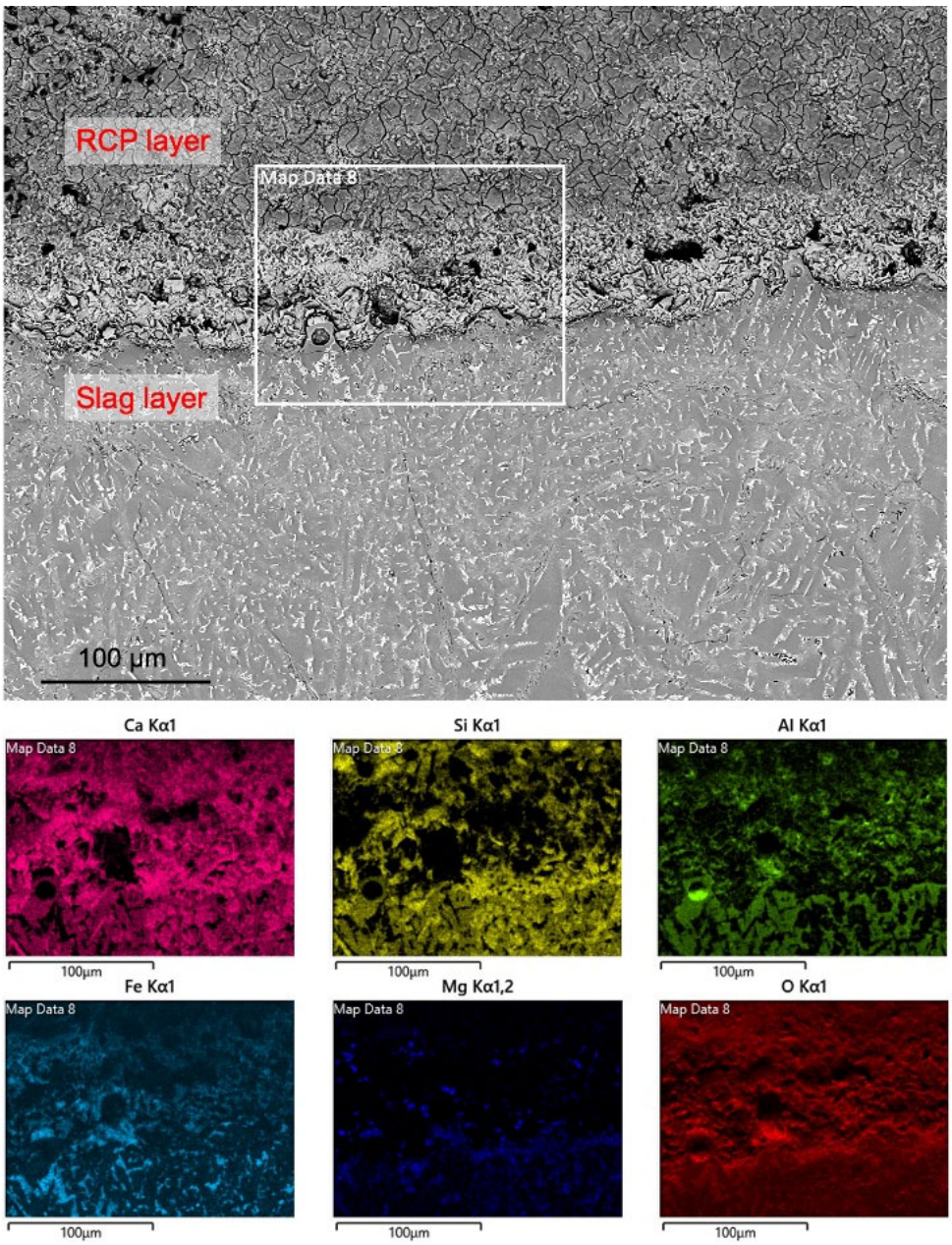

FIG 6 – SEM image and EDS results for dissolution interface of sample R2 (RCP, 1400°C, 60 sec).

CONCLUSIONS

The dissolution behaviours of recycled cement paste (RCP) and lime at temperatures of 1400°C and 1500°C were investigated under static conditions. The RCP could be completely dissolved into slag in 60 secs at 1500°C, and the dissolution rate of RCP is much higher than that of lime. The dissolution rate of lime was in range of 3.9×10^{-4} g/(cm^2·s) to 2.6×10^{-3} g/(cm^2·s), while that for RCP was in range of 1.5×10^{-3} g/(cm^2·s) to 4.9×10^{-3} g/(cm^2·s). A dense product layer of dicalcium silicate generated at the dissolution interface, with the dissolution of this dense C_2S layer identified as the limiting step for lime dissolution. Calcium ferrite could be observed at the interface between lime and C_2S layer. In the dissolution of RCP, there is no apparent product layer of C_2S formed at the dissolution interface. Fe^{2+} continuously diffuses into the RCP layer during the dissolution process. Generally, the dissolution rate of RCP in EAF slag was quite higher than that of lime, partially add RCP as flux in EAF could accelerate the liquid slag formation process in EAF.

ACKNOWLEDGEMENTS

The authors gratefully acknowledge the financial support from EPSRC Grant No. EP/W026104/1.

REFERENCES

Amini, S, Brungs, M and Ostrovski, O, 2007. Dissolution of Dense Lime in Molten Slags under Static Conditions, *ISIJ International*, 47(1):32–37.

Bordya, A, Younsib, A, Aggoun, S and Fiorioa, B, 2017. Cement substitution by a recycled cement paste fine: Role of the residual anhydrous clinker, *Construction and Building Materials*, 132:1–8.

Cho, W and Fan, P, 2004. Diffusional Dissolution of Alumina in Various Steelmaking Slags, *ISIJ International*, 44:229–234.

Deng, T and Du, S, 2012. Study of Lime Dissolution Under Forced Convection, *Metall Mater Trans B*, 43B:678–686.

Fruehan, R, Li, Y and Brabie, L, 2003. Dissolution of magnesite and dolomite in simulated EAF slags, Isstech Conference Proceedings, Iron And Steel Society.

Kitamura, S, 2017. Dissolution Behavior of Lime into Steelmaking Slag, *ISIJ Int*, 57(10):1670–1676.

Lesiak, S, Cheremisina, E, Rieger, J, Schenk, J, Firsbach, F, Johnson, W, Chopin, T and Nispel, M, 2022. Calcination Condition of Dolomite-Based Materials Influencing Static Dissolution in Synthetic Electric Arc Furnace Slag, *Steel Res Int*, 93:2100675.

Li, Z, Li, J, Spooner, S and Seetharaman, S, 2022. Basic Oxygen Steelmaking Slag: Formation, Reaction and Energy and Material Recovery, *Steel Res Int*, 93:2100167.

Li, Z, Whitwood, M, Millman, S and Boggelen, J, 2014. Dissolution of lime in BOS slag: from laboratory experiment to industrial converter, *Ironmaking and Steelmaking*, 4:112–121.

Martinsson, J, Glaser, B and Du, S, 2018. Lime Dissolution in Foaming BOF Slag, *Metall Mater Trans B*, 48B:3164–3170.

Oishi, Y, Cooper Jr, A R and Kingery, W D, 1965. Dissolution in ceramic systems: III, boundary layer concentration gradients, *Journal of the American Ceramic Society*, 48(2):88–95.

Sandhage, K H and Yurek, G J, 1988. Indirect Dissolution of Sapphire into Silicate Melts, *J Am Ceram Soc*, 71(6):478–489.

Silva, A, Nogueira, R, Bogas, A, Abrantes, J, Wawrzynczak, D, Sciubidło, A and Kucęba, I M, 2022. Valorisation of Recycled Cement Paste: Feasibility of a Short-Duration Carbonation Process, *Materials*, 15(17):6001.

Wang, J, Mu, M and Liu, Y, 2018. Recycled cement, *Construction and Building Materials*, 190:1124–1132.

Xiang, S, Lv, X, Yu, B, Xu, J and Yin, J, 2014. The dissolution kinetics of Al_2O_3 into molten CaO-Al_2O_3-Fe_2O_3 slag, *Metall Mater Trans B*, 45B:2106–2117.

Yang, M, Lv, X, Wei, R and Bai, C, 2018a. Wetting behavior of TiO_2 by calcium ferrite slag at 1523 K, *Metall Mater Trans B*, 49B:2667–2680.

Yang, M, Lv, X, Wei, R, Xu, J and Bai, C, 2018b. Wetting behavior of calcium ferrite slags on cristobalite substrates, *Metall Mater Trans B*, 49B:1331–1345.

Yu, B, Lv, W, Xiang, S and Xu, J, 2016. Dissolution Kinetics of SiO_2 into CaO-Fe_2O_3-SiO_2 Slag, *Metall Mater Trans B*, 47B:2063–2073.

Yu, B, Lv, W, Xiang, S, Bai, C and Yin, J, 2015a. Wetting behavior of calcium ferrite melts on sintered MgO, *ISIJ International*, 55(8):1558–1564.

Yu, B, Lv, W, Xiang, S, Bai, C and Yin, J, 2015b. Wetting behavior of Al_2O_3 substrate by calcium ferrite series melts, *ISIJ International*, 55(3):483–490.

Zhutovsky, S and Shishkin, A, 2021. Recycling of hydrated Portland cement paste into new clinker, *Construction and Building Materials*, 280:122510.

Experimental measurements of – Thermodynamic properties, multi-phase equilibria, minor element distributions

Experimental study and thermodynamic modelling of phase equilibria in the FeO-$FeO_{1.5}$-$SbO_{1.5}$-SiO_2 system in equilibrium with metal

DOI: 10.62053/GSGH9425

H Abdeyazdan[1], M Shevchenko[2], J Grogan[3], D Graf[4] and E Jak[5]

1. Postdoctoral Research Fellow, The University of Queensland, Brisbane Qld 4072. Email: h.abdeyazdan@uq.edu.au
2. Research Fellow, The University of Queensland, Brisbane Qld 4072. Email: m.shevchenko@uq.edu.au
3. Chief Technology Officer, Gopher Resource, Eagan, MN 55121, USA. Email: joe.grogan@gopherresource.com
4. Principal Engineer, Gopher Resource, Tampa, FL 33619, USA. Email: daniel.graf@gopherresource.com
5. Professor, The University of Queensland, Brisbane Qld 4072. Email: e.jak@uq.edu.au

ABSTRACT

An integrated experimental and thermodynamic modelling study of the phase equilibria in the FeO-$FeO_{1.5}$-$SbO_{1.5}$-SiO_2 system in equilibrium with liquid Sb and Sb-Ag metal has been undertaken to develop thermodynamic model of the Na-Si-Fe-O slag system with S-Sn-Sb-Pb-As minor elements based on the experimental investigation of the selected sub-systems. New experimental phase equilibria data at 575–1600°C were obtained for this system using high-temperature equilibration of synthetic mixtures with predetermined compositions in sealed silica ampoules, Fe_3O_4 basket in sealed silica ampoule, or Re foils, a rapid quenching technique, and electron probe X-ray microanalysis of the equilibrated phase compositions. Experimental results on phase equilibria in the Fe-Sb-Si-O+Sb metal system obtained helped to produce initial set of model parameters in the slag. The primary phase fields of quartz/tridymite/cristobalite (SiO_2), 2 high-SiO_2 immiscible liquids, olivine (Fe_2SiO_4), wustite (FeO_{1+x}), spinel (Fe_3O_4), schafarzikite ($FeSb_2O_4$) and valentinite/ senarmontite (Sb_2O_3) were identified in the binary Sb_2O_3-FeO, Sb_2O_3-SiO_2 and ternary FeO-Sb_2O_3-SiO_2 systems. Further refinement, particularly the distribution of excess Gibbs energy among the 'FeO'-Sb_2O_3-SiO_2 and '$FeO_{1.5}$'-Sb_2O_3-SiO_2 interactions, required the study at more oxidising conditions. Oxygen potential was increased using an inert metal (Ag) rather than using the gas flow due to the high volatility of Sb-containing gaseous species. Liquid Ag-Sb alloys with low concentrations of Sb of a few percent were used. At these conditions, the concentration of $AgO_{0.5}$ in slag was below 1 mol per cent, which had a small effect on observed phase equilibria in the system. In addition, important information on the solubility of silver in slags is produced, which can be valuable when treating electronic recycling materials or primary silver-containing ores through the Pb process. Two main areas were addressed: the spinel-tridymite boundary (40–70 per cent SiO_2 in slag) and spinel liquidus near 15 per cent SiO_2 in slag. This allowed to deconvolute the separate contributions of the FeO-Sb_2O_3(-SiO_2) and Fe_2O_3-Sb_2O_3(-SiO_2) systems.

INTRODUCTION

Antimony, tin, arsenic and other critical valuable as well as unwanted metals are found in a range of streams within primary and secondary smelters. These elements are typically concentrated in dusts and other streams, resulting in process challenges within industrial smelters. To improve the recovery of Sb, Sn and other critical metals, as well as to remove hazardous metals from the slag, fuming of these elements needs to be controlled and optimised. The fuming process depends on a number of factors including kinetics at the gas-slag interface, diffusive and convective mass transfer in the slag and gas phases at micro- and macro-scales, fluid flow pattern in the reactor as well as the properties of the slag, in particular thermodynamics (that determines the driving force) and phase equilibria (directly linked to thermodynamics).

To optimise the fuming of secondary lead slags, a detailed understanding of the thermochemistry of the slag system including phase equilibria, thermodynamics, fuming mechanisms and kinetics for these elements is required. Slags generated in these smelters typically belong either to the Ca-Si-Fe-O system or the Na-Si-Fe-O system, with the two systems behaving differently. The present

research program is focused on the Na-Si-Fe-O system as it is most commonly used for the smelting of side streams and by-products from smelters, typically enriched in these critical metals.

The characterisation and modelling of fuming mechanisms and kinetics requires reliable detailed knowledge of the thermodynamics (determining the driving force) and phase equilibria of the slag system. It is not possible to characterise kinetics without reliable knowledge on thermodynamics and phase equilibria. Preliminary review of literature on phase equilibria and thermodynamics indicated the lack of data. It is therefore recommended to focus the major part of this initial stage of the research in this area on the characterisation of phase equilibria and thermodynamics followed up by study of the kinetics of fuming.

This research provides new phase equilibria in the FeO-$FeO_{1.5}$-$SbO_{1.5}$-SiO_2 system in equilibrium with liquid Sb and Sb-Ag metal to develop thermodynamic model of the Na-Si-Fe-O slag system with S-Sn-Sb-Pb-As minor elements based on the experimental investigation of the selected sub-systems.

METHODOLOGY

The experimental apparatus and technique used in this study have been detailed in previous publications (Hidayat *et al,* 2012; Jak, Hayes, and Lee, 1995; Jak, 2012). The initial chemical mixtures were prepared by blending selected proportions of high-purity powders of Fe_2O_3, Sb_2O_3, Sb and Ag metal (99.9 wt per cent purity), SiO_2 (99.9 wt per cent purity, pre-dried at 400°C for 1 hr before mixing), supplied by Alfa Aesar, MA, USA. The mixtures were pelletised and divided into 0.2–0.4 g samples for the experiments. The initial compositions were selected to ensure that the liquid slag was in equilibrium with at least one crystalline phase, and the crystalline solid phase(s) fraction in the final sample at the equilibration temperature was preferably ~10 vol per cent and not greater than 50 vol per cent to promote the retention of the liquid as an amorphous phase during quenching. The substrates used for equilibration were: i) vacuum sealed silica ampoules for high-SiO_2 mixtures that were in equilibrium with tridymite and cristobalite at the target temperature; and ii) Re foils for low-SiO_2 mixtures. In some cases, Fe_3O_4 (spinel) baskets (obtained by controlled oxidation of Fe foil), or MgO crucibles sealed inside SiO_2 ampoules, were used. The experiments were conducted in a high-temperature vertical tube resistance PYROX furnace using lanthanum chromite heating elements under air or argon atmosphere. The samples were suspended in the centre of the uniform hot zone of the furnace on a Kanthal (Fe-Cr-Al alloy) wire (0.7 or 1 mm diameter), with 15–20 cm platinum wire added to the Kanthal wire for T > 1450°C to avoid failure at high temperatures. The samples were first pre-melted at 20–50°C above the target temperature for 5 min to support the formation of a homogeneous liquid. The samples with high antimony oxide partial pressure (low-SiO_2) area were not pre-melted to decrease the overall loss of Sb_2O_3.

Following equilibration, the samples were rapidly quenched in calcium chloride brine at -20°C, washed with water and ethanol, dried, and mounted in epoxy resin. Polished cross-sections were prepared using conventional metallographic techniques. The samples were examined using optical microscopy and then carbon-coated. The compositions of the phases were measured using electron probe X-ray microanalysis (EPMA) (JEOL 8200 L EPMA; Japan Electron Optics Ltd., Tokyo, Japan). The EPMA was operated with a probe current of 20 nA and acceleration voltage of 15 kV. The Duncumb–Philibert atomic number, absorption, and fluorescence correction (ZAF correction) was applied. Wollastonite ($CaSiO_3$), hematite (Fe_2O_3), Sb metal and Ag metal (supplied by Charles M. Taylor Co., Stanford, CA, USA) standards were used for Si, Fe, Sb and Ag calibration of the EPMA, respectively. Only the concentrations of metal cations were measured with EPMA; the proportions of Fe^{2+} and Fe^{3+} were not measured directly, Fe^{2+} ('FeO') is assumed to be predominant.

RESULTS

Typical microstructures for the selected experiments in the 'FeO'-$SbO_{1.5}$-SiO_2 system are shown in Figure 1. Liquidus surface of the 'FeO'-$SbO_{1.5}$-SiO_2 system according to the new experimental results and estimated with database developed for this system is given in Figure 2.

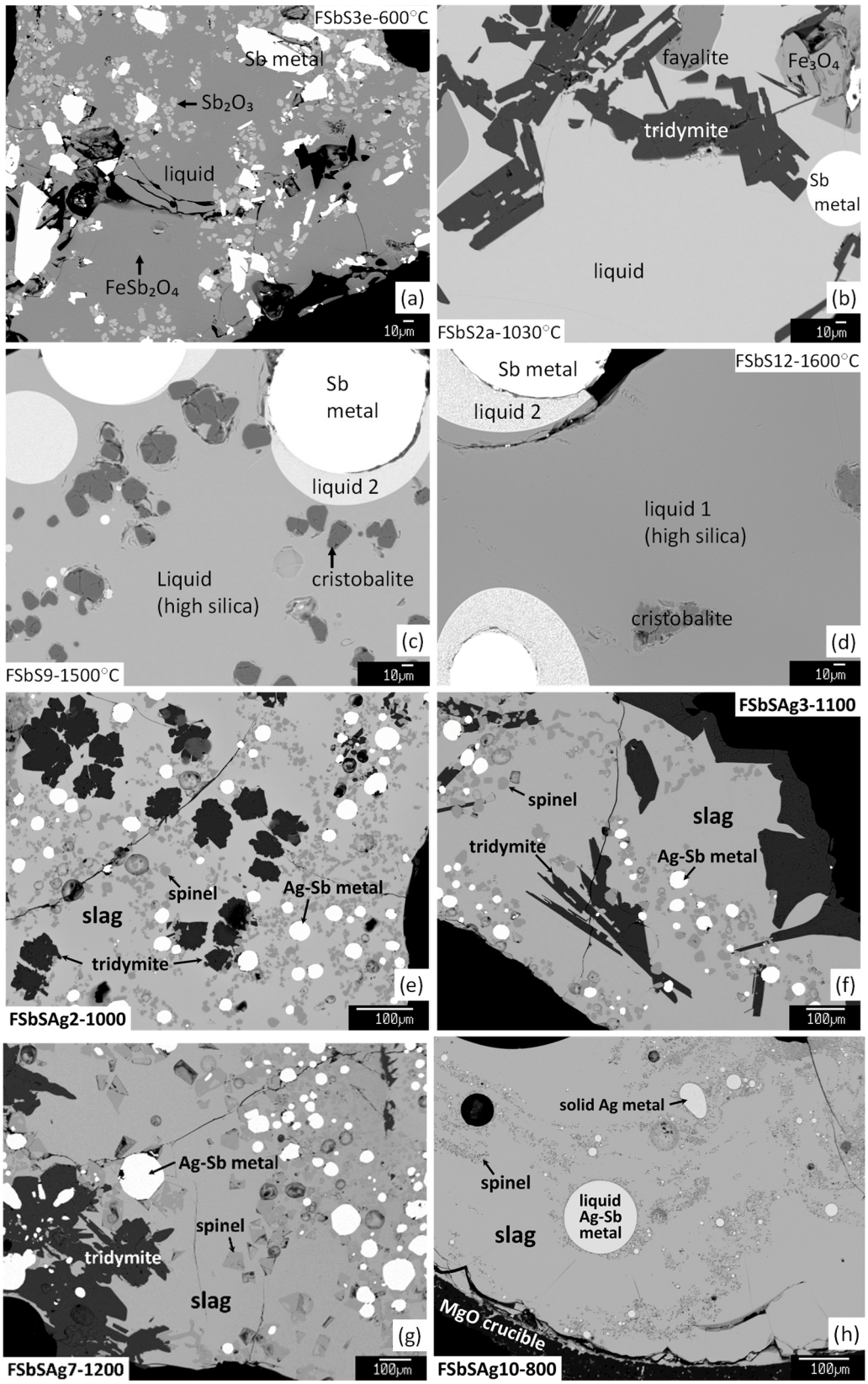

FIG 1 – Typical back-scattered electron micrographs for selected samples in the 'FeO'-$SbO_{1.5}$-SiO_2(-$AgO_{0.5}$) system in equilibrium with Sb-Fe(-Ag) metal, illustrating: (a) liquid slag, Sb_2O_3 (valentinite), $FeSb_2O_4$ (schafarzikite) and Sb metal (solid) at 600°C; (b) liquid slag, Fe_2SiO_4 (fayalite), SiO_2 (tridymite) and Sb metal (liquid) at 1030°C; (c) liquid slag 1, liquid slag 2, SiO_2 (cristobalite) and Sb metal at 1500°C; (d) liquid slag 1, liquid slag 2, cristobalite and Sb metal at 1600°C; (e) liquid slag, Ag-Sb metal, Fe_3O_4 (spinel) and SiO_2 (tridymite) at 1000°C; (f) liquid slag, Ag-Sb metal, spinel and tridymite at 1100°C; (g) liquid slag, Ag-Sb metal, spinel and tridymite at 1200°C; and (h) liquid slag, liquid Ag-Sb metal, solid Ag metal and spinel at 800°C.

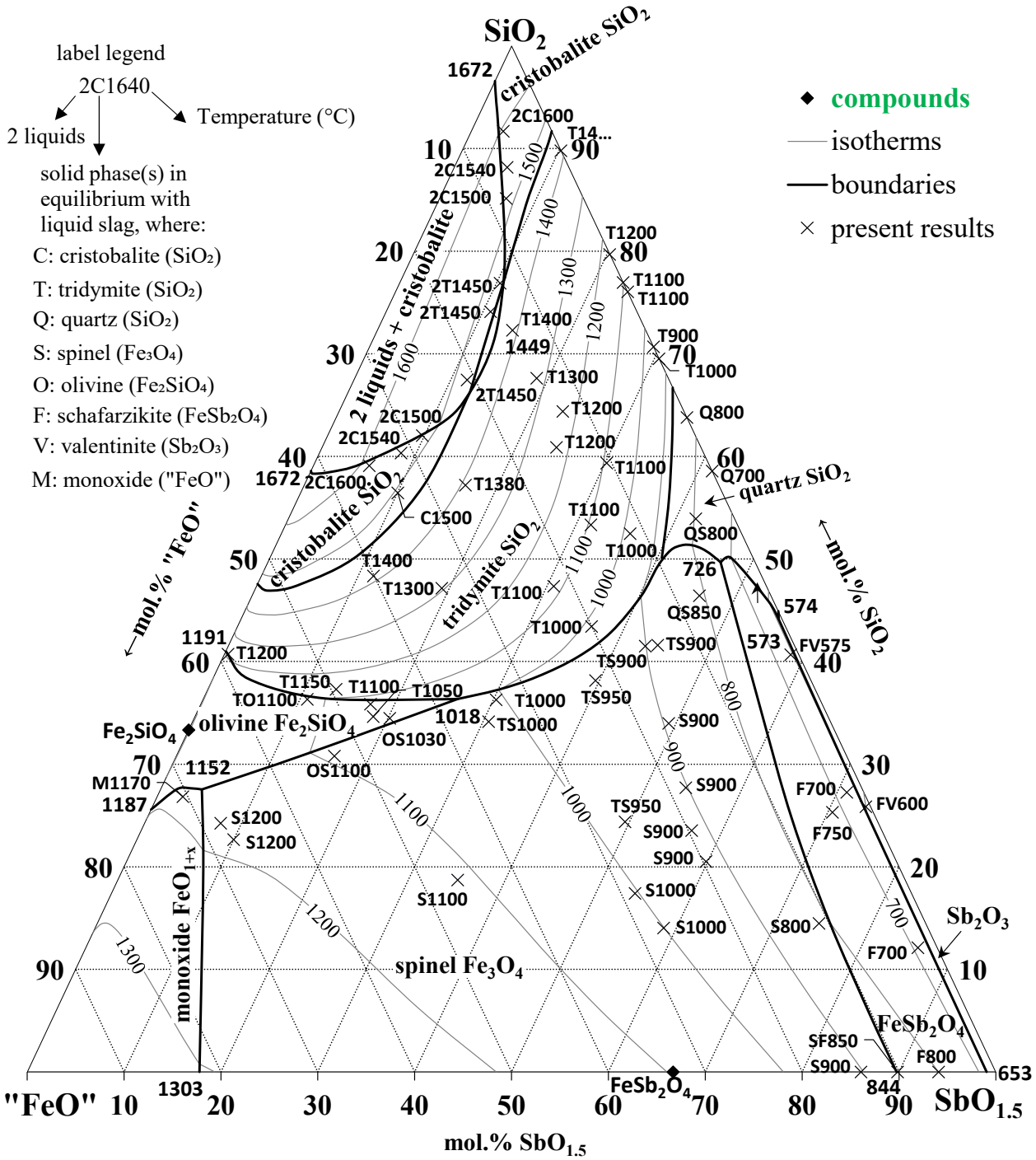

FIG 2 – Liquidus surface of the 'FeO'-$SbO_{1.5}$-SiO_2 system according to the new experimental results at 575°C to 1600°C and estimated with the thermodynamic database.

The 'FeO'-$SbO_{1.5}$-SiO_2 liquidus is dominated by spinel and quartz/tridymite/cristobalite primary phase fields. The spinel-olivine-tridymite-slag-metal invariant point is located in the central part of the triangle at 1018°C. Due to the 'oxygen buffer' nature of this point, correct description of its composition and temperature by the present thermodynamic model indicates its good quality compared to initial versions of thermodynamic parameters (Shishin *et al,* 2019, 2020) that resulted in significantly underestimated temperature for this invariant point. This improvement was achieved through revision of thermodynamic properties of the $SbO_{1.5}$ liquid endmember.

An iron antimonite phase, schafarzikite $FeSb_2O_4$ ($FeO{\cdot}Sb_2O_3$), was found at liquidus between the spinel and valentinite (Sb_2O_3) fields. This compound melts incongruently at ~844°C in the 'FeO'-$SbO_{1.5}$ pseudobinary system in equilibrium with Sb metal. A significant area of two immiscible liquids

was found over the cristobalite primary phase field, extending from the 'FeO'-SiO_2 binary monotectic at 1672°C (Wen *et al,* 2022) to a critical point at ~1449°C and 13 mol per cent $SbO_{1.5}$.

Prediction of the trend of mol per cent Fe in metal was carried out using the thermodynamic database and is given in Figure 3a. It can be seen that the trend of mol per cent Fe in Sb metal is consistent to the experimental results; however, the model overestimates the mol per cent Fe in metal. The eutectic of the $SbO_{1.5}$-SiO_2 binary (Figure 3b) estimated by thermodynamic database to form at 574°C and ~45 mol per cent SiO_2. This system has not been studied before directly, most likely due to extremely high viscosity of slags, combined with Sb_2O_3 volatility, that caused significant scatter of observed quartz and tridymite points even in the present study despite multiple precautions. The miscibility gap in the low-SiO_2 area, predicted by (Kopyto *et al,* 2009), was not confirmed, although the $SbO_{1.5}$-SiO_2 system is characterised by small positive deviations from ideal solution.

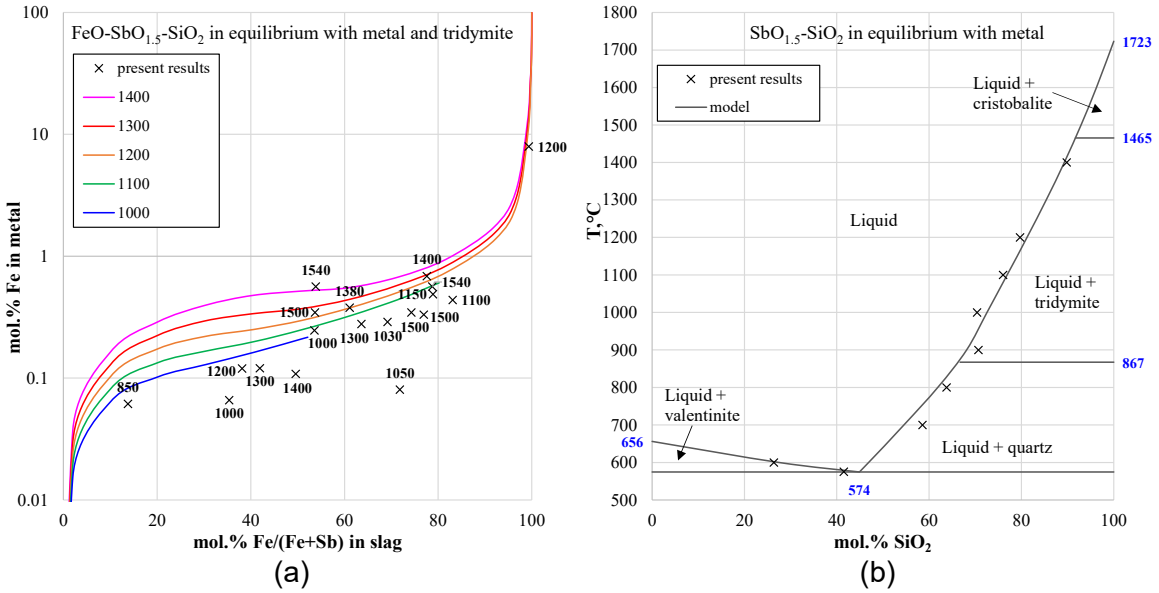

FIG 3 – (a) Prediction of trend of mol per cent Fe in metal using the thermodynamic database; (b) the eutectic of the $SbO_{1.5}$-SiO_2 binary estimated by thermodynamic database.

Experimental results on phase equilibria in the Fe-Sb-Si-O+Sb metal system served well to produce initial set of model parameters in the slag. Further refinement, particularly the distribution of excess Gibbs energy among the 'FeO'-Sb_2O_3-SiO_2 and 'Fe_2O_3'-Sb_2O_3-SiO_2 interactions, required the study at more oxidising conditions, compared to those typically observed during slag fuming. Often for systems containing iron, extremely oxidising conditions (eg in air atmosphere) are used to provide the limiting case when most of iron is Fe^{3+}. In the present project, this type of study would not provide the necessary information for the 'Fe_2O_3'-Sb_2O_3-SiO_2 interactions, because Sb can also exhibit higher oxidation state of Sb^{5+}. Thus, a study at moderately oxidising conditions was designed, where significant amount of Fe^{3+} is expected, but Sb is still predominantly in a form of Sb^{3+}.

The flow of gas with fixed $p(O_2)$ cannot be used due to high volatility of Sb-containing gaseous species. Alternatively, the oxygen potential can be increased by the addition of an inert metal, silver or gold to liquid Sb. According to the equation Sb (metal) + $0.75O_2$ = $SbO_{1.5}$ (slag), for a fixed activity of $SbO_{1.5}$ in slag, decreasing the activity of Sb by dissolution in inert metal would cause an increase in $p(O_2)$. This method would not provide the value of $p(O_2)$ directly, but in combination with thermodynamic modelling, it will give the necessary data for the model. Silver (Ag) was chosen as an inert alloying metal due to its affordability and low melting temperature. Liquid Ag-Sb alloys with low concentrations of Sb of a few percent were used. At these conditions, the concentration of $AgO_{0.5}$ in slag is expected to be <1 mol per cent, which would have a small effect on observed phase equilibria in the oxide system. In addition, important information on the solubility of silver in slags is produced, which can be valuable when treating electronic recycling materials or primary silver-containing ores through the Pb process. Two main areas were addressed: the spinel-tridymite

boundary (high-SiO_2 slag, Figure 4) and spinel liquidus (low-SiO_2 slag, Figure 5). The SiO_2-free slags were not attempted to study due to their extreme volatility.

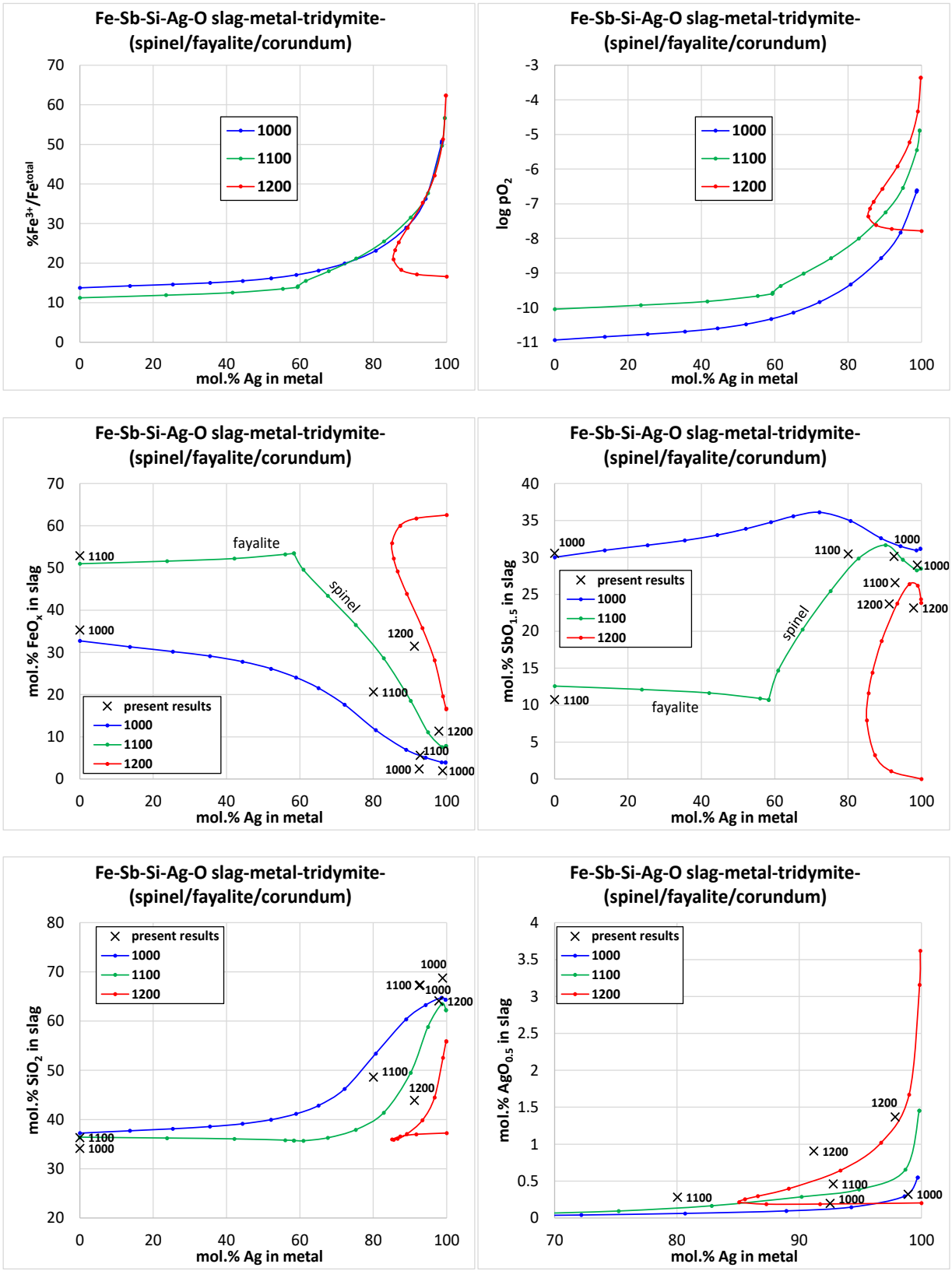

FIG 4 – Phase equilibria in the FeO-$FeO_{1.5}$-$SbO_{1.5}$-SiO_2-(Ag) system. Composition of slag and $p(O_2)$ in equilibrium with Ag-Sb metal, tridymite and either spinel, or fayalite, or corundum at 1000, 1100 and 1200°C are shown as a function of Ag in metal (the rest is Sb with traces of Fe). Lines are calculated using the thermodynamic model of the present study, black squares are experimental results, obtained in this study.

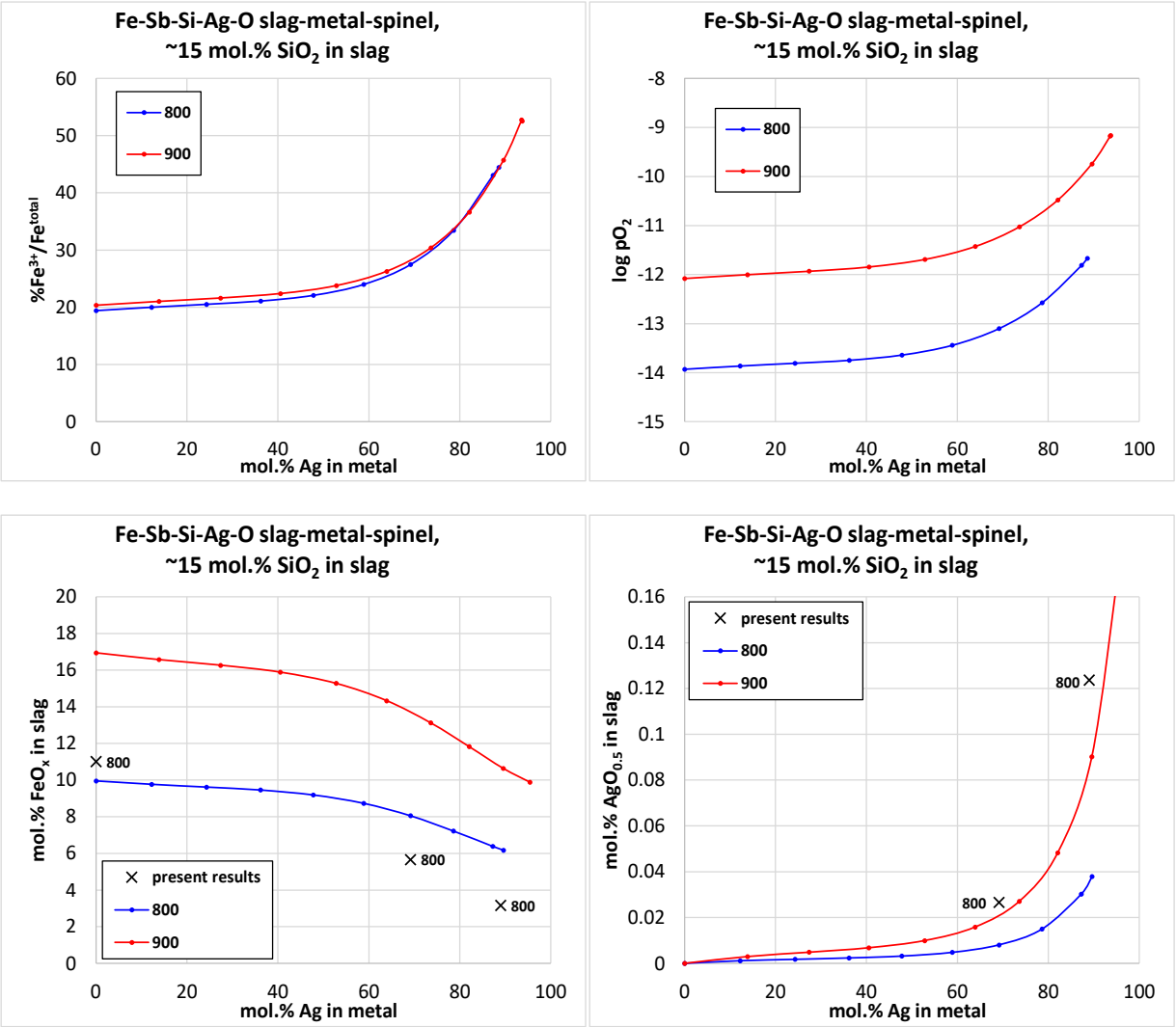

FIG 5 – Phase equilibria in the FeO-$FeO_{1.5}$-$SbO_{1.5}$-SiO_2-(Ag) system (low-SiO_2 slag). Composition of slag and p(O_2) in equilibrium with Ag-Sb metal and spinel 800 and 900°C are shown as a function of Ag in metal (the difference is Sb). Lines are calculated using the thermodynamic model of the present study, black squares are experimental results, obtained in this study.

As can be seen, the studied area covers a significant range of Fe^{3+}/Fe^{total} (from 10–20 per cent in the Fe-Sb-Si-O system in equilibrium with Sb metal, to 60–70 per cent in equilibrium with high-Ag, low-Sb metal. This allowed to deconvolute the separate contributions of the FeO-Sb_2O_3(-SiO_2) and Fe_2O_3-Sb_2O_3(-SiO_2) systems. The fact that total Fe solubility in slag at spinel liquidus dramatically decreases with replacing Sb by Ag in metal (more oxidising conditions) means that there are positive interaction parameters (Gibbs energy) in the Fe_2O_3-Sb_2O_3(-SiO_2) system compared to FeO-Sb_2O_3(-SiO_2).

CONCLUSIONS

While no previous publication could be found on liquidus of the FeO-$FeO_{1.5}$-$SbO_{1.5}$-SiO_2 system in equilibrium with metal, this study provided experimental results and thermodynamic modelling of the liquidus in this system. There are minor discrepancies between the experimental tridymite(quartz)-spinel boundary and the line calculated with the thermodynamic model (overestimated SiO_2 by up to 5 mol per cent). In this study, a new phase $FeSb_2O_4$ (schafarzikite) was found and added to the FactSage compounds list. No solid solutions (eg Sb in spinel, tridymite etc) were found in the system. Study of the $SbO_{1.5}$-SiO_2 binary system is challenging. This system is characterised by extremely high viscosity. Compositional gradients were observed in the samples at quartz/tridymite liquidus even after 1–2 weeks of equilibration. When amorphous SiO_2 (crushed ampoules) is used as a reagent, in all systems it usually instantly transforms to a crystalline phase on interaction with other

components. With $SbO_{1.5}$, however, it fails to crystallise for very long time. Instead, chunks of amorphous (supercooled liquid) SiO_2 remain surrounded by a continuum of slags with gradually increasing $SbO_{1.5}$ concentration. Further development of the technique is required to overcome this issue.

ACKNOWLEDGEMENT

The authors would like to thank Australian Research Council Linkage programs LP180100028 and LP190101020 as well as consortium of lead and copper producers: Aurubis, BHO OD, Boliden, Glencore Technology, Kazzinc Ltd. Glencore, Nyrstar, Peñoles, RHI Magnesita, Rio Tinto Kennecott and Umicore for the financial support for this study. The authors are very grateful to Professor Peter Hayes for initiating and contributing in this research program. The authors would like to thank Mrs Suping Huang and Mrs Samaneh Ashjaa for assistance in the experiments and also the staff at the Centre for Microscopy and Microanalysis (CMM), University of Queensland for technical support.

REFERENCES

Hidayat, T, Henao, H M, Hayes, P C and Jak, E, 2012. Phase Equilibria Studies of the Cu-Fe-O-Si System in Equilibrium with Air and with Metallic Copper, *Metall Mater Trans, B,* 43:1034–45.

Jak, E, 2012. Integrated experimental and thermodynamic modelling research methodology for metallurgical slags with examples in the copper production field, in *Proceedings of the 9th Intl Conf on Molten Slags, Fluxes and Salts*, 28 p (The Chinese Society for Metals).

Jak, E, Hayes, P C and Lee, H-G, 1995. Improved methodologies for the determination of high temperature phase equilibria, *Korean Journal of Minerals and Materials Institute (Seoul)*, 1:1–8.

Kopyto, M, Przybylo, W, Onderka, B and Fitzner, K, 2009. Thermodynamic properties of Sb_2O_3-SiO_2 and PbO-Sb_2O_3-SiO_2 liquid solutions, *Arch Metall Mater,* 54:811–822.

Shishin, D, Hidayat, T, Chen, J, Hayes, P C and Jak, E, 2019. Combined Experimental and Thermodynamic Modeling Investigation of the Distribution of Antimony and Tin between Phases in the Cu-Fe-O-S-Si System, *CALPHAD*, 65:16–24.

Shishin, D, Hidayat, T, Sultana, U, Shevchenko, M and Jak, E, 2020. Experimental measurement and thermodynamic model predictions of the distributions of Cu, As, Sb and Sn between liquid lead and PbO-FeO-Fe_2O_3-SiO_2 slag, *International Journal of Materials Research*, 111:733–743.

Wen, X R, Cheng, S, Shevchenko, M and Jak, E, 2022. Experimental Study of the Cu_2O-FeO-Fe_2O_3-SiO_2 and FeO-Fe_2O_3-SiO_2 Slag Systems at fixed oxygen partial pressures, in COPPER 2022, Santiago, Chile.

Overview of the experimental phase equilibria studies of the Ni-Sn-S, Cu-Sb-S, Cu-Sn-S, Fe-Sb-As and Fe-Sn-As systems

DOI: 10.62053/WTUW4662

M Akhtar[1], M Shevchenko[2] and E Jak[3]

1. PhD student, Pyrometallurgy Innovation Centre (PYROSEARCH), School of Chemical Engineering, The University of Queensland, Brisbane Qld 4072, Email: m.akhtar@uq.edu.au
2. Senior Research Fellow, Pyrometallurgy Innovation Centre (PYROSEARCH), School of Chemical Engineering, The University of Queensland, Brisbane Qld 4072. Email: m.shevchenko@uq.edu.au
3. Professor, Pyrometallurgy Innovation Centre (PYROSEARCH), School of Chemical Engineering, The University of Queensland, Brisbane Qld 4072. Email: e.jak@uq.edu.au

ABSTRACT

This article presents an overview of the experimental phase equilibria studies of S-containing systems (Ni-Sn-S, Cu-Sb-S, and Cu-Sn-S) and As-containing systems (Fe-Sb-As and Fe-Sn-As). These systems improve the prediction capabilities of FactSage in a 20-component 'Cu_2O'-PbO-ZnO-FeO-Fe_2O_3-CaO-SiO_2-S-(Al_2O_3-MgO-CrO-Cr_2O_3-Na_2O)-(As, Sn, Sb, Bi, Ag, Au, Ni, Co) system for complex pyrometallurgical operations during both refining and recycling. Experiments involved equilibration at predetermined temperatures (300–1200°C) with or without preheating, followed by rapid quenching in a brine. Quenched samples were then directly measured using an electron probe microanalyser. For the Ni-Sn-S system, liquid phases (NiS- and SnS-rich mattes and liquid metal) and solid phases ($Ni_{1+x}Sn$, SnS, Ni_3Sn, FCC-Ni, $Ni_{1-x}S$, NiS_2, Ni_3Sn_4, SnS_2, Sn_2S_3 and β-Ni_3S_2) were observed. A new $Ni_3Sn_2S_2$ phase was found to melt incongruently. For the Cu-Sb-S system, liquid metal, matte, FCC-Cu, digenite, Sb, $CuSbS_2$, Cu_3SbS_3 and Cu_3SbS_4 phases were observed. For the Cu-Sn-S system, liquid metal, matte, digenite, SnS and Cu_3Sn phases were found at liquidus. Also, the immiscibility gaps spread from:

1. The Sn-S binary toward the Ni-rich side in the Ni-Sn-S system.
2. The Cu-S binary toward the Sb-S binary in the Cu-Sb-S system.
3. The Cu-S binary toward the Sn-S binary in the Cu-Sn-S system.

The immiscibility gap in the Cu-Sn-S system is wider than in the Cu-Sb-S system. For the Fe-Sb-As system, liquid metal, $FeAs_2$, $Fe_{1-x}Sb$, Fe_2As, FeAs, $FeSb_2$ and BCC-Fe phases were found. For the Fe-Sn-As system, an immiscibility gap near the Fe-Sn system was observed with liquid metal (Fe-rich and Sn-rich) and $Fe_5(Sn, As)_3$, Fe_2As, FeAs and $FeAs_2$ phases.

INTRODUCTION

The steady decline in the availability of high-grade ores has led to enhanced interest in metal recovery through recycling (Seitkan *et al*, 2020). Pyrometallurgy is a proficient route for metal recovery (Rudnik, 2016).

For the Ni-Sn-S system, Peacock and McAndrew (1950) reported the Sn isomorph of shandite ($Ni_3Sn_2S_2$) compound. Bok and Boeyens (1957) reported Ni_2SnS_4 and $NiSn_2S_4$ compounds. Brower, Parker and Roth (1974) reported incongruently melting $Ni_3Sn_2S_2$ compound. Nitta *et al* (1976) synthesised a Ni_3SnS_7 compound.

Jumas *et al* (1977) reported Ni_2SnS_4 compound. Kusumoto, Fujimoto and Fujitani (2001) reported Cu, V, Cr, Mn, Fe, Co, Ni, Sn and S containing lithium secondary battery, having $Ni_{0.2}Sn_{0.8}S_2$ compounds. Ma and Beckett (2018) reported Ni_6SnS_2 compound.

For the Cu-Sb-S system, Pelabon (1905) studied the Cu_2S-Sb_2S_3 system. Groth (1908) reported Cu_3SbS_3 and $CuSbS_2$ compounds. Meisner (1921a) studied the Cu-Sb-S isotherms and reported Cu_3SbS_3 and $CuSbS_2$ compounds. Asano and Wada (1968) reported a miscibility gap at 1200°C. Godovikov and Il'yasheva (1969) studied the Cu_2S-Sb_2S_3-S system.

Skinner, Luce and Makovicky (1972) studied liquidus of the Cu-Sb-S system. Gather and Blachnik (1976) studied the Cu_2S-Sb system. Chang, Newmann and Choudary (1979) reported isotherms of

the Cu-Sb-S system. Karup-Moller (2000) reported isothermal section of Cu-Sb-S system at 700°C. Braga *et al* (2008) studied invariant reactions. Mammadli *et al* (2021) studied the $CuSbS_2$-Cu_3SbS_4-Sb_2S_3 system. Mammadli, Gasimov and Babanly (2022) studied the Cu_3SbS_4-Sb_2S_3-S system. Mammadli *et al* (2022) studied the $CuSbS_2$-Sb_2S_3-Sb system.

For the Cu-Sn-S system, Meisner (1921b) studied the Cu-Sn-S system. Moh and Ottemann (1962) studied the Cu-Sn-S system. Gerlach, Hennig and Trettin (1969) reported a Cu-Sn-S phase diagram with 1 per cent Ag at 1200°C.

Khanafer, Rivet and Flahaut (1974) studied different quasi-binaries, *viz* Cu_2S-SnS, Cu_2S-Sn_2S_3 and Cu_2S-SnS_2. Fiechter *et al* (2003) studied quasi-binary Cu_2S-SnS_2. Pogue *et al* (2019) studied isotherms of the Cu-Sn-S system at 25°C and 400°C.

For the Fe-Sb-As system, Landon and Mogilnor (1933) reported colusite mineral, containing Sb, As, Fe, Zn, Sn, Te, Mo, Cu, S and traces (Cr and W). Nurbaev, Toguzov and Onaev (1981) reported impurities removal from lead by adding Fe powder. Toguzov *et al* (1984) studied the liquidus of the Fe-Sb-As system. Peterson and Twidwell (1985) reported removal of As by roasting with pyrite from Sb-As-Bi-Ag-Au-Cu containing lead bullion. Jurkovic *et al* (2019) reported Fe-Sb-As mineral in soils as the Fe-Sb-As-Zn-Pb oxides with few minor elements. Sorulen *et al* (2019) reported Fe-Sb and Fe-Sb-As oxide minerals.

For the Fe-Sn-As system, Okunev *et al* (1975) reported an addition of alloys like ferro-chromium, silico-chromium and their mixtures improve the recovery of Sn in the Fe-Sn-As alloy. Chumarev, Sholokhov and Okunev (1979) reported activities of Sn and As and distribution of Sn and As between Fe-Sn-As-(Si-Cr-Mn) alloy and lead. Mueller *et al* (1979) reported tin recovery from ores at 1000–1100°C by removing As and S. Kovrigin, Chursin and Pichugin (1985) reported temperature dependence of dross formation. Jiang *et al* (2011) reported removal of As and Sn from Sn-As containing iron concentrated. Zheng *et al* (2019) reported recovery of Fe and Cu at 1300°C by removing Sn and As through selective oxidation.

No literature about the liquidus and solidus of the Ni-Sn-S and Fe-Sn-As systems was found. For the Cu-Sb-S and Cu-Sn-S systems, literature about liquid-solid phase equilibria along the Cu_2S-Sb_2S_3, Cu_2S-SnS, Cu_2S-SnS_2 joins are mostly available. Therefore, an attention is required towards new technologies for Ni, Sn, Cu, Sb, Fe and As elements for enhanced refining from complex feeds. So far, without the knowledge of matte-liquid metal phase equilibria, metals can be targeted separately.

The scope of this research was to investigate the liquidus and solidus of the Ni-Sn-S, Cu-Sb-S, Cu-Sn-S, Fe-Sb-As and Fe-Sn-As systems. This work will support the 20 component 'Cu_2O'-PbO-ZnO-FeO-Fe_2O_3-CaO-SiO_2-S-(Al_2O_3-MgO-CrO-Cr_2O_3-Na_2O)-(As, Sn, Sb, Bi, Ag, Au, Ni, Co) system in Cu, Zn, Fe and Pb smelting (Jak *et al*, 2023) for enhanced prediction of both complex feeds and products at different extraction stages.

EXPERIMENTAL AND ANALYTICAL METHODOLOGIES

Experimental and analytical methodologies are based on the publication from (Jak, 2012).

Materials

High purity Fe, Cu, Sb, Sn, CuS, Cu_2S, S, Ni and NiS powders and As lump were used as shown in Table 1 with manufacturer's details. To prevent S evaporation and fast achievement of thermodynamic stable phases, Sb_2S_3, SnS, Sn_2S_3 and SnS_2 master compounds were prepared as explained later.

TABLE 1

Purity and supplier of elements and a compound as powders.

Element/ compound	Purity (%)	Manufacturer
As lump	99.999	Alfa Aesar, USA
Fe	99.998	
Cu	99.9	
Sb	99.999	
Sn	99.85	
CuS	99.8	
Cu_2S	99.5	
S	99.999	Aldrich Chemical Company, USA
Ni	99.99	Sigma Aldrich, Germany
NiS	99.99	Changsha Easchem Co. Ltd., China

Preparation of powder mixtures to pelletising

The bulk compositions were calculated using the internal FactSage database where 2- or 3-phase assemblages were targeted with a minimum of one liquid phase. The proportion of solid was always lowered by picking a bulk composition to realise equilibration fast with enhanced quenching rate.

A 10 g mixture was used for master compounds while a 400 mg mixture was used for bulk compositions. These mixtures were made by blending in an agate mortar using a pestle, followed by compression under pressure of ~80–150 bar using a tool steel die.

Apparatus

All experiments were performed in a vertical impervious alumina tube, surrounded by four resistance heating elements. Before proceeding to the experiments, a hot zone in the furnace was calibrated at 1000°C±1°C, followed by temperature calibration by using B and R-type thermocouples simultaneously in the air. These thermocouples were calibrated against standard thermocouples, supplied by National Measurement Institute of Australia, NSW, Australia.

Experimental procedure

For better quenching practice, the bottom of the quartz ampoules was expanded by carefully reducing its thickness by controlled heating from all sides in the presence of controlled pressurised air inside. This improves fracturability on quenching.

These modified ampoules were evacuated and sealed in vacuum. Due to the small sample size and the small ampoule in both height (~1.5–2 cm) and weight (4–6 g), an additional weight as a high-temperature corrosion-resistant tube was placed on an ampoule. A Kanthal-D (FeCrAl alloy) wire (diameter = 0.7 mm) was used to hang ampoules inside the hot zone of the furnace. Some length of the wire at the bottom end was always cut to ensure its strength.

Experiments are based on a closed system (controlled by condensed phases). Experiments were performed by hanging the ampoules at a specific temperature (300–1200°C) in a predetermined hot zone in the air by using Kanthal wire. The test was completed after elapsing a certain time (minimum 1 hr for 1200°C, 2 hrs for 1100°C, 4 hrs for 700–1000°C, 6 hrs for 600°C and 2–4 days for 500°C equilibration temperature). Equilibration time was determined for a particular system by equilibrating a fixed bulk composition for different time and temperatures. The wire was pulled from the upper side of the tube, causing a free fall under gravity on an alloy cylinder that was immersed in 25 per cent $CaCl_2$ or 25 per cent $MgCl_2$ brine at -20°C. This resulted in a quick fracture of the

ampoule due to load and expanded bottom. Thus, brine was in contact with quenched phases. The samples were cleaned with tap water, followed by cleaning with ethanol and finally dried in the forced convection oven.

Manufacturing master compounds

Pelletised elemental powders corresponding to the molar ratio of SnS, Sn_2S_3, SnS_2 and Sb_2S_3 master compounds were used. Each mixture was sealed in an ampoule in a vacuum, followed by inserting it in a furnace.

SnS and Sb_2S_3 mixtures were heated from 400°C to 500°C at the rate of 0.5 K/min, followed by equilibration for 3 hrs and then natural air cooling to room temperature.

Sn_2S_3 mixture was heated from 300°C to 800°C at a rate of 0.2 K/min, followed by 3 hrs of equilibration. After equilibration, the temperature was dropped to 750°C with a rate of 0.5 K/min, where it was re-equilibrated for another 1 hr, followed by cooling to 400°C with a rate of 1 K/min. SnS_2 mixture was heated from 300°C to 790°C with a rate of 0.2 K/min, followed by 71 hrs of equilibration. After that, the temperature was dropped to 400°C with a 1 K/min rate. Finally, both Sn_2S_3 and SnS_2 were naturally air-cooled from 400°C to room temperature.

Two-step pre-heating

As sublimation during equilibration retards equilibrium. Therefore, to attain equilibrium fast, it is essential to allow the formation of arsenide before equilibration. Accordingly, preheating at 600°C for 1 hr was given for each bulk mixture.

The pre-heating of a bulk mixture at a temperature was given to undergo full or partial melting of bulk composition. This step ensures an accomplished mass diffusion between or among in-contact phases so that only a thermodynamic stable phase form. In this work, Fe-As and Fe-Sb compounds have higher melting points than many equilibration experiments performed. Also, a few experiments (containing master compounds in bulk mixtures) were performed below the melting point of the used master compounds. These are the potential reasons for this uncertainty. Therefore, many samples were given a second pre-heating to ensure fast attainment of equilibrium between or among stable phases.

Analysis of samples

Different faces of a quenched sample were mounted in an epoxy resin. Conventional metallography was performed to get mirror-like polishing, followed by optical microscopy. Before electron probe microanalysis (EPMA) measurements, optical microscopy provides three information types:

1. Surface roughness.
2. Abrasive residues.
3. Phases formed on quenching; checking all of that ensures that samples are ready for EPMA.

The samples were kept in a vacuum desiccator most of the time between polishing and EPMA.

Phase identification and microanalyses

Samples were transported to the EPMA lab (Centre for Microscopy and Microanalysis (CMM), The University of Queensland) after observing under an optical microscope, followed by sealing them in a portable vacuum jar. The resin blocks were carbon coated.

Compositions of quenched phases were directly measured using EPMA. Employment of EPMA by using the wavelength dispersive spectrometer increases the accuracy of the composition of the quenched phases as compared to energy dispersive X-ray spectroscopy and bulk wet chemistry methods.

JEOL JXA 8200L EPMA, manufactured by Japan Electron Optics Ltd., Tokyo was used for this study. In each EPMA session, standards were freshly calibrated and were put in every set of experiments as an unknown at the start, intermediate, and end of measurements, depending upon the number of points in a particular set.

Reference standards (Cu K_α, Sb L_α, Fe K_α, and Ni K_α as pure elements, S K_α as $CuFeS_2$, As L_α as InAs, and Sn L_α as SnO_2) were provided by Charles M Taylor Co., Stanford, CA. SiO_2 as a standard for Si K_α was also added in each set to monitor any contamination due to the usage of ampoules and abrasives.

Probe current = 38 nA at an accelerating voltage = 15 kV with various probe diameters, ranging from 0 to 200 μm were selected for measurement. The selection of probe diameter depends on:

1. Solid or liquid.
2. Homogeneity and heterogeneity of phase.

For example, solids are mostly homogeneous in each range of solid solutions or stoichiometric. Hence, any probe diameter is applicable, depending upon the physical size of the phase. However, extensive care was given to select the probe diameter for a liquid for uncertainty minimisation of chemical composition as follows.

Depending on the size of the liquid phase area

If liquid metal of 100 μm was observed, then 90 μm of probe diameter was considered to measure the liquid metal. Otherwise, new bulk composition was selected and experiment was repeated.

Quenching quality

When dendritic structures or precipitates or both was found then grid option was selected with 90 μm, 150 μm and 200 μm of probe diameter.

Presence of another stable liquid or solid phase

When excessive proportion of solid or second liquid phase (say matte) was observed, which sometimes causes an insufficient area for the measurement of liquid metal by EPMA. In such cases, bulk composition was modified, and experiment was repeated.

The Duncumb-Philibert ZAF correction integrated with EPMA software was applied. 5–70 points per phase were measured.

After measuring at a particular probe diameter with standards as unknowns, a second correction was performed for each measured element in a stable phase against standard reference material. Copper, antimony, iron and nickel were corrected against their pure elemental standard, sulfur was corrected against $CuFeS_2$, As was corrected against InAs and tin was corrected against SnO_2.

Confirmation of equilibrium accomplished with four-point assessments

Jak (2012) reported assurance of equilibrium attainment using four-point assessments of phase equilibria.

Varying equilibration time

It assists in observing thermal and chemical equilibrium over time. It also ensures the dissolution of any metastable phase that leads to a final and no change in the chemical composition of each phase formed over elapsing time.

Direct measurement of quenched phases to determine homogeneity by using EPMA with WDS

Measuring using EPMA is the second step in getting confidence in the achievement of equilibration of phases formed during ‘producing final equilibrium point with different bulk compositions’ against their chemical homogeneity. It also reflects a transition from non-equilibrium to metastable and finally equilibrium.

Producing final equilibrium point with different bulk compositions

It confirms the studied system is approaching thermodynamic equilibrium irrespective of the direction adopted like the different bulk mixtures, different equilibration temperatures with mandatory first preheating and optional second pre-heating of the starting mixture, etc.

Systematic analyses of specific phase equilibrium reactions

It involves in-depth analyses of reactions occurring in the area of temperature interest to confirm both equilibrium achievement and results accuracy. The previous three subheadings (varying equilibration time, direct measurement of quenched phases to determine homogeneity by using EPMA with wavelength dispersive spectrometry (WDS), and producing final equilibrium point with different bulk compositions) lack in confirming the achievement of thermodynamic equilibrium as proximity to an equilibrium point of a system minimises its driving force to accomplish the same. In many systems, a phase of fixed solid solution or stoichiometry, either cannot be quenched to room temperature or transform into another phase within an hour to months. Sophisticated analytical techniques like EPMA contribute to identifying possible complete or incomplete reactions that occurred during equilibration, followed by their correlations at various temperatures of interest. One possible way is the line analysis of composition by using EPMA.

Further planning to complete analyses

The experimental direction was from liquidus to solidus, where equilibration at high temperature was first done and then advanced towards a lower temperature. This methodology reduces the possibility of the formation of metastable phases. It allows the fast accomplishment of thermodynamic equilibrium and eases the systematic analyses of possible phase equilibria reactions. After analysing the first set of results, further experiments were planned based on:

1. Target phases and primary phase field.
2. Number of phases (minimum two-phase assemblage was selected to move further).
3. The presence of solid fraction and its type.
4. Target phase equilibria reaction.

When solid fraction was observed to increase with a decline in equilibration temperature then at some point, the bulk composition was modified.

RESULTS AND DISCUSSIONS

All experimental results were in agreement with the average and standard deviation (mathematically calculated using measured five points for the solids and 70 points for the liquids) of measured phases.

Ni-Sn-S system

In this system, liquidus, solidus, boundaries and primary phases field(s) of liquid phases (NiS- and SnS-rich mattes and liquid metal), MeX ($Ni_{1+x}Sn$), SnS, Ni_3Sn, FCC-Ni, $Ni_{1-x}S$, NiS_2, Ni_3Sn_4, SnS_2, Sn_2S_3 and β-Ni_3S_2 phases were studied with incongruently melting $Ni_3Sn_2S_2$ ternary compound (Figure 1). Here, the immiscibility gap spreads from the Sn-S binary towards the Ni-rich side. Microstructures of different phases are shown in Figure 2. The point E in the diagrams is eutectic, the point U is peritectic, the point P is quasi-peritectic, the point S is syntectic, the point M is monotectic and the point Sa is the saddle point.

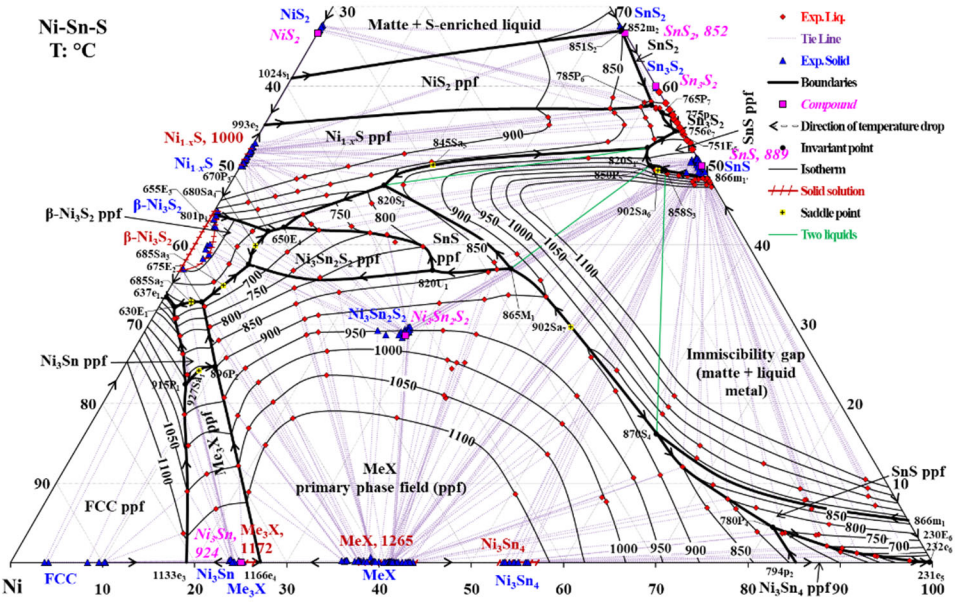

FIG 1 – Ni-Sn-S ternary phase diagram, showing experimental liquids and solids with liquidus, solidus, boundaries, isotherms and primary phase fields.

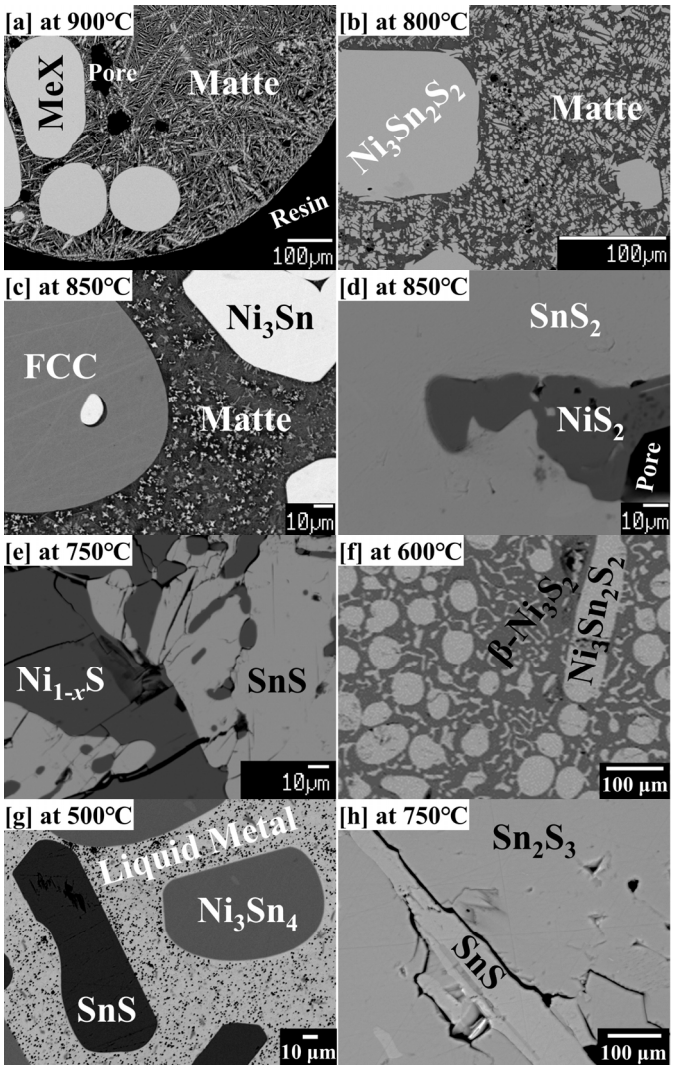

FIG 2 – Microstructures in backscattered electron mode for Ni-Sn-S system, showing: (a) matte and MeX, (b) matte and $Ni_3Sn_2S_2$, (c) matte, FCC-Ni and Ni_3Sn, (d) NiS_2 and SnS_2, (e) $Ni_{1-x}S$ and SnS, (f) $Ni_3Sn_2S_2$ and β-Ni_3S_2, (g) liquid metal, SnS and Ni_3Sn_4, and (h) SnS and Sn_2S_3 phases.

Cu-Sb-S system

For the liquid metal, matte, FCC-Cu, digenite (Cu_2S_{1+x}), Sb, Cu_3SbS_4, $CuSbS_2$ and Cu_3SbS_3 phases, liquidus, solidus, boundaries and primary phases fields were investigated (Figure 3). Here, the immiscibility gap spreads from the Cu-S binary towards the Sb-S binary at all compositional ranges of the Cu-Sb binary. Microstructures of phases found are shown in Figure 4.

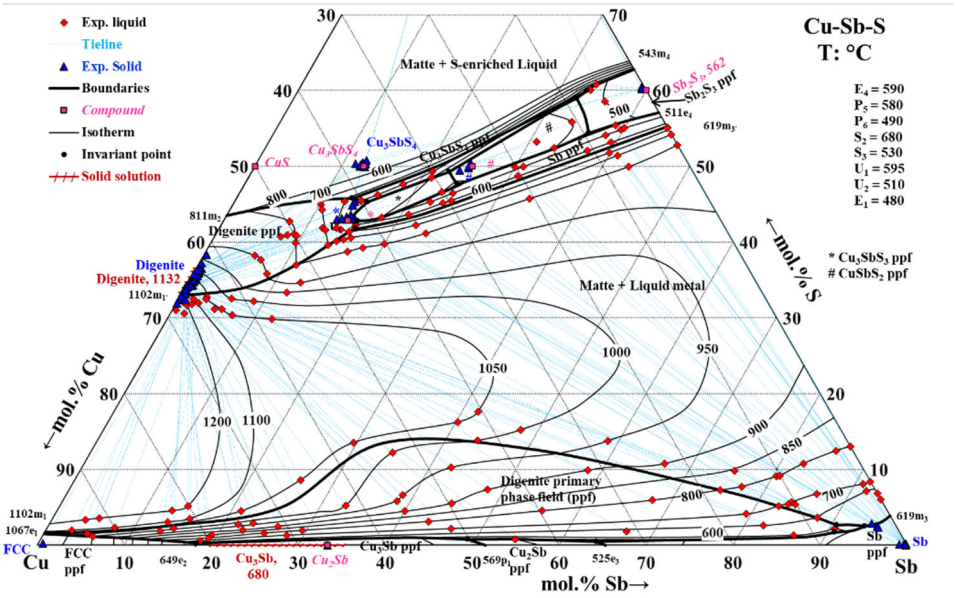

FIG 3 – Cu-Sb-S ternary phase diagram, showing experimental liquids and solids with liquidus, solidus, boundaries, isotherms and primary phase fields.

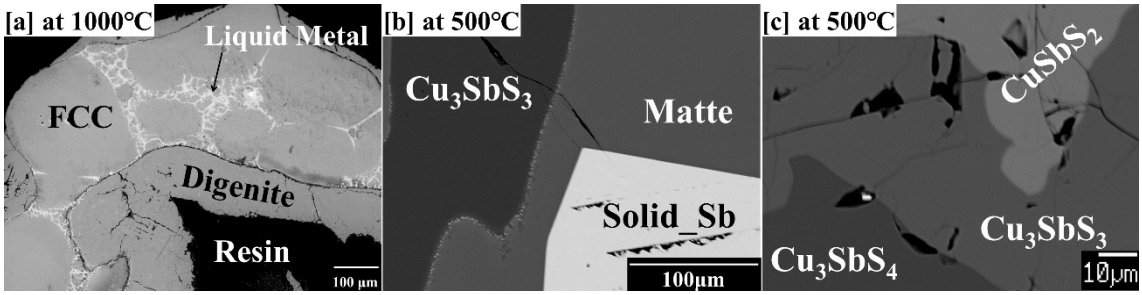

FIG 4 – Microstructures in backscattered electron mode for Cu-Sb-S system, showing: (a) liquid metal, FCC-Cu and digenite (Cu_2S_{1+x}), (b) matte, Cu_3SbS_3 and solid_Sb, (c) $CuSbS_2$ and Cu_3SbS_3 and Cu_3SbS_4.

Cu-Sn-S system

For this system, liquidus, solidus, boundaries and primary phases field(s) of liquid metal, matte, digenite (Cu_2S_{1+x}), SnS and Cu_3Sn phases were studied (Figure 5). Study of liquidus involving the Cu_2SnS_3, Cu_4SnS_4, $Cu_5Sn_2S_7$ and $Cu_2Sn_3S_7$ ternary compounds is in progress. Here, the immiscibility gap spreads from the Cu-S binary towards the Sn-S binary at all compositional ranges of the Cu-Sn binary, which is wider than the immiscibility gap observed for the Cu-Sb-S system. Microstructures of different observed phases are shown in Figure 6.

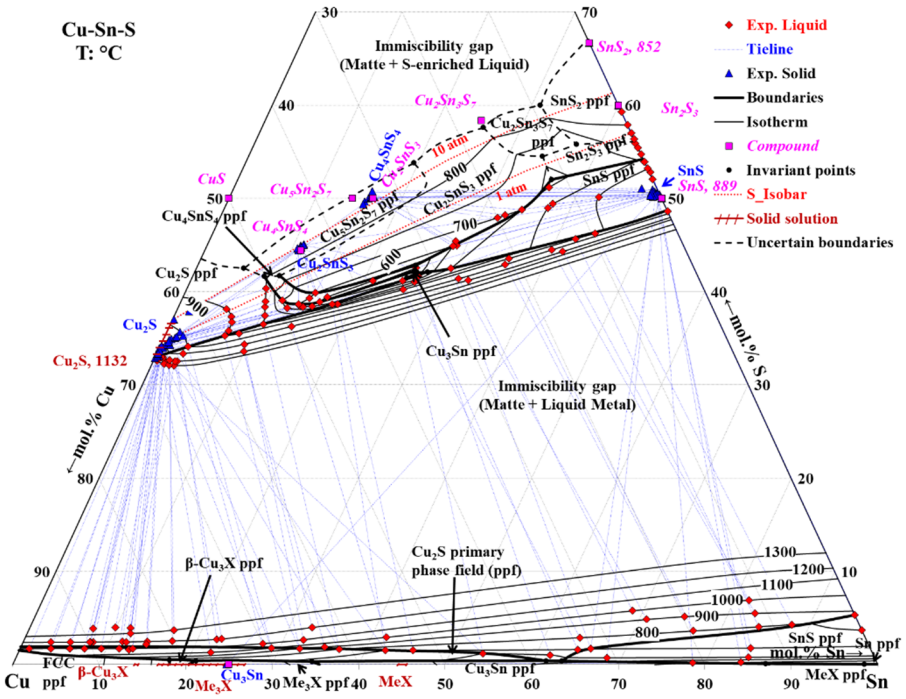

FIG 5 – Cu-Sn-S ternary phase diagram, showing experimental liquids and solids with liquidus, solidus, boundaries, isotherms and primary phase fields.

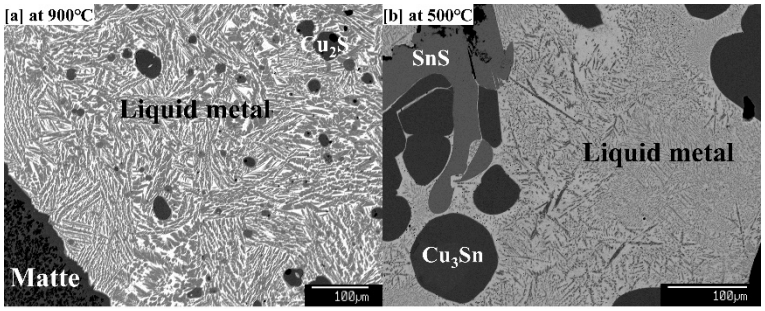

FIG 6 Microstructures in backscattered electron mode for Cu-Sn-S system, showing: (a) matte, digenite (Cu_2S) and liquid metal, and (b) liquid metal, SnS, Cu_3Sn.

Fe-Sb-As system

In this system, liquidus, solidus, boundaries and primary phases field(s) for liquid metal, $FeAs_2$, $Fe_{1-x}Sb$ (MeX), Fe_2As, FeAs, $FeSb_2$ and BCC-Fe phases were studied (Figure 7). Here, an immiscibility gap between the Fe_2As-rich and the Sb-rich liquids was found. Microstructures of different phases are shown in Figure 8.

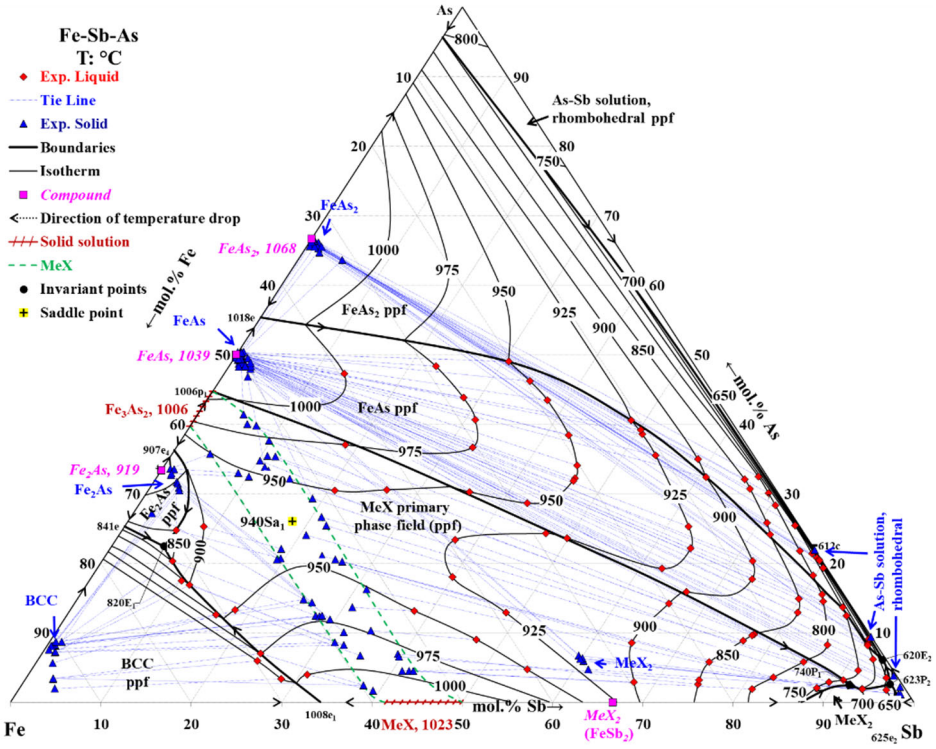

FIG 7 – Fe-Sb-As ternary phase diagram, showing experimental liquids and solids with liquidus, solidus, boundaries, isotherms and primary phase fields.

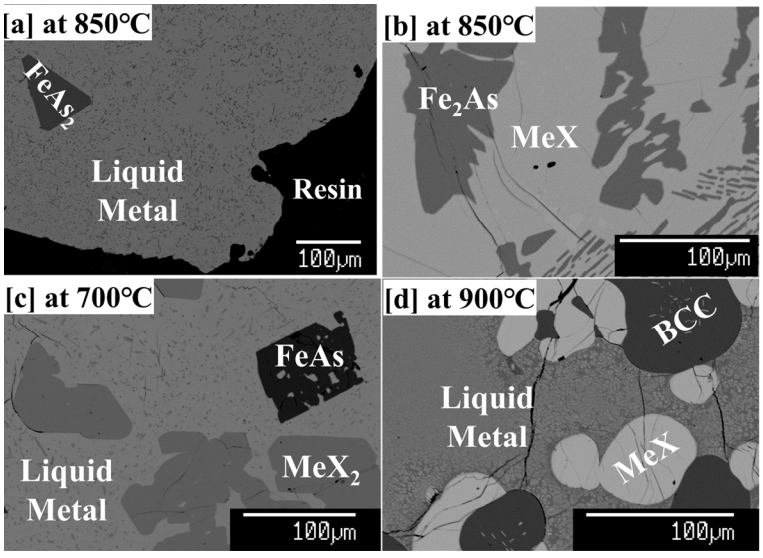

FIG 8 – Microstructures in backscattered electron mode for Fe-Sb-As system, showing: (a) liquid metal and $FeAs_2$, (b) MeX and Fe_2As, (c) liquid metal, MeX_2 ($FeAs_2$) and FeAs, and (d) liquid metal, MeX and BCC-Fe.

Fe-Sn-As system

In this system, liquidus, solidus, boundaries and primary phases field(s) for liquid metal (Fe-rich and Sn-rich), Me_5X_3 ($Fe_5(Sn, As)_3$), Fe_2As, FeAs and $FeAs_2$ phases were studied with an immiscibility gap near the Fe-Sn system spreading towards the As-side (Figure 9). Microstructures of different phases are shown in Figure 10.

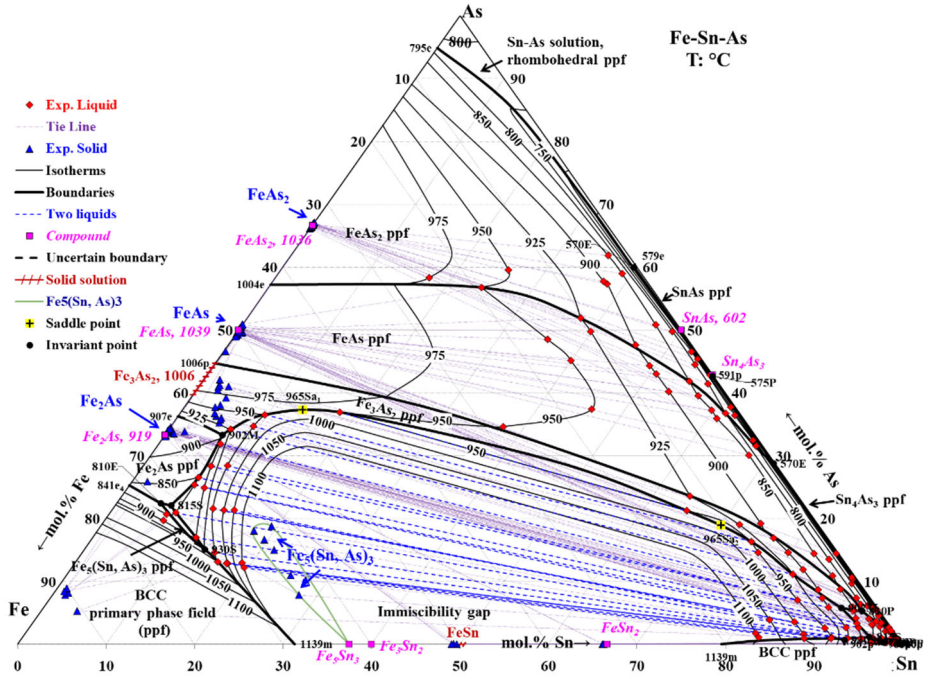

FIG 9 – Fe-Sn-As ternary phase diagram, showing experimental liquids and solids with liquidus, solidus, boundaries, isotherms and primary phase fields.

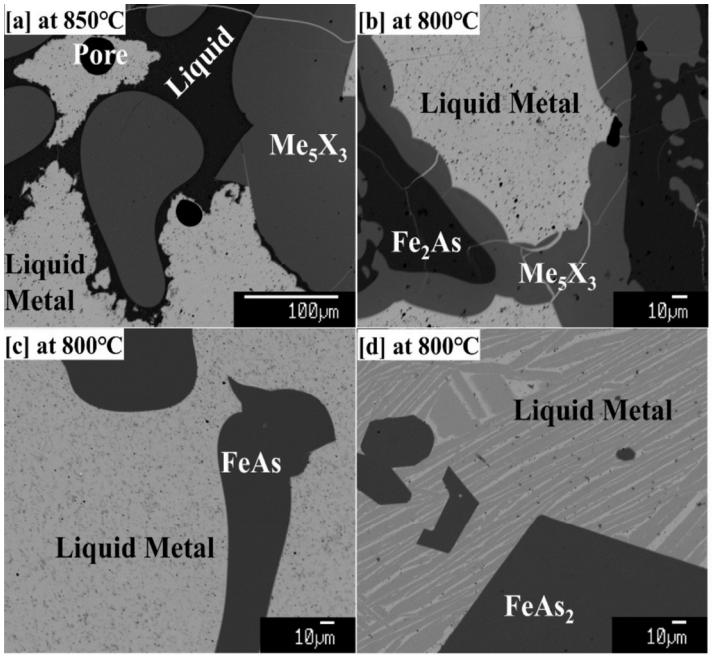

FIG 10 – Microstructures in backscattered electron mode for Fe-Sn-As system, showing: (a) liquid metal (Fe-rich) and liquid metal (Sn-rich) and Me_5X_3, (b) liquid metal, Me_5X_3, Fe_2As, (c) liquid metal and FeAs, and (d) liquid metal and $FeAs_2$.

CONCLUSIONS

Phase equilibria of S-containing systems (Ni-Sn-S, Cu-Sb-S and Cu-Sn-S) and As-containing systems (Fe-Sb-As and Fe-Sn-As) were studied to improve the prediction capabilities of FactSage in a 20-component system for complex pyrometallurgical operations. Different phases for each system were found with their liquidus, solidus, boundaries and primary phase fields. Different immiscibility gap for each system was observed. The immiscibility gap was the widest for the Cu-Sn-S system among all the studied systems. For the Ni-Sn-S system, two immiscible mattes, liquid metal, $Ni_{1+x}Sn$, SnS, Ni_3Sn, FCC-Ni, $Ni_{1-x}S$, NiS_2, Ni_3Sn_4, SnS_2, Sn_2S_3, β-Ni_3S_2 and $Ni_3Sn_2S_2$ phases were found. For the Cu-Sb-S system, matte, liquid metal, FCC-Cu, digenite, Sb, $CuSbS_2$, Cu_3SbS_3

and Cu_3SbS_4 phases were found. For the Cu-Sn-S system, liquid metal, matte, digenite, SnS and Cu_3Sn phases were found. For the Fe-Sb-As system, liquid metal, $FeAs_2$, $Fe_{1-x}Sb$, Fe_2As, FeAs, $FeSb_2$ and BCC-Fe phases were found. For the Fe-Sn-As system, two liquid metals (Sn and Fe-As speiss), $Fe_5(Sn, As)_3$, Fe_2As, FeAs and $FeAs_2$ phases were observed.

ACKNOWLEDGEMENTS

The authors would like to thank Australian Research Council Linkage program LP180100028 and consortium of copper and lead producers: Anglo American Platinum (South Africa), Aurubis (Germany), BHP Olympic Dam (Australia), Boliden (Sweden), Glencore (Australia), Kazzinc Ltd. (Kazakhstan), Outotec (Finland), Nyrstar (Australia), Peñoles (Mexico), RHI Magnesita (Austria), Rio Tinto Kennecott (USA) and Umicore (Belgium) for the financial support for this study. The authors are very grateful to Professor Peter Hayes for initiating and contributing to this research program. The authors would like to thank the staff at the Centre for Microscopy and Microanalysis (CMM), The University of Queensland, Australia for technical support.

REFERENCES

Asano, N and Wada, M, 1968. Distribution of Arsenic, Antimony and Bismuth between Liquid Copper and Cuprous Sulfide, *Suiyokaishi*, 16:385–388.

Bok, L D C and Boeyens, J C A, 1957. Preparation of double metal sulfides of the type AB2S4, II, Compounds of tin, *J S Afr Chem Inst*, 10:49–53.

Braga, M H, Ferreira, J A, Lopes, C and Malheiros, L F, 2008. Phase transitions in the Cu-Sb-S system, *Mater Sci Forum*, 587–588:435–439.

Brower, W S, Parker, H S and Roth, R S, 1974. Reexamination of synthetic parkerite and shandite, *Amer Mineral*, 59:296–301.

Chang, Y A, Newmann, J P and Choudary, U V, 1979. INCRA Series on the Metallurgy of Copper, Phase diagrams and thermodynamic properties of ternary copper-sulfur-metal systems, International Copper Research Association.

Chumarev, V M, Sholokhov, V M and Okunev, A I, 1979. Effect of silicon, chromium and manganese on tin and arsenic distribution between iron-arsenic-tin melts and lead, *Izv Akad Nauk SSSR Met*, pp 58–61.

Fiechter, S, Martinez, M, Schmidt, G, Henrion, W and Tomm, Y, 2003. Phase relations and optical properties of semiconducting ternary sulfides in the system Cu-Sn-S, *J Phys Chem Solids*, 64:1859–1862.

Gather, B and Blachnik, R, 1976. Temperature-composition diagrams in the Cu_2(VIb)-Vb) sections of the ternary copper-(Vb)-(VIb) systems (Vb = arsenic, antimony, bismuth; VIb = sulfur, selenium, tellurium), *J Less-Common Met*, 48:205–212.

Gerlach, J, Hennig, U and Trettin, K, 1969. Distribution of silver to matte and speiss: investigations of the systems copper-cobalt-arsenic-sulfur, copper-iron-arsenic-sulfur, copper-tin-sulfur, copper-arsenic-tin-sulfur, *Erzmetall*, 22:119–122.

Godovikov, A A and Il'yasheva, N A, 1969. New data on the copper sulfide-antimony sulfide-sulfur system, *Eksp Issled Mineral*, pp 58–60.

Groth, P, 1908. *Chemische Krystsllographie.* 2 *Teil*, *Die anorganischen Oxo und Sulfosalze* (Chemical Crystallography, Vol. 2: The Inorganic Oxo and Sulfo Salts), in German (Engelmann: Leipzig).

Jak, E, 2012. Integrated experimental and thermodynamic modelling research methodology for metallurgical slags with examples in the copper production field, in *Proceedings of the 9th Intl Conf on Molten Slags, Fluxes and Salts* (The Chinese Society for Metals: Beijing).

Jak, E, Shishin, D, Shevchenko, M and Hayes, P C, 2023. University R*ese*arch, Implementation and Education in support of the Sustainable Metals Production and Recycling, *European Metallurgical Conference (EMC 2023)*, (GDMB Gesellschaft der Metallurgen und Bergleute eV).

Jiang, M, Sun, T, Qin, X, Ji, Y and Wang, Z, 2011. Study on removing arsenic and tin from As-Sn bearing iron concentrates by direct reduction roasting with coal, *Kuangye Gongcheng*, 31:86–89.

Jumas, J C, Ribes, M, Philippot, E and Maurin, M, 1977. Preparation and ternary phase characterization of M_2SnS_4 in SnS_2-MS systems, (M = Ti, Cr, Mn, Fe, Co and Ni), *Comptes rendus hebdomadaires des séances de l'Académie des sciences*, *Ser C*, 284:845–847.

Jurkovic, L, Majzlan, J, Hiller, E, Klimko, T, Volekova-Lalinska, B, Meres, S, Gottlicher, J and Steininger, R, 2019. Natural attenuation of antimony and arsenic in soils at the abandoned Sb-deposit Poproc, Slovakia, *Environ Earth Sci*, 78:672.

Karup-Moller, S, 2000. The Cu-Sb-S phase system at 700°C, *Neues Jahrb Mineral Monatsh*, pp 333–336.

Khanafer, M, Rivet, J and Flahaut, J, 1974. Ternary copper-tin-sulfur, Equilibrium diagrams of the copper(I) sulfide-tin sulfide, copper(I) sulfide+tin(IV) and copper(I) sulfide-tin(IV) sulfide systems, Crystallographic study of the copper-tin-sulfur compounds (Cu_4SnS_4, Cu_2SnS_3, Cu_2Sn_4Sa and $Cu_4Sn_3S_8$), *Bull Soc Chim Fr*, pp 2670–2676.

Kovrigin, V A, Chursin, V M and Pichugin, B A, 1985. Dross formation on melts of copper and its alloys, *Tsvetn Met (Moscow)*, pp 79–82.

Kusumoto, Y, Fujimoto, M and Fujitani, S, 2001. Secondary lithium battery using mixed sulfide as active mass, JP patent application.

Landon, R E and Mogilnor, A H, 1933. Colusite, a new mineral of the sphalerite group, *Am Mineral*, 18:528–533.

Ma, C and Beckett, J R, 2018. Nuwaite (Ni_6GeS_2) and butianite (Ni_6SnS_2), two new minerals from the Allende meteorite: Alteration products in the early solar system, *Am Mineral*, 103:1918–1924.

Mammadli, P R, Gasimov, V A and Babanly, D M, 2022. Phase relations in the Cu_3SbS_4-Sb_2S_3-S system, *Chemical Problems*, 1:40–47.

Mammadli, P R, Gasimov, V A, Mashadiyeva, L F and Babanly, D M, 2022. Phase relations in the $CuSbS_2$-Sb_2S_3-Sb system, *New Mater Compd Appl*, 6:37–43.

Mammadli, P R, Mashadiyeva, L F, Gasimov, V A, Dashdiyeva, G B and Babanly, D M, 2021. Phase Relations in the $CuSbS_2$-Cu_3SbS_4-Sb_2S_3 System, *Azerbaijan Journal of Chemical News*, 3:100–108.

Meisner, K L, 1921a. The equilibrium between metal-pairs and sulfur, III, The system copper-antimony sulfur, *Met Erz*, 18:410.

Meisner, K L, 1921b. The Equilibrium between metal-pairs and sulfur, V, The system copper-tin-sulfur, *Met Erz*, 18:466–468.

Moh, G H and Ottemann, J, 1962. New investigations of stannite and related minerals, *Neues Jahrb Mineral Abh*, 99:1–28.

Mueller, L, Trinks, W, Brand, K H and Behrendt, H P, 1979. Development of tin production at the VEB Mining and Metallurgical Plant Albert Funk at Freiberg, *Neue Huette*, 24:374–378.

Nitta, T, Hayakawa, S, Kasahara, Y and Hirakata, T, 1976. Sulfide-ceramic bodies, DE patent application.

Nurbaev, M, Toguzov, M Z and Onaev, I A, 1981. Removal of impurities from lead, SU patent application.

Okunev, A I, Chumarev, V M, Sholokhov, V M, Shashmurin, V A, Gus'kov, V A, Kiryushkin, B N, Denisov, V I, Orlov, A F and Potapov, M V, 1975. Processing of tin-containing iron-arsenic alloys, SU patent application.

Peacock, M A and McAndrew, J, 1950. Parkerite and shandite and the crystal structure of $Ni_3Pb_2S_2$, *Am Mineral*, 35:425–439.

Pelabon, H, 1905. Fusibility of Mixtures of the Antimony Sulfide with Copper Sulfide and Mercury Sulfide, *Comptes rendus de l'Académie des Sciences*, 140:1389–1392.

Peterson, M and Twidwell, L G, 1985. Removal of arsenic from lead smelter speiss, *J Hazard Mater*, 12:225–229.

Pogue, E A, Sutrisno, A, Johnson, N E, Goetter, M B, Jiang, Z, Johnson, N E, Shoemaker, D P and Rockett, A A, 2019. Phase stability and structural comparison of phases in the Cu-Zn-Sn-S system using solid-state NMR, *Sol Energy Mater Sol Cells*, 190:37–48.

Rudnik, E, 2016. Collection and recycling of spent nickel and lithium batteries and accumulators in Poland, *Metall Foundry Eng*, 42:127–137.

Seitkan, A, Lampronti, G I, Widmer, R N, Casati, N P M and Redfern, S A T, 2020. Thermal Behavior of Iron Arsenides Under Non-Oxidizing Conditions, *ACS Omega*, 5:6423–6428.

Skinner, B J, Luce, F D and Makovicky, E, 1972. Studies of the Sulfosalts of Copper III, Phases and Phase Relations in the System Cu-Sb-S, *Econ Geol*, 67:924–938.

Sorulen, T T, Takahashi, R, Tanaka, S, Suzuki, K, Imai, A, Watanabe, Y and Kikuchi, S, 2019. Mineralogical and Geochemical Characteristics of the Utanobori Gold Deposit in Northern Hokkaido, Japan, *Resour Geol*, 69:402–429.

Toguzov, M Z, Nurbaev, M, Minkevich, S M, Zhaglov, V S and Onaev, I A, 1984. Physicochemical studies of the refining of lead by iron, *Kompleksn Ispol'z Miner Syr'ya*, pp 43–47.

Zheng, Y-X, Lv, J-F, Lai, Z-N, Lan, Z-Y and Wang, H, 2019. Innovative methodology for separating copper and iron from Fe-Cu alloy residues by selective oxidation smelting, *J Cleaner Prod*, 231:110–120.

Distribution behaviour of B and P in Si-slag system at 1500°C

DOI: 10.62053/YSSB9404

K Avarmaa[1], A Putera[2], J Chen[3], G Brooks[4] and M A Rhamdhani[5]

1. Postdoctoral Research Fellow, Fluid and Process Dynamics (FPD) Research Group, Swinburne University of Technology, Melbourne Vic 3122. Email: kavarmaa@swin.edu.au
2. PhD Student, Fluid and Process Dynamics (FPD) Research Group, Swinburne University of Technology, Melbourne Vic 3122. Email: aputera@swin.edu.au
3. Researcher, School of Chemical Engineering, The University of Queensland, Brisbane Qld 4072. Email: jcanu2018@gmail.com
4. Professor, Fluid and Process Dynamics (FPD) Research Group, Swinburne University of Technology, Melbourne Vic 3122. Email: gbrooks@swin.edu.au
5. Professor, Fluid and Process Dynamics (FPD) Research Group, Swinburne University of Technology, Melbourne Vic 3122. Email: arhamdhani@swin.edu.au

ABSTRACT

Silicon-based photovoltaic cells are currently the most dominant types applied to convert solar energy to electricity. In solar-grade silicon (SG-Si), the control of boron (B) and phosphorus (P) is very critical. Generally, these elements are difficult to remove into acceptable sub-ppm levels from lower grade Si. This study investigates slag treatment as a process for Si refining, focusing on the behaviour of P and B. The experiments were conducted by equilibrating Si-B-P alloys with 43 wt per cent SiO_2 – 47 wt per cent CaO – 10 wt per cent Al_2O_3 slag under inert atmosphere at 1500°C. Different crucible materials were used (Al_2O_3, SiO_2 and MgO), which determined the primary saturation phase for the system and modified the final slag composition accordingly. The samples were equilibrated and analysed with microanalysis techniques (EPMA (electron probe microanalysis) and LA-ICP-MS (laser ablation inductively coupled plasma mass spectrometry)). New standards were prepared and applied in the LA-ICP-MS analyses. Experimental results show that silver is essentially fully dissolved in silicon, as well as most phosphorus with LP (= wt per cent P in slag/wt per cent P in Si) between 0.1–0.3. The distribution coefficient of boron was measured to be between 1 and 2. The crucible material used had an influence on the phase compositions and slight influence on the distribution coefficients of boron and phosphorus. The experimental results provided new accurate data when considering applicability of slag treatment as a technique for Si refining and Si PV cell recycling.

INTRODUCTION

Boron and phosphorus naturally occur in the ore deposits used for silicon and ferrosilicon production. Their removal is very challenging and metallurgical grade silicon (>98 wt per cent purity) produced in electric arc furnace need to be refined via complex and energy-intensive Siemens process (>200 kWh/kg, (Braga *et al*, 2008; Chigondo, 2018) into higher purity solar grade silicon (>99.99 wt per cent). Potential secondary Si include various Si scraps, such as kerf slurry and end-of-life Si PV cells. These materials contain varying concentrations of B and P (a few ppm to thousands of ppm) (Chen *et al*, 2019; Yang *et al*, 2019; Liu, Huang and Zhu, 2017). Silver do not naturally occur in the silicon ore resources but exist in high concentrations end-of-life silicon PV cells, ~500–8000 ppm wt (Latunussa *et al*, 2016; Wang *et al*, 2022).

Different technologies for refining MG-Si and Si scraps have been investigated and proposed, such as slag treatment (Chigondo, 2018) and electrically-enhanced slag treatment (Wang *et al*, 2018; Islam, Rhamdhani and Brooks, 2014). Several studies investigating boron distribution behaviour in Si-slag systems can be found from the literature, but very limited is available for phosphorus. There exist various types of slags investigated for boron removal from molten silicon or silicon alloy, such as CaO-SiO_2/MgO, CaO-SiO_2-Al_2O_3/MgO/CaF_2/TiO_2/BaO/Na_2O/LiF/Li_2O and CaO-SiO_2-Al_2O_3-MgO (Chen *et al*, 2019; Jung, Moon and Min, 2011; Zhou *et al*, 2019). Table 1 presents the best comparable studies (limited to CaO-SiO_2-Al_2O_3-MgO slags) conducted to study boron and phosphorus distribution behaviour between molten silicon and slag.

TABLE 1

Literature on B and P distribution behaviour in Si alloy-slag systems.

Elements	Si alloy	Slag	Conditions	Result	Reference
B	Si	$CaO-SiO_2$, $CaO-SiO_2-Al_2O_3$	1450–1600°C, Al_2O_3 cru, 4 g (slag/Si: 1–3), t: 0–4 hrs, Ar	L_B: 1.6–3.2	Islam (2015)
B	MG-Si	$CaO-SiO_2-LiF/Li_2O$	1550°C, gr cru, 70 g slag (slag/Si: 0.5–5), t: 0–4 hrs, Ar	L_B = 1 for $CaO-SiO_2$, for Li-containing L_B = 1.2–2.8	Ding *et al* (2012)
B	Si	SiO_2-CaO/MgO, $SiO_2-CaO-MgO/Al_2O_3$	1600°C, gr cru, 30 g (slag/Si: 1), t: 0–9 hrs, Ar	L_B = 2–2.5, for high alumina L_B = 1.3	Jakobsson and Tangstad (2018, 2014)
B	Si	$CaO-SiO_2-Al_2O_3/CaF_2/MgO/BaO$	1600°C, Al_2O_3 cru, t: 0–5 hrs, Ar	L_B = 0.35–1.1	Fujiwara *et al* (1996)
B	Si	$CaO-SiO_2$	1550°C, gr cru, 9.7 g (slag/Si: 2.2), t: 18 hrs, Ar	L_B = 2–5	Teixeira and Morita (2009)
B	Si	$CaO-SiO_2$	1550°C, gr cru, 4 g slag (slag/Si: 0.4–0.8), t: 0–3 hrs, Ar or Ar-Cl_2	L_B = 2-2.2 (under Ar and Ar-Cl_2)	Nishimoto *et al* (2012)
B	Si	$CaO-SiO_2$/-MgO/BaO/CaF_2	1450–1550°C, gr cru, 20 g (slag/Si: 2), 2 hrs, CO, Ar or Ar-CO_2	L_B = 0.4–2, T and CaO concentration in slag increased L_B	Suzuki and Sano (1991)
B	Si	SiO_2-CaO	1500°C, SiO_2 cru, t: 4–6.5 hrs, Ar	L_B = 1.7	Weiss and Schwerdtfeger (1994)
B	Si	$SiO_2-CaO/-Al_2O_3/Na_2O/CaF_2$	1450–1600°C, quartz ceramic cru, 3.3 kg (slag/Si: 10), 0.5–2 hrs, Ar	L_B = 2–9	Luo *et al* (2011)
B	Si-20 wt per cent Fe	$CaO-SiO_2-Al_2O_3$	1600°C, Al_2O_3 cru, 10 g (slag/Si: 1), 8 hrs, Ar	L_B = 1–11 (mainly around 1–2)	Hosseinpour and Khajavi (2018)
B	Si-Fe (0–85 wt per cent Fe)	$CaO-SiO_2-CaO$	1600°C, gr cru, 8–11 g (slag/Si: 1, slag/Si-Fe: 0.6), t: 0–4 hrs, Ar	L_B = 2 (up to 75 wt per cent Fe in Si), 6 for 85 wt per cent Fe in Si	Krystad *et al* (2017)
B	Si kerf/Si kerf ceramics	$SiO_2-CaO/-CaF_2$	gr cru, 50 g (slag/Si kerf: 1), 40 min	L_B = 2.8–6.8 depending on optical basicity and CaF_2	Zhang *et al* (2020)
B	Mg-Si	$CaO-SiO_2$	1550°C, gr cru, 140 g (slag/Si: 1), 0.5–3 hrs, Ar	L_B = 0.7–1.6 depending on optical basicity	Wei *et al* (2015)
B, P	Mg-Si	$CaO-SiO_2-Al_2O_3-MgO$, $Al_2O_3-SiO_2-BaO$	1500°C, MgO/Al_2O_3 cru, 13 g (slag/Si: 1.4), t: 0–6 hrs, Ar	L_B = 1–2, LP = 0.1–0.4 at Al_2O_3-sat, LP = 1–9 at MgO-sat (when SiO_2/Al_2O_3>1)	Johnston and Barati (2010)
P	Si-20 wt per cent Fe	$CaO-SiO_2-Al_2O_3/-Na_2O$	1300°C, Al_2O_3 cru, 10 g (slag/Si-Fe: 1), t: 2–10 hrs, Ar	LP = 0.2–1.2 (Na_2O, CaO/SiO_2 and SiO_2/Al_2O_3 increased LP)	Taposhe and Khajavi (2021)
P	Si(-Al-Ca)	$CaO-SiO_2-Al_2O_3$.	1600°C, Al_2O_3 cru, 6–9.5 g (slag/Si: 2), 5 hrs, Ar	LP = 0.01–3 ($CaO/(CaO+SiO_2)$ increased LP)	Fujiwara *et al* (1996)
P	Si-20 wt per cent Fe	$CaO-SiO_2-Al_2O_3$	1600°C, Al_2O_3 cru, 10 g (slag/Si: 1), 8 hrs, Ar	LP = 0.01–0.2	Hosseinpour and Khajavi (2019)

Overall, the results on the influence of slag treatment on the boron and phosphorus removal from molten silicon are not clear and vary between different studies as shown in Table 1. All the previous studies have used 5–30 g sample primary chemical bulk analyses that can increase the risk of distorted results due to entrained phase droplets within wrong phase analysis. This study investigated the distribution behaviour of B and P between molten silicon and SiO_2-CaO-Al_2O_3/-MgO slags at 1500°C by using experimental technique of drop-quenching followed by microanalyses.

EXPERIMENTAL

The drop-quenching technique followed by microanalyses has been used in great extent for equilibrium studies and on minor element investigations in copper and nickel smelting conditions (Chen *et al*, 2022; Piskunen *et al*, 2018; Sineva *et al*, 2021, 2023). It enables to measure *in situ* ppm wt or even ppb wt concentration of elements in different phases and without risk of having entrapped 'wrong' phase distorting the analysis results, as can occur in bulk chemical analyses.

Materials

Si-P-B master alloys, as well as SiO_2-CaO-Al_2O_3 master slag were prepared for the experiments. The reagent materials were high-purity powders (99.9 per cent or above) supplied by Merck Life Science Pty Ltd and Thermo Fisher Scientific Australia Pty Ltd. Si-P-B powder mixtures were weighted into BN-painted alumina crucible and melted for 2 hrs in a vertical tube furnace under Ar gas atmosphere at 1500°C. The master slag was mixed into homogeneous powder mixture, melted in Pt crucible for 1 hr in a muffle furnace and cast to a steel rail. The final compositions of the master alloys and slag measured by inductively coupled plasma – atomic emission spectroscopy (ICP-AES) and scanning electron microscope - energy dispersive x-ray spectroscopy (SEM-EDS) are presented in Table 2.

TABLE 2

Si master alloy compositions by ICP-AES and normalised slag composition results by ICP-AES and SEM-EDS.

Si master alloys	B / ppm wt	P / ppm wt	Ag / ppm wt	Al / ppm wt	Ca / ppm wt
Si-P-B	570	150		685	320
Slag	CaO / wt%	SiO_2 / wt%	Al_2O_3 / wt%		
ICP-AES	47.1	43.2	9.7		
SEM-EDS	45.6	44.0	10.4		

As a new experimental technique for silicon-slag systems, appropriate standards for LA-ICP-MS analyses were prepared for silicon. Silicon standards were melted in alumina crucibles under Ar at 1500°C and drop-quenched into ice water. The final compositions of the standards are presented in Table 3.

TABLE 3

Si standard compositions measured by ICP-AES.

	B / ppm wt	P / ppm wt	Ag / ppm wt	Al / ppm wt	Ca / ppm wt
S1	555	845	1260	1780	30
S2	540	1540		1980	35
S3	720	165		1310	45

Three different crucibles were used in the experiments; Al_2O_3 (99.53 per cent), SiO_2 (99.99 per cent) and MgO (97.18 per cent) all supplied by Nanyang Yaki, China. The used crucible material will define the primary phase field of the system and slag composition will change accordingly.

Experiments

The experiments were carried out in a vertical tube furnace Nabertherm RHTV 120-300/18 and Nabertherm controller unit C42. The furnace temperature was measured with a calibrated B-type thermocouple (TC Measurement and Control Pty Ltd, Australia) inserted next to the sample and the followed through the experiment by using digital thermometer Anzeiger 32h8i (Eurotherm controller 32h8). The schematics of the experimental assembly is presented in Figure 1.

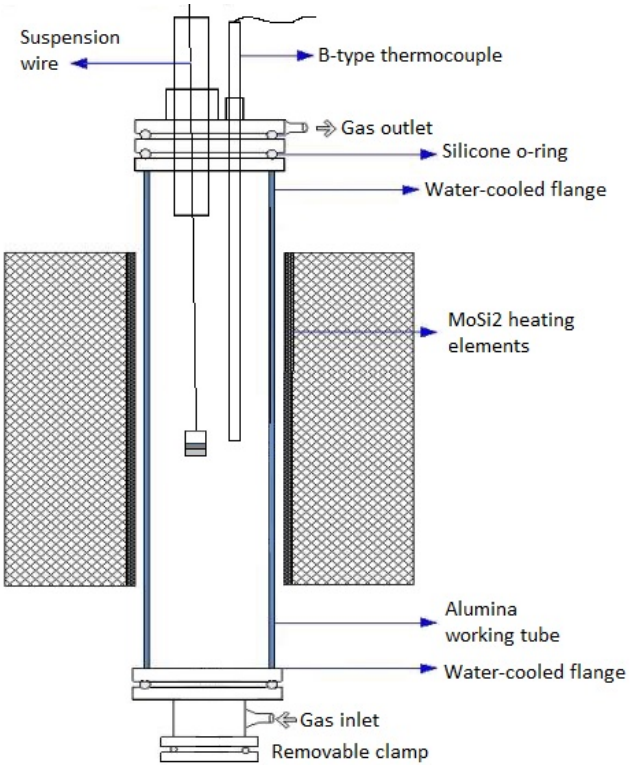

FIG 1 – Experimental apparatus.

First 0.2 g of master Si alloy and 0.4 g of master slag were measured in a crucible (initial slag/Si ratio = 2). A CaO-SiO_2-Al_2O_3 slag system was used in the study as this resembles a typical slag in the blast furnace ironmaking. The crucible was attached to the suspension wire which was a combination of Kanthal A1 and Mo or Pt wires. The hot zone of the furnace was measured at 1500°C, and the suspension wire combo was carefully measured for each experiment to be assure that the sample was in the hot zone during the experiment. The crucible attached to the suspension wire was first lowered into the guiding tube, that was large enough to fit the crucible through it and kept in the cold zone for 30 min while Ar gas atmosphere was created. Argon flow was controlled with a mass-flow controller (Aalborg DFC26, USA; accuracy ±1 per cent) and set to flow rate of 200 mL/min. After 30 min, the sample was lowered to the hot zone and the experiment started. After required time was full, the sample was drop-quenched into an ice water bucket. Time series to determine the equilibration times required at each crucible was conducted. The system was considered to reach the equilibrium when the slag composition was stabilised and homogenous throughout the sample. It was found that equilibration time of 8 hrs was enough for the Si-B-P alloy equilibrated with slag at silica-saturation at 1500°C; while 16 hrs equilibration time was enough for the Si-B-P alloy equilibrated with slag at alumina-saturation and magnesia-saturation at 1500°C.

Analytical techniques

Samples were mounted into epoxy resin and their cross-sections were prepared for microanalyses by using traditional wet-metallographic techniques and imaged by optical microscope. The microanalyses included electron microprobe analysis and laser ablation inductively coupled plasma mass spectrometer measurements.

Microstructure examination and quantitative elemental analysis were performed on the experimental samples using a JEOL 8530F Plus field-emission electron microprobe at the Centre for Advanced

Microscopy, Australian National University. For the major elements (>0.5 m per cent), an acceleration voltage of 15 keV and a probe current of 40 nA were used; for the minor and trace elements (<0.5 wt per cent), a probe current of 1000 nA were used. A probe size of 50–100 μm was chosen for slag and alloy phase. A list of elements, their emission lines analysed and the minimum detection limited are given in Table 4.

TABLE 4

List of elements, their emission lines analysed and the minimum detection limit by EPMA.

Slag	**Ca**	**Mg**	**Al**	**Si**	**Y**	**Zr**	**P**
Emission line	Kα	Kα	Kα	Kα	Lα	Lα	Kα 2nd order
Detection limit (ppm wt)	60	50	100	120	60	80	10–15
Si alloy	**Al**	**P**	**Ca**	**Mo**	**Zr**	**Fe**	**Ag**
Emission line	Kα	Kα	Kα	Lα	Lα	Kα	Lα
Detection limit (ppm wt)	12	15	5	16	25	12	55

Trace elements in the samples collected were determined by LA-ICP-MS at the Research School of Earth Sciences, ANU using an Agilent Technologies 7700 ICP-MS coupled to an ANU HelEX laser-ablation system with a 193-nm-wavelength EXCIMER laser (110 (ArF) COMPex, Lambda Physik). The elements determined and the isotopes used for these determinations were ^{11}B, ^{26}Mg, ^{27}Al, ^{31}P, ^{43}Ca, ^{57}Fe, ^{89}Y, ^{90}Zr, ^{95}Mo and ^{107}Ag. Data acquisition involved a 15 sec background measurement followed by 30 sec of ablation, with a 7 Hz repetition rate. The laser spot size was set to 81 μm. For the slag phase, NIST SRM 612 was used as the external reference standard and NIST SRM 610 was used for quality control standard; for the Si alloy phase, three Si alloy standards made-in-house doped with different levels of B, P and Ag were used as both external and quality control standards. Si concentrations in the slag and alloy determined by EPMA were used as internal standards. Data were processed and quantified using the Iolite v4 software package. The minimum detection limits for the elements analysed are given in Table 5.

TABLE 5

Minimum detection limits for the elements analysed by LA-ICP-MS.

	B	**Mg**	**Al**	**P**	**Ca**
Slag (ppm wt)	0.2–0.6	1–7	1–10	0.9–2	-
Alloy (ppm wt)	0.3–0.6	-	0.2–10	1–4	0.4–1
	Fe	**Y**	**Zr**	**Mo**	**Ag**
Slag (ppm wt)	0.5–1.5	0.003–0.05	0.01–0.1	0.01–0.05	0.01–0.03
Alloy (ppm wt)	10–40	-	-	-	0.05–1.5

RESULTS AND DISCUSSION

The equilibrated samples involved and discussed in this study are:

- Si-B-P – SiO_2-CaO-Al_2O_3 slag at silica-saturation at 1500°C equilibrated 8 hrs.
- Si-B-P – SiO_2-CaO-Al_2O_3 slag at alumina-saturation at 1500°C equilibrated 16 hrs.
- Si-B-P – SiO_2-CaO-Al_2O_3 slag at magnesia-saturation at 1500°C equilibrated 16 hrs.

Backscatter images of the samples at different saturations, as well as an optical microscope image of the cross-section of the alumina-saturated system is shown in Figure 2.

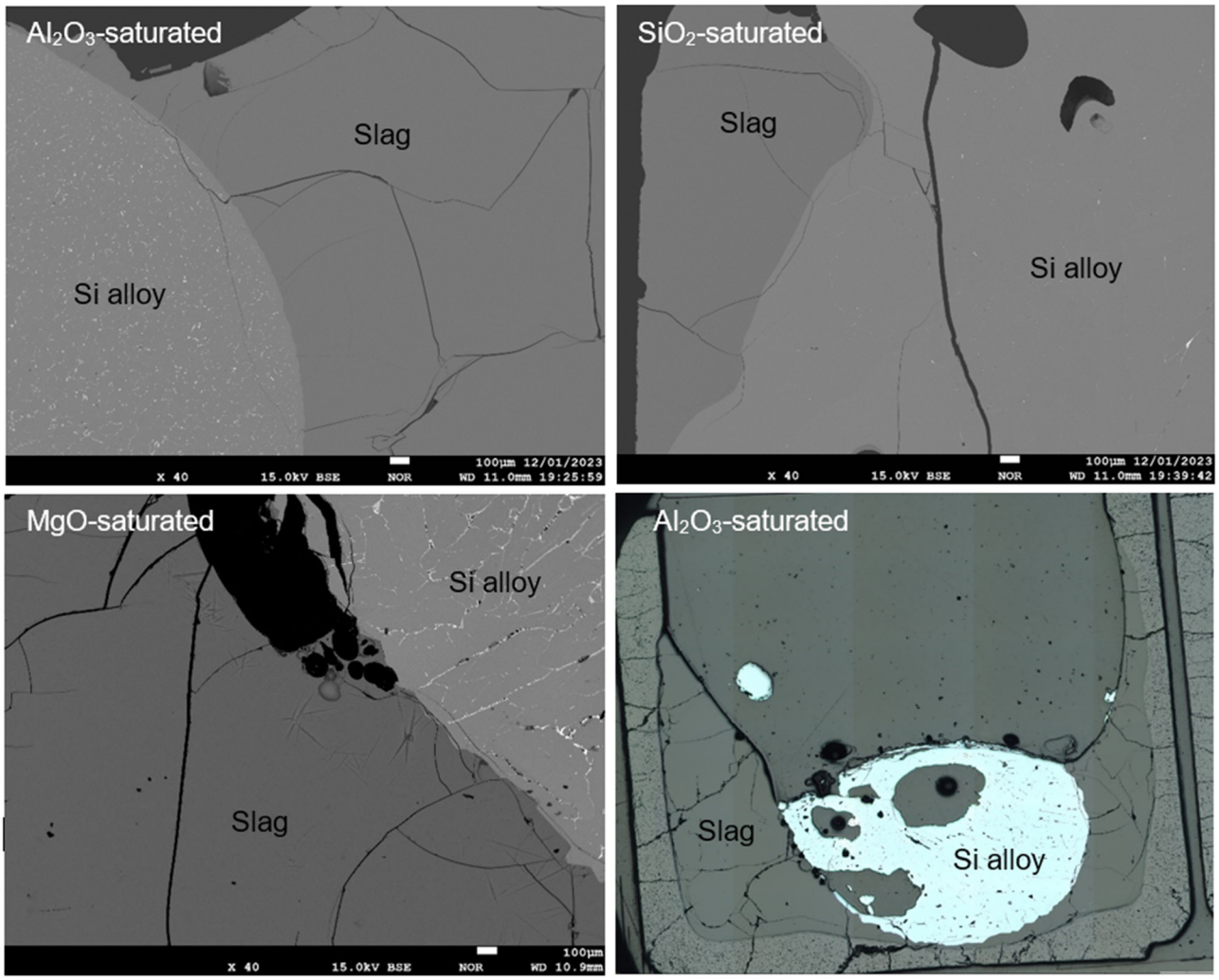

FIG 2 – BSE-images of the samples at different saturations and an optical microscope image of the cross-section of the alumina-saturated sample.

As shown in Figure 2, slag phase was quenched well and formed a homogeneous phase, whereas Si alloy had bright segregations, especially at alumina and magnesia-saturated systems (most likely caused by primary precipitations of Si intermetallics). As the brighter segregations are part of the Si alloy, the beam sizes of microanalyses were chosen larger to evaluate the overall phase composition. Nevertheless, this heterogeneity of the phase caused discrepancy within the taken Si alloy analyses causing in some cases rather high standard deviations for certain elements. Some needle formations were visible in slag phase in MgO-saturated samples that were excluded from the analyses. Slag analyses were taken from homogeneous slag areas and close to Si alloy. The Si alloy was typically as a droplet formation on the top and middle of the slag as shown in the cross-section in Figure 2. Molten silicon has somewhat lower density when compared to the used slags that explains the behaviour. Literature (Krystad *et al*, 2017; Zhou *et al*, 2019) presents that Si and Si-rich alloys (up to 75 per cent Fe) formed a droplet in the middle of the crucible and on top of slag similarly as in our study. The final slag compositions for main components are presented in Table 6. Traces of Zr, Y and Mg (30–90 ppm wt) were also measured in the slags. The final compositions are clearly different to the initial slag composition presented in Table 2. Each have dissolved crucible material, and the equilibrium slag compositions present the tie line conditions for the slag-primary phase field at 1500°C.

TABLE 6

The slag compositions of equilibrated samples, in wt per cent.

	CaO	SiO_2	Al_2O_3	MgO	Y_2O_3
Silica-saturated	27.7	66.8	5.5		
Alumina-saturated (P, B)	29.4	26.0	44.3		0.3
Alumina-saturated (Ag)	28.5	27.6	43.6		0.3
Magnesia-saturated	22.9	40.0	12.4	24.6	0.2

Phosphorus concentration was measured by EPMA and LA-ICP-MS techniques in both phases of interest. The comparison of EPMA and LA-ICP-MS results for P in slag is shown in Figure 3 and for Si alloy in Figure 4. EPMA results for phosphorus in slag at MgO and Al_2O_3-saturations were somewhat higher than measured by LA-ICP-MS, but relatively well in agreement. Si alloy phase with its segregations (ie heterogeneous phase structure), and lack of known standards for Si alloy required by LA-ICP-MS, made the measurements challenging. LA-ICP-MS results are extrapolated in relation to the standard used, and as the standard 1 (S1) included much higher P concentration than expected in the samples, the measured value might be exaggerated upwards. As can be noticed S1 gave clearly higher values than EPMA and LA-ICP-MS with S3, thus the results by S1 can be ruled out. When comparing the measured P concentrations in Si between EPMA and LA-ICP-MS with S3, alumina and magnesia-saturated system had a noticeable difference. This can be partially or fully related to the heterogeneous Si phase structure, whereas for more homogeneous Si alloy at silica-saturated system, EPMA and LA-ICP-MS provided better fit.

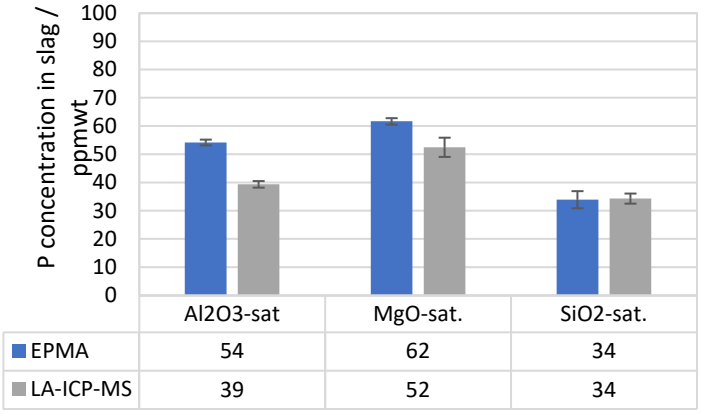

FIG 3 – Phosphorus concentration in slag measured by EPMA and LA-ICP-MS at different saturation phases at 1500°C.

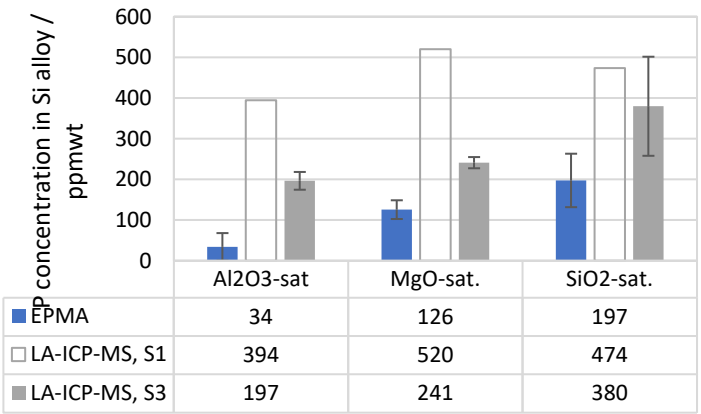

FIG 4 – Phosphorus concentration in Si alloy measured by EPMA and LA-ICP-MS (two different standards) at different saturation phases at 1500°C.

Boron was measured only by LA-ICP-MS technique and the results are presented in Figures 5 and 6 for slag and Si alloy, respectively. Boron concentration was radically higher in both phases in MgO-saturated system when compared to silica and alumina-saturated systems, even though the used master Si alloy and master slag were same for all systems. Possibly MgO-crucible contained boron as an impurity and thus had higher concentration in the system. Another reason might be that MgO-slag might retain boron from vaporisation more compared to other systems investigated. Both standards S1 and S3 provided rather similar results for B in Si alloy, which can be expected as they have rather similar concentrations in the used standards.

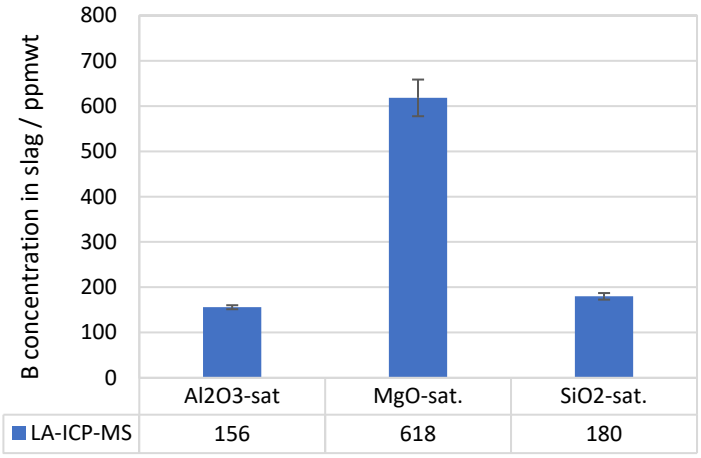

FIG 5 – Boron concentration in slag measured by LA-ICP-MS at different saturation phases at 1500°C.

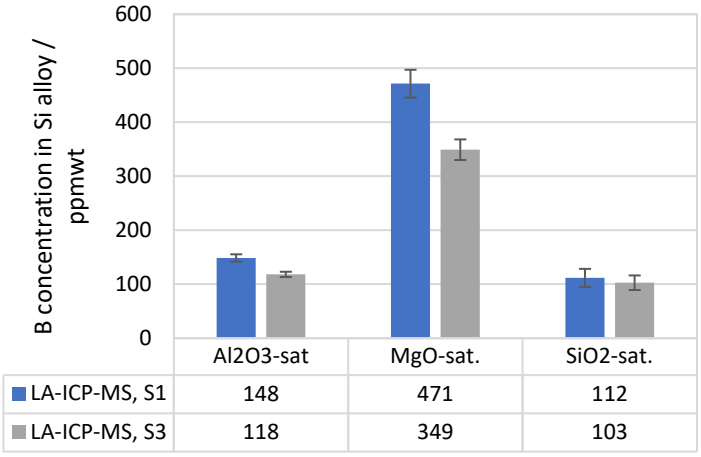

FIG 6 – Boron concentration in Si alloy measured by LA-ICP-MS (two different standards) at different saturation phases at 1500°C.

The distribution coefficient of element is determined as:

$$L_M = (M)_{\text{in slag}} / [M]_{\text{in Si alloy}} \quad (1)$$

When considering minor element behaviour in molten Si- slag system, the distribution behaviour relates to its oxidation reaction as follows:

$$[M] + x/2\ O_2 = (x\ MO_2) \quad (2)$$

or

$$[M] + (SiO_2) = [Si] + (MO_2) \quad (3)$$

By employing the equilibrium constant of the Reaction 2, the distribution coefficient of element can be defined thermodynamically as follows:

$$K = \frac{a_{MO_X}}{a_M p_{O_2}^{x/2}} = \frac{\gamma_{MO_x}(m-\%M)/\cancel{M_M}(n_T)}{\gamma_M[m-\%M]/\cancel{M_M}[n_T]p_{O_2}^{x/2}} \quad (4)$$

$$L_M = \frac{(m-\%M)_{slag}}{[m-\%M]_{silicon}} = \frac{K[n_T]\gamma_M^o p_{O_2}^{x/2}}{(n_T)\gamma_{MO_x}} \quad (5)$$

When minor element exists in dilute form in silicon, it can be estimated to follow Henry's law, ie $\gamma_M^o \sim constant$. Additionally, the total number of moles (n_T) per 100 g of each phase can be considered constant when slag is presented in mono-cationic form. If the partial pressure of oxygen is known and the L_M, the activity coefficient of oxidic minor element can be evaluated. Other approach is via Reaction 3 to evaluate the properties of the system and the minor element. Figures 7 and 8 presents the distribution coefficient of boron and phosphorus, respectively. L_B was calculated using results by both standards (S1 and S3), whereas LP by using LA-ICP-MS results for Si alloy (S3), while EPMA and LA-ICP-MS results for slag phase.

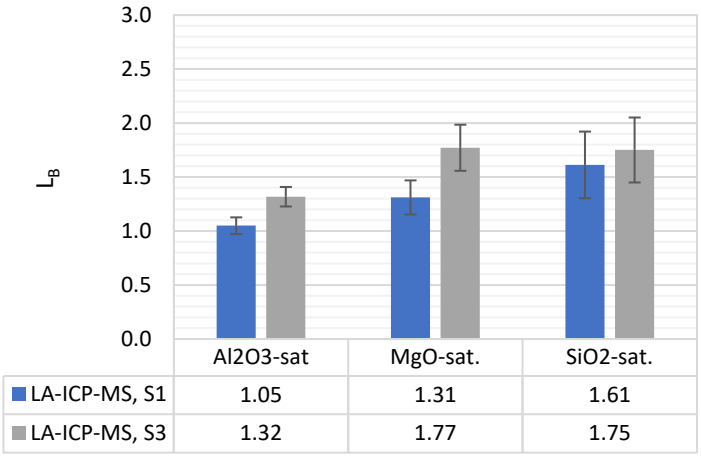

FIG 7 – Distribution coefficient of boron at different saturation phases at 1500°C by LA-ICP-MS (two different standards).

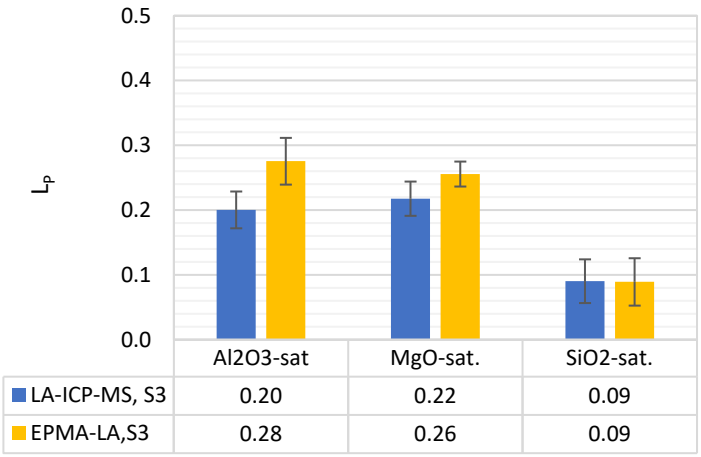

FIG 8 – Distribution coefficient of phosphorus at different saturation phases at 1500°C by EPMA and LA-ICP-MS.

Some differences depending on the technique and standard can be seen for alumina- and magnesia-saturated systems, that mainly can be explained by the heterogeneous Si alloy microstructure. Nevertheless, they still fit quite well with each other. Silica-saturate system had even more consistent results independent on the analysis technique or standard (more homogeneous Si alloy). Silica- and magnesia-saturated systems provided the highest L_B that indicates higher removal rate for boron between these three systems. Phosphorus was systematically distributed more on the silicon alloy, but the silica-saturated system provided the least favourable conditions for phosphorus removal.

When comparing measured L_B results to the literature, they are similar results by various studies (Ding *et al*, 2012; Jakobsson and Tangstad, 2018; Johnston and Barati, 2010; Suzuki and Sano, 1991; Weiss and Schwerdtfeger, 1994). Nevertheless, many studies have measured higher L_B values between 2–5 (Islam, 2015; Luo *et al*, 2011; Teixeira and Morita, 2009; Nishimoto *et al*, 2012; Zhang *et al*, 2020), and even up to 10 (Luo *et al*, 2011; Hosseinpour and Khajavi, 2018). The investigated systems, experimental conditions (T, slag composition, crucible material) and techniques have varied in literature that have influenced more or less the results. In this study, the slag composition did not seem to have a major impact on the L_B. Similar conclusion was presented eg the study by Jakobsson and Tangstad (2014). Most of the studies conducted for phosphorus, even with different type of slags and Fe-Si alloy provided distribution coefficients in the same range with our results (Fujiwara *et al*, 1996; Hosseinpour and Khajavi, 2019; Johnston and Barati, 2010; Taposhe and Khajavi, 2021).

CONCLUSIONS

This study investigated the behaviour of B and P in molten Si alloy and slag systems under different saturations at 1500°C. Experimental technique of drop-quenching followed by microanalyses; EPMA and LA-ICP-MS, were used for the first time to measure the minor element concentrations Si alloy and slag phases. Phosphorus and silver results by EPMA and LA-ICP-MS techniques were compared and discussed. Both techniques were applicable for phosphorus measurements. The distribution coefficients of P and B were not influenced radically by the slag composition and the crucible material, LP varied between 0.1–0.3 and L_B between 1–2.

ACKNOWLEDGEMENTS

The authors are grateful to Australia Renewable Energy Agency (ARENA), Grant number 2020RND011. Additionally, Mr. Andreas Putera is grateful on the Swinburne University SUPRA PhD Scholarship. The authors acknowledge the help of Mr. Aidan O'Keeffe, the manager of Swinburne workshop (Fabrication and laboratory).

REFERENCES

Braga, A, Moreira, S, Zampieri, P, Bacchin, J and Mei, P, 2008. New processes for the production of solar-grade polycrystalline silicon: A review, *Solar Energy Materials and Solar Cells*, 92(4):418–424.

Chen, H, Morita, K, Ma, X, Chen, Z and Wang, Y, 2019. Boron removal for solar-grade silicon production by metallurgical route: A review, *Solar Energy Materials and Solar Cells*, 203:110169.

Chen, J, Fallah-Mehrjardi, A, Specht, A and O'Neill, H, 2022. Measurement of minor element distributions in complex copper converting slags using quantitative microanalysis techniques, *JOM,* 74:185–194.

Chigondo, F, 2018. From metallurgical-grade to solar-grade silicon: an overview, *Silicon*, 10:789–798.

Ding, Z, Ma, W, Wei, K, Wu, J, Zhou, Y and Xie, K, 2012. Boron Removal from Metallurgical-Grade Silicon Using Lithium Containing Slag, *Journal of Non-Crystalline Solids,* 358(18–19):2708–2712. https://doi.org/10.1016/j.jnoncrysol.2012.06.031

Fujiwara, H, Liang, J, Takeuchi, K and Ichise, E, 1996. Reducing removal of phosphorous from calcium containing silicon alloys (in Japanese), *Materials transactions, JIM,* 37(4):923–926.

Hosseinpour, A and Khajavi, L, 2018. Thermodynamics of boron removal in slag refining of Fe-Si alloy, *Journal of Alloys and Compounds*, 768:545–552.

Hosseinpour, A and Khajavi, L, 2019. Phosphorus Removal from Si-Fe Alloy Using SiO_2-Al_2O_3-CaO Slag, *Metallurgical and Materials Transactions B,* 50:1773–1781.

Islam, M, 2015. Electrically Enhanced Slag-Metal Reactions, Doctoral thesis, Swinburne University of Technology, 242 p.

Islam, M, Rhamdhani, M and Brooks, G, 2014. Electrically enhanced boron removal from silicon using slag, *Metallurgical and Materials Transactions B,* 45:1–5.

Jakobsson, L and Tangstad, M, 2014. Distribution of boron between silicon and CaO-MgO-Al_2O_3-SiO_2 slags, *Metallurgical and Materials Transactions B,* 45:1644–1655.

Jakobsson, L and Tangstad, M, 2018. Thermodynamics of Boron Removal from Silicon Using CaO-MgO-Al_2O_3-SiO_2 Slags, *Metallurgical and Materials Transactions B,* 49:1699–1708.

Johnston, M and Barati, M, 2010. Distribution of impurity elements in slag–silicon equilibria for oxidative refining of metallurgical silicon for solar cell applications, *Solar Energy Materials and Solar Cells*, 94(12):2085–2090.

Jung, E, Moon, B and Min, D, 2011. Quantitative evaluation for effective removal of phosphorus for SoG-Si, *Solar Energy Materials and Solar Cells*, 95(7):1779–1784.

Krystad, E, Jakobsson, L, Tang, K and Tranell, G, 2017. Thermodynamic behavior and mass transfer kinetics of boron between ferrosilicon and CaO-SiO_2 slag, *Metallurgical and Materials Transactions B,* 48:2574–2582.

Latunussa, C, Ardente, F, Blengini, G and Mancini, L, 2016. Life Cycle Assessment of an innovative recycling process for crystalline silicon photovoltaic panels, *Solar Energy Materials and Solar Cells*, 156:101–111.

Liu, S, Huang, K and Zhu, H, 2017. Source of boron and phosphorus impurities in the silicon wiresawing slurry and their removal by acid leaching, *Separation and Purification Technology*, 172:113–118.

Luo, D W, Liu, N, Lu, Y P, Zhang, G L and Li, T J, 2011. Removal of Boron from Metallurgical Grade Silicon by Electromagnetic Induction Slag Melting, *Transactions of Nonferrous Metals Society of China (English Edition),* 21(5):1178–1184. https://doi.org/10.1016/S1003-6326(11)60840-6

Nishimoto, H, Kang, Y, Yoshikawa, T and Morita, K, 2012. The Rate of Boron Removal from Molten Silicon by CaO-SiO2 Slag and Cl2 Treatment, *High Temperature Materials and Processes,* 31(4–5):471–477. https://doi.org/10.1515/htmp-2012-0083

Piskunen, P, Avarmaa, K, O'Brien, H, Klemettinen, L, Johto, H and Taskinen, P, 2018. Precious metal distributions in direct nickel matte smelting with low-Cu mattes, *Metallurgical and Materials Transactions B,* 49:98–112.

Sineva, S, Shishin, D, Prostakova, V, Lindgren, M, Starykh, R, Chen, J and Jak, E, 2023. Experimental Study and Thermodynamic Modelling of Equilibrium Distributions of Ni, Sn and Zn Between Slag and Black Copper for E-Scrap Recycling Applications, *JOM,* 75(10):4254–4268.

Sineva, S, Shishin, D, Starykh, R, Hayes, P C and Jak, E, 2021. Equilibrium Distributions of Pb, Bi and Ag between Fayalite Slag and Copper-Rich Metal, Calcium Ferrite Slag and Copper-Rich Metal, Thermodynamic Assessment and Experimental Study at 1250°C, *Journal Of Sustainable Metallurgy*, 7(2):569–582.

Suzuki, K and Sano, N, 1991. Thermodynamics for removal of boron from metallurgical silicon by flux treatment, in *Tenth EC Photovoltaic Solar Energy Conference*: *Proceedings of the International Conference*:273–275.

Taposhe, G I A and Khajavi, L T, 2021. Removal of Phosphorus from Si-Fe Alloy by CaO-Al2O3-SiO2-Na2O Slag Refining, *JOM,* 73(2):729–735. https://doi.org/10.1007/s11837-020-04496-8

Teixeira, L A V and Morita, K, 2009. Removal of Boron from Molten Silicon Using CaO-SiO2 Based Slags, *ISIJ International,* 49(6):783–787. https://doi.org/10.2355/isijinternational.49.783

Wang, X, Tian, X, Chen, X, Ren, L and Geng, C, 2022. A review of end-of-life crystalline silicon solar photovoltaic panel recycling technology, *Solar Energy Materials and Solar Cells*, 248:111976.

Wang, Z, Ge, Z, Liu, J, Qian, G and Du, B, 2018. The mechanism of boron removal from silicon alloy by electric field using slag treatment, *Separation and Purification Technology*, 199:134–139.

Wei, K, Lu, H, Ma, W, Li, Y, Ding, Z, Wu, J and Dai, Y, 2015. Boron removal from metallurgical-grade silicon by CaO–SiO_2 slag refining, *Rare Metals*, 34:522–526.

Weiss, T and Schwerdtfeger, K, 1994. Chemical equilibria between silicon and slag melts, *Metallurgical and Materials Transactions B,* 25:497–504.

Yang, H, Liu, I, Liu, C, Hsu, H and Lan, C, 2019. Recycling and reuse of kerf-loss silicon from diamond wire sawing for photovoltaic industry, *Waste Management*, 84:204–210.

Zhang, Y, Sheng, W, Huang, L, Zhang, S, Chen, G, Zhang, C, Cai, H, Meng, J and Luo, X, 2020. Preparation of low-boron silicon from diamond wire sawing waste by pressure-less sintering and CaO–SiO_2 slag treatment, *ACS Sustainable Chemistry and Engineering*, 8(31):11755–11763.

Zhou, Q, Wen, J, Wu, J, Ma, W, Xu, M, Wei, K, Zhang, Z, Zhang, L and Xu, J, 2019. Recovery and purification of metallic silicon from waste silicon slag in electromagnetic induction furnace by slag refining method, *Journal of Cleaner Production*, 229:1335–1341.

Phase diagram study and thermodynamic modelling of the CaO-TiO_2-CaF_2 system

DOI: 10.62053/BPZS8985

J Bang[1] and I-H Jung[2]

1. Department of Materials Science and Engineering, Seoul National University, Seoul, South Korea, 08826. email: lpiok@snu.ac.kr
2. Department of Materials Science and Engineering, Seoul National University, Seoul, South Korea, 08826. email: in-ho.jung@snu.ac.kr

ABSTRACT

Ti is an important constituent for steels and superalloys. During the continuous casting process and ElectroSlag Remelting process (ESR), Ti in molten steel and superalloy can have chemical reactions with casting flux and ESR slag containing CaO and CaF_2. In order to investigate such exchange reactions, the understanding of the (Ca,Ti//O,F) reciprocal slag system is prerequisite. In the present study, a coupled phase diagram experiment and thermodynamic modelling of the (Ca,Ti//O,F) reciprocal system was performed. In particular, the phase diagram of the CaF_2-TiO_2 system was experimentally investigated by Differential Thermal Analysis (DTA) experiment and quenching experiments followed by Electron Probe MicroAnalysis (EPMA) phase analysis. The Gibbs energy functions of all solid and liquid phases in the (Ca,Ti//O,F) reciprocal system were optimised to reproduce the present data and all available reliable experimental data in literature.

INTRODUCTION

ElectroSlag Remelting (ESR) process is widely used in the refining process of superalloy and special steel due to its superior advantages such as homogenisation, desulfurisation, non-metallic inclusion removal and macro/micro-segregation control in alloy products (Arh, Podgornik and Burja, 2016; Shi *et al*, 2021). However, chemical reaction between liquid metal and slag can take place during ESR process, which induces the change in alloy composition in liquid metal (Chen, Wang and Hu, 2013). In particular, the content of strong oxidising element such as Ti, Al and Si can be readily varied by the reaction with ESR slag. Therefore, the understanding of the chemical reaction between liquid metal and ESR slag is important for accurate control of final target product composition in ESR process. Previous studies (Hou *et al*, 2016, 2018; Jiang *et al*, 2016; Pateisky, Biele and Fleischer, 1972) on the equilibration between slag and molten metal showed that the chemical composition of ESR slag and remelting condition influence the final liquid metal composition significantly.

Conventional ESR slag is composed of CaO, CaF_2 and Al_2O_3. In order to understand the distribution of Ti between liquid metal and ESR slag, the understanding of CaO-CaF_2-Al_2O_3-TiO_2 slag system is essential. Jung *et al* (2015) performed the thermodynamic modelling of the oxyfluoride system CaO-MgO-Al_2O_3-SiO_2-Na_2O-K_2O-Li_2O-ZrO_2-F, which is already available in FactSage FTOxid database (Bale *et al*, 2016). However, the system containing Ti oxide has not been assessed well for oxyfluoride system. Experimentally the CaF_2-CaO-TiO_2 system has not been well investigated yet.

The purpose of this study is to investigate the phase diagram of the CaF_2-CaO-TiO_2 system and develop a thermodynamic database for the system. Due to the high vapour pressure of CaF_2 and strong reactivity of CaO-containing slag, the phase diagram experiment was conducted using sealed Pt crucible. Based on the phase diagram data in this study, the thermodynamic modelling of the CaF_2-CaO-TiO_2 system was performed using the Calculation of the PHAse Diagram (CALPHAD) method. All thermodynamic calculations were conducted using FactSage thermochemical software (Bale *et al*, 2016).

LITERATURE REVIEW

Thermodynamic assessments of binary CaF_2-CaO (Kim *et al*, 2012) and CaO-TiO_2 (Du and Jung, personal communications, 2023) have been well-conducted. The phase diagram of the CaF_2-CaO-TiO_2 system was previously investigated by Hillert (1965) and Hillert *et al* (1965). He conducted equilibrium experiments on the CaF_2-TiO_2 and CaF_2-CaO-TiO_2 system using the quenching method. The microstructures of samples were analysed using optical microscopy and X-Ray diffraction (XRD)

method. The phase diagram of the CaF_2-TiO_2 reported by Hillert (1965) is presented in Figure 1. Hillert (1965) presented the existence of liquid miscibility gap between 0.46 ~ 0.94 CaF_2 mol fraction and reported an eutectic reaction of L → TiO_2 + CaF_2 at 0.42 CaF_2 and 1360°C. However, because the experiments were conducted using open Pt crucibles, the composition of initial samples could be changed due to the possible evaporation of CaF_2. In addition, there would be a high chance of quenched crystals formation during quenching process, which would mislead the interpretation of the results.

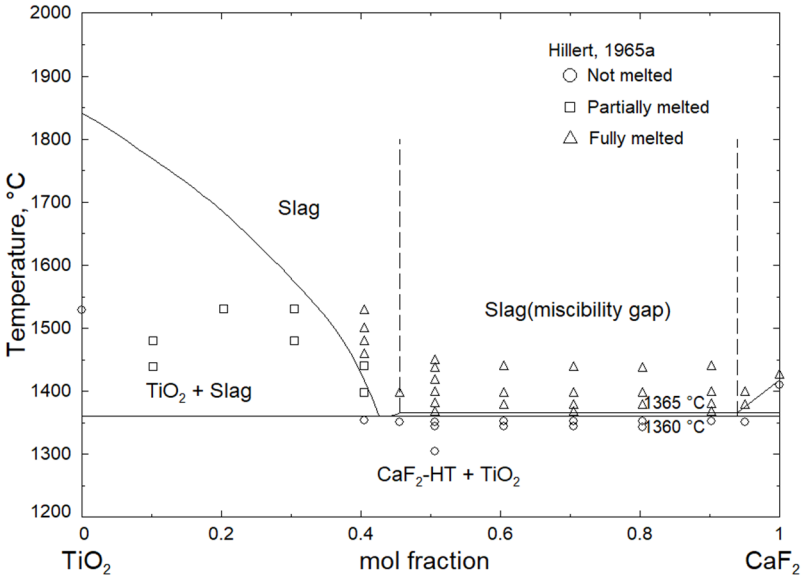

FIG 1 – Phase diagram of the CaF_2-TiO_2 system reported by Hillert (redrawn from original diagram by Hillert, 1965).

PHASE DIAGRAM EXPERIMENTS

Experimental challenges

There were three major challenges in conducting the phase diagram experiment of the CaF_2-CaO-TiO_2 system: (i) high vapour pressure of CaF_2 and gas reactivity of CaO-rich slag, (ii) difficulty in oxyfluoride sample composition analysis using electron probe micro-analyser (EPMA) and (iii) formation of quenched crystals due to low viscosity of CaF_2-containing melt. These experimental challenges were resolved by employing sealed Pt crucible and oxyfluoride standard in EPMA analysis. Unfortunately, quenched crystal formation cannot be avoided. In order to resolve difficulty in EPMA composition analysis due to quenched crystal formation, a large beam size of 10~30 μm was employed in the analysis to measure overall composition of original liquid phase. Potential sample damage due to evaporation of F in EPMA was minimised by employing a low voltage and amperage condition, 10 kV and 10 nA.

Starting materials

The mixtures of pure CaF_2 (Sigma-aldrich; 99.99 wt per cent purity), TiO_2 (Sigma-aldrich; 99.9 wt per cent purity) powders were prepared for the starting materials. To prevent hydration of starting samples, each powder was dried separately at high temperature before preparing the mixtures: drying of CaF_2 at 800°C and TiO_2 at 1200°C for 1 day. Dried powders were stored in vacuum desiccator to prevent moisture pickup. Starting samples were prepared by mixing dried powders using an alumina mortar with C_6H_{12}-cyclohexane to prevent moisture pickup. In order to confirm no oxidation of CaF_2 powder to CaO before sample preparation, XRD analysis was conducted and no CaO peaks were detected. To prevent vapourisation of CaF_2 during equilibration experiment and hydration during quenching process, samples were put in sealed in Pt crucibles (4 mm in outer diameter, 3 mm inner diameter and 10 mm length). The leakage of the sealed crucibles was checked by sonicating the crucibles in water for 10 mins and monitoring mass changes before and after sonication.

Differential Thermal Analysis (DTA) experiments

DTA experiment was conducted using the Netsch STA 449 F5 equipment. Temperature calibration on DTA was performed using phase transition temperatures of Ag_2SO_4, $BaCO_3$, $C_7H_6O_2$, $C_{12}H_{10}$, CsCl, $CaMgSi_2O_6$, K_2CrO_4, $KClO_4$ and $RbNO_3$. Experiment was conducted with a sealed Pt crucible directly placed into DTA alumina crucible. To minimise the effect of Pt crucible in the analysis, a reference was taken with empty Pt crucible and DTA alumina crucible.

Sample with $0.5CaF_2$–$0.5TiO_2$ in mol fraction was used for DTA experiments. Sample was heated and cooled at a rate of 10 K/min up to 1400°C under an Ar gas with 20 ml/min flow rate. Possible leakage of Pt crucible was continuously monitored using simultaneous thermogravity analysis in DTA equipment and weight change of Pt crucible before and after experiment was also checked to confirm no vapourisation loss of CaF_2.

Quenching experiments

Equilibration and quenching experiments were performed in a vertical tube furnace. Temperature of the furnace was measured by using a B-type thermocouple and maintained within 3°C range of the target temperature using PID controller. Sealed Pt crucibles were hanged in the hot zone (1200~1400°C) of the vertical furnace for equilibrium for 2~3 hr using Pt wire. After equilibration, samples were quenched by dropping into cold water. Possible leakage of the sample during experiment was checked by measuring the mass change of sealed Pt crucibles before and after the experiments. Due to high vapour pressure of the CaF_2-containing slag, ordinary Pt crucibles (3.3 mm outer diameter, 3 mm inner diameter and 10 mm length) were broken during long equilibration experiments at high temperature. Therefore, thick Pt crucibles (4 mm in outer diameter, 3 mm inner diameter and 10 mm length) were used in this experiment.

Phase analysis

After quenching experiments, sample were examined by XRD analysis (Bruker D8 Advance) and EPMA (JEOL-8530F). For XRD analysis, the samples were grounded and examined using Cu-Kα source (λ = 1.54 Å). Measured peaks were compared with powder diffraction files (PDF) of Bruker AXS DIFFRAC.EVA software. For EPMA, samples were mounted using epoxy and polished longitudinally using SiC paper of 400, 800, 1200, 2000 grit and diamond based oil. Oil-based polishing was conducted to exclude moisture pickup. After polishing, sonication using cyclohexane-C_6H_{12} was conducted and carbon coating was conducted. For EPMA, accelerating voltage of 10 kV and beam current of 10 nA was implemented. As finely distributed quenched crystals were inevitably formed in liquid region of quenched sample, a large beam size of 10~30 μm was used to obtain the overall liquid composition by averaging fluctuations in the sample composition caused by quenched crystals.

As the present samples have oxyfluoride chemistry, both mass balance and charge balance should be accomplished to determine the exact composition of the samples. However, when calibrating raw data using PRZ Armstrong algorithm with oxide and CaF_2 as standards, charge balance of the sample could not be easily accomplished. Therefore, a quenched liquid sample of 0.7 CaF_2–0.3 TiO_2 mol fraction was intentionally prepared from 1400°C and used for internal standard of EPMA for Ca, Ti, O and F concentration. It should be noted that very fine and homogenous quenched crystals of CaF_2 and TiO_2 were dispersed in the reference standard sample, as shown in Figure 2.

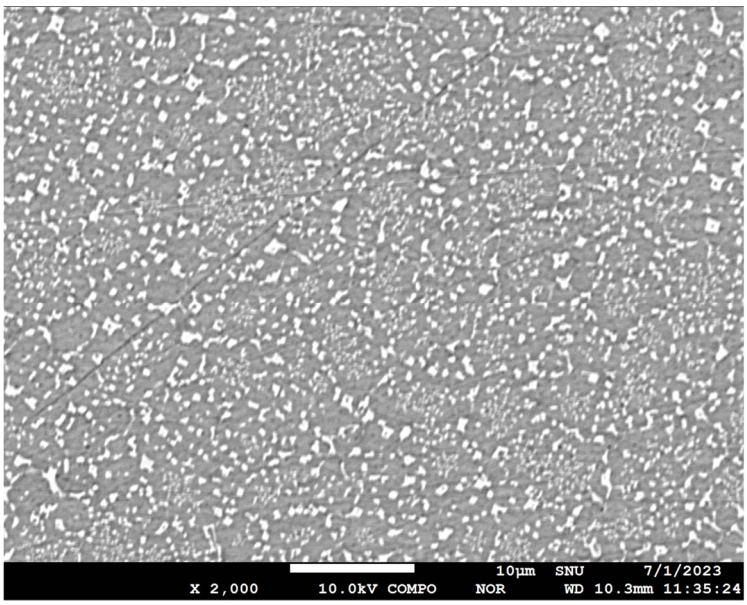

FIG 2 – Microstructure of the EPMA standard sample (0.7 CaF_2–0.3 TiO_2 in mol fraction) quenched at 1400°C. White crystals and dark crystals are TiO_2 and CaF_2, respectively.

THERMODYNAMIC MODEL

The Gibbs energy of pure elements and stoichiometric compounds can be expressed by heat capacity(Cp) and standard enthalpy of formation (ΔH^o_{298K}) and standard entropy (S^o_{298K}) at 298.15 K as following Equation 1.

$$G^o_T = \Delta H^o_{298K} + \int_{298}^{T} C_{p,T} dT - T(S^o_{298K} + \int_{298}^{T} \frac{C_{p,T}}{T} dT) \quad (1)$$

The Gibbs energy of liquid oxyfluoride solution was described by using Modified Quasichemical Model (MQM) (Pelton *et al*, 2000; Pelton and Chartrand, 2001) which considers the Short Range Ordering (SRO) of the nearest-neighbour atoms. The advantages of MQM compared with Bragg-Williams Random Mixing Model (BRWMM) are (i) the automatic change of non-ideal mixing entropy of solution depending on ordering tendency by interaction between solution species, (ii) freedom to modify the coordination number of component to reproduce SRO in binary liquid solution depending on system by system, and (iii) flexible choice of ternary interpolation technique depending on thermodynamic behaviour of each ternary system.

For oxide system, SRO between cations with a common oxygen anion is considered. However, as CaF_2-CaO-TiO_2 system is a reciprocal (Ca,Ti//O,F) system with two cations and two anions, two sublattice quadruplet approximation was implemented on MQM to consider first-nearest neighbour and second nearest neighbour SRO simultaneously (Chartrand and Pelton, 2001; Pelton, Chartrand and Eriksson, 2001). In the (Ca,Ti//O,F) reciprocal system, Ca^{2+} and Ti^{4+} are considered to be located in imaginary cationic sublattice and O^{2-} and F^- are considered to be located in imaginary anionic sublattice in the melt, as shown in Figure 3. The SRO of Ca^{2+} and Ti^{4+} cations can be expressed by binary interaction term of $\Delta g_{CaTi/OO}$ or $\Delta g_{CaTi/FF}$ which could be optimised for CaO-TiO_2 melt and CaF_2-TiF_4 melt, respectively. Similarly, binary model parameters of $\Delta g_{Ca/OF}$ and $\Delta g_{Ti/OF}$ can be optimised for binary CaO-CaF_2 and TiO_2-TiF_4, respectively. Reciprocal interaction parameters of $\Delta g_{CaTi/OF}$ and ternary interaction parameters can be also added to optimise the Gibbs energy of reciprocal melt.

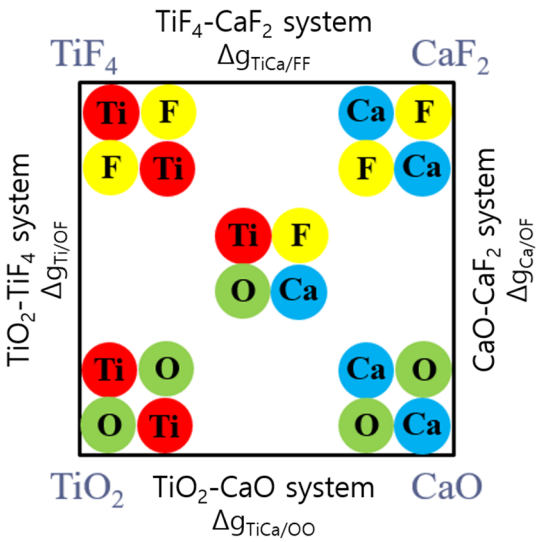

FIG 3 – Schematic diagram of two sublattice approximation of (Ca,Ti//O,F) reciprocal system. Ca^{2+} and Ti^{4+} located in cation sublattices and O^{2-} and F^{-} located in anion sublattices.

EXPERIMENTAL RESULTS AND THERMODYNAMIC MODELLING

Experimental results

The phase diagram of the CaF_2-TiO_2 system based on the present experimental data and thermodynamic modelling results is presented in Figure 4.

The DTA results for $0.5CaF_2$–$0.5TiO_2$ sample is presented in Figure 4a. As shown in the DTA curves for all three cycles, the transition peaks for the sample were not very discrete enough to ensure a clear phase transformation. Other DTA results for CaF_2-containing samples showed similar trend. Based on the heating curve data, the onset temperature for the phase transition was identified at 1349.5°C. The transition temperature in cooling curves was also the same as the value from heating curves.

In order to clearly determine the transition occurring at this transition temperature, quenching experiments at 1250 and 1400°C were conducted for the same samples and the BSE images of the quenched samples are presented in Figure 4b and 4c, respectively. Based on both XRD and EPMA results, the equilibrium phases at 1250°C and 1400°C were determined to be CaF_2 + TiO_2 and TiO_2 + liquid, respectively. EPMA results indicate that no mutual solubility between CaF_2 and TiO_2 in solid state. The liquidus of TiO_2 at 1400°C was determined to be $0.7CaF_2$–$0.3TiO_2$. In order to confirm the liquidus of this system, a sample of $0.8CaF_2$–$0.2TiO_2$ was prepared and equilibrated at 1400°C. The resultant phase confirmed no solid TiO_2 formation.

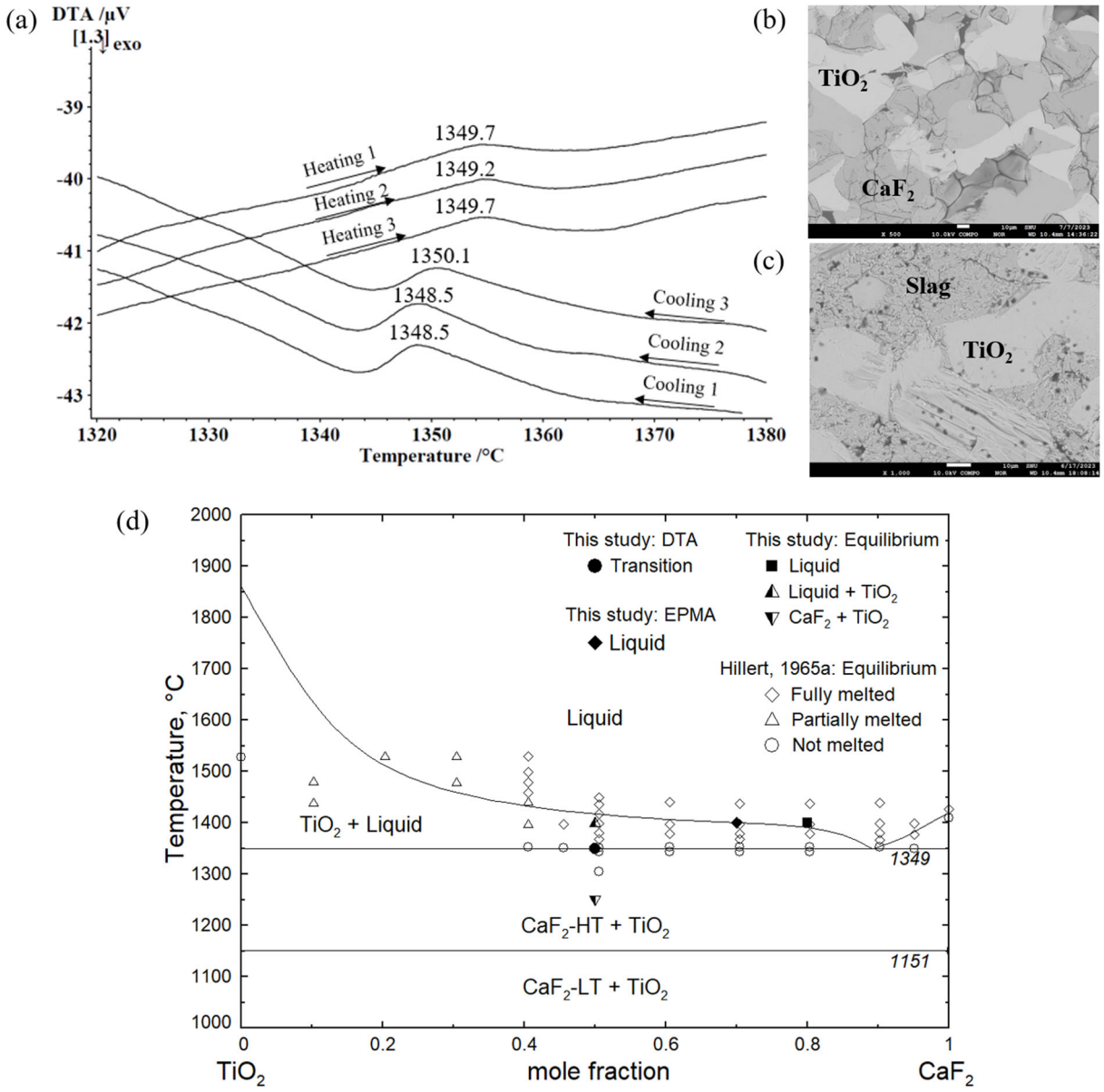

FIG 4 – Phase diagram of the CaF_2-TiO_2 system optimised in this study. (a) DTA result and BSE images of sample equilibrated at (b) 1250°C and (c) 1400°C with starting composition of $0.5CaF_2$–$0.5TiO_2$. (d) Optimised phase diagram based on the present experimental data along with previous experimental results by Hillert (1965).

Thermodynamic modelling

For thermodynamic modelling, the Gibbs energies of solid phases were taken from constituent binary system of the CaO-TiO_2 and CaF_2-CaO in FactSage FTOxide 8.3 database. No ternary or reciprocal solids were found in the (Ca,Ti//O,F) reciprocal system. To reproduce the phase diagram data in this study for the entire of (Ca,Ti//O,F) reciprocal system including the phase diagram information in Figure 4 and other pseudo-binary and isopleth sections (not presented here), reciprocal MQM parameters were optimised.

The calculated phase diagram from optimised model parameters is in good agreement with experimental data in this study, as shown in Figure 4. Several points are need to be highlighted regarding the differences between the previous experimental results (Hillert, 1965) and this optimised phase diagram. First, the miscibility gap reported in previous study was not substantiated in this study because a miscibility gap could not be observed in this experiment. As the previous study analysed sample using optical microscopy and XRD, the quenched crystals of CaF_2 and TiO_2 shown in Figure 2 could be misunderstood as a liquid immiscibility. Second, several experimental points reported as partially melted region were found to be a liquid single phase region in the present

phase diagram study. Considering the high vapour pressure of CaF_2, sample composition of the previous study with open crucible might be shifted toward TiO_2-rich composition, which induces this misinterpretation. Finally, considerable number of experimental data reported single phase at the range of $0.46CaF_2$ to $0.80CaF_2$ in mol fraction at 1365°C, 1380°C and 1400°C. However, in the present experiment, liquid + TiO_2 phase assemblage is found in the $0.5CaF_2$ mol fraction sample at 1400°C. We found that solid TiO_2 crystals settled down on the bottom of the sample and leave liquid phase in the upper side. This seems to happen because of very low viscosity of CaF_2 containing slag. This kind of settling of solid TiO_2 crystal in a large sample size might lead to the wrong interpretation of the equilibrium results in the previous study by Hillert (1965). Solid crystal settlement was also observed in other experiments (unpublished results by the present authors) for oxyfluoride systems containing CaF_2.

CONCLUSIONS

The phase diagram of the CaF_2-TiO_2 system was experimentally determined using DTA and quenching experiments followed by EPMA and XRD phase analysis. Sealed Pt crucible was employed for the experiment to overcome experimental challenges in oxyfluoride system. It is found that the previously reported phase diagram of the CaF_2-TiO_2 system is inaccurate. More reliable phase diagram of the CaF_2-TiO_2 system was constructed from the present coupled phase diagram experiment and thermodynamic modelling study. The resultant thermodynamic database can be integrated to the existing FactSage database to calculate the multicomponent phase diagram for oxyfluoride slag system containing TiO_2 and also for slag-metal equilibrium calculation for continuous casting steel process and ESR process.

ACKNOWLEDGEMENTS

This research was supported by Manufacturing and Evaluation Technology of Premium Quality Inconel 718 Alloy Ingot and Forging Product for Turbofan Rotor Disk funded by Ministry of Trade, Industry and Energy (No. RS-2023-00256058). Financial supports from Tata Steel Europe, Posco, Hyundai Steel, Nucor Steel, RioTionto Iron and Titanium, Nippon Steel Corp., JFE Steel, Voestalpine, RHI Magnesita, SeAH Besteel, Doosan Heavy Industry and Construction, and SCHOTT AG are also gratefully acknowledged.

REFERENCES

Arh, B, Podgornik, B and Burja, J, 2016. Electroslag remelting: A process overview, *Mater Technol*, 50(6):971–979.

Bale, C W, Bélisle, E, Chartrand, P, Decterov, S A, Eriksson, G, Gheribi, A E and Van Ende, M A, 2016. Reprint of: FactSage thermochemical software and databases, 2010–2016, *CALPHAD*, 55:1–19.

Chartrand, P and Pelton, A D, 2001. The modified quasi-chemical model: Part III. Two sublattices, *Metallurgical and Materials Transactions A*, 32:1397–1407.

Chen, C Y, Wang, G and Hu, Y, 2013. Composition variation in Incoloy 800H alloy ingot during ESR process, China Steel Technical Report, 26:7–12.

Hillert, L, 1965. Phase Diagram TiO_2-CaF2, *Acta Chemica Scandinavica*, 19(6):1516.

Hillert, L, Bo, H, Magnéli, A and Kallner, A, 1965. The phase diagram (81% TiO_2+ 19% CaO)-CaF2, *Acta Chemica Scand*, 19:1986–1987.

Hou, D, Jiang, Z, Dong, Y, Cao, Y, Cao, H and Gong, W, 2016. Thermodynamic design of electroslag remelting slag for high titanium and low aluminium stainless steel based on IMCT, *Ironmaking and Steelmaking*, 43(7):517–525.

Hou, D, Liu, F B, Qu, T P, Jiang, Z H, Wang, D Y and Dong, Y W, 2018. Behavior of alloying elements during drawing-ingot-type electroslag remelting of stainless steel containing titanium, *ISIJ International*, 58(5):876–885.

Jiang, Z H, Hou, D, Dong, Y W, Cao, Y L, Cao, H B and Gong, W, 2016. Effect of slag on titanium, silicon, and aluminum contents in superalloy during electroslag remelting, *Metallurgical and Materials Transactions B*, 47:1465–1474.

Jung, I-H, Van Ende, M-A, Kim, D-G, Konar, B and Kwon, S-Y, 2015. Thermodynamic database for oxy-fluoride mold flux, CaO-MgO-Na2O-K2O-Li2O-Al_2O_3-SiO_2-ZrO2-F, *Asia Steel*, 2015:476–477.

Kim, D G, van Hoek, C, Liebske, C, van der Laan, S, Hudon, P and Jung, I H, 2012. Phase Diagram Study of the CaO–CaF2 System, *ISIJ international*, 52(11):1945–1950.

Pateisky, G, Biele, H and Fleischer, H J, 1972. The reactions of titanium and silicon with Al_2O_3-CaO-CaF_2 slags in the ESR process, *Journal of Vacuum Science and Technology*, 9(6):1318–1321.

Pelton, A D and Chartrand, P, 2001. The modified quasi-chemical model: Part II, Multicomponent solutions, *Metallurgical and Materials Transactions A*, 32:1355–1360.

Pelton, A D, Degterov, S A, Eriksson, G, Robelin, C and Dessureault, Y, 2000. The modified quasichemical model I–Binary solutions, *Metallurgical and Materials Transactions B*, 31:651–659.

Pelton, A D, Chartrand, P and Eriksson, G, 2001. The modified quasi-chemical model: Part IV, Two-sublattice quadruplet approximation, *Metallurgical and Materials Transactions A*, 32:1409–1416.

Shi, C B, Huang, Y, Zhang, J X, Li, J and Zheng, X, 2021. Review on desulfurization in electroslag remelting, *International Journal of Minerals, Metallurgy and Materials*, 28:18–29.

Chemical- and micro-analytical techniques for molten slags, mattes, speisses and alloys

DOI: 10.62053/SCVK8806

J Chen[1], P Hayes[2] and E Jak[3]

1. Theme Leader – Analytical Methods, PYROSEARCH, University of Queensland, Brisbane Qld 4072. Email: j.chen5@uq.edu.au
2. Emeritus Professor, PYROSEARCH, University of Queensland, Brisbane Qld 4072. Email: p.hayes@uq.edu.au
3. Professor, Centre Director, PYROSEARCH, University of Queensland, Brisbane Qld 4072. Email: e.jak@uq.edu.au

ABSTRACT

The paper provides an overview of the various analytical and microanalytical techniques currently in use to characterise the outcomes of pyrometallurgical processes, examining the advantages and limitations of these approaches. Specific focus with be given to quantitative microanalysis techniques including electron probe microanalysis and laser ablation, covering general principles, capabilities and limitations and recent development to address specific challenges associated with analysing molten slag, matte, and alloys, highlighting the necessity of embracing the application of these and other innovative analytical methodologies.

INTRODUCTION

In the field of pyrometallurgy, obtaining accurate analyses of metallurgical materials, particularly slag, matte, speiss and alloys, is imperative for advancing our understanding, and for developing quantitative descriptions, of metallurgical processes. The complex nature of these materials necessitates the application of analytical techniques capable of characterising their chemical compositions, structural properties, mineralogy/phase assemblages, and where appropriate, elemental speciation.

At industrial pyrometallurgical plants, a range of analytical methods are commonly used to facilitate both quality assurance/quality control (QA/QC) processes and assist research and development (R&D). For instance, X-ray fluorescence (XRF), Inductively coupled plasma in conjunction with optical emission spectroscopy (ICP-OES), or inductively coupled plasma in conjunction with mass spectroscopy (ICP-MS) are routinely applied for the bulk chemical analysis of intermediate and final products (eg Cu matte and blister), as well as by-products and waste materials (eg slag). These bulk analyses in practice are used to ensure that these materials meet specified quality standards, and the data can be used for overall elemental mass balances across processes and process operations.

To provide a deeper and more complete understanding of these processes it is necessary to utilise more advanced and more specific analytical techniques capable of identifying the phases that are present in the materials and the distribution of elements within these phases. For example, slags are not necessarily homogeneous molten materials, they can contain solids and entrained liquid phases. Detailed analysis of molten materials quenched from the operating temperatures in reactor enable these important details to be identified and accurately characterised and their impacts on, for example, elemental distribution and slag viscosity to be understood and quantified.

The necessity for abundant and accurate experimental data for the development of advanced thermodynamic modelling tools also hinges directly on the availability of suitable analytical techniques. The adaptation of quantitative microanalytical methods such as Electron Probe Micro Analysis (EPMA) and Laser Ablation Inductively Coupled Plasma Mass Spectrometry (LA-ICP-MS) have notably expanded the range of measurable conditions and enhanced data accuracy for phase equilibrium studies. These techniques have proven vital for characterising heterogeneous processes, meeting emerging demands and opening avenues for refining industrial systems. These techniques enable detailed microstructural analysis and accurate composition measurement, detecting elements at minimum levels of ~300 ppm and ppb, with spatial resolutions ranging from sub- to hundreds of microns. Microanalysis of quenched industrial samples also presents a unique

opportunity to understand reactor processes, offering insights into kinetic reactions and facilitating the integration of thermodynamic models into real industrial operations.

SAMPLING AND INITIAL INSPECTION

Before embarking on extensive and time-consuming examination of samples it is critically important to ensure that the proposed procedures and practices for obtaining samples for analysis are consistent with the aim of the study. This is especially important at the outset of a new study.

If this is an equilibrium study, then the chemical and physical properties, the chemical composition and proportion of phases of all samples taken from the reaction system should be identical. If there are potentially variations in the reaction or process conditions at the time of sampling, these should be recognised and documented by sampling at appropriate times and positions within the reactor.

Obtaining accurate online chemical and analytical measurements in pyrometallurgical systems is extremely difficult in practice. The approach taken in most studies is to take representative samples and remove them from the reactor and cooling to room temperature, preserving them in a form that reflects their condition at the process temperature. Two typical methods are used to sample slag and other melts.

Water-quenching method

A preheated steel spoon can be used to collect molten slag samples at tapping, small aliquots of which are then quickly poured into cold water. This method allows effective quenching of the samples to preserve the phase assemblage at high temperature. However, caution should be taken when quenching samples reactive (sometimes aggressively enough to cause explosion) to water such as slag with high alkaline concentration, and those containing matte, molten salt or molten alloy. Modification to the quenching media is often needed to safely quench these materials.

Dip-bar method

A cold metal bar (steel or copper) is quickly submerged and removed into the molten bath, the molten sample in contact with the surface of the metal bar is quenched immediately and the high temperature phase assemblage is preserved. This method allows the sampling conducted in a safe manner. However, typically only tens to hundreds of micrometres of sample next to the sample-metal bar interface are effectively quenched, and therefore requiring careful microanalysis of the sample for characterisation. An example is show in Figure 1.

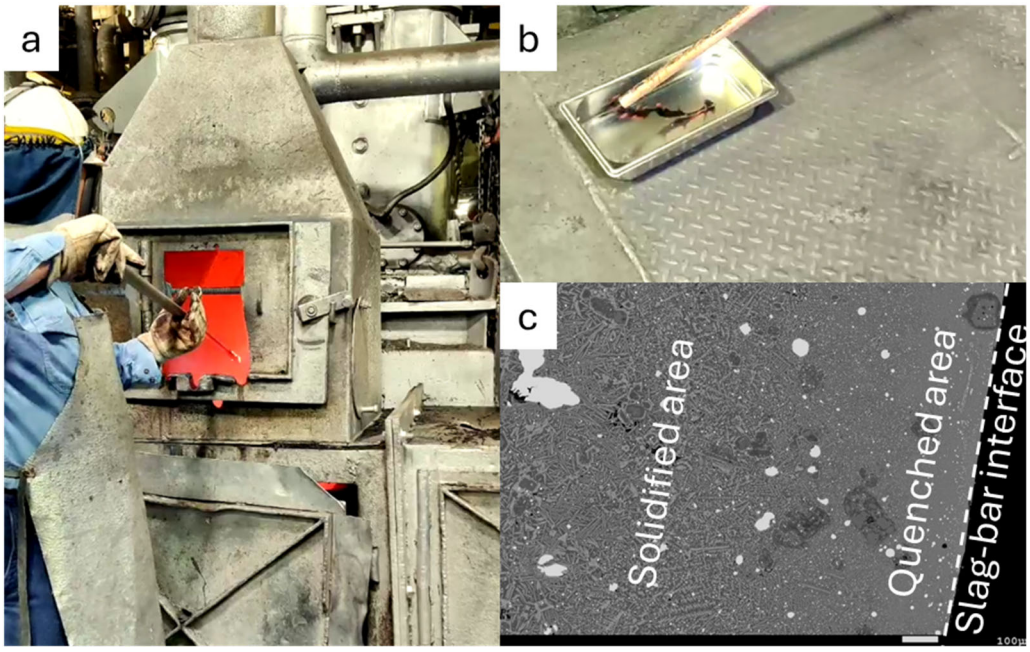

FIG 1 – (a) and (b) Slag sampling by dip-bar– sampling procedure; (c) microstructure of the sample taken showing the fully quenched area, representative of the sample at temperature, in the region immediately adjacent to the quench bar.

An important check to undertake when a sample has been obtained is to first examine the polished section under the metallurgical optical microscope. This immediately provides a checkpoint to establish the characteristics of the sample, to establish whether the sample is a single phase and uniform in appearance. If the sample appears uniform at this scale it may be sufficient to rely on bulk property measurements described in the following section to characterise the sample. If more than one phase is identified at this stage when only one phase is anticipated then further review of process conditions, sampling and preparation procedures should be undertaken to avoid the formation or presence these artefacts. In some cases, microscopic changes in sample structure can take place during the sampling procedure, particularly during cooling of samples from the process temperature; more detailed examination is recommended in all cases to fully characterise the samples. The use of advanced high-resolution techniques is discussed in a later section below.

CLASSIFICATION OF ANALYTICAL TECHNIQUES

Bulk chemical (elemental) analysis

Bulk chemical analysis is a process used to determine the mean elemental composition of a sample. It involves identifying and quantifying the concentrations selected elements present in a material or substance. This can be done through various well-established techniques, including wet chemical, spectroscopy, chromatography, and mass spectrometry.

Table 1 summarises the underlying principles and capabilities of these various techniques, with reference to appropriate texts addressing this topic.

Bonding structural/speciation analysis

Bonding structural/speciation analysis techniques are used to study the types of bonds at an atomic level, molecular structures, and chemical species present in materials. Typical techniques include Fourier Transform Infrared (FTIR) Spectroscopy, Raman Spectroscopy, Nuclear Magnetic Resonance (NMR) Spectroscopy and X-ray Absorption Near Edge Spectroscopy (XANES). References and applications of these techniques are also provided in Table 1.

Both FTIR and Raman Spectroscopy have been used to study the chemical bonding in silicate melts. Different types of chemical bonds (eg Si-O-Si, Si-O-Al) have characteristic spectra, which can be used to identify the types of bonds present and their relative proportions. These data can be used to identify and better understand the slag structure and its relation to physico-chemical properties, such as, viscosity for different bulk compositions and process conditions.

XANES is a technique used to identify the speciation of multivalent metal cations in the solid materials. To date, it’s application has been largely limited to the characterisation of crystalline geological materials.

Deriving quantitative information from these techniques is not a straightforward process and the accuracy heavily relies on:

- The use of matrix-matching standards to establish reliable calibration curve.
- The reliability of reference spectra in the handbook of the respective techniques.
- Peak fitting and spectra deconvolution process used, which introduce additional assumptions in the quantification of these phenomena.

QUANTITATIVE MICROANALYSIS TECHNIQUES

Quantitative microanalysis techniques stand apart from bulk analysis methods by allowing the characterisation of small samples, typically at the micrometer or even nanometer scale. They excel in examining individual phases and features within complex samples where distinct phases cannot be feasibly separated for bulk chemical analysis. Table 2 offers a compilation of references and applications highlighting the utility of these microanalytical methods.

TABLE 1

Summary of bulk analytical techniques used for metallurgical materials and references for further reading.

			Elements can be measured	Detection limit	Spatial Resolution	Sample preparation	Quantitative/Qualitative	Example of application
Bulk analysis techniques	Elemental	XRF (Beckhoff et al., 2007)	Na - U	10ppm	N/A	pressed pellet/fused glass	Typically quantitative; fused glass gives more accurate results	Slag, matte, speiss, alloy bulk assay
		ICP-OES (Olesik, 1991)	All except C, H, O, N and halogens	high ppbs		aqueous digestion	Quantitative	Slag, matte, speiss, alloy bulk assay
		ICP-MS (Olesik, 1991)	All except H, O, N, F and noble gas element	down to ppt		aqueous digestion	Quantitative	Trace elements
		AAS (Christian and Epstein, 1980)	All metal elements	low ppbs		aqueous digestion	Quantitative	Trace Au and Ag in slag
	Phase/ mineralogy	XRD (Epp, 2016)		1 wt%		grinding to make fine powder	Qualitative but can be quantitative	type and proportion of solids in molten slag
	Structural / speciation	Mossbauer Spectroscopy (May, 2012)	Fe, Sn, Sb, Te, I, Au, Ni, Ru, Ir, W, REEs	1 wt%		grinding to make fine powder	Qualitative but can be quantitative	Fe speciation in silicate melt/slag
		EXAFS/XANES (Teo, 2012)	Multivalent elements	0.1wt%		fine powder or bulk solid	Qualitative but can be quantitative	Ionic structure information of molten slag and salt
		NMR (Stebbins, 1995)	molecular structure	100 µmol/g		fine powder	Qualitative but can be quantitative	
	Surface	XPS (Stevie and Donley, 2020)	All except H and He	0.1-1 at%		fine powder or bulk solid	Qualitative but can be quantitative	surface elemental characterisation of slag, matte and metal/Transition metal speciation in silicate melt/slag

TABLE 2

Summary of micro-analytical techniques used for metallurgical materials and references for further reading.

			Elements can be measured	Detection limit	Spatial Resolution	Sample preparation	Quantitative/Qualitative	Example of application
Micro-analysis techniques	Elemental	SEM/EDS (Goldstein et al., 2017)	All except H, He, Li*	0.1-1wt%	1-5um	any vacuum-stable solid/powder	Semi-quantitative but can be quantitative	composition analysis of microscale phase in slag, matte, speiss, alloy
		SEM/WDS (Goldstein, 1969)	All except H, He, Li**	100-300 ppm	1-5um	mounted and polished solid	Quantitative	composition analysis of microscale phases in slag, matte, speiss, alloy
		u-XRF (Beckhoff et al., 2007, Papadopoulou et al., 2006)	Na - U	20ppm	30um	any solid/powder	Semi-quantitative but can be quantitative	elemental mapping of large areas
		LA-ICP-MS (Walsh, 2002)	All except H, O, N, F and noble gas element	low ppbs	10s to 100s um	any solid/powder	Quantitative for oxide slags, qualitative for other phases	trace elements measurement of microscale phase in slag, matte, speiss, alloy
		LIBS (Singh and Thakur, 2020)	All elements	down to ppm	10s to 100s um	any solid/powder	Qualitative but can be quantitative	Hydration of slags
	Phase/ mineralogy	Optical Microscopy (Geels et al., 2007)	N/A		down to 1um	mounted and polished solid sample	Qualitative but can be quantitative	Initial fast microstructural examination of slag, matte, alloy samples
		u-XRD (Flemming, 2007)	N/A	1 wt%	10s um	mounted and polished solid sample	Qualitative but can be quantitative	identification of SFCA in iron ore sinters
		QEMSCAN/MLA /TIMA (Sutherland and Gottlieb, 1991)	All except H, He, Li*	5wt%	1-5um	mounted and polished solid sample	Quantitative	quantitative analysis of phases in slags
	Structural /speciation	RAMAN (Long, 1977)	N/A	ppm	down to 1um	mounted and polished solid sample	Qualitative but can be quantitative	structural information of silicate slag
		FTIR (Berthomieu and Hienerwadel, 2009)	Si-O, Me-Si-O, O-Si-O groups	1-5 wt%	down to 1um	mounted and polished solid sample	Qualitative but can be quantitative	structural information of silicate slag
	Surface	TOF-SIMS (Fearn, 2015)	All elements	down to 1ppm	down to 0.1um	mounted and polished solid sample	Qualitative	surface elemental characterisation of slag, matte and metal

SEM-based X-ray microanalysis

General principles and capabilities

Electron microscope-based microanalysis is a non-destructive technique based on the interaction between a focused electron beam and a solid sample. As the electrons collide with atoms in the sample, characteristic X-rays are emitted due to inner-shell electron transitions. EPMA typically employs wavelength dispersive spectrometry (WDS), crystal monochromators for high resolution wavelength separation of incoming X-rays so that the intensity of the radiation from each element can be measured and quantified. An alternative approach to the measurement of X-rays emitted is the use of Energy Dispersion Spectrometer (EDS) in which characteristic X-rays from all elements present in the sample are simultaneously captured for rapid elemental analysis. EDS can be used in scanning electron microscopy (SEM) mode or transmission electron microscopy (TEM) mode.

Both WDS and EDS offer qualitative and quantitative analysis at high spatial resolution (typically 1–3 μm), making it suitable for examining small features. For quantitative analysis, the measured X-ray intensities of unknown samples are compared to that of known standards applied with a well-established matrix correction algorithm (eg atomic number, absorption, fluorescence (ZAF)) to determine the concentration of the element of interest. Sample preparation involves mounting solid samples in epoxy resin, exposing cross-sections through grinding and polishing. A thin carbon layer (20 nm) is often applied to samples before analysis to avoid charging of the sample. Table 3 shows the comparison of analytical capabilities between WDS and EDS.

TABLE 3

Comparison of the analytical capabilities between wavelength dispersive spectrometry (WDS) and energy dispersive X-ray spectroscopy (EDS) measurement techniques.

	EDS	WDS
Spatial resolution	Down to 0.5 μm	
Energy resolution	~125 ev	~ 5–10 ev
Elements can be measured	Be to U	
Typical detection limit	0.1 wt%	0.01 wt%
Data acquisition	All elements at same time (rapid)	One element per spectrometer at a time (slow)
Calibration	Every 3–12 months	Every 24–48 hrs

Applications

EPMA typically finds applications in determining high temperature phase equilibria and chemical compositions of individual phases in multi-phased pyrometallurgical materials. The EPMA analysis is typically navigated by high resolution backscattered electron imaging, which makes the investigation of elemental process taking place during the metallurgical process highly efficient.

Challenges and development

Measurement of trace elements

Notwithstanding its superior spatial resolution, EPMA has often been perceived as reliable only for major elements (>1 wt per cent). In fact, recent advances in EPMA instrumentation such as the field-emission electron gun, large-size diffraction crystals, and the automation of aggregated intensities from multiple spectrometers (Donovan, Singer and Armstrong, 2016) have made it feasible to use EPMA to measure at least the more abundant trace elements (>100 ppm) on a regular basis. Reviews on trace element measurement using EPMA are readily available in literature typically for geological materials (Batanova, Sobolev and Magnin, 2018; Donovan, Singer and Armstrong, 2016; Jercinovic *et al*, 2012). The principles are normally applicable to metallurgical materials. Over the

years, authors have developed analytical protocols to measure minor/trace elements in chemically complex phases, such as industry slag samples (Chen *et al*, 2022). These protocols address major issues associated with trace element analysis by EPMA, such as minimal detection limit (MDL), spectral interferences, beam damage and background corrections to ensure the accuracies of the measurements.

Measurement of light elements

Metallurgical research has long sought accurate determination of light elements, such as oxygen (O), fluorine (F), and boron (B) in for example, matte, mould flux, and slag. However, the available analysis techniques for these elements using electron microscope techniques are quite limited. Quantitative measurement of elements with atomic numbers less than or equal to 9 (eg fluorine) has been a persistent challenge for X-ray-based microanalysis (Bastin and Heijligers, 1992). This is due to several factors, including low X-ray emission, high sensitivity to surface contamination, poorly established mass absorption coefficients for matrix correction, and bonding-dependent peak shift of characteristic X-rays.

Protocols been proposed to measure light elements, such as fluorine (F), oxygen (O), nitrogen (N), carbon (C), boron (B), and beryllium (Be) in geological materials (Newbury and Ritchie, 2015; Zhang *et al*, 2016; Nash, 1992; Fonseca *et al*, 2008; Cheng *et al*, 2019; Wu *et al*, 2022). However, there is limited information available regarding how these challenges have been addressed and how the accuracy of the analysis has been evaluated.

Measurement of beam sensitive materials

Analysing beam-sensitive materials, such as alkaline-rich slags and halogen-bearing minerals, with SEM-based X-ray microanalysis technique requires careful consideration of several principles to ensure accurate results without damaging the sample. These principles have been discussed and measures taken to minimise the uncertainty due to beam damage have been extensively discussed in the literature (Willich and Bethke, 1996; Chen *et al*, 2020, 2022; Henderson, 2011). In general, the following analytical conditions are preferred: low beam voltage and current, short analysis time and avoiding high magnification for navigation. Modern software like Probe for EPMA (http://www.probesoftware.com/) has allowed the monitoring and the correction of time dependent intensity if required.

Measurement of melt with microcrystalline precipitation

In the process of sampling molten materials, not all phases can be effectively quenched and retained as a homogeneous glassy phase. Ionic liquids, including calcium ferrite slag, matte, speiss, alloy, and molten salt, crystallise much more rapidly than silicate melt, leading to a microcrystalline textured phase upon quenching.

To determine the composition of phases that exhibit micron/submicron-scale heterogeneity, some researchers have used a defocused electron beam with a fixed beam diameter during measurement. However, this approach has been controversial due to the matrix correction procedure of EPMA analysis, which assumes the sampling volume of the analysis area to be homogeneous. A previous study (Barkman *et al*, 2013) adopting this approach observed errors of up to 6 per cent in obtaining the average composition of a heterogeneous material. Conversely, other studies have shown that analysis accuracy is not affected by this approach. Fallah-Mehrjardi *et al* (2017) analysed the copper concentration in slag samples containing finely precipitated Cu-rich particles from gas/slag/matte/tridymite phase equilibrium experiments using EPMA with varying beam sizes. The authors observed improved analysis precision with no significant impact on analysis accuracy when employing larger beam sizes. Similarly, Chen *et al* (2022) measured the industry copper-converting slag with quench precipitations using a defocused beam. The authors evaluated the extent of potential error by measuring the areas of the slag phase with different extents of quench crystallisation. No systematic difference was observed between measurement results from different areas, suggesting that the potential error in minor element concentration measurement in the slag phase due to heterogeneity within the sampling volume is negligible.

In practice, the potential error in the measurement results due to heterogeneity within the sampling volume should be evaluated on a case-by-case basis. We suggest two possible ways to evaluate this potential error:

1. Measure the areas of the same phase with different extents of heterogeneity and compare the results. The smaller the difference in the results, the less uncertainty due to the sample heterogeneity.
2. Use alternative methods, such as LA-ICP-MS, to verify the measurement results by EPMA.

Systematic errors could be observed in certain cases and should be documented and included when reporting the analytical results.

Dealing with boundary secondary fluorescence

The boundary secondary fluorescence effect (BSF) is a known phenomenon in electron-induced X-ray microanalysis in SEM-EDS/WDS and is well recognised in materials and geoscience research (Borisova *et al*, 2018). The primary X-rays generated by electron-material interaction can travel within the sample and further produce characteristic X-rays of lower energies, extending the range of secondary X-ray fluorescence beyond that of primary X-ray generation. While the impact of secondary fluorescence is generally corrected for during matrix correction in X-ray microanalysis, there's uncertainty near phase boundaries. When analysing a phase close to a boundary with another phase containing a significantly higher level of the same element, the element of interest is often measured at a higher level than the true value. This is because some primary X-rays generated within Phase A travel across the phase boundary and excite secondary X-rays of lower energies inside Phase B. Some of these emitted secondary X-rays, characteristic of Element α from Phase B, are collected by the X-ray detector, leading to an apparent higher concentration of Element α in Phase A than its actual concentration. A schematic description of the BSF effect is shown as Figure 2.

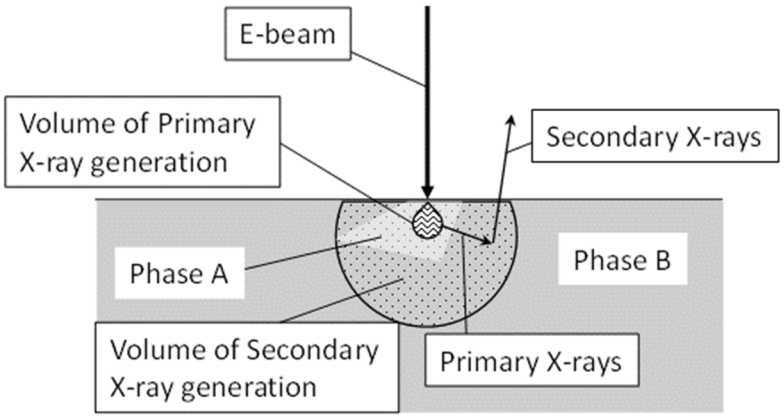

FIG 2 – Schematic description of the boundary secondary fluorescence (BSF) effect.

Despite numerous proposed methods to mitigate this issue, existing approaches have inherent limitations and lack of universal efficacy. Many methods assess BSF through computer or experimental simulations. These methods rely heavily on precise knowledge of the geometrical and dimensional characteristics of the phase under analysis and its surrounding matrix, which is extremely challenging to obtain itself in real-world scenarios. Other methods exhibit effectiveness only for specific elements.

A rapid and effective method aimed to eliminate the secondary fluorescence effect at boundaries in quantitative X-ray microanalysis has recently been developed by the authors (Chen *et al*, 2024). Utilising a focused ion beam – scanning electron microscope (FIB-SEM) dual-beam system, separate phase/features less than 10 µm of interest can be separated from their original matrix and remounted onto a suitable substrate for subsequent EPMA analysis as shown in Figure 3.

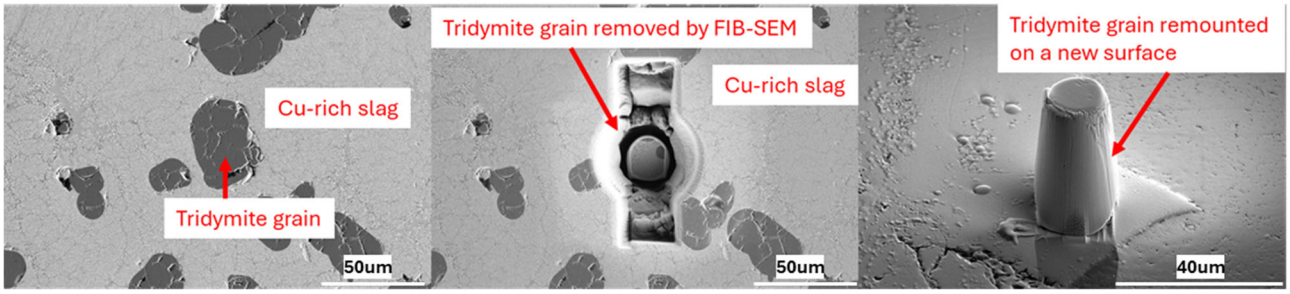

FIG 3 – Demonstration of removing and remounting of targeted phase for EPMA analysis to eliminate the SBF effect.

LA-ICP-MS

General principles and capabilities

LA-ICP-MS is an analytical technique for elemental analysis of solid samples. The process begins with a focused laser beam ablating material from the sample's surface. The ablated material is then transported into an ICP as an aerosol, where it undergoes ionisation at high temperatures. The resulting ions are then introduced into a mass spectrometer for precise elemental identification and quantification based on their mass-to-charge ratios. LA-ICP-MS offers significant advantages over EPMA, notably superior detection limits (down to ppb), enabling precise measurement of trace elements within targeted phases. To ablate sufficient material for ICP-MS analysis, the spot size and sampling depth of LA-ICP-MS analysis is typically in the range of tens of μm, as opposed to 1–3 μm for EPMA. Accurate quantification of the raw data often requires:

- Well-characterised standard reference materials that are generally available in the form of oxide glass or pressed-powder-pellets from National Institute of Standards and Technology and US Geological Survey.
- Separate measurement of the concentration of a major element in the sample served as internal standard – typically by EDS or WDS.

Applications

Originally developed for earth science research, LA-ICP-MS has found recent adoption within the metallurgical research community. The two groups that have been actively utilising the technique in extractive metallurgy research are thermodynamics and modelling group at Aalto University, Finland and Pyrosearch at University of Queensland, Australia since 2015 (Avarmaa *et al*, 2015; Chen *et al*, 2016) studies by these groups have showcased LA-ICP-MS's efficacy in accurately measuring trace elements in slag phases, contributing new fundamental data, and resolving discrepancies in literature regarding minor element distributions in non-ferrous melt smelting and converting processes.

Challenges and development

Analysis of matte, speiss and alloy

While LA-ICP-MS has demonstrated excellent analysis precision and accuracy when analysing oxide phases. There has been an on-going challenge in the measurement of sulfide and metal phases with consistent accuracy. It has been well documented (Sylvester, 2008) that the ablation and mass transportation processes of sulfides and alloys are very different from oxide minerals/glasses during the analysis, thus the relative proportions of element present in the material being detected and measured can vastly differ. Therefore, the LA-ICP-MS analysis accuracy heavily relies on the use of appropriate standard reference materials. However, the availability of high-quality metal and sulfide standards for LA-ICP-MS has been very limited compared to the oxide standards. Over the years, a number of solutions have been proposed to address this issue:

- Use non-matrix matching external standards (ie NIST 610/612 for non-silicate materials), establish correction factor for each element and apply to the results – the method has very limited applicability and is dependent on analytical conditions and sample-standard pair.

- Development of other matrix correction methods, such as multivariate regression algorithms for using non-matrix matching external standards – this method has broader applicability, but large calibration library needed for good analysis accuracy.
- Development and use of matrix-matching standards – the solution for the best analytical accuracy, however standard synthesis can be challenging and requires expertise to ensure the homogeneity of the standard at microscopic level is achieved.
- Use Femtosecond-LA-ICP-MS – the femtosecond laser ablation reduces matrix effect in the ablation process, but not as widely available as nano-second laser and laser energy output stability needs to be more closely monitored throughout the analytical session.

Chen, Jak and Misztela (2023) developed a Cu-based reference materials doped with minor elements of interest for laser ablation ICP-MS using high temperature melting/equilibration and fast quenching method. The composition and homogeneity of the sample was measured by EPMA. The standard deviation for most doped minor elements is within 5 per cent except for Se and Pb which exsolved significantly from Cu phase during the quenching due to their low solubility in Cu. LA-ICP-MS analysis of the sample show the analysis accuracy is analytical condition dependent and could introduce over 200 per cent error for certain elements (Figure 4) when using non-matrix matching standard (eg NIST610 glass).

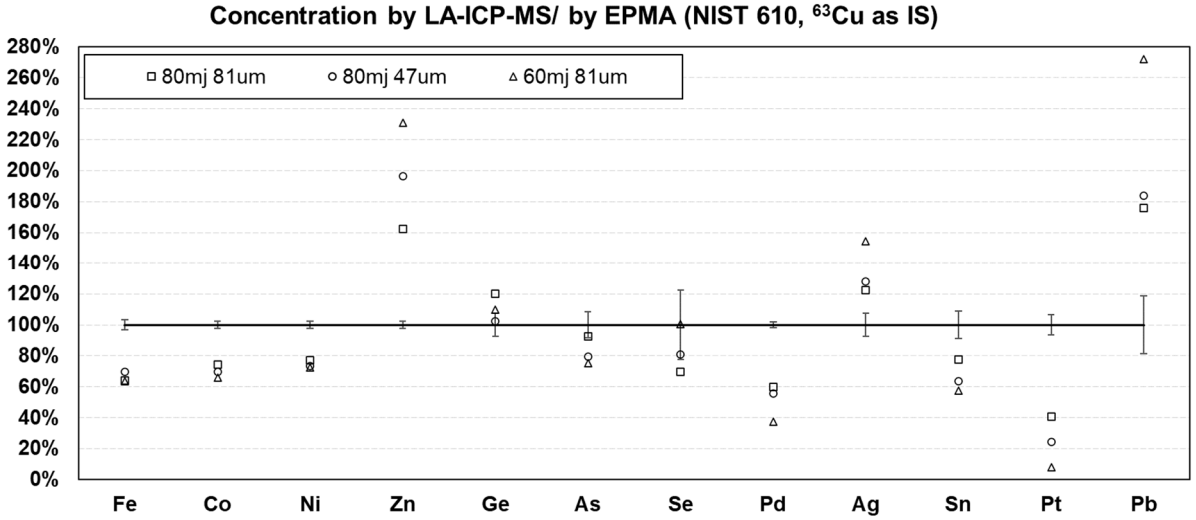

FIG 4 – Analytical error of LA-ICP-MS measurement of minor elements in Cu metal when using NIST 610 as reference material (Chen, Jak and Misztela, 2023).

Spatial resolution

To ablate sufficient material for ICP-MS analysis, the spot size and sampling depth of LA-ICP-MS analysis is typically in the range of tens of μm, as opposed to 1–3 μm for EPMA. This adds to the possibility of error due to the increased chance of sampling inclusions of another phase beneath the sample surface (ie entrained matte/metal in slag phase). Typically, this type of error can be identified by examination of time-resolved ablation spectra, allowing their effects to be minimised by removing the affected time segments for these elements (as show in Figure 5).

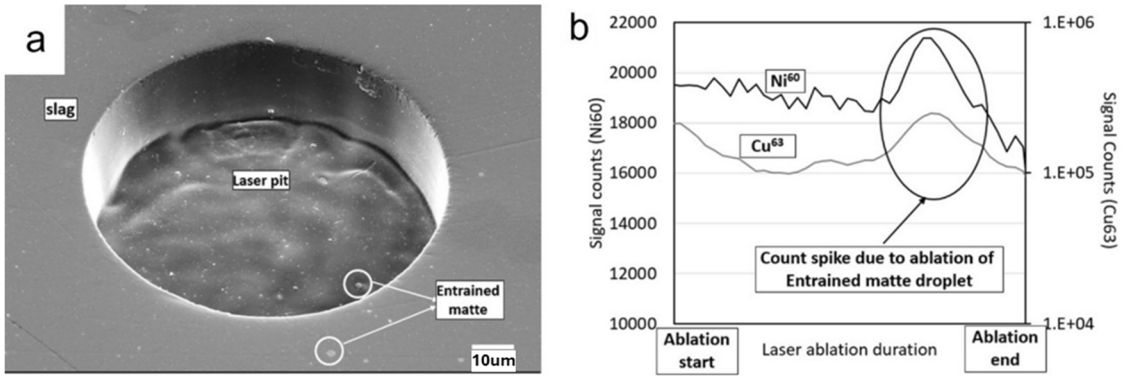

FIG 5 – (a) Ablation crater in slag phase; (b) LA-ICP-MS time-resolved intensity showing count spikes for Cu63 and Ni60 (Chen *et al*, 2022).

Better spatial resolution/smaller sampling volume may also be achieved by adopting femtosecond laser ablation ICP-MS. Femtosecond laser pulses can generate smaller ablation craters compared to conventional nanosecond pulses. This finer spatial resolution (down to 1 μm) allows for more precise sampling of small features within a sample, resulting in improved spatial resolution in elemental mapping and analysis (Russo *et al*, 2002).

MEASUREMENT OF HETEROGENOUS MATERIALS AND PHASES

PXRD

PXRD is a technique used to determine the crystal structure of a material. It is widely used to identify mineral phases present in ores, slags, and other materials. When X-rays are directed at a sample, they diffract at specific angles according to the crystal lattice structure, producing a diffraction pattern. By analysing the positions and intensities of these diffraction peaks, the crystalline phases and their relative abundances in the sample can be determined. Detection limits depend on mean atomic number but typically difficult to quantify materials containing lets than 2 wt per cent of individual crystalline solids.

Quantification by PXRD relies on the relationship between the intensity of X-ray diffraction peaks and the concentration of crystalline phases in a sample. Generally, this process involves comparing the intensities of diffraction peaks from the sample with those of known standards of known compositions. By calibrating the instrument and using appropriate mathematical models, such as the Rietveld refinement method or the internal standard method (Epp, 2016), it's possible to quantitatively determine the relative concentrations of different crystalline phases in the sample. However, caution should be taken when trying to determine the proportion of crystalline phases (solids) in the melt cooled (even quenched) from high temperature as the technique typically is unable to distinguish between the primary phase present at temperature and crystalised phase formed on upon cooling.

Quantitative phase analysis by microscopy

Optical microscopy

Optical microscopy has been widely used to examine the microstructure of metallurgical materials. It has been proven to be a fast, effective and low-cost tool for initial examination of samples particularly for quality control. Sections of the material are prepared and polished to create a flat surface for observation. By illuminating the sample with visible light, and adjusting magnification and focus, microstructural features are analysed. Modern instrument equipped with automated stage and image analysis software allows fast examination of large representative area of the sample and extracting quantitative information, such as phase size distribution, phase proportions and phase relations at high resolution (down to 1 μm). This is particularly of interest for evaluating metal loss in the slag in the form of entrained metal and/or matte.

Automated SEM

Automated SEM techniques are now available that combine imaging with EDS to characterise the mineralogy and texture of a sample. This technique is conventionally used for characterising ores, tailings, and concentrate samples, but also valuable in pyrometallurgy. The technology requires the integration of the SEM measurement system and advanced software programs that store, then analyse and display the analytical data produced in useful formats. Current systems include AMICS, TIMA, Maps Min and Mineralogic. The approach is useful for several reasons:

- Phase Identification: Automated SEMs can identify solid/mineral phases in a sample, including their abundance and size distribution as well as their chemical composition – eg steel inclusions
- Phase Texture Analysis: Information can be provided on mineral textures, such as grain size, shape, and associations. This information can be crucial for optimising the process condition for example for further recovering of Cu or Ni from smelting slag via slow cooling + crushing + flotation methods.
- Elemental Analysis: The EDS component of SEM also allows for the elemental analysis of each mineral grains at microscopic level, providing information on the chemical composition of the phase. This is important for accurate determination of elemental partitioning information of a heterogeneous material (typically flue dust) when performing phase identification analysis.

In addition to above, the automated SEM techniques allow for high-throughput data collection. This can significantly speed up the analysis process compared to manual methods such as point and count method.

SUMMARY

A range of advanced analytical techniques have been developed for the characterisation of the chemical compositions and physico-chemical properties of materials. These tools have been primarily used to date to measure the properties of geological materials and to assist in the further development of new materials, for example ceramics and alloys. It has been shown however that these tools can be used in determining chemical equilibria in complex phase assemblages, the measurement of the kinetics of reaction processes occurring at the microscopic levels and in the characterisation of complex heterogeneous materials encountered in industrial pyrometallurgical practice. The ability to undertake accurate measurements at the microscopic and atomic levels has provided the opportunity to obtain important new fundamental information about these systems thereby increasing the potential to improve process performance in technical and economic terms. The paper has provided an overview of the analytical tools currently available, their capabilities and limitations with a view to guiding the selection of the appropriate methods and procedures when embarking on examination of phenomena taking place in high temperature molten systems.

ACKNOWLEDGEMENTS

The research funding and technical support is provided by the consortium of copper and lead producing companies: Anglo American Platinum (South Africa), Aurubis AG (Germany), BHP Billiton Olympic Dam Operation (Australia), Boliden (Sweden), Glencore Technology (Australia), Metso Oy (Finland), Peñoles (Mexico), RHI Magnesita (Austria), Rio Tinto Kennecott (USA) and Umicore NV (Belgium), as well Australian Research Council Linkage program LP190101020 ‘Future copper metallurgy for the age of e-mobility and the circular economy’. Present study would not be possible without the facilities and technical assistance of the staff of the Centre for Microscopy and Microanalysis in The University of Queensland.

REFERENCES

Avarmaa, K, O’Brien, H, Johto, H and Taskinen, P, 2015. Equilibrium distribution of precious metals between slag and copper matte at 1250–1350C, *Journal of Sustainable Metallurgy*, 1:216–228.

Barkman, J E, Carpenter, P, Zhao, J-C and Donovan, J J, 2013. Electron microprobe quantitative mapping vs defocused beam analysis, *Microscopy and Microanalysis*, 19:848–849.

Bastin, G F and Heijligers, H J, 1992. Quantitative EPMA of the ultra-light elements boron through oxygen, *Electron Microbeam Analysis*, pp 19–36.

Batanova, V, Sobolev, A and Magnin, V, 2018. Trace element analysis by EPMA in geosciences: Detection limit, precision and accuracy, IOP Conference Series: Materials Science and Engineering, paper 012001.

Beckhoff, B, Kanngießer, B, Langhoff, N, Wedell, R and Wolff, H, 2007. *Handbook of Practical X-ray Fluorescence Analysis*, Springer Science and Business Media.

Berthomieu, C and Hienerwadel, R, 2009. Fourier transform infrared (FTIR) spectroscopy, *Photosynthesis Research,* 101:157–170.

Borisova, A Y, Zagrtdenov, N R, Toplis, M J, Donovan, J J, Llovet, X, Asimow, P D, De Parseval, P and Gouy, S, 2018. Secondary fluorescence effects in microbeam analysis and their impacts on geospeedometry and geothermometry, *Chemical Geology*, 490:22–29.

Chen, J J, Allen, C, Hayes, P C and Jak, E, 2016. Experimental study of slag/matte/metal/tridymite four phase equilibria and minor elements distribution in 'Cu-Fe-Si-SO' system by quantitative microanalysis techniques, *Advances in Molten Slags, Fluxes and Salts: Proceedings of the 10th International Conference on Molten Slags, Fluxes and Salts 2016*, pp 961–970.

Chen, J, Diao, H, O'Neill, H and Jak, E, 2024. A novel method for minimizing the boundary secondary fluorescence in X-ray microanalysis by FIB-SEM, Unpublished material.

Chen, J, Fallah-Mehrjardi, A, Specht, A and O'Neill, H S C, 2022. Measurement of minor element distributions in complex copper converting slags using quantitative microanalysis techniques, *JOM*, pp 1–10.

Chen, J, Jak, E and Misztela, M, 2023. Development of Cu-based Reference Materials for Laser Ablation ICP-MS, The 27th Australian Conference on Microscopy and Microanalysis, Australia.

Chen, Q, Dwyer, C, Sheng, G, Zhu, C, Li, X, Zheng, C and Zhu, Y, 2020. Imaging beam-sensitive materials by electron microscopy, *Advanced Materials*, 32:1907619.

Cheng, L, Zhang, C, Li, X, Almeev, R R, Yang, X and Holtz, F, 2019. Improvement of electron probe microanalysis of boron concentration in silicate glasses, *Microscopy and Microanalysis*, 25:874–882.

Christian, G D and Epstein, M S, 1980. *Atomic Absorption Spectroscopy* (Springer).

Donovan, J J, Singer, J W and Armstrong, J T, 2016. A new EPMA method for fast trace element analysis in simple matrices, *American Mineralogist*, 101:1839–1853.

Epp, J, 2016. X-ray diffraction (XRD) techniques for materials characterization, Materials characterization using nondestructive evaluation (NDE) methods, Elsevier.

Fallah-Mehrjardi, A, Hidayat, T, Hayes, P C and Jak, E, 2017. Experimental Investigation of Gas/Slag/Matte/Tridymite Equilibria in the Cu-Fe-O-S-Si system in Controlled Gas Atmospheres: Development of Technique, *Metall Mater Trans B*, 48:3002–3016.

Fearn, S, 2015. An introduction to time-of-flight secondary ion mass spectrometry (ToF-SIMS) and its application to materials science, Morgan and Claypool Publishers.

Flemming, R L, 2007. Micro X-ray diffraction (μXRD): a versatile technique for characterization of Earth and planetary materials, *Canadian Journal of Earth Sciences*, 44:1333–1346.

Fonseca, R O C, Campbell, I H, O'Neill, H S C and Fitzgerald, J D, 2008. Oxygen solubility and speciation in sulphide-rich mattes, *Geochim Cosmochim Acta*, 72:2619–2635.

Geels, K, Fowler, D B, Kopp, W-U and Ckert, M R, 2007. Metallographic and materialographic specimen preparation, light microscopy, image analysis and hardness testing, ASTM International West Conshohocken, PA.

Goldstein, J I, Newbury, D E, Michael, J R, Ritchie, N W, Scott, J H J and Joy, D C, 2017. *Scanning electron microscopy and X-ray microanalysis* (Springer).

Goldstein, M, 1969. Viscous Liquids and the Glass Transition: a Potential Energy Barrier Picture, *J Chem Phys,* 51:3728–3739.

Henderson, C E, 2011. Protocols and pitfalls of electron microprobe analysis of apatite.

Jercinovic, M, Williams, M, Allaz, J and Donovan, J, 2012. Trace analysis in EPMA, IOP conference series: materials science and Engineering, paper 012012.

Long, D A, 1977. *Raman Spectroscopy*, 310 p.

May, L, 2012. *An introduction to Mössbauer spectroscopy* (Springer Science and Business Media).

Nash, W, 1992. Analysis of oxygen with the electron microprobe: Applications to hydrated glass and minerals, *American Mineralogist*, 77:453–457.

Newbury, D E and Ritchie, N W, 2015. Quantitative electron-excited X-ray microanalysis of borides, carbides, nitrides, oxides and fluorides with scanning electron microscopy/silicon drift detector energy-dispersive spectrometry (SEM/SDD-EDS) and NIST DTSA-II, *Microscopy and Microanalysis*, 21:1327–1340.

Olesik, J W, 1991. Elemental analysis using ICP-OES and ICP/MS, *Analytical Chemistry*, 63:12A–21A.

Papadopoulou, D, Zachariadis, G, Anthemidis, A, Tsirliganis, N and Stratis, J, 2006. Development and optimisation of a portable micro-XRF method for in situ multi-element analysis of ancient ceramics, *Talanta*, 68:1692–1699.

Russo, R E, Mao, X, Gonzalez, J J and Mao, S S, 2002. Femtosecond laser ablation ICP-MS, *Journal of Analytical Atomic Spectrometry*, 17:1072–1075.

Singh, J P and Thakur, S N, 2020. *Laser-induced breakdown spectroscopy* (Elsevier).

Stebbins, J F, 1995. Dynamics and structure of silicate and oxide melts: nuclear magnetic resonance studies, *Reviews in Mineralogy*, 32:191–246.

Stevie, F A and Donley, C L, 2020. Introduction to x-ray photoelectron spectroscopy, *Journal of Vacuum Science and Technology A*, vol 38.

Sutherland, D and Gottlieb, P, 1991. Application of automated quantitative mineralogy in mineral processing, *Minerals Engineering*, 4:753–762.

Sylvester, P, 2008. Matrix effects in laser ablation-ICP-MS, Laser ablation ICP-MS in the earth sciences: Current practices and outstanding issues, Mineralogical Association of Canada Québec.

Teo, B K, 2012. *EXAFS: basic principles and data analysis* (Springer Science and Business Media).

Walsh, J, 2002. *Laser-ablation-ICPMS in the Earth Sciences: principles and applications* (ed: P Sylvester), Mineralogical Society of Canada Short Course Series, 66:375–375.

Willich, P and Bethke, R, 1996. *Practical aspects and applications of EPMA at low electron energies* (Springer).

Wu, R-Q, Rao, C, Wang, R-C, Che, X-D, Li, X-F, Wang, Q and Zhang, Z-Q, 2022. In situ quantitative analysis of beryllium by EPMA: analytical conditions and further insights into beryllium geochemistry, *Journal of Analytical Atomic Spectrometry*, 37:1824–1834.

Zhang, C, Koepke, J, Wang, L X, Wolff, P E, Wilke, S, Stechern, A, Almeev, R and Holtz, F, 2016. A practical method for accurate measurement of trace level fluorine in Mg-and Fe-bearing minerals and glasses using electron probe microanalysis, *Geostandards and Geoanalytical Research*, 40:351–363.

Coupled phase diagram experiments and thermodynamic modelling of the CaO-SiO_2-Ga_2O_3 system for Ga recycling

DOI: 10.62053/UNCV9107

W O Choe[1] and I H Jung[2]

1. Department of Materials Science and Engineering, Seoul National University, Seoul 08826, South Korea. Email: 6565oh@snu.ac.kr
2. Department of Materials Science and Engineering, Seoul National University, Seoul 08826, South Korea. Email: in-ho.jung@snu.ac.kr

ABSTRACT

Gallium (Ga)-containing compounds such as Gallium Arsenide (GaAs) and Gallium Nitride (GaN) are widely used in electronic devices due to their superior electro-optical properties and their usages increase rapidly. For the sustainable supply of Ga to electronic industry, therefore, the recycling of Gallium becomes essential. Pyrometallurgical Ga recycling process involves the complex chemical reactions between slag, matte, liquid metal, gas, refractories, etc. Therefore, the accurate thermodynamic information and phase diagram data for the oxide system containing Ga_2O_3 is important. In the present study, new phase diagram experiments for binary SiO_2-Ga_2O_3 and ternary CaO-SiO_2-Ga_2O_3 system are carried out using Differential Thermal Analysis (DTA) and quenching experiments followed by Electron Probe Micro-Analyser (EPMA) and X-Ray Diffraction (XRD) phase analysis. Based on new phase diagram data and available literature data, the thermodynamic modelling of the entire CaO-SiO_2-Ga_2O_3 system is performed for the first time.

INTRODUCTION

The consumption of Gallium (Ga), a constituent of Gallium Arsenide (GaAs) and Gallium Nitride (GaN) materials with superior electro-optical properties, has increased steadily. More than 90 per cent of Ga is currently produced as a by-product from the aluminium production and zinc smelting process, so the current mainstream production will not be sufficient to meet the demand in future. Therefore, recycling of Ga from electronic scrap becomes important for sustainable supply chain for Ga.

The CALPHAD (CALculation of PHAse Diagram) type thermodynamic database is very useful for new materials design and process optimisation. Thermodynamic database allows to perform complex thermodynamic equilibrium calculations for pyrometallurgical process involving multi-component and multi-phases of solid, liquid and gas. In particular, electronic scrap containing Ga can be processed in copper (Cu) smelting, the thermodynamic database for molten slag, matte and liquid Cu containing Ga can be important for optimising Ga recycling process.

In the present study, a coupled phase diagram experiment and thermodynamic modelling of the CaO-SiO_2-Ga_2O_3 system is conducted using the CALPHAD method. The CaO-Ga_2O_3 system can be modelled using the available phase diagram and thermodynamic property data in literature. Because the available data in the SiO_2-Ga_2O_3 system and the CaO-SiO_2-Ga_2O_3 system are inaccurate and insufficient, new phase diagram experiments are conducted in this study to assist the thermodynamic database development. All thermodynamic calculations are performed using the FactSage thermochemical computing program (Bale *et al*, 2016; Jung and Van Ende, 2020).

PHASE DIAGRAM EXPERIMENTS

Starting materials

For the binary and ternary phase diagram study within CaO-SiO_2-Ga_2O_3 system, $CaCO_3$ (Sigma Aldrich; 99.95 per cent purity), SiO_2 (Sigma Aldrich; 99.995 per cent purity) and Ga_2O_3 (Alfa Aesar; 99.99 per cent purity) powders were used to prepare starting sample materials. Due to the highly hygroscopic nature of CaO, $CaCO_3$ was used intentionally. Starting materials with target compositions were prepared by grinding appropriate amount of each powders in an alumina mortar for 20 mins. In order to grind them well in a mortar, cyclohexane (Sigma Aldrich; 99.5 per cent purity) liquid containing nearly zero H_2O was applied. Ground samples were dried in the vacuum oven at

70°C. The powder mixtures were stored in sealed Argon (Ar)-filled vials with cyclohexane to prevent any hydration and were dried in the vacuum oven before usage. If necessary, $xCaO{\cdot}yGa_2O_3$ compounds were synthesised by heating the mixtures of $CaCO_3$ and Ga_2O_3 mixture at 1100°C in a Platinum (Pt) cup and used as starting materials.

For main phase diagram experiments, the dried powder samples were put in sealed Pt capsules to prevent vapourisation loss of Ga_2O_3 and the hydration of sample during quenching process. First, 20 ~ 40 mg of the powder mixtures were put in one-side welded Pt capsules, which were made from Pt tube (10 mm length, 3 mm inner diameter and 0.3 mm wall thickness). The powder-packed Pt capsules were put in the box furnace at 1000°C for minimum 20 hours to decarbonise the $CaCO_3$ into CaO. The completion of decarbonisation of the samples were confirmed by mass changes before and after the heating. After the decarbonisation, the other side of the Pt capsule was welded to seal the Pt capsule. The sealed Pt capsules were sonicated in water for five mins to check any leakage by measuring their mass changes.

Quenching experiments

The quenching experiments were conducted in a vertical tube furnace equipped with $Pt_{87}Rh_{13}$-Pt (type R) thermocouples. The temperature was controlled using a PID (Proportional – Integral – Derivative) controller and maintained within ± 3°C at the target temperature. The sealed Pt capsules were hanged in an alumina tube using a Pt wire and equilibrated at target temperature between 1400–1600°C for 2–20 hrs. After the equilibration, the samples were quenched in cold water by releasing Pt wire. The mass of the quenched samples was again checked to confirm no weight changes during the whole equilibration and quenching process.

Differential Thermal Analysis (DTA) experiments

Differential Thermal Analysis (DTA) experiments were carried out with the NETZSCH STA 449 F5 Jupiter equipment. Temperature was calibrated with several standard materials. The sealed Pt capsule containing starting materials was placed in DTA alumina crucible and DTA experiments were carried out up to 1500°C with the heating and cooling rate of 10 K/min in an Ar atmosphere with 20 mL/min flow rate. At least two cycles of heating and cooling were conducted for each sample. Thermogravimetric analysis (TGA) was also performed simultaneously to ensure no weight loss by vapourisation of Ga_2O_3.

Characterisations

The phase characterisations for quenched samples and DTA samples were carried out using X-Ray Diffraction (XRD) and Electron Probe Micro-Analyser (EPMA). Bruker New D8 advance with Cu Kα radiation at Research Institute of Advanced Materials (RIAM) in Seoul National University (SNU) was used for XRD analysis. All peaks of the XRD patterns were identified with Powder Diffraction Files (PDF) from the International Centre for Diffraction Data (ICDD) using Bruker AXS DIFFRAC.EVA software. The compositional analysis was carried out using EPMA attached to JEOL JXA-8530F at National Centre for Inter-University Research Facilities (NCIRF) in SNU. The exact composition of each phase was measured using Wavelength Dispersive Spectroscopy (WDS) with a 15 kV accelerating voltage, 10 nA beam current and 1 μm beam diameter. Raw data were reduced with the PRZ Armstrong algorithm employing standard samples of Gadolinium Gallium Garnet ($Gd_3Ga_5O_{12}$) and Wollastonite ($CaSiO_3$) provided by NCIRF.

THERMODYNAMIC MODEL

As shown in Figure 1, there are four stoichiometric compounds in the $CaO\text{-}SiO_2$ system and four in the $CaO\text{-}Ga_2O_3$ system. No binary solid phase has been reported in the $SiO_2\text{-}Ga_2O_3$ system. Two ternary compounds, $Ca_2Ga_2SiO_7$ and $CaGa_2Si_2O_8$, are found in the $CaO\text{-}SiO_2\text{-}Ga_2O_3$ system. No solid solution phase has been reported in this ternary system.

The $CaO\text{-}SiO_2$ system was optimised previously and the optimised data are stored in FactSage FToxid database (Bale *et al*, 2016). The Gibbs energy data of all solids and liquid phase for the system are adopted from FToxid database without any modification. Binary $CaO\text{-}Ga_2O_3$ system and $SiO_2\text{-}Ga_2O_3$ system and ternary $CaO\text{-}SiO_2\text{-}Ga_2O_3$ system are newly optimised in the present study.

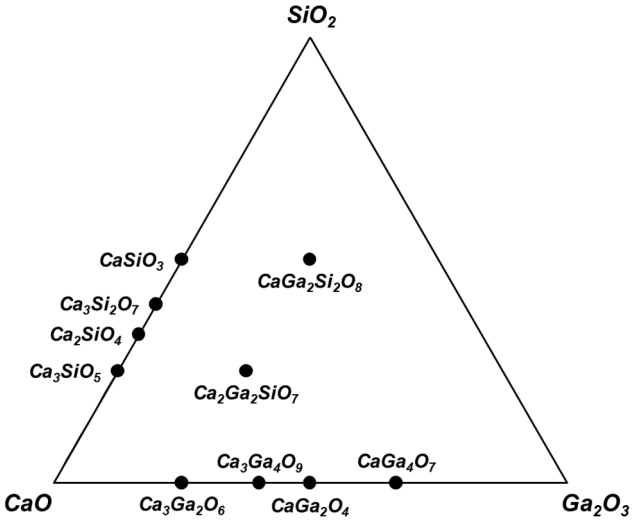

FIG 1 – Schematic diagram of the CaO-SiO_2-Ga_2O_3 system with all the stoichiometric compounds.

Stoichiometric compounds

The Gibbs energies of stoichiometric compounds can be expressed as follows:

$$G_T^o = H_T^o - TS_T^o \tag{1}$$

$$H_T^o = \Delta H_{298.15K}^o + \int_{298.15K}^{T} C_p \, dT \tag{2}$$

$$S_T^o = S_{298.15K}^o + \int_{298.15K}^{T} \frac{C_p}{T} \, dT \tag{3}$$

where $\Delta H_{298.15K}^o$ and $S_{298.15K}^o$ are the standard formation enthalpy and standard entropy at 298.15 K, respectively and C_p is the heat capacity which is a function of temperature.

Liquid solution (slag)

The Gibbs energy of liquid solution phase in the CaO-SiO_2-Ga_2O_3 system is described by the Modified Quasichemical Model (MQM) (Pelton *et al*, 2000; Pelton and Chartrand, 2001). In the MQM, a quasi-chemical pair exchange reaction between A and B cations in oxide melt can be expressed as:

$$(\mathrm{A}-\mathrm{A}) + (\mathrm{B}-\mathrm{B}) = 2(A-B): \Delta g_{AB} \tag{4}$$

where A and B are cations in the solution and $(A-A)$, $(B-B)$ and $(A-B)$ represent each pair containing O^{2-} anion between the cations.

In the present study, the cation species are Ca^{2+}, Si^{4+} and Ga^{3+}. Δg_{AB} represents the Gibbs energy of pair exchange reaction. Then, the Gibbs energy of the solution phase is expressed in MQM as following:

$$G_{sol} = \sum_i n_i g_i^o - T\Delta S^{config} + \sum_{i<j} \left(\frac{n_{ij}}{2}\right) \Delta g_{ij} \tag{5}$$

where n_i and g_i^o are the number of moles and molar Gibbs energy of solution component i and n_{ij} is the number of moles of $(i-j)$ pair at equilibrium. ΔS^{config} is the configurational entropy for the random distribution of the cation pairs and Δg_{ij} can be expressed a function of composition and temperature.

In the binary solution, Δg_{AB} can be expressed by the pair fraction X_{ij}:

$$\Delta g_{AB} = \Delta g_{AB}^o + \sum_{i\geq 1} g_{AB}^{io} X_{AA}^i + \sum_{i\geq 1} g_{AB}^{oj} X_{BB}^j \tag{6}$$

where Δg_{AB}^o, g_{AB}^{io} and g_{AB}^{oj}, which are model parameter of MQM, can be optimised as a function of temperature.

In this study, the Gibbs energies of liquid solution in binary CaO-Ga_2O_3 system and SiO_2-Ga_2O_3 system were optimised based on all phase diagram data and thermodynamic data available in each system.

The Gibbs energy of ternary liquid solution can be predicted from the binary Gibbs energy expression using the so-called geometric interpolation model. There are several geometric interpolations to be used in the prediction for the Gibbs energy of ternary system. Depending on the nature of constituents in ternary system, a proper interpolation method should be determined. In this ternary CaO-SiO_2-Ga_2O_3 system, Kohler-Toop type interpolation method with SiO_2 as an asymmetric component was used for the prediction. It should be noted that the same interpolation method was used for the CaO-SiO_2-Al_2O_3 solution (Eriksson and Pelton, 1993). The detailed explanation regarding the Gibbs energy for ternary solution can be found elsewhere (Pelton and Chartrand, 2001).

RESULTS AND DISCUSSIONS

The CaO-Ga_2O_3 system

Jeevaratnam and Glasser (1961) conducted quenching experiments using Mercury (Hg) as a quenching media and reported three stoichiometric compounds in the binary CaO-Ga_2O_3 system: $Ca_3Ga_2O_6$, $CaGa_2O_4$ and $CaGa_4O_7$. However, their experimental results are less reliable because the number of phases in equilibrated sample sometimes disobeyed the Gibbs phase rule. Later, Young (1979) reported a new stoichiometric compound $Ca_3Ga_4O_9$, located between $Ca_3Ga_2O_6$ and $CaGa_2O_4$. Daminova and Kadyrova (1997) observed the solid-state phase transition of $CaGa_2O_4$ at 1300°C using DTA experiment. Based on all available literature data, it can be confirmed that total four solid intermediate compounds are stable in this binary system: $Ca_3Ga_2O_6$, $Ca_3Ga_4O_9$, $CaGa_2O_4$ (low and high temperature polymorphs) and $CaGa_4O_7$. The melting point of each compound was measured using quenching method (Jeevaratnam and Glasser, 1961) or DTA (Young, 1979; Kovba, Lykova and Kalinina, 1980; Scolis *et al*, 1981). The melting points reported by Jeevaratnam and Glasser (1961) are quite different from other DTA results, but it is hard to tell exactly why such discrepancies among existing experimental data. When the samples are less well quenched, solid crystals can form during quenching and lead misinterpretation of the experimental liquidus temperature. Considering that liquid CaO-Ga_2O_3 solution is not very viscous like silicate melt, DTA results can be considered to be reliable in this system. All phase diagram results from DTA experiments are plotted in Figure 2a.

Scolis *et al* (1981) performed the electromotive force (EMF) experiments using electrochemical cells with CaF_2 electrolyte to determine the Gibbs energies of four stoichiometric compounds at 800~1100°C. CaO-stabilised zirconia ($0.17CaO{\cdot}0.83ZrO_2$)+$CaZrO_3$ was used as a reference electrode for the determination of the activity of CaO in working electrodes by EMF measurement. In the EMF experiments, Scolis *et al* (1981) also confirmed the existence of all four compounds. The enthalpies and entropies of formation of the compounds from CaO and Ga_2O_3 were obtained from the EMF data and the reported data are plotted in Figure 2b and 2c.

Thermodynamic modelling of the CaO-Ga_2O_3 system is performed based on the DTA results of Young (1979) and Kovba, Lykova and Kalinina (1980), and the thermodynamic properties of compounds from EMF measurements of Scolis *et al* (1981). The Gibbs energies of liquid solution and four stoichiometric compounds are optimised in the present study to reproduce the experimental data. The calculated phase diagram and thermodynamic properties from the present optimised model parameters are shown in Figure 2 in comparison to the experimental data. As shown in Figure 2a, the phase diagram data are well reproduced except the liquidus points at $X_{Ca}O > 0.7$. It is known that CaO-rich oxide melt, especially when it is saturated with solid CaO, can readily dissolve gas species like N_2 and CO_2 from atmosphere during the equilibrium experiment and be easily stabilised and show lower liquidus than real equilibrium liquidus. The enthalpy and entropy of solid stoichiometric compounds are also well reproduced within experimental error range. In the thermodynamic description, the heat capacities of solid compounds are estimated from constituent oxides, CaO and Ga_2O_3, using the Neumann-Kopp rule. It should be noted that the phase diagram of the CaO-Ga_2O_3 system is quite similar to that of the CaO-Al_2O_3 system.

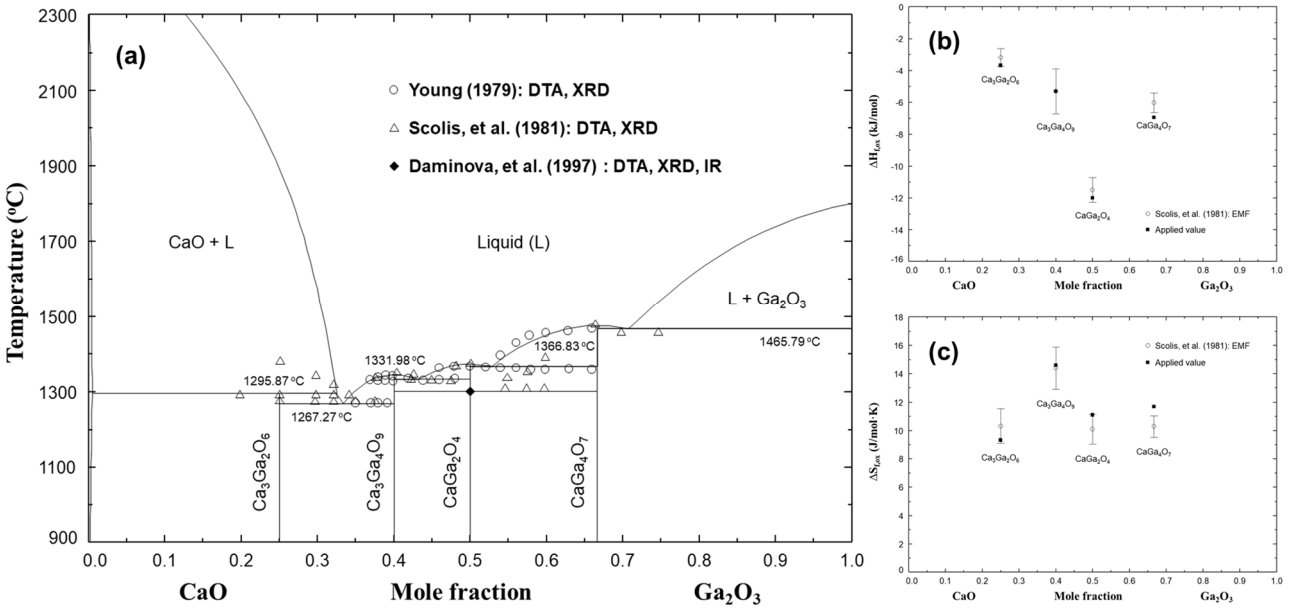

FIG 2 – Optimised results of the CaO-Ga_2O_3 system along with experimental data: (a) phase diagram, (b) enthalpy of formation, (c) entropy of formation of stoichiometric compounds.

The SiO_2-Ga_2O_3 system

Glasser (1959) and Toropov and Ling (1960a) performed the phase diagram study of the SiO_2-Ga_2O_3 system using quenching method. In both studies, no binary intermediate phase was found, but the phase diagrams proposed by two studies are completely different each other. Glasser (1959) reported the possibility of a large miscibility gap with a monotectic reaction L1 → L2 + Ga_2O_3 at about 1650°C, and a eutectic reaction of L → SiO_2 + Ga_2O_3 in the SiO_2-rich region at about 1635°C. On the other hand, Toropov and Ling (1960a) reported a simple eutectic reaction of L → SiO_2 + Ga_2O_3 in the SiO_2-rich region at about 1560°C. The SiO_2-Ga_2O_3 melt should be very viscous so it requires a long equilibration time. However, the equilibrium experiments of Glasser (1959) were held for only several minutes most probably due to the evaporation of Ga_2O_3, and the experiments of Toropov and Ling (1960a) lasted one hr to several hrs. Therefore, both results might be less reliable. Therefore, new phase diagram experiments are conducted in the present study.

Key samples are prepared to determine the phase diagram of the SiO_2-Ga_2O_3 system. The temperature range of the quenching experiments is 1530–1650°C. The equilibrations of key samples are conducted for minimum four hrs and maximum 20 hrs. The present experimental results are summarised in Figure 3a. The backscattered electron (BSE) images of two key samples are shown in Figure 3b and 3c. The microstructure of the quenched sample of $0.6SiO_2$-$0.4Ga_2O_3$ in mol fraction equilibrated at 1580°C (Figure 3b) shows two phases of pure Ga_2O_3 and liquid phase with $0.954SiO_2$-$0.046Ga_2O_3$. Two distinctive liquid phases in term of composition are observed in the sample of $0.8SiO_2$-$0.2Ga_2O_3$ equilibrated at 1650°C (Figure 3c). That is, the liquid miscibility gap is found in this binary system as reported by Glasser (1959). The monotectic reaction of L1 → L2 + Ga_2O_3 at about 1620~1630°C and the eutectic reaction of L → SiO_2 + Ga_2O_3 at about 1560~1575°C are determined from the present quenching experiment. No noticeable mutual solubility between SiO_2 and Ga_2O_3 are found.

Based on the new phase diagram results in the present study, thermodynamic modelling of the SiO_2-Ga_2O_3 system is carried out. The Gibbs energy of the liquid solution is optimised to reproduce the present experimental data, and the phase diagram calculated from the present modelling results is plotted in Figure 3a. As can be seen, the phase diagram with liquid miscibility gap is well reproduced in the modelling study.

The liquid composition in the condition of Figure 3b is calculated as $0.941SiO_2$-$0.059Ga_2O_3$, which shows small error of $0.013Ga_2O_3$ with experimental value. This can be caused by the sluggish kinetics due to viscous nature in SiO_2-rich region and it requires much longer equilibration time to measure the exact composition of liquid. However, the closed Pt capsule can't endure the high

vapour pressure of Ga_2O_3 at high temperature near 1600°C for a long time. Considering these experimental challenges, that small error is actually negligible in terms of thermodynamic optimisation.

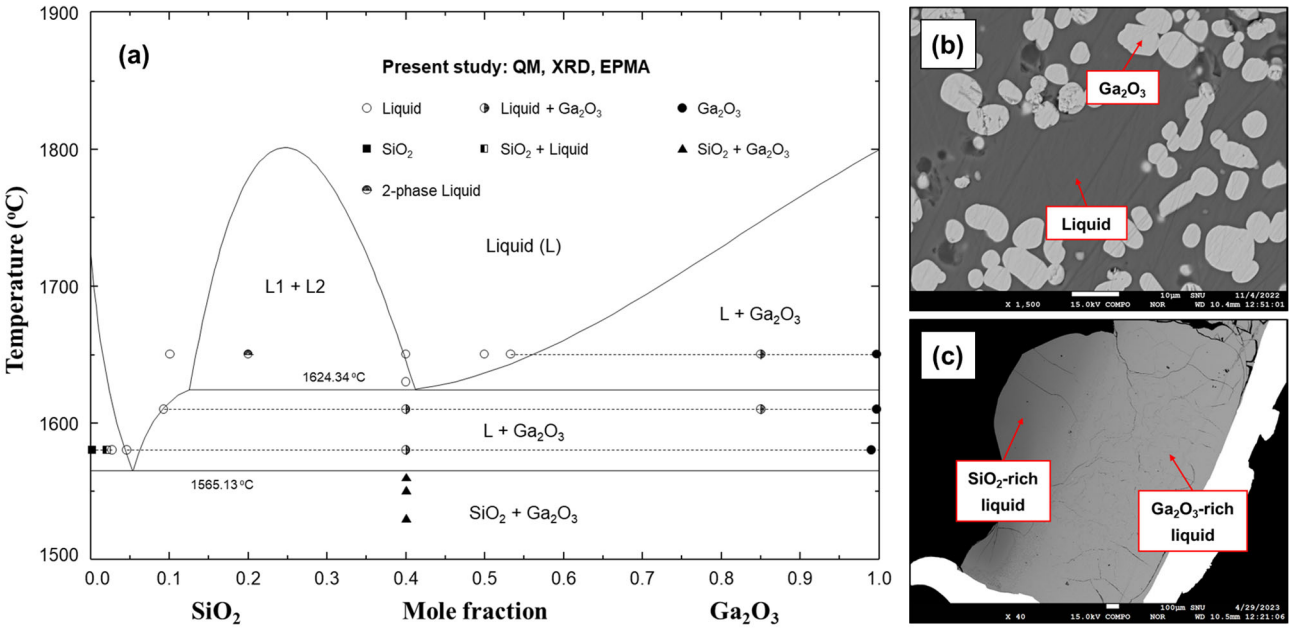

FIG 3 – Phase diagram experimental data and optimisation results of binary SiO_2-Ga_2O_3 system: (a) phase diagram along with all experimental data. BSE images of quenched samples of (b) $0.6SiO_2$-$0.4Ga_2O_3$ equilibrated at 1580°C, and (c) $0.8SiO_2$-$0.2Ga_2O_3$ at 1650°C.

The CaO-SiO_2-Ga_2O_3 system

Two ternary stoichiometric compounds are reported in the ternary CaO-SiO_2-Ga_2O_3 system: $Ca_2Ga_2SiO_7$ and $CaGa_2Si_2O_8$. These two compounds are almost identical to the ternary compounds, gehlenite $Ca_2Al_2SiO_7$ and anorthite $CaAl_2Si_2O_8$, in the CaO-SiO_2-Al_2O_3 system.

$Ca_2Ga_2SiO_7$ was first synthesised by Toropov and Ling (1960b), as part of continuous solid solution between $Ca_2Al_2SiO_7$ and $Ca_2Ga_2SiO_7$. Melting point of $Ca_2Ga_2SiO_7$ was first determined to be 1465°C by Toropov and Ling (1960b). On the other hand, Korczak and Raaz (1967) reported the melting point as 1485°C by observing crystal growth from oxide melt during solidification process. In order to resolve this discrepancy, phase diagram experiments are conducted in this study to determine the melting temperature using classical quenching method. Eitel, Herlinger and Tromel (1930) synthesised $CaGa_2Si_2O_8$ phase for the first time. The melting point of $CaGa_2Si_2O_8$ has not been reported yet. Therefore, the melting temperature of $CaGa_2Si_2O_8$ is also studied in the present study.

In general, no phase diagram study has been conducted for the ternary CaO-SiO_2-Ga_2O_3 system so far. In the present study, the preliminary phase diagram is predicted from the thermodynamic models with optimised model parameters of three binary systems. Then, based on the preliminary phase diagram, key sample compositions are chosen for three-phase equilibria or two-phase equilibria including liquid phase. Both quenching experiments and DTA experiments are performed for the ternary CaO-SiO_2-Ga_2O_3 system.

The melting points of $Ca_2Ga_2SiO_7$ and $CaGa_2Si_2O_8$ are determined from several quenching experiments. It is found that $Ca_2Ga_2SiO_7$ melts congruently at 1485°C and $Ca_2Ga_2SiO_7$ melts incongruently at 1225°C to liquid and Ga_2O_3. Isothermal phase diagrams at 1400°C and 1500°C are studied using quenching experiments. Several invariant reactions in the ternary system are determined using DTA. The examples of quenching and DTA experiment are presented in Figure 4a and 4b. The composition of liquid phase in Figure 4a is measured as $0.41CaO$-$0.16SiO_2$-$0.43Ga_2O_3$. The onset temperature of second and third heating peak in Figure 4b is 1374.4°C.

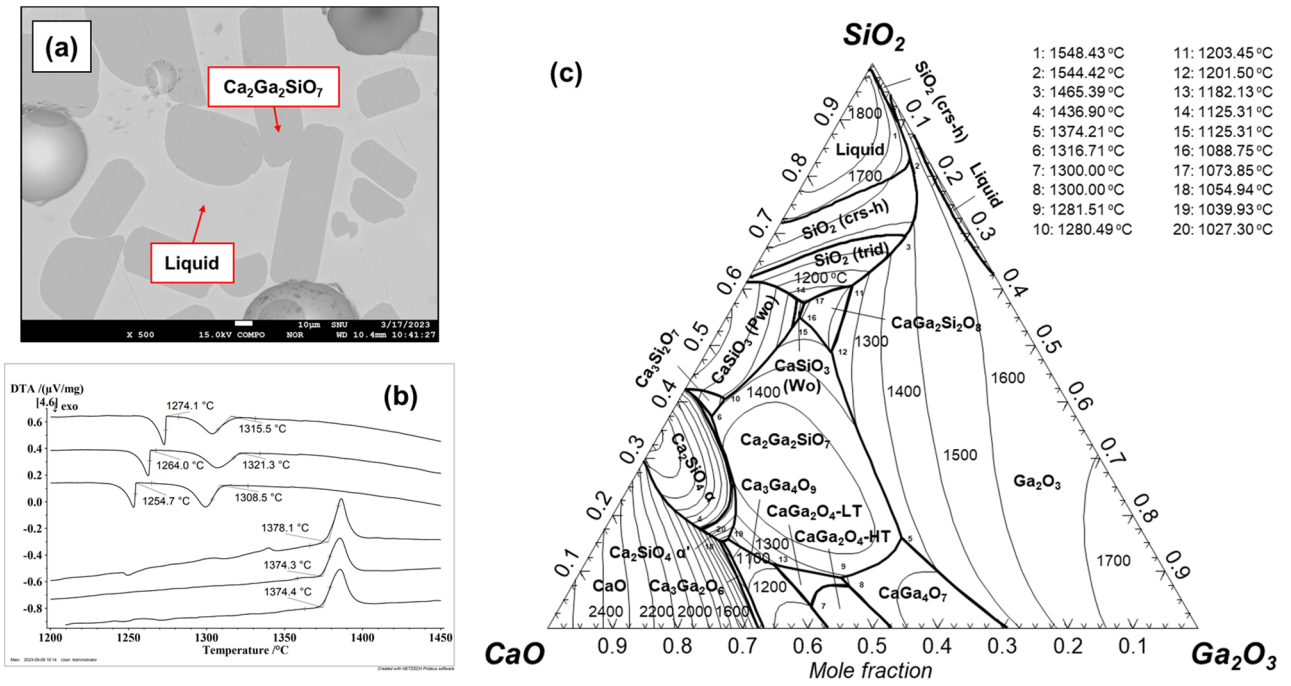

FIG 4 – Phase diagram experiments and calculated phase diagram of ternary CaO-SiO_2-Ga_2O_3 system: (a) BSE image for the quenched sample of $0.44CaO$-$0.19SiO_2$-$0.37Ga_2O_3$ equilibrated at 1400°C, (b) DTA results of sample of $0.35CaO$-$0.17SiO_2$-$0.48Ga_2O_3$, and (c) calculated liquidus projection of ternary system.

Experimental results of the present study are used for the thermodynamic optimisation of the ternary CaO-SiO_2-Ga_2O_3 system. The Gibbs energy of the liquid solution and two ternary compounds are optimised in the present study. The heat capacities of two ternary compounds $Ca_2Ga_2SiO_7$ and $CaGa_2Si_2O_8$ are estimated from CaO, tridymite SiO_2 and Ga_2O_3 using the Neumann-Kopp rule. The formation entropy of two ternary compounds are set to be the same value as those of ternary compounds $Ca_2Al_2SiO_7$ and $CaAl_2Si_2O_8$ in the CaO-SiO_2-Al_2O_3 system. Then, the standard enthalpy of formation of ternary compounds are optimised to reproduce their melting points. The Gibbs energy of liquid solution is optimised to reproduce entire phase diagram data in the present study.

The calculated value of liquid composition in Figure 4a is $0.415CaO$-$0.153SiO_2$-$0.432Ga_2O_3$. This matches well with the experimental value within the small error range less than 0.01. The invariant point expressing the reaction in Figure 4b is the point number 5 at 1374.21°C in Figure 4c. This also matches very well with the present experimental data.

CONCLUSIONS

Phase diagrams of the binary SiO_2-Ga_2O_3 and ternary CaO-SiO_2-Ga_2O_3 system are investigated using quenching experiments and DTA experiments and accurate phase diagrams are determined for the first time. Based on reliable phase diagram data and thermodynamic data in literature and the present study, the CALPHAD-type thermodynamic modellings of binary CaO-Ga_2O_3, SiO_2-Ga_2O_3 and ternary CaO-SiO_2-Ga_2O_3 system are carried out. The optimised thermodynamic database can be integrated to the commercial FactSage thermodynamic database to calculate complex chemical reaction in pyrometallurgical Ga recycling process.

ACKNOWLEDGEMENTS

This work is supported by the Korea Institute of Energy Technology Evaluation and Planning (KETEP) grant funded by the Korean government (MOTIE) (20217510100080, Development of critical metal recovery technologies (capacity of 200 kg/day) from low-grade solid wastes for the foundation of open access recycling platform). Financial support from Tata Steel Europe, Posco, Hyundai Steel, Nucor Steel, RioTionto Iron and Titanium, Nippon Steel Corp., JFE Steel,

Voestalpine, RHI Magnesita, SeAH Besteel, Doosan Heavy Industry and Construction, and SCHOTT AG is also gratefully acknowledged.

REFERENCES

Bale, C W, Belisle, E, Chartrand, P, Decterov, S A, Eriksson, G, Cheribi, A E, Hack, K, Jung, I H, Kang, Y B, Melancon, J, Pelton, A D, Petersen, S, Robelin, C, Sangster, J, Spencer, P and Van Ende, M A, 2016. FactSage thermochemical software and databases, 2010–2016, *Calphad*, 54:35–53.

Daminova, D A and Kadyrova, Z R, 1997. $Ca_3Al_{2(1-x)}Ga_{2x}O_6$ Solid Solutions, *Uzbekskii Khimicheskii Zhurnal*, 5:3–6.

Eitel, W, Herlinger, E and Tromel, G, 1930. The Crystal Chemistry of Aluminosilicates; Relations between the Anorthite Group and the Nephelin Group, *Naturwissenschaften*, 18:469–474.

Eriksson, G and Pelton, A D, 1993. Critical Evaluation and Optimization of the Thermodynamic Properties and Phase Diagrams of the CaO-Al_2O_3, Al_2O_3-SiO_2, and CaO-Al_2O_3-SiO_2 Systems, *Metallurgical and Materials Transactions (B)*, 24:807–816.

Glasser, F P, 1959. The System Ga_2O_3-SiO_2, *The Journal of Physical Chemistry*, 63(12):2085–2086.

Jeevaratnam, J and Glasser, F P, 1961. The System CaO-Ga_2O_3, *Journal of the American Ceramic Society*, 44(11):563–566.

Jung, I H and Van Ende, M A, 2020. Computational Thermodynamic calculations: FactSage from CALPHAD thermodynamic database to virtual process simulation, *Metallurgical and Materials Transactions (B)*, 51:1851–1874.

Korczak, P and Raaz, F, 1967. Refining of Gehlenite Crystal Structure on the Basis on Gallium Gehlenites, *Anzeiger der Oesterreichischen Akademie der Wissenschaften, Mathematisch-Naturwissenschaftliche Klasse*, 13:383–387.

Kovba, L M, Lykova, L N and Kalinina, T A, 1980. Physicochemical Study of Some Alkaline Earth Element Gallates and Indates, *Zhurnal Neorhanicheskoi Khimii*, 25(3):725–728.

Pelton, A D and Chartrand, P, 2001. The Modified Quasi-Chemical Model: Part II, Multicomponent Solutions, *Metallurgical and Materials Transactions (A)*, 32:1355–1360.

Pelton, A D, Decterov, S A, Eriksson, G, Robelin, C and Dessureault, Y, 2000. The Modified Quasichemical Model I – Binary Solutions*, Metallurgical and Materials Transactions (B)*, 31:651–659.

Scolis, Y Y, Levitskii, V A, Lykova, L N and Kalinina, T A, 1981. Thermodynamics of Double Oxides III. Study of the CaO-Ga_2O_3 System by the EMF Method and X-Ray Analysis, *Journal of Solid State Chemistry*, 38(1):10–18.

Toropov, N A and Ling, T H, 1960a. The Binary System Ga_2O_3-SiO_2, *Zhurnal Neorhanicheskoi Khimii*, 5(11):2462–2465.

Toropov, N A and Ling, T H, 1960b. The System $Ca_2Al[AlSiO_7]$-$Ca_2Ga[GaSiO_7]$, *Zhurnal Neorhanicheskoi Khimii*, 5(11): 2466–2470.

Young, I M, 1979. The Central Region of the Calcium Oxide – Gallium Oxide System, *Journal of Materials Science*, 14(12):3008–3010.

Increasing the deportment of titanium species to, and the stability field of pseudobrookite phase for valourisation of titaniferous slags

DOI: 10.62053/NLUH3099

X C Goso[1], J Petersen[2] and J Nell[3]

1. Mintek, Johannesburg 2125, South Africa. Email: xolisag@mintek.co.za
2. University of Cape Town, Cape Town 7701, South Africa. Email: jochen.petersen@uct.ac.za
3. Johannes Nell Consulting, Johannesburg 2194, South Africa. Email: drnell@outlook.com

ABSTRACT

The feasibility of increasing the deportment of titanium species and the stability of the pseudobrookite solid solution (M_3O_5) in a titaniferous slag was investigated, to facilitate the valourisation of titaniferous slags. Thermochemical simulations using FactSage™ software, ver 8.3 (by Thermofact/CRTC and GTT-Technologies), and equilibration-quench experiments were conducted using an appropriate synthetic titaniferous slag composition in an oxygen partial pressure (pO_2) ranging from air to 10^{-16} atm under non-isothermal conditions. The temperature-pressure phase stability diagram for the synthetic slag containing 37.19 per cent TiO_2, 19.69 per cent SiO_2, 13.12 per cent Al_2O_3, 16.00 per cent CaO and 14.00 per cent MgO showed that the spinel solid solution (M_3O_4) was the primary phase until a pO_2 of $10^{-10.5}$ atm, thereafter M_3O_5 was the primary phase until a pO_2 $10^{-13.2}$ atm. M_3O_4 again was the primary phase between a pO_2 $10^{-13.2}$ and 10^{-16} atm. The changeover of the primary phase coincided with an increase in the liquidus surface. When cooling the slag in a pO_2 of 10^{-16} atm, M_3O_5 crystallised as a ternary phase that showed a rapid increase in mass while that of the primary M_3O_4 phase decreased and that of the secondary perovskite ($CaTiO_3$) phase increased at a slower rate. At 1300°C under sub-liquidus conditions, the contents of M_3O_5, M_3O_4 and $CaTiO_3$ were about 20 per cent, 15 per cent, and 11 per cent, respectively. Experimental results showed that the Ti^{3+}/Ti^{4+} mass ratio in the M_3O_5 phase, ie a measure of the reduction of titanium species, is not considerably sensitive to equilibration temperature in the reviewed range. Slow cooling and minimum/no oxidation during cooling of titaniferous slag would increase the deportment of titanium species to, and the growth and stability of the M_3O_5 phase.

INTRODUCTION

Titaniferous magnetite (titanomagnetite) mineral deposits occur as accumulations of ilmenite and magnetite, with significant contents of vanadium (Fischer, 1975). Titanomagnetite is the primary source of vanadium throughout the world and an established source of steel (Taylor *et al*, 2006; Roskill Information Services Ltd, 2010). It is typically processed using the steel and vanadium coproduction process, which accounted for about 73 per cent of global vanadium production in 2021 (Bushveld Minerals, 2022). Coproduction operations are found in many countries, including in:

- New Zealand by New Zealand Steel (NZS) (involving smelting iron sands) (Kelly, 1993).
- Russia by EVRAZ Nizhny Tagil Iron and Steel (NTMK) (NTMK, 2003).
- China by Panzhihua Iron and Steel Company (Pangang) and Chengde Iron and Steel (CHMP) (Zhang *et al*, 2007).
- South Africa by the now-defunct EVRAZ Highveld Steel and Vanadium Corporation (EHSV) (Steinberg, Geyser and Nell, 2011) and the recently established Ironveld Smelting (Bokone Smelting) (Ironveld Group, 2023).

The steel and vanadium coproduction process essentially involves the smelting of titanomagnetite in an electric arc or blast furnace in the presence of limestone, dolomite, and/or quartz flux and carbonaceous reductant to produce vanadium-bearing pig iron and titanium-bearing slag, known as titaniferous slag (Roskill Information Services Ltd, 2003; Jochens, 1967; Bleloch, 1949). A fluxless coproduction process has also been proposed (Geldenhys, Akdogan and Reynolds, 2020; Boyd, Schoukens and Denton, 1993). Molten vanadium-bearing pig iron from the furnace is transferred to a converting process to produce vanadium slag and steel products (Taylor *et al*, 2006; Moskalyk and Alfantazi, 2003). Titaniferous slag typically forms a by-product stream. The size of the abandoned

EHSV slag dump is estimated to be about 45 million tonnes (Mt) (Mining Review Africa, 2017) whereas the size of the slag produced in China was estimated to be about 7400 Mt in 2019 (Lv and Bai, 2019). Only Ironveld reported the production of a marketable titaniferous slag from their coproduction operation. The technical details and compositions of the product streams from the Ironveld operation are not readily available in the public domain, perhaps due to that the operation was successfully commissioned only in January 2023. This operation is still undergoing further developments (Ironveld Group, 2023).

Titaniferous slags produced around the world are generally described by the CaO-MgO-Al_2O_3-SiO_2-TiO_x system and have 20 per cent to 40 per cent TiO_2 content, making them attractive for upgrading to a suitable feedstock for the production of titania pigment and other titanium products. These slags typically comprise titanaugite [$(Ca,Mg,Al,Ti,Si)_2O_6$], perovskite ($CaTiO_3$), spinel [$(Mg,Fe)(Al,V,Ti)_2O_4$ or M_3O_4], pseudobrookite [$(Mg,Al,Ti,V)_3O_5$ or M_3O_5] (Goso, Nell and Petersen, 2016; Pistorius, 2011; Zhang *et al*, 2006, 2007). Of all these phases, $CaTiO_3$ and M_3O_5 are the main phases that generally have the highest titanium contents. The existence and dominance of the specific phases in the slags depend on several factors including the chemical composition of the feed titanomagnetite, flux composition and addition, and smelting technology and conditions. The slag produced by Pangang using blast furnace technology has a high calcium content, with perovskite being the primary phase. Wang *et al* (2006) and Zhang *et al* (2006, 2007) reported that the deportment of titanium species from other phases to the $CaTiO_3$ phase in the slag and growth of the perovskite phase field could be achieved by aeration/oxidation of molten titaniferous slag during cooling. Two sets of studies by Zhang *et al* (2006) and Wang *et al* (2006) reported that it is technically feasible to recover perovskite from titaniferous slag by flotation. Wang *et al* (2010) further showed that a high-purity titania (TiO_2) feedstock can be produced from the perovskite concentrate by alkaline roasting and acid leaching process through the removal of calcium and other impurities. These studies have thus presented a technically viable option for the production of titania feedstock from high calcium titaniferous slags produced in China (Wang *et al*, 2006, 2010; Zhang *et al*, 2006, 2007).

Titaniferous slag produced by the now-defunct EHSV using dolomite and quartz as flux during smelting of the South African titanomagnetite in EAFs comprised M_3O_5 as one of the significant phases, with the lower titania content spinel being the other significant phase. The M_3O_5 phase in the slag has more than 80 per cent TiO_2 content (Goso, Nell and Petersen, 2016). M_3O_5-based titania slags, like ilmenite slags, are typically used as feedstock for pigment production (Pistorius, 2008).

The objective of the current study was therefore to investigate the feasibility of increasing the deportment of titanium species from other phases to the M_3O_5 phase in a typical fluxed South African titaniferous slag, and the stability field of this M_3O_5 phase. The effect of state variables such as temperature and pressure (partial pressure of oxygen, pO_2) on the stability of the M_3O_5 phase was evaluated using FactSage™ thermochemical simulation software and experimental work involving a synthetic titaniferous slag. Investigation into the separation of the M_3O_5 phase from the titanium-deficient phases in the slag fell outside the scope of the current work.

METHODOLOGY

Thermochemical simulations

Thermochemical simulations of the stability field of the M_3O_5 phase under various temperatures and pO_2 were conducted using FactSage™ software (Bale *et al*, 2016). The latest version of FactSage™, ver 8.3, was used to complete the calculations in the current study, mainly using the 'Phase Diagram' and 'Equilib' modules. 'FactPS' and 'FToxid' thermodynamic databases were used to complete the calculations. The 'FToxid' thermodynamic database in FactSage™ 8.3 is equipped with an appropriate pseudobrookite solid solution with tialite (Al_2TiO_5) included as an endmember in this solid solution, unlike in an earlier version used in previous studies (Goso, Nell and Petersen, 2016).

Experimentation

Materials and equipment

Analytical reagent grade powders of TiO_2, SiO_2, Al_2O_3, MgO and CaO with respective purities of >99 per cent after drying were supplied by Merck for the preparation of a synthetic titaniferous slag. Due to the hygroscopic nature of CaO, the required amount to make a synthetic slag was dried at 105°C just before it was used. Platinum foil with 0.127 mm thickness (99.9 per cent pure) and Pt/Rh wires with 0.5 mm diameter (Pt/Rh 6 per cent and Pt/Rh 30 per cent) were purchased from Merck for making sample capsules and B-type thermocouples, respectively. Another platinum wire of 99.9 per cent purity was also obtained for holding the samples inside the test furnace.

Bulk chemical analyses of raw and processed samples were conducted using a Varian Vista-PRO CCD simultaneous inductively coupled plasma optical emission spectrometer (ICP-OES). Mineralogical characterisation was conducted using a Bruker D8 advanced X-ray diffractometer (XRD), Zeiss EVO® MA15 scanning electron microscope (SEM) coupled with a Bruker energy-dispersive spectrometer (EDS), and Cameca SX50 electron probe microanalysis (EPMA) instrument.

Equilibration-quench tests were conducted using a set-up equipped with:

- A vertical sealable tube furnace equipped with an alumina tube with a 27 mm internal diameter.
- Ar, CO and CO_2 gas cylinders for pO_2 control in the furnace.
- 'Hydrosorb' for drying of gases
- 'Oxysorb' for residual oxygen removal from gases.
- Gas pre-heating horizontal tube furnace equipped with titanium metal turnings for removal of trace oxygen from the gases at 700°C.
- Mass flow controllers for gas flow regulations.
- Quenching water bath.

Thermocouples and mass flow metres used in the study were calibrated using the procedures detailed by Goso (2019). Temperature measurements were accurate to within ±2°C relative to a standard thermocouple (Goso, 2019). Test temperatures and prevailing pO_2 in the vertical tube furnace were verified using a DS oxygen probe supplied by Australian Oxytrol Systems (AOS) (Goso, 2019; Australian Oxytrol Systems Pty Ltd, 2017). The reaction tube was so small that the oxygen probe and test sample could not be fitted at the same time. Thus, the furnace reaction zone and purging period of 30 mins for the attainment of the target pO_2 with the CO and CO_2 gas mixture with a total flow rate of 1000 standard cubic centimetres per min (sccm) were determined without the sample before the execution of the experiments. The temperature of the hot zone and pO_2 were verified after completing five tests.

Preparation of synthetic slag

The relevant chemical composition of the titaniferous slag for current investigations was deduced from historical fundamental work on phase equilibria of fluxed titaniferous slags produced from SA titanomagnetite resources (Jochens, 1967) and the chemical composition of EHSV slag (Steinberg, Geyser and Nell, 2011). Thus, a synthetic slag comprising 37.19 per cent TiO_2, 19.69 per cent SiO_2, 13.12 per cent Al_2O_3, 16 per cent CaO and 14 per cent MgO was produced (Jochens, 1967). The procedure for preparing a 100 g mass of the synthetic slag involved weighing the respective masses of the high-purity metal oxide constituents, and blending them using a mechanical mixer over 24 hrs. The mixture was compacted into a cylindrical pellet of about 30 mm in diameter and height using a hydraulic press unit equipped with a relevant size steel hardened die operating at 20 MPa pressing pressure. To form preliminary phases and avoid difficulties in the attainment of liquidus temperatures and equilibrium phases in the subsequent equilibration-quench experiments, the pellet was sintered by heating at 1200°C over 24 hrs using a chamber furnace. The pellet was crushed, re-agglomerated and heated three times more, following the same procedure. The final synthetic slag was analysed by ICP-OES and XRD.

Attainment of pO_2 of 10^{-16} atm

In the current study, equilibration-quench experiments were conducted at pO_2 of 10^{-16} atm, which, in the absence of a measured value was estimated to be the prevailing pO_2 in the defunct EHSV titanomagnetite smelting furnaces. Estimated pO_2 was obtained from the equilibrium pO_2 of 10^{-16} atm attained for the reduction of V_2O_3 to metallic V at 1500°C (Goso, 2019; Bale *et al*, 2016), which is a close approximation to the tapping temperature of EHSV titaniferous slag (Steinberg, Geyser and Nell, 2011). This approach does not suggest that the pO_2 for the titanomagnetite smelting operation at EHSV was exclusively defined by the reduction of V_2O_3 to metallic V, but it was adopted in the absence of an empirical value.

Deines *et al* (1974) reported that carbon deposition would be experienced from a CO/CO_2 mixture that is equivalent to a pO_2 of 10^{-16} atm when the temperature reaches about 1435°C. This work indicated that it would be technically challenging to attain a pO_2 of 10^{-16} atm using a CO/CO_2 gas mixture at 1500°C. However, direct measurement of pO_2 using an oxygen probe showed that the target pO_2 of 10^{-16} atm using CO/CO_2 mixture at 1500°C was attained in the current study. In view of the carbon deposition field in literature (Deines *et al*, 1974), the target pO_2 in the current study was closer to the reported limits where measurement uncertainties were anticipated to be significant. This was therefore the reason it was possible to attain the target pO_2 in the current study.

Experimental

To complete each equilibration-quench experiment, the vertical tube furnace was pre-heated to 1200°C, which was used as the minimum operating temperature of this furnace during this study. A sample of the pulverised pre-heated synthetic slag was transferred into a capsule made using the Pt foil. The mass of the slag that was transferred in each test was about 500 mg – the use of smaller samples allowed for rapid attainment of thermal equilibrium and effective quenching. Smaller samples were analysed in their entirety to eliminate sampling uncertainties (Goso, 2019). The charged Pt capsule was introduced to the pre-heated furnace by suspending it in the reaction zone using a Pt wire. The furnace was sealed, followed by flowing a CO and CO_2 gas mixture to purge the system. Previous work showed that the sub-liquidus region of similar fluxed titaniferous slags ranged between 1200°C and 1550°C (Jochens, 1967). Thus, a test slag in the Pt capsule was pre-melted at 1600°C for 30 mins followed by lowering the temperature to the test equilibration temperature. CO and CO_2 flow rates were adjusted for attainment of target pO_2 of 10^{-16} atm at the test temperature. As established and reported in previous work (Goso, 2019), a minimum equilibrium time of 16 hrs was adopted. At the end of equilibration time, the Pt wire holding the charged capsule was released to slip through the furnace for instantaneous quenching of the sample in a bath of ice water to preserve the phases that existed at the equilibration temperature.

Equilibration-quench experiments conducted at pO_2 of 10^{-16} atm caused the Pt capsule containing the sample to be rigid and brittle. The test sample was however not lost. Quenched samples were recovered and mounted in epoxy resins, polished and subjected to analyses using SEM-EDS for the identification of distinct phases in the slag and EPMA for the analysis of the different phases.

RESULTS AND DISCUSSION

FactSage™ simulation

Phase stability diagram

A phase stability diagram for a dolomite-quartz-fluxed titaniferous slag containing 37.19 per cent TiO_2, 19.69 per cent SiO_2, 13.12 per cent Al_2O_3, 16.00 per cent CaO and 14.00 per cent MgO as deduced from previous development study (Jochens, 1967) is shown in Figure 1 in the form of temperature-partial pressure diagram (T-p diagram). These results show that Ti-spinel (M_3O_4) solid solution (ss) crystallised as the primary phase throughout the reviewed pO_2 range, except at pO_2 ranging from $10^{-10.5}$ to $10^{-13.2}$ atm where pseudobrookite (M_3O_5) ss was the primary phase. The changeover of the primary phase from M_3O_4 at higher pO_2 to M_3O_5 as pO_2 decreased, coincided with an increase in the liquidus surface from a fairly consistent range of 1335°C to 1350°C to a more rapid increase throughout the M_3O_5 crystallisation range. The primary phase changed back to M_3O_4

at a lower pO_2 than $10^{-13.2}$ atm. The initial M_3O_4 likely contained the Mg_2TiO_4 endmember with oxidised titanium species whereas the latter M_3O_4 formed at a lower pO_2 likely contained the $MgTi_2O_4$ endmember with reduced titanium species. When the latter M_3O_4 started to form at a pO_2 of $10^{-13.2}$ atm, the liquidus surface increased at a higher rate until the end of the reviewed range at a pO_2 of 10^{-16} atm. The observed behaviour of the liquidus surface and primary phase changes is in concurrence with previous work, in which the equilibrium phases were calculated using FactSage™ 7.0 that operated with a private $MgTi_2O_5$-Al_2TiO_5 (M_3O_5) thermodynamic database (Goso, Nell and Petersen, 2016).

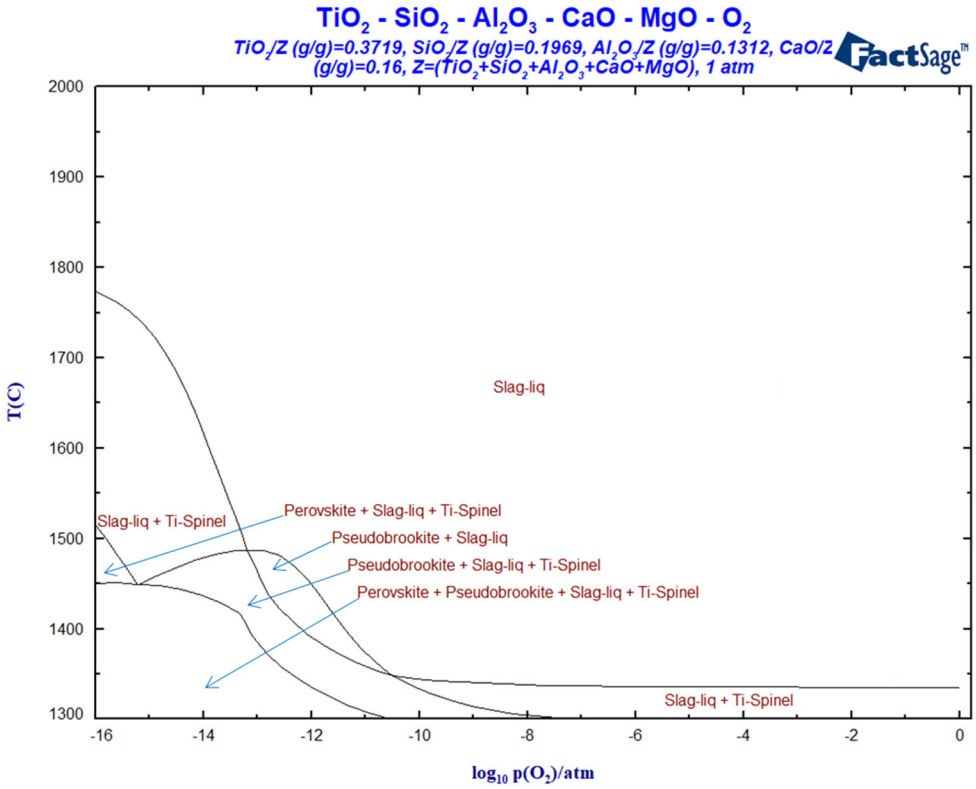

FIG 1 – Phase stability diagram for a titaniferous slag with chemical composition: 37.19 per cent TiO_2, 19.69 per cent SiO_2, 13.12 per cent Al_2O_3, 16.00 per cent CaO and 14.00 per cent MgO.

At pO_2 of $10^{-10.5}$ to 10^{-16} atm, over a temperature range of 1300°C to 1772°C, the prominent phase fields are those of 'slag-liq+M_3O_5', 'slag-liq+M_3O_4', 'M_3O_5+slag-liq+M_3O_4', '$CaTiO_3$+slag-liq+M_3O_4', and '$CaTiO_3$+M_3O_5+slag-liq+M_3O_4'. The reviewed pO_2 and temperature range covers the sub-liquidus systems, thus the three solid phases, ie M_3O_5, Ti-M_3O_4, and $CaTiO_3$ coexist with a molten slag (slag-liq) in different phase fields.

The solubility of titanium in the M_3O_4 is generally low, as reported in previous work, with the TiO_2 content in the M_3O_4 phase generally below 10 per cent TiO_2 (Jing *et al*, 2023; Shi *et al*, 2020). Wang *et al* (2006) and Zhang *et al* (2006, 2007) reported that $CaTiO_3$ is effectively precipitated under an oxidising atmosphere when the CaO content in the slag is high. As shown by the smaller secondary phase field of '$CaTiO_3$+slag-liq+Ti-M_3O_4' in the T-p diagram, the precipitation of $CaTiO_3$ from the SA titaniferous slag is not anticipated to be substantial under the low pO_2 levels of 10^{-16} atm. Thus, in the reviewed range of pO_2 and temperature, M_3O_5 is likely the main phase that hosts most of the titanium species. The results indicate that for improved collection of titanium species in the M_3O_5 and the growth of the M_3O_5-bearing phase region, dolomite-fluxed titaniferous slag should be cooled under low pO_2 levels of $10^{-10.5}$ atm and below.

Equilibrium phase composition of synthetic titaniferous slag

Figure 2 shows the distribution of equilibrium phases in the titaniferous slag containing 37.19 per cent TiO_2, 19.69 per cent SiO_2, 13.12 per cent Al_2O_3, 16.00 per cent CaO and 14.00 per cent MgO, in an atmosphere with a pO_2 of 10^{-16} atm at temperatures ranging from 1300°C

to 1800°C. The liquid region already contained about 96.5 per cent of the feed content, with about 3.5 per cent of the starting content removed as oxygen allegedly due to the reduction of TiO_2 to lower oxidation state titanium species. The results show that the ternary M_3O_5 phase started to crystallise at about 1448°C at a rapid rate and quickly caught up with the $CaTiO_3$ phase at about 10 per cent of feed slag mass, after which the $CaTiO_3$ growth became very slow. The amount of the primary M_3O_4 phase decreased from about 25 per cent of the feed slag mass when the M_3O_5 crystals started to form. At 1300°C, the amount of the M_3O_4 phase had decreased during cooling under reducing conditions to about 15 per cent of the feed slag while the amount of the M_3O_5 phase increased to about 20 per cent of the feed slag.

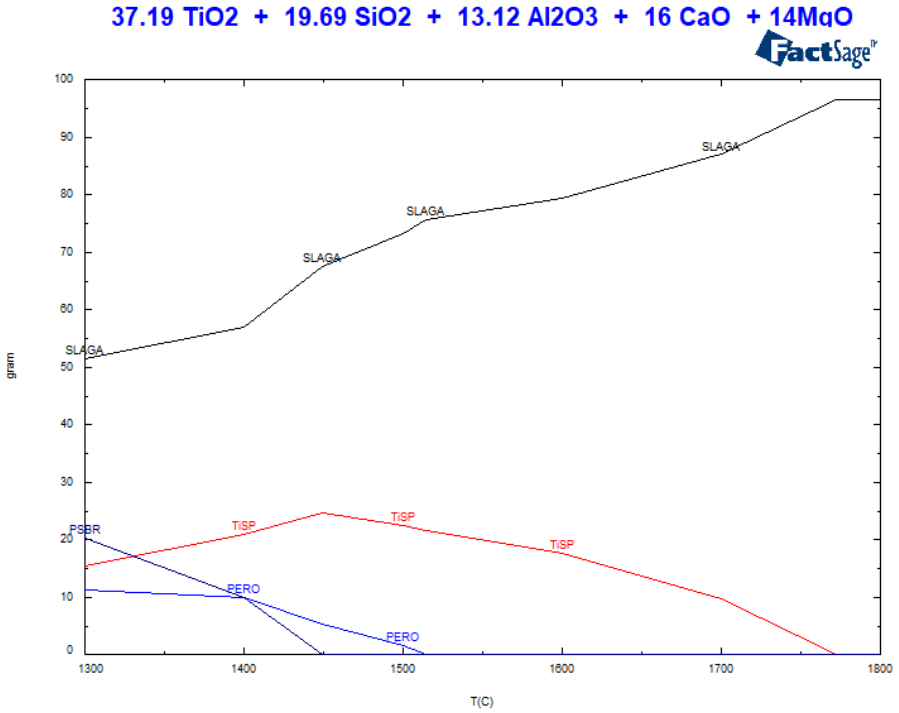

FIG 2 – Distribution of phases in the titaniferous slag containing 37.19 per cent TiO_2, 19.69 per cent SiO_2, 13.12 per cent Al_2O_3, 16.00 per cent CaO and 14.00 per cent MgO, at a pO_2 of 10^{-16} atm in a temperature range of 1300°C to 1800°C.

The results shown in the hypothetical reference, ie Figure 2, show that during cooling, the M_3O_5 phase grows and becomes stable. Slow cooling of the titaniferous slag would thus be recommended to avoid the formation of the glass phase and to maximise the growth of the M_3O_5 crystals. It is also important to prevent oxidation of the titaniferous slag during slow cooling to maximise the growth of the titanium-rich M_3O_5 phase, and thus the deportment of titanium species in the M_3O_5 phase.

Experimental results in relation to simulation results

Chemical analysis results showed that the synthetic titaniferous slag contained 37.41 per cent TiO_2, 19.11 per cent SiO_2, 12.38 per cent Al_2O_3, 15.52 per cent CaO and 12.90 per cent MgO. XRD analysis results showed that the preheated synthetic slag contained the following non-equilibrium phase assemblage: titanate ($CaTiSiO_5$), armalcolite ($MgTi_2O_5$), forsterite (Mg_2SiO_4), perovskite ($CaTiO_3$), anorthite ($CaAl_2Si_2O_8$), spinel ($MgAl_2O_4$), aluminium oxide (Al_2O_3), and quartz (SiO_2). Replicate pre-heating of the synthetic composition did not completely help to incorporate the respective starting metal oxides into intermediate phases as discrete Al_2O_3 and SiO_2 phases were still observed after preheating. This was not a significant problem for the subsequent equilibration-quench experiments as the equilibrium was mainly approached from above, ie the synthetic slag was melted first at 1600°C, followed by lowering the temperature to the target equilibration temperature.

EPMA results showing the equilibrium phase compositions for the synthetic slag processed at a pO_2 of 10^{-16} atm and equilibration temperatures ranging between 1320°C and 1500°C are presented in

Table 1. Equilibration-quench results agree with the simulated phase stability results presented in Figure 1 in that for this slag composition processed in an atmosphere with a pO_2 of 10^{-16} atm, the primary phase is the titanium-bearing M_3O_4 phase. However, the two sets of results disagree in terms of the liquidus temperature of the primary phase. Equilibration-quench and FactSage™ simulation results showed the liquidus temperatures to be about 1440°C and 1772°C, respectively.

TABLE 1

Equilibrium phase compositions for the synthetic slag processed at pO_2 of 10^{-16} atm and equilibration temperatures ranging between 1320°C and 1500°C (mass%).

Equilibration temperature, °C	MgO	Al_2O_3	SiO_2	CaO	TiO_2	Equilibrium phases
1500	15.37	14.57	21.62	17.84	30.84	Slag liquid
1450	15.20	14.70	22.19	17.76	30.83	Slag liquid
1440	11.24	13.94	27.13	19.44	28.16	Slag liquid
	28.96	66.76	0.14	-	3.66	M_3O_4
1430	11.27	14.05	26.93	19.75	28.09	Slag liquid
	28.51	67.33	0.11	-	3.56	M_3O_4
1410	11.70	13.90	28.96	20.33	25.05	Slag liquid
	28.82	67.19	0.11	-	3.80	M_3O_4
1400	11.33	13.83	26.76	19.58	28.05	Slag liquid
	29.89	67.72	0.08	-	3.38	M_3O_4
	11.88	4.15	0.05	0.30	82.79	M_3O_5
1390	11.10	14.40	27.71	19.95	26.73	Slag liquid
	29.37	66.84	0.10	0.04	3.54	M_3O_4
	11.15	3.94	0.16	0.43	84.65	M_3O_5
1360	12.62	13.50	29.49	20.80	23.42	Slag liquid
	30.24	65.19	0.20	0.06	5.24	M_3O_4
	12.92	5.16	0.12	0.43	81.90	M_3O_5
1350	14.73	11.37	26.08	20.59	27.65	Slag liquid
	29.03	68.90	0.28	0.14	2.85	M_3O_4
	13.36	4.39	0.04	0.31	82.60	M_3O_5
	0.13	0.12	-	41.68	58.04	$CaTiO_3$
1340	12.49	13.45	29.48	20.62	23.19	Slag liquid
	29.40	66.40	0.14	-	3.55	M_3O_4
	13.14	4.04	-	0.24	82.79	M_3O_5
	0.13	0.17	0.08	41.57	58.27	$CaTiO_3$
1320	16.20	11.37	29.77	23.81	19.55	Slag liquid
	31.05	63.06	0.22	0.04	6.35	M_3O_4
	12.99	4.67	-	0.19	82.57	M_3O_5
	0.15	0.17	-	41.57	58.29	$CaTiO_3$

"-": below detection limit.

In addition, equilibration-quench results showed the crystallisation of M_3O_5 as the secondary phase at about 1400°C whereas simulation results showed $CaTiO_3$ as the secondary phase crystallising at about 1512°C. In the equilibration-quench work, $CaTiO_3$ crystallised as the ternary phase at about 1350°C, contrary to the simulation results that indicated the crystallisation of M_3O_5 at about 1450°C as the ternary phase. However, both sets of results agreed in terms of the phase assemblage at temperatures of 1320°C and above as '$CaTiO_3$+M_3O_5+slag-liq+M_3O_4'.

Goso, Nell and Petersen (2016) and Pistorius (2011) reported titanaugite [$(Ca,Mg,Al,Ti,Si)_2O_6$], $CaTiO_3$, M_3O_4, and M_3O_5 as the phase assemblages of real plant titaniferous slags that were cooled under non-controlled atmospheres. This phase assemblage is similar to that reported above from thermochemical simulation and experimental work. Preventing or minimising the oxidation of the titaniferous slag during cooling would maintain a similar assemblage, with the M_3O_5 phase content increased with decreasing pO_2 or when the conditions become more reducing. M_3O_5 is the main titanium-bearing phase while M_3O_4 typically has lower contents of titanium species, and the contents of $CaTiO_3$ and liquid slag in the slag are anticipated to be lower, especially towards lower temperatures during cooling.

The differences between equilibration-quench and simulation results relating to liquidus temperature of the primary phase and actual secondary phase at low pO_2 conditions indicated a need for the development and validation of thermodynamic databases of titanium-bearing systems at lower pO_2 applicable to titanomagnetite smelting conditions. Goso, Nell and Petersen (2016) reported on FactSage™ simulation results, which showed that the Ti^{3+}/Ti^{4+} mass fraction ratio in the overall slag, ie a measure of the reduction of titanium species in the slag, increased with decreasing pO_2 to the lowest reviewed point of 10^{-16} atm. In the current study, the Ti^{3+}/Ti^{4+} mass ratios in the M_3O_5 phase found in the slags produced during the equilibration quench experiments were estimated by normalising the metal and oxygen atoms to the respective stoichiometry of 3 and 5, with the excess oxygen to the stoichiometry attributed to reduced titanium (Ti^{3+}) species. Figure 3 shows the effect of equilibration temperature on the Ti^{3+}/Ti^{4+} mass ratio in the M_3O_5 phase. The Ti^{3+}/Ti^{4+} mass ratio in the M_3O_5 phase is not considerably sensitive to equilibration temperature variation in the reviewed range. It is important to note that during the cooling of titaniferous slag under low pO_2, the Ti^{3+}/Ti^{4+} mass ratio in the M_3O_5 phase will likely remain the same or increase. Thus, the M_3O_5 phase would be stabilised. Oxidising cooling conditions would support the stabilisation of $CaTiO_3$ (Zhang *et al*, 2006, 2007; Wang *et al*, 2006).

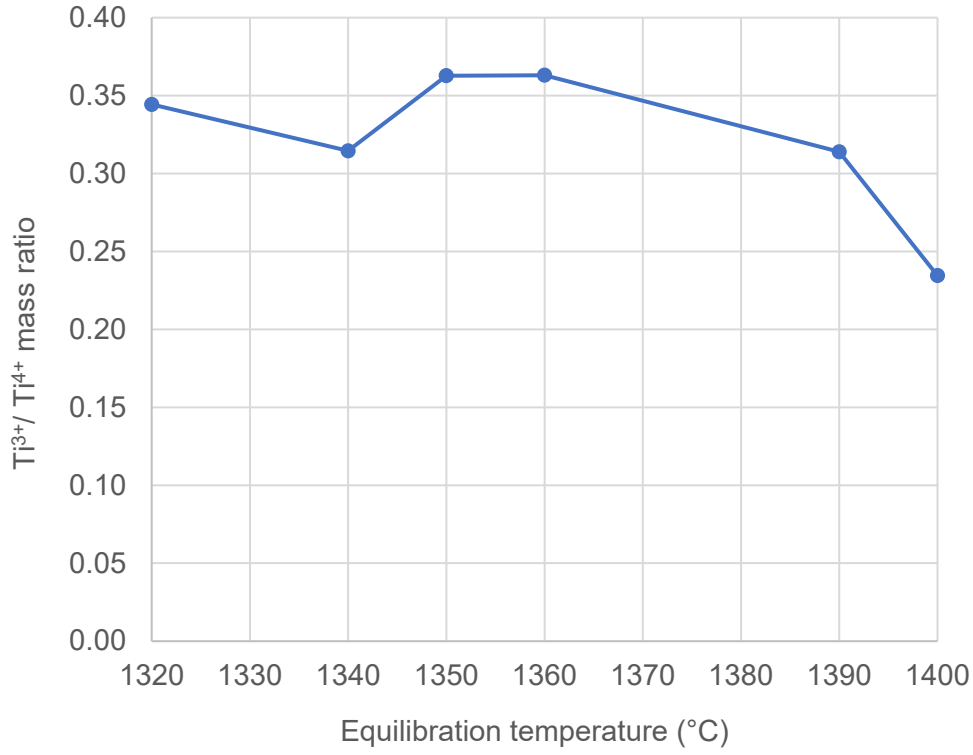

FIG 3 – Effect of equilibration temperature on the Ti^{3+}/Ti^{4+} mass ratio in the M_3O_5 phase.

CONCLUSIONS

Thermochemical simulations and equilibration-quench experiments were conducted to investigate the feasibility of increasing the deportment of titanium species from other phases, and the growth and stability of the M_3O_5 phase in a titaniferous slag. The T-p phase stability diagram for a titaniferous slag containing 37.19 per cent TiO_2, 19.69 per cent SiO_2, 13.12 per cent Al_2O_3, 16.00 per cent CaO and 14.00 per cent MgO showed that M_3O_4 crystallised as the primary phase over the review pO_2 range from air to 10^{-16} atm, except in pO_2 range of $10^{-10.5}$ to $10^{-13.2}$ atm where M_3O_5 was the primary phase. During cooling of the slag in a pO_2 of 10^{-16} atm, M_3O_5 crystallised as a ternary phase with its mass increasing rapidly as the temperature decreased. At the same time, the content of the primary M_3O_4 phase decreased and that of the secondary $CaTiO_3$ phase increased at a slower rate. Thermochemical simulation and experimental results agreed about the phase assemblage during slag cooling towards the solidus temperature, namely '$CaTiO_3$+M_3O_5+slag-liq+M_3O_4'. At 1300°C under sub-liquidus conditions, the contents of the M_3O_5, M_3O_4 and $CaTiO_3$ phases were about 20 per cent, 15 per cent, and 11 per cent, respectively. Experimental results showed that the Ti^{3+}/Ti^{4+} mass ratio in the M_3O_5 phase was not considerably sensitive to equilibration temperature in the reviewed range, but will remain the same or increase to support the growth and stability of the M_3O_5 phase. It can be concluded that slow cooling and minimum/no oxidation during cooling of the titaniferous slag would increase the deportment of titanium species to, and the growth and stability of the M_3O_5 phase. Future work will investigate the separation of M_3O_5 from low-titania-bearing phases such as $CaTiO_3$ and M_3O_4, most likely using a physical beneficiation process.

ACKNOWLEDGEMENTS

The paper is published with the permission of Mintek.

REFERENCES

Australian Oxytrol Systems Pty Ltd, 2017. Oxygen probe - SIRO2 C700 DS probe, Australian Oxytrol Systems Pty Ltd.

Bale, C W, Belisle, E, Chartrand, P, Decterov, S A, Eriksson, G, Gheribi, A E, Hack, K, Jung, I H, Kang, Y B, Melancon, J, Pelton, A D, Petersen, S, Robelin, C, Sangster, J, Spencer, P and Van Ende, M A, 2016. FactSage thermochemical software and databases, 2010–2016, *CALPHAD: Computer Coupling of Phase Diagrams and Thermochemistry*, 54:35–53.

Bleloch, W, 1949. The electric smelting of iron ores for production of alloy irons and steels and recovery of chromium and vanadium, *Journal of the Chemical Metallurgical and Mining Society of South Africa*, 49:363–408.

Boyd, M D, Schoukens, A K and Denton, G M, 1993. The recovery of titanium from titanomagnetite, South Africa, Patent no P11756.

Bushveld Minerals, 2022. Vanadium overview [online]. Available from: <https://www.bushveldminerals.com/about-vanadium/> [Accessed: 10 December 2022].

Deines, P, Nafziger, R H, Ulmer, G C and Woermann, E, 1974. Temperature-oxygen fugacity tables for selected gas mixtures in the system C-H-O at one atmosphere total pressure, *Bulletin of the Earth and Mineral Sciences Experiment Station: Number 88.*

Fischer, R P, 1975. Vanadium resources of titaniferous magnetite deposits, Geological Survey Professional Paper 926-B, pp B1–B10.

Geldenhys, I J, Akdogan, G and Reynolds, Q G, 2020. Towards sustainable processing of vanadium-bearing titaniferous magnetite deposits - an overview of barriers and opportunities, IMPC 2020: XXX International Mineral Processing Congress, Cape Town.

Goso, X C, 2019. Phase equilibria studies and beneficiation of titaniferous slags, PhD thesis, University of Cape Town, Department of Chemical Engineering.

Goso, X C, Nell, J and Petersen, J, 2016. Review of liquidus temperature and phase equilibria of titaniferous slags at pO2 applicable to titanomagnetite smelting, Seattle, USA, in *Proceedings of the 10th International Conference on Molten Slags, Fluxes and Salts (MOLTEN16)*, pp 101–114 (The Minerals, Metals, Materials Society).

Ironveld Group, 2023. Our Project [online]. Available from: <https://ironveld.com/ironveld-group/> [Accessed: 25 November 2023].

Jing, J, et al, 2023. An experimental study on the phase equilibria of the CaO-MgO-SiO2–13%Al2O3–50%TiO2 system in air at 1450°C, *CALPHAD: Computer Coupling of Phase Diagrams and Thermochemistry*, 83:1–8.

Jochens, P R, 1967. Contribution to the knowledge of the equilibrium and non-equilibrium behaviour of titaniferous slags, PhD thesis, University of Witwatersrand, Department of Metallurgy.

Kelly, B F, 1993. Ironmaking at BHP New Zealand Steel Limited, Glenbrook, New Zealand, in *Monograph 19 - Australasian Mining and Metallurgy, The Sir Maurice Mawby Memorial Volume,* second edition, pp 348–353 (The Australasian Institute of Mining and Metallurgy: Melbourne).

Lv, C and Bai, S, 2019. Upgrading of raw vanadium titanomagnetite concentrate, *Journal of Southern African Institute of Mining and Metallurgy*, 119:957–961.

Mining Review Africa, 2017. Nyanza Light Metals' plant to provide titanium dioxide pigment to Africa, *Mining Review Africa* [online]. Available from: <https://www.miningreview.com/news/nyanza-light-metals-plant-to-provide-titanium-dioxide-pigment-to-africa/> [Accessed: 4 December 2023].

Moskalyk, R R and Alfantazi, A M, 2003. Process of vanadium: a review, *Minerals Engineering*, 16:793–805.

NTMK, 2003. Specialization: Nizhniy Tagil Iron and Steelworks [online]. Available from: <htt://www.ntmk.ru/en/manufacture/specialization.php> [Accessed: 24 March 2015].

Pistorius, P C, 2008. Ilmenite smelting: the basics, *The Journal of The Southern African Institute of Mining and Metallurgy*, 108:35–43.

Pistorius, P C, 2011. Titania slag smelting and calcination of crude zinc oxide: examples of processing under thermodynamic and kinetic constraints, Leuven Belgium, in *Proceedings of the Second International Slag Valorization Symposium*, pp 263–270.

Roskill Information Services Ltd, 2003. *The Economics of Titanium Minerals and Pigments*, Roskill Reports on Metals and Minerals, Roskill Information Services Ltd, 400 p.

Roskill Information Services Ltd, 2010. Vanadium: Global Industry Market and Outlook, Roskill Reports on Metals and Minerals, 12th Edition, Roskill Information Services Ltd, 203 p.

Shi, J, et al, 2020. Phase equilibrium study of the CaO-SiO2-MgO-Al2O3-TiO2 system at 1300°C and 1400°C in air, *JOM*, 72(9):3204–3212.

Steinberg, W S, Geyser, W and Nell, J, 2011. The history and development of the pyrometallurgical processes at Evraz Highveld Steel and Vanadium, *Journal of the Southern African Institute of Mining and Metallurgy*, 111:63–79.

Taylor, P R, Shuey, S A, Vidal, E E and Gomez, J C, 2006. Extractive metallurgy of vanadium-containing titaniferous magnetite ores: a review, *Minerals and Metallurgical Processing*, 23(2):80–86.

Wang, M, et al, 2006. Selective enrichment of TiO2 and precipitation behavior of perovskite phase in the titania bearing slag, *Trans Nonferrous Met Soc China*, 16:421–425.

Wang, Y, Qi, T, Chu, J and Zhao, W, 2010. Production of TiO2 from CaTiO3 by alkaline roasting method, *Rare Metals*, 29(2):162–167.

Zhang, L, et al, 2006. Effect of perovskite phase precipitation on viscosity of Ti-bearing blast furnace slag under the dynamic oxidation condition, *Journal of Crystalline Solids*, 352:123–129.

Zhang, L, et al, 2007. Recovery of titanium compounds from molten Ti-bearing blast furnace slag under the dynamic oxidation condition, *Minerals Engineering*, 20:684–693.

Effect of MgO concentration on phase evolution during steelmaking slag cooling process

DOI: 10.62053/AFSW1040

W F Gu[1], J Diao[2], H Qin[3], H F Yu[4], Y Sasaki[5] and S Ueda[6]

1. Doctoral candidate, Chongqing University, College of Materials Science and Engineering, Chongqing 400044, China; and Tohoku University, Institute of Multidisciplinary Research for Advanced Materials, Sendai 980-8577, Japan. Email: guwengfeng@163.com
2. Associate professor, Chongqing University, College of Materials Science and Engineering, Chongqing 400044, China. Email: diaojiang@163.com
3. Master candidate, Chongqing University, College of Materials Science and Engineering, Chongqing 400044, China. Email: qh1240980784@163.com
4. Associate Professor, University of Science and Technology Beijing, State Key Laboratory of Advanced Metallurgy, Beijing 100083, China. Email: yuhuafang@ustb.edu.cn
5. Professor, Tohoku University, Institute of Multidisciplinary Research for Advanced Materials, Sendai 980-8577, Japan. Email: ironyaz@gmail.com
6. Professor, Tohoku University, Institute of Multidisciplinary Research for Advanced Materials, Sendai 980-8577, Japan. Email: shigeru.ueda.a5@tohoku.ac.jp

ABSTRACT

The main reason for the underutilisation of steelmaking slags is their instability, which is influenced by their complex phase structure. Recycling and sustainable steelmaking slag face challenges due to the presence of magnesium oxide (MgO), a crucial component in steelmaking slag. This study investigates the phase evolution of steelmaking slag during the cooling process with different MgO contents, using high-temperature experiments and FactSage™ software, ver 8.1, (by Thermfact/CRCT and GTT-Technologies) thermodynamic equilibrium calculations. X-ray diffraction (XRD) and scanning electron microscope - energy dispersive x-ray spectroscopy (SEM-EDS) analyses identified main phases in steelmaking slag, including Ca_2SiO_4 (C_2S), RO (MgO-FeO solid solution), $Ca_2Fe_2O_5$ (C_2F), and Ca_3SiO_5 (C_3S). The study reveals that RO phase increases as the MgO content increases. C_3S precipitates from steelmaking slag with a 12 mass per cent MgO content at a reduced temperature of 1400°C. It is important to note that C_3S remains in the steelmaking slag even after slow cooling. This may be due to the substitution of Ca^{2+} in C_3S by Fe^{2+} and Mg^{2+} ions. Intriguingly, the precipitation of *f*-CaO in steelmaking slag with 10 mass per cent of MgO content occurred after one year, while there was no manifestation of *f*-CaO precipitation in the steelmaking slag with 12 mass per cent of MgO content even after one year. This discrepancy suggests a potential stabilising effect of an appropriate amount of MgO in steelmaking slag. However, it is crucial to emphasise that this inference lacks supporting data, necessitating further research to validate this hypothesis. The significance of this work is in uncovering the complexities of steelmaking slag behaviour, providing essential insights for optimising recycling processes. The research sheds light on the factors that influence the phase composition and stability of steelmaking slag, contributing to the utilisation of steelmaking slags, promoting environmental sustainability, and enhancing the overall efficiency of metallurgical processes in the current industrial landscape.

INTRODUCTION

In China, the steel industry annually generates a substantial 130–160 million tons of steelmaking slag, yet its utilisation rate is less than 30 per cent (Carvalho *et al*, 2017; Guo, Bao and Wang, 2018; Oge *et al*, 2019). Utilising steelmaking slag in building materials can alleviate disposal challenges and reduce reliance on natural resources. However, its application has been hindered by characteristics such as volume expansion during storage (Park, Choi and Min, 2019; Ruan *et al*, 2022; Zhao, Yan and Wang, 2017). The expansion in volume is attributed to the hydration of free lime (*f*-CaO) and dusting resulting from the conversion of α'-Ca_2SiO_4 (α'-C_2S) to γ-Ca_2SiO_4 (γ-C_2S) within the slag (Benarchid *et al*, 2005; Brand and Roesler, 2018; Fix Heymann and Heinke, 1969).

A comprehensive understanding of the chemical, mineralogical, and morphological properties of steelmaking slag is crucial, as these properties directly impact its cementitious and mechanical attributes, influencing its utilisation potential. Given the significant variability in chemical composition

among different sources of steelmaking slag, substantial differences in mineralogical composition are expected (Deng *et al*, 2020; Kim and Azimi, 2022; Shen, Forssberg and Nordström, 2004; Yu *et al*, 2022). To enhance steel/slag reactions and dephosphorisation kinetics during the steelmaking process, considerable amounts of dolomite are introduced into the converter (Tayeb *et al*, 2015; Shi *et al*, 2004). The addition of dolomite, coupled with the loss of MgO refractory in the basic oxygen furnace (BOF) lining, results in a slag containing 0.4–14 per cent MgO, resulting in a stability issue for steelmaking slag (Yildirim and Prezzi, 2011).

The decomposition of Ca_3SiO_5 (C_3S) during the cooling process of steelmaking slag is a major source of *f*-CaO (Li *et al*, 2022; Shim *et al*, 2016; Tossavainen *et al*, 2007). However, Ca_3SiO_5 is also a vital component in Portland cement clinker. Consequently, the stability steelmaking slag directly influences its suitability for civil engineering and building materials. Research indicates that MgO content affects the crystal structure of C_3S, with low MgO stabilising the triclinic polymorph, while high MgO favours the formation of the monoclinic (Chen *et al*, 2014; Liu, Li and Zhang, 2002; Ma *et al*, 2015). This study investigates the phase evolution of steelmaking slag with varying MgO content during the cooling process, employing thermodynamic equilibrium phase calculations and molten steelmaking slag cooling experiments. The aim is to understand the influence of MgO content on the formation of phases and stability, optimising the mineral phase of steelmaking slag and enhancing its stability. This research will contribute a theoretical foundation for the treatment of steelmaking slag.

MATERIALS AND METHODS

Steelmaking slags with different magnesium oxide (MgO) contents were prepared using analytical reagents, and their chemical composition is detailed in Table 1. The raw mixtures, weighing 40 g, were dried and then subjected to burning at 1500°C for 40 mins. The temperature decrease occurred at a rate of 5°C/min, as shown in Figure 1. After the sample reached the target temperature, a connected quartz tube and pipette are used to extract the steelmaking slag sample for analysis of the precipitate phases during the steelmaking slag cooling process. Upon reaching 1000°C, the molten steelmaking slag had completely solidified. Subsequently, the slags were cooled to room temperature at a rate of 30°C/min. The experimental process was conducted under an argon (Ar) atmosphere to prevent the oxidation of the steelmaking slag, and all samples were rapidly cooled with water. The phases and microstructure of slag samples were analysed by scanning electron microscopy, SEM-EDS, (VEGA 3 LMH, TESCAN, Brno, Czech) and X-ray diffraction (PANalytical X'Pert Power, PANalytical BV, Netherlands).

TABLE 1

Chemical compositions of steelmaking slags (mass%).

No	MgO	CaO	Fe_xO	SiO_2	Al_2O_3	P_2O_5	MnO	TiO_2
1	8.00	44.53	28.63	12.72	2.04	2.04	1.02	1.02
2	10.00	43.56	28.00	12.44	2.00	2.00	1.00	1.00
3	12.00	42.59	27.37	12.16	1.96	1.96	0.98	0.98

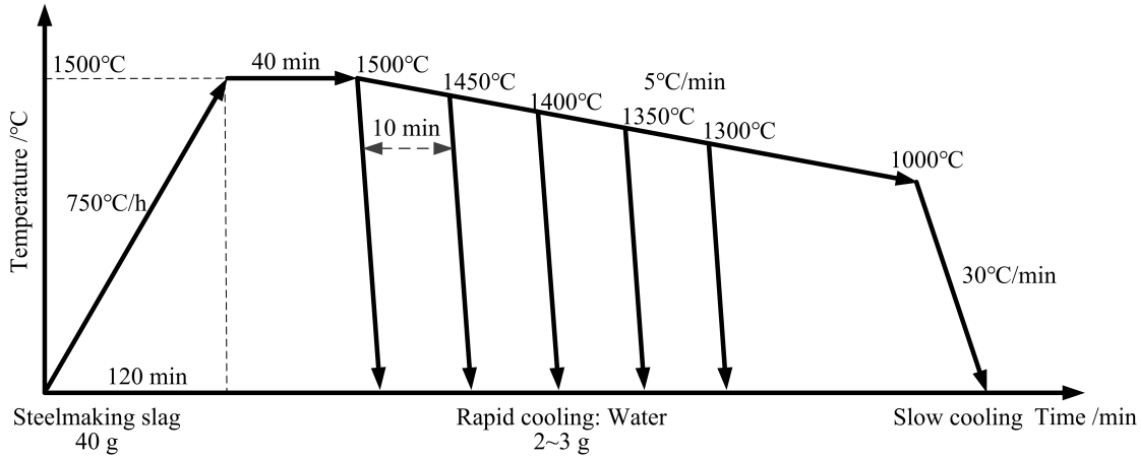

FIG 1 – Scheme of the heat patterns in this experiment.

RESULT AND DISCUSSION

Equilibrium phase of steelmaking slag

The thermodynamic equilibrium calculation results depicted in Figure 2 illustrate the predominant phases in steelmaking slags with 8 mass per cent and 12 mass per cent MgO. These phases encompass RO, C_2S, C_3S, C_2S-C_3P (solid solution of Ca_2SiO_4 and $Ca_3(PO_4)_2$), C_2F, and *f*-CaO. Notably, RO emerges as the initial precipitation phase in molten steelmaking slag, with its content at 1600°C escalating from 5.46 mass per cent to 10.91 mass per cent with an increase in MgO content from 8 mass per cent to 12 mass per cent. Correspondingly, the RO contents in fully solidified steelmaking slag exhibit a range of 35.84 mass per cent to 38.32 mass per cent. The findings in the figure unequivocally establish the RO phase as the exclusive form of MgO post-solidification of the steelmaking slag.

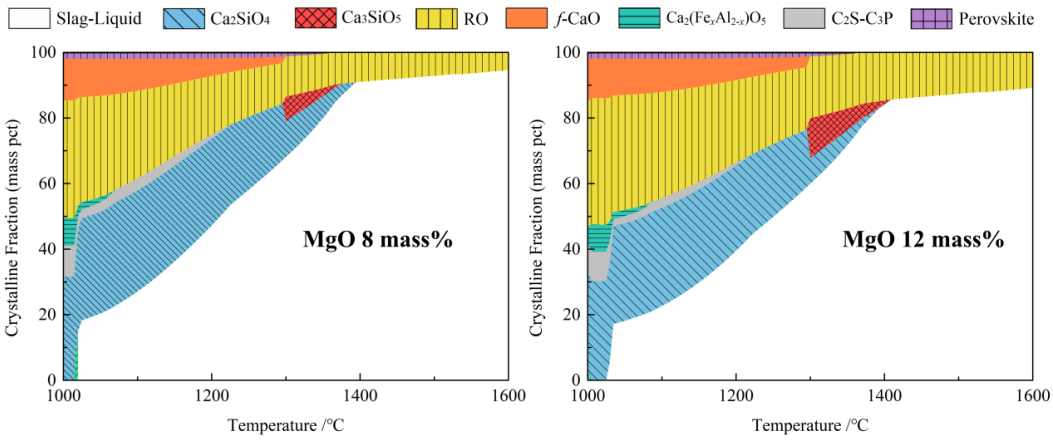

FIG 2 – Thermodynamic calculation based on a normal equilibrium calculation model for steelmaking slag with different MgO content. Fe_2O_3 content is 10 mass per cent of iron oxides in all steelmaking slags.

As shown in Figure 2, the increase of MgO content results in a reduction of the liquid phase in molten steelmaking slag. Consequently, there is an elevation in the concentration of CaO in the liquid phase, facilitating the precipitation of C_3S. At an MgO content of 8 mass per cent, C_3S precipitates in the steelmaking slag at 1375°C. With a further increase in MgO content to 12 mass per cent, the precipitation temperature of C_3S rises to 1405°C. As the temperature decreases, the C_3S content increases to 7.50 mass per cent and 12.19 mass per cent, respectively, before ultimately decomposing into C_2S and *f*-CaO at 1300°C. The data in Figure 2 conclusively suggests that the increasing in MgO content does not exert a significant influence on the *f*-CaO content in steelmaking slag.

Mineral phase structure

The XRD patterns for steelmaking slags containing 12 mass per cent MgO at different temperatures are depicted in Figure 3. It can be deduced that the primary phases in the steelmaking slag include C_2S, RO, C_2F, and C_3S. Figure 3 illustrates the precipitation of C_3S from the steelmaking slag with 12 mass per cent MgO content at a reduced temperature of 1400°C.

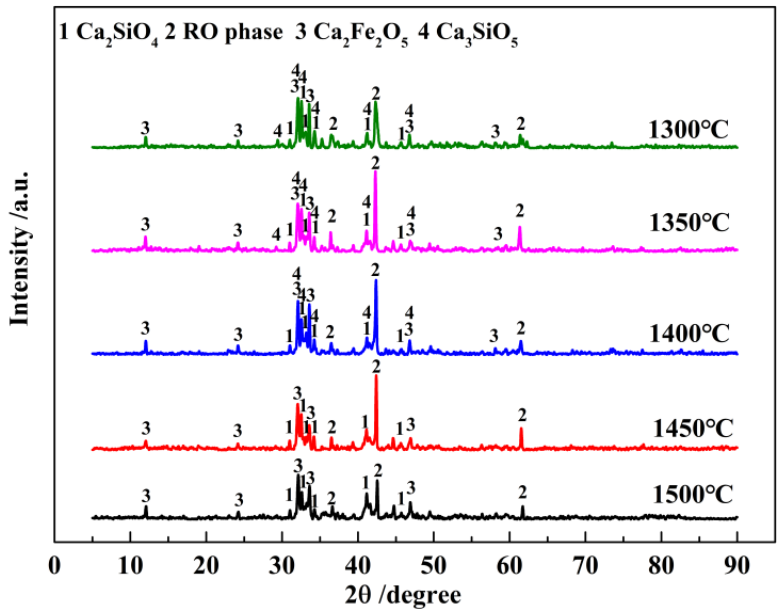

FIG 3 – XRD patterns of steelmaking slags of 12 mass per cent MgO during cooling.

Figure 4 displays SEM images of slowly cooling steelmaking slag with different MgO contents, revealing C_3S in bulk structures. Interestingly, the increase in MgO content has an insignificant impact on the composition and phases of the steelmaking slag. After cooling, steelmaking slag maintains phases such as C_2S, RO, C_2F, and C_3S, with no precipitation of C_3S in the case of 8 mass per cent MgO content. The persistence of C_3S in steelmaking slag after slow cooling, as observed, indicates that, under the experimental conditions, the kinetics required for the decomposition of C_3S have not been achieved.

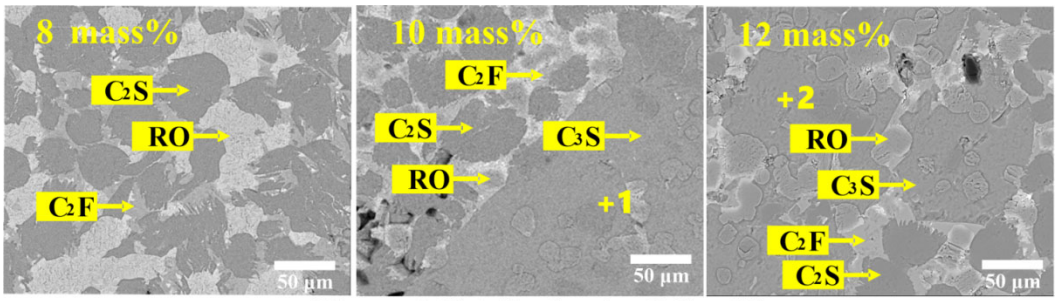

Element distribution in C_3S, at%

No.	O	Mg	Si	Ca	Fe
1	65.2	0.5	7.1	25.1	2.2
2	53.1	0.7	11.8	32.1	2.3

FIG 4 – SEM of the slowly cooled steelmaking slags with different MgO mass per cent (NB: the table shows the EDS results for points 1 and 2 in the figure).

As shown in Figure 4, EDS results demonstrate the presence of Mg and Fe in C_3S, suggesting the possibility of Fe^{2+} and Mg^{2+} substituting for Ca^{2+} in the C_3S crystal lattice. Notably, Mg serves not only as a substitutional atom but also as an interstitial atom. The addition of an appropriate amount of MgO to steelmaking slag has the potential to alter the formation kinetics of C_3S, influencing its crystal structure.

Stability of steelmaking slag

As already mentioned, steelmaking slag has been of limited use due to its characteristics of volume expansion during storage. The volume expansion is caused by the hydration of free lime (f-CaO) in the slag, which exhibits around 10 per cent swelling (Bazzoni *et al*, 2014; Stephan and Wistuba, 2006). Samples were polished and placed in air to investigate the stability of steelmaking slag at room temperature. The steelmaking slag surface starts to precipitate some black phase, as shown in Figure 5. Based on the SEM-EDS results in Figure 6, the black phase is considered to be gradually precipitated *f*-CaO. As shown in Figures 5 and 6, the MgO in the slag was 10 mass per cent and a large amount of *f*-CaO precipitated from the slag surface after one year. However, when the MgO content was increased to 12 mass per cent, there was no significant change in slag surface after one year. It suggests a potential stabilising effect of an appropriate amount of MgO in steelmaking slag. Nevertheless, it is crucial to emphasise that this inference lacks empirical support, and additional studies are imperative to validate this hypothesis and provide a more comprehensive understanding of the underlying mechanisms.

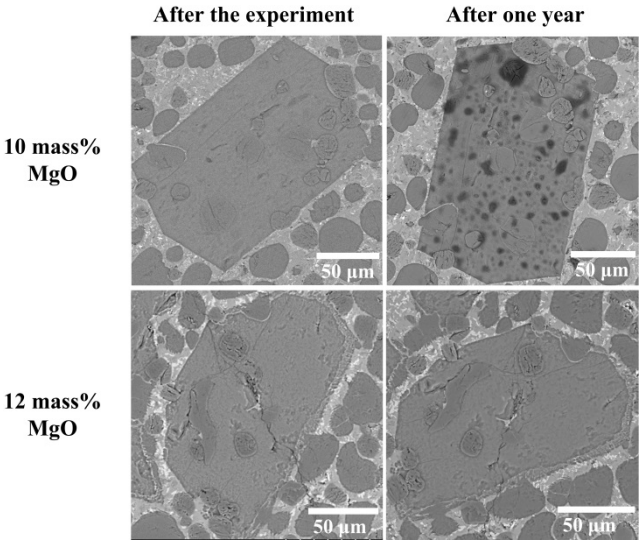

FIG 5 – SEM of steelmaking slag after one year for different MgO contents.

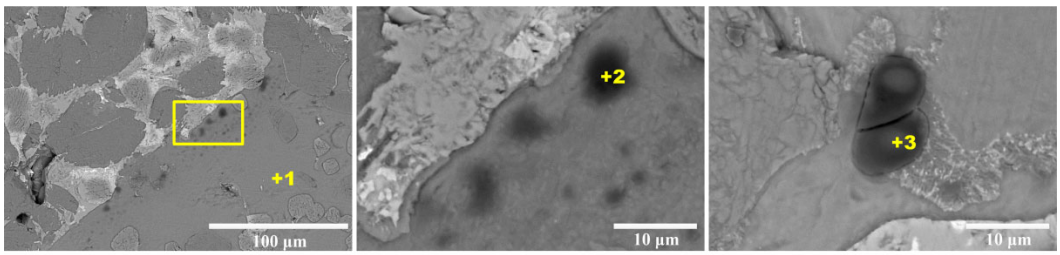

EDS result of slag with 10 mass% MgO, at%

NO.	O	Mg	Si	Ca	Fe	Ca/Si
1	61.38	0.57	7.37	28.62	2.06	3.88
2	68.14	0.87	5.05	23.55	2.39	4.66
3	77.33	0.81	1.90	18.30	1.65	9.63

FIG 6 – SEM and EDS of steelmaking slag with 10 mass per cent MgO after one year.

CONCLUSIONS

The investigation systematically examined the evolution of mineral phases and microstructures during the cooling of steelmaking slag with varying MgO contents, aiming to enhance the efficient recycling of steelmaking by-products. The principal findings are outlined as follows: the dominant phases in steelmaking slag encompass C_2S, RO, C_2F and C_3S. RO phase, representing the main

form of MgO in steelmaking slag, exhibited an increase from 35.84 mass per cent to 38.32 mass per cent with the MgO content rising from 8 mass per cent to 12 mass per cent. Simultaneously, an increasing in MgO content also heightened the C_3S precipitation content in steelmaking slag. Cooling experiments revealed that C_3S in steelmaking slag did not decompose into C_2S and CaO with decreasing temperature, possibly attributed to the ability of certain Fe^{2+} and Mg^{2+} to substitute Ca^{2+} in C_3S. Interestingly, the precipitation of *f*-CaO in steelmaking slag with 10 mass per cent of MgO content occurred after one year, while the precipitation of *f*-CaO in steelmaking slag with 12 mass per cent of MgO content did not manifest even after one year. This discrepancy implies a potential stabilising effect of an appropriate amount of MgO in steelmaking slag. However, it is essential to note that this inference lacks supporting data, and further research is required to validate this hypothesis.

REFERENCES

Bazzoni, A, Ma, S, Wang, Q, Shen, X, Cantoni, M and Scrivener, K L, 2014. The Effect of Magnesium and Zinc Ions on the Hydration Kinetics of C, 3S, *Journal of the American Ceramic Society*, 97(11):3684–3693. https://doi.org/10.1111/jace.13156

Benarchid, My, Y, Diouri, A, Boukhari, A, Aride, J and Elkhadiri, I, 2005. Hydration of iron–phosphorus doped dicalcium silicate phase, *Materials Chemistry and Physics*, 94(2–3):190–194. https://doi.org/10.1016/j.matchemphys.2005.04.047

Brand, A S and Roesler, J R, 2018. Interfacial transition zone of cement composites with steel furnace slag aggregates, *Cement and Concrete Composites*, 86:117–129. https://doi.org/10.1016/j.cemconcomp.2017.11.012

Carvalho, S Z, Vernilli, F, Almeida, B, Demarco, M and Silva, S N, 2017. The recycling effect of BOF slag in the Portland cement properties, *Resources, Conservation and Recycling*, 127:216–220. https://doi.org/10.1016/j.resconrec.2017.08.021

Chen, L, Wang, X, Shen, X D, Ma, S H and Zhou, W Q, 2014. Crystal Structure and Hydration Characteristics of Tricalcium Silicate Doped with Magnesium Oxide, *Advanced Materials Research*, 936:1336–1341. https://doi.org/10.4028/www.scientific.net/AMR.936.1336

Deng, L, Yun, F, Jia, R, Li, H, Jia, X, Shi, Y and Zhang, X, 2020. Effect of SiO_2/MgO ratio on the crystallization behavior, structure and properties of wollastonite-augite glass-ceramics derived from stainless steel slag, *Materials Chemistry and Physics*, 239:122039. https://doi.org/10.1016/j.matchemphys.2019.122039

Fix, W, Heymann, H and Heinke, R, 1969. Subsolidus Relations in the System $2CaO{\cdot}SiO_2$-$3CaO{\cdot}P_2O_5$, *Journal of the American Ceramic Society*, 52(6):346–347. https://doi.org/10.1111/j.1151-2916.1969.tb11948.x

Guo, J, Bao, Y and Wang, M, 2018. Steel slag in China: Treatment, recycling and management, *Waste Management*, 78:318–330. https://doi.org/10.1016/j.wasman.2018.04.045

Kim, J and Azimi, G, 2022. Selective Precipitation of Titanium, Magnesium and Aluminum from the Steelmaking Slag Leach Liquor, *Resources, Conservation and Recycling*, 180:106177. https://doi.org/10.1016/j.resconrec.2022.106177

Li, Y, Guo, K, Xiang, J, Pei, G and Lv, X, 2022. Effect of Cooling Method on the Mineralogy and Stability of Steel Slag, *ISIJ International*, 62(11):2197–2206. https://doi.org/10.2355/isijinternational.ISIJINT-2022-101

Liu, X, Li, Y and Zhang, N, 2002. Influence of MgO on the formation of Ca_3SiO_5 and $3CaO{\cdot}3Al_2O_3{\cdot}CaSO_4$ minerals in alite–sulphoaluminate cement, *Cement and Concrete Research*, 32(7):1125–1129.

Ma, S, Zhou, W, Wang, S, Li, W and Shen, X, 2015. Polymorph transformation kinetics of Ca_3SiO_5 with MgO, *Phase Transitions*, 88(9):888–896. https://doi.org/10.1080/01411594.2015.1030746

Oge, M, Ozkan, D, Celik, M B, Sabri Gok, M and Cahit Karaoglanli, A, 2019. An Overview of Utilization of Blast Furnace and Steelmaking Slag in Various Applications, *Materials Today: Proceedings*, 11:516–525. https://doi.org/10.1016/j.matpr.2019.01.023

Park, T J, Choi, J S and Min, D J, 2019. Investigation of Effects of SiO_2 Content and Cooling Rate on Crystallization in Fe_2O_3-CaO-SiO_2 System Using In Situ Confocal Laser Scanning Microscopy, *Metallurgical and Materials Transactions B*, 50(2):790–798. https://doi.org/10.1007/s11663-019-01518-y

Ruan, W, Ma, Y, Liao, J, Ma, T, Zhu, Y and Zhou, A, 2022. Effects of steel slag on the microstructure and mechanical properties of magnesium phosphate cement, *Journal of Building Engineering*, 49:104120. https://doi.org/10.1016/j.jobe.2022.104120

Shen, H, Forssberg, E and Nordström, U, 2004. Physicochemical and mineralogical properties of stainless steel slags oriented to metal recovery, *Resources, Conservation and Recycling*, 40(3):245–271. https://doi.org/10.1016/S0921-3449(03)00072-7

Shi, C, Inc, C T, Dr, U and On, B, 2004. Steel Slag—Its Production, Processing, Characteristics and Cementitious Properties, *Journal of Materials in Civil Engineering*, 16(3):230–236. https://doi.org/10.1061/(ASCE)0899-1561(2004)16:3(230)

Shim, G-I, Kim, S-H, Paik, D-J, Hong, M-H and Choi, S-Y, 2016. Influence of cooling rate on the crushing efficiency of solidified iron ore for recycled aggregates, *International Journal of Mineral Processing*, 150:9–15. https://doi.org/10.1016/j.minpro.2016.03.002

Stephan, D and Wistuba, S, 2006. Crystal structure refinement and hydration behaviour of $3CaO{\cdot}SiO_2$ solid solutions with MgO, Al_2O_3 and Fe_2O_3, *Journal of the European Ceramic Society*, 26(1–2):141–148. https://doi.org/10.1016/j.jeurceramsoc.2004.10.031

Tayeb, M A, Assis, A N, Sridhar, S and Fruehan, R J, 2015. MgO Solubility in Steelmaking Slags, *Metallurgical and Materials Transactions B*, 46(3):1112–1114. https://doi.org/10.1007/s11663-015-0352-8

Tossavainen, M, Engstrom, F, Yang, Q, Menad, N, Lidstrom Larsson, M and Bjorkman, B, 2007. Characteristics of steel slag under different cooling conditions, *Waste Management*, 27(10):1335–1344. https://doi.org/10.1016/j.wasman.2006.08.002

Yildirim, I Z and Prezzi, M, 2011. Chemical, Mineralogical and Morphological Properties of Steel Slag, *Advances in Civil Engineering*, 13 p. https://doi.org/10.1155/2011/463638

Yu, H, Lu, X, Miki, T, Matsubae, K, Sasaki, Y and Nagasaka, T, 2022. Sustainable phosphorus supply by phosphorus recovery from steelmaking slag: A critical review, *Resources, Conservation and Recycling*, 180:106203. https://doi.org/10.1016/j.resconrec.2022.106203

Zhao, J, Yan, P and Wang, D, 2017. Research on mineral characteristics of converter steel slag and its comprehensive utilization of internal and external recycle, *Journal of Cleaner Production*, 156:50–61. https://doi.org/10.1016/j.jclepro.2017.04.029

Studying the smelting behaviour of bauxite residue pellets reduced by hydrogen using high temperature thermal analysis

DOI: 10.62053/GACJ7735

D Hariswijaya[1] and J Safarian[2]

1. PhD candidate, Norwegian University of Science and Technology, Trondheim 7034, Norway. Email: dali.hariswijaya@ntnu.no
2. Professor, Norwegian University of Science and Technology, Trondheim 7034, Norway. Email: jafar.safarian@ntnu.no

ABSTRACT

Treating bauxite residue as an alternative source of metals for iron and aluminium industry is an approach to promote circular economy in metal industries. Reduction of metal oxides with H_2-based process is an important step on decarbonisation of metal industry. In this study bauxite residue pellets were prepared and were reduced with different H_2-H_2O gas compositions at different temperatures which yielded with various degrees of reduction. The bauxite residue pellets were made from a mixture of bauxite residue and $Ca(OH)_2$ powders and sintered at 1150°C. Hydrogen reduction was carried out on the oxide pellets using a resistance furnace at elevated temperatures in controlled reduction atmosphere of H_2-H_2O gas mixtures which resulted in reduction of iron oxides in the pellets. Unreduced and reduced pellets were subsequently heated to 1400°C to study their smelting behaviour using differential thermal analysis (DTA) and thermogravimetric analysis (TGA) technique to investigate the evolution of phases related to slag formation via smelting. Equilibrium module of Factsage™ ver 8.1 was utilised to analyse results of thermal analysis. It was observed that Tricalcium phosphate-β (CaP_2O_8), Bredigite ($Ca_7Si_4MgO_{16}$), Rankinite ($Ca_3Si_2O_7$), and calcium alumino ferrite ($Ca[Al,Fe]_6O_{10}$) were formed during thermal analysis as intermediate phases. The initial slag formation for sintered and reduced pellets occurred at 900°C which mainly contains calcium and small amount of strontium component. The slag formation rate increases significantly starting from 1100°C when iron oxides started to form initial molten slag phase which then followed by other oxides dissolution in the system. Gas formation was observed at 1180°C and it was found that the gas to be released from unreduced pellets is O_2 meanwhile the gas to be released from reduced pellets is SO_2 gas. Gas formation rate for both pellets start to increase at 1280°C when the remaining chemically bonded gas start to be released from the system.

INTRODUCTION

Bayer process and bauxite residue

The Bayer process was invented and patented by Carl Josef Bayer in 1888 and has since then been the leading process for alumina (Al_2O_3) production in the world. The process consists of eight main stages: milling, desilication, digestion, clarification, precipitation, evaporation, classification and calcination. In the milling step, the bauxite ore is crushed down into finer particles. Additionally, limestone is added to create a pumpable slurry. After the milling step, the slurry moves through a process called desilication, which involves removing silica (SiO_2). The slurry is then digested using a NaOH solution, which dissolves the aluminium bearing minerals in the bauxite. These minerals include gibbsite ($Al(OH)_3$, boehmite (γ-AlO(OH)) and diaspore (α-AlO(OH)). When the solution is added, the following reactions take place with gibbsite and boehmite/diaspore, given by Equation (1) and Equation (2) respectively (Smallman and Bishop, 1999):

$$Al(OH)_{3(s)} + NaOH_{(aq)} \rightarrow Al(OH)^-_{4(aq)} + Na^+_{(aq)} \quad (1)$$

$$AlO(OH)_{(s)} + NaOH_{(aq)} + H_2O_{(l)} \rightarrow Al(OH)^-_{4(aq)} + Na^+_{(aq)} \quad (2)$$

After the processing step, the slurry is cooled down using a series of flash tanks at 1 atm. The slurry is then prepared for clarification where the bauxite residue (BR) is separated away through sedimentation, where chemical additives assist in driving the BR to the bottom of the settling tanks. BR is transferred to washing tanks, where the goal is to recover the caustic soda used in the digestion step. The saturated liquid undergoes a series of filtration steps and BR is left in disposal areas. After

clarification, alumina is recovered through crystallisation during precipitation step. The precipitation reaction is shown in Equation (3) (Smallman and Bishop, 1999):

$$Al(OH)^{-}_{4(aq)} + Na^{+}_{(aq)} \rightarrow Al(OH)_{3(s)} + NaOH_{(aq)} \quad (3)$$

Evaporation of the liquid used during crystallisation takes place in heat exchangers, where it is subsequently cooled down afterwards in flash tanks. The condensate that is created through this process is reused for BR washing or as feed water. Recovered caustic soda is then re-added to the digestion step. The crystals are classified into size ranges, using cyclones and gravity classification tanks. For the coarse crystals, separation from liquid and calcination is performed. For the finer crystals, washing to remove organic impurities and re-addition to the precipitation step is performed. Calcination of the coarse crystals is done by roasting in calciners. The roasting process takes place at temperatures up to 1100°C. This drives off moisture and water, which eventually creates alumina solids. The calcination reaction is shown in Equation (4) (Smallman and Bishop, 1999):

$$2Al(OH)_{3(s)} \rightarrow Al_2O_{3(s)} + 3H_2O_{(g)} \quad (4)$$

Smelting reduction of bauxite residue

Red mud, also known as bauxite residue (BR) in dewatered form, is the main by-product generated in the Bayer process. Typically, for each tonne of produced alumina from bauxite ore, about 1.5 t of BR is produced (Pandey and Prakash, 2020). The generated BR from the Bayer process is stored in large holding ponds, where only 1 per cent to 2 per cent is being recycled (Brunori *et al*, 2005). Dried BR typically contains up to 50 per cent of iron oxides. Other compounds found in BR includes silica oxides, titanium oxides, aluminium oxides and other oxides. It is also highly alkaline, with a pH level ranging from 12–13. Due to its high alkalinity, red mud that is stored away in holding ponds poses a great environmental threat to its surroundings. The main way of treating the alkaline BR, is to attempt neutralising by adding acidic substances, such as HCl (Brunori *et al*, 2005).

Smelting reduction of BR opens opportunities for recovery of its metal content, especially iron (Liu *et al*, 2021), aluminium (Lazou *et al*, 2021) and rare-earth elements (REEs) (Borra *et al*, 2016). It is to be understood from previous research that removal of iron content is a necessary preliminary step for effective recovery of alumina and REEs in BR (Lazou *et al*, 2021; Borra *et al*, 2016) and smelting reduction is believed to be the most efficient method for removal of iron in BR. Several studies on smelting reduction of BR have been conducted within the past decade which mainly tries to recover iron content in BR either in the form of magnetite (Lazou *et al*, 2021) or metallic iron (Kar, van der Eijk and Safarian, 2022; Skibelid *et al*, 2022; Lazou *et al*, 2021; Ekstroem *et al*, 2021; Borra *et al*, 2016).

Smelting reduction of BR with H_2 at low temperature (480°C) was able to produce magnetite with 87 per cent conversion degree with insignificant metallic iron production (Samouhos *et al*, 2017). Meanwhile smelting reduction with H_2 at high temperature (1000°C) was able to completely reduce Fe content in BR to metallic Fe (Kar, van der Eijk and Safarian, 2022; Skibelid *et al*, 2022). However, the recovery of Fe-containing phases from solid-state reduced BR remains an issue due to its physical nature which exists in miniscule spots with less than 20 μm in particle diameter (Kar, van der Eijk and Safarian, 2022; Skibelid *et al*, 2022). Carbothermic reduction of BR beyond Fe melting point (>1538°C) was able to reliably produce pig iron in its own separated phase (Lazou *et al*, 2021; Ekstroem *et al*, 2021). The remaining issue was recovery of Al content from its slag where almost half of it was trapped in Gehlenite ($Al_2Ca_2O_7Si$) phase which is difficult to recover via hydrometallurgical means (Lazou *et al*, 2021).

Previous studies showed that temperature of smelting reduction plays a key role in determining final phase composition and state of reduced BR. Smelting reduction beyond Fe melting point can reliably produce pig iron in separated phase, but it will also produce unleachable slag which significantly lowers its valourisation potential. Meanwhile heat treating in solid state has its own challenges which mainly revolves around separation process of metallic iron which distributed throughout BR in miniscule spots (Kar, van der Eijk and Safarian, 2022; Skibelid *et al*, 2022). Thus, the aim of present study is to assess change in phase compositions of BR and smelted BR with increasing temperature through comparison of experimental data and thermochemistry simulation.

MATERIALS AND METHODS

An experimental procedure was designed to study smelting behaviour of BR pellets which has been reduced by hydrogen. A mix of BR and $Ca(OH)_2$ was made and pelletised, then they were sintered. The sintered pellets were reduced under different H_2-H_2O gas mixtures. X-ray diffraction (XRD) and X-ray fluorescence (XRF) were employed to analyse phase composition of sintered pellets, meanwhile only XRD was employed to analyse phase composition of reduced pellets. A single pellet from the sintered pellets and reduced pellets was then crushed and sieved under 1 mm for differential thermal analysis (DTA) and thermogravimetric analysis (TGA) to analyse smelting behaviour of sintered and reduced pellets with increasing temperature up to 1400°C.

Pelletising and sintering

BR fines were deagglomerated and screened (<250 μm) to obtain uniform sizing on the mixing process. Raw $CaCO_3$ powder was calcined to make CaO powder. Resulting CaO powder was ground and screened (<250 μm) before it was hydrated to make $Ca(OH)_2$ powder. BR fines were mixed with $Ca(OH)_2$ powder with a mass ratio of 1:0.38 respectively. The ratio was decided based on the stoichiometric ratio of CaO needed to effectively produce calcium aluminate phase in the reduced pellets to allow effective recovery of alumina through leaching. The green pellets were made using a disc pelletiser and screened to obtain pellets with diameter of 4–10 mm which then air-dried for one day and subsequently sintered at 1150°C for 2 hrs in a muffle furnace. The sintered pellets were cooled down naturally inside the furnace for 8 hrs before taken out. Flow sheet of the pelletising and sintering process is shown in Figure 1, meanwhile XRF analysis of raw BR, $CaCO_3$ powder and sintered pellet are shown in Tables 1 to 3, respectively.

TABLE 1

XRF analysis of raw BR, dry basis (normalised).

Composition	Wt%	Composition	Wt%
CaO	9.98	TiO_2	5.67
MgO	0.26	Na_2O	3.51
SiO_2	8.05	K_2O	0.10
Al_2O_3	24.94	P_2O_5	0.13
Fe_2O_3	46.20	SO_3	1.07
MnO	0.09	**Total**	**100**

*Excluding Loss of Ignition (LOI)

TABLE 2

XRF analysis of raw $CaCO_3$ powder, dry basis (normalised).

Composition	Wt%	Composition	Wt%
CaO	98.632	TiO_2	0.005
MgO	0.547	Na_2O	0.037
SiO_2	0.208	K_2O	0.035
Al_2O_3	0.175	P_2O_5	0.009
Fe_2O_3	0.084	SO_3	0.263
MnO	0.005	**Total**	**100**

*Excluding Loss of Ignition (LOI)

TABLE 3

XRF analysis of sintered BR pellet.

Composition	Wt%	Composition	Wt%	Composition	Wt%
CaO	29.01	Cr_2O_3	0.18	P_2O_5	0.12
MgO	0.37	V_2O_5	0.15	SO_3	1.03
SiO_2	7.66	TiO_2	3.87	ZrO_2	0.11
Al_2O_3	23.12	NiO	0.06	SrO	0.03
Fe_2O_3	30.52	Na_2O	3.61	Co_3O_4	0.02
MnO	0.04	K_2O	0.10	**Total**	**100**

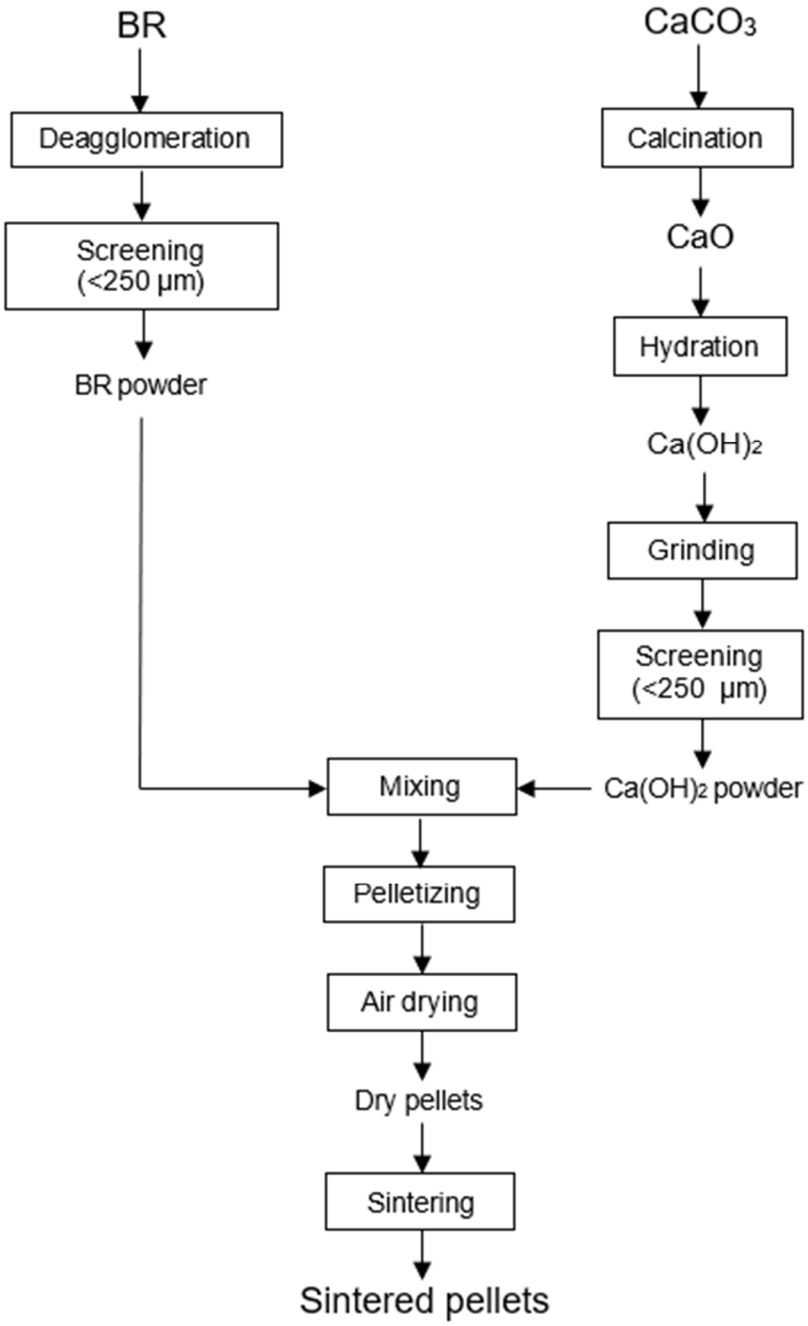

FIG 1 – Flow sheet of the pelletising and sintering process.

H2 reduction

The reduction experiments were conducted using a vertical alumina tube resistance furnace with an outer metallic alloy heating element. Around 20 g of sintered pellet was used in every experiment. Shown in Figure 2 is both the furnace and a schematic of its inside. The furnace consists of a cylinder-shaped alumina tube, surrounded by an element that is twined around the furnace. A thermocouple is inserted from the top of the furnace to measure the temperature of the sample holder. The sample holder is made from alumina with gas distributor attached at the bottom to ensure uniform gas distribution to the sample bed. The furnace features a reduction gas inlet positioned at its lower section which goes directly to the sample holder, while the gas, having interacted with the sample, is subsequently leaves through the top gas outlet of the furnace. Another gas inlet at lower section of the furnace which does not go to the sample holder is used to flush the furnace with Argon gas at all times of the experiment to prevent water vapor accumulation in the furnace chamber. The heating and cooling were programmed, while the temperature changes were collected by data logging.

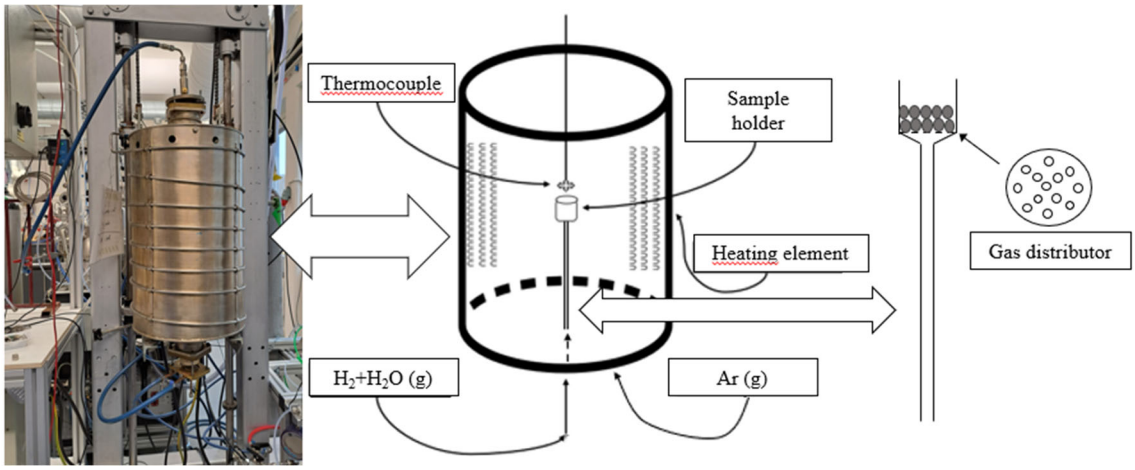

FIG 2 – Picture and schematic diagram of reduction furnace.

H_2-H_2O gas mixture composition was controlled by flowing H_2 gas through a humidifier with set humidity value. The humidifier is P-10 model made by Cellkraft™ AB with membrane technology. Experiments were done in three different H_2-H_2O gas compositions at 600°C as shown in Table 4. Heating rate of the furnace was 10°C/min and held for 2 hrs at set reduction temperature. Total flow of H_2-H_2O gas mix was kept at 1 L/min at all experiments and the furnace was flushed with 1L/min of argon at all times, including the cooling and heating period. Schematic heating diagram of the experiment is shown in Figure 3.

TABLE 4

Experiment conditions for H_2 reduction.

No.	Gas composition (vol%)	Reduction temperature (°C)
1	95% H_2 – 5% H_2O	600
2	85% H_2 – 15% H_2O	600
3	75% H_2 – 25% H_2O	600

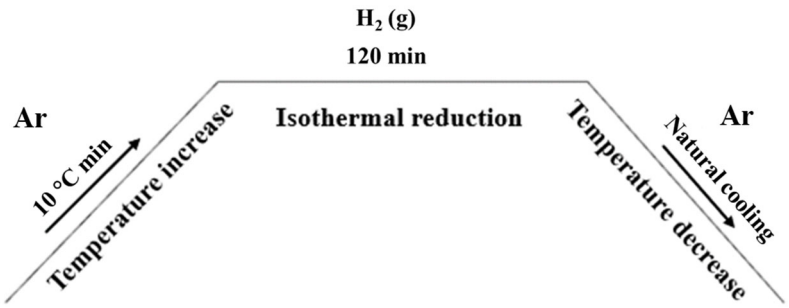

FIG 3 – Heating diagram of H_2 reduction experiment.

Thermal analysis

To simulate a smelting process, samples from sintered and reduced BR were subjected to heat treatment up to 1400°C under inert atmosphere. A single pellet from each hydrogen reduction experiment and the sintered pellet were grinded and sieved to <1 mm in preparation for DTA and TGA analysis. Two hundred milligrams of sample were used for every analysis. Both DTA and TGA analysis were carried out at the same time using LINSEIS™ TG-DTA equipment by putting the sample inside an alumina crucible. It is expected that the surface of alumina crucible which is in contact with the sample might react with the sample, promoting reactions with alumina as reactant or hindering reactions with alumina as product. However, considering the alumina content in the sample, although quantitative analysis on the result would be inaccurate due to reaction between the sample and the alumina crucible, it should not incur major interference in qualitative analysis. The analysis was carried out under argon flow of 27.8 cc/min for the whole time with heating rate of 20°C/min up to 1000°C and 10°C/min from 1000°C to 1400°C. The sample was cooled naturally inside the furnace with argon flow of 27.8 cc/min.

RESULTS AND DISCUSSION

XRD analysis

XRD analysis for sintered BR pellets and those reduced at 600°C is shown in Figure 4. Major phases in the sintered pellets were Brownmillerite ($Al_{0.441}Ca_2Fe_{1.559}O_5$), Gehlenite ($Al_2Ca_2O_7Si$), Lawsonite ($Al_2CaO_{10}Si_2$), Wollastonite ($CaO_3Si$), Melilite($Ca_{5.95}Na_{2.05}O_{15}Si_4$), Perovskite ($CaTiO_3$) and Hematite ($Fe_2O_3$). Meanwhile major phases in the reduced pellets were Srebrodolskite ($Ca_2[Fe,Al]_2O_5$), Gehlenite ($Al_2Ca_2O_7Si$), Perovskite ($CaTiO_3$), Magnetite (Fe_3O_4), Wüstite (FeO) and metallic iron. Brownmillerite and Srebrodolskite peaks were in similar positions due to their similar chemical composition and both belongs to the Brownmillerite subgroup, but with different crystallography. Based on XRD analysis all the Brownmillerite phase in sintered pellets were transformed into Srebrodolskite during H_2 reduction process. It was also observed that most of the calcium silicate-containing phases in the sintered pellets were absorbed into Gehlenite during H_2 reduction, leaving only Gehlenite as the only calcium silicate-containing phase in reduced pellets.

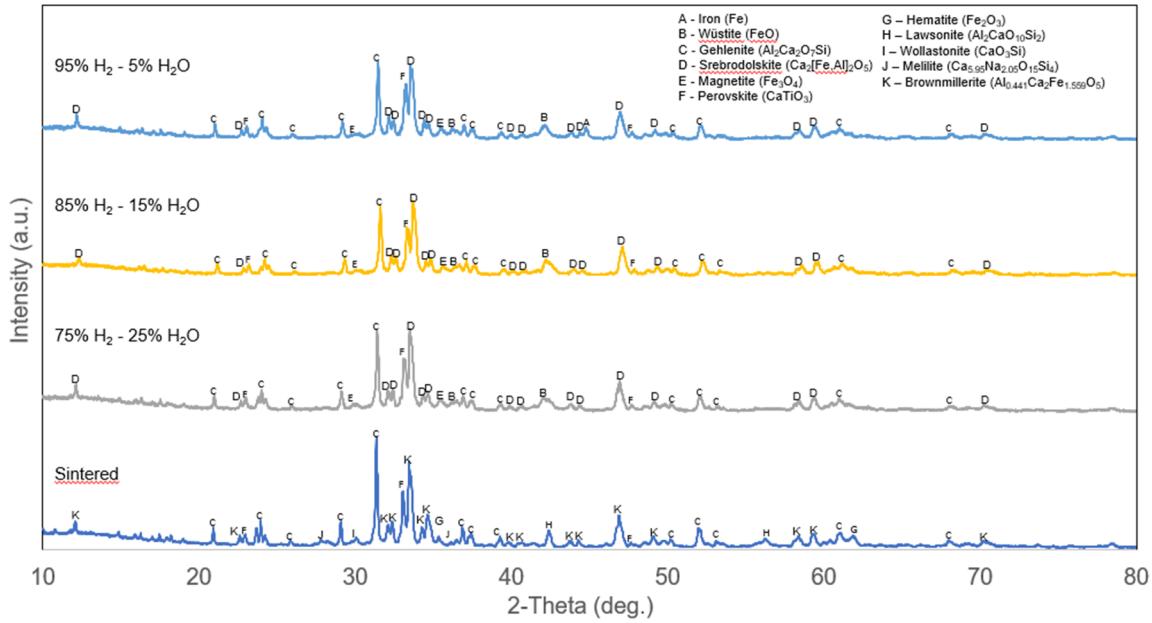

FIG 4 – XRD analysis of sintered BR pellets and pellets reduced at 600°C.

By analysing chemical composition of the phases between sintered pellets and reduced pellets it can be concluded that only iron oxides were reduced during H_2 smelting reduction at 600°C. Magnetite and Wüstite peaks were observed in all the reduced pellets suggesting slow kinetics of the reduction reaction. Meanwhile metallic iron peaks were observed only in pellets reduced with 95 per cent H_2 – 5 per cent H_2O gas composition, suggesting that the equilibrium for reduction of metallic iron at 600°C exists between 85 per cent to 95 per cent H_2 and 5 per cent to 15 per cent H_2O gas composition.

DTA analysis

DTA analysis for sintered and reduced BR pellets is shown on Figure 5. There are 12 temperature points of interests which are signified by occurrence of troughs in DTA curves.

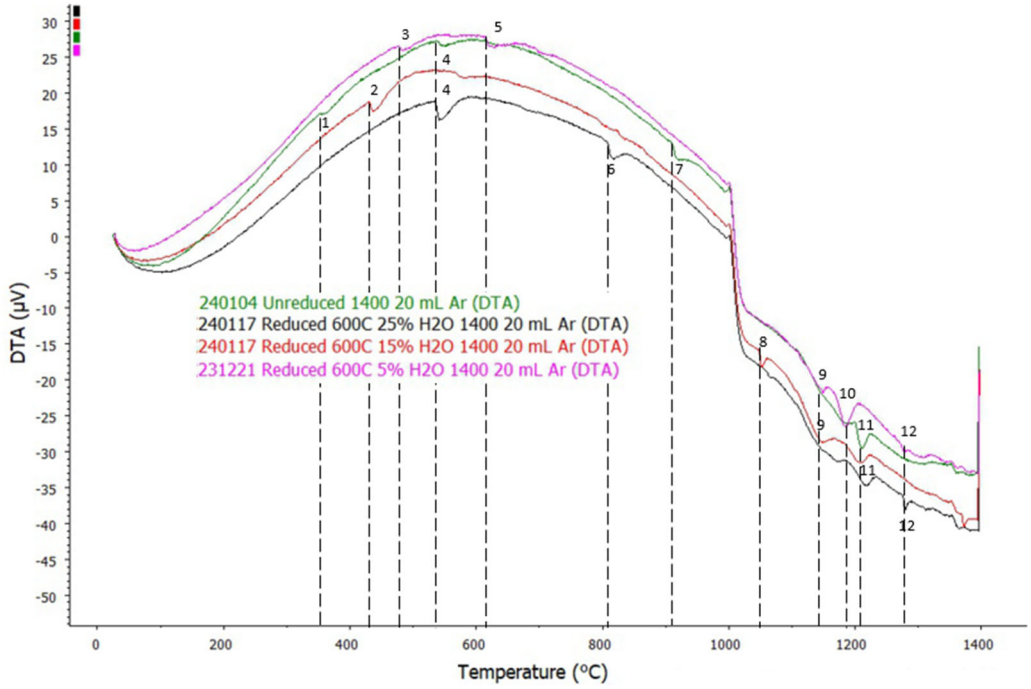

FIG 5 – DTA analysis of sintered BR pellets and pellets reduced at 600°C.

Phase equilibrium module of Factsage™ 8.1 was used to analyse and simulate melting process of sintered and reduced pellets. The simulation for sintered pellets was done based on chemical composition of XRF analysis for sintered pellets as shown in Table 3 in a basis of 100 g total mass. Whereas for simulation of reduced pellets 10 mol per cent and 5 mol per cent of initial Hematite composition in sintered pellets were converted into Wüstite and Magnetite, respectively. Amount of Wüstite and Magnetite for simulation of reduced pellets was estimated based on XRD result of BR pellets reduced at 600°C with 95 per cent H_2 – 5 per cent H_2O gas composition. Components input for simulation of reduced pellets is shown in Table 5.

TABLE 5

Components input for simulation of reduced BR pellets using Factsage™ 8.1.

Component	Mass (gr)	Component	Mass (gr)	Component	Mass (gr)
CaO	29.01	MnO	0.04	P_2O_5	0.12
MgO	0.37	Cr_2O_3	0.18	SO_3	1.03
SiO_2	7.66	V_2O_5	0.15	ZrO_2	0.11
Al_2O_3	23.12	TiO_2	3.87	SrO	0.03
Fe_2O_3	25.94	NiO	0.06	Co_3O_4	0.02
Fe_3O_4	1.48	Na_2O	3.61	**Total**	**99.65**
FeO	2.75	K_2O	0.10		

The simulation was done from 300°C to 1400°C to investigate the temperature points of interests in the DTA curves. Resulting Factsage™ 8.1 phase equilibrium simulation for sintered pellets is shown on Figure 6 and result of simulation for reduced pellets is shown on Figure 7.

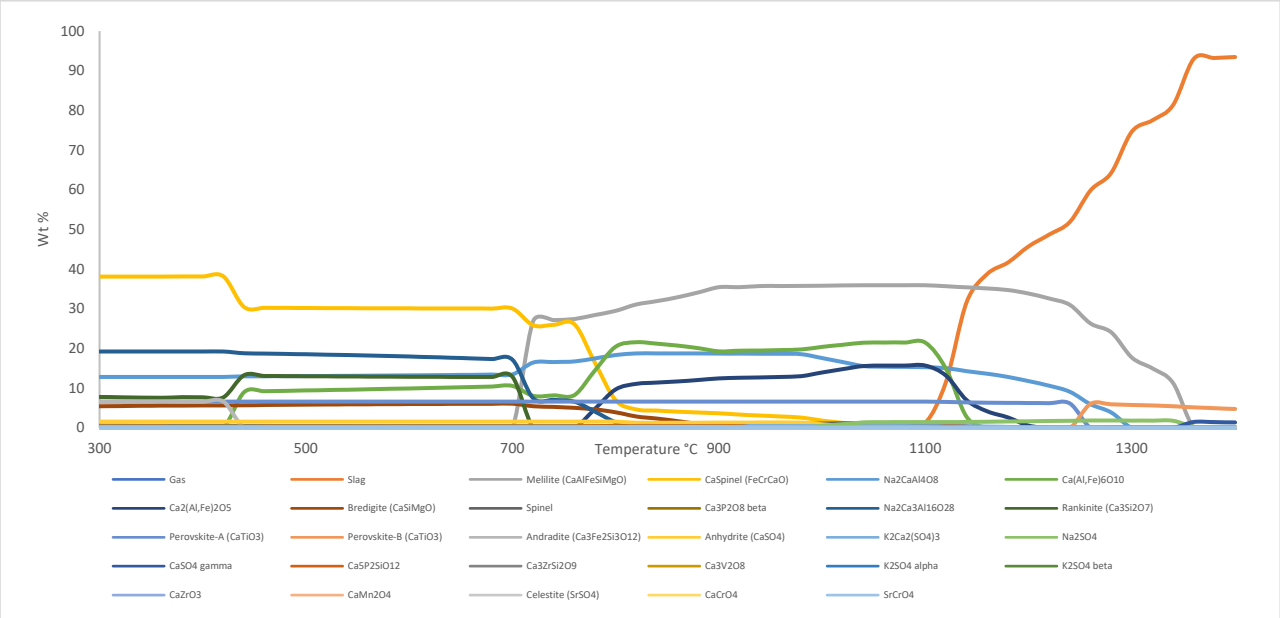

FIG 6 – Phase equilibrium simulation of sintered BR pellets from 300°C to 1400°C.

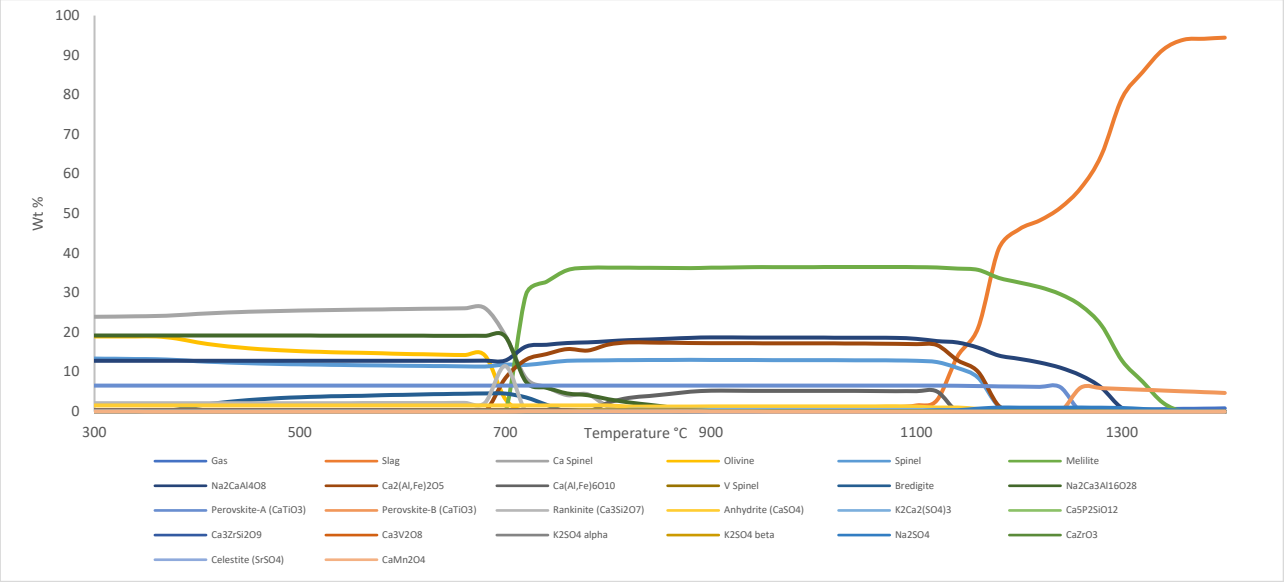

FIG 7 – Phase equilibrium simulation of reduced BR pellets from 300°C to 1400°C.

The first temperature point of interest occurred at T ≈ 350°C was signified by occurrence of a small trough in DTA curve of sintered (unreduced) pellet. Based on Factsage™ 8.1 simulation, $Ca_5P_2SiO_{12}$ breaks down into tricalcium phosphate-β (CaP_2O_8) on the first temperature point of interest which is at T ≈ 350°C. It is proposed that excess calcia and silicon from the reaction immediately dissolved into either Bredigite ($Ca_7Si_4MgO_{16}$) or Rankinite ($Ca_3Si_2O_7$) in the system. The reaction that occurred on this temperature is shown in Equation (5):

$$Ca_5P_2SiO_{12} \rightarrow CaP_2O_8 + 4 \cdot CaO + Si \quad (5)$$

Tricalcium phosphate-β is an unstable phase and based on the simulation its reverse reaction occurs at T ≈ 460°C, which is evidenced by occurrence of crest starting from T ≈ 470°C on the DTA curve of sintered sample.

The second temperature point of interest occurred at T ≈ 425°C where a trough occurred on DTA curve of the sample reduced with 85 per cent H_2 – 15 per cent H_2O gas composition. Formation of Bredigite from part of Olivine phase in the sample is supposed to occur around this temperature based on the simulation of sintered pellets. It is possible that olivine reacted with free CaO in the system to form Bredigite with excess magnesium oxide or iron oxide as shown in Equation (6):

$$7 \cdot CaO + 4 \cdot (Mg,Fe)_2SiO_4 \rightarrow Ca_7Si_4MgO_{16} + 3 \cdot (Mg,Fe)O \quad (6)$$

The third temperature point of interest at T ≈ 475°C is signified by occurrence of trough on DTA curve of sample reduced with 95 per cent H_2 – 5 per cent H_2O gas composition. Based on the simulation of reduced pellets a brief formation of Vanadium rich spinel occurred at T ≈ 480°C, however, it immediately breaks at T ≈ 500°C which explains the occurrence of trough at this temperature.

The fourth temperature point of interest at T ≈ 540°C is signified by occurrence of trough on DTA curve of the sintered sample and sample reduced with 75 per cent H_2 – 25 per cent H_2O gas composition. There was another nearby trough occurrence as well on the samples reduced with 85 per cent H_2 – 15 per cent H_2O and 95 per cent H_2 – 5 per cent H_2O gas composition, which suggests the same reaction is happening on all samples. Based on the simulation results of both sintered and reduced samples, transformation of potassium sulfate-α (K_2SO_4-α) into potassium sulfate-β (K_2SO_4-β) occurred around this temperature. The reaction is shown in Equation (7):

$$K_2SO_4\text{-}\alpha \rightarrow K_2SO_4\text{-}\beta \quad (7)$$

The fifth temperature point of interest is at T ≈ 620°C, which is signified by occurrence of trough on DTA curve of sample reduced with 95 per cent H_2 – 5 per cent H_2O gas composition. Considering its close proximity with the previous temperature point of interest and the sample is the only one with significant difference in chemical composition compared to other reduced samples, where it is the only one containing metallic Fe. There is a probability that the same reaction occurred where

potassium sulfate-α (K_2SO_4-α) transformed into potassium sulfate-β (K_2SO_4-β) since there is no other change occurred in the simulation around 620°C.

The sixth temperature point of interest at T ≈ 810°C is signified by the occurrence of trough on samples reduced with 75 per cent H_2 – 25 per cent H_2O and 85 per cent H_2 – 15 per cent H_2O gas composition. From the simulation of sintered samples it was observed that significant formation of calcium alumino ferrite ($Ca[Al,Fe]_6O_{10}$) and Rankinite occurred around this temperature. It is believed that part of Ca-rich spinel in the sample reacted with Andradite ($Ca_3Fe_2Si_3O_{12}$) and CaO in the system to form calcium alumino ferrite and Rankinite as shown in Equation (8):

$$3 \cdot CaO + CaFe_2O_4 + 2 \cdot Ca_3Fe_2Si_3O_{12} \rightarrow Ca(Al,Fe)_6O_{10} + 3 \cdot Ca_3Si_2O_7 \quad (8)$$

The seventh temperature point of interest occurred at T ≈ 920°C, which signified by the occurrence of trough on DTA curve of sintered sample. Based on simulation of sintered sample, Celestite ($SrSO_4$) and $Na_2CaAl_4O_8$ starts to melt around this temperature to form slag phase which may explain the sudden increase in endothermic nature of the system. It is worth noting that Sr content in the sample is quite low hence only a few Sr-containing intermediate phases occurred in the simulation at a very low amount.

The eighth temperature point of interest is at T ≈ 1050°C, which is signified by occurrence of trough on DTA curve of sample reduced with 85 per cent H_2 – 15 per cent H_2O gas composition. Based on the simulation of reduced pellets, formation of sodium sulfate (Na_2SO_4) are supposed to occur around this temperature. It is proposed that $Na_2CaAl_4O_8$ in the system breaks down to form slag and reacts with free SO_3 in the system to form sodium sulfate as shown in Equation (9):

$$SO_3 + Na_2CaAl_4O_8 \rightarrow Na_2SO_4 + 2 \cdot Al_2O_3 + CaO \quad (9)$$

The ninth temperature point of interest at T ≈ 1150°C is signified by the occurrence of trough on DTA curve of sample reduced with 85 per cent H_2 – 15 per cent H_2O and 95 per cent H_2 – 5 per cent H_2O gas composition which are followed by the occurrence of crest soon after, suggesting exothermic reaction occurred on the system. Based on the simulation of reduced sample a significant amount of calcium alumino ferrite and brownmillerite ($Ca_2[Al,Fe]_2O_5$) broke down to form slag around this temperature, which may explain the exothermic nature of the system.

The 10th and 11th temperature point of interest is occurring at T ≈ 1180°C and T ≈ 1220°C, which is evidenced by occurrence of trough on DTA curve of all the samples. The close proximity between these temperatures suggests that a similar event is happening with small difference in chemical composition of the sample reduced with 95 per cent H_2 – 5 per cent H_2O due to presence of metallic iron in it causing the event to occur in a slightly lower temperature compared to others. Based on simulations of both sintered and reduced sample gas phase start to occur around these temperatures. The release of gas phase from solid components is generally exothermic which may explain formation of trough in the DTA system.

The 12th temperature point of interest is at T ≈ 1270°C, which signified by the occurrence of trough on DTA curve of sample reduced with 75 per cent H_2 – 25 per cent H_2O and 95 per cent H_2 – 5 per cent H_2O gas composition. Based on simulation of sintered samples transformation of Perovskite-A into Perovskite-B occurred around this temperature as shown in Equation (10):

$$CaTiO_3\text{-}A \rightarrow CaTiO_3\text{-}B \quad (10)$$

Perovskite-A is a very stable phase which relatively remain unchanged from the beginning up to its transformation Perovskite-B. Meanwhile Perovskite-B is less stable than Perovskite-A and as soon as it formed it starts to slowly break down into slag phase.

Based on the simulation, most of the events occurred at each temperature point of interest should apply to all of the samples, however, due to the heterogenous nature of the sample and small amount of sample used in the analysis (~200 mg) obtaining uniform distribution of element in the sample is almost impossible, which explains why some events occurred in one sample but not on the other albeit similar phase composition based on XRD analysis.

TGA analysis

TGA analysis for sintered and reduced BR pellets is shown on Figure 8.

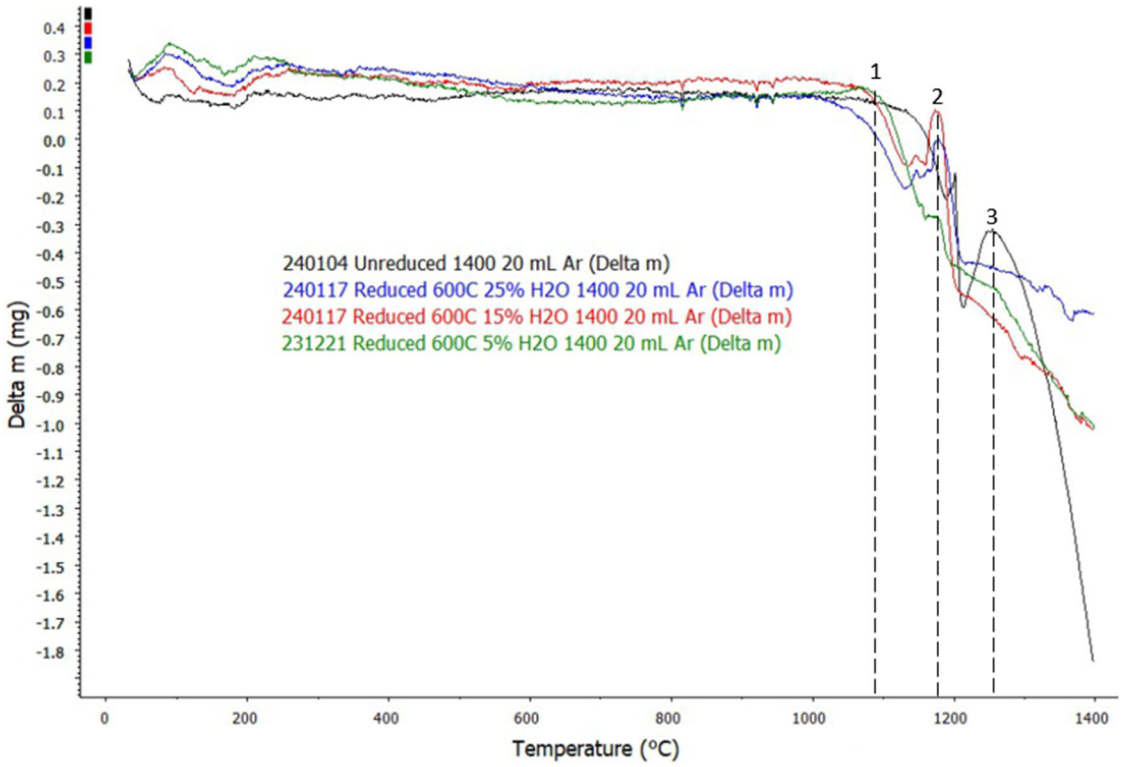

FIG 8 – TGA analysis of sintered BR pellets and pellets reduced at 600°C.

The curves in Figure 8 showed that there are three temperature points of interests where all of them are signified by significant increase in mass loss rate of the samples. All samples, both sintered and reduced, showed the same trend where the first significant increase in mass loss rate occurred at T ≈ 1080°C, followed by the second significant increase in mass loss rate at T ≈ 1180°C and the third significant increase in mass loss rate at T ≈ 1280°C. The same simulation results from Factsage™ 8.1 for sintered and reduced pellets was used to analyse the events happening on same temperature points of interest.

Based on simulation results, liquid slag formation starts to occur at T ≈ 900°C for both sintered and reduced sample, however, the initial amount is really small since only Celestite and small amount of $Ca_5P_2SiO_{12}$ formed the slag at 900°C. At this point the slag consists of mostly CaO, CaS, SrO and SrS which originated from Celestite and $Ca_5P_2SiO_{12}$. It is not until T ≈ 1100°C where the slag starts to pick up iron oxides in the system and increase its amount significantly with increasing temperature. It is proposed that most gases, which are trapped physically in the system are released during this process where larger number of solid phases are getting molten, forming the molten slag phase with lower viscosity and less hold-up potential, subsequently causing the first significant increase in mass loss rate of all systems at the first temperature point of interest which is at T ≈ 1080°C.

The second temperature point of interest is at T ≈ 1180°C which correlates to the DTA curve where a trough which followed by crest occurred at similar temperature, as mentioned previously gas phase start to from around this temperature. To properly analyse composition of gas phase with increasing temperature from 1180°C to 1400°C another simulation was conducted using Factsage™ 8.1 with addition of 10 L of argon gas. Similar to simulation of phase equilibrium, components input for sintered pellets was done based on chemical composition of XRF analysis for sintered pellets as shown in Table 3 in a basis of 100 g total mass and simulation of reduced pellets was done using components input shown in Table 5. Resulting simulation for equilibrium of gas phase composition for sintered pellets is shown on Figure 9 and result of simulation for equilibrium of gas phase composition for reduced pellets is shown on Figure 10.

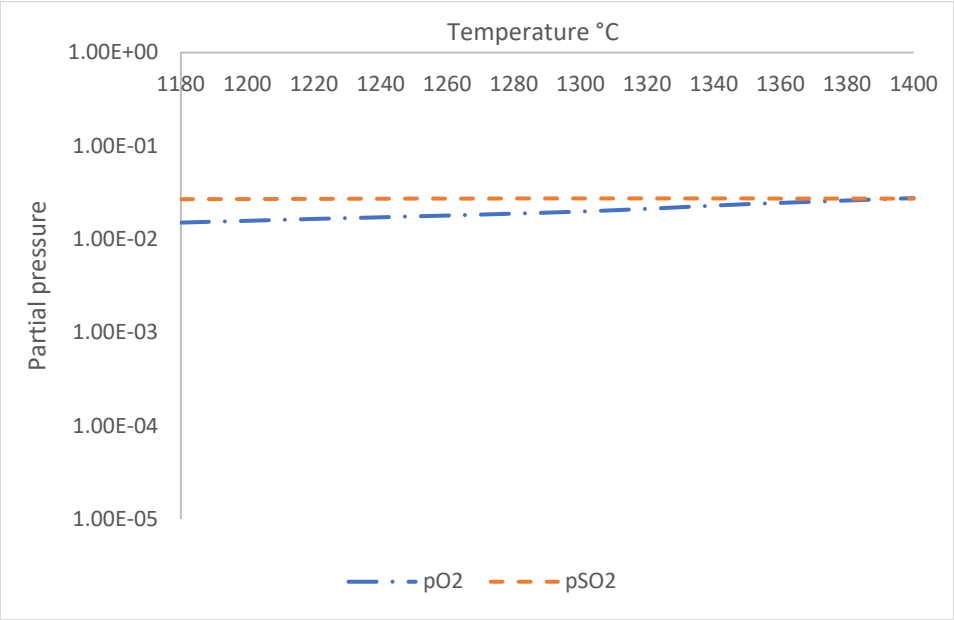

FIG 9 – Equilibrium simulation for gas phase composition of sintered BR pellets from 1180°C to 1400°C.

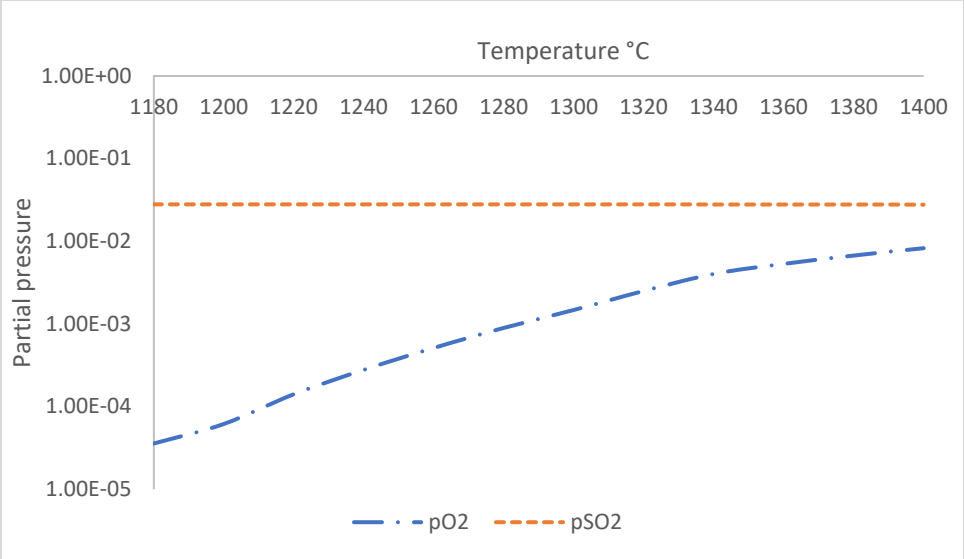

FIG 10 – Equilibrium simulation for gas phase composition of reduced BR pellets from 1180°C to 1400°C.

Based on simulation gas phase that are discharged by both sintered and reduced samples mainly consists of O_2 and SO_2 gas since partial pressure of other gases such as SO, SO_3, Na_2SO_4 and K_2SO_4 are at least lower by two orders compared to either O_2 or SO_2. Simulation for gas phase composition of sintered sample suggests that both O_2 and SO_2 gas are released at T = 1180°C meanwhile for simulation of gas phase composition of reduced sample the discharged gas consists of mostly SO_2 at T = 1180°C since partial pressure of O_2 at this temperature is lower by three orders. The difference in gas phase composition is due to reduced samples has significantly less chemically bonded O_2 since more O_2 has been removed during H_2 reduction leaving more chemically bonded SO_2 to be released into the atmosphere in comparison with O_2.

Based on the phase equilibrium simulation, the amount of gas phase in sintered samples is supposed to increase significantly with increasing temperature starting from T ≈ 1280°C and for reduced samples its amount of gas phase start to increase from T ≈ 1260°C. In correlation, simulation result for gas phase composition of sintered sample showed that partial pressure of O_2 starts to increase more significantly with increasing temperature at T = 1300°C, suggesting that higher

reaction kinetics starts to force higher amount of O_2 gas to be released from the sample despite of oxidative atmosphere due to existing SO_2 gas in the atmosphere, which eventually amplifies gas phase formation with increasing temperature. Simulation result for reduced sample also showed that partial pressure of O_2 is lower by less than one order compared to partial pressure of SO_2 at $T \geq 1320°C$, increasing the likeliness for remaining O_2 in the sample to be discharged into the atmosphere. It is suggested that increased kinetics of gas phase formation and the release of remaining O_2 from the sample are followed by an increase in mass loss rate of the system which explains the third temperature point of interest at $T \approx 1280°C$.

CONCLUSIONS

- Transformation of Brownmillerite into Srebrodolskite and dissolution of calcium silicate-containing phases into Gehlenite occurred during H_2 reduction of BR pellets.
- $Ca_5P_2SiO_{12}$ breaks down into tricalcium phosphate-β (CaP_2O_8), CaO and Silicone at $T \approx 350°C$, however, since tricalcium phosphate-β is an unstable phase, it reverts into $Ca_5P_2SiO_{12}$ at $T \approx 460°C$ which are evidenced by corresponding trough and crest on DTA curve of sintered sample.
- Formation of Bredigite occurred at $T \approx 425°C$ where olivine reacted with CaO to form Bredigite. Significant amount of calcium alumino ferrite and Rankinite were formed at $T \approx 810°C$ which originates from Ca-rich spinel phase in the system. $Na_2CaAl_4O_8$ in the pellet yields molten slag and reacts with free SO_3 in the system to form sodium sulfate at $T \approx 1050°C$.
- Transformation of potassium sulfate-α (K_2SO_4-α) into potassium sulfate-β (K_2SO_4-β) occurred at $T \approx 540°C$ and transformation of Perovskite-A into Perovskite-B occurred at $T \approx 1270°C$.
- Initial formation of slag phase for both sintered and reduced pellets occurred at $T = 900°C$ with a small liquid slag formation that contains mostly CaO, CaS, SrO and SrS. Amount of slag phase start to increase significantly with increasing temperature at $T \approx 1100°C$ where it starts to pick up iron oxides in the system which then followed by other oxides dissolution/melting in the system.
- Initial discharge of gas phase from both sintered and reduced pellets occurred at $T \approx 1180°C$ where sintered samples started to release both O_2 and SO_2 gas in the system and reduced samples released SO_2 gas. Amount of gas phase for both samples start to increase significantly with increasing temperature starting from $T \approx 1280°C$ when increased reaction kinetic forces remaining O_2 in the sample to be released into the atmosphere.

ACKNOWLEDGEMENTS

The current research is funded by HARARE project.

REFERENCES

Borra, R C, Blanpain, B, Pontikes, Y, Binnemans, K and Van Gerven, T, 2016. Smelting of Bauxite Residue (Red Mud) in View of Iron and Selective Rare Earths Recovery, *Journal of Sustainable Metallurgy*, 2:28–37.

Brunori, C, Cremisini, C, Massanisso, P, Pinto, V and Torricelli, L, 2005. Reuse of a Treated Red Mud Bauxite Waste: Studies on Environmental Compatibility, *J Hazard Mater*, 117(1):55–63.

Ekstroem, K E, Voll Bugten, A, van der Eijk, C, Lazou, A, Balomenos, E and Tranell, G, 2021. Recovery of Iron and Aluminum from Bauxite Residue by Carbothermic Reduction and Slag Leaching, *Journal of Sustainable Metallurgy*, 7:1314–1326.

Kar, M K, van der Eijk, C and Safarian, J, 2022. Hydrogen Reduction of High Temperature Sintered and Self-Hardened Pellets of Bauxite Residue produced via the Addition of Limestone and Quicklime, *Proceedings of 40th International Conference of ICSOBA*, Athens, Greece, *TRAVAUX* 51, pp 823–833.

Lazou, A, van der Eijk, C, Tang, K, Balomenos, E, Kolbeinsen, L and Safarian, J, 2021. The Utilization of Bauxite Residue with a Calcite-Rich Bauxite Ore in the Pedersen Process for Iron and Alumina Extraction, *Metallurgical and Material Transactions B*, 52B:1265.

Liu, X, Han, Y, He, F, Gao, P and Yuan, S, 2021. Characteristic, Hazard and Iron Recovery Technology of Red Mud – a Critical Review, *Journal of Hazardous Materials*, 420:126542.

Pandey, A K and Prakash, R, 2020. Opportunities for Sustainability Improvement in Aluminum Industry, *Engineering Reports*, e12160.

Samouhos, M, Taxiarchou, M, Pilatos, G, Tsakiridis, P E, Devlin, E and Pissas, M, 2017. Controlled Reduction of Red Mud by H_2 followed by Magnetic Separation, *Minerals Engineering*, 105:36–43.

Skibelid, O B, Velle, S O, Vollan, F, van der Eijk, C, Hosseinpur-Kermani, A and Safarian, J, 2022. Isothermal Hydrogen Reduction of a Lime-Added Bauxite Residue Agglomerate at Elevated Temperatures for Iron and Alumina Recovery, *Materials*, 15:6012.

Smallman, R E and Bishop, R J, 1999. Chapter 10 – Ceramics and Glasses, *Modern Physical Metallurgy and Materials Engineering*, 6th edition, pp 320–350 (Butterworth-Heinemann).

The effect of iron oxide on sulfide capacities of CaO-based molten slags

DOI: 10.62053/QHZQ1288

M Hasegawa[1] and K Saito[2]

1. Associate Professor, Kyoto University, Kyoto 606–8501, Japan.
   Email: hasegawa.masakatsu.7r@kyoto-u.ac.jp
2. Graduate Student, Kyoto University, Kyoto 606–8501, Japan.
   Email: saito.keijiro.x38@kyoto-u.jp

ABSTRACT

Removing sulfur and phosphorus from molten iron can be expressed by the following reactions, respectively.

$$[S]F_e + (O^{2-})_{slag} = (S^{2-})_{slag} + [O]F_e$$

$$[P]F_e + (3/2)\,(O^{2-})_{slag} + (5/2)\,(FeO)_{slag} = (PO_4^{3-})_{slag} + (5/2)\,Fe(liquid)$$

These equations indicate that desulfurisation and dephosphorisation have opposite oxygen potential conditions. If a small amount of desulfurisation slag not removed is carried over to dephosphorisation process, the reaction of sulfur mentioned above proceeds toward left hand resulting in increasing sulfur content in molten iron. For better understanding of such re-sulfurisation reaction in hot metal pre-treatments, the present study aimed at evaluating the effect of iron oxide on the sulfur distribution ratio between slag and hot metal. To measure sulfide capacities and FeO activities simultaneously at temperatures below the melting point of pure iron, CaO-SiO_2-FeO and CaO-Al_2O_3-FeO ternary molten slags were brought into equilibria with copper-iron-sulfur liquid alloys, and the equilibrium oxygen partial pressures were determined with an electrochemical technique involving the stabilised zirconia solid electrolyte. The experimental results showed that the sulfide capacity increased with an increase in FeO content, and this trend was consistent with the fact that FeO was basic. Although the addition of FeO raised the FeO activity and oxygen potential, the calculated value for sulfur distribution ratio between slag and hot metal increased with increasing FeO content.

INTRODUCTION

In hot metal pre-treatments, impurities of sulfur and phosphorus are removed from liquid iron and these reactions are given as follows.

$$[S]F_e + (O^{2-})_{slag} = (S^{2-})_{slag} + [O]F_e \quad (1)$$

$$[P]F_e + (3/2)\,(O^{2-})_{slag} + (5/2)\,(FeO)_{slag} = (PO_4^{3-})_{slag} + (5/2)\,Fe(liquid) \quad (2)$$

Where $[i]F_e$ and $(j)_{slag}$ represent chemical species *i* in liquid iron and *j* in slag, respectively.

According to Equations 1 and 2, it has been well known that the thermochemical conditions for effective desulfurisation are high basicity slag and low oxygen potential, while those for efficient phosphorus removal are high basicity slag and high oxygen potential (high FeO activity). Thus, desulfurisation and dephosphorisation have opposite oxygen potential conditions. When a small amount of desulfurisation slag not removed is carried over to dephosphorisation process, Reaction 1 proceeds toward left hand resulting in increasing sulfur content in hot metal, because FeO in dephosphorisation slag raises oxygen potential. This phenomenon is called re-sulfurisation. On the other hand, FeO is a basic oxide and increases sulfide capacities of slags (Richardson and Fincham, 1954; Pierre and Chipman, 1956; Bronson and Pierre, 1981; Shim and Ban-ya, 1982; Nagabayashi, Hino and Ban-ya, 1990; Nzotta, Sichen and Seetharaman, 1999a, 1999b; Jung, 2003). For better understanding of re-sulfurisation reaction in hot metal pretreatments, it is necessary to clarify the effect of FeO on sulfur distribution ratio between slag and hot metal, L_S, defined by Equation 3, at temperatures lower than the melting point of pure iron:

$$L_S \equiv \frac{(\%S^{2-})_{slag}}{[\%S]_{Fe}} \quad (3)$$

In Equation 3, $(\%S^{2-})_{slag}$ and $[\%S]_{Fe}$ represent mass per cent concentrations of sulfur in slag and liquid iron, respectively.

Sulfide capacity, $C_{S^{2-}}$, is a thermochemical property of slag to hold sulfur as sulfide and is defined based on the following reaction (Fincham and Richardson, 1954; Richardson and Fincham, 1954):

$$(1/2)\ S_2(gas) + (O^{2-})_{slag} = (S^{2-})_{slag} + (1/2)\ O_2(gas) \quad (4)$$

$$C_{S^{2-}} \equiv (\%S^{2-})_{slag} \cdot \frac{{P_{O_2}}^{1/2}}{{P_{S_2}}^{1/2}} = K(4) \cdot \frac{(a_{O^{2-}})_{slag}}{(f_{S^{2-}})_{slag}} \quad (5)$$

where:

P_i is the partial pressure of gaseous specie *i*,

$K(4)$ is the apparent equilibrium constant of Reaction 4

$(a_{O^{2-}})_{slag}$ is the activity of O^{2-}

$(f_{S^{2-}})_{slag}$ is the activity coefficient of S^{2-} in slag

The value for $C_{S^{2-}}$ increases when $(a_{O^{2-}})_{slag}$ is high, ie slag basicity is high and $(f_{S^{2-}})_{slag}$ is low, ie slag contains components with high chemical affinity for sulfur. The relationship between L_S and $C_{S^{2-}}$ can be derived as follows. The equilibrium partial pressure of oxygen between slag and liquid iron is fixed by:

$$Fe(liquid) + (1/2)\ O_2(gas) = (FeO)_{slag} \quad (6)$$

$$K(6) = \frac{(a_{FeO})_{slag}}{a_{Fe} \cdot {P_{O_2}}^{1/2}} \quad (7)$$

Where $(a_{FeO})_{slag}$ and a_{Fe} represent the activities of FeO in slag and iron, respectively. The dissolution of gaseous diatomic sulfur into liquid iron is given as:

$$(1/2)\ S_2(gas) = [S]F_e \quad (8)$$

$$K(8) = \frac{[f_S]_{Fe} \cdot [\%S]_{Fe}}{{P_{S_2}}^{1/2}} \quad (9)$$

In Equation 9, $[f_S]_{Fe}$ is the Henrian activity coefficient of sulfur in liquid iron. Combining Equations 3, 5, 7 and 9, we obtain:

$$L_S = C_{S^{2-}} \cdot {P_{O_2}}^{-1/2} \cdot \frac{[f_S]_{Fe}}{K(8)} = C_{S^{2-}} \cdot \frac{K(6) \cdot a_{Fe}}{(a_{FeO})_{slag}} \cdot \frac{[f_S]_{Fe}}{K(8)} \quad (10)$$

The values for $C_{S^{2-}}$ have been reported in the CaO-FeO based slags. However, there is still lack of the data at temperatures in hot metal pretreatments. It could be also pointed out here that, when $C_{S^{2-}}$ of FeO-containing slag is measured with the gas-slag equilibrium method based on Equation 4, the oxygen partial pressure, P_{O_2}, should be higher than the equilibrium value between Fe and FeO in order to avoid reducing FeO to form metallic Fe. Such an experimental condition would result in an increase in trivalent iron and then a decrease in slag basicity.

Based on the considerations above, this study aimed at determining $C_{S^{2-}}$ and FeO activities, $(a_{FeO})_{slag}$, in the CaO-SiO_2-FeO and CaO-Al_2O_3-FeO ternary slags under the oxygen partial pressure close to the equilibrium value between Fe and FeO. For this purpose, firstly, the activity coefficients of S and Fe in Cu-Fe-S liquid alloy were determined in order to be used as a reference metal. Subsequently the equilibrium oxygen partial pressures between slag and Cu-Fe-S liquid alloy were measured with an electrochemical technique involving the stabilised zirconia solid electrolyte at 1573 K and 1673 K. In this paper, '$\ln$' and '$\log$' represent natural and common logarithms, respectively.

EXPERIMENTAL ASPECTS

Activity coefficient of component in Cu-Fe-S alloy

The experimental apparatus and procedures have been described elsewhere (Matsushita *et al*, 2021). Figure 1a schematically shows the experimental set-up. An alumina container charged with about 0.5 g Cu-Fe-S alloy samples was heated in a mullite reaction tube in which the gas mixtures

of Ar + H_2 + SO_2 were introduced to fix P_{S_2} at 1573 K and 1673 K. The calculation method of the equilibrium partial pressures was based on the conventional thermochemical consideration. The reaction underlying the present experiments is given as:

$$(1/2)\ S_2(gas) = [S]_{Cu} \tag{11}$$

$$K(11) = \frac{[f_S]_{Cu} \cdot [\%S]_{Cu}}{{P_{S_2}}^{1/2}} \tag{12}$$

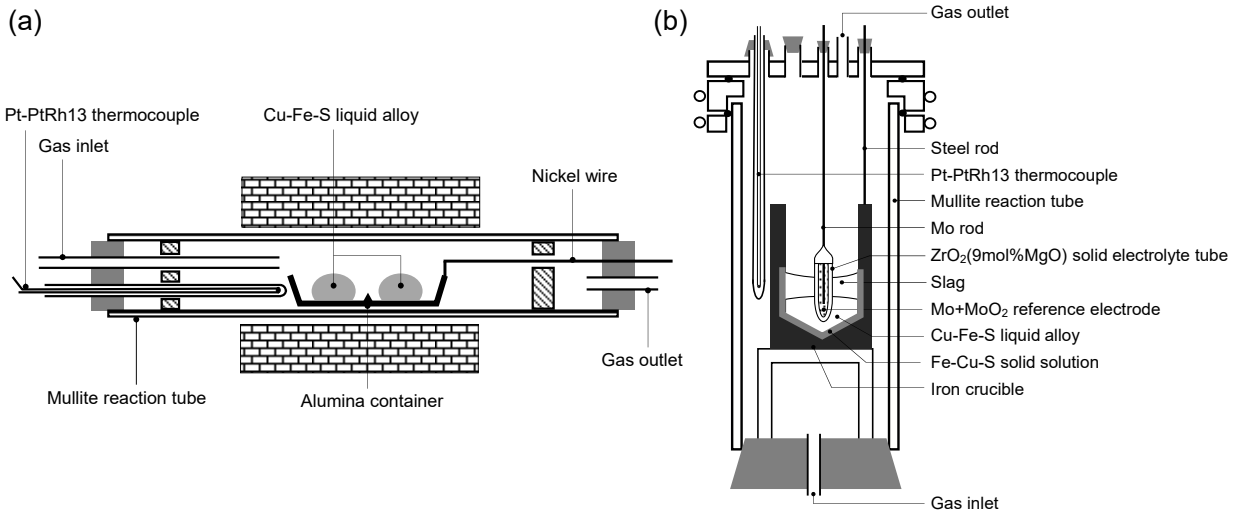

FIG 1 – Experimental apparatus: (a) activity coefficient of component in Cu-Fe-S alloy; (b) sulfide capacity and FeO activity in slag.

$[\%S]_{Cu}$ and $[f_S]_{Cu}$ are the mass content and Henrian activity coefficient of sulfur in Cu-Fe-S liquid alloy. Samples were held at constant temperature under a stream of Ar + H_2 + SO_2 gas mixture for at least seven hours, and then moved to the end of the mullite reaction tube with the aid of a nickel rod for quenching. The sulfur contents in alloy samples were analysed with an inductive-coupled plasma spectrometer (ICP-OES, Optima 5300 DV, PerkinElmer Inc.). It was confirmed that seven hours was long enough for Reaction 11 to reach equilibrium, which was attained from increasing and decreasing sulfur contents in alloy samples. Any unexpected reactions between alloy sample and alumina could not be observed. Temperatures were measured with a Pt-PtRh13 thermocouple placed beside samples and controlled to ±1 K by using a control thermocouple and a PID-type temperature regulator. The overall errors in temperature measurements and control were estimated to be less than ±2 K.

Sulfide capacity and FeO activity in slag

The experimental apparatus has been shown elsewhere (Awaya *et al*, 2023). Figure 1b illustrates the experimental set-up. An iron crucible charged with initial Cu-S alloy and powdery slag sample was heated at 1573 K or 1673 K under a stream of purified argon in a SiC resistance furnace. The gas purification train for argon consisted of silica gel, phosphorus pentoxide and magnesium chips held at 823 K. During heating, iron would dissolve into Cu-S alloy to a small extent resulting in a formation of Cu-Fe-S ternary liquid alloy, while Fe-Cu-S solid solution would form on the inner wall of the iron crucible.

The oxygen cell consisted of a zirconia tube stabilised by 9 mol per cent of magnesia as the solid electrolyte and a Mo + MoO_2 two-phase mixture as the reference electrode. A molybdenum rod was used as an electrical conductor to the reference electrode, while a steel rod soldered to the iron crucible and Cu-Fe-S liquid alloy made electrical contact to the outer electrode of the cell. An oxygen sensor was immersed into Cu-Fe-S liquid alloy to measure the electromotive force (*emf*) between Mo and Fe rods. After the stable value for *emf* could be obtained, the Cu-Fe-S alloy sample was withdrawn by means of a silica sampling tube and the slag sample was collected by immersing an iron rod into the crucible. The iron rod with the molten slag was pulled out of the furnace and cooled rapidly in air. Then, FeO was added into slag to change the concentration of FeO in slag. In CaO-

SiO_2-FeO slags the mole ratio of CaO/SiO_2, X_{CaO}/X_{SiO_2}, was fixed to be 0.53 or 1.1, while the CaO/Al_2O_3 mole ratio, $X_{CaO}/X_{Al_2O_3}$, remained as 2 in CaO-Al_2O_3-FeO slags. *Emf* measurements, collecting samples and adding FeO were repeated during an experimental run.

The open circuit emf, E, of the cell used in this study is given by:

$$E = \frac{RT}{F}\ln\frac{P_{O_2}(ref.)^{1/4}+P_e{}^{1/4}}{P_{O_2}{}^{1/4}+P_e{}^{1/4}} + E_t \qquad \text{(Schmalzried, 1962)} \quad (13)$$

where:

E_t is thermo-*emf* between Mo(+) and Fe(-)

R is the gas constant

T is temperature

F is the Faraday constant

P_e is the oxygen partial pressure at which the ionic and the *n*-type electronic conductivities are equal

$P_{O_2}(ref.)$ represents the oxygen partial pressures at the reference electrode of Mo + MoO_2. Values for these parameters have been reported as:

$$\frac{E_t}{\text{mV}} = -14.69 + 0.0227 \times \left(\frac{T}{\text{K}}\right)$$
(Iwase *et al*, 1984b) (14)

$$\log(P_e/\text{atm}) = +20.40 - 6.45 \times 10^4/(T/\text{K})$$
(Iwase *et al*, 1984a) (15)

$$\log[P_{O_2}(ref.)/\text{atm}] = +8.84 - 30{,}100/(T/\text{K})$$
(Iwase, Yasuda and Mori, 1979) (16)

By using Equations 13 through 16, the equilibrium oxygen partial pressures, P_{O_2}, can be determined between slag and Cu-Fe-S alloy.

The slags were submitted to chemical analysis for sulfur, which was based upon conventional combustion method using self-made equipment. The concentrations of the other elements in the slag and alloy samples were determined with inductively coupled plasma – optical emission spectroscopy (ICP-OES).

EXPERIMENTAL RESULTS AND DISCUSSION

Activity coefficient of component in Cu-Fe-S alloy

Equation 12 can be rewritten as:

$$\log[\%S]_{Cu} = (1/2)\log P_{S_2} - \log[f_S]_{Cu} + \log K(11) \quad (17)$$

Where $[\%i]_{Cu}$ represents the mass content of *i* in Cu-Fe-S liquid alloy. Equation 17 indicates that, when the Henrian activity coefficient of S in Cu-Fe liquid alloy, $[f_S]_{Cu}$, is constant at infinite dilute solution of sulfur, a plot of $\log[\%S]_{Cu}$ against $\log P_{S_2}$ is linear with a slope of $1/2$ and an intercept of $-\log[f_S]_{Cu} + \log K(11)$. Such plots at 1573 K and 1673 K are shown in Figure 2. As seen in this figure, a linear relation could be observed at a constant temperature and a fixed $[\%Fe]_{Cu}/[\%Cu]_{Cu}$ mass ratio, and the slope of each line was close to $1/2$. When the standard state of S in Cu-Fe liquid alloy is taken to be S in molten Cu at 1 mass per cent solution, $[f_S]_{Cu}$ in Cu-S alloy ($[\%Fe]_{Cu} = 0$) is unity and the intercept of the regression line corresponds to $\log K(11)$. Therefore, from the intercepts of the regression lines for Cu-S alloys, the values for $\log K(11)$ were determined as follows:

$$\log K(11) = 2.74 \pm 0.03 \qquad \text{at 1573 K} \quad (18)$$

$$\log K(11) = 2.55 \pm 0.01 \qquad \text{at 1673 K} \quad (19)$$

$$\Delta G°(11) = G_S(1\%\ \text{S in Cu}) - (1/2)G_{S_2} = -RT\ \ln K(11) \quad (20)$$

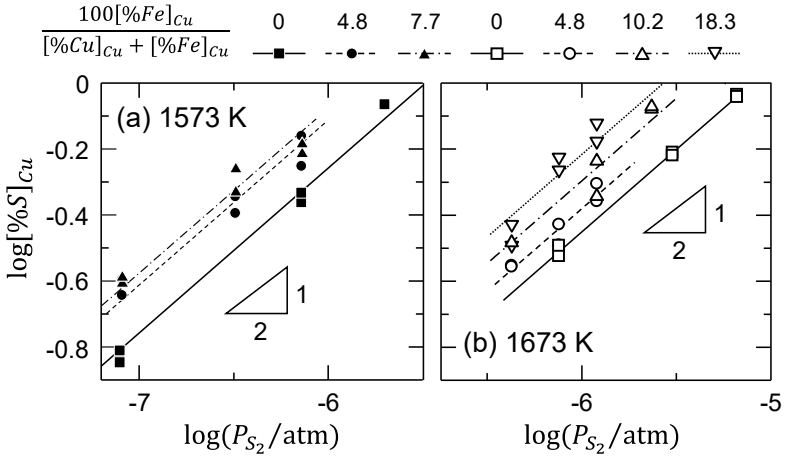

FIG 2 – Relation between $\log[\%S]_{Cu}$ in Cu-Fe-S liquid alloy and $\log P_{S_2}$.

Figure 3 shows that the present results of $\Delta G°(11)$ plotted against temperature were in good agreement with those reported by Alcock (1958) and Ohta, Kubo and Morita (2003) and were not inconsistent with the other literature data (Umetsu, 1950; Yagihashi and Sato, 1962; Sigworth and Elliott, 1974a).

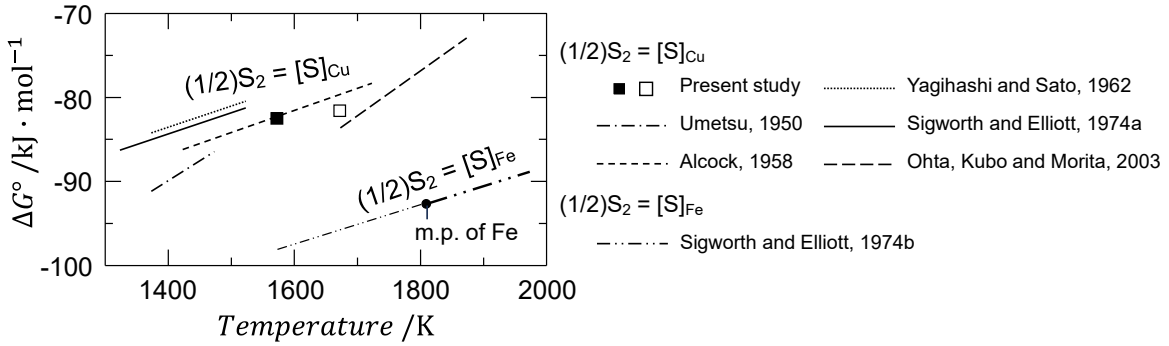

FIG 3 – Standard Gibbs energy change of the dissolution of gaseous sulfur into liquid metal.

Combining Equations 17 to 19, we have:

$$\log[\%S]_{Cu} = (1/2)\log P_{S_2} - \log[f_S]_{Cu} + 2.74 \pm 0.03 \quad \text{at 1573 K} \tag{21}$$

$$\log[\%S]_{Cu} = (1/2)\log P_{S_2} - \log[f_S]_{Cu} + 2.55 \pm 0.01 \quad \text{at 1673 K} \tag{22}$$

Substituting values for the intercepts of the regression lines into Equations 21 and 22, $\log[f_S]_{Cu}$ could be derived. Figure 4 shows $\log[f_S]_{Cu}$ plotted against $[\%Fe]_{Cu}$ with the Cu-Fe binary phase diagram (Okamoto, 2010). As seen in this figure, $\log[f_S]_{Cu}$ decreased with an increase in iron content. The standard Gibbs energy change of the dissolution of gaseous sulfur into liquid Fe, $\Delta G°(8)$, has been reported as follows and is also illustrated in Figure 3:

$$\Delta G°(8) = G_S(1\%\ \text{S in Fe}) - (1/2)G_{S_2} \tag{23}$$

$$\Delta G°(8)/\text{J} \cdot \text{mol}^{-1} = -135100 + 23.43 \times (T/\text{K}) \quad \text{(Sigworth and Elliott, 1974b)} \tag{24}$$

By extrapolating $\Delta G°(8)$ to temperature below the melting point of pure iron, it could be considered that $\Delta G°(8)$ is lower than $\Delta G°(11)$. This is consistent with the negative value for $\log[f_S]_{Cu}$, because both properties indicate that the chemical affinity between Fe and S is stronger than that between Cu and S.

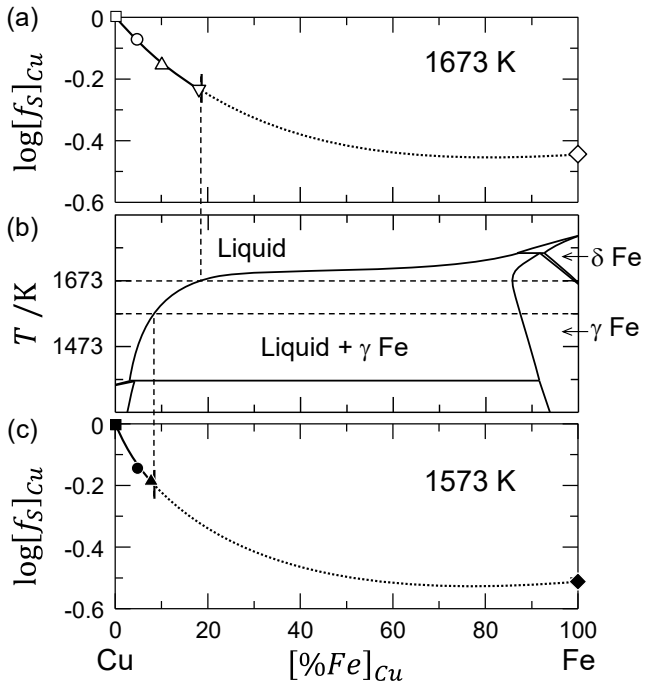

FIG 4 – (a) Henrian activity coefficient of sulfur in Cu-Fe-S liquid alloy at 1673 K; (b) Cu-Fe binary phase diagram (Okamoto, 2010); (c) Henrian activity coefficient of sulfur in Cu-Fe-S liquid alloy at 1573 K.

When the standard state is taken to be S in molten Cu at $[\%S]_{Cu} = 1$, the Henrian activity coefficient of S in liquid Fe at $[\%S]_{Fe} = 1$ is given by:

$$RT \ln[f_S]_{Fe} = G_S(1\%\ \text{S in Fe}) - G_S(1\%\ \text{S in Cu}) = \Delta G°(8) - \Delta G°(11) \quad \text{at } [\%S]_{Fe} = 1 \tag{25}$$

By inserting Equations 18, 19 and 24 into Equation 25, the Henrian activity coefficient of S in hypothetical liquid Fe, $[f_S]_{Fe}$, can be calculated as follows, and they are plotted on Figures 4a and 4c:

$$\log[f_S]_{Fe} = -0.52 \quad \text{at 1573 K} \tag{26}$$

$$\log[f_S]_{Fe} = -0.44 \quad \text{at 1673 K} \tag{27}$$

By connecting smoothly the present experimental results and $\log[f_S]_{Fe}$ given in Equations 26 and 27, the relations between $\log[f_S]_{Cu}$ at definite dilute sulfur concentration and $[\%Fe]_{Cu}$ in hypothetical homogeneous Cu-Fe liquid alloys at 1573 K and 1673 K can be drawn by dotted curves in Figures 4a and 4c, respectively. In this paper, the following quadratic formulae can be recommended tentatively:

$$\log[f_S]_{Cu} = -3.18 \times 10^{-2} \times [\%Fe]_{Cu} + 8.90 \times 10^{-4} \times {[\%Fe]_{Cu}}^2 \quad \text{at 1573 K} \tag{28}$$

$$\log[f_S]_{Cu} = -1.67 \times 10^{-2} \times [\%Fe]_{Cu} + 2.23 \times 10^{-4} \times {[\%Fe]_{Cu}}^2 \quad \text{at 1673 K} \tag{29}$$

When the standard state of iron in Cu-Fe-S liquid alloy is taken to be pure solid iron, the activity coefficient of iron, $[\gamma_{Fe}]_{Cu}$, is formulated by:

$$\ln[\gamma_{Fe}]_{Cu} = \ln[\gamma_{Fe}°]_{Cu} + \varepsilon_{Fe}^{Fe} \cdot [X_{Fe}]_{Cu} + \rho_{Fe}^{Fe} \cdot {[X_{Fe}]_{Cu}}^2 + \varepsilon_{Fe}^{S} \cdot [X_S]_{Cu} \tag{30}$$

Where $[X_i]_{Cu}$ is the mole fraction of *i*, ε_i^j and ρ_i^j are the first- and second-order interaction parameters in liquid copper. In Equation 30, $[\gamma_{Fe}°]_{Cu}$ represents the activity coefficient of iron when the iron activity obeys Henry's law and is obtainable by using the standard Gibbs energy change of the dissolution of iron into molten copper as follows:

$$\text{Fe(pure solid)} = [\text{Fe}]_{\text{Cu}} \tag{31}$$

$$\Delta G°(31)/\text{J} \cdot \text{mol}^{-1} = 54270 - 47.45 \times (T/\text{K}) = -RT \ln \frac{100 \cdot M_{Cu}}{[\gamma_{Fe}°]_{Cu} \cdot M_{Fe}}$$

(Sigworth and Elliott, 1974a) (32)

Where M_i is the atomic weight of *i*; $M_{Fe} = 55.847$ and $M_{Cu} = 63.546$. Based on Equation 32 and the literature data on $[\gamma_{Fe}]_{Cu}$ (Taniguchi, Morita and Sano, 1997; Hasegawa, Wakimoto and Iwase, 2002), the values for $[\gamma_{Fe}^{\circ}]_{Cu}$, ε_{Fe}^{Fe} and ρ_{Fe}^{Fe} can be estimated as follows:

$$\ln[\gamma_{Fe}^{\circ}]_{Cu} = 2.92 \qquad \text{at 1573 K} \qquad (33)$$

$$\varepsilon_{Fe}^{Fe} = -6.88 \qquad \text{at 1573 K} \qquad (34)$$

$$\rho_{Fe}^{Fe} = 0 \qquad \text{at 1573 K} \qquad (35)$$

$$\ln[\gamma_{Fe}^{\circ}]_{Cu} = 2.76 \qquad \text{at 1673 K} \qquad (36)$$

$$\varepsilon_{Fe}^{Fe} = -9.48 \qquad \text{at 1673 K} \qquad (37)$$

$$\rho_{Fe}^{Fe} = 14.36 \qquad \text{at 1673 K} \qquad (38)$$

Equations 28 and 29 indicate that the first-order interaction coefficients, e_S^{Fe}, at 1573 K and 1673 K are -3.18×10^{-2} and -1.67×10^{-2}, respectively. Therefore, the values for ε_{Fe}^{S} can be derived as:

$$\varepsilon_{Fe}^{S} = \varepsilon_{S}^{Fe} = 230 \cdot \frac{M_{Fe}}{M_{Cu}} \cdot (-3.18 \times 10^{-2}) + \frac{M_{Cu} - M_{Fe}}{M_{Cu}} = -6.29 \qquad \text{at 1573 K} \qquad (39)$$

$$\varepsilon_{Fe}^{S} = \varepsilon_{S}^{Fe} = 230 \cdot \frac{M_{Fe}}{M_{Cu}} \cdot (-1.67 \times 10^{-2}) + \frac{M_{Cu} - M_{Fe}}{M_{Cu}} = -3.25 \qquad \text{at 1673 K} \qquad (40)$$

Then, inserting Equations 33 to 40 into Equation 30, the formulae of $[\gamma_{Fe}]_{Cu}$ are given as follows:

$$\ln[\gamma_{Fe}]_{Cu} = 2.92 + (-6.88) \cdot [X_{Fe}]_{Cu} + (-6.29) \cdot [X_S]_{Cu} \qquad \text{at 1573 K} \qquad (41)$$

$$\ln[\gamma_{Fe}]_{Cu} = 2.76 + (-9.48) \cdot [X_{Fe}]_{Cu} + 14.36 \cdot [X_{Fe}]_{Cu}^{\,2} + (-3.25) \cdot [X_S]_{Cu} \qquad \text{at 1673 K} \qquad (42)$$

Sulfide capacity and FeO activity in slag

Substituting Equation 12 into Equation 5, we have:

$$C_{S^{2-}} = (\%S^{2-})_{slag} \cdot P_{O_2}^{\,1/2} \cdot \frac{K(11)}{[fS]_{Cu} \cdot [\%S]_{Cu}} \qquad (43)$$

Equations 28, 29 and 43 indicate that $C_{S^{2-}}$ can be determined by using the measured values for $(\%S^{2-})_{slag}$, $[\%S]_{Cu}$, $[\%Fe]_{Cu}$ and P_{O_2}. The experimental results are summarised in Table 1.

Figures 5a and 5b show the logarithmic value for $C_{S^{2-}}$ plotted against the mole fraction of FeO, $(X_{FeO})_{slag}$, in CaO-SiO_2-FeO slag at 1573 K and at 1673 K, respectively. The value for $C_{S^{2-}}$ increased with an increase in the CaO/SiO_2 mole ratio at a fixed $(X_{FeO})_{slag}$ and a constant temperature. The present result that $C_{S^{2-}}$ increased with an increase in $(X_{FeO})_{slag}$ was consistent with what was reported in the literatures based on FeO being a basic oxide (Richardson and Fincham, 1954; Pierre and Chipman, 1956; Bronson and Pierre, 1981; Shim and Ban-ya, 1982; Nagabayashi, Hino and Ban-ya, 1990; Nzotta, Sichen and Seetharaman, 1999a, 1999b; Jung, 2003). Figures 5a and 5b also show the values for $\log C_{S^{2-}}$ calculated by using the prediction model (Nzotta, Sichen and Seetharaman, 1999b). Although the parameters in this model were optimised by the data in a temperature range of 1673 K to 1923 K, the present experimental results at 1573 K and 1673 K were not inconsistent with the calculated values.

TABLE 1

Experimental results of sulfide capacity and FeO activity.

$(X_{FeO})_{slag}$	$\log\left(\frac{P_{O_2}}{\text{atm}}\right)$	$(\%S^{2-})_{slag}$	$[\%S]_{Cu}$	$[\%Fe]_{Cu}$	$\log C_{S^{2-}}$	$(a_{FeO})_{slag}$	$\log L_S$
CaO-SiO_2-FeO, 1573 K, $X_{CaO}/X_{SiO_2} = 0.53$							
0.212	-11.49	0.094	0.339	9.56	-3.34	0.310	-0.831
0.411	-11.17	0.147	0.264	9.86	-2.87	0.455	-0.531
0.437	-10.96	0.161	0.200	9.61	-2.61	0.578	-0.375
0.546	-10.78	0.194	0.112	9.38	-2.19	0.718	-0.048
CaO-SiO_2-FeO, 1573 K, $X_{CaO}/X_{SiO_2} = 1.1$							
0.202	-11.19	0.239	0.610	9.22	-3.05	0.415	-0.667
0.449	-10.87	0.182	0.163	10.98	-2.41	0.659	-0.229
0.478	-10.81	0.206	0.156	11.83	-2.29	0.717	-0.150
0.475	-10.79	0.201	0.139	10.78	-2.25	0.729	-0.119
0.552	-10.75	0.172	0.087	10.80	-2.10	0.761	0.014
CaO-SiO_2-FeO, 1673 K, $X_{CaO}/X_{SiO_2} = 0.53$							
0.270	-10.48	0.058	0.245	11.42	-3.16	0.291	-0.826
0.425	-9.90	0.162	0.202	11.74	-2.33	0.573	-0.297
0.768	-9.55	0.179	0.048	9.62	-1.51	0.820	0.366
CaO-SiO_2-FeO, 1673 K, $X_{CaO}/X_{SiO_2} = 1.1$							
0.213	-10.29	0.088	0.423	20.41	-3.03	0.411	-0.850
0.290	-10.01	0.156	0.401	19.32	-2.63	0.559	-0.580
0.409	-9.88	0.236	0.286	18.84	-2.24	0.650	-0.257
0.361	-9.96	0.178	0.385	23.07	-2.50	0.630	-0.505
0.473	-9.84	0.198	0.201	20.92	-2.13	0.705	-0.181
0.560	-9.81	0.186	0.127	20.59	-1.94	0.730	-0.011
CaO-Al_2O_3-FeO, 1573 K, $X_{CaO}/X_{Al_2O_3} = 2$							
0.229	-11.40	0.182	0.169	8.57	-2.72	0.335	-0.246
0.682	-10.83	0.501	0.171	7.94	-2.01	0.628	0.190
0.313	-11.45	0.633	0.197	8.68	-2.27	0.316	0.230
0.616	-10.90	0.472	0.133	7.71	-1.97	0.575	0.272
0.521	-11.04	0.559	0.183	8.30	-2.09	0.500	0.208
0.417	-11.19	0.599	0.208	8.32	-2.19	0.420	0.183
0.371	-11.21	0.251	0.096	9.34	-2.23	0.432	0.136

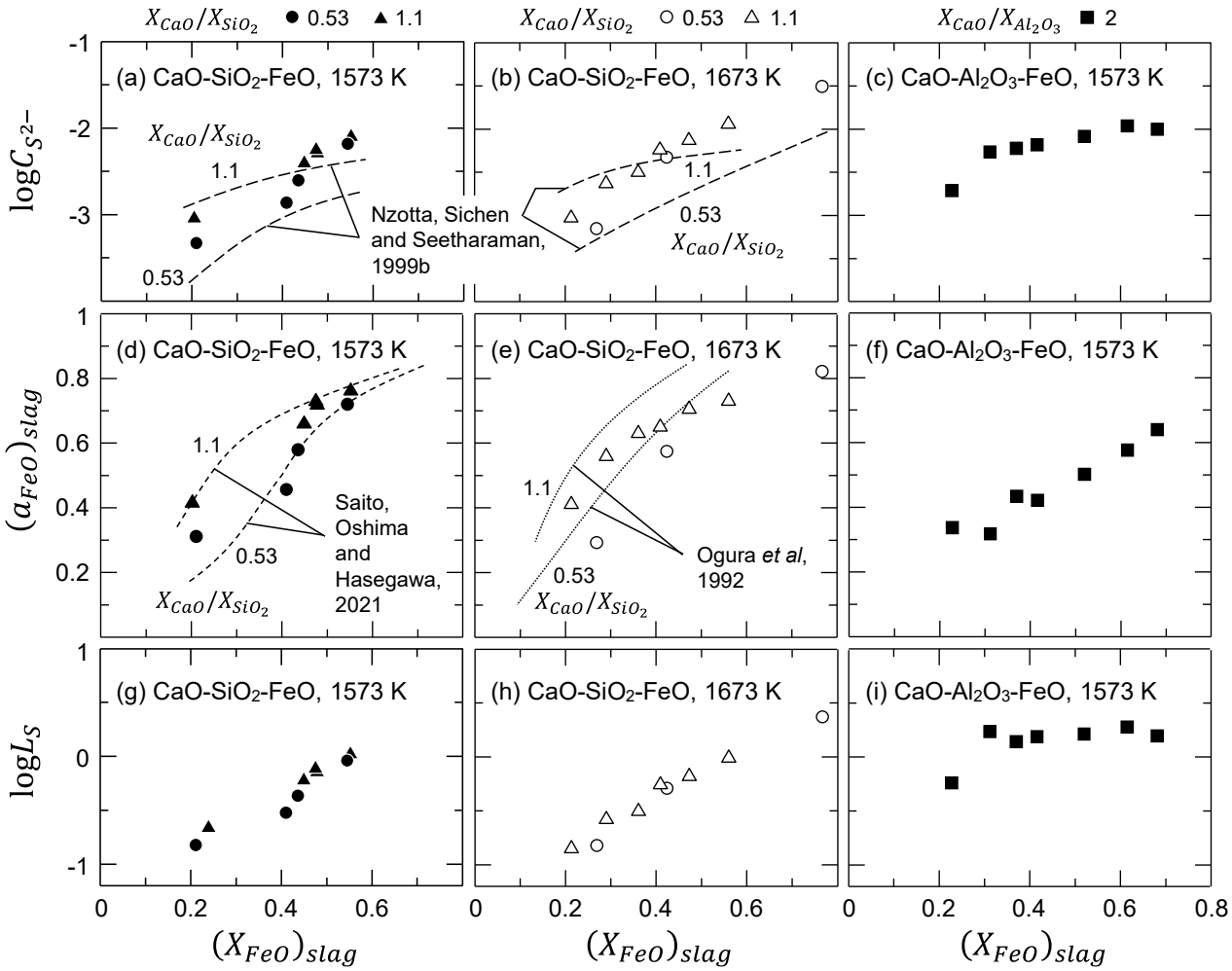

FIG 5 – Experimental and calculation results at 1573 K and 1673 K: (a) to (c) logarithmic value of sulfide capacity; (d) to (f) FeO activity; (g) to (i) logarithmic value of sulfur distribution ratio between slag and hot metal.

The comparisons of the present results with the literature data were conducted in Figures 6a and 6b. In the CaO-SiO_2-FeO ternary slags of the same CaO/SiO_2 mole ratio and $(X_{FeO})_{slag}$, the present values for $C_{S^{2-}}$ measured at 1573 K and 1673 K were agreement with those at higher temperatures (Nzotta, Sichen and Seetharaman, 1999b). It could be concluded that $C_{S^{2-}}$ in the CaO-SiO_2-FeO ternary slag decreased with an increase in reciprocal temperature. This agrees with the knowledge that the desulfurisation reaction proceeds more easily at higher temperatures. Figures 6a and 6b also show $C_{S^{2-}}$ for the CaO-SiO_2-MgO (Nzotta *et al*, 1997), CaO-SiO_2-$AlO_{1.5}$ (Fincham and Richardson, 1954; Abraham and Richardson, 1960; Berryman, Sommerville and Ishii, 1988; Drakaliysky, Sichen and Seetharaman, 1997) or CaO-SiO_2-CaF_2 (Uo *et al*, 1989; Ferguson and Pomfret, 1989) ternary liquid slags which contains MgO, $AlO_{1.5}$ or CaF_2 at the same concentration as FeO in the CaO-SiO_2-FeO ternary slag. As seen in this figure, replacing MgO, $AlO_{1.5}$ or CaF_2 with FeO at a fixed CaO/SiO_2 mole ratio raises $C_{S^{2-}}$ significantly.

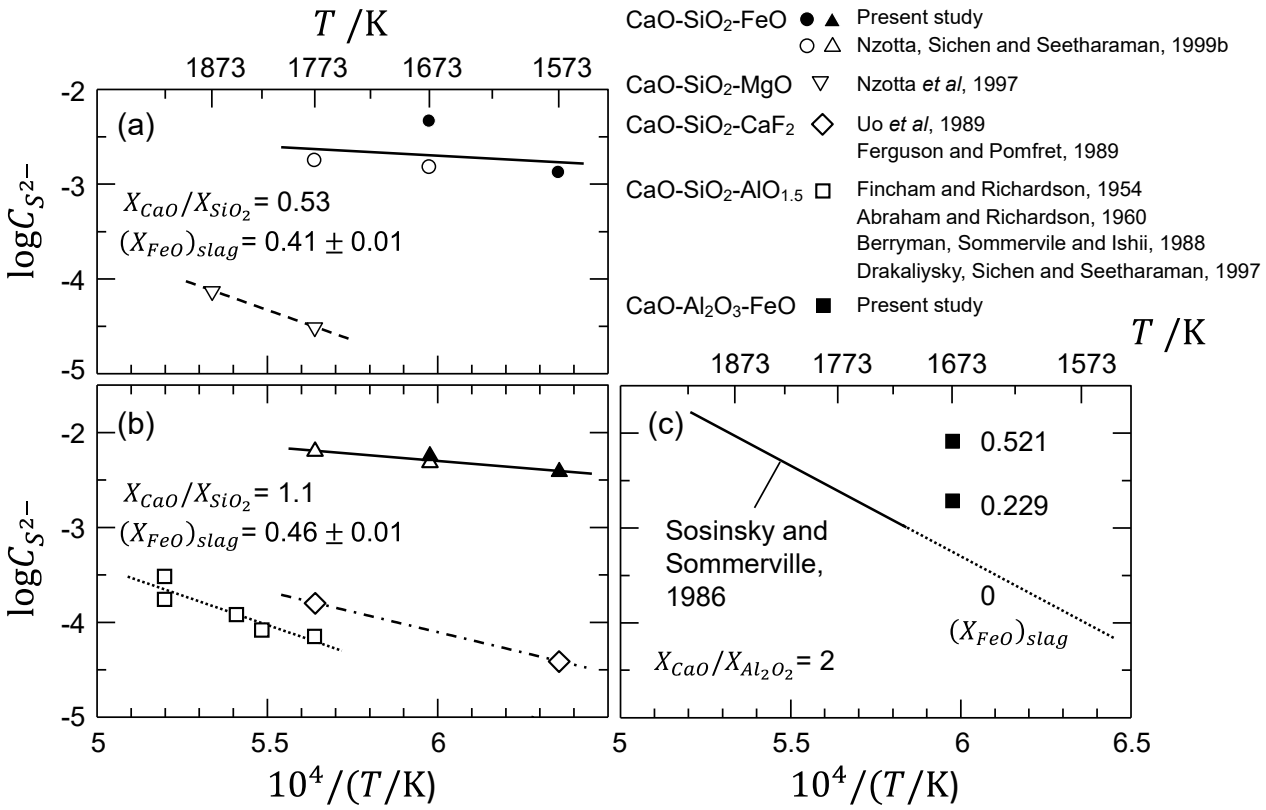

FIG 6 – Logarithmic value of sulfide capacity plotted against reciprocal temperature.

Figure 5c shows that $\log C_{S^{2-}}$ increased with an increase in $(X_{FeO})_{slag}$ in CaO-Al_2O_3-FeO slag at 1573 K. Figure 6c illustrates the present measured values for $\log C_{S^{2-}}$ with the literature data on CaO-Al_2O_3 binary system (Sosinsky and Sommerville, 1986). At 1573 K, CaO-Al_2O_3 binary oxide of $X_{CaO}/X_{Al_2O_3} = 2$ does not melt, while CaO-Al_2O_3-FeO ternary slag becomes homogeneous liquid with higher sulfide capacity than that of CaO-Al_2O_3 binary slag.

The reaction of iron between slag and Cu-Fe-S liquid alloy is formulated as:

$$[\mathrm{Fe}]_{\mathrm{Cu}} + (1/2)\ \mathrm{O_2(gas)} = (\mathrm{FeO})_{\mathrm{slag}} \tag{44}$$

$$K(44) = \frac{(a_{FeO})_{slag}}{[\gamma_{Fe}]_{Cu}\cdot[X_{Fe}]_{Cu}\cdot {P_{O_2}}^{1/2}} \tag{45}$$

$$\mathrm{Log}K(44) = -2.20 + \frac{11750}{\frac{T}{\mathrm{K}}}$$

(Iwase *et al*, 1984b) (46)

The standard states of Fe in Cu-Fe-S liquid alloy and FeO in slag are taken to be pure solid iron and pure non-stoichiometric liquid FeO coexisting with pure solid iron. The value for $(a_{FeO})_{slag}$ can be calculated from Equations 41, 42, 45 and 46 with the measured values for $[X_{Fe}]_{Cu}$, $[X_S]_{Cu}$ and P_{O_2}. The experimental results are listed in Table 1, and the relation between $(a_{FeO})_{slag}$ and $(X_{FeO})_{slag}$ is illustrated in Figures 5d, 5e and 5f with the activity curves reported in the literatures (Ogura *et al*, 1992; Saito, Oshima and Hasegawa, 2021); the present results are not inconsistent with the literature data.

Sulfur distribution ratio between slag and hot metal

In this section, the distribution ratios of sulfur between slag and hot metal, L_S, were calculated from the experimental results of $C_{S^{2-}}$ and $(a_{FeO})_{slag}$. When the standard states of a_{Fe} and $(a_{FeO})_{slag}$ are taken as pure liquid iron and pure non-stoichiometric liquid FeO, the equilibrium constant of Reaction 6 is given as (Iwase *et al*, 1984b; Kubaschewski, Alcock and Spencer, 1993):

$$\log K(6) = -2.59 + 12470/(T/\mathrm{K}) \tag{47}$$

Assuming that hot metal is Fe-C-S liquid alloy, a_{Fe} obeys Raoult's law and $[f_S]_{Fe}$ does not depend on $[\%S]_{Fe}$ due to low sulfur concentration, a_{Fe} and $[f_S]_{Fe}$ can be formulated as follows:

$$a_{Fe} = 1 - [X_C]_{Fe} - [X_S]_{Fe} \tag{48}$$

$$\log[f_S]_{Fe} = e_S^C[\%C]_{Fe} \tag{49}$$

$[X_i]_{Fe}$ and $[\%i]_{Fe}$ represent the mole fraction and mass content of *i* in Fe-C-S liquid alloy, respectively. Thus, the value for L_S can be obtained inserting Equations 47 through 49 into Equation 10 with the measured data on $C_{S^{2-}}$ and $(a_{FeO})_{slag}$. The calculation results are listed in Table 1 and shown in Figures 5g, 5h and 5i. In both of CaO-SiO_2-FeO and CaO-Al_2O_3-FeO ternary slags, L_S increased with an increase in $(X_{FeO})_{slag}$. These results mean that the effect of increasing $C_{S^{2-}}$ by adding iron oxide would be greater than the effect of increasing $(a_{FeO})_{slag}$.

Figure 7 shows the comparisons of L_S for CaO-SiO_2-FeO and CaO-SiO_2-CaF_2 ternary slags which occur at homogeneous liquid at 1573 K. The solid triangle for the CaO-SiO_2-FeO system indicates L_S when P_{O_2} is fixed by FeO in slag and Fe in hot metal. On the other hand, the open rhombus for the CaO-SiO_2-CaF_2 system gives L_S at P_{O_2} fixed by C in hot metal and CO gas of 1 atm. As seen in this figure, the value for L_S for CaO-SiO_2-FeO slag is lower than that for CaO-SiO_2-CaF_2 slag, because $C_{S^{2-}}$ of CaO-SiO_2-FeO slag is two orders of magnitude larger than $C_{S^{2-}}$ of CaO-SiO_2-CaF_2 slag (see Figure 6), but P_{O_2} fixed by FeO + Fe is more than five orders of magnitude larger than P_{O_2} fixed by C + CO.

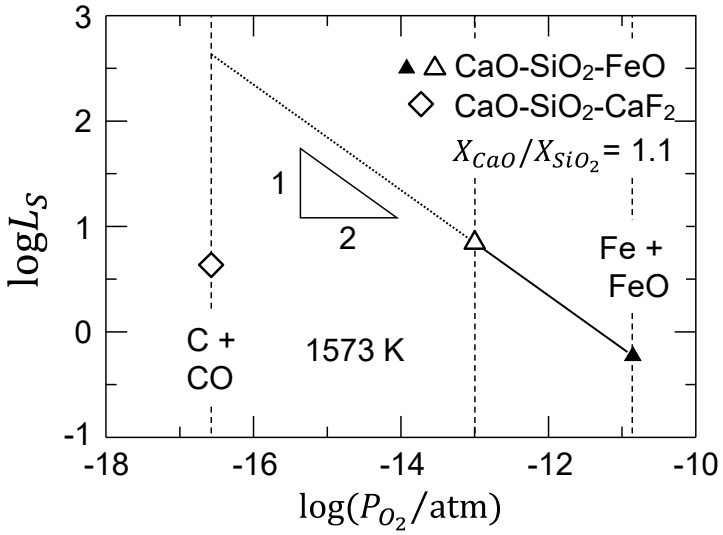

FIG 7 – Relation between $\log C_{S^{2-}}$ and $\log P_{O_2}$ at 1573 K.

The oxygen partial pressure between slag and hot metal in the practical operation is considered to take values between the Fe/FeO equilibrium and the C/CO equilibrium and is here assumed to be $\log(P_{O_2}/\mathrm{atm}) \fallingdotseq -13$ based on the study by Negishi ***et al*** (2023). In Figure 7, L_S for the CaO-SiO_2-FeO ternary system at $\log(P_{O_2}/\mathrm{atm}) = -13$ is shown by an open triangle and is almost equal to L_S for the CaO-SiO_2-CaF_2 ternary system. It is noteworthy that the relationship between $\log L_S$ and $\log P_{O_2}$ is linear with a slope of (–1/2) considering Equation 10.

CONCLUSIONS

For better understanding of re-sulfurisation reaction in hot metal pre-treatments, the present study aimed at evaluating the effect of iron oxide on the sulfur distribution ratio between slag and hot metal by measuring sulfide capacities and FeO activities in the CaO-SiO_2-FeO and CaO-Al_2O_3-FeO ternary slags simultaneously at 1573 K and 1673 K. The activity coefficients of components were also determined in Cu-Fe-S liquid alloy used as a reference metal. The results are summarised as follows.

The Herian activity coefficient of sulfur in Cu-Fe-S liquid alloy decreased with an increase in iron content. This indicated that the chemical affinity between iron and sulfur would be stronger than that between copper and sulfur.

The trend that the sulfide capacities in the $CaO\text{-}SiO_2\text{-}FeO$ and $CaO\text{-}Al_2O_3\text{-}FeO$ ternary slags increased with an increase in FeO content was consistent with the fact that FeO was a basic oxide.

The value for sulfide capacity of the $CaO\text{-}SiO_2\text{-}FeO$ system was significantly larger than those of the $CaO\text{-}SiO_2\text{-}MgO$, $CaO\text{-}SiO_2\text{-}AlO_{1.5}$ and $CaO\text{-}SiO_2\text{-}CaF_2$ ternary systems.

At 1573 K, $CaO\text{-}Al_2O_3\text{-}FeO$ ternary slag becomes homogeneous liquid with higher sulfide capacity than that of $CaO\text{-}Al_2O_3$ binary slag.

Although the addition of FeO raised the FeO activities in the $CaO\text{-}SiO_2\text{-}FeO$ and $CaO\text{-}Al_2O_3\text{-}FeO$ ternary slags, the calculated sulfur distribution ratios increased with increasing FeO content.

ACKNOWLEDGEMENTS

The authors express their sincere thanks to Mr Naoya Matsushita, Mr Kosuke Awaya, Mr Domu Mitsuyama and Mr Kazushi Tamaki, Graduate Students, Department of Energy Science and Technology, Kyoto University, for experimental assistance.

REFERENCES

Abraham, K P and Richardson, F D, 1960. Sulfide capacities of silicate melts Part II, *Journal of the Iron and Steel Institute*, 196:313–317.

Alcock, C B, 1958. An accurate radiochemical method for the measurement of high temperature equilibria involving H_2S/H_2 gas mixtures, *The International Journal of Applied Radiation and Isotopes*, 3:135–142. https://doi.org/10.1016/0020-708X(58)90008-5

Awaya, K, Mitsuyama, D, Tamaki, K, Saito, K, Kashiwaya, Y and Hasegawa, M, 2023. Sulfide Capacity and Activity of Iron Oxide in $CaO\text{-}SiO_2\text{-}FeO$ Ternary System at 1573 K, *ISIJ International*, 63:822–827. https://doi.org/10.2355/isijinternational.ISIJINT-2022-560

Berryman, R, Sommerville, I D and Ishii, F, 1988. The influence of Oxygen Potential on the Sulfide Capacity of Slags, *Trans Iron Steel Soc*, 9:61–66.

Bronson, A and Pierre, G R S, 1981. The sulfide capacities of $CaO\text{-}SiO_2$ melts containing MgO, FeO, TiO_2 and Al_2O_3, *Metallurgical Transactions B*, 12:729–731. https://doi.org/10.1007/BF02654142

Drakaliysky, E, Sichen, D and Seetharaman, S, 1997. An Experimental Study of The Sulfide Capacities in the System $Al_2O_3\text{-}CaO\text{-}SiO_2$, *Canadian Metallurgical Quarterly*, 36:115–120. https://doi.org/10.1179/cmq.1997.36.2.115

Ferguson, G and Pomfret, R J, 1989. Sulfur partition between carbon-saturated iron and $CaF_2\text{-}CaO\text{-}SiO_2$ slags, in *Proceedings of the 3rd Int Conf on Molten Slags and Fluxes 1988*, pp 323–326 (Institute of Metals: London).

Fincham, C J B and Richardson, F D, 1954. The behaviour of sulfur in silicate and aluminate melts, in *Proceedings of the Royal Society A*, 223:40–62. http://doi.org/10.1098/rspa.1954.0099

Hasegawa, M, Wakimoto, K and Iwase, M, 2002. Activities of Iron in Liquid Copper-Iron Alloys Saturated with Copper-Iron Solid Solutions, *High Temperature Materials and Processes*, 21:243–249.

Iwase, M, Ichise, E, Takeuchi, M and Yamasaki, T, 1984a. Measurements of the Parameter, P-, for the Determinations of Mixed Ionic and N-Type Electronic Conduction in Commercial Zirconia Electrolytes, *Transactions of the Japan Institute of Metals*, 5:43–52. https://doi.org/10.2320/matertrans1960.25.43

Iwase, M, Yamada, N, Ichise, E and Akizuki, H, 1984b. A Thermodynamic Study of $CaO+CaCl_2+Fe_xO$ Fluxes Used for the External Dephosphorisation of Hot Metal, *ISS Transactions*, 5:53–59.

Iwase, M, Yasuda, M and Mori, T, 1979. Free energy of formation of MoO_2 at steelmaking temperature from EMF measurements, *Electrochimica Acta*, 24:261–266. https://doi.org/10.1016/0013-4686(79)85043-4

Jung, S, 2003. Equilibria of manganese and sulfur between liquid iron and $CaO\text{-}SiO_2\text{-}Fe_tO\text{-}MgO\text{-}MnO$ slags saturated with $2CaO{\cdot}SiO_2$ and MgO, *ISIJ International*, 43:216–223. https://doi.org/10.2355/isijinternational.43.216

Kubaschewski, O, Alcock, C B and Spencer, P J, 1993. *Materials Thermochemistry*, 6th edition, pp 257–323 (Pergamon Press: UK).

Matsushita, N, Awaya, K, Saito, K and Hasegawa, M, 2021. Thermochemical Properties of Copper-Iron-Sulfur Alloy as Reference Metallic Phase for Analyzing Resulfurisation, *ISIJ International*, 61:2929–2936. https://doi.org/10.2355/isijinternational.ISIJINT-2021-247

Nagabayashi, R, Hino, M and Ban-ya, S, 1990. Distribution of Sulfur between Liquid Iron and Fe_tO-(CaO+MgO)-(SiO_2+P_2O_5) Phosphate Slags, *Tetsu-to-Hagané*, 76:183–190. https://doi.org/10.2355/tetsutohagane1955.76.2_183

Negishi, H, Kawabata, R, Hino, Y and Yokoi, Y, 2023. Development of torpedo car type dephosphorisation method without using fluorine, *CAMP-ISIJ*, 36:487.

Nzotta, M M, Nilsson, R, Sichen, D and Seetharaman, S, 1997. Sulfide capacities in MgO-SiO_2 and CaO-MgO-SiO_2 slags, *Ironmaking and Steelmaking*, 24:300–305.

Nzotta, M M, Sichen, D and Seetharaman, S, 1999a. Sulfide Capacities of FeO-SiO_2, CaO-FeO and FeO-MnO Slags, *ISIJ International*, 39:657–663. https://doi.org/10.2355/isijinternational.39.657

Nzotta, M M, Sichen, D and Seetharaman, S, 1999b. A study of the sulfide capacities of iron-oxide containing slags, *Metallurgical Transactions B*, 30:909–920. https://doi.org/10.1007/s11663-999-0096-4

Ogura, T, Fujiwara, R, Mochizuki, R, Kawamoto, Y, Oishi, T and Iwase, M, 1992. Activity determinator for the automatic measurements of the chemical potentials of FeO in metallurgical slags, *Metallurgical Transactions B*, 23:459–466. https://doi.org/10.1007/BF02649665

Ohta, M, Kubo, T and Morita, K, 2003. Effects of CaF_2, MgO and SiO_2 addition on sulfide capacities of the CaO-Al_2O_3 slag, *Tetsu-to-Hagané*, 89:742–749. https://doi.org/10.2355/tetsutohagane1955.89.7_742

Okamoto, H, 2010. *Phase Diagrams for Binary Alloys*, 2nd edition, p 308 (ASM International: OH).

Pierre, G R S and Chipman, J, 1956. Sulfur Equilibria Between Gases and Slags Containing FeO, *JOM*, 8:1474–1483. https://doi.org/10.1007/BF03377850

Richardson, F D and Fincham, C J B, 1954. Sulfur in silicate and aluminate slags, *Journal of the Iron and Steel Institute*, 178:4–15.

Saito, K, Oshima, Y and Hasegawa, M, 2021. Reevaluation and Measurements of Fe_xO Activities in Fe_xO-CaO-SiO_2 Pseudo-ternary System at 1573 K, *ISIJ International*, 61:697–704. https://doi.org/10.2355/isijinternational.ISIJINT-2020–349

Schmalzried, H, 1962. Über Zirkondioxyd als Elektrolyt für elektrochemische Untersuchungen bei höheren Temperaturen [in German] (On zirconium dioxide as an electrolyte for electrochemical investigations at higher temperatures), Zeitschrift für Elektrochemie, Berichte der Bunsengesellschaft für physikalische Chemie (Journal of Electrochemistry, Reports of the Bunsen Society for Physical Chemistry), 66:572–576. https://doi.org/10.1002/bbpc.19620660710

Shim, J D and Ban-ya, S, 1982. Equilibria of Sulfur between Liquid Iron and Fe_tO-SiO_2-CaO-MgO Slags Saturated with MgO, *Tetsu-to-Hagané*, 68:251–260. https://doi.org/10.2355/tetsutohagane1955.68.2_251

Sigworth, G K and Elliott, J F, 1974a. The thermodynamics of dilute liquid copper alloys, *Canadian Metallurgical Quarterly*, 13:455–461. https://doi.org/10.1179/cmq.1974.13.3.455

Sigworth, G K and Elliott, J F, 1974b. The Thermodynamics of Liquid Dilute Iron Alloys, *Metal Science*, 8:298–310. https://doi.org/10.1179/msc.1974.8.1.298

Sosinsky, D J and Sommerville, I D, 1986. The Composition and Temperature Dependence of the Sulfide Capacity of Metallurgical Slags, *Metallurgical Transactions B*, 17:331–337. https://doi.org/10.1007/BF02655080

Taniguchi, Y, Morita, K and Sano, N, 1997. Activities of FeO in CaO-Al_2O_3-SiO_2-FeO and CaO-Al_2O_3-CaF_2-FeO Slags, *ISIJ International*, 37:956–961. https://doi.org/10.2355/isijinternational.37.956

Umetsu, Y, 1950. Physico-chemical Research on some Fundamental Reactions of Copper Metallurgy, Report II, On the Equilibrium of Copper, Sulfur and Hydrogen et High Temperature, *Journal of the Mining Institute of Japan*, 66:335–340. https://doi.org/10.11508/shigentosozai1885.66.335

Uo, M, Sakurai, E, Tsukihashi, F and Sano, N, 1989. The CaS solubility in the CaO bearing slags, *Steel Research*, 60:496–502. https://doi.org/10.1002/srin.198901692

Yagihashi, T and Sato, T, 1962. The Equilibrium between Sulfur in Molten Copper and H_2-H_2S Gas Mixture, *Journal of the Mining and Metallurgical Institute of Japan*, 78:43–48. https://doi.org/10.2473/shigentosozai1953.78.883_43

Effect of alumina on microstructures of iron ore sinters from the perspective of the phase equilibria of the CaO-SiO_2-Fe_2O_3-Al_2O_3 system

DOI: 10.62053/TXSW1160

M Hayashi[1], A Takahashi[2], Y Uchisawa[3], T Watanabe[4] and M Susa[5]

1. Professor, Tokyo Institute of Technology, Tokyo 152-8552, Japan. Email: hayashi.m.ae@m.titech.ac.jp
2. Student, Tokyo Institute of Technology, Tokyo 152-8552, Japan. Email: takahashi.a.az@gmail.com
3. Student, Tokyo Institute of Technology, Tokyo 152-8552, Japan. Email: rintaro9773@gmail.com
4. Assistant Professor, Tokyo Institute of Technology, Tokyo 152-8552, Japan. Email: watanabe.t.ai@m.titech.ac.jp
5. Emeritus Professor, Tokyo Institute of Technology, Tokyo 152-8552, Japan. Email: susa.m.aa@m.titech.ac.jp

ABSTRACT

Owing to the deterioration of iron ore, the Al_2O_3 concentration in iron ore increases, and thus it is important to investigate the effect of increment in Al_2O_3 concentration on the microstructures of iron ore sinters. During the sintering process, a melt is present in the sinter for only a few minutes, and therefore the microstructure of the sinter doesn't reach thermodynamic equilibrium. Nevertheless, the formation process of the microstructures can be interpreted and predicted to some extent from the equilibrium phase diagram. This study investigated the liquidus isotherm in the CaO-SiO_2-Fe_2O_3-5 mass% Al_2O_3 system at 1240°C in air and the phase equilibria of silico-ferrite of calcium and aluminium (denoted by SFCA) and SFCA-I by XRD (X-ray diffraction analysis) and electron probe micro analyzer (EPMA). The following results were obtained:

1. The ferrite melt region with a high Fe_2O_3 concentration shifts to the lower Fe_2O_3 side than the liquidus isotherm in the CaO-SiO_2-Fe_2O_3 system.
2. The compositional region of SFCA extends in the $CaO{\cdot}3Fe_2O_3$-$4CaO{\cdot}3SiO_2$ direction than the silico-ferrite of calcium (denoted by SFC) composition region with a 0 mass% Al_2O_3.
3. SFCA-I is observed in the present system, which suggests that the increment in the Al_2O_3 concentration contributes to the stability of SFCA-I.

These results imply that an increment in Al_2O_3 concentration in iron ore leads to a decrement in the volume fraction of the bonding phase and that the fraction of the SFCA phase increases, and those of $2CaO{\cdot}SiO_2$ and slag phases decrease in the bonging phase. The SFCA-I phase is also precipitated from the slag with an Al_2O_3 concentration around 5 mass%.

INTRODUCTION

The qualities of the sinter such as strength and reducibility affect the CO_2 emissions of the ironmaking process. Thus, the production of high-quality sinters is highly desirable. The quality depends significantly on the sinter microstructures (Oyama *et al*, 1996), which are composed of calcium ferrite, hematite, magnetite and amorphous silicate (Sasaki and Hida, 1982; Scarlett *et al*, 2004; Patrick and Lovel, 2001). In particular, the silico-ferrite of calcium and aluminium (SFCA), consisting of CaO, SiO_2, Fe_2O_3, Al_2O_3 and MgO, plays the role of a bonding phase connecting the coarse hematite ores and contributes significantly to the quality of sinters (Hayes, Chen and Jak, 2016; Tonžetć and Dippenaar, 2011; Shigaki, Sawada and Gennai, 1986).

During the sintering process, a melt is present in the sinter for only a few minutes which is a very short time for convection mass transfer, and consequently, the microstructure of the sinter cannot reach thermodynamic equilibrium. Nevertheless, the formation process of the microstructures, such as the melting and precipitation of SFCA, can be successfully interpreted and predicted from the equilibrium phase diagram of the CaO-SiO_2-Fe_2O_3 system, which is the main component of sinters (Hayashi *et al*, 2022). Recently, the deterioration of iron ore has progressed and the Al_2O_3 concentration in iron ores has increased. Thus, it is important to investigate the effect of Al_2O_3 on the compositional region of SFCA and the liquid phase as well as the phase equilibria, including

SFCA in the CaO-SiO_2-Fe_2O_3-Al_2O_3 system to control the microstructures of sinters for the production of high-quality sinters.

To the best of our knowledge, however, there are no reports on the phase equilibria of the CaO-SiO_2-Fe_2O_3 system containing Al_2O_3 concentrations exceeding 1 mass% at temperatures below 1270°C which can be attributed to the high viscosity of the high Al_2O_3-containing slag melt (Machida *et al*, 2005) which results in slow mass transfer and reaction rates and thus a long time is required for the system to reach equilibrium. SFCA may precipitate at temperatures lower than 1300°C during the cooling cycle of the sintering process (Sasaki and Hida, 1982). Thus, a phase diagram with such a high Al_2O_3 concentration at temperatures lower than 1270°C may be necessary to control the microstructure of the sinter and produce high-quality sinters.

This study investigates the effect of Al_2O_3 on the compositional regions of SFCA and the liquid phase, and the phase equilibria including SFCA in a CaO-SiO_2-Fe_2O_3-5 mass% Al_2O_3 system at 1240°C in air (Takahashi *et al*, 2023) and estimates the effect of alumina on microstructures of iron ore sinters.

EXPERIMENTAL

Table 1 lists the chemical composition of the samples. The samples were prepared from reagent-grade $CaCO_3$, SiO_2, Fe_2O_3 and Al_2O_3 powders. To obtain the desired compositions, the reagents were weighed and then mixed using an alumina mortar and pestle.

TABLE 1

Initial compositions of the samples.

Sample No.	Composition (mass%)				Ratio (at%)	
	CaO	SiO_2	Fe_2O_3	Al_2O_3	Ca/Si	Fe/Si
1	29.45	15.20	50.35	5.00	2.08	0.62
2	24.00	9.00	62.00	5.00	2.86	1.30
3	24.00	7.50	63.50	5.00	3.43	1.59
4	19.92	9.36	65.72	5.00	2.28	1.32
5	24.00	4.80	66.20	5.00	5.36	2.59
6	18.81	5.17	71.06	5.00	3.90	2.59
7	18.81	3.00	73.19	5.00	6.72	4.59
8	12.90	7.60	74.50	5.00	1.82	1.84
9	18.81	1.50	74.69	5.00	13.44	9.37
10	16.50	0.00	77.00	5.00	-	-
11	11.83	1.34	81.84	5.00	9.46	11.49
12	6.96	1.56	86.49	5.00	4.78	10.43
13	5.39	0.00	89.61	5.00	-	-
14	18.53	16.58	62.40	2.50	1.20	0.71

The sample holder was prepared by spirally winding a Rh/Pt wire (0.5 mm diameter, 13 mass%) (Hayes, Chen and Jak, 2016), on which a sample mixture (approximately 0.4 g), which was uniaxially cold-pressed to a tablet diameter of 10 mm, was placed. Using a spiral sample holder, the molten sample was maintained in the form of a film between the gaps of the wire by surface tension during the equilibrium experiment, to ensure good contact with water during quenching and prevent crystallisation (Hayes, Chen and Jak, 2016). A sample tablet placed on the sample holder was suspended using the same wire in the maximum temperature zone of the furnace and was maintained at 1240°C for more than 48 hours in air to attain equilibrium. Preliminary experiments indicate that 48 hours is sufficient for the samples to reach equilibrium at 1240°C. As for samples No. 1, 3, 4 and 8, a sample was kept at 1300°C or higher for more than 30 mins to promote mass

transfer. After that, the furnace temperature was lowered to 1240°C (the equilibrium temperature) at a rate of 1°C/min and then the sample was kept at that temperature for more than 48 hours in air to attain equilibrium. After equilibration, the crucible containing the sample was quenched into water. For samples No. 11–13 (which have no equilibrium liquid phase), the sample mixture was uniaxially pressed to form a tablet. The tablet was placed in a Pt crucible and heated at 1240°C in air for at least 24 hours. Then, the tablet was thoroughly crushed and mixed. The mixture was uniaxially pressed to form a tablet and heated in the same manner. The heat treatment was repeated three times. Metastable phases such as calcium aluminate and gehlenite were formed in the sample after one heat treatment; however, these phases disappeared after two or three treatments, thus indicating that the sample reached equilibrium.

Each obtained sample was divided into two parts: one was pulverised into a powder and analysed by XRD to determine the phase present and the other part was analysed by an EPMA to observe the microstructure and for compositional analysis. The XRD analyses were carried out with CuKα radiation at an accelerating voltage of 40 kV and a filament current of 250 mA. The diffraction scanning rate was 0.005°/step or 0.02°/step, at 1°/min or 5°/min and the diffraction angle 2θ was between 5° and 70°. The microstructures were measured by EPMA at an accelerating voltage of 15 kV and a probe current of 3 nA for the backscattered electron images (BEI) and 20 or 50 nA for elemental mapping, where the analysis area was ϕ1 μm. The composition of each phase was quantitatively analysed by point analysis, where the analysis area was ϕ5 μm for some liquid phases and ϕ1 μm for others. The ZAF (Z: atomic number effect, A: absorption effect, F: fluorescence effect) correction was performed. For quantitative analyses by EPMA, a glassy sample of 32.83CaO-35.71SiO_2-24.46Fe_2O_3-5.00Al_2O_3-2.00MgO (mass%) was used as the standard sample.

RESULTS

Table 2 shows the measured compositions of the phases, where $2CaO{\cdot}SiO_2$ and $CaO{\cdot}SiO_2$ are denoted by C_2S and CS, respectively. Figure 1 shows a plot of the measured composition of the phases of each sample projected onto the CaO-SiO_2-Fe_2O_3-5mass% Al_2O_3 plane. SFCA contained Al_2O_3 concentrations in the range of 5.47–9.35 mass% and the Al_2O_3 concentrations in the liquid and SFCA-I in equilibrium with SFCA were lower than those of SFCA, thus indicating that the preferential distribution of Al_2O_3 in SFCA. However, when SFCA-I is in equilibrium with the liquid or hematite and SFCA is not present, the Al_2O_3 concentration in SFCA-I can reach 9.59 mass%, which is much higher than that of SFCA-I equilibrated with SFCA. The SiO_2 concentration of SFCA-I is lower than that of SFCA. In this study, the SiO_2 concentrations of SFCA-I and SFCA were 0.00–1.31 mass% and 1.55–6.30 mass%, respectively. In Figure 1, samples No. 1–3, 5–7 and 9 indicate equilibria between liquid and SFCA. The liquid phase compositions have a C/S ratio of larger than 2, which is a critical ratio determining the saddle point between the two liquid regions on the Alkemade join between Fe_2O_3 and C_2S. The presence of the saddle point is predicted by thermodynamic theory. Nevertheless, it is noteworthy that the liquid phase compositions of samples No. 4 and 8 have a C/S ratio of less than 2, which suggests that the SFCA primary phase field exists in the low C/S region. Figures 2 and 3 show the XRD profiles and elemental mappings of samples No. 4 and 8, respectively. As shown in Figures 2 and 3, the solid precipitations during the cooling cycles are not observed in liquid phases. The phenomenon that the SFCA primary phase field extends to the low C/S region may be relevant to the high Al_2O_3 concentration – a part of Fe ions in the SFCA phase with high Al_2O_3 concentrations may be Fe^{2+} ions by the reaction $2(Fe^{3+}, Al^{3+}) = (Ca^{2+}, Fe^{2+}) + Si^{4+}$ (Patrick and Pownceby, 2002). Thus, the stable compositional region of SFCA extends to the lower C/S.

SFCA-I was formed in samples No. 7, 9–11 and 13. In this study, the presence of SFCA-I was confirmed by XRD and EPMA. For example, Figure 4a shows the XRD profile of sample No. 11. In addition to the SFCA-I peaks, hematite and SFCA peaks were observed in this sample. Figure 4b and 4c show the XRD profiles of sample No. 7. Figure 5 shows the elemental mappings of samples No. 11 and 7, respectively, where SFCA-I and SFCA coexist. The brightest phase with the highest Fe concentration in the BEI of No. 11 was hematite. In samples No. 11 and 7, SFCA and SFCA-I exhibited almost the same brightness and the BEIs were not sufficient to distinguish them. Thus, they were distinguished based on the differences in the concentration of each element. SFCA-I is in the Fe- and Ca-rich and Al- and Si-poor regions, while SFCA is in the Fe- and Ca-poor regions and the Al- and Si-rich regions.

TABLE 2

Measured compositions of the phases.

Sample No.	Phases	Composition (mass%)				Ratio (mass%)
		CaO	SiO_2	Fe_2O_3	Al_2O_3	CaO/SiO_2
1	Liquid	35.45	22.18	38.29	4.08	1.60
	SFCA	16.38	6.30	70.77	6.55	2.6
	C_2S	64.04	35.18	0.78	0.00	1.82
2	Liquid	30.76	8.29	57.94	3.00	3.71
	SFCA	15.45	4.54	74.21	5.80	3.40
	C_2S	64.97	33.05	1.98	0.00	1.97
3	Liquid	29.70	8.81	58.00	3.49	3.37
	SFCA	15.41	4.31	72.49	7.79	3.58
4	Liquid	35.76	26.26	34.07	3.90	1.36
	SFCA	15.19	5.94	72.92	5.94	2.56
5	Liquid	28.17	4.85	63.29	3.69	5.81
	SFCA	15.11	3.53	73.85	7.51	4.28
6	Liquid	29.75	6.88	60.62	2.75	4.32
	SFCA	15.24	4.32	74.96	5.47	3.53
7	Liquid	26.82	3.40	66.91	2.87	7.89
	SFCA	13.89	3.07	76.77	6.27	4.52
	SFCA-I	16.08	1.31	79.74	2.87	12.3
8	Liquid	35.83	29.56	28.63	5.99	1.21
	SFCA	14.85	6.13	71.31	7.71	2.42
	Hematite	0.21	0.02	98.42	1.36	10.5
9	Liquid	23.89	1.38	71.97	2.77	17.31
	SFCA	13.16	2.09	78.18	6.58	6.30
	SFCA-I	13.82	0.53	80.57	5.08	26.08
10	Liquid	23.81	0.00	73.47	2.72	-
	SFCA-I	13.94	0.00	80.89	5.16	-
11	SFCA	12.50	1.55	80.24	5.71	8.06
	SFCA-I	12.86	0.38	82.09	4.67	33.84
	Hematite	0.35	0.01	98.65	0.99	35
12	SFCA	13.54	2.79	74.32	9.35	4.85
	Hematite	0.15	0.04	98.32	1.49	3.75
13	SFCA-I	11.96	0.00	78.45	9.59	-
	Hematite	0.13	0.00	97.87	2.00	-
14	Liquid	34.50	31.16	29.98	4.36	1.11
	Hematite	0.13	0.02	98.96	0.89	6.5
	CS	47.20	52.00	0.81	0.00	0.91

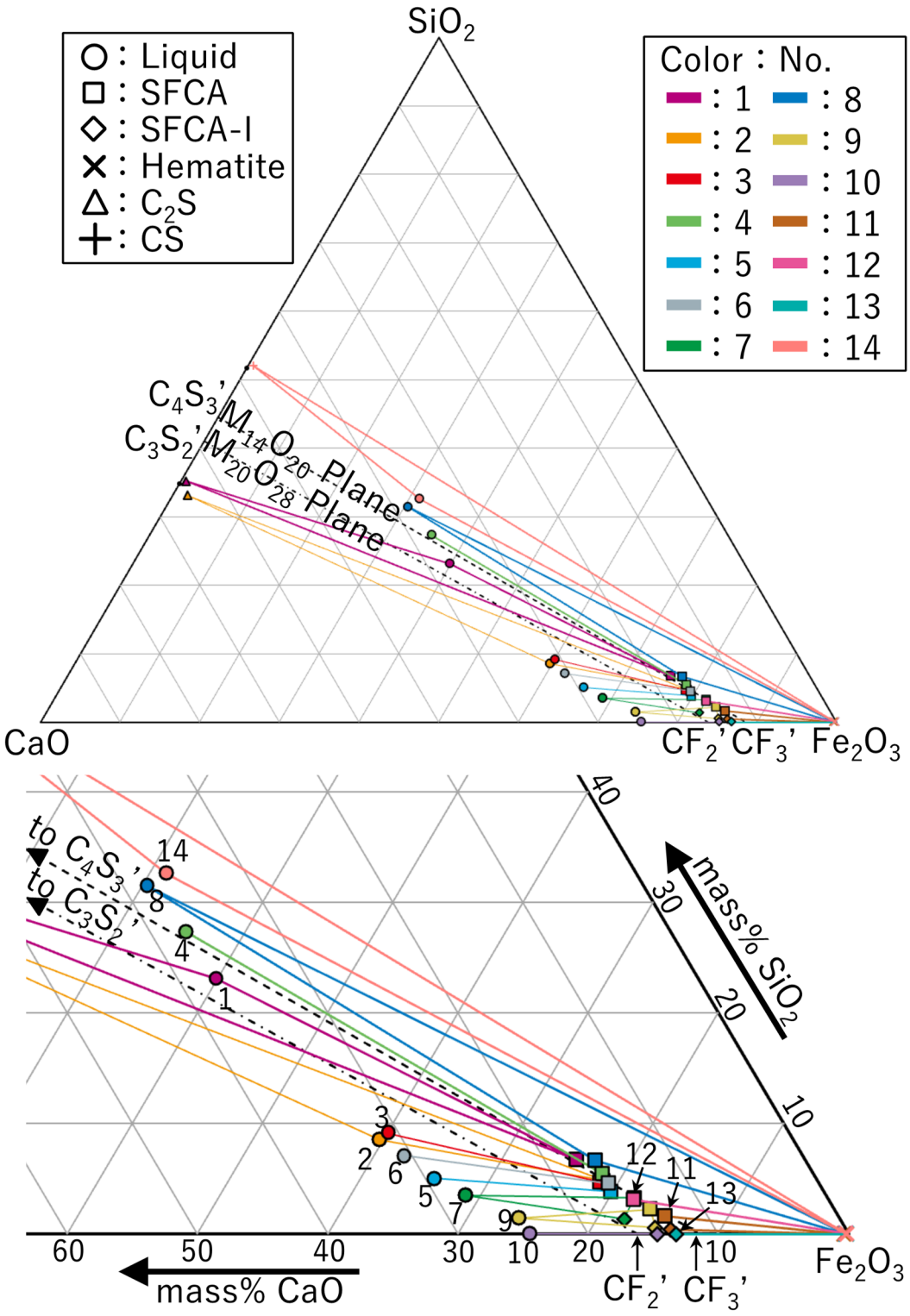

FIG 1 – Measured compositions of the phases for samples No. 1–14 on the iron-rich corner of the CaO-SiO_2-Fe_2O_3-5 mass% Al_2O_3 system in air at 1240°C (Takahashi *et al*, 2023).

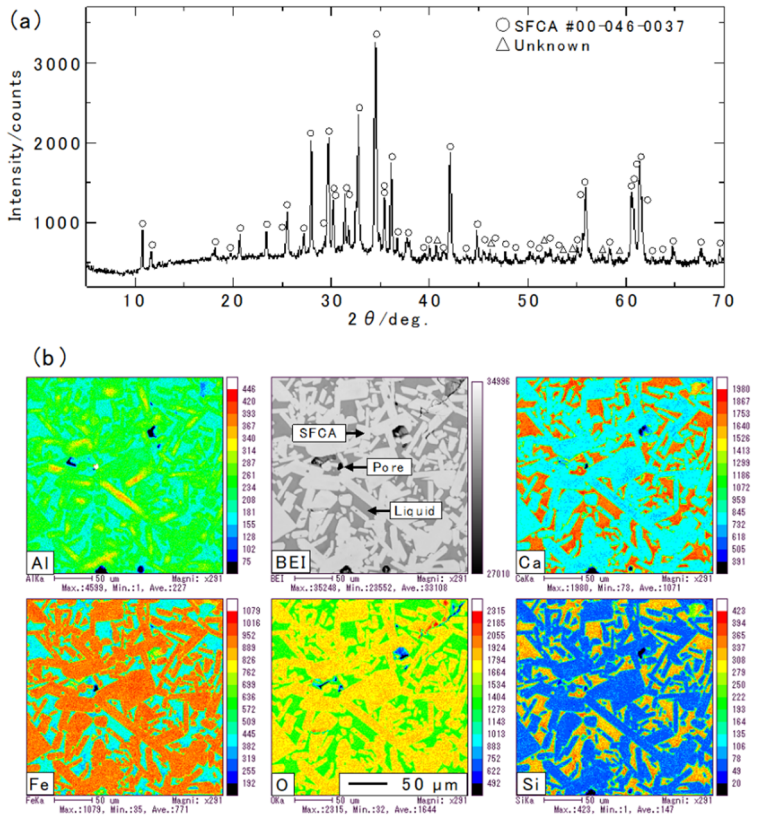

FIG 2 – XRD profile and elemental mappings of sample No. 4.

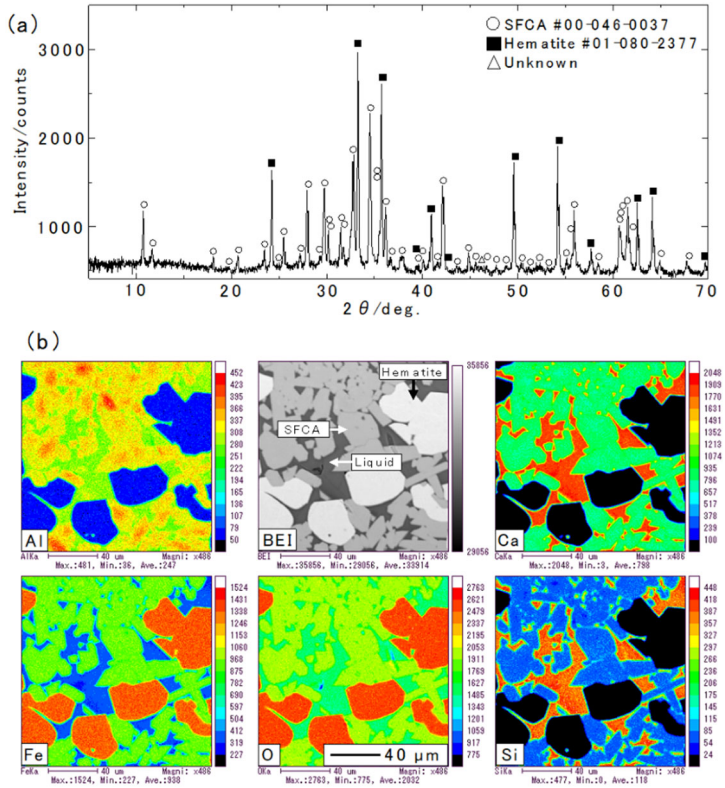

FIG 3 – XRD profile and elemental mappings of sample No. 8.

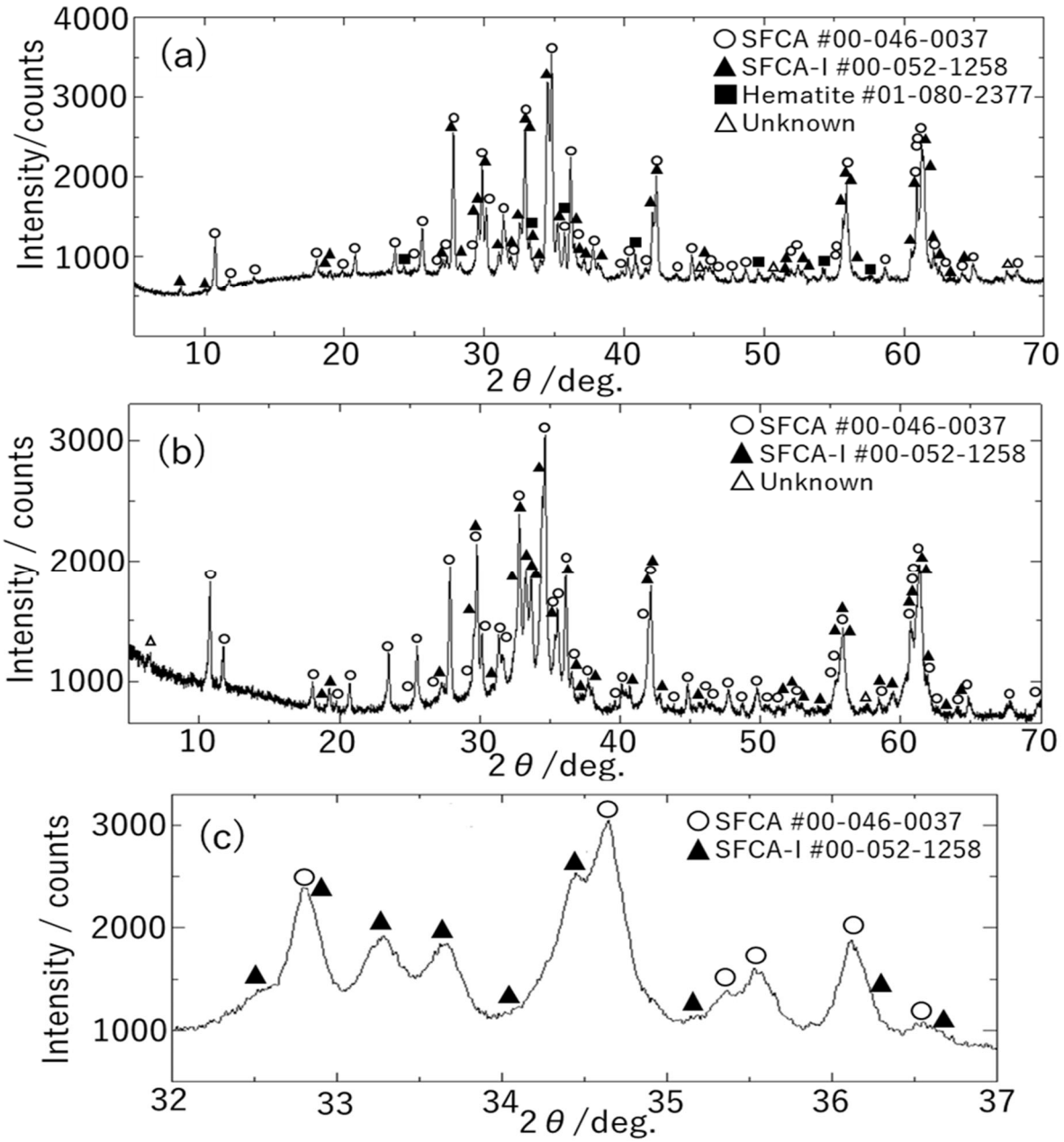

FIG 4 – (a) XRD pattern of sample No. 11; (b) XRD pattern of sample No. 7; and (c) XRD pattern of sample No. 7 (2θ = 32°–37°) (Takahashi *et al*, 2023).

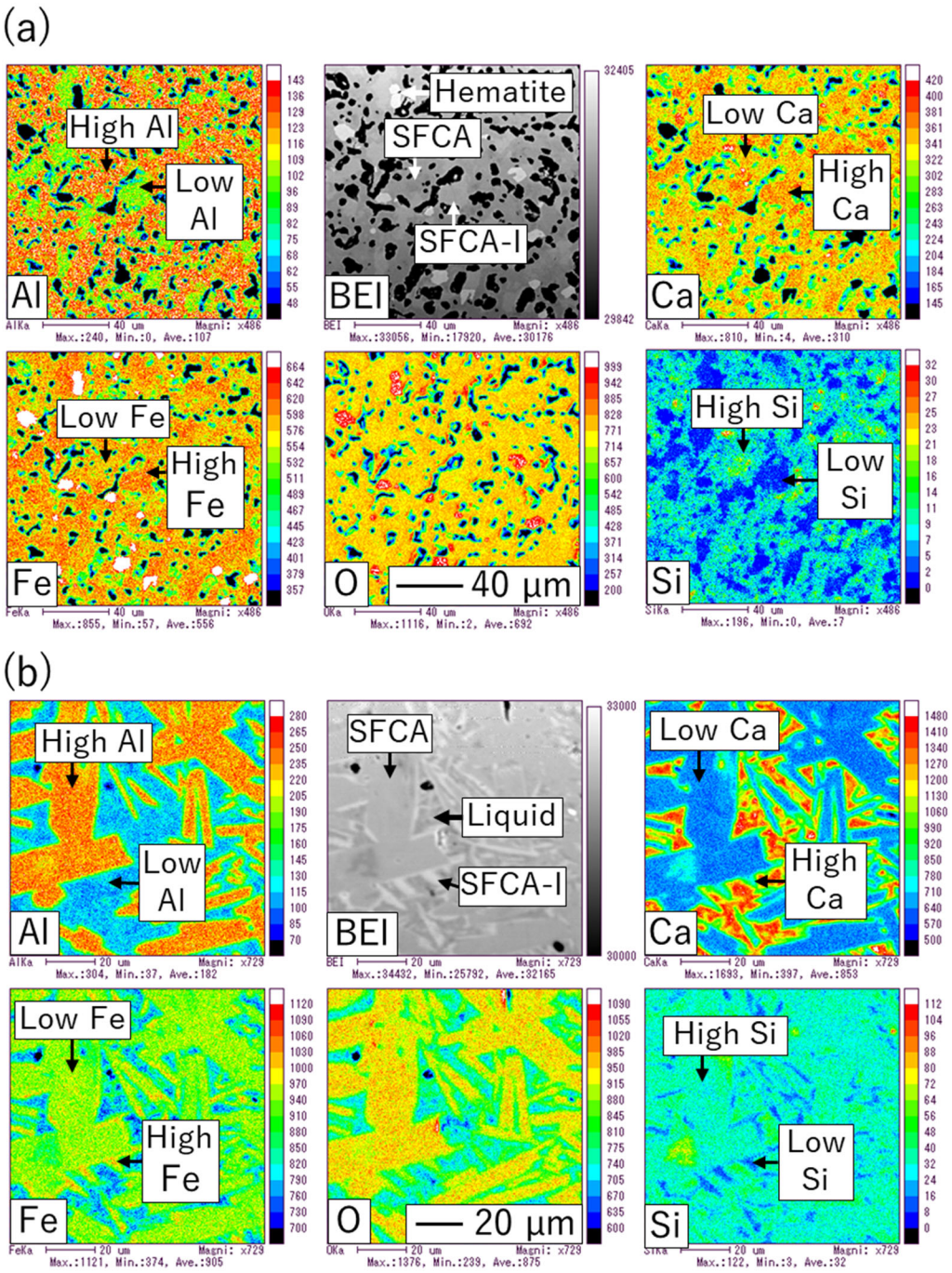

FIG 5 – (a) Mapping analysis of sample No. 11; (b) Mapping analysis of sample No. 7 (Takahashi *et al*, 2023).

DISCUSSION

In this study, the initial composition was CaO-SiO_2-Fe_2O_3-5 mass% Al_2O_3. However, since Al_2O_3 was preferentially distributed in SFCA, an Al_2O_3 concentration higher than 5 mass% was obtained. Figure 6 shows the relationship between the mass ratio of CaO/SiO_2 (denoted by C/S) and the Al_2O_3 concentration for the SFCA compositions. Chen *et al* (2019) reported that the C/S ratio of the SFC composition region is in the range of 2.92 to 4.322, which are plotted in Figure 6 as values at 0 mass% Al_2O_3. The highest C/S ratio of the SFCA composition region at 5 mass% Al_2O_3 was determined by interpolation using a straight line drawn by connecting the results of Chen *et al* (2019) and those of this study, while the lowest C/S ratio was determined using a straight line drawn by the least-square fitting of four plots obtained in this study, passing through the plot of Chen *et al* (2019) at 0 mass% Al_2O_3. It was thus found that the C/S ratio of the SFCA compositional region was in the range of 2.77 to 7.60 at 5 mass% Al_2O_3. Figure 6 reveals the expansion of the SFCA compositional

region upon the addition of Al_2O_3 which is also consistent with the results of Patrick and Pownceby (2002), while the compositional region of the SFCA with 5 mass% Al_2O_3 determined in this study was even wider than that reported by Patrick and Pownceby (2002).

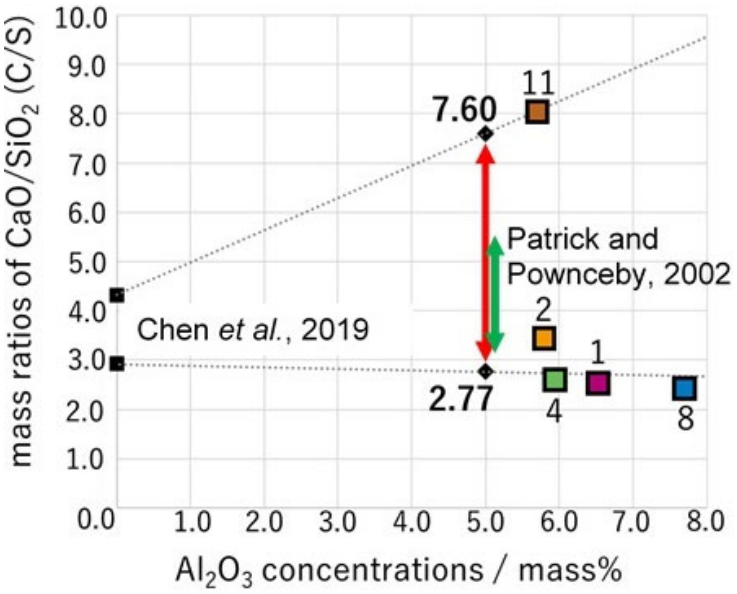

FIG 6 – Estimation of the SFCA composition range in 5 mass% Al_2O_3.

Figure 7 shows the isothermal cross-section of the CaO-SiO_2-Fe_2O_3-5 mass% Al_2O_3 at 1240°C superimposed on that of the CaO-SiO_2-Fe_2O_3 system reported by Chen *et al* (2019) and the liquidus isotherm in the CaO-SiO_2-Fe_2O_3 system reported by Philips and Muan (1959). Compared to these systems, the liquidus isotherm in the CaO-SiO_2-Fe_2O_3-5 mass% Al_2O_3 system shifted toward a low Fe_2O_3. This shift attributed to the addition of Al_2O_3 is consistent with the results of Cheng *et al* (2021), who investigated the CaO-Fe_2O_3-Al_2O_3 system and those of Chen *et al* (2021), who studied the effects of the addition of 1, 2 and 4 mass% Al_2O_3 on the CaO-SiO_2-Fe_2O_3 system. Furthermore, Yang, Shoji and Takenouchi (1978) reported that the addition of 2 mass% Al_2O_3 shifted the composition range of the silicate melt toward low Fe_2O_3 in the CaO-SiO_2-Fe_2O_3-2 mass% Al_2O_3 system at 1300°C. Thus, the results of the present study are consistent with those of the previous studies, thus indicating that the addition of Al_2O_3 contributes to the shift of the liquid-phase line to the low Fe_2O_3 side.

The end points of the low Fe_2O_3 side of the SFCA composition region were in equilibrium with the liquid phase, C_2S and hematite, whereas those of the high Fe_2O_3 side were in equilibrium with hematite and SFCA-I. The SFCA-I compositional region existed in a region with a lower SiO_2 concentration than that of the SFCA compositional region. The end point of the low Fe_2O_3 side of the SFCA-I compositional region was in equilibrium with SFCA and the liquid phase. The high Fe_2O_3 end point with the low-CaO side was in equilibrium with hematite and that with the high-CaO side was in equilibrium with the liquid phase. Chen *et al* (2021) reported that the end points on the high Fe_2O_3 side of SFCA at 1255°C and 1265°C for 1 mass% Al_2O_3 and at 1275°C for 2 mass% Al_2O_3 were in equilibrium with the liquid phase and hematite, suggesting that SFCA-I did not exist. The results of this study suggest that the addition of Al_2O_3 contributes to the stability of SFCA-I in the CaO-SiO_2-Fe_2O_3 system.

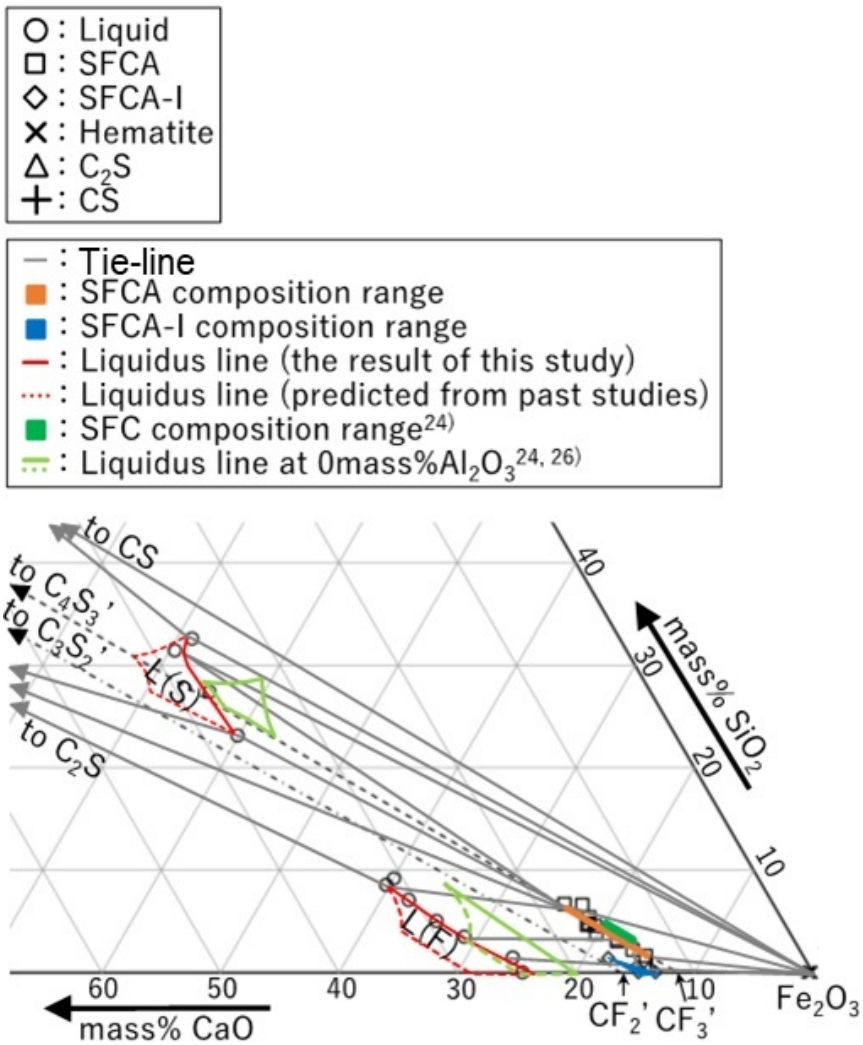

FIG 7 – Isothermal section of the CaO-SiO_2-Fe_2O_3-5 mass% Al_2O_3 system in air at 1240°C based on the present study and its comparison with previous studies (Chen *et al*, 2019; Dayal and Glasser, 1967; Takahashi *et al*, 2023).

Let us consider the microstructure formation of iron ore sinters from the perspective of the phase diagram of the CaO-SiO_2-Fe_2O_3 system reported by Chen *et al* (2019). Figure 8a shows the phase equilibrium of the iron-rich corner of the CaO-SiO_2-Fe_2O_3 system in air including liquidus, the SFC and C_2S primary phase fields, the SFC solid solution and a common iron ore composition (Chen *et al*, 2019). The straight lines connecting $4CaO{\cdot}3SiO_2$ (denoted by C_4S_3, not present as a compound) and $CaO{\cdot}3Fe_2O_3$ (denoted by CF_3, not present as a compound) and SiO_2 and iron ore composition are denoted by Line A and Line B, respectively. SFC solid solution is on Line A. T1 and T2 correspond to the temperatures at the intersections of the boundary between SFC (SFCA) and Fe_2O_3 primary phase fields with the extensions of straight lines connecting LC(1) and Fe_2O_3 and LC(2) and Fe_2O_3, respectively. T3 corresponds to the eutectic temperature of SFC (SFCA), Fe_2O_3 and C_2S. In general, some SiO_2 gangue minerals in iron ore remain unreacted during sintering and the local composition of iron ore sinter shifts away from the SiO_2 corner of the CaO-SiO_2-Fe_2O_3 system along Line B. Figure 8b shows schematic illustrations of the equilibrium microstructures for LC(1) and LC(2). For both compositions, Fe_2O_3 and liquid phases are equilibrated at 1300°C and then during the cooling cycle, SFC (SFCA) phases are precipitated from the liquid phase at T1 and T2 for LC(1) and LC(2), respectively. For LC(1), when the temperature decreases to T3, C_2S is precipitated from the residual liquid. On the other hand, as for LC(2), Fe_2O_3 and SFC (SFCA) phases are equilibrated below T2. Because Lines A and B approach each other as the C/S ratio is larger, the fraction of SFC (SFCA) is larger for LC(2) than for LC(1).

The effect of alumina on microstructures of iron ore sinters can be estimated from Figure 7. The liquidus isotherm in the CaO-SiO_2-Fe_2O_3-5 mass% Al_2O_3 system shifted toward a low Fe_2O_3 than

that in the $CaO\text{-}SiO_2\text{-}Fe_2O_3$ system. Thus, an increment in Al_2O_3 concentration in iron ore leads to a decrement in the volume fraction of the bonding phase. It can also be found from Figure 7 that the compositional region of SFCA extends in the $CaO\cdot 3Fe_2O_3\text{-}4CaO\cdot 3SiO_2$ direction than the silico-ferrite of calcium (denoted by SFC) composition region with a 0 mass% Al_2O_3. The compositions of the iron ore sinters are heterogeneous from place to place, with local compositions extending from the LC(1) to LC(2) composition range or beyond. Thus, the expansion of the compositional range of SFCA from SFC implies that the fraction of the SFCA phase increases and those of $2CaO\cdot SiO_2$ and slag phases decrease in the bonding phase. The SFCA-I phase is also precipitated from the slag with an Al_2O_3 concentration around 5 mass%.

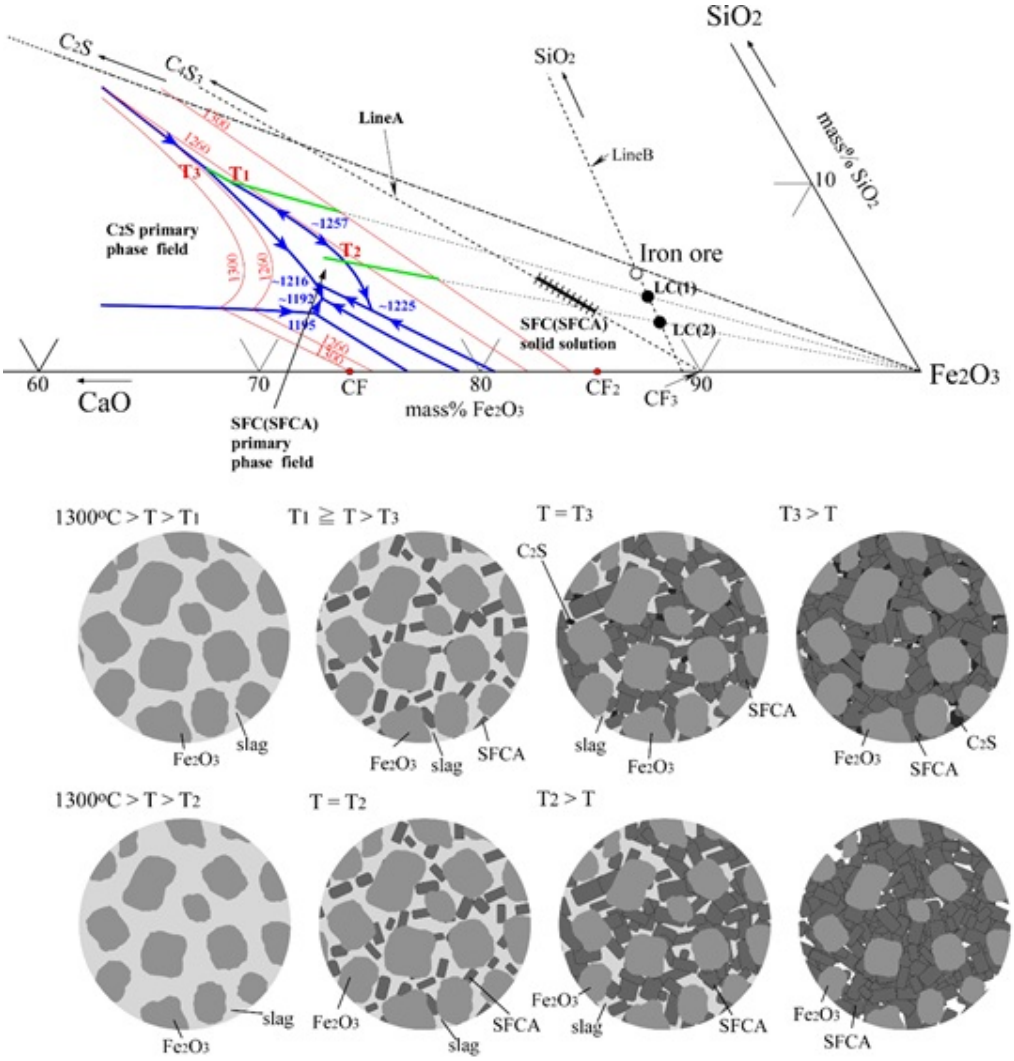

FIG 8 – (a) Phase equilibrium of the iron-rich corner of the $CaO\text{-}SiO_2\text{-}Fe_2O_3$ system in air including liquidus, SFC primary phase field, SFC solid solution and the sample composition (Chen *et al*, 2019). The straight lines connecting $4CaO\cdot 3SiO_2$ (C_4S_3) and $CaO\cdot 3Fe_2O_3$(CF_3) and SiO_2 and sample composition are denoted by Line A and Line B, respectively; (b) Schematic illustration of the equilibrium microstructures for samples having the chemical compositions of LC(1) and LC(2), which are both on Line B (Hayashi *et al*, 2022).

CONCLUSIONS

This study investigated the effect of alumina on microstructures of iron ore sinters from the perspective of the phase equilibria of the $CaO\text{-}SiO_2\text{-}Fe_2O_3$-5 mass% Al_2O_3 system at 1240°C in air including the compositional range of a four-component calcium ferrite (SFCA, SFCA-I), the liquidus isotherm and the phase equilibria of SFCA and SFCA-I.

The compositional region of SFCA lies on the $CF_3\text{-}CA_3\text{-}C_4S_3$ plane and is C/S = 2.77–7.60 for 5 mass% Al_2O_3. Compared to the SFC composition region with a 0 mass% Al_2O_3 (C/S = 2.92–4.32,

Chen *et al* (2019)), that of SFCA extended in the CF_3-C_4S_3 direction, indicating that the addition of Al_2O_3 contributes to SFCA stability.

The liquid-phase region was divided into a ferrite melt with a high Fe_2O_3 concentration and a silicate melt with a high SiO_2 concentration, both of which shifted to the lower Fe_2O_3 side compared to the liquidus isotherm in the CaO-SiO_2-Fe_2O_3 system (Chen *et al*, 2019; Dayal and Glasser, 1967).

Unlike the CaO-SiO_2-Fe_2O_3 (0 mass% Al_2O_3) system (Mumme, 2003), SFCA-I (SFC-I) was observed in the CaO-SiO_2-Fe_2O_3-5 mass% Al_2O_3 system. This suggests that the addition of Al_2O_3 contributes to the stability of SFCA-I. The compositional region of SFCA-I was not on the CF_2-CA_2-C_3S_2 plane owing to the presence of Fe^{2+}.

The aforementioned results imply that an increment in Al_2O_3 concentration in iron ore leads to a decrement in the volume fraction of the bonding phase and that the fraction of the SFCA phase increases and those of $2CaO{\cdot}SiO_2$ and slag phases decrease in the bonging phase. The SFCA-I phase is also precipitated from the slag with an Al_2O_3 concentration around 5 mass%.

REFERENCES

Chen, J, Cheng, S, Shevchenko, M, Hayes, P C and Jak, E, 2021. Investigation of the thermodynamic stability of $C(A,F)_3$ solid solution in the FeO-Fe_2O_3-CaO-Al_2O_3 system and SFCA phase in the FeO-Fe_2O_3-CaO-SiO_2-Al_2O_3 system, *Metall Mater Trans B*, 52B:517–527.

Chen, J, Shevchenko, M, Hayes, P C and Jak, E, 2019. A phase equilibrium of the iron-rich corner of the CaO-FeO-Fe_2O_3-SiO_2 system in air and the determination of the SFC primary phase field, *ISIJ Int*, 59:795–804.

Cheng, S, Shevchenko, M, Hayes, P C and Jak, E, 2021. Experimental phase equilibria studies in the FeO-Fe_2O_3-CaO-Al_2O_3 system in air, *Metall Mater Trans B*, 52B:2416–2429.

Dayal, R R and Glasser, F P, 1967. Phase relations in the system CaO-Al_2O_3-Fe_2O_3, *Sci Ceram*, 3(1967):191–214.

Hayashi, M, Zhou, D, Iwami, Y, Higuchi, T, Watanabe, T, Endo, R and Susa, M, 2022. Effect of $2CaO{\cdot}SiO_2$ addition on reaction behavior of iron ore sinters, *ISIJ Int*, 62:1785–1791.

Hayes, P C, Chen, J and Jak, E, 2016. Phase Equilibria Study of the CaO-"Fe_2O_3"-SiO_2 System in Air to Support Iron Sintering Process Optimisation, in *Proceedings 10th International Conference on Molten Slags, Fluxes and Salts 2016*, pp 707–714 (Springer).

Machida, S, Nushiro, K, Ichikawa, K, Noda, H and Sakai, H, 2005. Experimental evaluation of chemical composition and viscosity of melts during iron ore sintering, *ISIJ Int*, 45:513–521.

Mumme, W G, 2003. The crystal structure of SFCA-II, $Ca_{5.1}Al_{9.3}Fe^{3+}_{18.7}Fe^{2+}_{0.9}O_{48}$ a new homologue of the aenigmatite structure-type, and structure refinement of SFCA-type, $Ca_2Al_5Fe_7O_{20}$. Implications for the nature of the 'ternary-phase solid-solution', previously reported in *N Jahrb Mineral Abh*, 178:307–335.

Oyama, N, Nushiro, K, Konishi, Y, Igawa, K and Sorimachi, K, 1996. Influence of matrix strength and pore structure on sinter cake strength, *Tetsu-to-Hagané*, 82:719–724.

Patrick, T R C and Lovel, R R, 2001. Leaching dicalcium silicates from Iron ore sinter to remove phosphorus and other contaminants, *ISIJ Int*, 41:128–135.

Patrick, T R C and Pownceby, M I, 2002. Stability of silico-ferrite of calcium and aluminum (SFCA) in air-solid solution limits between 1240°C and 1390°C and phase relationships within the Fe_2O_3-CaO-Al_2O_3-SiO_2 (FCAS) system, *Metall Mater Trans B*, 33B:79–89.

Phillips, B and Muan, A, 1959. Phase equilibria in the system CaO-Iron Oxide-SiO_2 in air, *J Am Ceram Soc*, 42:413–423.

Sasaki, M and Hida, Y, 1982. Consideration on the properties of sinter from the point of sintering reaction, *Tetsu-to-Hagané*, 68:563–571.

Scarlett, N V Y, Pownceby, M I, Madsen, I C and Christensen, A N, 2004. Reaction sequences in the formation of silico-ferrites of calcium and aluminum in iron ore sinter, *Metall Mater Trans B*, 35B:929–936.

Shigaki, I, Sawada, M and Gennai, N, 1986. Increase in low-temperature reduction of iron ore sinter due to hematite-alumina solid solution and columnar calcium ferrite, *Trans Iron Steel Inst Jpn*, 26:503–511.

Takahashi, A, Uchisawa, Y, Sato, H, Watanabe, T, Endo, R, Susa, M and Hayashi, M, 2023. Effect of alumina on the phase equilibria of the Iron-rich corner of the CaO-SiO_2-Fe_2O_3 system at 1240°C in air, *ISIJ Int*, 63:1825–1833.

Tonžetć, I and Dippenaar, A, 2011. An alternative to traditional iron-ore sinter phase classification, *Miner Eng*, 24:1258–1263.

Yang, C K, Shoji, T and Takenouchi, S, 1978. Phase relations in the system CaO-Al_2O_3-Fe_2O_3-SiO_2 – Mineralogical study on sintered iron ores (2nd report), *J Min Metall Inst Jpn,* 94:575–580.

The possibility of using an autogenous Hydrogen-DRI slag as a raw material for vanadium extraction

DOI: 10.62053/SHTQ4045

J Huss[1], A Vickerfält[2] and N Kojola[3]

1. Researcher, Swerim AB, Isafjordsgatan 28A, 164 40, Stockholm, Sweden. Email: joar.huss@swerim.se
2. Researcher, Swerim AB, Isafjordsgatan 28A, 164 40, Stockholm, Sweden. Email: amanda.vickerfalt@swerim.se
3. Researcher, Hybrit Development AB, Klarabergsviadukten 70, E6, 101 21, Stockholm, Sweden, Email: niklas.kojola@hybrit.se

ABSTRACT

The possibility of using an acidic autogenous hydrogen direct reduced iron (H-DRI) slag as a basis for vanadium extraction is investigated. For a raw material to be suitable for producing high-quality FeV, the vanadium oxide content should be sufficiently high and the phosphorus oxide content in a tolerable range. Therefore, the feasibility for vanadium extraction relies on fulfilling two demands: the predominate partitioning of phosphorus to the metal and vanadium to the slag. Correspondingly, the behaviours of phosphorus and vanadium in the Al_2O_3-SiO_2-FeO_x-V_yO_z-P_2O_5-Fe system were studied experimentally. Slag, 10 g, was put in contact with liquid iron, 30 g, for different durations (2–24 hrs) in closed alumina crucibles at 1873 K. The slag composition was varied between 33.1–49.3 wt per cent Al_2O_3, 27.1–46.7 wt per cent SiO_2, 16.6–30.1 wt per cent FeO_x, and 2.5–8.8 wt per cent V_2O_3. The equilibrium phosphorus distribution was 0.42, while the vanadium distribution ranged from 7.6 to 43.4, increasing with the Al_2O_3- and the FeO_x-content.

INTRODUCTION

Ferro vanadium (FeV) is used to alloy steels of many grades during secondary steelmaking (Moskalyk and Alfantazi, 2003). The oxygen potential in this process step is intentionally kept very low to maximise the yield of the alloying element. The ability to refine steel from phosphorus is virtually non-existent in environments with low oxygen potential. Since phosphorus will contaminate the steel during secondary steelmaking, the quality of the alloying element is, among other factors, determined by its phosphorus content (Tao *et al*, 2020). Correspondingly, it is desirable to minimise the P-content in the FeV.

Converter slag has been seen as a largely untapped resource for vanadium production. The production of a high-quality, low phosphorus FeV from converter slag has therefore been of interest for previous studies, and while some innovative approaches have been proposed, none have seen industrial adoption (Lindvall *et al*, 2010, 2017; Gupta and Krishnamurthy, 1992). The main difficulty originates from the parallel transfer of vanadium and phosphorus from the liquid pig iron to the converter slag (Lindvall *et al*, 2010, 2017). At the same time, it is challenging to remove phosphorus during the extraction process (Tao *et al*, 2020). The amount of phosphorus in a slag intended for V-extraction should, therefore, be minimised during steelmaking. The future fossil-free production route could offer an opportunity for this purpose. In the novel fossil-free production route, where hydrogen direct reduced iron (H-DRI) will be the principal material, the initial conditions are different compared to the blast-furnace route. In the H-DRI, vanadium and phosphorus are initially in oxide phases originating from the iron ore (Jonsson *et al*, 2013; Lövgren, 2005). Vanadium is then concentrated in the autogenous slag during melting. Unfortunately, when fluxed, typically with CaO, the slag will also dephosphorise the steel made from H-DRI (Vickerfält, Martinsson and Sichen, 2021; Huss, Berg and Kojola, 2020). A future autogenous slag must be specially engineered for a high V- and low P-content for feasible vanadium extraction. In other words, the autogenous slag should satisfy two demands for it to be suitable as raw material for vanadium extraction, *viz* (a) the vanadium content should be sufficiently high, and (b) the phosphorus content should be in a tolerable range. The basis for a potential slag design is briefly outlined below.

The two main demands could be met by designing the autogenous slag for (a) a suitable oxygen potential during steelmaking and (b) a low dephosphorisation power. Firstly, a suitable oxygen

potential during steelmaking must be established to achieve the desired P and V distributions. Since the FeO content determines the oxygen potential, the FeO content in the slag should be designed. Secondly, the dephosphorisation power of the slag is, in addition to the oxygen potential, dependent on the oxygen anion activity (Herasymenko, 1941). Correspondingly, a future autogenous slag should be engineered for a low oxygen anion activity to decrease the dephosphorisation power of the slag. It is well established that the oxygen anion activity is strongly limited in acidic slag systems due to the high degree of structural linkage. Hence, in theory, an acidic slag could be a suitable basis for vanadium extraction. For efficient material use, the specially designed acidic autogenous slag should be based on the gangue found in the H-DRI. The main components of the gangue are silica and alumina (Lövgren, 2005). Thus, the pseudo-quaternary Al_2O_3-SiO_2-FeO_x-V_yO_z system is an interesting candidate to study, summarising the outline.

Some previous studies have been carried out on related systems, *viz* the CaO-Al_2O_3-V_2O_3 and the CaO-Al_2O_3-SiO_2-V_2O_3 systems (Lindvall, Gran and Sichen, 2014; Vermaak, Pistorius, 2000). Vermaak and Pistorius (2000) found that the activity coefficient of vanadium(III)oxide in the liquid slag phase decreased substantially with increasing CaO/Al_2O_3 ratios. Lindvall, Gran and Sichen (2014) observed that vanadium oxide was predominantly found in the solid phases of the slag, while the concentration in the liquid slag phase was close to 0 wt per cent. As the present system is hardly studied, this work presents novel and relevant results to determine whether an appropriately engineered autogenous H-DRI slag could provide new possibilities for vanadium extraction. Unfortunately, no commercial DR-grade pellets specially engineered for this purpose are available. The future possibility is, therefore, investigated by employing synthetic slags.

In summary, this exploratory study aims to assess the possibility of using an acidic autogenous slag as a raw material for vanadium extraction by investigating the distribution between relevant synthetic slags and liquid iron of (1) vanadium and (2) phosphorus and (3) by investigating the present slag phases to understand the behaviours better.

EXPERIMENTAL

Experimental set-up

A vertical resistance heated tube furnace was employed to study the distributions and slag phases. A schematic drawing of the set-up is given in Figure 1. The alumina reaction tube was fitted in the lower end with a water-cooled aluminium cap and in the upper end with an interconnected water-cooled aluminium cooling chamber. Argon gas (99.999 per cent purity) was passed to the reaction tube through an inlet situated in the aluminium cap and led out through an outlet placed in the cooling chamber. The cooling chamber was equipped with an additional inlet to allow a separate high flow of argon gas to be injected directly into the cooling chamber to enhance the heat transfer from the sample during cooling. A B-type thermocouple with an outer alumina sheath was installed through a compression seal fitting in the aluminium cap and positioned close to the sample in the even temperature zone (+/- 4 K over 10 cm) to monitor the temperature. The samples were suspended in the furnace using an arrangement consisting of a lifting system, a steel tube, a Mo-tube, and a Mo-crucible holder. The steel tube was attached to the lifting system and entered the furnace through the cooling chamber. The upper end of an intermediate Mo-tube was connected to the steel tube, while a Mo-crucible holder was connected to the lower end. The Mo-crucible holder held one recrystallised double-sintered alumina crucible, 60 mm hr × 36 mm Ø at a time, in which the sample resided. The orifice of the crucible was covered with a Mo-lid, thus closing the system. The suspension arrangement was, in turn, connected to a lifting system, enabling the movement of the samples in the vertical direction. Additionally, simmerings were fitted to the steel rod. Thus, the atmosphere was prevented from being altered by the movement of the rod. A gas-tight seal of the reaction tube was ensured by sealing the other set-up components using O-rings.

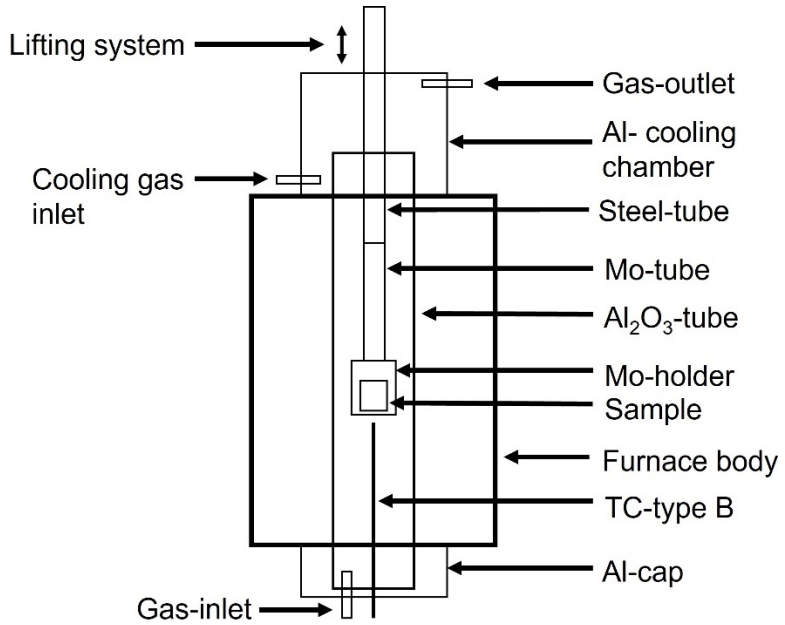

FIG 1 – Schematic drawing of the experimental set-up.

Sample preparation

The samples consisted of metal and slag. The metal phase was prepared by mixing 30 g of Fe- (99.9 per cent purity) and Fe_3P-powder (99.5 per cent) in an agate mortar. The total amount of phosphorus was varied by adding different amounts of Fe_3P and Fe. The corresponding P concentration, should all phosphorus commit to the metal phase, was thus varied between 0.1 to 0.82 wt per cent. The slag phase was prepared by mixing FeO_x and commercially available Al_2O_3 (99.97 per cent purity), SiO_2 (99.5 per cent), and V_2O_3 (99.7 per cent) powders. FeO_x was made in-house by thoroughly mixing Fe-powder (99.9 per cent) and Fe_2O_3-powder (99.9 per cent) to an oxygen content of 51.4 at per cent, followed by sintering in a closed iron crucible at 1373 K for 8 hrs. An argon atmosphere protected the iron crucible from oxidation throughout the sintering. The Al_2O_3 and SiO_2 powders were heated to 1173 K for 72 hr prior to usage. 10 g of the slag components were then mixed in an agate mortar for 15 min. Phosphorus was added to the slag side in one experiment, Sample 10, using $Mg_2P_2O_7$, to check the reliability of the experiments. Moreover, a specific procedure of adding the sample to the crucible was used to limit the reaction between the slag and the crucible during heating. A ~5 g portion of the Fe-mixture was first added to the crucible covering its base. The slag mixture was pressed into three cylindrical pellets using a hydraulic press and a steel die (23 mm ID) with an applied pressure of 30 MPa. The slag pellets were then stacked and centred in the crucible. Subsequently, the gap between the crucible wall and slag pellets was filled with the remaining Fe-mixture. Considering the limited contact between the slag and the crucible, the reaction between the two is expected to be minimised during heating. The system was then sealed by placing a polished Mo-lid on the crucible orifice, which was also polished beforehand. The weighed-in slag and metal compositions and the experimental durations are given in Table 1.

TABLE 1

Weighed-in slag and metal compositions and the corresponding experimental durations. *P added as $Mg_2P_2O_7$ given as the corresponding $[P]F_e$ content.

Sample no	Duration hrs	Al_2O_3 wt%	SiO_2 wt%	FeO_x wt%	V_2O_3 wt%	$Al2O_3/SiO_2$	$[P]F_e$ wt%
1	6	18.75	31.25	40.00	9.99	0.6	0.20
2	2	17.10	42.85	30.01	10.04	0.4	0.82
3	2	31.79	52.95	10.18	5.08	0.6	0.20
4	24	30.00	50.00	10.00	10.00	0.6	0.10
5	4	30.00	50.00	10.00	10.00	0.6	0.10
6	6	30.00	50.00	10.00	10.00	0.6	0.20
7	6	26.25	43.75	20.00	10.00	0.6	0.20
8	2	26.05	43.35	10.74	19.85	0.6	0.89
9	2	42.83	37.23	9.90	10.04	1.2	0.80
10	2	30.00	50.01	10.01	9.98	0.6	0.80*
11	2	29.99	49.93	10.06	10.01	0.6	0.81
12	2	10.00	49.78	30.16	10.08	0.2	0.81
13	2	50.25	29.52	10.33	9.91	1.7	0.82
14	2	54.42	24.70	11.05	9.84	2.2	0.82

Experimental procedure

The sample was mounted to the lifting system and suspended in the water-cooled aluminium chamber. The furnace was then sealed. The reaction tube was evacuated, and the seal was checked for vacuum. Argon gas was subsequently passed to the reaction tube to atmospheric pressure. The reaction tube was evacuated again and backfilled with argon gas. This process was repeated five times to ensure the desired atmosphere was acquired. A flow of 0.1 L min^{-1} was then kept throughout the experiment. The furnace was heated up to the experimental temperature of 1873 K at a rate of 1.7 K min^{-1}. The sample was preheated to avoid shocking the reaction tube by slowly lowering the sample to a preheating position (1573 K), followed by a 10-min thermal equilibration period. The sample was then quickly lowered to the even temperature zone and kept for different durations, 2-24 hrs, see Table 1. After the experimental duration, the sample was raised to the aluminium cooling chamber in a matter of seconds, where a separate high flow of argon gas was injected to enhance the cooling. The furnace was then cooled down, and the sample was extracted. The slag was found attached to the crucible wall and needed to be mechanically separated by grinding the crucible wall before chemical analysis. After separation, the composition of the slag was analysed using X-ray fluorescence (XRF), and the present phases were studied using a scanning electron microscope with supplementary energy dispersive spectroscopy (EDS) functionality. The metal phase released readily from the crucible and the slag. After separation, the metal composition was analysed using optical emission spectroscopy (OES).

RESULTS

The phosphorus and vanadium distributions in the closed Al_2O_3-SiO_2-FeO_x-V_yO_z-Fe system were studied as a function of slag composition. The compositions of the slag and the metal phase are given in Table 2. Omitted from the table are minor oxidic constituents, ie with a content of <0.2 wt per cent, except for P_2O_5. Note that phosphorous was added to the slag side as $Mg_2P_2O_7$ in one experiment, Sample 10, resulting in a MgO content of 1.9 wt per cent. Moreover, the determination of valences was not within the scope of this work. The content of vanadium and iron oxide is, therefore, given in the Fe^{2+} and V^{3+} valence states even though the presence of multiple

valences is likely (Wang, Li and Sichen, 2011; Allertz, Selleby and Sichen, 2015). The P_2O_5 content was found to be low or below the detection limit for all slag compositions, Table 2, while the content of V_2O_3 varied between 2.5–8.8 wt per cent. The distributions of P and V between slag and metal were calculated by virtue of Equations 1 and 2, respectively, to further the examination.

$$L_P = \frac{2M_P \times (wt\%P_2O_5)}{M_{P_2O_5} \times [wt\%P]_{Fe}} \quad (1)$$

where LP is the phosphorus distribution between slag and metal, (wt% P_2O_5) the analysed content of phosphorus oxide in the slag phase, [wt% P]F_e the analysed concentration of phosphorus in the metal phase, and MP, MP_2O_5 the molar masses of phosphorus and phosphorus oxide respectively.

$$L_V = \frac{2M_V \times (wt\%V_2O_3)}{M_{V_2O_3} \times [wt\%V]_{Fe}} \quad (2)$$

where L_V is the vanadium distribution between slag and metal, (wt% V_2O_3) the analysed content of vanadium oxide in the slag phase, [wt% V]F_e the analysed concentration of vanadium in the metal phase, and M_V, $M_{V2}O_3$ the molar masses of vanadium and vanadium oxide respectively.

TABLE 2

Analysis of the slag (XRF), metal phase (OES), and present phases.

	XRF						OES				
Sample no	**Al_2O_3 wt%**	**SiO_2 wt%**	**FeO_x wt%**	**V_2O_3 wt%**	**P_2O_5 wt%**	**Al_2O_3/SiO_2**	**[P]F_e wt%**	**[V]F_e wt%**	**L_V**	**LP**	**Phases**
1	38.2	27.3	30.1	4.4	<0.01	1.40	0.159	0.069	43.4		S, L
2	36.6	33.4	24.8	5.2	<0.01	1.09	0.297	0.144	24.6		S,L
3	33.3	46.7	17.5	2.5	<0.01	0.71	0.300	0.223	7.6		M, L
4	37.1	39.3	18.2	5.3	0.082	0.95	0.085	0.380	9.5	0.42	S, L, M
5	33.4	42.3	18.7	5.6	<0.01	0.79	0.090	0.390	9.7		S, L, M
6	35.2	42.6	16.8	5.4	<0.01	0.82	0.174	0.419	8.8		S, L, M
7	40.0	34.2	20.3	5.4	<0.01	1.17	0.154	0.234	15.5		S, L, M
8	37.9	31.3	21.9	8.8	<0.01	1.21	0.300	0.329	18.2		S, L, M
9	43.5	32.8	17.1	6.6	<0.01	1.33	0.289	0.309	14.5		S, L, M
10	36.6	37.1	20.8	5.2	0.265	0.99	0.288	0.208	16.8	0.40	S, L, M
11	33.1	43.8	17.6	5.5	<0.01	0.76	0.299	0.422	8.9		S, L, M
12	37.1	34.0	23.8	5.1	<0.01	1.09	0.293	0.175	19.7		S, L, M
13	48.3	28.3	16.6	6.8	<0.01	1.71	0.298	0.221	20.8		S,L,M,C
14	49.3	27.1	16.9	6.7	<0.01	1.82	0.300	0.153	29.7		S,L,M,C

The LP was calculated for Samples 4 and 10 to 0.42 and 0.40, respectively, while the L_V varied between 7.6 and 43.4. The calculated distributions are given together with the respective slag compositions in Table 2.

Furthermore, it was found that the vanadium distribution increased with an increase in the FeO- and in the Al_2O_3 content. To ease the detailed examination, L_V is shown as a function of the FeO content in Figure 2a. As indicated in the figure, the slag compositions have been divided into subsets of similar mass ratios of Al_2O_3/SiO_2. In Figure 2b, L_V is given as a function of the Al_2O_3/SiO_2 ratio for slags with similar FeO contents. By examining the figures, it is clear that the vanadium distribution increases with increasing contents of FeO and with increasing Al_2O_3/SiO_2 mass ratios.

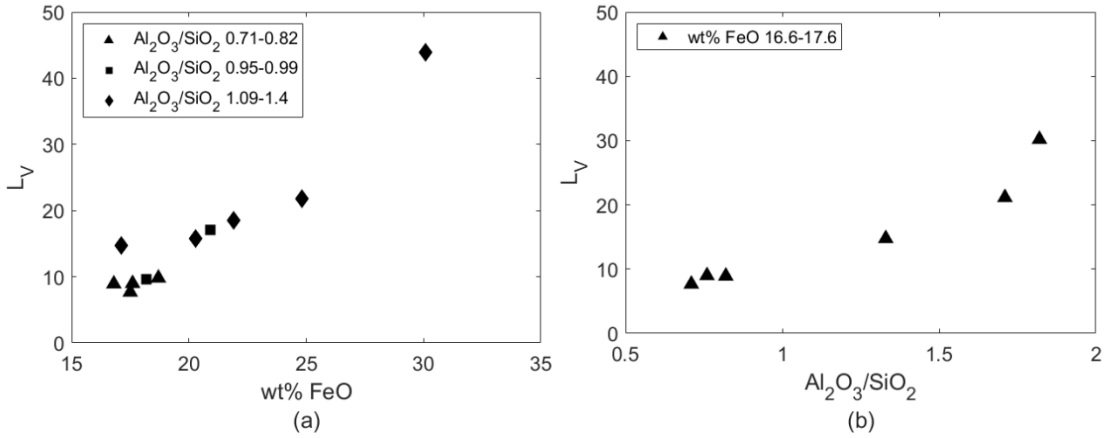

FIG 2 – L_V as a function of (a) the FeO content and (b) the Al_2O_3/SiO_2 mass ratio.

Further, the L_V data can be used to estimate the vanadium oxide content in an autogenous slag where the H-DRI is based on an iron ore with a vanadium(V)oxide content of 0.25 wt per cent. A mass balance approach was used for the calculation where the slag-to-metal mass ratio was varied between 3 and 4.2 per cent depending on the amount of alumina needed to modify the autogenous slag and the mass of FeO. It is calculated that the vanadium oxide content could vary between 2 and 5.5 wt per cent. The estimated vanadium oxide content in the autogenous slag is given as a function of FeO in Figure 3, where some relevant examples of the Al_2O_3/SiO_2 mass ratios are given next to the data points.

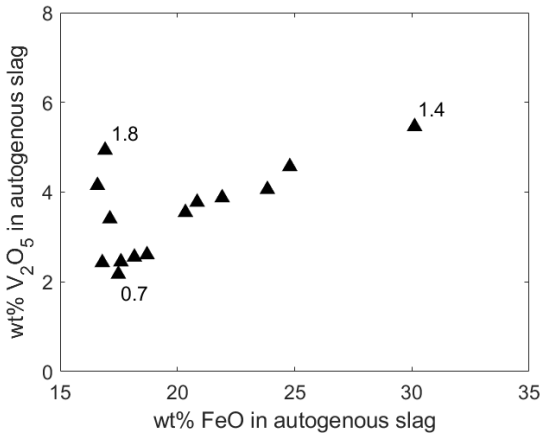

FIG 3 – Calculated vanadium oxide content in the autogenous slag as a function of FeO content.

The present slag phases were examined to better understand the effect of Al_2O_3 and FeO on L_V. When analysed by SEM-EDS, a total of four different phases were found: spinel phase, ‘S’, liquid phase, ‘L’, mullite phase, ‘M’, and corundum phase, ‘C’. The phases present in each sample are given in Table 2. As the table shows, four different phase relations were encountered: L-S, L-M, L-S-M, and L-S-M-C. Figure 4 shows an example micrograph of each phase relationship.

A microstructure consisting of two phases, a liquid phase (grey) and a vanadium-containing spinel phase (light grey), was found in slags with a FeO content of 27.5 +/- 2.6 wt per cent (Samples 1, 2) Figure 4a. A different microstructure containing a liquid- (grey) and a mullite phase (dark grey) was found for a slag containing 17.5 wt per cent FeO, Sample 3, see Figure 4b. For slags containing 33.1–43.4 wt per cent Al_2O_3, 31.3–43.7 wt per cent SiO_2, and 16.8–21.9 wt per cent FeO_x (Samples 4–12), a microstructure containing three phases, the bright spinel phase, the angular dark grey mullite, and the grey liquid phase was found, see Figure 4c. For slags containing 47.5–48.3 wt per cent Al_2O_3 (Samples 13, 14), the Al-corundum phase was present in addition to the previously mentioned phases; see Figure 4d. Furthermore, it was found that the composition of the phases varied depending on the total slag composition. Given the uncertainties associated with EDS analysis, the composition of the present phases for all slag compositions is not reported. Instead, to

illustrate the composition of the present phases, the EDS analysis of the phases for one sample containing all phases, Sample 13, is provided in Table 3.

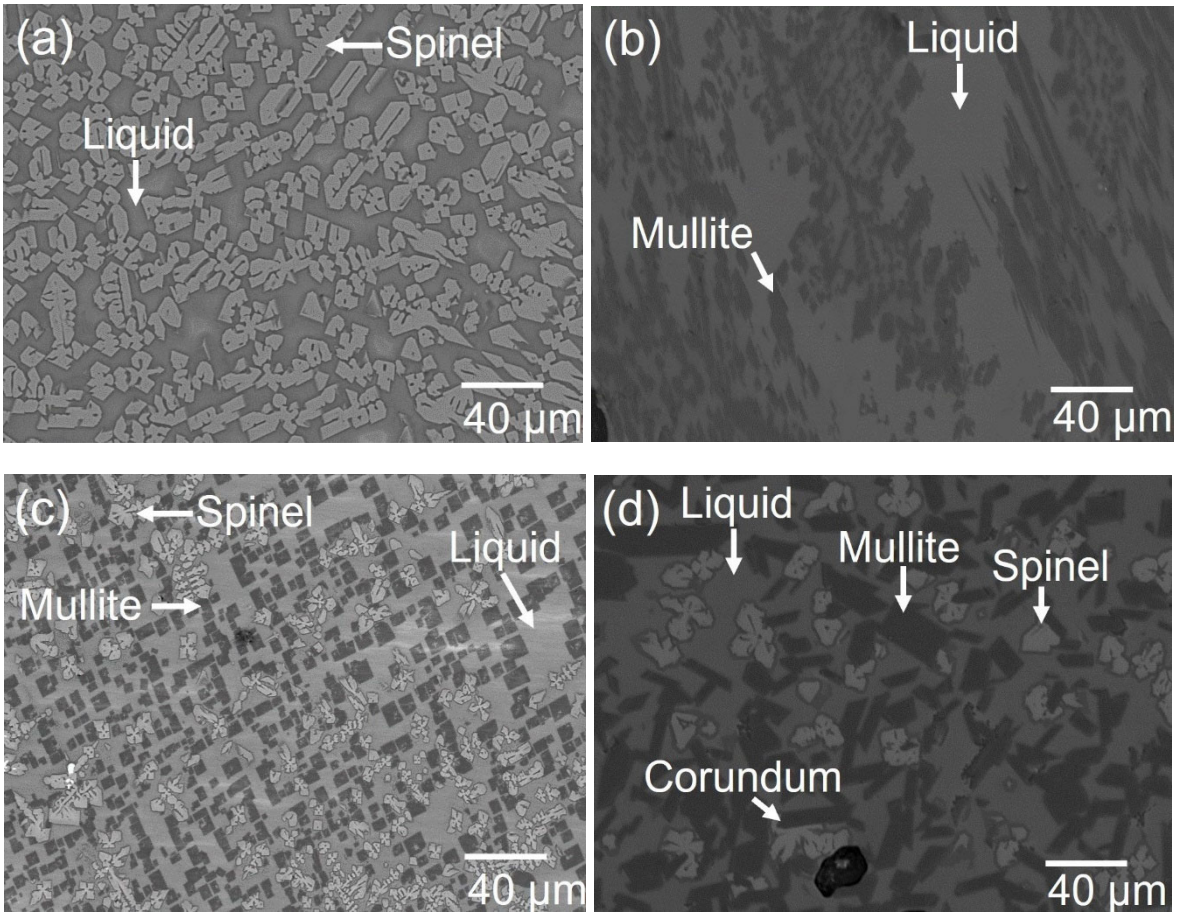

FIG 4 – Microstructures containing (a) the liquid- and spinel phase, (b) the liquid- and mullite phase, (c) the liquid-, mullite- and spinel phase, and (d) in addition the corundum phase.

DISCUSSION

Phosphorus distribution

The distribution expression in Equation 1 is, to some extent, dependent on the ratio of slag to metal mass. For practical convenience, the ratio of slag to metal in the present study was set to 1:3, while the ratio is commonly around 1:6–10 in the EAF (Horii *et al*, 2013). In remedy, a far greater concentration of phosphorus than expected in the industry was employed. The phosphorus oxide content in the slag will, therefore, be exaggerated in this experimental study compared to industrial conditions. Despite this fact, the phosphorus content in the slag was low or below the detection limit. This shows that the experimental observations would apply to the industrial case even though the slag-to-metal ratio is different.

Sample 4 was kept for 24 hrs, which is considerably longer than needed to establish equilibrium between metal and slag (Basu, Lahiri and Seetharaman, 2008; Suito, Inoue and Takada, 1981). Therefore, the observed phosphorus partition is considered the equilibrium distribution. The phosphorus content at equilibrium was 0.1 wt per cent with an LP of 0.42, whereas the content was below the detection limit for slags kept at a shorter duration. The difference indicates that equilibrium was not established during the shorter experimental time. Regardless, the very low phosphorus contents in the slag show that its dephosphorisation power is undoubtedly low. This is expected considering the low oxygen anion activity in acidic slags. Additionally, phosphorus was added to the slag side in one experiment, Sample 10. The experimental duration was 2 hrs, which resulted in a phosphorus distribution of 0.40. This is similar to Sample 4 (0.42), which indicates that phosphorus initially in the slag phase is transferred at a faster rate to the metal phase than *vice versa*. Potentially,

this is an aspect that should be considered in industrial applications. Nevertheless, it is evident that the proposed slag system is efficient in partitioning phosphorus to the metal phase, which unconventionally is the desired outcome. One of the necessary conditions for the possible vanadium extraction from an autogenous slag of the present slag system is thereby met. The second condition is the predominant partitioning of vanadium to the slag phase.

Behaviour of vanadium

The vanadium content in the autogenous slag must be sufficiently high for feasible vanadium extraction. Ultimately, the vanadium oxide concentration in the ore determines V-content in the slag and, thereby, whether the autogenous slag can feasibly be used for vanadium extraction. The feasibility should correspondingly be evaluated based on the ore. For this purpose, the vanadium oxide content in the autogenous slag was estimated based on the experimentally determined L_V and an iron ore containing 0.25 wt per cent of vanadium(V)oxide. It is estimated that the vanadium oxide content in the autogenous slag could vary between 2 wt per cent and 5.5 wt per cent, Figure 3. A vanadium content of 2 wt per cent is likely less than needed for an economically feasible extraction today, while 5.5 wt per cent could constitute, for this purpose, a sufficient portion of the slag.

Both demands have been satisfied since phosphorus is predominantly partitioned to the metal and the autogenous slag could contain a significant vanadium oxide content. It is, therefore, possible that an autogenous H-DRI slag based on the present system could provide a new opportunity for vanadium extraction. Further, to aid in the future process design, the behaviour of vanadium is discussed in detail based on the phases in the slag. The main focus of the discussion is given to the effect of slag composition and the impact of oxygen potential.

Vanadium-containing slag phases

To help the discussion in the later section, the phases in the slag will be discussed first. The present phases were identified based on the respective compositions. The mullite phase is of the $3Me_2O_3{:}2MeO_2$ form, corresponding to a molar ratio of Me^{3+} to Me^{+4} of 1.5 (Schneider, Schreuer and Hildmann, 2008). It is reasonable to assume that solid solution could lead to a shift in the ratio. For this reason, some thermodynamic calculations were carried out in the Al-Si-O system, which showed that the ratio between Me^{3+} and Me^{+4} can vary between 1.38 and 1.77 (Andersson *et al*, 2002). The observed ratio, specifically the $(Al_2O_3+V_2O_3)/SiO_2$ molar ratio, was 1.38, see Table 3, and is thus in line with the calculated boundaries. In addition, around 1–2 wt per cent of FeO_x was detected in the mullite phase, which could come from background interference in EDS analysis. This, nevertheless, shows that the amount of Me^{2+} lattice positions is limited, in line with the established understanding of the mullite phase (Schneider, Schreuer and Hildmann, 2008).

TABLE 3

Example of phase compositions by EDS.

Phase	Al_2O_3 wt%	SiO_2 wt%	FeO_x wt%	V_2O_3 wt%
Spinel	40.3	3.3	35.3	21.1
Liquid	18.8	52.2	28.9	0.1
Mullite	60.6	28.6	1.2	9.6
Corundum	86.9	0	1.0	12.1

A similar approach was employed in identifying the spinel phase. The spinel phase consists of alumina, iron-, and vanadium oxide. By not allowing silica, Si^{4+}, into the lattice, it is concluded that the Me^{4+} positions are limited, in line with the established understanding of the 2–3 spinel structure (Tsurkan *et al*, 2021). The measured phase composition also agreed with the V-Fe-Al-O phase diagram, further supporting the argument. Moreover, vanadium was found almost exclusively in the solid phases of the slag, see Table 3, which is similar to what Lindvall, Gran and Sichen (2014) observed for a related slag system. This could be due to the activity coefficient of vanadium(III)oxide

being significantly higher in the acidic liquid slag phase than in the solid phases (Vermaak, Pistorius, 2000). A systematic study regarding the activity coefficients of vanadium(III)oxide in the different phases is needed to explain this phenomenon fully. Further, it is noted that the spinel phase was suppressed as the content of vanadium oxide in the system was low, Sample 3, Figure 4b, and that the mullite phase did not form at higher FeO contents, Samples 1 and 2, Figure 4a. The principal vanadium-carrying phase could, therefore, depend on the ingoing material and the used praxis. Considering that the difference in the present phases will likely impact the subsequent vanadium extraction process, it is essential to consider the phases together with the employed praxis. The corresponding phase diagrams of the spinel, mullite, and corundum phases and the respective roasting and leaching properties will be integral to study to orientate a future process better.

Vanadium distribution

Effect of vanadium oxide content on LV

The effect of vanadium oxide content on the vanadium distribution between slag and metal was investigated by varying the amount of added V_2O_3. Samples 7 and 8 contained similar alumina to silica ratios and FeO contents, while the final V_2O_3 content differed (5.4–8.8 wt per cent). A similar distribution of vanadium was observed for the samples (15.5 and 18.2). This shows that the amount of V_2O_3 in the system does not profoundly change the vanadium distribution in the system over the mentioned range. Similarly, Samples 3 and 5 display a similar behaviour over the final V_2O_3 content range of 2.5–5.6 wt per cent. This shows that a variation in V_2O_3 content in a small range does not profoundly impact the vanadium distribution of the system. In contrast, when the full range of final V_2O_3 contents (2.5–8.8 wt per cent) is examined, there is a measurable difference. As vanadium is added to the slag side, a portion of the vanadium is reduced and dissolved in the metal phase. In the closed system, the chemical potentials are set by the ingoing components, which means the reduction of vanadium is achieved by the parallel oxidation of iron. This leads to a dynamic stabilisation of the chemical potentials where the FeO concentration initially increases and is followed by the dissolution of the crucible material. Hence, the stabilisation of the potentials results in an increase in the alumina-to-silica ratio, which significantly impacts the vanadium distribution.

Effect of alumina to silica ratio and FeO on Lv

The ability to vary the silica-to-alumina ratio is limited under the equilibrium condition. Therefore, to investigate the distribution of vanadium over a broader range of compositions, a duration of 2 hrs was chosen for most of the experiments. To ensure the experiments can be used for semi-quantitative determination of V and P distributions, four separate experiments were carried out where the distributions were examined over a duration range of 2–24 hrs, Samples 4, 5, 6, and 11. No profound change in the distribution of vanadium and phosphorus was apparent over the duration range. This strongly suggests that the results obtained over a 2 hour experimental duration will be suitable for semi-quantitative determination of the distribution of vanadium at different Al_2O_3/SiO_2 ratios.

Due to the dissolution of the crucible material, it is not possible to quantitatively distinguish the effect of FeO_x from the impact of the alumina to silica ratio (Al_2O_3/SiO_2) on L_V. The effects are, therefore, discussed separately in a qualitative manner. With increasing FeO contents, the FeO activity will increase, resulting in a higher oxygen potential. The increase in the partial pressure of oxygen will drive the oxidation reaction of vanadium, Equation 3, to the right-hand side, thus increasing L_V. The effect is evident when examining Figure 2a, where the vanadium distributions of similar ratios of Al_2O_3/SiO_2 are shown as a function of the FeO_x content.

$$[V]_{Fe} + \frac{x}{2}O_2 \leftrightarrow (VO_x) \tag{3}$$

In addition, it is clear from Figure 2b that an increase in the Al_2O_3/SiO_2 ratio has resulted in an increase in the vanadium distribution. Principally, two mechanisms operate simultaneously, resulting in the observed effect. The first is related to the oxygen potential in the system, and the second is the varying fraction of the solid phase. Considering the mechanisms operate simultaneously and interdependently, they will be discussed together. As a first step in the discussion, only the mullite phase is considered.

Systems with higher Al_2O_3/SiO_2 ratios will contain a larger fraction of mullite phase than systems with a lower ratio. As the solubility of FeO in mullite is very low, for any given FeO concentration, the liquid slag phase of high-ratio systems will contain more FeO and have higher oxygen potential compared to the corresponding low-ratio systems. To support the argument, the activity of FeO, at a fixed FeO content, of slags in equilibrium with liquid iron was calculated as a function of the Al_2O_3/SiO_2 ratio for the Al-Si-Fe-O system, using a commercial thermodynamic software (Andersson *et al*, 2002). The FeO activity for a high-ratio system (1.6) was double that of a low-ratio system (0.6), see Table 4. As discussed, the higher FeO-activity will, in turn, result in a higher oxygen potential. The corresponding oxygen potentials were, therefore, calculated by virtue of Equations 4–6 and are also presented in Table 4 (Basu, Lahiri and Seetharaman, 2007). This ultimately entails that a higher Al_2O_3/SiO_2 ratio drives the oxidation reaction of V, thus increasing L_V.

$$Fe(l) + \frac{1}{2}O_2(g) \rightarrow FeO(l) \tag{4}$$

with the corresponding free energy function:

$$\Delta G^{\circ} = -256061 + 53.831 \times T \ (\frac{J}{mole}) \tag{5}$$

where the equilibrium constant is defined as:

$$K = \frac{a_{FeO}}{a_{Fe} \times {p_{O_2}}^{1/2}} \tag{6}$$

where K is the equilibrium constant of Equation 6, aF_eO is the activity of FeO, aF_e the activity of iron and pO_2 the partial pressure of oxygen.

TABLE 4

Calculated oxygen potential as a function of the Al_2O_3/SiO_2 ratio of the slag in equilibrium with liquid iron at 1873 K for the Al-Si-Fe-O system.

Al_2O_3 wt%	SiO_2 wt%	FeO wt%	Al_2O_3/SiO_2	Mullite phase fraction	aF_eO	pO_2 atm
33.75	56.25	10.00	0.6	0.056	0.056	6.48E-12
45.00	45.00	10.00	1	0.241	0.072	1.07E-11
57.00	33.00	10.00	1.7	0.450	0.113	2.64E-11

To further the discussion, the spinel phase is also considered. Unfortunately, no detailed and reliable thermodynamic description of the vanadium-containing spinel was available. The effect of the fraction of spinel phase on the oxygen potential is therefore discussed qualitatively. The higher oxygen potential due to the mullite phase fraction could, to some extent, be lessened should the spinel phase also be present. The spinel phase consisted of alumina, iron-, and vanadium oxide. It is, therefore, expected that systems with a relatively high Al_2O_3/SiO_2 ratio will also contain a larger fraction of spinel phase compared to the low ratio system. The spinel phase contains a similar iron oxide content as the liquid phase, while the Al_2O_3 content is higher, see Table 3. Higher spinel phase fractions will, therefore, lead to the liquid phase containing more silica, which will, correspondingly, lower the FeO concentration in the liquid. It should be kept in mind that V is almost exclusively found in the solid phases of the slag. A higher fraction of solid phase(s) means the number of available lattice positions that vanadium can occupy is greater. More vanadium is allowed into the slag, resulting in a higher vanadium distribution between slag and metal. This reasoning implies that the highest vanadium distribution will be found at the highest total content of FeO and the highest Al_2O_3/SiO_2 ratio. The present reasoning is, therefore, in line with the experimental results.

While it is important to consider the vanadium distribution in the industrial implementation, it should be considered together with other aspects, such as the physical properties of the slag, reaction kinetics, and the content of V, especially. Apart from the concentration of V in the ore, when a substantial amount of alumina and FeO_x is present in the slag, V could be diluted to the detriment of the subsequent extraction process, even though the L_V is relatively high. Correspondingly, it is

essential to consider the L_V and the dilution effect simultaneously to optimise the V_yO_z content in the slag. Slags with high contents of vanadium oxide would, therefore, be an interesting topic for further studies.

SUMMARY

The possibility of using Al_2O_3-SiO_2-FeO_x-V_yO_z slags as a basis for vanadium extraction was investigated. The possibility was evaluated based on the fulfillment of two overarching criteria: the predominant phosphorus partitioning to the metal phase and vanadium to the slag phase. It was found that the dephosphorisation power of the slag was very low, with nearly all phosphorus partitioned to the metal phase. A significant amount of vanadium was kept in the slag, found almost exclusively in the solid phases. The distribution of vanadium increased with increasing ratios of Al_2O_3/SiO_2 and with increasing contents of FeO_x. The increase was discussed based on the oxygen potential in the system, the different vanadium-bearing solid phases, the fraction of solid phase, and the interplay between the fraction of solid phases and the oxygen potential. Ultimately, it was concluded that the studied slag system is a promising candidate for vanadium extraction as both criteria were satisfactorily met.

ACKNOWLEDGEMENTS

The authors gratefully acknowledge the financial support of HYBRIT Development AB.

The authors would like to express their gratitude to Prof. Pär Jönsson for his support. Also, we would like to express our most sincerest of thanks to Prof. Du Sichen for his never wavering patience in all discussions.

REFERENCES

Allertz, C, Selleby, M and Sichen, D, 2015. Sulfide Capacity in Ladle Slag at Steelmaking Temperatures, *Metallurgical and Materials Transactions B*, 46(6):2609–2615.

Andersson, J, Helander, T, Höglund, L, Shi, P and Sundman, B, 2002. Thermo-Calc and DICTRA, computational tools for materials science, CALPHAD, 26:273–312.

Basu, S, Lahiri, A and Seetharaman, S, 2008. Activity of Iron Oxide in Steelmaking Slag, *Metallurgical and Material Transactions B*, 38B(3):357–366.

Basu, S, Lahiri, A and Seetharaman, S, 2007. Phosphorus partition between liquid steel and CaO-SiO_2-FeOx-P_2O_5-MgO slag containing 15 to 25 Pct FeO, *Metallurgical and Material Transactions B*, 38B:623–630.

Gupta, C and Krishnamurthy, N, 1992. *Extractive Metallurgy of Vanadium* (Elsevier Science Publishers: Amsterdam, The Netherlands).

Herasymenko, P, 1941. Fremdionen-Wirkung auf die Gleichgewichte zwischen Stahl und flüssigen Schlacken (The effect of foreign ions on the equilibrium between steel and liquid slags), *Zeitschrift für Elektrochemie (Journal of Electrochemistry)*, 47(8):588–594.

Horii, K, Tsutsumi, N, Kitano, Y and Kato, T, 2013. Processing and Reusing Technologies for Steelmaking Slag, Nippon Steel Technical Report No. 104:123–129.

Huss, J, Berg, M and Kojola, N, 2020. Experimental Study on Phosphorus Partitions Between Liquid Iron and Liquid Slags Based on DRI, *Metallurgical and Material Transactions B*, 51B:786–794.

Jonsson, E, Troll, V, Högdahl, K, Harris, C, Nilsson, K and Skelton, A, 2013. Magmatic origin of giant 'Kiruna-type' apatite-iron-oxide ores in central Sweden, *Scientific Reports*, 3(1):1–8.

Lindvall, M, Gran, J and Sichen, D, 2014. Determination of the vanadium solubility in the Al_2O_3-CaO (25 mass%)-SiO_2 system, CALPHAD, 47:50–55.

Lindvall, M, Rutqvist, E, Ye, G, Björkvall, J and Sichen, D, 2010. Possibility of Selective Oxidation of Vanadium from Iron and Phosphorus in Fe-V-P Melt, *Steel Research International*, 8(2):105–111.

Lindvall, M, Tikka, J, Berg, M, Ye, G and Sichen, D, 2017. Vanadium Extraction from a Fe–V (2.0 Mass%)–P (0.1 Mass%) Melt and Investigation of the Phase Relations in the Formed FeO–SiO_2-Based Slag with 20 Mass% V, *Journal of Sustainable Metallurgy*, 3:808–822.

Lövgren, J, 2005. Metallugisk studie av pellets avsedda för LRI tillverkning (A metallurgical study of pellets intended for Less Reduced Iron (LRI) production), Master thesis, Luleå University of Technology.

Moskalyk, R and Alfantazi, A, 2003. Processing of vanadium: a review, *Minerals Engineering,* 16(9):793–805.

Schneider, H, Schreuer, J and Hildmann, B, 2008. Structure and properties of mullite - A review, *Journal of the European Ceramic Society*, 28:329–344.

Suito, H, Inoue, R and Takada, M, 1981. Phosphorus Distribution between Liquid Iron and MgO Saturated Slags of the System CaO-MgO-FeOx-SiO_2, *Transactions of the Iron and Steel Institute of Japan*, 21:250–259.

Tao, C, Yu, Q, Liu, Z, Peng, Y, He, W and Deng, R, 2020. Directional conversion and removal of complex phosphorus compounds from acidic leaching solution containing vanadium, *Journal of Water Process Engineering*, 37:1–8.

Tsurkan, V, Krug von Nidda, H, Deisenhofer, J, Lunkenheimer, P and Loidl, A, 2021. On the complexity of spinels: Magnetic, electronic and polar ground states, *Physics Reports*, 926:1–86.

Vermaak, M and Pistorius, P, 2000. Equilibrium slag losses in ferrovanadium production‘, *Metallurgical and Material Transactions B*, 31B:1091–1097.

Vickerfält, A, Martinsson, J and Sichen, D, 2021. Effect of Reduction Degree on Characteristics of Slag Formed by Melting Hydrogen-Reduced DR I and Partitions of P and V between Slag and Metal, *Steel Research International*, 92(3):1–11.

Wang, H, Li, F and Sichen, D, 2011. Development of an Analytical Technique to Determine the Fractions of Vanadium Cations with Different Valences in Slag, *Metallurgical and Material Transactions B*, 42:9–12.

Solubility of nitrogen and inclusion characteristics in high aluminium steels

DOI: 10.62053/IJND8579

M Ishfaq[1] and M M Pande[2]

1. Institute Post Doctoral Fellow, Department of Metallurgical Engineering and Materials Science, Indian Institute of Technology Bombay, Mumbai, Maharashtra 400076, India. Email: ishfaqibnghmohammad@gmail.com
2. Associate Professor, Department of Metallurgical Engineering and Materials Science, Indian Institute of Technology Bombay, Mumbai, Maharashtra 400076, India. Email: manish.pande@iitb.ac.in

ABSTRACT

The effect of aluminium on nitrogen solubility was investigated by equilibrating melt comprising master alloy of Fe-Al with pure electrolytic iron in a controlled atmosphere (pure argon) at 1873 K. Nitrogen in the samples was measured by sampling technique using inert gas fusion absorptiometry. It was found that nitrogen content decreases steadily with aluminium concentration and gradually, becomes close to 1 ppm for very high aluminium steels. Wagner's second order interaction parameter formalism has been used to estimate the equilibrium constant and interaction parameters. Scanning electron microscopy (SEM) investigation showed, dual-phase inclusions comprising AlN phase surrounding alumina core. The 3D morphology of inclusions was studied by extracting the sample from the top and the central bottom portion of the solidified ingot. A sparse distribution of nitrogen was found for most of the inclusions which manifested the presence of almost pure alumina inclusions with different morphologies and sizes.

INTRODUCTION

Solubility of nitrogen in very high aluminium steels has been rarely studied so far. During secondary steelmaking, most of the focus is on removal of oxygen by adding aluminium wire and minimising the unwanted impurities like alumina inclusions and sulfur by adding lime to the melt. However, nitrogen dissolution in steels also impact the properties of the metal. The nitrogen dissolution in steels happens as per Sievert's law where molecular nitrogen dissociates into atomic nitrogen as shown in Equations 1and 2 (Sieverts and Zapf, 1935; Turkdogan, 1980):

$$\frac{1}{2}\mathrm{N_2(g)} = \underline{\mathrm{N}} \tag{1}$$

$$\Delta \mathrm{G}^\circ = -RT \ln K = 3598 + 23.89\ \mathrm{T}\ \text{J/mole} \tag{2}$$

The affinity of nitrogen towards metals especially aluminium is lower as compared to that of oxygen towards aluminium due to difference in electronegativity. However, aluminium is known to form a stable nitride in steels (Hsiao, 1958). Both aluminium nitride and alumina inclusions have detrimental effects on the mechanical properties of the steel and hence both are undesirable. It is therefore crucial to study the evolution of their morphology, size, and growth. Presence of nitrogen however in steels can appreciably enhance interstitial solid solution strengthening. Nitrogen occupies an interstitial site and can lock the movement of dislocations. Examining the solubility of nitrogen is crucial, similar to investigating the solubility of oxygen, in relation to varying concentrations of aluminium as nitrogen plays a significant role in determining the physical and mechanical properties of metal after solidification. During solidification, excess nitrogen can come out as bubbles thus causing solidification defects like blowholes in metal. Some nitrogen may react with alloying elements like aluminium and form nitrides. The remaining nitrogen stays in the interstitial sites promoting austenitic (γ) structure. Nitrogen, similar to oxygen, exists in two forms: the soluble nitrogen which occupies interstitial sites and the insoluble nitrogen that forms nitride inclusions.

Most of the researchers have investigated the solubility of nitrogen in low aluminium steels at different partial pressures of nitrogen and have determined nitrogen either by using Sievert's method or sampling technique. A substantial work has been carried out in determining the solubility of nitrogen in liquid iron containing different alloying elements (Pehlke and Elliott, 1960; Wada and Pehlke, 1977; Ishii, Ban-ya and Fuwa, 1982; Kim *et al*, 2007; Paek *et al*, 2013) at different partial

pressures of nitrogen. In the present work, the prime focus is on the effect of aluminium on the dissolved nitrogen using sampling method. At aluminium concentration >5 wt per cent, there is hardly any reported data on the solubility of nitrogen in Fe-Al alloy. Sievert's method is based on gas solubility in molten metal at a particular gas pressure while in sampling method, the analysis of nitrogen is done after analysing the solidified metal. The analysis of nitrogen involves various methods, for example, using either Kjeldahl method or using inert gas fusion method. Beeghly (1949) determined nitrogen from aluminium nitride present in aluminium killed Bessemer steel and open-hearth steel using micro-Kjeldahal method. Kim *et al* (2007) studied the thermodynamics of AlN formation at various nitrogen partial pressures. Nitrogen solubility in high manganese, high aluminium steels was investigated by Paek *et al* (2013) at varying partial pressures of nitrogen (0.1–0.8 atm). Both used inert gas fusion method for determination of nitrogen and oxygen in the samples. Nitrogen content in the previous work was in the range of several hundred to even thousands of ppm however in the present work, it was limited in the range of 17 ppm (initial) to less than a ppm (final).

EXPERIMENTAL METHODOLOGY

Electrolytic iron chunks (weighing around 60–90 grams) along with Fe-Al master alloy were melted in the pure alumina crucible (99.99 per cent pure) at 1873 K using a vertical tube furnace (Carbolite Gero) as shown in Figure 1. The temperature, heating rate, cooling rate and dwelling time was set by a Nanodac controller. Detailed experimental procedure can be found in our previous work (Ishfaq and Pande, 2024). The equilibration time of 2 hr was provided for the melt. The sample underwent heating, melting, and cooling in the furnace in an inert (purified argon) atmosphere. Analysis of aluminium and nitrogen was conducted on samples extracted from the central bottom (CB) portion of the ingot. The thickness of CB region was 1 cm and it was sliced away from the bottom most region (thickness 0.5 cm), as shown in Figure 2. The quantitative determination of aluminium content was carried out using Inductively Coupled Plasma-Atomic Emission spectroscopy (ICP-AES, SPECTRO ARCOS). In the CB region, two cuboidal samples (4 mm × 5 mm × 8 mm) each with a mass of ~1 gram were taken for the nitrogen analysis using inert gas fusion infrared absorptiometry (LECO ON-736).

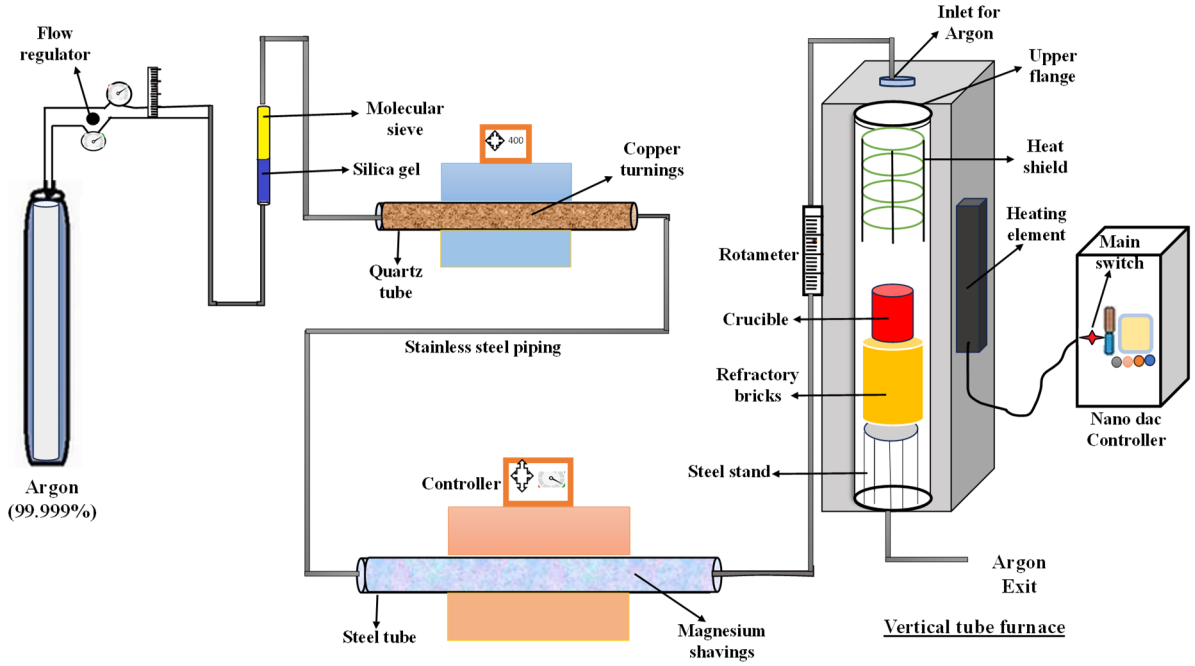

FIG 1 – Schematic of the high temperature experimental set-up.

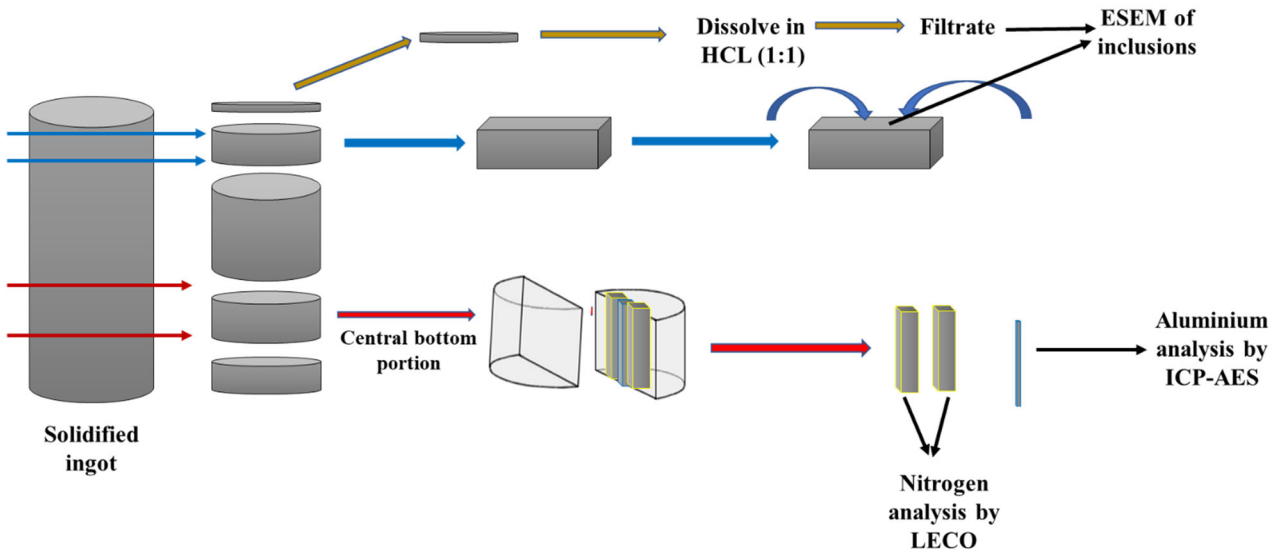

FIG 2 – Sampling methodology.

Initial nitrogen (melted electrolytic iron) was in the range of 46–50 ppm. Prior to melting, the total oxygen was found to be in the range of 93–115 ppm with accuracy of ±4 ppm in the electrolytic iron flakes using LECO while the total oxygen measured in the solidified samples (after melting in the furnace without any addition) was in the range of 100–120 ppm. For nitrogen analysis, the average of the two samples from the central bottom region of the solidified ingot was considered. However, for inclusion analysis, samples were taken from the top portion and CB region. These samples were examined using environmental scanning electron microscope (ESEM-FEI Quanta 200) for inclusion characteristics. For investigating the 3D morphology of inclusions, the sliced portion from the top and CB portion of ingot was dissolved in HCl (dilute 1:1 v/v). The filtrate was allowed to remain on Whatman filter paper with a pore size of 2.5 microns. The residue was then dried and placed over the carbon tape. Platinum coating was applied over it, and the inclusions were analysed using the SEM in secondary electron (SE) mode. The morphology, size, and elemental mapping of the inclusions were investigated and are elaborated in the 'Results and discussion' section. The detailed sampling methodology is depicted in Figure 2.

RESULTS AND DISCUSSION

The nitrogen content in the present experiments was limited as the high temperature experiments were carried out in a high-purity argon atmosphere rather than maintaining nitrogen at various partial pressures. This gives an important advantage of determining solubility of nitrogen in an inert atmosphere and therefore, formation of a fine deposit of aluminium nitride over the melt surface is prevented at higher aluminium concentration. The vapor pressure of aluminium at 1873 K is 182 pascals which is much more than that of liquid iron. In nitrogen atmosphere, some portion of vaporised aluminium may react with nitrogen present in the surrounding atmosphere and form a stable nitride layer or deposit over the melt surface (Pehlke and Elliott, 1960; Kim *et al*, 2007). In the present study, Al-N data from the selected experiments was considered as shown in Table 1. Al concentration range was much wider as compared to the nitrogen range. While establishing the equilibrium between aluminium and oxygen (Al-O), the oxygen concentration exhibited rapid fluctuations even with minor changes in aluminium concentration (Kang *et al*, 2009; Paek *et al*, 2015; Ishfaq and Pande, 2024). However, in assessing nitrogen solubility in the current experiments across varying aluminium concentrations, there was no discernible change in nitrogen concentration for the initial ten experiments outlined in Table 1. Moreover, considering the narrow nitrogen concentration range and calibration of nitrogen against a standard within ±3 ppm, resulted in the minimal variation in a N content for the increasing Al concentrations.

TABLE 1

Equilibrium concentration of Al and N in steel measured after solidifying the samples.

wt% Al	Nitrogen in wt% (±3 ppm)
0.0735	0.00162
0.14	0.001685
0.256	0.001925
0.279	0.001763
0.519	0.002445
1.132	0.00213
1.386	0.001575
1.704	0.00205
5.462	0.001555
5.985	0.001648
8.375	0.000133
9.518	0.000065
11.78	0.000089
13.013	0.000121
15.097	0.000095
21.56	0.000118
23.35	0.000057

As the aluminium content in the sample increases beyond a certain critical concentration, the dissolved nitrogen decreases. The change in nitrogen content is not prominent in the beginning as the nitrogen concentration fluctuates between 24 to 15 ppm. However, the trend was quite dissimilar to that of Al-O equilibria where oxygen was minimum in the certain concentration range of aluminium (Kang *et al*, 2009; Paek *et al*, 2015; Ishfaq and Pande, 2024). Beyond a particular concentration of aluminium, the oxygen started to increase again. It should be mentioned here that Kim *et al* (2007) found similar behaviour of decrease in nitrogen with increase in aluminium content in their experiments. In the present work, the nitrogen content was close to 1 ppm in all the samples when aluminium content was more than 8.375 wt per cent. Interestingly Ishii, Ban-ya and Fuwa (1982) and Paek *et al* (2013) found out a contrasting feature with addition of manganese. In their experiments, addition of manganese increased the solubility of nitrogen.

Thermodynamic assessment of aluminium nitrogen

The thermodynamics of Fe-Al-N system can be assessed by considering $\underline{Al}$ and $\underline{N}$ as two solutes dissolved in solvent iron. It is important to consider iron and aluminium along with O or N while considering the thermodynamics of ternary system. In the present study, Fe-Al-O and Fe-Al-N ternary systems can be separately considered instead of a quaternary Fe-Al-O-N system because it is unlikely that nitrogen and oxygen would contribute to any mutual interaction. Thermodynamics of Fe-Al-O ternary system has been already elucidated in our previous work using different formalisms (Ishfaq and Pande, 2024). For Fe-Al-N system, the formation of aluminium nitride has been considered by the following reaction:

$$\underline{Al} + \underline{N} = AlN \quad (3)$$

The equilibrium constant for Reaction 3 can be written as:

$$K_1 = \frac{a_{AlN}}{a_N\, a_{Al}} \tag{4}$$

The Henrian activity of component j (relative to 1 mass per cent) can be written as the product of activity coefficient (f_i) and wt per cent.

Considering AlN as pure, the activity of AlN can be taken as unity. Further, the Henrian activity of component 'j' relative to the hypothetical 1 mass per cent standard in liquid iron can be taken as the product of activity coefficient (f_j) and weight per cent of component j (wt per cent j). Expanding Equation 4:

$$\log(f_N) + \log(wt\%N) + \log(f_{Al}) + \log(wt\%Al) = \log\frac{1}{K_1} \tag{5}$$

Considering the Wagner's 2nd order interaction parameter formalism (WIPF 2nd order) for expansion of $\log(f_N)$ and $\log(f_{Al})$ (ignoring the 3rd and higher order ones),

$$e_{Al}^{Al}(wt\%Al) + e_{Al}^{N}(wt\%N) + r_{Al}^{Al}\,(wt\%Al)^2 + r_{Al}^{N}\,(wt\%N)^2 + r_{Al}^{Al,N}\,(wt\%Al)(wt\%N) + \log(wt\%Al) + e_N^{Al}(wt\%Al) + e_N^{N}(wt\%N) + \log(wt\%N) + r_N^{N}\,(wt\%N)^2 + r_N^{Al}\,(wt\%Al)^2 + r_N^{Al,N}(wt\%Al)(wt\%N) = \log K \tag{6}$$

Where K is the inverse of K_1.

Taking atomic weights of Fe, Al and N as 55.85, 27 and 14 respectively, the relationship between different interaction parameters (Lupis relationship) can be obtained as follows (Lupis, 1983):

$$e_{Al}^{(N)} = 1.92856\, e_N^{(Al)} - 4.0373 \times 10^{-3} \tag{7}$$

$$r_{Al}^{(Al,N)} = 3.857\, r_N^{(Al)} - 0.0192856\, e_N^{(Al)} + 0.01\, e_{Al}^{(Al)} \tag{8}$$

$$r_N^{(Al,N)} = 1.037\, r_{Al}^{(N)} - 0.01\, e_N^{(Al)} + 0.01\, e_N^{(N)} - 2.0933 \times 10^{-5} \tag{9}$$

The values of self-1st and 2nd order interaction parameters e_N^N and r_N^N have been taken as 0 (Sieverts and Zapf, 1935). The values of e_{Al}^{Al} and r_{Al}^{Al} have been taken as 0.045 and -0.001 (Sigworth and Elliott, 1974).

Substituting Equation 7, 8 and 9 in Equation 6:

$$0.045(wt\%Al) + \left[1.92856\, e_N^{(Al)} - 4.0373 \times 10^{-3}\right](wt\%N) - 0.001\,(wt\%Al)^2 + r_{Al}^{N}\,(wt\%N)^2 + \left[3.857\, r_N^{(Al)} - 0.0192856\, e_N^{(Al)} + 0.01\, e_{Al}^{(Al)}\right](wt\%Al)(wt\%N) + \log(wt\%Al) + e_N^{Al}(wt\%Al) + \log(wt\%N) + r_N^{Al}\,(wt\%Al)^2 + \left[1.037\, r_{Al}^{(N)} - 0.01\, e_N^{(Al)} + 0.01\, e_N^{(N)} - 2.09332 \times 10^{-5}\right](wt\%Al)(wt\%N) = \log K \tag{10}$$

Rearrangement of Equation 10 gives:

$$0.045(wt\%Al) - 4.0373 \times 10^{-3}(wt\%N) - 0.001\,(wt\%Al)^2 + \log(wt\%Al) + \log(wt\%N) + 4.29067 \times 10^{-4}(wt\%Al)(wt\%N) = e_N^{(Al)}[-1.92857(wt\%N) + 0.0292856\,(wt\%Al)(wt\%N) - (wt\%Al)] + r_N^{Al}[-3.857\,(wt\%Al)(wt\%N) - (wt\%Al)^2] + r_{Al}^{N}[-1.037\,(wt\%Al)(wt\%N) - (wt\%N)^2] + \log K \tag{11}$$

For determining the values of interaction parameters ($e_N^{(Al)}$, r_N^{Al} and r_{Al}^{N}) and equilibrium constant ($\log K$), Equation 11 can be represented by the form:

$$y = \lambda_1 x_1 + \lambda_2 x_2 + \lambda_3 x_3 + C$$

where:

$$y = 0.045(wt\%Al) - 4.0373 \times 10^{-3}(wt\%N) - 0.001\,(wt\%Al)^2 + \log(wt\%Al) + \log(wt\%N) + 4.29067 \times 10^{-4}(wt\%Al)(wt\%N)$$

$$x_1 = -1.92857(wt\%N) + 0.0292856\,(wt\%Al)(wt\%N) - (wt\%Al)$$

$$x_2 = -3.857\,(wt\%Al)(wt\%N) - (wt\%Al)^2$$

$$x_3 = -1.037\,(wt\%Al)(wt\%N) - (wt\%N)^2$$

$\lambda_1, \lambda_2, \lambda_3$ and C represent $e_N^{(Al)}$, r_N^{Al}, r_{Al}^{N} and $\log K$ respectively

Based on the present experimental data as compiled in Table 1, the values of all the unknowns in Equation 11 have been estimated using multiple linear regression. The value of R^2 was found to be 0.83. The plot on log scale is shown in Figure 3. The values of unknowns obtained on regression analysis are given as:

$$\text{Intercept} = \log K = -3.355 \pm 0.114$$

$$\lambda_1 = e_N^{(Al)} = -0.071 \pm 0.03$$

$$\lambda_2 = r_N^{(Al)} = 0.0015 \pm 0.0014$$

$$\lambda_2 = r_{Al}^{(N)} = -141.8 \pm 24.96$$

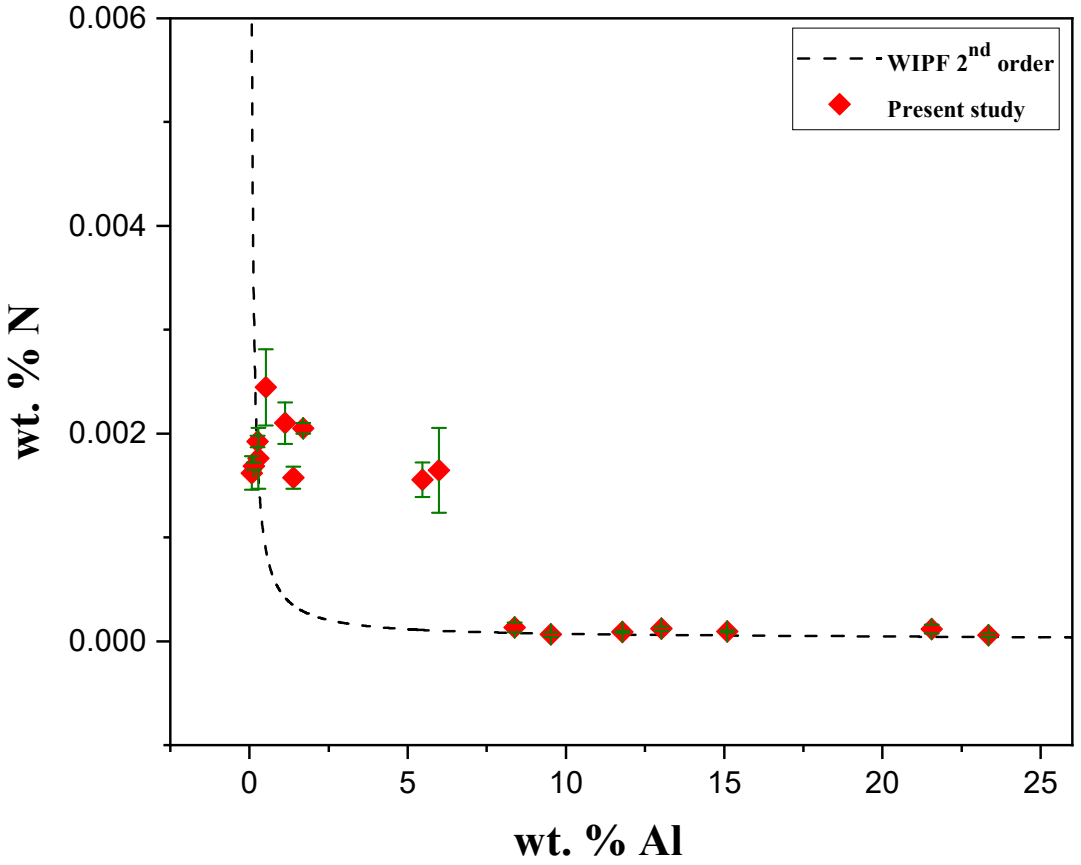

FIG 3 – Solubility of nitrogen at varying concentration of Al in steels. Symbols denote the experimental data and the solid line represent the curve obtained by WIPF 2nd order formalism.

The value of log *K* obtained in the present study is -3.355 using WIPF 2nd order. The values of log *K* obtained by the different researchers at 1873 K are -1.361 (Evans and Pehlke, 1964), -1.606 (Adachi, Morita and Wada, 1966), -1.267 (Wada and Pehlke, 1978) and -1.44 (Kim *et al*, 2007) while the values of 1st order interaction parameter $e_N^{(Al)}$ have been reported by some researchers as positive and others have reported its value as negative. The value of $e_N^{(Al)}$ at 1873 K as reported by different researchers are 0.017 (Kim *et al*, 2007), -0.028 (Evans and Pehlke, 1964), -0.025 (Adachi, Morita and Wada, 1966), -0.023 (Wada and Pehlke, 1978). The absolute value of log *K* and $e_N^{(Al)}$ in the present study is roughly three times greater than the values obtained by previous researchers. The present experiments were nitrogen deficient and aluminium concentration was much higher for most of the samples.

Inclusion analysis

The top central portion was examined under SEM for inclusion analysis. A cuboidal sample from two different experiments containing 5.985 and 11.78 wt per cent of aluminium were extracted close to the top region. The samples preparation is explained in the section Experimental Methodology. SEM-EDS investigation revealed the presence of dual-phase inclusions in the samples comprising of nearly spherical alumina in the centre and AlN at the periphery.

Figure 4 shows dual phase inclusions: Figure 4a with a ripsaw morphology, and Figure 4b a globular shape with a composition AlN at the outer periphery and Al_2O_3 in the centres. As mentioned by Alba (2021) that AlN is not stable at 1873 K at low nitrogen content. The aluminium nitride therefore grows over the pre-existing alumina inclusions. These alumina inclusions act as nucleating sites for nitrides to grow as can be seen in Figure 4. The EDS of the oxide inclusion located in the core of Figure 5 showed pure alumina.

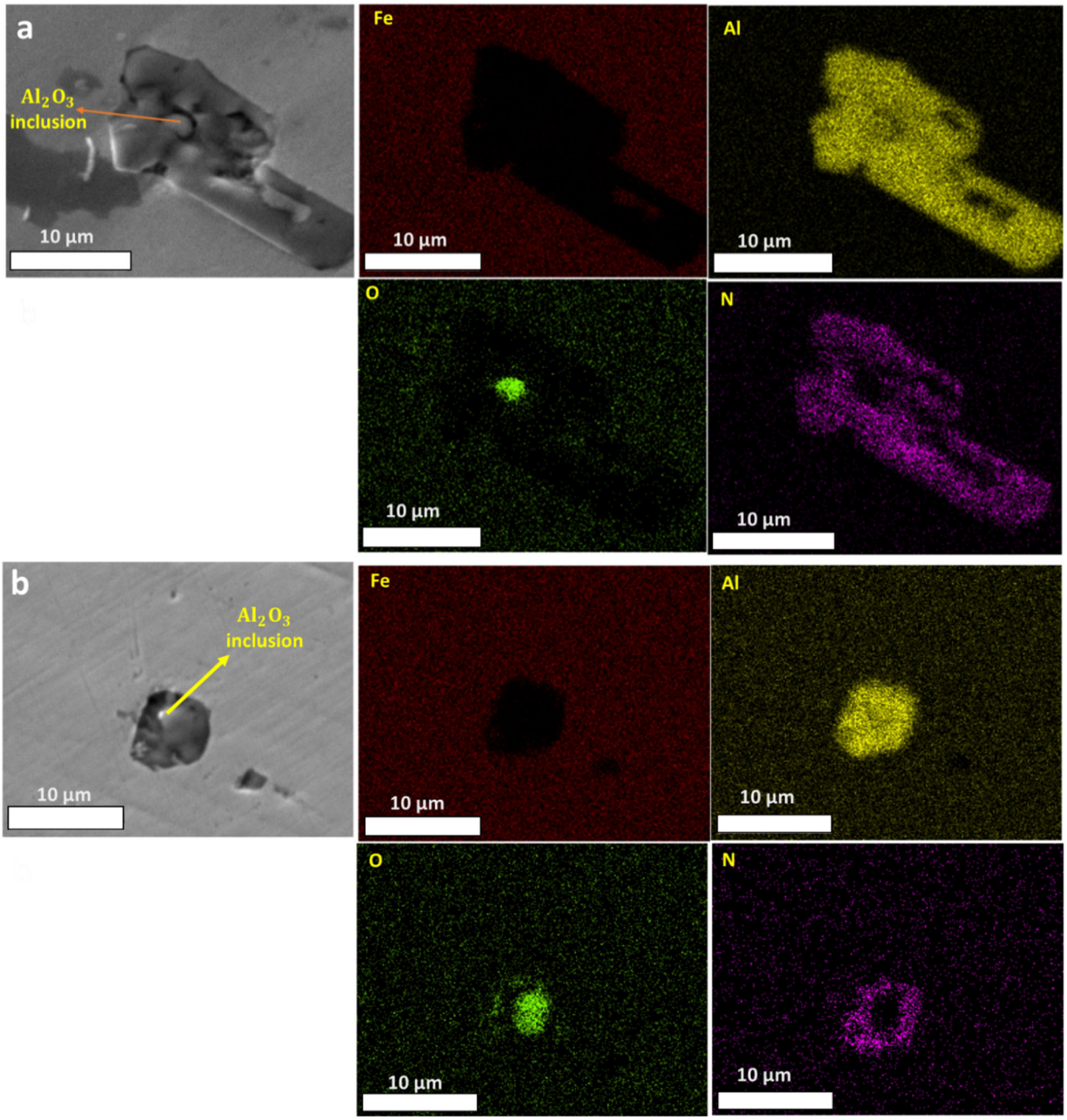

FIG 4 – BSE image and elemental mapping of aluminium nitride containing Al_2O_3 inclusion in its core while as AlN occupies the peripheral region: (a) sample with (Al – 5.985 wt per cent Al); (b) sample with (Al – 11.78 wt per cent Al).

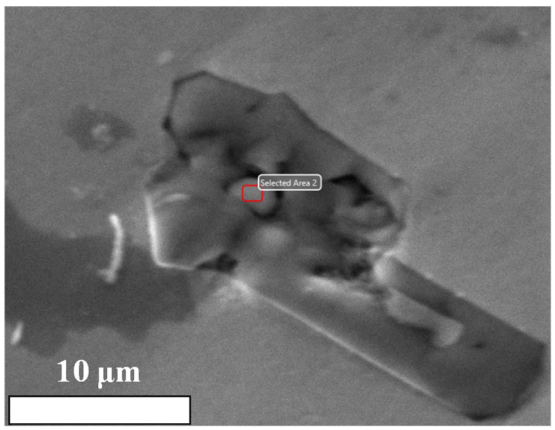

Element	Weight %	Atomic %
O	50.8	63.5
Al	49.2	36.5

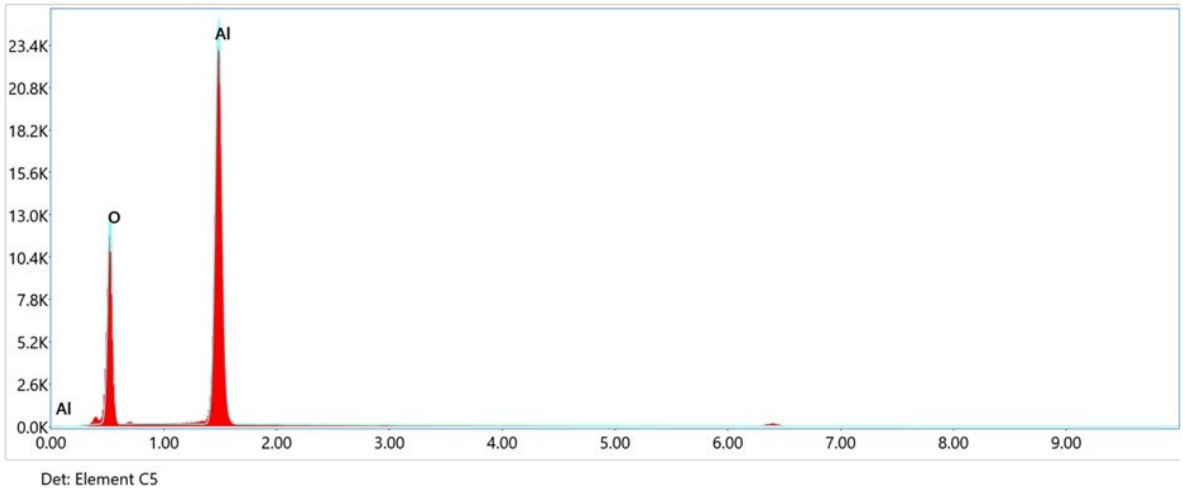

FIG 5 – EDS of the centred alumina inclusion (located in the core) of Figure 4a.

Alba (2021) and Guo *et al* (2023) obtained similar results. Using SEM analysis, they found out that AlN inclusions grow on the alumina inclusions. A heterogenous nucleation site thus promotes the growth of aluminium nitrides. Willems *et al* (1992) found out that single phase Al-O-N inclusion is stable only above 1923 K and dissociates into alumina and alumina nitride below this temperature. Nucleation of one type of inclusion over the other requires closeness in lattice fit. Bramfitt (1970) propounded that any nucleating site can be effective for a different inclusion to grow on its surface if lattice disregistry between the nucleating inclusion and substrate is less than 12 per cent. The lattice disregistry between (0001) AlN plane and (0001) alumina plane is about 12 per cent which indicates that AlN could grow on alumina substrate (Dovidenko *et al*, 1996). Presence of more oxygen in the melt decreases the contact angle between inclusion and steel. This can affect the size of inclusions as well. The relationship between contact angle (θ) and weight percentage of oxygen (Kawai and Shiraishi, 1988) can be given as:

$$\theta = 132 - 6.3\ln(1 + 400(\text{wt\%O})) \quad (12)$$

Since equilibrium concentration of oxygen in the melt is dependent on aluminium, so contact angle will also depend on aluminium. Further, aluminium will have its own individual effect on the surface tension of melt. The average size of aluminium nitride reported by Hsiao (1958) was in the range of 10–80 nm. However, aluminium concentration was in the deoxidation range (850 ppm). More oxygen in the melt decreases the contact angle of inclusions with steel thus promoting smaller sizes of inclusions. In the present experiments, oxygen concentration was in the 10 ppm range so the contact

angle of alumina inclusions was higher (130–136°). This clearly indicates the tendency of alumina inclusions to agglomerate and minimise contact with the steel.

It can be envisaged that the agglomerate was the outcome of accumulation of various particle sizes after the acid dissolution of the top surface of solidified ingot as filtrate residue. Such inclusion clusters were not found in polished surface of CB sample during SEM analysis. The elemental mapping was also done to confirm the presence of elements (Al, O and N).

Pure alumina inclusions were observed at the top surface after examining the filtrate using SEM-EDS (Scanning Electron Microscopy with Energy Dispersive X-ray Spectroscopy). Figure 6 illustrates a sparse distribution of nitrogen in the inclusions. These observations confirm that any nitrogen contamination from the atmosphere can be ruled out completely.

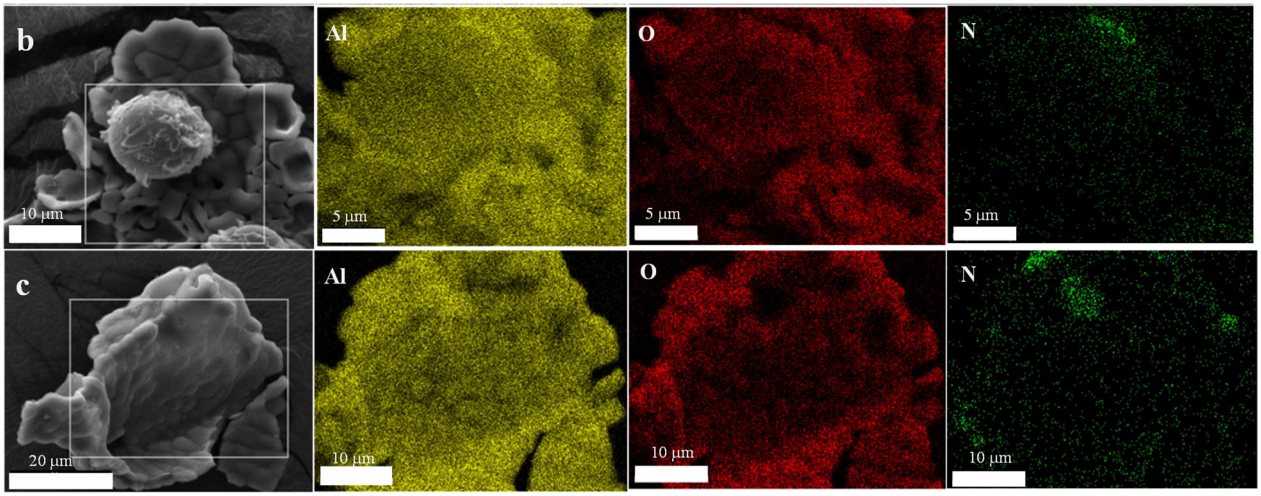

FIG 6 – The elemental mapping of the extracted inclusions (taken from the top portion of ingot as shown in Figure 2) shows presence of Al and O with minute distribution of nitrogen.

CONCLUSIONS

- The examination of nitrogen solubility at various aluminium concentrations in steels was conducted within a controlled atmosphere of pure argon, as opposed to nitrogen atmosphere. The initial nitrogen concentration was notably low.
- Increase in aluminium led to the decrease in the nitrogen levels, which was not prominent in low aluminium concentration range. However, in samples containing more than 8 wt per cent of aluminium, the nitrogen levels consistently remained around 1 ppm for all samples.
- Using 2nd order Wagner's interaction parameter formalism, the value of log *K* was found to be -3.355 while the first cross order interaction parameter $e_N^{(Al)}$ was found to be -0.071. The value of 2nd order interaction parameters $r_N^{(Al)}$ and $r_{Al}^{(N)}$ were found to be 0.0015 and -141.79 respectively.
- SEM-EDS analysis revealed the presence of nitride inclusions, which exhibited a tendency to grow over pre-existing alumina inclusions, forming dual-phase inclusions.

ACKNOWLEDGEMENTS

The authors express their appreciation to IIT Bombay for the resources made available for the experimental work conducted in the current study. The financial support provided by Industrial Research and Consultancy Center (IRCC) IIT Bombay, Mumbai; and Science and Engineering Research Board (SERB), Department of Science and Technology, Government of India is also gratefully acknowledged.

REFERENCES

Adachi, A, Morita, Z and Wada, J, 1966. The 19th Comm (Reaction), Japan Soc Promotion Sci (JSPS), report 19-8134.

Alba, M, 2021. Experimental investigation on inclusions in medium manganese steels and high manganese steels, PhD thesis, McMaster University, Hamilton.

Beeghly, H F, 1949. Behavior of nitrogen and some of its compounds in steel, *Analyt Chem,* 21:1513−1519.

Bramfitt, B L, 1970. The effect of carbide and nitride additions on the heterogeneous nucleation behavior of liquid iron, *Metall Trans*, 1:1987–1995.

Dovidenko, K, Oktyabrsky, S, Narayan, J and Razeghi, M, 1996. Aluminium nitride films on different orientations of sapphire and silicon, *J Appl Phys,* 79:2439–2445.

Evans, D B and Pehlke, R D, 1964. The Aluminium nitrogen equilibrium in liquid Iron, *Trans TMS-AIME,* 230:1651–1656.

Guo, Y, Cao, L, Wang, G and Liu, C, 2023. Precipitation behaviors of AlN inclusion in high-Al Steel, *Metall Mater Trans B*, 54:275–286.

Hsiao, C C, 1958. Fine Aluminium Nitride Precipitates in Steel, *Nature*, 181:1527–1528.

Ishfaq, M and Pande, M M, 2024. Establishing Aluminum-Oxygen (Al-O) Equilibria in Liquid Iron at 1873 K: An Experimental Study and Thermodynamic Analysis, *Metall Mater Trans B*, 55:1635–1655. https://doi.org/10.1007/s11663-024-03054-w

Ishii, F, Ban-ya, S and Fuwa, T, 1982. Solubility of nitrogen in liquid iron alloys, *Testu-to-Hagane*, 68:1551–1559.

Kang, Y, Thunman, M, Sichen, D, Morohoshi, T, Mizukami, K and Morita, K, 2009. Aluminum deoxidation equilibrium of molten iron–aluminum alloy with wide aluminum composition range at 1873, *ISIJ Int*, 49:1483–1489.

Kawai, Y and Shiraishi, Y, 1988. *Handbook of Physico-chemical Properties at High Temperatures*, 158 p (ISIJ).

Kim, W Y, Kang, J G, Park, C H, Lee, J B and Pak, J J, 2007. Thermodynamics of aluminum, nitrogen and AlN formation in liquid iron, *ISIJ Int*, 47:945–954.

Lupis, C H P, 1983. *Chemical Thermodynamics of Materials* (North Holland, New York).

Paek, M K, Jang, J M, Do, K H and Pak, J J, 2013. Nitrogen solubility in high manganese-aluminium alloyed liquid steels, *Met Mater Int*, 19:1077–1081.

Paek, M K, Jang, J M, Kang, Y B and Pak, J J, 2015. Aluminum deoxidation equilibria in liquid iron: Part I, Experimental, *Metall Mater Trans B*, 46:1826–1836.

Pehlke, R D and Elliott, J F, 1960. Solubility of nitrogen in liquid iron alloys, 1 – Thermodynamics, *Trans Met Soc AIME,* 218:1088–1101.

Sieverts, A and Zapf, G, 1935. Iron and nitrogen, *Zeitschrift Phys Chemie*, 172:314–315.

Sigworth, G K and Elliott, J F, 1974. The Thermodynamics of Liquid Dilute Iron Alloys, *Metal Science*, 8:298–310.

Turkdogan, E T, 1980. Physical Chemistry of High Temperature Technology, 81 p (Academic Press: New York).

Wada, H and Pehlke, R D, 1977. Nitrogen solution and titanium nitride precipitation in liquid Fe-Cr-Ni alloys, *Met Trans B*, 8:443–450.

Wada, W and Pehlke, R D, 1978. Nitrogen solubility and aluminum nitride precipitation in liquid iron, Fe-Cr, Fe-Cr-Ni and Fe-Cr-Ni-Mo alloys, *Met Trans B*, 9:441–448.

Willems, H X, Hendrix, M M R M, de With, G and Metselaar, R, 1992. Thermodynamics of Alon II: Phase relations, *Journal of the Eu Cer Soc*, 10:339–346.

Carbon distribution behaviour between molten iron and CaO-Al_2O_3-FeO-SiO_2-MgO slag at 1873 K

DOI: 10.62053/UQZR8470

Y J Jun[1], G H Park[2] and J H Park[3]

1. Student, Department of Materials Science and Chemical Engineering, Hanyang University, Ansan 15588, South Korea. Email: banana4368@gmail.com
2. Senior Researcher, Research and Development Center, Hyundai Steel, Dangjin 31719, South Korea. Email: slagmaker@hyundai-steel.com
3. Professor, Department of Materials Science and Chemical Engineering, Hanyang University, Ansan 15588, South Korea. Email: basicity@hanyang.ac.kr

ABSTRACT

The carbon solubility of the CaO-Al_2O_3-FeO-SiO_2-MgO slag, the main system formed in the Ruhrstahl-Heraeus (RH) vacuum degasser, was measured at 1873 K to understand the effect of slag compositions on the carbon contamination in the ultra-low carbon (ULC) steels. The stable form of carbon was demonstrated to be carbonate by plotting the log [(wt%C)/a_C] ratio against the log $p(O_2)$ which ranged -11 < log $p(O_2$,atm) < -9. The carbon solubility of the CaO-Al_2O_3-FeO-SiO_2-MgO slag can be estimated using thermodynamic model. The distribution ratio of carbon increased with increasing concentration of FeO due to the FeO reduction reaction and increased basicity of slag. The carbonate capacity of the CaO-Al_2O_3-FeO-SiO_2-MgO slag can be expressed as a linear function of the activity of lime and the optical basicity.

INTRODUCTION

Ultra-low carbon (ULC) steel sheets are widely used in the automotive industry due to its superior performance such as superior ductility or formability. There have been many improvements in the decarburisation reaction in Ruhrstahl-Heraeus (RH) process for the production of ULC steel. However, after decarburisation stage, carbon contamination has frequently occurred due to changes in the slag composition during the deoxidation stage. Therefore, understanding the solubility of carbon in RH-type molten slag is highly important.

Many researchers investigated the carbide solubility in various slag systems using graphite crucibles. Schwerdtfeger and Schubert (1977) reported the solubility of carbon in the CaO-Al_2O_3 slag following gas-slag equilibration. The carbide (C_2^{2-}) solubility increased with increasing basicity (ie CaO/Al_2O_3 ratio) of the slag. Park and his coworkers (Park and Min, 1999, 2004; Park, Park and Lee, 2010) reported that carbide solubility in the CaO-Al_2O_3-CaF_2, CaO-B_2O_3 and CaO-SiO_2-MnO systems also increased with increasing content of CaO.

Kuwata and Suito (1996) reported the carbon solubility in molten slag using slag-metal equilibrium with CaO or Al_2O_3 crucible. The carbide ion was found to exist as a (C^{2-}) single anion in the slag as shown in Equation 1. Consistent with other studies, the carbon solubility increased with increasing basicity.

$$C(s) + (O^{2-}) = (C^{2-}) + 1/2\, O_2(g) \quad (1)$$

Many researchers have demonstrated that carbonate solubility increased with increasing basicity, following reaction in gas-slag experiments in various systems (Ikeda and Maeda, 1989; Rachev, Tsukihashi and Sano, 1991; Simeonov, Fukita and Maeda, 1992).

$$CO_2(g) + (O^{2-}) = (CO_3^{2-}) \quad (2)$$

Ikeda and Maeda (1989) showed that carbonate solubility increased with increasing contents of basic oxides such as CaO in the CaO-CaF_2-$CaCl_2$ and CaO-CaF_2-SiO_2 systems. Additionally, Simeonov, Fukita and Maeda (1992) found that if CaO is replaced by Li_2O, the carbonate capacity is decreased due to the apparent basicity of CaO being higher than Li_2O. Rachev, Tsukihashi and Sano (1991) showed that carbonate capacity also increased with increasing contents of BaO. Moreover, the carbonate capacity increased with increasing optical basicity.

No published experimental data was found on the carbon solubility of FeO-containing slags. For this reason, the distribution ratio of carbon between FeO-containing slag and molten iron was measured at 1873 K in MgO crucible.

EXPERIMENTAL PROCEDURE

Carbon-saturated iron was prepared to ensure a uniform carbon concentration in the metal. The carbon-saturated iron was made by heating electrolytic iron in a carbon crucible using a high frequency induction furnace and stirring at 1723 K for one hour under an Ar (99.999 per cent) atmosphere. The carbon concentration of the carbon-saturated iron was confirmed to be 5.3 wt per cent using a combustion analyser. The slags were prepared using reagent grade Al_2O_3, FeO, SiO_2, MgO and CaO calcined from $CaCO_3$ at 1273 K. The equilibration experiments with 7 g slag, 4.95 g electrolytic iron and 0.05 g C-saturated iron were performed in MgO crucibles. The equilibration time was 24 hr under purified Ar atmosphere at 1873 K. After equilibration, the samples were quenched by Ar flushing and water.

A Super-Kanthal electric resistance furnace, shown in Figure 1, was used for the equilibration of the CaO-Al_2O_3-FeO-SiO_2-MgO slag with molten iron at 1873 K under an Ar (99.999 per cent) atmosphere. The temperature was controlled within ±2 K using a B-type thermocouple.

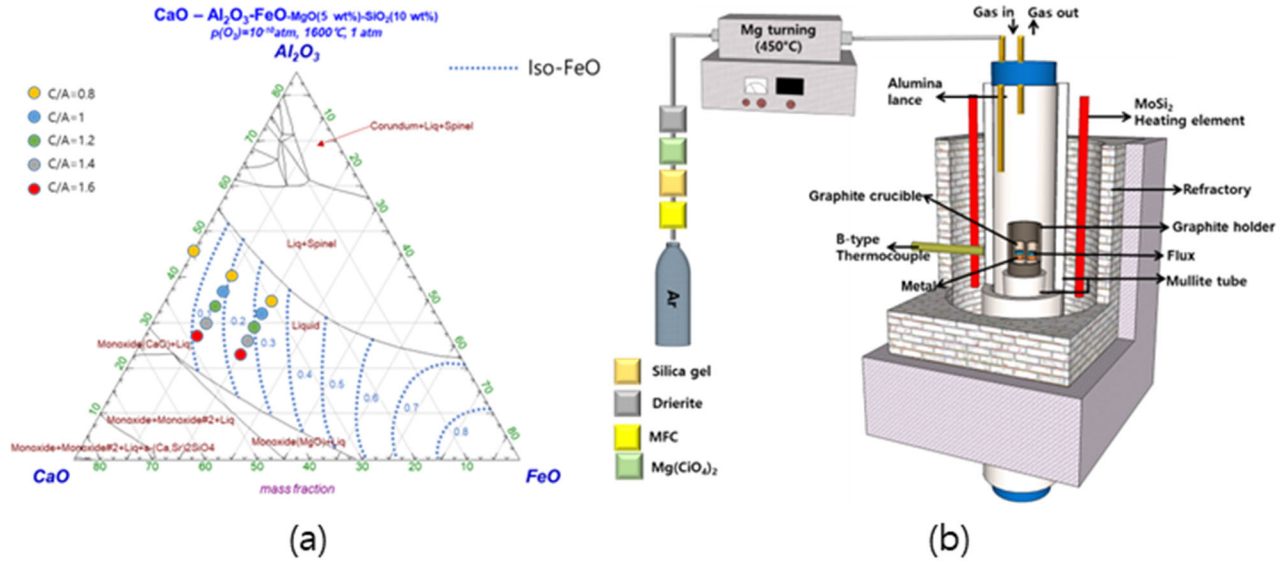

FIG 1 – (a) Experimental slag compositions, (b) schematic diagram of the experimental apparatus.

After the equilibration, the carbon concentrations of the slag and metal samples were determined by using the combustion analyser (CS 800, ELTRA) and each component in the slags were determined by using an ICP-AES (ACROS II, Spectro). The N/O combustion analyser (ONH-p, ELTRA Co.) was used to determine oxygen content in metal samples.

RESULTS AND DISCUSSION

Kuwata and Suito (1996) reported that carbon dissolves as carbide ion following Equations 3 to 5, and dissolves as carbonate ion following Equations 6 to 8 when $\log(wt\%C)/a_C$ is plotted against $\log p_{O_2}$. If the carbon dissolves as carbide ion, the slope is -1/2 from Equation 5, and dissolves as carbonate with the slope of unity from Equation 8.

$$[\mathrm{C}] + (O^{2-}) = (C^{2-}) + 1/2O_2(g) \quad (3)$$

$$K_{[3]} = (a_{C^{2-}} \cdot p_{O_2}^{1/2})/(a_C \cdot a_{O^{2-}}) \quad (4)$$

$$\log(wt\%C)/a_C = -(1/2)\log p_{O_2} + \log(K \cdot a_{O^{2-}}/f_{C^{2-}}) \quad (5)$$

$$[\mathrm{C}] + (O^{2-}) + O_2(g) = (CO_3^{2-}) \quad (6)$$

$$K_{[6]} = a_{CO_3^{2-}}/(a_C \cdot a_{O^{2-}} \cdot p_{O_2}) \quad (7)$$

$$\log(wt\%C)/a_C = \log p_{O_2} + \log\left[(M_C/M_{CO_3})\,K \cdot a_{O^{2-}}/f_{CO_3^{2-}}\right] \quad (8)$$

To investigate the general form of carbon in the slags, Figure 2 shows both the $\log(wt\%C)/a_C$ plotted against the oxygen partial pressure calculated with the Fe-FeO equilibrium reaction and carbon solubility calculated with Pelton-Eriksson-Serrano model (ie capacity model) (Pelton, Eriksson and Serrano, 1993). The activity of carbons was calculated from Wagner formalism using the first-order interaction parameters, which are listed in Table 1 (Hino and Ito, 2010). The slope of the linearly fitted line was about 0.8, which was close to the slope of unity expected from Equation 8. Therefore, the carbon in the RH-type molten slag can be defined as carbonate ion in the present study.

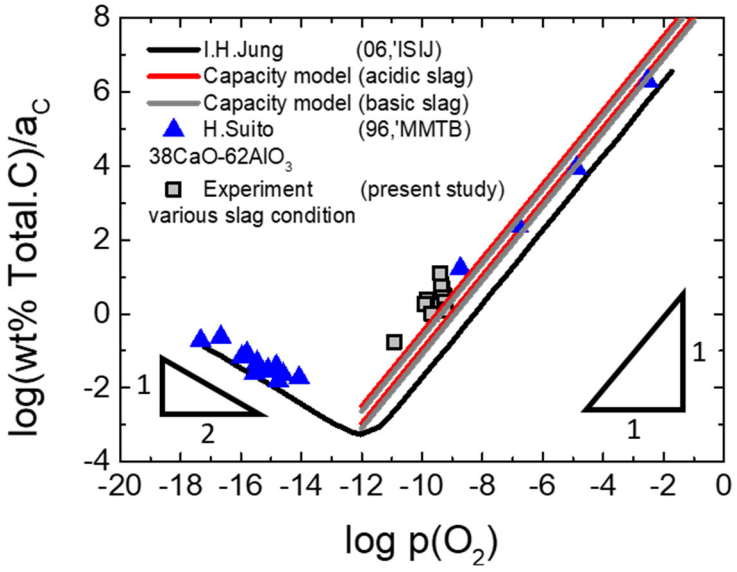

FIG 2 – Experimental and calculated results of carbon solubility plotted against oxygen partial pressure in logarithmic form for the FeO-containing slags.

TABLE 1

Interaction parameters used in the present study.

e_i^j	j = C	O
i = C	0.14	-0.34
O	-0.45	-0.17

Jung (2006) calculated the carbide and carbonate capacities in the CaO-Al_2O_3 binary slag system using the capacity model and found that the calculated results were well matched with the experimental data. In the present study, the carbonate capacities calculated with the capacity model were also in good agreement with the measured data as shown in Figure 2.

The carbonate dissolution reaction can be defined as given in Equation 2 and thus carbonate capacity is given below (Ikeda and Maeda, 1989; Rachev, Tsukihashi and Sano, 1991; Simeonov, Fukita and Maeda, 1992).

$$C_{CO_3^{2-}} = K \cdot a_{O^{2-}}/f_{CO_3^{2-}} = (wt\%\,CO_3)/p_{CO_2} = (M_{CO_3}/M_C)\cdot[(wt\%C)/p_{CO_2}] \quad (9)$$

$$\mathrm{Log}C_{CO_3^{2-}} = log a_{O^{2-}} - log f_{CO_3^{2-}} + constant \quad (10)$$

Because the activity of free oxygen cannot be directly measured due to thermodynamic constraints, the activity of basic oxide such as CaO can be used as an indirect basicity index. Figure 3 represents the relationship between the carbonate capacity and the activity of CaO. The activity of CaO was calculated using FactSage™ (ver 8.2.). A good linear correlation between them on a logarithmic

scale can be found with the slope of 0.85. Although there are some experimental scatters, the slope of the fitted line is relatively close to the theoretical value of unity even though there are some scatters.

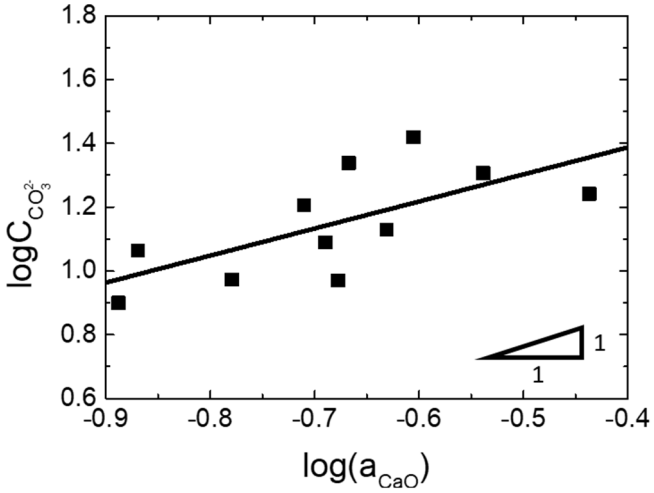

FIG 3 – Dependence of the carbonate capacity on the activity of CaO in molten slag.

CONCLUSIONS

Carbon solubility in the CaO-Al_2O_3-FeO-SiO_2-MgO slag was measured at 1873 K at oxygen partial pressure between $-11 \leq \log p_{O_2} \leq -9$ to determine the dissolution mechanism of carbon in the FeO-bearing slags by using the slag-metal equilibration reaction. The carbon solubility was plotted in terms of $\log (wt\%C)/a_C$ against $\log p_{O_2}$ to determine the stable form of carbon in the slag. Carbon was found to be dissolved as CO_3^{2-} and the carbonate capacity $C_{CO_3^{2-}}$ increased with increasing activity of CaO which can be the basicity index. Also, the calculated results using a capacity model were well matched with the experimental data.

REFERENCES

Hino, M and Ito, K, 2010. *Thermodynamic for Steelmaking*, pp 76–89 (Tohoku University Press: Sendai).

Ikeda, T and Maeda, M, 1989. Solubility of Carbon Dioxide in CaO-$CaCl_2$-CaF_2 Molten Fluxes, *Tetsu-to-Hagané*, 75(5):742–749.

Jung, I H, 2006. Thermodynamic modeling of gas solubility in molten slags (I) — carbon and nitrogen, *ISIJ International*, 46(11):1577–1586.

Kuwata, M and Suito, H, 1996. Solubility of carbon in CaO-Al_2O_3 melts, *Metallurgical and Materials Transactions B,* 27(1):57–64.

Park, J H and Min, D J, 1999. Solubility of carbon in CaO-B_2O_3 and BaO-B_2O_3 slags, *Metallurgical and Materials Transactions B,* 30(6):1045–1052.

Park, J H and Min, D J, 2004. Carbide Capacity of CaO-SiO_2-CaF_2(-Na_2O) Slags at 1773 K, *ISIJ International*, 44(2):223–228.

Park, J H, Park, G H and Lee, Y E, 2010. Carbide capacity of CaO–SiO_2–MnO slag for the production of manganese alloys, *ISIJ International*, 50(8):1078–1083.

Pelton, A D, Eriksson, G and Romero-Serrano, A, 1993. Calculation of sulfide capacities of multicomponent slags, *Metallurgical Transactions B,* 24(5):817–825.

Rachev, I P, Tsukihashi, F and Sano, N F, 1991. The thermodynamic behavior of sulfur in BaO-BaF_2 slags, *Metallurgical Transactions B,* 22(3):333–338.

Schwerdtfeger, K and Schubert, H G, 1977. Solubility of nitrogen and carbon in CaO-Al_2O_3 melts in the presence of graphite, *Metallurgical Transactions B,* 8(3):535–540.

Simeonov, S, Fukita, K and Madea, M, 1992. Influence of Li_2O on the carbonate capacity of CaO-CaF_2-Al_2O_3 Melts, *Metallurgical Transactions B,* 23(2):183–187.

Thermodynamic behaviour of TiO_2 in $CaO-Al_2O_3-MgO-TiO_2$ slag at high temperatures

DOI: 10.62053/EFMD9314

D Y Jung[1], Y J Jun[2], M J Lee[3], S J Park[4], S C Kang[5], Y-B Kang[6] and J H Park[7]

1. Student, Department of Materials Science and Chemical Engineering, Hanyang University, Ansan 15588, South Korea. Email: dy3572@naver.com
2. Student, Department of Materials Science and Chemical Engineering, Hanyang University, Ansan 15588, South Korea. Email: banana4368@gmail.com
3. Student, Department of Materials Science and Chemical Engineering, Hanyang University, Ansan 15588, South Korea. Email: dlalswn06@gmail.com
4. Principal Researcher, Steelmaking Research Group, Technical Research Laboratories, Pohang 37859, South Korea. Email: ssambbak@posco.com
5. Group Leader, Steelmaking Research Group, Technical Research Laboratories, Pohang 37859, South Korea. Email: sckang@posco.com
6. Professor, Graduate Institute of Ferrous and Eco Materials Technology (GIFT), POSTECH, Pohang 37673, South Korea. Email: ybkang@postech.ac.kr
7. Professor, Department of Materials Science and Chemical Engineering, Hanyang University, Ansan 15588, South Korea. Email: basicity@hanyang.ac.kr

ABSTRACT

High-Cr and Ti-bearing ferritic stainless steel (FSS) has superior corrosion resistance compared to other steels. The Ti-bearing FSS requires not only high corrosion resistance and formability, but also high cleanliness of the cold rolled sheet. Specifically, the cleanliness of Ti-bearing FSS has been improved through the vacuum oxygen decarburisation (VOD) and the ladle treatment (LT) processes. Nevertheless, there are still unsolved problems such as large fluctuations in Ti yield due to various factors including Al deoxidation practice and slag-metal reactions after Ti alloying. The activity of TiO_2 in the $CaO-Al_2O_3$-based slag must be measured to determine the equilibrium of the reaction between Ti and O in the molten steel and TiO_2 in the slag. Moreover, in continuous casting tundish, the internal cleanliness of molten steel is significantly affected by the reoxidation due to the reaction with the atmosphere as well as tundish flux and insulation cover powder. Therefore, the present study aims to provide a systematic understanding the reaction between Ti-bearing FSS melt and the slag and to investigate the thermodynamic behaviour of TiO_2 in the $CaO-Al_2O_3-MgO-TiO_2$ slag.

INTRODUCTION

In the vacuum oxygen decarburisation (VOD) and the ladle treatment (LT) processes, a systematic understanding the slag-metal reaction is required to control the Ti yield and cleanliness of high-Cr and Ti-bearing ferritic stainless steel (FSS) melt. Therefore, it is important to investigate the thermodynamic behaviour of TiO_2 in the $CaO-Al_2O_3$-based slag.

Several studies have been performed to investigate the activity coefficient of TiO_2 in the slag. Park, Lee and Gaye (2008) reported the thermodynamic behaviour of TiO_2 in the $CaO-SiO_2-Al_2O_3$-based slag in equilibrium with Fe-11 per cent Cr melt using MgO crucible. The activity coefficient of TiO_2 decreases with increasing basicity when the modified basicity (= (per cent CaO + per cent MgO) / (per cent SiO_2)) was above 0.7. Sun *et al* (2018) reported the activity coefficient of TiO_2 in the $CaO-SiO_2-Al_2O_3$-based slag in equilibrium with C-saturated molten iron. The activity coefficient of TiO_2 decreases with increasing basicity (= (per cent CaO) / (per cent SiO_2)) from 1.0 to 1.3.

However, because there are few experimental data for the thermodynamic behaviour of TiO_2 in the $CaO-Al_2O_3$-based slags, the activity of TiO_2 in the $CaO-Al_2O_3-MgO-TiO_2$ slag in equilibrium with molten silver as well as molten Fe-Cr melts was measured at 1823 K using MgO crucible.

EXPERIMENTAL PROCEDURE

A super-kanthal electric resistance furnace, shown in Figure 1 was used for equilibrium experiments between slag and metal at 1823 K. The temperature was controlled within ±2 K using a B-type

thermocouple. The slag samples were prepared using reagent grade Al_2O_3, MgO, TiO_2 and CaO calcined from $CaCO_3$ at 1273 K.

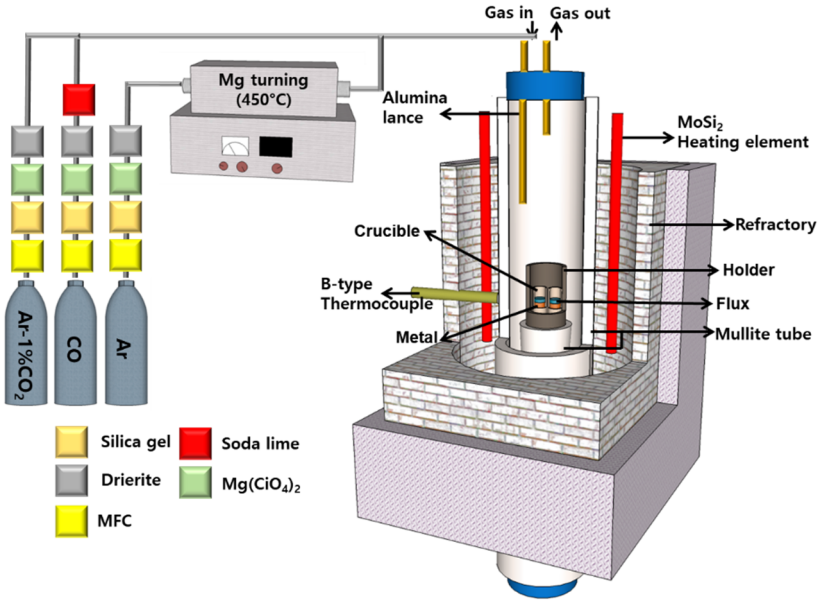

FIG 1 – Schematic diagram of the experimental apparatus.

In order to perform the equilibrium experiment between pure silver and Ti_3O_5 phase, Ti_3O_5 pellet was prepared by inserting TiO_2 pellet in a graphite crucible at 1573 K under CO atmosphere for four days in a vertical tube furnace (Figure 1) based on the Ti-O phase diagram (Kang and Lee, 2005).

First experiments were performed with 0.3 g Ti_3O_5 pellet and 10 g pure silver to measure the Henrian activity coefficient of Ti in silver using Al_2O_3 crucible. The equilibration time was 24 hrs under p_{O_2} = 10^{-13} *atm* using CO and Ar-1 per cent CO_2 gas mixture.

Second experiments were performed with 3 g slag and 5 g pure silver to measure the activity coefficient of TiO_2 in the CaO-Al_2O_3-MgO-TiO_2 slag using a graphite crucible under CO atmosphere (p_{O_2} = 10^{-16} *atm*) at 1823 K. The compositions of slags are shown in Figure 2.

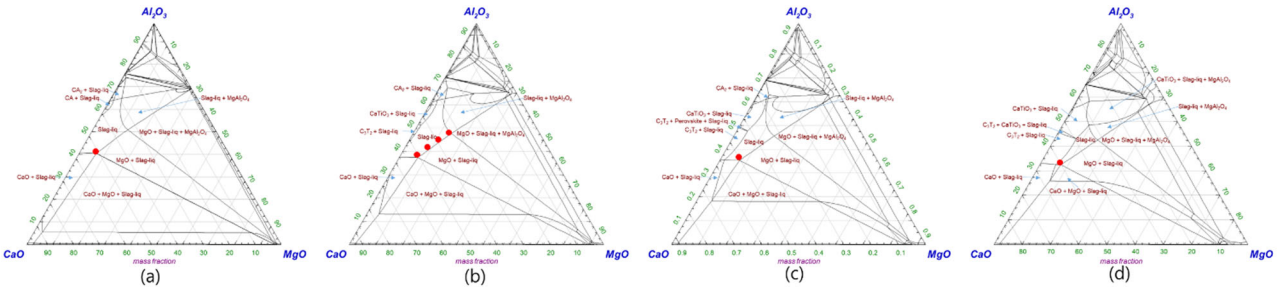

FIG 2 – Composition of slags in different TiO_2 content: (a) 2 wt per cent, (b) 5 wt per cent, (c) 7 wt per cent, and (d) 10 wt per cent in the CaO-Al_2O_3-MgO-TiO_2 system for the silver-slag equilibrium experiments at 1823 K.

After equilibrium, all samples were quenched by Ar flushing and water. The components in the slags and silver samples were determined using the Inductively Coupled Plasma – Atomic Emission Spectroscopy (ICP-AES) (ACROS II, Spectro). The N/O combustion analyser (ONH-p, ELTRA Co.) was used to determine oxygen content in metal samples. The ionic speciation of titanium oxide in the slag was confirmed by employing an XPS (Nexsa G2 Co.) analysis with quenched slag samples.

RESULTS AND DISCUSSION

In Ag-Ti_3O_5 equilibrium experiment, Ti_3O_5 pellet was in equilibrium with [Ti] and [O] in pure silver by Equation (1). Henrian activity coefficient of Ti in silver can be calculated by Equation (2). The oxygen

partial pressure (p_{O_2} = 10^{-13} *atm*) at 1823 K was set by controlling CO and Ar-1 per cent CO_2 gas flow rate according to Equations (3) and (4) (Stull, 1965; Turkdogan, 1980):

$$Ti_3O_{5(s)} = 3Ti_{(s)} + \frac{5}{2}O_{2(g)}, \Delta G^{\circ}_{[1]} = 2435{,}100 - 420.5\,T\ (J/mol) \quad (1)$$

$$K_{[1]} = \frac{(\gamma^{\circ}_{Ti(Ag)} \cdot X_{Ti(Ag)})^3 \cdot p_{O_2}^{5/2}}{a_{Ti_3O_5}(=1.0)} \quad (2)$$

$$CO_{(g)} + \frac{1}{2}O_{2(g)} = CO_{2(g)}, \Delta G^{\circ}_{[2]} = -281{,}900 - 87.3\,T\ (J/mol) \quad (3)$$

$$K_{[3]} = \frac{p_{CO_2}}{p_{CO} \cdot p_{O_2}^{1/2}} \quad (4)$$

Figure 3 shows the temperature dependency of the Henrian activity coefficient of Ti in molten silver and the linearly fitted data are given in Equation (5).

$$\ln \gamma^{\circ}_{Ti(Ag)} = -\frac{91{,}180(\pm 230)}{T} + 48.1(\pm 0.1) \quad (5)$$

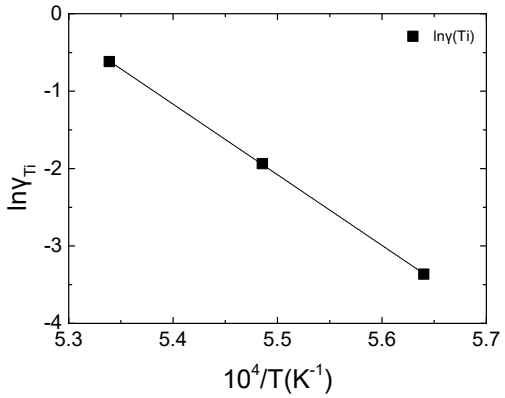

FIG 3 – Dependence of logarithmic form of the activity coefficient of Ti in silver on the reciprocal temperature.

From XPS spectra for Ti 2p shown in Figure 4, it was confirmed that the oxidation state of Ti was Ti^{4+} in the present $CaO\text{-}Al_2O_3\text{-}MgO\text{-}TiO_2$ slag system from the observation of Ti^{4+} peaks (458.5 eV) in Table 1 (Rotole *et al*, 2001; Yang and Park, 2017; Cho *et al*, 2021).

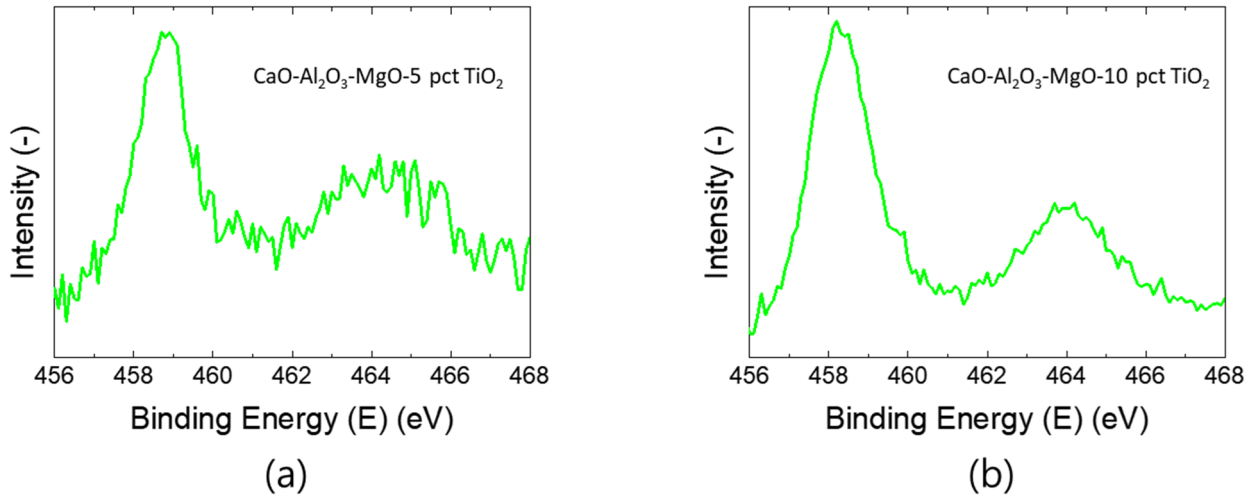

FIG 4 – X-ray photoelectron spectroscopy spectra of quenched slag samples with different content of titanium oxide; (a) 5 wt per cent and (b) 10 wt per cent.

TABLE 1

Binding energy of titanium oxides at different valances.

	Ti^{2+}	Ti^{3+}	Ti^{4+}
Binding Energy	455.0 eV	457.0 eV	458.5 eV

In Ag-slag equilibrium experiment, the activity of TiO_2 in the slag can be calculated by Equations (6) and (7) using Henrian activity coefficient of Ti in molten silver given in Equation (5). The oxygen partial pressure (p_{O_2} = 10^{-16} *atm*) at 1823 K was controlled by Equations (8) and (9) (Stull, 1965; Turkdogan, 1980).

$$TiO_{2(s)} = Ti_{(s)} + O_{2(g)}, \Delta G^{\circ}_{[6]} = 941{,}000 - 177.6\,T\ (J/mol) \tag{6}$$

$$K_{[6]} = \frac{\gamma^{\circ}_{Ti(Ag)} \cdot X_{Ti} \cdot p_{O_2}}{\gamma_{TiO_2} \cdot X_{TiO_2}} \tag{7}$$

$$C_{(s)} + \frac{1}{2}O_{2(g)} = CO_{(g)}, \Delta G^{\circ}_{[8]} = -112{,}900 - 86.5\,T\ (J/mol) \tag{8}$$

$$K_{[8]} = \frac{p_{CO}}{a_C \cdot p_{O_2}^{1/2}} \tag{9}$$

The activity coefficient of TiO_2 in the CaO-Al_2O_3-MgO-5 per cent TiO_2 slag decreases with increasing slag basicity (= per cent CaO / per cent Al_2O_3) shown in Figure 5a and FactSage™, ver 8.2 (by CRCT-ThermFact Inc. and GTT-Technologies) calculation shows similar tendency (but less sensitive) to the present work. The activity coefficient of TiO_2 in the CaO-Al_2O_3-MgO-TiO_2 slag close to the CaO-MgO double saturation condition sharply decreases with increasing TiO_2 content as shown in Figure 5b, while the calculated result from FactSage™ software exhibits nearly constant value irrespective of TiO_2 content.

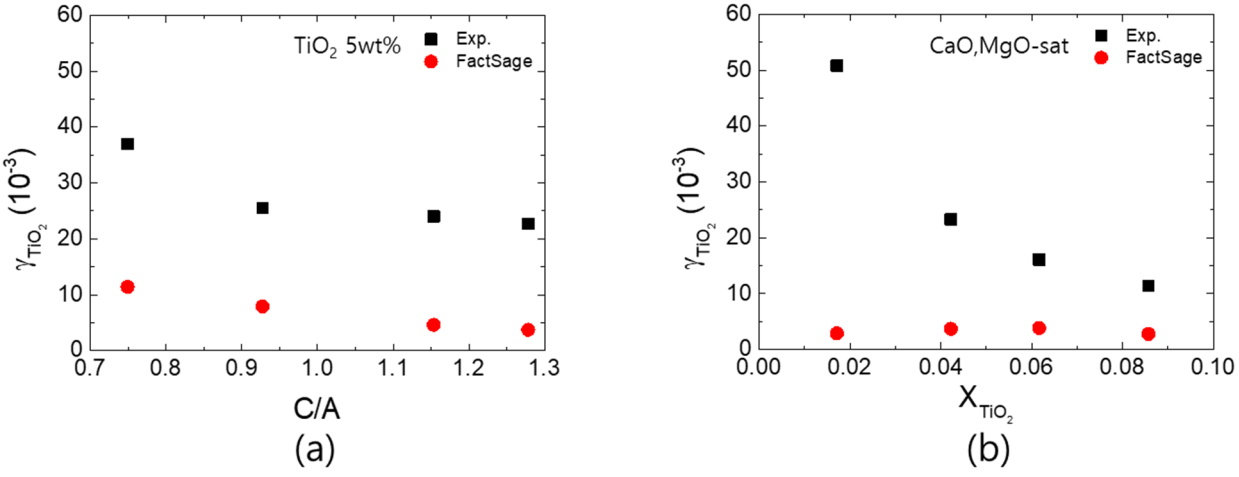

FIG 5 – Effect of (a) basicity and (b) TiO_2 content on the activity coefficient of TiO_2 in the CaO-Al_2O_3-MgO-TiO_2 slag measured in the present study and comparison with the values calculated by FactSage™.

CONCLUSIONS

The activity coefficient of TiO_2 in the CaO-Al_2O_3-MgO-TiO_2 slag was measured and compared with FactSage™ calculations at 1823 K. The major findings of present study can be summarised as follows:

- The Henrian activity coefficient of Ti in silver ($\gamma^{\circ}_{Ti(Ag)}$) can be expressed as a function of the reciprocal temperature.
- It was found that Ti was stabilised as TiO_2 (Ti^{4+}) in the present slag system, which was confirmed by XPS analysis.

- The activity coefficient of TiO_2 in the CaO-Al_2O_3-MgO-5 per cent TiO_2 system decreases with increasing C/A ratio at C/A>0.7 and FactSage™ shows similar tendency. Especially, there is a small change in activity of TiO_2 in the range of C/A ratio greater than 0.9.
- The activity coefficient of TiO_2 in the CaO-Al_2O_3-MgO-TiO_2 system close to the CaO-MgO double saturation condition sharply decreases with increasing TiO_2 content, while calculated result from FactSage™ software exhibits nearly constant value irrespective of TiO_2 content.

REFERENCES

Cho, J H, Martinsson, J, Sichen, D and Park, J H, 2021. Desulfurization behavior of Incoloy® 825 superalloy by CaO-Al_2O_3-MgO-TiO_2 slag, *Metallurgical and Materials Transactions B*, 52:3660–3670.

Kang, Y B and Lee, H G, 2005. Experimental study of phase equilibria in the MnO-"TiO_2"-"Ti_2O_3" system, *ISIJ International*, 45:1543–1551.

Park, J H, Lee, S B and Gaye, H R, 2008. Thermodynamics of the formation of MgO-Al_2O_3-TiO_x inclusions in Ti-stabilized 11Cr ferritic stainless steel, *Metallurgical and Materials Transactions B*, 39:853–861.

Rotole, J A, Gaskell, K, Comte, A and Sherwood, P M, 2001. Formation of potentially protective oxide-free phosphate films on titanium characterized by valence band x-ray photoelectron spectroscopy, *Journal of Vacuum Science and Technology A: Vacuum, Surfaces and Films*, 19:1176–1181.

Stull, D R, 1965. *JANAF Thermochemical Tables* (Clearinghouse).

Sun, J, Wang, S, Chu, M, Chen, M, Zhao, Z, Zhao, B and Liu, Z, 2018. Titanium distribution between blast furnace slag and iron for blast furnace linings protection, *Ironmaking and Steelmaking*, 47:545–552.

Turkdogan, E T, 1980. *Physical chemistry of high temperature technology* (Academic Press).

Yang, J G and Park, J H, 2017. Distribution behavior of aluminum and titanium between nickel-based alloys and molten slags in the electro slag remelting (ESR) process, *Metallurgical and Materials Transactions B*, 48:2147–2156.

Equilibrium distribution of Pb between copper metal and slags

DOI: 10.62053/FGBR2966

T Kan[1] and C Chen[2]

1. Research Scientist, CSIRO Mineral Resources, Clayton Vic 3168. Email: tao.kan@csiro.au
2. Principal Research Scientist, CSIRO Mineral Resources, Clayton Vic 3168. Email: chunlin.chen@csiro.au

ABSTRACT

The distribution ratio of Pb ($L_{Pb}^{s/m}$) between three types of slags (FeO_x–SiO_2, CaO–FeO_x and FeO_x–CaO–SiO_2) and molten copper after equilibrium was measured at 1300°C and oxygen partial pressure (pO_2) of 10^{-10}–10^{-6} atm. Results showed that for FeO_x–SiO_2 slag, the $L_{Pb}^{s/m}$ increased from 0.024 to 2.57 with pO_2 increased from 10^{-10} to 10^{-6} atm. The $L_{Pb}^{s/m}$ with CaO–FeO_x slag was lower than the FeO_x–SiO_2 slag at the same pO_2, ranging between 0.015 and 0.53. Using the FeO_x–CaO–SiO_2 slag generated $L_{Pb}^{s/m}$ values (0.02–1.6) in between. The oxygen partial pressure in the investigated range had no obvious effect on the activity coefficient of PbO (γP_bO) which was averagely 0.44, 1.70 and 0.71 for FeO_x–SiO_2, CaO–FeO_x and FeO_x–CaO–SiO_2 slags, respectively. The increases in the (CaO+MgO)/SiO_2 mass ratio of the FeO_x–CaO–SiO_2 slag induced the decrease in the $L_{Pb}^{s/m}$ and the increase in the γP_bO value. However, the variation in the Fe/SiO_2 mass ratio didn't exert obvious effects.

INTRODUCTION

Waste Electrical or Electronic Equipment (WEEE) or electronic waste (e-waste), denoted as 'any type of non-functional and abandoned electrical or electronic equipment', has been one of the fastest growing hazardous waste streams (Nithya, Sivasankari and Thirunavukkarasu, 2021). The global e-waste amount was 53.6 Mt in 2019 with a potential number of more than 70 Mt in 2030; however, only 17.4 per cent of e-waste was recycled formally (Forti *et al*, 2020; Nithya, Sivasankari and Thirunavukkarasu, 2021). E-waste has a general composition of 65–70 per cent of metals, ~20 wt per cent of plastics and ~5 wt per cent of glass (Babu, Parande and Basha, 2007). It has been deemed as a reservoir of common valuable metals such as Cu, Fe, Al and Ni and less common or trace elements such as Au, Ag, Pt, Sn, Ge and Se (Ebin and Isik, 2016). Metals of concern/hazardous metals (Be, As, Cd, In, Sb, Hg and Pb) may also be present in the e-waste (Hagelüken, Umicore and Co, 2006). For example, Pb can be present in the e-waste with a high content (eg 1.3–6.3 wt per cent in printed circuit boards) and is generally considered as a deleterious heavy metal with environmental concerns (Chakraborty *et al*, 2022; Khaliq *et al*, 2014). Improper handling of e-waste such as landfilling or incineration without suitable pollutant control will exert significant negative effects on the environment (Tian *et al*, 2021). E-waste recycling and reclamation are an imperative and challenging task for most countries.

E-waste can be processed through pyrometallurgical processes such as primary copper smelting or secondary copper smelting. Secondary copper smelting treats e-waste through different routes involving a number of metallurgical processes, eg reduction (at pO_2 of ~10^{-10} atm) of copper oxides followed by oxidation (at pO_2 of ~10^{-6} atm) of impurities, or *vice versa*, depending on the copper contents of the secondary materials (Yamasue *et al*, 2009). Besides the copper recycling, simultaneous recovery of minor elements is also significant. Secondary copper smelting including 'black copper' smelting featuring the utilisation of copper as the valuable metals collector, is still in the preliminary development (Ghodrat *et al*, 2018). Impurities such as Fe, Pb and As may be removed to the slag phase as oxides with residual amounts reporting to the copper. However, the presence of impurities such as Pb in the copper metal products if not removed will compromise their physical properties and workability. Elements with high volatilisation such as Pb, Sn, Zn and As may also partition to exhaust gas phase. The main fluxing agents are FeO_x, SiO_2 and CaO, forming slag systems of FeO_x-SiO_2 (fayalite slag, briefly F slag) and CaO-FeO_x (calcium ferrite slag, briefly CF slag). The addition of CaO into FeO_x-SiO_2 system to form FeO_x-CaO-SiO_2 (ferrous calcium silicate slag, briefly FCS slag) was also investigated in some studies and industrial practices to gain benefits such as a lower viscosity of slag (Ghodrat *et al*, 2016; Shuva *et al*, 2016; Ye, Liu and Xia, 2021).

Substantial Al_2O_3 is generally present in the e-waste smelting slag. Other additives such as MgO, B_2O_5 and Na_2O could also be present to alter the slag properties.

In Australia, a significant amount of e-waste is being generated with an estimated number at ~22 kg/capita (or 554 kt in total) in 2019 which was much higher than the world average at 6–7 kg/capita (Baldé *et al*, 2017; Forti *et al*, 2020). Substantial amounts of e-waste are still not successfully collected and recycled. The associated revenue potential from recoverable metals and other materials was estimated at US$3.59 billion in 2015 in Australia (Islam and Huda, 2019). In Australia, only a few primary smelters are in commission currently, ie BHP Billiton's Olympic Dam flash smelter in South Australia and Glencore's Mt Isa top submerged lance (TSL) bath smelter in Queensland which are remote from cities where e-waste collection takes place (Islam, Haque and Somerville, 2021).

Extensive research has been done on the thermodynamic behaviour of impurities originating from the primary copper concentrate materials. Gaining more thermodynamic knowledge about recycling or removing impurities from secondary resources such as e-waste is of high interest (Khaliq *et al*, 2014; Shuva *et al*, 2016). The published data with focus on thermodynamics of Pb in secondary copper smelting (eg black copper smelting) is still limited and needs further investigation (Shuva *et al*, 2016). In the meantime, discrepancies in Pb data are found in previous studies (Sineva *et al*, 2021). The obtained new data in this study is expected to bridge the gap of some existing data. In this study, experiments were carried out at T = 1300°C and pO_2 of 10^{-10}–10^{-6} atm to simulate the black copper smelting processes. The effects of oxygen partial pressure, different slag systems (F, CF and FCS slags), and composition of FCS slag with varied (CaO+MgO)/SiO_2 (taking into account of dissolved MgO from crucibles) and Fe/SiO_2 ratios on the thermodynamic behaviour of Pb were investigated.

EXPERIMENTAL

The master copper-lead alloy was first prepared by adding around 1 wt per cent of Pb metal to molten copper in a magnesia crucible at 1150°C in inert N_2 in an induction furnace. Afterwards, a silica tube was used to suck the molten alloy which was then collected after cooling down. The F, CF and FCS master slags were prepared in magnesia crucibles from analytical reagents, ie Fe_3O_4 with SiO_2, $CaCO_3$ with Fe_3O_4, and Fe_3O_4 with $CaCO_3$ and SiO_2, respectively. FCS slags with varied CaO/SiO_2 and Fe/SiO_2 ratios were also proposed.

Figure 1 shows the schematic diagram of the experimental set-up. The equilibrium experiments were performed in a vertical tube furnace equipped with an alumina tube and water-cooled end-caps. A refractory platform with an inserted thermocouple from the bottom was placed in the hot zone inside the alumina tube.

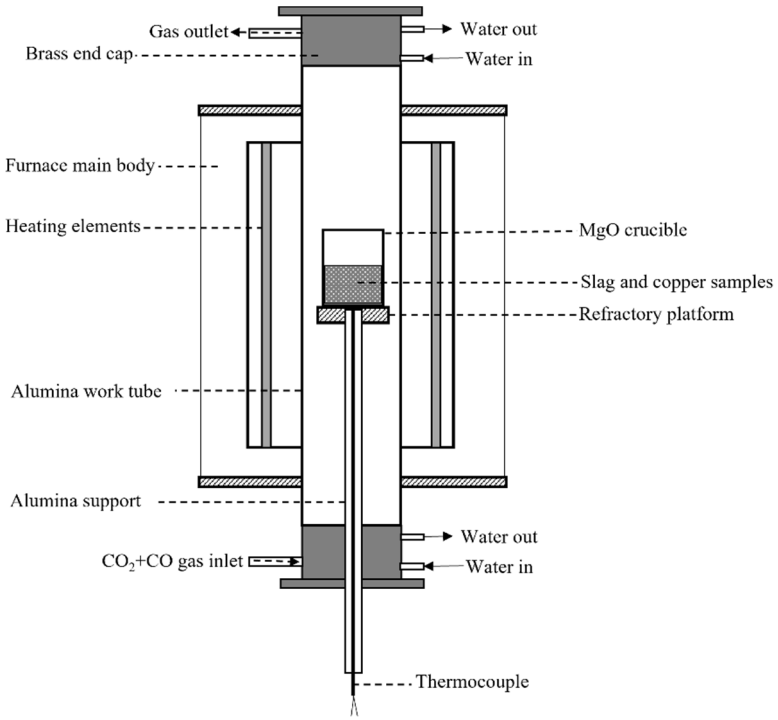

FIG 1 – Schematic diagram of vertical tube furnace with slag-copper equilibrium experimental set-up.

The hot zone was preheated to 1300°C and kept at this temperature. In each run, around 5 g of copper alloy and 5 g of master slag were placed in a magnesia crucible which was then mounted onto the platform from the top of the alumina tube. Magnesia crucibles were used for reasons. This study aimed to investigate the F, CF and FCS slags without the addition of other additives such as alumina which is although more likely to be present in industrial e-waste smelting slags. In the meantime, the magnesia crucible is highly resistant to the attack from slags. The addition of alumina and/or other additives into slags, or the use of alumina crucible, has been considered in the next stage of the study. CO and CO_2 mixture gas at a specified flow rate ratio was introduced into the tube to maintain the desired pO_2 (10^{-10} to 10^{-6} atm) based on Equations 1 and 2 (Yazawa and Takeda, 1982).

$$2CO\ (g) + O_2\ (g) = 2CO_2\ (g) \quad (1)$$

$$\log pO2\ (atm) = 2\log\left(\frac{pCO_2}{pCO}\right) - \frac{29510}{T} + 9.05 \quad (2)$$

The samples were maintained at 1300°C in a desired pO_2 (10^{-10} to 10^{-6} atm) continuously for 20 hrs for complete equilibration. Afterwards, the hot crucible was removed and quenched in cold water promptly. The obtained slag and copper phases were separated physically after drying. The slag was crushed to less than 210 µm and the contained copper droplets were removed carefully. Subsequently, the slag particles were ground manually to less than 45 µm before being analysed. Elemental compositions of slag and copper samples were tested through acid digestion followed by ICP-OES (model: Agilent 5900) and ICP-MS (model: Agilent 8900). The contents of Fe, Ca and Si in the slag were tested by XRF with fused bead method.

RESULTS AND DISCUSSION

Pb distribution ratio with oxygen partial pressure

The distribution of a minor element (Pb in this study) between slag and copper phases can be simply described by the following Equation 3:

$$[Pb] + \upsilon/2O_2 = (PbO_\upsilon) \quad (3)$$

where:

[ ] = value in copper phase

( ) = value in slag phase

2υ = valence state of Pb in slag

This reaction is commonly described as below (Takeda, Ishiwata and Yazawa, 1983):

$$Pb\ (l) + ½\ O_2\ (g) = PbO\ (l)\ \Delta G° = -195100 + 77.7T\ (J/mol) \quad (4)$$

The equilibrium constant K can be defined in Equation 5:

$$K = \alpha\ P_bO_{\upsilon/}(\alpha\ P_b * P_{O_2}^{\upsilon/2}) \quad (5)$$

where:

$\alpha\ P_bO_\upsilon$ = activity of PbO_υ in slag

$\alpha\ P_b$ = activity of Pb in copper

Also, K can be calculated based on the following Equation 6 and the obtained ΔG° from Equation 4.

$$\Delta G° = -RT\ lnK \quad (6)$$

The distribution ratio of Pb ($L_{Pb}^{s/m}$) between slag (s) and copper metal (m) is defined as the mass percentage of Pb in slag divided by its mass percentage in copper metal as below:

$$L_{Pb}^{s/m} = \frac{(Pb\%)}{[Pb\%]} = \frac{K(n_T)[\gamma P_b]\ P_{O_2}^{\upsilon/2}}{[n_T]\ (\gamma P_bO_\upsilon)} \quad (7)$$

where:

n_T = total number of moles in constituents in 100 g of each phase

γP_b is the activity coefficient of Pb in metal

γP_bO_υ is the activity coefficient of PbO_υ in slag

The activity coefficient of PbO_υ in slag can be calculated according to:

$$\gamma P_bO_\upsilon = \frac{K(n_T)[\gamma P_b]\ P_{O_2}^{\upsilon/2}}{[n_T]\ L_{Pb}^{s/m}} \quad (8)$$

where $[\gamma P_b] = 4.8$ is used in this study (Kaur, Swinbourne and Nexhip, 2009; Shuva *et al*, 2016).

The experimental results as well as the calculated $L_{Pb}^{s/m}$ and γP_bO_υ are summarised in Table 1.

Rearranging Equation 5 produces the following:

$$\log L_{Pb}^{s/m} = \log \frac{K\ (n_T)[\gamma P_b]}{[n_T]\ (\gamma P_bO_\upsilon)} + \frac{\upsilon}{2} \log pO2 \quad (9)$$

The logarithmic plot between $L_{Pb}^{s/m}$ and pO_2 will give a straight line with a slope of υ/2, which will indicate the oxidation state of Pb in the slag. As shown in Figure 2, the Pb distribution ratio was plotted against the oxygen partial pressure over the range of 10^{-10} to 10^{-6} (ie log pO_2 of -10 to -6) atm for F slag-copper, CF slag-copper and FCS slag-copper equilibrium systems. The data of previous studies on these three slag systems was also exhibited in each sub-figure for comparison.

TABLE 1

List of experiments and analysis results of slag and copper after equilibrium.

ID	Slag	pO_2 (atm)	Slag composition (wt%)						Pb (mg/kg)		(CaO+MgO)/SiO_2	Fe/SiO_2	$L_{Pb}^{s/m}$	γP_bO
			FeO	Fe_2O_3	CaO	SiO_2	MgO	Cu	Slag	Copper alloy				
F-O2(-6)	FeO_x-SiO_2	10^{-6}	35.89	16.59	0.24	25.78	11.79	5.22	3600	1400	NC	NC	2.57	0.45
F-O2(-7)	FeO_x-SiO_2	10^{-7}	37.44	16.62	0.20	27.20	11.92	4.30	1700	1200	NC	NC	1.42	0.27
F-O2(-8)	FeO_x-SiO_2	10^{-8}	48.50	8.38	0.10	27.77	10.54	1.73	1100	3600	NC	NC	0.31	0.40
F-O2(-9)	FeO_x-SiO_2	10^{-9}	50.69	8.02	0.12	27.49	9.92	0.82	340	5400	NC	NC	0.06	0.61
F-O2(-10)	FeO_x-SiO_2	10^{-10}	54.42	5.51	0.09	28.67	8.61	0.50	180	7400	NC	NC	0.02	0.50
CF-O2(-6)	CaO-FeO_x	10^{-6}	18.65	47.24	18.43	0.30	3.69	5.35	640	1200	NC	NC	0.53	1.92
CF-O2(-7)	CaO-FeO_x	10^{-7}	26.37	39.49	18.28	0.33	6.28	2.95	410	2700	NC	NC	0.15	2.25
CF-O2(-8)	CaO-FeO_x	10^{-8}	32.16	34.94	19.51	0.28	5.11	2.12	270	4900	NC	NC	0.06	1.99
CF-O2(-9)	CaO-FeO_x	10^{-9}	40.14	28.54	19.71	0.26	4.72	1.35	140	6400	NC	NC	0.02	1.61
CF-O2(-10)	CaO-FeO_x	10^{-10}	48.12	21.51	20.04	0.27	4.38	0.97	39	2600	NC	NC	0.02	0.75
FCS-a-(-6)	CaO-FeO_x-SiO_2	10^{-6}	19.30	8.15	13.95	37.77	13.89	3.81	2400	1500	0.74	0.55	1.60	0.80
FCS-a-(-7)	CaO-FeO_x-SiO_2	10^{-7}	19.43	9.15	14.51	38.37	12.80	2.39	1700	2500	0.71	0.56	0.68	0.60
FCS-a-(-8)	CaO-FeO_x-SiO_2	10^{-8}	23.80	6.83	14.97	39.87	10.96	1.40	1000	4800	0.65	0.58	0.21	0.62
FCS-a-(-9)	CaO-FeO_x-SiO_2	10^{-9}	26.50	4.24	15.15	40.58	11.10	0.75	260	5600	0.65	0.58	0.05	0.90
FCS-a-(-10)	CaO-FeO_x-SiO_2	10^{-10}	27.79	2.50	15.80	40.66	10.51	0.54	140	7000	0.65	0.57	0.02	0.66
FCS-b	CaO-FeO_x-SiO_2	10^{-8}	23.54	6.82	20.65	34.80	10.93	1.09	490	4900	0.91	0.66	0.10	1.31
FCS-c	CaO-FeO_x-SiO_2	10^{-8}	20.71	10.88	29.00	27.63	8.64	0.92	320	7600	1.36	0.86	0.04	3.07
FCS-d	CaO-FeO_x-SiO_2	10^{-8}	28.43	8.21	15.58	34.00	10.20	1.40	620	4400	0.76	0.82	0.14	0.91
FCS-e	CaO-FeO_x-SiO_2	10^{-8}	29.72	11.66	15.42	27.96	11.04	1.19	520	5700	0.95	1.12	0.09	1.38

NC: not calculated.

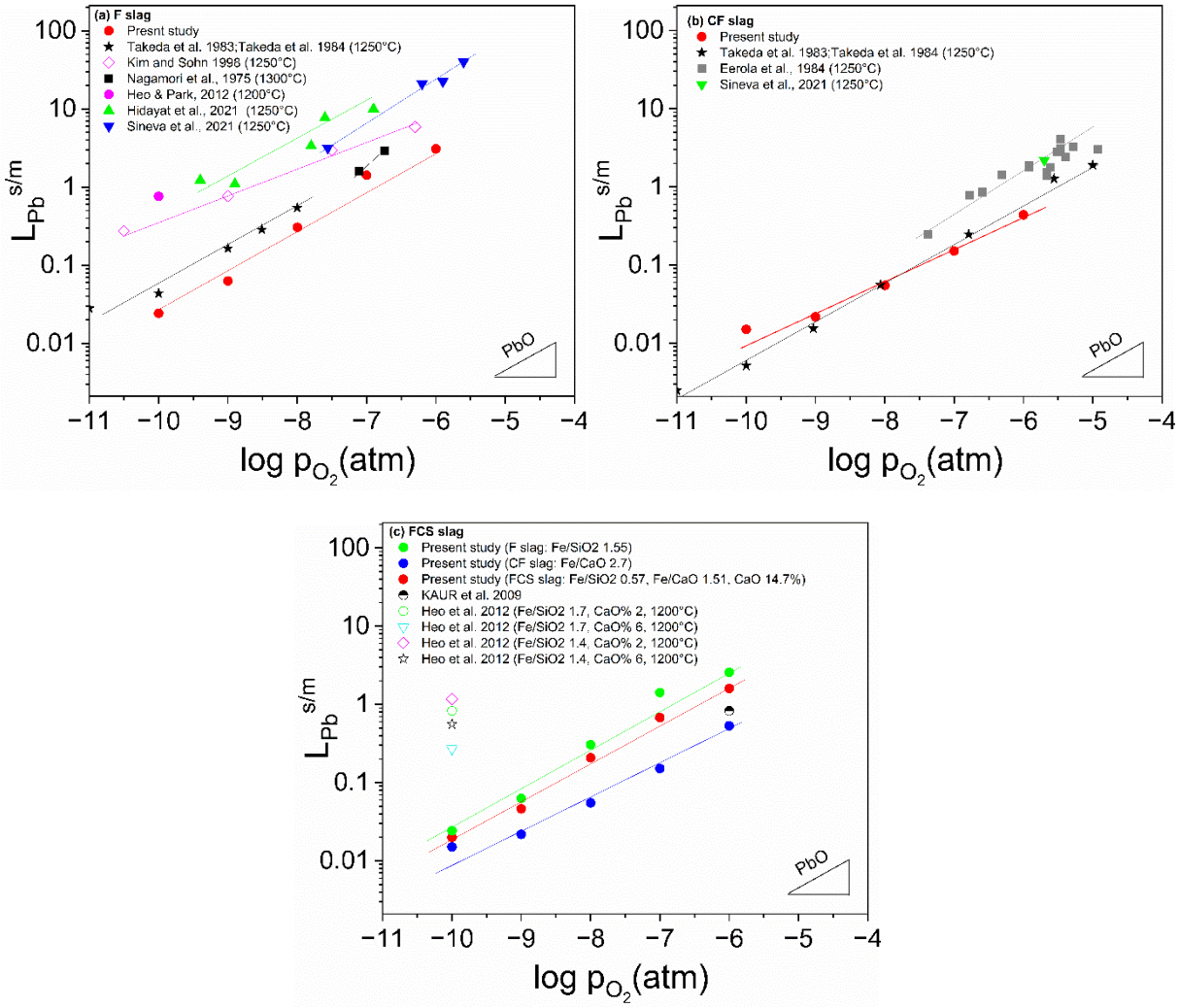

FIG 2 – Pb distribution ratio with oxygen partial pressure.

The distribution ratio of Pb generally relies on several parameters such as properties of the element itself, slag composition, oxygen partial pressure and temperature. In present study using F slag, the $L_{Pb}^{s/m}$ value was very low (0.024) at $pO_2 = 10^{-10}$ atm and climbed to 3.08 at $pO_2 = 10^{-6}$ atm. Pb preferentially dissolved into copper at $pO_2 < 10^{-7}$ atm while Pb mostly reported to slag ($L_{Pb}^{s/m} > 1$) at $pO_2 > 10^{-7}$ atm. At a higher pO_2, the Pb oxidation reaction (Equation 3) moves rightwards to form more Pb oxide. Compared to Cu, Pb is more reactive with oxygen to form stable PbO in slag at increased pO_2, thus can be separated from copper phase into slag (Ghodrat *et al*, 2018). Being similar to previous studies, a linear relationship between $\log L_{Sn}^{s/m}$ and $\log pO_2$ was obtained with a slope (υ/2) of 0.5 as an indicator for the bivalence of lead (ie PbO). As the figure shows, the $L_{Pb}^{s/m}$ values among most previous studies were inconsistent. The results in this study were close to the data from studies by Nagamori, Mackey and Tarassoff (1975) and Takeda, Ishiwata and Yazawa (1983) which adopted Al_2O_3 and SiO_2 crucible, respectively. Heo and Park (2012) used Al_2O_3 crucible to obtain an average $L_{Pb}^{s/m}$ value of 0.76 at $pO_2 = 10^{-10}$ atm and a low temperature of 1200°C. Recently, Hidayat *et al* (2021) and Sineva *et al* (2021) investigated the equilibrium thermodynamics of Pb in in a sealed silica ampoule to minimise the vaporisation of Pb, and used tridymite and Fe_3O_4 spinel materials respectively rather than crucibles, acquired much higher $L_{Pb}^{s/m}$ values than this study. Compared to previous studies, the $L_{Pb}^{s/m}$ value in this study was lower to different extents, suggesting that Pb was more likely to retain in the copper at the same oxygen partial pressure. The discrepancy could arise from the variation in slag composition and experimental conditions among various studies. In present study MgO crucibles were used while in previous studies SiO_2 crucibles were mostly employed with a few studies using Al_2O_3 crucible or Fe_3O_4 substrate wrap. In the meantime,

in most previous studies equilibration experiments were conducted at the temperature of 1250°C, which is lower than 1300°C for this study. Generally, a lower temperature can increase the K value (see Equation 7) thus increase the $L_{Pb}^{s/m}$ value and promote Pb to move into the slag phase (Chen *et al*, 2021; Taskinen and Avarmaa, 2021). In the meantime, the slag in this study could contain solids such as olivine, decreasing the concentration of Pb in the slag and therefore the $L_{Pb}^{s/m}$ values.

For Pb distribution between the CF slag and copper, data from this study ranged within 0.02 to 0.44, which is significantly lower than that with F slag. PbO is well recognised as an alkaline compound and is inclined to combine with the acidic SiO_2 in the F slag to generate stable compounds like $PbO{\cdot}SiO_2$ and $2PbO{\cdot}SiO_2$, therefore producing much higher $L_{Pb}^{s/m}$ values than those with the CF slag (Kuxmann and Fischer, 1974). The data in present study is in good agreement with that by Takeda, Ishiwata and Yazawa (1983). Higher $L_{Pb}^{s/m}$ values were observed in studies by Eerola, Jylha and Taskinen (1984) and Sineva *et al* (2021). However, the difference between these two studies and the present one is not significant.

All the $L_{Pb}^{s/m}$ values with F, CF and FCS slags were plotted in the same sub-figure Figure 2c FCS slag for comparison. FCS slag combines the benefits of both F and CF slags CF slags, giving medium $L_{Pb}^{s/m}$ values between 0.02 ($pO_2 = 10^{-10}$ atm) and 1.6 ($pO_2 = 10^{-6}$ atm) as expected. So far, limited work has been reported on the thermodynamic behaviour of Pb in FCS slag–copper system. Takeda and Yazawa (1989) reported that the lead solubility to slag (log%Pb in slag) increased with the oxygen partial pressure linearly at 1300°C. Kaur, Swinbourne and Nexhip (2009) obtained a $L_{Pb}^{s/m}$ value of 0.93 at 1300°C and $pO_2 = 10^{-6}$ atm in MgO crucible. Both the experimental conditions and the $L_{Pb}^{s/m}$ value are in line with the present study. Heo and Park (2012) employed FCS slags with 2–6 per cent CaO at 1200°C and $pO_2 = 10^{-10}$ atm to gain $L_{Pb}^{s/m}$ values higher than the present study. This could be due to the lower CaO content of FCS slag and lower temperature, compared to the present study (avg. 14.7 per cent CaO in slag and 1300°C).

In the industrial practice, it is significant to separate Pb from copper to slag as much as possible. The Pb content in cathode copper of higher than a few ppm will produce negative effects such as copper cracking during casting and hot rolling as well as the annealability of copper (Davenport *et al*, 2002). According to the above observations in the present study, the distribution ratio of Pb between slag and copper was significantly larger in F slag than in CF slag under continuous converting conditions (1300°C and ~10^{-6} atm) in the black copper process. The high risk of slag foaming and other disadvantages related to the F slag should be handled properly. The results suggest FCS slag could be a suitable replacement for F slag due to its improved properties and similar $L_{Pb}^{s/m}$ values in comparison to F slag. The resultant decrease in the impurity level (eg Pb) of the black copper will benefit to the enhanced concentration of copper and precious metals with higher stability. However, the loss of Cu in slag as Cu_2O will also increase simultaneously which needs to be taken into account. Undering the reducing smelting conditions (1300°C and ~10^{-10} atm), similar $L_{Pb}^{s/m}$ values for all three slags at low levels were obtained.

Activity coefficient of PbO

The activity coefficient of PbO (γ_{PbO}) in all three slags versus log pO_2 is calculated based on Equation 8 then exhibited in Figure 3.

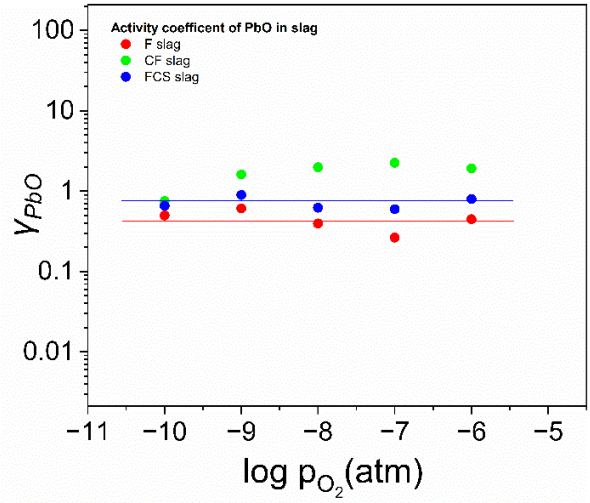

FIG 3 – Activity coefficient of PbO with oxygen partial pressure.

In the present work, the γP_bO value in three slags was not obviously affected by the pO_2. This trend was in good agreement with most previous studies. For the F slag, Nagamori, Mackey and Tarassoff (1975) and Takeda, Ishiwata and Yazawa (1983) obtained a constant γP_bO value of 0.07 and 0.4, respectively. The value in the present study (0.44) was in good accord with that from Takeda, Ishiwata and Yazawa (1983). Both of these two previous studies came to the same conclusion that the γP_bO value was independent of pO_2. Instead, the γP_bO value relies on the properties of both PbO and slag. However, Kim and Sohn (1998) observed that the γP_bO value (0.01–0.1) increased with the increase in pO_2 and explained that *'a strong dependence of γP_bO on pO_2 or even the presence of atomic Pb in iron silicate slag, might not be ruled out at low oxygen potentials (especially below 10^{-10} atm)'.*

In terms of the CF slag, a constant γPbO value versus pO2 was also observed by previous studies. Takeda, Ishiwata and Yazawa (1983) obtained the value of 3.2 and found it increased with the increase in the CaO content of slag. The same research team investigated the CF slag with molar ratios of FeO_x/(nCaO+nMgO+nFeO_x) at 0.7 and 0.84, and obtained a γP_bO value of 4.0 and 2.0, respectively (Takeda and Yazawa, 1989). A lower value from present study (avg. 1.70) was in line with the value of 1.7±0.6 by Eerola, Jylha and Taskinen (1984).

Regarding the FCS slag, Takeda and Yazawa (1989) studied the Pb distribution at varied slag composition with molar ratios of Q = (nCaO+nMgO)/(nCaO+nMgO+nSiO_n) and R = nFeO_x/(nCaO+nMgO+nSiO_n+nFeO_x). The γP_bO value was 0.3–0.5 (Q = 0.1, R = 0.5–0.8) and 3.0–1.0 (Q = 0.55, R = 0.2–0.6), respectively. Kaur, Swinbourne and Nexhip (2009) acquired a γP_bO value of 1.4 at 1300°C and $pO_2 = 10^{-6}$ atm. The γP_bO value in present study was 0.71 which was of the same order of magnitude as those in previous studies.

The γP_bO value was calculated to be in the order of CF slag (avg. 1.70) > FCS slag (avg. 0.71) > F slag (avg. 0.44). Obviously, the acidic F slag showed the strongest affinity to PbO thus decreased it activity coefficient while the CaO component in the CF slag could provide more basicity and weaken the ability of CF slag to dissolve the PbO.

Beside the data of previous studies in sections 3.1 and 3.2, Table 2 more comprehensively summarises previous studies on Pb distribution in various slag-copper systems to give an overall picture of experimental conditions and key findings. Beside the F, CF and FCS slag systems, other slag systems including CaO-SiO_2-Al_2O_3 (Matsuzaki *et al*, 2000) and SiO_2-CaO-Al_2O_3-MgO-FeO (Botor, Czernecki and Zajączkowski, 2000) were also attempted to equilibrate the copper phase. The γP_bO value increased with increasing the slag basicity (X_{CaO}/X_{SiO_2}). From Table 2, it can be seen that there is an disagreement on the effect of Al_2O_3 addition in slag on the behaviour of Pb. Nagamori, Mackey and Tarassoff (1975) found a higher content of Al_2O_3 lowered the γP_bO value while Kim and Sohn (1998) confirmed that distribution behaviour of Pb was not significantly affected by a small amount of Al_2O_3 addition. Heo and Park (2012) observed that the $L_{Pb}^{s/m}$ changed with the Al_2O_3 content of slag without a clear trend however.

TABLE 2

Summary of previous studies on thermodynamic behaviour of Pb in various slag-copper systems.

Slag system	Slag composition	Crucible	log pO_2/atm	T/◦C	$L_{Pb}^{s/m}$	γP_bO	Findings/notes	Ref.
F slag								
FeO_x-SiO_2-(Al_2O_3)	Fe/SiO_2 = 1.51 (or 1.97), Al_2O_3 8.5±0.2% (or 24.5±2.5%)	Al_2O_3	-7.1 to-6.7 (or-9.1 to-7.7)	1300	1.6 to 2.9 (or 4.5-1.7)	0.07	Fe/SiO_2 didn't obviously affect γP_bO. Higher content of Al_2O_3 lowered γP_bO. The γP_bO was independent of pO_2 and T.	Nagamori, Mackey and Tarassoff (1975)
FeO_x-SiO_2	/	SiO_2	-11.5 to-8	1250	0.021 to 0.544	0.4	Constant γP_bO value within Log pO_2/atm =-10 to-7	Takeda, Ishiwata and Yazawa (1983, 1984)
FeO_x-SiO_2-(CaO/Al_2O_3/MgO)	Pre-melted slag (58.8% FeO, 5.2% Fe_2O_3 and 36.0% SiO_2) with or without CaO/Al_2O_3/MgO	SiO_2	-12 to-6.3	1250	0.085 to 5.89	0.01-0.1	Distribution behaviour of Pb was not significantly affected by small additions of CaO, Al_2O_3, MgO, or a mixture thereof. The γP_bO increased with increase in pO_2.	Kim and Sohn (1998)
FeO_x-SiO_2-(Al_2O_3)	Fe/SiO_2 = 1.3/1.5, Al_2O_3% = 2–6%	MgO or SiO_2	-10	1200	Avg. 0.76	/	$L_{Pb}^{s/m}$ changed with Al_2O_3 content; however, the trend was not clear.	Heo and Park (2012)
FeO_x-SiO_2 with tridymite	FeO 60%, SiO_2 37% (tridymite 0.02–0.2%)	SiO_2	-9.4 to-6.9	1250	1.1–10	/	Higher concentration of Pb was found in slag than in copper.	Hidayat *et al* (2021)
FeO_x-SiO_2	FeO 56±5%, SiO_2 29±2%	Fe_3O_4 (spinel) substrate	-7.6 to-5.6	1250	3.2 to 39.8	/	Experiments were undertaken in a closed system at relatively high oxidising conditions typical for copper refining. Results were in agreement with prediction.	Sineva *et al* (2021)

Table 2 continued …

Slag system	Slag composition	Crucible	log pO_2/atm	T/◦C	$L_{Pb}^{s/m}$	γP_bO	Findings/notes	Ref.
CF slag								
$CaO\text{-}FeO_x$	CaO 20–32%	MgO	-11 to -5	1250	0.0025 to 1.91	3.2	$L_{Pb}^{s/m}$ decreased with increased CaO content of slag. The γP_bO increased with increase in CaO content.	Takeda, Ishiwata and Yazawa (1983, 1984)
$CaO\text{-}FeO_x$	Composition of primary slag: 25% CaO, 60% Fe_2O_3 and 15% FeO	CaO	-7.4 to -4.6	1250	0.25 to 3.1	1.7±0.6	No oxygen partial pressure dependence was found for γP_bO.	Eerola, Jylha and Taskinen (1984)
$CaO\text{-}FeO_x$ (saturated with MgO)	Composition with different values of R = Fe/(Fe+Ca+Mg)	MgO	-12 to -5	1300	/	4.0 (R = 0.7); 2.0 (R = 0.84)	Equilibrium experiments between slag and Pb metal	Takeda and Yazawa (1989)
$CaO\text{-}FeO_x$	$FeO_{1.5}$ 63.7%, CaO 23.5%	$Ca_2Fe_2O_5$ substrate	-5.7	1250	2.2	/	Pb distribution among copper, slag and solid phases (Fe_3O_4 spinel or $Ca_2Fe_2O_5$) was analysed.	Sineva *et al* (2021)
FCS slag								
$FeO_x\text{-}CaO\text{-}SiO_2$ (saturated with MgO)	Composition with different values of Q = (Ca+Mg)/(Ca+Mg+Si) and R = Fe/(Fe+Ca+Mg+Si)	MgO	-12 to -5	1300	/	0.3 or 0.5 (Q = 0.1, R = 0.5 or 0.8); 3.0 or 1.0 (Q = 0.55, R = 0.2 or 0.6)	Equilibrium experiments between slag and Pb metal. The solubility of Pb is affected by the activity of SiO_2.	Takeda and Yazawa (1989)
$FeO_x\text{-}CaO\text{-}SiO_2(\text{-}Cu_2O)$	35% total Fe, 18% SiO_2, 26% CaO and 4% Cu_2O (master slag)	MgO	-6	1300	0.93	1.4	For Pb deportment, replacing CF slag with FCS slag will not produce negative effects during copper converting.	Kaur, Swinbourne and Nexhip (2009)
$FeO_x\text{-}CaO\text{-}SiO_2$	Fe/SiO_2 = 1.7 (or 1.4), CaO 2–6%	MgO or SiO_2	-10	1200	0.83–0.27 (or 1.17–0.56)	/	$L_{Pb}^{s/m}$ decreases with increasing CaO content (~6 wt.%) irrespective of Fe/SiO_2 ratio (1.4 to 1.7).	Heo and Park (2012)
$FeO_x\text{-}SiO_2\text{-}CaO\text{-}Al_2O_3$	Fe/SiO_2 = 0.8–1.4 FeO_x 32.71 wt.% CaO 17.35 wt.% Al_2O_3 6.83 wt.% MgO 2.21 wt.%	TSL	Not reported	1280 ±50	/	/	Partitioning of Pb in slag/copper/dust = 13.8%/9.5%/76.7%	Ye, Liu and Xia (2021)

Table 2 continued …

Slag system	Slag composition	Crucible	log pO_2/atm	T/◦C	$L_{Pb}^{s/m}$	γP_bO	Findings/notes	Ref.
Other slags								
SiO_2-CaO-Al_2O_3-MgO-FeO	CaO 18.72 SiO_2 46.72 Al_2O_3 16.14 MgO 11.42 Fe_2O_3 7.15	Al_2O_3	$3\cdot10^{-11}$ to $2.42\cdot10^{-7}$	1400	0.009–0.24	/	Two separate slag phases could occur at $pO_2 > 10^{-8}$ atm.	Botor, Czernecki and Zajączkowski (2000)
CaO-SiO_2-Al_2O_3	X_{CaO}/X_{siO_2} = 0.5–1.3	Al_2O_3	-11.5 to-6	1350	0.03–4.0 (X_{CaO}/X_{siO_2} = 0.77±0.6)	0.06–1.03	Lead existed in slag as PbO at $pO_2 = 10^{-10} – 10^{-6}$ atm and Pb_2O at $pO_2 < 10^{-10}$ atm. The γP_bO increased with increasing slag basicity (X_{CaO}/X_{siO_2}).	Matsuzaki *et al* (2000)

Effects of (CaO+MgO)/SiO_2 and Fe/SiO_2 mass ratios in slag

The thermodynamic behaviour of minor elements during the black copper smelting process is highly dependent on the slag composition. Figure 4 shows the effects of (CaO+MgO)/SiO_2 and Fe/SiO_2 mass ratios in slag on the Pb distribution ratio and activity coefficient of PbO. It is noteworthy that the MgO was from the crucible and included into the calculation of basicity degree of the slag.

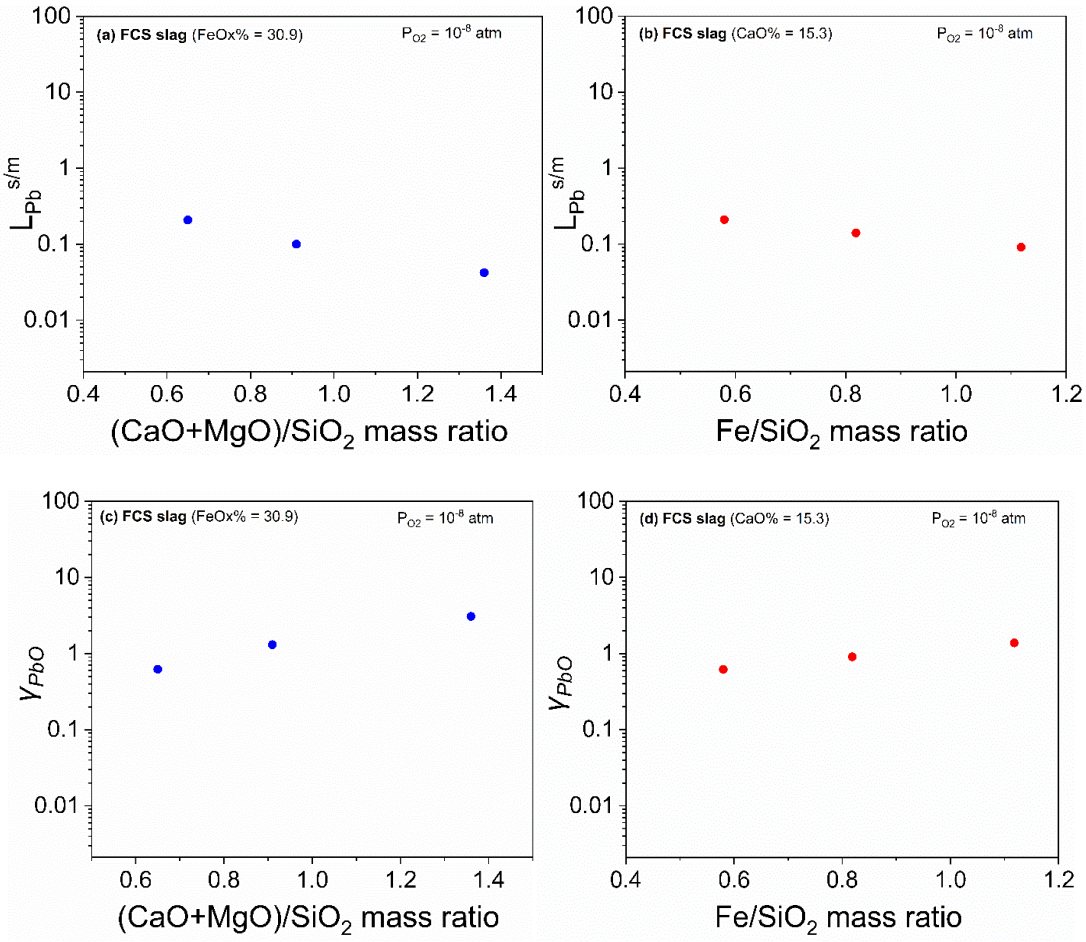

FIG 4 – Effects of (CaO+MgO)/SiO_2 and Fe/SiO_2 mass ratios on Pb distribution ratio and activity coefficient of PbO in slag.

In industrial practices, the slag composition is carefully designed to regulate the distribution of elements between slag and copper which is reflected by the activity coefficient of elements with high relevance to the slag composition (Nakajima *et al*, 2011). When increasing the CaO content in the slag as indicated by the rising (CaO+MgO)/SiO_2 ratio, SiO_2 was gradually neutralised by the added CaO with a declining absorbing ability towards PbO. Thus, a decreasing $L_{Pb}^{s/m}$ value with increased (CaO+MgO)/SiO_2 mass ratio was observed. An increasing γP_bO with rising (CaO+MgO)/SiO_2 mass ratio was determined. The γP_bO value is governed by the interactions between CaO and SiO_2 and between PbO and SiO_2 (Takeda and Yazawa, 1989). Results from Takeda and Yazawa (1989) indicated that γP_bO increased with the increase in the total content of CaO and MgO in the FeO_n-CaO-SiO_2 slag system in magnesia crucible at 1300°C.

In the present work, the Fe/SiO_2 mass ratio had no obvious effects on the $L_{Pb}^{s/m}$ and *γPbO* (averagely 0.97) within the Fe/SiO_2 range of 0.6–1.1. Nagamori, Mackey and Tarassoff (1975) observed that the γP_bO did not show obvious change for two F slags with Fe/SiO_2 = 1.51 and 1.97 at 1300°C. In a modelling study, the γP_bO value was constant in FCS slags of varied Fe/SiO_2 ratios with a fixed CaO content (Yazawa, 1994). However, the increase in the Al_2O_3 addition into F slag will lower the γP_bO value, which might be due to compounds formation among PbO, Al_2O_3 and SiO_2, such as binary compounds of $PbAl_2O_4$ and $PbAl_{12}O_{19}$ as well as ternary compounds of $PbAl_2Si_2O_8$ and $Pb_3Al_{10}SiO_{20}$ (Chen *et al*, 2001).

CONCLUSIONS

The distribution behaviour of Pb between slag and copper was investigated at 1300°C and varied pO2 of 10^{-10} to 10^{-6} atm. For all three slags of FeO_x–SiO_2 (F slag), CaO–FeO_x (CF slag) and FeO_x–CaO–SiO_2 (FCS slag), the logarithmic distribution ratio increased linearly with an increasing pO2. The distribution ratios in the acidic F slag were much higher than the alkaline CF slag due to the alkaline nature of PbO while FCS slag had a Pb capacity in between. The calculated activity coefficient of PbO in three slags followed the order of CF (1.70) > FCS (0.71) > F (0.44) which were comparable to previous studies. Differences in the Pb distribution ratio and activity coefficient of PbO between the present work and previous studies were observed possibly due to the different crucible, slag composition, possible presence of solids (eg olivine) in slag and operation conditions. Present study suggested that the FCS slag is a suitable substitute for F and CF slags for reducing smelting and oxidising converting during secondary e-waste smelting. A higher (CaO+MgO)/SiO_2 mass ratio (when MgO refractory is used) could adversely affect the Pb segregation from copper phase. The variation of Fe/SiO_2 mass ratio in the FCS slag didn't exert significant effects on the Pb distribution ratio and the activity coefficient of PbO.

ACKNOWLEDGEMENTS

Authors are thankful for the financial support and paper submission approval from Mineral Resources, CSIRO. Authors also would like to express thanks to Steve Peacock from CSIRO Mineral Processing for XRF analysis as well as Chris Sheedy and team members from CSIRO Manufacturing for ICP-OES/MS analyses.

REFERENCES

Babu, B R, Parande, A K and Basha, C A, 2007. Electrical and electronic waste: a global environmental problem, *Waste Management and Research*, 25(4):307–318.

Baldé, C, Forti, V, Gray, V, Kuehr, R and Stegmann, P, 2017. The Global E-waste Monitor 2017: Quantities, Flows and Resources [technical report], United Nations University, International Telecommunication Union, and International Solid Waste Association. Available from: <https://collections.unu.edu/view/UNU:6341>

Botor, J, Czernecki, J and Zajączkowski, A, 2000. Distribution of Cu and Pb between copper alloys and flash smelting slag, in *Proceedings of the Sixth International Conference on Molten Slags, Fluxes and Salts* (eds: S Seetharaman and Du Sichen), Sweden: Division of Metallurgy, KTH.

Chakraborty, S C, Qamruzzaman, M, Zaman, M W U, Alam, M M, Hossain, M D, Pramanik, B K, Nguyen, L N, Nghiem, L D, Ahmed, M F, Zhou, J L, Mondal, M I H, Hossain, M A, Johir, M A H, Ahmed, M B, Sithi, J A, Zargar, M and Moni, M A, 2022. Metals in e-waste: Occurrence, fate, impacts and remediation technologies, *Process Safety and Environmental Protection*, 162:230–252.

Chen, M, Avarmaa, K, Taskinen, P, Klemettinen, L, Michallik, R, O'Brien, H and Jokilaakso, A, 2021. Handling trace elements in WEEE recycling through copper smelting-an experimental and thermodynamic study, *Minerals Engineering*, 173:107189.

Chen, S, Zhao, B, Hayes, P C and Jak, E, 2001. Experimental study of phase equilibria in the PbO-Al_2O_3-SiO_2 system, *Metallurgical and Materials Transactions B*, 32(6):997–1005.

Davenport, W G, King, M J, Schlesinger, M E and Biswas, A K, 2002. *Extractive metallurgy of copper* (Elsevier).

Ebin, B and Isik, M I, 2016. Pyrometallurgical Processes for the Recovery of Metals from WEEE, in *WEEE Recycling* (eds: A Chagnes, G Cote, C Ekberg, M Nilsson and T Retegan), pp 107–137 (Elsevier).

Eerola, H, Jylha, K and Taskinen, P, 1984. Thermodynamics of impurities in calcium ferrite slags in copper fire-refining conditions, *Trans Inst Min Metall*, 93:193–199.

Forti, V, Baldé, C P, Kuehr, R and Bel, G, 2020. The Global E-waste Monitor 2020: Quantities, flows and the circular economy potential. Available from <https://ewastemonitor.info/wp-content/uploads/2020/11/GEM_2020_def_july1_low.pdf> [Accessed: 02 June 2024].

Ghodrat, M, Rhamdhani, M A, Brooks, G, Masood, S and Corder, G, 2016. Techno economic analysis of electronic waste processing through black copper smelting route, *Journal of Cleaner Production*, 126:178–190.

Ghodrat, M, Rhamdhani, M A, Khaliq, A, Brooks, G and Samali, B, 2018. Thermodynamic analysis of metals recycling out of waste printed circuit board through secondary copper smelting, *Journal of Material Cycles and Waste Management*, 20(1):386–401.

Hagelüken, C, Umicore, A and Co, K, 2006. Improving metal returns and eco-efficiency in electronics recycling, in *Proceedings of the 2006 IEEE International Symposium on Electronics and the Environment*, pp 218–223.

Heo, J and Park, S, 2012. Effect of Slag Composition on the Distribution Behavior of Pb between FetO-SiO_2 (-CaO, Al_2O_3) Slag and Molten Copper, *Metallurgical and Materials Transactions B*, vol 43.

Hidayat, T, Chen, J, Hayes, P C and Jak, E, 2021. Distributions of As, Pb, Sn and Zn as minor elements between iron silicate slag and copper in equilibrium with tridymite in the Cu–Fe–O–Si system, *International Journal of Materials Research*, 112(3):178–188.

Islam, M K, Haque, N and Somerville, M A, 2021. Characterisation and Techno-Economics of a Process to Recover Value from E-waste Materials, in *TMS 2021 150th Annual Meeting and Exhibition Supplemental Proceedings*, pp 995–1006.

Islam, M T and Huda, N, 2019. E-waste in Australia: Generation estimation and untapped material recovery and revenue potential, *Journal of Cleaner Production*, 237:117787.

Kaur, R R, Swinbourne, D R and Nexhip, C, 2009. Nickel, lead and antimony distributions between ferrous calcium silicate slag and copper at 1300°C, *Mineral Processing and Extractive Metallurgy*, 118(2):65–72.

Khaliq, A, Rhamdhani, M A, Brooks, G and Masood, S, 2014. Metal Extraction Processes for Electronic Waste and Existing Industrial Routes: A Review and Australian Perspective, *Resources*, 3(1):152–179.

Kim, H G and Sohn, H Y, 1998. Effects of CaO, Al_2O_3 and MgO additions on the copper solubility, ferric/ferrous ratio and minor-element behavior of iron-silicate slags, *Metallurgical and Materials Transactions B – Process Metallurgy and Materials Processing Science*, 29(3):583–590.

Kuxmann, U and Fischer, P, 1974. Beitrag zur Kenntnis der Zustandsdiagramme PbO-Al_2O_3, PbO-CaO und PbO-SiO_2, *Erzmetall (Z.Erzbergbau Metallhuettenwes)*, 27(11):533–537.

Matsuzaki, K, Ishikawa, T, Tsukada, T and Ito, K, 2000. Distribution equilibria of Pb and Cu between CaO-SiO_2-Al_2O_3 melts and liquid copper, *Metallurgical and Materials Transactions B*, 31(6):1261–1266.

Nagamori, M, Mackey, P J and Tarassoff, P, 1975. Copper solubility in FeO−Fe_2O_3−SiO_2−Al_2O_3 slag and distribution equilibria of Pb, Bi, Sb and As between slag and metallic copper, *Metallurgical Transactions B*, 6(2):295–301.

Nakajima, K, Takeda, O, Miki, T, Matsubae, K and Nagasaka, T, 2011. Thermodynamic Analysis for the Controllability of Elements in the Recycling Process of Metals, *Environmental Science and Technology*, 45(11):4929–4936.

Nithya, R, Sivasankari, C and Thirunavukkarasu, A, 2021. Electronic waste generation, regulation and metal recovery: a review, *Environmental Chemistry Letters*, 19(2):1347–1368.

Shuva, M A H, Rhamdhani, M A, Brooks, G A, Masood, S and Reuter, M A, 2016. Thermodynamics data of valuable elements relevant to e-waste processing through primary and secondary copper production: a review, *Journal of Cleaner Production*, 131:795–809.

Sineva, S, Shishin, D, Starykh, R, Hayes, P C and Jak, E, 2021. Equilibrium Distributions of Pb, Bi and Ag between Fayalite Slag and Copper-Rich Metal, Calcium Ferrite Slag and Copper-Rich Metal, Thermodynamic Assessment and Experimental Study at 1250 °C, *Journal of Sustainable Metallurgy*, 7(2):569–582.

Takeda, Y and Yazawa, A, 1989. Dissolution Loss of Copper, Tin and Lead in FeO sub n--SiO sub 2--CaO Slag, in, *Productivity and technology in the metallurgical industries* (eds: M Koch and J C Taylor), pp 227–240 (The Minerals, Metals and Materials Society).

Takeda, Y, Ishiwata, S and Yazawa, A, 1983. Distribution Equilibria of Minor Elements between Liquid Copper and Calcium Ferrite Slag, *Transactions of the Japan Institute of Metals*, 24(7):518–528.

Takeda, Y, Ishiwata, S and Yazawa, A, 1984. Distribution of Minor Elements between Slag and Metallic Copper: Equilibrium Study on Calcium Ferrite slags (4th Report), *Journal of the Mining and Metallurgical Institute of Japan*, 100(1152):103–108.

Taskinen, P and Avarmaa, K, 2021. Simulation of Slag–Matte/Metal Equilibria for Complex and Low-Grade Raw Materials, *Sustainability*, 13(22):12826.

Tian, H, Guo, Z, Pan, J, Zhu, D, Yang, C, Xue, Y, Li, S and Wang, D, 2021. Comprehensive review on metallurgical recycling and cleaning of copper slag, Resources, Conservation and Recycling, 168:105366.

Yamasue, E, Minamino, R, Numata, T, Nakajima, K, Murakami, S, Daigo, I, Hashimoto, S, Okumura, H and Ishihara, K N, 2009. Novel Evaluation Method of Elemental Recyclability from Urban Mine – Concept of Urban Ore TMR, *Materials Transactions*, 50(6):1536–1540.

Yazawa, A and Takeda, Y, 1982. Equilibrium Relations between Liquid Copper and Calcium Ferrite Slag, *Transactions of the Japan Institute of Metals*, 23(6):328–333.

Yazawa, A, 1994. Thermodynamic Interpretation on Oxidic Dissolution of Metal in Slag, *Australian Asian Pacific Course and Conference – Pyrometallurgy for Complex Materials and Wastes*, Melbourne, Australia.

Ye, F C, Liu, Z H and Xia, L G, 2021. Materials and Energy Balance of E-Waste Smelting – An Industrial Case Study in China, *Metals*, 11(11):1814.

Distribution of Pb, Zn, Fe, As, Sn, Sb, Bi and Ni between oxide liquid and metal in the '$CuO_{0.5}$'-CaO-$AlO_{1.5}$ system in equilibrium with Cu metal at 1400°C

DOI: 10.62053/RVWR6385

G Khartcyzov[1], M Shevchenko[2] and E Jak[3]

1. PhD candidate, Pyrosearch, School of Chemical Engineering, the University of Queensland, Brisbane Qld 4072. Email: g.khartcyzov@uq.edu.au
2. Research Fellow, Pyrosearch, School of Chemical Engineering, the University of Queensland, Brisbane Qld 4072. Email: m.shevchenko@uq.edu.au
3. Professor, Pyrosearch, School of Chemical Engineering, the University of Queensland, Brisbane Qld 4072. Email: e.jak@uq.edu.au

ABSTRACT

The increasing complexity of ore resources and recycled materials in the feed of pyrometallurgical processes present a technical challenge to the metallurgical engineers working on maximising the recovery of the valuable elements and minimising the environmental impact of the processes. To address this challenge, the availability of computational tools that can predict the mass and energy balance in complex systems is required. Then the accurate description of phase equilibria in the complex multicomponent systems describing the chemistry of the pyrometallurgical processes becomes critical for the correct implementation of the indicated tools and facing the outlined industrial challenges.

In the present study the distribution of selected elements (Pb, Zn, Fe, As, Sn, Sb, Bi and Ni) between oxide liquid and metal in the '$CuO_{0.5}$'-CaO-$AlO_{1.5}$ system in equilibrium with Cu metal at 1400°C (liquidus of $CaAl_2O_4$) was experimentally studied using the equilibration and quenching technique followed by the electron probe X-ray microanalysis of the resulted samples. The study covered a wide range of effective $p(O_2)$ over the system from 10^{-11} to $10^{-3.5}$ (corresponding to formation of immiscible $CuO_{0.5}$-rich slag). To avoid loss of volatile elements (Pb, Zn, As, Sn, Sb and Bi), a correlation between '$CuO_{0.5}$' in oxide liquid and $p(O_2)$ in open system was obtained first, followed by studying the volatile elements distribution in closed conditions (Al_2O_3 crucible sealed in SiO_2 ampoule), where '$CuO_{0.5}$' concentration was used as a marker to evaluate the effective $p(O_2)$ over the system.

The experimental results were then used for the optimisation of the thermodynamic model parameters of the system as part of the integrated experimental and self-consisting thermodynamic modelling research program of phase equilibria in the Cu-Pb-Zn-Fe-Ca-Si-Al-Mg-O-S-(As, Sn, Sb, Bi, Ag, Au, Ni, Cr, Co and Na) gas/oxide liquid/matte/speiss/metal/solids system.

INTRODUCTION

The recycling of nonferrous metals, an essential component for sustainable development, faces significant challenges due to the variability of the feedstock and the complex chemistry of the elements involved (Loibl and Tercero Espinoza, 2021). The development of new processes and the optimisation of existing processes require computational tools capable of predicting phase equilibria, energy balance and partitioning of all chemical elements. In turn, the accuracy of the predictions is improved by the integrated experimental and thermodynamic modelling study of the chemical system characterising the process of interest. The present study focuses on the distribution of the Cu, Pb, Zn, Fe, As, Sn, Sb, Bi and Ni between the oxide liquid and metallic phases of the '$CuO_{0.5}$'-CaO-$AlO_{1.5}$ system to help describe the complex phase equilibria in non-ferrous recycling slags.

The present study is a part of a broader research program supported by an international consortium of copper, lead, zinc and iron producing companies and focused on the integrated experimental and thermodynamic modelling study of phase equilibria in the Cu-Pb-Zn-Fe-Ca-Si-Al-Mg-O-S-(As, Sn, Sb, Bi, Ag, Au, Ni, Cr, Co and Na) gas/oxide liquid/matte/speiss/metal/solids system, and the development of a self-consistent set of the thermodynamic parameters for the described system (Shevchenko *et al*, 2021; Shishin, Hayes and Jak, 2018, 2019). The new experimental data on the presented subsystems will enable these and the larger multicomponent systems to be described

using chemical thermodynamic models. Phase equilibria data and other thermodynamic properties of these systems will then provide an important foundation for the improved understanding and, importantly, prediction of the behaviour of these slags in the industrial processes.

Similar works were found in the literature studying the distribution of the different elements in the iron silicate (Yazawa, 1981; Hidayat *et al*, 2021), iron alumina silicate (Nagamori and Mackey, 1977), iron calcium silicate (Anindya *et al*, 2013, 2014) and calcium ferrite (Yazawa, 1981) slags. The present work is considered to be the first to study the distributions of Cu, Pb, Zn, Fe, As, Sn, Sb, Bi and Ni in the calcium aluminate slags.

Figure 1 demonstrates the liquidus projection diagram of the '$CuO_{0.5}$'-CaO-$AlO_{1.5}$ system in equilibrium with metallic copper calculated using the FactSage™ software ver 8.2 (by CRCT-ThermFact Inc. and GTT-Technologies) (Bale *et al*, 2016) and internal thermodynamic database (Shevchenko *et al*, 2021; Shishin *et al*, 2018, 2019) with the area of the interest for the present study highlighted on the diagram. This area was chosen for several reasons:

- It is located in the low-temperature region of the diagram.
- It covers the range of concentrations of '$CuO_{0.5}$' in the oxide liquid (wide range of oxygen partial pressures).
- The $CaAl_2O_4$-$AlO_{1.5}$ side of the CaO-$AlO_{1.5}$ system promotes the formation of the layer of calcium aluminates on the Al_2O_3 crucible or Al_2O_3-based refractory material for all corresponding bulk compositions.

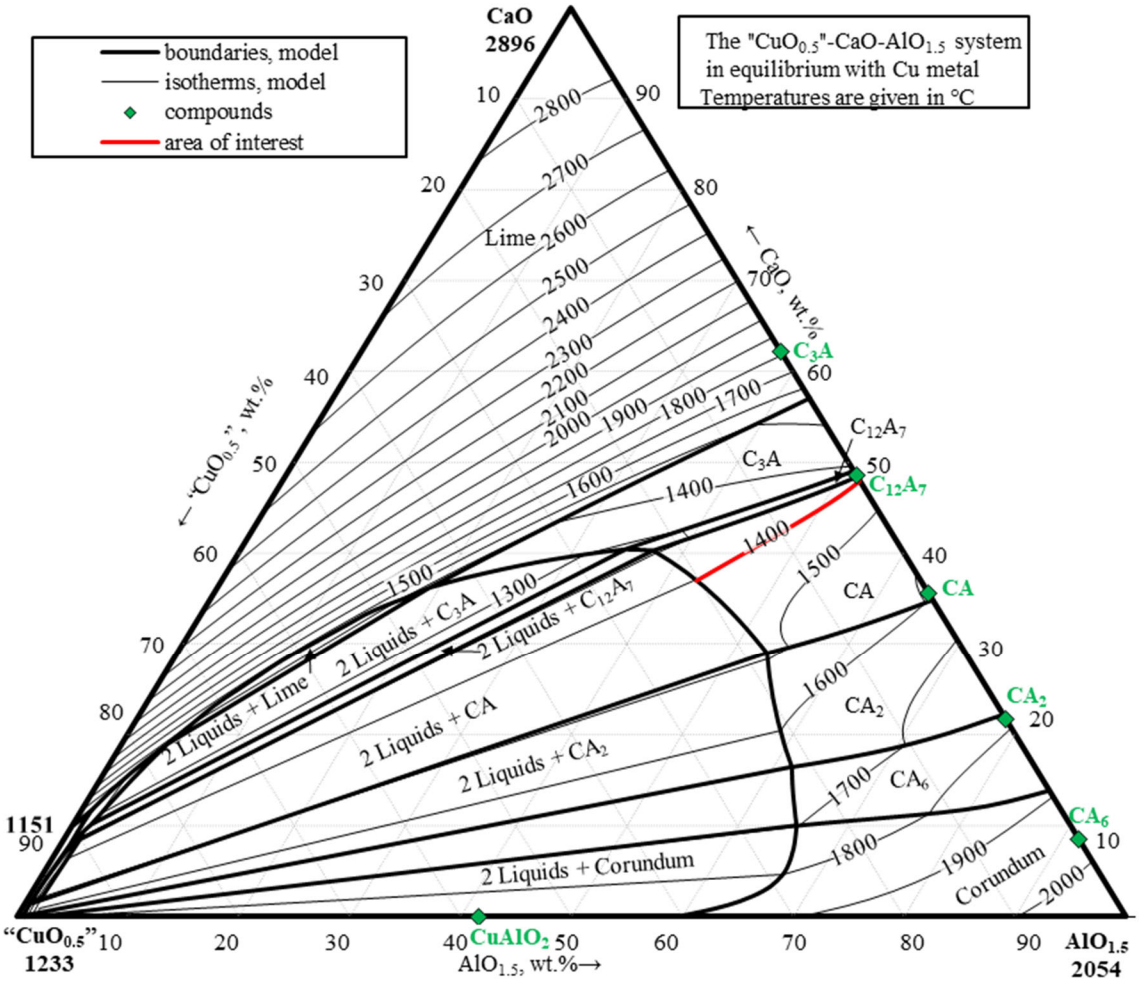

FIG 1 – Calculated phase diagram of the '$CuO_{0.5}$'-CaO-$AlO_{1.5}$ system in equilibrium with Cu metal with highlighted area of interest for the present study.

These reasons make the chosen area suitable and beneficial for the possible WEEE (waste electronic and electrical equipment) recycling processes.

The present study provides the experimental description of the phase equilibria in the '$CuO_{0.5}$'-CaO-$AlO_{1.5}$-(Pb, Zn, Fe, As, Sn, Sb, Bi and Ni) system in equilibrium with metallic phase and $CaAl_2O_4$ at 1400°C, including:

- Correlation between the concentration of copper oxide in the '$CuO_{0.5}$'-CaO-$AlO_{1.5}$ oxide liquid in equilibrium with $CaAl_2O_4$ at 1400°C and effective oxygen partial pressure ($p(O_2)$) over the system.
- The distributions of the Cu, Pb, Zn, Fe, As, Sn, Sb, Bi and Ni among the oxide liquid and the metallic phase in the '$CuO_{0.5}$'-CaO-$AlO_{1.5}$ system in equilibrium with $CaAl_2O_4$ at 1400°C in the wide range of oxygen partial pressures from 10^{-11} to $10^{-3.5}$.

RESEARCH METHODOLOGY

The experimental procedure and apparatus used in the present study were described earlier by the authors (Jak, Hayes and Lee, 1995; Jak, 2012; Khartcyzov *et al*, 2022, 2023). The initial mixtures were made of high-purity Cu_2O, ZnO, Fe_2O_3 and Al_2O_3 (all ≥99.9 wt per cent purity, supplied by Alfa Aesar, MA, USA or by Sigma-Aldrich, MO, USA) oxide and Cu, Pb, Sn, Sb, Bi and Ni (≥99.9 wt per cent purity; supplied by Alfa Aesar, MA, USA) metallic powders. As was added to the mixture in a form of Cu_3As (prepared by heating Cu and As powders at 5°C/min to 900°C (with 1 hr hold at 300, 500, 700 and 800°C) and keeping over 2 hrs, then allowing to cool with the furnace). CaO was added to the mixture in a form of the 'master slag' CaO-$AlO_{1.5}$, 55:45 molar ratio, prepared in advance by high-temperature sintering of mixed $CaCO_3$ and Al_2O_3 powders (≥99.9 wt per cent purity; supplied by Alfa Aesar, MA, USA). About 0.5 g of mixture was used in each equilibration experiment. The initial compositions of the mixtures were selected so that $CaAl_2O_4$ was present in equilibrium with liquid slag and metals. The initial predictions of the targeted phase compositions were made for every sample using FactSage™ 8.2 software (Bale *et al*, 2009, 2016) and continuously updated internal thermodynamic database (Shevchenko *et al*, 2021; Shishin *et al*, 2018, 2019). The volume fraction of solids in the final sample after equilibration was targeted to be in the range from 10 to 50 per cent and preferably about 10 per cent. Low proportion of solids ensures faster equilibration time and facilitates quenching of liquid slag into amorphous material without change in composition. Solid phases acted as heterogeneous nucleation centres, so that a minimum distance of 10–20 μm between solid grains was necessary to ensure that an amorphous slag of uniform composition, unaffected by dendritic crystal growth during quenching, was obtained. The correlation between the proportion of the solid phases present in equilibrium and the distance between solid grains was described previously by the authors (Khartcyzov *et al*, 2022). An iterative procedure involving preliminary experiments was required to achieve the targeted phase proportions for a given equilibration temperature and bulk slag composition, since the exact liquidus compositions at a given temperature were not initially known. Homogenous slag areas, not affected by the growth of the 'quench crystals', were analysed and included in the present study.

The mixtures were pressed into pellets using a tool steel die before being mounted on a substrate. Alumina crucibles (1.5 cm long, 1 cm outer diameter, 99.7 wt per cent purity, supplied by Xiamen Wintrustek Advance Materials Co., LTD, China) were used as sample support substrates for equilibration. For the closed system experiments the alumina crucibles were additionally sealed inside silica ampoules (5 cm long, 1.3 cm outer diameter, 99.999 per cent, supplied by GY, Jiangsu, China) to prevent the contamination of the samples with the suspension support materials and to limit the evaporation of the volatile species from the melt. The ceramic crucibles were previously found to be reliable as substrates (Khartcyzov *et al*, 2022; Hidayat *et al*, 2012; Chen *et al*, 2020). The precipitation of the primary phase on the ceramic substrate prevents the excessive dissolution of the substrate material into the slag ensuring little change in the bulk composition of the system during the equilibration time (Shevchenko and Jak, 2020; Klemettinen, Avarmaa and Taskinen, 2017).

Each equilibration experiment was carried out in an electrical-resistance heated vertical tube furnace with an impervious recrystallised alumina (30 mm inner diameter) reaction tube with silicon carbide (SiC) heating element; the upper temperature limit for the furnace operation was 1700°C. The

samples were placed immediately adjacent to a working thermocouple (type B) that was encased in a recrystallised alumina sheath in the uniform hot zone of the furnace to monitor the actual sample temperature. The working thermocouple was calibrated against a standard thermocouple (supplied by the National Measurement Institute of Australia, NSW, Australia). The overall absolute temperature accuracy of the experiment was estimated to be ±3 K.

The samples were suspended in the hot zone of the furnace by Kanthal support wire (Fe-Cr-Al alloy, 0.7 (Kanthal D) or 1-mm (Kanthal A-1) diameter; melting temperature 1500°C; suitable for operating up to $p(O_2)$ = 1 atm; supplied by Vulcan Stainless, VIC, Australia). High purity CO and CO_2 gases (>99.995 per cent purity, supplied by Coregas, NSW, Australia) were used for the open system experiments. The samples were then equilibrated at the final target temperature for the required time. For the open system experiments the $p(O_2)$ was maintained by an accurate control of the CO/CO_2 ratio in the gas flow phase using calibrated U-tube capillary flowmeters. The desired flow rates of gases, corresponding to the indicated $p(O_2)$ were calculated using FactSage™ 8.2 FactPS database (Bale *et al*, 2016) for the ideal gas phase. The accuracy of the oxygen potential was confirmed using a DS-type oxygen probe (supplied and calibrated by Australian Oxygen Fabricators, Melbourne, Vic, Australia). At the end of the equilibration process, the samples were released and rapidly quenched into $CaCl_2$ brine solution at -20°C. Brine solution was chosen over water due to the higher cooling rates (Pizetta Zordão *et al*, 2019; Luty, 1992). The samples were then washed thoroughly in water and ethanol, dried on a hot plate, mounted in epoxy resin and cross-sectioned and polished using conventional metallographic techniques.

The cross-sectioned samples were examined by optical microscopy, carbon-coated, and the compositions of the phases were measured by electron probe microanalysis (EPMA) using wavelength-dispersive detectors (JEOL 8200L EPMA; Japan Electron Optics Ltd., Tokyo, Japan) operated at 15 kV accelerating voltage and 20 nA probe current. The standard Duncumb–Philibert atomic number, absorption, and fluorescence (ZAF) correction supplied by JEOL (Philibert, 1963; Duncumb and Reed, 1968; Duncumb, 1971) was used. Copper (Cu) (for Cu and '$CuO_{0.5}$' measurements), zincite (ZnO) (for Zn and ZnO measurements), hematite (Fe_2O_3) (for Fe, FeO and $FeO_{1.5}$ measurements), wollastonite ($CaSiO_3$) (for CaO measurements), corundum (Al_2O_3) (for $AlO_{1.5}$ measurements), indium arsenide (InAs) (for As and $AsO_{1.5}$ measurements), cassiterite (SnO_2) (for Sn and SnO_2 measurements), antimony (Sb) (for Sb and $SbO_{1.5}$ measurements), bismuth (Bi) (for Bi and $BiO_{1.5}$ measurements) and nickel (Ni) (for Ni and NiO measurements) (supplied by Charles M. Taylor Co., Stanford, CA) and K456 lead-silica glass (71.4 wt per cent PbO) (for Pb and PbO) (supplied by NIST) were used as EPMA standards. The measurement uncertainties corresponded to the use of metals as standards for oxide measurements and *vice versa* did not exceed 0.2 per cent. Only concentrations of metal cations were measured using EPMA; no data on the oxidation states of the metal cations in slag were obtained in the present study.

It was shown (Fallah-Mehrjardi *et al*, 2017) that the increase from fully focused electron beam (zero probe diameter) to 50 μm decreased the uncertainty of the copper slags compositions measured with EPMA and did not affect the accuracy of measurements. Thus, the probe diameter was selected depending on the size of the phase under investigation. The slag compositions reported in this study were measured mainly using 30 μm probe diameter, while the metallic phases were measured mainly with 50 to 100 μm probe diameters. The compositions of the phases reported in the present study are the average values of a number (from 15 to 25, usually 20) of independent measurements from different regions of the samples rather than single measurements.

The accuracy of the compositional measurements was improved using the standard JEOL ZAF correction following an approach similar to that described previously by the authors (Shevchenko and Jak, 2017, 2018, 2019; Shevchenko, Chen and Jak, 2017; Khartcyzov *et al*, 2022, 2023). This involved using stoichiometric compounds of known composition (Cu_2PbO_2, Ca_2CuO_3, $CuAlO_2$, $ZnAl_2O_4$, Ca_2PbO_4, $Ca_2Fe_2O_5$, $CaFe_2O_4$, $CaFe_4O_7$, $FeAl_2O_4$, $Ca_3Al_2O_6$, $CaAl_2O_4$, $CaAl_4O_7$) as secondary internal standards. The following Equations (1–6) were then developed and applied to correct all cations concentrations in the target system of the present study:

$$x_{CuO_x}^{corrected} = x_{CuO_x}(1 - 0.0336x_{PbO} + 0.035x_{CaO} + 0.116x_{AlO_{1.5}}), \quad (1)$$

$$x_{ZnO}^{corrected} = x_{\mathrm{ZnO}}(1 + 0.06x_{AlO_{1.5}}), \quad (2)$$

$$x_{PbO}^{corrected} = x_{\mathrm{PbO}}(1 + 0.0336x_{CuO_x} + 0.0192x_{CaO}), \quad (3)$$

$$x_{FeO_x}^{corrected} = x_{FeO_x}(1 + 0.0208x_{CaO} + 0.0119x_{CaO}^2 - 0.0119x_{FeO_x}x_{CaO} + 0.038x_{AlO_{1.5}}), \quad (4)$$

$$x_{CaO}^{corrected} = x_{\mathrm{CaO}}(1 - 0.035x_{CuO_x} - 0.0192x_{\mathrm{PbO}}$$
$$-0.0208x_{FeO_x} - 0.0119x_{FeO_x}^2 + 0.0119x_{CaO}x_{FeO_x} - 0.044x_{AlO_{1.5}}), \quad (5)$$

$$x_{AlO_{1.5}}^{corrected} = x_{AlO_{1.5}}(1 - 0.116x_{CuO_x} - 0.06x_{ZnO} - 0.038x_{FeO_x} + 0.044x_{\mathrm{CaO}}), \quad (6)$$

where x(CuO_x, PbO, ZnO, FeO_x, CaO, $AlO_{1.5}$) are the cation molar fractions after the standard JEOL ZAF corrections, and x(CuO_x, PbO, ZnO, FeO_x, CaO, $AlO_{1.5}$)^{corrected} are the corrected cation molar fractions respectively.

To ensure the achievement of equilibrium in the samples, the '4-point test' (Jak, 2012; Shevchenko *et al*, 2016) was used including:

1. Variation of equilibration time.
2. Assessment of the compositional homogeneity of the phases by EPMA.
3. Approaching the final equilibrium point from different starting conditions.
4. And, importantly, consideration of reactions specific to this system that may affect the achievement of equilibrium or reduce the accuracy.

The presence of volatile elements (Pb, Zn, As, Sn, Sb and Bi) in the system made it impossible to run the equilibration experiments in the open system at the controlled $p(O_2)$. To overcome this issue, the experimental methodology similar to the one described before by the authors (Hidayat, Hayes and Jak, 2018) was developed and used in the present study. The methodology involves closed system experiments in the sealed ampoules using the Cu_{metal}/Cu_2O_{slag} couple as internal measure of the effective $p(O_2)$ over the system. In the presence of metallic Cu, the change in the oxidation potential of the system results in the change of the solubility of '$CuO_{0.5}$' in the slag phase, according to the following reactions (Hidayat, Hayes and Jak, 2018):

$$2Cu_{metal} + O_{slag} \leftrightarrow Cu_2O_{slag} \quad (7)$$

The Cu_{metal}/Cu_2O_{slag} couple then reflects the effective $p(O_2)$ of the slag phase as per the following reaction:

$$2Cu_{metal} + \frac{1}{2}O_{2\,gas} \leftrightarrow Cu_2O_{slag} \quad (8)$$

According to Equation 8, it is possible to estimate the effective $p(O_2)$ over the system based on the concentration of '$CuO_{0.5}$' in the oxide liquid, that is in equilibrium with Cu metal. The correlation between the $p(O_2)$ over the system and the concentration of '$CuO_{0.5}$' in the oxide liquid for the system of interest is required. In the present study the following approach was used:

- Establishing the correlation between '$CuO_{0.5}$'in oxide liquid and $p(O_2)$ over the system for the volatile-free '$CuO_{0.5}$'-CaO-$AlO_{1.5}$ system in equilibrium with Cu metal using accurate experimental data obtained with the open-system gas equilibration technique in the composition area of interest.
- Performing closed-system equilibration experiments for the '$CuO_{0.5}$'-CaO-$AlO_{1.5}$-(Pb, Zn, As, Sn, Sb, Bi and Ni) chemical system.
- Deriving the effective $p(O_2)$ over the system based on the experimental information obtained in steps 1–3.

RESULTS AND DISCUSSION

Preliminary experiments were carried out to find the conditions of achievement of equilibrium using the '4-point test' (Jak, 2012; Shevchenko *et al*, 2016) including:

1. Variation of equilibration time.
2. Assessment of the compositional homogeneity of the phases by EPMA.

3. Approaching the final equilibrium point from different starting conditions.
4. And, importantly, consideration of reactions specific to this system that may affect the achievement of equilibrium or reduce the accuracy.

For open system experiments, equilibration time varied from 1–5 hrs to ensure that no further reactions between the condensed and gaseous phases take place in the sample. Homogeneity of the phases was examined in different locations of the samples. When compositional trends were observed, results were rejected and equilibration time was increased. The dissolution of the substrate material into the liquid which could have potentially affected phase equilibria in the system was found to be not a problem, because no compositional trends were observed for the samples after equilibration and the targeted phases were obtained. Final equilibration times for the open system experiments are given in Table 1. For the closed system experiments, the equilibration time varied from 3–16 hrs: 3 hrs of equilibration were found enough for all samples, while some were equilibrated for 16 hrs to study the achievement of equilibria with time or for the experimental convenience. Final equilibration times are listed in Table 1. For selected experiments, different starting compositions were used, or samples were preheated by 50°C; the measured compositions of liquids agreed within the standard deviation of measurements.

TABLE 1

Experimental results for the distribution of Cu, Pb, Zn, Fe, As, Sn, Sb, Bi, Ni between oxide liquid and metal phase in the '$CuO_{0.5}$'-CaO-$AlO_{1.5}$ system in equilibrium with $CaAl_2O_4$ at 1400°C.

Element	Preheat	Final	Time	Phases present	Compositions (wt%)				Ox/*Met*	$Log_{10}L^1$	Log_{10} $p(O_2)$
MeO_x/*Me*	Temperature, °C		hour		'$CuO_{0.5}$'	CaO	$AlO_{1.5}$	MeO_x	Ox		
					Cu	*Ca*	*Al*	*Me*	*Met*		
none	-	1400	5	oxide liquid	0.10±0.00	47.2±0.1	52.7±0.1	-	Ox	-3.1	-11[C]
				$CaAl_2O_4$[2]	0.02±0.02	35.0±0.1	65.0±0.1	-	Ox		
				metal	***99.98±0.05***	***0.01±0.01***	***0.01±0.04***	***-***	***Met***		
	-	1400	5	oxide liquid	0.18±0.03	47.3±0.3	52.5±0.2	-	Ox	-2.9	-10[C]
				$CaAl_2O_4$[2]	0.70±0.08	33.8±0.2	65.5±0.3	-	Ox		
				metal	***99.99±0.01***	***0.01±0.00***	***0.00±0.00***	***-***	***Met***		
	-	1400	5	oxide liquid	0.30±0.06	47.4±0.3	52.3±0.2	-	Ox	-2.6	-9[C]
				$CaAl_2O_4$[2]	0.12±0.00	35.3±0.0	64.6±0.0	-	Ox		
				metal	***99.98±0.00***	***0.02±0.02***	***0.00±0.01***	***-***	***Met***		
	-	1400	5	oxide liquid	0.82±0.39	46.9±0.4	52.2±0.2	-	Ox	-2.2	-8[C]
				$CaAl_2O_4$[2]	0.07±0.00	36.7±0.0	63.2±0.0	-	Ox		
				metal	***99.98±0.02***	***0.02±0.03***	***0.00±0.01***	***-***	***Met***		
	-	1400	5	oxide liquid	1.0±0.2	47.1±0.3	51.9±0.2	-	Ox	-2.1	-7[C]
				$CaAl_2O_4$[2]	0.12±0.03	35.1±0.0	64.8±0.1	-	Ox		
				metal	***99.96±0.00***	***0.01±0.00***	***0.03±0.00***	***-***	***Met***		
	-	1400	5	oxide liquid	1.8±0.3	46.4±0.3	51.8±0.2	-	Ox	-1.8	-6[C]
				$CaAl_2O_4$[2]	0.18±0.00	35.1±0.1	64.7±0.1	-	Ox		
				metal	***99.97±0.02***	***0.03±0.02***	***0.00±0.00***	***-***	***Met***		
	-	1400	4	oxide liquid	2.2±0.2	46.0±0.1	51.9±0.1	-	Ox	-1.8	-6[C]
				$CaAl_2O_4$[2]	0.23±0.05	35.2±0.1	64.5±0.1	-	Ox		
				metal	***99.81±0.07***	***0.13±0.08***	***0.07±0.01***	***-***	***Met***		
	-	1400	5	oxide liquid	3.4±0.6	45.2±0.5	51.4±0.2	-	Ox	-1.6	-5[C]
				$CaAl_2O_4$[2]	0.08±0.04	36.5±0.2	63.4±0.1	-	Ox		
				metal	***99.94±0.2***	***0.02±0.04***	***0.04±0.05***	***-***	***Met***		
	-	1400	4	oxide liquid	6.4±0.1	43.0±0.2	50.6±0.1	-	Ox	-1.3	-4.5[C]
				$CaAl_2O_4$[2]	0.13±0.05	35.1±0.1	64.8±0.1	-	Ox		
				metal	***99.96±0.03***	***0.01±0.00***	***0.03±0.03***	***-***	***Met***		

Table 1 continued …

Element	Preheat	Final	Time	Phases present	Compositions (wt%)				Ox/*Met*	$Log_{10}L^1$	Log_{10} $p(O_2)$
MeO_x/*Me*	Temperature, °C		hour		'$CuO_{0.5}$'	CaO	$AlO_{1.5}$	MeO_x	Ox		
					Cu	*Ca*	*Al*	*Me*	*Met*		
PbO/*Pb*	1450	1400	16	oxide liquid	1.6±0.2	46.5±0.2	51.6±0.1	0.23±0.07	Ox	-1.4	-6.5[E]
				$CaAl_2O_4$[2]	0.06±0.02	35.0±0.1	64.9±0.1	0.04±0.00	Ox		
				metal	***95.0±0.7***	***0.03±0.01***	***0.01±0.02***	***5.0±0.7***	***Met***		
	-	1400	16	oxide liquid	5.9±0.1	43.8±0.1	50.2±0.2	0.15±0.08	Ox	-0.3	-4.4[E]
				$CaAl_2O_4$[2]	0.16±0.01	35.1±0.3	64.6±0.5	0.22±0.22	Ox		
				metal	***99.70±0.13***	***0.01±0.02***	***0.02±0.02***	***0.26±0.13***	***Met***		
ZnO/*Zn*	1450	1400	16	oxide liquid	1.2±0.1	45.7±0.1	52.2±0.1	0.89±0.05	Ox	0.7	-7[E]
				$CaAl_2O_4$[2]	0.00±0.00	34.7±0.0	65.3±0.0	0.00±0.00	Ox		
				metal	***99.79±0.08***	***0.02±0.01***	***0.02±0.02***	***0.17±0.06***	***Met***		
FeO/*Fe*	-	1400	5	oxide liquid	0.08±0.05	46.2±0.2	51.0±0.2	2.7±0.1	Ox	0.1	-11[C]
				$CaAl_2O_4$[2]	0.03±0.03	35.4±0.2	64.4±0.2	0.15±0.04	Ox		
				metal	***98.3±0.1***	***0.01±0.01***	***0.01±0.02***	***1.7±0.1***	***Met***		
	-	1400	5	oxide liquid	0.32±0.05	42.6±0.2	48.6±0.2	8.4±0.1	Ox	1.3	-9[C]
				$CaAl_2O_4$[2]	0.02±0.03	34.7±0.2	64.6±0.2	0.63±0.04	Ox		
				metal	***99.60±0.05***	***0.02±0.02***	***0.02±0.02***	***0.36±0.04***	***Met***		
$AsO_{1.5}$/*As*	-	1400	16	oxide liquid	2.7±0.1	45.9±0.2	50.5±0.1	0.88±0.06	Ox	-0.4	-5.6[E]
				$CaAl_2O_4$[2]	0.07±0.00	34.7±0.2	65.2±0.2	0.00±0.00	Ox		
				metal	***98.6±0.3***	***0.02±0.02***	***0.04±0.05***	***1.4±0.3***	***Met***		
	1450	1400	16	oxide liquid	3.7±0.1	45.1±0.1	49.9±0.1	1.4±0.1	Ox	0.1	-5.1[E]
				$CaAl_2O_4$[2]	0.12±0.08	34.8±0.1	65.1±0.1	0.00±0.00	Ox		
				metal	***99.12±0.06***	***0.02±0.01***	***0.01±0.01***	***0.85±0.06***	***Met***		
	1450	1400	16	oxide liquid	4.3±0.1	44.8±0.1	48.7±0.1	2.2±0.1	Ox	0.4	-4.9[E]
				$CaAl_2O_4$[2]	0.09±0.01	34.9±0.1	65.0±0.1	0.00±0.00	Ox		
				metal	***99.07±0.38***	***0.13±0.23***	***0.02±0.01***	***0.79±0.16***	***Met***		
SnO_2/*Sn*	1450	1400	16	oxide liquid	1.3±0.0	46.8±0.1	51.6±0.1	0.26±0.02	Ox	-0.8	-6.8[E]
				$CaAl_2O_4$[2]	0.06±0.02	34.9±0.1	65.0±0.1	0.00±0.00	Ox		
				metal	***98.9±0.1***	***0.01±0.01***	***0.01±0.01***	***1.0±0.1***	***Met***		
	1450	1400	16	oxide liquid	2.6±0.0	45.8±0.2	50.9±0.2	0.76±0.04	Ox	0.2	-5.7[E]
				$CaAl_2O_4$[2]	0.04±0.03	35.2±0.1	64.8±0.1	0.02±0.02	Ox		
				metal	***99.56±0.19***	***0.01±0.01***	***0±0.03***	***0.43±0.21***	***Met***		
	1450	1400	16	oxide liquid	4.4±0.2	43.6±0.1	50.5±0.1	1.5±0.1	Ox	1.0	-4.8[E]
				$CaAl_2O_4$[2]	0.05±0.04	34.8±0.0	65.1±0	0.02±0.03	Ox		
				metal	***99.85±0.06***	***0.01±0.01***	***0.01±0.02***	***0.13±0.07***	***Met***		
$SbO_{1.5}$/*Sb*	-	1400	16	oxide liquid	2.1±0.3	45.4±0.2	50.9±0.2	1.6±0.1	Ox	-1.0	-6.0[E]
				$CaAl_2O_4$[2]	0.07±0.08	34.8±0.0	65.1±0.1	0.02±0.03	Ox		
				metal	***89.0±1.4***	***0.01±0.01***	***0.01±0.02***	***11.0±1.4***	***Met***		
	-	1400	16	oxide liquid	3.4±0.1	44.6±0.1	48.2±0.2	3.9±0.1	Ox	-0.5	-5.2[E]
				$CaAl_2O_4$[2]	0.16±0.02	35.3±0.1	64.6±0.1	0.00±0.00	Ox		
				metal	***90.0±3.2***	***0.03±0.02***	***0.01±0.02***	***9.9±3.2***	***Met***		
$BiO_{1.5}$/*Bi*	-	1400	16	oxide liquid	4.0±0.2	45.1±0.2	50.8±0.1	0.08±0.03	Ox	-1.7	-5.0[E]
				$CaAl_2O_4$[2]	0.05±0.05	35.0±0.1	65.0±0.1	0.03±0.04	Ox		
				metal	***96.9±0.5***	***0.06±0.18***	***0.03±0.1***	***3.0±0.4***	***Met***		
	-	1400	16	oxide liquid	5.5±0.1	43.6±0.2	50.8±0.1	0.02±0.04	Ox	-1.2	-4.5[E]
				$CaAl_2O_4$[2]	0.16±0.02	34.7±0.1	65.1±0.1	0.02±0.04	Ox		

Table 1 continued …

Element	Preheat	Final	Time	Phases present	Compositions (wt%)				Ox/*Met*	$Log_{10}L^1$	Log_{10} $p(O_2)$
MeO_x/*Me*	Temperature, °C		hour		'$CuO_{0.5}$'	CaO	$AlO_{1.5}$	MeO_x	Ox		
					Cu	*Ca*	*Al*	*Me*	*Met*		
				metal	*99.69±0.10*	*0.02±0.01*	*0.04±0.05*	*0.26±0.1*	*Met*		
NiO/*Ni*	-	1400	16	oxide liquid	0.81±0.08	47.4±0.1	51.6±0.1	0.2±0.05	Ox	-1.7	-7.6[E]
				$CaAl_2O_4$[2]	0.04±0.03	35.4±0.0	64.6±0.0	0.03±0.03	Ox		
				metal	*93.7±0.4*	*0.01±0.01*	*0.03±0.03*	*6.3±0.4*	*Met*		
	-	1400	16	oxide liquid	1.7±0.1	45.8±0.1	51.8±0.1	0.64±0.05	Ox	-1.1	-6.4[E]
				$CaAl_2O_4$[2]	0.06±0.06	34.8±0.0	65.1±0.1	0.00±0.00	Ox		
				metal	*94.9±0.2*	*0.01±0.01*	*0.02±0.02*	*5.1±0.2*	*Met*		
	1450	1400	16	oxide liquid	3.7±0.1	43.8±0.1	50.4±0.1	2.1±0.1	Ox	-0.5	-5.1[E]
				$CaAl_2O_4$[2]	0.07±0.03	34.9±0.1	64.9±0.1	0.07±0.02	Ox		
				metal	*95.6±0.5*	*0.00±0.00*	*0.01±0.01*	*4.4±0.5*	*Met*		

[1] – for '$CuO_{0.5}$'-CaO-$AlO_{1.5}$ only system: L = wt%$Cu_{oxide\ liquid}$/wt%Cu_{metal} = wtfr.$Cu_{oxide\ liquid}$ for the system with Pb, Zn, Fe, As, Sn, Sb, Bi, Ni – L = wt%$Me_{oxide\ liquid}$/wt%Me_{metal}, where Me = [Pb, Zn, Fe, As, Sn, Sb, Bi, Ni]

[2] – the measurement of the phase composition was affected by secondary X-ray fluorescence and close presence of other phases

[E] – $p(O_2)$ over the system was estimated using the established correction (Equation 1)

[C] – $p(O_2)$ over the system was controlled during the experiment

The results of the experiments in the '$CuO_{0.5}$'-CaO-$AlO_{1.5}$ system in equilibrium with Cu metal in the controlled gas atmosphere were given in Table 1. The comparison of the discussed experimental results with the thermodynamic predictions of the current thermodynamic model (Shevchenko *et al*, 2021; Shishin *et al*, 2018, 2019) was presented in Figure 2.

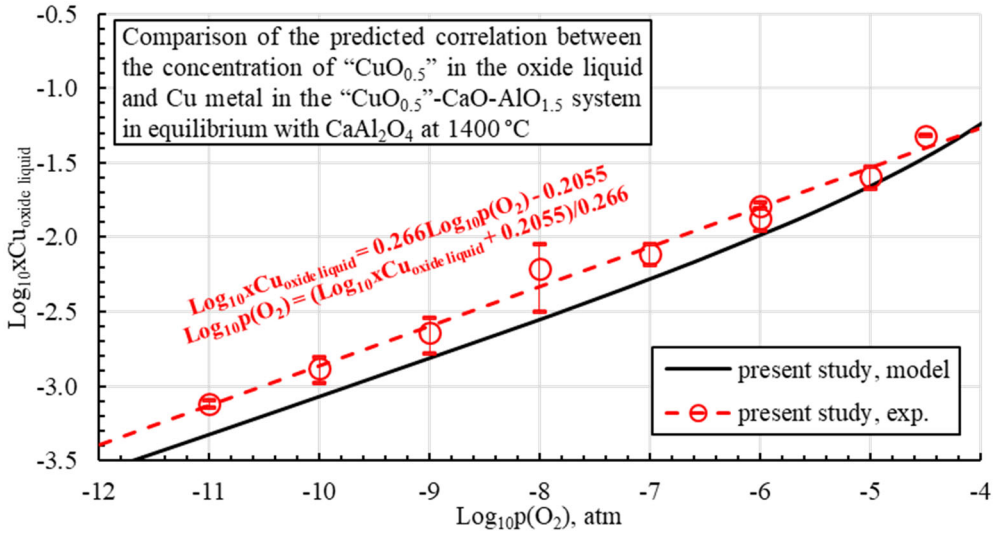

FIG 2 – Comparison of the experimental correlation between the solubility of Cu in the oxide liquid of the '$CuO_{0.5}$'-CaO-$AlO_{1.5}$ system in equilibrium with Cu metal with the corresponding thermodynamic predictions (Shevchenko *et al*, 2021; Shishin *et al*, 2018, 2019). In Y-axis, 'xCu' is the molar ratio '$CuO_{0.5}$'/('$CuO_{0.5}$'+CaO+$AlO_{1.5}$).

The presented comparison indicates that the solubility of Cu at the described conditions is underestimated by the internal thermodynamic database (Shevchenko *et al*, 2021; Shishin *et al*, 2018, 2019) and should be corrected in the future studies to comply with the recent experimental findings. Based on the obtained experimental results, the following equation was introduced to calculate the effective $p(O_2)$ over the system based on the concentration of '$CuO_{0.5}$' in the oxide liquid in equilibrium with Cu metal and $CaAl_2O_4$ solid:

$$Log\ {}_{10}p(O_2)_{estimated} = (Log_{10}xCu_{oxide\ liquid} + 0.2055)/0.266 \quad (9)$$

Examples of typical microstructures observed in the studied samples were given in Figure 3. These micrographs were obtained using backscattered electron microscopy (BSE) to provide compositional contrast based on the mean atomic number. Figure 3a demonstrates phase equilibria among oxide liquid, $CaAl_2O_4$ and metallic phase, representing the microstructure of most of the samples presented in Table 1 and Figure 3b shows oxide liquid, $CaAl_2O_4$ and the metallic phase equilibrium in the part of the sample close to the Al_2O_3 crucible, demonstrating the isolation of the Al_2O_3 crucible by the consequently growing calcium aluminates, preventing further dissolution of the substrate into the melt.

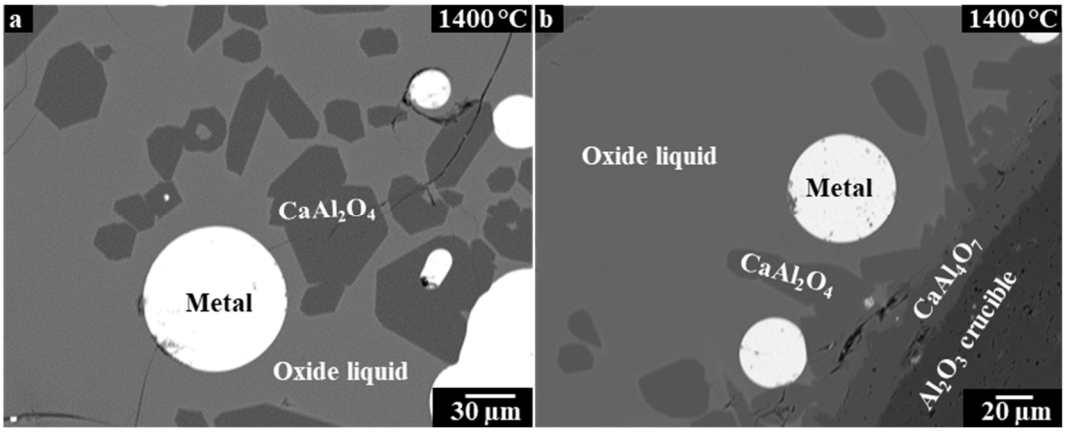

FIG 3 – Examples of backscattered scanning electron microscope (SEM) micrographs of the quenched '$CuO_{0.5}$'-CaO-$AlO_{1.5}$-(Pb, Zn, Fe, As, Sn, Sb, Bi and Ni) samples in equilibrium with metal phase: (a) oxide liquid-$CaAl_2O_4$-metal; (b) oxide liquid-$CaAl_2O_4$-metal, demonstrating isolation of the Al_2O_3 crucible with consequently forming layers of calcium aluminates.

The results for the experiments in the '$CuO_{0.5}$'-CaO-$AlO_{1.5}$-(Pb, Zn, Fe, As, Sn, Sb, Bi and Ni) system in equilibrium with metallic phase were given in Table 1. The experimental findings were graphically compared with the thermodynamic predictions for the distribution of the selected elements among the oxide liquid and metallic phases calculated using the FactSage™ software (Bale *et al*, 2016) and internal thermodynamic database (Shevchenko *et al*, 2021; Shishin *et al*, 2018, 2019) in Figure 4.

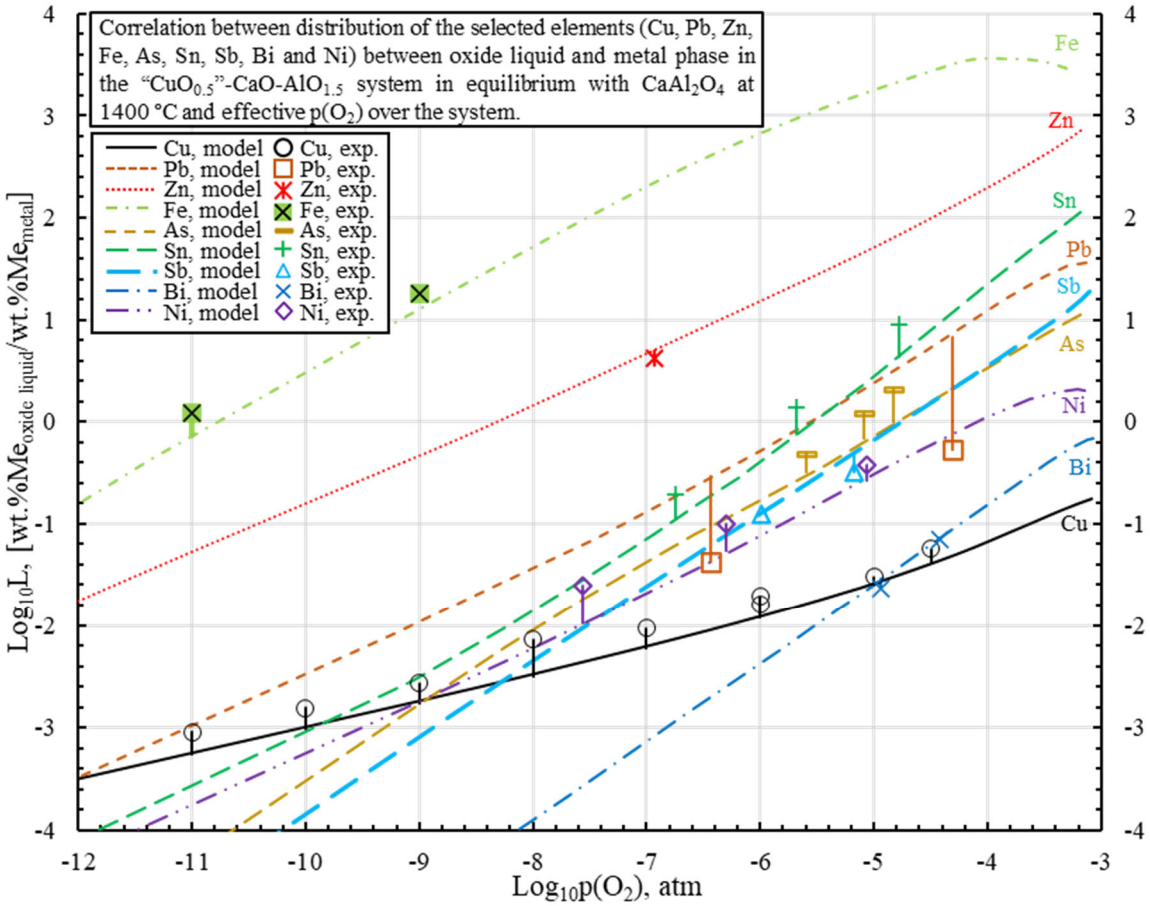

FIG 4 – Comparison of the experimental correlation between the distribution of the selected elements (Cu, Pb, Zn, Fe, As, Sn, Sb, Bi and Ni) between oxide liquid and metal phase in the '$CuO_{0.5}$'-CaO-$AlO_{1.5}$ system in equilibrium with $CaAl_2O_4$ and effective $p(O_2)$ over the system. In Y-axis, 'L' is the distribution coefficient [$wt\%Me_{oxide\ liquid}/wt\%Me_{metal}$].

It can be seen from Figure 4 that the predictions of the internal database (Shevchenko *et al*, 2021; Shishin *et al*, 2018, 2019) for some of the elements such as Fe, Zn, Sb and Bi are in a great agreement with the experimental results. At the same time predictions for Sn, As, Ni and Cu are in a moderate agreement with the experiment. The predictions for the distribution of Pb were found to be inconsistent with the experimental findings and overestimated by an order of magnitude.

The outlined disagreements between the experimental results and the model predictions are to be corrected in the future studies during the systematic revision and reoptimisation of the Cu-Pb-Zn-Fe-Ca-Si-Al-Mg-O-S-(As, Sn, Sb, Bi, Ag, Au, Ni, Cr, Co and Na) gas/oxide liquid/matte/speiss/metal/solids system. The results presented for the distribution of the selected elements between the oxide liquid and metallic phases of the '$CuO_{0.5}$'-CaO-$AlO_{1.5}$ system can be used as a powerful 'diagnostic' tool to outline inconsistencies among selected binary, ternary and quaternary systems during the process of the model parameters optimisation.

CONCLUSIONS

Experimental data on the distribution of the Cu, Pb, Zn, Fe, As, Sn, Sb, Bi and Ni among the oxide liquid and the metallic phase in the '$CuO_{0.5}$'-CaO-$AlO_{1.5}$ system were obtained for the first time. Concentration of copper oxide in the '$CuO_{0.5}$'-CaO-$AlO_{1.5}$ oxide liquid in equilibrium with $CaAl_2O_4$ at 1400°C was measured as a function of effective oxygen partial pressure ($p(O_2)$) over the system. The distributions of the Cu, Pb, Zn, Fe, As, Sn, Sb, Bi and Ni among the oxide liquid and the metallic phase in the '$CuO_{0.5}$'-CaO-$AlO_{1.5}$ system were obtained in the wide range of oxygen partial pressures from 10^{-11} to $10^{-3.7}$.

The experimental results were compared to the existing thermodynamic predictions to outline areas of inconsistency to be corrected in the future studies devoted to the systematic revision and

reoptimisation of the Cu-Pb-Zn-Fe-Ca-Si-Al-Mg-O-S-(As, Sn, Sb, Bi, Ag, Au, Ni, Cr, Co and Na) gas/oxide liquid/matte/speiss/metal/solids system.

ACKNOWLEDGEMENTS

The research funding and technical support are provided by the consortium of copper producing companies: Anglo American Platinum (South Africa), Aurubis AG (Germany), BHP Billiton Olympic Dam Operation (Australia), Boliden (Sweden), Glencore Technology (Australia), Metso Outotec Oy (Finland), Peñoles (Mexico), RHI Magnesita (Austria), Rio Tinto Kennecott (USA) and Umicore NV (Belgium), as well as Australian Research Council Linkage program LP190101020 'Future copper metallurgy for the age of e-mobility and the circular economy'; and consortium of lead producing companies: Aurubis AG (Germany), Boliden (Sweden), Kazzinc Ltd. (subsidiary of Glencore, Kazakhstan), Nordenham Metal (subsidiary of Glencore, Germany), Nyrstar (Australia), Peñoles (Mexico), Umicore NV (Belgium), as well as Australian Research Council Linkage program LP180100028 'New copper lead processes for critical metals recovery from complex sources'.

Authors would like to thank staff of the University of Queensland Centre for Microanalysis and Microscopy (CMM) for their support in maintenance and operation of scanning electron microprobe and XRD facilities in the Centre and Professor Peter Charles Hayes for his valuable contributions to the research done at the Pyrometallurgy Innovation Laboratory. Authors would also like to thank Mr Max Walshaw for taking part in the presented project as part of his summer research studies at the University of Queensland.

REFERENCES

Anindya, A, Swinbourne, D, Reuter, M and Matusewicz, R, 2013. Distribution of elements between copper and FeOx – CaO–SiO_2 slags during pyrometallurgical processing of WEEE Part 1 – Tin, *Mineral Processing and Extractive Metallurgy IMM Transactions Section C,* 122:165–173.

Anindya, A, Swinbourne, D, Reuter, M and Matusewicz, R, 2014. Distribution of elements between copper and FeOx – CaO–SiO_2 slags during pyroprocessing of WEEE Part 2 – Indium, *Mineral Processing and Extractive Metallurgy: Trans Inst Min Metall C*, 123:43–52.

Bale, C W, Belisle, E, Chartrand, P, Decterov, S A, Eriksson, G, Gheribi, A E, Hack, K, Jung, I H, Kang, Y B, Melancon, J, Pelton, A D, Petersen, S, Robelin, C, Sangster, J, Spencer, P and Van Ende, M A, 2016. FactSage thermochemical software and databases, 2010–2016, *CALPHAD,* 54:35–53.

Bale, C W, Bélisle, E, Chartrand, P, Decterov, S A, Eriksson, G, Hack, K, Jung, I H, Kang, Y B, Melançon, J, Pelton, A D, Robelin, C and Petersen, S, 2009. FactSage thermochemical software and databases — recent developments, *CALPHAD,* 33:295–311.

Chen, M, Avarmaa, K, Klemettinen, L, Shi, J, Taskinen, P and Jokilaakso, A, 2020. Experimental Study on the Phase Equilibrium of Copper Matte and Silica-Saturated FeO_x-SiO_2-Based Slags in Pyrometallurgical WEEE Processing, *Metall Mater Trans B,* 51:1552–1563.

Duncumb, P, 1971. Quantitative electron probe microanalysis, *Electron Microsc Anal Proc Anniv Meet*, pp 132–137.

Duncumb, P and Reed, S J B, 1968. Calculation of stopping power and backscatter effects in electron probe microanalysis, Tube Investments Res Lab, Cambridge, UK.

Fallah-Mehrjardi, A, Hidayat, T, Hayes, P C and Jak, E, 2017. Experimental Investigation of Gas/Slag/Matte/Tridymite Equilibria in the Cu-Fe-O-S-Si system in Controlled Gas Atmospheres: Development of Technique, *Metall Mater Trans B,* 48:3002–3016.

Hidayat, T, Chen, J, Hayes, P C and Jak, E, 2021. Distributions of As, Pb, Sn and Zn as minor elements between iron silicate slag and copper in equilibrium with tridymite in the Cu-Fe-O-Si system, *Int J Mater Res,* 112:178–188.

Hidayat, T, Hayes, P C and Jak, E, 2018. Phase Equilibria in the ZnO-'FeO'-SiO_2 System in Reducing Atmosphere and in the ZnO-'FeO'-SiO_2-'Cu_2O' System in Equilibrium with Liquid Copper Metal at 1250°C (1523 K), *Metall Mater Trans B,* 49:1766–1780.

Hidayat, T, Henao, H M, Hayes, P C and Jak, E, 2012. Phase Equilibria Studies of Cu-O-Si Systems in Equilibrium with Air and with Metallic Copper and Cu-Me-O-Si Systems (Me = Ca, Mg, Al and Fe) in Equilibrium with Metallic Copper, *Metall Mater Trans B,* 43:1290–1299.

Jak, E, 2012. Integrated experimental and thermodynamic modelling research methodology for metallurgical slags with examples in the copper production field, in *Proceedings of the 9th Intl Conf on Molten Slags, Fluxes and Salts,* pp 1–28 (The Chinese Society for Metals).

Jak, E, Hayes, P C and Lee, H-G, 1995. Improved methodologies for the determination of high temperature phase equilibria, *Korean Journal of Minerals and Materials Institute (Seoul),* 1:1–8.

Khartcyzov, G, Shevchenko, M, Cheng, S, Hayes, P C and Jak, E, 2022. Experimental phase equilibria studies in the '$CuO_{0.5}$'-CaO-SiO_2 ternary system in equilibrium with metallic copper, *Ceram Int,* 48:9927–9938.

Khartcyzov, G, Shevchenko, M, Cheng, S, Hayes, P C and Jak, E, 2023. Experimental phase equilibria study and thermodynamic modelling of the '$CuO_{0.5}$'-AlO1.5-SiO_2 ternary system in equilibrium with metallic copper, *Ceramics International,* 49:11513–11528.

Klemettinen, L, Avarmaa, K and Taskinen, P, 2017. Slag Chemistry of High-Alumina Iron Silicate Slags at 1300°C in WEEE Smelting, *J Sustain Metall,* pp 772–781.

Loibl, A and Tercero Espinoza, L A, 2021. Current challenges in copper recycling: aligning insights from material flow analysis with technological research developments and industry issues in Europe and North America, *Resources, Conservation and Recycling,* 169:105462.

Luty, W, 1992. Types of Cooling Media and Their Properties, in *Theory and Technology of Quenching*: *A Handbook* (eds: B Liščić, H M Tensi and W Luty) (Springer Berlin: Heidelberg).

Nagamori, M and Mackey, P J, 1977. Distribution Equilibriums of Tin, Selenium and Tellurium Between Iron(II) Oxide-Iron(III) Oxide-Silicon(IV) Oxide-Alumina-Copper Oxide ($CuO_{0.5}$) Slag and Metallic Copper, *Metall Trans B,* 8B:39–46.

Philibert, J, 1963. Method for calculating the absorption correction in electron-probe microanalysis, *X-Ray Opt, X-Ray Microanal,* 3*rd Intl Symp Stanford Univ,* pp 379–392.

Pizetta Zordão, L H, Oliveira, V A, Totten, G E and Canale, L C F, 2019. Quenching power of aqueous salt solution, *Int J Heat Mass Transf,* 140:807–818.

Shevchenko, M, Chen, J and Jak, E, 2017. Establishing additional correction for quantitative EPMA measurements in the system PbO-SiO_2, in *Proceedings of the 14th Biennial Australian Microbeam Analysis Symposium (AMAS)*, pp 94–95.

Shevchenko, M, Hidayat, T, Hayes, P and Jak, E, 2016. Liquidus of 'FeO'-SiO_2-PbO slags in equilibrium with air and with metallic lead, in *Proceedings of the 10th Intl Conf on Molten Slags, Fluxes and Salts,* pp 1221–1228.

Shevchenko, M and Jak, E, 2017. Experimental Phase Equilibria Studies of the PbO-SiO_2 System, *J Am Ceram Soc,* 101:458–471.

Shevchenko, M and Jak, E, 2018. Experimental Liquidus Studies of the Pb-Fe-Si-O System in Equilibrium with Metallic Pb, *Metall Mater Trans B,* 49:159–180.

Shevchenko, M and Jak, E, 2019. Experimental Liquidus Studies of the Binary Pb-Cu-O and Ternary Pb-Cu-Si-O Systems in Equilibrium with Metallic Pb-Cu Alloys, *J Phase Equilib Diff,* 40:671–685.

Shevchenko, M and Jak, E, 2020. Experimental Liquidus Studies of the ZnO-'$CuO_{0.5}$' and ZnO-'$CuO_{0.5}$'-SiO_2 Liquidus in Equilibrium with Cu-Zn Metal, *J Phase Equilib Diff,* 41:207–217.

Shevchenko, M, Shishin, D, Hayes, P C and Jak, E, 2021. Recent Developments in Experimental and Thermodynamic Modelling Techniques for the Characterisation of Phase Equilibria in Complex High Temperature Oxide Systems, *The 11th International Conference on Molten Slags, Fluxes and Salts* [virtual].

Shishin, D, Hayes, P and Jak, E, 2018. Multicomponent Thermodynamic Databases for Complex Non-ferrous Pyrometallurgical Processes, in *Proceedings of Extractions 2018*, pp 853–868.

Shishin, D, Hayes, P and Jak, E, 2019. Development And Applications Of Thermodynamic Database In Copper Smelting, in *Proceedings of Copper 2019,* pp 1–13.

Yazawa, A, 1981. Extractive metallurgical chemistry with special reference to copper smelting, in *Proceedings of the 28th Congress of IUPAC,* pp 1–21.

In situ observation of phase transition of silico-ferrite of calcium and aluminium

DOI: 10.62053/RQIH1996

H Kim[1], J Park[2] and J Lee[3]

1. Masters Student, Korea University, Seoul 02841, South Korea. Email: gkdmsskfk789@korea.ac.kr
2. Researcher, POSCO, Gwangyang 57807, South Korea. Email: j_park@posco.com
3. Professor, Korea University, Seoul 02841, South Korea. Email: joonholee@korea.ac.kr

ABSTRACT

Silico-ferrite of calcium and aluminium (SFCA) is a bonding phase in the iron ore sinter. The phase transition upon melting of SFCA was investigated with Differential Scanning Calorimetry and Confocal Laser Scanning Microscope. The initial melting of SFCA occurred at 1183.2°C and a massive melting was found at around 1351.1–1358.2°C. A phase transition-melting was investigated at 1476.5–1478.7°C. The liquid phase was composed of immiscible phases. The present results would be utilised to design a new iron ore sinter for better processing performance in a hydrogen-enriched ironmaking process.

INTRODUCTION

Iron ore sinter is a feeding material used in the blast furnace (BF) ironmaking process. Iron ore sinter is made of iron ore fines, flux and coal. Ignition of the coal by oxygen increases the temperature to 1300°C, resulting in liquid phase sintering of the iron ore particles. A complex mosaic structure is typically found in the iron ore sinter as shown in Figure 1, where the silico-ferrite of calcium and aluminium (SFCA) is the bonding material. Since the reduction of the iron ore sinter in BF starts from the reduction of hematite, SFCA would make the first liquid slag. Research on CO_2 emission reduction efforts in the BF operation is continuously conducted (Park *et al*, 2020). When hydrogen is introduced in BF to reduce CO_2 emission, the role of SFCA becomes more critical in forming a liquid slag phase (Park *et al*, 2023; Geleta *et al*, 2018).

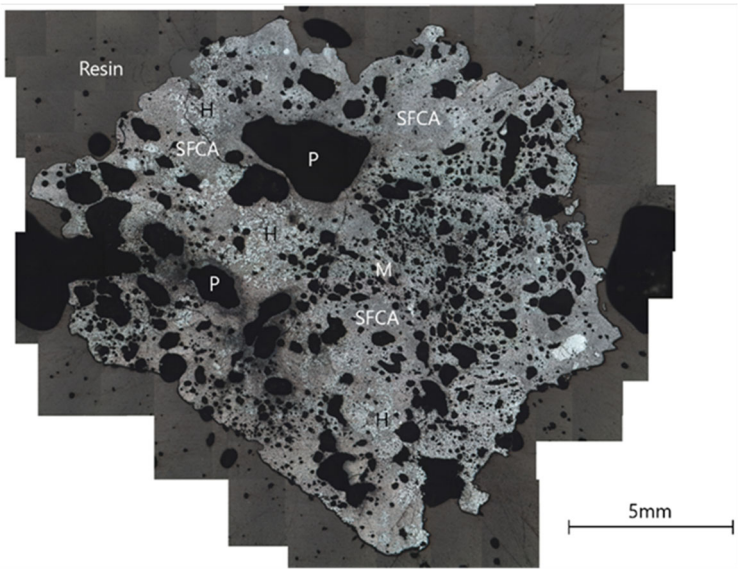

FIG 1 – Commercial iron ore sinter (H: Hematite, M: Magnetite, P: Pore, SFCA).

Figure 2 shows a schematic of the crystal structure of SFCA in the polyhedral model. SFCA (ICDD: 01-080-0850) comprises 14 metal atoms and 20 oxygen atoms, with each metal atom occupying either an octahedral or tetrahedral site and forming bonds with oxygen atoms (Hamilton *et al,* 1989). The triclinic space group characterises the structure of SFCA (Hamilton *et al,* 1989). Figure 2 provides a schematic representation of the crystal structure of SFCA, featuring alternating stacking of spinel planes and pyroxene planes (Park *et al,* 2022). The unit cell of SFCA possesses lattice

parameters a = 9.061Å, b = 10.020Å, and c = 10.920Å (Hamilton *et al,* 1989). In specific sites, Ca^{2+}, Fe^{2+}, and Mg^{2+} are located in the octahedral sites (M1, M2, M3, M7, M10 and M11), while Si^{4+}, Fe^{3+}, and Al^{3+} occupy the tetrahedral sites (M4, M5, M6, M8, M9 and M12) (Hamilton *et al,* 1989). The tetrahedral sites exhibit distinct categorisations: (1) Fe and Al substitution at the M6 site, (2) Si and Al substitution at the M12 site, and (3) Ca and Fe substitution at the Ca1 site. Takayama, Murao and Kimura (2018) and Murao *et al* (2018) identified the Mg substitution site based on Hamilton's crystal structure. SFCA has been studied extensively by many researchers. However, most of them focused on the microstructure of the iron ore sinter and the corresponding crystalline structures.

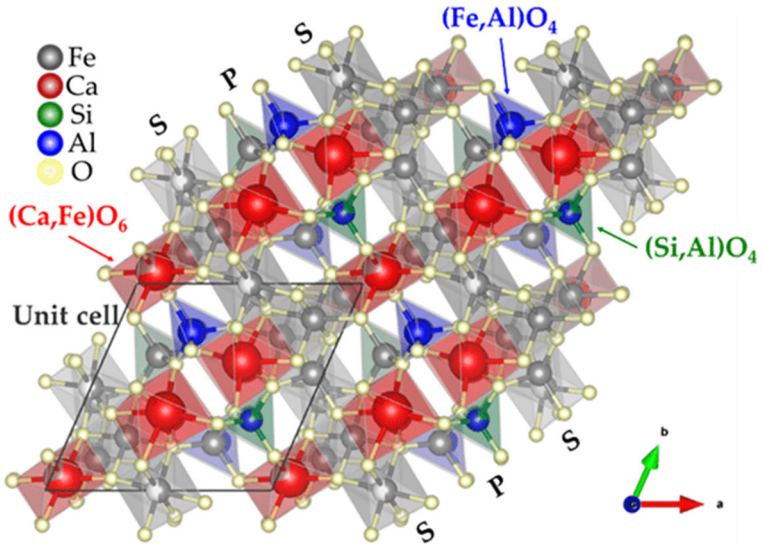

FIG 2 – Schematic of the crystal structure of SFCA in the polyhedral model (with the ball and stick model) indicating the atom substitution position of the tetrahedral ((Si, Al)O_4, (Fe, Al)O_4) sites and octahedral ((Ca, Fe)O6) sites, and the sequence of spinel (S) and pyroxene (P) (Park *et al,* 2022).

For the effective utilisation of the iron ore sinter in BF, it is essential to understand the phase transitions, especially liquid phase formation. In this study, the phase transition of SFCA with liquid phase formation is investigated using both differential scanning calorimetry (DSC) and confocal laser scanning microscope (CLSM). This new technique is helpful for understanding the liquid phase formation in BF to stabilise the operation condition by achieving a high gas permeability through the coke bed.

EXPERIMENTAL

Sample preparation

Reagent grade chemicals (Fe_2O_3, $CaCO_3$, SiO_2, Al_2O_3, 99.99 per cent purity, <100 µm) were used. $CaCO_3$ was calcinated to obtain CaO at 1273 K for 2 hrs in advance. Calcinated CaO was crushed and particles under 100 µm were collected for sample preparation. The composition of the samples used in the experiment is shown in Table 1. Figure 3 shows a schematic illustration of the experimental apparatus. A $MoSi_2$ electric resistance furnace of a maximum temperature of 1600°C was used. A mixture of chemicals with a pre-determined ratio is placed in a platinum-10 per cent rhodium crucible and kept at 1420°C for 12 hrs to form a liquid phase under a 300 mL/min air gas (21 per cent O_2–79 per cent N_2). The sample is then quenched in a distilled water.

TABLE 1

The composition of SFCA was used in the present experiments.

Composition (mole conc, %)			
Fe_2O_3	CaO	SiO_2	Al_2O_3
48.77	28.74	4.99	17.50

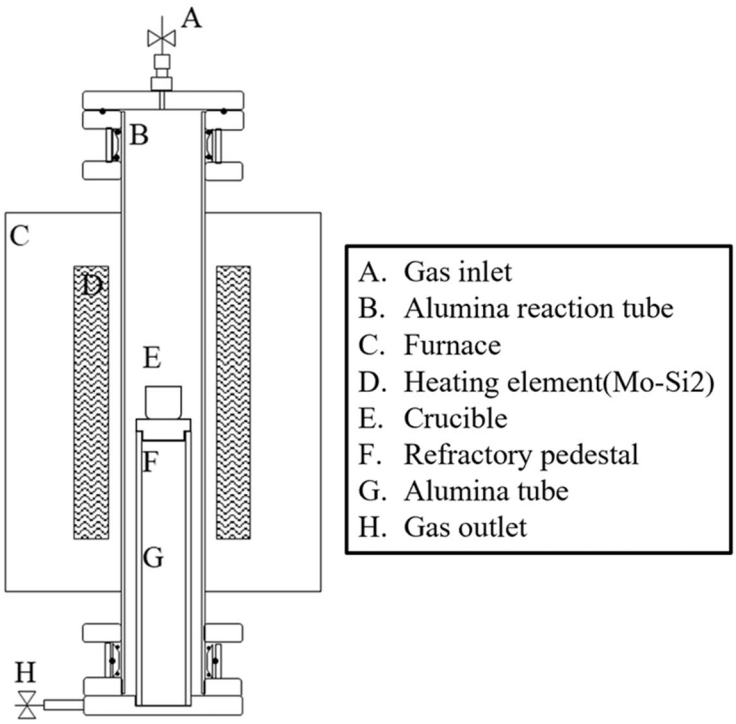

FIG 3 – Schematic diagram of the experimental set-up.

For the successive DSC analysis, synthesised SFCA was crushed under 100 μm using mortar and pestle. For the *in situ* observation with CLSM, the bulk SFCA was shaped into a cylindrical sample about 3–4 mm in diameter and 1 mm in height.

Phase transition analysis using DSC

DSC analyses were carried out in a simultaneous thermal analyser STA 449 F5 Jupiter (Netzsch, Germany), as shown in Figure 4. The temperature was calibrated with Benzoic Acid, $BaCO_3$, Ag_2SO_4 and CsCl, all supplied by Netzsch-Gerätebau GmbH. A sample was heated in a platinum-10 per cent rhodium crucible covered with an Al_2O_3 crucible at a heating rate of 50°C/min up to 1000°C. The sample was then heated at different heating rates (5, 10, 20, 25°C/min) up to 1500°C under a purified Ar gas (99.9999 per cent purity) flowing at 50 mL/min.

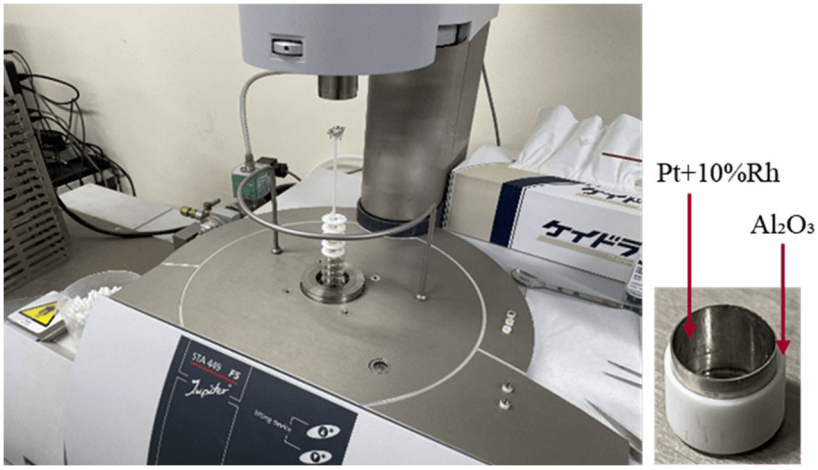

FIG 4 – (L) Differential Scanning Calorimetry equipment (STA 449 F5 Jupiter, Netzsch, Germany); (R) the crucibles used for DSC analysis.

In situ observation of the phase transition using CLSM

Phase transition of the SFCA was visually observed with CLSM (SVFSP; Yonekura MFG. Co. LTD, Japan), as shown in Figure 5. The observation temperature was calibrated with Au and Ni. The

sample temperature increased at 500°C/min up to 1000°C and held at this temperature for 60 sec and then it was heated at 10°C/min up to 1600°C, under a purified Ar gas (99.9999 per cent purity) at a flow of 200 mL/min. After experiments, the samples were analysed with a scanning electron microscope (SEM) (SU5000, HITACHI, Japan) and energy dispersive X-ray spectroscopy (EDS) (AZteclive Ultim Max40, Oxford, UK). As an exception, some samples are analysed with SEM (FEI Quanta FEG 250, Philips, USA) – energy dispersive X-Ray analysis (EDX) (Apollo 10, Ametek, USA).

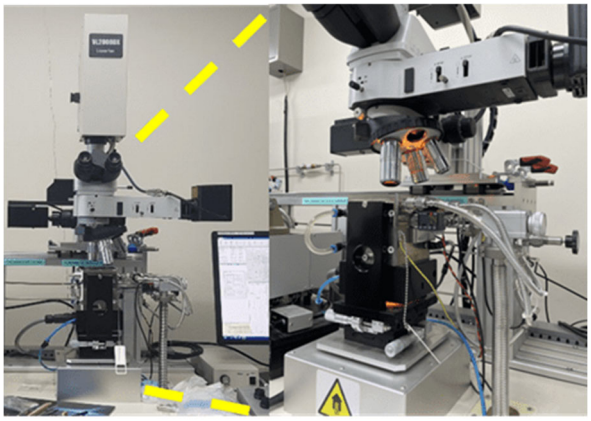

FIG 5 – CLSM equipment (SVFSP; Yonekura MFG. Co. LTD, Japan).

RESULTS AND DISCUSSIONS

Synthesised SFCA

The synthesised SFCA sample was investigated with SEM-EDS. The quenched sample was composed of a Fe-rich SFCA phase and a Ca-Si-Al-rich phase, as shown in Figures 6 and 7. Webster *et al* (2021, 2022) characterised the phase transition of the SFCA by using synchrotron X-ray diffraction (XRD) during heating and cooling cycles (Webster *et al,* 2021, 2022). Webster *et al* (2012) reported that once SFCA is molten to form a liquid phase and Fe_3O_4, Fe-rich SFCA, and SFCA are generated successively. Table 2 shows the EDS mapping and point analysis results of the synthesised SFCA. EDS mapping confirmed that the overall composition was similar to the target composition in Table 1. In addition, EDS point analysis confirmed that the bright area was the Fe-rich area with high Fe components and low Si and Al components and the dark part was SFCA. Accordingly, the present observation results show a good agreement with those of Webster *et al* (2022).

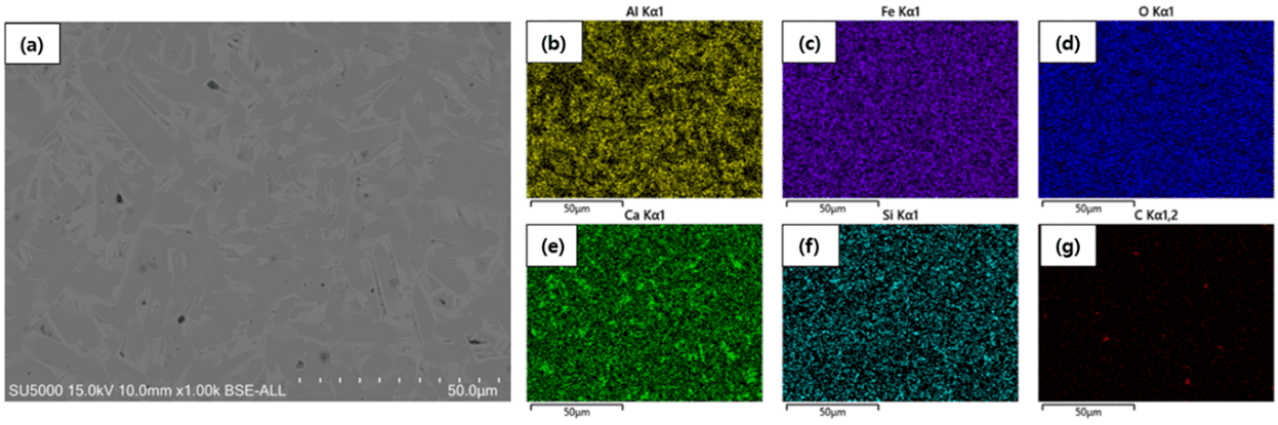

FIG 6 – Results of SEM-EDS analysis of synthesised SFCA: (a) backscattered electron (BSE) micrograph of synthesised SFCA; (b) Al signals of EDS of (a); (c) Fe signals of EDS of (a); (d) O signals of EDS of (a); (e) Pt signals of EDS of (a); (f) Ca signals of EDS of (a); (g) Si signals of EDS of (a); (h) C signals of EDS of (a).

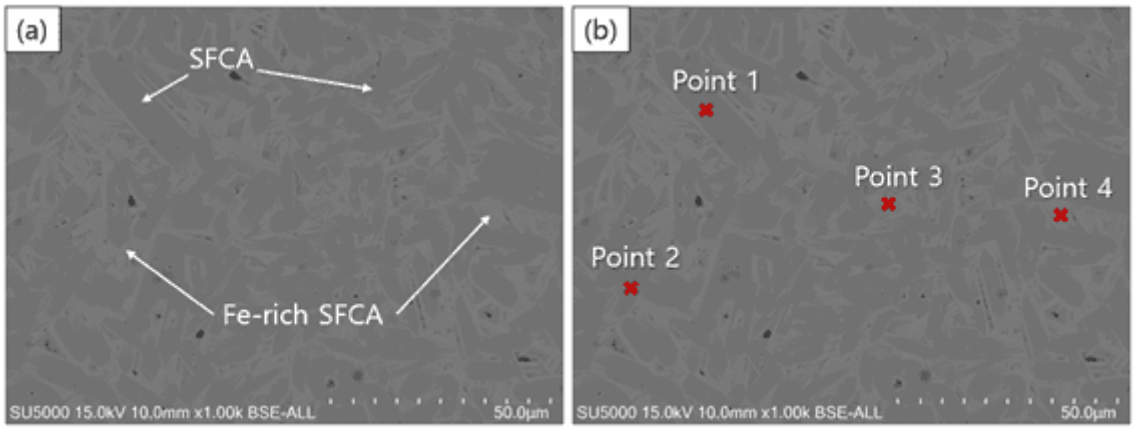

FIG 7 – Microstructure of synthesised SFCA: (a) identification of SFCA (dark) and Fe-rich SFCA (bright); (b) analysed points of synthesised SFCA.

TABLE 2

EDS results of mapping/point analysis of synthesised SFCA in Figure 7.

	Elemental Compositions (Atomic Conc, %)							Calculated Compotisions (Mole Conc, %)			
	Fe	Ca	Si	Al	O	C	Pt	Fe_2O_3	CaO	SiO_2	Al_2O_3
Mapping	24.55	7.21	1.33	9.29	49.88	7.29	0.49	48.27	28.35	5.11	18.27
Point 1	22.16	6.36	1.46	12.38	50.07	7.12	0.45	44.16	25.35	5.82	24.67
Point 2	22.22	6.34	1.4	12.24	49.58	7.53	0.23	44.49	25.39	5.61	24.51
Point 3	25.76	6.49	1.06	9.32	50.05	6.85	0.48	51.34	25.87	4.22	18.57
Point 4	30.47	6.34	0.59	5.13	48.84	8.12	0.52	61.61	25.64	2.39	10.37

Phase transition analysis results using DSC

Figure 8 shows the DSC curves obtained in the present study. The heating rate was set to 5, 10, 20 and 25°C/min, respectively. Table 3 summarises the onset point of the first peak, the peak points and the end points of the second and third peaks. The regression of the data points yields data at 0°C/min for the onset, peak 2, end 2, peak 3 and end 3 to be 1183.2, 1351.4, 1358.2, 1476.5 and 1478.7°C, respectively. Consequently, it is concluded that SFCA begins to melt at around 1183.2°C and massive melting occurs through 1351.1–1358.2°C and complete melting was found at 1476.5–1478.7°C, respectively.

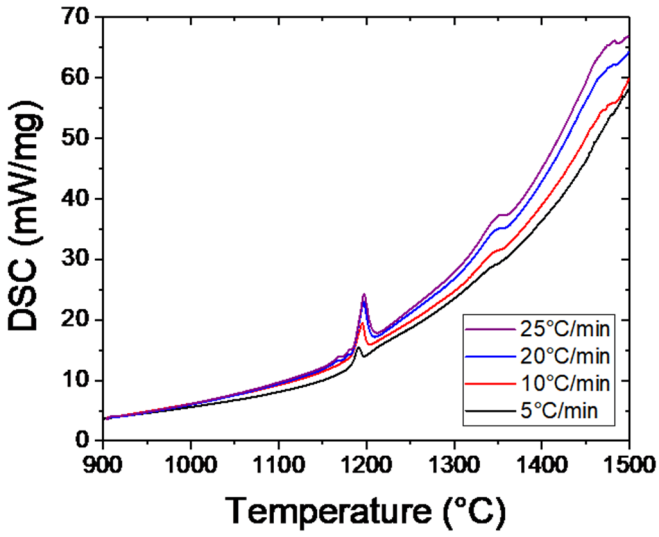

FIG 8 – DSC analysis results by heating rate.

TABLE 3

DSC analysis results at different heating rates.

	Heating Rate (°C/min)			
Peaks	5	10	20	25
Onset	1183.9	1184.7	1186.0	1186.8
Peak 2	1352.8	1351.9	1353.9	1355.1
End 2	1359.5	1360.0	1363.0	1363.6
Peak 3	-	1479.4	1478.3	1483.4
End 3	-	1483.2	1487.5	1489.9

In situ observation of the phase transition using CLSM

SFCA of this composition had several notable changes during the melting process. It was analysed by dividing it into four stages: initial surface modification, initial melting, massive liquid phase formation and phase transition-melting.

Step 1 – Initial surface modification

The initial surface modification observation results are shown in Figure 9. The scratch on the polished SFCA surface was modified due to thermal etching and the grain boundary of the SFCA was revealed.

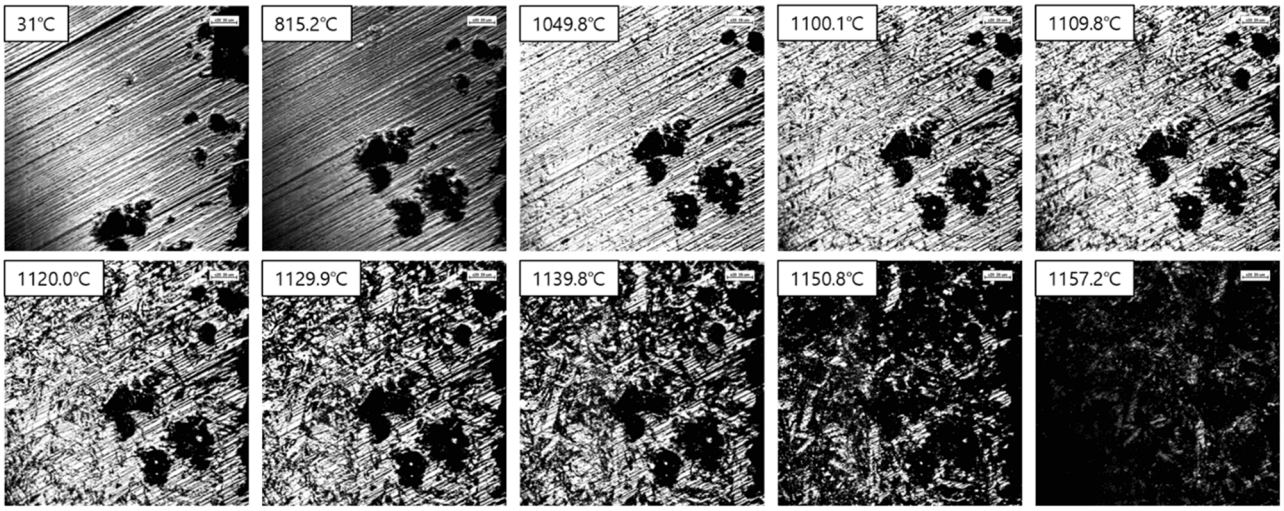

FIG 9 – *In situ* observation of initial surface modification using CLSM.

After observing the surface change up to the temperature before the first peak of the DSC result, the sample was rapidly cooled to analyse the surface SEM-EDS. This sample was quenched at 1157.2°C, for a successive EDS mapping. The results of the analysis are shown in Figure 10. Notably, a Ca-Si-Al-rich region is found near the pores. Eventually, this area was found to be the initial melting position from the successive analysis.

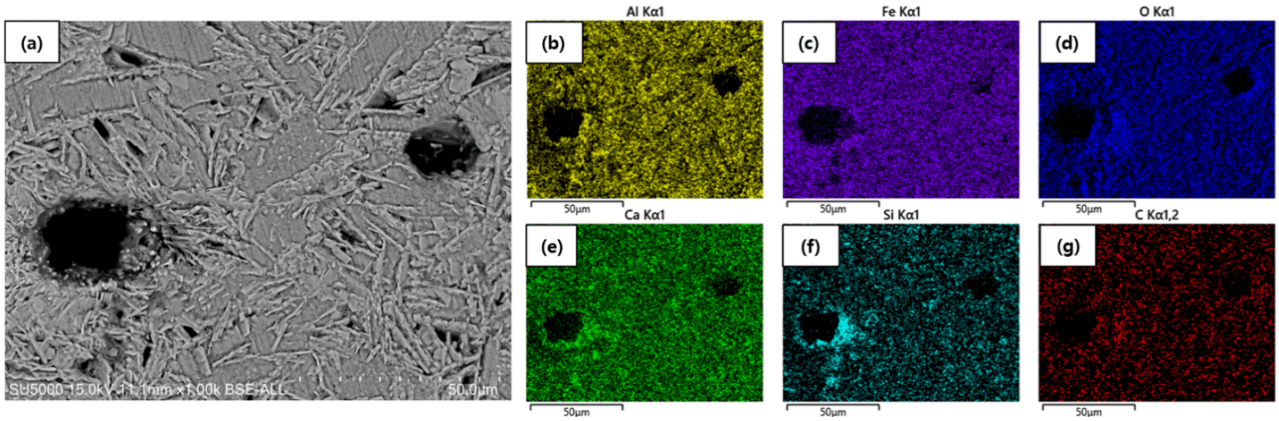

FIG 10 – Results of SEM-EDS analysis of the specimen after the observation of initial surface modification near pore side: (a) BSE micrograph of the specimen after the observation of initial surface modification; (b) Al signals of EDS of (a); (c) Fe signals of EDS of (a); (d) O signals of EDS of (a); (e) Pt signals of EDS of (a); (f) Ca signals of EDS of (a); (g) Si signals of EDS of (a); (h) C signals of EDS of (a).

Step 2 – Initial melting

The observations of initial melting with CLSM are shown in Figure 11. The initial surface melting was observed at around 1196°C, slightly higher than the point (1183.2°C) investigated with DSC. Nevertheless, this difference of 12.8°C is acceptable when we consider a typical error in temperature measurements with CLSM. The sample quenched at 1278.6°C was analysed with SEM-EDS, shown in Figure 12. It is found that Ca, Si and Al were segregated on several points, which were indicated with a dark grey colour in the SEM image. As shown in Table 4, EDS point analysis verified that the initial melting phase was a Ca-Si-Al-rich phase, whereas the matrix was a Fe-rich phase.

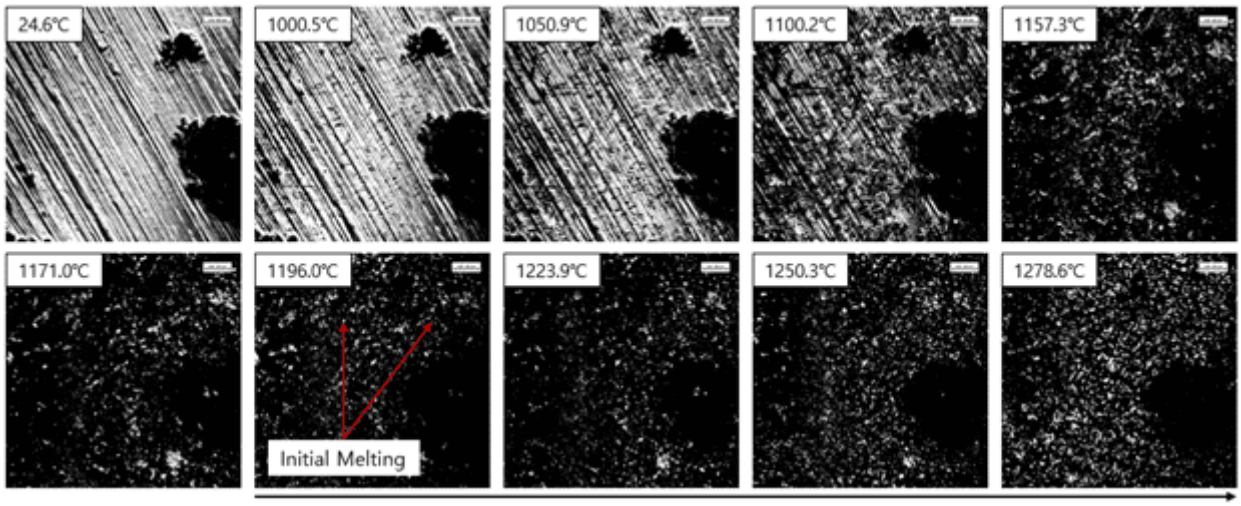

FIG 11 – *In situ* observation of initial melting using CLSM.

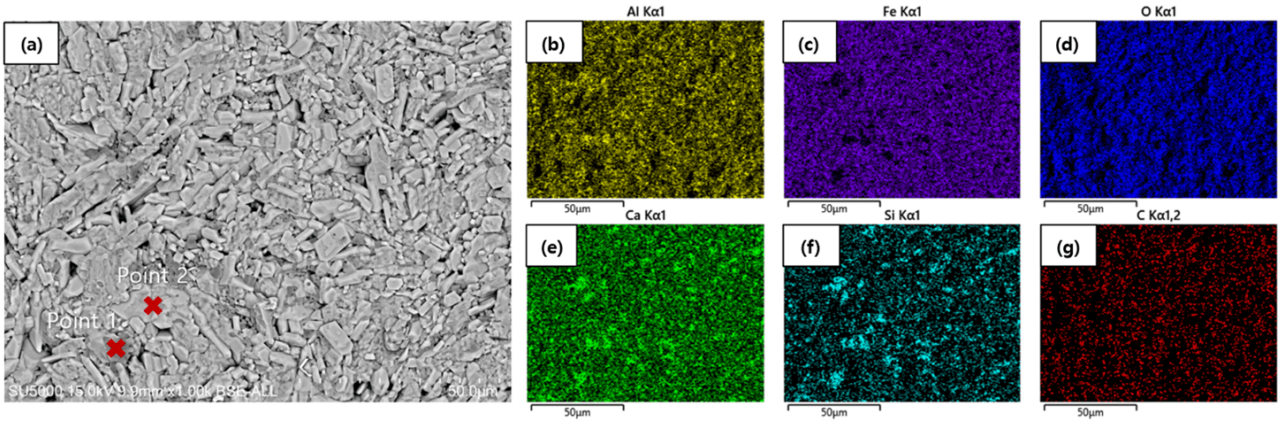

FIG 12 – Results of SEM-EDS analysis of the specimen after the observation of initial surface modification. Dark grey colour regions correspond to the initial melting points.

TABLE 4

EDS results of mapping/point analysis of the specimen after the observation of initial melting shown in Figure 12.

	Elemental Compositions (Atomic Conc, %)							Calculated Compositions (Mole Conc, %)			
	Fe	Ca	Si	Al	O	C	Pt	Fe_2O_3	CaO	SiO_2	Al_2O_3
Mapping	24.68	7.54	1.61	9.09	48.84	7.5	0.73	47.4	28.96	6.18	17.46
Point 1	12.96	19.63	6.79	11.43	42.85	5.5	0.84	16.78	50.84	17.58	14.8
Point 2	30.23	6.35	0.65	8.14	47.36	6.53	0.75	57.72	24.25	2.48	15.54

Step 3 – Massive liquid phase formation

DSC results showed a massive phase transition occurs at around 1351.1–1358.2°C. Further investigation with CLSM was carried out by 1362.4°C, as shown in Figure 13. It was found that a massive liquid phase formation occurred at 1351.6°C, which shows reasonable agreement with the DSC data. A liquid phase between small solid islands covered a wide range of the sample. The sample was quenched at 1362.4°C and SEM-EDS analysis was carried out successively. As shown in Figure 14 and Table 5, the light grey region is CF and CFA, while the dark grey region is indicated to be the liquid Ca-Si-Al-rich phase.

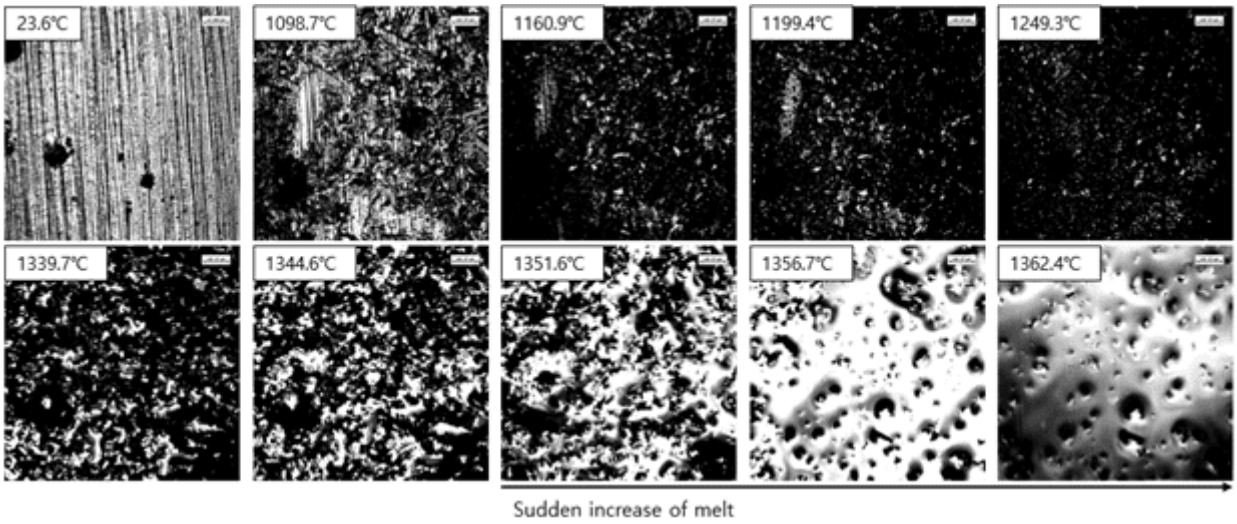

FIG 13 – *In situ* observation of an increase of liquid phase using CLSM.

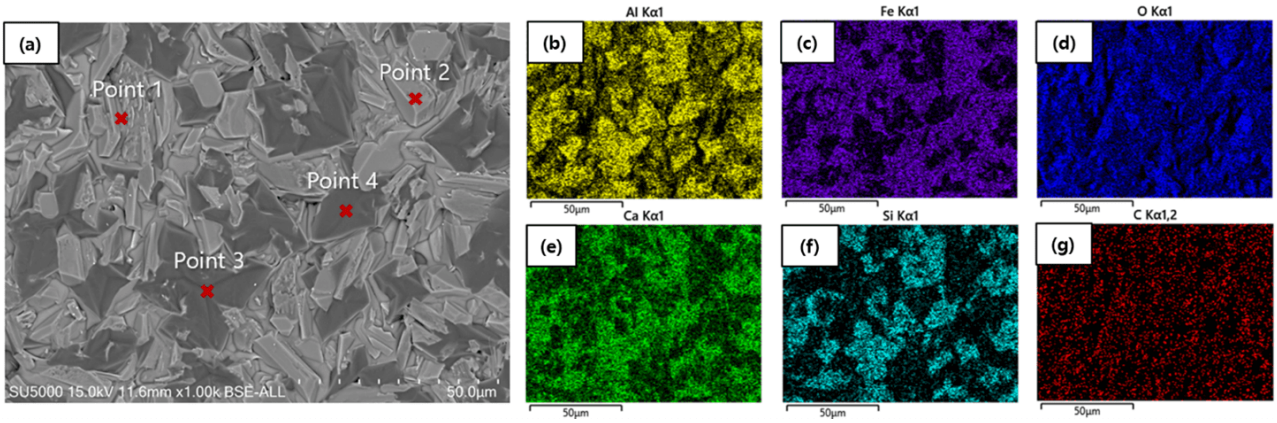

FIG 14 – Results of SEM-EDS analysis of an increase of the liquid phase.

TABLE 5

EDS results of mapping/point analysis of Figure 14.

	Elemental Compositions (Atomic Conc, %)							Calculated Compositions (Mole Conc, %)			
	Fe	Ca	Si	Al	O	C	Pt	Fe_2O_3	CaO	SiO_2	Al_2O_3
Mapping	18.18	10.89	3.32	10.22	49.46	7.28	0.65	32	38.33	11.69	17.99
Point 1	52.46	22.29	0.49	2.82	17.09	3.68	1.17	52.02	44.21	0.97	2.8
Point 2	24.75	3.82	0.64	9.21	52.81	8.18	0.59	57.72	17.82	2.99	21.48
Point 3	3.3	14.63	7.06	13.92	53.18	7.48	0.44	5.45	48.28	23.3	22.97
Point 4	5.34	15.16	7.01	13.73	50.55	7.77	0.45	8.42	47.82	22.11	21.65

Step 4 – Phase transition-melting

DSC results revealed that the last phase transition occurred at 1476.5~1478.7°C. The CLSM observation shown in Figure 15 supported the fact that the transition was related to the phase transition and successive melting. The cross-section of the quenched sample was investigated with SEM-EDX. The EDX results in Figures 16 and 17, and Table 6, show elemental segregation. There were two immiscible phases: the Fe-Al-rich phase and the Ca-Si-Al-rich phase. The Fe-Al-rich phase is considered a Fe_3O_4 solid solution and the Ca-Si-Al-rich phase is liquid. Webster *et al* (2012) reported a similar result that Fe_3O_4 could appear in SFCA at high temperatures. Accordingly, it is considered that CF and CFA transformed to Fe_3O_4 solid solution and some amount of CaO and Al_2O_3 dissolved in liquid slag.

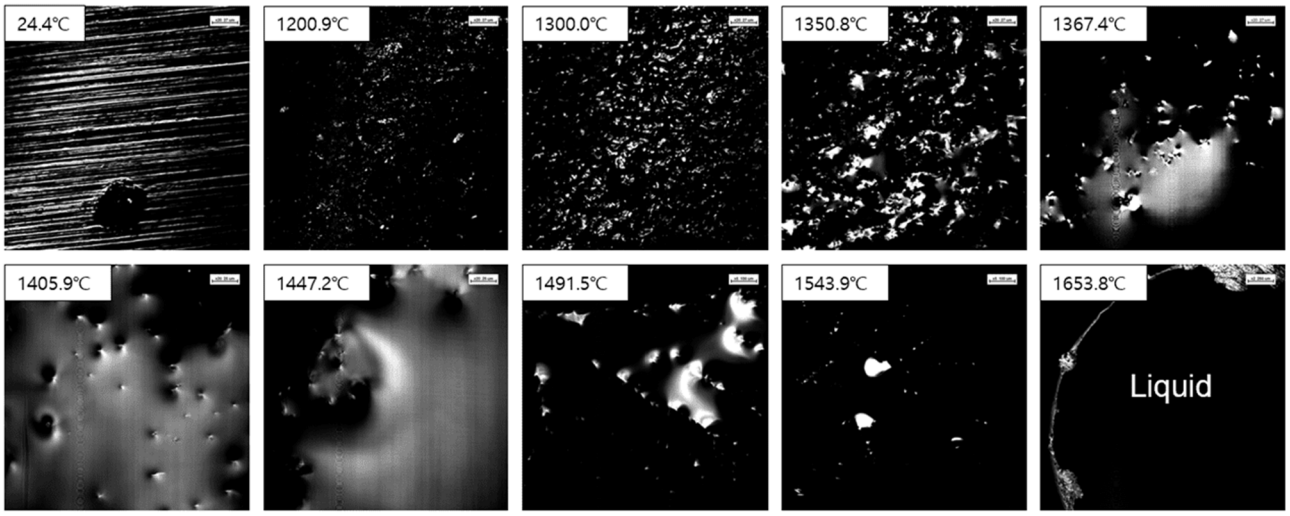

FIG 15 – *In situ* observation of complete melting using CLSM.

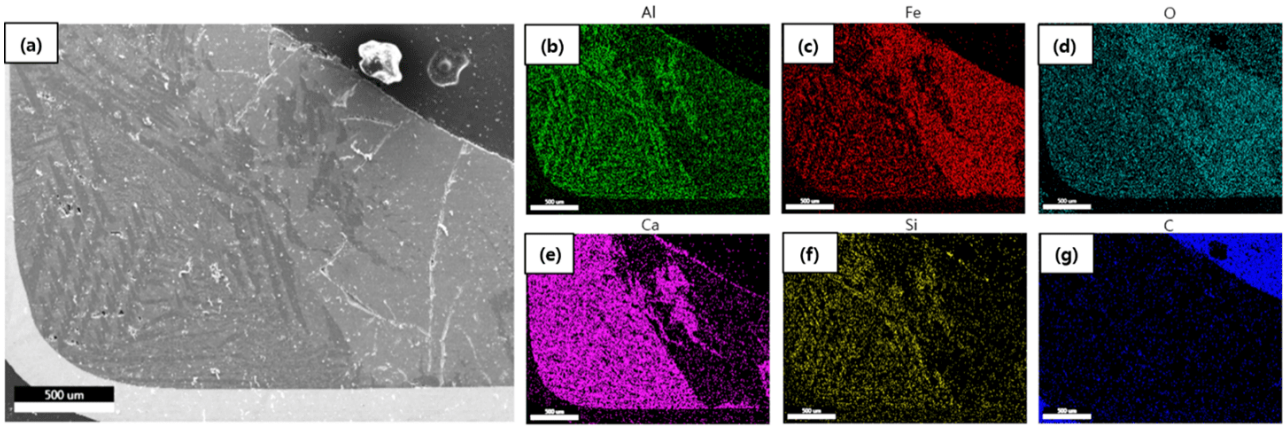

FIG 16 – Locations for EDX analysis for the specimen after the observation of initial surface modification.

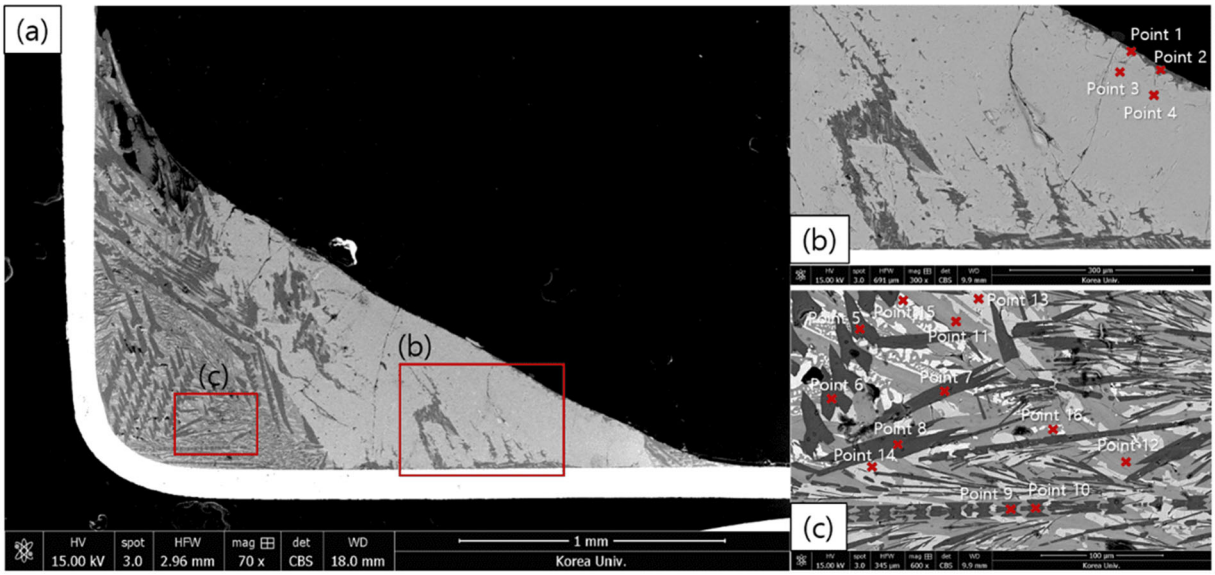

FIG 17 – SEM-BSE analysis of the quenched sample after phase transition-melting melting.

TABLE 6

EDX results of point analysis of Figure 17.

	Elemental Compositions (Atomic Conc, %)						Calculated Compositions (Mole Conc, %)			
	Fe	Ca	Si	Al	O	C	Fe_2O_3	CaO	SiO_2	Al_2O_3
Point 1 (Dark grey)	4.56	14.69	4.08	16.95	52.54	7.18	7.72	49.75	13.82	28.7
Point 2 (Dark grey)	8.28	12.27	4.29	14.54	50.69	9.94	14.8	43.87	15.34	25.99
Point 3 (Light grey)	28.37	0.52	-	9.6	50.08	11.43	72.72	2.67	-	24.61
Point 4 (Light grey)	28.04	0.49	-	9.21	49.26	13	73.35	2.56	-	24.09
Point 5 (Dark grey)	3.29	14.8	4.98	16.67	52.83	7.42	5.53	49.73	16.73	28.01
Point 6 (Dark grey)	3.04	14.9	5.2	16.5	52.3	8.06	5.09	49.88	17.41	27.62
Point 7 (Dark grey)	2.95	14.74	5.36	16.21	51.84	8.9	4.97	49.66	18.06	27.31
Point 8 (Dark grey)	3	14.82	5.04	16.53	53.03	7.58	5.06	50.03	17.01	27.9
Point 9 (Dark grey)	3.28	14.98	4.92	16.72	52.94	7.15	5.48	50.1	16.45	27.96
Point 10 (Dark grey)	3.47	14.94	4.9	16.69	52.95	7.04	5.8	49.93	16.38	27.89
Point 11 (Medium grey)	13.51	20.58	0.68	6.26	51.14	7.82	21.69	66.08	2.18	10.05
Point 12 (Medium grey)	11.91	20.48	0.59	8.16	51.45	7.41	19.14	65.84	1.90	13.12
Point 13 (Medium-light grey)	31.04	0.94	-	6.39	50.94	10.69	78.96	4.78	-	16.26
Point 14 (Medium-light grey)	30.98	0.98	-	6.17	50.66	11.21	79.21	5.01	-	15.78
Point 15 (Light grey)	38.49	1.68	-	1.15	47.12	11.56	89.51	7.81	-	2.67
Point 16 (Light grey)	38.06	1.57	-	1.05	47.45	11.87	90.08	7.43	-	2.49

CONCLUSIONS

The phase transition of SFCA was investigated with DSC and CLSM. The *in situ* observation with CLSM was focused on the peak positions observed with DSC. It was found that the peak position was related to the liquid phase formation: initial melting, massive liquid phase formation and phase transition-melting. The quenched sample revealed that the Fe_3O_4 solid solution appeared as a result of the phase transition of CF and CFA. The results of the present observation can be utilised in designing a new iron ore sinter, which can be used in a hydrogen-enriched ironmaking process.

ACKNOWLEDGEMENTS

This work was supported by the Industrial Strategic Technology Development Program (RS-2023-00262421, Development of basic design technology for hydrogen based ironmaking) funded by the Ministry of Trade, Industry and Energy in the Republic of Korea. This work was also supported by the Korea Institute for Advancement of Technology(KIAT) grant funded by the Government of the Republic of Korea(MOTIE, P0023676, HRD Program for Industrial Innovation).

REFERENCES

Geleta, D D and Lee, J, 2018. Effects of Particle Diameter and Coke Layer Thickness on Solid Flow and Stress Distribution in BF by 3D Discrete Element Method, *Metallurgical and Materials Transactions B-process Metallurgy and Materials Processing Science*, 49:3594–3602.

Hamilton, J G, Hoskins, B, Mumme, W, Borbidge, W and Montague, M, 1989. The crystal structure and crystal chemistry of Ca2. 3Mg0. 8Al1. 5Si1. 1Fe8. 3O20 (SFCA): solid solution limits and selected phase relationships of SFCA in the SiO_2-FeO3-CaO (-Al_2O_3) system, *Neues Jahrbuch für Mineralogie, Abhandlungen*, 161:1–26.

Murao, R, Harano, T, Kimura, M and Jung, I-H, 2018. Thermodynamic modeling of the SFCA phase Ca2 (Fe, Ca):6 (Fe, Al, Si):6O20, *ISIJ International*, 58:259–266.

Park, J, Ramaraghavulu, R, Suh, I-K, Jeon, J, Son, S and Lee, J, 2020. Effects of Basicity and Al_2O_3 Content on the Chemistry of Phases in Iron Ore Sinter Containing ZnO, *Metallurgical and Materials Transactions B-process Metallurgy and Materials Processing Science*, 51:3016–3020.

Park, J, Kim, E, Suh, I-K and Lee, J, 2022. A Short Review of the Effect of Iron Ore Selection on Mineral Phases of Iron Ore Sinter, *Minerals*, 12:35.

Park, J, Kim, E, Suh, I-K and Lee, J, 2023. Effects of basicity and Al_2O_3 content on the crystal structure of silico-ferrite of calcium and aluminium, *ISIJ International*, 63:235–243.

Takayama, T, Murao, R and Kimura, M, 2018. Quantitative Analysis of Mineral Phases in Iron-ore Sinter by the Rietveld Method of X-ray Diffraction Patterns, *ISIJ International*, 58:1069–1078.

Webster, N A S, Pownceby, M I, Fan, R and Brand, H E A, 2022. Fundamentals of Silico-Ferrite of Calcium and Aluminium (SFCA) and SFCA-I Iron Ore Sinter Bonding Phase Formation: Effects of MgO Source on Phase Formation during Heating, *ISIJ International*, 62:652–657.

Webster, N A S, Pownceby, M I, Madsen, I C and Kimpton, J A, 2012. Silico-ferrite of Calcium and Aluminum (SFCA) Iron Ore Sinter Bonding Phases: New Insights into Their Formation During Heating and Cooling, *Metallurgical and Materials Transactions B-process Metallurgy and Materials Processing Science*, 43:1344–1357.

Webster, N A S, Pownceby, M I, Madsen, I C and Kimpton, J A, 2021. Silico-ferrite of Calcium and Aluminum (SFCA) and SFCA-Iron Ore Sinter Bonding Phase Formation: Effects of MgO on Phase Formation During Heating, *JOM*, 73:299–30.

Phase equilibrium study in the sodium metasilicate primary phase field of PbO-Na_2O-SiO_2 system between 800 and 1000°C

DOI: 10.62053/FOVH3002

X Ling[1], E Moosavi-Khoonsari[2] and M Barati[3]

1. PhD Candidate, University of Toronto, Toronto Ontario M5S 1A1, Canada. Email: xi.ling@mail.utoronto.ca
2. Professor, École de technologie supérieure (ÉTS), Montreal Quebec H3C 1K3, Canada. Email: elmira.moosavi@etsmtl.ca; Adjunct Professor, University of Toronto, Toronto Ontario M5S 1A1, Canada.
3. Professor, University of Toronto, Toronto Ontario M5S 1A1, Canada. Email: mansoor.barati@utoronto.ca

ABSTRACT

In the pyrometallurgical process of secondary lead recycling, a desulfurising agent, such as Na_2CO_3 is added to minimise the emissions of sulfur into the atmosphere, while silica is introduced into the smelter as a fluxing material. Subsequently, a significant amount of Na_2O and SiO_2 remains in the downstream reverberatory furnace and blast furnace slags. However, there is limited understanding of the thermodynamic behaviour of silicate-based lead slags rich in Na_2O, posing challenges in accurately determining the optimal condition for targeted metal recovery and final slag composition. In this work, the equilibrium phase relations of the PbO-Na_2O-SiO_2 system in the primary phase field of Na_2SiO_3 are studied from 800 to 1000°C via equilibration-quenching method. Samples with different compositions were prepared and held in platinum capsules in air at these temperatures to reach equilibrium. The equilibrated samples were subsequently quenched and the phase compositions were measured by electron probe microanalysis (EPMA). The results were then compared to those of previous studies and any discrepancies were resolved.

INTRODUCTION

The lead-acid battery (LAB) has a history of over 150 years since its invention in the mid-18th century (Rand and Moseley, 2015). In 2019 (pre-pandemic), the global production of refined lead was around 11.8 million metric tonnes, 80 per cent of which went to the LAB industry. LAB accounts for nearly 50 per cent of the secondary battery market with a market size of US$50 billion in 2019 (Zhao *et al*, 2021). With the growing demand of LABs in the automotive industry, the LAB market is forecasted to grow at an annual rate of over 8 per cent, to reach US$116 billion in 2030 (Yanamandra *et al*, 2022). LABs are considered an example of circular economy, evidenced by the fact that the recycling of LABs is economically feasible with a recycling and reuse rate of 99 per cent (EDR Group, 2019; Yanamandra *et al*, 2022). The recycling of LABs is not only economically significant but also environmentally crucial. If not recycled, the lead contained in LABs might enter landfills and contaminate the water and ecosystems. As a result, the recycling of LABs is an essential and critical practice as it serves both the purpose of conserving finite resources and preventing environmental contamination.

The recycling process of LABs usually includes a critical desulfurisation process where lead sulfate is converted to carbonate by a desulfurising agent such as Na_2CO_3. The representative equation can be written as follows:

$$\mathbf{PbSO_{4(s)} + Na_2CO_{3(aq)} = Na_2SO_{4(aq)} + PbCO_{3(s)}}$$

To maintain the desired low sulfur content, excess Na_2CO_3 is added, which partly makes it to the furnace and is eventually decomposed to Na_2O during the smelting process (Lyakov *et al*, 2007; Zhang *et al*, 2016). In a typical two-step smelting process, the desulfurised lead paste and lead grids are firstly melted and partially reduced in a reverberatory furnace and then charged into a blast furnace. The reverberatory furnace slag contains 45–65 wt per cent Pb, 5–10 per cent Na and 4–7 per cent Si, while the blast furnace slag generally contains 1–6 per cent Pb, 10–15 per cent Na and 10–18 per cent Si (Nicol *et al*, 2020). In this complex slag system, some of the subsystems have been extensively studied and their thermodynamics were well established. However, the

thermodynamic behaviour of silica-based lead slags that contain Na_2O, represented by the PbO-Na_2O-SiO_2 system remains underexplored.

One of the limited research works conducted on this subject was by Krakau, Mukhin and Heinrich (1949), who studied the phase equilibria of the binary subsystems at different primary phase saturations, including PbO, SiO_2, $PbSiO_3$, Pb_2SiO_4, $Pb_3Si_2O_7$, Pb_3SiO_5 and Na_2SiO_3 using heating and cooling curves method. Later, Santoso (2017) revisited the work on liquidus temperatures of the PbO-Na_2O-SiO_2 system from 900 to 1100°C at SiO_2 saturation using quenching method. Their results revealed significantly lower liquidus points than those determined by Krakau, Mukhin and Heinrich (1949), Santoso suggested that the difference could be attributed to the limitations of the dynamic method employed by Krakau's group.

In this work, the phase equilibria of PbO-Na_2O-SiO_2 system in the primary phase field of Na_2SiO_3 was studied in air between 800 and 900°C using equilibration-quenching-microanalysis technique. The results are compared with the above two studies.

METHODOLOGY

The current work utilises the static method, also known as the equilibration-quenching technique. In this approach, samples are equilibrated at specific temperatures until reaching equilibrium. Subsequently, the samples are quenched to room temperature to preserve the phase assemblage present at high temperatures. The composition of the equilibrium phases is then determined with electron probe micro-analysis (EPMA).

Samples were prepared by mixing various amounts of PbO (99.0 per cent purity, Fisher Scientific), Na_2SiO_3 (200 level quality, Sigma Aldrich) and SiO_2 (99.5 per cent purity, Sigma Aldrich) in an agate mortar and pestle. The well-mixed powders were pressed into Pt capsules of 6 mm in diameter, 6 mm long and 0.15 mm in thickness. The two ends of the capsule were folded to minimise the loss of volatile material at high temperatures. The capsules were then put in an alumina tray and suspended in the hot zone of a vertical resistance heating furnace under an air atmosphere. The sample temperature was continuously monitored by a type K thermocouple, the tip of which comes into contact with the Pt capsule. The schematic of the experimental set-up is shown in Figure 1.

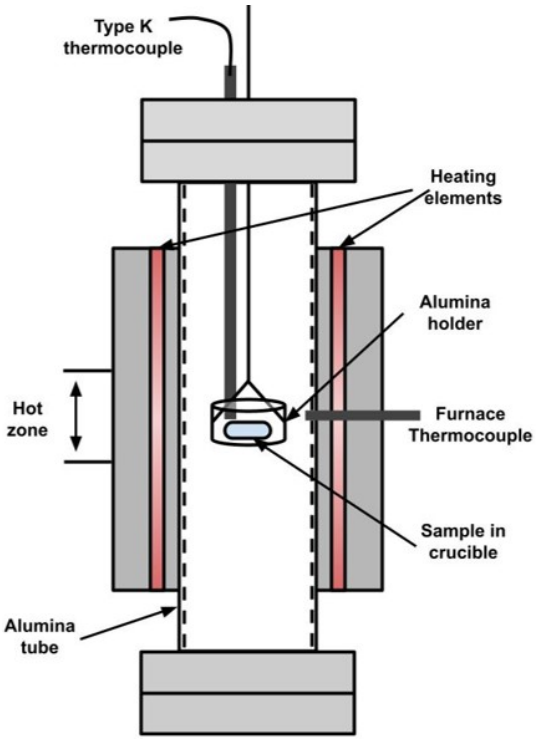

FIG 1 – Schematic diagram of equilibrium test set-up.

After the test, the specimens were quenched in oil due to the hygroscopic nature of the Na_2O-containing products. Solidified samples were mounted in epoxy and were then grinded and polished

using ethylene glycol as lubricant to avoid reaction between water and Na_2O. The samples were quickly transferred to the EPMA (JEOL, Japan) employing a JXA8230 probe. Compositions of each phase were measured by wavelength-dispersive spectrometry (WDS) function at an accelerating voltage of 15 KV, 20 nA beam current, 20 μm beam size, 40 sec on-peak counting time and 20 sec on each side of the background. Albite ($NaAlSi_3O_8$) was used as reference material for Na and Si and crocoite ($PbCrO_4$) was used as reference material for the determination of Pb. The average was taken from at least ten measurements on each phase of the sample.

RESULTS AND DISCUSSION

Samples with various $PbO:Na_2O:SiO_2$ ratios were equilibrated at 800, 900 and 1000°C under an air atmosphere. The material was held in platinum crucibles and quenched in oil. The bulk composition of samples was determined to lie in the sodium metasilicate primary phase field based on previous research by Krakau, Mukhin and Heinrich (1949). The composition of starting materials, experimental conditions, product phases and their compositions are listed in Table 1. The backscattered electron (BSE) images of typical samples at different temperatures are presented in Figure 2. The isothermal sections of the ternary phase diagram including the data from the present work and the previous studies are shown in Figure 3.

TABLE 1

Test conditions and compositions of each phase.

Temperature (°C) and sample number	Sample Composition ($PbO:Na_2O:SiO_2$ mol%)	Sample Composition ($PbO:Na_2O:SiO_2$ wt%)	Duration (h)	Phase	Composition ($PbO:Na_2O:SiO_2$ mol%)	Composition ($PbO:Na_2O:SiO_2$ wt%)	Raw EPMA (sums before normalisation wt%)	Standard deviation ($PbO:Na_2O:SiO_2$ wt%)
800-S1	11:36:53	16:34:50	40	Liquid	20:24:56	48:16:35	98.9	1:0.4:0.7
				Na_2SiO_3	0:48:52	0:49:48	97.2	0:2:1.6
800-S2	16:34:50	41:24:35	40	Liquid	26:23:51	55:14:29	98.5	1:0.2:0.6:
				Na_2SiO_3	0:49:51	0:48.5:49	97.7	0:0.4:0.2
800-S3	23:36:41	52:23:25	40	Liquid	60:13:27	85:5:10	101.6	1.7:0.7:1
				Na_2SiO_3	0:48:52	0:48:50	98	0:0.8:0.2
900-S1	8:8:84	24:7:69	40	Liquid	12.5:12:75.5	34:9:55	97.3	0.3:0.1:0.2
				SiO_2 (tridymite)	0:0:100	0:0:97.4	97.4	0:0:0.6
900-S2	2.5:43:54.5	9:41:50	20	Liquid	7:32:61	21:27:50	97	2:2.8:1.1
				Na_2SiO_3	0:49:51	0:48:49	97	0:1:0.5
900-S3	10:40:50	29:32:39	20	Liquid	24:26:50	53:16:30	99.1	0.8:1:0.6
				Solid Na_2SiO_3	0:48:52	0:48.4:49	100.2	0:3:2.7
900-S4	16:42:42	41:30:29	20	Liquid	33:31:36	64:17:19	100.2	3.7:2.3:1.6
				Solid Na_2SiO_3	0:49:51	0:48:49	97	0:0.6:0.3
1000-S1	4:45:51	13:41:45	10	Liquid	16.5:29:54.5	41:21:37	99	5:4:2
				Solid Na_2SiO_3	0:50:50	0:50:50	100.04	0:0.5:0.4

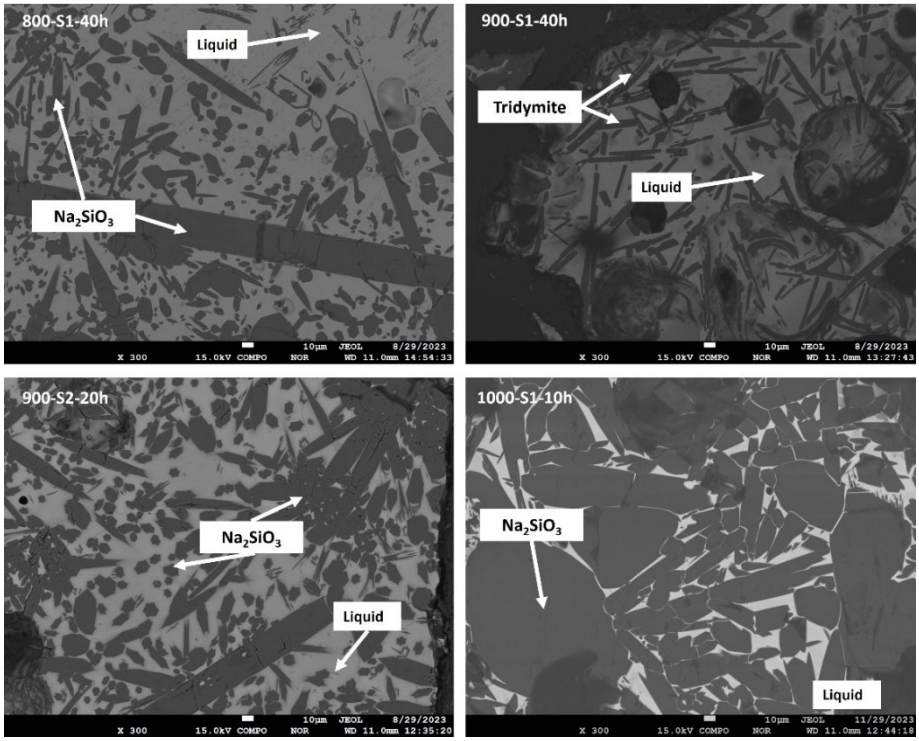

FIG 2 – Backscattered electron images of samples 800-S1, 900-S1, 900-S2 and 1000-S1.

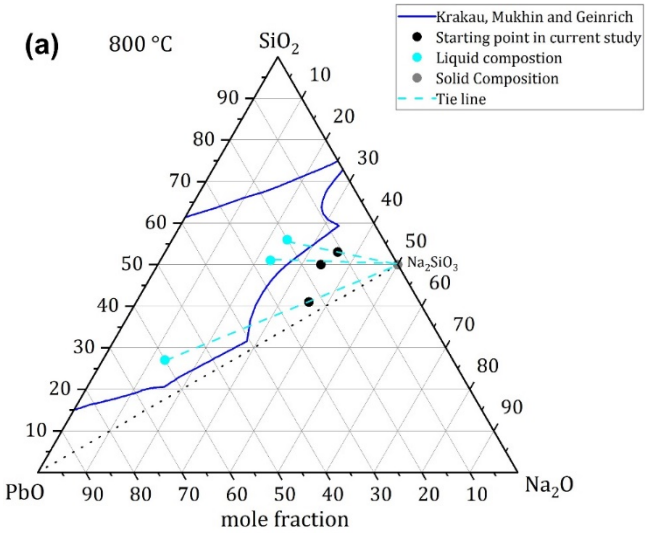

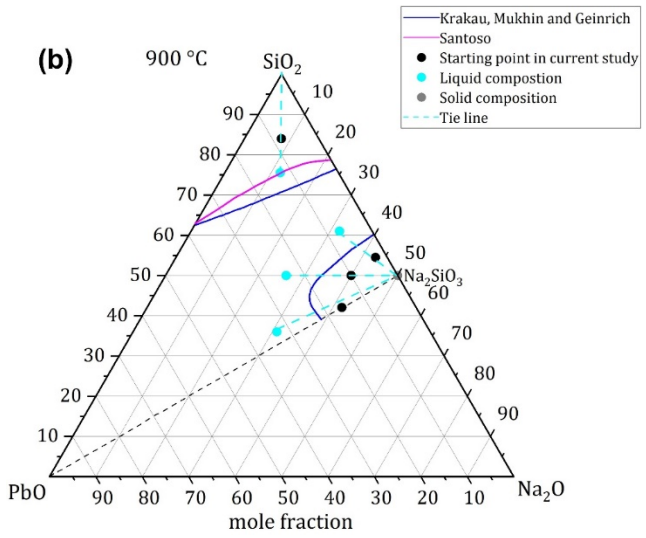

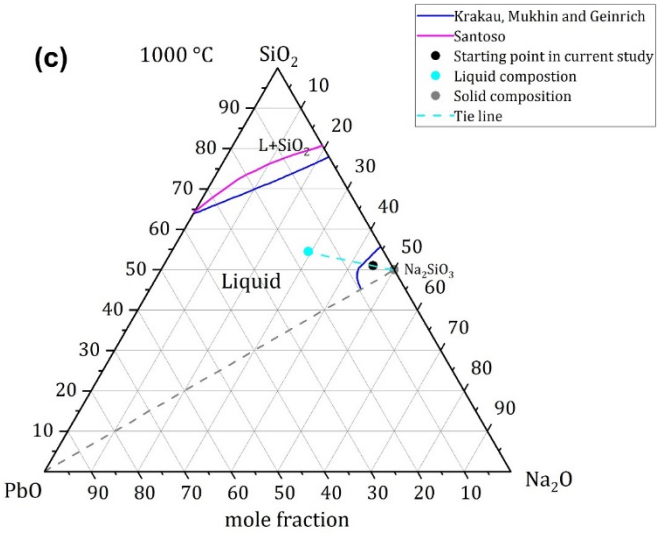

FIG 3 – Isothermal sections of PbO-Na_2O-SiO_2 system at (a): 800°C, (b): 900°C and (c): 1000°C.

Sample 900-S1 is a comparison test with previous studies in the SiO_2 primary phase field by holding the sample in Pt capsule under air atmosphere at 900°C for 40 hrs. The BSE images show that the liquid phase is in equilibrium with the needle-like solid tridymite (Figure 1). The composition of the liquid phase in 900-S1 closely aligns with the data reported by Santoso (2017), shown in Figure 2b, who employed a different methodology involving the use of quartz crucibles to establish a silica-saturated composition. The consistency between the results obtained from distinct approaches underscores the reliability of the approach employed in this work. The compositions determined by Santoso (2017) and the current study both measured higher SiO_2 content in the liquid phase compared to Krakau, Mukhin and Heinrich (1949). This discrepancy likely arose from the difference between static and dynamic techniques. Samples especially those with high SiO_2 content, might not have reached equilibrium in dynamic experiments.

Except for sample 900-S1, all other samples were measured to be in the two-phase region where liquid was in equilibrium with solid Na_2SiO_3. In samples tested at 800 and 900°C, the solid grains displayed two distinct structures: polygonal and lath-shaped, both of which had identical compositions, suggesting that these crystalline structures were Na_2SiO_3. The polygonal shape is likely a cross-section of the crystal, whereas the larger lath-like structure may result from viewing the lateral section of the solid phase. According to the isothermal sections in Figure 2, tie lines pass through the starting points in all samples, suggesting negligible sample loss during high temperature tests and negligible Na loss during the electron beam analysis. Compared to the results reported by Krakau, Mukhin and Heinrich (1949), the liquid phase with much higher PbO content was observed. The liquid-solid two-phase region of Na_2SiO_3 primary phase field is much larger, indicating a higher melting point of mixture in this region. From practical point of view, when the slag composition falls between the liquidus lines established by Krakau, Mukhin and Heinrich (1949) and the current study, it is likely that slag might not achieve complete melting at the designated temperature. This incomplete melting can result in increased viscosity, thereby causing challenges during the tapping process. Consequently, it is essential to determine an accurate liquidus and other associated properties.

CONCLUSIONS

The current work studied the liquidus temperatures of the Na_2SiO_3 primary phase field between 800 and 1000°C on the PbO-Na_2O-SiO_2 system using the equilibration-quench-analysis method. The liquid-solid two-phase region established in the current study is significantly larger than the one observed by Krakau, Mukhin and Heinrich (1949), suggesting a higher melting point within this primary phase field.

REFERENCES

EDR Group, 2019. Economic Contribution of the US Lead Battery Industry, report, 22 p. Available from: <https://batterycouncil.org/wp-content/uploads/2019/10/Economic-Impact-of-Lead-Batteries-in-the-United-States-Sept-2019.pdf>

Krakau, K A, Mukhin, E Y and Heinrich, M S, 1949. Equilibrium diagram of the system Na_2O-PbO-SiO_2, Physicochemical Properties of the Ternary System Sodium Oxide-Lead Oxide-Silica, *Izd Akad Nauk*, pp 15–38.

Lyakov, N K, Atanasova, D A, Vassilev, V S and Haralampiev, G A, 2007. Desulphurization of damped battery paste by sodium carbonate and sodium hydroxide, *Journal of Power Sources*, 171:960–965. https://doi.org/10.1016/J.JPOWSOUR.2007.06.014

Nicol, S, Grogan, J, Davis, B and Lebel, T, 2020. Slag Reduction Kinetics of a Lead Slag from a Secondary Lead Smelter, in (eds: A Siegmund, S Alam, J Grogan, U Kerney and E Shibata), in *Proceedings of the 9th International Symposium on Lead and Zinc Processing, PbZn 2020*, pp 41–50.

Rand, D A J and Moseley, P T, 2015. Energy Storage with Lead–Acid Batteries, *Electrochemical Energy Storage for Renewable Sources and Grid Balancing*, pp 201–222. https://doi.org/10.1016/B978-0-444-62616-5.00013-9

Santoso, I, 2017. Phase Equilibria of Na2O-PbO-SiO2 system between 900 and 1100°C, *Proceedings of EMC 2017,* pp 317–326.

Yanamandra, K, Pinisetty, D, Daoud, A and Gupta, N, 2022. Recycling of Li-Ion and Lead Acid Batteries: A Review, *J Indian Inst Sci*, 102:281–295. https://doi.org/10.1007/s41745-021-00269-7

Zhang, J, Yi, L, Yang, L, Huang, Y, Zhou, W and Bian, W, 2016. A new pre-desulphurization process of damped lead battery paste with sodium carbonate based on a surface update concept, *Hydrometallurgy*, 160:123–128. https://doi.org/10.1016/J.HYDROMET.2015.12.016

Zhao, Y, Pohl, O, Bhatt, A I, Collis, G E, Mahon, P J, Rüther, T and Hollenkamp, A F, 2021. A Review on Battery Market Trends, Second-Life Reuse and Recycling, *Sustainable Chemistry*, 2:167–205. https://doi.org/10.3390/suschem2010011

Fusion of molten phase R&D into the metallurgical industry to drive circularity

DOI: 10.62053/MTIB9896

S Nikolic[1], A Burrows[2], S L Nicol[3], O J Mendoza[4] and B J Hogg[5]

1. Manager- Technology, Glencore Technology, Brisbane Qld 4000.
   Email: stanko.nikolic@glencore.com.au
2. Project Lead – Smelters, Glencore, Baar 6340, Switzerland
   Email: alistair.burrows@glencore.com
3. Senior Metallurgist, Glencore Technology, Brisbane Qld 4000.
   Email: stuart.nicol1@glencore.com.au
4. Senior Metallurgist, Glencore Technology, Brisbane Qld 4000.
   Email: oscar.mendoza@glencore.com.au
5. Principal Metallurgist, Glencore Technology, Brisbane Qld 4000.
   Email: ben.hogg@glencore.com.au

ABSTRACT

The top submerged lance (TSL) technology, developed in the 1970s, is now widely used for the processing of a range of materials. The key advantage the ISASMELT™ TSL technology provided was the ability to process feed materials in a highly turbulent bath, reaching close to equilibrium conditions, uniquely allowing for operation below the liquidus of the molten slag phase. The details on what happened below the liquidus line in the phase diagram became critical for the successful operation of the technology. During the development of the ISASMELT™ technology this led to a collaboration between the Process Technology group of Mount Isa Mines, now part of Glencore Technology, and the Pyrometallurgy Research Centre (PYROSEARCH) at The University of Queensland. The fusion of the phase equilibria research into the technology development allowed for understanding of the behaviour of molten splash, reliable tapping of the furnace, and the ability to operate the furnace with a refractory lining and achieve a year campaign life in excess of four years. The outcome has allowed for the highly successful adaption of the ISASMELT™ technology to recycling of complex feed streams necessary to drive circularity in our modern global economy.

INTRODUCTION

The development of the top submerged lance (TSL) technology began in the 1970s and started with investigations on how to improve tin smelting processes. This work led to the development of the SiroSmelt lance, which through collaboration between the Commonwealth Scientific Industrial Research Organisation (CSIRO) and Mount Isa Mines, now part of Glencore, by the 1990s had expanded the TSL technology, ISASMELT™, to industrial implementations in both primary concentrate smelting and secondary recycling targeting the processing of the carrier metals copper, nickel, zinc and lead (Burford, 2009; Hogg, Nikolic and Voigt, 2018).

The ability of the ISASMELT™ technology to process a wide variety of feeds in the same furnace arrangement is because it is a turbulent molten slag reaction process. The slag phase itself is both continuously produced and continually provided with fresh oxidant or reductant, depending on the process reactions taking place, by the feed materials and the inlet air/oxygen/reductant being added down the centrally positioned lance. Unlike other high temperature processes, which either over or under oxidise the feed through a burner or pass the oxygen through a matte/metal layer, necessitating thermal control, slag phase reaction allows for near thermal and chemical equilibrium to be achieved. Proper understanding of the operation of the furnace requires detailed knowledge of the phase equilibria of the molten phases and their interactions.

Information present in the literature during the development of the technology was either focused on binary/ternary systems or analysis of the behaviour of complex phases taken from furnace rebuilds. The understanding of the fundamental compositional and physical properties of the molten slag in the multi-component systems, such as phase equilibria and viscosity, was missing from the earlier research and it would be vital for the process implementation, optimisation and control of the ISASMELT™ technology. This led to a collaborative effort beginning in the late 1990s between the

Process Technology group of Mount Isa Mines, now part of Glencore, and the Pyrometallurgy Research Centre (PYROSEARCH) at The University of Queensland for the purpose of investigating the fundamental phase equilibria of multi-component systems with their rapid quenching electron probe x-ray microanalysis technique (Jak, Hayes and Lee, 1995; Jak and Hayes, 2004; Ilyushechkin, Hayes and Jak, 2004).

UNDERSTANDING SLAG CHEMISTRY FOR REFRACTORY FREEZE LININGS

The main concerns in the early development of the Lead ISASMELT™ process were to minimise dust production from the vaporisation of the lead sulfide in the feed during the smelting step. This led to a minimisation of the operating temperature as this has a direct correlation with the fuming rate. A surprising observation on the demonstration plant scale, later confirmed on the commercial scale, was that there was effectively no refractory wear in the walls of the smelting vessel.

Samples taken from the operating furnace by PYROSEARCH staff as a part of an industry-sponsored research program in the mid-1990s shed light on this mystery. The samples showed that at typical smelting temperatures the ISASMELT™ slag in the lead smelter at Mount Isa Mines Ltd. was not a homogenous liquid. As shown in Figure 1, slags obtained by careful sampling, followed by rapid quenching, contained a mix of reaction products in both solid and liquid states as a result of the smelting process.

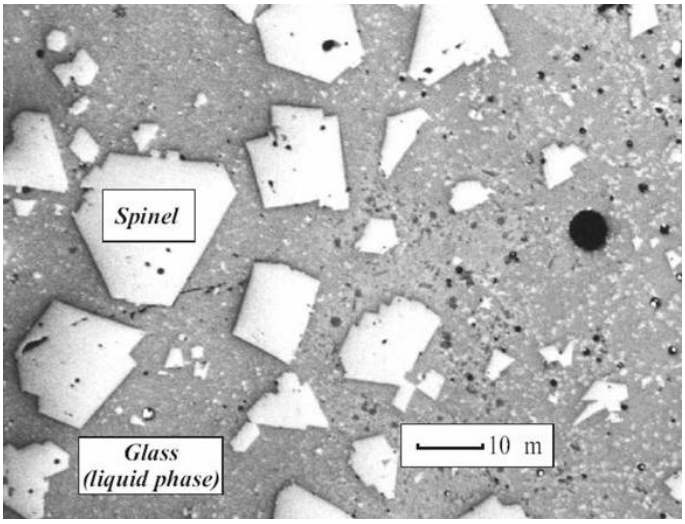

FIG 1 – Photomicrograph of slag from the lead ISASMELT™ process (Jak *et al*, 1994). Many euhedral spinel particles, up to a particle size of 10 μm, are suspended inside a liquid.

The lead ISASMELT™ furnace at that time operated, as those still operating do today, below the slag liquidus temperature. Tiny particles of solids, in addition to floating in the bath of high-density slag, gradually accumulate on solid surfaces inside the furnace that are exposed to splashed slag. The liquid part of the slag drains off quickly, leaving behind a few solid particles each time, developing a spinel coating that provides protection for the furnace side wall refractory from upset over temperature conditions that may occur. A view inside a nicely spinel coated ISASMELT™ furnace is shown in Figure 2.



FIG 2 – Lead ISASMELT™ Furnace side wall bricks, exposed mid-campaign, showing widespread spinel coating (Hogg *et al*, 2022).

It was later shown that the proportion of spinel present in the lead smelting slag in air for a given bulk composition and temperature could be deduced from the experimentally determined equilibria presented on pseudo-ternary sections Fe_2O_3-ZnO-(PbO+CaO+SiO_2) for given CaO/SiO_2 and PbO/(CaO+ SiO_2) ratios (Jak and Hayes, 2002).

Copper ISASMELT™ furnace lining development

When considering the copper ISASMELT™ furnace technology in Mount Isa it was initially justified on a two year campaign length. However, this target was not achieved for the first six campaigns from 1992 to 1998, refer to Figure 3, with most campaigns lasting between 45–65 weeks. A review was completed on implementing some form of copper cooling – either of the bricks, interwoven with the bricks, or direct freeze lining of the slag bath. However, experience from operation of the lead ISASMELT™ process and the demonstration plant for the copper ISASMELT™ process indicated that a 90 week refractory campaign life was achievable (Burford, 2009).

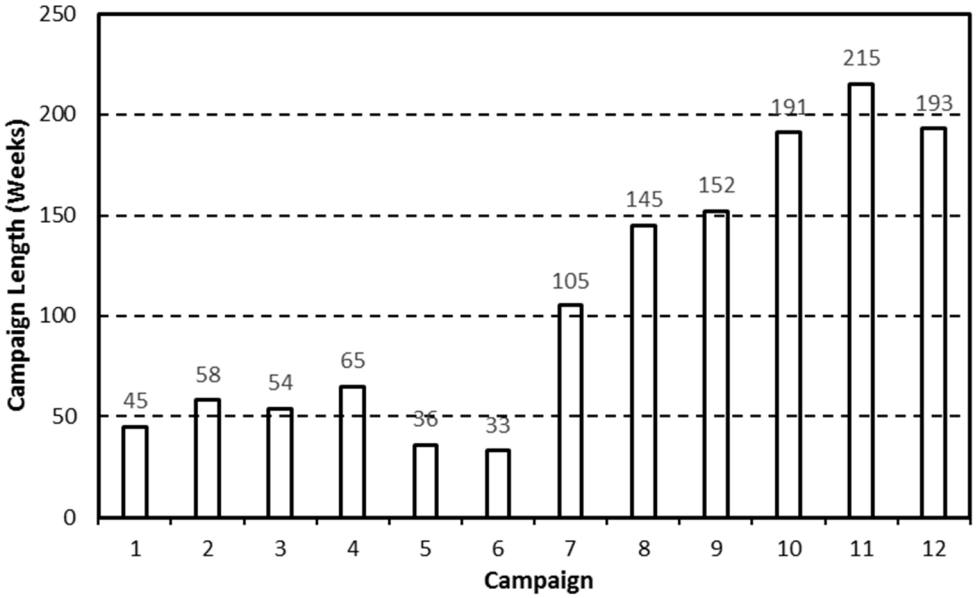

FIG 3 – Mount Isa copper smelting ISASMELT™ campaign life.

Although similar levels of solids, as seen in lead smelting, were not possible to be maintained in the copper process it led to a renewed focus on maximising the campaign life through temperature management and understanding of the slag phase equilibria to produce spinel crystal structures. Based on this daily review, plant operating set points were adjusted, and the result was an extension to the campaign length for a record 105 weeks. Management of the ISASMELT™ plant has continued to improve with a four year campaign life becoming the new standard for operation, refer to Figure 3.

Once the correct metallurgical recipe and operating temperature regime has been obtained, side wall brick-wear can be minimised in the Copper ISASMELT™ process. This has been proven time and again at ISASMELT™ furnaces around the world as is evident when operating temperatures are elevated, as shown on the left portion of Figure 4. Against when the furnace temperature control is optimised, to below the liquidus, as shown on the right side of Figure 4. The ISASMELT™ refractory wear can be minimised to a point where it is almost non-existent. This is possible, and highly repeatable, with the ISASMELT™ process due to the reaction zone location and the combination of the knowledge provided by the phase equilibria research with the process control incorporated within the technology.

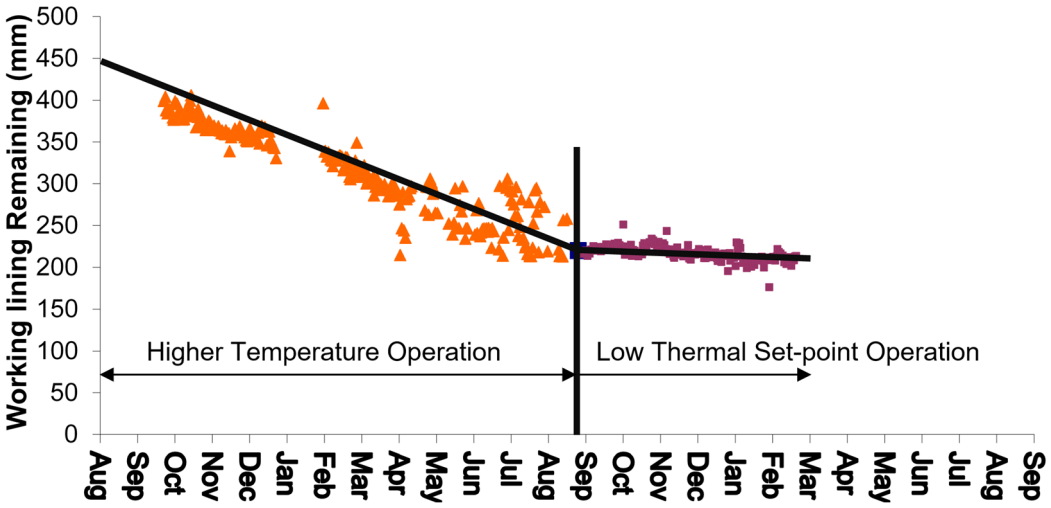

FIG 4 – ISASMELT™ brick wear trend showing high temperature operation and optimal temperature operation.

PHASE EQUILIBRIA AND TAPPING IN THE ISASMELT™ PROCESS

The lead ISASMELT™ process has been implemented in Australia, China, and Kazakhstan. The closely related ISASMELT™ process for recycling lead-acid batteries was developed in the late 1980s and has additionally been operated in England and Malaysia (Burford, 2009). In each case lead-rich feeds are smelted and slags are created that are rich in lead oxide. Removal of the slag through a tap hole in the wall of the furnace has been the subject of numerous efforts of design, improvement, re-design, and modification.

Operating the furnace with the aim to minimise lead fuming and maximise refractory life presented a challenge with the tapping of essentially a liquid molten slurry from the furnace. This came into focus during the period when the industrial-scale lead ISASMELT™ furnace in Mount Isa was being commissioned. The taphole in the oxidation furnace was to be operated as an overflow taphole, with a minimum head of liquid slag inside the oxidation furnace. Challenges with process constraints (unrelated to tapping) determined that continuously feeding the furnace and tapping the slag batchwise was a more appropriate option.

Tapping sub-liquidus slag was next tried in China when the Isa-YMG process was commissioned in Qujing (Errington *et al*, 2005). Although the production capacity of Chihong Zinc and Germanium Company's smelter in China was intended to be greater than that at Mount Isa Mines, there was a comparatively reduced amount of lead-rich slag owing to the high-grade of concentrate being smelted and the production of some lead bullion inside the ISASMELT™ furnace.

There was also a tendency for the slag at Qujing to change from 'tappable' to 'untappable' throughout the day, with little apparent change in temperature or bulk composition. This phenomenon was investigated further with the PYROSEARCH Centre through a sponsored research program. This work identified that at the microscopic level fluid slags, refer to Figure 5, tended to look very similar to those at Mount Isa a decade earlier: a slurry of spinel particles suspended in a lead oxide-rich liquid. But the viscous slags looked different. There were some additional particles with the approximate composition of willemite. The crystals of willemite tended to appear as acicular needles, which were very different from the shape of spinels.

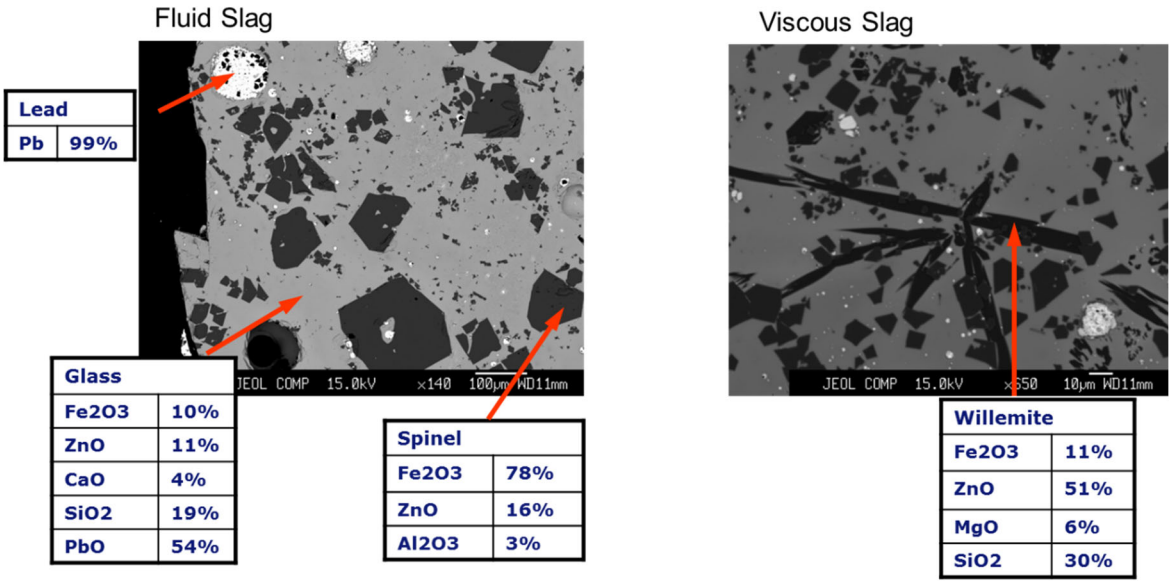

FIG 5 – Photomicrographs of slags, tapped at sub-liquidus temperatures, from Qujing lead ISASMELT™ furnace (Zhao *et al*, 2005).

The absence of acicular crystals was found to be a prerequisite for achieving a reliable slag flow. It was already known that the presence and crystal-shape of the suspended solid particles in a sub-liquidus lead oxide-rich slag could vary with slag composition. Zhao *et al* (2005) reported this observation with respect to melilite particles. Accumulated knowledge about sub-liquidus crystal types now seemed to be knowhow that was transportable to the more practical application of understanding whether a slag would exhibit good tapping behaviour at sub-liquidus temperatures.

The Campforts diagram

To be able to adapt this knowledge, so that it was understandable and relatable to the industrial process, a new approach had to be undertaken. Separate research being done in collaborations that PYROSEARCH completed with other universities and industry partners offered a new approach. In a series of published papers (Campforts *et al*, 2007, 2008; Campforts, Blanpain and Wollants, 2009) the authors calculated the proportion of phases present at various temperatures using the FactSage™ package and associated database (Jak *et al*, 1997, 1998; Bale, Pelton and Thompson, 2007). The proportion of solids was graphically presented as pseudo-unary phase diagrams, as shown in Figure 6. With a variation in the slag bulk composition, the nature and proportion of solids changes, with a unique pseudo-unary diagram for each slag composition and oxygen partial pressure. It was a useful method to explain the topic of freeze lining formation. By chance, it is also a useful method to explain the chemistry of sub-liquidus slags. In the interests of brevity, and because these cited papers are the first in which the authors saw this type of diagram, it is referred to hereafter as the ‘Campforts diagram’.

For two different slags rich in lead oxide, Campforts predicted different proportions of stable condensed oxide phases at each temperature (Campforts, Blanpain and Wollants, 2009). Compositions of slags M1 and S1 are shown in Table 1.

TABLE 1

Compositions used in analysis of the Campforts diagram (Campforts, Blanpain and Wollants, 2009).

Slag	CaO	SiO_2	PbO	ZnO	Fe_2O_3	Al_2O_3
M1	10.57	13.81	45.79	3.28	20.28	6.27
S1	3.70	9.56	55.80	4.44	21.35	4.90

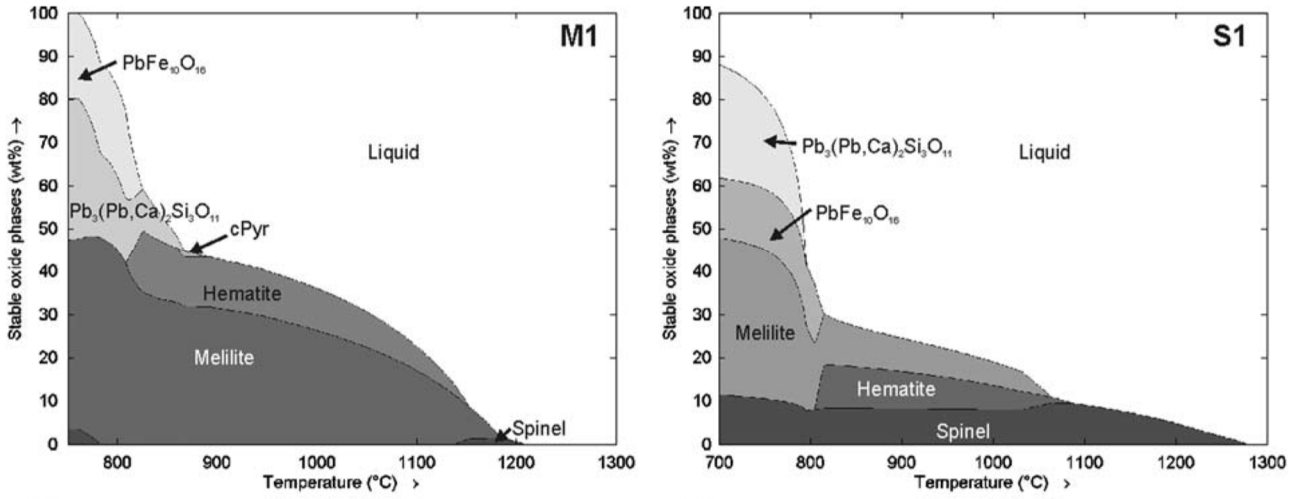

FIG 6 – Campforts diagrams for two different slags (denoted M1 and S1) (Campforts, Blanpain and Wollants, 2009).

For both of these slags it was predicted that only about 90 per cent of the mass of condensed oxides is going to be in liquid form at the temperature of 1150°C. However, it was also predicted that there were significant differences in the solid phases present. Referring to Figure 6, it is clear that for slag M1 at 1150°C the solids are predicted to be mostly melilites, whereas for slag S1 at the same temperature those solids will be exclusively spinels.

In the experiments performed by Campforts, Blanpain and Wollants (2009) and under the conditions investigated, melilite was observed to form acicular crystals that were able to be interlocked, while spinel was observed as individual and isolated crystals. This ability for spinel crystals to form individual phases whilst crystals involving silica formed interlocking structures was consistent with that observed by other researchers in other slag systems (Hidayat *et al*, 2012). From experience with sub-liquidus slag tapping, and informed by the Campforts diagrams of these two slags, it is possible to predict that slag M1 will need to be tapped at a temperature of about 1200°C, but it would be possible to tap slag S1 at a temperature of 1100°C. Note that this is completely the opposite of the conclusions that would be drawn if the liquidus temperature alone were considered. ie Slag S1 has a higher liquidus temperature than slag M1, but it is possible to tap slag S1 at a lower temperature.

MOLTEN PHASE RESEARCH DRIVING THE CIRCULAR ECONOMY AND RECYCLING

At the end-of-life of a given component, product or material, implementation into circularity involves a large number of steps- from the initial collection stage and preliminary sorting, which generally involves some degree of physical upgrading and separation, through to the final processing stages to produce pure renewed starting materials or by-products. In the case of complex intermediate streams, which cannot be separated or reused directly in the circular economy, recycling of the contained metal values is required. All steps in this process are important, but due to the energy intensity and requirement for extractive processing, the near-final recycling processing step producing a payable metal product, is the step that is ultimately the key to achieving sustainability.

The application of ISASMELT™ for the treatment/recycling of complex feed streams was implemented in Europe at the Umicore Precious Metals Refining Hoboken Plant in Belgium and the Aurubis AG Lünen plant in Germany in the 1990s (Vanbellen and Chintinne, 2006; Ayhan, 2001). Umicore focused on the processing of complex lead/copper materials, containing valuable minor elements in a two-step smelting and converting ISASMELT™ process, shown in Figure 7. The Aurubis Lünen plant (Aurubis, 2011), focused on treating copper secondary and recycling materials in a process that can involve a number of steps in a single ISASMELT™ reactor – such as smelting, reduction and converting to maximise the recovery of the targeted elements to the gas phase, slag phase or copper phase in each stage of the batch process. This is shown in Figure 8.

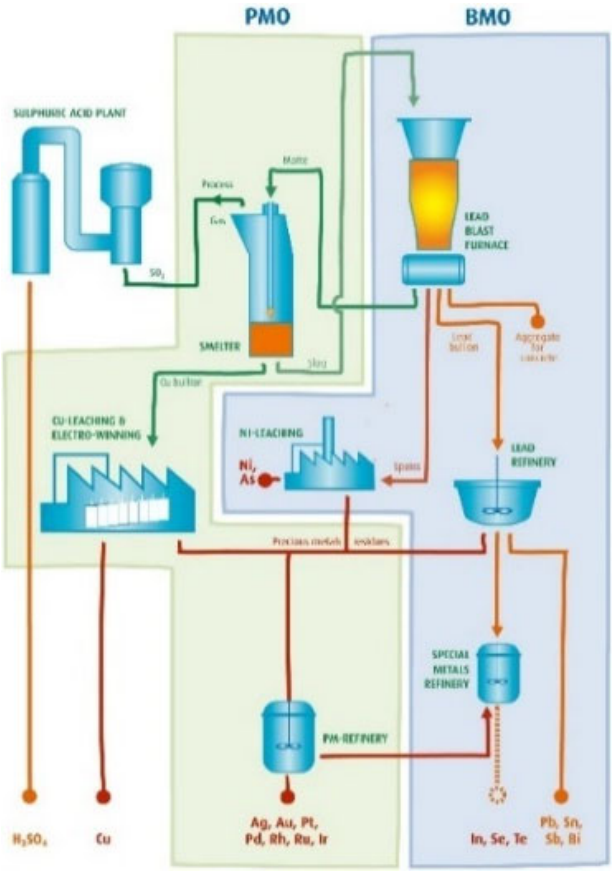

FIG 7 – ISASMELT™ Furnace in the Umicore, Hoboken plant operations flow sheet (Vanbellen and Chintinne, 2006).

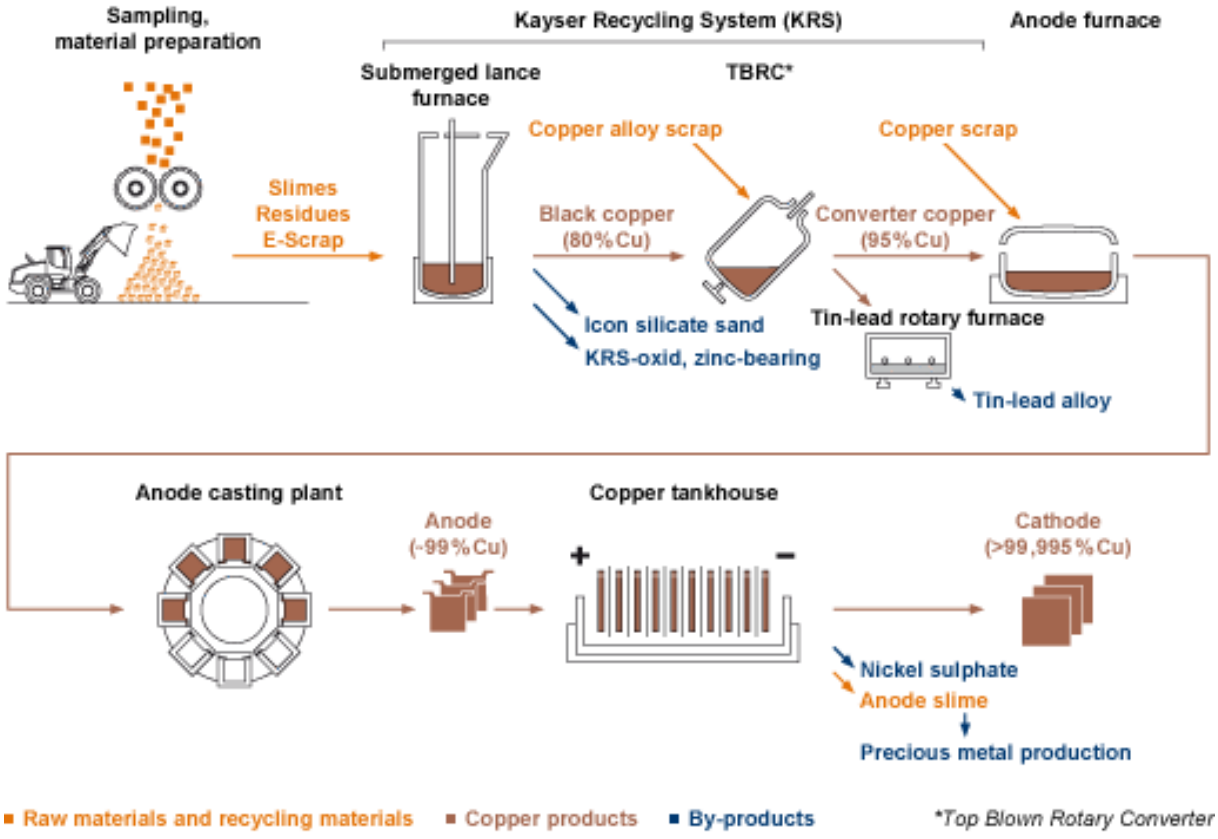

FIG 8 – ISASMELT™ Furnace in the KRS flow sheet at Aurubis Lünen, Germany (Aurubis, 2011).

The core of the application of the ISASMELT™ within both flow sheets was the ability of the technology to maintain a turbulent slag bath that allows for rapid integration of all feed materials to their molten metal equivalents. Both sites used this to their advantage as once in the molten phase base metals can then be used as the collectors for the contained value, predominately the precious and platinum group metals present in the feed. Recovery of these, as well as the base metals, can only be optimised through the selective oxidation possible with a batch ISASMELT™ process. Thermodynamic calculation packages can be used to simulate these requirements. For example, under appropriate oxygen and sulfur potentials conditions (oxidative smelting) lead can be selectively oxidised and transferred to the slag as copper remains in a sulfide/metallic phase as oxidation progresses.

To be able to take advantage of the ability of the ISASMELT™ to operate across the oxidative range a more robust thermodynamic calculation process was required than what was offered by generic databases and software. As illustrated in the previous examples maintaining a spinel crystal presence in the ISASMELT™ melt is critical to the longevity of an operation. The work of the PYROSEARCH Centre to increase the available information used in thermodynamic packages has been critical to the ability to calculate the multi-component phase equilibria in these types of systems. To illustrate this a set of ternary diagrams, produced by FactSage™ (Bale, Pelton and Thompson, 2007) and using databases developed from the outcomes of work at PYROSEARCH, calculating the impact of oxygen partial pressure, representing operational conditions from reductive smelting to converting at a fixed alumina content in a typical fayalite slag at 1200 and 1300°C is shown in Figure 9.

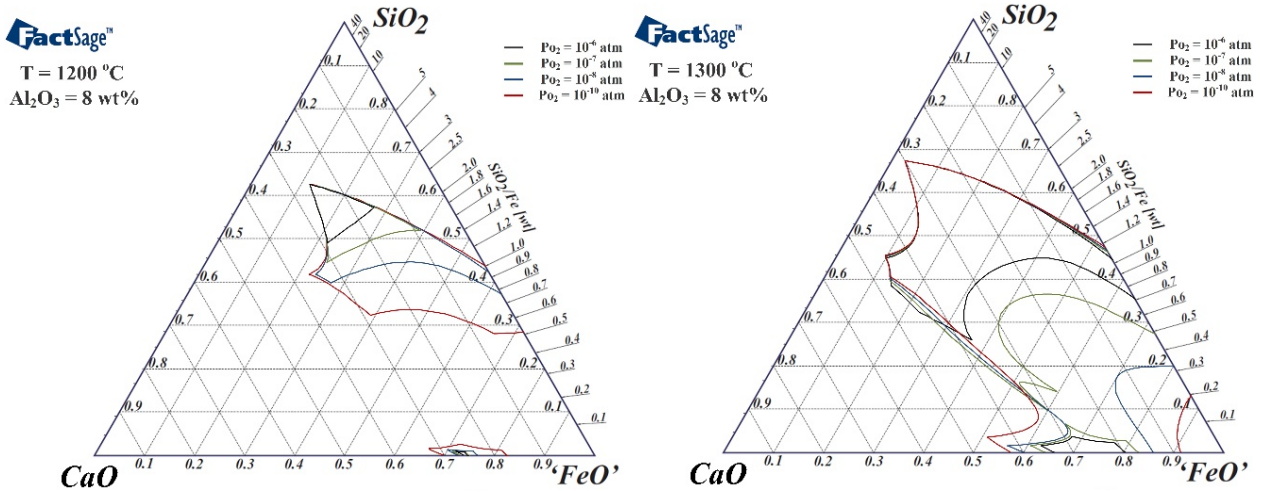

FIG 9 – FactSage calculations for the effect of oxygen partial pressure on slag liquidus on alumina containing fayalite slag at 1200°C and 1300°C.

Within a batch process, typically in the first step the furnace is run in pseudo-continuous operating conditions whilst one of the molten phases is built up in the vessel. During this period the operational targets of slag fluxing and operating temperature of the furnace would be conducive to building a protective spinel lining. This would represent the base condition and, for example, would be operating at 1200°C with a low oxygen partial pressure of 10^{-10} atm and a SiO_2/Fe ratio in the slag of 0.7, when considering the lime concentration. During the subsequent step in the batch cycle a more oxidative oxygen partial pressure would normally be practiced. When considering the impact of oxygen potential on the proportion of solids in the melt at 1200°C this would reach unacceptable levels if the slag operating temperature and fluxing are not managed. Using the information in the calculations it is possible to calculate the necessary increase in temperature against the oxygen potential of the bath to maintain the proportion of solids in the melt required to maintain the integrity of the furnace.

Although these changes can be predicted it should be noted that slag liquidus alone is not sufficient in this regard. Operating regions need to be selected that allow for the most sustainable outcome. One where appropriate levels of metals are recovered, whilst the versatility and usability of the waste

materials from the process is maximised by allowing them to be used as feed materials for other industries.

CONCLUSIONS

ISASMELT™ technology's vertical submerged lance injection, with a resulting highly turbulent bath, allows for a different approach to be taken for the design and implementation of a furnace system. To be able to take full advantage of this the understanding of the fundamental compositional and physical properties of the molten slag in the multi-component systems was required to be applied to the technology process development. Through the collaborative efforts, beginning in the late 1990s, between Glencore Technology and PYROSEARCH, this allowed for the understanding of the behaviour of freeze linings on refractories through molten splash, reliable tapping of the furnace and the adaptation of the technology to recycling of complex feed streams.

ACKNOWLEDGEMENTS

The ISASMELT™ licensees and PYROSEARCH supporters and industry partners, who are part of the continuous evolution and development of the industry. The authors wish to acknowledge Kazzinc Limited and Glencore Technology for permission to publish this paper.

REFERENCES

Ayhan, M, 2001. Das neue HK-Verfahren für die Verarbeitung von Kupfer-Sekundärmaterialien, 2000 (The new HK process for the treatment of copper secondary materials, 2000), *Intensivierung metallurgischer Prozess* (*Intensification of Metallurgical Processes*), 87:197–207 (GDMB: Germany).

Bale, C W, Pelton, A D and Thompson, W T, 2007. Facility for the Analysis of Chemical Thermodynamics, Ecole Polytechnique de Montreal. Available from: <http://www.crct.polymtl.ca>

Burford, B, 2009. The ISASMELT™ Technology Package: Over 30 Years of Innovation, AusIMM Bulletin, *Journal of the Australasian Institute of Mining and Metallurgy*, 1(Feb):26–30.

Campforts, M, Blanpain, B and Wollants, P, 2009. The Importance of Slag Engineering in Freeze-Lining Applications, *Metall Mater Trans B*, 40B(5):643–655.

Campforts, M, Verscheure, K, Boydens, E, Van Rompaey, T, Blanpain, B and Wollants, P, 2007. On the Microstructure of a Freeze Lining of an Industrial Nonferrous Slag, *Metall Mater Trans B*, 38B(Dec):841–851.

Campforts, M, Verscheure, K, Boydens, E, Van Rompaey, T, Blanpain, B and Wollants, P, 2008. On the Mass Transport and the Crystal Growth in a Freeze Lining of an Industrial Nonferrous Slag, *Metall Mater Trans B*, 39B(June):408–417.

Errington, B, Arthur, P, Wang, J and Dong, Y, 2005. The ISA-YMG Lead Smelting Process, *Proc Intl Symp on Lead and Zinc Processing*, *MMIJ*, pp 581–599.

Hidayat, T, Henao, H M, Hayes, P C and Jak, E, 2012. Phase Equilibria Studies of Cu-O-Si Systems in Equilibrium with Air and Metallic Copper and Cu-Me-O-Si Systems (Me = Ca, Mg, Al and Fe) in Equilibrium with Metallic Copper, *Metall Trans B*, 43B:1290–1299.

Hogg, B, Prince, M, Letchford, M, Burrows, A, Tokzhigitov, T and Azekenov, T, 2022. Successful Development and Optimisation of Lead ISASMELT™ Furnace Slag Tapping System at Kazzinc Ltd, in (eds: J D Steenkamp, D Gregurek, Q G Reynolds, G R Alvear Flores, H Joubert and P J Mackey) *Furnace Tapping 2022*, pp 245–259 (The Minerals, Metals and Materials Series) https://doi.org/10.1007/978-3-030-92544-4_18

Hogg, B, Nikolic, S and Voigt, P, 2018. ISASMELT™ Technology for Sulfide Smelting, in *Proceedings Extraction 2018 Symp*, pp 149–158.

Ilyushechkin, A, Hayes, P C and Jak, E, 2004. Liquidus Temperatures in Calcium Ferrite Slags in Equilibrium with Molten Copper, *Metall Mater Trans B*, 35B:203–215.

Jak, E and Hayes, P C, 2002. Experimental liquidus in the PbO-ZnO-Fe_2O_3-(CaO+SiO_2) system in air with CaO/SiO_2 weight ratio of 0.35 and PbO/(CaO + SiO_2) = 5.0, *Metall Trans B*, 33B:817–825.

Jak, E, Degterov, S, Hayes, P C and Pelton, A D, 1998. Thermodynamic optimisation of the systems CaO-Pb-O and PbO-CaO-SiO_2, *Can Metall Quart*, 37(1):41–47.

Jak, E, Degterov, S, Wu, P, Hayes, P C and Pelton, A D, 1997. Thermodynamic optimisation of the systems PbO-SiO_2, PbO-ZnO, ZnO-SiO_2 and PbO-ZnO-SiO_2, *Metall Transactions*, 28B:1011–1018.

Jak, E, Liu, N, Lee, H G and Hayes, P C, 1994. Application of phase Equilibria Studies to Describe Behaviour of Lead Smelting Slags, in *Proceedings of the 6th AusIMM Extractive Metallurgy Conference,* pp 261–268.

Jak, E and Hayes, P C, 2004. Phase Equilibria Determination in Complex Slag Systems, in *Proc Intl Symp Molten Slags and Fluxes*, pp 85–104 (SAIMM).

Jak, E, Hayes, P C and Lee, H G, 1995. Improved Methodologies for the Determination of High Temperature Phase Equilibria, *Korean Journal of Metals and Materials*, 1:1–8.

Vanbellen, F and Chintinne, M, 2006. The Precious Art of Metals Recycling, *Advanced Processing of Metals and Materials* (eds: F Kongoli and R G Reddy) 1:43–52 (TMS: Warrendale).

Zhao, B, Errington, B, Yang, G, Wang, J, Dong, Y, Jak, E and Hayes, P C, 2005. Characterisation of ISASMELT™ Slag and Lead Blast Furnace Sinters, in *Proc Intl Symp on Lead and Zinc Processing*, pp 571–586.

Phase equilibria of Al_2TiO_5–Ti_3O_5 pseudobrookite solid solution in the Al_2O_3–TiO_x system under various oxygen partial pressures

DOI: 10.62053/MCAM4452

Y-J Park[1], W-Y Kim[2] and Y-B Kang[3]

1. PhD candidate, Pohang University of Science and Technology, Pohang, Gyeongbuk 37673, Republic of Korea. Email: yjpark92@postech.ac.kr
2. Senior Researcher, POSCO Holdings, Pohang Gyeongbuk 37673, Republic of Korea. Email: wanyikim911@posco-inc.com
3. Professor, Pohang University of Science and Technology, Pohang, Gyeongbuk 37673, Republic of Korea. Email: ybkang@postech.ac.kr

ABSTRACT

The phase equilibria in the Al_2O_3–TiO_x system were investigated in wide ranges of temperature and oxygen partial pressure: 1300~1600°C and $10^{-16.6}$~10^{-8} atm, respectively. The equilibrium phases and their compositions were identified using X-ray diffraction (XRD) and electron probe micro-analysis (EPMA), respectively. Most noticeably, a wide range of pseudobrookite solid solution was found in equilibrium with almost pure alumina. At each temperature, the cationic ratio expressed as $R_{Ti} = n_{Ti}/(n_{Al} + n_{Ti})$) of the pseudobrookite solid solution showed a noteworthy dependency on the oxygen partial pressure. This resulted in the formation of a broad range of pseudobrookite solid solutions, ranging from Al_2TiO_5 (R_{Ti} = 1/3) to Ti_3O_5 (R_{Ti} = 1.0). Complete miscibility within the pseudobrookite solid solution was observed at 1600°C, with only a minor miscibility gap becoming evident below 1500°C. Based on the results obtained in the present study, the behaviours of Al_2TiO_5 pseudobrookite have implications in two key domains: (1) understanding changes in the physical properties of the materials, and (2) elucidating the evolution of Al–Ti complex oxide inclusions in liquid steel which can deteriorate the steel cleanliness.

INTRODUCTION

Various metallic and oxide phases have been documented in the Al-Ti-O system (Das, 2002). Within the boundaries of the Al_2O_3-TiO_2-Ti_2O_3 system, commonly referred to as Al_2O_3-TiO_x, several stable oxide phases have been identified. These include corundum (Al_2O_3), rutile (TiO_2), pseudobrookite (Ti_3O_5), ilmenite (Ti_2O_3), and tialite (Al_2TiO_5) and Magnéli phases (Ti_nO_{2n-1}, $4 \leq n \leq 10$). The formation of titanium oxide is influenced not only by temperature (T), but also by the oxygen partial pressure (P_{O_2}) in the system due to the transition metal nature of Ti. Among these phases, ceramics materials based on Al_2TiO_5 have become popular for use in diesel particulate filters and foundry crucibles due to their significant thermal shock resistance and corrosion-resistant properties (Aneziris *et al*, 2010; Fruhstorfer *et al*, 2016; Gehre *et al*, 2015). Additionally, Al_2TiO_5 ceramics are suitable for various applications, including port liners, piston bottoms, and turbochargers (Gugel, 1984; Heinrich, Langer and Siebels, 1988; Wright, 1972).

The Al_2TiO_5 phase has been also identified as non-metallic inclusions in Ti-added ultra-low carbon (Ti-added ULC) steel, which is commonly utilised as the outer panel in automotive applications due to its exceptional formability (Fekete, Strugala and Yao, 1992; Mao, 2019). In the steelmaking process, liquid Ti-ULC steel is deoxidised by Al, followed by the addition of Ti during the RH (Ruhrstahl-Heraeus) process. The purpose of adding Al is to deoxidise the liquid steel, which then leads to the formation of alumina inclusions, primarily Al_2O_3. Ti is subsequently introduced to enhance the formability of the sheet steel, acting as a potent binder for interstitial elements such as C and N (Mao, 2019). It is important to note that the addition of Ti occurs after the Al deoxidation process, as Ti is not intended to react with oxygen. Despite the intention, both Al and Ti exhibit a strong affinity for O, resulting in the formation of various oxides (Al_2O_3, Ti_2O_3, Ti_3O_5, Al_2TiO_5 etc). Despite extensive research, the origin of Al-Ti complex inclusions in Ti-added ULC steel within the Al-Ti-O system remains unclear due to a lack of comprehensive thermodynamic equilibrium studies. Previous studies present conflicting views, with some literature (Matsuura and Tsukihashi, 2012) suggesting the stable existence of Al_2TiO_5, while others (Kang and Lee, 2017) propose that Al_2TiO_5 will not be unstable in molten steel and exists only as Al_2O_3 or Ti_3O_5 solid oxide.

The phase equilibria of the Al_2O_3–TiO_x system are highly influenced by temperature (T) and oxygen partial pressure (P_{O_2}) due to the presence of titanium (Ti). Phase equilibria of the Al_2O_3-TiO_x system were investigated by some studies in air condition (Ilatovskaia, Savinykh and Fabrichnaya 2017; Panda and Jung, 2020) and strong reducing conditions using H_2 gas (McKee and Aleshin, 1963), Ar-5 per cent.H_2 (Yasuda, Aoki and Sakuma, 1998), high-purity Ar (Horibe and Kuwabara, 1964), and vacuum. Although these conditions are strongly reducing, it is not possible to precisely define an accurate P_{O_2}. However, no intermediate phases were reported under these conditions, indicating that Al_2TiO_5 is no longer stable. It should be noted that a specific P_{O_2} range was not provided.

Seifert and Aldinger (1996) examined Al_2TiO_5 under air as a $(Al^{3+})_2\{Ti^{4+}\}_1[O^{2-}]_5$ stoichiometric phase. They suggested that, with decreasing P_{O_2} (z decreases from 1), the decomposition reaction leads to the formation of Ti_3O_5 and corundum (***z*** = 0) as:

$$(3-2z)(Al^{3+})_2\{Ti^{4+}\}_1[O^{2-}]_5 = (Al_z^{3+}Ti_{1-z}^{3+})_2\{Ti^{4+}\}_1[O^{2-}]_5 + 3(1-z)Al_2O_3 + \frac{1}{2}(1-z)O_2 \quad (1)$$

This means that Al_2TiO_5 should be considered as a part of a wider solid solution with Ti_3O_5 and not as the stoichiometric compound. Despite a thorough literature survey, no experimental data were found showing the transition in stability from the Al_2TiO_5 phase to Ti_3O_5 in the pseudobrookite phase. Addressing this gap is crucial for understanding the evolution of non-metallic Al–Ti complex inclusions in liquid steel. Therefore, the present study aims to provide precisely determined phase diagram data in the Al_2O_3–TiO_x system, particularly under precisely controlled P_{O_2}. This will help identify the conditions under which Al_2TiO_5 remains stable and how it decomposes into other phases.

EXPERIMENTAL

The experimental procedure involved high-temperature equilibration under controlled P_{O_2} and temperature (T), followed by quenching and subsequent analysis using electron probe micro analysis (EPMA) and X-ray diffraction (XRD). The experimental apparatus used in the present study is shown in Figure 1. All high-temperature equilibrations were conducted in a vertical resistance heating furnace with a $LaCrO_3$ heating element. The furnace comprised a recrystallised alumina tube sealed by a water-cooled brass end cap. The temperature, maintained within ±2°C, was monitored using a B-type thermocouple after ensuring a uniform temperature range in the heat zone. The P_{O_2} in the chamber was controlled by flowing a gas mixture of CO (g), CO_2 (g), Ar-10 per cent.H_2, and Ar-1 per cent.CO_2. P_{O_2} was calculated by using FactSage™ with the FactPS database (Bale ***et al***, 2009, 2016). It was also monitored in some runs using a yttria-stabilised zirconia sensor with air as the reference. The observed difference between calculated and measured P_{O_2} was within ±0.2 on a logarithmic scale.

Samples were prepared by mixing high-purity Al_2O_3 and TiO_2 powders, weighed in desired proportions and blended using a turbula mixer. The mixed powders were dried, weighed (1.2 to 1.5 g), and pelletised at 20 MPa pressure. Pellets were placed in either alumina or graphite crucibles, along with shielding materials (Pt wire for oxidising or Mo wire for reducing conditions) to prevent contamination. A graphite crucible was used under C(s)-CO(g) equilibrium gas, and a porous alumina crucible otherwise. The crucible with samples was loaded into the chamber, heated to the target temperature in a vertical resistance furnace, and then lowered at a speed of 3 cm min^{-1} to the heat zone. After annealing at 1650°C for 12 hrs, equilibration at the designated temperature occurred at a rate of 2°C min^{-1} for 24–48 hrs, with additional initial annealing. Following equilibration, pellets were rapidly pulled up and quenched in iced water. Quenched samples were dried, with some subjected to polished for EPMA quantitative analysis, and others ball-milled into the powder for XRD analysis.

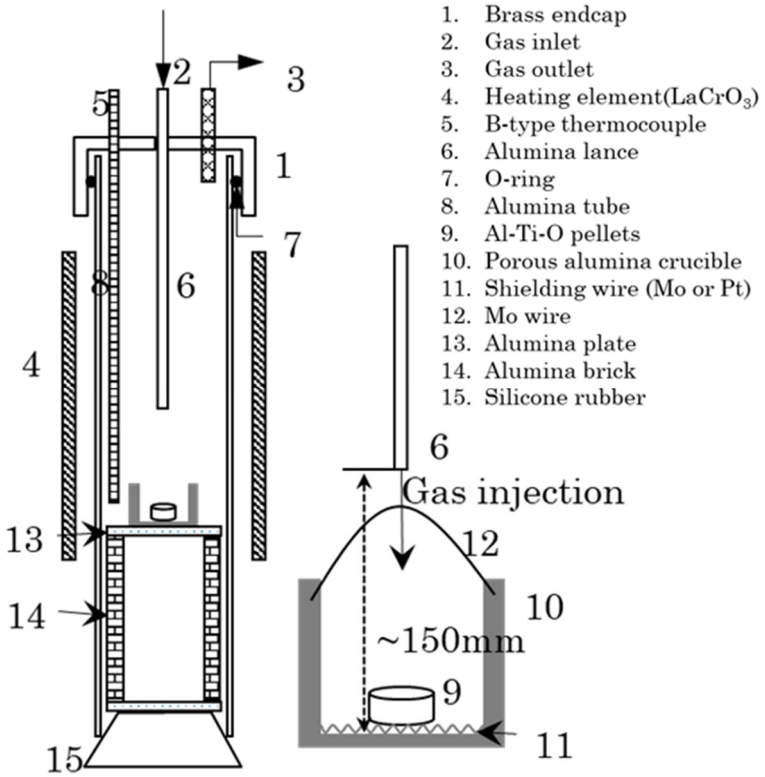

FIG 1 – Experimental apparatus of the high-temperature equilibrium experiments.

RESULTS

All the data obtained in the present study are shown in the phase diagram at each temperature as composition (cationic ratio, $R_{Ti} = n_{Ti}/(n_{Al} + n_{Ti})$) versus oxygen potential (log P_{O_2}) Type-II diagram in Figure 2. Both open and closed circles are the analysed composition of each phase measured in the present study: the closed circles for the single-phase and the open circles for phase boundary in two-phase mixtures at the equilibrium. Experimental data from the literature were also shown. In addition to this, thermodynamic calculation was carried out using FactSage with FTOxide database, shown by dashed lines. In this calculation, the Al_2TiO_5 phase was treated as a stoichiometric compound as is available in the database.

The experiments were mainly conducted at 1600°C, as shown in Figure 2a. According to established literature, the R_{Ti} of the pseudobrookite solid solution under air is approximately 0.33 (Das, 2002; Panda and Jung, 2020; Ilatovskaia, Savinykh and Fabrichnaya, 2017). The highest log P_{O_2} used in this study was -7.97, which was achieved by mixing CO and CO_2 gases in a 4:1 ratio. At this P_{O_2}, the known stoichiometry of Al_2TiO_5 (R_{Ti} = 0.33) was no longer valid. The R_{Ti} of the pseudobrookite solid solution was higher than 0.33. 0.37 and 0.44 when in equilibrium with corundum and rutile, respectively. Therefore, it is confirmed that Al_2TiO_5 is not a stoichiometric compound, and decreasing P_{O_2} increases the R_{Ti} of the pseudobrookite solid solution. At a log P_{O_2} of -12.67 (achieved by mixing CO and Ar-1 per cent CO_2 gases at a 9:1 ratio), it was observed that the pseudobrookite solid solution remained stable over a wider R_{Ti} range from 0.64 to 0.91, as confirmed by EPMA. Even under the lowest P_{O_2} atmosphere in C(s)-CO(g) equilibrium conditions, the stability of pseudobrookite was confirmed through XRD analysis, as shown in Figure 3. Consequently, this study considers the sample at the C(s)-CO(g) equilibrium to consist of the corundum solid solution and the pseudobrookite solid solution.

In contrast to the experiment conducted at 1600°C where the pseudobrookite solid solution was miscible over the composition range, the experiment at 1500°C revealed that the pseudobrookite separated into two phases, yielding a miscibility gap. As shown in Figure 2b, one pseudobrookite solid solution with R_{Ti} = 0.60–0.68 and another with $R_{Ti} \approx 0.95$ were observed. In Figure 4a, two different phases were shown but their crystal structures were those of pseudobrookite as shown in Figure 4b. This leads to the conclusion that the pseudobrookite solid solution exhibits a miscibility

gap at 1500°C. The present experimental data measured at 1400°C and 1300°C under reducing atmosphere were shown in Figure 2c and d, respectively. It is likely that the miscibility gap persists at the low temperature. This would result in the formation of Al-rich pseudobrookite solid solution (close to Al_2TiO_5) and Ti-rich pseudobrookite solid solution (close to Ti_3O_5).

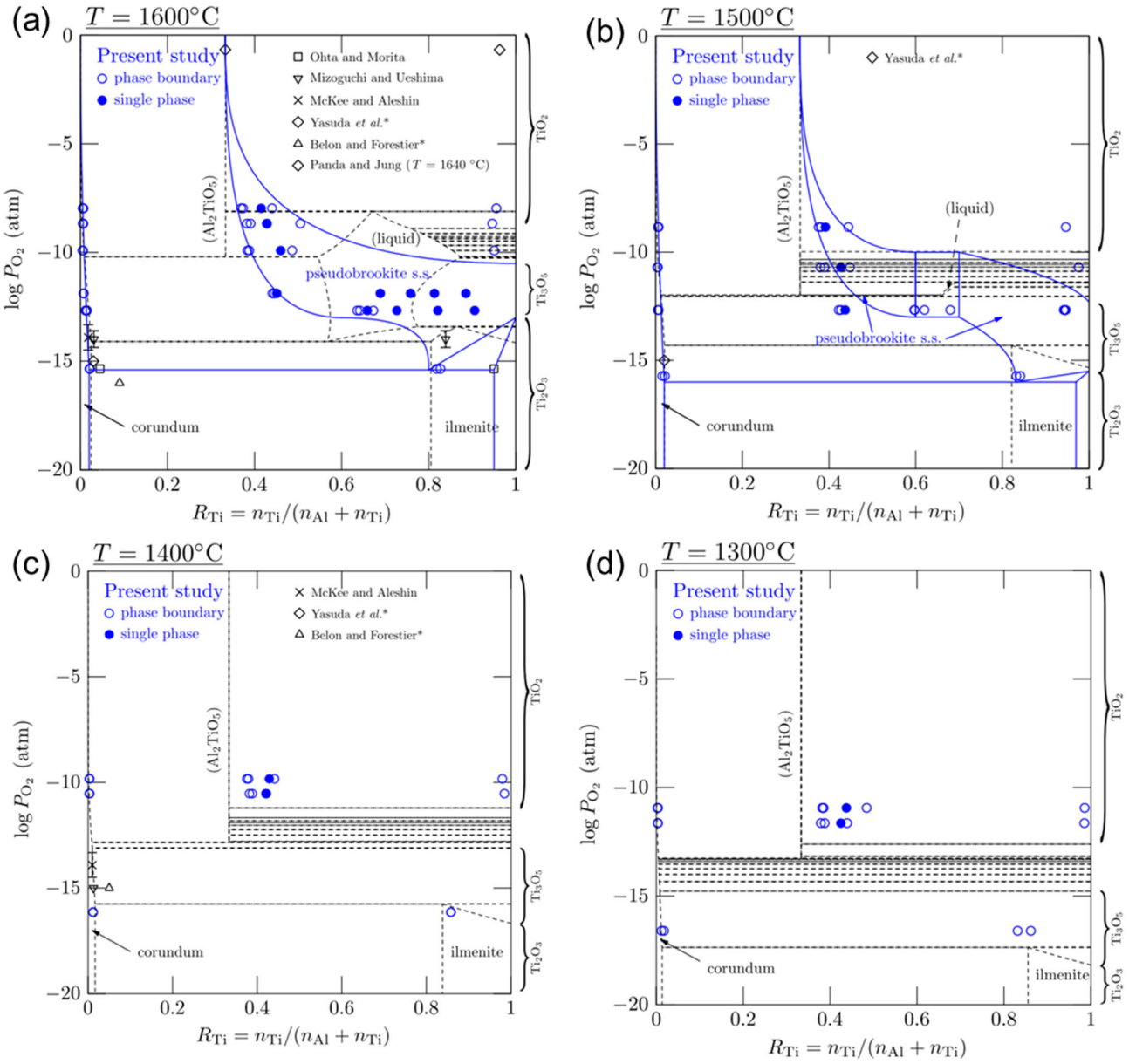

FIG 2 – Type II phase diagrams (R_{Ti} versus log P_{O_2}) of the Al_2O_3–TiO_x system at (a) 1600°C, (b) 1500°C, (c) 1400°C and (d) 1300°C (the figures were taken from Park, Kim and Kang (2021). The present experimental data are marked by open circles and closed circles in blue colour. Blue lines are to guide eye. Dashed lines are the calculated phase diagram using the FactSage FTOxid database (ver 8.0).

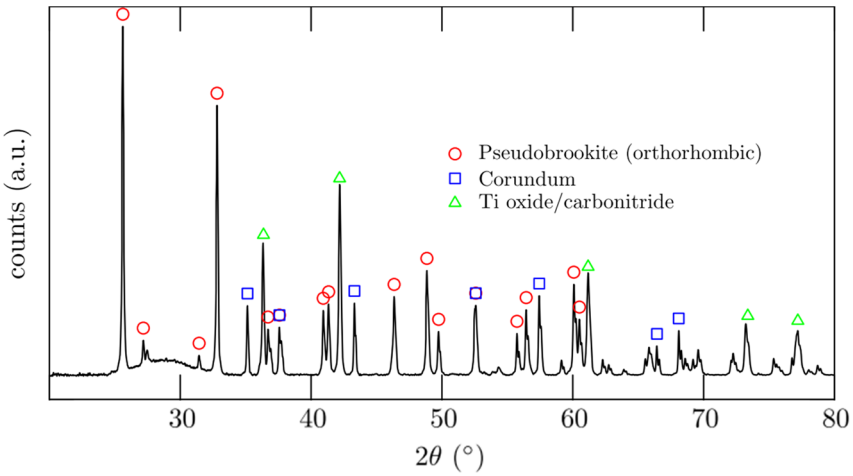

FIG 3 – XRD result for the sample equilibrated at 1600°C under C(s)-CO(g) equilibrium condition (the figure was taken from Park, Kim and Kang (2021)).

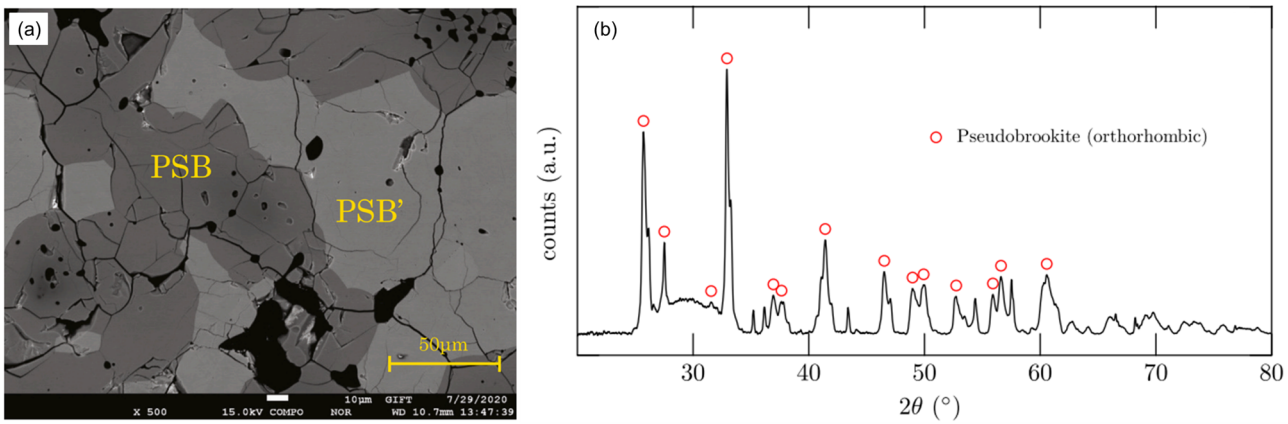

FIG 4 – (a) Microstructure of immiscible pseudobrookite oxide phase; and (b) its XRD results for the samples equilibrated at 1500°C under P_{H_2}/P_{CO_2} = 90 gas condition (the figures were taken from Park, Kim and Kang (2021)).

DISCUSSIONS

Stability of pseudobrookite oxide

Reaction 1 shows that a decrease in P_{O_2} results in an increase in R_{Ti} within the pseudobrookite solid solution. This shift moves the stable region towards the Ti-rich oxide side, indicating the reduction of Ti^{4+} to Ti^{3+} within the pseudobrookite solid solution. The present study shows that under reduced P_{O_2} conditions, Al_2TiO_5 (a pseudobrookite solid solution with R_{Ti} = 0.33) decomposes into corundum solid solution (Al_2O_3 with low Ti_2O_3 solubility) and a pseudobrookite solid solution with higher R_{Ti}. In an air atmosphere, the pseudobrookite solid solution is virtually Ti^{4+}, forming the stoichiometric compound $(Al^{3+})_2\{Ti^{4+}\}_1[O^{2-}]_5$. Therefore, decreasing P_{O_2} results in higher R_{Ti} in the pseudobrookite solid solution, which leads to the rejection of Al^{3+} from the pseudobrookite solid solution, forming Al_2O_3. The experimental results confirmed the validity of Reaction 1, demonstrating the progression from z = 1 (Al_2TiO_5) to z = 0 (Ti_3O_5).

However, the reduction in P_{O_2} did not exclude Ti oxide from the pseudobrookite solid solution. This can be proven as follows: if the excluded titanium oxide is $(Ti^{3+})_2(O^{2-})_3$, the subsequent decomposition reaction can be expressed upon decreasing P_{O_2}:

$$(Al^{3+})_2\{Ti^{4+}\}_1[O^{2-}]_5 = \alpha(Al^{3+}_{1-x}Ti^{4+}_x)_2\{Ti^{4+}_{1-y}Al^{3+}_y\}_1[O^{2-}]_5 + \beta Ti^{3+}_2O_3 + \gamma O_2 \quad (2)$$

where the reduced Ti^{3+} leaves out of the pseudobrookite solid solution while Al^{3+} enters both in first and second sub-lattice sites in the pseudobrookite solid solution. Considering mass balance of Al, Ti, and O gives the following relations 3 to 5:

$$2 = \alpha(2(1-x)+y) \ \ldots \text{(For Al mass balance)} \quad (3)$$

$$1 = \alpha\big(2x+(1-y)\big)+2\beta \ \ldots \text{(For Ti mass balance)} \quad (4)$$

$$5 = 5\alpha+3\beta+2\gamma \ \ldots \text{(For O mass balance)} \quad (5)$$

Solving the above equations revealed that β = 0 and γ = 0, indicating that Reaction 2 does not occur. Therefore, reducing the oxygen partial pressure (P_{O_2}) of the pseudobrookite solid solution while excluding Ti_2O_3 is not feasible. Instead, the pseudobrookite solid solution consistently transforms into a Ti-rich oxide solid solution by excluding Al_2O_3.

Al-Ti complex oxide inclusion in Ti-added ULC steel

The properties of the Al-Ti pseudobrookite solid solution in the Al_2O_3-TiO_x oxide system investigated in this study may provide insights into the evolution behaviour of Al-Ti complex oxides during the Ti-added ULC steelmaking process. The oxygen content in the molten steel during this process typically ranges from a few tens of ppm [O]. However, reoxidation can occur due to various reasons, such as the presence of high oxygen potential FeO-containing slag, tundish open eye, and CO gas from MgO-C refractory. This leads to a rapid increase in the oxygen potential (aO) of the molten steel, causing a transformation of stable Al_2O_3 inclusions into another phase.

This phenomenon can be schematically explained using the phase diagram measured in the present study. Figure 5 illustrates a schematic phase diagram of the Al_2O_3-TiO_x system at 1600°C, based on Figure 2a. The solubility of Ti oxide in corundum solid solution decreases as P_{O_2} increases, and the stable region of the pseudobrookite solid solution shifts toward the Ti oxide-rich side as P_{O_2} decreases. The corresponding [per cent O] at each P_{O_2} were calculated using FactSage FSStel database, assuming [per cent Al] and [per cent Ti] to be 0.03, which are typical values for Ti-ULC steel as shown in Figure 5b. If the corundum inclusion (initially marked by the filled triangle) is exposed to a reoxidation atmosphere, the solubility of Ti in the corundum solid solution would decrease, causing the rejected Ti to form a certain amount of pseudobrookite solid solution with R_{Ti} somewhat higher than 0.33. The mixture of corundum solid solution (Al-rich inclusion) and pseudobrookite solid solution (Al-Ti inclusion) results in a complex inclusion. This mixture is then re-entrapped in the low P_{O_2} liquid steel, causing the pseudobrookite solid solution to undergo a reaction similar to Reaction 1. As a result, additional Al_2O_3 inclusion (marked by the open circle) and excess oxygen are formed. The latter can serve as a source for additional inclusion information in the steel, in addition to the pseudobrookite inclusion (marked by an open square).

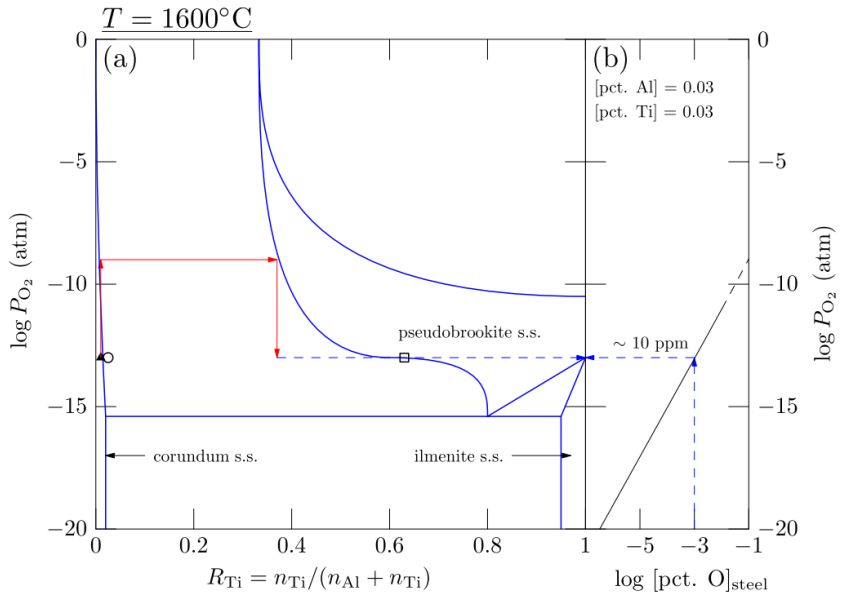

FIG 5 – (a) Estimated phase diagram of Al_2O_3-TiO_x system at 1600°C schematically drawn using the experimental data obtained in the present study (Figure 4); and (b) calculated equilibrium O content in liquid steel containing 0.03 per cent. Al and 0.03 per cent. Ti (the figures were taken from Park, Kim and Kang (2021)).

CONCLUSIONS

The phase equilibria of the Al_2O_3-TiO_x system were experimentally investigated in the temperature range from 1300 to 1600°C under reducing condition. The present study focused on the stability of the pseudobrookite solid solution, which is of practical importance both in ceramic materials development and non-metallic inclusions in steel. The observed phases included corundum s.s. (Al_2O_3 with limited Ti_2O_3 solubility), rutile s.s. (TiO_2), and pseudobrookite s.s. (Al_2TiO_5–Ti_3O_5). Al_2TiO_5 pseudobrookite is stable as a stoichiometric compound in air, but becomes non-stoichiometric at lower P_{O_2}, forming a wide range of pseudobrookite s.s. with Ti_3O_5. A miscibility gap appears at 1500°C in the pseudobrookite s.s. The change in pseudobrookite s.s. with varying P_{O_2} was discussed to understand Al_2TiO_5 instability under reducing conditions and oxide inclusion evolution in Ti-ULC steel. Non-metallic inclusions in Ti-ULC steel are prone to reoxidation, leading to a shift from the corundum phase to the pseudobrookite phase, potentially generating additional inclusions in liquid steel.

ACKNOWLEDGEMENTS

This investigation was carried out under the Steel Science Program, financially supported by POSCO, Rep. of Korea.

REFERENCES

Aneziris, C G, Patrick, G, Kratschmer, T and Berek, H, 2010. Thermal Shock Behavior of Flame-Sprayed Free-Standing Coatings Based on Al_2O_3 with TiO_2- and ZrO_2-Additions, *International Journal of Applied Ceramic Technology*, 8(4):953–964. https://doi.org/10.1111/j.1744-7402.2010.02535.x

Bale, C W, Bélisle, E, Chartrand, P, Decterov, S A, Eriksson, G, Hack, K, Jung, I-H, Kang, Y-B, Melançon, J, Pelton, A D, Robelin, C and Petersen, S, 2009. FactSage thermochemical software and databases — recent developments, *CALPHAD*, 33(2):295–311. https://doi.org/10.1016/j.calphad.2008.09.009

Bale, C W, Bélisle, E, Chartrand, P, Decterov, S A, Eriksson, G, Gheribi, A E, Hack, K, Jung, I-H, Kang, Y-B, Melançon, J, Pelton, A D, Petersen, S, Robelin, C, Sangster, J, Spencer, P and Van Ende, M-A, 2016. FactSage thermochemical software and databases, 2010–2016, *CALPHAD*, 54:35–53. https://doi.org/10.1016/j.calphad.2016.05.002

Das, S, 2002. The Al-O-Ti (Aluminum-oxygen-titanium) system, *Journal of Phase Equilibria*, 23(6):525–536. https://doi.org/10.1361/105497102770331271

Fekete, J R, Strugala, D C and Yao, Z, 1992. Advanced sheet steels for automotive applications, *JOM,* 44(1):17–21. https://doi.org/10.1007/bf03222745

Fruhstorfer, J, Dudczig, S, Gehre, P, Schmidt, G, Brachhold, N, Schöttler, L and Aneziris, C G, 2016. Corrosion of carbon free and bonded refractories for application in steel ingot casting, *Steel Research International*, 87(8):1014–1023. https://doi.org/10.1002/srin.201600023

Gehre, P, Aneziris, C G, Klinger, M, Schreiner, M and Neuroth, M, 2015. Influence of TiO_2-and ZrO_2-addition on the interaction of alumina castable with molten coal and gasifier slag, *Fuel*, 150:252–260. https://doi.org/10.1016/j.fuel.2015.02.024

Gugel, E, 1984. Ceramic materials for engine construction, Keram, Z, (Germany, Federal Republic of), 36:477–479.

Heinrich, H, Langer, M and Siebels, J E, 1988. Experimental results with Ceramic Components in passenger-car diesel engines, *Materialwissenschaft Und Werkstofftechnik*, 19(1):23–27. https://doi.org/10.1002/mawe.19880190104

Horibe, T and Kuwabara, S, 1964. Preliminary investigation of phase equilibriums in Al_2O_3–Ti_2O_3 system, *Kogyo Kagaku Zasshi*, 67:276–281.

Ilatovskaia, M, Savinykh, G and Fabrichnaya, O, 2016. Thermodynamic description of the Ti-Al-O system based on experimental data, *Journal of Phase Equilibria and Diffusion*, 38(3):175–184. https://doi.org/10.1007/s11669-016-0509-4

Kang, Y and Lee, J-H, 2017. Reassessment of oxide stability diagram in the Fe–Al–Ti–O system, *ISIJ International*, 57(9):1665–1667. https://doi.org/10.2355/isijinternational.isijint-2017-182

Mao, X, 2019. *Titanium Microalloyed Steel: Fundamentals, Technology and Products* (Metallurgical Industry Press: Beijing).

Matsuura, H and Tsukihashi, F, 2012. Compositional and morphological control of non-metallic inclusions in Fe–Al–Ti alloy, in *Proceedings of Clean Steel in the Future – Prof Hae-Geon Lee Symposium*, pp 14–26 (Korean Inst Met Mater).

McKee, W D and Aleshin, E, 1963. Aluminum Oxide-Titanium Oxide Solid Solution, *Journal of the American Ceramic Society*, 46(1):54–58. https://doi.org/10.1111/j.1151-2916.1963.tb13771.x

Panda, S K and Jung, I, 2020. Coupled Experimental Study and Thermodynamic Modeling of the Al_2O_3–Ti_2O_3-TiO_2 System, *ISIJ International*, 60(1):31–41. https://doi.org/10.2355/isijinternational.isijint-2019-006

Park, Y-J, Kim, W-Y and Kang, Y-B, 2021. Phase equilibria of Al_2O_3–TiO_x system under various oxygen partial pressure: Emphasis on stability of Al_2TiO_5–Ti_3O_5 pseudobrookite solid solution, *Journal of the European Ceramic Society*, 41(14):7362–7374. https://doi.org/10.1016/j.jeurceramsoc.2021.06.052

Seifert, H J and Aldinger, F, 1996. Applied Phase Studies / Angewandte Konstitution, *International Journal of Materials Research*, 87(11):841–853. https://doi.org/10.1515/ijmr-1996-871106

Wright, R E, 1972. Acoustic emission of aluminum titanate, *Journal of the American Ceramic Society*, 55(1):54. https://doi.org/10.1111/j.1151-2916.1972.tb13401.x

Yasuda, A, Aoki, J and Sakuma, T, 1998. Nano precipitation in Al_2O_3–3mol% Ti_2O_3 due to oxidation, *Ceramics International*, 24(7):483–487. https://doi.org/10.1016/s0272-8842(97)00037-0

Boron removal through multistage refining treatment using $CaO-SiO_2-Al_2O_3$ slag

DOI: 10.62053/FMNT9284

A D P Putera[1], K L Avarmaa[2], H T B M Petrus[3], G A Brooks[4] and M A Rhamdhani[5]

1. PhD Student, Swinburne University of Technology, Hawthorn Vic 3122.
   Email: aputera@swin.edu.au
2. Postdoctoral Researcher, Swinburne University of Technology, Hawthorn Vic 3122.
   Email: kavarmaa@swin.edu.au
3. Professor, Universitas Gadjah Mada, Yogyakarta 55281, Indonesia.
   Email: bayupetrus@ugm.ac.id
4. Professor, Swinburne University of Technology, Hawthorn Vic 3122.
   Email: gbrooks@swin.edu.au
5. Professor, Swinburne University of Technology, Hawthorn Vic 3122.
   Email: arhamdhani@swin.edu.au

ABSTRACT

Multistage slag treatment was carried out to investigate boron removal from metallurgical grade silicon. Boron is known to be one of the most difficult elements to remove from silicon. Depending on boron initial concentration, boron can be removed from silicon into certain level; most previous studies have attained final 50–100 ppmw (parts per million weight) boron in the silicon using slag treatment. The term 'multistage' refers to a process where the resulting silicon from the initial slag treatment is further refined multiple times using a new slag. In this study, an initial slag composition of $45CaO-45SiO_2-10Al_2O_3$ (wt per cent) was utilised. Using this technique, boron level in the silicon was expected to be gradually lowered because the new slag will always have more capacity to reach the equilibrium distribution coefficient ($L_B = (ppmwB)_{slag}/(ppmwB)_{Si}$). The current study was carried out through combined thermodynamic calculations (using FactSage™ ver 8.2, by Thermfact Ltd, thermochemical package) and high-temperature experimentation. The thermodynamic calculations were carried out for reactions at 1500, 1550, and 1600°C for three different scenarios:

1. Single stage refining with varied slag to Si ratio.
2. Multistage refining with slag to Si ratio of 1:1.
3. Multistage refining with slag to Si ratio of 2:1.

The multistage experimental work was carried out at 1550°C under inert gas atmosphere each time for 2 hrs, with slag to Si ratio of 2:1. The simulation results indicate that the boron distribution coefficient stay essentially constant with varying slag to Si ratio and temperature, around 1.8 to 2, and the experimental results measured L_B in the same range, between 1.5 and 2.5. By harnessing this feature, the simulation showed that boron can be removed by approximately 78 per cent in each stage. The experimental result confirmed that the boron concentration in the silicon was reduced by a total of 97.8 per cent from its initial value using four stages of slag treatment, from initial 270 ppmw down to 6 ppmw.

INTRODUCTION

Boron is one of the most difficult elements to remove from silicon (Chen *et al*, 2019; Hou *et al*, 2019; White, 2013). The element has a high segregation coefficient, meaning that it tends to concentrate in the solid phase during solidification. It also has a low vapor pressure, making it difficult to remove by evaporation. In addition, boron is chemically stable and does not form volatile compounds with common refining agents such as chlorine and oxygen (Betharia, 2014).

The difficulty of boron removal is a major challenge for the production of high-purity silicon by the semiconductor industry. Boron is used as a dopant to control the electrical conductivity of silicon (Betekbaev *et al*, 2016; Hwang *et al*, 2014), but even small distortion in boron concentration in the silicon wafer have a significant impact on the performance of the semiconductor device. Metallurgical grade silicon (MG-Si) has the boron concentration of approximately 80 ppmw (parts per million weight; Yang, 2019). Whereas, solar grade silicon (SOG-Si), the raw materials for silicon PV cell production, should have boron concentration below 0.38 ppmw (Karabanov *et al*, 2019).

There are a number of methods that have been developed for boron removal from silicon, specifically slag treatment. In the slag treatment processes, the extent of boron removal relies on the thermodynamic equilibrium between slag and silicon phase, which is represented as the boron distribution coefficient (L_B) (White, 2020, 2013). Boron distribution coefficient is affected by the basicity and composition of the slag which is reported to be as high as 2.1 for basic slag (40CaO-40SiO_2-20K_2CO_3, wt per cent) (Yang, 2019). The L_B can be described as:

$$L_B = \frac{(B)}{[B]} \quad (1)$$

where (B) and [B] are the boron concentrations in the slag and silicon phase in ppmw, respectively.

There are several studies of boron removal from silicon using slag treatment with majority of the results showing that the refined silicon still has considerably high concentration of boron. The summary of the previous relevant studies is given in Table 1. Krystad, Tang and Tranell (2012) refined silicon with the initial boron concentrations of 260–280 ppmw at 1600°C using SiO_2-CaO and SiO_2-CaO-MgO slags. The results show that the boron concentration in the silicon started to stabilise after 4000 secs at 50–80 ppmw. Nishimoto *et al* (2012) studied boron removal from silicon (318 ppmw) using 55CaO-45SiO_2 (wt per cent) at 1550°C and slag to silicon ratio of 1.25–2.5 and found that the boron concentration stabilised at 85–110 ppmw after approximately 4000 secs. Islam and Rhamdhani (2018) studied similar process with various slag compositions (CaO-SiO_2 with 0; 9.59; and 15.9 wt per cent Al_2O_3), various slag to silicon ratios (1.5 to 2.5, w/w), and temperatures (1500–1600°C) and found similar final boron concentrations in the silicon at 110–120 ppmw from the initially 370 ppmw boron in the silicon.

TABLE 1

Summary of initial and final boron concentrations in the silicon during slag treatment under various working conditions. *Approximated value by visual inspection.

Author	Slag system, wt%	Temp, °C	Slag to Si ratio, w/w	Initial [B], ppmw	Final [B], ppmw
Krystad, Tang and Tranell (2012)	50CaO-50SiO_2	1600	1	260*	75*
	50CaO-50SiO_2	1600	2	260*	49*
	40CaO-40SiO_2-20MgO	1600	2	260*	50*
	35CaO-65SiO_2	1650	1	280*	80*
Nishimoto *et al* (2012)	55CaO-45SiO_2	1550	1.25	318	85.1
	55CaO-45SiO_2	1550	1.33	318	118
	55CaO-45SiO_2	1550	2.5	318	100
Islam and Rhamdhani (2018)	49CaO-41SiO_2-9.6Al_2O_3	1500	2.5	370	130*
	49CaO-41SiO_2-9.6Al_2O_3	1550	2.5	370	120*
	49CaO-41SiO_2-9.6Al_2O_3	1600	2.5	370	100*
	46CaO-38SiO_2-15.9Al_2O_3	1500	2.5	370	110*
	46CaO-38SiO_2-15.9Al_2O_3	1550	2.5	370	120*
	46CaO-38SiO_2-15.9Al_2O_3	1600	2.5	370	125*
Wu *et al* (2016)	37.5CaO-37.5SiO_2-25K_2CO_3	1550	1	22	2.6
	40CaO-40SiO_2-20K_2CO_3	1550	1	22	1.8
	42.5CaO-42.5SiO_2-15K_2CO_3	1550	1	22	2.7
	45CaO-45SiO_2-10K_2CO_3	1550	1	22	3.8
	47.5CaO-47.5SiO_2-5K_2CO_3	1550	1	22	4.1
Fang *et al* (2014)	67Na_2O-33SiO_2	1700	0.5	10.6	1.8*
	67Na_2O-33SiO_2	1700	1	10.6	0.62*
	67Na_2O-33SiO_2	1700	1.5	10.6	0.4*
	67Na_2O-33SiO_2	1700	2	10.6	0.38*
	67Na_2O-33SiO_2	1700	2.5	10.6	0.36*

A work by Wu *et al* (2016) stated that the efficiency of boron removal using slag treatment can reach 90 per cent, with a final boron concentration in the silicon of 1.8 ppmw using 40CaO-40SiO_2-20K_2CO_3 (wt per cent) slag at 1550°C for 3 hrs. However, the initial boron concentration in this study was only 18 ppmw (Wu *et al*, 2016). Another method to effectively lower boron concentration has been shown to occur by combining the slag treatment method with Ar-H_2-O_2 gas blowing. The result shows that boron removal reached 96.6 per cent at 0.5 ppmw. However, the initial boron concentrations in this study were very low at 2–3 ppmw (Wu *et al*, 2017).

Multiple slag treatment method was attempted by Fang *et al* (2014) to remove boron from silicon, using Na_2O-SiO_2 slag at 1550–1700°C. The study shows that multiple slag operation consistently reduced boron concentration in the silicon to very low levels, at around 0.2 ppmw. However, this study also used a low initial concentration of boron, at 10.6 ppmw. In this study, an effort to decrease the boron concentration in the silicon from considerably high concentrations (above 100 ppmw) to very low concentrations (around 1–10 ppmw), with the removal rate >90 per cent, was done using multiple stages of slag treatment. The method was studied through combined thermodynamic calculation using FactSage and experimental work.

METHODOLOGY

Thermodynamics assessment

Thermodynamic assessment was carried out using FactSage® 8.2 with the Equilib module. The module calculates the equilibrium state of a system in a specific working condition, such as temperature and pressure based on chosen database(s) by utilising Gibbs energy minimisation. The built-in databases used in this study are:

- FactPS, for pure substances.
- FTOxid, for oxides.
- FSupsi, for silicon alloy.

The boron concentration in the Si alloy was at 300 ppm and the slag component compositions were 0.45 wt per cent CaO, 0.45 wt per cent SiO_2, and 0.1 wt per cent Al_2O_3. The resulting melts were saved as new mixtures using ‘Save Stream’ feature in the FactSage. This feature was also used to save the silicon melt in each stage of the multi-stage slag treatment. In this current study, only solid and liquid states are included in the modelling. Therefore, no vaporisation (either from silicon or boron) occurred in the simulation results.

Raw materials preparation

The following raw materials for slag making were supplied by Sigma Aldrich (Merck KGaA, Darmstadt, Germany): calcium oxide (CaO) 99 wt per cent, silicon dioxide (SiO_2) 99.5 wt per cent, aluminium oxide (Al_2O_3) 99.5 wt per cent Master slags were prepared by melting mixed oxides with appropriate composition (45CaO-45SiO_2-10Al_2O_3, wt per cent) in an SX2-2-17TP muffle furnace. The oxides were previously mixed in a ball mill using cylinder container and ceramic balls; rotated at 60 rev/min for 60 mins. After mixing, the mixture was placed in a Pt crucible (of approximately 30 g each run) and melted in a muffle furnace at 1550°C for 30 mins before casting on a steel mould. The casting process is shown in Figure 1.

The master silicon alloy materials were made from 99.99 wt per cent silicon from Sigma Aldrich and crystalline boron powder 99 wt per cent from Alfa Aesar (Thermo Fisher Scientific Inc. Australia Pty Ltd). The method to make the master silicon alloy (containing 300 ppmw boron) in presented in the previous work (Islam and Rhamdhani, 2018). Both master slag and master silicon were analysed using ICP-AES to confirm the compositions.



FIG 1 – Slag casting process.

Slag treatment experiment

The furnace configuration is shown in Figure 2. The sample included initially 7.2 g of Si-B master alloy and 14.3 g of master slag in an alumina crucible. The crucible was placed inside a sacrificial crucible that was attached to alumina pedestal. Initially, the sample was placed in the cold zone inside the vertical tube furnace and then, the furnace was sealed. Argon gas with a flow rate of 200 mL/min was flushed into the furnace for 15 mins to ensure an inert atmosphere. Gas bubbling was regularly checked to ensure the furnace was completely sealed. After 15 mins of stabilising the gas atmosphere, the pedestal-crucible set-up was inserted into the hot zone. It took approximately 1 min to insert the pedestal into the hot zone and re-seal the system gas tight. The samples were reacted for 120 mins under Argon gas after which they were lowered to the cold zone, for sample quenching, to stop the reactions. In this process, it took approximately 20 to 30 secs to move the pedestal to the cold zone.

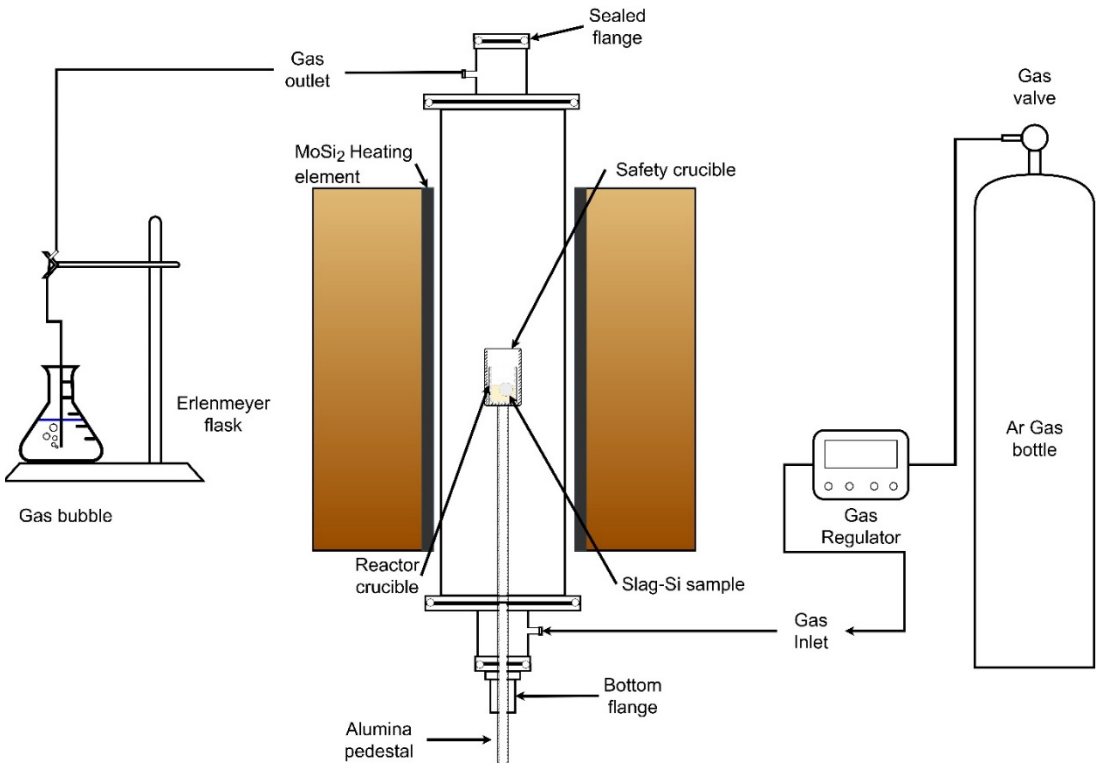

FIG 2 – Schematic diagram of the vertical tube furnace set-up for slag treatment experiment.

After approximately 60 mins, the bottom flange and the sample were removed from the furnace. The sample was crushed, and a small amount (approximately 1 g) of the silicon phase was taken to analyse by inductively coupled plasma atomic emission spectroscopy (ICP-AES). It is important to

note that ICP-AES is a destructive analysis, which means that the analysed sample cannot be used again in the next batch. In addition, a small portion of silicon was expected to be vaporised during the slag treatment (Fang *et al*, 2014). Therefore, in the second batch, approximately 5 g of silicon was reacted with 10 g of new slag with the same composition (the slag to Si ratio was kept at 2:1, w/w). The approach is depicted in Figure 3 and the multi-stage slag treatment was carried in four stages in this study. A complete record of measured weights after each stage is provided in Table 2.

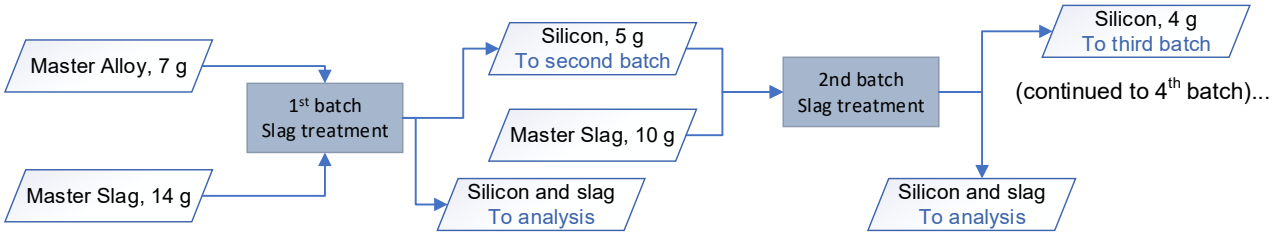

FIG 3 – Flow diagram for multi-stage slag treatment.

TABLE 2

Weight measurements of silicon and slag after each stage.

Stage	Silicon, g	Slag, g
1	7.1667	14.3285
2	5.2020	10.4815
3	3.0813	6.1589
4	1.2851	2.6200

Analysis

Master silicon, master slag, and the slag from 1st to 4th stage of the experiment were crushed, and a fraction of the sample was taken for ICP-AES analyses conducted at Spectrometer Services PTY. Ltd., Melbourne, Australia. Analysis preparation such as sample comminution, dilution, and standardisation were carried out at the company.

The multi-stage slag treatment samples were additionally analysed by laser ablation inductively coupled plasma spectrometer (LA-ICP-MS) at the Research School of Earth Sciences, Australian National University. Samples were mounted in epoxy resin and prepared by traditional wet metallographic techniques for microanalyses. The details on the equipment, analysis procedure and settings can be found in the other study (Avarmaa *et al*, 2024).

RESULT

Thermodynamic calculations

The thermodynamic calculations in this study are divided into two scenarios: (1) the single-stage process; and (2) multi-stage process. Figure 4 shows the boron distribution coefficient (L_B) of a single-stage slag treatment at temperatures from 1500 to 1600°C and slag to Si ratio from 1 to 20 (w/w). The line plot shows the boron distribution coefficient ranged between 1.84 to 1.96 for the observed temperatures. Slag to Si ratio had only marginal influence on the L_B and temperature influence was rather small as well.

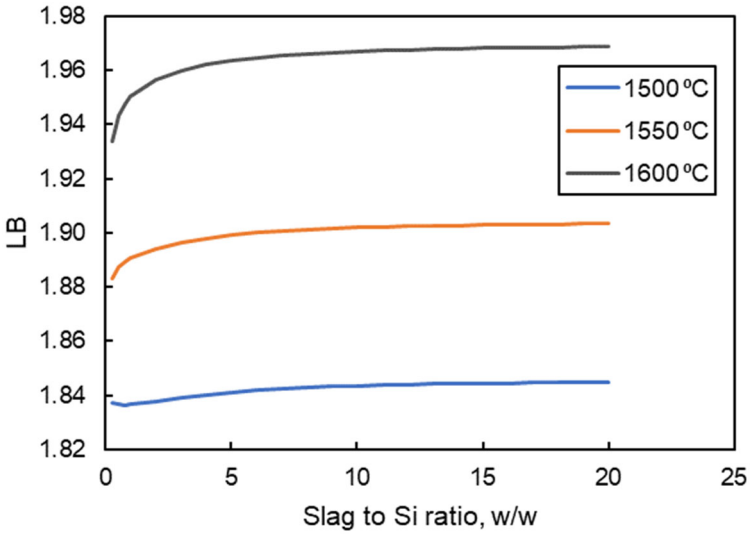

FIG 4 – Boron distribution coefficient of single-stage slag treatment at various temperatures and slag to Si ratios.

In terms of boron concentration in the silicon, [B], the result shows that it does not vary significantly between the different temperatures, although higher temperature generally yielded lower [B]. In addition, the result shows that the boron concentration decreased less significantly beyond slag to Si ratio of 5 (w/w). Boron concentration reached approximately 10 ppmw at slag to Si ratio of 20 (w/w). Boron concentration in the silicon for single-stage slag treatment at various temperatures and slag to Si ratios is presented in Figure 5.

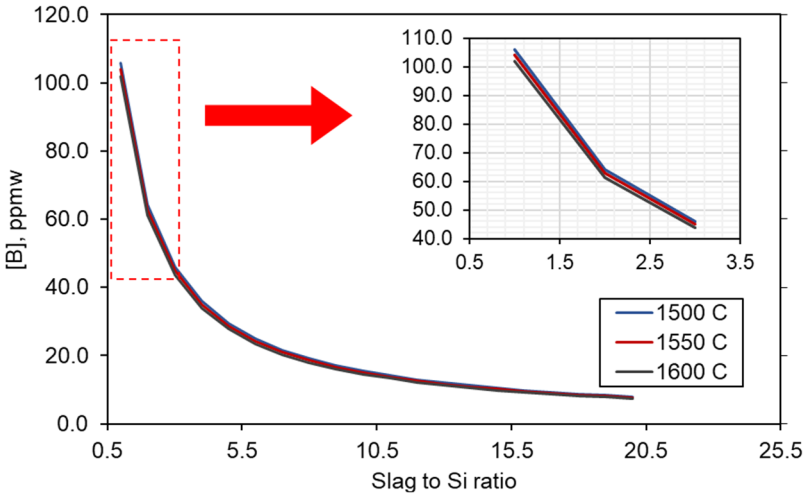

FIG 5 – Boron concentration in silicon after single-stage slag treatment at various slag to Si ratios at 1500–1600°C.

The multi-stage simulation was carried out using two different slag to Si ratios, ie 2 and 1 (w/w) at 1550°C. The results of the boron concentration for each different scenario are presented in Figure 6. The Y-axis in this figure represents boron concentration in the silicon as ppmw and the X-axis represents the amount of slag consumed (g) for each gram of silicon, in order to compare effectiveness of a single and multi-stage slag treatments. The results show that the multi-stage process can significantly lower the boron concentration in the silicon compared to the single-stage slag treatment. For slag to Si ratio of 2 (w/w), four stages of slag treatment can already yield boron concentration in the silicon of 0.63 ppmw, or approximately 78 per cent reduction in each stage. At the fourth stage, the slag to Si consumed is equal to 8 (w/w) in the single-stage process. However, in the single-batch process, boron concentration in the silicon was at 19.06 ppmw, which is very high compared to the multistage result.

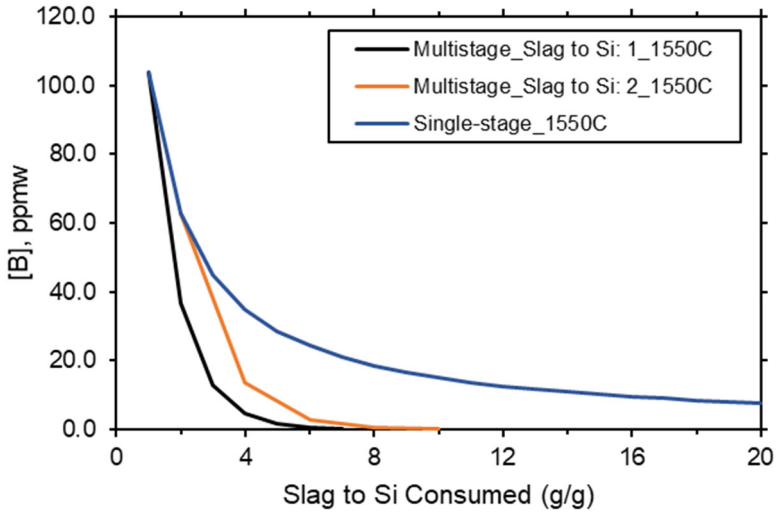

FIG 6 – Boron concentration in silicon after slag treatment for single-stage (blue), multi-stage with slag to Si ratio = 2:1 (orange), and multi-stage with slag to Si ratio = 1:1 (black) at 1550°C.

For slag to Si ratio of 1 (w/w), similar boron concentration was reached after six stages, or at six slag to Si consumed (w/w). Although one can achieve better boron removal using smaller slag to Si ratio in the multistage slag treatment, this scenario might have some issues in the applicability as numerous stages of slag treatment is also not favourable and a lot of slag would be produced. However, the result of this simulation generally demonstrates that multiple stage slag treatment is more effective to lower boron concentrations than a single-stage slag treatment.

Experimental result and discussion

Physical appearance

Silicon and slag exist as two immiscible melts in the crucible. In this case, silicon has lower density than the used slag, therefore, silicon floats as a droplet above-inside the slag melt. After cooling, the crucible was shattered using a hammer, and some parts of the sample detached from the crucible were preserved for further experiment and analysis. Due to evaporation, the weight of the sample always reduced in each stage, as shown in Table 2.

On one hand, slag samples can be used in a destructive analysis, such as the ICP-AES because it is not used multiple times. On the other hand, silicon is not as flexible as the slag sample. The physical appearance of the shattered sample is provided in Figure 7 and the prepared sample for LA-ICP-MS is provided in Figure 8.



FIG 7 – Silicon-slag sample after 1st stage of slag treatment at 1550°C for 2 hrs. A big portion of the silicon was taken for 2nd stage of slag treatment.

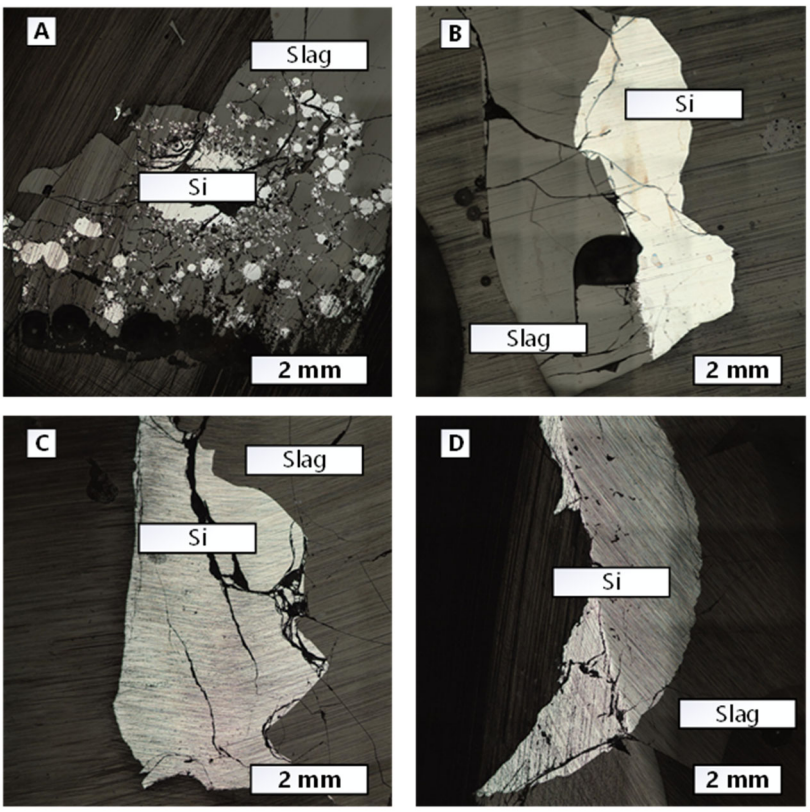

FIG 8 – Optical microscope images of silicon and slag samples from multistage slag treatment. (A) 1st stage, (B) 2nd stage, (C) 3rd stage, and (D) 4th stage.

Concentration results

The minor elements including boron, aluminium, calcium, and iron were measured by the LA-ICP-MS, whereas the major oxide concentrations were analysed by the ICP-AES. The results show that the boron concentration in the initial master silicon was 270 ppmw. This master silicon also contained traces of aluminium (810 ppmw) that primary have dissolved from the alumina crucible during the master alloy making and iron (930 ppmw) that may come from the comminution process or as an impurity from the chemicals used.

The boron concentration in the silicon from 1st to 4th stage were measured as 61.4; 12.0; 6.5; and 6.0 ppmw, respectively, showing a clear decrease of boron in the silicon alloy. In total, boron was successfully removed by approximately 97.8 per cent from the silicon alloy. The results indicate that the multistage slag treatment was successful to remove boron from the silicon more effectively than the previous works using a single slag treatment. Previous study of a single stage slag treatment with similar slag composition, temperature and initial boron concentration reached approximately 110–120 ppmw of boron concentration in the silicon (Islam and Rhamdhani, 2018).

However, the decrease of the boron concentration in the silicon was less significant in the latter stages, which may be caused by contamination from the furnace or evaporation of both silicon and slag phases. Also, boron can be considered to vaporise from the system, as especially in the first two stages, its concentration decreased in both phases in much higher extent than initial concentration of B would predict. This occurs, even though, clearly alumina dissolved to the slag from the crucible and more slag mass/volume is expected to exist after the melting indicating to lower B, see slag results in Table 3. Figure 9 presents the boron removal from silicon and boron behaviour in the Si-slag system by the multi-stage treatment. The result show that the boron distribution coefficient is rather constant, between 1.4 and 2.4 which indicates that the boon concentration in both phases is at equilibrium (or close to equilibrium) at each stage. The achieved L_B results from the experiments also fit with the simulation results.

TABLE 3

ICP-AES and LA-ICP-MS analysis result of the multistage experiments.

Sample	B, ppmw	Al, ppmw	Ca, ppmw	Fe, ppmw	SiO_2, %	CaO, %	Al_2O_3, %
Master Si	270	810	<20	930			
Si-1st stage	61.4	143.1	68.8	1563.5	-	-	-
Si-2nd stage	11.9	439.9	78.8	11.0	-	-	-
Si-3rd stage	6.5	4664.8	254.7	233.9	-	-	-
Si-4th stage	6.0	421.6	64.3	117.2	-	-	-
Master slag	-	-	-	-	43.9	47.6	8.34
Slag-1st stage	89.0	-	-	104.5	45.8	37.1	16.0
Slag-2nd stage	30.9	-	-	110.6	46.5	33.9	18.5
Slag-3rd stage	13.7	-	-	97.2	52.1	28.7	23.0
Slag-4th stage	8.6	-	-	97.6	45.8	30.2	23.0

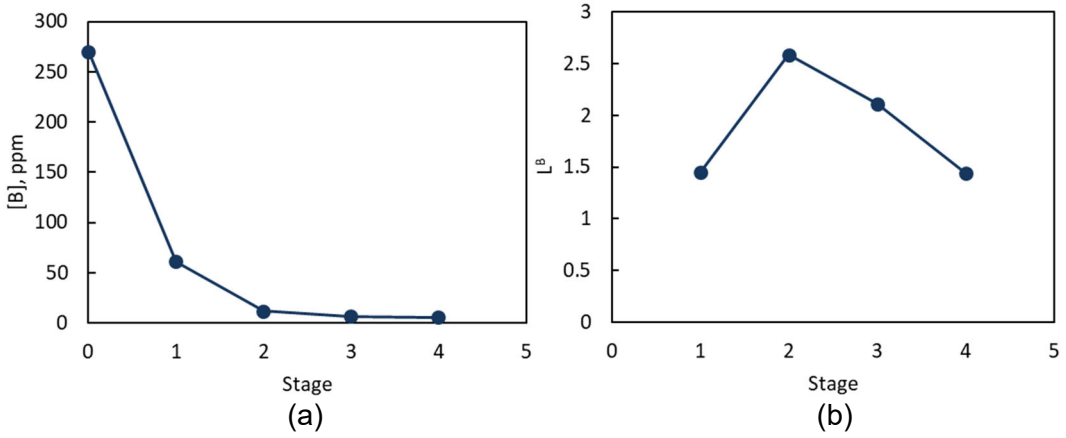

FIG 9 – Boron concentration in silicon (A) and boron distribution coefficient (B) in each stage of the multistage silicon slag treatment.

Other minor elements, such as aluminium and calcium appeared at higher concentrations in some of the silicon alloy samples, which may be caused by the reactions within the silicon-slag-crucible system. Iron also was measured at higher concentration in some stages, which may be caused by multiple comminution process. However, the fluctuating values of the mentioned minor elements show that the multistage slag treatment does not make any great impurity accumulation in the silicon sample.

CONCLUSIONS

Boron removal from silicon using multistage slag treatment was successfully simulated and experimentally investigated. Using the FactSage ® 8.2 (FactPS, FTOxid and FSupsi databases), it was demonstrated that the boron distribution coefficient is independent on slag to Si ratio. This feature was harnessed by applying multistage slag treatment process and the boron can be consistently reduced by approximately 78 per cent in each stage using slag to Si mass ratio of 2.

The laboratory experimentation was carried out by reacting master silicon (with 270 ppmw of boron) and $45SiO_2$-$45CaO$-$10Al_2O_3$ (wt per cent) slag at 1550°C and Ar gas atmosphere for 2 hrs. The experiment was carried out using slag to Si mass ratio of 2, in four stages by adding a new slag in each stage. Boron concentrations in the master silicon, 1st to 4th stage, can be reduced from 270 to 61.4; 12.0; 6.5 and 6.0 ppmw, respectively. The current study demonstrated that the multistage slag treatment can be utilised to gradually remove boron from silicon. Other minor element such as Al, Ca, and Fe contamination in the silicon showed no radical accumulation during the multiple slag treatment that was carried out.

ACKNOWLEDGEMENTS

The authors gratefully acknowledge financial SUPPORT from SUPRA (Swinburne University Postgraduate Research Award) scholarship; as well as from Australia Renewable Energy Agency (ARENA), Grant number 2020RND011. The authors are grateful to Dr. Jiang Chen on his help with the LA-ICP-MS analyses.

REFERENCES

Avarmaa, K, Putera, A, Chen, J, Brooks, G and Rhamdhani, M A, 2024. Distribution behaviour of B and P in Si-slag system at 1500°C, in *Proceedings of the 12th International Conference on Molten Slags, Fluxes and Salts (MOLTEN 2024)*, pp 301–312 (The Australasian Institute of Mining and Metallurgy: Melbourne).

Betekbaev, A A, Mukashev, B N, Pelissier, L, Lay, P, Fortin, G, Bounaas, L, Skakov, D M and Pavlov, A A, 2016. Doping optimization of solar grade (SOG) silicon ingots for increasing ingot yield and cell efficiency, *Modern Electronic Materials*, 2(3):61–65. https://doi.org/10.1016/j.moem.2016.10.002

Betharia, S, 2014. *Boron, Encyclopedia of Toxicology,* third edition, pp 536–539. https://doi.org/10.1016/B978-0-12-386454-3.00255-4

Chen, H, Morita, K, Ma, X, Chen, Z and Wang, Y, 2019. Boron removal for solar-grade silicon production by metallurgical route: a review, *Solar Energy Materials, Solar Cells*, 203:110169. https://doi.org/10.1016/j.solmat.2019.110169

Fang, M, Lu, C, Huang, L, Lai, H, Chen, J, Yang, X, Li, J, Ma, W, Xing, P and Luo, X, 2014. Multiple slag operation on boron removal from metallurgical-grade silicon using Na_2O-SiO_2 slags, *Industrial and Engineering Chemistry Research*, 53(30):12054–12062. https://doi.org/10.1021/ie404427c

Hou, Y, Wu, Y D, Zhang, G H and Chou, K C, 2019. Removal of boron from metallurgical grade silicon by CaO-SiO_2 based slags, *Metallurgical Research and Technology*, 116(4). https://doi.org/10.1051/metal/2019001

Hwang, S W, Park, G, Edwards, C, Corbin, E A, Kang, S K, Cheng, H, Song, J K, Kim, J H, Yu, S, Ng, J, Lee, J E, Kim, J, Yee, C, Bhaduri, B, Omennetto, F G, Huang, Y, Bashir, R, Goddard, L, Popescu, G, Kyung Mi, L and Rogers, J A, 2014. Dissolution chemistry and biocompatibility of single-crystalline silicon nanomembranes and associated materials for transient electronics, *ACS Nano*, 8(6):5843–5851. https://doi.org/10.1021/nn500847g

Islam, M S and Rhamdhani, M A, 2018. Kinetics Analysis of Boron Removal from Silicon through Reactions with CaO-SiO_2 and CaO-SiO_2-Al_2O_3 Slags, *Metallurgical and Materials Transactions B*: *Process Metallurgy and Materials Processing Science*, 49(6):3171–3185. https://doi.org/10.1007/s11663-018-1424-3

Karabanov, S M, Trubitsyn, A A, Suvorov, D V, Tarabrin, D Y, Belyakov, O A, Karabanov, A S, Slivkin, E V and Serebryakov, A E, 2019. Optimization of boron, phosphorus, carbon extraction from metallurgical-grade silicon, *AIP Conference Proceedings*, p 2147. https://doi.org/10.1063/1.5123880

Krystad, E, Tang, K and Tranell, G, 2012. The kinetics of boron transfer in slag refining of silicon, *JOM*, 64(8):968–972. https://doi.org/10.1007/s11837-012-0382-5

Nishimoto, H, Kang, Y, Yoshikawa, T and Morita, K, 2012. The rate of boron removal from molten silicon by CaO-SiO_2 slag and Cl_2 treatment, *High Temperature Materials and Processes*, 31(4–5):471–477. https://doi.org/10.1515/htmp-2012-0083

White, J F, 2013. Equilibrium and Kinetic Considerations in Refining of Silicon, KTH Royal Institute of Technology. Available from: <https://www.diva-portal.org/smash/get/diva2:662840/FULLTEXT02.pdf> [Accessed: 11/2023].

White, J, 2020. Fundamentals of Slag-Metal Reactions, Montana Tech. Available from: <https://digitalcommons.mtech.edu/public_lectures_mtech/169> [Accessed: 11/2023].

Wu, J, Wang, F, Ma, W, Lei, Y and Yang, B, 2016. Thermodynamics and Kinetics of Boron Removal from Metallurgical Grade Silicon by Addition of High Basic Potassium Carbonate to Calcium Silicate Slag, *Metallurgical and Materials Transactions B*: *Process Metallurgy and Materials Processing Science*, 47(3):1796–1803. https://doi.org/10.1007/s11663-016-0615-z

Wu, J, Zhou, Y, Ma, W, Xu, M and Yang, B, 2017. Synergistic Separation Behavior of Boron in Metallurgical Grade Silicon Using a Combined Slagging and Gas Blowing Refining Technique, *Metallurgical and Materials Transactions B*: *Process Metallurgy and Materials Processing Science*, 48(1):22–26. https://doi.org/10.1007/s11663-016-0860-1

Yang, D (ed), 2019. *Handbook of Photovoltaic Silicon* (Springer). https://doi.org/10.1007/978-3-662-56472-1

Activities of components in Ca_2SiO_4-$Ca_3P_2O_8$ solid solution at 1573 K

DOI: 10.62053/AOFK6956

K Saito[1] and M Hasegawa[2]

1. Graduate Student, Kyoto University, Kyoto, Japan, 606–8501.
   Email: saito.keijiro.x38@kyoto-u.jp
2. Associate Professor, Kyoto University, Kyoto, Japan, 606–8501.
   Email: hasegawa.masakatsu.7r@kyoto-u.ac.jp

ABSTRACT

In steelmaking processes, it is known that P_2O_5 in dephosphorisation slags often exists in solid solutions between Ca_2SiO_4 and $Ca_3P_2O_8$, $<C2S\text{-}C3P>_{SS}$, and thus the solid solutions play an important role in the dephosphorisation reaction. Hence, the knowledge of thermochemical properties, ie phase relations and activities of components, in slags containing $<C2S\text{-}C3P>_{SS}$ are necessary for the effective removal of phosphorus from hot metal. In this study, the P_2O_5 activities in $<C2S\text{-}C3P>_{SS}$ were measured through the gas equilibrium method.

In the present experiment, oxide samples were equilibrated with Cu-P liquid alloys at 1573 K under a stream of Ar + H_2 + H_2O or Ar + H_2 + CO_2 gas mixture in which oxygen potential was fixed and then equilibrium phosphorus concentrations in the Cu-P alloys, $[mass\%P]_{Cu}$, were analysed with ICP-OES. The underlying reaction can be expressed by:

$$2[P]_{Cu} + (5/2)O_2(gas) = P_2O_{5\ in\ oxide}$$

$$K = aP_2O_5\,(pO_2/atm)^{-5/2}\,[mass\%P]_{Cu}^{-2}$$

Where:

K	denotes the equilibrium constant
aP_2O_5	represents the P_2O_5 activity
pO_2	is the oxygen partial pressure in the gas phase

Firstly, the experiments were performed on MgO + $Mg_3P_2O_8$, in which the P_2O_5 activity has already been reported, to determine the value for the equilibrium constant, K. Subsequently, the P_2O_5 activities were measured in $<C2S\text{-}C3P>_{SS}$ + $CaSiO_3$ and $<C2S\text{-}C3P>_{SS}$ + CaO with the same experimental procedure.

The P_2O_5 activity in $<C2S\text{-}C3P>_{SS}$ coexisting with CaO was found to be about seven digits lower than that with $CaSiO_3$ even at the same composition of $<C2S\text{-}C3P>_{SS}$. This phenomenon was explained in terms of the activities of Ca_2SiO_4 and $Ca_{1.5}PO_4$ (= (1/2)$Ca_3P_2O_8$). These activities are determined depending on temperature and the composition of $<C2S\text{-}C3P>_{SS}$, while the P_2O_5 activity depends not only on these variables but also on the second phase coexisting with $<C2S\text{-}C3P>_{SS}$. The Ca_2SiO_4 and $Ca_{1.5}PO_4$ activities exhibited large negative deviations from Raoult's law, which implied the strong chemical affinity between the components. Experimental errors in these experiments would be cancelled out in calculating aP_2O_5 since they would be involved in both experimental procedures for MgO + $Mg_3P_2O_8$ and $<C2S\text{-}C3P>_{SS}$ + CaO or $<C2S\text{-}C3P>_{SS}$ + $CaSiO_3$, which makes the present results more reliable.

INTRODUCTION

Phosphorus is a typical harmful element in steel and is removed from molten iron by the following oxidation reaction in the steelmaking processes (Hino and Ito, 2009):

$$2[P]F_e + 5FeO_{\ in\ slag} = P_2O_{5\ in\ slag} + 5Fe(liquid) \quad (1)$$

$$\log K_1 = \log aP_2O_5 - 5\log aF_eO - 2\log([fP]F_e\,[mass\%P]F_e)$$

$$= 12730/(T/K) - 20.0 \quad (2)$$

Where $[P]F_e$ and $[fP]F_e$ denote phosphorus in molten iron and its Henrian activity coefficient, respectively, while a_i represents the Raoultian activity of component i in the slag. The standard states

of $a P_2O_5$ and $a F_eO$ are taken to be pure hypothetical liquid P_2O_5 and pure liquid FeO in equilibrium with metallic iron, respectively. It is known that P_2O_5 reacts with CaO and SiO_2 in slags to form solid solutions between di-calcium silicate, Ca_2SiO_4, and tri-calcium phosphate, $Ca_3P_2O_8$. The phosphorus oxides are enriched in such solid solutions, and thus the solid solutions have an important role in the dephosphorisation reaction (Kitamura, Shibata and Maruoka, 2008). Figure 1 gives a part of the CaO-SiO_2-P_2O_5 ternary phase diagram at 1573 K (Matsu-suye *et al*, 2007; Uchida, Watanabe and Hasegawa, 2021; Uchida, Watanabe and Tsuruoka, 2022) and the Ca_2SiO_4-$Ca_3P_2O_8$ pseudo-binary phase diagram (Fix, Heymann and Heinke, 1969). It can be seen that the solid solution between *α*-Ca_2SiO_4 and *ά*-$Ca_3P_2O_8$ can coexist with $CaSiO_3$ or CaO when the $Ca_3P_2O_8$ content is 10–40 mass per cent at 1573 K. In Figure 1 and hereafter, the following abbreviations are used:

C2S	= $2CaO \cdot SiO_2$	= Ca_2SiO_4
CS	= $CaO \cdot SiO_2$	= $CaSiO_3$
C3P	= $3CaO \cdot P_2O_5$	= $Ca_3P_2O_8$
M3P	= $3MgO \cdot P_2O_5$	= $Mg_3P_2O_8$
$<C2S\text{-}C3P>_{SS}$	= Ca_2SiO_4-$Ca_3P_2O_8$ solid solution	

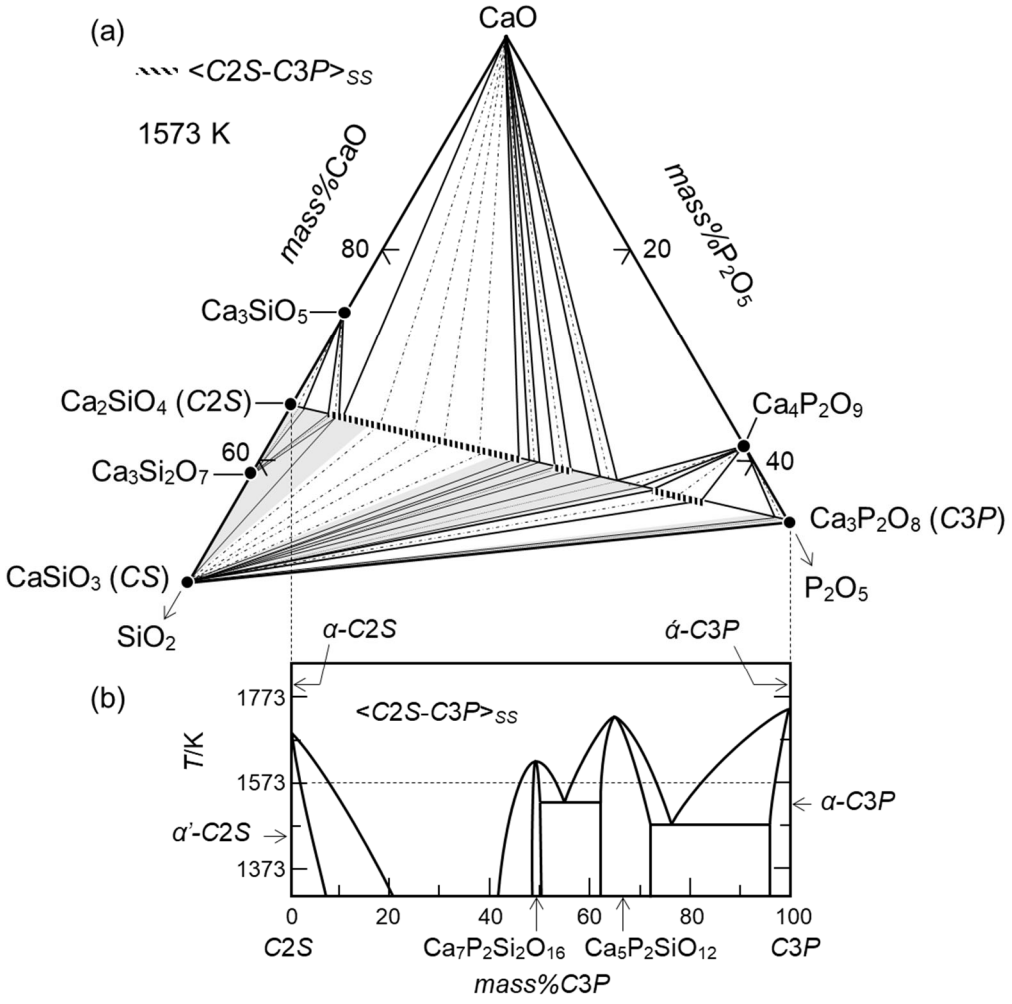

FIG 1 – (a) CaO-SiO_2-P_2O_5 ternary phase diagram at 1573 K. The grey-shaded areas are unknown and estimated. (b) Ca_2SiO_4-$Ca_3P_2O_8$ pseudo-binary phase diagram.

According to Le Chatelier's principle, Reaction 1 can proceed effectively in conditions of low temperature, high FeO activity, low P_2O_5 activity and high P activity coefficient. If the molten iron is regarded as a carbon-saturated Fe-C-P liquid alloy, the Henrian activity coefficient of phosphorus, $[f\mathrm{P}]F_e$, can be expressed by using interaction parameters, e_i^j (Hino and Ito, 2009):

$$\log[f\mathrm{P}]F_e = e\mathrm{P}^{\mathrm{C}}\,[mass\%\mathrm{C}]F_e + e\mathrm{P}^{\mathrm{P}}\,\mathrm{PP}[mass\%\mathrm{P}]F_e$$

$$= 0.126[mass\%C]_{Fe} + 0.054[mass\%P]_{Fe} \quad (3)$$

When iron ore is reduced by carbon, dissolving carbon in pig iron can decrease the liquidus temperature and increase $[f_P]_{Fe}$ in the iron alloy, which is advantageous to the phosphorus removal. On the other hand, concerning hydrogen reduction aiming at carbon-neutral refinings, phosphorus exists as an impurity also in hydrogen-reduced iron to the same extent as the carbon-reduced one (Kashiwaya and Hasegawa, 2012). The phosphorus content after dephosphorisation from the carbon- or hydrogen-reduced molten iron can be compared as follows. The refining temperatures were assumed to be 1573 K for the carbon-reduced iron and 1873 K for the hydrogen-reduced one. Compositions of the liquid slags saturated with *C2S* were determined as given in Table 1 based on the FeO-CaO-SiO_2 ternary phase diagram (Muan and Osborn, 1965), Figure 2, with the assumption that CaO/SiO_2 mole ratios were 2 and mole fractions of P_2O_5 were 0.02. The activities of FeO and P_2O_5 were calculated with a regular solution model (Ban-ya, 1993) and the phosphorus concentrations in the iron could be estimated by solving Equations 2 and 3.

TABLE 1

Comparison of the phosphorus contents in the C-reduced or H-reduced iron.

Reduced by	Mole fraction in liquid slag					Activity (Ban-ya, 1993)		Mass% content in iron	
	T/K	FeO	CaO	SiO_2	P_2O_5	FeO	P_2O_5	C	P
Carbon	1573	0.73	0.17	0.08	0.02	0.90	6.2×10^{-17}	4.5	0.0024
Hydrogen	1873	0.41	0.38	0.19	0.02	0.55	5.3×10^{-18}	0	0.039

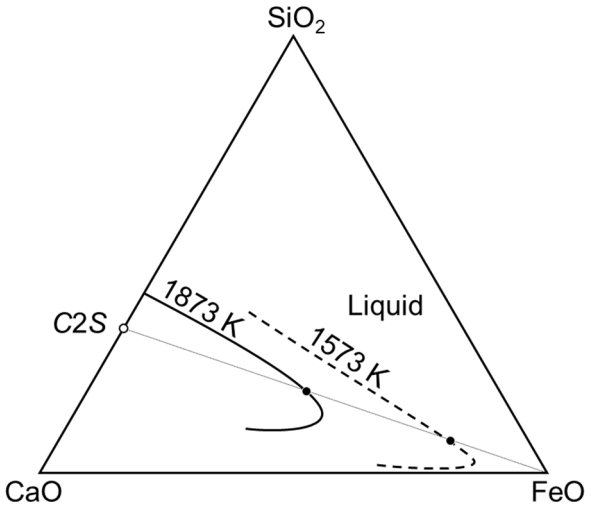

FIG 2 – Schematic phase diagram of the FeO-CaO-SiO_2 ternary system.

The equilibrium phosphorus content in the hydrogen-reduced iron was found to be 16 times higher than that in the carbon-reduced one. In order to overcome such a disadvantageous situation, it is essential to know accurately the basic thermochemical properties of the slags containing $<C2S\text{-}C3P>_{SS}$.

In the present study, the activities of P_2O_5 were measured in $<C2S\text{-}C3P>_{SS}$ coexisting with *CS* or CaO through the gas equilibrium method. The P_2O_5 activity depends on not only temperature and the *C3P* concentration in $<C2S\text{-}C3P>_{SS}$ but also the second phase coexisting with the solid solution, *CS* or CaO. Therefore, the thermochemical properties of the solid solution were discussed in terms of the *C2S* and *C3P* activities, which were determined by only temperature and the composition of $<C2S\text{-}C3P>_{SS}$. To improve the accuracy of the measurement, the same gas equilibrium method was applied to the MgO-P_2O_5 binary system, in which the P_2O_5 activity has been reported, as a reference system.

EXPERIMENTS

Experimental principle

In the present experiments, liquid Cu-P alloys were brought into equilibrium with MgO + *M*3*P*, <*C*2*S*-*C*3*P*>$_{SS}$ + *CS*, or <*C*2*S*-*C*3*P*>$_{SS}$ + CaO at 1573 K under a stream of Ar + H_2 + H_2O or Ar + H_2 + CO_2 gas mixture, in which the oxygen potential was fixed. The underlying reaction can be expressed as:

$$2[P]_{Cu} + (5/2)O_2(gas) = P_2O_{5\ in\ oxide} \quad (4)$$

$$\log K_4 = \log a P_2O_{5_} 2\log([f P]_{Cu}\,[mass\%P]_{Cu}) - (5/2)\log(pO_2/atm) \quad (5)$$

It was reported that phosphorus in the molten copper alloy obeyed Henry's law and hence $[fP]_{Cu}$ was unity in the composition range of $[mass\%P]_{Cu}$ <1 (Iwase, Ichise and Yamada, 1985). Thus, Equation 5 indicates that K_4 can be determined by analysing the phosphorus content in the copper alloy equilibrated with MgO + *M*3*P*, in which aP_2O_5 is well known, under the fixed oxygen potential. Now that the value for K_4 is available, unknown values for aP_2O_5 in the $CaO\text{-}SiO_2\text{-}P_2O_5$ ternary system can be derived from the phosphorus contents in the copper alloys equilibrated with the ternary oxides under fixed pO_2.

Materials and procedure

Regent grade MgO, $Mg(H_2PO_4)_2{\cdot}3H_2O$, $CaCO_3$ and *C*3*P* were obtained from Nacalai Tesque Inc Kyoto, Japan, while SiO_2 was obtained from Nacalai Tesque Inc Kyoto, Japan and FUJIFILM Wako Pure Chemical Co, Osaka, Japan. A mixture of MgO + $Mg(H_2PO_4)_2{\cdot}3H_2O$ at a mole ratio of 2:1 was heated slowly to 1273 K in air to prepare *M*3*P*. Lime was obtained by calcining $CaCO_3$ in air at 1373 K. To synthesise *C*2*S* and *CS*, $CaCO_3$ and SiO_2 were mixed at mole ratios of 2:1 and 1:1, respectively and heated in air at 1573 K. The resulting compounds were submitted to powder X-ray diffraction analyses to confirm the expected phases only. The obtained *C*2*S* was mixed with *C*3*P* and heated at 1573 K to prepare <*C*2*S*-*C*3*P*>$_{SS}$. The mole fraction of *C*3*P* in <*C*2*S*-*C*3*P*>$_{SS}$ was 0.20 (31 mass per cent $Ca_3P_2O_8$). Oxide mixtures of MgO + *M*3*P*, <*C*2*S*-*C*3*P*>$_{SS}$ + *CS*, and <*C*2*S*-*C*3*P*>$_{SS}$ + CaO were used for the following experiments. The starting materials for the metallic phase were copper shavings obtained from Nakalai Tesque Inc, Kyoto, Japan and Cu_3P from Hirano Seizaemon Co Ltd, Tokyo, Japan.

Table 2 summarises the experimental conditions. For some conditions, dense alumina crucibles (10 mm od, 8 mm id and 30 mm in height) were charged with the oxide mixtures and the copper shavings. For the other conditions, the oxide mixtures were pressed in a steel die to form crucible shapes (15 mm od, 8 mm id and 8 mm in height) and charged with Cu + Cu_3P. The latter is considered a better method that completely prevents contaminations of impurity from crucibles, although little difference was seen in the experimental results described later. Subsequently, the oxide and metallic samples were held at 1573 K in a mullite reaction tube equipped with a SiC resistance furnace, and then the metallic phase melted to form the Cu-P molten alloys coexisting with the oxides. A decomposition reaction of the mullite, $Al_6Si_2O_{13}$, under the reducing atmosphere is expressed as Reaction 6 (Davis, Aksay and Pask, 1972). From thermal data for Reaction 6 (Kubaschewski, Alcock and Spencer, 1993), the mullite tube had satisfactory resistance under the present experimental conditions and would not disturb the gas control:

$$Al_6Si_2O_{13}(solid) = 3Al_2O_3(solid) + 2SiO(gas) + O_2(gas) \quad (6)$$

$$\log K_6 = 2\log(p_{SiO}/atm) + \log(pO_2/atm) = -27.3 \text{ at } 1573\ K \quad (7)$$

TABLE 2

Experimental conditions and results at 1573 K.

Oxide sample	log(pO_2/ atm)	Holding time/hr	*[mass%P]*$_{Cu}$		
			initial	equilibrium	average
MgO + *M3P*	-11.45	42.0	0	0.0225	0.0248 ± 0.0016
		42.0	0.11	0.0264	
		42.0	0.26	0.0254	
MgO + *M3P*	-11.76	44.2	0	0.0543	0.0539 ± 0.0004
		44.2	0.59	0.0535	
MgO + *M3P*	-12.03	42.3	0	0.0765	0.0731 ± 0.0076
		42.3	0.20	0.0802	
		42.3	0.57	0.0625	
MgO + *M3P*	-12.31	45.6	0	0.154	0.159 ± 0.011
		45.6	0.22	0.149	
		45.6	0.64	0.174	
MgO + *M3P*	-12.60	49.1	0	0.395	0.395 ± 0.001
		49.1	0.68	0.394	
<*C2S-C3P*>$_{ss}$ + *CS*	-12.90	47.3	0	0.0166	0.0159 ± 0.0028
		90.6	0	0.0203	
		142.2	0	0.0137	
		122.8	0	0.0132	
<*C2S-C3P*>$_{ss}$ + *CS* [a]	-12.94	91.3	0	0.0197	0.0209 ± 0.0021
		139.2	0	0.0224	
		161.9	0	0.0248	
		185.1	0	0.0217	
		207.2	0	0.0194	
		230.5	0	0.0182	
		230.5	0	0.0203	
<*C2S-C3P*>$_{ss}$ + *CS*	-13.45	39.8	0	0.0688	0.0765 ±0.0077
		39.8	0.33	0.0842	
<*C2S-C3P*>$_{ss}$ + CaO	-15.35	7.0	0.024	0.00295	0.00288 ± 0.00012
		23.8	0	0.00272	
		23.8	0.013	0.00304	
		23.8	0.024	0.00282	
<*C.2S-C3P*>$_{ss}$ + CaO [a]	-16.10	640.0	0	0.0604	0.0619 ± 0.0055
		754.0	0	0.0619	
		830.0	0	0.0646	
		846.0	0	0.0487	
		851.0	0	0.0619	
		855.0	0	0.0683	
		869.0	0	0.0639	
		941.0	0	0.0658	

a – the samples were charged in the alumina crucibles.

Into the reaction tube, the Ar + H_2 + H_2O or Ar + H_2 + CO_2 gas mixture was introduced to fix the oxygen potential. The Ar + H_2 + H_2O gas mixture prepared by passing the Ar + 12 per cent H_2 gas mixture through distilled water kept at 283 K to 304 K in a thermostat bath was used for the experiments with MgO + *M3P*. On the other hand, for <*C2S*-*C3P*>$_{SS}$ + *CS*, the Ar + H_2 + H_2O gas mixture was prepared by passing the Ar + 12 per cent H_2 gas mixture through ether distilled water kept at 278 K or LiCl-saturated water kept at 303 K or 313 K. The partial pressures of H_2O and O_2 in these gas mixtures can be calculated from the following thermal data (Kubaschewski and Alcock, 1979; Takeshita, Hasegawa and Iwase, 2008):

$$\log(p_{H_2O}/\text{atm}) = 19.732–2900/(T_{bath}/\text{K}) - 4.65\log(T_{bath}/\text{K})$$

$$\text{distilled water, } 273\ \text{K} < T_{bath} < 373\ \text{K} \quad (8)$$

$$\log(p_{H_2O}/\text{atm}) = 5.94–2510/(T_{bath}/\text{K})$$

$$\text{LiCl-saturated water, } T_{bath} > 291.5\ \text{K} \quad (9)$$

$$H_2(\text{gas}) + (1/2)\ O_2(\text{gas}) = H_2O(\text{gas}) \quad (10)$$

$$\log K_{10} = -(1/2)\log(pO_2/\text{atm}) - \log(p_{H_2}/p_{H_2O}) = 5.32 \text{ at } 1573\ \text{K} \quad (11)$$

Where T_{bath} is the temperature of the thermostat bath. For the experiments with <*C2S*-*C3P*>$_{SS}$ + CaO, the much lower oxygen potentials were necessary, and thus the following Ar + H_2 + H_2O and Ar + H_2 + CO_2 gas mixtures were used. The Ar + H_2 + H_2O gas mixture was prepared by passing the Ar + 12 per cent H_2 gas mixture through $C_2H_2O_4$ + $C_2H_2O_4{\cdot}2H_2O$ two-phase mixture kept at 268 K. The water vapour pressure in equilibrium with the $C_2H_2O_4$ + $C_2H_2O_4{\cdot}2H_2O$ is given by (Takeshita, Hasegawa, and Iwase, 2008):

$$\log(p_{H_2O}/\text{atm}) = 6.88–2810/(T_{bath}/\text{K})$$

$$C_2H_2O_4 + C_2H_2O_4{\cdot}2H_2O \text{ two-phase mixture, } T_{bath} < 293\ \text{K} \quad (12)$$

The value for pO_2 in this Ar + H_2 + H_2O gas mixture can be obtained from Equation 11. The Ar + H_2 + CO_2 gas mixture was prepared by mixing Ar + 30 per cent H_2 and Ar + 1 per cent CO_2 gas mixtures. The calculating method for the equilibrium partial pressures of gaseous species has been described elsewhere (Iwahashi *et al*, 2021).

After being held at 1573 K, the phosphorus contents in quenched alloys were determined with ICP-OES. Initial compositions of alloys are also listed in Table 2. Except for several conditions, the alloy samples with different initial phosphorus contents were simultaneously held in the reaction tube. When the phosphorus concentration was higher or lower than the equilibrium value, Reaction 4 proceeded toward the right or left hand, respectively. The phosphorus concentrations in such alloys that matched each other within experimental uncertainties were able to be confirmed as the equilibrium value.

RESULTS AND DISCUSSION

Activity measurements of P_2O_5

A typical relationship between the compositions of copper alloys and duration time for MgO + $Mg_3P_2O_8$ is shown in Figure 3. The phosphorus concentrations in the alloys with different initial compositions agreed well after 42.0 hours and hence the equilibrium value for $[\text{mass\%P}]_{Cu}$ was determined to be 0.0248 ± 0.0016.

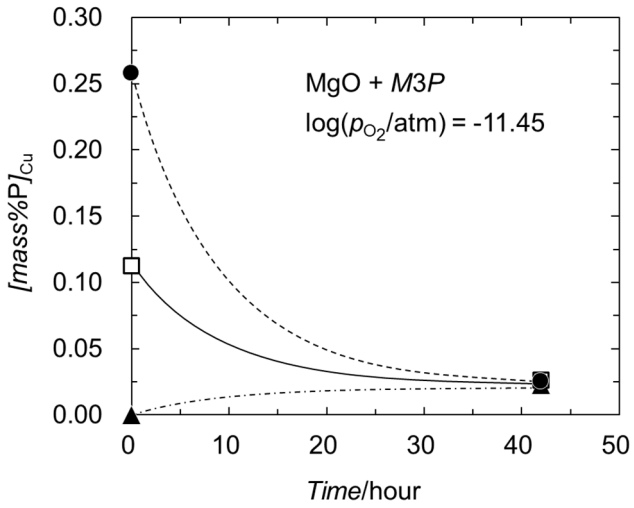

FIG 3 – Typical changes in the compositions of alloys over duration time.

All the experimental results are summarised in Table 2. Equation 13 given by rewriting Equation 5 indicates that the logarithmic relationship between $[mass\%P]_{Cu}$ and pO_2 should be linear with a slope of - 5/4 and an intercept of [- (1/2)logK_4 + (1/2)log$a_{P_2O_5}$]:

$$\log[mass\%P]_{Cu} = -(5/4)\log(pO_2/atm) - (1/2)\log K_4 + (1/2)\log a_{P_2O_5} \quad (13)$$

Figure 4 shows such relationships. Linear relations can be observed for the three types of oxide mixtures and their slopes are close to - 5/4.

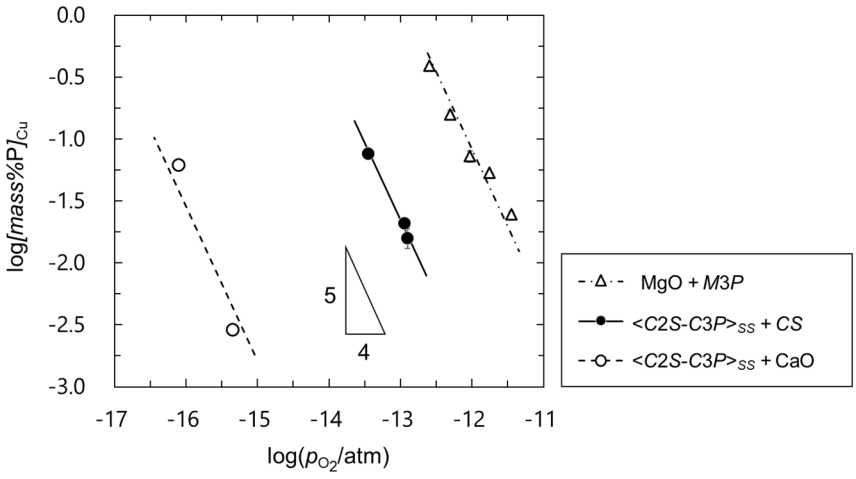

FIG 4 – Relationship between log$[mass\%P]_{Cu}$ and log(pO_2/atm) at 1573 K.

The P_2O_5 activity in the MgO + *M3P* two-phase mixture at 1573 K can be derived from the following formulae (Pandit and Jacob, 1995; Jung and Hudon, 2012):

$$3\ MgO(solid) + P_2O_{5\ in\ M3P} = M3P(solid) \quad (14)$$

$$\log K_{14} = -\log a_{P_2O_{5(MgO+M3P)}} = 13.6 \text{ at } 1573\ K \quad (15)$$

From Equation 13, K_4 was determined from the intercept of the regression line for MgO + *M3P* in Figure 4:

$$\log K_4 = -18.5 \pm 0.2 \text{ at } 1573\ K \quad (16)$$

By using the obtained value for K_4, the P_2O_5 activity in $<C2S\text{-}C3P>_{SS}$ coexisting with *CS* or CaO at 1573 K was determined from the intercept of the regression line for the corresponding oxide mixture in Figure 4:

$$\log a_{P_2O_{5(<C2S\text{-}C3P>_{SS}+CS)}} = -17.3 \pm 0.1 \text{ at } 1573\ K \quad (17)$$

$$\log a_{P_2O_{5(<C2S\text{-}C3P>_{SS}+CaO)}} = -24.5 \pm 0.4 \text{ at } 1573 \text{ K} \quad (18)$$

The P_2O_5 activity in $<C2S\text{-}C3P>_{SS}$ + CaO was found to be about seven digits lower than that in $<C2S\text{-}C3P>_{SS}$ + *CS* even at the same composition of $<C2S\text{-}C3P>_{SS}$, 31 mass per cent *C*3*P*.

The activities of Ca_2SiO_4, $Ca_{1.5}PO_4$, CaO and SiO_2 in the solid solution

The simple CaO-SiO_2 binary system is focused on at the beginning of this section. Figure 5 gives the CaO and SiO_2 activities against the composition in the binary system at 1573 K calculated by thermal data (Kubaschewski, Alcock and Spencer, 1993; Seetharaman, 2014) as well as assessed results by CALPHAD approach in the latest study (Abdul *et al*, 2023). Both values are in good agreement. As shown in this figure, the activities of components change drastically within the quite narrow composition ranges of the stoichiometric compounds ($CaSiO_3$, $Ca_3Si_2O_7$, Ca_2SiO_4 and Ca_3SiO_5). For example, at the composition of *CS*, the activity of *CS* is unity and hence a product of a_{CaO} and a_{SiO_2} is fixed by Equation 19:

$$CaO_{\text{ in } CS} + SiO_{2 \text{ in } CS} = CS(\text{solid}) \quad (19)$$

$$\log K_{19} = -\log(a_{CaO}\, a_{SiO_2}) = 2.92 \quad (20)$$

Nevertheless, each value for the CaO and SiO_2 activities in *CS* cannot be determined as shown in Figure 5:

$$-2.92 < \log a_{CaO_{(CS)}} < -2.07 \quad \text{at } 1573 \text{ K} \quad (21)$$

$$-0.85 < \log a_{SiO_{2(CS)}} < 0 \quad \text{at } 1573 \text{ K} \quad (22)$$

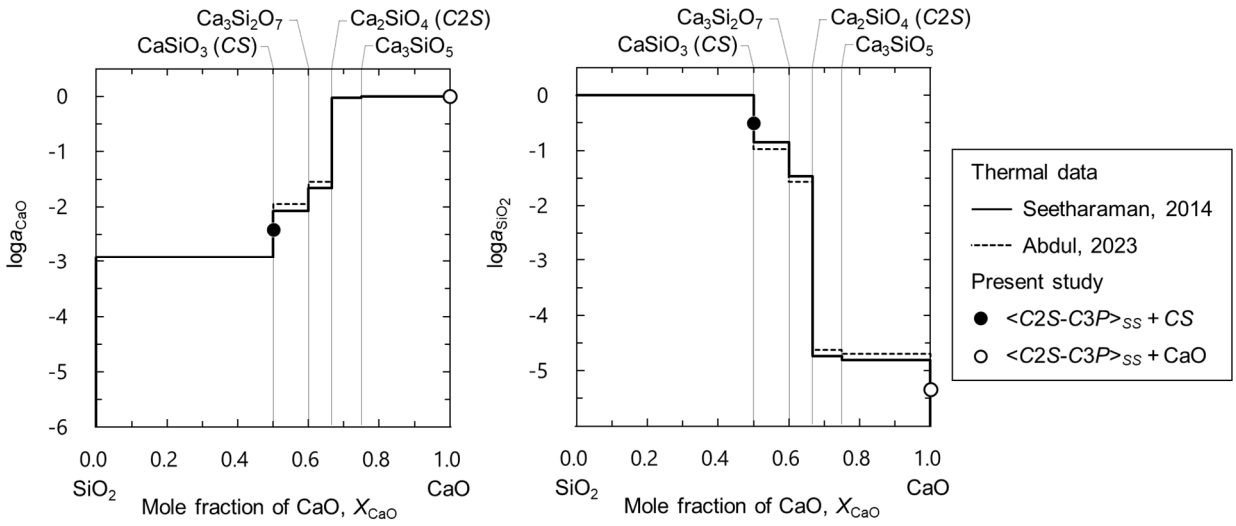

FIG 5 – Activities of components in the CaO-SiO_2 binary system at 1573 K.

Similarly, the *C*2*S* and *C*3*P* activities are determined depending on temperature and the composition of $<C2S\text{-}C3P>_{SS}$, while the P_2O_5 activity depends not only on these variables but also on the second phase coexisting with $<C2S\text{-}C3P>_{SS}$. In the $<C2S\text{-}C3P>_{SS}$ + *CS* and $<C2S\text{-}C3P>_{SS}$ + CaO two-phase regions, Reactions 23 and 25 achieve the equilibrium states, respectively and hence the P_2O_5 activities are determined through the *C*2*S* and *C*3*P* activities (Kubaschewski, Alcock and Spencer, 1993; Seetharaman, 2014; Jung and Hudon, 2012; Hudon and Jung, 2015):

$$P_2O_{5 \text{ in } SS} + 3\ C2S_{\text{ in } SS} = C3P_{\text{ in } SS} + 3\ CS(\text{solid}) \quad (23)$$

$$\log K_{23} = \log a_{C3P} - 3\log a_{C2S} - \log a_{P_2O_{5(<C2S\text{-}C3P>_{SS}+CS)}} = 16.50 \text{ at } 1573 \text{ K} \quad (24)$$

$$P_2O_{5 \text{ in } SS} + 3\ CaO(\text{solid}) = C3P_{\text{ in } SS} \quad (25)$$

$$\log K_{25} = \log a_{C3P} - \log a_{P_2O_{5(<C2S\text{-}C3P>_{SS}+CaO)}} = 21.99 \text{ at } 1573 \text{ K} \quad (26)$$

Therefore, the *C*2*S* and *C*3*P* activities should be considered in order to understand the thermochemical properties of the solid solution. From the experimental results, the *C*3*P* activity can be obtained by Equations 18 and 26:

$$\log a_{C3P} = -2.54 \quad (27)$$

In addition, the *C*2*S* activity can be derived by Equations 17, 24 and 27:

$$\log a_{C2S} = -0.59 \quad (28)$$

The standard states of a_{C3P} and a_{C2S} were taken to be pure supercooled solid *ά*-*C*3*P* and *α*-*C*2*S*, respectively. In the solid solutions, the anion SiO_4^{4-} is thought to be replaced by PO_4^{3-} (Suzuki, Umesaki and Ishii, 2022). Although tri-calcium phosphate has conventionally been treated as $Ca_3P_2O_8$, it should be better to consider the chemical compound containing a single PO_4^{3-}, ie $Ca_{1.5}PO_4$ (= (1/2)*C*3*P*); the relationship between the activities of $Ca_{1.5}PO_4$ and $Ca_3P_2O_8$ can be formulated as:

$$\log a_{(1/2)C3P} = (1/2)\log a_{C3P} = -1.327 \quad (29)$$

Figure 6 shows the activities of (1/2)*C*3*P* and *C*2*S* plotted against the mole fraction of (1/2)*C*3*P*, $X_{(1/2)C3P}$, in the *C*2*S*-(1/2)*C*3*P* binary system. The curves in this figure represent calculated values from a sub-regular solution model, Equations 30 and 31. The parameters, *A* and *B*, were determined based on the present results:

$$\log a_{(1/2)C3P} = \log X_{(1/2)C3P} + A(1 - X_{(1/2)C3P})^3 + B(1 - X_{(1/2)C3P})^2 \quad (30)$$

$$\log a_{C2S} = \log(1 - X_{(1/2)C3P}) - AX_{(1/2)C3P}^3 + (1.5A + B)X_{(1/2)C3P}^2 \quad (31)$$

$$A = -3.89 \quad (32)$$

$$B = 0.81 \quad (33)$$

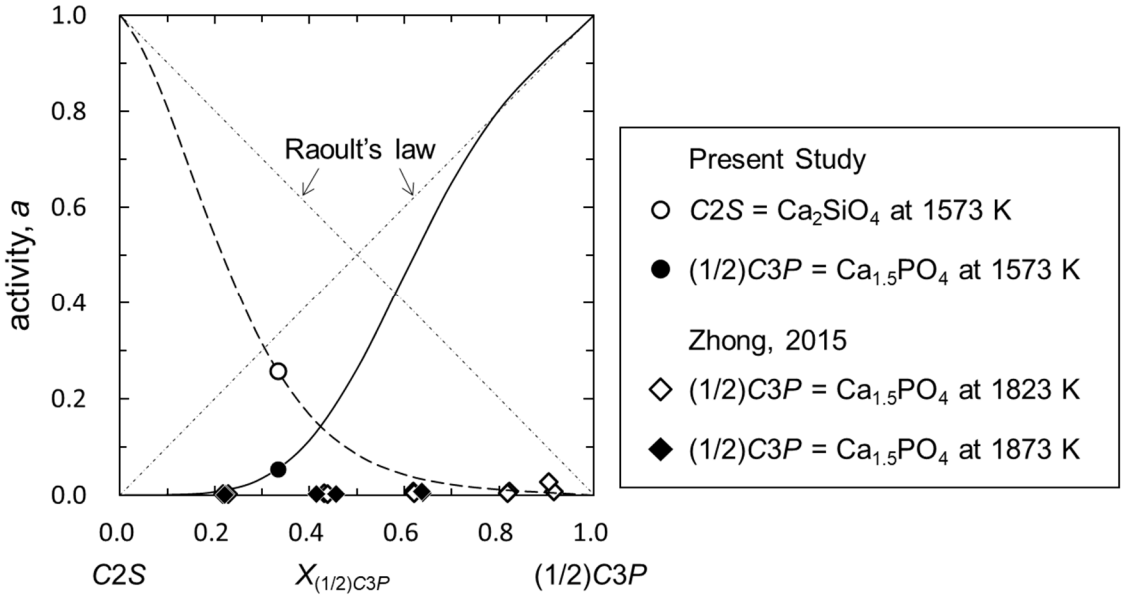

FIG 6 – Activities of components in the Ca_2SiO_4-$Ca_{1.5}PO_4$ binary system.

Figure 6 also shows literature data at higher temperatures, in which the P_2O_5 and *C*3*P* activities have been measured in <*C*2*S*-*C*3*P*>$_{SS}$ + CaO at 1823 K and 1873 K (Zhong, Matsuura and Tsukihashi, 2015). Although the activities of (1/2)*C*3*P* at higher temperatures were much lower than the present result, the activities of components in this system exhibited large negative deviations from Raoult's Law. It implies the strong chemical affinity between SiO_4^{4-} and PO_4^{3-} in the solid solution, which is consistent with the fact that *C*2*S* can incorporate *C*3*P* in the whole composition range as shown in Figure 1b.

Once the thermochemical properties of <*C*2*S*-*C*3*P*>$_{SS}$ are clarified, the CaO and SiO_2 activities can be calculated in the solid solutions coexisting with *CS* or CaO from the following reactions.

<*C2S-C3P*>$_{SS}$ + *CS* two-phase region:

$$CaO_{\text{ in } SS} + CS(\text{solid}) = C2S_{\text{ in } SS} \quad (34)$$

$$\log a_{CaO_{(<C2S\text{-}C3P>_{SS}+CS)}} = -\log K_{34} + \log a_{C2S} = -2.42 \text{ at } 1573 \text{ K} \quad (35)$$

$$SiO_{2\text{ in } SS} + C2S_{\text{ in } SS} = 2\ CS(\text{solid}) \quad (36)$$

$$\log a_{SiO_{2(<C2S\text{-}C3P>_{SS}+CS)}} = -\log K_{36} - \log a_{C2S} = -0.50 \text{ at } 1573 \text{ K} \quad (37)$$

<*C2S-C3P*>$_{SS}$ + CaO two-phase region:

$$2CaO(\text{solid}) + SiO_{2\text{ in } SS} = C2S_{\text{ in } SS} \quad (38)$$

$$\log a_{CaO_{(<C2S\text{-}C3P>_{SS}+CaO)}} = 0 \quad (39)$$

$$\log a_{SiO_{2(<C2S\text{-}C3P>_{SS}+CaO)}} = -\log K_{38} + \log a_{C2S} = -5.34 \text{ at } 1573 \text{ K} \quad (40)$$

The values for K_{34}, K_{36} and K_{38} were obtainable from the thermal data (Kubaschewski, Alcock and Spencer, 1993; Seetharaman, 2014). The calculated results are superimposed in Figure 5. The calculated result of the CaO and SiO_2 activities in the presence of *CS*, Equations 35 and 37, were within the activity ranges of 21 and 22, respectively. It can be said that the present results are not inconsistent with the literature data for the CaO-SiO_2 binary system.

Experimental error in the gas equilibrium method

The gas equilibrium method, in which the Cu-P liquid alloys are equilibrated with oxides, has been pointed out to involve relatively large experimental errors in analysing the compositions of the copper alloys because of the very low phosphorus contents in the alloys (Yamasue, Shimizu and Nagata, 2013). Such experimental errors are discussed in the last section. The equilibrium constants of Reaction 4 in the experiment for MgO + *M3P*, <*C2S-C3P*>$_{SS}$ + *CS*, and <*C2S-C3P*>$_{SS}$ + CaO are expressed as:

$$\log K_4 = \log a_{P_2O_{5(MgO+M3P)}} - 2\log [mass\%P]_{Cu} - (5/2)\log(p_{O_{2(MgO+M3P)}}/\text{atm}) \quad (41)$$

$$\log K_4 = \log a_{P_2O_{5(<C2S\text{-}C3P>_{SS}+CS)}} - 2\log [mass\%P]_{Cu} - (5/2)\log(p_{O_{2(<C2S\text{-}C3P>_{SS}+CS)}}/\text{atm}) \quad (42)$$

$$\log K_4 = \log a_{P_2O_{5(<C2S\text{-}C3P>_{SS}+CaO)}} - 2\log [mass\%P]_{Cu} - (5/2)\log(p_{O_{2(<C2S\text{-}C3P>_{SS}+CaO)}}/\text{atm}) \quad (43)$$

When the three regression lines in Figure 4 are compared with a fixed value for $\log [mass\%P]_{Cu}$ on the vertical axis, the differences between Equations 41 and 42 or 43 are written as:

$$\log a_{P_2O_{5(<C2S\text{-}C3P>_{SS}+CS)}} = \log a_{P_2O_{5(MgO+M3P)}} + (5/2)\log(p_{O_{2(<C2S\text{-}C3P>_{SS}+CS)}}/p_{O_{2(MgO+M3P)}}) \quad (44)$$

$$\log a_{P_2O_{5(<C2S\text{-}C3P>_{SS}+CaO)}} = \log a_{P_2O_{5(MgO+M3P)}} + (5/2)\log(p_{O_{2(<C2S\text{-}C3P>_{SS}+CaO)}}/p_{O_{2(MgO+M3P)}}) \quad (45)$$

Equations 44 and 45 indicate that the P_2O_5 activities in <*C2S-C3P*>$_{SS}$ + *CS* and <*C2S-C3P*>$_{SS}$ + CaO can be derived from the ratios of $p_{O_{2(<C2S\text{-}C3P>_{SS}+CS)}}$ and $p_{O_{2(<C2S\text{-}C3P>_{SS}+CaO)}}$ against $p_{O_{2(MgO+M3P)}}$. In other words, the experimental errors in analysing the alloy compositions would be cancelled out in calculating $a_{P_2O_5}$ since they would be involved in all the experimental procedures for MgO + *M3P*, <*C2S-C3P*>$_{SS}$ + *CS*, and <*C2S-C3P*>$_{SS}$ + CaO, which makes the present results more reliable.

CONCLUSIONS

For a better understanding of the dephosphorisation reaction in the steelmaking process, the present study focused on the thermochemical properties of the oxides containing the Ca_2SiO_4-$Ca_3P_2O_8$ solid solutions, <*C2S-C3P*>$_{SS}$. The P_2O_5 activities were measured in the solid solution coexisting with $CaSiO_3$ or CaO through the gas equilibrium method, in which the Cu-P liquid alloys were brought into equilibrium with the oxides under fixed oxygen potentials at 1573 K:

$$2\ [P]_{Cu} + (5/2)\ O_2(\text{gas}) = P_2O_5$$

$$\log a_{P_2O_{5(MgO+M3P)}} = 2\log[mass\%P]_{Cu} + (5/2)\log(pO_2/atm) + \log K$$

The value for K was determined by the same experimental method applied to the MgO + $Mg_3P_2O_8$ two-phase mixture, in which the P_2O_5 activity was well known. The obtained results at 1573 K are summarised as follows:

$$\log K = -18.5 \pm 0.2$$

$$\log a_{P_2O_{5(<C2S\text{-}C3P>_{SS}+CaSiO_3)}} = -17.3 \pm 0.1$$

$$\log a_{P_2O_{5(<C2S\text{-}C3P>_{SS}+CaO)}} = -24.5 \pm 0.4$$

Where $C3P$ contents are 31 mass per cent in $<C2S\text{-}C3P>_{SS}$. The P_2O_5 activity in $<C2S\text{-}C3P>_{SS}$ + CaO was found to be about seven digits lower than that in $<C2S\text{-}C3P>_{SS}$ + $CaSiO_3$. The experimental results can be understood in terms of the activities of Ca_2SiO_4 and $Ca_{1.5}PO_4$ (= $(1/2)Ca_3P_2O_8$). The activities of components in the Ca_2SiO_4-$Ca_{1.5}PO_4$ binary system exhibited negative deviations from Raoult's law, indicating the strong chemical affinity between the components in the solid solutions.

ACKNOWLEDGEMENTS

This work was supported by JSPS KAKENHI Grant Number 22KJ1689 and 21K04737. Experimental assistance was provided by Mr. Taihei SAITO, Graduate Student, Department of Energy Science and Technology, Kyoto University, Mr. Toru NISHIMURA, Graduate Student, Department of Energy Science and Technology, Kyoto University, and Ryunosuke KONDO, Undergraduate Student, Faculty of Engineering, Kyoto University. These are gratefully acknowledged.

REFERENCES

Abdul, W, Mawalala, C, Pisch, A and Bannerman, M N, 2023. CaO-SiO_2 assessment using 3rd generation CALPHAD models, *Cement and Concrete Research*, 173:107309. https://doi.org/10.1016/j.cemconres.2023.107309

Ban-ya, S, 1993. Mathematical expression of slag-metal reactions in steelmaking process by quadratic formalism based on the regular solution model, *ISIJ international*, 33:2–11. https://doi.org/10.2355/isijinternational.33.2

Davis, R F, Aksay, I A and Pask, J A, 1972. Decomposition of mullite, *Journal of the American Ceramic Society*, 55:98–101. https://doi.org/10.1111/j.1151-2916.1972.tb11218.x

Fix, W, Heymann, H and Heinke, R, 1969. Subsolidus relations in the system $2CaO{\cdot}SiO_2$-$3CaO{\cdot}P_2O_5$, *Journal of the American Ceramic Society*, 52:346–347.

Hino, M and Ito, K, 2009. Thermodynamic Data for Steelmaking, p 30, p 251, p 259 (Tohoku University Press: Sendai).

Hudon, P and Jung, I, 2015. Critical Evaluation and Thermodynamic Optimization of the CaO-P_2O_5 System, *Metallurgical and Materials Transactions B*, 46:494–522. https://doi.org/10.1007/s11663-014-0193-x

Iwahashi, K, Hashimoto, S, Yamauchi, R, Saito, K and Hasegawa, M, 2021. Phase relationship and activities of components in CaO-SiO_2-Cr_2O_3 ternary system at 1573 K, *ISIJ International*, 61:1404–1411. https://doi.org/10.2355/isijinternational.isijint-2020-752

Iwase, M, Ichise, E and Yamada, N, 1985. Activities of phosphorus in liquid copper by solid oxide galvanic cell, *Steel Research*, 56:319–326. https://doi.org/10.1002/srin.198500642

Jung, I and Hudon, P, 2012. Thermodynamic assessment of P_2O_5, *Journal of the American Ceramic Society*, 95:3665–3672. https://doi.org/10.1111/j.1551-2916.2012.05382.x

Kashiwaya, Y and Hasegawa, M, 2012. Thermodynamics of impurities in pure iron obtained by hydrogen reduction, *ISIJ International*, 52:1513–1522. https://doi.org/10.2355/isijinternational.52.1513

Kitamura, S, Shibata, H and Maruoka, N, 2008. Kinetic Model of Hot Metal Dephosphorization by Liquid and Solid Coexisting Slags, *Steel Research International*, 79:586–590. https://doi.org/10.1002/srin.200806170

Kubaschewski, O and Alcock, C B, 1979. *Metallurgical Thermochemistry*, 5th edition, pp 358–384 (Pergamon Press: Oxford).

Kubaschewski, O, Alcock, C B and Spencer, P J, 1993. *Materials Thermochemistry*, 6th edition, pp 257–323 (Pergamon Press: Oxford).

Matsu-suye, M, Hasegawa, M, Fushi-tani, K and Iwase, M, 2007. Phase Equilibrium of the System CaO-P_2O_5-SiO_2 between 1473 K and 1673 K, *Steel Research International*, 78:465–467. https://doi.org/10.1002/srin.2007062323

Muan, A and Osborn, E F, 1965. Phase Equilibria among Oxides in Steelmaking, p 113 (Addison-Wesley Publishing Company: Reading).

Pandit, S S and Jacob, K T, 1995. Thermodynamic Properties of Magnesium Phosphate ($Mg_3P_2O_8$) Correction of Data in Recent Compilations, *Metallurgical and Material Transactions A*, 26:225–227. https://doi.org/10.1007/BF02669808

Seetharaman, S, 2014. *Treatise of Process Metallurgy, Vol 1, Process Fundamentals*, pp 527–556 (Elsevier: Oxford).

Suzuki, M, Umesaki, N and Ishii, Y, 2022. Highly disordered ionic distribution in α-dicalcium silicate for structure relaxation, *Journal of the American Ceramic Society*, 105:700–711. https://doi.org/10.1111/jace.18096

Takeshita, H, Hasegawa, M and Iwase, M, 2008. Water Vapor Pressures of LiCl-$_2H_2O$-Saturated Solutions and $C_2H_2O_4$-$_2H_2O$-$C_2H_2O_4$ Mixtures, *High Temperature Materials and Processes*, 27:19–22. https://doi.org/10.1515/htmp.2008.27.1.19

Uchida, Y, Watanabe, C and Hasegawa, M, 2021. Phase Equilibria in High Phosphate-Containing Slag without CaO Saturation at Elevated Temperature, *Tetsu-to-Hagané*, 107:701–707. https://doi.org/10.2355/tetsutohagane.tetsu-2021-046

Uchida, Y, Watanabe, C and Tsuruoka, H, 2022. Basic Evaluation of Phase Relation in a Phosphorus-Containing System Saturated with $CaSiO_3$ at Elevated Temperatures for the Utilization of Steelmaking Slag and Sewage Sludge as Phosphorus Resources, *Minerals*, 12:266. https://doi.org/10.3390/min12020266

Yamasue, E, Shimizu, K and Nagata, K, 2013. Direct determination of standard Gibbs energies of the formation of $4CaO·P_2O_5$ and $3CaO·P_2O_5$ by transpiration method, *ISIJ International*, 53:1828–1835. https://doi.org/10.2355/isijinternational.53.1828

Zhong, M, Matsuura, H and Tsukihashi, F, 2015. Activity of phosphorus pent-oxide and tri-calcium phosphate in $2CaO·SiO_2$-$3CaO·P_2O_5$ solid solution saturated with CaO, *Materials Transactions B*, 56:1192–1198. https://doi.org/10.2320/matertrans.M-M2015813

Thermal analysis of molten salts and their mixtures with metals

DOI: 10.62053/SOOI6309

D Sergeev[1], J Qi[2], S Gezgin[3], D Rapp[3], A Lichtinger[3], F Beckstein[3] and M Müller[4]

1. Application Scientist, NETZSCH-Gerätebau GmbH, Selb D-95100, Germany. Email: dmitry.sergeev@netzsch.com
2. Post doctorate, Institute of Energy and Climate Research, Structure and Function of Materials (IEK-2), Forschungszentrum Jülich GmbH, Jülich D-52425, Germany. Email: j.qi@fz-juelich.de
3. Application Scientist, NETZSCH-Gerätebau GmbH, Selb D-95100, Germany
4. Group Leader, Institute of Energy and Climate Research, Structure and Function of Materials (IEK-2), Forschungszentrum Jülich GmbH, Jülich D-52425, Germany. Email: mic.mueller@fz-juelich.de

ABSTRACT

Salts and their mixtures play an important role for industrial and energy sectors, eg metallurgy, biomass gasification and combustion, nuclear and solar powerplants and electrochemical processes. Depending on the composition of salts (eg Li^+, Na^+, K^+, Mg^{2+}, Ca^{2+} // NO_3^-, F^-, Cl^-, CO_3^{2-}, SO_4^{2-}, etc), the temperature range for different applications can vary starting from room temperature and going up to 1500°C. For the proper design and modelling of heat exchangers and other equipment, it is necessary to have reliable and validated data sets of thermophysical properties.

The 50 mol per cent $NaNO_3$ – 50 mol per cent KNO_3 salt mixture as a well-studied composition was selected for validation of relevant thermophysical properties (heat capacity, enthalpy of phase transitions, thermal expansion, viscosity and thermal conductivity). To study these properties of the liquid phase, special crucibles and approaches should be implemented. Verification of these crucibles for different methods (differential scanning calorimetry (DSC), thermomechanical analysis (TMA), laser flash analysis (LFA) and rheometers) has been performed.

The low thermal conductivity of salts is one of the main problems in implementing latent heat storage. In this project, the authors intend to develop a fundamental solution to this problem using chemically bonded metals with salts. These are known as metal-salt solutions. To fit the main parameters of new phase change materials to the requirements of thermal energy storage, a wide variety of possible combinations should be considered. CALPHAD modelling is used together with thermal analysis for the development of a consistent thermodynamic database including chloride salts (Li, Na, K, Mg, Ca // Cl) and corresponding metals (Li, Na, K, Mg, Ca). The results of the study of quasi-binary and multicomponent metal-salt (eg Mg-KCl and Ca-KCl) systems as well as the selection of suitable crucible materials and challenges by studying of these systems will be discussed.

INTRODUCTION

The transition to renewable energy sources, including wind, solar, water, and biomass, necessitates advancements not only in the development of efficient and energy-storage technologies but, given the inherently variable nature of these sources, particularly in the realm of energy storage systems. Beyond electrical and electrochemical storage, thermal storage emerges as a pivotal facet on this new technological landscape. The concept of thermal energy storage (TES) is well known, exemplified by furnaces used for heating homes, and nowadays its contemporary significance lies in its diverse applications across varying temperature ranges. Thermal storage, for example, is integrated into a variety of applications, ranging from heat storage for solar-assisted heating of buildings (0–100°C), to applications in industrial processes (100–300°C), to high-temperature storage for powerplants (300–1000°C).

In recent decades, there has been a growing interest in thermal storage technologies, propelled by the advancement of Concentrated Solar Power (CSP) plants. CSP is one of the most promising renewable energy technologies and will play a key role in addressing current and future global electricity demand challenges. Recognising the potential for further advancements, the current ‘SaltMe’ project directs its focus toward increasing the capacity of CSP plants. The key strategy involves the development of latent thermal energy storage using innovative phase change materials with enhanced two main parameters: energy density and thermal conductivity.

Currently, in most CSP plants so called SolarSalt (mixture of 60 wt per cent $NaNO_3$ and 40 wt per cent KNO_3) is used for TES with a large amount of salt (up to several tons of salt). This type of TES uses the heat capacity of the liquid phase, known as sensible heat. There are two other types of TES, latent and thermochemical, which are still under development and have not been applied for CSP plants yet, because of the low thermal conductivity of salts (Cárdenas and León, 2013; Baharoon *et al*, 2015; Liu *et al*, 2016), which causes a relatively poor performance of the TES (Jegadheeswaran and Pohekar, 2009). In latent TES, phase change materials (PCMs) will be used. They can store a large amount of thermal heat in a narrow temperature range. As PCMs for latent TES, in particular salts and salt systems (Kenisarin, 2010; Cárdenas and León, 2013) are suitable due to thermodynamic, physical, chemical and economic aspects. Latent TES requires PCMs with a thermal conductivity preferably in the range of 5–20 W/(m·K) and additionally high volumetric heat capacity to guarantee high discharging power and high storage density (do Couto Aktay, Tamme and Müller-Steinhagen, 2008). By using different salt mixtures with a relatively high phase transition enthalpy, the energy density of latent TES can be improved. However, these systems usually have very low thermal conductivity (lower than 2 W/(m·K)), which means that charging and discharging of TES takes longer than for materials with higher thermal conductivity. From this point of view, metal systems are an interesting alternative to salts, because they have higher thermal conductivity. Nevertheless, the low energy density and relatively high price of metallic systems make the choice between these two groups of PCMs more complicated and ambiguous.

In the case of metal-salt systems, homogeneous mixtures can be easily prepared. It is sufficient to melt metals with salts according to the existing phase diagrams. There is a miscibility gap between the two liquids. However, if the critical (consolute) temperature is achieved, a homogeneous liquid phase is formed and the metal can be dissolved in the entire concentration range. It is possible to prepare homogeneous metal-salt solutions *in situ* with various concentrations of the metals. However, yet it is not clear how the thermal conductivity of these materials is changed by phase transitions, eg from liquid to solid. It may be the case that the thermal conductivity of the homogeneous liquid phase can be increased significantly. However, it must be determined how the metals are distributed in the salts after crystallisation, because it exerts a strong influence on the thermal conductivity of the solid phase.

Even if the thermal conductivity of metal salt solutions can be significantly increased, this does not mean that these materials can be used as PCMs in CSP plants due to the stringent requirements, eg low costs, no corrosion, thermal stability and suitable temperature of the phase transitions. Therefore, it is important to vary the parameters of metal-salt systems, which can be done by using multicomponent systems. Nevertheless, these systems have not undergone any comprehensive study. In this case, a different kind of possible combinations of components should be considered. Therefore, the fundamental principles of the formation of metal-salt solutions and influences on the phase transition temperatures and on the thermal conductivity need to be understood. Nowadays such tasks can be solved by using thermochemical modelling based on the CALPHAD method, which has been successfully applied in the last few decades for the development of superalloys and slag systems with three and more components. However, in the case of metal-salt systems, this is not yet possible because there is currently no such database that includes both metals and salts. The SaltMe project focuses on developing a consistent thermodynamic database and discovering new correlations between thermodynamic properties and thermal conductivity for metal-salt solutions.

SAMPLES

The pure salts LiCl (Alfa Aesar, ultra-dry, 99.995 per cent), KCl (Thermo Fisher Scientific, ultra-dry, 99.997 per cent), NaCl (Thermo Fisher Scientific, 99.998 per cent), $MgCl_2$ (Thermo Fisher Scientific, 99.9 per cent), $CaCl_2$ (Thermo Fisher Scientific, 99.99 per cent) and pure metals Li (Sigma-Aldrich, ultra-dry, 99 per cent), K (Thermo Fisher Scientific, ultra-dry, 99 per cent), Na (Thermo Fisher Scientific, 99.95 per cent), Mg (Carl Roth, ≥99.8 per cent), Ca (Sigma-Aldrich, 99 per cent) were used to prepare samples for the measurements. Preparation of the samples was performed inside a glove box with argon atmosphere (purity 99.9992 per cent).

The 50 mol per cent $NaNO_3$ – 50 mol per cent KNO_3 salt mixture was prepared from the two pure compounds with purity 99.995 per cent of $NaNO_3$ and 99.999 per cent of KNO_3 from Sigma-Aldrich

by mixing in a glazed porcelain crucibles and heating up to 300°C under air atmosphere. Thermogravimetric analysis of the prepared mixture shows minor mass loss (in total 0.06 per cent) by heating the sample up to 400°C with two cycles, which confirms low content of absorbed water.

INSTRUMENTS

Differential Thermal Analysis (DTA)

NETZSCH STA 449C device was used to measure the phase change temperature. Samples were tested at a heating and cooling rate of 5 K/min with an argon gas flow rate of 20 mL/min, the purity of the argon gas is 99.9992 per cent.

Differential scanning calorimetry (DSC)

NETZSCH STA449F3 (Type S thermocouple) and NETZSCH DSC204F1 (Type E thermocouple) have been used for determination of heat capacity of the 50 mol per cent $NaNO_3$ – 50 per cent KNO_3 mixture. The experiments were performed with a heating rate of 10 K/min and 40 mL/min flow rate of argon (purity of 99.999 per cent) and nitrogen (purity of 99.999 per cent).

X-ray diffractometry (XRD)

Samples were investigated by using XRD with an EMPYREAN diffractometer (Malvern Panalytical, Almelo, The Netherlands) equipped with a Cu LFF X-ray tube (operated at 40 kV and 40 mA), a Bragg Brentano HD mirror, a PIXcel3D detector in 1D mode and a HTK 1200N oven chamber (Anton Paar, Austria).

CRUCIBLE MATERIALS FOR SALT MIXTURES

The choice of crucible material and geometry is highly dependent on the specific requirements of the thermal analysis method (eg DSC, thermomechanical analysis (TMA), laser flash analysis (LFA) and rheology) to ensure the determination of reliable thermodynamic (heat capacity, enthalpy of phase transitions) and thermophysical (thermal conductivity, thermal expansion, viscosity) properties. The selection depends on several factors such as the temperature range, thermal stability (when using closed or open crucibles), possible reactions with the crucible material and the gas atmosphere. In addition, surface energy and roughness of crucible material can influence the creep behaviour of the sample (Grosu *et al*, 2019; Piro, Lipkina and Hallatt, 2021; Hallatt, 2019).

In the case of salt systems, the use of graphite and boron nitride crucibles is preferable for DSC and Dilatometric (DIL)/TMA analyses due to low reactivity and wettability. However, relatively high thermal conductivity of graphite and non-replicable structure can indeed impact the reliability and accuracy of results for the LFA measurements. The irregularities in the graphite structure can introduce variability in thermal properties, affecting the precision of thermal diffusivity measurements. Low wettability can also be considered as a disadvantage when selecting spindle materials for rheological viscosity measurements. In rheological measurements, the interaction between the sample and the spindle or geometry used is critical to obtaining accurate and reliable viscosity data. Spindles with low wettability may not fully immerse or cover the sample, resulting in incomplete interaction. This can result in inaccurate viscosity readings as the instrument may not measure the entire sample.

In the frame of this work, different crucibles were tested for various thermal analysis techniques, including DSC, TMA, LFA and rheometry. A 50 mol per cent $NaNO_3$ – 50 mol per cent KNO_3 salt mixture was used as the well-studied composition to verify the experimental values. Figure 1 shows the experimental results of heat capacity obtained for the first heating of the sample in aluminium and graphite crucibles. In both cases quite similar results within the uncertainty of 3 per cent can be obtained, however in both cases two different devices STA449F3 (Type S thermocouple) and DSC204F1 (Type E thermocouple) were used. The results are also compared with available heat capacity data from FTSalt and FTfrtz databases from FactSage.

The temperature dependence of the density, thermal diffusivity and viscosity as well as the calculated thermal conductivity of the 50 mol per cent $NaNO_3$ – 50 mol per cent KNO_3 mixture will be discussed in the presentation at the MOLTEN 2024 conference. One of the main problems for

the determination of these values in the solid phase is the appropriate sample preparation, which should minimise the formation of pores and irreversible solid phase transition in the samples. In the case of viscosity measurements by rotational rheometer, spindle geometries made of different materials have been tested and reliable values have been obtained by using a plate-plate geometry made of copper.

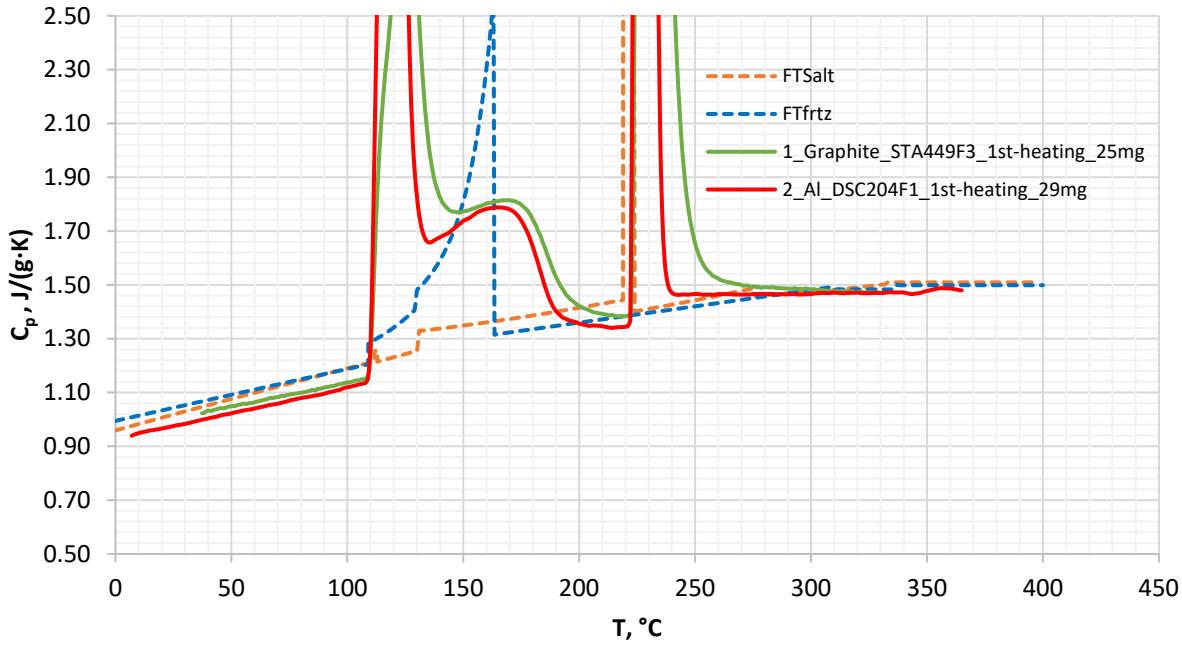

FIG 1 – Experimental values of the specific heat capacity of a 50 mol per cent $NaNO_3$ – 50 mol per cent KNO_3 mixture measured in aluminium and graphite crucibles and calculated values from FTSalt and FTfrtz databases from FactSage.

CRUCIBLE MATERIALS FOR METAL-SALT MIXTURES

The combination of salts and alkaline/alkaline earth metals introduces additional challenges in the selection of crucible materials, especially for high-temperature applications. The corrosive and reactive nature of certain salts, coupled with the reactivity of alkaline and alkaline earth metals, necessitates careful consideration when choosing materials for crucibles.

Table 1 shows the melting and boiling points of the metals, alongside the melting point of the salts. Notably, the boiling point of potassium (K) is lower than the melting points of NaCl and KCl. This implies that it is not advisable to conduct measurements of the K-KCl and K-NaCl mixture in open crucibles. Additionally, all metals within the system are prone to oxidation, and lithium (Li), sodium (Na), and potassium (K) are particularly susceptible to reacting with water (H_2O). To prevent undesirable interactions between the gas flow and the sample, as well as the vapourisation of the sample, it is preferable to use closed crucibles for the measurements.

TABLE 1

Melting and boiling temperatures of pure metals and salts.

Metal	Melting temperature, °C	Boiling temperature at 1 atm, °C	Salt	Melting temperature, °C
Li	181	1350	LiCl	610
Na	98	899	NaCl	801
K	64	768	KCl	770
Mg	650	1114	$MgCl_2$	714
Ca	842	1492	$CaCl_2$	772

The K-KCl system was experimentally investigated by Johnson and Bredig (1958) utilising stainless steel crucibles. Similarly, the Na-NaCl system was studied by Bredig, Johnson and Smith (1955) and Bredig and Bronstein (1960) using stainless steel crucibles. As an example, the phase diagram of K-KCl system studied by Johnson and Bredig (1958) is shown in Figure 2, which demonstrates the formation of a homogeneous solution between salt and metal in the liquid phase. The Li-LiCl system was measured by (Nakajima *et al*, 1974) using molybdenum (Mo) cells sealed by means of electron beam welding. For the measurement of the Ca-$CaCl_2$ system, tantalum and stainless-steel crucibles were used (Sharma, 1970; Staffanson, 1960). The effect of Mg on the corrosion of 316H stainless steel in molten salts $MgCl_2$-NaCl-KCl was investigated by (Zuo *et al*, 2021). These results are summarised in Table 2.

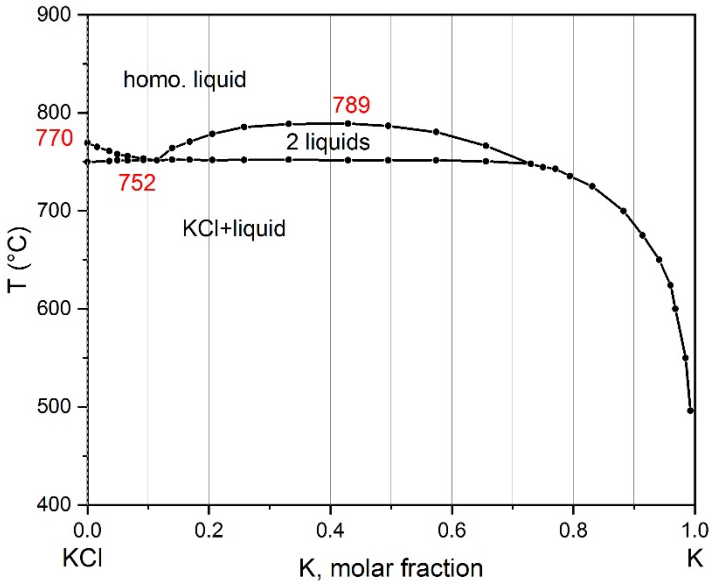

FIG 2 – Phase diagram of the metal-salt system K-KCl (Johnson and Bredig, 1958).

TABLE 2

Literature data on crucible materials used in previous studies.

System	Crucible	References
K-KCl	Stainless steel + glass	Johnson and Bredig, 1958
Na-NaCl	Stainless steel + glass	Bredig, Johnson and Smith, 1955
Li-LiCl	Mo cell sealed by means of electron beam welding	Nakajima *et al*, 1974
Ca-$CaCl_2$	Tantalum melt container/ stainless steel	Sharma, 1970; Staffanson, 1960
NaCl-KCl-$MgCl_2$-Mg	Stainless steel	Zuo *et al*, 2021

In studies involving liquid sodium (Na) as a heat transfer fluid, Pacio and Wetzel (2013) identified suitable structural materials. Their findings indicated that pure iron, ferritic stainless steel, austenitic stainless steel, chromium, nickel alloys (containing iron, chromium and molybdenum) and refractory metals (molybdenum, niobium, tantalum and tungsten) exhibited good compatibility with the liquid sodium at 300°C, 600°C and 800°C, ensuing a corrosion rate lower than 25.4 μm/a.

It is important to ensure that no reactions occur between the sample and the crucible when selecting crucible materials. This validation process involves consideration of the phase diagrams with the present components. If the analysis reveals the presence of intermediate compounds or solid solutions, the crucibles are subsequently excluded from the consideration. The assessment involved examining the phase diagram or the intermediate compounds that may form between the metals and

SiO_2, Al_2O_3, graphite and Pt. The phase diagram of metals and oxide crucible materials were calculated using the FToxid database and SGPS database. As an example, the results of Mg-Al_2O_3 are illustrated in Figure 3. While the liquid phase of the phase diagram may lack accuracy due to the absence of a shared database between metal and oxide, the representation of intermediate compounds and solid solution phases in the solid part of the diagram offers valuable insights into potential reactions between the samples and the crucible materials. Analogously, in the calculated phase diagrams of Al_2O_3 and other metals (ie Li, Na, K and Ca), intermediate compounds are found formed, eg Li_5AlO_4, $LiAlO_2$, $LiAl_5O_8$, $NaAlO_2$, $Na_2Al_{12}O_{19}$, $NaAl_9O_{14}$, $KAlO_2$, $K_2Al_{12}O_{19}$, $CaAl_2O_4$, $CaAl_{12}O_{19}$ and $CaAl_4O_7$. In the calculated phase diagrams between SiO_2 and sample metals (Li, Na, K, Mg and Ca), various intermediate compounds are found, such as Li_2SiO_3, $Li_2Si_2O_5$, Li_4SiO_4, Li_8SiO_6, Na_2SiO_3, $Na_2Si_2O_6$, Na_4SiO_4, $K_2Si_4O_9$, $K_2Si_2O_5$, K_2SiO_3, $CaSiO_3$, Ca_2SiO_4, $MgSiO_3$ and Mg_2SiO_4. In the case of Pt, numerous intermediate compounds such as LiPt, $LiPt_2$, $LiPt_7$, Li_2Pt, $NaPt_2$, MgPt, $MgPt_3$, Mg_2Pt, Mg_3Pt, Mg_3Pt_2, $CaPt_2$, $CaPt_5$ and Ca_2Pt_2 have been identified, as documented in the ICSD database (Belsky *et al*, 2002). Notably, no intermediate compound between Pt and K was found in this database. Besides, the phase diagram between other crucible material (Mo, Ni, Fe and graphite) and the sample metals (Li, Na, K Mg and Ca) were calculated with FTlite database in FactSage. In Table 3 possible compatibilities of crucible materials with salts and metals are shown.

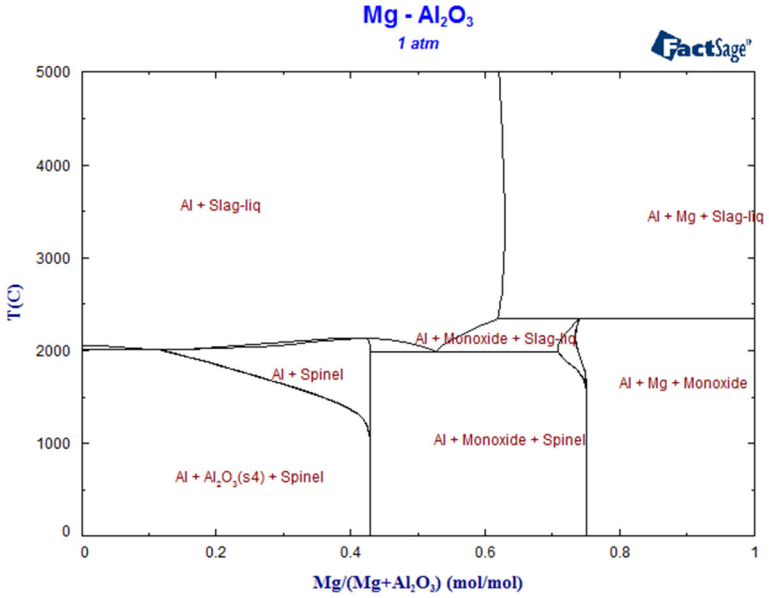

FIG 3 – Phase diagram of Mg-Al_2O_3 system.

TABLE 3

Compatibility of crucible materials with salts and metals.

Samples	Crucible materials							
	graphite	glass	Pt	Al_2O_3	Mo	Fe	Ni	Stainless steel 316L
Chloride salts	+	+	+	+	+	+	+	+
Na	-	-	-	-	+	+	+	+
K	-	-	+	-	+	+	+	+
Li	-	-	-	-	+	+	+	+
Mg	-	-	-	-	+	+	-	-
Ca	-	-	-	-	+	+	-	-

'+' = good compatibility, '-' = not compatible.

Two types of closed crucibles were designed for the DTA experiments of the salt-metal system, which are made of Fe-alloy-Mo crucible and of stainless steel 316L, as shown in Figure 4,

respectively. The threaded structure and the sealing gasket are used to increase the sealing ability of the crucibles. The similar structure was reported by Piro, Lipkina and Hallatt (2021).

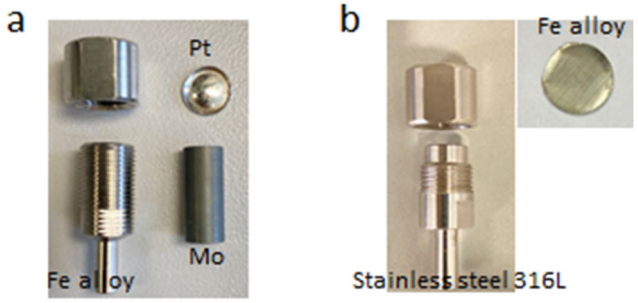

FIG 4 – DTA crucible from: (a) Fe-alloy with Mo liner; and (b) stainless steel 316L.

MULTICOMPONENT METAL-SALT SYSTEMS

In addition to quasi-binary metal-salt systems, multicomponent metal-salt systems have great potential for use as phase change materials or as heat transfer fluids. Such systems have not yet been investigated systematically. Binary metal-salt mixtures are limited and not suitable for various application conditions requiring lower phase transition temperatures. In the case of multicomponent systems, the melting temperature can be decreased significantly. For example, we can consider the reciprocal system Na-K-KCl-NaCl. This system includes four binary (K-Na (Figure 5), KCl-NaCl (Figure 5), K-KCl (Figure 2), Na-NaCl) systems. It can be seen, that in all these cases the lowest melting temperature is reduced. Therefore, it can be assumed, that the melting temperatures inside of the reciprocal system will be lower compared to the quasi-binary systems.

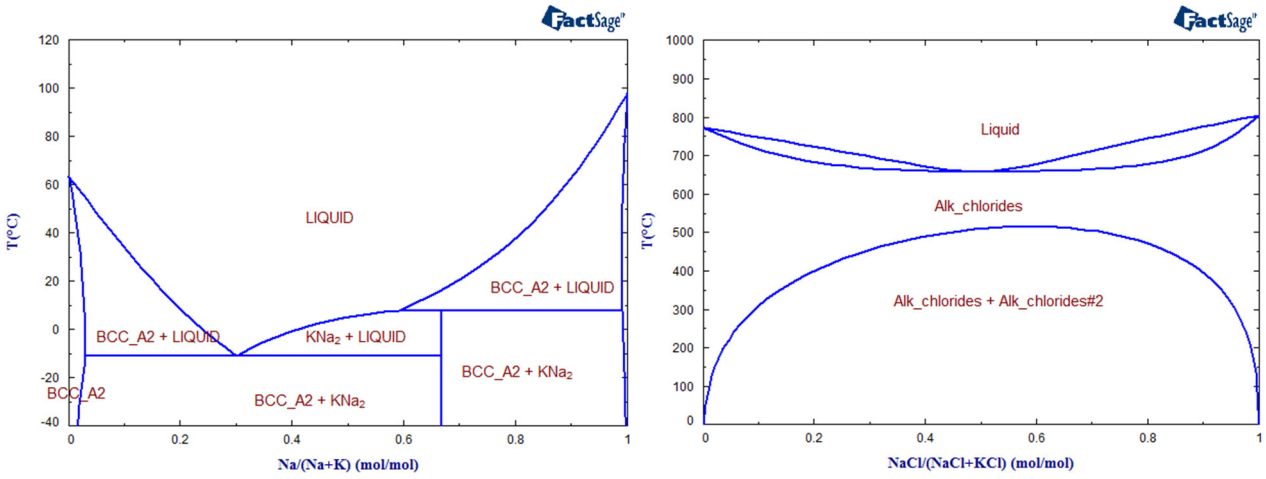

FIG 5 – Phase diagram of Na-K (SGTE database) and NaCl-KCl systems (PCM database).

One of the features of reciprocal systems is the reciprocal reaction, eg K+NaCl = KCl+Na. Equilibrium conditions of this reaction should be considered. For example, when studying the two-component K-NaCl or Na-KCl systems, four components can be formed according to the equilibrium conditions of the reciprocal reaction. That means it is sufficient to mix just three components, eg Na, KCl and NaCl, to produce all the compositions in the triangle Na-KCl-NaCl on the phase diagram. This allows the preparation of mixtures with more suitable components. It also avoids the use of highly reactive components such as potassium.

For the reciprocal system, the stable diagonal systems can be confirmed using Ellingham diagonal, calculated with FactSage Reaction using SGTE database, as shown in Figure 6. There are crossings in the Ellingham (Na-Li and Na-Ca). According to this calculation, the stable diagonals at room temperature are not correct for the (Na-Li-NaCl-LiCl) and (2Na-Ca-$(NaCl)_2$-$CaCl_2$) systems, when the temperature is above the cross point. The stable diagonals at 298 K are shown in Figure 7 and listed in Table 4. The reliability of this calculation needs to be tested experimentally. From the application point of view, according to these reactions, when small amounts of metals were added

to the salt mixture, only the stable metals remained. For example, when the metal mixture of Na, K and Mg is added into the salt mixture of NaCl, KCl and $MgCl_2$, Na and K will react with $MgCl_2$ to form NaCl and KCl. After the reaction, only Mg remains and the composition of the salt mixture will be changed. This composition change can lead to changing of transition temperature of the system. Therefore, only the stable diagonals can be used. The stable metal in the ternary systems is given in Table 4. This was also the case when the metals were added to the quaternary salt systems. The five quaternary salt systems and the corresponding metals are listed in Table 4. The information about the eutectic or lowest temperature and corresponding composition in binary and ternary systems are given in Tables 5 and 6.

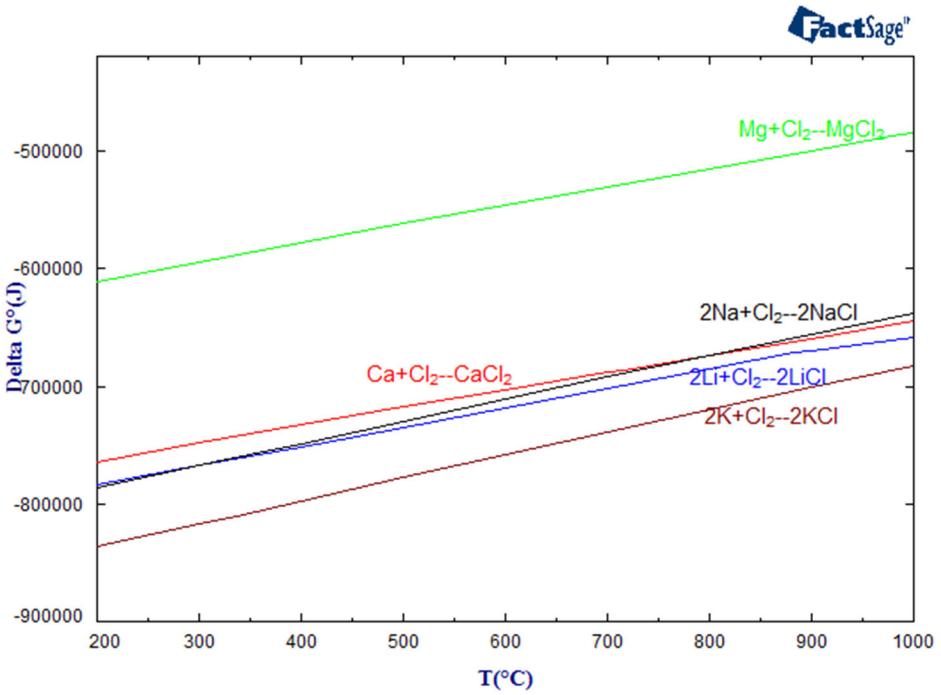

FIG 6 – Ellingham diagram for the chlorides.

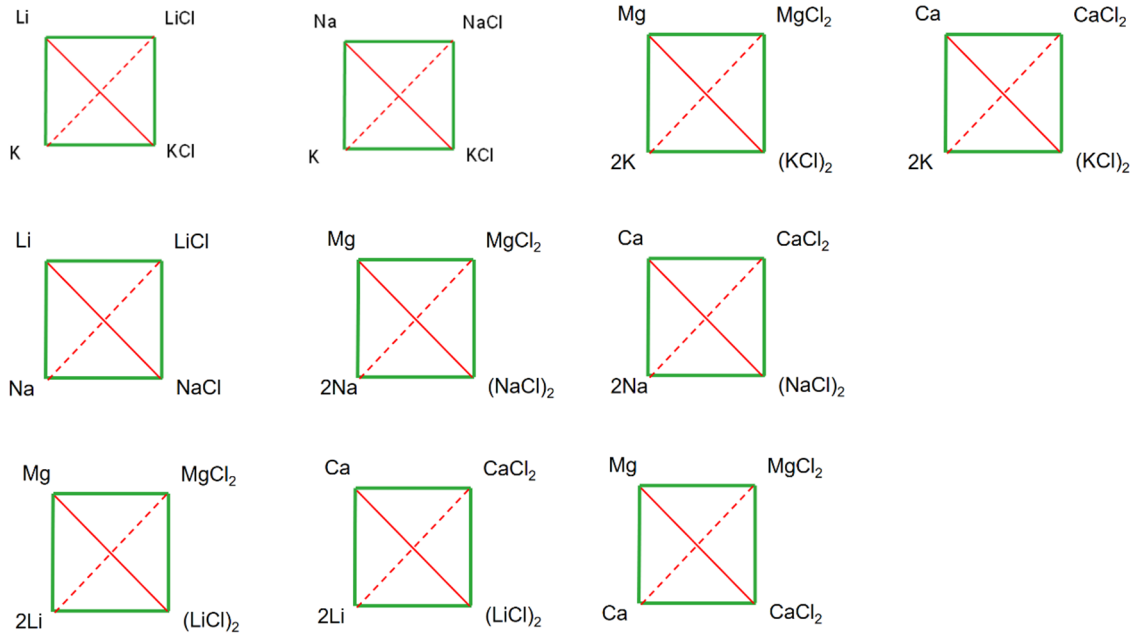

FIG 7 – Stable diagonals (solid lines) and unstable diagonals (dashed lines) at 298 K for different reciprocal systems.

TABLE 4

Stable diagonal systems in the reciprocal systems and stable metals in the ternary and quaternary systems.

Reciprocal system	Stable diagonal at 298 K	Ternary systems	Stable metal	Quaternary system	Stable metal
K-Li-KCl-LiCl	Li-KCl	KCl-NaCl-$CaCl_2$	Ca	KCl-NaCl-$MgCl_2$-$CaCl_2$	Mg
K-Na-KCl-NaCl	Na-KCl	KCl-NaCl-$MgCl_2$	Mg	LiCl-NaCl-$MgCl_2$-$CaCl_2$	Mg
Na-Li-NaCl-LiCl	Li-NaCl	NaCl-$CaCl_2$-$MgCl_2$	Mg	KCl-LiCl-$MgCl_2$-$CaCl_2$	Mg
2K-Mg-$(KCl)_2$-$MgCl_2$	Mg-KCl	KCl-$CaCl_2$-$MgCl_2$	Mg	KCl-NaCl-LiCl-$CaCl_2$	Ca
2Na-Mg-$(NaCl)_2$-$MgCl_2$	Mg-NaCl	KCl-NaCl-LiCl	Li	KCl-NaCl-$MgCl_2$-LiCl	Mg
2Na-Ca-$(NaCl)_2$-$CaCl_2$	Ca-NaCl	NaCl-LiCl-$MgCl_2$	Mg		
2K-Ca-$(KCl)_2$-$CaCl_2$	Ca-KCl	KCl-LiCl-$CaCl_2$	Ca		
Mg-Ca-$MgCl_2$-$CaCl_2$	Mg-$CaCl_2$	NaCl-LiCl-$CaCl_2$	Ca		
2Li-Mg-$(LiCl)_2$-$MgCl_2$	Mg-LiCl	KCl-LiCl-$MgCl_2$	Mg		
2Li-Ca-$(LiCl)_2$-$MgCl_2$	Ca-LiCl	LiCl-$CaCl_2$-$MgCl_2$	Ca		

TABLE 5

Eutectic or lowest temperature and corresponding composition in binary systems.

Binary system	Composition, molar fraction	Temperature, °C
KCl-LiCl (PCMJ)	0.413–0.587	351.9
KCl-NaCl (PCMJ)	0.512–0.488	657
KCl-$MgCl_2$ (FTsalt)	0.70–0.30	422.7
KCl-$CaCl_2$ (FTsalt)	0.751–0.249	601.4
NaCl-LiCl (PCMJ)	0.72–0.28	557
NaCl-$MgCl_2$ (FTsalt)	0.569–0.431	459.3
NaCl-$CaCl_2$ (FTsalt)	0.476–0.524	506.2
LiCl-$MgCl_2$ (FTsalt)	0.68–0.32	571
LiCl-$CaCl_2$ (FTsalt)	0.65–0.35	475.1
$MgCl_2$-$CaCl_2$ (FTsalt)	0.526–0.474	617.4

TABLE 6

Eutectic or lowest temperature and corresponding composition in ternary systems.

Ternary system	Composition, molar fraction	Temperature, °C
KCl-NaCl-LiCl (FTsalt)	-	347.5
KCl-NaCl-$MgCl_2$ (FTsalt)	0.273–0.284–0.444	382.1
KCl-NaCl-$CaCl_2$ (FTsalt)	0.080–0.405–0.515	483.1
KCl-LiCl-$CaCl_2$ (FTsalt)	0.424–0.529–0.047	340.9
KCl-LiCl-$MgCl_2$ (FTsalt)	0.454–0.464–0.08	335.8
KCl-CaCl2-$MgCl_2$ (FTsalt)	0.694–0.025–0.281	416.7
NaCl-LiCl-$MgCl_2$ (FTsalt)	0.431–0.236–0.332	414.4
NaCl-LiCl-$CaCl_2$ (FTsalt)	-	436.2
NaCl-CaCl2-$MgCl_2$ (FTsalt)	0.51–0.25–0.24	416.6
LiCl-CaCl2-$MgCl_2$ (FTsalt)	0.305–0.334–0.36	545.2

EXPERIMENTAL RESULTS

In this work, preliminary results on the study of the reciprocal (2K-Mg-$(KCl)_2$-$MgCl_2$) system will be presented. In this system, the stable diagonal is Mg-$(KCl)_2$ (see Figure 7). $MgCl_2$ and K react to form metallic Mg and KCl. The mixture of 0.2K-0.8$MgCl_2$ was studied by using DTA in a Fe-alloy crucible with Mo liner and Pt sealing (Figure 4a). The result is shown on Figure 8. In this case, the reaction can be represented in the following way:

$$20K + 80MgCl_2 \rightarrow 20KCl + 70MgCl_2 + 10Mg \quad (1)$$

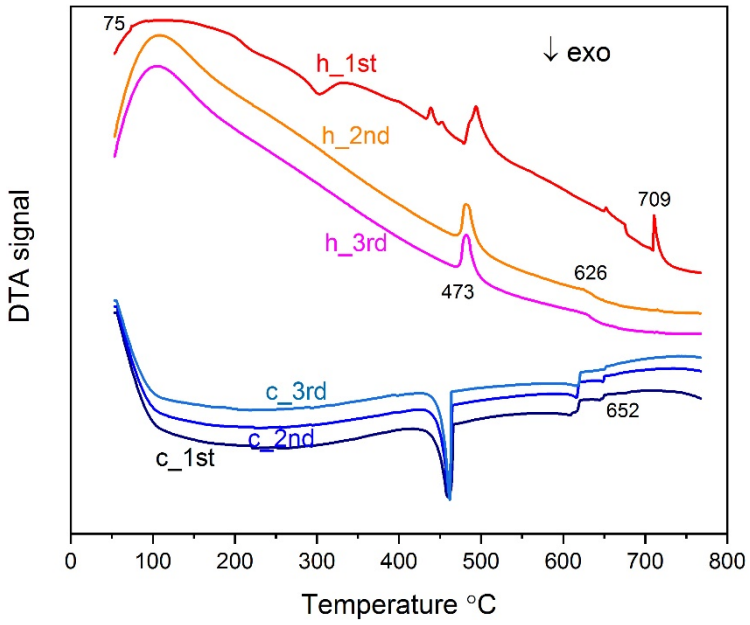

FIG 8 – DTA results of the 0.2K-0.8$MgCl_2$ composition measured in Fe-alloy-Mo closed crucible.

On the first heating curve the melting temperatures of K and $MgCl_2$ are visible, and the rest of the peaks showed that the reciprocal reaction (1) occurred during the heating. In the second and third cycles, the melting temperature of K was not visible (see Figure 8) and the area of the melting peak of $MgCl_2$ was reduced due to the reciprocal reaction (see Figure 9). In the second and third cycles, two reproducible phase transition temperatures (473°C and 626°C) were detected. According to the reaction (1), the composition of the salt mixture in the sample was recalculated to be 0.22KCl-

0.78$MgCl_2$. Therefore, the phase transition temperature of the sample 0.2K-0.8$MgCl_2$ measured by DTA is compared with the phase transition temperatures of the composition 0.22KCl-0.78$MgCl_2$ in the phase diagram calculated using FTsalt database (see Figure 10). The temperatures of phase transition of 0.2K-0.8$MgCl_2$ obtained from DTA (473°C and 626°C) agree well with the calculated eutectic temperature (472°C) and liquidus temperature (626°C) of the salt mixture. The melting of the metallic Mg, formed due to reciprocal reaction (1), was not detected in the heating curve, but in the cooling curves (652°C). The reason for the low signal of Mg may be due to the reaction between the Mg and Pt seal. The XRD results after the DTA experiment of the analysed 0.2K-0.8$MgCl_2$ mixture are shown in Figure 11. The mixture consists of 0.6 $KMgCl_3$ and 0.4 $MgCl_2$ in weight fraction, which is 0.54 $MgCl_2$-0.46 $KMgCl_3$ in molar fraction. In the phase diagram (Figure 10), the composition of the stable phase $MgCl_2$ and $KMgCl_3$ was calculated to be 0.56$MgCl_2$-0.44$KMgCl_3$ according to the lever rule. The XRD results agree well with the calculated composition.

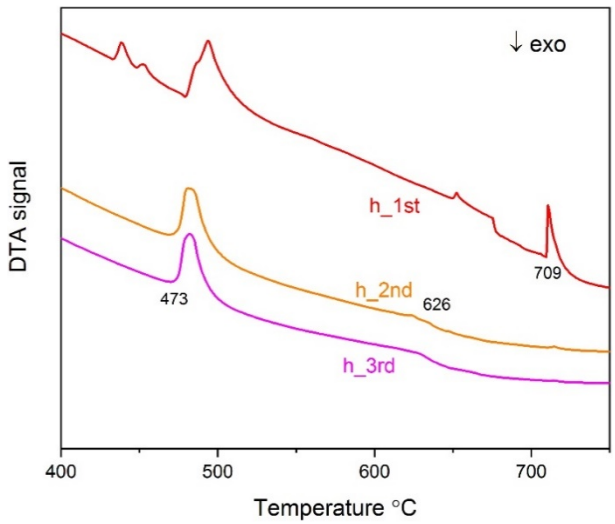

FIG 9 – DTA heating curves for 0.2K-0.8$MgCl_2$ composition measured in Fe-alloy-Mo closed crucible in the temperature range of 400–750°C.

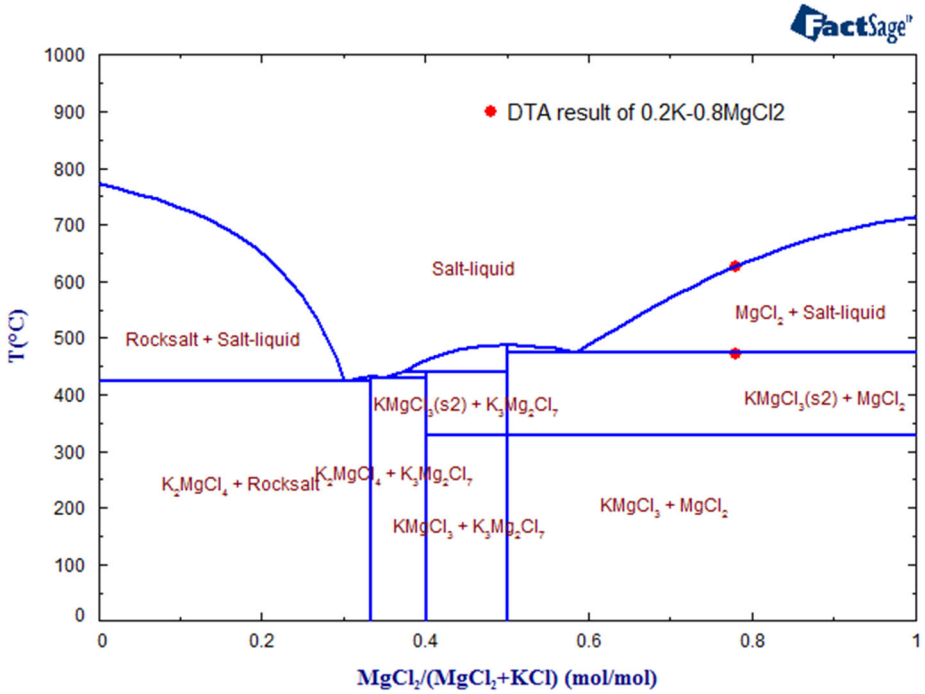

FIG 10 – Phase diagram of $MgCl_2$-KCl calculated with FTsalt database compared with the phase transition temperature of 0.2K-0.8$MgCl_2$ mixture detected by DTA.

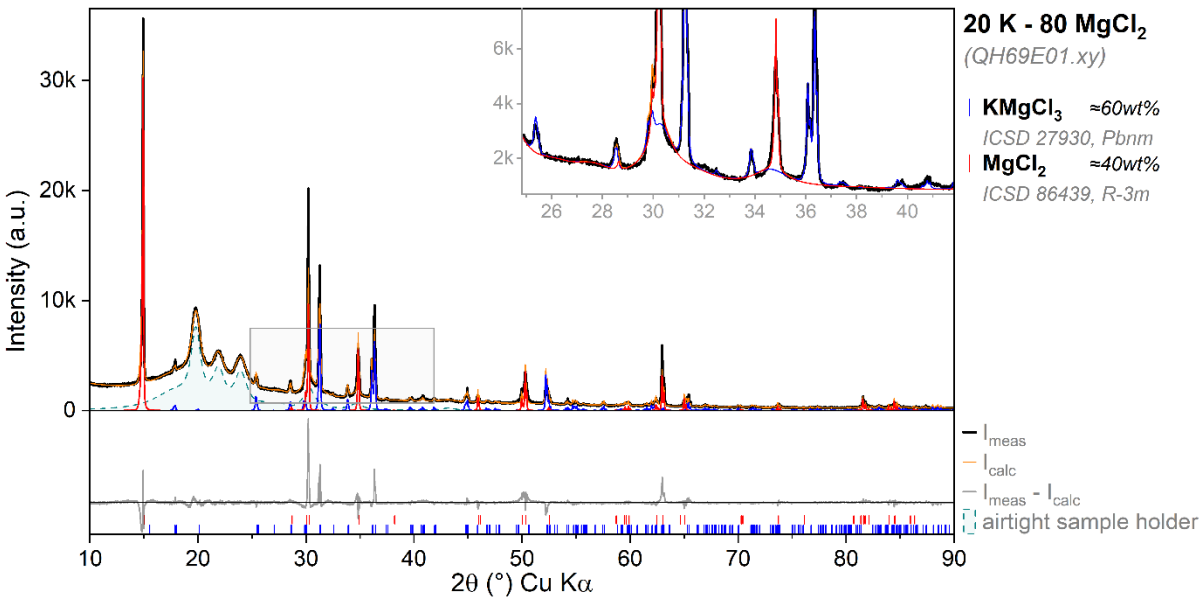

FIG 11 – XRD results of the mixture 0.2K-0.8$MgCl_2$ after DTA experiment.

The mixture of 0.2Mg-0.8KCl from the stable diagonal was measured in a Fe-alloy crucible (Figure 4b), the result is shown in Figure 12. On the DTA curve the melting temperatures of KCl (770°C) and Mg (655°C) are detected like for the pure substance, which means the solubility on both sides is neglectable. An additional peak at 512°C was detected on the heating and cooling curves, however no additional phases besides KCl were detected by XRD (Figure 13). This peak can be related to the Mg-Ni phase diagram, which corresponds to one of the eutectic temperatures. Nickel is one of the components of the stainless steel. Mg was not detected in the sample according to the XRD results (Figure 13) and the DTA peaks reduced in the second and third heating cycles. That is because the Mg reacts with Ni in the container and the rest of Mg is sticked in the wall of the crucible. Therefore, using Mo liners or crucibles could be the best option for the study of metal salt systems, which do not show any additional reactions with the samples.

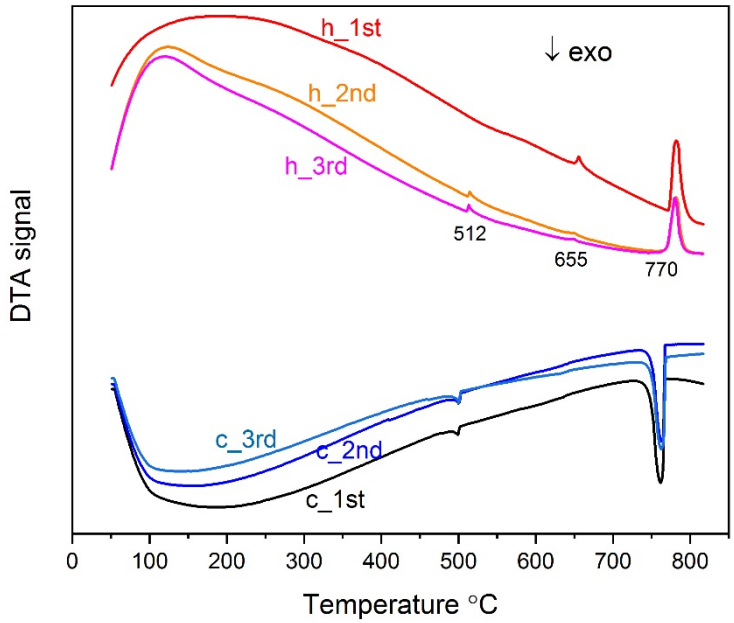

FIG 12 – DTA result of 0.2Mg-0.8KCl composition measured in SS316L closed crucible.

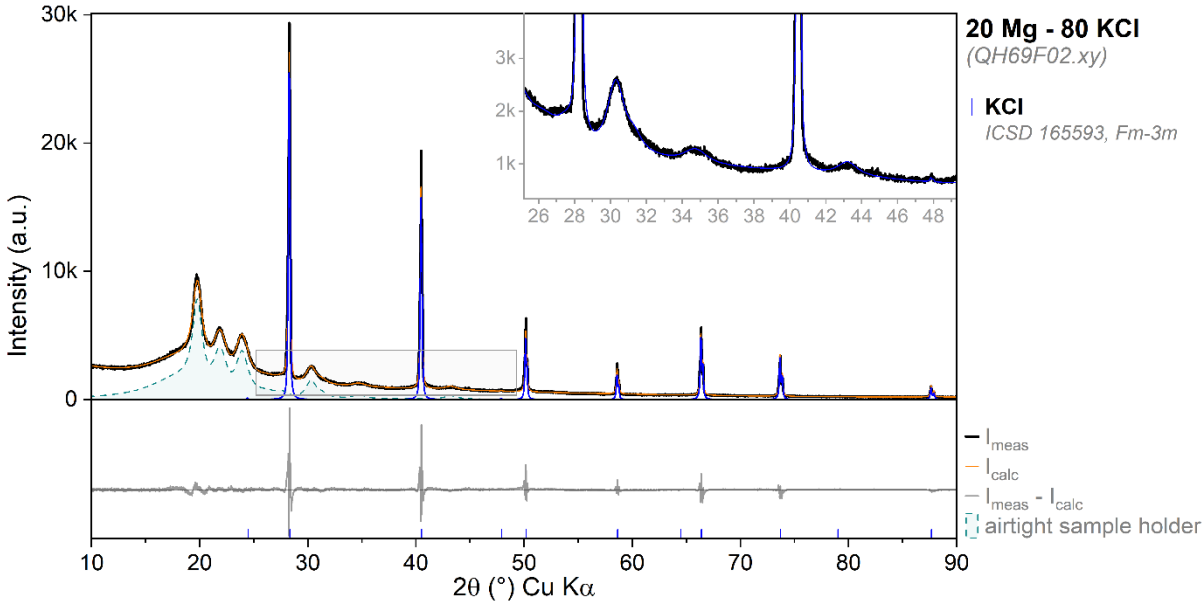

FIG 13 – XRD results of the mixture 0.2Mg-0.8KCl after the DTA experiment.

CONCLUSIONS

In this work, different crucible materials for studying of thermophysical properties of salt and metal-salt mixtures are discussed. Considerations such as temperature range, thermal stability, possible reactions, formation of solid solutions and intermediate compounds and surface properties influenced the choice of materials. A 50 mol per cent $NaNO_3$ – 50 mol per cent KNO_3 mixture was studied by using different techniques of thermal analysis (DSC, TMA, LFA and rheometry) and the detailed results will be presented on the MOLTEN 2024 conference. A significant challenge in determining these properties of the salt systems is ensuring proper sample preparation to minimise pore formation and consideration of metastable phases as well as creeping and wettability behaviour, which can be influenced by the materials in contact.

Metal-salt systems can play an important role in enhancement of thermal conductivity of salt systems, which is important from the application point of view. However, many challenging questions must be answered first. This work focuses on selecting appropriate crucibles for investigating the thermochemical properties of metal-salt systems and identifying suitable compositions for thermal conductivity tests. Based on the available data in thermodynamic databases, literature review and own experimental results it can be concluded that closed Mo-crucibles and liners are the best option for studying metal-salt systems. Fe-based alloys can be also used as well. DTA and XRD results for the reciprocal 2K-Mg-$(KCl)_2$-$MgCl_2$ system have been obtained and discussed. The formation of the stable Mg-$(KCl)_2$ diagonal in the frame of this system was confirmed, however no solubility between the end members of this system within the 0.2Mg-0.8KCl mixture was detected. Further study of other metal-salt systems will be performed and analysed. All collected data will be used for the development of the new thermodynamic database, which should allow the prediction of stable metal-salt compositions and their miscibility properties.

ACKNOWLEDGEMENTS

This work is supported by the German Research Foundation within the project ‘SaltMe’ (DFG 497349462).

REFERENCES

Baharoon, D A, Rahman, H A, Omar, W Z and Fadhl, S O, 2015. Historical development of concentrating solar power technologies to generate clean electricity efficiently – A review, *Renewable and Sustainable Energy Reviews*, 41:996–1027.

Belsky, A, Hellenbrandt, M, Karen, V L and Luksch, P, 2002. New developments in the Inorganic Crystal Structure Database (ICSD): accessibility in support of materials research and design, *Acta Crystallographica Section B: Structural Science*, 58(3):364–369. https://doi.org/10.1107/S0108768102006948.

Bredig, M A, Johnson, J and Smith, W T, 1955. Miscibility of Liquid Metals with Salts, I, The Sodium-Sodium Halide Systems 1, *Journal of the American Chemical Society*, 77(2):307–312. https://doi.org/10.1021/ja01607a016.

Bredig, M A and Bronstein, H R, 1960. Miscibility of liquid metals with salts, IV, The sodium–sodium halide systems at high temperatures 1, *Journal of Physical Chemistry*, 64(1):64–67. https://doi.org/10.1021/j100830a016.

Cárdenas, B and León, N, 2013. High temperature latent heat thermal energy storage: Phase change materials, design considerations and performance enhancement techniques, *Renewable and Sustainable Energy Reviews*, 27:724–737.

do Couto Aktay, K S, Tamme, R and Müller-Steinhagen, H, 2008 Thermal Conductivity of High-Temperature Multicomponent Materials with Phase Change, *International Journal of Thermophysics*, 29:678–692.

Grosu, Y, González-Fernández, L, Nithiyanantham, U and Faik, A, 2019. Wettability Control for Correct Thermophysical Properties Determination of Molten Salts and Their Nanofluids, *Energies*, 12:3765, https://doi.org/10.3390/en12193765.

Johnson, J W and Bredig, M A, 1958. Miscibility of Metals with Salts in the Molten State, III, The Potassium-Potassium Halide Systems, *Journal of Physical Chemistry*, 62(5):604–607. https://doi.org/10.1021/j150563a021.

Jegadheeswaran, S and Pohekar, S D, 2009. Performance enhancement in latent heat thermal storage system: A review, *Renewable and Sustainable Energy Reviews*, 13:2225–2244.

Hallatt, D, 2019. Developing a Framework for Thermodynamic Measurements of Fluoride Salt Nuclear Fuel, Masters' Thesis, University of Ontario Institute of Technology, Oshawa, Canada. Available from: <https://ir.library.ontariotechu.ca/handle/10155/1102>

Kenisarin, M M, 2010. High-temperature phase change materials for thermal energy storage, *Renewable and Sustainable Energy Reviews*, 14:955–970.

Liu, M, Steven Tay, N H, Bell, S, Belusko, M, Jacob, R, Will, G, Saman, W and Bruno, F, 2016. Review on concentrating solar power plants and new developments in high temperature thermal energy storage technologies, *Renewable and Sustainable Energy Reviews*, 53:1411–1432.

Nakajima, T, Minami, R, Nakanishi, K and Watanabe, N, 1974. Miscibility of Lithium with Lithium Chloride and Lithium Chloride–Potassium Chloride Eutectic Mixture, *Bulletin of the Chemical Society of Japan*, 47(8):2071–2072. https://doi.org/10.1246/bcsj.47.2071.

Pacio, J and Wetzel, T, 2013. Assessment of liquid metal technology status and research paths for their use as efficient heat transfer fluids in solar central receiver systems, *Solar Energy*, 93:11–22. https://doi.org/10.1016/j.solener.2013.03.025.

Piro, M H A, Lipkina, K and Hallatt, D, 2021. Exploring crucible designs for differential scanning calorimetry measurements of fluoride salts, *Thermochimica Acta*, 699:178860, https://doi.org/10.1016/j.tca.2021.178860.

Sharma, R A, 1970. Solubilities of calcium in liquid calcium chloride in equilibrium with calcium-copper alloys, *Journal of Physical Chemistry*, 74(22):3896–3900. https://doi.org/10.1021/j100716a009.

Staffanson, L I, 1960. The physical chemistry of metals in their molten halides, Doctoral dissertation, Imperial College London.

Zuo, Y, Cao, M, Shen, M and Yang, X, 2021. Effect of Mg on corrosion of 316H stainless steel in molten salts $MgCl_2$-NaCl-KCl, *Journal of Chinese Society for Corrosion and Protection*, 41(1):80–86. https://www.jcscp.org/article/2021/1005-4537/1005-4537-2021-41-1-80.shtml

Advancement in experimental methodologies to produce phase equilibria and thermodynamic data in multicomponent systems

DOI: 10.62053/FUJO2256

M Shevchenko[1], D Shishin[2] and E Jak[3]

1. Research Fellow, PyroSearch, University of Queensland, Brisbane Qld 4072. Email: m.shevchenko@uq.edu.au
2. Research Fellow, PyroSearch, University of Queensland, Brisbane Qld 4072. Email: d.shishin@uq.edu.au
3. Professor, Centre Director, PyroSearch, University of Queensland, Brisbane Qld 4072. Email: e.jak@uq.edu.au

ABSTRACT

One of the key aspects to develop sustainable metallurgical production is to ensure that the predictive power of thermodynamic tools is brought up to a new level of accuracy and reliability. Exploring new polymetallic processes, integrating primary and recycled materials, means utilising the uncharted areas within the Cu-Pb-Zn-Fe-Ca-Al-Mg-Si-O (major) – Cr-Na (slagging) – As-Sn-Sb-Bi-Ag-Au-Ni-Co (minor) slag-solids-metal-matte-speiss-sulfate system. This requires extensive integrated experimental and thermodynamic modelling study, which is underway at PyroSearch at the University of Queensland (UQ).

Recent improvements in experimental methodology allowed:

- Generating over a thousand equilibrium data points per annum by high-temperature (400–1750°C) equilibration, quenching, electron probe X-ray microanalysis (EPMA) technique at laboratory-controlled oxidation/reduction conditions.
- Studying previously impossible systems by smart choice of substrates corresponding to system conditions, one example being rhenium foil for Sn- and Sb-rich slags.
- Systematic updates in the properties of pure components/endmembers to provide self-consistent heat capacities from -273 to >3000°C in all phases, enthalpies of phase transition and melting points.

The accuracy of measurements also increased. For instance, selected compounds with well-known stoichiometry were systematically used as a set of secondary standards. Also, effects of secondary X-ray fluorescence were addressed. As the experimental techniques improve, new areas of compositions are revealed, which are not necessarily easy to describe using the existing thermodynamic model frameworks. Examples of these areas are: miscibility gaps in silicate systems, many of which never accurately measured before; multicomponent 4-phase liquid equilibria slag-matte-metal-speiss; liquidus temperatures for extremely high melting oxides CaO, MgO, NiO and SnO_2.

INTRODUCTION

Pyrometallurgy is an important sector of modern industrial society actively participating in solving current environmental, economic, materials scarcity and other challenges (Jak, 2018). Fundamental theoretical models can now be used to make a significant next step towards the development and implementation of computerised models describing real industrial processes. Recent trends determine the new challenges for the scientists including:

- stricter demand for the accuracy of the data
- more difficult systems for research
- more components of chemical systems (Jak, 2012).

The ultimate target is development of ‘Pyro-GPS’ multicomponent, multi-phase, wide range of conditions thermodynamic model (Jak *et al*, 2024).

An outline of the fundamental and applied research, through the expert analysis of processes of the industrial processes, to the implementation of the results of the research outcomes into industrial

operations, was provided by (Jak, 2012). The present paper attempts to present the developments of this approach that happened during the last 12 years. The integrated experimental/thermodynamic modelling approach developed in previous studies by the co-authors (Jak, 2012; Jak, Hayes and Lee, 1995; Jak *et al*, 2016), based on microanalysis of equilibrium phase compositions, represents a breakthrough in the accuracy, productivity and range of conditions to be studied (Jak *et al*, 2024).

New experiments are essential for development of the new model. Literature lacks both cover of systems/conditions and often accuracy. Experiments need to be planned to ensure sufficient: quantity and coverage of systems and conditions; and accuracy and reliability.

Which systems to investigate and how densely?

The range of characterised systems keeps extending each year. Due to large scope of possible studies (thousands of binary, ternary and quaternary systems, with 10–200 experiments potentially needed in each), it is essential to identify priorities and conduct minimum sufficient number of them in the most important systems first (Jak *et al*, 2024). This planning is driven by the model requirements – experiments location and quantity should adapt to the model needs.

Since most models in the currently available thermodynamic software packages have only binary and ternary parameters, it is essential to study all corresponding binary and ternary systems ('no experiments – no parameters' approach). Importantly:

- Thermodynamic data for pure components – H, G, S, Cp(T) for all stable and metastable phases (eg supercooled liquids as endmembers for slag) – are often not reliable due to high melting points (>2000°C: CaO, MgO, Al_2O_3, Cr_2O_3, SnO_2), instability (Ag_2O, Au_2O), volatility (As_2O_3, Sb_2O_3, SnO, ZnO), extreme reactivity (Na_2O), etc. Therefore, binary and often ternary or even quaternary data are needed just to understand the behaviour of pure components properly.
- Similarly, some areas of binary systems are not known directly. But they are required for description of ternary and higher-order systems – that is how the models work. Although ideally it would be desirable to have 20–30 reliable points in each binary system (at least one point per each 5 mol per cent), this can rarely be achieved in practice due to:
  - high liquidus temperature of many areas, particularly close to pure components, that exceeds the current technique limits (1750°C)
  - instability, volatility and reactivity of pure components as listed above
  - inability to quench liquids with compositions rich in some of the components that are poor glass-formers – particularly metals.

For example, Figure 1 for CaO-NiO-SiO_2:

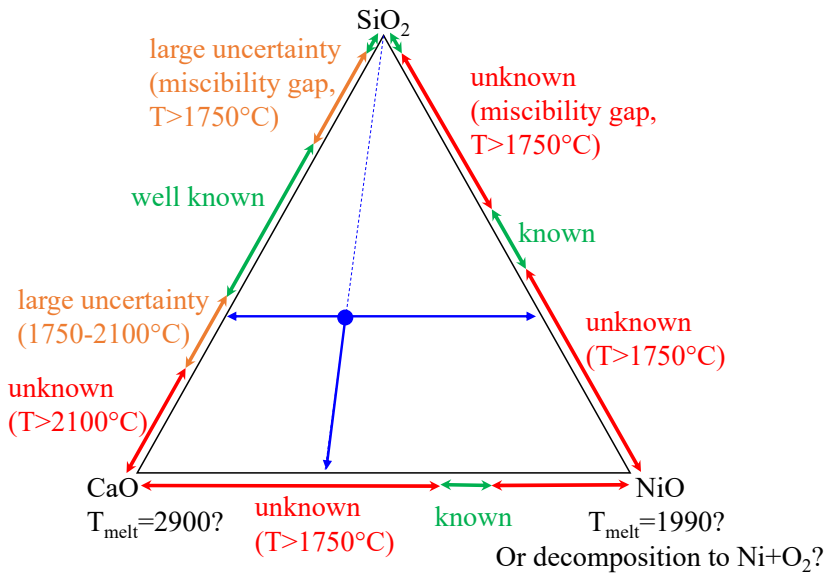

FIG 1 – Example of limited binary thermodynamic data for the CaO-NiO-SiO_2 system.

A random composition inside the area of realistic liquid slag, is shown using the blue dot in Figure 1. For this composition, thermodynamic properties are calculated by combining properties from three binaries as shown by the blue arrows, with further addition of ternary parameters. It is very likely, interpolation into ternary system is done from the unknown part of a binary sub-system. That is why ternary data may and should be used to double-check and evaluate the properties of binaries in the areas that cannot be studied directly.

Similarly, not all areas of each ternary system can be directly studied, but they may be revealed by experiments in the certain quaternary systems. Thus, quaternary systems must be studied and used to test the values of binary and ternary parameters.

Furthermore, a third or fourth component can sometimes be used as a flux added to the binary (or ternary) eutectic, to study the subsolidus behaviour in a more productive way. For instance, kinetically-limited solid-state experiments within the MgO-$AlO_{1.5}$-SiO_2 system would likely result in a sample, which is porous, contains compositional gradients and very hard to polish into smooth surface. For this system, the phases are also indistinguishable due to similar brightness in backscattered electron image, which relies on the difference in average atomic numbers of phases. Alternative approach involves the addition of PbO flux, as shown in Figure 2. PbO does not form any solid solutions with MgO-$AlO_{1.5}$-SiO_2 phases, neither it forms new stable solid phases. The addition of even small concentration of PbO to the liquid slag immediately makes it much brighter than all solids, giving the necessary contrast for effective sample much analysis. Some ternary invariant points involving slag have too high temperature to be studied directly. For instance liquid slag-lime-periclase-C_3S equilibrium within the CaO-MgO-SiO_2 system has the temperature of >1800°C. An addition of a fourth component, such as $AlO_{1.5}$, extends this invariant point as a lower temperature univariant line, allows measuring phase compositions accurately, and then extrapolate the quaternary results to obtain the compositions of all liquid and solid solutions in that point for the $AlO_{1.5}$-free ternary system.

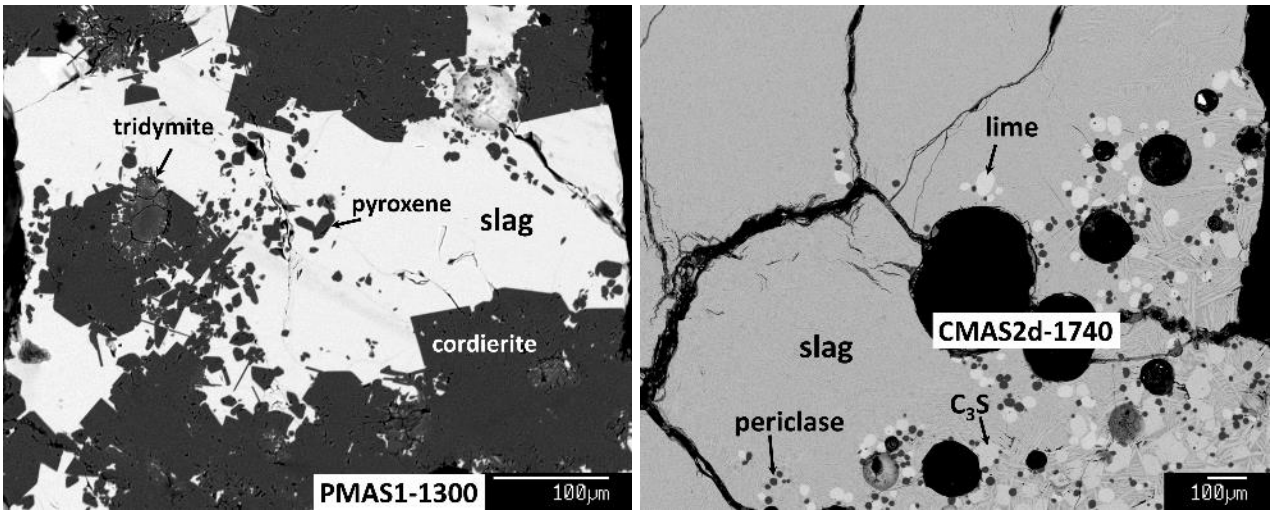

FIG 2 – Example microstructure of approaching the MgO-$AlO_{1.5}$-SiO_2 system (tridymite-pyroxene-cordierite solids) by addition PbO-rich flux (slag), and CaO-MgO-SiO_2 (lime-periclase-C_3S solids) with $AlO_{1.5}$ liquid slag.

High-order systems (4-, 5-, 6-component etc) are the ultimate target for thermodynamic predictions, relevant to the industrial purposes. The predictions must be confirmed by a certain number of experiments, preferably covering a large volume of the multidimensional compositional space. Traditional binary and ternary diagrams cannot represent the results of calculations and experiments in such systems. Several options exist to represent and analyse phase equilibria in these cases:

- Pseudoternary sections, where the concentrations or ratios of all components except three are fixed. Example: for the 6-component (PbO+CaO+SiO_2)-FeO-Fe_2O_3-ZnO systems, the ratio PbO/SiO_2 and CaO/SiO_2 can be fixed, furthermore the $p(O_2)$ is fixed at 0.21 atm to define the FeO/Fe_2O_3 ratio, allowing the (PbO-CaO+SiO_2)-(FeO+Fe_2O_3)-ZnO pseudo-ternary diagram (Jak and Hayes, 2002b, 2002a).

- Projections from the selected apex(es) of the multidimensional space. In the FactSage™ (Bale *et al*, 2016) calculation, this can be achieved by fixing the activity of the corresponding primary solid phase to 1, and analysing the secondary phase fields (Shevchenko and Jak, 2020b; Wen *et al*, 2023).
- Plotting the phase diagram based on three major components and analysing the behaviour (solubility, activity coefficients) of other minor components (Shevchenko, Chen and Jak, 2021).

Types of thermodynamic data

For each system, multiple types of thermodynamic data exist:

- Properties (H, G, S, Cp, vapour pressures etc) of pure components, compounds and solutions as functions of temperature, most importantly $\Delta_f H°_{298}$, $S°_{298}$.
- Properties of compounds and solutions (liquid, solid) as functions of temperature: integral and partial H, G, S, activities of components, vapour pressures.
- Phase equilibria: liquidus of each phase; extents of solutions; special points/lines of phase diagrams (phase transitions, eutectics, univariants etc); distributions of elements between phases.

Only rarely, all these types of data are available and even possible to measured directly. Lack of some types of data can be partially compensated by improved reliability and range of other types.

Current scope of study by PyroSearch team

Wide range of objects is studied simultaneously by the PyroSearch team: slag (including silica-free and other 'exotic' systems), matte, metal, speiss, liquid sulfates, solid solutions (Figure 3). Attempts are taken to develop other techniques: differential thermal analysis (DTA) / differential scanning calorimeter (DSC), viscosity, electrical conductivity, aqueous leaching.

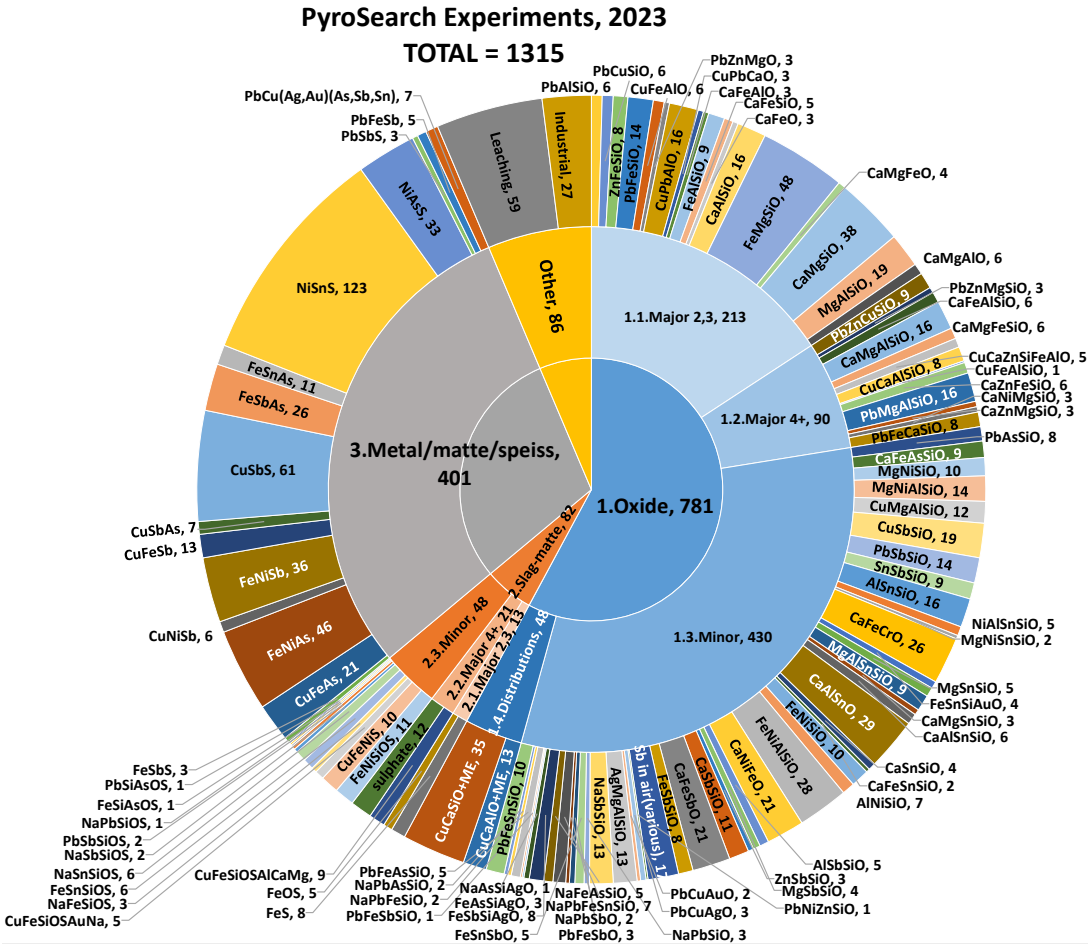

FIG 3 – Summary of all successful experiments done at PyroSearch in a typical year (2023).

Examples of microstructures of quenched high-temperature samples obtained in recent years are shown in Figure 4.

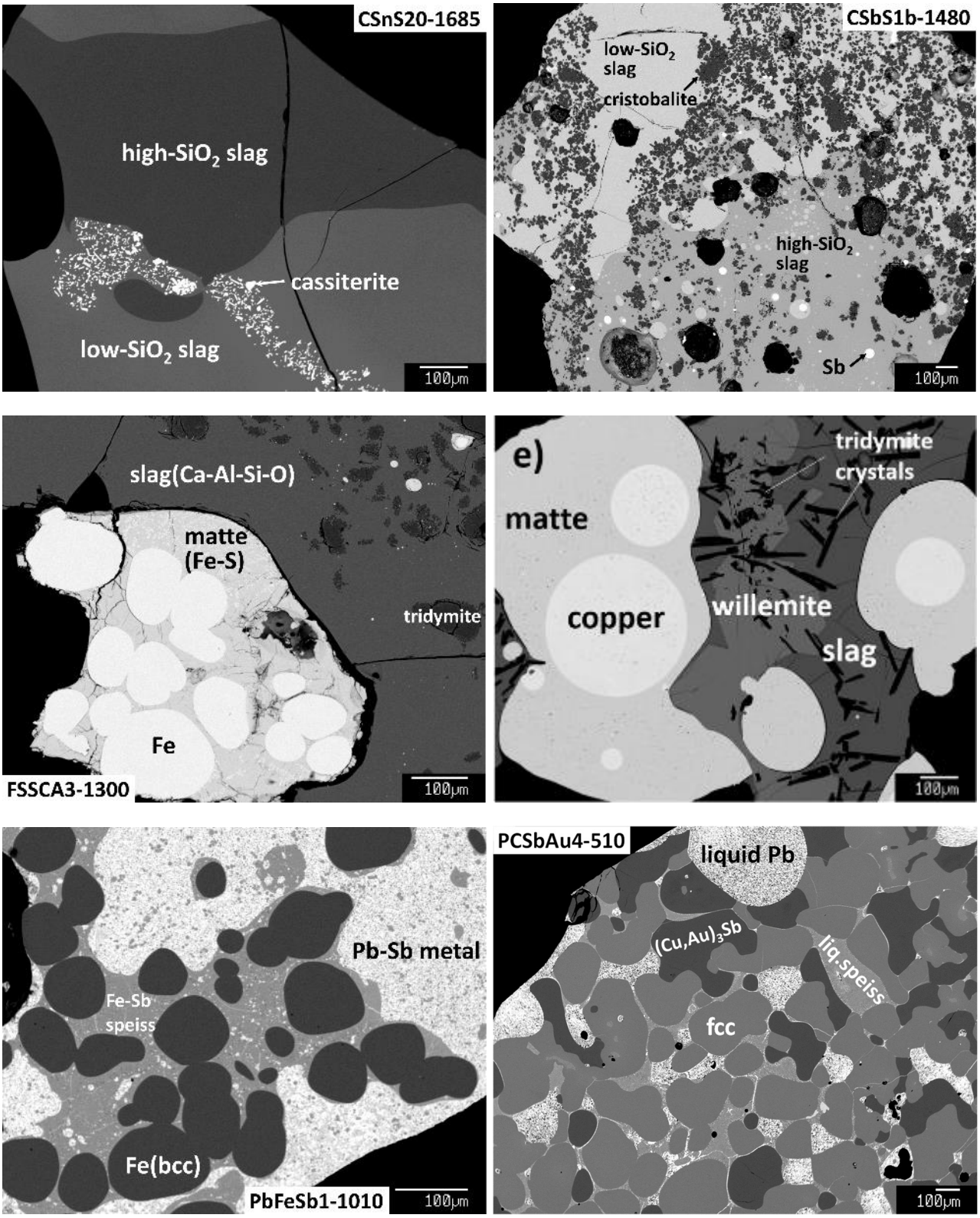

Continued…

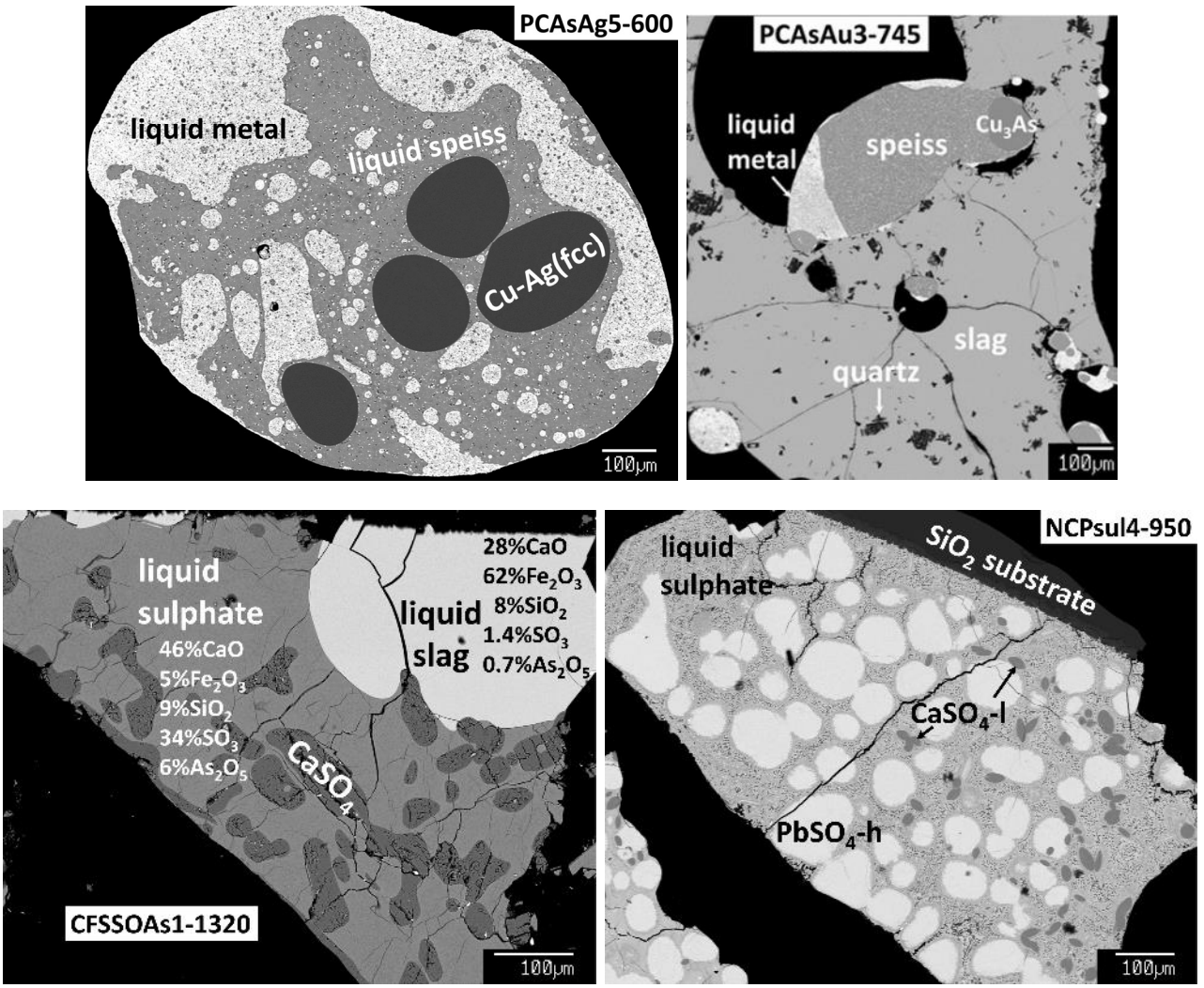

FIG 4 – Examples of microstructures in various types of systems studied at PyroSearch: immiscible liquid slags; liquid slag-matte-metal; metal-matte-speiss; metal-speiss-solids-slag; liquid sulfate-slag-solids.

Accuracy and reliability of experiments

Although the equilibration, quenching, electron probe X-ray microanalysis (EPMA) proved to be powerful, and seem easy to implement, there is a long list of possible issues that can lead to experiment failure or unreliable results. Each time a new type of object is studied, it is essential to prove that sample has reached equilibrium and that its quenched state properly represents that high-temperature equilibrium. Multiple stages of each experiment need a careful approach to avoid uncertainties, including:

- Experimental: impurities, achievement of equilibrium, temperature and gas composition uncertainties, quenching quality.
- Analytical: selection of area for analysis, effect of probe diameter, standards, characteristic line selection and interference, ZAF-correction, beam-sensitive elements, secondary fluorescence.

Conditions

Accuracy of temperature, p(O_2/SO_2/etc.), stability of substrates, absence of impurities. The impurities can be introduced from original materials, during the sample preparation, during the equilibration in impure atmosphere/dust, due to reaction with substrate and at post-quenching treatment due to hydration, oxidation.

A large variety of the starting materials is used:

- Pure powders, eg Fe, FeO_{1+x}, Fe_3O_4, Fe_2O_3, FeS, Cu, Cu_2O, CuO, Cu_2S, $CaCO_3$, CaO selected by optimising the purity, mixing efficiency, availability, price-to-value ratio.

These can be affected and controlled by:

- Reactions during heating/melting. For instance, CuO can de-compose upon heating, iron and lead oxides will react according to Fe + PbO = FeO + Pb.
- A thermal arrest at lower than target temperature, eg to melt a mixture of PbO + SiO_2, or Cu + As.

Master slags/matte/speiss are often prepared in advance. The PbO-SiO_2 master slag is necessary to minimise vaporisation of PbO in initial stages of experiment. The CaO-SiO_2, $Ca_2Fe_2O_5$ needs to be prepared to avoid residues of volatiles, $CaCO_3$ and $Ca(OH)_2$. Without complete removal of volatiles, sealed ampoule experiment can fail due to expansion. The synthesis of compounds like Cu_3As, FeAs, SnS, Sb_2S_3 may help avoiding the conditions where combined pressure of arsenic-sulfur containing gaseous species exceeds 1 atm and results in explosion.

The selection of a holding material for the sample equilibration is not straightforward. Over the years, many combinations substrates and samples has been developed at PyroSearch, which are summarised in Table 1 and Figure 5. Substrates made of 'inert' precious metals requires careful analysis of experimental conditions. Factors, such as temperature, $p(O_2)$, and possible reactions with corrosive metals, such as Cu, Pb, Sn, Sb etc, their oxides and mattes, often make them impractical to use. Both the melting points and the affinity for oxygen of most commonly used precious metals increase in the order Au < Pt < Ir < Re (Jak *et al*, 2022).

TABLE 1

List of substrates applied at PyroSearch for high-temperature phase equilibria studies.

Material	Advantages	Disadvantages	Systems studied, examples
SiO_2 ampoule 	Allows full protection from interaction with gas and evaporation of volatile materials. Used for quartz, tridymite, cristobalite liquidus, or others if second substrate enclosed inside. 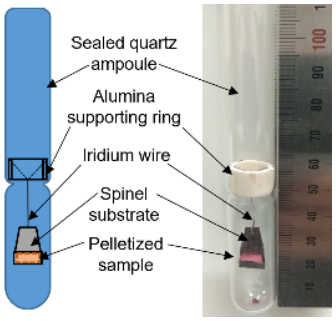	Sometimes infiltrated by slag (eg FeO-rich). Can expand and block the furnace at high T if any gas is released from sample.	Preferred for all oxide systems (high-SiO_2 ranges) where contact with gas is not needed. Also – slag-matte-metal, matte-metal-speiss...
SiO_2 ampoule with a hole	Allows the escape of released gas (CO_2, O_2, SO_2) and exposure to outside gas, which is not too far from composition inside.	The equilibration with gas is not fast enough in some cases.	Pb slag-matte-metal at high pSO_2 – limits evaporation of Pb. Fe-Sn-Si-O at high pO_2.

Table 1 continued…

Material	Advantages	Disadvantages	Systems studied, examples
SiO_2 open crucible 	Allows faster equilibration with gas (eg CO-CO_2).	Exposes a sample to dust contamination from above.	Large range of slag-metal, slag-metal-matte at fixed pO_2.
Al_2O_3 crucible 	Strong, not expensive, available in multiple sizes. Can be enclosed in SiO_2 ampoule (up to 1590°C) for volatile systems.	Relatively thick, may prevent fast quenching. May be infiltrated by slag.	Cu-Ca-Al-O.
MgO crucible 	Low solubility in most silicate, Cu- and Pb-slags. May be covered by protective layer of olivine. Can be enclosed in SiO_2 ampoule (up to 1540°C) for volatile systems.	Thick, may prevent fast quenching. May be infiltrated by slag. Contains ~3% Y_2O_3 impurity. Relatively brittle and expensive.	Cu-Mg-Si-O, Pb-Mg-Si-O.
Au foil 	Very stable to oxidation to slag, does not form any oxide compounds. Reusable.	Low T_{melt} = 1064°C, even lower in presence of Pb, Sn, Sb, ...	PbO-rich slags at low T.
Pt foil/wire/ crucible 	Easy to manufacture, thin – promotes fast quenching. Does not oxidise in air in contact with most slags.	Can form liquid or solid alloy in presence of Pb, Sn, Sb, Ni, Fe... at high T and reducing conditions. Can oxidise to slag (up to 0.3 wt%) or compounds (Pb-Pt-O, Ca-Fe-Pt-O) at low T and high $P(O_2)$. Expensive, not reusable.	Ca-Fe-Si-O, Pb-Fe-Si-O etc.

Table 1 continued…

Material	Advantages	Disadvantages	Systems studied, examples
Pt-25%Ir foil 	Stronger than Pt and less brittle than Ir, therefore reusable. High T_{melt} than Pt.	Intermediate resistance to alloy formation (reducing) and oxidation to slag/compounds between Pt and Ir.	Preferred for most oxide systems in air or mildly reducing/ inert atmosphere.
Ir wire/plates  	Stable to corrosion by Cu, Pb, Sn metals.	Can oxidise to compounds (Pb-Ir-O, Ca-Ir-O, spinel...) at low T and oxidising conditions. Relatively brittle. Expensive, not reusable. Plates are particularly expensive but reusable.	Cu, Pb, Sn systems. The only substrate to work in air above 1750°C, and in reducing atmosphere + corrosive metals.
Re foil/wire 	Stable to corrosion by liquid Cu, Pb, Sn, Sb, Bi, Ag, Au metals. Not brittle, reusable.	Can oxidise to slag, oxide compounds, and gas (eg in air it just gradually burns out).	SnO- and Sb_2O_3-rich systems in equilibrium with metal.
Ag wire	Easy to manufacture.	Low T_{melt} = 962°C. Easily oxidises to slag.	Pb-Ag-Si-O.
Pd wire	Similar to Pt, may be less prone to formation of certain oxide compounds, eg calcium ferrites.	Lower T_{melt} than Pt and higher solubility in most slags.	Ca-Fe-O.
Mo, W wire 	Very high T_{melt}, strong, not expensive.	Easy to oxidise and contaminate slag, form many stable solid compounds. Also form volatile MoO_3, WO_3 which cause persistent furnace contamination. Only for very reducing conditions.	Fe-Mg-Si-O.

Table 1 continued…

Material	Advantages	Disadvantages	Systems studied, examples
Cu foil/wire 	Cheap, easy to manufacture.	T_{melt} = 1085°C, further reduced by impurities.	Cu-Pb-Si-O.
Ni foil/wire 	Cheap, easy to manufacture.	T_{melt} = 1455°C, further reduced by impurities.	Ca-Ni-Al-O.
Co foil/wire 	Cheap, easy to manufacture.	T_{melt} = 1495°C, further reduced by impurities. Requires careful protection from oxidation.	Co-Si-O.
Fe foil/wire 	Cheap, easy to manufacture.	Requires careful protection from oxidation. Wetted by slag and liquid metals that creep into thin layer. Usually has some Mn contamination (~0.1%) that preferably goes to slag.	Ca-Fe-Si-O, Pb-Fe-Si-O (reducing – equilibrium with Fe).
FeO, Fe_3O_4 prepared from Fe foil/wire 	Can be reliably manufactured. Good choice for corrosive slag-metal combinations.	Brittle, very porous. Slag can be fully lost into pores. Not as good when slag has spinel-forming components (Al, Mg, Zn, Ni) – unclear if slag-spinel equilibrium distribution is reached.	Cu-Ca-Fe-O, Cu-Fe-Si-O, Pb-Fe-Si-O spinel and wüstite liquidus.
Other sintered oxides ($CaSiO_3$, ...)	Can be used in primary phase fields of respective compounds, when all other substrates are too reactive.	Brittle, very porous. Slag can be fully lost into pores. Complicated preparation with low success rate. Still requires other intermediate substrates (metal wires) for handing.	Cu-Ca-Si-O.

Table 1 continued…

Material	Advantages	Disadvantages	Systems studied, examples
Future plans – Cr_2O_3 	Very low solubility in most silicate slags, high T_{melt}.	Technique requires development.	Cr systems, multicomponent Pb slags.

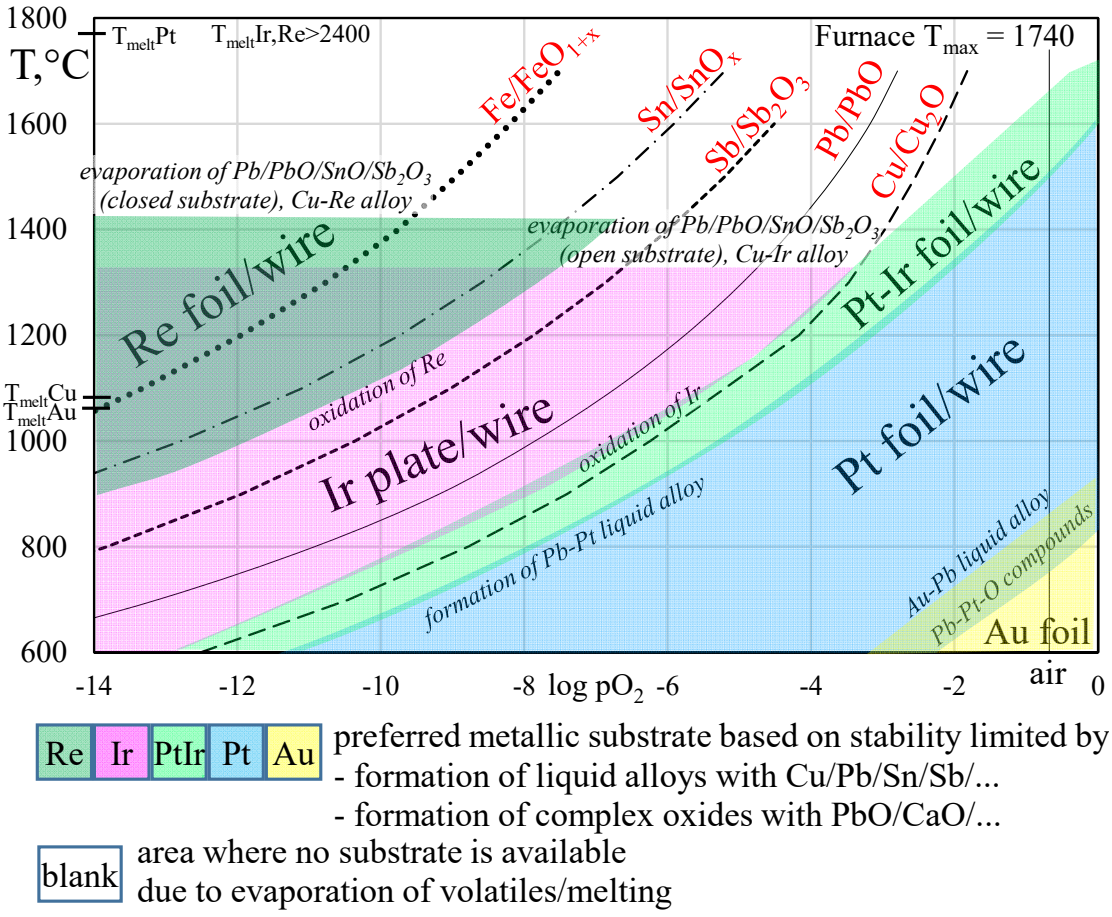

FIG 5 – Typical substrate preferences depending on pO_2 and T (Jak *et al*, 2022).

Achievement of equilibrium

Completion of reactions. General principles: macro- and micro-inhomogeneities, fast (liquid/solid) versus slow (gas/liquid, solid/solid) reactions.

Confirmation of achievement of equilibrium can be complicated, formulated as a '4-point test' (Jak, 2012; Shevchenko *et al*, 2016) including:

1. Variation of equilibration time.
2. Assessment of the compositional homogeneity of the phases by EPMA.
3. Approaching the final equilibrium point from different starting conditions.
4. Importantly, consideration of reactions specific to this system that may affect the achievement of equilibrium or reduce the accuracy.

Therefore:

- Direction of reactions towards equilibrium – should be investigated in preliminary experiments to avoid blocking mass transfer during equilibration (Hidayat *et al*, 2023).
- Distance to equilibrium point:
  - in initial experiments can be larger to ensure approach to equilibrium from different directions;
  - final experiments – better to be in the 'believed to be true'.

Planning may be assisted with FactSage™ with adjustment for 'believed to be true', but also can be done with a separate 'mass balance' model.

Preliminary short experiments (1–5 mins) are recommended at the initial stage of study of each system, to identify most important reactions on melting. Final equilibration time can vary from 10–15 mins (very high temperature ~1700–1750°C, fluid low-SiO_2 liquids, presence of volatile components such as ZnO, SnO_2) to 2–24 hrs (typical) and even several weeks (low temperature ~500–700°C, viscous liquids rich in SiO_2, PbO, Sb_2O_3, expected slow-forming compounds such as $PbSiO_3$).

Quenching

Selection of quenching medium. The best is not 'as cold as possible' but 'as far from boiling point as possible, in terms of enthalpy'. For example, liquid N_2 is very cold but close to the boiling point and thus a very bad quenching medium. Sometimes, is referred to as Leidenfrost effect. Water at room temperature is not as good as water at 0°C. Even better is the salt brine at -20°C. It is not just the low temperature, but also the prevention of continuous vapour cushion blanket due to the change in regime of boiling (Luty, 1992; Pizetta Zordão *et al*, 2019). Other possible, but less used quenching media is fluororganic liquid NOVEC1230, $C_6F_{12}O$, also known as 'dry water', which is applicable samples that are water-sensitive, such as high-Na_2O slags and molten salts. Oils are not used for quenching due to fire hazard and because the oil contamination is very bad for the electron microscopes.

Depending on the properties of phases and their combinations, the main uncertainty is either the achievement of equilibrium or preservation of equilibrium during the quenching (Figure 6). The former is limiting for highly viscous liquids or slow solid-state reactions, while the latter is a problem for very fluid liquids, or reactions happening fast at temperature drops.

- Fluid liquid – expected problems with quenching and no issues with equilibration – % solids should be minimum with maximum liquid exposed first to the quenching media and later found in the mounted sample, equilibration time can be shorter (unless gas is involved).
- Viscous liquid – expected problems with equilibration and no issues with quenching – % solids should be higher, but not blocking mass transfer access to other phases (eg gas, matte, slag).

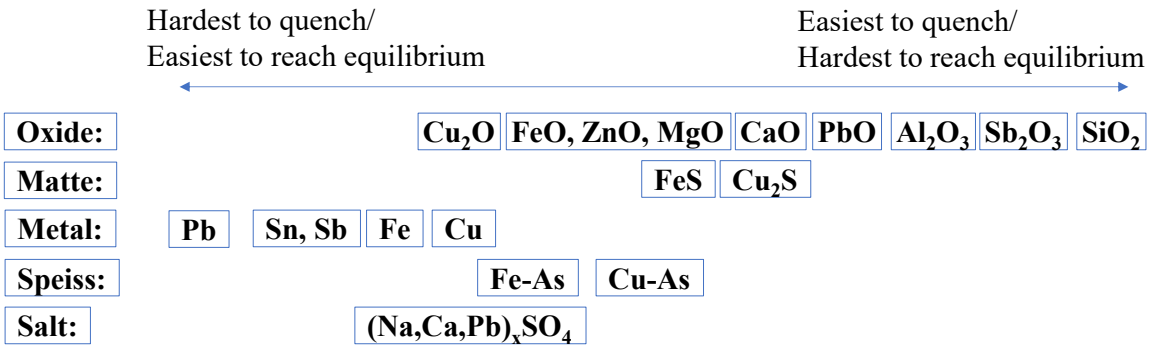

FIG 6 – Approximate rating of liquids by behaviour on quenching.

Analysis of phase compositions

EPMA is the main technique – it allows high accuracy after taking all necessary precautions.

Selection of area for analysis

It is recommended to avoid immediate proximity to solids, dendrites and micro-inhomogeneities. Areas closer to surface provide better quenching (Figure 7). Good areas must have all needed phases to be present within the diffusion path. When some expected phases are lacking in the area, it is sometimes referred to as macro-inhomogeneities. A number of separate areas in sample should be investigated. Within each area, at least five points should be measured for well-quenched samples and 15–20 for poorly quenched. Also, for poorly quenched samples, a non-zero probe diameter is selected, within the 20–100 micron. This helps to average minor local micro-inhomogeneities formed during the quenching.

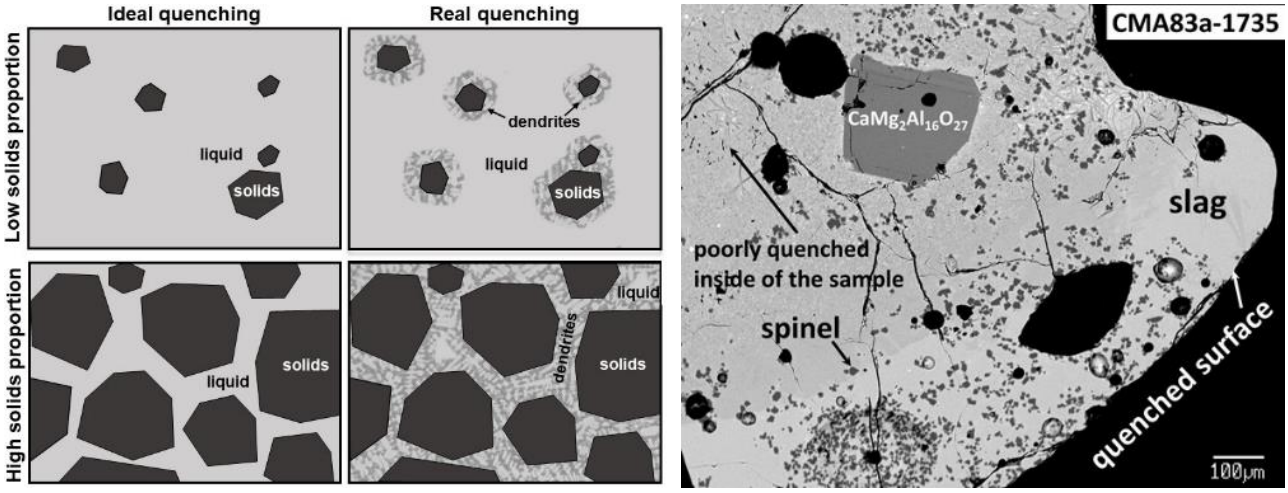

FIG 7 – A schematic diagram illustrating the correlation between the volume fraction of solid phases and the volume fraction of homogenous liquid phase (Khartcyzov *et al*, 2022), and example of microstructure with well-quenched slag on the surface and poorly quenched inside.

The volume fraction of solids is targeted to be below 50 per cent and preferably about 10 per cent, to achieve rapid equilibration and satisfactory quenching of the liquid phase into an amorphous material. The solid phases act as heterogeneous nucleation centres, and a minimum distance of 10–20 µm between solid grains is necessary to ensure that an amorphous slag of uniform composition exist between the grains. In this case, it is unaffected by dendritic crystal growth during quenching. The correlation between the volume fraction of the solid phases and the volume fraction of the liquid slag phase affected by the growth of the quenching crystals is schematically shown in Figure 7 (Khartcyzov *et al*, 2022): an increase in the volume of the solid phases will lead to a decrease in the volume of the liquid slag suitable for accurate measurement using the EPMA.

The steps to analyse of micro- and macro-inhomogeneity trends can be summarised as follows:

- Identify all phases. If unsure, use energy dispersive X-ray spectroscopy (EDS), literature, powder X-ray diffraction (XRD) database, first-principles predictions.
- Make a hypothesis of reactions occurring within the sample as it approached the equilibrium. Prove it by varying starting conditions, equilibration time, etc.
- Macro-inhomogeneity check: measure the trend in similar areas across the sample (Hidayat *et al*, 2023).
- Micro-inhomogeneity check: measure the trends in each location. A distance from solids must be kept as described above and supported by a micrograph.
- In the case of viscous liquid samples, which are at risk of equilibration issue, use areas close and exposed to solids – targets of liquid/solid equilibrium.
- In the case of fluid liquid samples, which are at risk of quenching issue, use liquid areas free from solids, and those first exposed to quenching medium.
- Tune contrast to the maximum to identify inhomogeneities and to find hidden phases.

- Non-equilibrium samples can only be accepted with a special proof that at least local equilibrium exists.
- Average of all measurements is not directly acceptable. Plotting the scattered points compositions against a phase diagram should reveal the existence or absence of a systematic trend. The points that are obviously further from equilibrium/or affected by poor quenching should be rejected, rather than averaged.

Over the years, some issues were identified with the standard EPMA ZAF-correction, used to recalculate X-ray counts into concentrations, considering complex effects of interaction between electrons and the sample, as well as X-rays and the sample. Many uncertainties can be resolved by introduction of secondary standards within the sample. Ideal secondary standard is a stoichiometric compounds existing within the system of interest. Good examples are: $PbSiO_3$, Pb_2SiO_4, Zn_2SiO_4, Fe_2SiO_4, $Ca_2Fe_2O_5$, $CaFe_2O_4$, $CaAl_2O_4$, $FeAl_2O_4$, $CuSiO_3$, $CuAlO_2$, Cu_2PbO_2 etc (Cheng *et al*, 2021; Khartcyzov *et al*, 2023; Shevchenko and Jak, 2017, 2018, 2019a, 2019b, 2021). When secondary standards are not available, using alternative types of ZAF-corrections, such as Mass Absorption Coefficients sets (MACs) were proved to be valuable. Using different EPMA machines for mutual check was tried in many cases. Some trends were revealed for neighbouring elements in periodic table, eg Fe-Al – Co-Al – Ni-Al – Cu-Al – Zn-Al. All of them had stoichiometric compounds (or approaching stoichiometric at certain conditions) – spinel ($FeAl_2O_4$, $CoAl_2O_4$, $NiAl_2O_4$, $ZnAl_2O_4$) and delafossite ($CuAlO_2$). For all of them, the concentrations of Al were overestimated if the existing MAC set was used. Larger overestimation was observed when Al is combined with heavier elements (Cu, Zn) than lighter (Fe, Co). This effect is not universal but depends on the local EPMA machine, software and settings used. Therefore, each machine/ software/settings combination needs to be calibrated against stoichiometric compounds and the correction developed accordingly.

The secondary X-ray fluorescence is a widely overlooked source of ‘fake solubility’. It is observed for transition elements (Cr, Mn, Fe, Co, Ni, Cu, Zn) in light element-rich phases (SiO_2, CaO, Al_2O_3) (Hamuyuni, Klemettinen and Taskinen, 2016; Hidayat, Hayes and Jak, 2012; Hidayat *et al*, 2012; Shevchenko and Jak, 2018; Xia, Liu and Taskinen, 2016). Interesting cases involved two neighbouring transition element-rich phases inside one another, such as overestimated %Fe in metallic Cu, which was surrounded by FeO-rich slag. Also, several per cent overestimation of Cu was noticed in zincite phase (ZnO), which was surrounded by the Cu-rich slag (Shevchenko and Jak, 2020a).

The progress in: (1) quantity and selection of studied systems; and (2) accuracy and reliability of results for each systems, has become a foundation for the next stage in thermodynamic modelling. It has allowed gradual improvement of the accuracy of thermodynamic models for all studied systems. But it also revealed some limitations of the thermodynamic models, which could not be resolved without the deep re-assessment of model parameters and even some concepts of the models themselves. Further in the paper, we describe the revision of properties of all end-members of model solutions.

REVISION OF THERMODYNAMICS OF END-MEMBERS

Since the early development of FactSage™ solution models, heat capacities of supercooled liquids below melting points were usually assigned the same functions of temperature as the corresponding solid phases. This often resulted in a discontinuous function for the pure liquid heat capacity (Cp) at the melting temperature. Typically, the heat capacity of liquids is about 10 per cent higher compared to the solid of the same composition (Figure 8a). The discontinuity is also present in the heat capacities of multicomponent liquids, which are mostly approximated as an additive sum of all liquid endmembers, with only a minor contribution from the quasichemical interaction. The experimental evidence accumulated later does not support any jumps in liquid heat capacities (Richet and Bottinga, 1985, 1986). Instead, most liquid silicates demonstrate constant heat capacities down to the lowest temperature of their stable existence, which can be closely approximated by the additive sum of liquid endmember heat capacities above their melting points. Moreover, for glass-forming liquids such as SiO_2, constant heat capacity (81.4 J/mol K) is observed down to glass transition point (Richet *et al*, 1982). The latter point (~1200°C for SiO_2) is not a thermodynamic but a kinetic phenomenon, ie shifts to lower temperature on longer time scales and is sensitive to even minor impurities. Therefore, constant high heat capacity for equilibrium (relaxed) supercooled SiO_2 liquid

may be extended below 1200°C, but not indefinitely, since the entropy of this supercooled liquid must not become lower than the entropy of the most stable solid at low temperature (low-quartz) – this condition known as 'Kauzmann paradox' (Johari, 2000; Speedy, 2003; Stillinger, 1988). While the heat capacity of supercooled SiO_2 can be measured due to its high viscosity, other pure oxide supercooled liquids could not be experimentally obtained, so their heat capacities may only be evaluated from the multicomponent data (Lange and Navrotsky, 1992; Stebbins, Carmichael and Moret, 1984). Similarly, the heat capacities of all other supercooled liquid endmembers between ~1000°C and their melting point need to be increased according to the literature for multicomponent melts – for example, for most divalent oxides (CaO, MgO, FeO, ZnO) from 50–60 J/mol K (as in solid phases) to at least 70–80 J/mol K. This allows a significant improvement of description of binary and multicomponent phase diagrams while simultaneously removing excessive negative interaction parameters, the only purpose of which was to compensate for underestimated liquid Cps. This compensation, however, can never be perfect and resulted in large discrepancies in slopes of liquidus that would accumulate to >100 K discrepancy in some areas (Figure 8b).

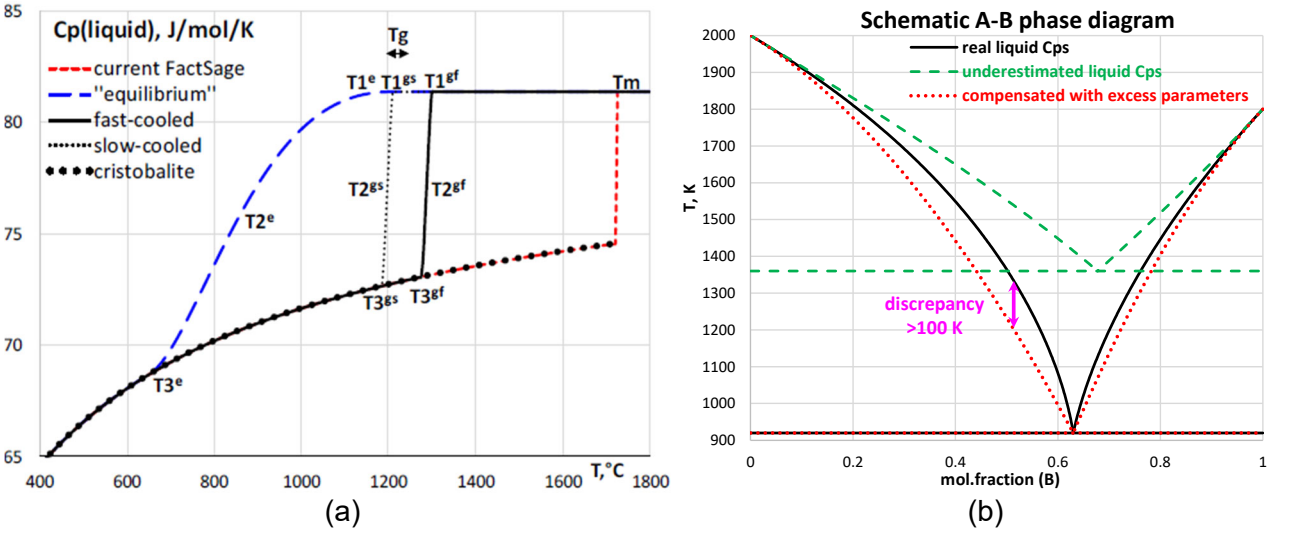

FIG 8 – Example of the supercooled liquid SiO_2 Cp improvement (a); and schematic effect of the liquid endmember Cps on the simple eutectic, ideal liquid solution binary A-B phase diagram (b).

PRINCIPLES IN REVISION OF ENDMEMBER THERMODYNAMIC PROPERTIES

Heat capacity must be a non-negative, monotonically increasing function on temperature

(*Unless there is solid experimental evidence of otherwise, eg due to magnetic transitions).*

Usually, in the revised version of thermodynamic model, the range 0–50 K is described by:

$Cp = aT + bT^2 + cT^3 + dT^4 + eT^5$ (no terms with T power <1 should be used, to avoid divergence),

50–298.15 K: $Cp = a + bT + cT^2 + dT^3 + eT^4$

298.15-X (X~1000–3000 K): $Cp = a + bT + cT^{-2} + dT^2$ + some other terms if needed

Mandatory term for highest T (X to >6000 K): $Cp = a + bT^{-0.5} + cT^{-1} + dT^{-2} + eT^{-3}$ (*no terms with T power >0 should be used, to avoid divergence*)

Heat capacities and entropies of solid allotropes and liquid endmember of the same composition should follow the same sequence as their stability ranges on the temperature scale

To ensure no unreasonable restabilisation of liquid or high-T solid at low T, or solid at high T.

Entropies of all solid and liquid endmembers should (*at least approximately*) tend to 0 at 0 K (third law of thermodynamics)

Although pyrometallurgy rarely encounters T < 25°C, this fundamental principle allowed to fix lots of issues over the last few years.

It is known that glasses/amorphous solids have small residual positive entropy at 0 K. This is due to incomplete relaxation – the viscosity below the glass transition (T_g) becomes so high that the lowest-entropy most-stable state is not achieved below T_g within reasonable experimental timescale. What is known for sure is:

- the difference of entropy between supercooled liquid and solid decreases below T_{melt}
- it must remain non-negative to avoid 'Kauzmann's paradox'.

There is no consensus in literature whether the entropy of liquid should be exactly 0 at 0 K (Benigni, 2021; Speedy, 2003), or may remain somewhat higher. There are recent examples of thermodynamic models where zero entropy of supercooled liquid at 0 K is assumed: (Bajenova *et al*, 2020; Bigdeli, Chen and Selleby, 2018; He and Selleby, 2022; Khvan *et al*, 2018, 2019, 2020, 2022; Khvan, Uspenskaya and Aristova, 2024; Li *et al*, 2017; Sergeev *et al*, 2019; Yazhenskikh *et al*, 2021). While there are different ways to extrapolate the thermodynamic properties of supercooled liquids below their observed glass transitions, they usually result in very similar outcomes, as long as the range between the glass transitions of most endmembers (~400–800°C) and their melting points (1700–2900°C) is described well.

Heat capacities and entropies of all chemically similar species should have similar tendencies, with physically sound dependence on the position in the periodic table

The currently used liquid slag model describes oxide and sulfide endmembers as unbreakable species (eg CaO, FeS), while matte/metal – as combinations of metal (eg Ca, Fe) + hypothetical liquid O or S.

For example, for trivalent oxides (Figure 9):

- Heat capacities (Cp) of all M_2O_3 liquid endmembers reach ~150–160 J/mol K above 500 K and do not change much anymore.
- Entropies S of all M_2O_3 liquid endmembers have systematic trend on periodic table position: low S (light Al) => high S (heavy Bi).

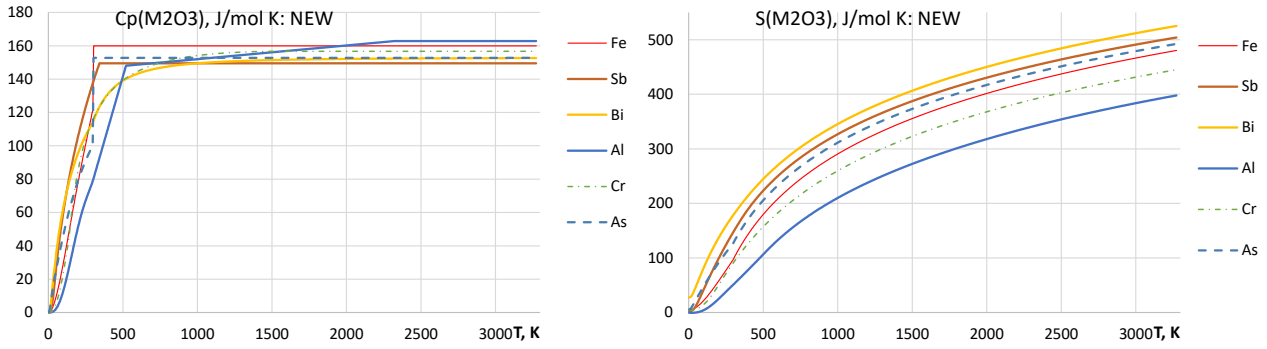

FIG 9 – Systematic change in heat capacities (Cp) and entropies (S) of trivalent liquid slag endmembers (M_2O_3) in the revised thermodynamic model, as function of temperature. All Cps stabilise at 150–160 J/mol K above ~500 K, while the entropies are usually ranked by atomic number (Al<Cr<Fe<As<Sb<Bi).

A systematic revision has been underway to ensure both approaches (ie oxide 'FeO' in slag and elemental 'Fe, O' in matte/metal) result in consistent thermodynamic properties over the whole temperature range (0 K – at least 2000 K)

This involved modifying the heat capacity of the hypothetical liquid O endmember in matte/metal to a lower value (29 J/mol K) at high T to avoid spurious formation of 'oxide matte' instead of liquid slag for many systems (Pb-O, Sb-O, Bi-O, ...)

All endmembers should be reviewed with regards to all recent literature

Some were inherited from early versions of FactSage™ (1980–1990s) and appeared to be obsolete.

Systematic analysis of pure oxide endmembers (Table 2, Figure 10):

- enthalpies/entropies of melting versus T_{melt}
- heat capacities of liquid and solids at T_{melt}

These should be consistent throughout the whole periodic table (Figure 11).

TABLE 2

List of updates in the properties of pure components (endmembers) of the oxide database within the recent major thermodynamic revision. Note: properties below 298 K were also described for all solids and liquids.

Component	Changed T_{melt}, ΔH_{melt}	Changed C_p(liq) (J/mol K)	Changed other; reference
SiO_2	-	Increased from 74 to 83. 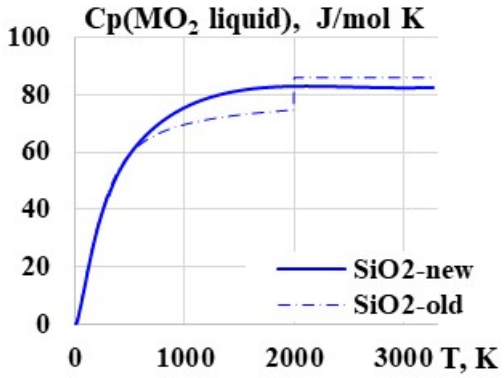	(Wen *et al*, 2023)
CaO	Increased T_{melt} from 2572 to 2896°C. Increased ΔH_{melt} from 79.5 to 83 kJ/mol.	Increased from 55 to 80. 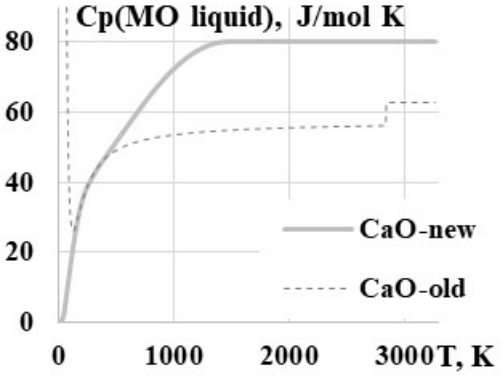	Increased Cp(solid) > 2000 K.

Table 2 continued…

Component	Changed T_{melt}, ΔH_{melt}	Changed C_p(liq) (J/mol K)	Changed other; reference
FeO	-	Increased from ~60 to 71. 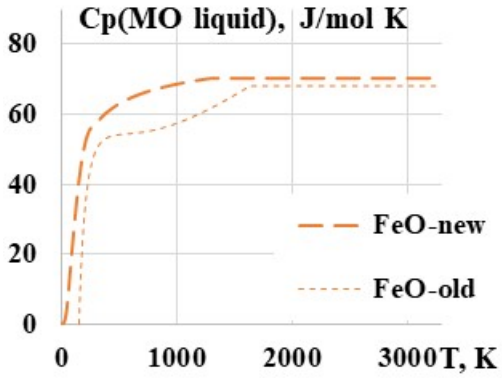	(Wen *et al*, 2024)
Fe_2O_3	Decreased T_{melt} from 1695 to 1673°C. Increased ΔH_{melt} from 77.2 to 98.6 kJ/mol.	Increased from 145 to 160. 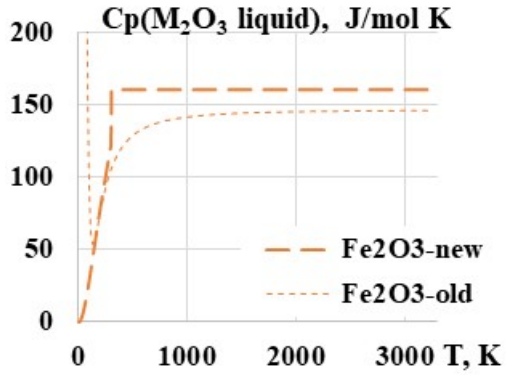	(Wen *et al*, 2024)
PbO	Increased ΔH_{melt} from 25.5 to 27.7 kJ/mol	Increased from <60 to 65. 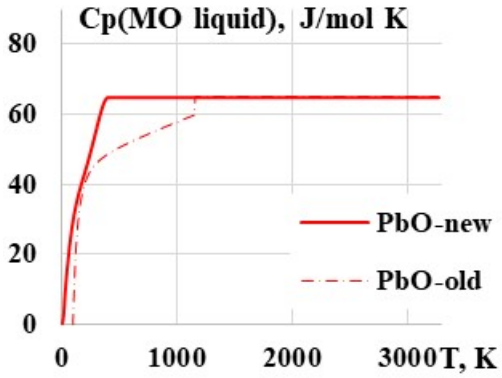	(Wen *et al*, 2023)
ZnO	-	Increased from 55–60 to 70. 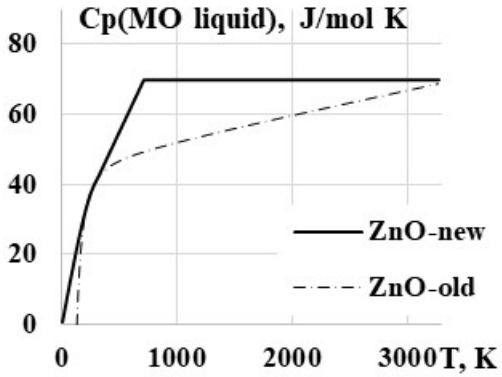	(Wen *et al*, 2023)

Table 2 continued…

Component	Changed T_{melt}, ΔH_{melt}	Changed C_p(liq) (J/mol K)	Changed other; reference
Cu_2O	-	Decreased from 120 to 103. 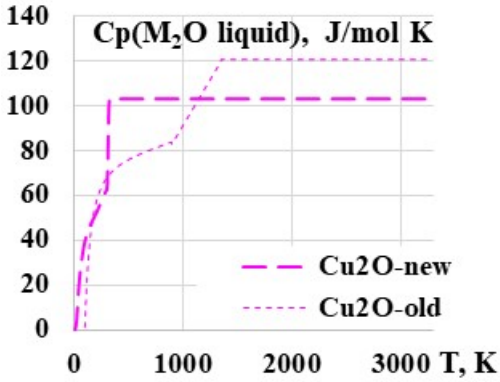	'Apparent MQM coordination number' from 1 to 2. (Wen *et al*, 2023)
Al_2O_3	-	Increased from ~145 to 155–160. 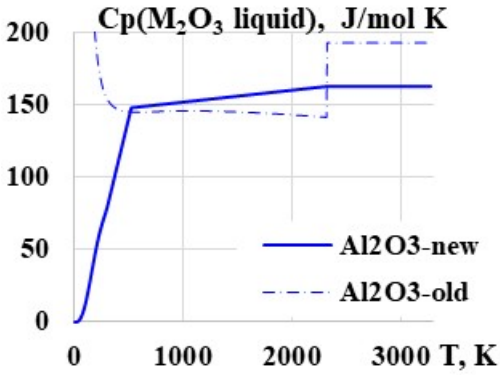	
MgO	Increased T_{melt} from 2825 to 2941°C. Increased ΔH_{melt} from 77.4 to 85.4 kJ/mol.	Increased from ~60 to 72 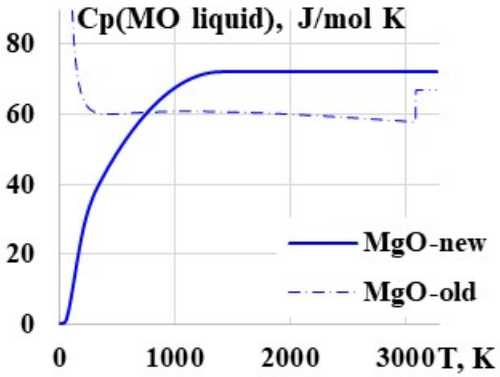	Increased Cp(solid) > 2000 K. Partially published by (Abdeyazdan *et al*, 2024)
Cr_2O_3	-	Increased from 130–135 to 157. 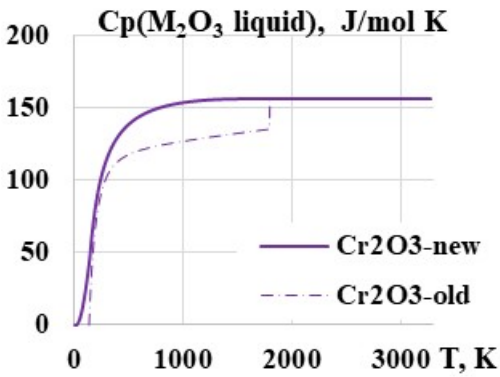	-

Table 2 continued…

Component	Changed T_{melt}, ΔH_{melt}	Changed C_p(liq) (J/mol K)	Changed other; reference
CrO	Increased ΔH_{melt} (from $Cr+Cr_2O_3$).	Increased from ~54 to 72. 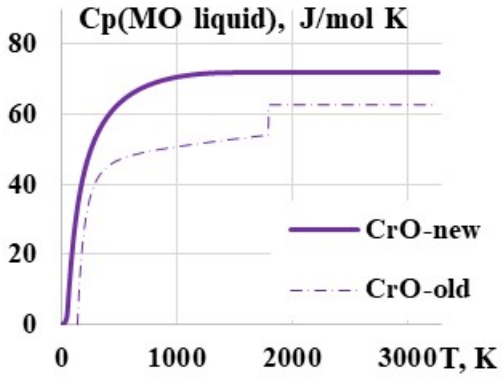	-
As_2O_3		Made smooth below 298 K. 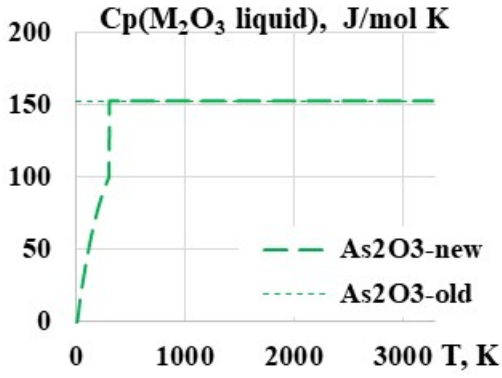	-
As_2O_5	Introduced first time.	Set as 205. 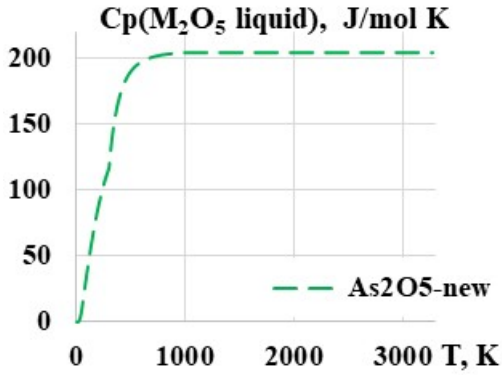	-
SnO	-	Made smooth below 1000 K. 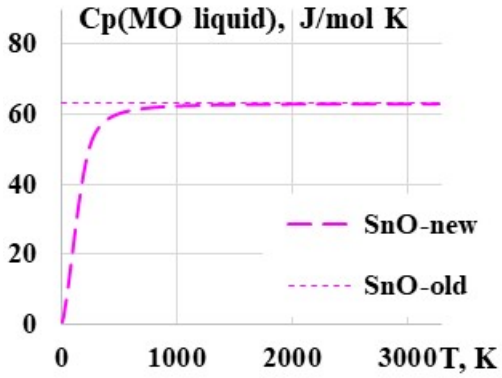	Partially published in (Shevchenko *et al*, 2021)

Table 2 continued…

Component	Changed T_{melt}, ΔH_{melt}	Changed C_p(liq) (J/mol K)	Changed other; reference
SnO_2	Increased T_{melt} from 1625 to 2349 and then to 2439°C. (Note: these are T_{melt} under closed conditions – at finite pO_2 they are lower, currently being set as 2144 at 1 atm O_2 and 2059°C at 0.21 atm O_2). Increased ΔH_{melt} from 41.1 to 49.8 and then to 55.5 kJ/mol.	Increased from 92 to 97. 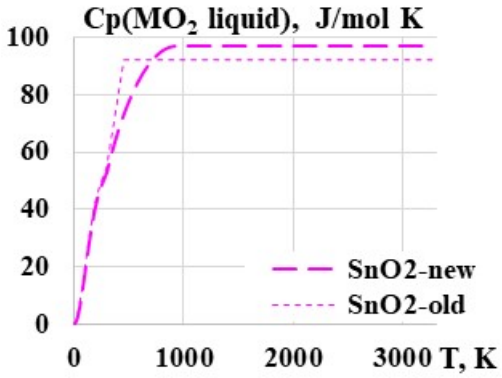	Partially published in (Shevchenko *et al*, 2021).
Sb_2O_3	-	Decreased from 157 to 150. 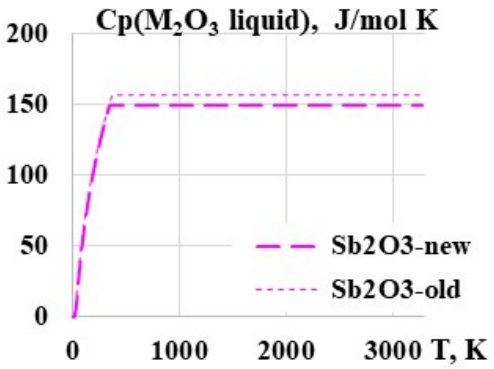	Revised Cp(solids), ΔH_{form} and $\Delta H_{transition}$ to destabilise Sb_2O_3 liquid.
Bi_2O_3	-	Increased from 140 to 144. 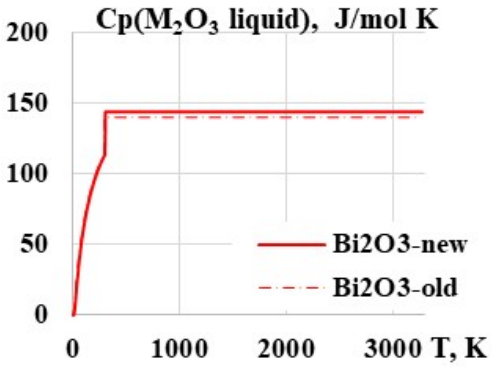	-
Ag_2O	-	No change. 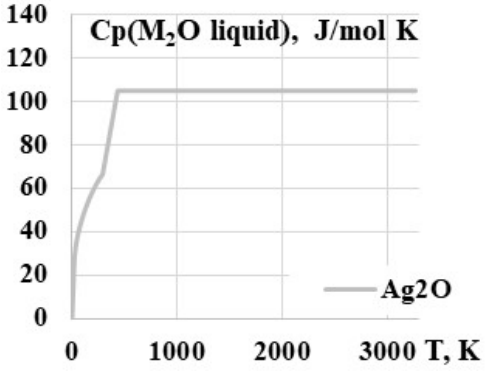	(Sultana, Shevchenko and Jak, 2021)

Table 2 continued…

Component	Changed T_{melt}, ΔH_{melt}	Changed C_p(liq) (J/mol K)	Changed other; reference
Au_2O	-	Decreased from 121 to 103. 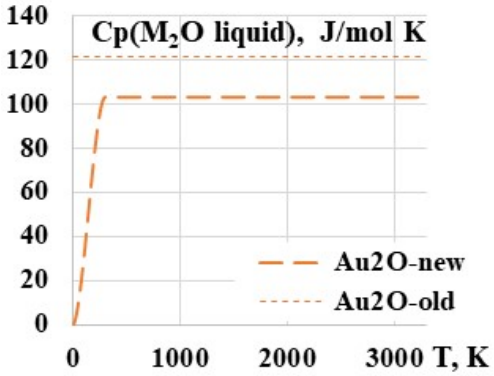	-
NiO	Increased T_{melt} from 1955 to 1990°C. (Note: these are T_{melt} under closed conditions – at finite pO_2 they are lower, currently being set as 1970 at 1 atm O_2 and 1947°C at 0.21 atm O_2). Increased ΔH_{melt} from 58.3 to 59.5 kJ/mol.	Increased from 67 to 71. 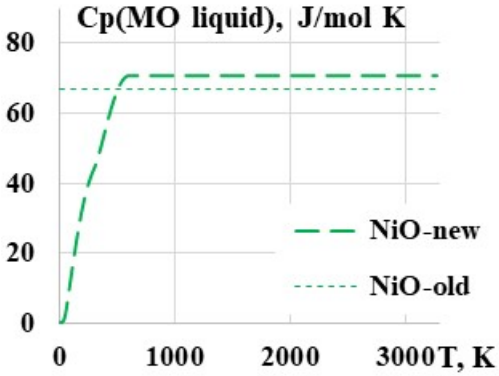	(Abdeyazdan, Shevchenko and Jak, in press).
CoO	T_{melt} = 1830°C. Increased ΔH_{melt} from 40 to 42.1 kJ/mol.	Made smooth below 1400 K. 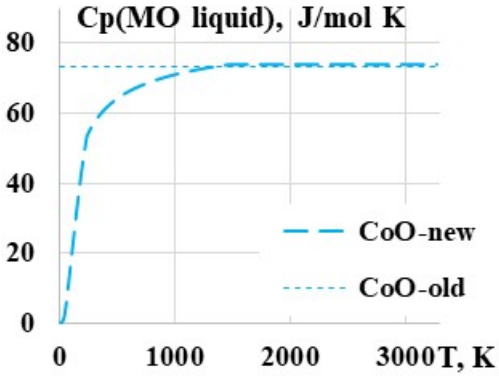	-
Na_2O	-	Increased from 99 to 105. 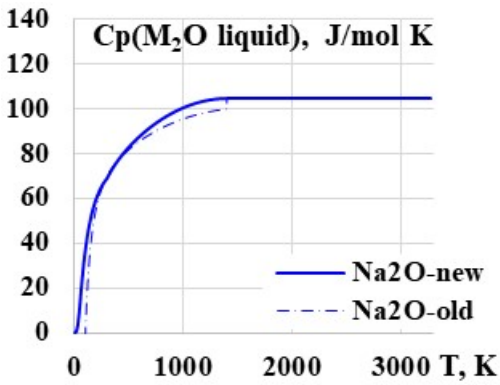	-

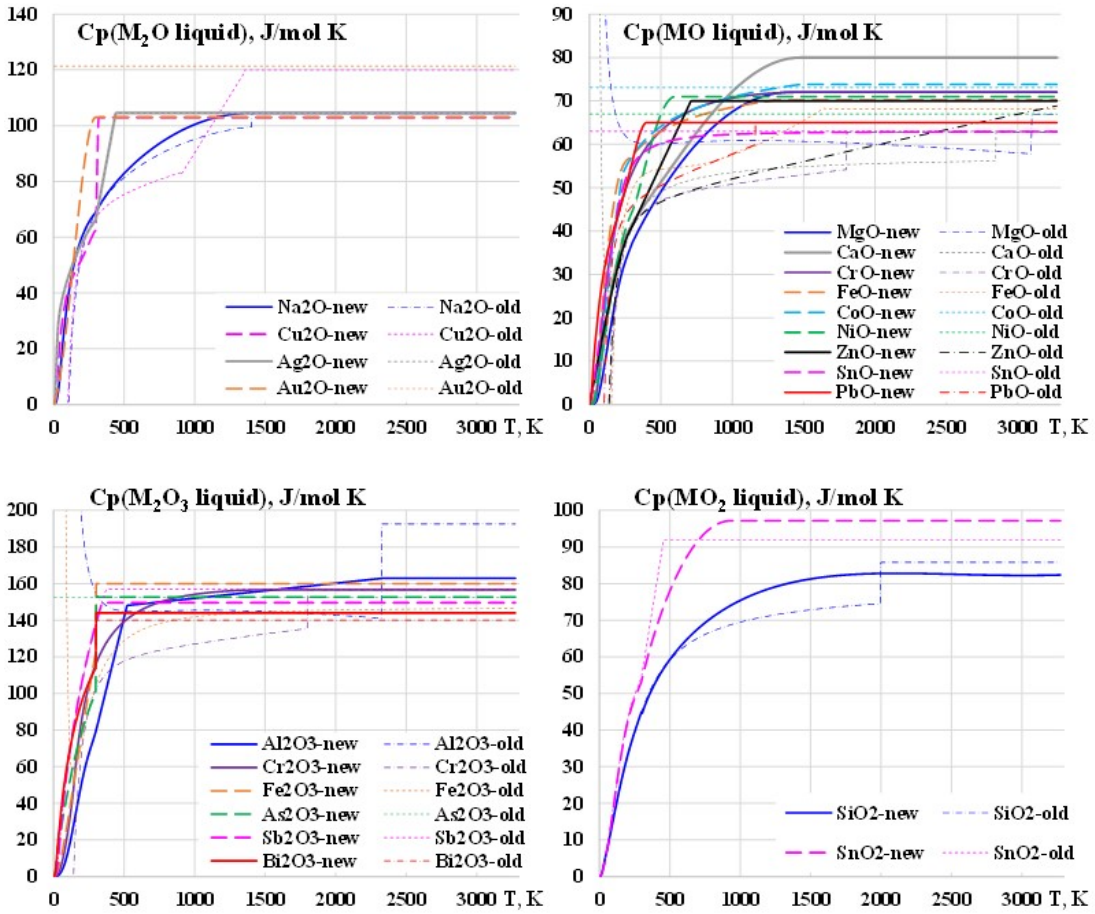

FIG 10 – Comparison of old and new heat capacities of liquid monovalent (M_2O), divalent (MO), trivalent (M_2O_3) and tetravalent (MO_2) liquid slag endmembers. Several unreasonable jumps (Na_2O, CrO, PbO, MgO, CaO, Cr_2O_3, Al_2O_3, SiO_2) and divergences to ±∞ (MgO, CaO, ZnO, Al_2O_3, Fe_2O_3) at low or high T have been corrected.

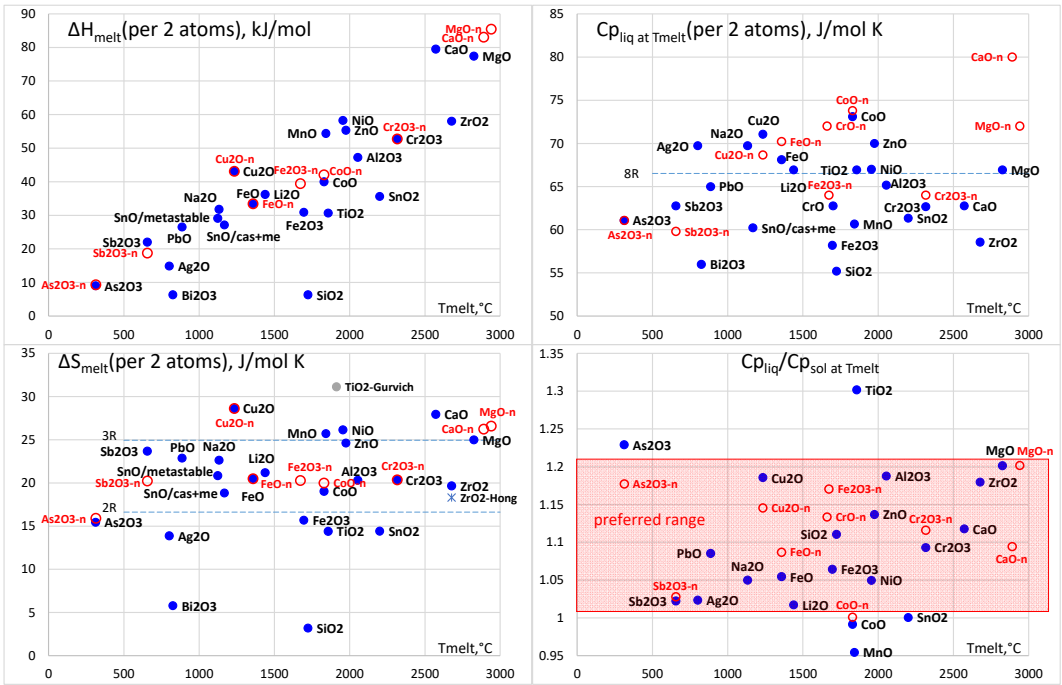

FIG 11 – Comparison of enthalpies of melting (ΔH_{melt}), entropies (ΔS_{melt}), heat capacities of liquids (Cp_{liq} at T_{melt}) and ratios of liquid to solid heat capacities at T_{melt}, all normalised to 2 atoms for presentation purpose. Red circles represent corrected properties for some endmembers (eg CaO-n).

Ideally, all elements should have (at least approximately) the same high-T heat capacities when expressed as (oxide – pure liquid O) and as (pure liquid metal) = ideal dashed line (y=x).

Existing discrepancies (Figure 12) provide clues for further improvement of the database robustness, and will make introduction of new species (eg As^{5+}, Sb^{5+}, other elements) more fundamentally supported. Note: this chart includes elements that are not in the current thermodynamic database – literature review was undertaken to plot Li^{+}, P^{5+}, K^{+}, Ti^{3+}, Ti^{4+}, V^{2+}, V^{3+}, V^{4+}, V^{5+}, Mn^{2+}, Mn^{3+}, Ge^{4+}, Zr^{4+}, Te^{4+}, Ba^{2+} – from public FactSage™ etc – to ensure consistency for all possible elements. Some of them (eg P^{5+}, V^{5+}, Te^{4+}, Zr^{4+}) do not align with the principles described here – indicating potential inaccuracies in properties from literature.

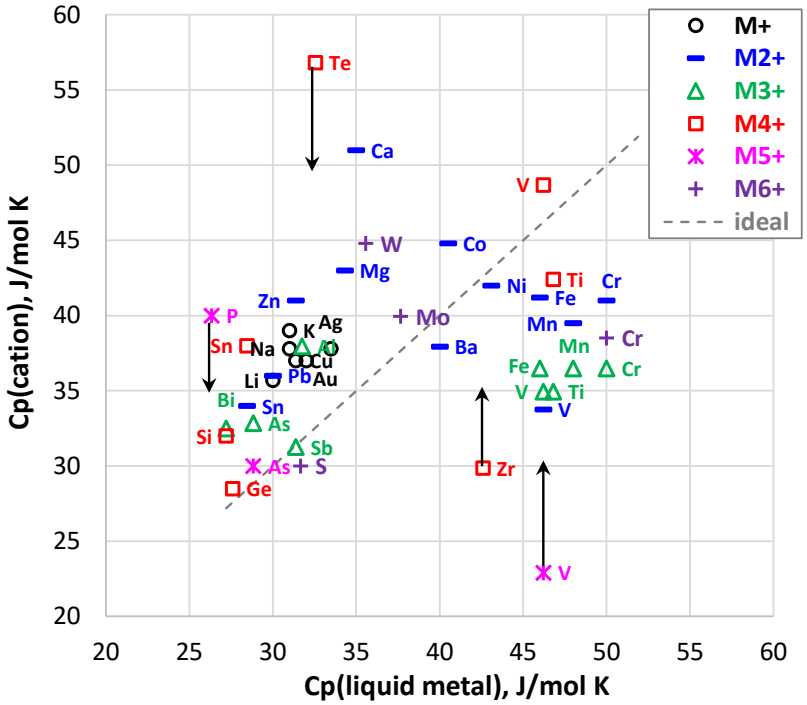

FIG 12 – Correlation between the heat capacities of pure liquid elements (metals and metalloids, eg P, Te, S) and their cations in liquid slag, calculated in assumption of $Cp(O^{2-}) = 29$ J/mol K or (for covalently bound in SiO_2, GeO_2, SO_3 groups) 25 J/mol K. Deviations from 'ideal' dashed line indicate likely uncertainties in presently accepted Cp of the liquid element and/or its liquid oxide, with arrows showing desired correction.

CONCLUSIONS

Advances in experimental technique and scope within the 20-component Cu-Pb-Zn-Fe-Ca-Al-Mg-Si-O (major) – Cr-Na (slagging) – As-Sn-Sb-Bi-Ag-Au-Ni-Co (minor) slag-solids-metal-matte-speiss-sulfate system have been demonstrated in this paper. Improved range, quantity and accuracy of experimental data have initiated major improvements in thermodynamic model, including revision of properties of pure components (endmembers) that has not been attempted since the 1990s.

ACKNOWLEDGEMENTS

The authors would like to thank Australian Research Council Linkage programs LP180100028 and LP190101020 as well as consortium of lead and copper producers: Aurubis, BHO OD, Boliden, Glencore Technology, Kazzinc Ltd. Glencore, Nyrstar, Peñoles, RHI Magnesita, Rio Tinto Kennecott and Umicore for the financial support for this study. The authors are very grateful to Professor Peter Hayes for initiating and contributing in this research program. The authors would like to thank Mrs Suping Huang, Mrs Marina Chernishova, Mrs Samaneh Ashjaa, Mrs Joanna Chang for assistance in the experiments, and also the staff at the Centre for Microscopy and Microanalysis (CMM), University of Queensland for technical support.

REFERENCES

Abdeyazdan, H, Shevchenko, M and Jak, E, in press. Phase equilibria in the NiO-ZnO-SiO_2 and PbO-NiO-ZnO-SiO_2 systems, *J Eur Ceram Soc*, 2024.

Abdeyazdan, H, Shevchenko, M, Chen, J, Hayes, P C and Jak, E, 2024. Phase equilibria in the ZnO-MgO-SiO_2 and PbO-ZnO-MgO-SiO_2 systems for characterizing MgO-based refractory - slag interactions, *J Eur Ceram Soc*, 44(1):510–531.

Bajenova, I, Khvan, A, Dinsdale, A and Kondratiev, A, 2020. Implementation of the extended Einstein and two-state liquid models for thermodynamic description of pure SiO_2 at 1 atm, *CALPHAD*, 68:101716.

Bale, C W, Belisle, E, Chartrand, P, Decterov, S A, Eriksson, G, Gheribi, A E, Hack, K, Jung, I H, Kang, Y B, Melancon, J, Pelton, A D, Petersen, S, Robelin, C, Sangster, J, Spencer, P and Van Ende, M A, 2016. FactSage thermochemical software and databases, 2010–2016, *CALPHAD*, 54:35–53.

Benigni, P, 2021. CALPHAD modeling of the glass transition for a pure substance, coupling thermodynamics and relaxation kinetics, *CALPHAD*, 72:102238.

Bigdeli, S, Chen, Q and Selleby, M, 2018. A New Description of Pure C in Developing the Third Generation of Calphad Databases, *J Phase Equilib Diffus*, 39(6):832–840.

Cheng, S, Shevchenko, M, Hayes, P C and Jak, E, 2021. Experimental Phase Equilibria Studies in the FeO-Fe_2O_3-CaO-SiO_2 System and the Subsystems CaO-SiO_2, FeO-Fe_2O_3-SiO_2 in Air, *Metall Mater Trans B*, 52(3):1891–1914.

Hamuyuni, J, Klemettinen, L and Taskinen, P, 2016. Experimental phase equilibrium data of the system Cu-O-CaO-Al_2O_3 at copper saturation, *CALPHAD*, 55(Part_2):199–207.

He, Z and Selleby, M, 2022. A third generation Calphad description of W-C including a revision of liquid, C, *CALPHAD*, 78:102449.

Hidayat, T, Fallah Mehrjardi, A, Shevchenko, M, Hayes, P C and Jak, E, 2023. Development of Experimental Techniques for the Phase Equilibrium Study in the Pb-Fe-O-S-Si System Involving Gas, Slag, Matte, Lead Metal and Tridymite Phases, *Processes*, 11(2):372.

Hidayat, T, Hayes, P C and Jak, E, 2012. Experimental Study of Ferrous Calcium Silicate Slags: Phase Equilibria at Between 10^{-8} atm and 10^{-9} atm, *Metall Mater Trans B*, 43(1):27–38.

Hidayat, T, Henao, H M, Hayes, P C and Jak, E, 2012. Phase Equilibria Studies of the Cu-Fe-O-Si System in Equilibrium with Air and with Metallic Copper, *Metall Mater Trans B*, 43:1034–1045.

Jak, E and Hayes, P C, 2002a. Experimental Liquidus in the PbO-ZnO-Fe_2O_3-(CaO+SiO_2) System in Air, with CaO/SiO_2=0.35 and PbO/(CaO+SiO_2)=3.2, *Metall Mater Trans B*, 33B(6):851–863.

Jak, E and Hayes, P C, 2002b. Experimental Study of Phase Equilibria in the PbO-ZnO-Fe_2O_3-CaO-SiO_2 System in Air for High Lead Smelting Slags (CaO/SiO_2=0.35 and PbO/(CaO+SiO_2)=5.0 by Weight), *Metall Mater Trans B*, 33B(6):817–825.

Jak, E, 2012. Integrated experimental and thermodynamic modelling research methodology for metallurgical slags with examples in the copper production field, in *Proceedings of the 9th Intl Conf on Molten Slags, Fluxes and Salts*, pp 1–28 (The Chinese Society for Metals).

Jak, E, 2018. The role of research in pyrometallurgy technology development - from fundamentals to process improvements - Future, Sulphide Smelting, in *Proceedings of Extraction 2018*, pp 19–37 (TMS/CIM: Ottawa).

Jak, E, Hayes, P C and Lee, H-G, 1995. Improved methodologies for the determination of high temperature phase equilibria, *Korean Journal of Minerals and Materials Institute (Seoul)*, 1(1):1–8.

Jak, E, Hidayat, T, Shishin, D, Mehrjardi, A F, Chen, J, Decterov S A, and Hayes, P C, 2016. Integrated experimental and modelling research for non-ferrous smelting and recycling systems, in *Proceedings of the 10th International Conference on Molten Slags, Fluxes and Salts (Molten16)* (eds: R G Reddy, P C Chaubal, P C Pistorius, U B Pal), pp 947–959.

Jak, E, Shevchenko, M, Shishin, D, Nekhoroshev, E, Chen, J and Hayes, P C, 2024. University Research on molten slags, matte, speiss and metal systems for high temperature processing, in *Proceedings of the 12th International Conference on Molten Slags, Fluxes and Salts (MOLTEN 2024)*, pp 1029–1060 (The Australasian Institute of Mining and Metallurgy: Melbourne).

Jak, E, Shishin, D, Shevchenko, M and Hayes, P C, 2022. Integrated Experimental Phase Equilibria and Thermodynamic Modelling Research and Implementation in Support of Pyrometallurgical Copper Processing, in *Proceedings of the 11th International Conference on Copper (COPPER 2022)*, pp 608–634.

Johari, G P, 2000. An equilibrium supercooled liquid's entropy and enthalpy in the Kauzmann and the third law extrapolations and a proposed experimental resolution, *J Chem Phys*, 113(2):751–761.

Khartcyzov, G, Shevchenko, M, Cheng, S, Hayes, P C and Jak, E, 2022. Experimental phase equilibria studies in the $CuO_{0.5}$-CaO-SiO_2 ternary system in equilibrium with metallic copper, *Ceram Int*, 48(7):9927–9938.

Khartcyzov, G, Shevchenko, M, Cheng, S, Hayes, P C and Jak, E, 2023. Experimental phase equilibria study and thermodynamic modelling of the $CuO_{0.5}$-$AlO_{1.5}$-SiO_2 ternary system in equilibrium with metallic copper, *Ceram Int*, 49(7):11513–11528.

Khvan, A V, Babkina, T, Dinsdale, A T, Uspenskaya, I A, Fartushna, I V, Druzhinina, A I, Syzdykova, A B, Belov, M P and Abrikosov, I A, 2019. Thermodynamic properties of tin: Part I Experimental investigation, ab-initio modelling of α-, β-phase and a thermodynamic description for pure metal in solid and liquid state from 0 K, *CALPHAD*, 65:50–72.

Khvan, A V, Dinsdale, A T, Uspenskaya, I A, Zhilin, M, Babkina, T, Phiri, A M, 2018. A thermodynamic description of data for pure Pb from 0 K using the expanded Einstein model for the solid and the two state model for the liquid phase, *CALPHAD*, 60:144–155.

Khvan, A V, Konstantinova, N, Uspenskaya, I A, Dinsdale, A T, Druzhinina, A I, Ivanov, A and Bajenova, I, 2022. A description of the thermodynamic properties of pure indium in the solid and liquid states from 0 K, *CALPHAD*, 79:102484.

Khvan, A V, Uspenskaya, I A and Aristova, N M, 2024. Critical assessment of the data for Pure Cu from 0 K, using two-state model for the description of the liquid phase, *CALPHAD*, 84:102637.

Khvan, A V, Uspenskaya, I A, Aristova, N M, Chen, Q, Trimarchi, G, Konstantinova, N M and Dinsdale, A T, 2020. Description of the thermodynamic properties of pure gold in the solid and liquid states from 0 K, *CALPHAD*, 68:101724.

Lange, R A and Navrotsky, A, 1992. Heat capacities of iron(3+) oxide-bearing silicate liquids, *Contrib Mineral Petrol*, 110(2–3):311–320.

Li, Z, Bigdeli, S, Mao, H, Chen, Q and Selleby, M, 2017. Thermodynamic evaluation of pure Co for the third generation of thermodynamic databases, *Phys Status Solidi B*, 254(2):1600231.

Luty, W, 1992. Types of Cooling Media and Their Properties, in *Theory and Technology of Quenching: A Handbook* (eds: B Liščić, H M Tensi and W Luty), pp 248–340 (Springer: Berlin Heidelberg).

Pizetta Zordão, L H, Oliveira, V A, Totten, G E and Canale, L C F, 2019. Quenching power of aqueous salt solution, *Int J Heat Mass Transf*, 140:807–818.

Richet, P and Bottinga, Y, 1985. Heat capacity of aluminium-free liquid silicates, *Geochim Cosmochim Acta*, 49(2):471–486.

Richet, P and Bottinga, Y, 1986. Thermochemical Properties of Silicate Glasses and Liquids: A Review, *Rev Geophys*, 24(1):1–25.

Richet, P, Bottinga, Y, Denielou, L, Petitet, J P and Tequi, C, 1982. Thermodynamic properties of quartz, cristobalite and amorphous SiO_2: drop calorimetry measurements between 1000 and 1800 K and a review from 0 to 2000 K, *Geochim Cosmochim Acta*, 46(12):2639–2658.

Sergeev, D, Reis, B H, Dreger, I, Baben, Mt, Hack, K and Mueller, M, 2019. Thermodynamics of the $Ca(NO_3)_2$ - $NaNO_3$ system, *CALPHAD*, 67:101688.

Shevchenko, M and Jak, E, 2017. Experimental Phase Equilibria Studies of the PbO-SiO_2 System, *J Am Ceram Soc*, 101(1):458–471.

Shevchenko, M and Jak, E, 2018. Experimental Liquidus Studies of the Pb-Fe-Si-O System in Equilibrium with Metallic Pb, *Metall Mater Trans B*, 49(1):159–180.

Shevchenko, M and Jak, E, 2019a. Experimental Liquidus Studies of the Binary Pb-Cu-O and Ternary Pb-Cu-Si-O Systems in Equilibrium with Metallic Pb-Cu Alloys, *J Phase Equilib Diff*, 40(5):671–685.

Shevchenko, M and Jak, E, 2019b. Experimental Liquidus Studies of the Pb-Fe-Ca-O System in air, *J Phase Equilib Diff*, 40(2):128–137.

Shevchenko, M and Jak, E, 2020a. Experimental Liquidus Studies of the ZnO-"$CuO_{0.5}$" and ZnO-"'$CuO_{0.5}$''-SiO_2 Liquidus in Equilibrium with Cu-Zn Metal, *J Phase Equilib Diff*, 41(3):207–217.

Shevchenko, M and Jak, E, 2020b. Experimental study and thermodynamic optimization of the ZnO-FeO-Fe_2O_3-CaO-SiO_2 system, *CALPHAD: Computer Coupling of Phase Diagrams and Thermochemistry*, 71:102011.

Shevchenko, M and Jak, E, 2021. Integrated experimental phase equilibria study and thermodynamic modelling of the binary ZnO-Al_2O_3, ZnO-SiO_2, Al_2O_3-SiO_2 and ternary ZnO-Al_2O_3-SiO_2 systems, *Ceramics International*, 47(15):20974–20991.

Shevchenko, M, Chen, L and Jak, E, 2021. Experimental phase equilibria study and thermodynamic modelling of the PbO-FeO-SiO_2-ZnO, PbO-FeO-SiO_2-Al_2O_3 and PbO-FeO-SiO_2-MgO systems in equilibrium with metallic Pb and Fe, *Ceram Int*, 48(11):15124–15135.

Shevchenko, M, Hidayat, T, Hayes, P and Jak, E, 2016. Liquidus of FeO-SiO_2-PbO slags in equilibrium with air and with metallic lead, in *Proceedings of the 10th Intl Conf on Molten Slags, Fluxes and Salts*, pp 1221–1228.

Shevchenko, M, Ilyushechkin, A, Abdeyazdan, H and Jak, E, 2021. Integrated experimental phase equilibria study and thermodynamic modelling of the PbO-SnO-SnO_2-SiO_2 system in air and in equilibrium with Pb-Sn metal, *J Alloys Compd*, 888:161402.

Speedy, R J, 2003. Kauzmann's paradox and the glass transition, *Biophysical Chemistry*, 105(2–3):411–420.

Stebbins, J F, Carmichael, O S E and Moret, L K, 1984. Heat Capacities and Entropies of Silicate Liquids and Glasses, *Contrib Mineral Petrol*, 86(2):131–148.

Stillinger, F H, 1988. Supercooled liquids, glass transitions and the Kauzmann paradox, *J Chem Phys*, 88(12):7818–7825.

Sultana, U, Shevchenko, M and Jak, E, 2021. Integrated Experimental Liquidus and Modelling Studies of the Ternary $AgO_{0.5}$-$FeO_{1.5}$-SiO_2 Systems in Equilibrium with Metallic Ag, *Journal of Alloys and Compounds*, 870:159333.

Wen, X, Shevchenko, M, Nekhoroshev, E and Jak, E, 2023. Phase equilibria and thermodynamic modelling of the PbO–ZnO-$CuO_{0.5}$-SiO_2 system, *Ceram Int*.

Wen, X, Shevchenko, M, Nekhoroshev, E and Jak, E, 2024. Phase Equilibria and Thermodynamic Modelling of the PbO-ZnO-FeO-FeO1.5-SiO_2 system and its subsystems in equilibrium with air/metallic lead/iron, *Ceram Int*, 50(6):8917–8951.

Xia, L, Liu, Z and Taskinen, P A, 2016. Equilibrium study of the Cu-O-SiO_2 system at various oxygen partial pressures, *J Chem Thermodyn*, 98:126–134.

Yazhenskikh, E, Jantzen, T, Kobertz, D, Hack, K and Mueller, M, 2021. Critical thermodynamic evaluation of the binary sub-systems of the core sulphate system Na_2SO_4-K_2SO_4-$MgSO_4$-$CaSO_4$, *CALPHAD*, 72:102234.

Experimental and thermodynamic study of the phase equilibria in the NiO-CaO-FeO-Fe_2O_3 system in air and in equilibrium with metal (Fe-Ni) alloy

DOI: 10.62053/OJQL4468

S Sineva[1], M Shevchenko[2], D Shishin[3] and E Jak[4]

1. Postdoctoral Research Fellow, Pyrosearch, The University of Queensland, Brisbane Qld 4068. Email: s.sineva@uq.edu.au
2. Senior Research Fellow, Pyrosearch, The University of Queensland, Brisbane Qld 4068. Email: m.shevchenko@uq.edu.au
3. Research Fellow, Pyrosearch, The University of Queensland, Brisbane Qld 4068. Email: d.shishin@uq.edu.au
4. Director, Pyrosearch, The University of Queensland, Brisbane Qld 4068. Email: e.jak@uq.edu.au

ABSTRACT

This study represents a part of comprehensive research aimed at integrating nickel into a thermodynamic database constantly developed at Pyrosearch. The behaviour of Ni in calcium-ferrite slags is considered. An integrated approach combining experimental and thermodynamic modelling methods has been employed to predict phase equilibria in the NiO-CaO-FeO-Fe_2O_3 system under oxidising conditions and in equilibrium with the metal FeNi phase.

The compositions of liquid slags and coexisting solid solutions have been determined through the analysis of equilibrated and quenched samples by electron probe microanalysis technique (EPMA). The research results are presented in the form of liquidus projections on the corresponding phase diagrams, considering both oxidising and reducing conditions. The solubility of Ni in spinel, dicalcium ferrite and calcium oxide as well as solubility of Fe and Ca in Ni monoxide, have been examined under several atmospheric conditions. Additionally, the compositions of the NiO-FeO monoxide in equilibrium with metal phase have been studied. The experimental data not only support the outcomes of thermodynamic modelling but also validate the parameters of the applied thermodynamic models, thus confirming the reliability and accuracy of the integrated approach.

INTRODUCTION

A comprehensive experimental and thermodynamic study of high-temperature phase equilibria in multicomponent systems, relevant to materials and products of non-ferrous metallurgy, is crucial for prediction, managing and optimisation industrial processes. Many applied studies rely on accurate thermodynamic descriptions. Therefore, fundamental studies of phase equilibria, supplemented by thermodynamic optimisation make the essential tools for metallurgists worldwide.

The multicomponent NiO-CaO-FeO-Fe_2O_3 system falls within a range of basic oxide systems that are related to Ni-containing slags of nonferrous metallurgy. Compounds of this system are present in slags formed during the recovery of Ni and other metals from WEEE (waste electrical and electronic equipment) (Bigum, Brogaard and Christensen, 2012; Coman, Robotin and Ilea, 2013). Under reducing conditions, when the slag phase reaches equilibrium with FeNi metal, it becomes relevant to Caron the process, widely utilised for treatment of nickel laterite ores (Rhamdhani *et al*, 2009; Meshram, Abhilash and Pandey, 2019). Optimising the slag composition is critical for achieving high nickel recovery rates, minimising energy consumption, and reducing environmental impacts associated with nickel production. Thus, a thorough understanding of phase equilibria in the NiO-CaO-FeO-Fe_2O_3 system enables researchers to tailor slag composition to enhance nickel recovery efficiency and overall process performance in both primary and secondary metallurgy.

Phase equilibria in boundary CaO-FeO-Fe_2O_3 system in air has been initially investigated by Phillips and Muan (1958), followed by Schurmann and Kraume (1976), laying the foundation for the thermodynamic description of the system. In 2016 this system has been optimised by Hidayat *et al* (2016), and further experimentally revised by Cheng *et al* (2021). The CaO-FeO system in equilibrium with Fe metal has also been extensively studied (Hidayat *et al*, 2016b). While the NiO-FeO-Fe_2O_3 system has been studied by less extent, some thermodynamic and calculated data have

been published in Prostakova's thesis (2013). However, there remains a lack of experimental data on phase equilibria in the high-temperature region close to the liquidus surface of the system. Regarding the studied quaternary NiO-CaO-FeO-Fe_2O_3 system, only two experimental papers have focused on measuring the solubility of CaO in FeNi spinel at 1200°C (Yamamura *et al*, 1981) and at 1300°C (Vasiliu, 1979). The calculated isothermal sections of the system at 1200 and 1300°C have been plotted in Prostakova's thesis (2013), but these data have not been supplemented by accurate experimental results.

Therefore, the aim of the present study is to define phase equilibria in the NiO-CaO-FeO-Fe_2O_3 system at high-temperatures in air and in equilibrium with the metal phase. The study will cover aspects such as defining the solubility of CaO in spinel and Ni monoxide solutions, defining the solubility of Ni in lime and dicalcium ferrite solutions and revising the positions of monovariant lines and locations of invariant points. In equilibrium with the metal phase, the temperature of the experiments will be limited by formation of liquid FeNi alloy (approximately 1450°C), and the operating partial pressure will range from $10^{-5.5}$ to 10^{-9} atm.

EXPERIMENTAL STUDY

The experimental methodology employed in this study involves high temperature equilibration under controlled conditions, rapid cooling (quenching) and direct measurement of the phase compositions using electron probe X-ray microanalysis (EPMA) (Jak, Hayes and Lee, 1995; Jak, 2012).

The obtain the desired phase assemblages, NiO, FeO, Fe_2O_3, CaO powder oxides, as well as Fe and Ni metals have been utilised in the mixtures. All reagents were sourced from Alfa Aesar company (MA, USA) and characterised with a purity of 99.9 wt per cent and higher. To simulate the composition of dicalcium ferrite a master slag with a CaO:FeO mass ratio of 1:1 was preliminary prepared. The proportions of reagents in the initial mixtures were determined through calculations using FactSage™ software ver 7.2 and a current version of confidential thermodynamic database to produce one or two solid crystalline phases (Ni monoxide, lime, spinel or dicalcium ferrite) in equilibrium with liquid slag and FeNi metal (for the second case). Prepared mixtures were pressed into 0.2–0.3 g pellets prior to equilibration.

Preliminary prepared substrates from high purity Fe_3O_4 (spinel), NiO (Ni monoxide), $Ca_2Fe_2O_5$ (dicalcium ferrite) and SiO_2 (tridymite) were used to support the mixtures for equilibration in air. Ni folded baskets were employed as substrates for equilibration in the presence of the FeNi phase. The overall illustration of the different types of substrates as well as details of substrates preparations are published by Sineva *et al* (2023). The idea was to apply substrates made of primary crystallised phase depending on the bulk composition of the initial sample.

To study samples in an air atmosphere, compressed air with a total flow of 500 mL/min has been passed through the furnace. For the system in equilibrium with FeNi phase over a range of $p(O_2)_s$, the oxygen partial pressure was controlled using mixtures of Ar/CO/CO_2 at different ratios depending on the target of $p(O_2)$ value. Furnaces temperatures ranged from 1200 to 1600°C for experiments in air and from the 1250 to 1450°C for those in equilibrium with the metal phase. Temperature measurements were verified using a Pt/PtRh 10 per cent thermocouple adjacent to the experimental sample and calibrated against a standard thermocouple supplied by the National Measurement Institute of Australia (NSW, Australia). The equilibration time was 6 hrs, determined through preliminary experiments. Following equilibration, samples were rapidly quenched into a 20 per cent $CaCl_2$-H_2O solution maintained at -20°C. Subsequently, samples were thoroughly washed in water and ethanol, dried, and mounted in epoxy resin for further polishing using conventional metallographic techniques.

A JEOL JXA8200L (trademark of Japan Electron Optics Ltd., Tokyo) electron probe X-ray microanalyser (EPMA) with wavelength dispersive detectors (WDD) was used to get the images of the microstructures of the experimental samples and to measure the concentrations of the elements in different phases. The EPMA was employed at an acceleration voltage of 15 kV and a probe current of 20 nA. Pure Fe_2O_3, $CaSiO_3$,SiO_2 and $NiSiO_3$ reference standards were used to measure the composition of the slags and solid oxides phases. Fe and Ni metals served as standards for measurement metal phases composition. All referenced materials were provided by Charles Taylor. The concentrations of the components in slag and solid oxide phases were recalculated to selected

oxidation states for presentation convenience and to unambiguously report the compositions of the phases, while Fe was expressed as FeO for experiments in equilibrium with metal phase and as Fe_2O_3 for experiments in air.

RESULTS AND DISCUSSIONS

NiO-CaO-FeO-Fe_2O_3 system in air

The typical microstructures illustrating phase compositions of the experimental samples are given in Figure 1. In each microstructure, the liquid slag exists in equilibrium with one or two solid phases, which represents spinel, Ni monoxide, dicalcium ferrite, or lime solutions. The compositions of all phases have been determined using EPMA, recalculated to mol per cent and then plotted on calculated version of liquidus surface of the NiO-CaO-$FeO_{1.5}$ system. The resulting phase diagram is illustrated in Figure 2. Compositions of the liquid slags in equilibrium are denoted by red circles, tie-lines are represented by blue dashed lines, connect to compositions of the corresponding solid phases. The calculated version of the phase diagram has been generated using the Equilib module of FactSage 7.3 software, utilising the most recent version of a confidential thermodynamic database. In is shown, that the compositions of the lime, spinel, Ni monoxide and dicalcium silicate (C_2F) solid solutions are predicted quite accurate with the current version of the database. Experimental validation confirms the solubility of Ni in lime, spinel, and C_2F solutions. However, slight deviations are observed between the experimental compositions of invariant points on the liquidus surface and the calculated version. Consequently, it is necessary to reoptimise the temperatures of the invariant reactions based on the acquired experimental data.

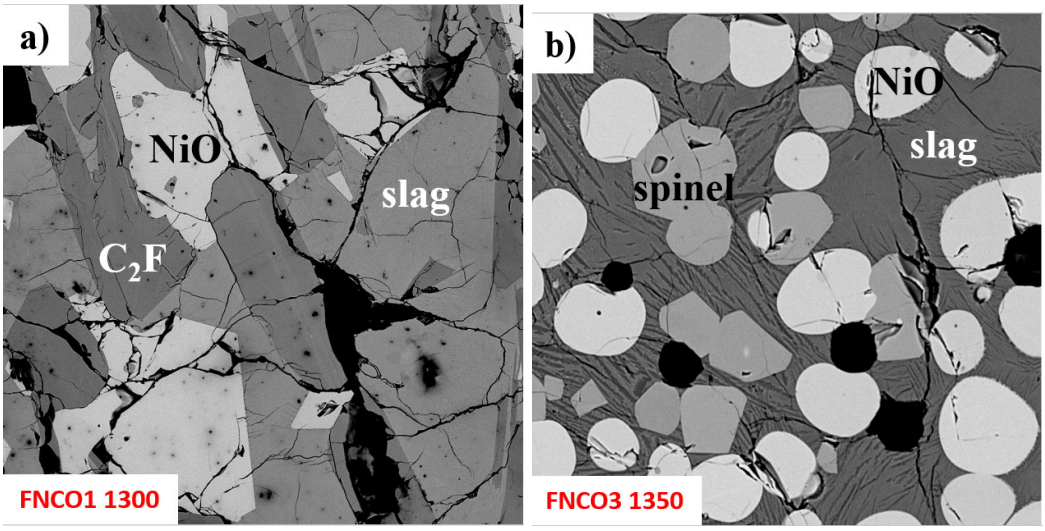

FIG 1 – Back-scattered electron images of the quenched samples, illustrating phase equilibria in the NiO-CaO-$FeO_{1.5}$ system in air at given temperatures: a) slag/NiO/C_2F at 1300°C; b) slag/NiO/spinel at 1350°C.

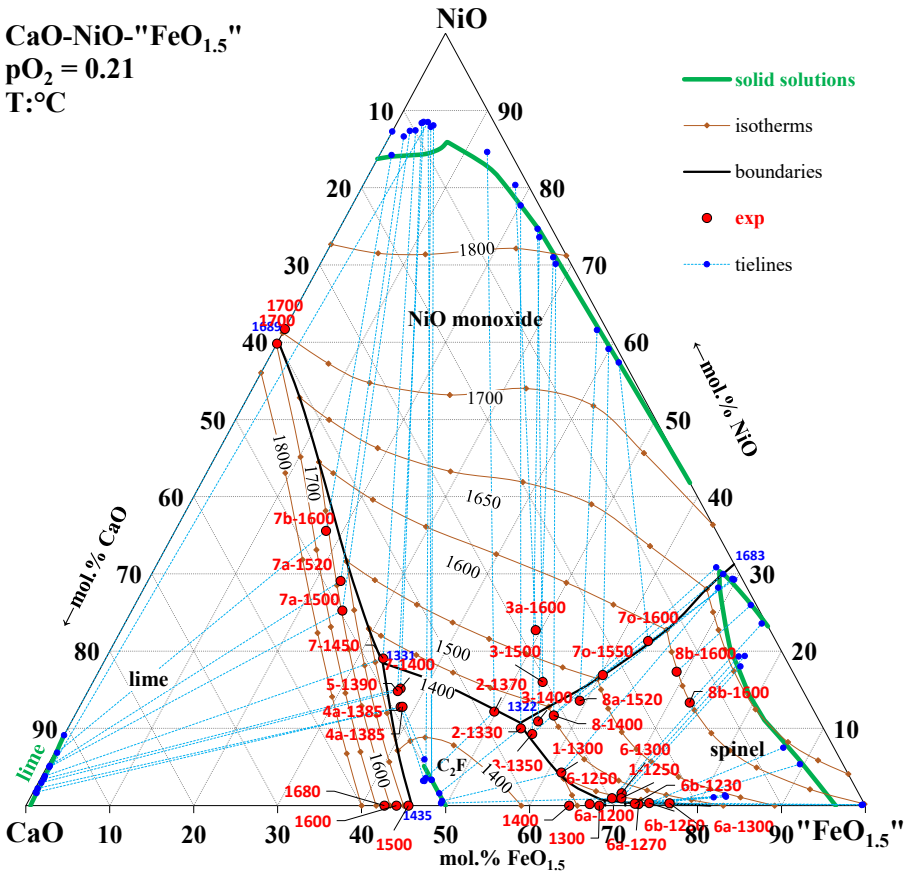

FIG 2 – Phase diagram of the NiO-CaO-$FeO_{1.5}$ system in air.

As it was mentioned before, all solid phases are characterised by homogeneity ranges. Figure 3 illustrates compositions of the solid phases in the NiO-CaO-$FeO_{1.5}$ system in air as functions of slag composition and temperature. Majority of the experimental points are located on the boundary lines between phases because most of the experimental slag is in equilibrium with two crystalline phases and located on monovariant line. It is shown that temperature trends, based on experimental points are in quite good agreement with calculated data.

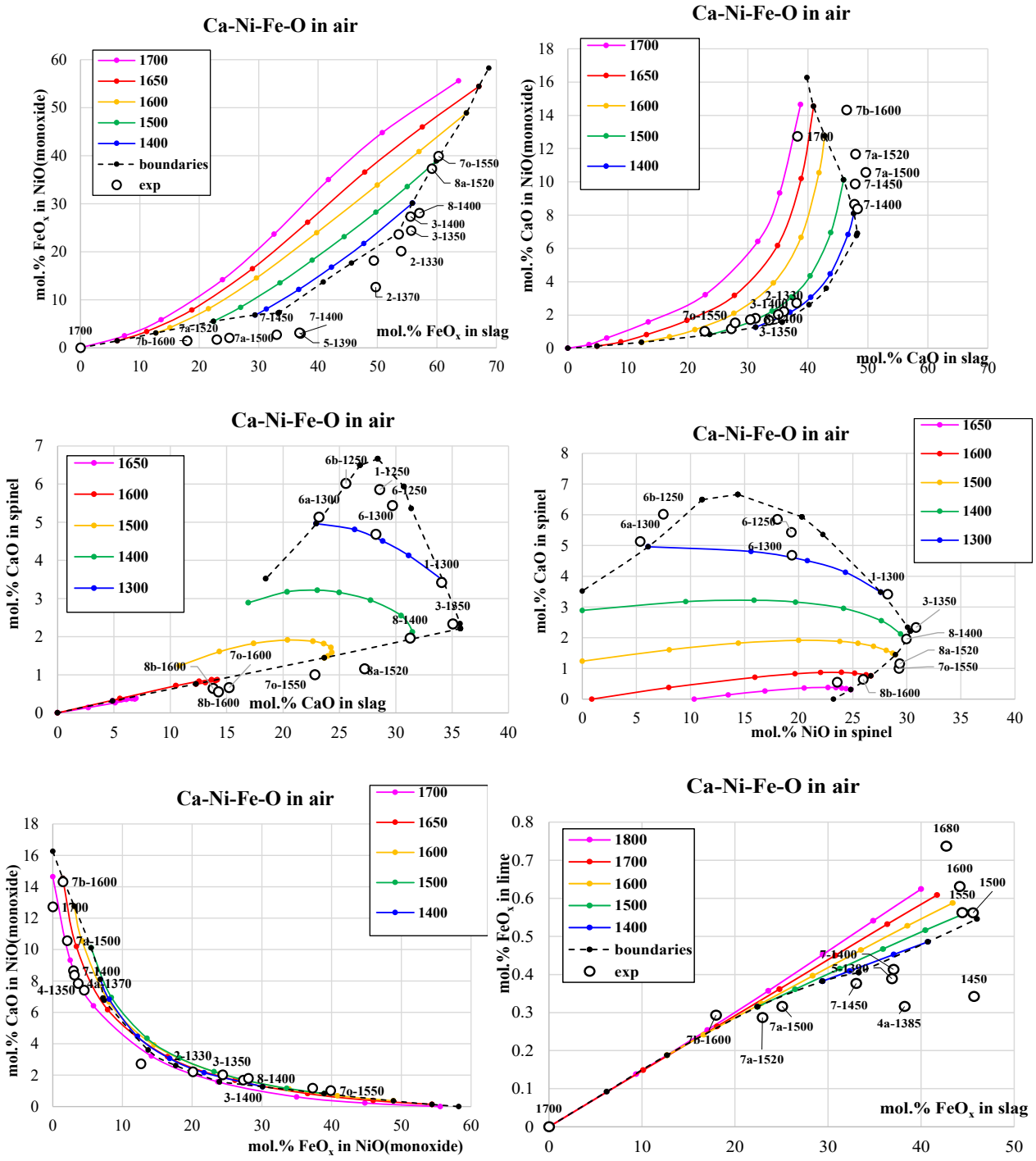

FIG 3 – Compositions of the solid phasess: (a, b, e) NiO monoxide; (c, d) spinel and (f) lime in the the NiO-CaO-FeO_x system in air as functions of slag or solid phases compositions and temperature (ºC). Lines and boundaries of all solid solutions are calculated with current version of confidential thermodynamic database, points are experimental data of the study.

Obtained experimental data allow to include Ni in the thermodynamic models for better description of lime and dicalcium ferrite solutions, as well as include Ca in Ni monoxide and Ni spinel phases.

NiO-CaO-FeOx system in equilibrium with metal FeNi phase

Figure 4 illustrates high-temperatures slag/FeNi metal/solid solution (lime, Ni monoxide or C_2F) phase equilibria. Due to fix both parameters at the same time (oxygen partial pressure and temperature) it's unable to get equilibrium of slag and metal with two solid phases (the system would be over fixed in that case). Therefore, all the points of liquid slags are located in the fields of primary phases crystallisations, but not on monovariant lines. Calculated small phase area of spinel and

CWF (CaO*FeO) solutions existed in low temperatures area (below 1250°C) have not defined experimentally.

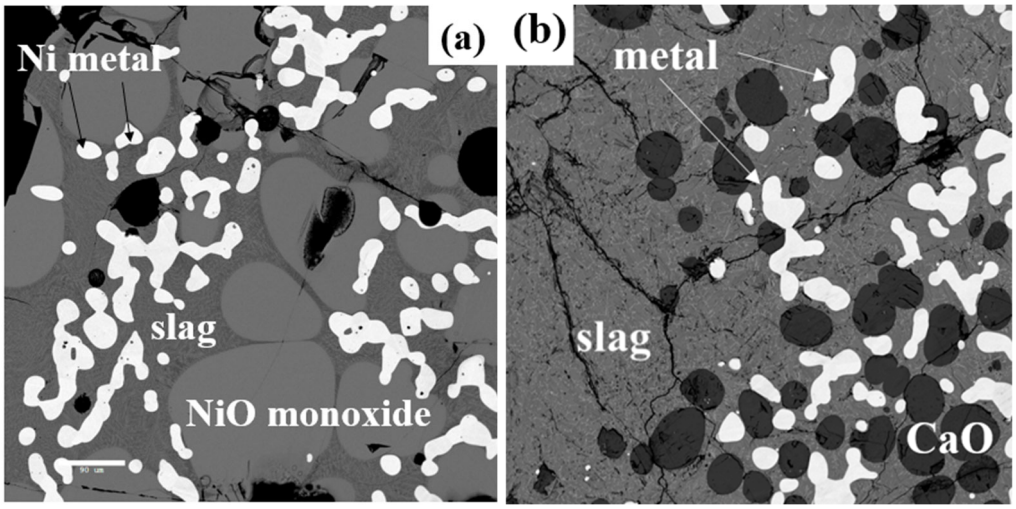

FIG 4 – Back-scattered electron images of the quenched samples, illustrating phase equilibria in the NiO-CaO-$FeO_{1.5}$ system in equilibrium with metal phase at given temperatures: a) slag/NiO monoxide/metal at 1500°C; b) slag/CaO/metal at 1400°C.

Obtained experimental data have been plotted on calculated version of the liquidus projection of the NiO-CaO-FeOx system. The resulting phase diagram is illustrated in Figure 5a. The zoomed area of phase diagram with low NiO concentration is illustrated in Figure 5b for better representation of small phase areas as well as compositions of lime, C_2F and monoxide solutions. Compositions of the liquid slags in equilibrium with other phases are identified by red circles, tie-lines are blue dashed lines ending with compositions of corresponding solid phases. Calculated version of the phase diagram calculated in Equilib module of FactSage 7.3 software with employing of current version of confidential thermodynamic database.

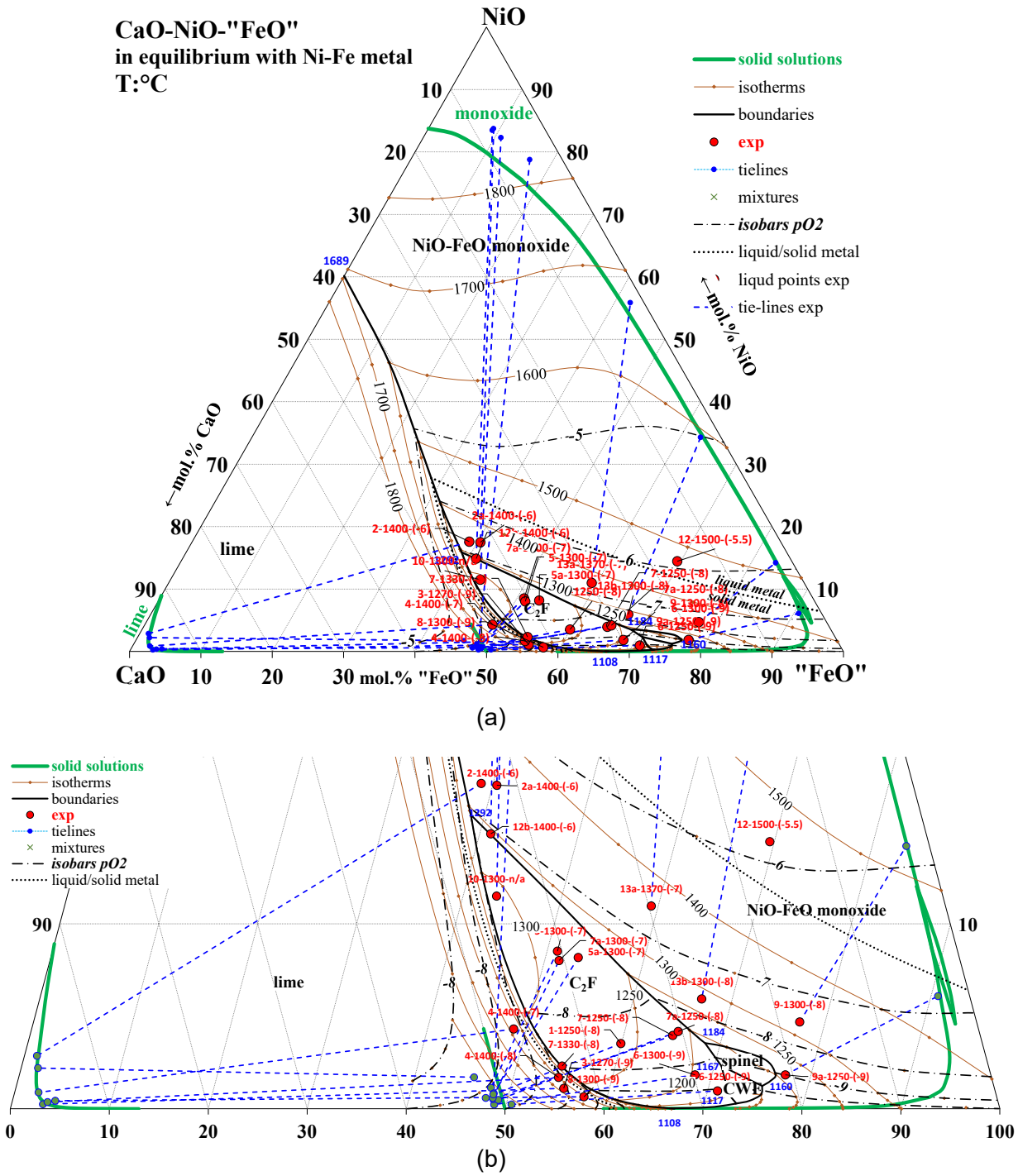

FIG 5 – (a) Phase diagram of the NiO-CaO-FeO_x system in equilibrium with metal Fe-Ni phase. (b) Zoomed area with low NiO concentration of the phase diagram of the NiO-CaO-FeO_x system in equilibrium with metal phase.

Based on the experimentally defined slag compositions the isotherms and isobars within the studied system will be corrected. A good agreement is observed between calculated and experimental compositions of lime, C_2F and NiO-FeO monoxide solutions. The only exception is dissolution of CaO in monoxide solution in high NiO-containing area.

Measured compositions of the slag, metal, and solid phases as functions of $P(O_2)$ and Ni concentration in slag have been plotted in Figure 6.

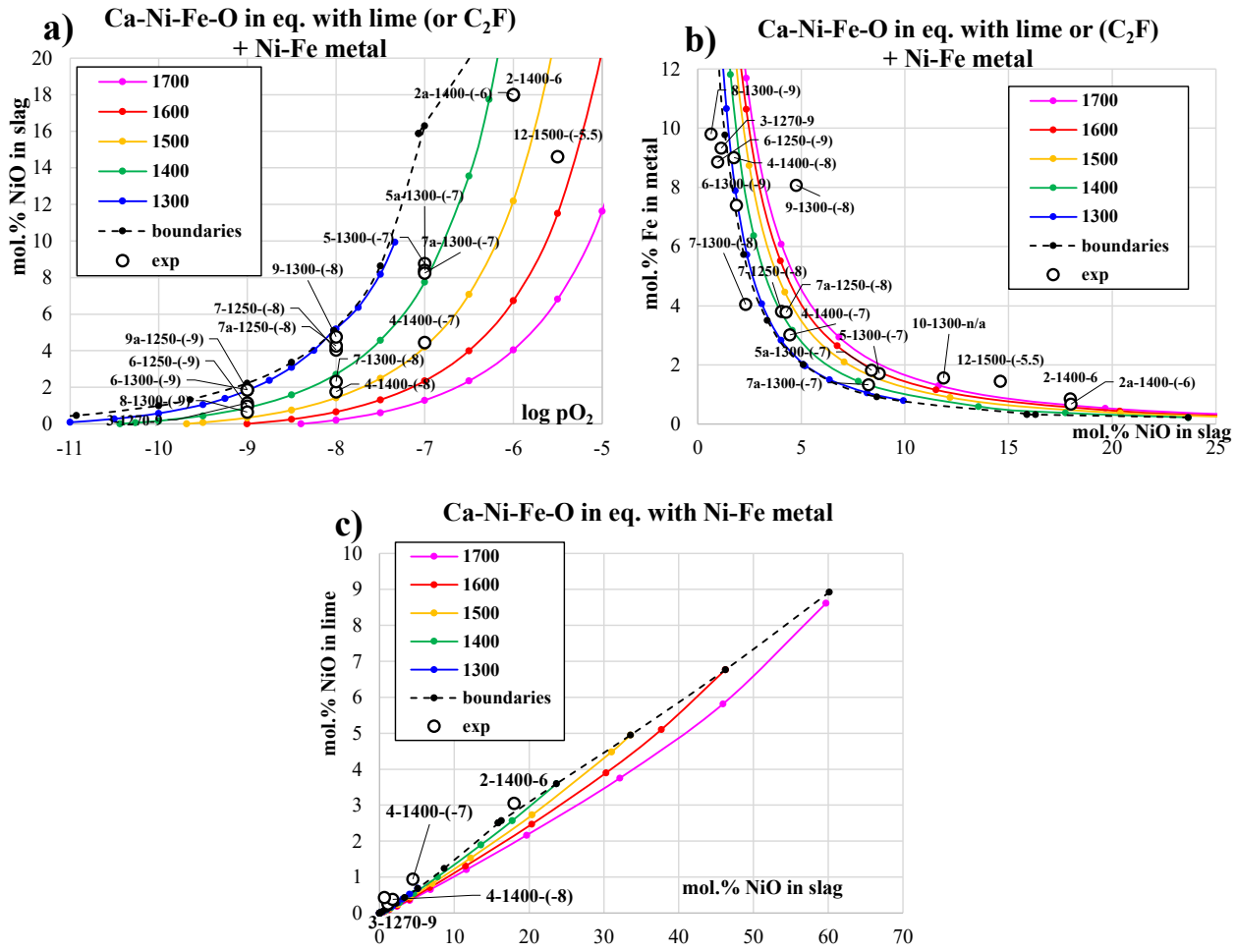

FIG 6 – Compositions of phases: (a) slag; (b) metal and (c) lime phases in mol per cent in the the NiO-CaO-FeO_x system in equilibrium with metal phase as functions of slag composition, $P(O_2)$ (atm) and temperature (ºC). Lines for all solid solutions are calculated with current version of the UQPY (beta-version) database.

CONCLUSIONS

Phase equilibria in the high-temperature region of the NiO-CaO-FeO-Fe_2O_3 system in air and in equilibrium with the metal phase have been studied using the integrated approach, which combines thermodynamic predictions with the 'equilibration-quenching-EPMA' experimental technique. The resulted liquidus surfaces of the NiO-CaO-Fe_2O_3 system and NiO-CaO-FeO/FeNi system have been plotted. Particular emphasis has been placed on defining the homogeneity ranges of lime, dicalcium ferrite, NiO-FeO monoxide and spinel solutions. The solubility of Ni in lime and C_2F solutions has been precisely characterised and validated through experimental data. The solubility of CaO in spinel and NiO-FeO monoxide solutions has been determined. When in equilibrium with metal phase the concentration of Ni in slag as a function of oxygen partial pressure has been defined experimentally.

This study has been performed as a part of integrated research program, aimed at complete characterisation of the gas-slag-matte-speiss-metal-solids equilibria in the Cu-Pb-Zn-Fe-O-S-SiO_2-(Al_2O_3-CaO-MgO-Cr_2O_3)-(As-Sn-Sb-Bi-Sn-Au-Ni-Co) system.

ACKNOWLEDGEMENTS

The research funding and technical support is provided by the consortium of copper producing companies: Anglo American Platinum (South Africa), Aurubis AG (Germany), BHP Billiton Olympic Dam Operation (Australia), Boliden (Sweden), Glencore Technology (Australia), Metso Outotec Oy (Finland), Peñoles (Mexico), RHI Magnesita (Austria), Rio Tinto Kennecott (USA) and Umicore NV (Belgium), as well Australian Research Council Linkage program LP190101020 'Future copper metallurgy for the age of e-mobility and the circular economy'. The authors are grateful to Ms Suping

Huang, Ms Marina Chernishova and Ms Samaneh Ashjaa for assistance with conducting experiments. Present study would not be possible without the facilities and technical assistance of the staff of the Australian Microscopy and Microanalysis Research Facility at the Centre for Microscopy and Microanalysis in The University of Queensland.

REFERENCES

Bigum, M, Brogaard, L and Christensen, T H, 2012. Metal recovery from high-grade WEEE: A life cycle assessment, *J of Hazardous Materials*, 207–208:8–14.

Cheng, S, Shevchenko, M, Hayes, P C and Jak, E, 2021. Experimental Phase Equilibria Studies in the FeO-Fe_2O_3-CaO-SiO_2 System and the Subsystems CaO-SiO_2, FeO-Fe_2O_3-SiO_2 in Air, *Metall Mater Trans B*, 52(3):1891–1914.

Coman, V, Robotin, B and Ilea, P, 2013. Nickel recovery/removal from industrial wastes: a review, *Recourses Conservation and Recycling*, 73:229–238.

Hidayat, T, Shishin, D, Decterov, S and Jak, E, 2016a. Critical thermodynamic re-evaluation and re-optimization of the CaO-FeO-Fe_2O_3-SiO_2 system, *CALPHAD*, 56:58–71.

Hidayat, T, Shishin, D, Decterov, S and Jak, E, 2016b. Thermodynamic optimization of the Ca-Fe-O system, *Metall Trans B*, 47(1):256–281.

Jak, E, 2012. Integrated experimental and thermodynamic modelling research methodology for metallurgical slags with examples in the copper production field, in *Proceedings of the 9th Intl Conf on Molten Slags Fluxes and Salts*, 28 p (The Chinese Society for Metals).

Jak, E, Hayes, P C and Lee, H-G, 1995. Improved methodologies for the determination of high temperature phase equilibria, *Korean Journal of Minerals and Materials Institute (Seoul)*, 1(1):1–8.

Meshram, P, Abhilash and Pandey, B D, 2019. Advanced review on extraction of nickel from primary and secondary sources, *Min Proc and Ext Met Review*, 40(3):157–193.

Phillips, B and Muan, A, 1958. Phase Equilibria in the System CaO-Iron Oxide in Air and at 1 atm O_2 Pressure, *J Am Ceram Soc*, 41(11):445–454.

Prostakova, V, 2013. Development of a thermodynamic database for nickel containing oxide systems for simulation of nickel extraction from laterite ores, PhD thesis, École Polytechnique de Montréal (Canada), 320 p.

Rhamdhani, M A, Chen, J, Hidayat, T, Jak, E and Hayes, P, 2009. Advances in research on nickel production through the Caron process, in *Proceedings of the EMC Conference 2009*, pp 899–912.

Schurmann, E and Kraume, G, 1976. Melting Equilibria in the System FeO-Fe_2O_3-CaO, *Arch Eisenhuttenwes*, 47(7):435–439.

Sineva, S, Shishin, D, Prostakova, V, Starykh, R, Chen, J and Jak, E, 2023. Experimental study and thermodynamic modelling of equilibrium distributions of Ni, Sn and Zn between slag and black copper for e-scrap recycling applications, *JOM*, 75(10):4254–4268.

Vasiliu, A, 1979. Initial Permeability and Curie Temperature in the Compounds of the Calcium Nickel Ferrite ($Ca_xNi_{1-x}Fe_2O_4$) System, *Bul Inst Politeh Iasi Sect*, 125(1–2):103–108.

Yamamura, H, Haneda, H, Watanabe, A, Moriyoshi, Y and Shirasaki, S, 1981. Magnetic Properties in the System Iron Nickel Oxide-Calcium Iron Oxide ($NiFe_2O_4$-$CaFe_2O_4$), *Yogyo Kyokaishi*, 89(11):595–598.

Slag chemistry on the Moon

DOI: 10.62053/LMTN3469

S P Singh[1], G A Brooks[2], M G Shaw[3], B Eisenbart[4], A R Duffy[5], M A Rhamdhani[6] and A K Shukla[7]

1. PhD Student, Swinburne University of Technology, Melbourne Vic 3122. Email: spsingh@swin.edu.au
2. Professor, Swinburne University of Technology, Melbourne Vic 3122. Email: gbrooks@swin.edu.au
3. Research Scientist, CSIRO Clayton, Melbourne Vic 3168. Email: matt.shaw@csiro.au
4. Professor, Swinburne University of Technology, Melbourne Vic 3122. Email: beisenbart@swin.edu.au
5. Professor, Swinburne University of Technology, Melbourne Vic 3122. Email: aduffy@swin.edu.au
6. Professor, Swinburne University of Technology, Melbourne Vic 3122. Email: arhamdhani@swin.edu.au
7. Associate Professor, Indian Institute of Technology, Madras, India. Email: shukla@iitm.ac.in

ABSTRACT

The field of astrometallurgy is a growing area of study. Metal production on the Moon is likely to begin in less than a decade as major space agencies such as NASA (National Aeronautics and Space Administration) and CNSA (China National Space Administration) are preparing to construct permanent lunar bases. The utilisation of regolith to generate oxygen and metals is expected to be important in the development of a sustainable lunar habitat. This paper provides an overview of potential metallurgical processing methods for lunar conditions, emphasising the impact of lunar factors on slag chemistry. The interaction between regolith and the extracted metals, as well as their impact on slag composition and refractory performance, are critical considerations in metal production on the lunar surface. The initial research on lunar metallurgical technologies is focused on oxygen extraction and Fe-Si alloys are reported as the by-products of these processes. This paper delves into the fundamental thermodynamics associated with the carbothermic reduction of lunar regolith. Thermodynamic analysis using the FactSage™ ver 8.2 software package indicates that the Fe-Si alloy can be produced as a metallic product from the lunar regolith at temperatures ranging from 1400°C to 1600°C under terrestrial conditions. However, under ultra-high vacuum conditions (3×10^{-15} bar) on the Moon, the required operating temperature for producing ferrosilicon would be significantly reduced. Thermodynamic modelling results indicate that under lunar vacuum conditions, Fe-Si alloys only exist as solid phases at lower temperatures below 650°C. At higher temperatures, both Fe and Si are expected to be present in the gas phase. In this work, the carbothermic reduction of the Lunar Mare Simulant (LMS-1) is conducted under terrestrial conditions. The findings indicate that the process can readily yield Fe-Si alloys with 7–10 wt per cent Si at 1600°C. Additionally, energy dispersive spectroscopy (EDS) analysis of the resulting Fe-Si alloy indicates the presence of phosphorus up to 1 wt per cent.

INTRODUCTION

Metallurgical engineering technologies have played a crucial role in the development of societies on Earth. Expanding to the Moon is now the intended stated goal for several nations and space agencies, such as NASA (National Aeronautics and Space Administration), ISRO (Indian Space Research Organization), ESA (European Space Agency) and CNSA (China National Space Administration), where they have already made their plans for sustainable lunar exploration (ESA, 2019; Mahoney, 2020; NASA, 2020). NASA's *Artemis* missions, China's *Change* missions, Russia's *Luna* missions and India's *Chandrayaan* missions represent some of the ongoing major programs in the lunar exploration series. Moreover, several commercial ventures, such as SpaceX, Blue Origin, ORBITEC, Cislunar Industries, Lunar Resources Inc. and Shimizu Construction Company, are actively engaged in lunar exploration efforts (Ignatiev and Freundlich, 2012; Mackwell, Neal and Pestak, 2019). For this kind of settlement, new metallurgical processes need to be developed that can work under extreme lunar conditions such as ultra-high vacuum of the order of 3×10^{-15} bar, low gravity (1/6th of that of the Earth) and large temperature fluctuations of 121°C to -133°C between lunar day and night near the Moon's equator. The knowledge of metallurgical processes on Earth

acquired over many years could help in the development of the lunar metallurgical processes. In particular, the vast knowledge and experience of steelmaking on Earth can be leveraged to inform lunar steel production. Recovery of iron from the lunar regolith and processing into steel can potentially contribute to the establishment of a permanent lunar base.

A permanent lunar base would require a sustainable supply of metals and alloys; In-Situ Resource Utilization (ISRU) of lunar resources can provide the necessary metals for the lunar base. The metal resources on the Moon can be grouped into three categories:

1. Metal produced from lunar regolith using ISRU.
2. Recycled end-of-life products on the lunar surface, such as metals from the landers and rovers.
3. Outsourced metals from the Earth.

Lunar regolith and rocks are source of oxygen and metals. Lunar regolith is primarily composed of metal oxides close in chemistry to mineral deposits found on Earth but with a relatively large content of fine glassy material formed from meteorite impacts. The composition of bulk lunar regolith varies across the lunar surface. The chemical composition of the lunar regolith suggests the presence of average 44.6 wt per cent oxygen and several metal(loid)s like Si, Fe, Ca and Al (Duke *et al*, 2006). Extraction of the metals from lunar regolith using ISRU technologies can minimise the dependency on Earth for material supplies. Another source of metals on the Moon could be the end-of-life products on lunar surface. In, 2012, NASA prepared a catalogue of human-made objects left on the lunar surface (NASA, 2012). It was estimated that about 200 000 kg of such human-made materials are available on the lunar surface. The amount of these end-of-life products like landers, rovers on the lunar surface will continue to grow with the future missions unless their raw materials are recuperated.

Existing ISRU techniques like Molten Regolith Electrolysis (MRE), solar pyrometallurgical reduction and vacuum pyrolysis have shown their potential for oxygen and metal production (Sargeant *et al*, 2020; Schreiner *et al*, 2016; Shaw *et al*, 2021a; Sirk, Sadoway and Sibille, 2019). These technologies are still in the development stage, with some prototypes having been tested under simulated lunar conditions (Shaw *et al*, 2021a; Sirk, Sadoway and Sibille, 2019). Alongside these metal extraction processes, the technologies for mining and beneficiation need to be proven to operate effectively in the lunar environment.

The literature published on ISRU technologies is primarily focused on extracting oxygen from the lunar soil as it is vital for human survival on the moon (Schlüter and Cowley, 2020). Ferrosilicon (Fe-Si) alloys are reported as the major by-product of these ISRU technologies (Grossman *et al*, 2019; Samouhos *et al*, 2022). In the MRE process, Fe and Si are the first elements to be reduced from FeO and SiO_2 due to their lower dissociation potential compared to other elements like Al and Ca (Schreiner *et al*, 2016). Carbothermal reduction is another potential ISRU technology to reduce lunar regolith (Gustafson *et al*, 2010; Kaur *et al*, 2024; Samouhos *et al*, 2022). This approach has been proposed for other extra-terrestrial application, such as iron production on Mars, where carbon is sourced from the CO_2 atmosphere (Nababan *et al*, 2022). Carbothermal reduction uses carbon sources such as C, CO, CH_4 etc to reduce oxide species of lunar regolith, forming metal and CO/CO_2 according to the following reactions:

$$MeO_{(S)} + CO_{(g)} \rightarrow Me_{(S/l)} + CO_{2(g)} \quad (1)$$

$$MeO_{(S)} + C_{(s)} \rightarrow Me_{(S/l)} + CO_{(g)} \quad (2)$$

On the moon the carbon needs to be supplied from the earth or it can be recycled from the carbonaceous lunar waste. Gustafson *et al* (2010) suggested that carbothermal reduction of molten regolith requires a temperature of over 1625°C. At this temperature oxides of both Fe and Si can be reduced and an oxygen yield of 28 kg per 100 kg regolith can be achieved. A recent study by Samouhos *et al* (2022) synthesised granulated Fe-Si alloy with an average of 23.78 wt per cent Si along with minor Al and Ti at 1300°C using BP-1 lunar regolith simulant and carbon. Kaur *et al* (2024) performed thermodynamic modelling study on carbothermal reduction of JSC-1A lunar simulant and predicted the favourable operating temperatures at three different pressures (10^{-1}, 10^{-8} and 3×10^{-15} bar) for Fe and Si production. They reported complete conversion of Fe_2O_3 to Fe gas above 850°C

and about 90 per cent conversion of SiO_2 to Si gas above 1000°C under lunar conditions of 3×10^{-15} bar.

In this study, thermodynamic calculations have been performed to understand the primary products and by-products of carbothermal reduction of lunar regolith under earth and lunar conditions. The report discusses the effect of various carbon percentages, temperature and lunar conditions on the product chemistry and recommends the optimum processing condition for producing Fe-Si alloys using ISRU. Additionally, preliminary experimental results on the carbothermal reduction of lunar regolith simulant, LMS-1, are presented, indicating the formation of ferro-silicon alloys.

THERMODYNAMIC PREDICTIONS

Thermodynamic modelling is a critical tool to predict the equilibrium compositions based on Gibbs free energy minimisation (Bale *et al*, 2016). In this study, FactSage™ ver 8.2 thermodynamic software was used to predict the composition of the products from the carbothermic reduction of lunar regolith under different pressures. FactPS, FSsteel and FToxid databases were used for the calculations. Thermodynamic modelling was conducted in three stages using the Equilibrium module. The first stage was to predict the optimum equilibrium conditions for the carbothermic reduction at Earth's conditions, ie at 1 bar pressure. These calculations were performed to design the experimental process on Earth and develop an understanding of the equilibrium phases and the possible metallic alloy extraction. These findings will also be potentially applicable for regolith processing inside a pressure-controlled human habitat on the Moon. The second stage of equilibrium calculations was performed on the lunar vacuum condition (3×10^{-15} bar). These calculations were aimed at predicting the slag composition, metallic alloy chemistry and off-gas composition over a range of temperatures and carbon content. The third stage of calculations was performed at an intermediate vacuum condition of 3×10^{-8} bar. The reason behind these calculations was that during a lunar carbothermal reduction process, the off-gas generated from the chemical reactions would potentially increase the pressure inside the reaction chamber. It is important to note that for such ultra-low pressures, the extrapolated thermodynamic data may not give the accurate results, as the experimental validation data becomes scarcer. However, qualitatively It will provide useful trends and insights of the process.

The composition of the lunar regolith varies across the lunar surface (Shaw *et al*, 2021b). The composition of the regolith obtained from different lunar missions is shown in Table 1. It is clear from the table that FeO content significantly varies from below 5 wt per cent to over, 20 wt per cent in all these samples. For this study, the composition utilised was that of LMS-1 regolith simulant provided by Exolith lab, which contains 8.6 wt per cent FeO and is commonly used in studies related to regolith processing.

TABLE 1

Compositions of Lunar Regolith samples (Duke *et al*, 2006; Shaw *et al*, 2021b).

Constituents (wt%)	Apollo 16 (Sample ID 64501)	Luna 24 (Sample ID 24999)	Apollo 17 (Sample ID 76501)	This study uses LMS-1 Simulant
FeO	4.4	20.3	11.1	8.6
Al_2O_3	27.6	11.1	18.2	12.4
SiO_2	45.2	45.9	42.8	46.9
TiO_2	0.4	1	3.3	3.6
MgO	4.7	10.4	11.9	16.8
MnO	0.1	0.3	0.1	0.2
CaO	16.6	10.7	12.3	7
Na_2O	0.4	0.3	0.4	1.7
K_2O	0.1	0.0	0.1	0.7
P_2O_5	-	-	-	0.2

Processing on the Earth

The equilibrium calculations for carbothermal processing of lunar regolith on the Earth were conducted for 100 g of regolith quantity and 1 bar pressure at different reduction temperatures and carbon content. Primary products obtained at different conditions were liquid alloy, liquid slag, gas and, in some cases, solid silicate phases. The percentage of these phases varied with carbon content and temperature. Figure 1 shows the predicted quantity of liquid alloy and slag as the carbon and temperature vary.

Figure 1 indicates that at 800°C, no liquid alloy or liquid slag formation is expected. The prediction suggests that liquid phases are anticipated to begin forming above 1000°C. As the temperature increased to 1200°C, a sharp rise in the quantities of both liquid alloy and liquid slag were observed, although the quantities remained unchanged with increasing carbon addition. As the temperature further increased to 1400°C, the amount of liquid alloy was predicted to increase slightly, while the quantity of slag more than doubled. A slight increase in the liquid alloy quantity of 0.1 g can also be observed in Figure 1a when the carbon increased from 2 g to 4 g. Figure 1b shows the slag quantity increased from 39 g to almost 88 g across all the carbon content. As the temperature increased further to 1600°C, the liquid alloy quantity is predicted to increase, however the slag quantity decreased. A clear declining trend can be seen for slag with increasing carbon content. This trend remains consistent at 1800°C. The liquid alloy on the other hand jumped to its highest values at 1800°C and at 10 g carbon. After 10 g carbon, the decline in liquid alloy quantity is attributed to the formation of carbide phases such as TiC and SiC. The predicted results also indicated that there was excess carbon remaining in the form of graphite.

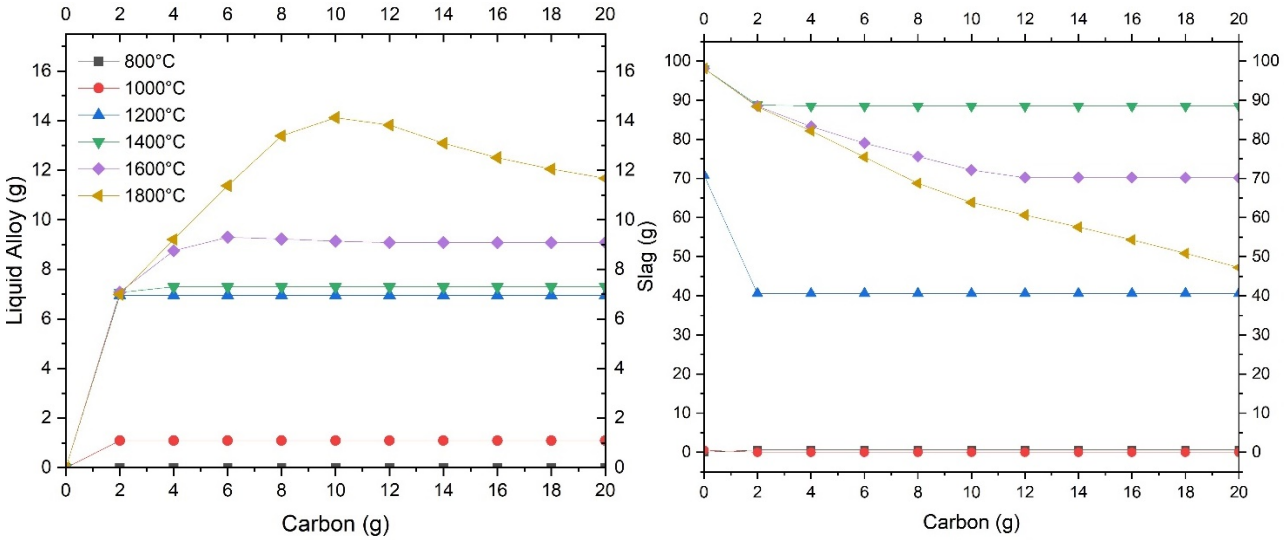

FIG 1 – (a) Predicted amount of liquid alloy, and (b) liquid slag from the carbothermic reduction of 100 g of LMS-1 simulant with variation in carbon content from 0 to 20 g and reduction temperature from 800°C to 1800°C at 1 bar.

To understand these trends further, the compositions of both liquid alloy and liquid slag were analysed. Figure 2 shows the predicted primary elements of the liquid alloy (Fe, Si and Ti) at four different temperatures, 1200°C, 1400°C, 1600°C and 1800°C. As can be seen from Figure 2, iron is the only major component of the liquid alloy at 1200°C. Other elements such as C and P are also present in the liquid alloy, for eg reduction at 2 g C, results in a liquid alloy with 3.96 wt per cent C and 1.26 wt per cent P, equivalent to 0.275 g C and 0.088 g P. These elements are not shown in Figure 2 due to their smaller quantity. As the temperature increases to 1400°C, silicon is predicted to start forming. With further rise in temperature to 1600°C and 1800°C, silicon quantity in Fe-Si alloy is predicted to increase. Silicon content in the Fe-Si alloy is also predicted to rise with increasing carbon content, reaching a maximum at about 6 g carbon for 1600°C and 10 g carbon for 1800°C. Titanium is also predicted to be present in Fe-Si alloy at 1600°C and its quantity starts to rise with

temperature. The graphs in Figure 2 illustrate that at temperatures exceeding 1600°C, liquid alloys are anticipated to contain higher quantities of titanium and silicon.

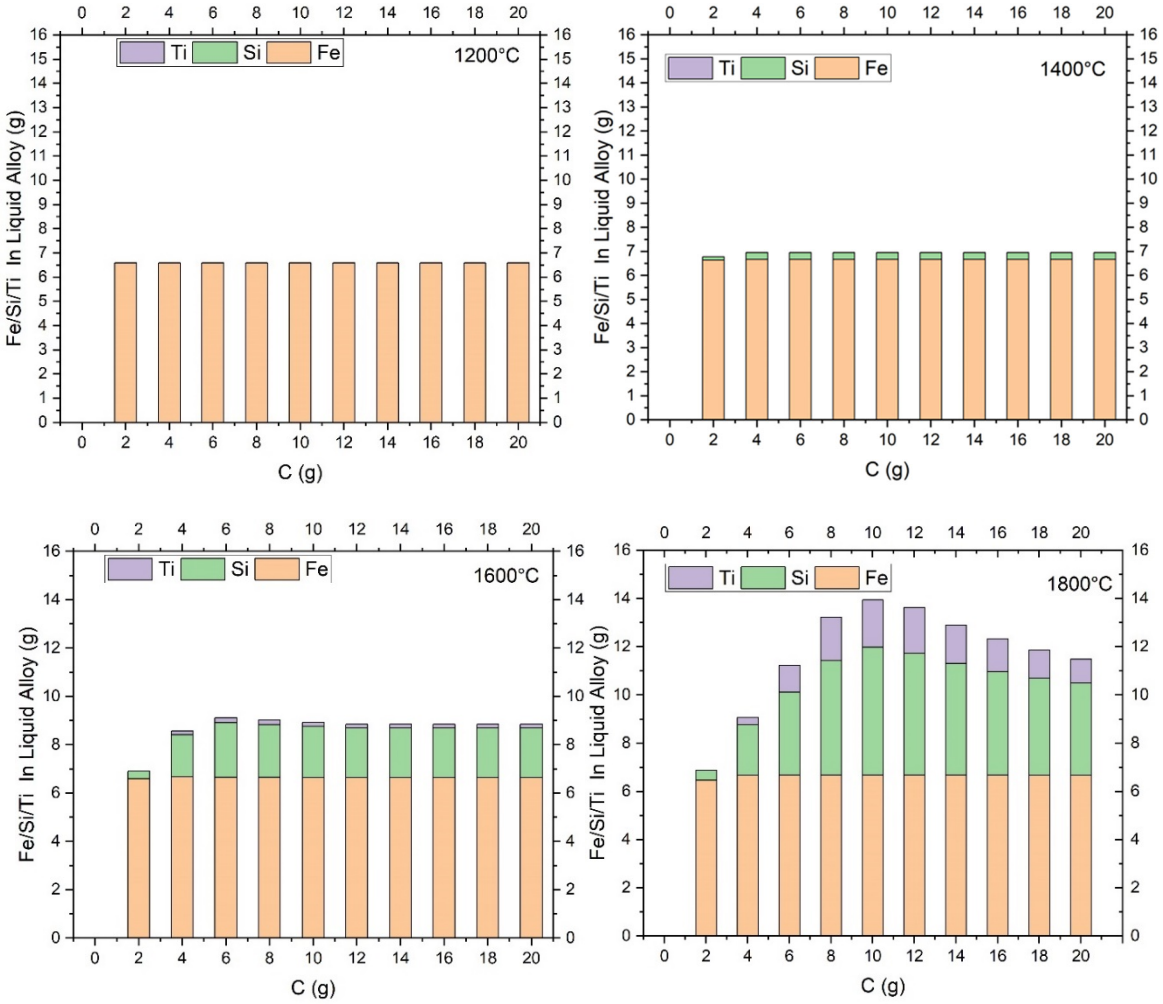

FIG 2 – Composition of liquid alloy predicted to be produced from the carbothermic reduction of 100 g of LMS-1 simulant with variation in carbon content from 0 to 20 g and reduction temperatures at 1200°C, 1400°C, 1600°C and 1800°C at 1 bar pressure.

These calculations indicate that the liquid alloys formed during the carbothermal reduction process of lunar regolith simulant LMS-1 consist of various compositions of Fe-Si alloy. Although the highest amount of liquid alloy is predicted to form at the highest reduction temperature of 1800°C, it contains higher percentages of silicon and titanium compared to lower temperatures. As the lower Si-containing Fe-Si alloys have a better balance between strength and ductility, lower temperatures of 1200 to 1400°C seem like an ideal temperature range. However, it is also important to look at other phases present in the products to determine the optimum temperature.

Figure 3 shows the predicted composition of liquid slag at 1400°C and 1800°C. As can be seen in Figure 3, at 0 g carbon, FeO is present in the slag. With carbon addition, FeO is the only component that is fully reduced. CaO and MgO are present at all conditions but are not reduced to metal and, therefore, were not observed in the liquid alloy. At 1800°C, the notable difference in slag composition lies in the reduction of SiO_2 and TiO_2 levels with carbon, compared to 1400°C. This is because at higher temperatures, both SiO_2 and TiO_2 are reduced by carbon, forming Si and Ti that go into the liquid alloy. In addition, the metallic Si and Ti reacts with excess carbon and forms carbide phases. From Figures 2 and 3, 1400°C and 4 g, carbon appears to be sufficient for producing Fe-rich ferrosilicon alloys. However, separating and extracting the liquid alloy from the other products is also crucial in the effective recovery of the Fe-Si alloy. Therefore, it is crucial to understand the other products during the reduction.

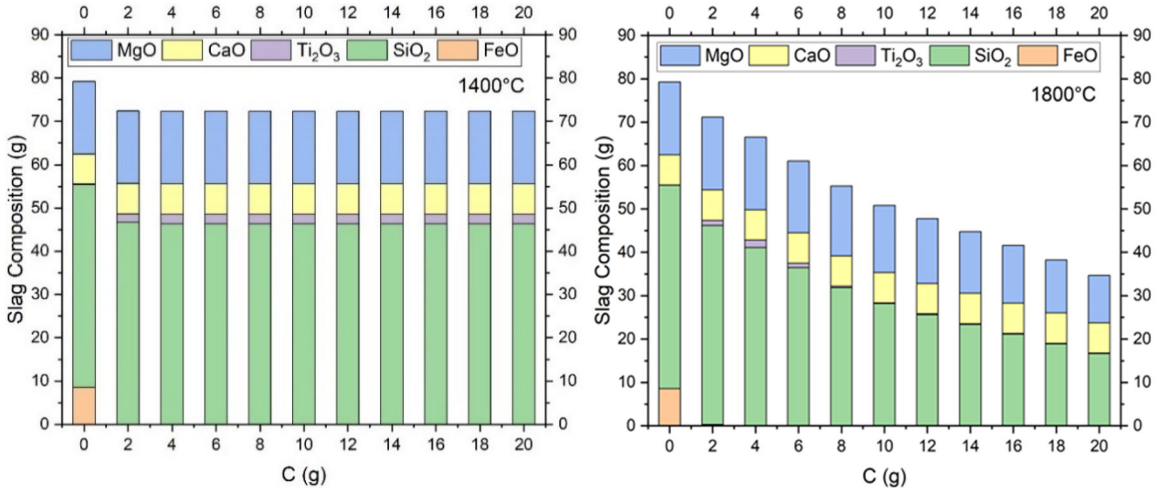

FIG 3 – Composition of liquid slag predicted to be produced from the carbothermic reduction of 100 g of LMS-1 simulant with variation in carbon content from 0 to 20 g and reduction temperatures at 1400°C and 1800°C at 1 bar pressure.

Figure 4 shows the stability of different phases that form during the carbothermal reduction of lunar regolith at 1200°C and 1400°C at 1 bar. At 1200°C, different silicate phases such as olivine, pyroxenes and feldspar are predicted to be present in the products in the solid state. These silicate phases coexist with liquid alloy, liquid slag and gas phases at all carbon percentages, as shown in Figure 4a. At 1400°C, these silicate phases are predicted to disappear. The liquid alloy phase will only coexist with liquid slag, and due to density difference, it can be separated from the slag. At higher temperatures, the quantity of slag is predicted to decrease, as shown in Figure 1b. This will increase both the quantity of liquid alloy and the gas phase. Therefore, 1400°C is the ideal temperature for processing the lunar regolith under the terrestrial conditions. In addition, the amount of slag, liquid alloy and gas plateaus after 4 g carbon at 1400°C.

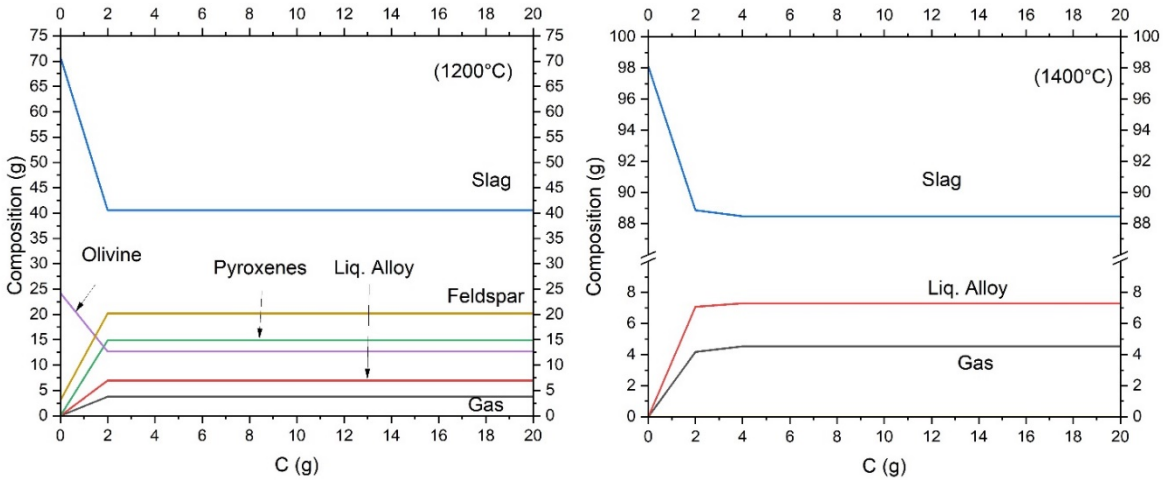

FIG 4 – Predicted equilibrium compositions from the carbothermal reduction of 100 g of LMS-1 simulant with variation in carbon content from 0 to 20 g and reduction temperatures at (a) 1200°C and (b) 1400°C at 1 bar.

It is important to note that the primary aim of the ISRU technologies on the moon is to produce oxygen. Therefore, the aim of the carbothermal reduction process is to generate as much gas as possible to recover the oxygen. Figure 5 shows the variation in equilibrium compositions with reduction temperature at fixed carbon amounts of 4 g and 6 g. The graph indicates that the amount of gas increases with temperature and carbon. Figure 5 shows that after about 1350°C, the primary constituents of the products are gas, liquid alloy and liquid slag. A small amount of carbide phases such as TiC and SiC are also predicted to form after 1450°C.

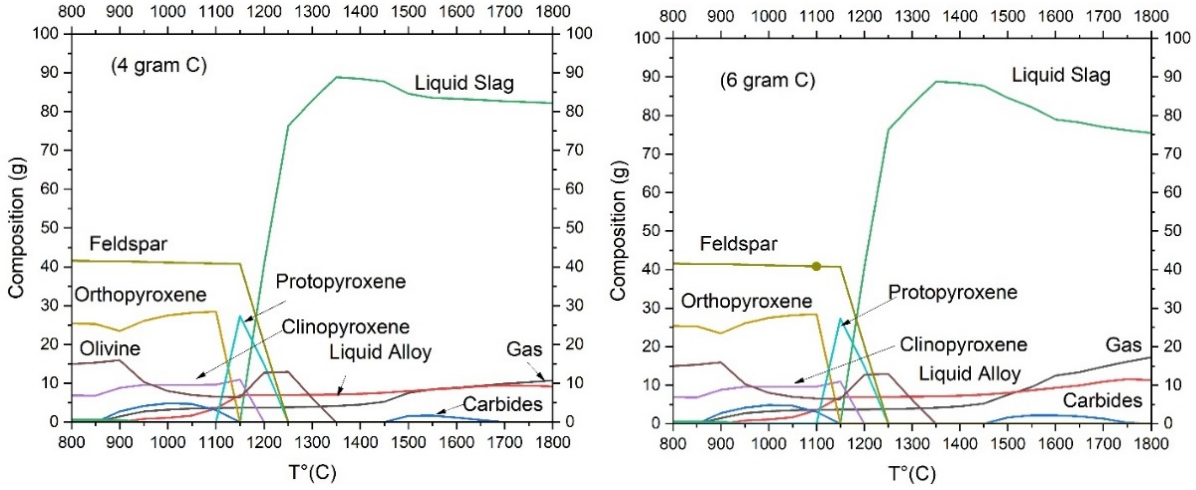

FIG 5 – Predicted equilibrium compositions of the products from carbothermal reduction of 100 g lunar regolith at various reduction temperatures at 4 g and 6 g carbon.

Processing on the Moon

The equilibrium calculations for carbothermal processing of 100 g lunar regolith simulant (composition shown in Table 1) were conducted at 3 × 10^{-15} bar pressure and 6 g carbon, and the equilibrium product composition under lunar vacuum conditions is shown in Figure 6. Few minor phases have been removed from the phase diagram to avoid clutter. As can be seen in Figure 6a, there is no liquid slag or liquid alloy phase in the product. Gas is the major phase. The products include various silicate phases, such as different types of pyroxenes and feldspar, at temperatures below 1000°C. Corundum forms between 1000°C to 1150°C. The quantities of Fe-containing phases are very small compared to the other phases. The magnified phase diagram shown in Figure 6b shows the presence of four different solid phases of Fe: BCC phase, FCC phase, Fe-Si and Fe_5Si_3 alloys. At lower temperatures of below 350°C, the majority of Fe is present in the BCC phase. After 350°C, the FCC phase starts to form. Both FeSi and Fe_5Si_3 alloys start to form at 400°C. Initially, the quantity of the FeSi phase increases with an increase in temperature, reaching its peak at 500°C, and then decreases, finally disappearing at 600°C. Similarly, the Fe_5Si_3 intermetallic compound initially increases until 450°C and disappears after 500°C. Beyond 600°C, no solid phases containing Fe are observed in the phase diagram, indicating that all the Fe is predicted to have evaporated. After 900°C Feldspar is predicted to vaporise into different gas components, few minor-concentration phases such as $Mg_4Al_{10}Si_2O_{23}$, $CaTiO_3$, $CaAl_4O_7$ have been omitted from the phase diagram to mitigate visual complexity in Figure 6.

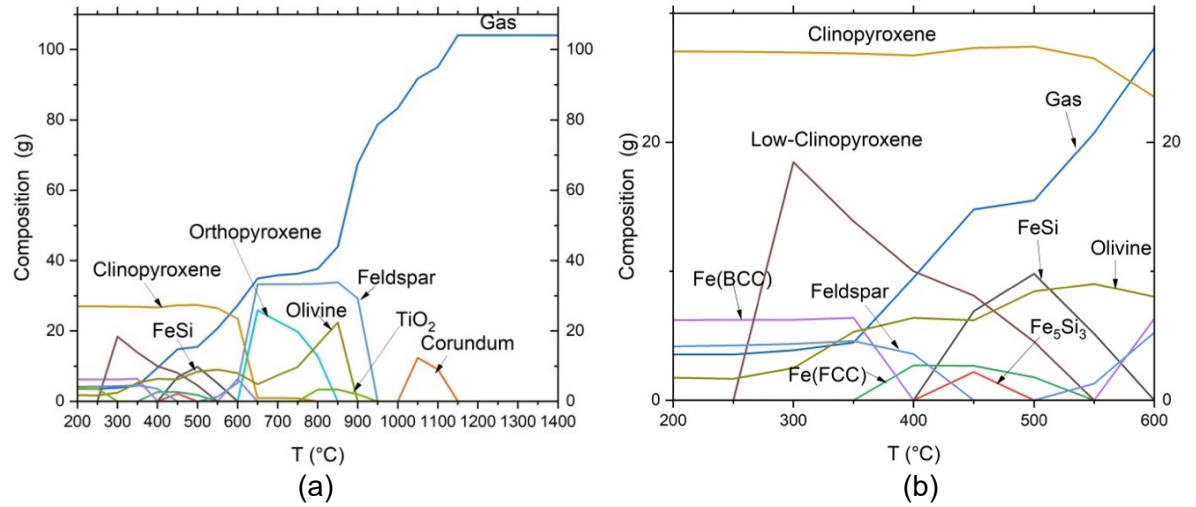

FIG 6 – (a) Predicted equilibrium compositions of the products from the carbothermal reduction of 100 g lunar mare simulant (LMS-1) at 6 g carbon and 3 × 10^{-15} bar pressure, (b) Magnified diagram.

As gas is the major product of the carbothermal reduction of regolith under lunar vacuum conditions, the predicted composition of the gas phase with temperature is shown in Figure 7. Figure 7a shows that the gas phase is predicted to start forming from as low as 200°C reduction temperature with CO gas as the major constituent. With the rise in temperature to over 350°C, Na and K are predicted to appear in the gas phase. The formation of SiO gas starts at about 500°C and increases as the temperature rises. Upon comparing Figures 6 and 7, it is evident that initially, the SiO gas forms from the Si present in the FeSi alloy. Subsequently, between 600°C to 950°C, the SiO gas is produced from all the silicate phases containing SiO_2. Figure 7b shows the magnified image of Figure 7a at higher temperatures. The figure suggests that Fe is predicted to vaporise at about 600°C, and the quantity of Fe gas reaches a plateau after about 700°C. With further rise in temperature, Mg evaporates, followed by Ca and Al. The quantity of gas phase reaches its maximum at 1150°C and plateaus afterwards. Vacuum distillation process can be used to recover these metallic vapour phases although it has its own technical challenges. In order to recover Fe metal and especially the FeSi alloys, a reduction temperature of 400°C to 600°C could be used, and the resulting product may undergo grinding and magnetic separation process to potentially eliminate silicate phases. It is crucial to highlight that these predictions have not taken reaction kinetics into consideration. Hence, experimental research is necessary to confirm these predictions and gain insights into the kinetics of the reaction.

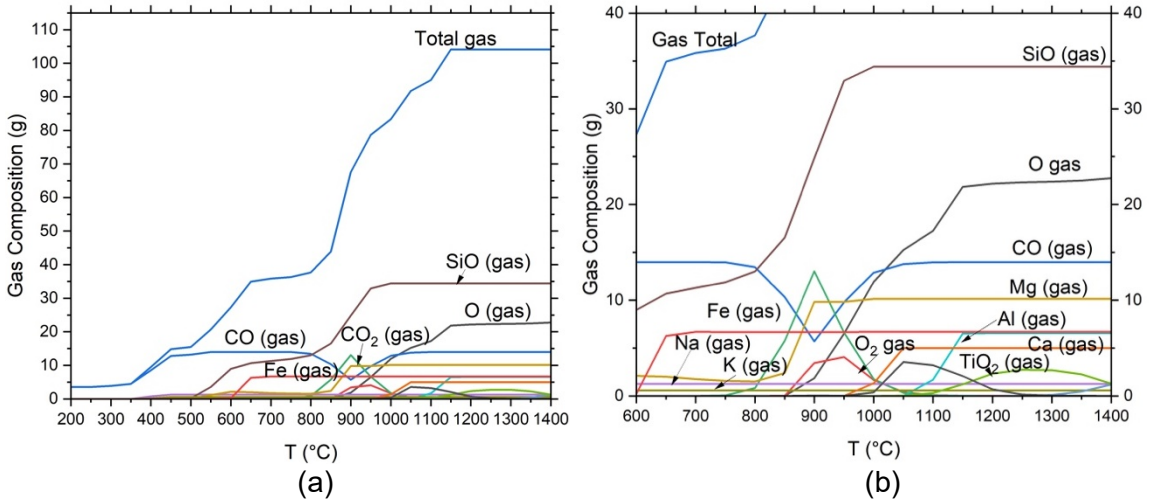

FIG 7 – (a) Equilibrium compositions of the products from the carbothermal reduction of 100 g lunar regolith at 6 g carbon and 3 × 10^{-15} bar pressure, (b) Magnified diagram.

Processing at intermediate vacuum condition

As mentioned earlier, the gases produced during the carbothermal reduction will increase the vacuum pressure inside the reaction chamber. Kaur *et al* (2024) assumed a pressure of 10^{-8} bar in their study to account for the pressure increases due to the evolving gases. In this study, equilibrium calculations were performed at 3 × 10^{-8} bar pressure to understand the products of carbothermic reduction. Like the previous equilibrium calculations, 100 g regolith was reduced using 6 g carbon and the equilibrium phases at different temperatures are plotted, as shown in Figure 8. Under this intermediate vacuum condition, although the liquid slag phase is forming in the temperature range of 1150°C to 1500°C, metals stay in the solid or gaseous form. As with the previous diagrams, different types of silicate phases are shown to form at different temperatures. The FeSi alloy is stable in the temperature range of 650°C to 900°C. The magnified image shown in Figure 8b suggests the presence of Fe_5Si_3 alloy until 950°C. The key takeaway from this figure is that even under this intermediate vacuum condition, the Fe and FeSi alloys are still in solid form and need to be ground and magnetically separated to extract the Fe/Fe-Si alloys from the silicate phases.

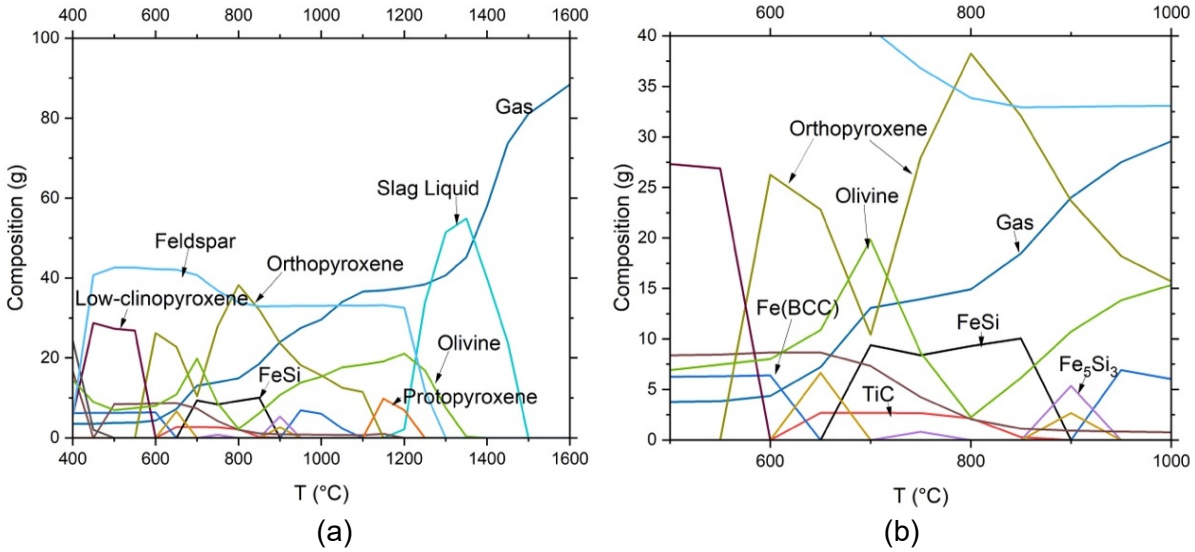

FIG 8 – (a) Equilibrium compositions of the products from the carbothermal reduction of 100 g lunar regolith at 6 g carbon and 3 × 10^{-8} bar pressure, (b) Magnified diagram.

In order to estimate the optimum vacuum pressure to recover liquid Fe-Si alloys, equilibrium calculations were performed at different pressures ranging from 1 bar to 10^{-15} bar and the results are shown in Figure 9. The figures suggest that at both 1200°C and 1400°C, the liquid alloy coexists with liquid slag in the pressure range of 1 to 10^{-5} bar. The amount of both liquid slag and liquid alloy is predicted to be higher at 1400°C. For both cases, the liquid slag is present until 10^{-9} bar. From these graphs, it is evident that the pressure inside the reaction chamber should be more than 10^{-5} bar to recover liquid Fe-Si alloys. The density difference between the liquid slag and liquid alloy should ensure easy separation. At higher vacuum conditions, FeSi alloys need to be extracted in solid form by grinding and magnetic separation. Fe vapour can also be extracted from the gas phase using vacuum distillation.

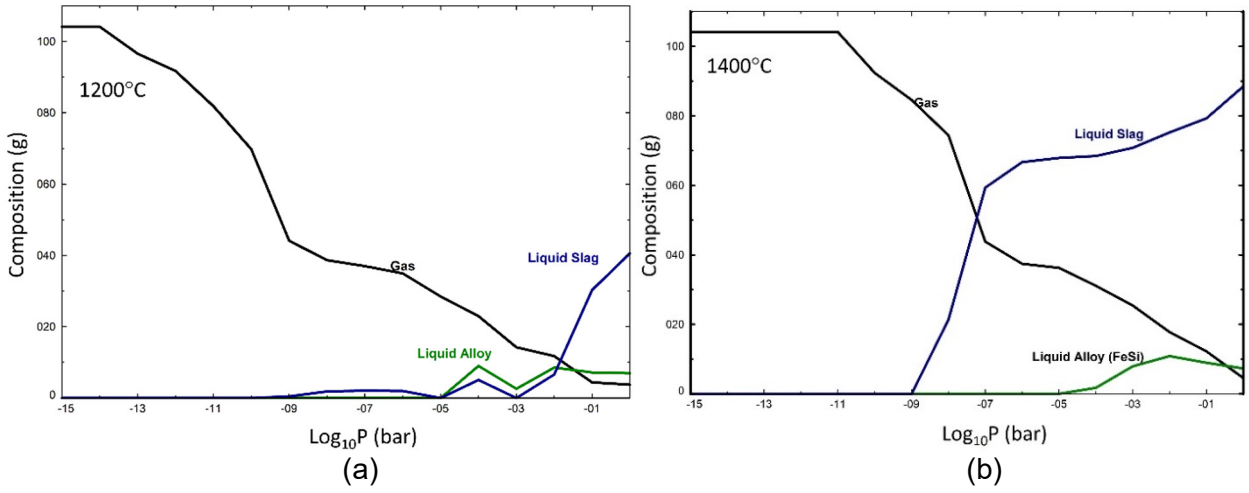

FIG 9 – (a) Predicted products of carbothermic reduction of 100 g LMS-1 simulant with 6 g carbon at different pressures at 1200°C, and (b) 1400°C.

Figure 10 presents a schematic summary of the predicted product phases resulting from carbothermal regolith reduction under three distinct pressure conditions at 1400°C. As explained earlier, under earth's conditions of 1 bar pressure, both liquid Fe-Si alloy and liquid slag phases forms, while at pristine lunar vacuum conditions and intermediate pressure of 3 × 10^{-8} bar, Fe and Si (in the form of SiO) joins the gas phase.

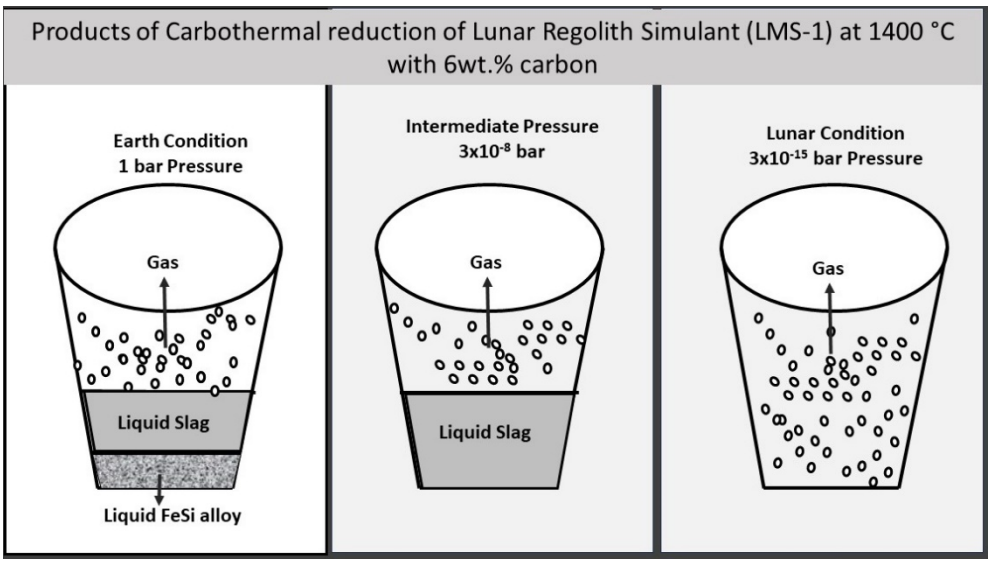

FIG 10 – Schematic diagram showing predicted results of carbothermal reduction of 100 g LMS-1 at 1400°C and 6 g C at different pressures.

EXPERIMENTAL FINDINGS

The thermodynamic calculations at Earth conditions suggests a minimum of 4 g carbon (ie 4 wt per cent of the regolith) and 1400°C temperature as the optimum condition to produce liquid Fe-Si alloy with less impurities. At higher reduction temperatures, higher amounts of Si and other elements are present in the Fe-Si alloy and increase the quantity of liquid alloy. For the experimental investigation presented in this study, the aim was to prove that a liquid FeSi alloy can be produced from the lunar regolith. Therefore, a higher reduction temperature of 1600°C and a higher carbon amount of 10 wt per cent was chosen to ensure liquid Fe-Si alloy forms during the experiment.

The experiments were conducted using a resistance-heated horizontal tube furnace from Nabertherm. A 30 g regolith sample was mixed with 10 wt per cent (ie 3 g) graphite using mortar and pestle, followed by loading the mixture in an alumina crucible. The crucible was then loaded into the hot zone of the furnace. The furnace was then heated at 200°C/hr until the desired 1600°C was achieved at the hot zone. The experiments were conducted under an inert atmosphere of argon gas and the sample was cooled inside the furnace. The next day, the sample was taken out in a cold condition. Figure 11 shows the sample before and after the experiment.

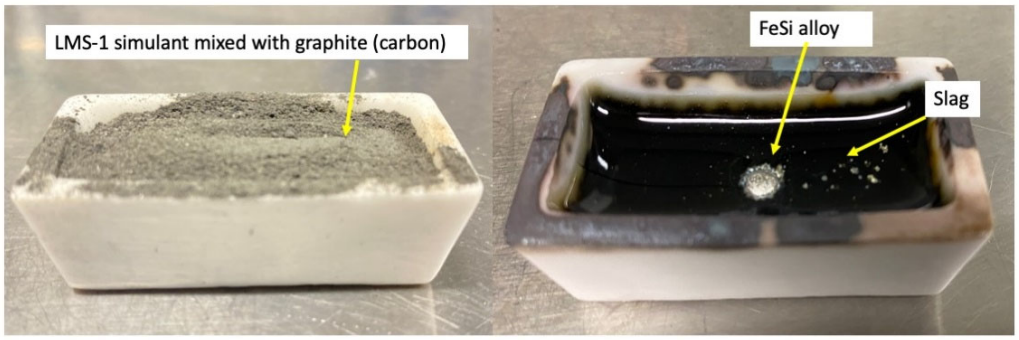

(a) (b)

FIG 11 – (a) Mixture of LMS-1 simulant and graphite before experiment, (b) product of carbothermal reduction showing FeSi alloy at centre.

The product, as shown in Figure 11b, contains a glassy slag phase and a metal phase. The appearance of the metal phase suggests that the metal was in liquid form at the temperature of 1600°C. The crucible was broken using a hammer, and the metal phase was collected and analysed using a scanning electron microscope (SEM) and energy dispersive spectroscopy (EDS) for microstructure and chemistry. The results are shown in Figure 12.

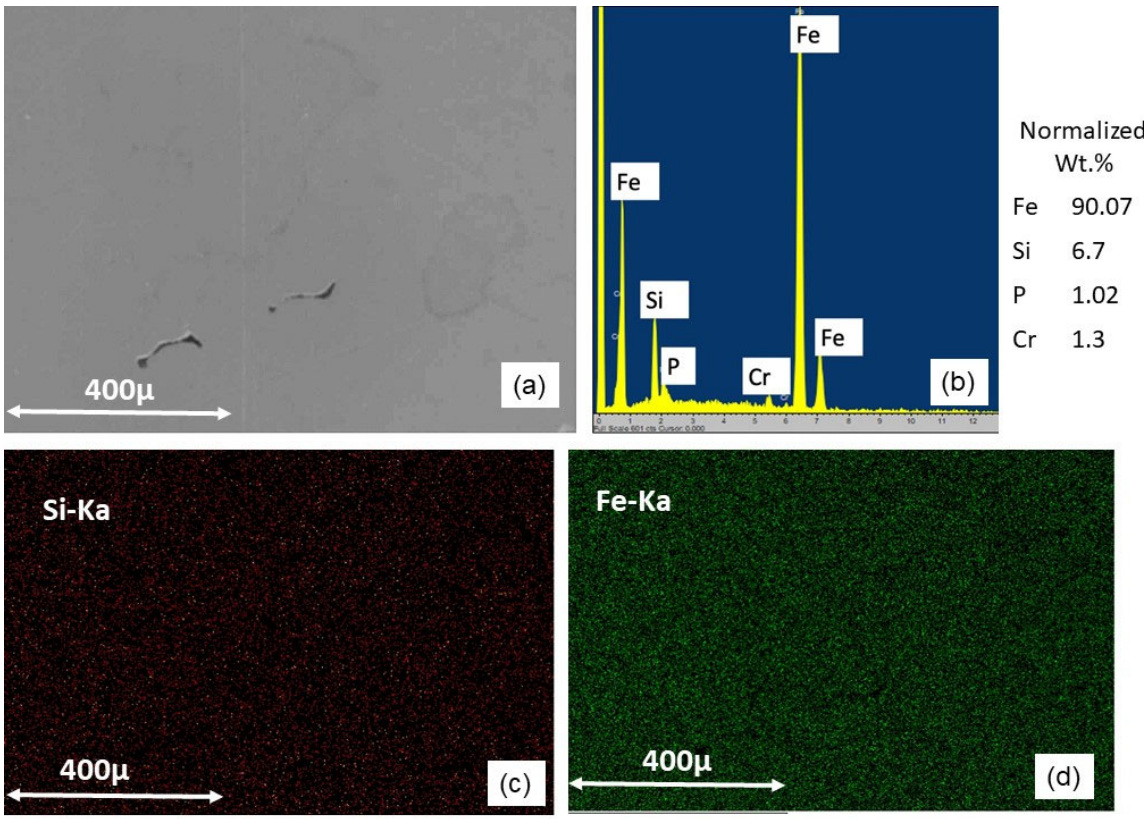

FIG 12 – (a) Mounted Fe-Si alloy in SEM (scanning electron microscope), (b) EDS (energy dispersive spectroscopy) spectrum and semi-quantitative analysis, (c) Si distribution map, and (d) Fe distribution map.

The EDS spectrum and the semiquantitative analysis suggest the metal phase is a Fe-Si alloy with 90 wt per cent Fe and about 7 wt per cent Si, with minor P and Cr presence. Although Chromium is seen in the EDS spectrum, it is likely to be an impurity added during the sample cutting process as the cutting blade contains chromium and the initial regolith did not contain chromium. The presence of phosphorous could be critical in the further refining process of the Fe-Si alloy. As indicated by the thermodynamically predicted results, titanium is expected to be present in the liquid alloy; however, it was not detected in the EDS analysis conducted in this study. This discrepancy might be attributed to the fact that only the bottom part of the solidified liquid alloy was analysed under EDS. Moreover, the inclusion of impurities such as water and oxygen in bottled argon gas could have impacted the findings, as titanium has the capacity to scavenge oxygen in argon, potentially resulting in its retention within the slag phase. A comprehensive investigation is necessary to ascertain the presence of titanium in the liquid alloy. The hardness of this metal phase was also measured using a Vicker Hardness tester, and the average hardness value was found to be 515 ± 1 per cent VHN.

CONCLUSIONS

In this paper, the thermodynamic study of the carbothermal reduction behaviour of lunar mare simulant LMS-1 was carried out under three different pressure conditions: 1 bar pressure to simulate Earth-like conditions, lunar vacuum condition of 3×10^{-15} bar pressure and an intermediate 3×10^{-8} bar pressure to account for the pressure rise due to gas evolution. The optimum thermodynamic conditions for carbothermal reduction of regolith and FeSi alloy extraction on the Earth are a minimum of 4 g carbon per 100 g regolith and a reduction temperature of 1400°C. Under both lunar conditions and an intermediate vacuum of 3×10^{-8} bar, iron can be extracted either in a vapour phase or as a solid phase in combination with other elements, as a liquid metal/alloy phase is not stable at these pressure conditions. In order to recover Fe-Si alloys in liquid form at this temperature, the vacuum pressure needs to be less than 10^{-5} bar. This paper also discusses the successful synthesis of Fe-Si alloy with 90 wt per cent Fe from the lunar mare simulant LMS-1.

ACKNOWLEDGEMENTS

The authors would like to acknowledge the financial support of Swinburne University of Technology to undertake this research.

REFERENCES

Bale, C W, Bélisle, E, Chartrand, P, Decterov, S A, Eriksson, G, Gheribi, A E, Hack, K, Jung, I H, Kang, Y B, Melançon, J, Pelton, A D, Petersen, S, Robelin, C, Sangster, J, Spencer, P and Van Ende, M A, 2016. FactSage thermochemical software and databases, 2010–2016, *CALPHAD,* 54:35–53.

Duke, M B, Gaddis, L R, Taylor, G J and Schmitt, H H, 2006. Development of the Moon, *Reviews in Mineralogy and Geochemistry*, 60(1):597–655.

European Space Agency (ESA), 2019, 23 May. ESA Space Resources Strategy [online], *European Space Agency*, 18 p. Available from: <http://exploration.esa.int/moon/61369-esa-space-resources-strategy/> [Accessed: 11 November 2021].

Grossman, K D, Sakthivel, T S, Sibille, L, Mantovani, J G and Seal, S, 2019. Regolith-derived ferrosilicon as a potential feedstock material for wire-based additive manufacturing, *Advances in Space Research*, 63(7):2212–2219.

Gustafson, R J, White, B C, Fidler, M J and Muscatello, A C, 2010. Demonstrating the Solar Carbothermal Reduction of Lunar Regolith to Produce Oxygen, in Proceedings of the 48th AIAA Aerospace Sciences Meeting Including the New Horizons Forum and Aerospace Exposition, AIAA 2010.

Ignatiev, A and Freundlich, A, 2012. The Use of Lunar Resources for Energy Generation on the Moon, in *Moon: Prospective Energy and Material Resources* (ed: V Badescu), pp 325–334 (Springer: Berlin). https://doi.org/10.1007/978-3-642-27969-0_13

Kaur, S, Aleksandrov, A B, Ready, W J, Orlando, T M and Loutzenhiser, P G, 2024. Thermodynamic and experimental study on carbothermal reduction of JSC-1A lunar regolith simulant for metal and metalloid production, *Advances in Space Research*, 73(8):4024–4039.

Mackwell, S, Neal, C and Pestak, C (eds.), 2019. *Proceedings of the Lunar ISRU 2019: Developing a New Space Economy Through Lunar Resources and Their Utilization*, LPI Contribution No. 2152 (Lunar and Planetary Institute: Houston).

Mahoney, E, 2020. NASA Selects Blue Origin, Dynetics, SpaceX for Artemis Human Landers [online], *NASA*. Available from: <http://www.nasa.gov/feature/nasa-selects-blue-origin-dynetics-spacex-for-artemis-human-landers> [Accessed: 1 June 2023].

Nababan, D C, Shaw, M G, Humbert, M S, Mukhlis, R Z and Rhamdhani, M A, 2022. Metals extraction on Mars through carbothermic reduction, *Acta Astronautica*, 198:564–576.

NASA, 2012. Catalogue of Manmade Material on the Moon, NASA History Program Office. Available from: <https://www.nasa.gov/wp-content/uploads/2024/02/final-catalogue-of-manmade-material-on-the-moon.pdf> [Accessed: 21 July 2022].

NASA, 2020. Artemis, NASA. Available from: <https://www.nasa.gov/specials/artemis/> [Accessed: 11 November 2021].

Samouhos, M, Tsakiridis, P, Iskander, M, Taxiarchou, M and Betsis, K, 2022. In-situ resource utilization: ferrosilicon and SiC production from BP-1 lunar regolith simulant via carbothermal reduction, *Planetary and Space Science*, 212:105414. https://doi.org/10.1016/j.pss.2021.105414

Sargeant, H M, Abernethy, F A J, Barber, S J, Wright, I P, Anand, M, Sheridan, S and Morse, A, 2020. Hydrogen reduction of ilmenite: Towards an in situ resource utilization demonstration on the surface of the Moon, *Planetary and Space Science*, 180:104751. https://doi.org/10.1016/j.pss.2019.104751

Schlüter, L and Cowley, A, 2020. Review of techniques for In-Situ oxygen extraction on the moon, *Planetary and Space Science*, 181:104753. https://doi.org/10.1016/j.pss.2019.104753

Schreiner, S S, Sibille, L, Dominguez, J A and Hoffman, J A, 2016. A parametric sizing model for Molten Regolith Electrolysis reactors to produce oxygen on the Moon, *Advances in Space Research*, 57(7):1585–1603. https://doi.org/10.1016/j.asr.2016.01.006

Shaw, M G, Brooks, G A, Rhamdhani, M A, Duffy, A R and Pownceby, M I, 2021a. Thermodynamic modelling of ultra-high vacuum thermal decomposition for lunar resource processing, *Planetary and Space Science*, 204:105272. https://doi.org/10.1016/j.pss.2021.105272

Shaw, M, Humbert, M, Brooks, G, Rhamdhani, A, Duffy, A and Pownceby, M, 2021b. Mineral Processing and Metal Extraction on the Lunar Surface - Challenges and Opportunities, *Mineral Processing and Extractive Metallurgy Review*, 43(7):865–891. https://doi.org/10.1080/08827508.2021.1969390

Sirk, A H, Sadoway, D R and Sibille, L, 2019. Direct Electrolysis of Molten Lunar Regolith for the Production of Oxygen and Metals on the Moon, *ECS Transactions*, 28(6):367–373. https://doi.org/10.1149/1.3367929

Phase relationship of quaternary system FeO-Al_2O_3-SiO_2-'V_2O_3' at 1873 K and its impact during melting of H-DRI for possible vanadium extraction

DOI: 10.62053/GBQB1648

A Vickerfält[1], J Huss[2] and J Martinsson[3]

1. Researcher, Swerim AB, Stockholm, 164 40 Kista, Sweden. Email: amanda.vickerfalt@swerim.se
2. Researcher, Swerim AB, Stockholm, 164 40 Kista, Sweden. Email: joar.huss@swerim.se
3. Group manager and researcher, Swerim AB, Stockholm, 164 40 Kista, Sweden. Email: johan.martinsson@swerim.se

EXTENDED ABSTRACT

The European Union has listed vanadium (V) as one of the critical raw materials for the transition to a future green society, as stated in the Critical Raw Material Act, written by Grohol and Veeh (2023). In the steelmaking industry based on V-containing iron ore, V is a possible by-product from the slag. A requirement for slags to be suitable for V extraction is a V content preferably above 8 wt per cent as V_2O_3 and a phosphorus (P) content below 0.1 wt per cent as P_2O_5. Hence, it is important to keep V in the slag phase while the P is moved to the metal phase during the steelmaking process.

The present research group has carried out parallel works to increase the understanding on how to concentrate V in the slag during steelmaking, while reaching a low P content. The works have been a part of the HYBRIT research program, a joint venture between the iron ore producer LKAB, steel producer SSAB and electricity producer Vattenfall, with the aim to pioneer fossil-free steel production. The starting point of the raw material has therefore been the existing high quality LKAB iron ore pellet named KPRS, designed for direct reduction (DR) shaft furnace technology. The composition of KPRS pellets can be seen in Table 1.

TABLE 1

Composition of KPRS, as written in the 2021 LKAB Product Catalogue.

	Fe	SiO_2	CaO	MgO	Residual oxides
wt%	67.8	0.80	0.90	0.65	1.01

KPRS was first reduced in pure hydrogen at 900°C to different reduction degrees in a vertical resistance-heated furnace. The hydrogen reduced iron pellets (H-DRI) were then melted, one by one, in a high temperature resistance-heated furnace at temperatures between 1500–1600°C, and quenched after different times, to study the melting progression. It was found that the unreduced oxidic components (CaO, SiO_2, MgO, remaining FeO etc) inside the H-DRI formed an autogenous slag inside the pellet already prior to the melting of the iron grains. The autogenous slag was found to flow in the porous network inside the H-DRI, between the reduced iron grains. Upon the melting of iron, numerous of autogenous slag droplets were found distributed in the liquid metal, generating a huge surface area between slag and metal.

The experimental results also showed that the autogenous slag system based on the present H-DRI contained in general terms FeO-CaO-SiO_2-MgO. The CaO/SiO_2 ratio was approximately 1.2, FeO content varying between approximately 20 and 70 wt per cent depending on reduction degree, and MgO saturated at approximately 10 wt per cent.

H-DRI was also melted batchwise to study the resulting V and P partitions based on oxygen potential fixed by the FeO/Fe equilibrium in the slag using a closed crucible. It was unfortunately found that it is difficult to sufficiently separate V and P using the KPRS as raw material, independent of the oxygen potential. Too much P was still found in the slag.

In the subsequent work, the separation of V and P was studied in a novel slag system based on FeO-Al_2O_3-SiO_2-V_2O_3, ie CaO is replaced by Al_2O_3. Examples of weigh-in slag compositions can be seen in Table 2.

TABLE 2

Examples of weigh-in slag composition.

	FeO_x wt%	SiO_2 wt%	Al_2O_3 wt%	V_2O_3 wt%	$[P]_{Fe}$ wt%
Slag 1	40	31.25	18.75	9.99	0.20
Slag 8	10.74	43.35	26.05	19.85	0.89
Slag 14	11.05	24.70	54.42	9.84	0.82

In the experiments, 10 g of slags were allowed to react with 30 g of iron containing P additions, as shown in Table 2, at a temperature of 1873 K inside a high temperature resistance-heated furnace. The oxygen potential was fixed by the system through the FeO/Fe equilibrium by closing the crucible with a lid. The pO_2 was calculated using Thermo-Calc, based on XRF analysis. Almost all P was found in the metal phase, while a V_2O_3 content higher than 8 wt per cent was obtained in the slag, as shown by Table 3. ie the system was found promising for the separation of V and P.

TABLE 3

Examples of slag and iron analysis after equilibration.

	XRF analysis					OES analysis		
	FeO wt%	SiO_2 wt%	Al_2O_3 wt%	V_2O_3 wt%	P_2O_5 wt%	$[P]_{Fe}$ wt%	$[V]_{Fe}$ wt%	$pO_2 \times 10^{11}$ atm
Slag 1	30.1	27.3	38.2	4.4	<0.01	0.159	0.069	9.41
Slag 8	21.9	31.3	37.9	8.8	<0.01	0.300	0.329	4.82
Slag 14	16.9	27.1	49.3	6.7	<0.01	0.300	0.153	4.12

The results also showed that V could be found in different phases in the slag. Unfortunately, the available literature of phase diagrams for vanadium containing slags are limited. Since the phase relationship is likely to impact the aftercoming V extraction, it is necessary to study which phases are stable at relevant oxygen partial pressures, and how much V each phase contain. Therefore, the pseudo ternary phase diagrams Al_2O_3-SiO_2-'V_2O_3', FeO-SiO_2-'V_2O_3' and Al_2O_3-FeO-'V_2O_3' were studied in another subsequent work. The fourth system Al_2O_3-FeO-SiO_2 was found sufficiently studied in the literature, compiled in the Slag Atlas (Allibert and Verein Deutscher Eisenhüttenleute, 1995). The construction of phase diagrams was based on experiments conducted at 1873 K and the different oxygen partial pressures 3.4×10^{-11}, 3.3×10^{-10} and 3.4×10^{-9} atm, controlled by a CO/CO_2 mixture. After equilibration, the samples were quenched in oil. The phase compositions, analysed by wavelength-dispersive spectroscopy (WDS), were used to construct relevant phase diagrams based on each slag system and oxygen partial pressure. Since V is multi-valent, its valence state at equilibrium can vary depending on oxygen partial pressure, temperature, and slag composition. In the present work, 'V_2O_3' is used for giving the content of vanadium. The valence state has although not been analysed, thus the use of citation marks around 'V_2O_3' to illustrate the uncertainty.

In the pseudo ternary phase diagrams based on the quaternary system Al_2O_3-FeO-SiO_2-'V_2O_3'; mullite, spinel Al_2O_3-corundum, V_2O_3-corundum, cristobalite, and liquid were found. Among these phases, only cristobalite had zero trace of V, and only small amounts were found in the liquid.

In this work, the Al_2O_3-SiO_2-'V_2O_3' system is presented as example. The oxygen potential had no profound effect on the Al_2O_3-corundum+V_2O_3-corundum+mullite and the V_2O_3-corundum+ cristobalite+liquid equilibria. On the other hand, the equilibrium between V_2O_3-corundum, mullite and liquid was affected. A decreased oxygen potential resulted in higher contents of Al_2O_3 and slightly higher contents of V_2O_3 in the liquid phase, as well as slightly higher contents of Al_2O_3 in V_2O_3-corundum and mullite. Since V is multi valent, the oxygen partial pressure will decide the fraction of the different valance states of V in the slag. The different valence states of V can be dissolved into

different phases, resulting in a change in the phase diagram as a result of changed oxygen partial pressure.

For vanadium extraction, V_2O_3 must first be roasted (oxidised) to V_2O_5 for the leaching process to work. It is therefore important to understand which phases that are easier, or even possible, to roast. The research must henceforth be carried out systematically. The phase diagrams constructed in the present work will be used to suggest slag compositions which result in high V content. The resulting slags will then be studied in a roasting process. The roasting process will in turn give feedback regarding if the resulting V-containing phases were easy to roast or not, which will result in new suggestions of slag compositions based on the phase diagram. The slag compositions that resulted in highest V content had V found in the solid phases spinel, mullite and corundum. These phases are therefore the most interesting in the initial stage of the future studies on roasting.

At the same time as V needs to be concentrated in the slag, P needs to be moved to the steel. The first study regarding melting mechanisms of H-DRI showed that an autogenous slag is formed and flows inside the H-DRI prior to the melting of iron. As iron melts, slag is distributed as droplets in the iron melt, generating a huge reaction surface area between the slag and metal. The kinetic conditions for moving P from the slag to metal is therefore potentially excellent and the separation of V and P is thus promising.

Since V is mainly found in solid phases, a slag suitable for V extraction will assumably result in a slag with high fraction of solids, resulting in high viscosity. In an industrial point of view, a highly viscous slag can be problematic to handle in the production and can be associated with high costs to ensure safe production. An optimised slag practice for maximum V extraction is therefore important to reach maximise profitability.

In addition, the proposed production route will result in an iron melt containing high content of P. A two-slag-practice is therefore necessary to produce a clean steel with low P and meet the demands of the steel producer. The first slag, based on the autogenous slag, will in this scenario extract V to the slag while P is moved to the steel melt. This slag would then be removed from the furnace, after which a second slag will be added. The second slag will be closer to a traditional slag for phosphorus removal, with high oxygen potential and a basicity of more than 2.

ACKNOWLEDGEMENT

The authors gratefully acknowledge the financial support of this research by Hybrit Development AB. HYBRIT (Hydrogen Breakthrough Ironmaking Technology) is a joint initiative of the three companies SSAB, LKAB and Vattenfall with the aim of developing the world's first fossil-free ore-based steelmaking route. For more information, please visit www.hybritdevelopment.com

The authors would also like to express their gratitude to Prof. Pär Jönsson at KTH Royal Institute of Technology, and Prof. Emeritus Du Sichen, senior advisor at Hybrit Development AB.

REFERENCES

Allibert, M and Verein Deutscher Eisenhüttenleute, 1995. *Slag Atlas*, 2nd edition, Verlag Stahleisen, 616 p.

Grohol, M and Veeh, C, 2023. Study on the critical raw materials for the EU 2023 – Final report. European Commission, Directorate-General for Internal Market, Industry, Entrepreneurship and SMEs, Publications Office of the European Union. Available from: <https://data.europa.eu/doi/10.2873/725585/> [Accessed: 17 January 2024].

Phase diagram of V_2O_3-Fe_tO-SiO_2-CaO(15 mass%) system at 1623 K

DOI: 10.62053/SJGR5273

B Yan[1], D Wang[2], T Deng[3], B Song[4] and Q Shu[5]

1. Professor, School of Metallurgical and Ecological Engineering, University of Science and Technology Beijing, Beijing 100083, China. Email: baijunyan@ustb.edu.cn
2. Senior Researcher, Safety and Environmental Engineering Technology Institute, Sinosteel Group, Maanshan 243071, China. Email: dayawangustb@126.com
3. Professor, State Key Laboratory of Silicate Materials for Architectures, Wuhan University of Technology, China 430070, Wuhan. Email: dengtf@whut.edu.cn
4. Professor, School of Metallurgical and Ecological Engineering, University of Science and Technology Beijing, Beijing 100083, China.
5. Professor, Research Unit of Process Metallurgy, University of Oulu, Oulu 90014, Finland. Email: qifeng.shu@oulu.fi

ABSTRACT

In view of the lack of phase equilibria data of vanadium-bearing oxide system and the desirability of them for design or optimisation of vanadium extraction process, the phase equilibria relationships of V_2O_3-FeO-SiO_2-CaO(15 mass per cent) system were determined experimentally and then an isothermal section phase diagram of this system was constructed. Totally, 81 samples of different composition were equilibrated at 1623 K for 48 hours in iron crucible under Ar atmosphere. The equilibrated samples were quenched quickly in cold water, and then the phase constituents of all the samples were identified by X-ray diffraction (XRD) combined with electron probe microanalysis (EPMA) measurements. 17 different types of phase equilibria relationship were determined, by using L to represent liquid phase they are summarised and numbered as follows:

1. single L
2. L + SiO_2
3. L + spinel + SiO_2
4. L + spinel + SiO_2 + $(V,Fe)_2O_3$
5. L + SiO_2 + $(V,Fe)_2O_3$
6. L + $(Ca,Fe)_3V_2Si_3O_{12}$ + SiO_2 + $(V,Fe)_2O_3$
7. L + $(V,Fe)_2O_3$
8. L + spinel + $(V,Fe)_2O_3$
9. L + spinel + $(Ca,Fe)_3V_2Si_3O_{12}$ + $(V,Fe)_2O_3$
10. L + $(Ca,Fe)_3V_2Si_3O_{12}$ + $(V,Fe)_2O_3$
11. spinel + $(Ca,Fe)_3V_2Si_3O_{12}$ + $(V,Fe)_2O_3$
12. $(Ca,Fe)_3V_2Si_3O_{12}$ + $(V,Fe)_2O_3$
13. L + Fe_tO + $(V,Fe)_2O_3$
14. L + spinel
15. L + Fe_tO
16. L + spinel + $(Ca,Fe)_3V_2Si_3O_{12}$
17. L + SiO_2 + $(Ca,Fe)_3V_2Si_3O_{12}$

Finally, based on the measured experimental data and the neighbouring phase field rule, the sectional diagram of V_2O_3-FeO-SiO_2-CaO(15 mass per cent) system at 1623 K composed of 17 phase equilibria areas was presented.

INTRODUCTION

Vanadium is an important transition metal element, which has been widely used in many areas, such as catalysis, electrode materials and laser materials etc (Du *et al*, 2018; Ejigu, Edwards and Walsh, 2015; Tomashchuk, Grevey and Sallamand, 2015). In the vanadium industry, about 80 per cent of the vanadium is extracted from the vanadium-bearing ores, while the reminder comes from the

secondary sources including residues and ashes from the petroleum industry, and recycled spent catalysts (Dai *et al*, 2012; Ketris and Yudovich, 2009). Of the production of vanadium by ores, the most commonly used ores are vanadium-titanium magnetite and vanadium-bearing black shale (Dai *et al*, 2018).

As for the extraction of vanadium from the vanadium-titanium magnetite, it is firstly smelted and reduced in blast furnace to obtain vanadium-bearing hot metal (Smirnov, Filatov and Rovnushkin, 2010). Then, the vanadium-bearing hot metal is oxidised in converter to transfer and concentrate the vanadium to slag which is mainly constituted of iron oxide, silica and vanadium oxide (Fang, Li and Xie, 2012; Dong, Zhang and Yan, 2021). Next, the vanadium rich slag is adopted as feedstock for production of vanadium. In this vanadium rich slag, the vanadium mainly occurs in a spinel solid solution phase with iron vanadate ($Fe_{3-x}V_xO_4$) as its parent mineral. To raise the recovery rate of vanadium from the hot metal, the conditions favourable to the formation of the spinel phase are desired in practice. As the basis of optimisation of the conditions, the thermodynamics of the SiO_2-Fe_tO-V_2O_3 system are essential.

Regarding the extraction of vanadium from the black shale, which is mainly composed of SiO_2, CaO, Al_2O_3, MgO and small amounts of V_2O_3,Fe_tO etc, the general process of vanadium extraction is direct soda roasting followed by leaching. However, due to the very low vanadium content in the shale, this process is faced with the environmental issues such as large production of effluent in leaching, high energy and soda consumption at roasting, etc (Seredin, 2012; Chen *et al*, 2014). To improve the vanadium grade, a novel beneficiation method of vanadium was developed by our group (Yan *et al*, 2018; Wang, Li and Yan, 2019). Where,Fe_2O_3 is added to the shale, and the vanadium occurred in shale is transformed into $Fe_{3-x}V_xO_4$ spinel phase by reducing roast. Then, the formed $Fe_{3-x}V_xO_4$ spinel phase is separated by magnetic method, and the acquired high-grade vanadium concentrate is used as feedstock for extraction of vanadium. To optimise the conditions and ensure the formation of $Fe_{3-x}V_xO_4$ spinel phase effectively, the thermodynamics of the CaO-SiO_2-Fe_tO-V_2O_3 system is required basically (Yan *et al*, 2020a, 2020b; Wang, Li and Yan, 2019; Wang *et al*, 2017).

In addition, the solid solution $Fe_{3-x}V_xO_4$ spinel phase possesses versatile properties and is with broad potential applications, its preparation also needs the related thermodynamic information as guideline. However, the thermodynamic studies on the oxide system containing both vanadium oxide and iron oxide are scarce and insufficient. Huang *et al* (2016) calculated a phase diagram of FeO-SiO_2-V_2O_3 system on base of the binary subsystem by using the FactSage software, ver 7.1 (by Thermfact/CRCT and GTT-Technologies). But, due to the lack of the thermodynamic data of the $Fe_{3-x}V_xO_4$ spinel phase, they can only use the stoichiometric compound FeV_2O_4 to substitute for $Fe_{3-x}V_xO_4$. This replacement definitely brings about a large uncertainty on the calculated phase diagram. Semykina, Dzhebian and Shatokha (2012) reported that vanadium ferrites (FeV_2O_4 and Fe_2VO_4) can be formed in CaO-SiO_2-FeO-V_2O_5 system at 1773 K in argon atmosphere. Li *et al* (2019) investigated the effect of CaO addition on the evolution of main phases in the Fe-Fe_2O_3-V_2O_3 system under argon atmosphere, but in alike manner, they treated the spinel solid solution phase as stoichiometric compound Fe_2VO_4. Fang *et al* (2015) investigated the influence of CaO on the occurrence state of vanadium in slag, and pointed out that with the increasing of CaO content the vanadium-bearing spinel phase transforms into goldmanite $Ca_3V_2(SiO_4)_3$ phase gradually.

From the above summarisation, it can be seen that the phase relations of the silicate system containing both vanadium oxide and iron oxide are interesting and important, whereas the available studies are not only scrappy but also deficient. Therefore, in the present study, the phase relations in the CaO(15 mass per cent)-SiO_2-Fe_tO-V_2O_3 system were investigated systematically at 1623 K, and an isothermal phase diagram of the system was constructed.

EXPERIMENTAL

Determination of experimental conditions

To get a correct phase diagram of a high-order system, it is crucial to choose correct variables which are adopted as the axes of the diagram. For a N-component system, due to the Gibbs-Duhem relation shown as Equation 1, only N+1 potential variables of *T*, *P* and μ_i are independent.

$$SdT - VdP + \Sigma N_i d\mu_i = 0 \quad (1)$$

Where, *S*, *V* and N_i are extensive variables representing the entropy, volume and the content of component *i*, respectively. *T*, *P* and μ_i are conjugate potentials of *S*, *V* and N_i, representing temperature, pressure and chemical potential of component *i* respectively.

As for the variables, which can be adopted as the axes of a phase diagram, a general way to determined them is as follows. For example, for a *N*-component system. Firstly, *n* potentials from the Gibbs-Duhem relation, $n \leq N+1$, are chosen, and these potentials are denoted as $\varphi_1, \varphi_2, \ldots, \varphi_n$. Secondly, from the remaining conjugate pairs, the variables N_i are used to form (N+1-n) independent ratios, which are denoted as $Q_{n+1}, Q_{n+2}, \ldots, Q_{N+1}$. The formula to form Q_i is shown as Equation 2.

$$Q_i = N_i / \sum_{j=n+1}^{N+2} N_j \ \ (n+1 \leq i \leq N+1) \tag{2}$$

Thirdly, a set of (N+1) independent variables $\varphi_1, \varphi_2, \ldots, \varphi_n, Q_{n+1}, Q_{n+2}, \ldots, Q_{N+1}$ is formed. Finally, any two variables in this set can be selected and the remainder are held constant to construct a true two-dimensional phase diagram.

In the present study, the following set of variables was formed: *T*, *P*, μFe, $N_{CaO}/(N_{SiO_2} + N_{V_2O_3} + N_{FeO} + N_{CaO})$, $N_{SiO_2}/(N_{SiO_2} + N_{V_2O_3} + N_{FeO} + N_{CaO})$, and $N_{V_2O_3}/(N_{SiO_2} + N_{V_2O_3} + N_{FeO} + N_{CaO})$. To construct a two-dimension phase diagram, the temperature was fixed at 1623 K, the pressure was fixed by equilibrating the sample in Ar atmosphere of 1 atm, the μFe was fixed by using pure Fe crucible to contain the sample, and $N_{CaO}/(N_{SiO_2} + N_{V_2O_3} + N_{FeO} + N_{CaO})$ was fixed to be 15 mass per cent. Then, the phase relationships of the system with various contents of SiO_2, V_2O_3 and FeO were measured, and a Gibbs triangle representing the compositions of SiO_2, V_2O_3 and FeO was adopted to demonstrate the measured phase relationships.

Materials and sample preparation

The chemical agents CaO, SiO_2 and V_2O_3 with purity higher than 99.9 mass per cent were used as reactants. Before weighing, CaO and SiO_2 were dried at 1273 K in air for 24 hours. FeO was prepared by using chemical agents Fe_2O_3 and Fe as the raw materials. The powders of Fe_2O_3 and Fe with molar ratio of 1 were mixed homogeneously and pressed into tablets, then the tablets were heated at 1323 K in the atmosphere of CO/CO_2 = 1 for 48 hrs.

Afterwards, about 1 g mixture of the four oxides were homogenised in an agate mortar and pressed into a tablet, and then the tablet was placed into a pure iron crucible (10 mm OD, 9 mm ID, 30 mm height) for high-temperature equilibrium.

Procedure of equilibration

A vertical-tube resistance furnace heated by $MoSi_2$ elements was used for the equilibration, and the detailed description of this furnace can be found in a previous publication (Fang *et al*, 2015). The temperature of the furnace was controlled by a proportional-integral-differential (PID) controller with an accuracy of ±1 K. The temperature of the sample was measured by a W-Re5/W-Re26 thermocouple positioned just beneath the bottom of the alumina crucible. The atmospheres used was pure Ar with purity higher than 99.999 per cent.

After the crucible containing the samples was hung in the even temperature zone of the furnace, the reaction chamber was sealed, evacuated and filled with Ar. Thereafter, the furnace was heated up at a rate of 3 K/min to 1623 K, and the flow rate of Ar was 100 mL/min. According to the results of the pre-experiments, the equilibration time was chosen to be 48 hrs. When the equilibration was completed, the samples were lifted from the even temperature zone to the water quenching chamber and cooled quickly in the pure Ar reaction atmosphere. The samples were not taken out from Fe crucibles, the sample and the crucible together were mounted and polished.

Characterisation of quenched samples

To identify the phases existed in the quenched samples, X-ray diffraction (XRD) measurement of the ground powder sample was performed firstly. A Bruker D8-Advance X-ray powder diffractometer with Cu Kα radiation (λ= 1.5406 Å) (Bruker AXS, Germany) was used, and the scattering angles was from 10° to 90°. Then, to determine the composition of the equilibrated phases, scanning electron

microscope (SEM) - electron probe microanalysis (EPMA) measurements were performed. A JEOL JXL-8230 instrument with wavelength dispersive spectrometers was adopted. The measurements were conducted with an accelerating voltage of 20 kV, a beam current of 10 nA, and a pot size of nearly 1 μm. Fe_2O_3, $CaSO_4$, $NaAlSi_3O_8$ and V-P-Pb glass (V_2O_5: 59.82 per cent, P_2O_5: 29.55 per cent, PbO: 11.50 per cent) were used as the standards for the quantitative analysis of Fe, Ca, Si and V in each mineral phase.

RESULTS AND DISCUSSION

Phase relations of V_2O_3-FeO-SiO_2-CaO(15 mass per cent) system at 1623 K

Totally, 81 samples with different composition were equilibrated at 1623 K under Ar atmosphere. All the equilibrated-quenched samples were observed by SEM, it could be found from the backscattered electrons micrograph that the microstructures of the quenched sample are composed of matrix and crystal phases. The matrix comes from the liquid phase in the equilibrated sample, which was super cooled in the process of quenching and formed the amorphous matrix. The crystal phase is the solid phase that is in equilibrium with the liquid phase at 1623 K, and the crystal phases were further identified by XRD.

From the combining measurements of SEM-EPMA and XRD, it can be found that, beside the liquid phase, five crystal phases can be found in the investigated samples. These five crystal phases are SiO_2, $(V,Fe)_2O_3$,$Fe_{3-x}V_xO_4$,Fe_tO and $(Ca,Fe)_3V_2Si_3O_{12}$. The Fe crucibles were adopted and the solid Fe phase must have been present in the sample. As for the phase equilibria relationships of these crystal phases and the liquid phase, totally 15 different phase equilibria relationships were found in the examined samples. The 15 phase equilibria relationships included one single-phase area of liquid, four two-phase areas of coexisting between solid and liquid, five three-phase areas of coexisting among two solids and liquid, three four-phase areas of coexisting among three solids and liquid, and two areas of coexisting only solid phases. The detailed information of the found 15 phase equilibria relations are shown in Table 1.

TABLE 1

The phase equilibria relations in CaO(15 mass per cent)-SiO_2-Fe_tO-V_2O_3 at 1623 K.

Coexisting phase	Phase equilibria relations
Single-liquid (one area)	L
Two-phase coexisting (four areas)	L+Tridymite(SiO_2), L+Wüstite(Fe_tO), L+Karelianite($(V,Fe)_2O_3$), L+Spinel($Fe_{3-x}V_xO_4$)
Three-phase coexisting (five areas)	L+Spinel($Fe_{3-x}V_xO_4$)+Tridymite(SiO_2), L+Spinel($Fe_{3-x}V_xO_4$)+Karelianite($(V,Fe)_2O_3$), L+Tridymite(SiO_2)+Karelianite($(V,Fe)_2O_3$), L+$(Ca,Fe)_3V_2Si_3O_{12}$+ Karelianite($(V,Fe)_2O_3$), L+ Spinel($Fe_{3-x}V_xO_4$)+Wüstite(Fe_tO)
Four-phase coexisting (three areas)	L+Spinel($Fe_{3-x}V_xO_4$)+Tridymite(SiO_2)+Karelianite($(V,Fe)_2O_3$), L+Spinel($Fe_{3-x}V_xO_4$)+$(Ca,Fe)_3V_2Si_3O_{12}$+Karelianite($(V,Fe)_2O_3$), L+ $(Ca,Fe)_3V_2Si_3O_{12}$+Karelianite($(V,Fe)_2O_3$)+ Tridymite(SiO_2)
only solid phases coexisting (two areas)	Spinel ($Fe_{3-x}V_xO_4$)+$(Ca,Fe)_3V_2Si_3O_{12}$+Karelianite($(V,Fe)_2O_3$), $(Ca,Fe)_3V_2Si_3O_{12}$+Karelianite($(V,Fe)_2O_3$)

The SEM micrograph and the XRD patterns of the investigated samples are shown according to the phase equilibria relationships.

Single liquid

At 1623 K, there was one single-liquid area in the CaO(15 mass per cent)-SiO_2-Fe_tO-VO_x system. The typical backscattered electron image and XRD pattern of the single-liquid sample are shown in Figure 1.

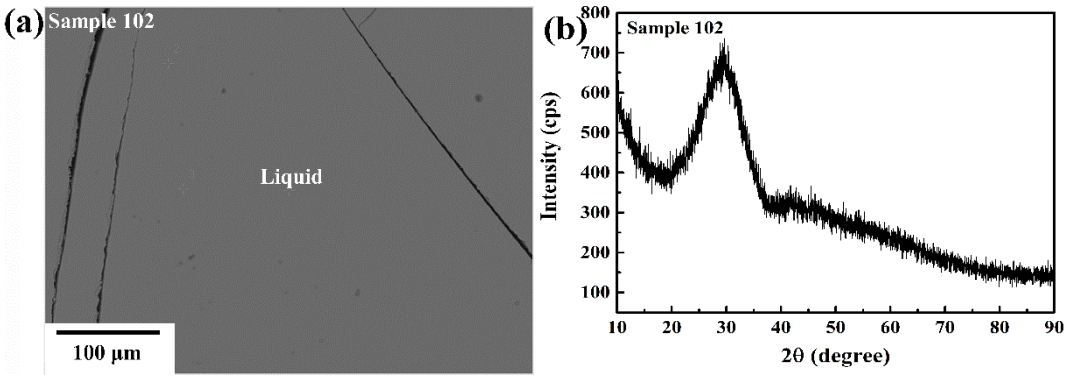

FIG 1 – The backscattered electron image (a), and XRD pattern (b) of single-liquid sample.

Coexisting of one solid phase and liquid

The typical backscattered electron image and XRD pattern of the sample containing one solid phase and one liquid phase simultaneously are shown in Figures 2 through 5. In Figure 2, that of the sample containing SiO_2 and liquid are presented. Figure 3 is for the case of coexisting between spinel phase ($Fe_{3-x}V_xO_4$) and liquid, Figure 4 for coexisting between Wüstite (Fe_tO) and liquid, Figure 5 for coexisting between Karelianite($(V,Fe)_2O_3$) and liquid.

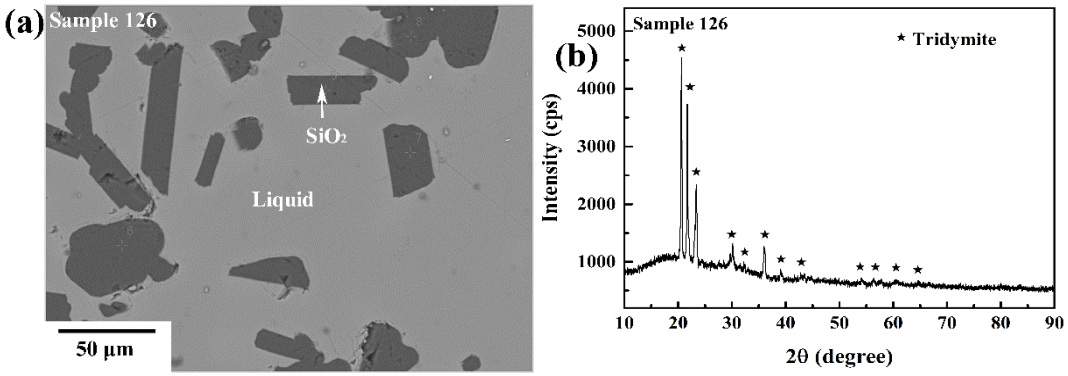

FIG 2 – Backscattered electron image (a), and XRD pattern (b) of SiO_2-liquid coexisting sample.

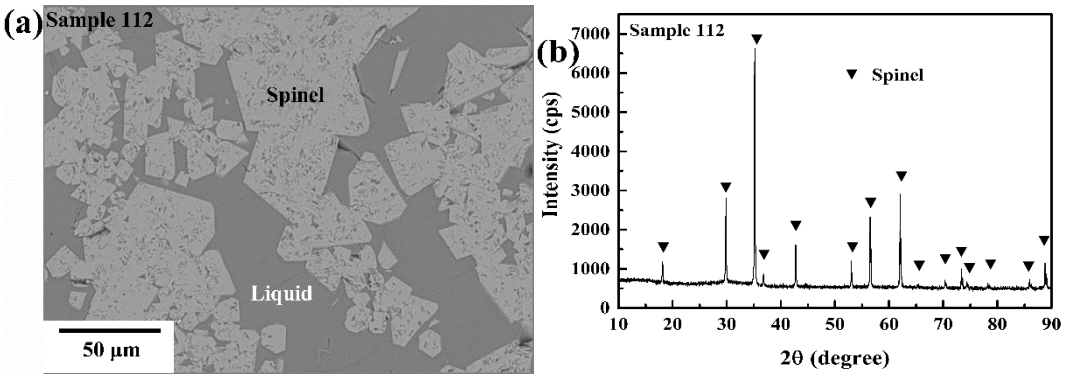

FIG 3 – Backscattered electron image (a), and XRD pattern (b) of $Fe_{3-x}V_xO_4$-liquid coexisting sample.

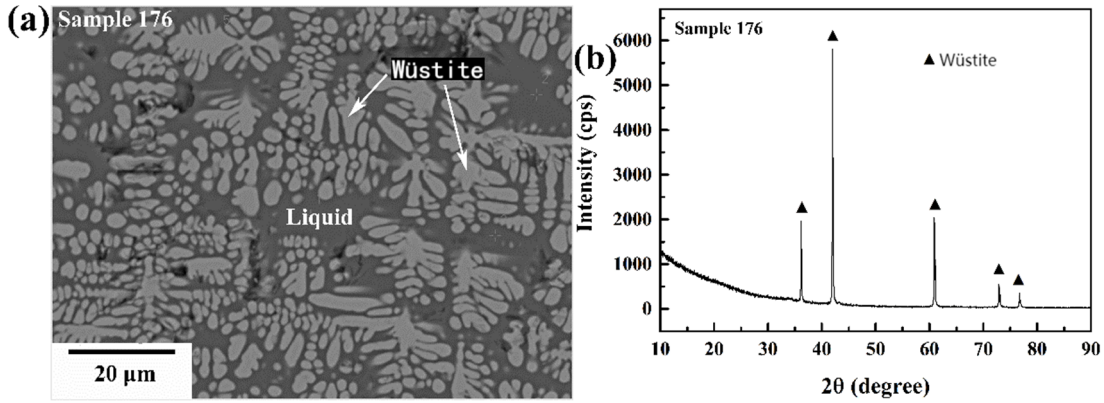

FIG 4 – Backscattered electron image (a), and XRD pattern (b) of Fe_tO-liquid coexisting sample.

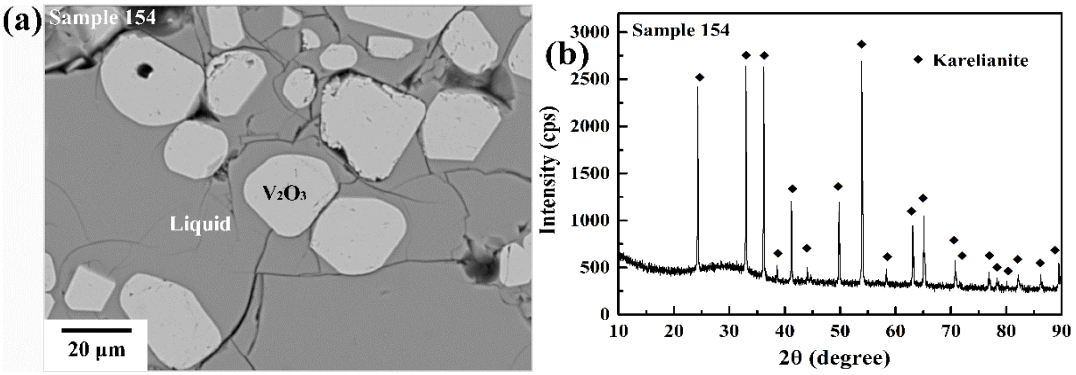

FIG 5 – Backscattered electron image (a), and XRD pattern (b) of $(V,Fe)_2O_3$-liquid coexisting sample.

Coexisting of two solid phases and liquid

Among the investigated samples, five cases of coexisting between two solid phases and liquid were found. The micrography and the XRD patterns of the representative samples were shown in Figures 6 through 10.

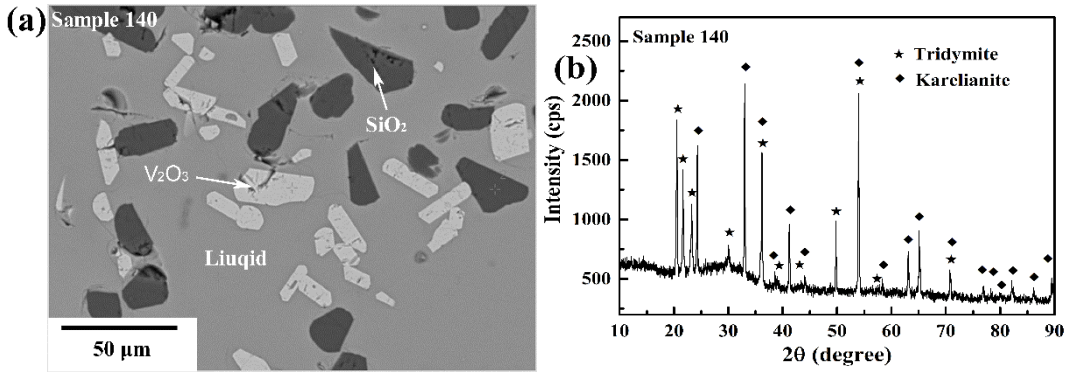

FIG 6 – Backscattered electron image (a), and XRD pattern (b) of $(V,Fe)_2O_3$-SiO_2-liquid coexisting sample.

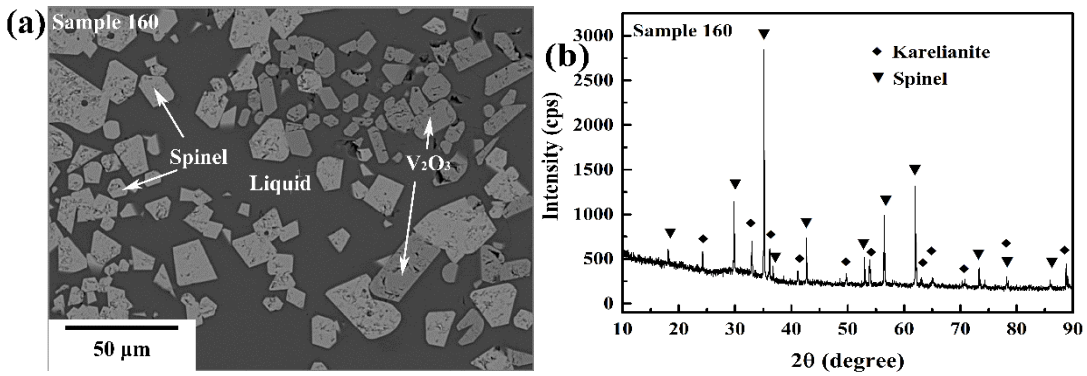

FIG 7 – Backscattered electron image (a), and XRD pattern (b) of $(V,Fe)_2O_3$-$Fe_{3-x}V_xO_4$-liquid coexisting sample.

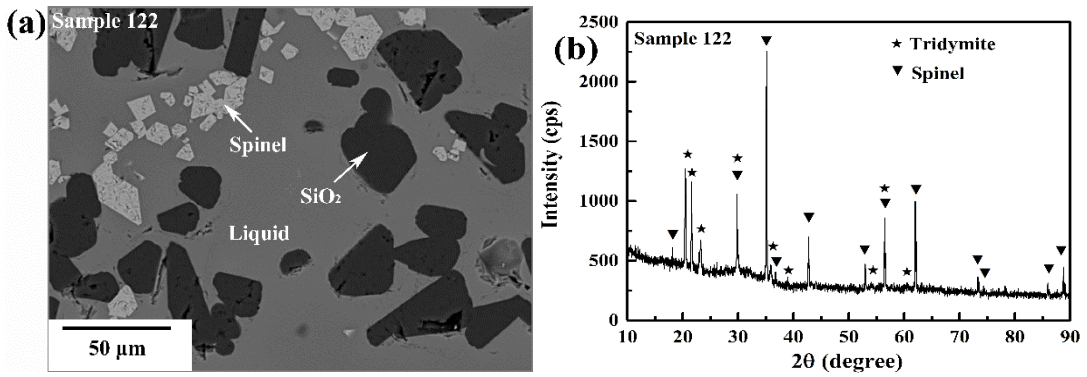

FIG 8 – Backscattered electron image (a), and XRD pattern (b) of SiO_2-$Fe_{3-x}V_xO_4$-liquid coexisting sample.

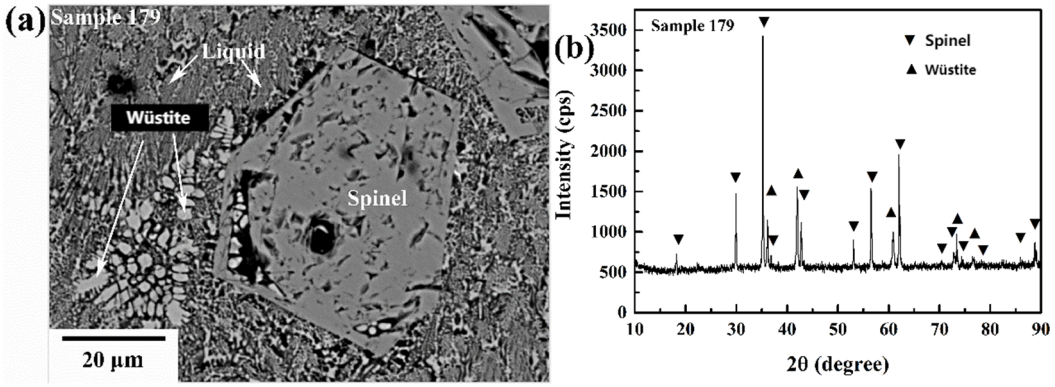

FIG 9 – Backscattered electron image (a), and XRD pattern (b) of Fe_tO-$Fe_{3-x}V_xO_4$-liquid coexisting sample.

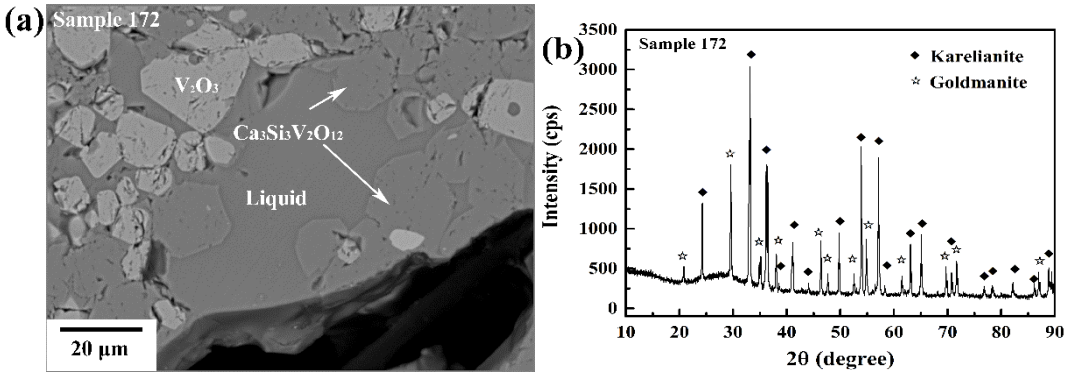

FIG 10 – Backscattered electron image (a), and XRD pattern (b) of $(V,Fe)_2O_3$-$(Ca,Fe)_3V_2Si_3O_{12}$-liquid coexisting sample.

Coexisting of three solid phases and liquid

Three different four-phase equilibria were found in the investigated sample. One is liquid phase equilibrating with solid phases SiO_2, $(V,Fe)_2O_3$ and $(Ca,Fe)_3V_2Si_3O_{12}$, as shown in Figure 11. The second is liquid phase equilibrating with solid phases SiO_2, $(V,Fe)_2O_3$ and $Fe_{3-x}V_xO_4$, as shown in Figure 12. The third is liquid phase equilibrating with solid phases $(Ca,Fe)_3V_2Si_3O_{12}$, $(V,Fe)_2O_3$ and $Fe_{3-x}V_xO_4$, as shown in Figure 13.

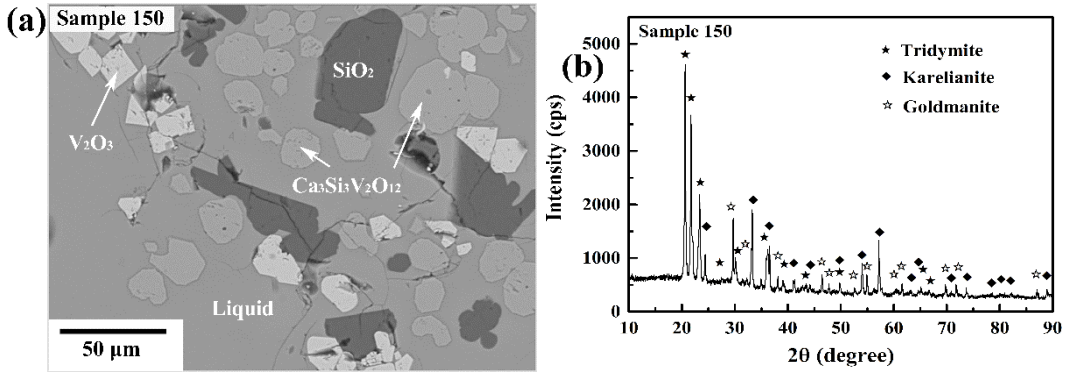

FIG 11 – Backscattered electron image (a), and XRD pattern (b) of $(V,Fe)_2O_3$-$(Ca,Fe)_3V_2Si_3O_{12}$-SiO_2-liquid coexisting sample.

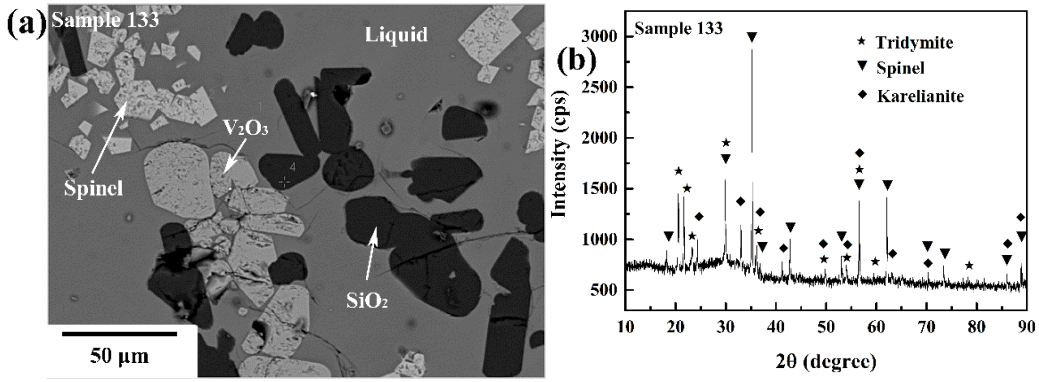

FIG 12 – Backscattered electron image (a), and XRD pattern (b) of $(V,Fe)_2O_3$- $Fe_{3-x}V_xO_4$-SiO_2-liquid coexisting sample.

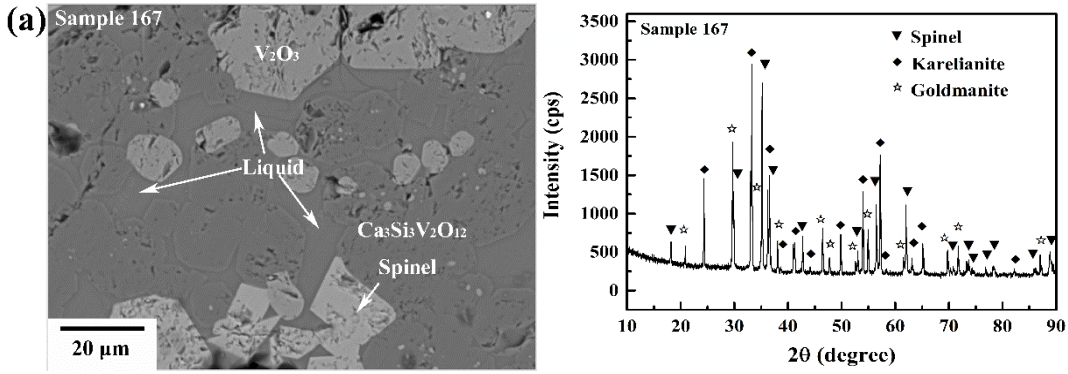

FIG 13 – Backscattered electron image (a), and XRD pattern (b) of $(V,Fe)_2O_3$-$(Ca,Fe)_3V_2Si_3O_{12}$-$Fe_{3-x}V_xO_4$-SiO_2-liquid coexisting sample.

Coexisting only solid phases

Two different solid-phase equilibria were found in the investigated sample. One is equilibrium among three solid phases, Goldmanite ($(Ca,Fe)_3V_2Si_3O_{12}$), Karelianite ($(V,Fe)_2O_3$) and Spinel ($Fe_{3-x}V_xO_4$), as shown in Figure 14. The other is equilibrium between Goldmanite ($(Ca,Fe)_3V_2Si_3O_{12}$) and Karelianite ($(V,Fe)_2O_3$), as shown in Figure 15.

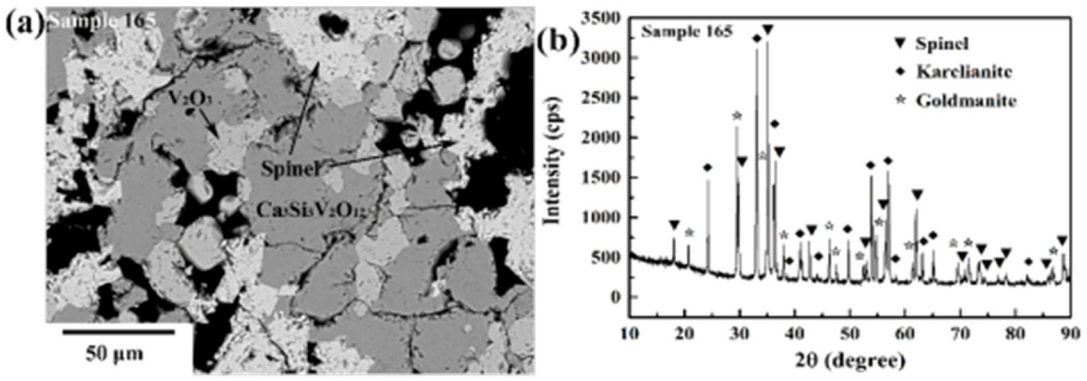

FIG 14 – Backscattered electron image (a), and XRD pattern (b) of $(V,Fe)_2O_3$-$(Ca,Fe)_3V_2Si_3O_{12}$-$Fe_{3-x}V_xO_4$ coexisting sample.

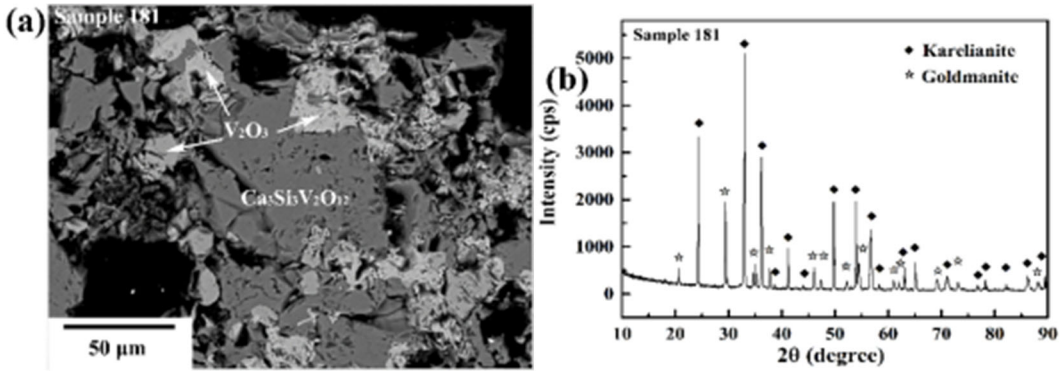

FIG 15 – Backscattered electron image (a), and XRD pattern (b) of $(V,Fe)_2O_3$-$(Ca,Fe)_3V_2Si_3O_{12}$ coexisting sample.

Phase diagram of V_2O_3-FeO-SiO_2-CaO(15 mass per cent) system at 1623 K

Based on the above-determined phase equilibria relationships, the iso-sectional phase diagram of V_2O_3-Fe_tO-SiO_2-CaO(15 mass per cent) system at 1623 K was constructed, which is shown in Figure 16.

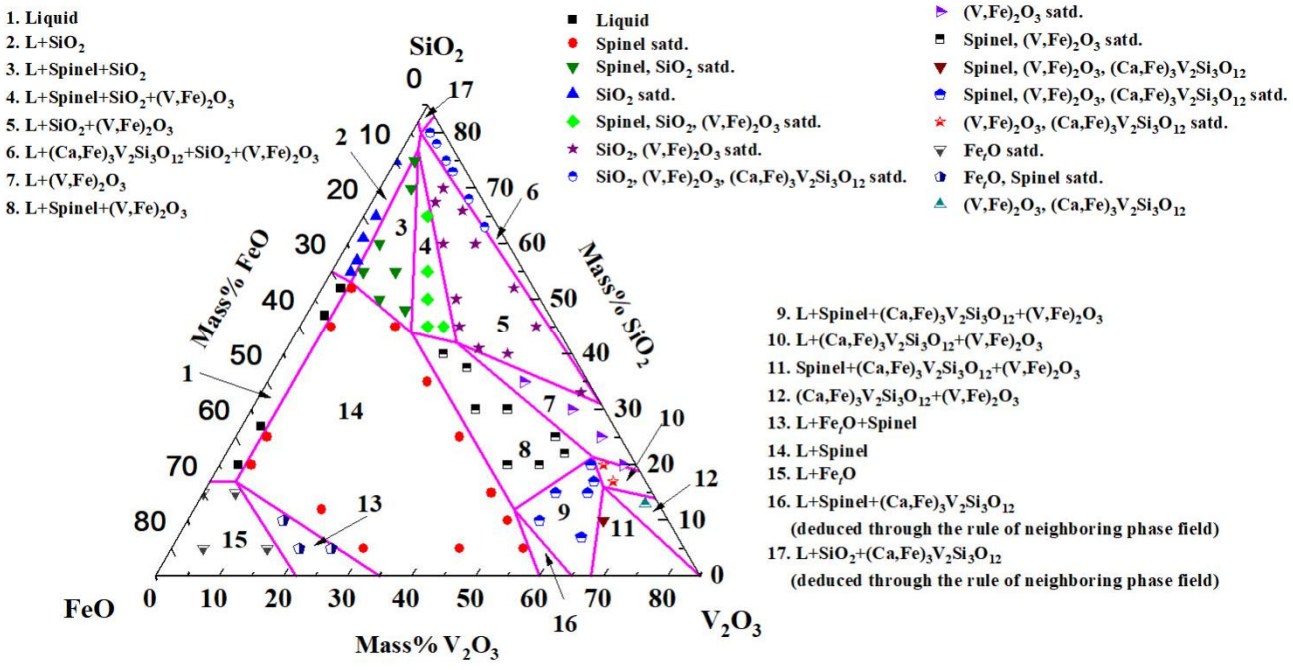

FIG 16 – The iso-sectional phase diagram of V_2O_3-Fe_tO-SiO_2-CaO(15 mass per cent) system at 1623 K.

In Figure 16, all the symbols such as the solid star, solid triangle, solid square etc represent the investigated samples, their positions represent the compositions of the samples, and different symbols represent different phase constituents. For example, the red solid circle symbols represent the samples which were constituted of spinel phase and liquid phase. According to the change of the phase constituents of the samples, the phase boundaries of different phase fields, which are lines in the two-dimensional phase diagram, were determined. Finally, the V_2O_3-Fe_tO-SiO_2-CaO(15 mass per cent) system was segmentalised into 17 areas, and the areas were numbered from 1 to 17. The phase constituents of each phase filed was also provided in Figure 16.

In Figure 16, it can also be seen that four linear phase boundaries meet at a point, which is the smaller unit composing the whole phase diagram. For each smaller unit, it was indicated by Mats Hillert (2008) that the numbers of phases in the phase fields around the intersection point have the relations as shown in Figure 17.

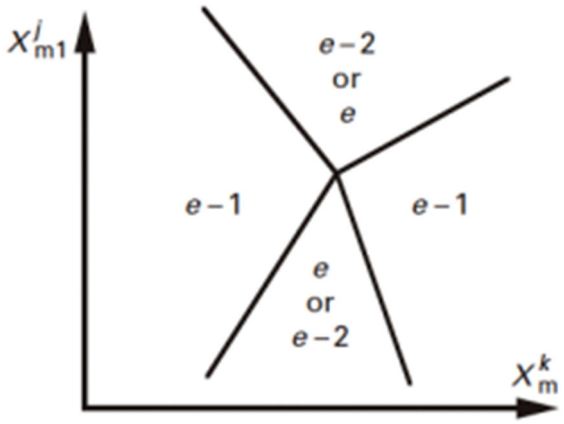

FIG 17 – Elementary unit of a molar phase diagram, the e values from 3 to a maximum determined by the number of sectioning.

As mentioned, totally 17 phase fields were indicated in Figure 16. However, only 15 different phase equilibria relationships were determined experimentally. For the un-experimental determined phase fields 16 and 17, they were deduced according to the rule of neighbouring phase field as shown in Figure 17. So, the phase constituents in the phase fields 16 and 17 should be confirmed by experiments in future.

CONCLUSIONS

In the present study, the traditional method of high temperature equilibration followed by quenching and combination of SEM and XRD measurements was adopted to identify the phase constituents of the samples. Then, based on the experimentally determined phase equilibria relationships, the iso-sectional phase diagram of V_2O_3-Fe_tO-SiO_2-CaO(15 mass per cent) system at 1623 K was constructed. The results revealed that the phase diagram is composed of 17 phase fields. The 17 phase fields are as follows:

1. single Liquid
2. Liquid + SiO_2
3. Liquid + spinel + SiO_2
4. Liquid + spinel + SiO_2 + $(V,Fe)_2O_3$
5. Liquid + SiO_2 + $(V,Fe)_2O_3$
6. Liquid + $(Ca,Fe)_3V_2Si_3O_{12}$ + SiO_2 + $(V,Fe)_2O_3$
7. Liquid + $(V,Fe)_2O_3$
8. Liquid + spinel + $(V,Fe)_2O_3$
9. Liquid + spinel + $(Ca,Fe)_3V_2Si_3O_{12}$ + $(V,Fe)_2O_3$

10. Liquid + $(Ca,Fe)_3V_2Si_3O_{12}$ + $(V,Fe)_2O_3$
11. spinel + $(Ca,Fe)_3V_2Si_3O_{12}$ + $(V,Fe)_2O_3$
12. $(Ca,Fe)_3V_2Si_3O_{12}$ + $(V,Fe)_2O_3$
13. Liquid + Fe_tO + $(V,Fe)_2O_3$
14. Liquid + spinel
15. Liquid + Fe_tO
16. L + spinel + $(Ca,Fe)_3V_2Si_3O_{12}$
17. L + SiO_2 + $(Ca,Fe)_3V_2Si_3O_{12}$.

ACKNOWLEDGEMENTS

The financial support from National Natural Science Foundation of China on the projects of 51534001 and 52174274 were gratefully acknowledged.

REFERENCES

Chen, J, Liu, G, Kang, Y, Wu, B, Sun, R, Zhou, C and Wu, D, 2014. Coal utilization in China: Environmental impacts and human health, *Environmental Geochemistry and Health*, 36(4):735–753.

Dai, S, Ren, D, Chou, C-L, Finkelman, R B, Seredin, V V and Zhou, Y, 2012. Geochemistry of trace elements in Chinese coals: A review of abundances, genetic types, impacts on human health and industrial utilization, *International Journal of Coal Geology*, 94(3–21).

Dai, S, Zheng, X, Wang, X, Finkelman, R B, Jiang, Y, Ren, D, Yan, X and Zhou, Y, 2018. Stone coal in China: a review, *International Geology Review*, 60(5–6):736–753.

Dong, Z H, Zhang, J and Yan, B J, 2021. Co-extraction of Vanadium Titanium and Chromium from Vanadium Slag by Oxalic Acid Hydrothermal Leaching with Synergy of Fe Powder, *Metallurgical and Materials Transactions B – Process Metallurgy and Materials Processing Science*, 52(6):3961–3969.

Du, X, Xue, J, Wang, X, Chen, Y, Ran, J and Zhang, L, 2018. Oxidation of Sulfur Dioxide over V_2O_5/TiO_2 Catalyst with Low Vanadium Loading: A Theoretical Study, *The Journal of Physical Chemistry C*, 122(8):4517–4523.

Ejigu, A, Edwards, M and Walsh, D A, 2015. Synergistic Catalyst–Support Interactions in a Graphene–Mn_3O_4 Electrocatalyst for Vanadium Redox Flow Batteries, *ACS Catalysis*, 5(12):7122–7130.

Fang, H X, Li, H Y and Xie, B, 2012. Effective Chromium Extraction from Chromium-containing Vanadium Slag by Sodium Roasting and Water Leaching, *ISIJ International*, 52(11):1958–1965.

Fang, H X, Li, H Y, Zhang, T, Liu, B-S and Xie, B, 2015. Influence of CaO on Existence form of Vanadium-containing Phase in Vanadium Slag, *ISIJ International*, 55(1):200–206.

Hillert, M, 2008. *Phase Equilibria, Phase Digrams and Phase Transformations* (Cambridge University Press: New York).

Huang, W, Chen, M, Shen, X, Yu, S, Wang, N and Xu, L, 2016. Phase Diagrams and Thermodynamic Properties of the FeO–SiO_2–V_2O_3 Systems, *Steel Research International*, 88(6).

Ketris, M P and Yudovich, Y E, 2009. Estimations of Clarkes for Carbonaceous biolithes: World averages for trace element contents in black shales and coals, *International Journal of Coal Geology*, 78(2):135–148.

Li, X, Meng, F, Dong, X, Liang, D, Gao, F and Wei, Y, 2019. Effect of CaO addition on phase formation in the Fe-Fe_2O_3-V_2O_3 system, *Journal of Alloys and Compounds*, 772:955–960.

Semykina, A, Dzhebian, I and Shatokha, V, 2012. On the Formation of Vanadium Ferrites in CaO–SiO_2–FeO–V_2O_5 Slags, *Steel Research International*, 83(12):1129–1134.

Seredin, V V, 2012. From coal science to metal production and environmental protection: A new story of success, *International Journal of Coal Geology*, 90–91:1–3.

Smirnov, L A, Filatov, S V and Rovnushkin, V A, 2010. Removal of vanadium from low-silicon hot metal, *Steel Transl,* 40.

Tomashchuk, I, Grevey, D and Sallamand, P, 2015. Dissimilar laser welding of AISI 316L stainless steel to Ti6–Al4–6V alloy via pure vanadium interlayer, *Materials Science and Engineering*: *A*, 622:37–45.

Wang, D, Li, F and Yan, B, 2019. Synthetic mechanism and kinetics of Fe_2VO_4 at 1273–1473 K from Fe_2O_3 and V_2O_3 under reducing atmosphere, *Journal of Alloys and Compounds*, 797:1050–1058.

Wang, D, Shu, Q, Yan, B, Wu, L, Wang, J and Dong, Y, 2017. Thermodynamics of the CaO–SiO_2–VO_x system at 1873 K under the oxygen partial pressure of 6.9×10^{-11} atm, *Journal of the American Ceramic Society*, 100(10):4912–4927.

Yan, B, Wang, D, Deng, T, Wu, L and Dong, Y, 2020a. Effects of oxygen partial pressure on the thermodynamics of CaO–SiO_2–VO_x system at 1873 K, *Journal of the American Ceramic Society*, 103(3):2114–2127.

Yan, B, Wang, D, Qiu, Q and Deng, T, 2020b. Phase relations in the FeO–V_2O_3 system at 1473 K and the magnetic properties of spinel phase $Fe_{3-x}V_xO_4$, *Ceramics International*, 46(5):6160–6167.

Yan, B, Wang, D, Wu, L and Dong, Y, 2018. A novel approach for pre-concentrating vanadium from stone coal ore, *Minerals Engineering*, 125:231–238.

Implementation of research outcomes by industry – Application of fundamental research to industrial practice

Understanding the side-blown furnace slag system at Glencore Nordenham's lead plant – from theory to industrial application

DOI: 10.62053/JWRI3272

A Abadias Llamas[1], A Kandalam[2] and C Zschiesche[3]

1. Process Engineer, Nordenham Metall GmbH, 26954 Nordenham (Lower Saxony), Germany. Email: alejandro.abadias@glencore.de
2. Process Engineer, Nordenham Metall GmbH, 26954 Nordenham (Lower Saxony), Germany. Email: avinash.kandalam@glencore.de
3. Chief Technology Officer, Nordenham Metall GmbH, 26954 Nordenham (Lower Saxony), Germany. Email: christoph.zschiesche@glencore.de

ABSTRACT

Lead has the ability to collect and carry valuable metals such as copper, bismuth, antimony, tin and precious metals for their downstream recovery. Therefore, lead metallurgy is key for the raw material supply that our society demands. Lead smelters, excluding lead-acid battery recyclers, tend to process more complex primary and secondary raw materials, which are mostly processed via the pyrometallurgy route. Accordingly, understanding the slag system of these metallurgical processes is key for the efficient industrial operation and recovery of minor elements.

Glencore Nordenham is an integrated lead and zinc smelter in northern Germany with a production of 92 000 t of lead and 164 700 t of zinc in 2022. The lead production line processes complex lead-bearing raw materials through the direct smelting process. Firstly, the feed mix is smelted in a Top Submerged Lance (TSL – Ausmelt®) furnace, where a lead bullion containing minor metals and a lead-rich slag are produced. Then, the lead-rich slag from the TSL is tapped (via launder) into a Side-Blown Furnace (SBF), where lead oxide is reduced to produce lead bullion (with minor elements) and discard slag. The lead bullion from both stages is refined to produce lead (>99.9 per cent) and recover the minor elements (Cu, Ag, Au, Sb, Te, Bi etc).

This paper reflects the experience of operating the SBF after the first five years of operation and describes its 'PbO-SiO_2-FeOx-CaO-ZnO' slag system. Firstly, the slag system, the furnace operating region and the potential solid phases present are discussed from a theoretical point of view. This theoretical study has been performed using FactSage™ 8.2 and the database developed by the Pyrosearch group at the University of Queensland, Australia (UQPY). Then, the FactSage™ simulations are compared with industrial slag measurements. Finally, some examples on how the slag knowledge gained at Glencore Nordenham can help the industrial operation of the SBF are discussed.

INTRODUCTION – GLENCORE NORDENHAM'S INTEGRATED LEAD AND ZINC PRODUCTION

The metallurgical infrastructure of non-ferrous base metals such as lead, zinc, copper or nickel is key for supplying the materials that society demands. Many minerals, alloys or technology products contain at least two of these metals together with other minor elements. These materials are often processed in the base metal's metallurgical infrastructure where the base metals are refined and the accompanying minor elements are recovered as by-products. The ability of base metals to dissolve and carry other minor elements throughout their refining process enables it.

Lead can collect valuable metals such as precious metals, copper, bismuth, antimony, tin and/or zinc for their downstream recovery. Furthermore, by-products containing copper, nickel, cadmium, lead or precious metals are obtained when zinc is produced. Therefore, there is a close interconnection within the non-ferrous metallurgical infrastructure to maximise metal recovery through the exchange and treatment of its by-products. This interconnection becomes more important day by day because of the increase on the complexity of raw materials and the necessity of moving towards a circular economy (Reuter, Matusewicz and van Schaik, 2015).

Ores are decreasing their grade and becoming more complex in terms of minor elements, while chemical elements representing half the periodic table can be present in other products such as

modern vehicles or waste electrical and electronic equipment (WEEE). Moreover, the processing of these complex materials generates higher quantities of by-products that should be treated to maximise material recovery. These are a few examples of raw materials that the metallurgical infrastructure has to process nowadays to supply the metals that society demands.

Glencore Nordenham is an integrated lead and zinc smelter aiming at becoming a modern and flexible polymetallic smelter that can process a wide range of complex materials by making the most out of the synergies between lead and zinc metallurgies. The zinc plant has a roasting-leaching-electrowinning (RLE) configuration combined with Glencore's Albion Process™ direct-leaching technology. The production of zinc was 164 700 t in 2022 as master and die-casting alloys, special high-grade (SHG) zinc and zinc alloys for continuous galvanising. Additionally, by-products such as sulfuric acid, lead and silver secondaries, copper cement or cadmium metal are also produced.

The lead smelter uses the direct smelting process to produce over 100 000 t of lead per annum as soft and fine lead and lead alloys. Additionally, sulfuric acid and silver-gold alloys are also produced. The flow sheet of the lead smelter is shown in Figure 1. The process starts with the feed blend preparation of primary and secondary materials. Different types of concentrates, residues and secondaries are blended with internal recycle materials and fluxes. This feed blend is then smelted in a top submerged lance (TSL) furnace, Ausmelt®, where a lead bullion containing minor elements and a lead-rich slag (~ 50 wt per cent Pb) are produced. The lead bullion is sent to copper drossing before being sent to the pyrometallurgical lead refinery. The lead-rich slag from the TSL flows via a launder to a side-blown furnace (SBF), where the lead oxide in the slag is reduced to recover the lead as lead bullion together with other minor metals. The SBF slag is then landfilled. The lead bullion of both furnaces is sent to a pyrometallurgical lead refinery to refine the lead and recover the dissolved minor metals such as Ag, Au, Bi, Cu, Sb, Sn or Te.

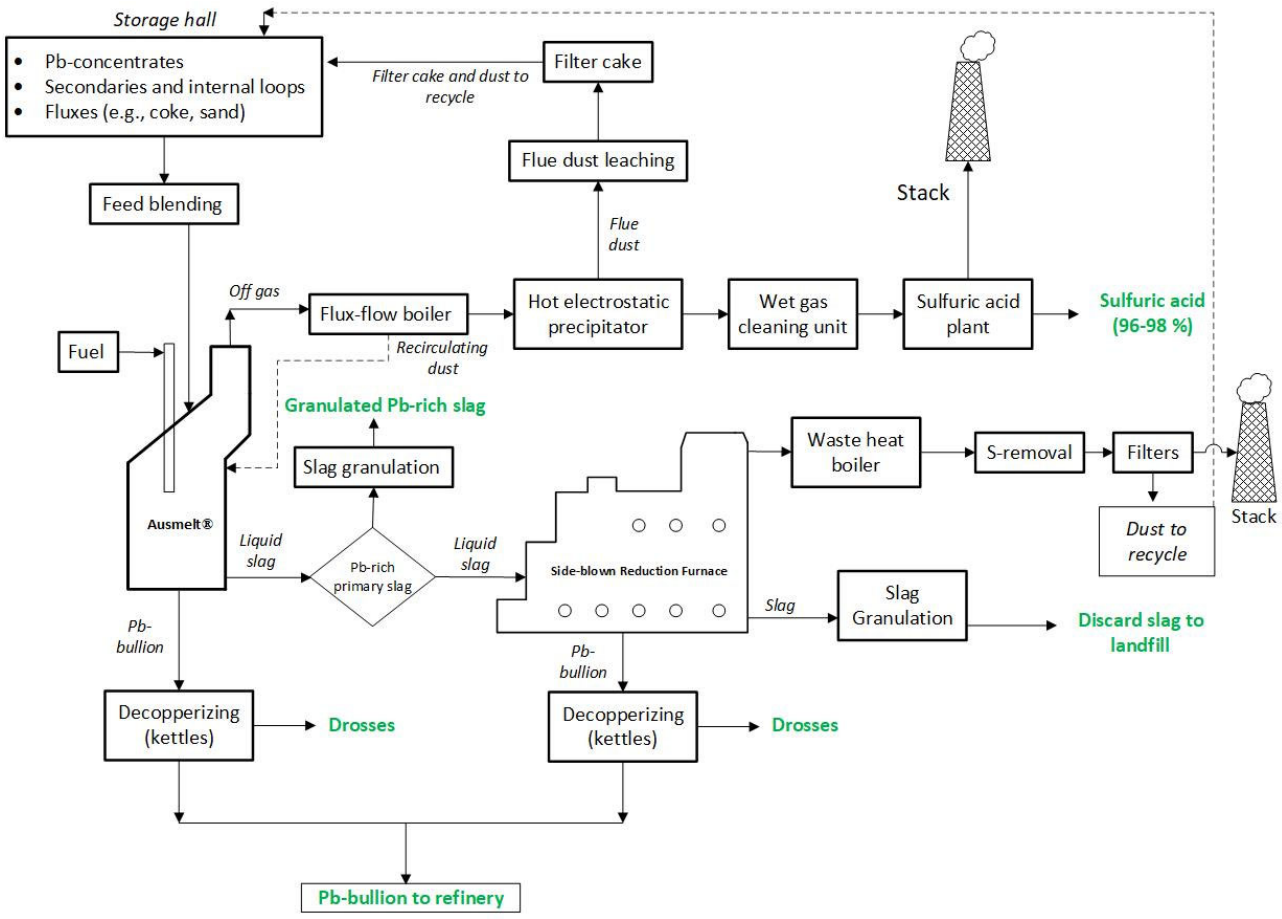

FIG 1 – Flow sheet of Lead plant at Nordenham Metall GmbH, Germany (Kandalam *et al*, 2023).

The TSL furnace and its latest upgrades at Glencore Nordenham have been already described by Kandalam *et al* (2023). Therefore, this paper describes the SBF and the experience after five years

of operation. Particularly, the 'PbO-SiO_2-FeOx-CaO-ZnO' slag system used in the SBF is described theoretically. Additionally, few examples on how the theoretical knowledge of the slag system is used in furnace operation are explained.

LEAD SLAG REDUCTION FURNACE AT GLENCORE NORDENHAM

The SBF at Glencore Nordenham is a submerged-tuyere furnace constructed with a long and narrow rectangular hearth that becomes wider at the top of the furnace (Wei *et al*, 2019). It was commissioned in 2018 to process the lead-rich slag of the TSL furnace, increase the lead recovery of the plant and enable the recovery of minor metals when complex raw materials are treated.

A schematic of the SBF is shown in Figure 2, while data of the furnace are gathered in Table 1. Four main regions can be distinguished in the SBF:

1. Lead region – a refractory-lined region at the bottom of the furnace and below the tuyeres where the lead bullion is settled and transferred to the copper drossing kettles via siphon.
2. Slag region – a water-cooled copper panels region in the middle part of the furnace. The tuyeres are situated in this region to blow enriched air into the slag.
3. Freeboard region – a water-cooled copper panels region above the slag region, where the gases in the furnace are post-combusted with air from the secondary tuyeres.
4. Off-gas region – lined with concrete and steel anchors, this region carries the post combustion gases to the waste heat boiler (WHB).

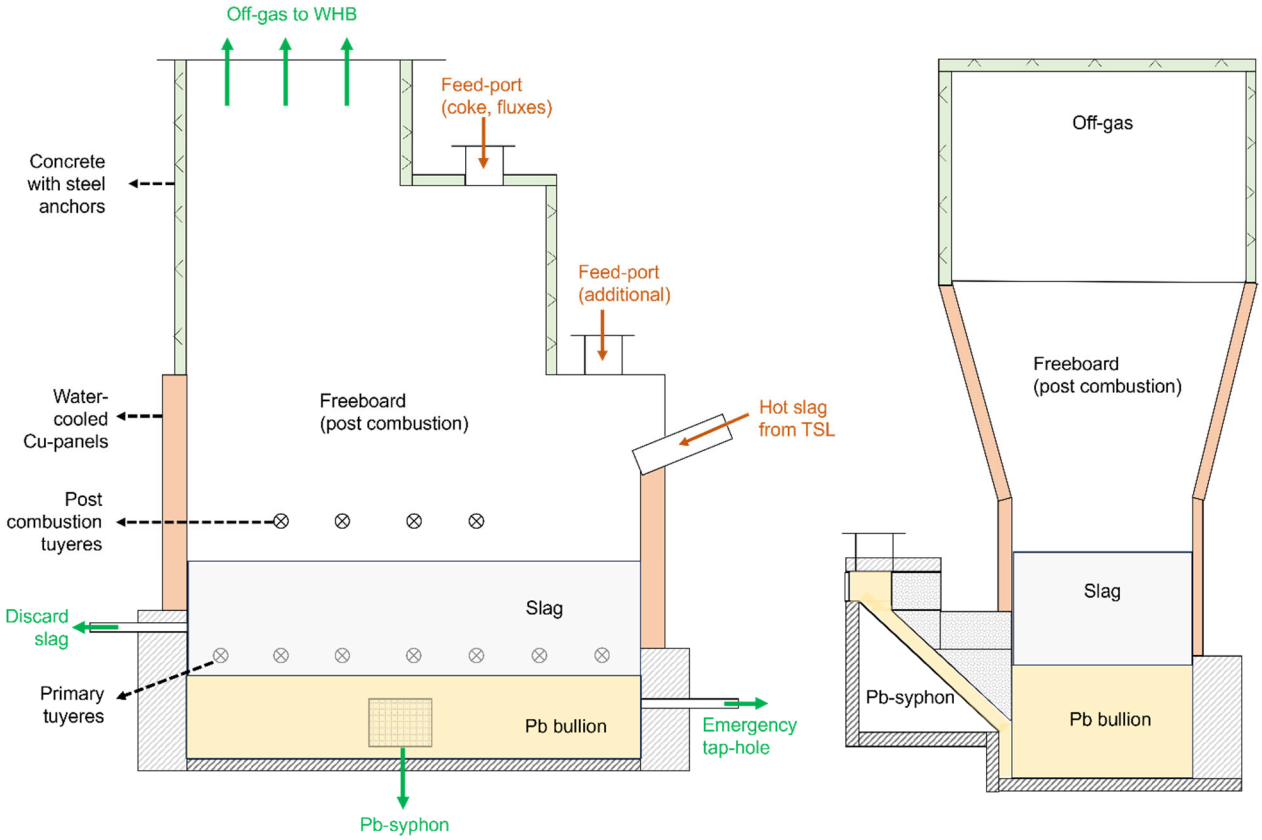

FIG 2 – Schematic representation of Side-Blown Furnace (SBF) at Nordenham Metall GmbH, Germany.

TABLE 1

Glencore Nordenham's SBF data.

Commissioned	August 2018
Length * width (m)	6.35 * 2.80
Height (m)	8
Number of tuyeres	22
Slag charge (t)	34–38
Pb in input TSL slag (wt%)	48–54
Pb in output slag (wt%)	<1.5
Slag tapping target temperature (°C)	1250
Batch time (min)	120
Slag treated per annum (t/a)	140 000

The slag flows from the TSL furnace via launder into the SBF hot slag feed port. Moreover, the coal for heating and reduction is fed through a feed port located at the top of the furnace. Fluxes and cold material can also be fed through this feed port if needed. Final slag is tapped through a taphole, granulated, and then landfilled, while a siphon transfers the lead bullion to two copper drossing kettles. The furnace operates in batch mode with three stages: (i) charging, (ii) reduction and (iii) tapping. The batch time is around two hours.

After five years of operations (from 2018 to 2023), the SBF has treated around 600 000 t of lead-rich slag from the TSL furnace with an availability of >98 per cent (excluding planned maintenance and shut-downs), producing a slag with a lead content below 1.5 wt per cent suitable for landfilling. Additionally, the SBF has enabled the recovery of accompanying metals such as Ag, Bi, Cu, Sb, Sn and Te when they are present in the TSL slag. Therefore, a wide range of complex raw materials can be treated at Glencore Nordenham. This flexibility has enabled the treatment of more than 50 different raw materials such as lead-bearing concentrates, residues and recyclates (excluding internal loops and fluxes).

SLAG SYSTEM OF THE SLAG REDUCTION FURNACE

The slag composition and phases present vary during the SBF batch, particularly, during the charging and reduction stages. The SBF works best when the slag is fluid, above the liquidus temperature. But owing to the batchwise operation of the SBF the slag temperature constantly changes throughout each batch. Moreover, the SBF is not refractory lined in the slag region. Therefore, a slag freeze lining forms on the water-cooled copper panels. The life of the water-cooled copper panels is long and does not determine the furnace campaign duration. However, an excessive freeze lining build-up might create issues during operations, eg a reduction of the SBF volume. Therefore, understanding the slag system of the SBF is essential for its optimal operation.

The major components of the slag at Glencore Nordenham are FeO_x, SiO_2, CaO, PbO and ZnO. Other slag components such as Al_2O_3 or MgO are also present but in lower concentrations (<1 wt per cent). To understand the SBF slag during a batch, the TSL slag should be discussed briefly. A simplified phase diagram containing the representative phase fields of the TSL slag (Figure 3) has been created using FactSage™ 8.2 (Bale *et al*, 2016) and the database of the Pyrosearch centre at the University of Queensland, Australia (UQPY). This database has been particularly developed for the slag/matte/metal systems of the copper and lead industries (Shishin *et al*, 2020, 2022; Hidayat *et al*, 2023). The TSL slag composition range (striped green circle) is also shown in Figure 3. The TSL slags operate below liquidus temperature and are in the 'liquid slag + melilite + spinel' phase field of the phase diagram. Therefore, the hot slag that is charged into the SBF is a source of some suspended solids.

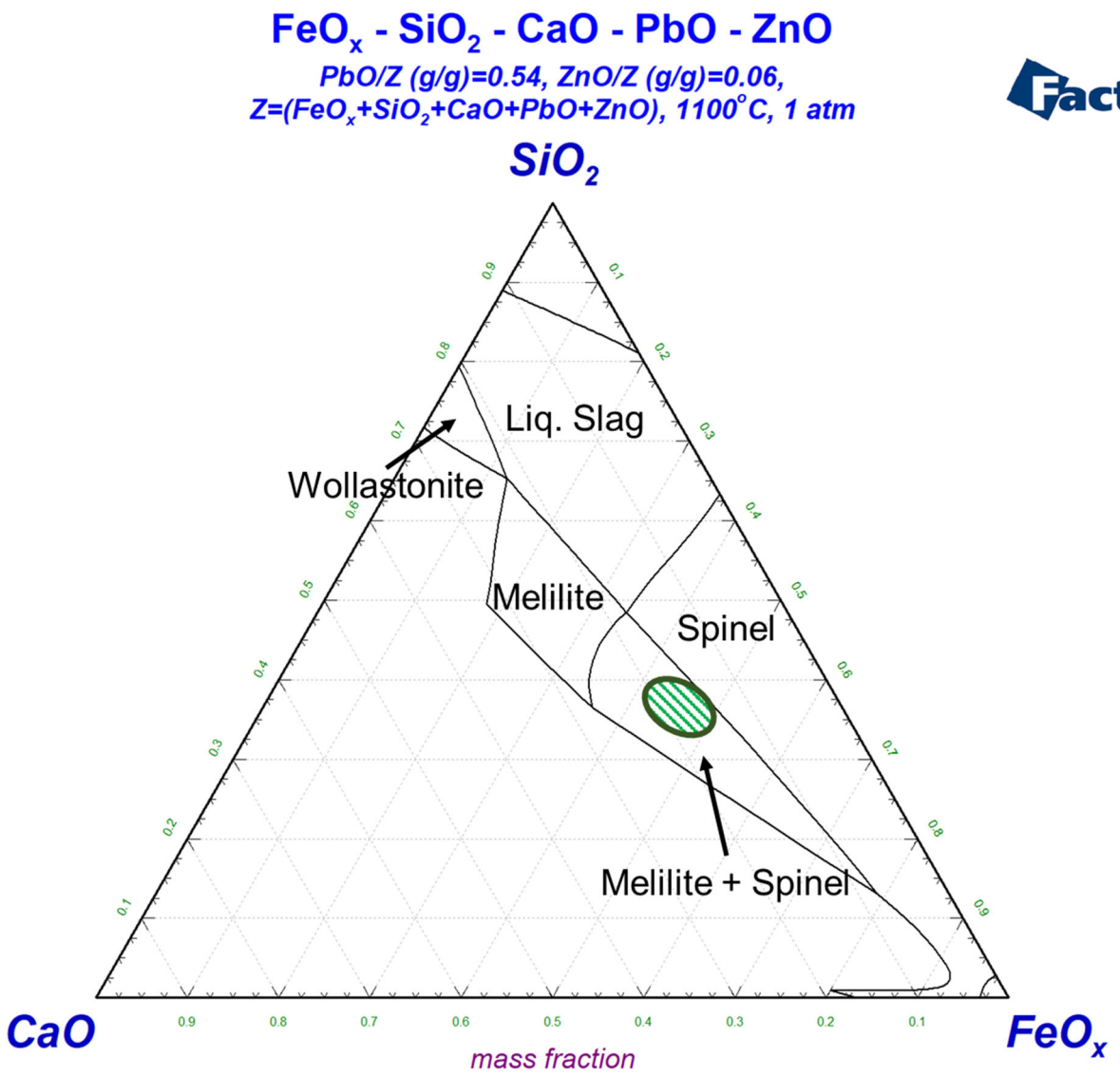

FIG 3 – Simplified phase diagram for the TSL slag at 1100°C showing the slag composition range (striped green area). Liquid slag is also present in the phase fields containing solid phases. A lead content of 50 wt per cent and zinc content of 5 wt per cent are set as constant values for this phase diagram calculation. The partial pressure of O_2 (pO_2) has been calculated and set for a slag in equilibrium with metallic lead.

When the lead-rich slag of the TSL flows to the SBF at the beginning of the batch (charging stage), it mixes with a slag heel from the previous batch (<2 wt per cent Pb). This results in the starting slag composition for the reduction stage in the SBF. The starting slag has a lead and zinc content around 20 wt per cent and 12 wt per cent respectively.

A phase diagram for the starting slag in the SBF after charging has been created for these conditions using FactSage™ and the UQPY database. This phase diagram (see Figure 4) shows how the liquid slag region becomes larger when the temperature of the starting slag increases. At the end of the charging phase, the temperature is between 1175°C and 1200°C. Therefore, the slag is in the 'liquid slag + spinel' area. As the bulk slag composition is close to the liquid slag phase field, the solids content in the bulk slag would be around 5 wt per cent based on FactSage™ calculations.

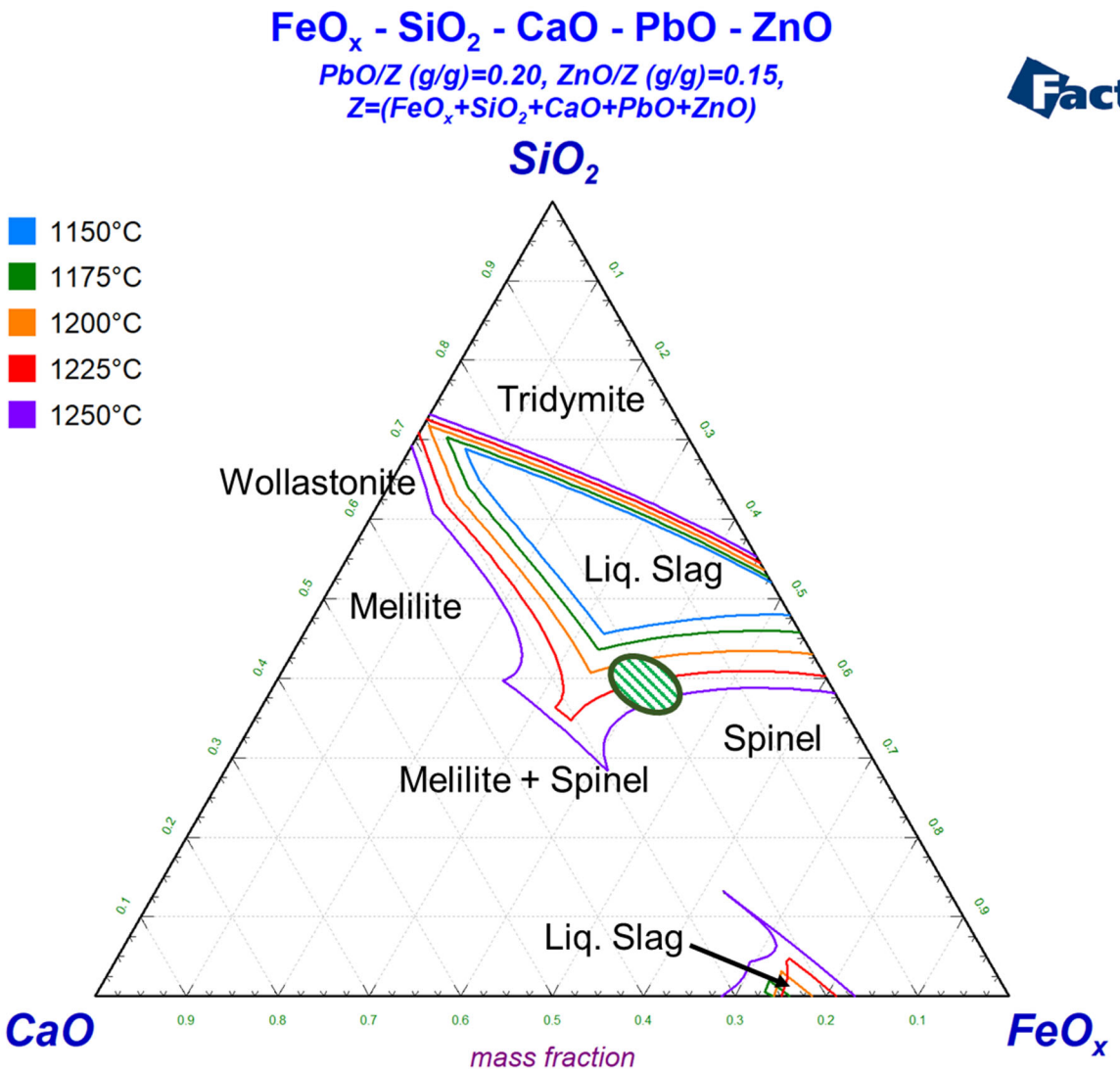

FIG 4 – Phase diagram for the starting SBF slag composition after slag charging showing the liquid slag area for different temperatures and the slag composition range (striped green area). A lead content of 19 wt per cent and zinc content of 12 wt per cent are set as constant values for phase diagram calculations. The pO_2 is calculated and set for a slag in equilibrium with metallic lead at the different temperatures.

Then, the reduction phase begins. During reduction, the lead content decreases from around 20 wt per cent to less than 2 wt per cent. The reduction process can be represented in a phase diagram if the ratio between CaO, FeO_x or SiO_2 is fixed and PbO is included in the ternary diagram. In this case, a phase diagram with a representative CaO/SiO_2 ratio has been plotted using FactSage™ and the UQPY database (see Figure 5). As discussed before, the starting slag composition is in the 'liquid slag + spinel' phase field below 1200°C. However, the final slag composition is inside the liquid slag phase field at this temperature. Moreover, the slag temperature increases slightly during the reduction phase. Therefore, a decrease in the solids content is expected to happen during the reduction phase.

When the lead content in the slag is reduced below 2 wt per cent, the tapping phase of the batch begins. Here, the temperature is increased to around 1250°C to produce a slag with good lead oxide reduction kinetics and free from entrained lead bullion. According to Figure 5, the slag is expected to be fully liquid at this temperature, which avoids the generation of solid phases and decreases the viscosity of the slag.

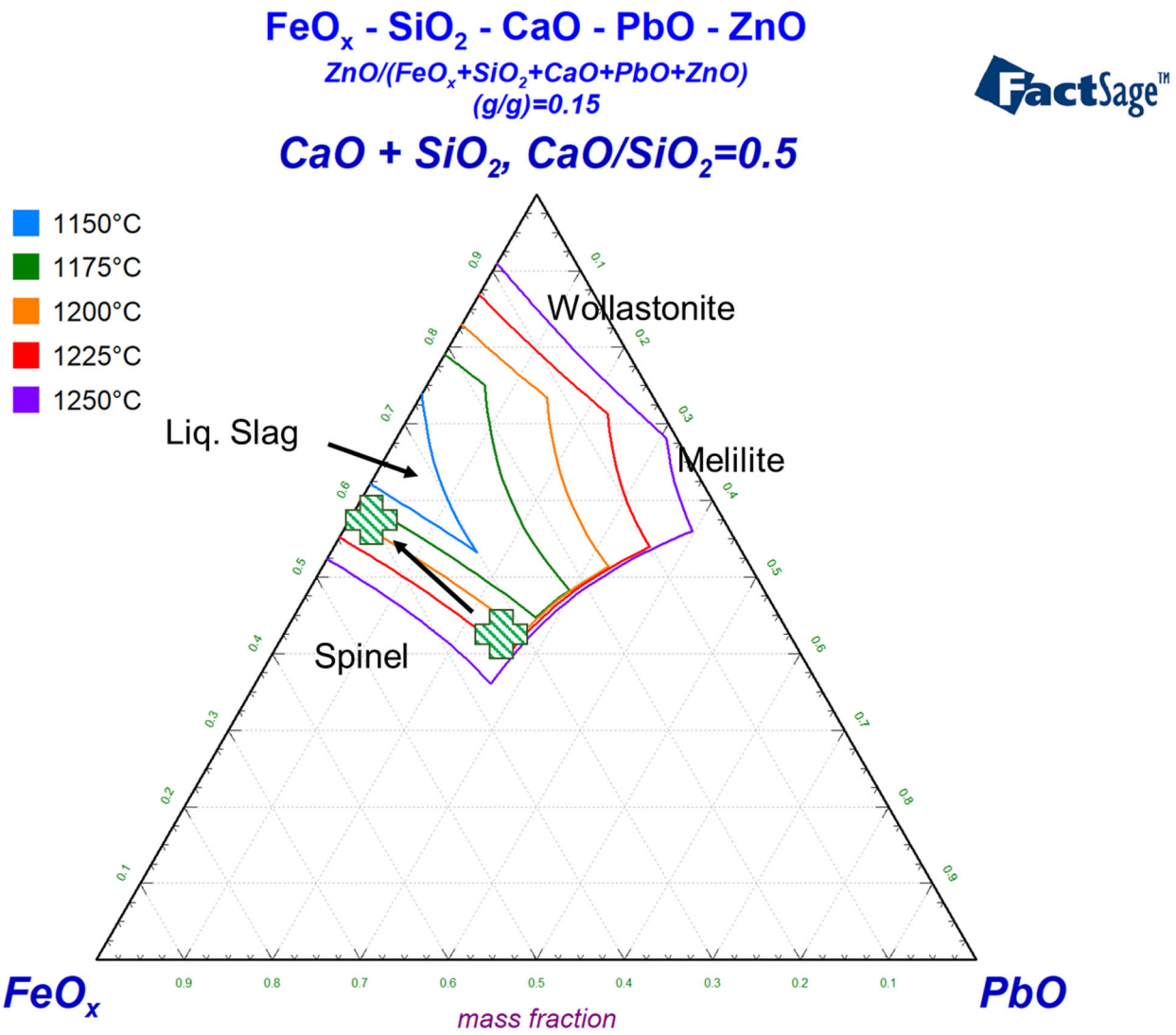

FIG 5 – Phase diagram for the reduction phase of the SBF batch showing the liquid slag area at different temperatures and the starting and final slag composition range (striped plus symbol). CaO and SiO_2 are combined as compound in the ternary diagram with a CaO/SiO_2 ratio of 0.5, while the zinc concentration is set to 12 wt per cent. The pO_2 is calculated and set for a starting slag in equilibrium with metallic lead at the different temperatures.

INDUSTRIAL APPLICATION OF SLAG CHEMISTRY FUNDAMENTALS

The previous section explains the slag chemistry of the SBF batch from a theoretical point of view based on FactSage™ modelling and the use of the UQPY database. When these theoretical results are compared with actual industrial samples, a good correlation exists. For example, the microscope images of two different TSL slags at Glencore Nordenham analysed by UQPY are shown in Figure 6. As expected, the solid phases present in the bulk slag are spinel (square/polygonal shape) and melilite (elongated shape). Some droplets of lead bullion can be also seen in both samples because of incomplete settling/entrainment. In terms of phase proportions, the proportion of solid phases calculated theoretically with FactSage™ and the UQPY database also correlates with the value range measured in industrial samples, which is around 10–15 wt per cent solids in bulk TSL slag.

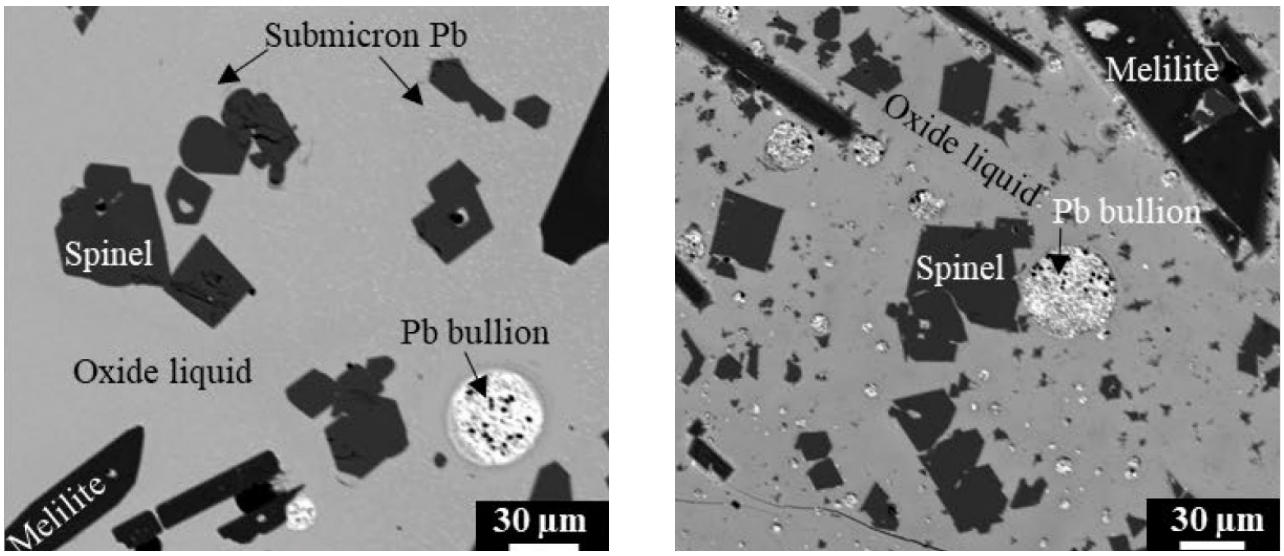

(a) (b)

FIG 6 – Optical microscope images of two TSL slag samples entering the SBF, analysed by UQPY.

This good correlation between modelling and actual industrial values allows the application of slag chemistry fundamentals through modelling for analysis, prediction and optimisation of the metallurgical processes performed at Glencore Nordenham. A few real examples will be discussed in this section.

As discussed before, the slags at Glencore Nordenham contain solid phases. The solid phases in the slag help the formation of a freeze lining in the furnaces that protects the refractory and water-cooled copper panels (see Figure 7), extending their campaign time before relining and maintenance. However, viscosity-related issues may appear if an excessive proportion of solids is present in the slag.



FIG 7 – Left: Freshly cleaned water-cooled Cu-panels inside SBF. Right: Slag freeze layer (~3 cm) on the Cu-panels observed during the maintenance shut-down of SBF.

During the slag charging phase of the SBF, only spinel is expected to be present in the slag (see Figure 4). However, a slight increase in the CaO content of the slag at 1175°C because of feed material variability might move the slag composition inside the ‘melilite + spinel’ phase field and

melilite would also be formed. The phase diagrams shown in the previous section and FactSage™ are used to predict the effect of these slag composition variations on the solid phase proportions.

The calculated proportion of spinel and melilite phases in the SBF slag after charging is shown in Table 2. A slight increase in the CaO content at 1175°C would lead to a melilite proportion in slag of 1.9 wt per cent, while the total proportion of solids would increase from 7.5 to 10.6 wt per cent. However, if the temperature of the SBF slag after charging is 1200°C, melilite would not be formed while the increase in the total proportion of solids would be lower than at 1175°C (from 4 to 4.9 wt per cent). These results can be used to help the furnace operations department develop a set of directions for the operators when variations in feed are expected.

TABLE 2

Solid phase proportions in bulk slag calculated with FactSage™ and the UQPY database for two different slags. Values in wt%.

	Solid phase	**1175°C**	**1200°C**
$SiO_2/(SiO_2 + CaO + FeO_x) = 0.40$	Spinel (wt%)	7.5	4
$CaO/(SiO_2 + CaO + FeO_x) = 0.19$	Melilite (wt%)	0	0
$FeO_x/(SiO_2 + CaO + FeO_x) = 0.41$	Total solids (wt%)	7.5	4
$SiO_2/(SiO_2 + CaO + FeO_x) = 0.39$	Spinel (wt%)	8.7	4.9
$CaO/(SiO_2 + CaO + FeO_x) = 0.21$	Melilite (wt%)	1.9	0
$FeO_x/(SiO_2 + CaO + FeO_x) = 0.40$	Total solids (wt%)	10.6	4.9

Another common consequence of processing a wide portfolio of lead-bearing raw materials at Glencore Nordenham is the variability of the zinc content in slag. Zinc in slag promotes the formation of zinc compounds/endmembers in the melilite and spinel solid phases present in lead slags such as hardystonite in melilite ($Ca_2ZnSi_2O_7$) or zinc ferrite in spinel ($ZnFe_2O_4$). Therefore, an increase in the solid phase proportion in the slag can be expected if the zinc content increases. This can be seen in the phase diagram plotted using FactSage™ and the UQPY database and shown in Figure 8. Here, the liquid slag phase field is plotted for different zinc content values in the slag after SBF charging. When the zinc content in the slag increases, the liquid slag phase field moves away from the slag composition range in the diagram.

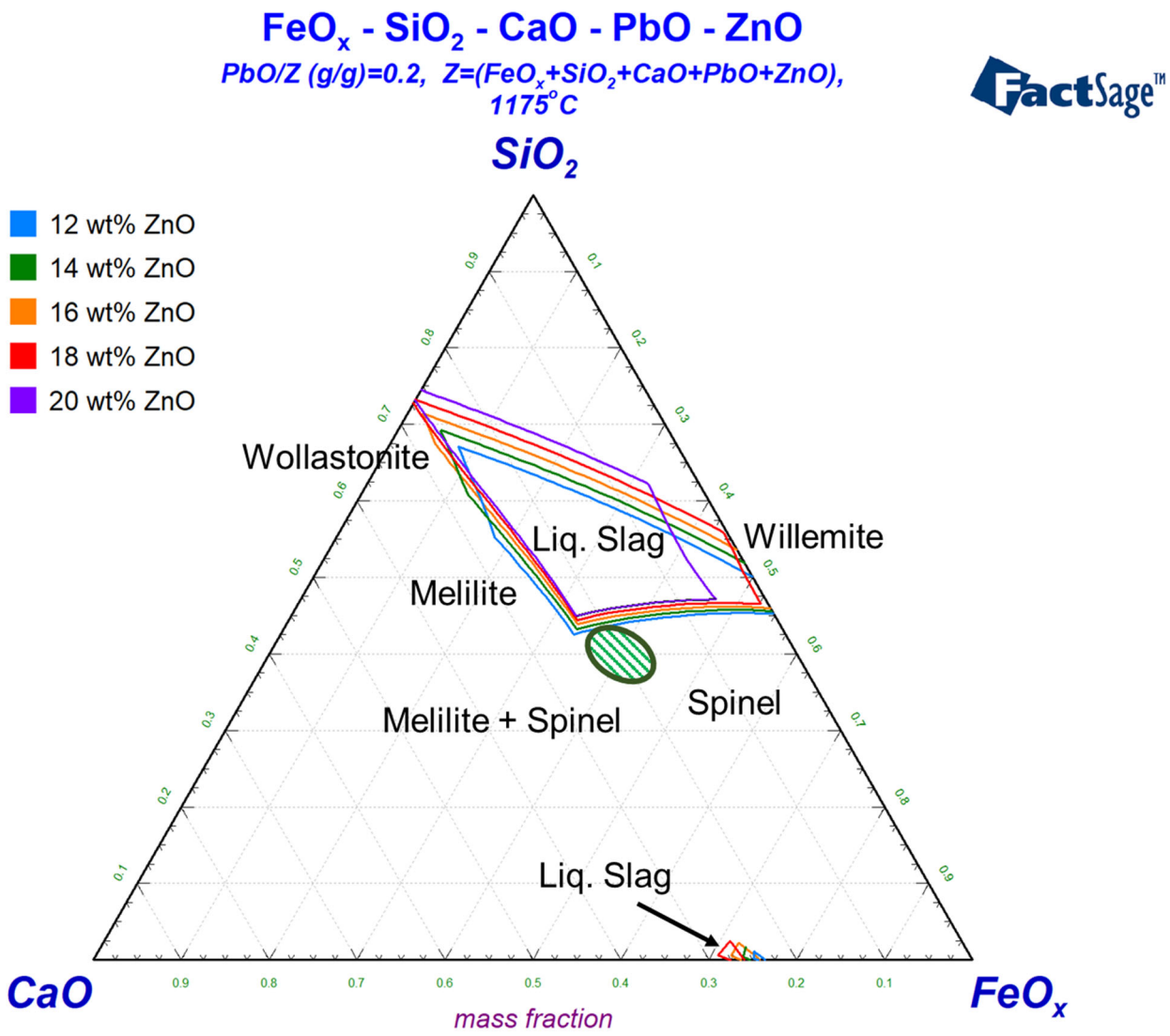

FIG 8 – Phase diagram for the starting SBF slag composition after slag charging showing the liquid slag area for different ZnO contents and the slag composition range (striped green area). A lead content of 19 wt per cent and a temperature of 1175°C are set as constant values for phase diagram calculations. The pO2 is calculated and set for a slag in equilibrium with metallic lead.

The proportion of solids can also be estimated for the different zinc content values in the slag using FactSage™ and the UQPY database. The results of the FactSage™ simulations are shown in Table 3. The solid phase formed for the selected slag composition would be spinel for all the simulated ZnO content values. The solid phase proportions would increase from 6.4 wt per cent in a slag containing 12 wt per cent of ZnO to 9.1 wt per cent for a ZnO value of 20 wt per cent. Therefore, a more viscous slag may be expected after SBF slag charging and the operations department can advise the operators how to operate the furnace under the specific batch conditions.

TABLE 3

Solid phase proportions in bulk slag calculated with FactSage™ and the UQPY database for different ZnO contents. Values in wt%.

Solid phase proportions (wt%)	12 wt% ZnO	14 wt% ZnO	16 wt% ZnO	18 wt% ZnO	20 wt% ZnO
$SiO_2/(SiO_2 + CaO + FeO_x) = 0.40$ $CaO/(SiO_2 + CaO + FeO_x) = 0.19$ $FeO_x/(SiO_2 + CaO + FeO_x) = 0.41$	6.4	7.1	7.8	8.5	9.1

CONCLUSIONS

Glencore Nordenham is transforming into a modern polymetallic smelter with high raw material flexibility. This is enabled by the integration of the lead and zinc smelters and their modern and innovative technology. The commissioning of the side-blown furnace (SBF) in 2018 for the reduction of lead-rich slags enabled the recovery of elements such as Ag, Au, Bi, Cu, Sb, Sn and Te and the treatment of more complex raw materials. Till the end of 2023, the SBF has treated around 600 000 t of lead-rich slag, has increased the overall secondary materials in feed to up to 80 per cent and has enabled the treatment of more than 50 different raw materials.

The transformation of Glencore Nordenham into a flexible smelter requires metallurgical knowledge of slags containing FeO_x, SiO_2, CaO, PbO and ZnO. Nowadays, there is chemical thermodynamics software such as FactSage™ containing comprehensive thermochemical databases for pyrometallurgical processes such as the one developed by the Pyrometallurgy Innovation Centre at the University of Queensland (UQPY), Australia. The ability of this software of representing the thermochemical processes occurring in industrial furnaces helps understand their slag systems, predict how variations in the operating conditions affect them and optimise the operating parameters. Two real examples on the application of this approach at Glencore Nordenham have been explained, showing how the knowledge on fundamental slag chemistry is applied to industrial operations. This way, the operations teams have more information on the furnace to act faster and with confidence, creating a safe working environment. These quick decisions taken confidently are essential for the optimal and safe furnace operation in flexible smelters like Glencore Nordenham.

ACKNOWLEDGEMENTS

The authors extend their heartfelt appreciation to the management of Glencore Nordenham, including Koen Demesmaeker, Chairman of the Supervisory Board, and Thomas Hüser, Managing Director, for their gracious permission to publish this work. Additionally, we are deeply thankful to the production managers, Mike Kittel, and Christian Laser, along with the entire team at the smelters. Their dedication, commitment to excellence, and consistent application of best practices have been pivotal in maintaining efficient operations and achieving our objectives. We also wish to convey our profound gratitude to the Pyrosearch team at the University of Queensland, Australia – Evgueni Jak, Denis Shishin, Jeff Chen, Georgii Khartcyzov, and Maksym Shevchenko – for their invaluable support with the FactSage™ UQPY database and the experimental analysis of slag systems.

REFERENCES

Bale, C W, Bélisle, E, Chartrand, P, Decterov, S A, Eriksson, G, Gheribi, A E, Hack, K, Jung, I-H, Kang, Y-B, Melançon, J, Pelton, A D, Petersen, S, Robelin, C, Sangster, J, Spencer, P and Van Ende, M-A, 2016. FactSage™ thermochemical software and databases, 2010–2016, *CALPHAD: Computer Coupling of Phase Diagrams and Thermochemistry*, 54:35–53. https://doi.org/10.1016/j.calphad.2016.05.002

Hidayat, T, Fallah-Mehrjardi, A, Abdeyazdan, H, Shishin, D, Shevchenko, M, Hayes, P C and Jak, E, 2023. Integrated Experimental and Thermodynamic Modeling Study of the Pb-Fe-O-S-Si System: Effect of Temperature and p(SO2) on Slag-Matte-Metal-Tridymite Equilibria, *Metallurgical and Materials Transactions B*: *Process Metallurgy and Materials Processing Science*, 54(2):536–549. Available from: <https://doi.org/10.1007/s11663-022-02707-y

Kandalam, A, Zschiesche, C, Burrows, A, Tesch, T and Lischeid, F, 2023. Upgrading the TSL smelter (Ausmelt®) at Nordenham to treat low-Pb and complex feed materials, Proceedings of the European Metallurgical Conference (EMC) 2023 (GDMB: Düsseldorf).

Reuter, M A, Matusewicz, R and van Schaik, A, 2015. Lead, zinc and their minor elements: Enablers of a circular economy, *World of Metallurgy - ERZMETALL,* 68(3):134–148.

Shishin, D, Hidayat, T, Sultana, U, Shevchenko, M and Jak, E, 2020. Experimental measurement and thermodynamic model predictions of the distributions of Cu, As, Sb and Sn between liquid lead and PbO–FeO–Fe_2O_3–SiO_2 slag, *International Journal of Materials Research*, 111(9):733–743. https://doi.org/10.3139/146.111942

Shishin, D, Mehrjardi, A F, Shevchenko, M, Hidayat, T and Jak, E, 2022. Experimental study, thermodynamic calculations and industrial implications of slag/matte/metal equilibria in the Cu-Pb-Fe-O-S-Si system, *Journal of Materials Research and Technology*, 19:899–912. https://doi.org/10.1016/j.jmrt.2022.05.058

Wei, W, Tao, L, Weiyan, Y, Bin, T and Wenjiang, L, 2019. Industrial application of side-blowing furnace smelting process in China Nerin, in *Proceedings of the* 58*th Annual Conference of Metallurgists (COM) Hosting the 10th International Copper Conference 2019*, pp 18–21.

Improving industrial copper processing operations through the application of thermodynamic fundamentals and advanced predictive tools

DOI: 10.62053/HQGK2707

G R F Alvear Flores[1,2]

1. President, Canadian Engineering Associates, Toronto, Canada.
   Email: gerardo.alvear@caeng.ca
2. Adjunct Professor, The University of Queensland, St Lucia Qld.
   Email: g.alvearflores@uq.edu.au

ABSTRACT

Mineral resources are becoming more complex in composition and structure making it more difficult to produce clean concentrates for primary metal smelting. In parallel, providing technological solutions to the recycling and recovery of end-of-life materials is becoming more important in moving towards the goal of increasing circularity. The availability of fundamental thermodynamic data and advanced thermodynamic tools greatly assists in evaluating these complexities and their impact on existing and new processes. In addition, it is fundamental to support the economic performance of smelters. This paper describes several examples on how fundamental work can be applied to industrial processing.

INTRODUCTION

Primary and secondary sources of base metals are gradually increasing complexity. This complexity is expressed in terms of lower grade materials and increase in concentration of minor metals and slagging elements. This pattern has clearly affected the non-ferrous metal production, increasing operating costs and investment required to ensure the sustainable production of metals.

Alvear Flores *et al* (2018) and Alvear Flores, Risopatron and Pease (2020) discussed some key elements associated with the increasing complexity for primary copper production. They pointed out that this behaviour was observed in the processing of primary and secondary materials, with increasing complexity and reduction in the concentration of base and precious metals in the sourced raw materials.

The processing of complex materials in non-ferrous smelting has traditionally been approached as a niche opportunity to capture the economic value contained in the mined resources (Alvear Flores, Risopatron and Pease, 2020). Mining companies, on one side, have sometimes adopted processing options, such as ultra-fine grinding, alternative flotation circuits, or hydrometallurgical processes to address the impact of the complexity on the value of their product. Smelters, on their side of the equation, have addressed complexity either by modifying their operational set points or when strictly necessary developing new processes.

In recent times, as sustainable solutions are more and more demanded, synergies and cooperation between base metal processing facilities have improved recovery and waste management. Good examples of these collaboration have been integrated processing, such as the efforts of Codelco and Ecometales to process complex dust from roasting and smelting, (Alvear Flores, 2018), the Albion dust leaching process at the Glencore Mount Isa Smelter (Alvear Flores, Hourn and Salas, 2013) and the Nutton process proposed by Rio Tinto (2023) among others.

Other examples of integrated operations across the globe, the Aurubis multi metal smelter network, the Kazzinc Pb-Zn-Cu integrated flow sheet and the Japanese non-ferrous smelting companies, have demonstrated how base metals integration can support more effective metal processing and recovery of valuable elements. Chinese non-ferrous processing companies have also developed integrated solutions following similar principles. The synergic, multi-metal process approach as shown in Figure 1, is required to ensure that maximum possible value is extracted from the natural resources. Examples of these flow sheets are discussed by (Schlesinger *et al*, 2021).

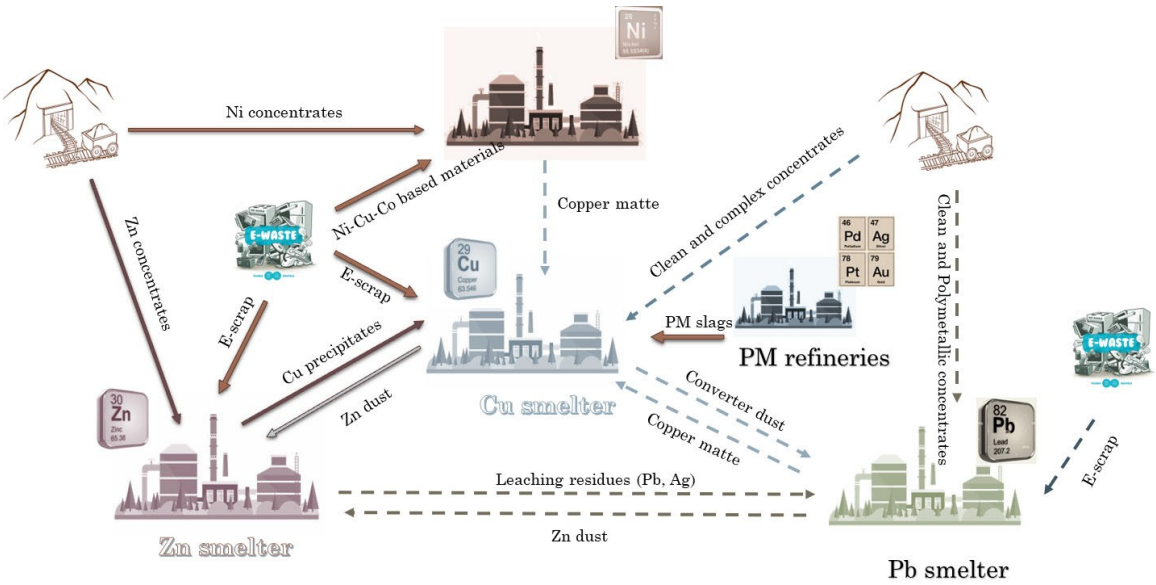

FIG 1 – Multi metal processing approach using base metals as collectors, modified from Alvear Flores, Risopatron and Pease (2020).

However, in most cases, the copper industry has used dilution as the main response, either by blending complex materials in central facilities or by diluting small quantities in large feed streams to smelters. This approach has gradually been challenged by the need to minimise waste, reduce the environmental footprint, and the need to develop different methods to valourise mining and metal projects.

This pattern places smelters in a constant questioning of their competitiveness and with the need of a regular evaluation of cost-effective measures to remain competitive. It is in here, where producers are facing the most critical question: 'How to differentiate from each other in a business that has been traditionally regarded as a commodity business with commodity-based technologies used for this purpose' (Alvear Flores, 2018).

Valid questions to ask are: 'How is fundamental knowledge evolving?', 'What research support is needed to be able generate the fundamental knowledge to enable industry to achieve this transformation?' and 'How can this fundamental knowledge be integrated with emerging approaches such as advanced analytics, and artificial intelligence to provide more effective integrated solutions?'

DEVELOPMENTS IN THE COPPER INDUSTRY

Figure 2 shows a timeline representing the copper smelting industry development for the last 50 years (Schlesinger *et al*, 2021). Over this period, the copper smelting processing has dramatically evolved. New bath smelting technologies have claimed their territory, and along with flash smelting, increased the processing intensity and proposed new slag chemistry targets.

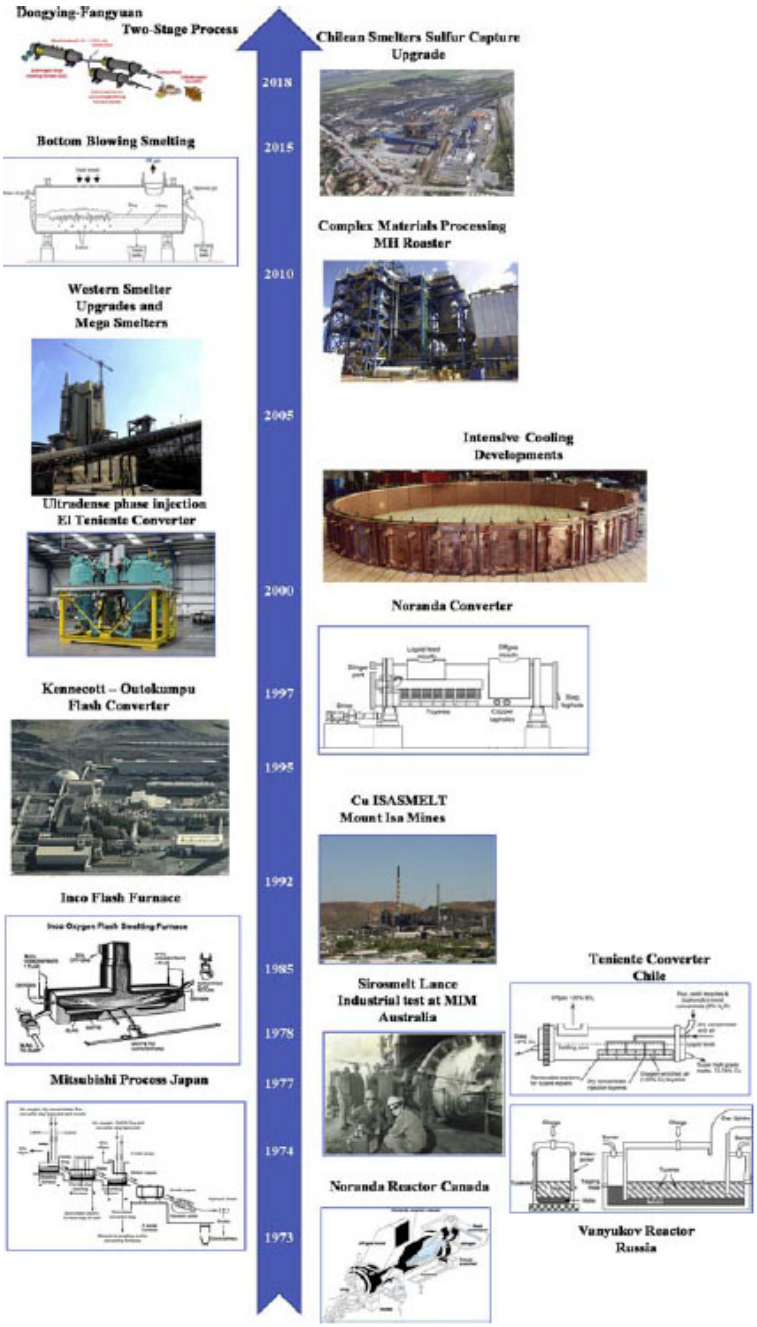

FIG 2 – Examples of some of the relevant technological developments in the copper smelting industry since 1973, Schlesinger *et al* (2021).

Copper technology developments have focused on increasing the process intensity by using tonnage industrial oxygen, this has translated into increasing processing capacities. An example of the processing intensity by means of the increasing of the copper concentrate smelting feed rates in a number of different technologies is shown in Figure 3. Modern smelting plants can achieve over 250 t/hr of fresh feed.

This path of increasing process intensity has been accompanied by a systematic improvement in the determination of the required thermodynamic properties. The development and consolidation of advanced thermodynamics database have allowed scientists to increase the accuracy of critical predominance and phase diagrams that play a relevant role in supporting the understanding of modern copper smelting. Some examples are shown in the next section of this paper.

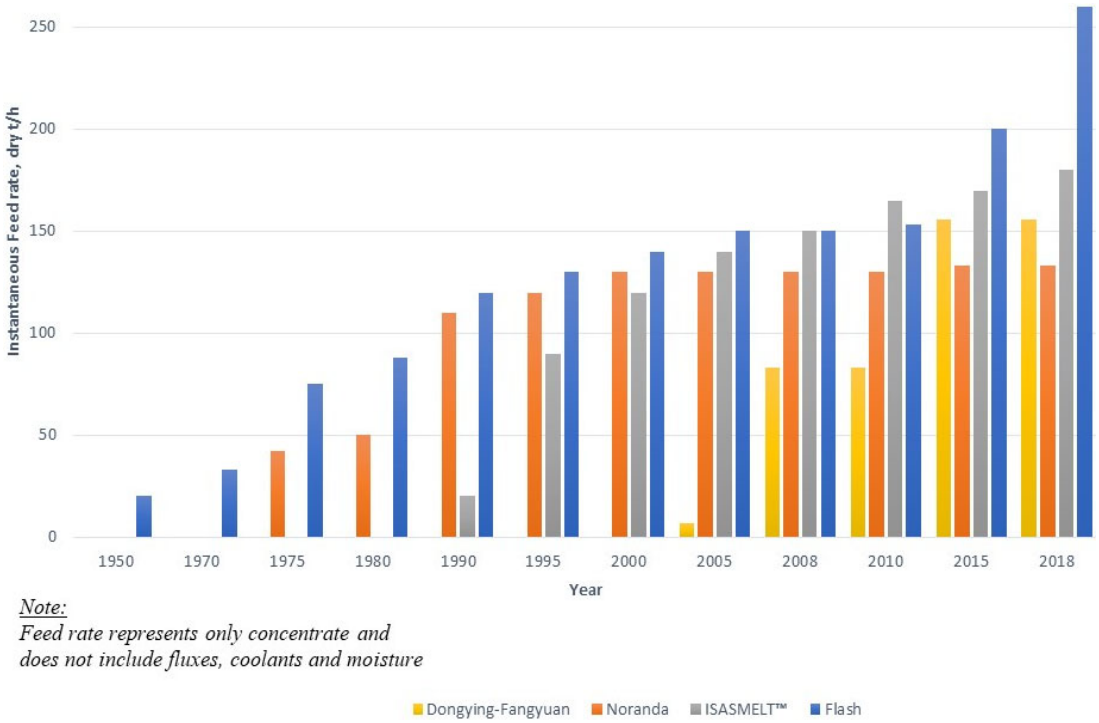

FIG 3 – Instantaneous concentrate feed rate evolution since 1950 in selected copper sulfide smelting technologies. Figure modified from Schlesinger *et al* (2021).

Example 1 – the Cu-S predominance diagram

A classic example of key fundamental knowledge is the Cu-S predominance diagram proposed by Professor Akira Yazawa. Despite the technical relevance of this diagram, still there are many metallurgists across smelters that they do not know how to use the contained information to better understand their processes. Figure 4 shows a newly recalculated Cu-S predominance diagram at 1300°C, prepared with support of Pyrosearch, University of Queensland, using the FactSage™ public database (Jak *et al*, 2016). The figure also shows the original boundary lines calculated by Yazawa (1979) and allows you to identify the main 'metallurgical road' for copper processing, A/B/C(C')/D/E and B/B', as follows:

- Copper smelting: Following the path A/B copper concentrates are gradually combusted (oxidised) to a given matte grade by controlled oxygen addition. Through this process, iron is oxidised, sulfur is combusted to SO_2, and slag is formed by adding silica as a flux.
- Slag/Matte separation: Following path B/B', matte and slag are, given appropriate process conditions, allowed settle and physically separate.

Batch converting

Slag blowing following path B/C: Copper matte is oxidised to finalise the controlled oxidation of iron.

Copper blowing following path C/D: After removal of slag generated in the previous step, the high-grade matte is converted to blister copper:

- *Continuous Converting* follows the path B (close to the 70 per cent Cu matte grade).
- *Direct to Blister*: Copper matte is directly converted to blister, avoiding an intermediate step.

For special concentrates, normally low in iron, it is possible to produce blister copper in a single step. This follows the path A/C'.

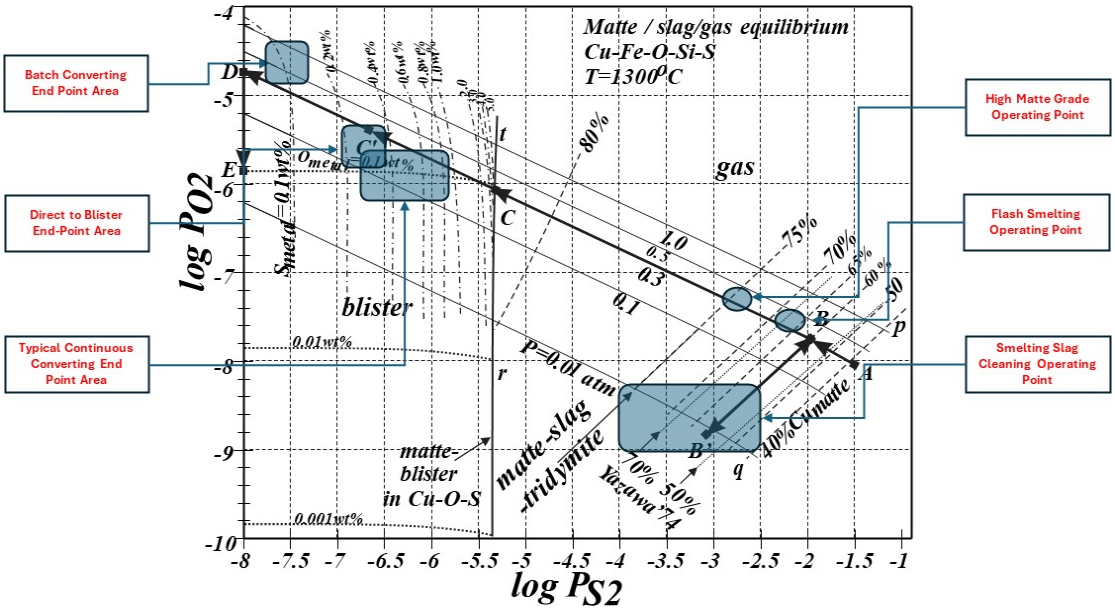

FIG 4 – Predominance diagram describing copper making process at 1300°C based on calculations using FactSage™ public database and original Yazawa diagram (Jak *et al*, 2016; Yazawa, 1979; Schlesinger *et al*, 2021).

Example 2 – the FeO-Fe_2O_3-SiO_2 phase diagram and copper smelting

The selection of an appropriate slag system is also important to maximise the capacity of slags for the required elements and minor oxides. The selection of the slag system is governed by the chemical and physical properties of the slags, such as liquidus temperature and viscosity. In primary copper smelting, the FeO-Fe_2O_3-SiO_2 phase diagram is the main system used to define the equilibrium conditions between copper matte and smelting slags.

The physical chemistry properties of slag in copper smelting were reviewed 40 years ago by Mackey (1982). In his review, Mackey commented: '*Despite many changes, the smelter man still relies largely on art and experience, especially with regard to slag control and in taking care of the slag*'. He also added: '*Copper smelting is still largely an art but is emerging into science of copper smelting and the understanding of processes develops on sound metallurgical engineering principles*'.

Mackey discussed chemical and physical properties of copper smelting and converting slags. Figure 5 shows a comparison of a section of the FeO-Fe_2O_3-SiO_2 phase diagram from his original publication and the re-calculated phase diagram using FactSage™ database (Mackey, 1982; Hidayat *et al*, 2017).

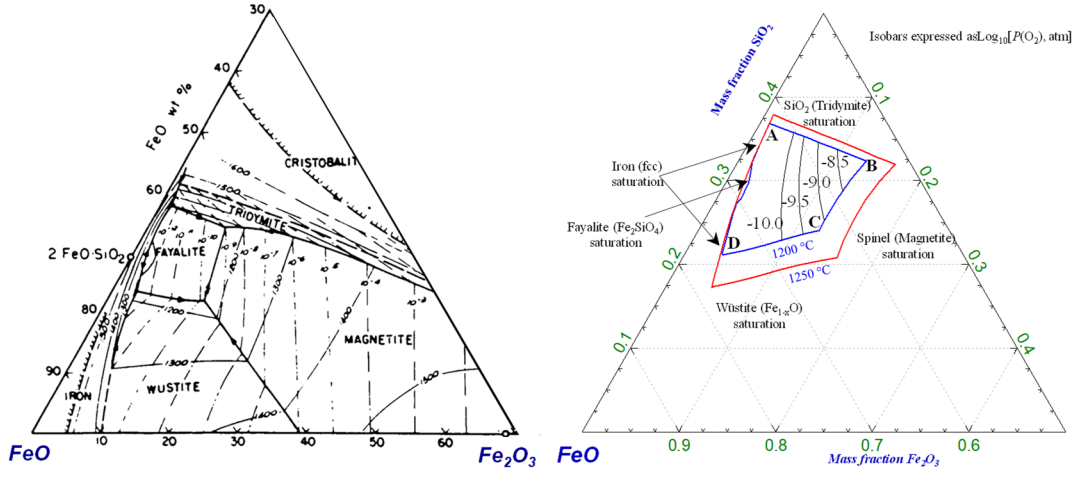

FIG 5 – Liquidus surfaces of the Fe-O-Si system describing copper smelting slags at 1300°C based on calculations using the FactSage™ public database and original Yazawa diagram (Mackey, 1982; Hidayat *et al*, 2017).

The slag system described by Figure 5 is a simplification of the real chemistry involved in the primary smelting. Moreover, as complexity is increasing, the participation of minor oxides becomes relevant not only to understand the real slag composition but also to determine, the required amount of fluxing, the heat load requirements of the process and the impact of these minor oxides into the overall chemical and physical properties of the system.

The work at Advanced Research Centres, such as Pyrosearch, developing a more accurate database evaluating impact of minor oxides in the system is enabling metallurgical engineers to design in a more precise fashion new metallurgical processes and estimate the impacts of complex feeds on well-established metallurgical processes.

Figure 6 shows the impact of minor oxides in the Fe/SiO_2 ratio as function of copper matte grade for the iron silicate slag system at 1200°C and pSO_2 = 0.25 atm (Shishin, Decterov and Jak, 2018). The figure shows the impact of minor oxides in the liquidus region for different Fe/SiO_2 ratios and highlights the importance of understanding these facts to properly estimate flux requirements for the process.

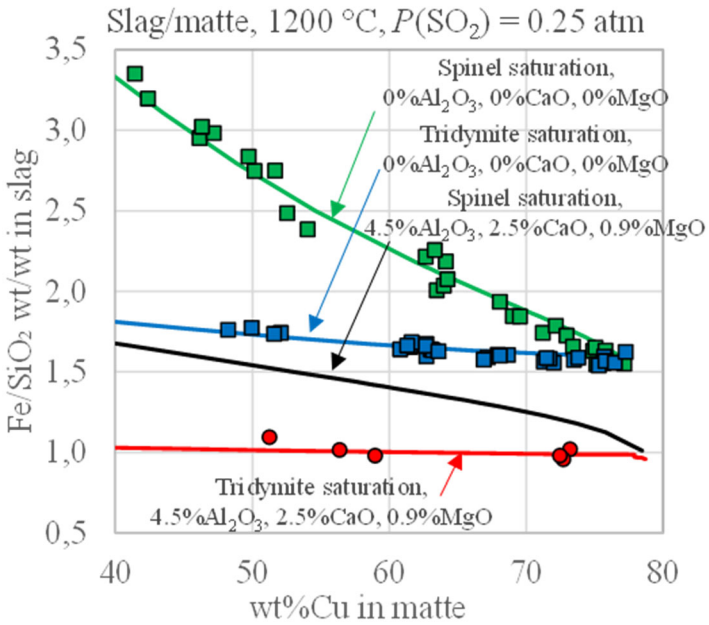

FIG 6 – Impact of minor oxides in the limiting Fe/SiO_2 ratios as function of copper matte grade for the iron silicate slag system at 1200°C and pSO_2 = 0.25 atm (Shishin, Decterov and Jak, 2018; Schlesinger *et al*, 2021).

An interesting example of the impact of minor oxides in primary and secondary copper smelting is the effect of alumina in the liquidus temperature, viscosity, and overall copper recovery of copper and other valuable elements.

In the primary copper, an increment in alumina has direct impact on the fluxing regime as additional silica is required to slag the alumina and the potential use of CaO requires revision. Alvear Flores and Nikolic (2013) reported the impact of alumina in the viscosity of fayalite slags. Figure 7 exemplifies the impact of minor oxides in the liquidus region for a 60 per cent copper matte grade and how lime impacts in the liquidus region. The viscosity calculations reported by Alvear Flores and Nikolic (2013) shows how viscosity is increased when alumina concentration increases and how the liquidus is affected at 8 per cent alumina in the slag at different oxygen partial pressures. Solids precipitation is avoided until over 5 wt per cent alumina in the slag.

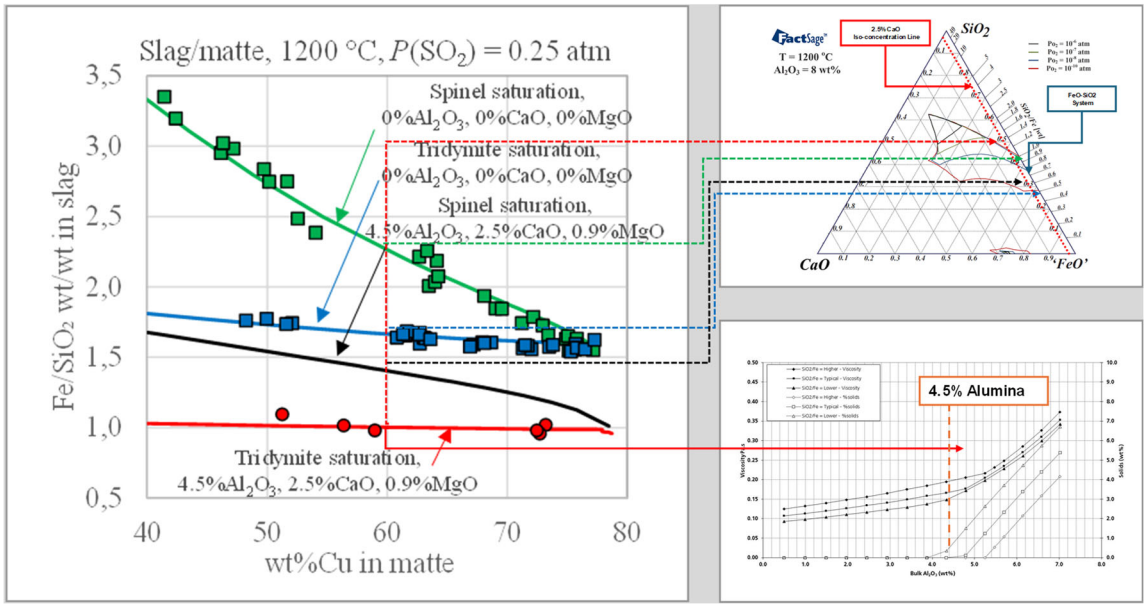

FIG 7 – Impact of minor oxides in the limiting Fe/SiO_2 ratios as function of copper matte grade for the iron silicate slag system at 1200°C and pSO_2 = 0.25 atm (Shishin, Decterov and Jak, 2018; Schlesinger *et al*, 2021) and viscosity of the slag for a given alumina and CaO concentration (Alvear Flores and Nikolic, 2013).

Defining a proper slag composition has direct impact on the overall economics of the smelting business. Fluxing must be maintained to the minimum requirements to maximise the copper recovery and the potential slag valourisation required for the slag as a subproduct of the smelting process. In this aspect, some smelters have decided to use slag flotation as the main process to recover the slag while others use the traditional slag cleaning by means of settling and reduction of magnetite in electric furnaces. Klaffenbach *et al* (2023) has undertaken extensive work on evaluating slag as product of economic use for other applications, such as the cement industry. Regardless of the used method, minimising copper content in the slag and amount of fluxing required will have a direct impact on the profitability of the business. This can be easily demonstrated using Value-in-use modelling to estimate the impact of copper losses on the overall profit margin of the smelting business.

As this author was preparing this manuscript, sadly the passing of Professor Bill Davenport was announced. Coincidentally, Mackey and Alvear Flores (2014) presented a review on the advances in copper smelting at the Davenport Symposium. In that work, gaps in fundamental knowledge were recognised and in the last ten years since then, Pyrosearch with the support of key industrial partners, has been assessing these gaps and generating the required fundamental work. A number of major industrial companies, such as Aurubis, Umicore, Boliden and other consortium members have also supported and worked in this field. Table 1 shows some of the gaps identified in 2014 and some advances since then.

TABLE 1

Gaps in fundamental knowledge in copper smelting identified in 2014 and some advances since.

Process/area	Gaps in fundamental knowledge in 2014	Some knowledge developed since 2014
Primary copper smelting	• Correction and refinement in minor element activity coefficients in matte phase. • Minor element partial pressure under smelting conditions.	• Review and thermodynamics analysis in copper smelting liquid mattes, metals, slags, speiss and solids phases (Shishin, Prostakova and Jak, 2022; Sineva *et al*, 2021). • Phase equilibria and minor element distributions in copper/slags/matte systems, (Sineva *et al,* 2020). • Thermodynamic consideration of copper matte smelting conditions with respect to minor element removal and slag valourisation (Klaffenbach *et al,* 2023). • Modelling of liquid phases and metal distributions in copper converters: transferring process fundamentals to plant practice (Jak *et al*, 2019)
Copper converting	• High matte grade batch converting process control and link with physico-chemical data.	• Equilibria of iron silicate slags for continuous converting copper-making process based on phase transformations (Sun *et al,* 2020).
Slag cleaning	• Electric furnace modelling. • Minor element distribution improvements.	• Comprehensive review on metallurgical recycling and cleaning of copper slag (Tian *et al,* 2021). • Copper smelting slag cleaning in an electric furnace by using waste cooking oil (Wei *et al,* 2020). • Sustainable and comprehensive utilisation of copper slag: a review and critical analysis (Klaffenbach *et al,* 2023).
Secondary copper smelting	• Minor element modelling at reducing conditions.	• Experimental study and thermodynamic modelling of modelling equilibrium distribution of Ni, Sn, and Zn between slag and black copper for e-scrap recycling applications (Sineva *et al,* 2023).
Anode refining	• Continuous anode refining.	• Dongying Fangyuan application for continuous converting and refining.
Polymetallic systems	• Further development in the Cu_2S-FeS-PbS-Cu-Fe-Pb system.	• Fundamental analysis of improved multi metal recovery by combining copper and lead metallurgy (Zschiesche, Alvear Flores and Ayhan, 2019).
General	• Incorporation of fundamental data in software packages for modelling.	• Effort done at Pyrosearch by updating FactSage™ with fundamental thermodynamic data generated in the Copper Consortium.

Example 3 – minor element distribution and recovery

Copper resources processed in the primary and secondary smelting processes are accompanied of minor oxides and minor elements. Minor oxides, such as alumina, magnesia or lime can be removed with appropriate fluxing as shown in the previous discussed example. In the case of minor elements, they will distribute in between the phases, with partitions define by the distribution equilibria between the molten phases and the volatilisation degree of these minor elements.

The topic minor elements distribution has been given a great degree of importance by Japanese researchers and thermodynamic models such as the Degree of Volatilisation, *S*, has been proposed by Professor Kimio Itagaki and A Yazawa (1982). CSIRO also did review thermodynamic properties of minor elements and incorporated them into their modelling tools (Chen, Zhang and Jahanshahi, 2010).

There have been a lot of discussions about the role of technology selection on the maximisation of the removal of impurities from copper sources. It is the opinion of the author that the maximisation of the removal of impurities is associated with the oxidation/reduction ability of the element to be removed, the reactor characteristics (plug reactor or equilibrium reactor) and the selection of appropriate slag systems.

A method to quantify the potential of removing a minor element in the secondary copper is the refining ability. Since almost all the impurities contained in the copper scrap have a high oxygen affinity, oxidation refining is normally used as an appropriate alternative method for the copper scrap refining after a first reductive smelting step.

Fujisawa *et al* (1997) proposed the Oxidising Refining Ability Index, as a parameter to preliminary qualify and quantify the potential for minor elements removal in copper scrap refining. The oxidation of a minor element was defined by Equation 1.

$$\mathrm{X}(\text{in metal}) + (\nu/4)\mathrm{O}_2 = \mathrm{XO}_{\nu/2}(\text{in slag}) \tag{1}$$

$$A_{\mathrm{X}} = K_{(1)} \cdot \gamma_{\mathrm{X}} \cdot p_{\mathrm{O}_2}^{\nu/4} \tag{2}$$

The refining ability of a minor element x, A_x, is defined by the expression of Equation 2, were $K_{(1)}$ is the equilibrium constant of Reaction (1), γ_i is the Raoultian activity coefficient of component i, in liquid copper and p_{O_2} is the standardised oxygen partial pressure at the slag-metal interface. The index was estimated based on the following approximations:

- $[n_T]$ defined as the molar amount of 100 g metal can be approximated to pure copper
- (n_T) defined as the molar amount of 100 g slag does not change so much among the slag systems under study
- p_{O_2} can be approximated to the equilibrium value for the Cu_2O/Cu system, since the main component of the slag is Cu_2O
- γ_{X} can be approximated to that at infinite dilution, $\gamma_{\mathrm{X}}^{\circ}$, when the impurity content in copper is low.
- Figure 8 shows the estimated refining ability index for several minor elements potentially contained in copper secondary sources at 1573 K at Cu/Cu_2O equilibrium. The index decreases in the following order: Al, Si, Cr, Fe, Zn, Sn, Co, Ni, Pb, Sb, Bi and As. Fujisawa *et al* (1997) stated that most of the above-mentioned elements can form stable complex oxides with Cu_2O-SiO_2, Cu_2O-B_2O_3 and Cu_2O-Fe_2O_3 slags. Following these estimations, several experimental distribution experiments were conducted to estimate the distribution ratio, L, between copper and slags. It should be mentioned that at the time of this research (In which the author of this paper was part of) tools like FactSage™ were not very well developed and a lack of fundamental data under these conditions was observed.

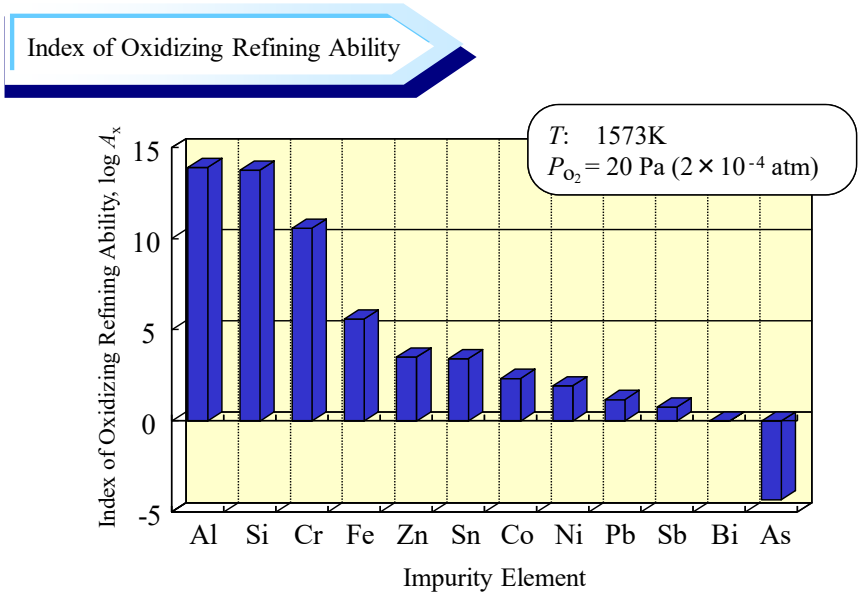

FIG 8 – Index of Oxidising Refining Ability (Fujisawa *et al,* 1997).

The early work conducted at Nagoya University as part of the Research Centre for Advanced Waste and Emission Management, was summarised and reported as part of the Super Smelter Project, an effort between Japanese universities and Japanese copper processing companies to evolve in the processing of copper secondary sources. Figure 9 shows the results reported by Fujisawa *et al* (1997) for different copper-based slag systems.

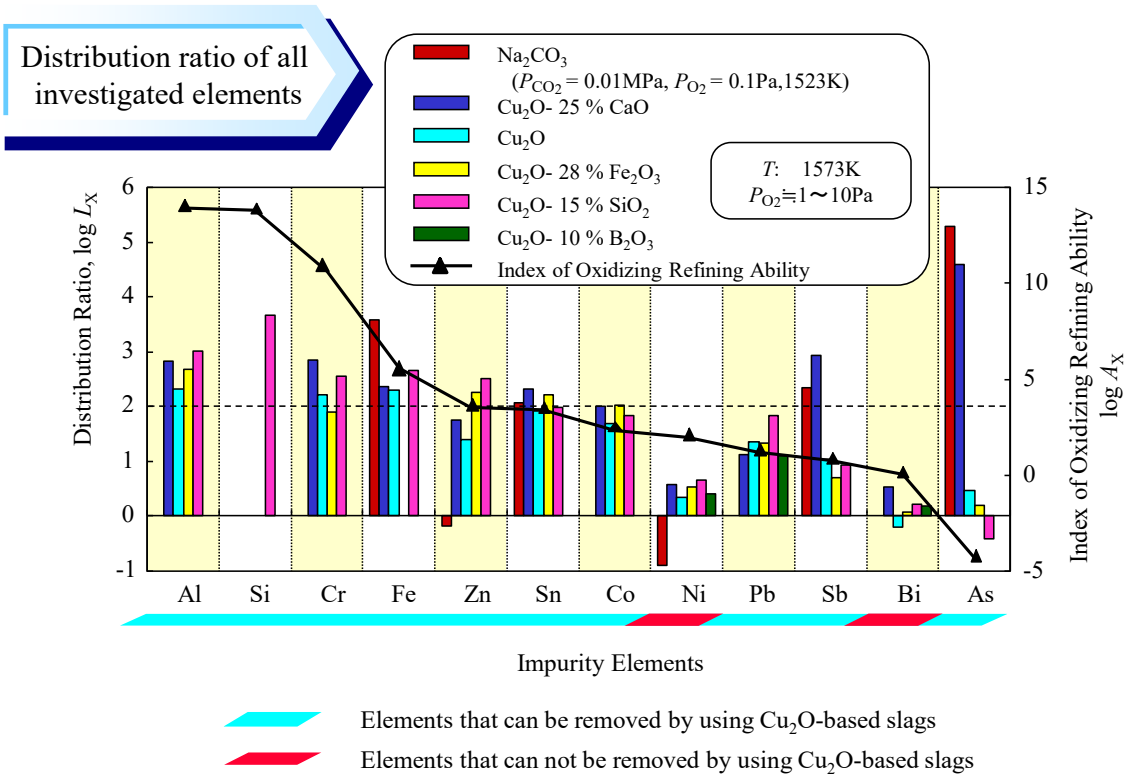

FIG 9 – Index of Oxidising Refining Ability (Fujisawa *et al,* 1997) for different copper-based slag systems.

The results indicated that:

- Al, Si and Cr present can be eliminated even without slag addition and by simply blowing oxygen or air into the scrap melt.

- Fe, Zn, Sn, Co and Pb can be efficiently removed by using Cu_2O-SiO_2 slags.
- Co, Sb and As, Cu_2O-CaO slag can be efficiently used for their elimination.
- Ni and Bi, the results indicate that their elimination cannot be expected by using Cu_2O-based slags.

A particular impurity of great concern for the primary concentrate process has been arsenic. Arsenic is present in most of copper concentrates exported by Chilean and Peruvian miners and in some cases, the concentration can exceed the import limits defined by local authorities (ie China has a maximum concentration of 5000 ppm in concentrates). The impact on As in the copper anode was reported by Moats *et al* (2016) in his surveys of copper refineries, in which he reported over 80 per cent increase in As concentration in anodes compared with levels in 2003.

Pyrosearch reported the As distribution between copper matte and slags between 60 and 75 per cent matte grade, showing good agreement with selected plant data. Their main conclusions indicated that the thermodynamic model demonstrate the decreasing order As > Pb > Bi for the distribution coefficient. Thermodynamic predictions indicate the decreasing order Zn > Sb > Sn > As > Pb > Bi > Ni > Ag > Au for the slag/matte distribution coefficient in the matte grade range up to 70 wt per cent Cu (Sineva *et al*, 2020).

In the refining of copper, Alvear Flores and Bafghi (1998) reported the impact of oxygen concentration on the simultaneous elimination of As and Sb from molten copper using sodium carbonate slags. A mechanism for the simultaneous elimination of As and Sb was observed, depending on the relative compositions of these elements and oxygen in the melt. For instance, under similar concentrations of impurities and oxygen, as shown in Figure 10, the removal of arsenic will occur until the arsenic concentration is low enough to enable free oxygen to react with antimony.

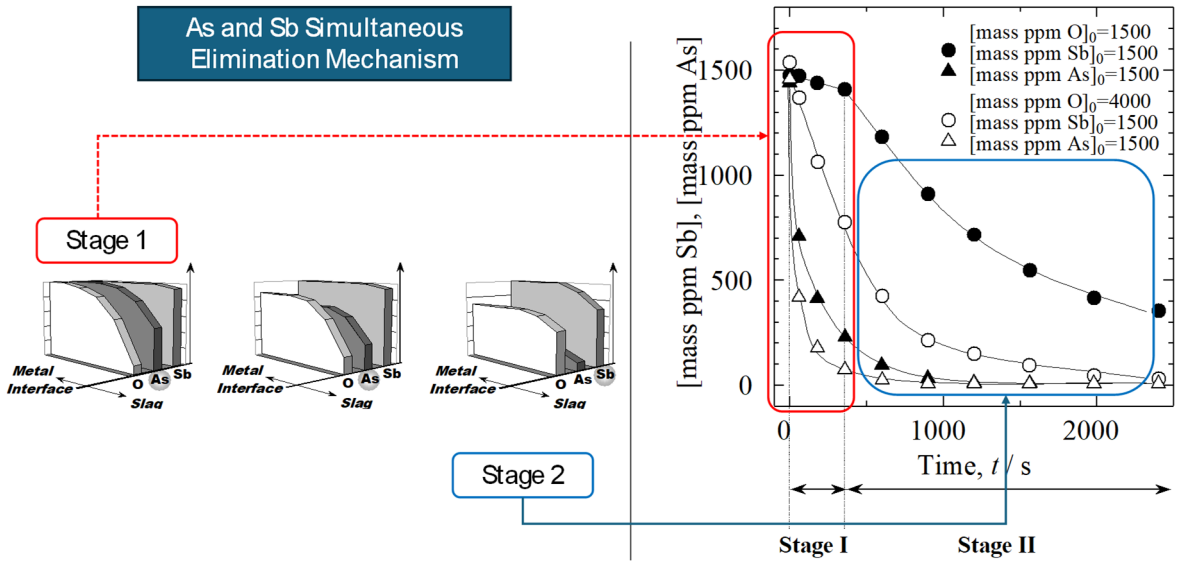

FIG 10 – Simultaneous Elimination Mechanism of As and Sb Mechanism from Molten Copper using Sodium Carbonate Slags at 1523 K, Alvear Flores and Bafghi (1998).

All the fundamental work undertaken to determine distribution ratios of minor elements, activity coefficients and physical properties need to be added to simulation tools to allow process engineers to estimate process indicators and anode impurity capacities in more robust fashion. Moreover, following these process fundamental estimations, these calculations are vital to estimate financial performance of the process and estimate the anode impurity capacities of each plant. These advanced predictive capacities will allow to determine the financial performance of each plant depending on the material portfolio they will be processing.

CONCLUSIONS

The copper industry has evolved in the last 50 years, significantly increasing process intensity. As processes have been developed, and resources are becoming more complex, highly advanced

thermodynamic tools are required to support scientist and process designers in the task of developing process operating windows.

Minor oxide and minor elements play an important in the chemical and physical properties of slags as well as in the final composition of copper produced in the pyrometallurgical processing of primary and secondary sources.

Despite this fact, there are some classical diagrams, such as the Cu-S stability diagram Yazawa Diagram and the FeO-Fe_2O_3-SiO_2 ternary diagram that still relevant to support the process development in copper smelting.

The knowledge developed at Pyrosearch to support the copper smelting industrial has been vital to the success of these companies in the copper business.

Integration of fundamental findings firstly to process modelling tool platforms is fundamental to allow process engineers and business analysts to balance material portfolios for different plants, assess potential processing of complex materials and evaluate synergies between plants to improve multi-metal recovery and extraction of valuable metals from primary and secondary resources.

There is still work to be done from the fundamental perspective, with the verification of physical properties, such as viscosities and partial pressures of minor elements under different conditions. In addition, properties of secondary products, such as dusts, and the recycling to primary and secondary vessels requires a deeper understanding of their respective mechanisms.

A more complete understanding of these properties will allow companies to better assess processing of complex materials at optimum processing cost, and maximum utilisation of their resources, with particular focus on the optimisation of multi-metal operations.

ACKNOWLEDGEMENTS

The author acknowledges the financial support from the Ministry of Education, Culture, Sports, Science and Technology Scholarship, that supported his initial immersion into the non-ferrous research and development and, in particular, to Professors Chikabumi Yamauchi and Toshiharu Fujisawa at Nagoya University from 1990 until 1999. This was the milestone that re-routed his academic and industrial life to the non-ferrous industry. The Ministry of Education, Culture, Sports, Science and Technology Scholarship, formerly known as Monbusho Scholarship that supports foreign students, is an academic scholarship offered by the Japanese Ministry of Education, Culture, Sports, Science and Technology (Monbu-kagaku-shō, or MEXT), and is selected on the recommendation of the Japanese.

The author also thanks researchers at the University of Queensland for the last 20 years of technical exchange and opportunities to discuss initiatives to increase the knowledge base of the copper industry.

REFERENCES

Alvear Flores, G R F and Bafghi, M S, 1998. Simultaneous removal of impurities from molten copper using sodium carbonate slag, *Resources and Materials*, (4):101–104.

Alvear Flores, G R F and Nikolic, S, 2013. ISASMELT™ for Recycling of Valuable Elements Contributing to a More Sustainable Society, in *REWAS 2013* (Springer). https://doi.org/10.1007/978-3-319-48763-2_11

Alvear Flores, G R F, 2018. Arsenic management for the Copper Smelting Industry, International Seminar on Impurities in Copper Raw Material, JOGMEC, Tokyo, Japan.

Alvear Flores, G R F, Löbbus, M, Springub, B, Fallah-Mehrjardi, A and Tappe, A, 2018. Sulfide Smelting: Thirty-Five Years of Continuous Efforts to Find New Value Adding Solutions, in *Extraction 2018 Proceedings of the First Global Conference on Extractive Metallurgy*, pp 39–56.

Alvear Flores, G R F, Hourn, M and Salas, J C, 2013. Xstrata Technology's Approach for the Processing of Copper Bearing Materials, *Copper 2013*, IIMCH, Santiago, 3:389–400.

Alvear Flores, G R F, Risopatron, C and Pease, J, 2020. Processing of Complex Materials in the Copper Industry: Challenges and Opportunities Ahead, *JOM*, 72:3447–3461. https://doi.org/10.1007/s11837-020-04255-9

Chen, C, Zhang, L and Jahanshahi, S, 2010. Thermodynamic Modeling of Arsenic in Copper Smelting Processes, *Metall Mater Trans B*, 41:1175–1185. https://doi.org/10.1007/s11663-010-9431-z

Fujisawa, T, Alvear Flores, G R F, Shinpo, Y and Yamauchi, C, 1997. Thermodynamic of Cu_2O-based Slag Treatment for Recycling of Copper, Tokyo Symposium, The University of Tokyo.

Hidayat, T, Shishin, D, Decterov, S A and Jak, E, 2017. Experimental Study and Thermodynamic Re-evaluation of the FeO-Fe_2O_3-SiO_2 System, *J Phase Equilib Diffus,* 38(4)477–492. https://doi.org/10.1007/s11669-017-0535-x

Itagaki, K and Yazawa, A, 1982. Thermodynamic Evaluation of Distribution Behaviour of Arsenic in Copper Smelting, *Transactions of the Japan Institute of Metals*, 23(12):759–767.

Jak, E, Hidayat, T, Shishin, D, Fallah Mehrjardi, A, Chen, J, Decterov, S and Hayes, P, 2016. Integrated experimental and thermodynamic modelling research methodology for metallurgical slags with examples in the copper production field, in *Advances in Molten Slags, Fluxes and Salts (MOLTEN16)* (ed: R G Reddy, P Chaubal, C Pistorius and U Pal), TMS, pp 947–959.

Jak, E, Hidayat, T, Shishin, D, Mackey, P J and Hayes, P C, 2019. Modelling of liquid phases and metal distributions in copper converters: transferring process fundamentals to plant practice, *Mineral Processing and Extractive Metallurgy*, 128(1,2):74–107. https://doi.org/10.1080/25726641.2018.1506273

Klaffenbach, E, Montenegro, V, Guo, M and Blanpain, B, 2023. Sustainable and Comprehensive Utilization of Copper Slag: A Review and Critical Analysis, *J Sustain Metall,* 9:468–496. https://doi.org/10.1007/s40831-023-00683-4

Mackey, P J, 1982. The Physical Chemistry of Copper Smelting Slags – A Review, *Canadian Metallurgical Quarterly*, 21(3):221–260.

Moats, M, Wang, S, Filzwieser, A, Siegmund, A, Davenport, W and Robinson, T, 2016. Survey of copper electrorefining operations, in *Proceedings of the 9th International Copper Conference, Copper 2016* (eds: H Nakano and K Muriase), paper IV-1, Japan.

Mackey, P J and Alvear Flores, G R F, 2014. Developments In Copper Smelting: A Discussion of Changes in Copper Technology and Science as Seen through the Lens of Professor Davenport's TEXTS, Canadian Institute of Mining, Metallurgy and Petroleum.

Rio Tinto, 2023. Nuton: A better way to produce copper, Rio Tinto, Available from: <https://www.riotinto.com/en/news/stories/nuton-a-better-way-to-produce-copper> [Accessed: 1 April 2024].

Schlesinger, M, Sole, K C, Davenport, W G and Alvear Flores, G R F, 2021. *Extractive Metallurgy of Copper*, sixth edition, ch 22.

Shishin, D, Decterov, S A and Jak, E, 2018. Thermodynamic assessment of slag-matte-metal equilibria in the Cu–Fe–O–S–Si system, *J Phase Equilib Diff*, 39(5):456–475.

Shishin, D, Prostakova, V and Jak, E, 2022. Review and thermodynamic analysis of As (arsenic) in copper smelting liquid mattes, metals, slags, speiss and solid phases, in *The Igor Wilkomirsky Symposium on Pyrometallurgy, Copper 2022*, Instituto de Ingenieros de Minas de Chile (IIMCh), pp 506–521.

Sineva, S, Shevchenko, M, Shishin, D, Hidayat, T, Chen, J, Hayes, P C and Jak, E, 2020. Phase Equilibria and Minor Element Distributions in Complex Copper/Slag/Matte Systems, *JOM*, 72:3401–3409. https://doi.org/10.1007/s11837-020-04326-x

Sineva, S, Shishin, D, Prostakova, V, Lindgren, M, Starykh, R, Chen, J and Jak, E, 2023. Experimental Study and Thermodynamic Modelling of Equilibrium Distributions of Ni, Sn and Zn Between Slag and Black Copper for E-Scrap Recycling Applications, *JOM*, 75(10):2023. https://doi.org/10.1007/s11837-023-06059-z

Sineva, S, Shishin, D, Prostakova, V, Lindgren, M, Starykh, R, Hayes, P C and Jak, E, 2021. Equilibrium Distributions of Pb, Bi and Ag between Fayalite Slag and Copper-Rich Metal, Calcium Ferrite Slag and Copper-Rich Metal, Thermodynamic Assessment and Experimental Study at 1250°C, *Journal of Sustainable Metallurgy*, 7:569–582, https://doi.org/10.1007/s40831-021-00360-4

Sun, Y, Chen, M, Cui, Z, Contreras, L and Zhao, B, 2020. Equilibria of Iron Silicate Slags for Continuous Converting Copper-Making Process Based on Phase Transformations, *Metall Mater Trans B*, 51:2039–2045. https://doi.org/10.1007/s11663-020-01901-0

Tian, H, Guo, Z, Pan, J, Zhu, D, Yang, C, Xue, Y, Li, S and Wang, D, 2021. Comprehensive review on metallurgical recycling and cleaning of copper slag, Resources, *Conservation and Recycling*, vol 168. https://doi.org/10.1016/j.resconrec.2020.105366

Wei, Y, Zhang, T, Li, B and Zhou, S, 2020. Copper Smelting Slag Cleaning in an Electric Furnace by Using Waste Cooking Oil, *Metall Mater Trans B*, 51:2756–2768. https://doi.org/10.1007/s11663-020-01986-7

Yazawa, A, 1979. Thermodynamic Evaluations of Extractive Metallurgical Processes, *Metall Mater Trans B*, 10:307–321.

Zschiesche, C, Alvear Flores, G R F and Ayhan, M, 2019. Fundamental Analysis for an Improved Multi Metal Recovery by Combining Copper and Lead Metallurgy, in *Proceedings of the 58th Annual Conference of Metallurgists (COM) 10th International Copper Conference 2019,* paper 594899.

Visualisation of calculated thermodynamic properties by integration of FactSage™ with SEM-EDS element maps

DOI: 10.62053/RQQG4392

N Barrett[1], S Mitra[2], E Copland[3], D O'Dea[4] and T Honeyands[5]

1. Research Associate, Centre for Ironmaking Materials Research, Newcastle NSW 2307. Email: nathan.barrett@newcastle.edu.au
2. Research Associate, Centre for Ironmaking Materials Research, Newcastle NSW 2307. Email: subhasish.mitra@newcastle.edu.au
3. Research Associate, Centre for Ironmaking Materials Research, Newcastle NSW 2307. Email: evan.copland@newcastle.edu.au
4. Principal Sustainability Marketing, BHP, Brisbane Qld 4000. Email: damien.p.odea@bhp.com
5. Co-Director, Centre for Ironmaking Materials Research, Newcastle NSW 2307. Email: tom.a.honeyands@newcastle.edu.au

ABSTRACT

This work describes a novel mapping technique that allows the direct overlay of calculated local phase equilibria on micrographs of the physical system. The technique demonstrated integrates FactSage™, ver 8.2 (by Thermfact Ltd. and GTT-Technologies) phase equilibria calculations with mapped compositions determined by Scanning Electron Microscope – Energy Dispersive X-ray Spectroscopy (SEM-EDS) to visually express calculated properties while preserving the spatial information of the sample. The developed methodology is used to analyse interrupted blast furnace softening and melting tests containing mixed burdens of lump and sinter. Tests are interrupted at 1300°C and cooled to room temperature for analysis. Phases present at room temperature are analysed to infer the liquid fraction and phases present at high temperature. Analysis of the interface regions between the dissimilar burdens allows insights to be gained into the interaction mechanism. During the transition from solid to liquid, migration and interaction of liquid oxide across the interfaces of the dissimilar burdens has been observed and demonstrated to impact softening and melting performance. Specifically, interaction of the oxides generated by lump (primarily FeO, SiO_2 and Al_2O_3) and sinter (primarily FeO, CaO, SiO_2, Al_2O_3 and MgO) are analysed, and the occurrence of a range of new mineral phases such as merwinite, melilite, olivine and bredigite observed.

INTRODUCTION

The ironmaking blast furnace currently provides ~72 per cent of the hot metal for steelmaking globally, the total production of which exceeded 1.8 billion tonnes (Bt) in 2023 (World Steel Association, 2023). While many blast furnaces operate with predominantly sinter (iron ore fines agglomerated with fluxes), supplementation with lump ore (natural iron ore of an appropriate size for direct charging) is beneficial, as it avoids emissions associated sinter production (Liu *et al*, 2018, 2019b). The natural gangue in lump ores is primarily SiO_2 and Al_2O_3, while sinter contains added CaO and MgO flux. As such, with the differing chemical composition of the two burdens, chemical interactions occur at high temperatures during softening and melting. These interactions have been demonstrated to be beneficial to cohesive zone performance, improving the permeability of ferrous burden to rising gas (Hoque *et al*, 2021; Liu *et al*, 2019b; Lu *et al*, 2020; Wu *et al*, 2018).

During its descent in the furnace stack, ferrous burden is reduced (oxygen is removed), resulting in the formation of metallic iron. From this, the microstructure at the onset of melting is an interconnected metallic iron network partitioned from oxide gangue (Kim *et al*, 2021; Vemdrame Flores *et al*, 2021). With the variation in composition at the interface between dissimilar burdens, liquid formation and interaction (>1200°C) depends on the local composition. As such, it is appropriate that methods of analysis consider the local interfacial compositions, rather than bulk composition.

Thermodynamics is used to describe the chemical processes that occur in extractive metallurgical operations. Of particular importance in the extraction and refining of metals is the properties of the formed slag – which acts to partition impurities from product metal. These slags are typically multicomponent metal oxides. Bulk compositions of slags produced by sinter and lump ore can be

plotted on ternary phase diagrams, allowing various thermodynamic variables to be analysed, such as liquidus temperature, stable phase fields, etc. Where more than three components are present (as is the case with most operations), pseudo-ternary diagrams are used, for which additional component compositions are fixed. These diagrams show 'slices' through the higher dimensional phase fields and as such their interpretation can be more difficult. This is especially the case in heterogenous systems, in which the range of compositions present may not be directly expressible in a single diagram.

While elemental mapping techniques (such as Scanning Electron Microscope – Energy Dispersive X-ray Spectroscopy (SEM-EDS) (Hoque *et al*, 2021; Liu *et al*, 2019a; Lu *et al*, 2020; Lyu *et al*, 2023a, 2023b; Ma *et al*, 2022; Wu *et al*, 2010) and EPMA (Electron Probe microanalysis) (Liu *et al*, 2018, 2019b)) have been used historically, thermodynamic analysis has only been performed for compositions determined by bulk chemical analysis (of initial material (Hoque *et al*, 2021; Liu *et al*, 2019a, 2018) or collected slags (Liu *et al*, 2014; Wang *et al*, 2022; Wu *et al*, 2018, 2020)) or point analysis (Lyu *et al*, 2023a; Wang *et al*, 2022). From these techniques, the interaction between lump and sinter has been generally described. The interaction is thought to be initiated by low temperature fayalitic (FeO/SiO_2) melts originating from the lump (Liu *et al*, 2019b; Wang *et al*, 2022; Wu *et al*, 2020). On contact with CaO and MgO rich sinter phases, these liquids re-solidify as new phases such as olivine ($CaFeSiO_4$), merwinite ($Ca_3MgSi_2O_8$) and melilite (mainly akerminite ($Ca_2MgSi_2O_7$) and gehlenite($Ca_2Al_2SiO_7$)) (Liu *et al*, 2019b, 2014).

In this study, a new approach to thermodynamic analysis of real systems is demonstrated through the investigation of an interface between dissimilar ferrous burdens during softening and melting (Barrett *et al*, 2024). The developed technique integrates element maps (acquired by SEM-EDS) with thermodynamic calculations (performed with FactSage™) to directly overlay the calculated phase equilibrium onto the imaged microstructure. The resulting images preserve the spatial composition information, allowing intuitive analysis of phase distribution in a multi-component heterogenous system. The developed technique has potential applications in the pyrometallurgy field far beyond the presented example.

METHODOLOGY

Softening and melting test

The Softening and Melting (S&M) test is designed to characterise ferrous burden behaviour in the blast furnace. During the tests, ferrous material is exposed to a temperature profile and reducing gas while under load. As the temperature increases, the material contracts (softens), restricting gas flow, before melting and dropping from the crucible. The bulk performance of the material is characterised through derived indices related to its temperature dependant contraction and pressure drop.

In this study, two ferrous burdens were used, designed around a mixed burden of 20 per cent lump and 80 per cent sinter previously studied (Barrett *et al*, 2023; Hoque *et al*, 2021; Liu *et al*, 2019b). The lump ore used was Newman Blend Lump, an Australian high-grade hematite-goethite (henceforth referred to as NBLL). The sinter was a high basicity plant sinter (henceforth referred to as SH1). The composition of the burdens are given in Table 1.

TABLE 1

Chemcial composition of burdens used in this study.

Burden	TFe (wt%)	FeO (wt%)	CaO (wt%)	SiO_2 (wt%)	Al_2O_3 (wt%)	MgO (wt%)
NBLL	62.8	-	0.05	3.70	1.4	0.1
SH1	56.7	7.6	10.04	5.43	1.87	1.76

The sample analysed in this study was subject to a standard S&M test, before being interrupted at 1300°C. Details of the experimental apparatus and conditions can be found elsewhere (Barrett *et al*, 2023; Hoque *et al*, 2021). After reaching 1300°C, the furnace was cooled under 14 L/min nitrogen, reaching 1100°C within approximately 30 minutes.

Thermodynamic analysis

In this study, a novel technique for analysis in heterogenous systems was developed, in which calculated phase equilibrium at specific local conditions was directly overlayed on the imaged microstructure. The developed technique is akin to repeated point analysis, for which an equilibrium calculation is performed for every point. An overview of the procedure is described in more detail.

Selection of interface

Samples from mixed burden S&M tests (reduced under a 70 per cent $N_{2,(g)}$ + 30 per cent $CO_{(g)}$ atmosphere) interrupted at 1300°C were used, the same as in a previous study (Barrett *et al*, 2023). The heating profile consisted of 10°C/min up to 600°C, followed by a 3.6°C/min up to 950°C, 1.9°C up to 1230°C and 4.7°C up to 1300°C. The resulting reduction degree was approximately 90 per cent (as approximated for the overall burden). The selected interruption temperature was above the temperature of the first formation of liquid slag (~1200°C), but below the temperature where significant movement and dynamic mixing of the bulk liquid is expected (~1450°C).

Following the interruption of the test, the crucibles were set in resin, sectioned longitudinally and polished for microscopic analysis. Figure 1 (left) shows the light optical microscopy image of the entire crucible of material. From the lump particles present, an interface contacting sinter was chosen for detailed analysis. A magnified view of the selected region is shown in Figure 1 (right), with the scanned area outlined in red. The phases present on cooling from 1300°C could then be analysed to infer conditions present at high temperature. It was assumed that no changes to the microstructure occur during cooling.

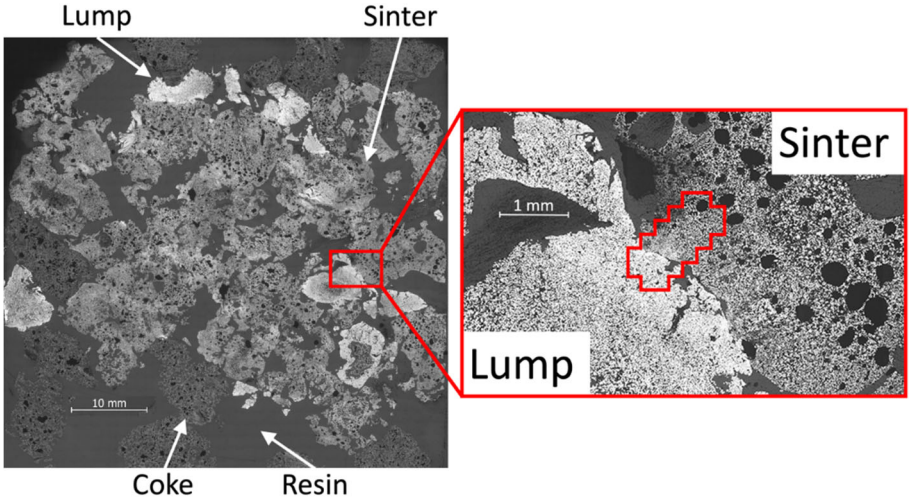

FIG 1 – Light optical microscopy images of sectioned crucible (left) and enlarged interface between lump and sinter (right). Scanned area for detailed analysis is outlined in red.

Data acquisition (SEM-EDS)

A Tescan Integrated Mineral Analyser (TIMA) was used for SEM-EDS data acquisition. The sample was carbon coated for use in the SEM. The TIMA was equipped with four EDS detectors, facilitating rapid analysis.

The selected scan area highlighted as the red region in Figure 1 (right) was composed of multiple 200 µm fields with a pixel spacing of 4 µm (close to the practical resolution/beam interaction volume). A working distance of 15 mm at an acceleration voltage of 25 keV was used, with 30 000 X-ray counts collected per pixel. Spectra were acquired for all pixels of which the Back Scattered Electron (BSE) intensity was greater than 15 per cent, to avoid scanning areas without material (resin or pores). The BSE image of the acquired scan is shown in Figure 2 (left), with an approximately marked interface between the lump and sinter marked in blue. In Figure 2 (right) an enlarged field is shown, with a selected pixel indicated in red.

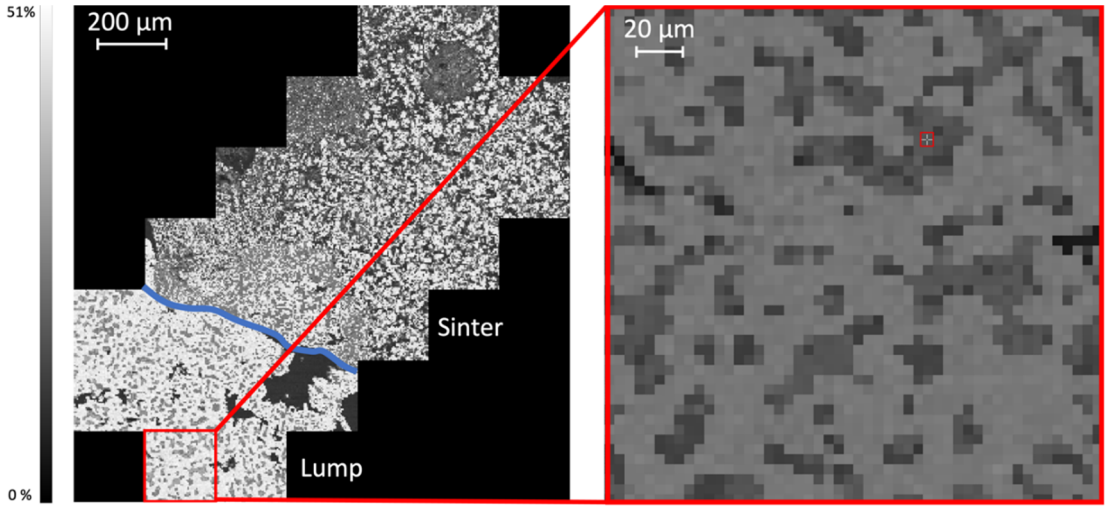

FIG 2 – BSE of scanned area for detailed analysis (left) and enlarged field (right). A single 4 µm pixel is outlined in red in the enlarged field (right). An approximate interface between the burdens is indicated by the freeform blue line (left).

Data processing

Following the acquisition scan, Python 3.1 scripts were used to automate the retrieval of spectra from each pixel. The corresponding elemental composition of each 4 µm pixel was determined from the measured EDS spectra using the standardless quantification tool in the TIMA software (version 2.8.1). For standardless quantification, carbon was specified as the coating element, with the removal of escape peaks and sum peaks (spectral artefacts). Analysis was performed for Mg, Ca, Fe, Al, Si and O (all measured) and results returned as normalised atomic percent compositions.

The Python scripts output pixel coordinates and their associated compositions. The collected data was processed using a MATLAB script (version 2022b), from which the respective element maps were reassembled and an input file was generated for use in FactSage™ calculations. As only the properties of the oxide slag were to be calculated, pixels of metallic iron (determined as >80 atomic per cent Fe) were excluded from the FactSage™ input file.

Equilibrium calculation

The generated input files from MATLAB were imported by a FactSage™ 8.2 Equilibrium Module macro (FToxid, FactPS). The macro sequentially performed equilibrium calculations for each pixel composition, writing results back to the input file. The input composition for the calculation was the quantified elemental composition as measured by EDS, ie no assignment of stoichiometry was assumed. All solution and solid phases were selected, with duplicates suppressed (priority order FToxid > FactPS). The calculation temperature was set as 1300°C (the experiment interruption temperature). The key outputs from the equilibrium calculations were the amount of liquid slag and solid oxides, as well as their composition.

Image reassembly and presentation of data

Results from FactSage™ calculations were imported back to MATLAB for reassembly into the final images. From the calculated quantities, properties such as the liquid fraction could be determined for each pixel by normalising to total oxide amount (ie excluding metallic iron). A summary of the above discussed workflow is shown in Figure 3.

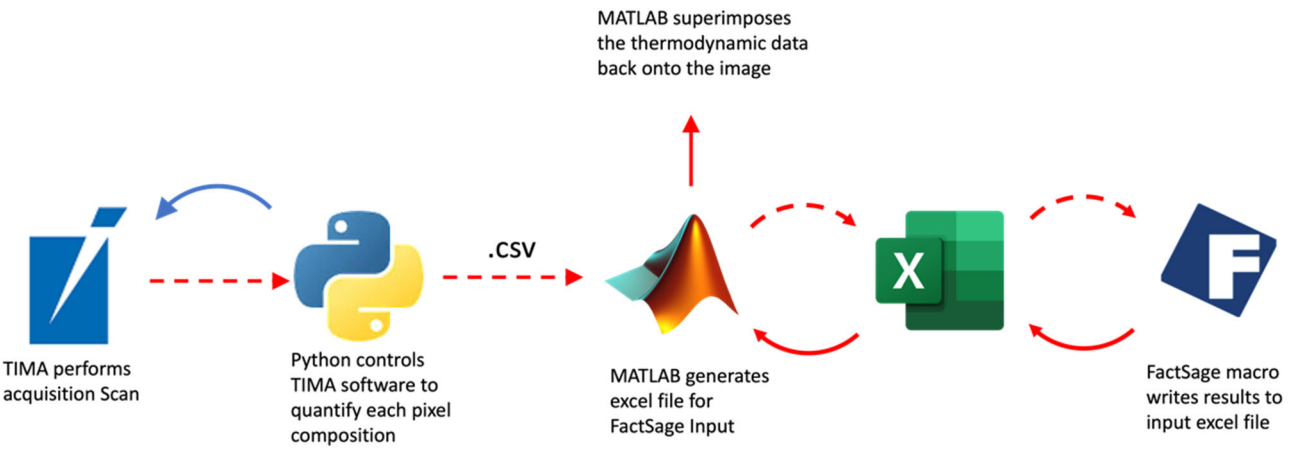

FIG 3 – Flow of information for developed workflow. Dotted red lines represent the flow of information leading up to the thermodynamic calculation, while solid red lines represent the processing of data into an image.

In addition to presenting calculated thermodynamic properties directly on the original microstructure, the data obtained during calculation can be presented in many formats to enhance interrogation of the data. One such method is to average the calculated compositions in a particular direction, allowing the system to be represented in a one-dimensional line. Analysis in such manner allows expression of multiple data sets on a single graph.

In the context of the interface analysed in this study, the compositions were averaged in the direction normal to the interface, so as to provide a one-dimensional representation of composition changes across the interface. To provide additional context to the determined properties, the averaged composition was inclusive of metallic iron and also demonstrates the change in liquid composition with distance from the interface.

RESULTS

To demonstrate the developed technique, calculated properties are presented for the interface of lump and sinter shown in Figures 1 and 2. The quantified element maps are first shown to provide context for the proceeding calculated properties. Following the element maps, the calculated liquid fraction is shown alongside the solid phase stability maps. Finally, the average line compositions across the interface are shown.

Element maps

The individual element maps as determined by standardless quantified SEM-EDS spectra (30 000 X-ray counts) is shown in Figure 4. Note that iron (Fe) and oxygen (O) are presented on a scale of 0–100 atomic per cent while gangue elements (Si, Ca, Al and Mg) are shown on a scale of 0–50 atomic per cent to allow for greater contrast. The dotted lines are included as a reference line for the averaged line compositions discussed later.

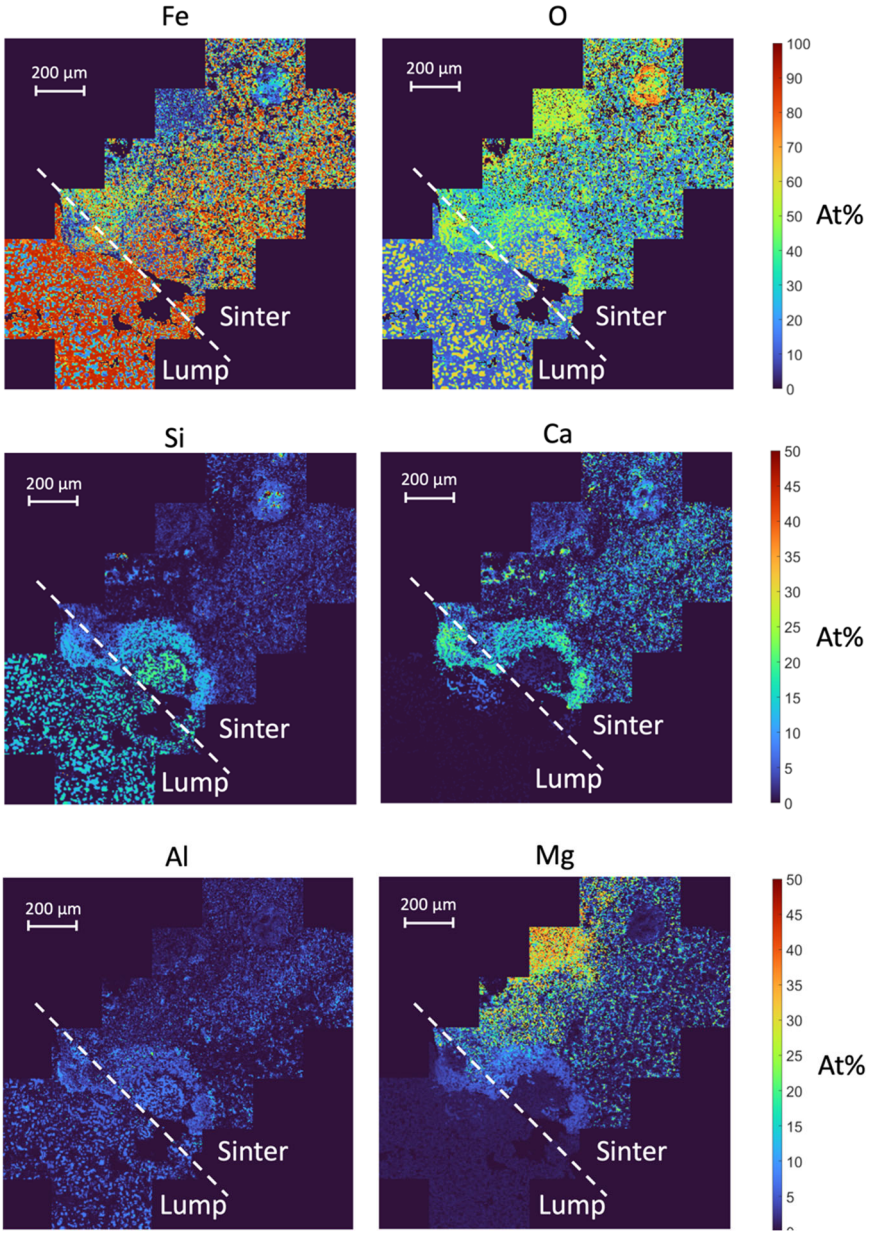

FIG 4 – Element maps as produced by standardless quantification of SEM-EDS spectra. Note that Fe and O are presented on a scale of 0–100 atomic per cent (At%), while Si, Ca, Al and Mg are on a scale of 0–50 atomic per cent.

From Figure 4, the local variation in composition across the interface is evident. It is worth noting that the local composition can vary quite significantly from the bulk composition reported in Table 1. From the Fe map, metallic iron in the lump ore is seen to be an interconnected network. Additionally, the primary gangue in the lump ore is silicon based. Conversely, the sinter is observed to contain well distributed calcium, as well as a local region of magnesium. These local variations in composition provide key context to the proceeding calculations.

The most interesting variations in composition occur at the interface between the dissimilar burdens. The element maps indicate that a region of increased silicon occurs within the sinter close to the interface, with a curved region of accumulated calcium. The properties of this region are of key importance to the interpretation of the burden interaction mechanism.

Oxide phase stability

The dominant equilibrium phases that are predicted to have existed at 1300°C, calculated from the compositions presented in Figure 4, are shown in Figure 5.

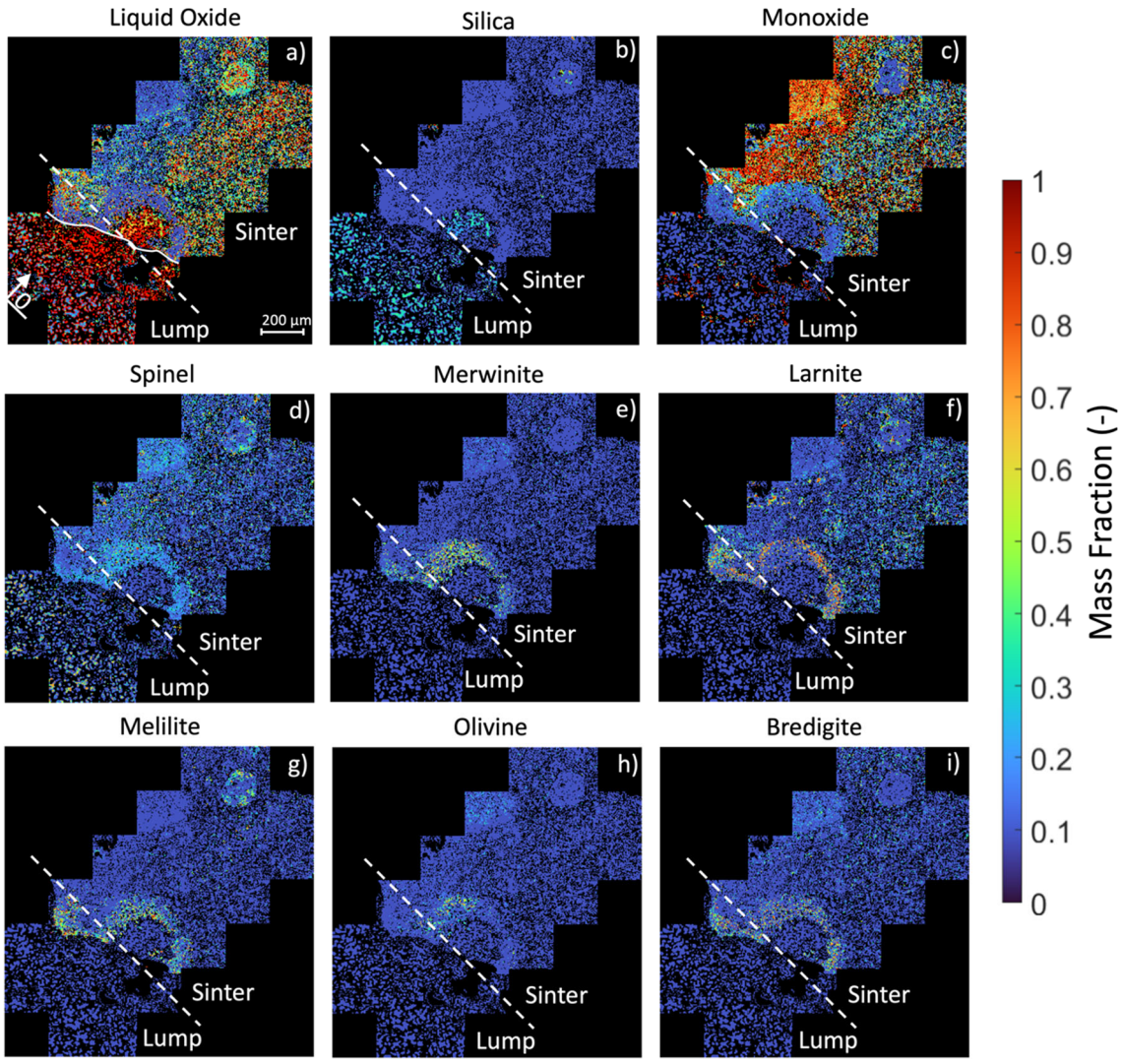

FIG 5 – Equilibrium phases determined by FactSage™ using composition input from element maps in Figure 4.

Figure 5 presents key insights into the spatial distribution of phases around the interface between the lump and sinter at 1300°C. Additionally, mechanisms of interaction are evident through comparison of phases present in the bulk of the respective burdens and those at the interface. In the analysis of the predicted phases in Figure 5, it is assumed that no changes to the microstructure occurred on cooling.

From Figure 5a, the lump ore is seen to contain a significant proportion of phases that would have been liquid at 1300°C. The liquid phase is dispersed through the metallic iron network, with some remaining solid phases present. Through comparison with Figures 5b and 5d, the solid phases remaining in the lump are primarily silica (SiO_2) and spinel ($FeAl_2O_4$). On the sinter side of the interface, the evenly distributed phases are partially molten (regions between 30–70 wt per cent liquid). A clear region with significantly lower liquid formation is seen in the upper left region of the sinter, directly correlating with the region containing magnesium in Figure 4. From Figure 5c, the primary phase in this region is monoxide (MgO). In other regions of the sinter, the remaining solid phases are mostly larnite (Ca_2SiO_4) and spinel ($(Mg,Fe)Al_2O_4$).

At the interface between the two burden particles, a curved band of low liquid formation (Figure 5a) is seen, which directly corresponds to a region of unique mineral phases (Figures 5e–5i). Specifically, where the oxide phases of the two burdens have interacted, merwinite ($Ca_3MgSi_2O_8$), melilite ($Ca_2(Mg,Fe)Si_2O_7$), olivine ($(Ca,Mg,Fe)_2SiO_4$) and bredigite ($Ca_7MgSi_4O_{16}$, $Ca_3Mg_5Si_4O_{16}$) are formed, as calculated by FactSage™.

The mapping of properties through the developed technique is advantageous as it visually demonstrates the previously hypothesised interaction mechanisms reported in literature around a real ferrous burden interface.

Averaged line composition

Through comparison of all phase distributions presented in Figure 5, it can be observed that the interaction of the oxide phases between the burdens acts to suppress liquid formation through the stabilisation of new solid phases. In order to further elucidate the driving mechanisms of interaction, the liquid composition across the interface boundary is presented in Figure 6.

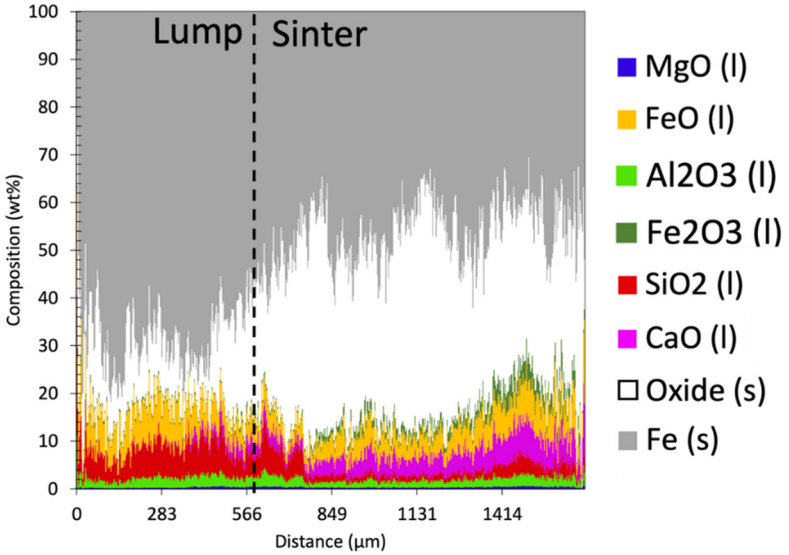

FIG 6 – Average line composition in direction normal to the interface between the burdens. Imposed coordinates are indicated at the bottom left of Figure 5a.

As previously discussed, Figure 6 presents the average composition across the interface between the burdens. The zero point of the imposed coordinates are marked at the bottom left of Figure 5a, with the direction of averaging indicated by an arrow. As a reference point, the approximate location of the interface (marked by a dotted white line in Figures 4 and 5) is marked in Figure 6 as a dotted black line.

In conjunction with Figures 4 and 5, the liquid composition in Figure 6 and the context of its surrounding microstructure (including the metallic iron presented in Figure 6) provide a holistic understanding of the interaction mechanisms occurring at the burden interface.

The lump liquids are primarily FeO/SiO_2 based (fayalitic), while the sinter liquids are dominated by $CaO/FeO/SiO_2$. An important insight from Figure 6 is that while the lump oxides have a higher fraction of liquids than the sinter (as also seen in Figure 5a), the oxide presence in the metallic structure is lower than that of sinter. This is in part due to the higher iron content of the lump (as seen in Table 1), as it does not contain additional oxide fluxes. Of note, MgO is not seen to participate significantly in the formed liquids at 1300°C.

With an understanding of the composition of the formed liquids in the bulk materials, a mechanism of interaction can be directly observed, supporting previously proposed mechanisms (Liu *et al*, 2019b, 2014) and providing additional insight. Of particular importance, the dependency of liquid formation characteristics on the locally available oxides is evident.

These findings emphasise the importance of thermodynamic analysis using real, measured conditions from a particular heterogenous system. With the restricted intuition of pseudo-ternary phase diagrams in these systems, the technique presented in this study proves extremely useful in applying and understanding the appropriate thermodynamic analysis.

CONCLUSIONS

A novel data processing technique for overlaying calculated phase equilibria onto microstructures was developed. The integration of compositions determined by SEM-EDS element mapping with thermodynamic calculations provides an alternative visualisation tool for enhanced analysis while preserving spatial information. This technique is particularly advantageous in multi-component, heterogenous metallurgical systems, for which compositions cannot be expressed in a single pseudo-ternary diagram.

The newly developed technique was demonstrated through detailed analysis of the interface between a lump and sinter particle in a softening and melting test at 1300°C. Mechanisms of interaction between the oxide phases of the dissimilar burdens were observed directly on the microstructure. Specifically, a region of suppressed liquid formation was seen, in which unique mineral phases (such as merwinite, melilite, olivine and bredigite) were stabilised.

The developed technique allows a visual application of the calculated thermodynamic properties, facilitating intuitive and automated interpretation of complex heterogenous microstructures. The further possibilities and applications of such an applied technique extend far beyond what is presented in this paper.

ACKNOWLEDGEMENTS

The authors gratefully acknowledge BHP for their financial support of the Centre for Ironmaking Materials Research and permission to publish this work.

REFERENCES

Barrett, N, Mitra, S, Chew, S, O'Dea, D and Honeyands, T, 2023. Effect of Hydrogen Addition on Softening and Melting Performance of Lump and Sinter Mixed Burden, *ISIJ International*, 63(10):1626–1636. https://doi.org/10.2355/isijinternational.ISIJINT-2023-190

Barrett, N, Mitra, S, Copland, E, Chew, S, O'Dea, D and Honeyands, T, 2024. Changes in Microscale Liquid Formation in Lump and Sinter Mixed Burden Softening and Melting Tests with the Addition of Hydrogen, *Metallurgical and Materials Transactions B*, 55:1712–1734. https://doi.org/10.1007/s11663-024-03062-w

Hoque, M M, Doostmohammadi, H, Mitra, S, O'Dea, D, Liu, X and Honeyands, T, 2021. High Temperature Softening and Melting Interactions Between Newman Blend Lump and Sinter, *ISIJ International*, 61(12):2944–2952. https://doi.org/10.2355/isijinternational.ISIJINT-2021-198

Kim, S-H, Zhang, X, Ma, Y, Souza Filho, I R, Schweinar, K, Angenendt, K, Vogel, D, Stephenson, L T, El-Zoka, A A, Mianroodi, J R, Rohwerder, M, Gault, B and Raabe, D, 2021. Influence of microstructure and atomic-scale chemistry on the direct reduction of iron ore with hydrogen at 700°C, *Acta Materialia*, 212:116933. https://doi.org/10.1016/j.actamat.2021.116933

Liu, X, Honeyands, T, Evans, G, Chen, J and O'Dea, D, 2019a. Chemical interaction between basic sinter and Newman blend lump analogues, in *Proceedings of the Eighth International Iron Ore Conference 2019*, pp 872–879 (The Australasian Institute of Mining and Metallurgy: Melbourne).

Liu, X, Honeyands, T, Evans, G, O'Dea, D and Ellis, B, 2018. Interaction Between Lump Ore and Sinter Under Simulated Blast Furnace Conditions, in *Proceedings of the Eighth* International Congress on Science and Technology of Ironmaking (ICSTI 2018), pp 583–589 (Austrian Society for Metallurgy and Materials).

Liu, X, Honeyands, T, O'Dea, D, Chen, J and Qiu, G-J, 2019b. Interaction between sinter and lump during softening and melting process, *Iron and Steel International*, 54:19–26. https://doi.org/10.13228/j.boyuan.issn0449-749x.20190094

Liu, X, Wu, S, Huang, W, Zhang, K and Du, K, 2014. Influence of High Temperature Interaction between Sinter and Lump Ores on the Formation Behavior of Primary-slags in Blast Furnace, *ISIJ International*, 54(9):2089–2096. https://doi.org/10.2355/isijinternational.54.2089

Lu, Y, Wu, S, Du, B and Zhou, H, 2020. Increasing the Softening as well as Melting Behaviors for Iron Ore Materials within the Blast Furnace Cohesive Zone through the High-temperature Interactivity, *ISIJ International*, 60(7):1461–1468. https://doi.org/10.2355/isijinternational.ISIJINT-2019-713

Lyu, B-B, Wang, G, Yang, F, Zuo, H-B, Xue, Q-G and Wang, J-S, 2023a. Softening and melting behaviors of ferrous burden in hydrogen-rich blast furnace cohesive zone, *Journal of Iron and Steel Research International*, 30:2366–2377. https://doi.org/10.1007/s42243-023-00951-3

Lyu, B-B, Yang, F, Wang, G, Zuo, H, Xue, Q and Wang, J, 2023b. Effect of Hydrogen-Rich Atmosphere on Softening and Melting Behaviors of Ferrous Burden in Blast Furnace Cohesive Zone, in *Proceedings of the Advances in Pyrometallurgy (TMS 2023)*, pp 95–106 (Springer: Cham). https://doi.org/10.1007/978-3-031-22634-2_9

Ma, L, Zhang, J, Wang, Y, Lu, M, Cai, Q, Xu, C, Li, Z and Liu, Z, 2022. Mixed burden softening-melting property optimization based on high-silica fluxed pellets, *Powder Technology*, 412:117979. https://doi.org/10.1016/j.powtec.2022.117979

Vemdrame Flores, I, Matos, O, Lima da Silva, A and Covcevich Bagatini, M, 2021. Microstructure and Porosity Evolution During the Reduction, Softening and Melting of Iron-Bearing Materials, *Metallurgical and Materials Transactions B,* 52(3):1716–1738. https://doi.org/10.1007/s11663-021-02140-7

Wang, Y, Diao, J, Xie, B, Qi, C and Du, P, 2022. Melting-Dropping Property of Blast Furnace Charge on the Basis of Its Slag Formation Behavior, *Metals*, 12(6):987. https://doi.org/10.3390/met12060987

World Steel Association, 2023. World Steel in Figures [press release]. Available from: <https://worldsteel.org/steel-topics/statistics/world-steel-in-figures-2023/>

Wu, S, Han, H, Xu, H, Wang, H and Liu, X, 2010. Increasing Lump Ores Proportion in Blast Furnace Based on the High-temperature Interactivity of Iron Bearing Materials, *ISIJ International*, 50(5):686–694. https://doi.org/10.2355/isijinternational.50.686

Wu, S, Lu, Y, Hong, Z and Zhou, H, 2020. Improving the Softening and Melting Properties of Ferrous Burden with High Al_2O_3 Content for Blast Furnace by Ore Blending, *ISIJ International*, 60(7):1504–1511. https://doi.org/10.2355/isijinternational.ISIJINT-2019-833

Wu, S, Su, B, Liu, X and Kou, M Y, 2018. Optimisation of the blast furnace burden based on its primary slag formation behaviour, *Ironmaking and Steelmaking*, 45(1):50–57. https://doi.org/10.1080/03019233.2016.1237073

Transient slag behaviour in the Direct Reduced Iron (DRI) and scrap-based Electric Arc Furnace (EAF) process – case study for high and low-grade DRI input

DOI: 10.62053/DBSU5458

S Chatterjee[1], S K Panda[2] and M A Van Ende[3]

1. Principal Researcher, Tata Steel, R&D, IJmuiden, Velsen-Noord, Noord-Holland 1951 JZ, The Netherlands. Email: saikat.chatterjee@tatasteeleurope.com
2. Principal Researcher, Tata Steel, R&D, IJmuiden, Velsen-Noord, Noord-Holland 1951 JZ, The Netherlands. Email: sourav.panda@tatasteeleurope.com
3. Research Professor, Department of Materials Science and Engineering and Research Institute of Advanced Materials, Seoul National University, Seoul 08826, Republic of Korea. Email: vanende@snu.ac.kr

ABSTRACT

Tata Steel Netherlands (TSN) aims to reduce its CO_2 emissions by 35–40 per cent by 2030 and become CO_2 neutral by 2045. A first step to reach these targets is via the utilisation of an Electric Arc Furnace (EAF), which will run on a mixture of high proportion of Direct Reduced Iron (DRI) and scrap.

For an EAF operation, optimisation of slag chemistry is important to achieve the right mix of basicity (for refining especially dephosphorisation), foaming, volume (rate) and refractory life. Slag composition and rate can vary widely depending on the process variables like charge mix, charge composition, feeding rate, oxygen lancing, external carbon injection/addition, fluxing and refractory erosion/corrosion. Moreover, it is important to note that the slag composition and rate are 'transient' parameters and change throughout the heat. This makes all the dependent phenomena and/or outcomes transient as well. To describe all these effects simultaneously and be able to realistically simulate the EAF operations, a validated dynamic process model is important in the absence of real plant data.

In this study, a validated dynamic EAF process model based on the concept of Effective Equilibrium Reaction Zone (EERZ) has been utilised to analyse the impact of high DRI industrial scale EAF operations on the transient slag characteristics – including slag volume (rate), composition, phases, solid fraction and viscosity. Simultaneously, the model is able to predict the impact on steel and off-gas characteristics. Case studies were performed with 70 per cent DRI:30 per cent scrap mix considering both low and high-grade DRI. Both melting and refining aspects of the process including continuous feeding, arcing program, carbon addition, fluxing and oxy-lancing were considered.

INTRODUCTION

The EU has embarked on a route to reduce its greenhouse gas (GHG) emissions in three steps – 20 per cent by 2020, 55 per cent by 2030 and 100 per cent by 2050, compared to the 1990 levels. While the 2020 target was achieved in 2019, achievement of the 2030 target looks challenging due to the post-COVID industrial bounce-back. Industrial processes in the EU contribute 9.1 per cent of its GHG emissions. The iron and steel industry is a major contributor, generating ~2 t CO_2 for each tonne of crude steel produced; most of it comes from the Blast Furnace (BF) ironmaking step.

Tata Steel Netherlands (TSN) is an integrated steel producer using the BF – Basic Oxygen Furnace (BOF) route to produce variety of steel products, including automotive and packaging grades. It emits 12.6 Mtpa CO_2 which is ~8 per cent of the total CO_2 emissions in the Netherlands. It aims to reduce the emissions by 4–5 Mtpa (35–40 per cent) by 2030 and become CO_2 neutral by 2045. It also aims to increase its utilisation of scrap to 30 per cent and maximise slag valorisation by 2030.

In order to meet these targets, TSN has decided to replace one of its existing BF with a combination of Direct Reduction Plant (DRP)-Electric Arc Furnace (EAF). Along with scrap addition, the Direct Reduced Iron (DRI) coming out of the DRP will be fed into the EAF.

Numerous integrated steel producers such as POSCO, Salzgitter, ArcelorMittal Dofasco, Voestalpine have opted for the EAF route (for their first phase of transition) charged with a high

proportion of virgin iron units (VIU). Although scrap input is important from the circularity standpoint, tramp elements such as Cr, Ni, Mo, Cu and Sn in the scrap can have adverse effects on the mechanical properties of the steel product (Memoli, Jones and Picciolo, 2015). Hence, high per cent scrap based EAF route is unable to produce the high-grade steel products that are typically made via the BF-BOF route (Mandal *et al*, 2018). In order to control the tramp element levels and address circularity at the same time, the charge material into an EAF needs to be a combination of scrap with a VIU, such as DRI. This strategy should also help in addressing the problem of producing the high-quality steel grades through the EAF route.

However, DRI comes with its own challenges. Factors such as chemical composition (gangue, C, S, P), metallisation degree and temperature of the DRI are critical as they greatly impact the EAF process parameters such as yield, fluxes, slag weight, energy, carbon, oxygen consumptions and raw material feeding rates (Memoli, Jones and Picciolo, 2015).

In this work, a dynamic EAF process model has been used to analyse the impact of DRI quality (high-grade versus low-grade) on the following factors of a continuously charged EAF process:

- product composition (liquid steel and slag)
- productivity (liquid steel and slag)
- yield and specific consumptions.

In terms of refining, the concept of controlling slag FeO and decarburisation rate by controlling oxygen lancing and carbon injection have been described under the section ‘Dynamic Process Control For Transient Slag Control’ in this paper. This knowledge has been applied during the simulations to optimise the slag FeO and decarburisation.

IMPACT OF USE OF DRI ON THE EAF PROCESS

The following characteristics of the DRI greatly impact the EAF process performance:

- Type of green iron-ore pellet: The green pellets (raw unreduced) are classified into two types: DR-grade pellets and BF-grade pellets. The DR-grade pellets contain 67 per cent+ Fe whereas the BF-grade pellets typically contain 65 per cent Fe or less (Linklater, 2021). The higher the iron content, the lower the gangue content, notably acidic components like SiO_2 and Al_2O_3.
- Acidic Gangue content: The gangue (SiO_2, Al_2O_3 etc) present within the green pellets becomes concentrated within the DRI – as it is not ejected into a liquid slag phase (like in a BF). The presence of a higher amount of acidic gangue in the DRI pellet necessitates higher electrical power and flux consumptions in the EAF – leading to a larger slag volume, higher iron loss to the slag and lower productivity. The gangue content also affects the degree of reduction or metallisation within the DRP, which also affects the electrical power consumption in the EAF process.
- Metallisation degree: The metallisation degree is defined as the percentage of metallic iron in the reduced pellet divided by the total iron in the reduced pellet. The amount of unreduced iron oxide depends on the degree of metallisation achieved during the direct reduction step.
- Carbon content: Carbon has multiple roles in the EAF process:
    - adds chemical energy to the system
    - reduces the remaining FeO in DRI: around 1 wt per cent C can reduce 6 wt per cent FeO in the DRI pellet
    - leads to slag foaming: Carbon, when present at sufficient levels within the DRI, yielded substantial improvements in slag foaming in the EAF process, by the promotion of carbon boil (Erwee and Pistorius, 2012). Slag foaming helps in shielding the bath from the atmosphere which reduces radiation loss, electrode loss and nitrogen absorption.
    - enhances nitrogen removal from the liquid steel bath via carbon boil.

- Sulfur and phosphorus levels: The presence of sulfur and phosphorus in DRI may require different slag practices in the EAF to remove these contaminants.
- Temperature: the initial temperature affects the energy balance and thus electrical power consumption and power-on-time.

IMPORTANCE OF EAF SLAGS AND SLAG ENGINEERING

The importance of slag foaming in EAF operations is well understood (Pretorius, 2023), including decreased heat loss from electric arc, improved heat transfer to bath, higher rate and magnitude of power input, increased arc length without increase in flare, reduced power and voltage fluctuations, reduced electrical and audible noise.

Attainment of a good foaming slag necessitates the right combination of slag basicity, FeO and MgO levels at any fixed temperature (Pretorius and Carlisle, 1998). A target EAF slag should have the following characteristics (Pretorius, Oltman and Jones, 2001; Pretorius, 2023):

- $1.3 < B_3 < 2$: the EAF slag should have a proper balance between basic and acidic oxides. Higher B_3 values are needed in case of stronger dephosphorisation. Note that B_3 = per cent CaO / (per cent Al_2O_3 + per cent SiO_2) and B_2 = per cent CaO / per cent SiO_2. The results are discussed in terms of B_3 as it includes both the acidic components (Al_2O_3 and SiO_2), unlike B_2. However, the variation of B_2 is also shown for convenience.
- Presence of second phase (solid or solid solution) particles: slag saturation with respect to CaO (Ca_2SiO_4) and/or MgO (MgO-FeO wüstite) should be aimed. A solid solution is a phase where the secondary components (for eg FeO, CaO etc) are dissolved in the crystal structure of the main component (for example MgO). These solid particles dispersed in the slag serve as gas nucleation sites, which lead to a high amount of favourable small gas bubbles in the foaming slag.
- CO gas bubbles: lifts the slag phase and increases the effective volume of the bubbling slag layer.
- Slag FeO: FeO in slag generates CO bubbles by reacting with injected carbon, but it should not be too high as it decreases the slag viscosity and promotes refractory wear.
- Slag MgO: Slag should be just saturated with MgO so as to prevent refractory wear.
- Slag viscosity: A highly fluidic slag (Al_2O_3, SiO_2 and FeO) attacks the refractories. As the effective slag viscosity (liquid slag + solid particles) is increased, the residence time of the gas bubbles in the slag is prolonged, extending the stability and the subsequent life of the foam. However, too high viscosities (high CaO and MgO) hamper refining and make the slag useless.
- Minimum slag volume: is necessary to cover the steel melt as well as the arc.

Thus, it is important to understand the relative phase stabilities to better control slag foaming in an EAF operation. Typically, the phase stabilities are obtained from Isothermal Stability Diagrams (ISDs), which are plots between per cent MgO and per cent FeO at a constant B_3 and temperature. A sample ISD at a B_3 of 1.5 and temperature of 1600°C is shown in Figure 1a (Oltmann and Pretorius 2002; Pretorius, 2023). The highlighted regions in colour are the inferred regions of good slag foaming – due to the presence of second phase particles. The blue-highlighted region indicates the MgO-saturation conditions while the light red-highlighted region the CaO-saturation conditions. Due to better refractory compatibility and flexibility over FeO levels, the MgO-saturated region is preferred over the CaO-saturated region.

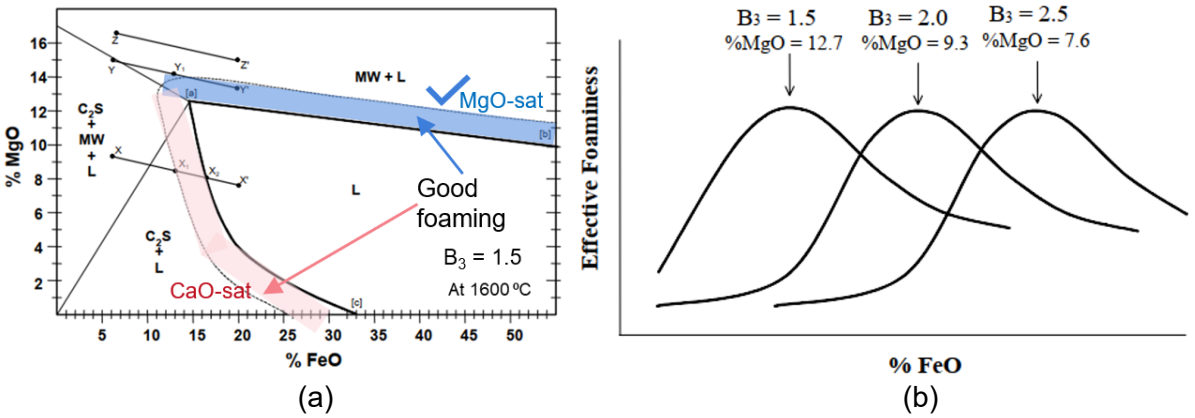

(a) (b)

FIG 1 – Slag foaming requirements: (a) Sample Isothermal Stability Diagrams (ISD); (b) Possibilities for good slag foaming (Oltmann and Pretorius, 2002; Pretorius, 2023).

In reality, various EAF operations have been able to achieve good foaminess under various combinations of B_3, FeO and MgO contents (Figure 1b). However, this choice depends on tap steel quality requirements, for example:

- For low-C heats, higher FeO content will be reached. This needs a high B_3 (Figure 1b), based on which the MgO content can be targeted.
- For high dephosphorisation requirements, high B_3 and high FeO content must be aimed.
- For not so low-C heats, the slag FeO content will be lower. In this case, it is possible to work under low B_3 values.

Present study

In the present study, a low-C heat has been considered which is likely to result in relatively high FeO content in slag. Assuming a FeO content of ~30 wt per cent, it is possible to select different B_3 values and still remain in the region of good foaming and MgO saturation. This is shown schematically in Figure 2. With decreasing values of B_3, lime requirements decrease – however, it increases the dololime requirement due to an increase in the MgO saturation point. This increases the risk of refractory wear.

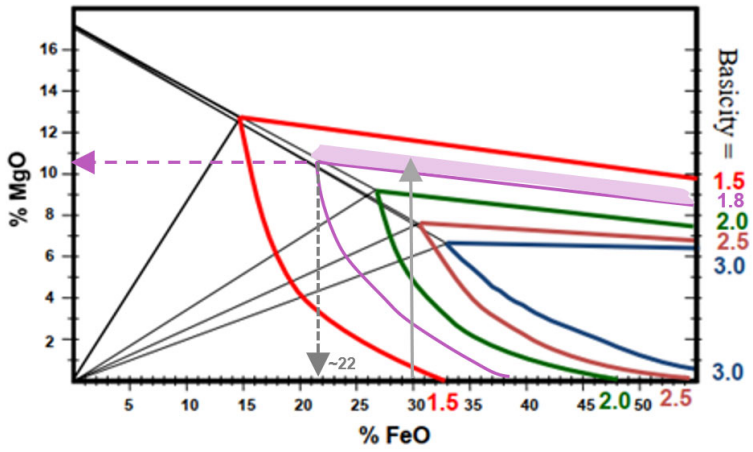

FIG 2 – ISD at different B_3 values (adapted and reprinted with permission from Pretorius, 2023).

Moreover, the use of a very low B_3 is restricted by the minimum slag volume requirement for steel bath coverage and foaming. Thus, a B_3 value of 1.8 was selected which is more of an average value observed in real operations. From Figure 2, it can be observed that the MgO saturation is obtained at ~10 wt per cent MgO and the minimum FeO content is ~22 wt per cent at this B_3. These values are good starting points for comparison to the model simulation results presented later.

Since slag foaming is not part of the current version of the model (described later), it had to considered indirectly. In the simulations, an average B_3 value of 1.8 and continuous MgO saturation throughout the heat were ensured. While the B_3 value was controlled by flux addition, MgO saturation was controlled by ensuring the presence of MgO solid solution. The assumption is that there is a good foaming slag during the process just by ensuring these two conditions.

DYNAMIC PROCESS CONTROL FOR TRANSIENT SLAG CONTROL

Sustenance of a good foaming slag throughout the power-on-time could be challenging due to the transient nature of the process (Oltmann and Pretorius, 2002). The slag foam can collapse due to increase in the slag FeO levels and bath temperature or decrease in the CO gas evolution rate. An imbalance between the feeding/melting rates of input materials (scrap, DRI, flux, carbon), oxygen and carbon injection, FeO formation or MgO dissolution from refractories can lead to transient changes in the composition and hence basicity and viscosity of the slag.

In a recent study (Kirschen, Hay and Echterhof, 2021) that analysed data from multiple EAF plants, it was observed that the slag FeO control was poorer in case of high DRI charged EAFs compared to scrap heats. The standard deviation of FeO was found to be 4.1–9.6 per cent for heats based on>50 per cent DRI (remaining scrap) heats, while it was in the range of 3.9–5.5 per cent for 100 per cent scrap heats. This was attributed to poor operational control of the furnace.

Hence, it is critical to analyse and control the transient changes in the process in order to obtain favourable outcomes. An example (Pretorius, 2023) showing the impact of dynamic operational control (oxygen lancing and carbon injection) on the slag FeO levels is shown in Figure 3. In this example, the tap (C) requirement is around 0.04–0.06 wt per cent. With a constant oxylancing throughout the refining cycle (Figure 3a), the slag FeO reaches 50 wt per cent.

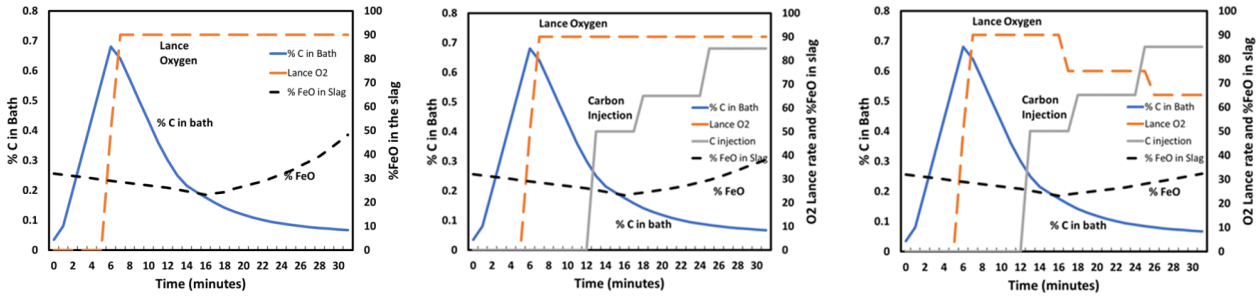

(a) (b) (c)

FIG 3 – Slag FeO control by controlling process conditions dynamically: (a) No FeO control: final FeO ~ 50 wt per cent; (b) FeO control by carbon injection: final FeO ~ 40 wt per cent; (c) FeO control by carbon injection and oxylancing: final FeO ~ 30 wt per cent (reprinted with permission from Pretorius, 2023).

As shown in Figure 3b, injecting carbon in the bath appropriately (time and rate) can reduce the slag FeO levels (to ~40 wt per cent in this example) since the injected carbon reduces slag FeO and increases the Fe yield. The starting point and rate of carbon injection need to be decided based on the slag FeO and bath (C) profiles.

The FeO levels can be further reduced (to ~30 wt per cent in this example) by controlling the oxylancing. This is because beyond the critical carbon value, the rate of decarburisation shifts from oxygen flow rate control to mass-transfer control. Under this regime, the oxygen reacts more with Fe to form FeO instead of taking part in the de-C reaction. Hence, a reduction of the oxylancing rates beyond the critical carbon value results in a decreased slag FeO.

Both the concepts of dynamic process control and slag engineering (discussed above) have been utilised in the present case study.

In this paper, it was decided not to discuss the slag refining capabilities and the concentration profiles of other elements such as S, P, Mn, Si etc. The scope of this study is limited to the influence of the

DRI grade on the main process conditions to obtain a final steel with a target temperature and carbon content and slag with adequate foamability during the EAF process.

EAF MODEL DESCRIPTION

A dynamic process model based on the concept of Effective Equilibrium Reaction Zone (EERZ) has been utilised to carry out the case study in the present work. EERZ is a concept (Ding *et al*, 2000; Van Ende *et al*, 2011) that has been successfully applied to other industrial processes such as BOF, EAF, Ladle Furnace (LF) and Ruhrstahl Heraeus (RH) degasser. Under this concept, mass and heat transfer are coupled with thermodynamic databases to simulate chemical reactions in the reaction zones (volumes). A schematic diagram of the 11 different reaction zones of the EAF dynamic model is shown in Figure 4. The EAF model employed in the present study is an extension of the model described in (Van Ende, 2022), in which the addition of hot metal, DRI and hot briquetted iron (HBI) and their reactions in the EAF have been included. This model has been validated for various cases such as 100 per cent scrap, up to 30 per cent hot metal and up to 40 per cent DRI inputs. However, it is yet to be validated for a high (~70 per cent) DRI input. Hence, the results for the 70 per cent DRI + 30 per cent scrap case (present work) should be considered as logical extrapolations between the validated extremes.

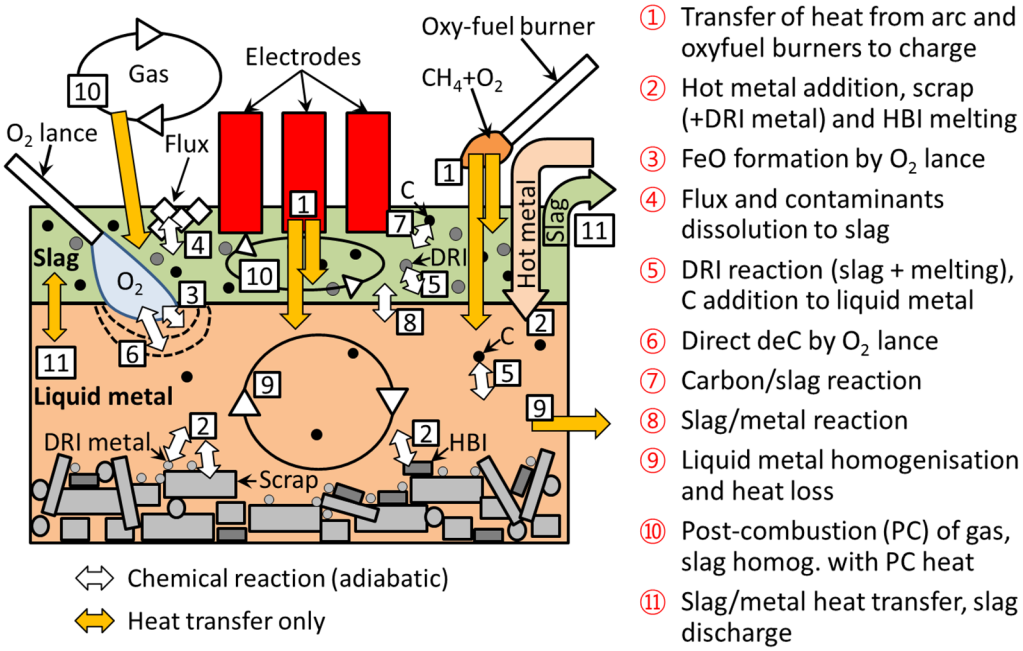

FIG 4 – Schematic representation of the reaction zones of EAF dynamic model (adapted from Van Ende, 2022).

The most important DRI reactions in the EAF process model are explained below. The DRI charged in the EAF will mainly undergo reactions in the EAF slag due to its relatively low density (Reaction 5 in Figure 4). In this reaction, heat is extracted from the slag to heat up the DRI and possibly melt the gangue and metallic fraction of the DRI. The C from the DRI reacts with the DRI gangue and the surrounding EAF slag to reduce FeO and other reducible components and produce CO bubbles in the slag. After the reaction, the oxide products are dissolved into the slag, while the metallic products (solid and/or liquid) travel through the slag to the liquid metal bath. The liquid metal products will mix with the liquid metal bath, whereas the solid metallic products will sink and continue to melt in the liquid metal bath (similarly to scrap, Reaction 2 in Figure 4). All heat transfer requirements associated with the above phenomena are considered in the model. In this way, imbalance in the amount of heat provided to the slag during DRI charging, which will result in the solidification of the slag (ferrobergs) and the accumulation of solid unmelted DRI metal in the liquid bath, can be identified during the simulations.

CASE STUDY SET-UP

A case study was performed with an input mix of 70 per cent DRI and 30 per cent scrap into a continuously fed EAF. The objective of this work was to estimate some of the unknowns using process modelling. The EAF model inputs and outputs for the case study are shown in Figure 5 and the other important considerations are provided in Table 1.

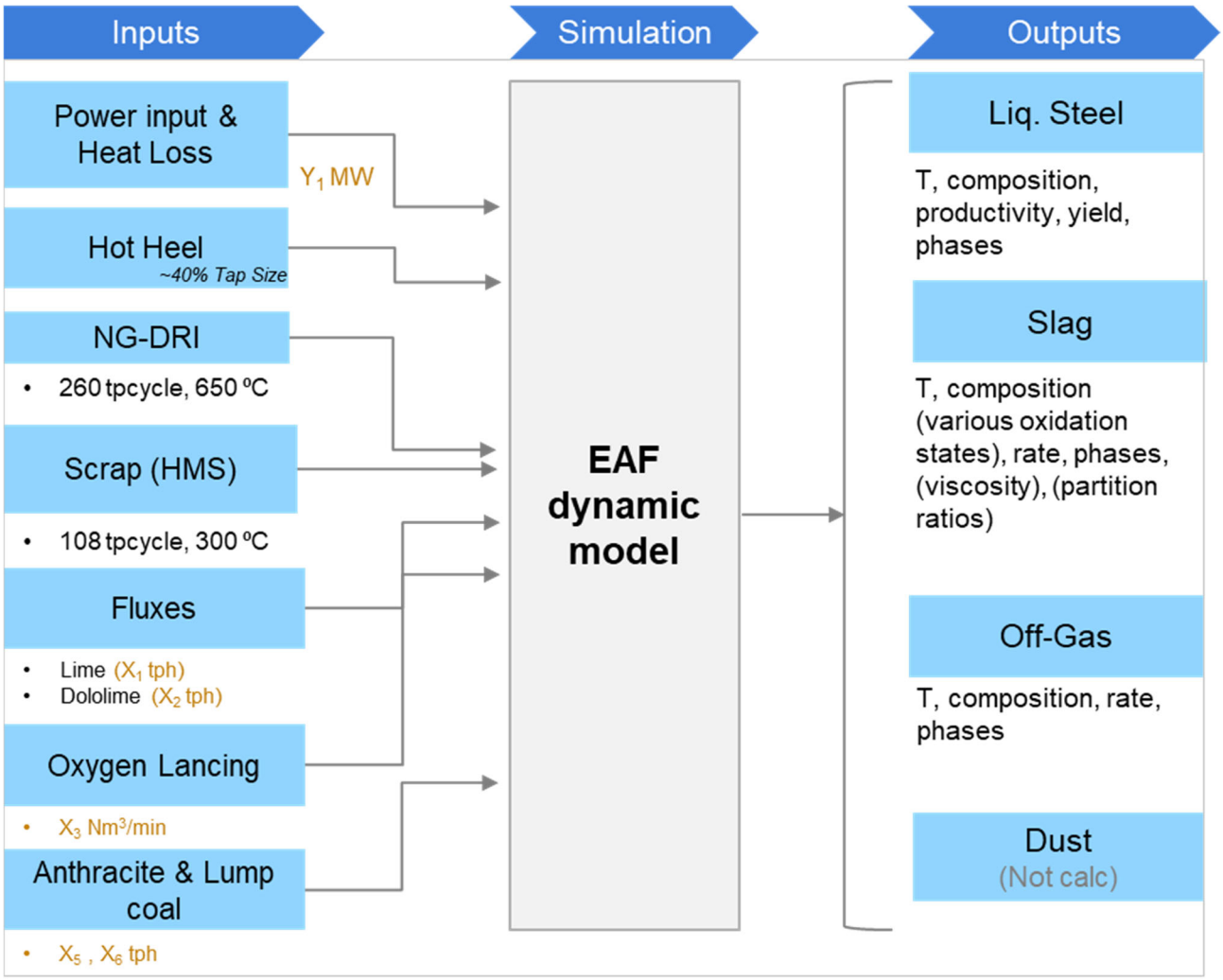

FIG 5 – Model Inputs and outputs for case study: 70 per cent DRI + 30 per cent Scrap into an EAF (continuous charge).

TABLE 1

Other key model inputs and considerations for case study: 70 per cent DRI + 30 per cent scrap into an EAF (continuous charge).

Parameter	Values/remarks

Input charge mix	• DRI pellet:
	  ○ T = 650°C
	  ○ 12 mm size
	  ○ High-grade:
	  ▪ Metallisation = 96 per cent, FeO ~ 4 per cent, C ~ 2.7 per cent
	  ▪ Total acidic gangue (Al_2O_3 + SiO_2) ~ 2.5 per cent
	  ○ Low-grade:
	  ▪ Metallisation = 94 per cent, FeO ~ 7 per cent, C ~ 2.7 per cent
	  ▪ Total acidic gangue (Al_2O_3 + SiO_2) ~ 5 per cent
	• Scrap:
	  ○ T = 300°C
	  ○ No oxides considered
	  ○ 0.4 m × 0.15 m × 0.15 m

Aim liquid steel (LS) quality	• ~ 1650°C • ~ 0.04–0.05 per cent C • <0.01 wt per cent P, <0.02 wt per cent S
Tap-to-Tap Time	50 mins
Power on Time	40 mins
Charging Cycle	36 mins
Slag foaming	considered indirectly
Aimed slag B_3	1.8 (explained earlier)

RESULTS AND DISCUSSIONS

Through this case study, the impact of DRI quality (high-grade versus low-grade) on the following EAF process metrics will be presented:

- product composition
- productivity and yield
- specific consumptions.

Both the concepts of dynamic process control and slag engineering have been considered in these case studies.

The process conditions and the model simulation results are presented in Figure 6 for the high-grade (solid lines) and low-grade DRI (dashed lines) cases. The feed rates (Figure 6a) of scrap and DRI were ramped up (or down) based on their melting behaviour. The electrical power was scaled to match the feed rates. This was an iterative procedure to find a balance between the two parameters. Higher than necessary power would result in higher tap temperatures while an insufficient power supply is unable to melt all the feed material, fluxes or slag. Around 108 t of scrap and 260 t DRI pellets were added per cycle. Since the ratio of DRI feed rate to scrap feed rate is quite high (almost 2.5), the requirement of electrical power (and its variation with time) in order to melt all the feed

material was primarily determined by the feed rate of DRI. This variation can be observed in Figure 6a. The higher power consumption for the case of low-grade DRI input (dashed green line) is due to the extra power needed to melt the additional acidic gangue in low-grade DRI and relatively higher amount of added fluxes.

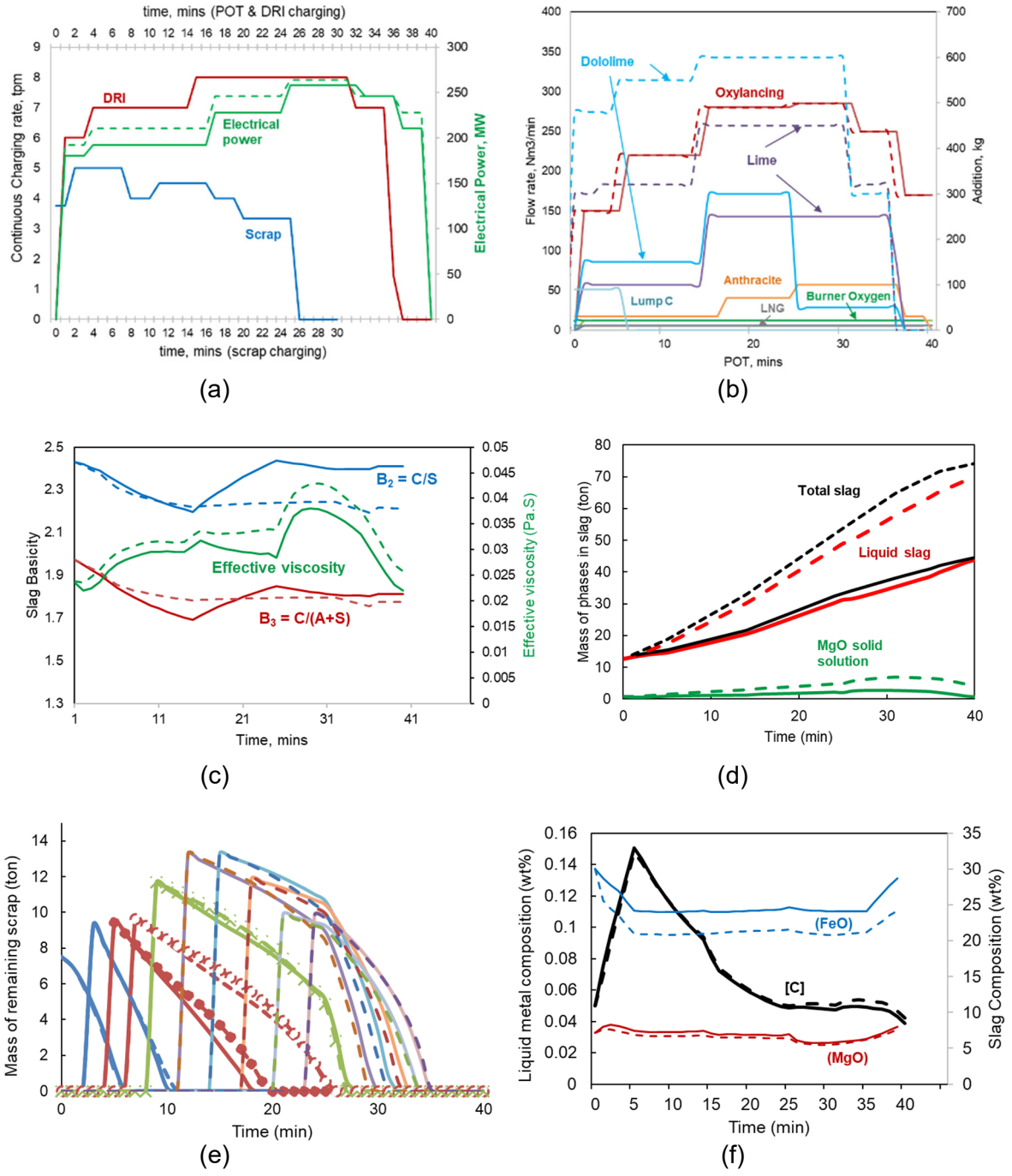

FIG 6 – Model Outputs: Dynamic profiles for the high-grade DRI (solid lines) and low-grade DRI (dashed lines) cases: (a) Charging and Electrical power profiles; (b) Additions (flux, C, O_2, NG); (c) Slag basicity and viscosity profiles; (d) Slag weight (no deslagging) and MgO saturation profiles; (e) Scrap melting profiles. Note: Each line shows a separate scrap feed into the furnace; (f) Chemistry:$(C)_{LS}$, $(FeO)_{slag}$ and $(MgO)_{slag}$.

The transient addition profiles of various other inputs to the process – such as fluxes, oxylancing, carbon, burner oxygen and natural gas – are shown in Figure 6b. The basic flux (lime and dololime) additions are matched with the incoming acidic oxides (present in DRI) as well as acidic component in scrap (Si in this case). Maintaining a MgO saturation throughout the heat was also considered a

necessity in order to: (i) protect the refractory wear, and (ii) generate second phase particles (solid and solid solution) needed to maintain a foamy slag. As clearly observed, the flux addition amounts are significantly higher for the low-grade DRI case, having much higher acidic gangue content (twice that of high-grade DRI).

For generation and sustenance of a foamy slag, the presence of a sufficient amount of CO gas bubbles is also necessary. The amount of gas to sustain foaming is higher when the slag amount increases. Hence, the carbon and oxygen consumption should be higher for the low-grade DRI case to compensate for the higher mass of slag. However, since the effect of slag foaming is not 'directly' included in this version of the EAF model, the carbon and oxygen consumptions are kept the same in both cases for simplification.

As shown in Figure 6c, the slag B3 (per cent CaO / (per cent Al_2O_3 + per cent SiO_2)) was kept at ~1.8 to accommodate slag foaming requirements, as explained earlier. The slag B_2 (per cent CaO / per cent SiO_2) varied in between 2.2 to 2.4. Evidence of MgO saturation can be observed from Figure 6d, which shows the presence of MgO solid solution throughout the process. The slag B_3 ratio and MgO saturation are controlled by adjusting the flux (lime and dololime) additions with time.

Based on the flux additions, the cumulative slag weight can be calculated as shown in Figure 6d. The weights of total slag (black dashed line) and liquid slag (red dashed line) for the low-grade DRI case are significantly higher than for the high-grade DRI case (solid lines). On a cumulative bases, ~70 t of total slag is generated in the low-grade DRI case, compared to ~40 t in the high-grade case. Usually, the slag is discharged towards the end of the heat. However, the effect of deslagging is not considered in this study.

The variation of the effective viscosity (liquid + solid slag), shown in Figure 6c, gives an idea of the foaminess of the slag (transient nature). The calculated viscosity of the liquid slag is based on a very extensive database of FactSage. The Einstein-Roscoe equation (Einstein, 1906) was then used to calculate the effective viscosity (liquid + solid slag) that considers the effect of the MgO solid fraction. The fraction of solid MgO in slag is in the range of 2–10 per cent under the present conditions (Figure 6d) and therefore has only a small contribution to the effective viscosity of the slag. The calculated values range from 0.025–0.035 Pa.s under the considered conditions. These values are in the range of experimental observations (Choi *et al*, 2021) for similar slag composition (~30 wt per cent FeO slags at 1600°C).

The kink in the viscosity curve at ~30 mins (Figure 6c) is most likely due to the increase in formation of the MgO solid solution. The viscosity curve follows the pattern of the MgO solid solution throughout as this is the only solid phase present.

The transient melting profile of various scrap feeds are shown in Figure 6e. As observed, there is no unmelted scrap remaining in the heat after ~35 mins.

As depicted in Figure 6f, the bath (C) and slag (FeO_x) and (MgO) levels are comparable to those obtained from the BOF process. It is also important to check the presence and behaviour of other important components such as (P), (Mn), (S) and (N). However, they are not part of the present study. This is especially important from the product point of view as the integrated steel producers are looking to cover their current product portfolio as much as possible with the DRP-EAF route. In this study, a bath (C) level of 0.04 wt per cent and slag (FeO_x) of 29 wt per cent are obtained in the high-grade DRI case – compared to 0.04 wt per cent (C) and 24 wt per cent (FeO_x) for the low-grade DRI case. A lower (FeO_x) level in the low-grade DRI case might seem counter-intuitive at first. However this is likely the result of dilution of its concentration due to the addition of very high amounts of fluxes (lime and dololime) in the low-grade DRI case. Although its concentration is lower, the specific mass of FeO_x formed is higher due to a relatively higher slag rate in the low-grade DRI case (52 kg FeO/tLS), compared to 29 kg FeO/tLS in case of the high-grade DRI case. The slag (MgO) level for both the cases is around 8 wt per cent.

One important point to note is that the (relatively) steady variations in process outputs, such as steel and slag compositions, slag B_3, slag viscosity (foaming), are obtained after carefully manipulating the control parameters such as flux additions, feed rates, power input, oxylancing and carbon addition.

Few selected parameters are listed in Table 2 for comparing the end point results from the high-grade and low-grade DRI cases. Few key points to note are as follows:

- For the low-grade DRI case:
  - lower productivity
  - higher electrical energy consumption
  - higher slag rate
  - higher flux consumption
  - the specific consumption figures can be used further to carry out cost calculations.

TABLE 2

Model simulation results (selected parameters) at LS tap.

Parameter	Ore type	With High-grade DRI ~ 2.5% acidic gangue	With Low-grade DRI ~ 5% acidic gangue
LS	Composition	387 ppm C, 503 ppm O	420 ppm C, 460 ppm O
Slag	Composition	• B_3 (C/A+S) = 1.8 • FeO_x ~ 29 wt.%	• B_3 (C/A+S) = 1.8 • FeO_x ~ 24 wt.%
	Rate	92 kg/tLS	186 kg/tLS
Electrical energy consumption	kWh/tLS	417	458
Flux consumption	Lime	20 kg/tLS	42 kg/tLS
	Dololime	17 kg/tLS	58 kg/tLS
Yield	%	93%	89%

CONCLUSION

In this work, a sample case study for a 70 per cent DRI + 30 per cent scrap input to a continuous charging EAF was performed using a dynamic EERZ process model. The model is not validated for this specific case, but results should be considered as logical extrapolations from the validated extremes (100 per cent scrap and 40 per cent DRI + 60 per cent scrap).

Two cases, one with a high-grade DRI (~2.5 per cent acidic gangue content) and another with a low-grade DRI (~5 per cent acidic gangue content), were simulated. Following conclusions can be drawn from this specific case study:

For the low-grade DRI case (compared to the high-grade DRI case), the following were observed:

- 4 per cent lower productivity of liquid steel (LS)
- 9 per cent higher electrical energy consumption
- 51 per cent higher slag rate
- 62 per cent higher flux consumption
- 4 per cent lower yield.

The higher electrical energy consumption for the case of low-grade DRI input is due to the extra power needed to melt the additional acidic gangue in low-grade DRI and relatively higher amount of added fluxes. Higher fluxes are needed in the low-grade DRI case to balance the higher incoming acidic gangue. Moreover, higher fluxes also generate higher slag rates and thus reduce the liquid steel productivity and yield. The specific consumption figures can be used further to carry out cost calculations and compare between various options on a techno-economical basis.

A lot of research and technology development is now being channelised towards getting an EAF liquid steel that is as close as possible to that of BOF liquid steel. Using a high amount of DRI in EAF is one of the steps towards it, but dynamic process control and slag engineering are also very important influencing factors. Through this study, the importance of these factors has been highlighted:

- Slag engineering:
  - It is possible to operate EAFs at different B_3 (slag basicity) values.
  - The target slag for a good EAF operation should ensure minimum volume requirement, refining requirement (dephosphorisation), slag foaming and MgO saturation.
- Dynamic process control:
  - It is important to understand the transient behaviour (and not just the end point) of the process characteristics: steel, slag and off-gas composition, rate and temperature.
  - Dynamic control over parameters such as carbon and oxygen injection enables hitting targets of bath (C) content, slag (FeO) content and yield.

REFERENCES

Choi, J S, Park, T J, Min, D J and Sohn, I, 2021. Viscous behavior of high-FetO-bearing slag systems in relation to their polymeric structural units, *Journal of Materials Research and Technology*, 15:1382–1394.

Ding, R, Blanpain, B, Jones, P T and Wollants, P, 2000. Modeling of the Vacuum Oxygen Decarburization Refining Process, *Metallurgical and Materials Transactions, B,* 31(1):197–206. https://doi.org/10.1007/s11663-000-0145-5.

Einstein, A, 1906. Eine neue Bestimmung der Moleküldimensionen, *Annalen der Physik*, 324(2):289–306. https://doi.org/10.1002/andp.19063240204.

Erwee, M W and Pistorius, P C, 2012. Nitrogen in SL/RN direct reduced iron: origin and effect on nitrogen control in EAF steelmaking, *Ironmaking and Steelmaking*, 39(5):36–41.

Kirschen, M, Hay, T and Echterhof, T, 2021. Process Improvements for Direct Reduced Iron Melting in the Electric Arc Furnace with Emphasis on Slag Operation, *Processes*, 9:402.

Linklater, J, 2021. Adapting to Raw Materials Challenges: Part 1 – Operating MIDREX Plants With Lower Grade Pellets and Lump Ores, Midrex Technologies, Inc. Available from: <https://www.midrex.com/tech-article/adapting-to-raw-materials-challenges-part-1-operating-midrex-plants-with-lower-grade-pellets-lump-ores/> (Accessed: 18 April 2024).

Mandal, T, Maity, A, Sinha, K K, Chatterjee, S and Mukherjee, A, 2018. A Comparative Analysis of Various Types of EAFs Based on Flexibility and Operational Performance, *AISTech 2018 Proceedings*, 14 p.

Memoli, F, Jones, J A T and Picciolo, F, 2015. The Use of DRI in a Consteel® EAF Process, *Iron and Steel Technology*, 12(1):72–80.

Oltmann, H and Pretorius, E, 2002. Improvements in EAF operation by the use of refining simulation tools and mass-balance programs for foaming slag, 60th Electric Furnace Conference.

Pretorius, E, Oltmann, H and Jones, J, 2001. EAF fundamentals, LWB Refractories. Available from: <https://docplayer.net/28531891-Eaf-fundamentals-eugene-pretorius-and-helmut-oltmann-process-technology-group-lwb-refractories-jeremy-jones-nupro-corporation.html>

Pretorius, E B and Carlisle, R C, 1998. Foamy slag fundamentals and their practical application to electric furnace steelmaking, *in Proceedings of the 56th Electric Furnace Conference*, pp 1–24.

Pretorius, E, 2023. AIST Modern EAF Training Seminar.

Van Ende, M-A, Kim, Y-M, Cho, M-K, Choi, J and Jung, I-H, 2011. A Kinetic Model for the Ruhrstahl Heraeus (RH) Degassing Process, *Metallurgical and Materials Transactions, B,* 42:477–489.

Van Ende, M-A, 2022. Development of an Electric Arc Furnace Simulation Model Using the Effective Equilibrium Reaction Zone (EERZ) Approach, *Journal of Metals*, 74:1610–1623.

Practicalities of the use of fayalite slags for recovery of metals from urban wastes

DOI: 10.62053/KJVT3477

J Chen[1], S Nicol[2], B Hogg[3], E Jak[4] and S Nikolic[5]

1. Theme Leader Analytical Methods, University of Queensland, Brisbane Qld 4067. Email: j.chen5@uq.edu.au
2. Senior Metallurgist, Glencore Technology, Brisbane Qld 4068. Email: stuart.nicol1@glencore.com.au
3. Principal Metallurgist, Glencore Technology, Brisbane Qld 4068. Email: ben.hogg@glencore.com.au
4. Professor, University of Queensland, Brisbane Qld 4067. Email: e.jak@uq.edu.au
5. Technology Manager, Glencore Technology, Brisbane Qld 4068. Email: stanko.nikolic@glencore.com.au

ABSTRACT

The quantity of post-consumer 'waste' materials generated each year is rapidly increasing. These materials can contain significant quantities of critical metals and present an environmental challenge if landfilled. The ISACYCLE™ technology is a proven solution for the processing of these materials. In the ISACYCLE™ furnace, the post-consumer materials are processed to recover energy along with any contained critical metals, in the form of a base metal alloy or matte. In addition, a clean aggregate (slag) is generated, which has the potential to be used for a range of applications in the construction industry. This slag is commonly based on a fayalite slag but is modified to manage the complex feed. This paper will review the fayalite slag system and the theoretical modifications required for treating urban wastes. Slags from an ISACYCLE™ furnace processing urban wastes have been sampled and characterised. The chemistry of these samples will be reviewed and compared to the expected theoretical modifications required.

INTRODUCTION

Critical metals are important for modern societies, with many of them used in niche applications. One of these applications is electronics, both consumer and non-consumer electronics. The critical metals in electronics include copper, nickel, tin, zinc, lead, and precious metals. Currently 17 per cent of tin, 21 per cent of silver and 7 per cent of gold produced annually is used in electronics. To move towards a sustainable society and circular economy, end of life electronics (E-Scrap) need to be responsibly processed to recover these critical metals.

ISASMELT™ technology is well established as one of the leading technologies for secondary copper smelting. The ISASMELT™ Technology was developed at Mount Isa Mines, in Queensland Australia, through rigorous lab testing, pilot testing, and demonstration-scale plant trials. This resulted in the first commercial ISASMELT™ plant being constructed in 1991. The technology was initially developed to process primary copper concentrates and primary lead concentrates, but it was quickly identified that the technology was able to be used for smelting and/or converting most primary and secondary base metal feed materials. The leading E-Scrap recyclers in Europe, Aurubis Lunen and Umicore Hoboken, both use ISASMELT™ Technology to recover critical metals from these types of feed materials – and have done for more than 20 years. The ISASMELT™ Technology is adaptable and suited to both continuous and batch processing of secondary base metal feeds, with the batch processing route enabling both smelting and converting to occur in a single vessel.

This paper will investigate an industrial slag from an ISACYCLE™ furnace.

SAMPLING

Dip bar-quenched slag samples were taken during reduction smelting and converting stage from a ISACYCLE™ furnace. The samples were mounted in epoxy resin and cross-sections were prepared using conventional metallographic techniques.

ANALYTICAL METHODS

EPMA

Quantitative elemental analyses were carried out using a JEOL 8530F Plus field emission electron microprobe housed at the Centre for Advanced Microscopy, The Australian National University. The analysis parameters included an acceleration voltage of 15 kV, a probe current of 80 nA, and a spot size ranging from 1 to 30 µm. achieving a detection limit better than 100 wt ppm for all elements analysed. Given the complex chemical composition of the samples, special attention was given to minimising spectral interferences using the protocol developed by Chen *et al* (2022).

LA-ICP-MS

The concentrations of minor/trace elements in the slag were measured by Laser Ablation ICP-MS on an Agilent Technologies 7700 quadrupole mass spectrometer coupled to a Lambda Physik (λ = 193 nm) laser ablation system at the Research School of Earth Sciences, The Australian National University. A 80 mJ output energy and 81 µm diameter spot-size was chosen for the quantitative spot analysis. Data acquisition involved a background pre- and post-ablation for 15 sec. The isotopes measured were: 29Si, ^{59}Co, ^{60}Ni, ^{63}Cu, ^{75}As, ^{118}Sn, ^{121}Sb and ^{206}Pb. Si concentrations determined by EPMA were used as the internal standard and the NIST reference glass SRM 610 was used as the primary standard. Reference glass SRM 612 was monitored as secondary standards. The data obtained were reduced using the Iolite v4 software package.

RESULTS

Microstructure of the samples

A typical microstructure of a reduction smelting slag sample is shown in Figure 1. Microstructural analysis indicated that phases present in the system at the temperature include slag, spinel and entrained copper metal. Measurement of the slag phase composition was conducted at the slag-dip bar interface where the slag was best quenched.

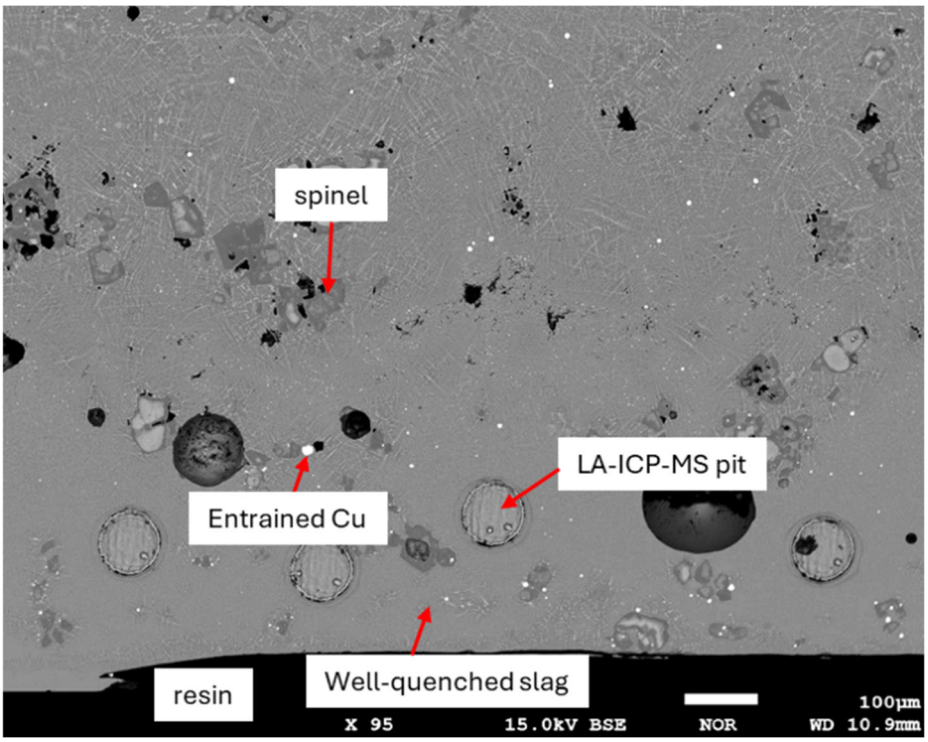

FIG 1 – Typical microstructure of a smelting slag.

Slag composition

As shown in Figure 2, the composition of the slag phase presented in the reduction smelting stage was plotted on the liquidus projection of the multicomponent system in equilibrium with metallic Cu and Fe onto the Al_2O_3-'FeO'-SiO_2-CaO pseudoternary section calculated by FactSage™ (Bale *et al*, 2002) using the current thermodynamic database developed by Prostakova *et al* (2019) and Shishin, Hidayat and Jak (2020). The measured liquid slag phase composition projected onto the section is in the spinel primary phase field and corresponds approximately to the liquidus temperature of ~1350°C and corresponds to ~10 wt per cent spinel at equilibrium at the process temperature of ~1250°C.

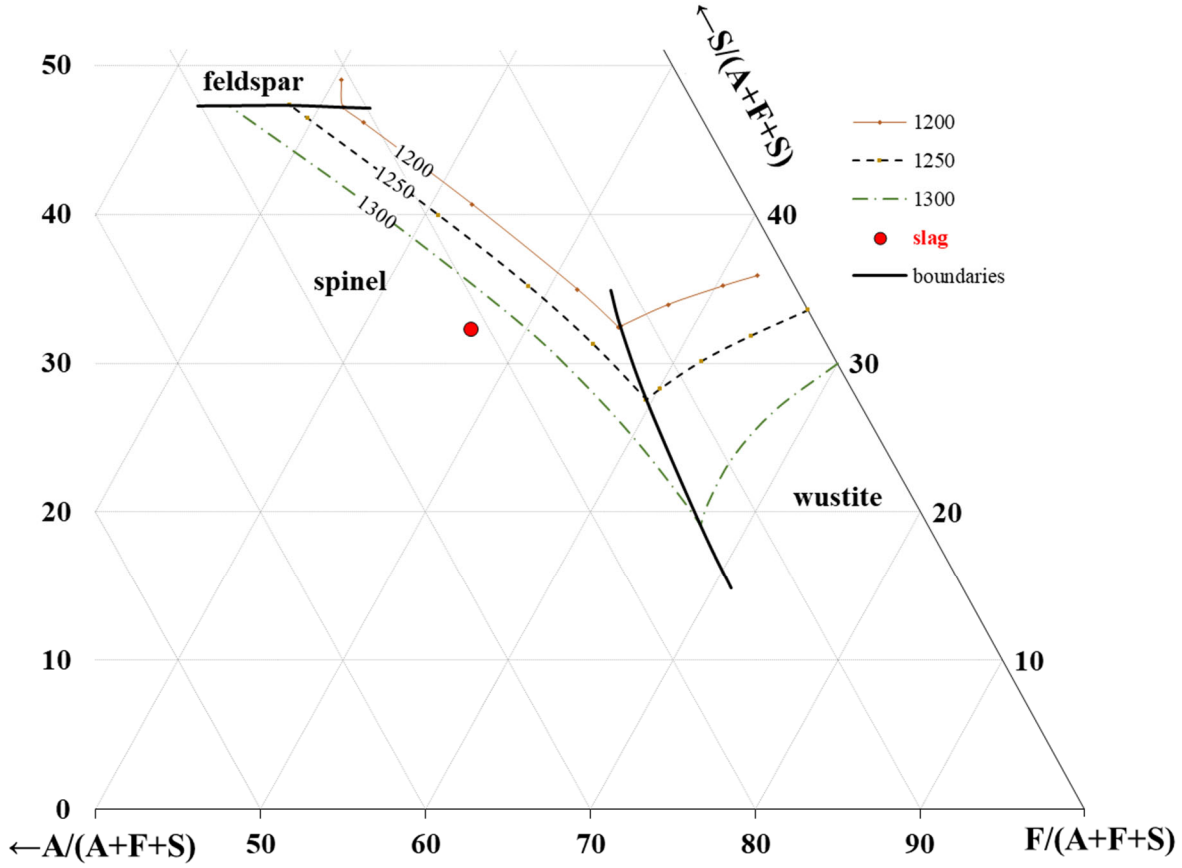

FIG 2 – Liquidus projection of the multicomponent system in equilibrium with metallic Cu and Fe onto the Al_2O_3-'FeO'-SiO_2-CaO pseudoternary section at a fixed CaO concentration, calculated with the current thermodynamic database (Prostakova *et al*, 2019; Shishin, Hidayat and Jak, 2020).

Minor element concentration in the slag phase after reduction smelting by LA-ICP-MS

Selected minor element concentrations measured by LA-ICP-MS in the slag phase are reported in Table 1. The values for the minor elements in Cu metal phase were approximately estimated from the LA-ICP-MS readings. It can be seen the Cu dissolved in the slag is as low as ~2000 ppm while all other minor elements are less than ~400 ppm.

TABLE 1

Minor element concentration in the slag phase after reduction smelting.

Element	Co	Ni	Cu	As	Sn	Sb	Pb
Concentration (ppm)	212	38	2221	4.75	334	0.39	76

Distribution coefficient of selected element

The calculated distribution coefficients ($L_{slag/metal}$) for the minor elements in the system at 1250°C as a function of Fe dissolved in metallic copper predicted with the thermodynamic database developed by Prostakova *et al* (2019) and Shishin, Hidayat and Jak (2020) are presented in Figure 3. The predicted sequence of minor element distribution coefficients (L) is Co > Pb > Sn > Ni > Sb, and these findings align with the sequence of values estimated from the measurements.

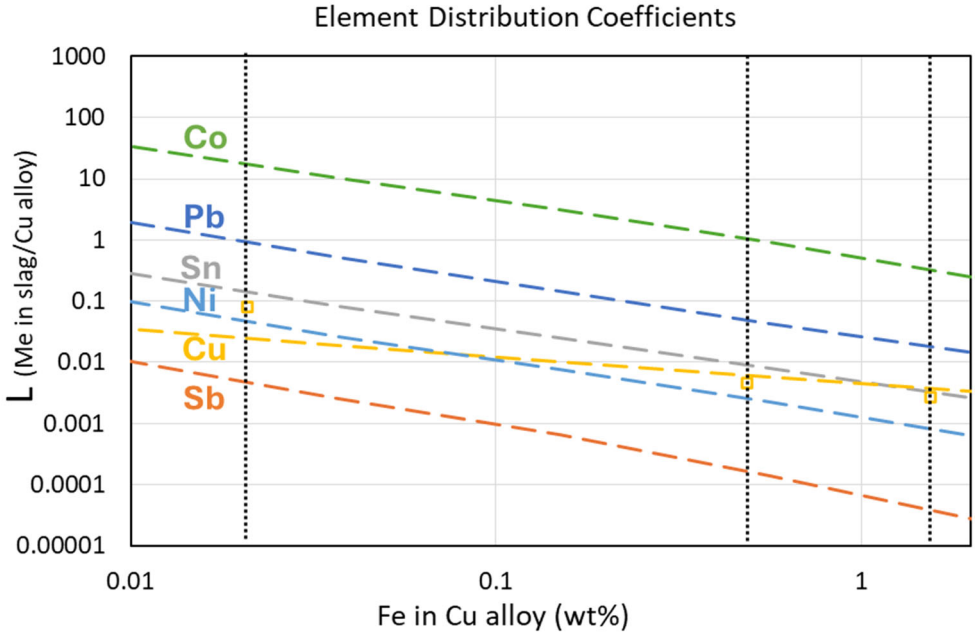

FIG 3 – The calculated distribution coefficients of selected minor elements as a function of Fe in Cu alloy in the present study. The measured distribution coefficients of Cu between slag and Cu alloy at different stages of the smelting/converting are also plotted on the diagram (open squares).

SUMMARY OF FINDINGS

- Microstructural analysis indicated that phases present in the system at the temperature include slag, spinel and entrained copper metal suggesting the spinel primary phase field.
- The predicted liquidus temperature of the slag phase presented in the reduction smelting slag is significantly higher (~100°C) than observed.
- The slag phase after reduction smelting contains very low level of minor elements.
- Th sequence of minor element distribution coefficients ($L_{slag/metal}$) is found to be Co > Pb > Sn > Ni > Sb; the measured distribution coefficient of selected elements at different stages of the smelting process follow the trend predicted by FactSage™ using the UQPY private database.
- The distribution coefficients (L) of minor elements between slag and Cu metal are strongly affected by the oxygen potential in the process – higher the PO_2, the less Fe in Cu metal and the higher L.

REFERENCES

Chen, J, Fallah-Mehrjardi, A, Specht, A and O'Neill, H S C, 2022. Measurement of minor element distributions in complex copper converting slags using quantitative microanalysis techniques, *JOM,* pp 1–10.

Bale, C W, Chartrand, P, Degterov, S A, Eriksson, G, Hack, K, Mahfoud, R B and Petersen, S, 2002. FactSage thermochemical software and databases, *CALPHAD,* 26(2):189–228.

Prostakova, V, Shishin, D, Shevchenko, M and Jak, E, 2019. Thermodynamic optimization of the Al_2O_3–FeO–Fe_2O_3–SiO_2 oxide system, *CALPHAD,* 67:101680.

Shishin, D, Hidayat, T and Jak, E, 2020. Thermodynamic assessment of the CaO–Cu2O–FeO–Fe_2O_3 system, *CALPHAD,* 68:101715.

Research on *in situ* recovery technology of hot-dip galvanised dross

DOI: 10.62053/XZPC8409
R Chu[1], X Deng[2] and X Li[3]

1. Chief Engineer, Shougang Group Co., LTD. Research Institute of Technology, 100043 Beijing, China. Email: churensheng@163.com
2. Chief Engineer, Shougang Group Co., LTD. Research Institute of Technology, 100043 Beijing, China. Email: dxx042@163.com
3. Engineer, Shougang Group Co., LTD. Research Institute of Technology, 100043 Beijing, China. Email: xiangyuli@163.com

ABSTRACT

The hot-dip galvanising industry is the largest consumer of zinc, with over 40 per cent of the world's total annual production of zinc used for galvanised steel. The dross generated in the hot-dip galvanising coating process is a valuable co-product, since it contains high quantities of recyclable metal. A new method to recover the metal from the industrial galvanising dross was proposed using supergravity separation. During the hot-dip galvanising process, the presence of zinc dross has a serious impact on the surface quality of the hot-dip galvanised sheet, forming zinc dross defects. To reduce the impact of zinc dross, the zinc dross on the surface of the zinc pool needs to be manually or mechanically removed at regular intervals. However, during the dross removal process, a large amount of metal zinc is inevitably carried out, resulting in low zinc utilisation rate and high zinc loss rate. This article proposes an efficient and low-cost technology for the recycling and utilisation of hot-dip galvanised dross, which uses super-gravity technology to recover hot-dip galvanised dross online. The metal in the hot-dip galvanised dross returns to the zinc pot *in situ*, while a small part of the dross remains in the super-gravity equipment, which can reduce the amount of zinc dross by more than 60 per cent and achieve a reduction in zinc loss from 17 per cent to less than 7 per cent.

INTRODUCTION

Hot-dip galvanising industry is the largest consumption field of metal zinc with more than 40 per cent of the total annual output of metal zinc in the world. In the process of hot galvanising, the dross accounts for about 10 per cent ~ 15 per cent of the total zinc input (Gao *et al*, 2017). With the rapid development of hot-dip galvanising industry, a large amount of hot-dip galvanising dross will be produced every year. Recycling hot dip galvanising dross can not only alleviate the current situation of zinc resource shortage, but also can reduce environmental pollution. From this point of view, the recycling of hot-dip galvanising dross is of great significance to improve the sustainable development and cleaner production and further reduces the CO_2 emission of the whole process of the steel production. Moreover, the energy consumption intensity and material efficiency are improved for the low-carbon development.

At present, the recovery methods of the dross mainly include electrolytic preparation of cathode zinc, evaporation condensation or vacuum distillation recovery of zinc, chemical preparation of zinc salt etc (Gao, Zhong and Guo, 2016). These methods can successfully recover the metal, but have some notable limitations such as large capital investment, waste of certain energy or complex process which is not the best way to recover the metal from the dross. Super-gravity, as a way to greatly strengthen the mass transfer processes, can be used to achieve the high-efficiency recovery and utilisation of hot-dip galvanised dross (Li, Gao and Guo, 2016; Li, Guo and Gao, 2014; Zhao, *et al*, 2010).

This paper is to examine the feasibility with super-gravity to recover metal from hot-dip galvanised dross. The dross particles with small amount of intermetallic compound can be removed from the molten alloy bath under super-gravity field, and the purified metal could be directly returned into the bath for the production (Figure 1). In this study, the influences of gravity coefficient (G), separation time (t) and separation temperature (T) on the separation efficiency were investigated as well as the mechanism of super-gravity separation of galvanised dross, which can reduce the amount of zinc dross by more than 60 per cent (Figure 2) and achieve a reduction in zinc loss from 17 per cent to less than 7 per cent.

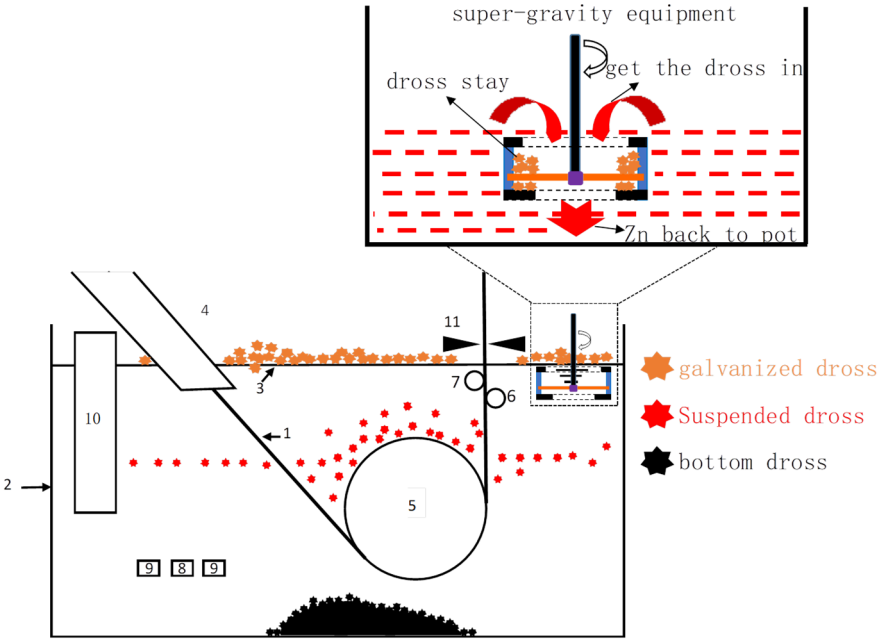

FIG 1 – Schematic diagram of online recycling and utilisation of zinc dross (1 - strip steel, 2 - zinc pot, 3 - zinc liquid level, 4 - furnace nose, 5 - sinking roller, 6 - correction roller, 7 - stabilisation roller, 8 - induction heater outlet, 9 - induction heater inlet, 10 - zinc ingot, 11 - air knife).

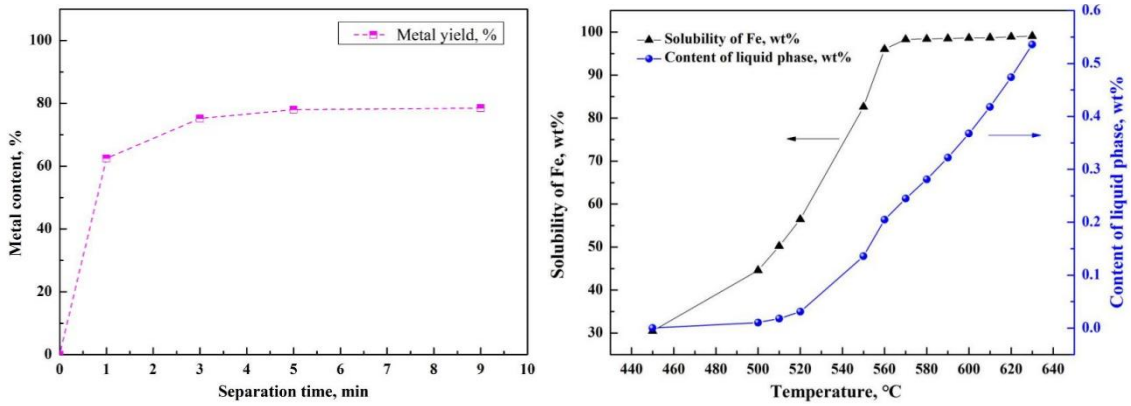

FIG 2 – The metal yield get from the super-gravity separation and calculate the solubility and liquid phase content of iron in the slag system using FactSage™ software.

CONCLUSIONS

- It examined the feasibility with super-gravity to recover metal from hot-dip galvanised dross.
- It was shown that it can reduce the amount of zinc dross by more than 60 per cent and achieve a reduction in zinc loss from 17 per cent to less than 7 per cent by the super-gravity equipment.

REFERENCES

Gao, J T, Li, Y, Xu, G L, Wang, F G, Lu, Y and Guo, Z C, 2017. Separation of olivine crystals and borate containing slag from CaO-SiO_2-B_2O_3-MgO-Al_2O_3 system by utilizing super-gravity, *ISIJ International*, 57(3):1–3.

Gao, J T, Zhong, Y W and Guo, Z C, 2016. Selective separation of perovskite (CaTiO3) from titanium bearing slag melt by super gravity, *ISIJ International*, 56(8):1352–1357.

Li, C, Gao, J T and Guo, Z C, 2016. Isothermal enrichment of P-concentrating phase from CaO-SiO_2-FeO-MgO-P2O5 melt with super gravity, *ISIJ International*, 56(5):759–764.

Li, J C, Guo, Z C and Gao, J T, 2014. Isothermal enriching perovskite phase from CaO-TiO_2-SiO_2-Al_2O_3-MgO melt by super gravity, *ISIJ International*, 54(4):743–749.

Zhao, L X, Guo, Z C, Wang, Z, *et al*, 2010. Removal of low-content impurities from Al by super-gravity, *Metall Mater Trans B*, 41(3):505–508.

Direct observation of the fayalite slag formation behaviour from large SiO_2 grains

DOI: 10.62053/JHAW7732

Y Goto[1,2], S Kawanishi[3], S Natsui[4], J Takahashi[5] and H Nogami[6]

1. Manager, Sumitomo Metal Mining Co., Ltd., Tokyo 105-8716, Japan. Email: yuko.goto.r4@smm-g.com
2. PhD student, Tohoku University, Miyagi, 980-8577, Japan. Email: goto.yuko.t7@dc.tohoku.ac.jp
3. Associate Professor, Kyoto University, Kyoto, 606-8501, Japan. Email: kawanishi.sakiko.6h@kyoto-u.ac.jp
4. Associate Professor, Tohoku University, Miyagi, 980-8577, Japan. Email: natsui@tohoku.ac.jp
5. Chief Staff, Research and Development, Sumitomo Metal Mining Co., Ltd., Tokyo, 105-8716, Japan. Email: junichi.takahashi.e4@smm-g.com
6. Professor, Tohoku University, Miyagi, 980-8577, Japan. Email: nogami@tohoku.ac.jp

ABSTRACT

The demand for copper increases yearly, and further improvements in copper smelting efficiency using flash furnaces are required. This study was conducted to understand and promote the interfacial reaction associated with the collision of silica flux and iron oxide particles, ie the formation reaction of fayalite slag, in the reaction shaft of the flash furnace. High-temperature microscopy was used to observe the reaction behaviour of a 2 mm granular SiO_2 reagent in contact with micrometre-order-sized FeO reagents *in situ*. When the amount of FeO was lower than the stoichiometric amount with SiO_2, the molten slag formed at the interface between FeO and SiO_2 diffused into the SiO_2 particle before dissolving the remaining FeO particles. It did not contribute to the subsequent reaction, and despite having the lowest amount of FeO among the samples in this study, many unreacted FeO particles remained on the surface of the samples after testing. On the other hand, under conditions with high FeO content and close to the eutectic composition of the FeO-SiO_2 system, a liquid phase formed from low temperatures, gradually increasing in volume and eventually completely dissolving the 2 mm SiO_2 grain. These results indicate that the early-stage slag is essential in increasing the interfacial area between FeO and SiO_2 and facilitating the supply of FeO to SiO_2. In other words, the FeO/SiO_2 determines the amount of liquid phase and significantly influences the subsequent interfacial reaction rate between FeO and SiO_2. Therefore, the local FeO/SiO_2 of the particles falling down the reaction shaft should also be optimised to ensure early slag formation. Meanwhile, the time required for 2 mm SiO_2 to complete the reaction for the temperature history employed in this study was significantly longer than the particle residence time in the reaction shaft. Further detailed investigation of the effects of silica flux particle size, composition, and reaction temperature on the reaction time will help find the conditions under which the reaction of silica flux can be completed in the reaction shaft. These kinetic approaches could contribute to future innovations in the copper smelting process using flash furnaces.

INTRODUCTION

Copper is mainly used in electrical and telecommunications infrastructure and small equipment. The demand for copper is increasing year by year due to the development of the global economy and the drive towards electrification (ICSG, 2023). With a new specific target of 'triple renewable energy by 2030' included in COP28 (Emirates 24/7, 2023), demand for copper is expected to grow further. In copper smelting, there is a need for technological innovations to increase smelting efficiency further.

Figure 1 shows a schematic diagram of the most common copper smelting furnace, the Outokumpu-type flash furnace (Kojo, Jokilaakso and Hanniala, 2000; Kojo, Reuter and Scheidema, 2015; ICSG, 2023). The copper concentrate consists of copper and iron sulfides, is injected through the concentrate burner with oxygen-enriched air and silica flux and reacts in the reaction shaft in the flash furnace. Sulfur in the concentrate is oxidised to SO_2 by oxygen-enriched air and separated into the gas phase. Iron in the concentrate is oxidised to iron oxide (FeO*x*), which further reacts with SiO_2 to form fayalite slag (FeO*x*-SiO_2). Copper in the concentrate is concentrated in copper matte (Cu_2S-FeS) by separating S and Fe. Copper matte is recovered from the slag by specific gravity separation

at the settler, tapped through the matte holes and sent to the converter. The viscosity of the molten slag and the presence of a spinel, eg Fe_3O_4, significantly affect the matte's settling rate, which in turn significantly affects the matte yield (De Wilde *et al,* 2016). For this reason, many studies on slag chemistry based on the equilibrium theory have been conducted, for example, by Muan (1955); Yazawa (1979); Vartiainen (1982); Taskinen, Dinsdale and Gisby (2005); Jak *et al* (2007); Shishin, Jak and Decterov (2018). Although the reaction shaft is the flash furnace's main reaction field, few studies still focus on slag formation behaviour in the reaction shaft. To the authors' knowledge, there are studies carried out by Takebe, Takahashi and Okura (2019); Nishioka *et al* (2022); Natsui *et al* (2023), but the discussions based on kinetics are insufficient.

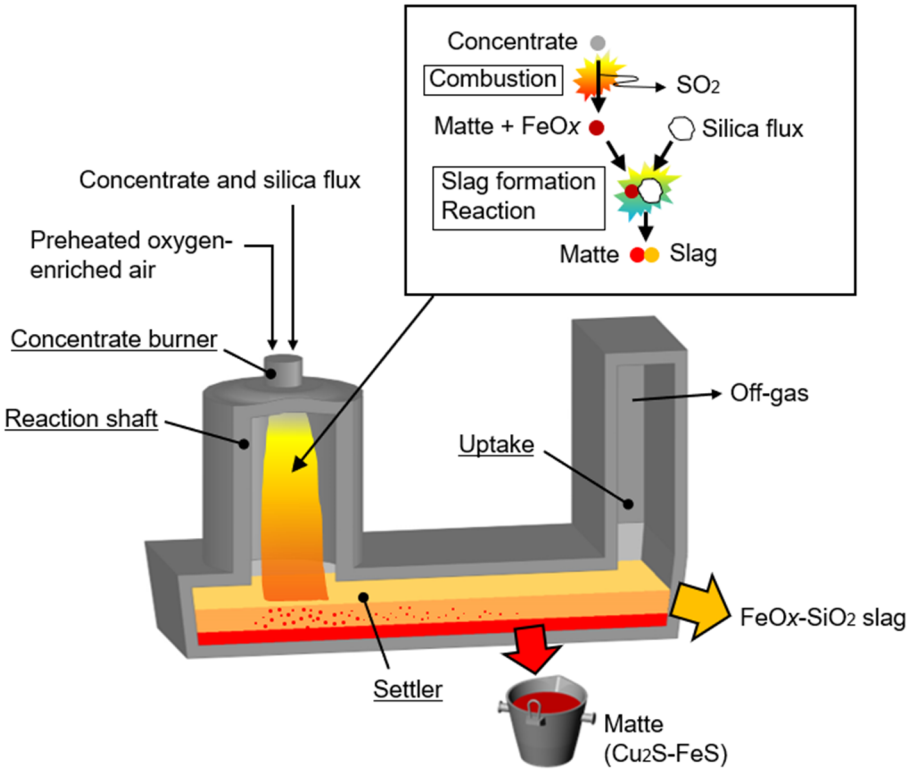

FIG 1 – Outokumpu type flash furnace and image of reaction mechanism in reaction shaft.

SiO_2, a raw material of fayalite slag, is supplied additionally to the flash furnace as silica flux. Silica flux can contribute to slag formation only if it is heated up to the reaction temperature and if it comes into contact with the iron oxides produced by the oxidation of the concentrate (Kemori, Denholm and Kurokawa, 1989; Goto *et al,* 2024). The silica fluxes, however, are unlikely to be heated quickly because their size is usually larger than that of the concentrates (Ahokainen and Jokilaakso, 1998; Taskinen and Jokilaakso, 2021). Furthermore, it is known that the residence time of the particles in the reaction shaft is extremely short, around 1 second or 2–3 seconds at most (Solnordal *et al,* 2006; Taskinen and Jokilaakso, 2021; Nirmal Kumar *et al,* 2022). A detailed understanding of the FeO*x*-SiO_2 interfacial reactions and the SiO_2 heating process is essential to complete the slag formation reaction within this short residence time.

To understand the formation behaviour of fayalite slag following the collision of silica flux and iron oxide particles in the flash furnace reaction shaft, this study observed the reaction behaviour of SiO_2 reagents in contact with FeO reagents *in situ* using high-temperature microscopy (Goto *et al,* 2024). Since the silica flux fed to the flash furnace generally has a larger grain size than the concentrate, this study used a 2 mm granular SiO_2 reagent and reacted with a micrometre-order-sized FeO reagent. The formation of fayalite slag from granular SiO_2 was directly observed and the effect of the FeO/SiO_2 ratio on fayalite slag formation behaviour was visualised.

EXPERIMENTAL WORK

Experimental apparatus

A schematic diagram of the high-temperature microscopy system used in this study is shown in Figure 2. The system consists of an infrared gold image furnace (SVF18SP, Yonekura MFG, Japan) for heating the sample, a microscope with a CMOS (Complementary Metal-Oxide Semiconductor) digital camera for observing the interface in the sample, a light source and an oxygen partial pressure controller (SiOC-200C, STLab Co., Ltd., Japan). The infrared gold image furnace has an oval-shaped chamber to which a dish-shaped sample holder with a thermocouple is attached at the upper focal point. The sample is heated by focusing infrared radiation. An observation window is mounted on the top of the chamber to observe the heated sample from outside the furnace. A microscope is installed above the observation window, and white light from the light source is irradiated through the microscope's objective lens onto the sample to obtain a bright-field image. A digital camera electronically records the variation of the sample appearance during the reaction. The oxygen partial pressure controller was used to control the oxygen partial pressure of the reaction atmosphere.

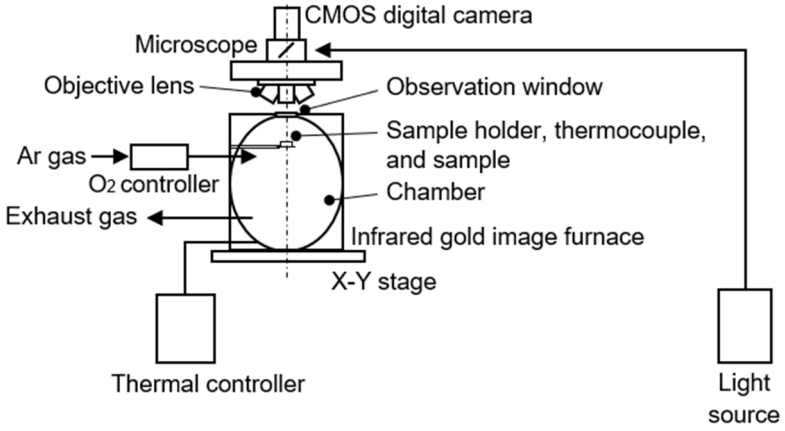

FIG 2 – Schematic diagram of the experimental apparatus.

Experimental procedures

The platinum pan (inner diameter 4.8 mm, depth 2.6 mm) with the sample was placed on the sample holder and the furnace was sealed. The furnace was depressurised to 5×10^{-2} Pa or less using an unshown vacuum pump. The gas in the furnace was then replaced by Ar gas with an adjusted oxygen partial pressure. The furnace was then heated while the temperature was measured using thermocouples. The melting behaviour of the samples was observed with a microscope through an observation window and an optical filter and recorded electronically using a CMOS digital camera. The image resolution was 960 × 600 and the frame rate was 30 fps.

Sample

In this study, FeO powder reagent (99.5 per cent purity, Kojundo Chemical Laboratory Co., Ltd., Japan) and cylindrical granular SiO_2 reagent with a diameter of 2 mm and a height of 2 mm (99.99 per cent purity, Kojundo Chemical Laboratory Co., Ltd., Japan) were used to prepare three different samples. The appearances of the samples before heating are shown in Figure 3. Each sample was prepared by placing FeO reagent on a single SiO_2 grain in a platinum pan, differing only in the amount of FeO reagent. Sample 1 was prepared by putting FeO reagent on a single SiO_2 grain with a molar ratio of FeO: SiO_2 = 2: 1 (Figure 3a). Sample 2 was prepared by placing a considerably smaller amount of FeO than the stoichiometric ratio on top of the SiO_2 grain as a small pile. Sample 3 was prepared by dispersing an even smaller amount of FeO than in Sample 2 on SiO_2 grain (Figure 3b). Samples 2 and 3 were prepared on the same platinum pan and heated simultaneously.

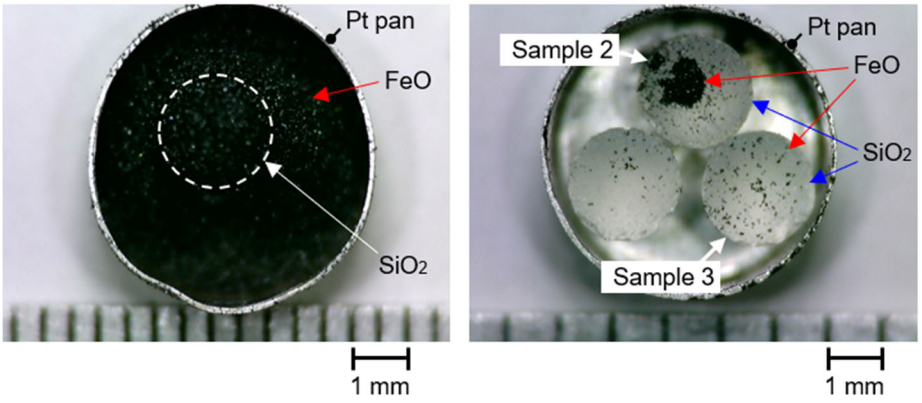

FIG 3 – Samples used in this study.

Experimental conditions

Ar gas of 99.999 per cent purity with a controlled oxygen partial pressure of around 10^{-9} atm was supplied at 200 cm^3/min. The furnace temperature was increased to a maximum of 1673 K, then held at 1673 K for 60 seconds before being lowered in the tests using Sample 1. In the tests using Samples 2 and 3, the furnace temperature was raised to a maximum of 1573 K and immediately lowered. The rate of temperature increase was 200 K/min from room temperature to 1273 K and 50 K/min from 1273 K to the maximum temperature for all samples.

The sample temperature was calibrated by the melting point of copper. The preliminary test of heating metallic copper on an alumina pan was conducted. The furnace temperature measured by the thermocouple at which the metallic copper began to melt was 5 K above the melting point of the copper. The following sections illustrate the results using sample temperatures corrected 5 K lower than the furnace temperature.

RESULTS AND DISCUSSION

Reaction behaviour of Sample 1

The morphological changes of Sample 1 (FeO/SiO_2 = 2) during heating up to 1668 K are shown in Figure 4. The elapsed time after the sample temperature reached 1268 K and the sample temperature are shown in the figure. At 1268 K (Figure 4a), the outline of the SiO_2 grain under the FeO can be seen. At 1413 K (Figure 4b), the outline of the SiO_2 grain is more clearly visible than in Figure 4a due to the furnace luminescence. Subsequently, the formation of a liquid phase at once around 1418 K (Figure 4c) can be seen on the SiO_2 grain. At 1423 K (Figure 4d), the SiO_2 grain starts tilting, suggesting that the reaction progresses at the bottom of the SiO_2 grain. At 1428 K (Figure 4e), the amount of the liquid phase further increases, and the FeO reagent, which appeared to be in a semi-molten state at the bottom of the Pt pan, started to deform as it peeled off from the Pt pan. The reaction progresses further in Figures 4f and 4g, and the SiO_2 grain tilts significantly. In Figure 4h, the SiO_2 grain is considerably soaked in the $FeO\text{-}SiO_2$ slag. Subsequently, as heating continues, the SiO_2 gradually becomes smaller, as shown in Figure 4i and Figure 4j, and at 1668 K (Figure 4k), the SiO_2 grain is almost invisible. The sample was then held at 1668 K for 60 seconds, but no significant change in the appearance of the molten sample was observed (Figure 4l). The time from the liquid phase formation (Figure 4c) to the completion of the reaction (Figure 4k) was 306 seconds. This is about two orders of magnitude longer than the typical residence time in the reaction shaft of a flash furnace.

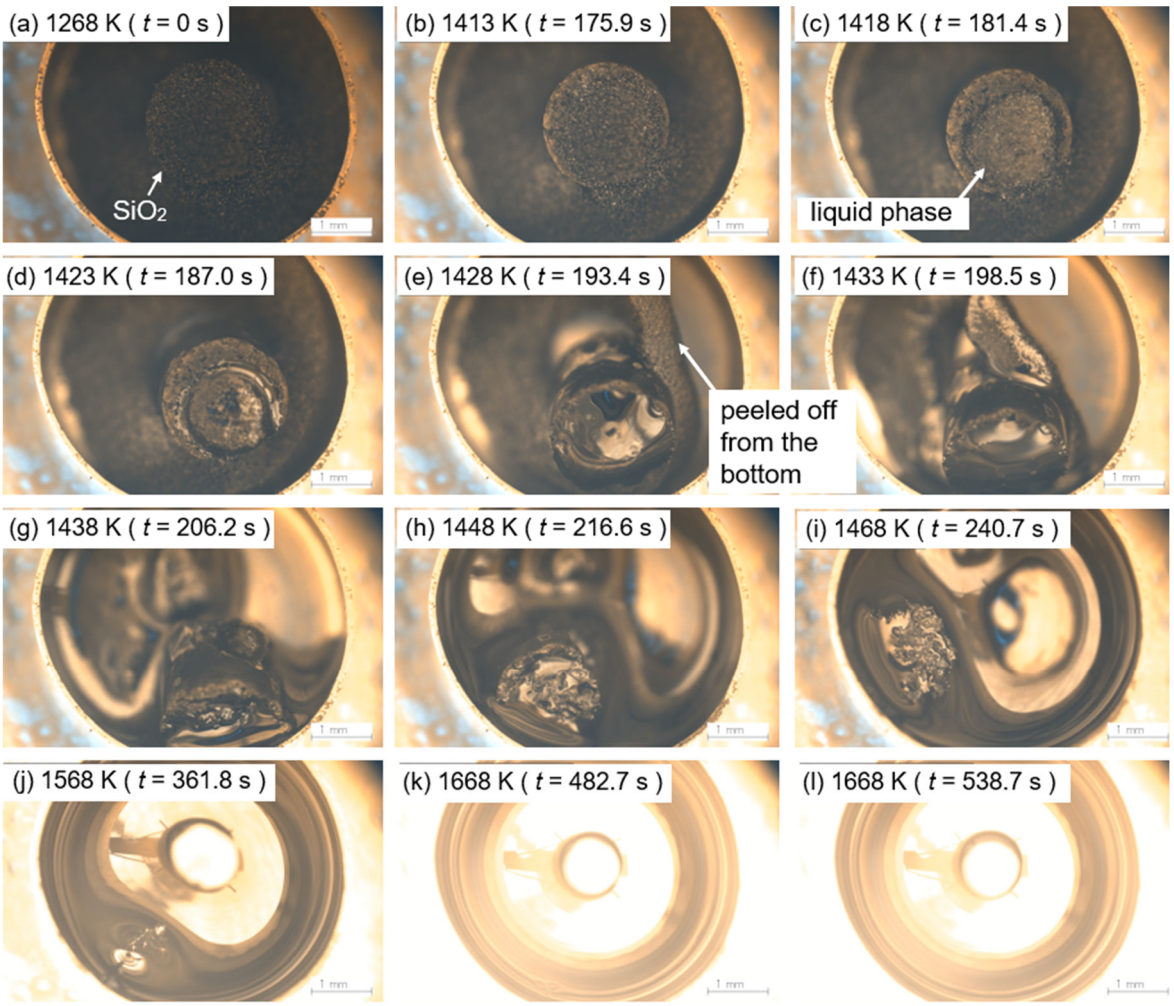

FIG 4 – The morphological change of Sample 1 during heating.

After the test, the sample was cut together with the Pt pan and an Electron Probe microanalysis (EPMA) of the vertical cross-section was performed. Figure 5 shows the elemental mapping of the cross-section of Sample 1 after the test. A material composed of Fe, Si and O can be seen in the corner of the platinum pan. The distribution of Fe, Si and O are uniform and the surface shape of the material is smooth. These results suggest that all the FeO and SiO_2 react and form a uniform melt, the FeO-SiO_2 slag.

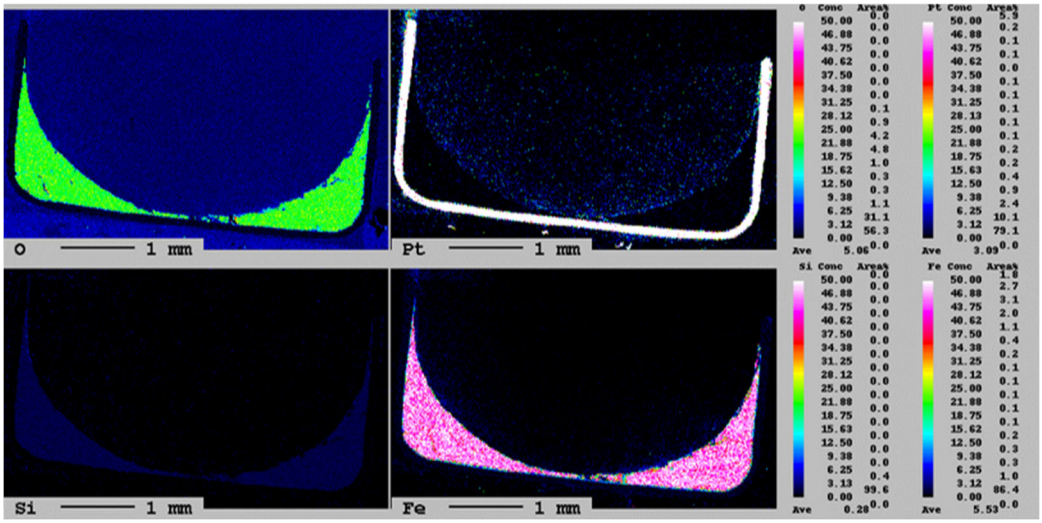

FIG 5 – EPMA image of a cross-section of sample 1 after the test.

Reaction behaviour of Samples 2 and 3

The reaction behaviour of samples with less amount of FeO was observed. Sample 2 is the sample with less than stoichiometric FeO placed as a pile on the SiO_2 grain, and Sample 3 is the sample with even less FeO sprinkled to disperse on the SiO_2 grain. They were placed on the same Pt pan and heated simultaneously to check the effect of the amount of FeO. Figure 6 shows the morphological change of Samples 2 and 3 during heating. Sample 2 is shown in the top right and Sample 3 in the bottom left. The elapsed time after the sample temperature reached 1268 K and the corresponding temperature are shown in the figure. At 1268 K (Figure 6a) and 1368 K (Figure 6b), angular FeO particles are visible on top of granular SiO_2 in Samples 2 and 3, suggesting that FeO exists in solid. At 1443 K (Figure 6c), some stains appeared near the FeO particles on the top surface of the SiO_2 grain in Sample 2, and at 1448 K (Figure 6d), the liquid phase became visible in the FeO reagent-rich areas. After that, the liquid phase quickly spread throughout the SiO_2 at 1451 K (Figure 6e). The liquid phase was absorbed by the SiO_2 grain at 1453 K (Figure 6f) and was almost invisible in Sample 2 by 1503 K (Figure 6g). Sample 3, on the other hand, showed no significant change in the appearance of FeO until 1503 K (Figure 6g). Further heating up to 1518 K (Figure 6h) resulted in several black stains spreading over Sample 3 at once. Subsequently, heating was continued up to 1568 K (Figure 6i), but no significant change in the sample appearance was observed for both Samples 2 and 3. In Samples 2 and 3, some particles remained in the central part of the stains on the SiO_2 grain surface.

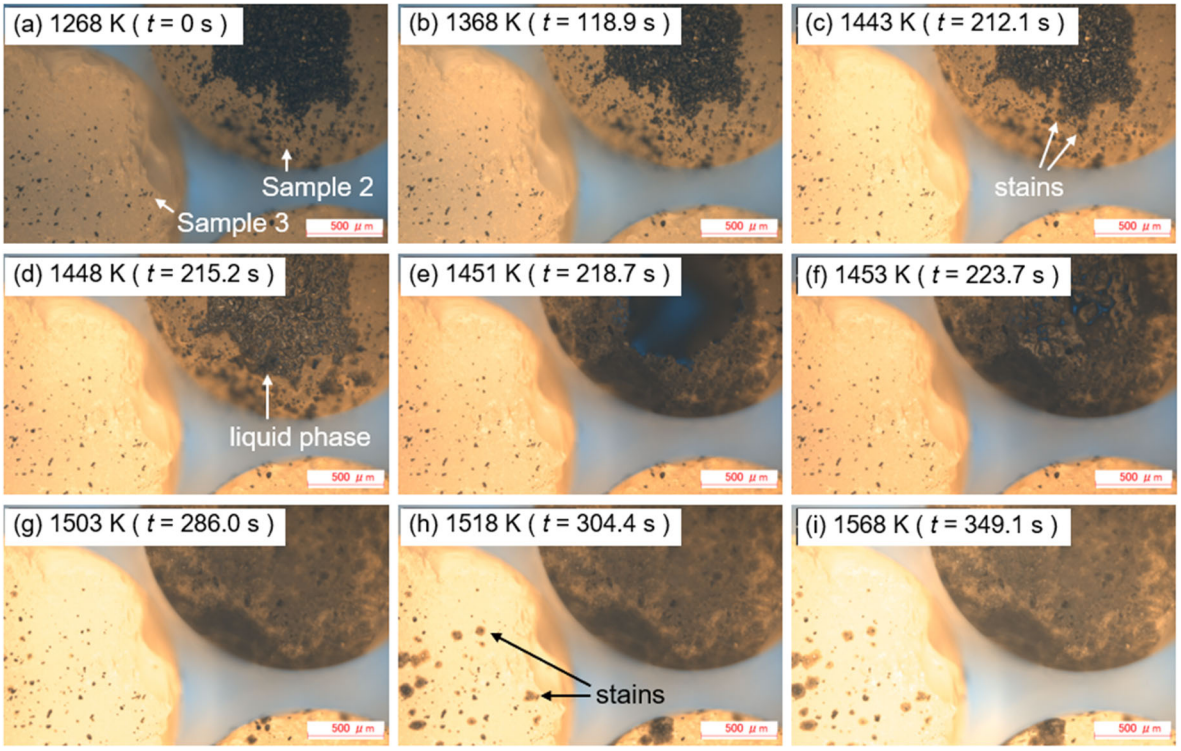

FIG 6 – The morphological change of Samples 2 and 3 during heating.

After the experiment, the surface of the samples was observed. The appearances of the post-test samples are shown in Figure 7. Figures 7a and 7b show the top surface of Samples 2 and 3, respectively. As in the observation image during heating shown in Figure 6, the stains produced by the reaction and several residual particles in the centre of the stains can be seen. In Sample 2, shown in Figure 7a, several stains were linked together to form a single mass. In the middle of the sample, where a large amount of liquid phase was generated, residual particles were hardly visible. On the other hand, in the areas where FeO was dispersed in Samples 2 and 3, the stains were dispersed, and residual particles could be seen in most stains.

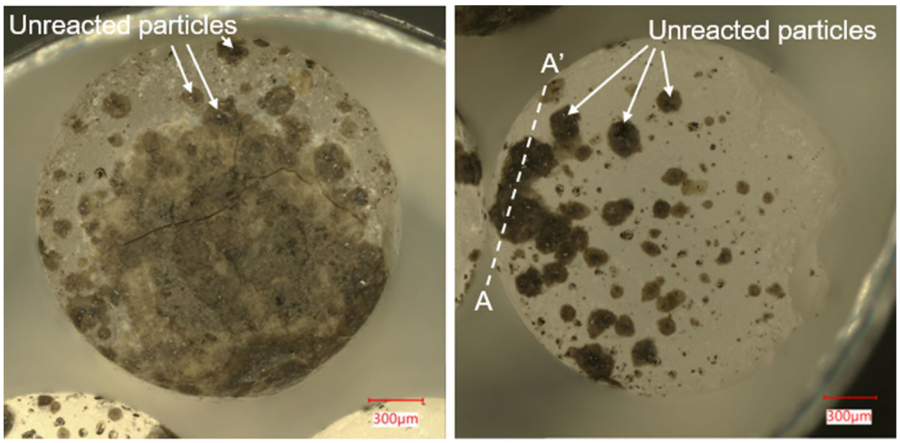

(a) Sample 2 (b) Sample 3

FIG 7 – Photos of Samples 2 and 3 after the experiment.

After the surface observation, Sample 3 was cut and a cross-section was observed by SEM (Scanning Electron Microscope). Figure 8 shows the SEM image of the cross-section A-A' of Sample 3 in Figure 7b. In Figure 8, white granular material can be seen on the bulk material. Under the white granule, the bulk material is cracked. The EDS (Energy Dispersive X-ray Spectroscopy) analysis shows that these are FeO particle, FeO-SiO_2 and SiO_2, respectively.

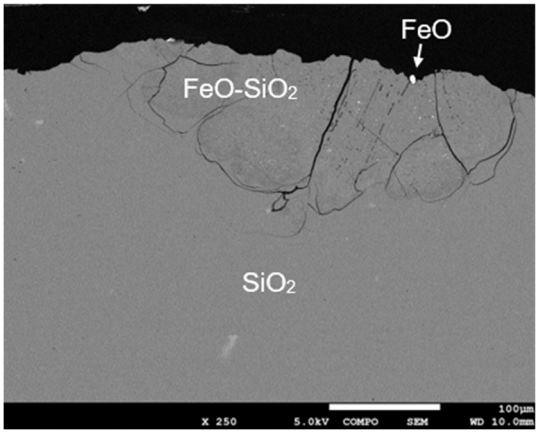

FIG 8 – SEM image of a cross-section of Sample 3 after the test.

Discussion

Table 1 summarises the test results of this study. Figure 9 shows the phase diagram of the FeO-SiO_2 system at pO_2 = 10^{-9} atm calculated by FactSage 8.3 (Bale *et al,* 2009) with the line corresponding to the overall composition of Sample 1 (FeO/SiO_2 = 2). Sample 1, with FeO/SiO_2 close to the stoichiometric ratio, had the lowest liquid formation temperature among the samples in this study. No unreacted FeO was identified in the post-test sample and the entire sample was in a completely liquid phase. This is because the overall composition of the sample was close to the eutectic composition, which allowed the liquid phase to form at low temperatures. The liquid phase further dissolved unreacted FeO and increased the volume. As a result, good contact between FeO and SiO_2 through the liquid phase was achieved. The FeO continued to be supplied to the unreacted bulk SiO_2 as there was sufficient FeO. Coexistence with FeO lowered the melting point of the SiO_2 interface and resulted in the dissolution of all of the SiO_2. On the other hand, in Sample 3, where the FeO was tiny relative to SiO_2, the temperature at which the liquid phase could be seen was 100 K higher than in Sample 1. Although Sample 3 had the lowest amount of FeO, many unreacted FeO particles remained on the sample's surface after the test. This is due to the few FeO particles, which resulted in a smaller contact interface area with SiO_2, delaying the progress of the reaction. Furthermore, the produced slag diffused into the SiO_2 before dissolving the remaining FeO particles. The composition of the SiO_2 inside was on the SiO_2-rich side of the eutectic point on the phase

diagram, resulting in a melting point higher than the test temperature reported here. This prevented the subsequent liquid phase formation and the complete dissolution of FeO.

TABLE 1

Comparison of reaction results for Samples 1–3.

		Sample 1	Sample 2	Sample 3
Experimental conditions	FeO/SiO_2	2	Smaller than 2	Extremely small
	Max furnace temperature	1673 K, 60 sec hold	1573 K, No hold	
Results	Temperature of liquid phase formation observed	1418 K	1448 K	1518 K
	The degree of reaction of FeO	All reacted	Partially remaining in areas with sparse FeO	Partially remaining

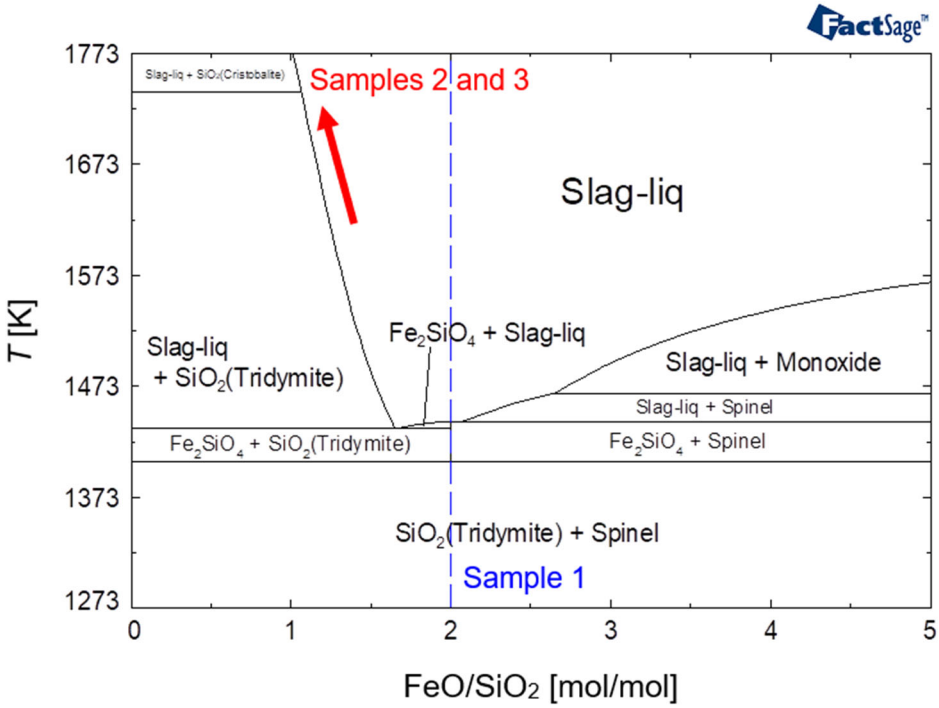

FIG 9 – $FeO\text{-}SiO_2$ phase diagram of $pO_2 = 10^{-9}$ atm calculated by FactSage 8.3.

To further improve the smelting efficiency of flash furnaces, it will be necessary to promote the slag formation reactions not only in the settler but also in the reaction shaft. This study shows that the reaction hardly proceeds when there is an excess of SiO_2 relative to FeO, even with small amounts of FeO. If the ratio of FeO to SiO_2 is close to the stoichiometric ratio, the reaction is accelerated because a liquid phase formed from low temperatures forms new reaction interfaces. In flash furnace operations, the raw material composition is usually controlled so that the FeO/SiO_2 ratio in the settler slag reaches the desired value, considering slag flowability. This study suggests that the local FeO/SiO_2 ratio in the reaction shaft should also be optimised to promote the formation of fayalite slag.

The 2-mm-size SiO_2 grain took 306 seconds to dissolve, even in Sample 1, which had the best reactivity among the test conditions in this study. This is considerably longer than the residence time in the reaction shaft. This means that if 2 mm pure SiO_2 were to be fed into the reaction shaft and the temperature history of this study, the slag formation reaction would not be complete in the residence time of the reaction shaft. Of course, a 2 mm feed is quite large in a flash furnace. In addition, the actual temperature history of the silica flux may be higher than the one in this study because there is a local high-temperature field in the reaction shaft (Hahn and Sohn, 1990; White *et al,* 2015). Future tests should provide a more detailed evaluation of the relationship between silica

flux particle size, reaction temperature and reaction time. This information could be combined with the temperature history of the particles and the frequency of collisions with iron oxides obtained from existing simulation techniques. The fayalite slag formation reaction in the reaction shaft could be predicted by this method, and the essential information could be obtained for completing the reaction of large silica fluxes within the shaft residence time. It could contribute to innovations in flash furnace technology in the copper smelting process.

CONCLUSIONS

In this study, to understand the fayalite slag formation reaction during a collision between iron oxide and silica flux in the reaction shaft of the flash furnace, the interfacial reaction behaviour between FeO powder and a large SiO_2 particle was directly observed by high-temperature microscopy. The FeO/SiO_2 significantly influences the rate of $FeO\text{-}SiO_2$ interfacial reaction because a liquid phase formed from low temperatures makes a new reaction interface and accelerates the reaction. The local FeO/SiO_2 in the reaction shaft must also be optimised to promote slag formation.

It is necessary to evaluate the effect of particle size, composition, and reaction temperature on the reaction rate in the future. These kinetic approaches may help to find the conditions under which the reaction can be completed, even with the large silica fluxes in the reaction shaft. It will contribute to future innovations in the copper smelting process using flash furnaces.

ACKNOWLEDGEMENTS

The authors are grateful to Mr Takashi Kamaya and Ms Miho Hayasaka of Tohoku University, who operated the SEM-EDS system at the Institute of Multidisciplinary Research for Advanced Materials (IMRAM), as well as Mr Hiroshi Takasuka of Sumitomo Metal Mining Co., Ltd., who operated the SEM-EDS system at the Sumitomo Metal Mining Co., Ltd.

REFERENCES

Ahokainen, T and Jokilaakso, A, 1998. Numerical Simulation of the Outokumpu Flash Smelting Furnace Reaction Shaft, *Canadian Metallurgical Quarterly,* 37(3–4):275–283.

Bale, C W, Bélisle, E, Chartrand, P, Decterov, S A, Eriksson, G, Hack, K, Jung, I H, Kang, Y B, Melançon, J, Pelton, A D, Robelin, C and Petersen, S, 2009. FactSage thermochemical software and databases – recent developments, *Calphad,* 33(2):295–311.

De Wilde, E, Bellemans, I, Campforts, M, Guo, M, Vanmeensel, K, Blanpain, B, Moelans, N and Verbeken, K, 2016. Study of the Effect of Spinel Composition on Metallic Copper Losses in Slags, *Journal of Sustainable Metallurgy,* 3(2):416–427.

Emirates 24/7, 2023, 13 December. COP28 delivers historic consensus in Dubai to accelerate climate action [online], from Emirates News Agency - WAM. Available from: <https://www.emirates247.com/sustainability/cop28/cop28-delivers-historic-consensus-in-dubai-to-accelerate-climate-action-2023-12-13-1.728660>

Goto, Y, Kawanishi, S, Natsui, S, Takahashi, J-I and Nogami, H, 2024. In Situ Microscale Observation of $FeOx–SiO_2$ Interfacial Reaction, *Metallurgical and Materials Transactions, B, Materials Science*. https://doi.org/10.1007/s11663-024-03063-9.

Hahn, Y B and Sohn, H Y, 1990. Mathematical Modeling of Sulfide Flash Smelting Process: Part, I, Model Development and Verification with Laboratory and Pilot Plant Measurements for Chalcopyrite Concentrate Smelting, *Metallurgical Transactions, B,* 21B:945–958.

ICSG, 2023. The World Copper Factbook 2023 [online], International Copper Study Group. Available from: <https://icsg.org/copper-factbook/> [Accessed: 14 Dec 2023].

Jak, E, Hayes, P, Pelton, A and Decterov, S, 2007. Thermodynamic optimisation of the $FeO\text{-}Fe_2O_3\text{-}SiO_2$(Fe-O-Si) system with FactSage, *Int J Mat Res,* 98(9):847–854.

Kemori, N, Denholm, W T and Kurokawa, H, 1989. Reaction Mechanism in a Copper Flash Smelting Furnace, *Metallurgical Transactions, B,* 20B:327–336.

Kojo, I V, Jokilaakso, A and Hanniala, P, 2000. Flash smelting and converting furnaces: A, 50 year retrospect, *JOM,* 52:57–61.

Kojo, I V, Reuter, M A and Scheidema, M N, 2015. Primary Copper Smelting Impact, *EMC*, pp 77–93.

Muan, A, 1955. Phase Equilibria in the System $FeO\text{-}Fe_2O_3\text{-}SiO_2$, *Journal of Metals*, pp 965–976.

Natsui, S, Goto, Y, Takahashi, J-I and Nogami, H, 2023. Pattern analysis of the combustions of various copper concentrate tablets using high-speed microscopy and video-based deep learning, *Chemical Engineering Science,* 276:118822.

Nirmal Kumar, S, Desai, B, Tathavadkar, V, Patel, Y, Patel, J, Singh, A, Vakil, K and Kanakanand, S, 2022. CFD modelling of copper flash smelting furnace – reaction shaft, *Mineral Processing and Extractive Metallurgy,* 132(1):49–61.

Nishioka, N, Tsurusaki, R, Hasegawa, S and Takebe, H, 2022. *Direct observation of the copper concentrates ignition and combustion reaction with a lab-scale experiment,* translated in Santiago, Chile.

Shishin, D, Jak, E and Decterov, S A, 2018. Thermodynamic Assessment of Slag–Matte–Metal Equilibria in the Cu-Fe-O-S-Si System, *Journal of Phase Equilibria and Diffusion,* 39(5):456–475.

Solnordal, C B, Jorgensen, F R A, Koh, P T L and Hunt, A, 2006. CFD modelling of the flow and reactions in the Olympic Dam flash furnace smelter reaction shaft, *Applied Mathematical Modelling,* 30(11):1310–1325.

Takebe, H, Takahashi, Y and Okura, T, 2019. Evaluation of Oxidation Reaction of Copper Concentrate Mixed with Silica Sand by Hot-Thermocouple Method, *Journal of Sustainable Metallurgy,* 5(2):210–218.

Taskinen, P and Jokilaakso, A, 2021. Reaction Sequences in Flash Smelting and Converting Furnaces: An In-depth View, *Metallurgical and Materials Transactions, B,* 52(5):3524–3542.

Taskinen, P, Dinsdale, A and Gisby, J, 2005. Industrial slag chemistry: A case study of computational thermodynamics, *Scandinavian Journal of Metallurgy,* 34(2):100–107.

Vartiainen, A, 1982. Schematic Presentation of Copper Losses within the Homogeneous Field of Fe-O-SiO_2 Slags, *Scandinavian Journal of Metallurgy,* 11:239–242.

White, M, Haywood, R, Ranasinghe, D J and Chen, S, 2015. The development and application of a CFD model of copper flash smelting, translated by CSIRO, Melbourne, Australia, pp 7–9.

Yazawa, A, 1979. Thermodynamic Evaluations of Extractive Metallurgical Processes, *Metallurgical Transactions, B,* 10B:307–321.

Combining the power of computational thermochemistry with the convenience of Python within the digital platforms of SMS group GmbH

DOI: 10.62053/HXTB3709

S Khadhraoui[1], M Reuter[2], A Akouch[3], C Kirmse[4], T Yusuf[5], R Degel[6], N Borowski[7] and E Hecker[8]

1. Senior R&D Engineer, RD Central Department, SMS Group GmbH, Duesseldorf 40266, Germany. Email: sabrine.khadhraoui@sms-group.com
2. Chief Expert Process and Technology, Department of Non-Ferrous Metallurgy, SMS Group GmbH, Duesseldorf 40266, Germany. Email: markusAndreas.reuter@sms-group.com
3. Data Expert, Department of Non-Ferrous Metallurgy, SMS Group GmbH, Duesseldorf 40266, Germany. Email: ali.akouch@sms-group.com
4. Senior Data Scientist, SMS Digital GmbH, Duesseldorf 40266, Germany. Email: christoph.kirmse@sms-group.com
5. Process Engineer, Department of Non-Ferrous Metallurgy, SMS Group GmbH, Duesseldorf 40266, Germany, Email: taopheeck.yusuf@sms-group.com
6. Vice President, Department of Non-Ferrous Metallurgy, SMS Group GmbH, Duesseldorf 40266, Germany. Email: rolf.degel@sms-group.com
7. Head of Technical Sales, Department of Non-Ferrous Metallurgy, SMS Group GmbH, Duesseldorf 40266, Germany. Email: nikolaus.borowski@sms-group.com
8. Head of Process Technology, Department of Non-Ferrous Metallurgy, SMS Group GmbH, Duesseldorf 40266, Germany. Email: erik.hecker@sms-group.com

ABSTRACT

For an optimal design and control of metallurgical processes, a deep understanding of the thermodynamics of the governing reactions is required. Modelling the thermochemical behaviour of those reactions is complex, as it involves multi-component and multi-phase systems. For this purpose, thermodynamic computing systems such as FactSage™ (Bale *et al*, 2016), which combine Gibbs energy minimisation routines with large databases of optimised thermodynamic data of solutions and compounds, have been used within the SMS group GmbH.

Recently, the successful integration of those thermodynamic computing systems into the digital platforms of SMS has been achieved through ChemApp, which made running complex thermochemical calculations in Python-integrated development environments possible. ChemApp is a programmer's package for thermochemistry and incorporates the Gibbs energy minimiser of FactSage™ as reported by Petersen and Hack (2007) as well as by Zietsman and Petersen (2018). The digital platforms link the fundamental and the industrial aspects together and can be applied as a process advisor, or for the evaluation of the environmental footprint and the economic implications of different process routes, as discussed by Reuter (2023). Two examples illustrating the progress of the developments in this regard will be introduced:

1. The Tilting Refining Furnace (TRF) for copper scrap recycling and refining to anode copper (the BlueControlApp).
2. Dephosphorisation control for the oxygen steelmaking process (Basic Oxygen Furnace (BOF)).

INTRODUCTION

The future of metals is circular and carbon neutral. To achieve this, a thorough evaluation of the thermodynamic behaviour of the systems involved is crucial. This evaluation is necessary for a comprehensive understanding of the system, allowing us to characterise its thermodynamic behaviour to the full extent, quantify its limitations and minimise the gap depicted in the top left of Figure 1.

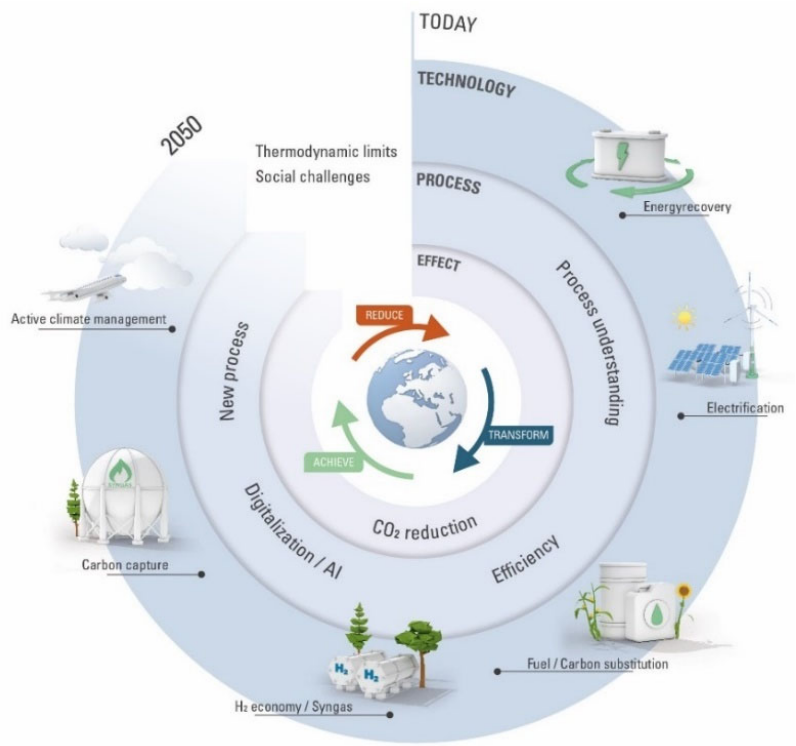

FIG 1 – Integration of process understanding, digitalisation and innovation via the digital platforms of the SMS group GmbH.

Figure 1 illustrates the necessity of robust digital platforms for accurately quantifying the limitations of larger systems. These platforms facilitate scaling the physics of reaction interfaces in metallurgical reactors, which are instrumental in processing and recycling systems and guiding the product design. Consequently, it's crucial to thoroughly quantify the exergy efficiency of the entire system. Here, thermodynamics also plays an integral and important part in quantifying the performance relative to a rigorous baseline laying the groundwork for a comprehensive understanding of green premiums and their role in driving innovation within the system (Reuter, 2023).

Using ChemApp (Petersen and Hack, 2007; Zietsman and Petersen, 2018), it has become possible to run complex thermochemical calculations within the Python-based Integrated development environment (IDE). ChemApp is a programmer's package for thermochemistry and incorporates the Gibbs energy minimiser of FactSage™.

Later, two examples illustrating the progress of the developments in this regard will be introduced.

APPLICATION FOR THE TRF FURNACE – THE BLUECONTROL APP

In order to refine copper scrap, the SMS group GmbH uses a tilting refining furnace (TRF). By combining the TRF with a casting wheel, high-quality anodes are produced. In other words, when combined with the casting wheel, TRF can execute the melting, refining and casting of copper scrap in one flexible unit. However, as discussed by Reuter (2023), despite multiple advances in the process control of such furnaces, a certain degree of operator intervention is still required. Although there are modern process control methodologies available such as artificial intelligence techniques, the current process control input is primarily based on the operator's and/or metallurgist's expertise and intuition, rather than solely relying on these advanced techniques.

As shown in Figure 2, the tilting refining furnaces operate through a series of stages. Initially, the scrap is melted. Subsequent stages involve the removal of impurities such as Al, Fe, Ni, Pb, Sn, Zn etc, which are transferred from the copper alloy into the slag by oxidation. This purification begins indirectly during the smelting of high-grade scrap, but due to limited slag uses, the final oxidation step(s) after charging and smelting are necessary.

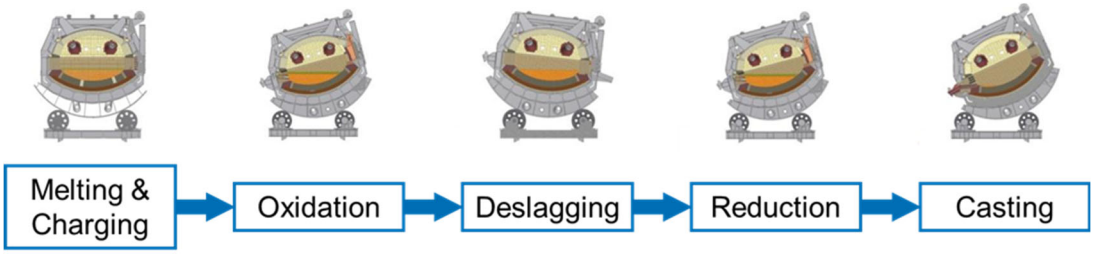

FIG 2 – Tilting refining furnace (TRF) and its various steps, oxidation can happen in 1 to 3 steps depending on the scrap feed quality and required anode quality.

Non-linear solution chemistry of slag and copper affects the distribution of elements from copper to slag and off-gas. Obviously, the flow of gas through the system especially affects the distribution of elements and compounds with higher vapour pressure. Inefficiencies due to mass and heat transfer and fluid flow also have an effect.

Although a TRF is seemingly a simple system, various non-linear interconnected physical processes complicate the prediction of possible outcomes, ie metal quality. A full cycle of melting, oxidising, refining and casting typically takes approximately 24 hours. Optimising the feed mix for a desired outcome requires substantial computational effort, as it involves repeatedly solving numerous 24-hour cycles using the Gibbs energy minimisation method. Typical operational parameters to be optimised can include:

- correct quantity and mix of fluxes to achieve the desired flux type, fayalite/olivine (Figure 3), calcium- or calcium silicate-based
- the processing steps and times
- lambda of the burner, which denotes the ratio of actual air supply to the stoichiometric air requirement for complete fuel combustion
- quantity and type of oxidising and reducing gases
- temperature
- indirect parameters, such as viscosity
- oxidation or reduction gas rate.

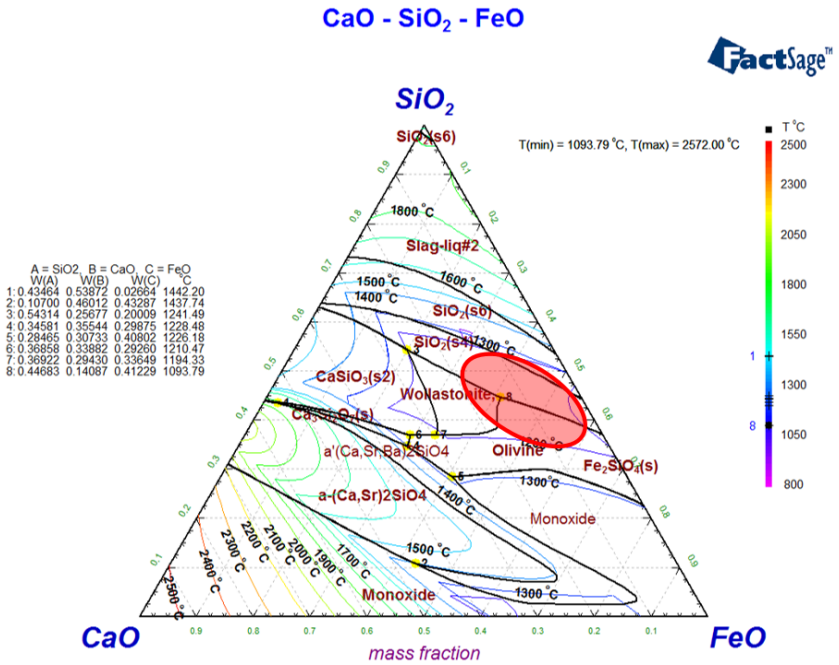

FIG 3 – Example target slag compositions for the copper refining for an operating point for an olivine.

The above said would suggest that the involvement of human intervention and decision-making in the production and refining processes of copper scrap may lead to various adverse outcomes. These might include inefficiencies in anode production mass, inconsistent anode quality, ie impurities outside of desired levels, unreliable parameters, eg slag viscosity, significant deviations from customer yield targets, suboptimal refining processes, ie not reaching the targets for an anode, lengthy decision-making periods and heavy reliance on skilled operators and metallurgists with specialised knowledge of these processes. These downsides can lead to increased costs and reduced productivity.

For this purpose, SMS has developed the BlueControl application, to support the metallurgists as well as the operators in designing, analysing, controlling and optimising the copper refining process. The application can be further used for the training of operators and for calculating the process outcomes under different operating conditions (linked directly to the thermochemical software library ChemApp). As shown in Figure 4, the BlueControlApp has two main calculation features:

1. Simulation: The executed dynamic simulations use thermochemical equilibrium software FactSage™ (Bale *et al*, 2016), with a ChemApp interface, to perform Gibbs free energy minimisation. Unfortunately, since the Gibbs free energy minimisation algorithm uses the constrained and non-linear optimisation method, the calculations can be time-consuming. For example, using FactSage™ with a ChemApp interface may take a single oxidation simulation (single refining cycle) up to 2 mins and about 20 sec to execute.
2. Optimisation: Based on the copper scrap weight and its composition, feed temperature, oxidation gas rate and reduction gas rate, the optimisation application finds the ultimate fluxes combination. The resulting flux combination assures the highest possible copper amount and the lowest possible amount of impurities at the end of the refining process (purest copper anode). This will improve production efficiency, yield, quality, throughput and reduce production costs.

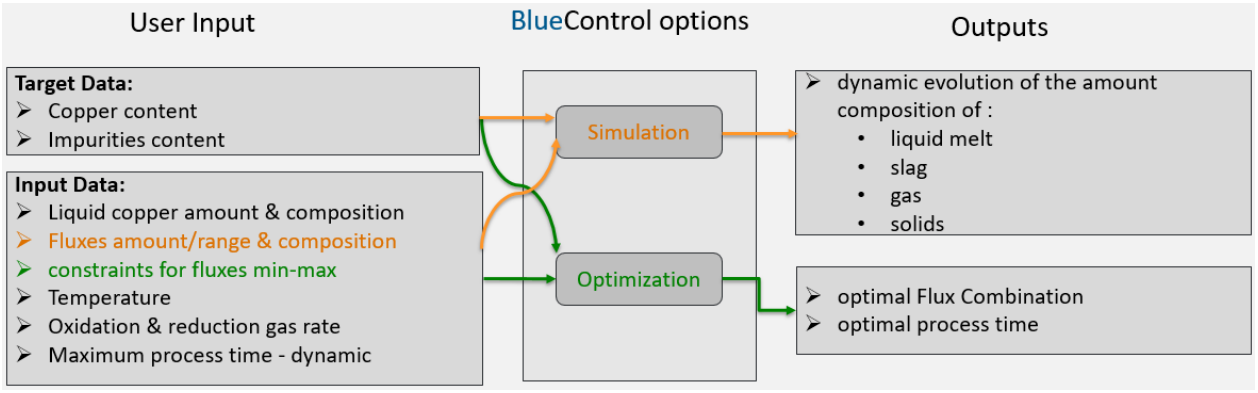

FIG 4 – Schematics of BlueControlApp.

Moreover, the optimisation process is based on the calculations done by the simulations, making it time-consuming. To illustrate more, using the BlueControlApp optimiser to find suitable fluxes combinations requires running a tremendous number of simulations, where each simulation resembles specific input values used during the copper refinement process. Recalling that such simulations are based on the time-consuming ChemApp interface, the optimisation process itself will be also time-consuming. This can lead to tremendous production delays and an increase in production cost, thus making such analyses infeasible. To handle this issue, Akouch *et al* (2023) developed a surrogate model, which corresponds to a statistical model that accurately approximates the FactSage-based simulation outputs within seconds and not minutes.

The surrogate model is considered as a supervised machine learning model, where the model is trained to recognise patterns and physical relationships between the input-outputs of the copper refining process. Using the surrogate model as a core model to run BlueControl simulations/optimisation, made it possible to accurately estimate in real-time the costly and time-consuming simulations/optimisation.

APPLICATION FOR THE BASIC OXYGEN FURNACE (BOF) PROCESS – DEPHOSPHORISATION CONTROL

The next example illustrating the need to integrate computational thermochemistry into digital platforms is the control of phosphorous removal from steel during the oxygen steelmaking route, denoted as ‘steel dephosphorisation’.

Phosphorus is introduced to the blast furnace through the charged iron ore and ends up almost completely in the discharged liquid metal. The dissolved phosphorus must be removed from the liquid metal up to levels below 150 ppm due to its detrimental effect on the quality of steel. This occurs in the next aggregate, the BOF process (Basic Oxygen Furnace) through oxidation of phosphorus to P_2O_5, which is then bound into the slag phase. To ensure that the phosphorous oxide remains in the slag, the process should be operated in a way that sets favourable conditions for P_2O_5 stability in the slag. Otherwise, P_2O_5 is reduced and the phosphorous returns to the liquid metal denoted as ‘steel rephosphorisation’. It is well established that the dephosphorisation potential of the slag increases with its CaO and FeO content while it decreases with temperature.

In previous works (Khadhraoui *et al*, 2018, 2019; Khadhraoui, 2021), it has been reported that BOF slags are heterogeneous for a large part of the process containing a liquid phase and a variety of solid phases. The solid phase $2CaO.SiO_2$ (C2S) is particularly interesting for dephosphorisation, as it is capable of dissolving phosphorous through the formation of the $2CaO.SiO_2$–$3CaO.P_2O_5$ (C2S_C3P) phase, which increases the dephosphorisation potential of the heterogeneous slag. The formation of other solid phases, which do not dissolve phosphorous such as the $3CaO.SiO_2$ (C3S) phase, as well as the MgO- and CaO-based solid monoxide solutions, decreases the dephosphorisation potential. Thus, the optimal slag zone for dephosphorisation is suggested to lie within the single C2S saturation regions, indicated by the blue-marked area in Figure 5, which presents the phase diagram of the main oxide system for BOF slags, the CaO-FeO_x-SiO_2. However, the ratio of the C2S phase in the heterogenous slag has to be controlled carefully below a certain value, otherwise, its positive effect on dephosphorisation can be counteracted by the negative effect on the kinetics of dephosphorisation, as it decreases the mass transfer coefficient of the slag. Thus, the target region for optimal dephosphorisation has to be narrowed further, as indicated by circle A in Figure 5.

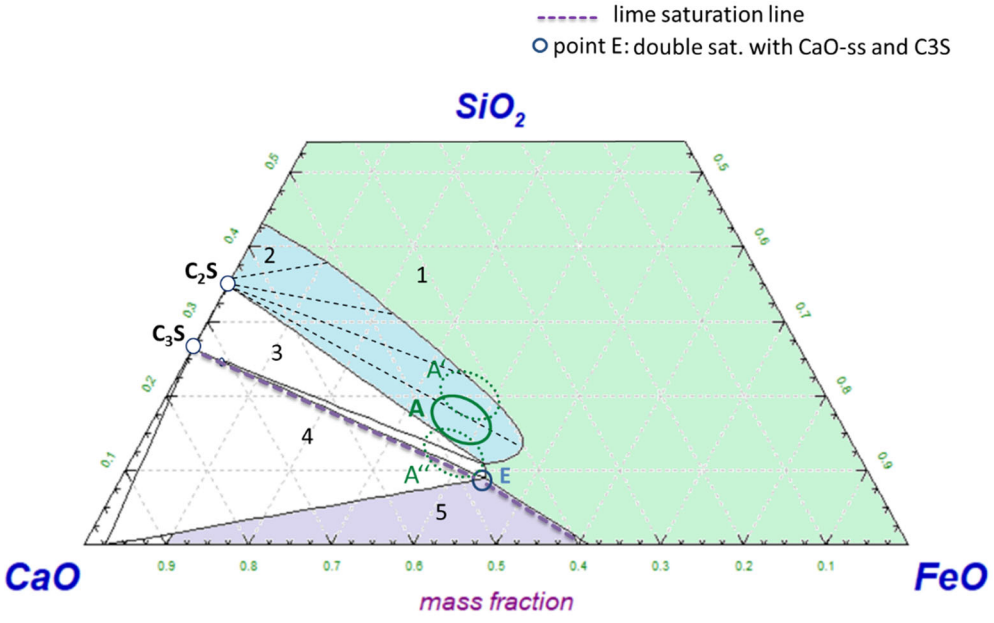

FIG 5 – Position of the alternative target slag regions A and B, suggested for optimal dephosphorisation results in the CaO-FeO_x-SiO_2 system, at 1973 K (1700°C) and for a reduced $p(O_2)$ state.

Controlling the slag composition during the BOF process towards the target region, indicated by region A in Figure 5, is associated with the following challenges:

- Identifying the actual composition of the slag: The CaO oxide is formed through the addition of CaO-containing fluxes such as lime and limestone. The further major components FeO and SiO_2 are formed through the oxidation of Fe and Si from the metal phase, respectively. Due to its high oxygen affinity, Si oxidises almost completely within the first minutes of the process and the mass of SiO_2 in the slag remains constant for the rest of the process. The FeO content of the slag is distinguished by a dynamic behaviour and is largely affected by the process operation (oxygen lance height, oxygen flowing rate etc) and the decarburisation rate. The FeO in the slag further acts as a fluidising agent for the slag and helps dissolve the lime charged into the furnace. Thus, in addition to temperature, the amount of CaO dissolved in the slag is a strong function of FeO evolution. For identifying the actual position of the slag in the phase diagram shown in Figure 5, functions or modules for the determination of the evolution of the main slag components as well as the temperature based on the actual process data are required.
- Identifying the target composition of the slag: The phase boundaries of the CaO-FeO_x-SiO_2 oxide system are a strong function of the process temperature, the p(O_2) levels as well as of the minor oxide contents such as MgO, MnO, Al_2O_3. This implies that the composition of the target slag region, indicated by circle A in Figure 5 should be adjusted accordingly. Examples of adjustment of the target composition in case of an increase in temperature, in the presence of 7 per cent MgO and 4 per cent Al_2O_3 are presented in Figure 6b, 6c and 6d respectively. For this purpose, ChemApp can be applied for the accurate determination of the thermochemical behaviour of the actual oxide system at the conditions prevailing in a furnace.

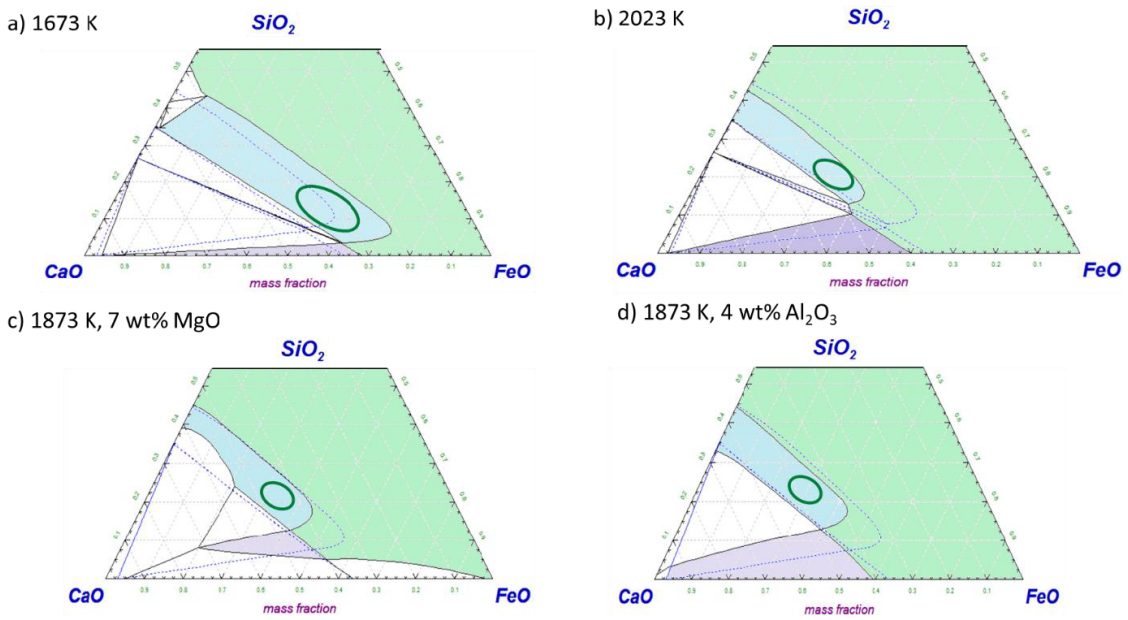

FIG 6 – Target slag compositions for optimal dephosphorisation in the BOF furnace. Examples of the adjustment of the position of the optimal target slag region (green circle) in the CaO-FeO_x-SiO_2 oxide system at reduced p(O_2) state as a function of temperature: (a) 1673 K (1400°C), (b) 2023 K (1750°C) and depending on the minor oxide content of the system: (c) 7 wt per cent MgO at 1873 K (1600°C), d) 4 wt per cent Al_2O_3 at 1873 K (1600°C). The dashed lines represent the phase boundaries of the ternary system at 1873 K.

In summary, the determination of the dynamic evolution of the slag composition and temperature, as well as the adjustment of the corresponding target zone are required for deciding on the necessary measures to be taken to achieve dephosphorisation targets. Figure 7 provides an example of how computational thermochemistry can be integrated into the dynamic dephosphorisation model through ChemApp. Actual process data, such as the oxygen blowing rate, the lance height profile, the input time, and the input amounts of fluxes define the input for dynamic process modules which are mainly based on mass and energy balance equations. The calculation output of other modules, such as the amount of dissolved lime is also required. The dynamic process modules deliver information on the evolution of the process temperature as well as on the evolution of the main slag

components, such as CaO, FeO, SiO_2, MnO and MgO. The results are fed into the ChemApp module, which, in turn, calculates the actual and the target slag compositions. The necessary corrective measures to be undertaken to minimise the deviation between actual slag and target slag state are determined and controlled by further dynamic modules. For example, the CaO content and/or the FeO content of the slag can be adjusted toward the target values by charging lime and/or modifying the blowing profile. The options available for undertaking the corrective measures may differ depending on the processing stage.

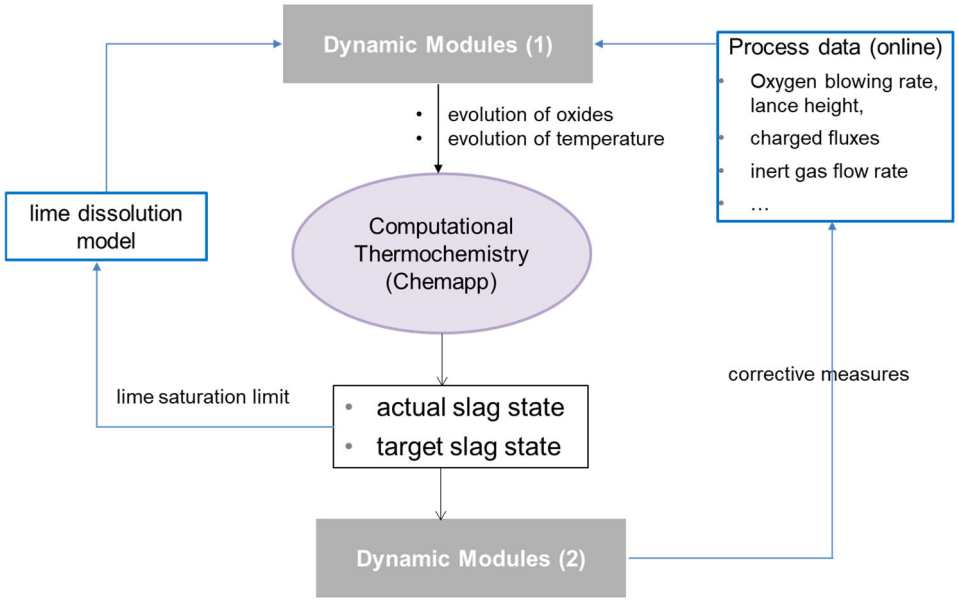

FIG 7 – Concept for the implementation of computational thermochemistry in the dynamic dephosphorisation model.

To overcome the limitations associated with the high computational effort, the surrogate model approach, introduced in the previous section for the TRF furnace, can be applied.

CONCLUSION

The development of robust digital platforms serves as a basis for the integration of process understanding, digitalisation and innovation into the industrial plants. The direct integration of computational thermochemistry into those digital platforms through ChemApp opens new possibilities for enhanced process control for the metallurgical industry. A surrogate-based modelling approach is adopted to overcome the limitations associated with the high computational efforts, thus making it suitable for online application. The examples discussed in this work illustrate the benefits for both the ferrous and non-ferrous metallurgical industry.

REFERENCES

Akouch, A, Reuter, M A, Kirmse, C, Bruns, M, Khadhraoui, S, Degel, R, Hecker, E and Borowski, N, 2023. Deep learning of thermodynamic equilibria for optimized process control, in *Proceedings European Metallurgical Conference 2023* (GDMB Gesellschaft der Metallurgen und Bergleute e.V: Duesseldorf).

Bale, E B C W, Chartrand, P, Decterov, S A, Eriksson, G, Gheribi, A E, Hack, K, Jung, I H, Kang, Y B, Melançon, J, Pelton, A D, Petersen, S, Robelin, C, Sangster, J, Spencer, P and Van Ende, M A, 2016. FactSage Thermochemical Software and Databases – 2010–2016, *CALPHAD*, 54:35–53.

Khadhraoui, S, 2021. A Contribution to Modeling and Control of Dephosphorisation, Doctoral thesis, University of Duisburg-Essen.

Khadhraoui, S, Hack, K, Jantzen, T and Odenthal, H, 2019. Study of the State of Industrial P_2O_5-Containing Slags Relevant to Steelmaking Processes Based on a New Thermodynamic Database Developed for CaO–FeOx–P_2O_5–SiO_2–MnO–MgO–Al_2O_3 Slags. *Steel Research Int*, 90:1900085. https://doi.org/10.1002/srin.201900085

Khadhraoui, S, Odenthal, H, Das, S, Schlautmann, M, Hack, K, Glaser, B and Woolf, R, 2018. A new approach for modelling and control of dephosphorization in BOF converter, *La Metallurgia Italiana*, (11–12):5–16.

Petersen, S and Hack, K, 2007. The thermochemistry library ChemApp and its applications, *International Journal of Materials Research*, 9:935–945.

Reuter, M A, 2023. The fundamental limits of circularity quantified by digital twinning, in *Handbook of Recycling: State-of-the-art for Practitioners, Analysts and Scientists* (eds: C Meskers, E Worrell and M A Reuter), second edition, chapter 2 (Elsevier).

Zietsman, J and Petersen, S, 2018. ChemAppPy - A Python interface to ChemApp, paper presented to the RCCM-GTT Users' Meeting, Tokyo, 7 November.

Hy^3 (Hy-cube) project – Hyundai Steel's carbon neutral strategy

DOI: 10.62053/ZJLY1406

H Kim[1] and M J Sun[2]

1. Team Leader, Hydrogen Reduction Research Team, Hyundai Steel, Dangjin-Si 31719, South Korea. Email: hyuk923@hyundai-steel.com
2. Research Engineer, Hydrogen Reduction Research Team, Hyundai Steel, Dangjin-Si 31719, South Korea. Email: minjoo8454@hyundai-steel.com

ABSTRACT

In order to reduce carbon emissions from the steelmaking process and achieve carbon neutrality, global steel companies are establishing their own medium to long-term strategies and implementation plans using competitive technological advantages held by each steel company. At this point, Hyundai Steel has formulated a product-oriented carbon-neutral strategy based on innovative processing that makes use of Hyundai Steel's own strength. Based on our experience in electric arc furnace product manufacturing and blast furnace operation in an integrated steel mill, Hyundai Steel is driving the Hy^3 (Hy-cube) project, which involves a unique hybrid production system utilising hydrogen and hydrogen-based renewable energy sources. This initiative aims to achieve carbon-neutral production and eventually specialise in producing premium carbon-neutral automotive parts. The project has originality in that it involves not only designing processes using electric furnaces to produce premium steel products such as car body panels and electrical steel sheets, but also aims to reduce carbon emissions from the process, developing carbon-neutral products based on market demand. To assess the feasibility of the Hy^3 project, Hyundai Steel conducted two pilot productions. The first pilot was producing a prototype of lower-arm part using electric arc furnace with three different kinds of raw materials: molten iron, HBI (hot briquetted iron), and scrap. Successful performance evaluation of auto parts with 1 GPa strength was achieved. The second pilot has been focused on tire cord steel, with the first-phase tests yielding a 33 per cent reduction in carbon footprint (CFP). Using the advantages of operating experience in electric arc furnace, Hyundai Steel is preparing for test operations producing various automotive parts using an electric arc furnace (EAF) to advance the Hy^3 concept. From a medium to long-term technological development perspective, Hyundai Steel's blueprint includes producing high-end carbon-neutral steel products using hydrogen-reduced iron as raw material.

INTRODUCTION

Hyundai Steel's journey has been marked by a dynamic shift in manufacturing methodologies. Founded in 1953 and later integrated into the Hyundai Group, the company initially operated a flat bath furnace. Over the years, its focus evolved, leading to the incorporation of electric arc furnaces for long product manufacturing. A pivotal moment occurred in 2004 when Hyundai Motors, Hyundai Steel's parent company, sought flat products for automobiles, prompting a strategic merger with Hanbo Steel. This move, however, entailed divesting the COREX process in favour of preparing blast furnaces. The subsequent years witnessed Hyundai Steel's foray into blast furnace operations, with the commissioning of the first blast furnace in 2010 and the simultaneous initiation of one more in 2010. Presently, the company operates three blast furnaces with identical inner volumes and capacities, forming the backbone of its steel production capabilities.

Hyundai Steel's product portfolio is a testament to its versatility and market adaptability. Approximately 50 per cent of its production caters to flat products, supplying critical components for automobiles, line pipes, and thick plates. Key clients include Hyundai and Kia Motors, as well as global automotive giants such as Volkswagen. The remaining production output, constituting long products, serves the construction sector with materials like H-beams and wire rods. Notably, Hyundai Steel also operates a mini mill line dedicated to special steel.

This balanced product mix positions Hyundai Steel as a robust player in the steel industry, enabling it to weather market fluctuations and meet diverse customer demands. This strategic balance lays the foundation for Hyundai Steel's distinctive approach to achieving carbon neutrality.

In response to the global imperative of reducing carbon emissions, Hyundai Steel has undertaken a strategic shift towards carbon neutrality. The steelmaking industry, traditionally reliant on blast furnace processes, is grappling with the challenge of minimising CO_2 emissions. Hyundai Steel recognises that achieving a zero-carbon footprint necessitates a departure from conventional blast furnace routes.

The carbon emissions associated with blast furnaces arise from the use of carbon as a reductant and fuel. To eliminate CO_2 emissions from this process, Hyundai Steel has embarked on a multifaceted strategy. This involves substituting coke with hydrogen, transitioning from blast furnaces to Direct Reduction (DR) plants, and replacing converters with electric arc furnaces.

THE HY-CUBE PROJECT

The global steel industry is undergoing a paradigm shift, with various companies exploring alternative iron and steelmaking processes to reduce CO_2 emissions. Hyundai Steel's counterparts, such as Voestalpine in Austria and POSCO in South Korea, are actively engaged in projects like H2FUTURE and HyREX, respectively, testing new processes utilising renewable energy sources.

Hyundai Steel, with its rich history in electric arc furnace operations dating back to 1953, identifies its strength in this area. Operating a maximum of 13 electric arc furnaces concurrently, including AC, DC, and TWIN types, the company has accrued extensive experience in both process technology and product development. Noteworthy is Hyundai Steel's use of HBI as an alternative to scrap in one of its electric arc furnaces in 2015, a testament to its commitment to innovation.

Considering Hyundai Steel's business structure and strengths, the company has devised a unique approach to carbon neutrality – the Hy-cube project (Figure 1). This project aligns with the global trend of exploring new steelmaking processes that leverage renewable energy sources. Hyundai Steel's answer to green steelmaking lies in its continued focus on the electric arc furnace.

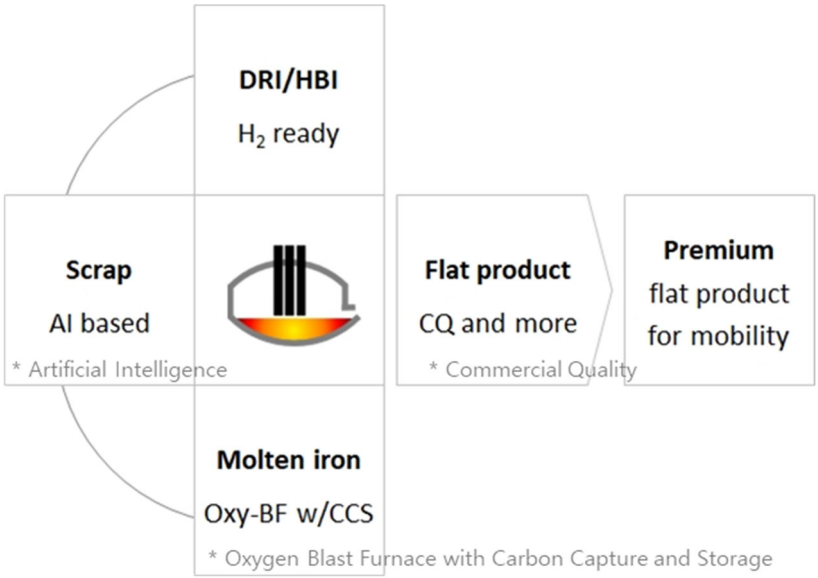

FIG 1 – A concept of Hy-Cube project for carbon neutral steelmaking.

The Hy-cube project, abbreviated for Hyundai, Hydrogen, Hybrid process, revolves around an electric arc furnace-oriented new process. The distinguishing feature of this process is its flexibility, encompassing material flexibility, process flexibility, and product flexibility.

- Material Flexibility: Hyundai Steel's Hy-cube project allows the blending of different raw materials in response to market trends in scrap or iron ore, as well as fluctuations in natural gas and hydrogen prices. This adaptability ensures a resilient supply chain.
- Process Flexibility: The project offers the flexibility to choose specific processes, from direct reduction processes (DRP) to secondary steelmaking, tailored to the requirements of valuable products. This adaptability is crucial in responding to dynamic market conditions.

- Product Flexibility: By maximising process flexibility, Hyundai Steel can produce a wide range of steel products, from commercial quality (CQ) to extra deep drawing quality (EDDQ), and even high-alloy products such as 9 per cent Ni steel, manganese steel, and stainless steel.

However, transitioning from the current steelmaking process to the EAF-oriented new process poses challenges. Hyundai Steel has therefore adopted a two-route approach, encompassing a gradual reduction of total CO_2 emissions while simultaneously advancing the Hy-cube project. This approach aligns with national and global goals, recognising the urgency to transform steel production methods.

While governmental initiatives, such as the plan for net zero by 2050, provide a framework for gradual transformation, the market demands proactive measures. Hyundai Steel acknowledges this reality and, in response, has undertaken the Hy-Cube project specifically to address the carbon footprint of its products. In anticipation of market and automotive customer expectations, Hyundai Steel is investing in new electric arc furnaces to produce products with a 70 per cent reduced CFP by 2030.

This phased approach involves the initial investment in new EAFs, focusing on operational technologies to reduce CO_2 emissions while maintaining existing blast furnace processes. Successful results will pave the way for the gradual replacement of blast furnaces with electric arc furnaces.

Prototypes and product development

To validate the concept of the Hy-cube project, Hyundai Steel has conducted trials, producing prototypes that showcase the project's viability. Two noteworthy trials include the production of a lower arm part and tire cord.

- Lower Arm Part: Hyundai Steel successfully produced a 1 GPa low-emission sheet product for the lower arm part. This achievement required precise control over chemical composition and properties, showcasing Hyundai Steel's adeptness in material engineering. The composition adhered to industry standards, and the resulting product achieved a notable 30 per cent reduction in CFP.
- Tire Cord: Tire cords, crucial components in tyre manufacturing, present a unique challenge due to their thin profile (under 0.5 mm) and the requirement for extreme tensile strength in clean steel. Traditionally produced from blast furnace steel, Hyundai Steel undertook the challenge of producing tyre cord using the Hy-cube concept. Initial successes include the production of standard tensile (ST) grade wire, with ongoing efforts to achieve high tensile (HT) grade steel wire.

H2-DRI TECHNOLOGY ACQUISITION PLAN

While EAF technology plays a pivotal role in Hyundai Steel's strategy, it alone is insufficient to achieve carbon-neutral steelmaking. The Hy-cube project recognises the limitations posed by scrap shortages and varying product quality in conventional EAF processes. Consequently, Hyundai Steel underscores the indispensability of Hydrogen direct reduced iron (H_2-DRI) technology.

Acknowledging its lack of experience in producing direct reduced iron, Hyundai Steel has devised a plan to obtain H2-DRI technology and facilities. The strategy involves two fundamental steps.

1. NG-HBI Commercial Plant Investment: The initial step entails investing in a natural gas - hot briquetted iron (NG-HBI) commercial plant. This investment serves a dual purpose – acquiring construction and operation technology while contributing to research and development from a technological standpoint.
2. Hydrogen Enhancement and H_2-DRI Production: The second step focuses on enhancing hydrogen capabilities and producing H_2-DRI. Leveraging a shaft reduction facility, the plan involves a phased transition from natural gas to hydrogen. This comprehensive strategy aligns with the overarching goal of securing leading-edge technologies for operational optimisation during the transition.

Hyundai Steel has systematically categorised the technology required for the DR plant into four key areas, emphasising raw materials, reduction kinetics, operation technology, and carburisation.

- Raw Materials for H_2-DRI: The effective handling of raw materials takes precedence in the DR process, particularly given the challenges associated with slags. Hyundai Steel is actively involved in standardising ore materials, collaborating with ISO methodologies, and incorporating novel approaches for H_2 reduction.
- H_2 Reduction Technology: Hydrogen reduction poses inherent challenges due to its strong endothermic nature. Hyundai Steel addresses this challenge through an in-depth exploration of H_2 reduction kinetics, estimating reduction mechanisms, and rates to enhance efficiency and cost-effectiveness. Simulation models and case studies contribute to upgrading existing blast furnace (BF) based models for the DR process.
- Operation Technology: The third facet focuses on operational technology, with Hyundai Steel developing a comprehensive balance tool for pre-studies on higher hydrogen operation. This tool, previously presented by a colleague, aids in assessing the feasibility of transitioning from natural gas to hydrogen, ensuring a smooth operational shift.
- Carburisation in H_2-DRI: To optimise EAF efficiency, carburisation of hydrogen-reduced iron is crucial. Hyundai Steel explores the use of biomass for carburisation, offering a sustainable alternative. Carburisation using carbon monoxide (CO) at specific temperatures, as demonstrated in technologies like MIDREX-ACT, is highlighted. Collaborative efforts with national funding projects, such as HyREX, underscore Hyundai Steel's commitment to advancing carburisation techniques.

CONCLUSIONS

In summary, Hyundai Steel's Hy^3 project embodies a holistic approach to achieving carbon-neutral high-end steel products. The strategic shift towards electric arc furnace technology, coupled with the innovative Hy-cube project, signifies the company's commitment to environmental sustainability and technological leadership. As Hyundai Steel navigates the complexities of steel production in the era of carbon neutrality, the Hy^3 project is poised to reshape the industry landscape, presenting 'HyECOsteel' as a symbol of excellence in low-carbon steel production. Hyundai Steel's journey underscores the intricate interplay between technological innovation, market dynamics, and environmental responsibility, positioning the company as a trailblazer in the global steelmaking arena.

Characterising bubble size distribution and generation position in iron oxide-containing slag smelting reduction

DOI: 10.62053/KGYQ5775
K Ohno[1] and T Kon[2]

1. Professor PhD, Kyushu University, Fukuoka 819-0395, Japan.
   Email: ohno.ko-ichiro.084@m.kyushu-u.ac.jp
2. Assistant Professor PhD, Kyushu University, Fukuoka 819-0395, Japan.

ABSTRACT

Slag foaming is an important control item in the process of refining molten steel. This study aims to investigate the factors controlling slag foaming by observing the bubble formation behaviour resulting from the chemical reaction between iron oxide and Fe-C alloy in the slag. In this study, 0.06 g of Fe-C alloy was introduced at the bottom of a BN crucible, and 6.0 g of slag (SiO_2:CaO:Fe_2O_3 = 40:40:30) was placed on top of it. The crucible was positioned inside an infrared image heating furnace, where the temperature was rapidly raised to 1370°C at a rate of 1000°C/min in a nitrogen stream, and then held at that temperature for a predetermined time before rapid cooling. Following rapid cooling, the internal structure of the sample was examined using a high-resolution X-ray CT device. The spherical equivalent volume was calculated based on the number of observed bubbles and their equivalent circle diameter. Additionally, the relationship between the volume ratio of small bubbles in the slag volume and the distance from the bottom of the crucible was determined, along with the calculation of bubble density and volume ratio. Under various experimental conditions, numerous bubbles with equivalent circular diameters ranging from 200 to 300 μm were consistently observed. The density and volume fraction of bubbles with circular equivalent diameters between 200 and 500 μm showed a tendency to increase as the distance from the bottom of the crucible increased. Bubbles with equivalent circular diameters of 500 μm or more consistently exhibited lower bubble densities, regardless of their height within the crucible. The formation of larger bubbles is attributed to a decrease in iron oxide concentration within the slag as the reaction progresses. However, this is believed to be due to their higher buoyancy, resulting in shorter residence times within the slag and a reduction in the number of encapsulated bubbles.

INTRODUCTION

Research into the steel refining process has delved into the effective utilisation and control of slag. Particularly, with the advent of the oxygen steelmaking process, steel production has grappled with challenges arising from the dispersion of slag and molten iron induced by slag foaming. Slag foaming, a phenomenon wherein gas is introduced into low-basicity slag, resulting in gas retention and a substantial increase in slag volume, has been identified as a significant concern. Notably, managing slag foaming in recycling processes involving the melting and reduction of slag using electric furnaces has emerged as a critical issue (Harada *et al*, 2018a, 2018b; Nakase *et al*, 2021). The judicious selection of the carbon source (Harada *et al*, 2018a, 2018b) plays a crucial role in regulating foaming behaviour. Addressing this challenge is integral to ongoing efforts in new iron source manufacturing processes, such as those integrating fluidised bed reduction and smelters like COREX (Yin *et al*, 2022). Additionally, research has highlighted the significance of employing estimation models based on machine learning to control the height of slag foaming (Son *et al*, 2021). The optimisation of these processes is pivotal in addressing current challenges and advancing the field of steelmaking.

The occurrence of slag foaming in molten slag during steel refining processes is a prevalent phenomenon in various refining procedures utilising top-blown oxygen, such as converters, hot metal pre-treatment, smelting reduction, and scrap melting with the use of fossil fuels (Hara and Ogino, 1992; Nakase *et al*, 2021). Specifically, during the dephosphorisation treatment conducted in hot metal pre-treatment, silicon within the hot metal undergoes desiliconisation before the dephosphorisation reaction, resulting in the formation of slag with low basicity. In situations where dephosphorisation treatment is executed in the presence of such low basicity slag, slag foaming occurs due to the CO gas generated by the concurrent decarburisation reaction and the carrier gas used to inject the dephosphorisation agent. Containers employed in the hot metal pre-treatment

process, such as torpedo cars and ladles, possess smaller freeboards compared to converters. Consequently, in the event of slag foaming, there is a risk of slag overflow from the container. This has a substantial impact on productivity and workability, as it necessitates time-consuming efforts to restore the lower part of the furnace (Mukai, 1991; Harada *et al*, 2018a). Moreover, the iron, intended as the final product, becomes emulsified within the slag, leading to a reduction in the yield of iron.

Due to these challenges, the phenomenon of slag foaming has garnered significant attention and research efforts since the early stages of basic oxygen furnace (BOF) steelmaking technology. When delving into the mechanism of slag foaming, it becomes imperative to categorise influencing factors, distinguishing those related to the generation process—such as the velocity of gas production resulting from reactions and the dimensions of bubbles—and those regulating the stability of the generated bubbles. To scrutinise the stabilising factors associated with bubbles, various approaches are conceivable. One approach involves measuring the elevation of the top surface of the slag by introducing gas into the molten metal at a constant flow rate. Alternatively, the cessation of gas injection post-foaming allows the top surface of the bubbles to ascend to a certain height due to bubble disruption.

In assessments utilising cold models designed to simulate foaming slag at ambient temperature, endeavours have been made to modulate foam generation behaviour through the incorporation of fine solid-phase powder and liquid-phase particles (Martinsson, Vickerfält and Sichen, 2022). Moreover, studies involving measurements of liquid-phase viscosity, encompassing the gas phase (Hatano *et al*, 2021) have indicated the significance of controlling the interfacial energy between solid-gas and liquid phases. There have also been investigations into the size and growth patterns of bubbles within cold models, as these aspects are pivotal in managing foaming behaviour and viscosity measurements (Zhang *et al*, 2021). It has been documented that bubbles ascending to the surface and persisting there tend to adopt non-spherical shapes.

In their study conducted at the elevated refining temperature, Cooper and Kitchener (1959) explored the slag-foaming characteristics of the $CaO\text{-}SiO_2\text{-}P_2O_5$ melt. The investigation revealed that binary $CaO\text{-}SiO_2$ melts do not exhibit foaming tendencies; however, the introduction of P_2O_5 to melts with more than 50 per cent SiO_2 content induces pronounced foaming. It was observed that the longevity of bubbles increased proportionally with higher P_2O_5 and SiO_2 concentrations. Subsequent research by Hara *et al* (1983) and Hara, Yunoki and Ogino (1989) involved the measurement of bubble lifetime and height in $CaO\text{-}SiO_2\text{-}FeO$ and $Na_2O\text{-}SiO_2$ melts through gas injection, establishing a significant correlation between bubble lifetime and surface tension. Studies have reported a substantial increase in bubble lifespan attributed to a reduction in surface tension. In a separate investigation, Ito and Fruehan (1989) derived the foaming index, representing the bubble lifetime, as a function of viscosity and surface tension in a $FeO\text{-}CaO\text{-}SiO_2$ melt. This experiment involved the introduction of Ar gas through a capillary tube. The foaming index proposed by Ito and Fruehan is presented below.

$$\Sigma = 570\,\frac{\mu}{\rho\sigma} \tag{1}$$

Here:

- Σ is the life of the foam (s)
- μ is the viscosity of the slag (Pa s)
- ρ is the density of the slag (kg/m^3)
- σ is the surface tension (N/m)

The foaming index facilitates an explication of the observation that the longevity of a bubble increases proportionally with escalating viscosity and diminishing surface tension. Notably, the investigations conducted employed blowing nozzles featuring relatively large inner diameters of 2.1 mm and 2.5 mm, resulting in the formation of correspondingly sizable bubbles. This raises concerns regarding the fidelity of the reproduction of bubble characteristics in the actual process. Mukai (1991) posits that bubbles generated through gas injection via a capillary tube differ from those originating from gaseous products formed in a chemical reaction within the authentic industrial process. In the industrial scenario, slag foaming transpires as iron oxide within the slag, floating atop the hot metal, reacts with the carbon present in the hot metal at the vessel's bottom due to

gravitational forces. Consequently, it becomes imperative to scrutinise bubbles generated through the chemical interaction between FeO and Fe-C alloy.

Moreover, predominant scholarly inquiries thus far have delved into the correlation between the physical attributes of slag and the stability of foam. These investigations have encompassed aspects such as the internal structure of foamed slag and the behaviour of CO bubbles regarding their generation and distribution. In the 1980s, the methodology of direct observation employing transmitted X-rays was employed to scrutinise the slag bubbling phenomenon induced by gases resulting from reactions mirroring actual operational conditions. Notably, an examination of the interaction between slag melt containing iron oxide and carbon-saturated iron (Ogawa and Tokumitsu, 2001) has revealed a discernible relationship between the height of slag foaming and alterations in bubble diameter. Specifically, heightened foaming was observed when small bubbles were generated, while a pronounced decrease in foaming occurred concomitantly with an increase in bubble diameter. This observation intimates that the progression involving the formation, coalescence, growth, and breakdown of microbubbles is integral to the lifespan of the bubbles. Additionally, scholars (Drain *et al*, 2021) have underscored the significance of regulating slag viscosity in assessing decarburisation and dephosphorisation reactions induced by emulsions dispersed in the slag. Nevertheless, owing to limitations in X-ray transmission resolution, attaining proximity to the formation processes of microscopic bubbles measuring 1 mm or less proves challenging. Therefore, an imperative need exists to elucidate the intricate mechanisms governing the formation of microscopic bubbles.

Our investigation endeavours to examine slag foaming resulting from the chemical interaction between FeO and Fe-C alloy within slag, emphasising physical attributes such as the size and distribution characteristics of CO bubbles comprising the foam. The primary objective of this study is to elucidate the mechanisms of slag foaming and identify the determinative factors governing slag foaming through an analysis of its internal structure. Specifically, our research centres on the dimensions and spatial arrangement of gas bubbles, with a novel emphasis on scrutinising the generation and distribution patterns of microscopic air bubbles measuring 1 mm or smaller in diameter.

EXPERIMENTAL METHOD

In this investigation, aimed at simulating slag foaming during hot metal pre-treatment arising from the interaction between slag and pig iron, particular attention was directed towards the microbubbles produced through the reduction reaction involving iron oxide in the molten slag and carbon in the Fe-C alloy. The distribution patterns of bubbles within the evolving slag were scrutinised employing the methodology outlined below.

Experimental sample

The basic system of slag generated during hot metal pre-treatment is the CaO-SiO_2-Fe_xO ternary system. In this investigation, the principal constituents of the slag comprised CaO, SiO_2, and Fe_2O_3, with a selected CaO/SiO_2 basicity ratio of 1 for simplicity. In consideration of the challenges associated with handling iron oxide, stemming from variations in iron valence during slag preparation and experimental execution, this study opted for the utilisation of Fe_2O_3 due to its straightforward nature. In order to observe bubbles smaller than 1 mm, this study adopted a Fe_2O_3 concentration of 40 mass per cent, which has a relatively lower viscosity, compared to lower iron oxide containing slag. Special grade reagents SiO_2, $CaCO_3$, (all reagents manufactured by Sigma-Aldrich Japan Co., Ltd., purity: ≥99.0) and Fe_2O_3 (99.8 per cent-Fe, manufactured by Strem chemicals) were used in the experiment. Taking into account the thermal decomposition of $CaCO_3$, each sample was weighed to have a predetermined composition and thoroughly mixed using an Al_2O_3 mortar. The mixed powder was filled into a platinum crucible and melted in an air atmosphere at 1500°C for 1 hr. Thereafter, it was poured onto a copper plate and rapidly cooled, and the resulting glassy slag sample was pulverised to under 600 μm.

The carbon concentration of the iron-carbon alloy specimen employed in this investigation was 0.63 mass per cent. The aforementioned iron-carbon alloy specimen constituted a standardised sample (fabricated by the Japan Iron and Steel Federation) and its compositional details are

delineated in Table 1. The iron specimens underwent preparation by grinding to achieve a particle size ranging from approximately 1 to 2 mm prior to utilisation.

TABLE 1

Chemical composition of Fe-C alloy (mass%).

C	Si	Mn	P	S	Cu	Al	N_2
0.63	0.24	0.48	0.0058	0.0027	0.008	0.03	0.0028

Experimental method

The objective of this experimental study was to investigate slag foaming, a critical issue in hot metal pre-treatment, with a focus on observing slag foaming at approximately 1400°C. To minimise the occurrence of reactions during temperature elevation and reduction processes and to observe the state in which slag foaming takes place, it was imperative to control reactions before slag foaming and rapidly cool the system while sustaining the slag foaming phenomenon. Consequently, an infrared image heating apparatus capable of swift heating and cooling was employed in this investigation.

The apparatus employed in this experiment comprised an infrared image heating furnace in the central stage, a furnace core tube, a lifting mechanism for the sample crucible in the lower stage, and a cooling chamber. The capability for rapid temperature rise and rapid cooling was achieved through the integration of an infrared image heating furnace, an elevating sample crucible, a cooling chamber, and an air-cooled quartz reaction tube known for its high resistance to thermal shock.

A R-type thermocouple, positioned inside the graphite rod as depicted in Figure 1a, was utilised for temperature measurement and control of the sample. Given that the height of the slag increases due to slag foaming, measures were taken to prevent direct contact between the slag and the graphite rod. To mitigate temperature differentials between the furnace interior and the thermocouple, the graphite rod was strategically positioned such that its lower end aligned with the upper end of the BN crucible, as illustrated in Figure 1b.

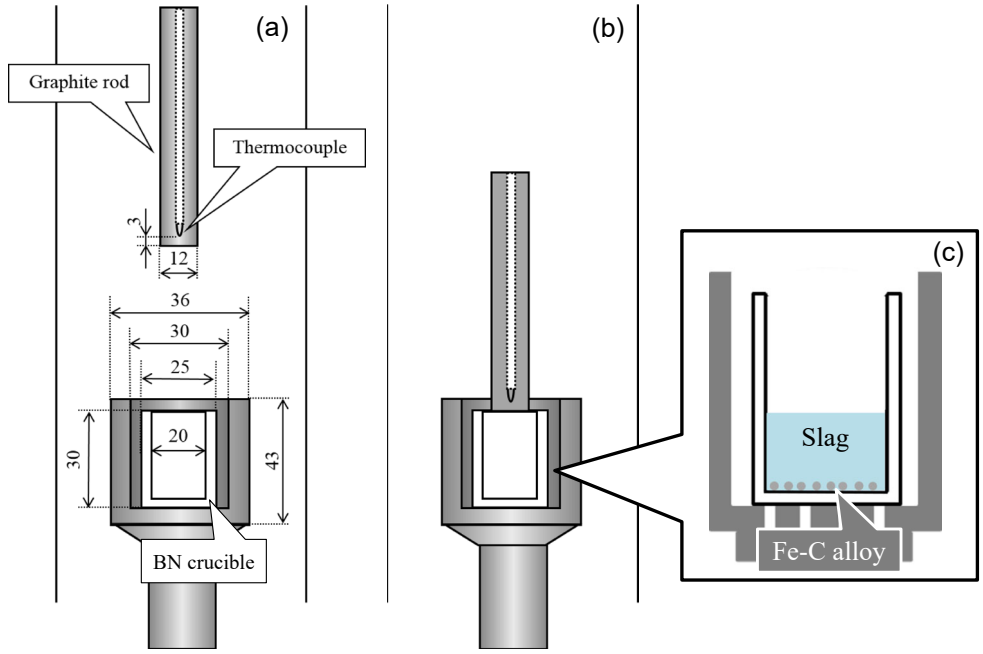

FIG 1 – Schematic illustration of sample holder part and sample setting.

The sample crucible employed consisted of a graphite crucible (outer diameter 36 mm, inner diameter 30 mm, height 40 mm), while a BN crucible (outer diameter 25 mm, inner diameter 20 mm, height 32.5 mm) was utilised. As depicted in Figure 1c, Fe-C alloy and slag were sequentially charged into the BN crucible, with the weights adjusted to 0.06 g for Fe-C alloy and 6.0 g for slag.

Following the sample charging, the crucible was placed in an infrared image heating furnace, where the temperature was rapidly elevated to 1370°C at a rate of 1000°C/min under an inert atmosphere with an N2 flow rate of 2NL/min. Subsequently, the sample was held at the set temperature for a predetermined duration and then swiftly cooled at 1000°C/min using a quenching chamber.

3D X-ray CT imaging

In the present investigation, we employed a high-resolution three-dimensional X-ray computed tomography (CT) apparatus, specifically the SKYSCAN 1172 model manufactured by BRUKER, to scrutinise the spatial distribution of bubbles within the cross-sectional profile of the foaming slag. The CT equipment exploits variations in X-ray transmittance and absorption coefficient to capture detailed structural information. This is achieved by situating the specimen on a revolving pedestal and subjecting it to X-ray irradiation during rotation. Consequently, regions of heightened X-ray absorption are discerned, allowing for the reconstruction of a tomographic cross-sectional view by compiling absorption data at specific positions on the object.

The experimental parameters were set as follows: Camera Pixel Size of 9.00 μm, Image Pixel Size of 20.00 μm, Source Voltage of 80 kV, Source Current of 100 μA, Exposure time of 2000 ms, and Rotation Step of 1.2 degrees. These conditions facilitated the acquisition of high-quality imaging data, enabling the accurate calculation of ratios and the subsequent construction of a detailed cross-sectional representation of the specimen.

RESULTS AND DISCUSSION

After conducting the experiment, a cross-sectional examination of each specimen was carried out utilising CT apparatus. An exemplar depiction of the observation of a specimen rapidly cooled and held for 2 mins is presented in Figure 2. Through CT imaging, both a horizontal cross-sectional perspective of the crucible (depicted in Figure 2a) and a vertical cross-sectional view (illustrated in Figure 2b) were acquired, enabling the discrimination of slag, iron, air bubbles, and voids. In the illustration, the grey region corresponds to slag, while the white masses represent iron. Additionally, the small black circular features within the slag indicate the presence of air bubbles, whereas the larger black regions signify voids.

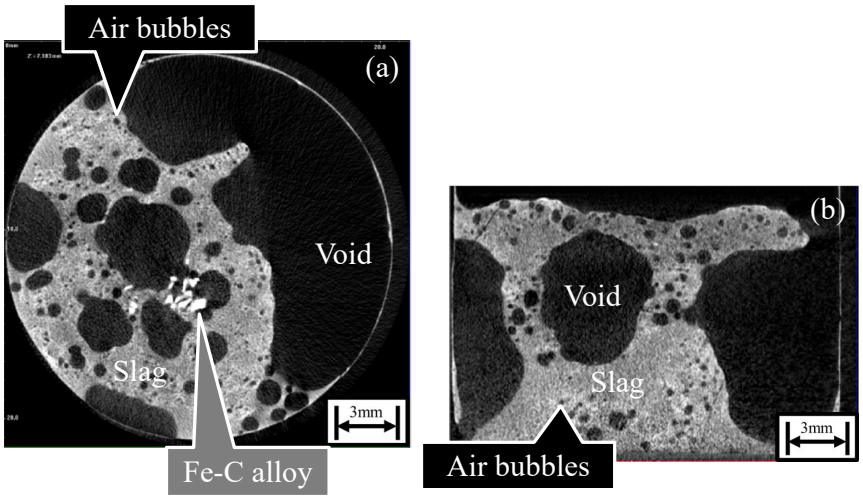

FIG 2 – Cross-sectioning photographs of quenched sample in BN crucible in (a) Radial section, and (b) Vertical section (hold for 2.0 mins).

Evaluation based on circle equivalent diameter distribution

The evaluation of slag foaming was conducted through the analysis of the distribution of equivalent circle diameters. The equivalent circle diameter distribution is defined as the distribution of diameters of circles corresponding to a specified area of a given cross-section. Following the acquisition of cross-sectional images of the crucible using CT imaging, these images were colourised and organised based on the range of equivalent circle diameters. To ensure a comprehensive analysis of the entire crucible cross-sectional direction, the minimum equivalent circle diameter was set

between 200 and 300 μm, accounting for the resolution and pixel count of the CT images obtainable. Additionally, areas in the crucible where the equivalent circle diameter range was not depicted were identified as slag. This methodology facilitated the organisation of the size, number, and positional relationship of bubbles. Figure 3 presents a horizontal cross-sectional view of the crucible captured using a CT device after each experimental run. Given the scarcity of bubbles exceeding 2 mm in size, the crucible cross-section was observed at 2 mm intervals.

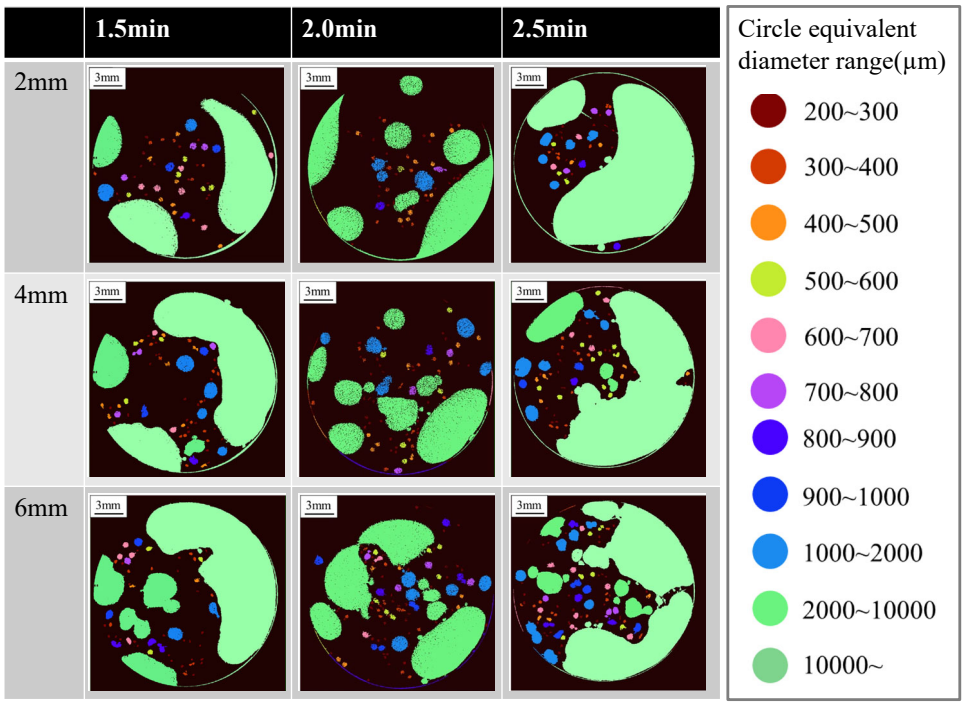

FIG 3 – Radial-sectional observation of quenched samples for each holding time and distance from the bottom of the crucible using micro-CT observation.

Three-dimensional evaluation of slag foaming

Three-dimensional evaluation is necessary to understand the internal structure of slag foaming in more detail. Therefore, as shown in Figure 4, the foaming slag was carved into 1 mm height increments, and the volume of air bubbles and cavities present in a 1 mm height cylinder was calculated and analysed from a two-dimensional cross-sectional view.

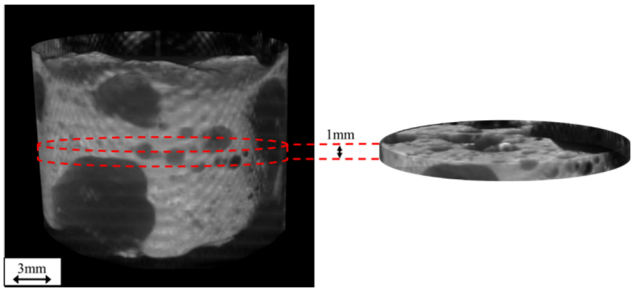

FIG 4 – 3D image of foaming slag and 3D evaluation method (hold for 2min).

The primary objective of this investigation was to assess the distribution characteristics of air bubbles within the slag. Consequently, the substantial voids evident in each cross-sectional analysis were omitted, and emphasis was placed on the evaluation of minute air bubbles embedded within the slag. As shown in Figure 5, denoting the volume of a cylinder with a 1 mm thickness, excluding portions exhibiting an equivalent circular diameter of 1 mm or greater as V (mm^3), and representing the number of small bubbles within each cross-section as n (-), the bubble density N ($/mm^3$) was articulated in the ensuing manner.

$$N = n/V \quad (/mm^3) \tag{2}$$

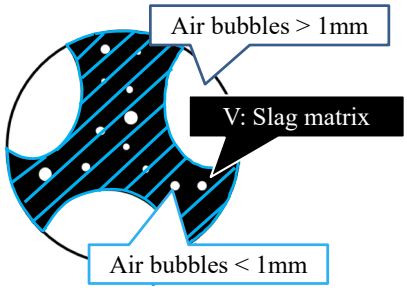

FIG 5 – Schematic illustration of small air bubbles evaluation method.

Figure 6 illustrates the correlation between bubble density and the distance from the bottom of the crucible for various bubble sizes. The data depicted in this figure indicates that a decrease in the equivalent circular diameter of bubbles is associated with an increase in bubble density. This observation suggests that smaller bubbles exhibit a lengthened residence time, while larger bubbles swiftly ascend and exit the slag due to the fact that, under uniform viscosity conditions, smaller bubbles have a lower terminal velocity. Across all experimental parameters, the bubble density of bubbles with an equivalent circular diameter ranging from 200 to 500 μm rises proportionally with the distance from the bottom of the crucible. Additionally, the bubble density of bubbles with an equivalent circular diameter of 500 to 1000 μm demonstrates an increasing trend independent of the height. Notably, a discernible tendency of density reduction becomes evident.

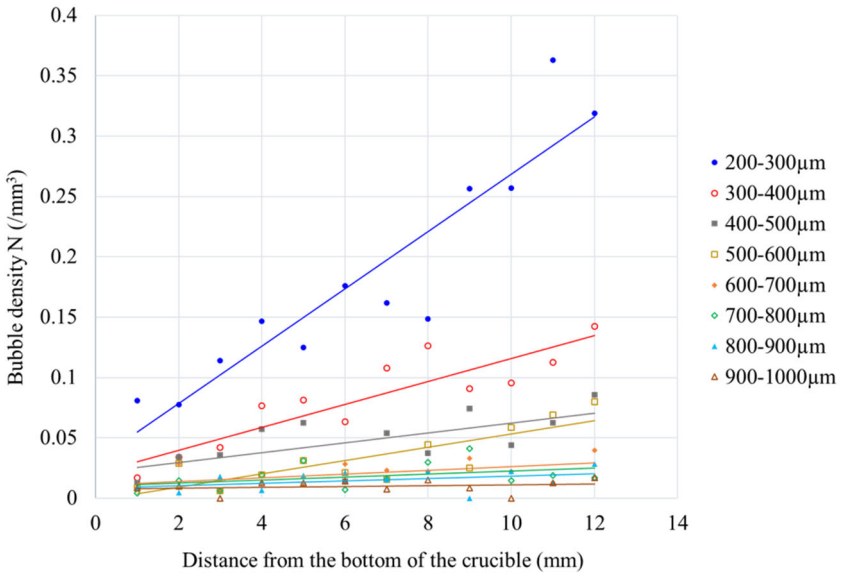

FIG 6 – Relationship between the distance from the bottom of the crucible and the bubble density for each bubble size (hold for 2.0 min).

Mechanism of bubble generation and distribution

Utilising the acquired results, Figure 7 illustrates a schematic depicting the progression of bubble generation and distribution.

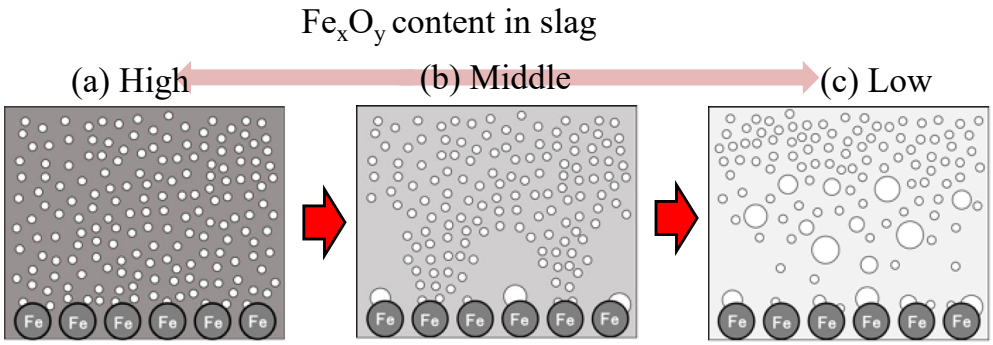

FIG 7 – Relationship between the distance from the bottom of the crucible and the bubble density for each bubble size (hold for 2.0 min).

Upon initiation of the reaction, diminutive bubbles manifest, as depicted in Figure 7a, leading to an elevation in the liquid level. The diminishing iron oxide concentration within the slag during the progression of the reaction is postulated. Notably, Ogawa and Tokumitsu (2001) conducted a study revealing an augmentation in the size of bubbles at the slag/metal interface as the iron oxide concentration diminishes. Terashima *et al* (1992) proposed that the size of generated bubbles is contingent upon wettability. Moreover, Mukai, Furukawa and Tsuchikawa (1977) quantified the contact angle between slag and molten iron, asserting an enhanced wettability with higher iron oxide concentration in the slag. Collectively, these reports suggest that as the iron oxide concentration diminishes, impeding the wetting of slag on molten iron, the bubbles burgeon in size. Conversely, when the iron oxide concentration is high, facilitating slag wetting on molten iron, the bubbles persist in a smaller size, forming at the interface. It is conceivable that these bubbles disengage from the interface and ascend to the surface. Consequently, as the iron oxide concentration wanes over time, larger bubbles may commence forming at the slag/metal interface, as illustrated in Figure 7b. As small bubbles are not generated at the slag/metal interface where large bubbles are prevalent, it is inferred that the quantity of small bubbles generated diminishes compared to the initial stages of the reaction. Moreover, it is hypothesised that the bubble density of small bubbles, characterised by an equivalent circle diameter of 200 to 500 μm, decreases with an increasing distance from the bottom of the crucible. Additionally, with the progression of the reaction from the state depicted in Figure 7b, the number of large bubbles generated intensifies, as evidenced in Figure 7c. However, owing to their rapid ascent, the temporal residency of large bubbles within the slag is abbreviated, resulting in a presumed reduction in the number of entrapped bubbles. Consequently, it is posited that the bubble density remains low irrespective of the height, emphasizing the transitory nature of large bubbles within the system.

CONCLUSIONS

In this investigation, simulated slag composed of CaO, SiO_2, and Fe_2O_3 was utilised, and the dimensions and distribution of bubbles resulting from the chemical interaction between iron oxide and Fe-C alloy in molten slag at 1370°C were assessed employing an infrared image heating apparatus. The subsequent observations were made by examining the cross-section of the specimen post-quenching. Irrespective of the experimental parameters, numerous bubbles with equivalent circular diameters ranging from 200 to 300 μm were consistently observed. This phenomenon can be attributed to the principle outlined in Stokes' equation, indicating that, under constant slag viscosity, smaller bubbles exhibit lower terminal velocities and consequently longer residence times. The density and volume fraction of bubbles with circular equivalent diameters within the range of 200 to 500 μm exhibited an upward trend as the distance from the crucible bottom increased. This behaviour is conjectured to stem from the temporal evolution wherein larger bubbles are progressively formed, leading to a reduction in the simultaneous generation of smaller bubbles. Bubbles with equivalent circular diameters exceeding 500 μm tended to manifest smaller bubble densities independent of their vertical position. The emergence of larger bubbles is attributed to the diminishing concentration of iron oxide in the slag as the chemical reaction advances, resulting in a heightened buoyant speed that curtails residence time in the slag and diminishes the count of bubbles.

ACKNOWLEDGEMENTS

The authors would like to express their gratitude to the research group ‘Slag Visualization Study Group for Understanding the Flow of Multiphase Melts’ established at the Japan Iron and Steel Institute for financial support and scientific advice.

REFERENCES

Cooper, C F and Kitchener, J A, 1959. The foaming of molten silicates, *J Iron Steel Inst,* 193:48–55.

Drain, P B, Gu, K, Dogan, N, Longbottom, R J, Chapman, M W, Monaghan, B J and Coley, K S, 2021. Dephosphorisation Kinetics of Bloated Metal Droplets Reacting with Basic Slag Containing TiO_2, *ISIJ-Int,* 61(3):734–744.

Hara, S and Ogino, K, 1992. Slag-Foaming Phenomena and the Suppression, *Tetsu-to-Hagané*, 78(2):200–208 (in Japanese).

Hara, S, Ikuta, M, Kitamura, M and Ogino, K, 1983. Foaming of Molten Slags Containing Iron Oxide, *Tetsu-to-Hagané*, 69(9):1152–1159 (in Japanese).

Hara, S, Yunoki, T and Ogino, K, 1989. Effect of Surface Viscosity on the Foaminess of Molten Oxides, *Tetsu-to-Hagané*, 75(12):2182–2187 (in Japanese).

Harada, T, Hirata, H, Arai, T, Toh, T and Shuto, C, 2018b. Development of the Molten Slag Reduction Process-2 Optimization of Slag Reduction Process with Molten Slag Charging, *ISIJ-Int,* 58(10):1943–1952.

Harada, T, Hirata, H, Arai, T, Toh, T and Yamada, T, 2018a. Development of the Molten Slag Reduction Process-1 Characteristics of Closed Type DC arc Furnace for Molten Slag Reduction, *ISIJ-Int,* 58(10):1934–1942.

Hatano, S, Hayashi, S, Saito, N and Nakashima, K, 2021. Viscosity Evaluation of Simulated Foaming Slag via Interfacial Reaction at Room Temperature, *ISIJ-Int*, 61(12):2904–2914.

Ito, K and Fruehan, R J, 1989. Study on the foaming of CaO-SiO_2-FeO slags: Part, I, Foaming parameters and experimental results, *Metall Trans B*, 20B:509–514.

Martinsson, J, Vickerfält, A and Sichen, D, 2022. Impact of Solid Particles and Liquid Droplets on Foams – Cold Model and High Temperature Experiments, *ISIJ-Int,* 62(1):104–111.

Mukai, K, 1991. Some Views on the Slag Foaming in Iron and Steelmaking Processes, *Tetsu-to-Hagané*, 77(6):856–858 (in Japanese).

Mukai, K, Furukawa, H and Tsuchikawa, T, 1977. Effect of Iron Oxide in CaO-SiO_2, Slag on Interfacial Tension between Liquid Dilute Fe-Si-O Alloys and the Slag, *Tetsu-to-Hagané*, 63(9):1484–1493.

Nakase, K, Matsui, A, Nakai, Y, Kikuchi, N, Kishimoto, Y and Tetsuyama, I, 2021. Development of Iron Recovery Technique from Steelmaking Slag by Reduction at High Temperature, *Tetsu-to-Hagané*, 107(9):693–700 (in Japanese).

Ogawa, Y and Tokumitsu, N, 2001. X-ray Fluoroscopic Observation of Slag Foaming, *Tetsu-to-Hagané*, 87(1):14–20 (in Japanese).

Son, K, Lee, J, Hwang, H, Jeon, W, Yang, H, Sohn, I, Kim, Y and Um, H, 2021. Slag foaming estimation in the electric arc furnace using machine learning based long short-term memory networks, *J Mater Res Tech,* 12:555–568.

Terashima, H, Nakamura, T, Mukai, K and Odawara, T, 1992. The Foaming Mechanism of Iron-Silicate Slag, *Shigen-to-Sozai*, 108(10):737–742.

Yin, C, Zhang, S, Gu, O Y, Wen, L and Bai, C, 2022. Effect of Top Gas Recycling Technology on the Softening, Melting and Dropping Behavior of V–Ti Bearing Burden in COREX Process, *ISIJ-Int,* 62(9):1777–1784.

Zhang, B, Wang, R, Hu, C, Liu, C and Jiang, M, 2021. Effect of Viscosity on Dynamic Evolution of Metallurgy Slag Foaming, *ISIJ-Int,* 61(5):1348–1356.

A study of heat and material balances in direct reduction plant with various conditions

DOI: 10.62053/ESWO9966

M J Sun[1] and H Kim[2]

1. Research Engineer, Hydrogen Reduction Research Team, Hyundai Steel, Dangjin-Si 31719, South Korea. Email: minjoo8454@hyundai-steel.com
2. Team Leader, Hydrogen Reduction Research Team, Hyundai Steel, Dangjin-Si 31719, South Korea. Email: hyuk923@hyundai-steel.com

ABSTRACT

Global steel companies are actively combating climate change by reducing carbon emissions. Traditional steel production, using the blast furnace (BF) – basic oxygen furnace (BOF) process, heavily depends on coal and emits substantial CO_2. To mitigate this, companies are transitioning to the more eco-friendly DRP (direct reduction plant) – EAF (electric arc furnace) process, which lowers CO_2 emissions. This study quantitatively evaluates the impact of increased hydrogen consumption on the carbon footprint of product (CFP) through an analysis of direct reduction process heat and mass balances. The study prioritises a comprehensive material balance based on mass conservation principles. The heat balance is calculated using differences in enthalpy through state energy properties, avoiding heat consumption. Validation using operational data from Hyundai Steel Dangjin works' blast furnaces shows close alignment between calculated results and actual data, with less than 1 per cent error. This methodology facilitates a detailed analysis of the direct reduction process, offering insights into its feasibility and efficiency. Analysis of the operational impact by increasing the hydrogen ratio demonstrates reduced CO_2 emissions and increased heat requirements due to the endothermic nature of hydrogen reduction, in contrast to the exothermic CO reduction. Possible solutions include raising reducing gas temperature or enhancing flow rate. The study effectively utilises designed heat and mass balances to assess material quantities and thermal balance under different operational conditions. It lays the foundation for the initial direct reduction process design, aiding in deriving and optimising operational parameters. Additionally, it provides valuable insights into the challenges of increased hydrogen, contributing to the production of greener steel by addressing these issues.

INTRODUCTION

In response to the global imperative for achieving carbon neutrality by 2050, the steel industry is undergoing a transformative shift from conventional blast furnace and basic oxygen furnace processes to advanced technologies such as DRP (direct reduction plant) coupled with electric arc or submerged arc furnaces (SAF). While the utilisation of natural gas-based DRP is already a commercial reality, the exclusive deployment of hydrogen for the entire reducing gas composition necessitates significant modifications to existing facilities. The complexity arises from the fact that hydrogen reduction is an inherently endothermic reaction, demanding intricate design considerations for heat and mass balances within the DRP and the concurrent development of process optimisation strategies, with a keen focus on hydrogen consumption.

LITERATURE REVIEW

Review of literature on heat and mass balances in blast furnaces

Historical investigations into the heat and mass balances of blast furnaces trace back to the early 1900s, utilising diverse methodologies for comprehensive evaluations. A pivotal contribution to this field is the Rist diagram, a graphical representation of blast furnace operations introduced by Rist and Meysson (1967). This innovative tool aimed at promoting stable operation and enhancing operational performance through mathematical analysis. Concurrently, studies led by Yatsuzuka *et al* (1960) delved into carbon consumption based on thermodynamics, marking a departure from traditional experience-based blast furnace operation methods. These studies provided essential insights into evaluating the heat balance of blast furnaces and deriving optimal reductant rates.

Literature gaps in heat and mass balances in direct reduction plants (DRP)

In stark contrast, a noteworthy gap exists in the literature concerning the heat and mass balances specific to DRP, particularly in the context of hydrogen consumption. Recent contributions have emerged, offering glimpses into the optimisation of the Iron Ore Direct Reduction Process. Notable among these is the work by Béchara *et al* (2018), which delves into multiscale process modelling, encompassing single pellet, shaft furnace and plant models. This research contributes significantly to understanding the intricate dynamics of the DR process, spanning from microscopic grains to the macroscopic scale of the shaft furnace, employing integrated plant simulation tools like Aspen Plus.

Another critical study, conducted by Xu *et al* (2019), addresses the emerging demand for research on direct reduction-based steelmaking to achieve decarbonisation. The study investigates the effect of H_2/CO ratio on gas consumption and energy utilisation rate in gas-based DR processes. By calculating energy and mass balances for typical shaft processes such as MIDREX and HYLⅢ, the researchers shed light on evaluating the heat and mass balance of DRP and identifying trends in balance variations.

OBJECTIVES OF THE CURRENT RESEARCH

Given the imminent transition to hydrogen-rich reducing gases in DRPs, this research seeks to bridge the existing gap in detailed reviews on balances based on hydrogen consumption. The primary objectives are threefold:

1. Development of a static tool for assessing heat and mass balance in DRP: The creation of a tool for rapid static assessments of heat and mass balances in DRP.
2. Case studies on balance with hydrogen increment: Conducting comprehensive case studies to understand the dynamic impact of hydrogen increment on the balance.
3. Optimisation of DR process conditions: Identification of methodologies to optimise DR process conditions, particularly focusing on hydrogen consumption.

STATIC MASS AND HEAT BALANCE IN DRP – AN IN-DEPTH EXPLORATION

The foundational principles involve the calculation of static mass balances using the law of mass conservation for various phases, including solids like pellets and direct reduced iron (DRI) and gases. Simultaneously, the heat balance employs the enthalpy difference between reactants and products. In this study, heat and material balances of DRP is designed using Microsoft Excel, with reference to MIDREX process as depicted in Figure 1.

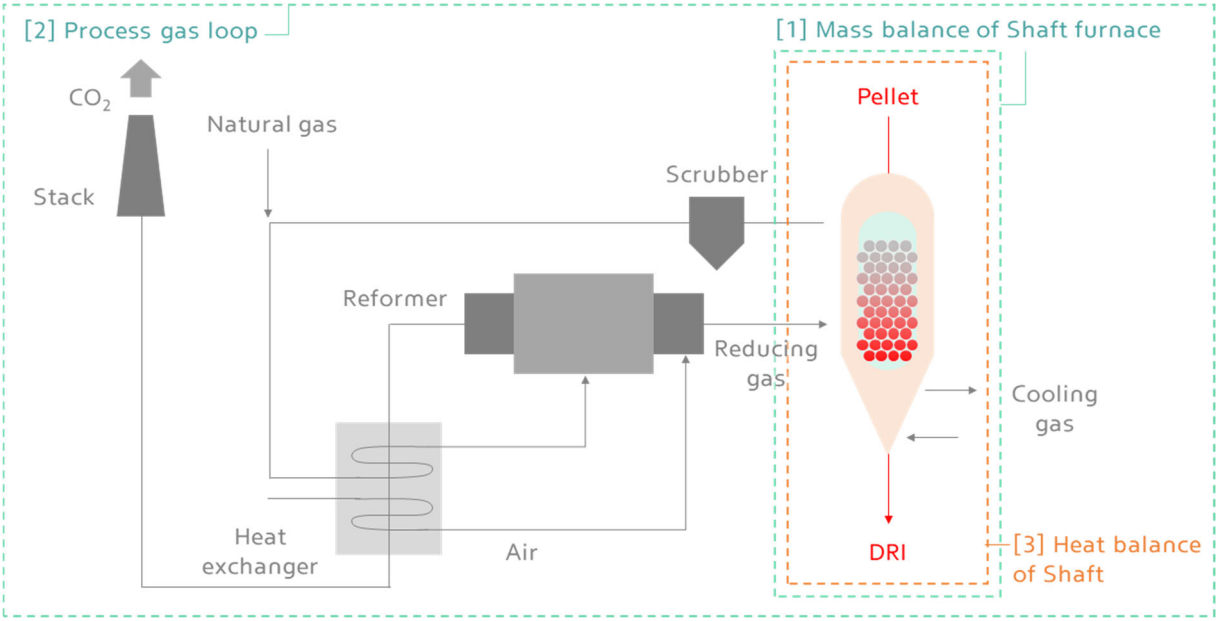

FIG 1 – The flow sheet and design scope of DRP heat and material balance.

Mass balance:

- Rigorous calculations of mass balance among major raw materials and products based on the law of mass conservation.
- Key results encompass the determination of the amount of raw materials required, the quantity of reducing gas considering efficiency and composition and the composition and amount of gas after the reaction (top and cooling gas).

Heat balance:

- The design of an energy balance using the enthalpy difference between reactants and products.
- Exclusion of considerations related to internal reactions and intermediate products.
- The utility of this approach lies in the comprehensive assessment of heat balance and the calculation of required energy.

APPLICATION OF BALANCE PRINCIPLES TO BLAST FURNACE AND DRP

The practical application of these principles to blast furnaces involves detailed burden calculations, setting blowing conditions and determining the composition of top gas and slag. This meticulous process ensures stable operation by inputting target production and raw material composition, calculating the burden, setting the efficiency of CO, hydrogen, and oxygen enrichment, and determining the composition and amount of top gas and slag.

Extending this sophisticated methodology to DRP, a robust tool is developed, incorporating shaft mass balance, process gas loop and shaft heat balance.

Shaft mass balance outputs:

- The quantity of pellet usage based on target DRI production and metallisation.
- Blowing conditions of reducing gas, calculated with the composition of reducing gas and the utilisation of hydrogen and CO.
- Composition and amount of outgoing cooling gas, determined by target DRI carbon content.

Process gas loop calculation:

- The quantity of pellet usage based on target DRI production and metallisation.
- Blowing conditions of reducing gas, calculated with the composition of reducing gas and the utilisation of hydrogen and CO.
- The comprehensive gas mass balance for the DR process is completed.

Shaft heat balance:

- Analogous to the approach in a blast furnace, the heat balance of the shaft furnace is calculated using enthalpy values for inputs, outputs and heat loss.
- The difference between output and input enthalpy facilitates the diagnosis of the heat balance of the direct reduction process.

CASE STUDY – ANALYSING THE IMPACT OF HYDROGEN INCREMENT

Based on the mass balance analysis, as shown in Figure 2, a decreasing trend in the carbon footprint of product (CFP) compared to the current commercial MIDREX plant (H_2/CO 64 per cent) was observed with the increase in the hydrogen ratio in the reducing gas. The reason for a 20 per cent CFP occurrence in the case of 100 per cent hydrogen is due to fixing the quantities of gases other than hydrogen and CO (CO_2, H_2O, N_2, CH_4) during the mass balance calculation and some of the cooling gas being introduced into the reducing gas stream. The amount of CO_2 generated is estimated through the flow of CO_2 in the flue gas discharged through the stack.

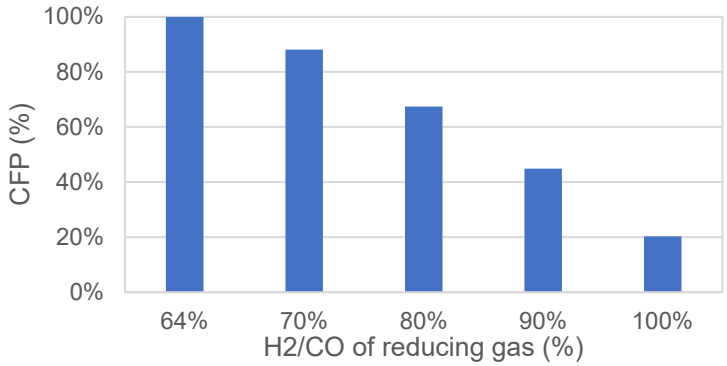

FIG 2 – The level of CFP from the DRP varies depending on the H_2/CO ratio in the reducing gas.

A meticulous analysis of the heat balance under varying hydrogen ratios reveals a discernible trend – as hydrogen content increases, the required heat also escalates. This phenomenon can be attributed to the endothermic nature of hydrogen reduction. The potential risks associated with insufficient heat in the shaft are multifold, including a decrease in gas utilisation, hindrance to reactions such as carburisation and internal reforming and an uptick in operating expenses if more heat is introduced.

Methods for heat compensation

Two pragmatic methods for compensating heat in the DRP are proposed:

Heating:

- Preheating pellets before charging.
- Elevating the reduction gas temperature.
- Challenges associated with this approach include issues such as sticking, limitations in temperature elevation using the reformer and inherent difficulties in increasing the temperature of hydrogen.

Increasing gas volume:

- Compensating heat by augmenting the gas volume.
- The challenges encountered revolve around the substantial amount of gas needed for heat compensation, particularly when the reducing gas consists predominantly of hydrogen.

ANTICIPATED ISSUES AND FUTURE CHALLENGES

In summation, the global steel industry's pivotal shift towards hydrogen-rich reducing gases in DRP to achieve carbon neutrality is not merely an ambition but an imminent reality. While the literature on this subject is still in its nascent stage, this study addresses the existing gaps and presents a comprehensive synthesis of the current state of knowledge. The proposed tool for assessing heat and mass balances, coupled with detailed case studies and innovative heat compensation methods, provides a robust foundation for future research endeavours and practical applications. The challenges and anticipated issues underscore the necessity of continuous investigations, not only in understanding hydrogen reduction characteristics but also in the operational implementation of these advancements.

At Hyundai Steel, our commitment to DRP technologies encompasses the diversification of raw materials, enhancement of reduction efficiency, acceleration of carburisation, optimisation of balance and stabilisation of product quality. By actively developing technologies in these areas, we aim to contribute significantly to the ongoing evolution of DR processes in the steel industry. The holistic understanding and proactive solutions presented in this study lay the groundwork for a sustainable and efficient future in direct reduction processes, aligning with the global imperative of carbon neutrality in steel production.

REFERENCES

Béchara, R, Hamadeh, H, Mirgaux, O and Patisson, F, 2018. Optimization of the Iron Ore Direct Reduction Process through Multiscale Process Modeling, *Materials*, 11(7):1094.

Rist, A and Meysson, N, 1967. A dual graphic representation of the blast-furnace mass and heat balances, *JOM*, 19:50–59.

Xu, C Y, Zheng, A Y, Zhang, J L, Wang, R R, Li, Y, Wang, Y Z and Liu, Z J, 2019. Effect of H2/CO Ratio on Gas Consumption and Energy Utilization Rate of Gas-Based Direct Reduction Process, *The Minerals, Metals and Materials Series*, 631–647.

Yatsuzuka, T, Sawamura, J, Ota, S and Fukuda, T, 1960. Studies on carbon and heat consumption in blast furnace-I, *Tetsu-to-Hagane*, 46(6):643–652.

Reducing CO_2 emissions from the ferro-alloy and silicon production

DOI: 10.62053/PJEW9367
M Tangstad[1] and G M Tranell[2]

1. Professor, Norwegian University of Science and Technology, Trondheim 7491, Norway. Email: merete.tangstad@ntnu.no
2. Professor, Norwegian University of Science and Technology, Trondheim 7491, Norway. Email: gabriella.tranell@ntnu.no

ABSTRACT

The CO_2 footprints in the production of Mn-ferroalloys and silicon/ferrosilicon are correlated with the fossil carbon consumption. The CO_2 emissions may be reduced in the Mn-ferroalloy process by increasing the degree of prereduction and reduction of carbonate materials, while the silicon/ferrosilicon process is optimised based on silicon yield. By changing the fossil reductant into biogenic reductants, the global warming potential will be decreased even more. Even if the reductants are biogenic reductants, there will still be a global warming potential (GWP) in eg the electrode consumption and the CH_4 emissions in the charcoal production. To reduce the use of fossil reductants there are also more disruptive technologies like the use of H_2 that at least for the silicon production is on a very low technology readiness level (TRL). Using metallothermic processes will reduce the use of carbon but requires carbon neutral metal reductants. Electrowinning can have low CO_2 emissions, and the electrowinning of pure Mn is a technology of high TRL. Salt and oxide electrolysis is under investigation for both Mn and Si production however the research is still on a low TRL. The use of CCS/CCU (carbon capture storage/utilisation) is a part of obtaining carbon neutral processes. Last, the energy mix used for these energy demanding processes is discussed.

INTRODUCTION

The production of metals is a vital part of the green transition, which the production of solar cells and windmills are examples of. Thus, to reach the goals of international agreements with respect to reducing greenhouse gas emissions, one expects an increased production of metals and other materials related to green technologies. At the same time, the production processes of metals are also responsible of emitting a high amount of CO_2 and other greenhouse gases, and this industry is now racing towards the goal of carbon neutral production. Most of the industry have ambitious goals both for 2030 and 2050, of reducing their CO_2 emissions. In this paper, the reduction of CO_2 emissions from the manganese alloy and silicon/ferrosilicon alloy industries will be discussed. The mitigation tasks range from activities in adjusting today's process to researching disruptive technologies that may be potential future processes.

Mn-ferroalloy and silicon alloy production are both carbothermic reduction processes operated in submerged arc furnaces (SAF). The raw materials are ore and/or quartz, some fluxes like lime, and carbon materials. The carbon materials added are the main origin of direct CO_2 emissions. As there is high gas production in the lower part of the furnace, the raw materials must be lumpy to achieve a permeable path for the gas through the charge.

Mn ferroalloys are mainly produced in SAF as many other ferroalloys. The most typical geometry is the circular furnace with three Søderberg electrodes. In the lower part of the furnace the electrical energy is provided by the electrodes, and here the temperature is between 1400–1600°C. At these high temperatures, the oxide materials are melted, mixed and reduced to metal, and then drained from the furnace as metal and slag. The slag/metal ratio is typically around 0.5–1.2. The raw material mix, containing Mn-sources, fluxes and carbon materials, are being fed to the charge by gravity at the top of the furnace, where the temperature is at its lowest, in the area of 200-600°C. As slag and metal are being tapped from the furnace the rest of the material in the furnace will descend while heated by the gas coming from the high temperature zone. The high temperature zone is called the coke-bed (1400–1600°C), due to a stagnant layer of carbon materials, while the low temperature zone (200–1400°C) is called the pre-reduction zone.

In the high temperature zone, the following carbon consuming reactions occur in the metal producing reactions during high carbon FeMn (HC FeMn) production:

$$MnO + C = Mn + CO \quad (1)$$

$$FeO + C = Fe + CO \quad (2)$$

$$C = C \text{ (carbon dissolves into the metal)} \quad (3)$$

The typical composition of HC FeMn is 76–79 per cent Mn, 7 per cent C and the rest is iron. As shown in Table 1, this will lead to a consumption of 273 kg carbon/tonne alloy, however only 203 kg will go the gas phase as CO, and the rest will be dissolved in the metal. There is however also some carbon consumption in the prereduction zone. The reduction of higher Mn- and Fe-oxides is reduced with CO gas to CO_2 (Reaction 4) and if this reaction happens above about 800°C, the CO_2 will subsequently react with the carbon materials according to the Boudouard reaction (Reaction 5), and the sum of these two reactions (Reaction 6) will consume carbon:

$$Me_yO_x + CO = MeO_{x-1} + CO_2 \quad (4)$$

$$CO_2 + C = 2CO \quad (5)$$

$$Me_yO_x + C = Me_yO_{x-1} + CO \quad (6)$$

CO_2 from the decomposition of carbonates may also react according to the Boudouard reaction (Reaction 5), and hence the total reaction will be according to Reaction 7:

$$CaCO_3 + C = CaO + 2CO \quad (7)$$

TABLE 1

Example of carbon consumption and subsequently CO_2 emission producing a metal with 79 per cent Mn, a slag/metal ratio of 0.7, 40 per cent MnO in the slag, 100 kg lime/ton metal and 0 per cent prereduction.

		kg C	**kg CO_2**
790 kg Mn	MnO+C=Mn+CO	173	633
140 kg Fe	FeO+C=Fe+CO	30	110
70 kg C	C dissolved in metal	70	0
C in cokebed zone		**273**	**743**
s/m=0,7, 40%MnO	Mn_3O_4+C=3MnO+CO	59	217
	Fe_3O_4+C=3FeO+CO	10	37
100 kg $CaCO_3$/tonne metal	$CaCO_3$+C=CaO+2CO	12	88
0% degree of prereduction		**81**	**341**
Total		**354**	**1084**

Based on industrial operation over five years and four different furnaces (Ishak and Tangstad, 2007) it has been seen that the CO_2 from the reduction of MnO_2, Mn_2O_3 and Fe_2O_3 with CO gas, will not react with solid carbon, and hence the total oxygen content of the charge mix will not affect the total carbon consumption. The CO_2 from Mn_3O_4 and Fe_3O_4 to MnO and FeO, as well as the CO_2 from the decomposition of lime ($CaCO_3$), may or may not react with carbon to CO gas. If none of this CO_2 is reacting with C, it has been defined as 100 per cent degree of prereduction, and if all of this CO_2 reacts, it has been defined as 0 per cent degree of prereduction. Industrially, it was seen that the typical degree of prereduction varied between 0 per cent to 60 per cent. The degree of prereduction is determined by type and size of Mn-sources as well as furnace operation (Ishak and Tangstad, 2007).

So far, we have discussed the carbon consumption, as this is proportional with the final CO_2 emissions (with the exemption of the carbon dissolved in the metal). This is always the case for open furnaces where all CO gas will burn on the charge top. There are however some notes that must be included on this issue. For closed furnaces the off-gas will be a mixture of CO and CO_2 gas. If the

gas is flared, again the carbon consumption will be proportional with the C consumption. As the off-gas from Mn-alloy production may contain high amounts of CO (50–90 per cent), this gas may be sold to other users of CO as eg fuel. When this gas is burned to CO_2 and emitted, the total amount of CO_2 emissions will again be proportional with the original carbon consumption. This CO_2 may however be reported as a part of the customers CO_2 emissions and not the metal producer. From an environmental point of view, the total CO_2 emission will still be proportional with the carbon consumption in the metal producing furnace, and hence this will be the focus in this article.

In Table 1 the carbon consumption needed in the HC FeMn is shown. In the high temperature zone 273 kg of carbon per ton of metal is required, however 70 kg of these will be dissolved in the metal and hence 203 kg C or 743 kg CO_2 will be emitted from the reactions in this zone. If no prereduction is occurring the additional carbon consumption in the prereduction zone is 81 kg C, that is 341 kg CO_2 will be emitted. This means that with these operating conditions, 31 per cent of the CO_2 emitted from the furnace will come from the prereduction zone. Figure 1 shows how the total emission will vary with the degree of prereduction. On a day-to-day basis it is hence important to increase the degree of prereduction and lower the use of carbonates.

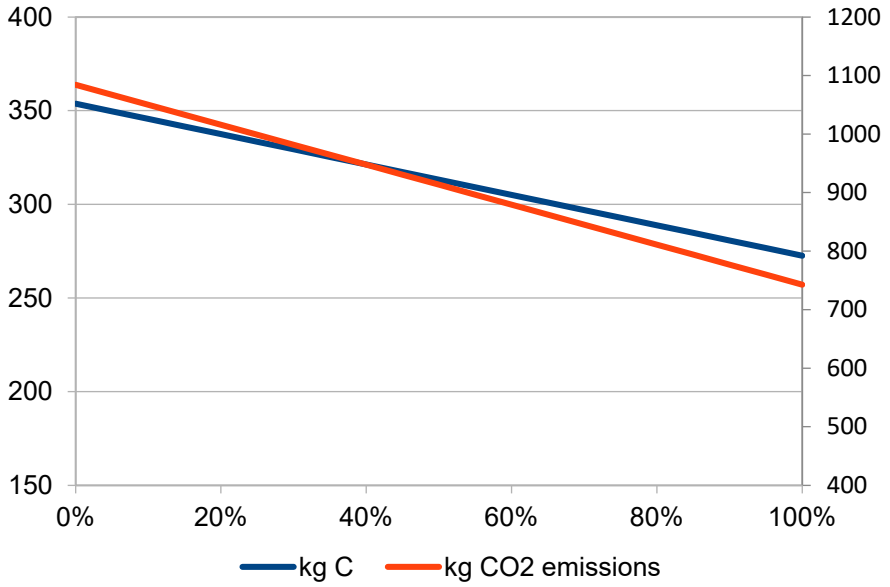

FIG 1 – Consumption of Fix C and CO_2 emissions from the fix C (volatiles and electrodes not included) for a given charge (slag/metal ratio=0.7, per cent MnO in slag=40 per cent, 100 kg $CaCO_3$ per ton metal, all Mn-sources are MnO_2, Mn_2O_3 or Mn_3O_4) as a function of degree of prereduction.

'High-silicon alloys' typically denote silicon-containing alloys in which silicon dominates the behaviour in the production furnace. This normally includes metallurgical grade silicon (MG-Si) with 96–99 per cent purity and ferrosilicon (FeSi) with a silicon content of 45–90 per cent. MG-Si is a precursor for pure Si (electronic grade, solar grade etc) and silicone production. MG-Si is also used as an alloy for aluminium while FeSi is typically used to de-oxidise or alloy steel or cast iron. Both MG-Si and FeSi alloys are produced through carbothermic reduction of quartz (and Fe-containing raw materials in the case of FeSi) in open or semi-open SAF.

In the Si furnace, most of the silicon is tapped from the furnace as liquid silicon, but some of the silicon escape from the charge as SiO gas. A simplified overall mass balance for the production of Si and SiO can be expressed by Reactions 8 and 9:

$$SiO_2 + 2C = Si + 2CO \quad (8)$$

$$SiO_2 + C = SiO + CO \quad (9)$$

The silicon furnaces are open or semi-closed furnaces, and hence the CO will burn with ambient air to CO_2. The Fix C consumption and the CO_2 emissions from the Fix C will hence be given by the Si-yield as seen in Figure 2.

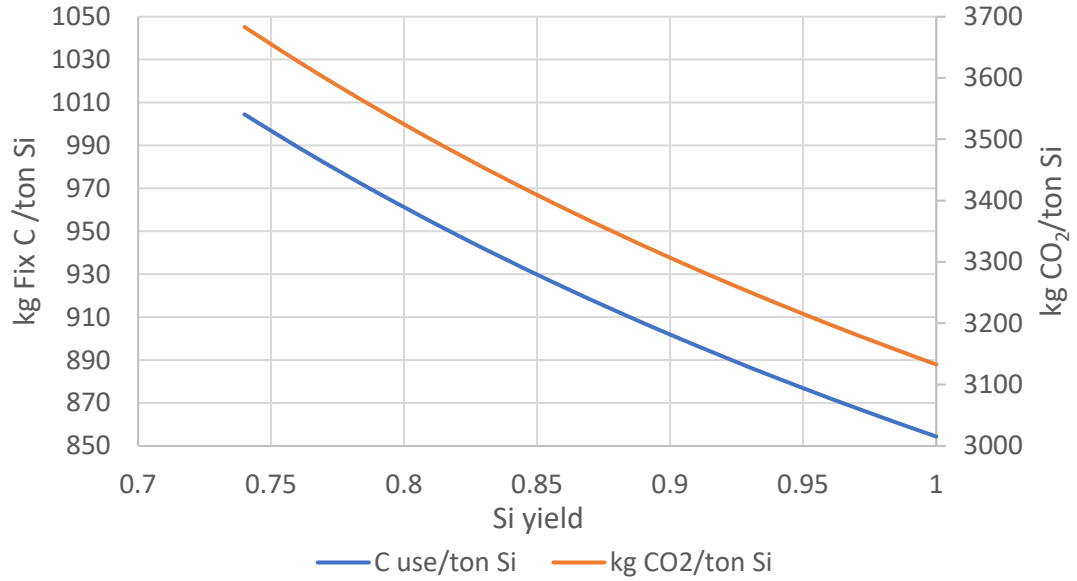

FIG 2 – Theoretical energy consumption and CO_2 emissions from the furnace not including the volatiles and the electrodes.

The Si yield (typically 85–92 per cent Si in metal alloy with respect to total input of Si), and hence the specific carbon consumption and thus the CO_2 emissions, is determined by the mode of operation and the carbon material properties. The rest of SiO_2-unit input is ending up as silica fume in the furnace off-gas, typically sold as a valuable bi-product. Typical carbon materials are coke/char, coal, charcoal and woodchips. The raw metal produced in the SAF is tapped into a ladle where dissolved Ca and Al is refined by oxidation, resulting in a Si alloy-infused (20–30 per cent Si) Al_2O_3-CaO-SiO_2 slag by-product, typically representing a Si-loss of up to 8 per cent Si. The CO gas produced in the furnace is combusted above the charge to CO_2 and released together with other hydrocarbons. The fixed C contributes to around 65 per cent of the CO_2 emissions, and carbon fines in the off-gas, volatiles in the carbon materials and the combustion of the electrode will be around 35 per cent. The standard emission factors for different Si-based alloys are listed in Table 2 where all the factors affecting the global warming potential (GWP) is included.

TABLE 2

Generic CO_2 emission factors for Si and FeSi alloys (ton CO_2/ton tapped metal) (Lindstad, 2007).

Type of alloy	Generic emission factors
Ferrosilicon 45% Si	2.5
Ferrosilicon 65% Si	3.6
Ferrosilicon 75% Si	4.0
Ferrosilicon 90% Si	4.8
MG-Si (>98% Si)	5.0

With the high electricity consumption involved in both Mn-alloy production and even more so the silicon alloy production as seen in Figure 3, the specific electricity mix clearly has a large impact on the total environmental footprint of the process (Saevarsdottir, Kvande and Magnusson, 2021). An life cycle assessment (LCA) study on the Si-process analysed the effect of energy mix. It was seen that with an almost 100 per cent renewable energy mix (like in Norway), the GWP decreases to about 55 per cent of an European mix, that still contains coal-based energy as seen in Figure 4. This number is of course very dependent on the amount of biogenic carbon used in the charge. Using mainly biogenic materials, this number would be down to 40 per cent (Nøstvold, 2022).

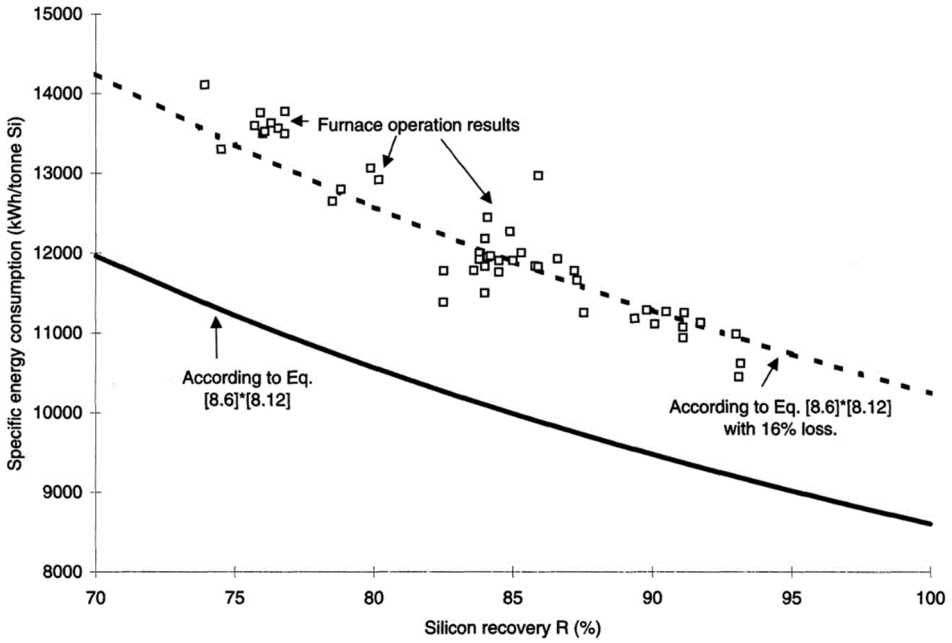

FIG 3 – Measured and calculated energy consumption. Dotted line is assuming an energy efficiency of 84 per cent (Schei, Tuset and Tveit, 1998).

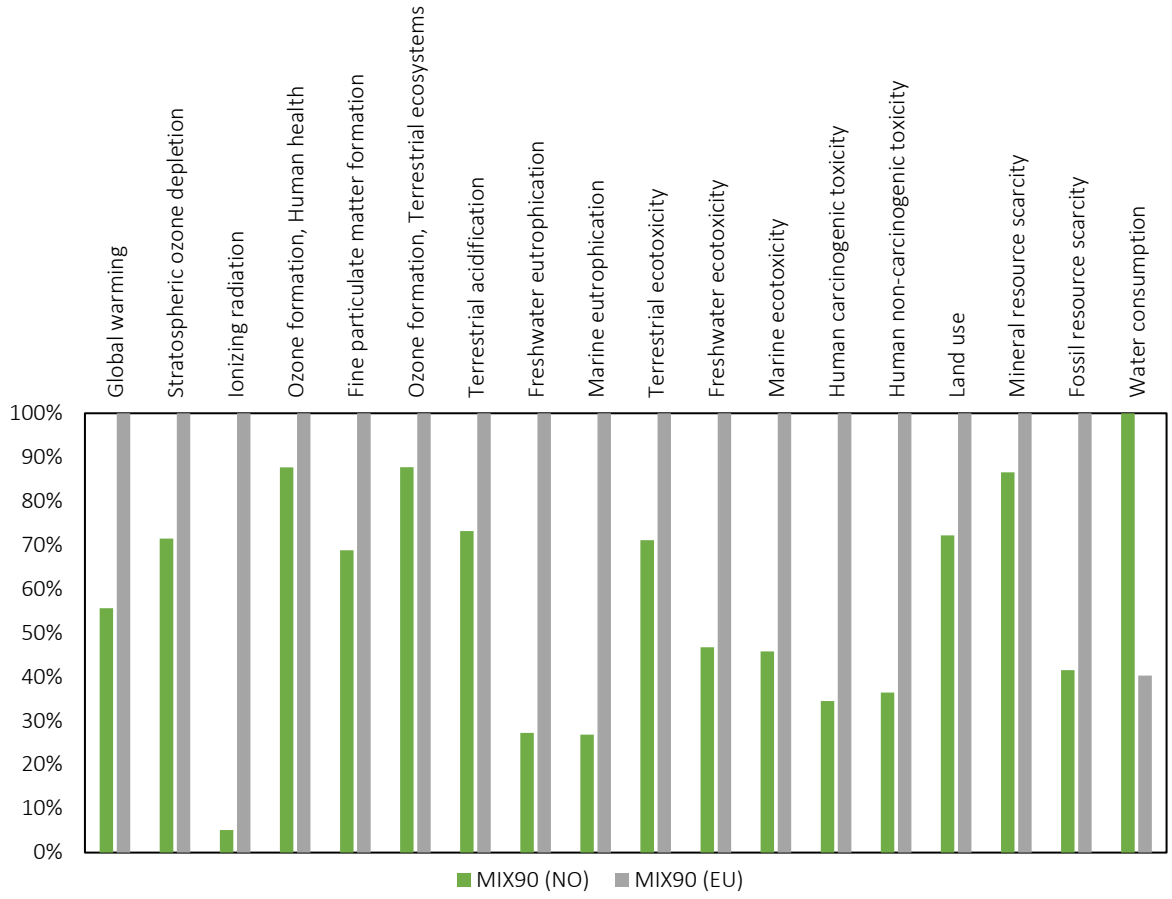

FIG 4 – Environmental impacts comparing the Norwegian and European energy mix for a fossil based carbon mix and silicon yield of 90 per cent (Nøstvold, 2022).

A significant part of the energy input to the furnace is contained in the furnace off-gas. Several of the Si-alloy plants in Norway have incorporated energy recovery systems, producing both electricity and

hot water for the grid and local community use. The energy consumption is decided by type of alloy, by silicon yield (as seen in Figure 3 for MG-Si) and energy losses.

CCS/CCU (Carbon Capture Storage/Utilisation) is part of the strategy to produce carbon neutral metals for many companies. The Mn-ferroalloy process can be, and is often, produced in closed furnaces, which means that the off-gas can eventually contain close to 100 per cent CO_2. The silicon and high ferrosilicon are today produced in semi-open furnaces. With an exhaust gas system designed to both optimise CO and hydrocarbon combustion and produce a high-quality silica fume, this means that the CO_2 content in the off-gas will be in the area of a couple of percentages. This gas can as an example be used to produce algae for fish feed (Giæver, 2024). If this gas will be used in CCS, the cost to pretreat the gas will be expensive due to the low CO_2 content. The CO_2 content can however be increased by recycling the flue gas as shown in Figure 5. Closed furnaces have also been investigated but the mechanical stoking and effect on off-gas temperature and silica product has prevented further development in this area.

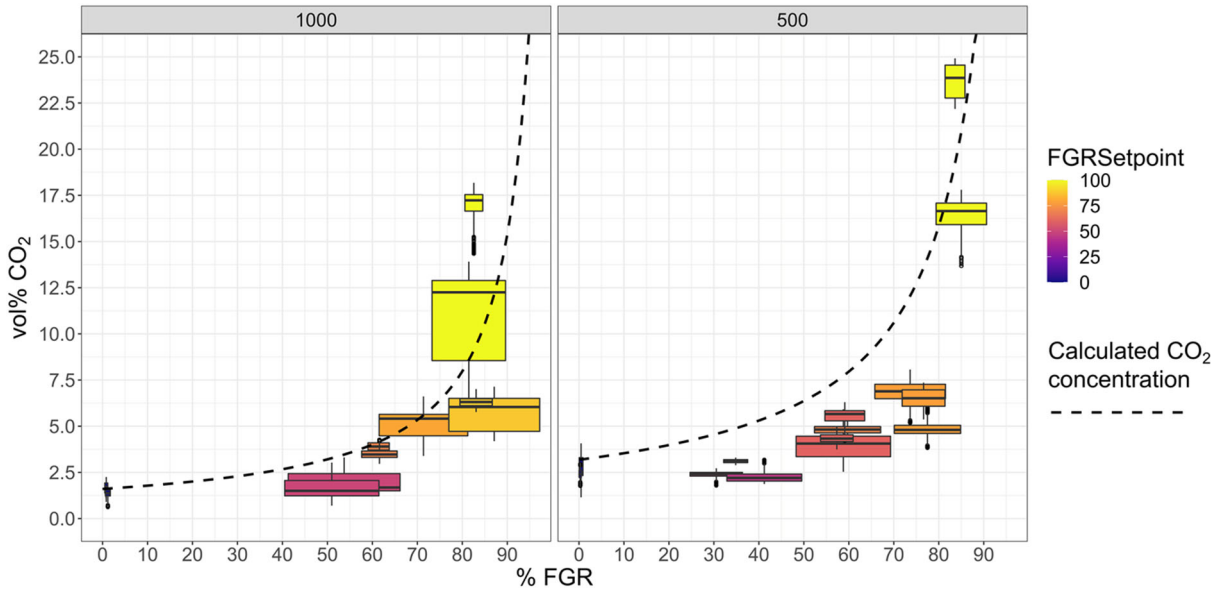

FIG 5 – Increased CO_2 content in off-gas by recycling. %FGR (Flue Gas Recycling) is fraction of off-gas recycled (Andersen, 2023).

BIOCARBON

Brazil has for many years used charcoal as the main reductant in Mn-ferroalloys. Using biomass, like charcoal, the CO_2 emitted will be consumed when growing new agricultural biomass and hence the CO_2 will not be enriched in the atmosphere. In addition to the issues regarding the availability of charcoal or other biomass addressed above, there are also some technical issues regarding the use of charcoal in the Mn-ferroalloy process in the SAF. The mechanical strength may be an issue in large furnaces. In addition to the dusting outside of the furnace and the subsequent HES (Health, Environment, Safety) issues, the issues inside the furnace will be the following:

1. The electrical energy is developed by the electrical voltage over the coke bed. It is hence important that the carbon in the coke bed is lumpy material with low amount of fines, both for the positions of the electrode-tips, but also for the slag flow-through the coke bed (Tangstad *et al*, 2021).
2. Fines in the prereduction zone clogs the voids and hence disrupts the gas flow. This will affect the degree of prereduction, and hence the energy consumption, but may also pose as a safety threat.
3. The density is low for charcoal (about 350 kg/m^3) versus coke (about 550 kg/m^3) (Ramos *et al*, 2021). This means that the volumetric carbon/ore ratio will be higher. This may lead to less agglomeration in the charge mix. This phenomenon may also affect higher electrical current paths, however as the charcoal at low temperatures are more or less insulating (Pedersen, 2020; Surup *et al*, 2020), this is not believed to be a problem. The higher descending rate, in

m/s, may cause a lower prereduction. The CO_2 reactivity will at the same time be higher for charcoal versus coke, and this may also increase the extent of the Boudouard reaction.

In the silicon process, many producers are partially using biogenic carbon. The goal is now to convert the fossil carbon-based reduction material charge. No fossil reductant in the charge is common in South America and Australia where there is local access to bio-carbon. While bio-based reductants are considered carbon neutral if the wood is responsibly regrown, a recent LCA study (Nøstvold, 2022) comparing the environmental impact of different carbon charge mixes and silicon furnace yields identified areas where also bio-based charge mixes have negative environmental impacts such as land use, water consumption etc, as illustrated in Figure 6. When the CO_2 emissions is reduced from 100 per cent fossil CO_2 to 8 per cent fossil CO_2 and 92 per cent biogenic CO_2, the total global warming potential will decrease with 40 per cent.

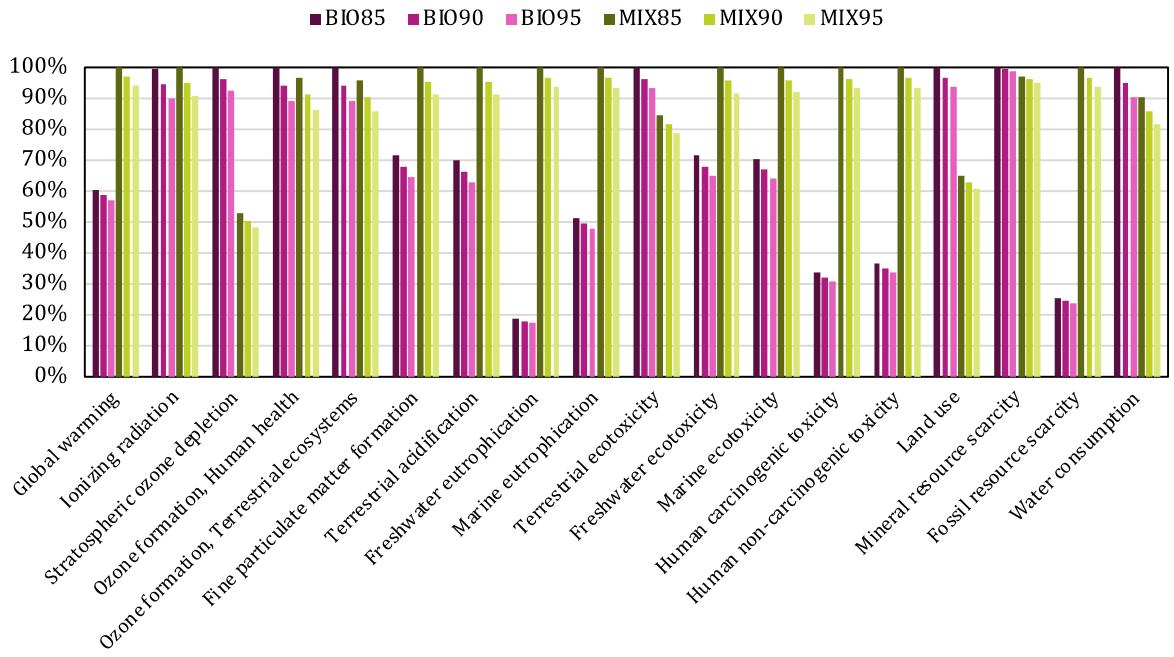

FIG 6 – Environmental impact when using biocarbon versus fossil reductant for various silicon yields (Nøstvold, 2022).

HYDROGEN

One of the strategies to reduce the CO_2 emissions in today's processes is to increase the degree of prereduction in the furnace, that is to reduce the extent of the Boudouard reaction, and hence the total carbon and energy consumption. Figure 1 shows the carbon consumption and the CO_2 emission for the same charge as shown in Table 1 as a function of degree of prereduction. As previously noted, the highest degree of prereduction seen industrially was in the area of 60 per cent (Ishak and Tangstad, 2007), and this would reduce the CO_2 emissions to 870 kg CO_2, that is 19 per cent. To obtain such numbers, the operation is optimal under today's conditions. The main factor for this to happen is first and foremost, optimal raw materials. If the raw materials could be developed further to obtain 100 per cent degree of prereduction, a total reduction of 31 per cent CO_2 emission compared to 0 per cent prereduction could be obtained.

MnO is a stable oxide and cannot be reduced with H_2, only with C as shown in Reaction 1, as seen in Figure 7. FeO and the higher manganese oxides can however be reduced with H_2 according to Reactions 10 and 11 (Davies *et al*, 2023; Tangstad, Schanche and de Preez, 2023). According to the above discussion between 20 and 30 per cent of the CO_2 emission could then be reduced:

$$Me_3O_4 + H_2 = MeO + H_2O \quad (10)$$

$$FeO + H_2 = Fe + H_2O \quad (11)$$

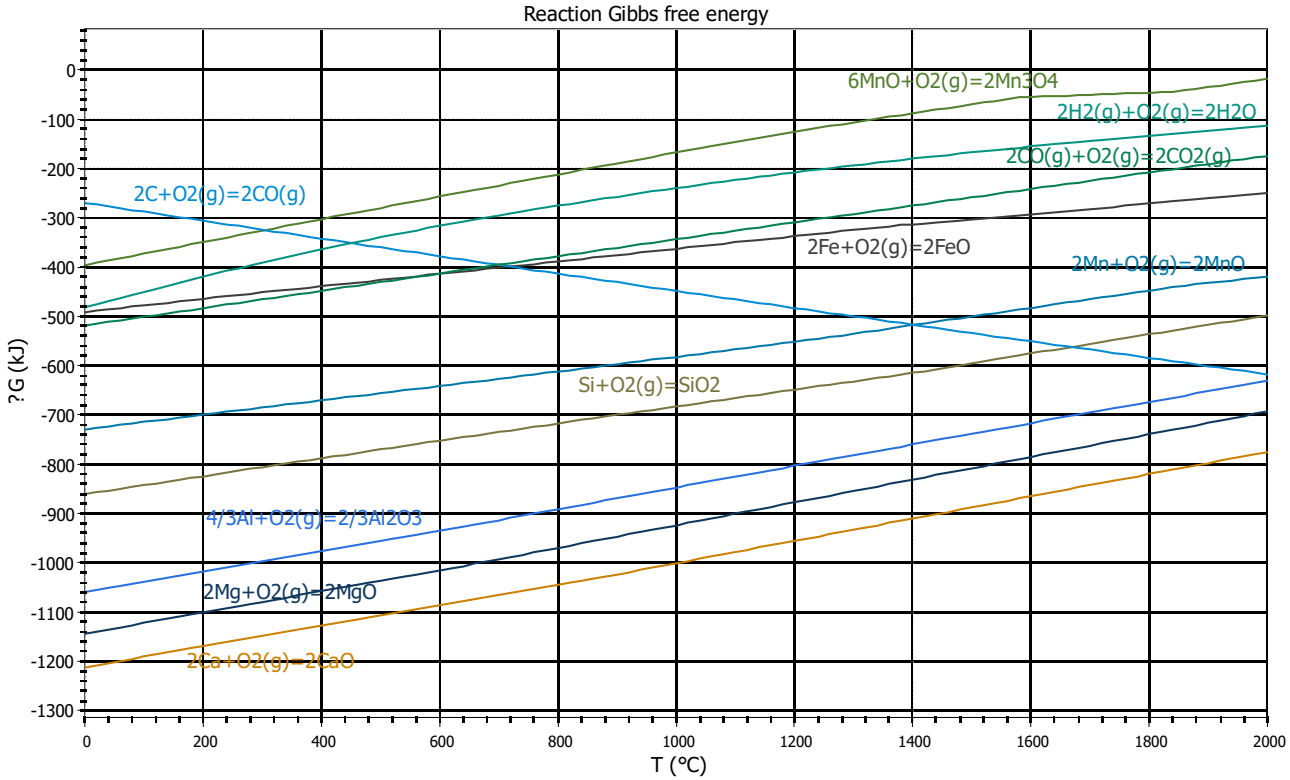

FIG 7 – Gibbs free energy diagram showing the stability of various oxides versus C, CO and H_2 (HSC Chemistry v9).

In a process where the reactions of the prereduction zone could be separated from the high temperature coke bed zone, like eg in a prereduction unit, H_2 could be used to reduce the higher manganese oxides and the FeO without any Boudouard reaction. A more possible scenario is to operate a prereduction unit with no solid carbon, and hence both the CO from the coke bed and/or additional H_2 may be used. In both cases, the total emitted CO_2 would now be down to 633 kg CO_2 per ton of metal produced (or 743 kg CO_2 if the iron is not reduced to metallic iron). The conditions, which is required to reduce the ore down to MnO and Fe is extensively investigated to mention a few (Davies *et al*, 2023; Larssen, Senk and Tangstad, 2021; Schanche, 2022).

In the silicon process, where SiO_2 is an even more stable oxide than MnO, hydrogen cannot be used directly as indicated in Figure 7. Hydrogen gas can, however, produce the silicon sub-oxide SiO and water according to Reaction 12:

$$SiO_2 + H_2 = SiO + H_2O \quad (12)$$

At atmospheric pressure and temperatures above 1800°C (Aarnæs, 2023; Dalaker, 2022). However, to directly convert SiO_2 with H_2 to Si and H_2O with reasonable yields require pressures > 10 000 bars and would need excessive amounts of H (typically 2500:1 H:Si at 2000°C), as shown in Figure 8.

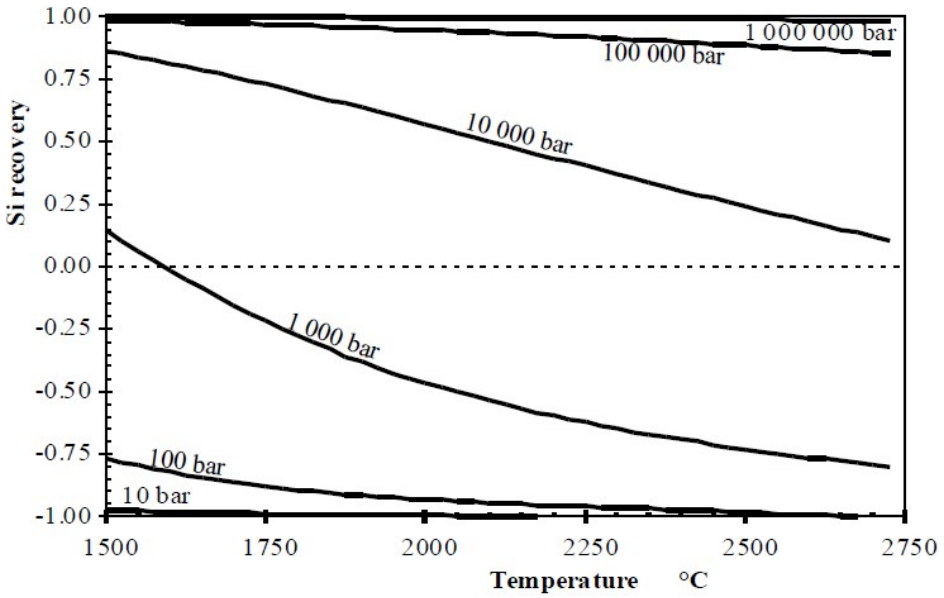

FIG 8 – Silicon recovery as a function of temperature for various pressures. A negative value means that the equilibrium reaction between SiO_2, Si and H_2 will consume Si and produce SiO (Schei, Tuset and Tveit, 1998).

As an alternative, in plasma, where H+ is stabilised (rather than H_2), direct production of SiH_4 may be viable at temperatures below 1400°C, although back reaction with the water vapour in the gas phase may be prohibitive. The use of hydrogen as a reductant in manganese production is currently under investigation where plasma is investigated, according to Reaction 13:

$$MnO + 2H \rightarrow Mn + H_2O \quad (13)$$

Dividing the silicon reduction in the two following reactions, Reactions 14 and 15, is also proposed as illustrated in Figure 9 (Svenum and Ringdalen, 2022).

$$Si + SiO_2 = 2SiO \quad (14)$$

$$2SiO + 2H_2 = 2Si + 2H_2O \quad (15)$$

$$SiO_2 + 2H_2 = Si + 2H_2O \quad (16)$$

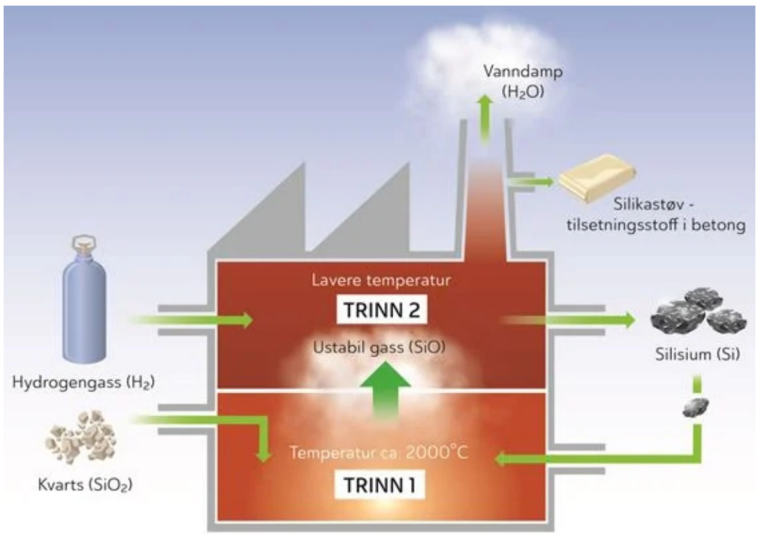

FIG 9 – The concept of a hydrogen producing silicon furnace (illustration: Knut Gangåssæter/ SINTEF) (Svenum and Ringdalen, 2022).

The overall reaction will then be the production of Si and water vapor according to Reaction 16. There are several challenging parts, as eg both the thermodynamics and the rates of the reactions.

The main challenge is that Reaction 15 requires a low temperature, and one has hence to stop the SiO gas from producing Si and SiO_2.

METALLOTHERIC PRODUCTION

While most of the metallic manganese is produced as manganese ferroalloys in Submerged Arc Furnaces by carbothermic reduction, manganese ferroalloys may also be produced in other processes eg in the blast furnaces. As the energy is here produced by combustion of carbon this may increase the carbon consumption by a factor of six to seven, and hence will typically not be a sustainable alternative for Mn-ferroalloy product. With the exception of the type of energy production, it is assumed that the chemical reactions are quite close to the reactions in the SAF as described above.

Another quite mature technology is the production of Mn-metal or Mn-ferroalloys using metallic reductants like Si or Al instead of using carbon according to Reaction 17:

$$2MnO + Si = 2Mn + SiO_2 \quad (17)$$

This process can be carbon free and hence CO_2 free. The raw materials, the Si and Al, will however be produced with the use of carbon, and hence again the metallothermic reduction will not globally reduce the CO_2 emissions, only locally. The exception may of course be either if the reductant is produced without any consumption of carbon (eg inert electrodes) or if waste Si or Al is used that is not being used for other purposes.

In the same way, it is possible to produce silicon by using metals with a higher affinity to oxygen than silicon as a reducing agent. The most relevant metals are aluminium, magnesium and calcium, where the most viable option from a material access perspective in Norway is aluminium. Research on Si production by aluminothermic reduction of SiO_2 has been carried out since the early 1900s (Islam, Rhamdhani and Brooks, 2011). As aluminium is an expensive reductant compared to carbon, this has not been widely acknowledged as a viable route to production of MG-Si. However, interest in the last decades in production of pure Si for PV applications, as well as a growing interest in Si nanoparticles for Li-ion batteries has created extensive activity within metallothermic reduction of Si oxides. For this purpose, aluminothermic reduction has been applied in Cl-solvents, enabling relatively low temperature processes (Liu, Giordano and Antonietti, 2012; Lin *et al*, 2015a; Ueda, Abe and Ohtsuka, 2005; Zhou *et al*, 2016). Si production through reaction between silicon tetrachloride (STC, $SiCl_4$) and Al has been investigated by several researchers and companies (Lin *et al*, 2015b). Reaction products include $AlCl_3$, which can be electrolysed for recycling. Aluminothermic reduction of SiO_2 in cryolite (Na_3AlF_6) to produce an Al-Si alloy has also been proposed (Gorji, Soltanieh and Hibabolahzadeh, 2007). Previous work also includes aluminothermic reduction of either quartz or silicate-glasses that are heated with Al to temperatures above the melting point of Al, and in some cases above the melting point of Si (Dietl *et al*, 1984; Smith, 1960; Thurmond, 1959; Wartenberg, 1956; Yusada and Okabe, 2010). Recently, an integrated process (SisAl) for production of silicon via alumino-thermic reduction of SiO_2-containing slag using different aluminium sources, such as for example scrap and Al dross, with subsequent processing of slag, followed by recycling of Al_2O_3 and CaO, has been developed (Tranell, Safarian and Wallin, 2020; Phillipson *et al*, 2022). This process, illustrated in Figure 10, has the ability of delivering different grades of silicon and Al-Si alloys, depending on the raw materials used. The process is currently developed in large scale pilot through the EU H2020 program.

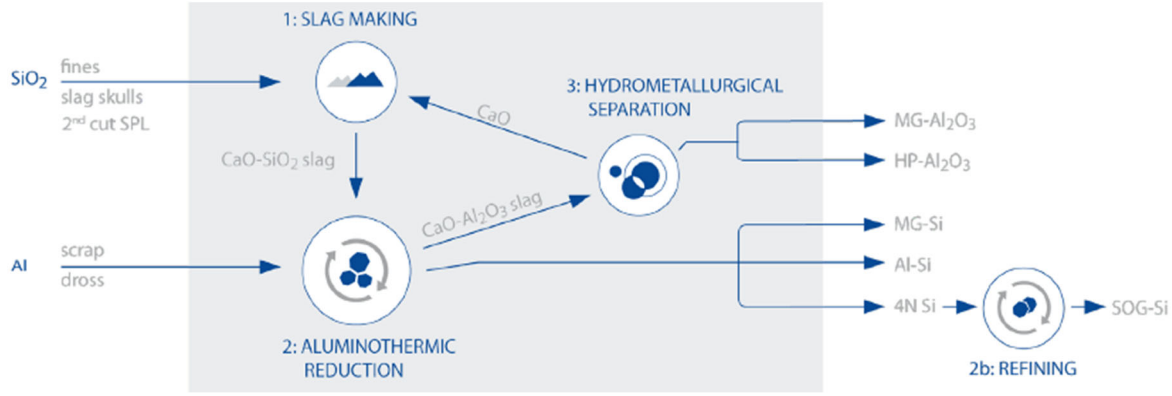

FIG 10 – Overview of the SisAl project where silicon is produced industrially from waste materials, will a following refining of both the silicon and the slag produced.

ELECTROWINNING

Mn-metal, 99 per cent pure, can also be produced by aqueous electrolyses (Kero *et al*, 2020). EMM (electrolytic manganese metal) is produced by hydrometallurgy, dissolving the Mn-source in acid followed by electrolyses. There are some advantages with this process, as eg very low CO_2 emissions. The main part of the CO_2 comes from the prereduction of the ore, but this can be done with H_2. The disadvantages are quite large amount of waste materials and the fact that it is a costly process. New electrowinning processes can be based on salt- or molten oxide-electrolyses (Kero *et al*, 2020).

At the start of the century, as a result of the increased demand for high purity silicon for solar cells, research on electrochemical processes for silicon production was intensified and new processes developed at the laboratory scale. Electrolytic production of silicon can be a low-carbon alternative if an inert anode can be used. An important reason why electrolysis processes have not been industrialised is the high melting point of silicon compared to other electrolysis processes such as aluminium. Various electrolytes have been investigated:

- fluoride/cryolite-based electrolytes
- oxide-based electrolytes
- chloride-based ($CaCl_2$, $AlCl_3$) electrolytes.

Chloride and fluoride electrolytes are typically very corrosive and will present significant material challenges if operated at temperatures above the melting point of silicon. While both chloride and fluoride electrolytes have comparatively low melting temperatures operating at such temperatures would mean that silicon would be deposited as a powder or in solid form at the cathode, prohibiting a continuous process. Powder-based Si products may however be interesting for the battery market, in which Si powder is currently produced by crushing and grinding of cast metallurgical silicon.

CONCLUSIONS

In the production of Mn-ferroalloys and silicon/ferrosilicon the daily production processes is optimised to minimise the CO_2 emissions. On a day-to-day basis the Mn-process is optimised based on increasing the degree of prereduction and reduction of carbonate materials, while the silicon/ferrosilicon process is optimised based on silicon yield. This may reduce the CO_2 emissions in the order 10 per cent. By changing the fossil reductant with biogenic reductants, the reduction of the global warming potential will be approximately 60 per cent. It can be pointed out that the emissions of CH_4 in the charcoal production will add to the global warming potential and also that the electrodes cannot, so far, be made with biogenic materials. To reduce the use of fossil reductants there are also more disruptive technologies like the use of H_2 that at least for the silicon production is on a very low technology readiness level (TRL). Using metallothermic processes requires carbon neutral metals which will be vital for the overall CO_2 emission. Electrowinning of Mn is a technology of high TRL, however salt and oxide electrolyses is also discussed and researched for both Mn and Si production where the research is still on a low TRL. Additionally, to the discussed technologies,

CCS/CCU is also a part of the industries plan, and especially for the open furnaces where the CO_2 level in the off-gas is low, research is ongoing to increase the CO_2 level in the off-gas to lower the resources needed for the treatment of the off-gas. Finally, as all these processes are energy intensive, the energy mix will be an important part of the total CO_2 emissions, and countries with a high amount of renewable energy will hence have a lower CO_2 footprint.

ACKNOWLEDGEMENTS

Acknowledgement will be given to the following project funded by the Norwegian Research Council: SFI Metal production (237738), HydrogenI (333118) BioMet (336175), Controlled Tapping (267621), Thanos (309475) and SisAl funded by EU in the Horizon 2020 programme under grant agreement No. 869268

REFERENCES

Aarnæs, T S, 2023. The Effect of Hydrogen and Methane Containing Gases on SiC and SiO formation, PhD thesis, Norwegian University of Science and Technology, 48 p.

Andersen, V, 2023. Flue Gas Recirculation for the Silicon Process, PhD thesis, Norwegian University of Science and Technology.

Dalaker, H, 2022. Silicon Production from SiO Gas via Gas-Phase Reactions, in: (eds: F Tesfaye, L Zhang, D P Guillen, Z Sun, A A Baba, N R Neelameggham, M Zhang, D E Verhulst and S Alam), *REWAS 2022*: *Energy Technologies and CO_2 Management (Volume II)*, pp 33–40 (Springer International Publishing).

Davies, J, Tangstad, M, Schanche, T L and du Preez, S P, 2023. Pre-reduction of United Manganese of Kalahari Ore in CO/CO_2, H_2/H_2O and H_2 Atmospheres, *Metall Mater Trans B,* 54:515–535. https://doi.org/10.1007/s11663-022-02705-0

Dietl, J, Holm, C, Kotilge, J and Wohlschlager, M, 1984. Semicontinuous process for the production of pure silicon, US Patent, US4457903A.

Giæver, I, 2024. Mass cultivation of diatoms at Finnfjord AS, UiT The Arctic University of Norway. Available from: <https://en.uit.no/prosjekter/prosjekt?p_document_id=564100> [Accessed: 16 Jan 2024].

Gorji, Y M, Soltanieh, M and Hibabolahzadeh, A, 2007. Production of Al-Si Master Alloy by Aluminothermic Reduction of Silica in Molten Cryolite, *Canadian Metall Qrtly,* 46:385–390. https://doi.org/10.1179/cmq.2007.46.4.385

Ishak, R and Tangstad, M, 2007. Degree of Prereduction Without Coke Consumption in Industrial Furnaces, Presented at INFACON XI, The Indian Ferro Alloy Producers' Association, pp 268–280.

Islam, M S, Rhamdhani, M-A and Brooks, G A, 2011. Solar-Grade Silicon: Current and Alternative Production Routes, *Chemeca*.

Kero, I, Dalaker, H, Osen, K S and Ringdalen, E, 2020. Some carbon-free technologies for manganese ferroalloy production, *Infacon XVI,* Trondheim, Norway.

Larssen, T A, Senk, D and Tangstad, M, 2021. Reduction of Manganese Ores in $CO\text{-}CO_2$ Atmospheres, *Metall Mater Trans B,* 52:363–381. https://doi.org/10.1007/s11663-020-02018-0

Lin, N, Han, Y, Wang, L, Zhou, J, Zhou, J, Zhu, Y and Qian, Y, 2015b. Preparation of Nanocrystalline Silicon from $SiCl_4$ at 200°C in Molten Salt for High-Performance Anodes for Lithium Ion Batteries, *Angew Chem Int Ed Engl*, 54(12):3822–3825.

Lin, N, Han, Y, Zhou, J, Zhang, K, Xu, T, Zhu, Y and Qian, Y, 2015a. A low temperature molten salt process for aluminothermic reduction of silicon oxides to crystalline Si for Li-ion batteries, *Energy Environ Sci*, 8:3187–3191.

Lindstad, T, 2007. Greenhouse gas emissions from ferroalloy production, *INFACON XI,* pp 457–466.

Liu, X, Giordano, C and Antonietti, M, 2012. A molten-salt route for synthesis of Si and Ge nanoparticles: chemical reduction of oxides by electrons solvated in salt melt, *J Mater Chem,* 22:5454–5459.

Nøstvold, C, 2022. Mass and Energy Balanced Life Cycle Assessment of Metallurgical Grade Silicon Production, MSc Thesis, Norwegian University of Science and Technology, Department of Material Science and Engineering.

Pedersen, T, 2020. Electrical Resistivity in Carbon Materials Converting to SiC, MSc Thesis, Norwegian University of Science and Technology, Department of Material Science and Engineering.

Phillipson, H, Blandhol, K, Engvoll, K, Djupvik, V, Wallin, M, Tranell, G and Haarberg, T, 2022. Preliminary Techno-Economic Considerations of the Sisal Process- Closing Materials Loops through Industrial Symbiosis, *Proceedings of the Silicon for the Chemical and Solar Industry XVI*.

Ramos, D C, Carneiro, A C O, Tangstad, M, Pereira, B L C, Saadieh, R, Oliveira, A C and Vital, B R, 2021. Reactivity assessment of charcoal for use in silicon production, *Eur J Wood Prod*, https://doi.org/10.1007/s00107-021-01683-5

Saevarsdottir, G, Kvande, H and Magnusson, T, 2021. Greenhouse gas emissions from silicon production- development of carbon footprint with changing energy systems, *Proceedings of the 16th International Ferro-Alloys Congress (INFACON XVI)*.

Schanche, T, 2022. Pretreatment of manganese ores in $CO/CO_2/H_2$ atmospheres, PhD thesis, Norwegian University of Science and Technology.

Schei, A, Tuset, J K and Tveit, H, 1998. *Production of High Silicon Alloys*, Tapir, Trondheim.

Smith, W E, 1960. Process for making purified silicon from silicon-containing substances, US Patent, US2955024.

Surup, G R, Pedersen, T A, Chaldien, A, Beukes, J P and Tangstad, M, 2020. Electrical Resistivity of Carbonaceous Bed Material at High Temperature, *Processes,* vol 8. https://doi.org/10.3390/pr8080933

Svenum, I-H and Ringdalen, E, 2022. Vi er storforbrukere av silisium, Nå er vi kanskje på sporet av en produksjonsmåte uten CO_2-utslipp (We are major consumers of silicon. Now we may be on the track of a production method without CO_2 emissions) [online], Forskersonen.no. Available from: <https://www.forskersonen.no/klima-materialteknologi-meninger/vi-er-storforbrukere-av-silisium-na-er-vi-kanskje-pa-sporet-av-en-mate-a-produsere-det-uten-co2-utslipp/2031126>

Tangstad, M, Bublik, S, Haghdani, S, Einarsrud, K E and Tang, K, 2021. Slag Properties in the Primary Production Process of Mn-Ferroalloys, *Metall and Mater Trans B,* 52:3688–3707. https://doi.org/10.1007/s11663-021-02347-8

Tangstad, M, Schanche, T and de Preez, F, 2023. Use of H_2 in Mn-Ferroalloy Production, in *Advances in Pyrometallurgy* (C Fleuriault, J D Steenkamp, D Gregurek, J F White, Q G Reynolds, P J Mackey, S A C Hockaday), pp 35–53 (Springer Nature Switzerland).

Thurmond, C D, 1959. Recovery of silicon from silicon dioxide, US Patent, US2904405.

Tranell, G, Safarian, J and Wallin, M, 2020. SisAl – A New Process for Production of Silicon, in *Proceedings of the Silicon for the Chemical and Solar Industry XV*, pp 129–139 (Norges Teknisknaturvitenskapelige Universitet: Trondheim).

Ueda, M, Abe, Y and Ohtsuka, T, 2005. Reduction of SiO_2 to Si by aluminium metal fog in NaCl–KCl-$AlCl_3$ molten salt, *Materials Letters,* 60:635–638.

Wartenberg, H V, 1956. Schwefel-Thermitverfahren zur Darstellung von Rein-Silicium (Sulfur-thermite process for the production of pure silicon), *Zeitschrift für anorganische und allgemeine Chemie (Journal of Inorganic and General Chemistry)*, 286(5–6):247–253.

Yasuda, K and Okabe, T H, 2010. Solar-grade silicon production by metallothermic reduction, *JOM*, 62(12):94–101.

Zhou, Z-W, Liu, Y-T, Xie, X-M and Yeb, X-Y, 2016. Aluminothermic reduction enabled synthesis of silicon hollow microspheres from commercialized silica nanoparticles for superior lithium storage, *Chem Commun*, 52:8401–8404.

Thermal phosphorus – it's a hot commodity with a hot process

DOI: 10.62053/TRLA2623

E Wingate[1], Y Liu[2], R Prasad[3], R Atmuri[4] and W Liang[5]

1. FAusIMM(CP), Principal Process Specialist, Bechtel Mining and Metals, Fortitude Valley Qld 4006. Email: ewingate@bechtel.com
2. Senior Process Engineer, Bechtel Mining and Metals, Fortitude Valley Qld 4006. Email: yliu15@bechtel.com
3. Senior Process Engineer, Bechtel Mining and Metals, Fortitude Valley Qld 4006. Email: rprasad2@bechtel.com
4. Senior Principal Process Engineer, Bechtel Mining and Metals, Fortitude Valley Qld 4006. Email: sratmuri@bechtel.com
5. Decarbonisation Specialist, Bechtel Mining and Metals, Fortitude Valley Qld 4006. Email: wliang1@bechtel.com

ABSTRACT

Yellow phosphorus (YP) has been commercially produced since the 1920s. First in the USA by the Tennessee Valley Authority (TVA), next in Russian (Kazakhstan) in the 1950s, and finally in China in the late 1970s and early 1980s. There are operations in Vietnam and Sarawak on a smaller scale.

YP has become very in vogue due to its use in the production of lithium iron phosphate battery cathode precursor materials by the Chinese and other western battery manufacturers. The YP is also used to produce purified phosphoric acid and higher grades of acid using a thermal oxidation process after smelting.

This paper will look at the basics of the smelting including slag chemistry, alloy chemistry and off-gas chemistry. The paper will look at the design of the furnaces used in the YP production process as well as the downstream recovery of phosphorus from the smelter off-gas stream to YP.

The next part of the discussion will focus on the operations of a YP smelter with regards to control of the furnace to optimise phosphorus recovery to YP. Will discuss tapping cycles for alloy and slag with a view to optimal phosphorus recovery.

The discussion will close out with a review of operational challenges in the smelter and a brief description of the downstream conversion of YP to high purity phosphoric acid.

INTRODUCTION

The production of phosphorus via the thermal route has seen a resurrection in popularity in the last few years due to the need for increased amounts of purified phosphoric acid (PPA) for use in lithium ion battery (LIBs) cathode assemblies utilising lithium iron phosphate (LFP). Operators do not need to rely on large wet process phosphoric acid production facilities for the production of purified phosphoric acid (PPA).

The technology employed today has remained unchanged for more than 80 years. The original thermal phosphorus production was conducted in small blast furnaces in the USA in the Tennessee Valley Authority (TVA) (Easterwood, 1933). Later in the late 1940s the production of thermal phosphorus began to appear in Russia in Kazakhstan (Karatau region). A series of phosphorus chemical facilities were developed around the low-grade sedimentary phosphate ores of the region. These same facilities are still in operation today. In the late 1970s and early 1980s the Russian based technology was seen to be developing in China in the eastern part of Yunnan Province. The metallurgical process for the production of thermal phosphorus relies on the use of hard lumpy ore combined with metallurgical coke (reductant) and silica (flux). It is worth noting that thermal phosphorus production facilities have been constructed in Vietnam and Sarawak where power costs (hydroelectric) are lower than countries using fossil fuel generated power.

The predominant furnace design is a closed top electric submerged arc furnace with twin slag tap holes and a single alloy tap hole located between the two slag tap holes.

METALLURGICAL BASICS OF THERMAL PHOSPHORUS PRODUCTION

The production of thermal phosphorus relies on thermal energy to liberate elemental phosphorus from its oxide form and subsequently produce phosphoric acid. This carbothermal reduction process is typically conducted within two major process units: the yellow phosphorus (YP) plant and the downstream thermal phosphoric acid (TPA) plant.

The reaction, which is endothermic, between phosphate rock, silica and coke (carbon source), is as shown in Equation 1 at a reaction temperature greater than 1100°C. Optimum reaction temperature is between 1400°C–1600°C. Temperatures over 1700°C will not only result in unwanted side-reactions but also increases energy consumption.

$$2Ca_3(PO_4)_2 + 6SiO_2 + 10C \rightarrow P_4 + 10CO + 6CaSiO_3 \quad (1)$$

Typical material characteristics

The production of YP requires phosphate ore, carbon reductant and silica. Tables 1, 2 and 3 illustrate some typical chemical analyses for the materials concerned.

TABLE 1

Phosphate ore specification.

Species	P_2O_5 (%)	S (%)	SO_3 (%)	MgO (%)	Al_2O_3 (%)	Fe_2O_3 (%)	As (ppm)	Na_2O (%)
Target	>= 28.0	N/A	<+1.75	<=0.35	<=0.65	<=1.90	<=20	<=0.45
Species	**K_2O (%)**	**Cl (%)**	**F (ppm)**	**LOI (%)**	**CaO (%)**	**SiO_2 (%)**	**H2O (%)**	**Pb (ppm)**
Target	<=0.06	<=0.06	<=27 500	<=6.25	<=46.5	>+10.0	<=4.0	N/A

TABLE 2

Carbon reductant specification (metallurgical coke).

Analysis item	Specification	Unit
Fixed Carbon	≥ 80.0	% w/w
Volatile Matter	≤ 1.5	% w/w
Ash	≤ 18.0	% w/w
Total Sulfur	≤ 1.0	% w/w
Moisture	≤ 5.0	% w/w
Particle size range	10–25	mm

TABLE 3

Silica specification.

Analysis item	Specification	Unit
SiO_2	≥ 95.0	% w/w
CaO	≤ 0.01	% w/w
Al_2O_3	≤ 0.2	% w/w
Fe_2O_3	≤ 0.5	% w/w
MgO	≤ 0.008	% w/w
Particle size range	20–50	mm

Thermodynamics of yellow phosphorus smelting

As stated in the introduction, this process is a carbothermal reduction process whereby phosphate ore (P_2O_5) is combined with a carbon reductant (metallurgical coke) and a flux (silica). The process reaction is illustrated in Equation 1.

Fluxing strategies for phosphate ore are based on the need to achieve fluid slags with a low liquidus temperature.

Potential operating temperatures have been observed between 1340°C and 1450°C, depending upon the ore chemistry and quantity of flux addition. Recovery of phosphorus to the furnace off-gas stream has been observed to decline as slag volumes increased, or if the Fe content in the ore increases above approximately 2.3 per cent.

The furnace conditions were noted by Kennedy *et al* (2017), as being highly reducing which is required to fume the phosphorus as P_2, and the CO/CO_2 ratio in the off-gas can be between 105 and 107, depending upon the temperature, chemistry and final phosphorus content of the slag.

Slag chemistry

It has been said that if you take care of your slag it will take care of you (and your process). YP smelting is no different. The slag chemistry of the phosphate smelting process relies on the carbothermal reduction of P_2O_5 to P. In ferro alloy smelting one is always watch the viscosity of the slag so as to minimise product losses to the slag.

In YP production the P losses are caused when the ore has >2.3 per cent Fe in the ore which readily complexes with the P to form an iron rich phosphorus (FeP) alloy.

As can be seen in Table 1, the ore specifications call for a low Fe, MgO and Al_2O_3 contents.

The key base slag systems are the Al_2O_3-CaO-SiO_2 system as shown in Figure 1 and the CaO-SiO_2-P_2O_5 system in Figure 2. The Al_2O_3-CaO-SiO_2 system has previously been extensively studied by Osborn and Muan (1964).

A typical slag analysis for YP smelter slag is shown in Table 4.

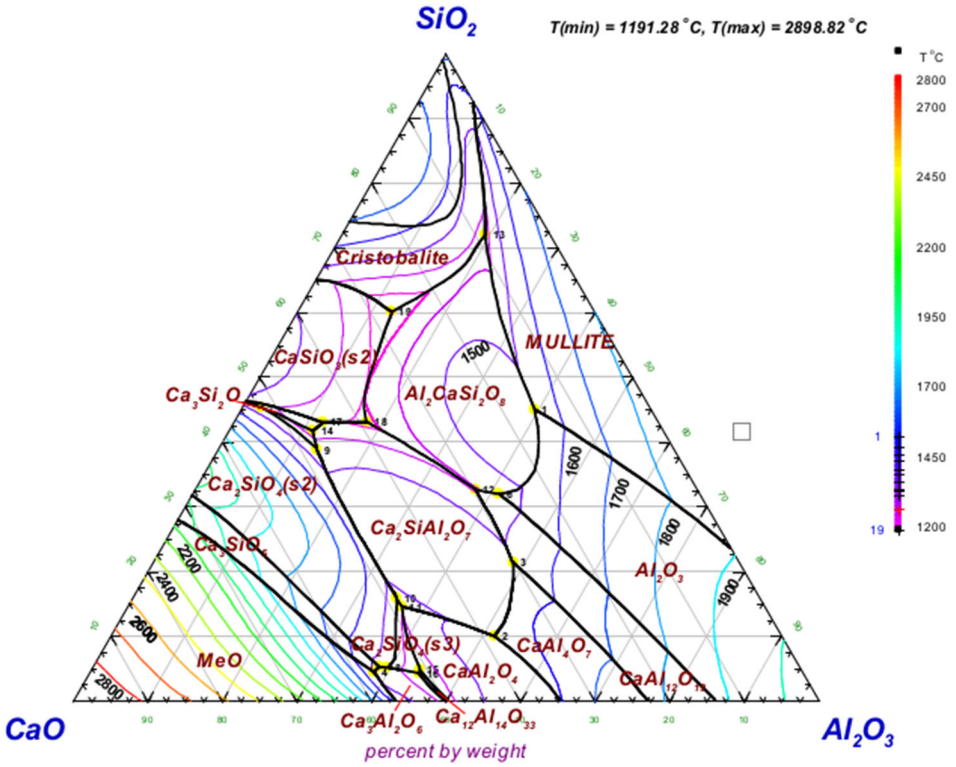

FIG 1 – Al_2O_3-CaO-SiO_2 phase diagram (weight %) (GTT Technologies, 2021).

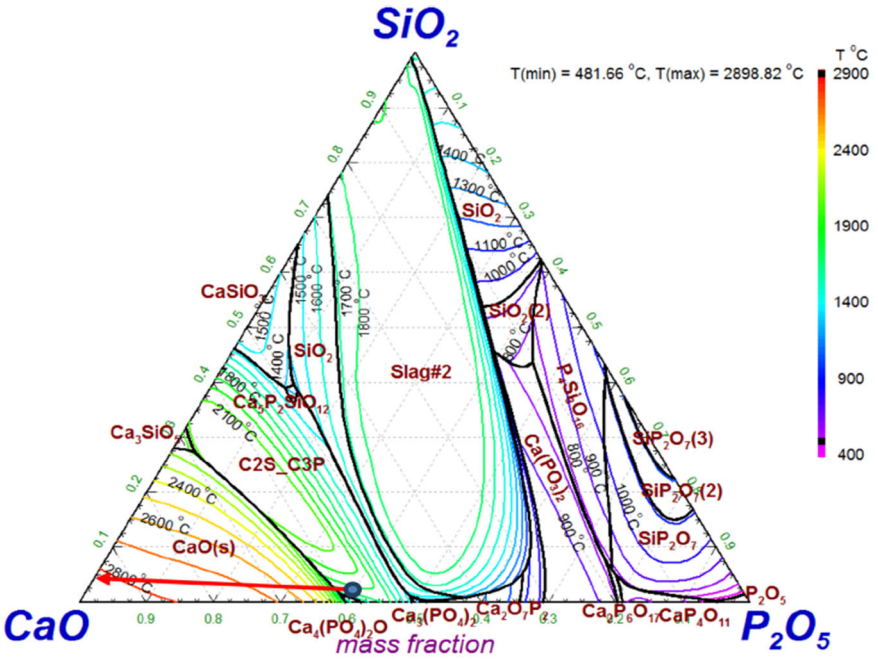

FIG 2 – CaO-SiO_2-P_2O_5 phase diagram (weight %) (GTT Technologies, 2021).

TABLE 4

Typical YP smelter slag analysis.

	P as P_2O_5 (%)	**Al as Al_2O_3 (%)**	**Mg as MgO (%)**	**Fe as Fe_2O_3 (%)**	**Sulfur, S (%)**
Control range	1.0–3.0	2.0–5.0			
Values	0.87	3.52	2.77	0.34	0.95
	Ca as CaO (%)	**SiO_2 (%)**	**Mk Ratio (SiO_2 + Al_2O_3) / (CaO + MgO)**	**Basicity (CaO + MgO) / SiO_2**	
Control range	40.0–50.0	35.0–42.0			
Values	48.81	38.75	0.82	1.34	

The Russian thermal phosphorus production industry derived a dimensionless metric to measure the basicity of the slag called the Mk value which is the ratio of acidic oxides (SiO_2 + Al_2O_3) to basic oxides (CaO + MgO) in the slag. The Chinese YP operations have adopted the same metric to assess their slag chemistry. In ferro alloy smelting use is made of the basicity ratio which is the ratio of basic oxides (CaO + MgO) versus acidic oxides (SiO_2). Noting that the basicity ratio treats Al_2O_3 as amphoteric and therefore is left out of the calculation.

Phosphorus fuming

The recovery of phosphorus from the ore to gaseous phosphorus is driven by the ability to remove the P gas from the furnace burden as quickly as the burden porosity allows (Scheepers *et al*, 2010).

The typical industrial furnace smelting operating temperatures are recorded as being between 1450°C and 1340°C, depending upon the ore chemistry and quantity of flux addition. Recoveries are reduced as slag volume increased or if the Fe content in the ore/concentrate increased.

The highest phosphorus recoveries to the fume were for ores which have low iron contents. As iron and phosphorus ‘like each other’, phosphorus will alloy with iron in the solid state as well as the liquid state, recovery will be affected by the iron content of the feed.

PROCESS PLANT OPERATION

Figure 3 illustrates the process flow for the production of YP via the smelting route. Phosphate rock (lump), silica and metallurgical coke is delivered to the YP plant where materials are unloaded and conveyed to their respective covered storage sheds. The phosphate rock, silica and metallurgical coke are recovered by front end loaders and conveyed via their respective sizing and screening circuits to the raw materials proportioning area storage bins. The sized raw materials are then batched according to a preset material recipe which caters for the amount of carbon required per tonne of phosphate ore, is conveyed and stored in dedicated furnace day storage bins.

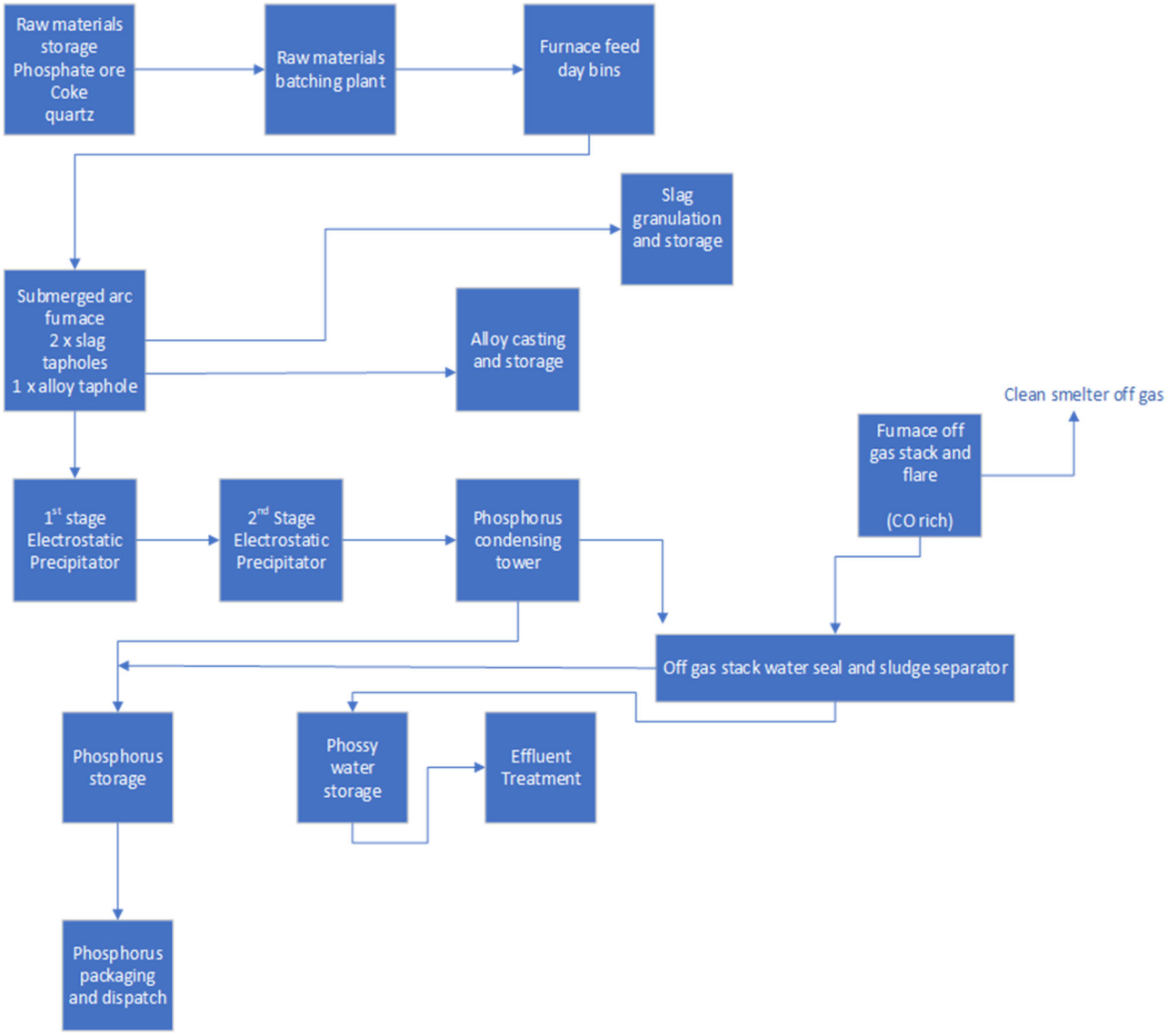

FIG 3 – Diagram of yellow phosphorus smelting system.

The proportioned feed is fed via vertical chutes into the furnace. The material feed proportions are primarily based on P_2O_5 to fixed carbon ratio as well as silica to calcium oxide ratio. However, contents of other species (eg sulfur and iron) should also be considered, which could affect silica and carbon (coke) feed rate relative to phosphate rock.

The furnace most commonly used is a closed top submerged electric arc furnace. The furnace is equipped with cylindrical, pre-baked graphite electrodes that are vertically hung via suspension cables or water-cooled electrode hoists and clamps.

Typical energy consumption data shows the average power consumption to be approximately 13 to 15 MW per tonne of YP. The furnace produces molten slag and ferro phosphorus alloy as by-products. The slag (calcium silicate) is typically tapped every four hours into a launder and directed

into a water granulation system. The ferro phosphorus alloy is tapped every eight hours into small sand moulds where the ingots are allowed to cool before being removed to a storage area. The furnace off-gas stream, which is rich in phosphorus, carbon monoxide, hydrogen and fine particulates exits the furnace via an off-gas duct to the gas scrubbing and phosphorus recovery circuit. The phosphorus rich off-gas is passed through an electrostatic precipitator where the fine particulates are removed ahead of the multistage phosphorus recovery condensers. The phosphorus gas in the condensers is condensed to liquid phase by water sprays.

The liquid phosphorus and the spray water from the condensers flows by gravity into a collection sump. Although most of the dust and particulates in the off-gas stream will have been captured by the electrostatic precipitators, some carryover of these contaminants can be expected in the condenser outlet stream. In the collection sump, the liquid phosphorus, which is denser than the water will separate out and settle at the bottom. The particulates, however, will be distributed between the water and phosphorus layers.

The water (plus fine particulates) is separated from the yellow phosphorus and transferred to holding tanks (settlers) to separate out the solids (sludge or mud) from the water. The water will then be recycled to the spray condensers. Neutralisation may be required depending on the pH of the water stream. The liquid YP is next pumped to purification tanks to separate out the remaining solids. The clean YP will be pumped to storage, while the sludge will be transferred to sludge (mud phosphorus) tanks. Low Pressure (LP) steam will be supplied to the tanks and piping system to maintain the temperature of the YP at ~80°C. Noting that YP solidifies at 45°C.

The clean YP is then pumped from the YP storage tanks to the downstream thermal phosphoric acid facility where technical grade phosphoric acid is produced.

PROCESS CHALLENGES

The production of YP from phosphate ores comes with its own set of challenges. These range from energy efficiency of the smelting process through contaminant management in the YP to ore and reductant quality and sources.

Ore

The traditional production of YP has relied on the availability and use of lump ore (25 mm to 75 mm) in electric submerged arc furnace smelting operations. As the availability of lump ore dwindles and the cost of lump ore increases, there is a need to look at the use of phosphate concentrates (fines) that have been agglomerated into similar sized briquettes as the lump ore. The briquetting of ore is simple and one of the better binders is phosphoric acid which acts with the calcium in the ore to produce hard mechanically robust lumps. The challenge lies in the fact that with China currently the leader in YP production they also have certain set ideas about ore substitution in the YP furnaces. Chinese YP production limits the mass of briquettes to a maximum of 30 per cent by total ore mass per batch. The reason given is that the furnace operation becomes unstable above 30 per cent.

It is worth remembering that in ferro chrome (FeCr) production in the years prior to the late 1980s, use was made of lump chromite ore in deep hearth submerged arc furnaces. As the lump chromite ore supplied dwindled, it became necessary to develop ways of using the chromite fine concentrates that were readily available. The result was the development of chrome ore pelletising followed by sintering to produce feed for the FeCr furnaces. Allied to the smelting of chromite pellets was the redesign of the furnace hearths to have a shallower hearth so as to allow the gases to exit the furnace.

This line of thinking needs to be tested and applied to the production of YP so as to be able to access cheaper phosphate ore supplies.

Carbon reductants

Metallurgical coke has been used as the reductant of choice for many years due to its availability and cost. Today there is a move towards using reductants that are manufactured from biomass thus creating bio chars and bio coke products. One of the key attributes for the reductant in the YP

smelting process is to have good mechanical strength so as to maintain the furnace burden porosity so that the P rich off-gas can easily exit the furnace.

Waste heat recovery

The smelting process produces a final scrubbed off-gas with a CO rich off-gas. Table 5 illustrates a typical off-gas chemistry as reported by Feng and Ma (2017). The energy from the off-gas can be used to raise steam for local district heating. In operations where briquetting is carried out, the waste heat can be used to dry the green briquettes. Alternatively, the steam can be used for local cogeneration of electrical power.

TABLE 5

Typical YP smelter off-gas analysis.

Species	CO (%)	CO_2 (%)	O_2 (%)	H_2 (%)	CH_4 (%)	N_2 (%)	H_2O (%)	H_2S (mg/m^3)	PH_3 (mg/m^3)
Range	87	1	0	1	0	2	0	800	500
	92	4	1	8	0.3	5	5	1100	1000

Yellow phosphorus process slag valourisation

The smelting of phosphate ore produces approximately 7–9 t of slag per tonne of YP during the smelting operations. The slag is usually granulated in water baths. The resultant product is a gravel like slag that is dumped on stockpiles to dewater. The slag is predominantly a calcium silicate slag which can be used as feedstock into cement manufacturing as a cement extender similar to the addition of fly ash to cement grinding.

Other uses of the slag are as aggregate replacement in cinder block manufacturing and in gravel replacement materials.

Alternative smelting technology for phosphate smelting

Research is being considered to investigate the use of direct current (DC) electric arc furnace technology for open bath smelting of phosphate ore. Given the main product is a fumed phosphorus gas in the furnace off-gas. The rationale draws on the experiences gained in South Africa at Mintek where open bath DC arc furnace smelting of zinc oxides was piloted to assess the fuming of zinc.

The potential to make use of open bath DC arc smelting for YP production means operators could possibly make use of phosphate fines directly with finer carbon reductant products. This would be a game changer in the YP production space as this would potentially reduce the cost of production due to cheaper ore prices.

Carbon footprint

The production of YP is highly energy intensive. It is therefore essential to conduct a preliminary estimation of the greenhouse gas (GHG) inventory or carbon footprint for the conversion of mined phosphate rock to YP and identify potential reductions and elimination where possible. The following should be considered in the design phase:

- Incorporate emissions impact into decision-making on logistics, facility location and process design.
- Carbon emission costs and tax calculations.
- Identify opportunities to potentially reduce the carbon footprint, which could also potentially improve the efficiency of the process. This may include alternatives to metallurgical coke as carbon reductant, waste heat recovery, electrification by way of renewables for operations where possible and gas scrubbing to remove CO_2 and inclusion of CCS technologies.
- Identify potential cost-saving opportunities.
- Demonstrate environmental and corporate responsibility to potential investors and off-takers.

CONCLUDING REMARKS

The smelting technology employed in the production of YP has remained the same for nearly 80 years. The use of submerged arc furnaces appears to offer the best process control for the fuming of the P from the ore.

The next stage in the evolution of the process will be the development of furnaces that can make use of concentrates rather than lumpy ore. This may lead to the potential use of DC arc furnaces for the fuming of P. Another area of development will be the adoption of bio coke in place of the traditional metallurgical coke manufactured from coking coal.

That said the YP process route for the production of purified phosphoric acid (PPA) for use in battery cathode assemblies will remain popular due to its lower capex than that associated with the traditional wet phosphoric acid production process.

ACKNOWLEDGEMENTS

Authors acknowledge the support of Bechtel Corporation and technical assistance by the Bechtel Mining and Metals Centre of Excellence for Critical Minerals and Operational Excellence.

REFERENCES

Easterwood, H, 1933. Manufacture of phosphoric acid by the blast furnace method, *Trans AIME*, 29:1–20.

Feng, X and Ma, H, 2017. Contrast Analysis of Recycling and Utilization Approaches of Yellow Phosphorus Tail Gas, *Chemical Engineering Transactions*, 61:451–456.

GTT Technologies, 2021. Slagatlas (Schlackenatlas), HotVeGas, version 16, GTT-Technologies, 1459 p.

Kennedy, M W, Sun, T, Yurramendi, L, Arnout, S, Aune, R E and Tranell, G, 2017. Pyrometallurgical Treatment of Apatite Concentrate with the Objective of Rare Earth Element Recovery: Part II, *Journal of Sustainable Metallurgy*, 3(4):846–857.

Osborn, E F and Muan, A, 1964. *Phase Diagrams for Ceramists* (eds: E M Levin, C R Robbins and H F McMurdie), 1:219 (The American Ceramic Society: Columbus).

Scheepers, E, Adema, A T, Boom, R, Reuter, M A and Yang, Y, 2010. Process Modeling and Optimization of a Submerged Arc Furnace for Phosphorus Production, *Metallurgical and Materials Transactions B*, 41(5):990–1005.

Mathematical descriptions of – Physico-chemical property models

Combined molecular dynamics – experimental investigation of oxidic slag properties

DOI: 10.62053/CHLJ8393

I Bellemans[1], A Maslov[2], D Seveno[3] and K Verbeken[4]

1. Assistant Professor, Gent University, Department of Materials, Textiles and Chemical Engineering, Gent 9052, Belgium. Email: inge.bellemans@ugent.be
2. PhD Researcher, KU Leuven, Department of Materials Engineering, Leuven 3001, Belgium. Email: andrea.maslov@kuleuven.be
3. Associate Professor, KU Leuven, Department of Materials Engineering, Leuven 3001, Belgium. Email: david.seveno@kuleuven.be
4. Professor, Gent University, Department of Materials, Textiles and Chemical Engineering, Gent 9052, Belgium. Email: kim.verbeken@ugent.be

ABSTRACT

Recycling and decarbonisation current metallurgical processes is key for our planet's future and in both cases, digital twinning will play an important role. However, the various modelling techniques being used for digital twinning require a lot of input values on variables such as viscosities, diffusion coefficients and surface energies that need to be known as a function of temperature, atmosphere and composition, but which are not widely available, such as in databases, for molten slag phases. The need for more accurate data on physical slag properties is clear and will be extremely relevant for making more realistic and quantitative simulations. Some of these properties are difficult to determine, which is inherent to the very high pyrometallurgical temperatures. Therefore, this work focuses on some aspects related to determining electrical conductivities, viscosities and surface tensions of slags via a combined experimental-modelling method.

Besides experimental work, molecular dynamics (MD) simulations can be used to investigate oxidic slag physical properties. With MD simulations, one can follow the time evolution of a system (consisting of atoms or molecules) by integrating Newton's equation of motion. The input for an MD simulation mainly consists of a force field as well as initial positions, velocities and mass of each atom. The determination of the transport properties in existing literature of MD simulations in oxidic systems, is typically based on incorrect assumptions. For example, to determine the ionic conductivity, the frequently-used Einstein-Stokes equation fails to take into account all ionic types and neglects correlated motion. Furthermore, the viscosity determination via the Einstein-Stokes formula also assumes independent motion of the different ions. This paper gives a brief overview of the opportunities and challenges related to the use of MD simulations for oxidic slag systems.

INTRODUCTION

Metals are indispensable in our future society as they will become even more important in the years to come, given the energy transition we are embarking on (Gregoir and van Acker, 2022). Their use has increased immensely in the past decennia due to the growing global demand for electronic consumer goods and high-tech solutions for the transition towards a carbon neutral society (Gregoir and van Acker, 2022). Pyrometallurgy (often in combination with electro- and hydrometallurgy) is one of the most important techniques used in extractive operations of ores and scrap (Ebin and Isik, 2016). Upon pyrometallurgical processing, the impurities are typically collected in a slag (metal oxide) phase which floats on top of a liquid metal or liquid matte (metal sulfides) phase (Mills, 2011).

In order to meet the climate objectives, more emphasis is put on recycling as well as on decarbonisation the existing metallurgical production methods. Current operations have been working fine for decades, but will need to be adapted when more scrap and carbon-less technologies are employed. For both recycling and decarbonisation, electric furnaces will play a key role (Allanore, 2013). For the operation and design of electric furnaces, the electrical conductivity of the slag is a crucial property as in electric furnaces, thermal energy is generated primarily by the Joule effect, which is inversely related to the slag conductivity. However, data on slag conductivity is unfortunately scarce.

The physical properties, except for the electrical conductivity, of slags from primary production are well studied as they have long been used in the industry. They are catalogued in the '*Slag Atlas*' (Allibert, 1995). In contrast, only limited research is available on slag conductivities and for all relevant properties, data for slags originating from feeds of secondary materials is scarce. The composition of these new types of slag can indeed vary significantly depending on the market supply of secondary resources. These great variations in slag composition result in a large variability in slag properties, amongst which the electrical conductivity. In pyrometallurgical slags, properties are rather described by structure-property relationships than purely as a function of composition. This is because slags have a very specific molecular structure, as discussed in the following section, and the slag property variations can be explained qualitatively with the variations in these structures.

SLAG PROPERTIES AND STRUCTURE

The slag composition has a direct influence on the slag structure and in turn physical slag properties depend on the slag structure. The dependence of slag properties on the slag structure has been described in a qualitative way, but not quantitatively as the relations are not yet fully understood. Furthermore, the various properties depend differently on the slag structure. As the network structure becomes more polymerised the resistance to viscous flow will increase and the viscosity will increase. The polymeric network also hinders the movement of cations and thus a more polymerised slag has a lower electrical conductivity (Mills *et al*, 2014). Electrical conduction in silicate slags results from an applied electrical field and takes place through two parallel mechanisms, ionic and electronic conduction. Ionic conduction involves the movement of cations through the silicate network. The structural dependence of the ionic conduction is currently assumed to be the same as for the slag's viscosity (Zhang *et al*, 2011; Li *et al*, 2016; Thibodeau and Jung, 2016).

Previous experiments of electrical conductivities showed a minor influence of substitution of MgO with CaO (Kawahara *et al*, 1978), which is in contrast to the substitution effect of these ions on the viscosity (Gao *et al*, 2014) (showing a increased viscosity when Ca^{2+} was substituted by Mg^{2+}). Furthermore, our recent work on electrical conductivity experiments showed that substitution of PbO with CaO clearly decreases the electrical conductivity (Figure 1 left), whereas viscosity predictions from Factsage indicate an increasing viscosity trend at a constant temperature. Hence, the trends observed in viscosity based on changes in the slag structure, cannot be directly translated into the same relationships for electrical conductivities, which has been the standard hypothesis and operating method for years (Zhang *et al*, 2011; Li *et al*, 2016).

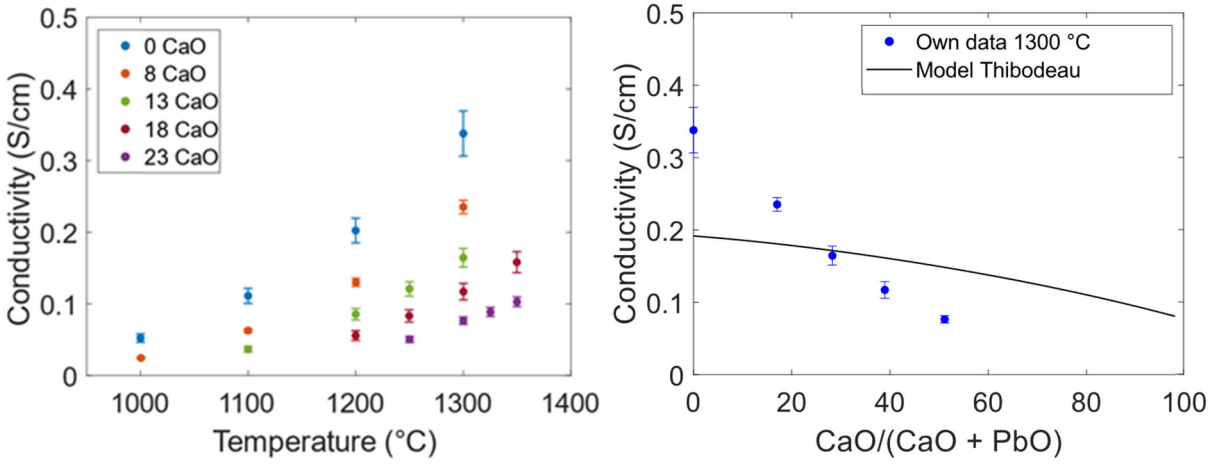

FIG 1 – Influence of the substitution of CaO with PbO on the electrical conductivity in a SiO_2-CaO-PbO slag (at 1300°C) at various temperatures (unpublished results), and compared with existing model by Thibodeau and Jung (2016).

The most recent structure-property model for electrical conductivities is the one by Thibodeau and Jung (2016) (black line in right part of Figure 1). It is a semi-empirical model, as is very common to use in slag property descriptions: it is based on the abovementioned description of the slag structure, assuming similar correlations as for the slag's viscosity with the slag's structure. This description contains several model parameters which are typically fitted to available experimental results. The

model uses temperature and slag composition as input parameters. However, for electrical conductivities, there is an insufficient amount of data, so that in the description of the ionic contribution, the following assumptions are made: (i) there is no interaction between different cations, (ii) the network is only generated via SiO_2 and Al_2O_3, the latter for which the amphoteric character is neglected, and (iii) the possible amphoteric effect of Fe_2O_3 is neglected.

To optimise this model, less assumptions, more data and more fundamental molecular insights into the slag properties are necessary. However, pyrometallurgical experiments remain very difficult to perform due to the extremely high temperatures. Molecular dynamics modelling of slag structures and their physical properties could reveal a lot of fundamental knowledge provided the simulations account for the complexity of the slag structure as observed experimentally, which can be checked by experimental validation of the simulations. That is why a combined experimental-modelling approach is very promising. More information on the experimental methodology, considering both the set-up development and an investigation of influencing parameters, can be found in the following references: (Boeykens, Bellemans and Verbeken, 2022; Boeykens *et al*, 2023). Specific focus was put on the reproducibility of the results, the measurement technique itself (comparing Electrochemical Impedance spectroscopy (EIS) versus single frequency measurements) and comparing crucible materials (Pt-Ir versus Al_2O_3). The crucible material had a clear influence on the conducting path, but the resulting conductivity values for the liquid PbO-SiO_2 slags were of similar order. It should be noted, however, that the measurements in Al_2O_3 are unstable over time as the conductivity decreases continuously during the experiment due to crucible dissolution.

MOLECULAR DYNAMICS SIMULATIONS

Given the fact that the slags are highly dynamic systems due to the high temperature conditions, it is highly desirable to perform atomistic level simulations at the temperatures of interest to capture the nature behind their peculiar behaviour. With Molecular Dynamics (MD) simulations, one can follow the time evolution of a given system of particles, atoms or molecules, by integrating Newton's equation of motion. In principle, the forces between the atoms have to be determined from first principles, ie based on underlying quantum mechanical techniques. Density Functional Theory (DFT) is the most popular method for this purpose thanks to its attractive trade-off between accuracy and computational efficiency. However, yet for the systems of interest, consisting of 10^3–10^4 atoms, DFT is still computationally very intensive. Therefore, initially classical force fields MD simulations can be used. These atomistic simulations are based on classical interatomic potentials and can account for a substantially larger number of atoms and allow calculation of dynamic properties for larger systems and at higher temperatures (Alder and Wainwright, 2004; Vandenhaute, Rogge and Van Speybroeck, 2021).

Overview of MD studies on slags

Molecular dynamics has already been used to study the properties of several slag systems, mostly molten silicate systems consisting of several thousands of atoms. The following paragraphs give a non-exhaustive overview of molecular dynamics studies focusing on various attention points for MD studies in slag systems.

The FeO-SiO_2 and CaO-SiO_2 systems were investigated by Seo and Tsukihashi (2004, 2005). The structural properties such as pair distribution functions and the fractions of oxygen ion species (bridging non-bridging and free oxygen), self-diffusion coefficients, enthalpy, entropy and the Gibbs free energy of mixing were determined. The results were in good agreement with the previously determined experimental values. Takei *et al* (2000) calculated the metastable immiscibility region in the Al_2O_3-SiO_2 system from the thermodynamic structural data obtained by MD simulations. The immiscibility gap range was narrower compared with previous reported data.

Wu *et al* (2015) also investigated several binary systems. They calculated the viscosity and electric conductivity of CaO-SiO_2 and CaO-Al_2O_3 systems with different CaO contents. With the increase of the CaO content, the melt viscosity decreased, while the electrical conductivity was enhanced in both systems. Belashchenko, Ostrovski and Skvortsov (2001) investigated structural, thermodynamic and transport properties of the binary CaO-FeO, MgO-SiO_2, FeO-SiO_2, CaO-SiO_2

and CaO-Al_2O_3 and the ternary CaO-FeO-SiO_2 systems. It should be noted that the electrical conductivity was derived based on the simplifying Nernst-Einstein equation.

However typically, no real systematic approach of binary to higher order systems can be found in literature and most other molecular dynamics investigations go immediately to complex systems with four, five or even seven components. One exception are the studies by Zheng *et al* (2012, 2014), who used MD simulations to model calcium aluminosilicate ternary systems, CaO-SiO_2-Al_2O_3. They first investigated systems with a fixed CaO content and varying molar ratios between SiO_2 and Al_2O_3, investigating the change of self-diffusion coefficients and structure. They used the Q^n species description to illustrate the polymerisation of the slag. The sequence of diffusivity for four atoms was Ca>Al>O>Si, with the self-diffusion coefficients of Al, Si and O sharing close values and similar variation trends with compositions, indicating that O atoms move cooperatively with network-forming atoms in (SiO_2) and (Al_2O_3) tetrahedra. It is one of the few studies investigating the network-forming tetrahedra, but unfortunately they missed on the opportunity to investigate the charge compensation effect in more detail.

Wu *et al* (2016) investigated the effect of CaO/SiO_2 ratio in a slag with five components (CaO-SiO_2-Al_2O_3-FeO) on structural properties and viscosity of the melt. The viscosity decreased and the atomic self-diffusion coefficients increased with the increase in basicity, which is in line with the expectations from structure-property relations in slags. However, when higher Al_2O_3 contents were used, more complex structures were obtained, indicating that not only SiO_2 was structurally incorporated into the polymer network, but that also Al_2O_3 is taking up a role as network forming component. This in turn requires charge compensating cations to retain charge neutrality within the melt, but this was not investigated in detail. It should be noted that the electrical conductivity was derived based on simplifying the Einstein-Stokes equation.

Gelchinski *et al* (2011) investigated the multicomponent SiO_2-CaO-Al_2O_3-MgO-CaF_2-Na_2O-K_2O-FeO mixture and compared their results to experimental density values. In this system, and in simpler systems with alkali ions, a more thorough investigation could result in more insights into the mixed alkali effect.

Zhang *et al* (2014b) investigated the structure of CaO-SiO_2-Al_2O_3-TiO_2 slags with varying amounts of TiO_2 and varying CaO/TiO_2 ratios. They validated the structural parameters of the liquid slag in the MD simulations with Fourier-transform infrared (FT-IR) spectroscopic analysis of quenched slags. They found that the replacement of CaO by TiO_2 has little effect on the degree of polymerisation in the system. However, it should be noted that they compared the structural parameters of the liquid slag from the MD simulations to the experimental structure obtained from quenched slag. It is highly probable that during the liquid-to-glass transition in experiments there is some sort of structural change taking place, so that a direct comparison between the two states is not optimal.

Zhang *et al* (2014a) further investigated the structure of the CaO-SiO_2-Al_2O_3-MgO-TiO_2 and the relationship with experimentally determined viscosity values for varying basicity and TiO_2 additions. Some of their results indicated the viscosity decreased with increasing basicity and TiO_2 content. They also found that TiO_2 had more network breaking than network forming characteristics, which is somewhat unexpected, but might be due to the relatively high Al_2O_3 amounts. This indicates the potential of molecular dynamics simulations, but it is clear from the different references and corresponding remarks above that attention should be paid on the MD simulation set-up and post-processing for validation.

MD simulations set-up

The force field is an essential ingredient for the MD simulations and should represent all interatomic interactions. So far, interactions in silicate melts are typically represented by a Born-Mayer-Huggins (BMH) potential function:

$$U_{ij}(r) = \frac{Z_i Z_j}{r_{ij}} + B_{ij} \exp\left(-\frac{r_{ij}}{\rho_{ij}}\right) - \frac{C_{ij}}{r_{ij}^6}$$

This potential is composed of the long-range Coulomb interaction, short range repulsion and attractive van der Waals force. This force field considers a melt as a completely ionic solution during the simulation. The charge distribution on each atom is represented by a point charge whose magnitude is identified with the formal charge of the ion in the corresponding oxide (eg for SiO_2: q_{Si}=+4e$^-$, qO=-2e$^-$). In this equation, $U_{ij}(r)$ is the interatomic-pair potential; Z_i and Z_j are the selected charges, and in order to ensure the transferability of the interaction potential with the melt composition, the valence assigned to the atoms is usually kept fixed for all compositions; r_{ij} represents the distance between atoms i and j; B_{ij} and C_{ij} are energy parameters for the pair ij describing the repulsion at short distances and van der Waals attractive forces, respectively; and $1/\rho_{ij}$ is a e-folding length characterising the radially symmetric decay of electron repulsion energy between atom pair ij. This BMH potential is sometimes also referred to as Buckingham potential, based on the description by Matsui (1996).

Aside from the BMH potential, other potentials have been mentioned in the context of oxidic slags. For example, Wu *et al* (2016) used a BMH potential function in combination with a Lennard-Jones (L-J) two-body potential function:

$$U_{ij}(r) = D_0\left\{\left(\frac{R_0}{r_{ij}}\right)^{12} - 2\left(\frac{R_0}{r_{ij}}\right)^{6}\right\}$$

With D_0 is the depth of the potential well; R_0 is the distance at which the potential reaches its minimum, at R_0 the potential function has the value − D_0. These authors claimed this is necessary because there are no accurate parameters for Fe-Fe, Fe-Al, Fe-Si and Fe-Ca pairs corresponding to the BMH function. Unfortunately, they did not carefully refer to the original paper for the BMH potential, as these parameters are well described for example for Fe-containing slags by Guillot and Sator (2007).

The work of (Mongalo, Lopis and Venter (2016) is also worth mentioning. They first used a Morse potential, based on the description by Pedone *et al* (2006), which corresponds to the second term in the following equation:

$$U_{ij}(r) = \frac{Z_i Z_j e^2}{r_{ij}} + D_{ij}\left[\left\{1 - \exp\left(-a_{ij}\left(r_{ij} - r_0\right)\right)\right\}^2 - 1\right] - \frac{C_{ij}}{r_{ij}^{12}}$$

The Morse function is typically used in modelling bonded interactions in covalent systems (eg the hydroxide ion in ionic systems) where the different parameters have a certain physical meaning. This is not the case here because the Coulomb term is explicitly included in the full potential expression, and D_{ij}, a_{ij}, and r_0 should be simply considered as parameters.

The study by Mongalo (2018) is one of the few studies mentioning a comparison of different force fields. Unfortunately, they seemed to have made a copying mistake for the parameter values for the BMH potential. Furthermore, originally, Pedone *et al* (2006) mentioned the following for O-O bound: The term C/r^{12} is needed only in MD simulations and in free energy calculation at high temperature and pressure. In fact, the COO term can range between 22 and 100 eV Å^{12} without altering the results of free energy minimisation at room temperature. Mongalo, on the other hand, stated for all C_{ij} terms that '*This term is only necessary to model the interactions at high temperature and pressure. Since the simulations were performed at atmospheric pressure, this term is not required and was therefore not used*'. It is clear that Pedone *et al* only made the remark referring to the O-O bond, where Mongalo interpreted it much broader. Therefore, it is not clear whether the conclusion of Mongalo (2018) is indeed correct. He concluded that the Morse potential predicts the experimental densities with better accuracy than the Buckingham potential.

This brings to the attention that various force field expressions and the corresponding parameters are typically developed by fitting to a certain aspect of the system being investigated. This can result in for example a very good correspondence of some of the structural or transport properties, but large deviations for other properties. A possible solution is the use of DFT-derived force field and parameters, which happens in ab-initio MD simulations. Since 2015 more and more ab-initio MD simulations have been used, as increased computational power now also allows calculations of this

type for the highly disordered slag systems (Harvey, Gheribi and Asimow, 2015; Sajid *et al*, 2020; He *et al*, 2021).

Besides the force field, the remainder of the simulations is more similar to MD simulations in other (non-slag) systems. Typically, the MD simulations are performed in isobaric and isothermal ensemble (NPT) which implies that the simulations run while keeping the number of particles, sample pressure and the temperature of the systems constant. Temperature is controlled by the velocity scaling method and pressure is controlled by Parrinello and Rahmann method (Parrinello and Rahman, 1998).

In the simulation process, an appropriate number (typically a couple of thousands) of atoms of each type are placed in the representative volume element with random initial configurations and then the volume of the cell is determined by the atom numbers and the density. Periodic boundary conditions are typically employed on all sides of the model box to create an infinite system with no boundaries. At the beginning of each simulation, the initial temperature is fixed at a certain very high value (eg 4000 K) for a few thousand steps to mix the system completely and eliminate the effect of the initial configuration. Then, the temperature is cooled down to the temperature of interest with a cooling rate that is extremely large compared to the experimental values. The control over the system temperature is achieved by rescaling the velocity of each particle. At equilibrium, the system is relaxed and finally different transport and structure properties for different systems can be calculated and analysed as described below.

Properties derivable by MD simulations and points of attention

In MD simulations, the atomic structure of melts is commonly described in terms of radial distribution functions (RDF), which represent the probabilities for finding pairs of atoms at a certain distance r. The peak positions of the RDF represent the most probable interatomic distances of the different coordination shells. In addition, the coordination numbers (CN) can be determined by a numerical integration of the first peak of the RDF.

As a first property, the diffusion coefficients are determined based on the mean square displacement (MSD). This MSD can be generated by statistical analysis of the particles trajectory. MSD indicates the average displacement of a certain atom during a fixed time t and is defined by the following equation:

$$MSD = \frac{1}{N}\left\langle \sum_{i}^{N} [\vec{r}_i(t) - \vec{r}_i(0)] \right\rangle^2$$

where N is the number of atoms, $r_i(t)$ is the position of atom i at time t and the angle brackets express an ensemble average taken over time. In literature, the self-diffusion coefficient of a selected ion i (D_i) is typically calculated from the slopes of MSD of ions as a function of time:

$$D_i = \frac{1}{6} \lim_{t\to\infty} \frac{d}{dt} \left\langle \sum_{i}^{N} [\vec{r}_i(t) - \vec{r}_i(0)]^2 \right\rangle$$

The determination of the other transport properties in the abovementioned references, is typically based on incorrect assumptions, such as independent motion of different ions. The electrical conductivity (σ) is typically calculated by combining the diffusion coefficient and the Nernst–Einstein equation:

$$\sigma = D \frac{nq^2}{k_B T}$$

Where n is the number of the carrier atoms in a unit volume and q is the charge of the ion. It should be emphasised that the frequently used Nernst-Einstein equation, should actually be extended to also take into account all ionic types:

$$\sigma^{NE} = \frac{e^2}{kTV} \sum_{j} N_j Z_j^2 D_j$$

With e the elementary charge, V the simulation box volume, Z_j the charge of the ion and N_j the number of ions of this type. However, this equation still assumes independent migration of ions and neglects correlated motion. As experimental results in Figure 1 have shown, this is not the case. Hence, a more accurate analysis requires the application of the more general Einstein relationship:

$$\sigma^E = \frac{e^2}{6kTV} \lim_{t\to\infty} \frac{d}{dt} \left\langle \sum_i^N \sum_j^N Z_i Z_j [\vec{r}_i(t) - \vec{r}_i(0)][\vec{r}_j(t) - \vec{r}_j(0)] \right\rangle$$

This more realistic analysis results in better correspondence with experimental values, as shown by the work of Mongalo, Lopis and Venter (2016). They compared experimentally measured slag conductivities reported in the *Slag Atlas* (Allibert, 1995) compared to MD values with either the Nernst-Einstein equation or the more general Einstein equation and they showed that the Nernst-Einstein approximation overestimates the experimental conductivities, by 40–100 per cent, which can be ascribed to neglecting the correlation between different atom types. However, it should also be noted that experimental data they investigated were derived from the slag atlas. Some compositions and conditions they addressed, should actually result in not-fully liquid slag systems. The presence of solids has a definite influence on the measured electrical conductivity (Zhang *et al*, 2023), but the slag atlas did not mention any presence of these solids.

CONCLUSION – OPPORTUNITIES AND CHALLENGES FOR MD SIMULATIONS IN SLAGS

With the increasing importance of electric furnaces, the need for new data on electrical conductivity of slags is high. As the experimental measurement of this data is extremely intricate, the benefit of using a combined modelling – experimental approach to determine slag electrical conductivities has been illustrated in this work. Of course, the experiments should be performed with the utmost care to ensure only measurement of the desired property so that no unwanted side effects are taken into account. These effects are not present during MD simulations, as long as they are executed in a dedicated way so that they represent the real systems. Hence, the molecular dynamics simulations should be post-processed in such a way that no *a priori* assumptions, of for example independent motion of different types of ions, are used to assure the resulting transport properties within the liquid slags are correct. For the experimental validation of structural properties, it should be emphasised that the liquid to glass transition could have had an effect on the structural parameters so that care should be taken in comparing these two states. It is also noted that the MD technique could elucidate many remaining questions regarding slag structure and specific structural effects such as the charge compensation effect and mixed alkali effect and their influence on the slag properties. However, a systematic investigation is currently lacking to allow for this. Finally, it should be mentioned that the ab-initio MD technique holds great promise, as the force field and the corresponding parameters are derived from first principles and thus are not derived with a specific focus property to be optimised for.

ACKNOWLEDGEMENTS

The author, I Bellemans, holds a grant from the Research Foundation Flanders (1239024N).

REFERENCES

Alder, B J and Wainwright, T E, 2004. Phase Transition for a Hard Sphere System, *The Journal of Chemical Physics*, 27(5):1208. https://doi.org/10.1063/1.1743957.

Allanore, A, 2013. Contribution of Electricity to Materials Processing: Historical and Current Perspectives, *JOM*, 65(2):130–135. https://doi.org/10.1007/s11837-012-0538-3.

Allibert, M, 1995. *Slag Atlas* (ed: Verein Deutscher Eisenhüttenleute), second edition, 616 p (Verlag Stahleisen).

Belashchenko, D K, Ostrovski, O I and Skvortsov, L V, 2001. Molecular dynamics simulation of binary CaO–FeO, MgO–SiO_2, FeO–SiO_2, CaO–SiO_2 and ternary CaO–FeO–SiO_2 systems, *Thermochimica Acta*, 372(1–2):153–163. https://doi.org/10.1016/S0040-6031(01)00451-8.

Boeykens, P, Bellemans, I and Verbeken, K, 2022. Methodological investigation of a four-electrode electrical conductivity set-up in a binary SiO_2-PbO system, in *Copper 2022*, Abstracts.

Boeykens, P-J, Bellemans, I, Scheunis, L and Verbeken, K, 2023. Parameter investigation of the experimental methodology of electrical conductivity measurements for PbO containing slags, *Electrochimica Acta*, 464:142846. https://doi.org/10.1016/j.electacta.2023.142846.

Ebin, B and Isik, M I, 2016. Pyrometallurgical Processes for the Recovery of Metals from WEEE, *WEEE Recycling*: *Research, Development and Policies*, pp 107–137. https://doi.org/10.1016/B978-0-12-803363-0.00005-5.

Gao, Y-M, Wang, S-B, Hong, C, Ma, X-J and Yang, F, 2014. Effects of basicity and MgO content on the viscosity of the SiO_2-CaO-MgO-9wt%Al_2O_3 slag system, *International Journal of Minerals, Metallurgy and Materials*, 21(4):353–362. https://doi.org/10.1007/s12613-014-0916-7.

Gelchinski, B, Belashchenko, D K, Dul'Dina, E V and Lozovskii, E P, 2011. Computer Model for a Multicomponent Slag-Forming Mixture Melt: Relation between Its Atomic Structure and Physicochemical Properties, *Russian Metallurgy (Metally)*, 2011(2):148–152. https://doi.org/10.1134/s0036029511020066.

Gregoir, L and van Acker, K, 2022. Metals for Clean Energy: Pathways to solving Europe's raw materials challenge, report prepared for KU Leuven, p 91. Available from: <https://www.connaissancedesenergies.org/sites/connaissancedesenergies.org/files/pdf-actualites/metals-for-clean-energy.pdf>

Guillot, B and Sator, N, 2007. A computer simulation study of natural silicate melts, Part I: Low pressure properties, *Geochimica et Cosmochimica Acta*, 71(5):1249–1265. https://doi.org/10.1016/j.gca.2007.05.029.

Harvey, J P, Gheribi, A E and Asimow, P D, 2015. A self-consistent optimization of multicomponent solution properties: Ab initio molecular dynamic simulations and the MgO-SiO_2 miscibility gap under pressure, *Geochimica et Cosmochimica Acta*, 161:146–165. https://doi.org/10.1016/j.gca.2015.04.004.

He, X, Ma, S, Wang, L, Dong, H and Chou, K, 2021. An *Ab Initio* Molecular Dynamics Simulation of Liquid FeO–SiO_2 Silicate System with Sulfur Dissolving, *Metallurgical and Materials Transactions B*: *Process Metallurgy and Materials Processing Science*, 52(5):3346–3353. https://doi.org/10.1007/s11663-021-02263-x.

Kawahara, M, Ozima, Y, Morinaga, K and Yanagase, T, 1978. The Electrical Conductivity of Na2O-SiO_2-MgO and CaO-SiO_2-MgO Melts, *Journal of the Japan Institute of Metals*, 42(6):618–623. https://doi.org/10.2320/jinstmet1952.42.6_618.

Li, W, Cao, X, Jiang, T, Yang, H and Xue, X, 2016. Relation between electrical conductivity and viscosity of CaO-SiO_2-Al_2O_3-MgO system, *ISIJ International*, 56(2):205–209. https://doi.org/10.2355/isijinternational.isijint-2015-502.

Matsui, M, 1996. Molecular dynamics simulation of structures, bulk moduli and volume thermal expansivities of silicate liquids in the system CaO-MgO-Al_2O_3-SiO_2, *Geophysical Research Letters*, 23(4):395–398. https://doi.org/10.1029/96GL00260.

Mills, K C, 2011. The Estimation Of Slag Properties, in *Proceedings of the Southern African Pyrometallurgy 2011 International Conference*, pp 1–52.

Mills, K, Hayashi, M, Wang, L and Watanabe, T, 2014. The Structure and Properties of Silicate Slags, in *Treatise on Process Metallurgy*, pp 149–286. https://doi.org/10.1016/B978-0-08-096986-2.00008-4.

Mongalo, L, 2018. Molecular dynamics simulations of the electrical conductivities of high temperature metallurgical slags, PhD thesis, University of Cape Town, Available from: <http://hdl.handle.net/11427/29784>

Mongalo, L, Lopis, A S and Venter, G A, 2016. Molecular dynamics simulations of the structural properties and electrical conductivities of CaO–MgO–Al_2O_3–SiO_2 melts, *Journal of Non-Crystalline Solids*, 452:194–202. https://doi.org/10.1016/j.jnoncrysol.2016.08.042.

Parrinello, M and Rahman, A, 1998. Polymorphic transitions in single crystals: A new molecular dynamics method, *Journal of Applied Physics*, 52(12):7182. https://doi.org/10.1063/1.328693.

Pedone, A, Malavasi, G, Menziani, M C, Cormack, A N and Segre, U, 2006. A new self-consistent empirical interatomic potential model for oxides, silicates and silicas-based glasses, *J Phys Chem B*, 110(24):11780–11795. https://doi.org/10.1021/jp0611018.

Sajid, M, Bai, C, Yu, W, You, Z, Tan, M and Aamir, M, 2020. First principle study of electronic structural and physical properties of CaO-SiO_2-Al_2O_3 ternary slag system by using Ab Initio molecular and lattice dynamics, *Journal of Non-Crystalline Solids*, 550:120384. https://doi.org/10.1016/j.jnoncrysol.2020.120384.

Seo, W G and Tsukihashi, F, 2004. Molecular Dynamics Simulation of the Thermodynamic and Structural Properties for the CaO-SiO_2 System, *ISIJ International*, 44(11):1817–1825. https://doi.org/10.2355/isijinternational.44.1817.

Seo, W G and Tsukihashi, F, 2005. Thermodynamic and Structural Properties for the FeO–SiO_2 System by using Molecular Dynamics Calculation, *Materials Transactions*, 46(6):1240–1247. https://doi.org/10.2320/matertrans.46.1240.

Takei, T, Kameshima, Y, Yasumori, A and Okada, K, 2000. Calculation of metastable immiscibility region in the Al_2O_3-SiO_2 system using molecular dynamics simulation, *Journal of Materials Research*, 15(1):186–193. https://doi.org/10.1557/jmr.2000.0030.

Thibodeau, E and Jung, I H, 2016. A Structural Electrical Conductivity Model for Oxide Melts, *Metallurgical and Materials Transactions B*: *Process Metallurgy and Materials Processing Science*, 47:355–383. https://doi.org/10.1007/s11663-015-0458-z.

Vandenhaute, S, Rogge, S M J and Van Speybroeck, V, 2021. Large-Scale Molecular Dynamics Simulations Reveal New Insights Into the Phase Transition Mechanisms in MIL-53(Al), *Frontiers in Chemistry*, 9:699. https://doi.org/10.3389/fchem.2021.718920.

Wu, T, He, S, Liang, Y and Wang, Q, 2015. Molecular dynamics simulation of the structure and properties for the CaO–SiO_2 and CaO–Al_2O_3 systems, *Journal of Non-Crystalline Solids*, 411:145–151. https://doi.org/10.1016/j.jnoncrysol.2014.12.030.

Wu, T, Wang, Q, Yu, C and He, S, 2016. Structural and viscosity properties of CaO-SiO_2-Al_2O_3-FeO slags based on molecular dynamic simulation, *Journal of Non-Crystalline Solids*, 450:23–31. https://doi.org/10.1016/j.jnoncrysol.2016.07.024.

Zhang, G-H, Yan, B-J, Chou, K-C and Fu-Shen Li, F-S, 2011. Relation between viscosity and electrical conductivity of silicate melts, *Metallurgical and Materials Transactions B*: *Process Metallurgy and Materials Processing Science*, 42(2):261–264. https://doi.org/10.1007/s11663-011-9484-7.

Zhang, L, Blanpain, B, Guo, M and Malfliet, A, 2023. In-situ electrical conductivity monitoring of slag solidification during continuous cooling for slag recycling, *Waste Management*, 161:234–244. https://doi.org/10.1016/j.wasman.2023.02.015.

Zhang, S, Zhang, X, Liu, W, Lv, X, Bai, C and Wang, L, 2014a. Relationship between structure and viscosity of CaO–SiO_2–Al_2O_3–MgO–TiO_2 slag, *Journal of Non-Crystalline Solids*, 402:214–222. https://doi.org/10.1016/j.jnoncrysol.2014.06.006.

Zhang, S, Zhang, X, Peng, H, Wen, L, Qiu, G, Hu, M and Bai, C, 2014b. Structure Analysis of CaO–SiO_2–Al_2O_3–TiO_2 Slag by Molecular Dynamics Simulation and FT-IR Spectroscopy, *ISIJ International*, 54(4):734–742. https://doi.org/10.2355/isijinternational.54.734.

Zheng, K, Yang, F, Wang, X and Zhang, Z, 2014. Investigation of Self-Diffusion and Structure in Calcium Aluminosilicate Slags by Molecular Dynamics Simulation, *Materials Sciences and Applications*, 5(2):73–80. https://doi.org/10.4236/msa.2014.52011.

Zheng, K, Zhang, Z, Yang, F and Sridhar, S, 2012. Molecular Dynamics Study of the Structural Properties of Calcium Aluminosilicate Slags with Varying Al_2O_3/SiO_2 Ratios, *ISIJ International*, 52(3):342–349. https://doi.org/10.2355/isijinternational.52.342.

Molecular dynamics simulation of viscosity of selected pure oxide melts

DOI: 10.62053/SKQK6306

A E Moiseev[1] and A Kondratiev[2]

1. PhD Scholar, Laboratory of Chemical Thermodynamics, Department of Physical Chemistry, Faculty of Chemistry, Lomonosov Moscow State University, Moscow 119991, Russia. Email: moiseev.ae@yandex.ru
2. Leading Researcher, Laboratory of Chemical Thermodynamics, Department of Physical Chemistry, Faculty of Chemistry, Lomonosov Moscow State University, Moscow 119991, Russia. Email: al.v.kondratiev@gmail.com

ABSTRACT

Viscosity of oxide melts is one of the fundamental physicochemical properties that plays a crucial role in important technological and natural processes like slag flow, slag/metal separation, volcano eruptions etc. However, many oxides melt at extremely high temperatures and are highly corrosive in the liquid state, which makes experimental measurement of melt viscosity by traditional experimental techniques a difficult and expensive, if not unachievable, task. In this case it might be useful to employ other methods of viscosity determination such as modelling or simulation. In the present paper the shear viscosity coefficients of selected pure refractory oxides (CaO, MgO, Al_2O_3 and others) have been simulated at temperatures above their melting points via the classical molecular dynamics and compared to the available viscosity data (eg experimental viscosities, other model predictions) collected by the authors. The simulation has been carried out using the non-commercial molecular dynamics simulation package LAMMPS and the Born-Mayer-Huggins potential, which parameters for the selected oxides were taken from the literature. Several viscosity calculation techniques (the Stokes-Einstein and Green-Kubo equations, the so called Einstein relations, and the non-equilibrium molecular dynamics methods) have been applied to ensure a more reliable viscosity calculation. It has been demonstrated that the simulated viscosity of the selected melts agrees with the available experimental data. It has also been shown that the simulated viscosity of a number of the oxide melts investigated is close to that calculated by phenomenological viscosity models, which supports viscosity extrapolation from the corresponding binaries and ternaries, if no experimental data is present for unary systems. In general, it has been demonstrated that the molecular dynamics simulation could provide a reasonable estimation of viscosity if no other viscosity data is available.

INTRODUCTION

The extreme melting temperatures and/or extreme reactivity in the molten state of many pure oxides preclude experimental investigation of important melt properties such as viscosity, density, etc. A number of practical, phenomenological models have been developed to calculate viscosity of oxide melts (or slags) as a function of temperature and chemical composition; in the present study four such models are used to compare with MD results: the FactSage (Grundy *et al*, 2008), GTT (Wu *et al*, 2015), Kondratiev-Jak (Forsbacka *et al*, 2007) and Starodub (Starodub *et al*, 2019) models. However, all these models are usually based on known viscosities of the pure oxides that are used then to calculate viscosity of binary, ternary and high-order melts. If viscosity of a pure oxide is not experimentally measured, it can be estimated *vice versa* from corresponding binary or ternary oxide systems. Typically, such estimation is not very reliable and can produce significant uncertainty in calculation of viscosity of multicomponent oxide melts. Therefore, it is necessary to obtain a more reliable estimation for viscosity of pure oxide melt. Among other methods, classical molecular dynamics (MD) simulation appears to be a reliable and powerful tool for evaluation of physical properties of molten pure oxides including viscosity.

A number of different techniques have been developed to evaluate the shear viscosity coefficient from MD simulation. These techniques include the equilibrium MD methods (Einstein, Green-Kubo) and non-equilibrium MD methods (periodic perturbation, SLLOD and Muller-Plathe). Compared to a phenomenological approach to viscosity modelling the approach based on MD simulation can provide more reliable and physically rigorous viscosity values.

In this study four different MD methods were used to calculate the shear viscosity of selected pure oxide melts (CaO, MgO, and Al_2O_3), and the Born-Mayer-Huggins potential was used to describe interatomic interactions for MD simulations. As no experimental data exists for liquid CaO, the shear viscosity of the pure CaO melt calculated in the present work for the first time is compared to viscosities predicted by the different practical models. Viscosities of other oxides calculated by MD simulation are also compared to the available data, which is discussed below.

COMPUTATIONAL METHODS

Viscosity calculation methods depend on the MD simulation, which is based on the interatomic potential, boundary conditions, number of atoms per simulation. The LAMMPS non-commercial package (CERN, Switzerland) was employed to carry out classical MD simulations. The details of calculations are provided below.

Viscosity calculation

The shear viscosity can be obtained from an equilibrium MD simulation via the stress tensor autocorrelation function (Allen and Tildesley, 2017) by the Green-Kubo formula:

$$\eta = \frac{1}{3}\frac{V}{k_B T}\sum_{\alpha,\beta}\int_0^\infty \langle P_{\alpha\beta}(t)P_{\alpha\beta}(0)\rangle\, dt \quad (1)$$

Following (Nevins and Spera, 2007), two independent stress tensor components ($P_{xx} - P_{yy}$ and $P_{yy} - P_{zz}$) were included to estimate the shear viscosity. The standard deviation of the calculated shear viscosity 'components' represents the error of estimation:

$$\Delta\eta = \sqrt{\frac{(\eta_{xy}-\eta_{av})^2+(\eta_{xz}-\eta_{av})^2+(\eta_{yz}-\eta_{av})^2+(\eta_{xxyy}-\eta_{av})^2+(\eta_{yyzz}-\eta_{av})^2}{5}}, \quad (2)$$

where η_{av} is the arithmetic mean of the five independently determined shear viscosity components η_{xy}, η_{xz}, η_{yz}, η_{xxyy} and η_{yyzz}.

The shear viscosity can also be determined via the following Einstein relation (Hess, 2002):

$$\eta = \lim_{t\to\infty}\frac{1}{6}\frac{V}{k_B T}\sum_{\alpha,\beta}\frac{d}{dt}\left\langle\left(\int_{t_0}^{t_0+t} P_{\alpha\beta}(t')dt'\right)^2\right\rangle_{t_0}, \quad (3)$$

where:

V	is the system volume
k_B	is Boltzmann's constant
T	is the absolute temperature
t	is the time
$P_{\alpha\beta}$	is the off-diagonal pressure tensor component, α, β refer to x, y, z and α≠β

Alternatively, the shear viscosity can be obtained from a non-equilibrium MD simulation by applying an external perturbation to the system. The shear viscosity relates the maximum shear rate s (equal to the gradient of x-component of the fluid velocity regarding z-direction) with the flux of transverse linear momentum $j_z(p_x)$ (Todd and Daivis, 2017):

$$\eta = \frac{-1}{s} j_z(p_x), \quad (4)$$

where $s = \left(\frac{\partial v_x}{\partial z}\right)$. It is important to use a high shear rate to obtain reliable statistics, but not so high that the system moves too far from its equilibrium. The system will be able to relax when the inverse shear rate is longer than the relaxation time.

The SLLOD method (Hess, 2002) is used to simulate the planar Couette flow by planar movement of the box wall. The momentum flux can be considered as an off-diagonal (eg xz) component of the stress tensor:

$$j_z(p_x) = \langle P_{xz}\rangle, \quad (5)$$

where P_{xz} is the off-diagonal pressure tensor component.

The periodic simulation box is divided into slabs along the z coordinate in the Müller-Plathe method (Muller-Plathe, 1999). A momentum flux (Equation 6) and a fluid velocity gradient are generated by momentum swaps between slabs.

$$j_z(p_x) = \frac{p_x}{2tA}, \tag{6}$$

where p_x *is* the total momentum transferred in a simulation, t is the simulation time and A is the box face area.

The error bar for the shear viscosity is calculated as follows (Bordat and Müller-Plathe, 2002):

$$\Delta\eta \leq \eta\left(\frac{\Delta J}{J} + \frac{\Delta G}{G}\right), \tag{7}$$

where J is the flux equal to the slope of the exchanged momentum with the simulation time, determined by a least squares fit, G is the slope of the linear velocity profile, also obtained by a least-squares fit, and the error bars ΔJ and ΔG were both obtained from a least squares fit.

Equations 8 and 9 can be used to obtain the shear rate and momentum flux, respectively, when a periodic external force creates a periodic force field in the periodic perturbation method (Hess, 2002):

$$j_z(p_x) = \rho\frac{a}{k}, \tag{8}$$

where ρ is the density, a is the external acceleration, and:

$$s = -vk, \tag{9}$$

where v is the velocity profile amplitude, $k=2\pi/l_z$, l_z is the box length.

Molecular dynamics simulation

Classical MD simulations were carried out using atomic interactions in the form of the Born–Mayer–Huggins (BMH) potential, for which the potential energy of interactions between atoms is given by the following equation:

$$u(r_{ij}) = \frac{q_i q_j}{r_{ij}} + A_{ij}\exp\left(\frac{\sigma_{ij} - r_{ij}}{\rho_{ij}}\right) - \frac{C_{ij}}{r_{ij}^6} + \frac{D_{ij}}{r_{ij}^8}, \tag{8}$$

with i and j being atomic species and r_{ij} being the interatomic distance between two ions of species i and j. It should be noted that only the van der Waals term was taken into account in the dipolar expansion. Parameters in Equation 10 with the corresponding references are given in Table 1. Parameters by Alvares *et al* (2020) are used for simulation of the CaO melt, while parameters by Arkhipin *et al* (in prep) are used for simulation of the MgO and Al_2O_3 melts. Parameters from Gutierrez *et al* (2000) are given for comparison.

Using this empirical potential, classical molecular dynamic simulations were performed with the LAMMPS code. At the first stage simulations were performed in the isobaric–isothermal ensemble (NPT) using a Nosé–Hoover thermostat coupled with an isotropic barostat (Martyna, Tobias and Klein, 1994) to determine the mean volume of system over a period of 100 ps. The system volume was adjusted to the mean value, and equilibration in the canonical (NVT) ensemble with coupling constant 0.1 ps was carried out for 100 ps. Periodic boundary conditions were applied in the three directions of space, and the long-range Coulomb interactions were treated within the Ewald summation method. Equations of motion were solved numerically by the Verlet algorithm in the velocity form using the time step of 1 fs. The simulation box contains different numbers of atoms in the initial crystalline configuration dependent on the MD method used for viscosity calculation. For example, the cubic box containing 729 Ca or Mg atoms and 729 O atoms for CaO or MgO and 600 Al atoms and 900 O atoms for Al_2O_3 was used for the Green-Kubo and Einstein viscosity calculations. The equilibration stage of non-equilibrium MD simulations by the SLLOD and Müller-Plathe algorithms lasts for 100 ps followed by the production stage lasting 100 ps. The orthorhombic box (L×L×3L) with 1029 Ca or Mg atoms and 1029 O atoms for CaO or MgO and 768 Al atoms and 1152 O atoms for Al_2O_3 was used for the Müller-Plathe method. The temperature ranges were 3200–4000 K, 3100–4000 K, and 2300–3200 K for CaO, MgO and Al_2O_3, respectively.

TABLE 1

Parameters of the Born-Mayer-Huggins potential.

Atom/ interaction	q	A_{ij}(eV)	ρ_{ij}(Å)	σ_{ij}(Å)	C_{ij}(eV Å^6)	Reference
Ca	1.2					Alvares *et al* (2020)
Mg	1.2					
Al	1.8					
O	-1.2					
Ca−Ca		0.0035	0.0800	2.3440	20.9856	
Ca−O		0.0077	0.1780	2.9935	42.2556	
O−O		0.0120	0.2630	3.6430	85.0840	
Mg−Mg		38868.5	0.2066	0.0	43.773	Arkhipin *et al* (in prep)
Mg−O		12655.4	0.2089	0.0	36.798	
Al−Al		0.00290	0.0680	1.5704	14.0498	
Al−O		0.0075	0.1689	2.6067	20.7448	
O−O		0.01015	0.2140	3.2678	5.0840	
Al	1.4175					Gutierrez *et al* (2000)
O	-0.9450					
Al−Al		0.00295	0.068	1.5704	14.0524	
Al−O		0.00746	0.172	2.6067	34.5814	
O–O		0.0120	0.276	3.643	85.1011	

RESULTS AND DISCUSSION

Selected examples of the MD simulation and viscosity calculation results obtained for three oxides (CaO, MgO and Al_2O_3) are presented here. Some MD simulations are still to be carried out; only the preliminary results are published in the paper.

General MD results

During the production stage of MD simulations used further for the Green-Kubo and Einstein calculations, the off-diagonal components of the stress tensor and the corresponding stress autocorrelation functions (SACF) were written into a file every five timesteps. Figure 1 demonstrates the normalised SACFs obtained for CaO, MgO and Al_2O_3 at temperatures of 3500, 3600 and 2800 K, respectively. The autocorrelation functions for CaO and MgO decay significantly after 0.5 ps, while for Al_2O_3 it decays after 1 ps. The autocorrelation functions obtained at other temperatures exhibit the same behaviour. The shear viscosity was calculated by integrating the SACF using Equation 1 and the trapezoidal integration method.

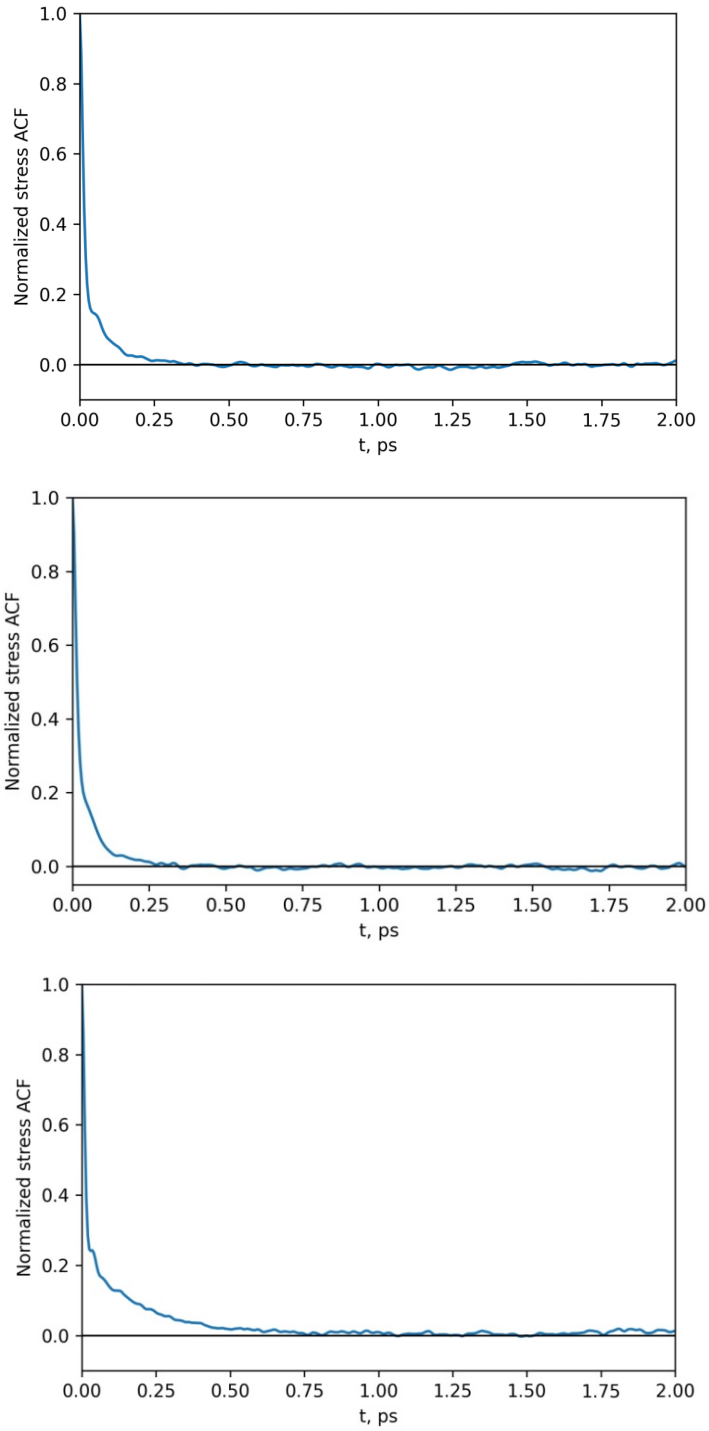

FIG 1 – Normalised stress autocorrelation functions for: (a) CaO at 3500 K, (b) MgO at 3600 K, (c) Al_2O_3 at 2800 K.

During MD simulations used for the Müller-Plathe method, the orthorhombic simulation box is divided into 20 slabs in the z direction, which is the direction of the momentum flux exchange. Momentum exchange periods (w) were chosen at intervals of 1, 10, 20 and 40 timesteps. During the production stage velocity profile, temperature profile, density profile and transferred momentum were written into a file every 100 timesteps. The duration of the production stage was 500 ps for a temperature interval of 3400–4000 K and 1 ns for a temperature interval of 3100–3300 K for MgO. The momentum when the system reached a steady state was controlled by a dependence of cumulative shear viscosity upon time (Figure 2). The viscosity calculation was based solely on data obtained in a steady state.

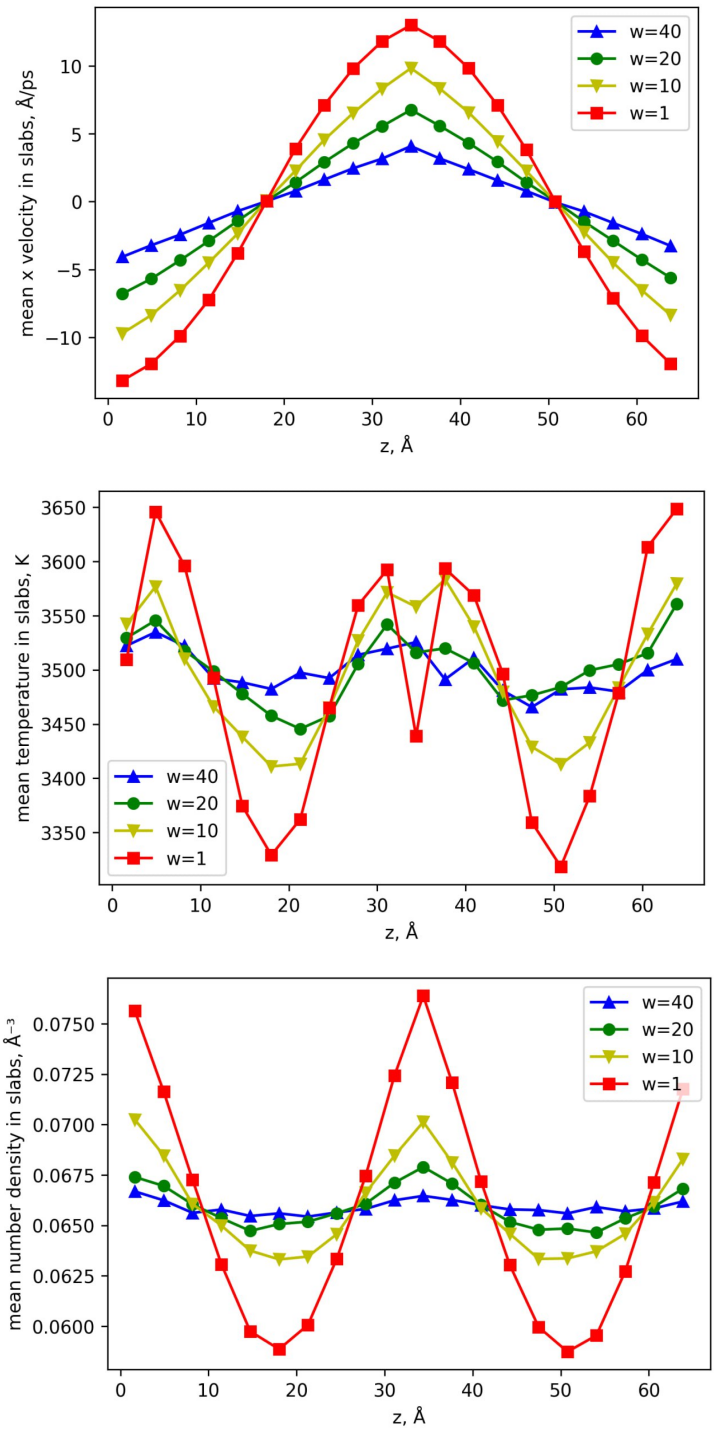

FIG 2 – The MD results for MgO at 3500 K: (a) velocity, (b) temperature, (c) density profiles.

Viscosity of the CaO melt

Figure 3 demonstrates viscosity of the CaO melt calculated by four different MD (Green-Kubo, periodic perturbation, SLLOD and Muller-Plathe) methods at different temperatures. Additionally shown a viscosity value at 3200 K calculated via the MD simulated oxygen diffusion coefficient and Stokes-Einstein equation. It can be seen that all the MD methods provide very close results, although one method uses equilibrium MD simulation and three use non-equilibrium MD simulation. It can also be seen that the viscosity value calculated via the oxygen diffusion coefficient is lower than that calculated by the Green-Kubo equation by an order of magnitude. The viscosity of pure CaO liquid is evaluated in the present work for the time, and it should be noted that the MD results usually underestimate measured viscosity values (eg Kondratiev *et al,* in prep).

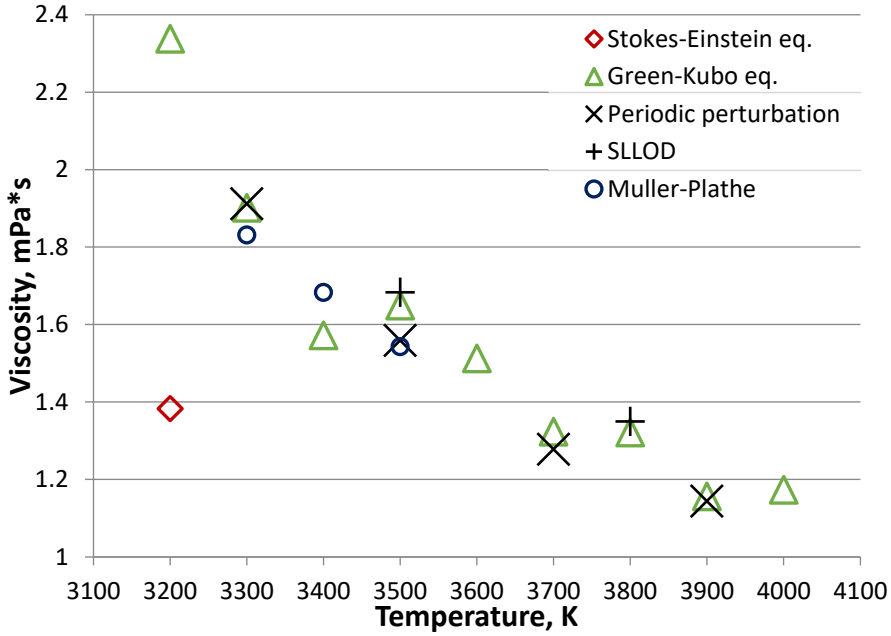

FIG 3 – Viscosity of the CaO melt calculated by four different MD methods.

The average Arrhenius dependence (logarithm of viscosity as a function of the reciprocal temperature) was obtained for the four MD calculations by fitting the classical Arrhenius equation to the MD results. Figure 4 shows comparison between viscosities calculated by four different (FactSage, Kondratiev-Jak, Starodub and GTT) viscosity models and the average MD dependence. It can be seen that the FactSage, GTT and Kondratiev-Jak models underestimate viscosity of the pure CaO melt, as these model curves lie substantially below the MD average curve. It demonstrates that extrapolation from the corresponding binary and ternary systems does not always provide a correct estimation of viscosity of pure oxides.

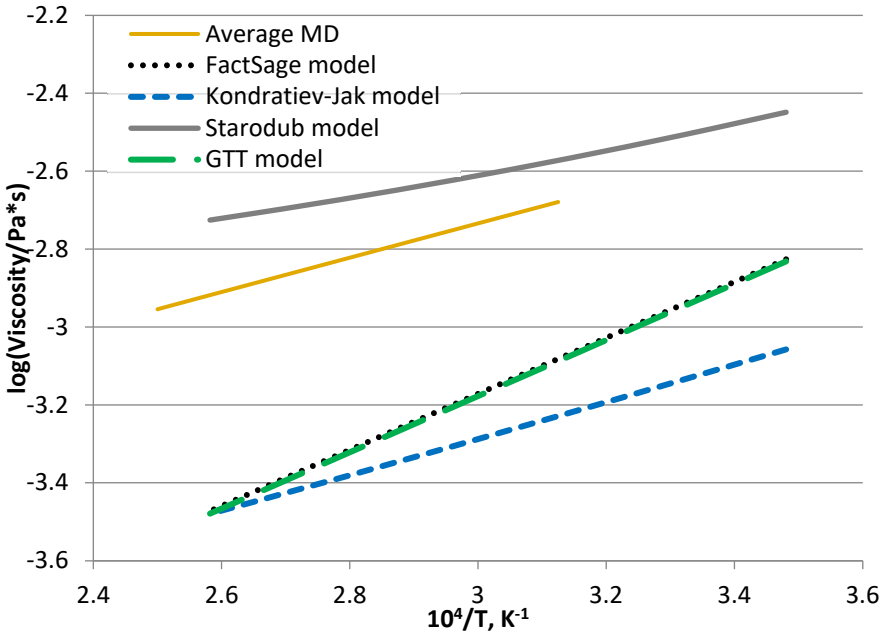

FIG 4 – Comparison of the CaO viscosity calculated via MD simulation and by different viscosity models.

Viscosity of the MgO melt

Figure 5 shows viscosities of the MgO melt calculated in this work by two equilibrium MD methods (Equations 1 and 3), in the study of Karki, Zhang and Stixrude (2013) using the *ab initio* MD simulation, and by Leu, Ma and Eyring (1975) using the significant structures theory. It can be seen that the MD results by Karki, Zhang and Stixrude (2013) are very close to the MD results obtained in the present work.

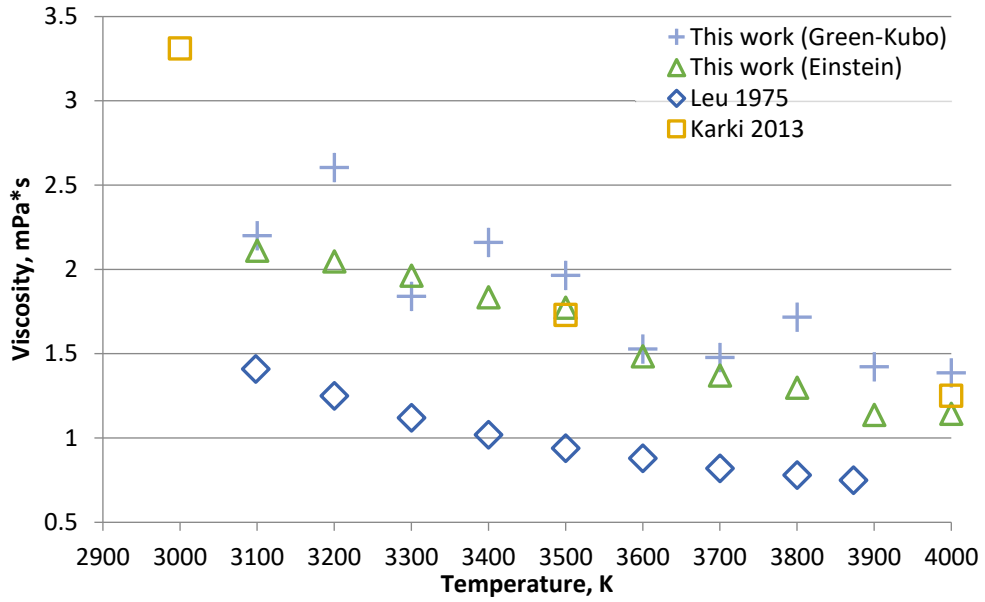

FIG 5 – Viscosity of the MgO melt calculated in different works.

Figure 6 shows the average Arrhenius viscosity for two MD methods used and calculations by different viscosity models in logarithmic format as a function of the reciprocal temperature. It can be seen that the GTT model might underestimate viscosity of pure MgO, while the viscosity curve by the Kondratiev-Jak model provides more realistic estimation of the MgO melt viscosity.

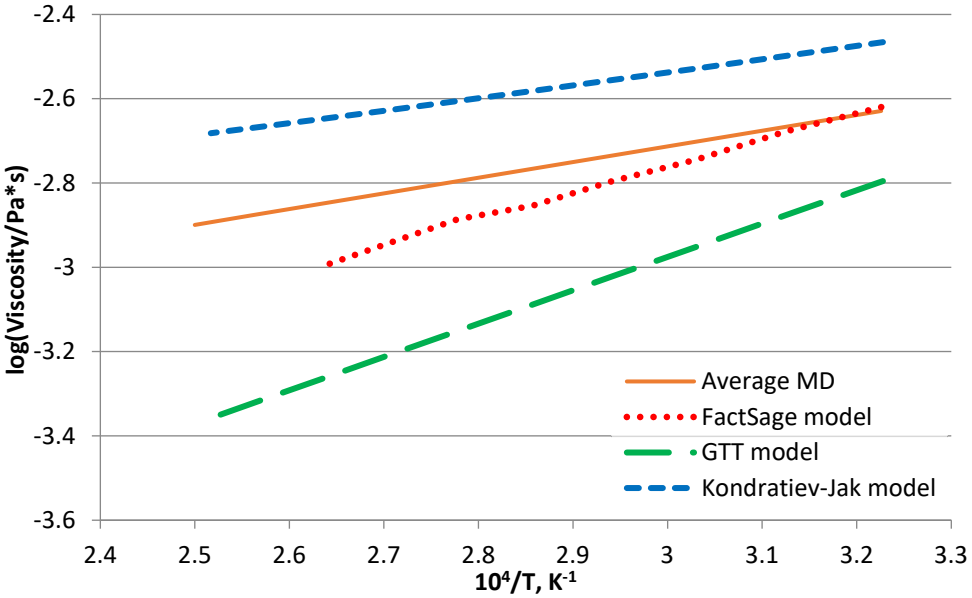

FIG 6 – Comparison of the MgO viscosity calculated via MD simulation and by different viscosity models.

Viscosity of the Al_2O_3 melt

Viscosity of the Al_2O_3 melt was calculated by two different methods: Green-Kubo (equilibrium MD) and Muller-Plathe (non-equilibrium MD). Only preliminary MD results are presented here. The available experimental data for Al_2O_3 can roughly be divided into two large groups dependent on a method used to determine viscosity: those obtained via conventional viscometry methods (eg rotational cylinder technique, oscillation technique) and those measured indirectly by levitation methods. Figure 7 demonstrates agreement of MD simulation results obtained in this work with the Al_2O_3 experimental data and other MD simulation by Jahn and Madden (2007) and Jahn (2008). The classical MD simulation with the BHM potential and the Green-Kubo formula (Equation 1) was used in the present work to estimate viscosity of pure Al_2O_3, while Jahn and Madden (2007) and Jahn (2008) employed an aspherical ion model potential with more complex interactions. It can be seen that viscosity calculated by the Green-Kubo equation is much lower than the most of the experimental points, while the Muller-Plathe method provides slightly higher values. In total, the viscosity calculation results obtained in the present work indicate that MD simulation with a simple interatomic potential can provide a lower estimation of viscosity.

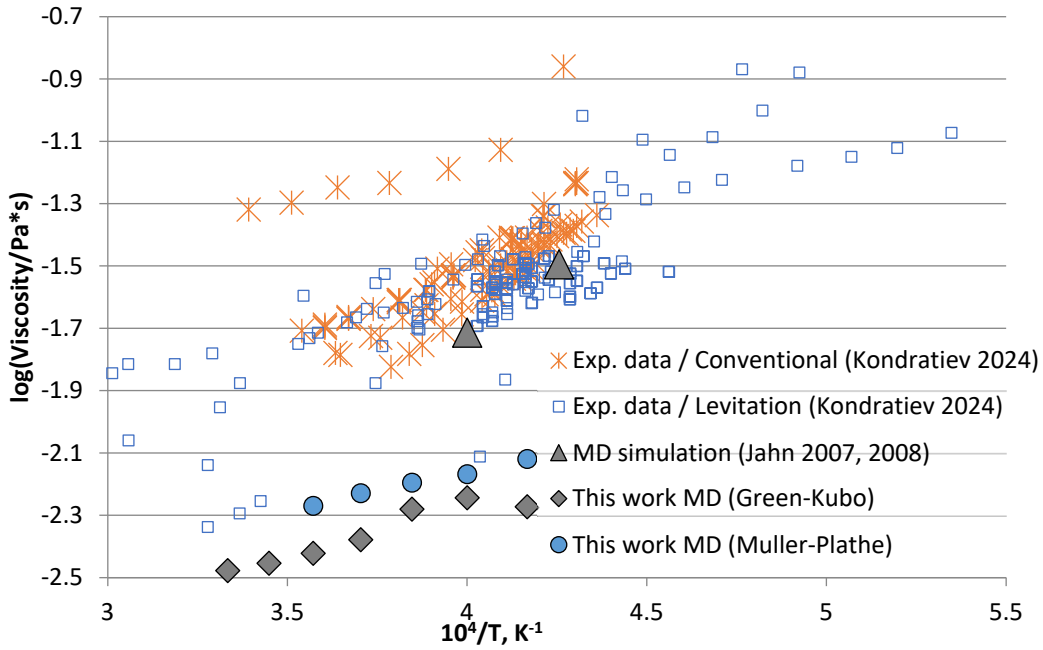

FIG 7 – Comparison of the calculated (MD) and experimental viscosity for the Al_2O_3 melt.

CONCLUSIONS

Equilibrium and non-equilibrium molecular dynamics simulation coupled with viscosity calculation was carried for the CaO, MgO, and Al_2O_3 melts using the Born-Mayer-Huggins interatomic potential. Parameters of the BHM potential were taken from the literature.

Viscosity of the pure CaO melt was evaluated by MD simulation for the first time and compared to predictions of the selected viscosity models. It was shown that the MD results are higher than most of the model predictions and can now be used as a more reasonable estimation for CaO viscosity.

Viscosity of the pure MgO melt evaluated by MD simulation was compared to other theoretical calculations and showed a reasonable agreement with other MD simulation.

Viscosity of the pure Al_2O_3 melt evaluated by MD simulation was compared to the available experimental data, and the comparison demonstrated that MD simulation with a simple interatomic potential (like BHM) can provide a lower estimation of viscosity in relation to the experimental points.

ACKNOWLEDGEMENTS

This work was financially supported within the framework of the State Program 'Chemical Thermodynamics and Theoretical Materials Science' at the Lomonosov Moscow State University (N◦121031300039-1).

REFERENCES

Allen, M P and Tildsley, D J, 2017. *Computer Simulation of Liquids*, 2nd edition, 641 p (Oxford University Press: New York).

Alvares, C M S, Deffrennes, G, Pisch, A and Jakse, N, 2020. Thermodynamics and structural properties of CaO: A molecular dynamics simulation study, *J Chem Phys*, 152:084503.

Arkhipin, A S, Morineau, F, Pisch, A, Uspenskaya, I A and Jakse, N, in prep. A molecular dynamics simulation study of crystalline and liquid MgO, to be published.

Bordat, P and Müller-Plathe, F, 2002. The shear viscosity of molecular fluids: A calculation by reverse nonequilibrium molecular dynamics, *J Chem Phys*, 116:3362–3369.

Forsbacka, L, Holappa, L, Kondratiev, A and Jak, E, 2007. Experimental study and modelling of viscosity of chromium containing slags, *Steel Res Int*, 78:676–684.

Grundy, A N, Liu, H, Jung, I-H, Decterov, S A and Pelton, A D, 2008. A model to calculate the viscosity of silicate melts, Part I: Viscosity of binary SiO_2-MeOx systems (Me = Na, K, Ca, Mg, Al), *Int J Mater Res*, 99:1185–1194.

Gutierrez, G, Belonoshko, A B, Ahuja, R and Johansson, B, 2000. Structural properties of liquid Al_2O_3: A molecular dynamics study, *Phys Rev E*, 61(3):2723–2729.

Hess, B, 2002. Determining the shear viscosity of model liquids from molecular dynamics simulations, *J Chem Phys*, 116:209–217.

Jahn, S and Madden, P A, 2007. Structure and dynamics in liquid alumina: Simulations with an ab initio interaction potential, *J Non-Cryst Solids*, 353:3500–3504.

Jahn, S, 2008. Atomic structure and transport properties of MgO-Al_2O_3 melts: A molecular dynamics simulation study, *Am Miner*, 93:1486–1492.

Karki, B B, Zhang, J and Stixrude, L, 2013. First principles viscosity and derived models for MgO-SiO_2 melt system at high temperature, *Geophys Res Lett*, 40:94–99.

Kondratiev, A, Zinoveev, D, Bajenova, I, Khvan, A, Uspenskaya, I and Ilyushechkin, A, in prep. A review of viscosity data for unary oxide systems, to be published.

Leu, A-L, Ma, S-M and Eyring, H, 1975. Properties of molten magnesium oxide, in *Proceedings of the Nat Acad Sci USA*, 72:1026–1030.

Martyna, G J, Tobias, D J and Klein, M L, 1994. Constant pressure molecular dynamics algorithms, *J Chem Phys*, 101(5):4177–4189.

Muller-Plathe, F, 1999. Reversing the perturbation in nonequilibrium molecular dynamics: An easy way to calculate the shear viscosity of fluids, *Phys Rev E*, 59(5):4894–4898.

Nevins, D and Spera, F J, 2007. Accurate computation of shear viscosity from equilibrium molecular dynamics simulations, *Mol Sim*, 33(15):1261–1266.

Starodub, K, Wu, G, Yazhenskikh, E, Mueller, M, Khvan, A and Kondratiev, A, 2019. An Avramov-based viscosity model for the SiO_2-Al_2O_3-Na2O-K2O system in a wide temperature range, *Ceram Int*, 45:12169–12181.

Todd, B D and Daivis, P J, 2017. *Nonequilibrium Molecular Dynamics, Theory, Algorithms and Applications* (Cambridge Univ Press).

Wu, G, Yazhenskikh, E, Hack, K, Wosch, E and Mueller, M, 2015. Viscosity model for oxide melts relevant to fuel slags, Part 1: Pure oxides and binary systems in the system SiO_2–Al_2O_3–CaO–MgO–Na2O–K2O, *Fuel Process Technol*, 137:93–103.

Evaluation of thermal conductivities of molten SiO_2-Al_2O_3-CaO slags

DOI: 10.62053/LTYL7744

K Tang[1], M Zhu[2], J You[3], X Ma[4] and G Tranell[5]

1. Senior Scientist, SINTEF AS, Trondheim N-7436, Norway. Email: kai.tang@sintef.no
2. Post-doc Researcher, Norwegian University of Science and Technology, Trondheim N-7491, Norway. Email: mengyi.zhu@ntnu.no
3. Professor, Shanghai University, Shanghai 200444, China. Email: jlyou@staff.shu.edu.cn
4. Senior Scientist, SINTEF AS, Oslo N-0373, Norway. Email: xiang.ma@sintef.no
5. Professor, Norwegian University of Science and Technology, Trondheim N-7491, Norway. Email: gabriella.tranell@ntnu.no

ABSTRACT

The thermal conductivity of slag is critical for the efficiency of high temperature metallurgical processes such as the smelting reduction of ferroalloys, the ladle refining and the continuous casting mold flux in steelmaking. Experimental determination of slag's thermal conductivity is fraught with challenges, as seen in yielding data for the SiO_2-Al_2O_3-CaO system that are often inconsistent and widely dispersed. In molten slags of this system, thermal transport occurs via phonons within the network structure. To quantitatively describe thermal conductivity based on the microstructure, high-temperature Raman spectroscopy was employed to measure the silicate tetrahedra Q_i (i = 0, 1, 2, 3), with Q_4 species inferred from mass balance. This study also integrated molecular dynamics simulations to provide a fundamental understanding of the microstructure units distributions. Machine learning algorithms, especially deep neural networks, were applied to establish the relationship between slag composition and the configuration of tetrahedra. The thermal conductivities were then connected with silicate tetrahedra Q_i using an Arrhenius-type formalism. This study sets the stage for extending our findings to more complex, multicomponent slags, enhancing their practical application in industrial processes.

INTRODUCTION

The thermophysical properties of molten slags, such as viscosity, conductivity, and diffusivity, are fundamentally linked to their microstructures. Thermal conductivity is crucial in various steelmaking processes including smelting reduction of ferroalloy, ladle slag and continuous casting mold flux. However, accurately determining the thermal conductivity experimentally for the entire SiO_2-Al_2O_3-CaO slag system poses challenges, caused by inconsistent and scattered data. Consequently, there is lack of robust, physically sound models for mathematically describing the thermal behaviour of this molten slag system.

In molten silicate melts, heat conduction occurs through the interplay of molecular movements, particularly the random motion of ions and the vibrational energy within the SiO_4 tetrahedral network, facilitating heat transfer (Wang *et al*, 2020). This process differs from crystalline solids, where heat transfer is more organised, primarily through lattice vibrations or phonons. The disordered, fluidic nature of molten silicates leads to a less structured heat transfer mode. The melt's structure and composition, influenced by various metal ions and silica content, significantly impact its thermal conductivity. Rising temperatures increase thermal agitation, disrupting regular heat transfer and reducing conductivity. Moreover, the viscosity of molten silicate, indicative of its internal structural complexity (Mills, Yuan and Jones, 2011), is a critical factor. Higher viscosity, associated with more complex network structures, typically results in lower thermal conductivity. Consequently, heat conduction in molten silicates is a dynamic process, intricately linked to the melt's molecular structure, temperature and viscosity.

Raman spectroscopy is a powerful tool for studying the structure of molten slag. It can be used to identify the different types of structural units present in the slag, such as SiO_4 tetrahedral Q_i (i = 0–4) units. The relative abundance of these different units can provide insights into the degree of polymerisation of the molten slag.

In the present work, the microstructure of molten SiO_2-Al_2O_3-CaO slags have been characterised by high-temperature Raman spectroscopy. To visualise the microstructure in these high-temperature

silicate melts, molecular dynamics (MD) simulations were carried out. The MD simulations have corroborated the experimentally determined relationships between silica tetrahedra and Al_2O_3 content as observed through Raman spectroscopy. We have also constructed a machine learning framework with a deep neural network architecture to establish a correlation between the silicate tetrahedra and the molar ratios of the slag.

Furthermore, we have devised a physical model that accurately describes the thermal conductivity of molten SiO_2-Al_2O_3-CaO slag within a temperature range of 1723−2073 K. The model can be used to describe the composition-temperature-thermal conductivity relations over entire SiO_2-Al_2O_3-CaO system.

LITERATURE

Mills, Yuan and Jones (2011) and Mills *et al* (2012) noted no existing models available for estimating the thermal conductivities of slags. However, it's observed that the thermal conductivity of liquid silicate slags at their liquidus temperature increases linearly as the ratio of non-bridging oxygens to tetrahedral cations (NBO/T) decreases, ie as Q increases. They believed that thermal conduction in slags was greater along covalent chains than across cationic bonds. This is due to slags exhibiting both covalent and ionic bonding. They also showed a link between thermal conductivity and viscosity. The temperature dependence of thermal conductivities of molten slags can be represented by the Arrhenius relation. They pointed out the measurements of thermal conductivity at temperatures on glassy and liquid slags included contributions from radiation conduction, which varied based on the measurement method. Attempts were made to estimating thermal conductivity with both Q and viscosity, but the results were not satisfactory.

Kang and Morita (2006) determined the thermal conductivity of the SiO_2-Al_2O_3-CaO molten slags system using the non-stationary hot wire method. The measurements in temperatures ranging from the liquidus temperature to 1873 K across various compositions. They found that thermal conductivity decreased with increasing basicity (CaO/SiO_2 ratio) and showed a maximum around 15–20 per cent Al_2O_3 content. They also noted that thermal conductivity decreased with rising temperature and discussed the effects of silicate structure depolymerisation at higher temperatures.

Kang, Lee and Morita (2014) further made a comprehensive review of various methods used to measure the thermal conductivity of molten silicate slags. The authors discussed various methods for measuring thermal conductivity of molten slags, particularly focusing on non-steady-state methods. The hot-wire and laser flash methods were emphasised due to their short measurement times and suitability for high-temperature liquid phases. They also assessed the impact of slag composition and temperature on thermal conductivity, emphasising the correlation between thermophysical properties like thermal conductivity and viscosity. The iso-thermal conductivity curves at 1673, 1773 and 1873 K, which were determined using the hot wire method, were presented.

Wang *et al* (2020) studied thermal conduction mechanism of molten slag by non-stationary hot wire experimental method and a reverse non-equilibrium molecular dynamic simulation. MD simulations showed that the majority of Si in the slag forms [SiO_4] tetrahedra, with a significant portion of Al and Fe forming [AlO_4] and [FeO_4] tetrahedra. The presence of NBOs enhances the anharmonicity in the tetrahedral structure, leading to a reduction in thermal conductivity. They also defined an equivalent molar concentration of the Q_4 tetrahedron (XQ_4) and finds a positive linear relationship between thermal conductivities and XQ_4.

The relationship between microstructure of molten coal slags and thermal conductivity was studied by Wang *et al* (2019). They found that thermal conductivity of slags was influenced by phonon vibration, which depended on the degree of polymerisation in the slags. The authors presented an equation for calculating the thermal conductivity of coal slags in relation to their degree of polymerisation, denoted as Q:

$$\lambda = Aexp\left(\frac{BQ}{T}\right), Q = \frac{4Q_4+3Q_3+2Q_2+Q_1}{100} \quad (1)$$

This equation establishes a mathematical relationship that quantifies how changes in the slag's microstructure, particularly the degree of polymerisation, affect its thermal conductivity. The

relationship is derived from empirical data and analysis, reflecting the intricate interplay between the slag's chemical composition and its thermal properties.

In our previous study (Tang *et al*, 2023), we utilised high-temperature Raman spectroscopy and Nuclear Magnetic Resonance (NMR) techniques to quantitatively analyse the microstructural characteristics of calcium aluminosilicate glasses. The results demonstrated a gradual increase in the fourfold coordinated aluminium (Al^{IV}) with the addition of Al_2O_3 to equal molar SiO_2-CaO mixtures. Additionally, significant adjustments were observed in the distribution of Q_i species, indicating notable changes in the SiO_2-Al_2O_3-CaO glass microstructure. Figure 1 shows the Q_i obtained from measured Raman spectra of SiO_2-Al_2O_3-CaO samples.

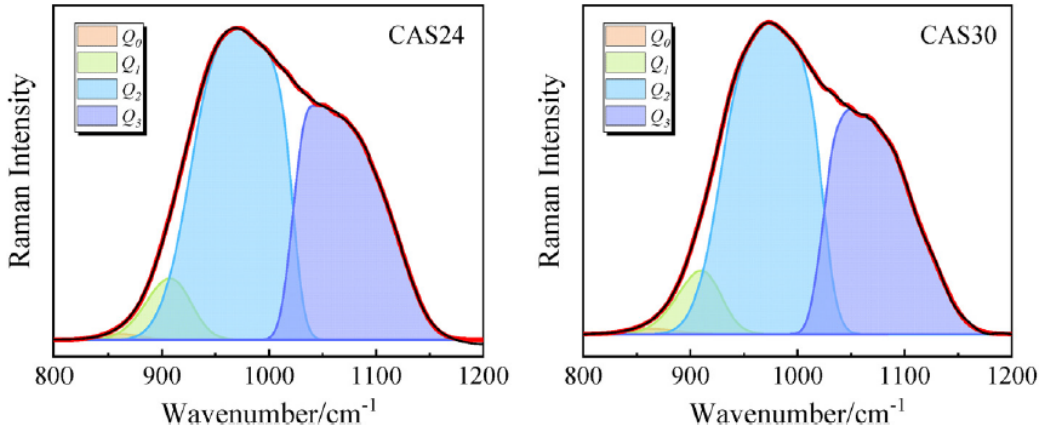

FIG 1 – Q_i (i = 0, 1, 2, 3) distributions of Raman spectra of calcium aluminosilicate samples.

A phenomenological viscosity model (Tang *et al*, 2022) has been proposed for the description of the rheological properties covering from homogenous liquid to heterogenous partial solidified SiO_2-Al_2O_3-CaO ternary system. The model has been developed by modification of the well-known Vogel–Fulcher–Tammann (VFT) formalism. As Figure 2 shows, good agreement exists between calculated and measured viscosities across a wide temperature range. This phenomenological viscosity model can be used to determination of the maximum in conductivity, usually occurs near glass transition temperature, T_g (Mills *et al*, 2012).

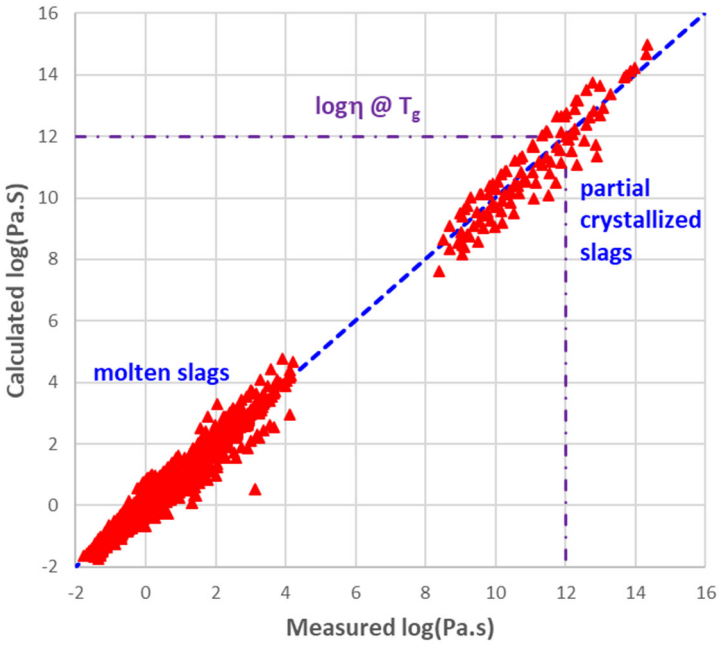

FIG 2 – Comparison of the experimental measured viscosities with calculated values by the phenomenological viscosity model.

Thermal conductivity measurements at temperatures on liquid slags contain a significant and unknown contribution from radiation conduction (RC). The RC contributions are much smaller in transient hot wire (THW) measurements than for those obtained with the laser pulse (LP) method, because the emitting surface area in LP experiments is ten more times higher than that in THW studies (Mills *et al*, 2012). Therefore, only thermal conductivity data from THW studies were accepted in the present work. Figure 3 shows the experimental data of thermal conductivity available in the literature. The experimentally determined thermal conductivities of molten SiO_2-Al_2O_3-CaO slags exhibit considerable variability: the relative differences in measurements for identical slag compositions by different researchers often exceed 50 per cent, and in some instances, these discrepancies can surpass 200 per cent.

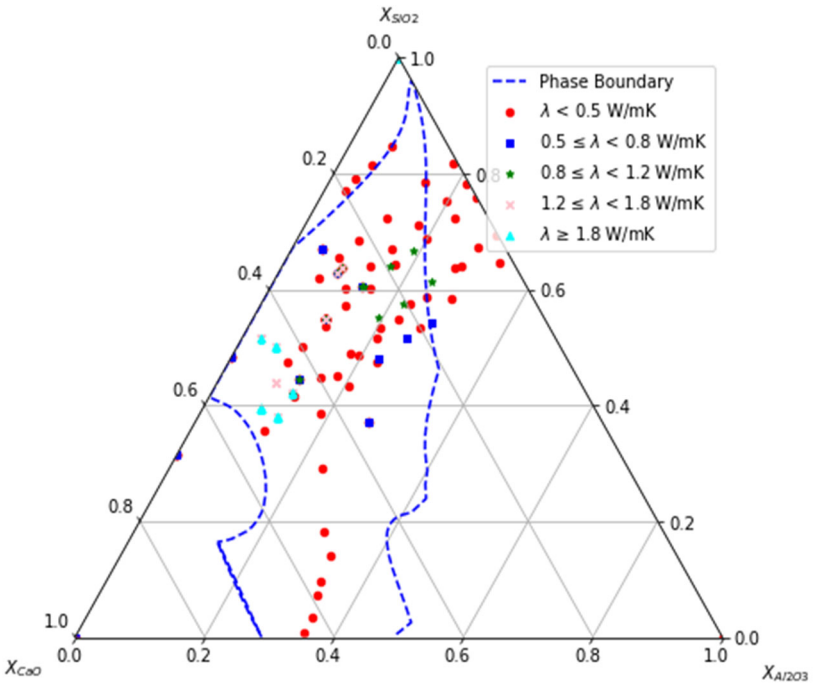

FIG 3 – Measured thermal conductivity of molten SiO_2-Al_2O_3-CaO slags reported in 1673–1973 K in the literature.

METHODOLOGY

A statistical model was first developed to estimate the distribution of silicon tetrahedra in SiO_2-Al_2O_3-CaO slags across various compositions. The model was based on the contents of nearest neighbour pairs, such as Si-Si, Si-Al, Si-Ca etc as defined by the modified quasichemical model and the commercial thermochemical database, FToxid (Bale *et al*, 2009). For more detailed insights into this model, the work of Grundy *et al* (2008) serves as a reference.

Unfortunately, the statistical model cannot give reasonable description of the silicon tetrahedra in the molten SiO_2-Al_2O_3-CaO oxides, as can be seen from Figure 4. Although the general tendencies of Q_i vary with Al_2O_3 content are rather similar, the statistical model calculations show the changing rules of Q_4 and Q_0 with the Al_2O_3 composition are exactly opposite to the measured results. The limitations of the statistical model have prompted the implementation of molecular dynamics (MD) simulations for more accurate analysis.

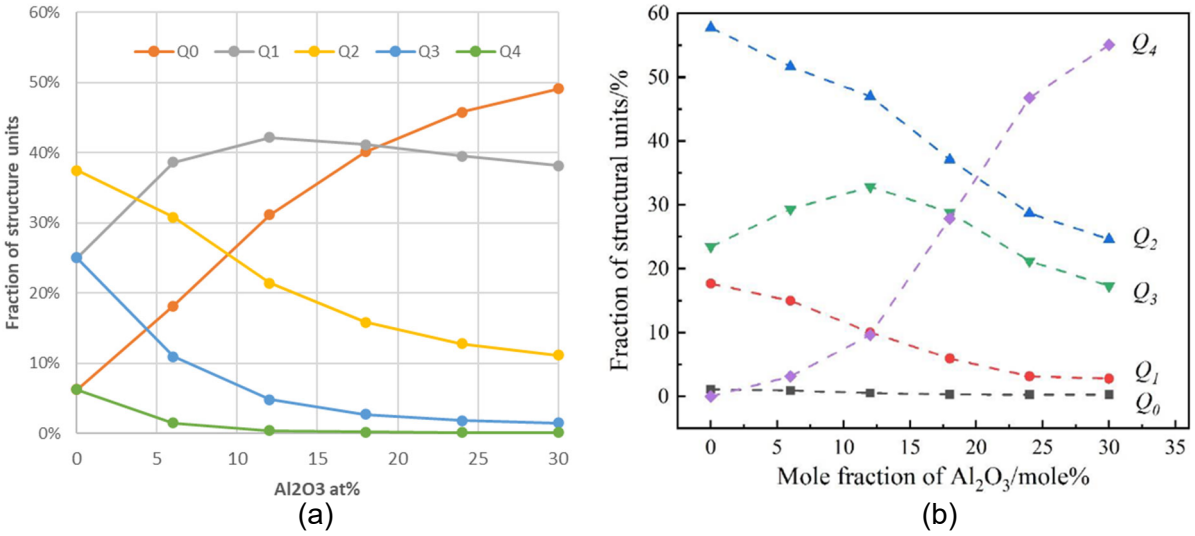

FIG 4 – Comparison of the statistic model calculated Q_i (a) versus Raman determined values (b).

Molecular dynamic calculation

To determine the silicon tetrahedra across the entire compositional range of the SiO_2-Al_2O_3-CaO ternary system, MD simulations have been carried out. High-throughput MD simulations of 231 samples were performed using the LAMMPS package (Plimpton, 1995), covering the SiO_2-Al_2O_3-CaO ternary system in 5 mol per cent increments. The known Jakse force field was adopted for its accuracy. Each simulated slag composition underwent a melt-quench approach from 4000 K to 2073 K in the NPT ensemble. Further equilibration was conducted in the NVT ensemble followed by the NVE ensemble. Slag configuration sampling was performed in the final NVE ensemble.

Owing to space limitation, the comprehensive methodology and additional results of the MD calculations will be detailed in a forthcoming publication.

Machine learning

Machine learning framework has been applied to further analyse and interpret the results obtained from the MD simulations. To model the relationship between molar fraction of species and Q_i (i = 0–4) at a constant temperature of 2073 K, a deep neural network (DNN) with a (30,30) architecture was employed. The training of this network achieved an error rate of 0.00030 and a score of 0.9809, indicating high accuracy.

Mathematic description of thermal conductivity

Since the silicon tetrahedra can now be described numerically, we are able to set-up a mathematic expression for thermal conductivity of molten calcium aluminosilicate slags. As mentioned above, the temperature dependence of thermal conductivity for molten silicate melts can be expressed as Arrhenius type relation.

Recent studies revealed that the compositional dependence of thermal conductivity can be characterised by the presence of silicon tetrahedra. Effect of composition on the thermal conductivity for the present work is expressed in term of silicate tetrahedra, Q_i. By examining the Q_i distributions in the entire SiO_2-Al_2O_3-CaO ternary system and using Lasso (Least Absolute Shrinkage and Selection Operator) regression (Tibshirani, 1996) for feature selection: the most important Q_i for thermal conductivity. As expect, Q_4 and Q_0 have been selected based primary on the experimental results reported by Kang and Morita (2006) and Kang, Lee and Morita (2014).

Integrating theoretical foundations with experimental observations, we propose a model for the thermal conductivity of the slag:

$$\lambda = (a_0 + a_1 Q_0 + a_2 Q_4) exp\left[\frac{e_0 + e_1 Q_0 + e_2 Q_4}{T}\right] \quad (2)$$

where a_i and e_i are the model parameters to be optimised from the experimental results.

RESULTS AND DISCUSSION

The MD simulations results can first be validated using the experimental results appeared in Figure 4b. Figure 5 shows the similar results obtained from machine learning modelling results. It fits rather well with the Raman observation.

On the other hand, data from both Raman/NMR spectroscopy and MD simulations reveal the substantial presence of fourfold-coordinated aluminium within the molten SiO_2-Al_2O_3-CaO slags, resulting in the formation of Al-tetrahedra. These structural units are expected to have a definitive impact on the thermal conductivity of the slags. However, due to constraints in manuscript length, an in-depth analysis of this effect is beyond the scope of the current discussion.

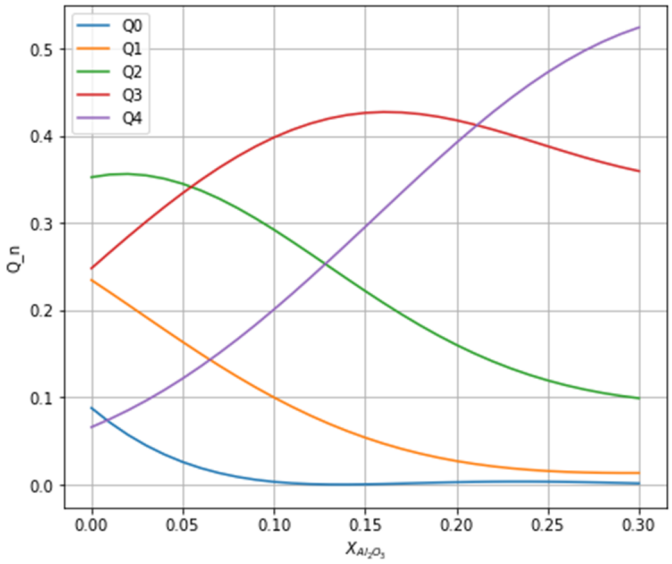

FIG 5 – Machine learning calculated effect of Al_2O_3 contents on the distribution of Q_i species in molten calcium aluminosilicate slag.

The calculated Q_0 distribution over the entire SiO_2-Al_2O_3-CaO composition range is shown in Figure 6. Similarly, for the most important species, the distribution of Q_4 is shown in following Figure 7.

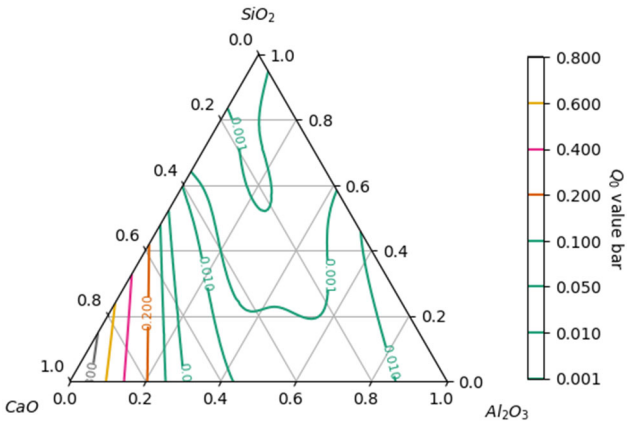

FIG 6 – Calculated iso-contours of Q_0 in the entire SiO_2-Al_2O_3-CaO system at 2073 K.

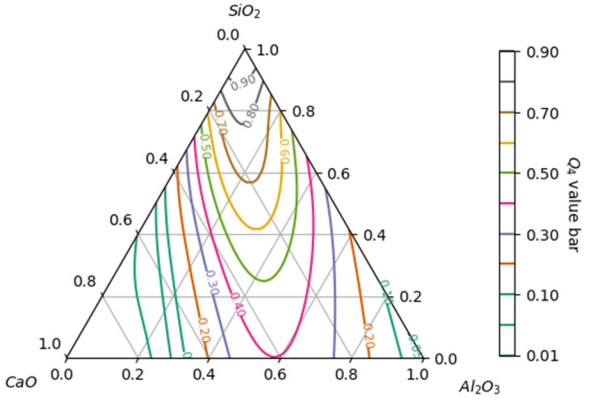

FIG 7 – Calculated iso-contours of Q_4 in the entire SiO_2-Al_2O_3-CaO system at 2073 K.

The modelled thermal conductivity of the molten SiO_2-Al_2O_3-CaO slag at 1773 K is depicted in Figure 8, alongside experimental data for comparative purposes. There is a commendable correlation between the two with a regression score of approximately 0.86 across all experimental data employed in this work.

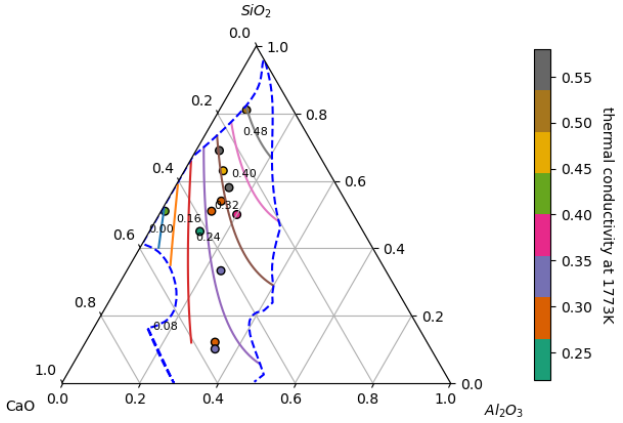

FIG 8 – Calculated iso-contours of thermal conductivity at 1773 K.

Figure 9 displays the calculated iso-contours of thermal conductivity at 1873 K. Once more, the computational data and the trend of the contours are consistent with the results obtained from non-stationary hot wire experiments.

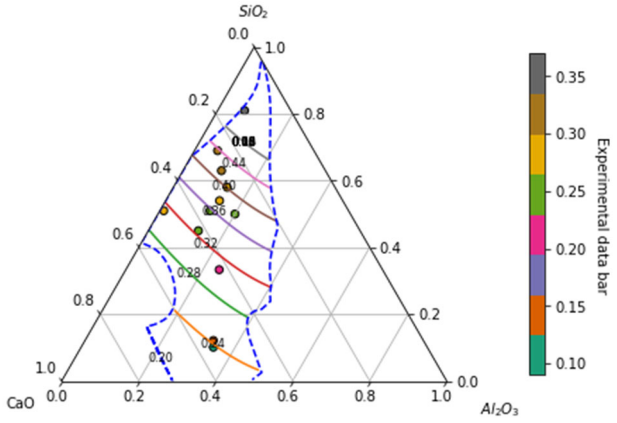

FIG 9 – Calculated iso-contours of thermal conductivity at 1873 K.

As mentioned earlier, thermal conductivity of liquid slag is closed related to its viscosity. Attempts have been made to include viscosity properties in the Arrhenius type relation. However, a simple implementation of the viscosity data modelled by the modified VFT model results in even worse

fitting results. However, coupling viscosity and silicon tetrahedron content into deep neural networks has initially shown some promising results. Therefore, machine learning is expected to give more accurate results compared to the physical model proposed in this manuscript.

CONCLUSIONS

This study has successfully elucidated the intrinsic relationships between the microstructural properties and thermophysical behaviours of the SiO_2-Al_2O_3-CaO slag system, which holds significant relevance in metallurgy and material processes. Employing Raman and NMR spectroscopy, the essential insights into the slag structures were garnered, identifying various Q_i (i = 0–3) units with given composition. A deep neural network model was then employed to reproduce the statistical model calculations. Furthermore, the study successfully connected thermal conductivities with the Q_i units and viscosity, utilising empirical Arrhenius-type and neural network models, amplifying our knowledge about heat conduction phenomena in molten slags. Essentially, this work paves the way to extend these integrated methods and findings to multicomponent slags, enhancing applicability and relevance in real metallurgical and materials processing scenarios.

ACKNOWLEDGEMENTS

The current work has received funding from the European Union's Horizon 2020 research and innovation program under grant agreement No 869268 (Sisal Pilot) and the Key Basic Research Projects of the Basic Strengthening Plan of the Commission of Science and Technology (2021-JCJQ-ZD-051-00-02).

REFERENCES

Bale, C W, Bélisle, E, Chartrand, P, Decterov, S A, Eriksson, G, Hack, K, Jung, I H, Kang, Y B, Melançon, J, Pelton, A D and Robelin, C, 2009. FactSage thermochemical software and databases—recent developments, *CALPHAD*, 33(2):295–311.

Grundy, A N, Liu, H, Jung, I H, Decterov, S A and Pelton, A D, 2008. A model to calculate the viscosity of silicate melts, Part I: Viscosity of binary SiO2#x2013;MeOx systems (Me = Na, K, Ca, Mg, Al), *International Journal of Materials Research*, 99(11):1185–1194. https://doi.org/10.3139/146.101752

Kang, Y, Lee, J and Morita, K, 2014. Thermal conductivity of molten slags: a review of measurement techniques and discussion based on microstructural analysis, *ISIJ International*, 54(9):2008–2016.

Kang, Y and Morita, K, 2006. Thermal Conductivity of the CaO–Al2O3–SiO2 System, *ISIJ International*, 46(3):420–426. https://doi.org/10.2355/isijinternational.46.420

Mills, K C, Yuan, Y, Li, Z, Zhang, G H and Chou, K C, 2012. A Review of the Factors Affecting the Thermophysical Properties of Silicate Slags, *High Temperature Materials and Processes*, 31(4–5):301–321. https://doi.org/10.1515/htmp-2012–0097

Mills, K, Yuan, L and Jones, R, 2011. Estimating the physical properties of slags, *Journal of the Southern African Institute of Mining and Metallurgy*, 111(10):649–658.

Plimpton, S, 1995. Fast Parallel Algorithms for Short-Range Molecular Dynamics, *Journal of Computational Physics,* 117(1):1–19.

Tang, K, van der Eijk, C, Gouttebroze, S, Du, Q, Safarian, J and Tranell, G, 2022. Rheological properties of Al2O3–CaO–SiO2 slags, *CALPHAD*, 77:102421. https://doi.org/10.1016/j.calphad.2022.102421

Tang, X, You, J, Wang, J, Zhang, F, Gong, X, Xie, Y, Canizarès, A, Bessada, C, Tang, K and Lu, L, 2023. Quantitative studies on the microstructure of ternary CaO–Al2O3–SiO2 glasses by Raman spectroscopy, 27Al MAS NMR and quantum chemistry ab initio calculation, *Ceramics International*, 49(22):34397–34408. https://doi.org/10.1016/j.ceramint.2023.07.150

Tibshirani, R, 1996. Regression shrinkage and selection via the lasso, *Journal of the Royal Statistical Society Series B*: *Statistical Methodology*, 58(1):267–288.

Wang, Q, Wang, D, Li, Q and Zhang, J, 2019. Relationship between Microstructure and Thermal Conductivity in Coal Slags with Variable Silica and Alumina, *Energy and Fuels*, 33(7):6226–6233. https://doi.org/10.1021/acs.energyfuels.9b01090

Wang, Q, Zhang, J, Liu, J, Wu, W, Qi, X and Deng, H, 2020. Thermal conduction mechanism based on microstructural transformations of molten slag: The role of calcium oxide, *International Journal of Heat and Mass Transfer*, 160:120167. https://doi.org/10.1016/j.ijheatmasstransfer.2020.120167

On the development of a viscosity model for molten multicomponent slag systems with several glass-forming, amphoteric and modifier oxides

DOI: 10.62053/TWUQ4893

G M Zhomin[1], A S Arkhipin[2] and A Kondratiev[3]

1. BSc Scholar, Faculty of Materials Science, Lomonosov Moscow State University, Moscow 119991, Russia. Email: georgy.zhomin@gmail.com
2. PhD Scholar, Laboratory of Chemical Thermodynamics, Department of Physical Chemistry, Faculty of Chemistry, Lomonosov Moscow State University, Moscow 119991, Russia. Email: arkhipinmsu@gmail.com
3. Leading Researcher, Laboratory of Chemical Thermodynamics, Department of Physical Chemistry, Faculty of Chemistry, Lomonosov Moscow State University, Moscow 119991, Russia. Email: al.v.kondratiev@gmail.com

ABSTRACT

Viscosity of multicomponent slags is one of the crucial physicochemical properties for many industrial processes and technologies. While the viscosity-temperature relationship of completely molten slags can well be described by an Arrhenian-type law, the compositional dependence of viscosity is still not fully understood, especially in compositional regions with the lack of experimental data (eg at the glass-former concentration of 90 molar per cent or higher). In the present work major compositional relationships of the activation energy of viscous flow have been revised for numerous binary and ternary slag systems on the basis of experimental data collected and stored in the viscosity database OxiVis. For example, it has been found that the activation energy relevant to the polymerisation effect in binary systems of the MO-GFO type, where MO is the modifier oxide (ie monovalent K_2O, Na_2O, Li_2O and bivalent CaO, MgO, BaO, MnO, PbO etc) and GFO is the glass-forming oxide (SiO_2 or B_2O_3) is not always proportional to the third power of X_GFO (contrary to the Urbain formalism) and can vary significantly dependent on the slag system. Also, the activation energy of the charge compensation effect has been revised for ternary systems of the AO-MO-GFO and AO-MO type, where AO is the amphoteric oxide (Al_2O_3, Fe_2O_3 or other). A simple polynomial model has been proposed on the basis of the carried-out analysis for estimation of viscosities of multicomponent slag systems. The model has been optimised against the experimental viscosities in the selected binary, ternary, and higher-order oxide systems and has been shown reasonable agreement with the experimental data.

INTRODUCTION

Viscosity of molten oxide mixtures commonly known in industry as slags plays the critical role in many industrial and natural processes. The main problem with experimental determination of viscosity is a high melting point of various oxides (>1500°C) and extreme reactivity of oxides in the liquid state. Therefore, modelling of viscosity can be applied to avoid experimental difficulties.

A number of practical viscosity models have been developed over last 30–40 years to calculate viscosity of multicomponent oxide melts (eg Kondratiev, Jak and Hayes, 2002; Jung, Jak and Lehmann, 2014). Among others, structural viscosity models are based on the melt structure usually described by concentrations of various structural units (eg bridging and non-bridging oxygens, silica tetrahedra, the second nearest neighbour bonds etc). However, these models are complicated, often cannot be used without additional data and demonstrate good agreement mostly for multicomponent melts.

It is well known that, based on their effect on viscosity, all oxides can roughly be divided into three groups: glass-forming oxides (GFO), modifier oxides (MO) and amphoteric oxides (AO). Glass-forming oxide melts have much higher viscosity than the rest of oxide melts due to formation of interconnected, continuous structural network in the molten state. This continuous structural network is sometimes referred to as the ‘fully polymerised melt’. Modifiers usually break (or ‘depolymerise’) that continuous network into fragments and thereby lower the melt viscosity.

Amphoteric oxides can either break the network or form a quasi-network structure depending on the other melt components.

One of the less complicated, polynomial models based on the above idea is the so called Urbain formalism (Urbain *et al*, 1981), in which the Weymann-Frenkel equation (Equation 1) is used for the viscosity-temperature dependence, and the compositional dependence of the parameter *B* in the ternary Al_2O_3-CaO-SiO_2 system is expressed as the polynomial (Equation 2) of the molar fraction of SiO_2 and the ratio of Al_2O_3 and CaO:

$$\log \eta = \log A + \log T + \frac{B}{T}, \tag{1}$$

$$B = \sum_{i=0}^{3} \sum_{j=0}^{2} b_{ij} \left(\frac{X_{Al_2O_3}}{X_{Al_2O_3} + X_{CaO}} \right)^j X_{SiO_2}^i. \tag{2}$$

The Urbain-type models (eg Kondratiev and Jak, 2001; Forsbacka *et al*, 2007) demonstrate good agreement for calculating viscosity of the systems with one GFO (SiO_2), one AO (Al_2O_3) and a number of divalent MOs (CaO, MgO, MnO etc). In the binary and ternary systems with monovalent modifiers (K_2O, Na_2O) this formalism is not generally capable to describe experimental data with a reasonable accuracy and other, more complex models have to be developed (eg Jak, 2009). To the authors' best knowledge the Urbain formalism has not been applied to the systems with two or more GFO. The major problem of development of phenomenological viscosity models is the experimental data, its existence, amount and quality.

In the present work the OxiVis viscosity database (Kondratiev, 2021) was used to extract and analyse experimental data for unary, binary and ternary systems. The OxiVis database is a big collection of the experimental viscosity data developed and maintained by one of the authors for 20 years (available on request, contact author A Kondratiev). It contains over 50 000 experimental points for over 9000 chemical compositions of 54 different oxides.

The main task considered in the present work is to construct a simplest possible polynomial model that is still capable to describe experimental data on viscosity of unaries, binaries and ternaries with a reasonable accuracy. Thus, some nonlinear viscosity effects other than polymerisation encountered in binary oxide systems, though be discussed, will not be taken into account during modelling. First, the available experimental data for binary systems will be analysed, and a polynomial model will be proposed for binary silicate, borate and other systems that takes into account different viscosity growth at the GFO concentrations approaching 1. Then additional terms will be proposed and discussed for the parameter B (Equations 1–2) in the ternary systems of the AO-MO-GFO type. Finally the model will be tested on high-order systems.

EXPERIMENTAL EVIDENCE ON THE PRESENCE OF LINEAR REGIONS IN BINARY SYSTEMS

Viscosity of binary systems, in which one component is a GFO, are generally characterised by the so-called polymerisation effect, which results in a rapid growth of viscosity by several orders of magnitude as the GFO concentration tends to 1. In terms of the activation energy (proportional to the parameter B in Equation 1) it results in an increase of the activation energy to the value that corresponds to the GFO parameter. In the Urbain formalism the polymerisation effect is expressed as the third power polynomial of the SiO_2 molar fraction (see Equation 2). However, the exact form of the effect is not well investigated for most of binaries, especially at higher GFO concentrations (see Kondratiev, 2021).

Analysis of the collected experimental data for binary silicates revealed the presence of a nearly linear region at the $\log \eta$ versus X_GFO dependence in each binary silicate system. The width of this region can expand from 0–0.3 to about 0.7–0.8 $X(SiO_2)$ and depends on a system. Figure 1 provides the experimental data for five silicate binary systems at constant temperatures against the molar fraction $X(SiO_2)$ (between 0 and 0.8) along with the linear fit for logarithm of viscosity. At $X(SiO_2) > 0.7$ a rapid growth of viscosity (the so-called polymerisation effect) usually takes place. At $X(SiO_2) < 0.3$ a similar, but less pronounced effect can be observed in systems like Al_2O_3-SiO_2 or PbO-SiO_2.

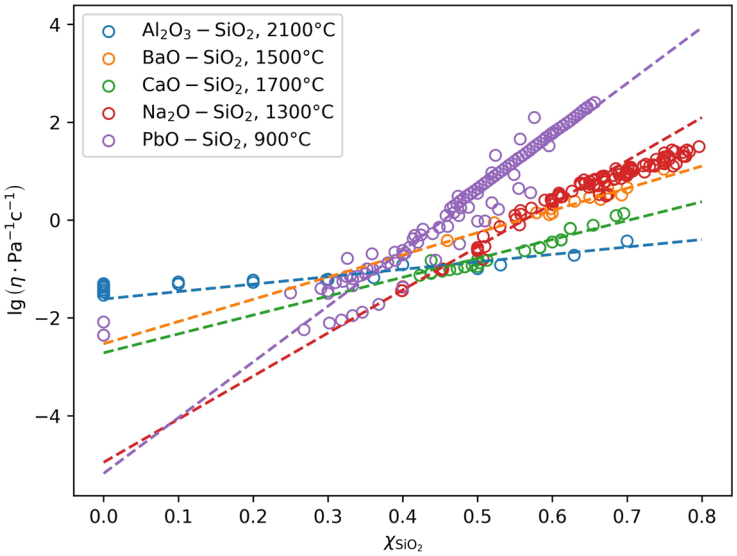

FIG 1 – The quasi-linear regions in the (Al_2O_3, BaO, CaO, Na_2O, PbO)-SiO_2.

Interpolation of the linear fit of the viscosity logarithm against X(SiO_2) was carried out for each system in selected silicate binaries (Al_2O_3-, BaO-, CaO-, K_2O-, MgO-, MnO-, Li_2O-, Na_2O- and PbO-SiO_2). The interpolation procedure was applied to all the experimental viscosity values at X(SiO_2) from 0.3 to 0.7, approximately and to all the temperatures above the melting point. Table 1 shows the linear fit coefficients (log*A* and *B*) obtained for each system and the root mean squared errors (RMSE) of the interpolation. Also the coefficient of determination (R^2) is included. It can be seen that the fit 'quality' ($R^2 > 0.8$, RMSE is low) is good for most of the systems, which implies that the quasi-linear regions exist at certain intervals of X(SiO_2) in silicate binaries. Also, it can be seen that the parameters of the linear fit are similar to each other: the parameter log*A* is negative for all systems and the parameter *B* is positive for all systems except for K_2O-SiO_2.

TABLE 1

Linear fit parameters and errors for selected silicate systems (Equation 1).

System	End-member	log(A/Pa*s)	10^3·B, kK	RMSE	R^2
Al_2O_3-SiO_2	Al_2O_3	-2.538	2.189	0.104	0.833
	SiO_2	-4.792	11.146		
BaO-SiO_2	BaO	-5.029	4.430	0.062	0.987
	SiO_2	-5.157	12.708		
CaO-SiO_2	CaO	-6.839	8.137	0.172	0.834
	SiO_2	-3.292	8.756		
K_2O-SiO_2	K_2O	-6.302	-0.896	0.172	0.973
	SiO_2	-5.540	17.028		
Li_2O-SiO_2	Li_2O	-5.775	3.065	0.103	0.969
	SiO_2	-3.227	9.411		
MgO-SiO_2	MgO	-2.801	0.524	0.101	0.987
	SiO_2	-6.454	15.189		
MnO-SiO_2	MnO	-6.601	6.812	0.118	0.811
	SiO_2	-0.110	2.925		
Na_2O-SiO_2	Na_2O	-6.923	3.100	0.153	0.983
	SiO_2	-3.319	11.289		
PbO-SiO_2	PbO	-8.468	3.857	0.293	0.921
	SiO_2	-1.606	9.175		

Figure 2 shows the 'log(Viscosity) versus 1/T' dependences of the pure SiO_2 obtained during interpolation for each silicate binary system. It can be seen that only two systems do not follow the mean trend: K_2O-SiO_2 and MnO-SiO_2. And PbO-SiO_2 is also slightly out at higher temperatures. A possible reason for deviation of the K_2O-SiO_2 and MnO-SiO_2 systems is the lack of experimental data at $X(SiO_2) < 0.5$ for K_2O-SiO_2 and at $X(SiO_2) > 0.5$ for MnO-SiO_2. The PbO-SiO_2 system can be characterised by a large scatter in the experimental data at $X(SiO_2)$ from 0 to 0.5. On the basis of the above analysis one set of parameters can be selected for the pure SiO_2 end (shown in Figure 2 as the mean line).

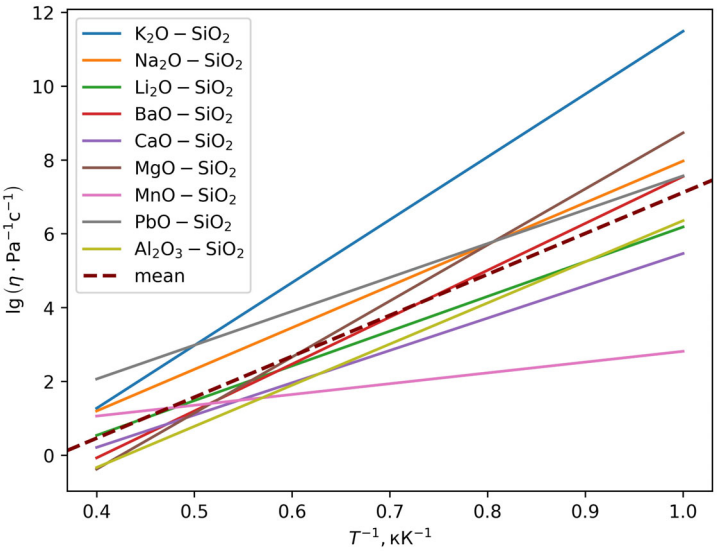

FIG 2 – Viscosity of pure SiO_2 obtained from each system optimisation.

Among all binaries molten silicates are by far the most investigated systems due to their significance for industry and geology. Binary borates, germanates and phosphates are less investigated, although these systems may also be important for glass-making industry or nuclear waste vitrification. Nevertheless, a lot of silicate systems are investigated only in a narrow compositional range (eg the CaO-SiO_2 viscosities are measured only in the range $0.4 \leq X(SiO_2) \leq 0.7$), at relatively low melting temperatures (Kondratiev, 2021). In the present study a number of binary silicate and borate systems will be analysed as well as few other GFO-containing systems.

MODEL CONSIDERATIONS

In the present study the classical Arrhenius equation (in a logarithmic format) is used to describe the temperature dependence of viscosity of molten oxide systems:

$$\log \eta = \log A + \frac{B}{T}, \tag{3}$$

where the parameters *A* and *B* depend on chemical composition. The *B* parameter is linked to the activation energy of viscous flow.

Parameters of Equation (3) can easily be calculated for those pure oxides, for which the experimental data is available. For the rest of pure oxides it is possible to use estimations from various viscosity models or molecular dynamics simulations (Kondratiev *et al*, in press).

The compositional dependence of viscosity in a binary system consists of two parts (called 'ideal' and 'excess' by the analogy to thermodynamics):

$$\log \eta = \log \eta^{id} + \log \eta^{ex} \tag{4}$$

$$\log \eta^{id} = X_1 \log \eta_1^{id} + X_2 \log \eta_2^{id} = X_1 \log A_1^{id} + X_2 \log A_2^{id} + \frac{X_1 B_1^{id} + X_2 B_2^{id}}{T} \tag{5}$$

$$\log \eta^{ex} = X_1^{\alpha_1} \log \frac{A_1^0}{A_1^{id}} + X_2^{\alpha_2} \log \frac{A_2^0}{A_2^{id}} + \frac{X_1^{\alpha_1}(B_1^0 - B_1^{id}) + X_2^{\alpha_2}(B_2^0 - B_2^{id})}{T} \tag{6}$$

Consequently, the following dependence can be written for the parameter *B* in a binary system MO-GFO:

$$B = B_1^{id}X_1 + B_2^{id}X_2 + \left(B_1^0 - B_1^{id}\right)X_1^{\alpha_1} + \left(B_2^0 - B_2^{id}\right)X_2^{\alpha_2}, \quad (7)$$

where indices 1 and 2 refer to the first and second components of a binary system, B^{id} describes the linear part of the experimental data and B^0 are the pure oxide values.

One of relatively well investigated binary systems without GFO is Al_2O_3-CaO, in which viscosity as a function of composition has a maximum approximately at Al_2O_3/CaO = 1. This non-monotonous behaviour is due to formation of quasi-tetrahedra $(AlCa_{0.5})O_4^{4-}$ that are linked together and generate a network similar to the silica tetrahedral network. This effect is usually referred to as the charge compensation effect in ternary systems, while it is not investigated in similar binary systems such as Al_2O_3-K_2O or Al_2O_3-Na_2O.

As mentioned, viscosity in the ternary systems of the AO-MO-GFO type is also characterised by the charge-compensation effect, when an amphoteric cation (eg Al^{3+}) coupled with a mono- or divalent modifier cation (eg Na^+) form additional quasi-network interlinked to the silica tetrahedral network, which results in an increase of viscosity. This effect is much more pronounced for monovalent cations (K^+, Na^+, Li^+), but also found in systems with divalent cations (eg Ca^{2+}, Mg^{2+}).

In a binary system AO-MO and a ternary system AO-MO-GFO the charge compensation term is proposed in the following form:

$$B \sim B^{ChC} \cdot \left(\frac{X_{AO}}{X_{AO}+X_{MO}}\right)^{\gamma_1} \cdot \left(\frac{X_{MO}}{X_{AO}+X_{MO}}\right)^{\gamma_2}, \quad (8)$$

where γ_1 and γ_2 are the adjustable parameters.

Thus, in the ternary system AO-MO-GFO, the parameter *B* (the Arrhenius activation energy reduced by the universal gas constant R) has the following general form:

$$B = B_{AO}^{id}X_{AO} + B_{MO}^{id}X_{MO} + B_{GFO}^{id}X_{GFO} + \left(B_{AO}^0 - B_{AO}^{id}\right)X_{AO}^{\alpha_{AO}} + \left(B_{MO}^0 - B_{MO}^{id}\right)X_{MO}^{\alpha_{MO}} + \left(B_{GFO}^0 - B_{GFO}^{id}\right)\left[\frac{X_{AO}}{X_{AO}+X_{MO}}X_{GFO}^{\beta_{AO}} + \frac{X_{MO}}{X_{AO}+X_{MO}}X_{GFO}^{\beta_{MO}}\right] + B_{AO\cdot MO}^{ChC}\left(\frac{X_{AO}}{X_{AO}+X_{MO}}\right)^{\gamma_{AO}}\left(\frac{X_{MO}}{X_{AO}+X_{MO}}\right)^{\gamma_{MO}}. \quad (9)$$

RESULTS AND DISCUSSION

Only a part of the results obtained for binaries and ternaries is presented and discussed here. Other results are still to be obtained and might be included into the conference presentation.

Viscosities of binary silicates

Tables 2 and 3 represent the model parameters for unary systems and binary silicate systems, respectively. Parameters for several pure oxides were taken from the review by Kondratiev *et al* (in press). In the present work the parameters of those pure oxides, for which no experimental data are available, were made equal to the corresponding linear parameters obtained as described above. Also, the α parameters for these oxides were not calculated, since it is not possible without experimental data. The 'ideal' SiO_2 parameters listed in Table 3 were calculated as the average for all systems from Table 1 except K_2O-SiO_2 and MnO-SiO_2.

TABLE 2

Model parameters for pure oxide melts.

	Al_2O_3	PbO	SiO_2	BaO	CaO	K_2O	Li_2O	MgO	MnO	Na_2O
log(A^0/Pa*s)	-3.20	-4.02	-7.73	-5.86	-6.18	-8.56	-4.31	-5.21	-3.73	-6.83
B^0 (kK)	4.13	2.30	28.54	5.24	5.85	7.49	0.06	4.53	0.74	4.50
Reference	Kondratiev *et al*, in press		This work							

TABLE 3

Model parameters for binary silicate melts obtained in this work.

System	Coefficients			
	$\log(A^{id}/Pa*s)$	B^{id} (kK)	α_1	α_2 (SiO_2)
SiO_2	-3.72	10.85	-	-
Al_2O_3-SiO_2	-3.07	1.63	3.46	11.46
BaO-SiO_2	-5.86	5.24	-	14.69
CaO-SiO_2	-6.18	5.85	-	12.00
K_2O-SiO_2	-8.56	7.49	-	67.98
Li_2O-SiO_2	-4.31	0.06	-	23.51
MgO-SiO_2	-5.21	4.53	-	12.00
MnO-SiO_2	-3.73	0.74	-	10.00
Na_2O-SiO_2	-6.83	4.50	-	45.26
PbO-SiO_2	-5.52	1.22	8.66	9.23

The parameter *B* in binary silicate systems is expressed by Equation (7) and the values of the parameters of Equation (7) can be found in Table 3. The polymerisation effect is introduced into the model simply as the difference between the pure oxide and linear ('ideal') *B* parameters multiplied by the SiO_2 concentration to a certain power (the α parameter). Figure 3 shows four examples of the compositional dependence of the parameter *B* (Equation (7)) for the CaO-SiO_2, Al_2O_3-SiO_2, Na_2O-SiO_2 and PbO-SiO_2 systems. Different symbols denote different temperatures (in °C). It can be seen that the polymerisation effect is more pronounced in the Na_2O-SiO_2 than in the Al_2O_3-SiO_2 or PbO-SiO_2 systems. The region that corresponds to the polymerisation effect in the CaO-SiO_2 is not investigated, so it is problematic to assume the exact form of the compositional dependence with increasing X(SiO_2). Therefore the parameter B was chosen arbitrarily from 10 to 15. For the PbO-SiO_2 system two structural effects can be observed: the polymerisation effect at higher SiO_2 and similar but less pronounced at lower SiO_2, with the quasi-linear region at intermediate SiO_2.

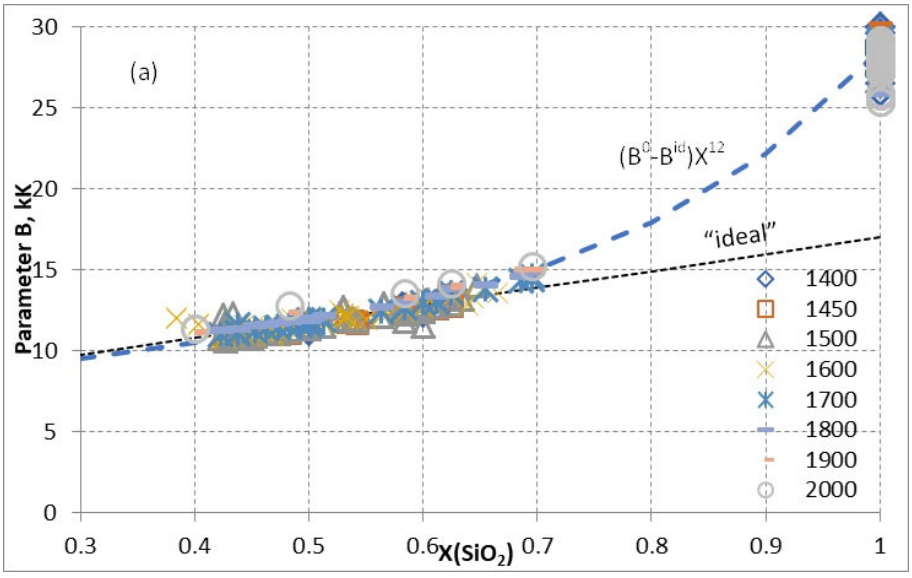

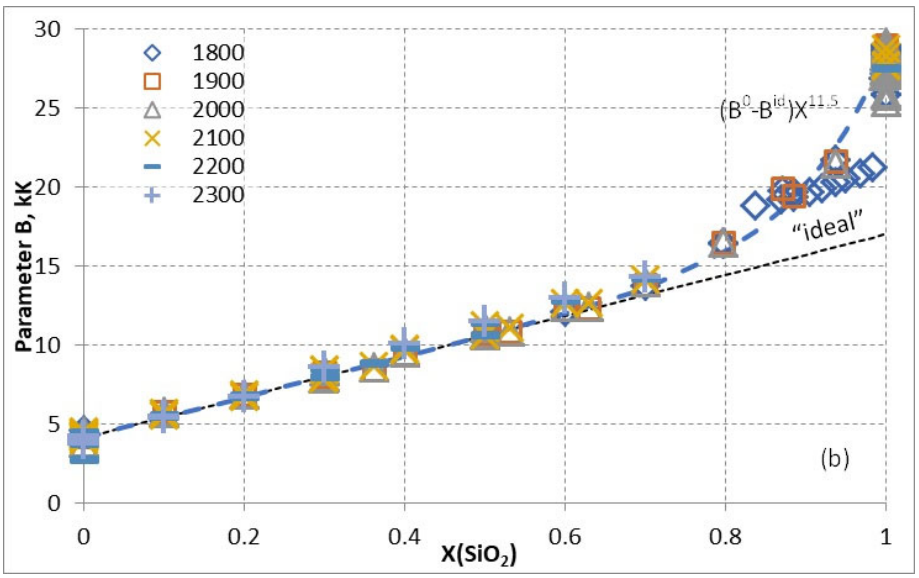

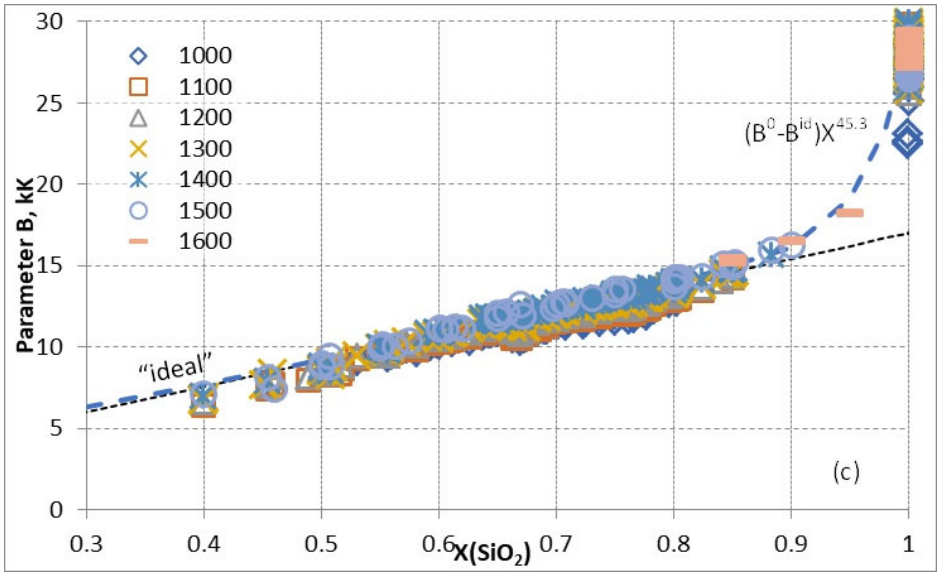

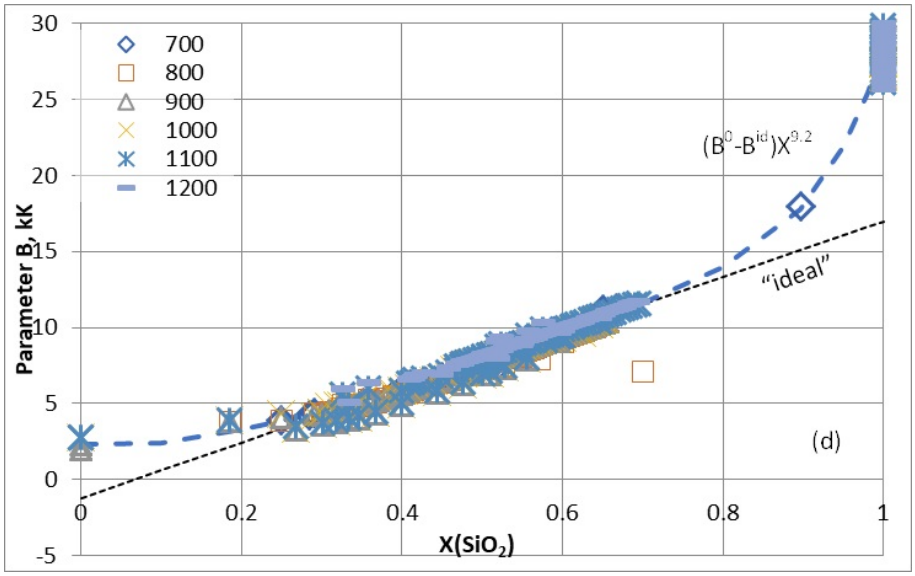

FIG 3 – The parameter *B* as a function of the SiO_2 molar fraction for: (a) CaO-SiO_2, (b) Al_2O_3-SiO_2, (c) Na_2O-SiO_2, (d) PbO-SiO_2.

This linear region at intermediate SiO_2 concentrations in binary silicate systems may be considered as the compositional region, in which no structural rearrangement takes place. Increasing SiO_2 leads to the polymerisation effect, while SiO_2 decreasing results in other, similar to polymerisation, effect of structural rearrangement. Both effects result in viscosity increasing. Polymerisation is a type of clustering, structural network formation. At the other end also some clustering occurs.

Figures 4–12 represent the experimental and calculated viscosities in the Al_2O_3-SiO_2, CaO-SIO_2, K_2O-SIO_2, Li_2O-SiO_2, MgO-SiO_2, MnO-SiO_2, Na_2O-SiO_2 and PbO-SiO_2 systems. It can be seen that the model describes the experimental data with a reasonable accuracy, although only two to three model parameters are used for each binary system.

Figures 4–12 demonstrate reasonably good agreement with the available experimental data. Perhaps, a poorest, but still reasonable agreement among all systems is shown in the Al_2O_3-SiO_2 system (Figure 4). This is mainly due to slightly lower values of the SiO_2 ideal parameters than for the Al_2O_3-SiO_2 system (see Table 1), and also because a low-temperature experimental data is described with a better agreement that the viscosity data at higher temperatures.

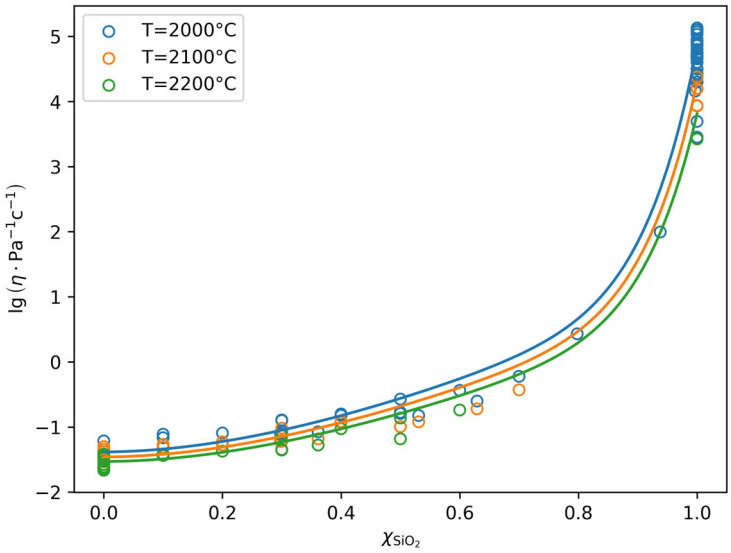

FIG 4 – Viscosities of the Al_2O_3-SiO_2 system.

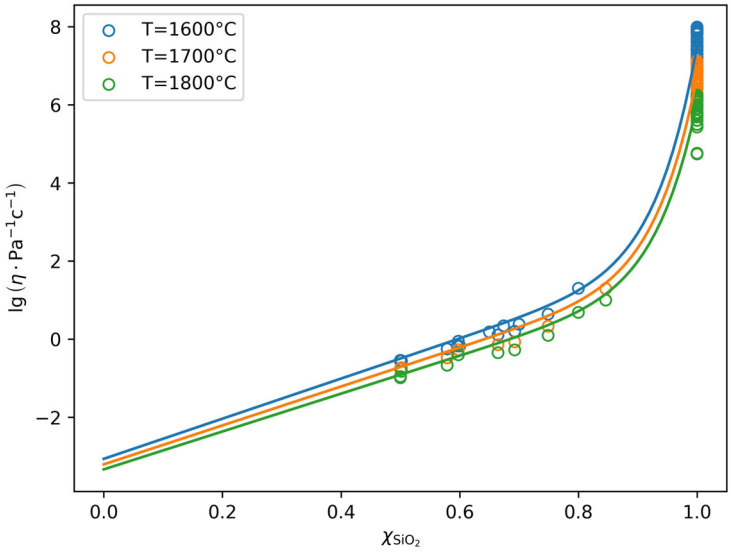

FIG 5 – Viscosities of the BaO-SiO_2 system.

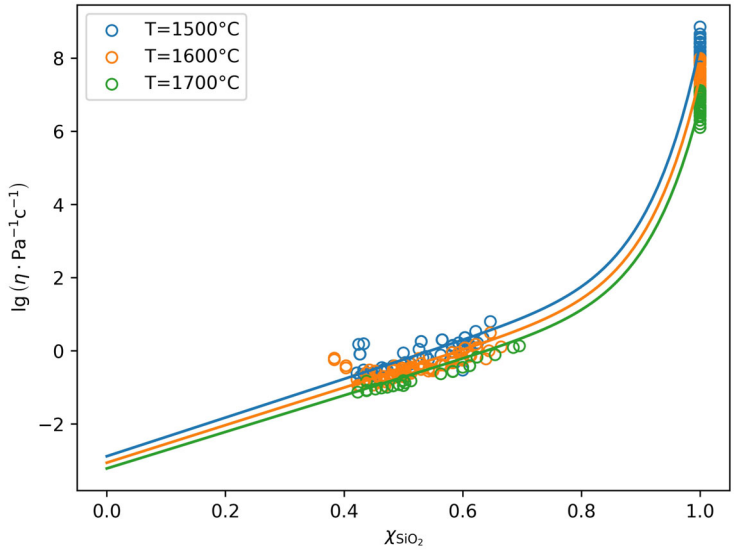

FIG 6 – Viscosities of the CaO-SiO_2 system.

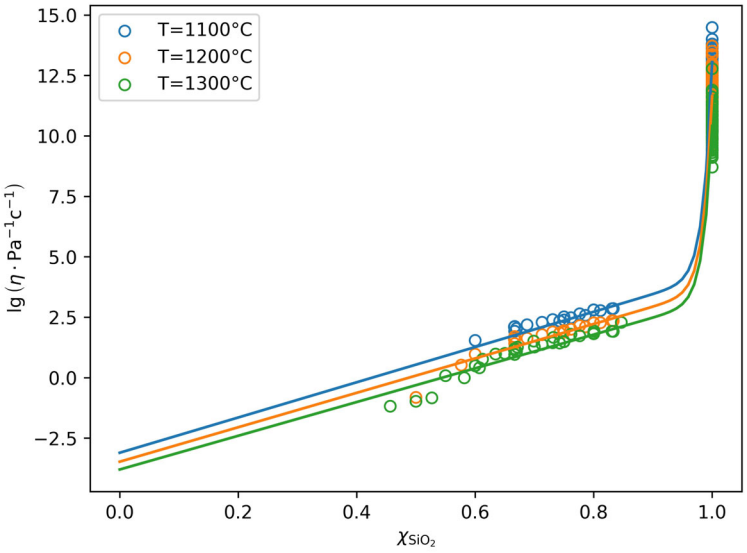

FIG 7 – Viscosities of the K_2O-SiO_2 system.

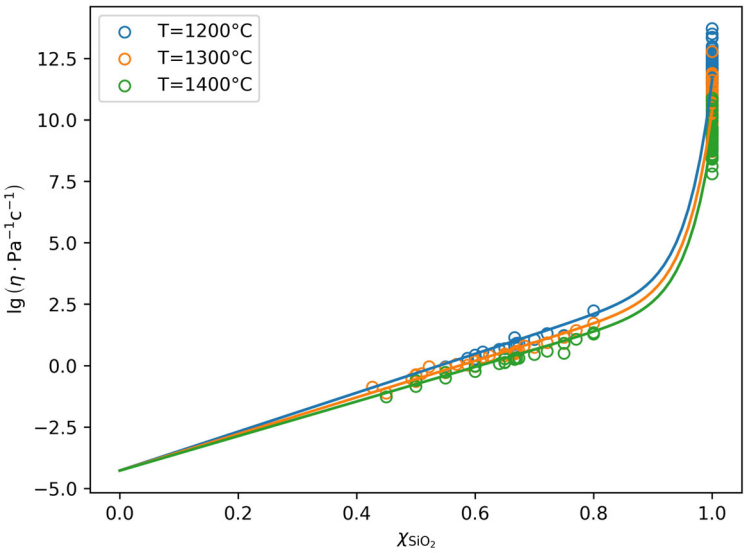

FIG 8 – Viscosities of the Li_2O-SiO_2 system.

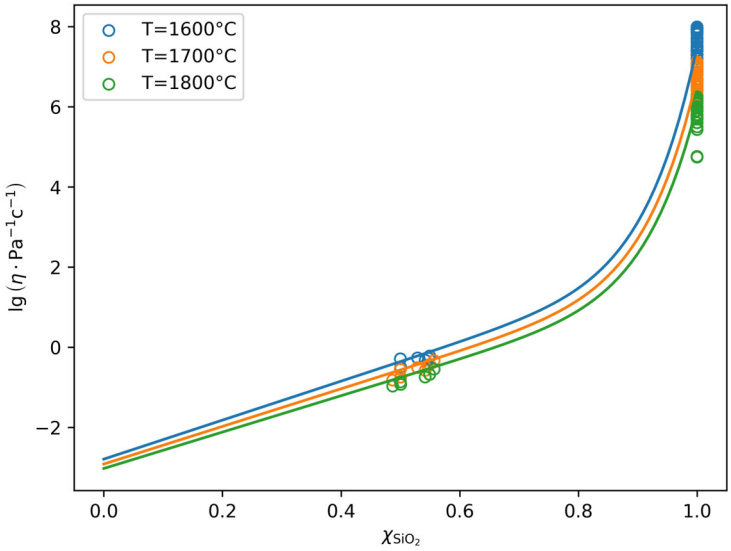

FIG 9 – Viscosities of the MgO-SiO_2 system.

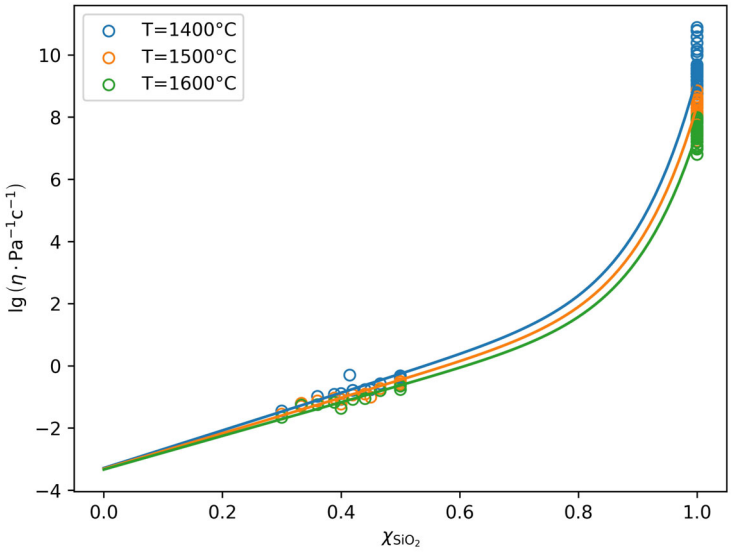

FIG 10 – Viscosities of the MnO-SiO_2 system.

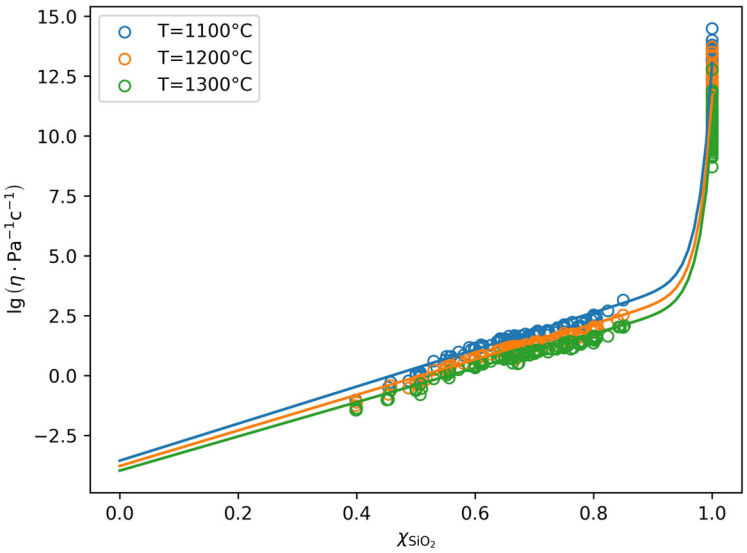

FIG 11 – Viscosities of the Na_2O-SiO_2 system.

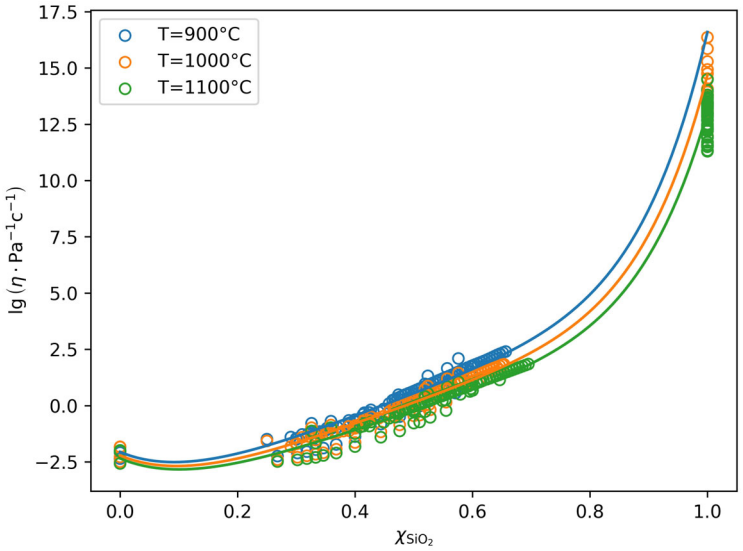

FIG 12 – Viscosities of the PbO-SiO_2 system.

Viscosities of binary borates and other binaries

Table 4 represents the model parameters for B_2O_3 and B_2O_3-SiO_2. The parameters for pure B_2O_3 are calculated using the experimental data at temperatures above the melting point and the Arrhenius Equation (1). The experimental data for borates are scarce and controversial, the only reliable data is found to be present in the B_2O_3-SiO_2 system. The B_2O_3 'ideal' parameters were optimised mainly on the basis of B_2O_3-SiO_2. The other end-member parameters for molten B_2O_3-BaO, B_2O_3-Na_2O, B_2O_3-PbO were taken from the corresponding silicates listed in Table 3.

TABLE 4

Model parameters for binary borate melts.

System	Coefficient					
	log(A^0/Pa*s)	**B^0 (kK)**	**log(A^{id}/Pa*s)**	**B^{id} (kK)**	**α_1**	**α_2**
B_2O_3	-2.14	3.96	-0.83	2.06	-	-
B_2O_3-SiO_2	-	-			4.64	4.61

Figures 13–15 represent the results of model calculation for two borate systems (B_2O_3-PbO and B_2O_3-Na_2O). Borate melts are less investigated and are characterised by larger experimental scatter than silicate melts. It can be seen that the model cannot describe complex compositional effects present in the borate binary systems. It should be mentioned that the model parameters for PbO and Na_2O (the linear part) were taken from the corresponding silicate binaries, while the model parameters for B_2O_3 were obtained on the basis of the B_2O_3-SiO_2 system.

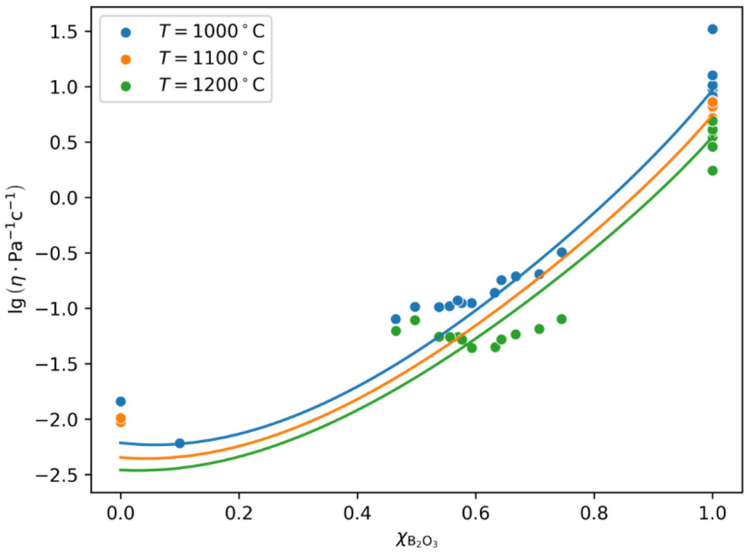

FIG 13 – Viscosities of the B_2O_3-PbO system.

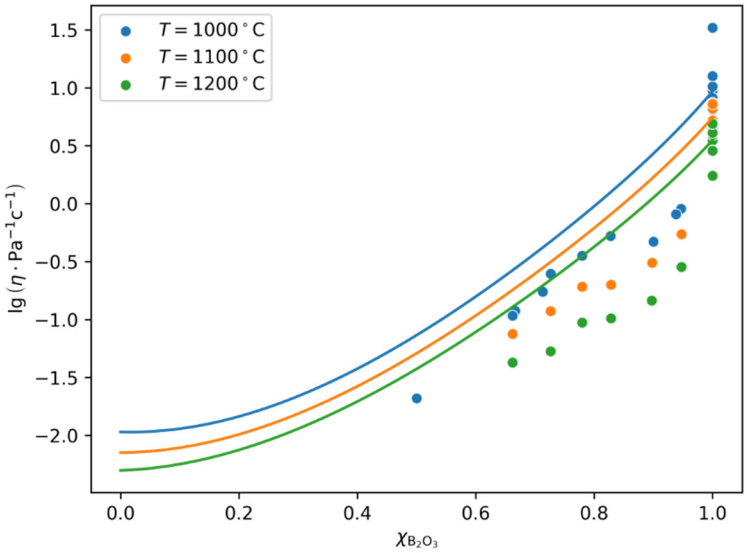

FIG 14 – Viscosities of the B_2O_3-Na_2O system.

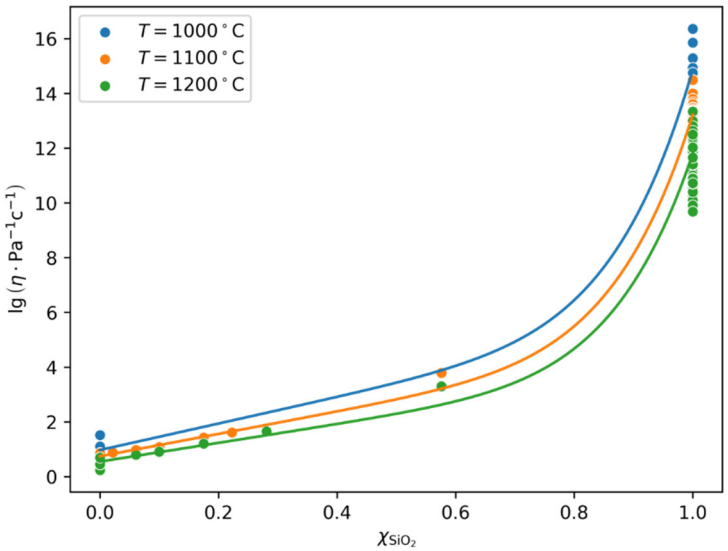

FIG 15 – Viscosities of the B_2O_3-SiO_2 system.

Viscosity of the B_2O_3-SiO_2 melt is shown in Figure 15. It can be seen that agreement between the experimental and calculated viscosities is reasonably well.

Viscosity of the Al_2O_3-CaO system is shown in Figure 16 as a function of the $Al_2O_3/(Al_2O_3+CaO)$ ratio. Parameters are listed in Table 5. The agreement between the experimental and calculated values is reasonable.

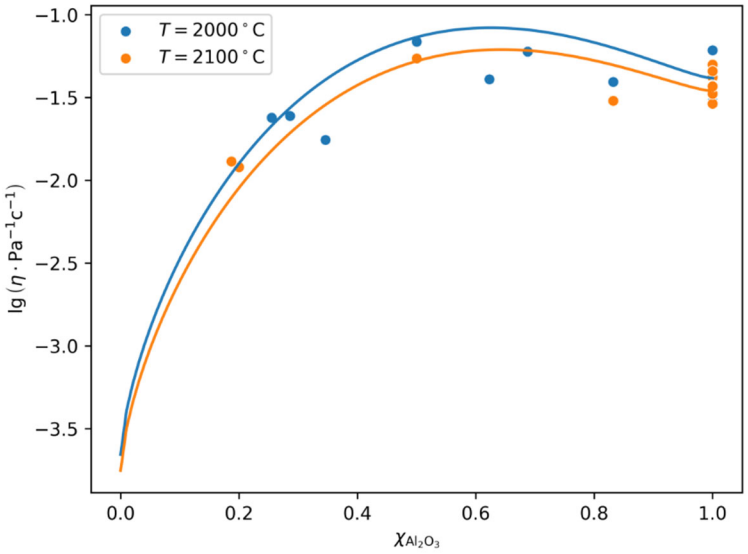

FIG 16 – Viscosities of the Al_2O_3-CaO system.

TABLE 5

The charge compensation model parameters for Al_2O_3-CaO and ternary oxide melts.

System	Coefficient		
	B^{ChC} (kK)	γ_1	γ_2
Al_2O_3-CaO	10.66	0.64	1.12
Al_2O_3-Na_2O-SiO_2	829.45	4.53	3.20
Al_2O_3-CaO-SiO_2	3.57	1	1

Viscosities of ternary systems

Table 5 provides the model parameters for the charge compensation term in one binary system, Al_2O_3-CaO, and two ternary systems, Al_2O_3-Na_2O-SiO_2 and Al_2O_3-CaO-SiO_2.

Viscosity of the Al_2O_3-Na_2O-SiO_2 is presented in Figure 17. The agreement between the calculated and experimental values is good.

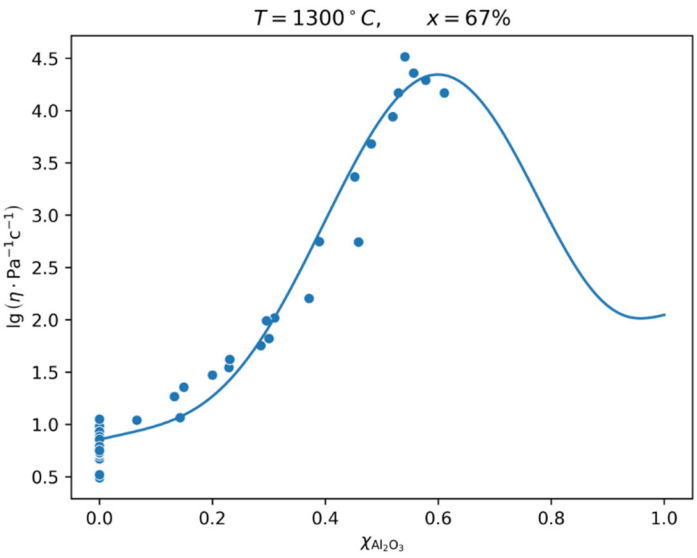

FIG 17 – Viscosities of the Al_2O_3-Na_2O-SiO_2 system at X(SiO_2)=0.67 and T=1300°C.

Experimental viscosities of Al_2O_3-CaO-SiO_2 are shown in Figure 18 with preliminary coefficients of the charge compensation term. It can be seen that agreement between calculated and experimental viscosities is reasonable.

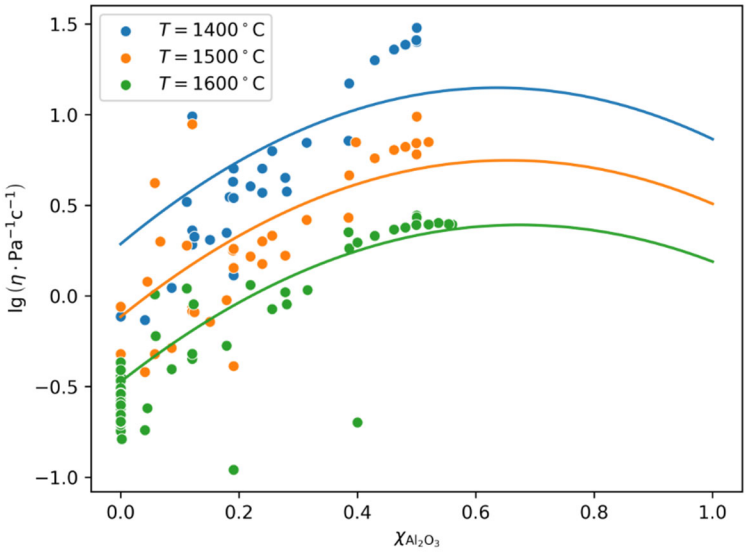

FIG 18 – Viscosities of the Al_2O_3-CaO-SIO_2 system at X(SiO_2)=0.5 and T=1400, 1500, 1600°C.

The experimental data and calculated viscosities for the other AO-MO-GFO systems (eg Al_2O_3-K_2O-SiO_2, Al_2O_3-Li_2O-SiO_2, Al_2O_3-MgO-SiO_2) might be added to the conference presentation.

CONCLUSIONS

The simple polynomial model is constructed on the basis of analysis of experimental data in binary silicate systems. The model introduces a linear compositional dependence and polymerisation effect for silicate systems. In ternary systems a charge compensation term is added to describe the experimental data.

A significant rise of viscosity with approaching pure SiO_2 (the so-called polymerisation effect) is described reasonably well in different binary silicate systems.

The presence of viscosity maximum in ternary systems of the AO-MO-GFO type (the charge compensation effect) is described reasonably well in two ternaries (Al_2O_3-Na_2O-SiO_2 and Al_2O_3-CaO-SiO_2) systems.

More complex viscosity effects (eg in binary borates) are not described. However, viscosity in the B_2O_3-SiO_2 system is described reasonably well.

ACKNOWLEDGEMENTS

This work was financially supported within the framework of the State Program ‘Chemical Thermodynamics and Theoretical Materials Science’ at the Lomonosov Moscow State University (N◦121031300039-1).

REFERENCES

Forsbacka, L, Holappa, L, Kondratiev, A and Jak, E, 2007. Experimental study and modelling of viscosity of chromium containing slags, *Steel Res Int*, 78:676–684.

Jak, E, 2009. Viscosity Model for Slags in the Al_2O_3-CaO-’FeO’-K2O-Na2O-MgO-SiO_2 System, in *Proceedings of the VIII International Conference on Molten Slags, Fluxes and Salts*, pp 433–448.

Jung, I-H, Jak, E and Lehmann, J, 2014. Slag Viscosity Model, in *Treatise on Process Metallurgy 2*, ch 5.2, pp 643–674.

Kondratiev, A and Jak, E, 2001. Predicting coal ash slag flow characteristics (viscosity model for the Al_2O_3-CaO-’FeO’-SiO_2 system), *Fuel*, 80:1989–2000.

Kondratiev, A, 2021. Experimental gaps (virtual), presented at 11th International Conference on Molten Slags, Fluxes and Salts 2020.

Kondratiev, A, Jak, E and Hayes, P C, 2002. Predicting slag viscosities in metallurgical systems, *JOM*, 54(11):41–45.

Kondratiev, A, Zinoveev, D, Bajenova, I, Arkhipin, A, Khvan, A, Uspenskaya, I and Ilyushechkin, A, in press. A review of viscosity data for unary oxide systems.

Urbain, G, Cambier, F, Deletter, M and Anseau, M R, 1981. Viscosity of silicate melts, *Trans J Br Ceram Soc*, 80:139–141.

Determining the properties of $CaO-Al_2O_3-SiO_2$ slags from molecular dynamics simulation

DOI: 10.62053/ZWPP8709
M Zhu[1] and J Safarian[2]

1. Postdoctoral Researcher, Norwegian University of Science and Technology (NTNU), Trondheim 7491, Norway. Email: mengyi.zhu@ntnu.no
2. Professor, Norwegian University of Science and Technology (NTNU), Trondheim 7491, Norway. Email: jafar.safarian@ntnu.no

ABSTRACT

Understanding the slag composition-structure-property relationship remains challenging due to the amorphous nature of slag melts and the difficulty of high-temperature experimental investigations. Since the $CaO-Al_2O_3-SiO_2$ slag system is maybe the most important slag system for various high-temperature metallurgical process, the present research employed high-throughput molecular dynamics (MD) simulations on the entire composition region of the $CaO-Al_2O_3-SiO_2$ slag system to determine physical properties like molar volume, density and diffusivity, structural properties such as distribution of different oxygen types for each simulated slag melt. The obtained slag properties result from the simulations displayed good consistency with experimental data, underscoring the reliability of the MD simulation as a novel tool to predict reasonable slag properties and to study slag behaviour from atomistic insight. The simulated results demonstrate a near-linear relationship between molar volume changes and composition, highlighting the predominant role of oxygen atoms, which is attributed to the significantly larger size of oxygen compared to other cations in the slag melts. This disparity in size leads to oxygen ions occupying most of the space in slags, thereby playing a major role in determining the overall molar volume. The simulation results of slag density revealed a decreasing trend with increased SiO_2 content and identified a local minimum at constant SiO_2 when Al_2O_3 content increases, also consistent with established slag density models. Furthermore, the simulated oxygen self-diffusion coefficients reveal a strong composition-structure-property relationship, where an increase in CaO content enhances slag diffusivity, while a minimum in diffusivity is observed near a CaO/Al_2O_3 ratio of unity. The diffusivity minimum also corresponding to the local viscosity maxima, indicating effective simulation of charge compensation effects and dynamic characteristics of slag melts. The simulated distribution of oxygen types in slag — bridging oxygen (BOs), non-bridging oxygen (NBOs), free oxygen (FOs) and tricluster oxygen (TOs) — reveals a composition-dependent pattern: BOs peak near $CaO/Al_2O_3 = 1$, NBOs and FOs are abundant in CaO-rich areas with NBOs peaking near the Ca_3SiO_5 composition, FOs in the CaO corner, and TOs predominantly in the Al_2O_3 corner, highlighting the complex interplay of network formers and modifiers for the charge compensation effects on the slag's structural properties. The successful application of MD simulations in this study paves the way for a powerful approach to explore the complex relationships in multicomponent slag systems and bridges the gap between mathematics modelling and experimental observations in high-temperature metallurgical processes.

INTRODUCTION

The emergence of the 'big data' era attracts widespread attention from metallurgical engineering industry and academia. However, it is notoriously challenging for metallurgists to obtain a complete materials database for multicomponent slag systems by way of experiments at high temperature. Nevertheless, in the past decades, considerable attention has been paid to metallurgical slag falling within the composition-property relations. It is now well-known that slag property is strongly dependent on its microscopic structure at atomistic level (Kondratiev, Jak and Hayes, 2002; Mills, Yuan and Jones, 2011; Min and Tsukihashi, 2017; Zhang, Chou and Mills, 2014). However, direct structure observation of slag melt remains an ongoing challenge due to the high temperature in metallurgical process. Therefore, introducing computational simulations to reveal and predict the slag composition-property relations is considerably urgent.

Molecular dynamics (MD) simulation has become an effective tool for predicting properties of multi-component glass and melts, facilitated by the development of high-quality and transferrable force

field for the multi-component systems (Bouhadja, Jakse and Pasturel, 2013; Cormack, Du and Zeitler, 2002; Guillot and Sator, 2007).

The CaO-Al_2O_3-SiO_2 slag system is renowned as the most crucial slag system in various high-temperature industrial processes. For instance, it is a key constituent in blast furnace slag, ladle slags and continuous casting mold fluxes. Additionally, the significance of the CaO-Al_2O_3-SiO_2 slag system extends to applications in metallurgical-grade Si refining. Its crucial role also evident in other fields such as glass science and geology, highlighting its fundamental importance. Moreover, its importance was also underscored in the recent developed novel SisAl process for silicon and alumina production (see <www.sisal-pilot.eu> for more details). In the SisAl process, aluminium is employed as the reducing agent for the aluminothermic reduction of a CaO-SiO_2 slag. This innovative approach leads to the production of CaO-Al_2O_3-(low) SiO_2 slag and a silicon alloy, both of which are subjected to further processing to produce various grades of silicon and alumina.

Therefore, it is vital to gain a comprehensive understanding of the system, especially by determining its properties and obtaining structural information across the entire composition range. In fact, due to the lack of an electron in trivalent Al cations to stabilise the Al-O tetrahedron configuration, the known charge compensation phenomenon widely occurs in the Al_2O_3-bearing slag system. This also results in a series of intriguing phenomena in systems containing Al_2O_3, such as the viscosity maxima near the CaO/Al_2O_3=1 composition line, the amphoteric behaviour of Al_2O_3, the formation of five-coordinated AlO_5 structural unit and three-coordinated tricluster oxygen. Consequently, this makes the study of the classic CaO-Al_2O_3-SiO_2 slag system is particularly important in academia. Thus, in the present work, high-throughput MD simulations were performed on the CaO-Al_2O_3-SiO_2 slag system to obtain the respective high temperature properties and structural information to further explore the composition-structure-property relationship.

METHODS

High-throughput MD simulations were performed by using the LAMMPS package (Plimpton, 1995). Totally 231 slags were simulated with 5 mol per cent increment of each component, evenly spanning the CaO-Al_2O_3-SiO_2 ternary diagram. The Jakse force field was employed to simulate the entire ternary slag system, renowned for its capability to well describe the structural and dynamic properties of the ternary system in good agreement with experimental data and *ab initio* MD simulations (Bouhadja, Jakse and Pasturel, 2013). The force field consists of both long-range Coulombic interaction and short-range interactions and is written as follows:

$$u_{ij}(r_{ij}) = \frac{q_i q_j}{4\pi\epsilon_0 r_{ij}} + A_{ij} exp\left(-\frac{r_{ij}\sigma_{ij}}{\rho_{ij}}\right) - \frac{C_{ij}}{r_{ij}^6}$$

where:

$\{i,j\} \in \{Ca, Al, Si, O\}$, and *r* denotes the distance between atom *i* and *j*

ϵ_0 represents the permittivity of vacuum

q_i is the effective charge of atom *i*, with the effective atomic charges for Ca, Al, Si, O assigned as 1.2, 1.8, 2.4, and -1.2, respectively

A_{ij}, ρ_{ij}, σ_{ij}, and C_{ij} are empirical parameters used to describe the short-range interaction between specific atoms pairs through a repulsive exponential term and an attractive $1/r^6$ term.

All parameters, which are composition-independent and remain the same for all slag simulations within the entire composition range of the ternary system, are listed in Table 1.

For each slag simulation, approximately 4000 atoms were randomly distributed within a box subject to periodic boundary conditions. The melt-quench process (Bauchy, 2014) was applied to prepare the slag simulation samples, where the system was initially equilibrated at 4000 K for 200 ps relaxation time to form the initial amorphous configuration and then cooled down to 2073 K at a cooling rate of 2 K/ps in the isothermal-isobaric NPT (Constant Number of particles, Pressure and Temperature) ensemble. At 2073 K, the slag systems were further equilibrated in the NPT ensemble. This stage allowed the system to further adapt its volume according to the preset temperature and

pressure conditions. After reaching equilibrium, the volume fluctuations of the simulated system were collected and averaged for the calculation of molar volume and density.

TABLE 1

Two-body coefficients for the adopted potential (Bouhadja, Jakse and Pasturel, 2013).

Pair	$A_{ij}(eV)$	ρ_{ij}(Å)	σ_{ij}(Å)	$C_{ij}(eV$ Å$^6)$
O-O	0.0120	0.263	3.6430	85.0840
O-Si	0.0070	0.156	2.5419	46.2930
O-Al	0.0075	0.164	2.6067	35.5747
O-Ca	0.0077	0.178	2.9935	42.2556
Si-Si	0.0012	0.046	1.4408	25.1873
Si-Al	0.0025	0.057	1.5056	18.8116
Si-Ca	0.0027	0.063	1.8924	22.9907
Al-Al	0.0029	0.068	1.5704	14.0498
Al-Ca	0.0032	0.074	1.9572	17.1710
Ca-Ca	0.0035	0.080	2.3440	20.9856

For the calculation of slag dynamic properties like self-diffusion coefficient, it is critical that the volume remains constant to avoid deviation in the diffusivity calculation due to compression or expansion of the system. Additionally, the canonical ensemble, also known as the NVT (Constant Number of particles, Volume and Temperature) ensemble, regulates the temperature by controlling the velocities of atoms within the system, which may also impact the diffusivity simulation. Consequently, the NVT ensemble was employed as an intermediate stage for a smooth transition from the NPT ensemble to the final microcanonical (NVE) ensemble with constant volume and energy. Each stage of the simulation was conducted over a period of 200 ps during which the statistical average of system properties reached a steady state. Then, a final simulation run covering 1 ns was conducted in the NVE ensemble for the sampling of slag configurations and atom diffusivity calculation. It should also be noted that only the results for the composition points located inside the single liquid phase region according to the phase diagram at 2073 K were considered valid for analysis.

RESULTS AND DISCUSSIONS

Evaluation of slag properties simulation

In the MD simulation, the choice of the potential function is of great importance, as it directly influences the accuracy of the simulation results. Consequently, it is also essential to validate these results. The accuracy of adopted potential was firstly verified by comparing simulated and experimentally measured density values of 40wt%CaO-20wt%Al_2O_3-40wt%SiO_2 slag as seen in Figure 1. The selection of this slag composition is because the slag melt under this composition has a relatively large amount of experimental data available for comparison.

It is seen that density obtained from MD simulation shows a good agreement by comparing with measured data, respectively, Exp. 1 (Winterhager, Greiner and Kammel, 1966) and Exp. 2 (Courtial and Dingwell, 1995) and developed density models (Courtial and Dingwell, 1999; Mills, Yuan and Jones, 2011). Furthermore, Figure 1 also clearly demonstrates the significant advantage of using MD simulation to calculate the properties of the melt, which is the absence of high temperature limitations that often encountered in experimental measurement. The study range for physical properties can even be extrapolated to several thousand kelvins, which is extremely difficult to measure experimentally. Furthermore, MD simulations have demonstrated a very powerful ability to obtain reasonable data in a time-efficient and labour-saving manner.

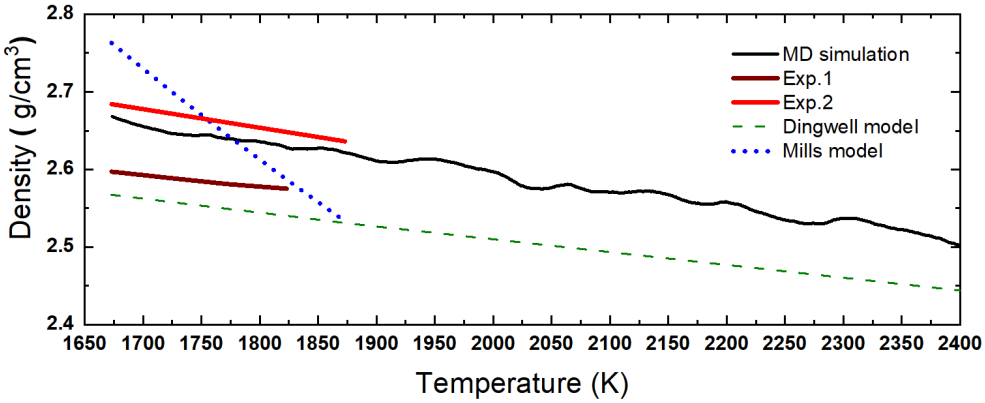

FIG 1 – Comparison of simulated and experimentally measured density of 40wt%CaO-20wt%Al_2O_3-40wt%SiO_2 slag system with varying temperature (Exp. 1 (Winterhager, Greiner and Kammel, 1966) and Exp. 2 (Courtial and Dingwell, 1995)).

Another important property for evaluation of the potential function in MD simulations is the accuracy of diffusivity simulations. We have also assessed the self-diffusion coefficients of all the ions in the slag system. The results are presented in Table 2 and Figure 2. It can be seen that the adopted potential can effectively reflect the diffusion behaviour of ions in slag melts.

TABLE 2

Comparison of simulated and measured self-diffusion coefficients of 40wt%CaO-20wt%Al_2O_3-40wt%SiO_2 under 1 atm.

Temperature [K]	D_{Ca} $\times 10^{-12}m^2s^{-1}$	D_{Al} $\times 10^{-12}m^2s^{-1}$	D_{Si} $\times 10^{-12}m^2s^{-1}$	DO $\times 10^{-12}m^2s^{-1}$
1673 K MD	65.5±3.0	8.1±0.6	4.2±0.5	7.25±0.7
1673 K Exp.	62, 68, 69[a]			
1723 K MD	106.6±3.5	15.0±3.1	7.4±1.8	12.2±2.9
1723 K Exp.	95, 100, 130[a]			
1773 K MD	153.6±11.4	21.8±2.5	11.3±0.3	18.3±0.6
1773 K Exp.	230±100[b]; 210[a]; 131.0±4.1[d]	67[c]	25[b]; 39.2±11.0[d]	38.0±6.8 [d]

NB: [a] from Goto, Sasabe and Kawakami (1977); [b] from Towers and Chipman (1957); [c] from Henderson, Yang and Derge (1961); [d] from Liang *et al* (1996).

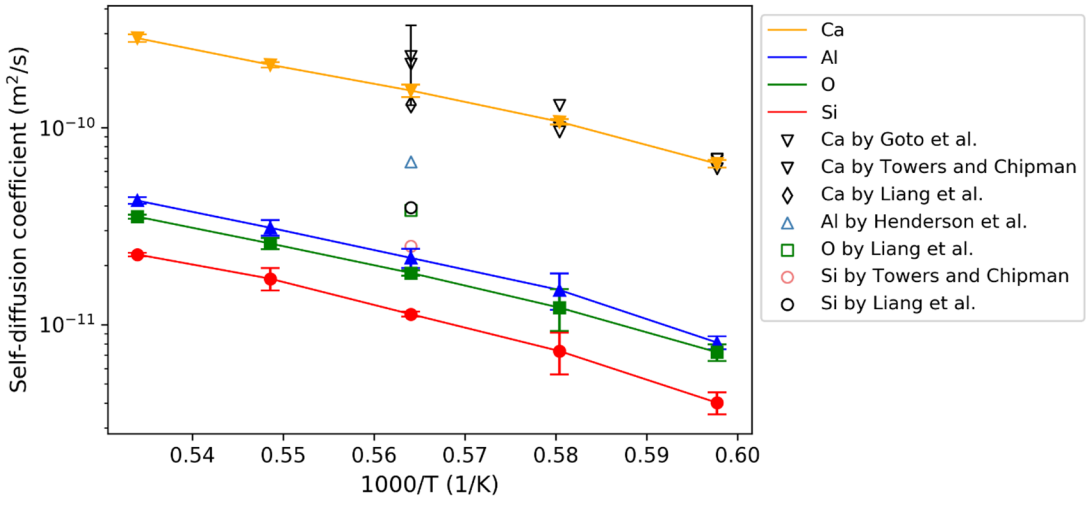

FIG 2 – Comparison of simulated and experimentally measured self-diffusion coefficients of 40wt%CaO-20wt%Al_2O_3-40wt%SiO_2 slag system with varying temperature.

From Table 2, it can be seen that the self-diffusion coefficient of Ca ions obtained from simulations falls within the range of experimental measurements by different researchers. Additionally, the self-diffusion coefficients of Al and Si ions are also close to experimental results, lying within the same order of magnitude. Furthermore, the diffusion capabilities of various ions in slag melts are also clearly observed with the trend: $D_{Ca} > D_{Al} > D_{Si}$. This is in agreement with experiments (Liang *et al*, 1996) and clearly demonstrates the structural characteristics of Ca as a network modifier and Al, Si as network formers, forming the complex tetrahedral networks. Furthermore, the linear relationship between the self-diffusion coefficient and the reciprocal of temperature also demonstrates the sensitivity of MD simulations to temperature, specially, the Arrhenius relationship between the self-diffusion coefficient and temperature.

Furthermore, the structure of the melt can be accurately described with changes in its composition. As illustrated in Figure 3, the basicity has a noticeable impact on the slag structure. In slags with high basicity, B=1.2 of 50wt%CaO-10wt%Al_2O_3-40wt%SiO_2, there are more depolymerised areas, and the network structure formed by network formers is mainly in simple chain forms. However, with the reduction of slag basicity, B=0.8 of 40wt%CaO-10wt%Al_2O_3-50wt%SiO_2, the melt structure becomes more complex, resulting in a higher number of complex polyhedral ring configurations.

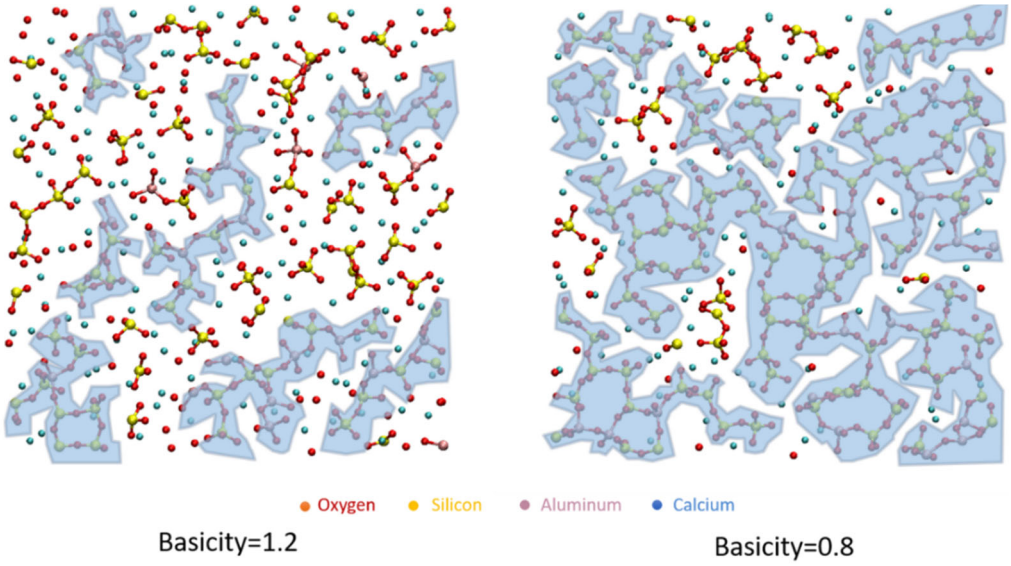

FIG 3 – Structural visualisation of depolymerised slag (left) and polymerised slag (right) with varying basicity (CaO/SiO_2 ratio).

High-throughput simulation results

The results of molar volume obtained through high-throughput MD simulations are shown in Figure 4. It can be observed that the molar volume changes of slag melts exhibit almost linear relationship with the composition. This indicates that the changes in the melt structure have a minor impact on the molar volume. In fact, this is because the radii of O^{2-}, which is about 1.40 Å, are much larger than those of other cations, such as Si^{4+}, which is only 0.40 Å, almost 3.5 times smaller. This means that the space occupied by one oxygen anion is about 40 times that of a Si^{4+} cation. In other words, although the ball-stick model is often used to describe the structure of slag melts, in fact, nearly 90 per cent of the space in slag melts is occupied by oxygen anions. As for the cations, they are more like fillers in the gaps between the oxygen anions. Therefore, we can see that the primary influencing factor of molar volume is the number of oxygen atoms, particularly the content of Al_2O_3, because 1 mol of alumina provides 3 mol of oxygen anions. Additionally, an empirical rule can also be proposed: the contribution of 2 mol per cent SiO_2 to the molar volume is equivalent to the sum of 1 mol per cent CaO and 1 mol per cent Al_2O_3 due to the oxygen atomic stoichiometric coefficients are identical. Certainly, it's undeniable that due to the non-ideality of the melt structure, deviations from the near-linear relationship can occur in regions with strong structural interactions. For instance, the presence of tricluster oxygen in areas with low SiO_2 and low CaO content can lead to a molar volume that is smaller than the ideal scenario. However, it can be ascertained that the most significant contribution to the molar volume comes from the oxygen ions, which are not only the most

abundant ion but also occupy the largest volume in the melt. This explains why numerous models for calculating slag molar volume are effective when they employ a simple linear additive function based on the partial molar volumes of individual slag components.

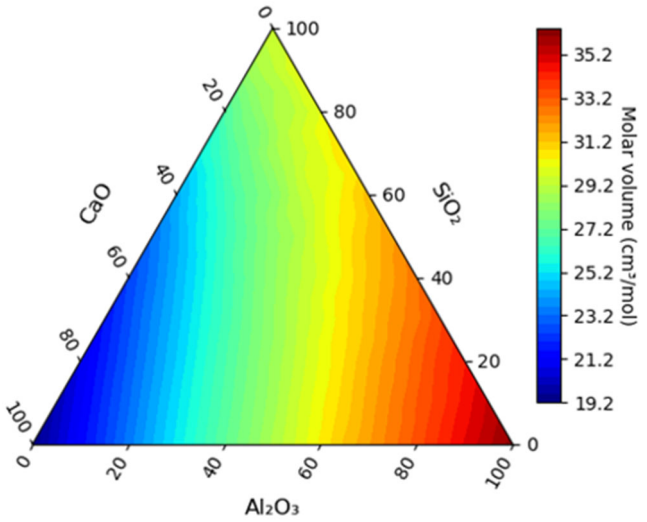

FIG 4 – Simulated molar volume values of CaO-Al_2O_3-SiO_2 slag system at 2073 K. Note that the region outside liquid slag area corresponds to the amorphous state.

Figure 5 shows the simulation results of slag density for the CaO-Al_2O_3-SiO_2 system. The calculation of density is obtained by dividing the molar mass of the slag melt by its molar volume. A clear trend can be seen that slag density decreases with increasing SiO_2 content. In addition, at constant SiO_2 content, slag density exhibits a minimum with increasing Al_2O_3 content. This trend in density variation is also consistent with the reported slag density model (Xin *et al*, 2017). The observed minimum in density at compositions with maximum charge compensation reflects the complex effects of charge compensation on the network structure; although Ca^{2+} ions bond closely with Al-tetrahedra to form more stable structural units, this interaction also facilitates the formation of a more complex spatial network structure, resulting in an acceleratingly increased molar volume and results in a decreased density. As the content of Al_2O_3 increases to the peraluminous area where Al_2O_3>CaO, Ca^{2+} becomes insufficient for charge compensation, leading to the formation of smaller and denser network, which consequently raises the density. The slag density local minimum phenomenon becomes more pronounced with the reduction in SiO_2 content and is particularly evident in the CaO-Al_2O_3 binary system where the charge compensation effect is the most intensive.

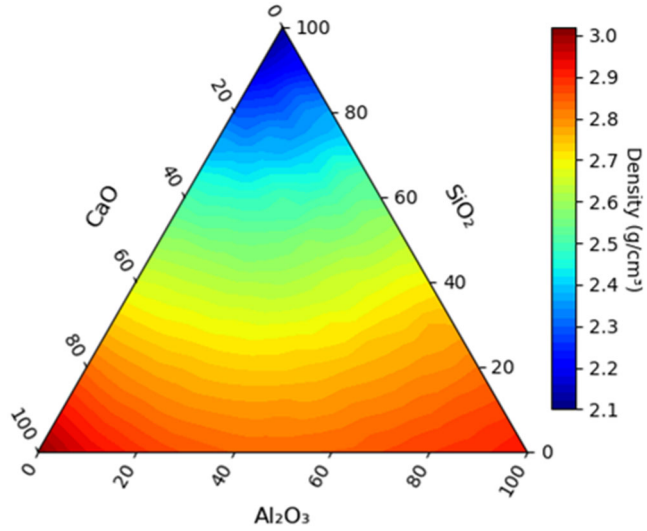

FIG 5 – Simulated density values of CaO-Al_2O_3-SiO_2 slag system at 2073 K. Note that the region outside liquid slag area corresponds to the amorphous state.

Figure 6 shows the results of obtained oxygen self-diffusion coefficients. A strong composition-structure-property relation can also be seen. No matter whether with constant SiO_2 or Al_2O_3 content, the network de-polymerisation caused by an increase in CaO content leads to a higher slag diffusivity and also, a lower viscosity. Therefore, it can be observed that near the Ca-rich corner, oxygen diffusivity becomes higher, which also reflects a lower viscosity at high basicity region. However, with constant SiO_2 content, it can be seen that with the increase in Al_2O_3 content, oxygen diffusivity initially decreases and then increases, indicating the presence of a diffusivity minimum. This also aligns with the maxima in slag viscosity obtained in experiments (Matsushita, Hayashi and Seetharaman, 2005). Moreover, it can be seen that this diffusivity minima occurs near the composition line of CaO/Al_2O_3=1, which clearly suggests that the potential function used in this work is capable of effectively simulating the occurrence of charge compensation effects and reflects the dynamic characteristics of the slag melt.

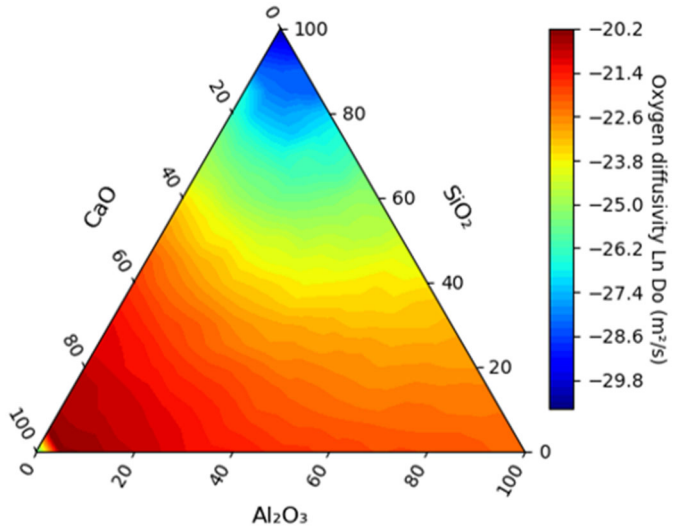

FIG 6 – Simulated oxygen self-diffusion coefficient values of CaO-Al_2O_3-SiO_2 slag system at 2073 K. Note that the region outside liquid slag area corresponds to the amorphous state.

It is known that the slag structure could be described as a 3D amorphous network topology composed by a number of [SiO_4] and [AlO_4] tetrahedral units which connect with each other through bridging oxygen (BO). Other cations behave as a network breaker to depolymerise the chains and to create non-bridging oxygen (NBO). The rest parts oxygen atoms are known as free oxygen (FO) and the tricluster oxygen (TO) where one oxygen is coordinated with three network formers. In this work, we have also obtained the distribution of various types of oxygen, as shown in Figure 7.

It can be observed that the distribution of these four types of oxygen shows sensitivity to the slag composition. For BOs, their local maxima appear near the compositional line of CaO/Al_2O_3=1, fully reflecting the impact of charge compensation effects on the melt structure. Under the fully charge compensation, the melt structure is the most polymerised and also corresponding to the occurrence of the maximum viscosity. For NBOs and FOs, they are more enriched in the CaO corner, as this area contains more Ca^{2+} acting as a network modifier. Additionally, it can be seen that the peak region for NBOs appears around CaO/SiO_2 = 3, which corresponds to the binary compound Ca_3SiO_5, the closest binary compound to CaO in the CaO-SiO_2 system. As for the distribution of TOs, it is also evident that they are predominantly concentrated in the Al_2O_3 corner due to the lack of Ca cation charge compensation.

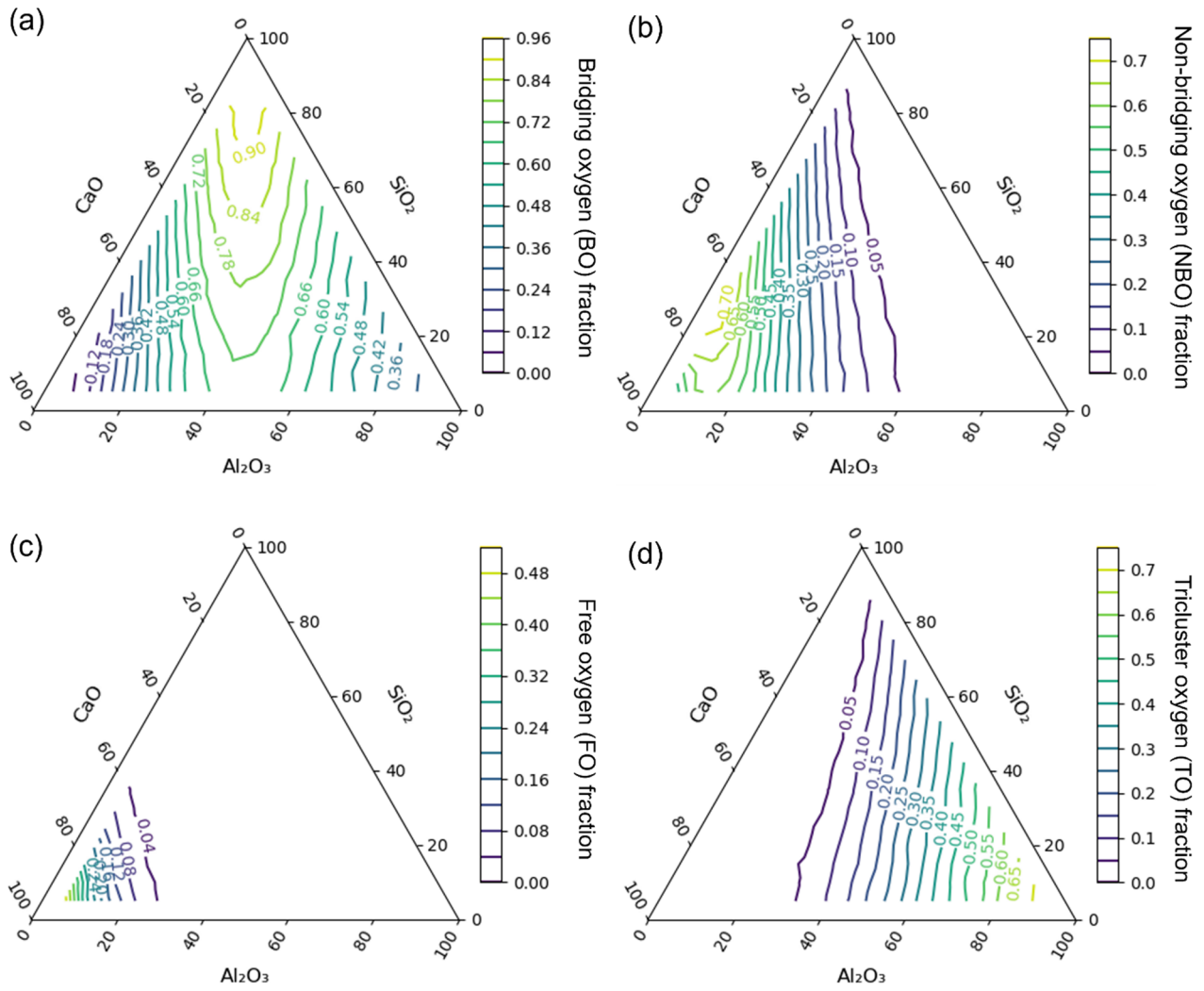

FIG 7 – Distribution of simulated oxygen types in the CaO-Al_2O_3-SiO_2 slag system at 2073 K: (a) BO, (b) NBO, (c) FO, (d) TO. Note that the region outside liquid slag area corresponds to the amorphous state.

CONCLUSIONS

In the present work, high-throughput MD simulations were performed on the CaO-Al_2O_3-SiO_2 system to obtain high temperature properties and decipher the composition-structure-property relationship. The simulated density and diffusivity show a good agreement with experimental results and demonstrate the promising feature of MD simulations for the slag database development. The distribution of different oxygen types further illuminated the structural characteristics of the slag, showcasing the critical role of Ca as a network modifier and charge compensator, Si and Al as network formers. This study not only provide a wealth of slag properties data on the CaO-Al_2O_3-SiO_2 ternary system, but also highlights the effectiveness of MD simulations in bridging the gap between theoretical predictions and experimental observations in high-temperature metallurgical processes.

ACKNOWLEDGEMENTS

The research leading to these results has been performed within the SisAl Pilot project (<www.sisal-pilot.eu/> [Accessed: 1 May 2023]) and received funding from the European Community's Horizon 2020 Programme (H2020/2014-2020) under grant agreement No 869268. Simulations were performed with computing resources granted by RWTH Aachen University under project p0200350.

REFERENCES

Bauchy, M, 2014. Structural, vibrational and elastic properties of a calcium aluminosilicate glass from molecular dynamics simulations: The role of the potential, *Journal of Chemical Physics*, https://doi.org/10.1063/1.4886421

Bouhadja, M, Jakse, N and Pasturel, A, 2013. Structural and dynamic properties of calcium aluminosilicate melts: A molecular dynamics study, *Journal of Chemical Physics*, 138(22):224510. https://doi.org/10.1063/1.4809523

Cormack, A N, Du, J and Zeitler, T R, 2002. Alkali ion migration mechanisms in silicate glasses probed by molecular dynamics simulations, *Physical Chemistry Chemical Physics*, 4(14):3193–3197. https://doi.org/10.1039/B201721K

Courtial, P and Dingwell, D B, 1995. Nonlinear composition dependence of molar volume of melts in the CaO-Al203-SiOz system, *Geochimica et Cosmochimica Acta*, 59(18).

Courtial, P and Dingwell, D B, 1999. Densities of melts in the CaO-MgO-Al2O3-SiO2 system, *American Mineralogist*, 84(4):465–476. https://doi.org/10.2138/AM-1999-0401

Goto, K S, Sasabe, M and Kawakami, M, 1977. Relation between Tracer Diffusivity and Electrical Conductivity on Multi-component Oxide Slags at 900° to 1600°C, *Transactions ISIJ,* 17:212–214.

Guillot, B and Sator, N, 2007. A computer simulation study of natural silicate melts, Part I: Low pressure properties, *Geochimica et Cosmochimica Acta*, 71(5):1249–1265. https://doi.org/10.1016/J.GCA.2006.11.015

Henderson, J, Yang, L and Derge, G, 1961. Self-diffusion of aluminium in CaO-SiO2-Al2O3 Melts, *Transactions of the Metallurgical Society of AIME*, 221:56–60.

Kondratiev, A, Jak, E and Hayes, P C, 2002. Predicting slag viscosities in metallurgical systems, *JOM*, 54(11):41–45. https://doi.org/10.1007/BF02709749

Liang, Y, Richter, F M, Davis, A M and Watson, E B, 1996. Diffusion in silicate melts: I, Self diffusion in CaO-AI2O3-SiO2 at 1500°C and 1 GPa, *Geochimica et Cosmochimica Acta*, 60(22):4353–4367.

Matsushita, T, Hayashi, M and Seetharaman, S, 2005. Thermochemical and thermophysical property measurements in slag systems, *International Journal of Materials and Product Technology*, 22(4):351–390. https://doi.org/10.1504/IJMPT.2005.006464

Mills, K C, Yuan, L and Jones, R T, 2011. Estimating the physical properties of slags, *Journal of the Southern African Institute of Mining and Metallurgy*, 111(March):6–9.

Min, D J and Tsukihashi, F, 2017. Recent advances in understanding physical properties of metallurgical slags, *Metals and Materials International*, 23:1:23(1):1–19. https://doi.org/10.1007/S12540-017-6750-5

Plimpton, S, 1995. Fast Parallel Algorithms for Short-Range Molecular Dynamics, *Journal of Computational Physics*, 117(1):1–19. https://doi.org/10.1006/JCPH.1995.1039

Towers, H and Chipman, J, 1957. Diffusion of Calcium and Silicon in a Lime-Alumina-Silica Slag, *JOM*, 9(6):769–773. https://doi.org/10.1007/BF03377932

Winterhager, H, Greiner, H L and Kammel, R, 1966. Investigations of the Density and Electrical Conductivity of Melts in the System CaO-Al2O3-SiO2 and CaO-MgO-Al2O3-SiO2, vol 23 (Westdeutscher Verlag: Cologne).

Xin, J, Gan, L, Jiao, L and Lai, C, 2017. Accurate density calculation for molten slags in SiO2-Al2O3-CaO-MgO systems, *ISIJ International*, 57(8):1340–1349. https://doi.org/10.2355/isijinternational.ISIJINT-2017-070

Zhang, G H, Chou, K C and Mills, K, 2014. A structurally based viscosity model for oxide melts, *Metallurgical and Materials Transactions B: Process Metallurgy and Materials Processing Science*, 45(2):698–706. https://doi.org/10.1007/S11663-013-9980-Z

Mathematical descriptions of – Process simulations

Process modelling and high-throughput thermochemical calculations using ChemApp for Python

DOI: 10.62053/JNQW7969
Ö K Büyükuslu[1], F Tang[1], M Baben[1] and S Petersen[2]

1. GTT-Technologies, 52134 Herzogenrath, Germany.
2. GTT-Technologies, 52134 Herzogenrath, Germany. Email: sp@gtt-technologies.de

ABSTRACT

GTT-Technologies' ChemApp for Python was developed to provide a powerful, easy to use interface to ChemApp for a programming language highly popular with scientists and engineers. It is used, for instance, by GTT to develop program modules such as the CALPHAD Optimiser for the FactSage™ software, by customers to move from interactive FactSage calculations to perform versatile scripting with Python, and by GTT and its partners in research projects in the area of materials informatics.

Computational thermochemistry is fundamental for advancing sustainable metallurgy and creating new alloy compositions for engineering applications. Materials informatics involves handling vast amounts of data and complex workflows.

GTT's approach uses ChemApp for Python and the FactSage thermodynamic databases to design recyclable alloys from the start, incorporating a higher percentage of scraps while aiming to simplify the workflows to simulate material design steps. Challenges arise due to recycling scraps, introducing more elements for consideration. CALPHAD-based databases accurately cover materials from primary metallurgy, but additional data for minority and critical elements is crucial for precise computational modelling.

GTT combines machine learning-based ab-initio databases with traditional CALPHAD databases to cover the complete chemical space with appropriate accuracy. The design of a hardfacing alloy through a high-throughput materials informatics approach is used as a demonstrator of the current possibilities.

INTRODUCTION

ChemApp is a thermochemical software library which enables the user to perform thermochemical calculations across a wide spectrum of applications by providing a programmable interface to perform complex equilibrium calculation techniques for multicomponent, multiphase chemical systems. It is based on Gunnar Eriksson's SOLGASMIX code, which was further developed into ChemSage (Eriksson and Hack, 1990), and became a widely used program for the calculation of complex chemical equilibria.

Since 1996, ChemApp has been available as a product and is not only used as a module for custom program development in research and industry, but also as an add-on to third-party software (Petersen and Hack, 2007). The wide range of application areas is supported by the amount of thermochemical data available for ChemApp. In particular, all thermochemical data accessible through FactSage (Bale *et al*, 2016) can be used with ChemApp by exporting a subset of the data for a particular chemical system from one or more databases to a data-file.

Initially, ChemApp was used primarily with programming languages such as FORTRAN, C/C++, Basic, and Object Pascal/Delphi. In the last years however, Python became more and more a programming language of choice for scientists and engineers, especially for scripting and prototyping tasks. It was thus decided to develop an interface to ChemApp in the form of a Python package to make ChemApp accessible to a larger group of users and applications.

CHEMAPP FOR PYTHON

Design goals

ChemApp for Python provides several augmentations and additional components that allow for ease of use and increased productivity. Special care was taken to help new users getting started with the

packages, without taking away from the accessibility of the raw API to the calculation core, which, due to the potential intricate nature of the calculations to perform, is also frequently used. Therefore, the package contains a *basic* module, which provides a direct link to the ChemApp subroutines, very similar to the well-established C/C++ and Fortran interfaces.

An addition to ChemApp for Python is the *friendly* module, which is exclusive to ChemApp for Python. It strives to simplify the process of setting up and running calculations, making it accessible to users with all levels of expertise.

Furthermore, a set of helper functions and classes are part of ChemApp for Python that allow for collaboration and combination with various typical components of the Python ecosystem, such as pymatgen (Ong *et al*, 2013), for instance by providing a compatible class for managing and manipulating chemical compositions.

Additionally, a technical necessity shapes a number of decisions regarding the implementation of ChemApp for Python. Since the ChemApp calculation kernel is very strictly procedural, it is unfeasible to keep state in a manner like how Python usually does, by reference-counting of objects and shallow copying. Therefore, an abstraction of result objects is introduced, which bridges the conceptual differences sufficiently well.

For most applications, including the high-throughput calculations introduced in this study, Python is not used for its performance, but rather for its flexibility of use. Nonetheless, performance is a critical feature of every software, and in a way a matter of sustainability, too. Therefore, ChemApp for Python strives to be as thin of a layer as possible, which, especially given the discrepancies in software architecture, is a challenging task.

Implementation details

The underlying ChemApp library is designed with the so-called TQ-Interface, for which all separate dimensions of a thermochemical system loaded from a data-file have to be addressed using an internal index. These indexes exist for phases, system components (which in most cases are the elements of the thermochemical system), but also phase constituents, which are generally phase model-specific countable entities such as species in a gas phase, or certain stoichiometric compositions for which individual modelling data exists.

The problem space is typically defined by several degrees of freedom that are determined by the dimensionality of the thermochemical system, eg the number of linearly independent system components, and the number of boundary conditions determined by the Gibbs phase rule.

Despite having its advantages, the set-up of calculations using indexes can be improved to increase user-friendliness. ChemApp for Python thus implements an interface that allows for the use of names of phases, system components, and phase constituents, thus increasing maintainability of the code significantly. Furthermore, some of the TQ-Interface functions use string literals. These have all been encapsulated into Python enumeration types, which allow for their type-checking by modern ‘linters’, which help to prevent coding errors by highlighting semantic and stylistic problems in the source code. As of the management of errors, failure modes of the ChemApp calculations are properly encapsulated into Python exceptions to allow for typical pythonic try-except idioms.

Despite these improvements, the procedural architecture of the ChemApp library and its inability to communicate the internal calculation state continuously are a big problem when trying to produce recreatable results. This means that the calculation path to a solution may be different depending on previous results and calculations, which can be helpful if calculations are similar and therefore the ‘proximity’ can be used as an advantage. However, it can be also detrimental to performance if, for instance, a randomised input parameter space is employed, for which the final conditions of a calculation are very dissimilar. It is computationally impossible to infer which of those cases is more likely to occur for a given calculational sequence without a deep understanding of the specific calculations.

ChemApp for Python in its entirety is written in Cython (Behnel *et al*, 2011), resulting in an elegant and efficient wrapping of the ChemApp library, as well as a statically compiled, performance-enhanced, fully C-compiled Python package.

In the design of ChemApp for Python, the developers tried to achieve a balance between the addition of 'verbose' commands that are close to natural language, and descriptions which are brief and clear. One example is the group of user-friendly class functions to retrieve specific results (Figure 1).

```
# set the amount of O2 in the gas phase of stream #2 to 'A'
casc.set_IA_pc("#2", "gas_ideal", "O2", A)

# calculate without printing results
casc.calculate_eq(print_results=False)

# get the amount for each phase constituent in the gas (as list)
amount_of_pcs_in_gas = casc.get_eq_A_pcs_in_ph("GAS")

# set the status of SLIQ phase as ENTERED
cats.set_status_ph("SLIQ#1", Status.ENTERED)
```

FIG 1 – Example calls for functions that ChemApp for Python provides. Notice that a few abbreviations are being used. These are used throughout the package, making the developer experience fully consistent. The 'caec' and 'casc' objects are abbreviated class names, with their full names being ChemApp.EquilibriumCalculation and ChemApp.StreamCalculation, respectively.

Having a consistent and concise, but at the same time clear way to retrieve result values was a main goal of the development.

Within the scope of this type of application, the efficiency of high-throughput computations is significantly enhanced by adopting a 'fail early' approach, which can be quickly implemented in Python. The 'brute force' of using nested iterations on certain compositions has to be organised in a way so that the most significant criteria can be evaluated first, and in case of failing validation, the nested iterations can be skipped. In Figure 2, an abbreviated example approach highlights how this approach removes a (potentially large) chunk of compositions that are known to fail the criteria later.

```
def critical_cost_reached(B, Mo, Ti):
    # this assumes a global dictionary 'cost' exists with the cost of each
    # element. The value 30 is arbitrarily chosen
    return cost[B] + cost[Mo] + cost[Ti] >= 30

for B in B_range:
    for Mo in Mo_range:
        for Ti in Ti_range:
            # when cost for B, Mo, Ti reaches a certain threshold, skip
            # the rest of the loop because it's going to be too expensive
            if critical_cost_reached(B, Mo, Ti):
                # skip the rest of the loop
                continue
            # otherwise, continue to sample the rest alloying elements
            for Cr in Cr_range:
                ...
```

FIG 2 – Slightly modified example of an early failing iteration of the calculation scheme, where injecting an additional condition early to omit certain iterations increases overall performance.

ChemApp calculations can produce vast amounts of reasonably informative data, but it is crucially important to be able to navigate these results. Therefore, a balance must be found between stored and discarded results. As some of the results aren't simple to recover without redoing a calculation,

a satisfactory amount of data needs to be stored to validate against all criteria. Typically, when using ChemApp for Python, a Python object that collects all obtainable results can be generated after each calculation. However, depending on the size of the thermochemical system (eg number of system components and phases), this object can reach sizes of a few megabytes per calculation relatively easily, which affects performance and agility of any further analysis. If enough consideration of later-applied criteria can be carried out beforehand, it may be more reasonable to only fetch those required results and omit the generation of the full object. The caveat for that strategy is obviously a loss of possible further evaluations that would require more information. As many strategies of data warehousing in industrial processes prioritise to keep as much data as possible, simply storing all result objects may be more feasible, and ChemApp for Python provides routines to serialise into common database compatible formats to address this need.

LEVERAGING THE PYTHON ECOSYSTEM

A major advantage of using ChemApp for Python for process modelling is the strength of the Python ecosystem that allows for easy data transformations. An example of such a strong incorporation of established data pipelines and the ease of inputting and outputting into adequate formats and plots is illustrated for a simple LD converter process, which can be modelled in a short amount of time. The code for this example can be found online (GitHub, Inc., 2024).

In this example, a specific aspect of the LD converter process of a hot iron melt is illustrated, namely the removal of carbon from the liquid phase by oxygen blowing. In real processes, the composition of the liquid metal varies, with the appropriate amount of oxygen and the reaction enthalpy being the technically interesting results. In Figure 3, an easy way to interact with an externally provided table of input values is illustratively shown to indicate the low threshold that is needed to combine external data sources with ChemApp for Python. Noteworthy is that the *friendly* interface performs all necessary conversions and datatype management issues internally.

```
import pandas as pd

# content of the hotmetal.csv file:
# > ID,mass,T,Fe,C,Si,Mn,P,S
# > 0,97.09,1306.1,94.88,4.01,0.54,0.43,0.109,0.019
# > 1,99.12,1361.6,94.71,4.28,0.51,0.39,0.096,0.02
#  ...

# read the input data from a CSV file
input_data = pd.read_csv("hotmetal.csv").set_index("ID")

for ID, composition in input_data.iterrows():
    total_mass, T, Fe, C, Si, Mn, P, S = composition
    casc.set_IA_pc("#1", "Fe_bcc(s)", "Fe_bcc(s)", Fe)
    casc.set_IA_pc("#1", "C_Graphite(s)", "C_Graphite(s)", C)
    casc.set_IA_pc("#1", "Si_solid(s)", "Si_solid(s)", Si)
```

FIG 3 – A simple way to include external data sources into a Python script, and subsequently into a ChemApp calculation. The code is abbreviated and does not show a fully working example, but simply highlights the few lines of code it takes to import values from a csv file for use as parameters to ChemApp calls.

All calculations, but especially large-dimension calculations benefit a lot from easy exploratory plotting and interaction with reduced data. In Figure 4, a brief example is shown that again highlights the construction of specific data views from a CalculationResultObject and its properties.

```
# create a DataFrame with the columns:
# A, Amount Fe-liq, Carbon content, wt% C, dH
carbon_content_in_Fe_liq = pd.DataFrame(
    columns=["A", "Amount Fe-liq", "Carbon content", "wt% C",
"dH"]).set_index("A")
for ID in input_data.index:
   # iterate over the dictionary of calculated result objects
    for amount_O2, calc_res in converter_results[ID].items():
        # the total phase amount
        amount_feliq = calc_res.phs["Fe-liq"].A
        # the total enthalpy change
        dH = calc_res.dH
        # the phase constituent amount
        amount_c = calc_res.phs["Fe-liq"].scs["C"].A
        # calculate carbon content
        wp_c = amount_c / amount_feliq * 100
```

FIG 4 – Using pandas' DataFrames, a table is filled with data specific to a query of the stored results is generated by iterating over the results objects and excerpting the respective values from the objects. The use of pandas' DataFrames allows for very convenient use of the data in subsequent processing pipelines, as they are a de facto standard for data analysis in Python.

HIGH-THROUGHPUT SCREENING USING CHEMAPP FOR PYTHON – A WORKFLOW FOR THERMODYNAMICALLY-INFORMED DECISION-MAKING

High-throughput screening (HTS) is a powerful approach in materials science that facilitates the rapid evaluation of numerous material candidates under varying process conditions. Using ChemApp for Python, researchers can systematically explore a wide range of materials and process parameters to make informed decisions. The decision-making process follows a number of steps to narrow down the initial compositional space to a reduced number of candidates for a more thorough examination. This approach is demonstrated below using a simplified example of a high-temperature alloy selection process in the Fe-Cr-Co metallic system.

Step 1 – Collect data

The first step in HTS involves gathering comprehensive data on the materials of interest and their associated process conditions. This data collection includes identifying the state-of-the-art materials and the specific conditions under which these materials will be processed. Key factors to consider are the chemical composition, phase stability, and potential reactions of the materials under certain conditions.

> ***Example:*** *The alloy system Fe-Cr-Co exhibits the sigma phase over a large composition range. The sigma phase is known to cause embrittlement at high temperatures and is not desired.*

Step 2 – Analyse

Once the data is collected, the next step is to translate the requirements for the material and the process into computable criteria. This involves defining the thermodynamic properties and constraints that are critical for the application. For instance, desired properties such as phase stability, reaction enthalpies, and Gibbs free energy changes are converted into specific criteria that can be analysed computationally.

> ***Example:*** *The compositional space for the Fe-Cr-Co system is generated based on the literature/plant data as shown in Table 1. The equilibrium calculations will be performed for a temperature of 800°C at ambient pressure. The activity of the sigma*

phase will be stored in a results database for each composition to assess the stability of the embrittling phase.

TABLE 1

Composition space for the Fe-Cr-Co system. 'Stepsize' represents the resolution of the calculations and corresponds to the increment of system component amounts from minimum to maximum (in wt per cent).

System component	Min (wt%)	Max (wt%)	Stepsize (wt%)
Fe	10	80	balance
Cr	20	80	2
Co	10	70	1

Step 3 – Calculate

With the criteria defined, the next step is to perform the thermochemical calculations using ChemApp for Python. This involves setting up and executing a series of equilibrium calculations to generate the necessary thermochemical results. ChemApp for Python allows for the automation of these calculations, enabling the efficient handling of a large number of scenarios. The results from these calculations, including equilibrium compositions, phase distributions, and thermodynamic properties, are stored for further analysis.

Example: *ChemApp for Python code snippet. The composition space is generated and fixed conditions are set (1). The incoming amount for each system component is defined (2) and the equilibrium for each composition is calculated (3) within a nested loop. The activities of the sigma phase are stored in a results dataframe (4). In case the equilibrium cannot be calculated, the exception handler is triggered (5).*

```
# Set fixed conditions (1)
Co_range = np.arange(10, 71, 1)
Cr_range = np.arange(20, 81, 2)
caec.set_eq_T(800)  # °C
caec.set_eq_P(1)  # bar
for Co in Co_range:
    for Cr in Cr_range:
        Fe = 100 - Co - Cr
        if Fe <= 80 and Fe >= 10:
            # Set chemical formula incoming amounts. (2)
            caec.set_IA_cfs(["Fe", "Co", "Cr"], [Fe, Co, Cr])
            try:
                # Calculate equilibrium (3)
                caec.calculate_eq()
                activity_sigma = caec.get_eq_AC_ph("SIGMA")
                # Assume the results are stored in a
                # dataframe with the composition as index (4)
                results_df.loc[Fe, Co, Cr] = activity_sigma
                print(f"composition {composition_ID} is calculated")
                        # Handle error (5)
            except ChemAppError:
                print("Equilibrium cannot be calculated!")
                results_df.loc[Fe, Co, Cr] = "None"
```

FIG 5 – High-throughput screening of alloy candidates using ChemApp for Python. The code snippet illustrates the procedure for setting conditions, calculating the equilibrium, and retrieving results.

Step 4 – Filter and select

The final step in the HTS workflow is to filter and select the most promising material candidates based on the predefined criteria. This involves comparing the calculated results against the desired properties and constraints. Candidates that meet the criteria are shortlisted for further experimental validation or a more detailed study. This step ensures that only the most viable materials, which satisfy all necessary thermodynamic requirements, are considered for further examination.

> ***Example:*** *Set a threshold for the activity of the sigma phase. The compositions that pass the criteria are stored in a new dataframe, which is subsequently used for a new set of calculations. Repeat the screening until all computable requirements are met based on the materials design and processing conditions.*

Input

```
threshold = 0.5
results_df_filtered = results_df[results_df["activity_sigma"] < threshold]
print(results_df_filtered)
print(
    f"""Out of {results_df.shape[0]}, {results_df_filtered.shape[0]}
    compositions have a sigma phase activity of less than {threshold}."""
)
```

FIG 6 – Postprocessing of equilibrium calculation results. The code snippet illustrates how the equilibrium calculation results are filtered to identify compositions where the sigma phase has an activity of less than 0.5. It then prints the filtered results and reports the number of compositions meeting the threshold criteria.

Output

```
                     activity_sigma
Fe_wt% Co_wt% Cr_wt%
21     59     20              0.497369
20     60     20              0.478664
19     61     20              0.461042
18     62     20              0.444460
17     63     20              0.428878
16     64     20              0.414260
15     65     20              0.400567
14     66     20              0.387766
13     67     20              0.375822
12     68     20              0.364705
11     69     20              0.354385
10     70     20              0.344834
```

FIG 7 – Output of results generated by the code snippet shown in the Figure 6.

By following the steps outlined above, researchers can make thermodynamically informed decisions that enhance the efficiency and effectiveness of material selection and process optimisation. Screening can be repeated to further refine the composition space of alloy candidates.

CASE SCENARIO – HARDFACING ALLOY DESIGN USING THERMOCHEMICAL SCREENING

In this example we introduce the design of a hardfacing alloy using a high-throughput 'materials informatics' approach. The objective is to identify successful compositions for an iron-based hardfacing alloy for mining and agricultural applications, which is also cheaper than a patented benchmark material. The project started with a sample space of 765 000 compositions based on a range of the benchmark alloy's reference composition space that involves 12 elements. As a result of the multi-step HTS process, 168 promising compositions were obtained.

The foundational step in the high-throughput approach involves the selection and integration of compatible thermochemical data within the chemical system of interest. FactSage provides a variety of databases which are particularly useful for various applications such as materials design, process metallurgy, and energy conversion. By combining CALPHAD (Calculation of Phase Diagrams) and ab-initio based thermochemical data for use with ChemApp calculations, users can address complex scenarios in material science, such as identifying critical elements in steel metallurgy, which require a comprehensive and accurate materials property database.

Following the selection of the appropriate thermochemical data, specifications must be clearly defined based on the intended application of the material. This corresponds to step 1 (see above), where data is collected for the calculations. Specifications can be material-, process- or cost-related based on the application case. A crucial step is the transformation of process specifications to thermodynamically computable criteria in order to generate a high-throughput calculation workflow (ie analyse the data and ensure that the specifications are met). For instance, the design of hardfacing alloys necessitates specific processes and properties such as austenitic solidification, martensitic transformation, and a narrow melting range. The melt range criterion is defined as the difference between the formation temperature of a first hard phase to solidify, and the liquidus temperature of a matrix phase. It is a fingerprint of the tendency for hot cracking during solidification. Additionally, it is vital to avoid conditions that result in the formation of phases such as carbides, borides, and intermetallics that can embrittle the alloy. Specific conditions also include physical properties such as low density and cost-effectiveness, which can be estimated using databases such as GTT's ab-initio Materials Project Database (aiMP). These specifications can serve as computable criteria for the subsequent material screening process.

The next phase involves navigating the chemical space to identify potential candidates that meet the defined specifications. ChemApp offers robust capabilities for exploring and manipulating chemical compositions. This allows researchers to rapidly scan through thousands of potential compounds to pinpoint those that align with the desired material properties. In the process of generating the compositional space for the design of a hardfacing alloy, it is initially defined to consist of 10 metals plus boron (B) and carbon (C). The composition range for each element is established with iron serving as the balancing element. The maximum and minimum values (in mol per cent) are set for each component. Iron is set to vary from 45 to 70 mol per cent, while additives like molybdenum, vanadium, and nickel vary from 0 to 20 mol per cent, and carbon and boron from 5 to 15 mol per cent. The step sizes for each element are set to values between 2.5 and 5 mol per cent. This structured approach allows for the systematic exploration and analysis of the defined chemical space.

Once the compositional space is generated, it is possible to calculate and perform the equilibrium calculations. The initial screening of 765 000 compositions involves two equilibrium calculations at temperatures of 500°C and 1000°C. This process aims to identify compositions that predict stability for the FCC (face-centred cubic) phase at high temperature (1000°C) and the BCC (body-centred cubic) phase at low temperature (500°C), aligning with the benchmark alloy and its FCC-BCC transformation criteria. Additionally, the screening checks for the predicted absence of the graphite phase, which is crucial for the desired material properties. Once the calculation results are stored in a dedicated database, the compositions can be subsequently refined, corresponding to the 'Filter and Select' step of the high-throughput approach. This efficiently narrows down the number of potential candidates by assessing their relevant phase stabilities under the specified thermal conditions.

After filtering out 92 per cent of compositions as a result of the initial screening, the focus shifts to more computationally intensive calculations, now manageable due to the reduced data set size. The

melt range of hard precipitates is determined through a two-step process that starts with the calculation of the liquidus temperature (Tliq) of the matrix phase. This temperature is critical for identifying the point at which the material begins to solidify. Following this, an equilibrium calculation is conducted at 250°C lower than Tliq to assess the stability of the matrix phase at reduced temperatures. The martensite start temperature (Tms) model, which predicts the temperature at which martensite (a harder, more brittle phase of steel) begins to form, is applied to successful candidates that pass the melt range criteria (van Bohemen and Morsdorf, 2017). This prediction is based on how the free energy of the material changes with temperature between two different Fe-matrix phases (FCC and BCC) at 1000°C.

Estimated Tms values agree well with experimental findings of our project partners within a range of ±50°C. The aiMP database is employed to calculate the bulk density of each alloy composition. The cost of each composition is calculated by the weighted average of phases and corresponding densities. Approximately 300 phases are identified for each composition and categorised into four groups: (1) Fe-matrix phase, (2) carbides and borides that cause strengthening, (3) carbides and borides that cause embrittlement, and (4) intermetallics. Consequently, any compositions that include phases leading to embrittlement (ie which belong to group 3 and 4) are filtered out. The remaining compositions are taken as the successful candidates that pass the screening criteria. Furthermore, the solidus and liquidus temperatures of the alloy are reported for each successful composition, as these temperatures define the range over which the alloy remains partially liquid and are thus crucial for processing techniques in additive manufacturing.

In the final screening step, alloy compositions which pass the thermochemical screening criteria are evaluated based on the criticality of the alloying elements. Criticality in the context of alloying elements refers to the assessment of risks associated with their supply, which includes factors such as scarcity, geopolitical risks, and environmental implications of their extraction and processing. As shown in Figure 8, the 'Substitution Index' (SI) is used as a metric for criticality, where the arrow indicates the tendency towards a lower substitution index that is the goal with respect to the alloy composition, as well as a lower production cost.

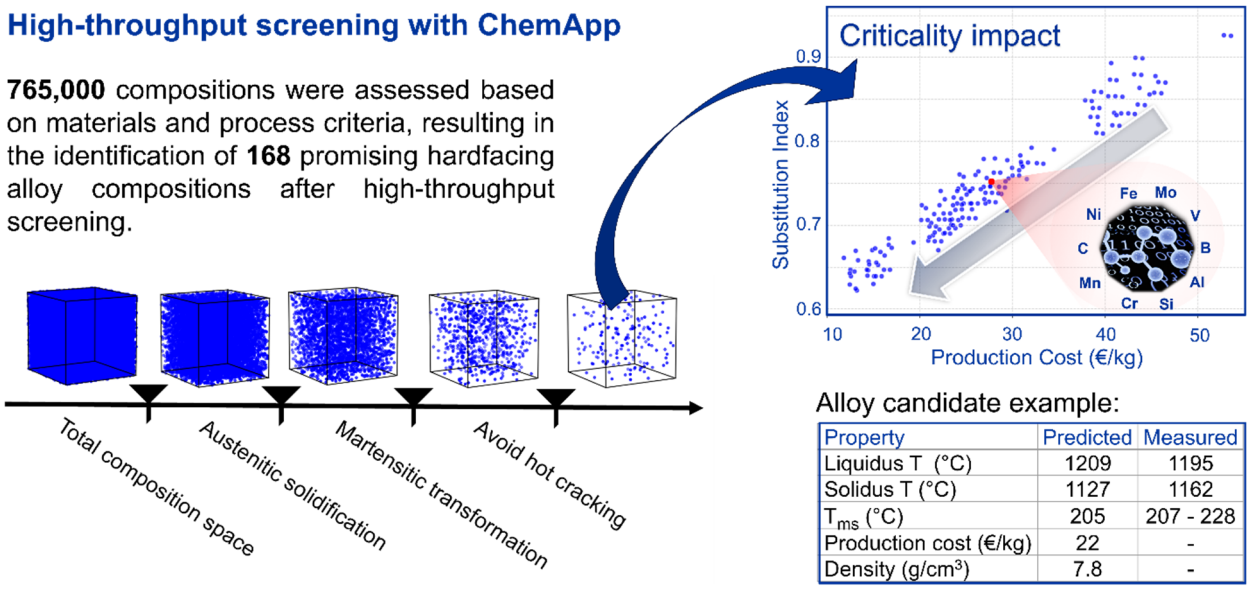

Alloy candidate example:

Property	Predicted	Measured
Liquidus T (°C)	1209	1195
Solidus T (°C)	1127	1162
T_{ms} (°C)	205	207 - 228
Production cost (€/kg)	22	-
Density (g/cm³)	7.8	-

FIG 8 – High-throughput screening of alloy candidates using ChemApp for Python. The figure demonstrates the process of identifying suitable alloys through high-throughput screening. The methodology encompasses evaluation within the total compositional space, austenitic solidification, martensitic transformation, and avoidance of hot cracking (eg melt range criteria). The criticality impact plot (top right) highlights the substitution index versus production cost (€/kg). The arrow indicates the intended tendency towards a lower substitution index and lower productions costs for the alloy composition. Predicted results and measured properties by subsequent processing of a single alloy candidate are given in the inserted table (bottom right). Liquidus, solidus and martensite start temperatures are compared and found to be in good agreement.

An average substitution index is calculated based on the aforementioned criteria for each composition and is found to be in good agreement with the low production costs associated with using fewer alloying elements.

The thermochemical screening methodology used in this work has proven to be effective in identifying potential alloy candidates for industrial applications, taking into account process specifications, production costs, as well as environmental and supply chain of issues of critical alloying elements. Successful alloy candidates already underwent experimental analysis by our project partners. It was found that the measured findings align well with the predicted results, providing corroborating evidence for the existence of novel alloy compositions that are more sustainable and cheaper than the benchmark alloy while maintaining structural performance.

CONCLUSIONS

In the rapidly evolving field of material science, the high-throughput materials informatics approach has emerged as a transformative methodology, significantly accelerating the discovery and optimisation of novel materials. With the automatic generation of ChemApp for Python scripts from FactSage, this approach is now easily accessible to every FactSage user, be it in an academic or industrial research context. The potential is demonstrated by screening millions of compositions for interesting properties as hardfacing alloys. The properties include application-related properties such as high hardness by formation of martensite and pre-defined volume fraction of carbides and borides, as well as properties related to processing, such as low liquidus temperature and low tendency for hot cracking during solidification. Besides the direct screening for application- or processing-related properties, the methodology can also be used to generate high-quality, homogeneous input data for machine learning models.

REFERENCES

Bale, C W, Bélisle, E, Chartrand, P, Decterov, S A, Eriksson, G, Gheribi, A E, Hack, K, Jung, I H, Kang, Y B, Melançon, J, Pelton, A D, Petersen, S, Robelin, C, Sangster, J, Spencer, P, Van Ende, M-A, 2016. FactSage Thermochemical Software and Databases 2010–2016, *CALPHAD*, 54:35–53. https://doi.org/10.1016/j.calphad.2016.05.002

Behnel, S, Bradshaw, R, Citro, C, Dalcin, L, Seljebotn, D S and Smith, K, 2011. Cython: The best of both worlds, *Computing in Science and Engineering*, 13(2):31–39. http://dx.doi.org/10.1109/MCSE.2010.118

Eriksson, G and Hack, K, 1990. ChemSage- A computer program for the calculation of complex chemical equilibria, *Metall Trans B*, 21:1013–1023. https://doi.org/10.1007/BF02670272

GitHub, Inc., 2024. GTT-Technologies / ChemApp-Examples [Public], GitHub, Inc. Available from: <https://github.com/GTT-Technologies/ChemApp-Examples/>

Ong, S P, Richards, W D, Jain, A, Hautier, G, Kocher, M, Cholia, S, Gunter, D, Chevrier, V L, Persson, K A and Ceder, G, 2013. Python Materials Genomics (pymatgen): A Robust, Open-Source Python Library for Materials Analysis, *Computational Materials Science*, 68:314–319. https://doi.org/10.1016/j.commatsci.2012.10.028

Petersen, S and Hack, K, 2007. The thermochemistry library ChemApp and its applications, *International Journal of Materials Research*, 98(10):935–945. https://doi.org/10.3139/146.101551

van Bohemen, S M C and Morsdorf, L, 2017. Predicting the Ms temperature of steels with a thermodynamic based model including the effect of the prior austenite grain size, *Acta Materialia*, 125:401–415. https://doi.org/10.1016/j.actamat.2016.12.029

An investigation of potential wear occurring on refractory lining and coating formation – a remedy of wear in a basic oxygen steelmaking furnace using CFD modelling

DOI: 10.62053/BJBS2609

R Chowdhury[1,7], S Mitra[2,7], G Evans[3,7], T Honeyands[4,7], B J Monaghan[5] and D Scimone[6,7]

1. Research Assistant, University of Newcastle, Callaghan NSW 2308. Email: raju.chowdhury@newcastle.edu.au
2. Research Academic, University of Newcastle, Callaghan NSW 2308. Email: subhasish.mitra@newcastle.edu.au
3. Conjoint Professor, University of Newcastle, Callaghan NSW 2308. Email: geoffrey.evans@newcastle.edu.au
4. Associate Professor, University of Newcastle, Callaghan NSW 2308. Email: tom.a.honeyands@newcastle.edu.au
5. Professor, University of Wollongong, Wollongong NSW 2522. Email: monaghan@uow.edu.au
6. Senior Refractory Technologist, BlueScope Steel, Port Kembla NSW 2505. Email: david.scimone@bluescopesteel.com
7. ARC Research Hub for Australian Steel Manufacturing, University of Wollongong, Wollongong NSW 2500.

ABSTRACT

Due to the harsh operating conditions, wearing of the inner refractory lining in a Basic Oxygen Steelmaking (BOS) furnace reduces the useful life of the refractories and incurs a significant cost component for relining. In this study, firstly, a combined compressible and incompressible computational fluid dynamics (CFD) model was developed to identify the potential wear prone zones in an industrial scale BOS system during the supersonic oxygen blowing phase by quantifying the wall shear stress distributions. Next, the retained slag splashing process was simulated by introducing an inert gas to residual slag mass to achieve a protective coating on the refractory walls. Effect of both design and operational parameters such as lance head configuration, lance position and the initial slag volume on the slag wall coating performance were quantified and most favourable conditions were determined.

INTRODUCTION

Wearing of the inner refractory lining of the Basic Oxygen Steelmaking (BOS) furnace is a known problem in the steelmaking industry. It reduces the useful life of BOS refractories. Replacing or repairing the refractory lining is quite a capital-intensive issue. Timely identification of the potential wear prone zones allows deployment of some targeted wear mitigation strategies to prolong the overall life of the furnace's working refractory lining.

BOS steelmaking is a complex process where oxygen gas is injected at a supersonic speed through a lance comprising multiple converging-diverging nozzles into a molten iron bath to reduce the carbon content and remove the impurities from the liquid metal phase to slag phase by oxidisation. The supersonic gas jet exhibits complex interactions with the liquid metal and slag phase involving deformation of slag/metal interface, cavity formation, bath oscillation, droplet generation and chemical reactions (Li *et al*, 2016a). The rate of the oxidation reactions greatly depends on the mixing of oxygen gas with the hot metal and is governed by momentum transfer from the gas jet which produces oscillatory motions in the liquid. The slag foaming (gas-slag-metal emulsions) that forms due to the chemical reactions influences the mixing performance by accelerating the process kinetics (Sattar, Naser and Brooks, 2014). The gas jet velocity that controls the mixing performance mainly depends on the nozzle design (Fruehan, 1998). Wear occurs in the inner lining of the converter over a prolonged period of operation due to the combined effect of chemical, mechanical and thermal attacks. Among these causes, mechanical wear occurs due to the bath oscillation motion during the steel refining process (Li *et al*, 2016b). Wear does not occur uniformly within the furnace; rather, it occurs locally and depends on the wall shear stress generated during the steelmaking operation.

Previously, some numerical studies have been conducted by (Odenthal, Falkenreck and Schlüter, 2006; Li *et al*, 2016b; Sun *et al*, 2022) to investigate the hydrodynamic behaviour of the main blowing process in a full-scale BOS system. These studies mainly examined the cavity profile, mixing time and effect of lance height variation, lance designs and bottom tuyere arrangements. A few of these studies (Li *et al*, 2016b, Sun *et al*, 2022) specifically quantified the wear prone zones due to the bath oscillation. (Li *et al*, 2016b) identified the wearing zone to exist between the slag-free surface and slag-metal interface while (Lee, O'Rourke and Molloy, 2001) reported that wear occurs at the knuckle region of the BOS furnace based on experiment.

Effective coating formation on the wearing zones ensures higher productivity by prolonging the life span of a BOS furnace. Slag splashing is a known cost-effective remedy for such purpose (Fruehan, 1998; Mills *et al*, 2005) compared to other coating formation methods such as gunning and slag coating. In this process, an inert gas such as nitrogen is blown through the lance into the retained slag pool periodically. The gas jet-slag interaction generates numerous slag droplets which deposit on the refractory wall, solidify and form a protective coating layer on the furnace wall. This process can be enhanced by adding bottom bubbling through the tuyeres mounted on the furnace floor (Mills *et al*, 2005). Achieving a good coating layer is case specific and depends on the slag composition, gas flow rate, quantity of residual slag, lance head design, lance position, converter shape and dimensions.

In slag splashing process, the main purpose is to coat a targeted region of BOS furnace utilising the optimal volume of slag in the shortest possible time. Determining such conditions through plant trials is quite expensive (Luomala *et al*, 2002). Some past numerical studies (Barron, Hilerio and Medina, 2015; Leão *et al*, 2016; Sinelnikov *et al*, 2021) investigated the potential of slag splashing method by assessing the influence of above stated operating conditions. It is however noted that these investigations focused on high gas flow rate (*Ma* = 1 or *Ma* > 1, where *Ma* is the Mach number – defined as the ratio of flow speed to the sound speed) while studies on the low flow rate (*Ma* < 1) scenarios with industrial conditions were quite limited. To address this knowledge gap, the present study aims to develop a comprehensive CFD model to investigate the hydrodynamic behaviour in an industrial scale BOS furnace utilising the actual operating conditions and determine the potential wear prone zones. Also, the study aims to quantify the effect of different operating conditions on the coating formation.

NUMERICAL MODELLING

A Computational Fluid Dynamics (CFD) model of an industrial scale BOS system was developed on the commercial CFD solver ANSYS-Fluent platform to simulate two main scenarios – a normal oxygen injection operation to determine the wear prone zones inside the furnace and a slag splashing operation with inert gas injection from both furnace top and bottom. The entire CFD modelling framework presented in this paper was divided into two separate parts comprising a compressible flow and incompressible flow component, respectively.

Flow modelling of lance head

First, a single phase CFD model was developed to quantify the flow behaviour in a 3D converging-diverging (CD) nozzle in the lance head of two different designs comprising five and six nozzles, as well as bottom tuyeres. The model included continuity, momentum and energy equations which were simultaneously solved using a compressible flow solver on a fixed Eulerian structured mesh. To account for the turbulence effect, a two-equation SST (shear stress transport) k–ω model was utilised. To simulate the high heat transfer rate between the impinging gas jet and the liquid metal, the value of turbulent Prandtl number was set to $Pr_t = 0.5$ in the energy equation (Alam, Naser and Brooks, 2010).

Taking advantage of the symmetric geometry (Figure 1a), only half domain of the lance head (Figure 1b) and a quarter domain of the tuyere (Figure 1c) was simulated to reduce the computational cost. A *pressure inlet* boundary condition was applied at the nozzle inlet whereas a *pressure outlet* boundary condition was applied at the outlet. A *no-slip* condition was adopted on the walls. Gas density was computed from the ideal gas law. First order upwind scheme was used

to discretise the pressure, momentum and energy equations and the solution convergence criterion for all residuals was set at 10^{-6}.

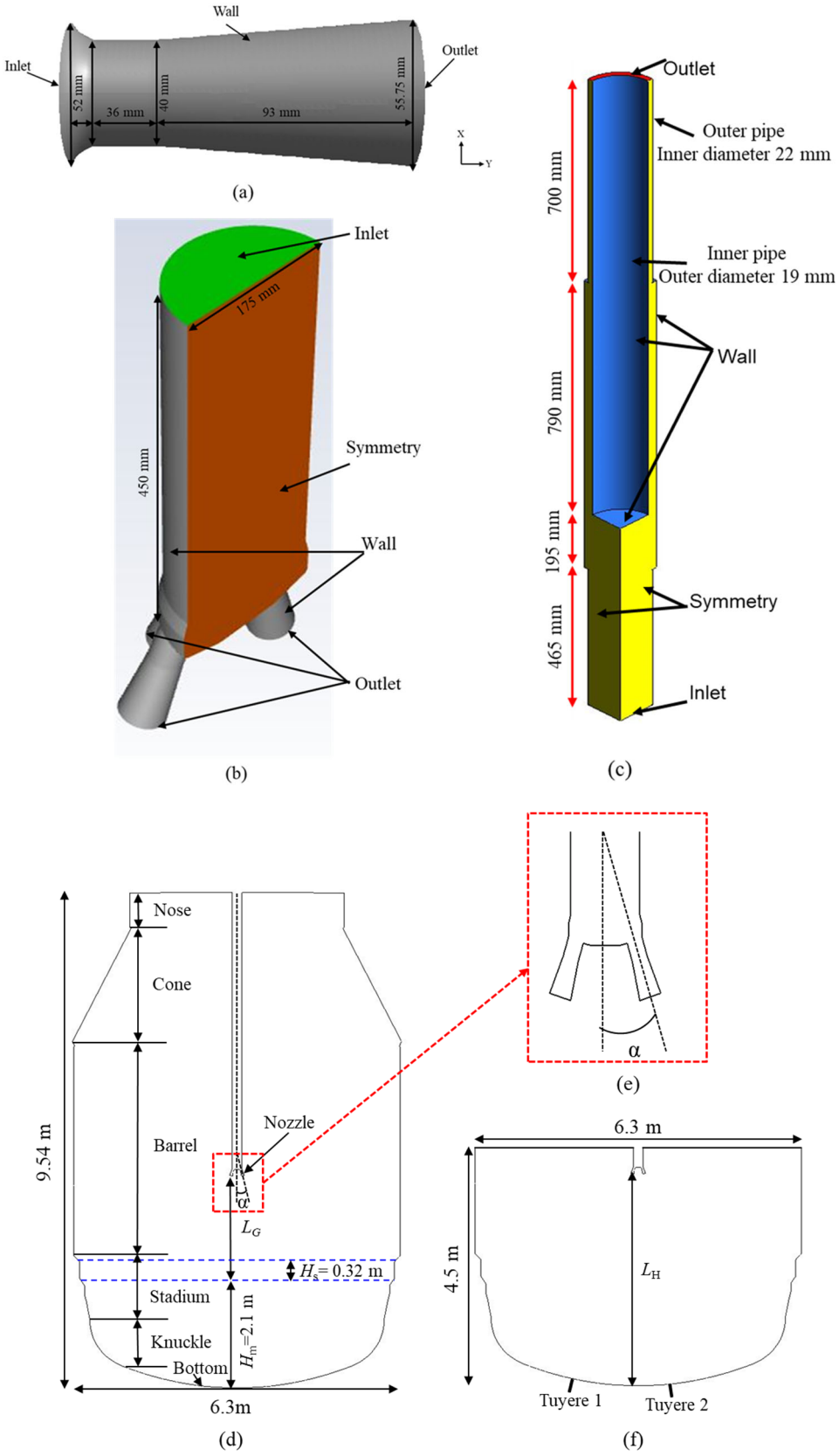

FIG 1 – Computational domains: (a) a 3D single CD nozzle used in *Lance1*, (b) a 3D 6-hole lance head, (c) bottom tuyere, (d) a 2D full-scale BOS furnace comprising a lance head to be used in main blowing simulation cases, (e) enlarged view of lance head, and (f) a 2D full-scale BOS furnace comprising a lance head and bottom tuyere to be used in slag splashing simulation cases.

Two low-pressure gas flow rate cases (11 600 Nm^3/hr and 250 Nm^3/hr nitrogen flow-through lance and tuyere, respectively) were simulated by applying *mass flow inlet* boundary condition at the inlet of lance and tuyere to determine the exit velocity and temperature. The model predicted velocity and temperature obtained at the lance and tuyere exit were used as boundary conditions for simulation of the overall hydrodynamic behaviour in a BOS system.

Flow modelling of BOS system

A 2D Eulerian-Eulerian multiphase CFD model was developed to simulate the flow dynamics of BOS system. Due to high computational cost involved in 3D modelling of a full-scale BOS system, a 2D model was instead considered. The computational domain for the main blowing process is shown in Figure 1d. The model comprised continuity, momentum with standard k–ε turbulence closure with standard wall function, and energy equation to account for the interactions between a gas jet and pool of liquid metal and slag phase. Any chemical reactions due to phase interactions were not considered.

For the slag splashing scenario, only the lower part however was considered (Figure 1f) keeping the governing equations same. *Velocity inlet* boundary condition was applied at the inlet and *pressure outlet* boundary condition was employed at the outlet. A no-slip condition was applied to the walls and the temperature was set to 1923 K. Solidification sub-model was not considered. Instead, it was assumed that where the slag will be in contact with the furnace wall, it will solidify.

The thermo-physical properties of BOS slag and metal used in the CFD model are given in Table 1. The properties of slag were computed using (Mills, Yuan and Jones, 2011) for the slag compositions (Drain, 2018) provided in Table 2. Before performing CFD simulations, a grid independency test was performed for each case considering three different grid levels to ensure the accuracy of the simulation results.

TABLE 1

Properties of slag and metal.

Physical properties	Slag	Metal
Density ρ_l ($kg{\cdot}m^{-3}$)	3067	7020
Dynamic viscosity μ_l (Poise)	0.24	0.05
Temperature T (K)	1923	1923
Thermal conductivity k_l ($W{\cdot}m^{-1}{\cdot}K^{-1}$)	0.05	40
Surface tension σ_l ($N{\cdot}m^{-1}$)	0.55	1.6
Specific heat Cp_l ($J{\cdot}kg^{-1}{\cdot}K^{-1}$)	1414	670

TABLE 2

Slag compositions.

Constituents	CaO	MgO	P	SiO_2	Fe_tO^*	MnO	Al_2O_3	TiO_2	S	V_2O_5
Mass (%)	42.7	9.5	1.0	13.0	23.3	4.6	2.0	1.2	0.1	1.6

*Fe_tO represents the total *Fe* in slag phase as *FeO.*

The governing equations were discretised using a first-order upwind scheme and spatial gradients were computed with a least-squares method. The pressure values at the cell faces were interpolated using the PRESTO (PREssure Staggering Option) scheme. Finally, pressure–velocity coupling was achieved by using a PC-SIMPLE (Phase Coupled Semi Implicit Pressure Linked Equation) algorithm. The initial time step size was set to 1×10^{-6} s and then switched to an adaptive scheme ensuring stability of the solution (global Courant number <1.0). The convergence criterion was set to 1×10^{-6} for the absolute residual of energy parameter, while a value of 1×10^{-3} was set for mass flow, velocity and turbulence parameters. All calculations were carried out on a high-performance computing Linux cluster deploying a maximum of 32 parallel processors. The required wall time was 144 hrs to simulate 1 sec physical time for both, main blowing and slag splashing

cases. Due to very long computation time required for these calculations, main blowing and slag splashing simulations were run for only 10 secs and 4 secs, respectively.

RESULTS AND DISCUSSIONS

Model validation

The developed CFD models were first validated with the theoretical solutions wherever applicable. For lance head, model predictions were validated by comparing with the isentropic theory as shown in Figure 2a. It can be seen the CFD model predicted Mach number along the nozzle axis agrees well with the isentropic theory showing only ~ 0.13 per cent deviation at the nozzle exit.

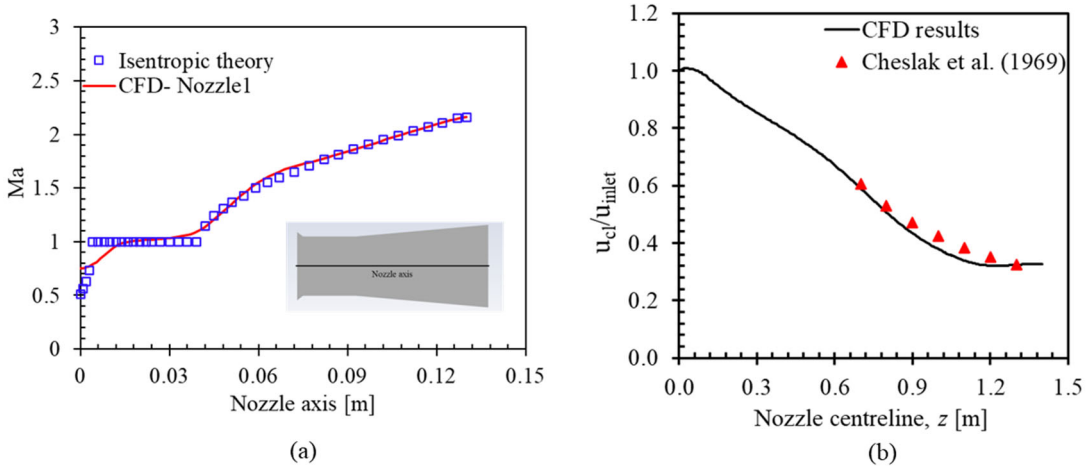

FIG 2 – (a) Single phase flow model comparison with isentropic theory and (b) multi-phase flow model comparison with theoretical prediction.

For the gas jet flow simulations, the model predictions were compared with the theoretical prediction of a single gas jet decay along the nozzle centreline (Cheslak, Nicholls and Sichel, 1969). The centre line gas velocity magnitude of a supersonic gas jet in its subsonic region (Ma < 1) can be written as:

$$\frac{u_{cl}}{u_0} = K_2 \frac{d_e}{L_G} \tag{1}$$

where:

- u_{cl} is the centreline gas jet velocity (m·s^{-1})
- u_0 is the released velocity at the nozzle exit (m·s^{-1})
- d_e is the diameter at the nozzle exit (m)
- L_G is the distance between the liquid bath surface to the nozzle tip (m)
- $K_2 = 6.4$ is a constant (Cheslak, Nicholls and Sichel, 1969)

The model predicted data were found in good agreement with the calculated velocity from Equation 1 as shown in Figure 2b.

Main blowing process

To simulate the main blowing process, an oxygen flow rate of 55 000 *Nm^3/hr* was used. Two lance head designs differing in number of nozzles and angle of inclination, were used to determine the effect of flow pattern on the potential wear prone zones. *Lance1* comprised of six CD nozzles with an inclination of 17.30° relative to the lance centreline while *Lance2* had five nozzles with an inclination angle of 15°. The *Lance1* design produced Ma ~ 2.10, jet velocity, V ~ 502 m/s, and temperature T_s ~ -117°C at the nozzle exit while *Lance2* design produced Ma ~ 1.97, jet velocity V ~ 482 m/s, and temperature T_s ~ -107°C. The flow induced high shear stress is thought to contribute to the wearing of the lining.

Hydrodynamic behaviour inside the furnace

Figure 3 presents the temporal evolution of the early stage of gas-liquid interface deformation during the jet impingement process in the *Lance1* case, where a lance gap, gap between the nozzle exits and surface of molten bath, L_G = 2.0 m was maintained. At a very early stage (t ~ 0.05 sec) a surface wave formed at the slag-gas interface due to the downward jet impingement. As time advances, impinging gas jets deforms the slag interface and a cavity is formed. With the increasing depth of the cavity, multiple ligaments formed at the edge of the cavity (t ~ 0.4 sec). Due to the shearing action of the impinging gas jet, these ligaments tore off and produced droplets leading to slag splashing on the furnace walls. Sabah and Brooks (2014) reported three distinct modes of cavity formation namely dimpling, splashing and penetration. CFD simulations showed that cavity formation enters the penetration mode at t ~ 1.25 sec. Similar interface deformation behaviour was observed in the cold model experiment (Sabah and Brooks, 2014) where compressed air was blown into a pool of water.

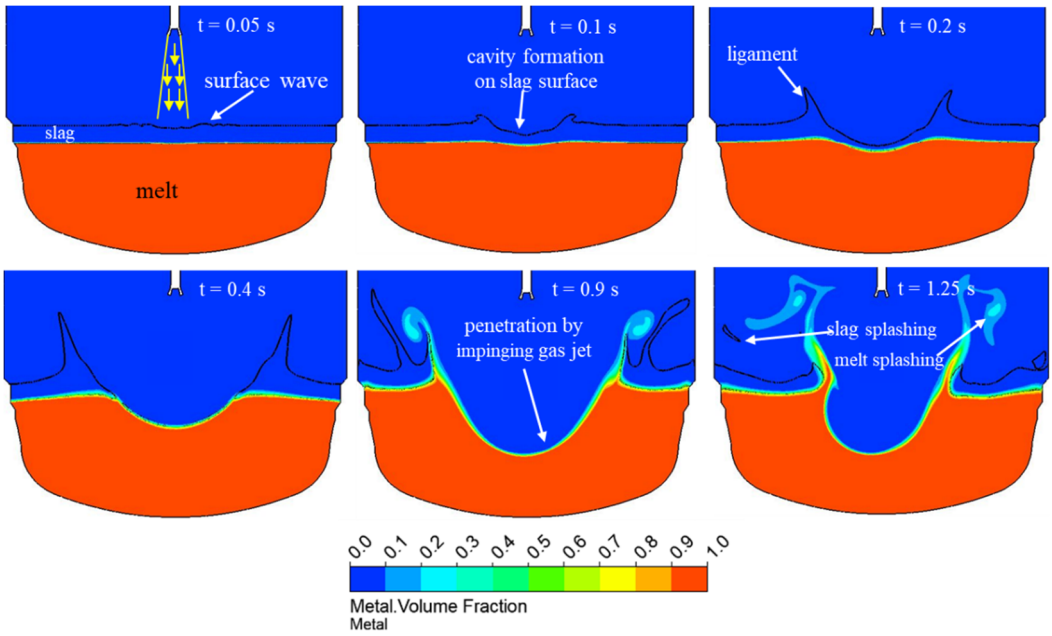

FIG 3 – Interface deformation behaviour due to supersonic oxygen gas jet impingement in the main blowing process using *Lance1*.

As the oxygen blowing process continues, the slag-metal interface and molten bath movement become more dynamic. Due to the presence of a strong shear and relative velocity between the fluid layers, distinct surface waves are predicted due to Kelvin–Helmholtz instability which propagates across the entire bath surface. The oscillatory turbulent motions of the liquid phases along the furnace wall is expected to contribute to mechanical erosion of the refractory lining (Li *et al*, 2016b). The sloshing behaviour at the gas-slag, slag-melt or gas-melt interface also contribute to premature wear of refractory lining around the perimeter of the furnace.

Effect of lance designs on wall shear stress

The continuous undulatory motions of the gas-liquid interface induce shear stress on the furnace wall (Sun *et al*, 2022). This wall shear stress was computed as:

$$\tau = \frac{\int (\mu+\mu_t)\frac{du}{dy}\,dA}{\int dA} \tag{2}$$

where:

- u is the fluid velocity (m·s^{-1}) at the wall adjacent cell
- y is the height (m) of wall adjacent cell

Figure 4a presents the maximum shear stress on the refractory wall imparted by the slag and melt phase. The shear stress induced by slag phase at the right stadium and knuckle were computed as ~52 Pa and ~58 Pa, respectively. The wall shear stress induced at the right furnace wall by the melt phase was found more than three times higher compared to the slag phase. The computed shear stresses were as follows: right stadium ~168 Pa, right knuckle ~240 Pa, left stadium ~65 Pa, and left knuckle ~20 Pa.

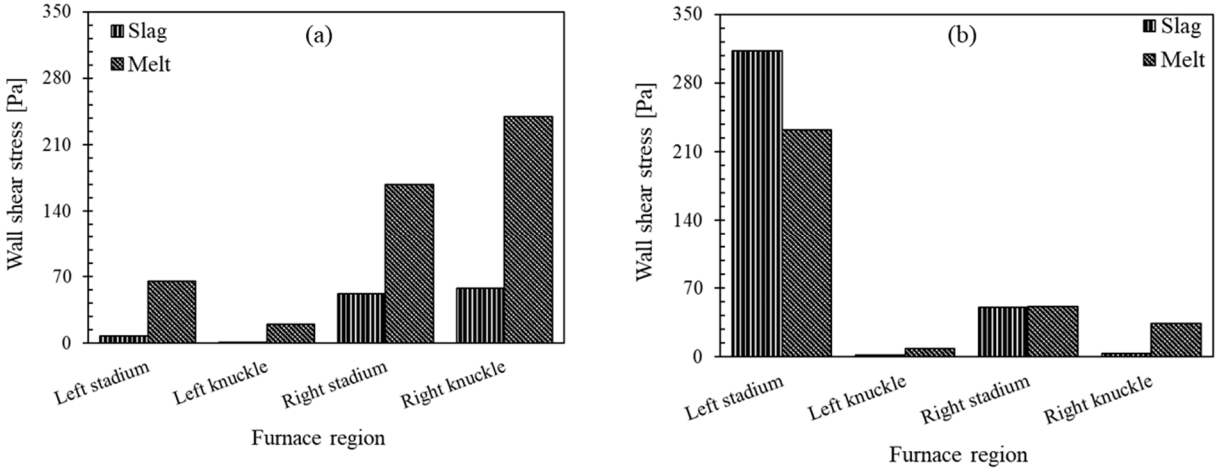

FIG 4 – Shear stress induced by slag and melt on furnace wall in main blowing process using (a) *Lance1* and (b) *Lance2* designs.

The nozzle design and inclination angle were different for the lance *Lance2* compared to *Lance1*. Due to different jet momentum created by these two designs, both cavity profile and molten bath oscillatory behaviour were different in these two cases. For the case of *Lance2*, the lance gas was 2.15 m. The computed values of maximum shear stress on the refractory wall based on *Lance2* design case is shown in Figure 4b. The continuous sloshing motions of the generated surface wave caused highwall shear stress at the left stadium region of the furnace. The maximum shear stress induced by slag were ~51 Pa at the right stadium and ~313 Pa at the left stadium. The computed maximum shear stress by melt phase were ~51 Pa at right stadium, ~34 Pa at right knuckle, and ~232 Pa at left stadium, respectively. These values were comparable with the suggested shear stress ~45 Pa in Fruehan (1998) required to form a crack on refractory surface. Model predicted potential wear prone zones agreed reasonably with the laser scan data obtained from the plant (not presented due to their confidentiality).

Slag splashing

Slag splashing cases were simulated by blowing nitrogen gas at a flow rate 11 600 Nm^3/hr and 250 Nm^3/hr through the top mounted lance and the bottom mounted tuyeres, respectively. Utilising these gas flow rates in the compressible flow model, *Lance1* provided a sub-sonic velocity, V ~260 m/s, and temperature, T_s ~-6°C at the nozzle exit whereas *Lance2* provided a sub-sonic velocity V ~246 m/s, and T_s ~-6°C. The tuyeres produced a choked flow condition at sonic velocity V ~300 m/s at the tip and the corresponding temperature was T_s ~-60°C. Simulations were run accounting for three lance heights (L_H = 3.1, 2.8 and 2.1 m), two initial slag volume (2 and 4 m^3), and two lance designs (*Lance1* and *Lance2*). Gas was blown through two bottom tuyeres in all cases.

Hydrodynamic behaviour during slag splashing

Figure 5 presents the transient hydrodynamic behaviour of downward gas jet interaction with the retained slag pool using *Lance1* for three different lance positions and initial slag volume of 2 m^3. After being discharged from the nozzle exit, gas jets travel through a freeboard region and entrain the surrounding gas. The accumulation of turbulent entrainment leads to the radial expansion and the mixing of the jet boundaries (Li *et al*, 2015) which causes merging of two jets into a single jet and significant deviation from the respective nozzle axes (t ~0.05 sec). Waves are generated at the slag surface due to impingement of gas jets from the lance and cavity formation occurs within the

slag pool due to bottom jetting from the tuyeres (*t* ~0.05 sec). The inside cavities expand with time and push the slag surface upwards along the walls (*t* ~0.2 sec). Finally, the slag pool ruptures into three parts (*t* ~0.5 sec). Gas jets move the separated slag mass towards the wall and form a thin coating layer on the wall (*t* ~1 sec). Due to the gravitational effect, the bulk slag moves back to the furnace floor (*t* ~2 sec).

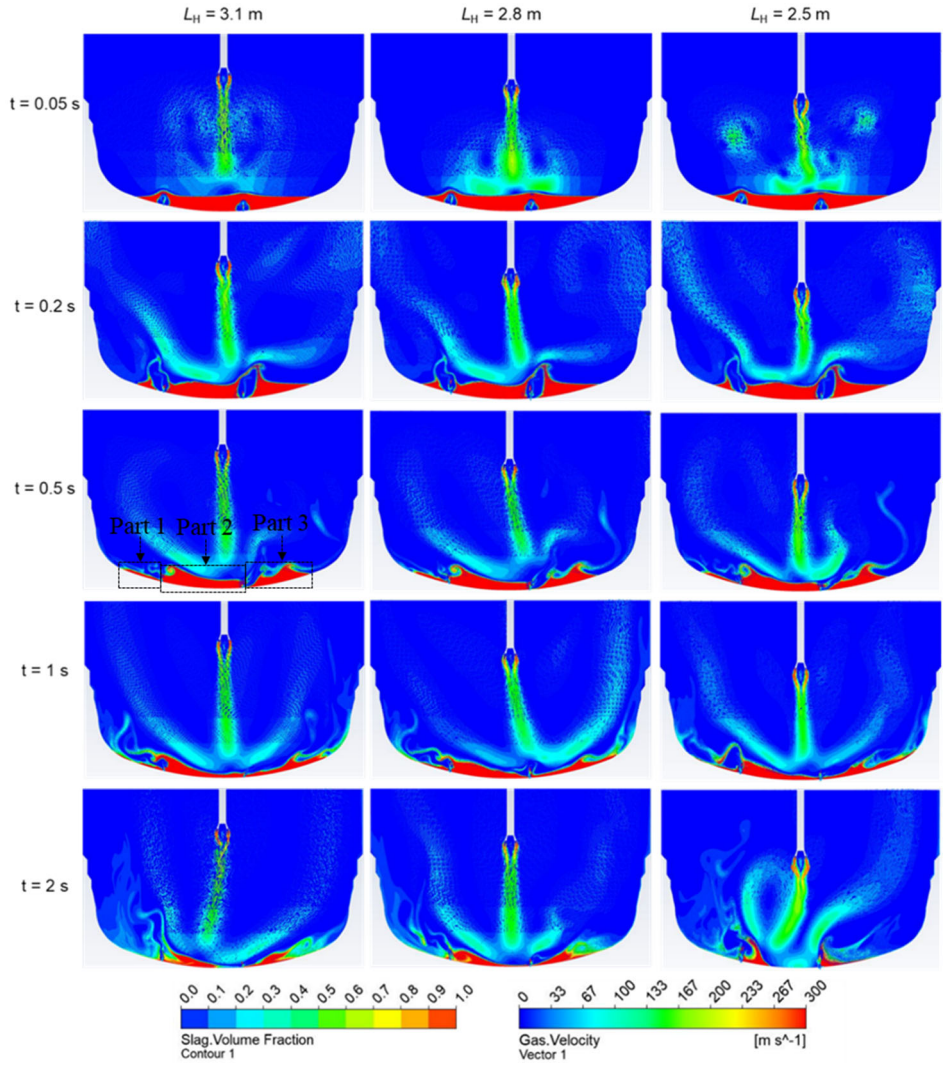

FIG 5 – Unsteady interaction of gas jets with the retained slag (initial slag volume 2 m^3) for three lance positions using *Lance1.*

Lowering the lance height from 3.1 m to 2.8 m, top gas jets impinge on the slag surface with a higher kinetic energy. Consequently, the gas jets push slag along the furnace wall much higher in both, left and right directions (*t* ~1 sec, L_H = 2.8 m) up to the stadium region. Further lowering the lance to 2.5 m, the higher energy jets completely rupture the slag pool and contacts the furnace floor (*t* ~2 sec).

Effect of lance position on slag coating

Figure 6 presents the energy flux on the slag surface as a function of lance position for the two different lance designs. The energy flux on the slag surface was computed as:

$$\text{Energy flux} = \frac{\int \rho_g V^3 dA}{\int dA} \quad (3)$$

where:

ρ_g is the density (kg·m^{-3})

V is the gas velocity (m·s^{-1})

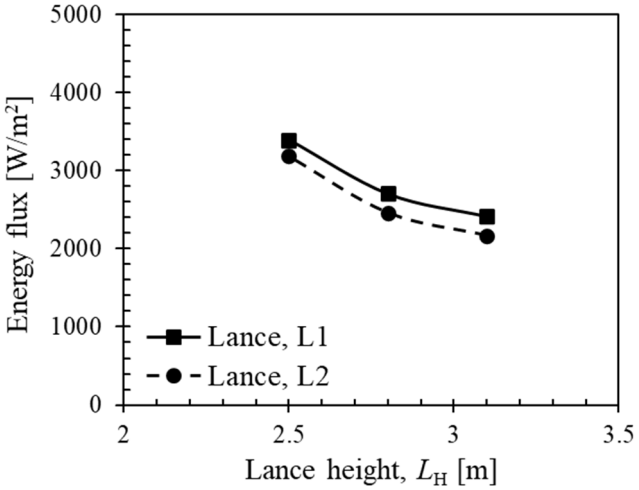

FIG 6 – Energy flux on slag surface for different lance designs and lance positions.

From Figure 6, it can be seen that the energy transfer rate per unit area on the slag surface decreased with the increase of lance height. The reason is that at lower lance height jet energy decay is lower due to low entrainment and the gas jet impinges on the slag surface at higher energy. At all lance heights, gas jets impinged on the slag pool with higher energy using *Lance1* compared to *Lance2* as shown in Figure 6. This is due to the higher gas jet velocity (velocity ~260 m/s) released from *Lance1* compared to *Lance2* (velocity ~246 m/s).

Effect of initial slag mass on slag coating

Figure 7 presents the coated area on refractory wall covered by slag splashing as a function of the lance height for different initial slag volume using *Lance1*. The coated area reported here is the average coated area of left and right walls of the furnace. Only knuckle, stadium and barrel walls were considered to compute the coated area which is given as:

$$\text{Coated area (\%)} = \frac{\int \varphi dA_{wall}}{\int dA_{wall}} \times 100 \quad (3)$$

where:

φ is the slag phase

A_{wall} is the area of the wall

In Figure 7a, for a fixed gas flow rate ~11 600 $Nm^3 \cdot hr^{-1}$ and slag volume 2 m^3, ~53 per cent of knuckle area was coated at lance position of 3.1 m. No significant change in coating formation on the knuckle region was found for subsequently lowering the lance position to 2.8 m and then to 2.5 m. Intuitively, a higher coating area would be expected due to lance position closer to the free surface allowing the gas jets to impinge on the slag surface with higher kinetic energy. This however did not happen in the simulations because of insufficient slag mass present in the system which could not be fully utilised to coat the furnace wall. Moreover, lowering the lance position, the high energy gas jet ruptured the slag pool leading to contact with the furnace floor and energy dissipation.

Increasing slag volume from 2 m^3 to 4 m^3, at the highest lance position (L_H = 3.1 m), coated area at knuckle region increased by ~27.7 per cent. Due to the increased slag volume, gas jets moved a higher amount of slag along the furnace wall and thus the coated area increased. At lance position of 2.8 m, the coated area at the knuckle region increased by ~43 per cent. The coated area however decreased by ~20 per cent for lowering lance position from 2.8 m to 2.5 m. This is again attributed to increasing energy flux on slag surface which led to complete penetration of the slag pool and contact with the furnace floor resulting in loss of jet energy and reduction in the amount of slag splashed (Mills *et al*, 2005).

Figure 7b shows the coated area at the stadium region for the variation of lance height. At L_H = 3.1 m, ~12 per cent of stadium region coated at the initial slag volume 2 m^3. For lowering the lance

height, the coated area at this region increased slightly which were obtained as follow: ~15 per cent at L_H = 2.8 m and ~16 per cent at L_H = 2.5 m. Although lowering lance height produces higher energy flux on slag pool, the amount of slag was not enough to travel to the stadium region. Increasing the slag volume 4 m^3, the coated area increased slightly which were as follow: ~14 per cent at L_H = 3.1 m, ~17 per cent at L_H = 2.8 m and ~14 per cent at L_H = 2.5 m.

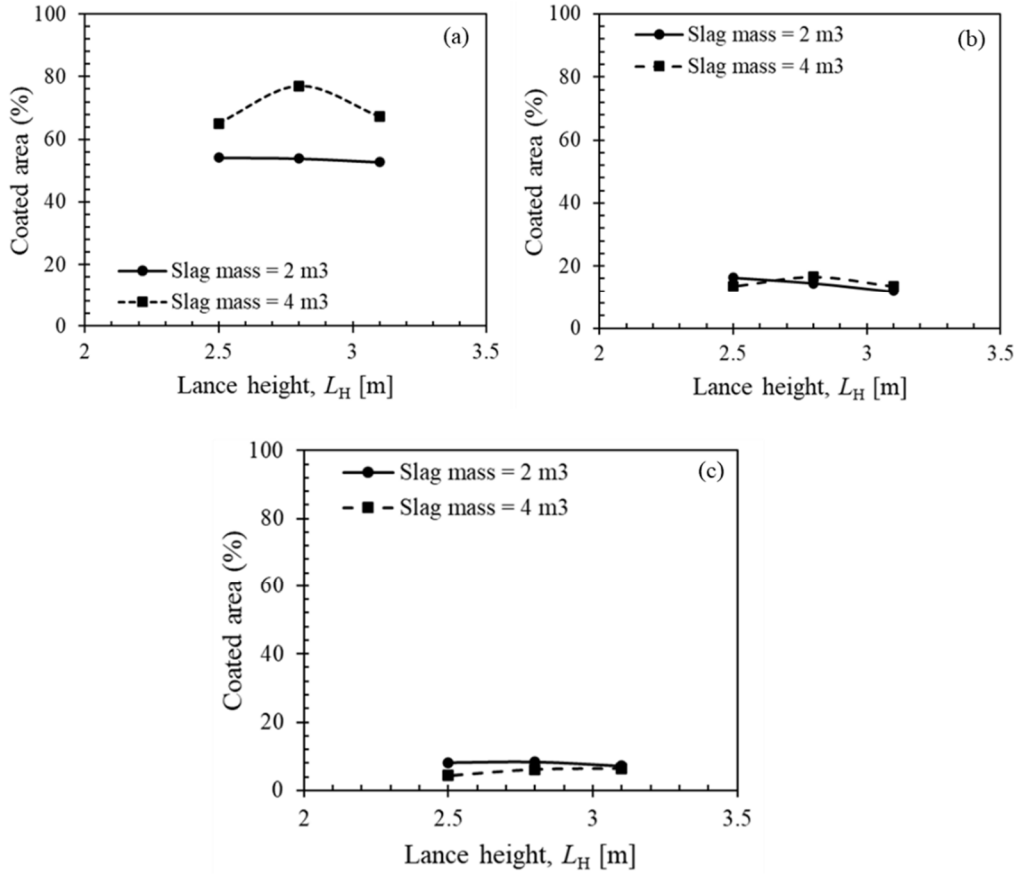

FIG 7 – Variation of coated area on: (a) knuckle wall, (b) stadium wall, and (c) barrel wall for the variation of lance height and initial slag volume utilising *Lance1*.

Utilising the initial slag volume of 2 m^3, the coated area at barrel region remains almost the same (~8 per cent) at all considered lance positions (Figure 7c). Increasing slag volume to 4 m^3 caused the coated area to decrease slightly which was ~6 per cent at lance position L_H = 3.1 m and L_H = 2.8 m. Further lowering it at L_H = 2.5 m, the coated area was only ~4 per cent.

Figure 8 presents the effect of *Lance2* on coated area for the variation of lance height and initial slag volume. Using slag volume of 2 m^3, coated area at knuckle region decreased slightly for lowering the lance height which were as follow: ~53 per cent at L_H = 3.1 m, ~50 per cent at L_H = 2.8 m and ~44 per cent at L_H = 2.5 m. The increase of slag volume aided to achieve a higher coated area for all lance heights. By lowering the lance position from L_H = 3.1 m to L_H = 2.8 m, coated area at the knuckle region increased by ~22 per cent. For further lowering lance position from L_H = 2.8 m to L_H = 2.5 m, coated area decreased by ~9 per cent.

Lance2 provided a similar coating performance at the stadium region (Figure 8b) and barrel region (Figure 8c) as *Lance1*. For slag volume of 2 m^3, coated area in the stadium region decreased by lowering lance height (~16 per cent at L_H = 3.1 m, ~13 per cent at L_H = 2.8 m and ~10 per cent at L_H = 2.5 m). Increasing initial slag volume to 4 m^3, the coated area remained almost the same at all lance positions (~12 per cent at L_H = 3.1 m, ~12 per cent at L_H = 2.8 m and ~16 per cent at L_H = 2.5 m). In the barrel region, the coated area was ~10 per cent for all lance positions using initial slag volume of 2 m^3. However, increasing slag volume to 4 m^3, ~7 per cent of the barrel area was coated for all lance positions.

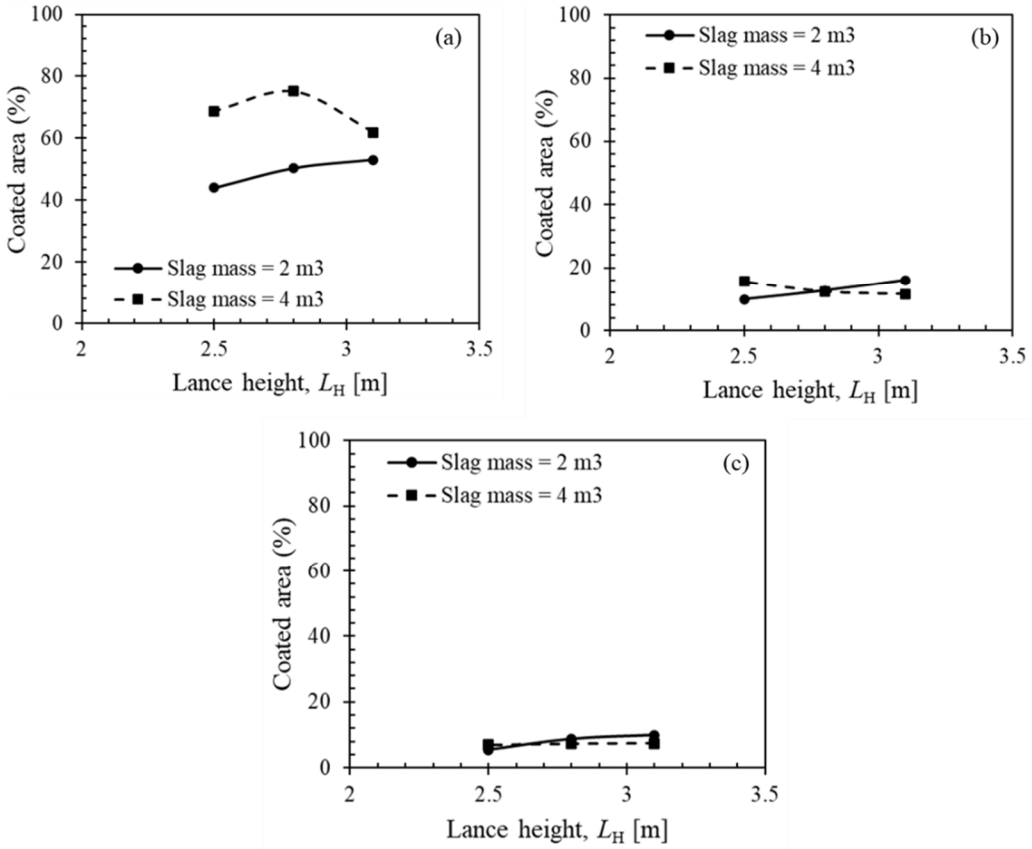

FIG 8 – Variation of coated area on: (a) knuckle wall, (b) stadium wall, and (c) barrel wall for the variation of lance height and initial slag volume utilising *Lance2*.

Effect of tuyere location on slag coating

Figure 9 shows the effect of tuyere location on coating formation on the refractory lining for the gas injection using *Lance1* and initial slag volume 4 m^3. Both tuyeres were located on either side of the furnace centreline, however *Tuyere2* is located closer to the furnace centreline (Figure 9a) compared to *Tuyere1*. The slag pool was completely ruptured at the tuyere locations and formed three separate parts because of gas jet-slag surface interactions. Due to the location of *Tuyere2*, part 3 contained higher slag mass compared to part 1. Both top and bottom gas jets aided movement of the slag mass (part 3) toward the right wall and formed a coating. However, due to less slag mass present in part 1, coating formation at the left region is lower compared to the right part. This result reflects in Figure 9b for all lance positions. At L_H = 2.8 m, ~64 per cent of left knuckle area was coated whereas ~90 per cent of right knuckle area was coated. A similar dependency of tuyere location on droplet generation was observed by (Qinglin, 1990).

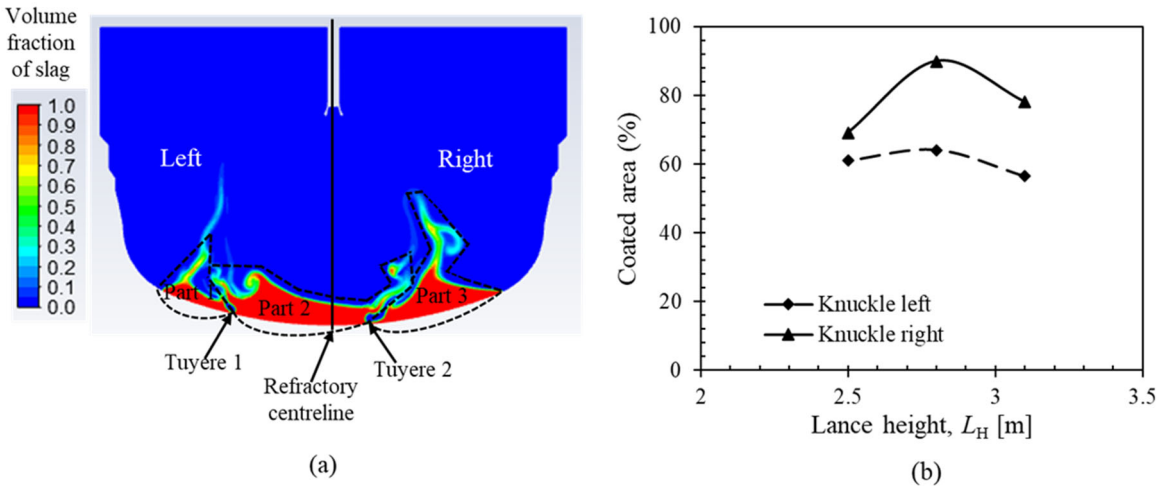

FIG 9 – (a) Location of tuyere at the furnace bottom, and (b) effect of tuyere location on coating formation using *Lance1* and initial slag volume 4 m^3.

CONCLUSIONS

In this study, CFD modelling was performed using actual plant data to identify the potential wear prone zones on the inner walls of an industrial scale BOS furnace during the main blowing process and determine the efficacy of slag splashing to coat these wear prone zones. The findings from these simulations are summarised as follow:

- The potential wear prone zones were characterised by the wall shear stress distribution for the two lance designs – *Lance1* and *Lance2* comprising six and five nozzles. The five-nozzle configuration produced larger stress compared to the six-nozzle configuration. Model predicted potential wear prone zones were left stadium, right stadium and right knuckle, which agreed well with the plant data.
- Simulation of slag splashing produced almost the same coated area in the knuckle region for both lance head design at the higher lance position. The five-nozzle configuration however produced a slightly higher coated area at the stadium and barrel region compared to the six-nozzle one.
- Utilising a larger initial slag volume of 4 m^3, optimal lance position was found to be 2.8 m in both lance head design cases which produced maximum coated area at the knuckle and stadium region. However, *Lance1* design was found to contribute slightly higher coating performance compared to *Lance2*.
- The tuyere position had a strong influence on coating formation. The coating area on the right knuckle was found to be greater than the left knuckle area due to proximity of the *Tuyere2* to furnace axis compared to *Tuyere1*.

ACKNOWLEDGEMENTS

Funding from the Australian Research Council Industrial Transformation Research Hubs Scheme (Project Number IH130100017) is gratefully acknowledged.

REFERENCES

Alam, M, Naser, J and Brooks, G, 2010. Computational Fluid Dynamics Simulation of Supersonic Oxygen Jet Behavior at Steelmaking Temperature, *Metallurgical and Materials Transactions, B,* 41:636–645.

Barron, M, Hilerio, I and Medina, D, 2015. Slag Splashing in a Basic Oxygen Furnace under Different Blowing Conditions, *Open Journal of Applied Sciences*, 5(12):819-825. https://doi.org/10.4236/ojapps.2015.512078.

Cheslak, F R, Nicholls, J A and Sichel, M, 1969. Cavities formed on liquid surfaces by impinging gaseous jets, *Journal of Fluid Mechanics,* 36:55–63.

Drain, P B, 2018. The effect of titanium on phosphorus removal during Basic Oxygen Steelmaking, PhD thesis, University of Wollongong.

Fruehan, R J, 1998. *The making, shaping and treating of steel* (AISE Steel Foundation: Pittsburgh).

Leão, P M G C, Rodrigues, E F, Da Silva, C A, Da Silva, I A and Seshadri, V, 2016. Influence of Physical Properties of Slag and Operational Parameters on Slag Splashing Process in an Oxygen Convertor, in *Advances in Molten Slags, Fluxes, and Salts: Proceedings of the 10th International Conference on Molten Slags, Fluxes and Salts 2016* (eds: R G Reddy, P Chaubal, P C Pistorius and U Pal), pp 1043–1051 (Springer: Cham). https://doi.org/10.1007/978-3-319-48769-4_111

Lee, M S, O'Rourke, S and Molloy, N A, 2001. Preferential refractory wear in top blown basic oxygen furnace, *Ironmaking and Steelmaking,* 28:244–249.

Li, M, Li, Q, Kuang, S and Zou, Z, 2016a. Computational Investigation of the Splashing Phenomenon Induced by the Impingement of Multiple Supersonic Jets onto a Molten Slag–Metal Bath, *Industrial and Engineering Chemistry Research,* 55:3630–3640.

Li, M, Li, Q, Kuang, S B and Zou, Z, 2015. Coalescence Characteristics of Supersonic Jets From Multi-Nozzle Oxygen Lance in Steelmaking BOF, *Steel Research International,* 86:1517–1529.

Li, Q, Li, M, Kuang, S B and Zou, Z, 2016b. Understanding Characteristic of Abrasion of Refractory Lining Caused by Bath Oscillation in BOF Steelmaking, *JOM,* 68:3126–3133.

Luomala, M J, Fabritius, T M J, Virtanen, E O, Siivola, T P, Fabritius, T L J, Tenkku, H, and Härkki, J J, 2002. Physical Model Study of Selective Slag Splashing in the BOF, *ISIJ International,* 42:1219–1224.

Mills, K C, Su, Y, Fox, A B, Li, Z, Thackray, R P and Tsai, H T, 2005. A Review of Slag Splashing, *ISIJ International,* 45:619–633.

Mills, K C, Yuan, L and Jones, R T, 2011. Estimating the physical properties of slags, *Journal of the Southern African Institute of Mining and Metallurgy,* 111:649–658.

Odenthal, H J, Falkenreck, U and Schlüter, J, 2006. CFD simulation of multiphase melt flows in steelmaking converters, in European Conference on Computational Fluid Dynamics, The Netherlands.

Qinglin, H, 1990. Fluid dynamics and droplet generation in the BOF steelmaking process, PhD thesis, University of Wollongong.

Sabah, S and Brooks, G, 2014. Splashing in Oxygen Steelmaking, *ISIJ International,* 54:836–844.

Sattar, M A, Naser, J and Brooks, G, 2014. Numerical simulation of slag foaming on bath smelting slag ($CaO–SiO_2–Al_2O_3–FeO$) with population balance modeling, *Chemical Engineering Science,* 107:165–180.

Sinelnikov, V, Szucki, M, Merder, T, Pieprzyca, J and Kalisz, D, 2021. Physical and Numerical Modeling of the Slag Splashing Process, *Materials,* 14:2289.

Sun, J, Zhang, J, Lin, W, Feng, X and Liu, Q, 2022. Effect of Bottom Blowing Mode on Fluid Flow and Mixing Behavior in Converter, *Metals,* 12:117.

Modelling of gas-slag flow behaviour in the ironmaking blast furnace – a review

DOI: 10.62053/UDRR3508

X F Dong[1], B J Monaghan[2] and P Zulli[3]

1. Research Fellow, ARC Research Hub for Australian Steel Innovation, University of Wollongong, Wollongong NSW 2522. Email: xuefeng@uow.edu.au
2. Professor, School of Mechanical, Materials, Mechatronic and Biomedical Engineering, University of Wollongong, Wollongong NSW 2522. Email: monaghan@uow.edu.au
3. Director, ARC Research Hub for Australian Steel Innovation, University of Wollongong, Wollongong NSW 2522. Email: paulz@uow.edu.au

ABSTRACT

In the lower zone of blast furnace (BF), slag trickles down through a packed bed of carbonaceous particles in the form of films, rivulets or droplets. During its downward flow, there are significant interactions occurring between slag and other phases, ie gas and packing particles. In particular, the interaction between gas and slag is closely associated with the key flow phenomena such as loading, flooding or channelling in the lower zone of the BF. With gas introduced laterally through tuyeres and slag flowing downward from the cohesive zone to the hearth, this interaction varies throughout the lower zone and in the cohesive zone:

- strong cross-flow of gas relative to the slag occurs in front of the raceway
- counter-current flow of gas and slag occurs in the upper parts of the lower zone
- both strong cross- and counter-current flow of gas and slag around and within the cohesive zone.

These interactions can be linked to furnace irregularities, affecting smooth operation and limiting production. Therefore, understanding the gas-slag interaction and its influencing factors remains critical for BF process control.

In the current review, the physical behaviour and key influencing factors of gas and slag flow are initially examined. Numerical models describing gas and slag flows in a packed bed at micro-, meso- and macro-scopic levels, are reviewed. Each simulation approach has its advantages and limitations, as well as unique assumptions when used in BF process modelling. Applications of these approaches to gas-slag flow in key identified functional zones will highlight the differences between approaches and modelling outcomes. As no single approach can fully address all aspects of gas-slag interactions, an integration of different approaches is considered an effective and beneficial method in providing a more complete understanding of gas-slag flow in the BF process.

INTRODUCTION

In the blast furnace (BF), the impurities (silica and alumina) in iron ore are removed in the form of blast furnace slag through the combination with flux materials such as limestone, dolomite and other slag forming agents. Slag is formed in the cohesive zone (CZ) of the BF process, together with the generation of liquid iron (hot metal). The liquid percolates through the coke in the lower zone, to the hearth. If pulverised coal injection or other solid injection technology is practiced, then at high rates, unburnt coal (or other remnant materials) may leave the raceway region via gas entrainment as a distinct powder phase. Thus, the multi-phases in the lower part of BF interact exist. During slag generation and removal from the furnace, physicochemical characteristics of slag and its interaction with other phases significantly influence BF operation in terms of furnace permeability, hot metal (HM) products quality and productivity, desulfurisation, coke consumption and production efficiency.

In terms of slag properties, different types of slags are usually identified across different regions, such as primary slag in the CZ, bosh slag in the dripping zone and final slag in the hearth. For smooth operation, the flow behaviour of slag in different regions needs to be understood. In this review, the physical behaviour and key influencing factors of gas-slag flow in the BF are initially examined – this is followed by a summary of the numerical approaches applied to the gas-slag flow in the process. General mathematical formulations are introduced with respect to the approaches used at micro-,

meso- and macro-scopic levels. Afterwards, the application of these approaches to gas-slag flow in major regions of interest is discussed in relation to key flow features. Finally, the challenges of modelling of gas-slag flow in the BF process are summarised, with emphasis on model development trends.

PHYSICAL PHENOMENA OF GAS-SLAG FLOW IN THE IRONMAKING BLAST FURNACE

Dissection studies of quenched blast furnaces demonstrate the existence of a CZ where the liquid iron and slag are generated from reduced and melted ferrous materials (Omori, 1987). The generated liquid trickles down through the coke bed to the hearth. During this process, very complex and intensive interactions occur, such as heat and mass transfer between liquid and other phases. From the dissection studies, specific phenomena were identified, including:

- Liquid generated in the CZ passing directly into the dripping zone or interacting with the cohesive layer beforehand, with metal icicles and slag droplets found in the coke slits of Hirohata No 1 and in Mannesmann No 5 BFs.
- Liquid holdup in Chiba No 1 BF was higher in the lower layers of the CZ than in the radially adjacent dripping zone.
- In Kukioka No 4 BF, a dense layer of metal and slag at the lower and back parts of the raceway cavity was found, suggesting that liquid had descended near the wall immediately above and below the raceway and between raceways.

Slag types

As the slag percolates through the coke zone, ie from the CZ, through the dripping zone, and to the hearth, slags with distinct compositions are produced eg primary slag, bosh slag and final slag. The formation of primary slag with high MnO and FeO content in the CZ is closely linked to the charged ferrous burden materials. As the descending primary slag incorporates lime and the FeO/MnO in the slag is reduced, the primary slag gradually transforms to bosh slag at tuyere level. After absorption of silica from coke ash and unburnt pulverised coal, bosh slag is converted to the final slag. This slag accumulates in the hearth until tapped. The final slag composition is primarily comprised of SiO_2, Al_2O_3, CaO and MgO.

Flow behaviour

Different slag flow behaviours have been identified around the CZ and near the gas inlet (raceway) through different studies, such as under two dimensional experimental conditions (Chew *et al*, 1997), ie:

- Molten slag percolates through a packed bed as a series of rivulets or drops.
- Slag/iron flow is significantly affected by the cross-flow of air near the gas inlet so that the dry region can be formed.
- Localised upflow of slag, complete filling of local void, and flooding may occur in the CZ, where strong gas flow and gas-slag interaction exist.

Influencing factors

The complexity of slag flow in the lower part of the BF is affected by these different slags, as well as zone-specific phenomena in the different flow regimes and the different phases states. These are influenced by various factors, including:

- Physical and chemical properties of slag which are functions of slag composition that changes during slag flow.
- Interactions with other phases (eg coke) including slag wettability, chemical reactions, heat, mass and momentum transfer.
- High temperature properties of ferrous materials and packing property of coke particles.

- Environmental and operating conditions such as temperature, blast volume and slag volume.

NUMERICAL MODELLING OF GAS-SLAG FLOW IN THE IRONMAKING BLAST FURNACE

Various numerical approaches have been used to simulate the complex flow behaviour of gas-slag in the BF. These may be classified into three categories: (1) continuum approach, (2) 'discrete' approach, and (3) miscellaneous approach.

Continuum approach

The key features/issues for continuum-based approaches are:

- Phases are generally considered as fully interpenetrating continuum media.
- Coupling between phases is represented by constitutive relations and interaction terms.
- Sum of volume fractions of phases is unity.
- Application is at a macroscopic level; hence suited for process modelling and applied research due to computational convenience and efficiency.

The general governing equations are within the framework of the two-fluid model (Gidaspow, 1994), as given by:

Conservation of mass:

$$\frac{\partial}{\partial t}(\varepsilon_i \rho_i) + \nabla \cdot (\varepsilon_i \rho_i \mathbf{u}_i) = S_i \tag{1}$$

Conservation of momentum:

$$\frac{\partial}{\partial t}(\varepsilon_i \rho_i \mathbf{u}_i) + \nabla \cdot (\varepsilon_i \rho_i \mathbf{u}_i \mathbf{u}_i) = -\varepsilon_i \nabla p + \nabla \cdot \boldsymbol{\tau}_i + \sum_j \mathbf{F}_i^j + \varepsilon_i \rho_i \mathbf{g} \tag{2}$$

The effective use of the continuum approach depends heavily on constitutive relations and the momentum exchange between phases. For gas-slag flow in the packed bed, the momentum exchanges between phases, $\mathbf{F}_i^j$, are mainly empirically based. A summary is provided in Table 1, for gas-solid (G-S), gas-liquid (G-L) and liquid-solid (L-S).

TABLE 1

Empirical correlations for the interaction forces between phases.

	Interaction forces	References
G-S	$\mathbf{F}_g^s = -\mathbf{F}_s^g = -\left[150\mu_g \frac{a_{gs}^2}{36\varepsilon_g} + 1.75\rho_g a_{gs}\lvert\mathbf{u}_g - \mathbf{u}_s\rvert\right](\mathbf{u}_g - \mathbf{u}_s)$	(Yagi, 1991)
G-L	$\mathbf{F}_g^l = -\mathbf{F}_l^g = -0.75 C_{d,gl} \frac{\varepsilon_l \rho_g}{\phi_l d_l}\lvert\mathbf{u}_g - \mathbf{u}_l\rvert(\mathbf{u}_g - \mathbf{u}_l)$	(Szekely and Kajiwara, 1979)
	$\mathbf{F}_g^l = -\mathbf{F}_l^g = -\left[150 f_{gl,1} \frac{(1-\varepsilon)^2 \mu_g}{d_s^2 \varepsilon_g} + 1.75 f_{gl,2} \frac{(1-\varepsilon)\rho_g}{d_s}\lvert\mathbf{u}_g - \mathbf{u}_l\rvert\right](\mathbf{u}_g - \mathbf{u}_l)$	(Iliuta *et al*, 2003)
L-S	$\mathbf{F}_l^s = -\mathbf{F}_s^l = -C_{d,ls}\mu_l\lvert\mathbf{u}_1 - \mathbf{u}_s\rvert(\mathbf{u}_1 - \mathbf{u}_s)$	(Sugiyama and Sugata, 1987)
	$\mathbf{F}_l^s = -\mathbf{F}_s^l = -\left[150 f_{ls,1} \frac{(1-\varepsilon)^2 \mu_l}{d_s^2 \varepsilon_l} + 1.75 f_{ls,2} \frac{(1-\varepsilon)\rho_l}{d_l}\lvert\mathbf{u}_l - \mathbf{u}_s\rvert\right](\mathbf{u}_l - \mathbf{u}_s)$	(Iliuta *et al*, 2003)

‘Discrete’ approach

In the ‘discrete’ approach, the phases are described based on the analysis of the motion of individual fluid elements such as small droplets. Hence, the approach can simulate the fluid flow at micro- or meso-scopic levels. To date, the ‘discrete’ approach has been applied to liquid phase modelling in the metallurgical field through the Smooth Particle Hydrodynamics (SPH) (Kon *et al*, 2012; Natsui *et al*, 2015) and Volume of Fluid (VOF) (Jeong, Kim and Sasaki, 2013; Geleta, Siddiqui and Lee, 2020; Dong *et al*, 2021a) methods.

Smooth particle hydrodynamics

The key features and issues for the SPH method are:

- A particle approach for modelling incompressible free surface flows at a microscopic level.
- The liquid phase comprises a finite number of individual particles.
- The motion of each particle is described using the continuity and navier-stokes equations, with the particle is tracked by a lagrangian method.
- Computationally, it is extremely demanding.

The basic equations of the SPH model (Kon *et al*, 2012) are given as follows:

$$\frac{D\rho}{Dt} = -\rho\nabla\cdot\boldsymbol{v} \tag{3}$$

$$\frac{D\boldsymbol{v}}{Dt} = -\rho\nabla p + \nu\nabla^2\boldsymbol{v} + \boldsymbol{g} + \frac{\boldsymbol{F}_s}{\rho} \tag{4}$$

The interaction between individual particles is based on the surface tension model (Kon *et al*, 2012). Gradient and Laplacian models are used to discretise the gradient and Laplacian of scalar and vector quantities. The pressure in the model has to be solved based on the derived Poisson’s equation. Some efforts have been made to reduce the pressure oscillation, such as the introduction of restricted compressibility in the Poisson equation to make the simulation stable.

The approach has been applied to dispersion, coalescence and distribution of liquid droplets in a packed bed (Kon *et al*, 2012; Natsui *et al*, 2015). However, SPH simulations are still limited to study at a small scale, such as the influence of solid-liquid wettability and viscosity on liquid flow in a packed bed. It is heavily dependent on the calculation of pressure. The effect of gas flow on liquid droplets has not been considered in the simulations.

Volume of Fluid model

The key features/issues for the Volume of Fluid model are:

- Capable of tracking the interface between immiscible phases.
- Simulation of steady or transient movement of multi-immiscible fluids with distinct physical properties is possible.
- Multi-physics simulations coupled with other physical models such as heat transfer and chemical reactions is feasible.
- Computationally expensive, especially for large-scale simulations.

The basic equations of the VOF model are given as follows:

$$\frac{\partial\varepsilon_i}{\partial t} + \nabla\cdot(\varepsilon_i\boldsymbol{u}) = 0 \tag{5}$$

$$\frac{\partial}{\partial t}(\rho\boldsymbol{u}) + \nabla\cdot(\rho\boldsymbol{u}\boldsymbol{u}) = -\nabla p + \nabla\cdot\boldsymbol{\tau} + \rho\boldsymbol{g} + S_m \tag{6}$$

Solution of the volume fraction equation, ie Equation (5), is used to track the interface between the phases. In the momentum equation, S_m refers to the surface tension force, $2\rho\kappa_i\sigma_{ij}\nabla\varepsilon_i/(\rho_i+\rho_j)$, which is used to account for the interaction between the phases. A single momentum equation is solved throughout the domain and the resulting velocity field is shared among the phases. The physical properties of the mixture such as density and viscosity are phase-volume-fraction-averaged.

The approach has been applied to liquid droplets flow in a packed bed (Jeong, Kim and Sasaki, 2013; Geleta, Siddiqui and Lee, 2020; Dong *et al*, 2021b), where studies at a laboratorial scale were carried out. The flow behaviour of slag droplets at a particle scale was visualised and investigated in terms of slag properties, holdup distribution and interactions with other phases. Due to the demanding computational capacity, previous investigations were limited to either small scale or two-dimensional studies when VOF is directly used to simulate liquid flow within the interstitial region between packing particles. However, this method has great potential for future application with the rapid development of computer technology. The same applies to the above SPH method.

The VOF model was also applied to simulate liquid flow in the hearth whilst considering the averaged transport equations in the packed bed (Nishioka, Maeda and Shimizu, 2005; Guo *et al*, 2006; Merten *et al*, 2023). In this case, an Ergun type of equation was applied to account for the strong interaction between liquid and packing particles (solids) and used for source term (S_m) in the momentum equation. However, the governing equations for the extended VOF model for bulk flow of slag in the packed bed are not consistent in the literature and further development is required.

Miscellaneous approach

Beyond the continuum and 'discrete' approaches, some specific models have been applied to simulate fluid flow patterns eg probability (Ohno and Schneider, 1988), tube network dynamic (Eto *et al*, 1994) and force balance (Wang *et al*, 1997) models for liquid flow. Rather than treating liquid as a pure continuous medium or 'discrete' elements, these models adopt more flexible methods. For example:

- In the probability model (Ohno and Schneider, 1988), the liquid downward flow is determined by distribution ratios/coefficients determined experimentally.
- In the force balance model (Wang *et al*, 1997), liquid flow is treated as discrete droplets or rivulets that percolate through the packed bed. For applications, in a computational cell equivalent to that used in the continuum approach, a force balance is used for the liquid flow. Through this approach, the liquid flow is determined by gravity and drag forces and the complex packing geometry.

In the last two decades, various comprehensive reviews (Yagi, 1991; Dong *et al*, 2007; Kuang, Li and Yu, 2017) have summarised the formulation, capabilities and application of numerical approaches applied for the slag flow in the BF process. Earlier reviews (Yagi, 1991) mainly focused on the continuum approach, whilst more recent reviews (Dong *et al*, 2007; Kuang, Li and Yu, 2017) focused on multi-scale approaches. However, there remain many challenges in the development and application of these numerical approaches. As no single approach can adequately address all aspects in the complex BF process, the following sections provide a summary of findings and capabilities of models with respect to features in major functional zones of BF, as well as their potential future development.

NUMERICAL MODELLING OF LOCAL GAS-SLAG FLOW BEHAVIOUR IN THE FUNCTIONAL ZONES OF A BLAST FURNACE

Based on the dissection study of Japanese BF in 1970s, slag generation and its subsequent downward flow and interaction with gas are linked within the key BF functional zones, (Omori, 1987). Modelling of gas-slag flow will be reviewed in the following sections in terms of the major identified functional zones: cohesive, dripping and hearth zones.

Cohesive zone

The cohesive zone works as a gas distributor and liquid generator with remarkable variations in fluid flow direction, pressure, temperature and species concentration, all of which affect the BF performance, operational stability and productivity.

BF dissection studies showed that the CZ has a layered structure consisting of molten, softening, lumpy and coke-only regions, as shown in Figure 1a. Iron-bearing materials are gradually transformed from a lumpy through to melt down state. The shape and position of the CZ can change significantly with operational conditions.

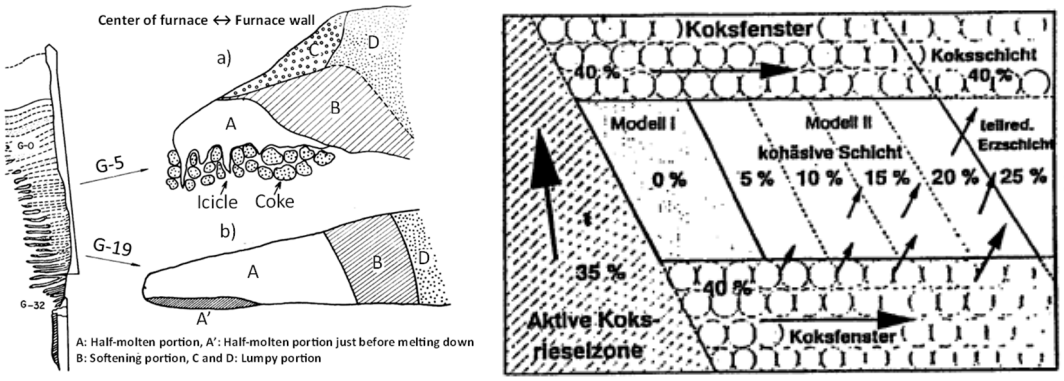

FIG 1 – (a) Schematic showing the internal state of the cohesive zone (Sasaki *et al*, 1977), and (b) model of the cohesive layer (Gudenau, Standish and Gerlach, 1992).
Note: Aktive Koksrieselzone – active coke zone, Koksfenster – coke window, Koksschicht – coke layer, Kohäsive Schicht – cohesive layer, teilred Erzschicht – partly reduced ore layer.

In order to better understand this zone, modelling of gas-slag flow was carried out through two ways: the CZ sub-model; and global modelling of BF process.

- In the CZ sub-model shown in Figure 1b, gas tends to flow preferentially through coke-slits. Liquid (primary slag and liquid iron) melts down from ore which is heated by gas passing through the coke-slits. For simplicity, a homogeneous model was applied for slag, iron and iron oxide in the cohesive layer, with an imposed porosity distribution along the horizontal direction of layer, dependent on melting temperature.
- Through global modelling, the CZ is treated either as a mixed region of iron-bearing materials and coke (Sugiyama and Sugata, 1987; Austin, Nogami and Yagi, 1997), or discrete layers (Dong *et al*, 2010). Continuum or Miscellaneous approaches were applied for gas-slag flow. However, these simulations were carried out under steady-state or pseudo steady-state conditions whilst ignoring the softening and melting process. It is difficult to understand the impact of transient processes occurring in the CZ – such as softening and melting of iron-bearing materials, phase transformation (eg soften-melting and solidification and flooding phenomena) and chemical reactions, based solely on a global modelling approach. Whilst in global modelling, the CZ region may be defined using solid temperatures or the shrinkage ratio of ferrous materials, in effect, it mainly represented a liquid (slag and liquid iron) source in the modelling.

The prediction of gas-slag flow in the CZ, where there is slag generation and a strong localised liquid flow involving downward, horizontal or even upward flow, remains a longstanding and challenging task.

Dripping zone

The dripping zone is featured by co-existing multiphases such as slag, liquid iron, coke, fine coke and unburnt coal. There are multiple states of each phase including static and dynamic holdup for liquid and powder, as well as complex solids flow regions. In terms of gas-slag flow, unique flow phenomena such as flooding and 'dry' areas may be present. Reactions occurring in this zone (including iron carburisation reaction and silicon transfer) determine the quality of final hot metal product.

In a numerical sense, the description of this zone is relatively poor. The development of global BF models either ignored the strong interaction between phases or invoked simplifications (Sugiyama and Sugata, 1987; Austin, Nogami and Yagi, 1997), especially for liquid flow.

In practice, the interaction between slag and other phases may cause flooding and accumulation – these phenomena are very likely to cause problems in BF operations. In fact, control of the BF process is, in part, constrained by knowledge of these complex phenomena.

In the dripping zone, different models have been proposed to describe the gas and liquid flows in the BF within the framework of continuum and miscellaneous approaches. These include potential flow (Szekely and Kajiwara, 1979; Sugiyama and Sugata, 1987), probability (Ohno and Schneider, 1988), probability-continuous (Wang, Takahashi and Yagi, 1991), tube network dynamic (Eto *et al*, 1994) and force balance (Wang *et al*, 1997) models. Among these, the force balance model is perhaps the most attractive because of its advantages in computation and representation of the relevant physics of liquid flows through a packed bed. As shown in Figure 2, both the liquid dry zone and liquid dispersion can be identified.

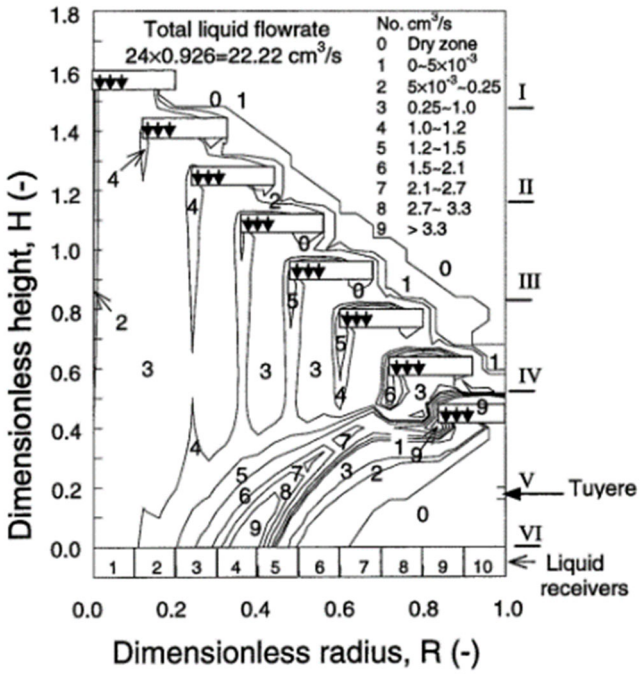

FIG 2 – Predicted liquid flow rate distribution in a simulated blast furnace lower zone (Wang *et al*, 1997). Note that this isothermal simulation is based on the water used at room temperature in the corresponding experiments.

To date, it remains difficult to simulate the division, collection, coalescence and deformation of liquid droplets using the continuum approach. In particular, for the high temperature conditions, the variation of phase properties together with the interactions between phases in relation to reactions and changing interfaces, make simulation more complex. In this respect, the 'discrete' approach has the capability to model and describe coalescence of droplets (Kon *et al*, 2012; Natsui *et al*, 2015; Dong *et al*, 2023). Although the study of the movement of liquid droplets is still at an early stage, the detailed micro-dynamic information provided by discrete techniques will assist in understanding the formation mechanisms of 'accumulation' phenomena and the influence of key factors. For example:

- The 'icicle' flow of iron under the cohesive zone was highlighted in the discrete simulation.
- Good wettability causes less liquid dispersion in the packed bed.
- Liquid (slag) viscosity controls the dynamic holdup.
- The significant influence of packing structure on the macroscopic flow behaviour of slag.

Figure 3 illustrates how the distribution of the slag flow path becomes narrower as viscosity increases. Regarding the effect of wettability on the slag flow (Figure 4), a more non-wetting slag (contact angle = 157°) flows predominantly around the less permeable (deadman) region (region of smaller diameter particles), with higher slag holdups near the interface. Note that deadman refers to a stagnant zone of coke particles in the centre of the lower part of the BF. As the contact angle decreases, slag can flow into the deadman region. In particular, the flow path for the more wetting slag (contact angle = 60°) appears stream-like rather than discrete droplets (Figure 4d).

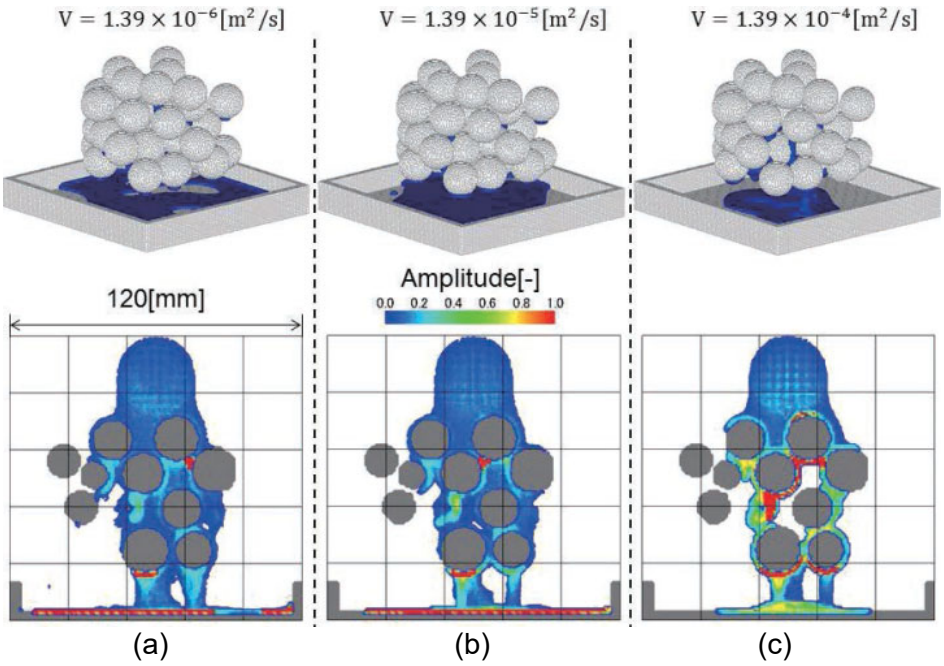

FIG 3 – Effect of viscosity on variation of flow path (Kon *et al*, 2012). Note that assumed liquid properties were used in this isothermal simulation, with surface tension coefficient of water and different viscosities.

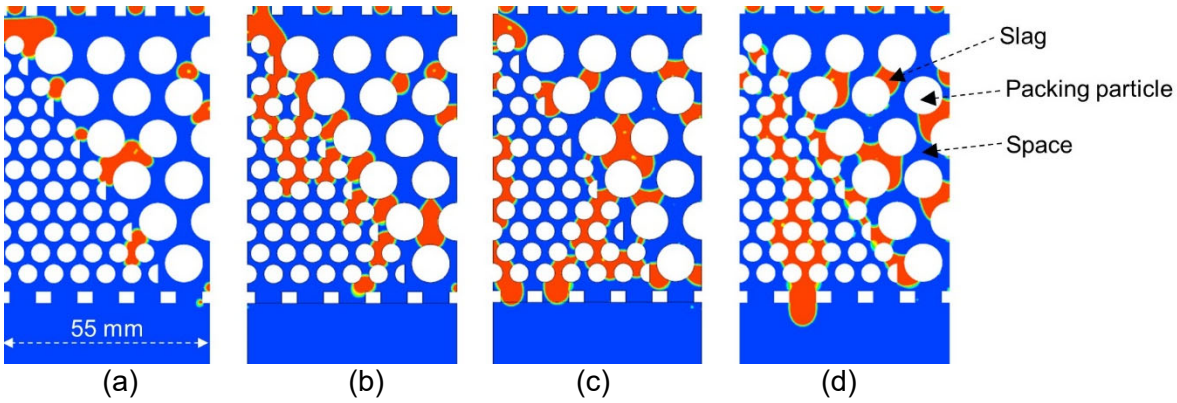

FIG 4 – Effect of wettability on variation of flow path in the packed bed in terms of different contact angles: (a) 157°, (b) 120°, (c) 90° and (d) 60° (Dong *et al*, 2023). Note that the four-component slag used in this simulation consists of CaO 40.7, SiO_2 37.4, Al_2O_3 12.5, MgO 8.8 wt per cent and the environmental temperature is constant 1500°C.

Applying the discrete approach to the dripping zone requires significant computational time due to a very high number of liquid droplets. In the literature, only very limited number of droplets are simulated within a small-scale computational domain (Kon *et al*, 2012; Dong *et al*, 2023). To reliably simulate the liquid flow at a microscopic level, the challenges are evident in terms of computational time. With rapid developments in computational technology, this should be gradually overcome. It is also anticipated that if the strong interaction between gas and slag phases in the lower part of BF is considered in such simulations, heat transfer and chemical reactions can be investigated in detail.

Hearth

Molten liquid products (slag and iron/hot metal) are collected in the hearth, where the large density difference between slag and hot metal leads to two immiscible liquid layers. The coke bed extends to the hearth refractory pad or floats partially or completely in the liquids bath. The flow, temperature and chemistry of liquids significantly influence the refractory wear of the hearth in terms of mechanical/thermal shock and chemical attack as well as the stability of the BF operation, product quality and productivity.

The simulation of coupled liquid flow and heat transfer in the hearth was mainly applied to understand the hot metal flow behaviour (eg Panjkovic, Truelove and Zulli, 2002). There are limited numerical studies (Nishioka, Maeda and Shimizu, 2005; Guo *et al*, 2006; Merten *et al*, 2023) on the slag flow and movement of gas-slag interface using an extended VOF model. These mainly focus on:

- Drainage behaviour of slag and hot metal in terms of taphole condition, coke bed permeability and coke size.
- Variation of gas-slag interface in relation to different operating conditions such as CZ location, blast condition and deadman properties (Figure 5).
- Coupled slag/hot metal flow, heat transfer and chemical reaction (carbon dissolution) in the hearth considering intermittent drainage.

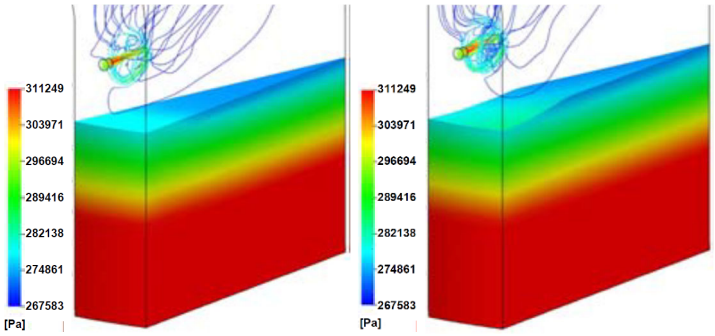

(a) (b)

FIG 5 – Pressure distribution in liquid versus liquid surface shape: (a) before deformation, (b) after deformation of liquid surface (Guo *et al*, 2006). Note that the slag density used in this isothermal simulation is 2500 kg·m^{-3} and the viscosity is 0.5 Pa·s.

CHALLENGES OF MODELLING OF GAS-SLAG FLOW IN THE IRONMAKING BLAST FURNACE

Based on this review, research and development areas identified for future consideration for modelling gas-slag flow in the ironmaking BF include the following.

Model development

- Integration of approaches used at different scales such as a continuum approach at the macroscopic level and a 'Discrete' approach at micro- and meso-scopic levels.
- Appropriate volume/time averaging of VOF model for the bulk flow of gas-slag in the packed bed.
- Further development of continuum and miscellaneous approaches enabling their application to special phenomena of slag flow such as flooding.
- Development of coupled SPH and continuum modelling for gas-slag flow.
- Appropriate incorporation of gas-slag and slag-coke reactions in the transient modelling of gas-slag flow in the coke packed bed considering heat transfer and chemical reactions.
- Derivation of the constitutive equations for the interactions between slag and other phases such as fine particles and liquid metal.

Phenomena understanding

- Transient process of gas-slag flow occurring in the CZ, considering softening and melting of iron-bearing materials, phase transformation and chemical reactions.
- Influence of CZ shapes on slag flow, slag properties and subsequent heat and mass transfer in the lower part of BF.

- Evaluation of conditions involving solidification and fluidisation of slag within and around the CZ, and operational CZ limitations in terms of coke slit length and cross-sectional area.
- Reliable prediction of residence time and distribution of slag in the dripping zone considering the complex operational conditions and coke bed structure.
- Quantitative analysis detailing gas-slag and slag-coke reactions on gas-slag flow in the dripping zone, particularly in terms of varying slag composition, surface tension, viscosity and wettability.
- Quantitative analysis of hot metal quality control in terms of interaction between slag and hot metal and slag-metal reaction in the hearth.
- Evaluation of flow behaviour in the slag layer and hot metal bath and gas-slag interface variation in the furnace.
- Investigation of the effect of liquid (slag/hot metal) flow on the coke renewal in the deadman.

The above research and development efforts should provide the basis for furthering the fundamental understanding and practical evaluation on flow behaviour of gas-slag in the lower part of BF.

CONCLUSIONS

Successful operation of a BF under quite different, potentially more critical, conditions (eg low carbon consumption, lower quality raw materials) is more likely to be achieved with a more complete understanding of the complex phenomena in the lower part of the furnace. In terms of liquid flow and its interaction with other phases, use of numerical modelling provides an excellent tool for investigating and determining the influence of such phenomena as dynamic wettability and liquid dispersion in the complex bed structure and functional zones – as well, the liquid distribution under high temperature conditions and various liquid properties can be quantified and potentially used for operational design. This review summarises the current status of gas-slag modelling and highlights the gaps and challenges in terms of model development and phenomena understanding. Although the developments/challenges are quite broad from the fundamental understanding to the process application, the outcome should provide direct guidance for the preparation of raw material and optimised lower zone control.

It is worth mentioning that the slag properties and the interaction between slag and other phases can significantly affect the numerical modelling results. Therefore, generating high-quality high-temperature thermophysical property data in key areas such as interfacial tension/wettability remains a challenge and imperative beyond the numerical modelling work discussed.

REFERENCES

Austin, P R, Nogami, H and Yagi, J I, 1997. A mathematical model of four phase motion and heat transfer in the blast furnace, *ISIJ International*, 37(5):458–467.

Chew, S J, Wang, G X, Yu, A B and Zulli, P, 1997. Experimental study of liquid flow in blast furnace cohesive zone, *Ironmaking and Steelmaking*, 24(5):392–400.

Dong, X F, Jayasekara, A, Sert, D, Ferreira, R, Gardin, P, Chew, S J, Pinson, D, Monaghan, B J and Zulli, P, 2023. Slag flow in the packed bed with varied properties and bed conditions: numerical investigation, *Metallurgical and Materials Transactions B*, 54(1):56–69.

Dong, X F, Jayasekara, A, Sert, D, Ferreira, R, Gardin, P, Monaghan, B J, Chew, S J, Pinson, D and Zulli, P, 2021a. Investigation of molten liquids flow in the blast furnace lower zone: numerical modelling of molten slag through channels in a packed bed, *Metallurgical and Materials Transactions B*, 52(1):255–266.

Dong, X F, Jayasekara, A, Sert, D, Ferreira, R, Gardin, P, Monaghan, B J, Chew, S J, Pinson, D and Zulli, P, 2021b. Numerical investigation of slag flow through a coke funnel analog and packed bed, *Metallurgical and Materials Transactions B*, 52(5):2926–2938.

Dong, X F, Yu, A B, Chew, S J and Zulli, P, 2010. Modeling of blast furnace with layered cohesive zone, *Metallurgical and Materials Transactions B*, 41(2):330–349.

Dong, X, Yu, A, Yagi, J I and Zulli, P, 2007. Modelling of multiphase flow in a blast furnace: Recent developments and future work, *ISIJ International*, 47(11):1553–1570.

Eto, Y, Takeda, K, Miyagawa, S, Itaya, H and Taguchi, S, 1994. Experiments and simulation of the liquid flow in the dropping zone of a blast furnace, *ISIJ International*, 33(6):681–686.

Geleta, D D, Siddiqui, M I H and Lee, J, 2020. Characterization of slag flow in fixed packed bed of coke particles, *Metallurgical and Materials Transactions B*, 51(1):102–113.

Gidaspow, D, 1994. *Multiphase Flow and Fluidization*, pp 1–8 (Academic Press: San Diego).

Gudenau, H W, Standish, N and Gerlach, W, 1992. Physical conditions in the area of the blast-furnace cohesive zone.2. measuring results and model development, *Stahl Und Eisen*, 112(9):113–119.

Guo, B Y, Zulli, P, Maldonado, D and Yu, A B, 2006. Numerical analysis of gas flow-slag surface interaction in blast furnace, in *Fifth International Conference on CFD in the Process Industries*, (CSIRO: Melbourne).

Iliuta, I, Grandjean, B P A, Piche, S and Larachi, F, 2003. Two-fluid model for countercurrent dumped packing-containing columns, *Chemical Engineering Science*, 58(7):1373–1380.

Jeong, I H, Kim, H S and Sasaki, Y, 2013. Trickle flow behaviors of liquid iron and molten slag in the lower part of blast furnace, *ISIJ International*, 53(12):2090–2098.

Kon, T, Natsui, S, Ueda, S, Inoue, R and Ariyama, T, 2012. Numerical simulation of dripping behavior of droplet in packed bed using particle method, *ISIJ International*, 52(9):1565–1573.

Kuang, S, Li, Z and Yu, A B, 2017. Recent developments in the modeling and simulation of blast furnace ironmaking, *Steel Research International*, 201700071.

Merten, H, Wirtz, S, Bartusch, H, Kaymak, Y, Hojda, S, Lin, R and Scherer, V, 2023. Analysis of the impact of carbon dissolution and energy transport on the flow in the hearth of an ironmaking blast furnace by transient CFD simulations, *Thermal Science and Engineering Progress*, 39:101747.

Natsui, S, Kikuchi, T, Suzuki, R O, Kon, T, Ueda, S and Nogami, H, 2015. Characterization of liquid trickle flow in poor-wetting packed bed, *ISIJ International*, 55(6):1259–1266.

Nishioka, K, Maeda, T and Shimizu, M, 2005. A three-dimensional mathematical modelling of drainage behavior in blast furnace hearth, *ISIJ International*, 45(5):669–676.

Ohno, Y and Schneider, M, 1988. Effect of horizontal gas flow on liquid dropping flow in two-dimensional packed bed, *Tetsu to Hagane*, 74:1923–1930.

Omori, Y, 1987. *Blast Furnace Phenomena and Modelling*, pp 24–30 (Elsevier Applied Science: London).

Panjkovic, V, Truelove, J S and Zulli, P, 2002. Numerical modelling of iron flow and heat transfer in blast furnace hearth, *Ironmaking and Steelmaking*, 29(5):390–400.

Sasaki, M, Ono, K, Suzuki, A, Okuno, Y and Yoshizawa, K, 1977. Formation and melt-down of softening-melting zone in a blast furnace, *Trans Iron Steel Inst Jpn*, 17(7):391–400.

Sugiyama, T and Sugata, M, 1987. Development of two-dimensional mathematical model for the blast furnace: 'BRIGHT', *Nippon Steel Technical Report*, (35):32–42.

Szekely, J and Kajiwara, Y, 1979. A mathematical representation of spatially non-uniform, countercurrent flow of gases and liquids in packed beds – relevance to flow phenomena in the bosh of iron blast furnaces, *Trans Iron Steel Inst Jpn*, 19(2):76–84.

Wang, G X, Chew, S J, Yu, A B and Zulli, P, 1997. Model study of liquid flow in the blast furnace lower zone, *ISIJ International*, 37(6):573–582.

Wang, J, Takahashi, R and Yagi, J I, 1991. Simulation model of the gas-liquid flows in the packed bed, *Tetsu to Hagane*, 77(10):1585–92.

Yagi, J I, 1991. Recent progress in fundamental and applied researches in blast furnace ironmaking in Japan, *ISIJ International*, 31(5):387–394.

Molten slag flow in an ironmaking blast furnace – a mesoscopic level investigation

DOI: 10.62053/RTCQ4781

X F Dong[1], A Jayasekara[2], D Sert[3], R Ferreira[4], P Gardin[5], S J Chew[6], D Pinson[7], B J Monaghan[8] and P Zulli[9]

1. Research Fellow, ARC Research Hub for Australian Steel Innovation, University of Wollongong, Wollongong NSW 2522. Email: xuefeng@uow.edu.au
2. Research Associate, ARC Research Hub for Australian Steel Innovation, University of Wollongong, Wollongong NSW 2522. Email: apsara@uow.edu.au
3. Ironmaking Specialist, ArcelorMittal Maizieres Research SA, Maizières-lès-Metz 57283, France. Email: dominique.sert@arcelormittal.com
4. Senior Technology Engineer, ArcelorMittal Maizieres Research SA, Maizières-lès-Metz 57283, France. Email: pascal.gardin@arcelormittal.com
5. Technology Engineer, ArcelorMittal Maizieres Research SA, Maizières-lès-Metz 57283, France. Email: rodolfopaulo.santosferreira@arcelormittal.com
6. Principal Technology and Development Engineer, Coke and Ironmaking Technology, BlueScope Ltd, Wollongong NSW 2522. Email: sheng.chew@bluescopesteel.com
7. Senior Technology and Development Engineer, Coke and Ironmaking Technology, BlueScope Ltd, Wollongong NSW 2522. Email: davidj.pinson@bluescopesteel.com
8. Professor, School of Mechanical, Materials, Mechatronic and Biomedical Engineering, University of Wollongong, Wollongong NSW 2522. Email: monaghan@uow.edu.au
9. Director, ARC Research Hub for Australian Steel Innovation, University of Wollongong, Wollongong NSW 2522. Email: paulz@uow.edu.au

ABSTRACT

In an ironmaking blast furnace (BF), molten slag and hot metal form in the softening-melting (cohesive) zone and then trickle through the coke packed bed before being discharged from the taphole. During their downward flow, there are significant interactions occurring between liquids and other phases, such as gas and packing particles. Overall, the formation, dripping and discharging of these liquid phases, particularly molten slag, have a significant impact on BF operations in terms of furnace permeability, fuel consumption, process stability, product quality and ultimately, productivity. Hence, understanding the liquid flow behaviour in the BF lower zone is critical for designing optimal operations.

In the current investigation, the flow behaviour of slag droplets was investigated at a mesoscopic level using a combined numerical and physical modelling approach. The interaction between slag and carbonaceous materials was studied using sessile drop wetting experiments, slag flow through a funnel and a high temperature packed bed and the Volume of Fluid (VOF) modelling technique. Molten slag flow and counter-current gas-slag flow in the packed bed was investigated in terms of superficial gas velocity, slag properties and packing structure. The gas-slag flow behaviour at a mesoscopic level was numerically visualised, with gas velocity gradually increased up to the flooding point. The strong interaction between gas and slag was uniquely identified, which can cause localised slag flooding as well as gas channelling. Detailed information concerning the effect on slag holdup distribution, residence time and flow patterns of wettability, slag properties and bed structure were obtained. The current investigation highlights the significant role of research at a mesoscopic level in understanding macroscopic slag flow behaviour. Gas channelling, which is a critical phenomenon in a packed bed with counter-current gas-slag flow, is predicted. It can be speculated that significant gas channelling in the BF can inevitably occur prior to operational limits being reached. In the BF process, the formation of permanent gas channelling and large slag rivulets should be avoided to maintain appropriate contact between phases and hence, furnace permeability.

INTRODUCTION

The lower zone of the blast furnace (BF), in particular, the dripping zone, plays a very important role in the furnace productivity, efficiency and stability, as well as product quality (Omori, 1987). In the lower zone, four phases, gas, solid, liquid and powder such as unburnt char, co-exist and interact in

many ways. Essentially, liquid iron and slag trickle down through a slow-moving or quasi-stagnant bed of coke particles, while hot gas, unburnt char and other powdered materials, ascend counter-currently to the coke and liquids. In addition, the hot gas exchanges heat with the descending phases and initiates several heterogeneous chemical reactions. Thus, flow phenomena and interactions in the BF lower zone are very complex.

Researchers have undertaken numerous studies, attempting to understand these complex phenomena and interactions, including those related to slag. These include the formation of molten slag in the BF cohesive zone, its flow-through the coke packed bed and ultimately, its discharge from the hearth together with hot metal. Some studies carried out using furnace dissections and tuyere-probe sampling, found indefinite shaped slag particles present in the coke bed, possibly indicating that the flow behaviour of slag in the lower zone may vary considerably along radial/vertical directions (Ichida *et al*, 2001). The composition of the initial slag formed can vary depending on the charged materials (sinter, lump ore, or pellets). The initial slag, often referred to as primary slag, can have an iron oxide (FeO) content up to 30 per cent. When slag flows through the coke packed bed, its composition changes further due to the reduction of metallic oxides and interactions with coke or remnant char mineral matter or the gas phase. The slag composition varies significantly in the lower zone, both radially and vertically. Similarly, the temperature distribution and the coke morphology also vary along the slag flow path.

To understand the molten liquids flow-through BF, several studies have been undertaken at the laboratory scale, both at low temperature (LT) (Chew *et al*, 1997) and high temperature (HT) (George, 2013). Amongst many causal factors, the behaviour and flow of liquids through the coke bed was found to be affected by:

- wetting behaviour of the liquids on coke particles (contact angle, θ)
- minimum distance between coke particles
- packing characteristics of coke particles.

Attempts to understand the effects of these factors were studied through the sessile drop experimental technique, HT funnel and packed bed experiments. The wettability can be measured and is a function of slag composition and the materials it contacts. It was observed in HT funnel experiments that the residual slag exists in the funnel in different forms, such as slag blockage within the funnel or held up below the funnel in terms of different wettability and pore size. Several HT packed bed experiments were reported to simulate the BF lower zone (Ohgusu *et al*, 1992; Husslage, 2004; George, 2013). These studies indicated that slag and hot metal may flow concurrently through the coke/coke analogue bed in a funicular flow where slag envelopes the hot metal. The liquid flows in rivulets and visits a limited number of possible flow paths/channels. For flow to occur, a critical hydrostatic pressure is required to overcome any resistance to flow. The liquid flow pattern and liquid hold up were affected by the liquid-coke/coke analogue contact angle, liquid chemistry, coke mineral distribution, coke particle sphericity and bed packing density (Husslage, 2004).

Numerically, liquid flow-through a packed bed can be modelled at both the mesoscopic level (Natsui *et al*, 2015; Geleta, Siddiqui and Lee, 2020; Dong *et al*, 2021a) and the macroscopic level (Sugiyama and Sugata, 1987; Wang, Takahashi and Yagi, 1991; Wang *et al*, 1997). At the macroscopic level, numerical models were developed within the framework of continuum, such as potential flow (Sugiyama and Sugata, 1987), probability-continuous (Wang, Takahashi and Yagi, 1991) and force balance (Wang *et al*, 1997) models developed for BF ironmaking and a two-fluid model approach (Sun *et al*, 2000) applied in the general chemical engineering field. Typically, numerical techniques such as Smooth Particle Hydrodynamic (Monaghan, 1988) and Volume of Fluid (VOF) (Hirt and Nichols, 1981) were applied to track the liquid droplets movement through the packed bed at a mesoscopic level. However, for strong gas and liquid flow-through a packed bed, the flow behaviour was mainly simulated based on the models developed within continuum frameworks, which generally provide macroscopic, steady-state analysis of flow phenomena, corresponding to experimental or furnace scale conditions, using empirical correlations to characterise the interaction between gas and liquid phases. The constitutive equations for different phases are suitable for a certain

application range; however, accuracy diminishes as the application condition approaches or reaches the flooding point.

In this study, an integrated approach that combines HT bench-scale experimentation and furnace-scale computational modelling was applied to study the molten slag flow. The HT experimental studies were carried out to measure the wettability and address liquid flow-through the funnel analogues and coke packed beds, and numerical studies were conducted to firstly investigate the slag flow behaviour, considering various bed permeability and more wide-ranging slag properties, and then simulate strong counter-current gas and liquid flow in the packed bed.

NUMERICAL AND PHYSICAL MODELLING APPROACH

The current methods used to study the interaction between slag and carbonaceous materials are presented, including sessile drop wetting experiments, funnel analogue and HT packed bed experiments, as well as VOF modelling technique. Slag flow and strong counter-current gas-slag flow in the packed bed were investigated in terms of superficial gas velocity, slag properties and packing structure.

Physical modelling and experimental set-up

Three experimental techniques were utilised to investigate the slag flow phenomena.

Sessile drop

Sessile drop experiments were carried out in a horizontal tube furnace in an Ar (99.99 per cent purity) atmosphere at 1500°C. A schematic of the sessile drop experimental set-up used to measure the contact angles is given in Figure 1, using the experimental technique (Abdeyazdan, 2016) consisted of four key steps:

1. Pre-assembly of the substrate and alumina tray.
2. Temperature stabilisation.
3. Slag melting.
4. Liquid slag addition.

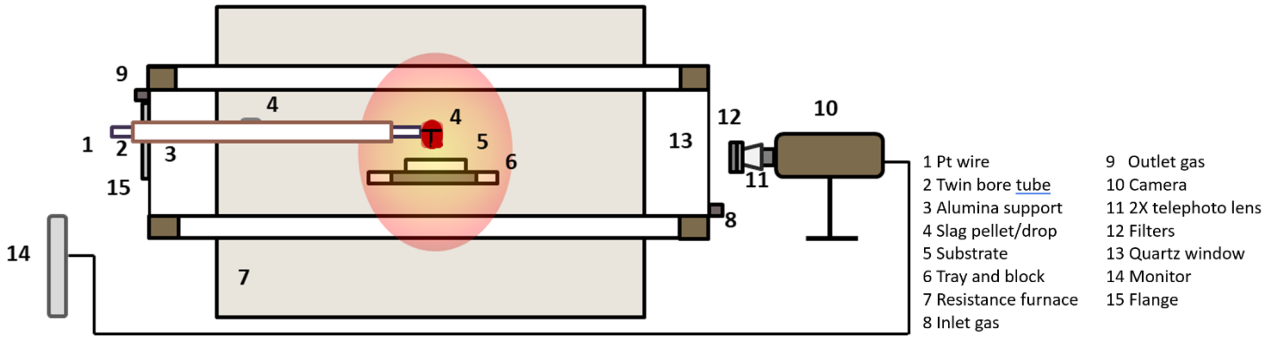

FIG 1 – A schematic of the sessile drop experimental set-up (Abdeyazdan, 2016).

Slags with the compositions given in Table 1 were prepared by mixing appropriate amounts of high purity laboratory grade reagents. The slags were primarily chosen to be representative of slags in the lower zone of the blast furnace, to be liquid at the experimental temperature. The properties of slag including surface tension, viscosity and density, were calculated via NPL (Mills, 1991) and Riboud (Riboud *et al*, 1981) models at 1500°C.

TABLE 1

Slag properties.

Phases	Composition, wt% CaO	SiO_2	Al_2O_3	MgO	Viscosity, μ, Pa·s	Surface tension, σ, N·m^{-1}	Density, ρ, kg·m^{-3}	T, °C
Slag 1	40.7	37.4	12.5	8.8	0.264	0.493	2675	1500
Slag 2	43.1	35.9	15.0	6.0	0.303	0.497	2686	1500

Funnel analogue

The funnel experiments were carried out in a vertical tube furnace (Figure 2a) in high purity (99.99 per cent) Ar gas at 1500°C. A slag pellet of ~1.4 g was placed on the funnel as shown in Figures 2b. The funnels were placed on a graphite holder plate with holes allowing the slag to drip freely into a graphite crucible. The entire set-up was fitted within the hot zone of the furnace.

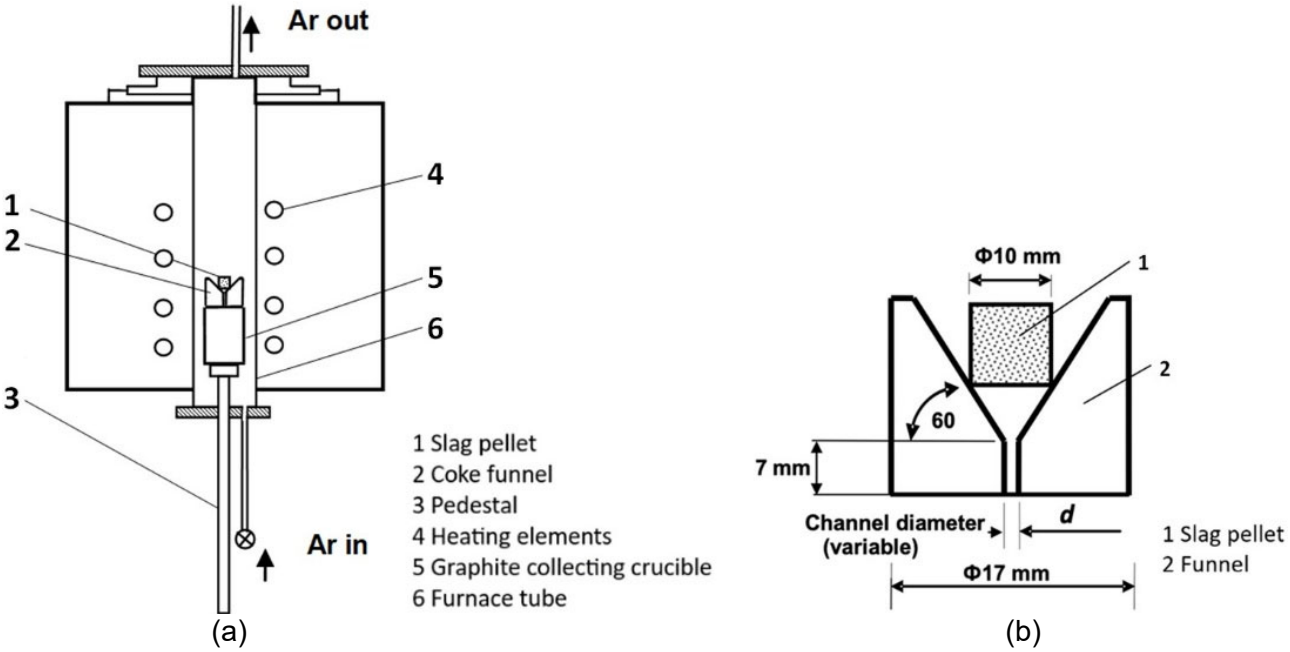

FIG 2 – Schematic diagrams of: (a) the furnace arrangement for funnel analogue experiments, and (b) a funnel and the placement of a slag pellet (George, 2013).

Packed bed

Packed bed experiments were carried out in a vertical tube furnace under high purity (99.99 per cent) Ar atmosphere at 1500°C. A schematic of the experimental set-up used is given in Figure 3. The slag addition rate was set to 3.3 g min^{-1} and Ar flow rate was 0.5 L min^{-1}. A slag particle size range of 250–1000 µm was used in the screw feeder. The coke packed bed height was 70 mm. It was made using ~100 g of coke particles of 8–10 mm diameter in size. In the experiments, the slag particles were added to the top of the packed bed via a screw feeder. The slag was then melted and passed through the bed, finally collected in a crucible placed on a micro-balance. Note that the valve in Figure 3a was connected to a vacuum pump to evacuate the air in the system before being purged with argon.

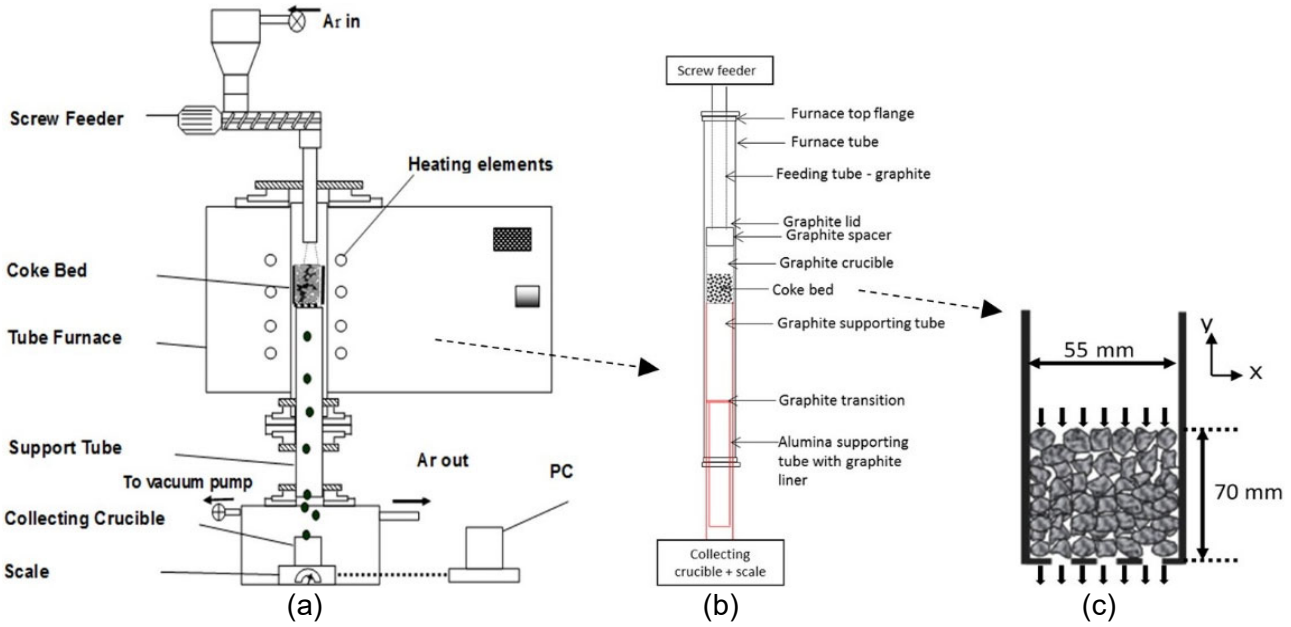

FIG 3 – (a) High temperature packed bed experimental facilities (George, 2013); (b) schematic of the detailed packed bed furnace arrangement; (c) a schematic of the coke bed.

Mathematical modelling and boundary conditions

The VOF method (Hirt and Nichols, 1981) was applied to simulate gas-slag flow in packed bed geometries. The simulations were carried out under a two-dimensional slot condition. The general governing equations for mass and momentum transfer were given in recent publications (Dong *et al*, 2021a, 2021b, 2023). Computations were carried out using the ANSYS-Fluent (v19.1) platform.

The following assumptions were imposed for the mathematical modelling of slag flow:

- incompressible multiphase flow
- no mass transfer between phases
- no variations in the surface tension coefficient
- phases are immiscible with a clearly defined interface
- no mass generation
- the system is in a thermal equilibrium
- phases share the same velocity field
- laminar flow.

The methodologies adopted in the simulation are summarised in Table 2.

TABLE 2

Methodologies used in the simulation.

Items	Schemes
Body force	Implicitly treated
Discretisation of convective terms	Second order upwind scheme
Gradient used to discretise the convection and diffusion terms	Green-Gauss node-based treatment
Velocity-pressure coupling	SIMPLE algorithm
Calculation of the volume fraction	Implicit formulation
Temporal derivation	First order implicit
Calculation of face fluxes	Modified HRIC (high-resolution interface capturing)

Computational domain and material properties

Two-dimensional simulations were carried out of slag flow based on the HT experimental packed bed geometry (Figure 3). Figure 4 shows the computational domain for slag flow in the different types of packed bed. The inlet, outlet, wall, opening and symmetric lines are highlighted via different colours, ie red, green, black, purple and light green colour, respectively.

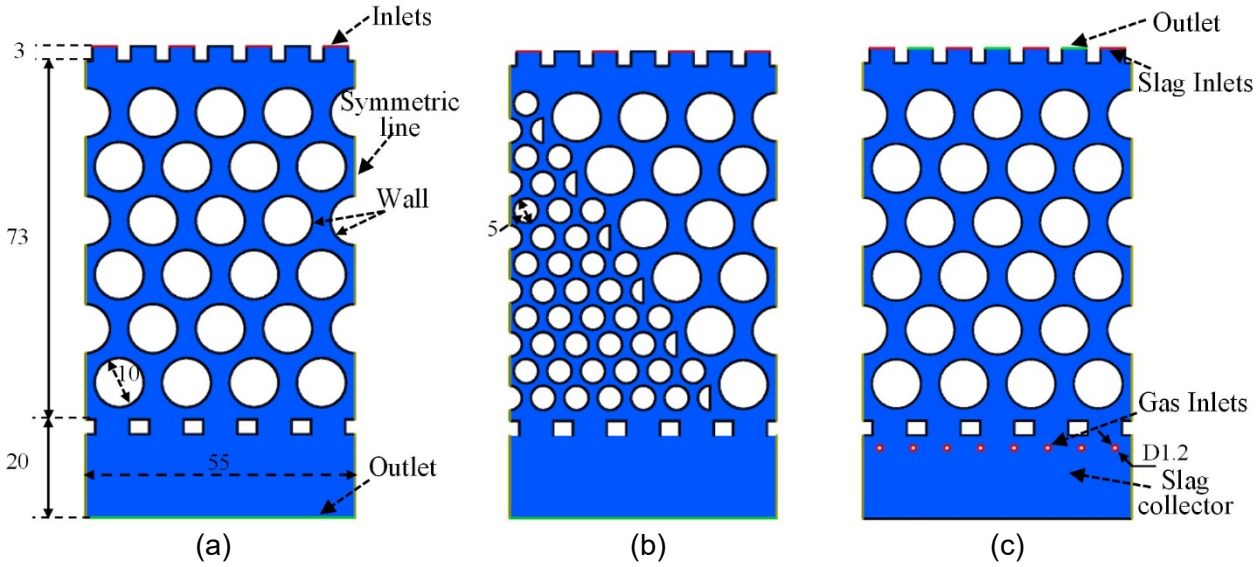

FIG 4 – 2D computational domain for slag flow in the packed bed: (a) base bed, (b) bed with deadman-shaped poor permeability region, and (c) counter-current gas and slag flow in the packed bed (unit: mm).

Slag 1 used in the experimental study was applied in the simulation. The gas properties used in the simulation approximate those under high temperature-high pressure conditions of the lower zone of a BF, ie gas viscosity (5.83×10^{-5} Pa·s) and density (0.648 kg·m^{-3}).

Initial and boundary conditions

At the beginning of each packed geometry simulation, a slag region was patched near the inlet in the computational domain. The patch was initialised with a volume fraction set to unity for the slag phase and a zero velocity. Each initial condition corresponds to the mass of slag that would flow into the bed within a period of 0.5 sec.

The slag is periodically introduced/fed into the packed bed from four inlets at the top. An inlet slag velocity of 5 mm·s^{-1} is used. For the case of counter-current gas-slag flow, gas continuously flows into the bed through the inlets below the packed bed.

For the walls, a no-slip boundary condition was imposed for the gas and slag velocities. A pressure outlet boundary condition was used.

RESULTS AND DISCUSSION

The typical experimental and numerical results are given in this section covering the measured contact angle, flow-through the funnel analogue and packed bed and counter-current gas-slag flow.

Experimental observation and measurement

Sessile drop

Sessile drop experiments were used to measure the contact angles of slags on graphite or coke. As an example, Figure 5a shows the original image captured from the recorded video during the experiment using Slag 1 and graphite substrate. Contact angles were then measured using ImageJ, ver 1.48 (public domain software, https://imagej.net/ij/index.html) image analysis software with DropSnake plugin. An example of the contact angle measurement using Image J is given in Figure 5b. The measured contact angles for Slags 1 and 2 on graphite substrates are 159 deg and 157 deg, respectively, which are average values based on the time series results.

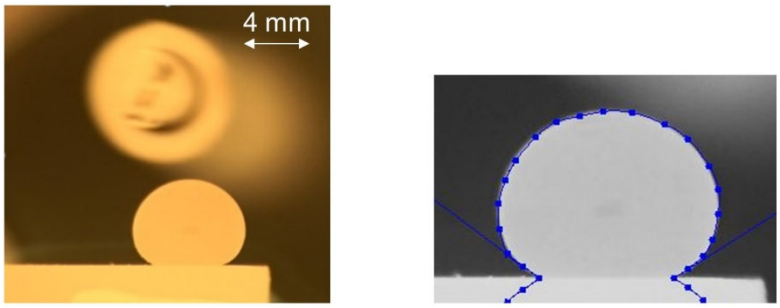

(a) (b)

FIG 5 – Depiction of contact angle measurement: (a) original image captured from video, and (b) drop analysis using Image J software with DropSnake plugin.

Sessile drop experiments allow characterisation of contact angle and the general interaction behaviour between the molten liquids and solids. Specifically, the contact angle values and key experimental observations will be used for the analysis of the interfacial mechanisms of liquid-solid interactions under representative BF conditions and subsequent numerical simulation.

Funnel analogue

Theoretically, the flow of liquids through a coke packed bed will be strongly affected by the gaps or the equivalent diameter of channels between coke particles. At the laboratory scale, the critical pore diameter for liquid flow in this study is investigated using funnel analogues with different neck diameters that approximate to the effective pore diameter between coke particles.

As an example, Figure 6 shows the blocked liquid flow behaviour in coke funnel with a funnel neck diameter of 4.5 mm. The critical funnel neck diameter, as defined by the neck diameter at which point no slag flowed, was determined. In this case using Slag 2, the critical funnel neck diameter was between 4.5 and 5 mm. The blockage phenomena for a highly non-wetting slag is similar to the previous studies (George, 2013), where the near-spherically shaped slag droplet can be observed to be easily held up above the channel of funnel if the funnel neck size is small.

These experiments provide the critical neck diameters associated with the onset of flow-through the funnel. In general, slag flow is affected by the slag properties (such as composition, interfacial tension, viscosity) and properties of the carbonaceous matter (ash/mineral content, roughness,

porosity, carbon structure). These factors then determine whether the slag can enter the channel and thereby the critical pore diameter.

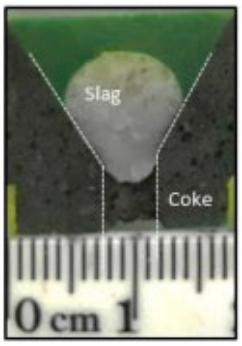

FIG 6 – Blocked slag droplet in coke funnels with a pore neck diameter of 4.5 mm.

Packed bed

Packed bed experiments were carried out to understand the slag flow behaviour and holdup distribution. As examples, two experimental results are given in Figure 7.

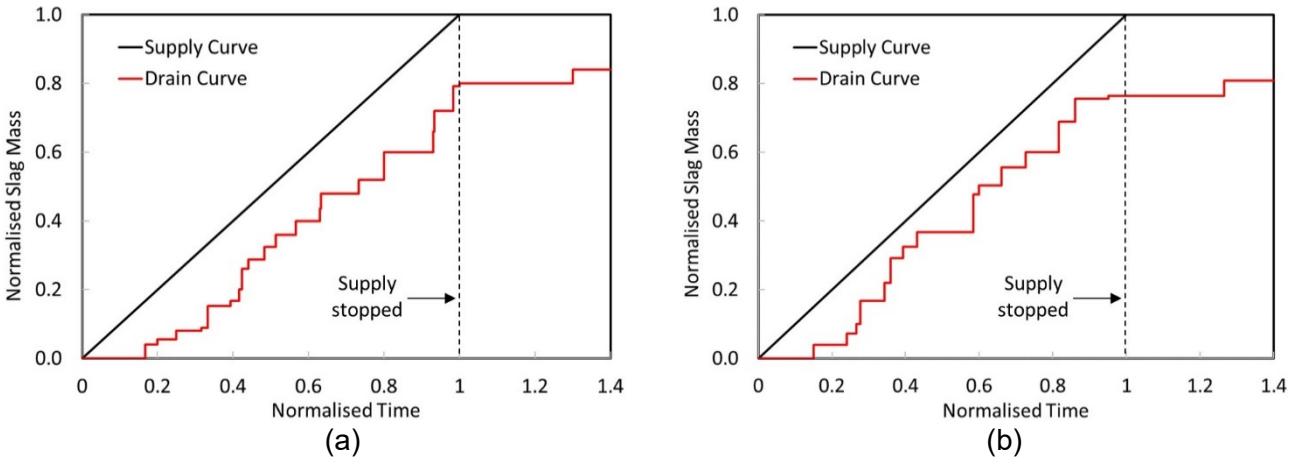

FIG 7 – Supply-drain curves of selected packed bed experiments of: (a) Slag 1 and (b) Slag 2.

The drain curves show a ‘step-like’ characteristic. It was not clear whether the presence of the steps represented stochastic flow in the bed, or an experimental artefact associated with the different packing structures around the crucible outlets (holes), number of outlets and packing properties. Additional experiments were carried out to investigate the effect of those properties on the appearance of steps. However, it was found that the steps remained despite varying the abovementioned properties.

To further investigate the cause of these steps, a two-dimensional modelling for Slag 1 was carried out. The detailed numerical investigation of the slag flow field showed that step changes in the drain curve are determined by the extent of slag accumulation within the interstitial space among the particles packed, which is closely related to the pore size, the shape and relative positioning of the particles, and slag properties ie they were not an experimental artefact but represent something fundamental about the character of the liquid flow. The features of the numerical modelling were detailed in the subsequent section.

Numerical simulation of slag flow in the packed bed

Slag flow in the base bed condition

A two-dimensional simulation for the base bed condition (Figure 4a) was carried out of slag flow in the HT experimental packed bed geometry, using a Cartesian coordinate system. The packing particles were assumed to be spherical and evenly distributed in the bed with a bed porosity of 0.51.

Figure 8 shows the transient simulation results at 0, 6, 12 and 18 seconds, respectively. As the slag trickles through the bed, some individual slag droplets are observed to pass through the bed; however, most droplets experience coalescence and breakup before exiting the bed. The droplets cannot maintain their spherical shapes after coalescence and easily deform and fill into the pore space between particles, causing local slag accumulation.

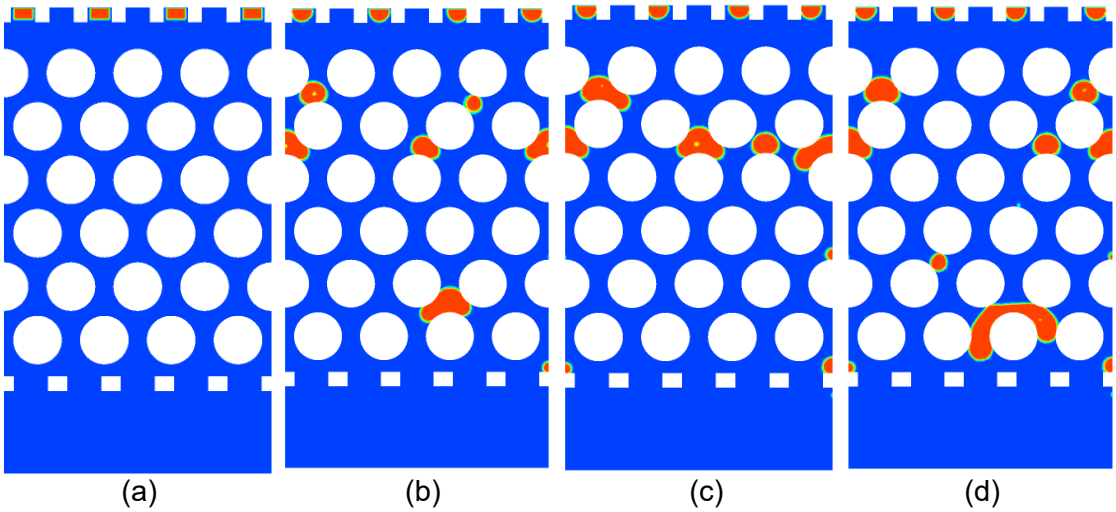

FIG 8 – Simulated slag flow in the base bed condition at different times: (a) 0 sec, (b) 6 sec, (c) 12 sec, and (d) 18 sec. Note that Slag 1 was used.

Based on such simulation results, supply–drain curves shown in Figure 9 can be generated. The black and red line in Figure 9 refer to the supply and drain curves, respectively. Compared with the supply curve, there are different step changes in the drain curve, which is consistent with experimental observations (Figure 7). The slag flow field in Figure 7 shows that step changes in the drain curve are determined by the extent of slag accumulation within the interstitial space among the particles packed in the specified domain (Figure 4a), which is closely related to the pore size, shape of particles and slag properties.

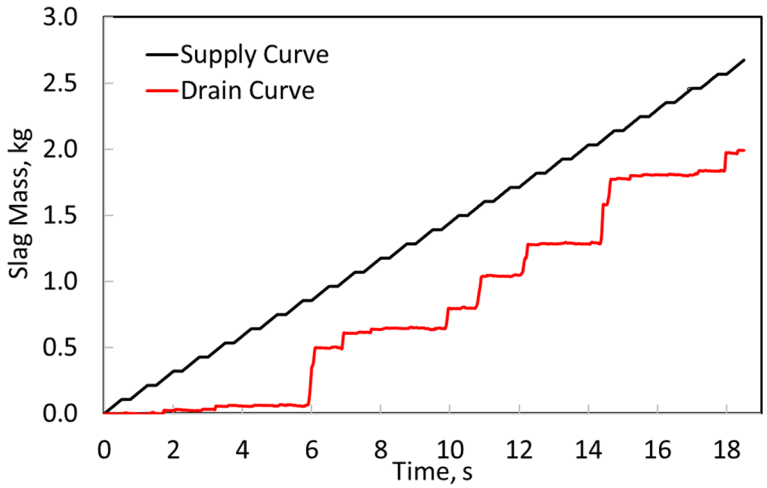

FIG 9 – A supply–drain curve from the simulation based on the base bed condition.

Figure 10 shows the slag flow fields at time t = 18 sec for different wettability reflected by the varied contact angles in the base packed bed condition. The contact angle changes from 157 to 60 deg characterises the relation between the acting adhesive and cohesive forces, and reflects reactions that may occur at the coke particle surface. With decreased contact angle, slag holdup in the packed bed increases and longer rivulets can be observed.

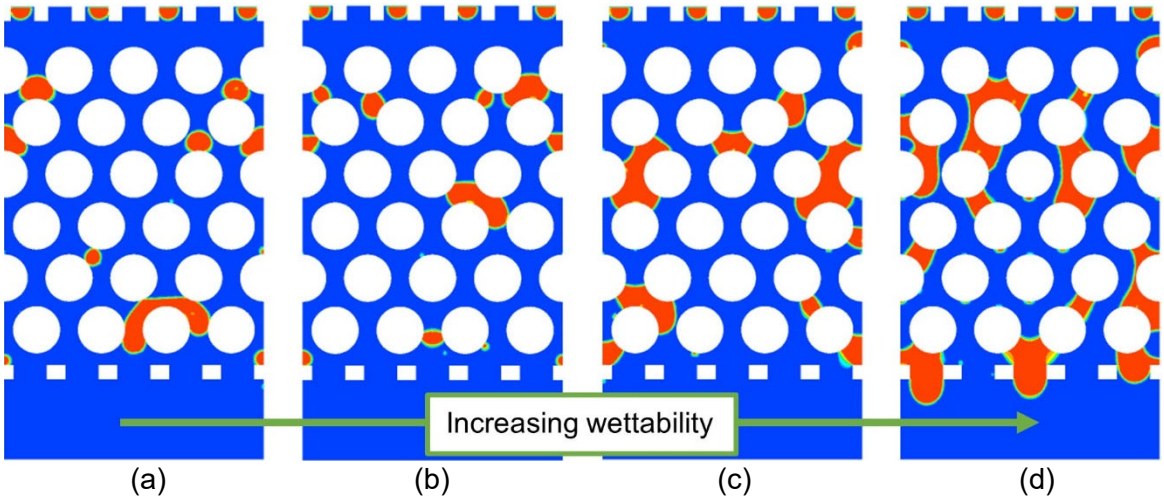

FIG 10 — Simulated slag flow in the packed bed at time t = 18 sec for different contact angles: (a) 157 deg, (b) 120 deg, (c) 90 deg, and (d) 60 deg.

Slag flow in the bed with a poor permeability region

To further investigate the effect of a poor permeability region on the slag flow behaviour, a bed with a deadman-shaped region (Figure 4b) was considered. In this deadman region, the overall porosity is the same as that in the base bed condition (Figure 4a). Figure 11 shows the slag flow fields at 0, 6, 12 and 18 sec in the bed with deadman-shaped poor permeability region. Most of the slag flows around the deadman region, with higher slag holdups near the interface. Slag flow in a packed bed is closely related to both particle morphology and liquid wettability. It can be expected that flow during the normal blast furnace operation, the region around surface of deadman is critical to the bed permeability and fluid flow.

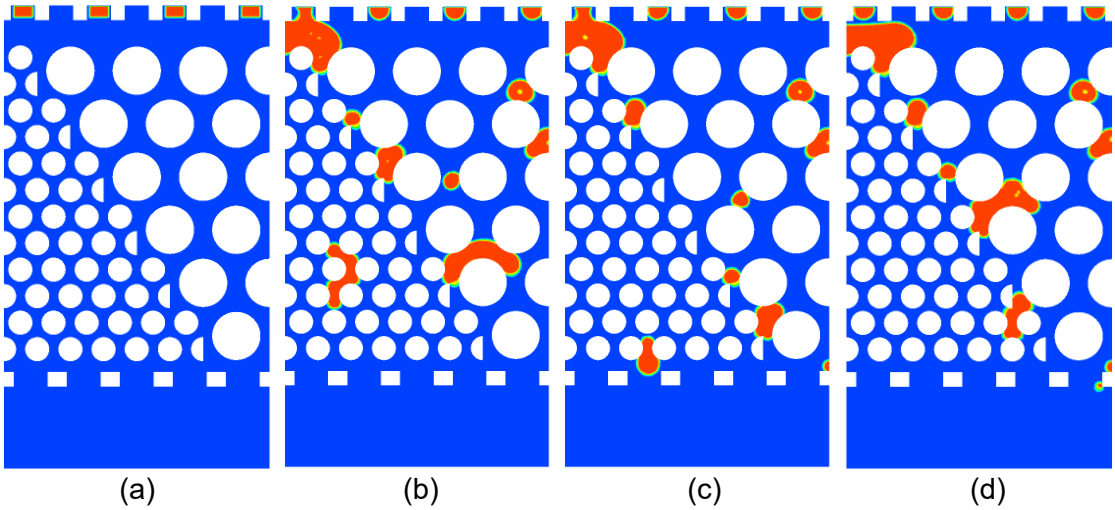

FIG 11 — Simulated slag flow in the packed bed with poor permeability region at different times: (a) 0 sec, (b) 6 sec, (c) 12 sec, and (d) 18 sec.

Counter-current gas and slag flow in the packed bed

The effect of gas flow on the counter-current gas-slag flow in the packed bed was studied using different gas inlet velocities, corresponding to superficial gas velocities, 0.33, 0.82 and 1.64 $m \cdot s^{-1}$ in the bed, respectively. In the simulation, gas continuously flows into the bottom and out of bed at the top outlets; slag is periodically fed into the bed from the top inlet and collected in the slag collector below the packed bed.

Figure 12 shows the calculated results of superimposed gas velocity and slag volume fraction fields at t = 9.5 sec. With increasing gas inlet velocity, local flooding near the top surface of the packed

bed becomes more frequent. It can be observed that gas prefers to flow along the paths of lower flow resistance, forming channelling. As the gas velocity increases, the downward flow of slag becomes more difficult and long rivulets has to be formed to generate sufficient hydrostatic pressure to overcome the strong upward gas-slag interaction force.

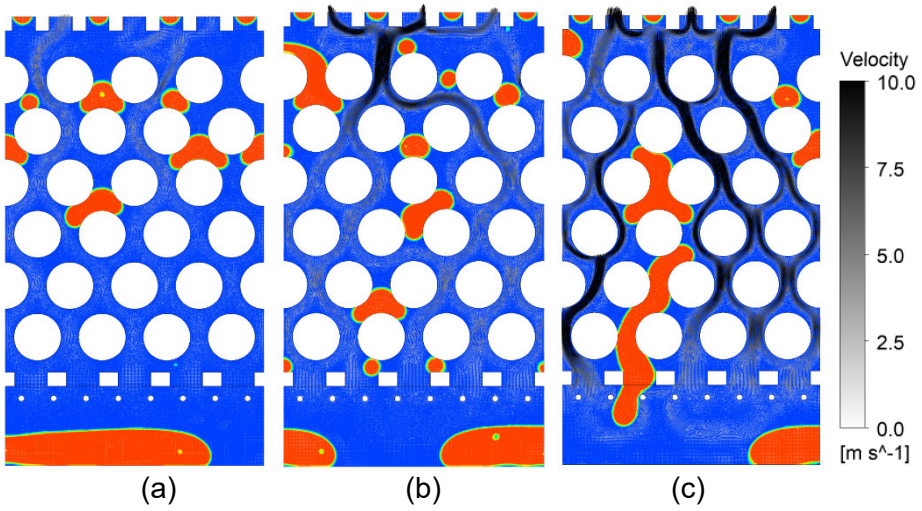

FIG 12 – Simulated counter-current gas and slag flow in the packed bed at time t = 9.5 sec for different superficial gas velocities: (a) 0.33 m·s^{-1}, (b) 0.82 m·s^{-1}, and (c) 1.64 m·s^{-1}. Note that the legend is used for gas velocity.

The local flooding of small liquid droplets near the bed surface can be observed, which is mainly due to relatively large contact areas between gas and slag and less influence of hydrostatic pressure for the small slag droplets.

In order to understand the flow status of the three current scenarios using the flooding diagram, flooding factor (*FF*), $\frac{U_g^2 a_t}{g\varepsilon^3}\frac{\rho_g}{\rho_l}\eta_l^{0.2}$, and fluid ratio (*FR*), $\frac{U_l}{U_g}\sqrt{\frac{\rho_l}{\rho_g}}$, were calculated based on the superficial gas velocity conditions, given in Table 3. In the calculation of *FF* and *FR*, the overall bed porosity, ie 0.51, and the particle size of 10 mm in the base bed were applied. As gas velocity increases from 0.33 to 1.64 m/s, the calculated (*FR*, *FF*) points, No. 1–3 (solid dots), approach the 'flooding limit' line. Note that the generation of flooding diagram based on published works was introduced in our previous report (Dong *et al*, 2009). The fluid ratio and flooding factor to achieve the flooding limit was provided in Table 3, with superficial liquid velocity of 0.97 mm·s^{-1}. No. 1–3 are highlighted in Figure 13 via solid dots.

TABLE 3

Flooding factors and fluid ratios based on the current VOF modelling and estimated values.

No.	Superficial gas velocity U_g, m·s^{-1}	Fluid ratio (-)	Flooding factor (-)
1	**0.33**	0.1895	0.0181
2	**0.82**	0.0758	0.1128
3	**1.64**	0.0379	0.4513

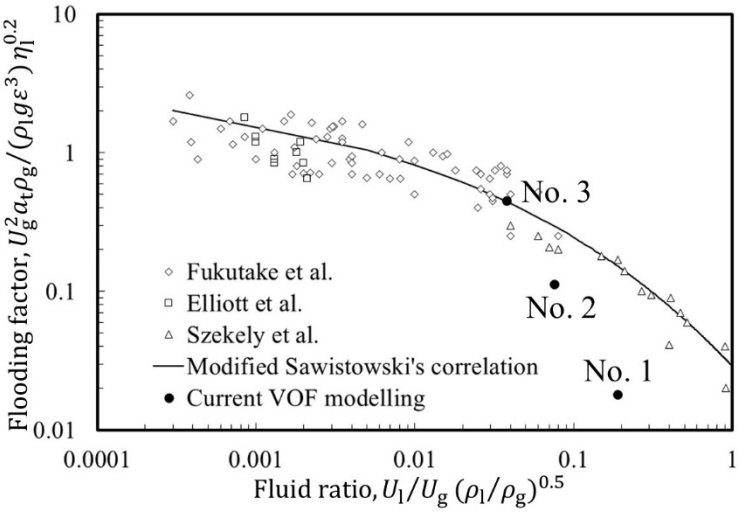

FIG 13 ─ Flooding data of published works (Dong *et al*, 2009), calculated (*FR*, *FF*) points for cases with different gas inlet velocities.

The comparison between calculated (*FR*, *FF*) points and flooding limit helps interpret the simulation results obtained previously at the particle scale. Observations based on current simulation results show the existence of gas channelling (at the mesoscopic level) even at a relatively low gas velocity (Point No. 1). As the points approach the 'flooding limit', gas channelling becomes pronounced. Likewise, the local flooding becomes more pronounced near the packed bed surface. At Point 3 on the empirical flooding line, slags still can enter the bed. However, the slag has to accumulate to achieve sufficient hydrostatic pressure to overcome the strong upward gas-liquid interaction force. Evidently, the large rivulets were formed at Point 3 (Figure 12c). It can be expected that gas channelling might be the reason for the occurrence of critical points and overall upward liquid flow cannot actually occur. Due to channelling, local flooding and the frequent occurrence of high pressure, the operation can become very unstable, which is consistent with the flooding limit obtained experimentally.

CONCLUSIONS

Numerical and experimental investigation of slag flow in a packed bed was carried out. The wettability between slag and carbonaceous materials can be measured at the laboratory scale. Local blockage and individual droplet flow of slag in the packed bed can be physically identified, which was further verified in numerical studies. A two-dimensional Volume of Fluid modelling technique was applied to simulate gas flow and movement of individual slag droplets. Localised slag flooding and gas channelling caused by the strong interaction between gas and slag were uniquely visualised. Such interactions cannot be ascertained using traditional macroscopic modelling techniques and are also difficult to study under high temperature experimental conditions with gas-slag flow. The current combined physical and numerical approach highlights the significant role of research at a mesoscopic level in understanding macroscopic slag flow behaviour. It can be speculated that significant gas channelling can inevitably occur in the blast furnace prior to operational limits being reached. In the blast furnace process, the formation of permanent gas channelling and large slag rivulets should be avoided to maintain appropriate contact between phases and hence, furnace permeability.

ACKNOWLEDGEMENTS

We acknowledge funding from the Australian Research Council (ARC) through the Industrial Transformation Research Hubs Scheme (Project Number: IH200100004). The funding support and permissions from ArcelorMittal and BlueScope Ltd to publish are gratefully acknowledged. This research was undertaken with the assistance of resources from the Australian Government's National Computational Infrastructure.

REFERENCES

Abdeyazdan, H, 2016. The wettability, interfacial tension and dissolution of alumina, spinel and calcium aluminate within Ladle and Tundish slags, University of Wollongong, Wollongong.

Chew, S J, Wang, G X, Yu, A B and Zulli, P, 1997. Experimental study of liquid flow in blast furnace cohesive zone, *Ironmaking and Steelmaking*, 24(5):392–400.

Dong, X F, Pham, T, Yu, A B and Zulli, P, 2009. Flooding diagram for multi-phase flow in a moving bed, *ISIJ Interntional*, 49(2):189–194.

Dong, X F, Jayasekara, A, Sert, D, Ferreira, R, Gardin, P, Monaghan, B J, Chew, S J, Pinson, D and Zulli, P, 2021a. Investigation of molten liquids flow in the blast furnace lower zone: numerical modelling of molten slag through channels in a packed bed, *Metallurgical and Materials Transactions B*, 52(1):255–266.

Dong, X F, Jayasekara, A, Sert, D, Ferreira, R, Gardin, P, Monaghan, B J, Chew, S J, Pinson, D and Zulli, P, 2021b. Numerical investigation of slag flow through a coke funnel analog and packed bed, *Metallurgical and Materials Transactions B*, 52(5):2926–2938.

Dong, X F, Jayasekara, A, Sert, D, Ferreira, R, Gardin, P, Chew, S J, Pinson, D, Monaghan, B J and Zulli, P, 2023. Slag flow in the packed bed with varied properties and bed conditions: numerical investigation, *Metallurgical and Materials Transactions B*, 54(1):56–69.

Geleta, D D, Siddiqui, M I H and Lee, J, 2020. Characterization of slag flow in fixed packed bed of coke particles, *Metallurgical and Materials Transactions B*, 51(1):102–113.

George, H L, 2013. Liquid flow through a reactive packed bed, PhD thesis (unpublished), University of Wollongong.

Husslage, W, 2004. Dynamic distributions – Sulphur transfer and flow in a high temperature packed coke bed, Delft University of Technology, The Netherlands.

Ichida, M, Orimoto, T, Tanaka, T and Koizumi, F, 2001. Behavior of pulverized coal ash and physical property of dripping slag under high pulverized coal injection operation, *ISIJ International*, 41(4):325–332.

Mills, K C, 1991. Slags Model (ed 1.07), National Physical Laboratory, UK.

Monaghan, J J, 1988. An introduction to SPH, *Computer Physics Communications*, 48(1):89–96.

Hirt, C W and Nichols, B D, 1981. Volume of fluid (VOF) method for the dynamics of free boundaries, *Journal of Computational Physics*, 39(1):201–225.

Natsui, S, Kikuchi, T, Suzuki, R O, Kon, T, Ueda, S and Nogami, H, 2015. Characterization of liquid trickle flow in poor-wetting packed bed, *ISIJ International*, 55(6):1259–1266.

Ohgusu, H, Sassa, Y, Tomita, Y, Tanaka, K and Hasegawa, M, 1992. Main factors affecting static holdup of molten slag in coke-packed bed, *Tetsu to Hagane*, 78(7):1164–1170.

Omori, Y, 1987. *Blast Furnace Phenomena and Modelling*, pp 546–547 (Elsevier Applied Science: London).

Riboud, P V, Roux Y, Lucas, L D and Gaye, H, 1981. Improvement of continuous casting powders, *Fachberichte Huttenpraxis Metallweiterverarbeitung*, 19(8):859–869.

Sugiyama, T and Sugata, M, 1987. Development of two-dimensional mathematical model for the blast furnace: ‘BRIGHT’, *Nippon Steel Technical Report*, 35:32–42.

Sun, C G, Yin, F H, Afacan, A, Nandakumar, K and Chuang, K T, 2000. Modelling and simulation of flow maldistribution in random packed columns with gas-liquid countercurrent flow, *Chemical Engineering Research and Design*, 78(3):378–388.

Wang, G X, Chew, S J, Yu, A B and Zulli, P, 1997. Modeling the discontinuous liquid flow in a blast furnace, *Metallurgical and Materials Transactions B*, 28(2):333–343.

Wang, J, Takahashi, R and Yagi, J, 1991. Simulation model of the gas-liquid flows in the packed bed, *Tetsu to Hagane*, 77(10):1585–92.

A phenomena-based model to investigate the possibility of scrap melting in an Open Slag Bath Furnace (OSBF) for green ironmaking

DOI: 10.62053/NCBM2380

A Emami[1], S van der Sluijs[2], M van Ende[3] and Y Tang[4]

1. Principal Researcher, Tata Steel, R&D, IJmuiden, The Netherlands, 1951 JZ Velsen-Noord, The Netherlands. Email: A.emami@tatasteeleurope.com
2. MSc Student, Eindhoven University of Technology, 5612 AE Eindhoven, The Netherlands. Email: s.t.m.sluijs@student.tue.nl
3. Associate Professor, Eindhoven University of Technology, 5612 AE Eindhoven, The Netherlands; Research Professor, Seoul National University, 08826 Seoul, Republic of Korea. Email: m.a.p.p.van.ende@tue.nl
4. Assistant Professor, Eindhoven University of Technology, 5612 AE Eindhoven, The Netherlands. Email: y.tang2@tue.nl

ABSTRACT

This paper presents a phenomena-based model for investigating the possibility of scrap melting in an Open Slag Bath Furnace (OSBF) for green ironmaking. The goal of this study is to enhance the circularity of the steelmaking process by utilising scrap as a green source of iron in OSBFs. The model takes into account the fundamental differences between OSBFs and traditional processes such as Electric Arc Furnaces (EAFs) and Basic Oxygen Furnaces (BOFs).

The model considers three primary regions where scrap heating and melting occur: the solid feed pile, slag and hot metal. It accounts for factors such as the furnace geometry, scrap charging mechanism and specific heat and mass transfer properties of the reactor. The model was validated using literature data and was used to investigate the heating and melting behaviour of individual scrap particles under various process parameters.

The study finds that the scrap melting process in OSBFs involves three stages: shell formation, shell remelting and subsequent melting of the parent scrap. The carbon content of the scrap and the liquid hot metal plays a critical role in determining the melting behaviour. Depending on the carbon concentration and temperature, the melting process can be heat transfer controlled or mass transfer controlled.

The paper also examines the scrap feeding methods in OSBFs, including direct charging into the slag or charging through a feed pile. The model provides insights into the melting rate of scrap compared to Direct Reduced Iron (DRI) in OSBFs and highlights the role of carbon in this process.

Overall, this phenomena-based model contributes to the understanding of scrap melting behaviour in OSBFs and provides valuable insights for optimising the circularity and efficiency of green ironmaking processes. The findings of this study can inform the design and operation of OSBFs, paving the way for increased utilisation of scrap as a sustainable feedstock in the steel industry.

INTRODUCTION

Tata Steel Nederland is committed to transitioning towards a clean, green and circular steel, using direct reduction of iron ore followed by electrical melting. Within the vision of the company, use of scrap as a green source of iron plays a central role. Conventionally, Electric Arc Furnace (EAF) and Basic Oxygen Furnace (BOF) are the main processes where scrap addition can take place. Open Slag Bath Furnaces (OSBFs) are primarily considered to be operated using Direct Reduced Iron (DRI) and believed to have a promising performance, especially with low-grade ores.

While the use of scrap as an additional feed material in OSBFs has not been demonstrated on an industrial scale, it holds tremendous potential for enhancing the circularity of this process. However, the degree in which such furnaces can be used as scrap melting units is unclear (Cavaliere *et al*, 2022). Therefore, it is increasingly important to understand the scrap melting behaviour in OSBFs given their fundamental differences from EAFs and BOFs.

In the present study, a phenomena-based model was developed, considering the key differences between the OSBF and EAF and BOF. These differences include the geometry of the furnace,

charging mechanism of scrap and the reactor's specific heat and mass transfer properties. The model encompasses three primary regions where scrap heating and melting occur: the solid feed pile, slag and hot metal. The model was validated and used to investigate the heating and melting behaviour of singular scrap particle under varying process parameters such as temperature, composition of hot metal and size of the scrap.

SCRAP MELTING IN LIQUID HOT METAL

The scrap melting process involves three stages: shell formation, shell remelting and subsequent melting of the parent scrap. Shell formation occurs due to flash absorption of heat by cold scrap particle upon contact with liquid bath. Key factors affecting the different stages of melting include coupled heat and mass transfer mechanisms and phase transformation (Wei *et al*, 2019). These factors are influenced by the chemical composition and temperatures of both the liquid hot metal and solid scrap particles. This melting phenomenon can be described as a dynamic moving boundary problem involving phase change otherwise known as Stefan problem (Chuang and Szekely, 1971).

The carbon content plays a critical role in determining the liquidus temperature and overall melting behaviour of scrap in liquid hot metal bath. When the scrap particle and the liquid bath have the same carbon concentration or the hot metal temperature is above liquidus temperature of scrap, the melting process is almost completely heat transfer controlled. In cases where the liquid hot metal carbon composition is higher than the scrap particle but its temperature is lower than the liquidus temperature of the scrap, diffusion melting comes to play. Carbon diffusion to the interface results in decrease in local liquidus temperature and enables the melting process. Therefore such melting condition is mass transfer controlled (Penz and Schenk, 2019).

SCRAP FEEDING IN OSBF

The main feeding material in the OSBF is DRI that is charged through feeding ports above the furnace. In principle, a fraction of DRI can be replaced with scrap without changing the electrical input or other major changes in the process parameters (Belford *et al*, 2022). The current model aims at determining the melting behaviour of a single scrap particle when it is charged in an OSBF unit. It is particularly interesting to understand the role of carbon and the difference it makes in the melting rate of scrap compared to DRI in OSBF.

Scrap can be introduced into an OSBF through two primary routes: directly into the slag or via a feed pile consisting of a mixture of scrap and primary feeding material (ie DRI and fluxes). The feed pile, located above the slag layer, represents a confined system that floats on top of the hot metal layer due to its lower density. In the direct charging method, scrap particles pass through the slag layer before entering the liquid hot metal layer (Figure 1). Scrap particles charged via a feed pile undergo heating during their descent through the pile and subsequently sink to liquid hot metal. The scrap particle descends within hot metal due to the higher density of the scrap.

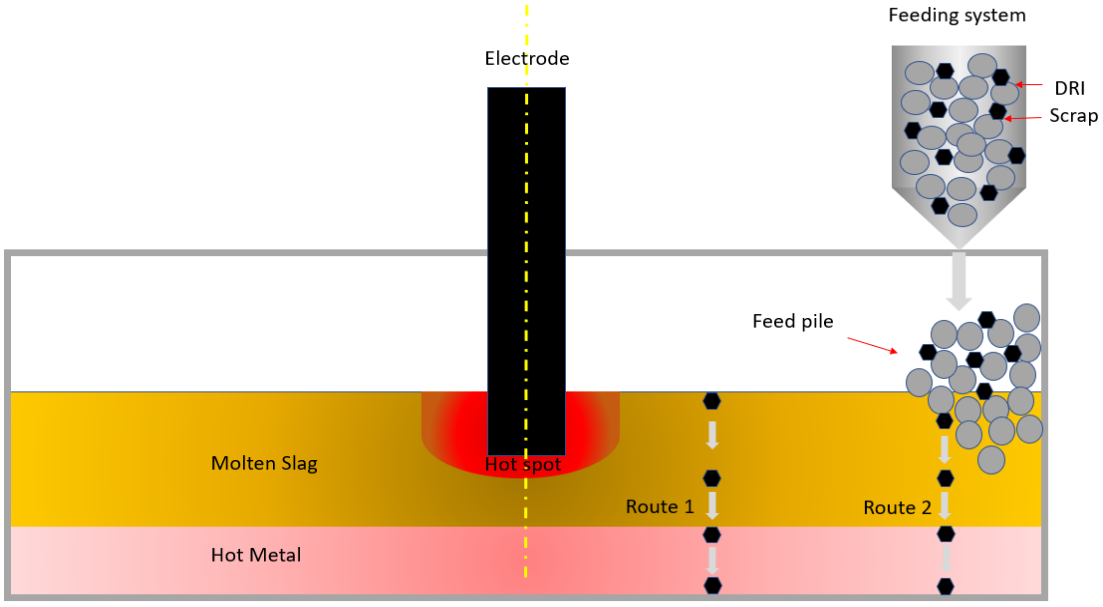

FIG 1 – Schematic of an OSBF cross-section. Left circles represents direct charging through slag; right circles show charging through feed pile.

MODEL DESCRIPTION

The model consists of three main parts; solid feed pile, slag and hot metal. The scrap particles are assumed to absorb heat in the feed pile and slag in radial direction. Therefore, no mass transfer or chemical interaction is considered in these layers. The main factors influencing the degree of pre-heating in these layers are the residence time and temperature profile. Given that feed pile is at sub-solidus temperature it is expected that scrap does not undergo any significant chemical interaction within the feed pile.

In the slag layer, the chemical interactions and the role of mass transfer are excluded due to very limited knowledge on the kinetics of such interaction between scrap and the slag. It will be clarified later that the residence time in the slag layer is very short and as such the impact of chemical interaction is limited.

To simulate the scrap melting behaviour in the hot metal, the problem is reduced to a one dimensional heat and mass transfer problem. It is assumed that the heat flow within the solid is purely radial. The explicit finite difference method (FDM) with fixed grid is used as modelling approach and several assumptions are made:

- The physical properties of liquid melt and solid steel scrap are considered to be constant.
- The scrap is assumed to be uniformly exposed over all its surfaces.
- Internal diffusion of carbon in the scrap particle is not taken into account.
- Only heating phenomenon is considered between the scrap and slag/feed pile.
- The carbon concentration of the shell is equal to liquid hot metal.

Mathematical description

Feed pile

The movement of the pellets and scrap within the feed pile is a function of various parameters such as density of feed material and the melting rate at feed pile boundaries. In order to describe this complex phenomenon the problem is reduced to uniform descent of scrap within this layer. Therefore, given a certain OSBF geometry, pile size and feeding rate one can estimate the descent velocity.

Another important factor in estimating the degree of pre-heating in the feed pile is the temperature profile. To estimate the temperature profile a one-dimensional linear gradient is assumed along the vertical axes where an interface temperature equivalent to the liquidus of DRI pellet is imposed at the bottom. The top temperature can be variable between ambient and the liquidus of DRI pellets.

Slag

To determine the residence time (*t*) in slag Stokes' law is used as represented in Equation 1.

$$t = \frac{2R^2}{9} \frac{\rho_{particle} - \rho_{fluid}}{\mu l} g \quad (1)$$

where:

R	is the radius of the particle [m]
l	is the slag thickness [m]
ρ	the density [kg/m^3]
μ	the viscosity [Pa·s]

For a small scrap particle (<20 mm) the terminal descent velocity is ~2.0 [m/s]. For a slag layer thickness of 1 m, a residence time of ~0.5 s can be estimated.

Only heat transfer is considered when the scrap particle travels solely through the slag layer. The temperature in the slag is considered to be constant and above the hot metal temperature since heating occurs in the slag via electrodes. Equation 2 describes the interface velocity or melting speed (v_{slag}) based on the heat transfer at the interface.

$$v_{slag} = \frac{1}{\rho \Delta H_0} \left[k \frac{\partial T}{\partial x}\Big|_{interface} - h(T_b - T_m) \right] \quad (2)$$

where:

ΔH_0	is the standard enthalpy of melting
k	the thermal conductivity [W/mK]
T_b	the bulk slag temperature [K]
T_m	liquidus temperature at interface [K]
h	the heat transfer coefficient [w/m^{2}K]

Hot metal

For the scrap melting in the hot metal bath a combined heat and mass transfer is considered. The heat and carbon mass transfer equations are coupled in order to calculate the velocity of the interface. Equation 3 describes the interface velocity in hot metal (v_{HM}) based on heat and mass transfer at the interface.

$$v_{HM} = \beta_0 \ln\left(\frac{C_i - C_{sc}}{C_b - C_{sc}}\right) = \frac{1}{\rho \Delta H_0} \left[\left[k \frac{\partial T}{\partial x} \right]_{interface} - h(T_b - T_m) \right] \quad (3)$$

where:

β_0	is the mass transfer coefficient at the interface [m/s]
C_i	the carbon concentration at the interface [wt per cent]
C_{sc}	the scrap carbon concentration [wt per cent]
C_b	the concentration in the hot metal [wt per cent].

Here T_b is the bulk temperature of hot metal.

SIMULATION RESULTS

First the results of the model were validated against a set of literature data. Then a parametric study was done of the melting behaviour of a singular piece of scrap when it is charged in an OSBF unit. The influence of important process parameters was studied using the model.

Model validation

Published experimental data were used to validate the model for scrap melting in hot metal. Xi *et al* (2020) studied the melting characteristics of singular round and square bars in hot metal (Figure 2a). The validation showed that the model is able to predict the experiments reasonably well. When simultaneous heat and mass transfer is considered, a deviation of 23–33 per cent was obtained in predictions of final melting time across various carbon concentrations in the hot metal (Figure 2b). Furthermore the model is capable of predicting the decrease in melting time as a function of carbon in the bath which follows the theory of scrap melting discussed earlier.

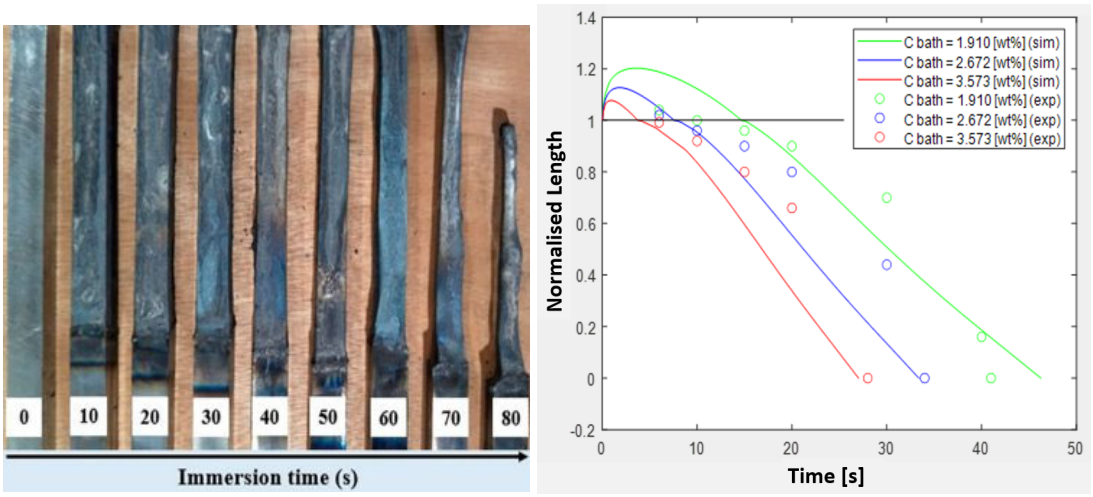

(a) (b)

FIG 2 – (a) An image of the scrap samples after several seconds from submersion in hot metal; (b) Validation of model using experimental data from Xi *et al* (2020).

There is some discrepancy in predicting the initial shell formation phase between the model and the experiments. This is partly due to the numerical approach and partly due to the inaccuracy in the acquired experimental measurements for the shell thickness. Such inaccuracies can arise as the freshly formed shell is removed during the extraction of the solid bar from the hot metal.

Parametric study

In this section a parametric study was conducted using the operational condition in Table 1 for a concept OSBF unit. The aim of the study is to understand the influence of the following process parameters: carbon concentration in hot metal, hot metal temperature, scrap size and pre-heating temperature on melting behaviour of scrap. The base case for the scrap size throughout the study was small particles. The large particles were used to demonstrate the influence of size in melting behaviour.

TABLE 1

The operational conditions of the concept OSBF process.

Process parameter	Value	Unit
Average hot metal temperature	1475	°C
Hot metal carbon concentration	4.0	wt%
Average slag temperature	1575	°C
Scrap temperature	25	°C
Scrap carbon concentration	0.1	wt%
Scrap Shape	Sphere	-
Scrap typical diameter	20 (small particle), 140 (large particle)	mm
Scrap liquidus temperature	1509	°C
Average feed pile temperature	875	°C

Carbon concentration in hot metal

In Figure 3, the melting time of small scrap particles is depicted for hot metal carbon concentration values between 1 and 4 wt per cent. The liquidus temperature of the scrap particle (1509°C) is higher than the liquid hot metal temperature (1475°C) and the hot metal has a higher carbon concentration (>1.0 wt per cent) compared to the scrap particle carbon concentration (0.1 wt per cent). Under such conditions the melting rate is controlled by mass transfer. Consequently, the carbon content has a significant influence on the total melting time of the scrap particle: with higher carbon content, the melting rate is higher.

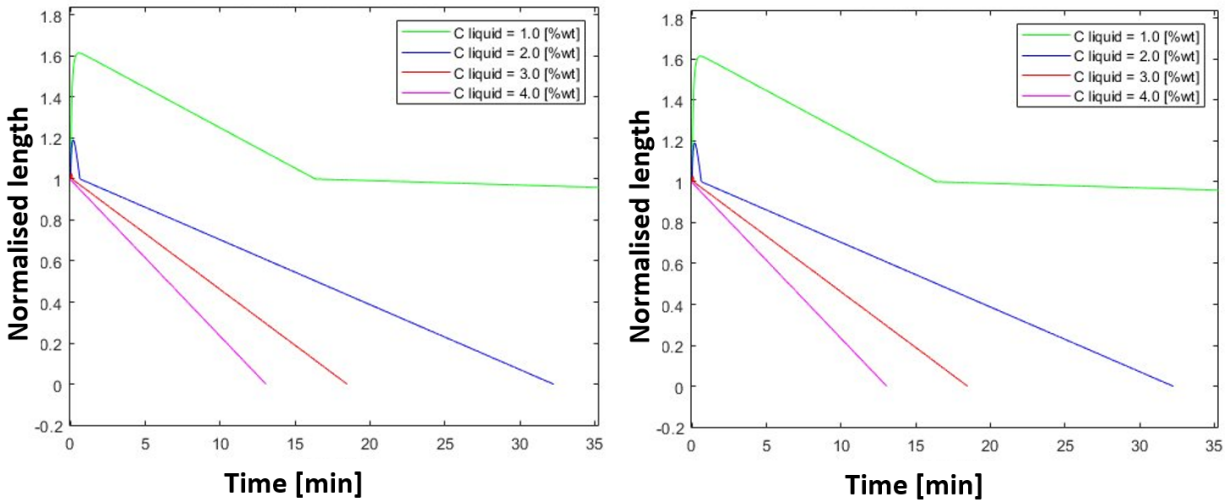

FIG 3 – (a) The influence of carbon concentration in hot metal on melting behaviour of small scrap particle; (b) Magnification of the early stage of the melting.

For small scrap increase in carbon from 1.0 wt per cent to 2.0 wt per cent results in ~15 times faster melting. Whereas for an increase from 3.0 wt per cent to 4.0 wt per cent the melting rate increases by 30 per cent. Therefore, the influence of carbon is more significant at lower carbon levels.

Hot metal temperature

Based on the data from Table 1, at temperatures below 1509°C the melting is mass transfer controlled. As depicted in Figure 4, the temperature of hot metal has a significant influence on the total melting time. The melting time is reduced by ~56 per cent when using 1600°C hot metal

temperature compared to 1500°C. While increasing the temperature from 1400°C to 1500°C results in ~72 per cent reduction in melting time. This behaviour indicates that increasing temperature in mass transfer controlled regime has more significant impact on melting than in the heat transfer controlled regime. While a unit change in temperature results in more improvements in melting time in mass transfer controlled regime, the melting at heat transfer controlled regime occurs at higher rates.

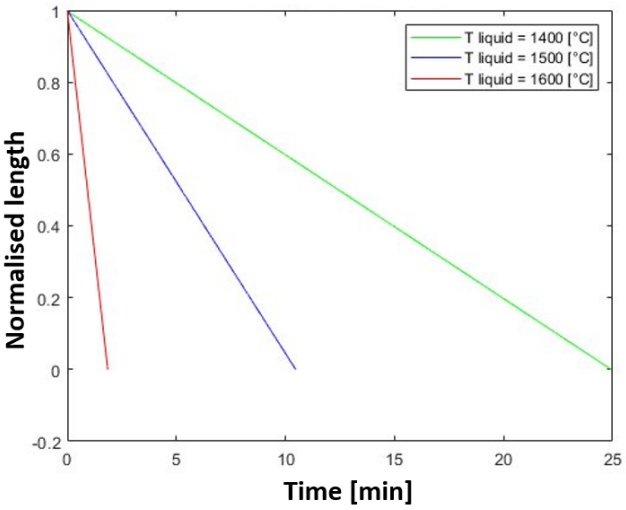

FIG 4 – The influence of hot metal temperature on melting behaviour of small scrap (from right to left 1400°C, 1500°C and 1600°C).

Scrap size

Figure 5 shows the total melting time for different feed pile heights for small (20 mm diameter) and large (140 mm diameter) scrap particles. The large scrap particle has approximately eight times longer melting time compared to small scrap particle. This is a result of larger surface-to-volume ratio for small particles.

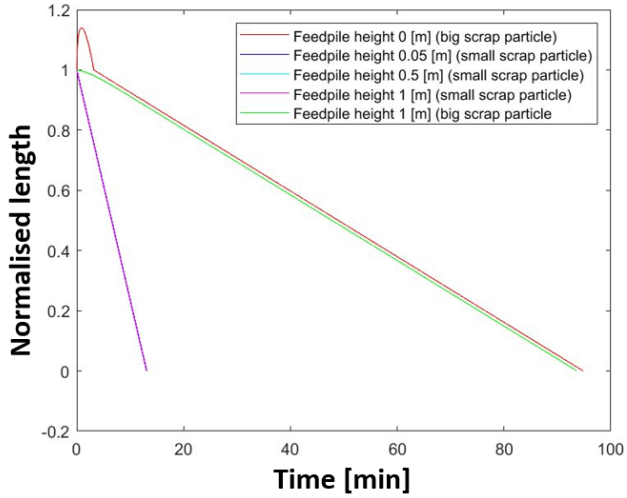

FIG 5 – The influence of scrap size for different feed pile height on melting behaviour of scrap.

A higher feed pile height does not have a significant influence on the total melting time for the scrap particles. There is only 3 per cent difference in total melting time between directly charged big scrap particle and those charged in the feed pile. For small scrap particles the difference is insignificant. This is because the majority of the heating and melting occurs in the molten hot metal after scrap particle is detached from the feed pile.

Even though, feed pile height does not have a significant influence on the total melting time, it reduces the initial shell formation phase for large scrap particles. The reason that such phenomenon

is not observed for small particles is the large surface-to-volume ratio of small particles, which in turn results in very short or no shell formation phase.

Preheating temperature

As explained in the previous section the preheating in the feed pile has no significant influence on the total melting time of small scrap. This holds for preheating of scrap before entering the OSBF as well. However, since the feed pile height had some influence on the shell formation phase of large scrap particles, the influence of the preheating temperature on large particles was studied separately.

Similar to the feed pile effect, Figure 6 shows that preheating the large scrap particle before entering the feed pile does not have a beneficial influence on total melting time and only influences the shell formation phase. Therefore, from purely melting time point of view it could be argued that pre-heating is not contributing to the scrap melting. However, if pre-heating is meant to increase the heat input to the system or decrease the electrical power input, then it might be beneficial.

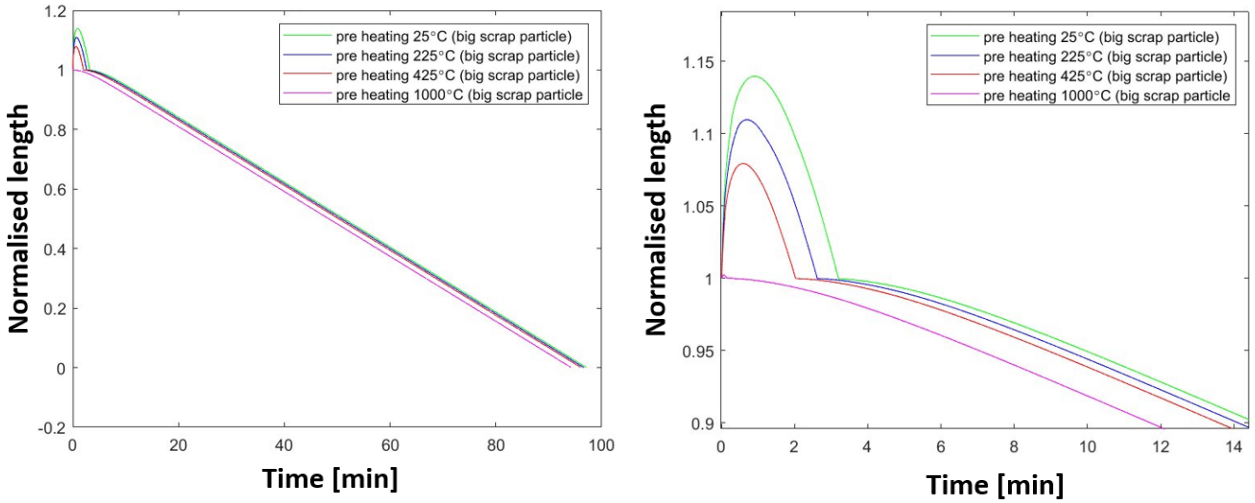

FIG 6 – (a) The influence of pre-heating temperature on melting behaviour of large scrap; (b) Magnification of the early stage of the melting.

CONCLUSIONS AND RECOMMENDATIONS

In this work, a phenomena-based model was built in order to simulate the heating and melting behaviour of a single scrap particle in an OSBF. Based on the validation study, it can be concluded that there is a reasonable agreement between the model and utilised experimental data. However, there is some discrepancy in predicting the initial shell formation phase between the model and the experiments partly due to the numerical approach used. Using a different FDM approach would allow a higher Fourier number, affording greater flexibility.

Furthermore, due to the inherent limitations of the model such as having a 1D approach and constant physical properties, 2D or 3D simulation with temperature and composition dependent physical properties would greatly improve the reliability of the simulation.

Based on the parametric study, the role of carbon in hot metal is proved to be critical for the total melting time. Specifically in mass transfer controlled melting regime when the liquid hot metal temperature is close to its liquidus temperature, increasing carbon content in the hot metal while keeping the same temperature significantly speeds up the melting process. In the case study, a 15 times increase in melting was observed for carbon increase in hot metal from 1.0 wt per cent to 2.0 wt per cent.

Similarly, the temperature of the hot metal has a considerable influence on the melting rate. In particular, increasing temperature from 1400°C to 1500°C results in ~72 per cent shorter melting

time. The role of temperature is more significant in mass transfer controlled regime than heat transfer controlled regime.

The scrap size was also found to be a key factor in scrap melting, with larger scraps requiring approximately nine times longer melting time. Pre-heating prior to entering the OSBF showed very little influence on the total melting time even though for large scrap particle the initial shell thickness was decreased at higher pre-heating temperatures.

The chemical interaction of the slag and cold scrap requires further fundamental research to clarify the underlying chemistry. This would bring further insight into the role of slag during the rather short contact time with scrap.

ACKNOWLEDGEMENTS

The valuable efforts and contributions of researchers at Tata Steel Ijmuiden, Technical University of Eindhoven and Seoul National University are highly appreciated in realising the current work.

REFERENCES

Belford, B, Farmer, G, Lötter, G and Kleier, T, 2022. Factors Affecting Throughput and Configuration of an Open Bath Furnace for the Production of Hot Metal, in Proceedings of the 8th ECIC and the 9th ICSTI 2022.

Cavaliere, P, Perrone, A, Silvello, A, Stagnoli, P and Duarte, P, 2022. Integration of Open Slag Bath Furnace with Direct Reduction Reactors for New-Generation Steelmaking, *Metals*, 12:203.

Chuang, K and Szekely, J, 1971. On the use of Green's functions for solving melting or solidification problems, Technical report, 12 p.

Penz, F M and Schenk, J, 2019. A Review of Steel Scrap Melting in Molten Iron-Carbon Melts, *Steel Research International,* 90:1900124.

Wei, G, Zhu, R, Tang, T and Dong, K, 2019. Study on the melting characteristics of steel scrap in molten steel, *Ironmaking and Steelmaking*, 46(7):609–617.

Xi, X, Yang, S, Li, J, Chen, X and Ye, M, 2020. Thermal simulation experiments on scrap melting in liquid steel, *Ironmaking and Steelmaking*, 47(4):442–448.

Modelling of liquid/liquid interface movement during spindle rotation of refractory – slag corrosion test

DOI: 10.62053/DXXZ4429
H Lee[1], B Choi[2] and Y Chung[3]

1. PhD student, Department of Advanced Materials of Engineering, Tech University of Korea, Siheung-si 15073, Gyeonggi Province, Republic of Korea. Email: rlghkemd369@tukorea.ac.kr
2. Senior Research Engineer, Hyundai Steel, Dangjin-si 31719, South Chungcheong Province, Republic of Korea. Email: bkchoi@hyundai-steel.com
3. Professor, Department of Advanced Materials of Engineering, Tech University of Korea, Siheung-si 15073, Gyeonggi Province, Republic of Korea. Email: ychung@tukorea.ac.kr

ABSTRACT

Numerous studies have explored refractory corrosion in the presence of slag and/or metal, utilising the Finger Rotating Test (FRT). Recent experimental results revealed that corrosion initially increased with rising rotation velocity but was then suppressed above a critical rotating speed, under conditions involving a two-liquid solution of slag and molten steel. This phenomenon indicated that the liquid/liquid interface movement occurred during spindle rotor. However, understanding of the phenomenon, known as the rod climbing effect, remains inadequate in the case involving slag, molten steel and refractories. To gain deeper insights, a simulation experiment was conducted on the phenomenon using silicon oil/water and the phenomenon was analysed using computerised simulation software (Ansys Fluent). Experimental modelling demonstrated that interfacial movement occurs even at low rotation velocity, as low as 200 rev/min, when the viscosity of silicone oil is at 100 cP. Computational analysis utilising the Volume of Fluid (VOF) method and a realisable k-ε turbulence model elucidated that interface elevation during rotor rotation arises due to viscosity disparities between the two fluids. Furthermore, this movement is more pronounced when the viscosity difference is lower. Additionally, the study findings suggest that higher density differences between two liquids suppress the phenomenon of interface movement.

INTRODUCTION

MgO-C refractories are mainly used as furnace lining materials. The workers (Liu *et al*, 2022; Liu *et al*, 2020) showed that MgO-C refractories have high mechanical strength, slag corrosion resistance and thermal shock resistance. The research reported that the furnace lining lifetime is determined by damage to the refractory due to chemical corrosion, thermal shock and mechanical wear (Zhang and Seetharaman, 1994; Lee and Zhang, 1999; Sniezek and Szczerba, 2020; Wang *et al*, 2022; Cui *et al*, 2022). Among these, Zhang and Lee (2000) reported chemical corrosion by slag is one of the main mechanisms causing serious wear of refractories. To improve the lining lifetime of the furnace, some researchers (Sniezek and Szczerba, 2020; Benavidez *et al*, 2015; Bavand-Vandchali *et al*, 2008; Guo *et al*, 2009; Um *et al*, 2014) have studied the corrosion mechanism of MgO-C refractories.

Methods for researching corrosion of refractory materials by slag can be divided into static and dynamic methods that embody the flow conditions of actual operation. A representative static method is the cup test, which processes refractory materials into a cup shape, adds solid slag and observes the reaction after melting. Meanwhile, a method of providing slag flow is the rotary slag test, which involves attaching a refractory material to a rotary furnace, putting molten slag in it and then rotating the furnace to check the corrosion phenomenon. However, Finger Rotating Test (FRT), which processes refractory materials into finger shapes and rotates them in molten slag and/or steel in a crucible, is the most widely used (Figure 1; Jeon *et al*, 2017; Harmuth and Vollmann, 2022).

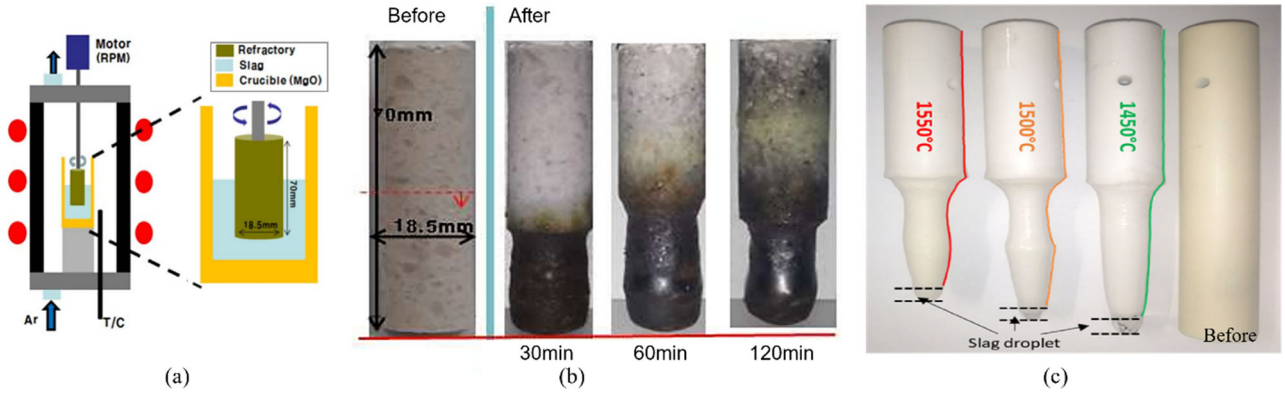

FIG 1 – Examples of Finger Rotating Test (FRT) studies.

Jürgen and Brüggmann (2012) revealed corrosion under operational conditions primarily arises due to the Marangoni effect at the interface between slag and molten steel. Previous research (Burhanuddin, Harmuth and Vollmann 2024) reported that an increase in rotational speed increases corrosion or reaction rates as a result of the combined effects of forced and Marangoni convection. However, recent findings by Um (2012) under a two-liquid solution condition comprising slag and molten steel, revealed that corrosion initially rose with increasing rotation velocity and was suppressed above a critical value.

This observed phenomenon, known as the rod climbing effect or Weissenberg effect, typically manifests in non-Newtonian fluids (Beavers and Joseph, 1977). However, recent studies (Chauhan and Yadav, 2021; Bonn *et al*, 2004) have demonstrated its occurrence in Newtonian fluids under specific circumstances. Despite this, research concerning the phenomenon among slag, molten steel and refractories remains insufficient. To complement this, our study delves into fluid dynamics and influencing factors utilising a water model and computational fluid dynamics using commercial software Ansys Fluent.

EXPERIMENTS

Water/silicone oil experimental

Experiments utilising water/silicone oil were conducted to simulate FRT involving slag and molten steel. Figure 2 depicts a schematic diagram of the simulation apparatus. Each experiment utilised 150 g of silicone oil and water, with a small quantity of red dye added to the water to enhance visibility. The rotating body consisted of MgO-C refractory material, processed to a diameter of 20 mm and a length of 50 mm and coupled with a metal rod connected to a motor to induce rotational motion. Transparent glass crucibles (outer diameter 50 mm, inner diameter 40 mm, height 130 mm) with internal monitoring capabilities were utilised. Real-time imaging was recorded by a CCD camera (charge-coupled device) to observe interface movement corresponding to rotation. Experiments were conducted under standard room temperature and atmospheric conditions.

Considering the viscosity effect, silicone oils with varying viscosities (100 cP and 1000 cP) were employed. The rotational velocity in both conditions was experimentally constrained to the maximum value that preserved the interface between the two fluids without inducing mixing due to rotation. each ranged up to 700 rev/min under conditions with 100 cP silicone oil and up to 1000 rev/min under conditions with 1000 cP silicone oil.

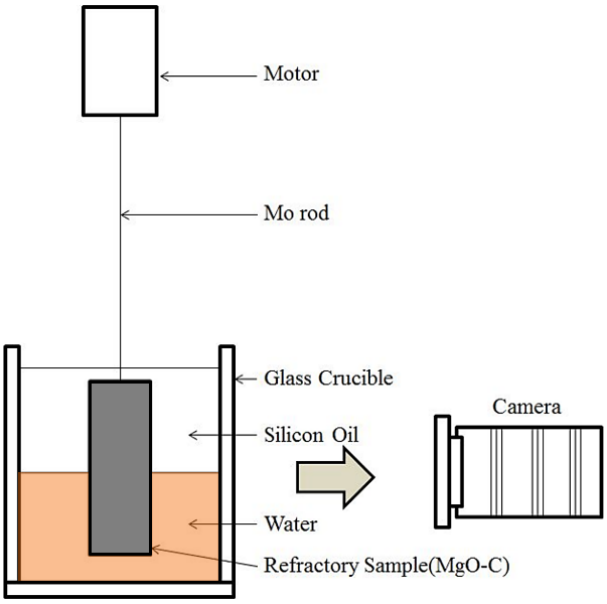

FIG 2 – A schematic of finger rotating test (FRT).

Computational Simulation

Ansys Fluent was used for computer simulation. The following assumptions and conditions were used to simulate the phenomenon.

Fundamental assumption

- The fluid is assumed to be an incompressible Newtonian fluid.
- The analysis of heat transfer under isothermal conditions is ignored.
- Unlike the actual reaction, the slag, molten steel and refractory material are assumed not to react with each other, so the initial form of the refractory material is maintained. Slag and molten steel are assumed to be in a uniform state, so there is no bias in the physical values.

Governing equations

The most basic governing equations used in computational fluid dynamics (CFD) simulations are as follows.

Continuity equation:

$$\frac{\partial \rho}{\partial t} + \nabla \cdot (\rho u) = 0 \tag{1}$$

where:

ρ is fluid density

t is time

u is the flow velocity vector field

Momentum equation:

$$\frac{\partial \rho u_i}{\partial t} + \frac{\partial}{\partial x_j}(\rho u_i u_j) = -\frac{\partial p}{\partial x_i} + \frac{\partial \tau_{ij}}{\partial x_j} \tag{2}$$

where:

ρ is fluid density

u is the velocity of fluid

P is static flow pressure

The Realised k-ε model was used to accurately simulate the rotation. This model was developed by Shih *et al* (1995) to improve the flow predictions of the standard k-ε model for boundary layer flows and separated flows and flows with rotational and vortex characteristics.

The equation of turbulent kinetic energy (k):

$$\frac{\partial}{\partial t}(\rho k) + \frac{\partial}{\partial x_j}(\rho k u_j) = \frac{\partial}{\partial x_j}\left[\left(\mu + \frac{\mu_t}{\sigma_k}\right)\frac{\partial k}{\partial x_j}\right] + G_k + G_b - \rho\varepsilon - Y_M + S_k \quad (3)$$

The equation of turbulent kinetic energy dissipation (ε):

$$\frac{\partial}{\partial t}(\rho\varepsilon) + \frac{\partial}{\partial x_j}(\rho\varepsilon u_j) = \frac{\partial}{\partial x_j}\left[\left(\mu + \frac{\mu_t}{\varepsilon}\right)\frac{\partial \varepsilon}{\partial x_j}\right] + \rho C_1 S_\varepsilon - \rho C_2 \frac{\varepsilon^2}{k+\sqrt{\nu\varepsilon}} + C_{1\varepsilon}\frac{\varepsilon}{k}C_{3\varepsilon}C_b + S_\varepsilon \quad (4)$$

where:

G_k is the generation of turbulence kinetic energy due to the mean velocity gradients

G_b is the generation of turbulence kinetic energy due to buoyancy

Y_M is the contribution of the fluctuating dilatation in compressible turbulence to the overall dissipation rate

σ_k, σ_ε are the turbulent Prandtl numbers for k and ε, respectively

S_k, S_ε are user-defined source terms

Computational simulation conditions

To perform a computational simulation of the experiment utilising water/silicone oil, the physical properties were obtained from the previous water/silicone oil experiment. For the modelling conditions, Volume of Fraction was utilised as a multi-phase condition and Multiple Reference Frame was employed for rotation, as depicted in Table 1. To reduce computation time, a 2D model was utilised, consisting of 73 236 quadrilateral meshes. The Realisable k-ε model was chosen and the roughness height was measured and implemented, with the default roughness constant applied. The simulation results were validated against those obtained from the water/silicone oil experiment, confirming the accuracy of the simulation.

Considering the differences in viscosity and density between liquid metal and slag, we investigated interfacial movement by varying the physical properties of silicone oil. Silicone oil viscosity was adjusted to match the experimental conditions, 100 cP and 1000 cP. Furthermore, density was expressed as a ratio. The density ratio of water to silicone oil set at 0.97 and 0.50, respectively.

TABLE 1

Physical properties, operation conditions for FRT computational simulation.

Parameter	Value
Physical properties of water	
Density (kg/m^3)	1000
Viscosity (cP)	1
Physical properties of silicone oil	
Density (kg/m^3)	970
Viscosity (cP)	100/1000
Tensions between the fluids	
Surface tension of water (N/m)	0.061
Surface tension of silicone oil (N/m)	0.024
Interfacial tension between water and silicone oil (N/m)	0.042 (Ismail *et al*; 2009)
Roughness of the MgO-C rotor	
Roughness height (μm)	0.42
Roughness constant	0.5
Operation conditions	
Rotation Speed ($\boldsymbol{rpm}$)	0 ~ 900
Initial interface height (cm)	4.2

RESULTS AND DISCUSSIONS

Water/silicone oil experimental results

Experimental investigations were conducted using water and silicone oil with viscosities of 100 cP and 1000 cP, respectively. Figure 3a depicts the initial appearance before the experiment, while Figure 3b depicts the experimental set-up under conditions of 700 rev/min and 1000 cP viscosity of silicone oil. To quantify the displacement of the interface, the height of the three-phase interface is defined ΔH.

$$\Delta H = H_{measured} - H_{inital} \tag{5}$$

Figures 3c and 3d represent the results for silicone oil viscosities of 100 cP and 1000 cP, respectively. In both cases, an increase in the rotational speed of the refractory material led to an upward movement of the three-phase interface between water, silicone oil and the refractory material. With 100 cP silicone oil, a gradual change in height was observed from 200 rev/min onwards, whereas with 1000 cP silicone oil, a sharp change in height occurred from 300 rev/min onwards. Hence, a smaller difference between the viscosities of silicone oil and water resulted in greater interfacial displacement.

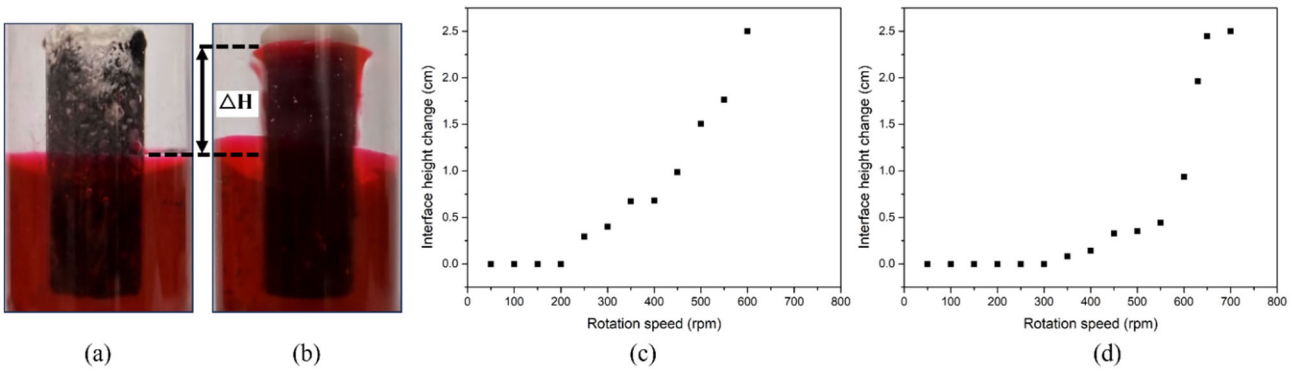

FIG 3 – (a) initial appearance preceding experiment, (b) appearance post-rotation at 700 rev/min, (c) plot depicting interface height variation with rotation velocity in water/silicone oil experiment under 100 cP silicone oil condition, (d) under 1000 cP silicone oil condition.

Computational simulation results

Computational simulations were conducted on water/silicone oil experiment when the viscosity of silicone oil was 100 cP and 1000 cP. The data set employed in the computer simulations is outlined in Table 1. Figures 4a and 4b present both experimental and simulated data for silicone oil viscosities of 100 cP and 1000 cP, respectively. In the case of 100 cP, a slight interfacial height change in height was observed even at 75 rev/min in the simulation and a sharp change occurred between 450 rev/min and 500 rev/min. Even in the case of 1000 cP, a slight interfacial movement was observed even below 100 rev/min, a phenomenon was not observed in the experimental results. In addition, the difference with the experimental results increased above 800 rev/min. Nevertheless, the trend of increasing interface heights with rising rotational speed of the refractory material well simulated that observed in the experiments.

Figure 4c illustrates the schematic representation of liquid flow under conditions of 1000 cP viscosity for silicone oil at 525 rev/min. Fluid velocities are depicted using a colour gradient, where red indicates high velocity and blue represents low velocity. Near the rotating body, silicone oil has high fluid velocities, while other regions experience relative stagnation. Conversely, water has slower fluid velocities near the rotor, with convection flow around it. As water flows move the interface near the rotating body, the silicone oil-water interface rises accordingly.

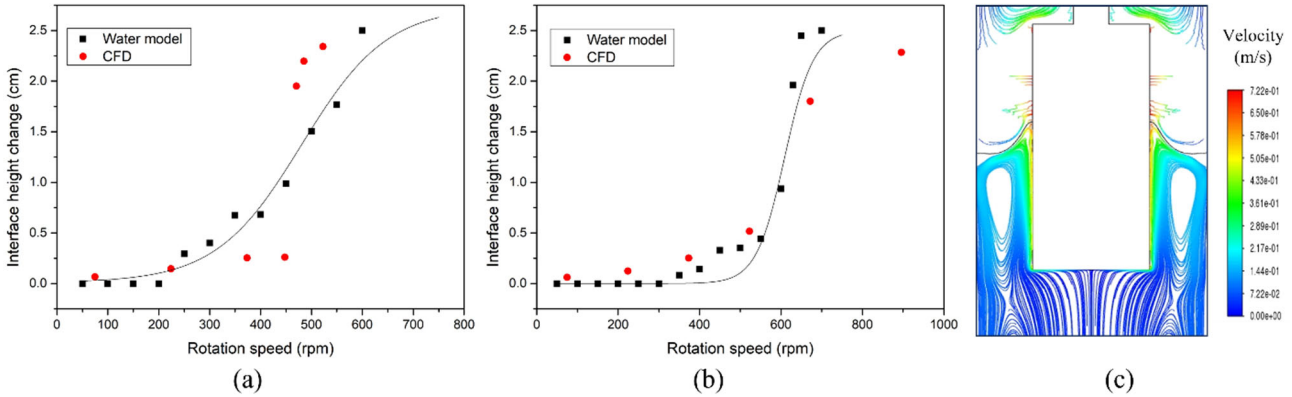

FIG 4 – (a) plot illustrating interface height variation with rotation velocity in experimental and simulated data under 100 cP silicone oil condition, (b) plot illustrating interface height variation with rotation velocity in experimental and simulated data under 1000 cP silicone oil condition, (c) schematic displaying velocity distribution with colour gradient under the condition of 1000 cP viscosity for silicone oil at 525 rev/min.

In industrial conditions, such as ladles containing molten steel and slag, there exists a notable density difference between the two liquids. To consider the effect of density difference, the density ratio is defined by Equation (6).

$$\rho_{ratio} = \rho_{silicone\ oil} / \rho_{water} \quad (6)$$

Figure 5a compares density ratios of 0.5 and 0.97 at a fixed viscosity of 100 cP in both cases. Below 400 rev/min, the similar results is observed between the two conditions. However, above 500 rev/min, significant interface movement is evident at a density ratio of 0.97, while less movement is evident at a ratio of 0.5.

Figure 5b depicts a schematic of liquid flow under conditions of density ratio 0.50 at 525 rev/min. While the velocity distribution resembles that of Figure 4c, convection of the silicone oil near the silicone oil/water interface is evident, suppressing interface movement. Consequently, insufficient force is exerted to raise the silicone oil/water/refractory interface compared to the case with a higher density ratio.

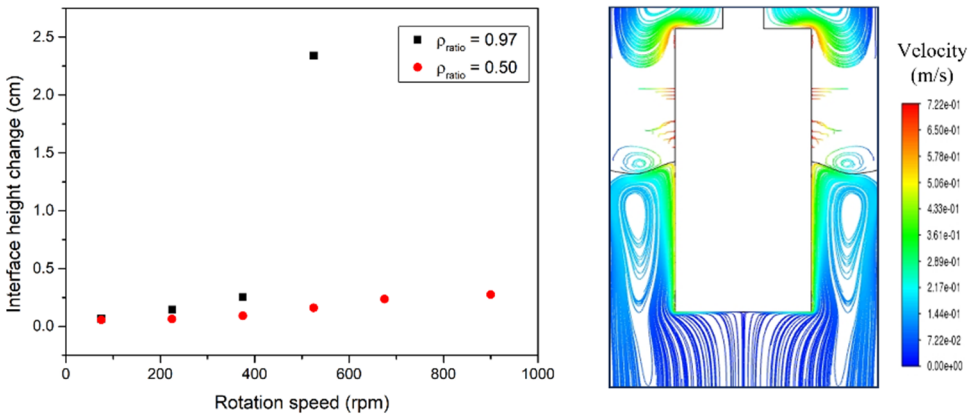

FIG 5 – (a) plot depicting difference in interface height variation based on density ratio, (b) schematic displaying velocity distribution with colour gradient under the condition of density ratio 0.50 and 1000 cP viscosity for silicone oil at 525 rev/min.

Under actual steelmaking conditions involving liquid molten steel and slag, density difference exist. Computational simulations indicate that simulation accuracy is accurate under conditions of significant high-density ratio. Therefore, it is worth considering additional variables such as interfacial tension and contact angle.

CONCLUSIONS

This study analysed fluid flow using both water/silicone oil experimental modelling and computational fluid dynamics (CFD) simulations to discern the factors influencing interfacial movement in the two-phase Finger Refractory Test (FRT) experiment involving molten steel and slag:

- In the water/silicone oil experimental model, the interface rose at rotational velocities of 200 rev/min or higher under 100 cP conditions and at 300 rev/min or higher under 1000 cP conditions. Furthermore, as rotational speed increased, the interface movement also increased.
- During computer simulations utilising Volume of Fluid (VOF), Multiple Reference Frames (MRF) and Realisable k-epsilon (k-ε) models, similar trends were observed in the water/silicone oil experiment. Water with low viscosity led to interface movement.
- In simulations comparing density ratio as a variable (0.97 and 0.5), reduced interfacial movement was noted with decreasing density ratio. To accurately simulate the fluid interaction in real operational conditions, additional factors such as interfacial tension or contact angle warrant consideration.

ACKNOWLEDGEMENTS

This paper was supported by Korea Institute of Energy Technology Evaluation and Planning (KETEP) Grant (20212010100060) and Korea Evaluation Institute of Industrial Technology (KEIT) Grant (00262191, 00262711) funded by the Ministry of Trade Industry and Energy (MOTIE).

REFERENCES

Bavand-Vandchali, M, Golestani-Fard, F, Sarpoolaky, H, Rezaie, H R and Aneziris, C G, 2008. The influence of in situ spinel formation on microstructure and phase evolution of MgO–C refractories, *Journal of the European Ceramic Society*, 28(3):563–569.

Beavers, G S and Joseph, D D, 1977. *Novel Weissenberg Effects*, pp 11–19.

Benavidez, E, Brandaleze, E, Musante, L and Galliano, P, 2015. Corrosion study of MgO-C bricks in contact with a steelmaking slag, *Procedia Materials Science*, 8:228–235.

Bonn, D, Kobylko, M, Bohn, S, Meunier, J, Morozov, A and Saarloos, W, 2004. Rod-climbing effect in Newtonian fluids, *Physical Review Letters*, 93(21):214503.

Burhanuddin, B, Harmuth, H and Vollmann, S, 2024. Determining the critical Reynolds number for suppressing Marangoni convection of alumina in silicate melt, *Ceramics International: CI*, 50(11):18323–18328.

Chauhan, V and Yadav, S S, 2021. Numerical Simulation of Rod Climbing Effect of Newtonian Fluids, *Fluid Mechanics and Fluid Power*, pp 565–568.

Cui, K, Wang, J, Wang, H, Zhang, Y and Fu, T, 2022. Erosion behavior and longevity technologies of refractory linings in blast furnaces for ironmaking: a review, *Steel Research International*, 93(11):2200266.

Guo, M, Parada, S, Jones, P T, Boydens, E, Dyck, J V, Blanpain, B and Wollants, P, 2009. Interaction of Al_2O_3-rich slag with MgO–C refractories during VOD refining—MgO and spinel layer formation at the slag/refractory interface, *Journal of the European Ceramic Society*, 29(6):1053–1060.

Harmuth, G J H and Vollmann, S, 2022. Application of an improved testing device for the study of alumina dissolution in silicate slag, *Journal of the European Ceramic Society*, 42(8):3652–3659.

Ismail, A E, Grest, G S, Stevens, M J, Heine, D R and Tsige, M, 2009. Interfacial structure and dynamics of siloxane systems: PDMS-vapor and PDMS-water, *Macromolecules*, 42(8):3186–3194.

Jeon, J, Kang, Y, Park, J H and Chung, Y, 2017. Corrosion-erosion behavior of $MgAl_2O_4$ spinel refractory in contact with high MnO slag, *Ceramics International*, 43(17):15074–15079.

Jürgen, P and Brüggmann, C, 2012. Premature wear of refractories due to Marangoni-convection, *Steel Research International*, 83(7):637–644.

Lee, W E and Zhang, S, 1999. Melt corrosion of oxide and oxide–carbon refractories, *International Materials Reviews*, 44(3):77–104.

Liu, Y, Wang, Q, Li, G, Zhang, J, Yan, W and Huang, A, 2020. Role of graphite on the corrosion resistance improvement of MgO–C bricks to MnO-rich slag, *Ceramics International*, 46(6):7517–7522.

Liu, Z, Yu, J, Wang, X, Ma, P, Gu, W, Wen, J, Wei, S, Zhang, X, Yan, Z, Wen, T, Yuan, L and Ma, B, 2022. Comparative study of B4C, Mg2B2O5, and ZrB2 powder additions on the mechanical properties, oxidation, and slag corrosion resistance of MgO–C refractories, *Ceramics International*, 48(10):14117–14126.

Shih, T-H, Liou, W W, Shabbir, A, Yang, Z and Zhu, J, 1995. A new k-ϵ eddy viscosity model for high Reynolds number turbulent flows, *Computers and Fluids*, 24(3):227–238.

Sniezek, R C E and Szczerba, J, 2020. Corrosion tests for refractory materials intended for the steel industry—A review, *Ceramics-Silikáty*, 64(3):278–288.

Um, H, 2012. Corrosion behavior of MgO-C Refractory in contact with ferromanganese slags and/or alloys, Master's Thesis, Tech University of Korea, pp 44–45.

Um, H, Lee, K, Kim, K Y, Shin, G and Chung, Y, 2014. Effect of carbon content of ferromanganese alloy on corrosion behaviour of MgO–C refractory, *Ironmaking and Steelmaking*, 41(1):31–37.

Wang, Q, Liu, C, Pan, L, He, Z, Li, G and Wang, Q, 2022. Numerical understanding on refractory flow-induced erosion and reaction-induced corrosion patterns in ladle refining process, *Metallurgical and Materials Transactions B*, 53(3):1617–1630.

Zhang, P and Seetharaman, S, 1994. Dissolution of MgO in CaO–'FeO'–CaF_2–SiO_2 slags under static conditions, *Journal of the American Ceramic Society*, 77(4):970–976.

Zhang, S and Lee, W E, 2000. Use of phase diagrams in studies of refractories corrosion, *International Materials Reviews*, 45(2):41–58.

CFD modelling of slag fuming, with focus on freeze-lining formation

DOI: 10.62053/WKWY2963

C M G Rodrigues[1], M Wu[2], M Chintinne[3], A Ishmurzin[4], G Hackl[4], N Voller[5], A Ludwig[2] and A Kharicha[2]

1. Montanuniversity of Leoben, 8700 Leoben, Austria.
   Email: christian.gomes-rodrigues@unileoben.ac.at
2. Montanuniversity of Leoben, 8700 Leoben, Austria.
3. Aurubis-Beerse, 2340 Beerse, Belgium.
4. RHI Magnesita, 8700 Leoben, Austria.
5. RHI Magnesita, 1120 Wien, Austria.

ABSTRACT

Slag fuming (SF) is a critical process for recycling zinc-containing slags, but the corrosive nature of molten slag poses challenges to the reactor durability. The freeze-lining (FL) technique offers a solution by forming a protective layer on the reactor wall. It requires intensive cooling using water-cooled jackets, which can stabilise the FL while compromising the energy efficiency of the process.

This study presents a computational fluid dynamic (CFD)-based model to optimise the SF process by considering FL formation and its impact on heat transfer and reactor wall temperature. A volume-of-fluid (VOF) model is coupled with a mixture continuum (MC) solidification model to capture the intricate multiphase flow dynamics within the SF furnace. Two FL types are considered: FL solidifying on the reactor wall in the slag bath region; and FL solidifying on the reactor wall in the freeboard region. The FL of the first type forms when the slag temperature drops below liquidus temperature. The FL of the second type only forms when a splash-induced slag droplet collides with the freeboard wall and solidifies. A series of splashing events are necessary to coat the freeboard wall.

The simulation was run until a global energy balance was reached. This means that the heat losses from the water-cooled jacket, bottom wall, outlet and fuming balance the heat gains from the hot gas injected through the submerged plasma torches. The increase in FL thickness, due to its low thermal conductivity, reduces the heat losses through the reactor walls. The calculated FL thickness and heat fluxes were in good agreement with industrial data, validating the model's credibility.

The simulation results provided valuable insights into the fuming process, including slag bath temperature evolution, slag splashing dynamics, FL formation patterns, local heat fluxes through the reactor wall and overall energy balance. These findings can inform process optimisation strategies to enhance the energy efficiency and sustainability of SF operations.

The authors have built a prior version of the model framework and applied it to simulate FL formation in an electric smelting furnace (ESF). The results from both the ESF and the current SF highlight the applicability of such model framework to a range of industrial processes involving FL formation. This model framework can ultimately contribute to more energy-efficient and sustainable industrial operations.

INTRODUCTION

Zinc, the world's fourth most consumed metal, plays a crucial role in various industries and in our daily life. Its annual global refined production surpasses 13.6 Mt (Kania and Saternus, 2023). However, the limited natural sources raise concerns about the sustainability of zinc production and its potential environmental impact. To address these challenges, a paradigm shift is needed, ie to prioritise zinc recycling. The recycling rate of 15–35 per cent for zinc is low (Worell and Reuter, 2014). Over the past decades, various technologies have emerged to recover zinc from slags and produce clean slags for value-added applications (Kaya, Hussaini and Kursunoglu, 2020). One such process is the slag fuming (SF) technology. It involves injecting coal and gas into molten slag to convert zinc oxides into metallic vapour (Verscheure *et al*, 2005). Optimal fuming rates can be achieved at high slag temperatures. However, the high temperature would rapidly erode furnace reactors or refractory linings, reducing their lifespan and increasing maintenance costs. To overcome this problem, modern SF furnaces often incorporate water-cooled jackets. These jackets promote

freeze-lining (FL) formation, a solidified layer of slag that acts as a protective barrier against the corrosive effects of molten slag (Verscheure *et al*, 2006).

FL formation has been extensively studied through both laboratory experiments and numerical models. Laboratory experiments have shown that the microstructure and thickness of FLs are determined by the solidification kinetics and slag chemistry (Campfort *et al*, 2009a, 2009b) and the FL front is influenced by the fluid flow (Fallah-Mehrjardi, Hayes and Jak, 2013a, 2013b; Nagraj *et al*, 2022). Modelling studies have also provided valuable insights into the governing mechanisms of FL formation. The early models had limited applicability due to their simplicity (Wei *et al*, 1997; Campbell, Pericleous and Cross, 2002), but numerical advancements over time have made models more capable of capturing the intricate mechanisms involved in FL formation (Guevara, 2007; Guevara and Irons, 2011; Feng *et al*, 2019).

Recently, the current authors developed a comprehensive model framework for simulating FL formation, extending the capabilities of previous numerical models by coupling FL formation with the flow dynamics, mass transfer processes and energy transport mechanisms. The model framework was applied to an electric smelting furnace (ESF) and accounted for the intricate energy balance between the electrode joule heating, matte production, FL formation or melting, feed presence and the cooling system (Rodrigues *et al*, 2023). This comprehensive representation of the system's energy balance was found crucial to accurately predict the FL layer behaviour. To further validate and expand the applicability of the model framework, the current authors applied it to the batch-type plasma-driven SF furnace operated at Aurubis-Beerse (Rodrigues *et al*, 2024). For an accurate representation of the multiphase flow with sharp interfaces between the gas and slag phases, the VOF formulation was integrated into the model framework. FL formation in both slag bath and freeboard was successfully captured. The simulation results were compared against industrial data and demonstrated a remarkable agreement that validated the model's accuracy.

This paper continues the authors' previous research on FL formation in the batch-type plasma-driven SF furnace. The primary focus of this work is to delve into the process dynamics, from furnace start-up to the establishment of a global net energy balance. The evolution of FL formation, slag temperature and heat flux patterns are analysed.

MODEL DESCRIPTION

Table 1 presents an overview of the model framework, which was described in detail in Rodrigues *et al* (2023, 2024). Here, only an outline is provided. Three phases (or phase states) are considered: gas, liquid bulk slag and solid slag (ie FL). The gas and the slag are captured with a volume-of-fluid (VOF) model. Their volume fractions add up to one ($\alpha_{\text{slag}} + \alpha_{\text{gas}} = 1.0$). The conservation equations for continuity, momentum and energy are shown in Equations 1–3.

The sensible enthalpy is defined by $h = \int_{298.15}^{T} c_p dT$.

Solidification occurs exclusively in the slag, which exists in two states (solid and liquid) and their volume fractions add up to one ($f_{\text{s}} + f_{\ell} = 1.0$). The solidification is solved with a mixture continuum (MC) model. The solidification path shown in Figure 1 is used to calculate f_{s} as function of T. The source term S_{H} (Equation 4) is the latent heat released/absorbed during solidification/re-melting. The drag term $\vec{S}_{\text{U}}$ (Equation 5) is included in the momentum conservation equation to dampen the flow in the mushy zone. The term S_{S} is the energy sink associated with the fuming rate. Owing to commercial reasons, details about this source term are omitted.

TABLE 1

Model overview.

Conservation equations	
$\frac{\partial \alpha_{\text{slag}} \rho_{\text{slag}}}{\partial t} + \nabla \cdot (\alpha_{\text{slag}} \rho_{\text{slag}} \vec{u}_{\text{slag}}) = 0 \qquad \text{with } \alpha_{\text{slag}} + \alpha_{gas} = 1$	(1)
$\frac{\partial}{\partial t}(\rho \vec{u}) + \nabla \cdot (\rho \vec{u} \vec{u}) = \rho \vec{g} - \nabla p + \nabla (\mu \nabla \cdot \vec{u}) + \alpha_{\text{slag}} \vec{S}_{\text{U}}$	(2)
$\frac{\partial}{\partial t}(\rho h) + \nabla \cdot (\rho \vec{u} h) = \nabla \cdot (k_{\text{c}} \nabla T) + \alpha_{\text{slag}} S_{\text{H}} + \alpha_{\text{slag}} S_{\text{S}}$	(3)
Source terms	
$S_{\text{H}} = \rho_{\text{slag}} L_{\text{slag}} \frac{\partial f_{\text{s}}}{\partial t}$	(4)
$\vec{S}_{\text{U}} = -K_0 \frac{f_{\text{s}}^2}{(1 - f_{\text{s}})^3} \vec{u}_{\text{slag}}$	(5)

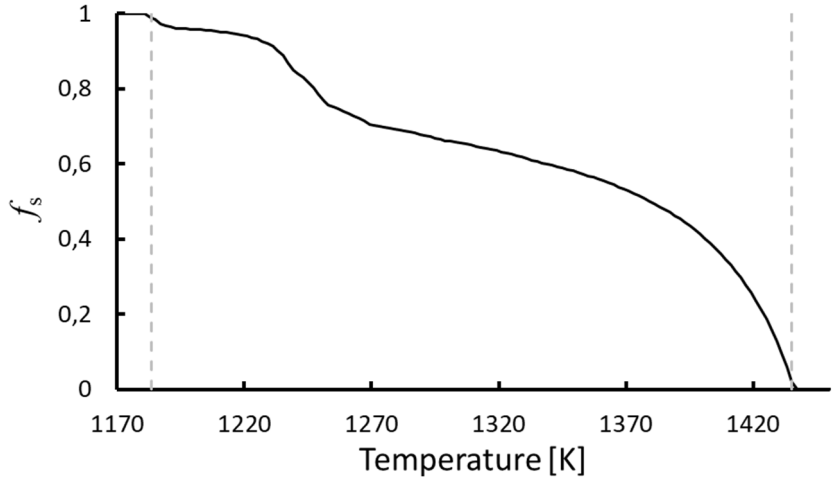

FIG 1 – Solidification path for the slag.

The simulation settings are summarised in Figure 2. Due to the large volume and the symmetry condition of the SF furnace, only one-third of the total furnace is considered. A mesh with 3.6 million cells is employed, with a local refinement near the wall (with 4 mm cells) to ensure adequate resolution of the FL layer. To effectively handle the complex flow dynamics near the furnace walls and the relatively high inlet gas velocity, a variable time stepping scheme between 10^{-5} and 10^{-4} seconds is employed. The computational domain is initialised with T_0 = 1473 K and a prescribed FL layer of 0.024 m on the reactor's inner walls in the freeboard region. This patched FL layer ensures that a global net energy balance can be established within a reasonable time frame.

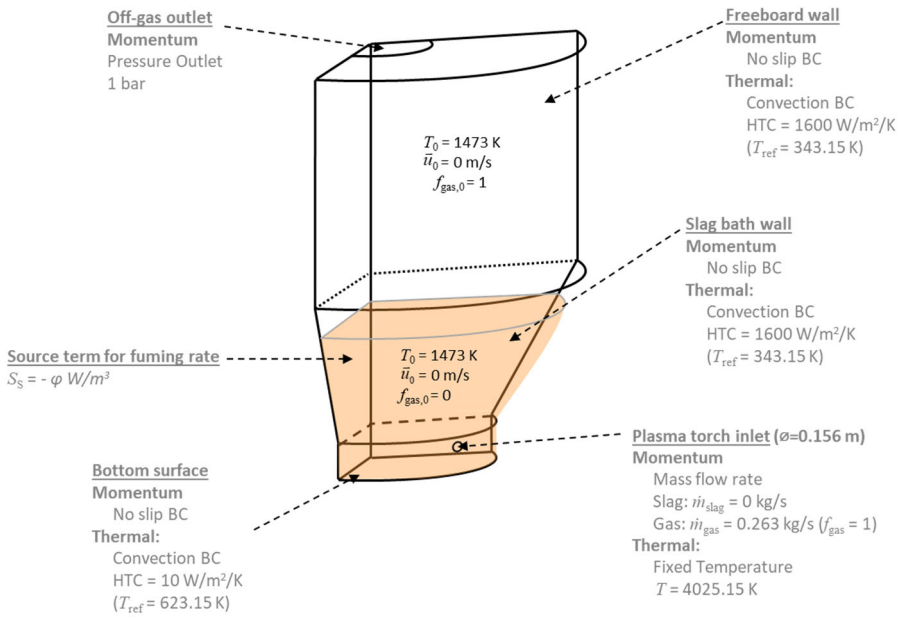

FIG 2 – Simulation settings for industrial slag fuming (SF) furnace.

RESULTS

Figure 3 shows the temporal evolution of the slag fuming process, from a completely static slag bath with significant superheat to a quasi-steady state with global net energy balance. The first column presents a series of snapshots of the 3D iso-surface at the slag/gas interface, which highlights the dynamics behaviour of the slag splashing onto the freeboard surface. The colour scale represents the temperature distribution. The second and third columns show snapshots in a 2D vertical plane of T and α_{slag} contours, respectively. The temperature contour demonstrates the gradual decline of superheat until the establishment of thermal equilibrium. The slag volume fraction contour is overlaid with streamlines to convey the dynamic behaviour of the flow both in the slag bath and in the freeboard. The fourth column shows snapshots of the 3D iso-surface depicting the thickness distribution of the FL layer on the reactor walls.

Early in the process (t = 30 sec), slag splashing is widespread and intense, as evidenced by the high and wide range of splashing occurrences (Figure 3: a1). This phenomenon stems from the high temperature (Figure 3: b1) and low viscosity of the slag phase. However, the relatively large superheat of the molten slag impedes FL formation in the freeboard region. This is evident from the uniform grey colour in the freeboard region in Figure 3: d1, which coincides with the thickness of the patched FL layer (2.4 cm). This indicates that no FL has formed on the freeboard surface. In contrast, in the slag bath region, where no patch was assumed, the FL has solidified to a maximum thickness of 0.4 cm, despite certain areas near the inlet remaining entirely devoid of FL.

At t = 100 sec, the temperature of the slag bath remains elevated. The splashing events traversing the freeboard increase the temperature locally (Figure 3: b2). Interestingly, slag flow is also quite dynamic within the slag bath, as indicated by the streamlines in Figure 3: c2. This dynamic flow is crucial for distributing heat across the slag bath and enhancing slag fuming efficiency. No splash-induced FL formation occurs on the freeboard. In the slag bath region, the FL thickness starts to increase in certain areas to 0.8 cm.

At t = 150 sec, the average slag bath temperature approaches 1445 K (Figure 3: b3) and the first splash-induced FL formations emerge in the freeboard region (Figure 3: d3). As a result, the FL thickness increases from 2.4 cm (assumed in the initial patch) to 3.0 cm in the darker areas. At this stage, FL formations primarily arise from splashing of individual slag droplets. This phenomenon can be attributed to the larger surface area-to-volume ratio, characteristic of smaller bodies, which expedites heat loss when the small slag droplet impacts on the freeboard surface. In contrast, larger bodies fail to reduce their temperature sufficiently to solidify upon impact and, instead, slide down the surface and merge with the bulk slag in the slag bath. In the slag bath region, the FL thickness increases to 1.8 cm, except in the region above the inlet, where the FL maintains a thickness of

1.3 cm due to the influence of the hot gas plumes generated by the submerged plasma torches (SPT).

At t = 180 sec, the average slag bath temperature decreases to approximately 1439 K (Figure 3: b4). This reduction in temperature significantly elevates the likelihood of FL formation in the freeboard region with each successive slag splashing/coating. For instance, in addition to the ongoing splashing event highlighted in Figure 3: a4, a distinct slag layer is visible coating the wall at a temperature lower than the bulk molten slag (as indicated by the green colour on the freeboard surface, contrasting with the orange colour in the molten slag). Correspondingly, the FL layer covers a larger area, as demonstrated in Figure 3: d4. Furthermore, the influence of slag splashing on gas flow dynamics becomes evident in the freeboard region (Figure 3: c4). The streamlines become more chaotic but tend to align with the trajectories of the molten slag bodies, highlighting the direct impact of splashing on the gas flow patterns within the system.

At t = 220 sec, a global net energy balance has been achieved in the simulation. Despite the transient nature of the flow dynamics beyond this stage, the overall energy balance persists in equilibrium over time. This means that a thermal equilibrium has been attained between the heat input (from the superheated slag bath and the injected hot gas), heat removal (by the cooling system, off-gas outlet, bottom surface and fuming reaction) and latent heat (associated with melting or solidification). The average slag temperature stabilises at approximately 1436.5 K (Figure 3: b5), which is 1.4 K above the liquidus temperature. The splashing-induced FL formation continues to expand its coverage area in the freeboard (Figure 3: d5). However, it is predominantly concentrated near the centreline of the domain, with the top corners of the reactor remaining untouched by splashing. This concentration pattern is attributed to the chosen gas density in the model, as discussed by Rodrigues *et al* (2024). The majority of the predicted FL thickness measures 3.0 cm, with some small areas appearing near the interface between the slag bath and the freeboard reaching 3.6 cm. This means that a newly created splash-induced FL layer was formed on top of a pre-existing FL layer. In the slag bath, the FL thickness increases to 3.0 cm, except in the vicinity of the inlet and along the vertical path near the surface, where the FL thickness is affected by the presence of the hot gas plumes.

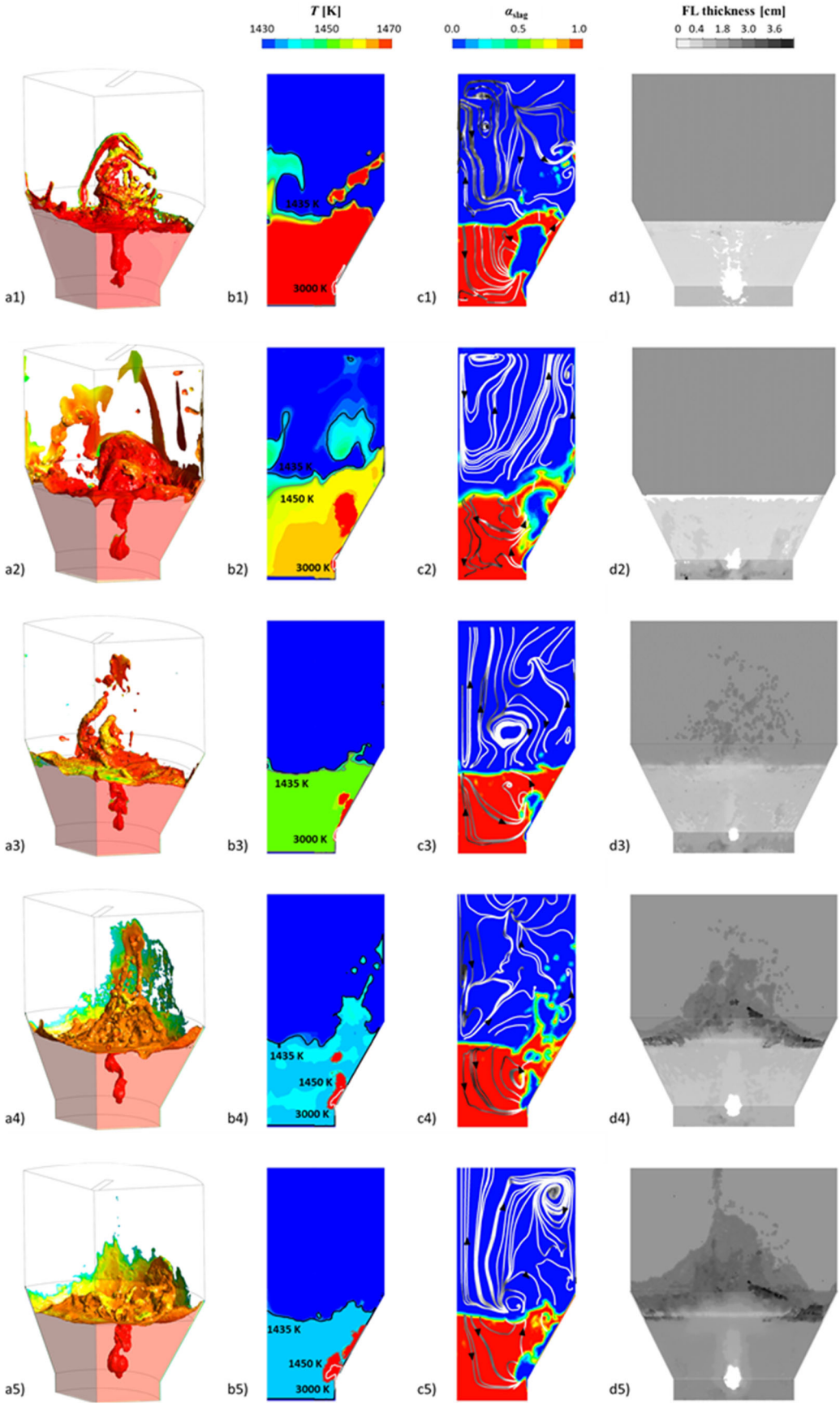

FIG 3 – Slag fuming process evolution at: 1) t = 30 sec; 2) t = 100 sec; 3) t = 150 sec; 4) t = 180 sec; 5) t = 220 sec. Simulation results for: a) iso-surface at slag/gas interface with temperature contour; b) contour of T overlaid with isotherms in 2D vertical plane; c) contour of α_{slag} overlaid with velocity streamlines in 2D vertical plane; d) distribution of FL thickness in grey scale on the furnace wall.

The final FL layer on the freeboard, shown in Figure 3: d5, is limited by the computational time constraints of the simulation. However, the evolution of the FL layer demonstrates that the model can capture FL formation in the freeboard region and that its evolution is directly dependent on the splashing number and range during the SF process. The simulation results for FL thickness in the slag bath and in the coated freeboard agree well with the estimated average 3 cm FL layer reported in industrial data. After reaching a global net energy balance, heat fluxes on specific reactor surfaces were compared against the industrial furnace heat balance data. The error is analysed in Table 2, revealing a clear agreement between simulation results and industrial data.

TABLE 2

Error percentage of heat fluxes on reactor walls after achieving a global net energy balance.

Heat fluxes [MW]	
Surfaces	**Error%**
Inlet	-0.4
Roof	-1.4
Walls	-0.4
Fuming reaction	-0.4

CONCLUSIONS

A CFD model framework has been developed to predict FL formation in a batch-type plasma-driven slag fuming furnace used for recycling Zn from slag. The FL is pivotal to protect the reactor walls and refractories from the corrosive molten slag and to act as an effective thermal barrier to enhance energy efficiency.

The model was successfully used to simulate FL evolution during the fuming process. The simulation results revealed a clear interplay between fluid flow, heat transfer and FL formation. Prediction of critical phenomena, including slag splashing, wall coating and freeze-lining formation, demonstrates the model's capability, providing valuable insights for a comprehensive understanding of the fuming process. Upon achieving a global net energy balance, the FL thickness and the heat fluxes through the main surfaces of the reactor agreed well with industrial data, validating the model's applicability in real-world scenarios.

The comprehensive understanding of fuming process dynamics facilitated by the model equips operators and engineers to make informed decisions, implement long-term targeted improvements and optimise operational parameters for enhanced efficiency and energy conservation. The model has proven capable of being used in a wide range of other industrial applications where FL formation plays a significant role.

ACKNOWLEDGEMENTS

This study was supported by the Austrian Research Promotion Agency (FFG) under the framework of Bridge 1 program (MoSSoFreez Project, F0999888120). We thank Dr Muxing Guo, Dr Annelies Malfliet, and Dr Zilong Qiu from KU Leuven, as well as Dr Samant Nagraj from Umicore for their discussions and valuable inputs. Approval from Aurubis-Beerse to publish manuscript is also acknowledged.

REFERENCES

Campbell, A P, Pericleous, K A and Cross, M, 2002. Modelling of freeze layers and refractory wear in direct smelting processes, in *Proceedings of the Ironmaking Conference*, pp 479–491.

Campforts, M, Jak, E, Blanpain, B and Wollants, P, 2009a. Freeze-Lining Formation of a Synthetic Lead Slag: Part I. Microstructure Formation, *Metall Mater Trans B*, 40:619–631.

Campforts, M, Jak, E, Blanpain, B and Wollants, P, 2009b. Freeze-Lining Formation of a Synthetic Lead Slag: Part II. Thermal History, *Metall Mater Trans B*, 40:632–642.

Fallah-Mehrjardi, A, Hayes, P C and Jak, E, 2013a. Investigation of Freeze-Linings in Copper-Containing Slag Systems: Part I. Preliminary Experiments, *Metall. Mater. Trans. B*, 44:534–548.

Fallah-Mehrjardi, A, Hayes, P C and Jak, E, 2013b. Investigation of Freeze-Linings in Copper-Containing Slag Systems: Part II. Mechanism of the Deposit Stabilization, *Metall. Mater. Trans. B*, 44:549–560.

Feng, Y, Gao, J, Feng, D and Zhang, X, 2019. Modeling of the Molten Blast Furnace Slag Particle Deposition on the Wall Including Phase Change and Heat Transfer, *Applied Energy*, 248:188–298.

Guevara, F and Irons, G, 2011. Simulation of slag freeze layer formation: Part II. Numerical study, *Metall Mater Trans B*, 42:652–663.

Guevara, F, 2007. Study of slag freezing in metallurgical furnaces, PhD thesis, McMaster University.

Kania, H and Saternus, M, 2023. Evaluation and Current State of Primary and Secondary Zinc Production—A Review, *Appl Sci*, 13(3):1–22.

Kaya, M, Hussaini, S and Kursunoglu, S, 2020. Hydrometallurgy, Critical review on secondary zinc resources and their recycling technologies, *Hydrometallurgy*, 195:105362.

Nagraj, S, Chintinne, M, Guo, M and Blanpain, B, 2022. Investigation of Bath/Freeze Lining Interface Temperature Based on the Rheology of the Slag, *JOM*, 74:274–282.

Rodrigues, C M G, Wu, M, Chintinne, M, Ishmurzin, A, Hackl, G, Voller, N, Ludwig, A and Kharicha, A, 2024 (in prep). Modeling freeze-lining formation: a case study in the slag fuming process.

Rodrigues, C M G, Wu, M, Ishmurzin, A, Hackl, G, Voller, N, Ludwig, A and Kharicha, A, 2023. Modeling Framework for the Simulation of an Electric Smelting Furnace Considering Freeze Lining Formation, *Metall Mater Trans B*, 54:880–894.

Verscheure, K, Kyllo, A, Filzwieser, A and Blanpain, B, 2006. Furnace cooling technology in pyrometallurgical processes in *Sohn International Symposium*, pp. 139–154.

Verscheure, K, Van Camp, M, Blanpain, B, Wollant, P, Hayes, P and Jak, E, 2005. Investigation of Zing Fuming Processes for the Treatment of Zinc-containing Residues in *John Floyd International Symposium*, pp. 137–250.

Wei, C, Chen, J, Welch, B and Voller, V, 1997. Modeling of dynamic ledge heat transfer, *Light Metals*, pp 309–316.

Worell, E and Reuter, M A, 2014. *Handbook of Recycling: State-of-the-art for Practitioners, Analysts, and Scientists*, pp 113–124 (Elsevier: Oxford).

Integrated process modelling for the Kalgoorlie Nickel Smelter

DOI: 10.62053/IUDM4601

G Sartor[1], A Rich[2], D Grimsey[3], M White[4] and R Forzatti[5]

1. Process Engineer, Hatch, Brisbane Qld 4000. Email: georgia.sartor@hatch.com
2. Smelter Development Manager, BHP Nickel West, Kalgoorlie WA 6430. Email: anthony.rich2@bhp.com
3. Principal Smelter Development Metallurgist, BHP Nickel West, Kalgoorlie WA 6430. Email: david.grimsey@bhp.com
4. Senior Mechanical Engineer, Hatch, Brisbane Qld 4000. Email: matthew.white@hatch.com
5. Project and Process Manager, Hatch, Perth, WA 6000. Email: ross.forzatti@hatch.com

ABSTRACT

An in-depth process model was developed for the pyrometallurgical, off-gas systems and water balance of the Kalgoorlie Nickel Smelter. This model was used to assess plant capacity with changing concentrate grades, increased throughput and tighter environmental emissions under a range of potential future operating conditions. Comparison of modelled results allowed for flow sheet optimisation across a range of metrics including sustainability, processing capacity and costs.

Process modelling software, METSIM® (ver 2020.06 by METSIM International), was used to simulate the flash furnace, integrated electric slag cleaning furnace, Pierce-Smith converters, matte granulation, waste heat boiler, hot gas handling equipment, wet gas cleaning plant and acid plant. The METSIM® model was divided into three separate, yet interconnected models: metals, off-gas and water balancing. This allowed for improved modelling efficiency and traceability while minimising manual error.

The METSIM® model was supported by inputs from other specialised software. Chemical thermodynamics software, FactSage™ (ver 8.2 by GTT Technologies), was used to establish relationships for the flash furnace fluxing strategy and determine the operating temperature. Arena® (ver 16.0 by Rockwell Automation), a discrete event modelling software, was used to simulate material movements within the aisle as well as Pierce-Smith converter operation, allowing for integration with upstream and downstream systems. A dynamic data exchange (DDE) was used to connect the results of each software package, interfacing through Excel® (version 4203 by Microsoft). The integration between models provided a streamlined approach to test capacity, bottlenecks, water consumption and emissions under a range of operating conditions, enabling a more robust process.

Further downstream modelling techniques were used to assess mechanical equipment. METSIM® outputs provided key parameters for combustion assessments using computational fluid dynamics and finite element analysis for the furnace mechanical design.

INTRODUCTION

The Kalgoorlie Nickel Smelter (NKS) was commissioned in December 1972 and has increased from a nameplate capacity of 30 to 100 kt/a Ni-in-matte. The final matte grade is approximately 68 per cent Ni, 2–3 per cent Cu and 1 per cent Co produced from a concentrate feed grade of 12 to 15 per cent Ni. Approximately 500 kt/a of concentrated sulfuric acid is also produced.

The original 1972 flow sheet included a flash furnace, separate electric slag cleaning furnaces, Peirce-Smith converters and off-gas heat recovery system to generate power. In December 1978 the smelter was upgraded to a unique, larger furnace incorporating flash smelting and slag cleaning within a single furnace, known as an integrated flash furnace (IFF), as described by Hastie *et al* (1984). Palmer, Malone and Loth (2005) summarise how NKS was progressively upgraded across several campaigns to increase capacity, align with technological developments, lengthen furnace campaign and meet environmental standards. The current flow sheet has been optimised around the 1978 IFF flow sheet, with the inclusion of a 525 t/day oxygen plant in 1993, an acid plant for SO_2 capture commissioned in 1996 and an upgraded furnace in 2008.

The current flow sheet is provided in Figure 1. The key areas include:

- Concentrate receival (by rail)
- Flux and revert preparation plant
- Oxygen production plant
- Air preheater
- Integrated flash furnace
- Peirce-Smith converters
- Matte granulation
- Power generation
- Off-gas cleaning including acid plant
- Effluent treatment.

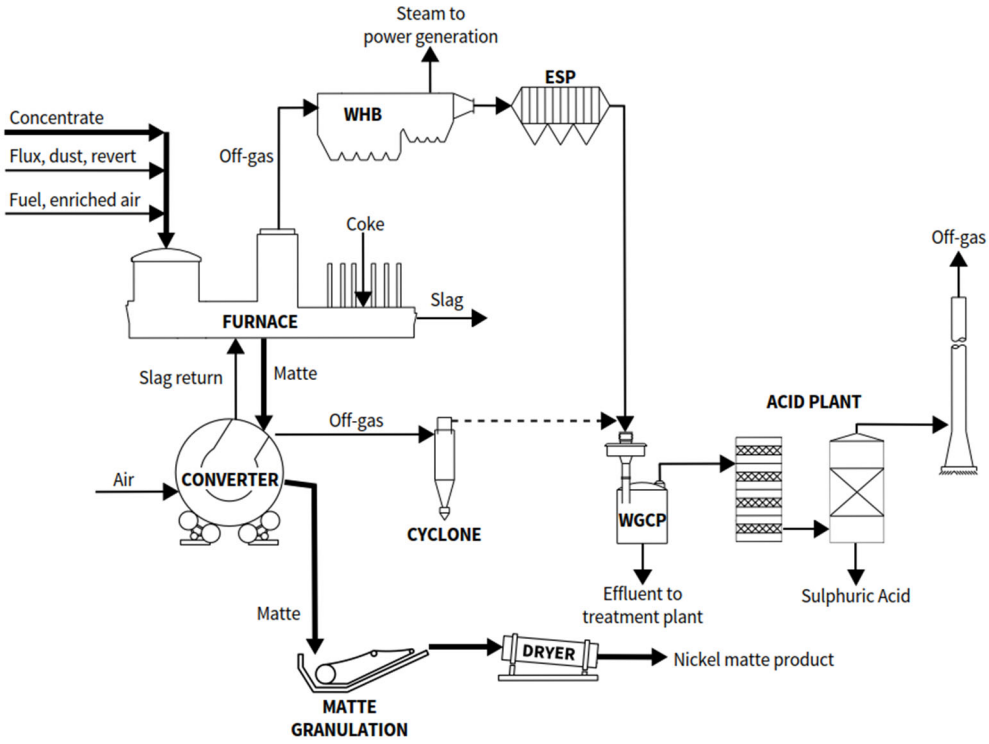

FIG 1 – Process flow diagram of Kalgoorlie Nickel Smelter.

The smelter receives nickel concentrate from Leinster, Mount Keith and the Kambalda concentrators. The flash furnace operates with a slag temperature of 1330°C, with the final slag heated to 1350°C as it passes two electrodes sets located in the slag cleaning end of the integrated furnace, known as the appendage. Low-grade matte containing 48 per cent Ni is produced along with discard final slag skimmed from the appendage. The matte is tapped from the furnace and blown through to final matte in three Peirce-Smith converters (PSCs) at 1250°C. The high-grade matte produced is granulated for further processing at the Kwinana nickel refinery or dried and packaged for export.

The smelting process produces SO_2-rich off-gas, the treatment of which includes heat and dust recovery, a wet gas cleaning plant (WGCP) and acid plant. A waste heat boiler (WHB) cools the furnace off-gas to approximately 350°C with superheated steam used to generate electricity for site use and sale to the grid. Electrostatic precipitators (ESPs) further remove dust before a series of scrubbers and wet ESPs remove halides and minor elements including arsenic and selenium. A double-contact double-absorption metallurgical acid plant produces 98.5 per cent sulfuric acid. Converter off-gas is treated with spray coolers and dust collection cyclones, then either discharged to the atmosphere via a stack when wind conditions are suitable to ensure populated areas are not impacted, or further treated in the acid plant. Weak acid effluent from off-gas cleaning is treated for

neutralisation and arsenic fixation before disposal to storage. The major sources of water loss from the process are from evaporative cooling water systems for the acid plant and furnace.

The last major furnace rebuild at the Kalgoorlie Nickel Smelter occurred in 2008, with the current campaign being the longest in the sites' history. The business is now in the planning stages for a rebuild, presenting the opportunity to make strategic investments aligned with future business objectives, such as increased operating range, operating expense (OPEX) reduction, and improved health, safety, environmental and community outcomes. A key process consideration was to evaluate the treatment of higher levels of magnesia in the feed, which typically requires higher furnace operating temperatures for processing.

Flow sheet optimisation generally requires an understanding of the interactions between metallurgical (concentrate, flux and molten metals), off-gas and water systems. For this purpose, a site-wide integrated model with equipment-level definition has been developed using multiple software packages. This paper outlines the development and applications of this model.

MODEL DEVELOPMENT

Process modelling of the smelter was developed primarily in METSIM®. Due to the complexity of the plant and software limitations, other software packages were used to supplement the modelling and provide metallurgical and scheduling based inputs. FactSage™ was used to establish relationships for the flash furnace fluxing strategy and determination of operating temperature. Arena® was used to simulate material movements within the converter aisle and the batch operation of the Pierce-Smith converters.

FactSage™

FactSage™ thermodynamic modelling software was used to determine the desired slag composition over a range of potential future operating temperatures and feed compositions. For a given operating slag temperature and superheat, the silica flux addition was varied with Fe/MgO in the concentrate blend supplied to the furnace. The concentrate Fe/MgO was then related to a target slag SiO_2/MgO, and this relationship was used within METSIM® to set the flash furnace fluxing requirements for all cases. This FactSage™ approach is similar to the methodology used to determine fluxing requirements for the current operation (Grimsey, Grimsey and Björklund, 2021). As shown in Figure 2, processing of higher MgO (low Fe/MgO) concentrates requires increased silica fluxing for a given slag temperature and superheat. Details of how this relationship is obtained can be found in Grimsey, Grimsey and Björklund (2021).

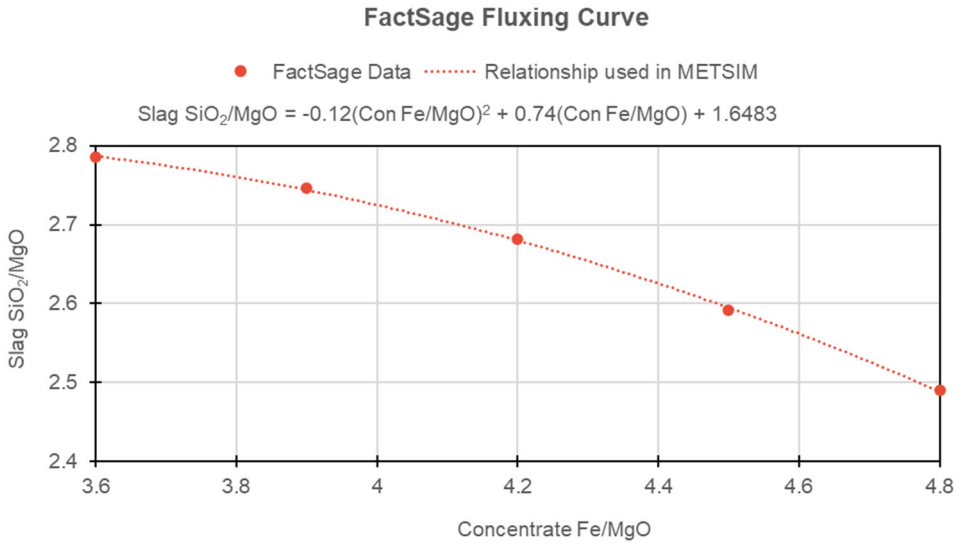

FIG 2 – Example fluxing curve generated using FactSage™.

Arena®

The PSCs operate batch processes and their production rate can be constrained by ladle movements within the crane aisle. To aid in debottlenecking and capacity analysis, Arena®, a discrete event modelling (DEM) software was used to model the system operations. An existing Arena® model was used, which had been developed and updated by OPTSIM®.

Key inputs to the Arena® model include furnace feed, maintenance schedules and personnel availability, physical constraints such as size and number of converters and ladles, metallurgical targets, number and speed of cranes, tuyere-line blast air rates, tapping times and the number of converters blowing at once due to limitations of the acid plant.

The model was used to ensure production targets can be met and for evaluating aisle productivity and bottlenecks. Sensitivity testing was completed to determine the optimal charge pattern, effect of number of converters, metallurgy and ladle sizes on aisle productivity. It was found that the converters were generally limited by the furnace matte production rate. Arena® outputs were fed into the METSIM® model; this included the converter charge pattern and ladle sizes in the pyrometallurgy model and blowing frequency in the off-gas model.

METSIM®

METSIM® is a process simulation software package used to facilitate modelling of complex processes for the metallurgical, chemical and minerals processing industries.

There are many pre-programmed blocks for specific unit operations available in METSIM®, with generic mixer and splitter blocks primarily used for this application. Chemical reactions and their extents, heat transfer, pressure changes, and phase separation are all manually inputted, allowing for complete visibility of the unit functionality. Reaction extents included partition coefficients of Ni, Cu and Co, metallurgical targets such as matte grades and vapour pressure correlations for off-gas systems. Set points and correlations were derived from plant operating data where possible, or from literature and in-house knowledge.

METSIM® uses a built-in thermodynamic database for a range of solids, liquid, molten and gas phase components from various references. Several additional components were added to the model database, for example, pentlandite from a FactSage™ database. The concentrate feed mineralogy was reproduced (including pentlandite, talc, serpentine and chlorite) instead of using simplified components, to account for the enthalpy of decomposition.

The smelter model was divided into three separate METSIM® models: pyrometallurgy, off-gas and water balance as depicted in Figure 3. This enabled the models to be built, calibrated and run separately by dedicated teams. The scope, inputs and interconnections between each model are described further.

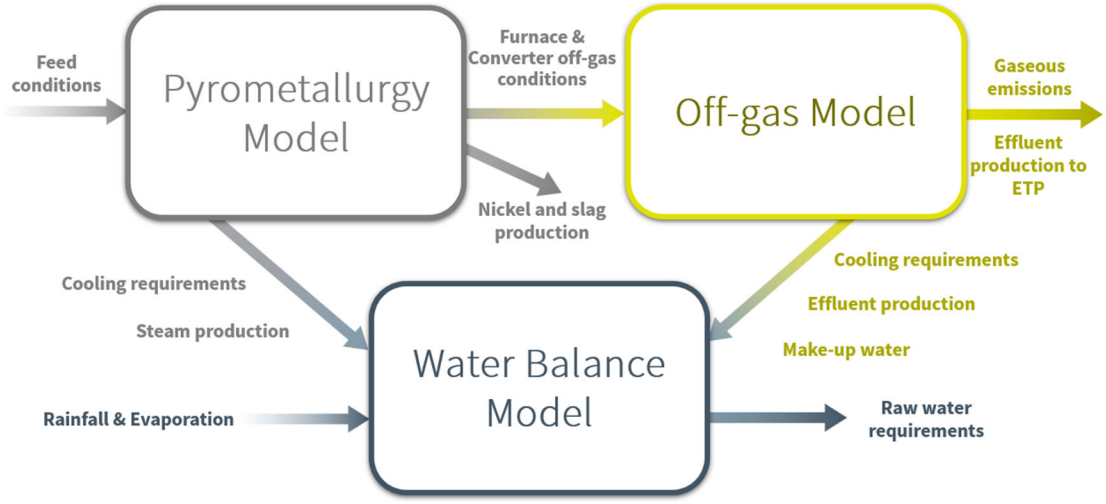

FIG 3 – Interconnection between METSIM® models.

The pyrometallurgy model contains the integrated flash furnace, PSCs, WHB, matte granulation and product dryer. Its primary inputs are the concentrate feed and furnace operating targets, from which the model calculates the production of matte and slag. The model outputs the furnace and converter off-gas flow rate, composition and temperature which are fed as inputs to the off-gas model. Furnace cooling requirements and steam production from the WHB are used in the water balance model. The off-gas model includes the furnace and converter hot gas handling systems, WGCP, acid plant and acid coolers. Key outputs from the off-gas model are the gaseous emissions and effluent production. It also calculates requirements of cooling water and make-up water which are used in the water balance model. In addition to requirements from the pyrometallurgy and off-gas models, the water balance model receives site rainfall and evaporation data to determine the total site raw water requirements as it varies across seasons. This involves quantification of the raw, demineralised, and recycled water grades used on-site, and variations in cooling requirement between summer and winter months.

Being an operating site, calibration of the model was critical to ensure accurate accounting and predictive capability for sensitivity testing of various operating scenarios. A comprehensive set of representative plant data was not always available. In the absence of reliable data from plant instruments, assays or log sheets, secondary sources of data such as existing equipment specifications, benchmarking and previous NKS studies were used to form the calibration basis. For example, the acid plant model was first calibrated to the original equipment manufacturer (OEM) design conditions which included a complete stream table, then validated to a partial set of plant operating data. The calibration process involved comparison of flow rates, temperatures, and compositions of solids, gas, and molten phases, pressures for gas systems, and estimation of heat losses. Critical parameters during calibration included the furnace heat balance and matte composition, PSC cycle times, and extent of SO_2 conversion in the acid plant.

A detailed equipment-level acid plant model had not been developed in METSIM® previously. This required various innovations in the modelling approach. Some of the notable challenges in model development are outlined below for the furnace, PSC and acid plant models:

- Due to the complexity of the furnace, it was divided into several blocks to assess the mass and energy balance, matte and slag compositions and the freeboard and bath reactions at each key stage in the furnace. This included dedicated blocks for the reaction shaft, settler and uptake shaft.
- The batch converting process had to be adapted to a steady-state model. Each blow of the converting cycle was modelled separately to target a progressively higher nickel grade, while charging additional matte ladles and skimming slag. The ‘per blow’ flow rates were then converted to an average continuous ‘per hour’ basis which could then be fed into the continuous furnace and off-gas models.
- Gas pressure drops across equipment and ductwork were manually built into METSIM®, as the software does not estimate pressure drops. These pressure drops were correlated to gas flow rate using constant K-factors determined during model calibration.
- Vapour pressure relationships were developed from literature and built into various units in the WGCP and acid plant model. These were used to determine reaction extents for halide removal, conversion of SO_3 to sulfuric acid and residual water and sulfuric acid in off-gas.
- The acid plant converter beds were modelled using the METSIM® Gibbs free energy minimisation reactor blocks to calculate chemical equilibrium reaction extents, instead of generic unit blocks used in the majority of the model.

Software integration

Inputs and outputs between models are shared using a dynamic data exchange (DDE) with Microsoft Excel®, providing a streamlined approach to running numerous cases to assess a range of operating scenarios. The Excel® interface is used to share inputs between the METSIM® models, as well as outputs from FactSage™ and Arena®, as shown in Figure 4. Furnace fluxing relationships derived from FactSage™ are used to determine the fluxing requirements in METSIM®, dependant on furnace operating temperature and concentrate Fe/MgO. The PSC matte charge pattern from Arena® defines

how many ladles of matte are charged for each blow of the PSC model. A complete set of modelling inputs for each case are listed in Excel®, which can be quickly imported into METSIM® without the need for manual transcribing. This provides an efficient, centralised and traceable method to run numerous cases with varying inputs.

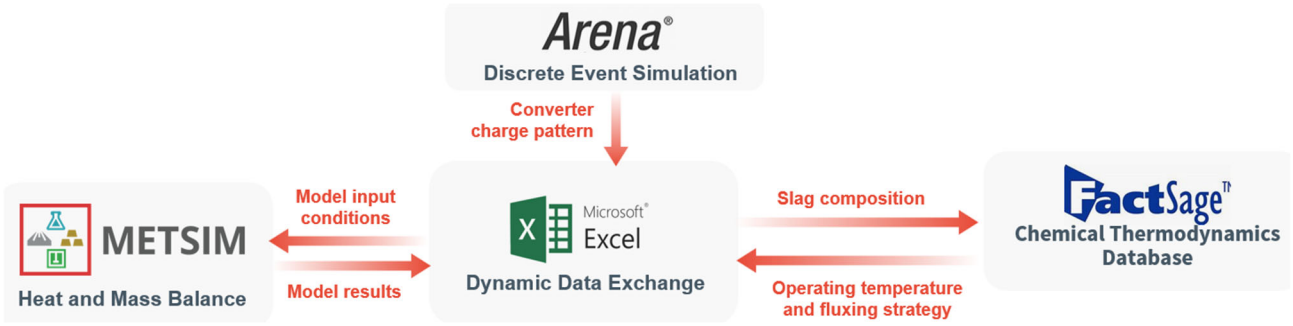

FIG 4 – Modelling software integration diagram.

While METSIM® was used for the majority of process modelling, additional specialised modelling software was selected for the effluent treatment and power generation areas of the plant. OLI Studio© (ver 11.0, by OLI Systems), a thermodynamic software package for aqueous chemistry analysis, was used to model the effluent treatment plant (ETP) and provide reagent consumptions, sludge production and water quality. A THERMOFLEX® (ver 30.0.4 by Thermoflow) model was developed for the steam power system. These packages are more suited to the chemistry and thermodynamics of these areas. These models use METSIM® outputs such as steam production and effluent composition to determine equipment sizing and reagent consumption. This approach utilises the strengths of each software, while maintaining an integrated model.

MODEL APPLICATIONS

The Kalgoorlie smelter is dependent on numerous ancillary systems to sustain the furnace operation and meet regulatory requirements. Equipment failure or under-sizing, environmental regulations, or water restrictions may prevent the furnace from reaching its target nickel throughput. Ancillary systems also contribute significantly to capital costs. Therefore, it is critical to assess and design these systems in parallel with primary pyrometallurgical equipment.

Smelter models developed using METSIM® are typically focused on pyrometallurgical equipment without integrating off-gas systems and water balancing at an equipment level. The development of an earlier NKS smelter model in METSIM® was discussed by Hunt, Grimsey and Gray (1991). The model scope was limited to the IFF, simplified modelling of PSCs and some hot gas cleaning equipment (WHB, ESPs, cyclone) for modelling dust recovery. The model was developed prior to the installation of the acid plant and WGCP, and did not include matte granulation and drying, blow-by-blow PSCs modelling, or water balances. A similar modelling approach combining METSIM®, FactSage™ and Arena® has previously been documented for the Sudbury nickel smelter (Tripathi *et al*, 2009). This was also limited to the pyrometallurgical equipment.

The comprehensive and integrated modelling approach developed for NKS can be used to assess individual equipment or the entire modelled flow sheet. Common parameters evaluated include nickel production, consumption rates of flux, oxygen and fuel, off-gas production, water consumption and effluent production. These parameters are assessed under various operating conditions and sensitivities, such as furnace operating temperature, oxygen enrichment, metallurgical targets, changes in concentrate throughput and composition. This provides a broader scope than existing site models, which are specialised to a particular area or equipment.

The modelling results provide a basis for trade-off studies, estimating operating expenditure and for sizing new equipment. It also assists with sustainability and regulatory assessments by quantifying energy consumption, gaseous emissions including SO_2, carbon intensity and water consumption. The range of modelled scenarios are used to robustly assess flow sheet capacity and optimise design across a range of metrics including sustainability, processing capacity and costs. This provides greater certainty of the design meeting the site business case.

Furnace design application example

Utilising METSIM® model outputs, a finite-volume computational fluid dynamics (CFD) assessment was performed to assess concentrate combustion and understand the flash furnace freeboard gas dynamics. A baseline assessment was performed on the existing furnace geometry and results were compared to future process and furnace options. This included assessing the transition from four jet-type concentrate burners, to a single dispersion-type burner.

Figure 5 illustrates velocity streamline between the existing furnace and a future process option with a single concentrate burner. Increases in oxygen enrichment and oil burner firing rates were noted to impact the gas dynamics in the reaction shaft (RS), settler and uptake shaft. Various changes to the furnace geometry (including settler and uptake geometry) were considered and tested using a combination of CFD modelling and industry benchmarking knowledge. The introduction of the single concentrate burner in Figure 5 was found to produce a large-scale upwards recirculation within the reaction shaft. This type of recirculation is common in flash smelting furnaces with a single concentrate burner and has been discussed by White, Gonzales and Anketell (2022).

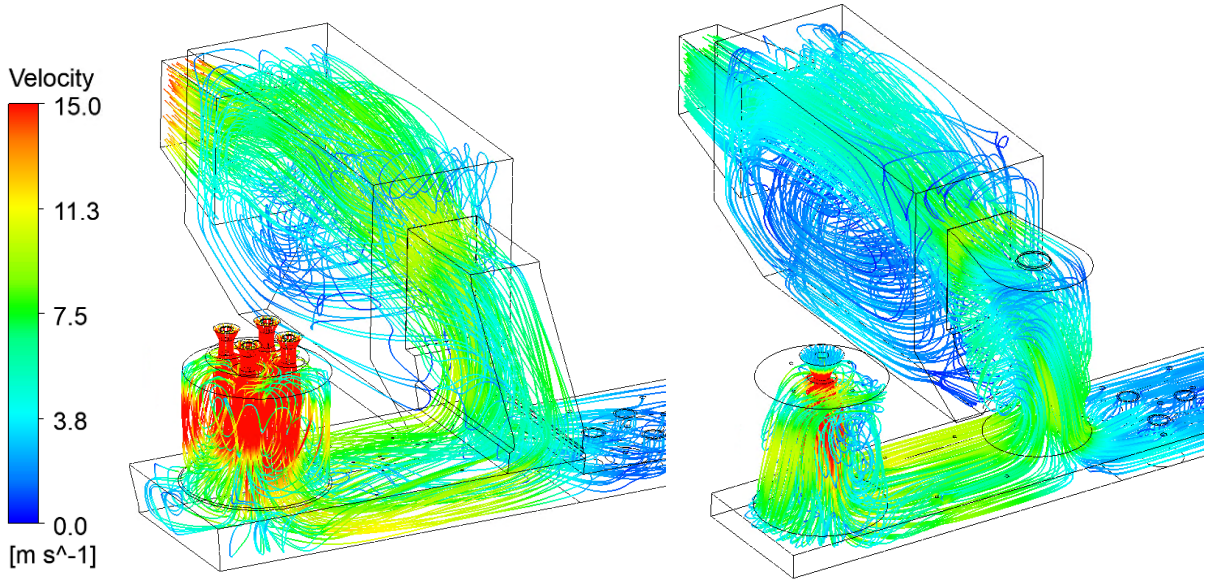

FIG 5 – Computational fluid dynamics (CFD) velocity comparison (left: existing, right: upgrade option).

For many years Hatch has modelled smelting processes and used process/metallurgical outputs to design furnaces. Across flash smelting and electric smelting, ongoing furnace innovations by Hatch have met challenges of increasingly intensive processes and throughputs. Ongoing improvements in furnace safety, extent of campaign and improved integrity are the core of Hatch's furnace designs.

Using process outputs (described above), the upgraded smelting process was benchmarked against the smelting industry. The upgraded furnace was evaluated against operating flash furnaces using comparison metrics such as RS residence time, as shown in Figure 6. The figure compares the reaction shaft velocity (m/s) relative to height (m), to understand the residence time to complete concentrate combustion for several cases. The Kalgoorlie upgrade cases for the maximum, nominal, and turndown cases (in addition to high and low Fe/MgO concentrate cases) were evaluated. Further parameters were assessed, including specific smelting intensity (t/h/m^3) and specific energy (MJ/h/m^3).

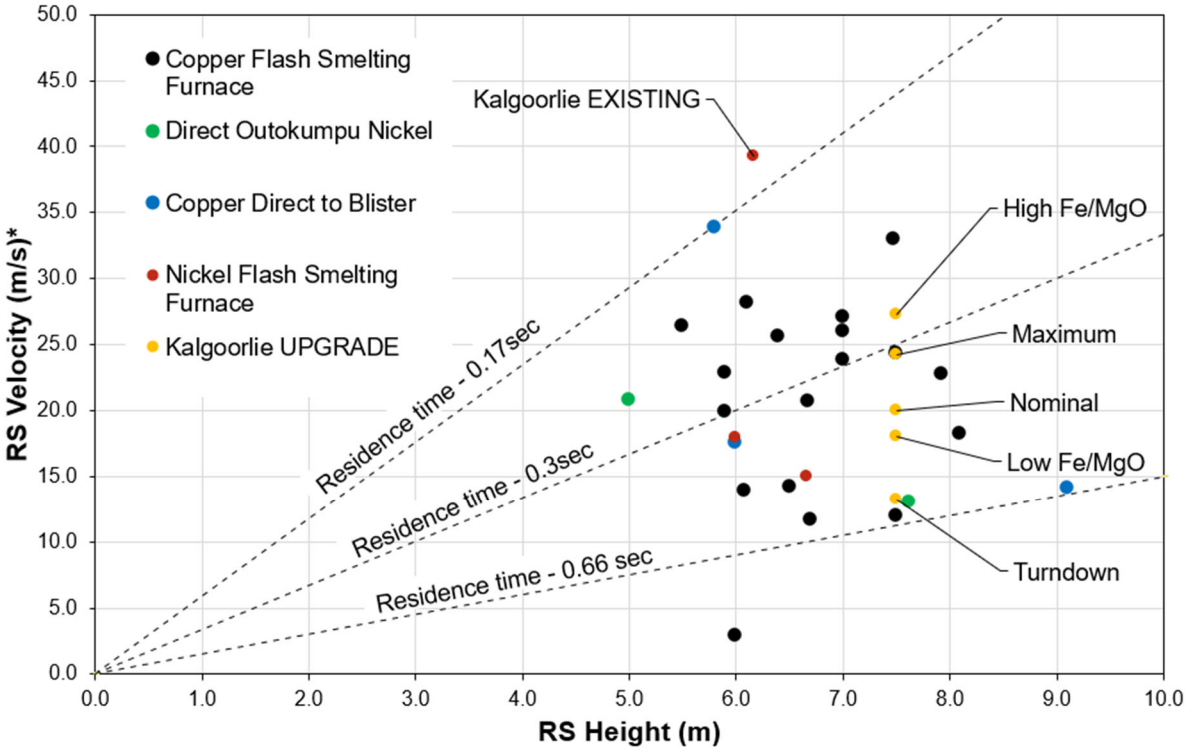

FIG 6 – Furnace reaction shaft residence time.

CONCLUSIONS

An in-depth METSIM® model has been developed by Hatch with the support of BHP for the Kalgoorlie Nickel Smelter. The interconnected model includes critical off-gas equipment and water balancing, not typically modelled alongside the core pyrometallurgical units. This enables broader flow sheet evaluation and optimisation in preparation for the next smelter rebuild including an investigation of increased throughputs, varying concentrate composition and higher oxygen enrichment to improve energy efficiency. To support the METSIM® modelling, FactSage™ was used to define the fluxing strategy and operating temperature for optimal processing of high magnesia feeds. Arena® dynamic simulation of the PSCs and aisle was used to optimise the operation. The specialised modelling packages were integrated through an Excel® interface to allow for streamlined simulation of numerous flow sheet options and sensitivity cases. The model results were used for equipment-level assessment across the smelter to define the operating window under future conditions, to quantify emissions and water consumption and as a key input to the detailed mechanical design of the flash furnace.

ACKNOWLEDGEMENTS

The authors would like to thank BHP for permission to publish this paper. The development of models involved valuable contributions of many Hatch engineers: Wendy Harris, Ahmed Hussein, Alison Imai, Tom Gonzales, Michael Bodley, Ellyce Wiliams, Kyle Lefebvre, Jordan Wilson, Kate Ellerby, Wiliam Yule and Daan Sauter.

REFERENCES

Grimsey, D, Grimsey, E and Björklund, P, 2021. Fluxing Optimisation and Control Improvements at the Kalgoorlie Nickel Smelter, in *Proceedings of Ni-Co 2021: The 5th International Symposium on Nickel and Cobalt* (eds: C Anderson, S Gostu, M Lundström, S Nicol, F Tesfaye, S Wang, G Goodall, D Gergurek, C Meskers, E Peuraniemi, P Tripathy and Y Zhang), pp 271–281 (The Minerals, Metals and Materials Society: TMS).

Hastie, C, Hall, J, Hohnen, C and Limerick, J, 1984. Kalgoorlie Nickel Smelter: Integration of Flash Smelting and Slag Cleaning within One Process Unit, in *Proceedings of the Symposium of Extractive Metallurgy*, pp 309–316 (The Australasian Institute of Mining and Metallurgy: Melbourne).

Hunt, A G, Grimsey, E J and Gray, N B, 1991. A Simulation of the Kalgoorlie Nickel Smelter Flowsheet using METSIM®, in *Proceedings of the Fifth AusIMM Extractive Metallurgy Conference*, pp 251–255 (The Australasian Institute of Mining and Metallurgy: Melbourne).

Palmer, J, Malone, J and Loth, D, 2005. WMCR – Kalgoorlie Nickel Smelter operations overview 1972–2005, in *Proceedings of the 44th Annual Conference of Metallurgists of CIM* (eds: J Donald and R Schonewille), pp 441–455 (Met Soc: Calgary).

Tripathi, N, Pandher, R, Barnes, A and Schonewille, R, 2009. Advanced Integrated Process Modelling of Ni-Cu Sulphide Treatment at the Xstrata Nickel Sudbury Smelter, in *Proceedings of the 50th Annual Conference of Metallurgists of CIM* (eds: B R Davis and J P T Kapusta), pp 441–455 (Met Soc: Montreal).

White, M, Gonzales, T and Anketell, A, 2002. Advanced Analysis of Flash Smelting Furnaces, in *Proceedings of Copper 2022 – The Igor Wilkomirsky Symposium on Pyrometallurgy,* vol 3, pp 705–716 (IIMCh: Santiago).

Pyrometallurgical process simulations using CALPHAD thermodynamic databases

DOI: 10.62053/BURK1637

M-A Van Ende[1], N Kumar[2] and I-H Jung[3]

1. Research Professor, Department of Materials Science and Engineering, and Research Institute of Advanced Materials, Seoul National University, Seoul 08826, South Korea. Email: vanende@snu.ac.kr
2. PhD student, Department of Materials Science and Engineering, Seoul National University, Seoul 08826, South Korea. Email: nishantk@snu.ac.kr
3. Professor, Department of Materials Science and Engineering, and Research Institute of Advanced Materials, Seoul National University, Seoul 08826, South Korea. Email: in-ho.jung@snu.ac.kr

ABSTRACT

In order to utilise the powerful thermodynamic databases for process simulations, a concept called Effective Equilibrium Reaction Zone (EERZ) was introduced to couple thermodynamic database calculations and reaction kinetics. Using the EERZ concept, many process simulation models for steelmaking processes have been developed within the FactSage steelmaking consortium. After validation of the simulation results by comparing with plant data, the simulation models have been applied to improve plant operations. Several success stories of the improvement of real steelmaking operations are shared. A new user-friendly FactProSim software developed for building process simulations is introduced.

INTRODUCTION

In pyrometallurgical processes, changes in phase amounts and their composition are mainly controlled by the thermodynamics of the system and reaction kinetics. In order to produce liquid metal in industrial scale, for example, the complex chemical reaction thermodynamics and kinetics between liquid metal and other phases (solid and liquid slag, sulfide, salt flux and inclusion, refractories and gas) should be considered. Most industrial processes involve multicomponent and multiphase systems, so even the thermodynamics of the system itself is difficult to understand.

Thermodynamic databases based on the CALPHAD (CALculation of PHAse Diagram) approach have been developed since 1960. Several commercial thermodynamic software packages containing extensive thermodynamic databases have been available since 1990 and widely used in both academic research and for industrial applications. One of the most well-known packages in particular for pyrometallurgical applications is FactSage™ software, ver 8.3 (by Thermfact and GTT Tech) and database (Bale *et al*, 2016). FactSage contains many critically evaluated and optimised thermodynamic databases for oxide, sulfide, salt, alloys etc, and allows to calculate complex multicomponent thermodynamic equilibrium involving solids, liquids and gas up to 40 elements. Although the thermodynamic calculations give good insight into chemical reactions at reaction interface and tell the direction and the final equilibrium state of overall reactions in the system, the variations in amount, composition and temperature of stable phases cannot be directly calculated from thermodynamic calculations.

In metal production and metal refining processes, the precise control of impurities and alloying elements in liquid metal and alloy is important. In classical kinetic studies, a simple chemical reaction involving a target impurity or alloying element was usually considered to solve the flux equations. However, in order to simulate an industrial scale process, the chemical reactions of all components in liquid metal and other existing phases should be simultaneously considered. The reaction kinetics should also vary with process parameters and temperature. The temperature variations of all phases should also be calculated considering the chemical reaction heats, heating by arcing, and heat loss during the process.

Van Ende *et al* (2011) proposed the ‘Effective Equilibrium Reaction Zone (EERZ) Model’ to couple the mass transfer kinetics with thermodynamic calculations based on CALPHAD-type databases to simulate high temperature materials processes. In the EERZ model, a complex process is divided

into a finite number of reaction zones in which equilibrium conditions are calculated. The reaction kinetic mechanism involving chemical reaction at the interface can be considered with the EERZ model, and heat evolutions can be considered simultaneously to track the temperature variation of each phase in the process. This model is well accepted and used for many process simulations in the recent years. Some of highlight works include the simulations by Van Ende (2022), Moosavi-Khoonsari, Van Ende and Jung (2022), Van Ende and Jung (2015a, 2015b, 2017, 2020, 2014, 2019), Van Ende *et al* (2011), Paek and Jung (2015), Van Ende, Jung and Harbers (2018), Kumar, Ahlborg and Pistorius (2019), Shin and Park (2020), Coetsee and De Bruin (2023) and Mason *et al* (2020).

In this study, the concept of the EERZ model and process simulation models for steelmaking developed based on the EERZ model are overviewed. A couple of success stories for the implementation of such process models to improve the real steelmaking process are shared. In addition, the new FactProSim software recently developed to assist in building process simulations is introduced.

CRITICAL WEAKNESS OF AI BASED MODEL FOR DIGITAL TWINS

Recently, artificial intelligence (AI) based predictions have been widely used for industrial process improvement. For the applications of the AI-based model, numerous sensors have been installed in pyrometallurgical processes to collect plant operation data. Although the sensors can collect a good amount of valuable data, the maintenance of sensors at high temperatures and reducing the noise in data constitute the main problems in high temperature processes. In addition, not only the total inputs but also the scheduling of input addition can significantly affect the quality (chemistry and temperature) of the final products. Therefore, it is rather difficult to implement an AI-based process model in pyrometallurgical processes.

The AI-based process model delivers the benefit of an accurate interpolation based on the available data. However, one of the critical weaknesses of AI-based model is the extrapolation capability. For example, the deoxidation of liquid steel is very important in the steelmaking process to reduce the amount of oxide inclusions in the final products. As shown in Figure 1, an AI-based model trained using the current operation data would predict a decreasing oxygen content with increasing Al content even above 1 wt per cent Al. But thermodynamics predict that the oxygen content increases again above 1 wt per cent Al in liquid steel. That is, a big data-based AI model can significantly mislead the oxygen prediction, but a thermodynamic-based model can improve the prediction accuracy at process conditions which have not been operated before. In particular, the process models based on thermodynamics and reaction kinetics can even be used as Digital Twins for the current and future plant operations.

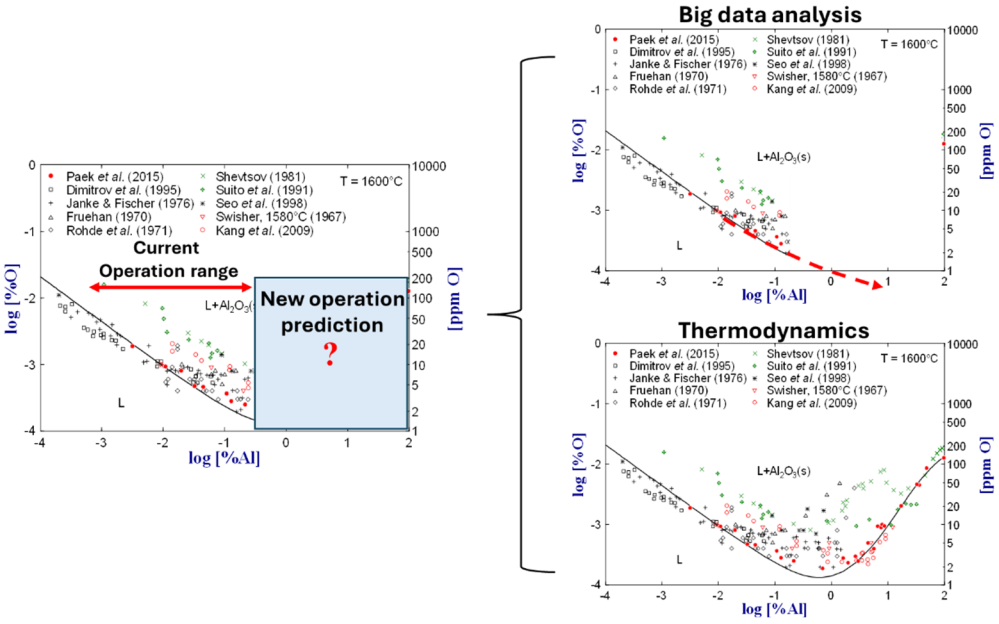

FIG 1 – AI deoxidation in liquid steel – comparison of AI model based on big data analysis and thermodynamics-based model.

OVERVIEW OF THE EERZ MODEL

Van Ende *et al* (2011) proposed the 'Effective Equilibrium Reaction Zone (EERZ) Model' to couple mass transfer kinetics with thermodynamic databases to simulate high temperature materials processes. In the EERZ model, a complex process is divided into a finite number of reaction zones in which equilibrium is calculated. For example, let's consider a slag and liquid steel reaction, as shown in Figure 2. The interfacial reaction zone size can be determined by the mass transfer coefficient which is influenced by the operation conditions. So, at each given time interval, the mass transfer coefficient is calculated using the operation conditions, and the effective volumes of steel (V2 in Figure 2) and slag (V3) participating in the interfacial reaction can be determined using the mass transfer coefficient of steel and slag, respectively. FactSage thermodynamic database can be used to calculate the interfacial equilibrium between V2 and V3. The reaction products after the interface reaction can be homogenised with remaining volumes of steel (V1) and slag (V4). If we run the calculation iteratively reflecting the change in the operation conditions, the evolution of the steel and slag composition and mass can be calculated with time.

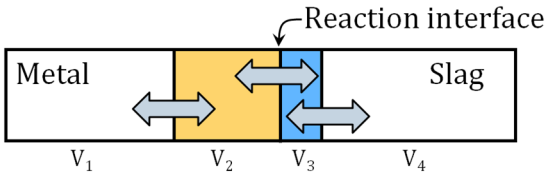

FIG 2 – Schematic diagram of the EERZ model – for the reaction between slag and liquid metal (Jung and Van Ende, 2020).

Using the thermodynamic database, the enthalpy change caused by the interface reaction can also be calculated, which can be used to predict the temperature profile of steel and slag. The heat loss and heat addition can also be included in the simulation. For example, we can add a certain amount of heat to liquid metal and slag due to arcing energy, which can increase the temperature of liquid metal and slag. As the heat capacities of liquid metal and slag are different, the temperatures of these phases can have very different values. Of course, heat transfer between liquid metal and slag can be considered too.

In steelmaking, complex reactions between slag/molten steel/inclusion/refractory/gas/input materials (fluxes, alloys, scraps etc) should be considered. In fact, to accurately analyse the thermodynamics between these reactions, kinetic concepts such as reaction efficiency, material mass and time of the input material additions must be considered. In the EERZ model, the reaction mechanism should be first defined based on literature laboratory study or plant sampling results.

For example, the change in the chemical composition of liquid steel and molten slag can be mainly determined by process kinetics at the slag/metal interface. In steelmaking process, the chemical reactions at reaction interface are usually fast enough so that reaction rates are mainly controlled by mass transfer of species to and/or from the reaction interface. If the interfacial reaction is the first order reaction, the change in composition at the interface can be calculated by:

$$J_i = k_i \, (\%C_{i,\,bulk} - \%C_{i,\,interface}) \tag{1}$$

Where: J_i and k_i are flux of i and mass transfer coefficient of i, respectively, and $\%C_i$, bulk and $\%C_i$, interface are concentration of i species at bulk and interface, respectively. That is, J_i is the flux of i species which can be consumed or gained by the interfacial reaction. $\%C_i$, interface can be determined by thermodynamic equilibrium at the interface. For nitrogen removal process involving liquid steel and gas interface, the adsorption of surface active elements like sulfur and oxygen can influence to the equilibration at the interface, which can be taken into account in the description of $\%C_i$, interface. If k_i of all species in the given solution are the same values regardless of species, the amount of each solution participating in chemical reaction at the interface can be simply derived as follows:

$$RW_{solution} = (k\rho A)_{solution} \, \Delta t \tag{2}$$

Where RW, k and ρ are reacting amount, overall mass transfer coefficient, and density of given solution, respectively, A is the area of reaction interface, and Δt is time step of reaction.

That is, if we consider that the interfacial reaction between slag and liquid metal, we can put the amount of reacting mass of slag ($(k\rho A)_{slag}\ \Delta t$) and liquid metal ($(k\rho A)_{metal}\ \Delta t$) at given time into the chemical equilibrium reaction. These slag and metal amounts can be assigned as effective reaction zone volumes at the interfacial reaction in Figure 2. This is the key concept of the EERZ model. k_{slag} and k_{metal} are the key parameters which can be varied with temperature, stirring energy etc, and can be determined from the plant operation data.

The overall mass transfer coefficient k in Equation (2) can vary with operation condition. For example, when the stirring energy of liquid metal becomes larger, k_{metal} becomes higher, which increases in general the reaction rate at the slag/metal interface. The k_{slag} can be also largely influenced by the viscosity of slag. The k value can be obtained from literature, or can be directly determined by the plant sampling data. Depending on the k values of slag and liquid metal, the rate determining step can be identified automatically in the calculations.

PROCESS SIMULATION MODELS – FACTSAGE STEELMAKING CONSORTIUM

Using the EERZ concept, we have developed many process simulation models in collaboration with our industrial partners of the FactSage Steelmaking Consortium. These include steelmaking processes simulation models for Electrical Arc Furnace (EAF) (Van Ende, 2022), hot metal treatment (powder injection) (Moosavi-Khoonsari, Van Ende and Jung, 2022), Basic Oxygen Furnace (BOF) (Van Ende and Jung, 2015a, 2015b), RH Degasser (Van Ende *et al*, 2011), Vacuum Tank Degasser (VTD) (Paek and Jung, 2015), Ladle Furnace (LF) (Van Ende and Jung, 2017; Van Ende, Jung and Harbers, 2018), Tundish (Van Ende and Jung, 2020), Continuous Casting (Van Ende and Jung, 2014) and Argon Oxygen Decarburisation (VOD) (Van Ende and Jung, 2019).

Originally, the process simulation models were developed using the FactSage macro processing code to connect thermodynamic calculations, but all of them were converted to ChemApp (by GTT Tech) based standalone programs to significantly improve the simulation speed. Most of the process simulations can be completed within 1/4 to 1/10 of real process operation time.

As shown in Figure 3, each process model has been tested using real plant data from several industrial members. When the model is applied to plant simulation, small tunings in the model parameters like mass transfer coefficient k and heat loss are usually necessary to more accurately reproduce the plant sampling data. The k and heat loss (heat transfer coefficient) parameters are mainly dependent on stirring condition, slag viscosity, reactor dimension etc. The influences of steel composition and additive schedule to the chemistries and temperatures of liquid steel, slag, inclusion and gas can be well predicted by EERZ model based on accurate thermodynamic database.

To validate and improve the model predictions, many sampling data of steel, slag and inclusions are necessary and the data and simulation results are analysed together with industrial partners. After the validation of model simulations, the process models can be applied to improve the plant operations. For example, the scheduling of flux addition, alloy addition and gas injection can be varied in the simulations to investigate their influences to the chemistry and temperature of liquid steel and slag. By employing the simulations, the current plant operation can be further optimised to improve the productivity and quality of the products and the future production scenarios can be designed virtually.

Some of the success stories by our industrial partners are presented.

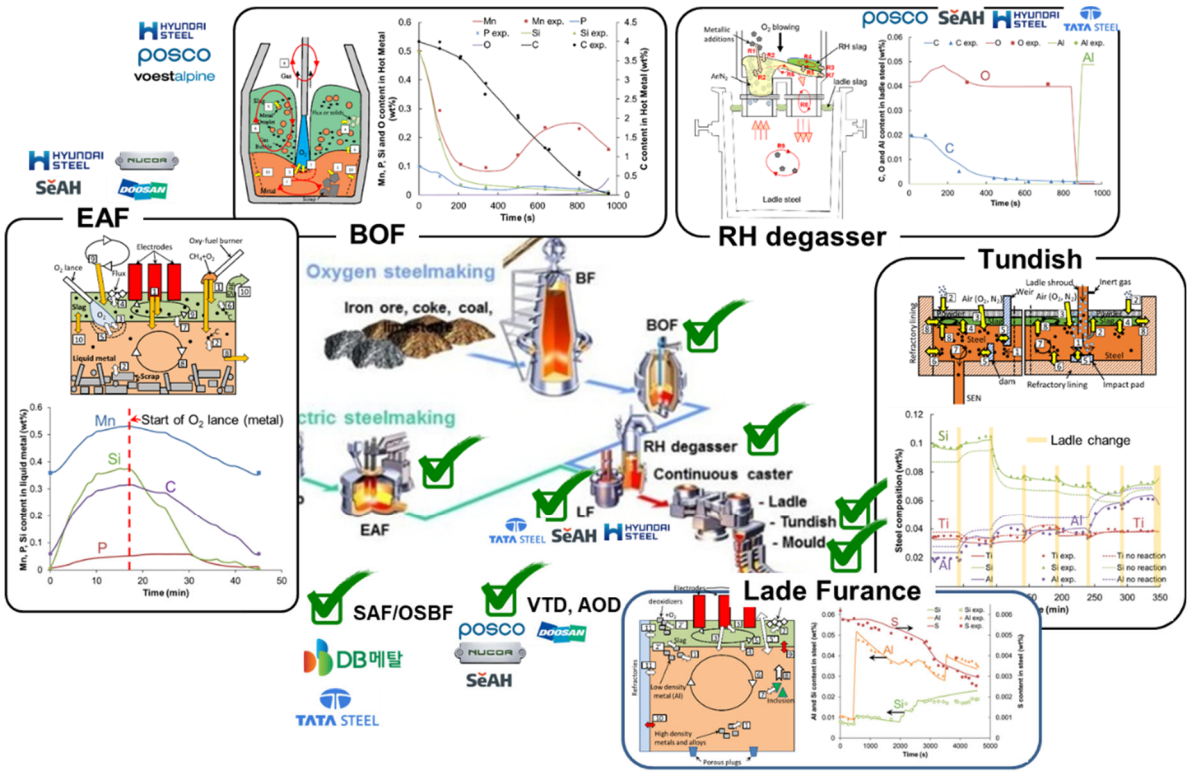

FIG 3 – Overview of the process simulation models (simulators) developed within the FactSage Steelmaking Consortium.

BOF process model

Figure 4 shows the schematic diagram of BOF process simulation model. In the BOF model, ten reaction zones are considered. For example, the semi-empirical drop generation model is incorporated in the present simulation to calculate the droplet generation rate depending on the process conditions. The decarburisation and oxidation of liquid steel, and reduction of Fe oxide in slag at hot spot and emulsion zone are calculated. A numerical simulation equation for scrap melting is taken into account. The dissolution rate of fluxes such as lime, dolomite, hematite, and other slag making flux is calculated considering thermodynamic driving force, temperature and slag viscosity. Other empirical parameters for interfacial reactions are fixed based on plant sampling data. In every time step, all these ten interfacial thermodynamic calculations are performed with the FactSage thermodynamic database, and heat loss/post combustion of the BOF is also considered for the accurate temperature calculations of slag and liquid metal.

- R1 : Scrap melting in metal bath and heat gain/loss
- R2: Burning of hot metal surface (O_2/metal reaction for FeO formation)
- R3: Hot spot (O_2/metal reaction for direct de-C)
- R4: Flux dissolution in slag
- R5: Metal droplet/slag reaction
- R6: Bulk metal/slag reaction
- R7: Bulk metal homogenization
- R8: Slag homogenization + post-combustion of the exhaust gas
- R9: Heat exchange between slag and metal
- R10: Mixing between active and dead zones in hot metal

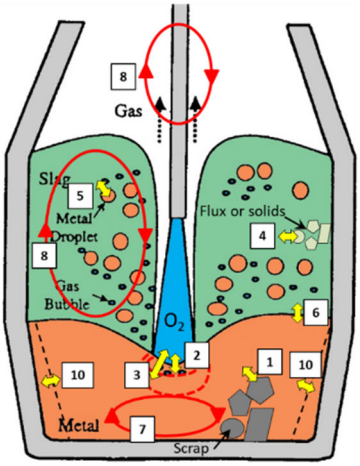

FIG 4 – Overview of the reaction zones for BOF process simulation model (Van Ende and Jung, 2015a).

BOF process model was applied to optimise the process and test the possible operation scenario of low quality hot metal. The main purpose of BOF is the decarburisation and dephosphorisation of hot metal to produce liquid steel. Due to the ever-decreasing availability of high quality BF (blast furnace) grade iron ores, many steel producers are looking alternative iron ores. For example, high P_2O_5 containing iron ore is one possibility. In order to evaluate whether it is possible to economically produce low P content liquid steel in BOF process or not, virtual operation patterns were studied with the BOF process model and operation cost could be calculated.

Figure 5 shows the BOF simulation results of hot metals containing different initial P content. The standard BOF operation condition is as follows (see the details in Figure 5a):

- Scraps: four kinds of scraps with 45.6 ton in total.
- Hot metal: 295 ton of hot metal (Fe-4.42C-0.214Mn-0.247Si-0.13P-0.003S in wt%) at 1350°C.
- Residual slag: 3 ton of the end of BOF slag at 1300°C.
- FeSi: 1.5 ton of Fe-Si (75 per cent Si).
- Flux: 11.65 ton of lump CaO, 2.94 ton of dolomite and 1.63 ton of ladle slag.
- Gas blowing: 15 690 Nm^3 of oxygen top blowing and 626 Nm^3 Ar bottom bubbling.
- Double slag operation: 20 min of total blowing time and 40 per cent of slag discharged after 6 min.

Residual Slag

total amount, kg	temperature (°C)	Al_2O_3	SiO_2	CaO	FeO	MgO	MnO	P_2O_5	S	Na_2O	V_2O_3	TiO_2	Cr_2O_3	total	tot CaS	C/S
3000	1300	2	15.4	46.5	23.6	7	3.5	2						100.00	100	3.02
	Normalized with CaS:	2.00	15.40	46.50	23.60	7.00	3.50	2.00	0.00 *CaS*	0.00	0.00	0.00	0.00	100.00		3.02

Hot Metal

total amount, kg	temperature (°C)	Fe	C	O	P	Mn	Si	S	Al	Ti	Cr	V	Total
295000	1350	94.9860	4.42		0.13	0.214	0.247	0.003					100

Fluxes

	Code	Type	Al_2O_3	SiO_2	CaO	FeO	Fe_2O_3	MgO	MnO	P_2O_5	$CaCO_3$	$MgCO_3$	$CaMg(CO_3)_2$	Na_2CO_3	V_2O_3	TiO_2	Cr_2O_3	CaS	amount, kg
1	CaO lump	CaO-based flux as lumps		1.00	90.00						9.00								11650
2	MgO	MgO-based flux						100.00											0
3	Dolom	Dolomite based flux											100.00						2940
4	Iron ore		3.00	3.00	1.00		90.00	3.00											0
5	Ladle_slag		32.00	7.20	40.00	11.71	1.19	5.50	1.90	0.50									1630
6	SiO2			100.00															0

Scrap

	Code	Type	Fe	C	O	P	Mn	Si	S	Al	Ti	Cr	V	Surface area (m2)	amount, kg
1	Scrap 1		99.5000	0.1000		0.0100	0.2500	0.1000	0.0100	0.0300				54.4	19600
2	Scrap 2		94.4680	4.5000		0.1300	0.2000	0.7000	0.0020					16.7	6000
3	Scrap 3		89.6000	0.0000	10.0000	0.1000	0.3000	0.0000	0.0000	0.0000				55.6	20000
4	Scrap 4		94.4900	1.0000	4.0000		0.2000	0.3000	0.0100					27.8	10000

Composition (normalized, wt%)

	Fe	C	O	P	Mn	Si	S	Al	Ti	Cr	V	amount, kg
FeSi alloy	25.0000					75.0000						1500

oxygen blowing (top blowing) 15690 QT (Nm3)

bottom blowing (Ar) 626 QT (Nm3)

(a)

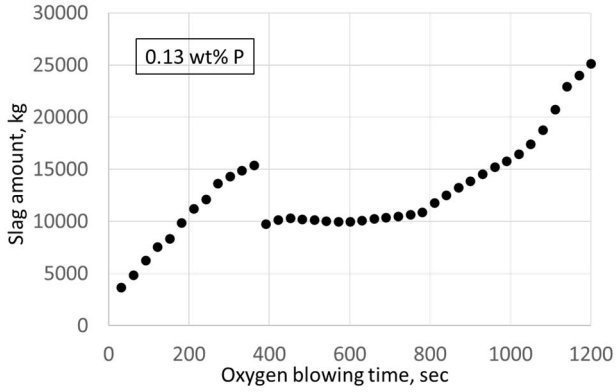

(b)

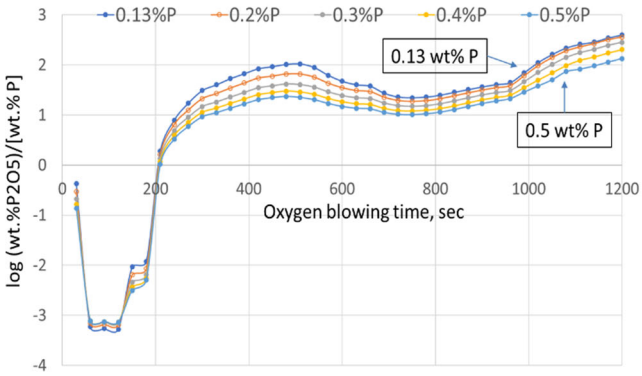

(c)

FIG 5 – BOF process simulation input and simulated results: (a) Input and overall operation condition, (b) slag amount in BOF, and (c) phosphorus distribution depending on the initial P content in hot metal.

In the simulations, only the initial P content in hot metal was varied from 0.13 to 0.5 wt per cent without changing any other operation conditions. Certainly the increasing P content in hot metal results in much lower phosphorus distribution (Lp = (per cent $P_2O_5)_{slag}$/[wt per cent P]$_{metal}$) in the end of BOF process: Lp = 396 for 0.13 wt per cent P to 135 for 0.5 wt per cent P hot metal. According to the simulations, the final P content in steel can be changed from 72 wt ppm for 0.13 wt per cent P to 817 wt ppm for 0.5 wt per cent P hot metal. Of course, the operation condition in Figure 5 is not optimised for each specific hot metal condition. This kind of simulation results can provide a plant operation team with the information whether a certain quality of liquid steel with low P can be still produced in BOF plant or not even when low quality hot metal is used, and if yes, how much operation cost can increase.

BOF simulation model was also used to analyse the slopping in BOF process. When excessive foam growth happens, it cannot be contained within the converter and flow down the outside of the converter. This phenomenon is the slopping. The model can calculate the CO generation rate, undissolved solid flux, formation of Ca_2SiO_4, and chemistry and temperature of slag. Using the information, viscosity of slag and slag foaming index can be calculated, which can be used to evaluate the slopping in BOF operation. A dynamic BOF model was also developed to predict the final carbon and oxygen content and temperature of liquid steel for online motoring of the BOF process. Recently, many virtual BOF operation simulations for processing low carbon hot metals (2.5 ~ 3.5 wt per cent) and operating low HMR (hot metal ratio: 70 to 80) have been carried out using the BOF model to more towards the carbon neutrality in steelmaking.

LF process model

The schematic diagram of the LF simulation model is presented in Figure 6. In total, 11 reaction zones are considered to describe LF process. The addition of ferro-alloy, shred Al and lump Al and slag flux are considered. The overall mass transfer coefficient of liquid steel and slag are allowed to be changed by the stirring energy determined by Ar bubbling. Arcing can provide heat to liquid steel and slag, and also induce more chemical reaction between slag and liquid steel. Steel reoxidation due to open eye formation and formation of non-metallic inclusion are also taken into account in the model. At each time step, all equilibrium reactions at each reaction zone are performed using the FactSage thermodynamic database.

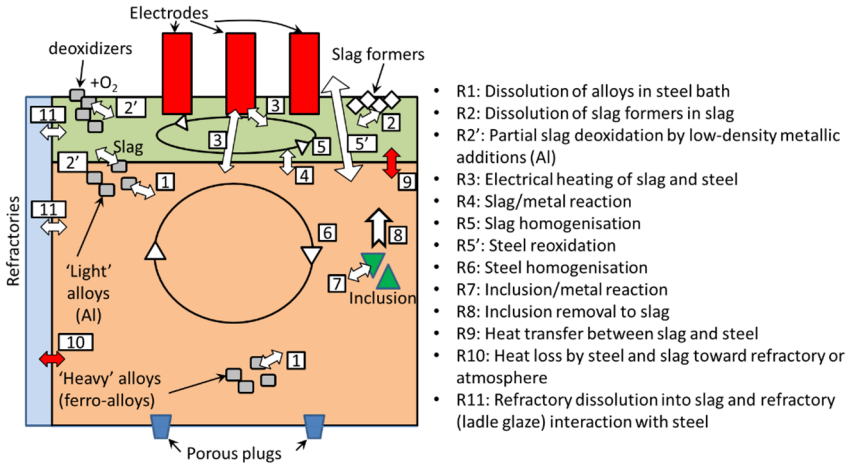

FIG 6 – Overview of the reaction zones for LF process simulation model (Van Ende and Jung, 2017).

LF is a secondary refining unit widely used in most of the steel plants for deoxidation, desulfurisation and alloying of liquid steel. In addition, the modification and removal of non-metallic inclusion can be carried out in LF. Accuracy in temperature prediction of liquid steel in LF process is presented in Figure 7a. In general, it is well predicted within ±5°C compared to the plant data. This is possible because the chemical reaction heat is well reflected from thermodynamic calculations. The precise control of temperature is important for the subsequent casting process. Therefore, when new high alloyed steel grades are developed, the process condition can be already well designed with LF simulation model. The modification of non-metallic inclusion can be also possible by changing the

operation condition and flux. Figure 7b shows a plant example of inclusion modification from high melting temperature inclusions to low melting temperature inclusions, which resulted in the improvement of steel castability. High melting temperature Al_2O_3 and $MgAl_2O_4$ spinel type inclusions can be modified by Ca injection to liquid inclusion. Instead of Ca injection, low quality ferro-alloy can be even employed to modify the inclusion as well, which can be well simulated by the LF simulation model.

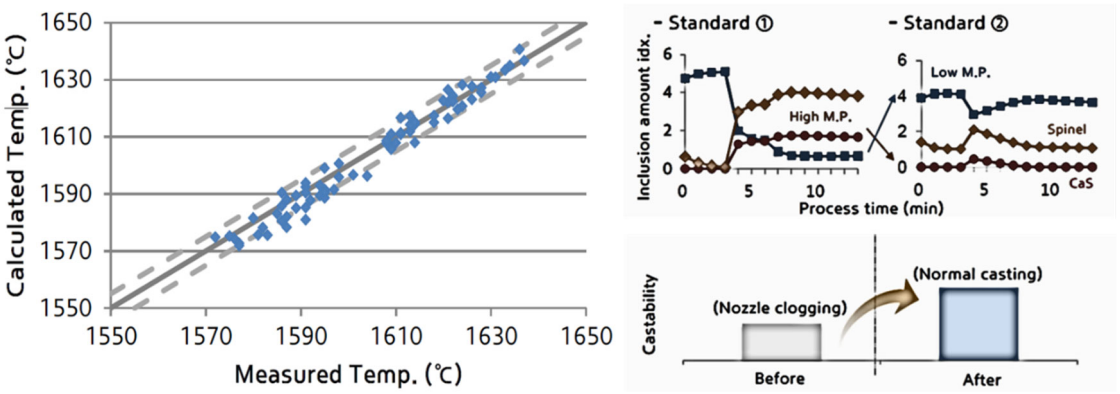

(a) (b)

FIG 7 – LF simulation results: (a) accuracy of temperature prediction, and (b) non-metallic inclusion modification by process optimisation and influence to castability.

The complex process optimisation to obtain ultra-low sulfur and low oxygen content in liquid steel can be also performed using the LF process model. In particular, when a company produces a wide range of steel grades from low carbon steel to special steel in a single steelmaking line, the LF operation is even more tricky because the delay in LF refining operation can affect the operation schedule of the entire plant. Therefore, operators prefer to adopt a conservative operation schedule to reduce the risk of operation delay instead of producing the best quality steel. In order to change the standard operation procedure (SPO), many trials in the plant are required but usually not possible in such a plant with a single steelmaking line. One of examples for the process optimisation is presented in Figure 8. Using the LF simulation model, flux addition and stirring condition for each specific steel grade were optimised to obtain higher desulfurisation and higher deoxidation level beyond the existing level, while the refining time, electrical energy and lime input amount were even reduced. These optimum operation conditions were applied to SPO in LF plant and contributed to improving the quality of steel as well as productivity. When new steel grades are ordered from clients, the plant engineers can use the LF process simulation to design the SPO to meet the specification of new steel too.

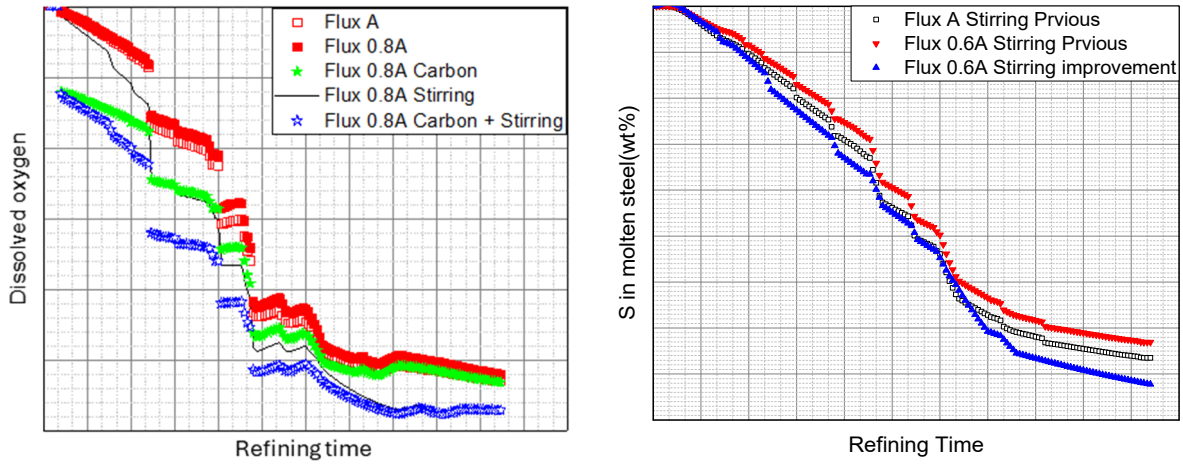

(a) (b)

FIG 8 – LF simulation results: Variations of (a) oxygen content and (b) sulfur content in liquid steel depending on the operation conditions.

Online monitoring system

As the simulation speed is faster than the real operation, online process simulation is possible by receiving the inputs of simulation from HMI (Human Machine Interface) in plants. One of consortium members already tested online LF simulation and VTD simulation to monitor the plant operations and also compare the simulation results with the plant sampling data for a long period. Eventually, the reliability of simulation prediction is confirmed, significant reduction in operating cost will be achieved by replacing intermediate samplings with model predictions.

Generation of virtual data to assist big data analysis for AI-based model

One of the critical weaknesses of AI model based on big data is the extrapolation capability. Using the simulation model, it is possible to generate virtual plant data for the operation conditions which are outside of the current operation range. By combining these virtual plant data to the real plant data set, the coverage of the available data set can be broadened and the prediction of AI model can be improved significantly.

FACTPROSIM – FLOW SHEET PROCESS SIMULATION SOFTWARE

The process simulation models we have developed so far were based on the FactSage macro processing code and ChemApp DLL (GTT-Tech). Although FactSage macro processing is rather easy to do the programming, the model can be only run under the FactSage environment and calculation speed is rather slow. On the other hand, process models based on ChemApp needs more programming skill for C++, Visual Basics, Python, etc.

In order to make process calculations without any coding, we have developed a new flow sheet program ‘FactProSim’ for process simulation applications based on our experience on the variety of process simulation models in steelmaking and other metallurgical processes. FactProSim software employs accurate and reliable FactSage thermodynamic databases and Gibbs Energy Minimizer (ChemSage) through ChemApp (internally available in FactSage program) to perform complex multiphase, multicomponent equilibrium calculations. FactProSim uses an intuitive flow sheet diagram approach to model the process with modules, which interact with each other through the flow of materials. It is designed with a drag-and-drop approach, providing a user-friendly interface with no coding required. This software will be available in FactSage 8.4 version in 2025.

FactProSim Features

As shown in Figure 9, the FactProSim software is designed with a complete graphical interface, allowing the user to interact with modules and the resulting flow sheet with relative ease. Modules can be added to the flow sheet by drag-and-drop operation, and modified through their respective windows, which also auto-populates relevant phases as and when needed. FactProSim is not process specific; it is a general-purpose process simulation tool. Flow sheeting is a systematic description of materials and energy flow in a process. A flow sheet is comprised of multiple streams interconnected to describe the process behaviour. A complex metallurgical process can be broken down into several local chemical equilibrium zones, where materials are assumed to be at equilibrium. Hence, a chemical equilibrium calculation is required to ascertain the local composition and enthalpy (heat) change using thermodynamic databases. This modelling approach based on local equilibrium is the basis of the EERZ model approach as shown in Figure 1.

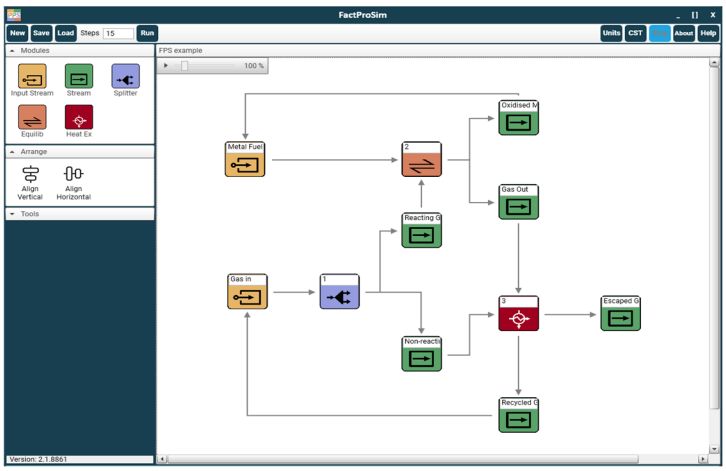

FIG 9 – Visualisation of the five main modules of FactProSim and the connections between them.

Any chemical reaction requires an equilibrium chemical reaction (Gibbs Energy minimisation), input materials (reactants) and output materials (reaction products). In some cases, material flow needs to be divided into several flow branches to bypass or to take part in other reactions, which is done by a splitter. These four flow sheet components are sufficient to describe the material flow and local chemical equilibria in a metallurgical process. As shown in Figure 9, these components are provided in FactProSim as five modules, namely, the Equilib module (orange module) to perform equilibrium calculation, the Input Stream module (yellow module) to define incoming material in the flow sheet, the Splitter module (purple module) to divide a material stream into several streams, the Stream module (green module) to save streams created by the Equilib and Splitter modules, and the Heat Ex module (red module) to allow the heat exchange between two streams without mass change or assign heat loss and heat gain. After chemical reactions at interfaces, the product streams can be allowed to mix with the remaining to begin the next cycle calculations. These modules can be easily added to the flow sheet diagram via drag-and-drop operation. Each module is connected by arrows to depict the flow of material in the flow sheet.

In addition, time-dependent process simulations can be performed with FactProSim by repeating a flow sheet for a certain number of time steps. The continuity in the simulation between the time step is carried out by designating the streams that will serve as input for the next time step.

FactProSim offers the possibility to enter various inputs in the flow sheet modules (such as material composition, amount and temperature, equilibrium calculation conditions etc) through spreadsheets by linking one or several Microsoft Excel spreadsheets to a flow sheet. Furthermore, the output of the simulation is also saved in Microsoft Excel spreadsheets to provide a convenient way to analyse and represent the output data.

A simple model demonstration

In order to demonstrate FactProSim, a simplified BOF process has been modelled. The schematic of the BOF process is presented in Figure 10a. The simplified process flow sheet is prepared in Figure 10b to represent the BOF process. In this simple simulation, three reactions are included: (R1) hot metal oxidation reaction by O_2 involving fractions of hot metal and slag with incoming O_2 gas, (R2) scrap dissolution in hot metal and hot metal homogenisation, and (R3) lime dissolution in slag and slag homogenisation. In addition, the heat recovery (H1) from the exhaust gas to slag is also considered.

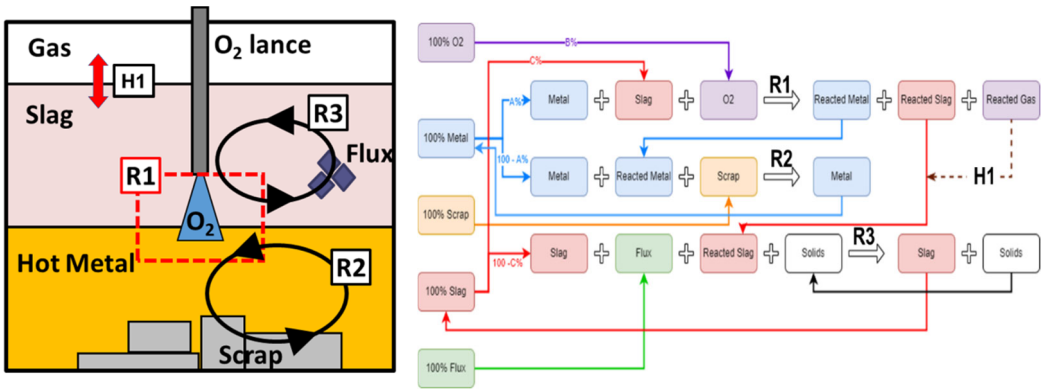

(a) (b)

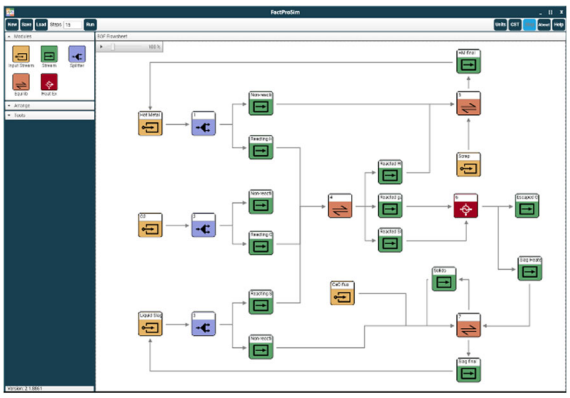

(c)

Inputs	Comp. (wt%)				Amount (kg)	Temp. (C)
Metal	Fe	C	Mn	Si		
	95	4	0.5	0.5	100	1300
Slag	CaO	FeO	SiO2			
	55	25	20		2	1300
Gas	O2					
	100					25
Flux	CaO					
	100					25
Scrap	Fe					
	100					25

	Kinetic factors					
Time (min)	O2 (kg)	CaO (kg)	Metal (A,%)	Gas (B,%)	Slag (C,%)	Scrap (kg)
1	0.57	0.25	10	50	50	2
2	0.57	0.25	10	50	50	2
3	0.57	0.25	10	50	50	2
4	0.57	0.25	10	50	50	2
5	0.57	0.25	10	50	50	2
6	0.57	0.25	30	80	80	2
7	0.57	0.25	30	80	80	2
8	0.57	0.25	30	80	80	2
9	0.57	0.25	30	80	80	2
10	0.57	0.25	30	80	80	0
11	0.57	0	30	80	80	0
12	0.57	0	30	80	80	0
13	0.57	0	30	80	80	0
14	0.57	0	30	80	80	0
15	0.57	0	30	80	80	0

(d)

FIG 10 – (a) Schematics of BOF process, (b) flow sheet of the BOF process model, (c) corresponding simulation flow chart in FactProSim, and (d) Excel file for input condition of process simulation.

As seen in Figure 10c, the process simulation in FactProSim can be constructed to be almost identical to the flow sheet in Figure 10b. All reactions are set to be calculated under adiabatic equilibrium conditions for simplicity. Simple kinetic parameters A per cent, B per cent and C per cent in Figure 10b are set to adjust the material flow between each reaction, as listed in Excel file (see Figure 10d).

The simulation results of a 100 ton hot metal with 4.0 wt per cent C, 0.5 wt per cent Si and 0.5 wt per cent Mn at 1300°C is shown in Figure 11. The metal and slag temperature profile during the BOF process can be predicted from the heat balance of all chemical reactions. The evolution of the C and Si content in hot metal is presented. Of course, this is a simple model and not directly applicable to the BOF operation analysis. The real model should be much more complex as shown in Figure 4. However, the present example can readily demonstrate the ease of simulating metallurgical processes with FactProSim.

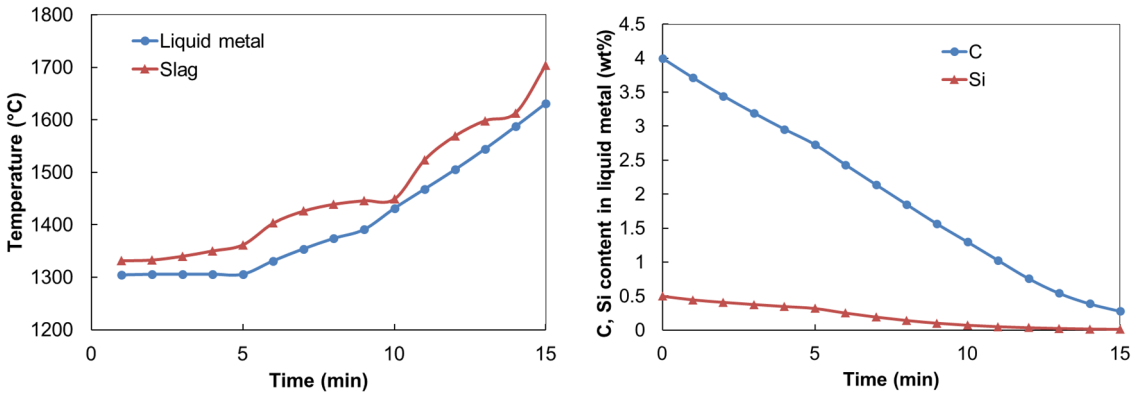

(a) (b)

FIG 11 – Simulated evolution of (a) slag and metal temperature, and (b) C and Si content in liquid metal.

FactProSim is designed to handle very complex industrial scale simulations. One of examples for complex process simulation is shown in Figure 12. This is a FactProSim flow sheet for the full scale LF model (Van Ende and Jung, 2017) shown in Figure 6. In order to facilitate the setting of the EERZ amounts of reactants in the reaction zone depending on the stirring energy and other factors, a function builder which allows to use complex mathematical equation is also implemented in the FactProSim.

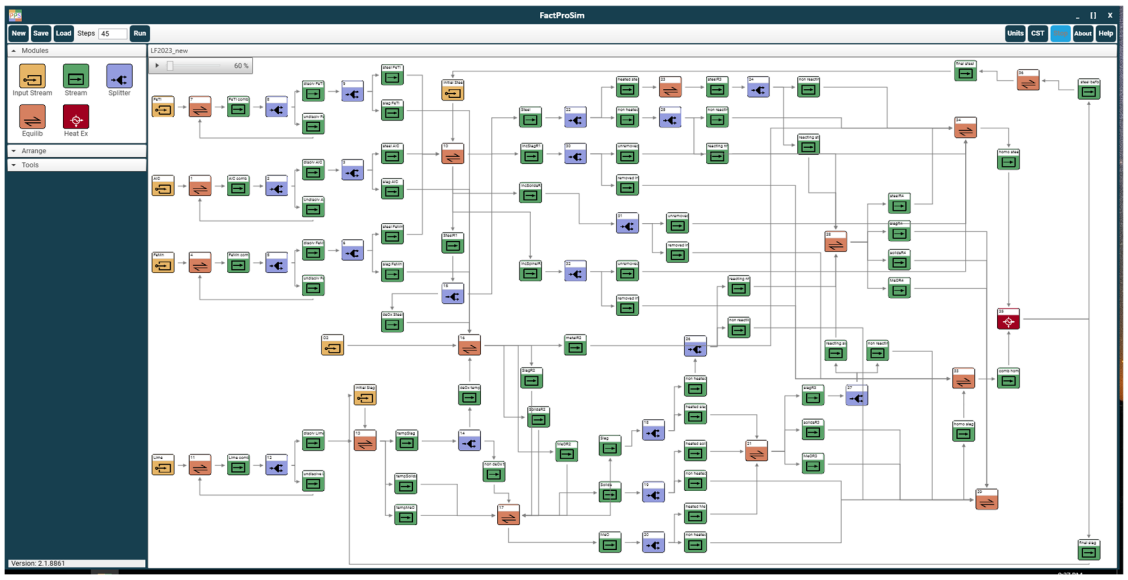

FIG 12 – FactProSim flow chart for LF process simulation.

We believe that FactProSim software can be a very useful tool for researchers and engineers in pyrometallurgy to build their own process simulation models to improve the current operation and design new process.

SUMMARY

The effective equilibrium reaction zone (EERZ) approach has been well applied to simulate the complex industrial processes that exhibit strong non-equilibrium and time-dependent characteristics. The steelmaking process simulation models for EAF, hot metal pre-treatment, BOF, LF, VTD, RH degasser, Tundish, continuous casting have been developed within the FactSage steelmaking consortium and applied to improving plant operations. New FactProSim software is also developed to assist in the development of process simulation models using the EERZ concept.

ACKNOWLEDGEMENTS

This work was supported by the Korea Planning and Evaluation Institute Of Industrial Technology (KEIT) and the Ministry of Trade, Industry and Energy (MOTIE) of the Republic of Korea (No. RS-2023-00262218). Financial supports from Tata Steel Europe, Posco, Hyundai Steel, Nucor Steel, RioTionto Iron and Titanium, Nippon Steel Corp., JFE Steel, Voestalpine, RHI Magnesita, SeAH Besteel, Doosan Heavy Industry and Construction, SCHOTT AG and Umicore are also gratefully acknowledged.

REFERENCES

Bale, C W, Belisle, E, Chartrand, P, Decterov, S A, Eriksson, G, Gheribi, A E, Hack, K, Jung, I H, Kang, Y B, Melancon, J, Pelton, A D, Petersen, S, Robelin, C, Sangster, J, Spencer, P and Van Ende, M A, 2016. FactSage thermochemical software and databases, 2010–2016. *CALPHAD,* 54:35–53.

Coetsee, T and De Bruin, F, 2023. EERZ (Effective Equilibrium Reaction Zone) Model of Gas-Slag-Metal Reactions in the Application of Unconstrained Al-Ni-Cr-Co-Cu Metal Powders in Submerged Arc Welding: Model and 3D Slag SEM Evidence, *Processes,* 11:2110.

Jung, I-H and Van Ende, M-A, 2020. Computational Thermodynamic Calculations: FactSage from CALPHAD Thermodynamic Database to Virtual Process Simulation, *Metall Mater Trans B,* 51:1851–1874.

Kumar, D, Ahlborg, K and Pistorius, P C, 2019. Development of a Reliable Kinetic Model for Ladle Refining, *Metall Mater Trans B,* 50:2163–2174.

Mason, P, Grundy, A N, Rettig, R, Kjellqvist, L, Jeppsson, J, Bratberg, J, 2020. The Application of an Effective Equilibrium Reaction Zone Model Based on CALPHAD Thermodynamics to Steel Making, in *Proceedings of the 11th International Symposium on High-Temperature Metallurgical Processing* (eds: Z Peng, J-Y Hwang, J P Downey, D Gregurek, B Zhao, O Yücel, E Keskinkilic, T Jiang, J F White, M M Mahmoud), The Minerals, Metals & Materials Series, pp 101–113.

Moosavi-Khoonsari, E, Van Ende, M-A and Jung, I-H, 2022. Kinetic Simulation of Hot Metal Pretreatment: Desulfurization Using Powder Injection, *Metall Mater Trans B,* 53:981–998.

Paek, M-K and Jung, I-H, 2015. Kinetic simulation model for Vacuum Tank Degasser, McGill University, Montreal, Canada, (unpublished work).

Shin, J H and Park, J H, 2020. Prediction of Inclusion Evolution During Refining and Solidification of Steel: Computational Simulation and Experimental Confirmation, *Metall Mater Trans B,* 51:1211–1224.

Van Ende, M-A and Jung, I-H, 2014. Development of a Thermodynamic Database for Mold Flux and Application to the Continuous Casting Process, *ISIJ Int*, 54:489–495.

Van Ende, M-A and Jung, I-H, 2015a. A kinetic process simulation model for Basic Oxygen Furnace (BOF): Importance of slag chemistry for BOF operation, *CAMP-ISIJ,* 28:527–530.

Van Ende, M-A and Jung, I-H, 2015b. A kinetic BOF process simulation model, in *Proceedings of the Asia Steel International Conference,* pp 596–597.

Van Ende, M-A and Jung, I-H, 2017. A Kinetic Ladle Furnace Process Simulation Model: Effective Equilibrium Reaction Zone Model Using FactSage Macro Processing, *Metall Mater Trans B,* 48:28–36.

Van Ende, M-A and Jung, I-H, 2019. Development of AOD process simulation model, Seoul National University, Seoul, South Korea, (unpublished work).

Van Ende, M-A and Jung, I-H, 2020. Development of Tundish process simulation model, Seoul National University, Seoul, South Korea, (unpublished work).

Van Ende, M-A, 2022. Development of an Electric Arc Furnace Simulation Model Using the Effective Equilibrium Reaction Zone (EERZ) Approach, *JOM,* 74:1610–1623.

Van Ende, M-A, Jung, I-H and Harbers, E, 2018. Applicability of the ladle furnace process model to plant operation, in 8th European Oxygen Steelmaking Conference (EOSC 2018).

Van Ende, M-A, Kim, Y-M, Cho, M-K, et al, 2011. A Kinetic Model for the Ruhrstahl Heraeus (RH) Degassing Process, *Metall Mater Trans B,* 42:477–489.

Development of a nitrogen prediction model for 320 tonne converter

DOI: 10.62053/BQWI2772
C M Yoon[1], C-H Eom[2], Y D Jeon[3] and K S Kim[4]

1. Senior Research Engineer, Hyundai Steel R&D Centre, Email: ferrous@hyundai-steel.com
2. Senior Research Engineer, Hyundai Steel R&D Centre, Email: cheom@ hyundai-steel.com
3. Senior Manager, Hyundai Steel R&D Centre, Email: jyd00@hyundai-steel.com
4. Senior Research Engineer, Hyundai Steel R&D Centre, Email: kimks@hyundai-steel.com

ABSTRACT

The carbon neutrality continues to require reduction of carbon usage in ironmaking and steelmaking processes. Specially, it is expected that the hot metal ratio (HMR) in the steelmaking process should be reduced essentially. Unfortunately, the reduction of the HMR in converter can bring about poor environment for nitrogen removal from molten Fe. From this situation, nitrogen prediction model has been developed to understand the fundamental of behaviour of nitrogen and quantitatively interpret its content changes in the converter process. Thermodynamic and kinetic approaches were improved based on existing mathematical model and attempted to predict nitrogen content in real-time by combining process data. In present study, heat supply from the oxidation (mainly carbon and silicon) and CO evolution in the converter are considered, and scrap melting due to the heat transfer from the molten Fe to the solid scrap charged in the converter also be considered.

INTRODUCTION

Nitrogen is widely known as that should be controlled in various levels for different steel grades production. Specially, the ultra-low carbon (ULC) steel requires very low nitrogen content in steelmaking process. However, it is difficult to prevent from pick-up because the nitrogen which is one of the interstitial elements is easily absorbed into molten steel from atmosphere. Recently, moreover, the carbon neutrality as a major environmental issue continues to require low hot metal ratio (HMR) in converter which is difficult condition for nitrogen removal. Thus, there were several efforts to understand the behaviour of nitrogen in steelmaking process including our previous research. Fruehan proposed mathematical model to calculate the nitrogen content during converter process based on thermodynamic and kinetic approaches. Based on basic concept of the model, we have proposed a nitrogen prediction model (NPM) for 320 tonne converter combined with operation condition and more sophisticated thermodynamic data using FactSage™. Furthermore, in present study, based on the previously developed NPM, several reactions such as oxidation, slag making, and scrap melting were additionally considered.

MODEL DESCRIPTION

Basic concepts for the NPM

Nitrogen removal mechanism

During decarburisation in converter, CO bubbles is mainly generated both in cavity and inside the molten steel as a by-product of the reaction. In particular, these internally generated CO bubbles locally have a significantly low nitrogen partial pressure compared to other liquid-gas interfaces and are therefore well known as a major source of nitrogen removal. So, it is important to quantify the CO evolution amount during oxygen blowing. Moreover, in the NPM, three stages for decarburisation are proposed. In the initial stage, which is desiliconisation step, most of the oxygen is consumed in oxidation of the silicon in molten Fe, and a small amount of CO bubbles can be generated. After that, decarburisation becomes main reaction of the oxidation. However, since most of the CO bubbles generated in this stage occur in the cavity region, it can be considered that the nitrogen removal is not as efficient as that of CO bubbles generated internally. In the dynamic stage where carbon content in molten Fe exists below the critical carbon level, decarburisation mechanism starts to change from interfacial chemical reaction to mass transfer in liquid phase. So, amount of the internal CO bubbles is increased, and nitrogen removal occurs strongly.

Scrap melting

From a viewpoint of nitrogen control, quantification of scrap melting during oxygen blowing is very important. Typically, the scrap contains about 80 ppm of nitrogen, and the longer the scrap melting is delayed, the longer the nitrogen pick-up period from scrap to molten Fe and carries the risk of increasing the nitrogen content at the end point. Wei *et al* (2019) have reported on the melting characteristics of scrap using melting experiments on the steel bars. According to their research, heat and mass transfer between molten Fe. So, it can be considered that not only would scrap be melted by heat transfer supplied from molten Fe, but the melting could be accelerated by carbon penetrated from molten Feo to scrap interface. This phenomenon would be described by a decrease in the melting point of solid scrap interface due to the carbon. Therefore, in present study, based on these heat and mass transfer model, scrap melting was quantified by considering stirring by oxygen blowing from top and Ar and N_2 blowing from bottom in the converter.

Nitrogen pick-up during tapping

After oxygen blowing in the converter, the molten steel is tapped into a ladle. During the tapping, the molten steel is exposed to atmosphere during falling into the ladle, and gas phase nitrogen, $N_2(g)$ would be picked up into the molten steel. As flux such as lime is added to inside of the ladle, it is possible to block the inflow of the air, but such nitrogen pick up could be occur in the falling part from the tapping hole to melting surface in the ladle. Unlike inside the converter, the molten steel during tapping has very high oxygen content (about 4~500 ppm), which is surface active element, and its nitrogen pick up is well known to be dominated by chemical reactions due to adsorption and desorption at the gas and liquid interface. Thus, the nitrogen picks up calculation during tapping was constructed based on the second-order reaction model.

THE NPM CALCULATION OUTLINE

Considering the converter process from the viewpoint of nitrogen removal, it can be divided into three stages (different from decarburisation stage), which are charging material, oxygen blowing, and tapping.

In the first stage, molten Fe (iron) and scrap are charged into the converter, and there is certain amount of nitrogen in them. The initial nitrogen content in the molten Fe can be inferred by composition and temperature information after KR process. It experimentally ranges between 50 and 60 ppm. In addition, the scrap melting by the heat and mass transfer would be start from this stage.

In the oxygen blowing stage, nitrogen removal is occurred by CO bubble. In this stage, since the molten Fe has low sulfur and oxygen content, it is possible to assume that the nitrogen removal reaction follows liquid phase mass transfer (LPMT) in molten Fe (1st order reaction). The average nitrogen partial pressure which is driving force for the nitrogen removal was calculated from CO gas, the impurities from oxygen, and the bottom blowing gases (Ar, N_2) which are combined with the real-time flow rates of the evolved. In addition, exothermic heat amount of the oxidation reaction can be derived separately. So, the temperature increase of molten Fe and slag can be calculated from the heat source, as well as the scrap melting can also be derived in conjunction. From these series calculation, nitrogen content of the molten Fe could be derived considering simultaneous removal from CO evolution and pick-up from scrap melting within a given reaction time (step). The outline of the nitrogen prediction model algorithm in the charging and oxygen blowing stage described so far is shown in Figure 1.

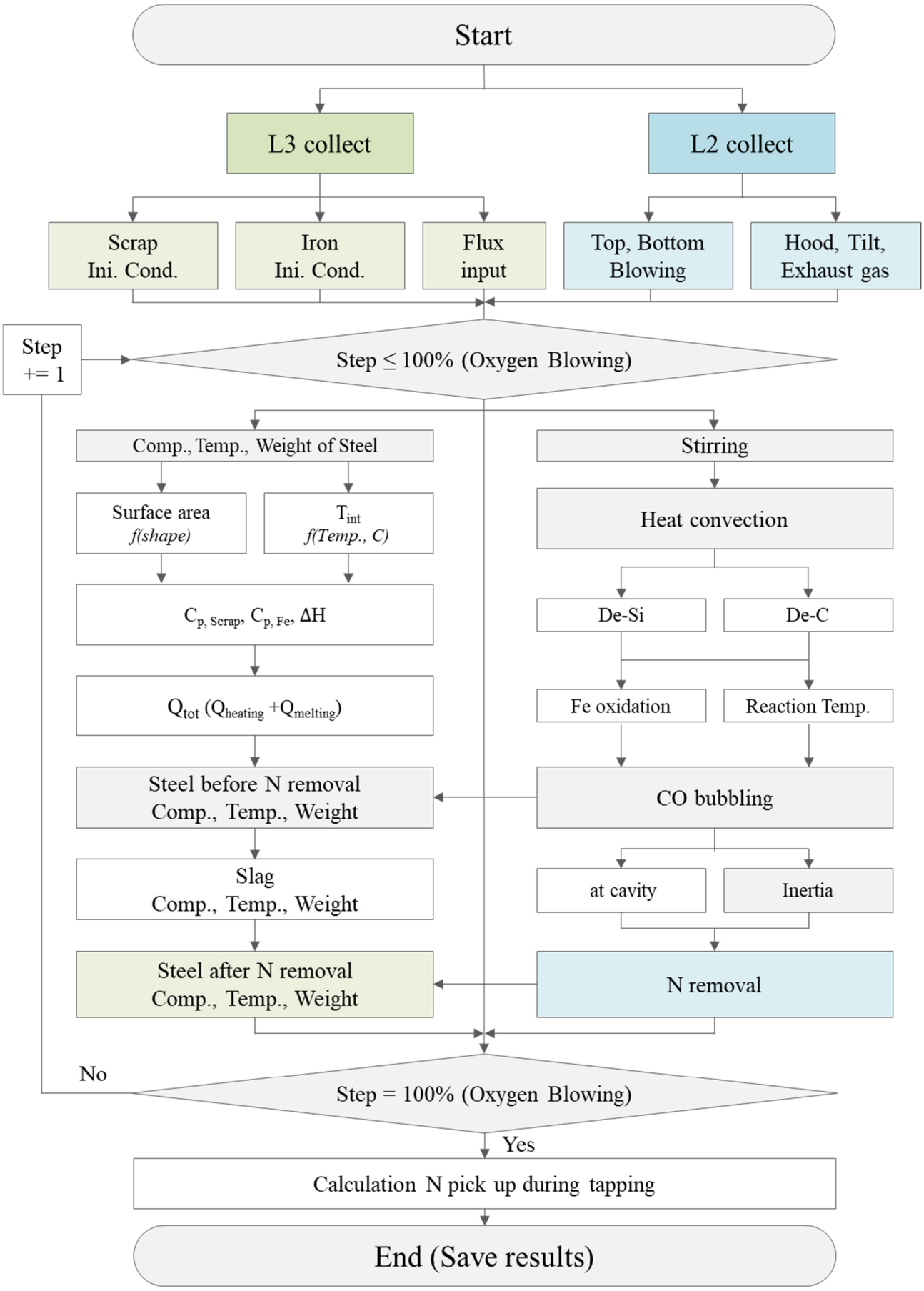

FIG 1 – outline of the nitrogen prediction model during converter process.

In the tapping stage, the activity of oxygen in molten steel can be calculated from composition and temperature data, and through this, the rate constant of nitrogen absorption during tapping finally could be derived. In case of calculating interfacial area, the falling height was derived from the average value of the maximum (H2) and minimum (H1) heights as shown in Figure 2. the total reaction time could be derived using the process time data.

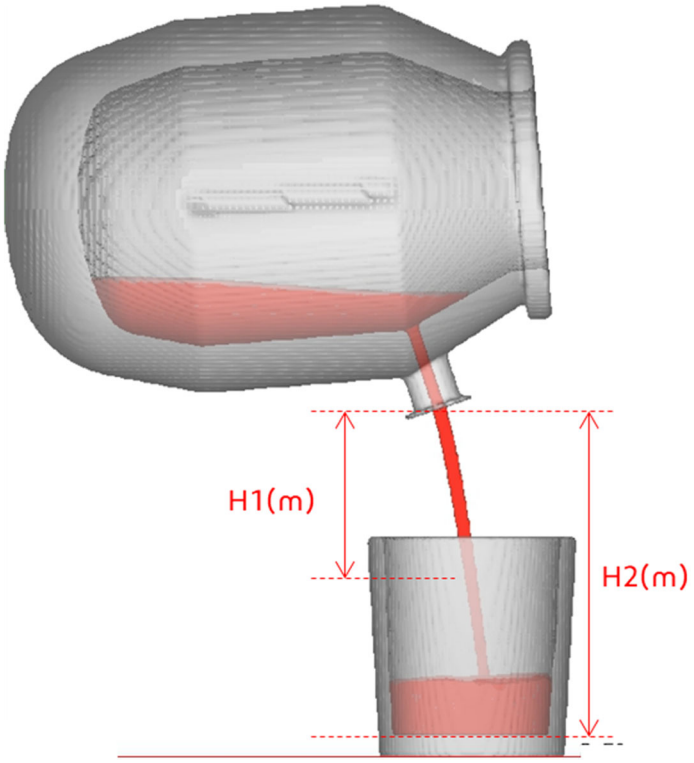

FIG 2 – schematic of the tapping process and definition of falling height.

As described above, the NPM includes the analysis of nitrogen content in raw materials charging in the converter, its removal during oxygen blowing and pick up during tapping process. Through this calculation series of processes, the behaviour of nitrogen in primary steelmaking can be predicted, and comparison of prediction results with operation performance will be explained and interpreted in the presentation.

SUMMARY

A NPM was developed to quantify the behaviour of nitrogen in molten Fe during converter process. This model can be proposed as a modified model through thermodynamic and kinetic approaches based on existing mathematical calculation model. The main concepts of the NPM are as follows.

- The main source of nitrogen removal in the converter process can be considered as a CO gas generated inside molten Fe. Therefore, in present study, quantification of the CO evolution phenomenon based on the properties of molten iron charged into converter and oxidation from oxygen blowing flow rate into the converter.
- A heat and mass transfer model between molten Fe and scrap was adopted to quantify the scrap melting in the converter. This is because if scrap melting during oxygen blowing is delayed until after the dynamic stage, it has a significant effect on nitrogen pick up in molten Fe.
- In addition to prediction the nitrogen content in molten Fe at end point of the oxygen blowing, an attempt was made to quantify the nitrogen pick up content during tapping from the converter to ladle using second-order reaction equation. In present study, it could be expressed as a function of tapping time regardless of the fluid properties. Thus, the interfacial area between the falling steel and atmosphere would be modified according to the lifespan of tap hole and refractories in the converter.

REFERENCES

Wei, G, Zhu, R, Tang, T and Dong, K, 2019. *Ironmaking and Steelmaking*, 46(7):609–619.

Efficient material descriptions for modelling high-temperature processes

DOI: 10.62053/TWUO7495
J H Zietsman[1,2]

1. CEO, Ex Mente Technologies, Pretoria, South Africa, 0081.
   Email: johan.zietsman@ex-mente.co.za
2. Research Associate, Department of Materials Science and Metallurgical Engineering, University of Pretoria, Pretoria 0002, South Africa.

ABSTRACT

The transition to more sustainable metal production is receiving much attention at present, and the iron and steel industry is at the centre of the conversation. New, more environmentally friendly production technologies, such as direct reduced iron (DRI) smelting furnaces, need to be developed in a short period of time. This necessitates increased use of computational modelling that incorporates more accurate material descriptions.

The combination of large-scale multiphysics models of high-temperature processes with CALPHAD material descriptions leads to infeasible computation times. This can be resolved with the previously reported RapidThermo framework, which has been demonstrated to make equilibrium calculations orders of magnitude faster, within controllable limits of accuracy.

In this paper, we explain how further material properties, which are important to modelling high-temperature reactors, can be added to the RapidThermo framework. This can improve the accuracy and usefulness of process and multiphysics models in the development of new technologies, which can significantly accelerate development cycles.

INTRODUCTION

To sustain and grow, modern society has a critical and growing need for metals to maintain and build infrastructure for accommodation, food production, transport, communication, etc. As we produce these metals, we emit waste and greenhouse gases that pollute water and the atmosphere, and influence the planet's climate, thereby threatening the very existence we aim to protect and expand. This is no longer a concern that lurks far into the future, but because governments have started to legislate emission reduction to combat climate change, it is a practical reality that we must face today. We need to find a balance between living, thriving, and growing, and destroying the environment without which we cannot exist.

To address this perceived existential threat, we need to change and improve how we do things... urgently. In pyrometallurgy this means we need to develop new processes that make better use of materials and energy, so that we can satisfy our needs for metals today, without destroying ourselves tomorrow.

Considering history, developing new high-temperature processes is difficult, costly, risky, and time-consuming. Given the magnitude and importance of this matter, though, it should be possible to (1) recruit talented people to take on these challenges and (2) obtain the required funding. The two realities that remain are high risk and the time required. The scale and complexity of this challenge require that we learn at a high rate and fail many times, so that we can successfully get more efficient and sustainable processes into operation – soon enough to protect our environment and ourselves.

To learn and develop new processes rapidly, we need to continue hypothesising, experimenting, and theorising, but faster than before, based on a greater reliance on computational methods. Physical measurements, experiments, and pilot-scale testing remain indispensable, but they are unlikely to yield the required pace on their own. Computer-based modelling (hypothesising) and simulation (experimenting) as the basis for developing new understanding (theorising) more realistically hold the potential for addressing the complexity and urgency of society's dilemma. Process and multiphysics models that describe the thermodynamics and kinetics of high-temperature processes and reactors are crucial for improving the efficiency and profitability of existing operations, and for developing more sustainable production technologies.

Computational models in pyrometallurgy, although already useful today, are fundamentally constrained by how accurately and efficiently we can describe the materials involved. Thermochemical equilibrium calculations along with composition- and temperature-dependent properties of materials like slags, alloys, and mattes are mostly omitted from multiphysics models that can be used for design, operation, and new technology development. This is mainly because of the complexity and computational expense of (1) equilibrium calculations, and (2) solving partial differential equations (PDEs) influenced by varying, non-linear material properties. Directly integrating Gibbs energy minimiser routines into PDE solvers generally lead to infeasible computation times, specifically for systems of industrial interest.

In this paper we consider the current urgency to transition to 'green steel' and the need to develop direct reduced iron (DRI) smelting furnaces. Rapid development of such new technologies creates a greater need for computational modelling of high-temperature reactors, which in turn makes more accurate and computationally efficient material descriptions a necessity. We then consider the current realities and constraints of CALPHAD and multiphysics models and explain how the RapidThermo framework can contribute to making more detailed computational models of pyrometallurgical processes feasible.

REPLACING THE BLAST FURNACE

The iron and steel industry, the world's largest metallurgical industry by production volume, is the second-largest greenhouse gas emitter, and contributes 7–9 per cent of global CO_2 emissions. These emissions result mainly from producing pig iron with a blast furnace (BF) from iron ore and converting it to crude liquid steel with a basic oxygen furnace (BOF), as shown in Figure 1a. This route emits close to 2 t CO_2/t liquid steel (LS) produced. Recycling scrap with the electric arc furnace (EAF) route can emit as little as 0.13 t CO_2/t LS, but this route can provide neither the required volume nor all the required grades (Wimmer, Fleischander and Voraberger, 2023).

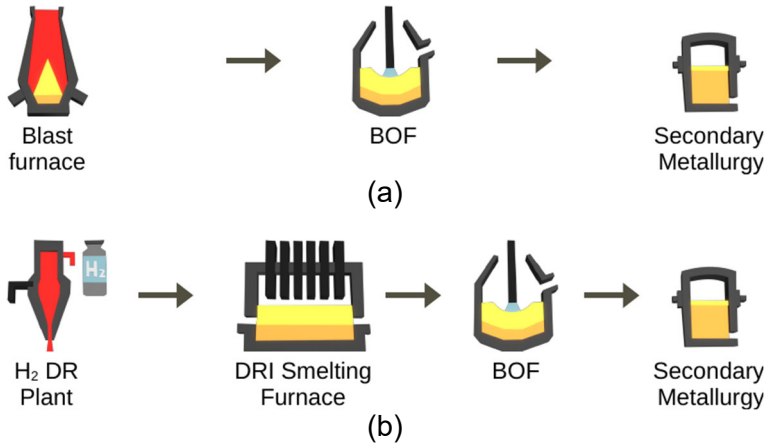

FIG 1 – Process routes for converting abundant low-grade iron ore to liquid steel: (a) Traditional route; (b) Proposed 'green steel' route (reproduced from Wimmer, Fleischander and Voraberger (2023)).

Directly reducing high-grade iron ore with hydrogen to produce H_2-DRI and melting it down in an EAF can yield as low as 0.2 t CO_2/t LS. Economically viable processing of low-grade iron ore, which is most abundantly available, into liquid pig iron via direct reduction requires a semi-continuous DRI smelting furnace (DSF), however, as shown in Figure 1b (Wimmer, Fleischander and Voraberger, 2023). DSF technology does not currently exist, and is a point of much attention in the iron and steel industry.

Some European countries, like the Netherlands and Germany, have legislated strict deadlines for the steel industry to adhere to. In some cases, DRI-DSF technology, with DSF units operating at about 100 MW to produce 1 Mt pig iron/a, needs to be operational by 2030, which leaves little time for developing the DSF concept into a successfully operating production technology.

DRI smelting

Several questions need to be answered to develop and ultimately design DSFs. These include:

1. What type of furnace should be used? eg rectangular 6-electrode AC, circular 3-electrode AC, circular single-electrode DC as shown in Figures 2a to 2c.
2. How should energy be discharged into the process? eg Immersed electrode(s), brush arc(s), open arc(s) as shown in Figures 2d to 2f.
3. What configuration should the furnace power supply have? eg number of taps, tap voltages, resistance, current.
4. Where should feed be discharged into the process? eg Close to the walls, close to the electrode(s) as shown in Figures 2g and 2h.
5. What will the furnace's energy consumption and efficiency be?
6. How should the process be contained? eg Slag saturated in refractory components, sidewall feed heaps, slag freeze lining as shown in Figures 2g and 2h.
7. What will the furnace's production capacity be? eg 1 Mt/a of tapped alloy.
8. What will the composition of the liquid alloy product be? Carbon and silicon contents are of specific importance for the downstream BOF process.

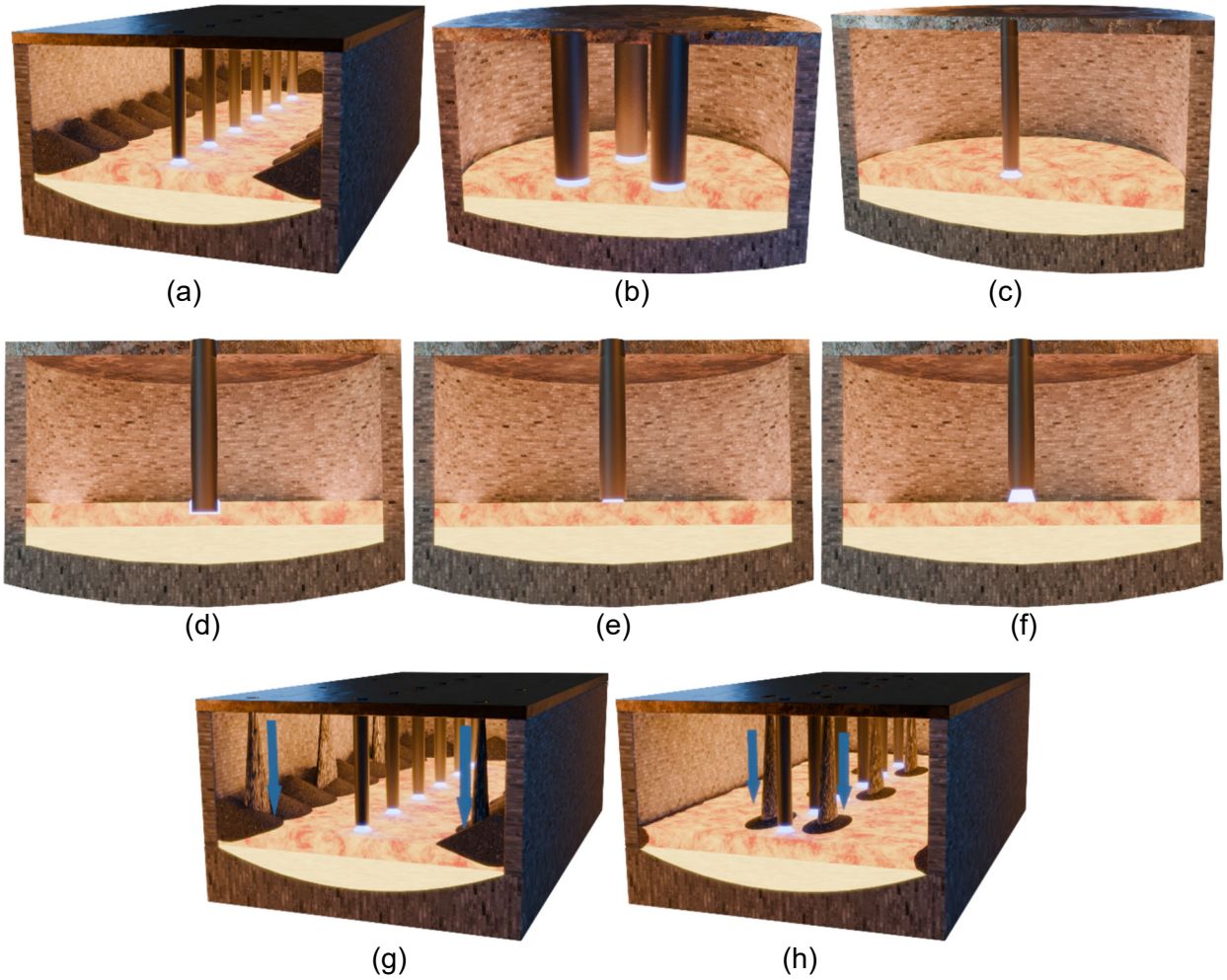

FIG 2 – Equipment and design choices relevant to DRI smelting furnaces: (a) Rectangular 6-in-line AC furnace; (b) Circular 3-electrode AC furnace; (c) Circular single-electrode DC furnace; (d) Immersed electrode; (e) Brush arc.; (f) Open arc; (g) Side feeding and sidewall feed heap containment; (h) Centre feeding and slag freeze lining containment.

Question 5 is easiest to answer based on mass and energy balance calculations and a heat transfer model of the furnace. Questions 1 to 4 are often driven by an equipment supplier's experience and capabilities, and by operational and scale considerations, and their answers have implications for questions 5 to 8. Questions 6 to 8 (the Key Questions) are the most difficult to answer. They are influenced by the preceding questions, and, very importantly, also by feed material properties, furnace operating conditions, and process material properties.

The development tasks are interdependent – furnace design depends on the process, which depends on material properties and operating conditions, which depend on raw materials and furnace design. To solve the problem, it is therefore necessary to iterate through different furnace designs, operating conditions, and process material compositions to converge to a configuration that will operate successfully. Within the time constraints, research and development iterations can feasibly involve laboratory experiments, and focused but limited pilot-scale testing. Extensive pilot-scale testing and demonstration-scale operation appear to be out of the question. It is therefore reasonable to conclude that computational modelling and simulation need to contribute substantially to DSF development for such furnaces to be in operation by 2030 or soon after.

Modelling a DSF

We can use process models to describe mass and energy balances (Zietsman, Steyn and Pretorius, 2018) and study dynamic process behaviour (Zietsman and Pistorius, 2006), thereby answering some of the questions posed in the previous section. The Key Questions require that we use multiphysics models to investigate the influences of and interactions between geometry, scale, transport phenomena, and material properties.

Table 1 and Figure 3 indicate the scope and complexity of a DSF multiphysics modelling endeavour, focusing only on the most important aspects – it is an ambitious task. The model needs to describe several physical phenomena, which involve several materials, as functions of varying temperature and composition. This means that a wide range of material property models are needed.

TABLE 1

Most important phenomena, materials, and material properties relevant to DSF multiphysics modelling. Most properties vary with temperature and composition. Gibbs energy $\bar{G}$ collectively refers to material thermodynamic properties, which also include $\bar{S}$ and $\bar{H}$. The slag bath region column and liquid slag material row are emphasised in blue.

			Region				Material properties	
Phenomenon	**EA**	**SB**	**AB**	**FB**	**FL**	**FH**	**Thermodynamic**	**Kinetic**
Electromagnetics:								
Magnetohydrodynamics	✓	✓	✓				ρ	$\mu_\mathrm{m}\sigma\mu$
Electrical current flow	✓	✓	✓					σ
Joule heating	✓	✓	✓					σ
Heat transfer:								
Thermal conduction	✓	✓	✓	✓	✓	✓	$\rho\ \bar{C}_P$	κ
Thermal radiation				✓				$\alpha_\mathrm{r}\ \rho_\mathrm{r}\ \tau_\mathrm{r}$
Momentum transfer:								
Fluid flow		✓	✓	✓			ρ	μ
Buoyancy		✓	✓	✓			ρ	
Lorenz forces		✓	✓					$\mu_\mathrm{m}\ \sigma$
Chemical changes:								
Chemical reactions		✓			✓	✓	$\bar{G}$	
Phase change		✓	✓		✓		$\bar{G}$	

			Region				Material properties	
Material	**EA**	**SB**	**AB**	**FB**	**FL**	**FH**	**Thermodynamic**	**Kinetic**
Raw materials:								
DRI particles		✓				✓	$\rho\ \bar{C}_P\ \bar{G}$	κ
Reductant particles		✓				✓	$\rho\ \bar{C}_P\ \bar{G}$	κ
Flux particles		✓				✓	$\rho\ \bar{C}_P\ \bar{G}$	κ
Process materials:								
Liquid slag		✓			✓	✓	$\rho\ \bar{C}_P\ \bar{G}$	$\mu_\mathrm{m}\ \sigma\ \kappa\ \mu$
Solidified slag		✓			✓	✓	$\rho\ \bar{C}_P\ \bar{G}$	κ
Liquid alloy		✓	✓			✓	$\rho\ \bar{C}_P\ \bar{G}$	$\mu_\mathrm{m}\ \sigma\ \kappa\ \mu$
Solidified alloy		✓	✓			✓	$\rho\ \bar{C}_P\ \bar{G}$	κ
Freeboard materials:								
Dust	✓			✓		✓	$\rho\ \bar{C}_P\ \bar{G}$	$\alpha_\mathrm{r}\ \rho_\mathrm{r}\ \tau_\mathrm{r}$
Fume	✓			✓			$\rho\ \bar{C}_P\ \bar{G}$	$\alpha_\mathrm{r}\ \rho_\mathrm{r}\ \tau_\mathrm{r}$
Gas	✓	✓		✓		✓	$\rho\ \bar{C}_P\ \bar{G}$	$\alpha_\mathrm{r}\rho_\mathrm{r}\tau_\mathrm{r}\kappa\ \mu$
Others:								
Plasma	✓			✓			$\rho\ \bar{C}_P$	$\sigma\ \kappa\ \mu$

EA: electric arc, SB: slag bath, AB: alloy bath, FB: freeboard, FL: slag freeze lining, FH: sidewall feed heap.

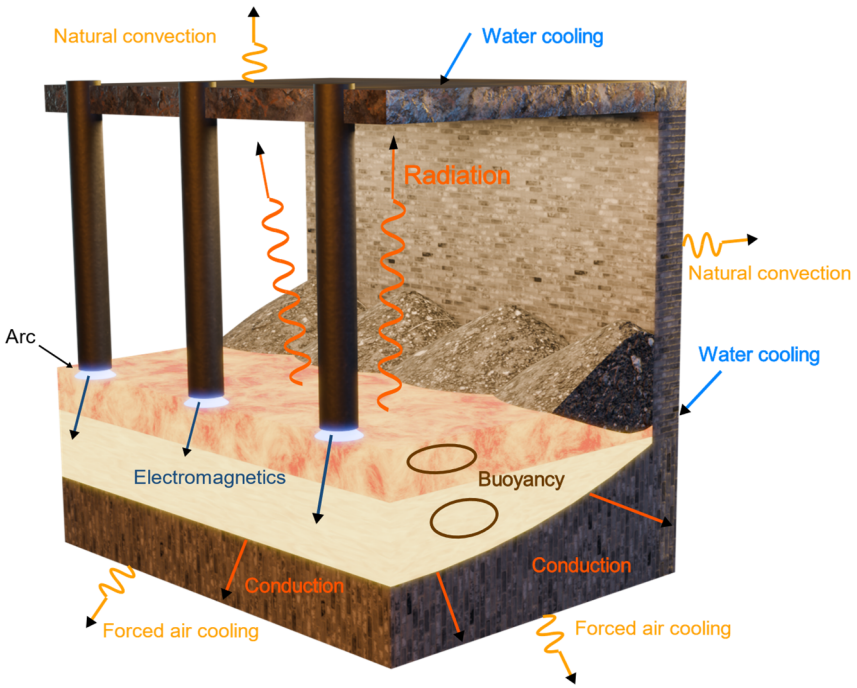

FIG 3 – Physical phenomena important to DSF modelling, design, and operation.

In the case of the slag bath (column highlighted in Table 1), for example, electrical current flow and joule heating release energy, which is transported through thermal conduction and fluid flow driven by buoyancy and Lorentz forces. Chemical reactions and phase change occur, which involve DRI, reductant, and flux particles, liquid and solid slag, liquid and solid alloy, and gas. Considering only the liquid slag material (row highlighted in Table 1), descriptions of density, heat capacity, Gibbs energy, magnetic permeability, electrical conductivity, thermal conductivity, and viscosity are required.

COMPUTATIONAL REALITIES

When considering comprehensively addressing the scope in Table 1 and focusing on liquid slag and other oxide phases in particular, we are confronted with a number of realities, which are true in the case of DSFs, but also in many, if not most, other pyrometallurgical scenarios.

Thermodynamic space

The Gibbs phase rule shown in Equation 1 shows the number of dimensions in which materials exist, and therefore the number of dimensions that we need to perform calculations in. A system's dimensionality is equal to $\hat{f}^{\rho}$ with $\hat{\varphi}^{\rho} = 1$:

$$\hat{f}^{\rho} = \hat{\psi}^{\rho} + \hat{\varepsilon}^{\sigma} + \sum_{i=1}^{\hat{\varphi}^{\rho}} \hat{\varepsilon}^{\varphi_i} - \hat{\varphi}^{\rho} - \hat{\zeta}^{\sigma} - \sum_{i=1}^{\hat{\varphi}^{\rho}} \hat{\zeta}^{\varphi_i} \quad (1)$$

In pyrometallurgy we usually work at constant pressure and varying temperature ($\hat{\psi}^{\sigma} = 1$), and with large numbers of system components. In the case of a DSF, iron ore combined with carbonaceous reductants commonly contain Al, C, Ca, Fe, H, K, Mg, Mn, N, Na, O, P, S, Si ($\hat{\varepsilon}^{\sigma} = 14$), when ignoring other minor elements. Assuming that there are no compositional constraints ($\hat{\zeta}^{\sigma} = \hat{\zeta}^{\varphi_i} = 0$), these elements combine with temperature to yield $\hat{f}^{\rho} = 14$ when $\hat{\varphi}^{\rho} = 1$... a 14-dimensional system. This results in the 'curse of dimensionality', which exponentially increases the required computation, memory, and storage space as the number of dimensions increase.

As an example, when generating a grid with 25 points in each dimension and storing the necessary independent and dependent parameters (each represented by a single double-precision floating point number of 8 B) at each grid location will require 17.50 to 144.5 TB of storage space. Such a data set will only sparsely cover the 14D domain and it will not capture detailed phase diagram features. Table 1 shows that values for several material thermodynamic properties (MTPs) and material kinetic properties (MKPs) need to be stored, and each of these will further increase the

required storage space. In comparison, the ChatGPT™, GPT-4 (by OpenAI) large language model (LLM) used a data set with 1 T tokens, and has about 1.76 T parameters (OpenAI, 2023; The Decoder, 2023) (NB: these figures were not formally released by OpenAI but are provided as a relatable reference).

Training a large neural network that can describe the example DSF system with all its thermodynamic and kinetic properties is possible in principle, but the enormity of thermodynamic space makes it practically infeasible. Exorbitant amounts of data (measured or calculated), computation, memory, and storage space would be required.

The limits of computation

When building a multiphysics model for answering the Key Questions related to DSF technology, we are primarily describing transport phenomena, and are therefore heavily dependent on kinetic properties. These properties are influenced by thermodynamic properties, which are determined by equilibrium behaviour as determined with Gibbs energy minimisation (GEM) calculations at the temperatures and compositions inside a DSF. These aspects are interdependent, which makes it necessary to solve such a model iteratively.

Roos and Zietsman (2022, Figure 2) showed that direct integration of GEM calculations with up to ten system components into realistically sized multiphysics models can result in computation times of up to hundreds of years for modest numbers of iterations. These durations only allowed for equilibrium calculations, and not for further material property calculations. Therefore, integrating partial differential equation (PDE) solver software and GEM software that are available today, yields infeasible computation times. This infeasibility is the thrust behind developing the RapidThermo material description framework (Roos and Zietsman, 2022).

The same authors showed that the burden of calculating and storing data across a DSF's entire 14D domain can be reduced in two ways. Firstly, the Gibbs phase rule reduces the number of dimensions by $(\widehat{\varphi}^{\rho} - 1)$ (Roos and Zietsman, 2022). For example, when liquid alloy, liquid slag, dicalcium silicate, and gas are stable, it is only necessary to work in 11 dimensions rather than 14. Secondly, only those regions of the phase diagram in which the process in question is active need to be populated with *in situ* tabulation (Roos, Bogaers and Zietsman, 2023). This is demonstrated in Figure 4 with simplified compositional spaces for ironmaking, steelmaking, and ilmenite smelting, which shows that large regions of compositional space will likely be unimportant for simulating such processes.

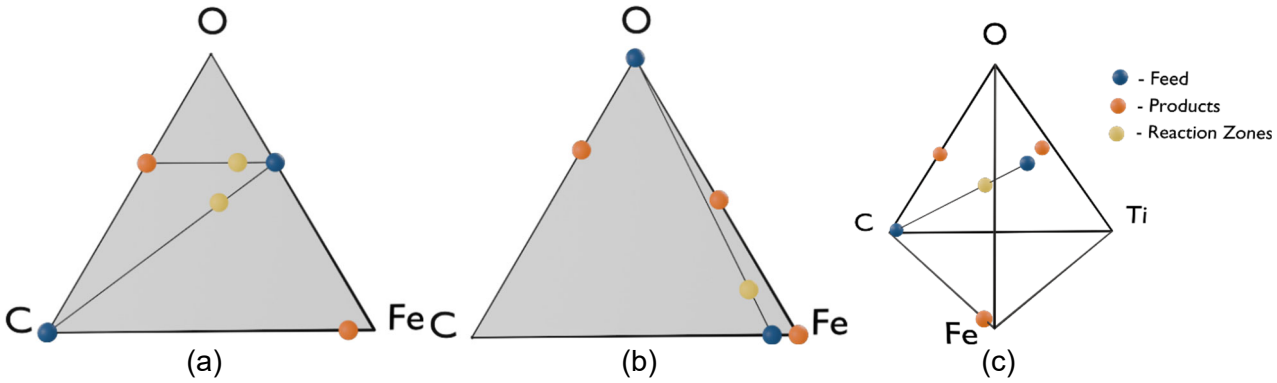

FIG 4 – Simplified compositional spaces indicating regions that need to be considered to describe feed and product materials, and process reaction zones: (a) Ironmaking; (b) Steelmaking; (c) Ilmenite smelting.

Thermodynamic properties

The thermodynamic behaviour (G, S, H) of the example 14D DSF system are fairly well (but not perfectly) described with thermochemical data in CALPHAD software such as FactSage™, ver 8.3 (by Thermfact Ltd. and GTT-Technologies). There are still regions of this system that are not well described, or described at all by the available data. Calculating the equilibrium state of a system

through GEM with such software is possible, but too slow for doing large numbers of calculations in short periods of time.

$\bar{C}_p, \Delta\bar{H}_{\mathrm{f},298K}$ and $\bar{S}_{298K}$ of pure substances and $\bar{G}$ of solutions are described reasonably well in CALPHAD software databases. Recent progress has been made with the description of molar volume and thermal expansivity that together describe density with a CALPHAD model (Thibodeau, Gheribi and Jung, 2016a, 2016b, 2016c) and density functional theory (DFT) (Liu, Wang and Shang, 2022) models, but these models are not yet readily available in CALPHAD software. Because density differences drive flow-through buoyancy, better descriptions of slag density can contribute to more accurate simulation of fluid flow and heat transfer in a DSF slag bath with multiphysics models.

Kinetic properties

When considering silicate slags relevant to the example 14D DSF system, the best described kinetic property is viscosity, with several models available in CALPHAD software or based on CALPHAD solution models (Grundy *et al*, 2008; Kim, 2011; Wu *et al*, 2015). Thibodeau and Jung (2016) reported a structure-based electrical conductivity model for slags. A similar model for thermal conductivity is not currently available. These properties combine to influence energy discharge, fluid flow, and heat transfer, all of which are relevant and important to developing DSFs.

General practice in multiphysics modelling is to select single values for these properties, and keep them constant throughout a simulation, without accounting for the influences of changing temperature and composition in a furnace over time. This is one of the core reasons why multiphysics models can only describe high-temperature systems with limited accuracy. To improve these models, these kinetic properties (μ, σ, and κ) need to be integrated along with thermodynamic properties and phase states at equilibrium. Accomplishing this through direct integration of CALPHAD and multiphysics software is infeasible at present.

Summary

The challenges stated can be summarised as follows:

1. It is infeasible to cover the vast thermodynamic space of a DSF process by pre-calculating data and, for example, fitting a neural network.
2. It is infeasible to use direct integration of equilibrium calculations in multiphysics models.
3. It is possible to calculate some thermodynamic properties with CALPHAD tools, but due to the dependence on equilibrium calculations, this is infeasible for high-throughput computation.
4. It is possible to calculate some kinetic properties of a system with CALPHAD tools, but due to the dependence on both equilibrium calculations and thermodynamic properties, it remains infeasible for high-throughput computation.

This leads to the conclusion that high-fidelity, high-resolution simulation of pyrometallurgical processes of industrial importance is currently infeasible. As shown in Table 2, the RapidThermo accelerator framework development by Roos and Zietsman (2022) addresses item 1 above through dimensional reduction and *in situ* tabulation, item 2 through tabulation of equilibrium calculation results, and item 3 partially through tabulation of phase thermodynamic properties.

TABLE 2

Current capabilities related to material property determination, description, and application. Shaded cells show the scope targeted by the RapidThermo framework.

Property	Property determination *Properties can be determined with physical measurements; computation, eg DFT, MD.*	CALPHAD descriptions *Descriptions are readily available in CALPHAD software.*	Efficient descriptions *Sufficiently efficient descriptions are available for high-throughput computation.*	Dependent models *Models that depend on these properties and descriptions.*
Pure substances/pure phases (PPs)				
Structural properties:				
Crystal structure	✓	✓		MP(SP)
Atomic/ionic radii	✓	✗		MP(SP)
Thermodynamic properties:				
$\bar{S}_{298K}$ $\bar{C}_P$ $\bar{G}$	✓	✓	✗	MP(TP) GM
$\bar{V}$ α_V ρ	✓	-	✗	MP(TP) GM
Kinetic properties:				
μ σ κ	✓	✗	✗	MP(KP) MP
Solution phases/mixture phases (MPs)				
Structural properties:				
Crystal structure	✓	✓		MP(TP,KP)
Atomic/ionic radii	✓	✗		MP(TP,KP)
Inter-atomic/ionic distances	✓	✗		MP(KP)
Thermodynamic properties:				
$\bar{S}^\circ$ $\bar{H}^\circ$ $\bar{G}^{ex}$	✓	✓	✓	GM PR MP
$\bar{V}^\circ$ $\bar{V}^{ex}$ α_V ρ	✓	✗	✗	MP
Kinetic properties:				
μ	-	✓	✗	MP
σ κ	-	✗	✗	MP
Equilibrium state				
System properties:				
Phase fractions	✓	✓	✓	SP(TP,KP) PM MP
Thermodynamic quantities	✓	✓	✓	PM MP
Phase properties:				
Molar composition	✓	✓	✓	PM MP
Thermodynamic quantities	✓	✓	✓	PM MP
Morphology:				
Particle size, surface area	✗	✗	✗	CM(KP) MP
Apparent TPs:				
$\check{H}$ $\check{C}_P$		✓	✓	PR MP
$\bar{V}$ α_V ρ		✗	✗	MP
Apparent kinetic properties:				
μ σ κ		✗	✗	MP

SP: structure property; TP: thermodynamic property; KP: kinetic property; MP: multiphysics models; PR: process models; GM: Gibbs energy minimisation; CM: composite material (multiple phases); ✓: good; -: ok; ✗: bad.

The following can also be noted based on Table 2.

1. Pure substances:

   Properties can be determined by experimental measurement and, more recently, with computational chemistry (Liu, Wang and Shang, 2022). CALPHAD descriptions provide crystal structure information, but not dimensions such as atomic/ionic radii, or kinetic properties. The latter is improving in, for example, FactSage™. The available descriptions are not suitable for direct inclusion in high-throughput computations such as multiphysics models.

2. Solution phases:

   Determining structure information, thermodynamic properties, and kinetic properties with physical measurements is possible but generally difficult for slags. Computational chemistry (eg DFT, MD) has made progress with determination of kinetic properties (Mongalo, Lopis and Venter, 2016), but much is still left to do. CALPHAD descriptions provide structure information, but not dimensional information, and not yet all required thermodynamic, and kinetic property descriptions. The available descriptions are not suited for high-throughput computation.

3. Equilibrium state:

   System and phase properties are described well with CALPHAD models, and these can be integrated into high-throughput computations with RapidThermo. Morphology influences the kinetic properties of composite materials (eg viscosity of slag with dispersed solids). This cannot be addressed with CALPHAD software at all because morphology is not determined by equilibrium. Some thermodynamic properties, and all the required kinetic properties are not yet accessible in high-throughput computation.

Continued RapidThermo development to incorporate further thermodynamic properties (item 3) and kinetic properties (item 4) is the focus of the next section.

EFFICIENT MATERIAL DESCRIPTIONS

Figure 5 shows that the RapidThermo accelerator accepts an independent system state $\mathbf{X}^{\sigma}$ as input. It returns a dependent equilibrium system state $\mathbf{Y}^{\sigma}$ directly calculated by CALPHAD software as result if its database contains insufficient data but returns interpolated values $\tilde{\mathbf{Y}}^{\sigma}$ once enough data is available. The database is populated *in situ*, which means it can start empty and be populated as the connected process or multiphysics models request calculation results; there is no need for a large number of pre-calculations. The interpolation routine is substantially faster than GEM calculations, and the benefit grows as the number of system components increases (Roos, Bogaers and Zietsman, 2023). This makes incorporating accurate material descriptions into such models more feasible.

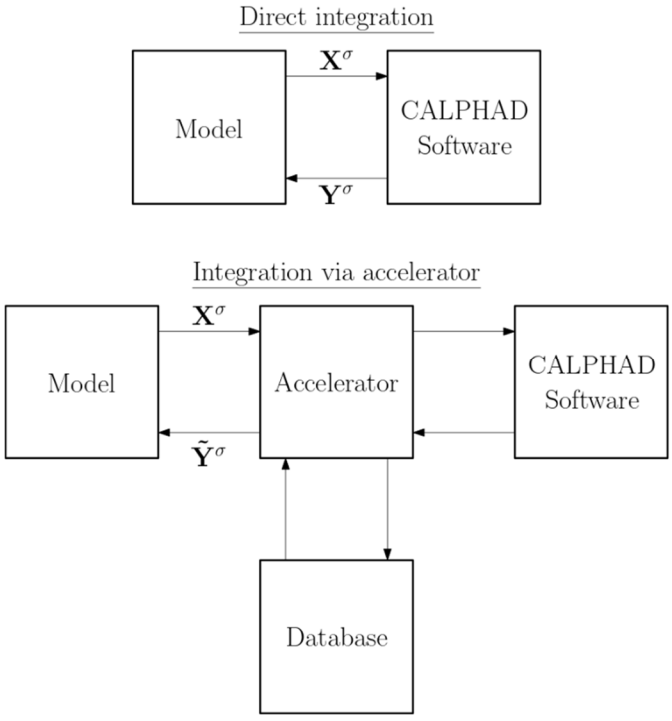

FIG 5 – The RapidThermo accelerator concept compared with direct integration between models and CALPHAD software (indicated as equilibrium calculation software) (Roos and Zietsman, 2022).

The accelerator discretises the system's phase diagram, which is 14-dimensional in the DSF example, into small thermochemical cells within which it can use interpolation based on the lever rule to calculate $\tilde{\mathbf{Y}}^{\sigma}$ results, which limits expensive CALPHAD software calculations. To be clear though, the RapidThermo accelerator does not aim to replace or eliminate the use of CALPHAD software. It acts as an intermediary between computationally intensive models and CALPHAD software to make more detailed, more accurate, and larger-scale investigation of pyrometallurgical processes feasible.

The core requirements of the RapidThermo algorithm are:

1. Configurability: The accelerator must:
    - be generic, so that it can function for any number of system components and nonchemical potentials.
    - use minimal configuration, including thermochemical system data and metadata, and discretisation ranges and cell sizes.
    - be modular, to allow changing sub-algorithms for discretisation, interpolation, and multiphase property calculation by changing configuration settings rather than changing source code.
2. Efficiency: The accelerator must:
    - perform calculations orders of magnitude faster than the CALPHAD software it integrates with, to allow feasible solution of the connected process and multiphysics models.
    - allow parallel execution, so that large numbers of $\mathbf{X}^{\sigma}$ can be specified and large numbers of $\mathbf{Y}^{\sigma}$ can be returned simultaneously.
    - require minimal computer memory and storage space to allow execution on reasonably-costed computer hardware.
3. Accuracy: The accelerator must:
    - produce calculation results that satisfy mass, element mass, and energy conservation within machine precision.
    - allow control over interpolation accuracy through configuration of discretisation cell ranges and sizes.

Table 2 shows that the accelerator reported by Roos, Bogaers and Zietsman (2023) can calculate system phase fractions and thermodynamic quantities, phase molar compositions and thermodynamic quantities, as well as $\bar{C}_p$ and $\Delta\bar{H}_P$ for combinations of multiple phases. These capabilities allow more sophisticated multiphysics model calculations that can describe, for example, phase change associated with slag freeze linings.

As indicated in Table 1, further properties that are required to describe DSFs include density, viscosity, electrical conductivity, and thermal conductivity, for both single phases such as liquid slag and multiple phases. Similar to $\bar{C}_p$and $\Delta\bar{H}_P$, these properties only need to be stored in single phase regions and on one-phase-fraction (OPF) boundaries for single phases. This has the benefit of reducing the number of data points that need to be calculated and stored. These properties are further addressed in the remainder of this section, with specific reference to liquid slag.

Slag structure

When oxides melt and mix to become a liquid slag, the cations and anions will with time arrange themselves into the most probable, or equilibrium, configuration $\Gamma_{\mathrm{eq}}^{\sigma}$. Considering a binary CaO-SiO_2 melt, Si-O-Si bonded oxygen ions are indicated as O^0 and referred to as bridged oxygens, Ca-O-Ca bonded ones are indicated as O^{2-} and referred to as free oxygens, and Ca-O-Si bonded ones are indicated as O^- and referred to as broken oxygens. The structure of this melt can be described with Q^0, Q^1, Q^2, Q^3, Q^4, and Ca-Ca species; the superscript indicates the number of oxygen atoms per Si tetrahedron that binds to another Si atom. The equilibrium mole fractions of the different species

change with composition and temperature, and can be determined experimentally or with CALPHAD software such as FactSage™ (Thibodeau, Gheribi and Jung, 2016a).

The structure of the melt directly influences its properties, such as molar volume, thermal expansivity, viscosity, electrical conductivity, and thermal conductivity. Some property models use equilibrium structure information from the Modified Quasichemical Model (MQM) (Pelton and Blander, 1986) in FactSage™ to estimate property values (Grundy *et al*, 2008; Thibodeau, Gheribi and Jung, 2016a; Thibodeau and Jung, 2016). Calculated equilibrium structure data would be too large to efficiently store in RapidThermo. This data must therefore be used to calculate property values, which can be stored efficiently, and then discarded.

Slag properties

Density, viscosity, electrical, and thermal conductivity are the most important properties that need to be accessible to multiphysics models, of DSFs for example. This additional information must be provided by RapidThermo at the lowest possible additional computational, memory, and storage cost.

Density

Phase density (Equation 2) varies with composition and temperature; it is determined by molar volume (Equation 3) and thermal expansivity (Equation 4):

$$\rho^{\varphi} = \frac{\sum_{\mu=1}^{\hat{\mu}^{\varphi}} x_{\mu}^{\varphi} \bar{m}_{\mu}}{\bar{V}^{\varphi}} \tag{2}$$

$$\bar{V}^{\varphi} = \frac{V_{T_{ref}}^{\varphi}}{\sum_{\mu=1}^{\hat{\mu}^{\varphi}} n_{\mu}^{\varphi}} \left(1 + \alpha_{V}^{\varphi}(T - T_{ref})\right) \tag{3}$$

$$\alpha_{V}^{\varphi} = \frac{1}{\bar{V}^{\varphi}} \frac{\partial \bar{V}^{\varphi}}{\partial T} \tag{4}$$

Liquid slag density can be calculated either directly based on structure data from GEM results and the model by Thibodeau, Gheribi and Jung (2016c), or interpolated with previously calculated data stored in the RapidThermo database. It is sufficient to store only ρ^{slag} rather than both $\bar{V}^{\mathrm{slag}}$ and $\alpha_{V}^{\mathrm{slag}}$, since the accelerator's discretisation scheme will implicitly store both composition and temperature dependence.

Density of a mixture of phases is not dependent on morphology. The combined density of the phases ρ can therefore be determined simply with Equation 5, based on either directly calculated or interpolated single-phase densities ρ^{φ}, which obviates storage of multi-phase density data:

$$\rho = \frac{m^{\sigma}}{\sum_{\varphi=1}^{\hat{\varphi}^{\rho}} \frac{m^{\varphi}}{\rho^{\varphi}}} \tag{5}$$

Viscosity

Single-phase dynamic viscosity μ^{φ} is only relevant to fluids such as gas, liquid slags, and liquid alloys. Together with the flow domain geometry, it determines the rate at which momentum is transferred. This is important for fluid flow and heat transfer in high-temperature reactors such as DSFs. Liquid slag viscosity can be calculated with models from Grundy *et al* (2008), Kim (2011) and Wu *et al* (2015), all of which use structure data from GEM calculations as basis.

Because viscosity is a kinetic property, the morphology of a mixture of phases influences the mixture's apparent viscosity μ (Schupsky *et al*, 2020). In the case of a single liquid phase with suspended solid phases, the Einstein-Roscoe equation (Roscoe, 1952) is often used (Equation 6). This equation omits the influence of solid particle morphology, and therefore the interfacial area between liquid and solid phases:

$$\mu^{\mathrm{apparent}} = \mu^{\mathrm{liquid}} \left(1 - 1.35 \frac{V^{\mathrm{solids}}}{V_{\mathrm{liquid}}}\right) \tag{6}$$

When the phase mixture only consists of liquids, such as a molten slag and alloy, Equation 7 can be used to calculate apparent viscosity as a volume weighted average (Muller, Zietsman and Pistorius, 2015), which also ignores morphology.

$$\mu^{\text{apparent}} = \frac{1}{V^{\sigma}} \sum_{\varphi=1}^{\hat{\varphi}^{\rho}} V^{\varphi} \mu^{\varphi} \tag{7}$$

Electrical conductivity

Single-phase electrical conductivity σ^{φ} together with domain geometry, and the electrical potential field determine the rate at which electrical charge is transferred. This releases energy through joule heating, which drives subsequent heat transfer, in high-temperature reactors such as DSFs. Liquid slag electrical conductivity can be calculated with the model from Thibodeau and Jung (2016), which uses equilibrium structure data as basis.

As a kinetic property, the morphology of a mixture of phases influences the mixture's apparent electrical conductivity σ^{apparent}. When ignoring morphology, an average weighted by volume fractions can be used as a simple approximation:

$$\sigma^{\text{apparent}} = \frac{1}{V^{\sigma}} \sum_{\varphi=1}^{\hat{\varphi}^{\rho}} V^{\varphi} \sigma^{\varphi} \tag{8}$$

Thermal conductivity

Thermal conductivity is the slag property that is most lacking in data and models. It is also of great importance to new technologies such as DSFs, since energy released through electrical heating must be transported, at least in part, through the slag bath. We suspect that heat transfer rates through the slag bath may be the fundamental capacity constraint of these new processes.

It may be possible to resolve some of these problems with computational methods such as MD and DFT for single phases. Multiple phases can be approached similar to electrical conductivity, due to the similarities between the two properties.

Summary

The availability of sophisticated material property models based on slag structure makes it feasible and relatively simple to add thermodynamic and kinetic material properties to the information stored by the RapidThermo framework. These models use equilibrium calculation results as basis and compute physical properties at limited additional cost. The calculated properties only need to be stored on OPF boundaries, as is the case with the compositions, heat capacities, and enthalpies of single phases.

Electrical conduction in slags involves transport of charge with ions and electrons (Equation 9). Similarly, slag thermal conduction involves transport of heat with phonons (lattice vibrations), photons (thermal radiation), and electrons (Equation 10). MQM structure information is used successfully as basis for describing σ_{ion}^{slag} (Thibodeau and Jung, 2016), and may similarly be able to support calculation of κ_{phn}^{slag}. It does not provide sufficient information, though, for estimating electronic and radiation components. It is therefore not yet possible to describe high-TiO_2 slags, for example, that have large electronic contributions to their electrical and thermal conductivities.

$$\sigma^{\text{slag}} = \sigma_{\text{ion}}^{\text{slag}} + \sigma_{\text{elc}}^{\text{slag}} \tag{9}$$

$$\kappa^{\text{slag}} = \kappa_{\text{phn}}^{\text{slag}} + \kappa_{\text{elc}}^{\text{slag}} + \kappa_{\text{pht}}^{\text{slag}} \tag{10}$$

All multiphase properties are re-calculated efficiently with interpolation based on density information and the lever rule, which obviates the need for excessive storage. Simple volume-based multiphase descriptions can be exchanged for more sophisticated models when morphology information is available. Simple descriptions can already improve multiphysics models significantly compared with assuming constant material property values.

Even though RapidThermo stores the minimum amount of data required for adequately accurate material descriptions, memory and storage requirements may increase to infeasible levels. In such cases, artificial neural networks (ANNs) may be fitted on OPF data to provide drastically compressed

phase boundary descriptions. Such non-linear fits will have to be constrained to ensure that they remain thermodynamically consistent, and that mass, element mass, and energy conservation are still adhered to.

CONCLUSION

The pressure to develop new production technologies for the iron and steel industry is clear, and a current reality. If DRI smelting furnaces are to be in successful operation as soon as 2030, computational modelling will have to play a large part in the development process. This, in turn, needs more comprehensive, accurate, and computationally efficient material descriptions as a crucial component. Combining multiphysics models and existing material descriptions with existing methods and software will, however, lead to infeasible computation times.

It has been demonstrated in earlier work that the RapidThermo framework can capture equilibrium phase compositions, heat capacity, and enthalpy, which can make substantially faster material descriptions available for process and multiphysics models. In this paper we explained how other material properties, including density, viscosity, electrical conductivity, and thermal conductivity can be added to the framework, to make more realistic models of high-temperature reactors possible.

The current work identified the following points for further investigation:

1. Large memory and storage requirements on OPF boundaries may make it necessary to compress this data. Artificial neural networks may provide a feasible solution, especially since large amounts of data would be available.
2. Solution models like the MQM do not yet provide sufficient information to describe the electronic components of electrical and thermal conduction, and the radiation component of thermal conduction. It may be useful to extend such models to produce additional structure, geometric and dimensional information that can be used as basis for estimating these properties.

ACKNOWLEDGEMENTS

The author gratefully acknowledges the contributions of Mr Stefan Koning in preparing visualisations and artwork for the manuscript, Mr Shane de Beer and Mr Hanno Muire in preparing physical property models to support the manuscript and presentation, and Mr Hanno Muire in preparing the final manuscript.

NOMENCLATURE

Extensive variables			Intensive variables		
U	internal energy	J			
S	entropy	JK^{-1}	T	temperature	K
V	volume	m^3	P	pressure	Pa
H	enthalpy	J			
G	Gibbs energy	J			
n	amount of substance	mol	μ	chemical potential	J mol^{-1}
			x	amount fraction	mol mol^{-1}
m	mass	kg	y	mass fraction	kg kg^{-1}

Arrays are indicated with boldface eg $\mathbf{n}$ is an array of n_{i}.

Extensive variable modifier notation					
$\bar{V}$	integral molar	V/n	$\hat{V}$	partial molar	$\frac{\partial V}{\partial n_i}$
$\check{V}$	integral mass-specific	V/m			

Material thermodynamic properties			Material kinetic properties		
$\bar{C}_P$	heat capacity	J K^{-1} mol^{-1}	μ	dynamic viscosity	Pa s
	molar volume	m^3 mol^{-1}	σ	electrical conductivity	S m^{-1}
	thermal expansivity	K^{-1}	κ	thermal conductivity	W m^{-1} K^{-1}
	mass density	kg m^{-3}	μ_{m}	magnetic permeability	H m^{-1}
			α_{r}	thermal radiation absorptivity	W W^{-1}
			ρ_{r}	thermal radiation reflectivity	W W^{-1}
			τ_{r}	thermal radiation transmissivity	W W^{-1}

Objects related to thermochemistry			
Υ	the universe	ς	the surroundings
σ	the system	ρ	phase region (unique set of phases) in a phase diagram
Γ^{σ}	a macrostate (macroscopic configuration) of σ	f	a degree of freedom
$\Gamma^{\sigma}_{\mathrm{eq}}$	an equilibrium state of σ	φ	a phase
γ^{Γ}	a microstate (microscopic configuration) of Γ	ε^{φ}	a component, eg an element or electron, local to φ
ψ^{σ}	a non-chemical potential of σ, eg T, P	ζ^{φ}	a compositional constraint of φ
ε^{σ}	a component (usually chemical element) of σ	ϵ^{φ}	an independent component of φ
ζ^{σ}	a compositional constraint of σ	μ^{φ}	a constituent of φ
ϵ^{σ}	an independent component of σ	λ^{φ}	a sublattice of φ
		μ^{λ}	a constituent of λ

Hat notation indicates 'the number of' an object, eg $\widehat{\varphi}^{\rho}$ is the number of phases in a phase region.

REFERENCES

Grundy, A N, Liu, H, Jung, I-H, Decterov, S A and Pelton, A D, 2008. A model to calculate the viscosity of silicate melts, Part I: Viscosity of binary SiO_2-MeO_x systems (Me = Na, K, Ca, Mg, Al), *International Journal of Materials Research,* 99(11):1185–1194. https://doi.org/10.3139/146.101752

Kim, W-Y, 2011. Modelling viscosity of molten slags and glasses, PhD thesis, Ecole Polytechnique de Montréal, Canada.

Liu, Z-K, Wang, Y and Shang, S-L, 2022. Zentropy Theory for Positive and Negative Thermal Expansion, *Journal of Phase Equilibria and Diffusion,* 43(6):598–605. https://doi.org/10.1007/s11669-022-00942-z

Mongalo, L, Lopis, A S and Venter, G A, 2016. Molecular dynamics simulations of the structural properties and electrical conductivities of CaO–MgO–Al_2O_3–SiO_2 melts, *Journal of NonCrystalline Solids,* 452(15):194–202.

Muller, J, Zietsman, J H and Pistorius, P C, 2015. Modeling of Manganese Ferroalloy Slag Properties and Flow During Tapping, *Metallurgical Materials Transactions B,* 46(2):2639–2651. https://doi.org/10.1007/s11663-015-0426-7

OpenAI, 2023. GPT-4 Technical Report, OpenAI. Available from: <https://arxiv.org/pdf/2303.08774.pdf> (Accessed: 08/02/2024).

Pelton, A D and Blander, M, 1986. Thermodynamic analysis of ordered liquid solutions by a modified quasichemical approach – Application to silicate slags, *Metallurgical and Materials Transactions B,* 17B:805–815.

Roos, W A and Zietsman, J H, 2022. Geometric acceleration of complex chemical equilibrium calculations — Algorithm and application to two- and three-component systems, *CALPHAD,* 77:102420. https://doi.org/10.1016/j.calphad.2022.102420

Roos, W A, Bogaers, A E J and Zietsman, J H, 2023. Geometric acceleration of complex chemical equilibrium calculations — Performance in two- to five-component systems, *CALPHAD,* 82:102584. https://doi.org/10.1016/j.calphad.2023.102584

Roscoe, R, 1952. The viscosity of suspensions of rigid spheres, *British Journal of Applied Physics,* 3:267–269.

Schupsky, J P, Saar, O, Wu, G, Dohrn, M and Müller, M, 2020. Viscosity and crystal morphology data of anorthite bearing synthetic coal slag systems, *Fuel,* 280:118663. https://doi.org/10.1016/j.fuel.2020.118663. Available from: <https://www.sciencedirect.com/science/article/pii/S0016236120316598>

The Decoder, 2023, 11 July. GPT-4 architecture, datasets, costs and more leaked. Available from: <https://the-decoder.com/gpt-4-architecture-datasets-costs-and-more-leaked/> (Accessed: 08/02/2024).

Thibodeau, E, Gheribi, A E and Jung, I-H, 2016a. A Structural Molar Volume Model for Oxide Melts Part I: Li2O-Na2O-K2O-MgO-CaO-MnO-PbO-Al_2O_3-SiO_2 Melts—Binary Systems, *Metallurgical and Materials Transactions B,* 47(2):1147–1164. https://doi.org/10.1007/s11663-015-0548-y

Thibodeau, E, Gheribi, A E and Jung, I-H, 2016b. A Structural Molar Volume Model for Oxide Melts Part II: Li2O-Na2O-K2O-MgO-CaO-MnO-PbO-Al_2O_3-SiO_2 Melts—Ternary and Multicomponent Systems, *Metallurgical and Materials Transactions B,* 47(2):1165–1186. https://doi.org/10.1007/s11663-015-0543-3

Thibodeau, E, Gheribi, A E and Jung, I-H, 2016c. A Structural Molar Volume Model for Oxide Melts Part III: Fe Oxide-Containing Melts, *Metallurgical and Materials Transactions B,* 47(2):1187–1202. https://doi.org/10.1007/s11663-015-0549-x

Thibodeau, E and Jung, I-H, 2016. A structural electrical conductivity model for oxide melts, *Metallurgical and Materials Transactions B,* 47:355–383.

Wimmer, G, Fleischander, A and Voraberger, B, 2023. Green Transition of the Iron and Steel Industry Impact on Slags and By-Products, in *Proceedings of the 21st ibausil International Conference on Building Materials*, 6(6):257–261. https://doi.org/10.1002/cepa.2954

Wu, G, Yazhenskikh, E, Hack, K, Wosch, E and Müller, M, 2015. Viscosity model for oxide melts relevant to fuel slags, Part 1: Pure oxides and binary systems in the system SiO_2–Al_2O_3–CaO–MgO–Na2O–K2O, *Fuel Processing Technology,* 137:93–103. https://doi.org/10.1016/j.fuproc.2015.03.025

Zietsman, J H and Pistorius, P C, 2006. Modelling of an ilmenite-smelting DC arc furnace process, *Minerals Engineering,* 19(3):262–279. https://doi.org/10.1016/j.mineng.2005.06.016

Zietsman, J H, Steyn, A and Pretorius, W, 2018. Evaluating pre-treatment and smelting options with EMSIM to improve production efficiency, Proceedings of INFACON XV, Southern African Institute of Mining and Metallurgy.

Mathematical descriptions of – Thermodynamic databases and models

Thermodynamic modelling of species distribution in $AlCl_3$:BMIC salts

DOI:10.62053/CQUY1573
M K Nahian[1] and R G Reddy[2]

1. Graduate student, The University of Alabama, Tuscaloosa AL 35487, USA. Email: mknahian@crimson.ua.edu
2. Professor, The University of Alabama, Tuscaloosa AL 35487, USA. Email: rreddy@eng.ua.edu

ABSTRACT

The thermodynamic model for species distribution in aluminium chloride ($AlCl_3$) and 1-butyl-3-methylimidazolium chloride (BMIC) system was developed. The experimental thermodynamic data, considering a range of aluminium chloride species, such as $AlCl_4^-$, $Al_2Cl_7^-$, $Al_3Cl_{10}^-$, $Al_4Cl_{13}^-$, and Al_2Cl_6 were used in developing the model. When the X_{AlCl3} was in the range of 0 to 0.50, only anion species Cl^- and $AlCl_4^-$ were existing in the solution. As the X_{AlCl3} value increased more than 0.50, the available anions were $Al_2Cl_7^-$, $Al_3Cl_{10}^-$, $Al_4Cl_{13}^-$, and Al_2Cl_6. Specifically, the concentration of $Al_2Cl_7^-$ increased in the composition range from 0.50 to 0.67 X_{AlCl3}, after which it decreased. This change in the concentration of $Al_2Cl_7^-$ was due to its reaction with excess $AlCl_3$, leading to the formation of $Al_3Cl_{10}^-$. The average cathode current density was determined by the electrochemical experiments varying X_{AlCl3} from 0.50 to 0.71 in the $AlCl_3$:BMIC solutions. The average cathode current density increased as the X_{AlCl3} increased from 0.50 to 0.67. However, it decreased when the X_{AlCl3} > 0.67. This trend can be attributed to the electroactive species $Al_2Cl_7^-$. The $Al_2Cl_7^-$ promotes the reduction rate at the cathode, resulting in an increase in the average cathode current density.

INTRODUCTION

Ionic liquids (ILs) exhibit distinctive chemical and physical characteristics such as extensive liquidus temperature range, high thermal stability, low melting point, and large electrochemical window (Pradhan and Reddy, 2014). Typically, ILs contain organic cations and either organic or inorganic anions with melting points less than 100°C. The adjustable nature of ILs enables the tailoring of specific properties to suit diverse fields, including batteries, fuel cells, and solvents in chemical processes. They are regarded as green electrolytes for metal deposition due to their low vapor pressure and less pollutant emission (Pradhan and Reddy, 2012, 2014). Among them, the 1-butyl-3-methyl-imidazolium chloride (BMIC) ionic liquid, when combined with aluminium chloride ($AlCl_3$), shows great promise in fields like batteries and low-temperature aluminium electrodeposition. In this IL, different important properties like density, viscosity, electrical conductivity, and diffusion coefficient are dictated by the species and their interaction with each other (Fannin *et al*, 1984). With changing $AlCl_3$ mole fraction (X_{AlCl3}) in the $AlCl_3$:BMIC system, species concentration changes which results in the change of the chloro-acidity. Depending on the content of X_{AlCl3}, $AlCl_3$:BMIC can be basic (X_{AlCl3} < 0.5), neutral, and acidic (X_{AlCl3} > 0.5) (Karpinski and Osteryoung, 1984). The molecular structures of $AlCl_3$ and BMIC are presented in the Figure 1.

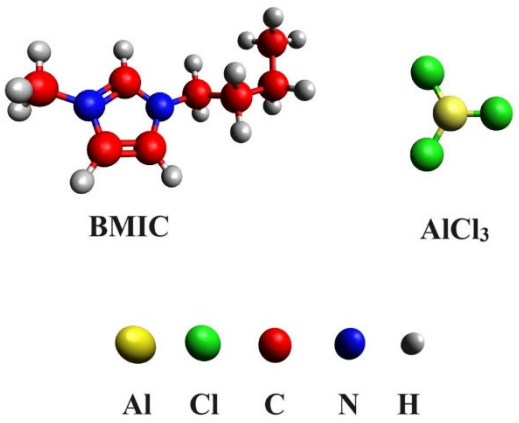

FIG 1 – Molecular structure of BMIC and $AlCl_3$ (drawn by Avogadro program (Hanwell *et al*, 2012).

Although there is a growing interest in low-temperature refining of aluminium using $AlCl_3$:BMIC, production of aluminium on a pilot scale using ILs is in progress (Pradhan, Mantha and Reddy, 2009). The average cathode current density during aluminium electrodeposition refers to the amount of electric current per unit area that flows to the cathode during the electrodeposition process. This parameter is a critical factor in controlling the rate at which metal ions are reduced and deposited onto the cathode surface. Parameters such as electrolyte composition, temperature, and applied voltage are varied to achieve the desired cathode current density for successful electrodeposition. To obtain maximum aluminium electrodeposition efficiently, it is crucial to understand the optimal composition of the $AlCl_3$:BMIC electrolyte.

This study discusses the species concentration profile of the $AlCl_3$:BMIC ionic liquid electrolyte with average cathode current density data during the aluminium electrochemical process. The species concentration profile was constructed across the X_{AlCl3} range from 0 to 1 (Nahian and Reddy, 2023). Average cathode current density in several literature with respect to X_{AlCl3} (Wang, 2020; Kamavaram, Mantha and Reddy, 2003, 2005). Understanding this correlation is vital as the species concentration profile influences the electrochemical behaviour of the electrolyte, while average cathode current density data provides insights into the rate of reduction reactions during aluminium electrodeposition.

MODELLING AND EXPERIMENTAL PROCEDURE

Thermodynamic modelling of $AlCl_3$:BMIC species

In $AlCl_3$:BMIC, BMIC dissociates and produces BMI^+ cation and Cl^-:

$$BMIC = BMI^+ + Cl^- \quad (1)$$

$AlCl_3$ prefers to form $0.5Al_2Cl_6$. This $0.5Al_2Cl_6$ reacts with Cl^- to produce $AlCl_4^-$:

$$Cl^- + 0.5Al_2Cl_6 = AlCl_4^- \quad (2)$$

$AlCl_4^-$ reacts with additional Al_2Cl_6 and produces $Al_2Cl_7^-$:

$$AlCl_4^- + 0.5Al_2Cl_6 = Al_2Cl_7^- \quad (3)$$

In a similar way higher order polymeric species form:

$$Al_2Cl_7^- + 0.5Al_2Cl_6 = Al_3Cl_{10}^- \quad (4)$$

$$Al_3Cl_{10}^- + 0.5Al_2Cl_6 = Al_4Cl_{13}^- \quad (5)$$

From above reaction the only cation is BMI^+ and the anions are Cl^-, $AlCl_4^-$, $Al_2Cl_7^-$, $Al_3Cl_{10}^-$, $Al_4Cl_{13}^-$. Al_2Cl_6 is the neutral species. Based on thermodynamic data, mass and charge balance anionic species concentration profile was developed for 25°C considering the anionic and the neutral species (Nahian and Reddy, 2023).

Electrodeposition of aluminium

The experimental procedure for aluminium electrodeposition using $AlCl_3$:BMIC is described somewhere else (Wang, 2020; Ahmed and Reddy, 2021; Pradhan and Reddy, 2014; Kamavaram, Mantha and Reddy, 2005). Electrolytes were prepared by mixing the required amount of $AlCl_3$ and BMIC. All experiments conducted in a 50 mL beaker. Cathode and anode were copper and aluminium alloys. Average cathode current density during this electrodeposition process was recorded for different X_{AlCl3}. As the electrolyte was sensitive to moisture, all experiments conducted under an argon atmosphere. The potential difference between two electrodes and the current of the electrochemical process measured using a Multimeter (Keithley Instruments Inc). Kepco power source (Kepco Programmable Power Supply) or Gamry potentiostat (Interface 1010E full-featured potentiostat) was used to apply the required potential. The temperature of the cell measured using thermometer by inserting into the electrolyte. The current was measured as a function of temperature. Electrochemical deposition time of aluminium was 2 hrs. The electrolyte was stirred at a constant speed. The current density was determined by dividing the current by the deposited aluminium area on the copper electrode. The schematic diagram of the electrochemical cell is represented in Figure 2.

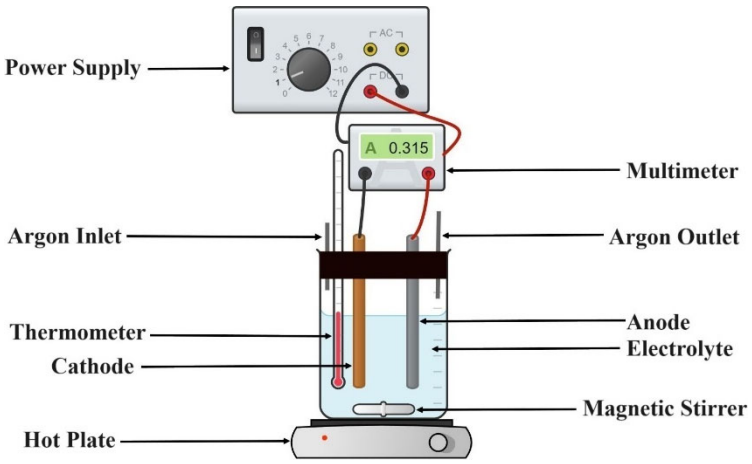

FIG 2 – Schematic of a typical electrochemical cell for aluminium deposition using IL electrolyte.

The average cathode current density for different experimental conditions is presented in Table 1. For experiments 2 and 3, the average cathode current density data were taken from the plots.

TABLE 1

Experimental conditions for aluminium deposition using $AlCl_3$:BMIC electrolyte.

Experiments	Anode	Cathode	Applied potential (V)	Temperature (°C)	X_{AlCl3}	Average cathode current density (A/m^2)	Reference
1	Al2020	Cu	1.5	100	0.50	6.4	Wang, 2020
					0.55	21.1	
					0.58	169.3	
					0.62	180.5	
					0.64	282.6	
					0.67	396.7	
					0.69	317.2	
					0.71	231.0	
2	Al MMC	Cu	1.0	103 ± 2	0.57	211	Kamavaram, Mantha and Reddy, 2005
					0.60	242	
					0.64	241	
					0.67	261	
3	A360	Cu/Al	1.3	100	0.60	169	Kamavaram, Mantha and Reddy, 2003
					0.62	183	
					0.64	183	

RESULTS AND DISCUSSIONS

The species concentration of $AlCl_3$:BMIC at 25°C is presented in Figure 3. X_{Cl^-}, $X_{AlCl_4^-}$, $X_{Al_2Cl_7^-}$, $X_{Al_3Cl_{10}^-}$, $X_{Al_4Cl_{13}^-}$, and $X_{Al_2Cl_6}$ represents the mole fraction of Cl^-, $AlCl_4^-$, $Al_2Cl_7^-$, $Al_3Cl_{10}^-$, $Al_4Cl_{13}^-$ and Al_2Cl_6 respectively.

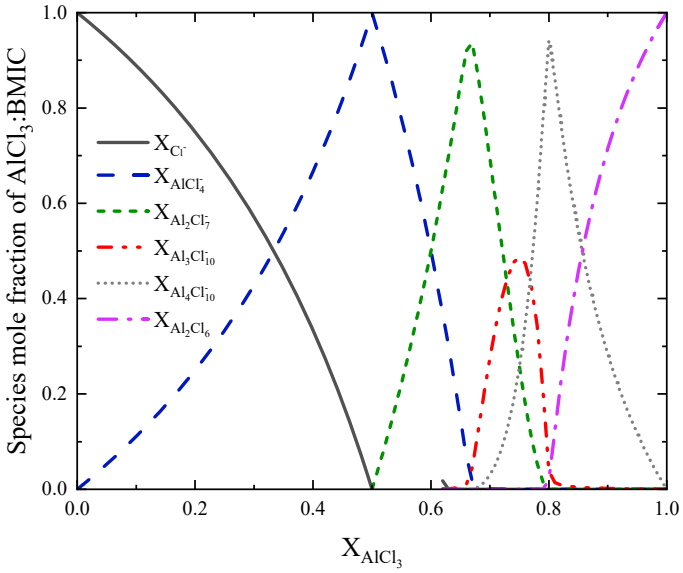

FIG 3 – Different species mole fraction of $AlCl_3$:BMIC as a function of X_{AlCl3} at 25°C (reproduced from (Nahian and Reddy, 2023).

When X_{AlCl3} varies from 0 to 0.5, the only anionic species are Cl^- and $AlCl_4^-$. Other anionic species $Al_2Cl_7^-$, $Al_3Cl_{10}^-$, $Al_4Cl_{13}^-$ exist when $X_{AlCl3} > 0.5$. The $AlCl_4^-$, $Al_2Cl_7^-$, $Al_3Cl_{10}^-$, $Al_4Cl_{13}^-$ exhibit peaks at X_{AlCl3} values of 0.50, 0.67, 0.75, and 0.80, respectively.

The average cathode current density as a function of X_{AlCl3} (varying from 0.50 to 0.71) in $AlCl_3$:BMIC electrolyte is given in Figure 4.

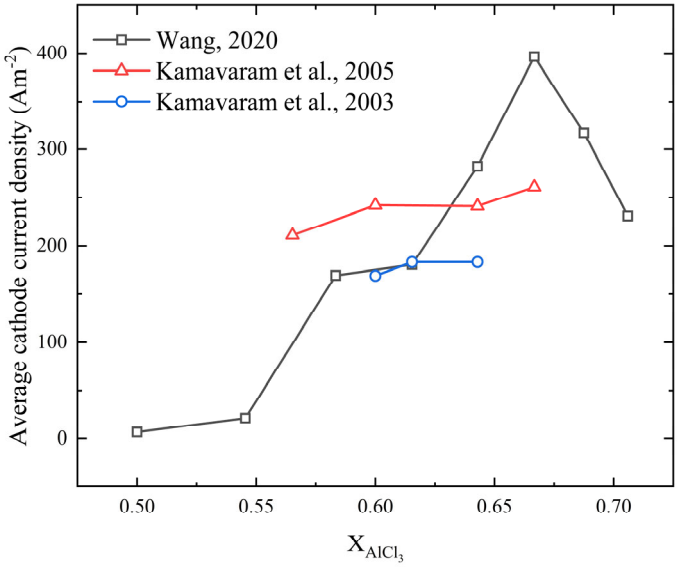

FIG 4 – Average cathode current density as a function of X_{AlCl3} during electrodeposition at 100°C, 120 rev/min, 1.5 V, and 2 hrs (Wang, 2020; Kamavaram, Mantha and Reddy, 2003, 2005).

In Figure 4, it is observed that the average cathode current density increases significantly with increasing X_{AlCl3} till $X_{AlCl3} = 0.67$. When $X_{AlCl3} > 0.67$, the average cathode current density starts to decrease. For experiment 1, the increase in average current density curve is steep X_{AlCl3} compared to experiments 2 and 3. Experiment 1 has also the highest average cathode current density at $X_{AlCl3} = 0.67$. This may be due to the composition of the anode. In experiment 1, Al2020 anode was used which has 93.43 wt per cent aluminium. On the other hand, Al MMC and A360 were used in experiments 2 and 3 which contain 66.22 and 76.2 wt per cent aluminium. Comparatively higher average current density was observed for experiment 2 at $X_{AlCl3} \geqslant 0.60$ because of the slightly high deposition temperature.

Species concentration profile is developed for 25°C and the average cathode current density data presented here is for 100°C. The effect of temperature on the species distribution of chloroaluminate IL, such as the mixture of 1-ethyl-3-methylimidazolium chloride (EMIC) or 1-butyl-3-methylimidazolium chloride with $AlCl_3$, is not significant, as evidenced in previous studies (Ahmed, Nahian and Reddy, 2023; Øye *et al*, 1991; Shi, Jiang and Zhao, 2021; Nahian and Reddy, 2023). Therefore, average cathode current density data obtained at 100°C can be effectively compared with the species concentration profile obtained at room temperature. Figure 5, presents a comparative analysis of the mole fractions of different species at 25°C alongside the average cathode current density for aluminium electrodeposition at 100°C using the $AlCl_3$:BMIC electrolyte system.

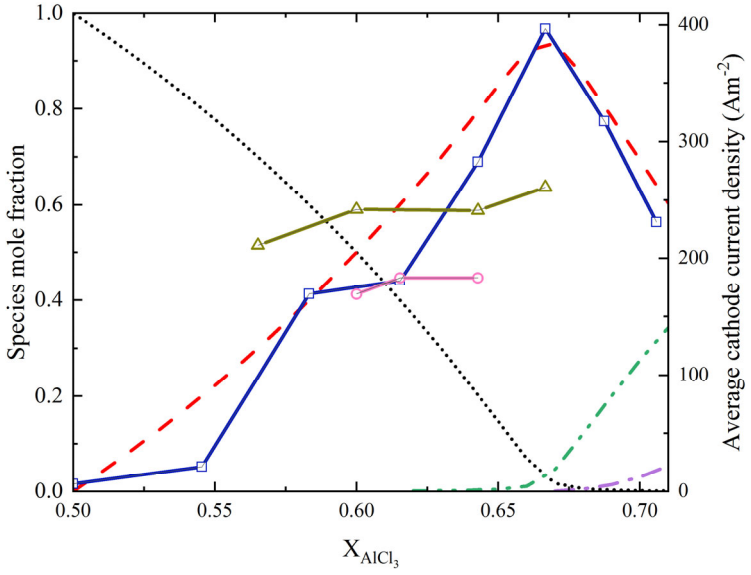

FIG 5 – Species mole fraction ($X_{AlCl_4^-}$, $X_{Al_2Cl_7^-}$, $X_{Al_3Cl_{10}^-}$, and $X_{Al_4Cl_{13}^-}$) at 25°C and average cathode current density at 100 and 103 ± 2°C for Al electrodeposition in $AlCl_3$:BMIC.

(····· $X_{AlCl_4^-}$, — — — $X_{Al_2Cl_7^-}$, — · · — $X_{Al_3Cl_{10}^-}$, — · — $X_{Al_4Cl_{13}^-}$, □ current density (Wang, 2020), △ current density (Kamavaram, Mantha and Reddy, 2005), ○ current density (Kamavaram, Mantha and Reddy, 2003).

In the aluminium electrodeposition using $AlCl_3$:BMIC electrolyte, the average cathode current density shows a good correlation with the concentration of electrolyte species. At $X_{AlCl_3} = 0.50$, where the only available anionic species is $X_{AlCl_4^-}$, it has been found that the deposition of aluminium is not possible due to the non-reducibility of $AlCl_4^-$ anion (Carlin, Crawford and Bersch, 1992; Kamavaram, Mantha and Reddy, 2003). Consequently, the average cathode current density is negligible at $X_{AlCl_3} = 0.50$. Beyond this composition ($X_{AlCl_3} > 0.50$), the $Al_2Cl_7^-$ anion starts to appear, concurrently with a decrease in $AlCl_4^-$. It is reported that $Al_2Cl_7^-$ is the electroactive species that is responsible for the deposition of aluminium (Kamavaram, Mantha and Reddy, 2005). The aluminium electrodeposition process involves the reduction of $Al_2Cl_7^-$ to $AlCl_4^-$, as shown in the following reaction:

$$4Al_2Cl_7^- + 3e^- = Al + 7AlCl_4^- \quad (6)$$

At $X_{AlCl_3} = 0.50$, the average cathode current density increases due to the increase in $X_{Al_2Cl_7^-}$. It reaches the maximum when $X_{Al_2Cl_7^-}$ is highest (at $X_{AlCl_3} = 0.67$). However, as X_{AlCl_3} exceeds 0.67, there is a decline in $X_{Al_2Cl_7^-}$ concentration resulting in a subsequent decrease in average cathode current density. It can be deduced that $Al_2Cl_7^-$ anionic species are determining species that control the overall average cathode current density.

CONCLUSIONS

A species concentration profile for the $AlCl_3$:BMIC electrolyte system based on thermodynamic modelling was discussed. The model was constructed incorporating species like Cl^-, $AlCl_4^-$, $Al_2Cl_7^-$, $Al_3Cl_{10}^-$, $Al_4Cl_{13}^-$ and Al_2Cl_6. The average cathode current density during the aluminium electrodeposition process using $AlCl_3$:BMIC electrolyte as a function of $AlCl_3$ mole fraction (X_{AlCl_3})

was also correlated with this species concentration profile calculated using a thermodynamic model to get insight into the aluminium deposition process. At X_{AlCl3} = 0.50, the average cathode current density was negligible. This is attributed to anion $AlCl_4^-$ which cannot be reduced during the electrochemical process. Hence there is no significant cathode current density was observed. Above X_{AlCl3} = 0.50, the average cathode current density increases and when X_{AlCl3} > 0.67, the average cathode current density starts to decrease. This trend is due to the $Al_2Cl_7^-$ which is responsible for the aluminium deposition. These findings contribute to the understanding of the intricate interplay between the electrolyte composition, species concentration, and average cathode current density in the aluminium electrodeposition process, providing valuable insight for optimising such electrochemical processes for the production of aluminium for practical applications.

ACKNOWLEDGEMENTS

The authors acknowledge the financial support from the National Science Foundation (NSF) award number 1762522 and ACIPCO for this research project. Authors also thank the Department of Metallurgical and Materials Engineering, the University of Alabama for providing the experimental and analytical facilities.

REFERENCES

Ahmed, A N and Reddy, R, 2021. Electrochemical separation of aluminum from mixed scrap using ionic liquids, *The Minerals, Metals and Materials Series*, pp 1036–1044.

Ahmed, A N, Nahian, M K and Reddy, R G, 2023. Chloro-aluminate species distribution correlation with electrical conductivity of 1-ethyl-3-methyl imidazolium chloride (EMIC)-aluminum chloride ($AlCl_3$) system, *The Minerals, Metals and Materials Series*, pp 1115–1120.

Carlin, R T, Crawford, W and Bersch, M, 1992. Nucleation and morphology studies of aluminum deposited from an ambient-temperature chloroaluminate molten salt, *Journal of The Electrochemical Society*, 139(10): 2720–2727.

Fannin, A A, Floreani, D A, King, L A, Landers, J S, Piersma, B J, Stech, D J, Vaughn, R L, Wilkes, J S and Williams, J L, 1984. Properties of 1,3-dialkylimidazolium chloride-aluminium chloride ionic liquids, part 2, phase transitions, densities, electrical conductivities and viscosities, *The Journal of Physical Chemistry*, 88(12):2614–2621.

Hanwell, M D, Curtis, D E, Lonie, D C, Vandermeersch, T, Zurek, E and Hutchison, G R, 2012. Avogadro: An advanced semantic chemical editor, visualization and analysis platform, *Journal of Cheminformatics*, 4(1).

Kamavaram, V, Mantha, D and Reddy, R G, 2003. Electrorefining of aluminum alloy in ionic liquids at low temperatures, *Journal of Mining and Metallurgy, Section B: Metallurgy*, 39(1–2):43–58.

Kamavaram, V, Mantha, D and Reddy, R G, 2005. Recycling of aluminum metal matrix composite using ionic liquids, *Electrochimica Acta*, 50(16–17):3286–3295.

Karpinski, Z J and Osteryoung, R A, 1984. Determination of equilibrium constants for the tetra chloroaluminate ion dissociation in ambient-temperature ionic liquids, *Inorganic Chemistry*, 23(10):1491–1494.

Nahian, M K and Reddy, R G, 2023. Electrical conductivity and species distribution of aluminium chloride and 1-butyl-3-methylimidazolium chloride Ionic Liquid Electrolytes, *Journal of Physical Organic Chemistry*, 36(10).

Øye, H A, Jagtoyen, M, Oksefjell, T and Wilkes, J S, 1991. Vapour pressure and thermodynamics of the system 1-methyl-3-ethyl-imidazolium chloride-aluminium chloride, *Materials Science Forum*, 73–75:183–190.

Pradhan, D and Reddy, R G, 2012. Dendrite-free aluminium electrodeposition from $AlCl_3$–1-ethyl-3-methyl-imidazolium chloride ionic liquid electrolytes, *Metallurgical and Materials Transactions B*, 43(3):519–531.

Pradhan, D and Reddy, R G, 2014. Mechanistic study of al electrodeposition from EMIC–$AlCl_3$ and BMIC–$AlCl_3$ electrolytes at low temperature, *Materials Chemistry and Physics*, 143(2):564–569.

Pradhan, D, Mantha, D and Reddy, R G, 2009. The effect of electrode surface modification and cathode overpotential on deposit characteristics in aluminium electrorefining using EMIC–$AlCl_3$ ionic liquid electrolyte, *Electrochimica Acta*, 54(26):6661–6667.

Shi, M, Jiang, J and Zhao, H, 2021. Electrodeposition of aluminium in the 1-ethyl-3-methylimidazolium tetra chloroaluminate ionic liquid, *Electrochem*, 2(2):185–196.

Wang, Y, 2020. Development of aluminium electrorefining in ionic liquids: The effects of experimental conditions on the deposition behaviour and microstructure, thesis, The University of Alabama.

Continuous method of thermodynamic optimisation using first-derivative matrices for large multicomponent systems

DOI: 10.62053/RPDV2805

E Nekhoroshev[1], D Shishin[2], M Shevchenko[3] and E Jak[4]

1. Theme Leader in Computational Thermodynamics, Pyrosearch group, University of Queensland, Brisbane Qld 4850. Email: e.nekhoroshev@uq.edu.au
2. Theme Leader in Thermodynamic Modelling, Pyrosearch group, University of Queensland, Brisbane Qld 4850. Email: d.shishin@uq.edu.au
3. Theme Leader in Experiments and Thermodynamic Optimization, Pyrosearch group, University of Queensland, Brisbane Qld 4850. Email: m.shevchenko@uq.edu.au
4. Professor of Chemical Engineering, Pyrosearch group, University of Queensland, Brisbane Qld 4850. Email: e.jak@uq.edu.au

ABSTRACT

Real-life applications require thermodynamic databases consisting of many elements. Currently, Pyrosearch supports a 20-component thermodynamic FactSage™, ver 8.2 (by Thermfact and GTT technologies) database for Cu-, Pb- and Fe-production provided to a group of industrial sponsors. The database development follows an agile cycle of experiment planning, modelling/update of database subsystems, quality tests and release. A unique challenge is development and maintenance of a database self-consistent across all binary/ternary and multicomponent systems. Practice shows that binary and ternary system data do not provide the necessary accuracy for predictions within multicomponent systems. Commercial databases are often developed using only available literature data and it is hard to estimate the prediction quality for industry-relevant multicomponent compositions. Therefore, to sustain a high reliability there is a need of targeted experiments including multicomponent data.

To support the continuous development process, a new optimisation methodology has been developed. After long years of optimisation experience, it is an authors' belief that for optimisation, it is essential to pinpoint a few trusted target points instead of using a whole cloud of available experimental data. In case if the optimisation procedure is automated, using all data, even with trust weights, still leads to inferior optimisation quality. This is caused by the fact that available optimisation algorithms usually assume a normal error distribution of experimental data which can be false in cases when experimental results are affected by sample contamination, evaporation, incomplete reactions, etc.

Typically, iterative optimisation involves multiple re-calculations of targets values which can take significant time and the whole procedure is not interactive. It is hard to find an exact combination of target weights to achieve desired outcomes. This problem has been solved by the authors by replacing slow FactSage™/ChemApp™ calculations by parameter value/target value relations using first-order derivative matrices. Precalculated derivative matrices allow fast analysis of parameter influence across multiple systems, selection of interaction combinations with superior performance, and analytical matrix solution to the optimisation problems using weighted linear least squares. The current optimisation system supports in-sheet ChemApp™ (by GTT-technologies, version 614) calculations for Microsoft® Excel® using custom Python® binding code, graphical and statistical representation of experimental data and target points, and real-time first-derivative matrix analysis of parameter sensitivity.

INTRODUCTION

This paper discusses results of development of a continuous optimisation methodology and a new efficient method of semi-automatic optimisation based on use of first derivative matrices of target points by model parameters, abbreviated JET (Jacobian of Experimental Targets).

Pyrosearch, UQ (University of Queensland) specialises in development of a 20-component thermodynamic database covering the Pb-Zn-Cu-Fe-Ca-Si-S-O-Al-Mg-Cr-As-Sn-Sb-Bi-Ag-Au-Ni-Co-Na system for various non-ferrous industrial applications. While development of most of the open and commercial thermodynamic databases relies heavily relies on the availability of experimental

data in the literature, Pyrosearch has a strong team of researchers specialising in high-precision measurements of phase equilibria including gas phase, slags, matte, speiss, metal, solids using electron probe microanalysis (EPMA) technique (Llovet *et al*, 2021). Rather than relying on availability of experimental data in the literature sources, the database development follows an agile cycle of experimental investigation of new systems, the initial optimisation, further experimental and modelling refining of these systems by cross-checking database prediction quality with multicomponent experimental data. Besides consistent experiment planning, systematic use of high-quality EPMA data for optimisation highlighted certain legacy inconsistencies and limitations in the thermodynamic database which eventually had to be resolved. For example, compared to FToxid database of FactSage™ software, all liquid slag end members now have consistent physical properties with proper extrapolation down to low temperatures.

The 20-component database includes 728 oxide systems, 123 Na_2O-containing systems, 345 metal-matte-speiss systems, with the total of 1196 2-, 3- and 4-metal component systems. There are over 450 stoichiometric compounds, around 100 large and small solution phases and more than 3000 excess parameters in solution phases. Development and maintenance of such a database is a huge effort from both experimental and modelling points of view. Higher order systems in a database depend on all lower-order subsystems which causes a pyramid dependence effect. Re-optimisation of a single binary system can result in a significant work of re-optimisation of all ternary and cross-checking quaternary systems including that binary system. For this reason, many systems, such as CaO-SiO_2, Al_2O_3-SiO_2 etc has not been updated in FToxid since 1990s (Eriksson and Pelton, 1993).

One of the goals of the work described in this paper was to, first, develop an overall methodology of continuous optimisation which allows to significantly reduce the effort and time of accessing new experimental data and second, develop a practical optimisation method suitable for dealing with large bodies of multicomponent data and able to simultaneously assess multiple subsystems and analyse parameter influence across multicomponent data sets.

OVERALL OPTIMISATION METHODOLOGY

The continuous optimisation methodology is based on the overall accepted CALPHAD methodology. A thermodynamic database consists of many individual stoichiometric and solution phases; solution models are chosen depending on chemistry, structure and type of interactions. Simple solid solutions are typically modelled using simple polynomial models, solid solutions with multiple sublattices and complex substitution mechanisms are expanded within the compound energy formalism (CEF) (Hillert, 2021). Slag and matte/liquid metal phase are modelled using Modified Quasichemical Formalism (Pelton *et al*, 2000), which is suitable to describe strong interactions such as metal oxide/silica in slag and metal/sulfur, metal/oxygen in matte and metals. Each model provides expressions for Gibbs free energy of a solution as a function of composition, temperature, and, optionally, pressure. These expressions include properties of pure solution end members and various interaction parameters which together comprise *model parameters* of a solution. Model parameters of all phases in a system, limited to the elements of that system, make up *model parameters* of that system.

Model parameters need to be evaluated during an optimisation procedure based on various experimental data available for a system. According to thermodynamics, it is possible to derive all thermodynamic properties of a system from its Gibbs free energy. Optimisation solves the inverse problem of finding parameters of Gibbs energy functions from existing experimental data.

Generally, there can be numerous combinations of model parameters based on the same thermodynamic data. To limit the uncertainty, it is highly desirable to consider multiple types of experimental data together: phase equilibria, calorimetry, activity measurements, etc. For example, phase equilibria alone should not be used to derive Gibbs energy parameters: there might be multiple combinations of phases with different individual stabilities which cancel each other at equilibrium resulting in similar phase diagrams.

In systems pertaining to pyrometallurgy, there is a limited number of solid phases with extensive cover of liquidus area: spinel, tridymite, monoxide, olivine, hematite/corundum, etc. There are referred to as *major* phases. The thermodynamic properties of major phases usually have been extensively studied and their known thermodynamic properties can be used to derive the parameters

in a liquid phase. There is also a much larger number of miscellaneous stoichiometric and slightly non-stoichiometric *minor* phases. While for some of them the thermodynamic properties are known, most of them are defined by the phase equilibria with a liquid and/or major solid phases.

Experimental data can have different quality depending on their source and the measurement method. The uncertainty in experimental data can be divided into *bias* and *scatter*. Biases can appear due to multiple reasons: incomplete chemical reactions, material losses, etc. Scatter is a random deviation due to individual history of a sample and its measurement. Because of the reasons explained in more detail later, for continuous optimisation it is preferred to use *target points* instead of raw experimental data.

Each target point can have one or more *target values*. It can be temperature, composition, partial pressure, or something else. For each target value, there should be an unambiguous way of calculating it. Similar target values are grouped together into *target groups*.

Ideally, all target points should be free from experimental biases, which are not handled well by optimisation algorithms, and scatter, which bloats the number of points necessary to derive reliable model parameters. For high-precision data, like EPMA measurements, target points can be the same as the experimental points. In case of highly scattered data (data clouds) and if there are several data groups with distinct biases, the best judgement and expertise of the researcher is required to carefully define custom target points (they do not have to be a subset of experimental points).

For composition areas where measurements are missing, *virtual target points*, introduced as a best estimate of thermodynamic properties, can be used to avoid unrealistic model parameters.

Ideally, for each subsystem there must be developed a set of target points that define its optimisation and can be reused multiple times to consistently update model parameters for that system.

Since target points, contrary to raw experimental data, are supposed to be free from bias and scatter, with target points it becomes possible to evaluate a quality of optimisation or compare the predictive ability of different versions of a database solely using predictions in target points: compact RMS (residual mean squares) tables with ΔT and Δx errors, detailed visualisations of individual deviations, scatter plots, etc.

JET (JACOBIAN OF EXPERIMENTAL TARGETS) OPTIMISATION ALGORITHM

Cost functions in thermodynamic optimisation

Let us take a simplified example of the CaO-SiO_2 system with just a few target points and a few variable parameter values. The complete optimisation of the system (Nekhoroshev *et al*, in prep) contains more target points and model parameters, but for illustrative purposes we consider only four target points in the phase diagram (Figure 1) and three parameters in Table 1.

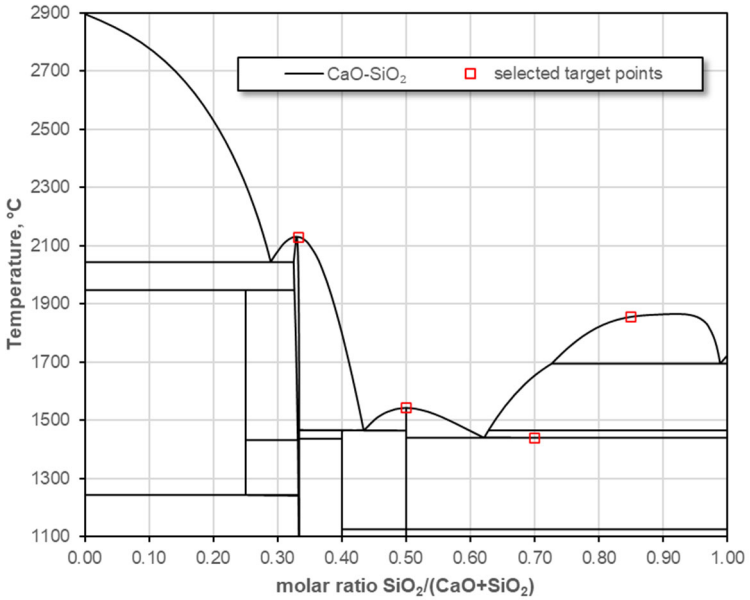

FIG 1 – Optimised phase diagram of the CaO-SiO_2 system (Shevchenko *et al*, in prep) together with a subset of target points: α-Ca_2SiO_4 and $CaSiO_3$ melting points, $CaSiO_3$-SiO_2 eutectic and a point on the miscibility gap.

TABLE 1

Optimal values of three selected parameters in slag phase of the CaO-SiO_2 system.

Parameter	Optimal value, J·mol^{-1}
$g^{00}_{Ca,Si}(T^0)$	-125520.8
$g^{01}_{Ca,Si}(T^0)$	+23544.7
$g^{07}_{Ca,Si}(T^0)$	-191208.8

The influence of parameters of the Modified Quasichemical Model in pair fraction expansion is mostly localised in composition domain. The main parameter $g^{00}_{Ca,Si}(T^0)$ mostly affects the area around the maximum short-range ordering composition at 33.33 mol per cent of SiO_2 (calcium disilicate liquidus). The auxiliary parameters $g^{01}_{Ca,Si}(T^0)$ and $g^{07}_{Ca,Si}(T^0)$ mostly affect the middle part of the diagram (pseudowollastonite liquidus) and the miscibility gap, correspondingly.

Figure 2 illustrates the dependencies of calculated temperatures in the target points obtained if the parameters are varied independently from each other starting from the optimal values in Table 1 as baseline references.

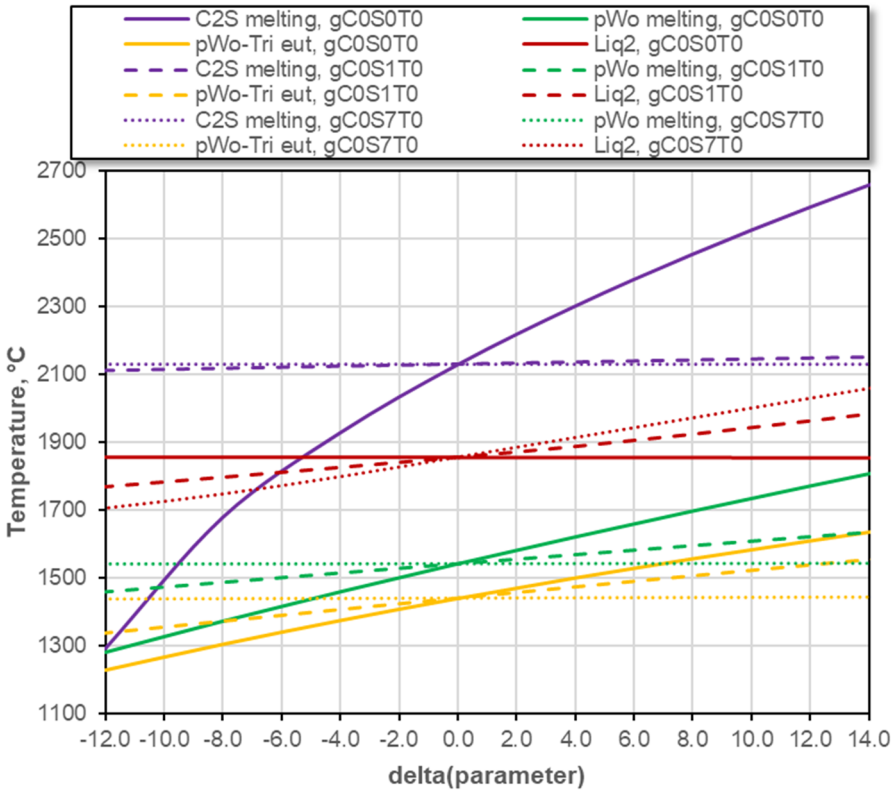

FIG 2 – Calculated formation target temperatures in selected target points on the CaO-SiO_2 phase diagram as functions of parameter deviations from the optimal values.

First, one should note the lines in Figure 2 are smooth and do not exhibit any breaks or kinks. For the most of them, the dependence is also approximately linear. It is always possible to make parameter dependencies exhibit smooth behaviour using a correct calculation set-up of target values.

The area of mathematical optimisation is extremely broad and covers various problems in engineering and physics. There are also multiple types of optimisation algorithms, each one of them is best suited for a certain type of task. Optimisation algorithms with certain assumptions about the cost function usually require less function evaluations to converge while algorithms which treat a cost function as a black box usually need more function evaluations. In thermodynamic optimisation, each function evaluation is performed using thermodynamic software such as FactSage™ or ChemApp™ and can be time-consuming. Phase target calculations generally take longer to calculate, especially in case of miscibility gaps. Isothermal calculations are usually much faster but in case of multicomponent systems can have limited applicability. Even if a single calculation is quite fast, multiple function evaluations can significantly slow down the whole optimisation procedure. It is important to find an appropriate trade-off between generality and efficiency.

To ensure the smoothness of the cost function one should pay attention to phase selection. As a rule, calculated thermodynamic properties exhibit breaks when a phase appears or disappears in a consequent iteration but generally, this situation can be avoided using a proper calculation set-up. For example, precipitation targets with multiple possible forming solids should be avoided and replaced with formation targets of a specific solid phase. Bulk compositions for isothermal targets should be selected in such a phase that a stable phase assemblage does not change when model parameters are updated.

Second, if set-up correctly, target values are smooth functions of model parameters and although the derivatives cannot be evaluated directly, they can be calculated using a finite difference method with an appropriate step size for each parameter. Numerical evaluation of second derivatives is usually too computationally expensive, though.

In general, the following information is required to choose an appropriate algorithm:

- Does the cost function have to be a scalar, or it can be written down as a vector of residuals?
- Is the cost function smooth and differentiable?
- If the first derivative exists, can it be evaluated analytically?
- Can we cheaply evaluate the second derivative of the target function?
- Does the target function have one global minimum or several local minima?

A scalar cost function, for example, a sum of squared residuals, loses some information compared to a vector cost function, which can result in more function evaluations.

Existence of first order derivatives greatly simplifies the optimisation task, giving rise to a group of optimisation methods related to the *gradient descent* algorithm. The gradient descent algorithm uses the direction of the maximum change in function value (the gradient) to update the solution. The extent of a step can be evaluated using information on the second derivative (Hessian matrix), giving rise to the Newton's method. If the Hessian matrix is not known, some information about its properties can be implicitly evaluated based on the change of gradient direction with consecutive iterations (quasi-Newton methods). In the limiting case when the second-order derivative of the cost function is zero (a linear system), the optimal solution can be found with one iteration.

The disadvantage of gradient descent methods is that they rely only on local information about the cost function and if multiple minima exist, the exact outcome of the optimisation routine will depend on the initial estimate. Usually, a set of initial points leading to the same minimum form a *basin of attraction* of this minimum.

To overcome this limitation, global optimisation methods can be used, such as Direct Search (Kolda, Lewis and Torczon, 2003), or genetic algorithms (Katoch, Chauhan and Kumar, 2020).

A typical scalar cost function in thermodynamic optimisation is illustrated in Figures 3 and 4. Since target value dependence on model parameters is mostly linear, as shown in Figure 2, the sum of squared residuals is supposed to have a near-parabolic shape (Figure 3). In case of two and more parameters, a parabolic valley can be more or less elongated indicating how fast residuals grow depending on parameters (Figure 4).

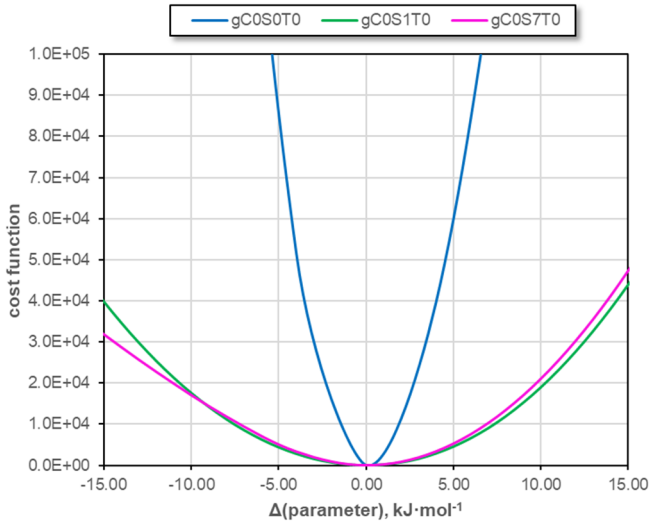

FIG 3 – The cost function (sum of squared residuals) as a function of deviation of a parameter from an optimal value with other parameters fixed at optimal values.

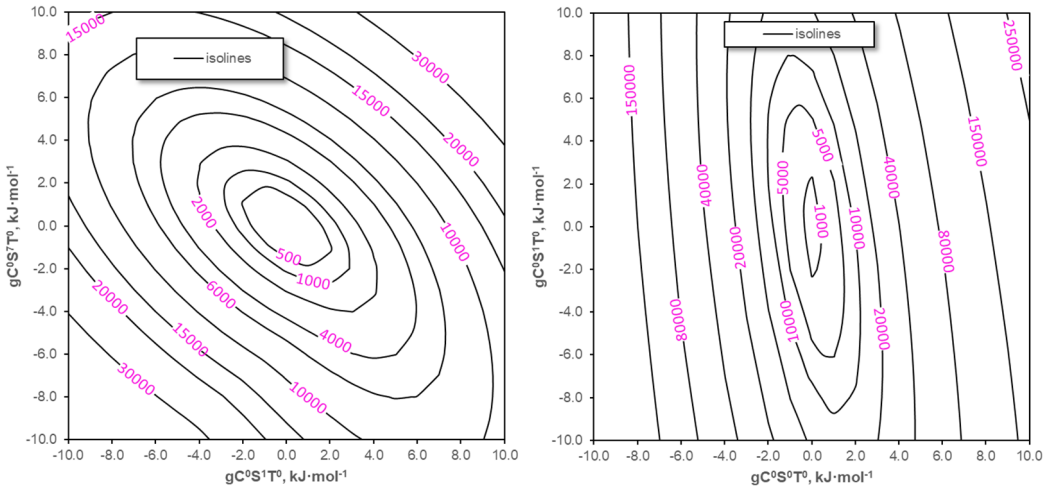

FIG 4 – Minimum valleys for the sum of squared residuals as a function of two parameters with the third parameter fixed: $S\left(g_{Ca,Si}^{01}(T^0), g_{Ca,Si}^{07}(T^0)\right)$ (a), $S\left(g_{Ca,Si}^{00}(T^0), g_{Ca,Si}^{01}(T^0)\right)$ (b).

Non-linear least squares method is an algorithm which, in our previous experience, works well for thermodynamic optimisation. It is available, for example, as *lsqnonlin* function in MATLAB or *least_squares* function in SciPy package for Python®. To use those functions, a rough initial guess for model parameters must be known which is usually found manually. The initial guess does not have to describe target points well, the only requirement is to be able to perform all thermodynamic calculations without errors and with a proper set of stable phases which ensures the existence of a smooth derivative in the initial point.

Non-linear least square optimisation with direct thermodynamic calculations is an acceptable solution for systems of small size (binary and ternary). However, it quickly becomes unfeasible for large multicomponent systems with thousands of target points. Also, maintenance of a multicomponent thermodynamic database implies that most subsystems are only slightly or moderately modified when new experimental data become available without a need of a total re-optimisation from scratch.

Also, it is very important to analyse parameter sensitivity and how model parameters influence target points across multiple subsystems and use this information to produce large self-consistent blocks of a thermodynamic database.

Derivation of Jacobian matrix and its use in optimisation

It was proposed by Professor Evgueni Jak that calculated target values can be efficiently approximated using linear relations between calculated values and model parameters. Let us suppose that any calculated values (temperatures, compositions, enthalpies, activities etc) are implicit functions of model parameters:

$$\begin{aligned} y_1 &= f_1(p_1, p_2, \dots, p_m) \\ y_2 &= f_2(p_1, p_2, \dots, p_m) \\ &\dots \\ y_n &= f_n(p_1, p_2, \dots, p_m) \end{aligned} \quad (1)$$

In a proximity of an *m*-dimensional model parameter vector $\bar{p}^0 = (p_1^0, p_2^0, \dots, p_m^0)$, *n f*-functions can be decomposed into linear parts of Taylor series of parameter deviations $\Delta\bar{p} = (\Delta p_1, \Delta p_2, \dots, \Delta p_m)$:

$$y_1 \approx y_1^0 + \frac{\partial f_1}{\partial p_1}(\bar{p}^0) \cdot (p_1 - p_1^0) + \frac{\partial f_1}{\partial p_2}(\bar{p}^0) \cdot (p_2 - p_2^0) + \dots + \frac{\partial f_1}{\partial p_m}(\bar{p}^0) \cdot (p_m - p_m^0)$$

$$y_2 \approx y_2^0 + \frac{\partial f_2}{\partial p_1}(\bar{p}^0) \cdot (p_1 - p_1^0) + \frac{\partial f_2}{\partial p_2}(\bar{p}^0) \cdot (p_2 - p_2^0) + \dots + \frac{\partial f_2}{\partial p_m}(\bar{p}^0) \cdot (p_m - p_m^0)$$

...

$$y_n \approx y_n^0 + \frac{\partial f_n}{\partial p_1}(\bar{p}^0)\cdot(p_1 - p_1^0) + \frac{\partial f_n}{\partial p_2}(\bar{p}^0)\cdot(p_2 - p_2^0) + \cdots + \frac{\partial f_n}{\partial p_m}(\bar{p}^0)\cdot(p_m - p_m^0) \quad (2)$$

The same relations can be written in a compact matrix form:

$$\bar{y} = \bar{y}^0 + A(\bar{p} - \bar{p}^0) \quad (3)$$

where the elements of matrix A are composed of partial derivatives in Equation 2.

Matrix A can be used for fast real-time updates of target values under conditions that parameter differences are not very large. It is important to note that once a derivative matrix is calculated, no consequent calls to thermodynamic software are needed. It can also be used for the inverse task of finding a new optimal set of parameters $\bar{p}^{opt}$ which satisfies the Linear Least Squares condition. To do that, we need to solve the following matrix equation:

$$(\bar{y} - \bar{y}^0) = A(\bar{p} - \bar{p}^0) \quad (4)$$

In general, matrix A is not square and cannot be inverted directly. To avoid this obstacle, Equation 4 is multiplied by a transposed matrix A on both sides:

$$A^T(\bar{y} - \bar{y}^0) = A^T A(\bar{p} - \bar{p}^0) \quad (5)$$

Now, matrix $D = A^T A$ is a symmetric square matrix (which can easily be shown) and we can take its proper inverse to find $(\bar{p} - \bar{p}^0)$:

$$\bar{p} - \bar{p}^0 = (A^T A)^{-1} A^T(\bar{y} - \bar{y}^0) = D^{-1} A^T(\bar{y} - \bar{y}^0) \quad (6)$$

A modification of Equation 6 accepts individual weights for target points as well:

$$\bar{p} - \bar{p}^0 = (A^T W A)^{-1} A^T W(\bar{y} - \bar{y}^0) \quad (7)$$

where W is a diagonal square matrix, whose diagonal elements are the corresponding target point weights.

From the practical point of view, direct matrix regression Equation 6 works well not only for a case when the initial guess is quite close to the optimal solution, but also in case when it is not – the only requirement is that all target values can be properly calculated initially (TD software converges). In this case, it is usually required to recalculate the derivative matrix two to three times before full convergence is achieved.

Derivation of the Linear Least Squares method assuming normal error distribution

This section covers in detail the mathematical reasons behind inefficiency of using raw experimental data for optimisation and why it is preferrable to replace it by target points.

Linear Least Squares (LLS) are so far one of the most popular methods of statistical analysis of experimental data. The usual way of deriving the formulas estimating the parameters a_0 and a_1 is writing down the expression of the sum of error squares and minimising it:

$$S(a_0, a_1) = \sum_{i=1}^{n}(y_i^{exp} - y_i^{calc})^2 = \sum_{i=1}^{n}(y_i^{exp} - (a_1 x_i + a_0))^2 \quad (8)$$

The condition of a minimum of Equation 8 is equivalent to the condition of partial derivatives of S by a_1 and a_0 being equal to zero:

$$\frac{\partial S}{\partial a_1} = -2\sum_{i=1}^{n} x_i^{exp}\left(y_i^{exp} - a_1 x_i - a_0\right) = 0$$

$$\frac{\partial S}{\partial a_0} = -2\sum_{i=1}^{n}\left(y_i^{exp} - a_1 x_i - a_0\right) = -2n(\bar{y} - a_1\bar{x} - a_0) = 0 \quad (9)$$

Solving for a_0 in the second equation of Equation 9 and substituting it in the first equation, after consequent rearrangement the final equations for a_1 and a_0 can derived:

$$a_1 = \frac{\sum_{i=1}^{n}(y_i - \bar{y})(x_i - \bar{x})}{\sum_{i=1}^{n}(x_i - \bar{x})^2}$$

$$a_0 = \bar{y} - a_1\bar{x} \tag{10}$$

From the standard definition it is unclear why, for example, the cost function must be expressed as a sum of squares of residuals. The reason behind this is that LLS is a method assuming *normal* error distribution. There is an alternative and more general approach to derive the LLS Equation 10 using maximum likelihood estimation (MLE) which explicitly uses error distributions and results in the same formulas for LLS.

Assuming a normal error distribution, we can write that the likelihood (estimated expectation) of an experimental point y^{exp} to correspond to a calculated point y^{calc} with added error value following a normal error distribution is:

$$L\left(y^{calc}, \sigma \middle| y^{exp}, x^{exp}\right) = L(a_1, a_0, \sigma | y^{exp}, x^{exp}) = \frac{1}{\sigma\sqrt{2\pi}} \exp\left[-\frac{\left(y^{exp} - y^{calc}\right)^2}{2\sigma^2}\right] =$$

$$\frac{1}{\sigma\sqrt{2\pi}} \exp\left[-\frac{(y^{exp} - a_1 x^{exp} - a_0)^2}{2\sigma^2}\right] \tag{11}$$

If for different points errors are independent, then for *n* points, the total likelihood is expressed as a product of individual likelihoods:

$$L\left(a_1, a_0, \sigma \middle| y_1^{exp}, x_1^{exp}, y_2^{exp}, x_2^{exp}, \ldots y_n^{exp}, x_n^{exp}\right) = \prod_{i=1}^{n} L\left(a_1, a_0, \sigma \middle| y_i^{exp}, x_i^{exp}\right) \tag{12}$$

For the maximum likelihood of a_1 and a_0, partial derivatives of the Equation 12 must be equal to zero; however, is it more convenient to use a logarithm of the likelihood Equation 13:

$$\ln L = \sum_{i=1}^{n}\left[-ln\left(\sigma\sqrt{2\pi}\right) - \frac{(y^{exp} - a_1 x^{exp} - a_0)^2}{2\sigma^2}\right] \tag{13}$$

$$\frac{\partial \ln L}{\partial a_1} = \frac{1}{\sigma^2}\sum_{i=1}^{n} x^{exp}(y^{exp} - a_1 x^{exp} - a_0) = 0$$

$$\frac{\partial \ln L}{\partial a_0} = \frac{1}{\sigma^2}\sum_{i=1}^{n}(y^{exp} - a_1 x^{exp} - a_0) = 0 \tag{14}$$

Equation 14, obtained by partial differentiation of Equation 13 are essentially the same as Equation 9 obtained independently except for a multiplier and they lead to the same working formulas as Equation 10.

The second derivation method explicitly states the implied error distribution of experimental data. It can be proven that only error distributions from so called *exponential family* (normal, Bernoulli, Poisson, chi-squared and some others) give rise to the same Equations 10.

Unfortunately, LLS cannot be effectively used for experimental data with non-normal distributions, such as data with experimental biases.

The most common source of errors in thermochemical measurements can be sample contamination, incomplete reactions, mass losses, kinetic hurdles, undesirable recrystallisation, etc. These kinds of uncertainties add a bias to the data which can be temperature and composition dependent. Since an experimental bias does not follow a normal error distribution, its presence quickly degrades the quality of optimisation predictions.

Although only shown for the case of ordinary least squares with one independent variable *x*, the same can be stated for the case of multivariate linear least squares as well as non-linear least squares and other optimisation methods.

In scientific community, it is usually assumed that the reliability of different data sets must be represented using *group weights*. However, we consider that even the weighted version of LLS cannot handle experimental biases well. To get reliable optimisation results, the optimisation algorithm should work on *unbiased* data, which can only be achieved by careful selection of *target points*.

CHEMAPP™ CALCULATIONS IN EXCEL® USING PYTHON® BINDING

Automated optimisation algorithms need to be able to read/write model parameters in a thermodynamic database, run thermodynamic calculations and read calculated values. Our optimisation process uses ChemApp™ library as a backend (https://gtt-technologies.de). ChemApp™ is preferred to FactSage™ because of much greater flexibility. However, it is harder to set-up and use for an average engineer because ChemApp™ use implies good skills in at least one of programming languages.

To overcome this problem and make ChemApp™ available for a user who is not familiar with programming, we developed a proprietary Excel® application called PyroApp which exports ChemApp™-related functionality together with rich additional functionality for optimisation purposes in form of ordinary Excel® functions.

From the programming point of view, there are three layers in PyroApp structure. In the lowest layer, a ChemApp™ library is hooked up to Python® environment using a foreign function interface (FFI) implemented in a third-party library called *ctypes*. Since the library version and name are not hard coded into the program during compilation, it is possible to customise ChemApp™ library selection and even load several copies of the same ChemApp™ library into a process memory for multithreaded calculations. The lowest layer library is called chemapp™ (not to confuse with a similar library from Ex Mente (https://ex-mente.com)). It exports all native calling routines from the original ChemApp™ documentation into Python® environment and also provides useful object-oriented abstractions, such as Component, Phase, Constituent and other classes. An analogous Python® library from Ex Mente has similar functionality, however, we use our own implementation which can be freely modified for our purposes.

The second layer Python® library is called *pyroapp* and it contains a rich collection of functions grouped according to their functionality. A non-exhaustive list of main functions is given in Table 2.

The life cycle of an Excel® function is different from a function life cycle in C++ or Python®.

First, it is impossible to make Excel® function execute in a particular order because of the way cell update mechanism in Excel® works. Also, it is impossible to pass any non-primitive parameters as function arguments (objects, structures, unions). Each Excel® function call must be self-contained: if ChemApp™ library is called, the whole cycle of initialisation, loading datafile into memory and execution of useful routines must be performed before the function returns. To comply with this requirement, every function in Table 2, starting with *ca_* prefix takes a datafile name as its first argument. To avoid repetitive datafile loading, similar operations should be organised into tables which are passed as an array input to a function, so ChemApp™ initialisation and datafile reading is done only once. Consequently, such a function usually outputs an array of results. For convenience, it is preferrable to work with dynamic Excel® arrays with variable length instead of the old-fashioned Ctrl + Shift + Enter fixed-size arrays. They have been first introduced into MS Office 365 and have a special syntax for cell addresses like A1# or A1#.

Second, Excel® runtime manages calls to Excel® functions in an automated way. Inside Excel®, cells with functions are mapped into a tree-like structure which keeps track of cell changes. If any cell in Excel® is updated, the runtime mechanism checks if this cell has dependencies and updates them if needed. This mechanism does not allow a user-defined function execution. Since PyroApp functions work with external objects (thermodynamic datafiles), Excel® runtime is not able to track down any changes that happen there. To enforce a proper update mechanism, most of ca_ functions have an optional last argument caller a *trigger*. A trigger can point to any cell or cell range and there are no restrictions on what values they contain. The only function of a trigger cell is to initiate function execution by changing its content to another arbitrary value. Properly set-up trigger cells allow a user to update thermodynamic calculations after model parameters have been updated in a datafile.

The third layer of PyroApp is Excel® binding created using third-party xlwings module. This module works both as an Excel® add-in and a Python® library. It creates a glue VBA code which allows to run Python® environment as a server and imports marked Python® functions as Excel® functions. Each Excel® book with activated PyroApp has a configuration sheet called xlwings.conf with settings for both xlwings (Python® installation and executable, imported Python® modules) and for PyroApp.

TABLE 2

Main functionality groups of PyroApp application.

Function group	Functions	Purpose
info	*ca_version*, *ca_islite*, *ca_dimensions_max*, *ca_user_id*, etc.	Functions related to retrieving general information from a ChemApp™ library: version, calculation size limitations, licence and dongle info, etc.
opt	*condition_number*, *linear_regression*, *best_combination*, *target_scores*, *pd_error_table*, etc.	Functions for Jacobian of experimental targets (JET) optimisation and analysis of a derivative matrix; also functions for custom pivot tables and residual mean squares (RMS) summaries
tdcalc	*ca_list_*... (*components*, *phases*, *solutions*, *compounds*, *species*) *ca_get_*... (*constituent_H298*, *constituent_S298*, *constituent_Cp*, *compound_H298*, *compound_S298*, *compound_Cp*, *interaction_parameters_g*, *interaction_parameters_m*), *ca_set_*... (the same as above), *ca_list_interactions* *ca_calculate*	The majority of ChemApp™ functionality, routines for reading and writing to open text datafiles and thermodynamic calculations adapted to the Excel® environment
utils	*data_change_basis*, *data_generate_mesh*, etc.	Utility functions which help generate multicomponent composition meshes and transform compositions from one chemical formula basis to another
factsage™	*factsage™_get_compound_H298*, *factsage™_get_compound_S298*, *factsage™_set_compound_H298*, *factsage™_set_compound_S298*, *factsage™_write_parameters*, etc.	Utility functions to write final optimised parameters to either a FactSage™ compound database or FactSage™ solution database

One of the remarkable options in PyroApp settings is the possibility to split a table calculation between a few copies of ChemApp™ library running concurrently in different threads. At optimal conditions, it can raise CPU occupancy up to 100 per cent compared to 15–20 per cent for a single threaded ChemApp™ or FactSage™. Modern operating systems kernels are capable of loading several copies of the same binary library into the computer memory. Usually, read-only code-containing parts (also called text sections) are loaded once for all processes and threads to lower memory usage while sections reserved for data (program variables etc) are loaded separately for each user process/thread.

In PyroApp, multithreading is done strictly inside the Python® code and for Excel® functions work the same way as if they were single threaded. Currently, PyroApp has a very simple dispatch mechanism which splits a calculation table into equal parts according to the number of threads indicated in xlwings.conf sheet. Possibly a more advanced mechanism with a task queue will be implemented in future to handle cases when some threads exit earlier and remain idle.

The main function which performs Gibbs Energy Minimization (GEM) calculations, called *ca_calculate*, requires special attention. A lot of thought and effort were spent to fit miscellaneous ChemApp™ calculations under the same hood and develop a unified set of function arguments for all of them.

Broadly, ChemApp™ calculations can be split into normal calculations and stream calculations. Stream calculations allow to pre-calculate some properties of input mass flows to use them later to output property differences. In Excel®, the same effect can be achieved by joining an output of one calculation to the input of another, so stream calculations have been deliberately left out in the Excel® interface, although it is still possible to use them in the lower level chemapp™ library.

Each ca_calculate call has four obligatory and two optional arguments. The obligatory arguments are *datafile* (absolute or relative path to a datafile), *input_header*, *input_values* and *output_header*. The optional arguments are *entered* (indicates default phase selection for the whole table, can be overridden by table entries) and *update_token*, whose purpose was explained earlier.

Input header is a 3xn cell array indicating n input conditions used for calculation. The first cell of a condition entry indicates its type. All native condition types from *tqsetc* routine of ChemApp™ are accepted; there are also multiple custom types, such as FORMATION (name of formation target phase), PRECIPITATION (name of a precipitation target phase), ENTERED, DORMANT, ELIMINATED (custom phase selection for each calculation in a table), THIGH, TLOW (values passed to *tqclim* function), etc. The second cell of a condition entry can contain a phase name, the third cell can contain a constituent/component name, if applicable.

Input_values is a table of different values of conditions defined in *input_header*. *Output_header* is a 3xm cell array with a structure similar to that of *input_header*. It accepts all native ChemApp™ output options for *tqgetr* routine and has custom-defined output options as well. It is worth noting that *ca_calculate* function can output calculated bond fractions for quasichemical models, a feature which, to the best of our knowledge, is missing from Equilib module of FactSage™ package. To output a bond fraction, BOND option is used together with a name of the phase and the name of the quadruplet (for example, Ca,Si//O,O).

DERIVATIVE MATRIX SET-UP FOR JET OPTIMISATION

A few things are required to calculate a matrix of first-order derivatives of target values by model parameters: First, corresponding *ca_get_* and *ca_set_* functions must be set-up with all variable parameters in one column; second, thermodynamic calculations have to be set-up as well with all calculated target values in one column. A derivative matrix is calculated by a special macro code called *derivative_matrix* which can be either called directly from Excel® as a VBA macro or from command line Python® environment (for example, ipython). The latter option is more convenient because it allows to track calculation progress for large calculations. A macro call is initialised with settings stored in the upper left corner of the sheet used for matrix calculations. It requires range addresses of model parameters, parameter steps, a residual vector, upper left coordinate for matrix output, a trigger cell to initiate recalculations as well as a binary mask to turn on/off recalculation of derivatives for certain parameters.

Once a derivative matrix is calculated, it can be used for multiple purposes. There is a PyroApp function called *linear_regression* which manages finding an optimal solution for model parameters based on a precalculated derivative matrix. As arguments, this function takes a matrix of derivatives, a vector of differences between target values and calculated values, a vector of combined weights (on/off target masks + group and individual weights), a binary array indicating which parameters are allowed to change and an array of manual increments for parameters. The output parameters (expressed as deltas and not absolute values) are multiplied by the derivative matrix using MMULT Excel® function and added to the vector of calculated target values.

The resulting vector is called a vector of predicted target values; predicted target values are then plotted and/or used in statistical analysis. This set-up allows to observe changes in predicted target values caused by changes in model parameters in a real-time mode. Arguments to *linear_regression* function are flexible and allow both manual experimenting with parameter selection as well as automatic solution within a chosen subset of parameters. If a suitable combination of parameters

has been found, the parameter deltas are added to the initial parameters for the datafile and everything is recalculated again. Non-linearity might cause slight disagreements between previously predicted and current calculated values. However, the cycle can be repeated one to two times until predicted deltas reach negligible values. Real time updates are indispensable for fine tuning of model behaviour across large data sets using target weights and selection/deselection of specific model parameters; it is a unique feature of JET optimisation. In conventional optimisers, the final result is not known until a complete cycle of iterations is performed and fine-tuning with those optimisers is not an easy task.

If the initial parameter set was far from optimal, the derivative matrix should be recalculated for consequent model refinement. In this case, JET is used similarly to conventional non-linear solvers. The number of matrix recalculations is usually not large, three to four times are enough to optimise a system from scratch. It is worth noting that if an initial estimate was close enough to the desired values in target points, the same derivative matrix allows to have significant changes in parameters if in total they do not result in large changes in target values. For example, parameters with certain powers can be replaced with parameters with other powers, which can prove to be very convenient.

For most of the systems in the 20-component database, a continuous refining is needed to keep the model updated with new experimental data coming in. Usually, the number of parameters and their powers are kept the same. Currently, it is possible to calculate matrices for many target points and a large number of components (five to six). Parameters for a subsystem can be change consistently with data sets for multicomponent system to ensure that the overall prediction quality does not deteriorate.

For a fewer number of newly investigated systems, an optimisation from scratch is required. If in the absence of model parameters some target values cannot be calculated (a phase is not stable etc), a very rough manual fit with two to three parameters for a binary or one to two parameters for a ternary system is required. For convenience, it can be done using FactSage™ Phase Diagram module. Once all target values can be calculated without errors, the quality of the initial estimate is not important (it is fine even if formation targets are 300–500°C off). In the first round, parameter selection is activated only for the existing non-zero parameters to further refine the system within the initial parameter set. Once a couple of iterations have passed, more parameters with different powers can be included. Usually, datafiles are created with many zero-valued parameters of different powers to avoid changing formulas; a zero-valued parameter is equivalent to not having the parameter at all. It is recommended to add parameters one by one; there is a special function of PyroApp, called *best_combination* which highlights a parameter which reduces the total cost function the most. Since regression with a calculated matrix is non-iterative, different parameters can be ranked quite fast. This method has recommended itself in course of many optimisations.

CONCLUSIONS

The current paper explains the principles of the continuous optimisation methodology, suitable for hybrid experimental and modelling development of a large multicomponent database. One of the key points of the continuous optimisation methodology is the use of target points instead of raw experimental data which allow to denoise input to an optimisation algorithm and make possible transparent automated assessment of optimisation quality of multiple subsystems across a database. Benefits and drawbacks of different optimisation algorithms are discussed. It is shown that thermodynamic calculations in optimisation process can be set-up in a way that first-order derivatives of target values by model parameters always exist.

The paper also explains the principles of using a first-order derivative matrix (jacobian) for real-time parameter sensitivity analysis and JET (Jacobian of Experimental Targets) optimisation. The main functionality of a proprietary application for Excel® with ChemApp™ backend, called PyroApp, is demonstrated together with data set-up and optimisation procedure.

REFERENCES

Eriksson, G and Pelton, A D, 1993. Critical Evaluation and Optimisation of the Thermodynamic Properties of the CaO-Al_2O_3, Al_2O_3-SiO_2, and CaO-Al_2O_3-SiO_2 Systems, *Metallurgy Transactions*, 24:807–816.

Hillert, M, 2001. The Compound Energy Formalism, *Journal of Alloys and Compounds*, 320(2):161–176.

Katoch, S, Chauhan, S S and Kumar, V, 2020. A review on genetic algorithm: past, present, and future, *Multimedia Tools and Applications*, 80:8091–8126.

Kolda, T G, Lewis, R M and Torczon, V, 2003. Optimisation by Direct Search: New Perspectives on Some Classical and Modern Methods, *SIAM Review*, 45(3):385–482.

Llovet, X, Moy, A, Pinard, P T and Fournelle, J H, 2021. Electron probe microanalysis: A review of recent developments and applications in materials science and engineering, *Progress in Materials Science*, 116:100673.

Pelton, A D, Decterov, S A, Eriksson, G, Robelin, C and Dessureault, Y, 2000. The Modified Quasichemical Model. I – Binary Solutions, *Metallurgical and Materials Transactions B*, 31(4):651–659.

Nekhoroshev, E, Shevchenko, M, Cheng, S, Shishin, D and, Jak, E, *in preparation*. Third generation CALPHAD re-optimisation of the CaO-SiO_2 system integrated with experimental phase equilibria studies, *Journal of Ceramics International*.

Thermodynamic modelling of the Fe-Al-Ti-O system and evolution of Al-Ti complex inclusions during Ti-added ultra-low carbon steel production

DOI: 10.62053/FWLU4527
Y-J Park[1] and Y-B Kang[2]

1. PhD candidate, Pohang University of Science and Technology, Pohang, Gyeongbuk 37673, Republic of Korea. Email: yjpark92@postech.ac.kr
2. Professor, Pohang University of Science and Technology, Pohang, Gyeongbuk 37673, Republic of Korea. Email: ybkang@postech.ac.kr

ABSTRACT

Ti-added ultra-low carbon (ULC) steel is produced by adding Al and Ti during the secondary refining process to deoxidise molten steel and to bind C and N which are detrimental to the deep drawing quality of the steel product. However, the production of Ti-added ULC steel faces challenges, including submerged entry nozzle clogging and surface defects on cold rolled coils. The troubles were often attributed to 'Al-Ti complex inclusions' in the molten steel. However, the evolution of oxide inclusions including their stability has been still unclear. In the present study, the evolution of these inclusions in Ti-added ULC steel was investigated by phase diagram measurement, CALPHAD thermodynamic modelling, high-temperature stability test for the oxides, and observation of transient behaviour of oxide inclusions in the steel. The phase diagram of the Al-Ti-O system was elucidated with an emphasis on oxygen potential, which significantly controls the stability of the oxides. CALPHAD thermodynamic models and a self-consistent database were developed. The transient behaviour of Al-Ti complex inclusions in Ti-added ULC steel was observed *in situ* using a confocal scanning laser microscope. This was additionally validated by the new thermodynamic model. The equilibrium phases of the oxide inclusions were investigated using a high-temperature resistance furnace, and were analysed using a secondary electron microscope, energy dispersive spectrometer, and electron back-scattered diffraction. By considering the morphology and crystal structure of these inclusions, the evolution of Al-Ti oxide inclusions was elucidated. Various behaviour of Al-Ti inclusions and their influence on steel cleanliness are discussed.

INTRODUCTION

Interstitial-free (IF) steel, also known as ultra-low carbon (ULC) steel, is widely used in automotive outer panels due to its excellent deep drawing quality (DDQ). In order to further enhance the DDQ, IF steel requires minimising interstitial elements such as C and N to the utmost extent. In particular, Ti is one of the most commonly used elements for improving the properties of IF steel. The addition of Ti has several beneficial effects, such as an increase in the plastic strain ratio (*r*-value), a decrease in the recrystallisation temperature, and reduced sensitivity to coiling temperatures (Gupta and Bhattacharya, 1989; Fukuda, 1973). As a result, the demand and supply of Ti-added ULC steel have been consistently increasing due to its excellent performance in maximising DDQ properties.

During the production of Ti-added ULC steel, the steel undergoes deoxidation in the RH (Ruhrstahl-Heraeus) process by adding Al: $2\underline{Al} + 3\underline{O} = Al_2O_3(s)$. Subsequently, Ti is added as Ti sponge or ferro-Ti alloy to achieve the target composition. While Ti-free ULC steel only considers Al_2O_3 oxide as the non-metallic inclusion, in the case of Ti-added ULC steel, Ti may also react with dissolved O. This could happen if the Al deoxidation was not enough to kill the O or reoxidation occurs during the secondary refining or continuous casting processes. This may induce Ti-containing inclusions and further, Al-Ti complex inclusions. It has been reported that Ti-added ULC steel encounters more severe submerged entry nozzle (SEN) clogging during continuous casting, compared Ti-free ULC steel (Basu, Choudhary and Girase*,* 2004; Cui *et al,* 2010; Lee *et al,* 2019). The accumulation of clogging deposits becomes more significant with increasing Ti content, resulting in poor productivity (Dorrer *et al,* 2019; Bernhard *et al,* 2019).

The origin of the severe SEN clogging due to Ti addition includes refractory-steel reaction, reoxidation from various sources (air aspiration, Ar gas quality, refractory carbothermic reaction etc), enhanced wettability, etc. In addition to this, the evolution of inclusions by Ti addition may play a significant role, however, the phase stability of Al-Ti complex inclusions is yet to be understood

clearly. Frequently mentioned oxide phase as the Al-Ti complex inclusion has been 'Al_2TiO_5' and there have been cases where Al_2TiO_5 was observed in Ti-added ULC steel melts (Wang, Nuhfer and Sridhar, 2009; Bai, Sun and Zhang, 2019). Several oxide stability diagrams of the Fe-Al-Ti-O system predicted by thermodynamic calculation included Al_2TiO_5, as a probable equilibrium phase in molten steel. However, there has been an experimental result showing the instability of Al_2TiO_5 in Ti-added ULC steel melts (Jo, 2011). Although the oxide stability diagram has been used to understand the inclusion evolution, published diagrams do not agree with each other and do not support experimental results on inclusion evolution. Therefore, the oxide stability of the Al-Ti complex inclusions has been a long-standing debate.

This is because the phase equilibria of the Fe-Al-Ti-O oxide system have not been fully investigated. The present authors recently carried out an experimental study on the phase equilibria in the Al-Ti-O system with an emphasis on the impact of oxygen partial pressure (Park, Kim and Kang, 2021). Al_2TiO_5, which was shown to form a pseudobrookite solid solution with Ti_3O_5 should decompose under low oxygen partial pressure relevant to the molten steel during the secondary refining process. This indicates that it is no longer a stoichiometric oxide. The decomposition behaviour of Al_2TiO_5 may provide insights into the understanding of inclusion evolution in Ti-added ULC steel. However, for further application to Ti-added ULC steel, it is necessary to complete the modelling of the Fe-Al-Ti-O system, including both molten metal and several oxide phases in the system, in order to study the behaviour of complex inclusions in molten steel.

In the present study, thermodynamic modelling of the Fe-Al-Ti-O system was carried out to evaluate the stability of Al-Ti complex inclusions in Fe-Al-Ti-O melts. The evolution of Al-Ti complex inclusions in Ti-added ULC steel was also investigated using various methodologies including Scanning-Electron Microscopy with Energy-Dispersive X-ray Spectroscopy (SEM-EDS), Electron Back-Scattered Diffraction (EBSD), and Confocal Scanning Laser Microscopy (CSLM).

THERMODYNAMIC MODELLING OF THE FE-AL-TI-O SYSTEM

Thermodynamic calculations and optimisation for the Fe-Al-Ti-O system were conducted using FactSage™ thermodynamic software (Bale *et al,* 2016). The Gibbs energies of pure substances were sourced from the SGTE compilation of Dinsdale (1991). The Fe-Al-Ti-O system was modelled by considering solution phases such as liquid alloy, liquid oxide, pseudobrookite, cubic spinel, ilmenite, rutile, monoxide, some metallic solutions, and stoichiometric compounds. The modelling assessed various sub-binary systems and extended to multi-component systems to cover the entire subsystem of the Fe-Al-Ti-O system. In certain instances, model parameters were adjusted slightly to meet the requirements of the phase diagrams and thermodynamic properties of solutions. Details of the models and parameter optimisation can be found elsewhere (Park and Kang, 2024).

Thermodynamic models

Liquid metal and liquid oxide

The Modified Quasichemical Model (Pelton *et al,* 2000; Pelton and Chartrand, 2001) was employed in modelling the liquid metal and the liquid oxide separately, aiming to consider short-range ordering (SRO) observed in the liquid solutions across a broader concentration range. For example, in the case of liquid metal, components A, B, C,... are distributed over a quasi-lattice as atoms. In the pair approximation, the pair-exchange reaction is considered as:

$$(\mathrm{A}-\mathrm{A})+(\mathrm{B}-\mathrm{B})=2(\mathrm{A}-\mathrm{B})\,\Delta g_{\mathrm{AB}} \quad (1)$$

where (A – A), (B – B), and (A – B) represent first-nearest-neighbour (FNN) pairs. The non-configurational Gibbs energy change for the formation of two moles of (A – B) pairs is Δg_{AB} which is used as a model parameter in each binary system. Gibbs energies of ternary and higher-order systems are then estimated using the appropriate interpolation method (Pelton and Chartrand, 2001), and a few of adjustable ternary model parameters can be added. The Gibbs energy of liquid oxide phase was modelled similarly.

Solid solutions including pseudobrookite, ilmenite, cubic spinel, etc

Solid phases having more than two sublattices such as pseudobrookite ($(Ti,Al,Fe)_3O_5$), cubic spinel ($Fe(Al,Ti)_2O_4$), and ilmenite ($(Ti,Al,Fe)_2O_3$) etc were modelled using the compound energy formalism (CEF) (Hillert, 2001) to described the Gibbs energies of the solutions in the Fe-Al-Ti-O system. For example, the model for the Fe-Al-Ti-O pseudobrookite is described below:

$$(Fe^{2+}, Fe^{3+}, Ti^{3+}, Ti^{4+}, Al^{3+})^{4c}(Fe^{2+}, Fe^{3+}, Ti^{3+}, Ti^{4+}, Al^{3+})^{8f}{}_2O_5 \quad (2)$$

where ions enclosed in parentheses occupy the same octahedral (*4c* and *8f*) sublattice.

The Gibbs energy of the pseudobrookite solution is expressed as:

$$G^m = \sum_i \sum_j Y_i^{4c} Y_j^{8f} G_{ij} - TS^{\text{config}} + G^{\text{excess}} \quad (3)$$

where Y_i^{4c} and Y_j^{8f} represent the site fractions of constituents '*i*' and '*j*' on the *4c* and *8f* octahedral sublattices, respectively; G_{ij} is the Gibbs energy of an 'end member $[i]^{4c}[j]^{8f}{}_2O_5$' in which *4c* and *8f* sites are occupied only by *i* and *j* cations, respectively; S^{config} is the configurational entropy which takes into account random mixing of cations on each sublattice. The Gibbs energies (G_{ij}) of end-members are the primary model parameters.

However, due to the presence of several non-neutral charged end-members, it is not feasible to ascertain the Gibbs energies of all end-members based solely on experimental data. To appropriately determine the values of these Gibbs energies, physically meaningful linear combinations of the end-members' Gibbs energies (G_{ij}) involved in specific site exchange reactions among cations are utilised as parameters in the model.

Taking the example of a Ti_3O_5 pseudobrookite oxide, the measurable Gibbs energy, $G^o(Ti_3O_5)$ (Gibbs energy of pure Ti_3O_5), is directly employed in the CEF modelling. The model parameters also encompass site exchange reactions between cations at the *4c* and *8f* sites, denoted by Δ and *I* parameters. These parameters are crucial in determining the Gibbs energies of end-members. Generally, these exchange energies are expected to be small and are frequently set to zero. This practice allows for a more controlled determination of the Gibbs energies of end-members, as opposed to arbitrary assignments without a rationale. Adopting this approach enhances the predictive capability and stability of the model, particularly for extensive solid solutions like pseudobrookite, ilmenite, and spinel phases.

The Gibbs energies of other solid phases without sublattice was described by a simple Bragg-Williams random mixing model.

Model calculation

Using the reported thermodynamic modelling of subsystems of the Fe-Al-Ti-O system, the present study extended the previous modelling to construct a model database for the Fe-Al-Ti-O system. Through model calculations of the Al-Ti-O oxide system, a definition of Al-Ti complex inclusions has been achieved. Considering the characteristics of Al_2TiO_5, formerly considered as an Al-Ti complex inclusion, the present study aimed to interpret the evolution and decomposition behaviours of Al-Ti complex inclusions under various oxygen pressure conditions (see section on 'Al-Ti-O oxide phase diagram at 1600°C').

Additionally, deoxidation equilibria in Ti-added ULC steel were described by modelling the deoxidation equilibria by Al and by Ti. While the previous research conducted by Paek *et al* (2016), using MQM for the liquid metal phase was adopted, additional modelling of Ti-deoxidation equilibria was performed using MQM to provide a more refined interpretation of equilibrium relationships in Ti-added ULC steel production (see section on 'Ti deoxidation equilibria at 1600°C').

At the final stage, the equilibrium [O] contents and corresponding inclusion phases in molten steel at 1600°C were interpreted based on the Al and Ti contents in the liquid steel. Unlike the model calculations investigated previously, the model database optimised in the present study allows for the calculation of not only the oxide phases in equilibrium with ULC liquid steel but also the Fe, Al and Ti solubilities within the oxide phase. This capability is expected to facilitate tracking the generation and transition behaviours of inclusions under reoxidation conditions.

Al-Ti-O oxide phase diagram at 1600°C

The calculated result of the Al-Ti-O_2 phase diagram (PO_2-R_{Ti}) is shown in Figure 1. It should be stressed that there is a wide solid solution encompassing 'Al_2TiO_5' (R_{Ti} = 0.33) and 'Ti_3O_5' (R_{Ti} = 1.0) over a wide range of PO_2 (1–10^{-14} atm), according to the present authors' experimental investigation (Park, Kim and Kang, 2021). These two oxides have the same crystal structure, therefore, these were treated in a single solid solution (pseudobrookite s.s.). However, this solid solution separates into two phases at lower temperatures (T < 1500°C), which was first revealed by the present authors (Park, Kim and Kang, 2021). This kind of phase equilibrium has not been known previously. According to this phase equilibria, Al_2TiO_5 should undergo the following phase transformation at lower PO_2 relevant to the steel refining process:

$$Al_2TiO_5 \text{ (at high } PO_2) \rightarrow (Ti,_{Al})_3O_5 + Al_2O_3 + O_2 \text{ (at low } PO_2) \quad (4)$$

where 'Al_2TiO_5 (at high PO_2)' and '$(Ti,_{Al})_3O_5$' represent Al-rich pseudobrookite s.s. and Ti-rich pseudobrookite s.s., respectively. This reaction would represent a situation that Al-Ti complex inclusions (near Al_2TiO_5) generated at high oxygen potential due to reoxidation in Ti-added ULC steel could generate Ti-rich oxide inclusion, Al_2O_3, and the additional O in the liquid steel. This suggests that the oxide inclusion reoxidised in Ti-added ULC steel may play as an O-carrier in the liquid steel.

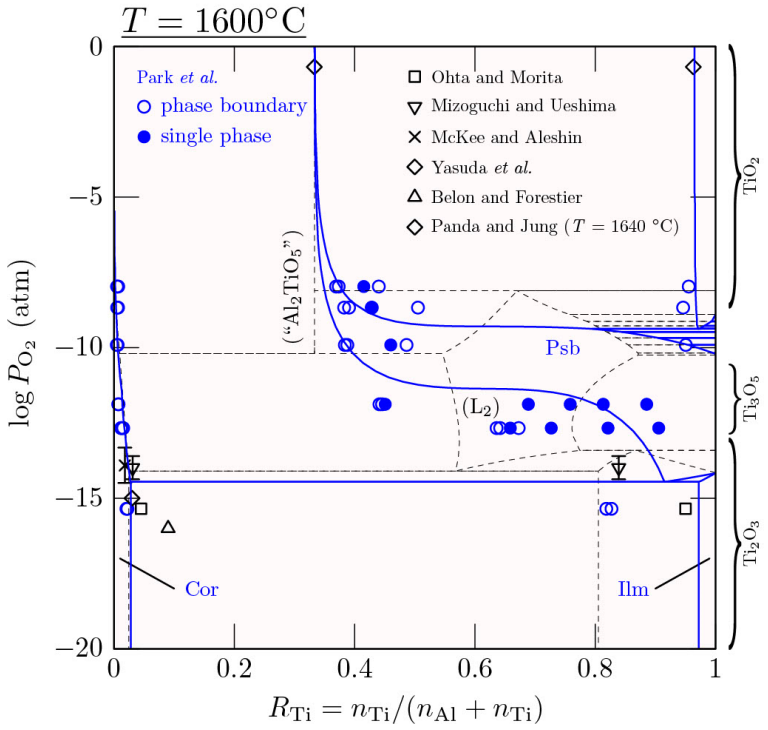

FIG 1 – Calculated phase diagram of the Al-Ti-O_2 system at 1600°C (Park and Kang, 2024). Blue solid lines were calculated using the present thermodynamic model, and black dotted lines were calculated using FactSage FTOxid database (ver. 8.2). Symbols are the reported experimental data (see Park, Kim and Kang, 2021).

These models were extended to incorporate Fe as a component. Detail modelling results can be found elsewhere (Park and Kang, 2024).

Ti deoxidation equilibria at 1600°C

By combining the existing thermodynamic model of the Fe-Al-O liquid metal, with that of the Fe-Ti-O liquid metal in the present study, the thermodynamic model for the deoxidation equilibria in the Fe-Al-Ti-O liquid metal could be completed. Figure 2 shows the Ti-deoxidation equilibria in the liquid Fe-Ti-O at 1600°C. Long-dashed, full, and short-dashed lines represent the equilibrium compositions of liquid metal in equilibrium with ilmenite, pseudobrookite, and liquid oxide, respectively. The present study describes the Ti-deoxidation equilibria over a wide composition range. The developed

thermodynamic model is now used to predict high-temperature equilibria between Ti-added ULC steel and oxide inclusions.

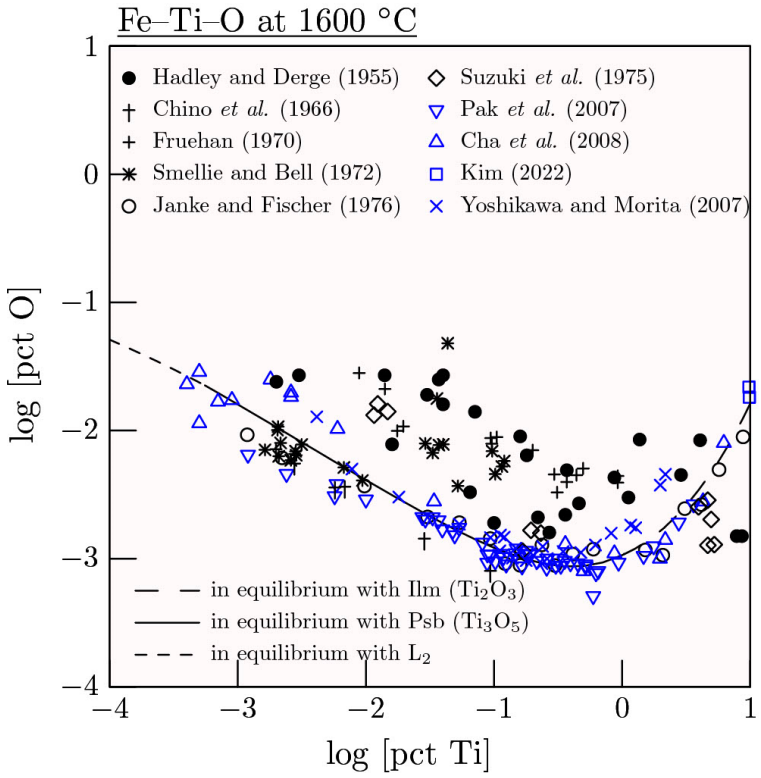

FIG 2 – Ti-deoxidation equilibria in liquid iron at 1600°C (Park and Kang, 2024). Solid lines were calculated using the present thermodynamic model.

Oxide stability diagram of the Fe-Al-Ti-O system

The calculated oxide stability diagram of the Fe-Al-Ti-O system at 1600°C using the thermodynamic models developed in the present study is shown in Figure 3. Thin black solid lines and blue solid lines are the iso-O (ppm) lines, and the phase boundaries between two different oxide phases, respectively. The most probable oxide phase formed during the Ti-added ULC steel production is obviously corundum ($(Al,Ti,Fe)_2O_3$) by typical compositions of this steel grade. Compared to the previous stability diagram by Kang and Lee (2017), the phase boundaries between corundum and pseudobrookite oxide are similar to each other: no separate Al_2TiO_5 phase region is seen. However, the incorporation of Fe in the pseudobrookite s.s. resulted in a somewhat wider stability region of the pseudobrookite s.s. This subsequently resulted in the stability region of the liquid oxide and ilmenite (Ti_2O_3) phases being reduced.

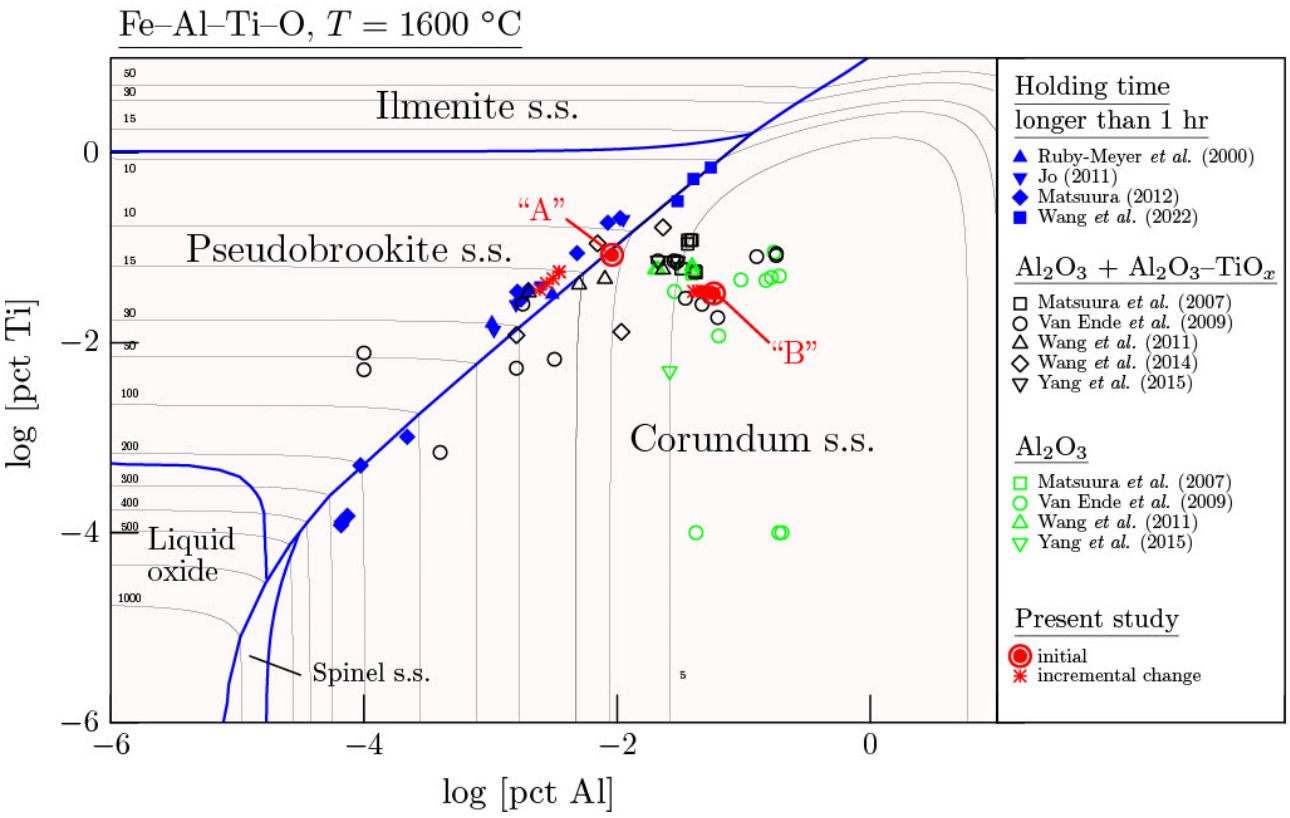

FIG 3 – Calculated oxide stability diagram of the Fe-Al-Ti-O system at 1600°C in the present study, modified from a figure from Park and Kang (2024). Symbols marked by 'A' and 'B' were obtained in the experimental work of the present authors. Other symbols were taken from literature (see Park and Kang, 2024).

EVOLUTION OF AL-TI COMPLEX INCLUSION IN LIQUID STEEL

Through the thermodynamic modelling of the Al-Ti-O system, the decomposition reaction of the Al-Ti complex oxide, as expressed in Reaction 4, was elucidated. Reaction 4 can be extended to the Fe-containing system, the Fe-Al-Ti-O system. In the reaction involving Fe, such as expressed in Reaction 5, the solubility of Fe in the pseudobrookite inclusion and the incorporation of the decomposition product O_2 into the molten steel can contribute to an increase in O contents.

$$(Fe,Al,Ti)_3O_5 \text{ (at high } PO_2) \rightarrow (Ti_{,Al})_3O_5 + Al_2O_3 + \underline{O} + Fe \text{ (at low } PO_2) \quad (5)$$

where '$(Fe,Al,Ti)_3O_5$ (at high PO_2)' represents a reoxidised pseudobrookite s.s. The O generated in Reaction 5 can react with Al and/or Ti in the liquid steel to produce additional inclusions. The Reaction 5 may be manipulated in the reverse order, which may represent the reoxidation of liquid Ti-added ULC steel:

$$Al_2O_3 + Fe + \underline{Ti} + \underline{O} \rightarrow (Fe,Al,Ti)_3O_5 \quad (6)$$

This reversed reaction would result in the formation of Fe-containing pseudobrookite s.s. from alumina inclusions. This scenario was experimentally investigated in the present study by employing CSLM. A Ti-added ULC steel sample that contains Al_2O_3 inclusions and dissolved Ti and O was observed. Figure 4a shows only alumina inclusion. On the other hand, the same steel sample was intentionally but mildly oxidised and the resultant oxide inclusions were shown in Figure 4b. Certainly, shape of the inclusions in the two figures was distinguished. Those in Figure 4b were identified as pseudobrookite phase. Details of the procedure of the experiment and post-analysis are presented elsewhere (Park and Kang, 2024).

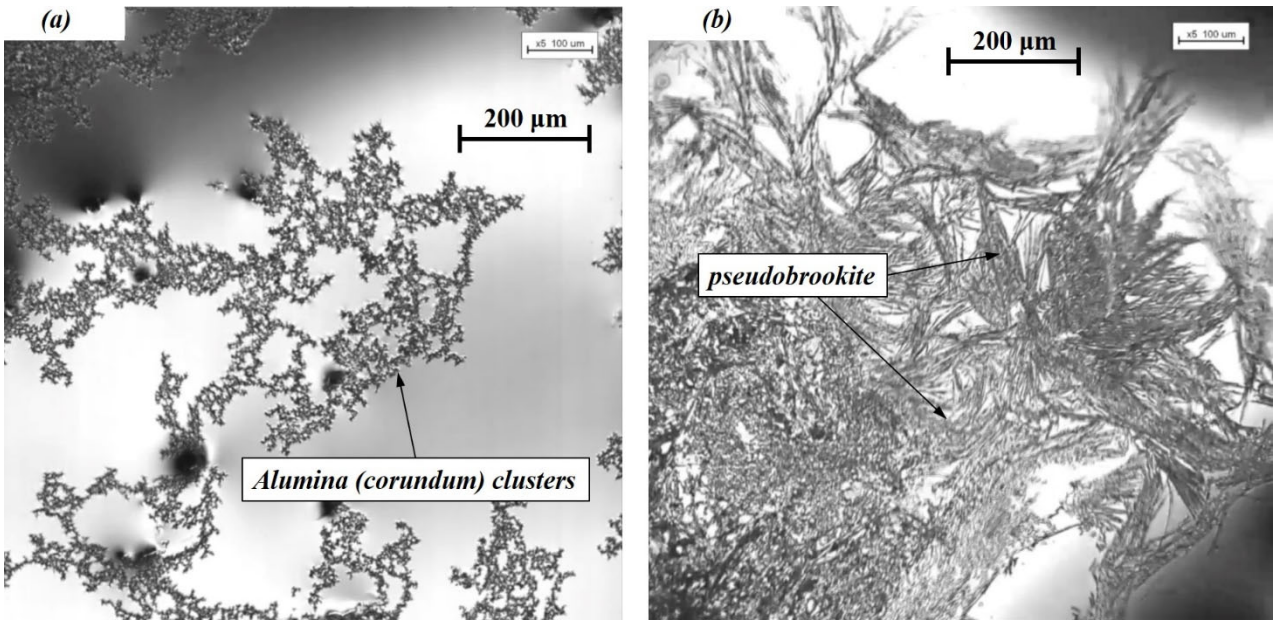

FIG 4 – Inclusions morphologies floating on a Ti-added ULC steel observed by CSLM: (a) without reoxidation and (b) with reoxidation.

The inclusions observed in Figure 4b, whose morphology seems to be a whisker-shape, were analysed using SEM-EDS after cooling the steel sample. The inclusions were composed of Al, Ti, Fe, and O Figure 5. According to the list of phases in the present system and the result of thermodynamic model calculation, this is most likely pseudobrookite phase.

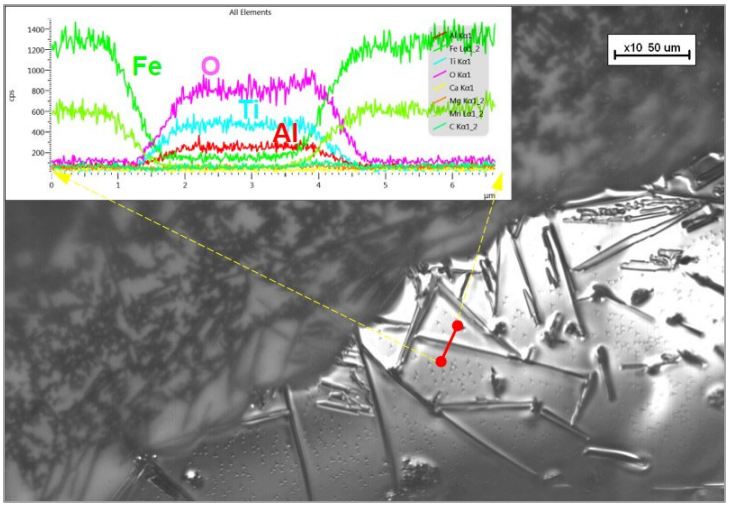

FIG 5 – Post analysis of inclusions seen in Figure 4b using SEM-EDS.

CONCLUSIONS

A self-consistent thermodynamic model of the Fe-Al-Ti-O system was developed, and the evolution of Al-Ti complex inclusions and their transition behaviours were investigated using various experimental techniques. It was shown that the Al-Ti complex inclusion should be defined as a part of pseudobrookite s.s. instead of the stoichiometric 'Al_2TiO_5', which is not stable in liquid steel. The predicted transition behaviours of the Al-Ti complex inclusions were postulated, and it was demonstrated that the complex inclusions can act as a reoxidation source, potentially deteriorating steel cleanliness.

REFERENCES

Bai, X-F, Sun, Y and Zhang, Y, 2019. Transient evolution of inclusions during Al and Ti additions in Fe-20 Mass pct Cr alloy, *Metals*, 9(6):702. https://doi.org/10.3390/met9060702

Bale, C W, Bélisle, E, Chartrand, P, Decterov, S A, Eriksson, G, Gheribi, A E, Hack, K, Jung, I-H, Kang, Y-B, Melançon, J, Pelton, A D, Petersen, S, Robelin, C, Sangster, J, Spencer, P and Van Ende, M-A, 2016. FactSage Thermochemical Software and Databases, 2010–2016, *CALPHAD*, 54:35–53. https://doi.org/10.1016/j.calphad.2016.05.002

Basu, S, Choudhary, S K and Girase, N U, 2004. Nozzle clogging behaviour of Ti-bearing Al-killed ultra low carbon steel, *ISIJ International*, 44(10):1653–1660. https://doi.org/10.2355/isijinternational.44.1653

Bernhard, C, Dorrer, P, Michelic, S K and Rössler, R, 2019. The role of FeTi addition to micro-inclusions in the production of ULC steel grades via the RH Process route, *BHM Berg-Und Hüttenmännische Monatshefte*, 164(11):475–478. https://doi.org/10.1007/s00501-019-00900-2

Cui, H, Bao, Y, Wang, M and Wu, W, 2010. Clogging behavior of submerged entry nozzles for Ti-bearing IF steel, *International Journal of Minerals, Metallurgy and Materials*, 17(2):154–158. https://doi.org/10.1007/s12613-010-0206-y

Dinsdale, A T, 1991. SGTE data for pure elements, *CALPHAD*, 15(4):317–425. https://doi.org/10.1016/0364-5916(91)90030-n

Dorrer, P, Michelic, S K, Bernhard, C, Penz, A and Rössler, R, 2019. Study on the influence of FeTi-addition on the inclusion population in Ti-stabilized ULC steels and its consequences for SEN-clogging, *Steel Research International*, 90(7). https://doi.org/10.1002/srin.201800635

Fukuda, N, 1973. Manufacture of Ti-stabilized extra low carbon steel for deep drawing quality, *Tetsu-to-Hagane*, 59(2):231–240.

Gupta, I and D, Bhattacharya. 1989. Metallurgy of formable vacuum degassed interstitial-free steels.

Hillert, M, 2001. The compound energy formalism, *Journal of Alloys and Compounds*, 320(2):161–176. https://doi.org/10.1016/s0925-8388(00)01481-x

Jo, J O, 2011. Thermodynamics of Titanium and Aluminum in Liquid Alloy Steel, PhD dissertation, Hanyang University.

Kang, Y-B and Lee, J-H, 2017. Reassessment of oxide stability diagram in the Fe–Al–Ti–O system, *ISIJ International*, 57(9):1665–1667. https://doi.org/10.2355/isijinternational.isijint-2017-182

Lee, J, Kang, M, Kim, S, Kim, J, Kim, M and Kang, Y, 2019. Influence of Al/Ti ratio in Ti-ULC steel and refractory components of submerged entry nozzle on formation of clogging deposits, *ISIJ International*, 59(5):749–758. https://doi.org/10.2355/isijinternational.isijint-2018-672

Paek, M, Jang, J, Pak, J and Kang, Y-B, 2015. Aluminum Deoxidation Equilibria in liquid iron: Part, I, Experimental, *Metallurgical and Materials Transactions B, Process Metallurgy and Materials Processing Science*, 46(4):1826–1836. https://doi.org/10.1007/s11663-015-0368-0

Paek, M, Pak, J and Kang, Y-B, 2015. Aluminum deoxidation equilibria in liquid iron: Part II, Thermodynamic Modeling, *Metallurgical and Materials Transactions B-process Metallurgy and Materials Processing Science*, 46(5):2224–2233. https://doi.org/10.1007/s11663-015-0369-z

Park, Y-J and Kang, Y-B, 2024. Evolution of Al–Ti Complex Oxide Inclusions in Interstitial-Free Steel Analyzed Using CALPHAD, SEM, EDS, EBSD and CSLM, submitted to *Metall Mater Trans B*.

Park, Y-J, Kim, W-Y and Kang, Y-B, 2021. Phase equilibria of Al_2O_3–TiO_x system under various oxygen partial pressure: Emphasis on stability of Al_2TiO_5–Ti_3O_5 pseudobrookite solid solution, *Journal of the European Ceramic Society*, 41(14):7362–7374. https://doi.org/10.1016/j.jeurceramsoc.2021.06.052

Pelton, A D and Chartrand, P, 2001. The modified quasi-chemical model: Part II, Multicomponent solutions, *Metallurgical and Materials Transactions A*, 32(6):1355–1360. https://doi.org/10.1007/s11661-001-0226-3

Pelton, A D, Degterov, S A, Eriksson, G, Robelin, C and Dessureault, Y, 2000. The modified quasichemical model I—Binary solutions, *Metallurgical and Materials Transactions B-process Metallurgy and Materials Processing Science*, 31(4):651–659. https://doi.org/10.1007/s11663-000-0103-2

Wang, C, Nuhfer, N T and Sridhar, S, 2009. Transient behavior of inclusion chemistry, shape and structure in Fe-Al-Ti-O melts: effect of titanium source and laboratory deoxidation simulation, *Metallurgical and Materials Transactions B-process Metallurgy Materials Processing Science*, 40(6):1005–1021. https://doi.org/10.1007/s11663-009-9267-6

Sulfur distribution ratio in iron and steelmaking slags

DOI: 10.62053/OSYH4816

R G Reddy[1] and A Yahya[2]

1. Professor, The University of Alabama, Tuscaloosa, 35487 Alabama, USA.
   Email: rreddy@eng.ua.edu
2. Graduate student, The University of Alabama, Tuscaloosa, 35487 Alabama, USA.
   Email: ayahya@crimson.ua.edu

ABSTRACT

The sulfur distribution ratio (Ls) is an expression of the amount of sulfur in slag to the amount of sulfur in molten metal. The sulfide capacities calculated from Reddy-Blander (RB) model were used to calculate the sulfur distribution ratio (Ls). A new Reddy model for sulfur distribution ratio (Ls) was developed for modelling Ls for ironmaking, steelmaking, and secondary steelmaking conditions. Besides calcium oxide, the major component in the ladle furnace (LF) slags is alumina. The Ls was calculated for typical LF slags as a function of temperature and composition. The model calculated Ls values are in good agreement with the experimental and industrial slags data. The extremely low oxygen potential in these furnaces after fully-killed steel is favourable for desulfurisation.

For any given slag's composition and temperature, its sulfide capacity can be calculated *a priori*. The equilibrium sulfur distribution ratio between this slag and liquid metal in a particular vessel can also be calculated *a priori*. The Ls for ladle furnace (LF) slags is about twice those for blast furnaces (BF) slags and ten times those of basic oxygen furnace (BOF) slags. The desulfurisation of pig iron in BF and desulfurisation of steel in LF during secondary steelmaking are recommended. Steel desulfurisation in steelmaking furnaces is not effective. Since the model used to calculate the sulfur distribution ratio (Ls) is *a priori*, it is a useful tool for the iron and steel makers in improving the product quality and optimisation of the industrial furnace operations.

INTRODUCTION

The sulfur distribution ratio (Ls) can be expressed as the amount of sulfur in slag to the amount of sulfur in molten metal. Sulfide capacity is of crucial importance to iron and steelmakers who are continuously trying to improve product quality. Sulfur drastically decreases the ductility and strength of steel, and it is undesirable except for free-cutting steels. Sulfur also causes hot-shortness and helps propagate hydrogen-induced cracks. In certain grades of clean steel, eg armour plates, plates for offshore oil installations and pipelines, the sulfur content should be less than 20 ppm (0.002 wt per cent S) to prevent hydrogen-induced cracking. The sulfide capacities calculated from the Reddy-Blander (RB) model were used to calculate the sulfur distribution ratio.

Reddy-Blander (RB) model for sulfide capacity

Reddy and Blander (RB) developed a model (Reddy and Blander, 1987, 1989; Chen, Reddy and Blander, 1989; Reddy, Hu and Blander, 1992; Reddy, 2003b), for calculating sulfide capacities of binary and multicomponent aluminate and silicate slags. They showed that sulfide capacities could be calculated *a priori* based on the knowledge of the chemical and solution properties of oxides and sulfides. In another publication, Zhao and Reddy (1995) extended the model to binary aluminate melts. Derin, Yucel and Reddy (2010) applied the model to ternary silicate melts containing FeO. RB model was extended to other slag systems, titania slags (Derin, Yucel and Reddy, 2004), lead industrial slags (Derin, Yucel and Reddy, 2005, 2006), multicomponent aluminosilicates (Yahya and Reddy, 2011; Pelton, Eriksson and Romero-Serrano, 1993) and phosphates (Yang *et al*, 2014; Pelton, 2000) and sulfates (Pelton, 1999), arsenates (Reddy and Font, 2003), antimonate (Font and Reddy, 2005), and prediction of sulfur and oxygen partial pressures in copper flash smelting slags (Derin and Reddy, 2003). In all systems, excellent agreement between the model and experimental data was observed. The RB model calculated the sulfide capacities of binary, ternary and higher order aluminate slags of the system CaO-FeO-MgO-MnO-Al_2O_3-SiO_2. In this work, the RB model predicted sulfide capacities were incorporated in developing a new Reddy model for sulfur distribution ratios in iron and steelmaking slags.

Basic oxides like CaO, FeO, MgO and MnO dissociate into cations and oxygen ions and on the other hand, acidic oxides such as SiO_2 and Al_2O_3 consume oxygen ions and form complex silicate and aluminate ions. Using CaO-$AlO_{1.5}$ as an example, the binary system is divided into two regions; one basic and one acidic. The model equations used to calculate the sulfide capacity are:

Basic binary ($0 \le X_{AlO_{1.5}} \le 0.33$)

$$C_S = 100 \bullet M_S \bullet K_{Ca} \bullet a_{CaO} \bullet \left(\frac{1-2X_{AlO_{1.5}}}{\overline{M}}\right) \quad (1)$$

Where M_S is the atomic weight of sulfur and K_{Ca} is the equilibrium constant for the reaction, $a_{Ca}O$ is the activity of the calcium oxide in the binary system, and $\overline{M}$ is the average molecular weight of solution. For a given slag's temperature and composition, K_{Ca} and $a_{Ca}O$ were obtained from thermodynamic data (Bale, Pelton and Thompson, 2002; Gokcen and Reddy, 1996).

Acidic binary ($0.33 \le X_{AlO_{1.5}} < 1$)

Acidic binary ($0.33 \le X_{AlO_{1.5}} \le 0.5$)

Acidic binaries are divided into two regions. For intermediate acidic binary ($0.33 \le X_{Al}O_{1.5} \le 0.5$), the solution is a mixture of polymeric species and monomer ions (Flory, 1953). The model equation for this region is:

$$C_S = 100 \bullet M_S \bullet K_{Ca} \bullet a_{CaO} \bullet exp\left(-1.25\left(1-\frac{1}{m}\right)\right) \bullet \frac{X_{AlO_{1.5}}}{\overline{M}} \quad (2)$$

Where m is the polymer chain length given by:

$$\frac{1}{m} = (1 - a_{CaO}) \bullet \left(\frac{1}{X_{AlO_{1.5}}} - 2\right) \quad (3)$$

Acidic binary ($0.5 \le X_{Al}O_{1.5} < 1$)

For the remaining portion of the acidic binary, the solution is mostly polymeric. The model equation for this region is:

$$C_S = 100 \bullet M_S \bullet K_{Ca} \bullet a_{CaO} \bullet exp(-1.25) \bullet \frac{X_{AlO_{1.5}}}{\overline{M}} \quad (4)$$

The most complicated multicomponent system investigated in this work has six components. In this system, four oxides are basic; CaO, FeO, MgO and MnO, while two oxides are acidic; SiO_2 and Al_2O_3. To calculate the sulfide capacity of this system, it is broken down into four ternaries: CaO-SiO_2-Al_2O_3, FeO-SiO_2-Al_2O_3, MgO-SiO_2-Al_2O_3 and MnO-SiO_2-Al_2O_3. Equations 1–4 were used to calculate the sulfide capacities of each ternary system. The activity of the basic component was obtained using the same mole fractions of the acidic components as in the multicomponent system. The average molecular weight of solution is obtained for the ternary system. Instead of using $X_{Al}O_{1.5}$, $X_{Al}O_{1.5}$ + $X_{S}iO_2$ was used, where these acidic mole fractions were the same as in the multicomponent system. Once the sulfide capacity of each ternary was calculated, the following equation was used to calculate the sulfide capacity of the multicomponent system:

$$\log C_S = y_{Ca} \log C_{S(Ca)} + y_{Fe} \log C_{S(Fe)} + y_{Mg} \log C_{S(Mg)} + y_{Mn} \log C_{S(Mn)} \quad (5)$$

Where y_i is the equivalent cationic fraction of species i. The comparison of Cs for available experimental data to RB model results of CaO-FeO-MgO-MnO-$AlO_{1.5}$-SiO_2 and several other multicomponent slag systems at various temperatures (Reddy, 2003a) were discussed. An excellent agreement was obtained between the experimental sulfide capacities to that of RB model *a priori* calculated sulfide capacities of the metallurgical process important slag systems.

Reddy model for sulfur distribution ratio

At normal iron and steelmaking conditions, sulfur is present in molten metal in a dissolved form. The gas/metal reaction is thus simply:

$$\frac{1}{2}S_{2(gas)} = [S] in\ iron \Delta G_6^\circ = -135\ 060 + 23.43T \text{(J/mol)} \quad (6)$$

The equilibrium constant of Reaction 6 is written as:

$$K_6 = exp\left(\frac{-\Delta G_6^\circ}{RT}\right) = \frac{a_S}{p_{S_2}^{1/2}} \quad (7)$$

The sulfur in equilibrium between slag and molten metal is written as the reaction:

$$[S] + (O^{2-}) = \frac{1}{2}O_{2(gas)} + (S^{2-}) \quad (8)$$

The equilibrium constant for the Reaction 8 is written as:

$$K_8 = \left(\frac{p_{O_2}^{1/2}}{a_{[S]}}\right) \bullet \left(\frac{a_{S^{2-}}}{a_{O^{2-}}}\right) \quad (9)$$

The gas/slag reaction for sulfur can then be written as:

$$\frac{1}{2}S_{2(gas)} + (O^{2-}) = \frac{1}{2}O_{2(gas)} + (S^{2-}) \quad (10)$$

The equilibrium constant for this reaction is:

$$K_{10} = \left(\frac{a_{S^{2-}}}{a_{O^{2-}}}\right) \bullet \left(\frac{p_{O_2}}{p_{S_2}}\right)^{\frac{1}{2}} \quad (11)$$

The expression for sulfide capacity (Fincham and Richardson, 1954) is:

$$C_S = (\text{wt.\% S in slag}) \bullet \left(\frac{p_{O_2}}{p_{S_2}}\right)^{\frac{1}{2}} \quad (12)$$

Combining Equations 11 and 12:

$$K_{10} = \left(\frac{a_{S^{2-}}}{a_{O^{2-}}}\right) \bullet \frac{C_S}{(wt.\%\ S \text{ in slag})} \quad (13)$$

Since sulfur is present in molten metal in small amounts (<0.2 wt per cent), dilute solution approximation can be used. Henry's law can then be applied to obtain the following expression for the activity of sulfur dissolved in liquid metal:

$$a_{[S]} = f_S \bullet [wt.\%\ S \text{ in metal}] \quad (14)$$

The value of the activity coefficient (f_S) can be calculated from the molten metal composition and interaction parameters. Using Equations 6, 8, 10, 12 and 14 and rearranging them, an expression for the distribution ratio is obtained:

$$L_S = \frac{(wt.\%\ S \text{ in slag})}{[wt.\%\ S \text{ in metal}]} = \frac{(S)}{[S]} = \frac{f_S \bullet C_S}{K_6 \bullet p_{O_2}^{1/2}} \quad (15)$$

For a given slag composition and temperature, the Cs can be calculated using the RB model as described above. The oxygen partial pressure depends on the process and operating conditions. It can be determined by considering each process separately.

RESULTS AND DISCUSSION

Sulfur distribution ratio in ironmaking

In the process of ironmaking, iron oxides are reduced by coke to produce pig iron. The oxygen partial pressure in such reducing conditions is low and can be determined by the following reaction:

$$\text{C (graphite)} + \tfrac{1}{2}\ O_2 \text{ (gas)} = \text{CO (gas)};\ \Delta G_{16}^\circ = -117\ 989 - 84.35T \text{(J/mol)} \quad (16)$$

The equilibrium constant of Reaction 16 is:

$$K_{16} = \frac{p_{CO}}{a_C \bullet p_{O_2}^{1/2}} = exp\left(\frac{-\Delta G^{\circ}_{16}}{RT}\right) \quad (17)$$

The partial pressure of carbon monoxide can be calculated considering the different gases present in the blast furnace. The gases such as hydrocarbons (ie methane) and air, liquids (ie oils), and solids (ie pulverised coal) are also injected through the tuyeres in the BF. Some plants may use certain hydrocarbons such as methane, but most gas input into the furnace is air. Air contains about 0.79 and 0.21 mole fractions of nitrogen and oxygen, respectively. Assuming that all the oxygen input into the furnace is consumed by Reaction 16, two moles of carbon monoxide will be produced for each mole of oxygen. Assuming that the total furnace pressure is 1 atm, the partial pressure of carbon monoxide can be calculated as: $p_{CO} = X_{CO} \bullet p_{Tot.} = 0.35 \bullet 1 = 0.35$ atm. For activity of carbon is unity, substituting Equation 17 into Equation 15, the Ls is given as:

$$L_S = \frac{K_{16} \bullet f_S \bullet C_S}{0.35 \bullet K_6} \quad (18)$$

The activity coefficient of sulfur in liquid iron (f_S) is determined from the metal composition using the following equation:

$$log(f_S) = \sum e_S^j \bullet [wt.\%\, j]_{in\ iron} \quad (19)$$

The term *e* is called interaction coefficient. Interaction coefficients slightly change with changes in temperature (Deo and Boom, 1993a, 1993b). A typical pig iron composition in weight percentages would be: 3 C, 1 Mn, 1 Si, 0.1 P and 0.1 S. Using Equation 19, the activity coefficient of sulfur is calculated as: f_S = 2.54. The Equation 18 then becomes:

$$L_S = \frac{2.54 \bullet K_{16} \bullet C_S}{0.35 \bullet K_6} \quad (20)$$

Equation 20 was used to calculate the sulfur distribution ratio of blast furnace slags in equilibrium with molten iron. The model calculated distribution ratios for liquidus slag/metal at 1400 and 1500°C are plotted against the experimental data (Filer and Darken, 1952; Hatch and Chipman, 1949) in Figure 1.

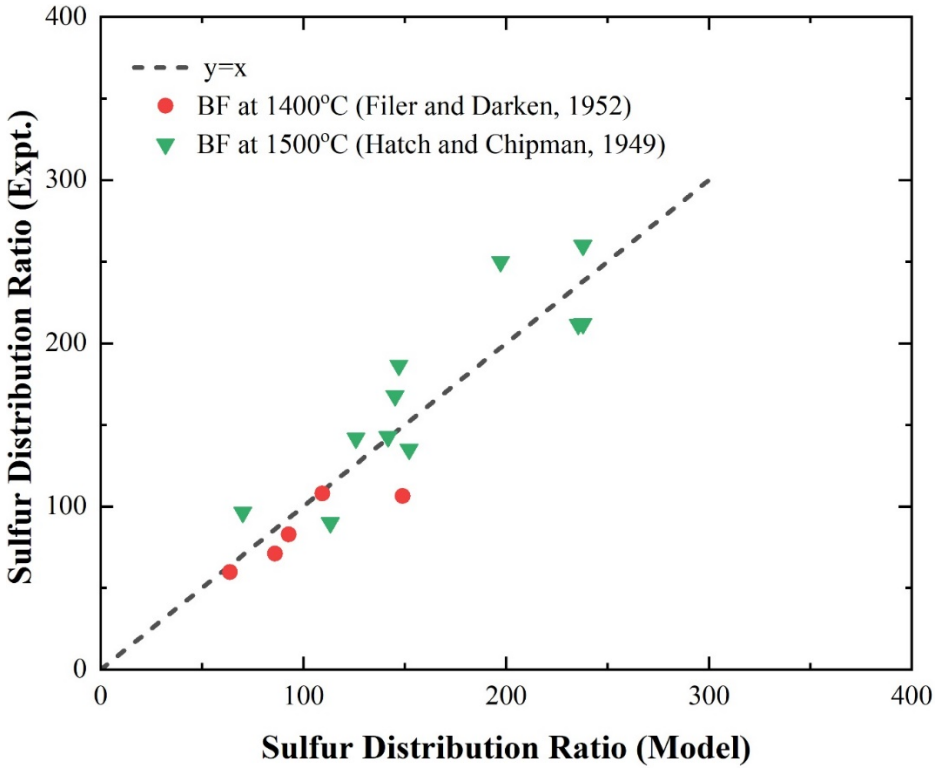

FIG 1 – Comparison of experimental data and model calculated data for sulfur distribution ratio (Ls) of BF ironmaking slags and iron.

The model calculated sulfur distribution ratio data are compared with the experimental data in the BF slags and liquid iron system over a wide compositions and two temperatures summarised in Figure 1. The present model reproduces most of the experimental data within experimental uncertainties, the average of relative value for this model was found to be 14.5 per cent. There are some points where the difference is noticeable. The method used here assumes equilibrium between slag and metal. It also assumes good mixing of each phase. These conditions are difficult to control and verify in laboratory experiments. Turkdogan (1996) reported that distribution ratios at turndown are about one-third to one-half of the slag/metal equilibrium values. There are two main observations that can be made from Figure 1. Increasing the temperature from 1400 to 1500°C nearly doubled the sulfur distribution ratio. The other observation is the large values of the distribution ratios, which were up to 300 at 1500°C.

Sulfur distribution ratio in steelmaking

Steelmaking is an oxidation process to remove the oxidisable elements from hot metal and scrap to the furnace slag as the steel is decarburised with oxygen blowing. Aluminium, silicon, phosphorous and manganese are all readily oxidised into the slag phase. The BOF charge normally contains only small amounts of Al, P and Mn. The oxidised silicon makes an important component of steelmaking slags. The oxidising conditions needed to decarburise the steel will also oxidise some of the iron. Lime is universally used as a fluxing agent to form steelmaking slags. Magnesia saturation of slag is needed to protect the furnace lining. The iron oxide goes into the slag phase and becomes an important component of slag. It follows that the main components of steelmaking slags are CaO, SiO_2, FeO and MgO. For a typical steel and steelmaking slag compositions used to determine the sulfur distribution ratio are Steel (wt per cent): 0.5 C, 0.3 Mn, 0.01 Si, 0.06 S and 0.01 P; and Slag (wt per cent): 47 CaO, 24 SiO_2, 15 FeO, 9 MgO, 3 MnO and 2 Al_2O_3. At or near turndown, among all other oxidation reactions, the iron oxidation reaction is what determines the oxygen potential:

$$\text{Fe (l)} + ½\ O_2\ \text{(g)} = \text{(FeO)};\ \Delta G^{\circ}_{21} = -238\ 070 + 49.45T\ \text{(J/mol)} \quad (21)$$

Since the calculations performed here are for slag/metal equilibrium, Reaction 21 is used to calculate the oxygen partial pressure. The equilibrium constant for Reaction 21 is then obtained from the equation:

$$K_{21} = \frac{a_{FeO}}{a_{Fe} \bullet p_{O_2}^{1/2}} = exp\left(\frac{-\Delta G^{\circ}_{21}}{RT}\right) \quad (22)$$

Equation 22 for the pressure of oxygen, activity of Fe equal to 1 and substituting into Equation 15, then Equation 23 can be obtained:

$$L_S = \frac{f_S \bullet C_S \bullet K_{21}}{K_6 \bullet a_{FeO}} \quad (23)$$

All parameters in Equation 23 can be calculated from the temperature and compositions of slag and metal. The calculation will be performed here at 1600°C for the above slag and metal compositions. The sulfur activity coefficient was calculated as: f_S = 1.122. The activity of iron oxide was obtained (Bale, Pelton and Thompson, 2002) and interaction parameters (Ghosh, 2001a) and Gibbs energy (Ghosh, 2001b; Gokcen and Reddy, 1996). The sulfide capacity of the slag was calculated using the RB model as described above. The sulfur distribution ratio was calculated as:

$$L_S = \frac{f_S \bullet C_S \bullet K_{21}}{K_6 \bullet a_{FeO}} = \frac{(1.122) \bullet (5.3430 \times 10^{-2}) \bullet (1.1383 \times 10^{4})}{(3.4887 \times 10^{2}) \bullet (2.4105 \times 10^{-1})} = 8.11 \quad (24)$$

The equilibrium sulfur distribution value for steelmaking is 8.11. The distribution ratio reported (Turkdogan, 1983) for similar system is 9.2. The model calculated data is in good agreement with the experimental data.

Sulfur distribution ratio in secondary steelmaking

In secondary steelmaking, the steel produced at the BOF or EAF is treated for impurity reduction and composition control in the ladle furnace (LF). The first step taken is usually to deoxidise the steel. When the aluminium bars with steel core are added at the top of the furnace, they sink to the

bottom as their density increases with aluminium melting. This process achieves very low contents of dissolved oxygen, and the product is called fully-killed steel.

The added aluminium will dissolve in steel and react with dissolved oxygen. This oxygen partial pressure is determined by the reaction:

$$[Al] + ¾\ O_2\ (g) = (AlO_{1.5})_{\text{(liquid slag)}};\ \Delta G^{\circ}_{25} = -722\ 358+165.795T(J/mol) \quad (25)$$

From Reaction 25, The equilibrium constant is written as:

$$K_{25} = \frac{a_{AlO_{1.5}}}{a_{[Al]} \bullet p_{O_2}^{3/4}} \quad (26)$$

Rearranging Equation 26 for the partial pressure of oxygen and substituting into Equation 15:

$$L_S = \left(\frac{f_S \bullet C_S}{K_6}\right) \bullet \left(\frac{K_{25} \bullet a_{[Al]}}{a_{AlO_{1.5}}}\right)^{\frac{2}{3}} \quad (27)$$

The activity of $AlO_{1.5}$ can be obtained for a given slag composition and temperature. The activity of aluminium dissolved in steel can be calculated as:

$$a_{[Al]} = f_{Al} \bullet [\%Al] \quad (28)$$

The activity coefficient is calculated form steel composition using:

$$log(f_{Al}) = \sum e_{Al}^{j} \bullet [wt.\%\ j]_{in\ iron} \quad (29)$$

A typical of steel composition (wt per cent) in the ladle furnace is: 0.4 C, 0.1 Mn, 0.1 Al, 0.01 Si, 0.01 P and 0.05 S. Substituting the interaction coefficients and the composition, the activity coefficient of aluminium f_{Al} = 1.1 and activity coefficient of sulfur f_S = 1.2 were calculated. A typical LF slag composition in (wt per cent) is: 47 CaO, 1 FeO, 9 MgO, 1 MnO, 32 Al_2O_3 and 10 SiO_2. By knowing the activity of $AlO_{1.5}$ in slag and Cs for slag was calculated using RB model at the temperature of steel in the ladle furnace, the distribution ratio calculated using Equation 27 as follows:

$$L_S = \left(\frac{f_S\ C_S}{K_6}\right) \bullet \left(\frac{K_{25} \bullet f_{Al}\ [\%Al]}{a_{AlO_{1.5}}}\right)^{\frac{2}{3}} = \left(\frac{1.2\ x\ 2.5247\times10^{-3}}{2.7844\times10^{2}}\right) \bullet \left(\frac{9.1268\times10^{10}\ x\ 1.1\ x\ 0.1}{2.8731\times10^{-2}}\right)^{\frac{2}{3}} = 670 \quad (30)$$

The equilibrium sulfur distribution value for secondary steelmaking is 670. The experimental distribution ratio reported by Inoue and Suito (1994) for similar system is 663. The experimental and model data are in good agreement.

The large Ls value for LF indicates that steel desulfurisation in the ladle furnace is very effective. Fully-killed steel can be desulfurised in the ladle furnace with lime-alumina slags to achieve very low sulfur contents (below 10 ppm). The sulfur distribution ratios for LF are about twice those for BF and about ten times those of BOF. It is clear that steel desulfurisation in steelmaking furnaces is not effective.

In industrial operations, many factors influence the sulfur distribution ratio. These factors include slag volume, gas bubbling practice, slag skimming practice, sampling procedure, analysis techniques, sample exposure to the environment and the location and time at which the sample was taken. The values calculated using Reddy model here are to give a general idea about the actual distribution ratio. The true distribution ratio can be higher or lower, but for the most part it should be close to the model calculated value. Calculation of Ls for all three systems for an extended compositions and temperatures are in progress. Since the method used here is *a priori*, it is a useful tool for the furnace operators. They can adjust the slag composition towards one with high distribution ratio and thus have high desulfurising power.

CONCLUSIONS

The sulfide capacities predicted using the Reddy-Blander model were used in calculation of sulfur distribution ratios for ironmaking, steelmaking and secondary steelmaking processes. The Reddy model calculated data shows good agreement with the experimental data. For a given slag's composition and temperature, its sulfide capacity can be calculated *a priori* using the RB model. Further, the sulfur distribution ratio between this slag and liquid steel in a particular vessel can also

be calculated *a priori* using the Reddy model. The sulfur distribution ratios for LF are about twice those for BF and about ten times those of BOF. The desulfurisation of pig iron in BF or desulfurisation of steel in LF during secondary steelmaking are recommended. Since the model used to calculate the sulfur distribution ratio (Ls) is *a priori*, it is a useful tool for the iron and steel makers in optimisation of the industrial furnace operations.

ACKNOWLEDGEMENTS

The authors acknowledge the financial support from the ACIPCO for this research project. Authors also thank the Department of Metallurgical and Materials Engineering, the University of Alabama for providing the experimental and analytical facilities.

REFERENCES

Bale, C W, Pelton, A D and Thompson, W T, 2002. FactSage 5.1: Thermochemical Software for Windows. TM Montreal, Quebec: Thermfact Ltd.

Chen, B, Reddy, R G and Blander, M, 1989. Sulfide Capacities of CaO-FeO-SiO_2 Slags, *Proceedings of the Third International Conference on Molten Slags and Fluxes*, pp 270–272.

Deo, B and Boom, R, 1993a. *Fundamentals of Steelmaking Metallurgy*, pp 205–206 (Prentice Hall: New York).

Deo, B and Boom, R, 1993b. *Fundamentals of Steelmaking Metallurgy*, pp 54–55 (Prentice Hall: New York).

Derin, B and Reddy, R G, 2003. Sulfur and Oxygen Partial Pressure Ratios Prediction in Copper Flash Smelting Plants Using Reddy-Blander Model, *TMS*, 1:625–632.

Derin, B, Yucel, O and Reddy, R G, 2005. Sulfide Capacities of PbO-SiO_2 and PbO-SiO_2-$AlO_{1.5}$ (sat.) Slags, *Mining and Materials Processing Institute of Japan (MMIJ),* pp 1279–1287.

Derin, B, Yucel, O and Reddy, R G, 2006. Predicting of Sulfide Capacities of Industrial Lead Smelting Slags, *Advanced Processing of Metals and Materials*, *TMS*, 1:237–244.

Derin, B, Yucel, O and Reddy, R G, 2010. Sulfide Capacity Modeling of FeOx-MO-SiO_2 (MO=CaO, MnO, MgO) Melts, *Minerals and Metallurgical Processing*, 28(1):33–36.

Derin, B, Yucel, O and Reddy, R G, 2004. Modeling of Sulfide Capacities of Binary Titanate Slags, *EPD Congress 2004*, TMS, pp 155–160.

Filer, E W and Darken, L S, 1952. Equilibrium between blast-furnace metal and slag as determined by remelting, *Transactions of AIME*, 194:253–257.

Fincham, C J B and Richardson, F D, 1954. The behaviour of sulphur in silicate and aluminate melts, *Proceedings of the Royal Society of London*, 223A, pp 40–62.

Flory, P J, 1953. *Principles of Polymer Chemistry* (Cornell University Press: New York).

Font, J M and Reddy, R G, 2005. Modelling of Antimonate Capacity in copper and Nickel Smelting Slags, *Trans Inst Min Metall C*, 114:C160–C164.

Ghosh, A, 2001a. *Secondary Steelmaking: Principles and Applications*, appendix 2.1 (CRC Press: New York).

Ghosh, A, 2001b. *Secondary Steelmaking: Principles and Applications*, appendix 2.2 (CRC Press: New York).

Gokcen, N A and Reddy, R G, 1996. *Thermodynamics, Thermodynamic simulator (TSIM) for thermodynamic calculations*, 371 p (Plenum Press: NY).

Hatch, G G and Chipman, J, 1949. Sulphur Equilibria between Iron Blast Furnace Slags and Metal, *JOM,* 1:185:274–284.

Inoue, R and Suito, H, 1994. Thermodynamics of Fe Equilibrated with O, N, and S in Liquid CaO-Al203-MgO Slags, *Metallurgical and Materials Transactions*, 25B:235–244.

Pelton, A D, 1999. Thermodynamic Calculation of gas solubilities in oxide melts and glasses, *Glastechnische Berichte*, 72:40–62.

Pelton, A D, 2000. Thermodynamic Modelling of Complex Solutions, *The Brimacombe Memorial Symposium*, ISS, CIM, TMS, pp 763–780.

Pelton, A D, Eriksson, G and Romero-Serrano, A, 1993. Calculation of Sulfide Capacities of Multi-component Slags, *Metall Trans B,* 24:817–825.

Reddy, R G and Font, J M, 2003. Arsenic Capacities of Copper Smelting Slags, *Metallurgical and Materials Transactions B*, 34B:565–571.

Reddy, R G and Blander, M, 1987. Modeling of Sulfide Capacities of Silicate Melts, *Metallurgical Transactions*, 18B:591–596.

Reddy, R G and Blander, M, 1989. Sulfide Capacities of MnO-SiO_2 Melts, *Metallurgical Transactions*, 20B:137–140.

Reddy, R G, 2003a. Impurity Capacities in Metallurgical Slags, *Materials Processing Fundamentals and New Technologies*, TMS, 1:25–48.

Reddy, R G, 2003b. Emerging Technologies in Extraction and Processing of Metals, *Metallurgical and Materials Transactions B*, 34B:137–152.

Reddy, R G, Hu, H and Blander, M, 1992. Sulfide Capacities of Silicate Slags, *Proceedings of the Fourth International Conference on Molten Slags and Fluxes*, pp 144–148.

Turkdogan, E T, 1983. *Physicochemical properties of molten slags and glasses*, The Metals Society, London, pp 298–301.

Turkdogan, E T, 1996. *Fundamentals of Steelmaking*, pp 237–244 (The Institute of Materials: London).

Yahya, A and Reddy, R G, 2011. Sulfide Capacities of CaO-MgO-$AlO_{1.5}$, MgO-MnO- $AlO_{1.5}$ and CaO-MgO-MnO-$AlO_{1.5}$ Slags, *Trans Inst Min Metall C*, 120(1):45–48.

Yang, X-M, Li, J-Y, Zhang, M, Chai, G-M and Zhang, J, 2014. Prediction model of sulfide capacity for CaO-FeO-Fe_2O_3-Al_3O_3-P_2O_5 slags in a large variation range of oxygen potential based on the ion and molecule coexistence theory, *Metallurgical and Materials Transactions*, 45B:2118–2137.

Zhao, W and Reddy, R G, 1995. Sulfide Capacities of CaO-$AlO_{1.5}$ Melts, *EPD Congress*, *TMS*, pp 39–47.

Challenges and limitations in development of large thermodynamic databases for multiple molten phases using the Modified Quasichemical Formalism

DOI: 10.62053/JXEX2673

D Shishin[1], M Shevchenko[2], E Nekhoroshev[3] and E Jak[4]

1. Research Fellow, PYROSEARCH, University of Queensland, Brisbane Qld 4072. Email: d.shishin@uq.edu.au
2. Research Fellow, PYROSEARCH, University of Queensland, Brisbane Qld 4072. Email: m.shevchenko@uq.edu.au
3. Postdoctoral Research Fellow, PYROSEARCH, University of Queensland, Brisbane Qld 4072. Email: e.nekhoroshev@uq.edu.au
4. Professor, Centre Director, PYROSEARCH, University of Queensland, Brisbane Qld 4072. Email: e.jak@uq.edu.au

ABSTRACT

In the field of pyrometallurgy, the presence of multiple molten phases with distinct chemical compositions, such as slags, mattes, speiss liquids, metals and molten salts, is a well-known phenomenon. These phases exhibit strongly non-ideal solution behaviour and are mutually miscible to varying degrees. To describe these complex molten liquids, the Modified Quasichemical Model (MQM) has proven effective and has been applied to numerous binary, ternary and several higher-order multicomponent systems related to pyrometallurgy. In recent decades, the complexity of high-temperature processes has escalated due to increased impurity concentrations in primary ores, the incorporation of recycled consumer products and the integration of metallurgical plants through by-product and waste exchanges. To address these issues, PYROSEARCH laboratory has been developing large 20-component thermodynamic database using a generalised CALPHAD (CALculation of PHAse Diagrams) methodology integrated with experimental investigations. Over the past decade, strategic decisions were made balancing the ability to generate experimental data, prediction power, accuracy, stability of calculations, as well as computational time, which are discussed in the paper. Examples provided for issues of >3 liquid immiscibility, non-ionic behaviour and exaggerated 'sharp' enthalpies of mixing in silicate slags, dealing with multiple oxidation states, as well as comparative analysis of pair and quadruplet approximation in MQM.

INTRODUCTION

Pyrometallurgical production of metals employs selective separation of metals and non-metals using their preference to one of the liquid phases, a gas phase, or rarely a solid phase. Commonly distinguished liquid types are molten salts, slags (oxide-based liquids), mattes (sulfide-based liquids), metallic liquids and speiss. Speiss liquids are formed between transition metals Fe, Co, Ni, Cu and Zn on the one side and metalloids As, Sb, (Sn) on the other side. Molten salts are based on pairing between alkali and alkali-earth metals on the one side and halogens, sulfates, phosphates, or carbonates on the other side. Molten salts are less common in primary pyrometallurgical production of metals from ores but applied in many electrometallurgical applications. They are also becoming increasingly important due to higher rates of recycling of e-waste, attempts to process tailings, incineration of waste, as well as in new emerging technologies for energy storage and generation.

In terms of the bond polarity these types of liquids can be ordered as follows:

Salts > Slags > Mattes > Speiss > Metals

Molten salts, slags and most mattes at stochiometric metal-to-sulfur compositions exhibit an ionic behaviour. Covalent bonds are observed within the anions of molten salts, ie SO_4^{2-} or CO_3^{2-}, and in slags with high proportion of silica or boron oxide. Incomplete dissociation into ions, with the portion of preserved covalent bonds is expected for matte and speiss. Also, when matte (Sundström, Eksteen and Georgalli, 2008) and speiss solutions deviate towards excess metal in

terms of stoichiometry, metallic type of bonds give important contribution to the observed physico-chemical properties.

The division of liquid into types is relative, they all are mutually miscible to a certain extent and bond types change with changing composition. The basis for distinction is the ability to form miscibility gaps and the formation of distinct layers. Separation of the liquid layers through skimming or taping is at the foundation of many pyrometallurgical processes. Examples are shown in Table 1. The microstructures of samples, containing all five types of liquids are shown in Figure 1. These come from lead production. Molten sulfate salt is not typical for lead smelting and appears due to the introduction of zinc tailings in primary lead production. Speiss forms due to introduction of recycled materials.

TABLE 1

Examples of pyrometallurgical processes bases on separation of liquid (molten) phases.

Process	Target production	Common design of furnaces	Liquid (molten) phases to be separated
Smelting from primary ores	Cu, Ni	Flash furnace, top-submerged lance, side and bottom-blown furnaces	Slag, matte
E-scrap smelting	Cu, Pb, Ni, Au, Ag, …	Top-submerged lance, top blown rotary furnace	Slag, metal
Smelting	Pb	Same as above	(Salt), slag, metal
Fuming	Zn	Side and bottom-blown, plasma, electric arc	Slag, metal (or speiss)
Converting	Cu, Ni	Peirce-Smith, side and bottom-blown	Slag, matte
Fire refining	Cu	Cylindrical anode furnace, tilting furnace	Slag, metal
Slag reduction	Pb	Lead blast furnace	Slag, matte, metal
Drossing	Pb	Kettles	(Liquid speiss), matte, metal
Doré process	Au, Ag	Bottom-blown oxygen cupel	Slag, metal
Smelting	Fe	Blast furnace	Slag, metal
Iron recycling	Fe	Electric arc furnace	Slag, metal
Steel production	Fe	Basic oxygen furnace	Slag, metal
Electrolysis (Hall-Héroult)	Al	Electrolytic cell	Salt, metal

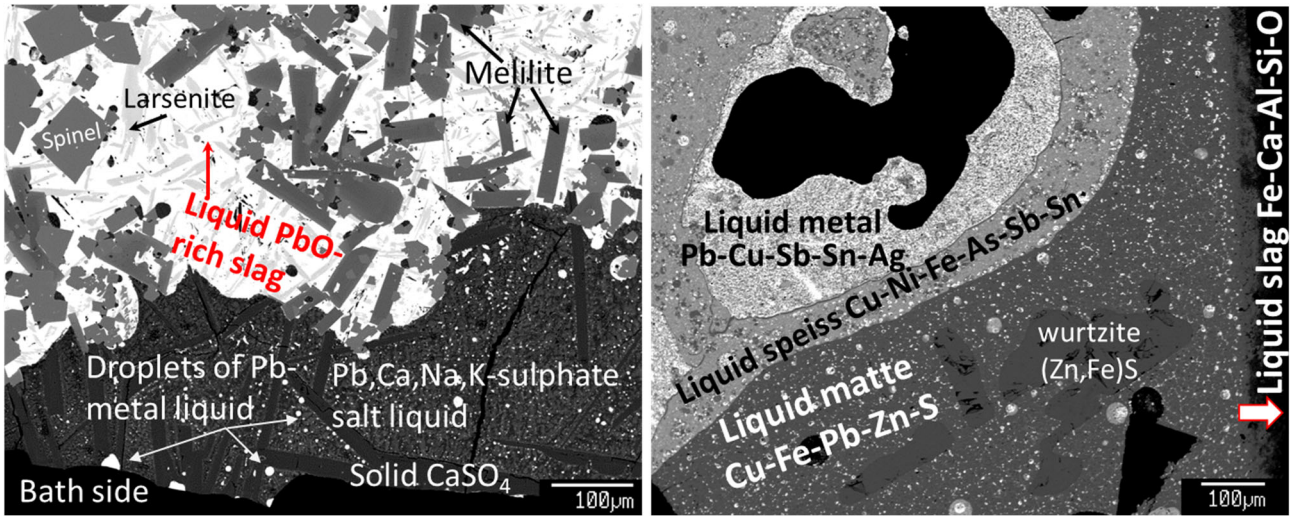

FIG 1 – Example of images obtained using backscattered electron microscopy of samples containing co-existing liquids with miscibility gaps. Left: liquid salt/slag/metal/solids equilibrium at conditions of lead sulfide smelting. Right: liquid slag/matte/speiss/metal/solids equilibrium at conditions of lead drossing. Slag phase is present, but not shown because it is too dark at the selected contrast.

Modern metallurgical production plants deal with rising impurity levels in primary ores. The recycled materials and wastes are also introduced in the process. The exchange of the by-products is used to increase the overall recovery, create new marketable products and reduce the environmental impact. These changes make the chemistry more complex. Any step-changes in existing operations can be performed more efficiently using predictive computational tools. But these tools should be applicable for a wide range of conditions in terms of composition, temperature, oxidation / reduction potential. They cannot be developed exclusively on the data from existing operations. Calculations of thermodynamic equilibrium based on Gibbs energy minimisations can provide such predictions. When combined with kinetic factors observed in real process, they may significantly reduce the need for costly pilot tests and trials (Castillo-Sanchez *et al*, 2023). Powerful thermodynamic software has been developed over the last decades. For practical predictions, thermodynamic software requires mathematical models describing the Gibbs energy of all potentially existing phases within the chemical system, as a function of temperature, pressure and composition.

Most mathematical models, including thermodynamic models, contain adjustable parameters. A combination of thermodynamic models together with the set of optimised adjustable parameters is often referred to as a thermodynamic database. High-quality models potentially have predictive power in complex systems with small number of adjustable parameters. But high-quality thermodynamic database is a product which must provide high accuracy. It is achieved by generating sufficiently abundant data used to fix the values of model parameters. The data used to optimise model parameters should be accurate and represent thermodynamic equilibrium. To achieve the accuracy and reduce the number of potential uncertainties, experimental studies are typically performed in less complex systems, which often means systems of smaller number of components. But the final goal is multi-component calculations. The aim of this publication is to demonstrate challenges we encountered during the development of thermodynamic models of liquid phases for the 20-component system directly relevant to non-ferrous pyrometallurgy applications. The first challenge was that the development had to be conducted in steps, with elements added in time:

Cu-Fe-O-S-Si (2014) + Ca-Al-Mg (2015) +
Pb-Zn-As-Sb-Bi-Sn-Ag-Au (2017) + Cr (2019) + Ni-Co (2020) + Na (2023) (System 1)

The decisions made in early stages of the project largely determined the direction of development of the models. As the size of the database grew, the larger resources required to introduce.

METHODOLOGY

Development of large multicomponent solution databases require the appropriate and strategic selection of the thermodynamic models and a method of obtaining model parameters while maintaining accuracy, predictive power and self-consistency. The models should be structurally based, so that model parameters are more than empirical mathematical expressions. For instance, they can correlate to the energy of interactions between the atoms in the phase.

Modified Quasichemical Formalism

The Modified Quasichemical Model (MQM) (Pelton *et al*, 2000; Pelton and Chartrand, 2001; Chartrand and Pelton, 2001; Pelton, Chartrand and Eriksson, 2001), a collaborative effort between CRCT (Montreal, Canada) and GTT (Germany), has demonstrated its ability to describe the thermodynamics of many chemical systems, binary, ternary and of more components. Over the years, the model has undergone several improvements, as detailed in recent publications (Jung and Van Ende, 2020). These enhancements now offer greater flexibility in choosing constituents, formulating expressions for excess Gibbs energy and interpolating binary parameters into ternary and higher-order systems. Notably, other established models, such as the Bragg-Williams ideal solution and the associate solution model can be reproduced within the MQM framework. These advancements warrant consideration of renaming MQM to the Modified Quasichemical Formalism (MQF), highlighting its ability to accommodate various models within its structure, as shown in Figure 2. Present publication will outline recent experience in model selection options within the MQF.

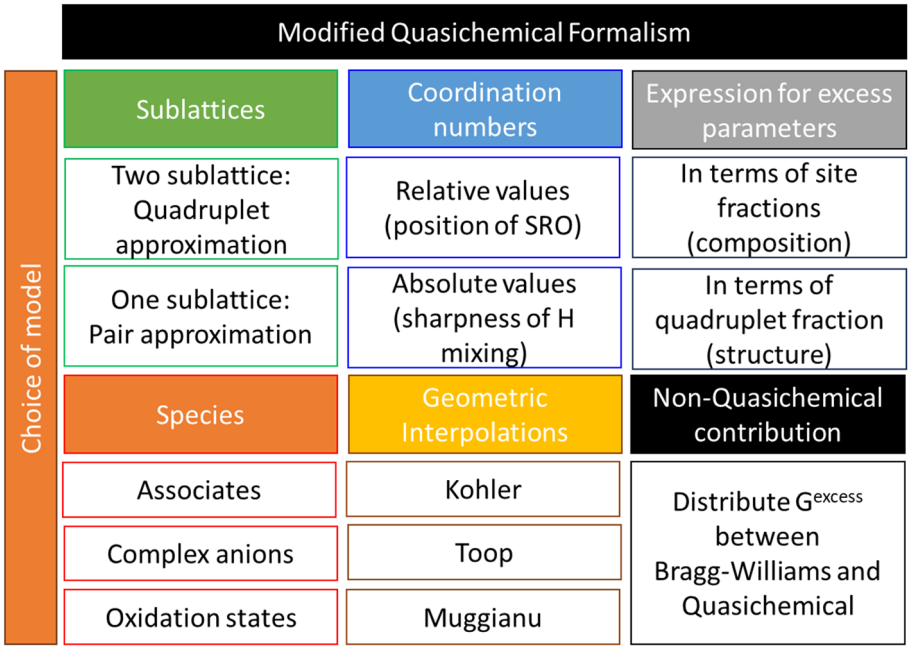

FIG 2 – Choice of model options within the Modified Quasichemical Formalism.

In many liquid solutions, strong attractive interactions between certain constituents at the atomic level result in the significantly higher than random probability of finding them next to each other. This phenomenon, known as Short Range Ordering (SRO), alters the probability distribution, leading to a deviation from ideal entropy of mixing (Pelton and Kang, 2007). The main purpose of the MQF is to take into account this deviation. By definition, the ideal Bragg-Williams model neglects the SRO effect. The Associate solution model, which is an alternative way to treat SRO, assumes that strongly interacting constituents are bonded to each other. As a result, it cannot reproduce the random mixing entropy once the molecular associate is introduced (Pelton and Kang, 2007). The full implementation of MQF is only available in FactSage™ software, versions 7.0 to 8.3 (Bale *et al*, 2016). Thermocalc™ software, version 2024a (Andersson *et al*, 2002), relies on the Ionic Two-Sublattice Model (ITSM) (Sundman, 1991). Unlike MQF, ITSM enables charged

and uncharged ions within the same solution, allowing the description of metallic and ionic solutions within the same model.

Ideas how to further improve the flexibility of MQF include the introduction of multiple compositions of SRO (Wang and Chartrand, 2021) and variable geometric interpolation technique, beyond the choice Kohler-, Toop- and Muggianu-types (Wang *et al*, 2023). But these ideas have not been implemented in thermodynamic databases developed by the authors.

Extended CALPHAD approach

Thermodynamic software requires expressions for the Gibbs energies of complex solution phases in the form of G = *f*(T, P, $x_1..x_n$). where T is temperature, P is total pressure and $x_1…x_n$ are compositional variables. The adjustable parameters, contained in these expressions, must be derived from experimental data, or in rare cases, from the first-principal methods. Enthalpy of formation, entropy and heat capacity expressions ($\Delta H_f°$, S°, CP) of solution components, as well as energy parameters for the interactions between them are all examples of model parameters. CALPHAD principles have become a standard for the thermodynamic description of a chemical system (Jung and Van Ende, 2020). The principles for a given system are as follows: a single set of model parameters for all potentially stable phases within the system should be obtained, which provides good description of all types of available experimental data, such as phase equilibria, activity measurements, the distribution of elements among phases, calorimetry and crystallography (Shishin *et al*, 2013).

Mathematical models of complex systems, in general, can include the simultaneous contributions of four and more factors. In contrast, in the thermodynamics of multicomponent liquids, decreasing probability of complex interactions among more than three atoms warrants the use of only binary and ternary interaction parameters (Gorsse and Senkov, 2018). This imposes a temptation to study and access only binary and ternary systems, relying on model extrapolation into multicomponent systems. While this may be applicable to metallic liquids, our experience showed that the values of ternary parameters in oxide systems must be verified inside several related quaternary, or even higher order systems. Extrapolations often did not provide the results which were accurate enough. The experimental methodology had to be improved to produce high quantity of experimental data in 4-, 5-components systems.

Thus, CALPHAD principles must be further extended when developing a large self-consistent multicomponent thermodynamic database. A larger single set of parameters need to be used and it should describe all data in all related systems. When performing predictions in multicomponent systems, it is necessary that model parameters are defined (fixed) for all the binary and eventually, for all ternary sub-systems and all solutions. For the database of 20-components, the theoretical number is 20!/2!/(20–2)! = 190 binary subsystems and 20!/3!/(20–3)! = 1140 ternary subsystems. Such huge numbers, especially for ternary systems, show the advantage of the model with high predictive power. Thermodynamic calculations using the current version of the database are used to determine the conditions of experiments and compositional areas are selected to improve the confidence of a given parameter. This helps to increase the number of successful experiments and reduce the need to mesh-type planning of experiments. In cases, when experiments cannot be performed due to challenging chemical nature, eg Au-O liquids not existing at ambient conditions, the values of parameters must be obtained indirectly, from the data of the multicomponent systems. High number of experiments and parameters means the process of development is inevitably iterative, requiring re-optimisation of previously assessed systems. Thus, the integrated experimental and modelling approach, is critical for the development of large thermodynamic databases.

Solid phases

At present, there are 95 solid solutions and 630 solid compounds with fixed stoichiometry in the database developed in PYROSEARCH. Models for liquids cannot be developed independently from solid phases. Phase equilibrium between the liquid and solid phase is one of the most important sources of thermodynamic information and typically can be measured more accurately, compared to activity or calorimetric information for molten solutions. For notoriously large and

complex solid solutions, such as spinel, the models are typically developed within the Compound Energy Formalism (CEF) (Hillert, 2001), which assumes the distinct crystal sublattices and random mixing within each sublattice. The main model parameters are the Gibbs energy functions of all solution end-members, as well as excess parameters for the interaction of atoms within the same sublattice. As in the case of MQF, different models can be developed within CEF. In CEF, more than two sublattices can be used, which MQF does not allow. This feature is used for pyroxenes, melilite, feldspar. The same components, even charged ions, can be present on several sublattices. This approach creates many 'virtual' end-members, necessitating the development of careful strategies to reduce the number of adjustable parameters though linear combinations and reciprocal reactions (Hillert *et al*, 2009). Still, for solutions like monoxide in the Fe-O system, simpler Bragg-Williams approach was preferred to describe the entropy of mixing (Hidayat *et al*, 2015). For non-stoichiometric solid speiss solutions, MQF with single sublattice demonstrated similar results as CEF with less parameters (Shishin and Jak, 2018) and more reasonable extrapolation of mixing properties outside of stoichiometry. This may be potentially beneficial for ternary and multicomponent systems.

OVERVIEW OF RESULTS AND ISSUES

Let us consider the selection of the models for important molten phases observed within the non-ferrous pyrometallurgy using the matrix in Figure 2. The summary is provided in Table 2 and the following sections discuss in more detail the selected models, their advantages and disadvantages.

TABLE 2

Selection of sublattice and species within the MQF, chosen for the molten phases within the 20-component System (1) targeted for non-ferrous pyrometallurgy.

Solution name	Selected model	Advantages	Limitations
Slag	(Cu^{+1}, Fe^{+2}, Fe^{+3}, Si^{+4}, Al^{+3}, Ca^{+2}, Mg^{+2}, Pb^{+2}, Zn^{+2}, Ni^{+2}, Co^{2+}, Sn^{+2}, Sn^{4+}, Sb^{+3}, As^{+3}, Bi^{+3}, Ag^{+1}, Au^{+1}, Cr^{2+}, Cr^{3+}, Na^{+}, $NaFe^{4+}$, $NaAl^{4+}$) (O^{-2}, S^{-2})	Takes into account Second Nearest Neighbour SRO between basic and acidic components	Cannot describe deviation from MeO_x and MeS_x stoichiometry, where x = 0.5, 1.0, 1.5, 2.0
		Compared to purely associate models, less ill-defined parameters	Does not contain Cu^{2+}, Cr^{6+}, Pb^{4+}
		Associate still can be introduced for particularly difficult systems (ie $NaFe^{4+}$)	Assumption of fully ionic liquid does not work near pure SiO_2
		Separate from liquid matte/metal/speiss and salt overcomes 3-phase immiscibility limit in FactSage™	
liquid matte/ metal/ speiss	(Cu^{I}, Cu^{II}, Fe^{II}, Fe^{III}, Pb^{II}, Zn^{II}, Ni^{II}, Sn^{II}, Sb^{III}, As^{III}, Bi^{III}, Ag^{I}, Au^{I}, Cr^{II}, Co^{II}, Ca^{II}, Mg^{II}, Na^{I}, O^{II}, S^{II})	Possible to describe complete stoichiometry range (even for oxides)	Cannot describe Second Nearest Neighbour SRO
		Easy to add new component no ill-defined end-members	Lack of flexibility of ternary parameters and geometric interpolations
		Easy to introduce Bragg-Williams parameters from literature	Separate from slag, creates conflicts with oxide liquids
Salt	(Ca^{+2}, Mg^{+2}, Pb^{+2}, Zn^{+2}, Na^{+1}, Cu^{2+}, Fe^{3+})(SO_4^{-2}, O^{-2})	Relatively easy to expand using existing molten salt assessments	Separate from slag, which is not the case for some systems

Slag

The slag solution was the original reason for the development of the MQM (Pelton and Blander, 1986; Wu, Eriksson and Pelton, 1993; Wu *et al*, 1993; Jak *et al*, 1997; Jak, Zhao and Hayes, 1997). Many binary and ternary oxide systems were reasonably well described at the time.

Sublattices

One sublattice model was chosen with O^{2-} being the only anion. Since the end-members of the solution were pure oxides, no deviation towards excess metal, or towards oxygen was allowed. For the systems containing Fe-O and Cr-O, species with several oxidation states were introduced (Decterov and Pelton, 1996), ie Fe^{2+} and Fe^{3+}, Cr^{2+} and Cr^{3+}, which partially solved the oxygen/metal non-stoichiometry within these sub-subsystems for a limited range of composition. Wide liquid-liquid miscibility gaps between metallic liquid and oxide liquids for most metal-oxygen systems justified the practicality of the model. This eventually grew into FToxid public database of FactSage™ (Bale *et al*, 2016), which is currently on of the largest self-consistent oxide database (Jung and Van Ende, 2020). The PYROSEARCH database (Jak *et al*, 2019) uses the same approach. It is not as big in terms of number of elements, but is continuously re-assessed iteratively, supported by new experimental results. For instance, new data have been generated even for foundational system of Ca-Fe-O-Si in 2022, resulting in major revision. At this point, the properties of all oxide end-members and all excess parameters in FToxid and the database of the PYROSEARCH database are different.

Alternatives for slags have been developed by Selleby and Sundman (1996), Selleby (1997) and Hillert, Sundman and Wang (1990), who used ITSM, which become the foundation of the Metal Oxide Solutions (TCOX) thermodynamic database from Thermo-Calc Software. Yet another approach was used by (Jantzen *et al*, 2021) who started the development of the independent GTOx (GTT oxide) database in 2000s, citing the need to 'give a second opinion to our customers who have licensed the FToxid (FACT oxide) database … and a better description for … high Na_2O- and K_2O- and vanadium-containing systems'. They used an associate model. For comparison, the models for the slag within the Ca-Fe-Si-O system, which is foundational for many non-ferrous pyrometallurgical processes, are given below:

MQF (FToxid and PYROSEARCH database): $(Fe^{+2}, Fe^{+3}, Si^{+4}, Ca^{+2})(O^{-2})$,

Ionic Two-Sublattice Model (TCOx): $(Fe^{+2}, Si^{+4}, Ca^{+2})P(O^{-2}, SiO_4^{-4}, FeO_{1.5}, SiO_2, Vacancy^{-Q})_Q$,

Associate model (GTOx): $(Ca_2O_2, Fe_2O_2, Fe_2O_3, Fe_3O_4/1.5, Si_2O_4, CaSiO_3, Ca_2SiO_4/1.5, FeSiO_3, Fe_2SiO_4/1.5, CaFe_2O_4/1.5, CaFeSi_2O_6/2)$

All these models have been further expanded to include more metals. The TCOx model can describe metallic liquid and slag using the same solution. The current model for slag in UQpy (Uncertainty Quantification with Python) is provided in Table 2.

Selection of species – oxidation states

Table 2 shows the selection of 'Species' for the PYROSEARCH slag model. A decision was made in 2013 to only include Cu^{+1}, but not Cu^{+2} in the slag model for non-ferrous applications. It was demonstrated (Shishin and Decterov, 2012) that the formation of Cu^{+2} is significant at $p(O_2)$ above 10^{-3} atm for temperature > 1100°C, as shown in Figure 3. These highly oxidising conditions are not encountered for most process steps in the pyrometallurgy of Cu, Ni, Pb, Zn, Fe, Sn or others. The decision significantly reduced the number parameters between Cu^{+2} and other components of the slag, which are difficult to define. Very little reliable experimental data existed for these high $p(O_2)$ conditions. The same logic applies to Pb^{+4}, Cr^{+6}, which are even less stable at high temperatures and are not expected in liquid slags, but are introduced as solid compounds, when necessary. Some applications, such as using molten copper oxide for high temperature for solar energy storage and oxygen production (Jafarian, Arjomandi and Nathan, 2017) do require correct predictions of Cu^{+2}/Cu^{+1} in liquid oxide. These are covered by the liquid matte/metal/speiss solution model (Shishin *et al*, 2013), which is discussed further. Some evidence exists that the formation of accretions close to the uptake shaft of the copper flash smelting furnaces may involve liquid slag phase equilibria within the Cu-Fe-O-Si system at oxygen partial pressures exceeding 10^{-2} atm. If

confirmed, the accurate description would require the introduction of Cu^{+2}. This in turn, would shift the stoichiometry of slags equilibrated with metallic copper further away from Cu^{0}, contrary to diagram in Figure 3. Introduction of both Cu^{0} and Cu^{+2} is not possible within the selected formalism, since charges and uncharged species together are not allowed. Even if was possible, that would create more calculation conflicts with liquid matte/metal/speiss solution model. The partial solution could be the possibility to turn on and off the Cu^{+2} species in FactSage™ software, but this makes phase selection complicated for metallurgical engineers.

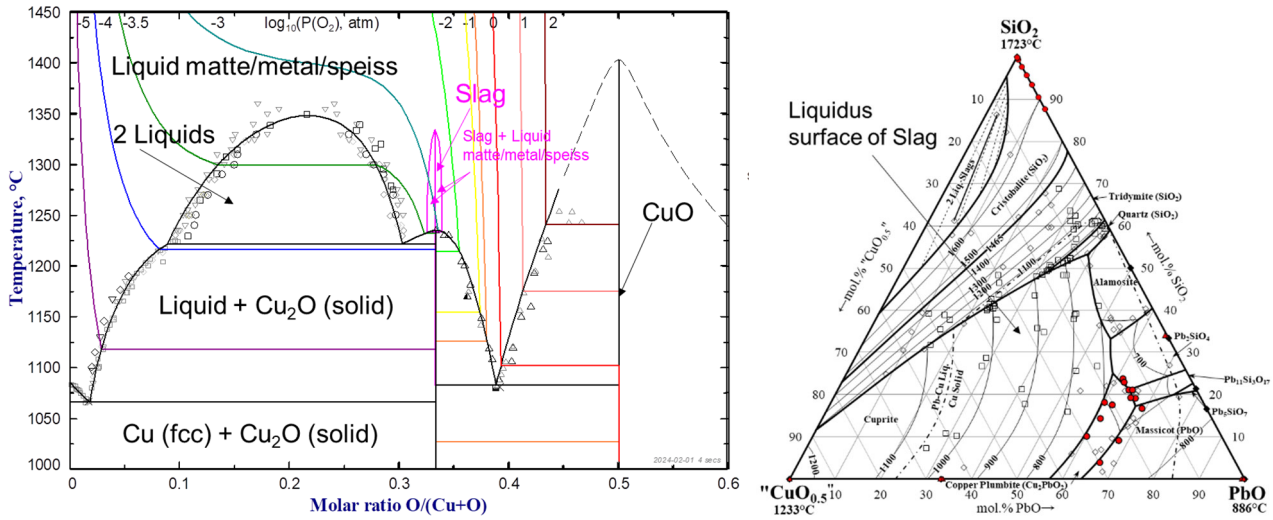

FIG 3 – Left: Phase diagram of the Cu-O system (Shishin and Decterov, 2012). The compositional domain of slag solution is much smaller than liquid/matte/metal solution. Right: Example of slag liquidus projection in the Cu-Pb-Si-O system (Wen *et al*, 2023) demonstrates the practicality of this approach for the description of multicomponent systems in non-ferrous pyrometallurgy.

Selection of species – associates

The presence of Na_2O in slags which also contain Al_2O_3 and SiO_2 result in the so called 'charge compensation' effect. Cations of Al^{+3} in the presence of Na^{+1}, assume the position of Si^{+4} and act as a network former (Decterov, 2018). This strong ternary effect cannot be satisfactory modelled without the introduction of $NaAl^{+4}$ associate in the MQF (Lambotte and Chartrand, 2013). The introduction did not require specific changes to the formalism and good results were achieved for systems exhibiting strong 'charge compensation'. Still, model parameters for the $NaAl^{+4}$ species are not well-defined. Thermodynamic properties of virtual liquid $NaAlO_2$ cannot be obtained from the Na_2O-Al_2O_3 data. They can be better fixed, when considering binary and ternary data within the Na_2O-Al_2O_3-SiO_2 simultaneously, but even so, the excess Gibbs energy parameters between $NaAl^{+4}$ and cations other than Si^{+4} are ill-defined. Predictions in multicomponent systems become less reliable and can result in spurious miscibility gaps, such as one observed by (Nekhoroshev, 2019) in the CaO-Na_2O-Al_2O_3-SiO_2 system. The decision to introduce $NaAl^{+4}$, (and $NaFe^{+4}$ for the same reasons), created a challenge. Significant resources are required to 'scan' the multicomponent systems for possible problems, generate experimental data and make sure the parameters involving these associates are fixed. This direction of work has not fully started yet, since Na^{+1} was the last element to be introduced in the chemical System (1).

Further evolution of the slag model within the MQF was largely driven by the need to describe the solubility of sulfur (Kang and Pelton, 2009), giving the rise of the two-sublattice model. The anion S^{-2} was introduced on the second sublattice as shown in Table 2 and used the mathematical expressions originally developed for molten salts. In addition to sulfide capacity, the resulting model could be used to predict phase equilibria involving sulfides (mattes) and oxysulfides (Jo, Lee and Kang, 2013), but limited to fixed sulfur-to-metal and oxygen-to-metal stoichiometry. For instance, within the Fe-O-S-Si system, no deviation of stoichiometry is possible near the composition of FeS, but the model was capable of describing miscibility between slag and matte. This approach is suitable to understand the formation of steel inclusions in the slag, but proved not applicable for slag/matte equilibria in copper, lead and nickel smelting. In the PYROSEARCH

database, mattes are described using a separate solution. Metal/sulfur non-stoichiometry in mattes is a significant factor for accurate predictions for non-ferrous processes. The introduction of sulfur-containing quadruplets, such as $Cu^{+1}Fe^{2+}O^{-2}S^{-2}$, allowed quantitative modelling solubility of copper in slags (Shishin *et al*, 2018b), as well as slag/matte equilibria involving Pb, Ni and other metals (Hidayat *et al*, 2023; Shishin *et al*, 2020; Sineva *et al*, 2023). Still, the selected model does not allow the description of complete miscibility between slag and matte, which is observed in Cu-free Fe-O-S-Si and Ca-Fe-O-S systems. As in the case of Cu^{2+}, the selection of the model was driven by multicomponent practical predictions, at the expense of lower order systems with small practical value. Example of alternative approach, describing slag, matte and metal with using single solution is available $(Fe^{+2}, Ca^{+2})P(O^{-2}, S^{-2}, S^{0}, FeO_{1.5}, Vacancy^{-Q})_{Q}$ (Dilner and Selleby, 2017) in the TCOx database. Large compositional areas of the system in question were not experimentally studied and the agreement with existing experimental data is semi-quantitative. The FToxid slag was further expanded towards F^{-}, SO_4^{-2}, PO_4^{-3}, CO_3^{-2} and other anions, with limited concentrations. Certain challenges in modelling oxyfluoride systems required formalism improvements (Lambotte and Chartrand, 2011), which later were generalised (Wang and Chartrand, 2021). The two-sublattice MQM in Quadruplet Approximation assumes the ionic nature of oxides and salts. It uses the Gibbs energy functions for solution end-members, ie Cu_2O, Cu_2S, FeO and FeS, to express the magnitude of First Nearest Neighbour SRO, while Second Nearest Neighbour SRO is taken into account by excess parameters.

Coordination numbers

The absolute values of coordination numbers were originally selected to provide the entropy of mixing to be zero at the composition of maximum short-range ordering for the system with infinitely negative enthalpy of mixing. The numerical values were calculated by (Pelton and Blander, 1984) and these values are still used for the coordination numbers of most species in present-day slag solution: 0.68872188 for +1 cations, 1.37744375 for +2 cations, 2.06616563 for +3 cations and 2.75488750 for +4 cations. The absolute values are not as important as the ratios of coordination numbers. Possibly due to the low importance, these absolute values are the only model parameters that have been preserved since the early versions of the model. The ratios of coordination numbers determine the composition of maximum short-range ordering. In later publication (Pelton *et al*, 2000), it was recommended that for the systems with small negative or positive values of enthalpy of mixing, the coordination numbers should be closer to their physical values. In the case of Cu^{+1}, this recommendation was originally not applied, so it was assigned the 'default' value for +1 cations. This worked relative well but required the introduction of the positive Bragg-Williams parameters to describe the tridymite liquidus related to the Cu_2O-SiO_2 system (Hidayat and Jak, 2014; Hidayat *et al*, 2017a). The latest systematic experimental work in the high-SiO_2 region studying the miscibility gas in slags for the systems like Cu-Fe-O-Si (Wen, Shevchenko and Jak, 2021), Cu-Pb-O-Si, Cu-Zn-O-Si demonstrated (Wen *et al*, 2023) the need for correction. Example is shown in Figure 3 (right) and labelled as 2 Liq. Slags. After the coordination number for Cu^{+1} was doubled, it was possible to improve the description of the miscibility gaps.

Sharp enthalpy and non-Quasichemical contribution

A large data set of new experimental data have been obtained for the foundational system Ca-Fe-O-Si, including all subsystems, in 2020–2024 (Cheng *et al*, 2019, 2021). With higher accuracy and large density of experimental points, it was quite difficult to achieve the desirable agreement by using the similar set of model parameters, as in the earlier assessment (Hidayat *et al*, 2016a, 2016b, 2017b). The major re-vision was initiated, which included the update in the properties of all liquid oxide end-members. Properties of many solid compounds also required updates. The principles are described in the parallel presentation (Shevchenko, Shishin and Jak, 2024). Furthermore, it became clear the liquidus of Ca_2SiO_4 in the Ca-Fe-O-Si and other systems could not be described even after the changes in thermodynamic properties of solids. The reasons for that were difficult to isolate, but in the end it turned out that for the slag phase, the Gibbs energy of mixing was too 'sharp' at the composition of Ca_2SiO_4. The phenomenon of sharp enthalpy of mixing was previously discussed for the metallic systems (Pelton and Kang, 2007), but not applied in slags. The solution was proposed by the present authors to combine the Bragg-Williams and Quasichemical contributions in slags, when required. After the Gibbs energy of mixing was

corrected by the combination of the Quasichemical and Bragg-Williams parameters for the CaO-SiO_2 system, as shown in Figure 4, better description in the area of Ca_2SiO_4 was obtained for the several systems containing CaO-SiO_2, such as ZnO-CaO-SiO_2, Al_2O_3-CaO-SiO_2 and MgO-CaO-SiO_2. These results are not yet published.

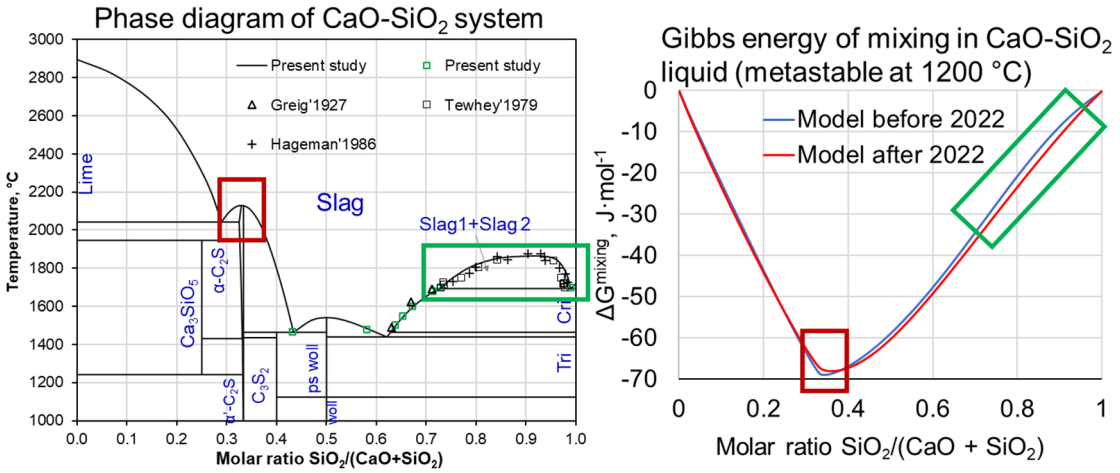

FIG 4 – Two regions in the CaO-SiO_2 system which required significant revision of model within the MQF, not just the revision of model parameters – enthalpy of mixing is too sharp near Ca_2SiO_4 and excess curvature of Gibbs energy of mixing near SiO_2.

Unusual excess parameters – non-ionic slags

The models for slags developed using the MQF typically require few model parameters to describe the main features of thermodynamic properties and phase diagrams. The use of multiple parameters to describe experimental data, especially series of negatively correlated parameters, is discouraged and may indicate internal inconsistencies in the experimental data series. Also, it is unusual to use excess parameters with high powers, ie $g_{AB}^{i,j}$ where *i* or *j* > 6, except for the Me-Si-O systems (Me = Li^+, Ca^{+2}, Mg^{+2}, Fe^{2+}, Fe^{3+}, Zn^{+2}, Cu, Ni^{+2}, Co^{+2}, Cr^{+2}...). Parameters with high power on SiO_2 have been commonly used for the to introduce the miscibility gaps in slag close to SiO_2 (Konar, Van Ende and Jung, 2017; Prostakova *et al*, 2012, 2013; Hidayat *et al*, 2017b; Wu *et al*, 1993; Jung, Decterov and Pelton, 2007). An example of miscibility gap in slag is shown in Figure 4 (left, green area). Furthermore, these parameters often contained large entropy terms to reproduce the closing the miscibility gaps at high temperature. For many systems the experimental data on the miscibility gaps were rare and controversial, so little attention was given to the values of these parameters. Recent Electron Probe microanalysis (EPMA) measurements in high-SiO_2 areas of the ternary and higher-order systems (Shevchenko, Shishin and Jak, 2022; Khartcyzov *et al*, 2022; Cheng *et al*, 2021) revealed that predicted miscibility gaps extended systematically too far into the multicomponent compositional space compared to experimental data and could not be described well enough using ternary parameters. This indicated that Gibbs energy of mixing was too concave in many Me-Si-O systems in the region shown using green area in Figure 4 (right). Less concave Gibbs energy of mixing, but similar shape of the miscibility gap could be achieved using excess parameters with higher power on SiO_2, more than 9. These parameters were never used before. It is believed the need to use unconventional parameter series is attributed to the fact that the model for slags assumes fully ionic behaviour. The high-SiO_2 liquids are not fully ionic (weak electrolytes) and exhibit long-range electrostatic interactions between the uncompensated charged Me^{x+} cations and O^{2-} anions, an effect similar to the Debye-Hückel model and clustering well known to be present in the diluted aqueous solutions. The Gibbs energy of mixing of the components can be better represented as a polynomial sequence, to simulate the long-distance ionic interactions (Figure 4). After the introduction of the polynomial sequences in some systems, unrealistic entropy contributions to excess parameters were no longer necessary, resulting in better description of tridymite liquidus at temperatures below the miscibility gap for many systems, particularly CaO-FeO-Fe_2O_3-SiO_2. Systematic replacement of parameters for high-SiO_2 liquids is expected to provide step-like improvement in many other systems.

An alternative approach was used in a PhD thesis by Nekhoroshev (2019), who introduced dimers of $(Na_2)^{+2}$ and $(K_2)^{+2}$ to better describe liquidus in high-SiO_2 region of the Na_2O-SiO_2 and K_2O-SiO_2 systems. Still, this approach, if applied to the multicomponent database, would result in many undefined excess parameters among dimers and other components of the solutions. In the PYROSEARCH model, a combination of $g^{0,8}_{Na^{+1}Si^{+4}}$ and $g^{0,15}_{Na^{+1}Si^{+4}}$ was tested for Na_2O-SiO_2 and good description of SiO_2-rich was achieved, as shown in Figure 5.

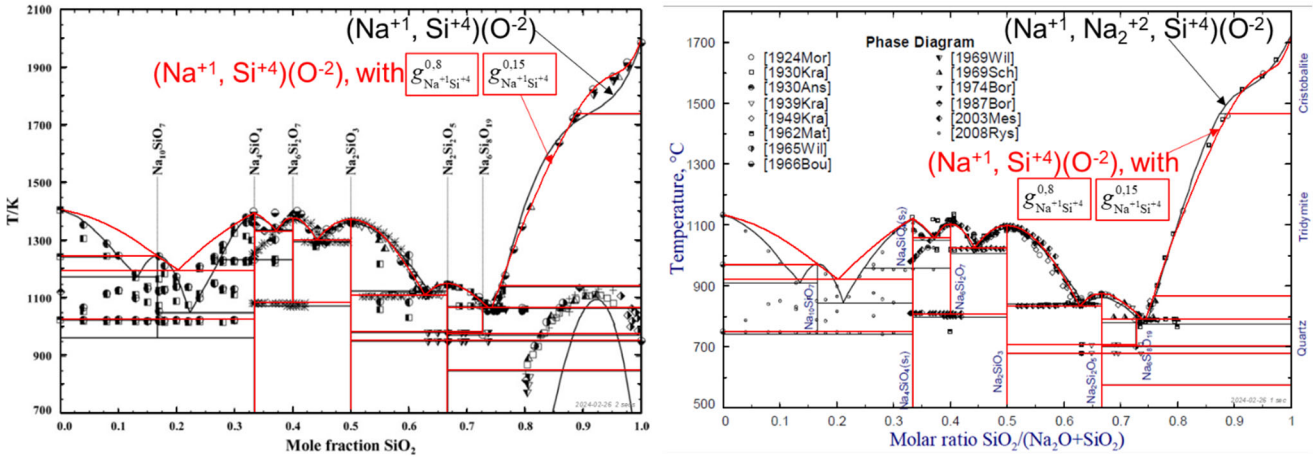

FIG 5 – Phase diagrams of the Na_2O-SiO_2 assessed using different models within the MQF – black lines are earlier works (Lambotte and Chartrand, 2011) and (Nekhoroshev, 2019), red lines are PYROSEARCH model results.

liquid matte/metal/speiss

Apart from differences in chemistry, the choice to treat liquid matte/metal/speiss as a separate model from slag and salt comes from the technical limitation of FactSage™. For the equilibrium calculations, a maximum of three immiscibilities within the same solution model is allowed, which is indicated by using the J-option in the user interface. In theory, more immiscible liquids of the same solution can be included in the calculation by creating copies of the same solution with different names and slightly different properties, but stability and speed of such calculations is questionable. Even three-phase equilibria in the multicomponent system pushes FactSage™ to the limit and sometimes gives incorrect results. A generalised model for slags, mattes, metals and speiss within the MQF is theoretically possible but not practical. We observe slag/matte/metal/speiss equilibrium in experimental results (see Figure 1, right). It would not be possible to reproduce this in the calculation, if all these phases were described using a single solution.

Sublattices and species

The first model for mattes within the MQF was developed in 1990s (Dessureault and Pelton, 1993; Decterov, Dessureault and Pelton, 2000; Kongoli, Dessureault and Pelton, 1998). One-sublattice approach was used, with the main goal of describing strong SRO between metals and sulfur. The species were not charged. In theory, this approach allows the description of liquids within the complete range of composition from metals to sulfides and to elemental sulfur. Still, in these publications, mattes were artificially separated from molten copper and from molten lead metal solutions to benefit from existing models for these metallic solutions. The one-sublattice approach was expanded by Waldner and Pelton (2004a, 2004b, 2005) and Waldner and Sitte (2011). Metallic copper and matte were merged and included in FactSage™ software as FTmisc database (FTsulf since version 8.2), but the results of this work were not published until much later (Waldner, 2020, 2022).

Multiple coordination numbers for elements

The concept of treating metals and mattes within the same solution was accepted by the developers of the PYROSEARCH model. When expanding the database towards non-ferrous applications, it was also necessary to describe the solubility of oxygen in metals and mattes. The

selected model within the MQF was also applicable to oxide liquids (see Figure 3 left) in cases when Second Nearest Neighbour SRO was not that important, ie for oxide liquids without SiO_2. The Cu-O and Fe-O systems had two compositions of SRO each, which was solved by introducing extra species intro the model. They had different thermodynamic properties and coordination numbers, ie Cu^{I} and Cu^{II}, Fe^{II} and Fe^{III} (Shishin and Decterov, 2012; Hidayat *et al*, 2015; Shishin *et al*, 2013). The notations ^{I}, ^{II} and ^{III} have the meaning of valency with O^{II} and S^{II} and determined by the ratio of coordination numbers. A drawback of this approach was that thermodynamic properties of pure liquid O^{II}, Cu^{II}, Fe^{III} were ill-defined, since they don't exist.

Heat capacity term in excess Gibbs energy

Within the selected model, the heat capacity of liquids at the compositions of maximum SRO, for instance at Cu_2S, is an additive function of endmembers, ie liquid Cu^{I} and S^{II}, which is not a very good approximation from the physical point of view. The bonds between atoms give a significant contribution towards heat capacity. Liquid copper has metallic bonds, Cu_2S is believed to have large proportion of ionic bonds, while S should retain much of covalent bonds in the liquid state. Still, uncertainties in heat capacities are significantly smaller compared to metal-sulfur and metal-oxygen interactions, so very good description of experimental results have been obtained by the introduction of composition-dependent excess Gibbs energy functions. Still, in the case of Cu_2S, a correction of heat capacity may be required, since the only experimental work on this topic indicates lower value (Figure 6). The problem of heat capacity was not addressed in a recent publication (Waldner, 2020). Typically, excess Gibbs energy dependence on temperature (T) is expressed as a + bT, but additional cTln$T$ term should be used in this case. Of course, such a correction would initiate the re-assessment of all parameters in systems related to the Cu-S, ie Cu-As-S (Prostakova, Shishin and Jak, 2021), Pb-Cu-S (Shishin, Chen and Jak, 2020) and dozens more. Optimistically this may help resolving some of the accuracy issues explained in sections below.

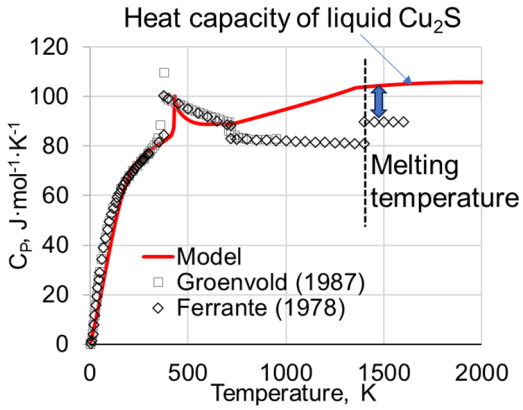

FIG 6 – Heat capacity of Cu_2S. Symbols are experimental data (Groenvold and Westrum, 1987; Ferrante *et al*, 1978). Line is calculated using the PYROSEARCH model for the liquid phase at the composition of Cu_2S. Double arrow indicates that heat capacity of liquid should be corrected using the cTln$T$ term in excess Gibbs energy.

Figure 6 shows another important concept. The reasonable function is used for liquid Cu_2S for temperatures below melting and down to 0 K. Large portions of FactSage™ public database do not have reasonable heat capacity functions far below melting temperatures, which is compensated by excess Gibbs energy functions. Further improvements in the accuracy of predictions demonstrated the need to revise these functions. In the CALPHAD community, the need to invest resources into re-assessments of the systems due to corrections in heat capacity below 298 K is often justified by using the term 'third generation' CALPHAD database, with publications appearing for single-component (He *et al*, 2022) and binary-system re-assessments. In some cases the use of this highly publicized term results in the publication of low-quality assessments (Abdul *et al*, 2023).

Lack of direct parameters between sulfides

The analysis of slag/matte equilibria with the Cu-Fe-O-S-Si and higher order systems (Shishin *et al*, 2018a, 2018b) indicates possible need for the re-assessment of the Cu-Fe-S system. The predicted $P(O_2)$ versus wt per cent Cu in matte, a systematic deviation of about +0.15 in $Log_{10}[P(O_2)$, atm] is observed, when compared to experimental data obtained using the equilibration with the flow of CO-CO_2-SO_2-Ar gas. No apparent reasons for this deviation can be found from the analysis of existing data within the Cu-Fe-S (matte) (Waldner, 2022) or Cu-Fe-O-Si (slag) (Hidayat *et al*, 2017a) subsystems. The data in the Cu-Fe-O-S system (Shishin, Jak and Decterov, 2015) is somewhat scattered and no systematic deviation is observed. So, the slag/matte data indirectly indicates the systematic deviation of the activity 'FeS' according to the reaction:

'FeS' (in Cu-Fe-S matte) + O_2 (activity fixed) = 'FeO' (in Fe-Si-O slag, activity predicted) + SO_2 (activity fixed)

This assumes the achievement of equilibrium and correct calibration of the gas flow in these complicated experiments.

Another case is the Cu-Ni-S system, where the data on the tie-lines between metallic phase and matte could not be successfully re-conciliated with the matte-digenite phase diagram data by Walder or in the PYROSEARCH database.

The current working theory is that accumulated deviation of Gibbs energy exist for the Cu_2S (as in Figure 6), or a misbalance in Gibbs energy between Cu_2S and other sulfides, ie FeS or NiS. In the case of Slag, these types of inconsistencies can be compensated by binary parameters between end-members. In one-sublattice model for mattes, ternary parameters must be used. As shown in Figure 7, main ternary parameters do not act along the line of maximum SRO, which makes it very hard to compensate issues in certain areas of the diagram, without affecting other areas. It is tempting to introduce the associates inside the MQF, such as Cu_2S, FeS, possibly NiS to get access more excess parameters. It would be possible to describe the existing binary system data and very likely, ternary data due to larger and more flexible set of available binary parameters. It is hard though, to predict how such model would behave in a system with many elements. Logically, Cu_2O, FeO etc associates would need to be introduced as well. Computational time will increase significantly, since FactSage™ still needs to calculate the bond fractions between all species on the sublattice, such as Cu-Cu_2S, Cu_2S-FeO etc.

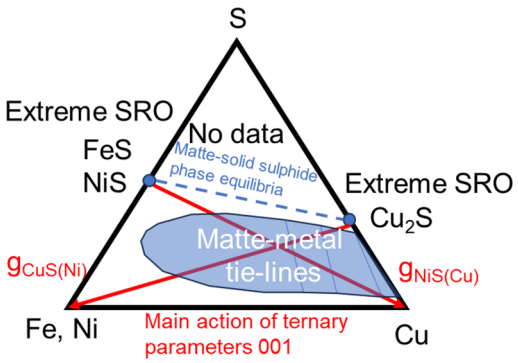

FIG 7 – The problem of ternary parameters in one-sublattice model for liquid matte/metal/speiss. No direct parameters along the FeS-Cu_2S and NiS-Cu_2S lines.

Geometric interpolation

Within the current model, the obvious interpolation method in binary parameters into higher-order space is Kohler-Toop with sulfur being an asymmetric component. With the expansion of the database towards As, Sb and Sn, the strong interaction between copper, iron and these metalloids (Shishin *et al*, 2019, 2023) was described using the same model within the QMF. Same model, but slightly different parameters were used in parallel studies by (Kidari and Chartrand, 2023b, 2023a). Unlike the sulfide systems, where barely any data exist for the sulfur-rich region beyond the composition of maximum SRO, the regions AsS-Cu_2S-S and AsS-Ag_2S-S were relatively well

studied experimentally. In these systems, the choice of geometric interpolation is not obvious. For the Ag-As-S, silver was selected as an asymmetric component (Kidari and Chartrand, 2023a). It is worth mentioning, that no liquid immiscibility experimental data within the Ag-Ag_2S-Ag_3As area of the diagram were available, even though the gap was predicted by the model. In the case of Cu-As-S, Muggianu-type of interpolation provided reasonable results, even though the mathematical expressions of the Muggianu-type interpolation of excess parameters written in terms of pair fraction may be incorrect in FactSage™ software. It was very challenging to describe experimental data on the immiscibility within the Cu-Cu_2S-Cu_3As together with other areas of the diagram, indicating that different types of interpolation techniques may be required for different areas of the diagram. This can only be achieved by introducing the associates within the existing MQF. While helping some systems, choice of geometric interpolations between associates and all other components can be a daunting task.

Salt

The choice of the model for salt was largely inspired by the works of Coursol *et al* (2005a, 2005b). It was decided not to merge slag and salt within the same solution but introduce the O^{-2} anions into the salt model (see Table 2). Antimony and arsenic in the +5 oxidation state will in all probability dissolve in sulfate liquids, forming antimonates and arsenates. Sulfate liquids have been demonstrated to remove As and Sb from copper metal (Coursol *et al*, 2004) and these studies are of interest for lead refining. Formation of liquid sulfates should be controlled, as it accelerates the hot corrosion of furnace components during the lead smelting and may also cause the formation of dust accretions in off-gas pathways. A possible further expansion is the introduction of SbO_4^{3-}, AsO_4^{3-} anions.

CONCLUSIONS

This review demonstrates the versatility of the Modified Quasichemical Formalism (MQF) for developing various molten phase models. The choice of the model is a balance between the predicting power of and the flexibility to provide the accurate description of reality through the optimisation of model parameters. When the focus is on multicomponent solutions, the developments in experimental techniques and generation of abundant and accurate experimental become critical. The data generated in 2014–2024 pushed the existing models to the limit in terms of accuracy and challenged some decisions that were made at the early stages of the development.

Examples of long standing issues that have been resolved recently by introducing unconventional model choices into MQF, including:

- combining Bragg-Williams and Quasichemical negative contributions into the slag model for the CaO-SiO_2, which made the tip at the enthalpy of mixing less sharp
- introducing the excess Gibbs energy parameters with powers of > 9 to describe non-ionic behaviour of slags near pure SiO_2.

An example of issue that has not been resolved yet is the inability to reconcile the activity, distribution of elements and phase equilibria for several Cu-S-containing systems. It is possible that the choice of one-sublattice approach without associates for liquid matte/metal/speiss limits the model flexibility and results in:

- incorrect heat capacity at the composition of maximum SRO requiring systematic introduction of the $T\ln T$ term in excess Gibbs energies
- inability to introduce direct excess binary parameters between two sulfides at the compositions of maximum SRO
- inability to create different geometric interpolation techniques for different areas of the ternary system X-Cu-S.

The issues and potential solutions often originate in systems of two or three components, but become evident only in multicomponent systems. For the established multicomponent thermodynamic database, any changes in low-order systems require significant efforts and iterative

re-assessment of model parameters in hundreds of related higher-order systems. This phenomenon is often compared in the CALPHAD community to re-building the foundation of the inverted pyramid. To perform re-assessments effectively, large data sets of hundreds of thousands experimental points and tools for their effective management must be developed. Newly obtained experimental information should trigger the semi-automated re-assessment. In this way, alternative model approaches potentially providing further improvements can be tested in timely manner.

ACKNOWLEDGEMENTS

The research funding and technical support is provided by the consortium of copper and lead producing companies: Anglo American Platinum (South Africa), Aurubis AG (Germany), BHP Billiton Olympic Dam Operation (Australia), Boliden (Sweden), Glencore Technology (Australia), Metso Oy (Finland), Peñoles (Mexico), RHI Magnesita (Austria), Rio Tinto Kennecott (USA) and Umicore NV (Belgium), as well Australian Research Council Linkage program LP190101020 'Future copper metallurgy for the age of e-mobility and the circular economy'. Present study would not be possible without the facilities and technical assistance of the staff of the Australian Microscopy and Microanalysis Research Facility at the Centre for Microscopy and Microanalysis in The University of Queensland.

REFERENCES

Abdul, W, Mawalala, C, Pisch, A and Bannerman, M N, 2023. $CaO\text{-}SiO_2$ assessment using 3rd generation CALPHAD models, *Cem Concr Res*, 173:107309.

Andersson, J, Helander, T, Höglund, L, Shi, P and Sundman, B, 2002. Thermo-Calc and DICTRA, Computational tools for materials science, *CALPHAD*, 26:273–312.

Bale, C W, Belisle, E, Chartrand, P, Decterov, S A, Eriksson, G, Gheribi, A E, Hack, K, Jung, I H, Kang, Y B, Melancon, J, Pelton, A D, Petersen, S, Robelin, C, Sangster, J, Spencer, P and Van Ende, M A, 2016. FactSage thermochemical software and databases, 2010–2016. *CALPHAD*, 54:35–53.

Castillo-Sanchez, J-R, Oishi, K, St-Germain, L, Ait-Amer, D and Harvey, J-P, 2023. The power of computational thermochemistry in high-temperature process design and optimization: Part 1 – Unit operations, *CALPHAD*, 82:102593.

Chartrand, P and Pelton, A D, 2001. The Modified Quasichemical Model III – Two Sublattices, *Metall Mater Trans A*, 32:1397–1407.

Cheng, S, Shevchenko, M, Hayes, P C and Jak, E, 2019. Experimental Phase Equilibria Studies in the $FeO\text{-}Fe_2O_3\text{-}CaO\text{-}SiO_2$ System in Air: Results for the Iron-Rich Region, *Metall Mater Trans B*, 51:1587–1602.

Cheng, S, Shevchenko, M, Hayes, P C and Jak, E, 2021. Experimental Phase Equilibria Studies in the $FeO\text{-}Fe_2O_3\text{-}CaO\text{-}SiO_2$ System and the Subsystems $CaO\text{-}SiO_2$, $FeO\text{-}Fe_2O_3\text{-}SiO_2$ in Air, *Metall Mater Trans B*, 52:1891–1914.

Coursol, P, Pelton, A D, Chartrand, P and Zamalloa, M, 2005a. The $CaSO_4\text{-}CaO\text{-}Ca_3(AsO_4)_2$ phase diagram, *Can Metall Q*, 44:547–553.

Coursol, P, Pelton, A D, Chartrand, P and Zamalloa, M, 2005b. The $CaSO_4\text{-}Na_2SO_4\text{-}CaO$ phase diagram, *Can Metall Q*, 44:537–545.

Coursol, P, Stubina, N, Carissimi, E, Zamalloa, M and Mackey, P J, 2004. Industrial development of a novel sulfate system for copper pyro-refining, *JOM*, 56:41–45.

Decterov, S A and Pelton, A D, 1996. Critical Evaluation and Optimization of the Thermodynamic Properties and Phase Diagrams of the $CrO\text{-}Cr_2O_3\text{-}SiO_2$ and $CrO\text{-}Cr_2O_3\text{-}SiO_2\text{-}Al_2O_3$ Systems, *J Phase Equilib*, 17:488–494.

Decterov, S A, 2018. Thermodynamic database for multicomponent oxide systems, *Chimica Techno Acta*, 5:16–48.

Decterov, S A, Dessureault, Y and Pelton, A D, 2000. Thermodynamic Modeling of Zinc Distribution among Matte, Slag and Liquid Copper, *Can Metall Q*, 39:43–54.

Dessureault, Y and Pelton, A D, 1993. An optimized thermodynamic database for matte, slag, speiss and metal phases in lead smelting, *Can Inst Min Metall Pet*, 143–151.

Dilner, D and Selleby, M, 2017. Thermodynamic description of the Fe-Ca-O-S system, *CALPHAD*, 57:118–125.

Ferrante, M J, Stuve, J M, Daut, G E and Pankratz, L B, 1978. Low-temperature heat capacities and high-temperature enthalpies of cuprous and cupric sulfides, Albany Metallurgy Research Centre, Bureau of Mines, Albany, Oregon, USA.

Gorsse, S and Senkov, O N, 2018. About the reliability of CALPHAD predictions in multicomponent systems, *Entropy*, 20:899.

Groenvold, F and Westrum Jr, E F, 1987. Thermodynamics of copper sulfides, I, Heat capacity and thermodynamic properties of copper(I) sulfide, Cu_2S, from 5 to 950 K, *J Chem Thermodyn*, 19:1183–1198.

He, Z, Haglöf, F, Chen, Q, Blomqvist, A and Selleby, M, 2022. A Third Generation Calphad Description of Fe: Revisions of Fcc, Hcp and Liquid, *Journal of Phase Equilibria and Diffusion*, 43:287–303.

Hidayat, T and Jak, E, 2014. Thermodynamic modeling of the "Cu_2O"-SiO_2, "Cu_2O"-CaO and "Cu_2O"-CaO-SiO_2 systems in equilibrium with metallic copper, *Int J Mater Res*, 105:249–257.

Hidayat, T, Fallah-Mehrjardi, A, Abdeyazdan, H, Shishin, D, Shevchenko, M, Hayes, P C and Jak, E, 2023. Integrated experimental and thermodynamic modelling study in the Pb-Fe-O-S-Si system: Effect of Temperature and p(SO2) on Slag-Matte-Metal-Tridymite Equilibria, *Metall Mater Trans B*, 54:536–549.

Hidayat, T, Shishin, D, Decterov, S A and Jak, E, 2016a. Critical thermodynamic re-evaluation and re-optimization of the CaO-FeO-Fe_2O_3-SiO_2 system, *CALPHAD*, 56:58–71.

Hidayat, T, Shishin, D, Decterov, S A and Jak, E, 2016b. Thermodynamic optimization of the Ca-Fe-O system, *Metall Trans B*, 47:256–281.

Hidayat, T, Shishin, D, Decterov, S A and Jak, E, 2017b. Experimental Study and Thermodynamic Re-evaluation of the FeO-Fe_2O_3-SiO_2 System, *J Phase Equilib Diffus*, 38:477–492.

Hidayat, T, Shishin, D, Decterov, S and Jak, E, 2017a. Critical assessment and thermodynamic modeling of the Cu-Fe-O-Si system, *CALPHAD*, 58:101–114.

Hidayat, T, Shishin, D, Jak, E and Decterov, S, 2015. Thermodynamic Reevaluation of the Fe-O System, *CALPHAD*, 48:131–144.

Hillert, M, 2001. The Compound Energy Formalism, *J Alloys Compd*, 320:161–176.

Hillert, M, Kjellqvist, L, Mao, H, Selleby, M and Sundman, B, 2009. Parameters in the compound energy formalism for ionic systems, *CALPHAD*, 33:227–232.

Hillert, M, Sundman, B and Wang, X, 1990. An assessment of the calcia-silica system, *Metall Trans B*, 21:303–312.

Jafarian, M, Arjomandi, M and Nathan, G J, 2017. Thermodynamic potential of molten copper oxide for high temperature solar energy storage and oxygen production, *Appl Energy*, 201:69–83.

Jak, E, Decterov, S A, Wu, P, Hayes, P C and Pelton, A D, 1997. Thermodynamic Optimisation of the Systems PbO-SiO_2, PbO-ZnO, ZnO-SiO_2 and PbO-ZnO-SiO_2, *Metall Mater Trans B*, 28B:1011–1018.

Jak, E, Hidayat, T, Prostakova, V, Shishin, D, Shevchenko, M and Hayes, P C, 2019. Integrated experimental and thermodynamic modelling research for primary and recycling pyrometallurgy, *EMC* Düsseldorf, Germany: GDMB Verlag.

Jak, E, Zhao, B and Hayes, P C, 1997. Experimental determination of phase equilibria in lead/zinc smelting slags and sinters, in *Proceedings of the 5th International Conference on Molten Slags Fluxes and Salts (MOLTEN '97)*, pp 719–726.

Jantzen, T, Yazhenskikh, E, Hack, K, Baben, M T, Wu, G and Mueller, M, 2021. Addition of V_2O_5 and V_2O_3 to the CaO-FeO-Fe_2O_3-MgO-SiO_2 database for vanadium distribution and viscosity calculations, *CALPHAD*, 74:102284.

Jo, Y, Lee, H-G and Kang, Y-B, 2013. Thermodynamics of the MnO-FeO-MnS-FeS-SiO_2 system at SiO_2 saturation under reducing condition: immiscibility in the liquid phase, *ISIJ Int*, 53:751–760.

Jung, I-H and Van Ende, M-A, 2020. Computational Thermodynamic Calculations: FactSage from CALPHAD Thermodynamic Database to Virtual Process Simulation, *Metall Mater Trans B*, 51:1851–1874.

Jung, I-H, Decterov, S A and Pelton, A D, 2007. Thermodynamic modeling of the CoO-SiO_2 and CoO-FeO-Fe_2O_3-SiO_2 systems, *Int J Mater Res*, 98:816–825.

Kang, Y-B and Pelton, A, 2009. Thermodynamic Model and Database for Sulfides Dissolved in Molten Oxide Slags, *Metall Mater Trans B*, 40:979–994.

Khartcyzov, G, Shevchenko, M, Cheng, S, Hayes, P C and Jak, E, 2022. Experimental phase equilibria studies in the "$CuO_{0.5}$"-CaO-SiO_2 ternary system in equilibrium with metallic copper, *Ceram Int*, 48:9927–9938.

Kidari, O and Chartrand, P, 2023a. Thermodynamic Evaluation and Optimization of the Ag-As-S system, *J Phase Equilib Diffus*, 44:269–299.

Kidari, O and Chartrand, P, 2023b. Thermodynamic evaluation and optimization of the As-Co, As-Fe and As-Fe-S systems, *CALPHAD*, 82:102589.

Konar, B, Van Ende, M-A and Jung, I-H, 2017. Critical evaluation and thermodynamic optimization of the Li-O and Li_2O-SiO_2 systems, *J Eur Ceram Soc*, 37:2189–2207.

Kongoli, F, Dessureault, Y and Pelton, A D, 1998. Thermodynamic Modeling of Liquid Fe-Ni-Cu-Co-S Mattes, *Metall Mater Trans B*, 29B:591–601.

Lambotte, G and Chartrand, P, 2011. Thermodynamic optimization of the (Na_2O + SiO_2 + NaF + SiF_4) reciprocal system using the Modified Quasichemical Model in the Quadruplet Approximation, *J Chem Thermodyn*, 43:1678–1699.

Lambotte, G and Chartrand, P, 2013. Thermodynamic modeling of the (Al_2O_3 + Na_2O), (Al_2O_3 + Na_2O + SiO_2) and (Al_2O_3 + Na_2O + AlF_3 + NaF) systems, *J Chem Thermodyn*, 57:306–334.

Nekhoroshev, E, 2019. Thermodynamic Optimization Of The Na_2O-K_2O-Al_2O_3-CaO-MgO-B_2O_3-SiO_2 System, PhD thesis, Polytechnique Montréal.

Pelton, A D and Blander, M, 1984. Computer-Assisted Analysis of the Thermodynamic Properties and Phase Diagrams of Slags, in *Proceedings of the Second International Symposium on Metallurgical Slags and Fluxes* (eds: H A Fine and D R Gaskell), pp 281–294 (TMS-AIME: Warrendale).

Pelton, A D and Blander, M, 1986. Thermodynamic Analysis of Ordered Liquid Solutions by a Modified Quasi-Chemical Approach, Application to Silicate Slags, *Metall Trans B*, 17B:805–815.

Pelton, A D and Chartrand, P, 2001. The Modified Quasichemical Model, II – Multicomponent Solutions, *Metall Mater Trans A*, 32:1355–1360.

Pelton, A D and Kang, Y-B, 2007. Modeling short-range ordering in solutions, *Int J Mater Res*, 98:907–917.

Pelton, A D, Chartrand, P and Eriksson, G, 2001. The modified Quasichemical Model, IV – Two Sublattice Quadruplet Approximation, *Metall Mater Trans A*, 32:1409–1415.

Pelton, A D, Decterov, S A, Eriksson, G, Robelin, C and Dessureault, Y, 2000. The Modified Quasichemical Model, I – Binary Solutions, *Metall Mater Trans B*, 31:651–659.

Prostakova, V, Chen, J, Jak, E and Decterov, S A, 2012. Experimental study and thermodynamic optimization of the CaO-NiO, MgO-NiO and NiO-SiO_2 systems, *CALPHAD*, 37:1–10.

Prostakova, V, Chen, J, Jak, E and Decterov, S, 2013. Experimental study and thermodynamic optimization of the MgO-NiO-SiO_2 system, *J Chem Thermodyn*, 62:43–55.

Prostakova, V, Shishin, D and Jak, E, 2021. Thermodynamic optimization of the Cu-As-S system, *CALPHAD*, 72:102247.

Selleby, M and Sundman, B, 1996. A Reassessment of the Ca-Fe-O System, *CALPHAD*, 20:381–392.

Selleby, M, 1997. An Assessment of the Ca-Fe-O-Si System, *Metall Trans B*, 28B:577–596.

Shevchenko, M, Shishin, D and Jak, E, 2022. Integrated phase equilibria experimental study and thermodynamic modeling of the Cr-Si-O, Fe-Cr-O and Fe-Cr-Si-O systems, *Ceram Int*, 48(22):33418–33439. https://doi.org/10.1016/j.ceramint.2022.07.286

Shevchenko, M, Shishin, D and Jak, E, 2024. Advancement in experimental methodologies to produce phase equilibria and thermodynamic data in multicomponent systems, in *Proceedings of the 12th International Conference on Molten Slags Fluxes and Salts (MOLTEN 2024)*, pp 531–558 (The Australasian Institute of Mining and Metallurgy: Melbourne).

Shishin, D and Decterov, S A, 2012. Critical assessment and thermodynamic modeling of Cu-O and Cu-O-S systems, *CALPHAD*, 38:59–70.

Shishin, D and Jak, E, 2018. Critical assessment and thermodynamic modeling of the Cu-As system, *CALPHAD*, 60:134–143.

Shishin, D, Chen, J and Jak, E, 2020. Thermodynamic Modeling of the Pb-S and Cu-Pb-S Systems with Focus on Lead Refining Conditions, *J Phase Equilib Diffus*, 41:218–233.

Shishin, D, Chen, J, Hidayat, T and Jak, E, 2019. Thermodynamic modelling of the Pb-As and Cu-Pb-As systems supported by experimental study, *J Phase Equilib Diff*, 40:758–767.

Shishin, D, Fallah Mehrjardi, A, Shevchenko, M, Hidayat, T and Jak, E, 2020. Experimental study, thermodynamic calculations and industrial implications of slag/matte/metal equilibria in the Cu-Pb-Fe-O-S-Si system, *J Mater Res Technol*, 19:899–912. https://doi.org/10.1016/j.jmrt.2022.05.058

Shishin, D, Hidayat, T, Chen, J, Hayes, P C and Jak, E, 2018a. Experimental Investigation and Thermodynamic Modelling of the Distributions of Ag and Au between Slag, Matte and Metal in the Cu-Fe-O-S-Si System, *Journal of Sustainable Metallurgy*, 5:240–249.

Shishin, D, Hidayat, T, Chen, J, Hayes, P C and Jak, E, 2018b. Integrated Experimental Study and Thermodynamic Modelling of the Distribution of Arsenic between Phases in the Cu-Fe-O-S-Si System, *J Chem Thermodyn*, 135:175–182.

Shishin, D, Hidayat, T, Jak, E and Decterov, S, 2013. Critical assessment and thermodynamic modeling of Cu-Fe-O system, *CALPHAD*, 41:160–179.

Shishin, D, Jak, E and Decterov, S A, 2015. Thermodynamic assessment and database for the Cu–Fe–O–S system, *CALPHAD*, 50:144–160.

Shishin, D, Shevchenko, M, Starykh, R, Sineva, S, Prostakova, V and Jak, E, 2023. Development and application of matte/speiss/metal thermodynamic database for optimization of processing of drosses, dusts and reverts from lead, zinc and copper production, in *Proceedings of the 10th International Conference on Lead and Zinc Processing (Lead-Zinc 2023)*, Journal of Physics: Conference Series, 2738:012032. https://doi.org/10.1088/1742-6596/2738/1/012032.

Sineva, S, Shishin, D, Prostakova, V, Fallah-Mehrjardi, A and Jak, E, 2023. Experimental Study and Thermodynamic Analysis of High-temperature Processing of mixed Ni-Cu sulfide feed, in *Proceedings of the 62nd Annual Conference of Metallurgists (COM 2023)*, pp 779–787. https://doi.org/10.1007/978-3-031-38141-6_102

Sundman, B, 1991. Modification of the Two-sublattice Model for Liquids, *CALPHAD*, 15:109–119.

Sundström, A, Eksteen, J J and Georgalli, G A, 2008. A review of the physical properties of base metal mattes, *Journal of The South African Institute of Mining and Metallurgy*, 108:431–448.

Waldner, P and Pelton, A D, 2004a. Critical Thermodynamic Assessment and Modeling of the Fe-Ni-S System, *Metall Mater Trans B*, 35:897–907.

Waldner, P and Pelton, A D, 2004b. Thermodynamic modeling of the Ni-S system, *Z Metallkd*, 95:672–681.

Waldner, P and Pelton, A D, 2005. Thermodynamic modeling of the Fe-S system, *J Phase Equilib Diff*, 26:23–28.

Waldner, P and Sitte, W, 2011. Thermodynamic modeling of the Cr-S system, *Int J Mater Res*, 102:1216–1225.

Waldner, P, 2020. Gibbs Energy Modeling of the Cu-S Liquid Phase: Completion of the Thermodynamic Calculation of the Cu-S System, *Metall Mater Trans B*, 51:805–817. https://doi.org/10.1007/s11663-020-01796-x

Waldner, P, 2022. The High-Temperature Cu-Fe-S System: Thermodynamic Analysis and Prediction of the Liquid–Solid Phase Range, *J Phase Equilib Diff*, 43:495–510. https://doi.org/10.1007/s11669-022-00988-z

Wang, K and Chartrand, P, 2021. Generic energy formalism for reciprocal quadruplets within the two-sublattice quasichemical model, *CALPHAD*, 74:102293.

Wang, K, Li, D, Zou, X, Cheng, H, Li, C, Lu, X and Chou, K, 2023. Generic bond energy formalism within the modified quasichemical model for ternary solutions, *J Mol Liq*, 370:120932.

Wen, X, Shevchenko, M and Jak, E, 2021. Experimental study of "$CuO_{0.5}$"-"FeO"-SiO_2 and "FeO"-SiO_2 systems in equilibrium with metal at 1400–1680°C, *J Alloys Compd*, 885:160853.

Wen, X, Shevchenko, M, Nekhoroshev, E and Jak, E, 2023. Phase equilibria and thermodynamic modelling of the PbO–ZnO-"$CuO_{0.5}$"-SiO_2 system, *Ceram Int*, 49(14)A:23817–23834. https://doi.org/10.1016/j.ceramint.2023.04.223

Wu, P, Eriksson, G and Pelton, A D, 1993. Critical Evaluation and Optimization of the Thermodynamic Properties and Phase Diagrams of the Calcia-Iron(II) Oxide, Calcia-Magnesia, Calcia-Manganese(II) Oxide, Iron(II) Oxide-Magnesia, Iron(II) Oxide-Manganese(II) Oxide and Magnesia-Manganese(II) Oxide Systems, *J Am Ceram Soc*, 76:2065–2075.

Wu, P, Eriksson, G, Pelton, A D and Blander, M, 1993. Prediction of the Thermodynamic Properties and Phase Diagrams of Silicate Systems – Evaluation of the FeO-MgO-SiO_2 System, *ISIJ Int*, 33:26–35.

Prognostic models for electroslag remelting process and slag engineering

DOI: 10.62053/TBYL4271

G Stovpchenko[1], L Medovar[2], L Lisova[3], D Stepanenko[4] and D Togobitskaya[5]

1. Chief Foreign Scientist, Tianjin Heavy Industries Research and Development Co, Ltd, Tianjin 300457, China; EO Paton Electric Welding Institute of National Academy of Sciences of Ukraine (NASU), Kyiv 03150, Ukraine. Email: anna_stovpchenko@ukr.net; stovpchenko@cfhi.com
2. Chief Foreign Scientist, Tianjin Heavy Industries Research and Development Co, Ltd, Tianjin 300457, China; EO Paton Electric Welding Institute of NASU, Kyiv 03150, Ukraine. Email: medovar@ukr.net; medovar@cfhi.com
3. Research Associate, Chair of Metal Forming and Casting, School of Engineering and Design, Technical University of Munich, Munich 80333, Germany; EO Paton Electric Welding Institute of NASU, Kyiv 03150, Ukraine. Email: llisova@ukr.net
4. Head of the Department of Physicochemical Problems of Metallurgical Processes, ZI Nekrasov Iron and Steel Institute NASU, Dnipro 49107, Ukraine. Email: d.gorodenskiy@gmail.com
5. Leading Researcher of Physicochemical Problems of Metallurgical Processes, ZI Nekrasov Iron and Steel Institute NASU, Dnipro 49107, Ukraine. Email: dntog@ukr.net

ABSTRACT

Classical electroslag remelting of consumable electrodes is a drop-by-drop melt feeding through a slag layer into a renewing molten metal bath, slowly solidifying into a homogeneous, dense, defect-free ingot in a copper water-cooled mould. The new look at the additive nature of the electroslag remelting (ESR) process in a protective atmosphere allowed us to formulate the principles of a comprehensive thermodynamic-based model that can predict dynamic changes in slag and metal composition at certain ingot remelting. The model considers drastically different slag-to-metal mass ratios at the beginning and end of remelting and predicts gas, slag and metal composition in a chain of thermodynamic subsystems. Despite consisting of calcium fluoride and stable oxides, the ESR slag can oxidise main and active elements from steel and alloys (primarily aluminium, titanium and silicon) due to chemical reactions between slag and metal. ESR is not an electrochemical process in its nature. However, slags are ionic melts and deviation in their composition causes a change in their properties, affecting both operation mode and ingot quality.

Another important understanding derived from the modern metallurgy technological route is that the ability to refine metal from impurities is not a priority for the ESR because consumable electrode has already passed all stages of refining and deep degassing at ladle treatment that changes ESR slags engineering principles. The critical importance became slag's ability to generate process heat and keep the melting composition in the metal bath unchanged (except for non-metallic inclusions assimilation). Slag engineering for ESR required a compromise between chemical inertness to a metal composition and desired physical properties deriving from technological reasons. The Directed Chemical Bonds Concept (DCBC) in a multicomponent oxide system was used to build predictive models of electric conductivity and the melting temperature of fluoride-oxide slag based on their chemical composition. Both models help to design a customised composition of effective slags for steel and alloy groups or individual grades, and they are significant steps in the development of a comprehensive model of electroslag remelting.

INTRODUCTION

In the technological chain of high-quality steel product manufacturing, electroslag remelting (ESR) takes one of the last but not least places. It refines the melt from impurities and inclusion and refines the ingot structure, increasing yield. That is exactly due to the homogeneity of the chemical composition and the dense dendritic structure over the cross-section and height of the ingot ESR metal, which is in demand for the most critical applications in modern industry (Medovar and Boyko, 2013; Hoyle, 1983).

The low rate of metal supply through the slag layer, which simultaneously performs the functions of an electric heater and thermal buffer for the process and refining media, guarantees a relatively small

depth of the liquid metal bath. The progressively replaced composition of the liquid metal bath provides significantly less segregation of elements than in a conventional same-diameter ingot. The second important feature of the ESR ingot is its dense dendritic structure, no shrinkage and smooth side surface, which ensures a high product yield. As a result, the low rate of ESR ingot formation in copper water-cooled mould (tens to hundreds of times lower than traditional ingots and continuously cast billets) is a prerequisite of well-recognised worldwide 'ESR quality'.

The electrical conductivity of the slag bath determines the performance and efficiency of the melting process, while the slag melting temperature and interval determine metal overheat, liquid metal bath depth, and ingot surface formation pattern, which in turn are efficiency factors for metal refining and homogeneity of ESR ingot. Thus, ESR slag is an indispensable component of the process, and its composition and properties are crucial for metal quality, process efficiency and cost. Knowledge of slag's chemical and physical properties and their impact on the remelting process is key to achieving high quality and efficiency. This article aims to provide a clear understanding of the changes that occur in the physicochemical system during the remelting of consumable electrodes in a protective gas atmosphere using a single slag charged at the start of the process. It emphasises the significant differences in slag-metal interaction conditions between ESR ingot formation's start and end points. The article asserts that slag is a critical component for ensuring consistency and stability in the ESR process and demonstrates the efficacy of an atomistic approach in predicting its crucial physical properties.

CONCEPT OF GAS-SLAG-METAL SYSTEM CHARACTERISATION AT ESR REMELTING IN INERT GAS

Electroslag remelting is an arc-less process powered by the heat generated by the passage of electric current through the electric conductive slag bath (Figure 1(3)). When slag temperature exceeds the melting point of a metal, the consumable electrode begins to melt. Metal drops go down from the electrode tip through a slag layer and accumulate in the metal pool (Figure 1(4)), which gradually solidifies, forming an ingot (Figure 1(6)). The reacting system at the ESR in each instant moment consists of a film on the edge of the consumable electrode, a liquid slag bath with falling metal drops inside, and a liquid metal pool whose bottom end solidifies, forming an ingot (Medovar and Boyko, 2013, Stovpchenko *et al*, 2020a).

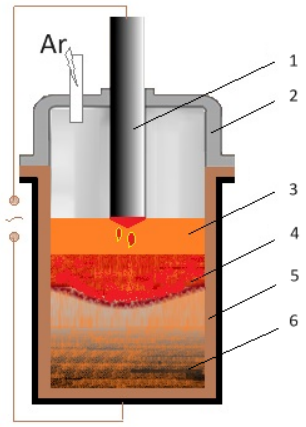

FIG 1 – ESR in argon protective atmosphere: (1) consumable electrode; (2) protective gas hood; (3) slag bath; (4) liquid metal pool; (5) mould; (6) solid ingot.

High temperatures of the melts and the developed surface of slag-metal interactions bring reactions closer to equilibrium (Mills, 2021; Hou *et al*, 2021; Duan *et al*, 2019). Nevertheless, specific features of gas-slag-metal system interactions at electroslag remelting must be outlined to clearly understand characteristic conditions that are a basis for further technological improvement.

Gas atmosphere contacts with slag only. Gaseous products of slag-metal reactions and evaporations from slag are removed in the furnace atmosphere (which is inert and slowly renewed). The gas atmosphere over the slag bath has no direct contact with liquid metal and does not participate in the

mentioned interactions, but in the case when it contains oxygen, the electrode surface can be oxidised. Using an oxygen-free atmosphere (mostly argon or nitrogen, depending on steel grade) solves this problem by preventing the growth of oxygen activity in a slag and oxygen transfer to the metal caused by variable valence oxides (primarily iron oxides) involving atmospheric oxygen. For this reason, the closed hood that covers a whole electrode to keep the protective gas atmosphere became a benchmark in today's ESR plants. Incrementally solidifying in the bottom of a liquid metal pool, the ingot leaves the reaction zone (after interacting with slag). On the contrary, molten slag continues to participate in refining processes and assimilates slag-metal interaction products and non-metallic inclusions from the consumable electrode.

The most common ESR practice must envisage charging the entire slag mass at the start of the remelting process and no additions of premelted slag (or slag components) are used. Thus, it is crucial to understand that the slag-to-metal ratio changes throughout the entire remelting process, as all the products of the interactions between the slag and metal and most of the nonmetal inclusions from consumable electrodes are accumulated in the slag bath.

From the formal logic, it is understandable that a permanent change and drastic difference in the slag-metal mass ratio (Figure 2) causes radically different conditions for slag-metal interaction during electroslag remelting.

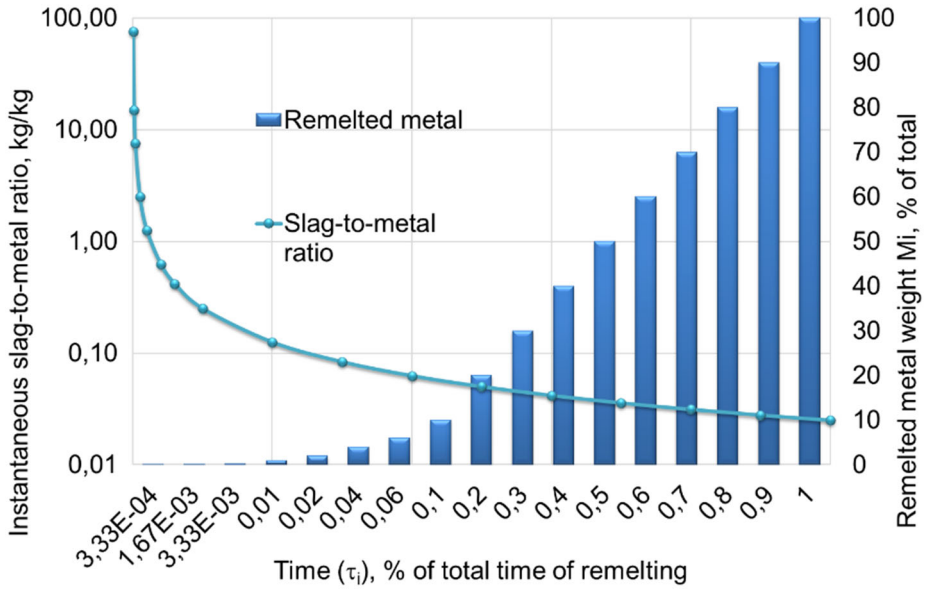

FIG 2 – Graphical representation of slag-metal interaction mass conditions at electroslag remelting (ESR) ingot formation (in an inert atmosphere) when a whole slag consumption makes 25 kg/ton of metal charged at the start.

The diagram summarises and demonstrates the characteristics of the physical and chemical processes that occur during ESR. The slag-to-metal ratio changes are shown for specific slag consumption of 25 kg/t of metal. However, the trend uncovered is general, regardless of its given value. Specific slag consumption usually makes 20–40 kg per ton, and exactly the last figure is usually used for thermodynamic calculations of the ESR, shoving just a very average result. However, due to the enormous slag-to-metal ratio in the first minutes of the remelting, the oxygen-bearing slag oxidates a metal the most at the beginning of the process. This effect cannot be neglected because the oxidative effect of slag remains tangible for quite a long time and can be a reason for ingot inhomogeneity along its height.

The physical properties of a slag itself are not less significant and they must be tested for their relevance to the requirements for an efficient ESR process. It is also important to find deeper dependencies between experimentally found values and chemical composition using atomistic approaches, which allows the prediction of molten slag physical properties and makes the choice of slags more deterministic. Directed Chemical Bonds Concept (DCBC) that was created by Professor E Prikhodko and continues to be developed by his followers at the ZI Nekrasov Institute of Ferrous

Metallurgy of the National Academy of Sciences of Ukraine (NASU) (Prikhodko, 1995a, 1995b; Prikhodko *et al*, 2013; Stepanenko, 2023; Stovpchenko *et al*, 2022) was chosen for these purposes.

METHODOLOGY OF RESEARCH

The first stage (Figure 3) of the evaluation procedure of slag-metal interaction is to construct the proposed 'quasi-dynamic' description (Figure 2) of the ESP process – a dynamic model of ESR in an inert atmosphere – in the form of a line of subsystems. This line of subsystems (masses of gas, slag and metal phases) for the predictive model of physicochemical interaction at ESR while consumable electrode remelting should be compiled using industrial data at certain ingot formation: typical slag consumption and rate of remelting. The input data is the mass of metal (mi) that is remelted to a certain point of time (τ_i), considering experimental data about the melting rate, the whole mass of slag and the volume of argon in the close chamber of the ESR plant. The proper time intervals (i), depending on the chosen purpose and number of calculations, should be determined, and for each conventional time, a subsystem of the whole masses of slag, gas and instantaneous mass of molten metal should be composed. For all subsystems, the remelted metal mass is only a variable (m_i); the primary mass of components of slag and gas phases are the same.

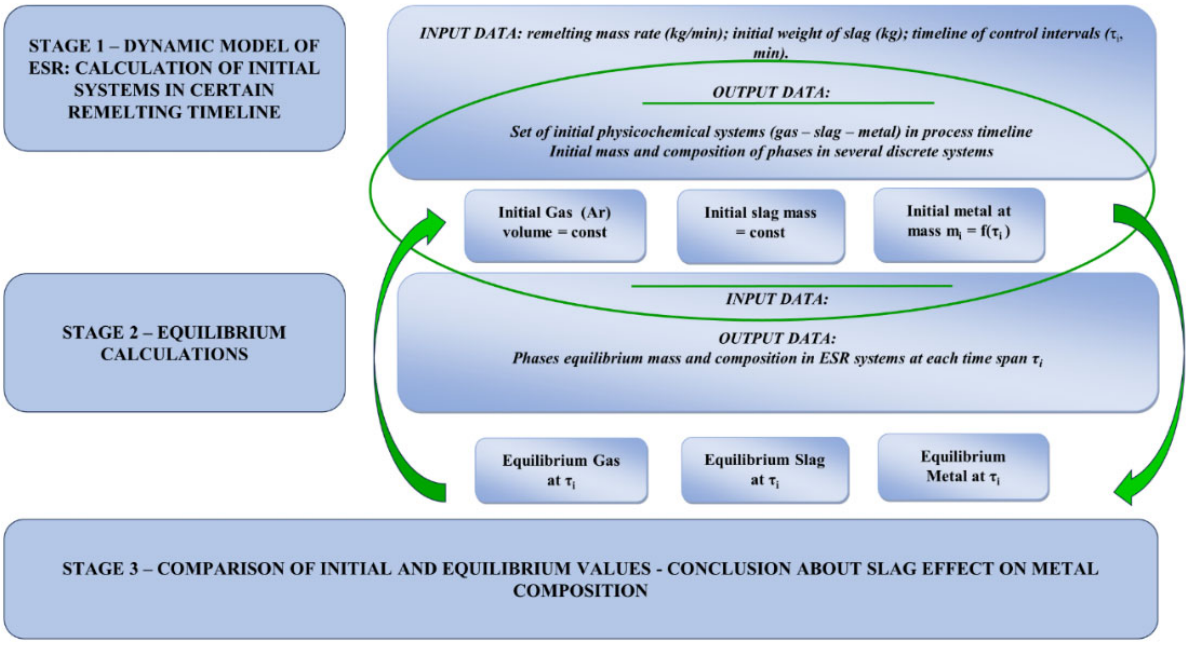

FIG 3 – The procedure of physicochemical modelling of the gas-slag-metal interaction in the inert atmosphere at the electroslag remelting (ESR) process course.

For each physicochemical subsystem, the masses and compositions of gas, slag, and metal phases at the chosen time of electroslag remelting should be calculated and used as initial data in software for equilibrium composition calculations. In the second modelling stage, thermodynamic calculations of the equilibrium state of the 'gas-slag-metal' system using CALPHAD Methodology (Lukas, Fries and Sundman, 2008; Sundman, 2016) implemented in HSC Chemistry, Pandat, ThermoCalc and similar possibility software can be used for this purpose. In the presented examples, thermodynamic calculations for the 'gas-slag-metal' system were made using HSC Chemistry software.

In the third stage, primary mass data of subsystems and equilibrium calculations are compared to recognise changes in phases' masses and composition. The overall analysis of received results allows for the finding of prospective slag compositions from a chemical point of view.

Changes in metal composition were calculated according to the proposed dynamic physicochemical model of ESR for comparative slag $34CaF_2/30Al_2O_3/27CaO/0.5SiO_2/2.5MgO/6TiO_2$ and Inconel 718 (Table 1) at 1873 K.

TABLE 1

The chemical composition of the Inconel 718 used in the calculation.

Elements content, wt%								
Ni	**Cr**	**Fe**	**Nb**	**Mo**	**Ti**	**Al**	**C**	**B**
53.7	18.2	18.2	5.4	3	1	0.5	0.03	0.004

The total system for dynamic ESR model demonstration comprised 300 kg of slag, 6.47 kg of argon atmosphere and a part of the total ingot mass (19 000 kg) of 1000 mm in diameter, corresponding to a certain time interval. This instantaneous metal mass and slag-to-metal ratio in a certain conditional time of remelting were found from the melting rate (14.2 kg/min), which was taken from the ESR practice of producing similar ingots. The main advantage of the proposed dynamic model is that it allows for predicting probable changes in ingot composition along its height caused by interaction conditions changes in gas-slag-metal. The main limitation is that it is very time-consuming (for ten times points and two slags, it would require creating and calculating 20 subsystems), making it impractical for cases when process dynamic is the same or ingot inhomogeneity is not a problem.

For example, a comparison of the effects of different slags on a metal composition could be done by traditional single-system thermodynamic estimation, slightly modifying it. Our approach involves using a higher slag-to-metal ratio typical for the stationary stage of the ESR. The suggested reacting system includes the entire slag mass and the mass of a liquid metal pool in a volume equal to a half-sphere with a depth equal to a certain ingot radius. Such a system gives more pronounced changes in phase composition than using a specific consumption value. The estimation presented here was made for an ingot 1000 mm in diameter. Such a single reacting system consisted of 2200 kg of liquid metal, 300 kg of a slag bath and 6.47 kg of argon. In the following calculations, the slag-to-metal ratio makes 0.14 (instead of a 0.016 value for the specific consumption at the above-described 19 000 kg ESR ingot). The single-system comparison was made for slags (#1–2, 1–3, 2–5 and 4–3) with the wider melting range whose compositions are given in Table 2.

TABLE 2

Composition and experimentally determined properties of slags system CaF_2-Al_2O_3-TiO_2-MgO.

Slag #	Components content, wt%				Melting temperature / melting range, K	Electrical conductivity at 1873 K
	CaF_2	Al_2O_3	TiO_2	MgO		
1–1	10	60	21	9	No data	625
1–2	20	54	18	8	1623 / 330	375
1–3	30	47	16	7	1653 / 190	279
2–1	70	0	30	0	No data	1064
2–2	63	10	27	0	1513 / 90	967
2–3	56	20	24	0	1543 / 80	760
2–4	49	30	21	0	1603 /80	449
2–5	42	40	18	0	1693 / 130	322
3–3	56	24	20	0	1533 / 60	541
4–1	50	22	18	10	1603 / 70	523
4–2	45	19	16	20	1473 /100	967
4–3	40	17	13	30	1583 / 110	625

Slags' physical properties should also be relevant to the ESR process. The molten slags' electrical conductivity and melting temperature range were measured experimentally (Table 2). The electrical

conductivity of slags was measured using a bridge-type three-electrode measuring cell (Kolisnyk *et al*, 1980) with KCL solution as the reference media. The melting interval was determined visually using an optical microscope to monitor slag particle behaviour on a heated molybdenum plate in argon. A tungsten rhenium thermocouple WRE5/20 was used to control the temperature.

The dependency between experimentally determined values and chemical composition was searched using the model of the ordered structure of oxide melts. The basics of Professor Prikhodko's physicochemical model (Prikhodko, 1995a, 1995b; Prikhodko *et al*, 2013) is the description of the act of elementary interaction of each pair of elements with unpolarised atomic radii R_{ui}, R_{uj} at a distance d between them in a multicomponent system by calculating a set of partial parameters in Equations 1–4:

$$\begin{cases} R_{u_i} + R_{u_j} = d \\ lgR_{u_i} = lg\dot{R}_{u_i} - Z_{ij} \cdot tg\alpha_i \\ lgR_{u_j} = lg\dot{R}_{u_j} - Z_{ij} \cdot tg\alpha_A \end{cases} \quad (1)$$

where Z_{ij} is calculated using the formula:

$$Z_{ij} = \frac{lg\frac{\dot{R}_{u_i} \cdot tg\alpha_i}{\dot{R}_{u_j} \cdot tg\alpha_j}}{(tg\alpha_i + tg\alpha_j)} + \frac{\Delta e_{ij}}{2} \quad (2)$$

The slags' chemical composition effect on their properties was assessed by the index of the cationic sublattice ΔZm non-equilibrium state, which is expressed by the equation:

$$\Delta Zm = \left(Z_{K(K-A)} - Z_{K(K-K)}\right) - \left(\frac{\frac{R_{u_A}}{R_{u_K}} - 0.53}{15{,}43(tg\alpha_K)^{1{,}5075}} + 0{,}51\right) \quad (3)$$

where R_{uK}, R_{uA} are the ionic radii of cations and anions; $Z_{K(K-A)}$ and $Z_{K(K-K)}$ are the average statistical charges of atoms in the cation-anion and cation-cation bonds, respectively, and $tg\alpha_K$ is a weighted average parameter characterising the change in the radii of cations when their charge changes:

$$tg\alpha_K = \sum_{i=1}^{n} tg\alpha_i \quad (4)$$

This semi-empirical approach considers slag a chemically united system whose melt properties depend on structure. Based on this concept, an oxide-fluoride melt composition can be transformed into integral criteria. Derived criteria are used to predict certain slag properties.

RESEARCH RESULTS

Outcomes of slag-metal interaction prediction in the course of electroslag remelting

Figure 4 presents the equilibrium content of elements in the metal phase that are most oxidised by sags' oxides and the slag-to-metal ratio corresponding to a certain conventional time of remelting in seven certain subsystems (shown as points on built curves).

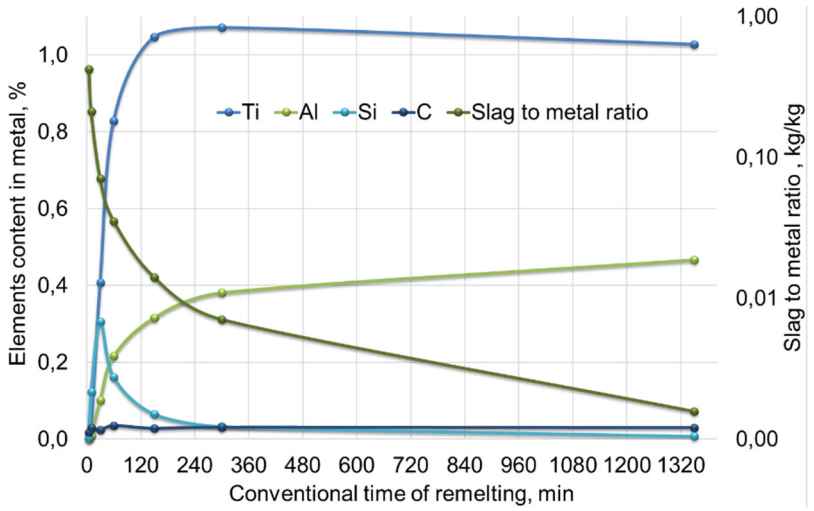

FIG 4 – Equilibrium content of active to oxygen elements in metal phase and slag to metal ratio at Inconel 718 remelting with slag $34CaF_2$-$30Al_2O_3$-27CaO-$0.5SiO_2$-$2.5MgO$-$6TiO_2$.

The slag-metal mass ratio at the fifth minute of remelting is nearly 42 kg/kg and drops throughout the process to 0.016 kg/kg at the completion of the melt. It is well visible that the system is most reactive when the slag-to-metal ratio is very high at the beginning of the remelting. Due to that, slag's oxidation action sufficiently affects the content of elements, which react with oxygen at this period. The content in the metal of active elements whose presence is critical for alloy properties (Ti, Al) at the process beginning (first 30–60 minutes) is close to zero. The sufficient changes in the content of both titanium and aluminium occur for around the first two hours, while the mass losses of the metal phase and gains of the slag phase mainly occur (Figure 5).

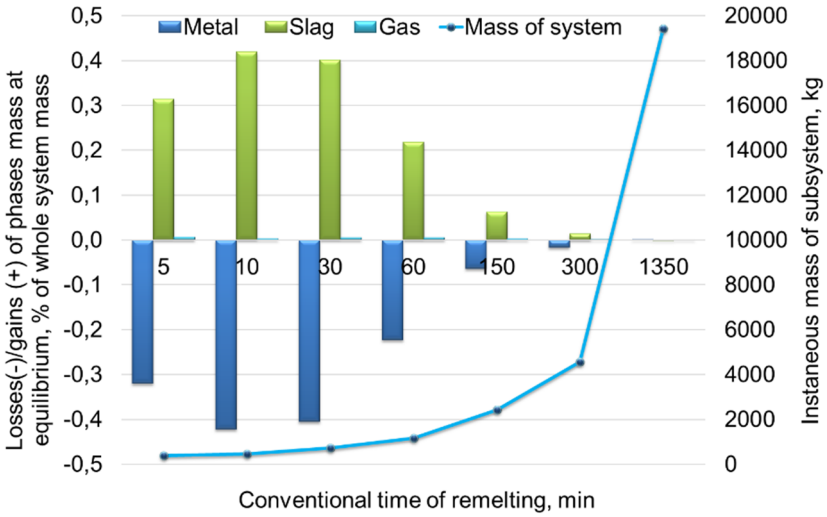

FIG 5 – Phases losses/gains in the reactive subsystems at a course of ESR in argon atmosphere (line is plotted by additional vertical axis).

After that period, when metal phase amounts start to be bigger (and the slag-to-metal ratio – smaller) than some critical values, the relative losses of equilibrium metal phase mass go down. This critical time can be supposed to be the time when the oxidative ability of slag is exhausted. Nevertheless, it does not mean that exchange reactions between slag and metal phases are stopped. It is visible (Figure 4) that titanium content grows during up to four hours. Despite a slight permanent reduction of its content during the lasting time, it is still higher than the initial value.

Aluminium content grows to the end of the remelting but doesn't reach the initial content due to silicon reduction from the slag, which goes most actively in the first minutes. At the start of the process, the silicon content goes to maximum and reduces during more than two hours of remelting and it is still in metal until the end of the melt. Carbon in metal shifts by 0.01–0.02 per cent from the

initial value in the period of metal losses. Thus, the calculations under the developed dynamic model of the gas-slag-metal interaction during the ESR process under a protective atmosphere show that even in an inert gas atmosphere, changes in oxygen-active elements content in the metal phase take place, which cause inhomogeneity of their content along ingot height.

When the dynamic of the ESR process is the same (same ingot, melting rate) or precise evaluation is not important, the assessment of interactions in the gas-slag-metal system can be done using a single system approach – the results of such a way for comparing four ESR slag actions (Figure 6).

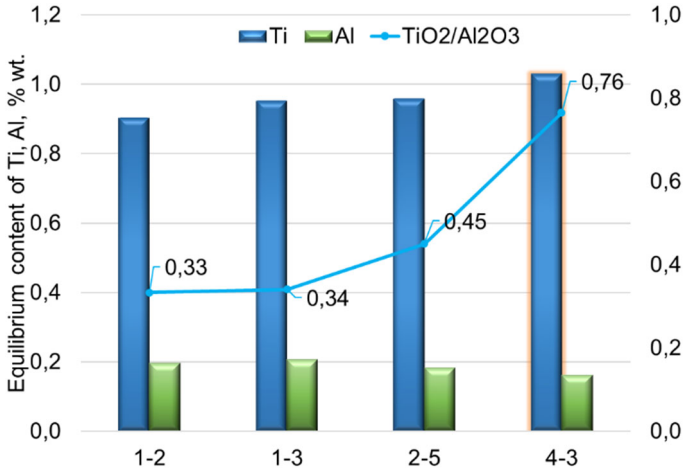

FIG 6 – Al and Ti equilibrium content in the metal phase interacted with slags having different TiO_2/Al_2O_3 ratios in their compositions (Table 2).

Inconel 718 has an extensive solidification range (1483–1617 K), so slags with the widest melting range (1–2, 1–3, 2–5 and 4–3) were compared. For slag with the highest TiO_2/Al_2O_3 ratio, the titanium content in the metal is slightly higher than the initial one (1 wt per cent), possibly due to the reduction of titanium from the slag. This version is also supported by the greatest loss in aluminium content in metal compared to other slags used. However, the cause may also be a metal loss, as was found for the comparative slag $34CaF_2$-$30Al_2O_3$-27CaO-$0.5SiO_2$-2.5MgO-$6TiO_2$. The titanium content close to the original was calculated using 1–3 and 2–5 slags. Aluminium losses in the metal are minimal for slags 1–2 and 1–3. Slag 1–3 is the most inert from the point of view of preserving both elements.

Outcomes of slag's physical properties modelling using Directed Chemical Bonds Concept

The atomistic approach was used to interpret slag's measured properties from the Directed Chemical Bonds Concept (DCBC) standpoint to build predictive models for slag engineering considering the physical properties of ESR slag melts. Table 3 lists the unpolarised radii of atoms ($\dot{R}_{u_i}$) and the gradient of changes in the radii of atoms from their charge ($t\dot{g}\alpha_i$) that belongs to elements in the studied slag system CaF_2-Al_2O_3-TiO_2-MgO (Table 2).

TABLE 3

Radii of elements ($\dot{R}_{u_i}$) and gradients of their change from their charge ($tg\alpha_i$) to interaction.

Element	$\dot{R}_{u_i}$, (10^{-1}nm)	$t\dot{g}\alpha_i$
Ca	2.02	0.151
Ti	1.45	0.085
Al	1.468	0.156
Mg	1.6	0.196
O	0.73	0.136
F	0.96	0.142

Table 4 presents the interatomic interaction parameters calculated for experimental slag compositions of the CaF_2-Al_2O_3-TiO_2-MgO system.

TABLE 4

The parameters of interatomic interaction in the studied slags' melts.

Slag #	d	Δe	tgα	ΔZm	Zka	Zkk	Zaa	Zak
1–1	3.2513	-2.7444	0.1502	0.0108	-0.23031	-1.32999	-3.57101	-2.5141
1–2	3.2274	-2.5349	0.1506	0.0062	-0.12664	-1.22344	-3.45441	-2.40823
1–3	3.2209	-2.3552	0.1505	0.0031	-0.04222	-1.13722	-3.3533	-2.3131
2–1	3.8161	-2.7419	0.1315	0.0269	-0.42814	-1.56892	-3.45975	-2.31482
2–2	3.6791	-2.6378	0.1351	0.0194	-0.33979	-1.46586	-3.42745	-2.2989
2–3	3.5347	-2.5097	0.1383	0.0125	-0.24118	-1.35587	-3.38104	-2.26926
2–4	3.3836	-2.3573	0.1413	0.0062	-0.13198	-1.2385	-3.32003	-2.22589
2–5	3.2256	-2.1782	0.1439	0.0007	-0.01087	-1.1124	-3.24295	-2.16775
3–3	3.4051	-2.2597	0.1412	0.0051	-0.08413	-1.18915	-3.26822	-2.17643
4–1	3.5018	-2.5083	0.15	0.0108	-0.14606	-1.2391	-3.41106	-2.3627
4–2	3.5744	-2.6832	0.1577	0.0111	-0.17787	-1.25373	-3.52106	-2.50572
4–3	3.6024	-2.7749	0.1649	0.0058	-0.16662	-1.2217	-3.59282	-2.60856

These parameters characterise the chemical and structural state of the slag systems: *d* (10^{-1} nm) is the average interatomic distance of interacting ions in the melt; *Δe* represents the number of electrons localised in the direction of their connection, e; *tgα* means the weighted average value of the gradients of changes in ion radii with changing its charge; *ρ* expresses the ratio of the number of cations to the number of anions; Δ*Zm*, as was mentioned above, is the indicator of non-equilibrium state of cationic sublattice.

The analysis showed that the parameter of the non-equilibrium state of cationic sublattice *ΔZm* demonstrates a close relationship with the chemical composition of the slags under study (Figure 7). The physicochemical essence of the parameter *ΔZm* characterises the stability of the cationic sublattice: the stability condition is that *ΔZm* tends to zero.

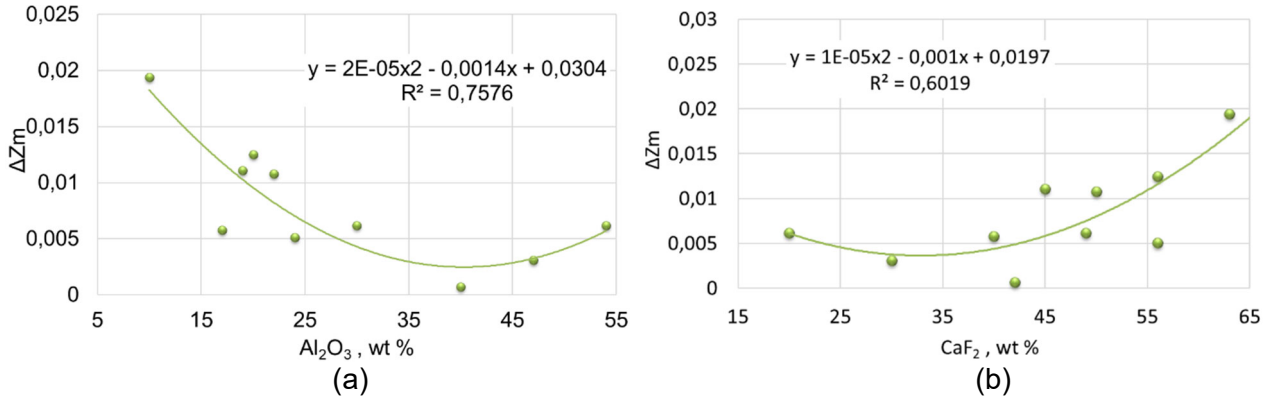

FIG 7 – Relationship between the content of Al_2O_3 (a) and CaF_2 (b) with the non-equilibrium index of the cationic sublattice *ΔZm*.

Combined with the established relationship *ΔZm* – Al_2O_3, the minimal value of integrated criteria is reached at Al_2O_3 content, approaching its maximum values from the investigated range (Figure 7a) and at CaF_2 content is close to the minimal level and TiO_2 13–18 per cent (for the system under study).

The established dependences between *ΔZm* parameter and composition of the slags' system under study and its properties (Figure 7) make it possible to consider slags with minimal content (wt%) of CaF_2-30 (Figure 7b) and TiO_2-13 (Figure 7c) having not very high melting temperatures range and also satisfactory melting range according to Table 2.

As shown in Figure 8, the parameter *ΔZm* has an acceptable relationship with slags' physical properties.

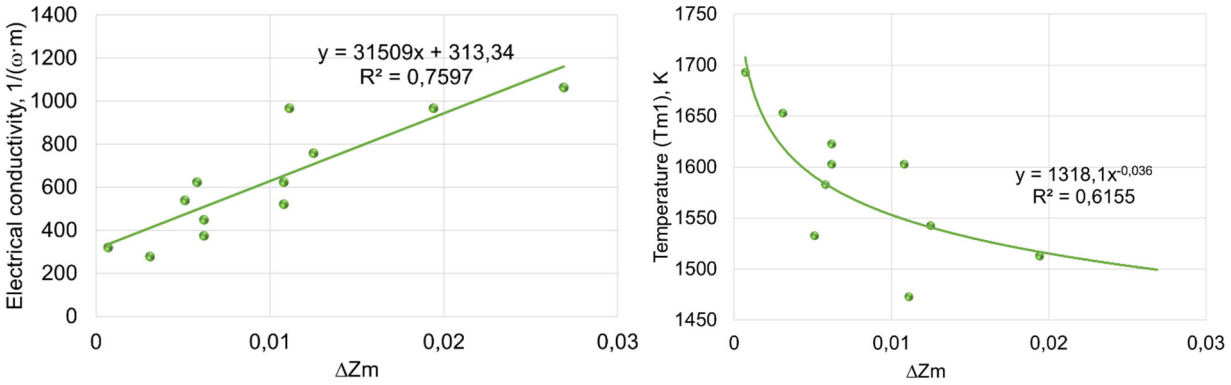

FIG 8 – Relationship between the non-equilibrium parameter of the cationic sublattice *ΔZm* and the properties of experimental slags: (a) electrical conductivity; (b) liquidus temperature of slag melting.

The involvement of the DCBC *ab initio* approach allows building models of electrical conductivity and temperature of melting from the integral parameter of the non-equilibrium state of cationic sublattice, *ΔZm*. Found dependencies are grounds for using this integral criterion when predicting these and other important properties of oxide-fluoride and other metallurgical slags.

DISCUSSION

Possibilities and limitations of the dynamic model of electrosalg remelting process

The current level of development of numerical methods for thermodynamic systems simulation has opened up new opportunities for improving existing and developing new industrial processes. However, digitalisation alone is insufficient since the simulation results must accurately reflect the real system. The accuracy of the system description and the reliability of thermodynamic programs play a decisive role in assessing complex processes, especially in the metallurgical industry, where sampling and analysis of samples are quite complex and expensive.

The provided view on ESR ingot composition formation while ESR differs from the traditional approach to the physicochemical calculation, which is usually used for ESR ingot composition estimation. Representation of this process as a line of subsystems allows for a step ahead in understanding the ESR ingot formation pattern and makes it possible to predict changes in slag-metal interaction during the process. The simpler single-system approach of thermodynamic calculations for the stable stage of electroslag remelting in argon is also relevant for comparing different slags under the same process conditions (same ingot, melting rate and temperature) or as a preliminary estimation. Calculations carried out using both the dynamic physicochemical model ESR process with several subsystems, and a single-system approach show that even with neutral gas and oxide-fluoride slags, gas-slag-metal interaction causes changes in the content of active-to-oxygen elements such as titanium and aluminium, silicon etc. The intensity of chemical composition changes is biggest at the higher slag-to-metal ratio. The highest slag-to-metal ratio is at the beginning of the process and permanently reduces during the process to the value of specific slag consumption usually used for thermodynamics estimation of the ESR.

The chemical composition of the phases changes as a result of oxidation-reduction reactions. Besides, slag's ability to desulfurise metal and assimilate non-metallic inclusions gradually reduces during the ESR process. Moreover, a slag bath accumulates all products of chemical interactions

between metal and slag, changing its chemical and, accordingly, physical properties, which are crucial for the stability of the process and the resulting quality of the ingot.

The slag is inert to metal when no or very minor oxidation occurs and it is usually good for ingot quality and technology operation. For such slags (with low content of stable oxides or fluorides only), the thermodynamic calculations show no changes outside the permissible range in the chemical composition of phases. Otherwise, when changes are significant, the composition of a consumable electrode should be adjusted, or slag should be changed for a less reactive one, or, in quite rare cases, metal alloying through the slag should be envisaged, requiring additional calculations.

The proposed more precise description of the electroslag remelting process as a line of subsystems can be used to predict changes in ingot composition along its height. The most important advantage of the dynamic model is its possibility to predict and exclude factors affecting the metal composition along the ESR ingot height or to respond to them properly. Such analysis can be done in different contexts depending on the purpose of the research (eg changes in the content of active components in the system). Summarising, the predictive physicochemical model of ESR ingot formation in dynamic can be used to achieve several goals:

- Adjust existing composition or search for new slags. For example, new slag composition could replace high CaF_2 composition at ESR of alloyed and high-alloyed steels in both stationary and short-collar moulds. The industrial tests conducted on the developed slag have shown the following benefits: oxide inclusion content was reduced by 0.5 points and power consumption – by 17 per cent. The more environmentally friendly with more than two times less calcium fluoride composition at a lower cost of 23–25 per cent was developed (Stovpchenko *et al*, 2020b; Lisova *et al*, 2020).
- Maintaining the active components content (Ti, Al etc) at high-alloyed steels and alloys while remelting (Stovpchenko *et al*, 2023) and a low level of oxygen in steel during ESR (Medovar *et al,* 2023a, 2023b; Stovpchenko *et al*, 2018a).
- Development of slags with specific properties, for example, self-disintegrating slag (Stovpchenko *et al*, 2018b).
- Development of slags for new steels and alloys (AHSS, superalloys etc) remelting (Stovpchenko, Gusiev and Medovar, 2014; Davidchenko *et al*, 2017; Medovar *et al*, 2023a).

In general, the proposed physicochemical dynamic model of the ESR process in the new paradigm could be a good tool for predicting how a slag composition affects an ingot's homogeneity on its height and the yield of a suitable metal. Such prediction is crucial in manufacturing high-alloyed steels and alloys by electroslag remelting. Uncontrolled changes in slag composition while remelting can cause ingot scrappage. However, it is even more dangerous when minor changes occur unheeded and are ignored, posing a significant risk of responsible parts damage at exploitation.

Possibilities and limitations of the Directed Chemical Bonds Concept in the prediction of electrical conductivity and melting temperature of ESR slags

Based on DCBC principles, atomistic models were developed to predict the physical properties of Ti-bearing ESR slags. Although these models were built using a limited amount of experimental data, the results demonstrate that the parameter of the non-equilibrium state of cationic sublattice ΔZm can be used to predict the properties of molten slags.

ΔZm parameter's validity explains that the crystal lattice restructuring of solid oxides at high temperatures occurs with a disordered liquid slag melt formation. The non-equilibrium state of the cationic sublattice of slag (Figure 9) can be caused by structural differentiation depending on the geometric sizes ratio of neighbouring ions and the relative arrangement of cation-anion clusters formed in complex composition melts.

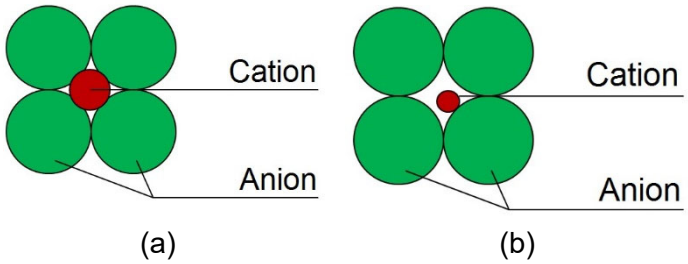

FIG 9 – Scheme of the cationic sublattice displacement inside the anion sublattice: (a) equilibrium state; (b) non-equilibrium state.

In the centre of such clusters are cations (calcium, aluminium, titanium, magnesium) surrounded by oxygen anions (fluorine and or complex anions). In a homogeneous melt, electron density distribution between cations and anions can be relatively stable. When an element is ionised, its radius changes significantly (Table 3): cations decrease in size due to transferring part of their electronic field to the anions in their immediate environment. In this case, the multicomponent slag system tends to the most favourable energy state, which can be described using the integral parameters of interatomic interaction (the model parameter ΔZm tends to zero). The bonds between cations and anions in a liquid melt at a given chemical composition and temperature retain short-range order, which determines the structure and complex properties of the liquid melt.

Atomistic models constructed using the integral parameter of the non-equilibrium state of cationic sublattice, ΔZm, offer promising possibilities for evaluating the physical properties of slags. ΔZm and other integral criteria offer promising possibilities for properties evaluation for other slags' and metals' melts (Togobitskaya, Bel'kova and Stepanenko, 2023; Muravyova *et al*, 2021; Stepanenko *et al,* 2017; Babachenko *et al*, 2020). Integral criteria are particularly effective when studying the multivariate compositions of melts, where more than one component is altered.

A proposed DCBC predictive model using *ab initio* principles helps develop a fundamental understanding of the phenomena occurring during slag melting and their interaction with metal melts in various metallurgical processes. It should be mentioned that slag engineering is now one of the trends because of the urgent necessity to be prepared for changes in the green transition of steelmaking, which is already ongoing. The issue is that an increased share of direct reduced iron (DRI) in electric arc furnaces increases the forming slag's volume and changes its composition. To keep efficient steel production, it became very important to have the possibility to make theoretical predictions of different slag (and alloys as well) characteristics. The melting temperature and electric conductivity were considered in this article, and viscosity, sulfide capacity, surface tension, and others can be predicted for various multicomponent molten slags whose composition changes in a wide range. The proposed concept makes it possible to reduce experimental measurements and tests, which are time-consuming and resource-consuming. This methodology is particularly relevant in metallurgy and materials science, where a detailed understanding of the underlying principles of chemical composition's effect on properties is essential for developing new materials and technologies.

Future works include experimental proof of dynamic models using slag and metal sampling at heavy ESR ingot producing and improvement of accuracy of DCBC models for physical properties of slag prediction using a sufficiently larger amount of experimental data for Ti-bearing and other metallurgical slags.

CONCLUSIONS

Both the dynamic physicochemical model ESR process in neutral gas presented as a chain of subsystems and a single-system estimation revealed that despite using neutral gas and oxide-fluoride slags participate in gas-slag-metal interaction, causing changes in the content of active-to-oxygen elements such as titanium, aluminium and silicon in a metal. The highest intensity of chemical composition changes occurs at the higher slag-to-metal ratio, which is at the start of the process and permanently reduces at its end to the value of a specific slag consumption.

The dynamic model is promising to study the composition changes along ingot height caused by the oxidative action of slag during the process, making it possible to predict ready ESR ingot's homogeneity and increase the yield of a suitable metal.

DCBC presenting a semi-empiric system providing effective concentration and convolution of the ab initio information on the type of bonds in multicomponent systems was employed to find integral criteria for predicting physicochemical and thermophysical properties of slags from their composition. The parameter *ΔZm* characterising the non-equilibrium state of the cation sublattice in the oxide melt is the suitable predictor of electric conductivity and melting temperature of studied slags.

The developed physicochemical dynamic model of the ESR combined with an ab initio approach of the DCBC that can predict slag properties becomes a step towards a comprehensive model of the ESR ingot formation and tailored functional slags development for specific compositions of alloys whose homogeneity is crucial for quality.

REFERENCES

Babachenko, A I, Togobitskaya, D N, Kononenko, A A, Snigura, I R and Kuksa, O V, 2020. Justification for choosing alloying and Micro-Alloying elements to improve the mechanical properties of railway wheels, *Steel in Translation*, 50(11):815–821. https://doi.org/10.3103/s0967091220110029

Davidchenko, S, Stovpchenko, G, Salnikov, A, Medovar, L, Logozinskii, I and Kuzmenko, A, 2017. Potentials of the Acid Slag for ESR, in *Proceedings of the Liquid Metal Processing and Casting Conference 2017*, pp 145–148.

Duan, S-C, Shi, X, Wang, F, Zhang, M-C, Sun, Y, Guo, H-J and Guo, J, 2019. A review of methodology development for controlling loss of alloying elements during the electroslag remelting process, *Metallurgical and Materials Transactions B,* 50(6):3055–3071. https://doi.org/10.1007/s11663-019-01665-2

Hou, D, Wang, D-Y, Jiang, Z-H, Qu, T-P, Wang, H-H and Dong, J-W, 2021. Investigation on Slag–Metal-Inclusion multiphase reactions during electroslag remelting of die steel, *Metallurgical and Materials Transactions B,* 52(1):478–493. https://doi.org/10.1007/s11663-020-02032-2

Hoyle, G, 1983. *Electroslag Processes, Principles and Practice*, 512 p. (Applied Science Publishers: London/New York).

Kolisnyk, V, et al. 1980. Patent #957081 USSR, G01 N27/02, Device for measuring the 07.09.82 electrical conductivity of molten slag, Bulletin #33:07.09.82.

Lisova, L O, Stovpchenko, G P, Goncharov, I O, Gusiev, Ia V and Medovar, L B, 2020. Thermodynamics of interactions and physical properties of slags of 30CaF2/30CaO/30Al2O3 (SiO2, MgO) system at electroslag remelting, *Sovremennaja Èlektrometallurgija*, 2020(1):8–13. https://doi.org/10.37434/sem2020.01.01

Lukas, H L, Fries, S G and Sundman, B, 2008. Computational thermodynamics: the CALPHAD method, *Choice Reviews Online*, 45(11):45–6195. https://doi.org/10.5860/choice.45-6195

Medovar, B I and Boyko, G A, 2013. *Electroslag Technology* (Springer Science and Business Media).

Medovar, L, Stovpchenko, G, Lisova, L, Jiang, Z, Dong, Y and Kang, C, 2023a. Features and Restrictions of Electroslag Remelting with Silica-Bearing Slags for Lightweight High Manganese Steel, *Steel Research International,* 94(11). https://doi.org/10.1002/srin.20230016

Medovar, L, Stovpchenko, G, Sybir, A, Gao, J, Ren, L and Kolomiets, D, 2023b. Electroslag hollow ingots for nuclear and petrochemical pressure vessels and pipes, *Metals*, 13(7):1290. https://doi.org/10.3390/met13071290

Mills, K C, 2021. Metallurgical slags, in *Encyclopedia of Glass Science, Technology, History and Culture* (eds: P Richet, R Conradt, A Takada and J Dyon), pp 843–855. https://doi.org/10.1002/9781118801017.ch7.4

Muravyova, I G, Togobitskaya, D N, Bel'kova, A I, Ivancha, N G and Nesterov, A S, 2021. Prediction of composition and properties of final smelting products based on integral indices of the blast furnace burden and temperature blasting mode, *Steel in Translation*, 51(8):531–537. https://doi.org/10.3103/s096709122108009x

Prikhodko, E V, 1995a. Metallokhimiya mnogokomponentnykh system (Metal chemistry of multicomponent systems), Moscow: *Metallurgiya*, 1995.

Prikhodko, E V, 1995b. Methodology for determining the parameters of directed interatomic interaction in molecular and crystalline compounds, *Metallophysics and Newest Technologies*, 17:(1)54–60.

Prikhodko, E, et al. 2013. Prediction of physical and chemical properties of oxide systems, Dnepropetrovsk, Porohi (*Thresholds*), 339 p.

Stepanenko, D, 2023. Calculation of activation energy of viscosity for evaluation of metallurgical slag melts structure, *Lithuanian Journal of Physics*, 63(1). https://doi.org/10.3952/physics.2023.63.1.6

Stepanenko, D A, Volkova, O, Heller, H-P, Otorvin, P I and Chebykin, D A, 2017. Selecting optimal slag conditions in the blast furnace, *Steel in Translation*, 47(9):610–613. https://doi.org/10.3103/s0967091217090133

Stovpchenko, G, Davidchenko, S V, Lisova, L O, Gusiev, Ya V and Medovar, L B, 2020b. Investigation of manufacturability and effectiveness of the new slag for electroslag remelting, *Sovremennaâ Èlektrometallurgiâ*, 2020(3):11–17. https://doi.org/10.37434/sem2020.03.01

Stovpchenko, G, Lisova, L, Medovar, L, Polishko, G, Brun, N, Bourson, P, Strelchuk, V and Nasieka, I, 2018a. Electroslag remelting for low oxygen metal manufacturing, in *Proceedings of the 7th International Congress on science and technology of steelmaking, The challenge of industry*, pp 1–10.

Stovpchenko, G P, Lisova, L O, Goncharov, I O and Gusiev, I V, 2018b. Physico-chemical properties of the ESR slags system CaF2-Al2O3-(MgO, TiO2), *Journal of Achievements in Materials and Manufacturing Engineering*, 2(89):64–72. https://doi.org/10.5604/01.3001.0012.7110

Stovpchenko, G P, Sybir, A V, Polishko, G O, Medovar, L B and Gusiev, Ya V, 2020a. Mass Transfer in Electroslag Processes with Consumable Electrode and Liquid Metal, *Uspehi Fiziki Metallov*, 21(4):481–498. https://doi.org/10.15407/ufm.21.04.481

Stovpchenko, G, Togobitskaya, D, Lisova, L, Stepanenko, D and Medovar, L, 2022. Predictive models for molten slags viscosity and electrical conductivity based on directed chemical bonds concept, *Ironmaking and Steelmaking*, 49(6):572–580. https://doi.org/10.1080/03019233.2022.2026043

Stovpchenko, G P, Lisova, L O, Medovar, L B and Goncharov, I O, 2023. Thermodynamic and physical properties of CAF2–(AL2O3–TIO2–MGO) system slags for electroslag remelting of Inconel 718 alloy, *Materials Science*, 58(4):494–504. https://doi.org/10.1007/s11003-023-00690-6

Stovpchenko, G, Gusiev, I and Medovar, L, 2014. Features of Slag-Metal interaction at electroslag remelting of superalloys, in *Proceedings of the 8th International Symposium on Superalloy 718 and Derivatives*, pp 47–56. https://doi.org/10.1002/9781119016854.ch4

Sundman, B, Kattner, U R, Sigli, C, Stratmann, M, Tellier, R L, Palumbo, M and Fries, S G, 2016. The Open CALPHAD thermodynamic software interface, *Computational Materials Science*, 125:188–196. https://doi.org/10.1016/j.commatsci.2016.08.045

Togobitskaya, D N, Bel'kova, A I and Stepanenko, D O, 2023. Model decision-making system in the task of choosing the optimal composition of the blast furnace burden under specific operating conditions of BF, *Acta Metallurgica Slovaca*, 29(2):67–74. https://doi.org/10.36547/ams.29.2.1764

Research on –
Industrial slag / flux / molten salt design and optimisation

Recent advances in understanding phosphorus in oxygen steelmaking

DOI: 10.62053/YAPV8986
G Brooks[1]

1. Professor, Swinburne University of Technology, Melbourne Vic 3160.
   Email: gbrooks@swin.edu.au

ABSTRACT

The control of phosphorus in steelmaking is one of the famous challenges of pyrometallurgy. It is well established that highly basic slags, the presence of FeO in the slag and lower temperatures (less than 1650°C) are favourable for phosphorous removal. The thermodynamics of this reaction have been extensively studied under laboratory conditions and the general trends confirmed through industrial trials. However, in general, phosphorus slag/metal distributions measured in industry are far from equilibrium and quite specific to the oxygen steelmaking technology being used. This variability was quantified by Urban, Weinberg and Cappel (2015), who found that the phosphorus partition ratio measured in plants varied with blowing practice, stirring intensity and even converter life. Some recent kinetic studies by Gu, Dogan and Coley (2017) have shown how the kinetics of these reactions vary with FeO content and dissolved sulfur at the droplet scale. A global kinetic model by Rout *et al* (2018) provides meaningful predictions of where dephosphorisation occurs in an industrial basic oxygen furnace (BOF) and some recent heat transfer modelling by Madhavan *et al* (2021, 2022) implies that temperature difference between droplets and slag has a role to play in explaining why equilibrium is not achieved. This paper will review the current state of knowledge and provide suggestions on predicting phosphorous removal for industrial operations and how greater removal could be achieved.

INTRODUCTION

The control of phosphorus is one of the central challenges facing steelmakers. In oxygen steelmaking, it is well established that maintaining a slag with high basicity (high CaO and MgO), low tapping temperatures (<1650°C) and high FeO will promote the removal of phosphorus from steel. High basicity also means high flux additions and added expense, low tapping temperatures may necessitate reheating the steel between steelmaking and casting and high FeO contents in the slag will adversely affect yield. As a result, steelmakers are always looking for ways to minimise phosphorus coming into their feed materials and the adverse effects associated with removing phosphorous.

Phosphorus in even low quantities (above 0.1 wt per cent) can adversely affect ductility, fracture toughness and cause hot shortness. Ironmaking conditions are not ideal for removing phosphorous, that is, reducing conditions encourage both Fe and P formation from their oxide states. In general, phosphorus is either removed from hot metal from a post blast furnace operation before entering the oxygen steelmaking or in the oxygen steelmaking furnace, typically below 0.010 wt per cent in the tapped steel depending on the requirement of the grade being produced (Turkdogan, 1996). Some steelmakers use a two staged oxygen steelmaking process to remove phosphorus from hot metal, as a means of minimising flux addition, though this is also likely to lower overall productivity.

The thermodynamics of phosphorus removal has been extensively studied (Assis *et al*, 2015). A recent review identified 24 different equilibrium relationships proposed in the literature (Urban, Weinberg and Cappel, 2015), based on different models for dealing with the complex solution behaviour of PO_4^{3-} anion in slags. It is well beyond the scope of this paper to critically review this vast literature but to note that many of the equilibrium relationships take the following form:

$$\log (\%P)/[\%P] = A/T + 2.5 \log (\%Fe) + B.(\%CaO) + C.(\%MgO) - D \quad (1)$$

Where () indicates slag, [] metal, T is temperature in Kelvin, concentrates are in wt per cent and A, B, C and D are constants.

This equation shows:

- The importance of temperature on phosphorus partition in slags – phosphorous oxide becoming less stable with temperature – with the ratio (%P)/[P] decreasing from approximately

50 at 1620°C for a commercial basic oxygen furnace (BOF) operation to below 35 at 1690°C (Urban, Weinberg and Cappel, 2015). High tapping temperatures (>1650°C) reflect processing requirements post steelmaking and the superheat required at the casting machine.

- The importance of FeO in the slag to provide dissolved oxygen into the metal for reaction with dissolved P (ie the least stable oxide in the slag will be accompanied by significant dissolved oxygen), other relatively unstable oxides (SiO_2 and MnO) will also provide dissolved oxygen but FeO content in the slag is major variable. Increasing the FeO content of the slag from 14 wt per cent to 24 wt per cent can typically double the partition ratio in industrial furnaces (Urban, Weinberg and Cappel, 2015). Increasing FeO in the slag effects yield from the operation and is itself controlled by the carbon content of the steel, so in many cases not a variable that can be easily manipulated ie the FeO content of the slag is set by the grade of the steel being tapped (Turkdogan, 1996).
- The importance of providing basic oxide fluxing agents to stabilise the phosphorus in the slag phase. Lime/silica weight ratios (an approximate measure of 'basicity' commonly used in industry) range from two to four depending on the grade of the steel and the operating temperature of the steelmaking furnace. Increasing the lime/silica ratio from 2.6 to 4.0 in BOFs can typically double the partitioning ratio of phosphorus but at the cost of extra flux and the risk of creating a high liquidus temperature slag that may not be practical to melt or easily tap from the vessel (Urban, Weinberg and Cappel, 2015).

There are variations to the relationship shown in Equation 1 (eg a temperature term is introduced to reflect the impact temperature on the activity of CaO and MgO) and significant debate about which is the most accurate formulae but these debates, in part reflect the variation in experimental data and difficulties in controlling and measuring all variables accurately in high temperature experiments (Assis *et al*, 2015). An important complication is the tendency of phosphorus oxide to dissolve into a solid solution with solid calcium silicate phases that can exist in steelmaking conditions, particularly early in the blow when temperatures in the vessel can be below 1600°C and various researchers have attempted to measure this behaviour in experiments and pilot plant testing (Millam *et al*, 2013).

The large body of work in quantifying the behaviour of phosphorus in steelmaking systems whilst providing an excellent basis by which to qualitatively understand the general trends of oxygen steelmaking furnaces, they do not allow direct control of the process because these thermodynamic relationships over predict phosphorus partitioning significantly in industrial operation. Most industrial furnaces are not at equilibrium regarding phosphorus and this paper explores the reasons for this and recent work in trying to provide a better predictive basis for phosphorous behaviour in oxygen steelmaking.

NON-EQUILIBRIUM CONDITIONS IN OXYGEN STEELMAKING

There is clear evidence that industrial oxygen steelmaking operations are not at equilibrium regarding phosphorus at the completion of the blow. An extensive review of plant data from around the world (including data from 30 plants) by Urban, Weinberg and Cappel (2015) found that tapped phosphorus partitioning ratios (P)/[P]) for oxygen steelmaking operations are far from equilibrium. For top blown (BOF) operations the (P)/[P] ratio may vary from 50 to 100, whilst combined blowing operations vary between from 80 to 140 and bottom blown between 100 to 200. Urban, Weinberg and Cappel reported that calculated equilibrium ratios over the range of conditions considered for these industrial systems ranged from 200 to 700. Turkdogan (1996) also recognised these differences had plant data showing that the greatest deviation from equilibrium could be found for top blown BOFs producing steel below 0.1 wt per cent C, where-as, bottom blowing operators were tapping close to equilibrium regarding phosphorous.

Urban, Weinberg and Cappel (2015) provided industrial data show that tapped phosphorus partition ratios in top blown BOFs were influenced by slag splashing, introduction of inert gas bottom stirring and converter life. They concluded that phosphorus partitioning in most oxygen steelmaking vessels is kinetically controlled, that bottom blown vessels are closest to equilibrium (which is consistent with Turkdogan (1996)) and that increased stirring in the vessel is important to improving the kinetics. They also concluded that equilibrium-based relationships could not be used to control industrial

operations and that each plant needed to develop empirical models based on statistical techniques to predict their phosphorous partitioning ratios at tapping.

In addition to plant data, which is dominated by at 'turn down' (a few minutes before tapping) and/or 'at tap' data, there has an extensive pilot plant study carried at Luleå using a 6 t top blown converter in which samples from different positions within the furnace were removed at regular intervals during the blow (Millam *et al*, 2013). This is the only known study in the open literature which quantified how phosphorus distributes itself in different phases at different stages of an oxygen steelmaking blow. The data generated from the study is detailed and difficult to interpret but the major findings regarding how dephosphorisation proceeded in this pilot plant study can be summarised:

- Early in the blow (under ten minutes), the majority of phosphorus removed from the metal was present in a solid solution phase containing Ca_2SiO_4 and $Ca_3(PO_4)_2$.
- After ten minutes, the liquid slag phase dominates the make of the slag layer and phosphorus previously in the solid solution phase is dissolved into the liquid phase.
- That amount of phosphorus in the slag phase is maximised below ten minutes and then is stable in the molten slag layer until tapping.
- The amount of phosphorus found in metal droplets in the slag emulsion reaches a maximum total quantity at the ten minute mark in the blow and then decreases to zero after 15 minutes.

This analysis implies that the formation of a solid solution phase early in the blow (when the temperature in the slag layer well below 1600°C and solid phases are thermodynamically stable) is the dominant mechanism in controlling the overall removal of phosphorous. This conclusion does not consider the possibility that the solid solution samples measured from the samples were formed during the cooling of the samples post-sampling, as these are the very phases expected to form upon cooling of a molten steelmaking slag. Also, the recognition of the potential importance of the solid solution in removing phosphorus is difficult to relate to the overall observations of Urban, Weinberg and Cappel (2015) that increased mixing in the vessel is key to the kinetics of dephosphorisation. It is also hard to understand why the total phosphorous removal is stable after ten minutes given that gas injection is still mixing the overall system beyond ten minutes. The indication that droplets found in the slag emulsion have less and less phosphorous further suggests that the role of droplets in dephosphorisation may be crucial in the slowdown of dephosphorisation observed in the pilot plant study.

DROPLET KINETICS AND DEPHOSPHORISATION

The role of droplet formation and the chemical behaviour of these droplets in steelmaking slags has been the subject of extensive study in the last 20 years, with groups at McMaster University and Swinburne University of Technology working on both modelling and fundamental experimental aspects of these systems (Gu, Dogan and Coley, 2017; Rout *et al*, 2018). Fully reviewing this literature is beyond the scope of this paper but a few key points from the most recent published studies from these groups can be summarised, as follows:

- Droplets of iron containing carbon and phosphorus readily 'bloat' when reacted within steelmaking slag, with nucleating CO gas bubbles being entrapped with the metal droplets, effectively lowering the density of droplets and promoting their movement upwards in a slag. The buoyant droplets spend between 30 to 60 seconds in a bloated state depending on the amount of carbon available, the FeO content of the slag and other parameters (Gu, Dogan and Coley, 2017). These observations have been made using X-ray fluoroscopy in laboratories and there is also plant sample that support this observation (ie iron droplets in the slag emulsion 'bloat').
- Small droplets (1 g) of iron containing carbon and phosphorus react very quickly in a steelmaking slag, with phosphorous in the metal being reduced from 0.088 wt per cent to below 0.04 wt per cent within 20 seconds.
- After an initial rapid dephosphorisation, the formation of CO starts consuming dissolved oxygen available for phosphorus oxidation and some reversion of phosphorus can occur within

the droplet. Both the nucleation of gas bubbles and the blocking of reaction sites at the gas/metal interface is influenced by slight changes in sulfur content in the metal droplets.

- Models of the bloating behaviour extended to the industrial BOF scenario by Rout *et al* (2018) calculated the rate of different refining reactions in three different regions of the furnace, namely: (i) the jet impact region, (ii) the slag-bulk metal zone and (iii) the slag metal droplet emulsion zone and predicted that the reaction between droplets and the slag dominated the dephosphorisation kinetics. The model further predicted that the rate of dephosphorisation slowed down after ten minutes in the blow because there was insufficient carbon in the metal to 'bloat' droplets and this resulted in significant less residence time of the droplets and thus slower kinetics. When validating the models developed against industrial data, there was some evidence to suggest that variations in the FeO content in the emulsion slag layer could influence the final phosphorus level of the product steel through both changes in the thermodynamic drive and kinetics of the droplet reaction kinetics. In the modelling of Rout *et al* (2018), the temperature at the droplets and emulsion was estimated using simplistic models and the droplets were assumed to be uniform in temperature during their time in the emulsion.

The modelling work of Rout *et al* (2018) did successfully capture several key aspects of steelmaking kinetics but the models were limited by a lack of reliable kinetic model for predicting FeO formation in steelmaking conditions – the kinetics of FeO were estimated by difference (ie calculate the kinetics of the other reactions and assume the remaining oxygen reacts with iron to form FeO) – and a simplistic treatment of heat transfer during the steelmaking process, particularly, in relation to the temperature of droplets generated from the impact region of the furnace and the gradients in the droplets as they react in the slag emulsion.

The modelling work of Madhavan *et al* (2021, 2022) attempted to combine the insights around droplet kinetics from Rout *et al* (2018) and recent experimental work by Gu, Dogan and Coley (2017), with a rigorous treatment of heat transfer within the system. From available plant data and modelling of heat transfer in the impact region, Madhavan *et al* (2022) estimated that the hot spot reaches a maximum of 2300°C in the middle of a blow (approximately ten minutes) and that droplets generated from the impact region heat the slag in the emulsion mainly by radiation, particularly in the first ten minutes of the blow. The model further predicts that the slag layer is consistently hotter than the hot metal bath, notably in the middle of the blow (50 to 100°C) because of the heat transfer from the droplets to the slag emulsion region. The model further predicts that the slag and hot metal get closer in temperature in the last five minutes of the blow. There is limited industrial data available to confirm this prediction but these results do suggest that some of the slowing of the overall kinetics observed in dephosphorisation could be explained by the slag region near the reacting droplets in the emulsion becoming hotter, resulting in lowering of the thermodynamic drive to remove phosphorus, which in turn could expected to slow the kinetics. Certainly, there is a complex interplay between droplet generation, reaction within the droplets whilst in the emulsion and the transfer of heat between droplets and the surrounding slag and this is likely to be important to understanding the overall kinetics of dephosphorisation in oxygen steelmaking.

CONCLUSIONS

There is significant evidence that top blown oxygen steelmaking vessels are far from equilibrium regarding phosphorus at the end of the blow. There is pilot plant data that suggests the majority of phosphorous removed from the metal is present in a solid solution phase containing Ca_2SiO_4 and $Ca_3(PO_4)_2$ and that metals droplets in the emulsion play a significant role in kinetic processes. Fundamental studies of droplet kinetics suggest that the 'bloating' of droplets is significant in understanding the behaviour of phosphorus in steelmaking and that the low residence time of droplets towards the end of the blow may explain why the system is far from equilibrium. Heat transfer modelling of droplets in the slag emulsion show that the droplets transfer significant heat to that layer and this is likely to affect the local kinetics of dephosphorisation. Models of oxygen steelmaking kinetics are limited by a lack of understanding of the kinetics of FeO formation, which is important as key phenomena such as decarburisation, 'bloating' and phosphorus removal are strongly related to the FeO content in the slag.

In general, there is a lack of plant data particularly relating to behaviour of droplets in the emulsion, the temperature gradients within the process and how they change with time. The recent developments in understanding droplet behaviour have the potential to accurately model key aspects of the process but improved industrial data will assist in refining and improving these models. Insights into the kinetics of this reaction would allow more efficient use of fluxes and reduced environmental impact of the process.

ACKNOWLEDGEMENTS

The author would like to acknowledge of the contribution of collaborators from Tata Steel, Swinburne University of Technology and McMaster University to my understanding of steelmaking kinetics, particularly, Akbar Rhamdhani, Ken Coley, Neslihan Dogan, Bapin Rout, Nirmal Madhavan and Aart Overbosch. The author is particularly grateful to the long-term support of the Tata Steel Ijmuiden for much of the work described in this paper.

REFERENCES

Assis, A, Tyler, M, Seetharman, S and Fruehan, R, 2015. Phosphorous Equilibrium Between Liquid Iron and CaO-SiO_2-MgO-Al_2O_3-FeO-P2O5 Slag Part 1, *Met Mat Trans B*, 46B:2255–2263.

Gu, K, Dogan, N and Coley, K, 2017. The Influence of Sulfur on Dephosphorization Kinetics Between Bloated Metal Droplets and Slag Containing FeO, *Met Mat Trans B*, 48B:2343–2353.

Madhavan, N, Brooks, G, Rhamdhani, M, Rout, B and Overbosch, A, 2022. Global Heat Transfer in Oxygen Steelmaking Process, *Metals*, 12:992.

Madhavan, N, Brooks, G, Rhamdhani, M, Rout, B, Overbosch, A, Gu, K, Kadrolkar, A and Dogan, N, 2021. Droplet Heat Transfer in Oxygen Steelmaking, *Met Mat Trans B*, 52B:4141–4155.

Millam, M S, Overbosch, A, Kapilashrami, Malmberg, D and Bramming, M, 2013. Some Observations and Insights on BOS refining, *Ironmaking and Steelmaking*, 40(6):460–469.

Rout, B, Brooks, G, Rhamdhani, A, Li, Z, Schrama, F and Sun, J, 2018. Dynamic Model of Basic Oxygen Steelmaking Process Based on Multi-Zone Reaction Kinetics: Model Derivation and Validation, *Met Mat Trans B*, 49B:537–557.

Turkdogan, E, 1996. *Fundamentals of Steelmaking* (Institute of Materials: London).

Urban, W, Weinberg, M and Cappel, J, 2015. Dephosphorisation Strategies and Modelling in Oxygen Steelmaking, *Iron and Steel Technology*, April 2015, pp 91–102.

Reoxidation of Al-killed ultra-low C steel by Fe_tO in $CaO\text{-}Al_2O_3\text{-}MgO_{sat.}\text{-}Fe_tO$ slag representing RH slag by experiment and kinetic modelling

DOI: 10.62053/PFJK7627

Y-M Cho[1], W-Y Cha[2] and Y-B Kang[3]

1. Graduate Student, Pohang University of Science and Technology, Pohang, Gyeongbuk 37673, Republic of Korea. Email: minn907@postech.ac.kr
2. Senior Researcher, POSCO, Pohang, Gyeongbuk 37673, Republic of Korea. Email: chawoo@posco.com
3. Professor, Pohang University of Science and Technology, Pohang, Gyeongbuk 37673, Republic of Korea. Email: ybkang@postech.ac.kr

ABSTRACT

Molten slag used in the secondary refining process (RH process) for the production of Ultra-Low C (ULC) steel is typically composed of $CaO\text{-}Al_2O_3\text{-}MgO_{sat.}\text{-}Fe_tO$ with minor constituents. Fe_tO in the RH slag is the main source of reoxidation of the molten ULC steel in the ladle by $2\underline{Al} + 3(Fe_tO) = (Al_2O_3) + 3Fe$, thereby serving as the source of the alumina inclusions. On the other hand, Fe_tO also enhances the fluidity of the slag, thereby increasing inclusion absorption capacity. Optimum slag chemistry design is therefore required to produce clear ULC steel. The reoxidation kinetics was investigated in the present study by employing high-temperature experiments and developing the reaction rate model. Initial compositions of slag ($(\%\ CaO)_0/(\%\ Al_2O_3)_0$ and $(\%\ Fe_tO)_0$) and reaction temperature were varied and change of [% Al] in the molten steel was measured. The rate-controlling step was analysed. It was found that the rate-controlling step in some cases changed during the reoxidation: from a mass transport of Al in the molten steel to a mixed transport including Al_2O_3 in the molten slag. The experimental data validated the reaction rate model based on the elucidated reaction mechanism and FactSage thermodynamic database. The model suggested that high $(\%\ CaO)_0/(\%\ Al_2O_3)_0$ suppresses the reoxidation only when $(\%\ Fe_tO)_0$ is low (5 or lower in the present study).

INTRODUCTION

Ultra-Low carbon (ULC) steel is distinguished as clean steel with exceptional formability and ductility, finding application in the production of various structural components for automobiles, necessitating intricate shaping and forming processes. The low carbon content (typically within the range of 10 to 30 mass ppm) in this steel grade makes it susceptible to oxidation during steelmaking and casting procedures. The production of ULC steel involves successive steps, including Blast Furnace (BF), Basic Oxygen Furnace (BOF), Ruhrstahl Heraeus (RH), and Continuous Casting (CC), with reoxidation posing a significant challenge during the RH and CC processes, resulting in the generation of non-metal inclusions (NMI).

ULC steel undergoes deoxidisation by Al alloys during the RH process. Once the liquid steel is adequately refined, it proceeds to a casting machine via a tundish. Reoxidation during the RH and casting processes can occur due to various factors, such as reactions with the RH slag/tundish flux, open-eye formation in the tundish, reactions with tundish and submerged entry nozzle refractories and aspiration through the sliding gate (Park and Kang, 2023). Consequently, Al in the liquid steel is depleted, resulting in the production of NMIs, such as alumina. This compromise not only hampers process efficiency but also adversely impacts the quality of the final products.

Narrowing the focus of the present study to reoxidation caused by RH slag reveals that Fe_tO, SiO_2 and MnO may be accountable for this phenomenon. Higher concentrations of these weak oxides can accelerate the reoxidation reaction. Conversely, since the slag absorbs non-metallic inclusions (NMI) at the steel–slag interface, a faster dissolution rate of NMI is necessary. Previous reports have summarised the dissolution rate of alumina inclusion in various slags (Park *et al*, 2020). Specifically, the dissolution rate of alumina inclusion in Fe_tO-containing RH slag was investigated using a high-temperature dissolution experimental technique coupled with the modified invariant interface approximation (Feichtinger *et al*, 2014). Findings indicate that a decrease in slag viscosity is a key factor in increasing the dissolution rate, aligning with proposals for various slag types. Given that the

primary components of RH slag are CaO, Al_2O_3 and Fe_tO, an increase in Fe_tO content ((% Fe_tO)) would enhance the dissolution rate. However, simultaneously, increasing the (% Fe_tO) would compromise the cleanliness of the liquid steel. Therefore, a comprehensive understanding of both phenomena – the dissolution of alumina into the RH slag and the reoxidation of the liquid steel by the RH slag – is crucial concerning (% Fe_tO) in the RH slag. The role of (% Fe_tO) from a dissolution perspective was recently discussed by the authors (Park *et al*, 2020).

The present article reports the authors' results that explore the reaction kinetics between ULC-Al killed liquid steel and Fe_tO-containing slag (representing RH slag) through high-temperature chemical reaction experiments and rate model analysis (Cho, Cha and Kang, 2021). Various rate-controlling steps were considered, compared with experimental data and a gradual change in the rate-controlling step was highlighted. The study concludes with practical suggestions for RH operation based on these findings.

EXPERIMENTAL PROCEDURE

A series of high-temperature reactions between Fe–Al alloy and CaO-Al_2O_3-$MgO_{sat.}$-Fe_tO slag were carried out, mostly at 1550°C under a well-controlled atmosphere. The reaction represents an interfacial reaction between Al-killed ULC steel and RH slag. The initial Al content in the liquid steel ([% Al]$_0$) was set to about 0.1. Nine slag samples were synthesized by melting reagent grade of CaO (calcined from $CaCO_3$), Al_2O_3 and MgO in a graphite crucible. The melt was cooled, crushed and then burned under air to remove any residual C. Appropriate amount of reagent grade of FeO was then mixed to have various initial compositions of the slag samples: C/A ratio ((% CaO)$_0$/(% Al_2O_3)$_0$ and (% Fe_tO)$_0$ were varied, where $_0$ means the initial state. The initial MgO content ((% MgO)$_0$) was set to its saturation content, estimated by FactSage FTOxid database (Bale *et al*, 2016). The initial compositions of the slag samples are listed in Table 1. The compositions of the slag and the steel were given in mass per cent.

TABLE 1

Slag compositions used in the present study.

Name	C/A ratio	(% Fe_tO)$_0$	(% MgO)$_0$
A5	1.2	5	saturated
A10		10	
A15		15	
B5	1.0	5	
B10		10	
B15		15	
C5	0.8	5	
C10		10	
C15		15	

Some 500 g of Fe-0.01 per cent Al steel was melted in an induction furnace at 1550°C, under purified Ar atmosphere. The initial O content in the alloy was approximately 0.002 per cent. Then, 40 g of the synthesized slag prepared as above was charged onto the molten steel surface using an alumina guide tube through a hole available in the upper endcap. This moment was set to the beginning of the reaction (t = 0). After the pre-determined time, a small portion of the liquid steel was periodically sampled using a quartz tube, followed by quenching in water. The composition of the liquid steel was analysed by Inductively Coupled Plasma – Atomic Emission Spectroscopy (ICP-AES) for soluble Al content ([% S Al]) and total Al content ([% T Al]) by inert gas fusion infrared absorptiometry for total O content ([% T O]). The distribution of non-metallic inclusions in the alloy was analysed using field-emission scanning electron microscopy with an energy-dispersive X-ray spectroscopy. All the data were reported previously (Cho, Cha and Kang, 2021) and were reproduced in this paper.

EXPERIMENTAL RESULTS

The time evolution of the alloy's composition is shown in Figure 1 for the case of high C/A ratio (= 1.2): [% T Al], [% S Al], [% T O] versus reaction time *t* (seconds) of liquid steel reacted with slags (A5, A10 and A15) at 1550°C. Both decreased continuously and those decreased faster when (% $Fe_tO)_0$ was higher. The following chemical reaction occurred:

$$2\underline{Al} + 3(FeO) = (Al_2O_3) + 3Fe \quad (1)$$

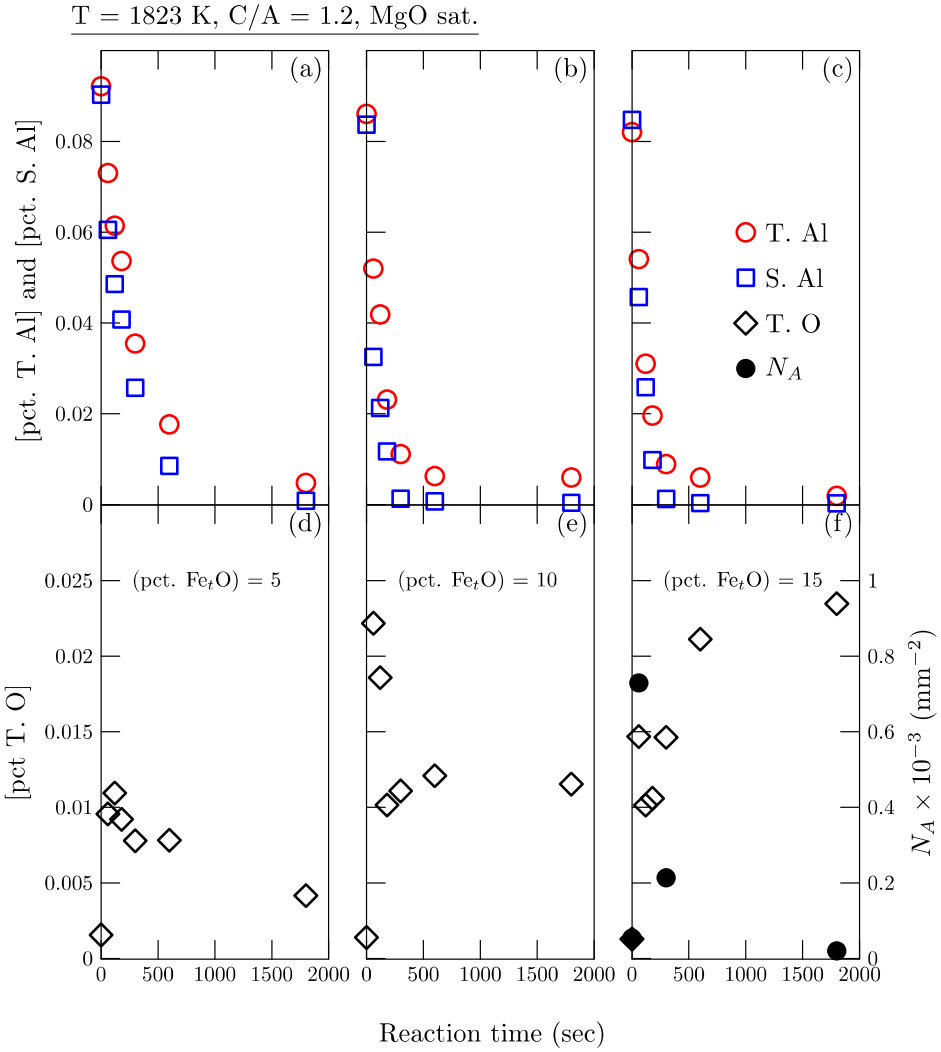

FIG 1 – Composition change of the liquid steel ([% Al]$_0$ = 0.1 reacted with CaO-Al_2O_3-$MgO_{sat.}$-Fe_tO slag): (a) to (c) [% T Al] and [% S Al], (d) to (f) [% T O] of the liquid steel reacted with the slag A5, A10 and A15, respectively, measured in the present study. Closed circles in (f) are the measured inclusion number density N_A, mm^{-2}) (Cho, Cha and Kang, 2021).

[% T Al] was slightly higher than [% S Al] and the difference should correspond to the insoluble Al content relevant to alumina inclusion in the steel. [% T O] is a sum of soluble O content ([% S O]) and insoluble O content ([% I O]) where the latter corresponds to the O content relevant to alumina inclusion in the steel. Although a simultaneous analysis technique of [% S O] and [% I O] in Al-killed steel was recently developed (Hong and Kang, 2021), it was not attempted in the present study. Therefore, the measured [% T O] should be treated carefully. When (% $Fe_tO)_0$ = 5, [% T O] first increased, showed a maximum, then decreased. It was thought that (Al_2O_3) in Equation 1 was mostly alumina inclusion, which gradually disappeared in the alloy due to buoyancy force. On the other hand, when (% $Fe_tO)_0$ = 15, [% T O] first increased, showed a maximum, then decreased. This was followed by a minimum in the [% T O], then [% T O] increased again. There should have been the following reaction:

$$(FeO) = Fe + \underline{O} \quad (2)$$

and the O can be attributed to the increase of [% T O]. Indeed, N_A, the measured inclusion number density by FE-SEM, showed different behaviour to that of [% T O]. Therefore, the measured [T O] after passing the minimum in the [% T O] is likely to correspond to soluble O content. It is evident that increasing (% $Fe_tO)_0$ increased O content in the liquid alloy and this results in 'reoxidation' in the liquid steel. Other cases (B5, B10, B15, C5, C10, C15) were also similar (Cho, Cha and Kang, 2021). Now, the task is to understand how the slag composition (C/A, (% $Fe_tO)_0$) influences the reoxidation reaction rate.

REOXIDATION KINETICS MODEL

The reoxidation reaction rate was represented by a temporal change of [% S Al], d[% S Al]/dt, as the soluble Al is the reactant of the reoxidation reaction (Equation 1). Assuming that: (1) local equilibrium at the slag-alloy interface is valid for Equation 1; and (2) mass balance in the system is kept thereby the change of the mass of slag components (FeO, Al_2O_3) can be calculated by the change of the mass of alloy components ([% S Al]); the reaction rate could be formulated in two ways:

$$\frac{d[\%\ \mathrm{S\ Al}]}{dt} = -\frac{A\rho_{\mathrm{steel}}}{W_{\mathrm{steel}}} k_{\mathrm{Al}}^{\mathrm{M}}\left([\%\ \mathrm{S\ Al}] - [\%\ \mathrm{S\ Al}]^i\right) \tag{3}$$

if the reoxidation reaction was only controlled by mass transport of Al (from bulk to the slag-alloy interface), or

$$\frac{d[\%\ \mathrm{S\ Al}]}{dt} = -\frac{A\mathrm{M_{Al}}}{W_{\mathrm{steel}}} k_{\mathrm{Al-Al_2O_3}}^{\mathrm{app}} \left(\frac{\rho_{\mathrm{steel}}}{\mathrm{M_{Al}}}[\%\ \mathrm{S\ Al}] - \frac{1}{L_{\mathrm{Al-Al_2O_3}}}\frac{\rho_{\mathrm{slag}}}{\mathrm{M_{Al_2O_3}}}(\%\ \mathrm{Al_2O_3})\right) \tag{4}$$

if the reoxidation reaction was only controlled by mass transport of Al and Al_2O_3 (from bulk to the slag-steel interface), simultaneously, where *t*, A, ρ_j, W_j, M_j, $k_{\mathrm{Al}}^{\mathrm{M}}$ and $L_{\mathrm{Al-Al_2O_3}}$ are the reaction time, the reaction area (interfacial area between the slag and the alloy), the density of the phase *j*, the mass of the phase *j*, the atomic or molecular mass of *j*, the mass transport coefficient of Al in the alloy and the distribution coefficient of Al between the alloy and the slag which is expressed as (Cho, Cha and Kang, 2021):

$$L_{\mathrm{Al-Al_2O_3}} = \frac{(\%\ \mathrm{Al_2O_3})^i}{[\%\ \mathrm{S\ Al}]^i}\frac{\rho_{\mathrm{slag}}}{\rho_{\mathrm{steel}}}\frac{\mathrm{M_{Al}}}{\mathrm{M_{Al_2O_3}}} \tag{5}$$

The superscript *i* means the 'interface'. The apparent rate constant for the mixed rate model in Equation 4 is:

$$k_{\mathrm{Al-Al_2O_3}}^{\mathrm{app}} \equiv \frac{1}{k_{\mathrm{Al}}^{\mathrm{M}}} + \left(\frac{1}{2L_{\mathrm{Al-Al_2O_3}}}\right)\frac{1}{k_{\mathrm{Al_2O_3}}^{\mathrm{S}}} \tag{6}$$

where $k_{\mathrm{Al_2O_3}}^{\mathrm{S}}$ is the mass transport coefficient of Al_2O_3 in the slag. As was proposed by Kim and Kang (2018), the mass transport coefficient of Al_2O_3 in slag phase was assumed to be inversely proportional to viscosity of the slag:

$$k_{\mathrm{Al_2O_3}}^{\mathrm{S}} = k_{\mathrm{Al_2O_3}}^{\mathrm{S},^\circ} \times \frac{\eta}{\eta^\circ} \tag{7}$$

where η is the viscosity of the slag, and $k_{\mathrm{Al_2O_3}}^{\mathrm{S},^\circ}$, and η° are the mass transport coefficient of Al_2O_3 and the viscosity of a reference slag. $k_{\mathrm{Al}}^{\mathrm{M}}$ and $k_{\mathrm{Al_2O_3}}^{\mathrm{S},^\circ}$ were optimised by fitting the experimental data to the model equation. It should be noted that the Equation 4 contains the interfacial concentration terms *via* $L_{\mathrm{Al-Al_2O_3}}$, which varies during the reaction. The interface compositions ([% S Al]^i and (% $Al_2O_3)^i$) also vary during the reaction and those can be calculated using CALPHAD approach without assuming the volume or thickness of the interface reaction zone. Detailed procedure to obtain the interface compositions and subsequent steps to calculate $L_{\mathrm{Al-Al_2O_3}}$, $k_{\mathrm{Al-Al_2O_3}}^{\mathrm{app}}$ and d[% S Al]/dt can be found in the present authors' article (Cho, Cha and Kang, 2021).

REOXIDATION KINETICS ANALYSIS

Figure 2 shows the extent of the reoxidation by temporal change of the normalised soluble Al content in the logarithmic scale (log [% S Al]/[% S Al]$_0$) (Cho, Cha and Kang, 2021). Closed symbols are the

measured data. Increasing (% $Fe_tO)_0$ from 5 to 15 (from bottom panel to top panel) decreased [% S Al] faster, therefor the reoxidation occurred faster.

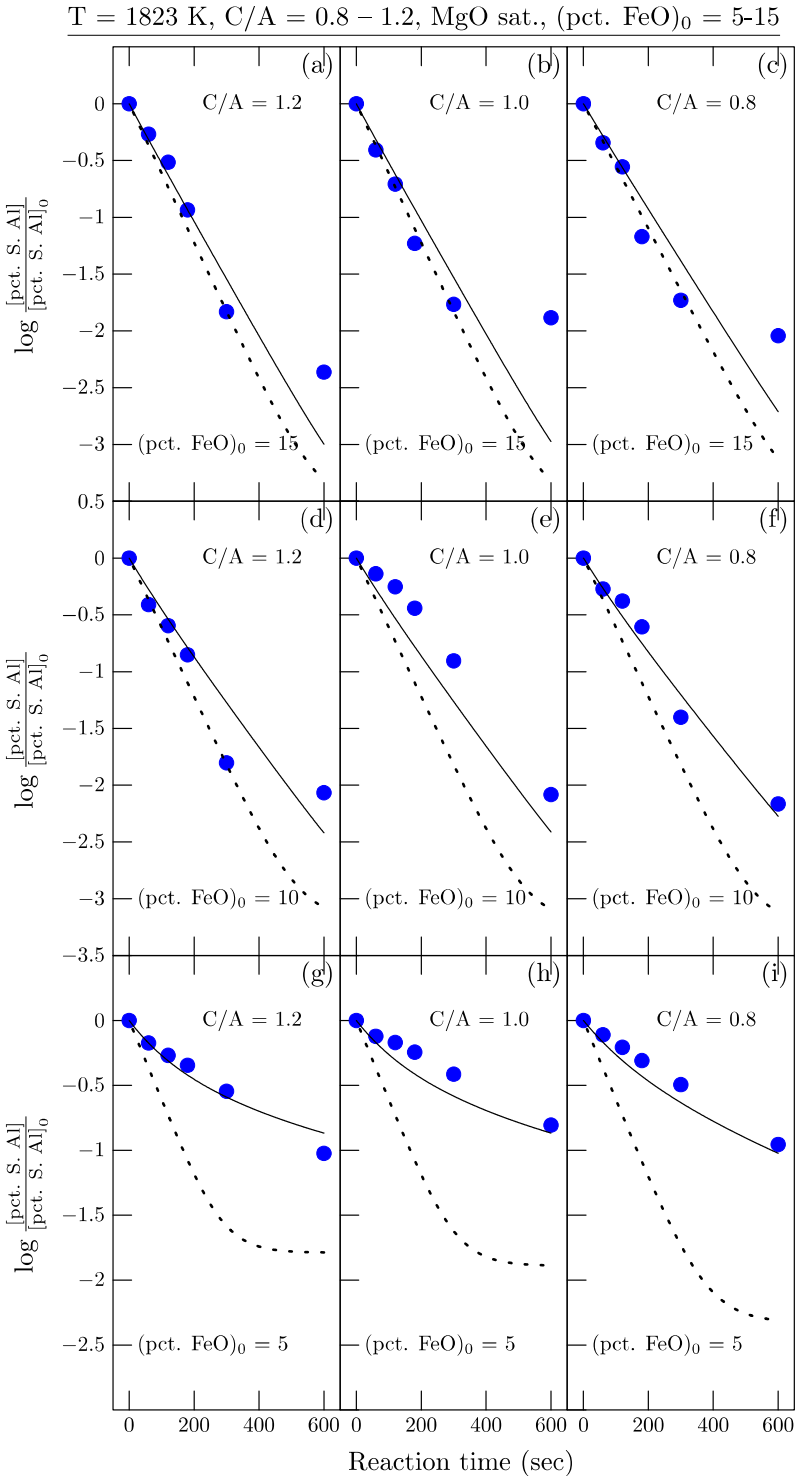

FIG 2 – Comparison between the experimental data and the model calculations for log [% S Al]. Symbols are the experimental data, the dotted lines from Equation 3 assuming the single rate controlling mechanism and the solid lines from Equation 4 assuming the mixed rate controlling mechanism (Cho, Cha and Kang, 2021).

The dotted lines were the calculated extent of the reoxidation by Equation 3, assuming the reoxidation was exclusively controlled by the mass transport of Al in the steel only. It was reasonable when (% $Fe_tO)_0$ was high (15), but deviated gradually from the experimental data as (% $Fe_tO)_0$ decreased. The lower (% $Fe_tO)_0$ means the higher viscosity of the slag. This suggests that the mixed controlling concept formulated by Equation 4 would be adequate. After a series of calculations, k_{Al}^{M}

and $k^{S,\circ}_{Al_2O_3}$ were optimised by fitting the experimental data to the model equation. The solid lines are the calculated extent of the reoxidation by Equation 4 in the context of the mixed controlling rate. A good agreement was achieved. It should be stressed that the extent of the reoxidation in view of the experiment and the model calculations does not clearly suggest the role of C/A on the reoxidation.

The developed model was manipulated to extract the reaction mechanism. The extent of reoxidation by Equation 4 requires $k^{app}_{Al-Al_2O_3}$ and $L_{Al-Al_2O_3}$ and these two properties require the property at the interface [% S Al]^i. Figure 3 shows the calculated [% S Al]^i, $L_{Al-Al_2O_3}$ and $k^{app}_{Al-Al_2O_3}$ for the nine slag samples (numbers near the curly bracket means (% Fe_tO)$_0$).

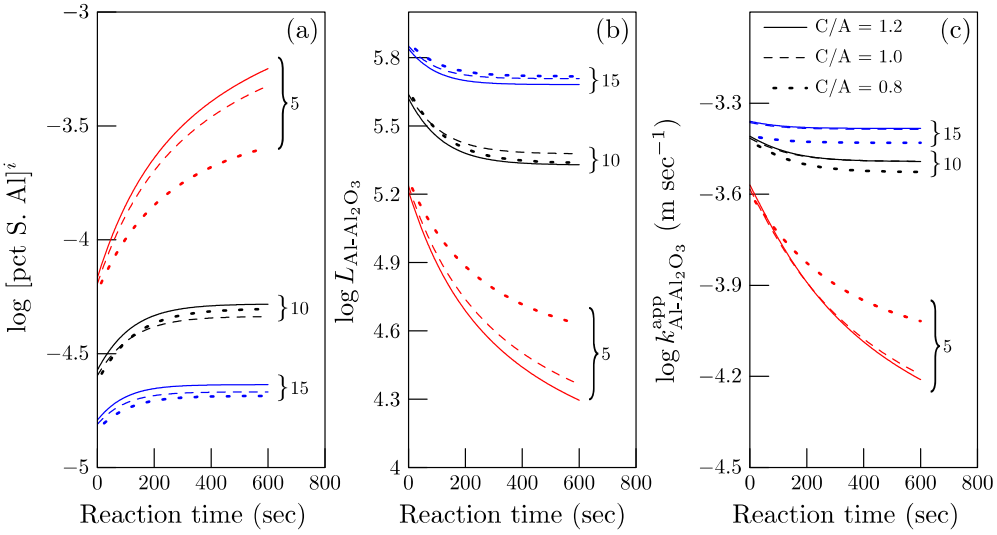

FIG 3 – Calculated various properties from during the reoxidation reaction at 1550°C: (a) [% S Al]^i, (b) $L_{Al-Al_2O_3}$ and (c) $k^{app}_{Al-Al_2O_3}$ (Cho, Cha and Kang, 2021).

The three properties depend on *t*, (% Fe_tO)$_0$ and C/A. In general, as the reoxidation proceeded, soluble Al at the interface increased, thereby decreasing the driving force of the reaction. This is reflected in the decrease in the Al distribution ratio, inducing a lower driving force. This lowers the apparent rate constant and finally, the reoxidation reaction ceased to proceed further. It should be stressed that the apparent rate constant is indeed not a constant, but varies during the reaction.

(% Fe_tO)$_0$ is the most dominant factor in the control of the reoxidation rate. When (% Fe_tO)$_0$ is high, the C/A ratio is not a critical factor in the three properties in Figure 2. However, at the lower (% Fe_tO)$_0$ = 5, C/A ratio does influence the three properties: increasing C/A ratio increased [% S Al]^i and decreased $L_{Al-Al_2O_3}$ and $k^{app}_{Al-Al_2O_3}$. Therefore, increasing C/A ratio would decrease the reoxidation rate. High C/A ration decreased the reoxidation rate because $L_{Al-Al_2O_3}$ is low, which is due to high [% S Al]^i. At the slag-steel interface, [% S Al]^i is determined by the equilibrium of Equation 1. It is known that increasing C/A in the CaO-Al_2O_3-Fe_tO slag lowers the activity of Fe_tO at the same (% Fe_tO). This results in a higher soluble Al content. Although the slag used in the present study and RH slags in practical operations contain some other minor components such as MgO, increasing C/A ratio in RH slag of low (% FeO)$_0$ (ie ~5) can lower the reoxidation rate. This conclusion is in agreement with recent reports (Ji *et al*, 2018; Ji *et al*, 2020).

In practical RH slag operation, Fe_tO originates from BOF slag, introduced due to partial entrapment during tapping. Fe_tO is a major cause of reoxidation during RH processing. Deoxidising the slag by eliminating Fe_tO using Al or C sources is a potential method to control reoxidation. However, reducing Fe_tO is challenging due to slag solidification and fume generation, impacting workability. Yet, higher Fe_tO aids in absorbing alumina inclusions, enhancing viscosity (Park *et al*, 2020). Balancing Fe_tO content is crucial, considering reoxidation prevention versus viscosity benefits. Alternatively, killing Fe_tO and adding a non-reducible flux can achieve the same goal, but cost and refractory life become additional considerations.

CONCLUSIONS

In the investigation of ULC steel reoxidation during the RH process, an analysis of the reaction rate and mechanism was conducted through a series of laboratory-scale experiments and the utilisation of a reaction rate model that integrates CALPHAD thermodynamics and mass transport theory (Cho, Cha and Kang, 2021). The observed increase in reoxidation rate with higher initial percentages of Fe_tO ((% $Fe_tO)_0$) and the significance of variations in the C/A ratio were particularly notable when (% $Fe_tO)_0$ was low (5 in this study). The predominant influence on the reoxidation rate was found to be the mass transport of Al in liquid steel. However, as (% $Fe_tO)_0$ decreased, the rate-controlling step shifted towards mixed transport control, involving Al_2O_3 transport. A new reaction rate model was developed, incorporating local equilibrium through the CALPHAD method, mixed transport rate in both phases and the viscosity effect on mass transport coefficients of Al_2O_3 or Fe_tO in the slag. This model demonstrated a good alignment with the experimental data. At high (% $Fe_tO)_0$, the C/A ratio in the slag had minimal impact on the reoxidation rate. Conversely, at low (% $Fe_tO)_0$, increasing C/A effectively reduced the reoxidation rate, showcasing its potential to suppress reoxidation.

ACKNOWLEDGEMENTS

This work was financially supported by POSCO, Republic of Korea.

REFERENCES

Bale, C W, Belisle, E, Chartrand, P, Decterov, S A, Eriksson, G, Cheribi, A E, Hack, K, Jung, I H, Kang, Y B, Melancon, J, Pelton, A D, Petersen, S, Robelin, C, Sangster, J, Spencer, P and Van Ende, M A, 2016. FactSage thermochemical software and databases, 2010–2016, *Calphad*, 54:35–53.

Cho, Y-M, Cha, W-Y and Kang, Y-B, 2021. Reoxidation of Al-killed ultra-low C steel by Fe_tO in RH Slag: experiment, reaction rate model development, and mechanism analysis, *Metallurgical and Materials Transactions B*, 52(5):3032–3044.

Feichtinger, S, Michelic, S K, Kang, Y B and Bernhard C, 2014. In situ observation of the dissolution of SiO_2 particles in CaO-Al_2O_3-SiO_2 slags and mathematical analysis of its dissolution pattern, *Journal of the American Ceramic Society*, 97(1):316–325.

Hong, H-M and Kang, Y-B, 2021. Simultaneous analysis of soluble and insoluble oxygen contents in steel specimens using inert gas fusion infrared absorptiometry, *ISIJ International*, 61(9):2464–2473.

Ji, Y, Liu, C, Lu, Y, Yu, H, Huang, F and Wang, X, 2018. Effects of FeO and CaO/Al_2O_3 ratio in slag on the cleanliness of Al-killed steel, *Metallurgical and Materials Transactions B*, 49(6):3127–3136.

Ji, Y, Liu, C, Lu, Y, Yu, H, Huang, F and Wang, X, 2020. Oxygen transfer phenomenon between slag and molten steel for production of IF steel, *Journal of Iron and Steel Research International*, 27:402–408.

Kim, M-S and Kang, Y-B, 2018. Development of a multicomponent reaction rate model coupling thermodynamics and kinetics for reaction between high Mn-high Al steel and CaO-SiO_2-type molten mold flux, *Calphad*, 61:105–115.

Park, J-H and Kang, Y-B, 2023. Reoxidation phenomena of liquid steel in secondary refining and continuous casting Processes – A Review, *Steel Research International*. https://doi.org/10.1002/srin.202300598.

Park, Y, Cho, Y M, Cha, W Y and Kang, Y B, 2020. Dissolution kinetics of alumina in molten CaO-Al_2O_3-Fe_tO-MgO-SiO_2 oxide representing the RH slag in steelmaking process, *Journal of the American Ceramic Society*, 103(3):2210–2224.

Effect of liquefaction controlling components in carbon-free mould powder for the continuous casting of ultra-low carbon steels

DOI: 10.62053/YPIX4601
N Gruber[1]

1. Senior Scientist, Montanuniversitaet Leoben – Chair of Ceramics, Leoben 8700, Austria. Email: nathalie.gruber@unileoben.ac.at

ABSTRACT

In the continuous casting of ultralow carbon (ULC) steels, free carbon is used to control the melting behaviour of mould powders. If the carbon is not completely removed during melting, it is enriched at the top of the slag pool. Liquid steel may come into contact with this layer because of the turbulence of the molten metal, resulting in its recarburisation, which negatively affects the desired product quality. Thus, a reduction in carbon input is desirable. For this purpose, SiC and/or Si_3N_4 with and without antioxidants were selected as melt-control additives to replace carbon in the mould powders. Thermodynamic calculations were performed to quantify their effect on the melting behaviour based on the chemical composition of a flux already applied to ULC steels. To experimentally assess the liquefaction behaviour, laboratory mould powders were prepared and annealed in steel crucibles closed with a lid. Crucibles were inserted into a furnace that was already preheated to selected temperatures between 900–1200°C for 10 mins and quenched to room temperature. Subsequently, the samples were mineralogically investigated. The results confirmed those obtained from the thermodynamic calculations. Si_3N_4, and SiC in particular, are suitable raw materials for delaying the solid-solid reactions of raw material components during melting. Owing to their stability at high temperatures, the necessary SiO_2 content to form a liquid phase is not available, resulting in lower amounts of the liquid phase. The addition of antioxidants to delay the oxidation of SiC further reduces this positive effect. Attempts to decrease the SiC content without negatively affecting the melting behaviour resulted in a reduction in the CO_2 emission by at least 27 g CO_2/kg of mould powder when compared to the carbon-containing standard mould powder. These investigations revealed differences in the melting behaviours of granules and loose powders, which are related to their respective production processes.

INTRODUCTION

In the continuous casting of steel mould powders added to the liquid steel pool form different horizontal layers during melting, a homogeneous liquid layer exists in contact with the steel and the original mould powder is still present on the upper surface. In between a sintered layer owing to the formation of liquid and new solid phases exists. The slag infiltrates the gap between the steel and the mould. A liquid layer is in contact with the strand, a glassy layer is close to the mould and a crystalline layer lies in between. In particular, the structure of the crystalline layer affects heat transfer from the strand to the mould (Mills *et al*, 2004).

A common approach for controlling the melting behaviour of mould powders is the addition of carbon particles of different types and sizes, for example, graphite or carbon black, to a mixture of raw-material components. At lower temperatures, they reduce the contact between raw material particles and delay solid-solid reactions. A liquid phase is formed with increasing temperature. Because of the nonwetting carbon particles, the liquid droplets remain separated and a continuous liquid is prohibited. This phenomenon is known as the skeleton effect (Mills, 1990; Kawamoto *et al*, 1994; Kölbl, Marschall and Harmuth, 2009; Kromhout, 2013). After the carbon is burned off, which depends on the oxygen supply in the high-temperature areas of the mould powder layers, a homogeneous liquid is formed. If the carbon is not completely oxidised, it accumulates on top of the liquid slag layer, resulting in a carbon-rich layer with a carbon content of more than 20 wt per cent for mould powders with carbon contents of solely 3.5 wt per cent when delivered (Supradist, Cramb and Schwerdtfeger, 2004). This effect has also been confirmed by laboratory investigations (Yan *et al*, 2015). Owing to the oscillation of the mould and the turbulence of the steel flow from the submerged entry nozzle, liquid steel may come into contact with the carbon-enriched layer, resulting in its recarburisation. In particular, for ultralow-carbon (ULC) steels, this reaction changes the steel properties, which reduces the strand quality. Various approaches have been proposed to inhibit this reaction. A thicker slag

layer increases the distance between the carbon-rich layer and steel bath, making contact more difficult. Furthermore, different efforts have been made to improve the raw material composition of the powders. Graphite is replaced by quick-burning or activated carbons to support its oxidation, and oxidising agents such as MnO_2 or catalysts such as Fe_2O_3 for reactions at low oxygen activity and high temperatures are added (Yi, Song and Peng 2013; Terada *et al*, 1991; Han *et al*, 2023; Nakato *et al*, 1991). Another approach is the replacement of free carbon in the mould powder by using alternative raw material components showing similar properties as carbon (Takeuchi *et al*, 1976, 1978; Debiesme *et al*, 1996, 1998). With respect to the skeleton effect, the non-wettability of slags is in the focus of these studies. In the first attempt, nitrides were added to the mixture instead of carbon and tested. For this purpose, BN, Si_3N_4, MnN, CrN, FeN, AlN, TiN, or ZrN were suggested (Terada *et al*, 1991; Takeuchi *et al*, 1976, 1978). Boron nitride (BN) is the most appropriate option owing to its similarity to carbon in terms of crystalline structure and wetting behaviour. Mould powder investigations in the laboratory showed that the sintering tendency of fluxes containing BN was reduced. The minimum amount required to effectively control the melting behaviour of the mould powders depends on the sizes of the BN particles and the oxidic and fluoridic base materials. A decrease in the raw material particle size resulted in decreased melting rates, which also accounted for the BN. The fusion rates were determined for the original mould powder with carbon and for mixtures containing different amounts of BN in the laboratory. Those containing 2.10 wt per cent of BN showed similar behaviour to the original sample. Furthermore, compared with carbon black, BN exhibited a reduced sintering tendency and reduced gas formation. In contrast, during the oxidation of boron nitride, B_2O_3 is formed, acting as a fluxing agent and causing the formation of the first liquid phase. Thus, antioxidants such as Al or CaSi were added to the samples to impede its oxidation at lower temperatures. However, boron oxide not only improves the sintering tendency but also lowers the slag viscosity. Therefore, solely for samples showing a CaO/SiO_2 (C/S) ratio of 0.9, proper viscosities for the continuous casting process were obtained. Based on the laboratory results, the mould powder was selected for testing with a defined steel grade in a continuous caster. After the trial, the surface of the strand was analysed with respect to surface quality. The results revealed that an increase in nitrogen content on the strand surface being as detrimental as the effect of recarburisation. Therefore, this amount must be reduced. The realisation was achieved by deliberating retaining some carbon from the mould powder to ensure controlled melting behaviour (Terada *et al*, 1991; Takeuchi *et al*, 1976, 1978).

Additionally, Si_3N_4 was considered to effectively control the melting of mould powders. The benefit compared with BN is that SiO_2, which is already included in the original mould powder composition, is formed during oxidation. Thus, the viscosity of the slag does not change after liquification. Investigations in the laboratory suggested a particle size of 5 µm and a specific surface of 2.5–3.5 m^2g^{-1} to meet the required demands. Subsequently, a mould powder was prepared for industrial trials. During operation, suitable melting rates were observed, but the surface of the steel strand also showed considerable nitride absorption (Debiesme *et al*, 1996, 1998; Lefebvre *et al*, 1996; Sun *et al*, 2019).

The concept of associating specially coloured mould powders with steel grades to facilitate on-site identification during operation requires the elimination of carbon from the mould powder composition. Carbon-free samples were investigated using a heating microscope. The results showed that the softening, melting and flow points agreed with those of the carbon-containing products. In contrast, the melting rate increased considerably. The authors (Macho *et al*, 2005) assumed sufficient thermal insulation of the steel in the mould, as long as a sufficiently thick mould powder layer rests on the mould slag.

Efforts have also been made by various research groups to replace free carbon with SiC (Lefebvre *et al*, 1996; Maillart, Chaumat and Hodaj, 2010; Ning and Jinghao, 1998; Safarian and Tangstad, 2009; Park *et al*, 2016). Similar melting rates were achieved for mould powders containing 2–2.5 wt per cent of carbon or 5–6 per cent SiC. A detailed investigation of the layers formed during the experiment revealed three layers. Contrary to the standard, solely carbon-containing product, the sintered layer increased considerably, whereas the original sample layer remained very thin. This was explained by the oxidation of SiC, resulting in a decrease in the basicity of the mould powder, thus accelerating liquid-phase formation. Consequently, carbon was partially replaced by SiC. These products, which contained different ratios of free carbon to SiC, were then tested in

contact with liquid steel. Analysis of the chemical compositions of the steel samples indicated an increasing tendency for recarburisation when the carbon content exceeded 1 wt per cent.

In the investigations quoted above, phenomenological methods were primarily used to compare the melting behaviour of mould powder compositions where carbon was partially or totally replaced as the melt-control additive. However, the effect of these additives during melting has not yet been described. Thus, in this study, SiC and/or Si_3N_4, with and without the addition of antioxidants, were selected to replace carbon in a mould powder already used for the continuous casting of steels for investigation in laboratory experiments.

EXPERIMENTAL

Mould powder, already used in the continuous casting of ultralow-carbon steels, was selected (hereafter denoted as MP0). Based on its chemical composition, this mould powder was reproduced as a mixture of raw material components that are generally used for the production of mould powders (MP2). As a reference, a sample without melt-controlling additives was prepared (MP1). Subsequently, to substitute the carbon content of MP2, SiC (MP3–6) and/or Si_3N_4 (MP9/MP8) were added to control the melting behaviour of the mixture. For this purpose, the composition was modified to achieve the chemical composition of MP1 after total oxidation of the carbide and nitride phases. An amount of 25 wt per cent of the total SiO_2 content in the mould powder was substituted by SiC and/or Si_3N_4. For refractory materials, the addition of antioxidants is the most common technology to prevent carbon oxidation and increase service lifetime owing to enhanced corrosion resistance. Additionally, the desired properties of the product, such as the mechanical properties, are improved (Ghosh, Jagannathan and Ghosh, 2001; Wang and Yamaguchi, 2001; Dai, Xiao and Ding, 2021). Laboratory mould powders MP4–MP6 contain Si and/or Al in addition to SiC, which prohibits the premature oxidation of SiC. A similar addition of Si and Al serves to protect carbon in refractories; so-called antioxidants (Ghosh, Jagannathan and Ghosh, 2001; Wang and Yamaguchi, 2001; Dai, Xiao and Ding, 2021).

Prior to laboratory investigations, thermodynamic calculations of the phase distribution with respect to temperature were performed using FactSage™, version 8.2 (by CRCT-ThermFact Inc. and GTT-Technologies). The mineral composition and possible liquid phase of each sample were calculated in equilibrium state up to 1550°C, which corresponds to the steel bath temperature in mould, while maintaining the total initial oxygen amount constant (no oxidation). As a result, the quantities of the phases formed in dependence on temperature are depicted in diagrams, and the amount of liquid phase at 1000°C was calculated, indicating the melting tendency of each sample for comparison. The experimental investigations of MP1–MP3 aimed to assess the effect of the additives used on the liquefaction behaviour, and it was revealed that, contrary to the calculations performed here, partial oxidation reactions occurred. To minimise the discrepancy between the chemical composition of the as-received commercially fabricated mould powder and the mixtures prepared in this study, the quantity of each raw material component was calculated based on its chemical composition. Quartz, feldspar, calcite, magnesite, fluorite, carbon, wollastonite, soda, corundum, fly ash, glass, blast furnace slag, and hematite were used as base materials, and SiC, Si, Al, and Si_3N_4 were added to control the melting behaviour of the specimen. The mixtures were prepared as listed in Tables 1 and 2. After homogenising, 20 g of each loose mould powder mixture were filled into steel crucibles (30·30·40 mm^3) closed by a steel lid and inserted into the furnace preheated to a selected temperature between 900 and 1200°C. Melt-control additives are expected to be partially oxidised in the crucible atmosphere. At least at lower temperatures, this reaction was incomplete. The oxygen supply was hindered by the lid, simulating the oxygen support under service conditions by diffusion. The crucibles were kept in the furnace for 10 mins before being removed and quenched at room temperature. Mineralogical investigations were conducted on polished sections using reflected light microscopy and scanning electron microscopy coupled with energy-dispersive X-ray microanalysis. The latter enables the identification of phases that are stable in dependence on temperature. The samples were ground for X-ray analysis. Finally, the results of the thermodynamic and laboratory investigations were compared.

TABLE 1

Raw material compositions of MP1–MP9 (in wt%).

	MP1	MP2	MP3	MP4	MP5	MP6	MP7	MP8	MP9
	no melt-control additive	with carbon	with SiC	SiC, antiox. Si	SiC, antiox. Al	SiC, antiox. Si and Al	antiox. Al	with Si_3N_4	with Si_3N_4 and SiC
Quartz	6.8	6.9	6.3		4.9	0.3			
Feldspar	4.3	4.9	3.8			3.6			
Calcite	2.1	3.3	17.8	7.6		12.0		3.0	15.3
Fly ash	13.3	11.1	13.0	7.4				16.0	7.7
Glass						8.1	22.7		15.3
Magnesite	9.4	9.1	8.1	9.5	10.9	9.3	9.9	9.3	7.7
Fluorite	19.5	18.7	18.7	19.5	20.4	19.2	20.3	19.8	19.1
Carbon		4.4							
Wollastonite	38.1	35.7	20.0	34.0	45.5	28.6	39.9	37.1	19.7
Soda	5.3	4.9	5.1	6.1	6.3	4.0	2.5	6.2	3.4
Corundum				2.4		0.7		0.5	1.7
Blast furnace slag				2.7	0.5	2.8			2.5
SiC			6.0	6.5	6.8	6.4			4.8
Hämatite	1.3	1.2	1.2	1.7	2.4	2.3	2.4	1.2	1.6
Si metallic				2.60		1.3			
Al metallic					2.3	1.3	2.3		
Si_3N_4								6.9	1.7

Owing to the suitable application of SiC to delay the reactions of the raw materials (Results), further attempts were made to reduce the SiC content of MP3 without negatively affecting its melting rate. For MP3, 25 wt per cent of the total SiO_2 content in MP0 was replaced with SiC. For MP10–MP13, this amount was continuously reduced. Mixtures were prepared according to Table 2, homogenised and granulated using a bottle roller to compare their melting behaviours. Subsequently, they were annealed in a preheated furnace according to the procedure described above.

TABLE 2

Raw material compositions of MP10–MP13 (in wt%).

	MP10	MP11	MP12	MP13
	20 wt% SiO_2 replaced by SiC	15 wt% SiO_2 replaced by SiC	10 wt% SiO_2 replaced by SiC	5 wt% SiO_2 replaced by SiC
Quartz			1.6	3.7
Feldspar	4.1	7.9	5.0	4.7
Calcite	4.14	3.5		
Fly ash	16.6	13.4	15.3	15.3
Magnesite	10.1	10.3	10.3	10.3
Fluorite	21.7	21.5	21.5	21.2
Wollastonite	40.1	41.2	44.1	43.9
Soda	6.0	5.3	5.8	5.8
SiC	5.8	4.3	2.8	1.4
Hämatite	1.3	1.5	1.3	1.4

RESULTS AND DISCUSSION

Thermodynamic calculations

Figure 1 summarises the phase compositions of MP0=MP2, MP3 and MP9 with increasing temperature. As expected, the phases differed only slightly among the calculated compositions; however, their stability ranges varied considerably. In all specimens, cuspidine ($Ca_4(Si_2O_7)(F,OH)_2$), formed by the reaction of the raw materials during heating, is the last solid phase that forms before a homogeneous liquid. If the iron oxide in the mould powder is reduced by another component, solid iron and iron silicide with diverse Fe/Si ratios are also formed. At low temperatures, nepheline ($Na_3KAl_4Si_4O_{16}$) is observed in all mixtures and combeite ($Na_2Ca_2Si_3O_9$) and fluorite (CaF_2) are observed in MP0–MP3 and MP8–MP9. MP3, MP8 and MP9 represent magnesium-fluoride silicates ($Mg_5F_2Si_2O_8$ or $Mg_9F_2Si_4O_8$).

In comparison to the carbon-containing mould powder, the replacement of SiO_2 by SiC and/or Si_3N_4 caused an increase in the quantity of cuspidine (MP3, MP8 and MP9). Owing to the incomplete oxidation of the melt-control components, the availability of SiO_2 was reduced in these samples. Thus, the formation of phases with a higher SiO_2 content was prohibited. Although diopside ($CaMgSi_2O_6$) can be found in MP0 and MP1, it is not stable in the samples containing SiC and/or Si_3N_4. The same applies to mixtures of SiC and antioxidants. Cuspidine and merwinite ($Ca_3Mg(SiO_4)_2$), olivine ($(Mg,Fe)_2SiO_4$) and melilite ($(Ca,Na)_2(Al,Mg,Fe^{2+})(Al,Si)SiO_7$) were present instead of clinopyroxene. Compared with the carbon-containing samples, the quantity of cuspidine did not increase significantly. Furthermore, because of the stability of SiC, particularly at lower temperatures, the CaO/SiO_2 ratio is low, and the formation of the liquid phase shifts to higher temperatures, where SiC oxidation is promoted, thus increasing the C/S ratio. This behaviour was not observed in the samples containing free carbon.

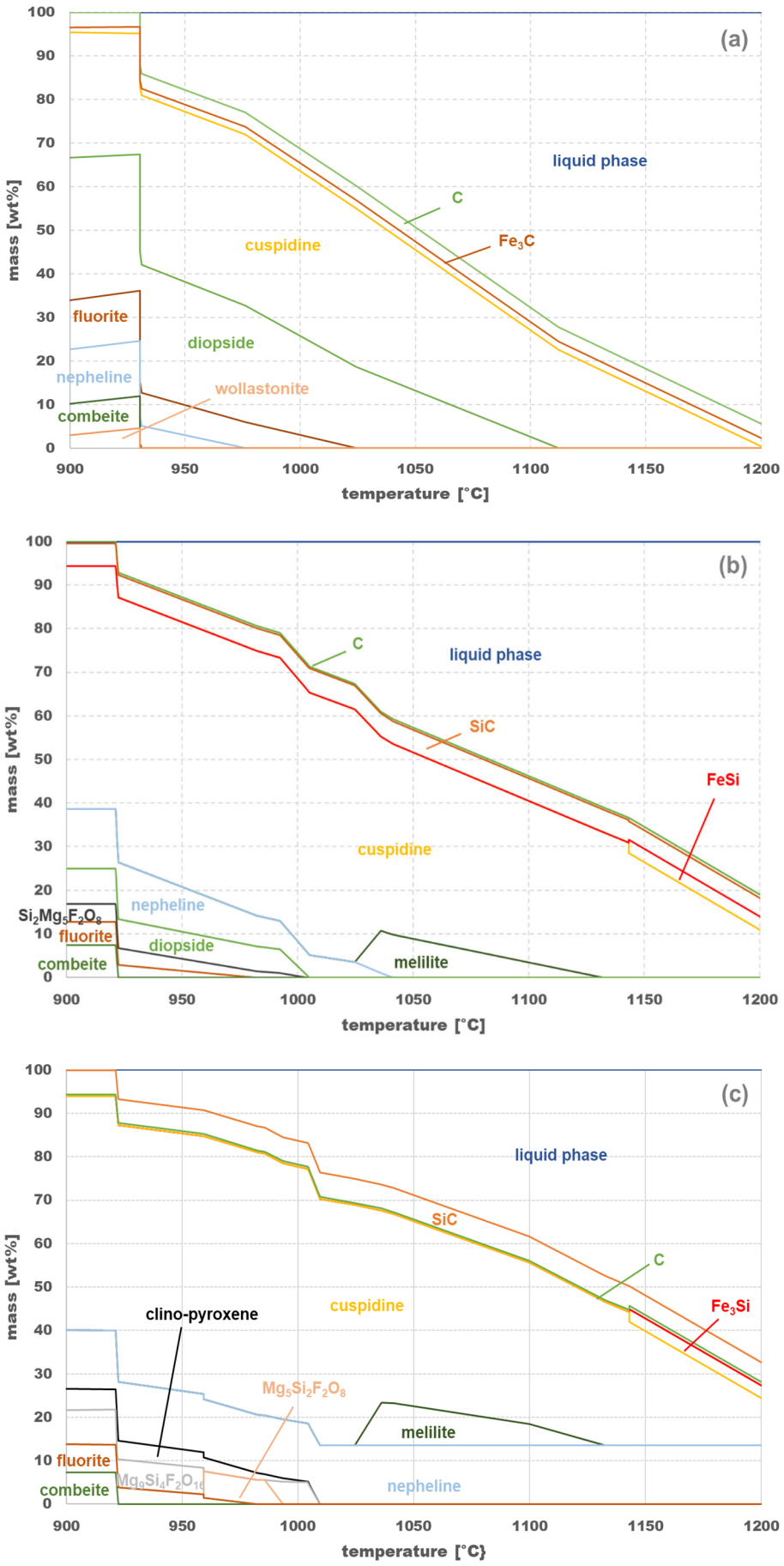

FIG 1 – Mineral compositions as a function of temperature for: (a) MP0 and MP2, (b) MP3, and (c) MP9.

For all the mould powders, the solidus (T_s) and liquidus (T_l) temperatures were determined using calculations. Additionally, the calculated amounts of liquid phase present at 1000°C (I_{1000}) were compared to enable the evaluation of the melting tendencies. The results are summarised in Table 3. In the equilibrium state, the temperature of the first liquid phase is not affected by the melting-controlling components. The amount of liquid phase at 1000°C is not significantly different for all mixtures, with the exception of MP5, which shows the lowest value. A more significant difference was observed in the liquidus temperature. The sample containing SiC (MP5) as the melt-control additive exhibits the highest T_l. By contrast, further addition of antioxidants results in an opposite effect and decreases the liquidus temperature by approximately 80°C again. In these samples, liquid phase formation is promoted, but its amount at 1000°C is only slightly higher and still lower than that of MP0 and MP2. The thermodynamic calculations do not end in a total liquefaction of the mould powders up to 1550°C because the melt-control additives (carbon, SiC, Si_3N_4) are not totally oxidised. Therefore, they are still stable at 1550°C. In Table 3, they are indicated by the subscript 'residual'. Additionally, their initial amount is given, which is marked by 'initial'.

TABLE 3

Melting tendency based on thermodynamic calculations.

	$I_{1000°C}$ [wt.%]	T_s [°C]	T_l [°C]	C $_{residual}$ [wt.%]	SiC $_{residual}$ [wt.%]	SiC $_{initial}$ [wt.%]	Si_3N_4 $_{residual}$ [wt.%]	Si_3N_4 $_{initial}$ [wt.%]
MP0	28.3	931	1202	3.2				
MP1	26.7	923	1190					
MP2	28.3	931	1202	3.2				
MP3	24.2	922	1235	0.8	4.3	6.0		
MP4	26.8	847	1209		7.1	7.1		
MP5	18.8	852	1225		7.0	7.0		
MP6	24.3	852	1210		7.0	7.0		
MP7	27.5	927	1216					
MP8	25.1	922	1235				4.9	6.9
MP9	23.8	921	1235	3.2	4.4	4.8	1.2	1.7

$I_{1000°C}$ amount of liquid phase at 1000°C

T_s solidus temperature

T_l liquidus temperature

$_{residual}$ quantity of the respective melt-control additive at 1550°C

$_{initial}$ initial quantity of the respective melt-control additive in the sample

Laboratory investigations of different mould powder compositions

The microscopical investigations of the standard mould powder MP0 after heat treatment at 900°C revealed the beginning reactions of the raw material components to form new phases. In this sample, the formation of cuspidine on the surface of the wollastonite particles is observed. The diffusion of Na_2O into the wollastonite results in the formation of sodium calcium silicates that separate the wollastonite in the centre from the cuspidine rim (Figure 2a). Fluorine does not only diffuse into wollastonite but also into albite to form fluorpectolite ($NaCa_2Si_3O_8F$) and into the partly decarburised magnesite (Figure 2a). Similar reactions were observed in MP1 and MP2. In addition, diopside ($CaMgSi_2O_6$) was formed. In contrast, no reaction between the raw material particles was observed in the sample containing SiC as the melting-control component (Figure 2b). However, this beneficial effect was reduced when antioxidants were added to the mixture. Al and/or Si are oxidised even at low temperatures. Furthermore, their oxides contribute to the melting of the raw materials, particularly fines. Thus, for MP4–MP6 liquid phase was already present owing to the reactions of the fines (Figure 2c). The cuspidine and sodium calcium silicate phases had already formed. The replacement of carbon with Si_3N_4 did not produce the desired effect. Due to the diffusion of Na_2O

into glassy phases, their melting temperature is reduced, which results in the formation of small amounts of liquid phase even at 900°C. Diffusion of F into the dissociated magnesite was also observed. When silicon nitride and silicon carbide were added together (MP9), the reactivity of the raw material components was marginally reduced. However, the diffusion of F into the magnesite and the diffusion of CaO, MgO and Na_2O into Si_3N_4 still occurred.

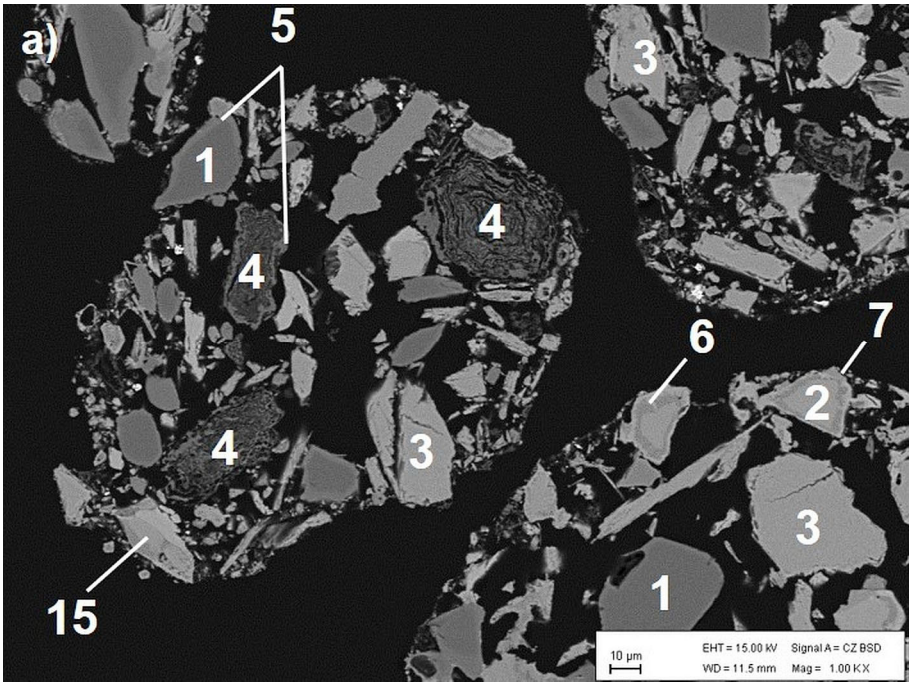

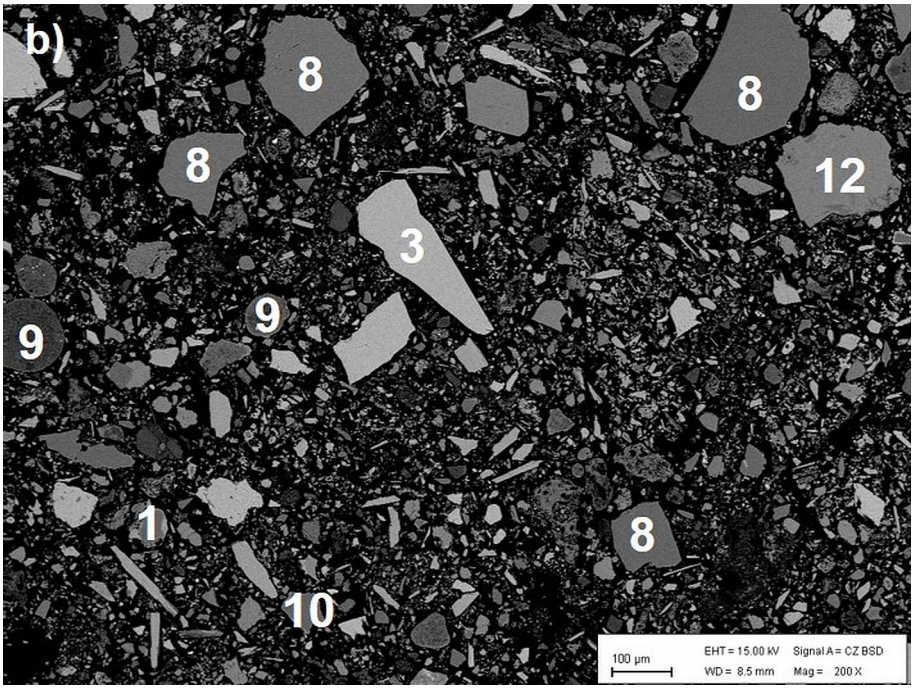

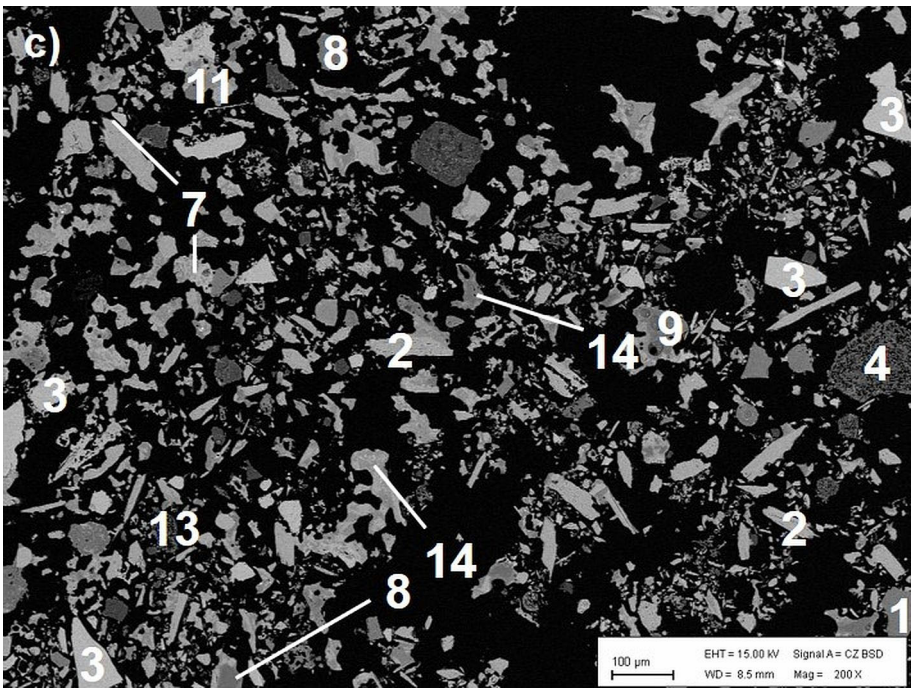

FIG 2 – Backscattered electron image of (a) MP0, (b) MP3, and (c) MP4 after temperature treatment at 900°C for 10 mins. (1) albite, (2) wollastonite, (3) fluorite, (4) dissociated magnesite, (5) fluorpectolite, (6) sodium calcium silicate, (7) cuspidine, (8) SiC, (9) fly ash, (10) quartz, (11) slag, (12) calcite, (13) corundum, (14) liquid phase, and (15) diopside.

Comparing the samples after the temperature treatment at 1000°C, considerable differences in the appearance of the respective mixtures could be observed. The mould powder MP0 used in the continuous casting process contained only the residuals of the initially larger raw material particles (Figure 3a). These were wollastonite, fluorite and albite. The cuspidine rim at the boundaries of the wollastonite and the area of the sodium calcium silicate separating the wollastonite in the centre increased. Furthermore, owing to the reaction of the fines, a considerable amount of liquid phase in contact with the newly formed cuspidine is observed. MP1, which contained no melt-control additives, exhibited the diffusion of primarily Na_2O and F into the other raw materials. The residuals of the decarburised magnesite are enriched in F, and silica-containing particles, especially at their surfaces, in Na_2O, but the liquid phase is hardly present. A similar behaviour was observed for MP2. In the SiC-containing sample (MP3), only small amounts of cuspidine were formed (Figure 3b). SiC inhibits the solid-solid reaction between the components. Thus, the formation of the new phases shifted to higher temperatures. The appearance of MP4 confirmed the previously described effect of Si addition, which resulted in an increased sintering tendency compared with MP3. New solid- and liquid-phase formations are observed. In contrast, if Si is replaced totally or at least partly by Al (MP5 and MP6), the amount of liquid phase is reduced, but is still higher than in MP3. Furthermore, the quantity of raw material particles increased at this temperature, as shown in Figure 3c. The use of Al alone as an additive resulted in the highest amount of the liquid phase, which is in accordance with the highest sintering tendency (Table 3). In MP8, silicon nitride also delays the solid-solid reactions of the raw materials but is less efficient than SiC. Hence, raw materials and new phases, such as cuspidine, are present. The MP9 showed a similar appearance (Figure 3d). For both MP8 and MP9 specimens, the oxidation of a substantial amount of Si_3N_4 was detected.

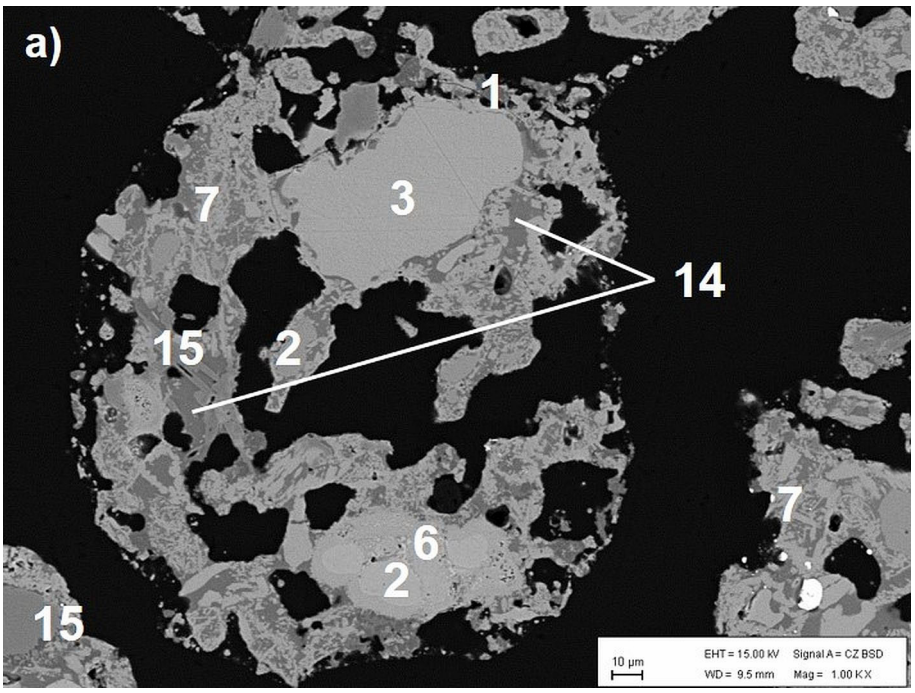
a)
1
7
3
14
15
2
7
6
2
15
10 µm
EHT = 15.00 kV
WD = 9.5 mm
Signal A = CZ BSD
Mag = 1.00 KX

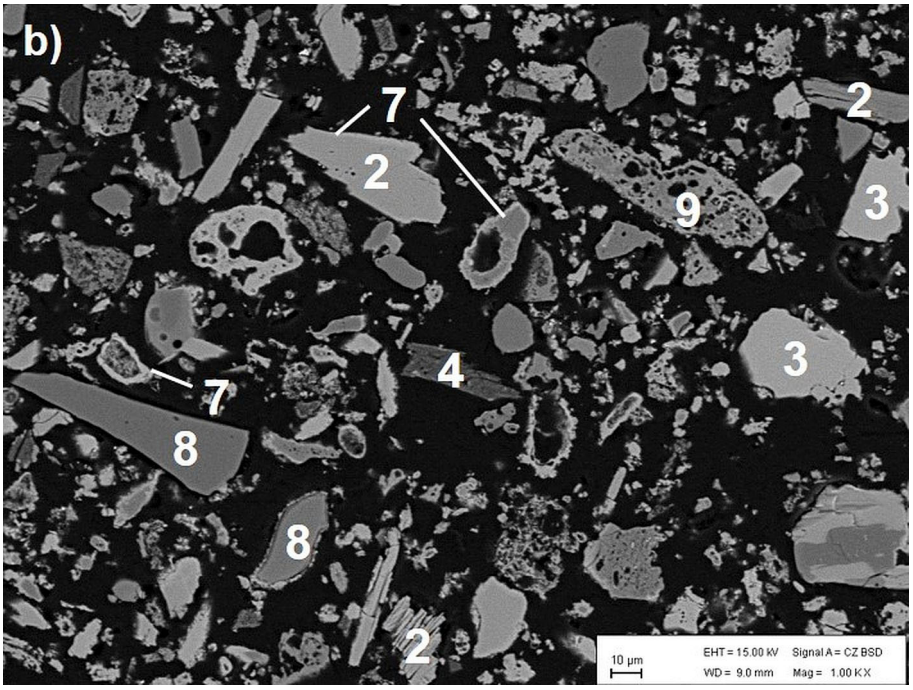
b)
7
2
2
9
3
4
3
7
8
8
2
10 µm
EHT = 15.00 kV
WD = 9.0 mm
Signal A = CZ BSD
Mag = 1.00 KX

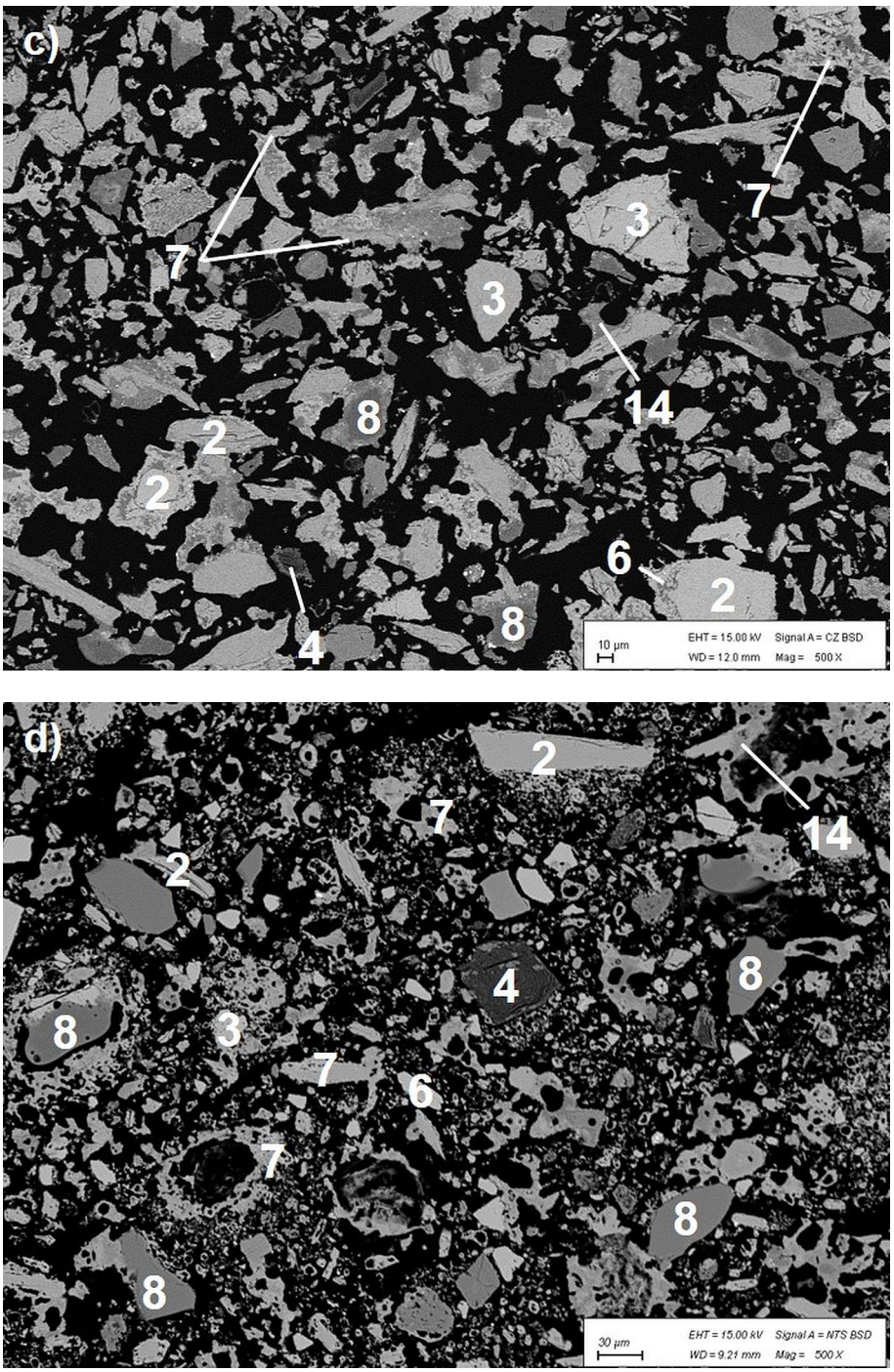

FIG 3 – Backscattered electron image of (a) MP0, (b) MP3, (c) MP6, and (d) MP9 after temperature treatment at 1000°C for 10 mins. (1) albite, (2) wollastonite, (3) fluorite, (4) dissociated magnesite, (6) sodium calcium silicate, (7) cuspidine, (8) SiC, (9) fly ash, (14) liquid phase, and (15) diopside.

After heat treatment at 1100°C, the samples contained mainly liquid phase and cuspidine (Figure 4). Residuals of large raw material particles were also observed. In MP1, additional fluoride dendrites were observed, which formed during quenching of the samples. A different appearance was observed for MP3 containing SiC. Large raw material particles showed small reaction boundaries on their surfaces, indicating a slow reaction rate. A liquid phase was present but was not coherent (Figure 3b). SiC was also detected in the samples containing additional antioxidants or silicon nitride (MP4–MP6 and MP9). In these specimens, SiC remained in direct contact with the already formed continuous liquid phase (Figure 4c). Locally, the SiC particles accumulated. Through oxidation, the melt-control additives caused the formation of pores in the liquid slag in all samples. This was particularly observed in MP8 and MP9, in which Si_3N_4 was used (Figure 4d).

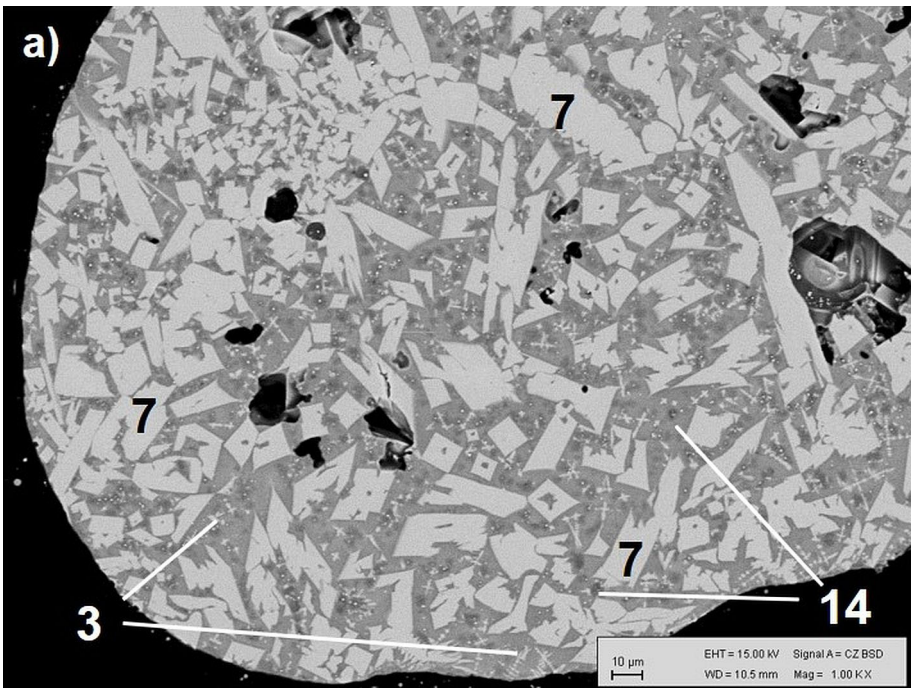
a)
7
7
7
3
14
10 µm
EHT = 15.00 kV
WD = 10.5 mm
Signal A = CZ BSD
Mag = 1.00 K X

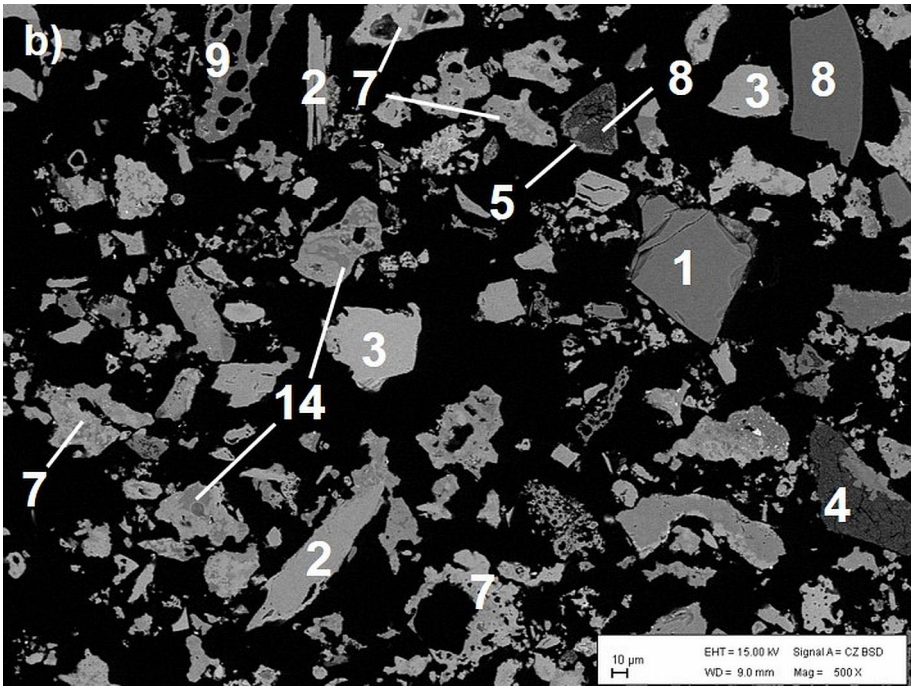
b)
9
2
7
8
3
8
5
1
3
14
7
4
2
7
10 µm
EHT = 15.00 kV
WD = 9.0 mm
Signal A = CZ BSD
Mag = 500 X

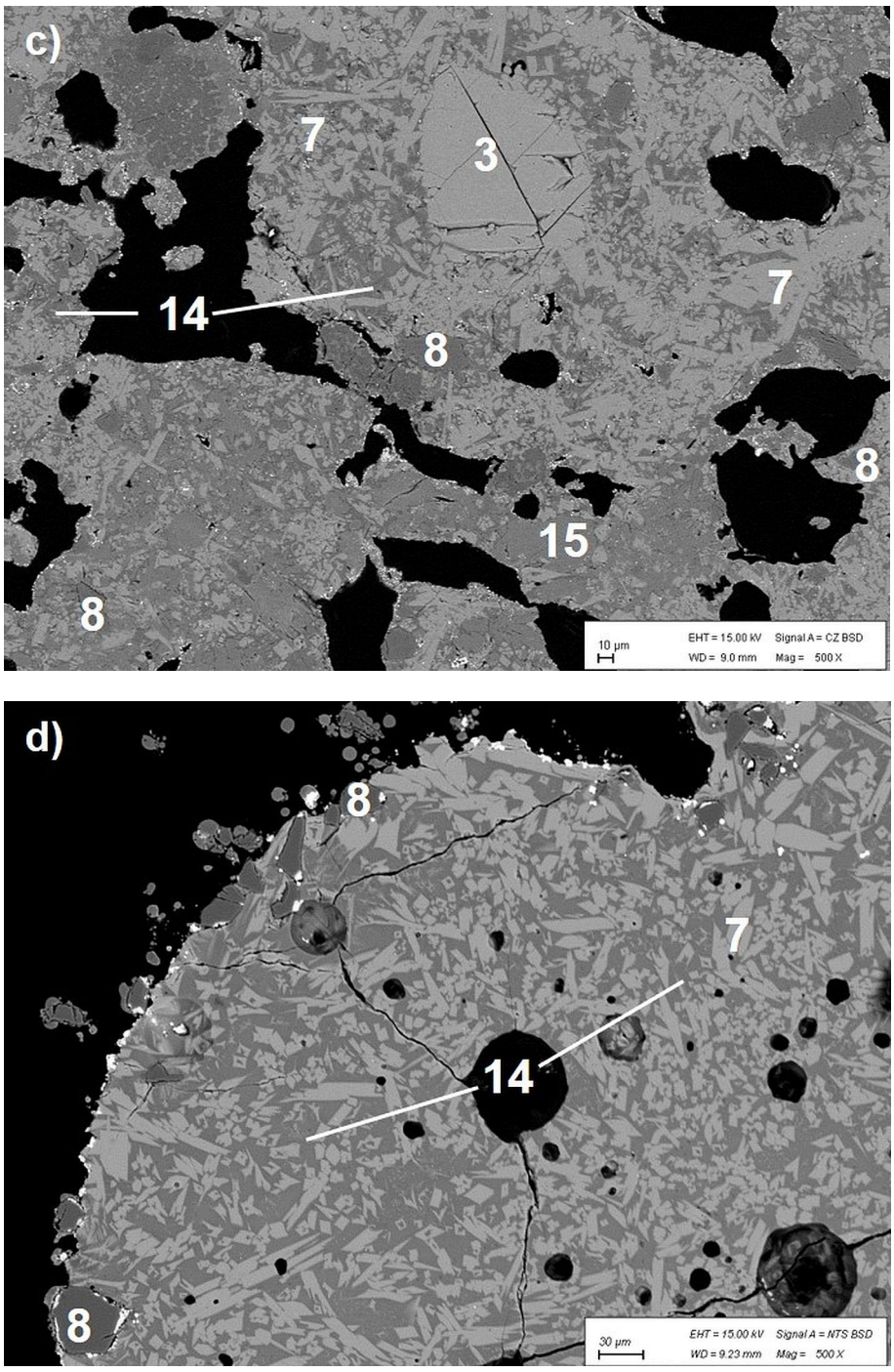

FIG 4 – Backscattered electron image of (a) MP0, (b) MP3, (c) MP4, and (d) MP9 after temperature treatment at 1100°C for 10 mins. (1) albite, (2) wollastonite, (3) fluorite, (4) dissociated magnesite, (5) fluoropectolite, (7) cuspidine, (8) SiC, (9) fly ash, (14) liquid phase, and (15) diopside.

After the treatment of the mould powder MP0 as received at 1200°C, the mineralogical investigations revealed the independent melting of each granule (Figure 5a). No continuous liquid phase was formed, even though all granules were at least partly liquefied. Some still showed cuspidine in the solid state, whereas others consisted only of the liquid phase. This can be explained by the slightly different chemical compositions of the granules with respect to their F and/or Na_2O contents, which influenced the melting temperature of the granules.

In general, the appearance of the mixtures was very similar. Except for MP0, MP3, and partly MP5, where small quantities of cuspidine in a stocky shape were still present (Figure 5a, 5b), a homogeneous liquid phase was formed (Figure 5d). Nevertheless, cuspidine was found in all other

samples. But due to its dendritic shape, it is indicated that it crystallised during cooling and was not present at 1200°C in the solid state (Figure 5a, 5b, 5c). When SiC was used, some residuals still existed within the liquid slag at this temperature. It was also present in samples containing antioxidants, but its particle size was smaller. This confirms the previously suggested assumption that the addition of Al and especially Si to SiC counteracts the beneficial properties of SiC by promoting reactions between the components. This was also observed when silicon carbide and silicon nitride are used together (MP9).

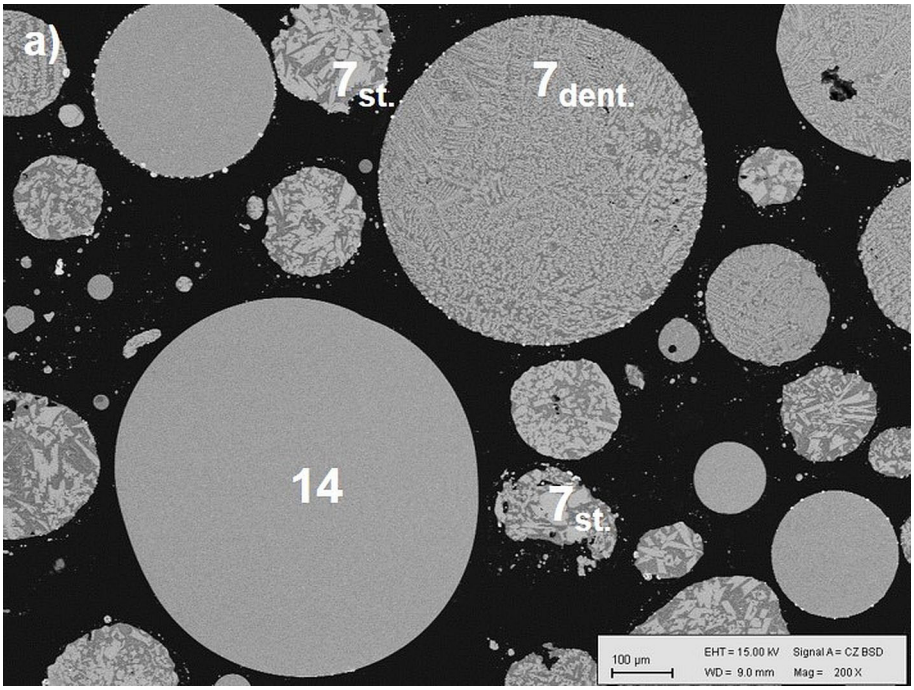

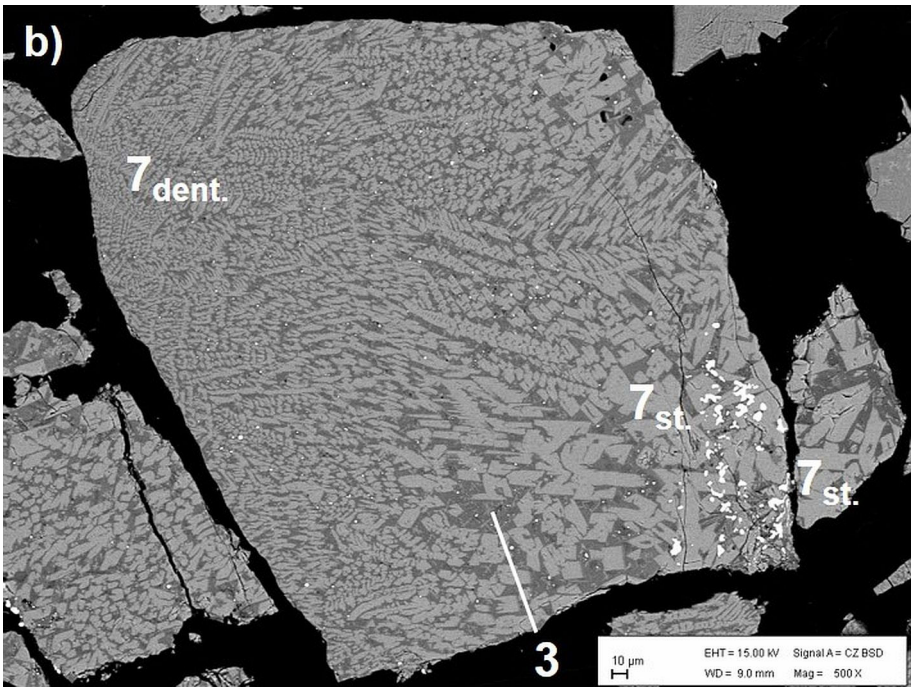

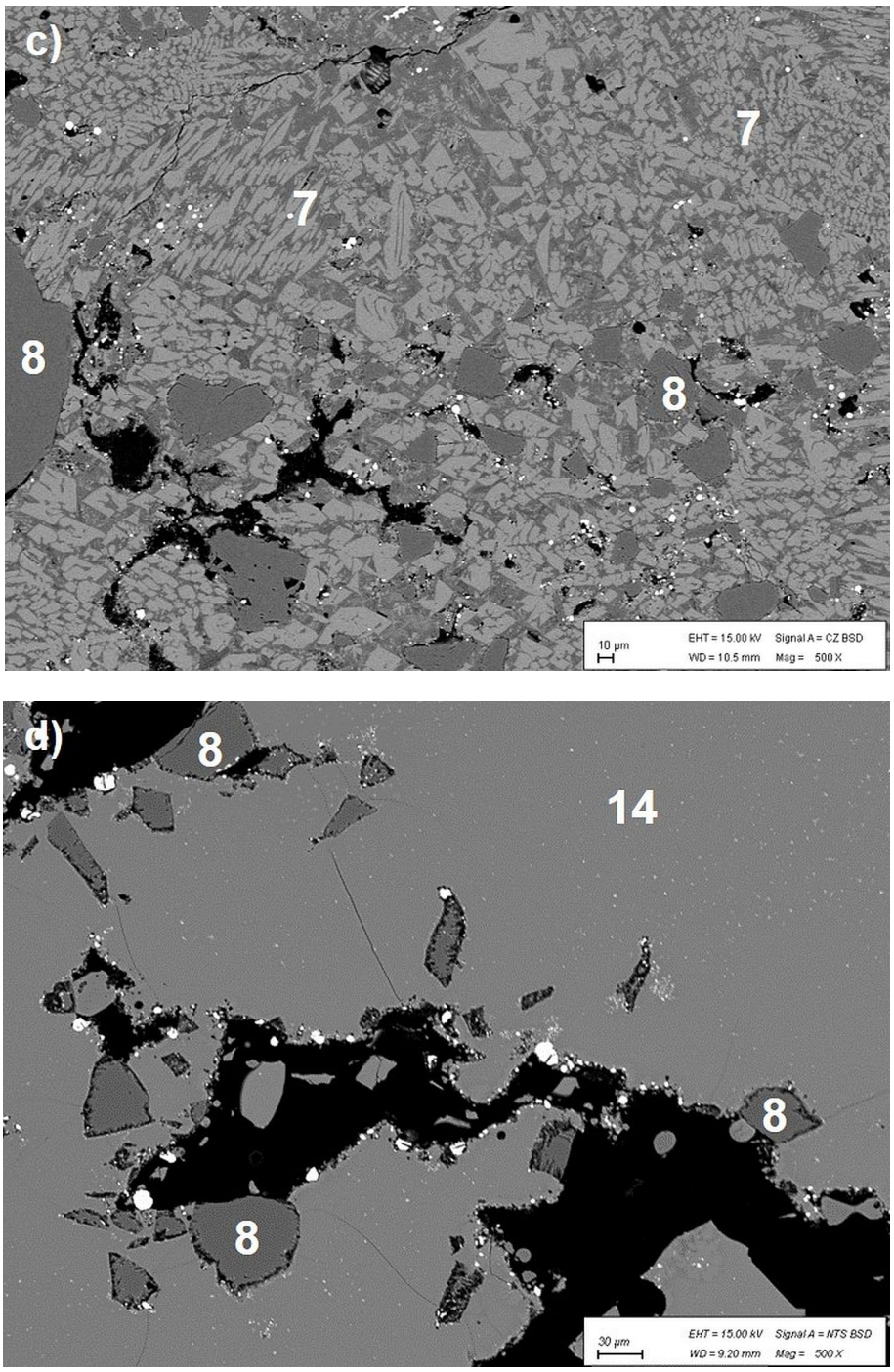

FIG 5 – Backscattered electron image of (a) MP0, (b) MP3, (c) MP5, and (d) MP9 after temperature treatment at 1200°C for 10 mins. (3) fluorite (7) cuspidine: stocky (st.) and dendritic (dent.), (8) SiC, and (14) liquid phase.

Reduction of the SiC content

To investigate the effect of the SiC content on the melting behaviour of the mould powder, mixtures were prepared according to the raw material composition given in Table 2. The investigations revealed that for this mould powder composition, SiC content >2.8 wt per cent did not have a significant further effect on reducing the reactions of the raw material particles. SiC particles were still present in the samples after the heat treatment at 1200°C. In contrast, the sample containing solely 1.4 wt per cent SiC (MP13) showed the same melting tendency as the mould powder without melt-control additives. On comparing the results of MP12 with those of the standard carbon-containing mould powder, it is evident that the residuals of the raw materials are detected at only higher temperatures and the amount of the liquid phase is reduced. This indicates that even small

amounts of SiC partially inhibited the reaction between the raw material particles and shifted the formation of new solid and liquid phases to higher temperatures. At 1200°C, SiC is the only solid phase, but its amount is considerably reduced.

CONCLUSIONS

Different melt-control components used to replace carbon in mould powders were investigated. Thermodynamic calculations and laboratory experiments at selected temperatures, together with mineralogical investigations, were conducted to compare their effects. The melting behaviours of the different mixtures were compared with those of the mould powder already used in the continuous casting of steel. These investigations revealed that SiC is a promising substitute for controlling the melting rate of mould powders. For temperatures below 1100°C, a reduced solid-solid diffusion was observed. This shifted the formation of new solid and liquid phases to higher temperatures and increased the stability of the raw material particles. Owing to its high oxidation resistance, SiC initially remains in a solid state. Thus, the amount of SiO_2 required to form the liquid phase is not available. With increasing temperature, SiC is partially oxidised and the availability of SiO_2 increases. This influences the formation of new phases. At lower temperatures, where SiC is unoxidised, phases with lower SiO_2 contents are formed. Comparing the amounts of liquid phase with those of the standard mould powder at temperatures below 1000°C, a lower value was obtained for the SiC-containing samples, even though their solidus temperatures were lower. This agrees with the thermodynamic calculations. Due to the oxidation of Al and Si at lower temperatures, the formation of new phases is supported, which also explains the higher amount of liquid phase at 900°C. In a subsequent study, the SiC content could be considerably reduced, which could lead to a reduction of at least 27 g CO_2/kg of mould powder compared to the carbon-containing product.

Another possible carbon replacement is silicon nitride. However, its effect is weaker than that of SiC. At temperatures below 1100°C the reactions between particles were prohibited, but with increasing temperatures, the appearance of the samples after heat treatment was similar to that of the standard mould powder (MP0), because it shows a lower stability than SiC and the necessary SiO_2 amount to form the liquid phase is available at lower temperatures. In addition, the combination of silicon nitride and silicon carbide did not meet expectations with respect to controlling melting behaviour.

The present investigations revealed that the melting rate was lower for loose powders. This can be explained by the close contact between the raw material particles in the case of granules and their production processes. During the production of granulated mould powders, raw material particles are added to a water/binder mixture and homogenised. Sodium carbonate is dissolved and distributed over the entire volume (Han *et al*, 2022). Thus, the formation of new phases during heating is promoted. Furthermore, the independent melting of the granules during temperature treatment at 1100°C and 1200°C is explained by the diffusion of Na_2O to the surface of the granules during spray drying. Owing to the increased sodium oxide content, the melting temperature is reduced and the granules start sintering from the boundaries. With an increasing amount of liquid phase, a nearly spherical drop is formed with minimal surface energy. The surface energy would further be reduced by the formation of a coherent liquid phase from single drops. However, owing to the lack of residence time at the annealing temperature, this process was only partially observed during the experiment.

The possible pick-up of carbon or nitrogen into the liquid steel during casting, if SiC or Si_3N_4 is used to control the melting behaviour is discussed below. In previous studies, carbon was only partly substituted by nitrides to prevent renitriding of the liquid metal (Debiesme *et al*, 1998). Thus, if Si_3N_4 is used to totally substitute carbon, nitriding will most probably take place during casting. Nevertheless, it was shown that its effect to control the melting rate of a mould powder is weaker than that of SiC being the preferred substitute for carbon. Even for this carbide, only partial substitution of carbon was suggested to ensure the same melting behaviour. If 3 wt per cent SiC was used, the carbon content was defined to be <1 wt per cent. Experiments in contact to the steel revealed a lower effect on recarburisation of the liquid metal (Ning and Jinghao, 1998). As shown in the present paper, similar melting rates were achieved by using solely 2.8 wt per cent SiC, which is even lower than in the samples mentioned before. Consequently, recarburisation is not expected to take place. Nevertheless, this assumption has to be confirmed by industrial trials.

ACKNOWLEDGEMENTS

The authors gratefully acknowledge the funding support of K1-MET GmbH, a metallurgical competence centre. The research program of the K1-MET competence centre is supported by the Competence Centre for Excellent Technologies (COMET), an Austrian program for competence centres. COMET is funded by the Federal Ministry for Climate Action, Environment, Energy, Mobility, Innovation, and Technology; the Federal Ministry for Labour and Economy; the Federal States of Upper Austria, Tyrol, and Styria; as well as the Styrian Business Promotion Agency (SFG) and the Standortagentur Tyrol. The Upper Austrian Research GmbH continuously supports K1-MET. In addition to public funding from COMET, this research project was partially financed by the scientific partner Montanuniversitaet Leoben and the industrial partners RHI Magnesita, voestalpine Stahl, and voestalpine Stahl Donawitz.

REFERENCES

Dai, L, Xiao, G and Ding, D, 2021. Review of Oxidation Resistance Technology of Carbon-containing Refractories. *Materials Reports*, 35(3):3057–3066.

Debiesme, B, Radot, J P, Coulombet, D, Lefebvre, C, Pontoire, J N, Roux, Y and Damerval, C, 1996. Mould cover for continuous casting of steel, especially very-low-carbon steels. US Patent 5876482A.

Debiesme, B, Radot, J P, Coulombet, D, Lefebvre, C, Pontoire, J N, Roux, Y and Damerval, C, 1998. Mould cover powder for continuous casting of steel, especially very-low-carbon steels. US Patent 6328781B1.

Ghosh, N K, Jagannathan, K P and Ghosh, D N, 2001. Oxidation of magnesia-carbon refractories with addition of aluminium and silicon in air, *Interceram - International Ceramic Review*, 50(3):196–202.

Han, F, Wen, G, Tang, P and Chen, F, 2023. Catalytic Effect of Iron Oxide on the Combustion of Carbonaceous Materials in Mold Flux for Continuous Casting, *Metallurgical and Materials Transactions B*, 54(5):2605–2613.

Han, F, Yu, L, Wen, G, Wang, X, Zhang, F, Jia, J and Gu, S, 2022. The effect of composition segregation of mold powder produced by spray granulation on the sintering performance, *Journal of Materials Research and Technology*, 20:448–458.

Kawamoto, M, Nakajima, K, Kanazawa, T and Nakai, K, 1994. Design Principles of Mold Powder for High Speed Continuous Casting, *ISIJ International*, 34(7):593–598.

Kölbl, N, Marschall, I and Harmuth, H, 2009. Investigation of the melting behavior of mould powders, in *Proceedings VIII International Conference on Molten Slags, Fluxes and Salts* (ed: M Sanchez), pp 1031–1040 (GECAMIN: Santiago).

Kromhout, J A, 2013. Mould powders for high speed continuous casting of steel, PhD Thesis, Technical University Delft, Delft. Available from: <http://resolver.tudelft.nl/uuid:4b52997d-9fc9-41b3-a4e8-70ffab1b3fdf> [Accessed: 20 November 2023].

Lefebvre, C, Radot, J P, Pontoir, J N and Roux, Y, 1996. Development of continuous casting mould powder for the limitation of recarburization in ULC steels, La Revue de Métallurgie-CIT, 93(4):489–496.

Macho, J J, Hecko, G, Golinmowski, B and Frazee, M, 2005. The development and evaluation of a new generation of no free carbon continuous casting fluxes, in *Preprints 33rd McMaster Symposium on Iron and Steelmaking*, pp 131–146 (McMaster University: Hamilton).

Maillart, O, Chaumat, V and Hodaj, F, 2010. Wetting and interfacial interactions in the CaO-Al_2O_3-SiO_2/silicon carbide system, *Journal of Material Science*, 45(8):2126–2132.

Mills, K C, 1990. NPLRep, DMM(A), ECSC Contract No. 7210.22/451, Report EUR 13177 EN, Teddington, UK.

Mills, K C, Fox, A B, Thackray, R P and Li, Z, 2004. The performance and properties of mould fluxes, in *Proceedings of the VII International Conference on Molten Slags, Fluxes and Salts*, pp 713–722 (The South African Institute of Mining and Metallurgy: Johannesburg).

Nakato, H, Takeuchi, S, Fujii, T, Nozaki, T and Washio, M, 1991. Characteristics of new mold fluxes for strand casting of low and ultra-low carbon slabs, in *Proceedings of the 75th Steelmaking Conference*, pp 639–646.

Ning, L and Jinghao, C, 1998. Study on SiC as the substitute of the mold fluxes in continuous casting of ULC steel, *Journal of Shaoguan University (Social Science)*, 19:112–120.

Park, J, Jeon, J, Lee, K, Park, J H and Chung, Y, 2016. Initial wetting an spreading rates between SiC and CaO-SiO_2-MnO slag, *Metallurgical and Materials Transactions B*, 47(3):1832–1838.

Safarian, J and Tangstad, M, 2009. Wettability of silicon carbide by CaO-SiO_2 slags, *Metallurgical and Materials Transactions B*, 40(6):920–928.

Sun, L, Liu, C, Fang, J, Zhang, J and Lu, C, 2019. Crystallization behavior and thermal properties of B_2O_3-containing MgO-Al_2O_3-SiO_2-Li2O glass ceramic and its wettability on Si3N4 ceramic, *Journal of the European Ceramic Society*, 39(4):1532–1539.

Supradist, M, Cramb, A W and Schwerdtfeger, K, 2004. Combustion of Carbon in Casting Powder in a Temperature Gradient, *ISIJ International*, 44(5):817–826.

Takeuchi, H, Mori, H, Nishida, T, Yanai, T and Mukunashi, K, 1978. Development of a Carbon-free Casting Powder for Continuous Casting of Steels, *Tetsu-to-Hagané*, 64(10):1548–1557.

Takeuchi, H, Nishida, T, Ohno, T, Kataoko, N and Hikara, Y, 1976. Kohlenstofffreies Gießpulver für Kokillen- und Strangguß von Stahl (Carbon-free casting powder for chill and continuous casting of steel), Deutsches Patent (26 26 354), München, Deutschland: eutsches Patentamt (DPMA: German Patent and Trade Mark Office).

Terada, S, Kaneko, S, Ishikawa, T and Yoshida, Y, 1991. Development of mold fluxes for ultra-low-carbon steels, *Iron and Steelmaker*, 18(9):41–44.

Wang, T and Yamaguchi, A, 2001. Oxidation Protection of MgO–C Refractories by Means of Al8B4C7, *Journal of the American Ceramic Society*, 84(3):577–582.

Yan, W, Yang, Y D, Chen, W Q, Barati, M and McLean, A, 2015. Design of mould fluxes for continuous casting of special steels, *Canadian Metallurgical Quarterly*, 54(4):467–476.

Yi, Z M, Song, J L and Peng, Q C, 2013. Analysis of Carbonization Mechanism in ULCS Continuous Casting and Control Measures, *Advanced Materials Research*, 739:214–217.

Fluxing options and slag operating window for Metso's DRI smelting furnace

DOI: 10.62053/NWKZ5785

J Hamuyuni[1], K Vallo[2], T Haimi[3], F Tesfaye[4], J Pihlasalo[5] and M Lindgren[6]

1. Product Manager, Metso, Espoo 28100, Finland. Email: joseph.hamuyuni@metso.com
2. Product Manager, Metso, Espoo 02230, Finland. Email: kimmo.vallo@metso.com
3. Senior Sales Manager, Metso, Espoo 02230, Finland. Email: timo.haimi@metso.com
4. Process Metallurgist, Metso, Espoo 02230, Finland. Email: fiseha.tesfaye@metso.com
5. Senior Metallurgist, Metso, Pori 28100, Finland. Email: jouni.pihlasalo@metso.com
6. Director R&D, Metso, Pori 28100, Finland. Email: mari.lindgren.@metso.com

ABSTRACT

Decarbonisation of the steel industry has recently attracted a lot of research and technological development. Most of the technological developments are centred around the replacement of blast furnace (BF), which has been the main primary smelting furnace in the ironmaking step of steel production. Replacement of the BF is not an easy task because of BF's many established capabilities over the years, especially its ability to use low-grade iron feed.

In this regard, Metso has developed its own technology, Metso's Outotec direct reduced iron (DRI) smelting furnace, to tackle this problem. The recently developed six-in line electric furnace for DRI smelting can be used for primary smelting of DRI from blast furnace grade iron ore. Unlike the electric arc furnace (EAF), the DRI smelting furnace can handle larger slag volumes that emanate from the high gangue in BF grade DRI. Therefore, fluxing plays an important role in operating the DRI smelting furnace. This paper presents fluxing options and proposes slag quality and operating windows for the DRI smelting furnace. Also, the effect of slag on refractory durability will be discussed.

INTRODUCTION

Decarbonising steel industry is one of the practical pathways to mitigate global warming. Carbon dioxide (CO_2) emissions from steel industry contribute a large share of greenhouse gases that leads to global warming. Carbon dioxide is responsible for about 73 per cent of all greenhouse gases, while the balance is mostly from methane (18 per cent), N_2O (6 per cent) and F-gases (2.5 per cent) (Olivier, Schure and Peters, 2017). Currently and depending on geographical location, it is estimated that between 5–14 per cent of all CO_2 emissions come from the steel industry alone (Gielen, 2003; Kuramochi, 2016). The Paris agreement puts an ambitious goal of limiting global temperature increase to 1.5°C. And while this is a daunting task, it also presents process technology development opportunities.

Currently, blast furnace which is the dominant technology for ironmaking step of the steel production, is the main source of CO_2 emissions. This is because of the consumption of large amount of fossil reductants. For every ton of pig iron, there is *ca* 0.5 tons of fossil reductants consumed (Fick *et al*, 2014). Opportunities for decarbonisation of steelmaking therefore, depends on finding a low CO_2 emission alternative process to the blast furnace. This can be built around existing secondary smelting processes or completely stand-alone process.

Metso's alternative to the blast furnace, is a high capacity 6-in line direct reduced iron (DRI) smelting furnace. When implemented together with a direct reduction process and current existing downstream processes, it is estimated to cut down CO_2 emissions by up to 60–80 per cent, depending on electricity sources. Metso's DRI smelting furnace is based on Outotec proven proprietary technologies and should offer competitive advantages towards greener steel industry. It offers capacities of hot metal more than 1.2 million tons per annum (Mt/a) and can handle larger than electric arc furnace (EAF) slag volumes, making it possible to use DRI from blast furnace grade iron ores. Also, various types of DRI from both natural gas and hydrogen based reducing processes can be used as feed.

DRI smelting furnace fluxing philosophy is built on using burnt dolomite and lime, in such proportion that regardless of the ore, the slag basicity stays within a narrow window. The fluxing philosophy also ensures that resultant slag can take impurities but stays within manageable viscosity.

Selection of suitable refractory is important, and Metso has conducted its own test work on various refractories on the market to determine the best candidate and operation mode for increased campaign life of furnace.

This paper presents data on fluxing philosophy and refractory selection for DRI smelting furnace. Operating window for resultant slag is assessed using thermodynamic software FactSage™, ver 8.2 (by GTT-Technologies, Germany) and the results are presented. Additionally, few observations made in ongoing refractory studies are discussed.

FEED FOR THE DRI SMELTING FURNACE AND FLUXING PHILOSOPHY

The design basis of the DRI smelting furnace is to target blast furnace grade iron ores, which have typically <67 per cent iron in the concentrate and much higher gangue content of >5 per cent. These types of ores are not suitable for smelting in EAF because of the low gangue tolerance of the EAF and globally only about 3 per cent of iron ores can be used to produce EAF grade DRI. Metso's ideal green steel flow sheet is by using hydrogen reduced DRI as in the Circored process, but the DRI smelting furnace can also handle DRI from shaft furnace and coal (Rotary kiln) based technologies. Table 1 shows typical feeds from the three DRI technologies. The numbers in the table are representative and not to be taken as standard for DRI available on the market today.

TABLE 1

Typical direct reduced iron (DRI) specification from different technologies.

	Natural gas reduced DRI	Solid carbon reduced DRI	Hydrogen reduced DRI
Total Fe (%)	>85	85–93	>85
Metallisation degree (%)	90–94	88–90	85–92
Carbon content (%)	0.5–3	0.1–2	0
Gangue (%)	2.8–6	3–8	3–8

The metal product quality targets of the DRI smelting furnace include carbon of 2–3 per cent and low in phosphorus and sulfur. Depending on the target carbon content, the metal and slag temperature are typically 1500–1600°C and 1600–1700°C, respectively. The DRI smelting furnace uses burnt dolomite and lime as flux, with the proportions of these varying according to the composition of types of feed. The main determining components are the amount of CaO, MgO, Al_2O_3 and SiO_2 contained in feed. By comparison, typical blast furnace flux is limestone. The main components of the resultant slag are therefore the above four oxides. The basicity (CaO/SiO_2) is typically targeted somewhere between 1.2–1.4 for most feeds. Additionally, it is important to keep the FeO content of slag at low levels (<5 per cent) that enables it acceptable as raw material for the cement industry.

Thermodynamic calculations for assessment of operating window

The thermodynamic calculations in this study were carried out with FactSage 8.1. Thermodynamic parameters for the chemical system (Al_2O_3-CaO-FeO-MgO-SiO_2) were obtained from FactPS and FToxid databases. Impurities MnO, P_2O_5 and TiO_2 were left out of the calculated chemical system, because their contents are so small and not considered to be significant factors regarding the thermodynamic properties of the slag.

Liquidus temperature projections were calculated with FactSage for different compositions. Four projections with a base diagram of CaO-SiO_2-MgO were calculated with constant content of FeO (2.00 per cent). Al_2O_3 content of the slag was 5.00, 10.00, 15.00 or 20.00 per cent in different projections. Calculated temperature range for all the projections was from 1200 to 1800°C (1473.15–2073.15 K). Interval between liquidus temperature isotherms was 20°C. The final calculation was

done with only those stable phases to make the final calculation faster and to produce smoother liquidus temperature isotherms.

Stable phases – solutions and compounds (pure substances PS) for the FactSage liquidus projections are listed in Appendix A.

Calculations with FactSage software package

The four liquidus projections calculated with FactSage are presented in Figures 1–4.

At 5.00 per cent Al_2O_3, the global liquidus temperature minimum of 1270–1280°C is located near the four-phase intersection point [Clinopyroxene#1 / SiO_2_Tridymite(h)(s4) / Wollastonite] with the liquid slag. The composition of this four-phase intersection point at 1270°C is 65.25 per cent SiO_2, 28.10 per cent CaO and 6.65 per cent MgO.

At 10.00 per cent Al_2O_3, the global liquidus temperature minimum of between 1192–1220°C is located near the four-phase intersection point Clinopyroxene#1 / SiO_2_Tridymite(h)(s4) / Wollastonite with the liquid slag. The composition of this four-phase intersection point at 1192.7°C is 68.46 per cent SiO_2, 27.84 per cent CaO and 3.70 per cent MgO.

At 15.00 per cent Al_2O_3, the global liquidus temperature minimum of between 1228–1240°C is located near the four-phase intersection points [$CaAl_2Si_2O_8$_Anorthite(s2) / Cordierite / Orthopyroxene] and [$CaAl_2Si_2O_8$_Anorthite(s2) / Cordierite / SiO_2_Tridymite(h)(s4)] with the liquid slag. The composition of these four-phase intersection points at 1233.5 and 1227.8°C are 70.33 per cent SiO_2, 16.97 per cent CaO and 12.70 per cent MgO and 73.45 per cent SiO_2, 16.61 per cent CaO and 9.94 per cent MgO, respectively.

At 20.00 per cent Al_2O_3, the global liquidus temperature minimum of between 1280–1300°C is located near the four-phase intersection point [$CaAl_2Si_2O_8$_Anorthite(s2) / Melilite / Spinel#1] with the liquid slag. The composition of this four-phase intersection points at 1280°C is 52.41 per cent SiO_2, 37.70 per cent CaO and 9.89 per cent MgO.

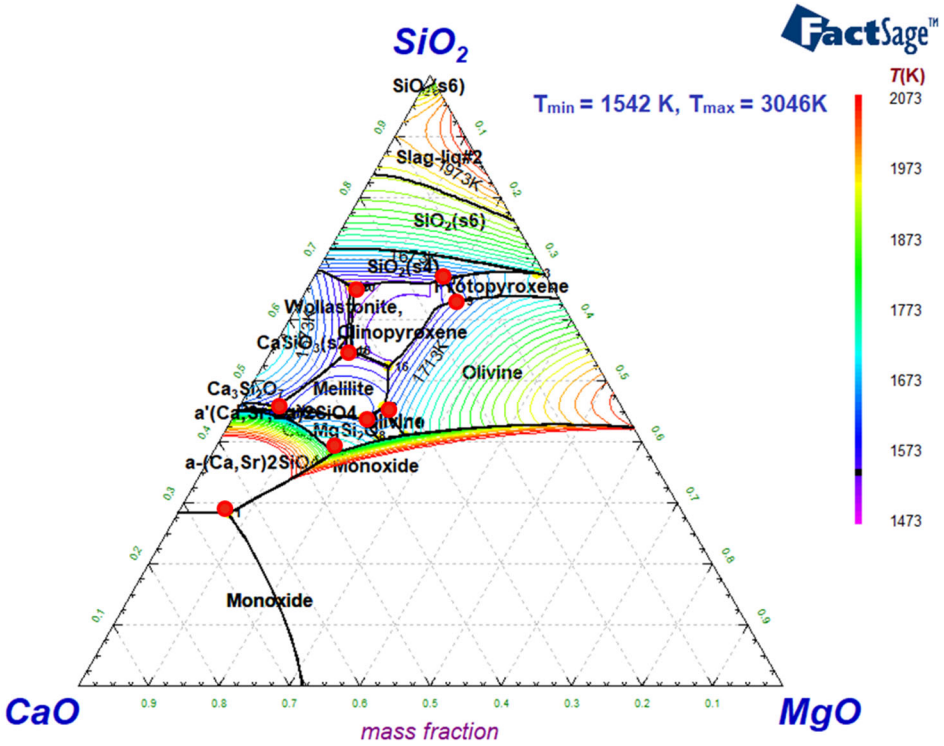

FIG 1 – Liquidus projection in system CaO-SiO_2-MgO with 2.00 per cent FeO and 5.00 per cent Al_2O_3 calculated with FactSage 8.1. The red dots indicate selected four-phase interaction points with the liquid slag.

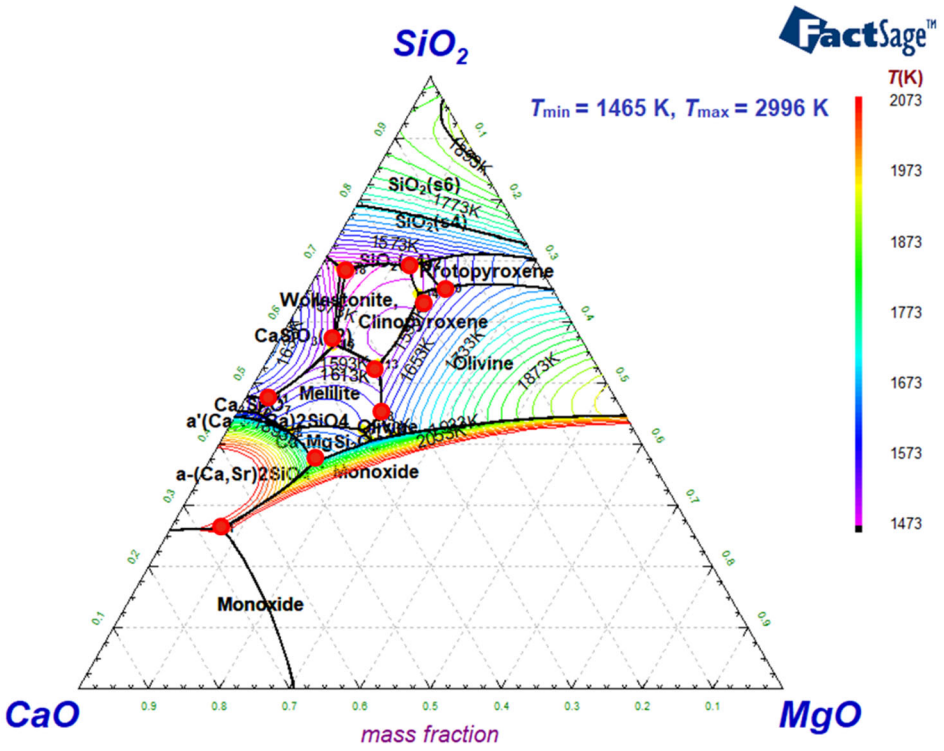

FIG 2 – Liquidus projection in system CaO-SiO_2-MgO with 2.00 per cent FeO and 10.00 per cent Al_2O_3 calculated with FactSage 8.1. The red dots indicate selected four-phase interaction points with the liquid slag.

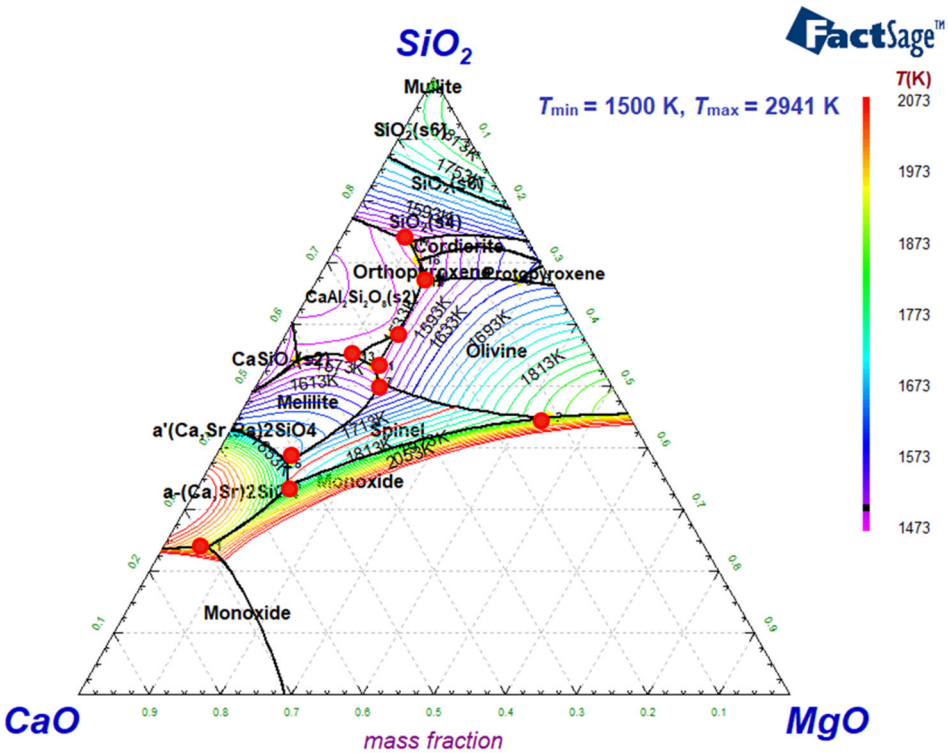

FIG 3 – Liquidus projection in system CaO-SiO_2-MgO with 2.00 per cent FeO and 15.00 per cent Al_2O_3 calculated with FactSage 8.1. The red dots indicate selected four-phase interaction points with the liquid slag.

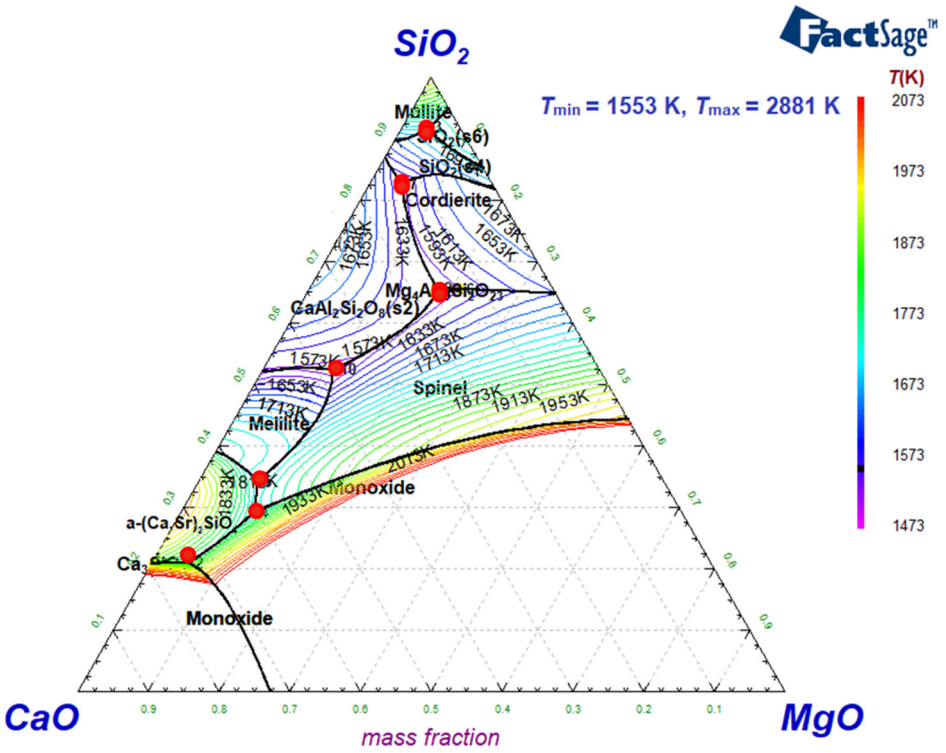

FIG 4 – Liquidus projection in system CaO-SiO_2-MgO with 2.00 per cent FeO and 20.00 per cent Al_2O_3 calculated with FactSage 8.1. The red dots indicate selected four-phase interaction points with the liquid slag.

Viscosity calculations with FactSage

Viscosity values have been calculated for certain slag compositions. Slag #1 has a CaO/SiO_2 ratio of 1.143 and slag #2 has a CaO/SiO_2 ratio of 1.5. For both slags, only the amounts of Al_2O_3 and MgO were varied in a proportional amount.

The results obtained are illustrated in Figure 5. In general, at any given composition of Al_2O_3 or MgO, slag #1 with lower CaO/SiO_2 ratio (dashed lines in Figure 5) has higher viscosity than that of slag #2. In all cases, substitution of Al_2O_3 with MgO resulted in lower viscosity. For the calculated slag compositions (Figure 5), viscosity at 1400°C remains below 0.65 Pa.s. Results are consistent with an earlier thermodynamic study conducted by Metso (internal report) (Pihlasalo and Tesfaye, 2022).

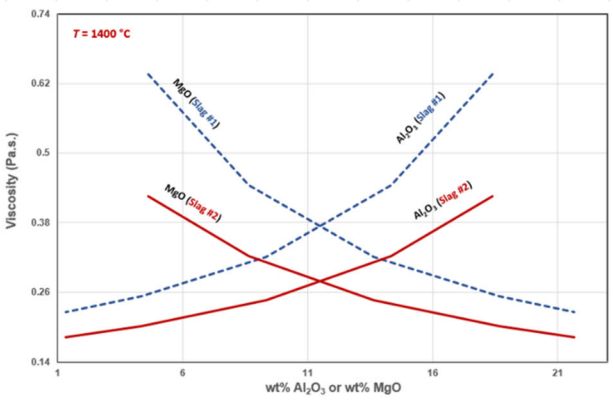

Slag #1 (CaO/SiO2)=1.143					
SiO2	Al2O3	CaO	MgO	FeO	Total
35	18.38	40	4.62	2	100
35	14.34	40	8.66	2	100
35	9.34	40	13.66	2	100
35	4.34	40	18.66	2	100
35	1.34	40	21.66	2	100

Slag #2 (CaO/SiO2=1.5)					
SiO2	Al2O3	CaO	MgO	FeO	
30	18.38	45	4.62	2	100
30	14.34	45	8.66	2	100
30	9.34	45	13.66	2	100
30	4.34	45	18.66	2	100
30	1.34	45	21.66	2	100

FIG 5 – Viscosities of two different slags (CaO/SiO_2 = 1.143 (dashed lines) and CaO/SiO_2 = 1.5 (solid lines)) with varying amounts of Al_2O_3 and MgO. Calculated with FactSage 8.1 software package.

Recommendation for DRI slag compositions at different operating temperatures

The operating temperature for the DRI smelting furnace is dependent on the liquidus temperature of the metal phase, which decreases as a function of carbon content of iron. Lowest liquidus temperature of Fe-C is 1147°C at 4.3 per cent C and melting temperature of pure Fe is 1538°C. The metal temperature is required to be 50°C higher than its liquidus temperature. The temperature difference between metal and slag is usually about 150°C. This means that the slag temperature (= operating temperature) is required to be in the range of 1350–1750°C. The slag needs 50°C superheat, which then corresponds to slag liquidus of temperature range of 1300–1700°C.

The suitable operating windows were found for operation temperatures between 1300 and 1500°C. At 1600°C, some operating windows were found but they are all high in MgO. At 1700°C, no suitable operating windows were found, because inside those areas suitable based on liquidus temperature, the isotherms are close to each other, which makes operation difficult.

REFRACTORY TESTING

Refractories play a crucial role in smelting furnaces by containing molten slag and metal for long periods extending to several years usually referred to as a campaign life. They must withstand chemical attack, must be thermal resistant and must maintain a certain minimum mechanical strength during the campaign life. Choosing the correct refractory for a process is therefore mandatory.

Metso has been conducting its own test work to understand the best refractory for the DRI smelting furnace. Finger tests and crucible tests were carried out on two types of refractories. The choice of refractory was based on preliminary assessment of potential candidate refractories.

A finger test is performed by dipping a piece of refractory that has been cut into a finger like shape, in hot slag at temperatures resembling typical operating conditions, Figure 6. In this study, the slag was heated to 1500°C and the samples were held in liquid slag for 6 hrs while stirring during the test was helped by induction.

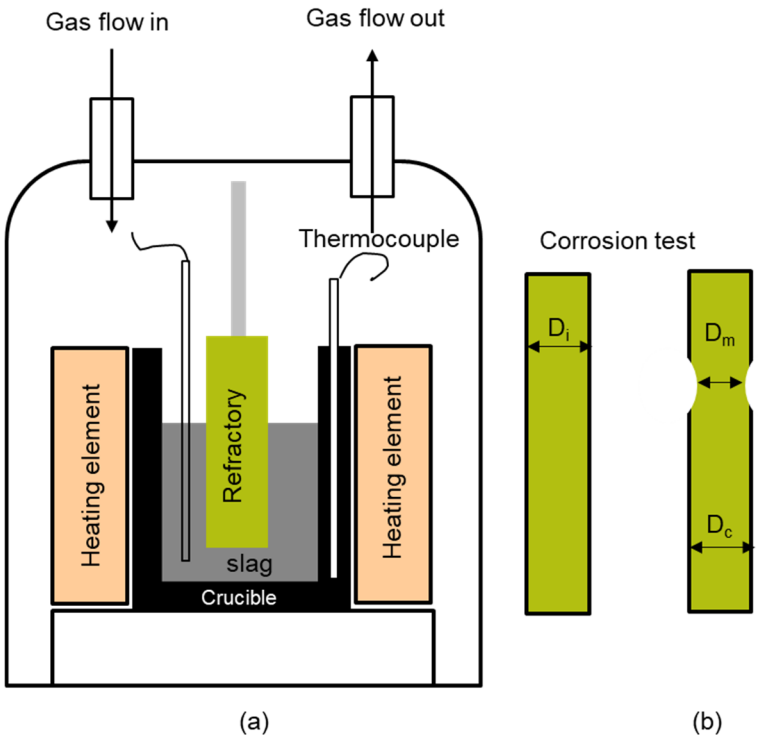

FIG 6 – Typical experimental set-up for finger tests: a) controlled inert atmosphere, sample evolution during tests in b), D_i is original dimensions of test sample, D_m, corrosion neck and D_c characteristic dimension of corroded piece in transverse direction sufficiently far off the corrosion neck, adapted from reference (Reynaert, Sniezek and Szczerba, 2020).

Crucible test (or cup test) is done by placing molten slag a in a cup or crucible shaped refractory. Although similar temperature for slag as in the finger test is used, the holding time for this test is much longer. In this study, the slag was held at 1500°C for about a week. Figure 7 shows the schematic of a crucible test set-up. Table 2 shows the conditions for the finger and crucible tests. The refractories tested are magnesia-chromite and pure magnesia grades.

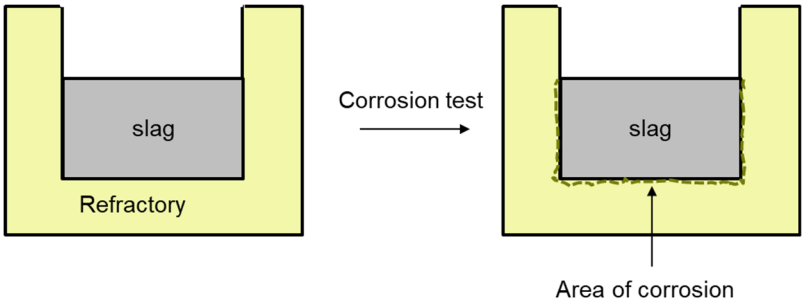

FIG 7 – Schematic of crucible test showing slag infiltration area. Adapted from reference (Reynaert, Sniezek and Szczerba, 2020).

TABLE 2

Test parameters for the refractory.

Type of test	Temperature (°C)	Holding time (hours)
Finger	1500	6
Crucible	1500	168

Results of finger tests are shown by the different forms of refractory degradation, especially in Figure 8. Figure 9 shows after test crucibles used for cup test. Microstructures of refractory after tests (not included here) were evaluated using scanning electron microscope - energy dispersive X-ray spectroscopy (SEM-EDS). Overall, the magnesia-chromite brick showed resistance to dissolution and cracking compared to the pure magnesia brick, which indicates that from the tested grades, magnesia-chromite is the recommended type of brick. In Figure 8, there is more degradation in pure magnesia brick. The worst case is observed when using this type of refractory in slag of higher basicity, as shown in Figure 8, the thin end of finger fell off during test.

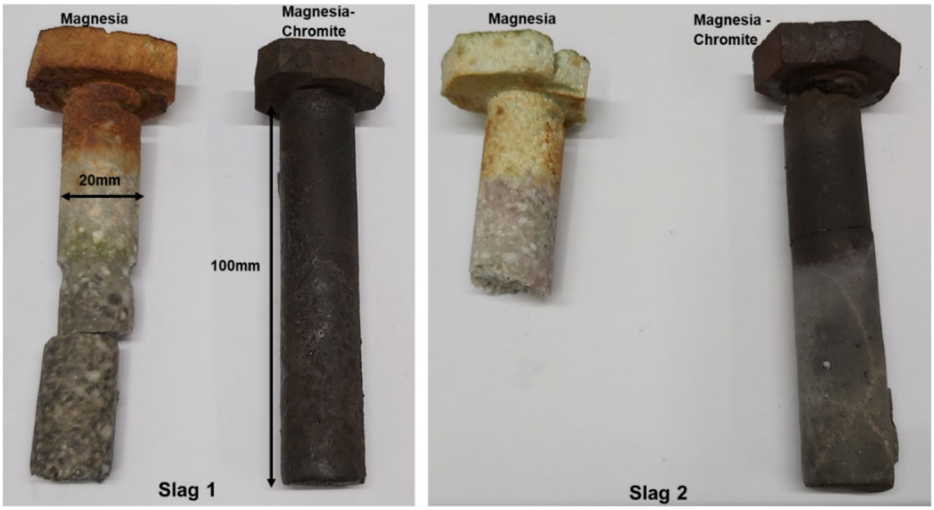

FIG 8 – Results of finger tests for two selected refractory types. Slag of two different basicities 1.2 and 1.4 have been used and are labelled slag 1 and 2, respectively.

However, this is an ongoing investigation and more information will be generated to fine-tune the selection and to understand the various types of loads caused by the industrial operation.

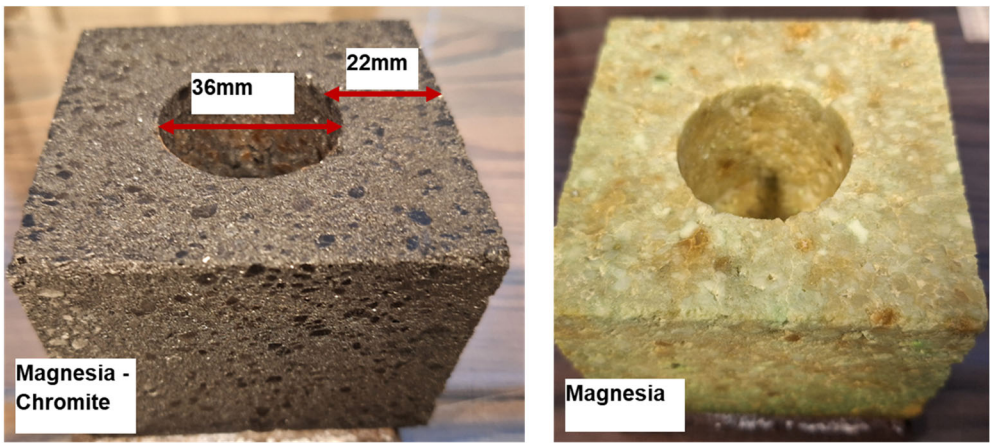

FIG 9 – Samples of crucible tests showing drilled hole for slag containment.

SUMMARY

Purpose of this paper was to present the fluxing philosophy of Metso's Outotec DRI smelting furnace. One of the main tasks was to identify operation window for smelting process, by using thermodynamic tools. The other purpose was to compare typical refractories for the DRI smelting furnace.

Suitable operation window in terms of liquidus temperature was found for production of iron metal with high carbon content. This operation window is large in terms of CaO/SiO_2 ratio, Al_2O_3 and MgO contents of the slag. However, operation area optimal in terms of liquidus temperature for iron metal with low carbon content is difficult to operate, because small changes in composition change operation temperature a lot. The slag obtained from Metso's DRI smelting furnace is of specification required for cement industry. For refractory selection, Magnesia chromite brick showed superior qualities for the DRI smelting furnace type of slag.

REFERENCES

Fick, G, Mirgaux, O, Neau, P and Patisson, F, 2014. Using biomass for pig iron production: A technical, environmental, and economical assessment, *Waste and Biomass Valorization*, 5:43–55.

Gielen, D, 2003. CO_2 removal in the iron and steel industry, *Energy Conversion and Management*, 44(7):1027–1037.

Kuramochi, T, 2016. Assessment of midterm CO_2 emissions reduction potential in the iron and steel industry: a case of Japan, *Journal of Cleaner Production*, 132:81–97.

Olivier, J G, Schure, K M and Peters, J A H W, 2017. Trends in global CO_2 and total greenhouse gas emissions, *PBL Netherlands Environmental Assessment Agency*, 5:1–11.

Pihlasalo, J and Tesfaye, F, 2022. Thermodynamic evaluation of the slag chemistry for DRI smelting, R2022–10677, confidential report.

Reynaert, C, Sniezek, E and Szczerba, J, 2020. Corrosion tests for refractory materials intended for the steel industry—A review, *Ceram–Silikáty*, 64:278–288.

APPENDIX A

Stable phases – solutions and compounds (pure substances PS) for the FactSage liquidus projections:

1 Slag-liq oxide [Al,Ca,Fe,Mg, (Mis.gap at high SiO_2)].

2 Spinel (Cubic): Al- Fe-Mg-O or Al-Fe-Mg-O. Replaces AlSp.Mis. gap if Al,Fe(3).

3 Monoxide Rocksalt-structure: Fe(2),Ca,Mg; dilute Al,Fe(3). Miscibility gap if CaO is present.

4 Clinopyroxene: (Ca,Mg,Fe) [Mg,Fe,Fe^{3+},Al]{Al,Fe^{3+},Si}SiO_6. Possible mis. gap when Ca is present.

5 Orthopyroxene: (Ca,Mg,Fe) [Mg,Fe,Fe^{3+},Al]{Al,Fe^{3+},Si}SiO_6. Possible miscibility gap when Ca is present.

6 Protopyroxene: (Ca,Mg,Fe) [Mg,Fe,Fe^{3+},Al]{Al,Fe^{3+},Si}SiO_6. Possible mis.gap when Ca is present.

7 Low-Clinopyroxene: {Ca,Mg}1{Mg}1$(Si)_2(O)_6$. Possible miscibility gap.

8 Wollastonite: $CaSiO_3$, dilute $MgSiO_3$, $FeSiO_3$.

9 Bredigite: $Ca_3(Ca,Mg)_4Mg(SiO_4)_4$.

10 a'$(Ca)_2SiO_4$: (alpha-prime $(Ca)_2SiO_4$); dilute Mg,Fe.

11 a-$(Ca)_2SiO_4$: (alpha-$(Ca)_2SiO_4$) – dilute Fe,Mg.

12 Melilite: $(Ca)_2$ [Mg,Fe^{2+},Fe^{3+},Al]{Fe^{3+},Al,Si}$_2O_7$.

13 Olivine [Ca,Mg,Fe]1[Ca,Mg,Fe]1[Si]1$[O]_4$. Possible mis. gap if Ca is present.

14 Cordierite: $Al_4(Mg,Fe)_2Si_5O_{18}$.

15 Mullite: [Al,Fe]2[Al,Si,Fe]$[O]_5$, accounts for non-stoichiometry.

16 $Ca_2(Al,Fe)_8SiO_{16}$: X-phase – $(CaO)_2[(Al,Fe)_2O_3]_4SiO_2$.

17 $Ca(Al,Fe)_{12}O_{19}$: $CaAl_{12}O_{19}$, dilute $CaFe_{12}O_{19}$.

18 $Ca(Al,Fe)_6O_{10}$: T-phase (pure end-members are not stable).

19 $Ca(Al,Fe)_4O_7$: $CaAl_4O_7$, dilute $CaFe_4O_7$.

20 Solution Phase $Ca(Al,Fe)_2O_4$. Possible miscibility gap (use [I] option).

21 Solution Phase $Ca_2(Al,Fe)_2O_5$: $Ca_2Fe_2O_5$, dilute $Ca_2Al_2O_5$.

22 Solution Phase $Ca_3(Al,Fe)_2O_6$: $Ca_3Al_2O_6$, dilute $Ca_3Fe_2O_6$.

23 Solution Phase M_2O_3(Corundum): Al_2O_3-Fe_2O_3 solid solution. Possible miscibility gap.

Mixed alkali effect on structure of Al_2O_3-based slags

DOI: 10.62053/XLFU2619

S H Hyun[1] and J W Cho[2]

1. Senior Researcher, POSCO Steelmaking Research Group, Pohang Gyeongbuk 37859, Republic of Korea. Email: sh.hyun@posco.com
2. Professor, POSTECH GIFT, Pohang Gyeongbuk 37673, Republic of Korea. Email: jungwook@postech.ac.kr

INTRODUCTION

Designing and optimising industrial slag, flux, and salt based on a detailed understanding of the atomic-scale structure of supercooled liquids is necessary to effectively control their physicochemical properties. However, the structural analysis of the industrial multi-oxide system is challenging due to the interaction between multiple network formers, intermediate oxides, and network modifiers. In particular, the Al_2O_3-based multi-oxide system presents additional complications due to the amphoteric nature of aluminate and the easy conversion of boron between the three- and four-coordinated states depending on the alkali composition. Furthermore, maintaining charge compensation between AlO_4 and alkali cation is very difficult at high temperatures.

Baek *et al* (2018) have reported that the AlO_4 structure preferentially bonded with Na ion is drastically decreased by increasing temperature in the sodium aluminoborosilicate system. If the alkali does not play a charge-compensating role for Al, the aluminium coordination increases to AlO_5 or AlO_6, which can act as network modifiers. In addition, the released alkali ions can reduce network connectivity by generating non-bridging oxygen.

However, establishing a highly stable network structure in the melt state at high temperatures is crucial for designing chemically stable slag that does not react with high aluminium molten steel and prevents the formation of undesirable crystal phases. The chemical reaction between Al of molten steel and SiO_2 of mold flux occurs very rapidly during the continuous casting of high Al steel. The chemical reaction of $3(SiO_2) + 4[Al] = 3[Si] + 2(Al_2O_3)$ changes the composition of the designed lime silica-mold flux and varies physical and chemical properties, eventually yielding problems with the essential functions. Permanent changes in the chemical composition of the mold flux will cause unexpected problems in the casting process, resulting in inadequate lubrication and severe product defects. Thus, Al_2O_3-based mold flux is an excellent alternative to prevent chemical reactions. However, controlling the size or morphology of crystals of an Al_2O_3-based system is difficult due to their thermodynamic characteristics.

Therefore, an innovative design method of Al_2O_3-based glass-forming liquid with a very stable network structure at high temperatures to retard chemical reactions with proper lubrication is essential. This work proposes exploiting the mixed alkali effect (MAE), which exhibits non-linear changes in chemical and physical properties such as ionic conductivity, viscosity, chemical durability, and glass transition temperature (T_g), as a key to enhancing the charge compensation stability at high temperatures. The mechanism of MAE has yet to be well understood, despite various physical and phenomenological models proposed over the past several decades. The main aim of this study is to develop the industrial composition with enhanced structural stability by MAE. To determine the MAE, we analysed the structure by changing the chemical composition and examined the relative bond stability between AlO_4 and alkali cation by increasing the temperature to 1550°C from 1350°C. The structure analysis was performed using solid-state magic angle spinning (MAS) nuclear magnetic resonance (NMR) and Raman spectroscopy to assess the structural changes of aluminate and borate according to temperature and composition.

EXPERIMENTAL

Table 1 gives the sample names and alkali oxide ratios of six Al_2O_3-rich glassy slag samples prepared for the present study. The relative proportions of the alkali oxides are changed to find the composition that maximises the stability of the AlO_4 structure by MAE. The molar ratio of the total alkali oxides to Al_2O_3 is designed to be 1:1 for all samples. The samples were prepared from regent-grade SiO_2, $CaCO_3$, Al_2O_3, Li_2CO_3, Na_2CO_3, K_2CO_3, B_2O_3, and CaF_2. The starting materials were

well mixed by a mixing machine for an hour, followed by homogenisation and melting in a graphite crucible using a box furnace at 1350°C and an induction furnace at 1550°C, respectively, with an air atmosphere. Then the melts were poured into a steel plate at room temperature to obtain 12 glass samples. After the conventional melting-quenching method, all glass sample was crushed to make powder for the NMR spectroscopy.

A solid-state ^{27}Al MAS NMR (Advance Ⅲ HD, Bruker, Germany) analysis was performed using a 4 mm CP MAS (Triple Resonance) probe operating at 130.32 MHz. The ^{27}Al spectra were recorded at a 10 kHz spinning rate. $AlCl_3$, as a reference, was set at 0 ppm. ^{11}B MAS NMR spectra were obtained with the same solid-state MAS NMR operated at 160.46 MHz and 10 kHz spinning rate with a 4 mm CP MAS probe. Boric acid in H_2O, as a reference, was set at 0 ppm.

A Raman spectrometer (LabRaman High Resolution, Horiba Jobin-Yvon, France) to investigate the structure of aluminate and silicate units analysed the Raman spectra of glass samples quenched at 1350°C and 1550°C. The Raman spectra were obtained at room temperature in 200–1600 cm^{-1} with a wavelength of 514 nm Ar ions as the excitation laser source for 300 secs.

TABLE 1

Alkali oxide ratios of the Al_2O_3-rich glassy slag samples.

Name	Alkali oxide ratio
LN	Li_2O:Na_2O = 1:1
L3N	Li_2O:Na_2O = 1:3
3LN	Li_2O:Na_2O = 3:1
LNK	Li_2O:Na_2O:K_2O = 1:1:1
L2N3K	Li_2O:Na_2O:K_2O = 3:2:1
3L2NK	Li_2O:Na_2O:K_2O = 1:2:3

RESULTS AND DISCUSSION

To assess the structure of aluminate and borate according to each alkali oxide ratio and temperature, the solid-state ^{27}Al and ^{11}B MAS NMR chemical shifts were analysed. Figure 1 show the ^{27}Al NMR data of 1350°C and 1550°C samples, respectively. It is well known that the ^{27}Al chemical shift depends on the coordination number of Al-O. Although this data has non-symmetric line shapes, there is almost a network former of AlO_4 structure rather than modifiers such as AlO_5 or AlO_6 units. This observation suggests that most of the alkali cations maintain a strong bonding with AlO_4 as a charge compensator even at the high temperature of 1550°C.

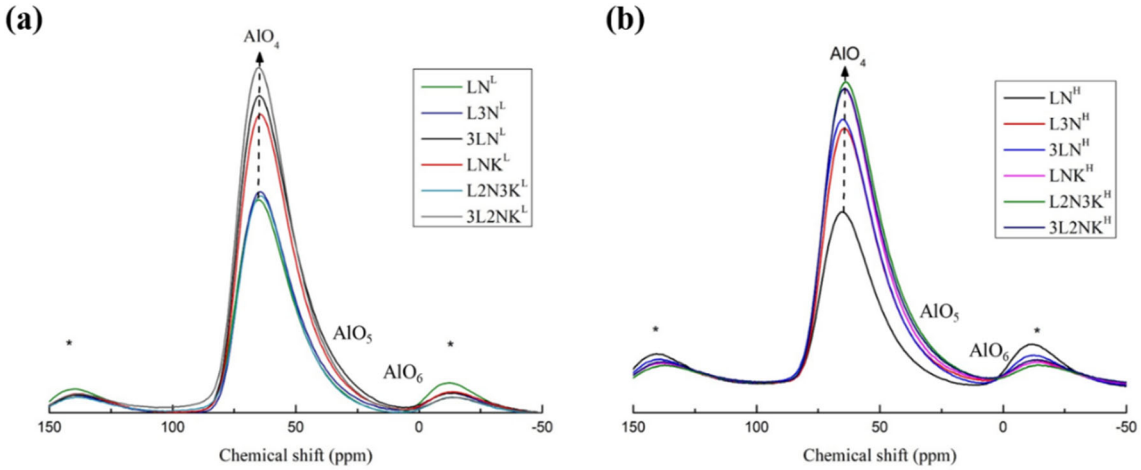

FIG 1 – ^{27}Al MAS NMR spectra of samples obtained at (a) 1350°C and (b) 1550°C.

Figure 2 show the ^{11}B MAS NMR chemical shift for the glass samples. The borate in the multi-oxide system generally exists as a BO_3 triangular ring or non-ring structure with a 3-coordinate boron and a BO_4 tetrahedron having a 4-coordinate boron. Among them, the tetrahedral borate structure can be formed only by charge compensation with alkali or alkaline earth cations, like the mechanism of AlO_4 formation. Moreover, both 3-coordinate boron and 4-coordinate boron can act as a glass former and do not significantly affect the glass-forming ability. Figure 2 shows a weak BO_4 peak compared to the BO_3 for all samples, which implies that most of the alkali cations are trying to achieve charge compensation with aluminate structure and not with borate. In the case of sample 3LN, it has slightly higher BO_4 peaks in both the 1350°C and 1550°C.

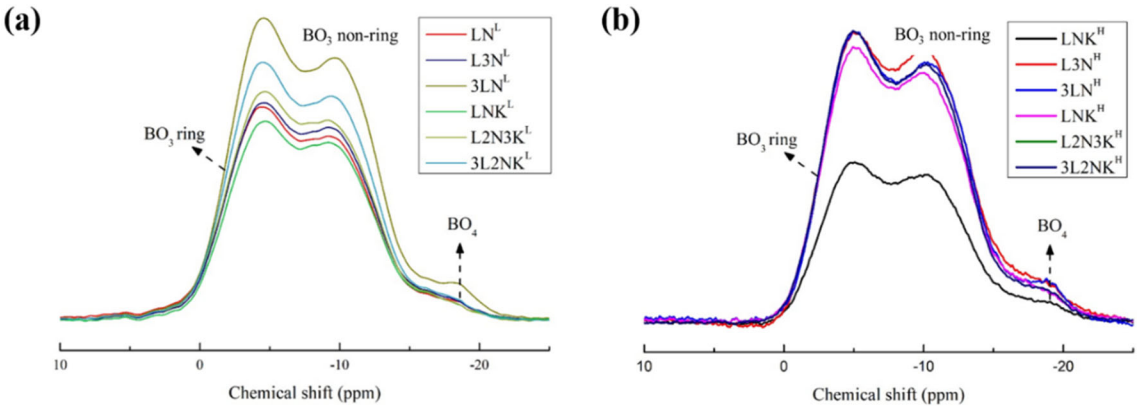

FIG 2 – ^{11}B MAS NMR spectra of samples obtained at (a) 1350°C and (b) 1550°C.

Alkali ions have good charge compensation ability with AlO_4 in the order of K>Na>Li. Therefore, due to the relatively large amount of Li_2O for the 3LN sample, Li cations will actively form a little more tetrahedral BO_4 without charge compensation with aluminate. Finally, these ^{11}B NMR results show the bonding tendency between the network former and alkali cation, consistent with the predominant consequence of AlO_4 bonding from ^{27}Al spectra.

The ^{27}Al NMR data show a featureless peak which indicates almost AlO_4 nature, but slight differences in line width were detected. The generation of different coordination environments contributes to an increase of full width at half maximum (FWHM). To determine structure variation depending on temperature and alkali mixing ratio, FWHM values of ^{27}Al NMR spectra were plotted in Figure 3. In Figure 3a, the FWHM was non-linearly decreased as the content of the stronger charge compensator Na increased due to the MAE. If the charge compensation for AlO_4 is not maintained, it will transition to the five- or six-coordinated Al. And then, the ^{27}Al spectrum broadens asymmetrically towards low chemical shift. In our previous work (Hyun *et al*, 2022), we demonstrated the new characteristic of the MAE, ie an increase in charge compensation stability of a small alkali when mixed with a large cation. Therefore, the non-linear variation of FWHM is due to the charge compensation stability of Li-Al being increased by the MAE. In Figure 3c, the FWHM values were nearly constant regardless of compositional changes.

However, it should be emphasised that the temperature affects the aluminium coordination environment. In Figures 3b and 3d, the minimum FWHM value was shown when the alkali molar ratio was equal (1:1 or 1:1:1) in the glasses quenched at a high temperature of 1550°C. The association between alkali and aluminium weakens with increasing temperature, and finally, the alkali cation easily dissociates from aluminium. Although the Na-Al charge compensation is stronger than that of Li-Al, Na inevitably tends to release from Al at high temperatures. However, the MAE enhances the charge compensation and is finally maximised in the 1:1 composition. This observation indicates that the MAE strengthens charge compensation even from K or Na.

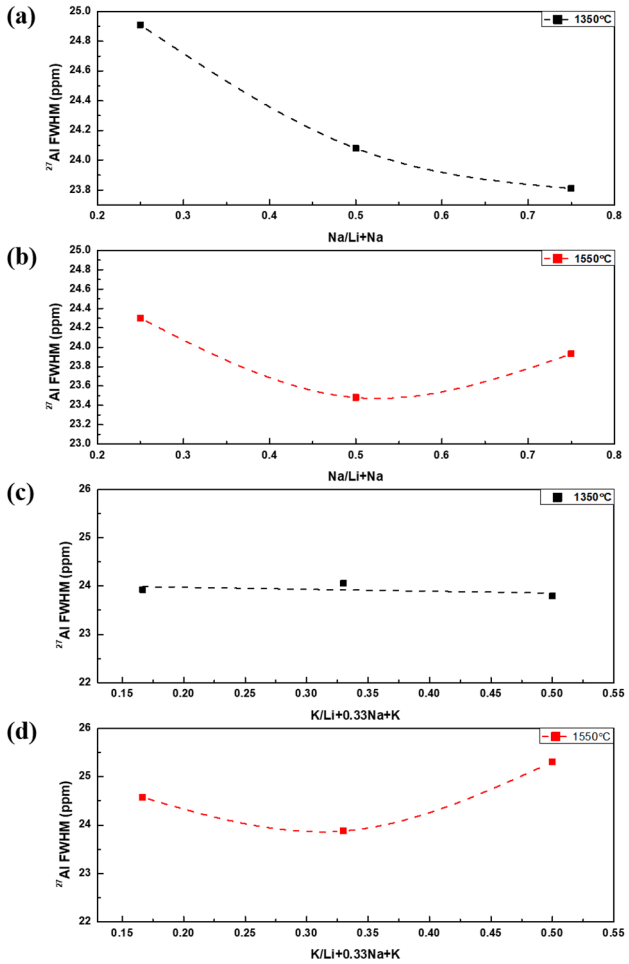

FIG 3 – FWHM values of ^{27}Al MAS NMR for glasses with different homogenisation holding temperatures (1350°C and 1550°C) and composition. (a) and (b): two types of alkalis were mixed. (c) and (d): three types of alkalis were mixed.

In Figure 4, The Raman peak at 770 cm^{-1} due to the presence of the AlO_4 revalidates this new knowledge. The relative intensities of the 770 cm^{-1} peaks from glass quenched at two different temperatures indicate precisely the opposite trend of the NMR results. The AlO_4 intensity was increased with the substitution of Na. However, the Raman feature related to AlO_4 is maximised in Li: Na = 1:1 glass-forming liquid at a high temperature of 1550°C. Therefore, the MAE is applicable to designing chemically stable Al_2O_3-rich slag systems for the continuous casting process.

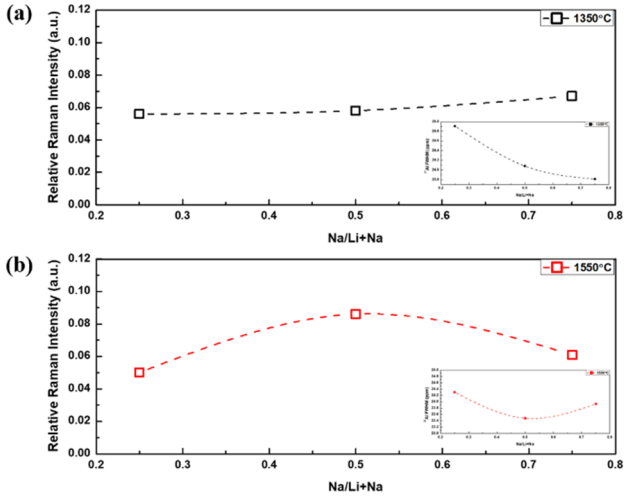

FIG 4 – Relative intensity of AlO_4 peak at 770 cm^{-1} in the Raman spectra for glassy slag samples obtained at (a) 1350°C and (b) 1550°C. Inset: ^{27}Al NMR results from Figure 3.

CONCLUSIONS

This study presents a structural study of multi-oxide systems for industrial aluminoborosilicate glassy slag systems. We provide insights into understanding complex structural changes of mixed alkali Al_2O_3-rich slag systems. To evaluate the compositional and temperature effect of the structural stability of Al, Al_2O_3-rich slags with various molar ratios of two or three alkali oxides were obtained at different temperatures of 1350°C and 1550°C. The stability of charge compensation between Al and alkali was significantly changed at high temperatures. Among them, Li:Na = 1:1 and Li:Na:K = 1:1:1 samples show the best charge compensation stability even at a high temperature which means the mixed alkali effect works most.

REFERENCES

Baek, J, Shin, S, Kim, S and Cho, J, 2018. Thermal history driven molecular structure transitions in alumino-borosilicate glass, *Journal of the American Ceramic Society*, 101(8):3271–3275.

Hyun, S, Yeo, T, Ha, H and Cho, J, 2022. Structural evidence of mixed alkali effect for aluminoborosilicate glasses, *Journal of Molecular Liquids*, 347:118319.

Effect of solid-solved FeO and MnO on hydration of free MgO in steelmaking slag

DOI: 10.62053/LKCS2487
R Inoue[1], N Kado[2], T Iwama[3] and S Ueda[4]

1. Researcher, Tohoku University, Sendai Miyagi 980-8577, Japan. Email: ryo.inoue.e2@tohoku.ac.jp
2. Researcher, JFE Mineral Company, Chiba Chiba 260-0835, Japan. Email: n-kado@jfe-mineral.co.jp
3. Assistant Professor, Tohoku University, Sendai Miyagi 980-8577, Japan. Email: takayuki.iwama.a6@tohoku.ac.jp
4. Professor, Tohoku University, Sendai Miyagi 980-8577, Japan. Email: tie@tohoku.ac.jp

ABSTRACT

Steelmaking slags are usually used as roadbed and civil engineering materials. However, the expansion phenomenon, which is caused by the volume expansion during hydration of free CaO and free MgO contained in steelmaking slag, is indispensable. Since the hydration of free MgO in steelmaking slag is much slower than that of free CaO, it is qualitatively considered that free MgO contributes to the hydration expansion of steelmaking slag over a long period of time. Similar to free CaO, free MgO consists of undissolved MgO and crystallised MgO in steelmaking slag. The latter precipitates during slag cooling. When divalent metal oxides (FeO, MnO, CaO) are dissolved in the crystallised MgO to form a MgO-based solid solution, it is expected to inhibit the hydration reaction similar to precipitated CaO. From the previous hydration test of Magnesioferrite, which was calcined after mixing MgO and Fe_2O_3 reagents, it was found that the higher the Fe_2O_3 concentration, the slower the hydration reaction progressed. In this study, by clarifying the influence of calcination conditions of MgO-FeO and MgO-FeO-MnO solid solutions, which were prepared by the calcination of mixture of MgO, FeO and MnO reagents, on their hydration reactivity, the effect of composition and thermal treatment on the formation of free MgO that is not hydrated (or easily hydrated) were discussed. To investigate the influence of MgO grain size, coarse MgO particles, which were obtained by crushing MgO crucible, were also used for heat treatment. With increasing the amount of FeO and MnO in the MgO-FeO-MnO solid solution, the hydration reaction became more suppressed. The expansion suppression effect was higher with solid-solved FeO than with solid-solved MnO. When the calcination temperature of the MgO-FeO solid solution was increased, the Fe^{3+}/Fe^{2+} concentration ratio increased, resulting in a higher hydration rate.

INTRODUCTION

To achieve a better global environment, a recycling-oriented society has to be built. From the perspective of effective resource utilisation, it is necessary to establish actively a reuse system for by-products and waste from industries.

With regard to the reuse of iron and steel slags, various technologies have been conducted. Slow-cooled blast furnace slag is mainly used as road construction material, and granulated blast furnace slag is used as a cement admixture by taking advantage of its latent hydraulic property. Therefore, the utilisation rate of blast furnace slag has reached almost 100 per cent in a report of Nippon Slag Association (2023a). On the other hand, steelmaking slag, whose annual amount is approximately 14 Mt in Japan in another report of Nippon Slag Association (2023b), can be reused as road construction materials, civil engineering materials, cement, concrete aggregate etc, due to its hard and dense properties, as described in the reports of Ichihara (2010) and Nippon Slag Association (2023c). When steelmaking slag is used as roadbed and landfill materials, lime phase (free CaO) and magnesia phase (free MgO) isolated in the slag react with water to form calcium hydroxide and magnesium hydroxide. From a report of Hori *et al* (2012), because the volume after the hydration expands to approximately double, it causes road upheavals and ground cracks. Michikawa, Ono and Eba (2016) investigated the hydration reactivity of steelmaking slag by estimating the expansion ratio of slag after hydration from the free CaO content in the slag.

Takayama *et al* (1996) and Hori *et al* (2012) said that aging treatments, which are performed to advance the slag expansion caused by free CaO before burial, include atmospheric aging and accelerated aging. In the former the slag is left in a slag yard for more than six months to promote hydration through rainfall, and in the latter the hydration reaction progresses by using steam or hot water. Sasaki and Hamasaki (2014) found that the higher the ambient temperature, the faster the slag expansion becomes stable, and in the case of steam aging, expansion stability is achieved in 48 hours. Namely, accelerated aging can be expected to provide stable hydration treatment in a short time. Inoue and Suito (1995) found that free CaO in steelmaking slag includes undissolved CaO and crystallised (precipitated during cooling) CaO, and in the latter divalent metal oxides (FeO, MnO, MgO) are solid-solved. The larger the amount of the solid-solved components, the more the hydration reaction of CaO was suppressed, and when the slag was slowly cooled below 1200°C, calcium ferrite precipitates in spots in the crystallised CaO, which significantly reduces the FeO concentration in the CaO matrix phase, showed that crystallised CaO becomes more easily hydrated.

On the other hand, regarding the hydration reaction of MgO, Ohira and Obata (2009) clarified the effect of particle size on the hydration of lightly calcined magnesia. Inoue *et al* (2021) noted that since the hydration reaction of pure MgO reagents proceeds slowly at room temperature and pressure, it is desirable to accelerate the hydration by thermal treatment under high temperature and pressure using an autoclave. Because of slow hydration rate of free MgO in steelmaking slag compared with that of free CaO, it has been qualitatively thought by Ichihara (2010) that MgO hydration contributes to the slow volume expansion of steelmaking slag over a long period of time. Similar to free CaO in steelmaking slag, free MgO includes undissolved MgO and crystallised (precipitated during cooling) MgO, and divalent metal oxides (FeO, MnO, CaO) are solid-solved in the crystallised MgO and affect the hydration reaction, as reported by Inoue *et al* (2021). They found that the higher the iron concentration, the slower the hydration reaction progressed, when Magnesiowüstite synthesised by the calcination of the mixture of MgO and Fe_2O_3 reagents was hydrated. On the other hand, Amita *et al* (1989) said that the size and morphology of crystals in MgO particle are influenced by heating.

In this study, the effect of calcination conditions on the hydration reactivity of MgO-FeO solid solution, which was prepared by calcination the mixture of MgO and FeO reagents, was clarified. Furthermore, by hydrating the MgO-FeO-MnO solid solution, the difference in hydration reactivity between MnO and FeO in solid solution was investigated. In addition, by comparing those results with the hydration properties of MgO reagent and heat-treated product of a commercially available dense MgO crucibles, the condition for producing free MgO that is not hydrated (or easily hydrated) was discussed.

EXPERIMENTAL

Sample preparation

Three types of MgO-FeO solid solutions with MgO/FeO mass ratio = 9/1, 8/2, and 7/3 were prepared. Their compositions are plotted with solid circle marks in the MgO-FeO phase diagram, which was presented by Wu *et al* (1993), in Figure 1. It can be seen that all of them are solid solutions at 1400 to 1600°C.

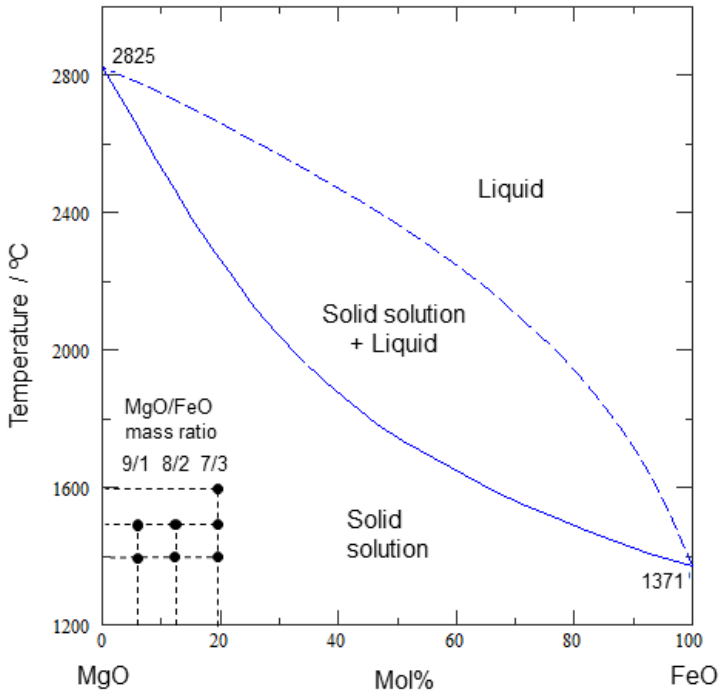

FIG 1 – Synthesised MgO-FeO solid solutions plotted in MgO-FeO phase diagram drawn by Wu *et al* (1993).

Figure 2 shows the synthesis of MgO-FeO solid solution. Appropriate amounts of special grade MgO reagent (manufactured by Wako Pure Chemical Industries, Ltd.) and FeO reagent (manufactured by Japan Pure Chemical Co., Ltd.) were weighed, mixed and pressed to a cylindrical shape at 8 ton/cm^2. To prevent direct reaction between the MgO calcination crucible and the solid solutions, pre-sintered MgO-FeO powder was placed on the inner bottom of the MgO crucible. The cylindrical sample was placed on the powder layer and slowly lowered to the soaking zone inside the vertical resistance furnace for calcination in an Ar flow (200 cm^3/min), which was deoxidised by Ti sponge at 1073 K. Heating temperature and holding time are summarised in Table 1. In this table, a pure Al_2O_3 crucible with thin wall (SSA-S, type-T3, manufactured by Nikkato) was used instead of pure MgO crucible with thick wall to promote temperature drop by reducing the heat accumulation on the crucible wall during rapid cooling. After a given time, the crucible was taken out of the furnace and quenched by He gas blowing (hereinafter abbreviated as ‘He quenching’) or dipping into water (hereinafter abbreviated as ‘water-quenching’). In addition, a MgO-FeO−MnO solid solution in which a part of FeO was replaced with MnO was also prepared using the same method. The obtained solid solution sample was ground to 75–150 μm for hydration treatment.

Two types of pure MgO were employed for hydration treatment: special grade MgO reagent (manufactured by Wako Pure Chemical Industries, Ltd.) and a dense MgO crucible (MG-12, manufactured by Nikkato) pulverised to 75 to 150 μm.

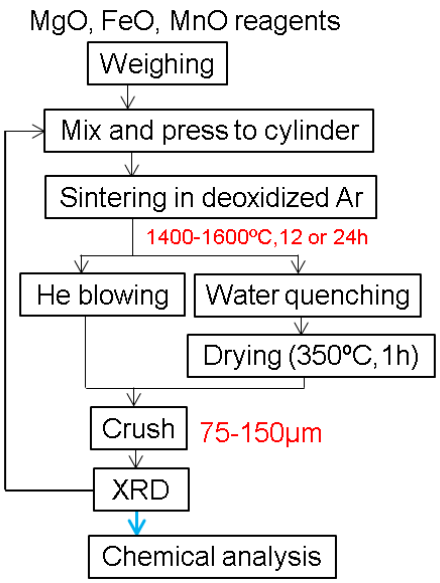

FIG 2 – Flow chart of preparation of MgO-FeO solid solution.

TABLE 1

Calcination conditions for preparation of solid solution samples.

MgO/FeO/MnO mass ratio	Temp. (°C)	Time (hrs)	Crucible
7 / 3 / 0	1400	12	Dense MgO with thick wall
		24	
	1500	12	Dense MgO with thick wall
	1600	12	Dense Al_2O_3 with thin wall
7 / 2 / 1	1400	12	Dense MgO with thick wall
8 / 2 / 0	1400		
	1500		
9 / 1 / 0	1400		
	1500		

Hydration treatment

An autoclave was used as the hydration reactor because hydration process is accelerated at high temperature and high pressure, as written in Dictionary of Research (2023).

At first, a Teflon test tube was weighed (w_1). After an appropriate amount of the solid solution powder was charged into the test tube, its weight was measured (w_2). The difference between w_1 and w_2 corresponds to the initial sample weight before the hydration reaction. Several drops of distilled water were added into the test tube to moisten the solid solution powder. The test tube was then placed in a pressure vessel of an autoclave and subjected to hydration treatment at 120°C for 12 hours. After the test tube removed from autoclave was heated at approximately 110°C for 2 hours in a drying oven to remove excess moisture, the weight of the test tube was measured to determine the sample weight after hydration. This autoclave treatment was repeated two more times in the same manner. For comparison, similar experiments were also conducted using a MgO reagent and a powder obtained by pulverising a dense MgO crucible.

Analysis

The mineral phases in solid solution samples were identified by powder X-ray diffraction (XRD) with the Crystallography Open Database (COD; <http://www.crystallography.net/cod/>; Downs and Hall-Wallace, 2003; Gražulis *et al*, 2009, 2012, 2015; Merkys *et al*, 2016, 2023; Quirós *et al*, 2018; Vaitkus, Merkys and Gražulis, 2021; Vaitkus *et al*, 2023).

Since it was found in preliminary experiments that the FeO amount in MgO-FeO solid solution cannot be evaluated from the relationships between MgO-FeO peak angle in XRD pattern and FeO concentration of MgO-FeO solid solution, which were given in Powder Diffraction File™ 4/Minerals supplied by JCPDS-International Centre for Diffraction Data (2020), it was determined by chemical analysis. The total iron and Fe^{2+} concentrations in the MgO-FeO and MgO-FeO-MnO solid solution powders were determined according to the potassium dichromate titration method of Japanese Industrial Standard JIS-M-8212 (1983) and JIS-M-8213 (1983), respectively. The MgO and MnO concentrations in the powder were determined by ICP emission spectrophotometry after dissolving 0.1 g of each powder with 10 mL of (1+1)HCl solution.

RESULTS AND DISCUSSION

Synthesis conditions of MgO-FeO solid solution

Number of calcinations

To investigate the change in the amount of solid-solved FeO with the number of calcination times of MgO-FeO solid solution, the following experiment was conducted. A mixture with MgO/FeO mass ratio = 7/3 was pressed to cylindrical shape and calcined in deoxidised Ar flow at 1400°C for 12 hours, then immediately quenched by He quenching. After pulverising this to less than 150 μm, it was pressed again and sintered using the same procedure as the first heating. Figure 3 shows the XRD results for those two samples. In this figure, only the (Mg, Fe)O peaks are observed in both samples despite the different number of calcination, indicating that one calcination is sufficient for the synthesis of MgO-FeO solid solution.

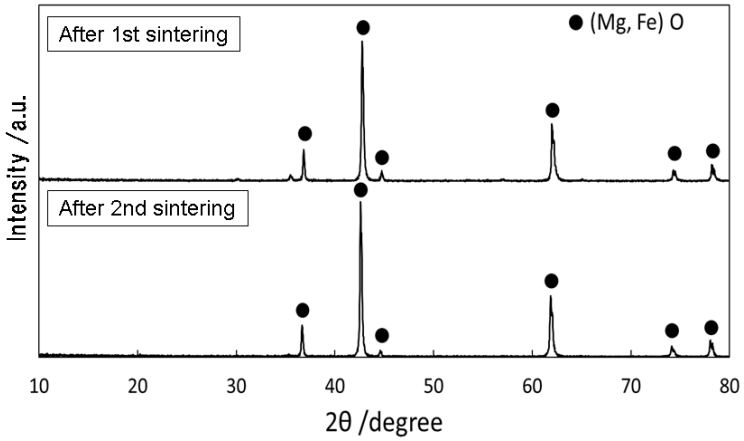

FIG 3 – Results of X-ray diffraction (XRD) analysis of MgO-FeO solid solution (MgO/FeO mass ratio = 7/3) calcined once and twice.

Table 2 shows the total iron and FeO concentrations determined by chemical analysis. In this table, the Fe^{3+} concentration is the difference between the total iron concentration and the Fe^{2+} concentration, and Fe_tO is the FeO concentration calculated assuming that all iron is present as FeO. It can be seen from the values listed in this table that the Fe^{3+} concentration is almost zero after second calcination, and that each solid solution contains approximately 30 mass per cent FeO. Therefore, one calcination is considered sufficient to synthesise MgO-FeO solid solution. In the subsequent solid solution synthesis, the calcination operation was performed only once. It should be noted that Fe^{3+} (Fe_2O_3) can dissolve in MgO according to MgO-Fe_2O_3 phase diagram reported by Phillips, Somiya and Muan (1961). The amount of solid-solved FeO and Fe_2O_3 will be explained later.

TABLE 2

Variations of chemical composition of MgO-FeO solid solutions (MgO/FeO mass ratio = 7/3) depending on calcination number and quenching method.

Quenching	Calcination number	T.Fe	Fe^{2+}	Fe^{3+}	Fe^{3+}/Fe^{2+} ratio	FeO	MgO	Fe_tO
		(mass%)				(mass%)		
He blowing	1	23.75	23.49	0.26	0.011	30.22	69.4	30.55
	2	22.64	22.63	0.01	0.0004	29.11	70.8	29.13
Water	1	24.13	21.24	2.89	0.136	27.33	68.5	31.05

Quenching method

In the previous section, the heated sample with MgO/FeO mass ratio = 7/3 was rapidly cooled by He quenching. To investigate the influence of the quenching method on the synthesis of MgO-FeO solid solution, the MgO crucible containing cylindrical sample subjected to the same calcination operation was quenched in water. The total iron and FeO concentrations in this MgO-FeO solid solution are listed in Table 2. According to XRD analysis, the sample obtained by water-quenching was also pure (Mg, Fe)O.

To clarify the influence of the quenching method on hydration behaviour, a sample with MgO/FeO mass ratio = 7/3, which was calcined once at 1400°C, rapidly cooled by He quenching or water-quenching, and crushed to a particle size of 75 to 150 μm, was subjected to the hydration treatment using an autoclave three times. Table 3 gives the sample weight changes after each hydration treatment.

TABLE 3

Mass change after hydration of MgO-FeO solid solutions (MgO/FeO mass ratio = 7/3) prepared by different quenching methods.

Hydration treatment	He quenching (69.4 mass%MgO)			Water-quenching (68.5 mass%MgO)		
	Weight (g)		Hydration rate (%)	Weight (g)		Hydration rate (%)
	Before hydration	After hydration		Before hydration	After hydration	
1st	0.5899	0.6021	6.67	0.7644	0.7924	12.0
2nd	0.6021	0.6095	10.7	0.7929	0.8135	21.0
3rd	0.6095	0.6118	12.0	0.8136	0.8328	29.2

The hydration rate of MgO can be determined by dividing the mass change after hydration by the mass when all MgO becomes $Mg(OH)_2$. For example, a sample of 0.5899 g (W_i) became 0.6021 g after the first autoclave treatment, so the mass change ΔW is expressed by Equation 1.

$$\Delta W = 0.6021–0.5899 = 0.0122 \text{ [g]} \quad (1)$$

When assuming that this ΔW is entirely due to the MgO hydration reaction, $MgO+H_2O = Mg(OH)_2$,

Reacted H_2O moles = ΔW / (H_2O molecular weight)

$= 0.0122 / 18.00 = 6.78 \times 10^{-4}$

= Reacted MgO moles

Mass of hydrated MgO = (Reacted MgO moles) × (MgO molecular weight)

$= 6.78 \times 10^{-4} \times 40.31 = 0.0273$ [g]

Mass of MgO in solid solution = W_i × (mass% MgO) / 100

$= 0.5899 \times 69.4 / 100 = 0.4094$ [g]

$$\begin{aligned}\text{Hydration rate} &= (\text{Mass of hydrated MgO}) / (\text{Mass of MgO in solid solution}) \times 100 \\ &= (\Delta W / 18.00 \times 40.31) / \{W_i \times (\text{mass\% MgO}) / 100\} \times 100 \\ &= 223.9\, \Delta W / \{W_i \times (\text{mass\% MgO}) / 100\} \\ &= 22390 \times 0.0122 / (0.5899 \times 69.4) = 6.67\ [\%]\end{aligned} \quad (2)$$

Table 3 shows the hydration rate of two types of MgO-FeO solid solutions with MgO/FeO mass ratio = 7/3, which were obtained by He quenching and water-quenching after the calcination at 1400°C, calculated by Equation 2 after each autoclave treatment. In those two MgO-FeO solid solutions, the hydration rate increases with the number of hydration treatment.

From the relationship between the hydration rate after third hydration treatment in Table 3 and the FeO concentration of solid solution (Table 2), the hydration rate is high in the water-quenched sample with low FeO concentration and high Fe^{3+}/Fe^{2+} concentration ratio. This is the same trend as the previous reports that the hydration of CaO (by Inou and Suito, 1995) and MgO (by Inoue *et al,* 2021) was suppressed by the solid solution of divalent metal oxides.

To clarify the reason for the difference in hydration rate depending on the quenching method, the presence of microcracks in the samples after hydration was examined by SEM observation. However, no microcracks were observed on the surface of any sample. Furthermore, when the specific surface area of the sample after third hydration was determined by the gas adsorption method (BET method), it was 0.7282 and 0.7352 [m^2/g] for the sample obtained by He quenching and water-quenching, respectively. Although the latter is slightly larger, it is difficult to conclude that the difference in specific surface area due to the quenching method would affect the hydration reactivity. Table 2 shows that the sample after He quenching is not oxidised and contains a higher amount of FeO compared with that after water-quenching. Therefore, He quenching is used as the cooling method in the following experiments.

Effect of calcination conditions on hydration reactivity of MgO-FeO solid solution

MgO-FeO solid solutions were calcined by varying the mixing ratio of MgO and FeO reagents, heating temperature and duration and the thickness of the crucible for calcination. The effects of those factors on the hydration reactivity of the solid solution were studied.

When XRD analysis was performed on the MgO-FeO solid solutions obtained under each calcination condition given in Table 1, only the (Mg, Fe)O peak was identified in all samples before hydration.

The mineral phases in the solid solution after third autoclave treatment were also identified using XRD. Figure 4 shows the results for the sample with MgO/FeO mass ratio = 7/3, which was calcined at 1400, 1500 or 1600°C for 12 hours and hydrated. Figures 5 and 6 show those with MgO/FeO mass ratio = 8/2 and 9/1, respectively, which were calcined at 1400 or 1500°C for 12 hours and hydrated.

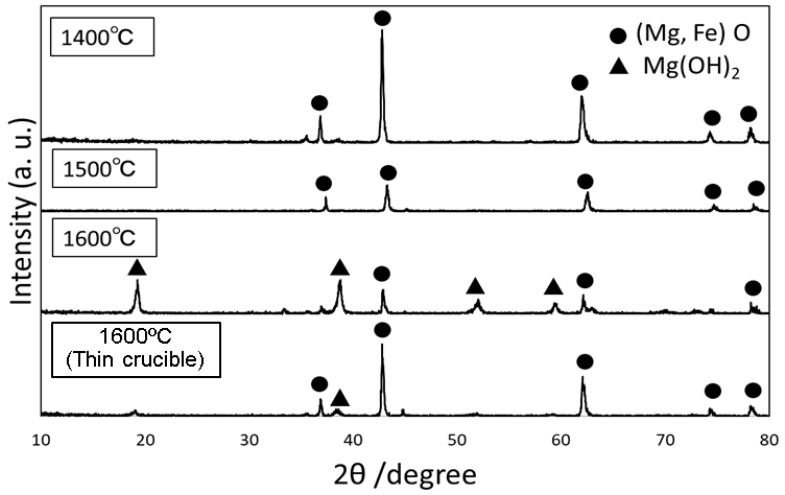

FIG 4 – XRD results after hydration of MgO-FeO solid solution (MgO/FeO mass ratio = 7/3) as a function of calcination temperature.

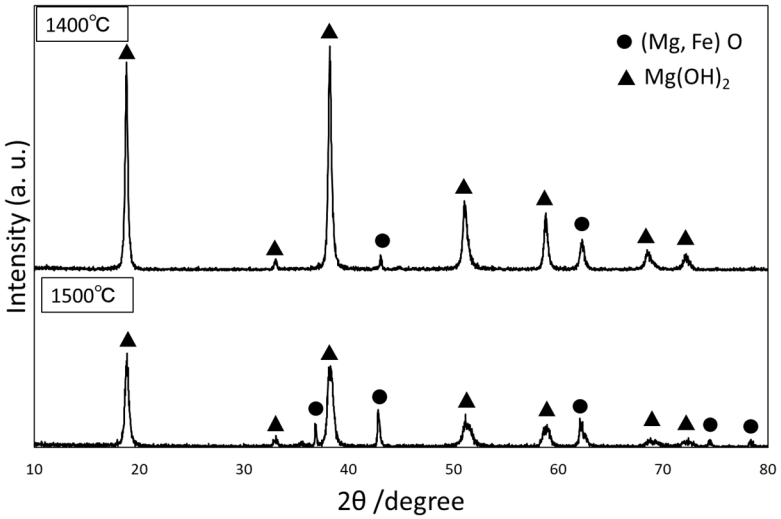

FIG 5 – XRD results after hydration of MgO-FeO solid solution (MgO/FeO mass ratio = 8/2) as a function of calcination temperature.

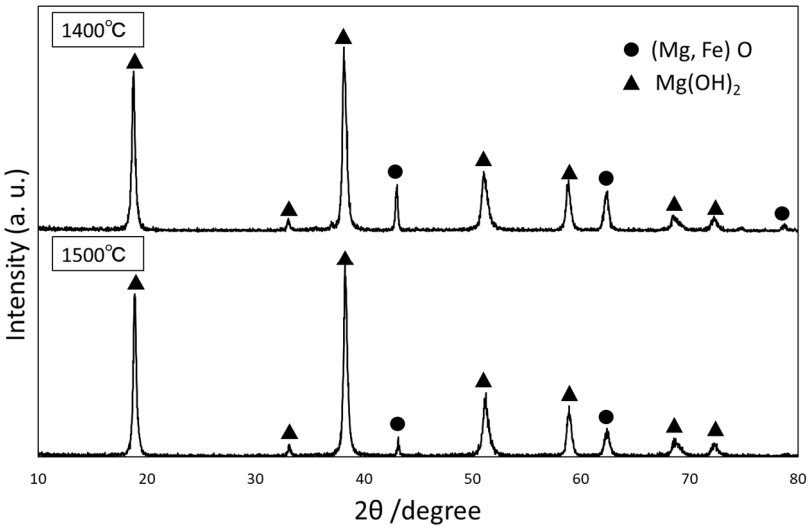

FIG 6 – XRD results after hydration of MgO-FeO solid solution (MgO/FeO mass ratio = 9/1) as a function of calcination temperature.

In all samples, only XRD peaks of (Mg, Fe)O and $Mg(OH)_2$ are observed. If only MgO in (Mg, Fe)O solid solution changes to $Mg(OH)_2$ during hydration, excess FeO should be generated as oxides or hydrates in terms of mass balance, but the XRD peaks of FeO, Fe_2O_3, $Fe(OH)_2$, FeO(OH), $Fe(OH)_3$, etc were not observed in Figures 4 to 6. Therefore, it is considered that amorphous Fe-based hydrates were generated. From the comparison of these figures, the $Mg(OH)_2$ peak becomes higher with increasing the MgO/FeO mass ratio, but clear correlation between the calcination temperature and the XRD peak height of $Mg(OH)_2$ was not found.

Table 4 shows the chemical compositions of solid solutions determined by chemical analysis. Figure 7 shows the relationship between the FeO concentration and calcination temperature, and Figure 8 shows that between the Fe^{3+}/Fe^{2+} concentration ratio and calcination temperature. In Figure 7, the effect of calcination temperature on the solid-solved FeO amount is small, while it can be seen from Figure 8 that the higher the calcination temperature and the lower the FeO concentration, the larger the Fe^{3+}/Fe^{2+} concentration ratio becomes. This might be thought to be because only a small portion of the sample surface is oxidised by the atmospheric oxygen caught in the He gas blow during He quenching.

TABLE 4

Chemical compositions of solid solutions prepared under various conditions.

MgO/FeO/MnO mass ratio	Temp. (°C)	Time (hrs)	T.Fe	Fe^{2+} (mass%)	Fe^{3+}	Fe^{3+}/Fe^{2+} ratio	FeO	MgO	MnO (mass%)	Fe_tO
7 / 3 / 0	1400	12	23.75	23.49	0.26	0.011	30.22	69.4	–	30.55
	1500		23.29	22.64	0.65	0.029	29.12	69.9	–	29.96
	1600		23.44	22.43	1.01	0.045	28.86	69.7	–	30.16
	1600*		23.62	22.14	1.48	0.067	28.48	69.4	–	30.39
	1400	24	23.97	23.26	0.71	0.031	29.92	69.0	–	30.84
7 / 2 / 1	1400	12	15.22	14.74	0.48	0.033	18.97	69.8	9.94	20.10
8 / 2 / 0	1400	12	15.55	14.50	1.05	0.072	18.65	79.8	–	20.00
	1500		15.80	13.89	1.91	0.14	17.86	79.3	–	20.33
9 / 1 / 0	1400	12	8.00	7.09	0.91	0.13	9.12	89.5	–	10.29
	1500		7.89	6.72	1.17	0.17	8.64	89.7	–	10.15

* Dense Al_2O_3 crucible with thin wall.

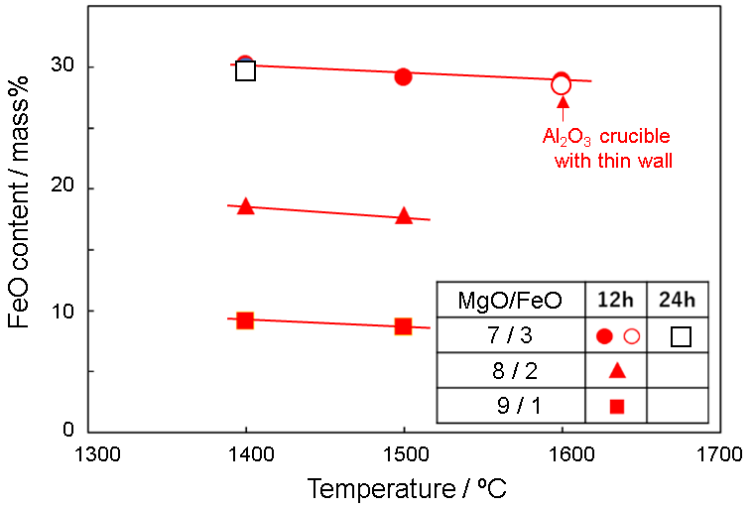

FIG 7 – Relationship between FeO content in MgO-FeO solid solution and calcination temperature.

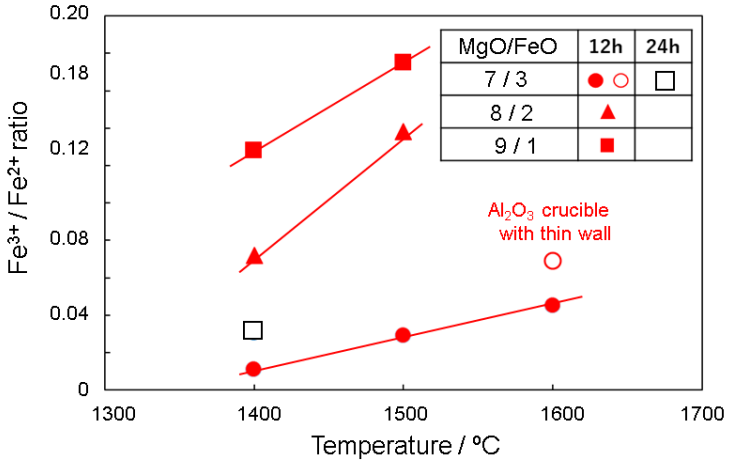

FIG 8 – Relationship between Fe^{3+}/Fe^{2+} ratio in MgO-FeO solid solution and calcination temperature.

Each sample was subjected to autoclave hydration three times. The results are listed in Table 5. The specific surface areas of MgO-FeO solid solutions (MgO/FeO mass ratio = 7/3, 8/2, 9/1) heated at 1400°C for 12 hours were determined by the BET method. The measured results are also shown in the same table. It can be seen from this table that the specific surface area increases with decreasing the amount of solid-solved FeO and the hydration rate increases accordingly.

TABLE 5

Mass change after hydration of MgO-FeO(-MnO) solid solutions prepared under various calcination conditions.

MgO/FeO/MnO mass ratio	Temp. (°C)	Time (hrs)	Weight (g)		Hydration rate (%)	Specific surface area (m^2/g)
			Before hydration	After third hydration		
7 / 3	1400	12	0.5899	0.6118	12.0	0.73
	1500		0.9009	0.9369	12.8	
	1600		1.0002	1.2408	77.3	
	1600*		1.0738	1.1565	24.8	
	1400	24	1.0642	1.1149	15.5	
7 / 2 / 1	1400	12	1.0542	1.1455	27.8	
8 / 2	1400	12	1.0080	1.2505	67.5	9.17
	1500		1.0631	1.3675	86.1	
9 / 1	1400	12	1.0958	1.4730	77.0	10.01
	1500		1.0043	1.4044	99.4	

* Dense Al_2O_3 crucible with thin wall.

Based on the values given in Table 5, the hydration rates plotted against FeO concentration and Fe^{3+}/Fe^{2+} ratio of sample are shown in Figures 9 and 10, respectively, where the hydration rate is the value after third autoclave treatment. From Figure 9, the hydration rate increases with decreasing FeO concentration. At almost the same FeO concentration, the hydration rate increases with the calcination temperature. In Figure 10, the larger the Fe^{3+}/Fe^{2+} concentration ratio, the higher the hydration rate becomes. This is thought to be because, as mentioned above, the higher the calcination temperature, the easier the sample is oxidised during He quenching, and the Fe^{3+}/Fe^{2+} ratio becomes larger, resulting in easier hydration. The effect of solid-solved MnO on hydration reactivity of MgO-FeO will be described later.

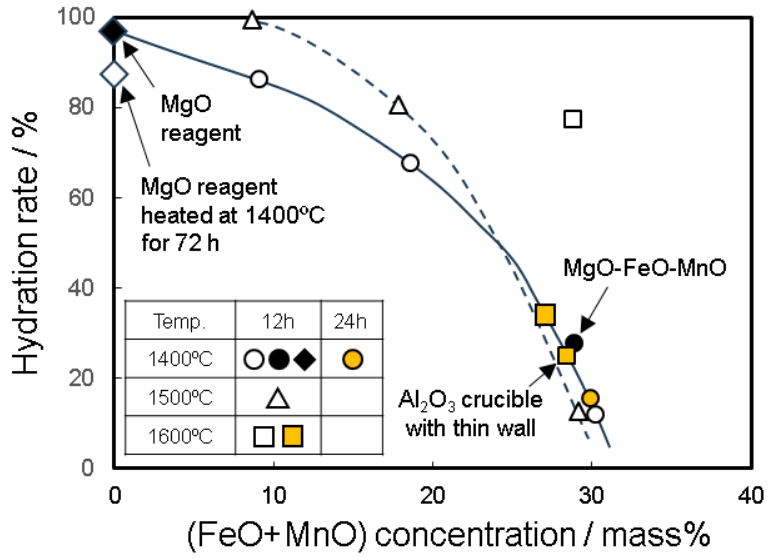

FIG 9 – Relationship between hydration rate and FeO (or FeO+MnO) content of MgO-FeO (MgO-FeO-MnO) solid solution as functions calcination temperature and time.

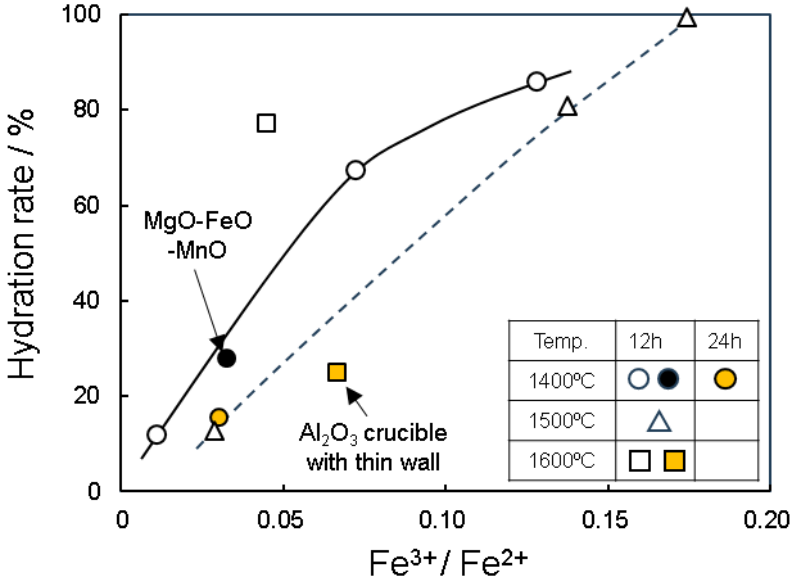

FIG 10 – Relationship between hydration rate and Fe^{3+}/Fe^{2+} ratio of MgO-FeO and MgO-FeO-MnO solid solutions as functions calcination temperature and time.

It is understood in the MgO-Fe_2O_3 system phase diagram, which was published by Phillips, Somiya and Muan (1961), shown in Figure 11 that the MgO-FeO sample with MgO/FeO = 7/3 calcined at 1400°C remains in the Magnesiowüstite region at rapid cooling, even if all FeO in this solid solution changes to Fe_2O_3 through oxidation. In contrast, at slow cooling, it will be in the coexistence region of Magnesiowüstite and Magnesioferrite at temperatures lower than point *a* (1374°C). In this region, when the iron concentration in Magnesiowüstite phase decreases toward point *b* with lowering temperature, the hydration reactivity of Magnesiowüstite increases with decreasing its iron oxide concentration, and the Magnesiowüstite/Magnesioferrite mass ratio of decreases. Therefore, the hydration rate increases by increasing Fe^{3+}/Fe^{2+} ratio due to the effect of hydration of the MgO-Fe_2O_3 system. It is concluded that by not only increasing the amount of solid-solved iron oxide but also rapidly cooling, the hydration of MgO−Fe oxide solid solution can be suppressed. In the samples obtained by calcination of MgO-FeO solid solution with MgO/FeO mass ratio = 7/3 at 1600°C for 12 hours using two types of crucibles with different wall thicknesses, it is found in Figure 9 that the hydration rate is lower when a thin-walled Al_2O_3 crucible is used, even though the Fe^{3+}/Fe^{2+} ratio is higher. The reason for this is not clear from this study, but it is presumed that the amount of heat

stored in the crucible was so small that the cooling was fast during He quenching. it is also possible that a small amount of Al_2O_3 was dissolved in the MgO-FeO solid solution and suppressed hydration.

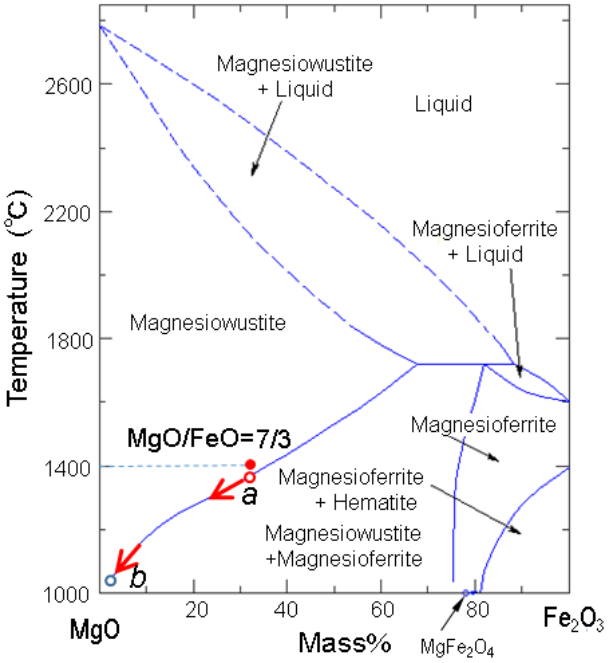

FIG 11 – Composition change of Magnesiowüstite during slow cooling in MgO-Fe_2O_3 phase diagram drawn by Phillips, Somiya and Muan (1961).

Effect of solid-solved MnO on hydration reactivity of MgO-FeO

The chemical composition and hydration rate of MgO-FeO-MnO solid solution are listed in Tables 4 and 5, respectively. Relationship between hydration rate and FeO+MnO content of MgO-FeO-MnO solid solution is shown in Figure 9, in which the hydration rate is not significantly different when solid-solving MnO instead of FeO. The relationship between hydration rate and Fe^{3+}/Fe^{2+} ratio for MgO-FeO-MnO solid solution shown in Figure 10 is near the line of that for the MgO-FeO solid solution. The relationship between Fe^{3+}/Fe^{2+} ratio and (FeO+MnO) content in the MgO-FeO-MnO solid solution was almost similar to that between Fe^{3+}/Fe^{2+} ratio and FeO content in the MgO-FeO solid solution, indicating that MnO did not affect the Fe^{3+}/Fe^{2+} ratio. It is said from Figures 9 and 10 that the ability of solid-solved MnO to the hydration of MgO-FeO solid solution is slightly inferior to that of FeO.

Effect of thermal history on hydration reactivity of MgO

Since Amita *et al* (1989) reported that the crystal size and morphology of MgO particles change with heating, it is expected that the hydration reactivity of pure MgO changes depending on the thermal history. In this study, two types of MgO powder, special grade MgO reagent powder and MgO crucible (MG-12 manufactured by Nikkato) pulverised to 75 to 150 μm, were heated at 1400°C for 12 or 72 hours in an Ar-1vol%H_2 flow, and then rapidly quenched with He blowing. The effect of thermal history on MgO hydration rate was investigated by performing hydration treatment three times in an autoclave. The obtained results are listed in Table 6.

TABLE 6

Changes in weight and hydration rate after hydration of MgO heated for various times.

Sample	Heating duration (h)	Before hydration		After third hydration	
		Weight (g)	Specific surface area (m^2/g)	Weight (g)	Hydration rate (%)
MgO reagent	0	1.0881		1.5631	97.8
	12	1.0374		1.4842	96.5
	72	1.0589		1.4758	88.2
Crushed MgO crucible	0	1.5541	4.34	2.0882	77.0
	12	0.9963	1.80	1.1177	27.3
	72	1.0571	0.68	1.0863	6.2

Figure 12 shows the relationship between heating time at 1400°C and hydration rate for MgO reagent and MgO crucible-pulverised powder. In Table 6 and Figure 12, even when the MgO reagent is heated at 1400°C for 72 hours, the hydration rate decreases by only about 10 per cent compared to the untreated one. However, when the MgO crucible powder is heated at 1400°C for 12 and 72 hours, the hydration rate is approximately 50 per cent and more than 70 per cent lower than that of the untreated one, respectively. The SEM observation revealed that calcination of the MgO reagent did not progress even after long-term heating, whereas calcination of the MgO crucible-pulverised particles powder easily progressed. This is thought to be because the MgO crucible contains a small amount of SiO_2 and Al_2O_3 as binders, which promotes fusion between the powders, making hydration difficult.

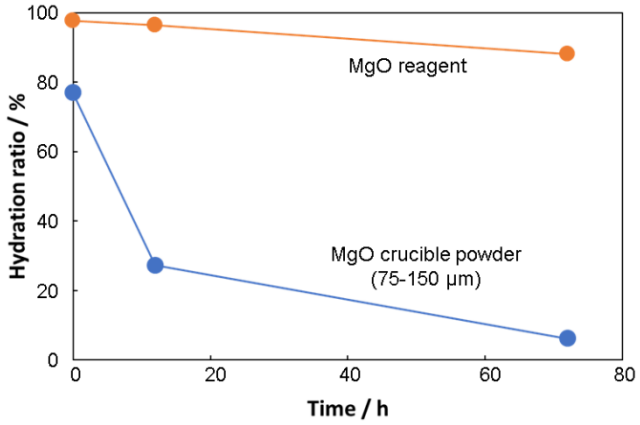

FIG 12 – Relationship between heating time at 1400°C and hydration rate for MgO reagent and MgO crucible powder.

To clarify the reason for the decrease in hydration reactivity due to calcination, the specific surface area of the MgO crucible powder (before hydration treatment) was measured using the BET method. The results are shown in Table 6. The specific surface area of the MgO crucible powder heated for a long time is significantly smaller than that of the unheated one. Since the specific surface area becomes smaller by calcination, hydration is suppressed. For the comparison of the hydration reactivity between MgO powders (Table 6) and MgO-FeO solid solutions prepared under various calcination conditions (Table 5), the hydration rates of MgO reagent powders heated for 12 and 72 hours are shown in Figure 9. The experimental point for MgO reagent heated for 12 hours is on the extrapolated curve of the relationship between FeO concentration and hydration rate of MgO-FeO solid solution heated for 12 hours. The relationship between hydration rate and the specific surface area is shown in Figure 13. In this figure, when comparing at the same specific surface area, the hydration rate of the MgO-FeO solid solution is lower than that of the unheated MgO crucible powder. This is also considered to be the effect of FeO solid solution.

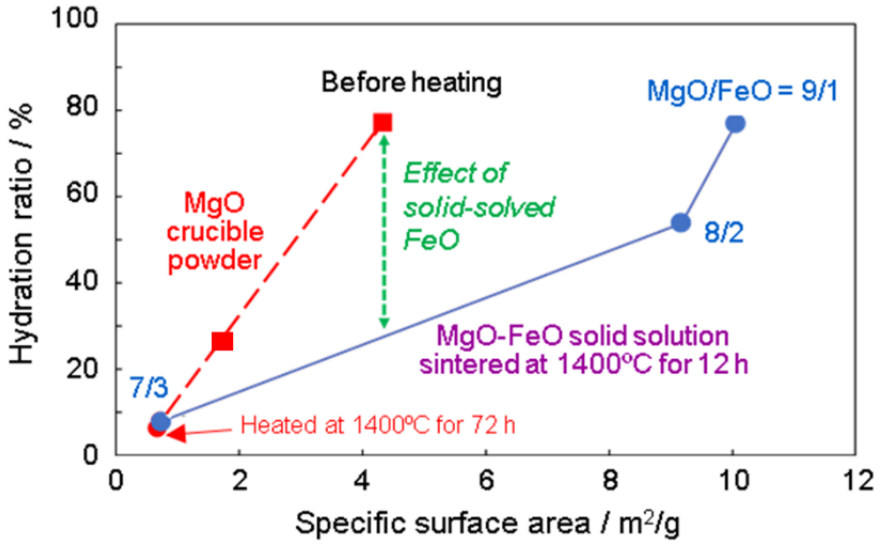

FIG 13 – Relationship between hydration rate and specific surface area for MgO-FeO solid solutions and MgO crucible powders.

CONCLUSIONS

To investigate the effect of solid-solved FeO on the hydration reactivity of free MgO in steelmaking slag, the preparation method of MgO-FeO solid solution was investigated, and conducted hydration experiments were performed on the synthesised MgO-FeO and MgO-FeO-MnO solid solutions using an autoclave. As a result, the following conclusions were obtained.

When the solid solution was rapidly cooled after calcination, a pure solid solution was obtained in one calcination process.

When MgO-FeO solid solution was hydrated under high temperature and pressure using an autoclave, the higher the amount of FeO dissolved in the MgO-FeO solid solution, the more the hydration reaction was suppressed.

When the calcination temperature of the MgO-FeO solid solution was increased, the Fe^{3+}/Fe^{2+} concentration ratio increased, resulting in a higher hydration rate.

Dense MgO crucible-pulverised powder had a lower hydration rate than commercially available MgO reagent.

The effect of heat treatment on the hydration rate of the MgO reagent was small. However, the longer the MgO crucible-pulverised powder was heated, the more the particles calcined and the specific surface area value decreased, resulting in a lower hydration rate.

ACKNOWLEDGEMENTS

We would like to express our gratitude by noting that a part of this research was conducted with the support of the Steel Environment Fund in 2018–2019.

REFERENCES

Amita, K, Nakagawa, K, Ikegami, Y, Ishihara, T and Hashizume, G, 1989. Effect of Additives on the shape of magnesium hydroxide obtained from hydration of magnesium oxide, *Gypsum and Lime*, 218:29–34.

Dictionary of Research, 2023. Autoclave. Available from:<https://www.wdb.com/kenq/dictionary/autoclabe> [Accessed: 6 January 2024].

Downs, R T and Hall-Wallace, M, 2003. The American Mineralogist Crystal Structure Database, *American Mineralogist*, 88:247–250.

Gražulis, S, Chateigner, D, Downs, R T, Yokochi, A T, Quiros, M, Lutterotti, L, Manakova, E, Butkus, J, Moeck, P and Le Bail, A, 2009. Crystallography Open Database – an open-access collection of crystal structures, *Journal of Applied Crystallography*, 42:726–729. https://doi.org/10.1107/S0021889809016690

Gražulis, S, Daškevič, A, Merkys, A, Chateigner, D, Lutterotti, L, Quirós, M, Serebryanaya, N R, Moeck, P, Downs, R T and Le Bail, A, 2012. Crystallography Open Database (COD): an open-access collection of crystal structures and platform for world-wide collaboration, *Nucleic Acids Research*, 40:D420–D427. https://doi.org/10.1093/nar/gkr900

Gražulis, S, Merkys, A, Vaitkus, A and Okulič-Kazarinas, M, 2015. Computing stoichiometric molecular composition from crystal structures, *Journal of Applied Crystallography*, 48(1):85–91. https://doi.org/10.1107/S1600576714025904

Horii, K, Tsutsumi, N, Kitano, Y and Kato, T, 2012. Processing and reusing technologies for steelmaking slag, *Shinnittetsu Giho*, 394:125–131.

Ichihara, A, 2010. Pressurized steam aging equipment for steelmaking slag, *Sanyo Technical Report*, 17(1):54–57.

Inoue, R and Suito, H, 1995. Hydration of crystallised lime in BOF slags, *ISIJ International*, 35(3):272–279.

Inoue, R, Uchidate, M, Kusukawa, S, Kado, N, Takasaki, Y and Ueda, S, 2021. Control of Hydration of Free Magnesia in Steelmaking Slag, *Journal of Sustainable Metallurgy*, 7:818–830.

Japanese Industrial Standard, 1983. JIS-M-8212. As 622.341.1-4:543.062:546.72 — Methods for Determination of Total Iron in Iron Ores, December 1983.

Japanese Industrial Standard, 1983. JIS-M-8213. As 622.341.1:543.242.5:546.722-31.062 — Methods for Determination of Ferrous Oxide in Iron Ores, December 1983.

JCPDS-International Centre for Diffraction Data, 2020. Powder Diffraction FileTM (PDF®) Search. Available from: <https://www.icdd.com/pdf-4-minerals/>

Merkys, A, Vaitkus, A, Butkus, J, Okulič-Kazarinas, M, Kairys, V and Gražulis, S, 2016. COD::CIF::Parser: an error-correcting CIF parser for the Perl language, *Journal of Applied Crystallography*, 49(1):292–301. https://doi.org/10.1107/S1600576715022396

Merkys, A, Vaitkus, A, Grybauskas, A, Konovalovas, A, Quirós, M and Gražulis, S, 2023. Graph isomorphism-based algorithm for cross-checking chemical and crystallographic descriptions, *Journal of Cheminformatics*, 15. https://doi.org/10.1186/s13321-023-0692-1

Michikawa, S, Ono, A and Eba, H, 2016. Determination of solid solubility and quantitative analysis of free-lime in steel slag by powder X-ray diffraction, *Tetsu-to-Hagané*, 102(11):623–629.

Nippon Slag Association, 2023a. Amounts of blast furnace slag produced and Used in FY 2021 [online]. Available from: <https://www.slg.jp/e/Statistics/Amounts of Blast Furnace Slag 2021FY.pdf> [Accessed: 6 January 2024].

Nippon Slag Association, 2023b. Amounts of steel slag produced and Used in FY 2021 [online]. Available from: <https://www.slg.jp/e/Statistics/Amounts of Steel Slag 2021FY.pdf> [Accessed: 6 January 2024].

Nippon Slag Association, 2023c. Characteristics and applications of iron and steel slag [online]. Available from: <https://www.slg.jp/e/slag/usage.html> [Accessed: 6 January 2024].

Ohira, Y and Obata, E, 2009. Effect of particle size on hydration rate of magnesium oxide, *Kagaku Kogaku Ronbunshu*, 35(5):543–547.

Phillips, B, Somiya, S and Muan, A, 1961. Melting relations of magnesium oxide-iron oxide mixtures in air, *J Am Ceram Soc*, 44(4):167–169.

Quirós, M, Gražulis, S, Girdzijauskaitė, S, Merkys, A and Vaitkus, A, 2018. Using SMILES strings for the description of chemical connectivity in the Crystallography Open Database, *Journal of Cheminformatics*, 10. https://doi.org/10.1186/s13321-018-0279-6

Sasaki, T and Hamazaki, T, 2014. Development of steam-aging process for steel slag, *Shinnittetsu-Sumikin Giho*, 399:21–25.

Takayama, S, Idemitsu, T, Aida N, Sugi M and Tokuhara H, 1996. The utilization of steel making slag improved by the method of steam aging as upper base materials, *Doboku-Gakkai Ronbunshu*, 544:177–186.

Vaitkus, A, Merkys, A and Gražulis, S, 2021. Validation of the Crystallography Open Database using the Crystallographic Information Framework, *Journal of Applied Crystallography*, 54(2):661–672. https://doi.org/10.1107/S1600576720016532

Vaitkus, A, Merkys, A, Sander, T, Quirós, M, Thiessen, P A, Bolton, E E and Gražulis, S, 2023. A workflow for deriving chemical entities from crystallographic data and its application to the Crystallography Open Database, *Journal of Cheminformatics*, 15. https://doi.org/10.1186/s13321-023-00780-2

Wu, P, Eriksson, G, Pelton, A D and Blander, M, 1993. Prediction of the thermodynamic properties and phase diagrams of silicate systems–evaluation of the FeO-MgO-SiO_2 system, *ISIJ International,* 33(1):26–35.

University research on molten slags, matte, speiss and metal systems for high temperature processing – challenges, opportunities and solutions

DOI: 10.62053/CYAH2875

E Jak[1], M Shevchenko[2], D Shishin[3], E Nekhoroshev[4], J Chen[5] and P Hayes[6]

1. Professor, Director, Pyrometallurgy Innovation Laboratory (Pyrosearch), The University of Queensland, Brisbane Qld 4072. Email: e.jak@uq.edu.au
2. Theme Leader, Pyrometallurgy Innovation Laboratory (Pyrosearch), The University of Queensland, Brisbane Qld 4072. Email: m.shevchenko@uq.edu.au
3. Theme Leader, Pyrometallurgy Innovation Laboratory (Pyrosearch), The University of Queensland, Brisbane Qld 4072. Email: d.shishin@uq.edu.au
4. Theme Leader, Pyrometallurgy Innovation Laboratory (Pyrosearch), The University of Queensland, Brisbane Qld 4072. Email: e.nekhoroshev@uq.edu.au
5. Theme Leader, Pyrometallurgy Innovation Laboratory (Pyrosearch), The University of Queensland, Brisbane Qld 4072. Email: j.chen5@uq.edu.au
6. Professor Emeritus, Pyrometallurgy Innovation Laboratory (Pyrosearch), The University of Queensland, Brisbane Qld 4072. Email: p.hayes@uq.edu.au

ABSTRACT

Recent decades have seen significant advancements in analytical and experimental techniques, thermodynamic theory, and computational capabilities in high temperature research which are particularly timely to address the challenges of increasingly complex and variable feedstocks in both primary and secondary pyrometallurgical processes, the need to optimise and improve them. Currently a research program is in progress on the development of the 20-component multi-phase thermodynamic database for pyrometallurgical smelting, refining and recycling systems describing thermodynamics and phase equilibria of molten slag, matte, speiss, salts, alloys and associated solids. The integrated experimental and modelling program has been supported for nearly two decades by several consortia of 14 major international companies with over 30 operations around the world, integrates many components, incorporates many in-house developments, and brings together many different groups of professionals of different levels from junior and mid-career to senior from both industry and university sectors. The aims of the paper are:

- to outline the many components and issues of the overall program including analytical, experimental and thermodynamic modelling research as well as implementation of the results in industrial practice, professional education, planning and organisation issues.
- to highlight the opportunities, challenges, and possible solutions.
- to present these to all different groups of professionals involved in the current program.
- and thus, importantly, to facilitate possible future further developments and collaborations in the field of phase equilibria and thermodynamics of complex high-temperature systems.

INTRODUCTION

Purpose of the paper

Significant technological society changes associated with decarbonisation, developments of renewable energy sources, electric vehicles, increasingly complex electrical and electronic devices have led to increasingly complex and variable pyrometallurgical processing streams. To address these challenges, optimise existing processes, and develop new pyrometallurgical technologies knowledge-based approaches are required. Fundamental information and powerful computer-based predictive tools can provide accurate and reliable descriptions of phase equilibria and thermodynamics in multi-phase multi-component systems. The Pyrosearch Laboratory (Pyrosearch) at The University of Queensland (UQ) developed and uses integrated experimental and thermodynamic modelling methodology to create computational tools used by Australian and international metal production and recycling industrial companies. The aim of the overall research

program is to support the industry in transition towards higher sustainability and efficiency. The current objectives of the program are to: i) develop a 20-component thermodynamic multiphase, multicomponent database for non-ferrous smelting, refining and recycling systems describing molten slag, matte, speiss, salts, alloys and associated solids using the integrated experimental and thermodynamic modelling approach; and ii) implement the research outcomes into industrial practice. The research program has been continuously supported over the last nearly two decades by the consortia of over a dozen of major international metallurgical and recycling companies with over three dozen industrial operations around the world, as well as by Australian and USA government grants. Significant progress has been achieved in fundamental and applied research, and in implementation of research outcomes into industrial practice.

The aims of this paper are to outline the developed research approach, different components integrated into one program, the issues encountered by the authors while working on this program, possible solutions and opportunities, and to present these to different groups of professionals to facilitate possible further developments and collaborations in the field.

The combination of many components in one overall research program is an important basis of the program.

The integrated experimental and modelling approach to develop thermodynamic databases presented by authors in this paper incorporates a *complex combination of many components* of different nature including but not limited to the: i) analytical, ii) experimental, iii) thermodynamic modelling, iv) computational science, v) organisational, vi) financial, vii) industrial implementation and viii) educational. This combination is an important basis of the program. Every component itself is complex and challenging, requires specific in-depth discussion and is of interest to a specific professional audience. The next level challenge is to bring together all these components into one integrated research program undertaken by a group of professionals with different but closely related complementary expertise. Each component therefore will be described at a high, generic, relatively simplified and superficial level to allow: a) to keep the focus on the combination of them; and b) to make it accessible to all different audiences of professionals of different spheres of expertise and levels. References will be given to the more detailed discussions on each component of interest to each specific group of professionals.

The combination of different groups of professionals in one team is another important factor, these include:

- Young undergraduate students – future industrial metallurgists and researchers learning and making their career choices.
- Junior, middle career and senior researchers involved in scientific developments, and assisting in implementation of the research outcomes into industrial practice and in education.
- Senior academics involved in the development of the research programs and in university education.
- University and scientific organisations senior management involved in major organisations decision-making.
- Young and middle career industrial research and development (R&D) metallurgists implementing the scientific and research advances into practice and improving metallurgical operations.
- Young and middle career industrial process metallurgists running the industrial processes, identifying and implementing improvements along with the R&D staff.
- Senior industrial executive R&D management leading industrial research and development programs.
- Senior industrial executive management making decisions on the companies' major developments and finance.
- Government officials looking after legislation and policies, as well as government funding.

Each of these groups is important for the sustainable development and operation of strategic and long-term research programs. The authors attempt to bring together all these groups in understanding of: a) the overall combination; and b) each component in order to facilitate further collaborative research and implementation developments in the field.

More on current challenges and opportunities for pyrometallurgy

As indicated above, significant technological changes are taking place in our societies right now and in the coming decades associated with decarbonisation and the developments of renewable energy sources, electric vehicles, and new increasingly complex electrical and electronic devices. The growth in the production of advanced materials used in these sophisticated technological devices has led to significantly increased demands in both volumes and variety of primary metals production and in metals recycling. As metal scarcity grows, primary concentrates are becoming increasingly complex. This is compounded by the rising number and diversity of metals found in recycled technological devices, which significantly increases the complexity and variability of metallurgical feed streams. Both short-term (daily-weekly-monthly) and long-term (multi-year) variations are observed. To address these challenges and minimise environmental impact, modifications to existing and development of new metallurgical technologies are crucial to enhance process efficiency and productivity. Adaptation of pyrometallurgical operations to these challenges requires implementation of a knowledge-based approaches using the fundamental information and powerful predictive computer tools for the accurate and reliable predictions of separation of the multi-component multi-phase process streams directly related to the phase equilibria and thermodynamics in multi-phase multi-component systems.

Significant gaps in knowledge on high temperature properties exist – these are due to difficulties associated with high-temperature research. *The demand* for the accurate fundamental information on phase equilibria, thermodynamic and physicochemical properties of the complex multi-component systems from metallurgical and recycling industries is growing due to the need to address: a) stricter environmental regulations, b) stronger economic competition, c) better equipment and options in process control and data management, and, importantly, d) increased complexity and variability of the process chemistry. *The supply* of the needed fundamental data on the chemistry of the processes is becoming possible since: a) new experimental techniques are becoming available due to b) the developments of modern advanced analytical techniques, dramatic improvement of their capabilities and availability, c) new theoretical modelling approaches, and d) the significantly increased computer capabilities. This demand/supply combination is the basis for *the renaissance in research on the high temperature chemistry of metallurgical systems.*

Phase equilibria and thermodynamics are critical for the high temperature processes modelling and optimisation

As illustrated in Figure 1, the optimisation and improvement of the existing processes and the development of new processes requires good control of the process parameters, that in turn requires adequate characterisation and modelling of all factors influencing the process output as a function of the input parameters. For pyrometallurgical operations the factors that require accurate characterisation for the stable operation include:

1. Thermodynamics and phase equilibria.
2. Physicochemical properties (eg viscosity etc).
3. Micro-kinetic (20–1000 μm).
4. Macro-kinetic (0.1–10 m) factors.
5. Plant data accuracy.
6. Plant control accuracy, where the thermodynamics and phase equilibria are particularly critical and important.

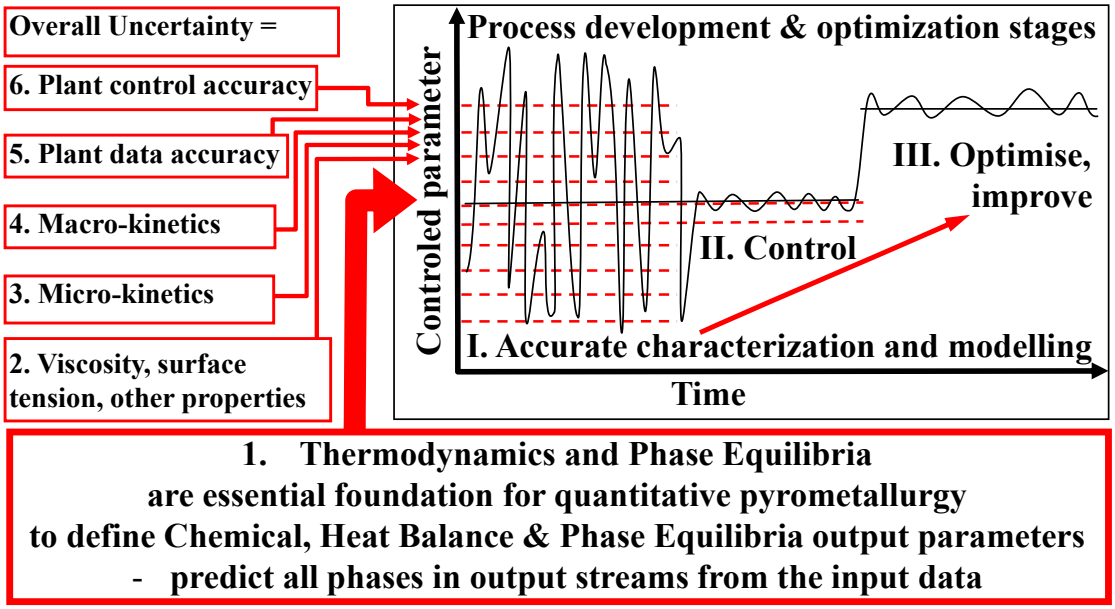

FIG 1 – Some factors influencing process uncertainty and the key stages in achieving process optimisation – characterisation/modelling and control.

In any pyrometallurgical process involving molten phases, adequate and simultaneous control of at least three key output parameters is essential (see Table 1):

1. *Chemical target* (product composition).
2. *Heat balance* (to control process temperature).
3. *Phase equilibria* (liquidus temperatures or proportion of solids) (Jak, 2018).

These three output parameters are directly controlled by the amounts and compositions of the materials introduced into the reactor. All these input and output parameters are interrelated- each output parameter depends on all input parameters with different sensitivities and is strongly determined by the thermodynamics and phase equilibria of the system. *Reliable models accurately describing thermodynamics and phase equilibria of the whole chemical system over a wide range of compositions, temperatures and pressures are therefore critical for the optimisation and control of existing and for the development of future pyrometallurgical processes.*

TABLE 1

Typical input, target and calibration parameters used in pyrometallurgical processing.

Examples of input parameters	Kinetic "calibration" parameters	Target output parameters
Oxygen coefficient (O_2/feed ratio) Duration of blow and rate	Oxygen efficiency	***Chemical*** - e.g. matte grade, Cu or Pb in slag, %S in blister
O_2 enrichment, fuel (coal, oil), dust and reverts, recycling, feed rate, composition (e.g. Cu/S/Fe), mineralogy, electric power	Heat loss	***Heat Balance*** - temperature
SiO_2 and CaO fluxes, slagging impurities levels (e.g. Al_2O_3, CaO, MgO)	Flux utilisation	***Phase equilibria*** - Liquidus, %solids, freeze-lining thickness, e.g. Fe/SiO_2, CaO/SiO_2 in slag

In industrial practice, a range of process models and predictive tools are used depending on the needs, availability of necessary data and other factors (Jak, 2018). For example, simplified thermodynamically-based models with the kinetic 'calibration' parameters valid for limited range of conditions specific for a given reactor, eg Nikolic *et al* (2018), can be very effective as process advisers for improved process control, preparation of blends, short- and long-term production planning, limited scale-up predictions, staff training, and, importantly, for the development of the feed-forward control. These thermodynamic predictive tools can further be used to develop process predictive tools (virtual reactors) and be incorporated into 'Pyro-GPS' systems (similar to the GPS systems) used for optimisation of complex plant flow sheets (see Figure 2).

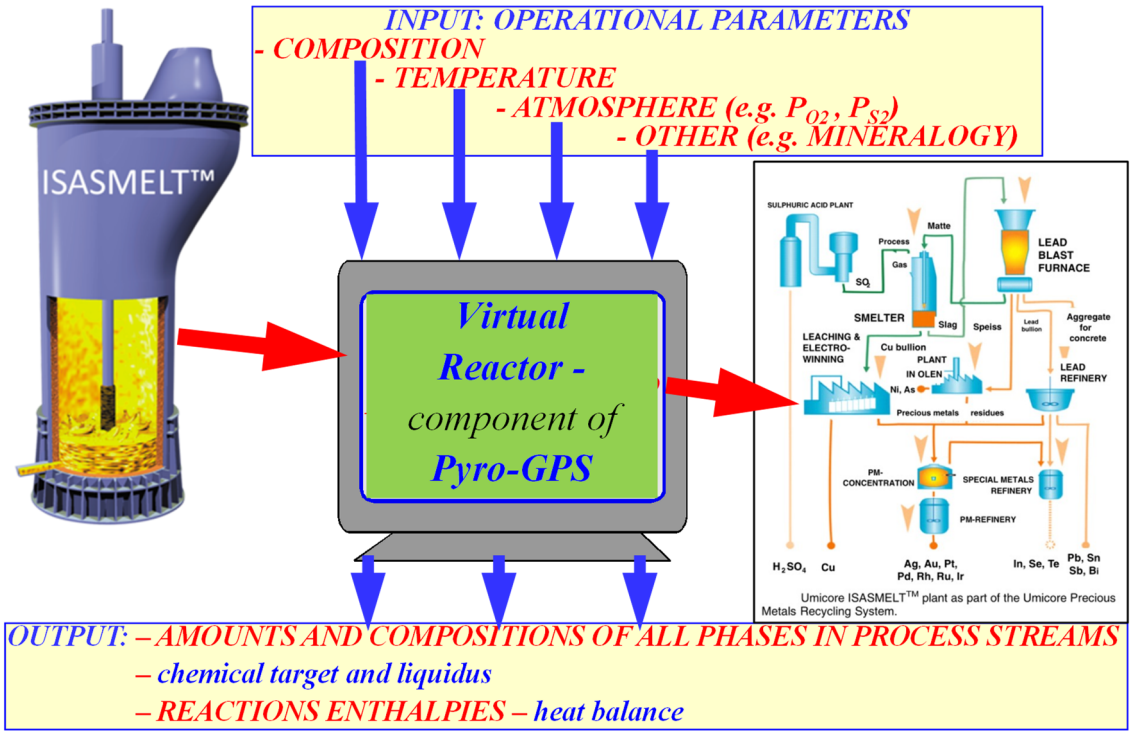

FIG 2 – Illustration of the key role of fundamentally based thermodynamic tools in predicting process outcomes and assisting in process optimisation (Jak, 2018).

The research program on the development of the multi-component multi-phase thermodynamic predictive tool outlined in this paper aims to provide the required strategic foundation for further developments in pyrometallurgy.

Research requirements for the development of computer predictive tool for pyrometallurgical thermodynamics and phase equilibria

Pyrometallurgical processing systems generally involve large number of phases with complex properties. The key liquid phases include slag, matte, speiss, salts (eg sulfates) and alloys. The majority of the key solid phases are solutions, many with wide ranges of compositions (eg spinels, melilites, olivines, pyroxenes, dicalcium silicate). Due to strong atomic-level interactions and intricate internal structures, most of these phases exhibit complex relationships between their thermodynamic properties, composition, and temperature. Accurately predicting the thermodynamic properties of key liquid and solid solution phases encountered in pyrometallurgy necessitates the use of suitable *theoretical thermodynamic models*. These models must be capable of capturing the complex dependence of thermodynamic functions on composition, temperature and pressure, and performing reliable extrapolations and interpolations beyond the range of available experimental data. Thermodynamic predictions for the multi-component multi-phase systems also require appropriate *computational capabilities* – the computer packages capable of performing complex and multiple calculations at practically acceptable speed and incorporating: i) adequate thermodynamic models, ii) Gibbs free energy minimisation module, iii) input/output interface and, importantly, iv) the databases containing thermodynamic model parameters on all possible phases including

stoichiometric compounds as well as solutions (slags, mattes, salts, speiss, alloys, solids etc). Prediction of the thermodynamic properties of the actual phases requires *experimental data* to fix model parameters. In summary, the critical research components necessary to predict equilibrium chemical behaviour of the pyrometallurgical processing systems include: a) appropriate theoretical thermodynamic models, b) adequate computational capabilities, and c) sufficient and accurate experimental data. The following sections will provide some comments relevant to these critical research components.

DEVELOPMENT OF THE TOOLS

Thermodynamic computer packages providing required computational capabilities in pyrometallurgy

Several commercial thermodynamic software packages have been developed for predictions in a field of pyrometallurgy. The most widely used are FactSage™ (Jung and Van Ende, 2020) (www.factsage.com) and Thermo-Calc (Andersson *et al*, 2002) (www.thermocalc.com). FactSage contains the databases for wide range of molten systems, including oxides, sulfides, molten salts, and metals, which are based on high-quality thermodynamic assessments. Thermo-Calc, in addition to extensive metallic thermodynamic databases, has oxide and molten salts databases, as well as capabilities in modelling physical properties for some molten phases and advanced kinetics for alloys. Other available products are MatCalc (www.matcalc-engineering.com), MTDATA National Physical Laboratory, UK, (Gisby *et al*, 2017), Pandat (www.computherm.com) and MPE (CSIRO, Australia (Chen, Zhang and Jahanshahi, 2013; Chen, 2015)). When customised user interface is needed, related software tools are often available for customised applications such as ChemApp (Petersen and Hack, 2007), ChemSheet (Koukkari *et al*, 2000), ChemAppPy (www.gtt-technologies.de) and SimuSage (Petersen *et al*, 2007), that are compatible with the FactSage databases. Thermo-Calc users can benefit from developer kits for Python, Matlab, and a collection of subroutines in a form of DLL called TQ-Interface.

Thermodynamic computer modelling – brief outline, experimental data needs and thermodynamic database development

A number of key points related to the thermodynamic modelling are listed below:

- The Gibbs energies of stoichiometric compounds including pure end members are calculated from the entropy at 298 K (S_{298}), the enthalpy at 298 K (ΔH_{298}) and heat capacities (Cp(T)) – these are generally considered as the most accurate and self-consistent data – important foundation of the solution models in thermodynamic databases (see Figure 3).
- A two-component thermodynamic solution model consists of: i) the expression for end-members (S_{298}, ΔH_{298} and Cp(T)), ii) adequate solution model expression related to the internal atomic-scale structure of the solution phase that determines an ideal entropy of mixing, and iii) binary excess parameters describing deviations from the corresponding ideal behaviour as a function of composition, temperature and pressure determined by the trends of internal interactions between the two components at atomic scale. The solution model expression must be sophisticated enough to adequately describe complex Gibbs free energy of mixing determined by the internal structure of the phase, eg M-shaped entropy of mixing in the solutions with strong internal atomic-scale interactions and ordering in phases such as silicate slag (molten oxide solution) (Pelton and Blander, 1986). For example: a) the Modified Quasichemical Model (Pelton *et al*, 2000; Pelton and Chartrand, 2001; Pelton, Chartrand and Eriksson, 2001) is used for the liquid slag and matte phases, b) the Compound Energy Formalism (or sublattice model) (Chartrand and Pelton, 2001; Hillert, 2001) is used for the solid solutions with complex crystal structure, and c) the Bragg-Williams random mixing model is used for solutions with weak or positive deviation from ideal in the present study within the FactSage computer package (Bale *et al*, 2016) or custom tools developed using ChemApp (Petersen and Hack, 2007).
- A three-component thermodynamic solution model incorporates mathematical expressions for the extrapolation of the Gibbs energy of binary systems into ternary space, as well as

mathematical formalism for the ternary excess thermodynamic parameters. The latter describes the effect of the third component on the binary interactions of the given two components. Generally, only binary and ternary thermodynamic parameters in the solution models of slag and other condensed phases are used since the effect of the next order interactions is negligible or does not exist at all. The extrapolation of the Gibbs energy of binary systems into ternary and higher order composition space is different for different components and is specific to a particular ternary system (Chartrand and Pelton, 2000; Pelton, 2001). The Gibbs free energies of the solutions with the number of components higher than three are generally described by binary and ternary parameters.

- Condensed phases in pyrometallurgy such as slag, matte, salts, speiss, solid oxide solutions are complex, non-ideal solutions, with strong interactions, so that the binary and ternary thermodynamic parameters for accurate description of solution properties cannot be derived without experimental data. Experiments over the whole range of conditions with adequate accuracy are necessary for the description of the thermodynamic properties of the multi-component solutions – so the *critical conditions for the accurate multi-component multi-phase model are: a) sufficiently abundant, and b) sufficiently accurate experimental data of all types*, including:
  - Heat capacities (Cp) as a function of temperature, S_{298}, ΔH_{298} for all stoichiometric compounds and all end-members of the solutions, calorimetric data.
  - Gibbs free energies of phases G_i and of reactions ΔG_R, thermodynamic activities.
  - Phase equilibria (liquidus/melting points, miscibility gaps, solid solubilities, distribution coefficients).
  - Structural information (such as, solid solutions, crystal structures, site occupancies etc).
- The lack of experimental data severely limits the development of accurate model parameters. This requirement can be summarised and will be further referred to in the paper by the slogan: '*No experiment, no model parameter*'.
- Thermodynamic databases of multi-component multi-phase systems are developed through thermodynamic 'optimisations' when all available thermodynamic and phase equilibrium experimental data for the system are evaluated simultaneously in order to obtain one set of model equations for the Gibbs energies of all phases as functions of temperature and composition. From these equations, all of the thermodynamic properties and the phase diagrams can be back-calculated. In this way, all the data are rendered self-consistent and consistent with thermodynamic principles. Thermodynamic property data, such as Cp(T), S_{298}, ΔH_{298}, G_i, ΔG_R and activity data, can aid in the evaluation of the phase diagram, and phase diagram measurements can be used to deduce thermodynamic properties. Discrepancies in the available data can be identified. These discrepancies can then be resolved through new experimental studies. The gaps in experimental data can in identified so that further experimental investigations are undertaken in areas essential for further thermodynamic optimisations.
- The self-consistent thermodynamic databases developed in this way are used for interpolations and extrapolations in a thermodynamically correct manner and for predictions of equilibrium phase compositions and phase assemblages in multi-component, multi-phase systems.

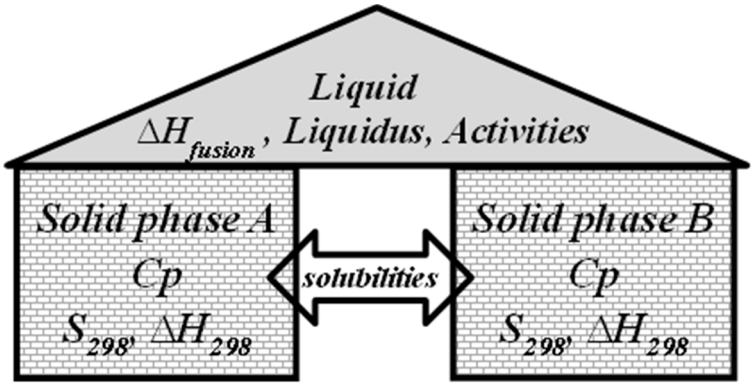

FIG 3 – Thermodynamic database structure.

Thermodynamic solution models used in the present program

Balance between predictive capability, complexity and accuracy of model predictions and available experimental data

The balance between predictive capability of a model, model complexity and accuracy of model predictions, extrapolations and interpolations depends on the available experimental data. Generally, the simpler the model (the less parameters it has) – the more predictive power it has, but at the same time the lesser capacity to describe complex trends and therefore the lesser accuracy the model has. The more complex model is—the more parameters generally it has—the more chances those parameters are not accurate enough when extrapolated, therefore significant additional experimental data are needed to determine parameters of more complex models. It is common that abundant and accurate experimental data set cannot be described with too simple and predictive model, therefore: a) sufficiently abundant, and b) accurate experimental data set requires more sophisticated model to be described, and therefore can fix parameters for such more sophisticated thermodynamic model, which in turn eventually results in more accurate and reliable description and predictions of the thermodynamics and phase equilibria of the multi-component systems. This can be re-formulated in an alternative way – the accurate and reliable sophisticated models with good predictive power require: a) sufficiently abundant, and b) sufficiently accurate experimental data set—supporting the statement indicated above 'no experiments—no model parameter'.

Brief outline of the thermodynamic models used in the present program

For the complex molten solutions with strong interactions and short range ordering at atomic scale, and corresponding complex trends in Gibbs free energy of mixing several approaches were developed, these are:

1. Introduction of associates at the composition of maximum ordering within the single sublattice.
2. Two-sublattice ionic models with complex ions corresponding to the composition of short-range ordering.
3. Quasichemical models in which the entropy of mixing takes into account the effect of short-range ordering.

The Modified Quasichemical Model (MQM) available in FactSage (Bale *et al*, 2016) used for the molten oxides (slags), sulfides and salts solutions in the present study incorporates many important additional complex functionalities, such as:

1. flexibility in the choice of pair (quadruplet) fractions or site fractions for the polynomial expansion for the Gibbs energy of quasichemical reactions (Pelton *et al*, 2000).
2. Freedom in the choice of coordination numbers, allowing the control in position and shape of short-range ordering for different systems sharing the same component (Pelton *et al*, 2000).
3. Combining quasichemical and Bragg-Williams random mixing contributions to the excess Gibbs energy (Pelton and Chartrand, 2001).

4. The opportunity to introduce associate species in cases when binary quasichemical interaction cannot describe the observed phenomenon, ie charge compensation effect.
5. Different interpolation methods of binary model parameters into multicomponent space (Pelton and Chartrand, 2001; Decterov, 2018).
6. Possible quadruplet formalism for ionic liquids with several cations and anions (Pelton, Chartrand and Eriksson, 2001).

All these modifications constitute a framework, which allows the description of the complex trends in the real solutions using Modified Quasichemical Formalism (MQF), which, in combination with sufficiently abundant and accurate experimental data, can achieve high levels of accuracy in multi-component compositional space.

For complex solid solutions such as spinels, melilites, pyroxenes, olivines and many other, the Compound Energy Formalism (CEF) (Hillert, 2001) is a widely accepted modelling method (Frisk and Selleby, 2001). The main two features of CEF are the assumption of distinct sublattices within the crystal structure, and the random mixing within each sublattice. The main model parameters are in the Gibbs energy functions of all solution endmembers, as well as excess parameters for the interaction of atoms (species) within the same sublattice. As in the case of MQF, different models can be developed within CEF. Large flexibility of CEF comes from the option of using more than two sublattices, which MQF does not allow. The same components, including charged ions, can be present on several sublattices. This approach creates many 'virtual' endmembers, necessitating the development of careful strategies to reduce the number of adjustable parameters through linear combinations and reciprocal reactions (Hillert *et al*, 2009). In multicomponent solutions, the introduction of a new solution component results in the dramatic increase in undefined endmembers, which makes expansion of solutions, such as Spinel, extremely challenging. In certain applications, such as non-stoichiometric solid speiss solutions, MQF with single sublattice demonstrated similar results to CEF with less parameters (Shishin and Jak, 2018). The MQF-based models for solid solutions are now being tested in ternary and multicomponent systems.

As indicated above, the Bragg-Williams random mixing model is used for simple solutions in the present study.

Further more detailed discussions on thermodynamic models are given in Shishin, Shevchenko and Jak (2024).

Overall experimental data requirements for constructing multi-component multi-phase thermodynamic database

As discussed earlier, a sufficiently abundant and accurate set of experimental data is crucial for a reliable thermodynamic description of pyrometallurgical systems. Some additional, more detailed points regarding data requirements are given below:

- All potential phases across the *entire composition and temperature range* need characterisation. This ensures the model's versatility for use by a diverse range of professionals to predict behaviour: i) at various stages throughout a pyrometallurgical process, and ii) within different reactor zones. Imagine a GPS system – if a specific area is not mapped, the route guidance might be inaccurate if your journey takes you through that unmapped region.
- At a minimum, *all binary systems* should be investigated. For simple binary systems with no intermediate compounds around 10–20 liquidus data points may be sufficient. However, complex and important binary systems containing multiple binary compounds and solid solutions may require 40–50 experiments to determine both the liquid slag's binary thermodynamic parameters and the solids' thermodynamic properties. As an example, the simple Sb_2O_3-SiO_2 binary system (no intermediate compounds) only required ten experimental points, while the more complex PbO-SiO_2 system (with four intermediate compounds at the liquidus and more at lower temperatures) needed 40 experiments (Wen *et al*, 2023).
- All ternary systems have to be investigated at least to a minimum level of ~20–30 liquidus points for a simple ternary and up to 200–300 experiments for a complex and important ternary

with binary and ternary compounds and solid solutions to determine ternary thermodynamic parameters for the liquid slag as well as thermodynamic properties of solids. For example, the simple PbO-Cu_2O-ZnO ternary system required only 12 experimental points (Wen *et al*, 2023) whereas a complex PbO-'Fe_2O_3'-SiO_2 ternary system required 146 experiments (Shevchenko and Jak, 2019c).

- Selected 4-component subsystems should be experimentally investigated to validate the extrapolation of ternary thermodynamic parameters.
- To ensure reliable and accurate model predictions for industrially relevant conditions, selected 4-component and higher-order subsystems should be experimentally characterised.
- The current 20-component, multi-phase gas-slag-matte-speiss-metal-solids systems with the PbO-ZnO-Cu_2O'-FeO-Fe_2O_3-CaO-Al_2O_3-MgO-SiO_2-S major and As-Sn-Sb-Bi-Ag-Au-Ni-Co-Cr-Na minor elements include:
  - 22!/(20!·2!) = 231 binaries and 22!/(19!·3!) = 1540 ternaries in the 22-component PbO-ZnO-'Cu_2O'-FeO-Fe_2O_3-CaO-Al_2O_3-MgO-SiO_2-As_2O_3-As_2O_5-SnO-SnO_2-Sb_2O_3-Bi_2O_3-Ag_2O-Au_2O-NiO-CoO-CrO-Cr_2O_3-Na_2O oxide system, and
  - 15!/(13!·2!) = 105 binaries and 15!/(12!·3!) = 455 ternaries in the 15-component Pb-Zn-Cu-Fe-S-As-Sn-Sb-Bi-Ag-Au-Ni-Co-Cr-Na metal/matte/speiss system.
- Complete experimental characterisation of all these binaries and ternaries would require many years of work of a laboratory such as Pyrosearch (these numbers do not even include 4- and higher order sub-systems nor combined slag-matte-metal systems). *Careful planning of the experimental work therefore is a critical factor* to ensure the continuing practical impact from this research program is delivered – this is discussed in the following sections.

Requirements for the overall experimental research program

As indicated above – adequate experimental characterisation of the current 20-component gas-slag-sulfate-matte-speiss-metal-solids systems is a very big task requiring significant efforts over extended period of time. Such significant research program, to be realistic, sustainable and practically executable requires a systematic planned gradual approach that would meet:

- the financial and organisational criteria would attract: i) continuing financial support with continuously returned value to the industrial and government sponsors, and ii) high-expertise continuous research expert team.
- the scientific or technical criteria.

These criteria are discussed as follows:

- Experimental and analytical methods should be available to generate: a) sufficient, and b) accurate data – this is the first necessary criterion.
- Intermediate, not fully optimised but, at the same time, accurate and reliable enough for some practical calculations thermodynamic database should be made available to the sponsors to provide immediate value to sponsors to justify continuing financial support – the *iterative approach* adopted in this program provides a practical solution of *bringing continuing value to sponsors* and thus maintaining the continuing financial support of the program.
- *Continuous support by research team of the implementation* of the intermediate results into the industrial practice is a critical factor to ensure this study is bringing the value to sponsors and thus maintaining the continuing financial support of the program.
- Criteria to produce the minimum number of experiments sufficient for model development is important given the large number of the overall experiments needed.
- Integration of experimental and modelling is critical to ensure: i) efficient progress of both experimental and modelling components, ii) high accuracy of both experiments and models are achieved, and iii) minimum but sufficient number of experiments is undertaken to develop the model of the required accuracy.

- Effective planning of experimental and modelling components is critical for the program with the large number of sub-systems being investigated, large number of experiments performed, large number of research staff involved and with the large number of sponsors and users of the database.
- Adequate computational method and computer tool for the experimental and modelling data management and manipulation in the process of the continuing iterative re-optimisation of the thermodynamic parameters is critical given the large number of experiments and large number of sub-systems continuously studied and re-optimised.
- Expert research team with adequate combined skills capable of running different components of the overall research program is a critical necessary factor.

As a summary – the following components are identified as critical combination to respond to the challenges:

- Financial and organisational criteria:
  - iterative approach in the thermodynamic database development
  - ongoing implementation into industrial practice
  - effective planning
  - minimum sufficient experimental data for the thermodynamic model development.
- Scientific or technical criteria:
  - experimental data: a) sufficiently abundant, and b) sufficiently accurate data for the thermodynamic model development
  - integration of experimental and modelling studies
  - adequate experimental and modelling data for computational management/ manipulation during re-optimisation
  - expert research team with necessary combined skills.

The following chapters will provide further comments by the authors on the above critical components.

METHODOLOGY

Integration of experiments and thermodynamic modelling is critical

The integrated experimental/thermodynamic modelling approach has been implemented at Pyrosearch and has enabled the rapid and efficient development of complex thermodynamic databases for the multicomponent systems: thermodynamic parameters are fixed by the new targeted experimental data points rather than by fitting into the pre-existing from literature and other sources experimental data. The continuously improved database is used for systematic assessment of completed experiments and identification of further new experiments that need to be carried out to accurately determine the binary and ternary model parameters. This systematic iterative procedure involves: i) the identification of priorities for experiments from thermodynamic assessment, ii) the development and application of advanced experimental and analytical techniques to characterise the required sub-systems, and performing experiments, and iii) the ongoing revision of thermodynamic parameters through re-optimisation of the required low- and corresponding high-order systems.

Steps i), ii) and iii) are repeated progressively improving predictions and database accuracy. The interval between planning and completing experiments in case of the Pyrosearch program is reduced to few days or weeks, and all tasks planning and undertaking of experiments and thermodynamic optimisations, are undertaken in many cases by the same researcher.

The integration of experimental and modelling components of the research ensures modelling is used: i) to analyse the agreement between different types of data, ii) to identify discrepancies in

previous and, importantly, recent experimental results, and iii) to suggest required further experiments if needed or to conclude the work on a given sub-system, as well as iv) to plan further experiments as need (bulk composition, proportion of solids, equilibration path). Experiments in turn are critical to continuously test and gradually improve model accuracy. It is critical that the interval between request for and execution of experiments is minimum to allow dynamic model development and dynamic continuous planning of further experiments. The model-focused and model-based experiments planning ensures minimum but sufficient number of experiments are undertaken for a given system and at the same time ensures consistency and accuracy of experiments as well as of the model are tested during the research program progress.

Experimental phase equilibria methodology – critical for the high temperature phase equilibria and thermodynamics

As discussed above, the thermodynamic model development requires different types of experimental data, phase equilibria are one of them but a critical type that is described in the present paper. The requirement for: a) the sufficiently abundant, and b) the sufficiently accurate high-temperature phase equilibria measurements poses significant experimental difficulties due to a number of issues including but not limited to the highly reactive/corrosive properties of liquid phases in these systems, issues with containment, the high vapour pressures of some metal species, changing composition during equilibration due to interaction with substrate, establishing gas/slag/matte/metal equilibria, evaporation etc. Previous experimental techniques cannot provide wide enough range of applicability and the accuracy required for thermodynamic database development at high temperatures, particularly for systems containing complex solutions and multicomponent systems.

The equilibration/quenching/microanalysis methodology developed by Pyrosearch (Jak, Hayes and Lee, 1995; Jak, 2012) has overcome all of these limitations and it is now the preferred approach to phase equilibria determination in these complex systems (Figure 4). The methodology involves equilibration of small synthetic samples (typically less than 0.5 g prepared by mixing pure powders and pelletising) at accurately controlled temperature and gas atmosphere conditions. The sample is then rapidly quenched to low temperature thus retaining the phase assemblage and phase compositions present at the equilibration temperature. The microstructures in the samples prepared using standard metallographic techniques are analysed with optical and scanning electron microscopy (SEM). The phase compositions present in the samples are measured using advanced microanalytical techniques including: i) electron probe X-ray microanalysis (EPMA), and ii) laser ablation inductively coupled plasma mass spectrometry (LA-ICPMS). The compositions and process conditions are deliberately selected so that multi-phase materials are formed in the equilibrated samples. Any change to the sample bulk composition only changes the proportions of the phases, not their compositions that are measured with microanalysis after the experiment. The methodology then has the important advantage that the results do not depend on the small bulk composition changes (within certain limits) that may take place during equilibration. Recent developments in experimental techniques now allow the phase equilibrium measurements and elemental distributions between phases to be obtained in slags/sulfates/mattes/speisses/metal alloys/solid solutions in closed and open systems over a wide and continuously extended range of conditions thus meeting the conditions of being: a) sufficiently abundant, and b) sufficiently accurate. Contamination from crucible materials is avoided by using synthetic substrates of the primary phase material. A range of metal substrates (Pt, Pd, Ir, Re, Rh/Pt, Au, Mo, W, Fe, Co, Ni, Cu) have also been used for specific systems and process conditions. Successful equilibrium experiments have been carried at temperatures up to 1740°C and now being extended to higher temperatures. In all cases, proof of equilibrium is established through the ‘4-point’ test that includes the following:

1. Changing the equilibration time to confirm that no further changes take place as the time is increased.
2. Confirming the chemical homogeneity of each of the phases.
3. Approaching equilibrium from different directions followed by analysis of the results.
4. Analysing possible reactions taking place during equilibration using available analytical techniques looking for possible signs of incomplete reaction pathways during equilibration.

SEM imaging and EPMA analysis of the trends of the compositions across the phases are particularly effective in this analysis.

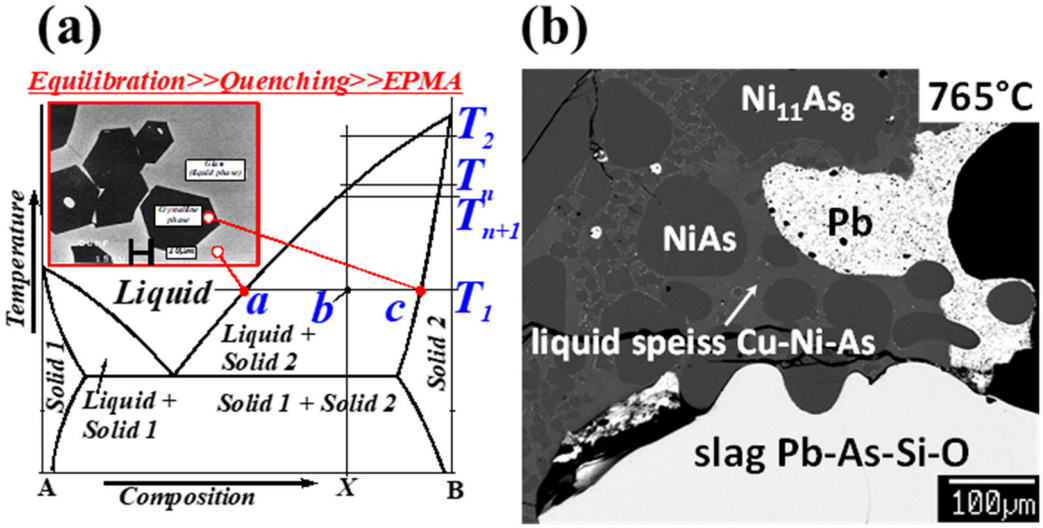

FIG 4 – (a) Illustration of the Pyrosearch approach to high temperature phase equilibria determination using equilibration-rapid quenching-microanalysis, enabling accurate measurement of phase compositions in multi-phase systems under defined process conditions, (b) An example of a complex multiphase, multicomponent system at equilibrium (Jak, 2018).

Overviews of the latest advances in the integrated experimental and modelling research approach to the thermodynamic database development for these pyrometallurgical systems are provided in Shevchenko, Shishin and Jak (2024). The use of these microanalysis techniques has provided breakthrough capabilities in phase equilibrium studies for pyrometallurgical applications, greatly extending the range of elements, bulk compositions and conditions that can be characterised and the accuracy achieved. Development and application of this experimental approach is the critical foundation of the overall research program.

Microanalytical techniques further developments

The availability of suitable analytical techniques is an important pre-requisite for obtaining: a) sufficiently abundant, and b) sufficiently accurate experimental data. The implementation of EPMA and LA-ICP-MS microanalytical techniques in the high-temperature phase equilibria has significantly expanded the range of measurable conditions and improved the accuracy of experimental data for phase equilibria studies. Therefore, the continuous development and refinement of these microanalytical methods is a crucial component of this research program. As an example of such advancements, the authors' experience with adapting and further improving these techniques is detailed below.

EPMA

The EPMA method involves the use of the electron microscope to both image the prepared cross-sections of the samples and simultaneously measure the compositions of the individual phases present. The impact of the electron beam on the samples results in the emission of X-rays characteristic of each of the elements present. Wavelength Dispersive Spectrometry (WDS) is used to select the wave lengths for particular elements for analysis. The measurement of intensities of the X-rays reflects the concentrations of the element present under the electron beam. Final analysis is obtained following corrections based on the overall matrix composition, for example, the ZAF correction where Z stands for the average atomic number, A – for absorption, and F – for fluorescence. The technique allows quantitative measurement of chemical compositions of both crystalline and amorphous phases on objects down to ~1 µm diameter. The region of interest is selected and navigated by scanning electron microscopy. EPMA also allows microanalysis of microcrystalline materials with non-zero diameter beam. Notwithstanding its superior spatial resolution, EPMA has often been perceived as reliable only for major elements with concentrations

>1 wt per cent. Recent advances in the EPMA instrumentation such as the field-emission electron gun, large-size diffraction crystals, and automation of aggregated intensity from multiple spectrometers (Donovan, Singer and Armstrong, 2016) have made it feasible to use EPMA to measure at least the more abundant trace elements (>100 ppm) on a regular basis.

Over the years, authors have developed a number of further custom improvements to this methodology for specific metallurgical applications.

One of the custom improvements are the analytical protocols to measure minor/trace elements in chemically complex phases (Chen *et al*, 2021). These protocols address major issues associated with trace element analysis by EPMA such as minimal detection limit (MDL), spectral interferences, beam damage and background correction to ensure the accuracy of the measurement.

The standard ZAF correction procedure was further improved. Systematic uncertainties of the standard ZAF correction were identified in many binary and ternary systems by measurement of the secondary standards – stoichiometric compounds existing within the system of interest, eg $PbSiO_3$, Zn_2SiO_4, Fe_2SiO_4, $Ca_2Fe_2O_5$, etc. The authors routinely synthesize and use stoichiometric compounds as secondary standards to monitor analytical uncertainties associated with the standard ZAF matrix correction parameters supplied with the commercial instruments. Improvement in analysis accuracy is achieved by applying further polynomial corrections to the measurement results (Shevchenko and Jak, 2017, 2018, 2019a, 2019b, 2021; Cheng *et al*, 2021; Khartcyzov *et al*, 2023). These corrections are specific for the same machine and standard procedures used, and allow back-correction of the data obtained in previous years before this ZAF correction bias was known. Alternative matrix correction parameters such as updated mass absorption coefficients (MACs) are also tested and applied where appropriate (Abdeyazdan *et al*, 2024).

Another potential issue affecting the analysis accuracy in multiphase systems is the Boundary secondary Fluorescence effect (BSF) – the element of interest was measured at a higher level than the true value when analysing a phase close to a boundary with another phase that contains a significantly higher level of the same element (Llovet *et al*, 2012). It was observed for transition elements (Cr, Mn, Fe, Co, Ni, Cu, Zn) in light element-rich phases (SiO_2, CaO, Al_2O_3) (Hidayat, Hayes and Jak, 2012; Hidayat *et al*, 2012; Xia, Liu and Taskinen, 2016; Hamuyuni, Klemettinen and Taskinen, 2016; Shevchenko and Jak, 2018), or when two neighbouring transition element-rich phases are adjacent to each other, such as over-estimated per cent Fe in metallic Cu surrounded by FeO-rich slag. The authors developed methods to first experimentally estimate the effect using cold-pressed minerals/materials then to apply correction to the unknown measurement results (Shevchenko and Jak, 2019d); in addition to that, authors demonstrated the effect could be minimised by measuring low energy < 5 keV characteristic lines (L lines of some of the transition metals, eg Cu, Zn) of element of interest (Shevchenko and Jak, 2021; Khartcyzov *et al*, 2023).

Focused Ion Beam – Scanning Electron Microscope (FIB-SEM)

An alternative approach to eliminate the secondary fluorescence effect at boundaries in quantitative X-ray microanalysis has recently been developed by the authors Chen *et al* (2024). Utilising FIB-SEM dual-beam system, the phase/features of interest with less than 10 µm size is physically extracted from the matrix and remount onto a suitable non-reactive substrate for subsequent EPMA analysis.

LA-ICP-MS

Originally developed for earth science research, Laser Ablation Inductively Coupled Plasma Mass Spectrometry has recently been adapted for use on the metallurgical systems for the quantitative analysis of trace/minor elements in solid materials (Avarmaa *et al*, 2015). This technique employs a focused laser beam to ablate a small portion of the sample, which is then ionised in an inductively coupled plasma and subjected to mass spectrometry for elemental identification and quantification. LA-ICP-MS offers significant advantages over EPMA, notably superior detection limits (down to ppb), enabling precise measurement of trace elements within targeted phases. Previous studies by the authors have showcased LA-ICP-MS's efficacy in accurately measuring trace elements in slag phases, contributing novel fundamental data and resolving discrepancies in literature regarding minor element distributions in non-ferrous melt smelting and converting processes. However, several

challenges have constrained the utility of LA-ICP-MS in metallurgy research. Primarily, its analytical precision heavily depends on the availability of matrix-matched standards, which are presently limited for sulfides and metals. Additionally, existing glass standards (eg NIST SRMs) lack certain elements crucial for metallurgical applications, notably the platinum group elements. Consequently, authors have dedicated ongoing efforts focused on developing in-house standards. The authors pioneered the creation of silicate glass standards encompassing all six platinum group elements, utilising an innovative high-temperature and high-pressure apparatus. Furthermore, the authors engineered copper alloy standards doped with various minor elements, specifically tailored for trace element analysis in copper metal via LA-ICP-MS (Chen, Jak and Misztela, 2023). Significant improvement in analysis accuracy has been demonstrated by Chen, Hayes and Jak (2024). In comparison to EPMA, LA-ICP-MS also suffers from inferior spatial resolution (>15 μm), posing challenges for measuring small features, particularly solids. To overcome this limitation, the authors are actively investigating new laser systems, such as femto-second laser systems, with the potential to enable analysis of features smaller than 5 μm. The downside to the use of LA-ICP-MS is that the material used for analysis is physically removed from the sample – the same area cannot be reanalysed as is the case with non-destructive EPMA analysis.

Speciation of multi-valent elements (eg Fe^{2+}/Fe^{3+})

The quantitative determination of multi-valent elements, particularly Fe^{2+}/Fe^{3+} in the slag phase, has long been crucial for thermodynamic modelling in pyrometallurgy. Traditional analysis methods involve wet-chemical titration, necessitating large quantities (over 1 g) of homogeneous slag material. Mossbauer Spectroscopy offers an alternative approach, requiring less material (~200 mg), but accurate quantification often entails complex spectra deconvolution and fitting, leading to potential ambiguities depending on the fitting methods utilised. Microanalysis techniques such as X-ray Absorption Near Edge Spectroscopy (commonly employing a synchrotron beam line) and the 'Flank Method' (utilising EPMA) have been developed to quantitatively measure Fe^{2+}/Fe^{3+} in specific geological materials, demonstrating good accuracy with the use of matrix-matching standards (Borfecchia *et al*, 2012; Hoefer and Brey, 2007). Currently, the authors are actively exploring these options for Fe^{2+}/Fe^{3+} measurement in slag and other oxide phases.

Further development of the microanalytical techniques is required: i) to extend the ranges of compositions that can be investigated, and ii) to further improve the accuracy of the measurements to meet for thermodynamic database development requirement for: a) sufficiently abundant, and b) sufficiently accurate data. More details are given in Chen, Hayes and Jak (2024).

Application of microanalytical techniques – new opportunities for high-temperature industrial R&D

As discussed above – implementation of the advanced thermodynamic modelling tools into industrial pyrometallurgical process control requires significantly more advanced characterisation of the actual processes to incorporate adequate calibration parameters to account for kinetic and other factors. The microanalytical techniques (EPMA, LA-ICP-MS) that became available relatively recently provide the capabilities to characterising heterogeneous processes responding to the new demands and created fresh possibilities to improve the characterisation of the industrial systems and thereby make further improvements to industrial practice and support implementation of the advanced models. Most of pyrometallurgical processes involve heterogeneous reactions taking place at microscopic scale at and around the phase interfaces. The microanalytical techniques EPMA and LA-ICP-MS enable advanced microstructural characterisation and accurate composition measurements minimum elemental detection limit down to ~300 ppm at spatial resolutions of approximately 0.5 to ~1–3 micron and down to ppb at spatial resolution of approximately 20 to 80 micron respectively. Microanalysis of industrial quenched samples provides an exceptional opportunity to characterise processes taking place in the reactors. Detailed analysis of the composition trends as microscopy scale of 10–30 micron from the phase boundaries and at larger scale across the quenched samples provides important information on the kinetic reactions taking place in the industrial process and therefore a basis for the incorporation of thermodynamic models to describe real industrial processes.

The examples of applications of microstructural analysis of industrial samples include: i) phase equilibria (melting etc), ii) reactions extents (eg Cu losses), iii) specific troubleshooting (eg freeze-lining, refractories, deposits).

The recent examples include the measurement of distribution of Co, Ni, Zn, Pb, Bi, Sn, As, Te, Se, Ga, In, and Ge in complex copper converting slags (Chen *et al*, 2021), analysis of iron sinter microstructure and their link to breakage characteristics (Cheng, Hayes and Jak, 2022), understanding the mechanism of refractory degradation in copper smelting (Fallah Mehrjardi *et al*, 2016), freeze-lining formation in non-ferrous applications (Fallah-Mehrjardi *et al*, 2014a, 2014b), investigation of reasons for the corrosion of steel walls in lead smelting (Watt *et al*, 2018), distribution of arsenic in industrial samples of nickel sulfide converting (Hidayat *et al*, 2017), conditions for the formation of spinels in nickel smelting and their effect on matte droplet settlement (Sineva *et al*, 2023).

Experimental data requirements and the importance of planning experiments

Effective planning of experimental and modelling components is a critical component for the program with large number of systems being investigated, large number of experiments performed, large number of research staff involved and with the large number of sponsors and users of the database. The following section presents further details on the planning derived by the authors from experience.

In case of the current Pyrosearch experience following up of the principle 'no experiments – no model parameters', the experimental component of the work takes approximately 75 per cent of resources and is a foundation of the overall program. The planning starts from the evaluation of the approximate number of possible experiments to be undertaken for a coming year for a given level of funding-each lead researcher in the team evaluates capabilities depending on experience as well as on the complexity of the system and commits to a particular number of successful experiments per week – this gives an approximate indication of a number of possible experiments and corresponding timing.

In order to prioritise the work to deliver more valuable outcomes, all elements in the overall multi-component system under investigation are divided into *major* elements (Me^{major}), *minor slagging* elements ($Me^{minor_slagging}$) and *minor other* elements ($Me^{minor\ other}$). The current program includes systematic phase equilibria studies of all low order 2- and 3- metal sub-systems from the major elements list, selected key multicomponent 4- and higher number of metals sub-systems from the major elements and slagging minor elements lists, all low order 2-metal sub-systems $Me^{minor\ other}$-Me^{major}, $Me^{minor\ slagging\ or\ other}$-$Me^{minor\ slagging}$ and 3-metal sub-systems $Me^{minor\ slagging\ or\ other}$-$Me_1^{major}$-$Me_2^{major}$, $Me^{minor\ other}$-Me^{major}-$Me^{minor_slagging}$, and minor elements distributions of elements between key phases (eg slag-metal, slag-matte, matte-metal). Transition from minor to major element list is done gradually after the all necessary major elements sub-systems have been characterised. For example, the current 20-component system at Pyrosearch has Me^{major} = Cu, Pb, Zn, Fe, Ca, Si, Al, Mg, S, O; $Me^{minor_slagging}$ =Cr, Na and Me^{minor} = As, Sn, Sb, Bi, Ag, Au, Ni, Co. Nickel Ni is included as a major element in matte/speiss/metal and selected oxide solid solution phases.

The following *key directions* are identified for the purpose of systematic planning: i) slag-solids (S-free) phase equilibria (with and without metal phase), ii) slag-matte or-sulfate (S-containing) equilibria (with and without metal phase), iii) matte-speiss-metal equilibria, and iv) and minor elements distributions of elements between key phases (eg slag-metal, slag-matte, matte-metal). The gaseous species equilibria are not currently in focus of the Pyrosearch program. Two types of experiments are performed – closed experiments undertaken in sealed ampoules for the slag/matte/metal, slag/metal and matte/metal systems; and open or semi-open experiments with the PO_2 and P_SO_2 in the gas/slag/matte and gas/slag/metal systems controlled by the $CO/CO_2/SO_2$ gas mixtures.

The techniques developed during this program for the first time enable the systematic accurate measurements of this kind to be undertaken, and these measurements provide an important foundation for the development of the thermodynamic database as well as for the overall quantitative description of the high-temperature thermochemistry. The total number of experiments needed to completely and quantitatively characterise the whole chemical system as functions of key operational parameters is very large and is increasing exponentially with further addition of new elements. The experimental needs therefore are carefully, critically and continuously reviewed.

The current criteria for priorities in selecting systems for further improvement are:

1. Importance for industrial sponsors.
2. Incorporation of all directions and elements.
3. Resolution of identified discrepancies in database predictions.
4. Finalising incomplete diagrams.
5. Prioritising possible, easy and high-success rate experiments.
6. Higher thermodynamic model parameters sensitivity/importance relative to the experimental accuracy.

Selection of experiments to be undertaken is facilitated by analysis of the sensitivity of the predicted values to the thermodynamic parameters relative to the achievable accuracy of experiments.

The issues indicated by the sponsors during the meetings are regularly summarised in a specific table, continuously reviewed and extended. In addition, to assess the accuracies of the databases at particular conditions relevant to the industrial practices, *systematic targeted programs on the laboratory-scale characterisation and modelling* of complex thermochemistry *of the key industrial processes of sponsors* are undertaken. This involves identifying/reconfirming chemistry of the main process streams and conditions, accurately characterising/reproducing complex industrial chemistry by undertaking series of experiments in the well-controlled laboratory conditions and analysing specially quenched industrial plant samples. The results are then used to analyse systematic uncertainties of the predictions against accurate and reliable data obtained in laboratory study and then to identify the needs and the ways for improvements of the models through the new targeted cycle of low order experiments and thermodynamic optimisations.

The integration of experimental and thermodynamic modelling studies helps to optimise the experimental program – to focus on what's needed and to minimise the overall number of experiments undertaken for the required accuracy of the thermodynamic predictions.

The actual program for the coming year is then developed based on the selected priorities and on the indication of a number of possible experiments indicated by the leading researchers.

The current focus of the research program of Pyrosearch is the 20-component development of the database for the system with the 'Cu_2O'-PbO-ZnO-FeO-Fe_2O_3-CaO-SiO_2-Al_2O_3-MgO-S major, Cr and Na slagging and As, Bi, Sn, Sb, Au, Ag, Ni, Co other minor elements containing gas, slag, sulfate, matte, speiss and metal alloy molten solution phases, 26 major oxide, sulfide and metallic solution phases such as spinel, melilites, olivines, pyroxenes and other, 79 solid solutions with limited ranges of solubility and over 380 oxide stoichiometric compounds.

In order to prepare an accurate description for all compositions and process conditions with the ten major elements following the criteria outlined above, the numbers of subsystems to be experimentally characterised is illustrated in Figure 5. The application of the priorities outlined above for the current list of major and minor elements, total 176 of binary and 694 ternary oxide sub-systems and several hundred more for the sulfates and matte/speiss/metal sub-systems are considered for experimental and further thermodynamic modelling characterisation.

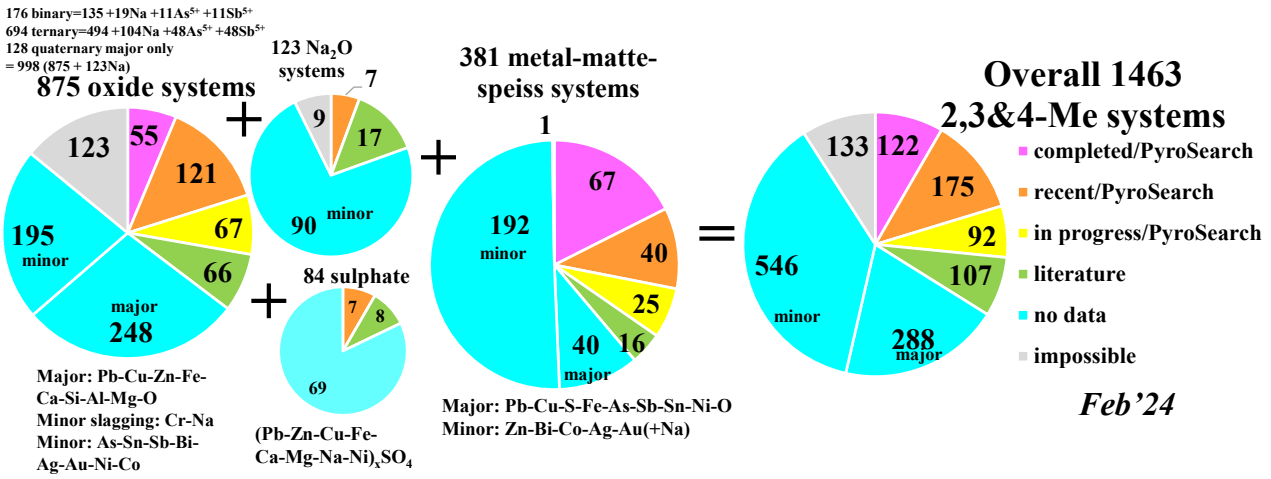

FIG 5 – Summary of chemical systems in 20-component system with 'Cu_2O'-PbO-ZnO-FeO-Fe_2O_3-CaO-SiO_2-Al_2O_3-MgO-S major, Cr and Na slagging and As, Bi, Sn, Sb, Au, Ag, Ni, Co, other minor elements and current status of database development.

Current experimental phase equilibria data status

Since early 1990s to date the Pyrosearch team has conducted ~20 000 experiments in 389 subsystems (122 completed, 175 studied at advanced level, and 92 in progress at initial level). Data from 107 systems are available in the literature, 133 systems are impossible to experimentally investigate using the current methodologies or they do not exist practically (eg Cu_2O-Fe_2O_3, FeO-SnO_2, Fe_2O_3-SnO). There are no measured phase equilibrium data on 288 major + 546 minor sub-systems. Pyrosearch team is currently undertaking approximately 1100–1300 successful experiments per annum in over >100 sub-systems.

Advanced thermodynamic optimisation methodology requirements and outline

Continuing re-optimisation of thermodynamic models using such significant number of experiments, management of the thermodynamic parameters and of experimental data is an important issue.

A major issue emerging in the *development* of multicomponent databases is the exponential increase in chemical interactions to be described with the increasing number of components. Adding a single component to a 20-component system results in the significant increase of the number of the sub-systems that require experimental and thermodynamic modelling characterisation from 171 to 190 binary and from 969 to 1140 ternary sub-systems. All types of experimental data from Cp's, enthalpies and entropies of endmembers and stoichiometric compounds to the multi-component phase equilibria data have to be described by the model simultaneously. Thus, any improvement in a given experimental value require fast and significant re-optimisation. Incorporating a new experimental data on a given binary sub-system into the database requires the iterative re-optimisation of all corresponding ~20 ternary and ~120 quaternary sub-systems – the so-called 'pyramid effect'. Experimental – thermodynamic modelling integration requires fast and frequent iterative re-optimisations, that in turn need continuous accumulation of optimisation results at each given stage for the use during the next iteration.

A semi-automated thermodynamic database development methodology has been developed and implemented to tackle these issues. The key points in this methodology are as follows. The sets of target experimental points to be described and corresponding weights are selected based on the experimental information available (note – not all available experimental data are included, and at the same time so called 'virtual' target points are included where no experiments are available). A matrix of first derivatives showing the sensitivity of each target point to each possible model parameter are calculated using traditional Gibbs energy minimisation calculations, which is a relatively slow step. Using the revised approach, the initial slow Gibbs energy minimisation calculations, are replaced by a fast analytical approach with linear extrapolation of the existing values through matrix multiplications of the form $\Delta\bar{y} = \boldsymbol{A} \cdot \Delta\bar{x}$, where A is the matrix of first-order derivatives

(n target values by k model parameters), $\Delta\bar{x} = \bar{x} - \bar{x}_0$ is the difference between the final set of model parameters and their initial approximation and $\Delta\bar{y} = \bar{y} - \bar{y}_0$ is the difference between the final model predictions and model predictions at $\bar{x}_0$. The optimum values of the model parameters $\bar{x}_{optimal}$ are then obtained by solving the relationship: $\bar{x}_{optimal} = \bar{x}_0 + \left(\mathbf{A}^T \cdot \mathbf{A}\right)^{-1} \cdot \mathbf{A}^T \cdot \left(\bar{y}_{\text{target}} - \bar{y}_0\right)$ for the condition $\bar{y} \to \bar{y}_{\text{target}}$. This non-iterative analytical (rather than numerical) optimisation approach is orders of magnitude faster than the combination of the thermodynamic calculations using Gibbs energy minimisation and numerical non-linear minimisation. The first derivative-based linear extrapolation approach enables immediate re-optimisation of model parameters for any single target or weight change. It also enables: a) the real-time graphical presentation of predicted and target points, as well as b) the real-time systematic tabular statistical analysis presentation of agreement between predictions and target values, which makes the optimisation process truly interactive. More details are given in Nekhoroshev *et al* (2024).

The accuracy of the database is analysed using a systematic set of graphical representations together with compact pivot tables across different primary phases/subsystems, including such information as average, min, max, temperature RMS + composition RMS, where RMS (root mean squares) are defined as a square root of average squared differences between target and predicted values.

The new formalised and semi-automated methodology makes it possible to increase the efficiency and flexibility of collaborative work between researchers by organising parallel simultaneous optimisations by several researchers, thus *distributing the database development intellectual efforts* between the research team members. Once formalised and semi-automated, the procedure can be used to optimise the model parameters by enabling each member of a group of researchers to contribute to the thermodynamic parameters optimisation by planning and undertaking new experiments, adding corresponding target points and correcting weights, rather than 'manually' optimising model parameters.

Thus, the discrepancies and conflicts within the system are resolved by the formalised semi-automated system significantly more efficiently and with less oversight. Only periodically the re-calculations using Gibbs energy minimisations are needed to update the matrix of derivatives. The new methodology enables researchers undertaking experimental work on a particular sub-system to personally contribute to the thermodynamic optimisation of that system and to select further experimental target points further increasing productivity. Optimisation is undertaken in iterative cycles, the major discrepancies are identified at each step, and new experiments are conducted to resolve discrepancies within time intervals from several days to several weeks rather than months and years using the more traditional approaches.

Outline of the thermodynamic database

The current 20-component database in focus includes the 'Cu_2O'-PbO-ZnO-FeO-Fe_2O_3-CaO-SiO_2-Al_2O_3-MgO-S major, Cr and Na slagging and As, Bi, Sn, Sb, Au, Ag, Ni, Co other minor elements in the gas, slag, sulfate, matte, speiss and metal alloy molten solution phases and many solid solution and stoichiometric phases. The database theoretically consists of 1540 binary and ternary oxide, 455 binary and ternary metal-matte-speiss, and several thousand quaternary systems as well as the systems including oxygen and sulfur together (oxygen in matte, sulfur in slag). Excluding systems of low importance (eg containing several minor elements together), there are currently considered 998 oxide binary, ternary and selected 4-component sub-systems (including 123 Na_2O-containing systems recently added), 381 metal-matte-speiss systems, 84 sulfate systems with the total of 1463 2-, 3-, and selected 4-metal component systems. The database includes over 450 stoichiometric compounds, >100 gaseous species, around 130 solution phases (among which there are 29 large solutions) with more than 3000 excess parameters. Most of compound and gaseous species have self-consistent CP functions over a wide range of temperatures, starting from 0 K and optimised S_{298} and ΔH_{298} values,. The largest liquid solutions in the system are Slag and Liquid Metal/Matte/Speiss, the latter being modelled as one thermodynamic solution with miscibility gaps. The Slag phase has 50 endmembers made up of 25 free metal cations (including Fe^{2+} and Fe^{3+}, Sn^{2+} and Sn^{4+}, As^{3+} and As^{5+}, Sb^{3+} and potentially Sb^{5+}, Cr^{2+} and Cr^{3+}, and two associates ($NaAl^{4+}$, $NaFe^{4+}$) multiplied by [O^{2-}

,S^{2-}] anions. There are 276 binary and 2024 ternary oxide systems in slag phase with around 990 excess parameters. Liquid Metal/Matte/Speiss solution consists of 20 endmembers on a single sublattice with over 730 interactions between them. A new liquid solution, Salt, has recently been introduced into the database, describing the interactions between molten sulfates, oxides, and arsenates. Currently, there are eight cations in the first sublattice and three anions in the second sublattice, making up 24 different end members with 33 interactions among them in the Salt solution model.

Most extensive solid solutions in the database are Spinel with 162 endmembers and 611 interaction parameters (some of them are identical for different combinations of elements in sublattices, though), Monoxide (12 endmembers, 74 interaction parameters), Melilite (63 endmembers, 23 interaction parameters), ortho- and clino-pyroxenes (36 and 75 endmembers, respectfully). Figure 6 provides a summary of the current Pyrosearch database.

Slag: (Cu^{+1}, Fe^{+2}, Fe^{+3}, Si^{+4}, Al^{+3}, Ca^{+2}, Mg^{+2}, Pb^{+2}, Zn^{+2}, Ni^{+2}, Co^{2+}, Sn^{+2}, Sn^{+4}, Sb^{+3}, As^{+3}, As^{+5}, Bi^{+3}, Ag^{+1}, Au^{+1}, Cr^{2+}, Cr^{3+}, Na^{+}, $AlNa^{+4}$, $FeNa^{+4}$)(O^{-2}, S^{-2}), MQM
Liquid matte/metal/speiss: (Cu^{I}, Cu^{II}, Fe^{II}, Fe^{III}, Pb^{II}, Zn^{II}, Ni^{II}, Sn^{II}, Sb^{III}, As^{III}, Bi^{III}, Ag^{I}, Au^{I}, Cr^{II}, Co^{II}, Ca^{II}, Mg^{II}, Na^{I+}, O^{II}, S^{II}), MQM
Liquid salt (Ca, Mg, Pb, Na, Zn, Fe, Cu, Ni)(SO_4, O, AsO_4, SiO_4), MQM
Spinel: [Cu^{+2}, Fe^{+2}, Fe^{+3}, Ni^{2+}, Al^{+3}, Mg^{+2}, Zn^{+2}, Cr^{2+}, Cr^{3+}, Co^{2+}, Co^{3+}]^{tet}
[Cu^{+2}, Fe^{+2}, Fe^{+3}, Ni^{2+}, Cr^{3+}, Al^{+3}, Ca^{+2}, Mg^{+2}, Zn^{+2}, Sn^{4+}, Co^{2+}, Co^{3+}, $Vacancy^{/2}$]$_2^{oct}O_4$, CEF
Monoxide: (FeO, $FeO_{1.5}$, NiO, CoO, $CrO_{1.5}$, $AlO_{1.5}$, CaO, MgO, CuO, ZnO, SnO_2, Na_2O), B-W
Corundum: ($FeO_{1.5}$, $AlO_{1.5}$, $CrO_{1.5}$, $SnO_{1.5}$), B-W
Mullite: (Al^{3+}, Fe^{3+}, Cr^{3+})$_2$(Al^{3+}, Sn^{4+}, Sn^{2+}, Si^{4+})(O^{-2}, $Vacancy^{/2}$)$_5$, CEF
Olivine: [Fe^{2+}, Ni^{2+}, Co^{2+}, Cr^{2+}, Ca^{2+}, Mg^{2+}, Zn^{2+}]^{M2}[Fe^{2+}, Ni^{2+}, Cr^{2+}, Co^{2+}, Ca^{2+}, Mg^{2+}, Zn^{2+}]$^{M1}SiO_4$, CEF
Melilite: [Ca^{2+}, Pb^{2+}, Na^{+}]$_2$[Al^{3+}, Zn^{2+}, Mg^{2+}, Fe^{2+}, Fe^{3+}, Ni^{2+}, Co^{2+}][Fe^{3+}, Al^{3+}, Si^{4+}]$_2O_7$, CEF
Pyroxenes (proto-, clino-, ortho-): [Fe^{2+}, Ca^{2+}, Mg^{2+}, Ni^{2+}, Zn^{2+}]^{M2}[Fe^{2+}, Fe^{3+}, Mg^{2+}, Al^{3+}, Ni^{2+}, Zn^{2+}]^{M1}[Fe^{3+}, Al^{3+}, Si^{4+}]$^{B}Si^{A}O_6$, CEF
Dicalcium silicates: (Ca_2SiO_4, Fe_2SiO_4, Mg_2SiO_4, Pb_2SiO_4, Zn_2SiO_4, Ni_2SiO_4, Co_2SiO_4, Sn_2SiO_4, CaO, $Ca_{1.5}AlO_3$, $Ca_{1.5}AsO_4$), B-W
Wollastonite, pseudowollastonite: ($CaSiO_3$, $FeSiO_3$, $MgSiO_3$, $ZnSiO_3$, $PbSiO_3$), B-W
SFCA: [CaO, FeO][Fe_2O_3, $CaSiO_3$, Va][Fe_2O_3,Al_2O_3]$_2$, CEF
Willemite: [Zn^{2+}, Fe^{2+}, Mg^{2+}, Ni^{2+}, Cu^{2+}][Zn^{2+}, Fe^{2+}, Mg^{2+},Ni^{2+}, Cu^{2+}]SiO_4, CEF
Feldspar: (Ca, Pb, Na, Va)[Al, Zn][Al, Si_3O_8, CEF
Zincite: (ZnO, FeO, Fe_2O_3, Al_2O_3, CaO, MgO, CuO, NiO, SnO_2, $Ca_2Fe_6Zn_6O_{17}$), B-W
Melanotekite: $Pb_2(Fe,Al)_2Si_2O_9$, B-W
Larsenite: Pb(Zn, Mg, Fe, Ni)SiO_4, CEF
Magnetoplumbite: (PbO,CaO)[Fe_2O_3,$PbFeO_2$,$PbZnO_2$,Al_2O_3][Fe_2O_3,Al_2O_3]$_5$, CEF
Delafossite: [Cu^{+}][Al^{3+}, Fe^{3+}, Cr^{3+}, Sn^{3+}]O_2, B-W
Fcc and bcc solids alloys: (Fe, Cu, Ni, Co, Cr, O, S, Pb, Zn, As, Sn, Sb, Bi, Ag, Au), B-W
Digenite-bornite: (Cu_2S, FeS, PbS, ZnS, Ni_2S, Ag_2S, $Vacancy_2S$), B-W
Villamaninite: (Cu, Ni, Fe)S_2, **Millerite** (NiS, CuS), B-W
Sphalerite, wurtzite (Zn, Fe)S
Pb-Ag-Au-Zn compounds and solutions
Pb-Ca-Mg-Bi compounds and solutions
MeS cubic: (FeS, PbS, CaS, MgS, Cu_2S, Vacancy, S), B-W
$(Cu, Ni)_7As_3$, B-W;
Cu_5As (solid speiss): (Cu^{I}, As^{III}, Ag^{I}, Au^{I}, Fe^{I}, Ni^{II}), MQMQA
ORTH [Fe, Ni][As, Sb, S]$_2$, CEF;
GAMM Cu_3X (Cu, Ni, Sb, Sn) MQMQA;
HEX MeX_(Fe,Ni,As, Sb, Sn, Cu), MQMQA
~450 solid Compounds and small solutions: sulfate, sulfide (FeAsS, Cu_3AsS_4), oxide, intermetallic, e.g. Ca_2Sb, Ca_5Sb_3, ZnSb, Sn_4Sb_3
Ideal gas: >150 species, including N_2, H_2O, CO, CO_2, SO_2, SO, As_2, AsS, AsO, Zn, ZnS, ZnO, AgS, Pb, PbS, PbO, Bi, Bi_2, BiO, BiS, Sn, SnO, SnS, Ag, AgO, AgS, Sb, Sb_2, SbO, SbS and more.

FIG 6 – Summary of phases in the current Pyrosearch database for the pyrometallurgical processing and the thermodynamic models used to describe these. MQM = Modified Quasichemical Model (Pelton *et al*, 2000; Pelton and Chartrand, 2001), CEF = Compound Energy Formalism (Hillert, 2001; Hidayat *et al*, 2015), B-W = Bragg-Williams ideal mixing model.

Current status of the thermodynamic database development

Recent accurate and abundant experimental measurements by Pyrosearch have provided sufficient data to identify and then rectify many significant systematic uncertainties in the previous thermodynamic database. These systematic uncertainties include thermodynamic descriptions of all liquid end-members as well as in the description of the silicate slag systems with the Modified Quasichemical model. The whole database therefore had to be fully revised starting from the properties of pure liquid endmembers such as SiO_2, CaO, MgO etc, key sub-systems such as CaO-SiO_2, FeO-Fe_2O_3-SiO_2 etc, and all other binary, ternary and higher order sub-systems. The

thermodynamic optimisation methodology developed at Pyrosearch had been critical to enable this significant task to be completed.

Brief outline of the major developments is given below.

Correcting the heat capacities of liquid end-members and of solid phases

Previous databases contained oversimplified descriptions of heat capacities of elements and compounds in which usually a single function of temperature is assigned to all phases of the same composition, ie all polymorphs and corresponding liquid (eg quartz, tridymite, cristobalite, and liquid/amorphous SiO_2). This approach does not accurately define the real experimental data on heat capacities of most phases. These over-simplified descriptions resulted in the step-like changes in heat capacities (and therefore entropies, enthalpies and Gibbs free energies) at melting points of the endmembers and corresponding uncertainties in the multicomponent solutions. Most importantly, the heat capacities of liquid solutions (slags) calculated from these liquid endmembers were typically 20–40 per cent higher than the real values for the range of temperatures relevant to industrial practices (700–1700°C). To compensate for these systematic uncertainties, artificial distortions to the interaction parameters between the liquid species were previously introduced thus significantly limiting the predictive power of the database; this becomes increasingly problematic with the increased solution complexity. These uncertainties have recently been corrected as one of the components of the major database revision, as shown in Figure 7. Also, heat capacities of all solid phases were revised to obtain physically relevant descriptions below the room temperature down to 0 K and at very high temperatures (above the melting point of solid endmembers) thus eliminating a number of erroneous predictions of liquid phase present at very low temperatures, solids at very high temperatures, and liquid miscibility gaps in the ranges of compositions and conditions where they are not actually observed.

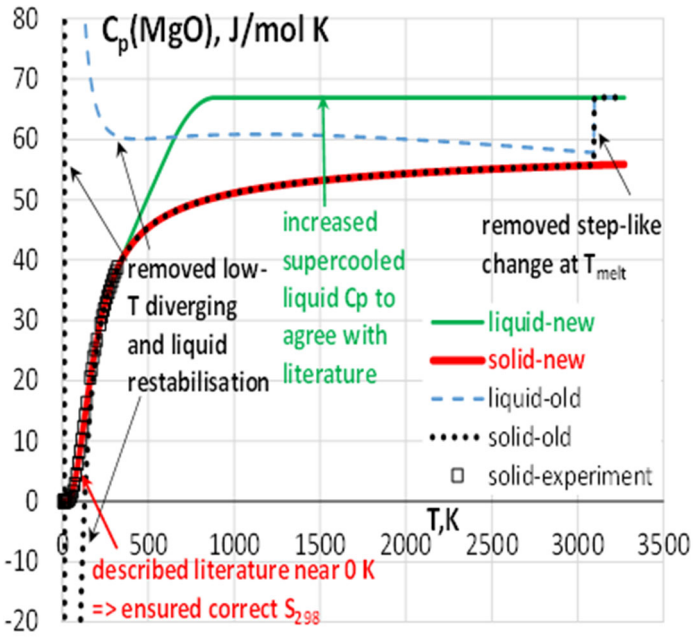

FIG 7 – Example of heat capacity versus temperature.

Gibbs free energies of solids at high temperatures

Extensive and accurate experimental results obtained by the Pyrosearch team at temperatures up to 1750°C have revealed significant uncertainties in the description of Gibbs free energies of high melting temperature of pure and binary compounds at higher temperatures (above 1750°C). The melting temperatures and enthalpies of several compounds (CaO, Ca_2SiO_4, Al_2O_3, MgO, SnO_2, Mg_2SiO_4, NiO etc) were corrected significantly. This correction, after overall major revision of the database, resulted in significant improvement of the description of phase equilibria in the temperature range important for industrial operations. For example, the melting temperature of SnO_2 in air was corrected from 1625°C to 2059°C (Shevchenko *et al*, 2021; Shevchenko, Shishin and Jak,

2024) that resulted in the improvement of the predictions of the cassiterite SnO_2 liquidus of 50–150°C for the range of temperatures relevant to industrial practice (700–1700°C).

Revising high-SiO_2 liquid

Accurate EPMA measurements of phase compositions and systematic high-temperature experiments in the high-SiO_2 areas recently performed by the Pyrosearch team have demonstrated that the currently used Quasi-chemical thermodynamic model of the SiO_2-containing liquids cannot accurately describe the experimental data in the areas of the tridymite/cristobalite liquidus, the monotectic and the miscibility gaps in a number of the Me-Si-O systems (Me = Ca, Mg, Fe^{2+}, Fe^{3+}, Zn, Cu, Ni, Co, Cr...). The reason for these systematic difficulties has been attributed to the fact that the Modified Quasichemical Formalism (MQM) only accounts for nearest neighbour interactions in the slag, assumed to be 100 per cent ionic liquid. The high-SiO_2 liquids, however, are not fully ionic (weak electrolytes), thus resulting in the long-range electrostatic interactions between the uncompensated charged M^{x+} cations and O^{2-} anions, an effect similar to the Debye-Hückel model and clustering well known to be present in dilute aqueous solutions. Identification and understanding of the underlying reasons for these behaviours provided the opportunity to adjust the models by: i) introducing a correction to the Gibbs energy of mixing (Figure 8) of the components in the form of a polynomial sequence so as to more closely simulate the long-distance ionic interactions (Debye-Hückel/clustering) in dilute MO_x solutions in SiO_2, that in turn enables ii) the minimisation or removal of the unrealistic temperature-dependent, excess entropy terms with high power on SiO_2 that were commonly used in previous optimisations for the binary systems and resulted in inaccurate extrapolation to the ternaries, and iii) making the entropy of mixing of the slag phase much closer to the ideal mixing limit in the experimentally determined immiscible regions. The introduction of these enthalpy and entropy of mixing corrections enabled the tridymite/cristobalite liquidus to be more accurately described in the key binary systems, such as 'FeO'-SiO_2, CaO-SiO_2, MgO-SiO_2, $CuO_{0.5}$-SiO_2, NiO-SiO_2. For example, these improvements enabled the elimination of the 2–5 wt per cent (~50–100°C) uncertainty in the prediction of the tridymite/cristobalite liquidus in the FeO-Fe_2O_3-CaO-SiO_2 system in reducing and oxidising conditions and thus significant improvement of the accuracy of the database. Introducing description of these long-range interactions also improved the description of the minor element distributions in multicomponent systems; it also allowed the use of smaller ternary parameters in the MO_x-$M'O_y$-SiO_2 systems, essentially treating them as near-ideal within the Quasichemical formalism. This approach was extended to all SiO_2-containing subsystems. This significantly improved the accuracy and predictive capability of the liquid slag model.

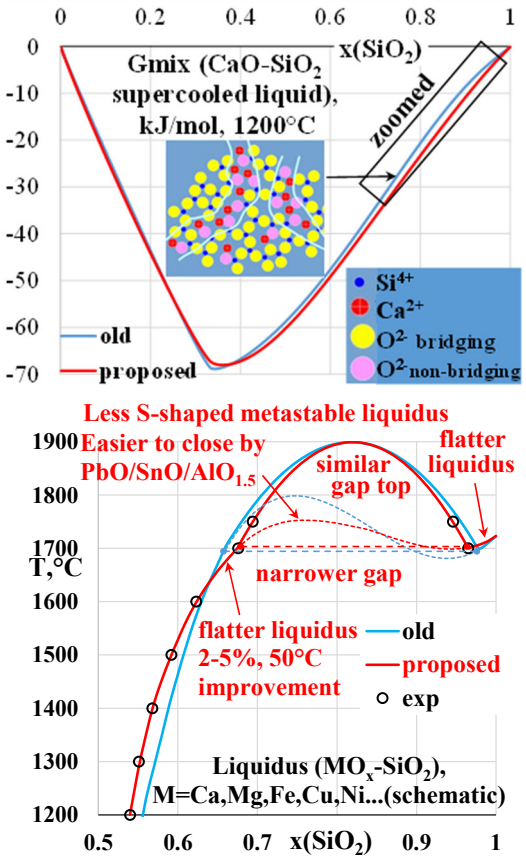

FIG 8 – Example of the correction of the high-SiO_2 slag model taking into account the different structure of the slags in high and low silica composition ranges.

Correcting the slag thermodynamic description around maximum ordering

The Modified Quasichemical Model (MQM) formalism adopts a one-dimensional solution (Ising model) as an approximate description of the correlation between the entropy of mixing and the strength of the second nearest bonds (the 3D solution of the Ising Model is not available). This 1D approximation works quite well for most systems, but in the cases of strong interactions the limitations of the 1D approximation can become significant, eg resulting in a sharp reversal in gradient at the minimum of the enthalpy/entropy of mixing and consequently of the Gibbs free energy of the slag (see Figure 8). For example, this sharp change means it was not possible using the MQM model alone to describe experimental data in the Ca_2SiO_4 primary phase field in the Fe_xO-CaO-SiO_2 system (Figure 9). The following approach was developed and implemented to rectify this issue: i) introduce a special polynomial sequence describing the enthalpy of mixing to reduce the 'sharpness' of the tip at the composition of maximum ordering, and ii) limit the configurational entropy of mixing to within ± 2 $J \cdot mol^{-1}$ K^{-1} based on the available statistical physics theory. Systematic corrections of the entropies of mixing for all relevant binary systems have been undertaken to improve the accuracy of the descriptions and predictions of the database (eg Figure 9).

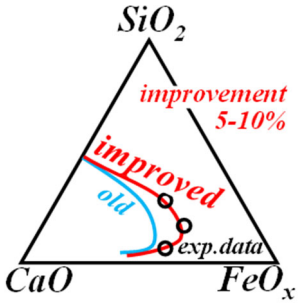

FIG 9 – Schematically shown Ca_2SiO_4 primary phase field in the CaO-FeO-Fe_2O_3 system at constant temperature.

Major revision of the whole thermodynamic database

Major revision of the whole (20 component) oxide database has been carried out a significant milestone that took substantial team efforts over several years; it included re-optimisation of ~250 subsystems using ~12 000 experimental phase equilibria points (including approximately ~10 000 experimental points by Pyrosearch) and significant number of other experimental thermodynamic data (Cp's etc), introduction of the new values for ~2500 thermodynamic parameters for 87 liquid and solid solution phases and ~700 stoichiometric solids. The new completely revised thermodynamic database forms an important basis for further developments.

Further more detailed discussions on thermodynamic optimisations are given in Shishin, Shevchenko and Jak (2024).

DEVELOPING THE TEAM

Multi-skilled team – critical factor for the strategic research program

Necessary components of the overall program of development of the thermodynamic database include application of the advanced theoretical models, development and application of appropriate sophisticated computational methodology, experimental methodology and analytical techniques as well as implementation of research results into industrial practice. Such program therefore requires a team with: i) high level expertise, ii) in different areas, and iii) of different levels (ie senior, intermediate and junior research academics, PhD students, qualified research assistants). The Pyrosearch current structure incorporates: i) five Theme leaders (advanced experts in high temperature experimentation, laboratory equipment and methods, analytical methods, thermodynamic optimisations and process modelling, and computational thermodynamics), ii) six Research Fellows; iii) seven to eight PhD and Masters students; iv) six well-trained continuing research assistants; v) seven casual undergraduate research assistants – current University metallurgy undergraduate students, and a few visitors. This is not a usual University group (many University groups have the majority of the research undertaken by PhD students). A strong continuing senior research academics core with the high level of expertise in different interrelated areas is the important factor. It is therefore critical to address the issues of continuity of the senior research academics within existing University system.

Industry support is critical for continuing research program

The long-term strategic research program requires continuing financial support, and industry therefore is a critical component providing long-term stability. *Continuous* implementation of the intermediate results into industrial practice is therefore a critical factor to ensure this study is *continuously* bringing the value to sponsors and thus helps to maintain the *continuing* financial support of the program. In the present research program this is achieved by: i) iterative, regular and frequent transfer of the intermediate thermodynamic database to sponsors, and ii) proactive implementation activity undertaken by the Pyrosearch staff.

The continuing focus on the industrial impact in turn guarantees the research is continuously directed at the practically important, priority industrial needs

The overall research program in case of Pyrosearch is organised through three consortia of industrial sponsors with common interests – Cu, Pb and Fe and slag recycling, where industry contributions are complemented by competitive government funds. The size of the overall program is beyond a capacity of a single industrial sponsor to support it. Pyrosearch important functions in this regard therefore are: i) to bring various industrial companies together into consortia and with common interests, and ii) obtain additional government and University support thus providing value to each individual industrial company.

Implementation of research outcomes into industrial practice is an important factor

The collaboration between the industry partners and Pyrosearch has enabled the development of a set of powerful predictive tools based on extensive experimental fundamental information, which can

be used to analyse a broad range of industrial systems independent of the technologies used. The collaborative program does not stop there – the important next step is implementation of these advanced tools and information into industrial practice. The tools can be used by companies to improve process efficiencies and productivities, optimise the utilisation of existing plant, predict changes to plant practice to adjust for changes in process feed compositions, design new processes or operations. It has been recognised and acknowledged that the successful implementation of the advanced tools and information into industrial practice requires adequate professional education and training in their use. This has been achieved through a variety of ways in collaboration with sponsor companies.

Upskilling of engineering professionals is achieved through providing:

- Dedicated courses in chemical thermodynamic theory, pyrometallurgy fundamentals and the application of FactSage tools to industrial problems, delivered by distance and in person.
- Extended visits, placements and secondments of engineers with the research team.
- Undertaking Research Masters and PhD studies at Pyrosearch.
- Undertaking one-on-one projects with the research team on industrial problems.

Significant progress has been achieved in this direction. For example, over the last few years over 160 engineers successfully completed an on-line Pyrometallurgy course, 182 completed in-person and on-line FactSage course, seven metallurgical engineers visited Pyrosearch for training or collaborative projects, ten Masters and PhD students from other local sponsor Universities did collaborative research in-person at Pyrosearch, four full time Pyrosearch UQ PhD students are now working in sponsor companies, 56 one-on-one focused industrial research projects were undertaken by Pyrosearch staff in collaboration with the sponsor's metallurgists.

The active collaborations between industry and the research team provide important opportunities to obtain high value from the capabilities of the predictive tools. Testing the tools against industrial practice provides: i) confidence in their potential for extended use in an industrial context – a critical factor in technology transfer, and ii) guidance in further research directions.

Metallurgical research-focused academics roles

Universities are viewed traditionally as institutions where knowledge is stored and passed on through teaching to the undergraduate and postgraduate students. Much less understood are other important roles played by the University academics; those with specialist knowledge in the metallurgical engineering can actively support the metallurgical industry in a number of other ways, by:

- Undertaking knowledge generation through fundamental and applied research.
- Developing and maintaining collaborative research links with industry.
- Attracting additional financial support for research from Government sources,.
- Developing research infrastructure within institutions, facilities that can be utilised to support industry related research.
- Facilitating communication and support relationships between the metallurgy industry and senior university management.
- Promoting the important role of the metallurgical industry to young people and the broader community.

In addition, by insuring the sustainability of strong research teams with specialist knowledge and expertise, University academics can:

- Develop and maintain industry consortia for research and education of common interest to sponsors.
- Actively assist in the optimisation of existing and development of new metallurgical processes.
- Ensure the successful implementation of research outcomes into industrial practice.

- Ensure the availability of expert capabilities and advanced technological for application to individual confidential R&D support.
- Facilitate active technological exchange and links between sponsors metallurgists and between sponsor-nominated Universities.
- Minimise the adverse impacts of periodic economic cycles on the retention of knowledge and expertise for the metallurgical industry.

Metallurgical undergraduate education – critical for future progress

Despite of the importance of metallurgical industry, the number of undergraduate students selecting studies in metallurgical engineering and the number of university programs offering educational opportunities in metallurgical engineering have been in decline for many years – this is a worldwide trend. There appear to be a number of contributing factors to this trend:

- Unfavourable public perceptions of the industry and lack of information on the role of metallurgy in our society.
- The lack of industry engagement and support in promoting studies and careers in the field.
- The funding formulae used by Government to support Universities, which are in the main based on the number of enrolments rather than industry or societal needs.
- University and Journal Ranking systems do not favour small specialist fields.

The lack of professionals in the field poses a significant threat to successfully implementing process improvements in existing operations and hinders the major changes needed for future economies. The public and students are increasingly aware of the impacts of climate change and the necessity of transforming our industrial practices to address these challenges. This shift in attitude presents an opportunity to reframe the narrative and public perception of the industry, shifting it from negative to positive. The dramatic shift towards electrification across all sectors – renewable energy, transportation, and electronic devices – has heightened awareness of the critical metals needed to enable these transitions. Additionally, there is a growing need for material conservation and increased metal recycling to minimise environmental impact, reduce energy consumption, and achieve circularity in the use of valuable, non-renewable resources. These are powerful messages the industry can leverage to explain how lead metallurgy plays a vital role in facilitating the recycling of critical, strategic, and precious metals.

Increasing public awareness of the key role of metallurgy is necessary but is not necessarily sufficient to attract students and graduates. The industry needs to be proactive in improving workplace environments and practices so that they are attractive to prospective students and engineers. Students are looking for opportunities where they feel they can make a positive contribution to the environment and are able to use the latest technologies to achieve this. Industry can take positive steps in attracting undergraduates in their early years at university when they have an opportunity to redirect their careers into the discipline, through for example, providing on-site experiences in the form of vacation work, plant visits and internships, financial support scholarships, professional development and social activities.

The allocation of university funding is for the most part determined by class size rather than strategic needs of industry or the country. Small classes for specialist courses are more likely to be removed from the curriculum, small programs are closed in the name of efficient use of limited financial resources. This is the pattern around the world – the only way to change the current trend and provide educational resources is for industry to be more proactive. Industry leaders need to inform university management and governments of the importance of the discipline and actively engage with and provide support to those institutions providing programs in metallurgical engineering.

We strongly believe there are opportunities to increase the number of metallurgy graduates if Industry, Universities and Governments are proactive and work collaboratively together to solve this problem to their mutual benefits.

University teaching- and research-focused academics potential important central role in triple academia-industry-government helix

The role of University academics in the research, education and implementation of the scientific advancements into industrial practice thus making real impact to the society is critical. University academics are in the centre of and are inherently connected to all stake-holders. University academics:

- by definition, are actual experts in a particular field
- have active links and knowledge of industry through research: a) at the applied R&D level, as well as b) at the industrial R&D management
- are in direct contact with the University management
- are in direct continuing contact and aware of the issues of the changing next generations of specialists
- and at the same time educate and directly influence the next generation of specialists
- and are in contact with the government policies and bodies through the research funding applications and schemes.

There is a great potential for more engagement of the University academics into the policy development and decision-making of the industry R&D and University management as well as government bodies.

EXTENDING THE METHODOLOGY

Thermodynamics and other physicochemical properties

An additional advantage of the use of structurally-based thermodynamic models, such as, the quasichemical formalism (QCF), is that they also provide important fundamental information about the behaviour of atoms within the materials. This information can be used to describe the physicochemical properties of the materials, for example, the viscosities of fluids (Kondratiev and Jak, 2005; Jak, 2009). Thermodynamic models are also critical to describe the viscosities of heterogeneous partly crystallised systems by predicting the proportion of solids and the composition of the remaining liquid phase (Kondratiev and Jak, 2001; Kondratiev, Jak and Hayes, 2002; Jak *et al*, 2003). Extending the thermodynamic computer database predictive capabilities to other slag physicochemical properties is an important development (Thibodeau, Gheribi and Jung, 2016a, 2016b; Kang and Chartrand, 2016; Smith *et al*, 2020; Kang, 2015).

Future needs in the high-temperature molten phases area

As outlined in the paper above, thermodynamic modelling: a) is the central and critical component in the mathematical description and further optimisation of the high-temperature industrial processes, b) has the required methodologies for the development of the accurate description of thermodynamic properties and of phase equilibria, c) has already progressed to the useful level of adequate prediction of high temperature processes, and at the same time d) has great further potential p close the gaps in knowledge. It is therefore an opinion of the authors that more efforts and resources should be invested into further experimental work and thermodynamic modelling, similar to the continuing program undertaken by Pyrosearch. International collaboration of various groups can facilitate faster overall progress.

Further potential exists in the wider use of the first principles (*ab-initio*) and molecular dynamic simulations in phenomenological modelling of the type presented by authors. Currently, these models do not allow accurate representation of complex solutions at high temperatures. However, they allow to find important reference points for the thermodynamic model, such as enthalpies of formation at 0 K and sometimes heat capacities as functions of T for individual pure compounds and endmembers, including those which were not studied experimentally due to their metastability. These theoretical predictions could become a valuable complement to the experimental techniques described above.

The incorporation of the thermodynamic modelling into description of the industrial processes with kinetics playing significant role is another challenge. Relatively long times (in some cases up to several seconds) are currently required for a thermodynamic calculation at a single condition in a multi-component multi-phase system. Kinetics modelling usually would require multiple thermodynamic calculations making the overall modelling critically slow for practical use. This issue may be and should be gradually solved using significantly more powerful computer capabilities as well as special computational approaches. Linear extrapolation using first derivatives outlined above in the thermodynamic optimisation section can be a useful approach in relation to this issue.

The incorporation of thermodynamic modelling into predictions and optimisations of complex multi-unit industrial flow sheets is another great opportunity and at the same significant challenge. Similarly to the kinetic modelling, the relatively long time (in some cases up to several seconds) required for a thermodynamic calculation at a single condition in a multi-component multi-phase system is a barrier for the implementation of thermodynamic modelling into flow-sheet packages such as ASPEN, SYSCAD, METSIM where multiple calculations are needed for numerical minimisation methods for flow sheets with recycling streams. Similar to the kinetic modelling, incorporation of thermodynamic models into the flow sheet modelling can be facilitated with the significantly more powerful computer capabilities as well as special computational approaches. Again, linear extrapolation using first derivatives outlined above in the thermodynamic optimisation section can be a useful approach in relation to this issue.

CONCLUDING STATEMENTS

The key messages to all groups of professionals is that the metallurgical and recycling industry needs complex computerised optimisation tools similar to the GPS systems now used widely. The development of such GPS-like systems in pyrometallurgy is now possible although the task is challenging. To achieve that- the following components are essential, the availability of: i) sufficiently abundant and sufficiently accurate experimental data (that in turn require analytical capabilities), ii) appropriate theoretical thermodynamic models, and iii) adequate computational capabilities. The development and implementation of the advanced fundamental information and advanced predictive tools requires long-term efforts of multi-skilled expert teams. To support such teams, the industry financial support and engagement as well as industrial implementation are essential. We believe that historically we are at the start of new digitalisation Pyro-GPS period. The tasks are significant, and the opportunities are significant. The risks not to progress in the direction of digitalisation are also significant.

The messages:

- to young researchers and metallurgists – the metallurgy field is important to the society.
- to industry R&D – more advanced information and tools are becoming available bringing more opportunities.
- to industry management – there are significant opportunities for improving efficiencies and profitability of the operations, pro-active research support is important, educated metallurgists are needed to convert opportunities into profits.
- to University management, government, broader community –metallurgy is important, and the risks not to act now and to miss those opportunities are high; it is important to maintain and expand metallurgy research and education.
- to metallurgy research academics – you can play a central role in the academia-industry-government triple helix.

Collaborative work of many specialists, many industrial companies and many research groups is critical – we are all part of the solution and we all can contribute to the solution.

ACKNOWLEDGEMENTS

The Pyrosearch team acknowledges the financial and technical support from:

- *Pb research industrial consortia* including Aurubis (Germany), Boliden (Sweden), Kazzinc Ltd, Glencore (Kazakhstan), Nyrstar (Australia), Peñoles (Mexico) and Umicore (Belgium).
- *Cu research industrial consortia* including Anglo American Platinum (South Africa), Aurubis (Germany), BHP Billiton Olympic Dam (Australia), Boliden (Sweden), Glencore Technology (Australia), Metso Outotec Oy (Finland), Peñoles (Mexico), RHI Magnesita (Austria), Rio Tinto Kennecott (USA) and Umicore (Belgium).
- *Fe and slag recycling research industrial consortia* including Aurubis AG (Germany), BHP Fe ore (Australia), Rio Tinto ore (Australia), SWERIM (Sweden) and Umicore (Belgium).
- Australian Research Council (ARC) Linkage program.
- US Defence program 'Materials Recovery Technology for Defense Supply Resiliency' and Gopher (USA).

Special acknowledgement to *Maurits Van Camp* (formerly from Umicore) for his immense input in this program – his legacy stays in this continuing program, in the significant impact it makes to the research and industry communities, and the overall society and in our memories.

REFERENCES

Abdeyazdan, H, Shevchenko, M, Chen, J, Hayes, P C and Jak, E, 2024. Phase equilibria in the ZnO-MgO-SiO_2 and PbO-ZnO-MgO-SiO_2 systems for characterizing MgO-based refractory - slag interactions, *J Eur Ceram Soc*, 44:510–531.

Andersson, J O, Helander, T, Hoglund, L, Shi, P and Sundman, B, 2002. Thermo-Calc and DICTRA, computational tools for materials science, *CALPHAD*, 26:273–312.

Avarmaa, K, O'Brien, H, Johto, H and Taskinen, P, 2015. Equilibrium Distribution of Precious Metals Between Slag and Copper Matte at 1250–1350ºC, *J Sustain Metall*, 1:216–228.

Bale, C W, Belisle, E, Chartrand, P, Decterov, S A, Eriksson, G, Gheribi, A E, Hack, K, Jung, I H, Kang, Y B, Melancon, J, Pelton, A D, Petersen, S, Robelin, C, Sangster, J, Spencer, P and Van Ende, M A, 2016. FactSage thermochemical software and databases, 2010–2016, *CALPHAD*, 54:35–53.

Borfecchia, E, Mino, L, Gianolio, D, Groppo, C, Malaspina, N, Martinez-Criado, G, Sans, J A, Poli, S, Castelli, D and Lamberti, C, 2012. Iron oxidation state in garnet from a subduction setting: a micro-XANES and electron microprobe (flank method) comparative study, *J Anal At Spectrom*, 27:1725–1733.

Chartrand, P and Pelton, A D, 2000. On the Choice of Geometric Thermodynamic Models, *J Phase Equilib*, 21:141–147.

Chartrand, P and Pelton, A D, 2001. The Modified Quasichemical Model, III - Two Sublattices, *Metall Mater Trans A*, 32:1397–1407.

Chen, C, 2015. Application of MPE Model to Iron Ore Sintering, Ironmaking and Steelmaking Processes, *Steel Res Int*, 86:612–618.

Chen, C, Zhang, L and Jahanshahi, S, 2013. Application of MPE model to direct-to-blister flash smelting and deportment of minor elements, in *Proceedings of Copper 2013*, pp 857–871.

Chen, J, Diao, H, O'Neil, Hugh and Jak, E, 2024. A novel method for minimizing the boundary secondary fluorescence in X-ray microanalysis by FIB-SEM, Unpublished material.

Chen, J, Fallah-Mehrjardi, A, Specht, A and O'Neill, H S C, 2021. Measurement of Minor Element Distributions in Complex Copper Converting Slags Using Quantitative Microanalysis Techniques, *JOM*.

Chen, J, Hayes, P C and Jak, E, 2024. Chemical- and micro-analytical techniques for molten slags, mattes, speisses and alloys, in *Proceedings of the 12th International Conference on Molten Slags, Fluxes and Salts (MOLTEN 2024)*, pp 321–334 (The Australasian Institute of Mining and Metallurgy: Melbourne).

Chen, J, Jak, E and Misztela, M, 2023. Development of Cu-based Reference Materials for Laser Ablation ICP-MS, The 27th Australian Conference on Microscopy and Microanalysis, Perth, Australia.

Cheng, S, Hayes, P C and Jak, E, 2022. Iron Ore Sinter Macro- and Micro-Structures and Their Relationships to Breakage Characteristics, *Minerals*, 12.

Cheng, S, Shevchenko, M, Hayes, P C and Jak, E, 2021. Experimental Phase Equilibria Studies in the FeO-Fe_2O_3-CaO-SiO_2 System and the Subsystems CaO-SiO_2, FeO-Fe_2O_3-SiO_2 in Air, *Metall Mater Trans B*, 52:1891–1914.

Decterov, S A, 2018. Thermodynamic database for multicomponent oxide systems, *Chimica Techno Acta*, 5:16–48.

Donovan, J, Singer, J and Armstrong, J, 2016. A new EPMA method for fast trace element analysis in simple matrices, *American Mineralogist*, 101:1839–1853.

Fallah Mehrjardi, A, Hayes, P C, Azekenov, T, Ushkov, L and Jak, E, 2016. Phase Chemistry Study of The Interactions Between Slag and Refractory in Coppermaking Processes, in *Advances in Molten Slags, Fluxes and Salts: Proceedings of the 10th Int Conf on Molten Slags, Fluxes and Salts 2016* (eds: R G Reddy, P Chaubal, P C Pistorius and U Pal), pp 1071–1076 (Springer International Publishing).

Fallah-Mehrjardi, A, Hayes, P C, Vervynckt, S and Jak, E, 2014a. Investigation of Freeze-Linings in a Nonferrous Industrial Slag, *Metall Mater Trans B*, 45:850–863.

Fallah-Mehrjardi, A, Jansson, J, Taskinen, P, Hayes, P C and Jak, E, 2014b. Investigation of the Freeze-Lining Formed in an Industrial Copper Converting Calcium Ferrite Slag, *Metall Mater Trans B*, 45:864–874.

Frisk, K and Selleby, M, 2001. The Compound Energy Formalism: Applications, *J Alloys Compd*, 320:177–188.

Gisby, J, Taskinen, P, Pihlasalo, J, Li, Z, Tyrer, M, Pearce, J, Avarmaa, K, Bjorklund, P, Davies, H, Korpi, M, Martin, S, Pesonen, L and Robinson, J, 2017. MTDATA and the Prediction of Phase Equilibria in Oxide Systems: 30 Years of Industrial Collaboration, *Metall Mater Trans B*, 48:91–98.

Hamuyuni, J, Klemettinen, L and Taskinen, P, 2016. Experimental phase equilibrium data of the system Cu-O-CaO-Al_2O_3 at copper saturation, *CALPHAD*, 55:199–207.

Hidayat, T, Hayes, P C and Jak, E, 2012. Experimental Study of Ferrous Calcium Silicate Slags: Phase Equilibria at Between 10^{-8} atm and 10^{-9} atm, *Metall Mater Trans B*, 43:27–38.

Hidayat, T, Henao, H M, Hayes, P C and Jak, E, 2012. Phase Equilibria Studies of the Cu-Fe-O-Si System in Equilibrium with Air and with Metallic Copper, *Metall Mater Trans B*, 43:1034–1045.

Hidayat, T, Shishin, D, Grimsey, D, Hayes, P and Jak, E, 2017. The Integration of Plant Sample Analysis, Laboratory Studies and Thermodynamic Modeling to Predict Slag-Matte Equilibria in Nickel Sulfide Converting, *Metall Mater Trans B*, 49:132–145.

Hidayat, T, Shishin, D, Jak, E and Decterov, S, 2015. Thermodynamic Reevaluation of the Fe-O System, *CALPHAD*, 48:131–144.

Hillert, M, 2001. The Compound Energy Formalism, *J Alloys Compd*, 320:161–176.

Hillert, M, Kjellqvist, L, Mao, H, Selleby, M and Sundman, B, 2009. Parameters in the compound energy formalism for ionic systems, *CALPHAD*, 33:227–232.

Hoefer, H E and Brey, G P, 2007. The iron oxidation state of garnet by electron microprobe: its determination with the flank method combined with major-element analysis, *Am Mineral*, 92:873–885.

Jak, E, 2009. Viscosity model for slags in the Al_2O_3-CaO-'FeO'-K_2O-Na_2O-MgO-SiO_2 system. in *Molten slags and salts 2009*, pp 434–448.

Jak, E, 2012. Integrated experimental and thermodynamic modelling research methodology for metallurgical slags with examples in the copper production field, in Ninth Intl Conf on Molten Slags, Fluxes and Salts (The Chinese Society for Metals).

Jak, E, 2018. Modelling Metallurgical Furnaces—Making the Most of Modern Research and Development Techniques, in *Extraction 2018* (eds: B Davis, M Moats and S Wang), pp 103–125 (Springer).

Jak, E, Hayes, P C and Lee, H-G, 1995. Improved methodologies for the determination of high temperature phase equilibria, *Korean Journal of Minerals and Materials Institute (Seoul),* 1:1–8.

Jak, E, Kondratiev, A, Christie, S and Hayes, P C, 2003. The prediction and representation of phase equilibria and physicochemical properties in complex slag systems, *Metallurgical and Materials Transactions B,* 34:595–603.

Jung, I-H and Van Ende, M-A, 2020. Computational Thermodynamic Calculations: FactSage from CALPHAD Thermodynamic Database to Virtual Process Simulation, *Metall Mater Trans B*, 51:1851–1874.

Kang, Y-B and Chartrand, P, 2016. Calculation of property diagram as a Zero-Phase Fraction line of auxiliary phase, *CALPHAD*, 55:69–75.

Kang, Y-B, 2015. Relationship between surface tension and Gibbs energy and application of Constrained Gibbs Energy Minimization, *CALPHAD*, 50:23–31.

Khartcyzov, G, Shevchenko, M, Cheng, S, Hayes, P C and Jak, E, 2023. Experimental phase equilibria study and thermodynamic modelling of the $CuO_{0.5}$-$AlO_{1.5}$-SiO_2 ternary system in equilibrium with metallic copper, *Ceram Int*, 49:11513–11528.

Kondratiev, A and Jak, E, 2001. Modeling of Viscosities of the Partly Crystallized Slags in the Al_2O_3-CaO-"FeO"-SiO_2 System, *Metall Mater Trans B*, 32B:1027–1032.

Kondratiev, A and Jak, E, 2005. A Quasi-Chemical Viscosity Model for Fully Liquid Slags in the Al_2O_3-CaO-'FeO'-SiO_2 System, *Metall Trans B*, 36B:623–638.

Kondratiev, A, Jak, E and Hayes, P C, 2002. Predicting slag viscosities in metallurgical systems, *JOM*, 54:41–45.

Koukkari, P, Penttila, K, Hack, K and Petersen, S, 2000. ChemSheet - an efficient worksheet tool for thermodynamic process simulation, *EUROMAT 99, Biann Meet Fed Eur Mater Soc (FEMS)*, 3:323–330.

Llovet, X, Pinard, P T, Donovan, J J and Salvat, F, 2012. Secondary fluorescence in electron probe microanalysis of material couples, *J Phys D Appl Phys*, 45:225301/1–225301/12.

Nekhoroshev, E, Shishin, D, Shevchenko, M and Jak, E, 2024. Continuous method of thermodynamic optimisation using first-derivative matrices for large multicomponent systems, in *Proceedings of the 12th International Conference on Molten Slags, Fluxes and Salts (MOLTEN 2024)*, pp 901–914 (The Australasian Institute of Mining and Metallurgy: Melbourne).

Nikolic, S, Shishin, D, Hayes, P C and Jak, E, 2018. Case study on the application of research to operations - calcium ferrite slags, in *Extraction 2018* (ed: B Davis) (Springer: Cham).

Pelton, A D and Blander, M, 1986. Thermodynamic Analysis of Ordered Liquid Solutions by a Modified Quasi-Chemical Approach, Application to Silicate Slags, *Metall Trans B*, 17B:805–815.

Pelton, A D and Chartrand, P, 2001. The Modified Quasichemical Model, II - Multicomponent Solutions, *Metall Mater Trans A*, 32:1355–1360.

Pelton, A D, 2001. A General Geometric Thermodynamic Model for Multicomponent Solutions, *CALPHAD*, 25:319–328.

Pelton, A D, Chartrand, P and Eriksson, G, 2001. The modified Quasichemical Model, IV - Two Sublattice Quadruplet Approximation, *Metall Mater Trans A*, 32:1409–1415.

Pelton, A D, Decterov, S A, Eriksson, G, Robelin, C and Dessureault, Y, 2000. The Modified Quasichemical Model, I - Binary Solutions, *Metall Mater Trans B*, 31:651–659.

Petersen, S and Hack, K, 2007. The thermochemistry library ChemApp and its applications, *Int J Mater Res*, 98:935–945.

Petersen, S, Hack, K, Monheim, P and Pickartz, U, 2007. SimuSage - the component library for rapid process modeling and its applications, *Int J Mater Res*, 98:946–953.

Shevchenko, M and Jak, E, 2017. Experimental Phase Equilibria Studies of the PbO-SiO_2 System, *J Am Ceram Soc*, 101:458–471.

Shevchenko, M and Jak, E, 2018. Experimental Liquidus Studies of the Pb-Fe-Si-O System in Equilibrium with Metallic Pb, *Metall Mater Trans B*, 49:159–180.

Shevchenko, M and Jak, E, 2019a. Experimental Liquidus Studies of the Binary Pb-Cu-O and Ternary Pb-Cu-Si-O Systems in Equilibrium with Metallic Pb-Cu Alloys, *J Phase Equilib Diff*, 40:671–685.

Shevchenko, M and Jak, E, 2019b. Experimental Liquidus Studies of the Pb-Fe-Ca-O System in air, *J Phase Equilib Diff*, 40:128–137.

Shevchenko, M and Jak, E, 2019c. Experimental Liquidus Studies of the Pb-Fe-Si-O System in air, *J Phase Equilib Diff*, 40:319–355.

Shevchenko, M and Jak, E, 2019d. Experimental Liquidus Studies of the Zn-Fe-Si-O System in air, *IJMR (International Journal of Materials Research)*, 110:600–607.

Shevchenko, M and Jak, E, 2021. Integrated experimental phase equilibria study and thermodynamic modelling of the binary ZnO-Al_2O_3, ZnO-SiO_2, Al_2O_3-SiO_2 and ternary ZnO-Al_2O_3-SiO_2 systems, *Ceramics International*, 47:20974–20991.

Shevchenko, M, Ilyushechkin, A, Abdeyazdan, H and Jak, E, 2021. Integrated experimental phase equilibria study and thermodynamic modelling of the PbO-SnO-SnO_2-SiO_2 system in air and in equilibrium with Pb-Sn metal, *J Alloys Compd*, 888:161402.

Shevchenko, M, Shishin, D and Jak, E, 2024. Advancement in experimental methodologies to produce phase equilibria and thermodynamic data in multicomponent systems, in *Proceedings of the 12th International Conference on Molten Slags, Fluxes and Salts (MOLTEN 2024)*, pp 531–558 (The Australasian Institute of Mining and Metallurgy: Melbourne).

Shishin, D and Jak, E, 2018. Critical assessment and thermodynamic modeling of the Cu-As system, *CALPHAD*, 60:134–143.

Shishin, D, Shevchenko, M and Jak, E, 2024. Challenges and limitations in development of large thermodynamic databases for multiple molten phases using the Modified Quasichemical Formalism, in *Proceedings of the 12th International Conference on Molten Slags, Fluxes and Salts (MOLTEN 2024)*, pp 931–948 (The Australasian Institute of Mining and Metallurgy: Melbourne).

Sineva, S, Shishin, D, Prostakova, V, Fallah-Mehrjardi, A and Jak, E, 2023. Experimental Study and Thermodynamic Analysis of High-temperature Processing of mixed Ni-Cu sulfide feed, The 62nd Annual Conference of Metallurgists: COM 2023 (MetSoc of CIM).

Smith, A L, Capelli, E, Konings, R J M and Gheribi, A E, 2020. A new approach for coupled modelling of the structural and thermo-physical properties of molten salts, Case of a polymeric liquid LiF-BeF_2, *J Mol Liq*, 299:112165.

Thibodeau, E, Gheribi, A E and Jung, I-H, 2016a. A Structural Molar Volume Model for Oxide Melts Part I: Li_2O-Na_2O-K_2O-MgO-CaO-MnO-PbO-Al_2O_3-SiO_2 Melts-Binary Systems, *Metall Mater Trans B*, 47:1147–1164.

Thibodeau, E, Gheribi, A E and Jung, I-H, 2016b. A Structural Molar Volume Model for Oxide Melts Part II: Li_2O-Na_2O-K_2O-MgO-CaO-MnO-PbO-Al_2O_3-SiO_2 Melts-Ternary and Multicomponent Systems, *Metall Mater Trans B*, 47:1165–1186.

Watt, W, Hidayat, T, Shishin, D and Jak, E, 2018. Advanced Thermochemical Fundamental and Applied Research to Improve Integrity of the Steel Water Jacketed Furnace at Port Pirie, in *Extraction 2018*.

Wen, X, Shevchenko, M, Nekhoroshev, E and Jak, E, 2023. Phase equilibria and thermodynamic modelling of the PbO–ZnO-$CuO_{0.5}$-SiO_2 system, *Ceram Int.*

Xia, L, Liu, Z and Taskinen, P A, 2016. Equilibrium study of the Cu-O-SiO_2 system at various oxygen partial pressures, *J Chem Thermodyn*, 98:126–134.

Genetic design of personalised slag for manufacturing die steel via electroslag remelting method and an industrial application case

DOI: 10.62053/ZDHS3978

Z H Jiang[1], Y M Li[2], J L Tian[3] and J W Dong[4]

1. Professor, Northeastern University, Shenyang 110819, China. Email: jiangzh@smm.neu.edu.cn
2. PhD candidate, Northeastern University, Shenyang 110819, China. Email: 15984327096@163.com
3. Associate Professor, Northeastern University, Shenyang 110819, China. Email: neujialong@163.com
4. PhD candidate, Northeastern University, Shenyang 110819, China. Email: neuemta@163.com

ABSTRACT

Electroslag remelting is widely used to produce various special steels, mainly because of its ability to provide high cleanliness and excellent homogeneity of ingot. Undoubtedly an optimal slag plays a key role in removing inclusions and enhancing the mechanical properties of a specific special steel. In order to improve the metallurgical performance of the slag in electroslag refining of die steel, a variety of slags have already been developed using traditional trial-and-error methods. Nonetheless, these slags may not be inherently optimal for the specific requirements of actual die steel refining processes. In this work, we have designed a CaF_2-CaO-Al_2O_3-SiO_2-MgO quinary slag system using genetic algorithms method aiming to remove the existing large size inclusions (D and Ds type) in high quality die steel. The comprehensive effects of five components (CaF_2, CaO, Al_2O_3, SiO_2 and MgO) were studied based on existing fundamental theory. The slag composition was screened considering the parameters such as melting point, electrical conductivity, calcium ion concentration, and appropriate viscosity etc. Furthermore, the candidate optimal slag was applied in the industrial production of die steel by electroslag remelting method. The detection results indicate that majority large inclusions (D and Ds type) have been successfully removed, showing significant advantage to traditional slags. This result has demonstrated the genetic method to be efficient and reliable. In addition, depending on the personalised demand of other steel and alloys, this method allows for the adjustment of the screening frameworks and processes to develop the candidate optimal slags. This method has not been reported previously in the field of electroslag composition design, and compared with the traditional trial-and-error method, the new method will save a lot of time and experimental costs.

INTRODUCTION

In steel production, the presence of non-metallic inclusions often results in the formation of micropores and cracks, initiating fatigue fracture and structural defects (Sabih, Wanjara and Nemes, 2005). To counteract this, the electroslag remelting (ESR) process is employed to achieve a uniform composition, structural densification, and the removal of inclusions, thereby increasing steel purity and quality (Jiang *et al*, 2023). In the ESR process, the role of slag is critically important, acting as a decisive factor in determining the quality of electroslag ingots (Sebastian and Bernd, 2015; Shi *et al*, 2015; Shi, 2020). Consequently, precise design and control of the slag composition are essential.

Traditionally, the design of slag composition relies on an empirical trial-and-error approach. While practical, this method can be time-consuming and may not yield optimal results, necessitating a more systematic and scientifically grounded strategy (Dong, Jang and Yu, 2016; Dong *et al*, 2014). In response to the diverse metallurgical requirements in the ESR process, modern slags have transcended traditional constituents such as CaF_2 and Al_2O_3 (Schneider *et al*, 2019; Sebastian and Bernd, 2015) and specific quantities of CaO, MgO, and SiO_2 have been incorporated. The concentrations of slag components could vary widely to meet the specific requirements of different steel categories (Sebastian and Bernd, 2015; Duan, 2020; Ju *et al*, 2020). The typical composition of CaF_2–CaO–Al_2O_3-based ESR slag includes 40 per cent–70 per cent CaF_2, 0 per cent–40 per cent CaO, and 20 per cent–40 per cent Al_2O_3, with small amounts of SiO_2 and MgO (Ju, Gu and Zhang, 2021; Wan *et al*, 2022).

In material design field, genetic algorithms have been extensively utilised (Campbell and Olson, 2000; Xu, del Castillo and van der Zwaag, 2009). This study pioneers genetic algorithms for optimising slag composition, a previously unexplored technique in slag composition design. Both considering the ESR ingots' metallurgical quality and surface quality, the slag's physical and chemical characteristics including melting point, viscosity, electrical conductivity, basicity, density, and ion/molecule concentrations have been identified as the slag system's crucial parameters ('genes'), leveraging genetic algorithms to select superior slag compositions.

In the conventional trial-and-error approach, optimising slag compositions is restricted to minor adjustments, typically limited to a few percentage points from the original composition. This method limits the number of experiments and frequently yields suboptimal outcomes. However, the application of genetic algorithms allows for a significantly broader range of variation for each component in the slag based on years of production experience. This approach, generating an extensive data set, considerably enhances the likelihood of identifying the optimal composition window in the new generation of slag compositions. Moreover, this approach can save time and material costs compared to conventional trial-and-error methods.

This novel slag design approach has been applied in the die steel production. When using traditional ANF-6 slag, excessive D and Ds inclusions in 1.2343 die steel were usually detected. The D and Ds inclusions are mainly composed of $CaO–Al_2O_3$ or $CaO–MgO–Al_2O_3$. These inclusions are challenging to remove during electroslag remelting and lead to minute point-like formations in ingots (Guo *et al*, 2021), detrimentally affecting the steel's plasticity, toughness, fatigue resistance, workability, and specific physical properties (Ragnarsson and Sichen, 2009). This work employs genetic algorithms for slag design, successfully developing a new slag used for manufacturing high cleanliness 1.2343 die steel. The newly developed slag preserves the surface quality of the ESR ingot and effectively mitigates the issue of excessive D and Ds inclusions.

METHODS

First, we created a comprehensive database incorporating all possible combinations of slag compositions. This study identified six physicochemical properties—density, melting point, electrical conductivity, optical basicity, viscosity, and ion/molecule concentration—as key parameters ('genes') of the slag system. Subsequently, genetic algorithms are utilised to determine slag compositions exhibiting superior performance. For instance, the calcium ion 'gene' activity is adjusted to mitigate excessive D and Ds inclusions in 1.2343 die steel. Figure 1 shows the process of the genetic algorithm employed to screen the slag composition.

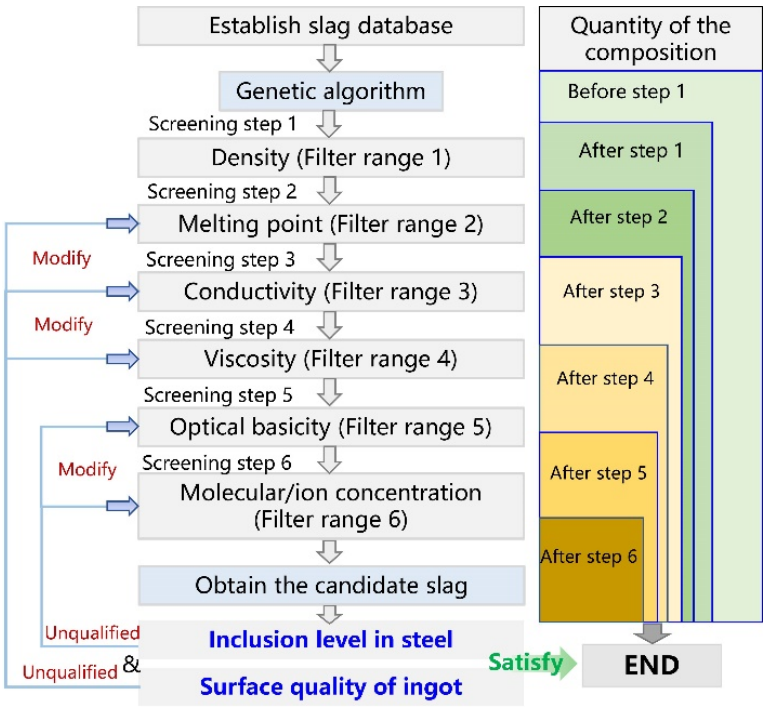

FIG 1 – Genetic algorithm employed in the selection of slag composition.

Establishment of slag composition combinations

Relying on extensive theoretical and practical experience, this study sets specific variation ranges for every component in the quinary slag system, as detailed in Table 1, to streamline calculations (Ju, Gu and Zhang, 2021; Duan, 2020; Wan *et al*, 2022; Dong, 2007). Employing a 1 per cent step increment for component variation, Python programming generated a total of 138 347 unique combinations.

TABLE 1

Concentration ranges for all components utilised in the optimisation (in weight fraction).

	CaO	SiO_2	Al_2O_3	MgO	CaF_2
Min	0	0	20	0	30
Max	40	15	40	15	70

Prediction of physical parameters of slag

Prediction of density of slag

The density of various slag compositions could be obtained based on the following empirical formula (Jang *et al*, 2015):

$$\frac{100}{\rho}=0.416m(SiO_2)+0.303m(CaO)+0.372m(MgO)+0.328m(Al_2O_3)+0.389m(CaF_2) \quad (1)$$

where m(i) represents the mass of substance i in 100 g of slag, expressed in grams, and the unit for density is grams per cubic centimetre (g/cm^3).

Prediction of melting point of slag

To calculate the melting point of various slags, the computational model has been proposed in previous work (Zhao, Zhang and Ju, 2013):

$$\begin{aligned} T = {} & 1682.9399+164.479X_1-162.6886X_2+250.209X_3-1415.624X_4 \\ & -819.2188X_5-7937.5X_1X_2+8687.5X_1X_3-8262.5X_1X_4 \\ & +146.875X_1X_5-12725X_2X_3+5075X_2X_4+1068.75X_2X_5 \\ & -1575X_3X_4+181.25X_3X_5+3906.25X_4X_5+1751.042X_1^2 \\ & +15.88542X_2^2-5495.84X_3^2+504.1668X_4^2+244.0104X_5^2 \end{aligned} \quad (2)$$

where:

X_1 is the mass percent of Al_2O_3

X_2 is the mass percent of MgO

X_3 is the mass percent of SiO_2

X_4 is the mass percent of CaO

X_5 is the mass percent of CaF_2

T represents the temperature in °Celsius

Prediction of conductivity of slag

The relationship between conductivity and slag composition could be quantified by the following formula (Ju, Lv and Jiao, 2012).

$$K\left(\Omega^{-1}\cdot cm^{-1}\right)=100\exp\left(1.911-1.38x_x-5.69x_x^{\ 2}\right)+0.39\left(T-1973\right) \quad (3)$$

$$x_x=x(Al_2O_3)+0.2x(CaO)+0.8x(MgO)+0.75x(SiO_2)+0.2x(CaF_2) \quad (4)$$

where X (i) represents the molar percentage of component i.

Prediction of optical basicity of slag

The optical basicity of slag containing calcium fluoride could be calculated using the following formula (Zhang, Chou and Pal, 2013):

$$\Lambda=\Sigma\Lambda_i\times X_i \quad (5)$$

$$X_i=\frac{A_i}{2}\times n_i\times\frac{N_i}{\Sigma\left[\frac{A_i}{2}\times n_i\times N_i\right]} \quad (6)$$

where:

A_i denotes the anionic charge of component i

n_i is the anionic number of component i

N_i denotes the mole fraction of component i

Λ_i denotes the optical basicity of component i

The optical basicities of each constituent element are specified in Table 2, offering comprehensive quantitative data (Zhang, Chou and Pal, 2013; Hao and Wang, 2016).

TABLE 2

Optical basicity value for each component.

Component	Optical basicity
CaO	1
MgO	0.92
Al_2O_3	0.66
SiO_2	0.47
CaF_2	0.67

Prediction of molecule and ion activity in the slag

To determine the activity of molecule and ions in CaF_2–Al_2O_3–CaO–SiO_2–MgO slag, this work employs the molecule ion coexistence theory (MICT), examining ternary phase diagrams such as CaO–CaF_2–SiO_2, CaO–CaF_2–MgO, CaO–CaF_2–Al_2O_3, CaO–SiO_2–MgO, CaO–SiO_2–Al_2O_3, CaO–MgO–Al_2O_3, CaF_2–SiO_2–MgO, CaF_2–SiO_2–Al_2O_3, CaF_2–MgO–Al_2O_3, and SiO_2–MgO–Al_2O_3 (Guillot and Guissani, 1996; Sun *et al*, 2021; Zhao, Li and He, 2022; Duan, 2020; Dong, 2007) Finally, the structural units in CaO–CaF_2–SiO_2–MgO–Al_2O_3 slag system are identified as four simple ions (Ca^{2+}, Mg^{2+}, O^{2-}, F^-), two simple molecules (Al_2O_3, SiO_2), along with 23 complex molecules. Using thermodynamic data provided in Table 3 and Python programming, the concentration of molecule and ions in the molten slags could be calculated.

TABLE 3

Chemical reaction formulas of complex molecules that may be formed, their standard Gibbs free energy changes, and mass action concentrations of structural units in the CaF_2–Al_2O_3–CaO–SiO_2–MgO system.

Reactions	ΔG_f° (J/mol)	Mass action concentration
$Ca^{2+}+O^{2-}=CaO$	/	$N_1=N_{Ca^{2+}}+N_{O^{2-}}=\frac{2x_1}{\Sigma X}$
$Mg^{2+}+O^{2-}=MgO$	/	$N_2=N_{Mg^{2+}}+N_{O^{2-}}=\frac{2x_1}{\Sigma X}$
$Ca^{2+}+2F^-=CaF_2$	/	$N_3=N_{Ca^{2+}}+2N_{F^-}=\frac{3x_1}{\Sigma X}$
SiO_2	/	$N_4=\frac{x_4}{\Sigma X}$
MgO	/	$N_5=\frac{x_5}{\Sigma X}$
$3(Ca^{2+}+O^{2-})+Al_2O_3=(3CaO\cdot Al_2O_3)$	ΔG_1^0=-21757-29.288T	$N_6=K_1N_1^3N_5$
$12(Ca^{2+}+O^{2-})+7Al_2O_3=(12CaO\cdot 7Al_2O_3)$	$\Delta G_2^0=617977-612.119T$	$N_7=K_2N_1^{12}N_5^7$
$(Ca^{2+}+O^{2-})+Al_2O_3=(CaO\cdot Al_2O_3)$	$\Delta G_3^0=59413-59.413T$	$N_8=K_3N_1N_5$
$(Ca^{2+}+O^{2-})+2Al_2O_3=(CaO\cdot 2Al_2O_3)$	ΔG_4^0=-16736-25.522T	$N_9=K_4N_1N_5^2$
$(Ca^{2+}+O^{2-})+6Al_2O_3=(CaO\cdot 6Al_2O_3)$	ΔG_5^0=-22594-31.798T	$N_{10}=K_5N_1N_5^6$
$(Mg^{2+}+O^{2-})+Al_2O_3=(MgO\cdot Al_2O_3)$	ΔG_6^0=-18828-6.276T	$N_{11}=K_6N_2N_5$

Table 3 – Continued …

Reactions	ΔG_f^o (J/mol)	Mass action concentration
$3\left(Ca^{2+}+O^{2-}\right)+2Al_2O_3+\left(Ca^{2+}+2F^-\right)=\left(3CaO\cdot 2Al_2O_3\cdot CaF_2\right)$	ΔG_7^0=-44492-73.15T	$N_{12}=K_7N_1^3N_5^2N_3$
$11\left(Ca^{2+}+O^{2-}\right)+7Al_2O_3+\left(Ca^{2+}+2F^-\right)=\left(11CaO\cdot 7Al_2O_3\cdot CaF_2\right)$	ΔG_8^0=-228760-155.8T	$N_{13}=K_8N_1^{11}N_5^7N_3$
$3\left(Ca^{2+}+O^{2-}\right)+SiO_2=\left(3CaO\cdot SiO_2\right)$	ΔG_9^0=-118826-6.694T	$N_{14}=K_9N_1^3N_4$
$3\left(Ca^{2+}+O^{2-}\right)+2SiO_2=\left(3CaO\cdot 2SiO_2\right)$	ΔG_{10}^0=-236814+9.623T	$N_{15}=K_{10}N_1^3N_4^2$
$2\left(Ca^{2+}+O^{2-}\right)+SiO_2=\left(2CaO\cdot SiO_2\right)$	ΔG_{11}^0=-102090-24.26T	$N_{16}=K_{11}N_1^2N_4$
$\left(Ca^{2+}+O^{2-}\right)+SiO_2=\left(CaO\cdot SiO_2\right)$	ΔG_{12}^0=-21757-36.819T	$N_{17}=K_{12}N_1N_4$
$2\left(Mg^{2+}+O^{2-}\right)+\left(SiO_2\right)=\left(2MgO\cdot SiO_2\right)$	ΔG_{13}^0=-56902-3.347T	$N_{18}=K_{13}N_2^2N_4$
$\left(Mg^{2+}+O^{2-}\right)+\left(SiO_2\right)=\left(MgO\cdot SiO_2\right)$	ΔG_{14}^0=-23849-29.706T	$N_{19}=K_{14}N_2N_4$
$3Al_2O_3+2SiO_2=\left(3Al_2O_3\cdot 2SiO_2\right)$	ΔG_{15}^0=-4354-10.467T	$N_{20}=K_{15}N_5^3N_4^2$
$2\left(Ca^{2+}+O^{2-}\right)+Al_2O_3+SiO_2=\left(2CaO\cdot Al_2O_3\cdot SiO_2\right)$	ΔG_{16}^0=-116315-38.911T	$N_{21}=K_{16}N_1^2N_5N_4$
$\left(Ca^{2+}+O^{2-}\right)+Al_2O_3+2SiO_2=\left(CaO\cdot Al_2O_3\cdot 2SiO_2\right)$	ΔG_{17}^0=-4184-73.638T	$N_{22}=K_{17}N_1N_5N_4^2$
$\left(Ca^{2+}+O^{2-}\right)+\left(Mg^{2+}+O^{2-}\right)+SiO_2=\left(CaO\cdot MgO\cdot SiO_2\right)$	ΔG_{18}^0=-124683+3.766T	$N_{23}=K_{18}N_1N_2N_4$
$\left(Ca^{2+}+O^{2-}\right)+\left(Mg^{2+}+O^{2-}\right)+2SiO_2=\left(CaO\cdot MgO\cdot 2SiO_2\right)$	ΔG_{19}^0=-80333+51.882T	$N_{24}=K_{19}N_1N_2N_4^2$
$2\left(Ca^{2+}+O^{2-}\right)+\left(Mg^{2+}+O^{2-}\right)+2SiO_2=\left(2CaO\cdot MgO\cdot 2SiO_2\right)$	ΔG_{20}^0=-73638+63.597T	$N_{25}=K_{20}N_1^2N_2N_4^2$
$3\left(Ca^{2+}+O^{2-}\right)+\left(Mg^{2+}+O^{2-}\right)+2SiO_2=\left(3CaO\cdot MgO\cdot 2SiO_2\right)$	ΔG_{21}^0=-205016-31.798T	$N_{26}=K_{21}N_1^3N_2N_4^2$
$2\left(Mg^{2+}+O^{2-}\right)+2Al_2O_3+5SiO_2=\left(2MgO\cdot 2Al_2O_3\cdot 5SiO_2\right)$	ΔG_{22}^0=-14422-14.808T	$N_{27}=K_{21}N_2^2N_5^2N_4^5$
$3\left(Ca^{2+}+O^{2-}\right)+2SiO_2+\left(Ca^{2+}+2F^-\right)=\left(3CaO\cdot 2SiO_2\cdot CaF_2\right)$	ΔG_{23}^0=-255180-8.20T	$N_{28}=K_{22}N_1^3N_4^2N_3$

Prediction of viscosity of slag

This work determined the viscosity of slag at 1550°C using FactSage™ 8.2, incorporating variations in slag components such as CaF_2 (30 per cent–70 per cent), Al_2O_3 (20 per cent–40 per cent), CaO (0 per cent–40 per cent), MgO (0 per cent–15 per cent), and SiO_2 (0 per cent–15 per cent) with 2 per cent step increments. This approach reduced the potential combinations to 9717, decreasing

computational requirements. A quadratic polynomial fitting analysis of these combinations, executed using Python, demonstrated high accuracy with an average absolute error of 1.7708 per cent, thereby validating its applicability to the larger data set of 138 347 combinations. The viscosity fitting results at 1550°C are as follows:

$$\begin{aligned}\eta = {} & 43342344120.47134 + 2260652.27797391 \cdot A \\ & -492659.33981768 \cdot B - 247519.83942283 \cdot C \\ & -442894.24850764 \cdot D - 465902.84576523 \cdot E \\ & -4356840.93482216 \cdot A^2 - 8686148.7534862 \cdot A \cdot B \\ & -8688600.14848205 \cdot A \cdot C - 8686646.40438652 \cdot A \cdot D \\ & -8686416.31844023 \cdot A \cdot E - 4329307.81862237 \cdot B^2 \\ & -8661067.03228913 \cdot B \cdot C - 8659113.28819614 \cdot B \cdot D \\ & -8658883.20218896 \cdot B \cdot E - 4331759.21364703 \cdot C^2 \\ & -8661564.683198 \cdot C \cdot D - 8661334.59722407 \cdot C \cdot E \\ & -4329805.46955192 \cdot D^2 - 8659380.8531375 \cdot D \cdot E \\ & -4329575.38355188 \cdot E^2\end{aligned} \quad (7)$$

where A, B, C, D, and E denote the mass percentages of CaF_2, Al_2O_3, CaO, MgO, and SiO_2, respectively, while η represents the slag system's viscosity at 1550°C, measured in Pa·s.

Screening method

The ESR product in this work is 1.2343 die steel and the chemical composition of this steel is presented in Table 4. Initially the 1.2343 die steel was remelted with ANF-6 slag, primarily composed of 70 per cent CaF_2 and 30 per cent Al_2O_3. Thus this work focused on optimising the slag composition based on ANF-6 slag.

TABLE 4

Chemical composition of 1.2343 die steel.

Element	C	Mn	Si	Cr	Mo	P	S
wt%	0.38–0.45	0.30–0.50	0.9–1.0	4.8–5.5	1.2–1.5	0.03 max	0.03 max

The initial step involves calculating various physical properties of the original slag (ANF-6 slag with 70 per cent CaF_2 and 30 per cent Al_2O_3), with values presented in Table 5. Upon calculating the physical property parameters of the original slag, we have chosen it as the reference slag system.

TABLE 5

Physical parameters of ANF-6 slag.

Physical parameters	Numerical value
Densities (g/cm^3)	2.7
Melting point (°C)	1466.8
Conductivity ($\Omega^{-1}\cdot cm^{-1}$)	2.0
Optical basicity	0.67
Calcium ion activity (mol/g)	0.0067
Viscosity (Pa·s)	0.027

During the process of ESR, metal droplets melting from the consumable electrode tip are subject to the buoyant forces of the slag, which can be quantitatively described by the buoyancy formula $F_{bouyangcy} = \rho_{slag} \cdot V_{metal\ drop}$,where $F_{bouyangcy}$ represents the buoyant force, ρ_{slag} denotes the density of the slag, and $V_{metal\ drop}$ is the volume of the metal (Duchesne and Hughes, 2017). The buoyancy force prolongs the slag-metal reaction time, significantly influencing the metal's purification and alloy composition, and impacts the final product's chemical and microstructural qualities. Thus, the objective is to select a slag composition with a higher density than the ANF-6 slag or the average of all combinations.

Regarding melting point, it is commonly accepted that the slag's melting point should be 100°C–200°C lower than the metal's melting point (Dong, 2007; Jang *et al*, 2023).

In terms of electrical conductivity, optimal conductivity is crucial for electroslag remelting efficiency and ingot quality. Lower conductivity decreases the electrode gap, increasing heat generation. However, lower conductivity may result in short-circuiting and unstable melting. Conversely, high conductivity enlarges the electrode gap, lowering the temperature and increasing heat loss, potentially causing an open arc (Birol, Polat and Saridede, 2015; Liu *et al*, 2016). Therefore, the slag's conductivity should be slightly lower than that of the ANF-6 slag or just below the median of all slag compositions to achieve a balance between efficiency, stability, and quality.

Concerning optical basicity, higher basicity slags, with elevated CaO content, enhance dephosphorization and desulfurisation but may increase gas content in steel; On the contrary, acidic slags are less effective in desulfurisation and facilitate gas content reduction, primarily hydrogen. Under protective or vacuum conditions, the advantages of acidic slag diminish (Birol, Polat and Saridede, 2015; Zhang, Chou and Pal, 2013; Hao and Wang, 2016; Dong, 2007). Thus, higher basicity slags are preferable, and the goal is to select a slag composition with optical basicity surpassing that of ANF-6 slag or exceeding the average of all slag combinations, ensuring that the selected basicity is the highest among these values.

Regarding inclusions in 1.2343 die steel, reducing the concentration of free calcium ions in the molten slag is crucial to addressing the excessive D and Ds inclusions. The aim is to lower calcium ion activity in the slag. The objective is to select slag compositions with calcium ion activity lower than that in ANF-6 slag and the average across all slag combinations.

In terms of viscosity, the slag needs to maintain an appropriate viscosity with minimal fluctuation under temperature changes. Optimal viscosity ensures good slag fluidity and is crucial for maintaining the surface quality of the ESR ingots (Sebastian, Johannes and Bernd, 2012). Generally, a lower viscosity is preferred (Dong, 2007; Li and Zhang, 2000). Therefore, the objective is to select slag compositions with a viscosity close to that of the ANF-6 slag or within the median viscosity value of all slag combinations.

Screening results of the new slag

Based on our analysis and calculations, the criteria for selecting slag compositions are as follows: density of 2.80–2.97 g/cm^3, melting point of 1150–1350°C, electrical conductivity of 1–2 $\Omega^{-1}\cdot cm^{-1}$, optical basicity of 0.70–0.82, free calcium ion concentration of 0.0035–0.0067 mol/g, and viscosity of 0.030–0.050 Pa·s.

In Figure 2, the sections highlighted with light blue shading represent the retained results after screening for each physicochemical parameter. After the screening, from the original 138 347 combinations, only 3961 remain, reducing the data set to 2.86 per cent of its initial data volume. The average, median, and model values for the filtered residue series are presented in Table 6.

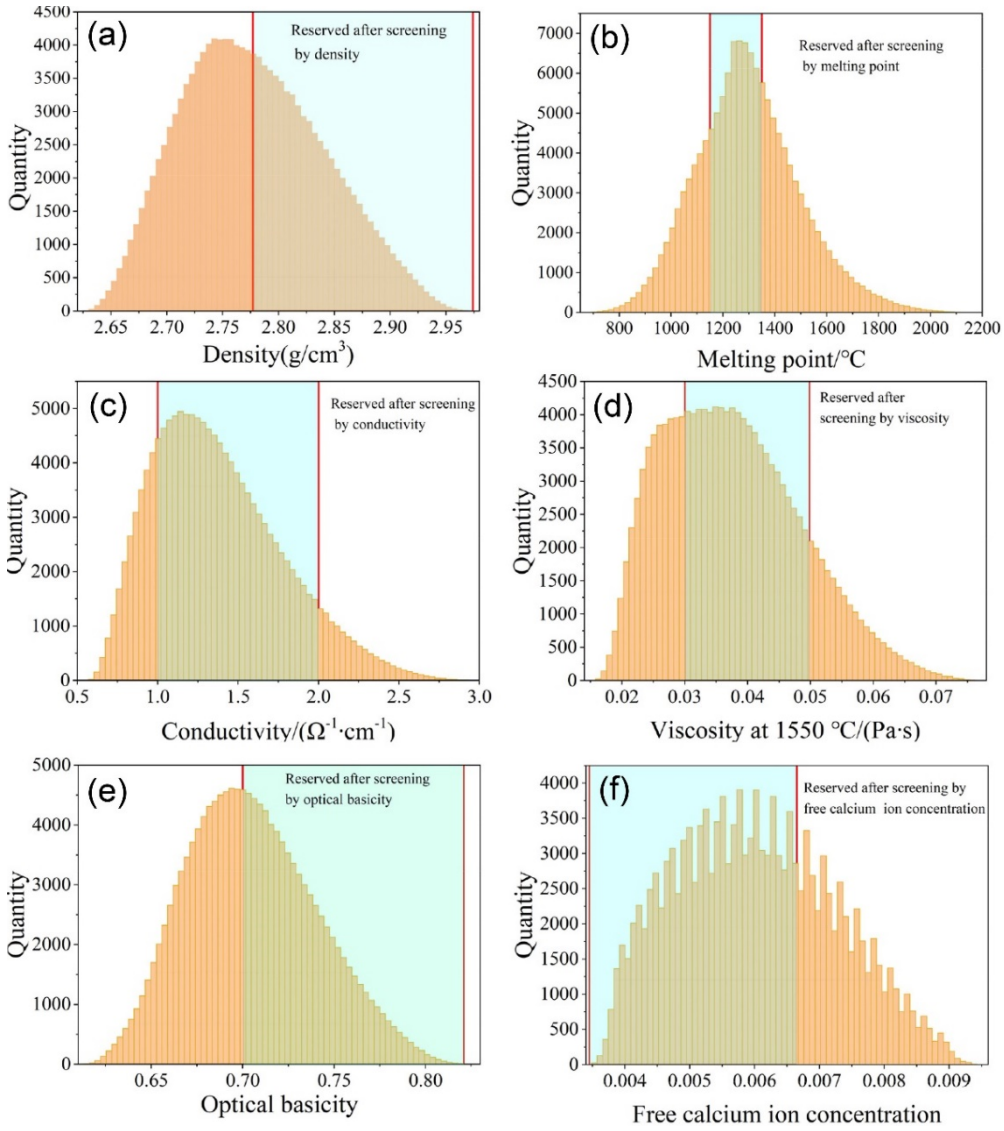

FIG 2 – Screening for each physical property parameter.

TABLE 6

The average, median, and model values for the filtered slag composition.

	CaF_2	Al_2O_3	CaO	MgO	SiO_2
Mean value/wt%	43.4	31.8	15.9	4.4	4.5
Median/wt%	43	32	15	4	4
Model/wt%	43	33	15	4	3

Despite narrowing down the viable slag combinations to 2.86 per cent of the original after screening, a wide range of options remains. Considering the limited experimental capacity, it's critical to choose a representative slag composition. To avoid extreme results and ensure experimental reliability, this study calculated the average content of each component, rounding to the nearest whole number for the target slag composition. This method balances the diverse slag characteristics, accurately representing average slag behaviour.

Based on the results presented in Table 6, the mass fraction composition of the slag system can be specified as follows: 43 per cent CaF_2, 32 per cent Al_2O_3, 16 per cent CaO, 4 per cent MgO, and 5 per cent SiO_2. This particular slag composition is denoted as the model slag.

INDUSTRIAL EXPERIMENTAL VALIDATION

Industrial experimental procedure

For slag used for industrial trial, it's essential to pre-melt the slag with specified granularity: ≥80 per cent of particles between 1-8 mm, and ≤10 per cent each for particles smaller than 1 mm or larger than 8 mm. The nominal compositions of the original (ANF-6 Slag) and experimental (Model slag) slags are outlined in Table 7.

TABLE 7

Compositions of the original (ANF-6 slag) and experimental (Model slag) slags.

Slag	CaF_2	Al_2O_3	CaO	MgO	SiO_2	FeO	P	S
Original	70±1%	30±1%	≤0.3%	≤0.3%	≤0.3%	≤0.3%	≤0.0005%	≤0.03%
Model	43±1%	32±1%	15±1%	4±1%	5±1%	≤0.3%	≤0.0005%	≤0.03%

Four ESR industrial experiments were performed at a steel plant in China using two different slags: ANF-6 slag and Model slag. Two ESR ingots have been remelted for each slag in a 5000 kg capacity furnace, and the chemical composition of the steel was shown in Table 4. The electrodes were melted in an electric arc furnace. After tapping of the melt, the ladle was transferred to a ladle furnace station to reach objective chemical composition and oxygen level. Thereafter, the ladle was sent to the vacuum degassing station to obtain the desired levels of sulfur and hydrogen contents in the melt. At casting station, the electrodes with 2600 mm in length and 550 mm in diameter have been cast using uphill casting technique. Before the experiments, the iron oxide scale was mechanically removed from the electrode surface. Approximately 150 kg of a slag mixture (CaF_2, Al_2O_3, CaO, SiO_2, and MgO) was prepared and introduced into the ESR furnace, initiating arcing with the consumable electrode. High-purity argon gas was used at 150–200 L/min to create an inert atmosphere. Once a steady state was achieved, melting parameters were recorded every minute and systematically logged in Table 8.

TABLE 8

Parameters for the electroslag remelting process.

Parameter	Value
Mold height/mm	3000
Mold diameter/mm	800
Slag mass/kg	150
Ar flow rate/(L·min^{-1})	150–200
Secondary voltage/V	42–52
Alternating current/A	10000–13000
Average melting rate/(kg·min^{-1})	10.0–10.5

Industrial experimental results

Figure 3 illustrates a smooth surface of the ESR ingot with an easily detachable thin slag skin during deslagging. This observation indicates that the physical properties of the model slag, such as melting point and viscosity, are well-suited for electroslag remelting, confirming its superior processability.



FIG 3 – The ESR ingot remelted by model slag.

After forging and heat treatment, samples with dimensions of 10 mm × 20 mm × 20 mm was cut from the axial centre of the slab with 180 mm × 1200 mm cross-section, used for inclusion detection. Figure 4 shows the calcium content of the electrode and ESR ingot, along with the inclusion rating results. Regarding inclusion rating, a notable reduction in the number and size of D/Ds inclusions was observed after adopting the model slag. In terms of elemental content, it was noted that the calcium concentration in ESR ingots significantly decreased with the introduction of the Model slag.

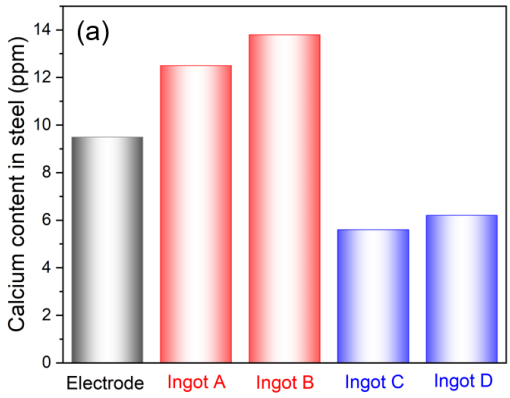

(b)	D(Thin)	D(Heavy)	Ds
Slab A	1.0	0.5	1.5
Slab B	1.0	0.5	1.5
Slab C	0.5	0.5	0
Slab D	0.5	0.5	0

FIG 4 – (a) Calcium content in electrode and ingots; (b) D and Ds inclusion rating results. Ingots A and B (Slabs A and B) were smelted using ANF-6 slag, while ingots C and D (Slabs A and B) were smelted using the model slag.

Data from Figure 4a indicates that, passing through the ANF-6 slag pool, the calcium content in Ingot A and Ingot B shows an increase trend relative to the raw consuming electrode. Conversely, when metal droplets traverse the Model slag pool to form Ingot C and Ingot D, there is a noticeable decrease in calcium content compared to the electrode. Given that calcium is not a required element in electrode alloys and primarily exists in the form of inclusions in the electrode, the reduction of calcium content during electroslag remelting is not attributable to the loss of dissociative calcium elements in the electrode matrix. This phenomenon suggests that the Model slag pool could effectively reduce the calcium content in the ingots by absorbing calcium-containing inclusions in the electrode. This is consistent with the results in Figure 5, which depicts electron microscopy scans of typical D and Ds inclusions in ESR ingots remelted using ANF-6 slag and Model slag. The results show a reduction in inclusion size and dramatically decreased concentrations of Ca in ingots remelted with the Model slag.

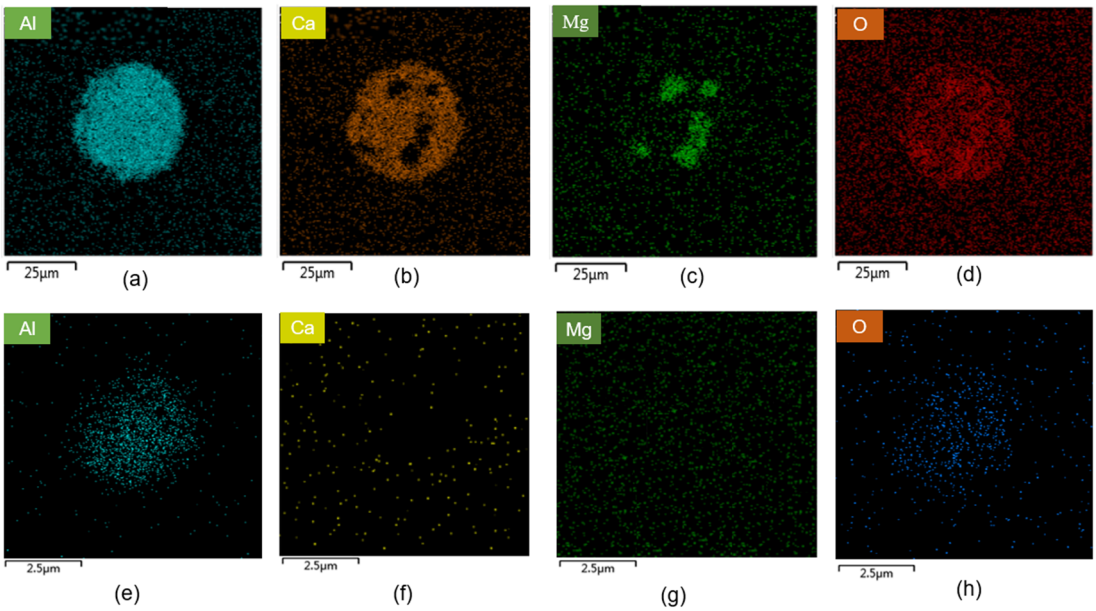

FIG 5 – (a), (b), (c), (d) SEM images of inclusions in Slab A remelted using ANF-6 slag; (e), (f), (g), (h) SEM images of inclusions in Slab C remelted using the model slag.

The industrial experimental results demonstrated that the utilisation of the Model slag not only preserved the excellent surface quality of the ingots but also effectively removed the excessive D and Ds inclusions in 1.2343 die steel.

Discussion

Based on MICT theory, the free calcium ions concentrations in ANF-6 slag and Model slag have been calculated. The results reveal a positive correlation between free calcium ion concentrations in molten slag and calcium content in ingots, as depicted in Figure 6. When remelting the steel with ANF-6 slag, due to sufficient slag-metal reaction, high free calcium ions in molten slag could lead to 'calcium treatment' on the original Al_2O_3 type inclusion in electrode. Thus, higher calcium content and excessive $CaO–Al_2O_3$ (D and Ds inclusions) have been detected in the slab. While, remelted with the Model slag with low free calcium ions concentration, the 'calcium treatment' effect have been effectively suppressed. Furthermore, calcium ions in liquid steel could diffuse into the molten slag driven by the concentration gradient. This could explain well that fewer calcium content and less D and Ds inclusions have been detected in the 1.2343 steel remelted with model slag.

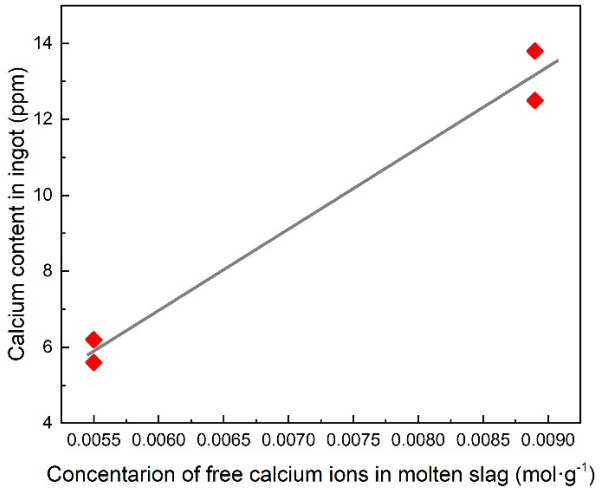

FIG 6 – Correlation between free calcium ion concentration in the slag and calcium content in the ESR ingot.

This work has utilised the molecule ion coexistence theory to calculate the effects of varying mass percentages of CaF_2, Al_2O_3, CaO, SiO_2, and MgO on the activity of calcium ions at 1550°C. Mass percentages of these components will range from 30 per cent to 70 per cent for CaF_2, 20 per cent to 40 per cent for Al_2O_3, 0 per cent to 40 per cent for CaO, 0 per cent to 15 per cent for SiO_2, and 0 per cent to 15 per cent for MgO, with each component varying in 1 per cent increments across all possible combinations. The calculated results presented in Figure 7a reveal that the correlation coefficient for CaF_2 is the highest, indicating that the concentration of CaF_2 in the slag directly affects the concentration of free calcium ions in the molten state. Furthermore, with the mass fraction of CaF_2 held constant, the impact of other components on the concentration of free calcium ions was calculated, shown in Figure 7b.

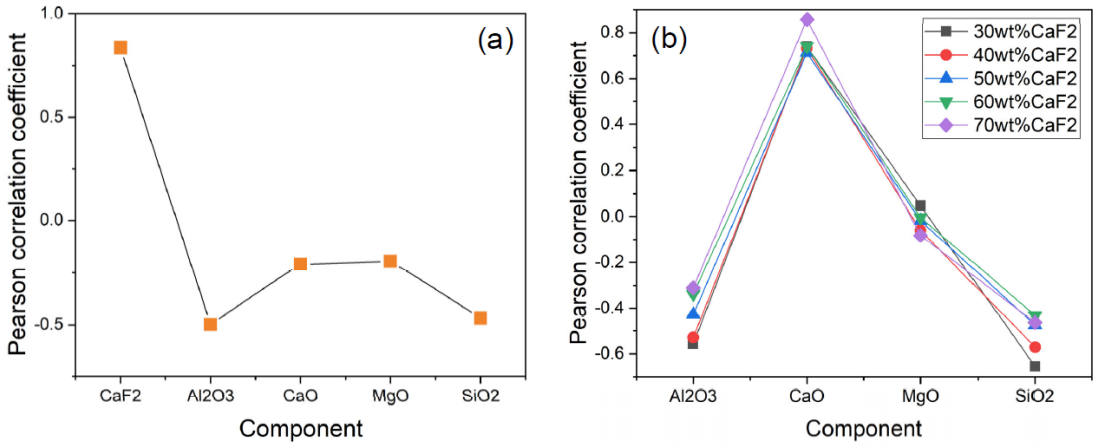

FIG 7 – Correlation coefficient for the relationship between each component and calcium ion concentration based on the molecule–ion coexistence theory: (a) Pearson correlation coefficients of each component with free calcium ion concentration; (b) Influence of other components on free calcium ion concentration when the CaF_2 mass fraction is fixed.

The Pearson correlation coefficients in Figure 7 show that CaF_2 significantly affects the concentration of free calcium ions in the slag. Additionally, the concentration of CaO also exerts an influence. Conversely, the concentration of MgO in the slag system has minimal impact on the concentration of free calcium ions. Moreover, Al_2O_3 and SiO_2 in the slag system moderately suppress the concentration of free calcium ions.

CONCLUSION

- Employing well-defined screening criteria, the slag composition exhibiting superior performance was theoretically selected. Subsequent experimental verification confirmed the exceptional performance of this new slag composition, thereby demonstrating the feasibility and efficiency of using genetic algorithms for slag system optimisation.
- CaF_2 and CaO were identified to increase the activity of calcium ions in the slag, with CaF_2 exerting a greater effect than CaO. SiO_2 and Al_2O_3 were observed to decrease calcium ion activity, with SiO_2 being slightly more effective than Al_2O_3 in this aspect. Meanwhile, MgO demonstrated no significant impact on calcium ion activity.
- To further reduce the concentration of free calcium ions and free alumina activity in the slag, it is recommended to decrease the content of CaF_2 and increase the contents of CaO and SiO_2.

ACKNOWLEDGEMENTS

This work was supported by Program of Introducing Talents of Discipline to Universities (No. B21001), Science and Technology Research Projects of Liaoning Province (2023JH1/10400051).

REFERENCES

Birol, B, Polat, G and Saridede, M N, 2015. Estimation Model for Electrical Conductivity of Molten CaF_2-Al_2O_3-CaO Slags Based on Optical Basicity, *JOM,* 67:427–435.

Campbell, C and Olson, G, 2000. Systems design of high performance stainless steels, I, Conceptual and computational design, *Journal of Computer-Aided Materials Design,* 7:145–170.

Dong, Y W, 2007. Mathematical Modeling of Solidification during Electroslag Remelting Process and Development of New Slags, PhD thesis, Northeastern University, Shenyang.

Dong, Y W, Jang, Z H and Yu, A, 2016. Dissolution Behavior of Alumina-Based Inclusions in CaF_2-Al_2O_3-CaO-MgO-SiO_2 Slag Used for the Electroslag Metallurgy Process, *Metals,* 6:272–279.

Dong, Y W, Jiang, Z H, Cao, Y L, Yu, A and Hou, D, 2014. Effect of Slag on Inclusions During Electroslag Remelting Process of Die Steel, *Metallurgical and Materials Transactions B*, 45:1315–1324.

Duan, S C, 2020. Fundamental Study on the Controlling Loss of Alloying Elements of Large IN718 Electroslag Remelting Ingots, PhD thesis, University of Science and Technology, Beijing.

Duchesne, M A and Hughes, R W, 2017. Slag density and surface tension measurements by the constrained sessile drop method, *Fuel,* 188:173–181.

Guillot, B and Guissani, Y, 1996. Towards a theory of coexistence and criticality in real molten salts, *Molecular Physics,* 87:37–86.

Guo, Y, Xia, Z, Shen, Z, Li, Q, Sun, C, Zheng, T and Ren, W, 2021. Enhancement of removing inclusions from liquid melt film during the ESR process assisted by a static magnetic field, *Journal of Materials Processing Technology,* 290:1–9.

Hao, X and Wang, X H, 2016. A New Sulfide Capacity Model for CaO-Al_2O_3-SiO_2-MgO Slags Based on Corrected Optical Basicity, *Steel Research International,* 87:359–363.

Jang, W F, Tian, L, Bo, H and Ma, T F, 2023. A new method for evaluating the melting performance of the slag, *Ironmaking and Steelmaking,* 50:775–781.

Jang, Z H, Dong, Y W, Geng, X and Liu, F B, 2015. *Physical Chemistry and Transport Phenomena During Electroslag Metallurgy*, pp 68–75 (Northeastern University Press: Shenyang).

Jiang, Z H, Dong, Y W, Geng, X and Liu, F B, 2023. Development and application of electroslag remelting technology for high quality special steels, *Iron and Steel,* 58:15–25.

Ju, J T, Gu, Y and Zhang, Q, 2021. Effect of CaF_2 and CaO/Al_2O_3 ratio on evaporation and melting characteristics of low-fluoride CaF_2–CaO–Al_2O_3–MgO–TiO_2 slag for electroslag remelting, *Ironmaking and Steelmaking*, 50:8.

Ju, J, Ji, G, Tang, C, Yang, K and Zhu, Z, 2020. Investigation of fluoride evaporation from CaF_2–CaO–Al_2O_3–MgO–TiO_2–(Li_2O) slag for electroslag remelting, *Scientific Reports,* 10:1–12.

Ju, J, Lv, Z L and Jiao, Z Y, 2012. Experimental Study on the Electrical Conductivity of CaF_2-SiO_2-Al_2O_3-CaO-MgO Slag System, *Journal of Iron and Steel Research International,* 24:27–31.

Li, J X and Zhang, J, 2000. CaO-MgO-CaF_2-Al_2O_3-SiO_2 Five-element slag system Calculation model of viscosity, *Journal of University of Science and Technology Beijing,* 22:316–319.

Liu, J H, Zhang, G H, Wu, Y D and Chou, K C, 2016. Study on electrical conductivity of FexO-CaOSiO_2-Al_2O_3 slags, *Canadian Metallurgical Quarterly,* 55:221–225.

Ragnarsson, L and Sichen, D, 2009. Inclusions Generated during Ingot Casting of Tool Steel, *Steel Research International,* 81:40–47.

Sabih, A, Wanjara, P and Nemes, J, 2005. Characterization of internal voids and cracks in cold heading of dual phase steel, *ISIJ International,* 45:1179–1186.

Schneider, R S E, Molnar, M, Kloesch, G and Schueller, C, 2019. Effect of the Al_2O_3 Content in the Slag on the Chemical Reactions and Nonmetallic Inclusions during Electroslag Remelting, *Metallurgical and Materials Transactions B,* 51:1904–1911.

Sebastian, R and Bernd, F, 2015a. Influencing the Electroslag Remelting Process by varying Fluorine Content of the utilized Slag, *The 8th European Metallurgical Conference (EMC).* Düsseldorf.

Sebastian, R and Bernd, F, 2015b. Process and Refining Characteristics of ESR using MgO containing Slag Systems, *International Symposium on Liquid Metal Processing and Casting,* Leoben/Germany.

Sebastian, R, Johannes, M and Bernd, F, 2012. The Influence of Selected Slag Properties and Process Variables on the Solidification Structure during ESR, *1st International Conference on Ingot Casting*, *Rolling and Forging (ICRF).* Aachen/Germany.

Shi, C B, Li, J, Cho, J W, Jiang, F and Jung, I H, 2015. Effect of SiO_2 on the Crystallization Behaviors and In-Mold Performance of CaF_2-CaO-Al_2O_3 Slags for Drawing-Ingot-Type Electroslag Remelting, *Metallurgical and Materials Transactions B,* 46:2110–2120.

Shi, C, 2020. Deoxidation of Electroslag Remelting (ESR) – A Review, *ISIJ International,* 60:1083–1096.

Sun, H, Yang, J, Zhang, R H and Yang, W K, 2021. Effect of Slag Basicity on Dephosphorization at Lower Basicity and Lower Temperature Based on Industrial Experiments and Ion-Molecular Coexistence Theory, *Metallurgical and Materials Transactions B,* 52:3403–3422.

Wan, X X, Shi, C B, Yu, Z and Li, J, 2022. Effect of CaF_2 and Li_2O on structure and viscosity of low-fluoride slag for electroslag remelting of rotor steel, *Journal of Non-Crystalline Solids,* 597:121914.

Xu, W, del Castillo, P E J R D and Van Der Zwaag, S, 2009. A combined optimization of alloy composition and aging temperature in designing new UHS precipitation hardenable stainless steels, *Computational Materials Science,* 45:467–473.

Zhang, G H, Chou, K C and Pal, U, 2013. Estimation of Sulfide Capacities of Multicomponent Slags using Optical Basicity, *ISIJ International,* 53:761–767.

Zhao, M G, Li, G and He, S P, 2022. Study of Thermodynamic for Low-Reactive CaO-BaO-Al_2O_3-SiO_2-CaF_2-Li_2O Mold Flux Based on the Model of Ion and Molecular Coexistence Theory, *Metals,* 12:1099.

Zhao, X H, Zhang, Z H and Ju, J T, 2013. Study on Melting Temperature of CaF_2-SiO_2-Al_2O_3-CaO-MgO Slag, *Hot Working Technology,* 42:81–84.

Flux smelting behaviour of pre-reduced Mn ore by hydrogen at elevated temperatures

DOI: 10.62053/LIOD4137
P Kumar[1] and J Safarian[2]

1. PhD candidate, Department of Materials Science and Engineering, NTNU, N-7034 Trondheim, Norway. Email: Pankaj.kumar@ntnu.no
2. Professor, Department of Materials Science and Engineering, NTNU, N-7034 Trondheim, Norway. Email: jafar.safarian@ntnu.no

ABSTRACT

Understanding how ore interacts with flux particles at elevated temperatures to create molten slag is crucial since it governs the dynamics of a chemical reaction. This study explores the smelting behaviour of pre-reduced Nchwaning manganese ore when combined with lime, with the objective of examining the evolving interaction between pre-reduced ore particles and lime over time. The research sheds light on the interaction between solid and liquid and the phases that emerge during this process. To achieve this, a sessile drop furnace was employed to rapidly heat the materials positioned adjacent to each other on an alumina substrate and to observe the smelting process as it unfolded over time. This method allowed for the direct observation of the melting temperatures and the flux-ore reaction progression rate, and the potential disruptive events that might occur. By comparing the molten interfaces of the fluxed materials at various time intervals, this study provides insights into the relative rate of slag formation from the two materials. The results indicate that the main slag formation initiated at approximately 1400°C and continued to advance with time, with complete mixing occurring around 1500°C. The possible phases formed were identified using Scanning Electron Microscopy and modelled using Fact Sage thermodynamic software. In addition, the iron particles in the pre-reduced Mn ore were separated and settled from a rich MnO-containing slag. It was found that the separation of molten iron droplets from the slag depends on the rate of solid MnO particles dissolution into the adjacent slag phase.

INTRODUCTION

Ferromanganese production consumes anywhere between 2400–2700 kWh energy per ton of metal produced (Tangstad and Olsen, 1995). Ferroalloys such as ferromanganese are mainly produced in submerged arc furnaces (Office of Air Quality Planning and Standards, 1992), where 50–70 per cent of the required thermal energy is given by electrical dissipation and the rest is met by carbon or other carbonaceous material like biomass and charcoal (Monsen *et al*, 2007), which is used as a reductant. The process of manganese production goes through series of reduction steps as shown in Equations 1–3 (Tangstad and Olsen, 1995). Where the higher manganese oxide is reduced to lower oxide by indirect reduction by CO gas followed by final step where the manganese monoxide is reduced to manganese metal by carbon Equation 4 (Tangstad and Olsen, 1995):

$$2MnO_2 + CO = Mn_2O_3 + CO_2 \ldots \Delta H^\circ_{298} = -203.007\ kJ \quad (1)$$

$$3Mn_2O_3 + CO = 2Mn_3O_4 + CO_2 \ldots \Delta H^\circ_{298} = -178.371\ kJ \quad (2)$$

$$Mn_3O_4 + CO = 3MnO + CO_2 \ldots \Delta H^\circ_{298} = -53.928\ kJ \quad (3)$$

$$MnO + C = Mn + CO \ldots \Delta H^\circ_{298} = 274.206\ kJ \quad (4)$$

The process emits huge amount of greenhouse gas (GHG) which greatly depends on the source of energy and reductant material (biomass, metallurgical coke, or coal (Haque and Norgate, 2013; Westfall *et al*, 2016). It was found from the previous studies that around 1.04 to 6.0 kg CO_2 is emitted per kg FeMn production (Haque and Norgate, 2013; Olsen, Monsen and Lindstad, 1998; Westfall *et al*, 2016). The CO_2 is responsible for 20 per cent of thermal absorption, which directly causes global warming (Schmidt *et al*, 2010) and climate change, which is recognised as a substantial threat to human health (Costello *et al*, 2009; Mora *et al*, 2017). With more awareness and stricter government rules, industries are forced to move towards greener alternative routes to produce these metal and alloys. One such route is the use of hydrogen, for the reduction of metal oxides like Cr_2O_3 (Davies *et al*, 2022), Fe_2O_3 (Heidari *et al*, 2021), MnO_2 (Barner and Mantell, 1968; Safarian, 2021),

to its lower oxides. The use of hydrogen produces water vapor as the main off-gas component which is safe and even can be further used, hence significantly reducing CO_2 emission. Manganese oxide can only be partially reduced with hydrogen following Equations 5–7,(Safarian, 2021) unlike iron oxide that can be completely reduced with hydrogen following Equation 8:

$$2MnO_2 + H_2 = Mn_2O_3 + H_2O \ldots \Delta H^\circ_{298} = -163.7 \text{ kJ/mol} \quad (5)$$

$$3Mn_2O_3 + H_2 = 2Mn_3O_4 + H_2O \ldots \Delta H^\circ_{298} = -135.1 \text{ kJ/mol} \quad (6)$$

$$Mn_3O_4 + H_2 = MnO + H_2O \ldots \Delta H^\circ_{298} = -16.6 \text{ kJ/mol} \quad (7)$$

$$Fe_2O_3 + 3H_2 = Fe + 3H_2O \ldots \Delta H^\circ_{298} = 85.6 \text{ kJ/mol} \quad (8)$$

The pre-reduction of manganese ore with hydrogen significantly reduces the net CO_2 emission from the process. In a recent approach, of which this manuscript is a part of, researchers have tried coupling the use of hydrogen for pre-reduction of manganese ore followed by aluminium for complete reduction of the pre-reduced ore following Equation 9. the process is referred to as HAlMan (Safarian, 2021):

$$3MnO + 2Al = Mn + Al_2O_3 \ldots \Delta H^\circ_{298} = -520 \text{ kJ/mol} \quad (9)$$

The reaction being highly exothermic in nature gives enough energy for slag metal formation and separation. The slag formed in the process mostly contains Al_2O_3, CaO and some unreduced MnO along with low amount of SiO_2 and MgO. One of the major aims in the HAlMan process is to generate slag which could be leached to recover alumina and calcia. The recovered alumina and calcia can be re-used in the process, hence further reducing the net energy consumption. But, for this to be achieved, the slag needs to be designed well to be easily leachable. It is found from the literature that calcium aluminate ($CaAl_2O_4$) phase is the most easily leached phase (Azof, Kolbeinsen and Safarian, 2017), while gehlenite phase ($Ca_2Al_2SiO_7$) is tough to be leached.

To achieve the required phase, it is of prime importance to understand the mechanisms of phases formation and transformation with time and temperature. The current manuscript focuses on studying the interaction of flux (CaO) with a pre-reduced Mn ore by H_2 gas on alumina. The study is performed in a sessile drop test furnace, where the lime and pre-reduced ore particles are placed on the alumina substrate and heated at various rates and durations to monitor softening, melting and interaction of material upon heating. After the tests, the microstructure and composition of samples are studied by microscopic examination.

EXPERIMENTAL

Method

The overall experimental procedure of this work is presented in Figure 1. The detail about the experiment is provided in later sections.

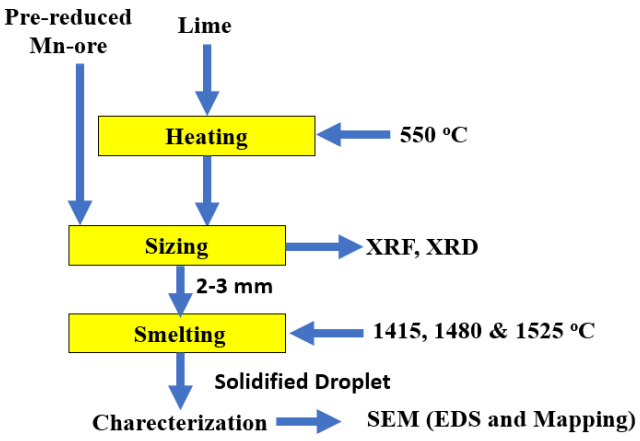

FIG 1 – Schematic of used methodology showing the materials flow.

Materials and preparation

A pre-reduced Nchwaning ore and lime was used for the study. The pre-reduction of the Nchwaning ore was carried out using a vertical tube resistance furnace, which is designed to reach a maximum temperature of 1100°C and can purge Ar, H_2 and CO gas. 50 g of dried Nchwaning ore in the size range of 4–10 mm was reduced with hydrogen at a flow rate of 4 Nl/min, held at 800°C for 1 hr. The reduced sample was then crushed and sieved to obtain particles of size 2–3 mm, which was then sealed in an airtight plastic bag to prevent any reoxidation. Similarly, the lime was pre-heated to 550°C under Ar atmosphere, to decompose any calcium hydroxide formed due to exposure to atmosphere for long time. Following the reaction in Equation 10:

$$Ca(OH)_2 = CaO + H_2O \ldots \Delta H^\circ_{298} = 104.903 \text{ kJ/mol} \quad (10)$$

After pre-heating, the lime samples were collected and sealed in airtight plastic to avoid hydration. The lime particles were carefully sized to 2–3 mm manually, as they are quite soft and may turn fine on pulverising mechanically. These sized particles were then kept for further sessile drop test study.

Sessile drop test

Particles of similar size, from the size range of 2–3 mm were taken from each pre-reduced Nchwaning ore and lime. One particle each of pre-reduced Nchwaning ore and lime was kept on alumina substrate, which was then kept on the graphite holder Figure 2. The sample holder was then pushed inside the furnace sealed, evacuated, and backfilled to atmospheric pressure with argon. The argon flow of 0.5 Nl/min was maintained throughout the test. For all the test similar schedule was used. The schedule comprised of four stages shown in Table 1. Starting of the interaction of lime and pre-reduced ore particle and the completion of melting of the samples were made the two end points of the experiment, and an intermediate stage between them was also considered for study. It was observed that the interaction started at 1415°C, and was completed at 1525°C, these two points were considered as the two end points and designated as T1 and T3, respectively, while the intermediate temperature 1480°C will be marked as T2 for ease of discussion.

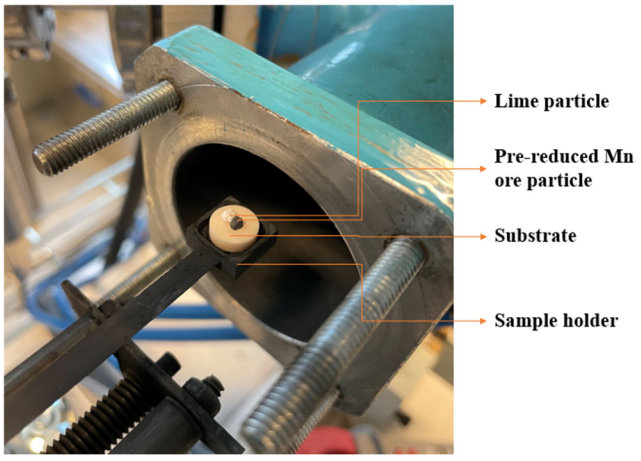

FIG 2 – Samples placed on sample holder.

TABLE 1

Program for sessile drop test furnace.

Total time [HH:MM:SS]	Time interval [HH:MM:SS]	End temp (°C)	Ar flow rate (Nl/min)
00:00:30	00:00:30	25	0.5
00:03:30	00:03:00	900	0.5
00:09:30	00:06:00	1200	0.5
00:49:30	00:40:00	1800	0.5
00:59:30	00:10:00	25	0.5

Figure 3 depicts the schematic of the sessile drop test furnace comprising three key components: the primary heating chamber equipped with heating element and a thermocouple, a firewire digital video camera with a telecentric zoom Lense capable of capturing images at 1280 × 960 pixels resolution situated to the right, and a pyrometer on the left for temperature measurement. The furnace offers a capability to purge CO, hydrogen, and inert gas, facilitating the examination of pre-reduction behaviour or properties such as melting point and surface tension. In this specific instance, the focus was solely on understanding the smelting characteristic of the pre-reduced Nchwaning manganese ore with lime particle and alumina substrate.

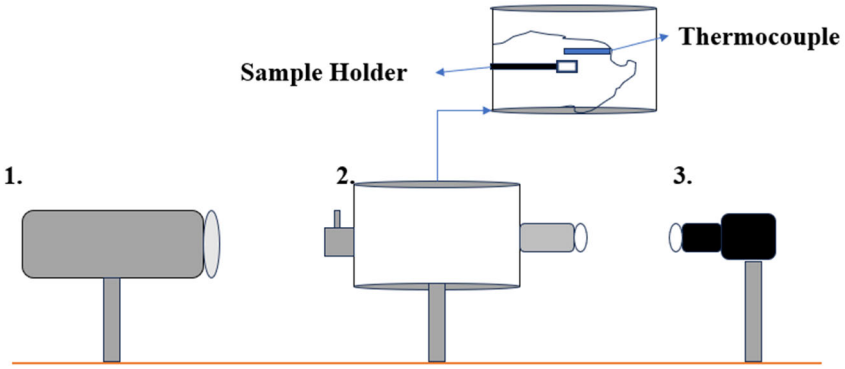

FIG 3 – Schematic of Sessile drop test furnace wherein: (1) represents the pyrometer, (2) main chamber and (3) the camera.

Characterisation technique

The pre-reduced Nchwaning ore and lime were powdered (<75 mm) in a ring mill for 1 min at a speed of 800 revolution per minute (rev/min) and sent for elemental analysis. Elemental analysis was done using the X-ray fluorescence (XRF) technique (Thermo fisher, Degerfors labortorium AB, Sweden). The mineralogical examination through X-ray diffraction (XRD) was done using the Bruker D8 A25 DaVinciTM equipment from Karlsruhe, Germany. For lime samples the XRD analysis was carried out both before and after pre-heating to be sure about complete decomposition of $Ca(OH)_2$ to CaO. The XRD for each sample was done for 2θ ranging from 0–80°, with a step size of 0.2°. The samples after sessile drop test were cold mounted using epoxy and polished using automatic polishing machine Tegrapol 30. The polished sample was observed under scanning electron microscope (SEM) (Zeiss ultra 55LE, Carl Zeiss, Jena, Germany) for microstructural analysis. While the elemental analysis and mapping was done using energy dispersive spectroscopy (EDS) (Bruker, AXS, microanalysis GmbH, Berlin, Germany).

The chemical composition of pre-reduced Nchwaning ore and lime is presented in Table 2. A major fraction of the weight of pre-reduced ore is composed of manganese monoxide and reduced iron. Limestone mostly contains CaO and small amount of MgO and SiO_2.

TABLE 2

XRF elemental analysis of pre-reduced Nchwaning ore and lime sample (wt per cent).

Sample	%MnO	%Fe	$\%Al_2O_3$	$\%SiO_2$	%CaO	%MgO	%LOI
Lime	-	-	0.16	0.19	90.20	0.50	8.45
Pre-reduced Nchwaning ore	72.22**	12.21*	0.43	4.66	8.93	1.48	-

*metallic iron, **in form of MnO.

RESULTS AND DISCUSSION

Melting behaviour

The lime and the pre-reduced manganese ore particle were kept on the alumina substrate and heated. It was observed that the lime particle started melting first, at around 1350°C near the contact

point with alumina substrate. Figure 4 shows different stages of melting of lime particle and pre-reduced manganese ore.

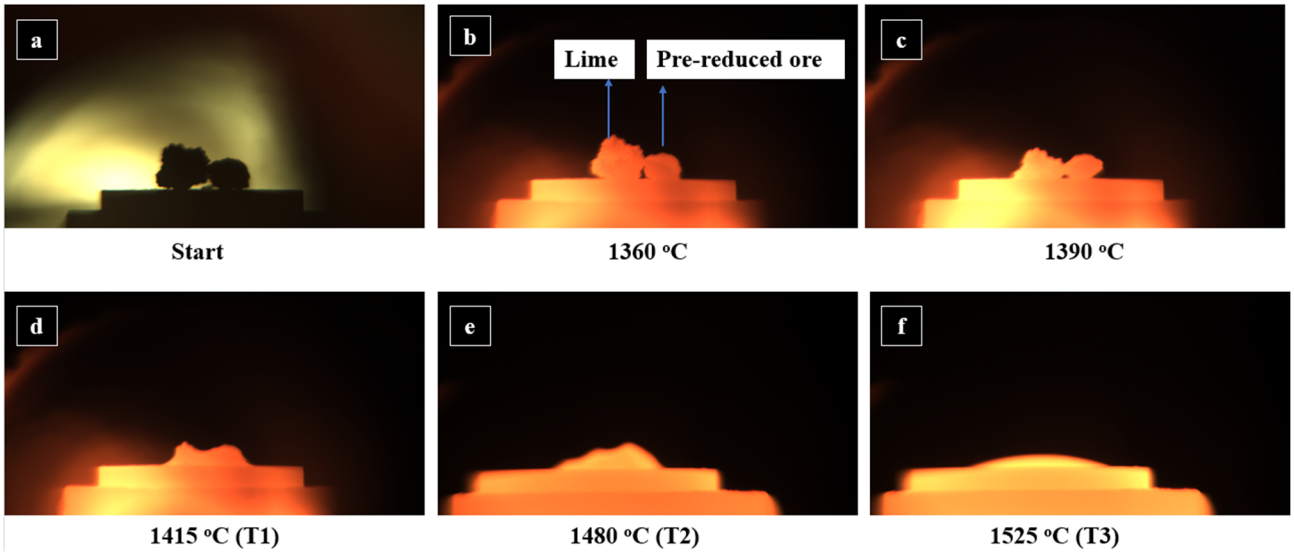

FIG 4 – Different stages of interaction between lime and pre-reduced ore particle.

The interaction of molten lime particle was observed to start at around 1415°C, while the complete melting occurred at around 1525°C Figure 4f, where a single molten pool was observed. To further understand the interaction of lime and ore particle, microscopic examination was done which is discussed in later section.

Microstructural analysis

Figure 5 shows the microstructure of test samples for test T2. From the microstructural images three distinct region were found in samples with lower holding time and temperature (T1 and T2), which was analysed further using EDS and mapping Figure 6. The outer most region (transformed) starting from the pre-reduced manganese ore particle, was mostly observed to be composed of (37–39 wt per cent) calcia and (55–57 wt per cent) alumina with very little (3–5 wt per cent) MnO. The middle region (partially transformed) was found to contain dendritic structure, made up of the ore particle, which shows small amount of undissolved ore particle in this region. While the inner portion (un-transformed) was found to contain larger circular undissolved ore particles. The width of the middle region (partially transformed region) was observed to decrease with increasing holding time and temperature. The width in case of samples heated till 1410°C was found to be around 250 mm which decreased to around 180 mm in case of sample heated till 1450°C and it completely vanished for the samples heated till 1500°C, Figure 6. The observation is obvious as the transformation is time and temperature dependent phenomenon. The reduced iron particles were mostly observed in the inner region, though there were few iron ore particles which was found suspending in the middle region. While no iron particles were observed in the outer region, the slag is already formed Figure 7. It is interesting to note that the iron particles were only observed attached to the manganese particles. As the outer region has no separate manganese particles hence no iron particle was observed as well. The iron particle was supposed to sink towards the bottom, because of the difference in density, tough the presence of small amount of iron particle in middle region was mostly because of higher viscosity due to presence of solid MnO particles in the slag phase. The good contact of metal droplets with solid MnO particles may indicate low interfacial energies between them that causes not detachment of metal droplets. Hence, we may conclude that the separation of tiny iron particles from the slag is dependent on the dissolution of solid MnO particles into the molten slag phase and hence the loss of the MnO/iron interfacial area.

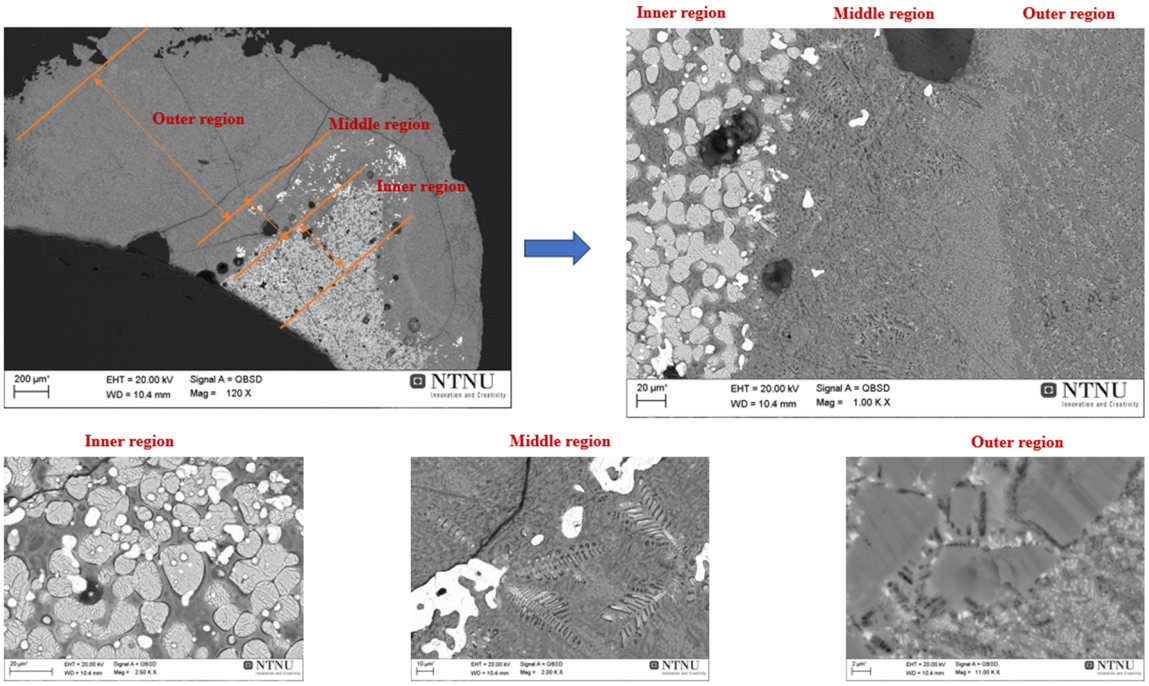

FIG 5 – Microstructure of test sample T2 showing different zones of transformation.

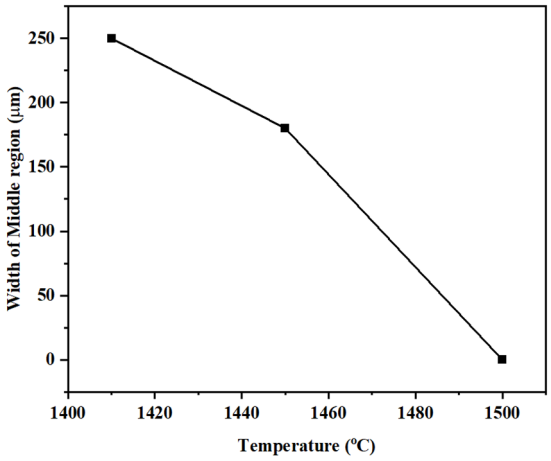

FIG 6 – Change in width of partially transformed zone (middle region), with temperature.

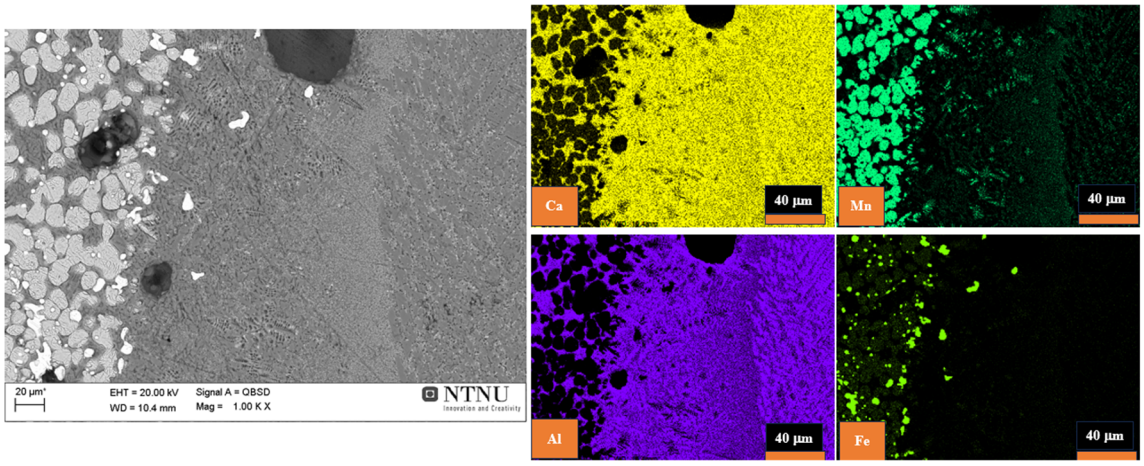

FIG 7 – Elemental X-ray mapping image of sample T2 showing the distribution of the main elements.

For the test sample T3, the phases were completely evolved and there was no demarcation of regions as was observed in other samples (T1 and T2). This shows that the melting and the phase formation was completed at 1525°C. The cross-sectional image of the sample shows a large single metal droplet at the bottom of the melted sample Figure 8, which also signifies complete melting and homogenisation of the molten bath. Two distinct phases were observed in the slag, a darker phase consisting of alumina and calcia, in the matrix of a brighter phase consisting of manganese, alumina and calcia. Figure 9 and Table 3 shows the difference in the chemical compositions of these two phases in higher magnification with small area analysis. The darker phase had a CaO/Al_2O_3 mass ratio close to 0.3, which is like that in $CaO.2Al_2O_3$ phase. While the CaO/Al_2O_3 mass ratio in case of brighter phase was close to 0.5, which is like that in $CaO.Al_2O_3$ phase. Hence, it can be very well said that the darker phases were $CaO.2Al_2O_3$, while the brighter ones were $CaO.Al_2O_3$.

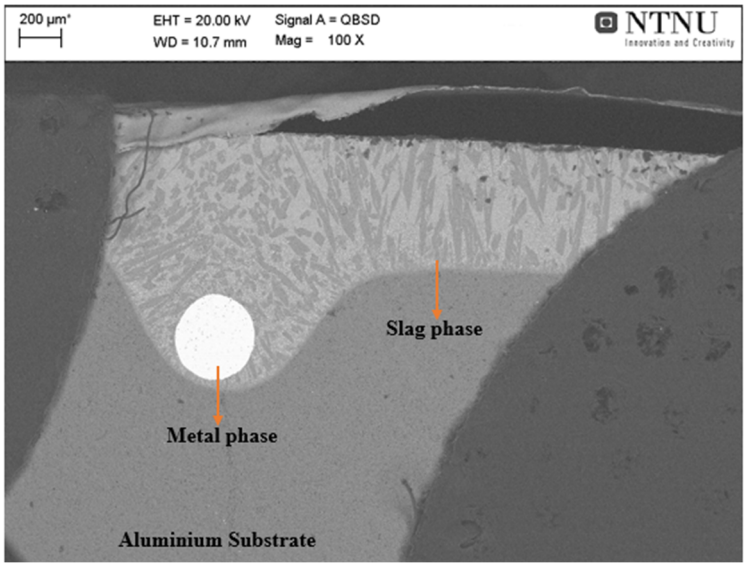

FIG 8 – Cross-section image of test T3 sample showing metal and slag phase.

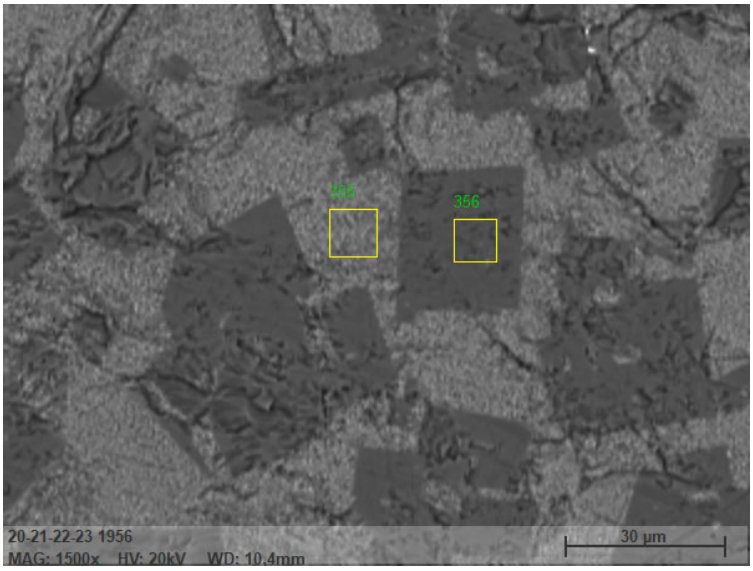

FIG 9 – SEM image showing two distinct phases in test T3.

TABLE 3

EDS result of darker and brighter phases formed in the slag of test T3.

Points/Elements	MnO	CaO	Al_2O_3	SiO_2	MgO
355	19.40	29.7	43.33	3.65	2.314
356	1.53	24.55	73.39	-	-

Probable mechanism

Figure 10 shows the probable mechanism of the melting and dissolution of lime and pre-reduced manganese ore on alumina substrate.

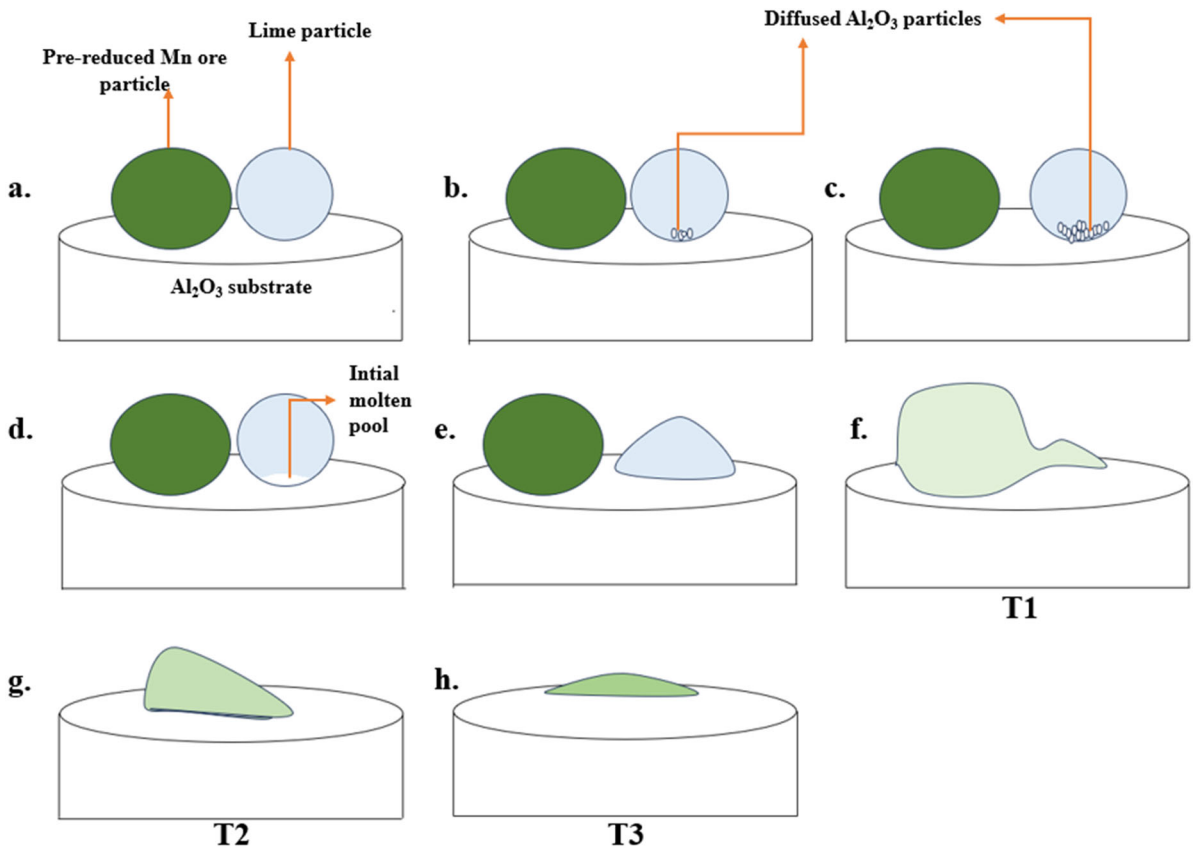

FIG 10 – Mechanism of Lime and pre-reduced manganese ore and Alumina substrate interaction.

As the temperature increases, more and more alumina particle from alumina substrate diffuses into the lime particle, which is obvious as diffusion is highly dependent on temperature Figure 11b and 11c. The diffusion of alumina particle would have been significantly easier, as the lime particles were highly porous. However, we may expect that the CaO and adjacent oxides in the lime such as MgO and Al_2O_3 and SiO_2 (Table 2) may yield some early slaggy phases formation in the lime particle, and the free surfaces of the particle and hence the lime/substrate interface. The slow increase in alumina concentration into the lime particle near the interface causes the CaO/Al_2O_3 ratio to decrease to lower ratios and eventually to 1, which reflects the eutectic point in $CaO\text{-}Al_2O_3$ phase diagram Figure 11, marked by arrow. It is at this point that the molten pool starts to form Figure 11d, which explains why the melting of lime particle was observed at 1360°C, much lower than the theoretical melting point of 2572°C. Once, the molten pool is formed, the further mechanism is a combination of diffusion and dissolution of lime and alumina into the molten pool. The further melting occurs rapidly and within a narrow temperature zone, because of the combined effect. The concentration of alumina in lime increases rapidly with time and temperature, Equations 11–13 show decreasing CaO/Al_2O_3 mass ratio from 1.66 to 0.2:

$$3CaO + Al_2O_3 = 3CaO.Al_2O_3 \ldots CaO/Al_2O_3 = 1.66 \quad (11)$$

$$CaO + Al_2O_3 = CaO.Al_2O_3 \ldots CaO/Al_2O_3 = 0.55 \quad (12)$$

$$CaO + 2Al_2O_3 = CaO.2Al_2O_3 \ldots CaO/Al_2O_3 = 0.28 \quad (13)$$

Once the lime is completely molten and spread over the substrate more it touches the solid pre-reduced manganese ore particle, and it covers the particle very rapidly, in a fraction of a second, so that a single molten pool is seen while there is an increase in temperature as shown in Figure 11f to 11h. The interaction of pre-reduced manganese ore particle with CaO and Al_2O_3 starts the slagging reactions with Mn oxide contribution via Equations 14 and 15 and the mass transport of MnO to the

slag occurs simultaneously via Equation 16, which is solid MnO dissolution into the adjacent molten slag:

$$SiO_2 + MnO = MnSiO_3 \quad (14)$$

$$SiO_2 + CaO.Al_2O_3 = CaO.Al_2O_3.SiO_2 \quad (15)$$

$$MnO\ (s) = MnO \quad (16)$$

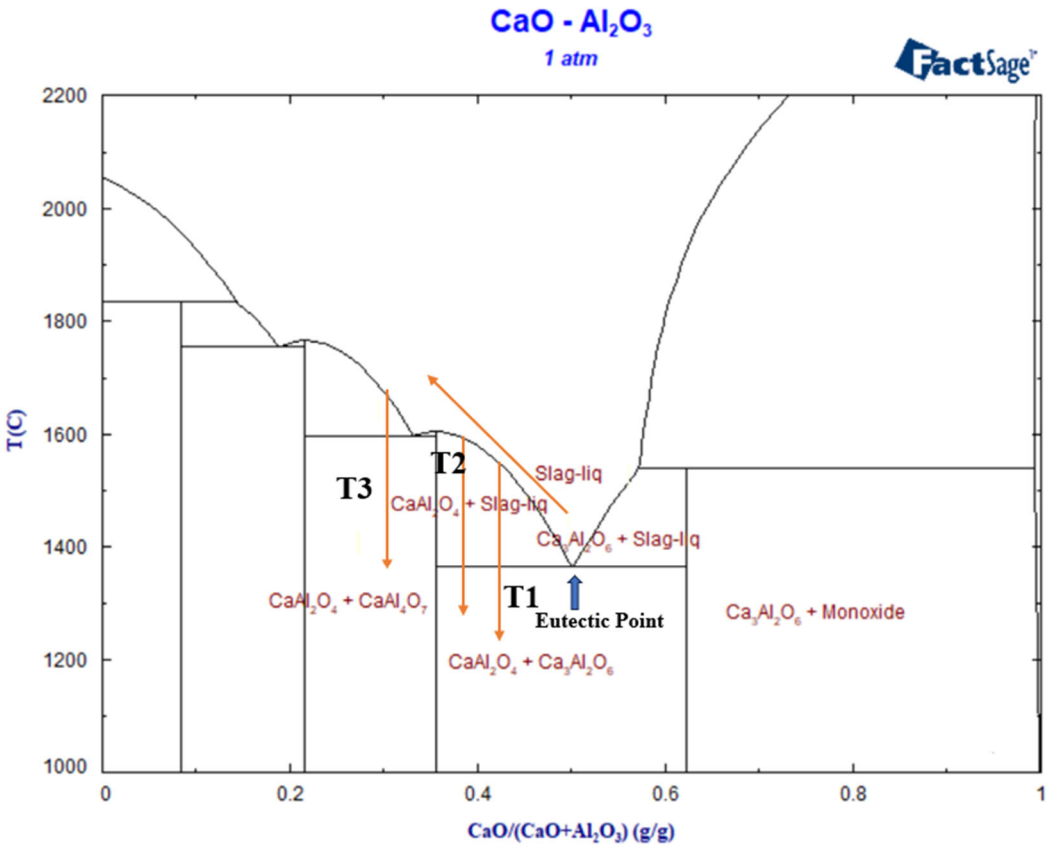

FIG 11 – $CaO\text{-}Al_2O_3$ phase diagram, showing possible phases formed during T1, T2 and T3.

At the beginning of the interaction two distinct humps were observed, which slowly reduces to single molten pool at around 1525°C, marking the end of the reaction. Throughout the reaction the concentration of alumina increases and follows the path marked by arrow on the $CaO\text{-}Al_2O_3$ phase diagram Figure 11. Upon cooling the phases formed during T1, T2 and T3 is marked on the phase diagram plot with arrow. The melting point increases with increase in Al_2O_3 content, and the melting point from the phase diagram seems higher than the original melting point during experiment, this is mainly because of impurity such as silica, which is present in the pre-reduced ore. The marked phases are like that observed using SEM analysis discussed earlier.

CONCLUSION

The interaction of lime particles with pre-reduced manganese ore particles on alumina substrate was studied using sessile drop approach. The main conclusions are summarised as follows:

- It was found that there is a significant drop in the melting point of lime (theoretically 2572°C) due to the presence of impurities and adjacent alumina substrate to temperature of 1380°C.
- It is proposed that CaO and Al_2O_3 interact at their contact and the two solids yield a molten interfacial phase that facilitates the rapid melting of CaO particle.
- The molten slag and solid Mn ore particle getting united rapidly in the moment the molten slag touches the ore particle. Melting is continued via the dissolution of MnO in the ore into the adjacent molten slag.

- The melting or the dissolution rate of Mn ore into the slag is depending on the applied temperature, not complete melting at around 1410°C, while complete melting at around 1525°C occurred within 2 mins.
- The separation of molten metal (iron) drops from the pre-reduced ore or slag during the smelting process is depending on the rate and extent of the dissolution of MnO solid particles to the bulk slag, when the solid oxide disappears, the metal is completely separated.

ACKNOWLEDGEMENTS

The authors would like to thank NTNU for providing the resources and supporting the research work. The authors would also thank all the supporting staff at NTNU. Special thanks to EU council for HalMan project, of which this is a part of.

REFERENCES

Azof, F I, Kolbeinsen, L and Safarian, J, 2017. The Leachability of Calcium Aluminate Phases in Slags for the Extraction of Alumina, in *Proceedings of the 35th International ICSOBA Conference*, pp 243–253.

Barner, H E and Mantell, C L, 1968. Kinetics of Hydrogen Reduction of Manganese Dioxide, *Ind Eng Chem Process Des Dev*, 7:285–294. https://doi.org/10.1021/i260026a023

Costello, A, Abbas, M, Allen, A, Ball, S, Bell, S, Bellamy, R, Friel, S, Groce, N, Johnson, A, Kett, M, Lee, M, Levy, C, Maslin, M, McCoy, D, McGuire, B, Montgomery, H, Napier, D, Pagel, C, Patel, J, De Oliveira, J A P, Redclift, N, Rees, H, Rogger, D, Scott, J, Stephenson, J, Twigg, J, Wolff, J and Patterson, C, 2009. Managing the health effects of climate change, *The Lancet*, 373:1693–1733. https://doi.org/10.1016/S0140-6736(09)60935-1

Davies, J, Paktunc, D, Ramos-Hernandez, J J, Tangstad, M, Ringdalen, E, Beukes, J P, Bessarabov, D G and Du Preez, S P, 2022. The Use of Hydrogen as a Potential Reductant in the Chromite Smelting Industry, *Minerals*, 12:534. https://doi.org/10.3390/min12050534

Haque, N and Norgate, T, 2013. Estimation of greenhouse gas emissions from ferroalloy production using life cycle assessment with particular reference to Australia, *J Clean Prod*, 39:220–230. https://doi.org/10.1016/j.jclepro.2012.08.010

Heidari, A, Niknahad, N, Iljana, M and Fabritius, T, 2021. A Review on the Kinetics of Iron Ore Reduction by Hydrogen, *Materials*, 14:7540. https://doi.org/10.3390/ma14247540

Monsen, B, Tangstad, M, Solheim, I, Syvertsen, M, Ishak, R and Midtgaard, H, 2007. Charcoal For Manganese Alloy Production, in *INFACON XI Conference*, 11:297–310.

Mora, C, Dousset, B, Caldwell, I R, Powell, F E, Geronimo, R C, Bielecki, C R, Counsell, C W W, Dietrich, B S, Johnston, E T, Louis, L V, Lucas, M P, McKenzie, M M, Shea, A G, Tseng, H, Giambelluca, T W, Leon, L R, Hawkins, E and Trauernicht, C, 2017. Global risk of deadly heat, *Nat Clim Change*, 7:501–506. https://doi.org/10.1038/nclimate3322

Office of Air Quality Planning and Standards, 1992. Background Report: AP-42 Section 12.4: Ferroalloy Production; Prepared for US Environmental Protection Agency. Available from: <https://www.epa.gov/sites/default/files/2020-11/documents/b12s04.pdf>

Olsen, S E, Monsen, B E and Lindstad, T, 1998. CO2 Emissions from the Production of Manganese and Chromium Alloys in Norway, in *Proc. 56th Electr Furn Conf*, pp 363–369.

Safarian, J, 2021. A Sustainable Process to Produce Manganese and Its Alloys through Hydrogen and Aluminothermic Reduction, *Processes*, 10:27. https://doi.org/10.3390/pr10010027

Schmidt, G A, Ruedy, R A, Miller, R L and Lacis, A A, 2010. Attribution of the present-day total greenhouse effect, *J Geophys Res*, 115. https://doi.org/10.1029/2010JD014287

Tangstad, M and Olsen, S E, 1995. The Ferromanganese process - Material and Energy Balance, in *INFACON 7 Conference*, pp 621–630.

Westfall, L A, Davourie, J, Ali, M and McGough, D, 2016. Cradle-to-gate life cycle assessment of global manganese alloy production, *Int J Life Cycle Assess*, 21:1573–1579. https://doi.org/10.1007/s11367-015-0995-3

Machine learning for predicting chemical system behaviour of $CaO-MgO-SiO_2-Al_2O_3$ steelmaking slags case study

DOI: 10.62053/EKON9161

B Laidens[1], W Bielefeldt[2] and D Souza[3]

1. Materials Engineer, RHI Magnesita, Contagem, Minas Gerais 32210-080, Brazil. Email: bruno.laidens@rhimagnesita.com
2. Metallurgical Engineer, Federal University of Rio Grande do Sul (UFRGS), Rio Grande do Sul 91501-970, Brazil. Email: wagner@ct.ufrgs.br
3. Metallurgical Engineer, RHI Magnesita, Contagem, Minas Gerais 32210-080, Brazil. Email: dickson.souza@rhimagnesita.com

ABSTRACT

The $CaO-MgO-SiO_2-Al_2O_3$ system, characterised by its intricate phases and thermodynamic properties, plays a pivotal role in steel secondary refining processes, encompassing desulfurisation, non-metallic inclusion capture, and refractory protection. Accurate predictions for diverse industrial applications, including metallurgy, ceramics, and materials science, are imperative. To address this challenge, a combination of machine learning techniques will be specifically applied to model the liquid fraction of the slag and the solid fraction of MgO. The development of an artificial intelligence (AI) system, leveraging various machine learning techniques, has gained momentum in this project. The focus of this work is on constructing an AI model, based on machine learning techniques, within the $CaO-MgO-SiO_2-Al_2O_3$ system, utilising simulation results from FactSage™, version 8.1 (by GTT Technologies). The primary objective is to train the AI model using these simulation outputs to predict the percentage of liquid fraction and MgO saturation based on chemical composition parameters. The AI model will undergo training with a comprehensive data set of simulations within the $CaO-MgO-SiO_2-Al_2O_3$ system, covering a diverse range of compositional at 1873 K. These simulations, conducted through FactSage™ 8.1 software, provide a robust foundation for AI model training, ensuring generalisability and precise predictions for the liquid fraction of the slag and the solid fraction of MgO, the solid fraction of MgO in this case is determined by the difference between the total MgO and the MgO in the liquid fraction, so it is not the objective of this study to determine which phase of MgO is in the solid state.. The predictive capabilities of this AI model hold significant implications for process optimisation, quality control, and decision-making in $CaO-MgO-SiO_2-Al_2O_3$-dependent industries. Precise estimations of the liquid fraction and MgO saturation empower researchers and engineers to enhance operational efficiency and quality. This paper explores the methodologies employed for AI model creation and training, achieved results in terms of prediction accuracy, and potential applications in the field. The development of this AI system signifies a notable advancement in utilising machine learning for better comprehension and control of complex chemical systems. Furthermore, to align the study with real-world steel production, we introduce FeO and MnO at concentrations of 2 per cent and 1 per cent at 1873 K, respectively, following the validation of model results using the $CaO-MgO-SiO_2-Al_2O_3$ system. This adjustment aims to bring the study closer to the observed reality in steel mills globally.

INTRODUCTION

In the contemporary landscape of the steel industry, the relentless pursuit of operational efficiency and sustainability has propelled the adoption of innovative technologies. In this context, artificial intelligence (AI) emerges as a transformative catalyst, facilitating significant advancements in the optimisation of complex processes (Rodriguez *et al*, 2022), With the collection of data from productive sectors and their relationships with artificial intelligence, especially in adoption, there is an expectation that artificial intelligence will be responsible for generating $15.7 trillion of the global gross domestic product by 2030 (Carvalho, 2021). This study aims to underscore the utilisation of AI trained on thermodynamic calculations' results conducted by FactSage™ 8.1 software, especially when applied in the specific context of the $CaO-MgO-SiO_2-Al_2O_3$ slag system. Precise prediction of MgO is crucial to enhance efficiency during the secondary refining of steel, such as adjustment of the sulfur level, capture of non-metallic inclusions (Bielefeldt, Vilela and Heck, 2014) and prolong the lifespan of ladles in steelmaking (Dahl, Brandberg and Sichen, 2006; Gran, 2011).

The steel industry, inherently linked to steel production, confronts considerable challenges related to the efficient consumption of inputs and waste reduction (Andrade, 2023). The manipulation of slag, composed of CaO-MgO-SiO_2-Al_2O_3, plays a critical role in the quality of produced steel (Zhao *et al*, 2016). However, optimising this process requires a profound understanding of the interaction among slag components, with a specific emphasis, for this study, on MgO.

In this context, this research proposes the implementation of AI developed from previously calculated data by FactSage™ 8.1 software. The main objective is to determine, through an AI model, the quantity of MgO in solid phase (indicating supersaturation) in the slag, facilitating the optimisation of the addition of sources of this fundamental oxide. This approach aims to avoid excesses or deficiencies in MgO addition, thus optimising the slag composition and, consequently, enhancing the efficiency of the steelmaking process. FactSage™ 8.1 stands out as a robust software solution with a well-established track record, having undergone a series of studies that validate its ability to interpret the CaO-MgO-SiO_2-Al_2O_3 system (Bielefeldt, Vilela and Heck, 2013; Bielefeldt, Vilela and Heck, 2014; Bale *et al*, 2016). The wealth of prior research and validations highlights the reliability of FactSage™ 8.1 in supporting the AI-driven analysis proposed in this study.

By precisely forecasting MgO requirements, the proposed AI contributes not only to input savings but also to the extension of ladle lifespan (Pretorius and Carlisle, 1998). Avoiding unnecessary or insufficient MgO additions not only results in economic benefits but also promotes more sustainable practices by reducing resource waste and minimising environmental impacts.

This article aims to assess the performance of an artificial intelligence (AI) model generated using data produced by FactSage™. The objective is to predict, based on the chemical composition of slag, the percentage of MgO in the solid phase and the percentage of liquid phase in the slag.

MATERIALS AND METHODOLOGY

While the CaO-MgO-SiO_2-Al_2O_3 system is crucial to this study, there are also other reducible oxides that may play a significant role in the solubilisation of MgO and the liquid fraction of the slag (Pretorius and Carlisle, 1998). Consequently, FeO and MnO were added into the system, with concentrations of 2 per cent and 1 per cent, respectively. These values are suggested as a starting point, and future research can further explore their impact. Typically observed in secondary metallurgy processes is the FeO content falling within the range of 1 to 3 per cent, and MnO ranging from 0.2 to 1 per cent. However, to better assess the methodology, a database was initially created solely for CaO-MgO-SiO_2-Al_2O_3, aiming to compare the results with existing literature. The same training methodology was employed for both systems. The system without the presence of FeO and MnO was trained solely to compare the data with the literature and verify if the calculations performed by FactSage™ align with the established literature. After training, the model's output consists of the MgO content in solid fractions and the percentage of liquid fraction in the slag. Thus, in practice, it would be possible to predict whether the slag used in secondary metallurgy is saturated with MgO, thereby preserving the refractory and with sufficient liquid content to promote reactions at the metal-slag interface.

The primary objective was to attempt to achieve results comparable to those found in the Slag Atlas (Allibert, 1995) using approximately 30 000 slags with different chemical compositions. The objective is to verify the feasibility of training a tool. Because of this, we chose to use a high sample volume. After this study, we will progress to optimise the training by varying the temperature and reducing the number of inputs to compare performance in terms of accuracy and computational resources. These slags were simulated using the Equilib mode of FactSage™. The machine learning method employed in this article is the Random Forest algorithm, which is a technique utilised for classification or regression problems. It relies on an ensemble of decision trees. Given the objective of obtaining numerical values, we are employing Random Forest Regression. The model's operation is elucidated by Lima and Amorin (2020). The step-by-step process is described in Figure 1's flow chart.

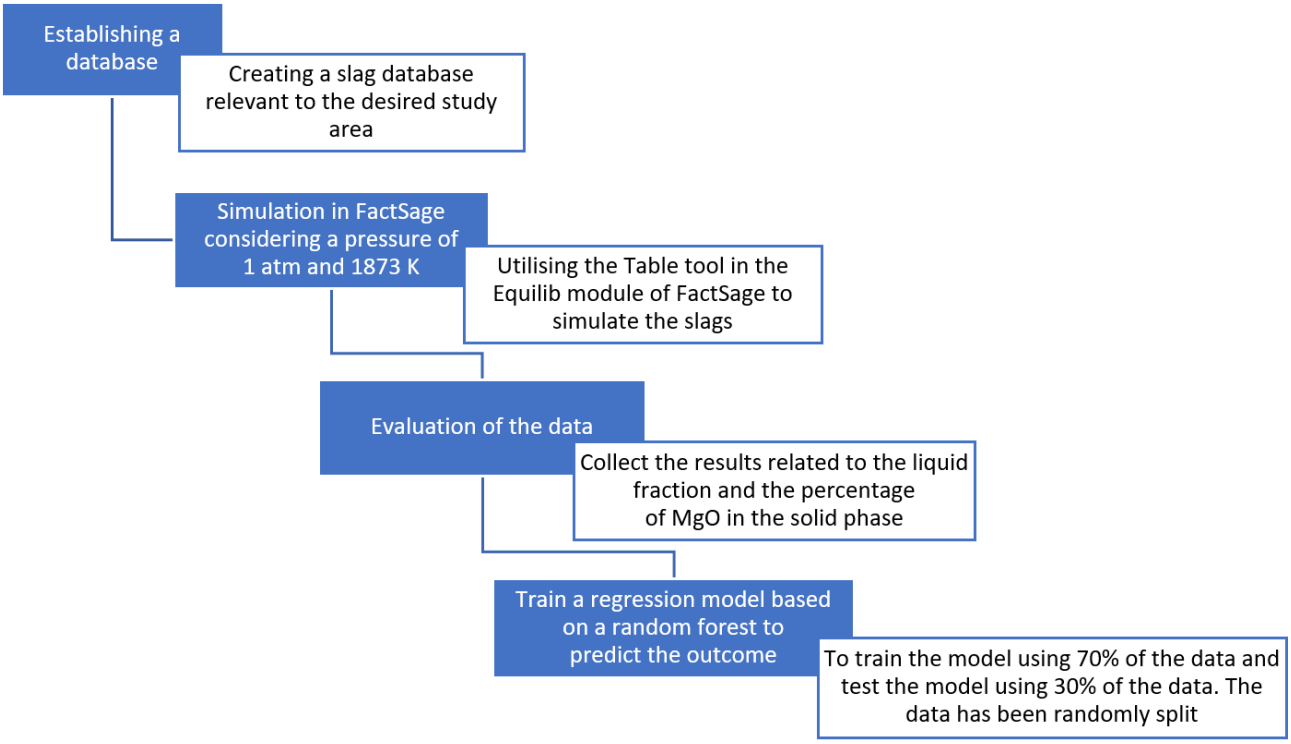

FIG 1 – Simplified flow chart of the methodology for data generation and AI model training.

This approach involved an extensive simulation process to generate a data set that could be compared with the literature data. The Equilib mode of FactSage™ was utilised to simulate the thermodynamic equilibrium of the slags under various conditions, aiming to replicate the range of compositions reported in the literature. The subsequent analysis and comparison of the simulated results with the literature findings constitute a crucial step in validating the accuracy and reliability of the simulation methodology employed in this study.

CaO-SiO_2-MgO-Al_2O_3 system

Understanding the intricacies of the CaO-SiO_2-MgO-Al_2O_3 system is of paramount importance in the context of the steel industry. Researchers such as Xu *et al* (2015), Zhao *et al* (2016), Bielefeldt, Vilela and Heck (2013), and Bielefeldt, Vilela and Heck (2014) have conducted seminal studies on this system, unravelling its critical role in various stages of the steelmaking process. Their works have contributed valuable insights into the thermodynamic and kinetic aspects of the interactions within the CaO-SiO_2-MgO-Al_2O_3 system, offering foundational knowledge for optimising steel production processes.

The Slag Atlas book (Allibert, 1995) provides diagrams of the CaO-MgO-SiO_2-Al_2O_3 system, which are commonly depicted and acknowledged in the literature. In consideration of this system outlined in the Slag Atlas, the primary objective of this study was to assess whether the methodology employed aligns with this significant body of literature. To achieve this, a dedicated AI model was constructed, utilising the same creation flow described in Figure 1, focusing solely on the oxides CaO-MgO-SiO_2-Al_2O_3.

Pseudo ternary diagrams were generated, highlighting the percentages of liquid fraction and MgO supersaturation. The aim was to compare these results with the diagrams presented in the Slag Atlas. Additionally, the data generated for machine learning training was also employed to generate pseudo ternary diagrams, where the information is entirely a result of calculations performed by the FactSage™ 8.1 algorithm.

This approach ensures a comprehensive evaluation of the presented methodology by juxtaposing it with established literature and utilising real-world data from FactSage™. The study not only validates the alignment of the AI model with the Slag Atlas but also provides insights into potential

enhancements or divergences in results, contributing to the ongoing discourse on the CaO-SiO_2-MgO-Al_2O_3 system within the steelmaking context.

In the following section, we delve into artificial intelligence (AI) trained using a data set generated from the combination of four different oxides: Al_2O_3, CaO, SiO_2, and MgO. The objective is to attempt the recreation of pseud oternary diagrams using the AI model's predictions. If the diagrams generated by the AI exhibit a strong resemblance to both existing literature and data obtained from FactSage™, we can consider expanding the scope of the study. This expansion involves the inclusion of additional oxides and the creation of alternative slag system configurations that closely mirror the reality of steel production.

For the establishment of the database, compositions of a slag were generated based on the oxides Al_2O_3, CaO, SiO_2, and MgO. The oxides CaO, SiO_2, and MgO vary from 0 to 100 in increments of 5 per cent, while the oxide Al_2O_3 varies from 0 to 30 in increments of 5 per cent. The objective in this phase of the study is not to achieve an extremely precise diagram but rather to demonstrate that the model is capable of handling intermediate values not present in the initial database. This capability allows for the construction of a pseudo ternary diagram akin to those found in the literature, showcasing the model's adaptability to a broader range of compositional inputs.

The AI model was trained using 1211 combinations of oxides, and the process of creating the AI is detailed in the flow chart depicted in Figure 1. In the model training phase, these slag compositions were randomly divided in a 70–30 proportion, with 70 per cent of the data employed for model training and the remaining 30 per cent utilised for testing the model's accuracy. The implementation of the AI model employed the Python library sklearn, utilising the DecisionTreeRegressor algorithm. The diagrams generated from the model are presented using the plotly.figure_factory library in Python.

The results of the simulations and the comparison of the generated diagrams with the literature will be described in Figures 2–9.

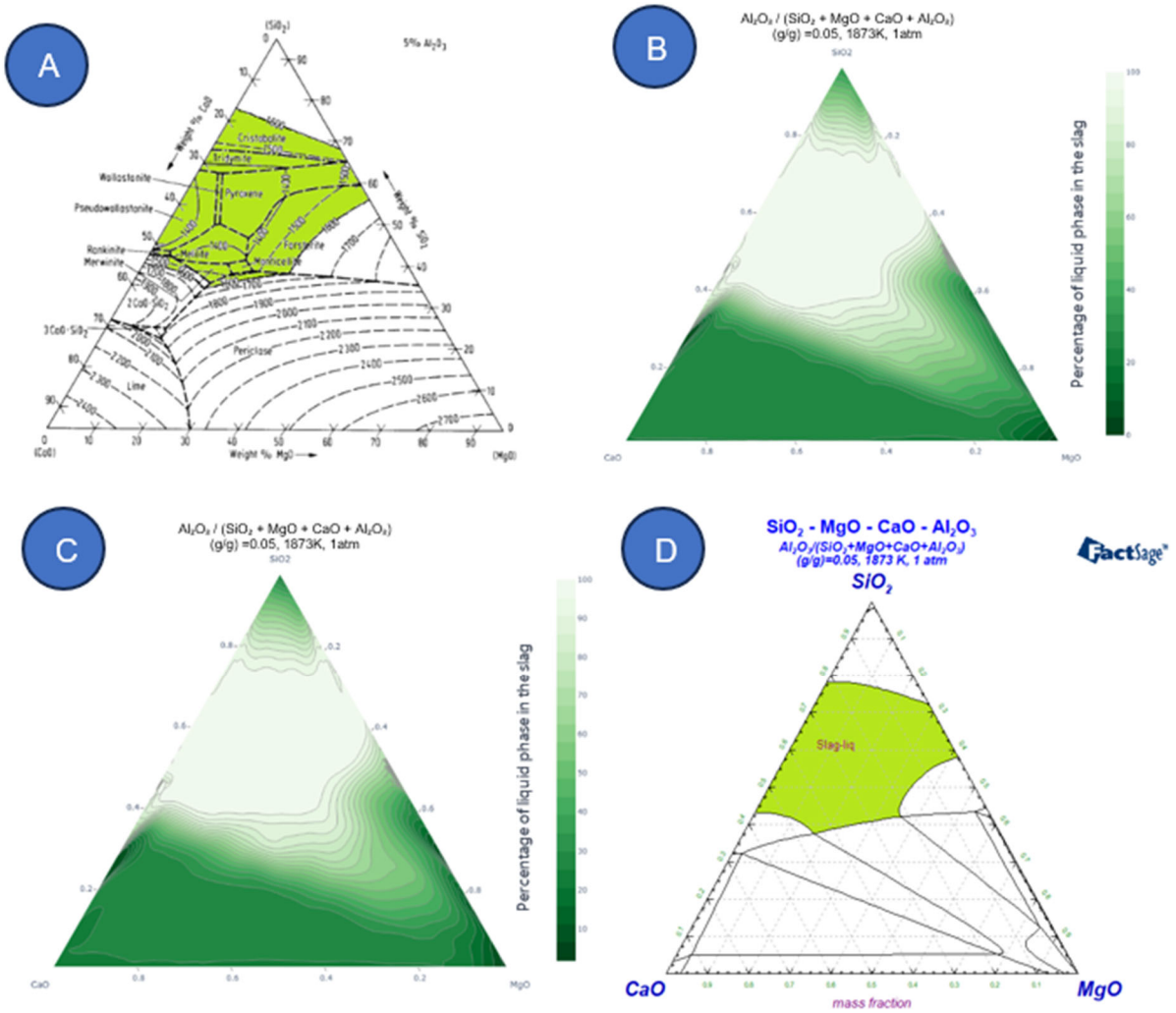

FIG 2 – (a) Liquidus surface: 100 per cent Liquid in green (Osborn *et al*, 1954); (b) Liquidus surface calculated by FactSage™; (c) Liquidus surface calculated by AI; (d) Liquidus surface calculated and built using the Phase Diagram mode in FactSage™. The diagrams are made in the CaO-MgO-SiO_2-Al_2O_3 system with 5 per cent Al_2O_3 by mass with temperature at 1873 K and pressure at 1 atm.

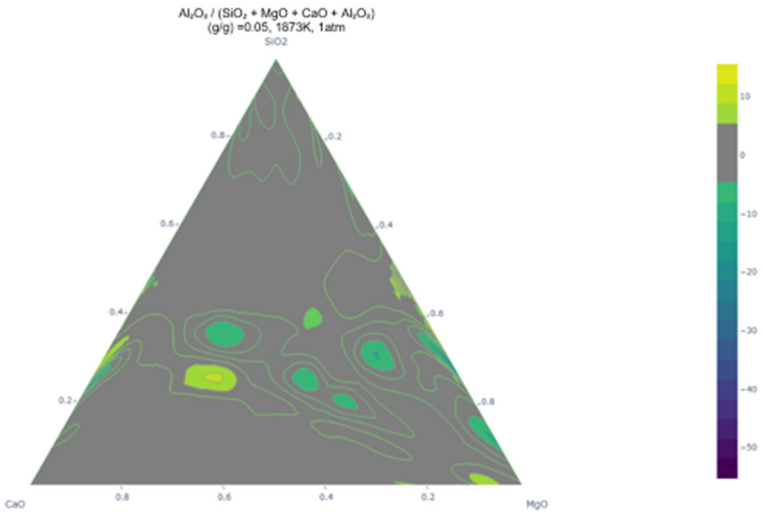

FIG 3 – Difference in the liquid phase (%) values between those calculated by FactSage™ and those predicted by the AI for a slag with 5 per cent Al_2O_3 at a temperature of 1873 K. The grey-shaded region represents areas where the difference between the values calculated by FactSage™ and those predicted by the AI falls between -5 and +5.

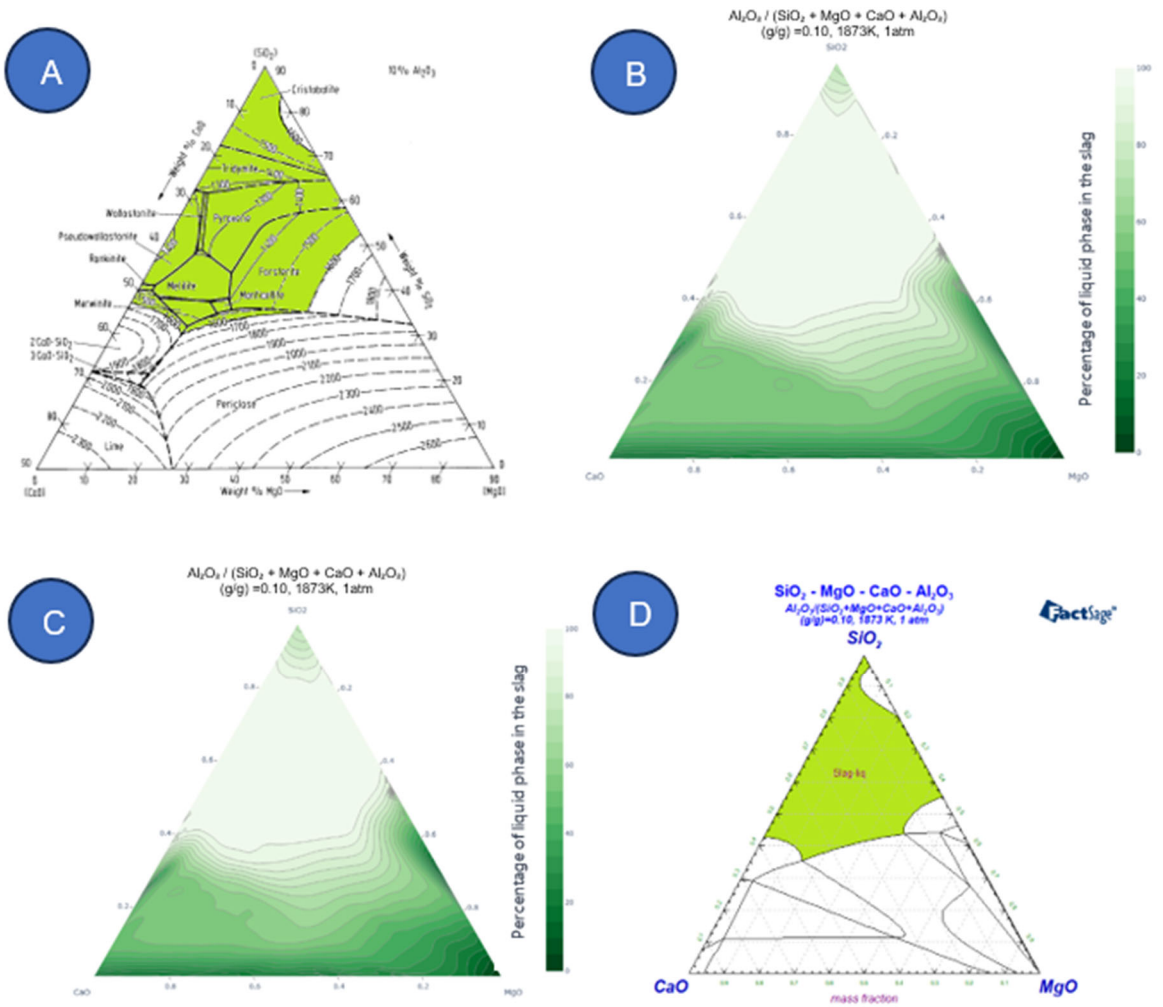

FIG 4 – (a) Liquidus surface: 100 per cent Liquid in green (Osborn *et al*, 1954); (b) Liquidus surface calculated by FactSage™; (c) Liquidus surface calculated by AI; (d) Liquidus surface calculated and built using the Phase Diagram mode in FactSage™. The diagrams are made in the CaO-MgO-SiO_2-Al_2O_3 system with 10 per cent Al_2O_3 by mass with temperature at 1873 K and pressure at 1 atm.

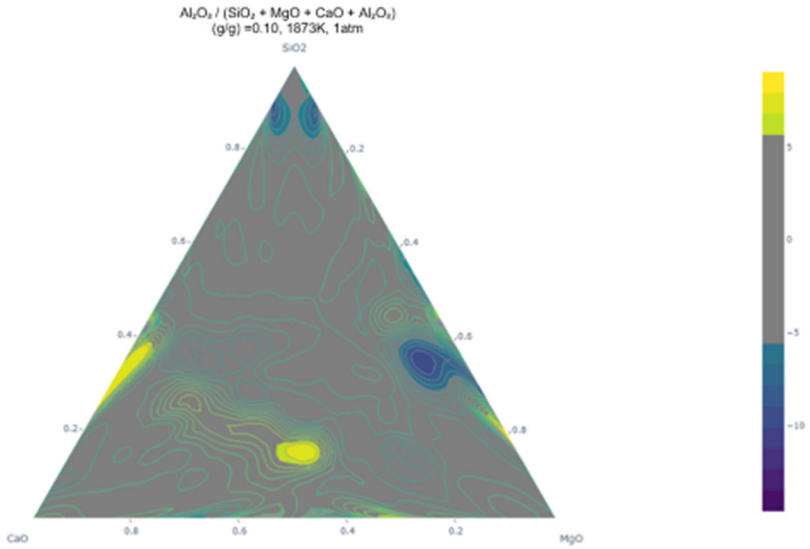

FIG 5 – Difference in the liquid phase (%) values between those calculated by FactSage™ and those predicted by the AI for a slag with 10 per cent Al_2O_3 at a temperature of 1873 K. The grey-shaded region represents areas where the difference between the values calculated by FactSage™ and those predicted by the AI falls between -5 and +5.

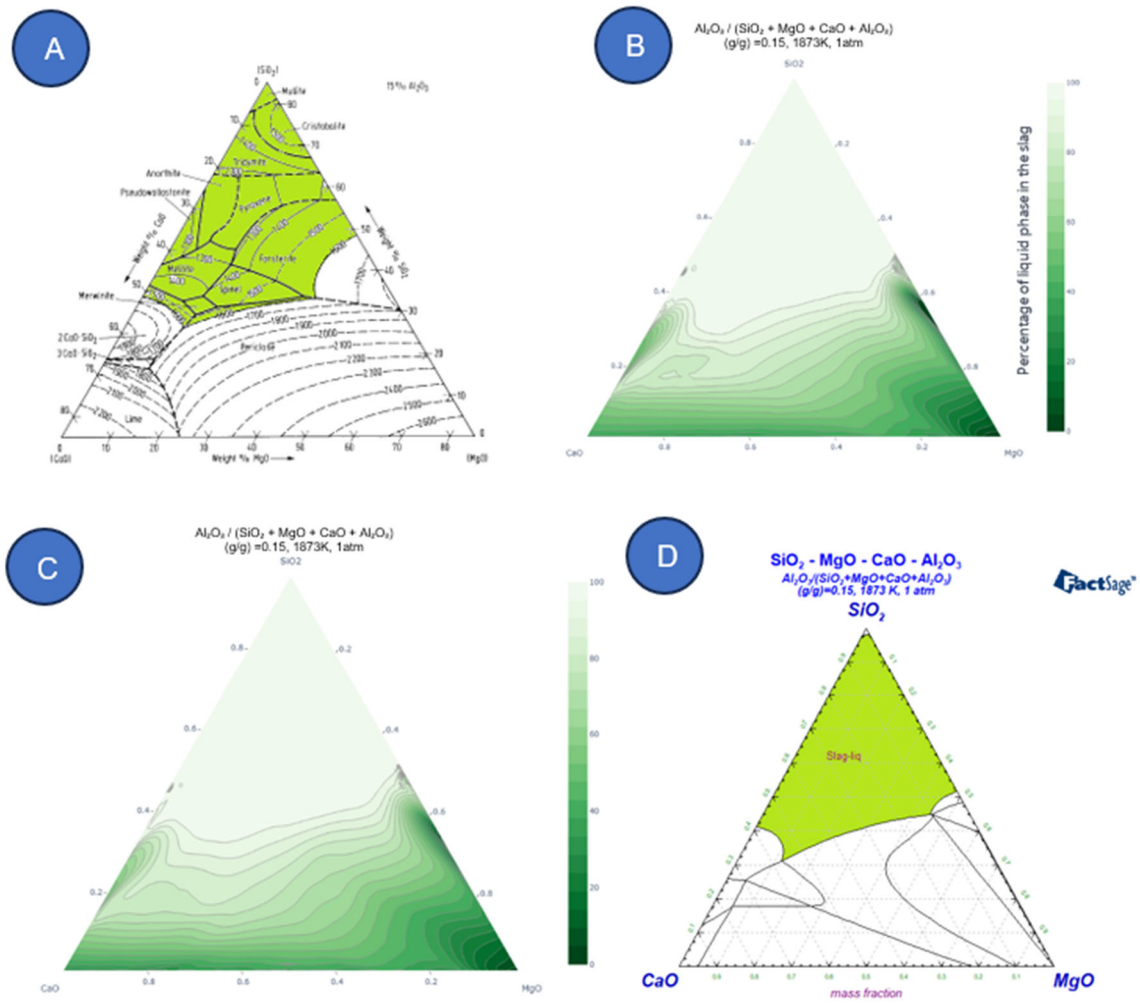

FIG 6 – (a) Liquidus surface: 100 per cent Liquid in green (Osborn *et al*, 1954); (b) Liquidus surface calculated by FactSage™; (c) Liquidus surface calculated by AI; (d) Liquidus surface calculated and built using the Phase Diagram mode in FactSage™. The diagrams are made in the CaO-MgO-SiO_2-Al_2O_3 system with 15 per cent Al_2O_3 by mass with temperature at 1873 K and pressure at 1 atm.

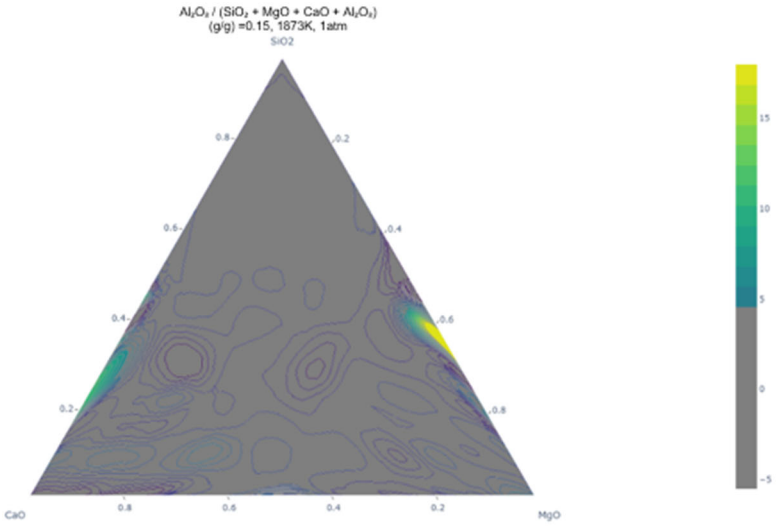

FIG 7 – Difference in the liquid phase (%) values between those calculated by FactSage™ and those predicted by the AI for a slag with 15 per cent Al_2O_3 at a temperature of 1873 K. The grey-shaded region represents areas where the difference between the values calculated by FactSage™ and those predicted by the AI falls between -5 and +5.

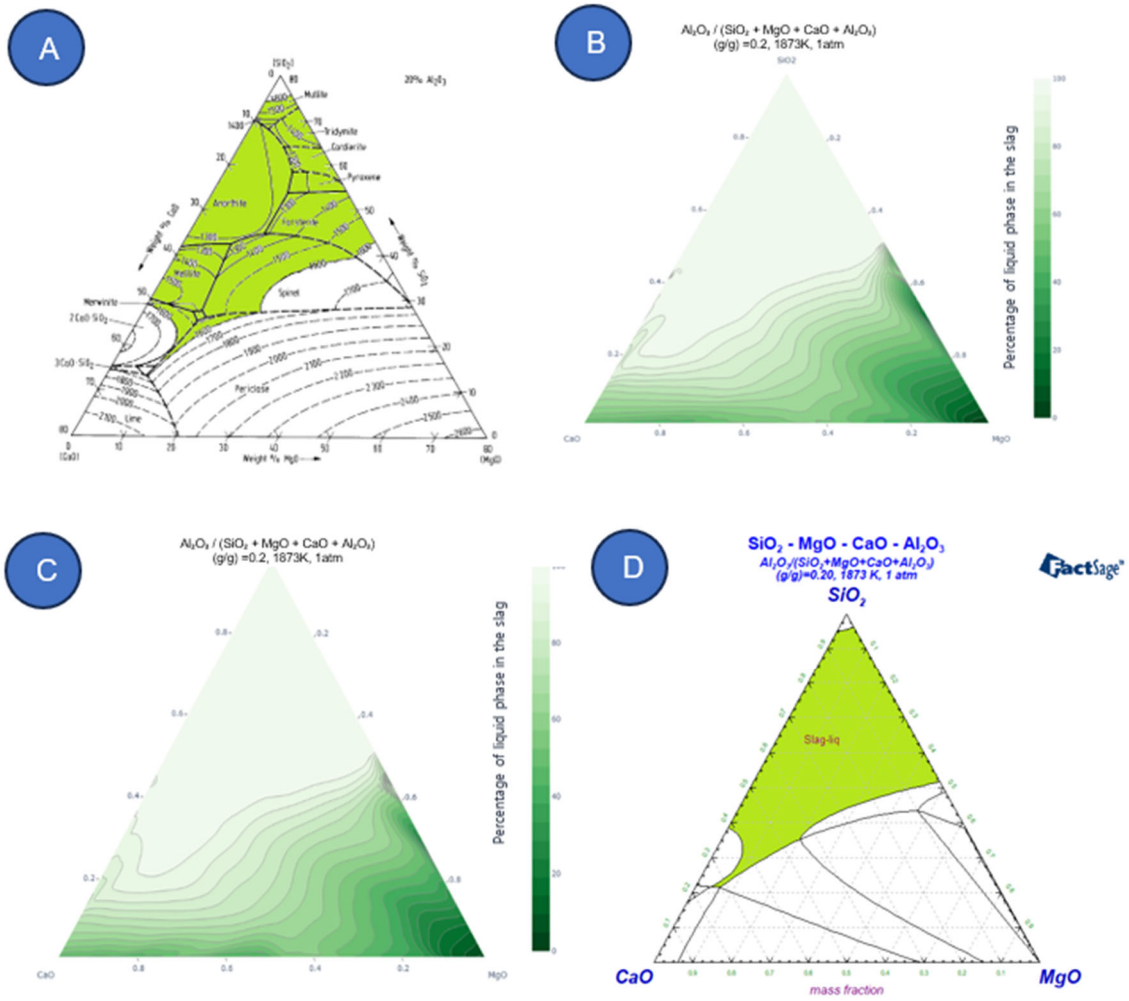

FIG 8 – (a) Liquidus surface: 100 per cent Liquid in green (Osborn *et al*, 1954); (b) Liquidus surface calculated by FactSage™; (c) Liquidus surface calculated by AI; (d) Liquidus surface calculated and built using the Phase Diagram mode in FactSage™. The diagrams are made in the CaO-MgO-SiO_2-Al_2O_3 system with 20 per cent Al_2O_3 by mas with temperature at 1873 K and pressure at 1 atm.

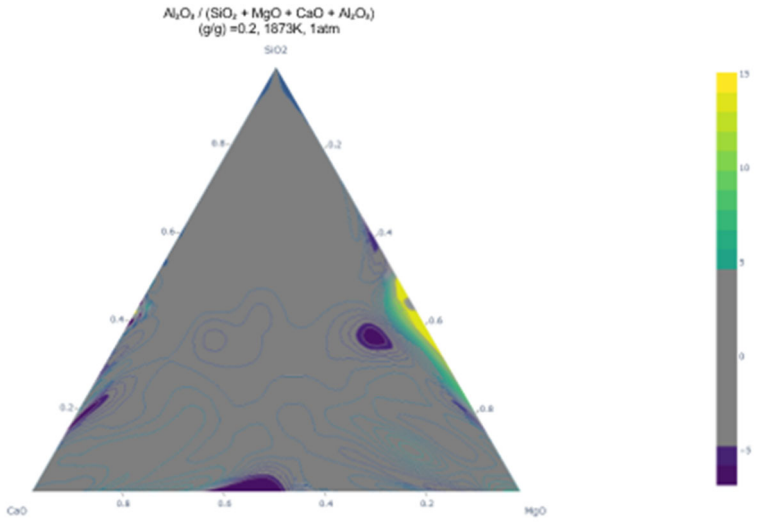

FIG 9 – Difference in the liquid phase (%) values between those calculated by FactSage™ and those predicted by the AI for a slag with 20 per cent Al_2O_3 at a temperature of 1873 K. The grey-shaded region represents areas where the difference between the values calculated by FactSage™ and those predicted by the AI falls between -5 and +5.

Through the analysis of the preceding figures, it can be concluded that, despite lacking precision in the 100 per cent liquid phase contour region, the silhouette of the graph generated by AI closely resembles that calculated by FactSage™ and depicted in the Slag Atlas diagram (Osborn *et al*, 1954). One possible factor contributing to this discrepancy is the database variation in five unit increments during slag generation. In an effort to enhance accuracy, the forthcoming section of this article, delving into the core theme of slag containing 2 per cent FeO and 1 per cent MnO, will adopt a revised approach. The variation will be reduced from five to one, with a specific focus on a chemical composition region based on the prevalent slags found in the steel industry, aiming to refine the model's precision.

$CaO-MgO-SiO_2-Al_2O_3$ system with 2 per cent FeO and 1 per cent MnO

In the literature, as previously described, there is a common occurrence of studies addressing the $CaO-MgO-SiO_2-Al_2O_3$ system. However, for the future development of a slag optimisation tool to be employed in real-time refining processes, it is imperative that other oxides present in the secondary refining slag are included in the system. Given that the training methodology of the AI has been validated in the previous section, we will now explore the system with the inclusion of 2 per cent FeO and 1 per cent MnO (Table 1). This system has been chosen for this article to showcase the accuracy of the simulation. However, for future endeavours, it is crucial to train the algorithm using various percentages of FeO and MnO to make the algorithm more comprehensive. It is highly relevant to consider other components such as Na_2O, K_2O, CaF_2, which should be included in future works.

TABLE 1

Variation of oxides in the database used for AI training. The variation steps for each oxide are set at 1. Temperature at 1873 K and pressure at 1 atm.

	Al_2O_3	CaO	FeO	MgO	MnO	SiO_2
Maximum	50	87	2	30	1	50
Minimum	0	20	2	0	1	10

More than 20 000 slag compositions were generated under these conditions. Using this, the artificial intelligence model has two objectives: determining the percentage of liquid fraction and the percentage of MgO in the solid phase of the slag. After performing the same procedure as in Figure 1, we evaluate the model's performance by comparing the predicted value with the calculated value from FactSage™ in Figures 10 and 11. It is important to note that we are using the 30 per cent of data that the model did not use for training.

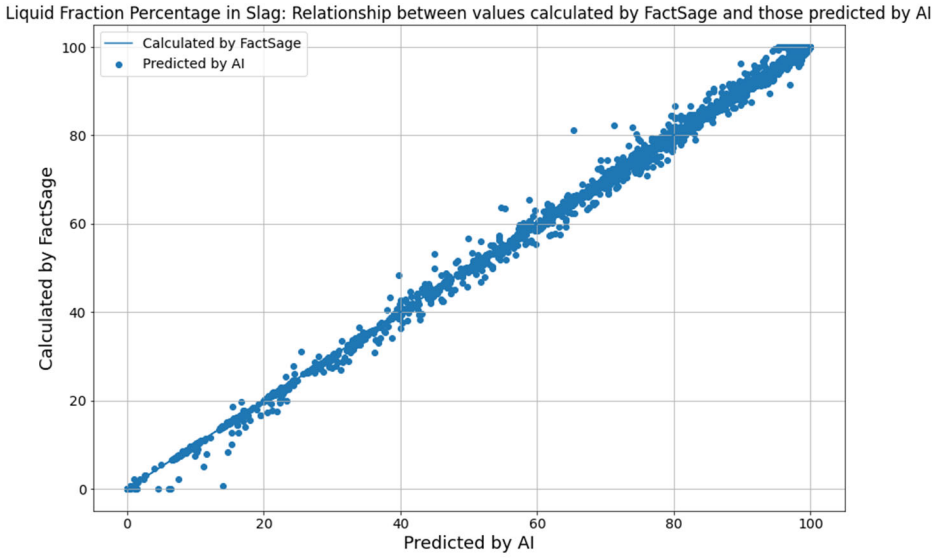

FIG 10 – Liquid fraction percentage in slag: relationship between values calculated by FactSage™ and those predicted by AI at 1873 K and 1 atm.

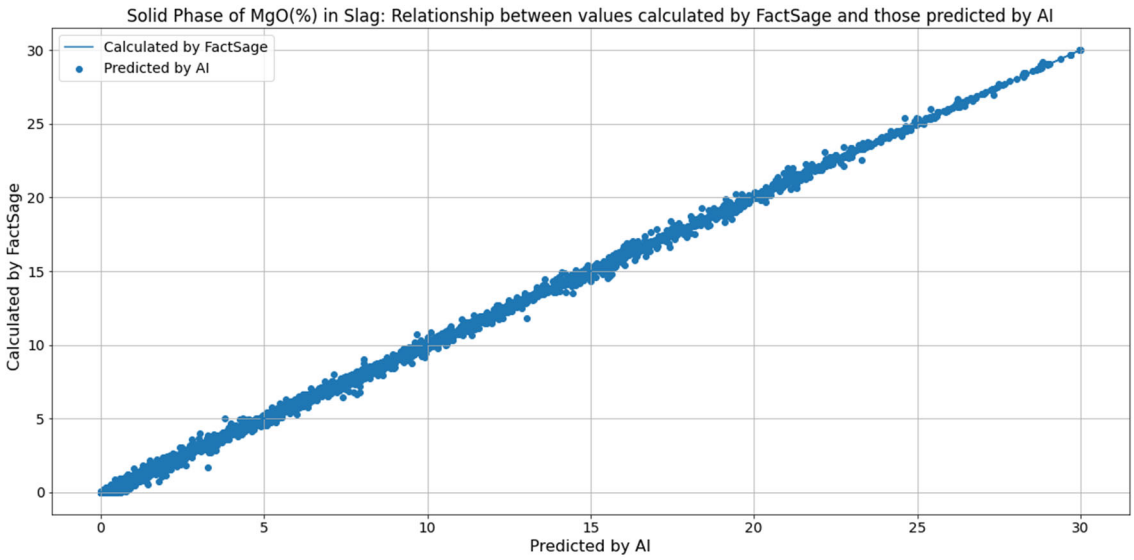

FIG 11 – Solid phase of MgO(%) in slag: relationship between values calculated by FactSage™ and those predicted by AI at 1873 K and 1 atm.

In order to compare the results, two histograms were generated, depicting the differences between the predicted values by the model and the values calculated by FactSage™. One histogram pertains to the prediction of the liquid fraction, while the other focuses on the prediction of the percentage of MgO in the solid phase (Figures 12 and 13).

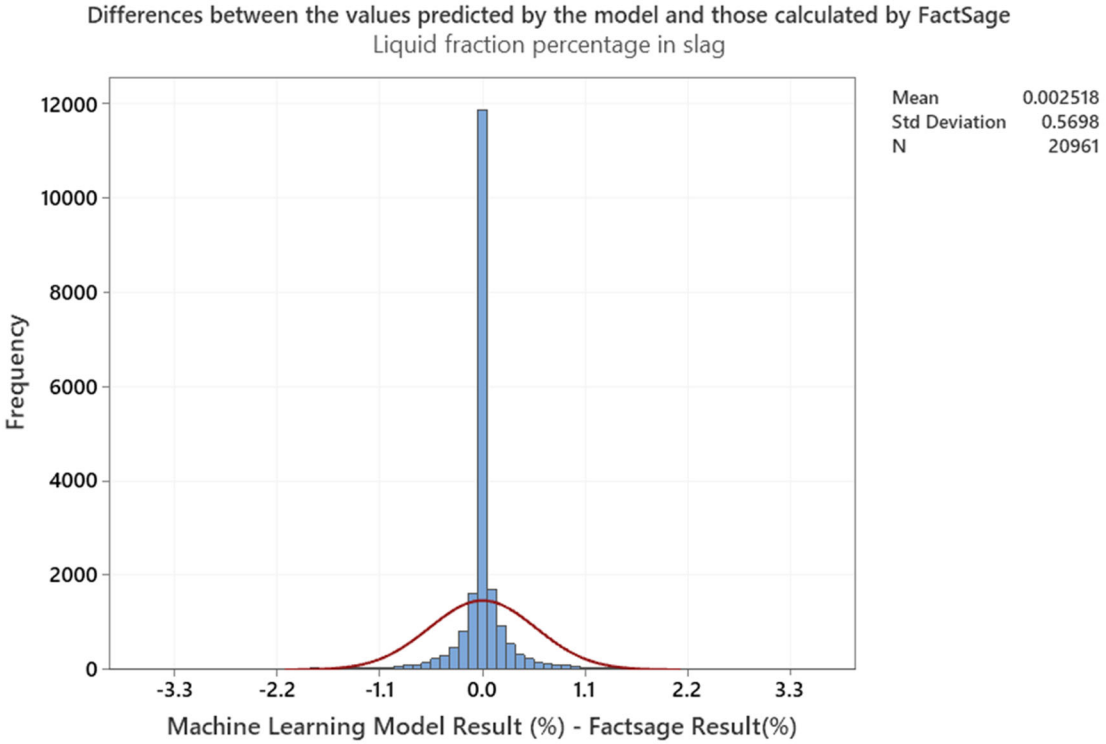

FIG 12 – Liquid Fraction percentage in slag – difference (%) between the value calculated by FactSage™ and the AI model result at 1873 K and 1 atm.

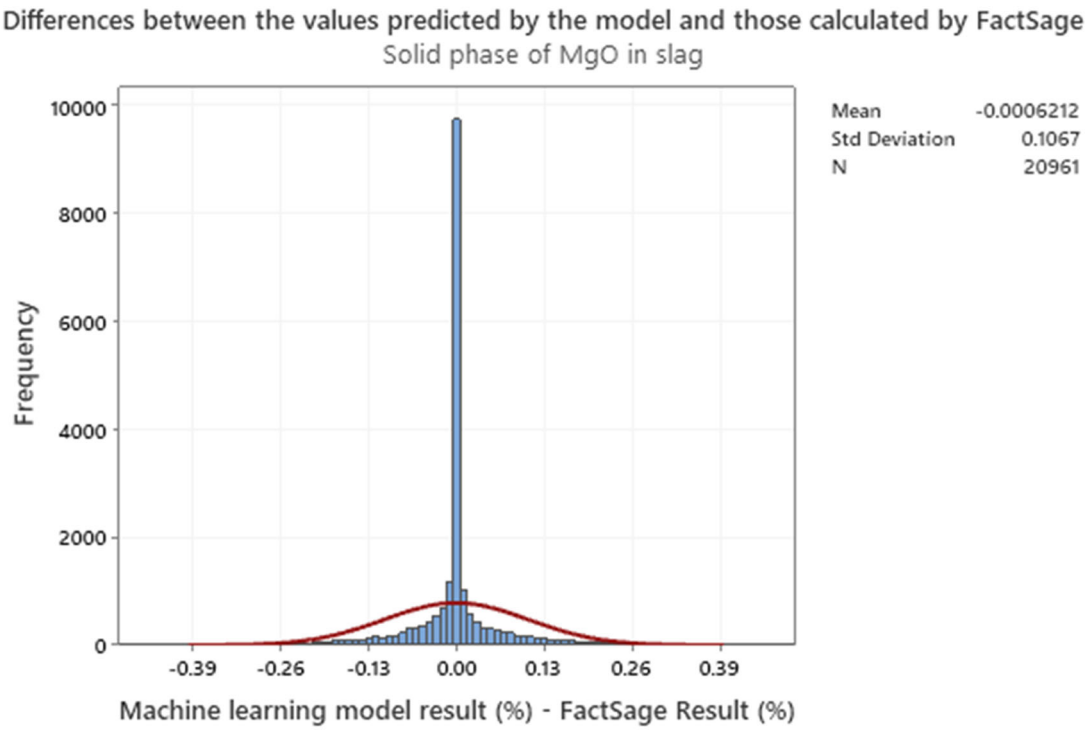

FIG 13 – Solid phase of MgO in slag – difference between the value calculated by FactSage™ and the AI model result at 1873 K and 1 atm.

Looking at the histogram depicting the differences in responses between FactSage™ and the model, it is evident that, for the liquid fraction, we observe an average difference very close to zero, with a standard deviation smaller than 1 per cent. In extreme cases, the error hardly exceeds +2 per cent or -2 per cent. Similarly, the AI model, when predicting MgO in the solid phase, also exhibits low error, with the vast majority of data falling between -0.4 per cent and 0.4 per cent. The implementation of a model with such accuracy seems to be sufficiently reliable to initiate an industrial-scale test.

It's important to note that the red line of the theoretical distribution is not aligned with the data from the histogram. This could indicate an error in the standard deviation generated by a very high number of values close to zero. Therefore, using the data generated by the model, we compare its results with those obtained by FactSage™, which will be displayed in the ternary diagrams described in these final figures.

Subsequently, the generated algorithm was employed to recalculate a diagram illustrating the evolution of the solid fraction of MgO in the slag and the percentage of liquid slag. In this approach, MgO was held constant at values of 5, 10, 15, and 20, while the oxides CaO, MgO, and SiO_2 were varied at the vertices of the ternary diagram. It is important to note that the system now incorporates 2 per cent of FeO and 1 per cent of MnO. The values of CaO, MgO, and SiO_2 needed to be normalised between 0 and 100 to enable the generation of the diagram. The outcomes concerning the liquid percentage in the slag will be elucidated in the diagrams presented in Figures 14–17. The grey regions represent areas outside the training range of the model.

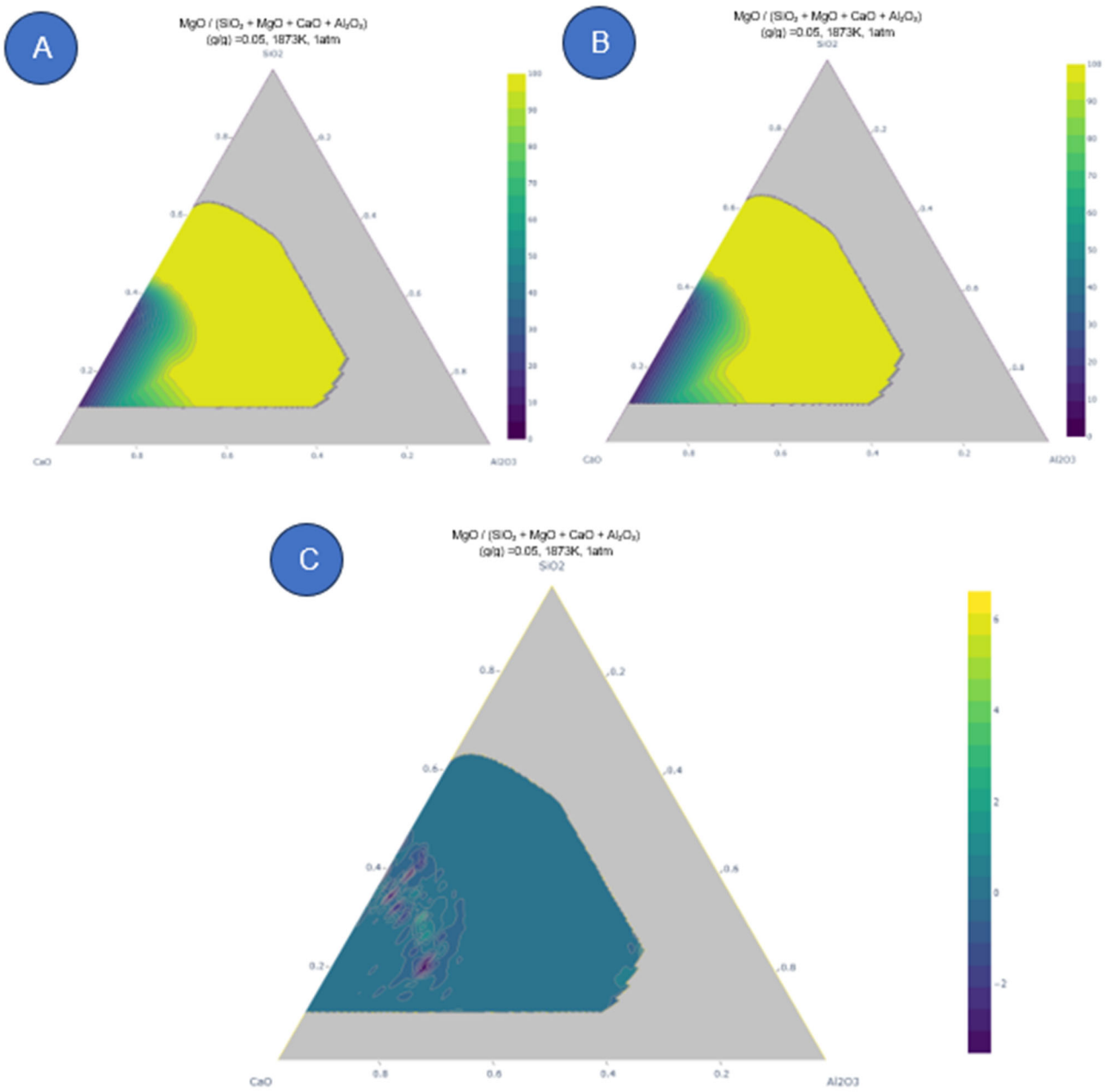

FIG 14 – (a) Diagram depicting the percentage of liquid phase of the slag calculated by FactSage™ at 1873 K and 1 atm with 5 per cent MgO; (b) Diagram illustrating the percentage of liquid phase of the slag predicted by the AI model at 1873 K and 1 atm with 5 per cent MgO; (c) Diagram showcasing the difference between the results calculated by the two methods at 1873 K and 1 atm with 5 per cent MgO.

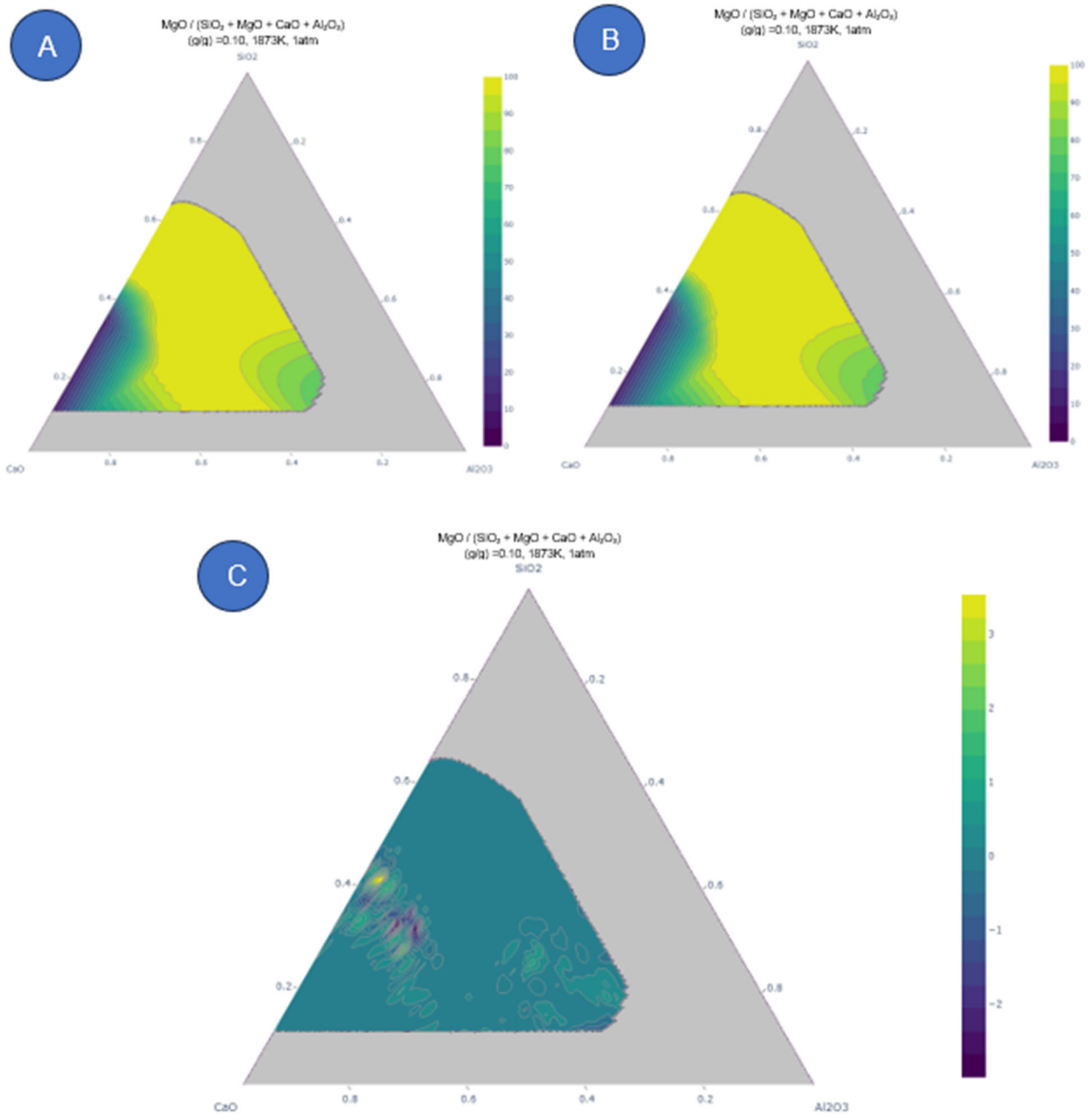

FIG 15 – (a) Diagram depicting the percentage of liquid phase of the slag calculated by FactSage™ at 1873 K and 1 atm with 10 per cent MgO; (b) Diagram illustrating the percentage of liquid phase of the slag predicted by the AI model at 1873 K and 1 atm with 10 per cent MgO; (c) Diagram showcasing the difference between the results calculated by the two methods at 1873 K and 1 atm with 10 per cent MgO.

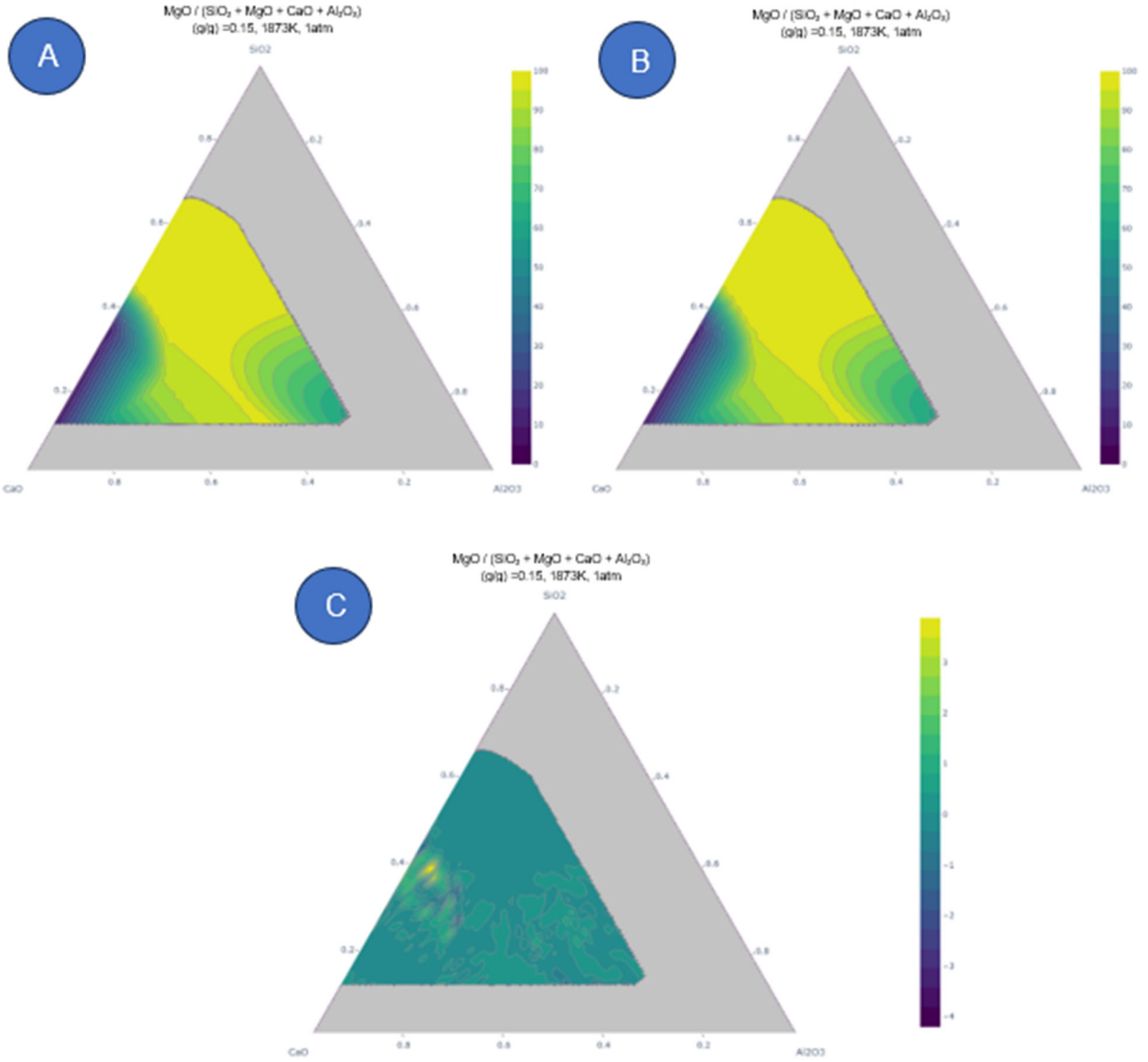

FIG 16 – (a) Diagram depicting the percentage of liquid phase of the slag calculated by FactSage™ at 1873 K and 1 atm with 15 per cent MgO; (b) Diagram illustrating the percentage of liquid phase of the slag predicted by the AI model at 1873 K and 1 atm with 15 per cent MgO; (c) Diagram showcasing the difference between the results calculated by the two methods at 1873 K and 1 atm with 15 per cent MgO.

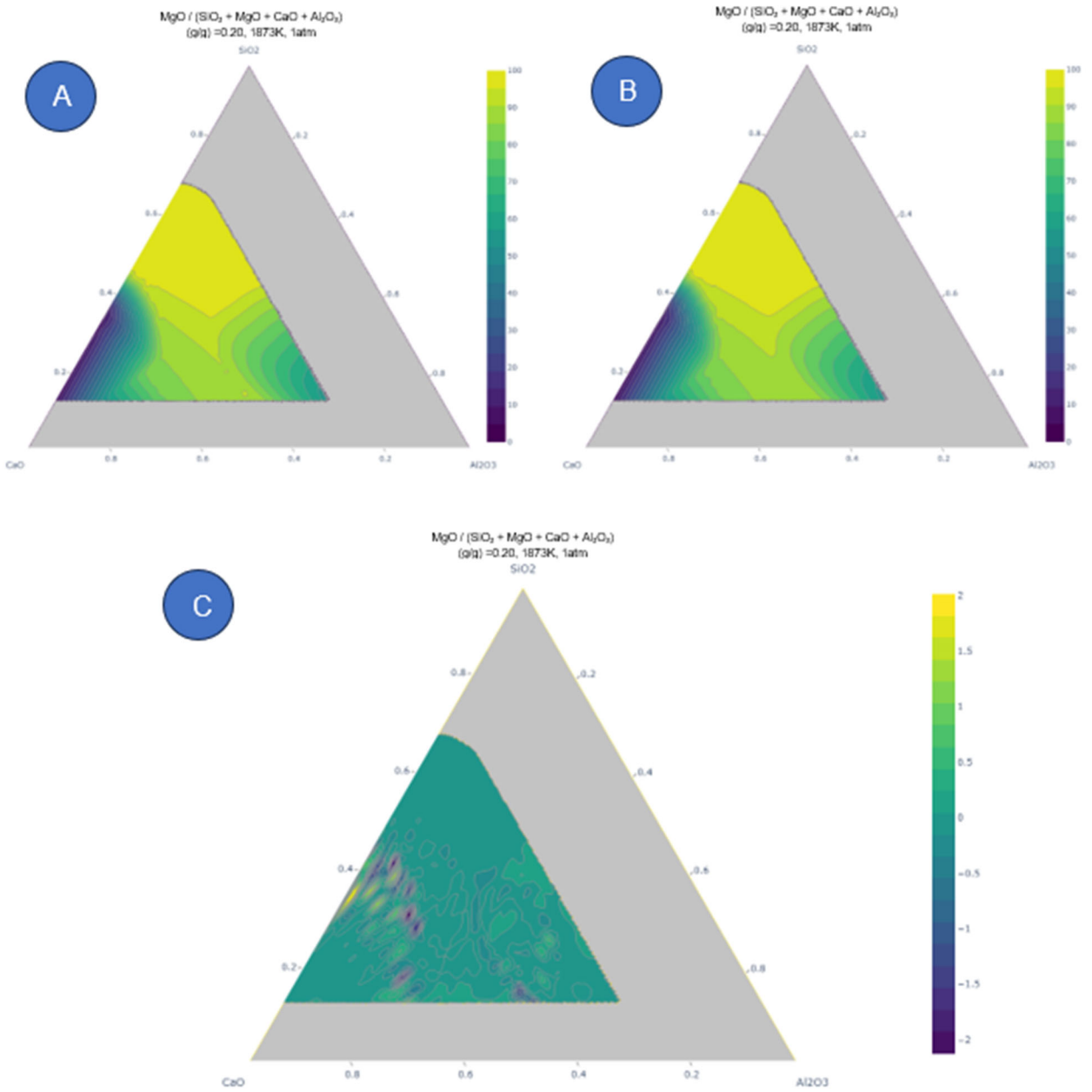

FIG 17 – (a) Diagram depicting the percentage of liquid phase of the slag calculated by FactSage™ at 1873 K and 1 atm with 20 per cent MgO; (b) Diagram illustrating the percentage of liquid phase of the slag predicted by the AI model at 1873 K and 1 atm with 20 per cent MgO; (c) Diagram showcasing the difference between the results calculated by the two methods at 1873 K and 1 atm with 20 per cent MgO.

Analysing the results concerning the liquid fraction in the slag, we can conclude that the AI model produces results very close to those generated by FactSage™. An important factor to note is that for slags with lower CaO content and higher Al_2O_3 levels (> 35 per cent), there are regions where solid precipitates are formed. It is observed that the liquid fraction content begins to decrease, possibly due to the formation of crystalline networks of Al_2O_3-rich oxides. The amount of solid formed in these regions is dependent on the MgO content in the slag; for lower MgO contents, the formation of solid fractions is less than for higher MgO contents.

Next, in Figures 18–21, we will present the data related to the MgO content in the solid fraction of the slag in a similar manner. Once again, we emphasise that the grey regions are not part of the study's sample space.

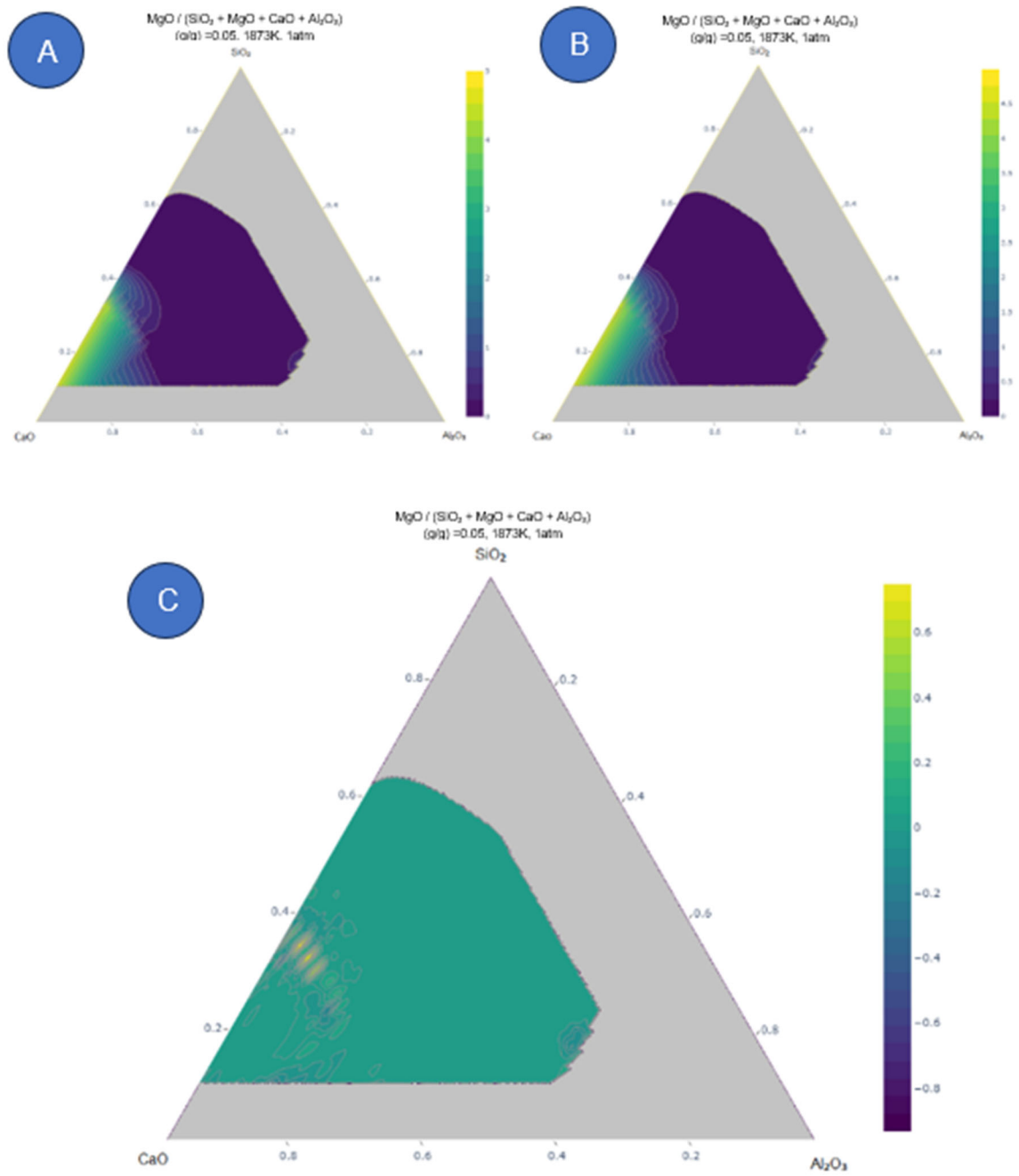

FIG 18 – (a) Diagram depicting the percentage of MgO in the solid fraction of the slag calculated by FactSage™ at 1873 K and 1 atm with 5 per cent MgO; (b) Diagram illustrating the percentage of MgO in the solid fraction of the slag predicted by the AI model at 1873 K and 1 atm with 5 per cent MgO; (c) Diagram showcasing the difference between the results calculated by the two methods at 1873 K and 1 atm with 5 per cent MgO.

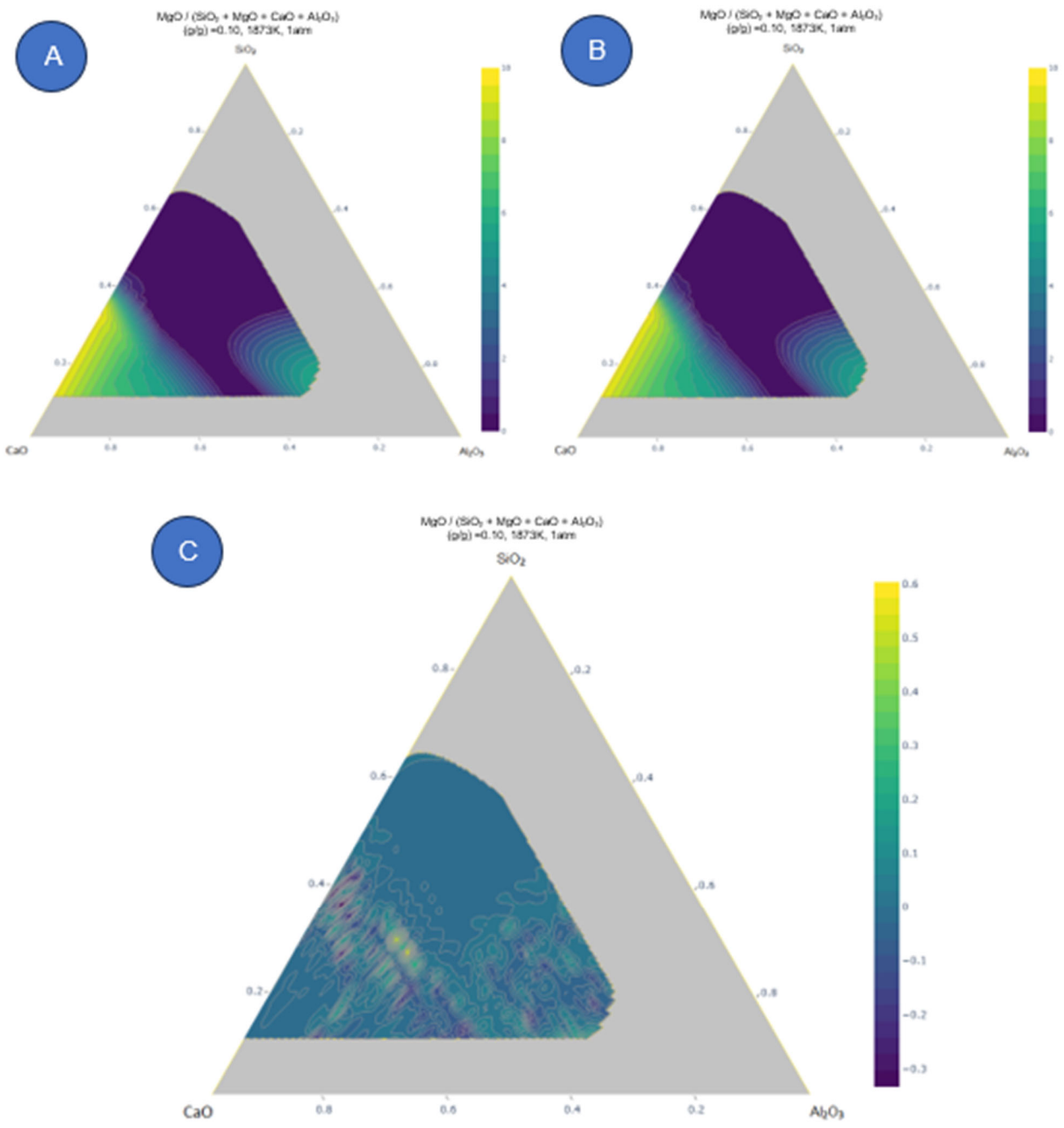

FIG 19 – (a) Diagram depicting the percentage of MgO in the solid fraction of the slag calculated by FactSage™ at 1873 K and 1 atm with 10 per cent MgO; (b) Diagram illustrating the percentage of MgO in the solid fraction of the slag predicted by the AI model at 1873 K and 1 atm with 10 per cent MgO; (c) Diagram showcasing the difference between the results calculated by the two methods at 1873 K and 1 atm with 10 per cent MgO.

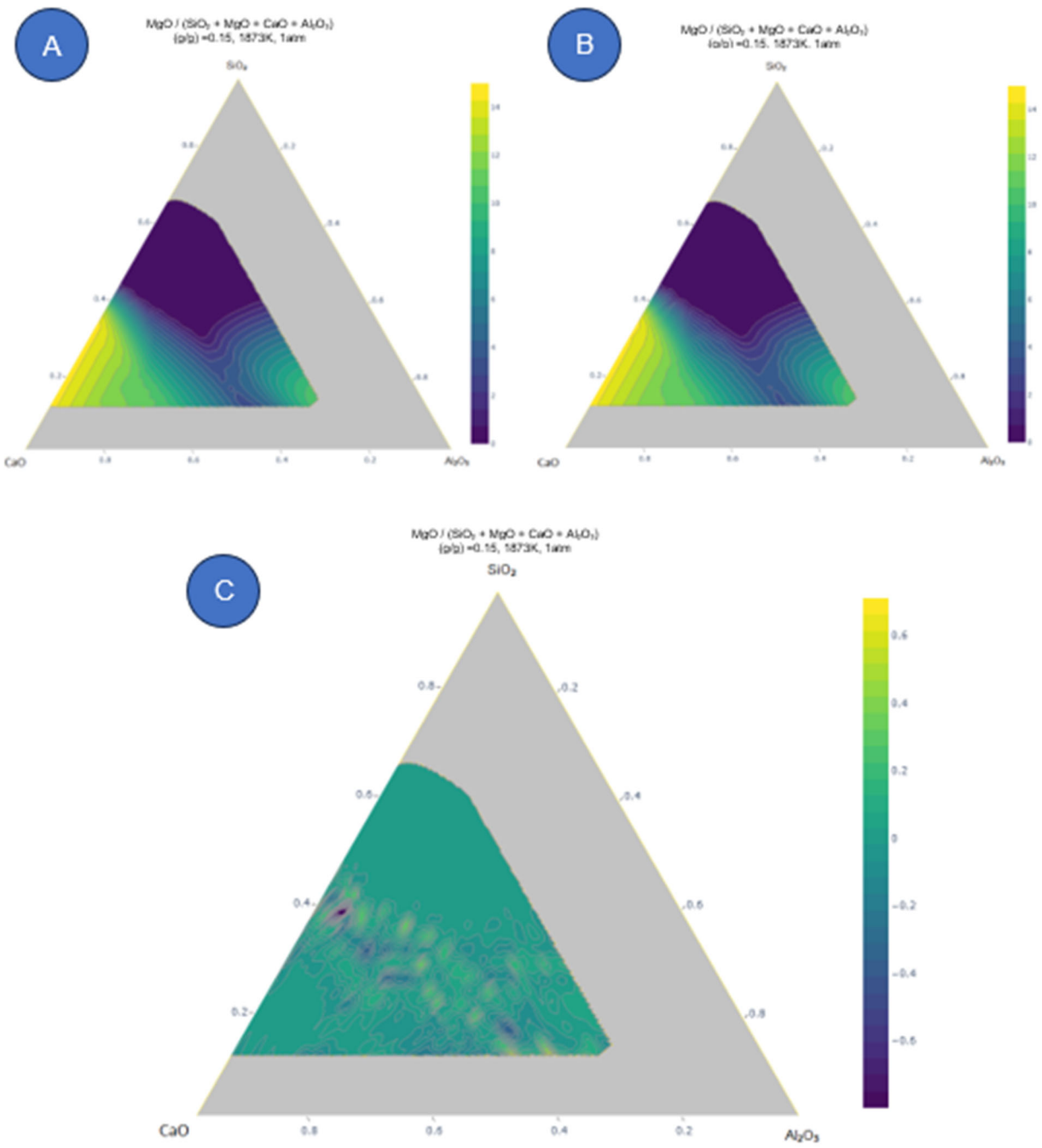

FIG 20 – (a) Diagram depicting the percentage of MgO in the solid fraction of the slag calculated by FactSage™ at 1873 K and 1 atm with 15 per cent MgO; (b) Diagram illustrating the percentage of MgO in the solid fraction of the slag predicted by the AI model at 1873 K and 1 atm with 15 per cent MgO; (c) Diagram showcasing the difference between the results calculated by the two methods at 1873 K and 1 atm with 15 per cent MgO.

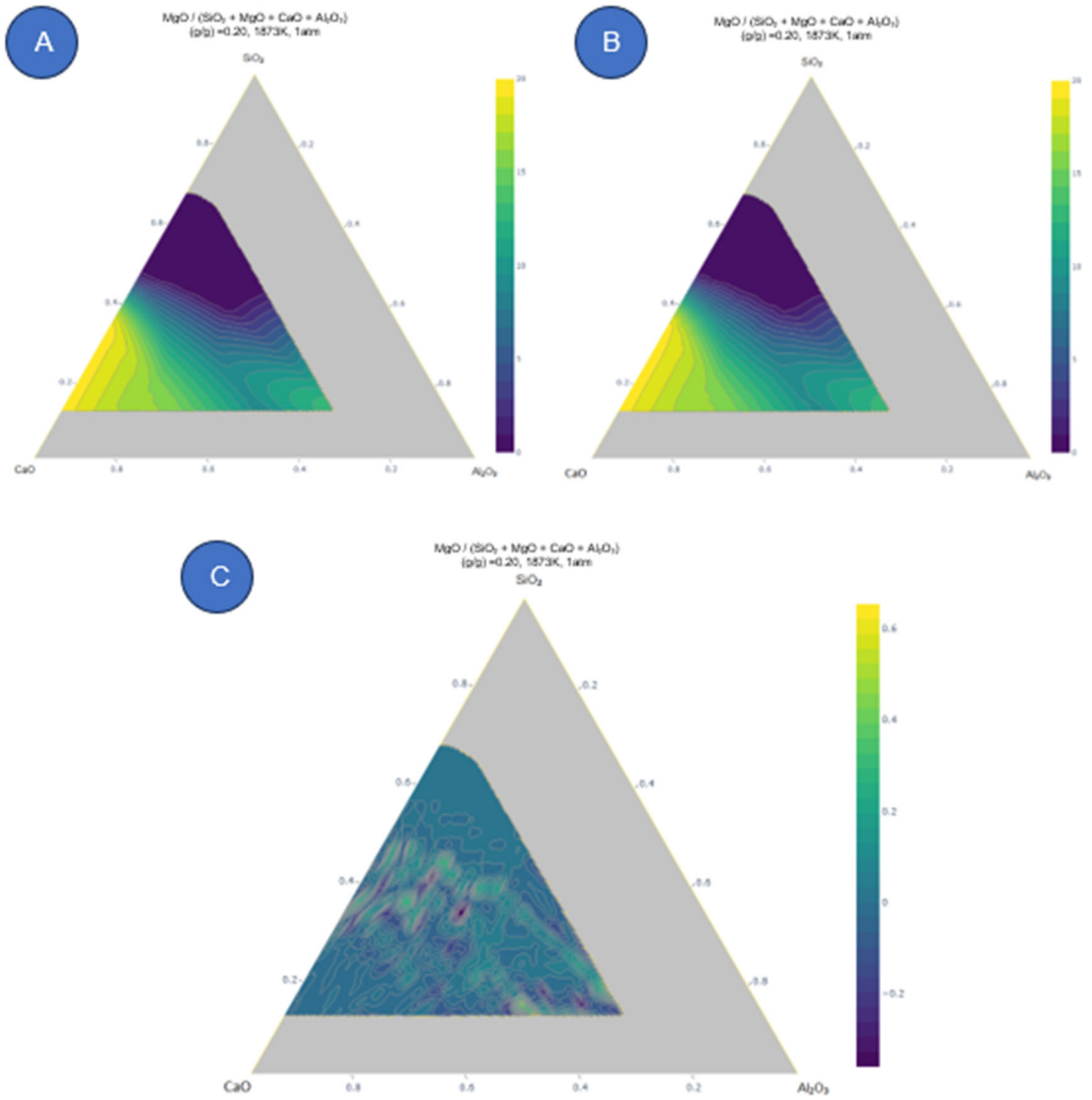

FIG 21 – (a) Diagram depicting the percentage of MgO in the solid fraction of the slag calculated by FactSage™ at 1873 K and 1 atm with 20 per cent MgO; (b) Diagram illustrating the percentage of MgO in the solid fraction of the slag predicted by the AI model at 1873 K and 1 atm with 20 per cent MgO; (c) Diagram showcasing the difference between the results calculated by the two methods at 1873 K and 1 atm with 20 per cent MgO.

Analysing the diagrams depicting the MgO content in the solid fraction as a function of CaO, Al_2O_3, and SiO_2, it is evident that the diagrams align with those in Figures 14–17. It is apparent that MgO plays a crucial role in reducing the liquid fraction, along with the addition of CaO and Al_2O_3. For higher total MgO contents, the amount of MgO increases in the solid phase and the liquid reaches a saturation value. The fraction of solids in the slag increases and that of liquid decreases. For instance, at 5 per cent MgO (Figures 14 and 18), there is no observed reduction in the liquid fraction in slags with elevated Al_2O_3 content. However, as the total MgO content in the slag increases, both the liquid fraction reduces, and the amount of MgO in the solid fraction increases, particularly with the addition of CaO and/or Al_2O_3 to the slag. In conclusion, MgO proves to be a crucial factor in the solid fraction content of the slag, especially when the slag requires higher additions of Al_2O_3 or CaO.

In order to gain a deeper understanding of the behaviour of Al_2O_3, CaO, and SiO_2 in MgO saturation, an alternative perspective was generated, as depicted in Figure 22. Only data calculated by FactSage™, where the MgO content in the solid fraction of the slag ranged between 1 and 2 per cent, was selected for this analysis. The graph considers the total MgO content in the slag (Y-axis) and the binary basicity (B_2) on the X-axis. To elucidate the influence of Al_2O_3, a colour gradient corresponding to the Al_2O_3 content was employed. The MgO supersaturation level ranging from 1 to

2 per cent is designed to have minimal impact on the liquid fraction of the slag (maintaining it close to 100 per cent), while concurrently mitigating the slag's propensity to corrode the refractory lining of the ladle due to its saturation in MgO.

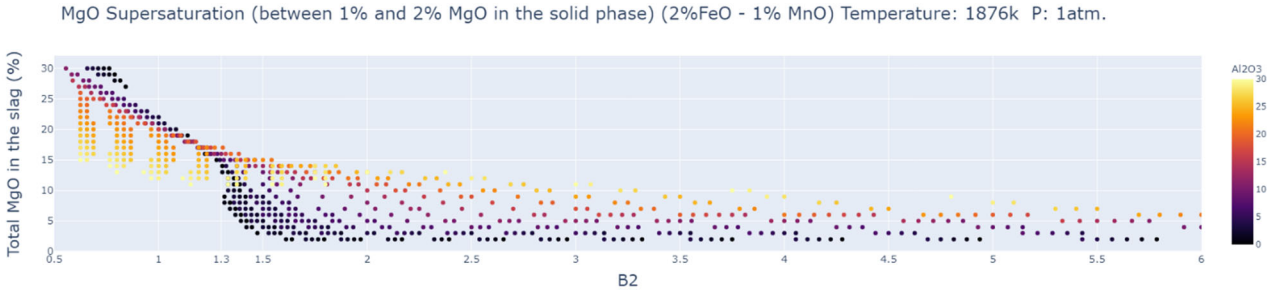

FIG 22 – The supersaturation range (between 1 and 2 per cent of solid MgO fraction at 1873 K) is examined in relation to the total MgO content in the slag, binary basicity (B_2), and the concentration of Al_2O_3.

Analysing Figure 22, it becomes evident that both basicity and the Al_2O_3 content play crucial roles in MgO saturation. It is observed that for lower basicities, a higher total MgO content in the slag is required to achieve saturation. It is noteworthy that Al_2O_3 plays a significant role for basicities below 1.3, where an increase in its content promotes the precipitation of solid MgO fractions. However, beyond a B_2 value of 1.3, an opposing effect is observed, wherein elevated levels of Al_2O_3 demand a higher total MgO content to saturate the slag.

CONCLUSIONS

The transformative impact of AI-focused technology on industrial processes is substantial, leading to heightened efficiency and providing prompt, nearly real-time responses. This article delves into the comparison of predictions generated by an AI model based on FactSage™ results with the actual outcomes obtained from FactSage™. It is crucial to underscore that FactSage™ remains pivotal for a comprehensive thermodynamic understanding of slag processes. Nonetheless, the integration of AI introduces significant advantages, especially in refining specific process parameters. In practical terms, as exemplified in this study, incorporating an AI system within a level 2 metallurgical framework in a steelmaking facility could effectively guide operations in fine-tuning the chemical composition of the slag. This optimisation ensures the efficient utilisation of inputs, minimising waste and ensuring the availability of slag for anticipated metallurgical processes.

Moreover, the impact of Al_2O_3, CaO, SiO_2, and MgO contents on both the liquid fraction and the solid-phase MgO content is discernible. Comparing these results with widely accepted diagrams from the literature reveals a remarkable similarity, highlighting the AI's potential to accurately predict and replicate the behaviour of slag compositions. This alignment with established theoretical frameworks in the literature further underscores the robustness of AI models.

In comparing the initial model, which solely addressed the CaO-MgO-SiO_2-Al_2O_3 system with limited training data, to the model incorporating FeO and MnO with a more extensive training data set, we observe a reduction in serrations in the contour regions of the graphs. This indicates that as the AI model is supplied with more data, its accuracy tends to improve. Consequently, there arises the possibility of developing specialised models for each region in the ternary phase diagram, continually augmenting data for a more confined space, thereby enhancing accuracy for specific purposes.

The aim of this work was to make a prediction of the liquid fraction and determine whether there is MgO saturation or not. A suggestion for future work in this study would be to understand how the model interprets the formation of solid precipitates by comparing it with laboratory tests and utilising thermodynamic tools.

ACKNOWLEDGEMENTS

I would like to extend my sincere gratitude, firstly to the approval team at AusIMM, for believing in and approving this article for participation in Molten 2024. I also want to express appreciation to RHI Magnesita for their steadfast support in fostering the development of new technologies aimed at

assisting their clients' processes. One notable contribution is the Ladle Slag Model, a tool designed to optimise customer slag. Additionally, special thanks are owed to the UFRGS Ironmaking and Steel Laboratory (LaSid), and specifically to Professor Bielefeldt, for his invaluable guidance in the writing of this article. Their collective support has been instrumental in advancing research and innovation in this field.

REFERENCES

Allibert, M, 1995. *Slag Atlas*, 2nd ed (Verlag Stahleisen GmbH: Düsseldorf).

Andrade, A, 2023. Main challenges regarding Steel Industries Operation and Maintenance, Vidya Technology. Available from: <https://vidyatec.com/blog/steel-industries-problems/>

Bale, C W, Bélisle, E, Chartrand, P, Decterov, S A, Eriksson, G, Gheribi, A E, Hack, K, Jung, I-H, Kang, Y-B, Melançon, J, Pelton, A D, Petersen, S, Robelin, C, Sangster, J, Spencer, P and Van Ende, M-A, 2016. FactSage™ thermochemical software and databases, 2010–2016, CALPHAD: Computer Coupling of Phase Diagrams and Thermochemistry, 54:35–53.

Bielefeldt, W V, Vilela, A C and Heck, N C, 2014. Termodynamic evaluation of the slag system CaO–MgO–SiO_2–Al_2O_3, in *Proceedings of the Iron Steel Technol Conf,* 2:1433–1445 (AISTech).

Bielefeldt, W V, Vilela, A C F and Heck, N C, 2013. Thermodynamic evaluation of the slag system CaO-MgO-SiO_2-Al_2O_3. in *Anais do Congresso Internacional of ABM* [Proceedings of the Annual Congress of ABM], pp 1630–1641.

Carvalho, G, 2021. Artificial Intelligence And The Perspectives Of The World Of Work, Ciência da Computação da Universidade do Sul de Santa Catarina.

Dahl, F, Brandberg, J and Sichen, D, 2006. Characterization of melting of some slags in the Al_2O_3-CaO-MgO-SiO_2 quaternary system, *ISIJ International*, 46(4):614–616.

Gran, J, Wang, Y and Sichen, D, 2011. Experimental determination of the liquidus basicity region in the Al_2O_3 (30 mass%)-CaO-MgO-SiO_2 system, *CALPHAD*, 35:249–254.

Lima, M and Amorin, F, 2020. Random Forest [in Spanish], Lamfo - UNB. Available from: <https://lamfo-unb.github.io/2020/07/08/Random-Forest/>

Osborn, E F, Devries, R C, Gee, K H and Kraner, H M, 1954. Optimum composition of blast furnace slag as deduced from liquidus data for the quaternary system CaO-MgO-Al2O3-SiO2, *JOM*, 6(1):33–45.

Pretorius, E B and Carlisle, R C, 1998. Foamy slag fundamentals and their practical application to electric furnace steelmaking, in *Proceedings of the Electric Furnace Conference*, pp 275–292.

Rodriguez, J, *et al*, 2022. Strengthening the steel industry with AI, BCG Global. Available from: <https://www.bcg.com/publications/2021/value-of-ai-in-steel-industry>

Xu, J, Su, L, Chen, D, Zhang, J and Chen, Y, 2015. Experimental investigation on the viscosity of CaO–MgO(–Al_2O_3)–SiO_2 slags and solid–liquid mixtures, *J Iron Steel Res Int*, 22(12):1091–1097.

Zhao, S, He, S P, Guo, Y T, Chen, G J and Lv, J C, 2016. Effect on cleanliness of molten steel with different refining slag systems for low alloy ship plate, *Ironmak Steelmak,* 43:790. https://doi.org/10.1080/03019233.2016.1223791

Perspectives of chemical metallurgy fundamentals in slag innovation

DOI: 10.62053/KMSR9620
S Lee[1] and I Sohn[2]

1. Research Professor, Yonsei University, Seoul 03722, Korea. Email: slag@yonsei.ac.kr
2. Professor, Yonsei University, Seoul 03722, Korea. Email: ilsohn@yonsei.ac.kr

ABSTRACT

The ferrous and non-ferrous metallurgical industries have been utilising slags, fluxes and mattes for process optimisation and quality improvements at high temperatures. Understanding the fundamentals of the thermodynamics and kinetics of chemical metallurgy regarding slags, fluxes and mattes has been essential to the technological developments of these optimisation and improvements. This work will discuss how these fundamentals have been studied in the reactions involved and implemented in the ferrous industry from primary refining to continuous casting. In particular, the chemical driving forces that allow these reactions to take place and the limitations of the kinetics that require optimisation to enhance the reactions. In addition, the future research direction for slag technology innovation and the role of these fundamentals will also be described.

INTRODUCTION

Ferrous metals including iron and steel are widely used for structural materials imbedded in nearly all industry sectors including construction, shipbuilding, transportation and many others. Non-ferrous metals are typically added into the basic materials of the ferrous metals to improve the various physical and chemical properties.

According to the World Steel Association (World Steel Association, 2023), approximately 1.9 Bt of crude steel was produced. For non-ferrous metals, the US Geological Survey notes that world aluminium output was 69 Mt (Merrill, 2023) and publications from the Government of Canada indicates global refined copper production to be 25 Mt. Depending on the metals processing method, large amounts of slags and mattes are produced. Global slag generation from these processes have been estimated to be approximately 500 Mt within the ferrous industry (Yang, Firsbach and Sohn, 2022).

The critical role of slags and mattes in chemical metallurgy cannot be overstated in terms of their importance to the final product quality. Although the humble beginnings of the slag and matte may have started out in part as gangue components in the raw materials, the product quality, energy benefits and protection from the environment with optimised design have become essential for process engineering. For slags in ferrous metallurgy, optimised slags have the ability to refine unwanted elements in the molten metal including sulfur, phosphorus, nitrogen, hydrogen and other elements. When a slag covers the molten metal, it acts as a barrier to the outside environment minimising the infiltration of dissolved gaseous elements into the molten metal and can also act as a thermal barrier for increased insulation of the molten metal. For mattes in non-ferrous metallurgy, optimised mattes can increase the recovery of the non-ferrous element and improve the separation efficiency of the oxide slags and also increase the purity of the target element. The typical sulfide mattes used for primary copper smelting operations and the slags that are formed during smelting of the concentrates comprised of oxy-sulfide minerals require process optimisation to ensure greater recovery of copper is possible, while maintaining greater purity with less ferrous impurities in the matte. With higher concentrations of Cu can be achieved in the matte, it can be sent to the converter for sulfur removal and subsequent blister Cu production.

The fundamentals that control the role in slags and mattes are based on thermodynamic and kinetic principles, which have been widely studied in chemical metallurgy. This review looks at some of the fundamentals of ferrous and non-ferrous chemical metallurgy that have been applied to ensure greater process efficiency and product quality.

THERMODYNAMIC FUNDAMENTALS

Slag capacities in steelmaking and refining

Slag capacity in steelmaking and refining is the ability of a slag to absorb and retain various impurities and elements during high temperature metallurgical processes. Several critical factors affect slag capacity, which in turn interacts with the chemical and physical properties of the slag. These factors have been widely studied and includes the slag chemical composition, temperature, and oxygen partial pressure.

Slags can typically be comprised of SiO_2, Al_2O_3, CaO, MgO, and FeO, which can influence the thermophysical properties of the slag including the viscosity and the chemical potential of the slag including the basicity, which have been known to directly impact the absorption and retainment of impurities from molten steel. Temperatures provide the thermal energy to the system for reaction and the kinetic energy of the bondings within the ionic slag melts to form new bonds. Depending on the exothermic or endothermic reactions between the slag and metal, reactions can be hindered or accelerated. Temperatures can also affect the viscosity and fluidity of slags, where higher temperatures lower the viscosity and increase the fluidity.

Oxygen partial pressure or oxygen potential of the system influences the redox reactions occurring at the slag-metal interface, where the impurities of sulfur and phosphorus can be exchanged. Low oxygen potentials or reducing conditions can promote the removal of certain impurities such as sulfur into the slag as sulfides, while high oxygen potentials or oxidising conditions may facilitate the removal of certain impurities such as phosphorus into the slag by forming stable oxide phases as phosphates. While not typical, slag viscosities and phase equilibria can be altered under high pressures, affecting the capacity of a slag to absorb impurities.

Basicity, which refers to the chemical potential of the free oxygen anions, is difficult to directly measure, but is one of the critical parameters determining the capacity of the ionic slag to remove impurities from metals during metallurgical processing. Thus, an indirect measure of the slag basicity was warranted and the Vee ratio defined as the mass ratio of basic oxides (eg CaO, MgO) to acidic oxides (eg SiO_2, Al_2O_3) in the slag composition was utilised. The basicity of an ionic slag influences both the chemical and physical properties, including the viscosity, fluidity, and slag capacity to absorb and retain impurities. Optimal slag basicity through slag composition design is often crucial for effective impurity removal and slag performance. The adage ‘Take care of the slag, and the steel will take care of itself’ emphasises the importance of managing the slag effectively in metallurgical processes to ensure the production of high-quality steel.

Considering the aforementioned slag capacity, two key impurities are closely controlled in the steelmaking operations, which include sulfur and phosphorus corresponding to the sulfide and phosphate slag capacities respectively.

Desulfurisation of steels typically involves the transfer of dissolved sulfur from the metal into the slag phase. The most common reaction under steelmaking conditions is the formation of calcium sulfide (CaS), when sulfur reacts with calcium oxide (CaO) in the slag, as expressed by Equation 1. The corresponding ionic reaction is express as Equation 2 and the subsequent sulfide capacity under reducing conditions is expressed by Equation 3. Depending on the slag composition, the activities of the reactants and products can be significantly modified. Thus, depending on the impurities existing in the steel, the activity of dissolved S can affect the reaction and the components such as Al_2O_3 or SiO_2 in the slag can also affect the activity of the CaO in the slag, which can inherently affect the S transfer to the slag phase.

$$CaO(slag)+S(metal)\rightarrow CaS(slag)+1/2O_2(g) \quad (1)$$

$$O^{2-}(slag)+S(metal)\rightarrow S^{2-}(slag)+1/2O_2(g) \quad (2)$$

$$C_{S^{2-}} = (\%S) \times \left\{\frac{P_{O_2}}{a_S}\right\}^{1/2} = K_2 \times \frac{a_{O^{2-}}}{f_{S^{2-}}} \quad (3)$$

According to Figure 1, the sulfide capacities according to the Vee ratio (corresponding to the basicity) and the activity of FeO are shown. It is clearly evident that the sulfide capacities for these systems

follow the expected thermodynamic interpretations and a slope of unity corresponding to Equation 3 is shown. Similar results have been identified for dephosphorisation with a slope of 1.5.

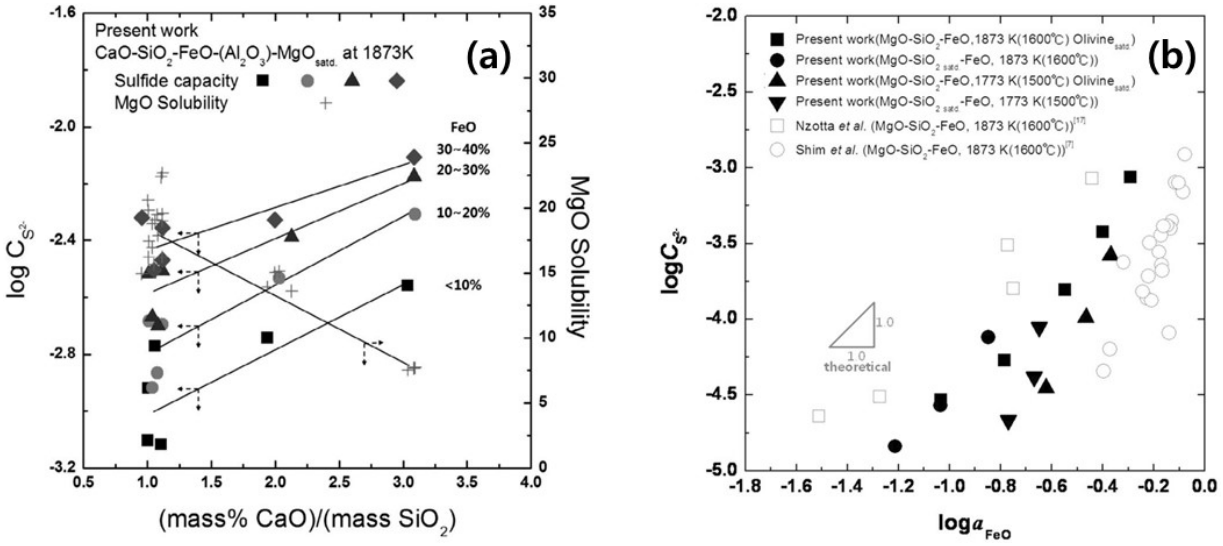

FIG 1 – Sulfide capacities of various slag systems as a function of: (a) Vee ratio (apparent basicity) (Park and Min, 2016); and (b) logarithm of the FeO activity (Kim, Huh and Min, 2014).

In Figure 2, the temperature dependence of the slag capacities are provided. Unlike the basicity, the sulfide and phosphate capacity show opposite trends with the temperature dependence. Higher temperatures are favourable for the sulfide capacity, but lower temperatures are favoured for the phosphate capacity. Dephosphorisation is the process of transferring the dissolved phosphorus in the molten metal to the slag phase resulting in the desired product specifications. Considering phosphorus removal in steelmaking occurs under a high oxygen partial pressure, the typical main reaction corresponds to the formation of a phosphate phase in the slag. Phosphorus reacts with CaO in oxidising conditions to form calcium phosphate ($Ca_3(PO_4)_2$), as described in Equation 4. The reaction in ionic form can be expressed as Equation 5. Accordingly, under oxidising conditions of steelmaking operations, the phosphate capacity can be expressed by Equation 6.

$$3/2CaO(slag)+P(metal)+5/4O_2(g)\rightarrow 1/2Ca_3(PO_4)_2(slag) \quad (4)$$

$$3/2O^{2-}(slag)+P(metal)+5/4O_2(g)\rightarrow PO_4^{3-}(slag) \quad (5)$$

$$C_{PO_4^{3-}} = (\%PO_4^{3-}) \times \frac{1}{a_P \times P_{O_2}^{1/2}} = K_5 \times \frac{a_{O^{2-}}^{3/2}}{f_{PO_4^{3-}}} \quad (6)$$

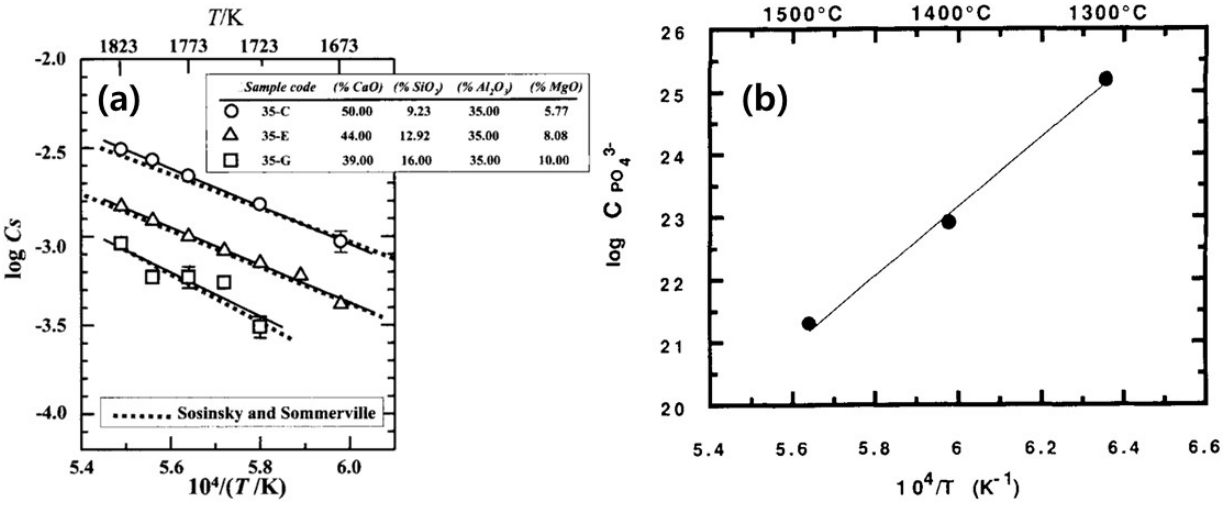

FIG 2 – (a) Sulfide capacity and (b) Phosphate capacity as a function of temperature (Nassaralla and Fruehan, 1992).

Similar to sulfur, the slag capacity for phosphorus removal from the metal to the slag depends on various factors including temperature, slag composition, and activities of the reactants and products. It should be noted that under a fixed temperature and oxygen partial pressure, the slag capacities are determined according to the slag system.

Overall, the thermodynamics of desulfurisation and dephosphorisation in slags involve complex interactions between the metal and slag phases, as well as the equilibrium between different chemical species. Understanding these fundamental thermodynamic principles is crucial to optimise steelmaking processes and achieving the levels of S and P removal into the designed slags for steel quality.

Matte optimisation in non-ferrous metallurgy

Beyond ferrous smelting operations, non-ferrous metallurgy is also a field for chemical metallurgists to make a significant impact on not only the industry, but also the environment considering the significant amount of emissions involved with smelting non-ferrous metals with relatively small concentrations of the product. Unlike ferrous raw materials, non-ferrous raw materials contains typically less than 5 mass per cent. of the target metals. Copper is one of the widely used non-ferrous metals that is critical to the electrification of the society. Copper smelting involves various processing stages, including matte production, converting, and refining. Matte, a sulfide-rich intermediate product before the production of blister copper after converting, plays a critical role in determining the efficiency and quality of copper extraction. Significant challenges are associated with matte optimisation in copper smelting, which can enhance process efficiency, reduce environmental impact, and improve product quality. Key optimisation parameters include flux addition, matte grading, and slag designing. These optimisation factors can maximise copper recovery and minimise energy consumption and emissions, ultimately contributing to sustainable copper processing and production.

Matte optimisation is challenged by the complexity of sulfide ore composition, feed variability, and impurities such as iron, sulfur, and arsenic. Blending different ore types, adjusting the sulfur-to-iron ratio, and flux additions assists in matte composition optimisation and minimise impurities.

Fluxes play a crucial role in copper smelting by facilitating slag formation, promoting metal separation, and controlling impurity levels. Optimising flux addition rates and compositions improves matte quality, reduces slag viscosity, and enhances metal recovery. Adjusting silica-to-alumina ratio, controlling slag basicity, and minimising iron oxide content can improve slag fluidity, reduce matte losses, and enhance overall process performance. Silica is a primary flux used in copper smelting to facilitate a liquid slag phase. It helps lower the melting point of the slag, promotes the dissolution of gangue minerals, and improves slag fluidity. Limestone is commonly added as a flux to neutralise acidic impurities such as S and As to form CaS and $Ca_3(AsO_4)_2$, which are then incorporated into the slag phase. Fayalite (Fe_2SiO_4) is a by-product of copper smelting and often recycled, which contribute to the formation of a stable slag phase, absorbing excess sulfur, and assists in controlling the slag viscosity. As described from Equations 7 and 8, copper smelting from sulfide ores is a stepwise oxidation of iron, where the oxygen activity increases resulting in blister copper production. (Taskinen *et al*, 2019).

$$[CuFeS_2] + 1x/2O_2(g) \rightarrow [(Cu, Fe_{(1-x)/2})_2S] + x(FeO) + SO_2(g) \quad (7)$$

$$[Cu_2S] + O_2(g) \rightarrow 2Cu + SO_2(g) \quad (8)$$

According to the results shown in Figure 3 the Cu content in the matte can be significantly affected by the amount of oxygen activity in the reactor and the subsequent Fe/SiO_2 slag formed during processing. It is generally known that the chemical dissolution affecting Cu loss can be of two possible types: oxidic and sulfidic. However, it is also known that when the grade of matte exceeds 60 per cent, it is influenced by oxidic copper dissolution (Cornejo Mardones, 2020). Therefore, higher flow rates, which correspond to higher oxygen potential and activity can increase the Cu content in the matte. However, excessive oxygen injection can not only oxidise the Fe in the chalcopyrite raw material, but can also oxidise the Cu into the slag phase resulting in lower recovery of Cu. As the Fe oxidises into the slag phase, there are some amounts of SiO_2 fluxing required to optimise the Cu content in the matte. As can be seen in Figure 3b, higher grade Cu mattes can be obtained with

Fe/SiO_2 reaching the ratios beyond 1.6. However, this needs to be balanced since higher oxygen potentials can lead to the formation of Fe_3O_4 in the slag phase, which can increase the melting point of the slag and reduce fluidity and also the separation between matte and slag phase during matte smelting and separation. An optimal Fe/SiO_2 ratio seem to be near the low temperature fayalite phase formation region and thus operations typically would target the slag composition to be in this range.

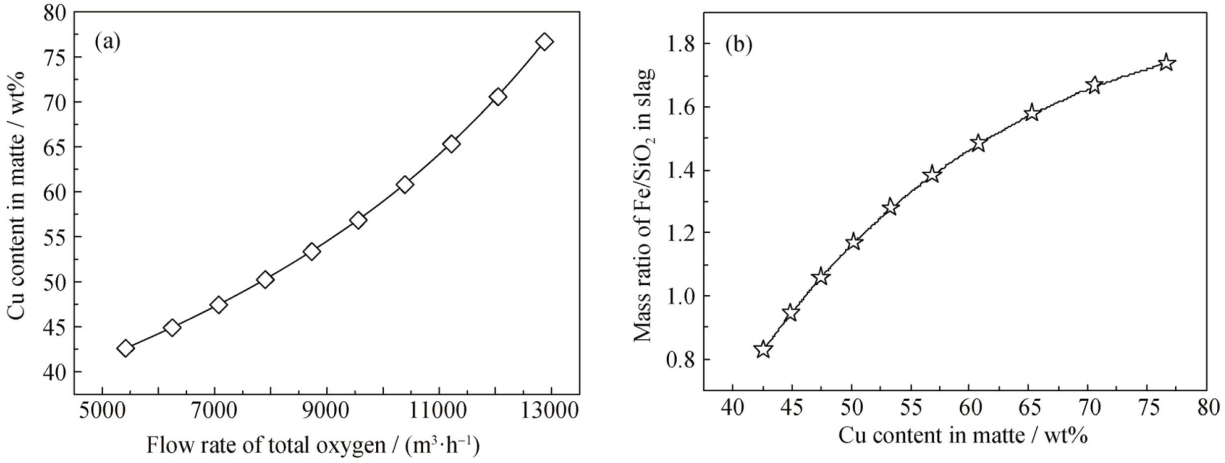

FIG 3 – (a) Cu content in matte as a function of oxygen and (b) relationship between the Fe/SiO_2 ratio to the Cu content in matte (Wang *et al*, 2019).

Thermophysical properties of slags and mattes

The thermophysical properties of slags and mattes play a significant role in determining their capacity to interact with molten metal and effectively absorb impurities. These properties influence the behaviour of slags during metallurgical processes, affecting their viscosity, thermal conductivity, heat capacity, and other characteristics.

Viscosity affects fluid flow behaviour and retention of the impurities in slags. Highly viscous slags can impede mass transfer kinetically reducing the slag capacity. This reduced mobility can hinder the absorption of impurities by the slag, limiting its capacity to remove contaminants from the metal. Lower viscosity enhances slag-fluid metal interactions, promoting impurity removal. The viscosity of slag is influenced by temperature, chemical composition, and phase composition. In addition, slags with high viscosity tend to have slower settling rates, prolonging the time required for slag-metal separation. Higher viscosities can also hinder convective heat transfer within the slag, leading to temperature gradients and non-uniform heating. Thus, optimising slag viscosity is essential for enhancing the slag capacity and improving the efficiency of impurity removal and other desired functions in metal production.

Slags and mattes with higher thermal conductivity can efficiently transfer heat from the surrounding environment, influencing temperature distributions within the system. Temperature gradients affect reaction kinetics and phase equilibria, consequently impacting the slag capacity. Like many of the thermophysical properties of slags and mattes, the thermal conductivity of slag is also influenced by its chemical composition, phase fractions, and temperature.

Slags and mattes with higher specific heat capacity can absorb more heat energy before significant temperature changes can be observed, which impact the energy needs of a reacting system in metallurgical processes. The heat capacity also depends on its chemical composition, phase fraction and temperature.

Understanding and controlling these thermophysical properties are essential for optimising metallurgical processes using slags and mattes. Slag and matte compositions and process conditions are often manipulated to achieve desired thermophysical properties and improve process performance.

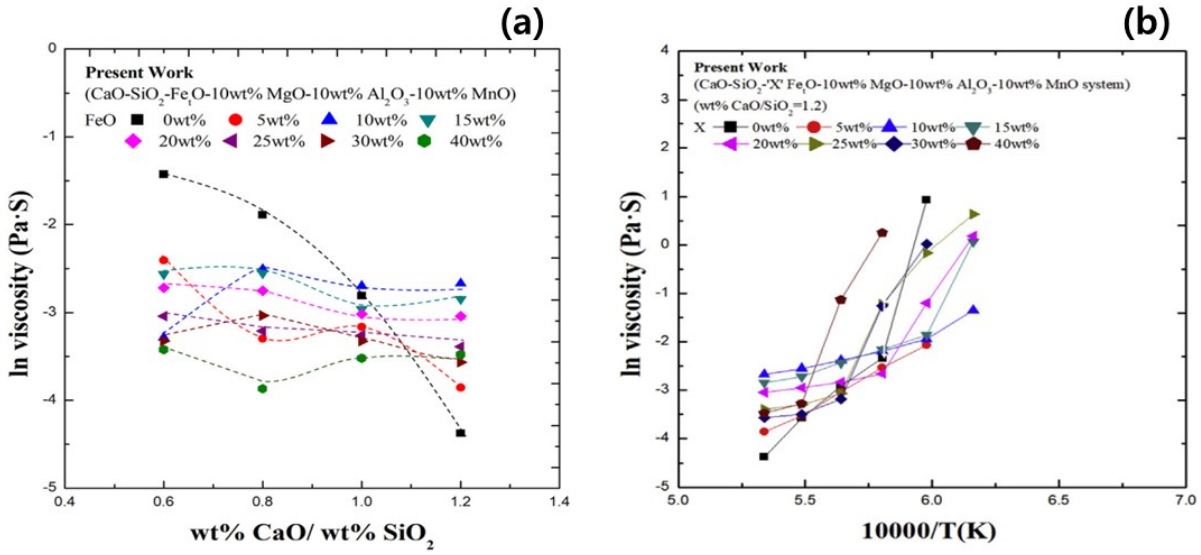

FIG 4 – Natural logarithm of the viscosity (Choi *et al*, 2021) as a function of (a) Vee ratio and (b) temperature.

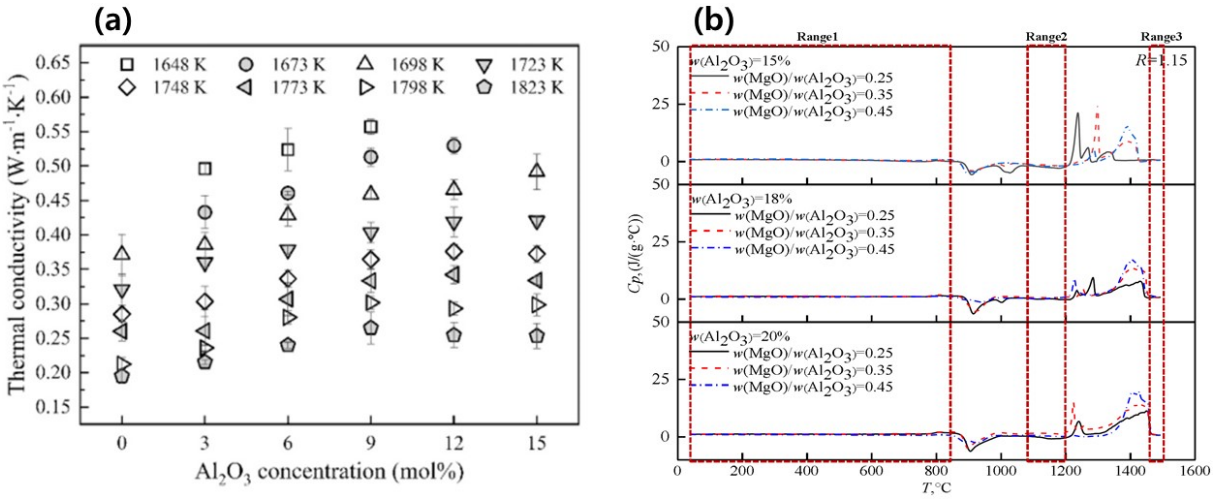

FIG 5 – (a) Thermal conductivity of slags as a function of Al_2O_3 content (Yang, Wang and Sohn, 2022) and (b) Specific heat capacities of slags as a function of temperature and composition (Zheng *et al*, 2021).

SUMMARY

This review looks briefly at the fundamental thermodynamics and thermophysical properties of slags and mattes for chemical metallurgy. Understanding the theory behind the various reactions and controlling the fundamental chemical potential allows the process engineer to achieve metals production at a more efficient and environmentally optimal way.

ACKNOWLEDGEMENTS

This work was supported by the Technology Innovation Program (Commercialization and development of new design on turbulent high temperature melting furnace (2000 tony pilot scale) and separation and (or) recovery of valuable metals from end of the xEV (ESS) battery pack) (20011183) funded by the Ministry of Trade, Industry and Energy (MOTIE, Korea).

REFERENCES

Choi, J S, Park, T J, Min, D J and Sohn, I, 2021. Viscous behavior of high-Fe_tO-bearing slag systems in relation to their polymeric structural units, *Journal of Materials Research and Technology*, 15:1382–1394.

Cornejo Mardones, K, 2020. Control of copper loss in flash smelting slags, Master's Thesis, School of Mechanical and Mining Engineering, The University of Queensland.

Kim, K D, Huh, W W and Min, D J, 2014. Effect of FeO and CaO on the Sulfide Capacity of the Ferronickel Smelting Slag, *Metall Mater Trans B,* 45B:889.

Merrill, A M, 2023. US Geological Survey, Aluminum.

Nassaralla, C and Fruehan, R J,1992. Phosphate Capacity of CaO-Al_20_3 Slags Containing CaF_2, BaO, Li_2O, or Na_2O, *Metall Trans B,* 23B:117.

Park, Y and Min, D J, 2016. Sulfide Capacity of CaO-SiO_2-FeO-Al_2O_3-MgOsatd Slag, *ISIJ Int*, 56:520–526.

Taskinen, P, Akdogan, G, Kojo, I, Lahtinen, M and Jokilaakso, A, 2019. Matte converting in copper smelting, *Mineral Processing and Extractive Metallurgy*, 128:58–73.

Wang, Q-M, Wang, S-S, Tian, M, Tang, D-X, Tian, Q-H and Guo, X-Y, 2019. Relationship between copper content of slag and matte in the SKS copper smelting process, *International Journal of Minerals, Metallurgy and Materials*, 26:301.

World Steel Association, 2023. World Steel in Figures 2023.

Yang, J, Firsbach, F and Sohn, I, 2022a. Pyrometallurgical processing of ferrous slag 'co-product' zero waste full utilization: A critical review, *Resources, Conservation and Recycling*, 178:106021.

Yang, J, Wang, Z and Sohn, I, 2022b. Topological understanding of thermal conductivity in synthetic slag melts for energy recovery: An experimental and molecular dynamic simulation study, *Acta Materialia*, 234:118014.

Zheng, H, Liang, L, Du, J, Zhou, S, Jiang, X, Gao, Q and Shen, F, 2021. Mineral Transform and Specific Heat Capacity Characterization of Blast Furnace Slag with High Al_2O_3 in Heating Process, *Steel Research Int*, 92:2000448.

Effect of slag composition on titanium distribution ratio between ferrosilicon melt and $CaO-SiO_2-Al_2O_3$ slag at 1773 K

DOI: 10.62053/NPON4744

M J Lee[1] and J H Park[2]

1. Student, Department of Materials Science and Chemical Engineering, Hanyang University, Ansan 15588, South Korea. Email: dlalswn06@gmail.com
2. Professor, Department of Materials Science and Chemical Engineering, Hanyang University, Ansan 15588, South Korea. Email: basicity@hanyang.ac.kr

ABSTRACT

Because the environmental problems are occurred by greenhouse gases such as CO_2, the industries have tried to increase electric motor efficiency to reduce CO_2 emissions. A core material of electric motor is high-silicon electrical steel. The ferrosilicon (FeSi) alloy, a raw material for the production of electrical steel, affects the electric properties of silicon steel. The main impurities such as Ca, Al and Ti make inclusions or precipitates that causes core loss. The slag treatment has been widely used to remove impurity elements. Thermodynamic principles for the refining of several impurities, specifically Ca and Al, have been investigated, whereas thermodynamic behaviour of Ti has not been fully understood yet. Therefore, in the present study, the titanium distribution ratio (L_{Ti}) between ferrosilicon and $CaO-SiO_2-Al_2O_3$ slag system at 1773 K was investigated.

The results show that L_{Ti} is influenced by both the basicity and stability of titanium ion in the slag. Specifically, L_{Ti} exhibits a minimum value at about C/S=0.7 indicating a shift in the titanate structure unit from $[TiO_5]$-square pyramid to $[TiO_4]$-tetrahedron because of lack of Ca^{2+} ions in a C/S<0.8 region, contributing to an increase in titanate capacity and L_{Ti}.

INTRODUCTION

The electric vehicle market is growing quickly and study of electric motor efficiency is in progress to reduce CO_2 emission and air pollutants. The raw material for production of high-silicon electrical steel, ie ferrosilicon (FeSi) alloy, affects the electric properties of silicon steel. The common impurities of Ca, Al, Ti, C and B form inclusions or precipitates that result in core loss by decreasing grain size (Nakayama and Tanaka, 1997; Nakayama and Honjou, 2000; Steiner Petrovič *et al*, 2010). These impurities in electrical steel are generally originated from FeSi alloy which have an adverse effect on the magnetic properties. Unfortunately, Ti equilibrium distribution data between silicon and slag are very limited. Moreover, the thermodynamics of the Ti distribution behaviour between FeSi melt and CaO-based slags has not been investigated. Therefore, in the present study, we measured the Ti distribution ratio between FeSi melt and the $CaO-SiO_2-Al_2O_3$ slag at 1773 K. Additionally, a structural analysis using Raman spectroscopy was performed to understand the stabilisation mechanism of titanium in aluminosilicate melts.

EXPERIMENTAL PROCEDURE

The slag-metal equilibrium experiments were performed using an electric resistance furnace with a $MoSi_2$ heating element. A schematic diagram of the experimental apparatus is shown in Figure 1. The temperature was controlled within ±2 K. A mixture of 5 g commercial low-carbon FeSi alloy (0.013 wt per cent Ti) and 3 g slag were loaded in a graphite crucible placed in an alumina porous holder at 1773 K. The furnace was filled with purified Ar gas controlled by a mass flow controller at a flow rate 500 mL/min. After the equilibration for 24 hrs, the sample was extracted from the furnace and quenched in water. The compositions of metal and slag samples were determined by X-ray fluorescence (XRF) and inductively coupled plasma – optical emission spectroscopy (ICP-OES).

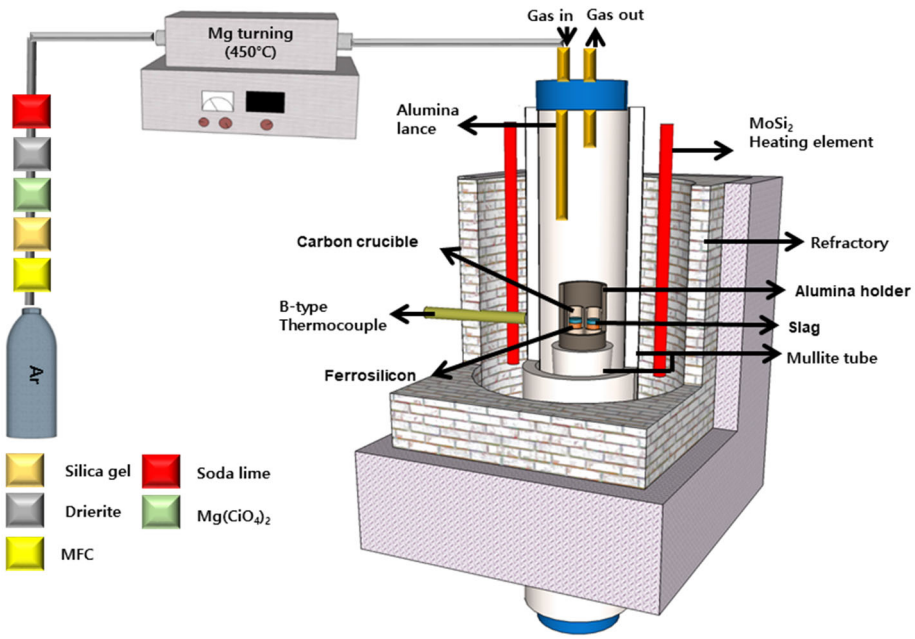

FIG 1 – Schematic diagram of the experimental apparatus.

RESULTS AND DISCUSSION

Influence of basicity on Ti distribution ratio between FeSi melt and CaO-SiO_2-Al_2O_3 slag

The distribution ratio of Ti (L_{Ti}) between FeSi and slags at 1773 K as a function of CaO/SiO_2 (=C/S) ratio is depicted in Figure 2. The distribution ratio of Ti is defined by the following equation.

$$L_{Ti} = \frac{(\text{wt\%TiO}_2)_{\text{slag}}}{[\text{wt\%Ti}]_{\text{metal}}} \quad (1)$$

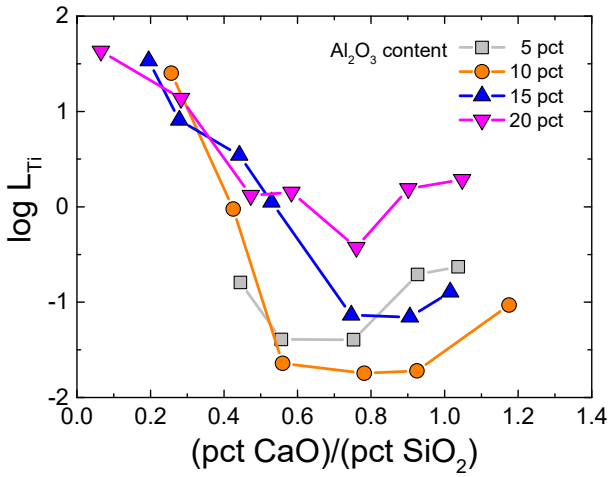

FIG 2 – Distribution ratio of Ti between CaO-SiO_2-Al_2O_3 slags and FeSi melts at 1773 K.

As shown in Figure 2, the V-shaped Ti distribution behaviour is observed in entire slags. In the 20 per cent Al_2O_3 system, the distribution ratio of Ti in a logarithmic scale is consistently greater than zero, ie $L_{Ti} > 1.0$, except for the C/S=0.8 system. This result suggests that the distribution ratio of Ti is significantly affected by the C/S ratio and Al_2O_3 content.

Effect of basicity and Al_2O_3 on titanate capacity and stability of titanium in slag

In the present study, it was assumed that the valence state of titanium is 4, ie Ti^{4+} is preferentially stable and the coordination number of titanium with oxygen is 5, ie $[TiO_5]$ square-based pyramid structure mainly exists in the present CaO-SiO_2-Al_2O_3 system (Romano *et al*, 2000; Le Cornec *et al*, 2021). Based on this assumption, the titanium refining reaction and titanate capacity of molten slag are represented as given in Equations 2 and 3, respectively. Here, the titanate capacity is the ability of a slag to absorb titanium as a function of slag basicity, stability of titanate ion in the slag and temperature. To our knowledge, few study have reported titanate capacity, C_{TiO_x}, of molten slag. Hence, in the present study, we propose the application of titanate capacity to understand the thermodynamic behaviour of titanium oxide in the slag.

$$[\mathrm{Ti}] + \mathrm{O}_2(\mathrm{g}) + 3(\mathrm{O}^{2-}) = (\mathrm{TiO}_5^{6-}) \tag{2}$$

$$C_{\mathrm{TiO}_5^{6-}} = \frac{K_{(2)} \cdot a_{\mathrm{O}^{2-}}^3}{f_{\mathrm{TiO}_5^{6-}}} = \frac{(wt\%TiO_5^{6-})}{f_{Ti} \cdot [wt\%Ti] \cdot p_{O_2}} = \frac{L_{Ti}}{f_{Ti} \cdot p_{O_2}} \tag{3}$$

where $K_{(2)}$ is the equilibrium constant of Equation 2, $a_{O^{2-}}$ and f_{Ti} represent the activity of free oxygen ion in slag and the Henrian activity coefficient of titanium in FeSi melt, respectively. In the present study, f_{Ti} was assumed to be unity because the concentration of Ti in FeSi melt is not more than 0.4 wt per cent. Here, $f_{TiO_5^{6-}}$ is the activity coefficient of titanate ion in slag, and p_{O_2} is the oxygen partial pressure, calculated from the following equilibrium (Turkdogan, 1980).

$$\mathrm{Si}(\mathrm{s}) + \mathrm{O}_2(\mathrm{g}) = \mathrm{SiO}_2(\mathrm{s}) \tag{4}$$

$$\Delta G^{\mathrm{o}}_{[4]} = -907{,}130 + 175.7\ \mathrm{T}\ (\mathrm{J/mol}) \tag{5}$$

On the other hand, it is suggested that CaO behaves as a basic oxide by contributing free oxygen ion in the slag as shown below (Sano, 1997).

$$(\mathrm{CaO}) = (\mathrm{Ca}^{2+}) + (\mathrm{O}^{2-}) \tag{6}$$

$$a_{\mathrm{O}^{2-}} = \frac{K_{(6)} \cdot a_{\mathrm{CaO}}}{a_{\mathrm{Ca}^{2+}}} \tag{7}$$

Therefore, the titanate capacity is a function of the basicity ($a_{O^{2-}}$) and the stability of titanate ion ($f_{\mathrm{TiO}_5^{6-}}$) at fixed temperature and it can be calculated using L_{Ti} and p_{O_2}. The activity of CaO in the slag system at 1773 K was calculated using Factsage software. By combining Equations 3 and 7, the relationship between CaO activity and titanate capacity can be described as follows:

$$\log C_{\mathrm{TiO}_5^{6-}} = 3log a_{\mathrm{CaO}} - 3log a_{\mathrm{Ca}^{2+}} - log f_{\mathrm{TiO}_5^{6-}} + Const. \tag{8}$$

Based on Equation 8, the titanate capacity is expected to exhibit a linear relationship with the activity of CaO by assuming that $a_{\mathrm{Ca}^{2+}}$ and $f_{\mathrm{TiO}_5^{6-}}$ terms are not significantly affected by slag compositions. As shown in Figure 3, the titanate capacity linearly increases with increasing activity of CaO in a logarithmic scale at $log a_{\mathrm{CaO}} > -2.2$, indicating that titanium oxide primarily acts as an acidic component in the relatively basic slag. The fitted lines have slopes of 2.7~3.0, indicating that $a_{\mathrm{Ca}^{2+}}$ and $f_{\mathrm{TiO}_5^{6-}}$ terms would be constant with increasing CaO activity. Therefore, in the basic slag system (ie $\log a_{CaO} > -2.2$), it is confirmed that titanate ion forms $[TiO_5]$-square pyramid based on Equation 2.

However, in the acidic slag system ($\log a_{CaO} < -2.3$), the titanate capacity increases with decreasing activity of CaO, suggesting that Ti dissolution reaction given in Equation 2 does not simply applicable in the relatively acidic region. Under the same activity of CaO condition, titanate capacity varies with Al_2O_3 content. This also implies that the Al_2O_3 concentration influences the $f_{\mathrm{TiO}_5^{6-}}$ term in the slag. Overall, the titanate capacity of the slag is significantly influenced by the activity of CaO and Al_2O_3 under the experimental conditions.

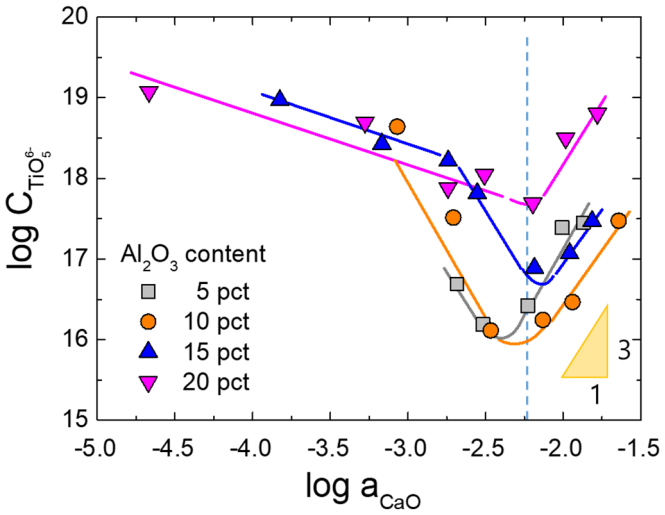

FIG 3 – Titanate capacity as a function of activity of CaO in the $CaO-SiO_2-Al_2O_3$ slags at 1773 K.

Effect of aluminosilicate structure on titanate stability

From the literature, titanium ion in aluminosilicate glasses have been studied and found that it is mainly Ti^{4+} and has five-fold coordination by Ti K-edge XAFS and thermodynamic analysis (Romano *et al*, 2000; Le Cornec *et al*, 2021). The five-coordinated Ti incorporated into the silicate framework through the Ti–O–Si bonds including the non-bonding oxygen of the short Ti=O titanyl bond requires a local charge compensation by Ca^{2+} ion. A distribution of titanium coordination region in the $CaO-SiO_2-Al_2O_3$ system is illustrated in Figure 4. The four-fold coordinated Al, ie $[AlO_4]$ tetrahedral unit also requires Ca^{2+} ion for charge balancing. When the Al_2O_3 is relatively low at C/S>0.8 region (Region A in Figure 4), the Ca^{2+} ion interacts with $[AlO_4]$ unit to keep the charge balance, and thus the activity coefficient of TiO_2 is increased by increasing the Al_2O_3 concentration due to deficiency of Ca^{2+} ion. Over the 10 per cent Al_2O_3 at C/S>0.8 (Region B in Figure 4), Ca^{2+} ion is mainly consumed for charge balance of $[AlO_4]$ structure, and thus some Ti in five-fold coordination is forced to transform to four-fold coordination (Romano *et al*, 2000). Transformation of titanium coordination from five to four also occurred in C/S<0.8 region (Region C in Figure 4) due to the lack of Ca^{2+} ion. Because $[TiO_4]$ group can be incorporated into the aluminosilicate network by replacing $[SiO_4]$ and $[AlO_4]$ tetrahedrons (Duan *et al*, 1998), the activity coefficient of TiO_2 is decreased by decreasing the C/S ratio and increasing Al_2O_3 concentration.

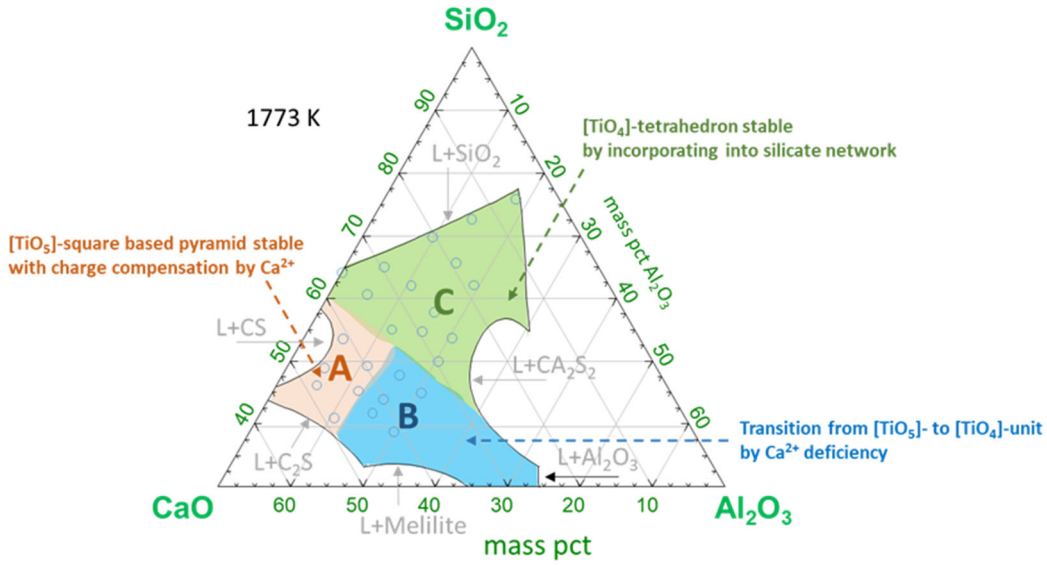

FIG 4 – Titanium coordinations in different regimes in the $CaO-SiO_2-Al_2O_3$ system at 1773 K.

CONCLUSIONS

The distribution behaviour of titanium between FeSi and CaO-SiO_2-Al_2O_3 slag was investigated at 1773 K. The major results of present study can be summarised as follows:

- The distribution behaviour of Ti is strongly influenced by slag basicity. The activity coefficient of TiO_2 decreases with an increase in C/S ratio at C/S>0.8, whereas it significantly decreases by decreasing the C/S ratio at C/S<0.8 system.
- At C/S>0.8 basic system, the addition of CaO stabilises five-fold coordinated Ti, but addition of Al_2O_3 depletes free Ca^{2+} ion due to charge balancing of [AlO_4]. Beyond 10 per cent Al_2O_3, Ti coordination partly shifts from five to four, resulting in a stabilisation of TiO_2 in slag.
- At C/S<0.8 acidic system, Ti in five-fold coordination is forced to transform to four-fold coordination because of Ca^{2+} depletion. The [TiO_4] group incorporates into the aluminosilicate network by replacing [SiO_4] and [AlO_4] structure, which increases the stability of TiO_2.

REFERENCES

Duan, R G, *et al,* 1998. The effect of Ti^{4+} on the site of Al^{3+} in the structure of CaO–Al_2O_3–SiO_2–TiO_2 system glass, *Materials Science and Engineering: A,* 249:217–222.

Le Cornec, D, *et al,* 2021. Structural role of titanium on slag properties, *Journal of the American Ceramic Society,* 104:105–113.

Nakayama, T and Honjou, N, 2000. Effect of aluminum and nitrogen on the magnetic properties of non-oriented semi-processed electrical steel sheet, *Journal of Magnetism and Magnetic Materials,* 213:87–94.

Nakayama, T and Tanaka, T, 1997. Effects of titanium on magnetic properties of semi-processed non-oriented electrical steel sheets, *Journal of Materials Science,* 32:1055–1059.

Romano, C, *et al,* 2000. Effect of aluminum on Ti-coordination in silicate glasses: A XANES study, *American Mineralogist,* 85:108–117.

Sano, N, 1997. *Advanced Physical Chemistry for Process Metallurgy* (Academic Press: New York).

Steiner Petrovič, D, *et al,* 2010. Correlation of titanium content and core loss in non-oriented electrical steel sheets, *Metalurgija,* 49:37–40.

Turkdogan, E T, 1980. *Physical Chemistry of High Temperature Technology* (Academic Press: New York).

Using novel methods to characterise slag films for continuously casting challenging and innovative steel grades

DOI: 10.62053/XEBQ4628

Z Li[1], T Zhang[2], S Qin[3], X Yang[4], Z Yan[5], P Wilson[6] and M A Williams[7]

1. Professor, University of Warwick, Coventry CV4 7AL, England. Email: z.li.19@warwick.ac.uk
2. Professor, Shanghai University, Shanghai 200444, China. Email: tongsheng_zhang@shu.edu.cn
3. Research Fellow, University of Warwick, Coventry CV4 7AL, England. Email: shiying.qin@warwick.ac.uk
4. Research Fellow, Brunel University London, Middlesex UB8 3PH, England. Email: xinliang.yang@brunel.ac.uk
5. Research Fellow, University of Warwick, Coventry CV4 7AL, England. Email: zhiming.yan@warwick.ac.uk
6. Research Fellow, University of Warwick, Coventry CV4 7AL, England. Email: paul.wilson@warwick.ac.uk
7. Professor, University of Warwick, Coventry CV4 7AL, England. Email: m.a.williams.1@warwick.ac.uk

ABSTRACT

Continuous development of complex new steel grades to meet the ever-increasing demand of high performance causes recurrent issues in steel continuous casting such as surface quality defects (eg cracks, depressions, deep oscillation marks) and productivity challenges (eg faster casting, near-net shape casting). Continuous casting of steel is a highly successful metallurgical process. Much of this success can be attributed to the performance of the casting powder that is added to the top of the mould, creates a liquid slag pool as it is heated, and forms a slag film between the water-cooled copper mould and steel shell during its passage down the mould.

Mould powder selection is a compromise between the conflicting requirements of heat transfer and lubrication. In an EU RFCS (Research Fund for Coal and Steel)-funded project, various techniques are developed to offer the opportunity to adapt the slag film to meet the conflicting needs in different parts of the mould such that mild cooling can be generated in the meniscus, mid-broad face or corner areas whilst maintaining lubrication and offering higher cooling rates in other areas of mould. This has significant potential to address the industrial issues in product quality and productivity of continuous casting.

This paper reports, as part of the EU RFCS project, the determination of crystallinity and porosity in slag films for casting challenging and innovative steel grades using new methods. In comparison with the methods such as X-ray powder diffraction (XRD) analysis and optical microscopy / scanning electron microscopy (OM/SEM) analysis that are currently adopted by the industries, EBSD (electron backscatter diffraction) has been employed to determine the crystallinity of the slag films taken from industry casters. X-ray computed tomography (XCT) plus 3D image reconstruction has been used to determine the slag film % porosity with pore volume, pore size distribution, and pore location, which can be linked with the performance of the slag films during casting different steel grades.

INTRODUCTION

The global crude steel production in 2022 is 1884.2 Mt, 96.8 per cent of which is casted by continuous casting technologies (Worldsteel Association, 2023). The success of the steel continuous casting can be attributed to the performance of the casting powder that is added to the top of the mould, creates a liquid slag pool as it is heated, and forms a slag film between the water-cooled copper mould and steel shell during its passage down the mould. Continuous development of complex new steel grades to meet the ever-increasing demand of high performance causes recurrent issues in steel continuous casting such as surface quality defects (eg cracks, depressions, deep oscillation marks) and productivity challenges (eg faster casting, near-net shape casting). Therefore, continuous endeavours have been made to develop new mould powders for the continuous casting of such challenging and innovative steel grades.

The slag film between the water-cooled copper mould and steel shell in its initial stage consists of a solid slag layer because of its freezing on the water-cooled copper and a liquid layer next to the high temperature steel shell. This structure fulfils the major functions of the mould powder in the continuous casting – the liquid slag layer provides the right level of lubrication to the steel shell and the solid layer determines the heat flux (ie heat transfer from the steel shell to copper mould). Major task for developing new mould powder has always been ensuring its physical and chemical properties (such as viscosity, solidification temperature or break temperature, melting behaviour) to balance the lubrication and horizontal heat transfer and avoid casting problems like longitudinal cracking and sticker breakouts (Sridhar *et al*, 1998). The slag film evolutes during its travelling down the mould. Depending on the steel grades casted and the designed chemistry of the mould powder, the liquid layer solidifies and may crystallise depending on the chemistry and thermal conditions and the solid layer also crystallises during the thermal processing. The crystals in the slag film scatter infrared radiation and consequently reduce the heat transfer from the steel shell to copper mould. Therefore, the crystallinity of slag film is a major factor controlling the horizontal heat flux in the mould (Susa *et al*, 2009). Pores are also found during the examination of the slag films taken from the industry mould (Li, Mills and Bezerra, 2004), although the formation mechanisms of pores in slag film have not been well understood. The increased porosity also results in the decrease in heat transfer from the steel shell to the mould (Mills and Dacker, 2017).

In summary crystallinity and porosity are two major characteristics determining horizontal heat transfer from the steel shell to copper mould, which is critically important to cast challenging and new steel grades without defects. This paper investigates the methods for determining the crystallinity and porosity of slag films taken from industrial casting moulds.

CRYSTALLINITY

The initial slag film formed consists of a glassy layer in the water-cooled mould side and a liquid layer in the high-temperature steel shell side. The thin liquid layer solidifies and the slag film crystallises over time until the crystallinity (f_{crys}) in the slag film reaches a steady state. The crystallinity in the slag film is one of the key parameters controlling the horizontal heat transfer from the steel shell to the mould. As summarised by Mills and Dacker (2017), three major parameters controlling the horizontal heat flux from the shell to mould are

1. The thickness of the slag film.
2. The fraction of crystalline phase (ie crystallinity, f_{cryst}) and the size of the crystallites in the slag film.
3. The interfacial resistance between the copper mould and slag film and porosity formed by the shrinkage of slag during crystallisation.

One of the major research topics on crystallinity is to manipulate the crystalline phase and consequently control the crystallinity (f_{cryst}) in the slag film. Cuspidine ($3CaO{\cdot}2SiO_2{\cdot}CaF_2$) is the primary crystalline phase in the conventional fluorine-containing casting powders but not in the environmentally friendly fluorine-free mould slag or calcium aluminate mould slags. Increasing the slag basicity (CaO/SiO_2) generally increases its crystallinity. Without being involved in too much detail in the mechanisms of crystallinity in slag film, this chapter focuses on the determination of the crystallinity in slag films taken from industry casting moulds. In this chapter, the authors will first determine the crystallinity of slag films using OM (optical microscopy), SEM (scanning electron microscopy) and XRD (X-ray powder diffraction) techniques, and then explore the use of EBSD (electron backscatter diffraction) in quantitatively analysing the crystallinity (f_{cryst}) of the slag film.

OM (Optical Microscopy) image analysis

The procedure to determine the crystallinity of slag film is to observe the well-prepared slag film sample under optical microscope, select the representative range/area(s) of the slag film for analysis, determine the crystalline and glassy phases, take photos of the selected area(s) and determine the crystallinity based on the estimation of the selected area(s). Figure 1 shows how OM is applied to determine the crystallinity of slag film B. Slag film B has two distinguished layers of glass and crystalline, which enables the researcher to estimate the crystallinity to be around 50 per cent.

The OM analysis can allow large areas of slag film to be analysed. This method is simple to provide comparative information for different slag films. However, this purely depends on the researcher's experience to choose the representative area(s) and distinguish the crystalline and glass phases. If there is no clear boundary between the glass and crystalline phases, or the crystallites scatter in the glassy phase or *vice versa*, its accuracy will be influenced.

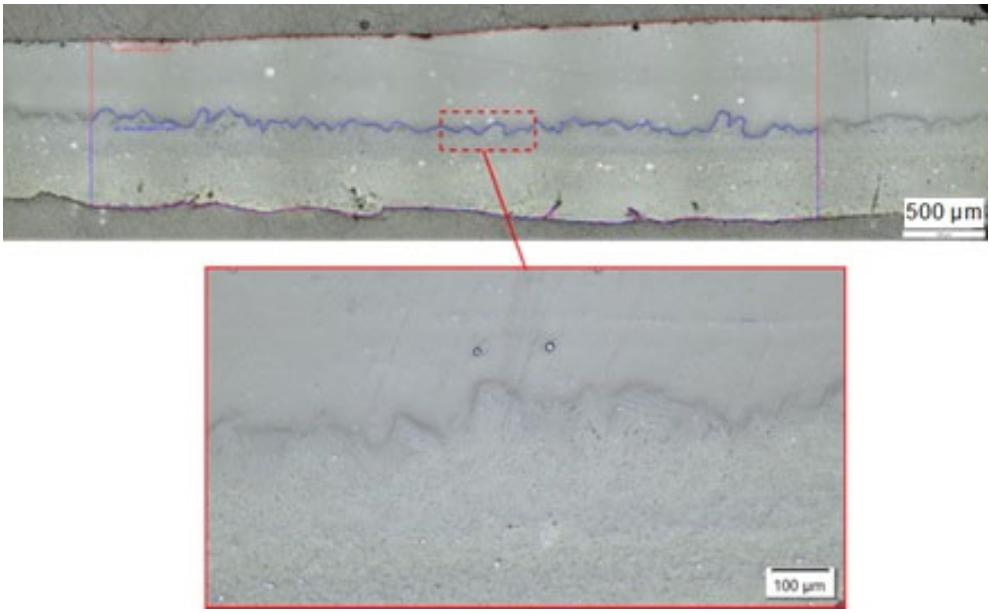

FIG 1 – Optical microscope (OM) image of slag film B for crystallinity estimation.

SEM image analysis

The procedure for SEM image analysis is similar to that for OM image analysis. However, SEM can go higher magnification than OM, which enables clear identification of crystalline phases in a focused area. Figure 2 illustrates the slag films A (top), B (middle) and C (bottom) respectively from industry casting moulds. The crystalline phase, glass phase and pores are clearly shown in the figures.

Slag film A has a thin layer in contact with steel shell consisting of crystalline phase (cuspidine), a thick glassy phase next to mould and pores (Figure 2 top). This thin layer could be the liquid layer in the initial formation of the slag film. Slag film B (Figure 2 middle) composes of two clear, similar thickness layers with the flat, glassy layer in contact with mould. The layer next to the steel shell is mainly crystalline phases (nepheline – $NaAlSiO_4$, cuspidine), pores and iron droplets. Dendrite crystalline is clearly observed to grow at the interface in the direction from the steel shell to the mould. Compared to Figure 1 by OM, SEM image clearly shows the morphology of the slag film. Slag film C (Figure 2 bottom) is mainly crystalline with large pores in the steel shell side.

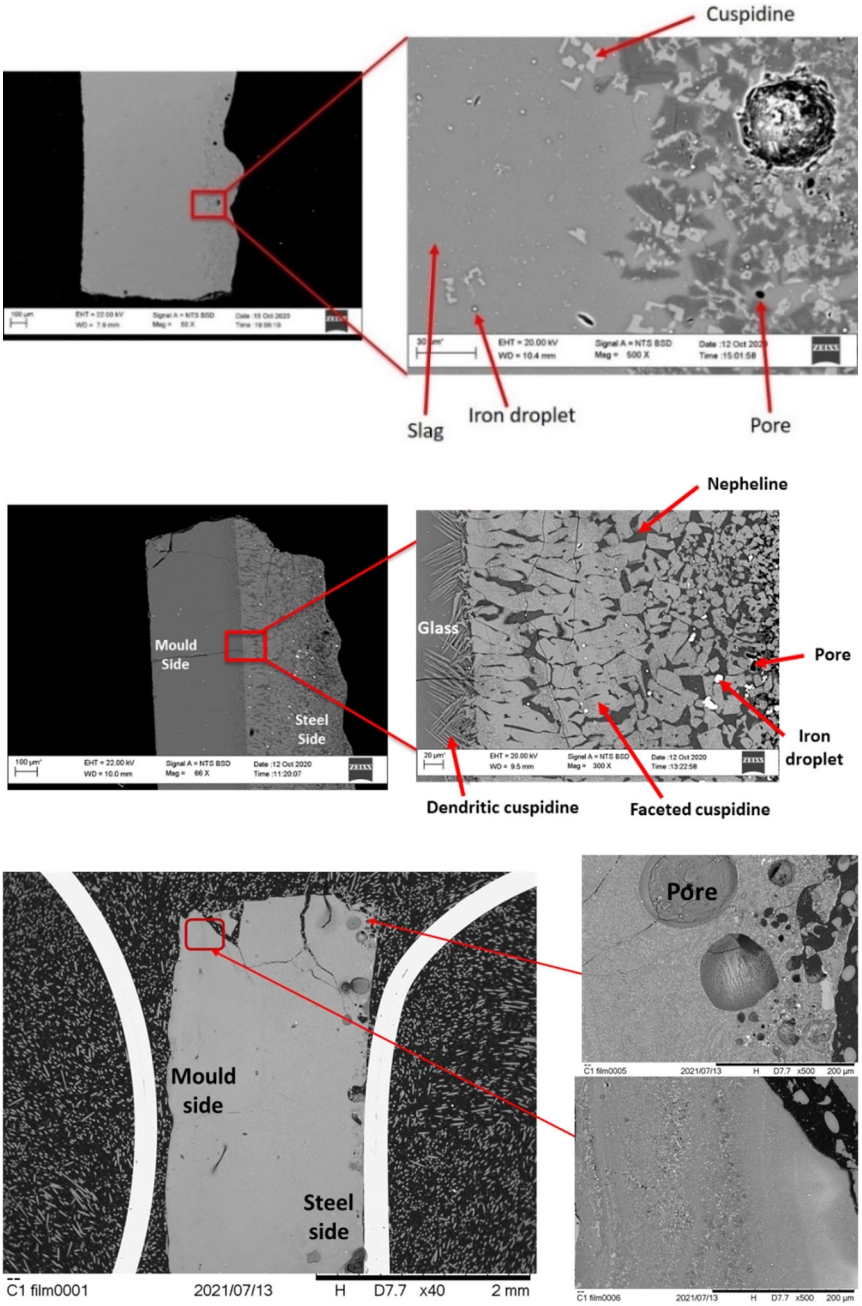

FIG 2 – SEM micrographs of slag films A (top), B (middle) and C (bottom). For each of the slag films, the left is its cross-section image and the right is the focused area.

SEM image can clearly show the crystalline and glassy phases in the slag films. However, the crystallinity determined is limited to the area(s) tested. Reliable results can only be obtained by examining an area which can represent the slag film. Therefore, macro photos of the whole slag film were taken, for example, as shown in Figure 3a. Then a thresholded image was obtained with the help of ImageJ (NIH Image, imagei.net) or other similar software, as shown in Figure 3b. Finally, the crystallinity of the industrial slag film can be calculated according to the colour difference, average f_{cryst} is then calculated using Equation 1:

$$\overline{f}_{cryst} = \frac{\sum f_{cryst} \cdot A_i}{\sum A_i} \quad (1)$$

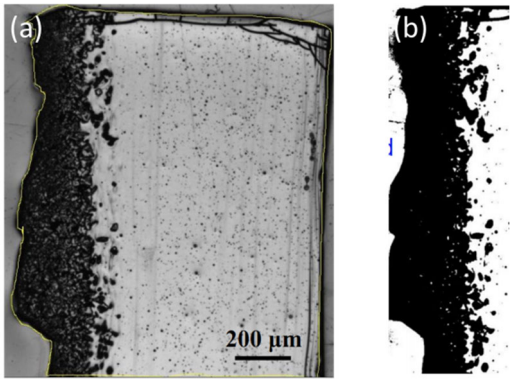

FIG 3 – Analysis process of SEM micrograph of a slag film at higher magnification: (a) SEM micrograph and (b) thresholded image.

Accordingly, the crystallinity determined by SEM image analysis is 21 per cent, 56 per cent and 100 per cent for slag films A, B and C respectively. In summary, OM or SEM can be used to determine the crystallinity of the slag films. The value and accuracy of the crystallinity determined depend on the representative area(s) selected. The difference between crystalline and glass phases may be subject to the researcher's experience. SEM, because of its better identification of crystalline phase, could give better outcomes compared to OM.

XRD analysis

XRD is a proven technique to determine the phases and their quantities in powders. The experimental procedure adopted in this study is to select representative pieces of the slag film and grind them to fine powders for XRD analysis. Panalytical X'Pert Pro MRD™ using a Cu-K_α radiation was employed with an accelerating voltage of 40 kV and a tube current of 40 mA. For XRD scans, the scanning angle was varied from 20° to 80° at a rate of 2°/min.

The type of the crystalline phases in the slag film samples can be obtained by analysing the XRD pattern of the sample, however, this study is more interested in the crystalline phase content (crystallinity f_{cryst}). The diffraction peak of crystal phase presents a high intensity in a narrow degree (ie crystalline area), by contrast, the diffraction peak of the glass phase looks like a steamed bread owing to the low intensity and wide degree (ie amorphous area). The degree of crystallinity (f_{cryst}) can be determined by the total integrated area of the crystal and glassy phase peaks in the XRD pattern of the sample. The f_{cryst} is then calculated by Equation 2:

$$fcryst = \frac{Crystalline\ Area}{Crystalline\ Area + Amorphous\ Area} \quad (2)$$

Figure 4 is the XRD patterns of three slag film powder samples obtained. For the slag film A, the crystallinity in the mould side and in the steel shell side varies as shown in Figure 4a. So the selected pieces of a slag film were fully crushed for the XRD test. The crystallinity for the three slag films determined is 22 per cent, 65 per cent and 100 per cent for slag films A, B and C respectively. It is concluded that XRD does provide reasonable, consistent results.

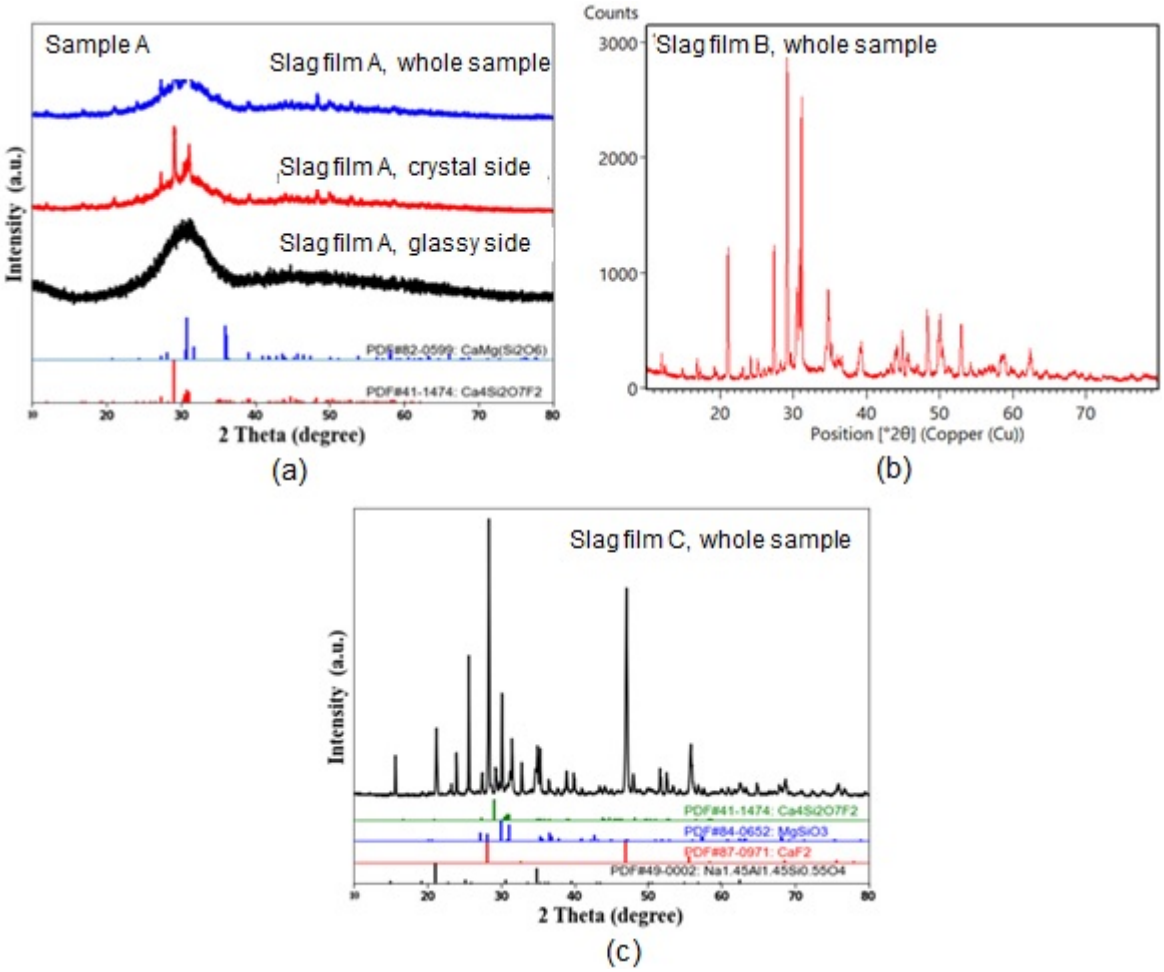

FIG 4 – XRD patterns of three slag film sample powders A, B and C.

EBSD analysis

Electron backscatter diffraction (EBSD), in addition to the conventional techniques of XRD analysis and OM/SEM image analysis, was attempted to obtain the crystallinity of slag film samples. EBSD is a scanning electron microscope-based microstructural-crystallographic characterisation technique commonly used in the study of crystalline or polycrystalline materials, which may be able to provide information about the crystallinity of slag films tested. The industrial slag film C is used as an example for the development. As shown in Figure 5, the presence of many small crystals only 1–2 μm in size (and glass phase if there is) can be detected. The crystalline phases and volumes in the area can be identified by using Kikuchi Patterns in EBSD (Figure 6). The total crystallinity of slag film C is about 71.1 per cent, which is lower than that determined by XRD analysis and SEM image analysis (100 per cent). The main reasons could be:

- To accurately determine the crystallinity of the slag film sample, pre-setting all the crystalline phases in the tested areas is essential, however, some minor phases in the tested areas might not be determined before EBSD analysis.
- The areas tested may not be sufficient in size.

All these factors can be further improved.

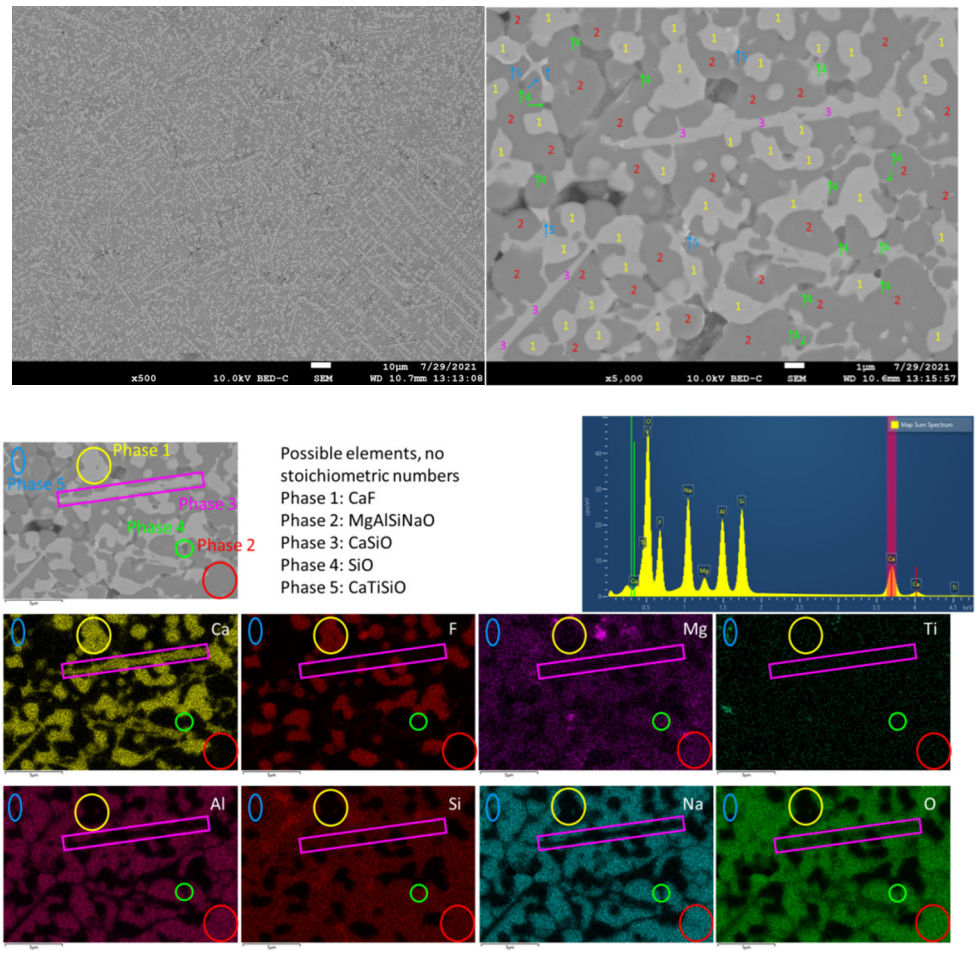

FIG 5 – SEM micrographs and the types of small size crystalline phases in slag film C. (Phase 1: CaF_2, Phase 2: MgAlSiNaO, Phase 3: CaSiO, Phase 4: SiO, Phase 5: CaTiSiO).

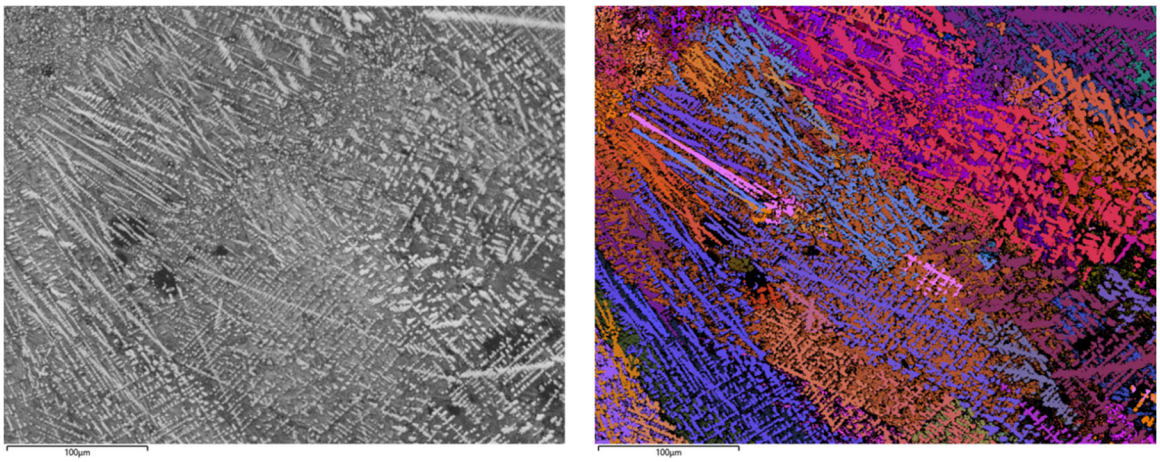

FIG 6 – Identification of crystalline phases using Kikuchi patterns in EBSD. Examination area: 0.4 mm × 0.3 mm, Step size: 0.5 mm, 503930 points measured in total. Acquisition time: 7 mins.

By comparing the crystallinity results from three methods of SEM image analysis, XRD analysis and EBSD analysis, it can be concluded that the values obtained by XRD analysis and SEM image analysis are in reasonably good agreement. The result from EBSD analysis is lower, which could be further improved by presetting all the crystalline phases in the tested area before EBSD scanning and increasing the size of areas. The advantage of SEM image analysis is its clear indication of crystallinity variation with position (tested area), however, due to the limitation of the field of vision, the results of different planes may have a large deviation. To obtain a reliable result, selecting representative area(s) is the key. XRD analysis, partially because of its easiness in selecting

representative samples, may be more suitable for the overall crystallinity analysis of slag film samples.

POROSITY

The porosity in the slag film can come from various sources although it is not well understood. Crystal is denser than glass, so crystallisation results in shrinkage and consequently creates micro-pores in the slag film. However, crystallisation is not the only cause of porosity. Casting powder with a high moisture content (or water leaks) can lead to hydrogen pores in the slag film. Blowholes containing $CO_{(g)}$ can be formed from reaction of C and FeO in the slag (Mills and Dacker, 2017). Also the potential reactions within the mould flux at high temperature such as evaporation of CaF_2 and formation of SiF_4 in fluorine-containing mould powder can also form pores. Different morphologies of pores have been observed in industrial slag films, which could be attributed to different formation mechanisms.

Mould flux is distributed between the mould and steel shell, which controls heat transfer and lubrication during continuous casting. The porosity in the slag films has a great influence on the heat transfer from the steel shell to the mould, and consequently affects the casting process and quality of the casting products. The increased porosity could lead to a decrease in heat flux from the shell to mould and to sticker breakouts. Because of the importance of porosity in controlling heat flux, Hunt and Stewart (2016) reported that the use of intumescent coatings on the copper mould could reduce heat transfer by up to 27 per cent in a laboratory cold finger simulation experiment.

Although the importance of porosity in slag film in heat flux is well known, their formation mechanisms are not very clear and the method to determine the porosity is not well established. In this chapter, the authors investigate the methods to determinate the porosity of industrial slag films using techniques from the OM/SEM image analysis to the innovative X-ray computed tomography (XCT) technique for 3D porosity determination. The number, size and distribution of the pores quantified in the three industrial slag films (A, B and C) are summarised in this section.

SEM image analysis

As shown in Figure 7, by applying appropriate threshold, SEM image (Figure 7a) can be processed to 2D image (Figure 7b) showing the porosity. The porosity in the thresholded image can be obtained by using commercial software such as Image J.

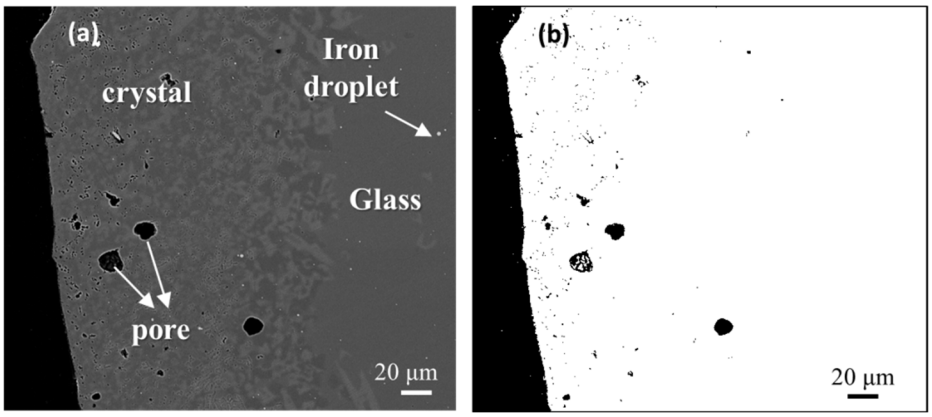

FIG 7 – SEM micrograph of slag film A at higher magnification: (a) SEM micrograph; (b) thresholded image.

As shown in Figure 8, small pores observed in SEM images of slag film C at high magnifications could be formed during crystallisation compared to the large blowholes observed in Figure 7 for slag film A. Using the SEM method, potentially pores in a wide range of size can be measured in a slag film, which may not be possible in the OM image analysis (which is not included in this paper).

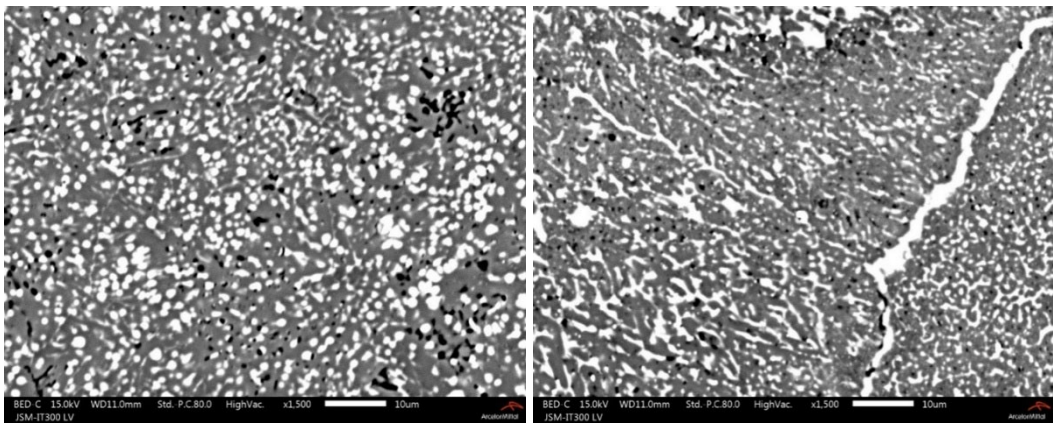

FIG 8 – SEM images at high magnification showing the pores (black spots) in the slag film C probably formed during crystallisation.

The characteristics of porosity in the three slag films A, B and C analysed by the above method are summarised in Figure 9. It should be pointed out that the analyses include all the pores in large areas from 16.18 mm^2 (slag film A) to 22.70 mm^2 (slag film C). The porosity obtained is 3.31 per cent (slag film A), 1.83 per cent (Slag film B) and 4.24 per cent (slag film C), respectively.

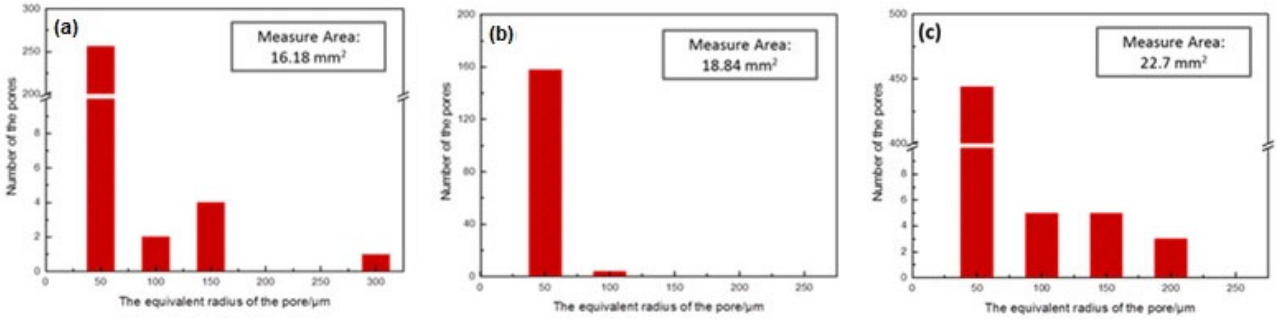

FIG 9 – Size distribution of all internal porosities in industrial slag films: (a) B, (b) A and (c) C. The equivalent radius of the pore is calculated by assuming the pore is circle. Radius 50 μm refers to the pores with radius between 0 and 50 μm and radius 100 μm refers to the pores with radius between 50 and 100 μm and so on. Measured area refers to the size of area measured for the % porosity.

Big difference in the % porosity even for the same slag film determined by different researchers was observed. The possible reasons are:

- The difficulty to balance the measurement area and accuracy due to the characteristics of the thresholded image detection.
- The selected areas – the size of the area and the representative of the area.

XCT analysis

X-ray computed tomography (XCT) is a non-destructive technique for visualising interior features within solid objects and for obtaining digital information on their 3D geometries and properties. An XCT image is typically called a slice, as it corresponds to what the object being scanned would look like if it were sliced along a plane. A complete volumetric representation of an object can then be obtained by acquiring a continuous set of CT slices. In the current study, XCT is used as a novel characterisation technique to visualise the slag films in 3D and identify the pores along with their size distribution. The XCT has the capability of identifying pores of very small dimensions with spatial resolutions of ~1/1000 times the thickness of the slag films. The samples used in the XCT tests are in ~20 mm square or round shape (which could be considered representative) cut from the industrial slag film samples. In this study, a lab-based CT scanner (Zeiss 620 Versa CT system) is used for scanning the industrial slag films prepared. The exposure voltage is 80 kV, exposure power 10 W

and exposure time 10 sec. The Voxel size is 9.0895 μm. The number of projections is 3201. Imaging processing including filtering, segmentation and quantification were carried out using the Avizo Software (Thermo Fisher Scientific). As an example, Figure 10 shows the morphologies of the slag film C and porosity in 3D images. From this 3D images, the porosity (%) and pore size distribution can be calculated and the pore distribution across the sample can be observed.

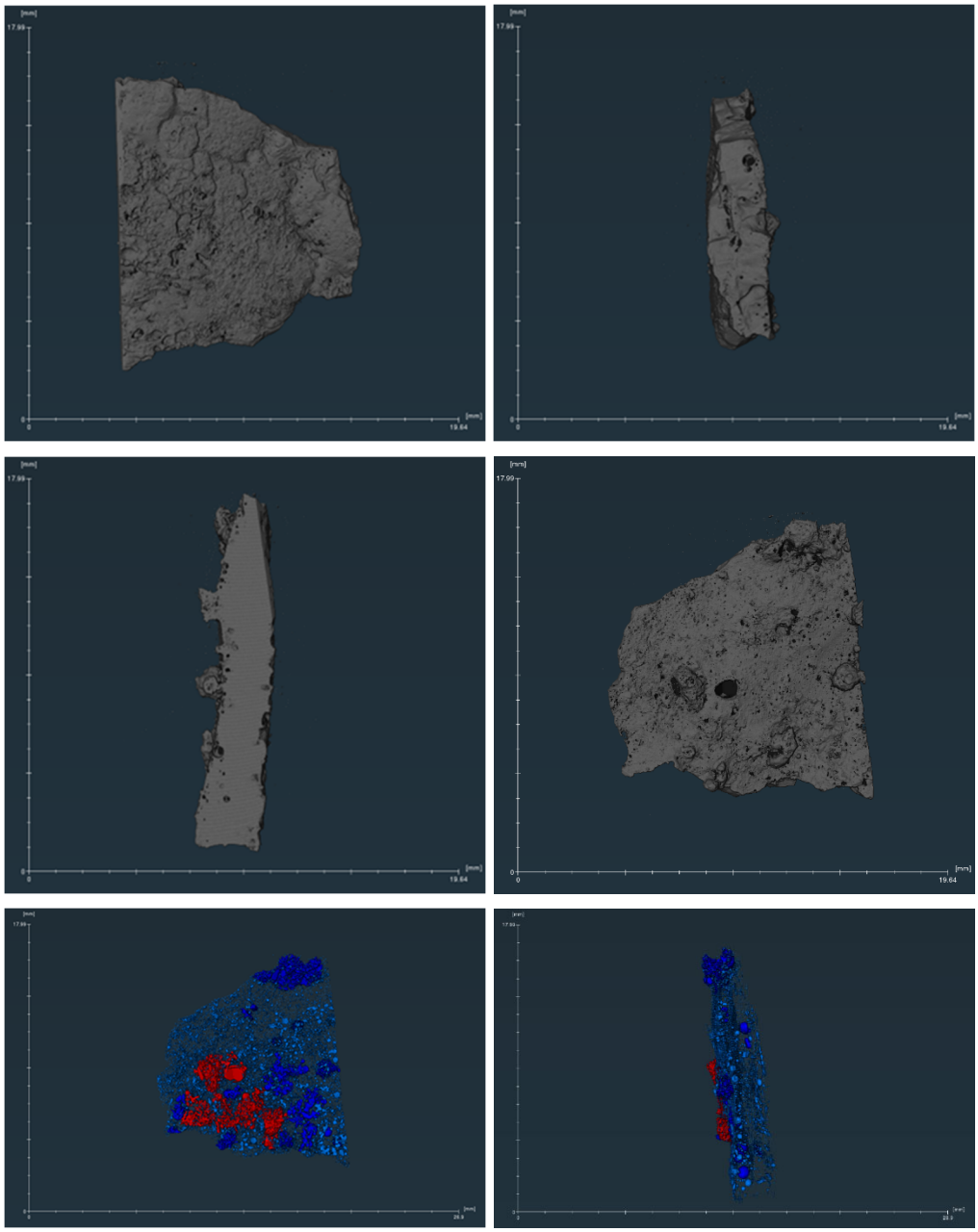

FIG 10 – XCT results for slag film C: morphology (top and middle) and pore distribution in 3D images (bottom).

The number of pores measured by XCT is large (3880 for slag film A sample, 539 for slag film B sample and 9344 for slag film C sample), which makes the data more truly reflect the characteristics of slag films. The measurement accuracy of XCT is 5 μm in this study, so the statistics range from 5 μm to 500 μm with intervals of 50 μm.

It was found that the sizes of all internal pores in slag film B are smaller than 100 μm and the proportion (number density percentage) of porosities with radius smaller than 50 μm is above 99 per cent. For slag film A, although the ratio (ie number density percentage) of the porosities smaller than 50 μm reached 98 per cent, their volume percentage is less than 7.5 per cent. The larger pores between 50 and 400 μm account for 92.5 per cent of the total volume of pores. Similar

phenomena are observed for slag film C. In slag film C, the proportion (number density percentage) of pores with radius below 50 μm almost reaches 60 per cent, but its volume percent is only about 3 per cent. The proportion of pores with a radius of 50–100 μm accounts for about 35 per cent and the volume percent accounts for more than 20 per cent. In other words, the larger pores (>50 μm) contributes more to its volume ratio. The proportion of varying pores detected by XCT agrees with that by SEM (Figure 9), at least in trend.

Overall, the pores in industrial slag film B are the smallest in all cases, both in average radius (20 μm) and volume ratio (0.05 per cent). The proportion of pores in industrial slag film A is obviously larger than that in slag film B with the average radius 35 μm and porosity 0.7 per cent. The effect of pores in slag film C is more significant. The proportion of pore volume in slag film C is 3 per cent (average pore radius 85 μm), being one order of magnitude larger than that of slag films A and B.

CONCLUSIONS

The authors have explored various methods to determine the crystallinity (f_{cryst}) and porosity (%) of the industrial slag film samples and the following conclusions can be obtained:

- OM/SEM can be used to determine the crystallinity of the slag film samples and the results does give similar trend to the XRD method. The value and accuracy depend on the representative area(s) selected.
- XRD does provide reasonably consistent results of the crystallinity of slag films.
- EBSD can be a useful tool to determine the crystallinity of the slag film samples, but further development is required for the application.
- The porosity can be measured by using SEM + image analysis, however, variation for the same sample occurs with different researchers. The possible reasons are:
    - the difficulty to balance the measurement area and accuracy due to the characteristics of the thresholded image detection
    - the selected area(s) to test.
- XCT has the advantages of determining % porosity, pore volume, pore size distribution and pore location (steel side or mould side). This could be a useful technique for porosity determination in slag film samples.

ACKNOWLEDGEMENTS

The authors would like to acknowledge the financial assistance received from the Research Fund for Coal and Steel (RFCS) under the Grant Number RFCS-2018–847269. The authors also would like to thank the partners in the project for providing industry slag films and discussions – Sidenor Aceros Especiales S. L., ArcelorMittal Maizières Research, SSAB, Sandvik Materials Technology, Proximion, the Materials Processing Institute, Swerim and the Open University.

REFERENCES

Hunt, A and Stewart, B, 2016. Techniques for controlling heat transfer in the mould-strand gap in order to use fluoride free mould powder for continuous casting of peritectic steel grades, in *Proceedings of the 10th International Conference on Molten Slags, Fluxes and Salts (MOLTEN16)* (eds: R G Reddy, P Chaubal, P C Pistorius and U Pal), pp 349–356 (The Minerals, Metals and Materials Society).

Li, Z, Mills, K C and Bezerra, M C, 2004. Characteristics of mould flux films for casting MC and LC steels, in *Anais do XXXVI Seminário de Fusão, Refino e Solidificação dos Metais (Proceedings of the XXXVI Seminar on Fusion, Refining and Solidification of Metals),* pp 13–24.

Mills, K C and Dacker, C-A, 2017. *The Casting Powders Book* (Springer: Switzerland AG).

Sridhar, S, Mills, K C, Ludlow, V and Mallaband, S T, 1998. A comparison of the mould powders used to cast slabs, billets and blooms, in *Proceedings of the 3rd European Conference on Continuous Casting*, pp 807–816.

Susa, M, Kushimoto, A, Toyota, H, Hayashi, M, Endo, R and Kobayashi, Y, 2009. Effect of both crystallisation and iron oxides on the radiative heat transfer in mould fluxes, *ISIJ International*, 49(11):1722–1729.

Worldsteel Association, 2022. World Steel in Figures 2023. Available from: <https://unesid.org/descargas_files/World-Steel-in-Figures-2023.pdf>

The recovery of pig iron from the Zimbabwean limonite-coal composite pellet

DOI: 10.62053/UGHB9737

S Maritsa[1], S M Masuka[2] and E K Chiwandika[3]

1. Master candidate, University of Zimbabwe; Teaching Assistant, Harare Institute of Technology, Harare 263, Zimbabwe. Email: steven.maritsa@gmail.com
2. Lecturer, University of Zimbabwe, Harare 263, Zimbabwe. Email: shebarmasuka@gmail.com
3. Lecturer, Harare Institute of Technology and Module Lecturer, University of Zimbabwe, Harare 263, Zimbabwe. Email: chiwandikae@gmail.com

ABSTRACT

The iron and steel industry is experiencing an increase in the use of iron and steel commodities within societies, decarbonisation pressures, depletion of high iron ore grades and high energy consumption. This necessitates scrap metal recycling, low-grade ore utilisation using the induction or electric arc furnace to achieve the global target of net zero CO_2 emission. The available high-quality scrap metal cannot sustain the steel industry but the world has unused hematite-goethite ores. It is the aim of this research that this resource be utilised using the induction furnace to sustain the steel industry in an environmentally friendly manner. Indurated pellets prepared from the hematite-goethite ore, 5 wt per cent limestone and 5 wt per cent coal addition were smelted in the induction furnace at 1350 ± 50°C with 25 mins holding time. The effects of basicity and carbon content were also investigated to optimise the smelting parameters. The results showed that the careful control of the basicity, and iron-to-carbon ratio maximised total metal recovery. The optimal basicity ratio was determined to be 1.3 and a carbon to iron ratio of 1.4 achieved a total metal recovery of 73 per cent. The metal recovery was closely related to the estimated slag melting temperature. The basicity ratio of 1.3 achieved the lowest slag melting temperature estimated to be around 1380°C based on the CaO-SiO_2-Al_2O_3 phase diagram. The recovered metal had a comparable chemical composition and microstructure to that products from an ITmk3 furnace.

INTRODUCTION

The world target of net zero emissions by 2050 has resulted in massive demand for equipment and infrastructure of clean-energy technologies where iron and steel products play a pivotal role (International Energy Agency, 2023). De Carvalho *et al* (2022) reported the global steel consumption to be around 2 5 billion metric tons and is expected to rebound by 1 per cent in 2023 from a decline of 2.3 per cent in the year 2022. This scenario coupled with the depletion of high-grade iron ores has forced the industry to utilise lower-grade iron ores that have previously been unexploited. The mineralogy of these underutilised ores is often very complex, and requires innovative processing techniques that can yield low-impurity molten metal from these low-grade iron ore resources (Liang *et al*, 2023).

The recycling of iron and steel has been a form of environmental management and a way of waste control in the industry, with up to 70 per cent recycling of scrap. This scrap is an essential raw material for small plants and foundries where in some instances, producers are almost totally dependent on scrap metal as a raw material (Rehlke, 2001). In such instances, where scrap metal becomes a critical raw material, the availability and prices of scrap metal carry a huge bearing on the productivity of such enterprises.

Zimbabwe is reported to host about 111 million tonnes (Mt) of iron ore at its Ripple Creek deposits in the Midlands Province, and of these deposits, 41 per cent are limonite ores (Magunda, Dube and Simbi, 2004). The Zimbabwean limonite ore was reported to have a total Fe concentrations of approximately 53 wt per cent (Chisahwira *et al*, 2023). Ores containing an iron (Fe) concentrations below 55 wt per cent are termed low-grade iron ores, where 60 to 70 per cent weight of these lump ores get converted to fines during mining and transportation of run-of-mine (ROM) (Reddy, Sahoo and Kumar, 2023). Limonite ores are also referred to as ‘low-grade ores’ because of the high amounts of gangue material associated with the ores, and the high α-FeOOH content which causes problems during sintering for the blast furnace iron-making operations (Mochizuki and Naoto, 2019).

The blast furnace has been the major method for the production of iron. However, the arising pressure on environmental resources has necessitated the exploration of other ironmaking technologies. Alternative ironmaking technologies are focusing mainly on reducing CO_2 emissions, lowering of energy consumption and production costs. Some of the new technologies being used include high intensity smelting (HIsmelt) reduction ironmaking, cool Earth 50 (COURSE50), Rotary hearth furnace (RHF) (Zhang *et al*, 2018). One of the technologies that utilises the RHF to produce iron nugget is the Iron-making Technology mark 3 (ITmk3). The ITmk3 technology utilises coal composite pellets that are fed into a RHF as a raw material, heating to temperatures between 1350–1450ºC and a residence time of about 8–10 mins (Upakare *et al*, 2018). Product from the ITmk3 technology is of high quality (Fe content > 96 wt per cent). The ability to separate metal and slag in one step via the ITmk3 process allows for effective concentration of the iron ore (Ghosh, Vasudevan and Kumar, 2021).

An investigation by Huang *et al* (2018), on the reduction of low iron ore composite pellets with a high silicon dioxide (SiO_2) of 40.61 wt per cent, sodium chloride (NaCl) was used as an additive to enhance the reduction process at experimental temperatures between 870°C and 990°C. It was concluded that the addition of NaCl increased the reduction of the iron oxide and hence suppressed the formation of the fayalite, a difficult-to-reduce phase, increasing metallisation by enhancing the reduction of wüstite to metallic iron. This was achieved by the enhancement of the gasification of coal, thus improving the reduction of iron oxides (Huang *et al*, 2018).

In smelting experiments at varying basicity conditions ranging from 0.46 to 1.91, where direct reduced iron (DRI) was formed into pellets and smelted at 1600°C for 1–2 hrs by Saleh and Rochani (2015), it was suggested that the reduction of FeO was favoured in alkaline conditions rather than in acidic conditions. At a basicity of 1.18, a recovery of 95.84 per cent was attained from the smelting of the DRI pellets to obtain pig iron with Fe content of 89.95 per cent. The basicity ratio of 1.18 was then considered the optimum basicity ratio. However, the amount of silica in the slag decreased with increasing basicity and the total Fe content in the slag was less than 10 per cent for the entire basicity range (Saleh and Rochani, 2015).

In another study by Sah and Dutta (2010) on the smelting reduction of iron ore-coal composite pellets in a liquid metal bath in an induction furnace, it was determined that the fractional reduction increased with a decrease in the total Fe to fixed C ratio, that is, the extent of reduction increased as the amount of reductant in the pellets increased. The average rate of reduction was calculated by dividing the fractional reduction by the time for which the pellets were in the bath and it was determined that initially the rate of reduction was very fast but decreased with time. This was attributed to the release of volatiles from the coal in the composites, which resulted in rapid solid-gas reaction (Sah and Dutta, 2010).

The aim of this paper was to study the reduction and recovery of cast iron from low-grade iron ore (limonite with 52 wt per cent Fe) by adopting the ITmk3 technology and determining the proper process parameters required to control quantity and quality of the produced iron nuggets. Careful control of basicity and carbon-to-oxygen ratio was studied to determine the best parameters required to produce metallic iron with similar properties to that of pig iron at a laboratory scale.

EXPERIMENTAL

Material preparation

Pellets used in this investigation were prepared using the Zimbabwean limonite ore, carbon, and limestone whose chemical composition is reported by Chisahwira *et al* (2023), according to the methods reported by the same. The iron ore was blended with 2.5 wt per cent coal and 2.5 wt per cent of limestone. The blend was then pelletised using a pelletisation disc and indurated at 1100°C for 25 mins. The indurated compressive strength of 250 kg/pellet was achieved. The chemical composition of the limonite ore and the limestone is shown in Table 1. The chemical composition of the pellets is shown in Table 2. The chemical analysis results were determined using atomic absorption spectrometry (AAS).

TABLE 1

Analysis of Zimbabwean limonite ore and limestone (Chisahwira *et al*, 2023).

Analyte	T-Fe	SiO_2	CaO	Al_2O_3	MgO	Mn	S	P	LOI
Zimbabwean Limonite Ore	52.51	8.78	1.32	1.30	0.59	2.1	0.005	0.04	11.87
Limestone	1.34	7.10	45.70	1.19	4.22	0.31	0.17	0.01	39.96

TABLE 2

Chemical composition of the indurated pellets made from the limonite ore.

Analyte	Total Fe	SiO_2	Al_2O_3	CaO	MgO	MnO
wt%	66.30	10.96	6.92	0.14	1.29	3.22

The results showed that the total iron concentration had increased from the 52.51 wt per cent in the ore to 66.30 wt per cent in the indurated pellets. Phase analyses in the ore was performed by X-ray diffraction (XRD) (Bruker AXS) using a Cu tube at a scan angle of 20° to 80°, scanning rate of 2°/min, voltage of 40 kV and current of 40 mA.

The results in Figure 1 showed that the major phases in the indurated pellets were Fe_3O_4, $MgO{\cdot}Fe_2O_3$, $Fe_{2.33}Si_{0.67}O_4$ and Fe_2O_3.

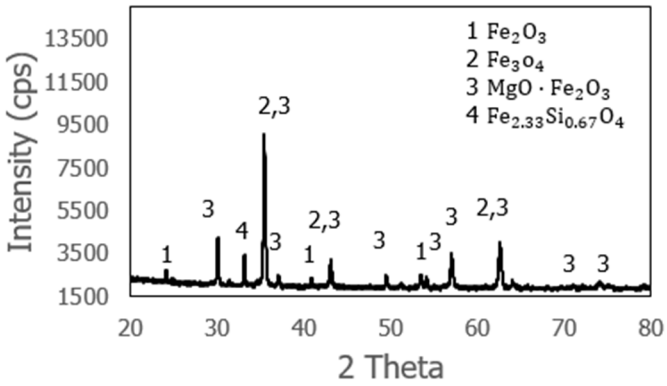

FIG 1 – Phase identification in the pellet by XRD.

Experimental procedure

About 250 g of the pellets were mixed with stoichiometric equivalent carbon to reduce the iron oxides, by placing the pellets in a crucible of 110 mm height and 60 mm diameter and placing the coal and limestone powder in the gaps between the pellets. The equivalent amount of carbon added was evaluated based on the amount of oxygen attached to Fe. The binary basicity of the charge was adjusted by the addition of some limestone with the chemical composition shown in Table 1. The binary basicity (CaO/SiO_2) was varied from 0.013 to 1.4, Table 3. The effect of basicity on the metal recovery had to be studied mainly in the alkali region because, smelting of low basicity burdens consumes high energy as compared to the alkali (Saleh *et al*, 2015). In a study conducted by Zhao *et al* (2017), an increase in basicity from 1 to 2 resulted in increasing recovery from 75.3 to 78.3 per cent and slightly decreased by adjusting basicity to 3.

TABLE 3

Evaluated chemical composition of the burden material.

Burden	wt%				Basicity ratio (CaO/SiO_2)
	T.Fe	CaO	SiO_2	Al_2O_3	
1	66.300	0.140	10.900	6.920	0.013
2	51.600	10.440	9.400	5.620	1.110
3	50.300	11.300	9.400	5.510	1.200
4	49.110	12.190	9.370	5.400	1.300
5	47.890	13.040	9.320	5.200	1.400

The mixed burden was then charged into a graphite crucible with the following dimensions: an inner diameter of 57 mm and a depth of 120 mm. The charged crucible was placed in an induction furnace. The temperature of the furnace was raised to 1350 ± 50 °C (Ishizaki, Nagata and Hayashi, 2006) and was held at that temperature for 25 mins to allow for the reduction of the pellets. The reduced samples were then removed from the furnace and quenched, the slag was then separated from the metal. The metal could be easily separated from the slag due to the difference in the densities. Figure 2 shows the image of the appearance of the slag and the metal before separation. The chemical composition of the slag and metal after separation is as shown in Tables 4 and 5 respectively to assist in providing a clear difference between the two phases



FIG 2 – Image showing metal and slag produced at a basicity of 1.3.

TABLE 4

Chemical composition of the slag phase after separation at a burden binary basicity of 1.3.

Analyte	MnO	TFe	CaO	MgO	Al_2O_3	SiO_2
wt%	4.0	9.55	36.20	2.41	10.30	28.03

TABLE 5

Chemical composition of the metal phase after separation at a burden binary basicity of 1.3.

TFe	C	Si	Al	Mn	P	S
96.37	3.24	0.002	0.001	0.148	<0.001	0.069
Cr	**Ni**	**Mo**	**V**	**Co**	**Ti**	**CaO/SiO_2**
0.005	<0.004	0.020	0.0011	0.009	<0.001	1.30

The burden material carbon content was also varied in order to investigate the effect of the burden carbon to oxygen ratio on the recovery of iron from the pellets. Since all the experiments were done using the graphite crucible it was assumed that the effect of the carbon from the crucible in all the samples were equal and therefore the burden carbon played a significant role in the reduction and smelting of the pellets. Metal recovery was determined using Equation 1.

$$Total\ metal\ recovery\ (\%) = \frac{W}{W_0 T_{Fe}} \times 100 \quad (1)$$

where:

- W is the weight of the metal separated from the slag
- W_0 is the total weight of the reduced pellets
- TF_e is the iron weight percent in the pellets

The final chemical composition of the cast iron produced was analysed using a spark emission spectrometry.

Microstructural examination was also carried out after some metallographic preparations that begun with sectioning of the samples using a Discotom cutting machine and then mounting the samples using a Struers mounting machine. Grinding and polishing of the samples were completed using the Struers machine. Lastly, etching of the samples was done using a 4 per cent nital reagent. Microstructural examination was carried out at 20× magnification using a metallurgical light microscope.

RESULTS AND DISCUSSION

Effect of basicity on the metal recovery

The effect of basicity on the metal recovery was investigated by varying the basicity using limestone. The results are as shown in Figure 3.

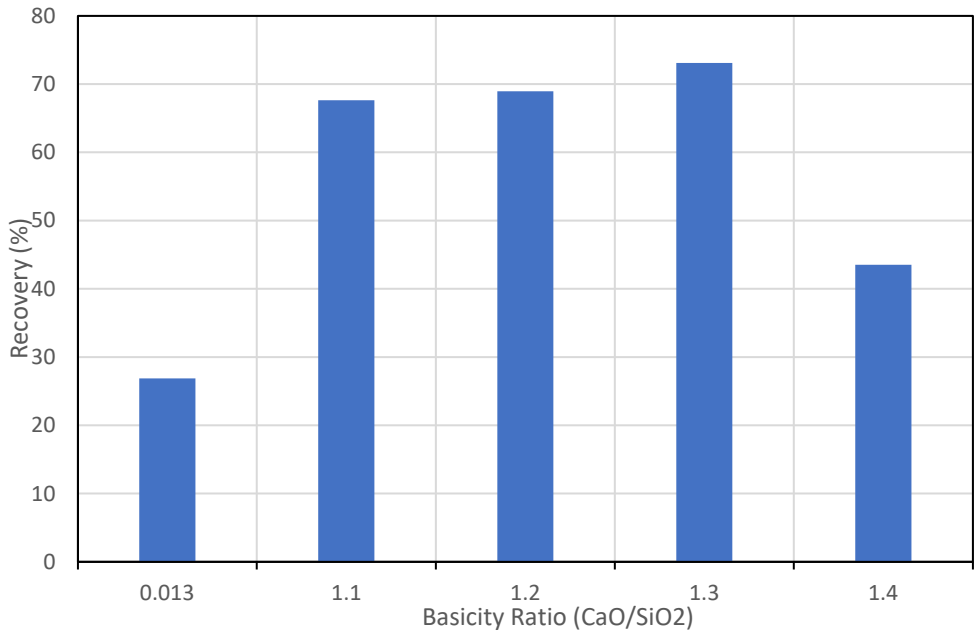

FIG 3 – Percentage metal recovery with increasing basicity.

It is clear from Figure 3 that the percentage metal recovery increased with increasing basicity up to 1.30 and above this value, the recovery decreased from about 73 per cent to about 44 per cent. These results obtained are comparable to those obtained by (Zhao *et al*, 2017) who studied slag/metal separation from H_2-reduced high phosphorus oolitic hematite. Optimal slag basicity gives the highest recovery of metal iron in smelting because it enhances the fluidity of slags and also suppresses the formation of highly stable compounds such as Fe_2SiO_4 (Saleh and Rochani, 2015).

An increase in basicity up to 1.30 in this current investigation might have facilitated for the easy separation of the metal and slag increasing percentage metal recovery due to the improved fluidity properties. Research has shown that enhanced fluidity in slag may result in higher diffusion coefficient of fine molten metal therefore making them easy to coalesce and form bigger drops that can easily and quickly drip below the slag as seen in Figure 4 where the amount of the total iron was varying inversely with the recovery (Tang *et al*, 2018). However more experimental investigations are required to validate the increased fluidity in this experiment. The binary basicity that gave the highest recovery was therefore determined to be 1.30 that yielded a percentage recovery of about 73 per cent. Large amounts of energy will be required to increase the metal recovery at low basicity, so as to trade-off with fluidity, thus more carbon source have to be used which will have a negative impact on the environment due to large CO_2 emission. A high basicity of 1.30 is favourable both on the energy requirement and on recovery. The total amount of Fe trapped in the slag was investigated using a handheld XRF and the results were as shown in Figure 4.

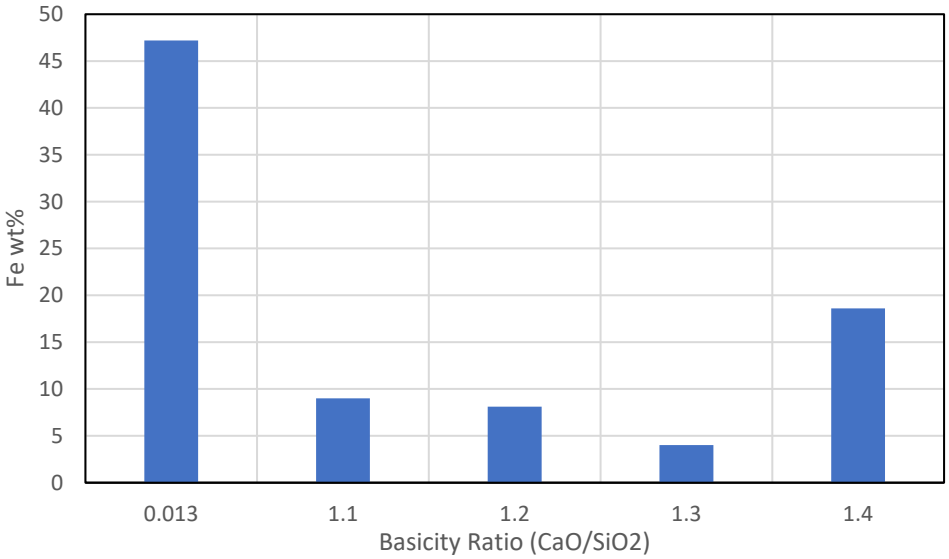

FIG 4 – Percentage of Iron content lost to slags with increasing basicity.

Iron by weight percent lost to slags decreased with increasing basicity from 0.013 to 1.3 following the opposite trend of the total metal recovery shown in Figure 3. Such a trend was observed because suppression of formation of the difficult-to-reduce compounds that might have occurred at suitable basicity increasing the metal recovery (Tang *et al*, 2018). Optimum basicity ratio was selected to be at 1.3 and the amount of Fe trapped in slag was only 4 wt per cent. Beyond the basicity of 1.3 the Fe wt per cent in slags rose to 18.6 wt per cent because of an increase in the slag to metal ratio which might cause the entrapment of more metal within the slags as shown in Figure 4. The recovered metal samples were taken for chemical analysis using spark emission spectrometry to understand the changes in the chemical composition of the cast iron recovered with increasing basicity and the results are shown in Table 6.

TABLE 6

Chemical composition of the cast iron with increasing burden basicity (wt per cent).

T.Fe	C	Si	Al	Mn	P	S	Cr	Ni	Mo	Co	Ti	CaO/SiO_2
97.45	2.270	0.034	0.006	<0.030	<0.02	<0.02	<0.01	0.034	0.052	0.019	<0.002	0.013
96.10	3.430	0.007	0.004	0.199	0.001	0.083	0.032	0.014	0.021	0.009	<0.001	1.110
95.76	3.730	0.009	0.018	0.122	<0.001	0.065	0.002	0.013	0.050	0.010	<0.001	1.200
96.37	3.240	0.002	0.001	0.148	<0.001	0.069	0.005	<0.004	0.020	0.009	<0.001	1.300
96.10	3.480	0.008	0.002	0.132	<0.00005	0.103	0.012	0.012	0.018	0.009	<0.001	1.400

The chemical analysis results showed an Fe concentration above 96 wt per cent in all the cast iron produced in the basicity range of 0.013 to 1.4. Silicon concentration in the metal was found to decrease with increasing basicity of up to 1.2 and increased thereafter. An iron-carbon phase diagram adopted from (Talla Padmavathi College of Engineering, 2017) was then used to predict the microstructure of the samples basing on metal carbon content.

The carbon content in the cast iron produced ranged from 2.27 to 3.73 wt per cent, which is less than the eutectic carbon content of 4.3 wt per cent, therefore the cast iron produced lies within the hypoeutectoid irons. From the iron carbon phase diagram, the samples produced were predicted to consist of a microstructure that include cementite, pearlite and transformed ledeburite. Micrographs in Figure 5, verified the predicted microstructures and confirmed that the castings are white cast irons by showing the ledeburite structure and a network of cementite grains. The ledeburite in Figure 5 is represented by the region with alternating dark and light layers whereas the cementite is the continuous threadlike light region.

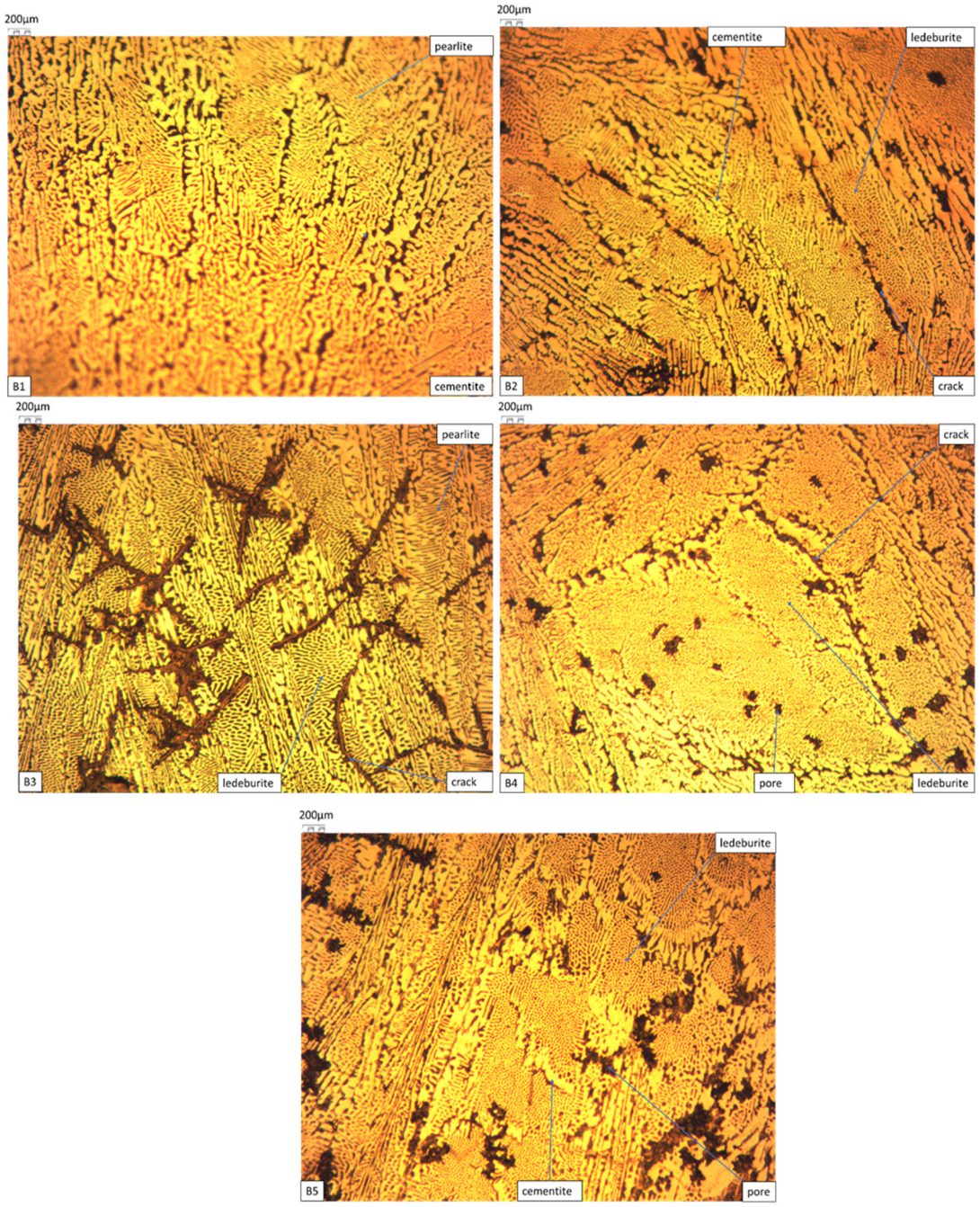

FIG 5 – Metal microstructure at 20× with increasing basicity ratio: B1: 0.034, B2: 1.11, B3: 1.20, B4: 1.30 and B5: 1.40.

The observed pores in Figure 5 in micrograph B4 and B5 may be as a result of the difference in molten metal viscosities as suggested by Cheng *et al* (2014) that viscosity is an important property in casting as it controls the rate of transport of liquid metals and may lead to defects like pores and hot tearing. Cheng *et al* (2014) went on to describe the Kaptay unified equation, which relates melting temperature of a metal to its viscosity. Tsepelev, Starodubtsev and Konashkov (2021) also discussed viscosity as a function related to temperature by associating viscosity to movement of liquid particles relative to each other which depends on diffusion mobility of the particles and in turn, linked to temperature by the Arrhenius equation. The different carbon in the samples shown in Table 6 indicates different melting temperatures of the samples as can be observed in Figure 5, this may lead us to conclude that the samples had different viscosities thus having pores in other castings as cited in literature (Cheng *et al,* 2014).

Effect of burden carbon on the metal recovery

The stoichiometric amount of carbon required for the reduction of iron oxide was evaluated based on the oxygen attached to iron and some excess carbon was added to the burden material in the first experiment to cater for the reduction of some other metal oxides components in the system at a basicity ratio of 1.30.

The percentage metal recovery was found to increase with the increase in the C/O ratio as shown in Figure 6, indicating an increase in the available amount of reducing agent which then became sufficient for the reduction of the metal oxide. The percentage metal recovery was found to decrease with the decrease in the C/O ratio showing a decrease in the available amount of reducing agent, which then became insufficient for the reduction of the metal oxide. The reduction of the iron oxide in this investigation occurred through direct and indirect reduction. The presence of large amounts of carbon might have resulted in an increased possibility of some additional energy through the increased possibility of the indirect reduction. The possibility of the reduction of the metal oxide is also highly expected to be near completion at high carbon content. This might have an effect on the fluidity of the molten material in the system allowing for more metal to drip out due to the increased temperature caused by the exothermic indirect reduction. The metal recovery decreased with the decrease in the amount of carbon due to the effect of the decreased chances of the exothermic reaction as well as an increased chance of incomplete reduction. The cast iron produced was also taken for chemical analysis using the emission spark spectrometry and the results were as shown in Table 7.

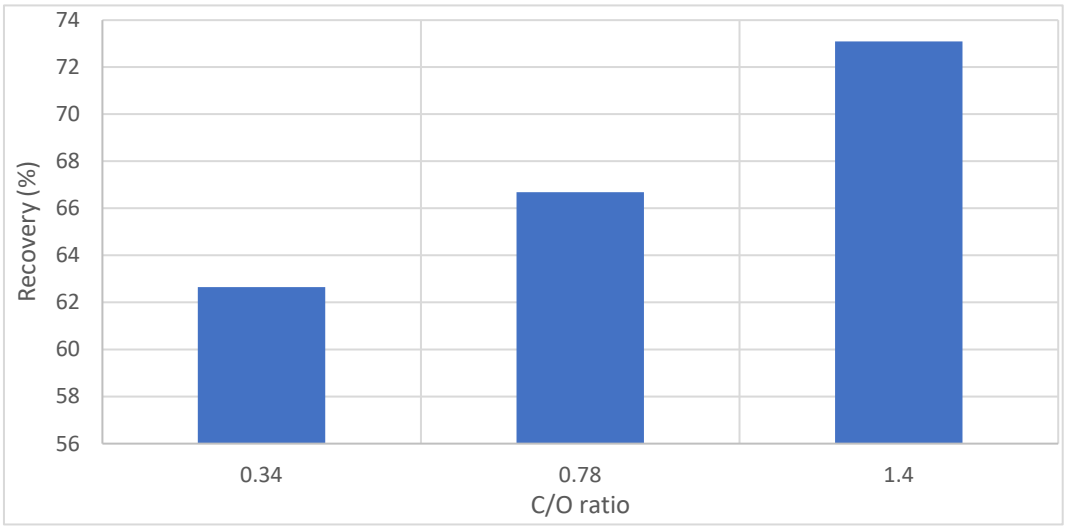

FIG 6 – Percentage metal recovery with change in C/O ratio.

TABLE 7

Chemical composition of the cast iron with decreasing burden carbon content.

TFe	C	Si	Al	Mn	P	S
96.37	3.24	0.002	0.001	0.148	<0.01	0.069
96.13	3.50	<0.001	0.0069	0.148	0.001	<0.001
95.3	4.16	0.003	0.0026	0.222	0.015	0.08
Cr	**Ni**	**Mo**	**V**	**Co**	**Ti**	**C/O ratio**
0.005	<0.004	0.020	0.0011	0.009	<0.001	1.40
<0.002	0.014	0.019	<0.0005	0.009	<0.001	0.78
0.004	0.034	0.019	0.0015	0.01	<0.001	0.34

The results clearly show a decrease in total Fe and an increase in C content in the metal with decreasing carbon content. The decrease in Fe might be an indication of the possibility of the incomplete reduction hence more Fe was trapped in the slag phase with decreasing reducing agent. The increase in C in metal observed might be related to the changes in the fluidity of the metal which might be related to the amount of indirect reduction in the system. A decrease in slag fluidity will offer more resistance to the dripping of the metal allowing more contact time of the metal with C which might result in increasing the amount of C observed in the metal indicated in Table 7. This was confirmed the slag chemical composition shown in Table 8 that showed a little more amount of Fe trapped in the slag with decrease in C/O ratio. The metal trapped in slag was higher when C/O ratio was lower than 1.40.

TABLE 8

Chemical composition of slag with decreasing burden C/O ratio (wt%).

T.Fe%	CaO	SiO_2	Al_2O_3	MgO	MnO	C/O ratio
6.68	36.20	20.03	10.30	2.41	4.55	1.40
9.09	31.00	28.00	13.00	2.50	4.40	0.78
10.80	31.64	29.55	13.67	2.30	4.55	0.32

Figure 7, clearly shows an increased generation of pearlite with a decrease in the burden carbon that resulted in an increase in C content within the metal. The micrographic images provide enough evidence of the increased C in metal that was shown in Table 7.

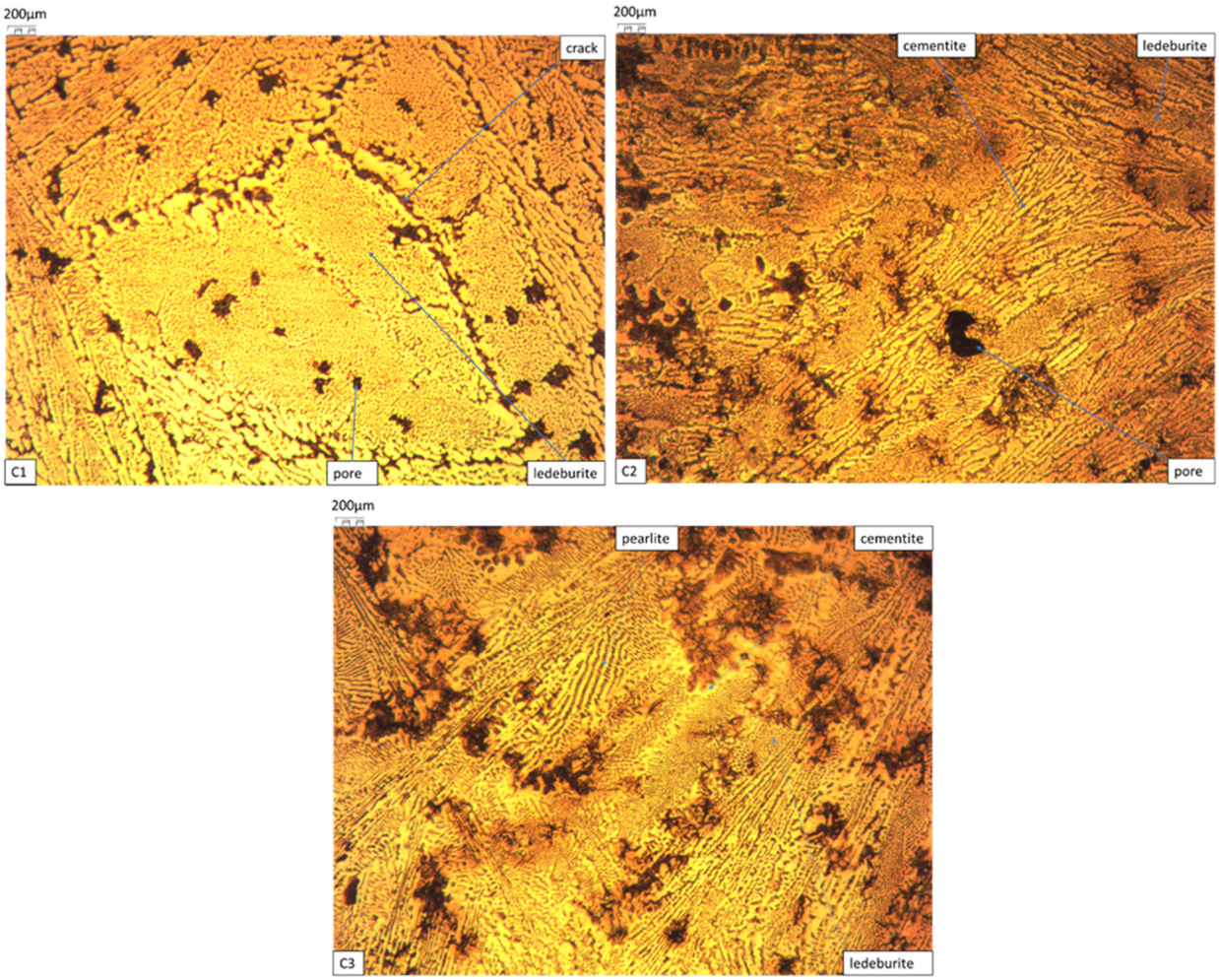

FIG 7 – Metal microstructure at 20× with change in burden C/O ratio: C1: 1.4, C2: 0.78 and C3: 0.34.

Estimation of slag melting temperature

Chemical analysis of slags produced at different basicity ratios was analysed using atomic absorption spectrometry and the results are presented in Table 9. It was important to carry out an analysis of the slags because slags contain unwanted impurities by forming oxides and floating them away from the metal.

TABLE 9

Slags chemical composition with increasing basicity (weight%).

T.Fe%	CaO	SiO_2	Al_2O_3	MgO	MnO	CaO/SiO_2
47.2	2.4	13.7	8.9	0.3	2.4	0.013
9.0	30.9	27.5	11.0	2.3	4.8	1.11
8.1	33.0	25.6	12.4	2.2	4.1	1.20
4.0	36.2	28.0	10.3	2.4	4.6	1.30
18.6	26.4	21.5	12.9	2.1	2.9	1.40

The major constituents of the slag were CaO, SiO_2 and Al_2O_3. The data from the slags chemical analysis was plotted on a CaO-Al_2O_3-SiO_2 phase diagram, Figure 8, to understand the oxide phases that may be in the slags and their melting temperatures at different basicity ratios.

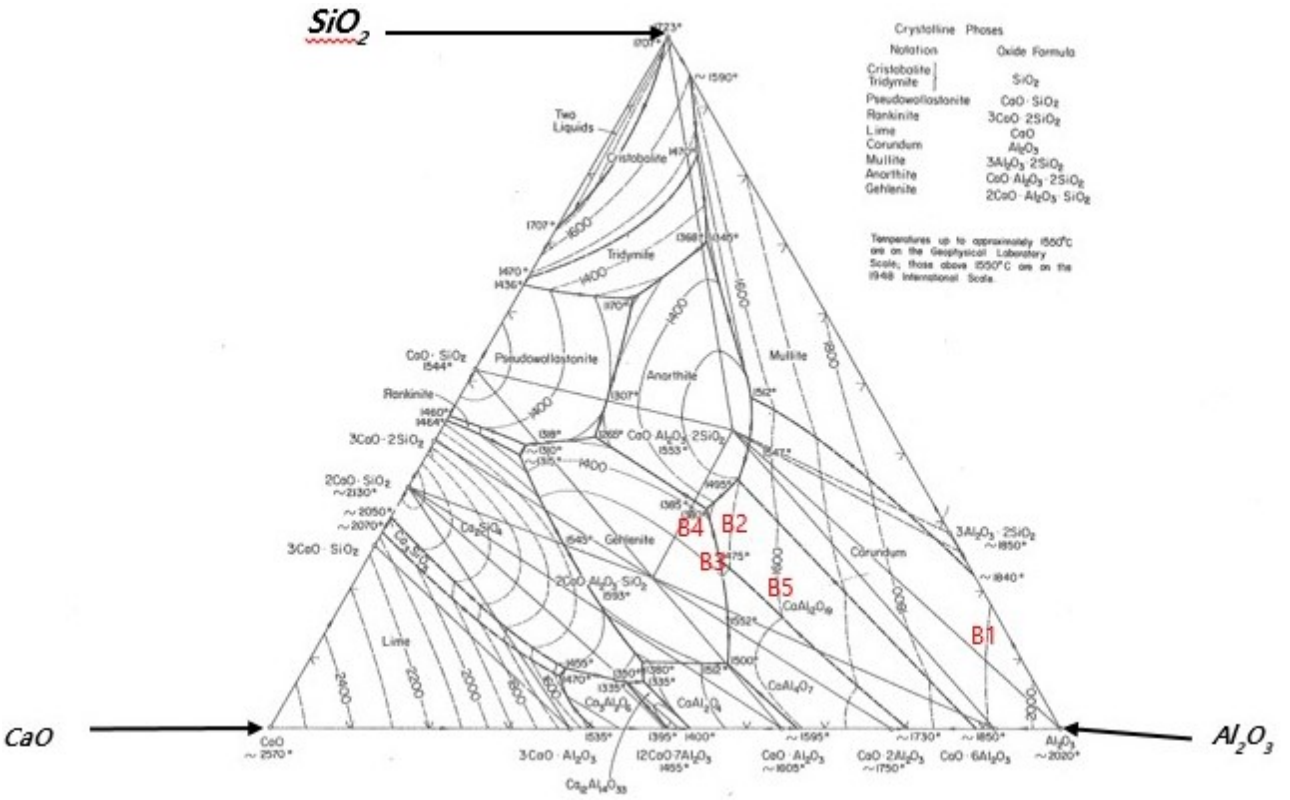

FIG 8 – CaO-Al_2O_3-SiO_2 phase diagram, adopted from (Draper, 1976): Approximate melting temperature with increase in basicity, B1: 0.034, B2: 1.11, B3: 1.20, B4: 1.30 and B5: 1.40.

The expected phases and their melting temperatures presented in Table 10 were estimated from the phase diagram shown in Figure 8.

TABLE 10

Slag's crystalline phases and melting temperature with increasing basicity ratio.

Estimated crystalline phases present	Approximate melting temperature (°C)	Basicity ratio (CaO/SiO_2)
$CaO{\cdot}6Al_2O_3$	1850	0.013
$CaAl_{12}O_9$ and $2CaO{\cdot}Al_2O_3{\cdot}SiO_2$	1475	1.11
$2CaO{\cdot}Al_2O_3{\cdot}SiO_2$ and $CaAl_{12}O_9$	1400	1.20
$2CaO{\cdot}Al_2O_3{\cdot}SiO_2$	1380	1.30
$CaAl_{12}O_9$	1600	1.40

Data from Table 6 was used to plot Figure 9 which shows the effect of the basicity ratio on the melting temperature of slags.

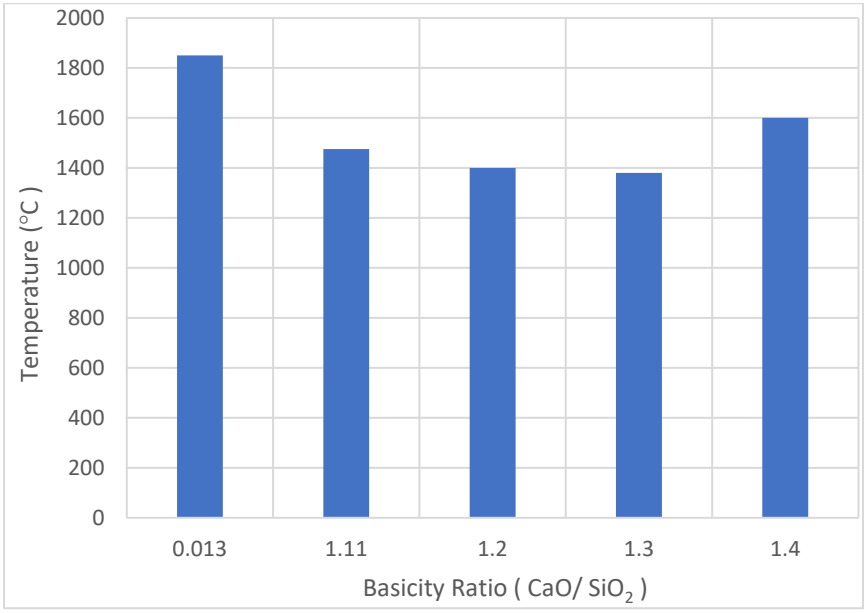

FIG 9 – Effect of basicity on melting temperature of slags.

Figure 9 shows a decrease in the melting temperatures of the slags as the basicity ratio increases. The melting temperature dropped from 1850°C at a basicity ratio of 0.013 to 1 380°C at an optimum basicity of 1.3. This trend is associated with the increase in metal recovery as basicity is increasing as shown in Figure 3 and in the results shown in Figure 4 where a decrease in iron content lost to slags with an increasing basicity ratio is observed. The melting temperature of slag is related to fluidity and viscosity as was discussed by Tang *et al* (2018) who stated that an increase in fluidity increases metal recovery by enhancing the diffusion coefficient of fine molten metal in the slag since there will be less drag due to decreased viscosity. From Figure 9, a clear drop in the melting temperature of the slags towards the induction's operating temperature indicates that the viscosity of the slags will be decreasing similar to the discussion by Cheng *et al* (2014) through the Kaptay unified equation which relates the melting temperature of a metal to its viscosity.

Muller and Erwee (2011) stated that slag viscosity determines metal yield, and impurity removal efficiency through its determination of the slag-metal separation efficiency. Data presented in Table 10 shows that the formed slags at the different basicity ratios do have different melting temperatures. Having furnace temperature fixed at 1350°C with accuracy ±50°C, it is highly likely that slags with melting temperature close to this value may have the best viscosity to allow for better slag-metal separation. Thus having the highest recovery at basicity ratio 1.3 where the slag melting temperature was 1380ºC unlike in other basicity ratios where the slags had melting temperatures above 1400ºC. Highly viscous slags tend to have reduced slag-metal separation efficiencies.

CONCLUSIONS

The reduction and recovery of cast iron from the Zimbabwean limonite carbon composite pellet was carefully studied at various burden basicity and carbon to oxygen ratio and it was found that:

- The careful control of burden basicity can improve the total metal recovery. The basicity with the highest recovery was determined to be 1.3.
- The total iron content in slag first decreased with the increase in burden basicity up to 1.3 and decreased with further increase in basicity.
- The optimal carbon to oxygen ratio was determined to be 1.4. A decrease in the carbon to oxygen ratio resulted in a decreased total metal recovery.
- The Zimbabwean limonite carbon composite pellet can potentially be used as a source of iron to produce cast iron with good quality to supplement the basic oxygen furnace, however more results are required to investigate the correlation between fluidity and the burden basicity in order to improve on metal recovery.

ACKNOWLEDGEMENTS

We would like to thank the Materials Technology and Engineering Department of the Harare Institute of Technology and the Institute of Mining Research of the University of Zimbabwe for providing laboratory equipment to carry out these investigations. We would also like to acknowledge Engineer Aron Mukuya and Mr Quinton Kadenge of Investcast Private limited for providing laboratory reagents.

REFERENCES

Cheng, J, Gribner, J, Hort, N, Kainer, K and Schmid-Fetzer, R, 2014. Measurement and calculation of the viscosity of metals—a review of the current status and developing trends, *Measurement Science and Technology*, (25):1–9.

Chisahwira, T, Masuka, S M, Maritsa, S and Chwandika, E K, 2023. The use of Zimbabwean limonite coal composite pellet as a sustainable feed for pig iron production, in *Proceedings of the Iron Ore 2023 Conference*, p 391 (The Australasian Institute of Mining and Metallurgy: Melbourne).

De Carvalho, A, Mercier, F, Mattera, G and Giua, L, 2022. Steel Market Developments, Q4 2022, Directorate for Science, Technology and Innovation Steel Committee, Organisation for Economic Co-operation and Development, 67 p. Available from: <https://one.oecd.org/document/DSTI/SC(2022)11/FINAL/en/pdf>

Draper, V F, 1976. Mullite Phase Equilibria in the System $CaO-Al_2O_3-SiO_2$, MS thesis, University of California, Berkeley.

Ghosh, A, Vasudevan, N and Kumar, S, 2021. Energy-Efficient Technology Options For Direct Reduction Of Iron Process (Sponge Iron Plants), The Energy and Resources Institute (TERI).

Huang, Z, Zhong, R, Yi, L, Jiang, T, Wen, L and Liang, Z l, 2018. Reduction Enhancement Mechanisms of a Low-Grade Iron Ore–Coal Composite by NaCl, *Metallurgical and Materials Transactions*, 49B:411–422.

International Energy Agency (IEA), 2023. Energy Technology Perspectives 2023, IEA. Available from: <https://www.iea.org/reports/energy-technology-perspectives-2023>

Ishizaki, K, Nagata, K and Hayashi, T, 2006. Production of Pig Iron from Magnetite Ore–Coal Composite Pellets by Microwave Heating, *ISIJ International*, 46(10):1403–1409.

Liang, Z, Peng, X, Huang, Z, Li, J, Yi, L, Huang, B and Chen, C, 2023. Innovative methodology for comprehensive utilisation of refractory low grade iron ores, *Powder Technology,* 418:118238, https://doi.org/10.1016/j.powtec.2023.118283

Magunda, S, Dube, N and Simbi, D J, 2004. Impact of Innovation Science and Technology on National Wealth Creation, paper presented at the HICC, Harare.

Mochizuki, Y and Naoto, T, 2019. Thermal Properties of Carbon-Containing Iron Ore Composite Prepared by Vapor Deposition of Tar for Limonite, *Metallurgical and Materials Transactions B,* 50B:2259–2272.

Muller, J and Erwee, M, 2011. Blast Furnace Control using Slag Viscosities and Liquidus Temperatures with Phase Equilibria Calculations, *Southern African Pyrometallurgy 2011* (eds: R T Jones and P den Hoed), pp 309–326 (Southern African Institute of Mining and Metallurgy: Johannesburg).

Reddy, A L, Sahoo, S K and Kumar, M, 2023. Studies on characterization of properties of low-grade hematite iron ores and their fired pellets, *Ironmaking and Steelmaking*, 50:1215–1223.

Rehlke, R D, 2001. Steel Plants: Size Location and Design, in *Encyclopedia of Materials*: *Science and Technology* (eds: K Buschow, R Cahn and B Ilschner), pp 8824–8832 (Elsevier: Amsterdam).

Sah, R and Dutta, S K, 2010. Smelting reduction of iron ore-coal composite pellets, *Steel Research International*, 81(6):426–433.

Saleh, N and Rochani, S, 2015. Study on basicity in direct reduced iron smelting, *Indonesian Mining Journal*, 18(2):59–70.

Talla Padmavathi College of Engineering (TPCE), 2017. IRON-CARBON Phase Diagram or Equilibrium Diagram, Talla Padmavathi College of Engineering – Mechanical Engineering Reference Books. Available from: <https://tpce-mechbooks.blogspot.com/2017/12/iron-carbon-phase-diagram-or.html> [Accessed: 2 March 2024].

Tang, Z, Ding, X, Yan, X and Dong, Y, 2018. Recovery of Iron, Chromium and Nickel from Pickling Sludge Using Smelting Reduction, *Metals*, 8(936):1–11.

Tsepelev, V S, Starodubtsev, Y N and Konashkov, V V, 2021. The Effect of Nickel on the Viscosity of Iron-Based Multicomponent Melts, *Metals*, 11(11):1724. https://doi.org/10.3390/met11111724

Upakare, R, Tupe, S, Tilak, A and Thosar, A, 2018. An Overview on ITmk3 (Iron-making Technology mark three) Process, *International Journal for Research in Engineering Application and Management*, 4:3.

Zhang, H, Wang, G, Wang, J-S and Xue, Q-G, 2018. Recent Development of Energy-saving Technologies in Ironmaking Industry, *IOP Conference Series: Earth and Environmental Science*, 233(5):052016. https://doi.org/10.1088/1755-1315/233/5/052016

Zhao, D, Li, G, Wang, H and Ma, J, 2017. Slag / Metal Separation from H2-Reduced High Phosphorus Oolitic Hematite, *ISIJ International*, 57(12):2161–2140. http://dx.doi.org/10.2355/isijinternational.ISIJINT-2017-304

Effect of SiO_2 on the structure and crystallisation of CaF_2-CaO-Al_2O_3 slag used in electroslag remelting

DOI: 10.62053/WSZG4852

P M Midhun[1] and S Basu[2]

1. Graduate student, Indian Institute of Technology Bombay, Powai, Mumbai 400076, India. Email: 214116001@iitb.ac.in
2. Professor, Indian Institute of Technology Bombay, Powai, Mumbai 400076, India. Email: somnathbasu@iitb.ac.in

ABSTRACT

Electro-Slag Remelting (ESR) is a process capable of producing ingots with much lower centre-line segregation and better internal soundness than conventional ingot casting processes, as well as lower inclusion and sulfur concentrations. This process is commonly used for alloyed steels intended for critical applications like components of marine turbines, supercritical powerplants and rocket motor casings. It involves melting a metal electrode using electrical resistive heating in a slag pool and re-solidification of the resulting metal droplets beneath the slag layer, forming an ingot. Conventional ESR fluxes consist primarily of CaF_2, Al_2O_3 and CaO, along with minor concentrations of SiO_2, MgO etc. The emission of fluoride vapour from the molten slag causes several environmental and health problems, triggering a need to develop and reduce the fluoride content in the ESR flux.

The present study aims to develop low-CaF_2 alternatives to commercial ESR fluxes without compromising on productivity and the surface quality of the refined ingot. Thus, the modification in chemical composition needs to satisfy properties like electrical resistivity, viscosity and liquidus temperature, essential for efficient ESR operation. Since electrical resistivity and viscosity are highly dependent on the ionic structure of the molten slag, it is important to understand the effect of compositional modification on the structure of the flux. The present study employs Fourier-transform infrared spectroscopy (FT-IR) and Raman spectroscopy to investigate the structural variations in the modified fluxes, especially the effect of changing SiO_2 concentration, in comparison with conventional CaF_2-rich fluxes. Additionally, thermal analysis (Differential Thermal Analysis (DTA) and Thermogravimetric Analysis (TGA)) has been carried out to characterise the melting behaviour of the fluxes. The findings are compared with simulations carried out using the FactSage™ software, ver 8.3 (GTT Technologies, Aachen, Germany). Simultaneous analysis of liquidus temperature and the structure is expected to help in identifying the practical suitability of modified ESR flux compositions for industrial implementation.

INTRODUCTION

Electro-Slag Remelting (ESR) is one of the processes employed for refining of speciality steels. The metal electrode that needs to be refined is subjected to electrical resistive heating within a slag pool, leading to its melting. Owing to density difference, the molten metal droplets descend through the slag pool, held within a water-cooled copper mould and re-solidify at the bottom to form an ingot. The slag plays multiple roles during the ESR process. It acts as the heat source through resistive heating, acts as a medium for refining reactions (eg sulfur removal), dissolves the non-metallic inclusions separating from the molten steel and controls the surface finish of the solidified ingot by forming a solid slag skin at the ingot-mould wall interface. Figure 1 presents a schematic view of the longitudinal section, showing the key components of the process. Commercially used ESR fluxes typically consist of CaF_2 (30–70 per cent), Al_2O_3 (20–40 per cent) and CaO (20–40 per cent); this range of composition is known to provide an optimal combination of liquidus temperature, viscosity and electrical conductivity in the molten slag. However, CaF_2-containing slags are prone to evaporation of fluoride vapours during the operation of the ESR, resulting in detrimental effects on the environment as well as the health of the operating personnel (Ju *et al*, 2022; Zheng, Li and Shi, 2020). Due to this concern, reduction in fluoride concentration in ESR fluxes is being attempted across the globe. However, this endeavour is not easy since the fluoride-containing molten slag offers an optimal combination of liquidus temperature, flow behaviour and electrical properties, thus enabling efficient operation of the ESR process. The key challenge is to identify suitable chemical composition(s) for the molten slag such that its electrical conductivity, viscosity and liquidus

temperature would remain within an optimal range, in spite of partial or total replacement of the fluoride content (Wroblewski *et al*, 2011, 2016).

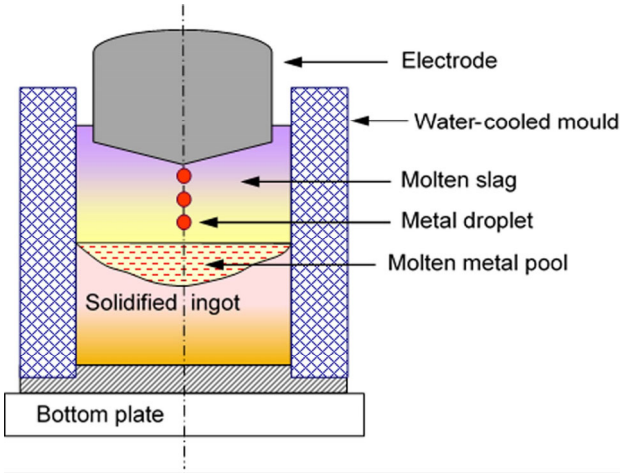

FIG 1 – Schematic view of longitudinal section of the ESR.

In addition to the major constituents (Al_2O_3, CaO and CaF_2), minor quantities of SiO_2, MgO etc are also added to the ESR flux for fine-tuning properties of the molten slag. The presence of SiO_2 in the slag is reported to have a contradicting influence on the ESR process; an increase in SiO_2 concentration tends to improve the surface quality but hinders the overall inclusion content and internal cleanliness of the solidified ingot. Consequently, in most electro-slag remelting practices, the presence of SiO_2 in the flux is considered permissible, but in low concentration (Shi *et al*, 2015).

Numerous studies have been carried out over the past few decades on the influence of varying concentrations of TiO_2, MgO etc on the properties and performance of commercial ESR fluxes (Shi *et al*, 2017; Ju *et al*, 2022; Zheng *et al*, 2020; Zheng, Li and Shi, 2020; Wan *et al*, 2022). However, relatively few reports on the modification of ESR flux through SiO_2 addition (Shi *et al*, 2015; Huang *et al*, 2021; Xu *et al*, 2022; Wan *et al*, 2023) are available in the public domain. Information on the structure as well as crystallisation behaviour of these ESR fluxes is also sporadic in literature. In the present study, SiO_2 concentration in a 20 per cent Al_2O_3 – 30 per cent CaO – 50 per cent CaF_2 commercial ESR flux, commonly employed for refining alloy steels, was modified through small increments, along with a simultaneous reduction in fluoride concentration. Since no studies have been investigated on this commercial flux composition until now, this work will be helpful for researchers and industries involved in ESR. Structural characteristics of the resulting slag were investigated through Raman and FT-IR spectroscopy. The results were crucial for understanding the polymerisation levels in the melt, which would influence the physico-chemical properties such as electrical conductivity and viscosity (Yan *et al*, 2021). The combination of these properties, in turn, would determine the overall suitability of the flux for use in the ESR process. Crystallisation studies were conducted through thermal analysis (Differential Thermal Analysis (DTA); Differential Scanning Calorimeter (DSC); Thermogravimetric Analysis (TGA)), which also allowed estimation of the liquidus and solidus temperatures. Thermodynamic simulations were carried out using the 'Equillib' module of FactSage™ software; the estimated values were compared with those obtained experimentally.

EXPERIMENTAL PROCEDURES

Sample preparation

The slag samples were synthesised using laboratory reagent extra pure grade powders of CaF_2 (≥97 per cent Purity), Al_2O_3 (≥99 per cent Purity), CaO (≥90 per cent Purity) and SiO_2 (≥99 per cent Purity) purchased from Loba Chemie Pvt Ltd. As-received Al_2O_3, CaO and SiO_2 powders were preheated at 1000°C in a muffle furnace to remove adsorbed moisture and decompose any hydroxide/carbonate that might have formed during exposure of the reagents to the ambient atmosphere. Preheating of CaF_2 was carried out at 700°C. A composition of 50 per cent CaF_2,

20 per cent Al_2O_3 and 30 per cent CaO (by mass) was chosen as the base mix for the flux. Requisite quantities of SiO_2 were added to the base mix, along with a corresponding decrease in CaF_2 content, to generate the entire range of compositions having varying concentrations of CaF_2 and SiO_2. The thoroughly mixed samples of the approximate total weight of 100 g were pre-melted in graphite crucibles (having inner diameter = 10 cm and depth = 10 cm) at 1480°C for two hours, followed by rapid quenching in liquid nitrogen. The fluoride content in the slag was measured using the fluoride ion-selective electrode (FISE) method, while calcium, aluminium and silicon concentrations were obtained using Inductively Coupled Plasma – Atomic Emission Spectroscopy (ICP-AES: ARCOS from SPECTRO Analytical Instruments, GmbH, Germany). Solution samples for ICP-AES and FISE analysis were prepared through the digestion of the slag samples via fusion method. Slag samples are well-mixed with lithium tetraborate and lithium metaborate in a ratio of 1:3:3. The platinum crucibles containing these premixed powders are kept inside a muffle furnace at 1050°C for 30 mins and consequently dissolved in 1N HCl. In the measurement of fluorine concentration using FISE method, an electrode has been dipped in the solution to be measured, and the resulting potential difference developed across the membrane has been correlated with the diffusion of fluorine ions from the solution. A few chelating agents (Solutions of Ammonium citrate dibasic, Ammonium tartrate dibasic, Citric acid, Ethylene diamine, EDTA and Sodium chloride) were added to the solution to facilitate the release of fluorine ions from the ionic complexes, ensuring accuracy in measurements (Yeager and Ramanujachary, 2007). Table 1 shows the chemical compositions of the fluxes premelted and the slag generated. After premelting, the CaF_2 concentration has been decreased, and the CaO concentration has been increased, corresponding to the fluoride evaporation (in forms of SiF_4, AlF_3, CaF_2, HF etc) during the chemical reactions at high temperatures (Persson and Seetharaman, 2007). Figure 2 presents the compositional variations within slag sample S2 measured before and after premelting. Even though the CaO/Al_2O_3 ratio in the as-mixed powder was initially 1.5, premelting at high temperature caused compositional variations due to the aforementioned reasons and the ratio was maintained within the range of 1.6–1.7 in every sample.

TABLE 1

Chemical composition of slag (in mass%).

Slag no	Composition before premelting				Composition after premelting			
	CaF_2	CaO	Al_2O_3	SiO_2	CaF_2	CaO	Al_2O_3	SiO_2
S1	50	30	20	0	44.34	35.46	17.52	0
S2	48.54	29.12	19.41	2.91	37.78	38.13	18.73	2.69
S3	47.16	28.31	18.86	5.66	41.49	32.42	18.22	5.21
S4	45.87	27.52	18.35	8.25	39.82	32.51	16.09	8.92

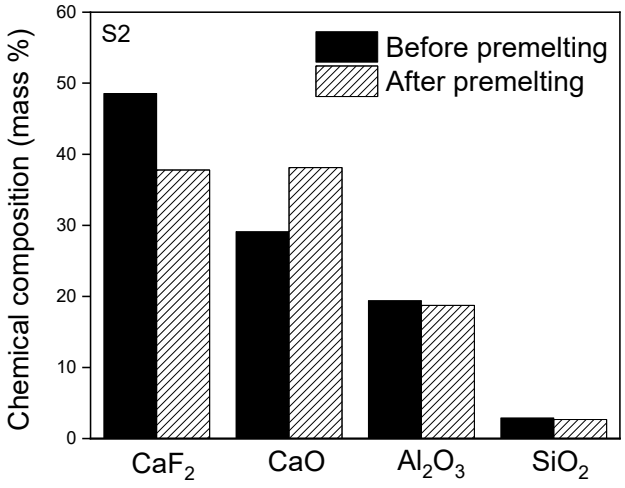

FIG 2 – Chemical composition of slag sample S2 before and after premelting.

Structural analysis using Raman and FT-IR Spectroscopy

Samples of the quenched slag were analysed using Raman Spectroscopy (Labram HR800 UV from Horiba Jobin Yvon, France) as well as Fourier-Transform Infrared (FT-IR) Spectroscopy (FT/IR-300E from JASCO).

Raman Spectroscopy

The Raman spectra for the slag samples were obtained at room temperature within the wavenumber range of 400–2000 cm^{-1}. A laser source with an excitation wavelength of 532 nm was used for all the measurements. The Raman spectra recorded were deconvoluted and fitted using the Fityk software with Gaussian bands.

FT-IR Spectroscopy

IR spectra of the samples were acquired in both absorption and transmission modes, over the wavenumber range of 4000–400 cm^{-1}, employing KBr detector. A spectral resolution of 4 cm^{-1} was chosen for all the measurements. The decision to use transmission and absorption modes arose from the fact that different structural aspects (eg Si-O-Si bond, O-Al-F bond etc) were better revealed under different spectroscopy modes. Each sample was prepared by mixing a particular slag with KBr in a mass ratio of 1:8 in an agate mortar, followed by pressing into pellets. The spectra obtained from the samples, each averaging 50 scans, are subsequently subtracted from the spectrum of 'pure' KBr powder in order to obtain the final spectra. The FT-IR absorbance spectra were deconvoluted using the Fityk and Origin software to better reveal the individual peaks and thus help in understanding the structural aspects. The features better revealed in the transmission spectra did not require any deconvolution.

Melting and solidification behaviour

DTA/TGA analysis

The liquidus temperature of each flux was determined through thermal analysis using a Netzsch™ STA 449 Jupiter unit (from Netzsch Instrument Inc., Germany). The samples were kept in argon atmosphere, with a purge rate maintained at 100 mL/min. For each measurement, close to 30 mg of the pre-melted flux sample was heated at a rate of 20°C/min from room temperature up to 800°C in an alumina crucible. Subsequently, it was further heated at 10°C/min up to 1450°C and held for 1 min for homogenisation. Following this, the melt was cooled at a uniform rate of 10°C/min until it reached 800°C after which it cooled to 100°C at the rate of 20°C/min. Typical temperature profile for the experiment is as shown in Figure 3. The DTA and TGA signals of the sample with time and temperature were captured automatically during each cycle and plotted.

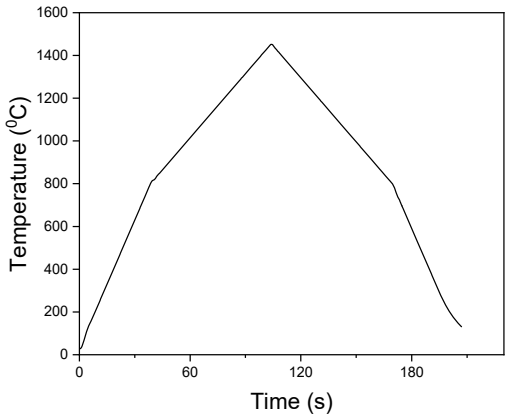

FIG 3 – Temperature profile for DTA/TGA experiment.

Thermodynamic simulations

FactSage™ was utilised to simulate the solidus and liquidus temperatures corresponding to the chemical composition of each sample. The Equilib module within FactSage™ was used, together with the FactPS and FToxid databases.

RESULTS AND DISCUSSION

Analysis of Raman spectra

Figure 4 shows the Raman spectra of the slag samples with varying SiO_2 concentrations. Each sample of molten slag was quenched in liquid nitrogen, with the objective of suppressing phase separations that might otherwise occur during slow solidification. Therefore, the samples were expected to be largely amorphous while retaining any crystalline phase and structural ordering that existed in the melt. In amorphous samples, Raman spectra are often present as envelopes, within which overlapped spectral peaks are responsible for various structural units (Hwa, Hwang and Liu, 1998).

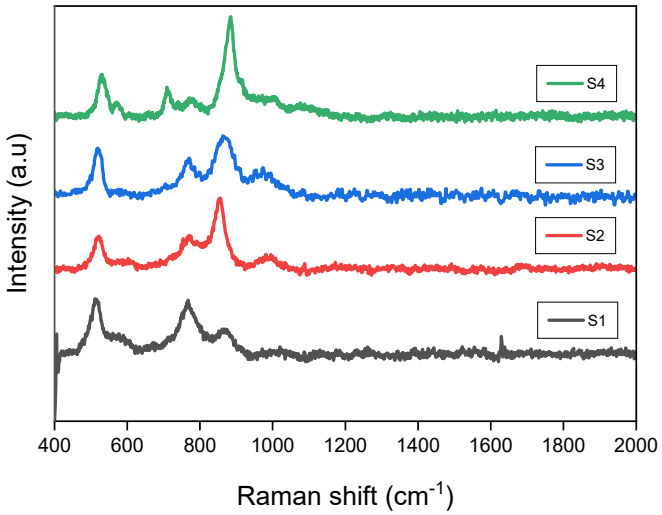

FIG 4 – Raman spectra of samples with various SiO_2 concentrations.

In the Raman spectra obtained from the slag samples, similar envelopes were deconvoluted through the Gaussian function to differentiate the individual structural components. The minimum value of the correlation coefficient (R^2) was maintained at 0.96 for this purpose. Fityk software, utilising Gaussian bands, was used for deconvoluting the Raman spectra and fitting the individual peaks. The resulting deconvoluted spectra for all four slag compositions, shown in Figure 5, provide insights into the relative proportions of the structural units and help to illustrate the influence of chemical composition (*viz* SiO_2 concentration) on the structural feature of each slag.

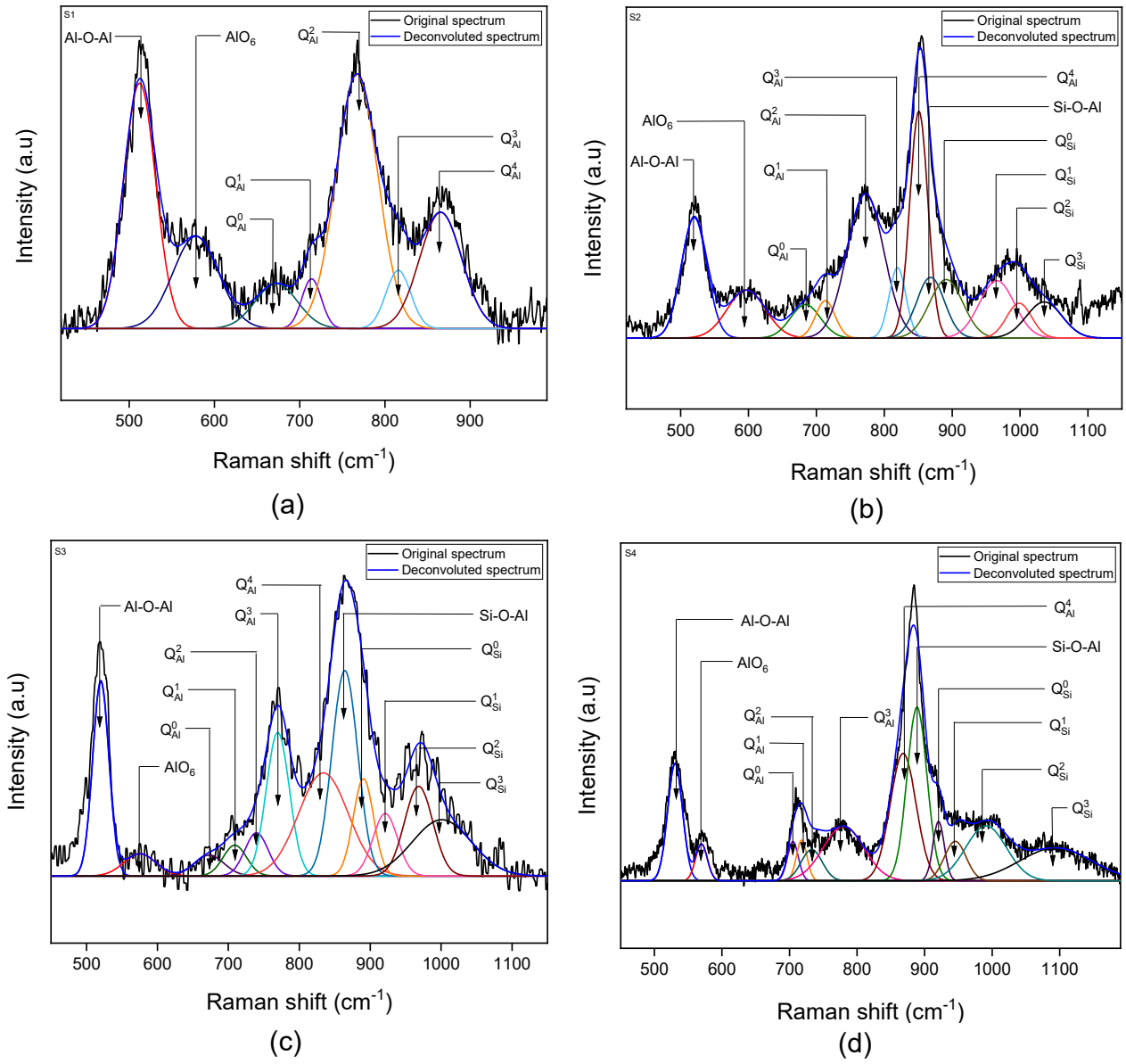

FIG 5 – Deconvolution results of Raman spectra: (a) S1; (b) S2; (c) S3; (d) S4.

In the silicate network, the absorption peak intensity corresponding to the vibrations of the Si-O covalent bonds in 'SiO_4' tetrahedral units varies depending on the population of bridging oxygen in the network. The quantity of bridging oxygens in the 'SiO_4' unit is denoted by 'n' in 'Q^n_{Si}', where n = 0, 1, 2 and 3, correspond to monomer, dimer, chain and sheet structures of silica, respectively. Similarly, 'Q^n_{Al}' is defined as the 'AlO_4' tetrahedral unit with bridging oxygens expressed as 'n', varying over the range 0–4. As an example, the Raman shift at ~525 cm^{-1} in the spectra corresponds to the transverse vibration of bridging oxygen within 'Al-O-Al' bonds. Absorption peaks at other Raman shift values similarly represent the vibrations associated with other bonds in the structural units. Table 2 lists the ranges of Raman shift identified in the slag samples bands and the corresponding structural information (Huang *et al*, 2021; Zheng *et al*, 2020; Haghdani, Tangstad and Einarsrud, 2022; McMillan and Piriou, 1983; Li, Shu and Chou, 2014; Hwa, Hwang and Liu, 1998; Kim and Park, 2014).

TABLE 2

Assignments of raman bands in spectra of CaF_2-Al_2O_3-CaO-SiO_2 slag (Huang *et al*, 2021; Zheng *et al*, 2020; Haghdani, Tangstad and Einarsrud, 2022).

Raman shift (cm^{-1})	Raman assignment and type of vibrations
500–552	Transverse motion of bridging oxygen in Al-O-Al linkages
578–609	AlO_6 stretching vibrations
665–695	Q^0_{Al}- symmetric stretching vibration of Al-O bonds in AlO_4 tetrahedra (zero bridging oxygen)
700–738	Q^1_{Al}- symmetric stretching vibration of Al-O bonds in AlO_4 tetrahedra (one bridging oxygen)
748–765	Q^2_{Al}- symmetric stretching vibration of Al-O bonds in AlO_4 tetrahedra (two bridging oxygen)
788–805	Q^3_{Al}- symmetric stretching vibration of Al-O bonds in AlO_4 tetrahedra (three bridging oxygen)
820–855	Q^4_{Al}- symmetric stretching vibration of Al-O bonds in AlO_4 tetrahedra (four bridging oxygen)
859–880	Si-O-Al stretching vibrations
890–910	Q^0_{Si}- symmetric stretching vibration of Si-O bonds in SiO_4 tetrahedra (zero bridging oxygen)
915–940	Q^1_{Si}- symmetric stretching vibration of Si-O bonds in SiO_4 tetrahedra (one bridging oxygen)
940–990	Q^2_{Si}- symmetric stretching vibration of Si-O bonds in SiO_4 tetrahedra (two bridging oxygen)
1000–1070	Q^3_{Si}- symmetric stretching vibration of Si-O bonds in SiO_4 tetrahedra (three bridging oxygen)

The integrated area under the curve for each deconvoluted peak may be considered as proportional to the fraction of the corresponding structural unit in the slag sample. Variations in these fractions with respect to the change in SiO_2 concentration in the slag samples are shown in Figure 6. From this figure, it is evident that a rise in SiO_2 concentrations in the slag leads to an enhancement in the intensity of the spectral peak associated with 'Si-O-Al' vibrations. This can be correlated with the more intense vibration of 'Si-O-' bonds with higher SiO_2 content. This vibration is conducive to the 'AlO_4' tetrahedral structures forming complex 'Si-O-Al' bonds in the slag structure. Consequently, there is a rise in complex networks and polymerisation in the slag increases. In the context of alumina-tetrahedral units, an increase in Q^3_{Al} and Q^4_{Al} networks was observed, along with a corresponding decrease in Q^0_{Al}, Q^1_{Al} and Q^2_{Al} networks, as shown in Figure 6. These observations suggest a noticeable increase in the polymerisation of alumina tetrahedra upon the addition of SiO_2 (up to 9 mass per cent) to the selected flux composition. In silicate networks, the simple networks Q^0_{Si} and Q^1_{Si} exhibit a decrease, while the proportions of complex Q^2_{Si} and Q^3_{Si} increase upon the addition of SiO_2. Thus, it can be inferred that the degree of polymerisation of both silicate and alumina networks was enhanced upon increasing SiO_2 concentration.

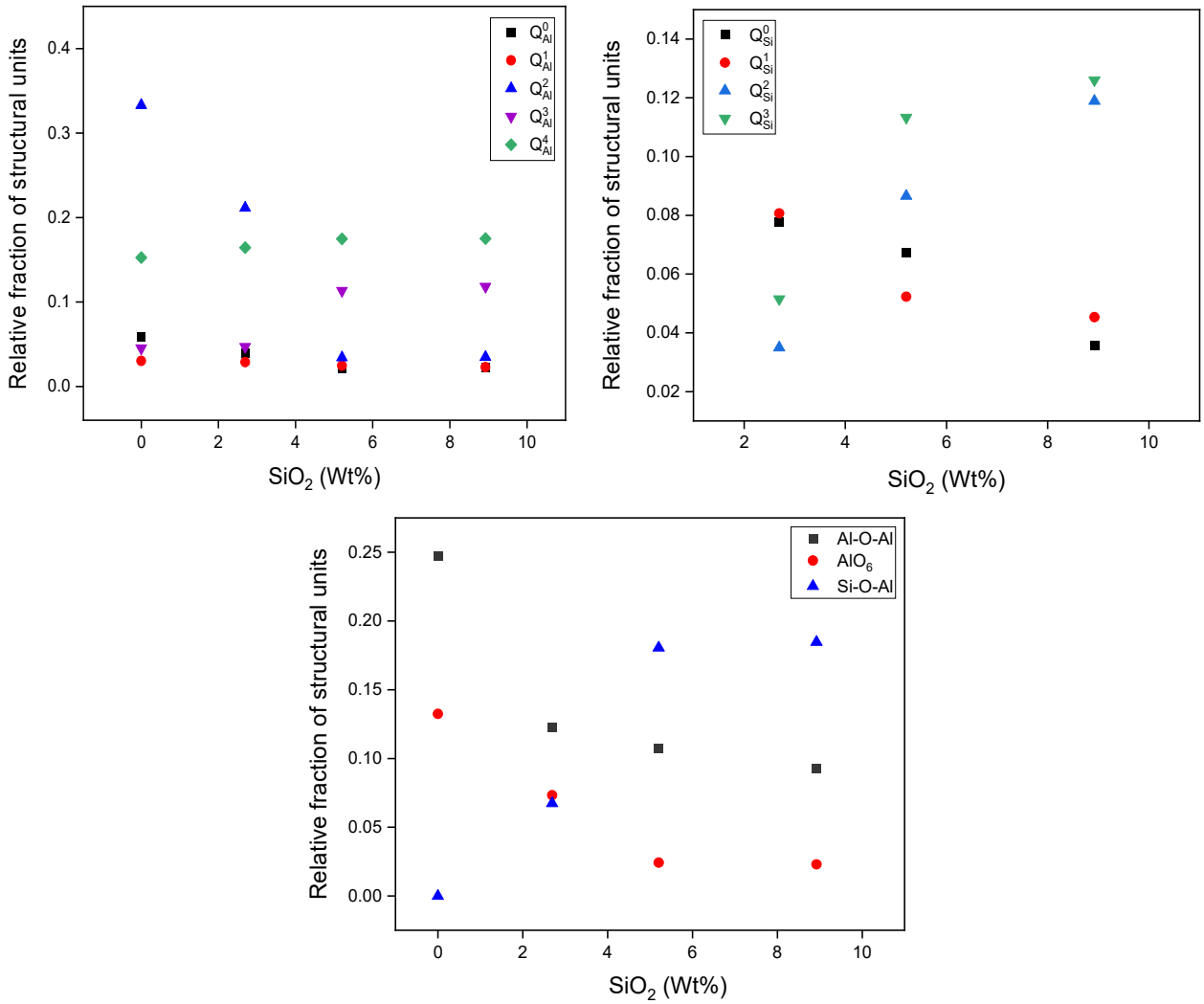

FIG 6 – Relative fraction of structural units in CaF_2-Al_2O_3-CaO-SiO_2 slag from Raman spectra with various SiO_2 concentrations.

Structural analysis of slag using FT-IR spectroscopy

Both the transmittance and absorbance spectra from the slag samples were obtained using FT-IR spectroscopy. Analysis of transmission depths corresponding to various structures present within the slag in the transmittance spectra provided information about changes in the polymerisation behaviour within each slag sample after SiO_2 addition, especially visible variations on the spectra associated with SiO_4 and AlO_nF_{4-n} structures. As well as, the deconvolution of curves from the absorbance spectra of each sample could provide quantitative information about the presence of distinct structural units inside AlO_4 and SiO_4 structures and gave better clarity about variation in absorption associated with AlO_nF_{4-n} structures, which was difficult to differentiate from some smaller structural units of SiO_4 from the analysis of transmission spectra due to overlapping. Combining both of these sets of information provides a more detailed understanding about the variation in the polymerisation behaviour of slag samples after silica addition.

Figure 7 presents the Fourier Transform Infrared (FT-IR) transmittance spectra of the quenched slag samples. By comparison with prior investigations, the different ranges of wave number associated with specific structural units of interest have been identified and are listed in Table 3. For example, the transmission characteristics over the wave number range of 1200–800 cm^{-1} represents the asymmetric stretching of 'Si-O' bonds within 'SiO_4' tetrahedral units, while that over the 800–600 cm^{-1} range is associated with the asymmetric stretching of 'Al-O' bonds in 'AlO_4' tetrahedral units (Park, Min and Song, 2002; Hwa, Hwang and Liu, 1998; Ju *et al*, 2022). Owing to the chemical composition, the slag samples investigated are likely to contain 'SiO_4' and 'AlO_4' tetrahedral units with varying

bridging oxygen, represented by the parameters 'Q^n_{Si}' for silicate units and 'Q^n_{Al}' for aluminate units ('n' = 0–4). A similar situation has been indicated in the previous section (on Raman spectra) as well.

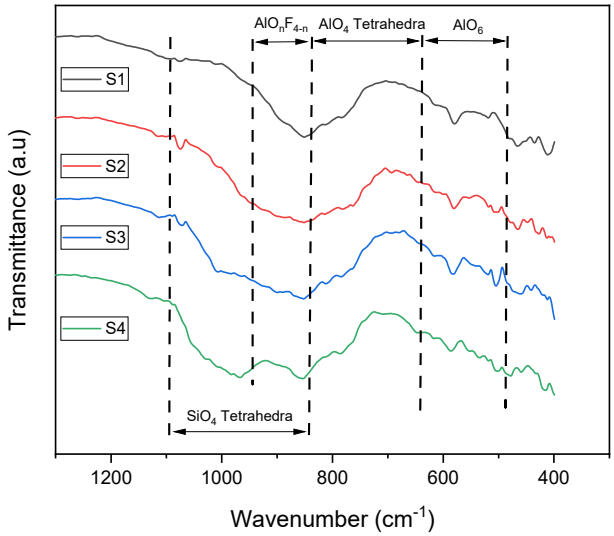

FIG 7 – The FT-IR spectra (transmittance) of the liquid nitrogen quenched CaF_2-Al_2O_3-CaO-SiO_2 flux samples with various SiO_2 contents.

TABLE 3

Assignments of FT-IR bands in spectra of CaF_2-Al_2O_3-CaO-SiO_2 slag (Park, Kim and Sohn, 2011; Lao *et al*, 2019; Ju *et al*, 2021).

Wavenumber range (cm^{-1})	Types of vibrations in FT-IR
850–890	Q^0_{Si}- asymmetric stretching vibration of Si-O bonds in SiO_4 tetrahedra (zero bridging oxygen)
910–930	Q^1_{Si}- asymmetric stretching vibration of Si-O bonds in SiO_4 tetrahedra (one bridging oxygen)
960–990	Q^2_{Si}- asymmetric stretching vibration of Si-O bonds in SiO_4 tetrahedra (two bridging oxygen)
1030–1070	Q^3_{Si}- asymmetric stretching vibration of Si-O bonds in SiO_4 tetrahedra (three bridging oxygen)
800–940	Asymmetric stretching vibrations of AlO_nF_{4-n}
490–600	Asymmetric stretching vibration of Al-O bonds in AlO_6 octahedra
610–630	Q^0_{Al}- asymmetric stretching vibration of Al-O bonds in AlO_4 tetrahedra (zero bridging oxygen)
650–670	Q^1_{Al}- asymmetric stretching vibration of Al-O bonds in AlO_4 tetrahedra (one bridging oxygen)
690–720	Q^2_{Al}- asymmetric stretching vibration of Al-O bonds in AlO_4 tetrahedra (two bridging oxygen)
730–760	Q^3_{Al}- asymmetric stretching vibration of Al-O bonds in AlO_4 tetrahedra (three bridging oxygen)
770–820	Q^4_{Al}- asymmetric stretching vibration of Al-O bonds in AlO_4 tetrahedra (four bridging oxygen)

It can be seen in Figure 7 that the transmission peak corresponding to 'AlO_nF_{4-n}' in sample S1 (0 mass per cent SiO_2) is stronger than in the SiO_2-containing samples over the wave number range

820–940 cm^{-1}. This may be attributed to the possibility of simpler silicate units (Q^0_{Si} and Q^1_{Si}) contributing to the transmission signal over the same wavenumber range in samples S2, S3 and S4, in addition to the contribution from 'AlO_nF_{4-n}' structural units. Based on this, it can be inferred that sample S1 contains a higher fraction of 'AlO_nF_{4-n}' units in comparison with the other slag samples. Upon careful observation around 1050 cm^{-1}, the transmission peak broadens and increases in intensity with increasing SiO_2 concentration, indicating vibrations associated with more complex Q^2_{Si} and Q^3_{Si} structural units. However, it was difficult to distinguish between the overlapping peaks associated with 'AlO_4' and 'AlO_6' structural units in the transmittance spectrum, for each of the slag samples. Therefore, FT-IR spectra of all the samples were acquired in the absorption mode as well. The resulting absorbance spectra were deconvoluted to identify the contributions from the individual structural units.

Figure 8 illustrates the deconvoluted FT-IR absorption spectra of all four slag samples, which were fitted using Gaussian functions with the Fityk software. Table 3 lists the FT-IR wave number ranges associated with the individual structural units that were identified after deconvoluting the absorbance spectra (Park, Kim and Sohn, 2011; Kim, Kim and Sohn, 2013; Lao *et al*, 2019; Ju *et al*, 2021).

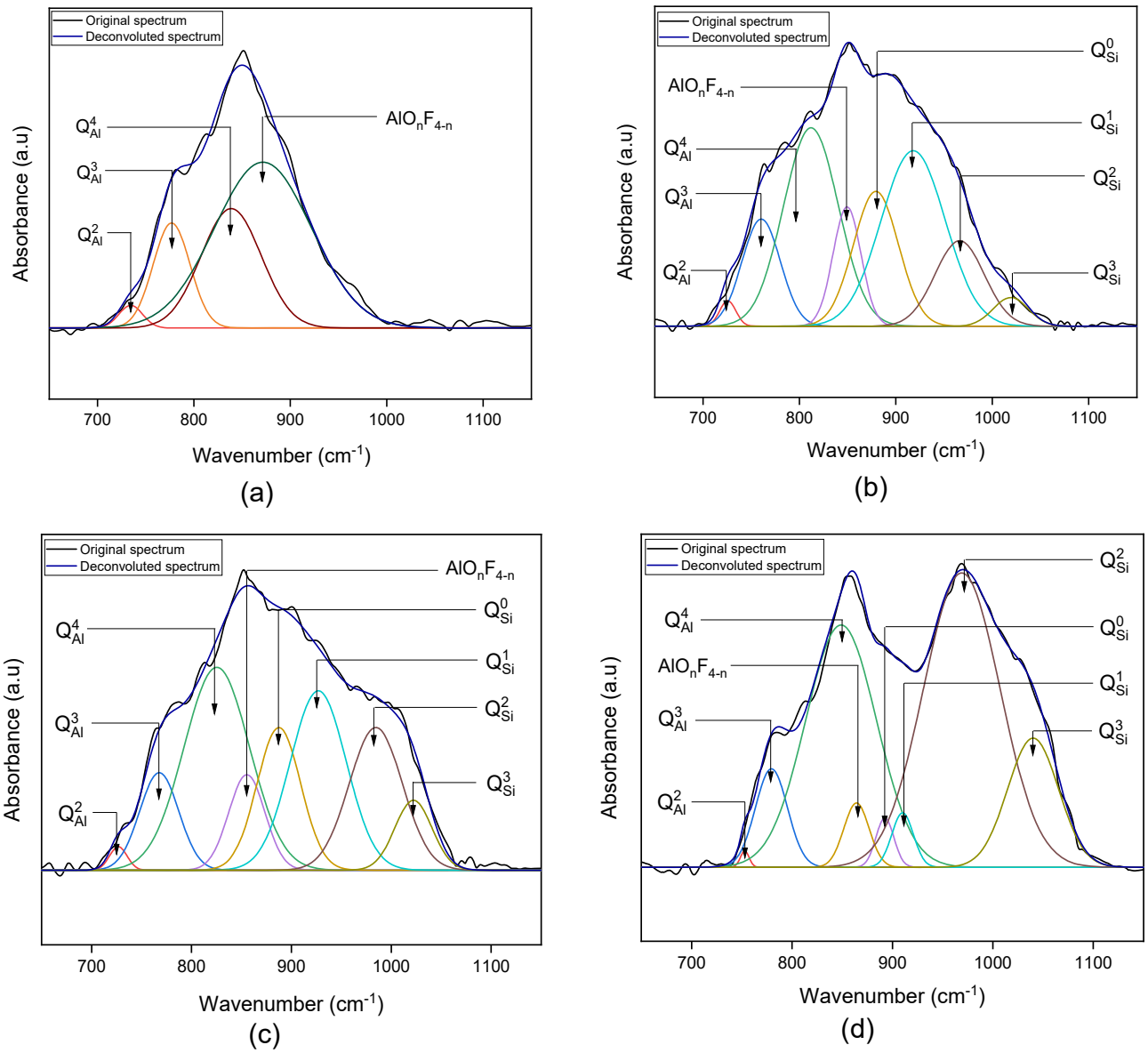

FIG 8 – The deconvolution results of FT-IR absorbance spectra: (a) S1; (b) S2; (c) S3; (d) S4.

In Figure 9, 'relative fraction of structural units' in each sample has been calculated from the deconvoluted peaks of absorption spectra and plotted against the increase in SiO_2 concentration in the slag samples. It has been observed from the plot that the addition of SiO_2 into the selected base

flux composition results in a continuous decrease in the presence of 'AlO_nF_{4-n}' networks. This can be attributed to the relative reduction in the fraction of fluorine and alumina in the system following the addition of SiO_2. From the analysis of the variation of different structural units within the silicate tetrahedral networks, it is observed that complex structural units, ie Q^3_{Si} and Q^2_{Si}, show an increase, while smaller structural units like Q^0_{Si} and Q^1_{Si} decrease. This trend signifies an increase in the polymerisation within silicate network structure. Upon further analysis of the graphs, it is observed that simple alumina tetrahedral units, Q^2_{Al} and Q^3_{Al}, decrease with the addition of SiO_2, while the complex network, Q^4_{Al} increases. These observations align with the inferences obtained from Raman spectroscopy, which also indicate behaviour of increase in the polymerisation of silicate and aluminate networks upon the addition of SiO_2 into the system.

Before introducing silica (SiO_2) into the '50 per cent CaF_2 – 20 per cent Al_2O_3 – 30 per cent CaO' flux system, the system predominantly contained alumina tetrahedral networks with calcium cations serve for charge balance. However, with the addition of SiO_2, silica forms tetrahedral network structures, and basic oxides/fluorides such as CaF_2 and CaO attempt to break these network structures, resulting in the formation of various simple/complex structural units of silica. In the presence of silica networks, aluminium in alumina units will try to enter silicate networks to form 'Si-O-Al' bonds, giving rise to the development of complex networks like Q^3_{Al} and Q^4_{Al}. In the case of silica tetrahedral networks, it is observed that the introduction of SiO_2 into the flux results in an increase in complex tetrahedral units (Q^2_{Si} and Q^3_{Si}), accompanied by a decrease in simple units, such as Q^0_{Si} and Q^1_{Si}. Because the basic oxides/fluorides available in the melt structure are almost constant and when more silica is introduced into the melt, available oxides/fluorides will try to break down more complex networks initially.

The results obtained from FT-IR spectroscopy and Raman spectroscopy show an increase in the level of polymerisation within both silica and Alumina tetrahedral networks due to the addition of SiO_2 into the selected base composition. These structural variations could influence the physicochemical properties such as viscosity and electrical conductivity of the slag. As the polymerisation level within the melt increased gradually upon adding SiO_2, viscosity and electrical resistivity values are expected to rise (Yan *et al*, 2021). However, further experiments are recommended to validate these inferences.

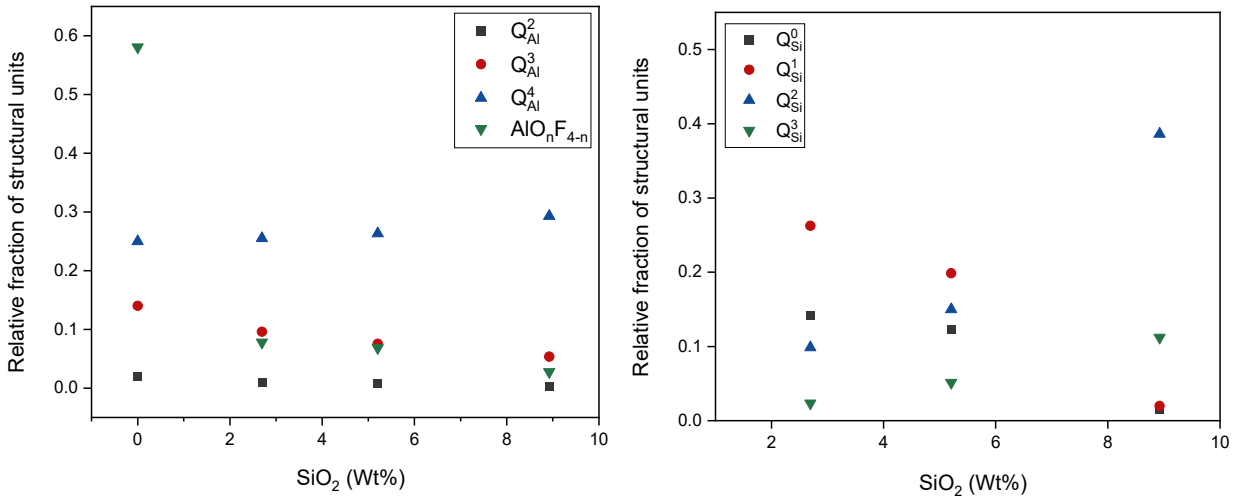

FIG 9 – Relative fraction of structural units in CaF_2-Al_2O_3-CaO-SiO_2 slag from FT-IR absorbance spectra with various SiO_2 contents.

Analysis of melting and solidification behaviour

Analysis of FactSage™ simulations

The Equillib module of FactSage™ software has been used to collect preliminary information on solidus-liquidus temperatures of the selected slag compositions, which can help identify the expected temperature range where the major phase transitions occur for the selected compositions.

Figure 10 shows the phase diagram plotted using FactSage™ simulation, where the X-axis shows the addition of SiO_2 concentration in mass per cent in a slag system containing 50 per cent CaF_2 – 20 per cent Al_2O_3 – 30 per cent CaO. Furthermore, from the Equillib module in the FactSage™, information on the formation of various product phases and their fractions under equilibrium conditions at different temperatures can be collected as output data, and this information has been used to plot the graphs showing the variation of the fraction of phases formed during the solidification of the slag samples, as shown in Figure 11. From these figures, liquidus and solidus temperatures for all four slag samples have been estimated. Liquidus temperature represents the temperature at which solidification initiates from 100 per cent liquid, and solidus temperature represents the temperature at which the whole liquid disappears on cooling.

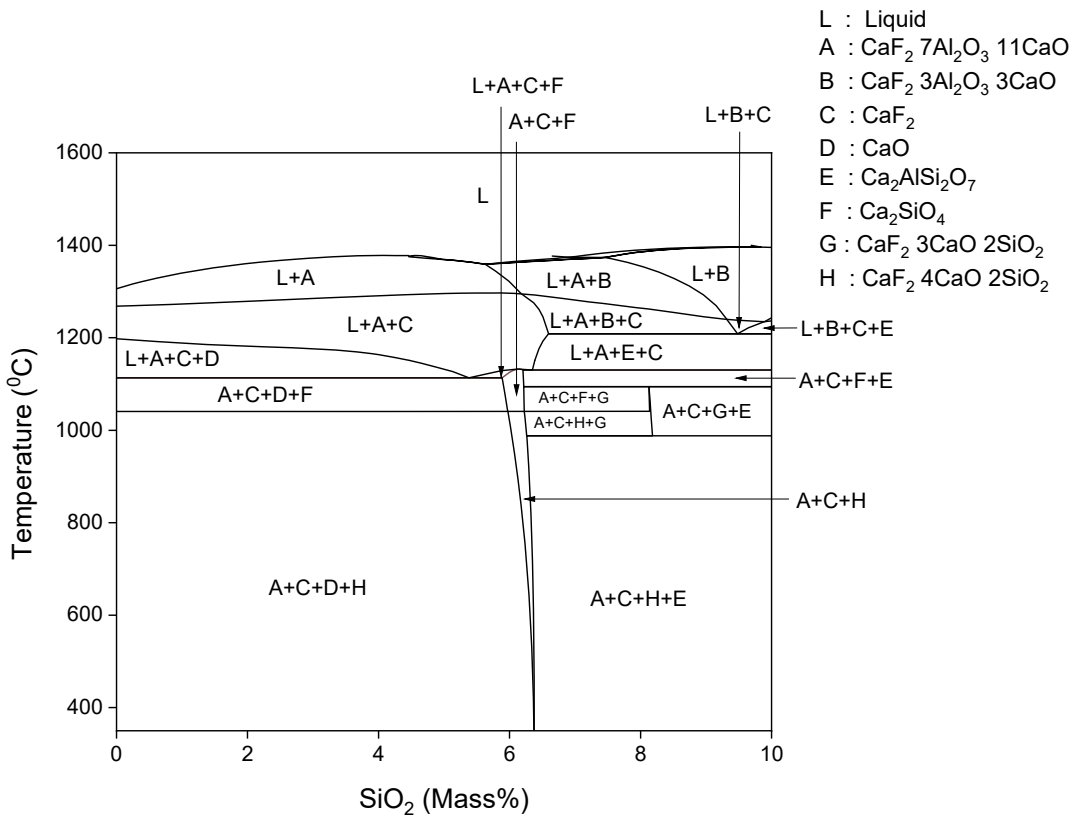

FIG 10 – The phase diagram plotted through FactSage™ simulation (X-axis indicates the concentration of SiO_2 added into 50 per cent CaF_2 – 20 per cent Al_2O_3 – 30 per cent CaO).

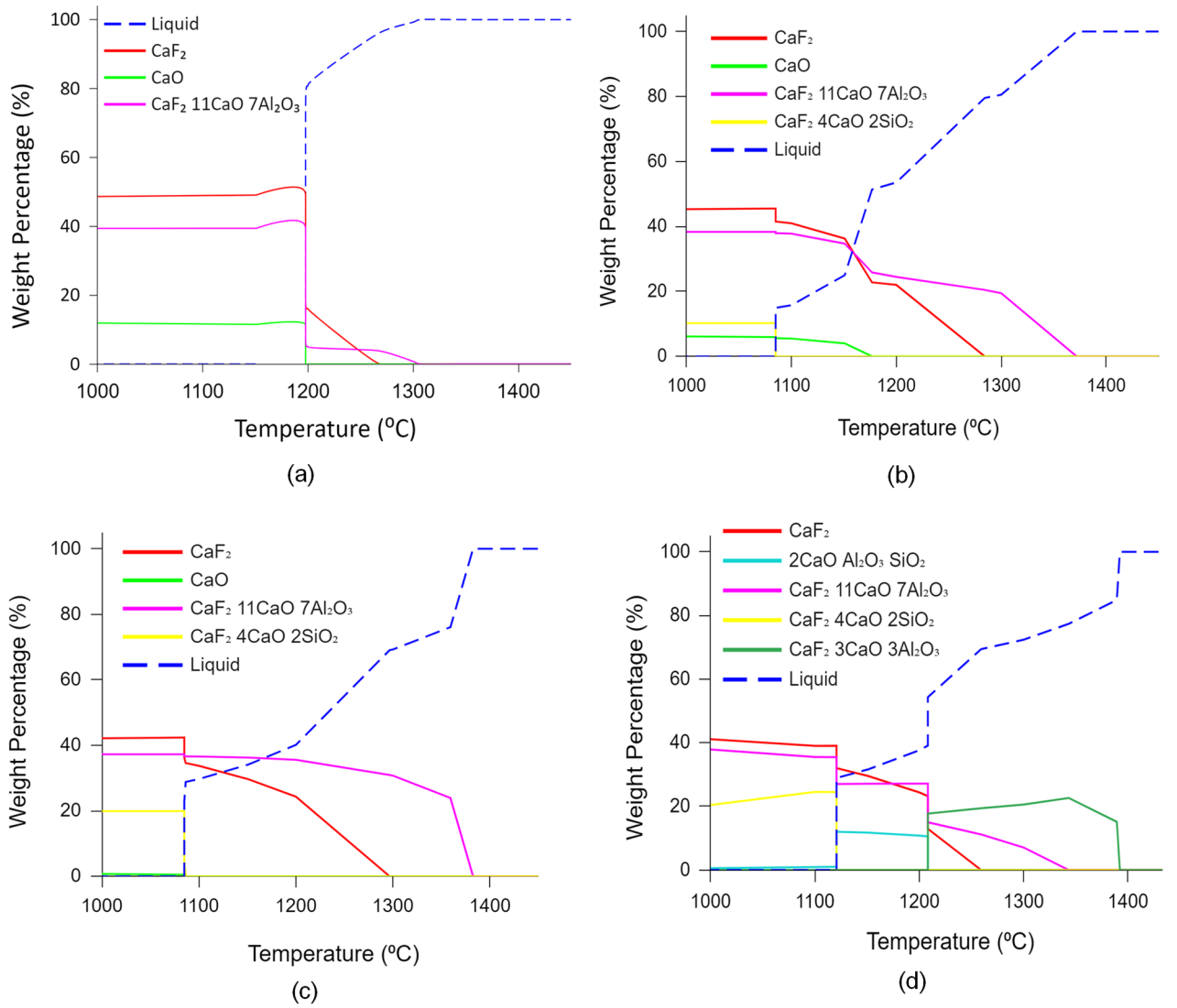

FIG 11 – Crystallisation behaviour of the fluxes calculated using FactSage™: (a) S1; (b) S2; (c) S3; (d) S4.

DTA/TGA analysis

Figure 12 shows the DTA and TGA curves of all four slag samples. The liquidus temperature of a slag is defined as the temperature at which the liquid phase initiates transformation to the solid phase during the cooling cycle or the temperature at which the solid sample is fully transitioned into liquid in the heating cycle. The solidus temperature is the temperature at which the first liquid phase forms in a heating cycle or the temperature at which the whole liquid phase transforms to the solid phase in the cooling cycle. Uniform heating and cooling rates of 10°C/min are performed for all fluxes in the temperature range of 800°C to 1450°C to determine and compare the liquidus and solidus temperatures. In the plots, the downward peaks are considered to be endothermic peaks. For example, from the DTA plots, the endothermic peaks observed during the heating cycle are analysed to estimate the liquidus temperature of the slag samples.

In Figure 12, the sudden variations from the DTA curve while changing the heating/cooling rate, represented by the symbol '#', can be associated with the thermal hysteresis. In the present work, these variations are not considered exo/endothermic peaks during the analysis. The symbols '•' and '×' in the curve denote estimated liquidus and solidus temperature, respectively. Further, the significant peaks observed between the temperature range of 800–1450°C in both heating and cooling cycles for all four slag samples are presented in Figures 13 and 14 respectively.

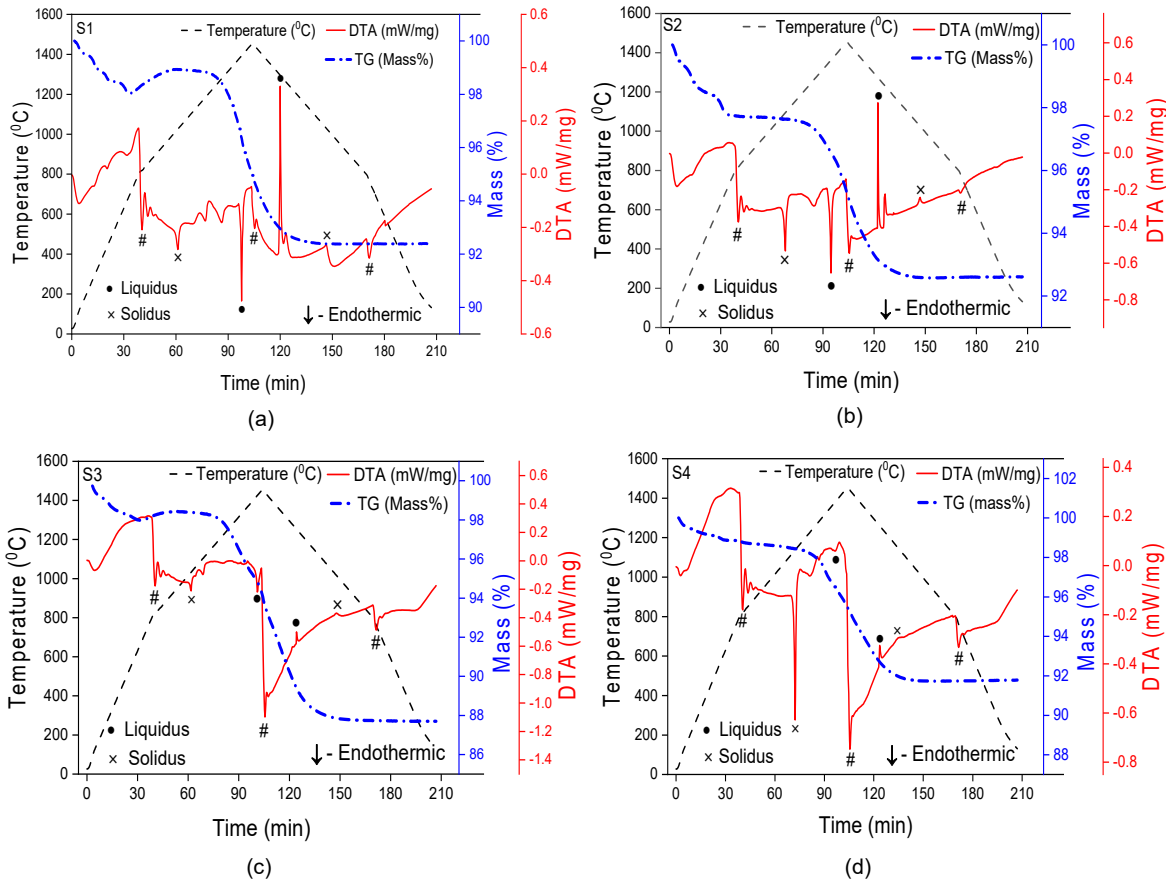

FIG 12 – DTA/TGA curves of the CaF_2-Al_2O_3-CaO-SiO_2 slag melts: (a) S1; (b) S2; (c) S3; (d) S4.

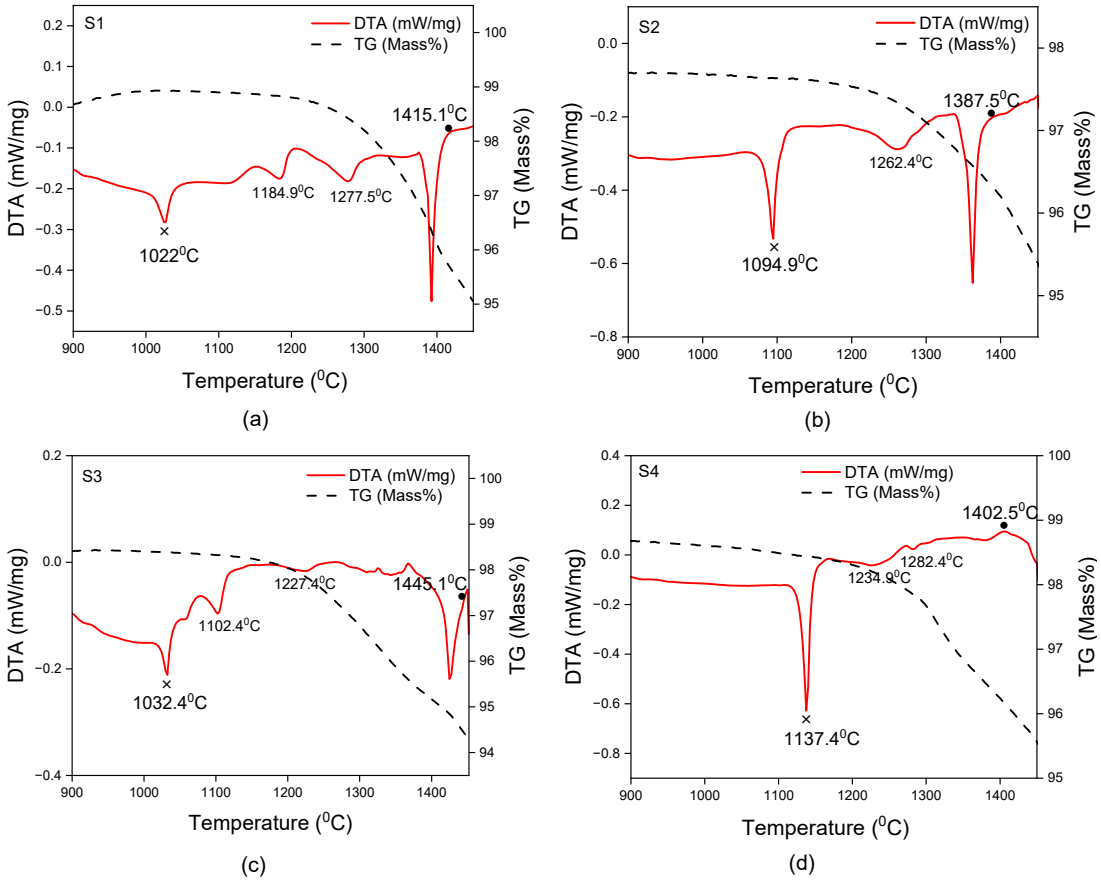

FIG 13 – DTA/TGA curves of the CaF_2-Al_2O_3-CaO-SiO_2 slag melts in heating cycle: (a) S1; (b) S2; (c) S3; (d) S4.

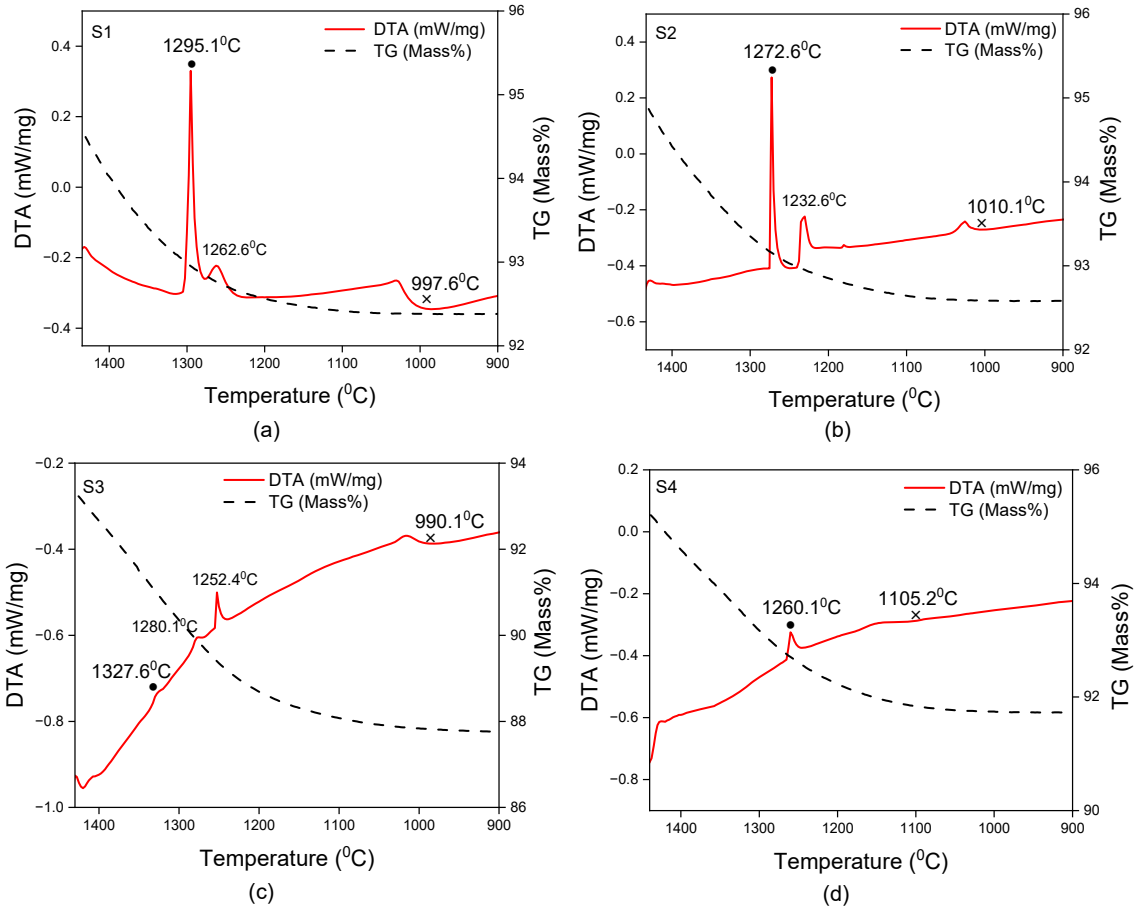

FIG 14 – DTA/TGA curves of the CaF_2-Al_2O_3-CaO-SiO_2 slag melts in cooling cycle: (a) S1; (b) S2; (c) S3; (d) S4.

In the heating cycle, following the energy required to overcome the nucleation barrier, the start of the formation of the liquid phase can be considered as the peak point of the first endothermic peak. Further, following the intermediate phase transformations during melting, the last endothermic peak observed in the cycle indicates the completion of solid-to-liquid phase transformation. The liquidus temperature is estimated from the point at which the curve regains its linearity following the final peak, showing that the slag sample is expected to be fully transitioned to the liquid phase. During the cooling cycle, crystallisation begins at the temperature associated with the first observed peak. After overcoming the energy required for the nucleation barrier, the temperature at which the first crystalline phase formed is considered as the peak point of the initial peak in the cooling cycle, representing the liquidus temperature. Following this, multiple peaks can be observed, corresponding to the possibility of crystallisation temperature of various intermediate phases formed, eventually leading to the last peak associated with the formation of the final phase and the complete solidification of slag. The solidus temperature in the cooling cycle is interpreted as the temperature at which the DTA curve regains its linearity following the final observed peak. Figures 13 and 14 present the estimation of liquidus and solidus temperature according to this convention.

After analysing the DTA curves, it is evident that the studied slag samples exhibit a high degree of undercooling in the cooling cycle, leading to the delayed observation of crystallisation peaks. Figure 15 shows the variation in the presence of exothermic peak associated with liquidus temperature in the cooling cycle due to undercooling from the slag sample S1. In the present work, considering these aspects of undercooling along with the knowledge of the mass loss due to fluoride evaporation at high temperature at the end of the heating cycle causing compositional changes, the selection of solidus-liquidus temperature values is determined from endothermic peaks from the heating cycle.

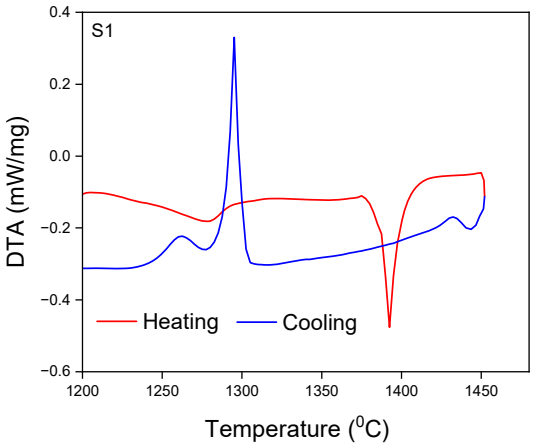

FIG 15 – DTA curve of slag sample S1 showing a high degree of undercooling.

Table 4 presents solidus and liquidus temperature information of all the slag samples determined from Figure 13, ie during the heating cycle. The peaks observed between the solidus and liquidus temperatures in DTA results can be due to the possible potential phase transformations within this temperature range, as reported by some previous works with similar slag samples (Huang *et al*, 2021). The plotted graphs from FactSage™ data shown in Figure 11 can further support this inference, as they show certain thermodynamically possible intermediate phase transitions between solidus and liquidus temperatures. For validating the presence of phases in the slag samples, the X-ray diffraction (XRD) characterisation has been performed on all four samples, quenched from 1000°C. Results are presented in Figure 16. The major phases identified in the analysis are 'CaF_2 11CaO $7Al_2O_3$' and 'CaF_2'. The results closely match with those of FactSage™ simulation as presented in Figure 11, where, in all the slag samples, major phases present below solidus temperature are these identified phases from XRD. However, further studies are recommended to confirm this and identify the reason for the formation of the aforementioned phases and the formation of peaks. TGA results indicate a mass drop of approximately ~10 per cent for all the slag samples following holding at 1450°C, which can possibly be due to the fluoride evaporation from the samples (Ju *et al*, 2023, 2021). Table 4 represents a comparison of the predicted solidus-liquidus temperatures from FactSage™ and results obtained from DTA analysis.

TABLE 4

Estimation of solidus and liquidus temperatures from DTA and FactSage™.

Slag No	Solidus (°C)		Liquidus (°C)	
	FactSage™	DTA	FactSage™	DTA
S1	1197.7	1022	1305.9	1415.1
S2	1084.9	1094.9	1371.8	1387.5
S3	1084.9	1032.4	1382.5	1445.1
S4	1120.7	1137.4	1392.2	1402.5

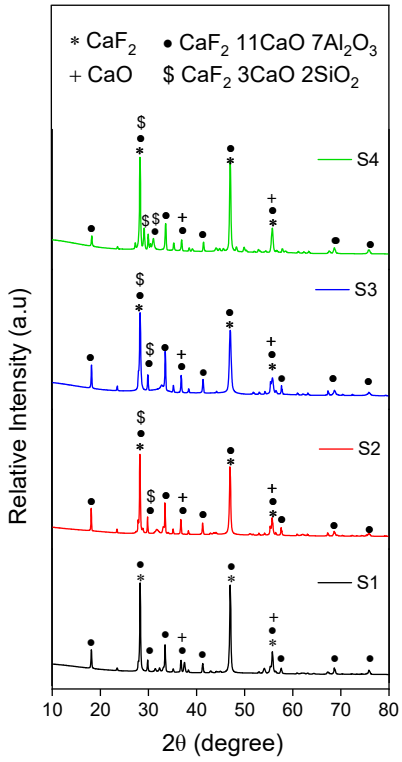

FIG 16 – XRD analysis of slag samples quenched from 1000°C.

After the addition of SiO_2 into the ESR slag selected for the study, which is used for refining special alloy steels, the liquidus temperatures of the fluxes undergo changes with respect to compositional and structural modifications. However, for refining commonly used special alloy steels, the measured values of liquidus and solidus temperatures are within acceptable range, as the liquidus temperatures of the fluxes are below those of commonly used alloy steel grades. Furthermore, it is suggested to conduct the ESR refining using the modified fluxes and analyse the efficiency of the ESR process as well as the quality of refined ingots for a better understanding of the suitability of these fluxes.

CONCLUSIONS

In this study, the influence of SiO_2 concentration on the structural characteristics and melting-solidification behaviour of the 'CaF_2-Al_2O_3-CaO-(SiO_2)' slag was systematically investigated. Structural analyses conducted through Raman spectroscopy and FT-IR spectroscopy techniques revealed significant changes in the polymerisation behaviour of alumina and silica units with varying SiO_2 concentrations. Changes in the relative fraction of structural units have been analysed through Raman and FT-IR spectroscopy techniques, indicating increased level of polymerisation in both alumina and silicate networks. The estimation of liquidus and solidus temperatures, performed using FactSage™ software and DTA/TGA analysis, further supported the suitability of the flux in ESR operation. The conclusions are summarised as follows.

- In raman spectroscopy results, within alumina-tetrahedral units, an increase in Q^3_{Al} and Q^4_{Al} networks was observed, with a corresponding decrease in Q^0_{Al}, Q^1_{Al} and Q^2_{Al} networks, suggesting an increase in alumina tetrahedra polymerisation with SiO_2 addition into the selected commercial flux composition. Silicate networks show a decrease in simple networks (Q^0_{Si} and Q^1_{Si}) and an increase in complex networks (Q^2_{Si} and Q^3_{Si}) after the addition of SiO_2, indicating an increase in the polymerisation of silicate tetrahedral networks.
- In FT-IR analyses, within silicate tetrahedral networks, an increase in complex structural units (Q^3_{Si} and Q^2_{Si}) and a decrease in smaller structural units (Q^0_{Si} and Q^1_{Si}) were observed, indicating increased polymerisation level of the silicate network. Within alumina networks, a decrease in simple alumina tetrahedral units (Q^2_{Al} and Q^3_{Al}) and an increase in the complex network Q^4_{Al} were observed, and results suggest that the addition of SiO_2 increases the

polymerisation of alumina tetrahedral networks, consistent with the results from Raman spectroscopy.

- After the addition of SiO_2 in the slag, silica forms tetrahedral networks, and basic oxides/ fluorides (CaF_2 and CaO) try to break these networks, creating various simple and complex structures in silica. Aluminium from alumina units will try to join silicate networks, forming 'Si-O-Al' bonds and leading to complex networks like Q^3_{Al} and Q^4_{Al}. In silica tetrahedral networks, the gradual addition of SiO_2 increases complex units (Q^2_{Si} and Q^3_{Si}) and reduces simpler ones like Q^0_{Si} and Q^1_{Si}. The reason for the rise in complex structural units can be that, after the addition of more silica, the basic oxides/fluorides in the melt, which is at a constant level across all compositions, initially break relatively more complex networks.
- Liquidus temperature measurements obtained from FactSage™ and DTA/TGA analyses show that the fluxes' liquidus temperatures are within permissible ranges, ie they were found to be below the melting point of the ingot to be refined, ensuring the suitability of the flux for the refining of various alloy steel grades.

ACKNOWLEDGEMENTS

The authors are thankful for the support received from the Science and Engineering Research Board (SERB), India, towards fellowship for one of the authors as well as the conduct of the experiments. We express our sincere gratitude to our colleagues in the Ferrous Process Laboratory and Geochemistry lab at IIT Bombay for their invaluable support in conducting this work.

REFERENCES

Haghdani, S, Tangstad, M and Einarsrud, K E, 2022. A Raman-structure model for the viscosity of SiO_2-CaO-Al_2O_3 system, *Metallurgical and Materials Transactions B,* 53(3):1733–1746.

Huang, Y, Shi, C B, Wan, X X, Li, J L, Zheng, D L and Li, J, 2021. Effect of SiO_2 and B_2O_3 on crystallisation and structure of CaF_2-CaO-Al_2O_3-based slag for electroslag remelting of ultra-supercritical rotor steel, *Journal of Iron and Steel Research International*, 28(12):1530–1540.

Hwa, L G, Hwang, S L and Liu, L C, 1998. Infrared and Raman spectra of calcium alumino-silicate glasses, *Journal of non-crystalline solids*, 238(3):193–197.

Ju, J T, Yang, K S, Gu, Y and He, K, 2022. Effect of Na_2O on Viscosity, Structure and Crystallization of CaF_2-CaO-Al_2O_3-MgO-TiO_2 Slag in Electroslag Remelting, *Russian Journal of Non-Ferrous Metals*, 63(6):599–609.

Ju, J, Gu, Y, Zhang, Q and He, K, 2023. Effect of CaF_2 and CaO/Al_2O_3 ratio on evaporation and melting characteristics of low-fluoride CaF_2-CaO-Al_2O_3-MgO-TiO_2 slag for electroslag remelting, *Ironmaking and Steelmaking*, 50(1):13–20.

Ju, J, Ji, G, Tang, C, Yang, K and Zhu, Z, 2021. The effect of Li_2O on the evaporation and structure of low-fluoride slag for vacuum electroslag remelting, *Vacuum*, 183:109920.

Kim, G H, Kim, C S and Sohn, I L, 2013. Viscous behavior of alumina rich calcium-silicate based mold fluxes and its correlation to the melt structure, *ISIJ international*, 53(1):170–176.

Kim, T S and Park, J H, 2014. Structure-viscosity relationship of low-silica calcium aluminosilicate melts, *ISIJ International*, 54(9):2031–2038.

Lao, Y, Gao, Y, Deng, F, Wang, Q and Li, G, 2019. Effects of basicity and CaF_2 on the viscosity of CaF_2-CaO-SiO_2 slag for electroslag remelting process, *Metallurgical Research and Technology*, 116(6):638.

Li, J, Shu, Q and Chou, K, 2014. Structural study of glassy CaO-SiO_2-CaF_2-TiO_2 slags by Raman spectroscopy and MAS-NMR, *ISIJ international*, 54(4):721–727.

McMillan, P and Piriou, B, 1983. Raman spectroscopy of calcium aluminate glasses and crystals, *Journal of Non-Crystalline Solids*, 55(2):221–242.

Park, H S, Kim, H and Sohn, I, 2011. Influence of CaF_2 and Li_2O on the viscous behavior of calcium silicate melts containing 12 wt pct Na_2O, *Metallurgical and Materials Transactions B,* 42:324–330.

Park, J H, Min, D J and Song, H S, 2002. Structural investigation of CaO-Al_2O_3 and CaO-Al_2O_3-CaF_2 slags via Fourier transform infrared spectra, *ISIJ International*, 42(1):38–43.

Persson, M and Seetharaman, S, 2007. Kinetic studies of fluoride evaporation from slags, *ISIJ International*, 47(12):1711–1717.

Shi, C B, Li, J, Cho, J W, Jiang, F and Jung, I H, 2015. Effect of SiO_2 on the crystallisation behaviors and in-mold performance of CaF_2-CaO-Al_2O_3 slags for drawing-ingot-type electroslag remelting, *Metallurgical and Materials Transactions B,* 46:2110–2120.

Shi, C B, Zheng, D L, Shin, S H, Li, J and Cho, J W, 2017. Effect of TiO_2 on the viscosity and structure of low-fluoride slag used for electroslag remelting of Ti-containing steels, *International Journal of Minerals, Metallurgy and Materials*, 24:18–24.

Wan, X, Shi, C, Huang, Y, Shu, Q and Zhao, Y, 2023. Effect of SiO_2 and BaO/CaO Mass Ratio on Structure and Viscosity of B_2O_3-Containing CaF_2-CaO-Al_2O_3-Based Slag for Electroslag Remelting of Rotor Steel, *Metallurgical and Materials Transactions B,* 54(1):465–479.

Wan, X, Shi, C, Zhao, Y and Li, J, 2022. Effect of CaF_2 and Li_2O on structure and viscosity of low-fluoride slag for electroslag remelting of rotor steel, *Journal of Non-Crystalline Solids*, 597:121914.

Wroblewski, K, DiBiaso, B, Fraley, J, Fields, J and Rudoler, S, 2016. Design of ESR Slags According to Requested Physical Properties; Part 2: Density and Viscosity, in *Proceedings of the 2013 International Symposium on Liquid Metal Processing and Casting*, pp 43–46.

Wroblewski, K, Fraley, J, Fields, J, Werner, R and Rudoler, S, 2011. Design of ESR Slags According to Requested Physical Properties; Part 1: Electrical Conductivity, in *Proceedings of the 2011 International Symposium on Liquid Metal Processing and Casting, Nancy, France*, pp 121–126.

Xu, R H, Guo, J, Zhang, M C and Guo, H J, 2022. Effect of SiO_2 and TiO_2 on the Crystal Morphology of CaF_2-Al_2O_3-CaO-Based Electroslag Remelting Slag, *Steel Research International*, 93(3):2100191.

Yan, X, Pan, W, Wang, X, Zhang, X, He, S and Wang, Q, 2021. Electrical conductivity, viscosity and structure of CaO-Al_2O_3-based mold slags for continuous casting of high-Al steels, *Metallurgical and Materials Transactions B,* 52(4):2526–2535.

Yeager, J and Ramanujachary, K, 2007. Method of Measuring Fluoride in Fluxes Using the Fluoride Ion-Selective Electrode, US Patent Application US11/456815.

Zheng, D, Li, J and Shi, C, 2020. Development of low-fluoride slag for electroslag remelting: role of Li_2O on the crystallisation and evaporation of the slag, *ISIJ International*, 60(5):840–847.

Zheng, D, Shi, C, Li, J and Ju, J, 2020. Crystallisation kinetics and structure of CaF_2-CaO-Al_2O_3-MgO-TiO_2 slag for electroslag remelting, *ISIJ International*, 60(3):492–498.

A machine learning model to predict non-metallic inclusion dissolution in the metallurgical slag

DOI: 10.62053/KBII2328

W Mu[1], C Shen[2,3], C Xuan[4], D Kumar[5], Q Wang[6] and J H Park[7]

1. Associate Professor, Royal Institute of Technology (KTH), Department of Materials Science and Engineering, Stockholm, SE-10044, Sweden. Email: wmu@kth.se.
2. Visiting scholar, Royal Institute of Technology (KTH), Stockholm SE-10044, Sweden. Email: chshen@kth.se
3. Associate Professor, Hebei University of Technology, Tianjin 300401, China. Email: cgshen@hebut.edu.cn
4. Technology Manager, Metso, Skellefteå SE-93157, Sweden. Email: xuanchangji@msn.com
5. Assistant Professor, IIT Bombay, Department of Metallurgical Engineering and Materials Science, Mumbai, India. Email: deepook@iitb.ac.in
6. Professor, Northeastern University, Shenyang 110819, China. Email: wangq@mail.neu.edu.cn
7. Professor, Hanyang University, Department of Materials Science and Chemical Engineering, Ansan 15588, Korea. Email: basicity@hanyang.ac.kr

ABSTRACT

Dissolution of non-metallic inclusions in the metallurgical slag is of vital importance for cleanliness control of the steel manufacturing. With the development of high temperature confocal laser scanning microscope (HT-CLSM), new insights have been obtained due to its *in situ* observation characteristics, higher resolution and precise control. However, HT-CLSM measurement has the limitation, eg the slag composition cannot include high amount of transition metal oxides. In addition, it is time consuming for the experimental procedure and not so simple to succeed for every measurement. It is known that digitalisation has made a significant progress in recent years. Machine learning (ML), a sub-domain of artificial intelligence (AI), is the key enabling technology for the digitalisation of the material science and industry. The database for ML model is collected using almost all available HT-CLSM experimental data and subsequently the established database is trained by different ML methods. Unseen data is used as the benchmark of the ML model. Al_2O_3 dissolution is the main process to be predicted in the current study. A good agreement between the HT-CLSM data and the ML model prediction results show the possibility to apply ML in process metallurgy.

INTRODUCTION

Inclusion (oxide) dissolution in the metallurgical slag is one of the key issues for the clean steel production. On the one hand, the main components in refractories, eg alumina, magnesia etc have the potency to be dissolved in the slag during contacting. Subsequently, the eroded refractory has a much lower chemical and physical stability at high temperature and tends to be a source for exogenous inclusions formation in the steel. On the other hand, the formed inclusion particles tend to flow up to pass the steel/slag interface and need to be dissolved quickly in the slag (Park and Zhang; 2020; Park and Kang, 2017; Reis, Bielefeldt and Vilela, 2014; Webler and Pistorius, 2020). If the remained inclusions entrapped back into the liquid steel, they may have the risk to make agglomerations resulting in serious industrial problems eg nozzle clogging. In this case, the study of inclusion dissolution attracts the attention of metallurgists during the past decades. Finger rotating test (also named as dip test) is the conventional method to investigate the dissolution of oxide (refractory or synthetic inclusion) in the liquid slag. This method provides a good freedom of varying the experimental conditions (slag composition, temperature, atmosphere etc), however the sample size is much larger than the real inclusion so the obtained knowledge cannot connect to the real steelmaking process directly (Cooper Jr and Kingery, 1964; Aneziris *et al*, 2013).

With the development of the instrumentation in recent 25 years, high temperature confocal laser scanning microscope (HT-CLSM) offers a path to the *in situ* observation of dissolution of inclusion particles in the steelmaking slag in real time. To track the particle dissolution, quasi-three-dimensional images with sharp boundary and good contrast could be taken from the video by the CCD camera equipped with HT-CLSM. Specifically, the size of the used particle which ranges from

a few tens to several hundreds of microns fits well with the actual inclusion size. Al_2O_3 dissolution in the slag is the most comprehensively studied by HT-CLSM and the early work can refer to Sridhar and Cramb (2000). They investigated the effect of the temperature on the dissolution of alumina particles in the CaO-Al_2O_3-SiO_2-MgO (CASM) slag. Subsequently, comprehensive research activities focusing on the effect of inclusion type, slag composition, slag viscosity, temperature etc are performed. Specifically, 1630°C is the maximum temperature which could be achieved so far to observe oxide dissolution (Liu *et al*, 2007b). Due to the development of furnace in HT-CLSM, this maximum temperature could be further challenged. CASM slag without transition metal (Fe, Mn etc) oxides is the mainly selected system since the slag needs to be transparent to enable the *in situ* observation, which is one main limitation for the application of HT-CLSM in this field. By utilising the advantage of HT-CLSM, dissolution kinetics of different kinds of non-metallic inclusions besides Al_2O_3, ie MgO, $MgAl_2O_4$, TiO_2, Al_2TiO_5, $CaO{\cdot}2Al_2O_3$ (CA2); SiO_2, SiC, TiN etc (Fox *et al*, 2004; Liu *et al*, 2007a, 2007b; Miao *et al*, 2018; Michelic *et al*, 2016; Michelic and Bernhard, 2017; Park *et al*, 2010; Ren *et al*, 2022; Sharma, Dabkowska and Dogan, 2019; Sharma, Mu and Dogan, 2018a, 2018b; Yi *et al*, 2003) have been investigated. Except for the chemistry of inclusion, other processing parameters, eg dissolution temperature, particle size, slag composition, have been studied, however, there are still many parameters need to worth further investigated. For instance, the HT-CLSM can only observe the particle dissolution in the transparent slag, which means the influence of some component, eg Fe_tO cannot be studied quantitatively, especially the Fe_tO content in slag is high (Um *et al*, 2022). In this case, the simulation and other technique needs to be performed to understand the inclusion dissolution mechanism with the comprehensive conditions.

Regarding the study of dissolution mechanism, shrinking core (SC) model is believed to be the most frequently applied approach. Using this model, the dissolution mechanism is usually identified through a proper fitting between the SC model prediction and the experimental observation data. If the observed dissolution profile is linear, the dissolution process is considered as the reaction-controlled dissolution (RCD). If the dissolution profile is in a parabolic shape, the boundary layer diffusion-controlled dissolution (BLDD) is the mechanism. When the dissolution profile shows a sigmoidal shape, shell layer diffusion-controlled dissolution (SLDD) may be the controlled mechanism. Alternatively, stationary interface diffusion model (SIM) could also obtain a sigmoidal profile which quite closes to SLDD. For the classical SC models, the experimental profile sometimes could not fit any mechanism curve which is a clear drawback, a few attempts have been made to modify the SC model. For instance, Feichtinger *et al* (2014) introduced a factor ‘f’ in the SIM model (also named ‘invariant interface diffusion control’), which improves the model performance significantly and ‘f’ is reported to relate to slag viscosity. Very recently, a modified SC-based physical model, ie diffusion-distance-controlled dissolution (DDD) model (Xuan and Mu, 2021) is developed to investigate the shape origin and variation of oxide dissolution in the slag. It is reported that the diffusion-related particle dissolution is actually one mechanism but not a few, the shape of the dissolution profile is controlled by the distance of diffusion region. This model has been verified with HT-CLSM data of different kinds of inclusions dissolution. However, the comprehensive application of this model is relied on the input of physical parameters to present different slag compositions, currently this is the only limitation for the DDD model.

In order to further extend the application of the theoretical model to predict inclusion dissolution in the comprehensive processing conditions, machine learning (ML) has been considered to use to combine with the current DDD physical model. Digitalisation has brought many significant changes to the manufacturing in the recent decade. ML is a sub-domain of artificial intelligence, which is the key enabling technology for industrial-driven research, eg material engineering and metallurgy. The database for ML model is collected using HT-CLSM experimental data, DDD model is used for the augmentation of the current database, to have a continuous distribution of data. Unseen experimental data is used as the benchmark of the ML model. Al_2O_3 is the most common inclusion, so its dissolution in the slag is performed in the current study, to test the accuracy of the current hybrid modelling methodology. The successful implementation of this model can be applied to predict the dissolution of other kinds of inclusions, eg MgO, SiO_2, $MgAl_2O_4$, $CaO{\cdot}2Al_2O_3$ etc in the further study.

METHODOLOGY

The current ML data set contains 1506 data points collected from the open literatures (Hagemann, Pettsold and Sheller, 2010; Lee *et al*, 2001; Liu *et al*, 2007a, 2007b; Monaghan, Chen and Sorbe, 2005; Michelic *et al*, 2016; Sharma, Mu and Dogan, 2018a, 2018b; Soll-Morris *et al*, 2009; Sridhar and Cramb, 2000; Yi *et al*, 2003), DDD physical model is used for the data augmentation, this combination methodology can be seen in the report by Mu *et al* (2021). The collecting data set is split into 80 per cent for training and 20 per cent for testing. Furthermore, 252 unseen data which are not included in the training and testing data sets (Liu *et al*, 2007a, 2007b; Yi *et al*, 2003; Michelic *et al*, 2016) is used as the validation data set for the benchmark. There are ten parameters including in the data set to predict Al_2O_3 dissolution, ie original inclusion size (radius), temperature, concentration of five components in slag (SiO_2, CaO, Al_2O_3, MgO and Fe_tO), density of inclusion, slag viscosity and radius change (R/R_0, R represents the radius at the certain time and R_0 is the initial radius). The time required for the dissolution of Al_2O_3 particles was selected as the output. For the further work to predict different kinds of inclusion dissolution, one more parameter, inclusion type needs to be added. The detailed information of training and testing data set as well as validation data set are listed in Tables 1 and 2.

TABLE 1

Data distribution in present data set (including training and testing sets).

Parameters	Min	Max	Mean	Std
Radius [μm]	41.3	250.2	176.6	76.9
Temperature [°C]	1673	1873	1772.3	56.7
SiO_2 [wt%]	0	62.4	33.4	19.8
CaO [wt%]	22.4	57.2	35.2	9.1
Al_2O_3 [wt%]	13.3	50.0	29.0	11.6
MgO [wt%]	0	7.5	2.0	3.1
Fe_tO [wt%]	0	9.2	0.4	1.7
Slag Density [kg.m]	3568	3640	3604	20.4
Slag viscosity [Pa.s]	0.1	100.5	4.7	16.4
R/R_0 [-]	0	1	0.7	0.3
Dissolution time [sec]	0	4490	925	1099

TABLE 2

Data distribution in validation set.

Parameters	Min	Max	Mean	Std
Radius [μm]	95.3	249.1	226.6	47.3
Temperature [°C]	1723	1873	1778.2	50.1
SiO_2 [wt%]	0	46.2	39.2	16.5
CaO [wt%]	29.7	49.5	32.7	7.1
Al_2O_3 [wt%]	24.1	50.0	28.0	9.3
MgO [wt%]	0	0.5	0.08	0.18
Fe_tO [wt%]	0	0	0	0
Slag Density [kg.m]	3568	3622	3602	18.0
Slag viscosity [Pa.s]	0.8	3.6	2.5	1.1
R/R_0 [-]	0	1	0.56	0.26
Dissolution time [sec]	0	4490	1527	1290

Standard normalisation was used in this work in order to eliminate the difference in numeric scale of features. Based on the previous modelling results, it is found that the prediction of the trained ML model fluctuates as the different partition of training data set and testing data set, so multiple hold-out method is used in order to reliably evaluate model's performance (Shen *et al*, 2019). In this study, the data set was randomly divided into training and testing sets by 50 times to develop 50 ML models. Moreover, common mean absolute error (MAE) and square correlation coefficient (R^2) were used to evaluate the model's performance (Pal, 2017). Besides, the suitable selection of ML algorithm is also important for good performance. In this work, six common ML algorithms were employed to develop three models, including Support Vector Regression (SVR) (Liu, Wang and Gu, 2021), Multi-Layer Perception (MLP) (Del Campo *et al*, 2021) and three kinds of ensemble learning algorithms, ie AdaBoost (Ada), decision tree regression (DTR), random forest regression (RFR) (Sammut and Webb, 2011) and the modelling results for testing data are plotted in Figure 1. It is seen that ensemble algorithms have the higher prediction accuracy than MLP and SVR algorithms. The R^2 values of these models were greater than 98 per cent, meaning a very good prediction performance. Finally, RFR algorithm was selected to predict the dissolve curve of Al_2O_3 particle owing to the relatively lowest MAE value.

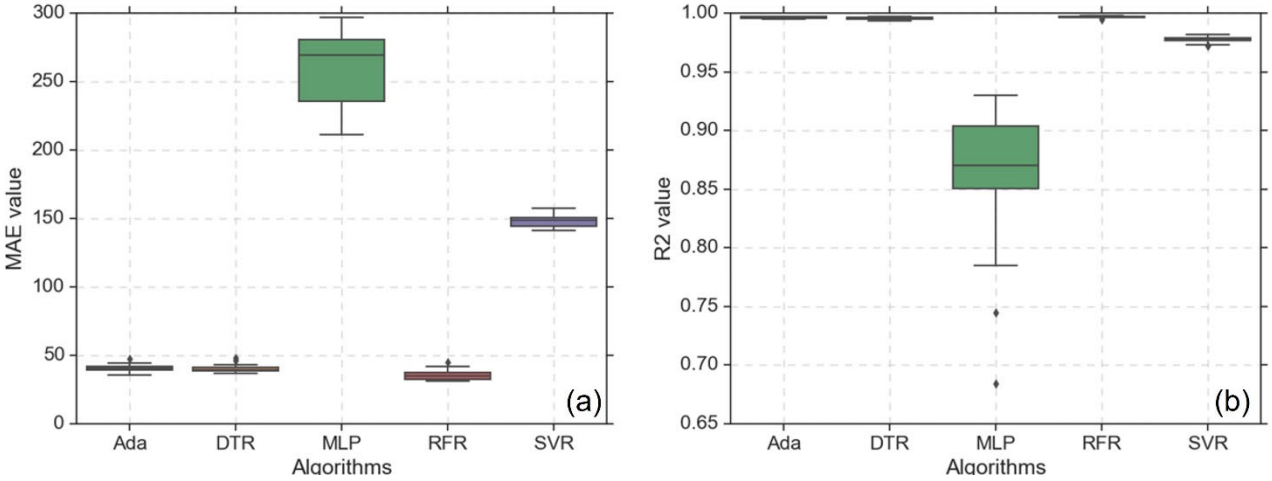

FIG 1 – Prediction performance of different ML algorithms: (a) MAE value; (b) R^2 value.

RESULTS AND DISCISSION

Pearson correlation is one of the simplest methods to determine the linear relation between features and the dependent variable. According to the method, the features that are uncorrelated with the dependent variable are good candidates to exclude from the data set before training the model (Rahaman *et al*, 2019). Here we apply the same methodology to determine the correlation between variables (radius, temperature, slag compositions, inclusion density, slag viscosity and R/R_0) with dissolution time. This method measures the linear correlation between two variables and the resulting value lies between -1 and 1. Negative values mean negative correlation; alternatively, positive values mean the opposite; 0 means that there is no linear correlation between the two variables. The Pearson's correlation coefficient for the inclusion dissolution data set is represented as a heat map in Figure 2. It can be seen that some parameters, eg original inclusion radius and SiO_2 have clear positive correlation with the dissolution time. It is obvious that the increasing inclusion original size as well as the SiO_2 content in slag will increase the dissolution time. The parameter, eg inclusion density has a less influence on the dissolution time. However, since the role of Pearson correlation is to check if some parameters can be removed but not the feature importance, we will discuss deeply on each parameter's linear correlation, also we keep all parameters in this ML model. For the current work, the data amount is not really large, more parameters are always good to use for the accuracy of ML modelling containing small size data set.

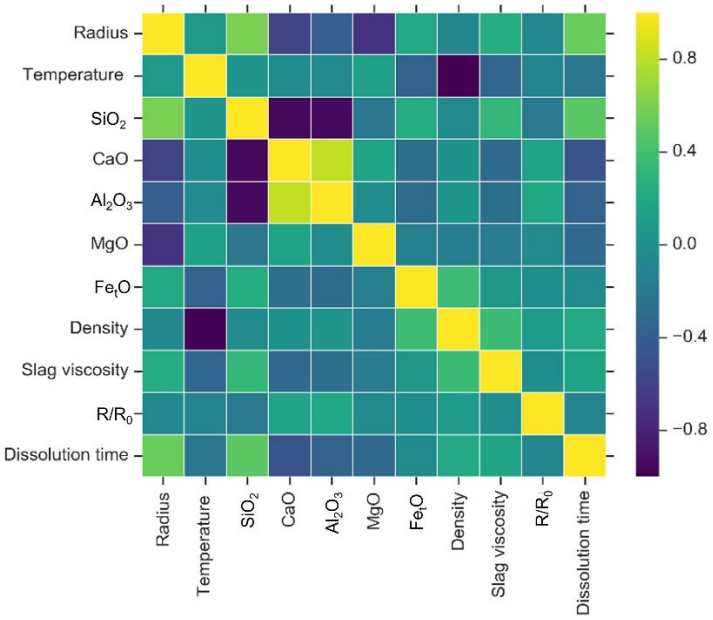

FIG 2 – Pearson correlation.

Figure 3 displays the prediction results of inclusion dissolution. The output is dissolution time of Al_2O_3 inclusion in the slag, and the X and Y axis strand for the actual dissolution time and predicted time by ML model, respectively. Figure 3a shows the actual value versus predicted value for training data. It can be seen that all data points basically concentrated around the diagonal, showing a very high prediction accuracy. The MAE and R^2 values are 17.0 sec and 99.8 per cent, demonstrating that the ML model has learned the reliable relation between dissolution time of inclusions and all input features based on training samples. In order to test the application ability of trained model, 20 per cent of the total data in the testing set were inputted into model and the prediction result is shown in Figure 3b. It is observed that most data points are also located in the line with the slope of 1, showing a good robustness of trained model. The MAE and R^2 values are 30.2 sec and 98.7 per cent. It is also seen that small number of data points deviates from the diagonal, but the largest MAE value is still less than 150 sec, which is within the acceptable scale. In order to further validate the robustness for new data, trained model was applied to the unseen 252 data in the validation data set with different parameters. The prediction result is shown in Figure 4. It can be seen that like training and testing data, present model also has a high prediction accuracy on validation data and most data points locate around the diagonal. The MAE and R^2 values are 70.8 sec and 97.7 per cent, respectively. Compared to training and testing data, the predicted accuracy on validation data slightly reduces, but present prediction level is still high enough to guide the actual experiments.

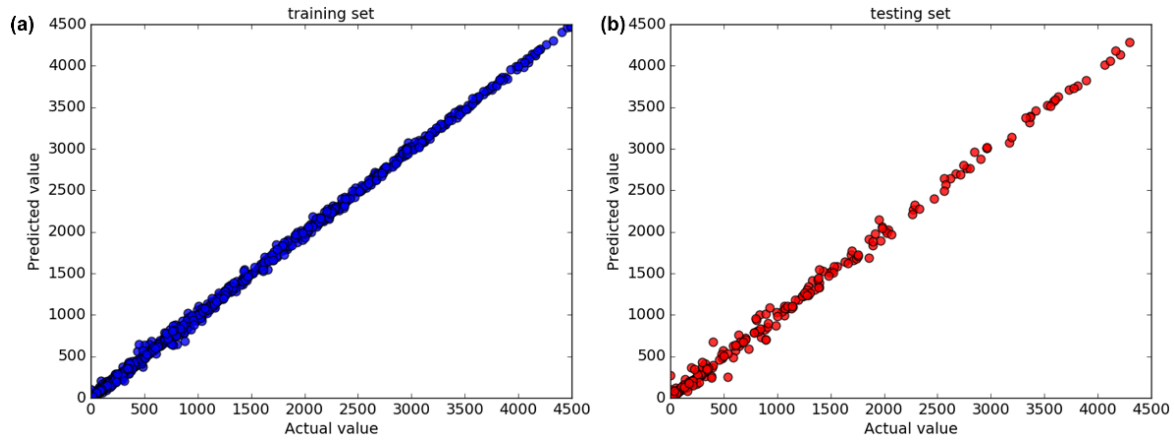

FIG 3 – Predicted results of dissolution time of inclusion using (a) training and (b) testing data set.

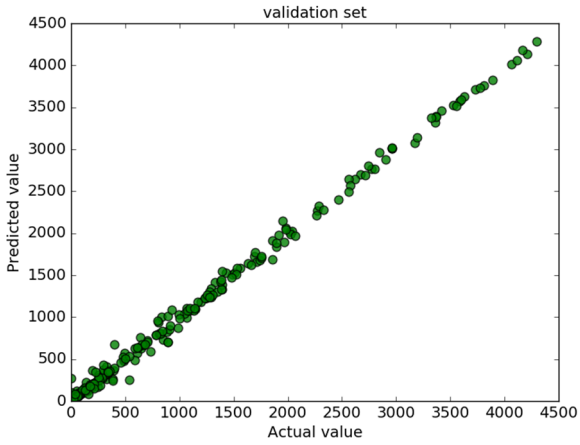

FIG 4 – Predicted results of dissolution time of inclusion using validation data set.

It is known that the parameters, eg slag viscosity is a joint function of temperature and slag composition and the inclusion density is also influenced by the temperature. Since these parameters are already included in the current database, new attempt to remove slag viscosity and inclusion density in the database has been made to see the model prediction performance. It seems the model accuracy decreases slightly but it is still quite acceptable (ie 41.66 of MAE and 98.41 per cent of R^2 for using testing data set in new model). In this case, the new model can be considered to use by inputting slag composition, temperature etc but without using physical parameters, eg slag viscosity, inclusion density etc which will be even easier to operate the model for the application perspective.

In addition, it needs to be mentioned that the correlation importance between dissolution time and each input parameter can be analysed. This type analysis is usually called feature importance (FI). FI is used to evaluate which parameter plays a more important role in within the specific data set (Rahaman *et al*, 2019; Mu *et al*, 2021). The importance of the same parameter can be different if the data set is changed. However, the current data set includes the experimental data are all collected from the HT-CLSM measurement. In this case, some parameters eg contents of different components in the slag are not such comprehensive due to the limitation of HT-CLSM (eg Fe_tO content should be almost zero). In this case, the feature importance may show different tendency compare with the physical understanding of inclusion dissolution, so FI analysis is not included in the current work.

CONCLUSIONS

The current hybrid methodology in combination of machine learning and physical modelling has been established to predict Al_2O_3 dissolution in the steelmaking slag. The successful implementation of applying the method to predict of dissolution time provides the possibility to further application of the model. Different kinds of inclusion dissolution data observed by HT-CLSM and measured by other methodology is needed to be used to establish a robust dissolution model.

ACKNOWLEDGEMENTS

Authors W Mu and C Shen would like to acknowledge the financial support provided by Jernkontoret Gerhard von Hofstens Stiftelse för metallurgisk Forskning foundation to support C Shen visiting at KTH Royal Institute of Technology, Swedish Foundation for International Cooperation in Research and Higher Education (STINT, Project No. IB2020-8781 and IB2022-9228) is acknowledged for the collaboration between KTH (Sweden), Hanyang University (Korea), Northeastern University (China) and IIT Bombay (India).

REFERENCES

Aneziris, C G, Dudczig, S, Emmel, M, Berek, H, Schmidt, G and Hubalkova, J, 2013. Reactive filters for steel melt filtration, *Advanced Engineering Materials*, 15(1–2):46–59.

Cooper Jr, A R and Kingery, W D, 1964. Dissolution in ceramic systems: I, molecular diffusion, natural convection and forced convection studies of sapphire dissolution in calcium aluminum silicate, *Journal of the American Ceramic Society*, 47(1):37–43.

Del Campo, F A, Neri, M C G, Villegas, O O V, Sánchez, V G C, Domínguez, H D J O and Jiménez, V G, 2021. Auto-adaptive multilayer perceptron for univariate time series classification, *Expert Systems with Applications*, 181:115147.

Feichtinger, S, Michelic, S K, Kang, Y B and Bernhard, C, 2014. In situ observation of the dissolution of SiO2 particles in CaO-Al2O3-SiO2 slags and mathematical analysis of its dissolution pattern, *Journal of the American Ceramic Society*, 97(1):316–325.

Fox, A B, Valdez, M E, Gisby, J, Atwood, R C, Lee, P D and Sridhar, S, 2004. Dissolution of ZrO2, Al2O3, MgO and MgAl2O4 particles in a B2O3 containing commercial fluoride-free mould slag, *ISIJ International*, 44(5):836–845.

Hagemann, R, Pettsold, L and Sheller, P R, 2010. The process of oxide non-metallic inclusion dissolution in slag, *Meta Min Indu*, 2:262–266.

Lee, S H, Tse, C, Yi, K W, Misra, P, Chevrier, V, Orrling, C, Sridhar, S and Cramb, A W, 2001. Separation and dissolution of Al2O3 inclusions at slag/metal interfaces, *Journal of Non-crystalline Solids*, 282(1):41–48.

Liu, J, Guo, M, Jones, P T, Verhaeghe, F, Blanpain, B and Wollants, P, 2007a. In situ observation of the direct and indirect dissolution of MgO particles in CaO-Al2O3-SiO2-based slags, *Journal of the European Ceramic Society*, 27(4):1961–1972.

Liu, J, Verhaeghe, F, Guo, M, Blanpain, B and Wollants, P, 2007b. In situ observation of the dissolution of spherical alumina particles in CaO-Al2O3-SiO2 melts, *Journal of the American Ceramic Society*, 90(12):3818–3824.

Liu, Y, Wang, L and Gu, K, 2021. A support vector regression (SVR)-based method for dynamic load identification using heterogeneous responses under interval uncertainties, *Applied Soft Computing*, 110:107599.

Miao, K, Haas, A, Sharma, M, Mu, W and Dogan, N, 2018. In situ observation of calcium aluminate inclusions dissolution into steelmaking slag, *Metallurgical and Materials Transactions B*, 49:1612–1623.

Michelic, S K and Bernhard, C, 2017. Experimental study on the behavior of TiN and Ti2O3 Inclusions in contact with CaO-Al2O3-SiO2-MgO Slags, *Scanning*, 2017.

Michelic, S, Goriupp, J, Feichtinger, S, Kang, Y B, Bernhard, C and Schenk, J, 2016. Study on oxide inclusion dissolution in secondary steelmaking slags using high temperature confocal scanning laser microscopy, *Steel Research International*, 87(1):57–67.

Monaghan, B J, Chen, L and Sorbe, J, 2005. Comparative study of oxide inclusion dissolution in CaO-SiO2-Al2O3 slag, *Ironmaking and Steelmaking*, 32(3):258–264.

Mu, W, Rahaman, M, Rios, F L, Odqvist, J and Hedström, P, 2021. Predicting strain-induced martensite in austenitic steels by combining physical modelling and machine learning, *Materials and Design*, 197:109199.

Pal, R, 2017. Chapter 4 – Validation methodologies, in *Predictive Modeling of Drug Sensitivity* (ed: R Pal), pp 83–107 (Academic Press).

Park, J H and Kang, Y, 2017. Inclusions in stainless steels− a review, *Steel Research International*, 88(12):1700130.

Park, J H and Zhang, L, 2020. Kinetic modeling of nonmetallic inclusions behavior in molten steel: A review, *Metallurgical and Materials Transactions B*, 51:2453–2482.

Park, J H, Park, J G, Min, D J, Lee, Y E and Kang, Y B, 2010. In situ observation of the dissolution phenomena of SiC particle in CaO-SiO2-MnO slag, *Journal of the European Ceramic Society*, 30(15):3181–3186.

Rahaman, M, Mu, W, Odqvist, J and Hedström, P, 2019. Machine learning to predict the martensite start temperature in steels, *Metallurgical and Materials Transactions A*, 50:2081–2091.

Reis, B H, Bielefeldt, W V and Vilela, A C F, 2014. Absorption of non-metallic inclusions by steelmaking slags-a review, *Journal of Materials Research and Technology*, 3(2):179–185.

Ren, Y, Zhu, P, Ren, C, Liu, N and Zhang, L, 2022. Dissolution of SiO2 inclusions in CaO-SiO2-based slags in situ observed using high-temperature confocal scanning laser microscopy, *Metallurgical and Materials Transactions B*, 53(2):682–692.

Sammut, C and Webb, G I (eds), 2011. *Encyclopedia of Machine Learning* (Springer Science and Business Media).

Sharma, M, Dabkowska, H A and Dogan, N, 2019. Application of Optical Floating Zone Method to Dissolution Kinetics of Inclusions in a Steelmaking Slag, *Steel Research International*, 90(1):1800367.

Sharma, M, Mu, W and Dogan, N, 2018a. In situ observation of dissolution of oxide inclusions in steelmaking slags, *JOM*, 70:1220–1224.

Sharma, M, Mu, W and Dogan, N, 2018b. In-Situ dissolution of aluminum titanate inclusion into Al2O3-CaO-SiO2-Type Slag, in *Proceedings of AISTech*, Philadelphia.

Shen, C, Wang, C, Wei, X, Li, Y, van der Zwaag, S and Xu, W, 2019. Physical metallurgy-guided machine learning and artificial intelligent design of ultrahigh-strength stainless steel, *Acta Materialia*, 179:201–214.

Soll-Morris, H, Sawyer, C, Zhang, Z T, Shannon, G N, Nakano, J and Sridhar, S, 2009. The interaction of spherical Al2O3 particles with molten Al2O3-CaO-FeOx-SiO2 slags, *Fuel*, 88(4):670–682.

Sridhar, S and Cramb, A W, 2000. Kinetics of Al2O3 dissolution in CaO-MgO-SiO2-Al2O3 slags: In situ observations and analysis, *Metallurgical and Materials Transactions B*, 31:406–410.

Um, H, Yeo, S, Kang, Y B and Chung, Y, 2022. The effect of FexO content on dissolution behavior of an alumina inclusion in CaO-Al2O3-SiO2-FexO slag by a single hot thermocouple technique, *Ceramics International*, 48(23):35301–35309.

Webler, B A and Pistorius, P C, 2020. A review of steel processing considerations for oxide cleanliness, *Metallurgical and Materials Transactions B*, 51:2437–2452.

Xuan, C and Mu, W, 2021. A mechanism theory of dissolution profile of oxide particles in oxide melt, *Journal of the American Ceramic Society*, 104(1):57–75.

Yi, K W, Tse, C, Park, J H, Valdez, M, Cramb, A W and Sridhar, S, 2003. Determination of dissolution time of Al2O3 and MgO inclusions in synthetic Al2O3-CaO-MgO slags, *Scandinavian Journal of Metallurgy*, 32(4):177–184.

Effect of C/A ratio on the crystallisation behaviour and structure of calcium-aluminate based alternative mold fluxes for casting medium and high Mn/Al steels

DOI: 10.62053/PVBH9528

A Nigam[1], K Biswas[2] and R Sarkar[3]

1. PhD Student, IIT Kanpur, Kanpur, Uttar Pradesh 208016, India. Email: amann21@iitk.ac.in
2. Professor, IIT Kanpur, Kanpur, Uttar Pradesh 208016, India. Email: kbiswas@iitk.ac.in
3. Assistant Professor, IIT Kanpur, Kanpur, Uttar Pradesh 208016, India. Email: rsarkar@iitk.ac.in

ABSTRACT

Because of the problems with 1st and 2nd generations of Advanced High-Strength Steels (AHSS), a 3rd generation of AHSS steels has become prominent and these steels have properties in between the 1st and 2nd generations of AHSS. However, although the 3rd generation of AHSS is a promising candidate as a replacement for its predecessors, there remain some challenges in processing these steels which are essentially medium Mn (Mn content ~ 5–7 wt per cent) and high Al (Al content ~ 1–3 wt per cent) steels. The use of conventional casting powders based on the $CaO\text{-}SiO_2$ system is unsuitable for high and medium Mn/Al steels. This work investigates the development of $CaO\text{-}Al_2O_3$-based mold fluxes for casting third-generation AHSS steel. Mold fluxes, with otherwise similar compositions but different C/A ratios, are tested and their crystallisation behaviour is examined using differential scanning calorimetry (DSC). A calcium aluminate phase having a composition $Ca_{12}Al_{14}O_{33}$ was found to be the main crystalline phase in the mold fluxes. A decrease in crystallisation temperature was observed as the CaO/Al_2O_3 ratio increased from 1.00 to 1.33. The effective crystallisation rate constant exhibited an increase with decreasing crystallisation temperature, indicating a potential influence of nucleation rate on the overall crystallisation rate and suggesting an anti-Arrhenius behaviour in the crystallisation process of these mold fluxes.

INTRODUCTION

Mold powders, either in granulated or non-granulated form, are introduced onto the top of liquid steel present within a copper mold. These mold powders generally have low melting point characteristics as their melting point lies usually below the pouring temperature of the liquid steel. Thus the superheat caused by the excessive temperature of the liquid steel helps the mold fluxes to undergo melting which creates a slag pool that infiltrates into the space between the solidifying steel shell and water-cooled copper mold. The primary role of these fluxes is to prevent the adhesion of the solidifying steel to the mold walls, ensuring efficient heat transfer and lubrication for the developing steel shell during solidification. The rapid cooling in the mold region results in the formation of a glassy slag film near the mold wall, which gradually transforms into a crystalline slag layer over time until reaching a stable state and near the shell region there will be liquid slag layer as shown in Figure 1. The solid part of the slag film governs the heat transfer because of its higher thermal conductivity and the liquid part helps in reducing the friction of the solidified steel shell which is moving down and thus will minimise the problems related to the surface quality of steels. Hence maintaining the thickness of the solid and liquid part of the slag film is important according to the type of steel being cast in the case of casting MC (medium carbon), peritectic steels, a thin, even shell is needed to avoid longitudinal and other surface cracking and this can be obtained with a low horizontal heat flux. Similarly in casting HC (high carbon) steels the shell is relatively weak and a thick shell is required to provide mechanical strength so a comparatively high heat flux is required. So for high horizontal heat flux thin slag film is required as heat flux is inversely proportional to thickness and *vice versa* for the low horizontal heat flux.

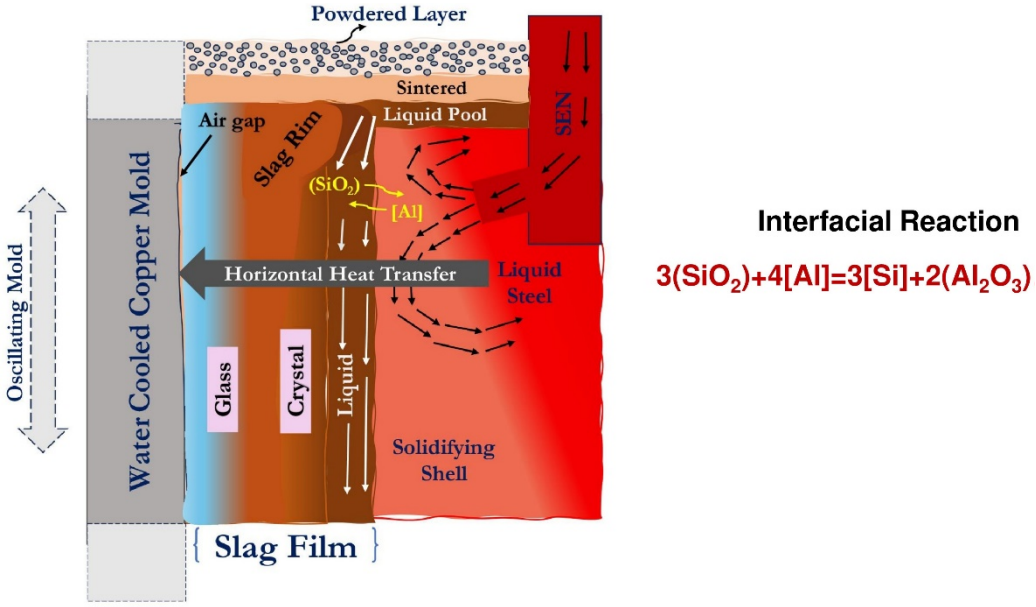

FIG 1 – Schematic diagram illustrating the function of mold flux in the continuous casting process.

Typically, mold powders are calcium silicate-based, augmented with fluxing agents to tailor their properties for specific steel types. Conventional CaO-SiO_2 mold fluxes are commonly employed for casting low C steels with low Al and Mn content. However, the evolving steel industry, driven by demands for lighter steel in the automotive and aerospace sectors, has led to the development of 3rd Generation AHSS (Advanced High-Strength Steel) with higher Al (0.5–2 wt per cent) and Mn (5–7 wt per cent) (Aydin *et al*, 2013). While using the traditional CaO-SiO_2 based mold fluxes in casting 3rd Generation AHSS there are certain interfacial reactions like the equation in Figure 1 (Kim and Park, 2012) involved between Al and Mn present in steel and SiO_2 present in the slag as Al and Mn has a more tendency to oxidise as they come below Si in the Ellingham Diagram. These interfacial reactions led to an increase in the Al_2O_3 content in the slag which led to an increase in the Al_2O_3/SiO_2 ratio of the slag by increasing the viscosity and melting temperature of the flux. This will create various surface defects in the cast steel like longitudinal cracks and break-out problems.

To address these challenges, there is a growing interest in using calcium aluminate-based mold fluxes, sometimes referred to as ‘non-reactive’ mold fluxes due to their minimal or absent silica content, eliminating interfacial reactions. Previous studies (Cho *et al*, 2013; Zhang, Wang and Shao, 2019) have found that lime-alumina-based mold fluxes exhibit physical characteristics similar to conventional fluxes, as long as the ratio wt per cent CaO / wt per cent Al_2O_3 remains close to 1.00. Furthermore, maintaining this wt per cent CaO / wt per cent Al_2O_3 ratio near 1.00 is crucial for ensuring that the fluxes have a low melting point because at that region low melting point phases lie, as depicted in Figure 2a. The low melting point area in the ternary phase diagram depicts the formation of a line compound $C_{12}A_7$ phase as can be seen in the binary phase diagram of the CaO-Al_2O_3 system (Figure 2b) indicating that the $C_{12}A_7$ phase has a high melting point depression. So $C_{12}A_7$ phase can be incorporated into the mold flux system while designing the composition, as this phase formation will be quite useful to maintain the low crystallisation temperature. Consequently, it is necessary to formulate these fluxes with a wt per cent CaO / wt per cent Al_2O_3 ratio near 1 and a SiO_2 content ranging from (3–6 per cent) to minimise the interfacial reactions (Liu *et al*, 2014). Also, by increasing the C/A ratio slightly greater than 1, an appropriate fraction of the primary crystalline phase ie may be achieved but this results in increasing the melting point of the flux. However, to reduce the melting point further fluxing agents like Na_2O, B_2O_3, CaF_2 and Li_2O are added to balance other thermophysical properties.

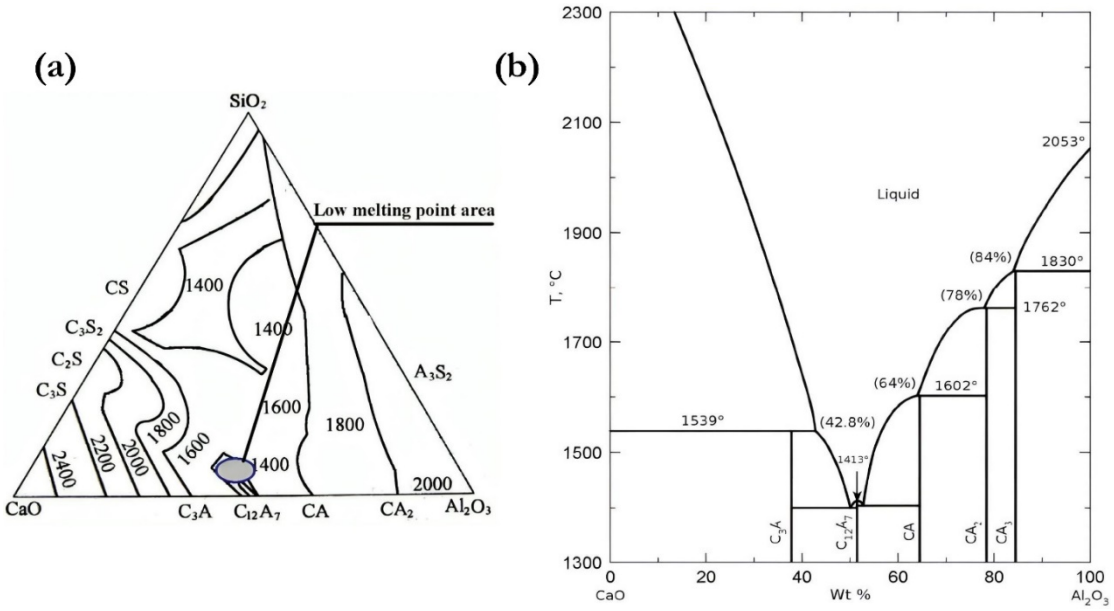

FIG 2 – (a) Liquidus projection of the SiO_2-CaO-Al_2O_3 system showing the low melting region (Liu *et al*, 2014), (b) Binary phase diagram of CaO-Al_2O_3 showing the eutectic composition phase $C_{12}A_7$ (Salasin and Rawn, 2017).

The crucial functions of mold fluxes—heat transfer and lubrication—are governed by the interfacial slag layer's resistance, particularly in horizontal heat transfer. This resistance is influenced by the fraction of crystal transformation (f_{crys}) as a function of temperature and time, which can be determined through methods such as confocal microscopy (CSLM) and DSC/DTA (Differential Thermal Analysis). Therefore, understanding the crystallisation kinetics of the forming phases is essential for comprehending heat transfer.

In the present study, two compositions of calcium aluminate mold fluxes with varying CaO/Al_2O_3 ratios (1.00 and 1.33) were developed. Isothermal crystallisation kinetics were investigated at different temperatures for both compositions and various crystallisation parameters were determined to characterise the type of crystallisation mode and the activation energy involved in that crystallisation phase.

EXPERIMENTAL DETAILS

Sample preparation

Mold flux samples were prepared on a laboratory scale using reagent grade CaO, Al_2O_3, Na_2CO_3, CaF_2, SiO_2 and B_2O_3. Compositional detail of the samples are mentioned in Table 1. Calcination of Na_2CO_3 to Na_2O was done by putting Na_2CO_3 at 800°C for 12 hrs in an air environment in a muffle furnace. The powders were then thoroughly mixed with the help of acetone in a mortar and pestle and then kept in the oven for 2 hrs at 100°C for the removal of moisture. Samples were then heated and melted in a graphite crucible inside a muffle furnace kept at 1400°C for 1 hr. Subsequently, the melted liquid flux was quenched in water and glassy cullets were obtained which was verified through X-ray diffraction (XRD) as seen in Figure 3a. These were then pulverised for further examination of the composition of the samples by X-ray fluorescence (XRF) to determine whether there was any evaporation loss or not. Pulverised samples were then used in the DSC experiments to study the crystallisation kinetics.

TABLE 1

Chemical composition of the mold flux (weight%).

Sample (wt/wt)%	CaO	Al_2O_3	Na_2O	B_2O_3	CaF_2	SiO_2
CaO/Al_2O_3 = 1.00	35	35	15	5	5	5
CaO/Al_2O_3 = 1.33	40	30	15	5	5	5

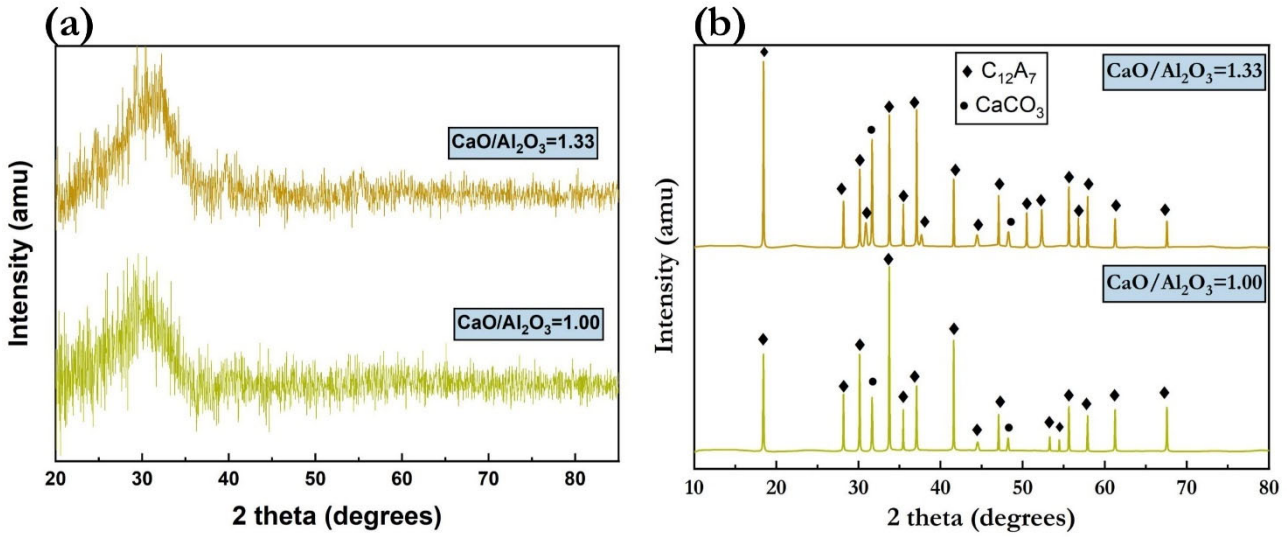

FIG 3 – (a) X-ray diffraction (XRD) plot of the two compositions after quenching, (b) XRD plot of the two compositions for the crystallised sample.

DSC measurements

The crystallisation kinetics of the fluxes were evaluated isothermally at different temperature ranges with DSC (STA 2500 Regulus; NETZSCH Instrument Inc, Germany). Measurement of the samples was done in a platinum crucible with a lid under an N_2 atmosphere at a flow rate of 60 mL/min. For each experiment 50 to 60 mg of the pulverised samples were subjected to a thermal cycle (Seo *et al*, 2015) as shown in Figure 4 under which the samples were heated at a constant rate of 25 K/min up to a target temperature (T_c) (determined by doing a normal DSC scan of the sample upto a temperature of 1400°C, Figure 5a) after which sample was isothermally held at that temperature for 2 hrs followed by subsequent cooling at a faster rate. After each experiment, samples were collected and examined in XRD and Scanning Electron Microscope – Energy Dispersive X-ray Spectroscopy (SEM-EDS) for phase determination.

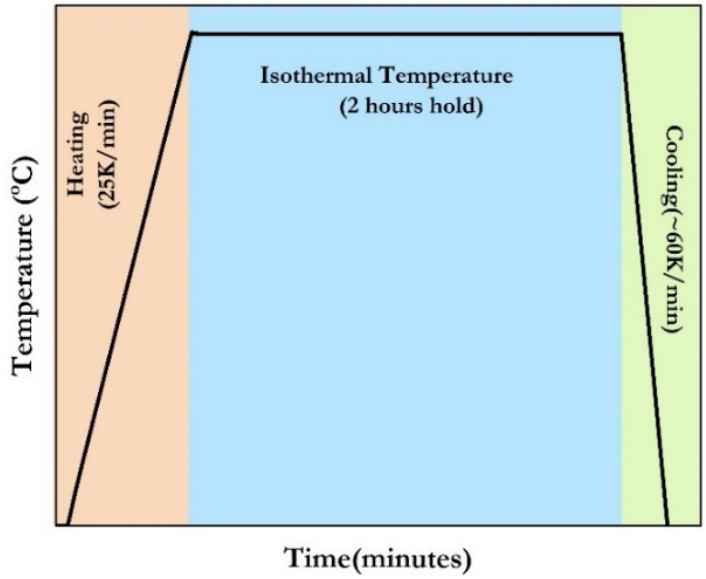

FIG 4 – Thermal cycle for the isothermal experiments.

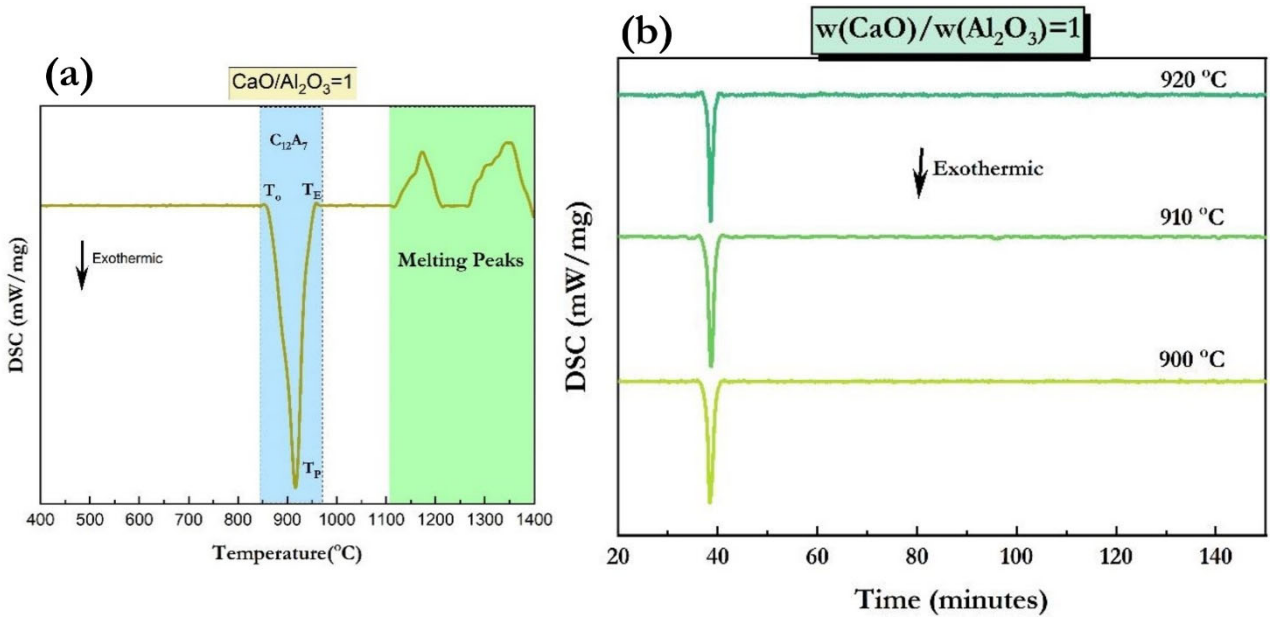

FIG 5 – (a) Differential Scanning Calorimetry (DSC) scan at 10 K/min for the identification of different peaks, (b) DSC scans for isothermal crystallisation of CaO/Al_2O_3 = 1.00.

RESULTS AND DISCUSSIONS

Isothermal DSC measurement

DSC experiments for two of the fluxes were carried out only after analysing the crystallisation temperature (T_c) through a normal DSC scan as seen in Figure 5. The crystallisation temperature is the peak temperature of the crystallisation event that occurred during the heating of the sample. Figure 5 shows the scans for the isothermal crystallisation of the flux wt per cent CaO / wt per cent Al_2O_3 = 1.00. There is only one peak of crystallisation which was identified through XRD as $C_{12}A_7$ ($Ca_{12}Al_{14}O_{33}$) (Figure 3b). DSC experiments for wt per cent CaO / wt per cent Al_2O_3 = 1.33 showed similar profiles.

Isothermal melt crystallisation kinetics

Crystallisation is an exothermic process as can be seen in the DSC scans (Seo *et al*, 2015). As the rate of heat release is proportional to the rate of crystallisation, the relative degree of crystallinity (α) can be obtained as:

$$\alpha(t) = \frac{\Delta Ht}{\Delta Htotal} = \frac{\int_0^t \left(\frac{\mathrm{d}H_c}{\mathrm{d}t}\right)\mathrm{d}t}{\int_0^\infty \left(\frac{\mathrm{d}Hc}{\mathrm{d}t}\right)\mathrm{d}t}$$

where:

ΔH_t is the enthalpy as a function of the time from initial to a given crystallisation time

ΔH_{total} is the total enthalpy reached at the end of the isothermal crystallisation process

Figure 6 shows the relative degree of crystallinity as a function of crystallisation time for CaO/Al_2O_3 = 1.00. So, we can say that the sigmoidal curve shifted towards the right with an increase in temperature indicating the overall crystallisation rate $\left(\frac{d\alpha}{dt}\right)$ for $C_{12}A_7$ phase formation decreases with an increase in the crystallisation temperature.

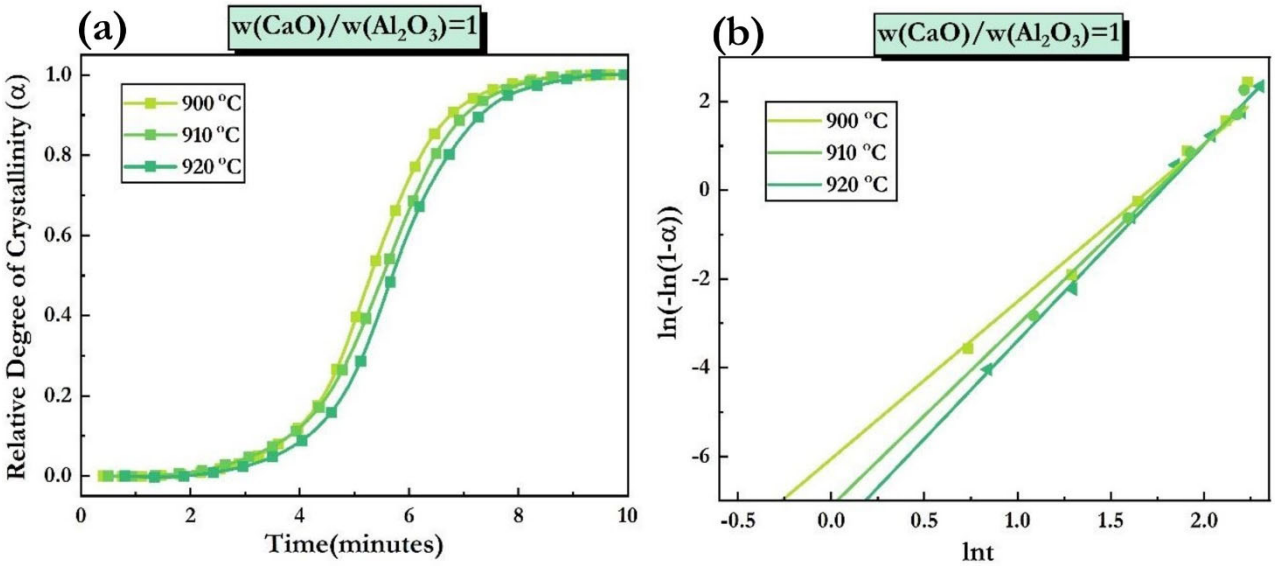

FIG 6 – (a) Relative degree of Crystallinity (α) with time, (b) $\ln\{-\ln[1-\alpha(t)]\}$ versus $\ln t$ plots for isothermal crystallisation of CaO/Al_2O_3 = 1.00.

The isothermal crystallisation kinetics of the flux can be understood with the help of the JMAK equation (Avrami, 1939):

$$\alpha(t) = 1 - \exp(-(kt)^n)$$

where:

α(t)	is the relative degree of crystallinity at time t (excluding incubation time)
n	is the Avrami exponent associated with the crystallisation mode
k	is the effective crystallisation rate constant, which is dependent on temperature and rate of nucleation and crystal growth

The values of n and k can be obtained by fitting the double logarithmic form as follows:

$$\ln\{-\ln[1-\alpha(t)]\} = n\ln k + n\ln t$$

The plots of $\ln\{-\ln[1-\alpha(t)]\}$ versus $ln\, t$ are also shown in Figure 6. From the slope and intercept the values of n and K can be obtained values of which are summarised in Table 2. The average value of n for CaO/Al_2O_3 = 1 lies around 4 and for CaO/Al_2O_3 = 1.33 value lies around 3.5. The crystallisation parameters, calculated from isothermal crystallisation experiments for both fluxes are reported in Table 2. It is noted from Table 2 that the values of effective crystallisation rate constant k for both the fluxes increase with the decreasing crystallisation temperature (T_c).

TABLE 2

Results of the Avarami analysis for isothermal crystallisation.

Sample	T_c (°C)	n	k (min^{-1})
CaO/Al_2O_3 = 1.00	900	3.548	0.1813
	910	4.082	0.1747
	920	4.144	0.1519
CaO/Al_2O_3 = 1.33	790	2.701	0.2119
	800	3.136	0.1919
	810	4.272	0.1832

The effective crystallisation rate constant k can be used to determine the crystallisation activation energy through the Arrhenius equation:

$$(\ln k) = \ln A - \frac{E}{RT_c}$$

where:

A	is the temperature-independent pre-exponential term
n	is the Avrami exponent
E	is the effective activation energy
R	is the universal gas constant
T_c	is the crystallisation temperature

Figure 7 shows the plot of $(\ln k)$ versus $(1/T_c)$ for the isothermal crystallisation of both mold fluxes. The effective activation energy determined from the slope of the plot for CaO/Al_2O_3 = 1 and 1.33 is -102.75 KJ/mol and -69.72 KJ/mol, respectively. These values indicate that the mold flux melt crystallisation may be controlled by the free energy change for nucleation related to the degree of undercooling. Activation energy represents the energy barrier that must be overcome for a reaction to occur. In the case of crystallisation, nucleation is the initial step where small clusters of atoms or molecules come together to form a stable nucleus, which then grows into larger crystalline structures. Lower activation energy values, such as those obtained (-102.75 kJ/mol for CaO/Al_2O_3 = 1.00 and -69.72 kJ/mol for CaO/Al_2O_3 = 1.33), imply that the energy barrier for nucleation is lower. This means that it requires less energy for the nucleation process to initiate, making it more favourable and easier for nuclei to form. Undercooling refers to the extent to which a liquid is cooled below its equilibrium melting point before crystallisation occurs. When undercooling is significant, nucleation becomes the rate-limiting step in the crystallisation process because it is the initial barrier that must be overcome for crystals to form. Given the lower activation energy values observed, it suggests that the energy barrier for nucleation is relatively low, indicating that nucleation is more likely to occur even at lower degrees of undercooling. Therefore, nucleation is expected to be the dominant factor governing the overall crystallisation rate for both mold fluxes, as it represents the crucial initial step in the crystallisation process (Vyazovkin and Sbirrazzuoli, 2003; Papageorgiou *et al*, 2005).

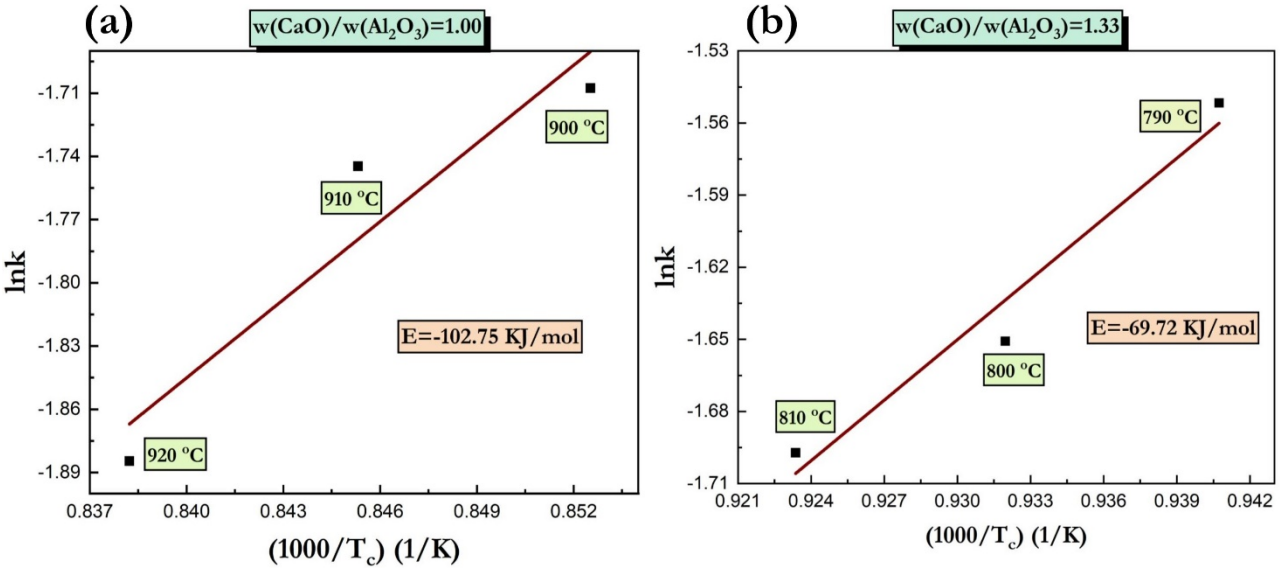

FIG 7 – Plots of $(\ln k)$ versus $1/T_c$ for isothermal crystallisation of (a) CaO/Al_2O_3 = 1.00, (b) CaO/Al_2O_3 = 1.33.

Structural analysis of the CaO-Al_2O_3 based fluxes

The melt structure of calcium aluminate-based mold fluxes plays a crucial role in influencing both viscosity and crystallisation tendencies. These factors, in turn, impact the lubrication and heat

transfer capabilities of the mold fluxes to the steel shell. The structural role of Al_2O_3 in the melt structure is intricate due to its amphoteric nature. The slag system's constituents, which can act as network formers or breakers, depend on the type of steel being cast. Understanding the melt structure of the calcium aluminate slag system and how it evolves with the replacement of SiO_2 by Al_2O_3 has been the subject of numerous studies (Zhou *et al*, 2021).

Figure 8a shows the deconvoluted Raman spectra for the CaO/Al_2O_3 = 1.00 glassy mold flux. The spectral pattern at approximately 460 cm^{-1} in the low-frequency range of the Raman spectra corresponds to the Al-O-Al stretching characteristics peak, indicative of the bridging oxygen in the aluminate network containing $[AlO4]^{5-}$ units. Within the mid-frequency range (700–1300 cm^{-1}), the spectra reveal the depolymerisation of the aluminosilicate structure, signifying $Al\text{-}O^-$ or $Si\text{-}O^-$ telescopic vibrations. Specifically, the peaks at 818 cm^{-1} and 921 cm^{-1} represent the symmetric $Al\text{-}O^-$ and Al-O-Si bonds, respectively. The degree of polymerisation or depolymerisation is denoted by Q^n, where 'n' signifies the number of bridging oxygen units. Q^0 corresponds to $[AlO4]^{5-}$ or $[SiO4]^{4-}$ units, with structural units $Q^0(Si)$ and $Q^1(Si)$ identified by peaks at 982 cm^{-1} and 1077 cm^{-1}, respectively (Nigam and Sarkar, 2023):

$$[AlO_4]^{5-} + O^{2-} = [AlO_5]^{7-}$$

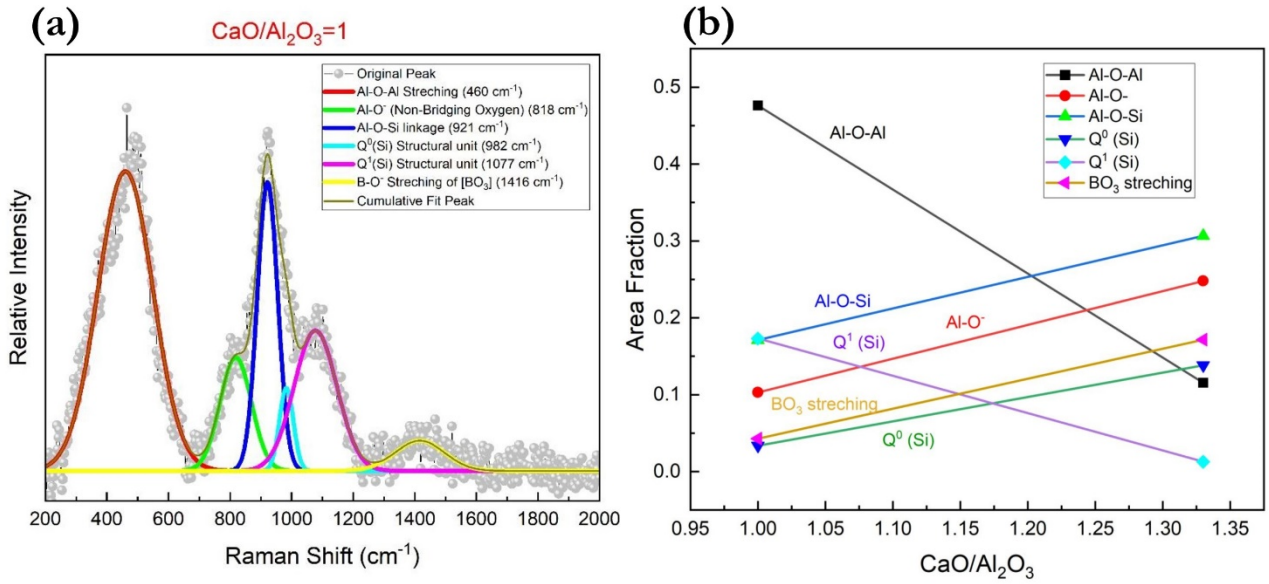

FIG 8 – (a) Deconvoluted Raman Spectra of CaO/Al_2O_3 = 1.00, (b) Area fraction of various structural units present in the two compositions.

The peak at 1416 cm^{-1} is assigned to the symmetric stretching vibrations of terminal oxygen atoms in orthoborate units $[BO_3]$. This suggests that the predominant formation of $[BO_3]$ groups in the mold flux is indicative of B^{3+} involvement in the structure.

Figure 8b shows that as wt per cent CaO / wt per cent Al_2O_3 increases from 1.00 to 1.33 the area fraction of Al-O-Al (bridging oxygen) and $Q^1(Si)$ decreases while $Al\text{-}O^-$, Al-O-Si, $Q^0(Si)$ and $[BO_3]$ increases, this indicates that more complex aluminate and silicate structure is transformed into the simpler one. As the $w(CaO)/w(Al_2O_3)$ increases weight fraction of CaO will increase, as there will be excess CaO the O^{2-} ions in the melt will depolymerise the chain. This indicates that higher CaO/Al_2O_3 ratios will decrease the viscosity of the melt as there will be more mobility of ions due to a higher number of non-bridging oxygen and this might also increase the crystallisation tendency (Shao *et al*, 2019).

CONCLUSIONS

The isothermal crystallisation kinetics of two mold fluxes of different CaO/Al_2O_3 ratios were investigated systematically. Based on the kinetic parameters of the JMAK model the crystallisation mode was determined. The main conclusions are summarised as follows.

- The average value of the Avarami exponent n for the wt per cent CaO / wt per cent Al_2O_3 = 1.00 is ~4 and for wt per cent CaO / wt per cent Al_2O_3 = 1.33 is ~3.5 indicating the $C_{12}A_7$ crystal growth is 3D with constant nucleation rate.
- The effective rate constant (k) for the formation of $C_{12}A_7$ in both mold flux compositions exhibits an increase as the crystallisation temperature decreases. This indicates that elevated temperatures impede the overall crystallisation rate, suggesting that the process is governed by nucleation across a range of crystallisation temperatures.
- The effective activation energy of $C_{12}A_7$ formation for the mold fluxes wt per cent CaO / wt per cent Al_2O_3 = 1.00 and 1.33 is -102.75 KJ/mol and -69.72 KJ/mol respectively. The negative value of activation energy means that it is showing anti-Arrhenius behaviour, indicating that crystallisation is determined by nucleation.
- As the wt per cent CaO / wt per cent Al_2O_3 ratio increased from 1.00 to 1.33 the peak crystallisation temperature of the $C_{12}A_7$ phase decreased 915°C to 800°C.
- The depolymerisation of the various structural units because of the various network breakers led to the formation of simpler structural units by increasing NBO, which in turn will enhance the crystallisation tendency of the melt as we increase the wt per cent CaO / wt per cent Al_2O_3 ratio from 1.00 to 1.33.

ACKNOWLEDGEMENTS

The author wishes to extend thanks to the multiple laboratories within the Department of Materials Science and Engineering at IIT Kanpur for generously providing the necessary facilities for the ongoing research.

REFERENCES

Avrami, M, 1939. Kinetics of phase change, I: General theory, *The Journal of Chemical Physics*, 7(12):1103–1112. https://doi.org/10.1063/1.1750380

Aydin, H, Essadiqi, H, Jung, I H and Yue, H l, 2013. Development of 3rd generation AHSS with medium Mn content alloying compositions, *Materials Science and Engineering A,* 564:501–508. https://doi.org/10.1016/j.msea.2012.11.113

Cho, J W, Blazek, K, Frazee, M, Yin, H, Park, J H and Moon, S W, 2013. Assessment of CaO-Al2O3 based mold flux system for high aluminum TRIP casting, *ISIJ Intl*, 53(1):62–70. https://doi.org/10.2355/isijinternational.53.62

Kim, D J and Park, J H, 2012. Interfacial reaction between CaO-SiO2-MgO-Al2O3 flux and Fe-xMn-yAl (x = 10 and 20 mass pct, y = 1:3 and 6 mass pct) steel at 1873 K (1600 °c), *Metallurgical and Materials Transactions B*: *Process Metallurgy and Materials Processing Science*, 43(4):875–886. https://doi.org/10.1007/s11663-012-9667-x

Liu, Q, Wen, G, Li, J, Fu, X, Tang, P and Li, W, 2014. Development of mould fluxes based on lime-alumina slag system for casting high aluminium trip steel, *Ironmaking and Steelmaking*, 41(4):292–297. https://doi.org/10.1179/1743281213Y.0000000131

Nigam, A and Sarkar, R, 2023. Development of a Low Silica Calcium Aluminate Based Mould Flux for Casting High Al/Mn Steels, in *Proceedings of the International Conference on Metallurgical Engineering and Centenary Celebration (METCENT 2023)*, pp 3–12 (Springer Nature Singapore). https://doi.org/10.1007/978-981-99-6863-3_1

Papageorgiou, G Z, Achilias, D S, Bikiaris, D N and Karayannidis, G P, 2005. Crystallization kinetics and nucleation activity of filler in polypropylene/surface-treated SiO2 nanocomposites, *Thermochimica Acta*, 427(1–2):117–128. https://doi.org/10.1016/j.tca.2004.09.001

Salasin, J R and Rawn, C, 2017. Structure property relationships and cationic doping in [Ca24Al28O64]4+ framework: A review, *Crystals*, 7(5). https://doi.org/10.3390/cryst7050143

Seo, M D, Shi, C B, Baek, J Y, Cho, J W and Kim, S H, 2015. Kinetics of Isothermal Melt Crystallization in CaO-SiO2-CaF2-Based Mold Fluxes, *Metallurgical and Materials Transactions B*: *Process Metallurgy and Materials Processing Science*, 46(5):2374–2383. https://doi.org/10.1007/s11663-015-0358-2

Shao, H, Gao, E, Wang, W and Zhang, L, 2019. Effect of fluorine and CaO/Al2O3 mass ratio on the viscosity and structure of CaO–Al2O3-based mold fluxes, *Journal of the American Ceramic Society*, 102(8):4440–4449. https://doi.org/10.1111/jace.16322

Vyazovkin, S and Sbirrazzuoli, N, 2003. Isoconversional Analysis of Calorimetric Data on Nonisothermal Crystallization of a Polymer Melt, *Journal of Physical Chemistry B*, 107(3):882–888. https://doi.org/10.1021/jp026592k

Zhang, L, Wang, W-L and Shao, H-Q, 2019. Review of non-reactive CaO–Al2O3-based mold fluxes for casting high-aluminum steel, *Journal of Iron and Steel Research International*, 26(4):336–344. https://doi.org/10.1007/s42243-018-00226-2

Zhou, L, Wo, H, Wang, W, Luo, H and Li, H, 2021. Crystallization behavior and melt structure of typical CaO–SiO2 and CaO–Al2O3-Based mold fluxes, *Ceramics Intl*, 47(8):10940–10949. https://doi.org/10.1016/j.ceramint.2020.12.213

Improving cobalt extraction through oxidative blowing of copper-nickel matte

DOI: 10.62053/ZFVS9836

R A Pakhomov[1], P V Malakhov[2], L V Krupnov[3] and I M Dymov[4]

1. Senior Researcher, Pyrometallurgy Laboratory, Gipronikel Institute LLC, Saint Petersburg 195220, Russia. Email: pakhomovra@gmail.com
2. Principal Specialist, Pyrometallurgical Technology, MMC Norilsk Nickel's Polar Division, Norilsk 663305, Russia. Email: malahovkm@nornik.ru
3. Principal Specialist, Pyrometallurgical Technology, MMC Norilsk Nickel's Polar Division, Norilsk 663305, Russia. Email: nordleon@mail.ru
4. Engineer 2 category, Gipronikel Institute LLC, Saint Petersburg 195220, Russia. Email: igor99smoke@yandex.ru

ABSTRACT

The article presents results of thermodynamic calculations and laboratory studies, focusing on the cobalt behaviour during oxidative smelting of copper-nickel mattes. The compositions of the studied solutions are related to the products formed during the second stage of the converting process of copper-nickel matte at the Nadezhdinsky Metallurgical Plant (NMP) of MMC Norilsk Nickel company. These sulfide products typically contain from 1.5 to 12 wt per cent of iron. The obtained experimental results and thermodynamic calculations indicate that adjusting the CaO ratio to increase the proportion of CaO or complete replacement of SiO_2 with fluxes containing CaO leads to a significant increase in cobalt recovery rates in the matte phase (with an iron concentration of 2.5 wt per cent) raising them from 30 per cent to 45 per cent. Meanwhile, the recovery rates of copper and nickel remain constant.

INTRODUCTION

Metallic cobalt ranks among the three most treated and valuable non-ferrous metals (Cu, Ni and Co), that are processed at the metallurgical plants of MMC Norilsk Nickel company. These metals are present in sulfide copper-nickel ores, with pentlandite or pyrite serving as the primary minerals containing cobalt. Cobalt concentration in certain particles can reach up to 2.5 wt per cent, averaging between 0.2 and 1.2 wt per cent (Genkin *et al*, 1981; Tsemekhman *et al*, 2010). Sulfide minerals extracted from the mineral deposits are subjected to flotational separation to produce Cu and Cu-Ni concentrates. During this stage approximately 14 per cent of all extracted cobalt is lost with tailings, attributed to technological losses.

The application of flotation separation methods results in the distribution of cobalt among various products: around 9 per cent of Co is transferred into the copper concentrate, while 77 per cent Co goes into copper-nickel concentrate, with the remaining 14 per cent ending up with tailings. Subsequent pyrometallurgical treatment of the copper-nickel concentrate yields a commercially valuable product known as the copper-nickel matte, characterised by a high copper concentration. The recovery rates for Cu and Ni in the final product exceed 95 per cent, whereas cobalt recovery is less than 55 per cent. The low Co recovery rates are primarily attributed to its low concentrations in the feed materials, and losses with slags. Figure 1 shows the schematic flow sheet of the pyrometallurgical treatment of sulfide materials.

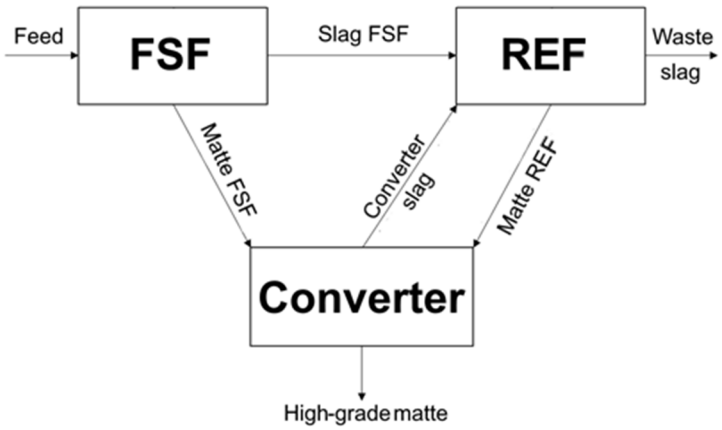

FIG 1 – Scheme of processing nickel-coper sulfide ore at Nadezhdinsky Metallurgical Plant (FSF-flash smelting furnace and REF- slag cleaning furnace).

Sulfide materials are oxidised in a converter to produce high-grade matte. Then the converter slag is conveyed to the slag cleaning furnace, while the matte is returning from the slag cleaning furnace back to converter, leading to circulation of cobalt between the furnaces. Figure 2 illustrates the distribution of cobalt between the materials supplied for converting stage and the products of the slag cleaning furnace. This figure is based on industrial data obtained from a Nadezhdinsky metallurgical plant. The concentration of cobalt in the products is determined by using analytical chemistry methods.

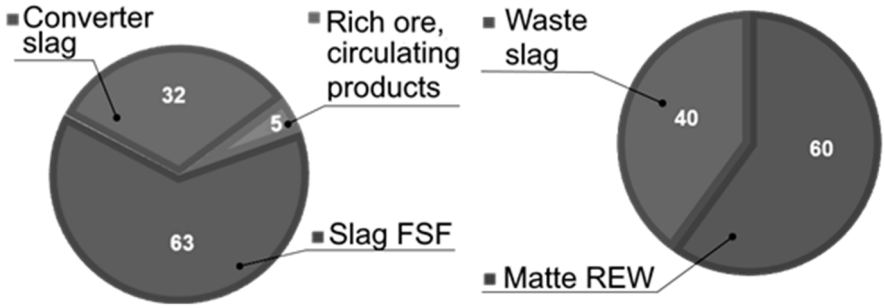

FIG 2 – Distribution of cobalt between processed and obtained products of converter (left image) or slag cleaning furnace (right image) of Nadezhdinsky Metallurgical Plant.

Increasing cobalt recovery at the converter process will reduce the amount of circulated cobalt and enhance overall recovery rates. During converting copper-nickel matte, SiO_2-based fluxes are used as additives to significantly lower the melting point of the formed slag, and to facilitate the bonding of resulting FeO and Fe_3O_4 during matte oxidation. However, the converting of matte into high-grade 'white matte' is accompanied by significant losses of non-ferrous metals into slag, particularly cobalt. Literature and metallurgical practice indicate that dissolved cobalt contributes significantly to total cobalt losses in slags (Krupnov *et al*, 2023; Tsemekhman *et al*, 2010). While iron and cobalt exhibit similar behaviour in these processes, they differ markedly from nickel and copper, where mechanical losses, such as entrained particles of sulfides or metals in slag greatly affect recovery rates. In ferrous metallurgy, fluorite (CaF_2), limestone or lime are the primary fluxing agents used in the processing of iron feed materials. Given the analogous behaviour of cobalt and iron in both non-ferrous and ferrous metallurgy, it is hypothesized that replacing SiO_2 flux with CaO-containing fluxing agents could alter the distribution of cobalt between slag and matte. This hypothesis requires verification through thermodynamic and experimental means.

At the initial stage, thermodynamic calculations were conducted to assess the oxidation of a cobalt-rich sulfide sample using SiO_2 and CaO-based additives in various ratios. Thermodynamic modelling was employed to provide an initial estimation of the distribution of non-ferrous metals. The calculation was focused on determining the required amount of flux and oxygen blow to achieve a matte with the desired composition.

THERMODYNAMIC CALCULATIONS

The calculation of the converting process was performed using the FactSage software version 6.4, utilising the thermodynamic databases FTmisc and FToxid (Bale *et al*, 2016). Throughout the matte oxidation calculation, the SiO_2/CaO ratio was varied within the range of 1 to 0.2 and only SiO_2. Operating conditions included a temperature of 1350°C, pressure at 1 atm, and pure oxygen as the oxidising agent. Table 1 outlines the composition of the matte employed for the calculations. Based on the computational outcomes, a series of graphs depicting the behaviour of non-ferrous metals in both matte and slag were generated and are presented in Figures 3 and 4.

TABLE 1

The concentrations of the main components in the matte used in the calculations.

The mass fraction of the component, wt%				
Cu	**Ni**	**Co**	**Fe**	**S**
17.19	43.78	2.68	12.68	23.67

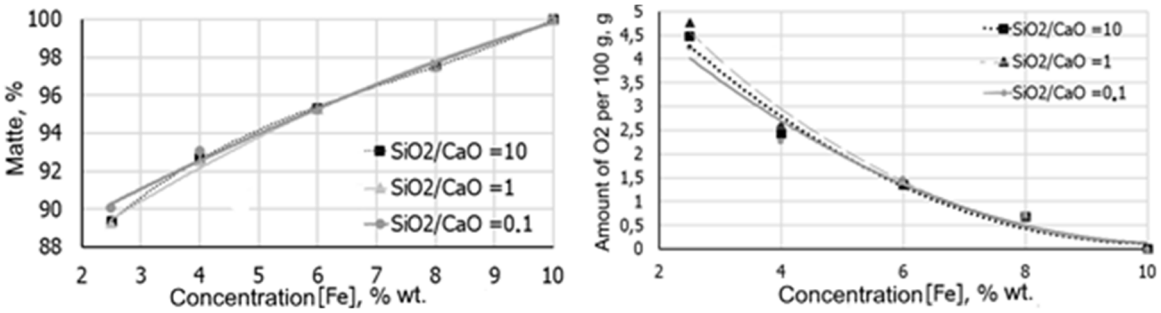

(a) (b)

FIG 3 – Output of the matte (a) and oxygen consumption (b) as functions of iron concentration in the matte.

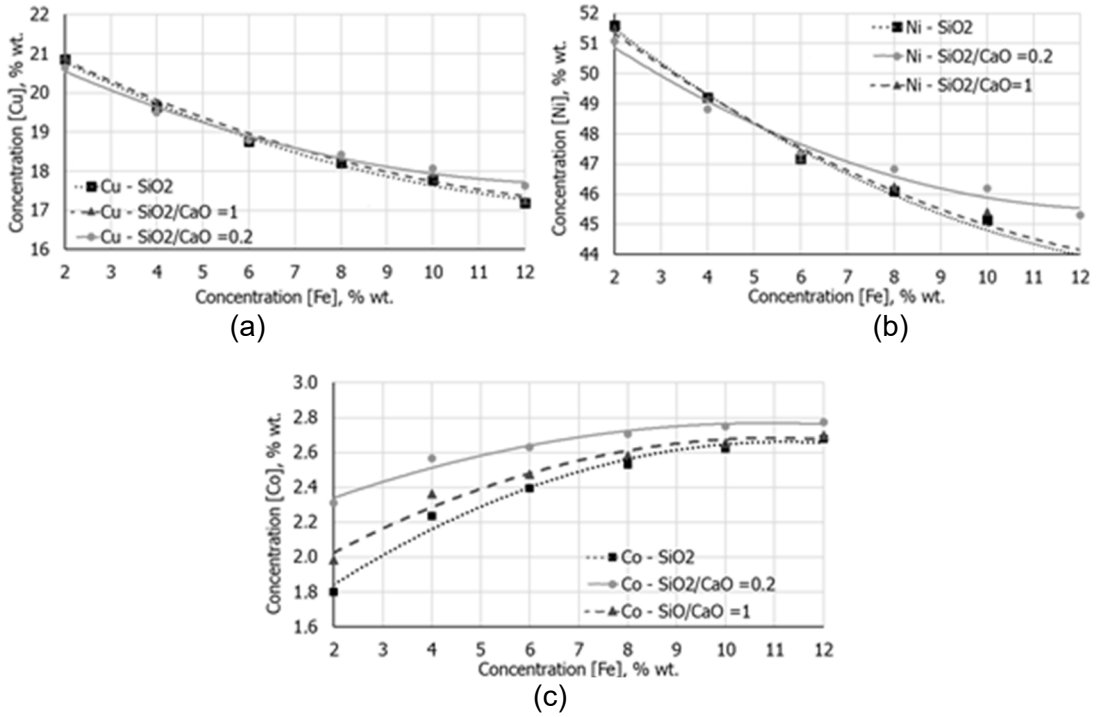

(a) (b)

(c)

FIG 4 – The concentrations (wt%) of Cu (a), Ni (b) and Co (c) in the matte as functions of iron concentration.

Figure 3 shows the amount of matte produced and oxygen consumption relative to the iron concentration in the matte phase. According to thermodynamic estimation, varying ratio of fluxing agents does not significantly impact matte output and oxygen consumption.

Figure 4 demonstrates that replacement SiO_2 with CaO has negligible effect on the Cu and Ni concentrations in the matte phase. However, there is a notable change in cobalt proportion with the substitution of SiO_2 by CaO. For instance, when obtaining copper-nickel matte with 2.5 wt per cent of Fe, the cobalt concentration increases by 0.5 wt per cent when using CaO. Based on the presented data, the evaluation of cobalt recovery into the matte phase suggests potential savings of cobalt up to 4.5 per cent compared to silicate slags.

Following the assessment of theoretical parameters for cobalt recovery, product compositions, and oxidation process conditions, a series of laboratory experiments were conducted.

RESULTS AND DISCUSSION

In total 11 experiments were performed, including six experiments with SiO_2-based slag (without Ca addition), and five experiments with CaO-based slag with a SiO_2/CaO ratio of 0.2. To estimate the distribution of non-ferrous metals between slag and matte, a synthetic flux composed of FeO, SiO_2 and CaO was used to simulate pyrometallurgical converting slag while maintaining a consistent SiO_2/CaO ratio. The experiments were conducted in an induction furnace at temperatures ranging from 1300 to 1350°C, under an overall pressure of is 1 atm, using pure oxygen as the oxidising agent and employing Al_2O_3 crucible. The compositions of the obtained samples were examined using methods of analytical chemistry and EDX-SEM (energy dispersive X-Ray – scanning electron microscope). Experimental conditions are detailed in Table 2, the results of the chemical analysis are presented in Table 3.

TABLE 2

Experimental conditions.

No	Feed composition, g				O_2		Mass of products, g		SiO_2/CaO
	Matte	SiO_2	CaO	FeO	Vol, L	Gas flow, L/min	Matte	Slag	
1	61.6	12	-	28	2.57	0.7	54.3	46.1	SiO_2
2	61.6	12	-	28	1.23	0.7	60.0	41.1	SiO_2
3	61.6	12	-	28	2.68	0.7	52.5	48.8	SiO_2
4	61.6	12	-	28	4.78	0.7	47.4	51.2	SiO_2
5	61.6	12	-	28	7.23	0.7	47.0	50.0	SiO_2
6	61.6	12	-	28	8.47	0.7	33.1	55.9	SiO_2
7	61.6	2	10.6	28	2.68	0.7	54.7	45.7	~0.2
8	61.6	2	10.6	28	1.46	0.7	57.4	44.6	~0.2
9	61.6	2	10.6	28	4.96	0.7	47.3	53.2	~0.2
10	61.6	2	10.6	28	6.35	0.7	43.8	40.7	~0.2
11	61.6	2	10.6	28	6.40	0.4	45.7	52.8	~0.2

TABLE 3

The concentrations of the main components in the matte and slag phases (wt%).

№	Composition of matte phase, wt%					Composition of slag phase, wt%					
	Cu	Ni	Co	S	Fe	Cu	Ni	Co	Fe	SiO_2	CaO
0	***16.9***	***42.9***	***2.95***	***23.0***	***12.45***						
1	17.4	46.6	2.06	24.0	7.18	0.59	1.47	1.38	47.2	25.2	-
2	16.6	43.9	2.16	24.5	8.97	0.56	1.24	1.18	48.0	25.8	-
3	18.0	47.9	1.97	23.7	6.69	0.88	2.33	1.43	47.5	24.2	-
4	19.0	48.7	2.01	23.0	6.81	1.23	3.25	1.72	44.6	19.8	-
5	20.1	52.4	1.50	22.4	3.25	0.95	3.45	2.03	47.9	20.6	-
6	22.9	55.4	0.81	19.3	1.47	1.62	8.19	2.40	41.9	16.7	-
7	17.8	47.2	2.31	23.6	6.6	0.69	2.02	1.09	46.6	3.8	16.8
8	17.1	45.6	2.46	24.3	8.33	0.67	1.41	0.88	46.3	3.4	18.2
9	20.1	52.0	1.60	24.1	2.2	0.64	2.34	1.12	38.2	2.4	15.6
10	20.8	52.7	1.76	22.0	2.18	3.98	1.05	1.73	42.6	3.6	17.7
11	21.3	53.5	1.57	21.7	1.9	0.83	3.61	1.94	49.3	1.8	16.7

Consider the behaviour of non-ferrous metals in the matte during oxidation and the use of additives based on SiO_2 and CaO, the results are shown in Figure 5.

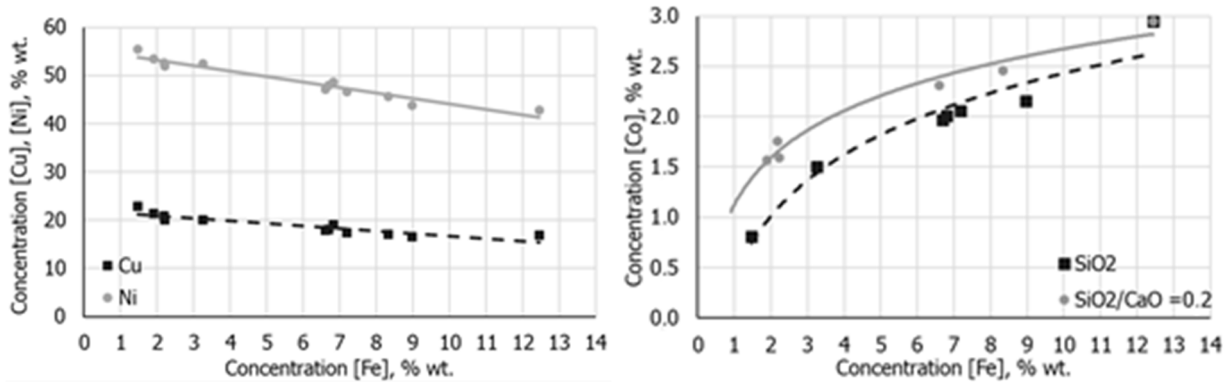

(a) (b)

FIG 5 – The concentrations of non-ferrous metals in the matte phase as functions of iron concentration (wt%): a – Cu, Ni; b – Co.

Analysis of the graphs in Figure 5 indicates that the choice of flux does not influence the tonne of copper and nickel concentration in matte, confirming the calculation results. However, the cobalt concentration varies significantly depending on the selected flux. For instance, in the copper-nickel matte (with 2.5 wt per cent Fe) the cobalt concentration increases from 1.24 wt per cent to 1.75 wt per cent. (at 40.5 rel per cent) with the addition of CaO-based slag. Evaluation of cobalt recovery rates using different types of slags is presented in Figure 6.

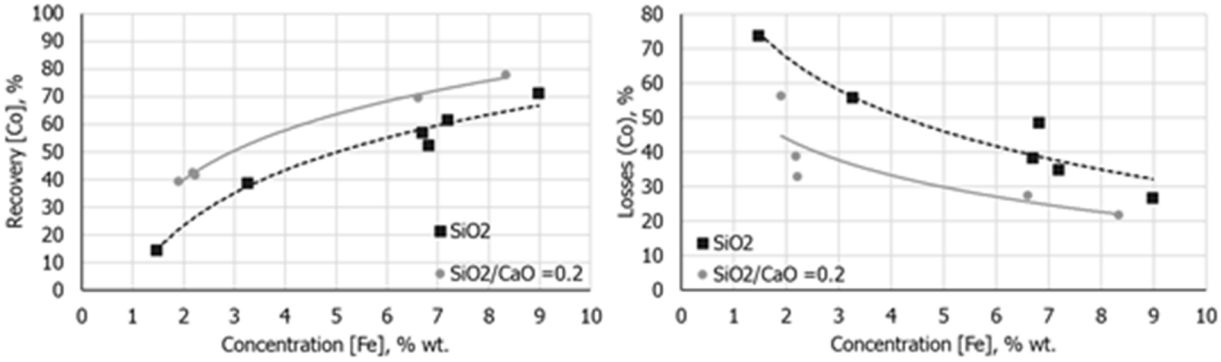

FIG 6 – Recovery of cobalt into the bottom phase (a) and losses with slag (b) from the iron content in the sulfide mass.

The recovery of cobalt in matte or the losses of cobalt with slag were calculated as the ratio of the amount of metal in high-grade matte or slag to the amount of metal in the initial sample, Equations 1 and 2.

$$[Co]_{rec} = \frac{[Co]_{hgm}}{Co_{matte}} \cdot 100\% \quad (1)$$

$$(Co)_{los} = \frac{(Co)_{slage}}{Co_{matte}} \cdot 100\% \quad (2)$$

Analysis of cobalt recovery and losses with slags during the second stage of converting reveals the effectiveness of incorporating CaO as fluxing additive. The recovery of Co within the examined range of matte compositions (with 2 to 10 wt per cent Fe) increases from 11 to 20 per cent with the utilising of calcium-ferrite slags. It's worth noting that the concentration of cobalt in the slag is assessed without considering mechanically entrained particles, utilising SEM-EDX methods for analysis. Detailed description of sample preparation methods for SEM-EDX are provided in previous works (Gouldstein *et al*, 1981; Krishtal *et al,* 2009). Figure 7 illustrates the cobalt concentration in slag as function of the iron concentration in the matte phase.

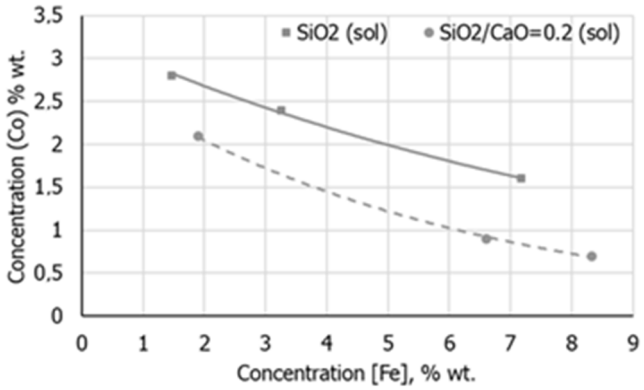

FIG 7 – Cobalt concentration in the matte phase according to SEM-EDX data.

The analysis of the microstructures of the samples reveals that in the first scenario, the matrix base comprises an iron-silicate solution with dispersed sulfide-metal particles of varying composition and structure. In the second scenario, the slag matrix consists primarily of the Fe-Ca-O system with a minor presence of residual silicate forming the slag base. Further analysis of the slags using EDX-SEM methods corroborates the potential benefits of employing CaO-based slags over SiO_2-based ones.

A comparison of the practical and calculated results of the behaviour of cobalt in slag and high-grade matte, the results are presented in Figure 8.

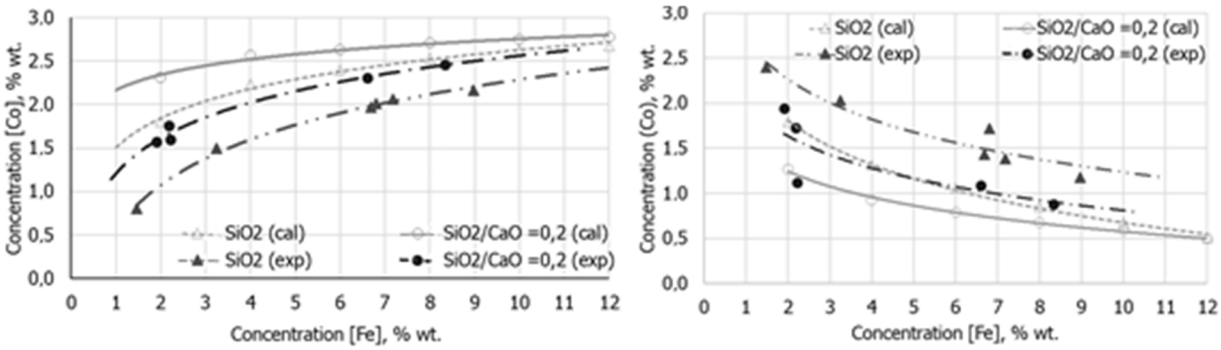

FIG 8 – Cobalt concentration in matte (a) and slag (b) according to calculation and experimental data.

The results of theoretical calculations of cobalt distribution presented in Figure 8 differ significantly from the practical data for two types of slags based on SiO_2 and CaO. The difference in results may be due to incomplete databases that lack data on the distribution of cobalt in sulfide solutions.

CONCLUSIONS

The assessment of cobalt distribution among the products of copper-nickel production of MMS Norilsk Nickel was carried out. The assessment involved thermodynamic calculations and laboratory studies on the converting process of copper-nickel matte to 'white' matte using additives based on SiO_2 and CaO. The utilisation of CaO-based slags resulted in an increase in cobalt concentration in the matte phase, while the concentrations of Cu and Ni remained unchanged. For instance, in high-grade matte with a 2.5 wt per cent Fe concentration, the cobalt concentration increased from 1.24 wt per cent to 1.75 wt per cent, that makes a 40.5 per cent rise, upon transition to calcium-ferrite slag. Furthermore, the recovery of Co within the considered range of Fe compositions from 10 to 2 per cent increases by 11–20 per cent upon switching to calcium-ferrite slag. Thus, the use of calcium oxide as the primary component of fluxing agents at the converting process of copper-nickel matte will have a positive impact on cobalt recovery rates.

REFERENCES

Bale, C W, Bélisle, E, Chartrand, P, Decterov, S A, Eriksson, G, Gheribi, A E, Hack, K, Jung, I-H, Kang, Y-B, Melançon, J, Pelton, A D, Petersen, S, Robelin, C, Sangster, J, Spencer, P and Van Ende, M-A, 2016. FactSage thermochemical software and databases 2010–2016, CALPHAD, 54:35–53.

Genkin, A D, Distler, V V, Gladyshev, G D, Filimonova, A A, Evstigneeva, T L, Kovalenker, V A, Laputina, I P, Smirnov, A V and Grokhovskaya, T L, 1981. *Sulfide copper-nickel ores of the Norilsk deposits* [in Russian], 234 p (Nauka: Moscow).

Gouldstein, J I, Newbury, D E, Etchlin, P, Joy, D C, Fiori, C and Lifshin, E, 1981. *Scanning electron microscopy and X-ray spectral microanalysis* (translated from English), Part 1, 296 p; Part 2, 348 p.

Krishtal, M M, Yasnikov, I S, Polunin, V I, Filatov, A M and Ulyanenkov, A G, 2009. Scanning electron microscopy and X-ray spectral microanalysis in practical application examples, *Technosphere*, 208 p.

Krupnov, L V, Malakhov, P V, Ozerov, S S and Pakhomov, R A, 2023. Analyzing Russian cobalt metallurgy and ways to raise recovery [in Russian], *Tsvetnye Metally*, (7):25–33. https://doi.org/10.17580/tsm.2023.07.03

Tsemekhman, L S, Fomichev, V B, Yertseva, L N, N G, Kaitmazov, S M, Kozyrev, V I, Maksimov, Schneerson Ya, M and Dyachenko, V T, 2010. Atlas of mineralogical raw materials, technological products and commercial products of the Polar Branch of the MMC Norilsk Nickel OJSC [in Russian], 336 p (Ore and Metals Publishing House).

Comparative study of oxide dissolution modelling in secondary steelmaking slags

DOI: 10.62053/UIXP9414
N Preisser[1] and S K Michelic[2]

1. PhD candidate, Christian Doppler Laboratory for Inclusion Metallurgy in Advanced Steelmaking, Leoben A-8700, Austria. Email: nikolaus.preisser@unileoben.ac.at
2. Full Professor, Christian Doppler Laboratory for Inclusion Metallurgy in Advanced Steelmaking, Leoben A-8700, Austria. Email: susanne.michelic@unileobane.ac.at

ABSTRACT

For certain applications, steels have to feature a very distinct and well-defined level of cleanness in terms of the number and composition of non-metallic inclusions. Therefore, one crucial aspect of steelmaking is removing and controlling said non-metallic inclusions during the process. Particle removal during ladle refining comprises three stages, namely:

1. Flotation
2. Transport through the steel/slag interface
3. Dissolution of the particle in the slag.

Only if all three stages are completed the particle can be considered as fully removed from the steel melt which, in turn, leads to the slag being one of the most influential parameters for inclusion removal and control. Depending on the composition of the particles and the slag, the dissolution can be controlled by different mechanisms. This study focuses on the diffusion-controlled dissolution of solid oxidic particles in slags. For this, a model of particle dissolution has been developed. For modelling diffusion, either the differential equation following Fick's second law can be solved, or an analytical solution to this equation valid for stationary interfaces can be used. Both approaches allow for calculations of concentration profiles of the dissolving species in surrounding slag. From this, the mass flux can be derived, which finally leads to calculating the boundary layer velocity due to considerations of mass balance. In this work, both methods as well as results of dissolution experiments using High Temperature Confocal Scanning Laser Microscopy are compared. This research aims to provide a framework for diffusion-based dissolution modelling in further expanding the understanding of particle dissolution in secondary metallurgy.

INTRODUCTION

The possible applications of steel and steel products are constantly rising. Much of this is due to the fact that enhanced steel cleanness is improving the mechanical, chemical and physical properties of the steel as shown by Garrison and Wojcieszynski (2007) and Chen *et al* (2019). One of the most essential aspects for steel cleanness is the secondary metallurgy in the steel plant especially the interaction of the steel with the slag phase. And as Sridhar and Cramb (2003) state, slags heavily influence the steel cleanness as the slag's properties are linked to multiple processes essential for steel cleanness. As non-metallic inclusions (NMI) are similar in composition to secondary metallurgical slags, there is a tendency towards chemical equilibrium between particles and slag and the chemical composition of NMIs can be influenced. Moreover, the slag's surface tension and viscosity is important for the transition of NMIs from the steel to the slag-phase as shown by Jimbo, Chung and Cramb (1996). And lastly, slags are responsible for the dissolution and, therefore the ultimate removal of NMIs from the system, as stated by Valdez, Shannon and Sridhar (2006) and Lee *et al* (2001). only if the NMIs can be transported to the steel-slag interface by mechanisms like flotation, move through this interface due to advantageous wetting conditions and surface tensions, and are then dissolved in the slag promptly to avoid re-entrapment in the steel, the particles can be considered entirely removed. For most applications especially hard and non-deformable NMIs are detrimental. Furuya, Abe and Matsuoka (2003) found that this is because especially with dynamic loads and many load cycles cavities can form around particles, which are not as deformable as the surrounding steel matrix. These cavities can then be the origin of cracks and lead to critical failure of the material. Therefore, it is of interest to gain a better understanding of the mechanisms which

are involved in the removal of such particles from the steel melt to ensure the highest possible steel cleanness, avoid fracture of the material, and enable smaller diameters, which in turn will lead to economic and ecological benefits. This work focuses on the last step of particle removal, the dissolution of NMIs in slags. Solid oxide particles like Al_2O_3, which are particularly harmful to the mechanical properties of steel, are studied. This is done by simulations of particle dissolution and experimentally, using high temperature confocal scanning laser microscopy (HT-CSLM), which allows *in situ* investigation of particle dissolution in slags at steelmaking temperatures.

From the work of Levenspiel (1999), it is clear that dissolution can be explained by different mechanisms that lead to very distinct dissolution curves. Suppose the dissolution is for example limited by some kind of chemical reaction between the particle and the matrix in which it dissolves. In that case, the dissolution takes place linearly, where the speed of dissolution can be directly found from the speed of the chemical reaction. In contrast, this work focuses on dissolution purely governed by the diffusion of solid particles into the liquid slag as Huo *et al* (2022) indicate that this shows promising results for the dissolution of solid oxide particles in steelmaking slags.

DESCRIPTION OF THE MODEL

The dissolution behaviour is portrayed in this work, assuming a stationary interface between the particle and the slag phase. According to Guo *et al* (2017) this approach models dissolution behaviour more accurately as the alternative to invariant field or reverse growth approximations. For this model, the interface where mass is transferred from the solid particle to the liquid slag is fixed at a position equal to the initial radius of the dissolving particle. Using this approach, the following calculations are simplified, as a homogeneous distance between spatial steps is used for a finite differences method. In contrast, a moving interface would lead to varying distances between calculation points.

For the diffusion simulation using this method, several parameters have to be provided. Parameters describing the system's spatial layout include the initial radius of the spherical particle, the width of the boundary layer and the number of spatial steps where calculations should be performed. The boundary layer describes a zone surrounding the solid particle where diffusive processes can occur. Outside of this boundary layer, the slag composition is assumed to be unchanged over the whole process of dissolution. All spatial steps where calculations of the concentration profile will be performed lie within this boundary layer between the particles' initial surface at time 0 and the edge of the boundary layer. A visual representation of the spatial layout of this simulation is represented in Figure 1.

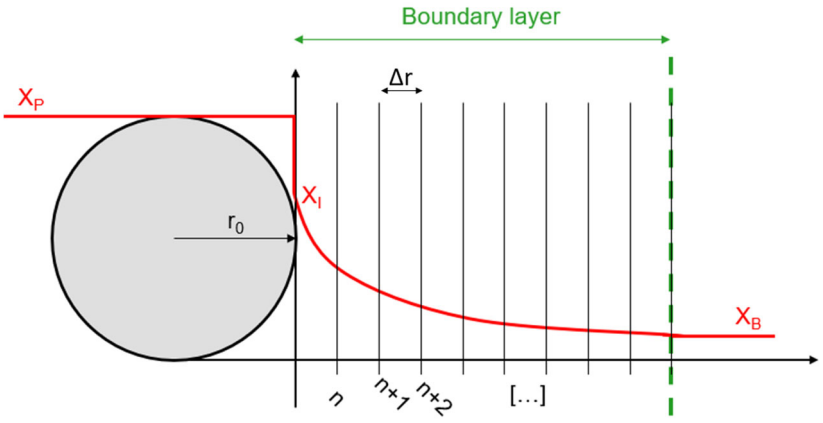

FIG 1 – Spatial layout of the diffusion model.

Additionally, chemical information about the system has to be provided, like the composition of the particle regarding the dissolving species as the dimensionless weight percentage xP (in this case, xP=1 as a homogeneous particle of one species is assumed), the weight percentage x_B of the dissolving species in the slag in the bulk zone (initial composition of the slag), as well as the weight percentage of the dissolving species in the slag saturated with the dissolving species (ie this is assumed to be the composition of the slag directly at the interface between particle and slag). The weight percentage of the dissolving species in the saturated slag is calculated via the thermodynamic

calculation software FactSage™ ver 8.3 (by Thermfact and GTT-Technologies) using the Equilib module. Lastly, the diffusion coefficient has to be provided to calculate the concentration profile around the dissolving particle at all times. The spatial stepsize can be calculated from the boundary layer thickness and the number of desired spatial steps. From this and the diffusivity the critical temporal stepsize can be calculated following Equation 1 were ∆t is the length of the temporal timestep ∆r is the size of the spatial step and D is the diffusion coefficient.

$$\Delta \boldsymbol{t} = \frac{\Delta \boldsymbol{r^2}}{\boldsymbol{2D}} \tag{1}$$

With the number of necessary timesteps and the defined number of spatial steps, the corresponding space and time matrices for the simulation of the concentration field around the particle can be set. The initial conditions for the concentration profile are set so that for all timesteps, the mass percentage of dissolving species at the interface is x_I. At the same time, it is x_B at any other spatial step. Additionally, the temporal derivative of the concentration field is set to be 0 at all spatial steps initially. The temporal derivative of the concentration field can be calculated for each timestep following Equation 2, as stated by Ogris and Gamsjäger (2022). Where x_{i-1}, x_i and x_{i+1} are the mass fractions of the dissolving species at a spatial position at different calculation times. The concentration field of the next timestep then follows as the sum of the concentration field of the current timestep and the calculated temporal derivative multiplied by the length of the timestep. Now, the spatial derivative of the concentration profile can be calculated at each spatial step for each timestep as seen in Equation 3. From this, the mass flux is calculated using Fick's second law of diffusion given in Equation 4 where J is the mass flux and $\dot{x}$ is the spatial derivative of the concentration profile. As the dimensionless mass percentage was used for the calculation of the concentration profile instead of actual concentrations, this flux would have to be multiplied with the slags density in order to resemble actual mass flux with unit $kgm^{-2}s^{-1}$. Due to this simplification the actual unit of this flux of weight fraction is ms^{-1} Now the reduction in diameter of the particle can be calculated for each timestep. This is performed using a mass balance equation called 'Stefan's interface condition' after Slovenian scientist Jozef Stefan as found in Glicksman (2000). This mass balance is given in Equation 5. On the left hand side, the mass leaving the interface is given as the product of the interface area multiplied by the mass flux at the interface $J(R_0)$, the length of the timestep ∆t and the slags density. On the right hand side, the respective difference in the spherical particle volume is multiplied by the particle density. For this simulation, the density of the solid particle and the density of the slag at the interface are assumed to be the same, which allows for simplification and rearrangement of Equation 5 to determine the radius of the particle in the next time step. This is shown in Equation 6.

$$\frac{\Delta \boldsymbol{x}}{\Delta \boldsymbol{t}} = \boldsymbol{D}\left(\frac{\boldsymbol{x_{i-1}+x_{i+1}-2x_i}}{\Delta \boldsymbol{r^2}} + \frac{\boldsymbol{x_{i+1}-x_{i-1}}}{\boldsymbol{r_i \Delta r}}\right) \tag{2}$$

$$\dot{\boldsymbol{x}} = \frac{\Delta \boldsymbol{x}}{\Delta \boldsymbol{r}} = \frac{\boldsymbol{x_{n+1}-x_n}}{\Delta \boldsymbol{r}} \tag{3}$$

$$\boldsymbol{J} = -\boldsymbol{D}\dot{\boldsymbol{x}} \tag{4}$$

$$\boldsymbol{4\pi\, R_0^2\, J(R_0)\, \Delta t\, \rho} = \frac{\boldsymbol{4}}{\boldsymbol{3}}\boldsymbol{\pi}\left(\boldsymbol{r_i^3 - r_{i+1}^3}\right)\boldsymbol{\rho} \tag{5}$$

$$\boldsymbol{r_{i+1}} = \sqrt[3]{\left(\boldsymbol{r_i^3 - 3\, J(R_0)\, \Delta t\, R_0^2}\right.} \tag{6}$$

PARAMETER ANALYSIS

The impact of changes of initial parameters is presented and discussed. This is necessary to further understand the models' capabilities and restrictions for further application. In Figure 2 the dissolution curves of various simulations are shown. In Figure 2a, the only difference in parameters is the number of spatial steps chosen between the interface and the outer edge of the boundary layer. As absolute values are plotted, it can be seen that with an increasing number of calculation points, the curve is shifted to slightly faster dissolution times. At the same time, the difference between simulations gets smaller as the number of spatial steps increases. Therefore, it can be assumed that the result of the simulation converges, and at some stage, increasing the number of calculation points does not result in significantly more accurate results.

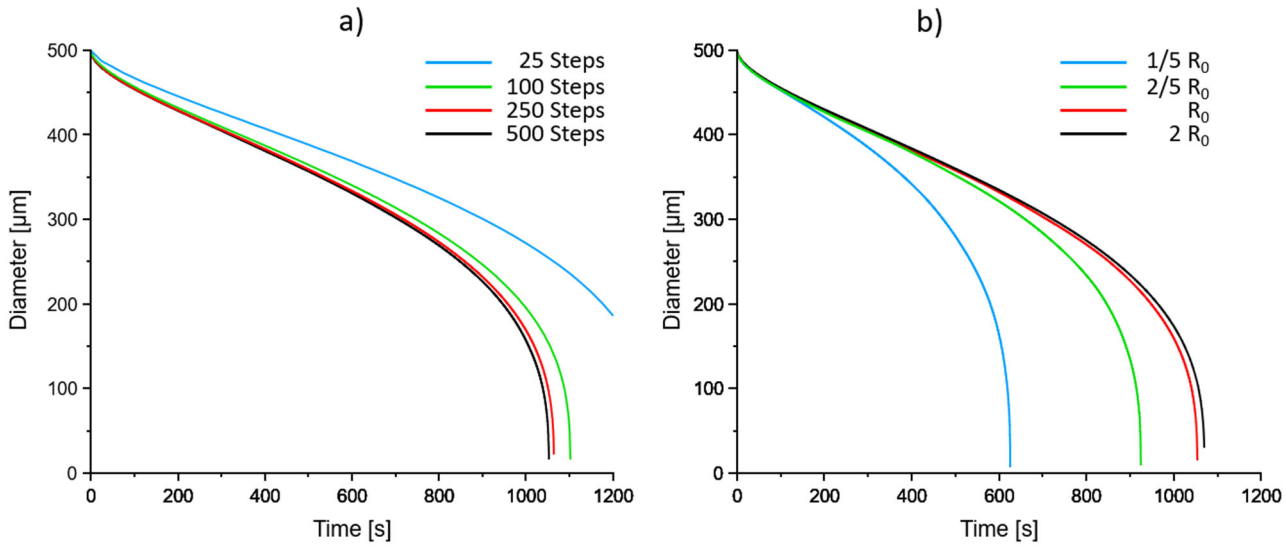

FIG 2 – Variation of number of spatial steps and boundary layer thickness.

In Figure 2b, the impact of the thickness of the boundary layer is shown. This parameter heavily influences the shape of the concentration profile, where smaller values lead to steeper gradients in concentration as the zone where an unchanged composition of the bulk medium is assumed moves closer to the interface between slag and particle. Therefore, smaller values for the boundary layer thickness result in faster particle dissolution. In this example, the slowest dissolution is achieved when the boundary layer thickness is double the initial radius of the particle. With decreasing boundary layer thickness, the dissolution of the particle rapidly speeds up, as the last line representing a boundary layer thickness of one fifth of the initial radius of the particle, shows much faster dissolution. Lastly, the influence of different diffusion coefficients was analysed with fixed amounts of spatial steps, boundary layer thickness and initial radius of the particle. In Figure 3a it can be seen that dissolution is faster with higher values for the diffusion coefficient, as would be expected. The normalised dissolution curves are depicted in Figure 3b. Normalised dissolution curves are derived by dividing particle diameters by their initial values at time zero and time by the total dissolution time. This normalisation technique allows for a direct comparison of dissolution behaviour across different scenarios, independent of specific particle sizes or dissolution durations. Here it is clear that a change in diffusion coefficient does not affect the general shape of the dissolution curve, as the normalised dissolution curves for all values for the diffusion coefficient are congruent. This observation suggests that while the diffusion coefficient influences the rate at which dissolution occurs, it does not alter the overall kinetics of the dissolution process.

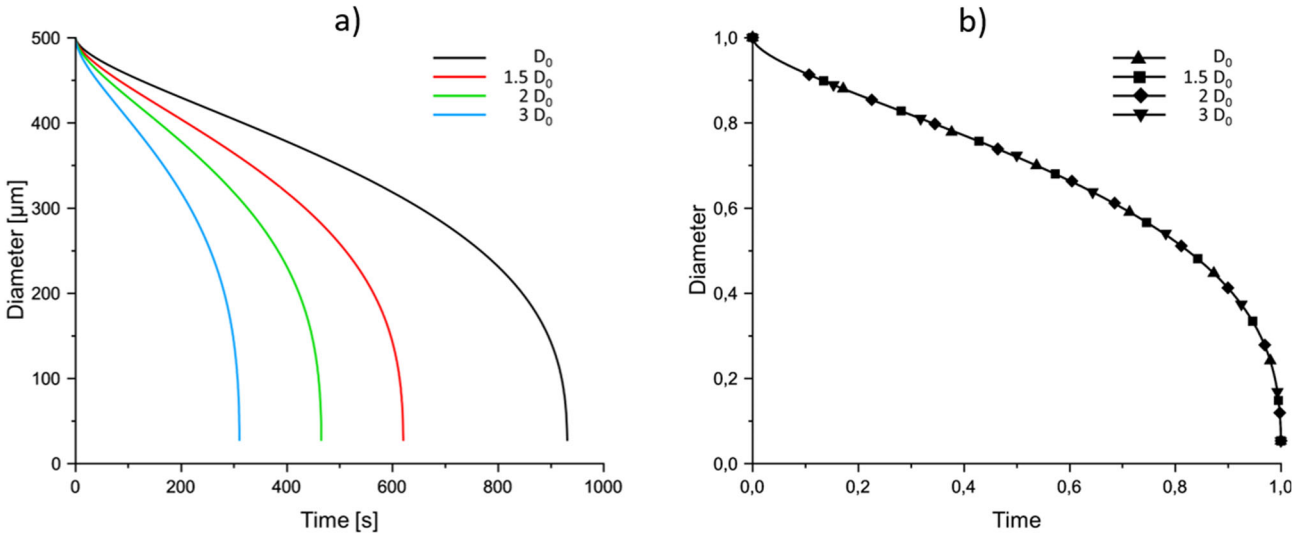

FIG 3 – Influence of changes in diffusion coefficient.

DESCRIPTION OF HT-CSLM AND EXPERIMENTAL SET-UP

For model validation, dissolution experiments have been conducted using high temperature confocal scanning laser microscopy (HT-CSLM). With this, the dissolution of particles in slags can be observed *in situ* and the dissolution curves can be gathered directly. The experimental set-up has already been widely discussed in previous work by Michelic *et al* (2016) as well as Feichtinger *et al* (2014) and will not be presented in detail. For validation of the model, a specific combination of particle, slag and temperature with a known diffusion coefficient has been selected from the literature. The slag composition is given in Table 1. The selection of slag is crucial for the analysis of the dissolution as it is paramount that the slag is transparent for the laser with a wavelength of 405 nm. Therefore, slags without tainting constituents like FeO or MnO should be used. The particles used for the dissolution experiment are synthetic Al_2O_3 particles with nearly perfect spherical geometry and an initial particle diameter of 500 µm. The slag is heated together with the particle to 1500°C. The particle is then manually tracked. The software directly logs the time and individual temperature. The corresponding particle diameter is gathered by extracting single frames from the video data afterwards and measuring the particle's dimensions. From this dissolution curves of diameter over time can be plotted. As time zero of dissolution, the time is chosen at which the experimental temperature of 1500°C is reached. Dissolution, which occurs before this point in time, is disregarded. Third-order polynomial smoothing of the data is performed using the SimpleFit Module of OriginPro (version 2023, OriginLab Corporation, Northampton, MA, USA). The data of both experiments are comparably close, which results in nearly identical dissolution curves after polynomial fitting. The total dissolution is achieved after approximately 900 seconds in both experiments. From both data sets it can be derived that the dissolution rate at the beginning as well as at the end of the dissolution is faster. This behaviour is quite common and must be expected if diffusion is assumed to be the limiting factor of dissolution. This is because of a steeper concentration gradient in the beginning of dissolution and a favourable relation of the particle's surface area to its volume.

TABLE 1

Slag composition.

Name	SiO_2 [wt.%]	CaO [wt.%]	Al_2O_3 [wt.%]	MgO [wt.%]
Slag 1	49.56	32.42	11.16	6.86

COMPARISON OF SIMULATION AND EXPERIMENTAL RESULTS

For validation of the simulation, the experimental results are compared with the dissolution curves calculated by the model using the presented stationary interface approach of dissolution modelling. The boundary layer thickness for the calculation was chosen to be 500 µm, which is double the synthetic particle's initial radius. The diffusion coefficient was set to $4.56*10^{-11,}$ as found in the work of Burhanuddin *et al* (2022) for the diffusion of Al_2O_3 in the specific slag used in the HT-CSLM experiments. As pure Al_2O_3 particles are dissolved, the mass fraction of Al_2O_3 of the particle is 1. The mass fraction of Al_2O_3 in the bulk slag is 0.1119 and the mass fraction of Al_2O_3 in the saturated slag is 0.3970, as calculated by Factsage™. For a relatively short computation time, 200 spatial steps were chosen for calculations between the interface and the outer edge of the boundary layer. With these parameters, a total dissolution time of approximately 600 s was calculated. At first glance, this would lead to the conclusion that the simulation does not describe the dissolution well, as this value is about a third lower than the dissolution time gathered from the HT-CSLM experiments. But by closer comparison, it becomes apparent that this discrepancy in dissolution time arises mainly in the second half of the dissolution when the diameter of the particles gets smaller. In contrast, the dissolution rate at the beginning of the dissolution is predicted with high accuracy. While the experimental data only shows a slight pick-up in the dissolution speed, the model leads to a drastic increase in dissolution rate to the point where the particle is expected to dissolve almost instantaneously after a decrease in diameter of about 75 per cent. In Figure 4 the data of both dissolution experiments and the calculated dissolution curve from the model are depicted.

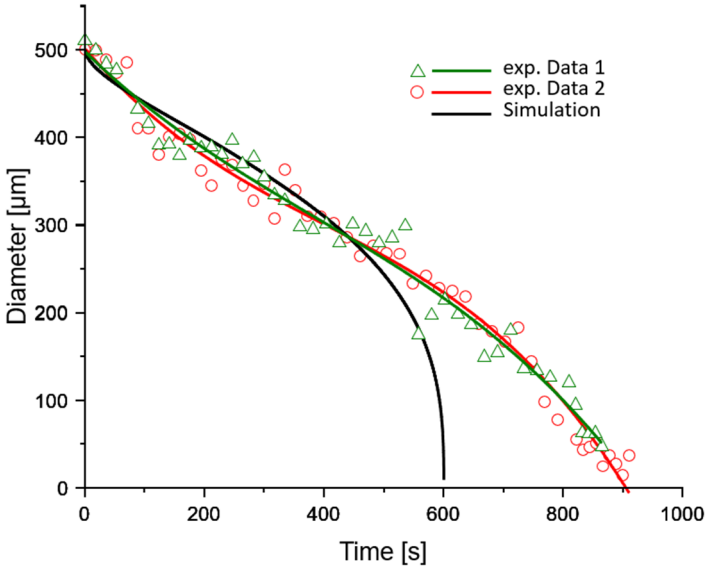

FIG 4 – Comparison of experimental results of dissolution curves and simulated dissolution curve.

DISCUSSION

In this work, a model for the simulation of diffusion-based dissolution of solid particles in liquid slags has been developed. The model follows a stationary interface approach, where for the sake of calculating the concentration profile around the particle and mass balance considerations, the interface is considered as not moving. This aids the calculation as the vectorised space for finite differences methods is homogeneous, where, in contrast, a moving interface would lead to inhomogeneous distances between nodal points of calculation and the concentration profile would need to be recalculated after each timestep as opposed to being calculated once upfront. For comparison, dissolution experiments have been conducted using HT-CSLM, where the dissolution of a synthetic particle in an experimental slag can be observed *in situ* at steelmaking temperatures. Dissolution rates of the experiments and the simulation are in good agreement at the beginning of the dissolution but deviate towards smaller diameters as the simulation predicts a faster pick-up in dissolution speed. This is believed to be an effect of the stationary interface approach, as the surface through which mass flux is assumed stays constant as the surface area of the initial particle, whereas in reality this also decreases in size throughout the dissolution. To clarify this effect, the ratio of surface area for mass flux and particle volume can be calculated for both a moving and a stationary interface approach. In Equation 7 this ratio is expressed for the case of a moving interface as γ_M. Equation 8 states the same ratio γ_S but for the case of a stationary interface.

$$\gamma_M = \frac{A}{V} = \frac{4\,\pi\,r^2}{\frac{4}{3}\pi\,r^3} = \frac{3}{r} \tag{7}$$

$$\gamma_S = \frac{A}{V} = \frac{4\,\pi\,R_0^2}{\frac{4}{3}\pi\,r^3} = \frac{3\,R_0^2}{r^3} \tag{8}$$

From these ratios, it is clear that with decreasing values of r the ratio γ_S will increase much faster than the ratio γ_M. This could in turn explain the difference between the experimental results and the simulation of dissolution in later stages of the dissolution process, as the mass flux through the surface area becomes overpronounced with decreasing particle diameters. To better understand the scope of this discrepancy between the different models, a critical radius can be calculated, which marks the radius at which the stationary interface approach theoretically overtakes the moving interface approach, given the concentration field would be the same for both calculations. This can be done by comparing the first derivative of both surface-to-volume ratios, shown in Equations 9 and 10.

$$\dot{\gamma}_M = -\frac{3}{r^2} \tag{9}$$

$$\dot{\gamma}_S = -\frac{9\,R_0^2}{r^4} \tag{10}$$

If these derivatives are compared, a critical value r_{crit} can be found. For values of r lower than r_{crit} the stationary interface approach leads to quicker dissolution of the particle. This is shown in Equations 11 and 12.

$$-\frac{3}{r_{crit}^2} = -\frac{9\,R_0^2}{r_{crit}^4} \tag{11}$$

$$r_{crit} = \sqrt{3\,R_0^2} = R_0\,\sqrt{3} \tag{12}$$

As Equation 12 states, this critical value is always higher than the initial particle radius R_0 as the square root of 3 is greater than 1. This shows that from the beginning, the stationary interface approach will already lead to faster dissolution of the particle than a moving interface approach, given the concentration profile would be the same. This assumption is not entirely correct, as a moving interface would lead to slightly different concentration profiles around the particle, but for further comparison of the models in this work, equal concentration fields are assumed. To grasp the magnitude of difference between the two models, log(Δγ) is plotted in Figure 5 over the particle radius. At the initial particle radius R_0 the difference is 0 as $\gamma_M=\gamma_S$ for $r=R_0$. As the particle dissolves, log(Δγ) grows rapidly at first, but soon the difference between the two modelling approaches somewhat stabilises for the central part of the dissolution. Only towards the end of the dissolution process, a massive increase in difference between γ_M and γ_S can be observed. To locate the radius at which Δγ starts to increase more rapidly, the second derivative of log(Δγ) can be set to 0 for calculating rPO_I, which represents the point of inflection of the function. This is done in Equations 13 and 14.

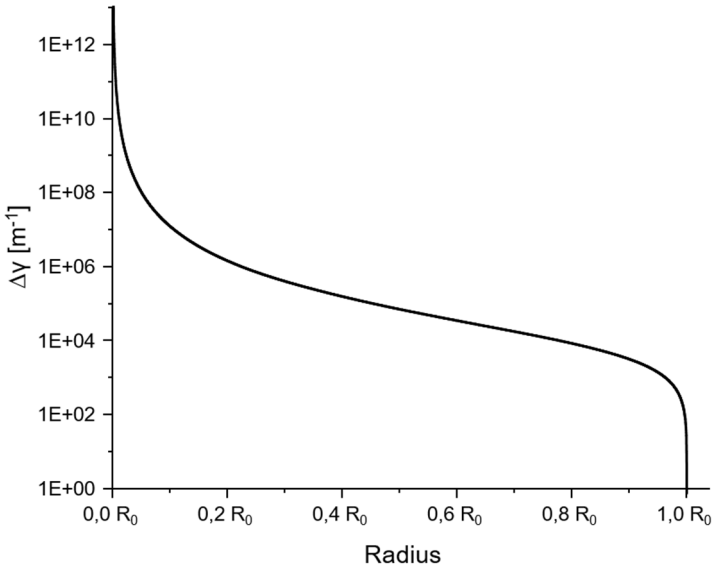

FIG 5 – Δγ plotted over particle radius.

$$\log_{10}(\Delta\gamma) = \log_{10}\left(\frac{3\,R_0^2}{r_{POI}^3} - \frac{3}{r_{POI}}\right) \tag{13}$$

$$\frac{d^2}{dr^2}(\log_{10}(\Delta\gamma)) = \frac{r_{POI}^4 - 8r_{POI}^2R_0^2 + 3R_0^4}{\left(r_{POI}^3 - r_{POI}R_0^2\right)^2} = 0 \tag{14}$$

If Equation 14 is solved for rPO_I, only one solution is positive and smaller than R_0. Only this solution presented in Equation 15 represents the point of inflection for the section of the function of log(Δγ) depicted in Figure 5. This shows that Δγ begins to grow faster as soon as a particle diameter of approximately 63 per cent of R_0 is reached. For an initial radius of R_0 = 250 µm as used for the calculations and HT-CSLM experiments presented in this paper, this leads to rPO_I = 157 µm or DPO_I=314 µm, respectively. In Figure 6 this value is marked as a horizontal line. Beyond this point in calculation, the deviation from the experimental results begins to increase rapidly, but before that the simulation is in good agreement to the experimental data.

$$r_{POI} = R_0\sqrt{(4-\sqrt{13})} \cong R_0 * 0.628 \quad (15)$$

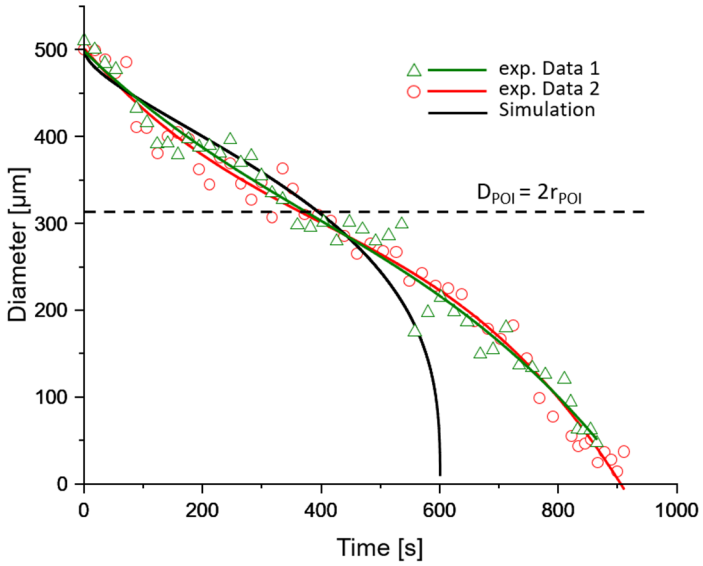

FIG 6 – Comparison of simulation and experimental data. The dashed line represents the diameter of the point of inflection of function log(Δγ).

CONCLUSION

Following these observations, it is proposed to expand the presented model to a moving interface approach as to better predict particle dissolution even at later stages of the dissolution. Additionally, the prediction of dissolution time could improve due to the implementation of more accurate density data of the slag and the dissolving particle. Furthermore, experiments for measuring boundary layer thickness around dissolving particles are of great interest as this is one of the most influential parameters apart from the diffusion coefficient. Once the adapted model is validated by further experimental data, the prediction of binary diffusion coefficients based on fitting the simulation data to experimental dissolution curves could be possible.

ACKNOWLEDGEMENTS

The financial support by the Austrian Federal Ministry for Labour and Economy, the National Foundation for Research, Technology and Development and the Christian Doppler Research Association is gratefully acknowledged. The authors declare no conflict of interest.

REFERENCES

Burhanuddin, B, Guarco, J, Harmuth, H and Vollmann, S, 2022. Application of an improved testing device for the study of alumina dissolution in silicate slag, *Journal of the European Ceramic Society*, 8:3652–3659.

Chen, C, Jiang, Z, Li, Y, Zheng, L, Huang, X, Yang, G, Sun, M, Chen, K, Yang, H, Hu, H and Li, H, 2019. State of the Art in the Control of Inclusions in Tire Cord Steels and Saw Wire Steels – A Review, *Steel Research International*, 8:1800547.

Feichtinger, S, Michelic, S K, Kang, Y-B and Bernhard, C, 2014. In-situ observation of the dissolution of SiO_2 particles in $CaO{-}Al_2O_3{-}SiO_2$ slags and mathematical analysis of its dissolution pattern, *Journal of the American Ceramic Society*, 1:316–325.

Furuya, Y, Abe, T and Matsuoka, S, 2003. 1010-cycle fatigue properties of 1800 MPa-class JIS-SUP7 spring steel, *Fatigue and Fracture of Engineering Materials and Structures*, 7:641–645.

Garrison, W M and Wojcieszynski, A L, 2007. A discussion of the effect of inclusion volume fraction on the toughness of steel, *Materials Science and Engineering: A*, 1–2:321–329.

Glicksman, M O, 2000. *Diffusion in Solids*, 142 p (John Wiley and Sons: New York).

Guo, X, Sietsma, J, Yang, Y, Sun, Z and Guo, M, 2017. Diffusion-limited dissolution of spherical particles: A critical evaluation and applications of approximate solutions, *AIChE J*, 7:2926–2934.

Huo, Y, Gu, H, Huang, A, Ma, B, Chen, L, Li, G and Li, Y, 2022. Characterization and mechanism of dissolution behavior of Al_2O_3/MgO oxides in molten slags, *J Iron Steel Res Int*, 11:1711–1722.

Jimbo, I, Chung, Y and Cramb, A W, 1996. Interfacial Tensions of Liquid Iron-alloys and Commercial Steels in Contact with Liquid Slags, *ISIJ Int*, Supplement:S42–S45.

Lee, S H, Tse, C, Yi, K W, Misra, P, Chevrier, V, Orrling, C, Sridhar, S and Cramb, A W, 2001. Separation and dissolution of Al_2O_3 inclusions at slag - metal interfaces, *Journal of Non-Crystalline Solids*, pp 41–48.

Levenspiel, O, 1999. *Chemical Reaction Engineering*, pp 582–586 (John Wiley and Sons: New York).

Michelic, S K, Goriupp, J, Feichtinger, S, Kang, Y-B, Bernhard, C and Schenk, J, 2016. Study on Oxide Inclusion Dissolution in Secondary Steelmaking Slags using High Temperature Confocal Scanning Laser Microscopy, *Steel Research International*, 1:57–67.

Ogris, D M and Gamsjäger, E, 2022. Numerical Treatment of Oxide Particle Dissolution in Multicomponent Slags with Local Gibbs Energy Minimization, *Steel Research International*, 2200056.

Sridhar, S and Cramb, A, 2003. Properties of Slags and Their Importance, in Manufacturing Clean Steels, *High Temperature Materials and Processes*, 5–6:275–282.

Valdez, M, Shannon, G S and Sridhar, S, 2006. The ability of slags to absorb solid oxide inclusions, *ISIJ International*, 3:450–457.

Impurity capacities of non-ferrous slags

DOI: 10.62053/VDZG2932

R G Reddy[1]

1. Professor, The University of Alabama, Tuscaloosa Alabama 35487, USA.
   Email: rreddy@eng.ua.edu

ABSTRACT

The complexity in treating environmentally harmful impurities such as As, Sb, Bi from the base metal matte or metal in the smelting stage are responsible for the high cost of the refining process. The impurity capacities (such as arsenic, antimony and bismuth) of slags were calculated *a priori* using Reddy-Blander (RB) model. The capacity predictions were for a wide range of matte and slag compositions in copper smelting conditions. The calculated impurities capacities and impurity distribution ratios results are in good agreement with the available experimental and industrial slags data. The *a priori* knowledge of impurities is useful for reduction of energy consumption and enhanced environmental control in the current and future non-ferrous metal processes.

INTRODUCTION

Impurity capacity of a slag is defined as a measure of the ability of slag to hold the impurity. The common minerals that contain As, Sb and Bi in copper are Arsenopyrite (FeAsS), Enargite (Cu_3AsS_4), Lautite (CuAsS), Tennantite [$(Cu,Fe)_{12}As_4S_{13}$], Famatinite (Cu_3SbS_4), Chalcostibite ($CuSbS_2$), Wittichenite (Cu_3BiS_3), Emplectite ($CuBiS_2$) and Aikinite ($PbCuBiS_3$). The lead impurity compounds are Jordanite ($Pb_{14}As_6S_{23}$) and Cosalite (Pb_2Bi_2S) (Larouche, 2001).

In copper, nickel and lead sulfide smelting and refining, removal of sulfur, arsenic, antimony, and bismuth cause metal losses in both entrained and chemically dissolved forms in the slags. As a result, an understanding of impurity capacity of slags is essential for the development of clean metal technology. The Reddy-Blander (RB) model, first proposed in 1987 (Reddy and Blander, 1987), predicted that sulfide capacities can be calculated *a prior* based on a simple solution model and on the knowledge of chemical and solution properties of sulfides and oxides.

The sulfide capacities of several binary silicate (Reddy and Blander, 1987, 1989; Reddy, Hu and Blander, 1992; Reddy, 2003b), aluminate (Reddy and Zhao, 1995), titanate (Derin, Yucel and Reddy, 2004), multi-component silicate (Yahya and Reddy, 2011; Chen, Reddy and Blander, 1989; Pelton, Eriksson and Romero-Serrano, 1993; Derin, Yucel and Reddy, 2011) and industrial slags (Derin and Reddy, 2003; Derin, Yucel and Reddy, 2005; 2006) were predicted using the RB model. The model was also applied for sulfate (Pelton, 1999, 2000), arsenate (Reddy and Font, 2003), antimonate, Font and Reddy, 2005) capacities in slags and sulfur and oxygen partial pressures in copper slags (Derin and Reddy, 2003). brief description of the RB model is presented on the thermodynamic modelling of impurity capacity section. Impurity capacity expressions for several impurities are presented in Table 1 (Reddy, 2003a).

TABLE 1

Capacities expression for different species.

Species, i	Reaction	Capacity, C_i
Sulfide, $[S^{2-}]$	$1/2S_2(g) + [O^{2-}] = [S^{2-}] + 1/2O_2(g)$	$C_S = (wt\%S)\left(\frac{P_{O_2}}{P_{S_2}}\right)^{\frac{1}{2}}$
Pyrosulfate, $[S_2O_7^{2-}]$	$S_2(g) + [O^{2-}] + 3O_2(g) = [S_2O_7^{2-}]$	$C_{S_2O_7^{2-}} = \frac{(wt\%S_2O_7^{2-})}{P_{O_2}^3 P_{S_2}}$
Sulfate, $[SO_4^{2-}]$	$1/2S_2(g) + [O^{2-}] + 3/2O_2(g) = [SO_4^{2-}]$	$C_{SO_4^{2-}} = \frac{(wt\%SO_4^{2-})}{P_{O_2}^{\frac{3}{2}} P_{S_2}^{\frac{1}{2}}}$
Carbide, $[C_2]$	$3C(gr) + [O^{2-}] = [C_2^{2-}] + CO(g)$	$C_{C_2} = wt\%C_2 \frac{P_{CO}}{a_C^3}$
Carbonate, $[CO_3^{2-}]$	$CO_2(g) + [O^{2-}] = [CO_3^{2-}]$	$C_{CO_3^{2-}} = \frac{(wt\%CO_3^{2-})}{P_{CO_2}}$
Hydroxyl, $[OH^-]$	$1/2H_2O(g) + 1/2[O^{2-}] = [OH^-]$	$C_{OH^-} = \frac{(wt\%OH^-)}{P_{H_2O}^{\frac{1}{2}}}$
Nitride, $[N^{3-}]$	$1/2N_2(g) + 3/2[O^{2-}] = [N^{3-}] + 3/4O_2(g)$	$C_N = (wt\%N^{3-})\frac{P_{O_2}^{\frac{3}{4}}}{P_{N_2}^{\frac{1}{2}}}$
Cyanide, $[CN^-]$	$N_2(g) + 3C + [O^{2-}] = 2[CN^-] + CO(g)$	$C_{CN^-} = (wt\%CN^-)\frac{P_{CO}^{\frac{1}{2}}}{a_C^{\frac{3}{2}} P_{N_2}^{\frac{1}{2}}}$
Phosphate, $[PO_4^{3-}]$	$P_2(g) + 3[O^{2-}] + 5/2O_2(g) = 2[PO_4^{3-}]$	$C_{PO_4^{3-}} = \frac{(wt\%PO_4^{3-})}{P_{O_2}^{\frac{5}{4}} P_{P_2}^{\frac{1}{2}}}$
Phosphide, $[P^{3-}]$	$1/2P_2(g) + 3/2[O^{2-}] = [P^{3-}] + 3/4O_2(g)$	$C_{P^{3-}} = (wt\%P^{3-})\frac{P_{O_2}^{\frac{3}{4}}}{P_{P_2}^{\frac{1}{2}}}$
Arsenate, $[AsO_4^{3-}]$	$3/2O^{2-} + As(l) + 5/4O_2(g) = AsO_4^{3-}$	$C_{AsO_4^{3-}} = \frac{(wt\%AsO_4^{3-})}{a_{As} P_{O_2}^{\frac{5}{4}}}$
Bismuthate, $[BiO_4^{3-}]$	$3/2O^{2-} + Bi(l) + 5/4O_2(g) = BiO_4^{3-}$	$C_{BiO_4^{3-}} = \frac{(wt\%BiO_4^{3-})}{a_{Bi} P_{O_2}^{\frac{5}{4}}}$
Antimonate, $[SbO_4^{3-}]$	$3/2O^{2-} + Sb(l) + 5/4O_2(g) = SbO_4^{3-}$	$C_{SbO_4^{3-}} = \frac{(wt\%SbO_4^{3-})}{a_{Sb} P_{O_2}^{\frac{5}{4}}}$
Telluride, $[Te^{2-}]$	$1/2Te_2(g) + [O^{2-}] = [Te^{2-}] + 1/2O_2(g)$	$C_{Te} = (wt\%Te)\left(\frac{P_{O_2}}{P_{Te_2}}\right)^{\frac{1}{2}}$
Selenide, $[Se^{2-}]$	$1/2Se_2(g) + [O^{2-}] = [Se^{2-}] + 1/2O_2(g)$	$C_{Se} = (wt\%Se)\left(\frac{P_{O_2}}{P_{Se_2}}\right)^{\frac{1}{2}}$

THERMODYNAMIC MODELLING OF IMPURITY CAPACITY

Reddy-Blander (RB) Model – impurity capacity

The Reddy-Blander model was used to predict the arsenic capacity of slags, metal and mattes. The arsenic capacity model (a measure of the ability of an oxide system or slag to hold arsenic), that can *a priori* predict the arsenic behaviour in copper mattes and slags was derived (Reddy and Font, 2003). For the MO-SiO_2 system, the arsenic equilibrium reaction can be written as:

$$\frac{3}{2}\mathrm{MO}(l) + \mathrm{As}(l) + \frac{5}{4}O_2(g) = M_{3/2}\mathrm{AsO_4}(l) \quad (1)$$

where, M is arsenate compound forming element (such as Fe, Ca, Mg,.). The most stable arsenic compound in copper smelting slags is $M_{3/2}AsO_4$. At high oxygen partial pressures, the arsenic dissolve into the slag as As_2O_5 (Kojo, Taskinen and Lilius, 1984). The equilibrium constant, K_M, for the above reaction is:

$$K_M = \frac{a_{M_{3/2}\mathrm{AsO_4}}}{a_{\mathrm{MO}}^{3/2}\, a_{\mathrm{As}}\, p_{O_2}^{5/4}} \quad (2)$$

The arsenic capacity, C_{As}, in terms of measurable quantities was defined by Reddy (2003a) as:

$$C_{\mathrm{AsO_4^{3-}}} = \frac{(\text{wt pct } \mathrm{AsO_4^{3-}})}{a_{\mathrm{As}}\, p_{O_2}^{5/4}} \quad (3)$$

Combining Equations 2 and 3, then Equation 4 can be obtained.

$$C_{\mathrm{AsO_4^{3-}}} = (\text{wt pct } \mathrm{AsO_4^{-}})\ \frac{K_M\ a_{\mathrm{MO}}^{3/2}}{a_{M_{3/2}\mathrm{AsO_4}}} \quad (4)$$

Development of this expression was made considering two compositions ranges.

A. Arsenic capacity for basic melts (0 $\leq X_{\mathrm{SiO_2}} \leq$ 0.33)

The arsenic capacity for the basic melt in the MO-SiO_2 binary system becomes:

$$C_{\mathrm{AsO_4^{3-}}} = \frac{100\ \mathrm{K}_M\ a_{MO}^{3/2}\ \mathrm{W}_{\mathrm{AsO_4}}\ (1-2\ \mathrm{X}_{\mathrm{SiO_2}})}{\gamma_{M_{3/2}\mathrm{AsO_4}}\ [W_{\mathrm{MO}}+X_{\mathrm{SiO_2}}(W_{\mathrm{SiO_2}}-W_{\mathrm{MO}})]} \quad (5)$$

Using RB model, similar expressions for the sulfide capacity of ferrous and non-ferrous slags in the silicate and aluminates systems were derived (Reddy and Blander, 1987, 1989; Reddy, Hu and Blander, 1992; Reddy, 2003b; Reddy and Zhao, 1995; Derin, Yucel and Reddy, 2004; Yahya and Reddy, 2011; Chen, Reddy and Blander, 1989; Pelton, Eriksson and Romero-Serrano, 1993; Derin, Yucel and Reddy, 2011; Derin and Reddy, 2003; Derin, Yucel and Reddy, 2005, 2006). By using the thermodynamic data for the equilibrium constant K_M, $\gamma_{M_{3/2}\mathrm{AsO_4}}$, a_{MO} in the MO-SiO_2 binary system, and W is molecular weight of compounds arsenic capacities were calculated for several binary arsenic systems and are discussed in the section B.

B. Arsenic capacity for acidic melts (0.33 $< X_{\mathrm{SiO_2}} <$ 1)

In this composition range, the arsenic is dissolved in the MO-SiO_2 binary acidic melt that contains polymeric species. It is also assumed that the AsO_4^{3-} ion and the SiO_4 units in the polymer are similar in size and forms a chain with no free O^{2-} ions. For dilute solutions, the volume fraction of As ions sites in solution can be expressed as:

$$\varphi_{\mathrm{As}} = \frac{n_{\mathrm{As}}}{n_{\mathrm{Si}}} \quad (6)$$

The $C_{\mathrm{AsO_4^{3-}}}$ for acidic melts is expressed as:

$$C_{\mathrm{AsO_4^{3-}}} = \frac{100\ \mathrm{K}_M\ a_{\mathrm{MO}}^{3/2}\ X_{\mathrm{SiO_2}} W_{\mathrm{AsO_4}}}{[W_{\mathrm{MO}}+X_{\mathrm{SiO_2}}(W_{\mathrm{SiO_2}}-W_{\mathrm{MO}})]}\ e^{\left[\frac{1}{m}-1-\mu\right]} \quad (7)$$

where m is the average polymer chain length and μ is the interaction energy between the ions. The arsenic capacity of binary MO-SiO_2 system can be predicted using Equations 5 and 7 for the entire composition range ($0< X_{SiO_2} <1$) and at a fixed temperature. As the composition crosses between the basic and acidic melts (at X_{SiO_2} of 0.33), the transition in the arsenic capacity is predicted by Equations 5 and 7 to a smooth and continuous.

For the FeO-SiO_2 binary system, the arsenate formation reaction can be written as:

$$\frac{3}{2}\text{FeO}(l) + \text{As}(l) + \frac{5}{4}O_2(g) = \text{Fe}_{3/2}\text{AsO}_4(l),\ \Delta\text{G}^\circ = \text{- 279.7 K J/mol at 1573 K} \quad (8)$$

It is important to note that in calculating the ΔG° for Equation 8, the values of ΔH° and ΔS° for As (l) and $Fe_{3/2}$ AsO_4(s) (Roine, 2022) were extrapolated from 1200 K and 811 K, respectively. The ΔG° for the liquid $Fe_{3/2}AsO_4$ (l) was estimated from the experimental arsenic solubility data at 1573 K. The aF_eO in FeO-SiO_2 binary system was calculated at 1573 K using FactSage software (Bale, Pelton and Thompson, 2002). The arsenic capacity, as predicted using Equation 5, depends on temperature and activity coefficient of $Fe_{3/2}AsO_4$ (l). At a constant $\gamma_{Fe_{3/2}AsO_4}$, the arsenic capacity of FeO-SiO_2 melts decreases with an increase in temperature. Also, at a constant temperature, the arsenic capacity deceases with increase in $\gamma_{Fe_{3/2}AsO_4}$. The calculated arsenic capacities of melts using Equations 5 and 7 at 1573 K and $\gamma_{Fe_{3/2}AsO_4}$ equal to 1. The arsenic capacity increases with increase in FeO content and shows a strong dependence on the activity of FeO in the melt. The K_M is the equilibrium constant for the R (arsenate, antimonate and bismuthate) forming reaction. The values of K_M arsenates, antimonates and bismuthate at 1573 K are given in Table 2 (Font and Reddy, 2003).

$$\frac{3}{2}\text{MO}\ (l) + \text{R}\ (l) + \frac{5}{4}O_2\ (g) = M_{3/2}\text{RO}_4\ \text{(s, l)} \quad (9)$$

TABLE 2

Equilibrium constants for impurity forming reactions at 1573 K.

	Log K_M		
M*	**Arsenate**	**Antimonate**	**Bismuthate**
Fe**	11.0	10.4	9.6
Ca	10.3	NA	NA
Mg	10.2	9.6	NA
Cu	-4.7	-6.0	NA
Ni	3.4	3.1	NA

NA: Not Available. * Reference state: Solid. ** Reference state: Liquid.

The arsenic capacities of CaO-SiO_2 and MgO-SiO_2 binary melts were calculated using Equations 5 and 7. The arsenic reactions for CaO-SiO_2 and MgO-SiO_2 melts are as follows:

$$\frac{3}{2}\text{CaO}(l) + \text{As}(l) + \frac{5}{4}O_2(g) = \text{Ca}_{3/2}\text{AsO}_4(s),\ \Delta\text{G}^\circ = \text{-362.50 KJ/mol at 1573 K} \quad (10)$$

$$\frac{3}{2}\text{MgO}(l) + \text{As}(l) + \frac{5}{4}O_2(g) = \text{Mg}_{3/2}\text{AsO}_4(s),\ \Delta\text{G}^\circ = \text{-338.14 KJ/mol at 1573 K} \quad (11)$$

The ΔG° for the reaction of $\text{Ca}_{3/2}\text{AsO}_4(s)$ in Equation 10 is taken from the reported data (Bale, Pelton and Thompson, 2002), and the ΔG° for Equation 11, the values of ΔH° and ΔS° for As(l) and $Mg_{3/2}AsO_4$(s) (Roine, 2022) were extrapolated from 1200 K and 1225 K, respectively. The activities of CaO and MgO in melts at 1573 K were calculated (Bale, Pelton and Thompson, 2002). The arsenic capacity in the hypothetical melts of CaO-SiO_2 and MgO-SiO_2 binary systems were calculated. In the CaO-SiO_2 system, a sharp increase in arsenic capacity above the X_{CaO} value of 0.6 was observed (Reddy and Font, 2003). At higher compositions X_{CaO} equal to 0.8 and greater, no significant changes in arsenic capacities were observed. This is mainly due to the variation in the activity of CaO, a_{CaO} in the CaO-SiO_2 binary melts, which shows a strong negative deviation. Similar observations were made for MgO-SiO_2 melts. But the decrease in arsenic capacity in MgO-SiO_2 melts with an increase in the concentration of SiO_2 is much smaller than in the CaO-SiO_2 melts.

C. Arsenic capacity in the multi-component systems

For multi-component system which contains only one acidic component such as SiO_2 (eg FeO-CaO-SiO_2 ternary system or FeO-CaO-MgO-SiO_2 quaternary system), the arsenate formation reactions for CaO- and FeO- can be expressed as:

$$\frac{3}{2}(\text{FeO, CaO})(l) + \text{As}(l) + \frac{5}{4}O_2(g) = (\text{Fe, Ca})_{3/2}\text{AsO}_4(l) \quad (12)$$

Using the Flood-Grjotheim approximation (Chen, Reddy and Blander, 1989; Flood and Grjotheim, 1952), the partial Gibbs energies of mixing for different oxidative species are comparably similar. Thus, for a ternary system, the standard Gibbs energy change of mixing is expressed as:

$$\Delta G_{(Fe,Ca)O} = N_{\text{FeO}}\Delta G_{\text{FeO}} + N_{\text{CaO}}\Delta G_{\text{CaO}} \quad (13)$$

where $\Delta G_{(\text{Fe, Ca})O}$, ΔG_{FeO} and ΔG_{CaO} are the Gibbs energy changes for Equations 12, 8 and 10, respectively. The N_{FeO} and N_{CaO} are the electrical equivalent cationic fractions ($N_{\text{FeO}} = \frac{X_{\text{FeO}}}{X_{\text{FeO}}+X_{\text{CaO}}}$ and $N_{\text{CaO}} = \frac{X_{\text{CaO}}}{X_{\text{FeO}}+X_{\text{CaO}}}$), and by considering the definition of Gibbs energy (ΔG = – RT ln K), Equation 13 is further simplified as:

$$\log \text{K}_8 = N_{\text{FeO}} \log \text{K}_5 + N_{\text{CaO}} \log \text{K}_6 \quad (14)$$

where K_8, K_5, and K_6 are the equilibrium constant for Equations 12, 8 and 10 respectively. For a constant X_{SiO_2} in the FeO-SiO_2 and CaO-SiO_2 binary systems, the arsenic capacity is expressed as $C'_{\text{AsO}_4^{3-}(\text{FeO})} = K_{\text{FeO}}\, a_{\text{FeO}}^{3/2}$ and $\text{C}'_{\text{AsO}_4^{3-}(\text{CaO})} = K_{\text{CaO}}\, a_{\text{CaO}}^{3/2}$. Thus, after substituting in Equation 14 and rearranging, Equation 15 is obtained.

$$\text{Log C}'_{\text{AsO}_4^{3-},\,(\text{Fe, Ca})O} - \frac{3}{2}\log \text{a}_{(\text{Fe, Ca})O} = N_{\text{FeO}}\left(\log \text{C}'_{\text{AsO}_4^{3-},\,\text{FeO}} - \frac{3}{2}\log \text{a}_{\text{FeO}}\right) + N_{\text{CaO}}\left(\log \text{C}'_{\text{AsO}_4^{3-},\,\text{CaO}} - \frac{3}{2}\log \text{a}_{\text{CaO}}\right) \quad (15)$$

Furthermore, taking into consideration only (Fe, Ca)O as a solution, then the integral Gibbs energy of solution for Equation 13 becomes $\log a_{(\text{Fe,Ca})\text{O}} = N_{\text{FeO}} \log a_{\text{FeO}} + N_{\text{CaO}} \log a_{\text{CaO}}$. After substituting in Equation 15 and rearranging it, the arsenic capacity for multi-component system is expressed as:

$$\log \text{C}_{\text{AsO}_4^{3-},\,(\text{Fe, Ca})O} = N_{\text{FeO}} \log \text{C}_{\text{AsO}_4^{3-},\,\text{FeO}} + N_{\text{CaO}} \log \text{C}_{\text{AsO}_4^{3-},\,\text{CaO}} \quad (16)$$

The arsenic capacity of multi-component system using Equation 16 can be calculated at a constant composition of acidic component (ie $X_{Si}O_2$ + $XF_eO_{1.5}$) and is further discussed in the following section.

Evaluation of the arsenic capacity model

The phase equilibrium studies for arsenic between the FeO-MgO-SiO_2, FeO-CaO-MgO-SiO_2 slags and copper mattes at 1573 K were reported (Roghani, Takeda and Itagaki, 2000). The arsenic experimental data were reported in the form of distribution coefficients and solubility of arsenic in the slag. In the present study, an expression was derived between the distribution coefficient and arsenic capacity of slags in equilibrium with copper mattes.

Expression between distribution coefficient (LAs) and arsenic capacity (CAsO43-)

The arsenic distribution coefficient between slag and matte phases is defined as:

$$L_{\text{As}} = \frac{\text{(wt pct As in slag-oxidic phase)}}{\text{\{wt pct As in matte – metal phase\}}} \quad (17)$$

The weight pct of As in matte is expressed as:

$$\{\text{Weight pct of As in matte}\} = \frac{a_{\text{As}(l)}\, \text{W}_{\text{As}}\{n_T\}}{\gamma_{\text{As}}} \quad (18)$$

where $a_{\text{As(l)}}$ is activity of arsenic in matte, γ_{As} is activity coefficient of As in matte and W_{As} is the molecular weight of As, and $\{n_T\}$ is the total number of moles of matte phase. Combining

Equations 17, 18 and 3, after making the conversion of weight pct of As in slag, and rearranging, the relationship between the arsenic capacity and the L_{As} is obtained as:

$$C_{AsO_4^{3-}} = \frac{L_{As}\, W_{AsO_4}\, \{n_T\}}{\gamma_{As}\, p_{O_2}^{5/4}} \tag{19}$$

The experimental arsenic capacities were derived using Equation 19 for each of the experimental L_{As} at 1573 K. The reported data of γ_{As} and p_{O_2} for Cu matte, were also used in the calculations.

Arsenic capacity and distribution ratios between Cu mattes and slags

The RB model calculated *a priori* and experimental data for arsenic capacity and distribution ratios for FeO-$FeO_{1.5}$-$CuO_{0.5}$-MgO-SiO_2 slags and Cu mattes at 1573 K are shown in Figures 1 and 2 respectively. The equilibrium constants for impurities reactions are presented in Table 2. The *a priori* predictions were calculated considering the reported data of γ_{As} for Cu matte, the a_{MO} for the MO-$FeO_{1.5}$-SiO_2 system and the experimental pO_2 and $\{n_T\}$. A good agreement between the experimental data and RB model *a priori* calculated arsenic capacity and distribution ratio.

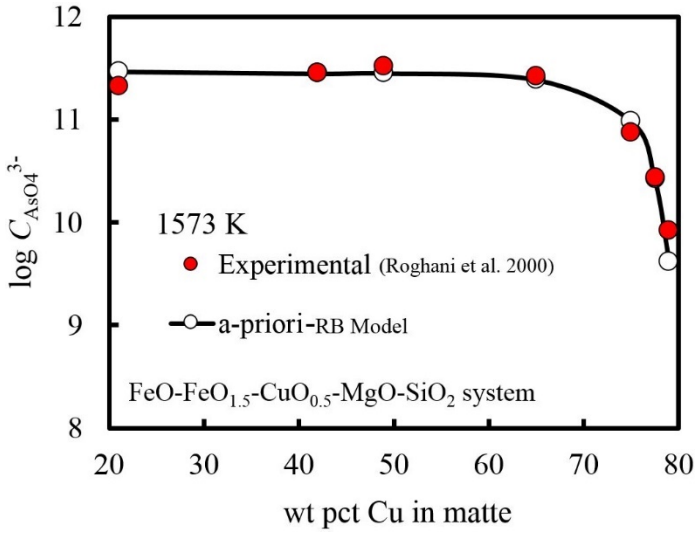

FIG 1 – Arsenic capacity of FeO-$FeO_{1.5}$-$CuO_{0.5}$-MgO-SiO_2 slag versus wt pct Cu in matte at 1573 K.

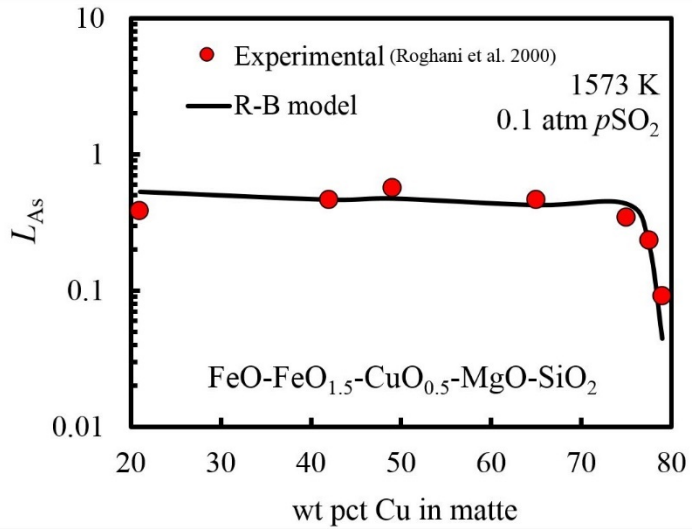

FIG 2 – Distribution coefficient of arsenic of FeO-$FeO_{1.5}$-$CuO_{0.5}$-MgO-SiO_2 slag versus wt pct Cu in matte at 1573 K.

The slight deviations between the experimental and the calculated arsenic capacity may be due to the corresponding uncertainties of the experimental L_{As} and the γ_{As} and p_{O_2} values (Roghani, Takeda

and Itagaki, 2000; Rosenqvist, 1978; Nikolov, Jalkanen and Kyto, 1992; Roghani, Hino and Itagaki, 1997) used in Equation 19 for deriving the experimental arsenic capacity. For the RB model arsenic capacity calculations using Equation 16, the MgO content in the multi-component system was estimated by using the data of the FeO-$FeO_{1.5}$-$CuO_{0.5}$-MgO-SiO_2 system (Font, Hino and Itagaki, 1998a, 1998b, 1999, 2000). Due to a lack of availability of thermodynamic data on liquid arsenates, the solid $Ca_{3/2}AsO_4$ and $Mg_{3/2}AsO_4$ data were used in calculating the Gibbs energy of the Equations 10 and 11. Use of liquids data for these compounds will lower the arsenic capacity of these systems. The availability of reliable thermodynamic data for impurities in slags and mattes is essential. Further studies are in progress for extending this model in *a priori* prediction of other impurities capacities such as Bi, Sb in copper matte and other non-ferrous metal smelting slags.

Antimonate capacity and distribution ratio between Cu mattes and slags

The antimonate capacities were calculated using RB model for each of the slag composition and corresponding distribution ratios of Cu matte in equilibrium with the FeO-$FeO_{1.5}$-$CuO_{0.5}$-MgO-SiO_2 slag at 1573 K and pSO_2 of 0.1 atm, using expressions similar to Equations 5, 7 and 16. The antimony dissolved into the slag as Sb_2O_5 (Kojo, Taskinen and Lilius, 1984). The equilibrium constants for impurities reactions are presented in Table 2. The calculated using RB model for antimonate capacities and distribution ratios are shown in Figures 3 and 4 respectively. The data of γ_{Sb} for the Cu matte, the a_MO in the MO-SiO_2 binary system and the experimental pO_2 and $\{n_T\}$ were used in the calculations. The *a priori* predictions and experimental data for antimony capacities and distribution ratios in slags and Cu mattes are in good agreement. The observed good agreement may be due to the including copper oxide data in slag system. This is particularly important at higher matte grades because higher solubility of copper into slags is reported (Roghani, Takeda and Itagaki, 2000).

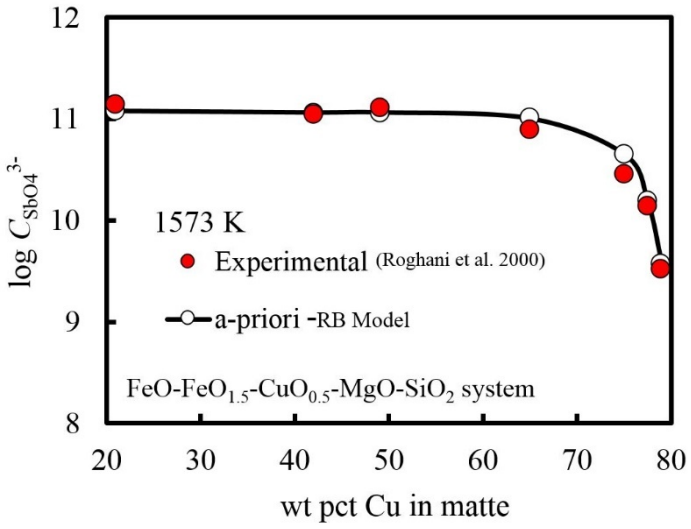

FIG 3 – Antimony capacity of FeO-$FeO_{1.5}$-$CuO_{0.5}$-MgO-SiO_2 slag versus wt pct Cu in matte at 1573 K.

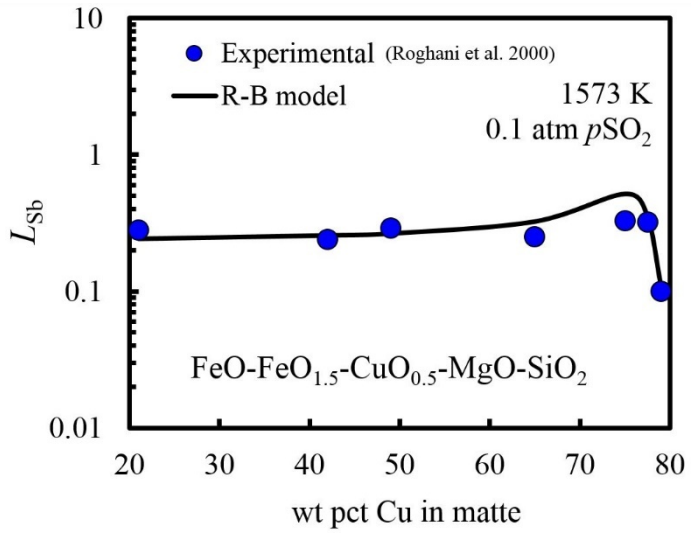

FIG 4 – Distribution coefficient of antimony of $FeO\text{-}FeO_{1.5}\text{-}CuO_{0.5}\text{-}MgO\text{-}SiO_2$ slag versus wt pct Cu in matte at 1573 K.

Bismuth capacity and distribution ratios between Cu mattes and slags

The bismuthate capacities and distribution ratios for Cu matte in equilibrium with the $FeO\text{-}FeO_{1.5}\text{-}SiO_2$ slag at 1573 K and pSO_2 of 0.1 atm were evaluated using the RB model, using an approach similar to arsenic expressions developed using expressions similar to Equations 5, 7 and 16. The calculated data for bismuthate capacities and distribution ratios are shown in Figures 5 and 6 respectively. The equilibrium constants for impurities reactions are presented in Table 2. The Gibbs Energy for the $M_{3/2}BiO_4$ (M = Mg, Cu) compounds are not available in the literature. Hence, the bismuthate capacity was calculated for a hypothetical $FeO\text{-}FeO_{1.5}\text{-}SiO_2$ slag. The equilibrium constant (KF_e) for the $Fe_{3/2}BiO_4$ formation reaction was used from the Table 2. Because an absence of data the quantities of MgO and $CuO_{0.5}$ in Equations 5, 7 and 16 were excluded from the slag composition at 1573 K and pSO_2 of 0.1 atm. The available experimental pO_2 and $\{n_T\}$, data of γ_{Bi} in the Cu matte and the aF_eO in the $FeO\text{-}FeO_{1.5}\text{-}SiO_2$ system were used in these calculations.

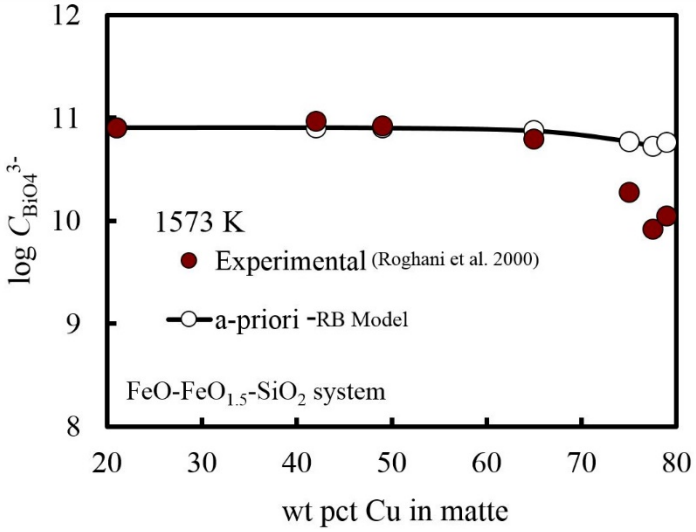

FIG 5 – Bismuth capacity of $FeO\text{-}FeO_{1.5}\text{-}CuO_{0.5}\text{-}MgO\text{-}SiO_2$ slag versus wt pct Cu in matte at 1573 K.

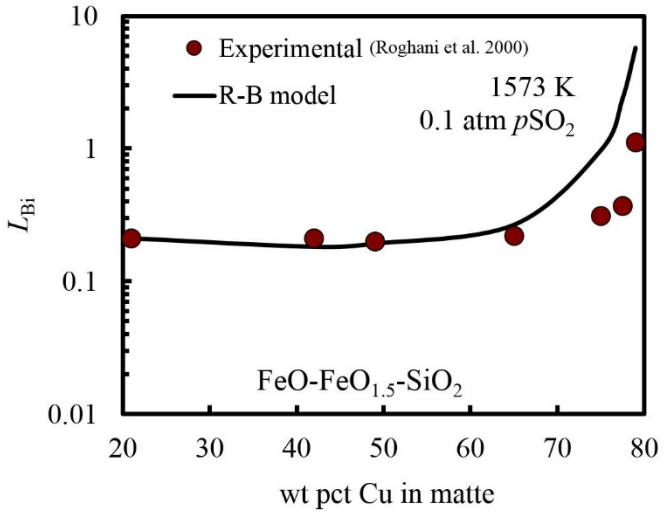

FIG 6 – Distribution coefficient of Bismuth of $FeO\text{-}FeO_{1.5}\text{-}CuO_{0.5}\text{-}MgO\text{-}SiO_2$ slag versus wt pct Cu in matte at 1573 K.

For the $FeO\text{-}FeO_{1.5}\text{-}SiO_2$ slags at 1573 K, the calculated RB model log $C_{Bi}O_4^{3-}$ and L_{Bi} shows that the model data agrees well with the experimental data below the Cu matte grade of 70 wt pct of Cu. But for the RB model data of log $C_{Bi}O_4^{3-}$ and L_{Bi} above the Cu matte grade of 70 wt pct of Cu are higher than the experimental data. As mentioned above, the data for $M_{3/2}BiO_4$ for M = Cu or Mg was not included in the calculations. The addition of basic oxides such as CaO to iron oxide slags increases the Fe_2O_3 content up to about 20 wt per cent (Rosenqvist, 1978), which decreases the capacity of the slag to retain the impurity. The Fe_2O_3, which is known as an acidic component due to its tendency to consume rather than supply oxygen, lowers the a_{FeO} value in slag, resulting in a decrease in the impurity capacity value. Thus, addition of MgO in the calculation of Bismuthate capacities using Equations 5, 7 and 16, expected to decrease the bismuthate capacity and also decrease the distribution ratios, by which their calculated data will be closer to the experimental data. Hence, the availability of reliable thermodynamic data for slag components and impurity compounds in slags and in mattes or liquid metals are essential for the accurate prediction of impurity capacities and their distribution ratios. Further studies are in progress in extending the RB model for the prediction of capacities and distribution ratios of other impurities, such as Se and Te in copper and other non-ferrous metal slags.

CONCLUSIONS

The impurity (As, Sb and Bi) capacities of iron silicate slags in equilibrium with copper mattes at 1573 K were calculated *a priori* using the RB model. The predicted impurity capacities are in very good agreement with the experimental data. An expression for the relationship between the impurity capacity and the impurity distribution ratio for copper slags and the copper mattes was derived. The derived impurity distribution ratios between the slags and the copper mattes found to be in particularly good agreement with the experimental data for multi-component slags. Such predictions are useful in understanding the behaviour of impurities in the current and eventually future non-ferrous metal process. The impurity capacities of slags are directly proportional: (i) to the equilibrium constant K_M, and (ii) to the values of a_MO, which are related to the solution properties. The availability of reliable thermodynamic data for slag components and impurity compounds in slags and in mattes or liquid metals are essential for the accurate prediction of impurity capacities and their distribution ratios.

The RB model is an invaluable tool for the optimisation of impurity removal in the existing processes and for the development of new processes. The *a priori* prediction of other impurity capacities such as Se and Te in non-ferrous metal smelting slags and mattes using RB model is possible and such predictions are very useful in understanding the behaviour of impurities in the current and eventually future non-ferrous metals technologies.

ACKNOWLEDGEMENTS

The author acknowledges the financial support from the National Science Foundation (NSF) and ACIPCO for this research project. Author also thanks the Department of Metallurgical and Materials Engineering, The University of Alabama for providing the experimental and analytical facilities.

REFERENCES

Bale, C W, Pelton, A D and Thompson, W T, 2002. FactSage 5.1: Thermochemical Software for Windows. TM Montreal, Quebec: Thermfact Ltd.

Chen, B, Reddy, R G and Blander, M, 1989. Sulfide capacities of CaO-FeO-SiO_2 Slags, *3rd International Conference on Molten Slags and Fluxes*, pp 270–272.

Derin, B, Yucel, O and Reddy, R G, 2006. Predicting of Sulfide Capacities of Industrial Lead Smelting Slags, *Advanced Processing of Metals and Materials*, 1:237–244.

Derin, B and Reddy, R G, 2003. Sulfur and Oxygen Partial Pressure Ratios Prediction in Copper Flash Smelting Plants Using Reddy-Blander Model, in *Yazawa International Symposium: Metallurgical and Materials Processing: Principles and Technologies; Materials Processing Fundamentals and New Technologies* (eds: F Kongoli, K Itagaki, C Yamauchi, H Y Sohn, F Kongoli, K Itagaki, C Yamauchi and H Y Sohn), 1:625–632.

Derin, B, Yucel, O and Reddy, R G, 2004. Modelling of Sulfide Capacities of Binary Titanate Slags, *EPD Congress 2004*. pp 155–160.

Derin, B, Yucel, O and Reddy, R G, 2005. Sulfide Capacities of PbO-SiO_2 and PbO-SiO_2-$AlO_{1.5}$ (sat.) Slags, *Mining and Materials Processing Institute of Japan (MMIJ),* Kyoto, Japan, pp 1279–1287.

Derin, B, Yucel, O and Reddy, R G, 2011. Sulfide Capacity Modelling of FeOx-MO-SiO_2 (MO=CaO, MnO, MgO) Melts, *Minerals and Metallurgical Processing*, 28(1):33–36.

Flood, H and Grjotheim, K, 1952. Thermodynamic calculation of slag equilibria, *Journal of the Iron and Steel Institute*, 171:64–70.

Font, J M and Reddy, R G, 2003. Modeling of Impurity Distribution between Mattes and Slags, *Copper 2003*, IV:301–313.

Font, J M and Reddy, R G, 2005. Modelling of Antimonate Capacity in copper and Nickel Smelting Slags, *Trans Inst Min Metall C*, 114:C160–C164.

Font, J M, Hino, M and Itagaki, K, 1998a. Thermodynamic Evaluation of Distribution Behaviour of VA Elements in Nickel Matte Smelting, *Met Rev of MMIJ*, 15(2):202–220.

Font, J M, Hino, M and Itagaki, K, 1998b. Minor Elements Distribution between Iron-Silicate Base Slag and Ni_3S_2-FeS Matte under High Partial Pressures of SO_2, *Mat Trans JIM*, 39(1998):834–840.

Font, J M, Hino, M and Itagaki, K, 1999. Phase Equilibrium Minor and Elements Distribution between Iron-Silicate Base Slag and Nickel-Copper-Iron Matte at 1573 K under High Partial Pressures of SO_2, *Mat Trans JIM*, 40:20–26.

Font, J M, Hino, M and Itagaki, K, 2000. Phase Equilibrium and Minor-Element Distribution between Ni_3S_2-FeS Matte and Calcium Ferrite slag under High Partial Pressures of SO_2, *Metall Trans B*, 31B:1231–1239.

Kojo, I V, Taskinen, P A and Lilius, K R, 1984. The Thermodynamics of copper fire refining by Sodium Carbonate, *Second international Symposium on Metallurgical Slags and Fluxes*, pp 723–737.

Larouche, P, 2001. Minor Elements in Copper Smelting and Electrorefining, MS thesis, Mining and Metallurgical Engineering, McGill University, 165 p.

Nikolov, S, Jalkanen, H and Kyto, M, 1992. Distribution of some impurity elements between high grade copper matte and calcium ferrite slag, *4th Inter Conf on Molten Slags and Fluxes*, *ISIJ*, pp 560–565.

Pelton, A D, 1999. Thermodynamic Calculation of gas solubilities in oxide melts and glasses, *Glastechnische berichte*, 72:40–62.

Pelton, A D, 2000. Thermodynamic Modelling of Complex Solutions, *The Brimacombe Memorial Symposium*, pp 763–780 (MetSoc: Canada).

Pelton, A D, Eriksson, G and Romero-Serrano, A, 1993. Calculation of sulfide capacities of multi-component slags, *Metall Trans B*, 24B:817–825.

Reddy, R G and Blander, M, 1987. Modeling of sulfide capacities of silicate melts, *Metallurgical Transactions*, 18B:591–596.

Reddy, R G and Blander, M, 1989. Sulfide capacities of MnO-SiO_2 slags, *Metallurgical Transactions,* 20B:137–140.

Reddy, R G and Font, J M, 2003. Arsenic Capacities of Copper Smelting Slags, *Metallurgical and Materials Transactions B*, 34B:565–571.

Reddy, R G and Zhao, W, 1995. Sulfide capacities of Na2O-SiO_2 melts, *Metallurgical and Materials Transactions*, 26B:925–928.

Reddy, R G, 2003b. Emerging Technologies in Extraction and Processing of Metals, *Metallurgical and Materials Transactions B*, 34B:137–152.

Reddy, R G, 2003a. Impurity Capacities in Metallurgical Slags, in *Yazawa International Symposium: Metallurgical and Materials Processing: Principles and Technologies; Materials Processing Fundamentals and New Technologies* (eds: F Kongoli, K Itagaki, C Yamauchi, H Y Sohn, F Kongoli, K Itagaki, C Yamauchi and H Y Sohn), 1:25–48.

Reddy, R G, Hu, H and Blander, M, 1992. Sulfide capacities of silicate slags, in *Proceedings of the Fourth International Conference on Molten Slags and Fluxes*, pp 144–148.

Roghani, G, Hino, M and Itagaki, K, 1997. Phase Equilibrium and Minor Elements Distribution between SiO_2-CaO-FeO_X-MgO Slag and Copper Matte at 1573 K under High Partial Pressures of SO_2, *Mater Trans Jpn Inst Met JIM*, 38:707–713.

Roghani, G, Takeda, Y and Itagaki, K, 2000. Phase Equilibrium and Minor Element Distribution between FeO_X-SiO_2-MgO-Based Slag and Cu_2S-FeS Matte at 1573 K under High Partial Pressures of SO_2, *Metall Trans B*, 31B:705–712.

Roine, A, 2022. HSC Chemistry software, ver. 7.1, Outokumpu Research Oy, Pori, Finland

Rosenqvist, T, 1978. Phase Equilibria in the Pyrometallurgy of Sulfide Ores, *Metallurgical Transaction B*, 9B:337–351.

Yahya, A and Reddy, R G, 2011. Sulfide Capacities of CaO-MgO-$AlO_{1.5}$, MgO-MnO- $AlO_{1.5}$ and CaO-MgO-MnO-$AlO_{1.5}$ Slags, *Trans Inst Min Metall C*, 120(1):45–48.

Flow investigation of multiphase manganese slags

DOI: 10.62053/ESHW9511

V Rimal[1] and M Tangstad[2]

1. PhD candidate, Department of Materials Science and Engineering, Norwegian University of Science and Technology (NTNU), Trondheim, Norway. Email: vishal.rimal@ntnu.no
2. Professor, Department of Materials Science and Engineering, Norwegian University of Science and Technology (NTNU), Trondheim, Norway. Email: merete.tangstad@ntnu.no

ABSTRACT

Multiphase slags form the basis of the reduction pathway for manganese ferroalloy production. The present work aims to understand the flow of slag through the coke bed based on experimentation in controlled conditions. Synthetic slags of different basicities were evaluated for their phase composition, viscosity, and flow. The two-phase slag will have two zones: a liquid slag zone and a multiphase zone. The multiphase zone will consist mostly of a solid phase with some liquid slag between the solid particles. The multiphase part will hence have a high viscosity. The liquid zone will flow into the coke bed while the multiphase area will stay. With increasing reduction, the multiphase area will decrease in size until the solid phase is gone and the whole slag will flow into the coke bed. The effective viscosity of slag will decrease with the lowering of the solid oxide phase. The results from flow experiments confirmed that the segregation of phases occurs when slag flows through the coke bed. It is observed that the flow is dependent both on the size of the void and the viscosity of slag.

INTRODUCTION

High-carbon ferromanganese are alloys containing Fe and C with a major proportion of Mn. They are produced by the carbothermic reduction of oxidic raw materials using coke in a submerged arc furnace (SAF). The SAF has two main reaction zones: (i) pre-reduction zone and (ii) reduction zone. In the pre-reduction zone, CO reduces iron oxides to metallic iron and higher Mn oxides to solid MnO. Carbonates will also decompose to basic oxides. Gas reduction of MnO to Mn is not possible due to the high stability of MnO. In the reduction zone, the pre-reduced components meet the coke bed. A slag mixture of liquid and solid phases is formed at this stage. The liquid phase consists of CaO, MnO, MgO, Al_2O_3, and SiO_2. The solid phase occurs due to the saturation of MnO in the liquid phase. The MnO present in the liquid phase reacts with the C in the coke bed through the following reaction to yield metallic Mn:

$$MnO_{liquid\ slag} + C_{solid} = Mn_{liquid} + CO_{gas}$$

As the reaction proceeds, the solid phase decreases and the reaction will rapidly slow down when a single-phase slag is achieved (Kumar, Ranganathan and Sinha, 2007; Tangstad *et al*, 2021; Hockaday, Dinter and Reynolds, 2023; Larssen and Tangstad, 2023).

In a SAF the coke bed does not act as a source of fuel rather it provides the carbon reductant, but more importantly the electrical resistance for energy development (Davies *et al*, 2023). The flow behaviour of the slag into the coke bed significantly affects the efficiency and the environmental emissions in the SAF (Oh and Lee, 2016). A consistent flow with characteristic fluid behaviour is desired for the smooth operation of SAF (Natsui *et al*, 2020; Dong *et al*, 2021). The coke bed can be described as a packed bed with the coke particles acting as the packing material. The packing is random and generally results in the formation of interconnected voids of variable sizes through which the liquids trickle down and gases flow upwards. The coke bed should be permeable to allow the flow of the different phases. The structure of the packed bed and packing density affects the size of voids, their interconnectivity as well as the permeability and liquid holdup (Geleta, Siddiqui and Lee, 2020; Natsui *et al*, 2021).

The flow of fluids through the coke bed is often interpreted in terms of void, micro-, and macro-scales. The majority of the studies on relations affecting the flow of slag have been based on cold models and non-moving packed beds, so inferences in high-temperature real-world conditions can vary significantly. Manuscripts have generally considered the coke bed as stationary since the descent of coke bed is very slow (Fukutake and Rajakumar, 1982). A number of studies at high

temperatures have been reported, however, the inconsistent physical and chemical properties of coke make it difficult to generalise the characteristics like reactivity, wetting, and strength (Safarian and Tangstad, 2009; George *et al*, 2014). The liquid slag/metal often flows as droplets or channels in the coke bed (Jeong, Kim and Sasaki, 2014). The size of voids has been found to influence the rate of flow of liquids as it progresses through the coke bed (George *et al*, 2014). Prior studies have shown that the overall resistance to the liquid flow increases with the decrease in particle size in the packed bed (Bando *et al*, 2005; Kawabata, Liu *et al*, 2006a; Kawabata, Shinmyou *et al*, 2006b).

For manganese ferroalloys, a significant portion of reduction generally takes place at the top section of the coke bed. The charge (oxides and coke) will settle on top of the permanent coke bed. The proportion of coke fed into the furnace will determine if the permanent coke bed is consumed in the process or not. The charge provides the necessary carbon source. According to theory, negligible reduction takes place when the slag has entered the coke bed as a single phase since the activity of MnO is very low when a single-phase slag is achieved (Olsen, Tangstad and Lindstad, 2007). The interaction of slag with the coke bed is thus dependent on the reduction of Mn in the upper sections of the coke bed.

The flow of slag through the coke bed will depend on the size of voids and the viscosity of Mn slag. The viscosity of Mn slag is high when the slag exists as a solid-liquid mixture and decreases with a decrease in the proportion of solid phase. When the melt initially encounters the coke bed, the viscosity of slag is high. As the reduction proceeds the viscosity decreases enabling the flow of slag through the coke bed (Tang and Tangstad, 2007; Muller, Zietsman and Pistorius, 2015).

This manuscript aims to understand the flow of slag in controlled conditions under the influence of gravity. Limited literature exists elucidating the Mn slag behaviour in the coke bed. The specific interest here is thus to comprehend the segregation of phases as the reduction proceeds and to find the parameters that affect the flow of slag.

EXPERIMENTAL DETAILS

Materials

MnO, SiO_2, Fe_2O_3, CaO, MgO, Al_2O_3, and CaS of analytical grade were procured from Sigma Aldrich and used as received. Double distilled water was used for the preparation of briquettes. Two types of graphite substrates were used for the experiments: (i) flat, and (ii) funnel (Figure 1). The flat substrate was used to evaluate the phase composition and thus calculate the viscosity. The funnel substrate was used to comprehend the flow of slag under the influence of gravity.

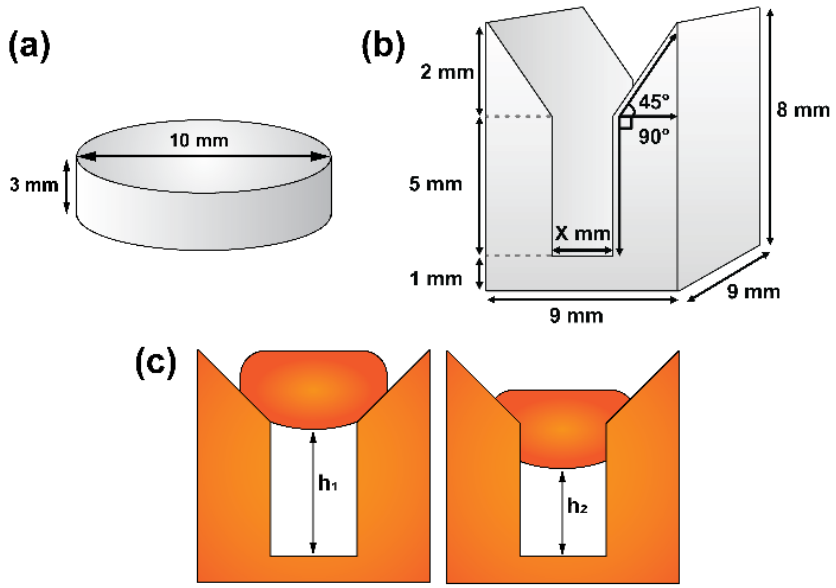

FIG 1 – Illustration of (a) Flat graphite substrate, (b) Graphite funnel diameter 'X = 2, 3, 4, 6 mm', (c) Displacement measurement protocol used in this study. Drawing not to scale.

Methodology

Synthetic slags of different basicity were prepared based on the ratio of chemical compounds as shown in Table 1. The basicity B, in this manuscript is defined using a wt per cent basis as:

$$B = \frac{CaO + MgO}{SiO_2 + Al_2O_3}$$

TABLE 1

Chemical composition of reactants used for experiments.

Basicity	Compound (%)						
	MnO	SiO_2	Fe_2O_3	CaO	MgO	Al_2O_3	CaS
0.8	72.86	10.28	7.85	7.26	1.27	0.30	0.17
1	70.31	9.71	9.31	8.60	1.51	0.36	0.20
1.22	76.45	6.69	7.85	7.26	1.27	0.30	0.17

The compounds 'as received' were mixed, briquetted using a press, and allowed to dry overnight. The samples were then placed on the graphite substrate and heated in a sessile drop furnace in an inert atmosphere with Ar airflow at 0.1 L/min. The heating rate was set at 300°C/min till 900°C followed by 50°C/min till 1500°C. The experiments were independently done for different holding durations (0 min, 20 min, 60 min, and 120 min) at 1500°C as shown in Figure 2. Additionally, slag was also prepared by (i) grinding the mixture before heating as well as by (ii) using a master slag powder of SiO_2, CaO, MgO, Al_2O_3, and CaS prepared at 1700°C. It was observed that identical slags were produced in all three routes. The master slag route was used for all experiments in this manuscript. The basicity was adjusted by adding additional SiO_2 to the mixture before heating.

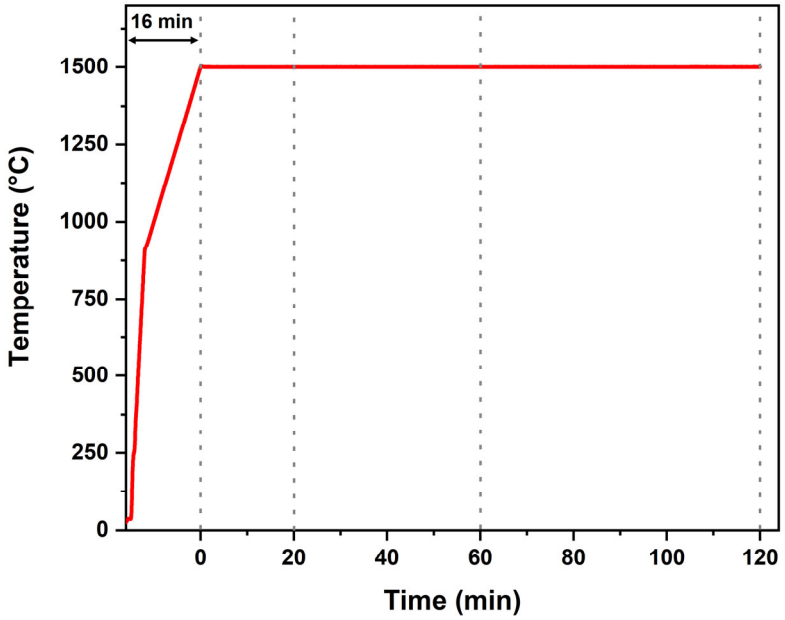

FIG 2 – Heat profile for experiments.

The proportions of the different phases were found from picture analyses from SEM micrographs. The area covered by the different phases was calculated using the measurement feature in Adobe Photoshop 2023. The flow was estimated from the wetting images by evaluating the y-axis displacement of the slag mixture with respect to the centre of the graphite funnel as shown in Figure 1c. The flow measurements were made till the completion of flow or 2 hrs of holding (whichever preceded earlier).

Apparatus

A sessile drop furnace equipped with a pyrometer and a C-type thermocouple was used for heating the samples. The wetting images were taken using a digital video camera (Allied Vision Prosilica GT2000, Edmund Optics, Inc, Barrington) with a telecentric lens (Navitar 1-50993D) at a resolution of 2048×1088 pixels. The distribution of different phases was obtained from SEM (Zeiss Ultra 55LE) images. The images were recorded at 200x magnification with an accelerating voltage of 10 kV. Due to the dimensional limitations, multiple images were captured to cover the periphery of the sample and subsequently compiled into a single image. EPMA (JEOL JXA-8500) was used for determining the composition.

RESULTS AND DISCUSSION

Phase composition and viscosity

The phase composition and viscosity were studied for a basicity of 0.8 and 1.22 on a flat substrate for different durations of holding ie 0 min, 20 min, 60 min, and 120 min at 1500°C. For all the holding durations, three phases *viz* liquid slag phase containing MnO-CaO-Al_2O_3-MgO and SiO_2, solid slag phase containing mainly MnO, and reduced Mn-Fe-metal could be observed in the SEM images (Figure 3). SEM image showing the solid particles surrounded by the liquid phase as well as the dendrites in the liquid slag, which are assumed to be the MnO phase precipitated during cooling is shown in Figure 4. The amount of solid phase was found to decrease with time as the reduction of MnO progressed. The composition analysis obtained using WDS/EPMA shows that the per cent MnO in the liquid phase is higher for 0.8 basicity (Figure 5). For the solid phase, the per cent MnO is the same for both basicities and close to 90 per cent. Here the solid phase does not include dendrites. The composition remains constant throughout holding for both phases except values at 0 min being found to deviate from others. The region has been highlighted in grey in the figure and represents the uncertainty in values in the studied range. Subsequent plots also have similar deviations at 0 min holding and are highlighted similarly. The per cent MnO in the liquid phase was also plotted against basicity (Figure 6). It is seen that the per cent MnO in liquid slag increases with a decrease in basicity. The experimental values were lower than theoretical predictions, however, the trend is comparable.

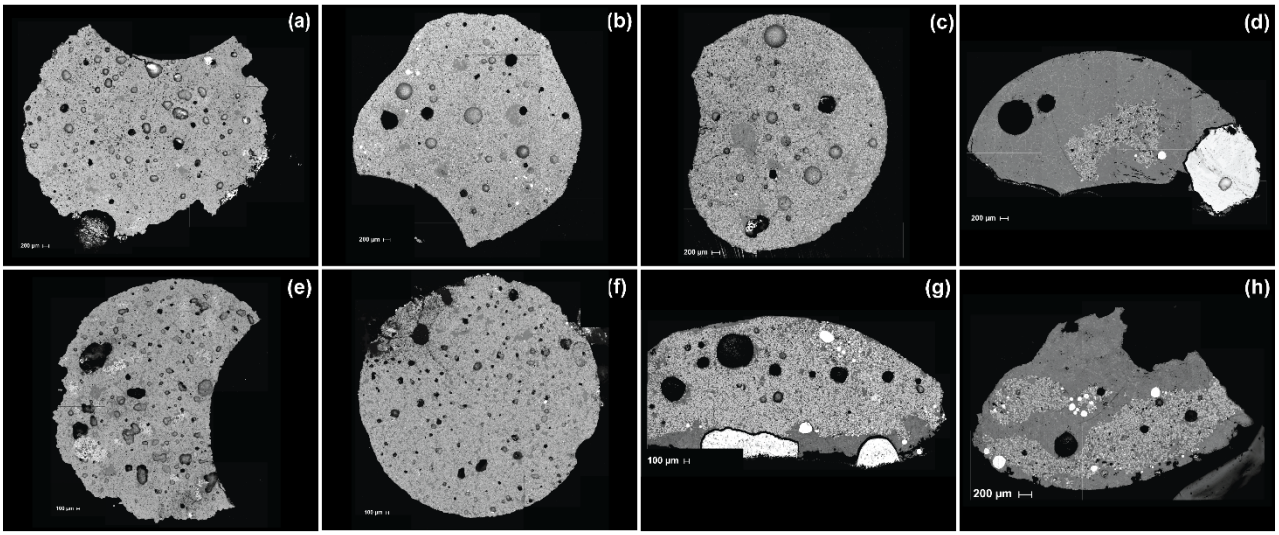

FIG 3 – SEM imaging of (a) 0.8 basicity at 0 min, (b) 0.8 basicity at 20 min, (c) 0.8 basicity at 60 min, (d) 0.8 basicity at 120 min, (e) 1.22 basicity at 0 min, (f) 1.22 basicity at 20 min, (g) 1.22 basicity at 60 min, (h) 1.22 basicity at 120 min.

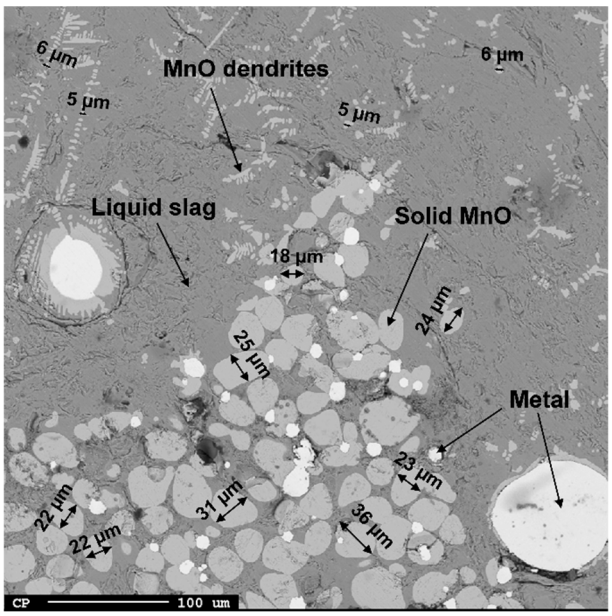

FIG 4 – SEM image showing the different phases. In the lower part one can see the multiphase, the mixture of solid MnO particles in a liquid, and in the top part the liquid.

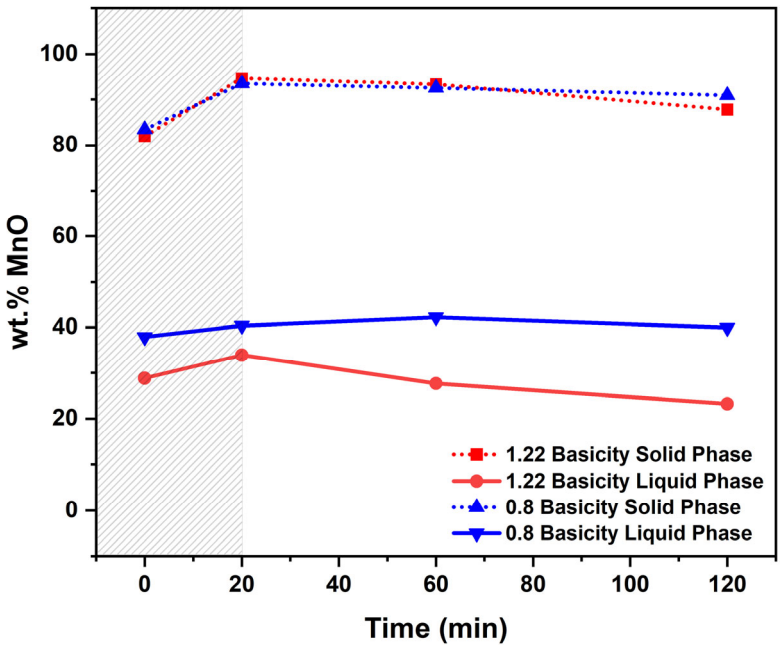

FIG 5 – wt per cent MnO versus Time for both solid MnO phase and liquid phase.

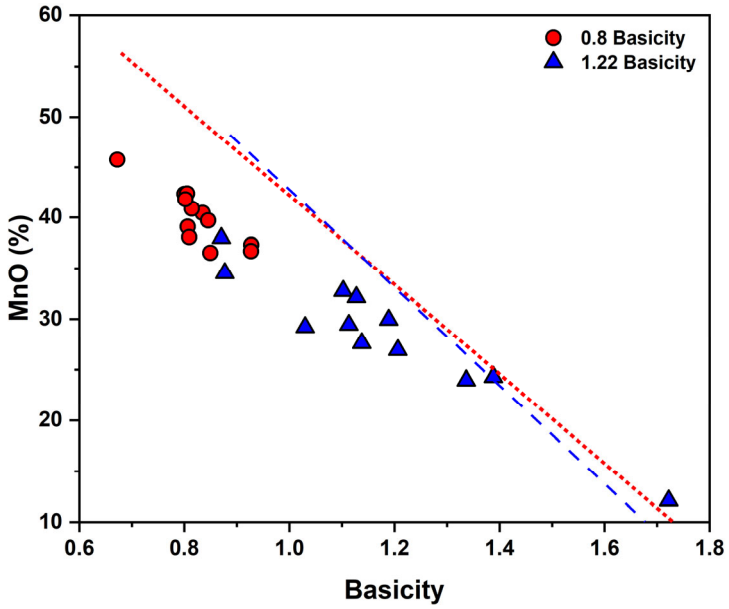

FIG 6 – per cent MnO versus Basicity (red and blue line indicate theoretical trend for 0.8 basicity and 1.22 basicity respectively).

The phase distribution is presented in Figure 7. As explained in the preceding paragraph, the solid phase decreases with reduction, that is the holding time. Using the phase distribution data, the overall MnO content was calculated using the formula:

$$\%MnO = \theta_{solid} \cdot \%MnO_{solid} + \theta_{liquid} \cdot \%MnO_{liquid}$$

where:

%MnO = total MnO content

θ_{solid} = fraction of solid phase

$\%MnO_{solid}$ = %MnO in the solid phase

θ_{liquid} = fraction of liquid phase

$\%MnO_{liquid}$ = %MnO in the liquid phase

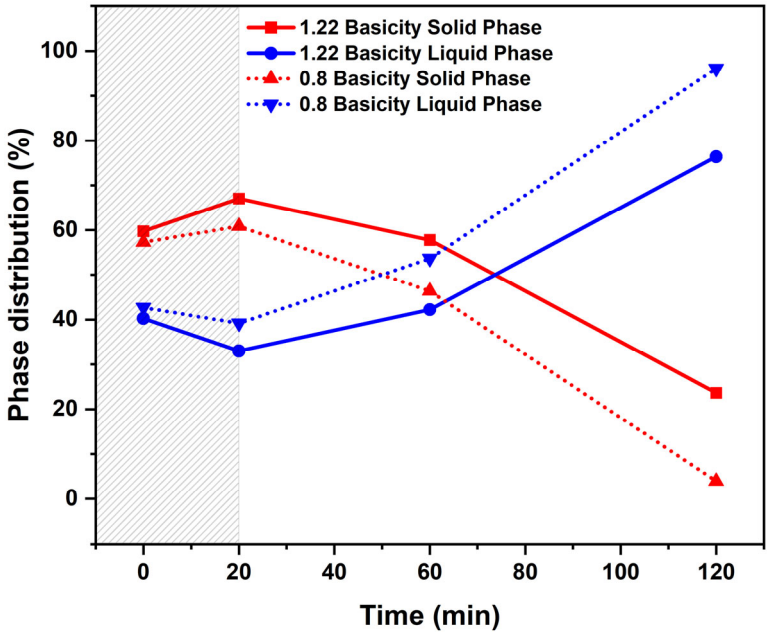

FIG 7 – Calculated amount of solid MnO phase and liquid phase.

Figure 8 shows the rate of MnO reduction with respect to time for 0.8 and 1.22 basicity. The rate of MnO reduction is constant for both basicities. The reduction of MnO is highly endothermic and literature suggests that the rate of reduction is chemically controlled and not transport-controlled (Ostrovski *et al*, 2002; Olsen, Tangstad and Lindstad, 2007). The present result counters earlier reports wherein the rate of reduction was found to be lower for high basicity solid-liquid mixture. Reports have also concluded that higher basicity was found to give a faster reduction in the case of a homogenous single-phase slag (Olsø, Tangstad and Olsen, 1998).

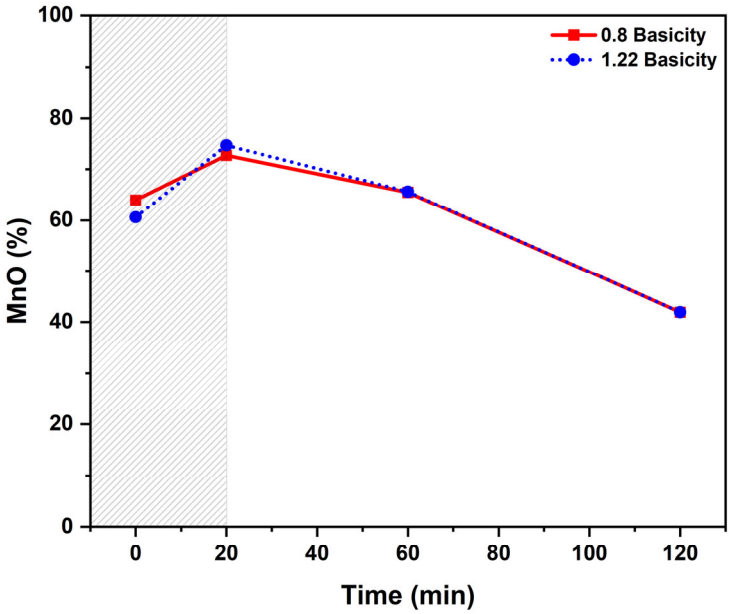

FIG 8 – Total per cent MnO versus Time showing the reduction of slag with time.

The viscosity of the liquid slag phase was calculated using the Urbain model developed by Mills, Yuan and Jones (2011). Figure 9 shows the viscosity of the liquid phase for 0.8 and 1.22 basicity at 0 min and 120 min of holding. The experimental composition at 1500°C was also extended for viscosity calculation at 1400°C and 1600°C. The effect of temperature on viscosity was well-defined in the model used. In the absence of a solid phase, the viscosity is higher for low-basicity systems and *vice versa*. However, for systems with a solid phase in existence the effective viscosity will have to be described using the Einstein-Roscoe equation (Roscoe, 1952):

$$\mu e \; = \; \mu(1 - 1.35\theta)^{-(\frac{5}{2})}$$

where:

μ_e = effective viscosity of the slag

μ = viscosity of liquid phase

θ = the fraction of precipitated solid phases

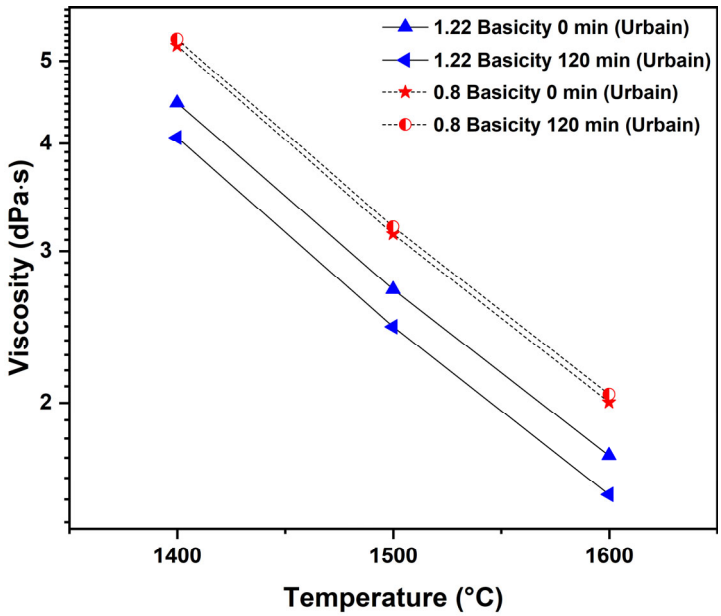

FIG 9 – Viscosity of liquid slag at different temperatures.

It is found that for a solid-liquid mixture, the effective viscosity is higher for high basicity systems as it contains a higher amount of solid MnO and the viscosity gradually lowers with lowering the amount of solid phase (Figure 10). For this calculation, the entire sample has been considered as a mixture of liquid and solid phases. Upon attainment of homogenous slag, the viscosity trend will reverse as discussed earlier.

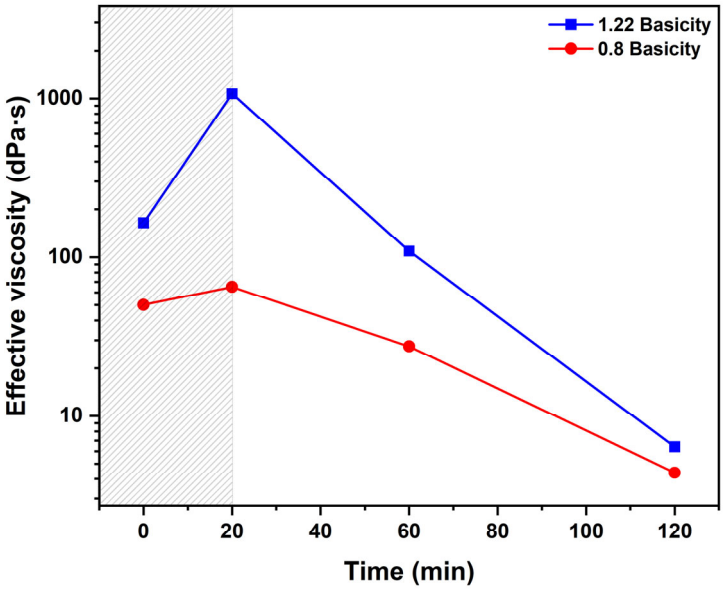

FIG 10 – Effective viscosity versus time.

The effective density of the slag was also determined using the equation:

$$\rho = \frac{(m_1 + m_2)}{(V_1 + V_2)}$$

where:

ρ = effective density

m_1 = mass of solid phase

m_2 = mass of liquid phase

V_1 = volume of solid phase

V_2 = volume of liquid phase

The effective density of the slag mixture was found to be roughly constant for 0.8 and 1.22 basicity at different holding durations (Figure 11). The effective density of the slag mixture lowers with the decrease in the solid phase.

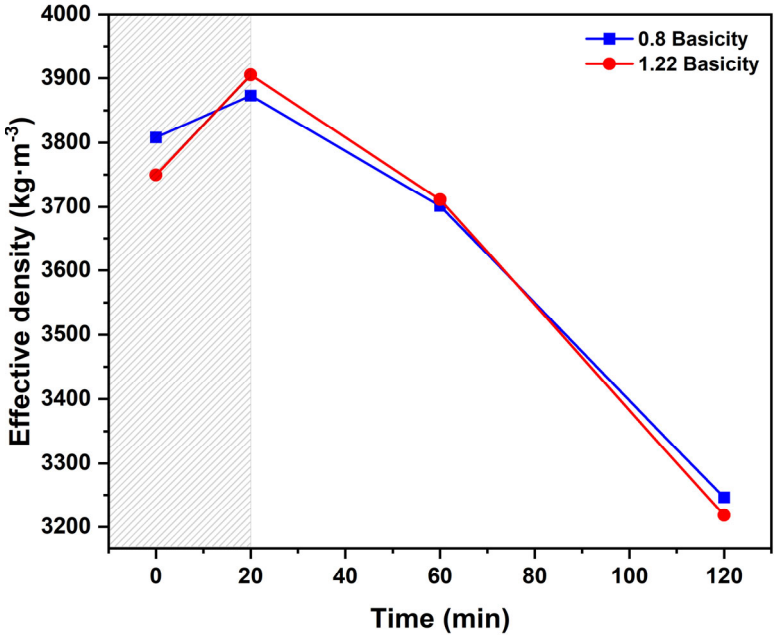

FIG 11 – Effective density versus time.

Flow measurement

Slags of three different basicities (0.8, 1, and 1.22) were evaluated using the funnel substrate to replicate the flow of slag through the coke bed in controlled conditions under the influence of gravity. The funnels of varying dimensions represent the different void sizes in the coke bed. The upper portion of the funnel represents the neck of the voids in the coke bed. The samples were heated using the same temperature profile as the flat substrate. Figure 12 shows the displacement of slag with respect to time at a constant temperature of 1500°C. The time ranges from 0 to 120 min of holding. The duration to complete the flow was typically quicker for funnels with larger dimensions like 3 mm and 4 mm. The slowest flow was observed for samples studied in 2 mm funnels for all basicities. This indicates that the flow of slag is influenced by the size of voids in the coke bed.

The live images obtained from the sessile drop furnace have been superimposed in the displacement plots (Figure 12). The reduction proceeds from the slag surface in contact with carbon and the produced metal phase typically appears away from the slag-carbon interface, here in our case the top or bottom portion of the funnel. The low-viscosity and higher-density metal phase is immiscible in the slag phase and separates as droplets that accumulate together resulting in a larger metal phase. Correlating the images and displacement, the metal phase is thus assumed to bring the sudden rapid displacement in the studied plots.

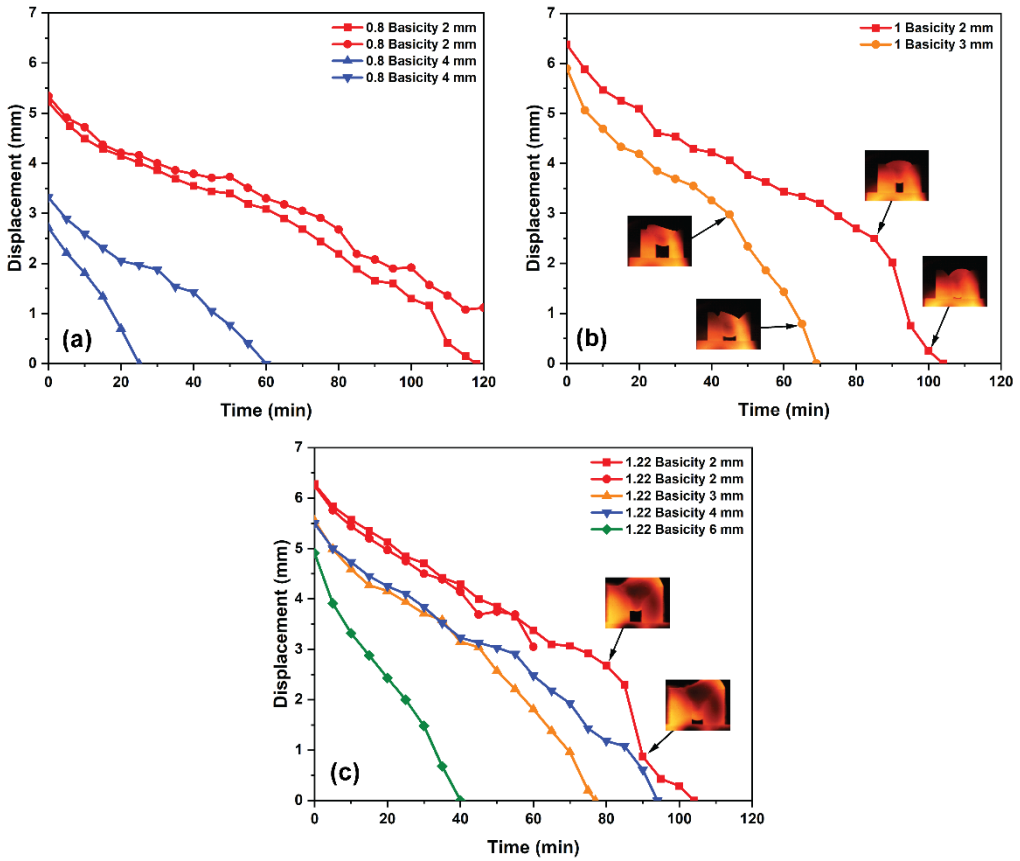

FIG 12 – Displacement versus time plots for different basicity and funnel dimensions.

SEM images of the funnels after completion of flow show the presence of solid, liquid, and metal phases (Figure 13). It is however observed that the phases segregate as the reduction proceeds. The slag is seen to comprise of two regions: a homogenous liquid slag of low viscosity and a multiphase solid-liquid mixture possessing high viscosity. The segregation pattern thus follows the trend of the multiphase slag at the top, homogenous slag in the middle, and metal phase at the bottom of the funnel. The region covered by the multiphase slag has high viscosity, which limits it from deforming. The low viscosity of the homogenous liquid slag allows it to seep under the multiphase region despite possessing a lower density. The immiscibility between the metal and liquid slag results in the clear demarcation between the two phases. A major portion of the metal phase is found at the bottom section of the funnel. However, it could be seen that in situations where the metal phase is produced in the upper sections of the funnel, the metal phase is unable to pass through the multiphase region. The viscosity of the multiphase region can be said to have a considerable impact on determining the flow of slag as it proceeds through the coke bed.

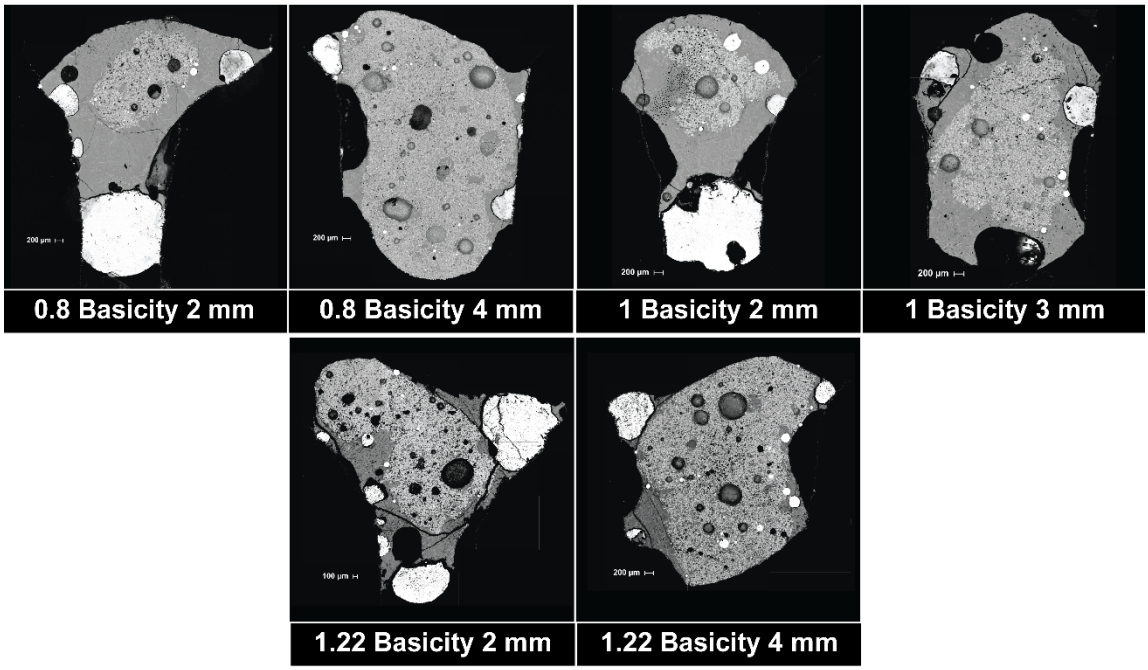

FIG 13 – SEM images of the different funnels after completion of flow.

As previously discussed, the proportion of solid phase decreases with increasing Mn reduction over time. It is seen in SEM images that for the samples investigated in funnel experiments, the quicker flow is generally accompanied with a greater fraction of multiphase. For the 2 mm funnels, the amount of multiphase is considerably less compared to 3 mm and 4 mm funnels. One presumption for this inference is that the dimension of the viscous multiphase in 2 mm is larger than the lower portion of the funnel, which prevents the slag from flowing and enables the reduction to proceed for longer durations. For 4 mm funnels, the multiphase region slides down enabling quick flow, accompanied with low reduction. Figure 14 shows the total per cent MnO after completion of flow for the studied funnels. The per cent MnO is greater for 4 mm funnel compared to 2 mm funnel for all basicities, which confirms the lowering in reduction with an increase in the size of funnels. It can be mentioned that 3 mm with 1.22 basicity is an outliner from this theory.

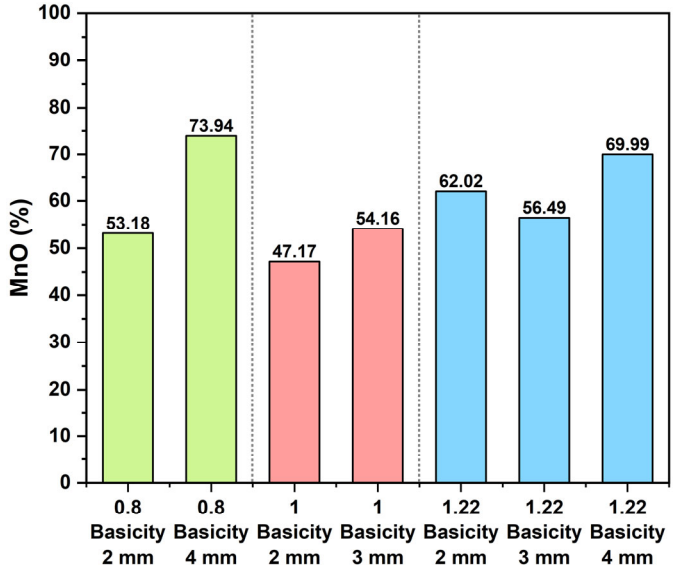

FIG 14 – Total per cent MnO for different basicities and funnel sizes.

The flow of Mn slag through the coke bed thus has two prime factors affecting its flow: (i) dimension of void neck, and (ii) the viscosity of slag. As discussed in the previous section, the flow rate increases with the increase in size of voids. For Mn slag, the high viscosity slag at first encounters

the top or outline of the coke bed. Initially, the flow will be extremely difficult even for big void neck dimensions primarily because the viscous forces will dominate and prevent the flow. As the reduction proceeds the metal phase would trickle down as droplets and eventually result in a metal phase with a clear demarcation with the slag phase. The multiphase slag on the other hand is unable to flow unless the void neck is larger than the multiphase volume at the neck. However, the homogeneous slag (with low viscosity) that is produced during the process drains into the voids. The situation is depicted in Figure 15. If the void neck is large enough to allow the multiphase to flow, this will result in a highly viscous slag being taken into the coke bed making it even more detrimental for smooth flow. Previous excavations have put explanations that the reduction generally completes at the upper sections and the coke bed is generally devoid of significant multiphase slag presence making the large void neck situation unlikely to be encountered in practical scenarios. The type of coke and ash percent are also influential during the flow of slags inside the coke bed however for Mn slag, the viscosity, wetting, and size of voids will most likely be the prime criterion that need to be optimised before other factors are taken into consideration.

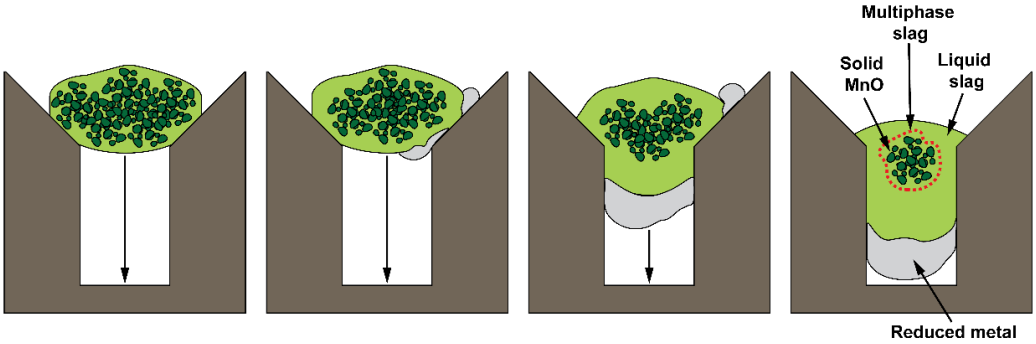

FIG 15 – Flow of slag in FeMn production.

Correlating with the discussion in the introduction, it can be safely concluded that the reduction generally proceeds at the top section of the coke bed in the presence of small voids. A single-phase slag and metal phase is anticipated inside the coke bed. The presence of small voids results in minimum reduction taking place inside the coke bed, but the majority on top of the coke bed.

CONCLUSION

The reduction rate was found to be constant for the studied basicity. The effective viscosity and density decrease with the lowering of the proportion of solid phase. The flow of slag was found to be influenced by the size of funnels, indicating that void size in the coke bed is an important parameter influencing the flow. It can be concluded that a slower flow is expected for coke bed with smaller voids. As the slags flow, the segregation of phases takes place. The solid-liquid multiphase possesses a distinct viscous character. For small voids, the multiphase is unable to flow until a substantial amount of solid phase is reduced whilst a larger void will result in quick flow at the expense of any substantial reduction.

ACKNOWLEDGEMENTS

This publication is funded by the Norwegian Research Council through the KPN project Recursive (326581), and the authors gratefully acknowledge the financial support received.

CONFLICT OF INTEREST

On behalf of all authors, the corresponding author states that there is no conflict of interest.

REFERENCES

Bando, Y, Hayashi, S, Matsubara, A and Nakamura, M, 2005. Effects of packed structure and liquid properties on liquid flow behavior in lower part of blast furnace, *ISIJ International*, 45(10):1461–1465. https://doi.org/10.2355/isijinternational.45.1461

Davies, J, Tangstad, M, Schanche, T L and du Preez, S P, 2023. Pre-reduction of United Manganese of Kalahari Ore in CO/CO_2, H2/H2O and H2 Atmospheres, *Metallurgical and Materials Transactions B*, 54(2):515–535.

Dong, X F, Jayasekara, A, Sert, D, Ferreira, R, Gardin, P, Monaghan, B J, Chew, S J, Pinson, D and Zulli, P, 2021. Investigation of Molten Liquids Flow in the Blast Furnace Lower Zone: Numerical Modelling of Molten Slag Through Channels in a Packed Bed, *Metallurgical and Materials Transactions B*: *Process Metallurgy and Materials Processing Science*, 52(1):255–266. https://doi.org/10.1007/s11663-020-02009-1

Fukutake, T and Rajakumar, V, 1982. Liquid Packed in the Holdup Beds Dropping and under Abnormal Conditions Flow Phenomena the in Flow Simulating Furnace Zone of a Blast, *Transactions ISIJ*, 22:355–364.

Geleta, D D, Siddiqui, M I H and Lee, J, 2020. Characterization of Slag Flow in Fixed Packed Bed of Coke Particles, *Metallurgical and Materials Transactions B*: *Process Metallurgy and Materials Processing Science*, 51(1):102–113. https://doi.org/10.1007/s11663-019-01750-6

George, H L, Longbottom, R J, Chew, S J and Monaghan, B J, 2014. Flow of molten slag through a coke packed bed, *ISIJ International*, 54(4):820–826. https://doi.org/10.2355/isijinternational.54.820

Hockaday, S A C, Dinter, F and Reynolds, Q G, 2023. The thermal decomposition kinetics of carbonaceous and ferruginous manganese ores in atmospheric conditions, *Journal of the Southern African Institute of Mining and Metallurgy*, 123(8):391–398. https://doi.org/10.17159/2411-9717/2527/2023

Jeong, I H, Kim, H S and Sasaki, Y, 2014. Trickle flow behaviors of liquid iron and molten slag in the lower part of blast furnace, *Tetsu-To-Hagane/Journal of the Iron and Steel Institute of Japan*, 100(8):925–934. https://doi.org/10.2355/tetsutohagane.100.925

Kawabata, H, Liu, Z, Fujita, F and Usui, T, 2006a. Characteristics of liquid hold-ups in a soaked and unsoaked fixed bed, *Tetsu-To-Hagane / Journal of the Iron and Steel Institute of Japan*, 92(12):885–892. https://doi.org/10.2355/tetsutohagane1955.92.12_885

Kawabata, H, Niina, K, Harada, T and Usui, T, 2006b. Influence of channeling factor on liquid hold-ups in an initially unsoaked bed, *Tetsu-To-Hagane / Journal of the Iron and Steel Institute of Japan*, 92(12):893–900. https://doi.org/10.2355/tetsutohagane1955.92.12_893

Kumar, M, Ranganathan, S and Sinha, S N, 2007. Kinetics of reduction of different manganese ores, in *Innovations In The Ferro Alloy Industry - Proceedings of the XI International Conference on Innovations in the Ferro Alloy Industry*, *Infacon XI,* pp 241–246.

Larssen, T A and Tangstad, M, 2023. Effect of Raw Materials on Temperature Development during Prereduction of Comilog and Nchwaning Manganese Ores, *Minerals*, 13(7):920.

Mills, K C, Yuan, L and Jones, R T, 2011. Estimating the physical properties of slags, *Journal of the Southern African Institute of Mining and Metallurgy*, 111(10):649–658.

Muller, J, Zietsman, J H and Pistorius, P C, 2015. Modeling of Manganese Ferroalloy Slag Properties and Flow During Tapping, *Metallurgical and Materials Transactions B*: *Process Metallurgy and Materials Processing Science*, 46(6):2639–2651. https://doi.org/10.1007/S11663-015-0426-7

Natsui, S, Tonya, K, Nogami, H, Kikuchi, T, Suzuki, R O, Ohno, K-I, Sukenaga, S, Kon, T, Ishihara, S and Ueda, S, 2020. Numerical study of binary trickle flow of liquid iron and molten slag in coke bed by smoothed particle hydrodynamics, *Processes*, 8(2). https://doi.org/10.3390/pr8020221

Natsui, S, Tonya, K, Hirai, A and Nogami, H, 2021. Comprehensive numerical assessment of molten iron–slag trickle flow and gas counter-current in complex coke bed by Eulerian–Lagrangian approach, *Chemical Engineering Journal*, 414(January):128606. https://doi.org/10.1016/j.cej.2021.128606

Oh, J S and Lee, J, 2016. Composition-dependent reactive wetting of molten slag on coke substrates, *Journal of Materials Science*, 51(4):1813–1819. https://doi.org/10.1007/s10853-015-9588-6

Olsen, S E, Tangstad, M and Lindstad, T, 2007. *Production of Manganese Ferroalloys*, 247 p (Tapir Academic Press).

Olsø, V, Tangstad, M and Olsen, S E, 1998. Reduction kinetics of MnO-saturated slags, in *8th International Ferroalloys Congress*, 8:279–283.

Ostrovski, O, Olsen, S E, Tangstad, M and Yastreboff, M, 2002. Kinetic modelling of MnO reduction from manganese ore, *Canadian Metallurgical Quarterly*, 41(3):309–318. https://doi.org/10.1179/cmq.2002.41.3.309

Roscoe, R, 1952. The viscosity of suspensions of rigid spheres, *British Journal of Applied Physics*, 3(8):267–269. https://doi.org/10.1088/0508-3443/3/8/306

Safarian, J and Tangstad, M, 2009. Wettability of silicon carbide by $CaO\text{-}SiO_2$ slags, *Metallurgical and Materials Transactions B*: *Process Metallurgy and Materials Processing Science*, 40(6):920–928. https://doi.org/10.1007/s11663-009-9292-5

Tang, K and Tangstad, M, 2007. Modeling viscosities of ferromanganese slags, *Innovations In The Ferro Alloy Industry - Proceedings of the XI International Conference on Innovations in the Ferro Alloy Industry*, *Infacon XI,* pp 344–357.

Tangstad, M, Bublik, S, Haghdani, S, Einarsrud, K E and Tang, K, 2021. Slag Properties in the Primary Production Process of Mn-Ferroalloys, *Metallurgical and Materials Transactions B*: *Process Metallurgy and Materials Processing Science*, 52(6):3688–3707. https://doi.org/10.1007/s11663-021-02347-8

Improvement of the copper flash smelting furnace (FSF) and the slag cleaning furnace (SCF) process by advice-based control of silica and coke addition

DOI: 10.62053/BACU4806

A Schmidt[1], S Winkler[2], E Klaffenbach[3], A Müller[4], V Montenegro[5] and A Specht[6]

1. Process Engineer, Aurubis AG, 20539 Hamburg, Germany. Email: am.schmidt@aurubis.com
2. Senior Process Engineer, Aurubis AG, 20539 Hamburg, Germany. Email: s.winkler@aurubis.com
3. Senior Manager R&D, Aurubis AG, 20539 Hamburg, Germany. Email: e.klaffenbach@aurubis.com
4. FSF/SCF Manager, Aurubis AG, 20539 Hamburg, Germany. Email: ar.mueller@aurubis.com
5. Senior Manager R&D, Aurubis AG, 20539 Hamburg, Germany. Email: v.montenegro@aurubis.com
6. Executive Director Pyrometallurgy R&D, Aurubis AG, 20539 Hamburg, Germany. Email: a.specht@aurubis.com

ABSTRACT

In the process of primary copper smelting in flash smelting furnace (FSF), the ratio of iron to silica (Fe/SiO_2 mass ratio) primarily determines the slag viscosity and magnetite formation. Viscous slag does not only cause difficulties in daily operation, such as in tapping, it also increases the copper losses to slag. Thus, keeping the Fe/SiO_2 mass ratio at the desired level is an important aspect of FSF and slag cleaning furnace (SCF) operation.

In this study, the improvement of the Fe/SiO_2 mass ratio was conducted in two steps: First, the optimal Fe/SiO_2 mass ratio was derived based on thermodynamic data. Based on this analysis, appropriate control limits were determined. Second, this range of favourable Fe/SiO_2 mass ratios was implemented into operation by an advice-based control system, which suggests the addition of silica based on the analysis of SCF slag. As this approach was successful, the same advice-based control system principle was adapted for the coke addition to the SCF.

After testing the new advice-based control for several months, the production data confirm the predictions by thermodynamics: since the prediction was implemented as an advisor, the copper and magnetite content in SCF slag is significantly reduced and viscous slag is reported less often by operations.

INTRODUCTION

In flash smelting furnace (FSF) operation, the Fe/SiO_2 mass ratio is an important target for controlling the slag quality, the balance is crucial as both too high and too low ratios can lead to undesirable effects. Too high Fe/SiO_2 mass ratios promote magnetite formation and increased slag viscosity, resulting in higher copper losses (Wang *et al*, 2021). This effect occurs also at too low Fe/SiO_2 mass ratios, as the excessive addition of silica increases the slag viscosity as well (Shen *et al*, 2022). An additional drawback of low Fe/SiO_2 mass ratios is that the overall slag amount increases with higher silica addition, leading also to additional copper losses. Moreover, the presence of magnetite and silica in the slag has been linked to the formation of mechanically entrapped matte particles, which contribute significantly to copper losses in the slag (Imris, Sánchez and Achurra, 2005). Research indicates that the concentration of copper and minor elements in slags can be optimised by controlling the slag composition (Klaffenbach *et al*, 2021). In this study a two-step approach is outlined: First, the optimal Fe/SiO_2 mass ratio is derived from thermodynamic calculations (Step 1). Secondly, this optimal Fe/SiO_2 mass ratio is implemented as a target for slag control into operations by an advice-based control system (Step 2). As an additional step, the same advice-based control system was adapted for the coke charging into the slag cleaning furnace (SCF) for improving the slag quality further and ensuring comprehensive control over the slag quality of both the FSF and the SCF. This study describes a case of optimising the industrial operation of Aurubis Hamburg's primary smelting process with the objective to reduce magnetite formation and hence copper losses to the slag.

Step 1 – Thermodynamic derivation of the optimal Fe/SiO_2 ratio

Equilibrium calculations are crucial procedure in determining the conditions, at which a fully liquid slag without solid particle formation is achieved within the FSF. The calculations were conducted using FactSage™ 8.0 using FactPS and UQPY private database. Various solution phases including matte/metal (Liq(Matte/Metal)), slag (UQPY-SLAG), spinel (UQPY-SPIN) were considered along with the stochiometric compounds tridymite (SiO_2) and fayalite (Fe_2SiO_4). Within the calculation, the operating conditions (such as feed composition, slag composition and oxygen enrichment) were set to model the behaviour of the metallurgical system in the FSF of Aurubis Hamburg. In Figure 1 the result of the calculation is illustrated, in which the impact of temperature and Fe/SiO_2 mass ratio on the calculated liquidus is shown.

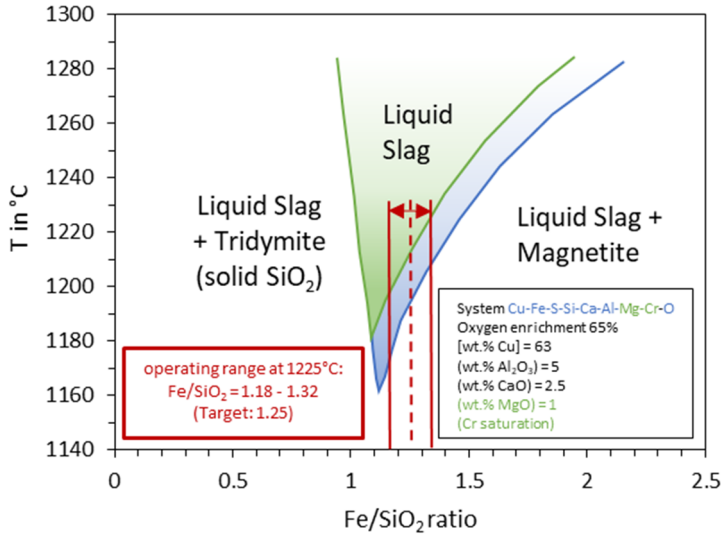

FIG 1 – Impact of temperature and Fe/SiO_2 mass ratio on the calculated liquidus of slag under conditions of Aurubis Hamburg flash smelter.

The calculation was conducted with and without presence of MgO and Cr_2O_3 in slag, in order to also consider the effect of interaction with magnesia chromite refractory on the slag liquidus. It can be seen that the presence of these components decreases the liquid range of the slag (green area in the diagram) as opposed to a slag without MgO and Cr_2O_3 components (blue and green area in the diagram combined). As MgO and Cr_2O_3 are likely to be present in an industrial slag, the derivation of the optimal Fe/SiO_2 mass ratios is derived from the respective liquid range.

At low Fe/SiO_2 mass ratios, tridymite (solid SiO_2) would be formed, meaning that in practice incomplete melting of silica would occur. At high Fe/SiO_2 mass ratios magnetite would be formed. Both should be avoided to achieve a slag with low viscosity, ensuring undisturbed settling of the copper containing particles within the given time. At the same time, only a minimum amount of slag should be produced, so that a high Fe/SiO_2 mass ratio is favoured. It was found that the Fe/SiO_2 mass ratio in operation has a variability of ±0.07 around the set point. For this reason, the targeted Fe/SiO_2 mass ratio at a process temperature of 1225°C is Fe/SiO_2 = 1.25 with an upper limit of 1.32 and a lower limit of 1.18. By the upper limit it is ensured that magnetite formation is prevented, the lower limit prevents excessive production of slag and also occurrence of non-molten silica.

Step 2 – Implementation into operation by an advice-based control system

The Fe/SiO_2 mass ratio in the FSF slag is controlled by sampling and analysing the SCF slag. Depending on the iron and silica content in slag, the ratio is then adjusted by manual changes to the silica addition to the feed. In practice, this leads to the following stages:

1. Sampling and analysis of SCF slag. Thereby, the chemical components are analysed by X-ray diffraction (XRD) and standard Satmagan.
2. Review of the SCF slag composition by the operators.
3. Manual calculation of the Fe/SiO_2 mass ratio and decision on the addition or reduction of silica.

4. Adjustment of the silica flow.

This process contains an inevitable time delay from sampling until the SCF slag analysis is available. Hence, the in-house developed advice-based control system for SiO_2 aims to shorten the reaction time from this point on until the ratio is adjusted by the operators by giving advice on the necessary addition or reduction of silica, thus simplifying step 2 and 3.

The slag analysis is directly retrieved from laboratory data into a separate calculation tool, which then calculates the instantaneous Fe-SiO_2 ratio. Afterwards, the Fe/SiO_2 mass ratio is compared automatically to the target Fe/SiO_2 mass ratio, giving direct advice to the operators in the control room, on whether to increase or reduce the silica flow.

As shown in Figure 2, this approach has been well accepted by the operators and was very successful in reducing the amplitude of fluctuations in the Fe/SiO_2 mass ratio, causing a reduction of outliers outside of the target Fe/SiO_2 mass ratio range by 70 per cent compared to before the implementation of the new advice-based control system.

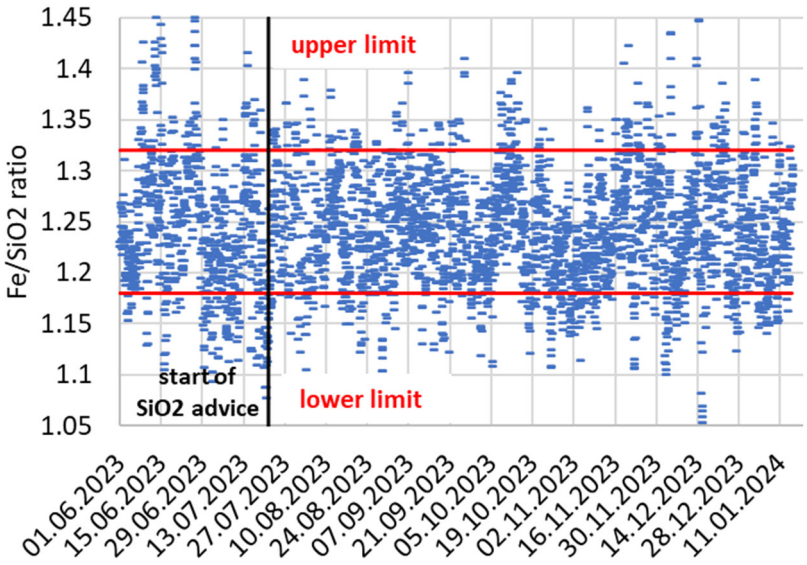

FIG 2 – Fe/SiO_2 mass ratio in SCF slag before and after implementation of the advice-based control system for SiO_2.

Since the Fe-SiO_2 was well implemented in the FSF, this control system was adapted to also give advice on the coke charging into the SCF in order to improve the slag quality further. Thereby, the coke already fed into the SCF is calculated based on the bunker weights, giving real-time advice on when and how much coke to charge until the daily target value is reached. The development of the coke charging is shown in Figure 3, proving the significant stabilisation of the process after implementation of the advice-based control system.

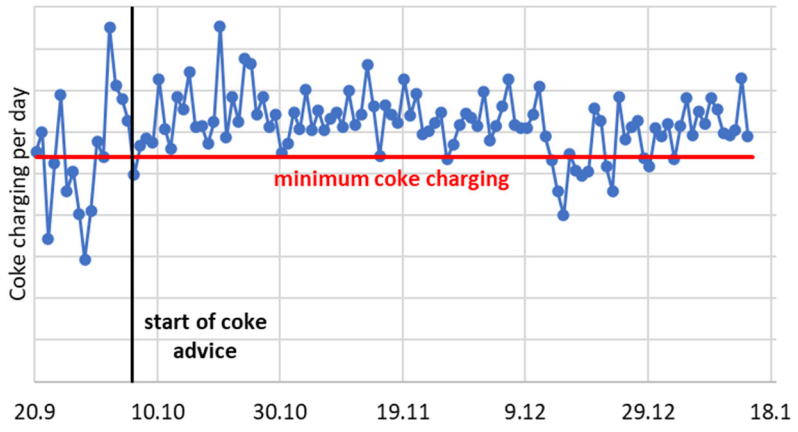

FIG 3 – Daily coke charging before and after implementation of the advice-based control system for coke.

In accordance with the thermodynamic predictions described in Step 1, the magnetite content of SCF stabilised and dropped significantly after the SiO_2 advice and the coke advice were implemented, as shown in Figure 4. Finally, a magnetite reduction by 41.9 per cent was observed, this improvement is stable for several months by now. Accordingly, the reports of viscous slag by operation have dropped by 56 per cent.

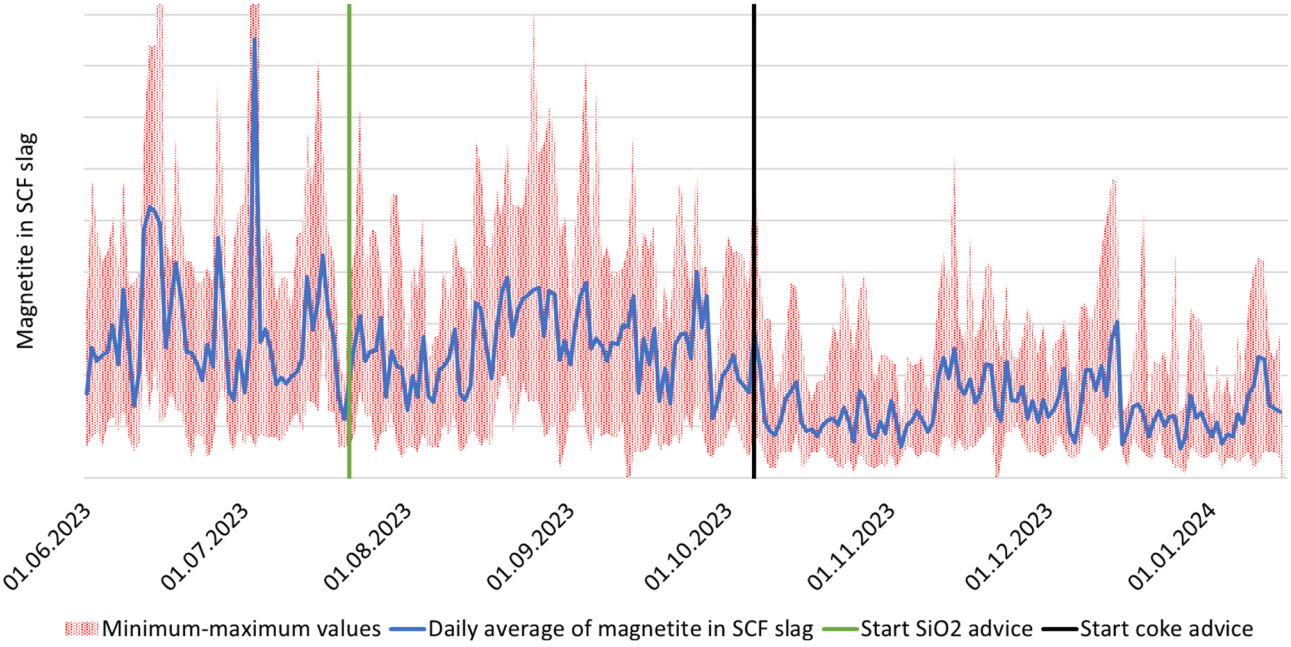

FIG 4 – Development of magnetite content in SCF slag after implementation of the SiO_2 advice and the coke advice.

The implementation of the advisors in the FSF and the SCF also caused a drop in copper losses, which currently accounts to a reduction of 6 per cent compared to before implementation of the advice-based control system.

CONCLUSIONS

The new advice-based control system was tested for several months and caused a visible stabilisation of the Fe/SiO_2 mass ratio and of coke addition to the SCF. In total, both measures caused a reduction of magnetite in SCF slag by 41.9 per cent. This reduction in magnetite led to a significant reduction in reports of viscous slag by operations and caused a reduction in copper losses by 6 per cent, proving that the thermodynamic predictions are correct and that they are an effective measure for improving slag quality. Both measures are still in operation and further data will be evaluated.

REFERENCES

Imris, I, Sánchez, M and Achurra, G, 2005. Copper losses to slags obtained from the El Teniente process, *Mineral Processing and Extractive Metallurgy,* 114(3):135–140. https://doi.org/10.1179/037195505X49769

Klaffenbach, E, Mostaghel, S, Guo, M and Blanpain, B, 2021. Thermodynamic Analysis of Copper Smelting, considering the Impact of Minor Elements Behavior on Slag Application Options and Cu-recovery, *Journal of Sustainable Metallurgy*, 7(2):664–683. https://doi.org/10.1007/s40831-021-00354-2

Shen, Y, Ma, Y, Peng, Y, Lu, B, Dou, Y, Tian, J, Guo, W and Zhang, Z, 2022. Effect of FeO content on melting characteristics and structure of nickel slag, *Journal of Mining and Metallurgy*, *Section B: Metallurgy*, 58(3):427–438.

Wang, L, Wei, Y, Zhou, S, Li, B and Wang, H, 2021. Matte separated behavior from slag during the cleaning process by using waste cooking oil as carbon neutral reductant, *Journal of Mining and Metallurgy Section B Metallurgy*, 57(3):379–388.

Characterisation and assessment of B_2O_3 added LF slag

DOI: 10.62053/QDUJ1311

S S Varanasi[1], S Kakara[2], B V R Mandalika[3], M B Shaik[4] and A Kamaraj[5]

1. Senior Manager (R&D), Rashtriya Ispat Nigam Limited, Visakhapatnam Steel Plant, Visakhapatnam 530031, India; PhD student, Department of Materials Science and Metallurgical Engineering, IIT Hyderabad 502285, India. Email: ms22resch14005@iith.ac.in
2. PhD student, Department of Materials Science and Metallurgical Engineering, IIT Hyderabad 502285, India. Email: ms23resch02001@iith.ac.in
3. General Manager, Corporate office, Rashtriya Ispat Nigam Limited, Visakhapatnam Steel Plant, Visakhapatnam 530031, India. Email: mbvenkatarao@vizagsteel.com
4. PhD student, Department of Materials Science and Metallurgical Engineering, IIT Hyderabad 502285, India. Email: ms22resch14003@iith.ac.in
5. Assistant Professor, Department of Materials Science and Metallurgical Engineering, IIT Hyderabad 502285, India. Email: ashokk@msme.iith.ac.in

ABSTRACT

The properties of top slags play a very important role in secondary steelmaking. Fluxes should be chosen based on the ladle furnace (LF) slag requirements like viscosity, melting temperature, sulfide capacity, etc. CaF_2 and $CaO\text{-}Al_2O_3$-based synthetic slags are the most used fluxes in secondary steelmaking to improve slag fluidity and interfacial chemical reactions. CaF_2 is obsolete due to fluorine pollution and $CaO\text{-}Al_2O_3$ based slags have 40–50 wt per cent Al_2O_3 and 30–40 per cent CaO which is not beneficial for desulfurisation. Yet another drawback is that LF slag disintegrates into fine powder during cooling due to phase transformation C_2S ($2CaO.SiO_2$). Hence, there is a need for the development of low melting fluxes with high CaO content and the capability to prevent slag disintegration. The current work studied the effect of 0–9 wt per cent B_2O_3 on physico-chemical properties and characterisation of LF slags. X-ray diffraction (XRD) analyses were carried out to identify mineralogical phases present in slag and Fourier-transform infrared spectroscopy (FT-IR) analysis was done to understand the changes in bonds of B_2O_3 added LF slag. The characteristic temperature of slag was determined by a hemispherical method using high-temperature microscopy. Empirical models were used to calculate viscosity, break temperature, and sulfide capacity. FactSage™, ver 8.2 (by GTT-Technologies) simulations were carried out to find the equilibrium phase fractions and percentage of liquid slag at different temperatures. New phases such as $Ca_{11}B_2Si_4O_{22}$ and $Ca_2B_3O_5$ were formed in LF slag with B_2O_3 addition. Based on the results, 0.5–1.0 wt per cent B_2O_3 was found to be sufficient to prevent C_2S-driven disintegration of LF slag. Also, the melting temperature and viscosity of LF slag were reduced by adding 3–8 wt per cent B_2O_3 due to the formation of BO_3 planar triangular structure and low melting eutectics in slag. Liquid slag started forming at a temperature as low as 800°C when B_2O_3 is >6 wt per cent. It was found that the sulfide capacity, viscosity, and break temperature of the slag decreased with increasing wt per cent B_2O_3. Based on the analysis carried out, B_2O_3 can be a promising fluxing material in secondary steelmaking, for improving the desulfurisation kinetics and valourisation potential of LF slag.

INTRODUCTION

Fluxes are important in the secondary steelmaking process, particularly in ladle furnace (LF) refining (Varanasi *et al*, 2019a). Conventional ladle fluxes are either CaF_2 or $CaO\text{-}Al_2O_3$ based which ensure optimum fluidity, viscosity, sulfide capacity, Liquidus temperature, thermal and and electrical conductivity etc (Varanasi *et al*, 2019b). However, the emission of fluorine causes corrosion to the equipment, environmental pollution, and health hazards (Yan *et al*, 2016). Even though $CaO\text{-}Al_2O_3$ based synthetic slags are good alternatives to CaF_2, the optical basicity of $CaO\text{-}Al_2O_3$ based synthetic slags is low and increased Al_2O_3 content in LF slag is not beneficial for desulfurisation, deoxidation, and absorption of impurities. So, the content of Al_2O_3 in refining flux should be controlled (Wang *et al*, 2011a). Another problem with LF slags is, that they crumble into fine powder during cooling, due to the volume expansion associated with phase transformation of $2CaO.SiO_2$ phase (Gollapalli *et al*, 2020). Even though LF slag has 50–60 wt per cent CaO and 15–30 wt per cent Al_2O_3 as major constituents, its valourisation potential is low due to the disintegrating phenomena

(Varanasi *et al*, 2022). There is a requirement for alternative fluxes, which help achieve optimum slag properties and prevent the disintegration of LF slag.

B_2O_3 is considered a promising fluxing material as an alternative to CaF_2 and CaO-Al_2O_3 based synthetic slags. It was reported by Babenko *et al* (2017) and Wang *et al* (2011c) that B_2O_3 reduces the melting point and viscosity of CaO-Al_2O_3-SiO_2-MgO based slags and for CaO-based refining flux, the fluxing action of B_2O_3 is better than that of Al_2O_3 and CaF_2. The viscosity of (composition per cent) 53–62 CaO, 7.5–12 SiO_2, 15–28 Al_2O_3, 8 MgO, 4 B_2O_3 slags did not exceed 0.8 Pa.s at 1500–1600°C range and are very much suitable for steel desulfurisation. Even though B_2O_3 is an acidic oxide and network former, it simplifies the complex silicate structure by forming BO_3^{3-} planar triangular structure (Bi *et al*, 2021). It was reported by Pontikes *et al* (2010) that the addition of B_2O_3 prevents the β-Ca_2SiO_4 to γ-Ca_2SiO_4 transformation in slags due to the replacement of SiO_4^{4-} units by BO_3^{3-} units. However, B_2O_3 can also form BO_4^{5-} tetrahedral structure and lead to complex structures in slag. Wang *et al* (2010a) reported that B_2O_3 may react with CaO present in slag to form low melting point eutectics such as $CaO.2B_2O_3$, $CaO.B_2O_3$, $2CaO.B_2O_3$ with melting points 986°C, 1154°C, 1298°C respectively. Bi *et al* (2021) reported that $[SiO_4]^{4-}$-$[BO_3]^{3-}$ structures are formed due to addition of B_2O_3 and polymerisation degree of the system will decrease. In addition, $[BO_3]^{3-}$ is a planar triangular structure that is unstable as the bond energy of B-O (787 kJ/mol) is much larger than that of Si-O (600 kJ/mol) and Al-O (485 kJ/mol). Wang *et al* (2012) reported that B_2O_3 has significant fluxing effect on CaO-($2CaO{\cdot}SiO_2$)-B_2O_3 slag system. When the content of B_2O_3 is more than 5 per cent, the melting temperature of $2CaO{\cdot}SiO_2$-B_2O_3 system is lower than 1300°C. CaO-B_2O_3 slags were used by Wang *et al* (2007) to prevent sticking of slag to the snorkel refractory. They reported that the viscosity of CaO (26–42 wt per cent) – Al_2O_3(40–65 Wt per cent) – SiO_2 (9–15 wt per cent) based slag decreased from 6.5 Pa.s to < 2 Pa.s at 1500°C. Also, the melting temperature of the slag decreased by 100°C with the addition of 10 wt per cent CaO-B_2O_3 (mass ratio 1:1) to the slag. The addition of B_2O_3 helps in improving slag metal reaction kinetics and hence desulfurisation efficiency. A highly basic slag with a low melting temperature can be achieved by the addition of B_2O_3 to the LF slag system. It was reported elsewhere (Wang *et al*, 2011d, 2011b, 2010b) that, just by 4 per cent B_2O_3 addition in the high basicity (5.75~7.75) CaO-based refining flux, melting temperature as low as 1250°C can be achieved. From studies conducted by Zhuchkov, Salina and Sychev (2019) there is a possibility of boron microalloying using B_2O_3 based slags. Boron can be reduced from B_2O_3 present in slag by Al or Si present in steel. Zhang *et al* (2019) reported that the addition of B_2O_3 to CaO-SiO_2 based slags increased the electrical conductivity due to the formation of BO_3^{3-} and BO_4^{5-} units whose effect is stronger than the increase in degree of polymerisation caused by B_2O_3. Babenko *et al* (2019) reported that for slags with basicity (CaO/SiO_2) 4–5, the MgO saturation concentration was <7 per cent for 4 wt per cent B_2O_3. Hence, by using B_2O_3 as a fluxing agent, there is a possibility to develop a slag system with ultra-high basicity (>5), ultra-low alumina content as well as low melting temperature and low viscosity.

However, the structure-property correlation of B_2O_3 modified LF slags was not reported clearly. In the present study, an attempt was made to study the effect of B_2O_3 additions on CaO-MgO-SiO_2-Al_2O_3 based LF slag for slag stabilisation and properties of slag. High-end characterisation techniques such as FT-IR, scanning electron microscope (SEM), X-ray diffraction (XRD), and high-temperature microscopy were used to study the effect of B_2O_3 addition on CaO-MgO-SiO_2-Al_2O_3 based LF slag collected from an integrated steel plant. Empirical models were used for calculating sulfide capacity, viscosity, and break temperature. Thermodynamic calculations were performed using FactSage™ ver 8.2 to estimate equilibrium phases of slag.

MATERIALS AND METHODS

Melting experiments

LF slag was collected from an integrated steel plant and laboratory grade boric acid (H_3BO_3) with min purity of 95 per cent is used as the source of B_2O_3. The composition of raw materials is given in Table 1.

TABLE 1

Chemical composition of raw materials.

Material/wt%	CaO	MgO	SiO_2	Al_2O_3	FeO	MnO	B_2O_3
LF slag	55	10.3	17.12	9.97	1.55	1	-
H_3BO_3	-	-	-	-	-	-	56

B_2O_3 was added in 0.25, 0.5, 1, 2, 3, 4, 6, 8 wt per cent in LF slag and mixed thoroughly. The samples each weighing 100 g were put into a graphite crucible and loaded in a muffle furnace with a capacity of 1700°C. The slags were melted at 1600°C with a heating rate of 5°C/min for 30 mins. After heating, the crucible was removed, and air-cooled at room temperature as shown in Figure 1.

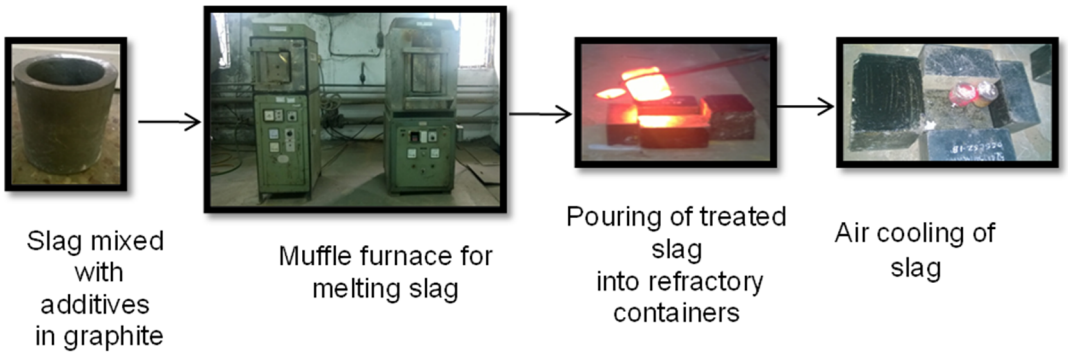

FIG 1 – Schematic of slag melting experiments carried out in a muffle furnace.

SPECTROSCOPY ANALYSIS

Elemental chemical analysis was done for slag before and after stabilisation using Panalytical axios wavelength dispersive X-ray fluorescence (WD-XRF). Particle size analysis of LF slag was carried out using ROTAP sieve shaker. XRD analysis was carried out in Rigaku ultima IV with 2θ between 10–90°, Cu Kα radiation with a wavelength of 1.54A and step size of 0.02. High-temperature microscopy was used to measure the melting temperature of slag. The hemisphere method was followed to estimate slag melting temperature. Ash fusion equipment with a heating rate of 8°C/min was used to analyse slag melting properties and the hemispherical temperature was considered as a base for comparison. FT-IR was carried out to study molecular vibrations and rotation related to covalent bonds. FT-IR spectra were recorded in the wavenumber range of 600 to 1600 cm^1.

THERMODYNAMIC CALCULATION

The effect of B_2O_3 addition on crystallisation phase fractions formed in the slag and melting temperature was studied by thermodynamic software FactSage™ 8.2. The composition of the slag considered is given in Table 2. At constant basicity ie 2.9, equal amounts of Al_2O_3 is replaced by B_2O_3 for analysis.

TABLE 2

Composition of slags considered for thermodynamic calculation.

CaO	MgO	SiO_2	Al_2O_3	B_2O_3	Basicity
56	12	19	13	0	2.9
56	12	19	12.5	0.5	2.9
56	12	19	12	1	2.9
56	12	19	10	3	2.9
56	12	19	7	6	2.9
56	12	19	4	9	2.9

RESULTS

Particle size analysis

Some 200 g of LF slag is taken, and sieving is done for 20 min using ROTAP sieve shaker. Weight retained on each sieve is measured, and graphs are plotted for mesh No versus weight retained on each sieve and Mesh No versus Cumulative weight as shown in Figure 2. It was found that 80 per cent of slag fell in the 53–106 µm size range. This fine slag as shown in Figure 3 is very difficult to recycle, store and handle. It also increases suspended particulate matter in the shop floor.

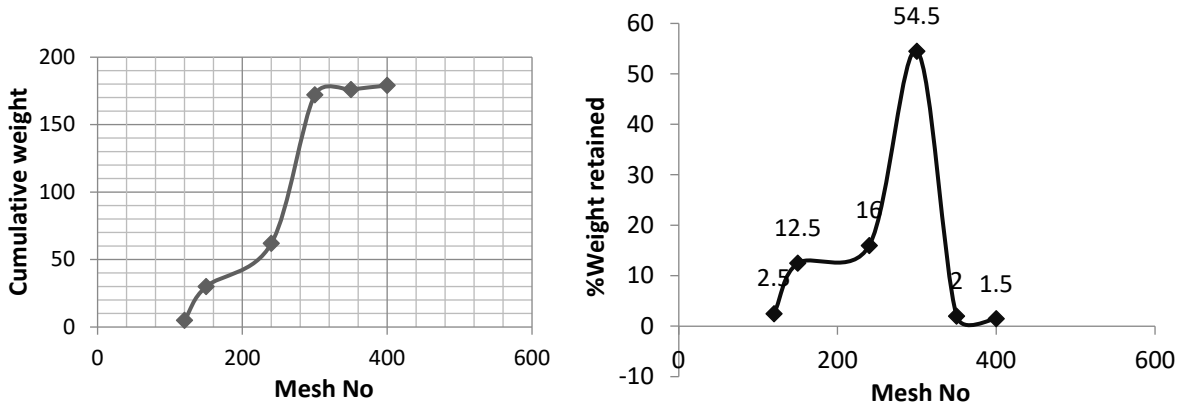

FIG 2 – Sieve analysis of as received LF slag.



FIG 3 – As received disintegrated LF slag.

EFFECT OF B_2O_3 ON C_2S STABILISATION

The amount of B_2O_3 in LF slag for C_2S stabilisation was varied from 0.25 to 2 wt per cent. The treated slags are presented in Figure 4. After melting the slag, the slag was allowed to cool in the air to study the effect of B_2O_3 on the disintegration of LF slag. The figure reveals that with 0.25 wt per cent B_2O_3, some part of the slag disintegrated and for 100 per cent slag stabilisation minimum of 0.5 wt per cent B_2O_3 addition is required. The treated slag is hard like a rock and can be used as a replacement for natural rock for road construction purposes. This process of slag stabilisation is very economical as a very small quantity of borate is required and there is no need for an additional heat source to melt borates in slag. The addition of B_2O_3 can be done during steel refining or in slag pots before dumping the slag. The addition of borate sources needs to be optimised depending on slag composition and logistics in the steel industry. The compact slag generated is easier to handle and more environmentally friendly as it can be used as a partial replacement to lime and CaO-Al_2O_3 based synthetic slags, or else sold to the construction industry for use as a filler. However, optimisation of B_2O_3 addition should be done as there is a chance of B pickup in steel from slag.



(a) (b) (c) (d)

FIG 4 – Visual appearance of B_2O_3 modified LF slag: (a) 0.25 wt per cent B_2O_3; (b) 0.5 wt per cent B_2O_3; (c) 1 wt per cent B_2O_3; (d) 2 wt per cent B_2O_3.

EFFECT OF B_2O_3 ON LF SLAG MELTING TEMPERATURE

A slag sample of 14 mm in size was prepared in the form of a cone. It is then heated in a reducing atmosphere to analyse the melting behaviour. Temperature is recorded at four points, when the rounding off of the sample tip is observed it is called deformation temperature (DT), when the height of the sample equals to width it is called softening temperature (ST), when the height of the sample is half the with it is called hemisphere temperature (HT) considered as melting temperature. And lastly, when the slag fuses and flows, it is called flow temperature (FT) as shown in Figure 5.

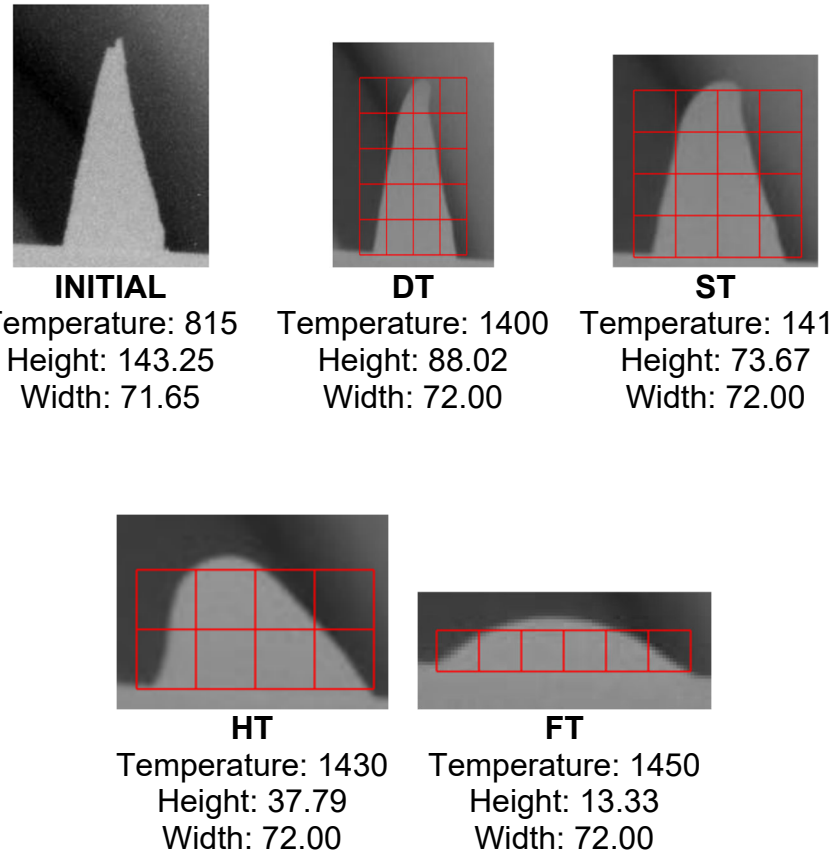

FIG 5 – High temperature microscopy for estimating slag melting temperature. (DT) deformation temperature; (ST) softening temperature; (HT) hemisphere temperature; (FT) flow temperature.

From lab scale experiments, we found that with 3–8 wt per cent B_2O_3 addition, the melting temperature of slag reduced from 1400 to 1110°C as shown in Figure 6. This may be due to the formation of low melting point eutectics such as $CaO.B_2O_3$, $MgO.B_2O_3$, $CaO.2B_2O_3$, etc. When the content of B_2O_3 is 3 wt per cent the melting temperature is reduced from 1380 to 1300°C. When the content of B_2O_3 is from 3–6 wt per cent there is a gradual decrease in melting temperature from 1270 to 1225°C. When the content of B_2O_3 is 6 wt per cent the slag melting temperature is 1225°C. When

the content of B_2O_3 exceeds 6 wt per cent, the temperature is reduced drastically to 1110°C. Comprehensively considering the fluxing effect and cost economics, 3–4 wt per cent B_2O_3 is sufficient to induce the slag fluxing effect. As a result, the melting speed of lime can be improved, which is beneficial for steel desulfurisation and refining efficiency.

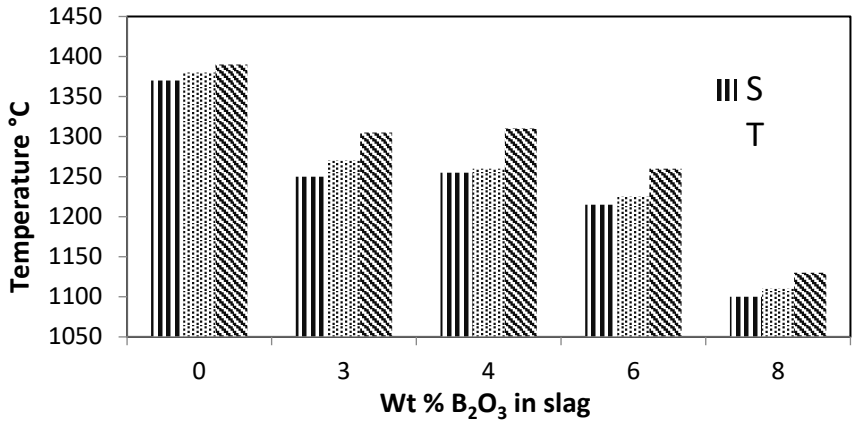

FIG 6 – Effect of B_2O_3 on LF slag melting temperature from lab scale experiments.

Effect of B_2O_3 on structural changes in LF slag

According to extensive studies, three basic units existed in the B_2O_3 bearing slag melts: boroxol ring, non-ring BO_3 triangular, and non-ring BO_4 tetrahedral, as shown in Figure 7. To investigate the influence of B_2O_3 addition on the structure and viscosity variation, FT-IR analysis was carried out. The results are shown in Figure 8. The FT-IR spectra curves were divided into three domains: the 600–800, 800–1200, and 1200–1600 cm^{-1} bands (Lai, Yao and Li, 2020) as shown in Table 3.

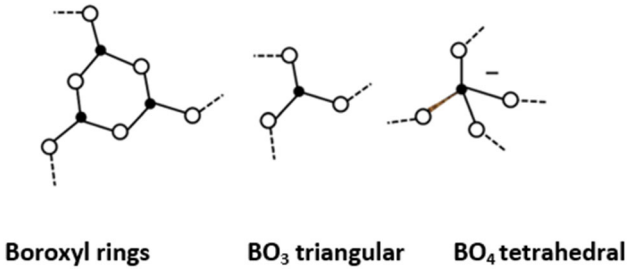

FIG 7 – Basic structural units of B_2O_3 in slag melts.

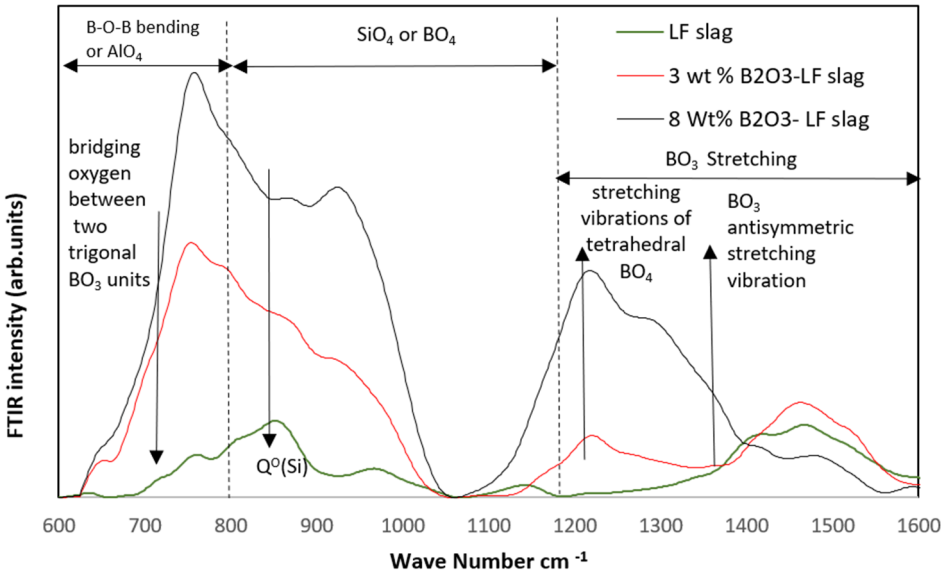

FIG 8 – FT-IR spectra of B_2O_3 added CaO-MgO-SiO_2-Al_2O_3 based LF slag between 600–1600 cm^{-1}.

TABLE 3

Assignments of FT-IR bands associated with B-O, Al-O, Si-O bonds (Sun *et al*, 2014; Lai, Yao and Li, 2020; Sadaf *et al*, 2020; Huang *et al*, 2014).

Wave number (cm^{-1})	FT-IR assignment
600–800	bending vibrations of $[AlO_4]^{5-}$ and B–O–B
800–1200	SiO_4, AlO_4, BO_4
1200–1600	BO_3 Stretching vibrations
~710	bending vibrations of bridging oxygen formed by two trigonal BO_3 units
~845	Q^0 (Si)
~1210	stretching vibrations of tetrahedral BO_4
~1350	BO_3 antisymmetric stretching vibration

The signal of the absorption region at 710 cm^{-1} became more pronounced as the B_2O_3 content increased, which indicated that BO_3 may be the main structural unit. It was observed that the intensity of the band centred at about 845 cm^{-1} gradually weakened with the increase of B_2O_3, which was assigned to Q^0(Si). The signal of trigonal BO_3 and BO_4 gradually became stronger with the increase of B_2O_3. It can be concluded that trigonal BO_3 and BO_4 were the main types of boron-related structural groups in the investigated LF slag.

Effect of B_2O_3 on LF slag mineralogy

The XRD of slags with different B_2O_3 from 0.5 to 8 wt per cent in LF slag is shown in Figure 9. The addition of B_2O_3 significantly influences the slag mineralogy. It depresses the formation of the crystalline phase and induces the formation of an amorphous glassy phase beyond 6 wt per cent. Similar results were reported by (Yan *et al*, 2014; Priven, 2001) and consequently improves the valourisation of LF slag where glass content is important. The major phases present in LF slag are mayenite, merwinite, gehlenite, and γ-dicalcium silicate. By addition of 0.5–2 wt per cent B_2O_3 in LF slag disintegration was minimised and slag β-dicalcium silicate was formed due to partial replacement of SiO_4^{4-} units by BO_3^{3-} units. This replacement suppresses the Ca^{2+} migrations and SiO_4^{4-} rotations required for the β to γ transformation (Seki *et al*, 1986). When B_2O_3 wt per cent was increased from 3–8 in LF slag, phases such as $CaO.B_2O_3$, $CaO.MgO.B_2O_3$ were formed. These are low melting phases and help in decreasing the melting point of slag. Analysis of mineralogical phases is given in Table 4.

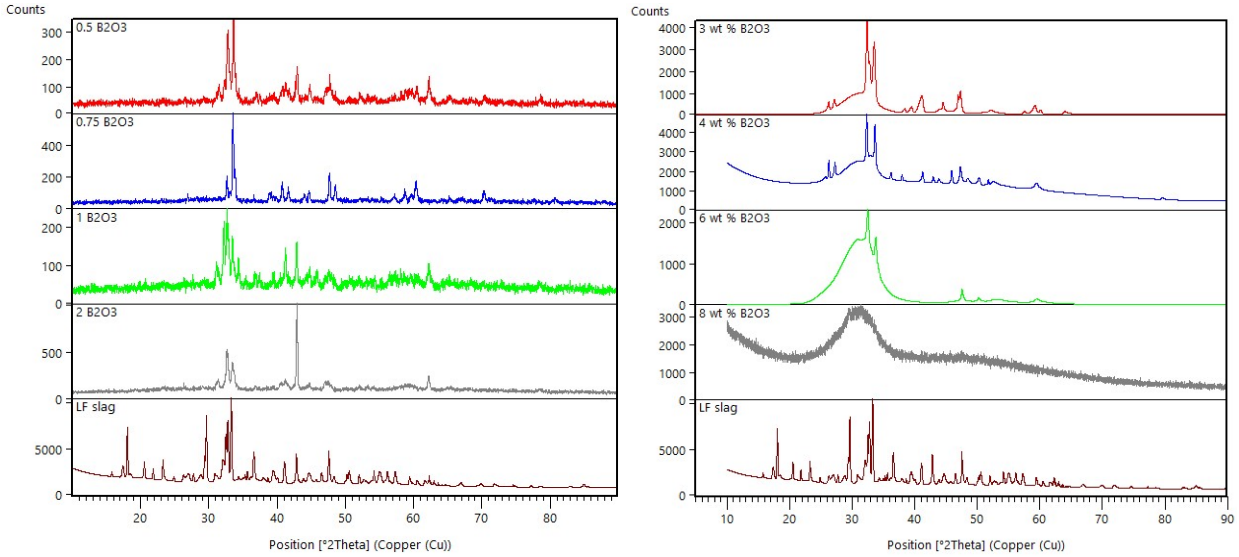

FIG 9 – XRD pattern of 0.5–8 wt per cent B_2O_3 added CaO-MgO-SiO_2-Al_2O_3 based LF slag.

TABLE 4

Mineralogical phases present in as received LF slag and B_2O_3 added LF slag.

Mineral phase	**LF slag**	**LF slag stabilised with 0.5–2 wt%B_2O_3**	**LF slag stabilised with 3–8 wt%B_2O_3**
Mayenite ($Ca_{12}Al_{14}O_{33}$)	✓	✓	✓
Merwinite ($Ca_3MgSi_2O_8$)	✓	✓	-
γ-dicalcium silicate (Ca_2SiO_4)	✓	-	-
β-dicalcium silicate (Ca_2SiO_4)	✓	✓	✓
Hatrurute (Ca_3SiO_5)	✓	✓	-
Akermanite ($Ca_2MgSi_2O_7$)	✓	✓	-
Gehlenite ($Al_2Ca_2SiO_7$)	✓	✓	-
Spinel (Mg_2SiO_4)	✓	✓	-
Periclase (MgO)	✓	-	-
Lime (CaO)	✓	-	-
calcium bisborate ($CaO.B_2O_3$)	-	-	✓
Kurchatovite ($CaO.MgO.B_2O_3$)	-	-	✓
$Ca_{11}B_2Si_4O_{22}$	-	✓	✓

FactSage™ analysis

From the analysis it was found that the main phases in LF slag when B_2O_3 is 0 wt per cent are Ca_2SiO_4, Ca_3SiO_5, and Ca_3MgAlO_4. The effect of B_2O_3 on LF slag at 500°C was studied to understand the phase changes during slag cooling as shown in Figure 10. With the addition of B_2O_3 a new phase, $Ca_{11}B_2Si_4O_{22}$ was found at 500°C. The per cent of this new phase increased with B_2O_3 content from 0.5 to 6 wt per cent and remained constant thereafter. When B_2O_3 is >6 wt per cent a new phase $Ca_3B_2O_6$ is formed. With the increase in B_2O_3 from 0.5 to 3 wt per cent, the per cent of Ca_2SiO_4 decreased from 55 to 25, and with further increase of B_2O_3, Ca_2SiO_4 phase disappeared completely at 500°C.

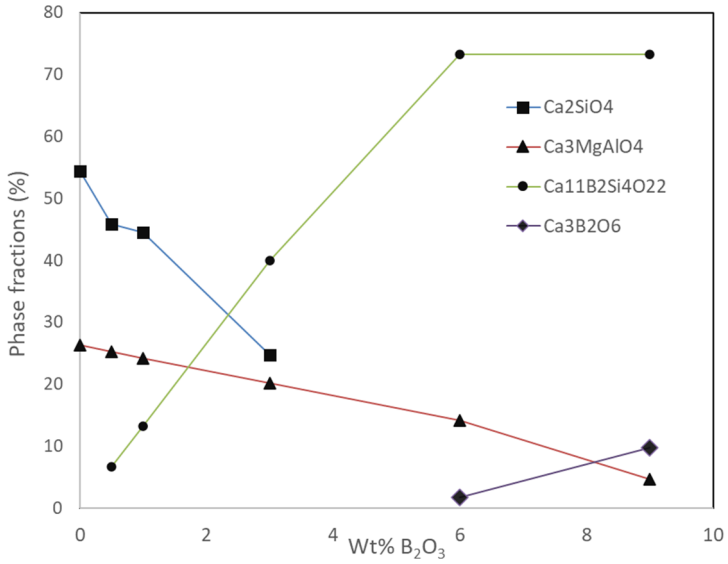

FIG 10 – Effect of B_2O_3 on phase equilibria of LF slag at 500°C.

The percentage of liquid phase slag formed with B_2O_3 addition was studied as shown in Figure 11. Analysis was carried out in slag with basicity of 2.9 by replacing equal amounts of Al_2O_3 with B_2O_3. When B_2O_3 is 0 wt per cent, the liquid phase slag started forming at 1350°C. With the addition of B_2O_3, liquid phase slag started forming at 1100°C. When 6 wt per cent Al_2O_3 is replaced with B_2O_3, liquid phase slag started forming at temperatures as low as 800°C. The solidus temperature of the slag decreased with increase in wt per cent B_2O_3 in slag. At 1550°C, around 80 per cent of slag is liquid when B_2O_3 is 9 wt per cent whereas with 0 wt per cent B_2O_3 only 68 per cent of slag is liquid. Whereas with 6 wt per cent B_2O_3 only 45 per cent of slag is liquid. Even though there is decrease in solidus temperature the per cent of liquid slag at steelmaking temperatures ie at 1550°C decreased till 6 wt per cent B_2O_3 and then increased at 9 wt per cent B_2O_3 as shown in Figure 12. This shows that different structural units are formed in slag when Al_2O_3 is replaced with B_2O_3. However, to understand the effect of B_2O_3 on slag melting temperature, further analysis needs to be carried out by varying slag basicity.

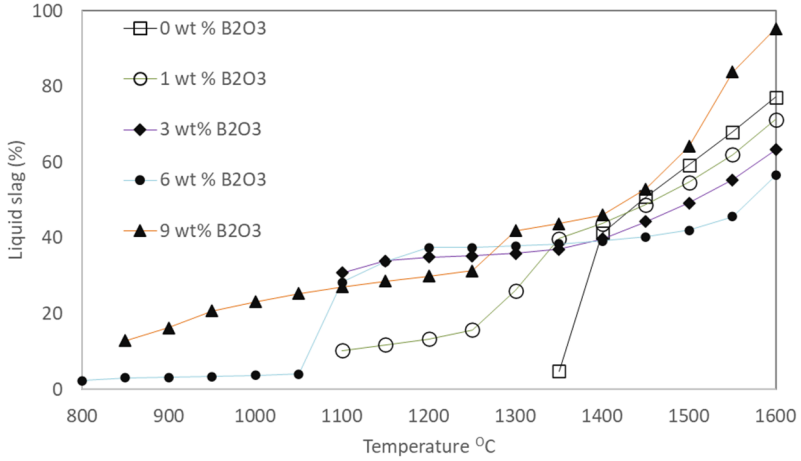

FIG 11 – Effect of replacing Al_2O_3 with B_2O_3 on percentage of liquid phase slag formed at different temperatures in 56 per centCaO, 12 per cent MgO, 19 per cent SiO_2, 13 per cent (Al_2O_3+B_2O_3)-slag wt per cent.

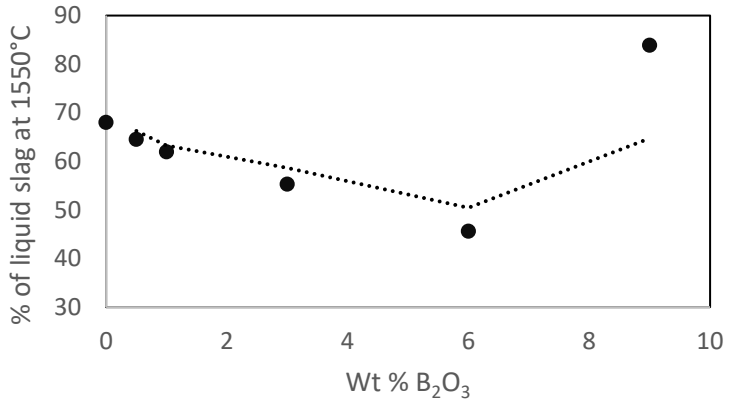

FIG 12 – Effect of replacing Al_2O_3 with B_2O_3 on percentage of liquid phase slag formed at 1550°C in 56 per centCaO, 12 per cent MgO, 19 per cent SiO_2, 13 per cent (Al_2O_3+B_2O_3) slag- wt per cent.

Effect Of B_2O_3 on LF slag viscosity, sulfide capacity, and break temperature

Several models have been developed by various researchers to estimate the sulfide capacity of slags. Earlier models were empirical and depended mainly on the optical basicity of slag and temperature. The optical basicity of various glassy and slag systems (denoted Λ) can be determined from their Pauling electronegativities. The optical basicity of a slag can be calculated from the optical basicity of individual oxides present in the slag using could be derived from Equation 1 where:

$$\boldsymbol{\Lambda} = \frac{\sum(\boldsymbol{X_1 n_1 \Lambda_1 + X_2 n_2 \Lambda_2 + \cdots})}{\sum(\boldsymbol{X_1 n_1 + X_2 n_2 + \cdots})} \quad (1)$$

Where Λ is the optical basicity of the slag; Λ^{th} is the optical basicity of individual oxides as shown in Table 5; as calculated from Pauling electronegativities. X is the mole fraction of individual oxides and n is the number of oxygen atoms associated with acidic and basic oxides, respectively. The sulfide capacity of B_2O_3 based LF slags was calculated from a model developed by (Sosinsky and Sommerville, 1986) as shown in Equation 2 where C_S is the sulfide capacity of the slag:

$$\log C_S = \frac{(22690 - 54640\Lambda)}{T} + 43.6\Lambda - 25.2 \quad (2)$$

TABLE 5

Optical basicity values of individual oxides (Sosinsky and Sommerville, 1986).

Oxide	CaO	MgO	SiO_2	Al_2O_3	B_2O_3
Optical basicity	1	0.78	0.48	0.61	0.42

The sulfide capacity of CaO, MgO, SiO_2, Al_2O_3, FeO, MnO (55, 11, 19, 5–14, 1, 1 wt per cent respectively) was calculated at 1773 K by varying B_2O_3 from 0–9 wt per cent where an equal amount of B_2O_3 replaced with Al_2O_3. Sulfide capacity was also calculated at constant basicity by varying wt per cent CaO and SiO_2 (CaO/SiO_2 = 2.5) with MgO, Al_2O_3, FeO, MnO, B_2O_3 (10, 11, 1, 1, 0–9 wt per cent respectively). For both cases, it was found that the sulfide capacity of slag decreased with B_2O_3 wt per cent as shown in Figure 13 indicating that B_2O_3 is an acid oxide and decreases the sulfide capacity. Similar results were reported by (Yan *et al*, 2014).

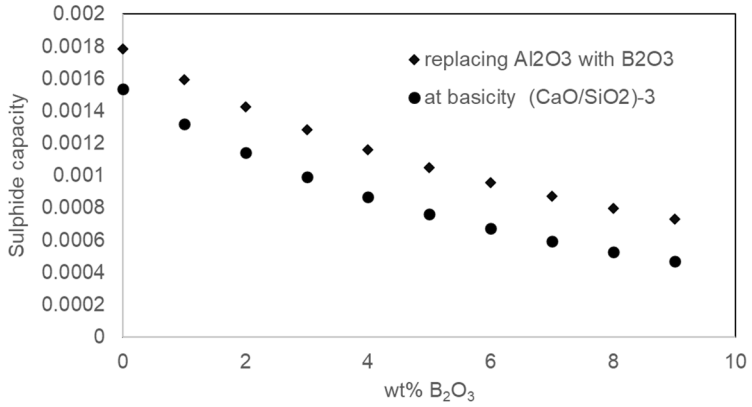

FIG 13 – Effect of B_2O_3 on sulfide capacity of CaO-MgO-SiO_2-Al_2O_3-FeO-MnO based LF slags.

The viscosity of slag plays an important role in kinetic conditions of steel refining particularly in desulfurisation as it is slag-metal interfacial reaction.

The viscosity of molten slag depends on the internal structure of oxide melt and is affected by changes in temperature, slag composition, and oxygen partial pressure. Many models have been developed for estimating viscosities for molten oxide slag systems. For the B_2O_3 based LF slag system, the Riboud model modified by (Wang *et al*, 2013) was used.

$$\eta = \mathrm{ATexp}\left(\frac{\mathrm{B}}{\mathrm{T}}\right)$$

where:

$$\mathrm{A} = \exp[-22.47 - 2.46\left(\mathrm{X_{CaO}} + \mathrm{X_{MgO}}\right) + 43.07\,\mathrm{X_{TiO_2}} + 72.61\mathrm{X_{B_2O_3}} + 7.02\left(\mathrm{X_{Na_2O}} + \mathrm{X_{K_2O}}\right) - 35.76\mathrm{X_{Al_2O_3}}]$$

$$\mathrm{B} = 34428 - 7342\left(\mathrm{X_{CaO}} + \mathrm{X_{MgO}}\right) - 84121\mathrm{X_{TiO_2}} - 130586\mathrm{X_{B_2O_3}} - 39159\left(\mathrm{X_{Na_2O}} + \mathrm{X_{K_2O}}\right) + 68833\mathrm{X_{Al_2O_3}}$$

T is temperature in K

η is viscosity in Pa.S

The viscosity of CaO, MgO, SiO_2, Al_2O_3 (60, 10, 17, 4–13 wt per cent respectively) based slag was calculated by varying B_2O_3 from 0–9 wt per cent, where an equal amount of B_2O_3 is replaced with Al_2O_3. Viscosity was also calculated at constant basicity varying wt per cent CaO and SiO_2 (CaO/SiO_2 = 2.6) with MgO, Al_2O_3, B_2O_3 (10, 10, 0–9 wt per cent respectively). For both cases, the viscosity of slags decreased with increasing wt per cent B_2O_3 as shown in Figure 14. This confirms that B_2O_3 can be used as a slag fluxing agent despite being an acidic oxide. This may be due to the formation of the BO_3 planar triangular structure. Similar results are reported by (Wang *et al,* 2006, 2015).

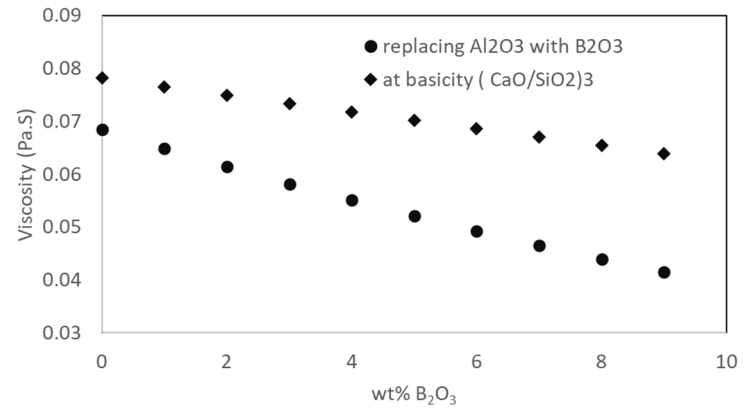

FIG 14 – Effect of B_2O_3 on viscosity of CaO-MgO-SiO_2-Al_2O_3 based LF slags.

The break temperature is the temperature below which there is a dramatic increase in viscosity and the slag becomes non-Newtonian in behaviour. The addition of B_2O_3 plays an important role in affecting the break temperature. Break temperature (T_{br}) of the LF type slags with CaO/SiO_2 = 3, Al_2O_3, B_2O_3 (15, 0–9 mol per cent respectively) were calculated using a model developed by (Huang *et al*, 2014) as shown in Equation 3 where T_{br} is in K. The break temperature reduced with an increase in B_2O_3 per cent as shown in Figure 15.

$$T_{br} = 1502.73 + 0.56\%\ CaO + 0.54\%\ SiO_2 - 1.41\%\ Al_2O_3 - 4.49\%\ Na_2O - 15.3\%\ B_2O_3 \quad (3)$$

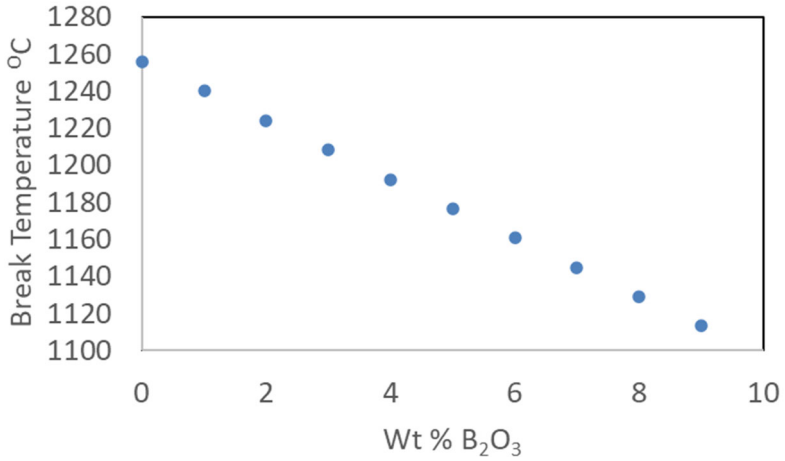

FIG 15 – Effect of B_2O_3 on break temperature of CaO, SiO_2, Al_2O_3 LF slag system.

CONCLUSIONS

- From the study, it was found that B_2O_3 can act as a slag stabiliser and slag fluxing agent.
- Around 0.5–1 wt per cent B_2O_3 in the studied slag system is sufficient to prevent di-calcium silicate-driven disintegration as only β-C_2S was present in B_2O_3 added LF slag. By increasing B_2O_3 wt per cent in LF slag, the melting point reduced from 1380°C to 1100°C with 8 wt per cent B_2O_3.
- From XRD analysis it was found that the slag slowly transformed from crystalline to amorphous/glassy phase after 6 wt per cent B_2O_3 addition and melting temperature reduced drastically beyond 6 wt per cent B_2O_3. Low melting phases such as $CaO.B_2O_3$ and $CaO.2B_2O_3$ were also formed in investigated LF slag. Considering cost economics, and requirements in steel desulfurisation 3–5 wt per cent B_2O_3 may be sufficient to induce a fluxing effect in LF slag.
- FT-IR analysis also confirmed the fluxing effect of B_2O_3 as trigonal BO_3 was the main type of boron-related structural group present in the investigated LF slag. However, the effect of B_2O_3 on the properties of slag depend on CaO/SiO_2 and CaO/Al_2O_3 ratios.
- FactSage™ analysis also confirmed the formation of liquid slag phases at 800°C when B_2O_3 is >6 wt per cent. New phases such as $Ca_{11}B_2Si_4O_{22}$ and $Ca_2B_3O_5$ were formed in slag. At 500°C when B_2O_3 is >3 wt per cent, Ca_2SiO_4 phase disappears proving that B_2O_3 helps in preventing slag disintegration. The solidus temperature of slag decreased by replacing equal amounts of Al_2O_3 with B_2O_3.
- From empirical models, it was found that with B_2O_3 addition the sulfide capacity, viscosity, and break temperature of LF slag decreased. As desulfurisation is a kinetic phenomenon compromise should be made between sulfide capacity and slag fluidity for effective interfacial chemical reactions.
- Further studies need to be carried out to optimise B_2O_3 content for different LF slag systems considering the slag fluxing effect, sulfide capacity, and effect on basic refractory. However, B_2O_3 additions should be optimised based on slag composition and process parameters by carrying out industrial trials.

- There is also a need for the development of a reliable model for predicting viscosity, melting temperature, sulfide capacity, and break temperature of CaO, MgO, SiO_2, Al_2O_3, B_2O_3 based LF slag systems.

REFERENCES

Babenko, A A, Istomin, S A, Zhuchkov, V I, Sychev, A V, Ryabov, V V and Upolovnikova, A G, 2017. Construction of viscosity diagrams for CaO-SiO2-Al2O3-8% MgO-4% B2O3 slags by the simplex lattice method, *Russian Metallurgy (Metally)*, 2017:372–375. https://doi.org/10.1134/S0036029517050020

Babenko, A A, Smetannikov, A N, Zhuchkov, V I and Upolovnikova, A G, 2019. Influence of B2O3 and Basicity of CaO-SiO2-B2O3-Al2O3 Slag on the Saturation Concentration of Magnesium Oxide, *Steel in Translation*, 49:87–90. https://doi.org/10.3103/S0967091219020037

Bi, Z, Li, K, Jiang, C, Zhang, J, Ma, S, Sun, M, Wang, Z and Li, H, 2021. Effects of B2O3 on the structure and properties of blast furnace slag by molecular dynamics simulation, *J Non Cryst Solids*, 551. https://doi.org/10.1016/j.jnoncrysol.2020.120412

Gollapalli, V, Tadivaka, S R, Borra, C R, Varanasi, S S, Karamched, P S and Venkata Rao, M B, 2020. Investigation on Stabilization of Ladle Furnace Slag with Different Additives, *Journal of Sustainable Metallurgy*, 6:121–131. https://doi.org/10.1007/s40831-020-00263-w

Huang, X H, Liao, J L, Zheng, K, Hu, H H, Wang, F M and Zhang, Z T, 2014. Effect of B2O3 addition on viscosity of mould slag containing low silica content, *Ironmaking and Steelmaking*, 41:67–74. https://doi.org/10.1179/1743281213Y.0000000107

Lai, F, Yao, W and Li, J, 2020. Effect of B2O3 on Structure of CaO-Al2O3-SiO2-TiO2-B2O3Glassy Systems, *ISIJ International*, 60:1596–1601. https://doi.org/10.2355/isijinternational.ISIJINT-2019-679

Pontikes, Y, Jones, P T, Geysen, D and Blanpain, B, 2010. Options to prevent dicalcium silicate-driven disintegration of stainless steel slags, *Archives of Metallurgy and Materials*, 55:1167–1172. https://doi.org/10.2478/v10172-010-0020-6

Priven, A I, 2001. Calculation of the viscosity of glass-forming melts: VI, The R2O-B2O3-SiO2 and RO-B2O3-SiO2 ternary borosilicate systems, *Glass Physics and Chemistry*, 27:360–370. https://doi.org/10.1023/A:1011372328059

Sadaf, S, Wu, T, Zhong, L, Liao, Z and Wang, H C, 2020. Effect of basicity on the structure, viscosity and crystallization of CaO-SiO2-B2O3 based mold fluxes, *Metals (Basel)*, 10:1–12. https://doi.org/10.3390/met10091240

Seki, A, Aso, Y, Okubo, M, Sudo, F and Ishizaka, K, 1986. Development of Dusting Prevention Stabilizer for Stainless Steel Slag, Kawasaki Steel Technical Report.

Sosinsky, D J and Sommerville, I D, 1986. The Composition and Temperature Dependence of the Sulfide Capacity of Metallurgical Slags, *Metallurgical and Materials Transactions B: Process Metallurgy and Materials Processing Science*, 17:331–337.

Sun, Y, Liao, J, Zheng, K, Wang, X and Zhang, Z, 2014. Effect of B2O3 on the Structure and Viscous Behavior of Ti-Bearing Blast Furnace Slags, *JOM*, 66:2168–2175. https://doi.org/10.1007/s11837-014-1087-8

Varanasi, S S, More, V M R, Rao, M B V, Alli, S R, Tangudu, A K and Santanu, D, 2019a. Recycling Ladle Furnace Slag as Flux in Steelmaking: A Review, *Journal of Sustainable Metallurgy*. https://doi.org/10.1007/s40831-019-00243-9

Varanasi, S S, Pathak, R K, Sahoo, K K, More, V M R, Santanu, D and Alli, S R, 2019b. Effect of CaO-Al2O3-Based Synthetic Slag Additions on Desulphurisation Kinetics of Ladle Furnace Refining, *Transactions of the Indian Institute of Metals*, 72:1447–1452. https://doi.org/10.1007/s12666-019-01616-0

Varanasi, S S, Rao, M V M, Santanu, D, Alli, R, Kumar, D S, Tangudu, A K, Gollapalli, V, Pathak, R K and Santhamma, C S, 2022. Effect of recycling ladle furnace slag as flux on steel desulphurization during secondary steel making secondary steel making, *Ironmaking and Steelmaking*, 8 p. https://doi.org/10.1080/03019233.2022.2060459

Wang, H M, Li, G R, Dai, Q X, Li, B, Zhang, X J and Shi, G M, 2007. CAS-OB refining: Slag modification with B2O3-CaO and CaF2-CaO, *Ironmaking and Steelmaking*, 34:350–353. https://doi.org/10.1179/174328107X155277

Wang, H M, Li, G R, Li, B, Zhang, X J and Yan, Y Q, 2010a. Effect of B2O3 on Melting Temperature of CaO-Based Ladle Refining Slag, *Journal of Iron and Steel Research International*, 17:18–22. https://doi.org/10.1016/S1006-706X(10)60177-X

Wang, H M, Li, G R, Li, B, Zhang, X J and Yan, Y Q, 2010b. Effect of B2O3 on Melting Temperature of CaO-Based Ladle Refining Slag, *Journal of Iron and Steel Research International*, 17:18–22. https://doi.org/10.1016/S1006-706X(10)60177-X

Wang, H M, Li, G, Dai, Q, Lei, Y, Zhao, Y, Li, B, Shi, G and Ren, Z, 2006. Effect of Additives on Viscosity of LATS Refining Ladle Slag, *ISIJ International*, 46(5):637–640. https://doi.org/10.2355/isijinternational.46.637

Wang, H M, Li, P S, Li, G R, Zhang, M, Zhao, Z and Zhao, Y, 2012. The melting temperature of CaO-(2CaO·SiO2)-B2O3-SiO2-(Al2O3) slag system, *App Mech Mat*, pp 35–38. https://doi.org/10.4028/www.scientific.net/AMM.217-219.35

Wang, H, Yang, L, Zhu, H and Yan, Y, 2011a. Comparison of effects of B2O3 and CaF2 on metallurgical properties of high basicity CaO-based flux, *Adv Mat Res*, pp 966–969. https://doi.org/10.4028/www.scientific.net/AMR.311-313.966

Wang, H, Yang, L, Zhu, H and Yan, Y, 2011b. Comparison of effects of B2O3 and CaF2 on metallurgical properties of high basicity CaO-based flux, *Advanced Materials Research*, 311–313:966–969. https://doi.org/10.4028/www.scientific.net/AMR.311-313.966

Wang, H, Zhang, T, Zhu, H, Li, G, Yan, Y and Wang, J, 2011c. Effect of B2O3 on Melting Temperature, Viscosity and Desulfurization Capacity of CaO-based Refining Flux, *ISIJ International*.

Wang, H, Zhang, T, Zhu, H, Li, G, Yan, Y and Wang, J, 2011d. Effect of B2O3 on melting temperature, viscosity and desulfurization capacity of CaO-based refining flux, *ISIJ International*, 51:702–706. https://doi.org/10.2355/isijinternational.51.702

Wang, L, Cui, Y, Yang, J, Zhang, C, Cai, D, Zhang, J, Sasaki, Y and Ostrovski, O, 2015. Melting Properties and Viscosity of SiO2-CaO-Al2O3-B2O3 System, *Steel Res Int*, 86:670–677. https://doi.org/10.1002/srin.201400353

Wang, Z, Shu, Q and Chou, K, 2013. Viscosity of Fluoride-Free Mold Fluxes Containing B2O3 and TiO2, *Steel Res Int*, 84:766–776. https://doi.org/10.1002/srin.201200256

Yan, P, Nie, P, Huang, S, Blanpain, B and Guo, M, 2014. Sulphide capacity and mineralogy of BaO and B2O3 modified CaO-Al2O3 top slag, *ISIJ International*, 54:1570–1577. https://doi.org/10.2355/isijinternational.54.1570

Yan, W, Chen, W, Yang, Y, Lippold, C and McLean, A, 2016. Evaluation of B_2O_3 as replacement for CaF_2 in CaO-Al_2O_3 based mould flux, *Ironmaking and Steelmaking*, 43:316–323. https://doi.org/10.1179/1743281215Y.0000000062

Zhang, P, Liu, J, Wang, Z, Qian, G and Ma, W, 2019. Effect of B2O3 Addition on Electrical Conductivity and Structural Roles of CaO-SiO2-B2O3 Slag, *Metallurgical and Materials Transactions B: Process Metallurgy and Materials Processing Science*, 50:304–311. https://doi.org/10.1007/s11663-018-1472-8

Zhuchkov, V I, Salina, V A and Sychev, A V, 2019. The Study of the Process of Metal-Thermal Reduction of Boron from the Slag of the System CaO-SiO2-MgO-Al2O3-B2O3, *Materials Science Forum* (Trans Tech Publications Ltd), pp 423–429. https://doi.org/10.4028/www.scientific.net/MSF.946.423

Slag-steel reactions in the refining of advanced high-strength steel

DOI: 10.62053/AFYH5639
P Su[1], P C Pistorius[2] and B A Webler[3]

1. PhD candidate, Carnegie Mellon University, Pittsburgh PA 15213, USA. Email: panwens@andrew.cmu.edu
2. POSCO Professor, Carnegie Mellon University, Pittsburgh PA 15213, USA. Email: pistorius@cmu.edu
3. Professor, Carnegie Mellon University, Pittsburgh PA 15213, USA. Email: webler@cmu.edu

ABSTRACT

Advanced high-strength steels (AHSS) typically have much higher aluminium concentrations (by an order of magnitude or more) than conventional low-carbon aluminium-killed steels. The resulting lower oxygen activity at the steel-slag interface changes the kinetics and thermodynamics of steel-slag reactions. Previous work showed that the rapid transformation of alumina inclusions to spinel inclusions, and spinel to periclase, occurs because of the relatively high concentration of dissolved magnesium. In this paper, experimental results on nitrogen removal by ladle slag are compared with predictions based on the available thermodynamic databases. As in previous work, the kinetics was modelled by assuming mass transfer control, with steel or slag mass transfer limiting. The results show that significant removal of nitrogen by steel-slag reaction is possible.

INTRODUCTION

The third-generation advanced high-strength steels (3rd GEN AHSS), with ≥ 1 GPa tensile strength and ~30 per cent elongation (World Steel Association, 2021), contain intermediate levels of alloying elements (0.05 to 0.5 per cent C, 0–4 per cent Al, 0–12 per cent Mn and 0–4 per cent Si) (Tang and Pistorius, 2021). Nitrogen control is important for steel quality: Al, Si and Mn are strong nitride formers (Paek *et al*, 2016). The resulting high solubility of nitrogen in these steels precludes nitrogen removal by vacuum degassing (Tang and Pistorius, 2022). A method was proposed to remove nitrogen by intentionally forming AlN precipitates that can be removed in the slag (Tada and Matsumura, 2011), but the AlN precipitates may redissolve before leaving the liquid steel. Instead, in the work presented here, the focus is on slag-based nitrogen removal from liquid 3rd GEN AHSS, using conventional calcium aluminate ladle slag. To study nitrogen removal, thermodynamic and kinetics calculations with FactSage 8.1 (Bale *et al*, 2016) and laboratory experiments with liquid steel and slag were employed.

For the conditions in this work (steel, not carbon saturated, temperature around 1600°C, CaO-rich slag), nitrogen can dissolve in the slag by the following equations (Jung, 2006):

$$[N]_{steel} + 1.5(O^{2-})_{slag} = 0.75\ O_2 + (N^{3-})_{slag} \quad (1a)$$

$$[Al]_{steel} + 0.75\ O_2 = 0.5(Al_2O_3)_{slag} \quad (1b)$$

Combination of Equations (1a) and (1b) gives the following net reaction:

$$[N]_{steel} + [Al]_{steel} + 1.5(O^{2-})_{slag} = (N^{3-})_{slag} + 0.5(Al_2O_3)_{slag} \quad (2)$$

Equation (2) illustrates why nitrogen removal by slag from AHSS steels might be feasible: the high aluminium concentration in these steels (one to two orders of magnitude higher than in conventional low-carbon aluminium-killed steel) would drive the nitrogen removal reaction to the right.

The high aluminium concentration in such steels leads to rapid transformation of alumina (initial deoxidation production), to spinel (approximately $MgAl_2O_4$) and periclase (MgO). The rapid transformation results from the relatively high concentration of dissolved magnesium (several tens of parts per million) at the steel-slag interface (Tang and Pistorius, 2021).

CALCULATIONS AND EXPERIMENTAL PROCEDURE

Kinetics calculations

The expected rate of steel-slag reactions – for the conditions of the laboratory trials – was calculated based on the assumption that mass transfer in the steel or slag (to the steel-slag interface) was rate-controlling, with local equilibrium at the steel-slag interface. The calculations were performed with FactSage macros, based on the effective equilibrium reaction zone (EERZ) approach (Van Ende *et al*, 2011): within a chosen time interval, portions of slag and steel are transported to the slag-steel interface to equilibrate; the amount of the phase reacting is equal to the product of the time interval, the effective mass transfer coefficient, the projected slag-steel area and the density of the phase (Pistorius and Vermaak, 1999). After equilibration, the reaction products are mixed back into the slag and steel and each phase is homogenised. Gaseous reactions were not considered, given the low rate of gas-based removal of nitrogen from AHSS (Tang and Pistorius, 2022). The databases and parameters employed for the FactSage simulations are listed in Table 1. The initial slag and steel compositions for the simulations and for the laboratory slag-steel reactions are given in Tables 2 and 3. The slag compositions were chosen to be close to double saturation with both periclase and lime (based on FactSage calculations), with different initial SiO_2 concentrations. The FTOxCN slag database was found to agree with previous experimental results for slag-based nitrogen removal (Jung, 2006) (albeit not for higher-Al steels as considered in this work).

TABLE 1

Solution models and simulation parameters for modelling slag-steel reactions.

Phase		Solution model
Liquid steel		FTmisc FeLQ
Slag		FTOxCN-slag
Solid oxides		FToxid-A-monoxide; FToxid-B-spinel; FToxid-corundum; FToxid-a-$(Ca,Sr)_2SiO_4$
Simulation parameters	Slag density, ρ_{slag}	2500 kg/m^3
	Steel density, ρ_{steel}	7000 kg/m^3
	Slag-to-steel mass ratio	1:5 to 1:12
	Steel mass transfer coefficient, m_{steel}	3.1×10^{-5} m/s (Piva and Pistorius, 2021)
	Slag mass transfer coefficient, m_{slag}	$0.1m_{steel}$

TABLE 2

Initial steel compositions for simulations and steel-slag reactions (mass percentages).

Version	Fe	Al	C	Mn	N	O	S	Si
High Al	Balance	0.83	0.2	2.1	0.002-0.02	0.01	~0.001	0.45
Low Al	Balance	0.087	0.2	2.1	0.002-0.02	0.01/0.15	~0.001	0.45

TABLE 3

Initial slag compositions and temperatures for experiments and simulations, with the experimental steel-to-slag mass ratio and the estimated increase in slag area by emulsification (A/A_0).

Experiment	T (°C)	%Al_2O_3	%CaO	%MgO	%SiO_2	W_{steel}/W_{slag}	A/A_0
E1	1550	35	54	6	5	12.8	5
E2	1600	42.3	51.2	6.5	0	6.3	2
E3	1600	36.9	53.5	5.6	4	4.6	2
E4	1600	35	54	6	5	5.0	1.5
E5	1600	42.3	51.2	6.5	0	5.3	2
E6	1600	42.3	51.2	6.5	0	5.0	5

Note: Experiments E1 to E5 used the higher-Al steel (0.83 per cent Al before reaction), while E6 used the lower-Al steel (0.087 per cent Al before reaction).

For reactions involving substantial transfer of oxygen between slag and steel (as in this work, due to reduction of SiO_2 from the slag, by reaction with Al in the metal), emulsification can be expected at the slag-steel interface (Riboud and Lucas, 1981; Assis *et al*, 2015; Song *et al*, 2021). To approximate the observed time constants of the steel-slag reactions, it was necessary to increase the interfacial area in the simulations (to be larger than the cross-sectional area of the crucible); the extent of this increase is given by the column 'A/A_0' in Table 3.

To match the final Al and Si concentrations in the steel, it was needed to add additional oxygen to the initial steel composition, for the kinetic simulations. This reflects entry of oxygen into the furnace chamber when the slag is added. The total oxygen load in the steel at the start of steel-slag reaction was taken to be 2000 ppm for the results shown here.

Slag-steel reactions

Experiments were performed in an induction furnace, as described previously (Mu *et al*, 2018; Piva, Kumar and Pistorius, 2017; Roy, Pistorius and Fruehan, 2013; Song *et al*, 2021). These experiments were performed in slip-cast MgO crucibles (OD = 64 mm, ID = 56 mm, height = 138 mm), using approximately 600 g of metal and 120 g of slag, in a high-purity argon atmosphere (flow rate ~0.6 dm^3/min at room temperature and ambient pressure). Raw materials for the metal were placed into the crucible before the experiment. Electrolytic iron (with ~400 ppm O, based on previous work (Piva, Kumar and Pistorius, 2017)), Al shot, graphite powder, electrolytic Mn pieces, pure Si pieces and crushed pieces of nitrided electrolytic manganese were used to make up the metal composition. Although the nominal nitrogen concentration in the nitrided manganese was approximately 6 per cent, the actual nitrogen at melt-in varied (likely because of inhomogeneity of the manganese briquettes), as the results show.

Slag for the experiments was prepared from pure oxides that were mixed, pressed into pellets and then premelted in a graphite crucible under argon (heating to and holding at approximately 1600°C for 10 mins). After cooling to room temperature, the graphite crucible was broken to remove the premelted slag. The slag was broken up and ground using a tungsten carbide puck mill. Following grinding, the slag was decarburised in air at 1000°C for 24 hrs. The decarburised slag powder was then pelletised and sintered at 1000°C for 12 hrs in an alumina crucible (62×56×60 mm) before the slag-steel experiments.

The slag-steel reactions were conducted in an induction furnace (maximum power = 10 kW). The MgO crucible containing the steel was placed in a graphite susceptor (OD = 71.5 mm, ID = 65.5 mm, height = 160 mm, bottom thickness = 15 mm) on an insulating alumina pedestal. Alumina felt was used as thermal insulation around the outside of the susceptor. A disc cut from porous alumina brick was used as a radiation shield on top of the crucible (with holes through which the sheath of the upper thermocouple and the feeding tube passed). The atmosphere was controlled by enclosing the susceptor in a fused-quartz tube (80 mm ID, 85 mm OD, 430 mm long), with a water-cooled stainless-steel end cap sealing onto Viton gaskets at each end of the fused-quartz tube. Temperature

was monitored with both upper and lower B-type thermocouples, sheathed with 6.35 mm OD alumina tubes. The sheathed tip of the bottom thermocouple (B-type) ended in a shallow hole (7.5 mm diameter, 9 mm deep) in the bottom centre of the graphite susceptor. The offset between the reading of the bottom thermocouple and the interior of the MgO crucible was measured with an empty crucible and found to be approximately 150°C. The tip of the upper thermocouple was placed approximately 5 mm above the estimated top of the slag layer. An alumina feeding tube passed through the upper end cap and was sealed with a silicone rubber stopper when slag was not being fed into the crucible.

After charging the crucible and sealing the working tube with the end caps, the crucible with the steel mixture was heated to the experimental temperature (1600°C for all but the first case; see Table 3) at a rate of approximately 30 K/min, by manually adjusting the power of the induction supply. The steel was held for 10 mins for melting and homogenisation, before taking the first steel sample.

Steel rod samples were taken by inserting the tip of a fused-quartz tube (4 mm ID, 6.35 mm OD, length 600 mm) through the feeding tube into the crucible and using a manual pipette pump to draw liquid steel into the fused-quartz tube.

After taking the first steel sample, slag pieces (diameter ≤ 3 mm) were added to the crucible through the unplugged feeding tube. The addition took several minutes, during which time the Ar flow was turned off to avoid slag powder blowing out of the feeding tube. During slag addition, oxygen would have entered the working tube, affecting the aluminium balance (as mentioned earlier). After slag addition, the feeding tube was sealed with the silicone stopper and Ar flow restarted at 0.6 dm^3/min. The system was subsequently held for ~10 mins for complete melting of the slag, before taking the first sample after slag addition. Several samples were taken subsequently while maintaining a constant temperature, for total times up to 3 hrs.

The nitrogen concentrations in the steel rod samples were analysed by IGA (instrumental gas analysis) at an external laboratory. The steel remaining in the crucible was analysed at another laboratory, using spark optical emission spectroscopy (OES) for all elements other than nitrogen and IGA for nitrogen. Slag was manually separated from the crucible, crushed and analysed by X-ray fluorescence (for all except experiment E6). Given uncertainties around the analysis of nitrogen in slag, the analysed nitrogen concentration in the steel was used to calculate the nitrogen distribution coefficient between the steel and slag, as follows:

The nitrogen distribution coefficient is given by:

$$L_N = (\%N)_{slag}/[\%N]_{steel}, \quad (3)$$

where $(\%N)_{slag}$ is the mass percentage of nitrogen in the slag, and $[\%N]_{steel}$ is the mass percentage of nitrogen in the steel. From a simple mass balance, based on the assumptions that the steel and slag are homogeneous, and that the slag contained no nitrogen before reaction, the nitrogen distribution coefficient after the steel-slag reaction can be calculated as follows from the measured steel compositions:

$$L_N = ([\%N]_i/[\%N]_f - 1)\,(W_{steel}/W_{slag}), \quad (4)$$

where $[\%N]_i$ is the nitrogen concentration in the steel before reaction, $[\%N]_f$ the nitrogen concentration after reaction, and W_{steel} and W_{slag} are the total masses of steel and slag.

Microscopy

Selected steel and slag samples were examined by scanning electron microscopy after the experiments. To test for possible AlN formation, a steel rod sample (N content = 190 ppm as given by IGA analysis) was mounted in conductive bakelite and polished to a 1 μm finish with diamond. Possible slag-crucible reactions were examined by mounting a piece of crucible (with attached slag) in cold-mounting epoxy resin, followed by grinding and polishing (with diamond) while avoiding any contact with water. Samples were examined by back-scattered electron imaging, using an accelerating voltage of 10 kV. The slag sample was carbon-coated before microscopy.

RESULTS AND DISCUSSION

Extent of steel-slag reactions

The time variation of %N in steel, for both FactSage simulations and experiments, are given in Figure 1; the measured steel and slag compositions after reaction are given in Tables 4 and 5. The measured MgO concentration in the samples of runs E2-E4 was much higher than expected for MgO-saturated slags; a likely reason is incomplete separation of slag from the MgO crucible before the slag was crushed for X-ray fluorescence (XRF) analysis.

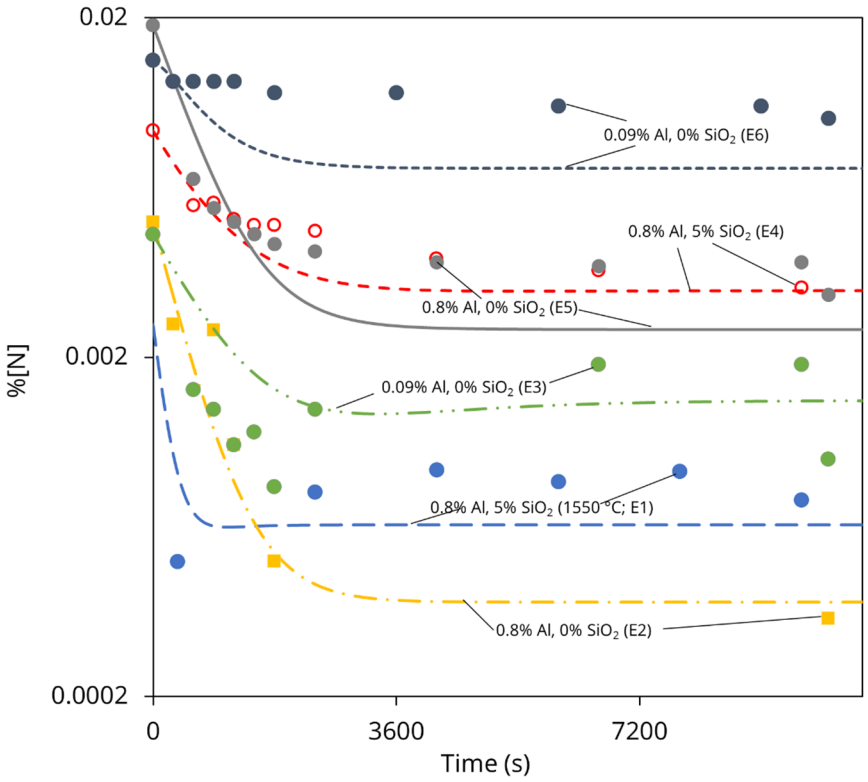

FIG 1 – Change in [%N] over time, for slag-steel experiments. Markers show the experimental results and the lines the results of FactSage simulations.

TABLE 4

The final steel composition after slag-steel experiments (nitrogen measured by IGA; other elements by spark OES; mass concentrations).

Experiment	Al%	C%	Mn%	Mg (ppm)	Si%	N (ppm)
E1	0.33	0.19	2.0	43	0.63	4.1
E2	0.41	0.15	1.9	49	0.53	3.4
E3	0.11	0.14	2.0	15	0.78	10
E4	0.36	0.20	2.4	71	0.58	47
E5	0.48	0.19	2.6	44	0.54	31
E6	0.06	0.20	2.4	12	0.37	101

TABLE 5

Initial slag compositions (double-saturated with CaO and MgO, based on FactSage) and the actual final slag compositions as analysed by XRF.

Slag	Al_2O_3%		CaO%		MgO%		SiO_2%	
	Initial	Final	Initial	Final	Initial	Final	Initial	Final
E1	35.6	42.53	53.95	48.66	5.45	7.72	5	1.09
E2	41.81	42.9	51.04	45.72	7.15	10.41	0	0.97
E3	36.45	33.6	53.26	40.61	6.29	24.97	4	0.81
E4	35.15	29.04	53.71	39.29	6.14	30.4	5	1.27
E5	41.81	43.98	51.04	49.42	7.15	6.61	0	0

Note that a large decrease in aluminium concentration occurred (from around 0.9 per cent to 0.4 per cent, for experiments E1 to E5), with a slight increase in silicon concentration in the steel (from 0.45 per cent to around 0.6 per cent on average) and greatly reduced silica concentration in the slag. However, the decrease in [%Al] is larger than can be accounted for just by the reduction of SiO_2: From stoichiometry, the reaction of 4 moles of Al with 3 moles of SiO_2 would yield 3 moles of Si (and 2 moles of Al_2O_3), with result that the ratio of the change in [%Al] to the change in [%Si] would be -1.3. The larger observed ratio of the aluminium to silicon changes (around -3) indicates that additional oxygen entered the experiment, causing additional loss of aluminium from the steel; this is also shown by the decrease of both [%Al and [%Si] in the low-Al experiment (E6). As mentioned earlier, oxygen likely entered during slag addition. The resulting loss of aluminium would have decreased the extent of nitrogen removal (as shown by Equation 2). (As Equation 2 indicates, some Al would also have been consumed by the nitrogen removal reaction, but this amount is small: given the 1:1 stoichiometry of Al and N in the reaction, removal of up to 200 ppm N would have resulted in consumption of less than 400 ppm of Al.)

Despite the loss of aluminium, substantial nitrogen removal did occur, as illustrated by Figure 1 and by the summary of nitrogen distribution coefficients in Table 6. The extent of nitrogen removal was insignificant only in the case of the low-Al control experiment (E6; distribution coefficient approximately 2). In the cases with higher final [%Al], the L_N values were much larger.

TABLE 6

Nitrogen distribution coefficients between slag and steel, as predicted from FactSage and observed in experiments.

Experiment	$[N]_{initial}$, ppm	$[N]_{final}$, ppm		W_{steel}/W_{slag}	L_N	
		FactSage	Expt.		FactSage	Expt.
E1	25	3.5	4.6	12.8	79	56.8
E2	50	3.8	3.4	6.3	77	86.3
E3	46	5.0	10.3	4.6	38	15.9
E4	93	12.9	32.0	5.0	31	9.5
E5	190	12.9	30.5	5.3	73	27.7
E6	150	53/80 (for initial [O] 100/1500 ppm)	101	5.0	9.2/4.3 (for initial [O] 100/1500 ppm)	2.4

The strong effect of [%Al] on nitrogen removal is emphasised by Figure 2, which shows the experimental L_N values for the different final [%Al]. The relationship is scattered, because not only [%Al] varied between experiments, but also slag composition – which would have changed the

activities of Al_2O_3 and O^{2-} and the N^{3-} activity coefficients in the slag. Despite the scatter, fitting a power-law expression to the data shows that L_N is approximately proportional to [%Al] (the fitted exponent is 1.17, similar to the expected value of 1). The conclusion is that nitrogen can be removed from high-Al AHSS by reaction with ladle slag.

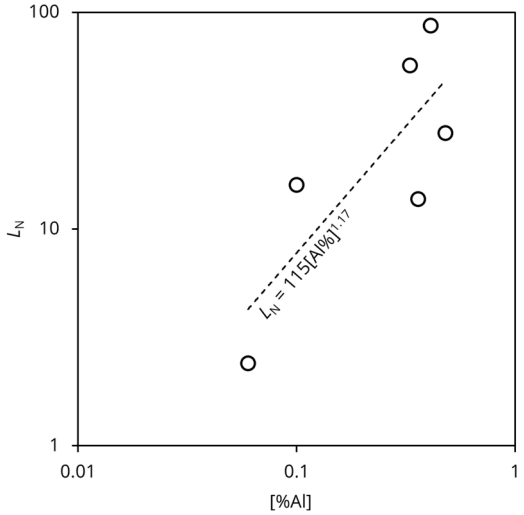

FIG 2 – Observed relationship between the nitrogen distribution coefficient and the final Al concentration in the steel, for all the experiments.

The extent of nitrogen removal in the experiments was large also because of the high mass ratio of slag to steel. This high mass ratio was essential to ensure that the steel was fully covered by slag. However, significant nitrogen removal would also be possible under industrial conditions, with much lower slag-to-steel mass ratios. Taking a typical ladle slag to steel mass ratio of $W_{slag}/W_{steel} = 0.015$ and $L_N = 60$ (feasible for [%Al]=1 per cent, as indicated by the experiments), the fraction of nitrogen removed from the steel (if the slag contained zero nitrogen before reaction) would be $1 - 1/(1+L_N W_{slag}/W_{steel}) = 0.47$. That is, approximately half of the nitrogen would be removed from the steel.

Figure 1 indicates that the observed time constants for nitrogen removal could be matched approximately by increasing the modelled steel-slag interfacial area (by the factors listed in Table 3). This increased area is expected for a system such as this, where high-Al steel reduces SiO_2 from the slag (Riboud and Lucas, 1981).

However, Figure 1 indicates that the observed extent of nitrogen removal was smaller than that predicted with FactSage. Part of this difference is due to the larger-than-predicted loss of aluminium due to the presumed ingress of oxygen. However, even when compensating for the loss of Al, the observed nitrogen distribution coefficients are generally smaller than those predicted by FactSage, as illustrated by Table 6. The conclusion is that, while the FactSage databases used here give useful indications of the reaction trends, the actual nitrogen removal – while substantial – would be less than predicted.

Slag microstructure

The solidified slag (after reaction with the Al-bearing steel at 1600°C) (Figure 3) contained the expected phases. As noted in Table 1, matching the observed nitrogen removal rate required increasing the effective steel-slag contact area by a factor of 2 (for the slag example in Figure 3). However, no emulsification was observed in the steel and slag after the experiments, likely because of the long duration of the experiments: Once the steel-slag reactions cease, no driving force for emulsification remains.

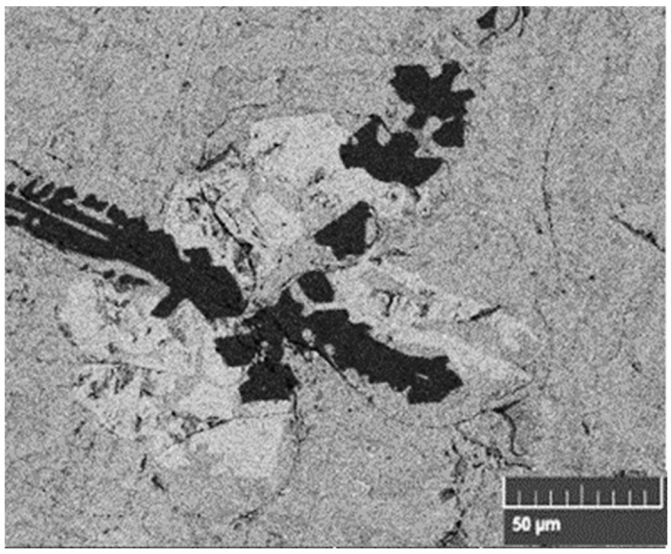

FIG 3 – SEM-BSE image of the 0 per cent SiO_2 slag after reaction at 1600°C with higher-Al steel (E5). The major phases are $Ca_3Al_2O_6$ (brightest phase), $Ca_3MgAl_4O_{10}$ (mid-grey region) and MgO (darkest dendrites).

Aluminium nitride in solidified steel

Given the high Al and N concentrations in the experimental steels (before nitrogen removal by the slag), the solid AlN may form in the steel (Paek *et al*, 2013). Scanning electron microscopy (10 kV accelerating voltage) of the first sample taken from Run E5 (containing 190 ppm) did show the presence of small AlN precipitates; examples are given in Figure 4. In some cases, the AlN appeared to have precipitated on an MgO-containing oxide core, as indicated by the energy dispersive X-ray (EDX) spectra in the figure. The predicted phase equilibria, calculated with Thermo-Calc 2024a (TCFE13 database) (Andersson *et al*, 2002) support the formation AlN during solidification (Figure 5). While some AlN forms during solidification, it is not stable in the liquid steel during ladle treatment (for the compositions considered here) and does not contribute to nitrogen removal during steel refining.

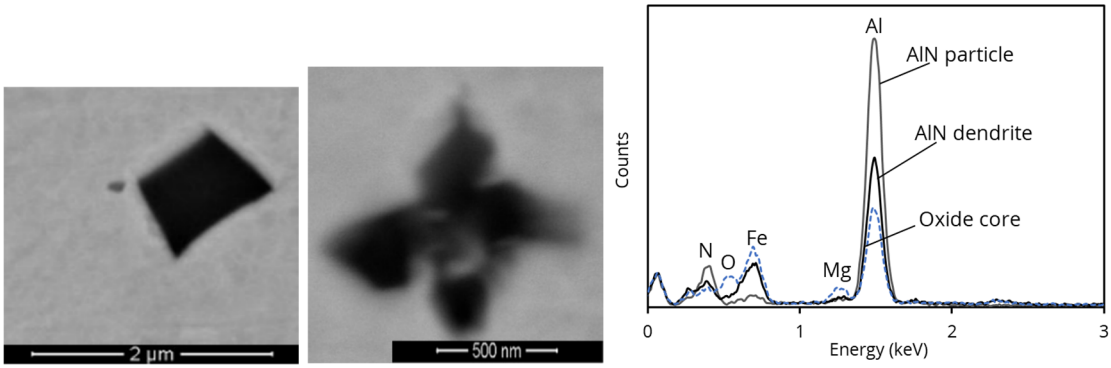

FIG 4 – Backscattered electron micrographs of AlN precipitates in the first steel sample from run E5, with EDX spectra at right.

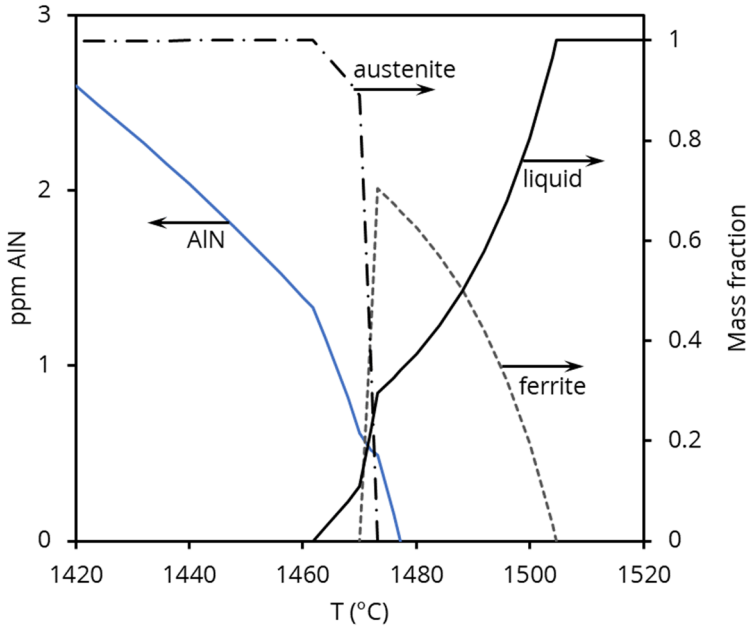

FIG 5 – Calculated equilibrium phases in the steel of run E5, with 190 ppm nitrogen.

Comparison of IGA and OES analysis of nitrogen in steel

Optical emission spectroscopy (OES) provides rapid analyses, but is less accurate for low concentrations of nitrogen. However, comparison of the reported compositions of the final steel samples (Table 7) shows close agreement between the IGA and OES results, for samples containing more than approximately 30 ppm nitrogen. This indicates that suitably calibrated OES can be used to rapidly assess nitrogen removal (or pick-up) during industrial ladle processing of liquid steel.

TABLE 7

Comparison of nitrogen analyses of the final steel samples, obtained by IGA and Spark-OES.

Experiment	N ppm, IGA	N ppm, Spark OES
E1	4.6	<5
E2	3.4	<5
E3	10.3	13.6
E4	32	32
E5	32	37
E6	110	101

CONCLUSIONS

Considerable nitrogen removal with calcium aluminate slag is possible during the ladle processing of AHSS containing >0.1 per cent dissolved aluminium. The available FactSage database provides a useful indication of the expected reactions, though it slightly overpredicts the extent of nitrogen removal.

ACKNOWLEDGEMENTS

The authors acknowledge use of the Materials Characterization Facility at Carnegie Mellon University supported by grant MCF-677785, and support of this work by the industrial members of the Center for Iron and Steelmaking Research.

REFERENCES

Andersson, J-O, Helander, T, Höglund, L, Shi, P and Sundman, B, 2002. Thermo-Calc and DICTRA, computational tools for materials science, *CALPHAD*, 26:273–312. https://doi.org/10.1016/S0364-5916(02)00037-8

Assis, A N, Warnett, J, Spooner, S, Fruehan, R J, Williams, M A and Sridhar, S, 2015. Spontaneous Emulsification of a Metal Drop Immersed in Slag Due to Dephosphorization: Surface Area Quantification, *Metall Mater Trans B,* 46:568–576. https://doi.org/10.1007/s11663-014-0248-z

Bale, C W, Bélisle, E, Chartrand, P, Decterov, S A, Eriksson, G, Gheribi, A E, Hack, K, Jung, I-H, Kang, Y-B, Melançon, J, Pelton, A D, Petersen, S, Robelin, C, Sangster, J, Spencer, P and Van Ende, M-A, 2016. FactSage thermochemical software and databases, 2010–2016, *CALPHAD,* 54:35–53. https://doi.org/10.1016/j.calphad.2016.05.002

Jung, I-H, 2006. Thermodynamic Modeling of Gas Solubility In Molten Slags (I)- Carbon and Nitrogen, *ISIJ International*, 46:1577–1586. https://doi.org/10.2355/isijinternational.46.1577

Mu, H, Zhang, T, Fruehan, R J and Webler, B A, 2018. Reduction of CaO and MgO Slag Components by Al in Liquid Fe, *Metall Mater Trans B*, 49:1665–1674. https://doi.org/10.1007/s11663-018-1294-8

Paek, M-K, Chatterjee, S, Pak, J-J and Jung, I-H, 2016. Thermodynamics of Nitrogen in Fe-Mn-Al-Si-C Alloy Melts, *Metall Mater Trans B*, 47:1243–1262. https://doi.org/10.1007/s11663-016-0588-y

Paek, M-K, Jang, J-M, Jiang, M and Pak, J-J, 2013. Thermodynamics of AlN Formation in High Manganese-Aluminium Alloyed Liquid Steels, *ISIJ Int*, 53:973–978. https://doi.org/10.2355/isijinternational.53.973

Pistorius, P and Vermaak, M, 1999. Modelling pyro metallurgical kinetics: ladle desulphurization, *South African Journal of Science*, 95:377–380.

Piva, S P T and Pistorius, P C, 2021. Ferrosilicon-Based Calcium Treatment of Aluminium-Killed and Silicomanganese-Killed Steels, *Metall Mater Trans B,* 52:6–16. https://doi.org/10.1007/s11663-020-02017-1

Piva, S P T, Kumar, D and Pistorius, P C, 2017. Modeling Manganese Silicate Inclusion Composition Changes during Ladle Treatment Using FactSage Macros, *Metall and Materi Trans B*, 48:37–45. https://doi.org/10.1007/s11663-016-0764-0

Riboud, P V and Lucas, L D, 1981. Influence of Mass Transfer Upon Surface Phenomena in Iron and Steelmaking, *Canadian Metallurgical Quarterly,* 20:199–208. https://doi.org/10.1179/cmq.1981.20.2.199

Roy, D, Pistorius, P C and Fruehan, R J, 2013. Effect of Silicon on the Desulfurization of Al-Killed Steels: Part II, Experimental Results and Plant Trials, *Metall Mater Trans B*, 44:1095–1104. https://doi.org/10.1007/s11663-013-9888-7

Song, S, Tang, D, Kumar, D and Pistorius, P C, 2021. Recycling of Chromium-Containing Waste Oxide as Alloying Addition in Ladle Metallurgy, *Metall Mater Trans B*, 52:2612–2618. https://doi.org/10.1007/s11663-021-02212-8

Tada, C and Matsumura, C, 2011. Removal method of nitrogen in molten steel, US Patents, US7901482B2.

Tang, D and Pistorius, P C, 2021. Non-metallic Inclusion Evolution in a Liquid Third-Generation Advanced High-Strength Steel in Contact with Double-Saturated Slag, *Metall Mater Trans B*, 52:580–585. https://doi.org/10.1007/s11663-021-02084-y

Tang, D and Pistorius, P C, 2022. Kinetics of Nitrogen Removal from Liquid Third Generation Advanced High-Strength Steel by Tank Degassing, *Metall Mater Trans B*, https://doi.org/10.1007/s11663-021-02417-x

Van Ende, M-A, Kim, Y-M, Cho, M-K, Choi, J and Jung, I-H, 2011. A Kinetic Model for the Ruhrstahl Heraeus (RH) Degassing Process, *Metall Mater Trans B*, 42:477–489. https://doi.org/10.1007/s11663-011-9495-4

World Steel Association, 2021. Advanced High-Strength Steel (AHSS) Definitions [online], *WorldAutoSteel News*. Available from: <https://www.worldautosteel.org/steel-basics/automotive-advanced-high-strength-steel-ahss-definitions/> [Accessed):13 April 2024].

Crystallisation control of $CaO-SiO_2-Al_2O_3-MgO$ system inclusion

DOI: 10.62053/XQXM9056

Y Wang[1,3,4], S Sukenaga[3], W Z Mu[4], H Zhang[2], H W Ni[2] and H Shibata[3]

1. The State Key Laboratory of Refractories and Metallurgy, Wuhan University of Science and Technology, Wuhan 430081, China. Email: wangyong6@wust.edu.cn
2. The State Key Laboratory of Refractories and Metallurgy, Wuhan University of Science and Technology, Wuhan 430081, China.
3. Institute of Multidisciplinary Research for Advanced Materials, Tohoku University, Sendai, Miyagi 980-8577, Japan.
4. Department of Materials Science and Engineering, KTH Royal Institute of Technology, Stockholm 10044, Sweden.

ABSTRACT

The crystallisation behaviour of low melting point $CaO-SiO_2-Al_2O_3-MgO$ inclusions greatly affect the deformability of inclusions during the rolling process. The crystallisation characteristics of $CaO-SiO_2-Al_2O_3-MgO$ melts representing the oxide inclusions in Si-Mn killed steel were systematically investigated. The effect of Al_2O_3 and MgO contents on the crystallisation change were analysed under a fixed CaO/SiO_2 in the complex inclusions. The continuous-cooling-transformation (CCT) and time-temperature-transformation (TTT) experiments were conducted. The results showed that the increase of MgO content increases the crystallisation ability of $CaO-SiO_2-Al_2O_3-MgO$ inclusions, while the increase of Al_2O_3 content has the opposite effect. The viscosity, liquidus temperature of oxide melt and also the initial crystallisation potential might be the reasons for the change in crystallisation behaviour. Also, the crystallisation activation energy could semi-quantitatively characterise the crystal growth during the crystallisation of inclusions. To obtain low melting point plasticized $CaO-SiO_2-Al_2O_3-MgO$ (CaO/SiO_2=1) system inclusions, the Al_2O_3 content of the system needs to be controlled larger than 15 wt per cent and the MgO content should be kept at a small amount.

INTRODUCTION

Inclusion control is one of the key areas in the clean steel production research since it directly affect the quality of final steel products. Till now, the inclusion evolution during refining and solidification processes has been widely studied in various steel grades (Zhang and Thomas, 2003). Therefore, there is quite enough information on the inclusion control in the molten and solidification state of steel. However, the inclusion characteristics in the final products are usually not the same as them in the as cast steel. This is due to the fact that inclusions can also evolve changes in the heating and rolling process because the combined effect of thermal and mechanical treatments. Kitamura (2011) pointed out the new directions of inclusion control should be focused on the heating, rolling deformation and cooling processes instead of refining and casting processes. Recent years, the inclusion characteristics during heat treatment as well as hot and cold rolling process have been investigated (Zhang *et al*, 2018; Yang *et al*, 2022). The deformation ability of inclusions has a direct impact on the fatigue resistance of steel. Controlling the deformation performance of inclusions is one of the keys to improving the quality of high-end special steel. In order to improve the deformability of inclusions, the high melting point and non-deformable inclusions (such as Al_2O_3, $MgO-Al_2O_3$ spinel) should be removed as much as possible in steel (Kirihara, 2011). This is especially important in some specific steel types, such as spring steel and tire cord steel (Chen et al, 2019; 2020). Therefore, Si-Mn deoxidation is used instead of Al deoxidation in these steels (Kim, Kim and Kim, 2021; Lyu *et al*, 2019). $CaO-SiO_2-Al_2O_3-MgO$ system oxide is a typical inclusion type in Si-Mn deoxidised steel (Bertrand *et al*, 2003). A larger number of studies aimed to control these inclusions in low melting point region to obtain better deformability. However, low melting point inclusions with high crystallisation ability tend to crystalise during the soaking process before hot rolling, which can greatly decrease the deformation ability of inclusions during the rolling process. The crystallisation behaviour of oxide melts is commonly studied in glass ceramics, mold fluxes, and molten slags. However, there are few studies concerning the crystallisation of oxide non-metallic inclusions in steel (Meng *et al*, 2022; Rocabois *et al*, 2001; Li *et al*, 2022; Liang *et al*, 2022).

In this study, the effects of MgO and Al_2O_3 contents on the crystallisation behaviour of CaO-SiO_2-Al_2O_3-MgO system inclusions were investigated using the sessile drop technique and thermodynamic calculations. This study provides a theoretical basis for understanding the crystallisation behaviour of CaO-SiO_2-Al_2O_3-MgO system inclusions and optimisation of its compositions with the lowest crystallisation ability.

EXPERIMENTAL METHODS

Sample preparation

The compositions of oxide melt were firstly designed based on the typical compositions of the inclusions in Si-Mn killed steel, the range of composition is presented in Table 1. In total, there are seven groups of sample, where the basicity (CaO/SiO_2) keeps as one. In groups S1, S2, S3, S4, the MgO content fixes as 8 per cent, and Al_2O_3 content varies from 5 per cent to 20 per cent. While in groups S2, S5, S6, S7, the Al_2O_3 content fixes as 10 per cent, and MgO content varies from 4 per cent to 16 per cent. The oxide samples were prepared using reagent-grade powders of $CaCO_3$ (≥99.0 mass per cent), Al_2O_3 (≥99.99 mass per cent), MgO (≥98.50 mass per cent), SiO_2 (≥99.99 mass per cent). About 20 g oxide mixtures were placed in a platinum crucible and melted in $MoSi_2$ furnace at 1600°C for 1 hr to ensure the homogenisation of chemical composition. Thereafter, the molten melt was quickly quenched on copper plate to obtain glass samples. The chemical compositions of the quenched samples were analysed using X-Ray fluoroscopy (XRF) and listed in Table 1.

TABLE 1

Chemical compositions of oxide mixtures before and after pre-melting (mass per cent).

Sample No.	Designed composition			
	CaO	SiO_2	Al_2O_3	MgO
S1	43.5	43.5	5	8
S2	41	41	10	8
S3	38.5	38.5	15	8
S4	36	36	20	8
S5	43	43	10	4
S6	39	39	10	12
S7	37	37	10	16

The crystallisation behaviour of the oxide melt was determined using a sessile drop measurement apparatus, which widely used for the wettability measurements (Xuan *et al*, 2015a, 2015b) as well as crystallisation control (Tashiro, Sukenaga and Shibata, 2017). The gas-tight furnace with customised apparatus is shown in Figure 1, which can allow us to observe the morphology change of melt and crystallisation behaviour in both vertical and horizontal directions. The whole heating and cooling process of samples were recorded by a CCD camera at the top, which was connected to a computer. About 50 mg glass sample was placed on a platinum substrate, which in turn, was placed on a platinum plate (diameter 13.0 mm; thickness 1.4 mm) on an Al_2O_3 tube pedestal. A sapphire plate was placed between the two-platinum holder. The temperature was measured using a thermocouple that was welded to the back of the platinum plate. Before the start of the experiment, the chamber was cleaned thoroughly by a cycle of vacuum and purging with a high purity Ar (purity > 99.9999 per cent). Then, the samples were heated up through quartz plates by two halogen lamps under an Ar protected atmosphere. The temperature profile for continuous-cooling-transformation (CCT) and time-temperature-transformation (TTT) experiments are shown in Figure 2. For both CCT and TTT experiments, the sample was heated to 1500°C and kept for 3 mins to eliminate the bubbles and uniform the chemical composition. Thereafter, the molten samples were continuously cooled at different cooling rates ranging from 5°C/min to 900°C/min in the CCT tests. In TTT experiments, the

molten melt was cooling down rapidly to different temperatures ranging from 950°C to 1250°C at a cooling rate of 900°C/min. The iso-thermal treatment time for TTT tests are about 2 hrs. In TTT experiments, the temperature and time at which 5 vol per cent. of melt crystallised was determined as the start crystallisation temperature and time, respectively.

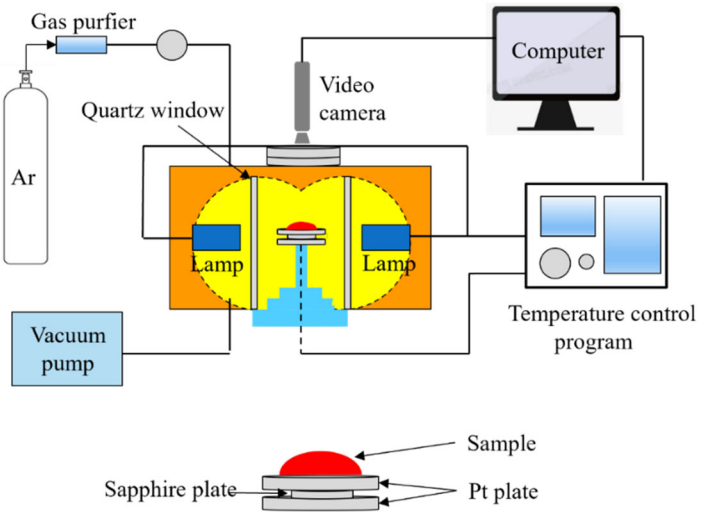

FIG 1 – Schematic diagram of the apparatus used to observe crystallisation behaviour.

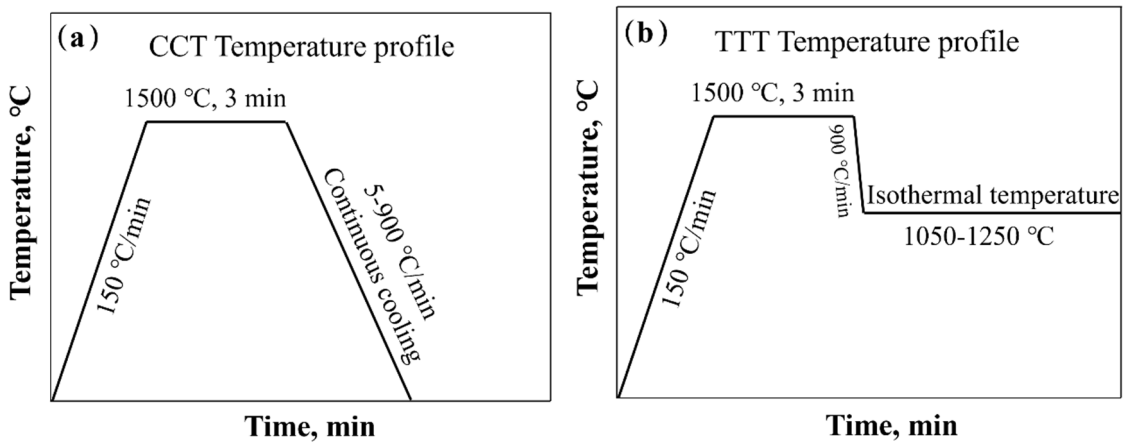

FIG 2 – Temperature profile of: (a) CCT and (b) TTT tests.

Characterisation methods

The crystallisation characteristics of each sample were measured by ImageJ software, according to the difference of brightness and contrast between the crystals and the melt. In this study, the structures of the quenched oxide melt were analysed using a laser confocal Raman spectrometer in order to reveal the relationship between the composition change and structure. The Raman spectra of the samples were recorded in the range of 200^{-1} to 2000 cm^{-1} at room temperature with the light source of a 1 mW semiconductor and an excitation wavelength of 500 nm. The solidified samples after the isothermal heat treatment experiments were divided into two parts, one part was crushed and grounded for X-ray diffraction (XRD) analysis in order to obtain the information of crystalline phases. The XRD data were collected using Cu Kα radiation in a range of 2θ = 10–90°. The other part was cold mounted in epoxy resin, and grinded, polished, then the crystallised phases were determined by a field-emission scanning electron microscope (FESEM) equipped with energy dispersive X-ray spectroscopy (EDS; Bruker).

RESULTS AND DISCUSSION

Continuous cooling crystallisation behaviour

During the continuous cooling experiment, the crystallisation happens under a certain supercooling degree. Besides, the supercooling degree varies with the cooling rates and chemical compositions. Figure 3 shows the morphology of the crystals in the samples with varying MgO contents and cooling rates after the CCT experiment. It can be clearly seen that crystallisation easily happens at a lower cooling rate and the crystallisation tendency decreases with the cooling rate. When the MgO content is 4 per cent, fully crystallisation can be seen for the sample at a cooling rate of 7.5°C/min. Two bulk crystals can be found for the sample at a cooling rate of 25°C/min, and the samples is transparent with no crystals at a cooling rate of 45°C/min. A higher cooling rate results in a higher supercooling degree, which decreases the driving force for the crystallisation. Moreover, the crystallisation tendency greatly increases with the increase of MgO contents. This is due to the fact that the fully crystallisation happens under a cooling rate of 7.5°C/min with 4 per cent MgO content, and it happens under a cooling rate of 240°C/min with 16 per cent MgO content. In terms of Al_2O_3 effect, the crystallisation tendency greatly decreases with the increase of Al_2O_3 contents.

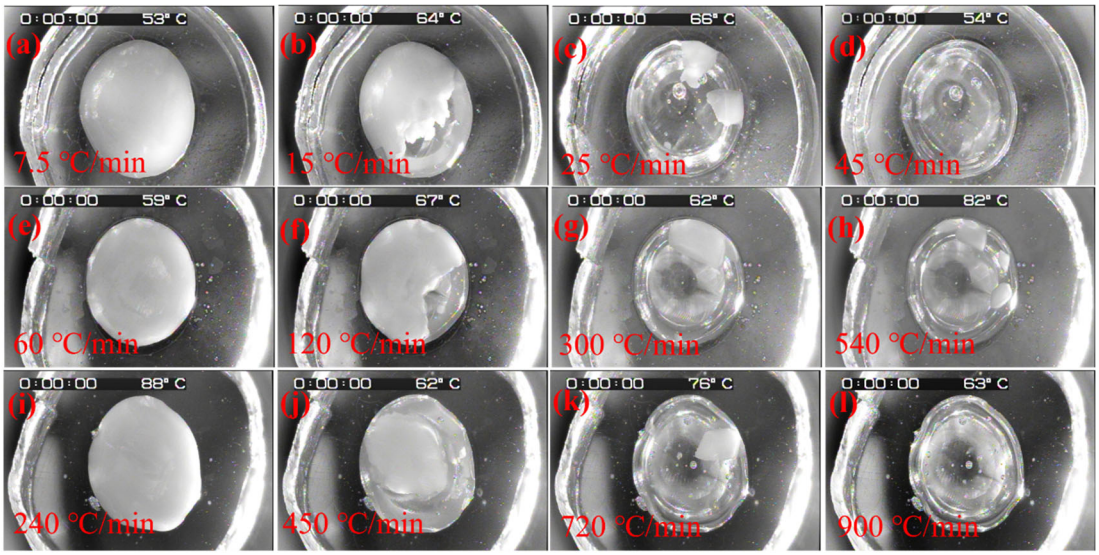

FIG 3 – The morphology of crystals after the CCT experiments with varying MgO contents.

Systematic analysis of the crystallisation characteristics based on the CCT experiments were performed. Figure 4 presents the CCT diagrams of the samples with varying Al_2O_3 and MgO contents. There are three obvious areas, a liquid area in a higher temperature, a crystallisation area in the middle and a glass area in a lower temperature. The critical cooling rate and the start crystallisation temperature are important parameters for evaluating the crystallisation ability of the samples. Taken the sample with 5 per cent Al_2O_3 as an example (Figure 4a), crystals can be formed when the cooling rate smaller than 180°C/min, and the sample will be glass when the cooling rate larger than 180°C/min. Thus, the critical cooling rate can be determined to be 180°C/min. It should be noticed that the critical cooling rate greatly increases from 30°C/min to 600°C/min when the MgO content increases from 8 per cent to 12 per cent. Further increase of MgO to 16 per cent slightly increases the critical cooling rate. Figure 5 shows the start crystallisation temperature of the samples with varying Al_2O_3 and MgO contents. The start crystallisation temperature under a lower cooling rate decreases approximately 100°C when the Al_2O_3 content increases from 10 per cent to 20 per cent, while that increases approximately 120°C when the MgO content increases from 8 per cent to 16 per cent. In addition, the start crystallisation temperature decreases with the increase of cooling rate under each composition due to the nucleation and growth of crystals are closely related to the change of viscosity and undercooling degree of the samples, which is discussed in detail later. It should be noticed that the start crystallisation temperature only slightly decreases with the increase of the cooling rate under higher MgO contents (eg 12 per cent and 16 per cent), which is still above 1200°C at a condition close to the critical cooling rate. It means that

cooling rate has a small effect on the crystallisation temperature when the sample has a larger crystallisation tendency.

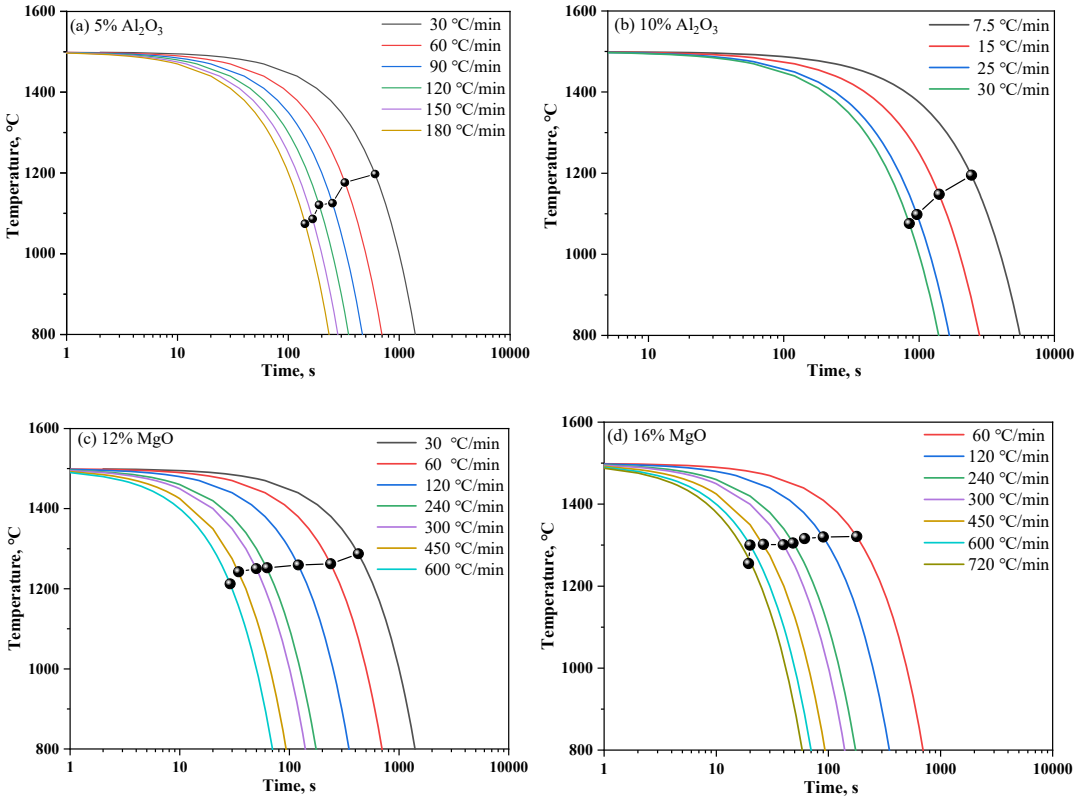

FIG 4 – CCT diagrams of CaO-SiO_2-Al_2O_3-MgO system inclusions with different compositions of (a) 5 per cent Al_2O_3, (b) 10 per cent Al_2O_3, (c) 12 per cent MgO, and (d) 16 per cent MgO.

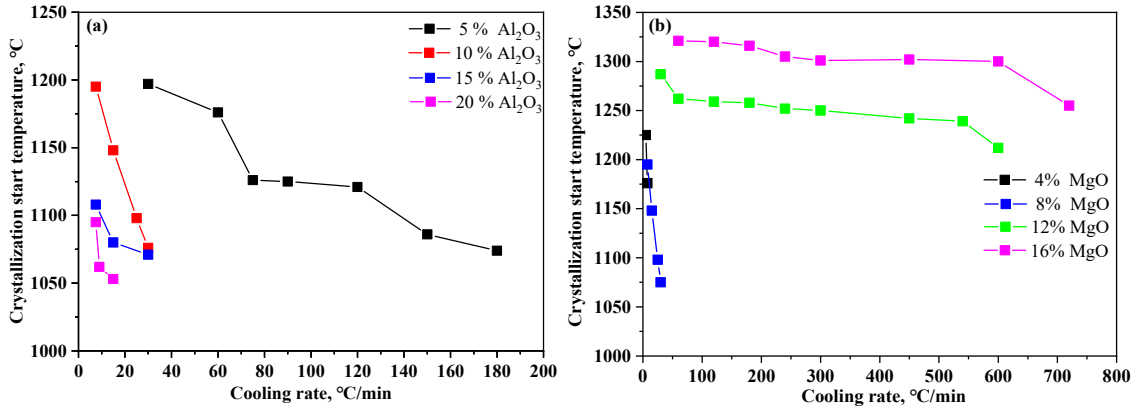

FIG 5 – The start crystallisation temperature in sample with varied (a) Al_2O_3 and (b) MgO contents.

Specifically, the increase of MgO content has a smaller effect on the start crystallisation temperature than the change of Al_2O_3 content. This indicates that the crystallisation ability greatly increases with the increase of MgO content, especially the MgO content is larger than 8 per cent. Under different conditions of cooling rates and compositions, the final area fractions of crystallisation phases can be obtained, as shown in Figure 6. The larger cooling rate, which result in lower crystallisation ability and therefore smaller area fractions of crystallisation phases can be obtained. This can partially reflect the nucleation and growth ability of crystals. The sample with more than 15 per cent Al_2O_3 and less than 4 per cent MgO under the CaO/SiO_2 ratio of 1 has the lowest crystallisation tendency. The change of cooling rate and composition can result in the change of viscosity, melting temperature and structure, which can directly affect the crystallisation behaviour. The detailed discussion of different factors on the crystallisation behaviour will be explained together with the TTT results in the following section.

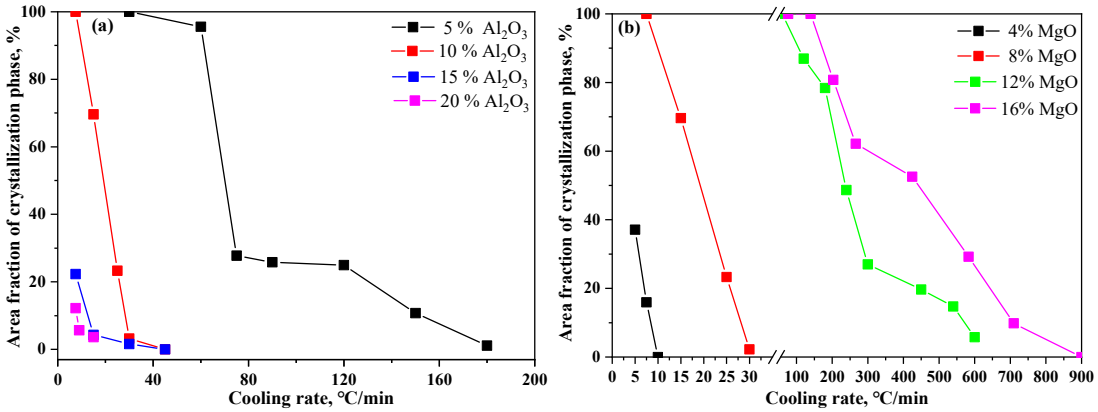

FIG 6 – The area fractions of crystallisation phases in sample with varied (a) Al_2O_3 and (b) MgO contents.

Isothermal crystallisation behaviour

The TTT diagrams of the samples with varying Al_2O_3 and MgO contents are shown in Figure 7 and Figure 8. It can be seen that the crystallisation period (time between the start crystallisation and the end of crystallisation) first decrease and then increase with the increase of temperature when the Al_2O_3 content is less than 10 per cent. Higher temperature greatly delays the crystallisation process due to the smaller supercooling degree and lower driving force for nucleation of crystals. This can be obviously seen in Figure 7c and 7d, since no crystallisation can be observed after two hrs holding time when the temperature is larger than 1150°C and 1100°C, respectively. With the increase of Al_2O_3 content, the crystallisation process becomes much later as the start crystallisation time becomes larger. Moreover, the crystallisation period (time between the start of crystallisation and the end of crystallisation) expands with the increase of Al_2O_3 content. Specially, fully crystallisation cannot be observed when the Al_2O_3 content is 20 per cent.

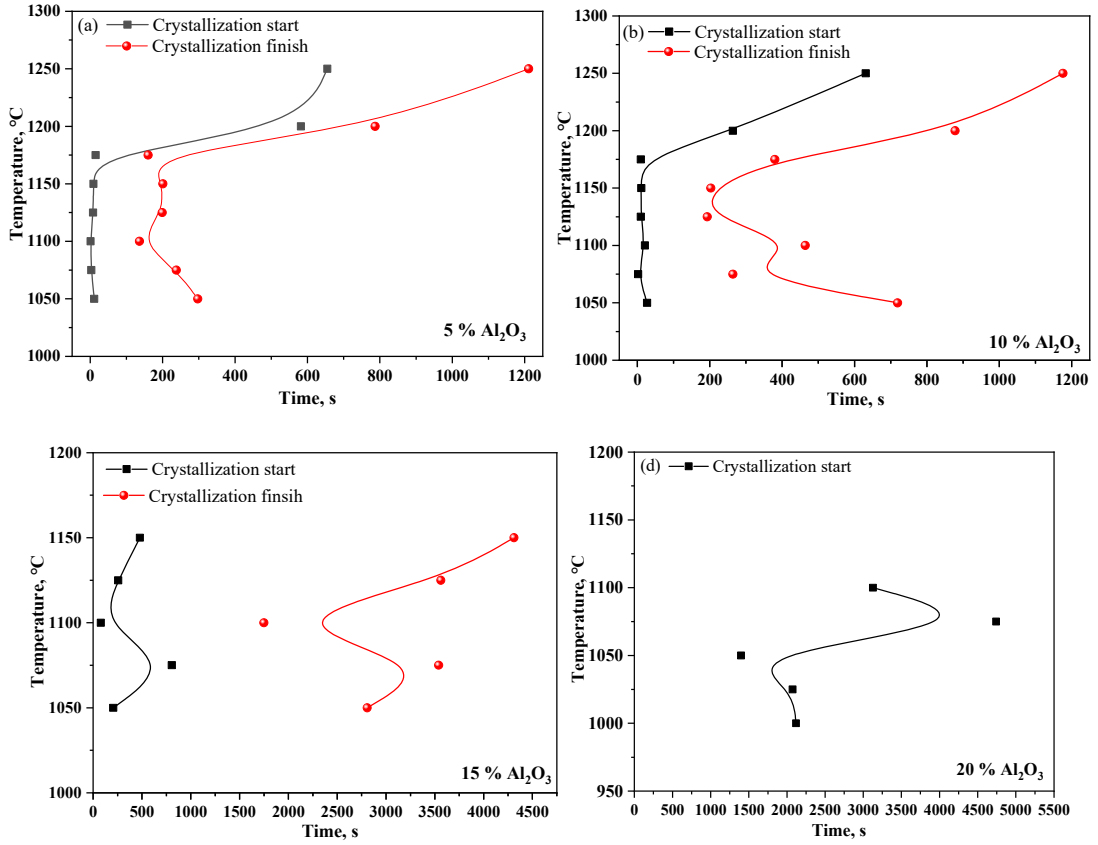

FIG 7 – TTT diagram for samples with varied Al_2O_3 contents (a) 5 per cent, (b) 10 per cent, (c) 15 per cent, (d) 20 per cent.

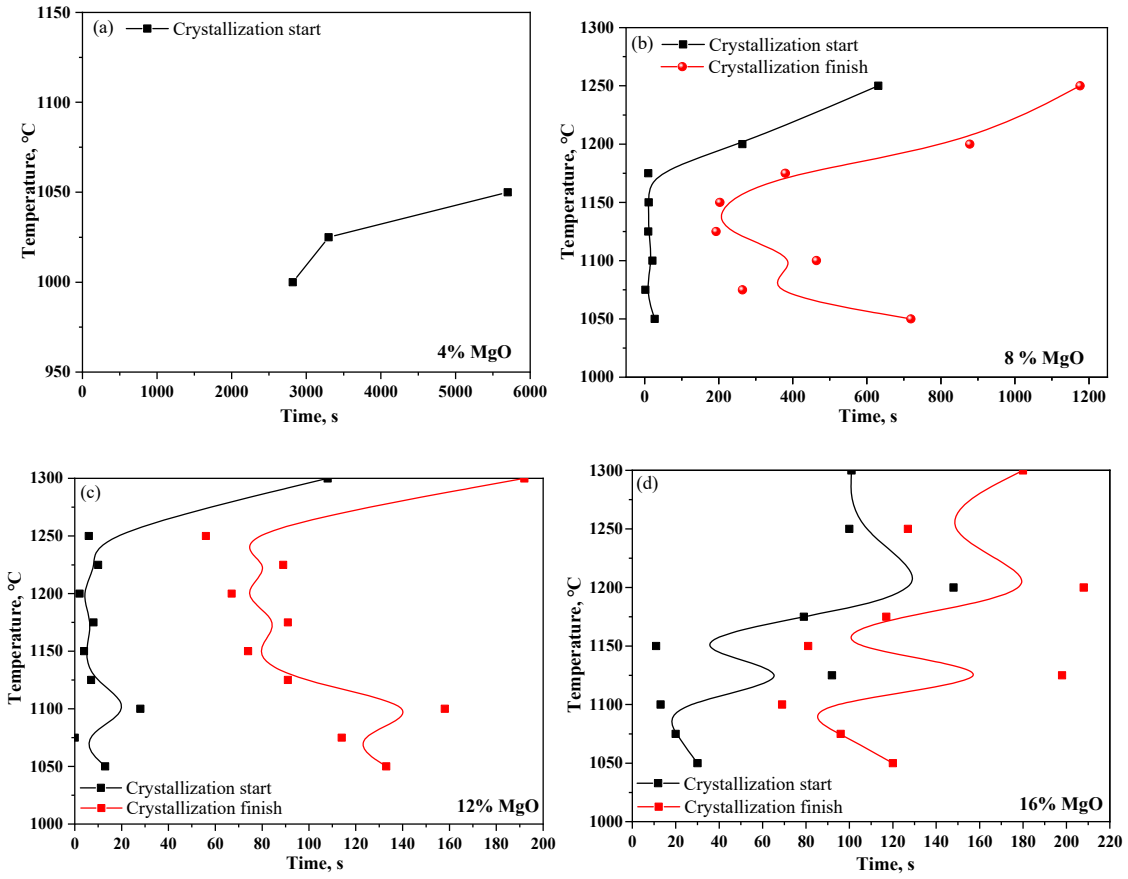

FIG 8 – TTT diagram for samples with varied MgO contents (a) 4 per cent, (b) 8 per cent, (c) 12 per cent, (d) 16 per cent.

In terms of MgO effect, an opposite tendency can be obtained. When the MgO content is about 4 per cent, crystallisation can only be observed at lower temperatures, and the start crystallisation time is much larger compared to those when the Al_2O_3 content is 20 per cent. The start crystallisation time becomes much smaller when the MgO content increases from 4 per cent to 8 per cent. With further increase of MgO content, the crystallisation period getting shorter, indicating that the crystallisation of inclusions occurred relatively easily. Moreover, the crystallisation period of inclusions under different MgO contents is much shorter compared to those with different Al_2O_3 contents in the similar temperature range. This indicates that the change of MgO content has a larger effect on the crystallisation rate compared to that of Al_2O_3. Thus, the increase of Al_2O_3 content and decrease of MgO content can greatly suppress the crystallisation of the CaO-SiO_2-Al_2O_3-MgO system inclusions (CaO/SiO_2 = 1).

Besides, the TTT curve of inclusions shows multiple ‘C’ shape, especially for the case of different MgO content, indicating that different crystallisation processes occurred in different temperature zones. However, it is difficult to identify the different phases since single crystallisation cannot be easily obtained. Based on the TTT results, the proper holding temperature, time and inclusion composition can be controlled to obtain the optimised soaking process.

CONCLUSIONS

- The increase of MgO content increases the crystallisation ability of CaO-SiO_2-Al_2O_3-MgO inclusions, while the increase of Al_2O_3 content has an opposite effect.
- The Al_2O_3 content of the system needs to be controlled larger than 15 wt per cent and the MgO content should be kept at a small amount (less than 5 wt per cent) to obtain low melting point plasticized CaO-SiO_2-Al_2O_3-MgO (CaO/SiO_2=1) system inclusions.

ACKNOWLEDGEMENTS

The authors are grateful for support from the National Natural Science Foundation of China (52304355 and U21A20113) and Japan Society for the Promotion of Science (JSPS).

REFERENCES

Bertrand, C, Molinero, J, Landa, S, Elvira, R, Wild, M, Barthold, G, Valentin, P and Schifferl, H, 2003. Metallurgy of plastic inclusions to improve fatigue life of engineering steels, *Ironmaking and Steelmaking*, 30:165–169.

Chen, C, Jiang, Z, Li, Y, Sun, M, Wang, Q, Chen, K and Li, H, 2020. State of the Art in the Control of Inclusions in Spring Steel for Automobile-a Review, *ISIJ International*, 60:617–627.

Chen, C, Jiang, Z, Li, Y, Zheng, L, Huang, X, Yang, G, Sun, M, Chen, K, Yang, H and Hu, H, 2019. State of the art in the control of inclusions in tire cord steels and saw wire steels–A Review, *Steel Research International*, 90:1800547.

Kim, W Y, Kim, K S and Kim, S Y, 2021. Evolution of Non-metallic Inclusions in Si-Killed Stainless Steelmaking, *Metallurgical and Materials Transactions B,* 52:652–664.

Kirihara, K, 2011. Production technology of wire rod for high tensile strength steel cord, *Kobelco Technol Rev*, 30:62–65.

Kitamura, S Y, 2011. Preface to the special issue on fundamentals and applications of non-metallic inclusions in solid steel, *ISIJ international*, 51:1943–1943.

Li, Z, Yang, W, Yao, H and Zhang, L, 2022. Effect of Na2O addition on crystallization behavior and properties of 25 wt% Al_2O_3–SiO_2–CaO non-metallic inclusion-type oxides, *Ceramics International*, 48:23849–23861.

Liang, Y, Shi, C, Huang, Y, Ju, J and Li, J, 2022. Effect of CaO/SiO_2 mass ratio and Li_2O on structure and phase precipitation behaviors of CaO–SiO_2–MgO–Al_2O_3 oxide inclusions, *Journal of Non-Crystalline Solids*, 597:121911.

Lyu, S, Ma, X, Huang, Z, Yao, Z, Lee, H-G, Jiang, Z, Wang, G, Zou, J and Zhao, B, 2019. Understanding the formation and evolution of oxide inclusions in Si-deoxidized spring steel, *Metallurgical and materials Transactions B,* 50:1862–1877.

Meng, Y, Li, J, Wang, K and Zhu, H, 2022. Effect of the Bloom-Heating Process on the Inclusion Size of Si-Killed Spring Steel Wire Rod, *Metallurgical and Materials Transactions B,* 53:2647–2656.

Rocabois, P, Pontoire, J, Lehmann, J and Gaye, H, 2001. Crystallization kinetics of Al_2O_3–CaO–SiO_2 based oxide inclusions, *Journal of Non-Crystalline Solids*, 282:98–109.

Tashiro, M, Sukenaga, S and Shibata, H, 2017. Control of crystallization behaviour of supercooled liquid composed of lithium disilicate on platinum substrate, *Scientific Reports*, 7:6078.

Xuan, C, Shibata, H, Sukenaga, S, Jönsson, P G and Nakajima, K, 2015a. Wettability of Al_2O_3, MgO and Ti_2O_3 by liquid iron and steel, *ISIJ International*, 55:1882–1890.

Xuan, C, Shibata, H, Zhao, Z, Jönsson, P G and Nakajima, K, 2015b. Wettability of TiN by liquid iron and steel, *ISIJ International*, 55:1642–1651.

Yang, Y, Zhan, D, Qiu, G, Li, X, Jiang, Z and Zhang, H, 2022. Inclusion evolution in solid steel during rolling deformation: A review, *Journal of Materials Research and Technology*, 18:5103–5115.

Zhang, L and Thomas, B G, 2003. State of the art in evaluation and control of steel cleanliness, *ISIJ international*, 43:271–291.

Zhang, L, Guo, C, Yang, W, Ren, Y and Ling, H, 2018. Deformability of oxide inclusions in tire cord steels, *Metallurgical and Materials Transactions B,* 49:803–811.

Effect of Al_2O_3/SiO_2 ratio on structure and properties of mould flux for high-Al steel continuous casting

DOI: 10.62053/FXJW8608

Q Wang[1], J Zhang[2], O Ostrovski[3], C Zhang[4] and D Cai[5]

1. The University of New South Wales, Sydney NSW 2052; Midea Group Laundry Appliance Division, Wuxi, 214028 Jiangsu, China.
2. The University of New South Wales, Sydney NSW 2052. Email: j.q.zhang@unsw.edu.au
3. The University of New South Wales, Sydney NSW 2052.
4. Baosteel Group Corporation Research Institute, Baoshan, 201900 Shanghai, China.
5. Baosteel Group Corporation Research Institute, Baoshan, 201900 Shanghai, China.

ABSTRACT

The conventional $CaO-SiO_2$-based mould fluxes are not suitable for high-Al steel casting because of the strong reaction between silica in the flux and aluminium in the steel strand. In the process of casting of high-Al steel, flux composition changes; with the decrease of the silica concentration and increase of alumina. Knowledge and understanding of the effect of the Al_2O_3/SiO_2 ratio on flux structure and properties are useful for flux design for the high Al-steel continuous casting.

This paper investigated the effect of the Al_2O_3/SiO_2 ratio on structure, viscosity, phase composition of fluxes quenched at different temperatures and heat transfer of $CaO-Al_2O_3-SiO_2-B_2O_3-Na_2O-Li_2O-MgO-F$ fluxes. It was found that flux melting temperature increased with the increase in Al_2O_3/SiO_2 ratio. Viscosity of the flux melts increased significantly with the increase of the Al_2O_3/SiO_2 ratio from 0.7 to 1.2, reaching the maximum value, and then decreased with further increase of the Al_2O_3/SiO_2 ratio. Raman spectroscopy analysis revealed that the change of the Al_2O_3/SiO_2 ratio led to the change of aluminate and silicate structural units. The turning point for viscosity was attributed to the change in the degree of flux polymerisation. X-ray diffraction (XRD) analysis showed that increasing Al_2O_3/SiO_2 ratio increased crystallisation tendency of the fluxes. Heat transfer measurement by infrared emitter technique (IET) revealed that increasing Al_2O_3/SiO_2 ratio led to the decrease in heat flux which is correlated well with the increased crystallinity of the flux. The results suggested that the flux with Al_2O_3/SiO_2 ratio 4.3 is the best candidate among the studied $CaO-Al_2O_3$-based mould fluxes for casting of high-Al steel.

INTRODUCTION

Conventional $CaO-SiO_2$-based mould fluxes contain high concentrations of SiO_2 (up to 56 mass per cent (Brandaleze *et al*, 2012)) which is essential to ensure the required flux properties for steel casting. However, for casting of high aluminium steel such as advanced high strength steel (0.5–2.0 mass per cent Al), [Al] in the steel can react with (SiO_2) in the flux, increasing the Al_2O_3 content and decreasing the SiO_2 content in the mould flux, ie increasing the ratio of Al_2O_3/SiO_2. As a result, it leads to an inevitable variation of flux properties, and consequently, affecting the casting of high-Al steel (Kim *et al*, 2013; Cho *et al*, 2013; Kang *et al*, 2013; Chung and Cramb, 2000; Zhou *et al*, 2017; Zhou, Wang and Zhou, 2015).

This work investigated the effect of Al_2O_3/SiO_2 ratio on the physicochemical properties, structure, and heat transfer of mould fluxes for continuous casting of high-Al steel. The ratio of Al_2O_3/SiO_2 changed from a relatively low value to a high one to reflect the flux composition change during high-Al steel casting process. The information of the effect of this ratio on flux structure and properties is useful for the flux design for high Al-steel continuous casting.

MATERIALS AND EXPERIMENTAL PROCEDURE

Materials

Flux samples were prepared by using reagent grade $CaCO_3$, Na_2CO_3, Li_2CO_3, SiO_2, Al_2O_3, B_2O_3 and CaF_2 which were fully mixed, and then melted in a high-purity graphite crucible at 1400°C for 20 mins. After that, the melted flux was quenched into water, then dried at 120°C for 2 hrs, and ground into fine powders using a ring mill. The contents of B_2O_3 and Li_2O were analysed using

inductively coupled plasma (ICP, Thermo Scientific IRIS Intrepid II, MA), while the other flux components were determined by X-ray fluoroscopy (XRF, PANalytical AXIOS-Advanced WDXRF spectrometer, Netherland). The measured flux compositions are shown in Table 1. The Al_2O_3/SiO_2 ratio of fluxes varied from 0.7 to 10.8 while concentrations of all other components were set as constants. All five flux samples are based on the CaO-Al_2O_3-SiO_2-B_2O_3 quaternary system with the addition of Na_2O, Li_2O, MgO, and F. It should be mentioned that variation of the Al_2O_3/SiO_2 mass ratio changed the CaO/Al_2O_3 mass ratio within the range 2.2–1.1.

TABLE 1

Measured chemical composition of mould fluxes, mass per cent and Al_2O_3/SiO_2 ratio.

Flux	CaO	Al_2O_3	SiO_2	Na_2O	B_2O_3	Li_2O	MgO	F	Al_2O_3/SiO_2
1	32.7	15.1	21.5	6.0	12.4	3.9	2.1	6.3	0.7
2	32.6	19.8	16.5	6.1	12.7	3.8	2.0	6.5	1.2
3	33.2	24.6	11.8	6.1	11.7	3.7	2.1	6.8	2.1
4	31.6	30.0	7.0	6.2	12.7	4.1	2.0	6.3	4.3
5	33.6	32.0	2.9	6.4	12.4	4.0	2.1	6.5	10.8

Experimental procedure

Melting properties of mould fluxes were investigated using a hot stage microscopy. As-quenched flux powders were pressed to pellets (Φ 3×3 mm). The pellets were continuously heated in a horizontal tube furnace at a rate of 15°C/min; their appearance change was monitored by a video camera. To characterise the melting properties of mould fluxes, the softening, hemispherical, and fluidity temperatures were defined as the temperatures at which the height of the flux pellet dropped to 75, 50 and 25 per cent of its original height, respectively. The details of melting property measurement were described elsewhere (Yang *et al*, 2017, 2018).

Viscosity of mould fluxes was investigated using a rotation viscometer (model ZC-1600, China). Approximately 140 g pre-melted flux was heated up to 1400°C in a graphite crucible in nitrogen atmosphere. After holding the molten flux at 1400°C for 1200 secs, a Mo bob was slowly submerged into the homogenised melt and rotated at a rate of 12 rev/min for the measurement of viscosity. After measurement of the flux viscosity at 1400°C, the viscosity was measured in the process of flux continuous cooling with a rate of 5°C/min until the Mo bob stopped rotation.

The structure of as-quenched mould fluxes from 1400°C was studied using Raman spectroscopy (Renishaw inVia Raman Microscope, UK). The pulverised mould flux was illuminated by Ar-ion laser beam. The excitation wavelength of Ar-ion laser was 514 nm with a beam spot size of 1.5 μm. The measurement was conducted in the Raman shift range from 400 to 1700 cm^{-1}. The obtained Raman spectra were deconvoluted using WiRE 4.4 software.

The heat transfer rate across the mould fluxes was measured using infrared emitter technique (IET, Central South University, China). The details of IET system were described elsewhere (Wang and Cramb, 2005). The flux disk was prepared using 13 g as-quenched flux powders which were melted at 1400°C and held for 1200 secs before pouring into a copper cylinder (Φ 40 mm) and pressing to a disk. The pressed mould flux disk was immediately placed in a muffle furnace in which the temperature gradually decreased from 800°C to 25°C with a slow cooling rate of 1°C/min to minimise the internal stress within the disk. The fabricated flux disk was ground to the thickness of 4 ± 0.01 mm using a diamond grinding wheel, and then carefully polished using sandpapers from 300 to 1200 grits. In the heat flux measurement, the mould flux disk was placed on the copper base of the IET system. The incident thermal radiation was increased up to 1.6 MW/m^2, which is close to the radiation released from the steel strand in the continuous casting. The temperatures recorded by the embedded thermocouples were used for the heat flux calculation according to the Fourier's law (Park *et al*, 2016):

$$q = \frac{-1}{n}\sum_i k\left(\frac{dT}{dx}\right)_i \quad (1)$$

where:

q	is the heat flux
n	presents the total number of thermocouples
k	is the thermal conductivity of copper

The heat fluxes measured at an incident radiation of 1.6 MW/m^2 were compared to reflect the heat transfer ability of fluxes during continuous casting.

The crystalline phases in the mould fluxes heated to different temperatures and quenched were determined using X-ray diffraction (XRD) with Cu-Kα radiation in the scanning range of 2θ from 10 to 80 degree with a scanning speed of 0.021 deg/s. Eight-gram samples for the XRD analyses were prepared separately by holding the fluxes at 950°C (low temperature zone), 1050°C (medium temperature zone), and 1150°C (high temperature zone) for 30 mins. Then the heat-treated samples were quenched into water and subjected to the XRD analysis. The selection of these three temperatures was based on the TTT measurement to reflect the phase changes at low, medium and high temperatures. The XRD spectra were analysed using HighScore Plus 4.2.

RESULTS

Melting properties

Figure 1 illustrates the influence of Al_2O_3/SiO_2 ratio on softening temperature (T_s), hemispherical temperature (T_h) and fluidity temperature (T_f) of the CaO-Al_2O_3-based mould fluxes.

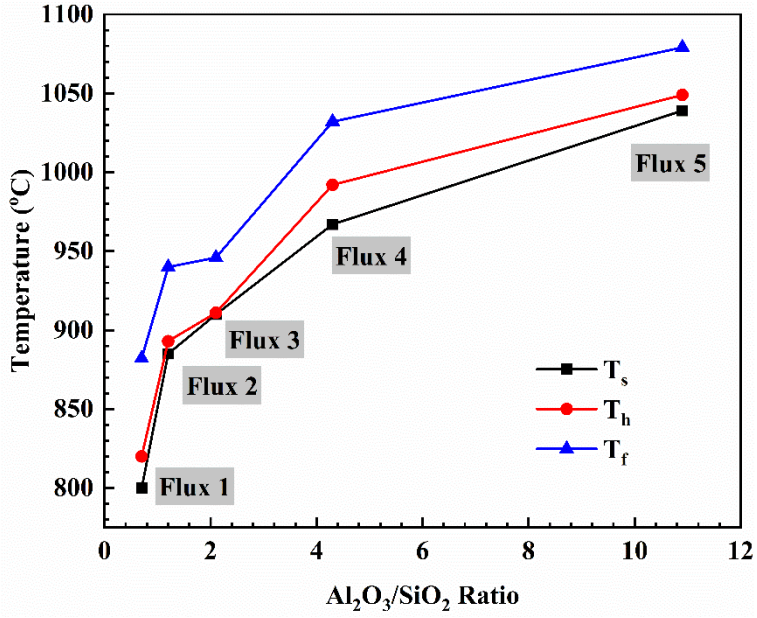

FIG 1 – Softening temperature (T_s), hemispherical temperature (T_h) and fluidity temperature (T_f) as functions of the Al_2O_3/SiO_2 ratio.

With the increase in the mass ratio of Al_2O_3/SiO_2 from 0.7 to 10.8, all three characteristic temperatures T_S, T_h and T_f continuously increased (Figure 1). The value of T_f is much higher than those of T_s and T_h in all cases.

Viscosity

Figure 2 shows the measured viscosity as a function of temperature. It was observed that for all mould fluxes, viscosity increased with the decrease in temperature. The enlarged scale of viscosity in the high-temperature zone from 1300 to 1400°C is shown in Figure 3. It was observed that when increasing the mass ratio of Al_2O_3/SiO_2 from 0.7 to 1.2, the viscosity increased significantly. With further increasing this ratio, the viscosity decreased. As a result, Flux 8-2 had the highest viscosity in all the fluxes. The viscosities at 1400°C (η_{1400}) of all examined mould fluxes are presented in

Table 2, further confirming that the viscosity reaches the highest point when Al_2O_3/SiO_2 = 1.2, and reduces gradually with further increase in Al_2O_3/SiO_2 ratio.

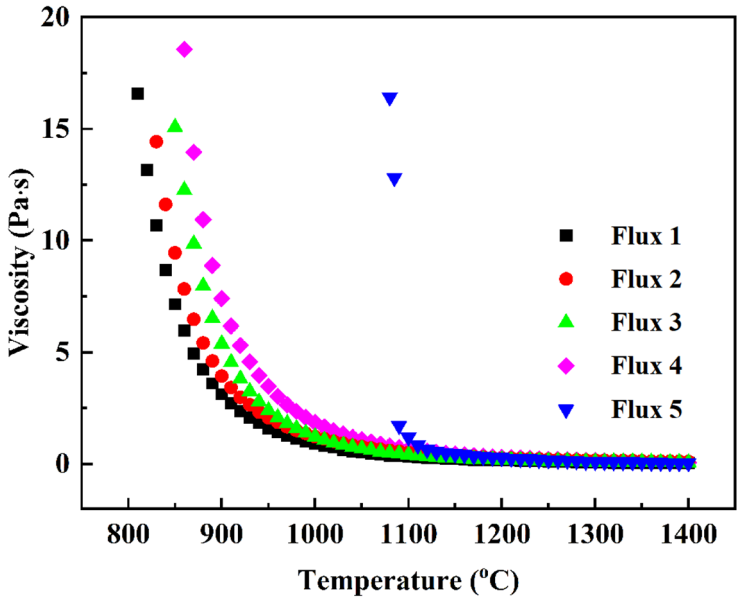

FIG 2 – Viscosity of mould flux with different Al_2O_3/SiO_2 ratios at different temperatures.

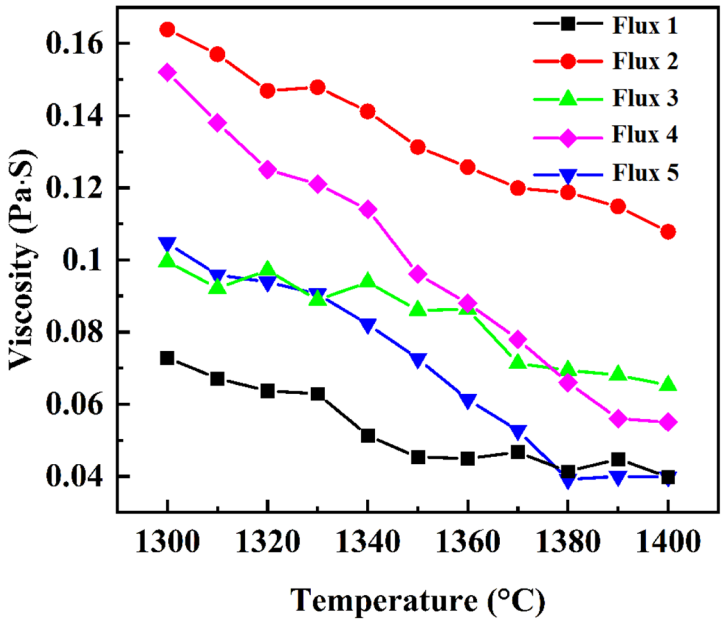

FIG 3 – Highlight the viscosity at temperatures 1300–1400°C.

TABLE 2

Calculated apparent activation energy (*Ea*), break temperature (T_{br}), and viscosity at 1400°C (η_{1400}) for the fluxes with different Al_2O_3/SiO_2 ratios.

Flux	*Ea* (kJ·mol^{-1})	R^2	T_{br}, °C	η_{1400}, Pa·s
1	137	0.991	-	0.040
2	98	0.996	-	0.108
3	117	0.989	-	0.065
4	156	0.978	-	0.055
5	188	0.985	1105	0.039

Liquid flux can be assumed to be a Newtonian fluid and its viscosity can be fitted by the Arrhenius equation.

$$\ln \eta = \ln A + \frac{Ea}{RT} \quad (2)$$

where:

η	represents viscosity
A	is viscosity constant
T	is the temperature
*E*a	activation energy

Figure 4 shows the Arrhenius plot of $\ln\eta$ as a function of 1/*T*. It appears that only Flux 5 shows a clear break temperature at 1105°C, while all other fluxes do not have apparent break temperatures. The activation energies determined in the temperature range of 1100–1330°C are 137 kJ·mol^{-1} for Flux 1, 98 kJ·mol^{-1} for Flux 2, 117 kJ·mol^{-1} for Flux 3, 156 kJ·mol^{-1} for Flux 4, and 188 kJ·mol^{-1} for Flux 5 in temperature range of 1100–1330°C. All these results are shown in Table 2**.**

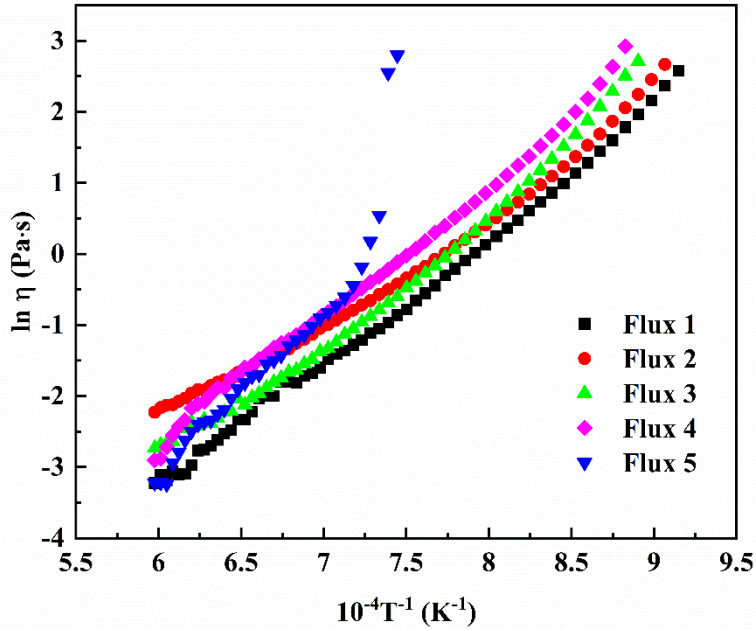

FIG 4 – Plots of $\ln\eta\ vs\ \frac{1}{T}$ for fluxes with Al_2O_3/SiO_2 ratio increased from 0.7 to 10.8.

Raman analysis

The structure of mould flux with varying Al_2O_3/SiO_2 mass ratios was studied using the Raman spectroscopy. Figure 5 illustrates the Raman spectra of as-quenching mould fluxes and Table 3 lists the assignments of deconvoluted Raman bands. In the low frequency region (between 400 and 800 cm^{-1}) the deconvoluted bands were assigned to aluminate group in which peaks around 500 cm^{-1} were assigned to Al-F stretching vibration in AlF_6; peaks centred around 550 cm^{-1} correspond to Al-O-Al linkage which is the major bond in the 3D aluminate network; peaks located around 590 cm^{-1} are related to Al-O$^-$ stretching vibration in AlO_6 units; peaks located around 770 cm^{-1} are related to Al-O$^-$ stretching vibration in Al-NBO units with 1 or 2 NBOs (non-bridging oxygen); peaks centred around 865 cm^{-1} correspond to Al-O-Si linkage. Among these characteristic peaks, structural units with Al-O-Si and Al-O-Al linkages had the most prominent peaks; with the increase of Al_2O_3/SiO_2 mass ratio, peaks assigned to AlF_6 and Al-O-Al linkages became more and more prominent, while peaks assigned to Al-O-Si linkage became weaker.

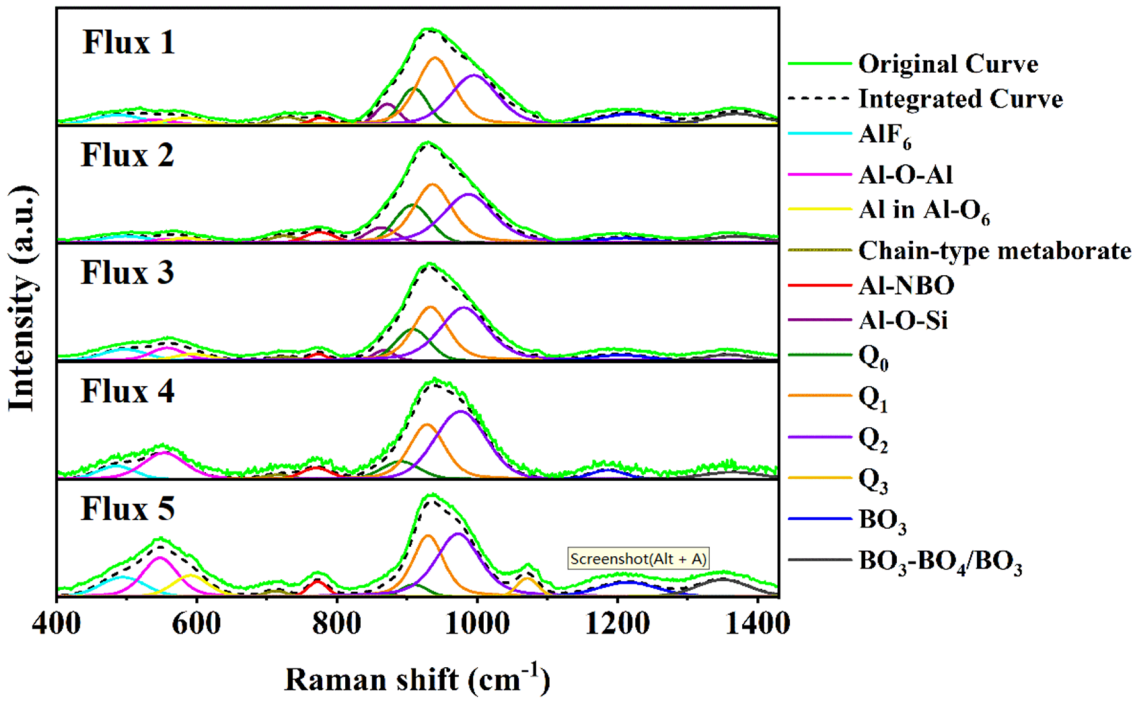

FIG 5 – Deconvoluted Raman spectra for mould flux with various Al_2O_3/SiO_2 ratios.

TABLE 3

Assignments of deconvoluted Raman bands.

Flux 1	Flux 2	Flux 3	Flux 4	Flux 5	Structural unit	Reference
488.1	498.5	497.0	485.2	494.3	AlF_6	Park, Min and Song (2002); Ma *et al* (2018)
539.3	558.0	557.8	553.5	547.5	Al-O-Al	Park, Min and Song (2002)
582.2	584.1	594.2	-	590.9	AlO_6	Park, Min and Song (2002); McMillan and Piriou (1983)
729.2	724.4	724.7	715.6	712.9	Chain-type metaborate	Kim and Sohn (2014); Kamitsos, Karakassides and Chryssikos (1987)
777.0	775.4	772.9	770.2	772.4	Al-NBO	Gao, Wang and Zhang (2017); Kim and Park (2014)
872.0	863.1	866.8	851.0	870.4	Al-O-Si	Gao (2016a, 2016b)
909.5	907.0	908.0	890.9	910.0	Q^0	Kim and Sohn (2012); Zheng *et al* (2014)
940.0	936.2	933.3	928.5	930.0	Q^1	
995.1	987.4	980.7	976.3	972.6	Q^2	
-	-	-	-	1071.5	Q^3	
1217.8	1210.9	1205.0	1186.3	1214.8	BO_3	Kim and Sohn (2014); Kamitsos, Karakassides and Chryssikos (1987)
1370.7	1371.8	1358.1	1364.2	1350.3	BO_3-BO_4/BO_3	

In the medium frequency range (900 to 1100 cm^{-1}), the deconvoluted Raman peaks were assigned to silicate structures, including Si-O stretching vibration in SiO_4^{4-} (Q^0), $Si_2O_7^{6-}$ (Q^1), SiO_3^{2-}(Q^2) and $Si_2O_5^{2-}$ (Q^3). In all fluxes, Q^1 and Q^2 were the dominant units, Q^0 and Q^3 were less noticeable in the

Raman spectra. No Q^4 unit was detected for all fluxes. Based on the spectra profile between 900 and 1100 cm^{-1} (Figure 5), with the increase of Al_2O_3/SiO_2 ratio, the area fraction of Q^0 decreased while the fraction of Q^2 increased, which means the simple silicate structure became less significant with the increase of Al_2O_3/SiO_2 mass ratio; the fraction of Q^1 did not change.

In the high frequency range, the Raman bands were assigned to different borate structures, where the peaks around 1210 cm^{-1} correspond to the B-O stretching vibration in BO_3 units which was a necessary component to form 3D borate groups, while the peak around 1360 cm^{-1} was assigned to B-O stretching vibration in BO_3^- units attached to other 3D borate groups. There is also a borate band located around 720 cm^{-1}, corresponding to chain-type metaborate groups. With the increase of Al_2O_3/SiO_2 ratio from 0.7 to 1.2, the fractions of these two borate units became depressed; with further increase the ratio to 10.8, the fractions of these units gradually increased.

The percentage of some main peaks from deconvoluted Raman spectra is shown in Figure 6. Increasing Al_2O_3/SiO_2 ratio increased the fraction of Al-O-Al, AlF_6 and Q^2, but decreased that of Q^0, Al-O-Si. The fraction of Q^1 remained no change.

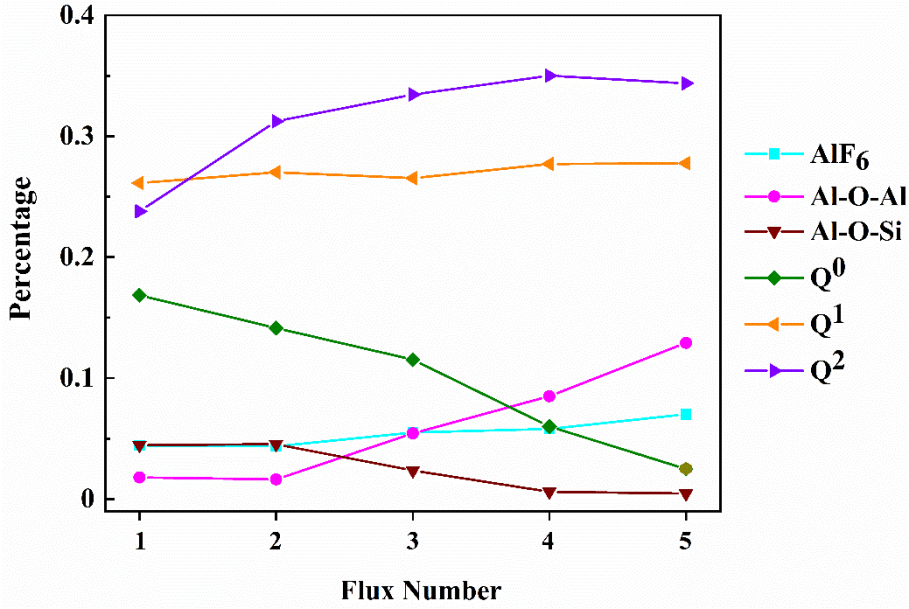

FIG 6 – Percentage of main peaks based on the deconvoluted Raman spectra.

Flux phase analysis by XRD

Figures 7 and 8 show the XRD patterns of mould fluxes 1 to 5 heat treated at 900°C and 1000°C; the XRD patterns of Flux 4 heat-treated at 950°C and 1050°C were also shown in these two figures, respectively. Table 4 lists the crystal phases identified by XRD at different temperatures. For Fluxes 2 and 3 (Al_2O_3/SiO_2 ratio of 1.2 and 2.1, respectively), $Ca_2Al_2SiO_7$ was the only phase at both 900°C and 1000°C. However, for other fluxes, different phases formed. At 900°C, $Ca_4Si_2O_7F_2$ (cuspidine) was detected to be the main phase in Flux 1 with Al_2O_3/SiO_2 ratio of 0.7, while the crystalline phases of Flux 5 with Al_2O_3/SiO_2 ratio of 10.8 were $Ca_5B_3O_9F$, $CaSiO_3$ and $LiAlO_2$ ($LiAlO_2$ was the main phase). For Flux 4, $Ca_2Al_2SiO_7$, $MgAl_6O_{10}$, $LiAlO_2$ were detected at 950°C. At 1000°C, the crystal phases detected in Flux 4 were the same as those at 900°C, while there was only trace amount of $Ca_4Si_2O_7F_2$ (cuspidine) detected in amorphous matrix for Flux 1 after heat treatment at 1000°C. For Flux 4 at 1050°C, $MgAl_6O_{10}$, $LiAlO_2$, and $Ca_2Al_2SiO_7$ were identified.

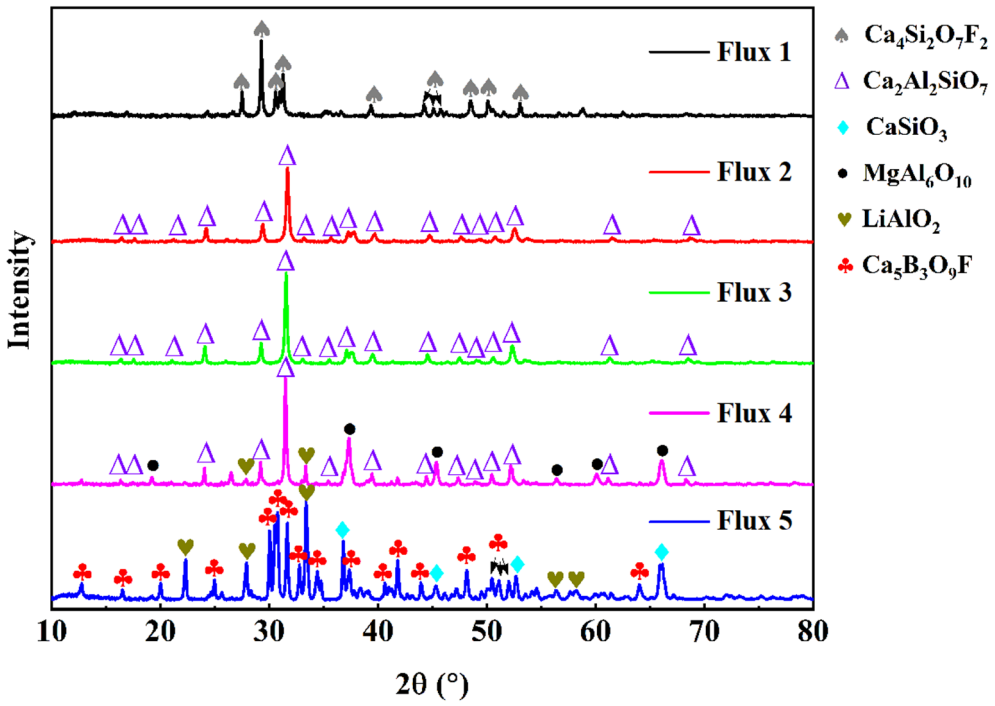

FIG 7 – XRD patterns of Fluxes 1, 2, 3 and 5 heated at 900°C and Flux 4 at 950°C.

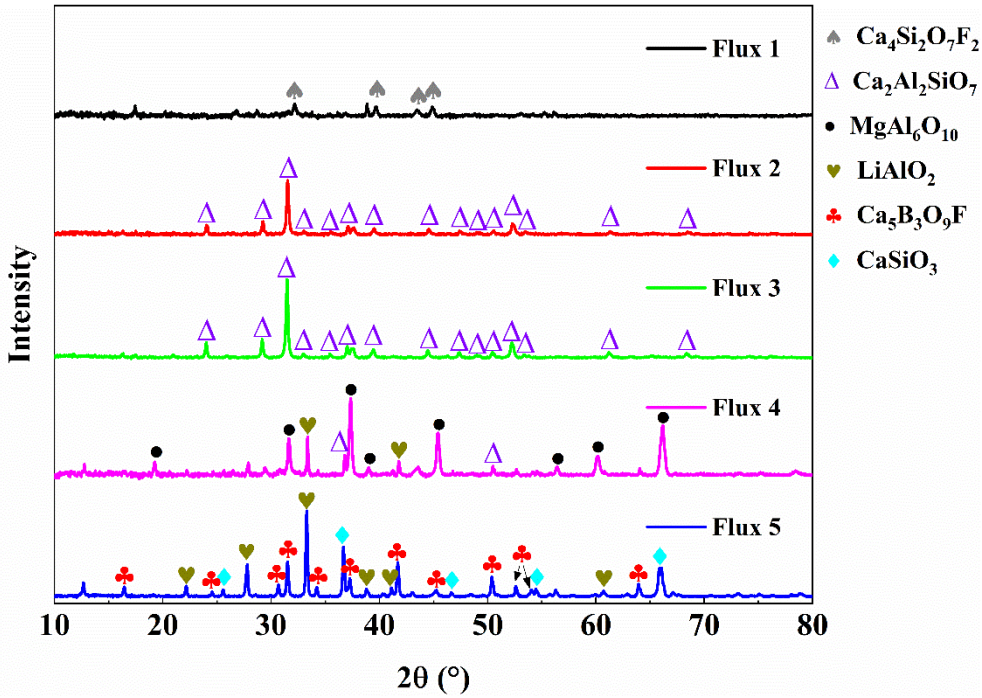

FIG 8 – XRD patterns of Fluxes 1, 2, 3 and 5 heated at 1000°C and Flux 4 at 1050°C.

TABLE 4

Summary of the XRD results at different temperatures.

T/°C	900	1000
Flux 1	$Ca_4Si_2O_7F_2$	Amorphous + trace amount of $Ca_4Si_2O_7F_2$
Flux 2	$Ca_2Al_2SiO_7$	$Ca_2Al_2SiO_7$
Flux 3	$Ca_2Al_2SiO_7$	$Ca_2Al_2SiO_7$
Flux 4	(950°C) $Ca_2Al_2SiO_7$, $MgAl_6O_{10}$, $LiAlO_2$	(1050°C) $MgAl_6O_{10}$, $LiAlO_2$, $Ca_2Al_2SiO_7$
Flux 5	$LiAlO_2$, $Ca_5B_3O_9F$, $CaSiO_3$	$LiAlO_2$, $CaSiO_3$, $Ca_5B_3O_9F$

Heat transfer of mould flux

Figure 9 shows results of IEF experiments for five mould fluxes. The heat flux tended to be stable after 2100 secs. The average heat flux values of the five fluxes at the final stage were 760.6, 720.0, 700.1, 686.0, 440.3 kW/m^2, respectively. It means that with the increase of Al_2O_3/SiO_2 ratio from 0.7 to 10.8 the heat flux decreases. Among these values, the heat flux for Flux 5 had a much lower value than those for other fluxes.

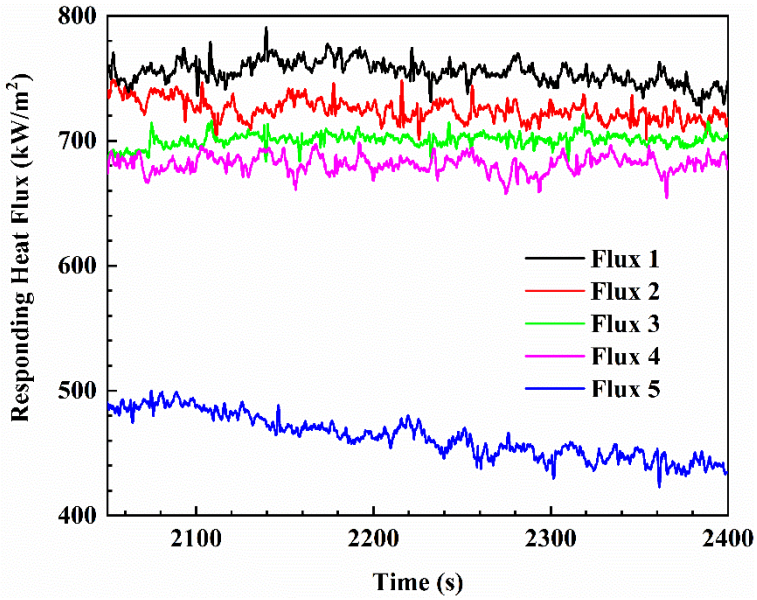

FIG 9 – Heat fluxes of five mould fluxes determined in IET experiment.

Flux discs after IET experiments were subjected to XRD analysis; the results are shown in Figure 10. Flux 1 was fully amorphous, and Flux 2 was basically amorphous with a couple of very small peaks. With the increase of Al_2O_3/SiO_2 ratio, more crystal peaks appeared with the increased intensity, indicating the crystallisation tendency of the mould flux was enhanced. The main phases identified were $Ca_2Al_2SiO_7$ for Flux 3; $LiAlO_2$, $MgAl_6O_{10}$, $Ca_2Al_2SiO_7$ and $Ca_5B_3O_9F$ for Flux 4; and $LiAlO_2$, $Ca_5B_3O_9F$, $CaAl_4O_7$ for Flux 5.

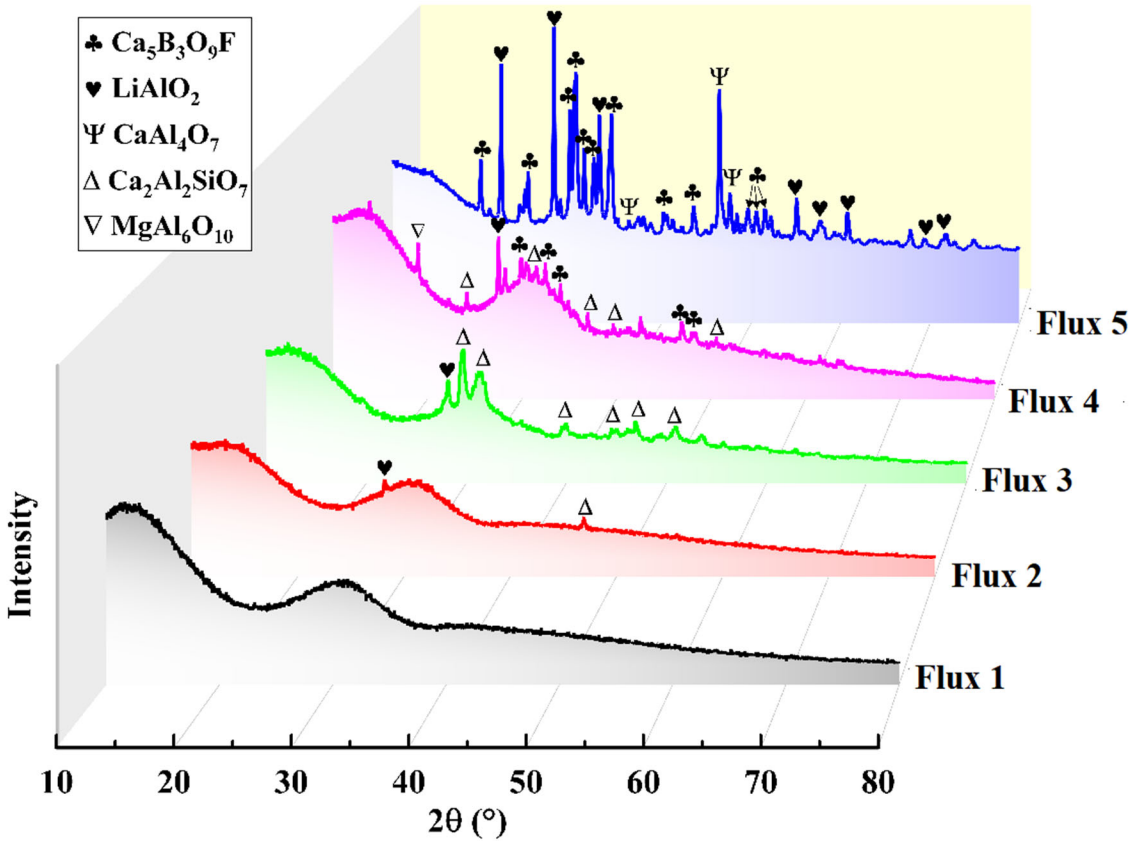

FIG 10 – XRD patterns of the flux discs after IET experiments.

DISCUSSION

Experimental results showed that the change of Al_2O_3/SiO_2 ratio led to the variation of flux properties. With the increase of Al_2O_3/SiO_2 ratio, the flux melting temperature and viscosity increased, while the heat transfer decreased. The dominate silicate structure shifted to the aluminate structure, affecting the viscosity. The increasing Al_2O_3/SiO_2 ratio raised the crystallisation tendency of fluxes, which explains a decreasing trend of heat transfer and an increasing flux melting temperatures.

Effect of Al_2O_3/SiO_2 ratio on the structure and the viscosity of mould fluxes

According to the results of Raman spectroscopy shown in Figures 5 and 6, the increase of Al_2O_3/SiO_2 ratio, ie the increase of Al_2O_3 content and the decrease of SiO_2 content, promoted the formation of aluminate structural units, eg AlF_6, AlO_6, and Al-O-Al, but decreased the Al-O-Si linkage. Both Al-O-Al and Al-O-Si were 3D structure components, while AlF_6, and AlO_6 were 2D structure components in the melt with octahedral coordination. The increased Al-O-Al 3D structural units lead to an increased degree of polymerisation, while the decreased Al-O-Si (3D structure) and the enhanced AlF_6 and AlO_6 2D structural units result in a decreased degree of polymerisation. Overall, the increasing Al_2O_3 content in the flux facilitated the accumulation of Al-related network.

In addition to Al-O related structures, with the increase of Al_2O_3/SiO_2 ratio, the silicate structures were also changed (Figures 5 and 6). The area fraction of Q^2 increased, and the area fraction of Q^0 decreased. There was even Q^3 presented in Flux 5. The degree of polymerisation referring to the silicate structure can be characterised by non-bridging oxygen per silicon NBO/Si, which is determined as:

$$\mathrm{NBO/Si} = 4X_{Q^0} + 3X_{Q^1} + 2X_{Q^2} + X_{Q^3} \quad (3)$$

The values of NBO/Si are shown in Figure 11 where NBO/Si decreased slightly with the increase in the Al_2O_3/SiO_2 ratio from 0.7 to 10.8, indicating an increased polymerisation of silicate structures. (Zhang *et al*, 2008) also found that the increase in Al_2O_3/SiO_2 ratio increased the $[SiO_4]$-tetrahedral structure and therefore increased polymerisation.

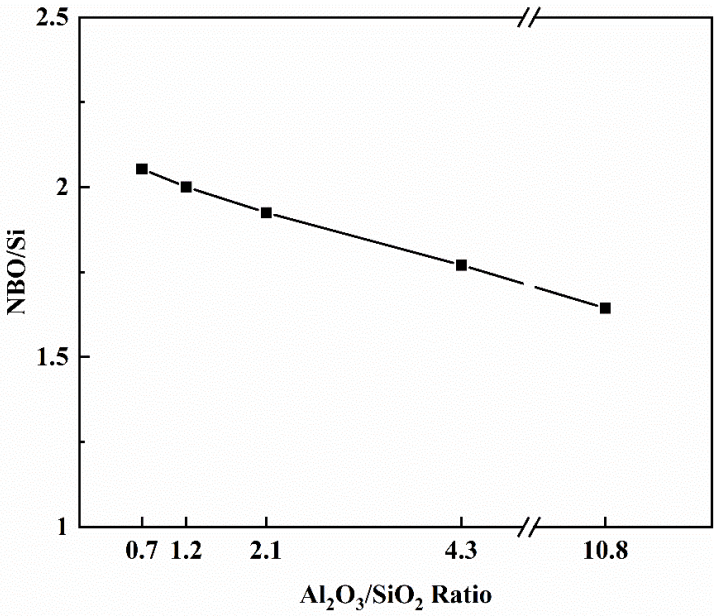

FIG 11 – Values of NBO/Si as a function of Al_2O_3/SiO_2 ratio.

For borate region, within the range of Al_2O_3/SiO_2 ratio from 0.7 to 2.1, changes of the area fractions of borate-related structural units were marginal compared to those of aluminate-related and silicate-related structural units. With further increasing Al_2O_3/SiO_2 ratio from 2.1 to 10.8, the area fraction of borate-related structures increased, correlating with the decrease of SiO_2 content. Silicate and aluminate structure can be treated as the backbone of the whole melt (Mills, 1993). The borate structure change is much less significant than those of aluminate and silicate structures. The effect of Al_2O_3/SiO_2 ratio on polymerisation of the whole flux depends mainly on the combined contribution of aluminate and silicate structures.

The viscosity of mould fluxes is generally correlated well with the flux structures, or more specifically, with the degree of polymerisation. As shown in Figure 3, viscosity sharply increased first when Al_2O_3/SiO_2 ratio increased from 0.7 to 1.2, but then rapidly decreased when Al_2O_3/SiO_2 ratio further increased from 1.2 to 10.8. This observation indicates that the flux polymerisation experiences a turning point when Al_2O_3/SiO_2 reaches 1.2 (Al_2O_3 20.5 mass per cent, Flux 2). Similar results were also reported by Kim *et al* (2012) in their work on $CaO\text{-}SiO_2\text{-}Al_2O_3\text{-}Na_2O\text{-}Li_2O$ flux and Chen *et al* (2019) on $CaO\text{-}SiO_2\text{-}MgO\text{-}Al_2O_3$ slag where they found that the viscosity initially increased to a maximum at about 20 mass per cent Al_2O_3 and then decreased with further addition of Al_2O_3. This phenomenon cannot be explained by the decreased NBO/Si shown in Figure 11 which indicates an increased degree of polymerisation. Similarly, NBO/T ratio (non-bridging O/tetragonal O) calculated using the following equation:

$$\frac{NBO}{T} = \frac{2\left(X_{CaO}+X_{MgO}+X_{Na2O}+X_{Li2O}-X_{Al2O3}-X_{B2O3}\right)}{X_{SiO2}+2X_{Al2O3}+2X_{B2O3}} \quad (4)$$

also showed the decreased NBO/T with the Al_2O_3/SiO_2 ratio (Figure 12). Therefore, there are other factors to cause this change.

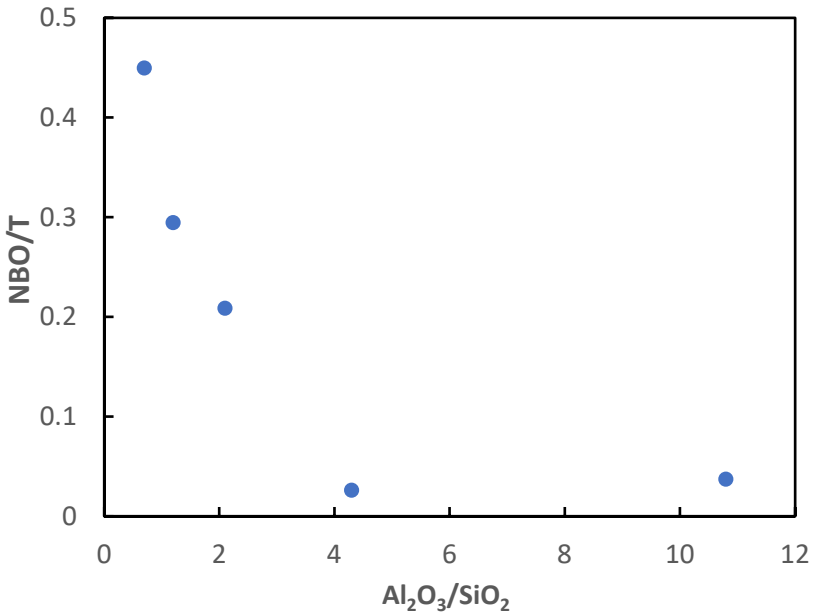

FIG 12 – NBO/T versus Al_2O_3/SiO_2.

When Al_2O_3 is introduced into the silicate network, the Al^{3+} ions can be absorbed into the silicate structure, exhibiting fourfold coordination like Si^{4+}. However, there is a charge difference between Al^{3+} and Si^{4+} which needs to be compensated by M^{2+} and/or M^{+} ions, eg Na^{+}, Li^{+}, Ca^{2+} and Mg^{2+}. Thus, Al_2O_3 additions act principally as network formers, eg in the case of Fluxes 1 and 2. However, when large amounts of Al_2O_3 are added to the slag (eg Fluxes 4 and 5), the Al^{3+} ions can also act as network breakers forming five- or sixfold coordination (Stebbins Farnan and Xue, 1992). Therefore this phenomenon can be attributed to the amphoteric effect of Al_2O_3, serving as a network former when Al_2O_3 content is low but a network modifier when its concentration is high. The turning point is when the Al/M ratio ($=2X_{Al2}O_3/(2X_{Na2}O+2X_{Li2}O+X_{Ca}O+X_{Mg}O)$) approaches 1 which is the case of Flux 4 (Al/M = 0.9).

Chen *et al* (2019) found a transition point (minimum) in the molar Gibbs energy of the mixing of the $CaO-SiO_2-MgO-Al_2O_3$ slag system at 17 mass per cent Al_2O_3. This calculated transition point is close to the viscosity turning point observed in this work and other reports (Zhang *et al*, 2008; Kim *et al*, 2012).

Effect of Al_2O_3/SiO_2 ratio on heat transfer of mould flux

XRD analysis of isothermally treated fluxes in Figures 7 and 8 reveals that changing Al_2O_3/SiO_2 ratio changes the phase composition of the fluxes. For the highest SiO_2 content (Flux 1, lowest Al_2O_3/SiO_2 ratio), caspidine appeared which is a key component of $CaO-SiO_2-Al_2O_3$-based commercial mould fluxes. Because of high SiO_2 concentration, this flux and Flux 2 were converted to predominantly amorphous phases after a fast cooling after the heat transfer measurements (Figure 10). In the Flux 3 with Al_2O_3/SiO_2 ratio 2.1, no cuspidine was observed but only $Ca_2Al_2SiO_7$ was detected at both 900 and 1000°C and in the samples after heat transfer measurements (Figure 10). Further increasing Al_2O_3/SiO_2 ratio to 4.3 and 10.8 led to a more complex multi-crystal phase formation, including $LiAlO_2$, $MgAl_6O_{10}$, $CaSiO_3$ or $Ca_5B_3O_9F$ (Figures 7, 8 and 10). Clearly, increasing Al_2O_3/SiO_2 ratio increases significantly the crystallisation tendency of the fluxes.

Heat transfer of mould flux depends strongly on flux crystallinity and types of crystals. With the increase in Al_2O_3/SiO_2 ratio, the heat flux through the slag film decreased gradually first (Flux 1 to Flux 4) and then dropped tremendously (Figure 9, Flux 5). As discussed above, increasing Al_2O_3/SiO_2 ratio increased flux crystallinity which therefore led to the decrease in heat transfer because of the heat scattering effect by grain boundaries and defects. The higher the crystallinity, the lower the heat flux. The significant decrease in the heat flux when Al_2O_3/SiO_2 is 10.8 could be also related to the crystals morphology although it is not the crucial factor in the heat transfer.

Flux selection in terms of Al_2O_3/SiO_2 ratio

As discussed above, $CaO\text{-}SiO_2$-based mould fluxes cannot be used for casting of high-Al steel because of the strong flux-steel reaction, leading to the significant variation of the flux properties demonstrated in this work. Above discussion reveals that the turning point of the viscosity reflects the difference in the flux properties and structure between $CaO\text{-}SiO_2$ based fluxes and $CaO\text{-}Al_2O_3$ based mould fluxes. This work also indicates that when SiO_2 is very low, eg Flux 5, flux crystallisation is too strong to provide an appropriate lubrication. Therefore, Flux 3 (Al_2O_3/SiO_2 = 2.1 mass per cent ratio) and Flux 4 (Al_2O_3/SiO_2 = 4.3 mass per cent ratio) could be considered to provide suitable structure and crystallinity to achieve optimal flux properties. By minimising the flux-steel reaction, the lower SiO_2 flux is preferred, ie Flux 4.

CONCLUSIONS

The effect of Al_2O_3/SiO_2 ratio on structure, viscosity, crystallisation behaviour and heat transfer of $CaO\text{-}Al_2O_3\text{-}SiO_2\text{-}B_2O_3\text{-}Na_2O\text{-}Li_2O\text{-}MgO\text{-}F$ fluxes was investigated. The major findings are summarised as follows:

- Flux melting temperatures increase with the increase in the Al_2O_3/SiO_2 ratio.
- Viscosity of the flux melts increase significantly with the increasing Al_2O_3/SiO_2 ratio from 0.7 to 1.2, reaching the maximum value, and then decrease with the further increase of Al_2O_3/SiO_2 ratio. Raman spectroscopy analysis revealed that the change of Al_2O_3/SiO_2 ratio leads to the change of flux structures. The turning point for viscosity can be attributed to the amphoteric effect of Al_2O_3, serving as a network former when Al_2O_3 content is low but a network modifier when its concentration is high.
- XRD analysis showed that increasing Al_2O_3/SiO_2 ratio increased crystallisation tendency of the fluxes. Heat transfer measurement by IET revealed that increasing Al_2O_3/SiO_2 ratio led to the decrease in the heat flux which is correlated well with the increased crystallinity of the flux.
- It can be concluded from this work that Al_2O_3/SiO_2 = 4.3 (SiO_2 7 mass per cent, Flux 4) is the best candidate among studied $CaO\text{-}Al_2O_3$-based mould fluxes to provide optimal flux properties but minimise the flux-steel reaction.

ACKNOWLEDGEMENTS

Financial supports from Baosteel-Australia Joint Research and Development Centre (BAJC) and Australian Research Council (ARC) Industrial Transformation Hub are greatly acknowledged.

REFERENCES

Brandaleze, E, Di Gresia, G, Santini, L, Martín, A and Benavidez, E, 2012. Mould fluxes in the steel continuous casting process, in *Science and Technology of Casting Processes*, 1st ed, InTech, pp 205–233.

Chen, Z, Wang, H, Sun, Y, Liu, L and Wang, X, 2019. Insight into the Relationship Between Viscosity and Structure of $CaO\text{-}SiO_2\text{-}MgO\text{-}Al_2O_3$ Molten Slags, *Metallurgical and Materials Transactions B,* 50(6):2930–2941.

Cho, J W, Blazek, K, Frazee, M, Yin, H, Park, J H and Moon, S W, 2013. Assessment of $CaO–Al_2O_3$ Based Mold Flux System for High Aluminum TRIP Casting, *ISIJ Int*, 53:62.

Chung, Y and Cramb, A W, 2000. Dynamic and equilibrium interfacial phenomena in liquid steel-slag systems, *Metall Mater Trans B*, 31B:957.

Gao, E, Wang, W and Zhang, L, 2017. Effect of alkaline earth metal oxides on the viscosity and structure of the $CaO\text{-}Al_2O_3$ based mold flux for casting high-al steels, *Journal of Non-Crystalline Solids,* 473:79–86.

Gao, J, Wen, G, Huang, T, Bai, B, Tang, P and Liu, Q, 2016a. Effect of slag-steel reaction on the structure and viscosity of $CaO\text{-}SiO_2$-based mold flux during high-Al steel casting, *Journal of Non-Crystalline Solids,* 452:119–124.

Gao, J, Wen, G, Huang, T, Bai, B, Tang, P and Liu, Q, 2016b. Effect of Al Speciation on the Structure of High-Al Steels Mold Fluxes Containing Fluoride, *Journal of the American Ceramic Society,* 99(12):3941–3947.

Kamitsos, E I, Karakassides, M A and Chryssikos, G D, 1987. Vibrational spectra of magnesium-sodium-borate glasses, 2, Raman and mid-infrared investigation of the network structure, *The Journal of Physical Chemistry,* 91(5):1073–1079.

Kang, Y B, Kim, M S, Lee, S W, Cho, J W, Park, M S and Lee, H G, 2013. A Reaction Between High Mn-High Al Steel and $CaO\text{-}SiO_2$-Type Molten Mold Flux: Part II. Reaction Mechanism, Interface Morphology, and Al_2O_3 Accumulation in Molten Mold Flux, *Metall Mater Trans B*, 44B:309.

Kim, G H and Sohn, I, 2012. Effect of Al_2O_3 on the viscosity and structure of calcium silicate-based melts containing Na_2O and CaF_2, *Journal of Non-Crystalline Solids,* 358(12–13):1530–1537.

Kim, G H and Sohn, I, 2014. Role of B_2O_3 on the Viscosity and Structure in the CaO-Al_2O_3-Na_2O-Based System, *Metallurgical and Materials Transactions B,* 45(1):86–95.

Kim, H, Matsuura, H, Tsukihashi, F, Wang, W, Min, D J and Sohn, I, 2012. Effect of Al_2O_3 and CaO/SiO_2 on the Viscosity of Calcium-Silicate–Based Slags Containing 10 Mass Pct MgO, *Metallurgical and Materials Transactions B,* 44(1):5–12.

Kim, M S, Lee, S W, Cho, J W, Park, M S, Lee, H G and Kang, Y B, 2013. A Reaction Between High Mn-High Al Steel and CaO-SiO_2-Type Molten Mold Flux: Part I, Composition Evolution in Molten Mold Flux, *Metall Mater Trans B*, 44B:299.

Kim, T S and Park, J H, 2014. Structure-Viscosity Relationship of Low-silica Calcium Aluminosilicate Melts, *ISIJ International,* 54(9):2031–2038.

Ma, N, You, J, Lu, L, Wang, J, Wang, M and Wan, S, 2018. Micro-structure studies of the molten binary K_3AlF_6–Al_2O_3 system by in situ high temperature Raman spectroscopy and theoretical simulation, *Inorganic Chemistry Frontiers,* 5(8):1861–1868.

McMillan, P and Piriou, B, 1983. Raman spectroscopy of calcium aluminate glasses and crystals, *Journal of Non-Crystalline Solids,* 55(2):221–242.

Mills, K C, 1993. The Influence of Structure on the Physico-chemical Properties of Slags, *ISIJ International,* 33(1):148–155.

Park, J H, Min, D J and Song, H S, 2002. Structural Investigation of CaO-Al_2O_3 and CaO-Al_2O_3-CaF_2 Slags via Fourier Transform Infrared Spectra, *ISIJ International,* 42(1):38–43.

Park, J Y, Kim, G H, Kim, J B, Park, S and Sohn, I, 2016. Thermo-Physical Properties of B_2O_3-Containing Mold Flux for High Carbon Steels in Thin Slab Continuous Casters: Structure, Viscosity, Crystallization, and Wettability, *Metallurgical and Materials Transactions B,* 47:2582.

Stebbins, J F, Farnan, I and Xue, X, 1992. The structure and dynamics of alkali silicate liquids: A view from NMR spectroscopy, *Chem, Geol*. 96:371–385.

Wang, W and Cramb, A, 2005. The Observation of Mold Flux Crystallization on Radiative Heat Transfer, *ISIJ International*, 45:1864.

Yang, J, Zhang, J, Ostrovski, O, Zhang, C and Cai, D, 2018. Effects of B_2O_3 on Crystallization, Structure, and Heat Transfer of CaO-Al_2O_3-Based Mold Fluxes, *Metallurgical and Materials Transactions B,* 50:291.

Yang, J, Zhang, J, Sasaki, Y, Ostrovski, O, Zhang, C, Cai, D and Kashiwaya, Y, 2017. Effect of B_2O_3 on Crystallization Behavior, Structure, and Heat Transfer of CaO-SiO_2-B_2O_3-Na_2O-TiO_2-Al_2O_3-MgO-Li_2O Mold Fluxes, *Metall Mater Trans B,* 48B:2077.

Zhang, Z, Wen, G, Tang, P and Sridhar, S, 2008. The Influence of Al_2O_3/SiO_2 Ratio on the Viscosity of Mold Fluxes, *ISIJ International,* 48(6):739–746.

Zheng, K, Zhang, Z, Liu, L and Wang, X, 2014. Investigation of the Viscosity and Structural Properties of CaO-SiO_2-TiO_2 Slags, *Metallurgical and Materials Transactions B,* 45(4):1389–1397.

Zhou, L, Li, J, Wang, W and Sohn, I, 2017. Wetting Behavior of Mold Flux Droplet on Steel Substrate With or Without Interfacial Reaction, *Metall Mater Trans B*, 48B:1943.

Zhou, L, Wang, W and Zhou, K, 2015. Effect of Al_2O_3 on the Crystallization of Mold Flux for Casting High Al Steel, *Metallurgical and Materials Transactions E,* 2:99.

Pushing the boundaries of slag operability – processing of high-MgO nickel concentrates with the Ausmelt TSL process

DOI: 10.62053/QMUM1347

J Wood[1], J Coveney[2], S Creedy[3], D Grimsey[4] and A Rich[5]

1. Manager Technology, Metso Australia, Melbourne Vic 3175. Email: jacob.wood@metso.com
2. Principal Process Engineer, Metso Australia, Melbourne Vic 3175. Email: james.coveney@metso.com
3. Customer Account Manager, Metso Australia, Melbourne Vic 3175. Email: stefanie.creedy@metso.com
4. Principal Smelter Development Metallurgist, BHP, Kalgoorlie WA 6430. Email: david.grimsey@bhp.com
5. Smelter Development Manager, BHP, Kalgoorlie WA 6430. Email: anthony.rich2@bhp.com

ABSTRACT

In 2021, BHP and Metso examined processing of high-MgO nickel sulfide concentrates using Metso's Ausmelt Top-Submerged-Lance (TSL) technology. Test work was conducted in Metso's pilot test work facility in Dandenong, Australia to explore operability of the SiO_2-FeO-MgO-CaO-NiO slag system across a wide range of compositions, temperatures and bath oxygen potentials. Pilot-scale testing aimed to define slag 'operability limits', representing the lowest bath temperature at which stable process and equipment operation could be maintained. This work was supported by FactSage™, version 8.2 (by Thermfact/CRCT and GTT-Technologies) thermodynamic modelling, slag viscosity measurements, physical characterisation of quenched slag samples performed by the University of Queensland and benchmarking of commercial-scale TSL nickel smelting operations.

A wide range of slag compositions were examined, with Fe/SiO_2 ratios varying from 0.4–1.1, CaO content from 0.8–7.0 wt per cent and MgO content from 6–19 wt per cent. Slag SiO_2/MgO ratio, wt per cent CaO and matte grade were found to have the greatest impacts on identified operability limits.

Operability limits were found to be influenced by both the solids content in slag and viscosity of the remaining liquid slag phase, with the relative contribution of these parameters heavily influenced by the slag composition. In the majority of trials, limits were defined by a theoretical solids content of 40–50 per cent, however in trials with a low Fe/SiO_2 ratio and/or low wt per cent CaO, limits were characterised by a much lower solids content due to the increased effect of the liquid slag viscosity in determining the behaviour of these slags.

The test work highlighted inherent flexibility of the Ausmelt TSL process to operate across a wide slag range of slag compositions and recover from process disturbances without an interruption to feeding. The trials also demonstrated the possibility for Ausmelt TSL technology to process concentrates with an Fe/MgO ratio as low as 1.4, which has important implications to the commercial-scale processing of high MgO feeds. Arsenic rejection across the trials was very good, with only 30 per cent of arsenic in the feed inputs reporting to the matte phase. Such high levels of arsenic removal provide the Ausmelt TSL process with a notable advantage over alternative smelting technologies.

INTRODUCTION

Metso's Ausmelt TSL process has achieved widespread acceptance as a leading smelting technology for the treatment of copper, nickel, lead, tin and zinc bearing feeds (Wood, Hoang and Hughes, 2017). Core to the technology is a vertically suspended lance operated with its tip submerged in the slag layer of the molten bath (Figure 1). Oxygen enriched air and fuel are injected via the lance resulting in significant bath mixing and agitation with consequently high rates of energy and mass transfer. The Ausmelt TSL process is used at more than 50 non-ferrous metals production facilities globally.

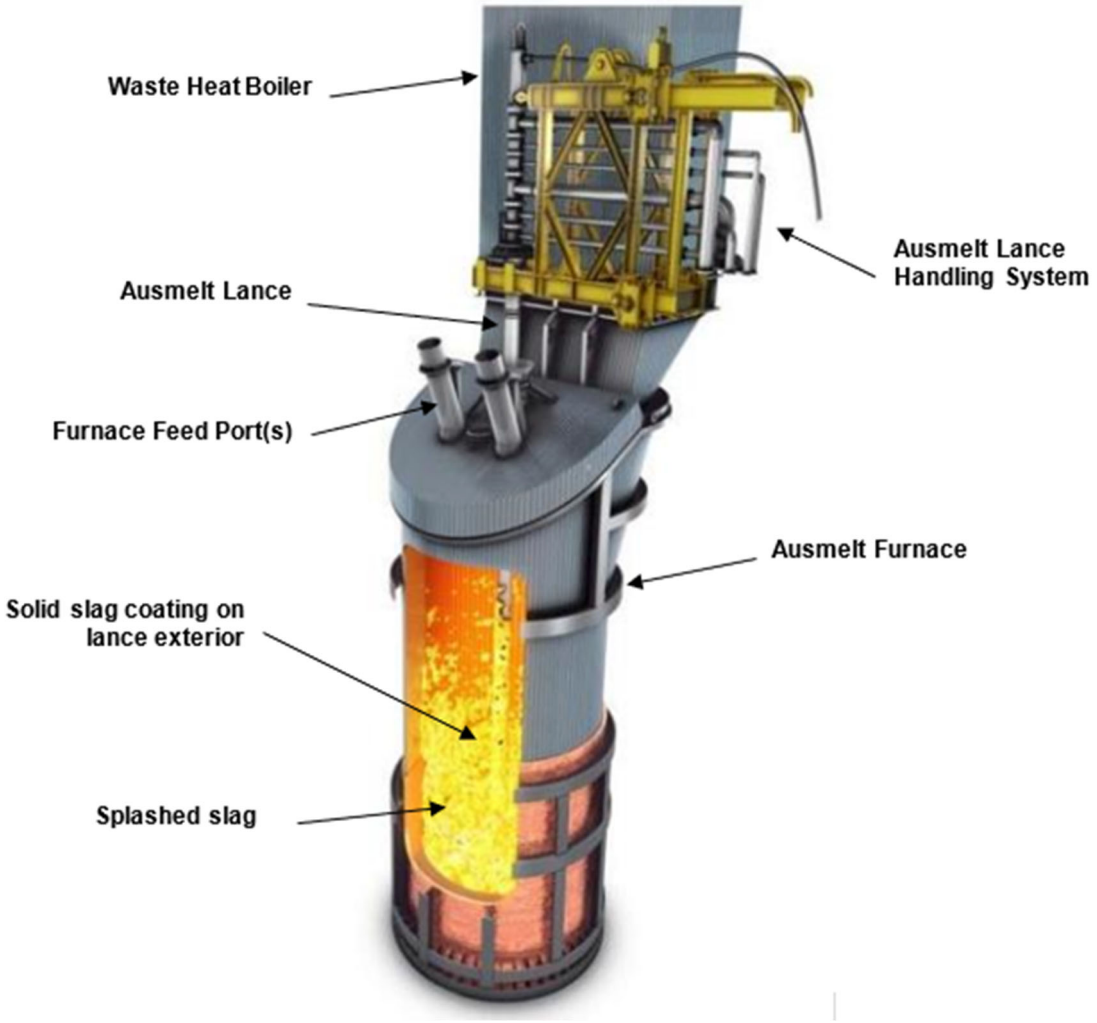

FIG 1 – Ausmelt TSL process schematic.

The Ausmelt TSL process has been applied at commercial scale for the treatment of nickel-bearing concentrates, matte and residues (Table 1). Jinchuan Nickel Mining Company (JNMC) utilises Ausmelt TSL technology to process more than 1 100 000 t/a of nickel sulfide concentrates to produce a low-grade matte, which is further upgraded in downstream Peirce Smith (PS) converters (Zhou *et al*, 2010). Jilin Ji'en Nickel Industry Co. Ltd. (JJNI) employ a similar process flow sheet for the processing of 275 000 t/a of nickel concentrates (Aspola *et al*, 2012).

TABLE 1

Ausmelt TSL nickel references.

Customer	Location	Start-up	Feed	Capacity (t/a)
Jilin Ji'en Nickel (JJNI)	China	2009	Concentrates	275 000
Jinchuan Nickel (JNMC)	China	2008	Concentrates	1 100 000
Anglo American Platinum	South Africa	2002	Matte	213 000
Bindura Nickel	Zimbabwe	1995	Residues	10 000
Rio Tinto Zimbabwe	Zimbabwe	1992	Residues	7700

Anglo American Platinum have installed two Ausmelt TSL converting furnaces to upgrade approximately 210 000 t/a of low-grade electric furnace matte via a continuous converting process (Hundermark *et al*, 2011). The resultant composition of the high-grade matte from the TSL process is critical to recovery of contained platinum and palladium.

As with other bath smelting processes, the Ausmelt process relies on regulation of the slag fluidity to ensure effective mass and energy transfer (Wood and Hughes, 2016), straightforward transfer of molten products to downstream handling/refining operations and to minimise the propensity for bath foaming. The process typically aims to achieve operation at the lowest possible temperature through a combination of slag compositional and bath temperature control. Silica, limestone and in some cases hematite flux addition as part of the overall furnace charge is used to regulate the slag composition whilst bath temperatures are controlled by adjusting lance fuel and/or oxygen flow rates.

Unlike some other smelting technologies, the Ausmelt TSL process is capable of operating at temperatures well below the slag liquidus, with elevated concentrations of solids in slag. The highly turbulent nature of the Ausmelt TSL process means solid particles remain suspended, without settling out to form a layer of build-up on the furnace hearth.

TEST WORK

In 2021, BHP and Metso conducted 15 individual trials in Metso's pilot scale test work facility in Dandenong, Australia to examine the processing of high-MgO nickel concentrates using Ausmelt TSL technology. The test work examined operability of the SiO_2-FeO-MgO-CaO-NiO slag system across a wide range of compositions, temperatures and bath oxygen potentials and aimed to define slag 'operability limits', representing the lowest bath temperature at which stable process and equipment operation could be maintained.

Materials and equipment

The following materials were used in the test work:

- Leinster nickel sulfide concentrate
- Mt Keith nickel sulfide concentrate
- magnesia powder
- silica-revert flux mixture
- limestone flux.

The feed rates of Leinster concentrate, Mt Keith concentrate and magnesia powder were varied during the test work to achieve a specific Fe/MgO ratio in feed blend for each trial. Magnesia powder was used to simulate processing of high-MgO concentrates, to achieve a target MgO concentration in slag. A mixture of silica and crushed revert from BHP's Kalgoorlie Nickel Smelter was introduced to achieve the target Fe/SiO_2 ratio, with limestone flux also added in the majority of trials to achieve a target wt per cent CaO in slag. Concentrates and fluxes were dispensed individually and combined with a small quantity of water in a screw mixer to minimise material carryover with the process offgas. The combined feed charge was then directed to the furnace roof with an inclined conveyor. Figure 2 depicts the arrangement of equipment used for concentrate and flux handling in the test work.

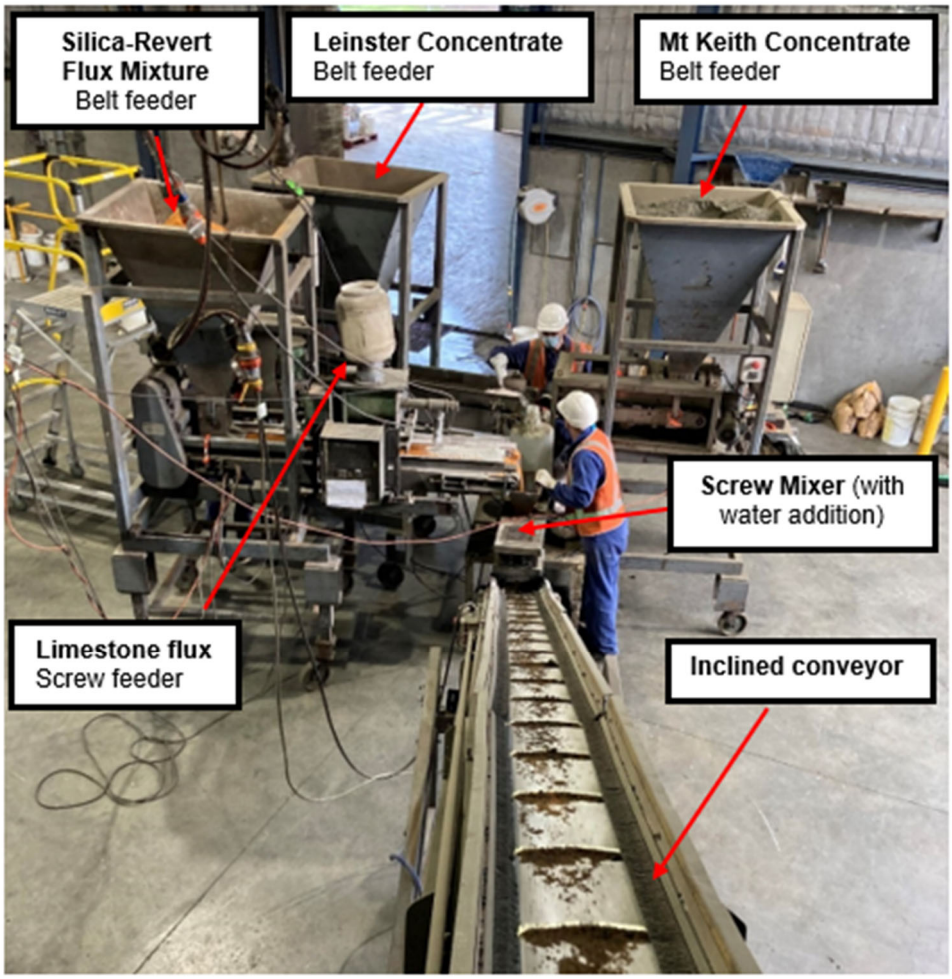

FIG 2 – Feed system arrangement.

The test work employed a refractory-lined furnace with internal dimensions of 1900 mm height and 500 mm diameter. The furnace roof contained four openings; the gas offtake, lance port, feed port and sampling/inspection port. The furnace was lined with magnesia-chrome refractories. A single water-cooled, copper taphole block with graphite inserts was employed in the trials. The taphole had two openings, one at the hearth level and another at a height of 200 mm. Figure 3 presents furnace equipment used in the test work.

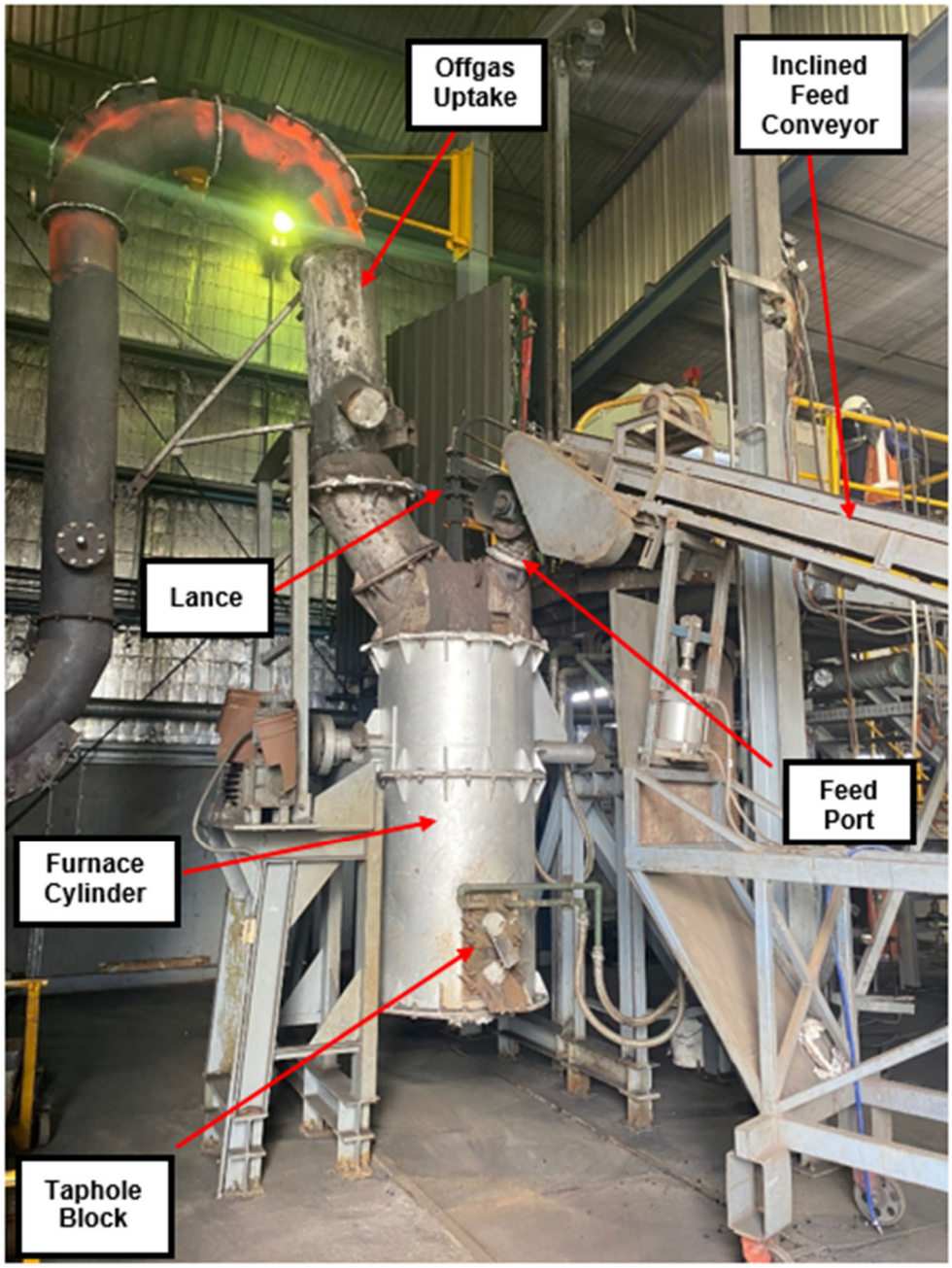

FIG 3 – Furnace arrangement.

Natural gas was used as a fuel in all trials. Flow rates of natural gas and oxygen, delivered via the Ausmelt lance were adjusted to achieve the desired bath temperature and to maintain a relatively consistent lance injection volume between the trials.

Matte and slag were tapped into sand-lined moulds (Figure 4) from both the top and bottom tapholes. The tapholes were opened using oxygen tapping rods and closed (when required) using fireclay. In instances where a mixture of slag and matte were tapped, these phases were subsequently separated once the mould contents had solidified and cooled sufficiently.



FIG 4 – Molten product handling.

Process offgas was directed to downstream cooling, de-dusting and cleaning operations, prior to discharge to the atmosphere. Two induced draught fans provided suction to maintain the furnace under constant negative pressure.

Objectives

The primary objective of the test work was to define ‘operability limits’ across a wide range of slag compositions and matte grades. The ‘operability limit’ represented the lowest bath temperature for which stable process and furnace operation could be maintained. In particular, the test work examined links between these identified operability limits and the following process parameters:

- feed Fe/MgO ratio
- slag Fe/SiO_2 ratio
- slag MgO/SiO_2 ratio
- slag wt per cent CaO
- slag wt per cent MgO
- matte wt per cent Fe.

Four main indicators were used to determine when an operability limit had been reached, namely:

1. Difficulties tapping slag and/or matte.
2. Formation of build-up (‘mush’) on the furnace hearth.
3. Rapid and excessive accretion formation around the furnace roof ports and/or offtake.
4. ‘Foamy’ bath condition due to injected gases being unable to disengage from the slag bath.

Methodology

Prior to commencing each trial, FactSage™ software was used to calculate the slag liquidus temperature, based on target slag and matte compositions for the trial, with this information used to enable exploration of process operability limits in a controlled manner as follows:

- Commence operation with a bath temperature at or slightly above the slag liquidus.
- Confirm slag composition and matte grade are stable and within the target range.
- Progressively reduce the bath temperature (measured via immersion thermocouple and confirmed with optical pyrometer during tapping) until the operability limit for a particular set of conditions has been identified.
- Collect quenched (water-granulated) slag samples during tapping and/or via the furnace roof inspection port at the identified operability limit.
- Increase the bath temperature slightly and maintain stable operation at or slightly above the identified operability limit for as long as possible.

Quenched slag samples taken during the test work were subsequently analysed by the University of Queensland (UQ) using an Electron Probe Micro-Analyser (EPMA) to visually determine the slag solids content for operability limits identified in each trial (Figure 5). This work was supported by results from FactSage™ thermodynamic modelling, which was used to calculate the expected solids content in slag at a particular set of operating conditions (slag composition, matte grade and bath temperature).

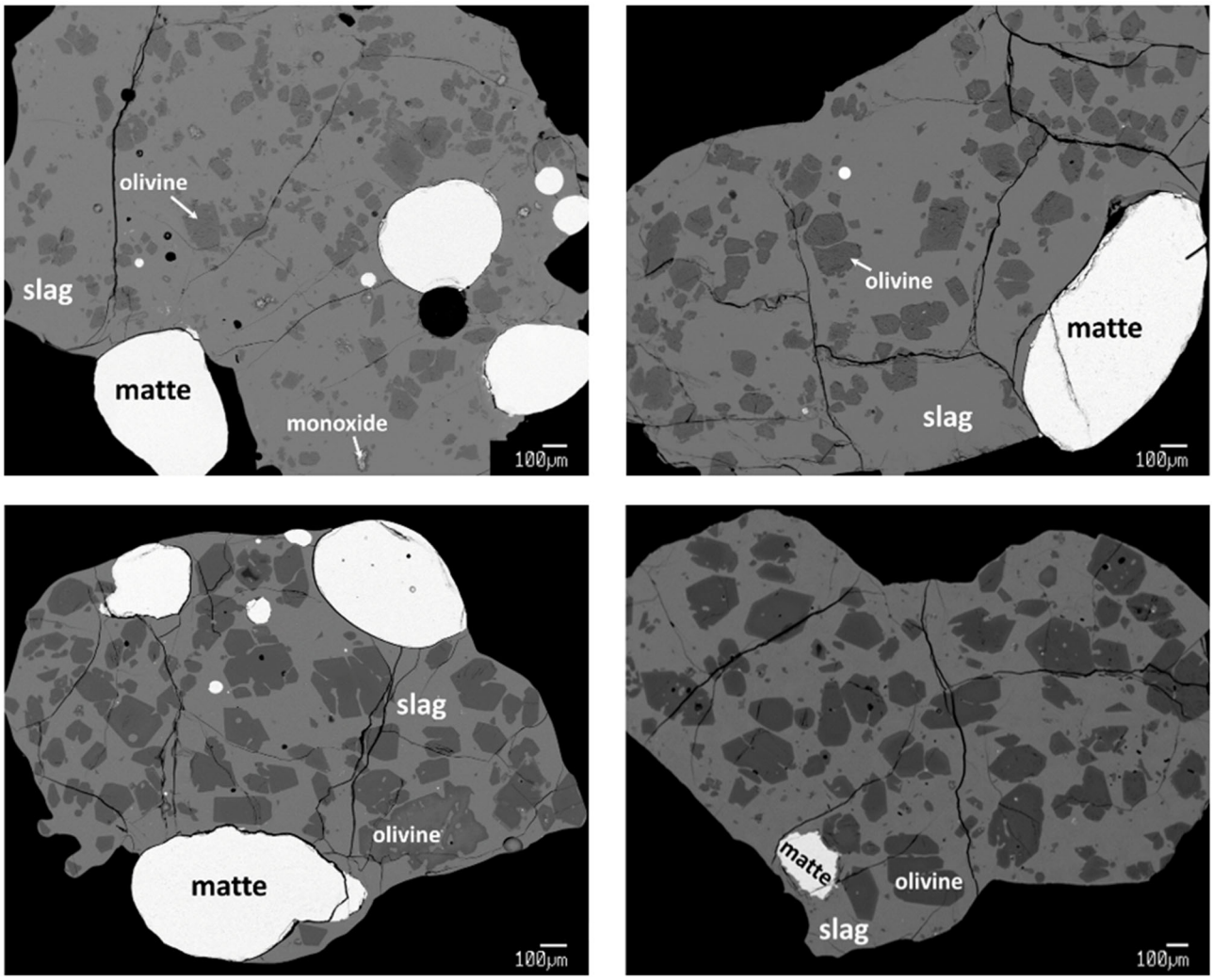

FIG 5 – Quenched slag analysis with EPMA.

Operating conditions

A wide range of slag compositions and matte grades were examined in the test work (Table 2). This presented challenges in directly comparing operability limits for each trial, particularly given the combined effects of multiple parameters in determining the limit for a particular set of conditions. An isothermal phase diagram generated with FactSage™ is also shown in Figure 6, with the slag compositional range investigated in the test work presented by the shaded area of the figure. The $p(O_2)$ chosen for this diagram is typical for slag in equilibrium with matte containing 15 wt per cent Fe at a temperature of 1300°C.

TABLE 2

Test work operating conditions.

Parameter	Minimum	Maximum
Feed Fe/MgO	1.4	3.0
Matte wt% Fe	2.2	32.1
Slag SiO_2/MgO	1.6	5.6
Slag Fe/SiO_2	0.4	1.3
Slag wt% CaO	0.6	8.4

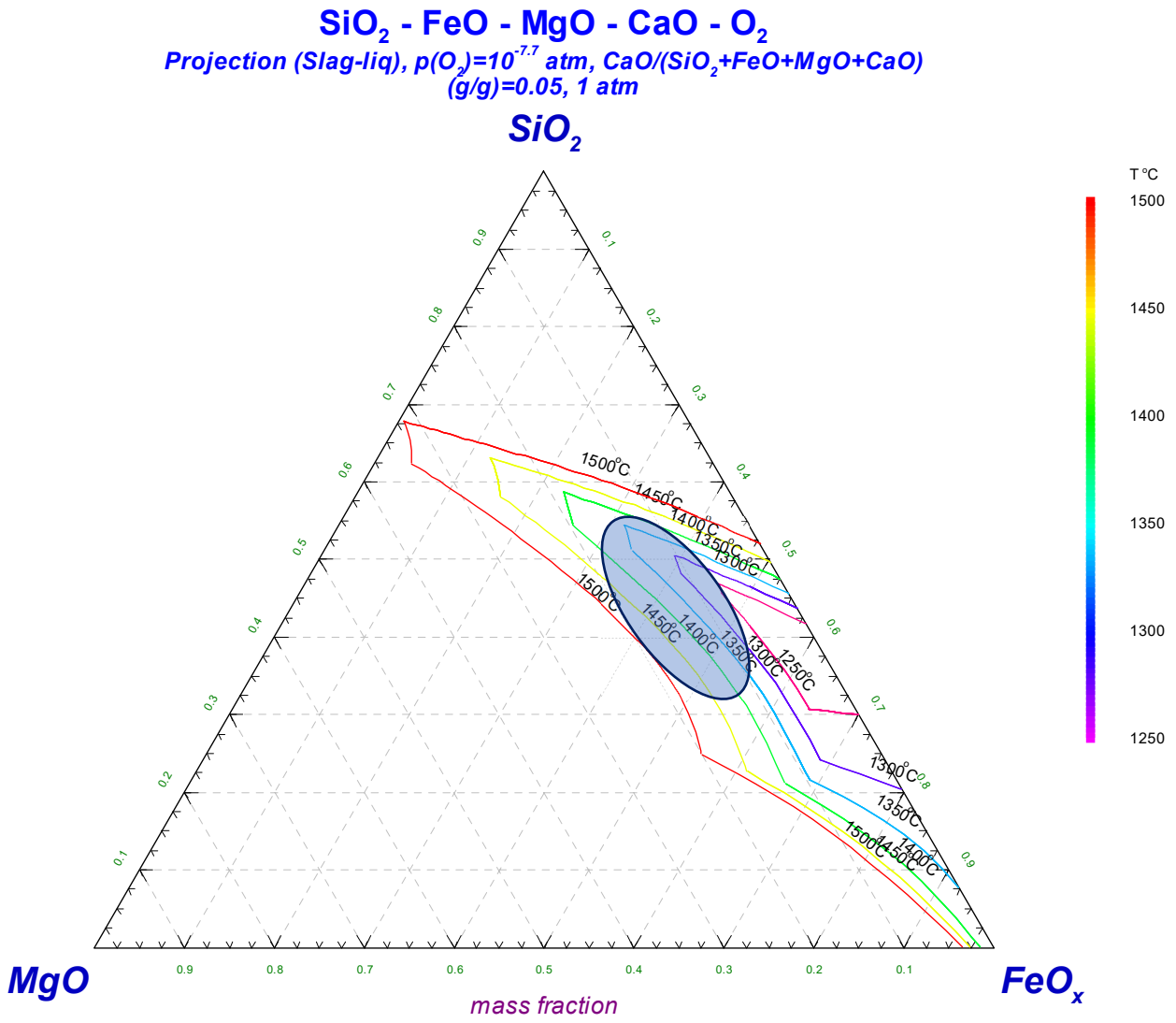

FIG 6 – Isothermal phase diagram.

Results and discussion

Operability limits were successfully identified in ten of the trials. Prior to the test work, it was hypothesised that the slag solids content would be the dominant parameter influencing the operability limit for a particular set of conditions. Results from the test work indicated however, that limits were defined by both the slag solids fraction and viscosity of the remaining liquid slag phase, with the relative contribution of these parameters heavily influenced by the slag composition. Operability limits were found to be largely dictated by the slag SiO_2/MgO ratio, bath oxygen potential (matte wt per cent Fe) and slag wt per cent CaO (Figure 7), with minimal impact from the slag Fe/SiO_2 ratio. Based on this finding, operability limits were grouped into three distinct data subsets (Table 3). The effects of these parameters are discussed in more detail in the following sections.

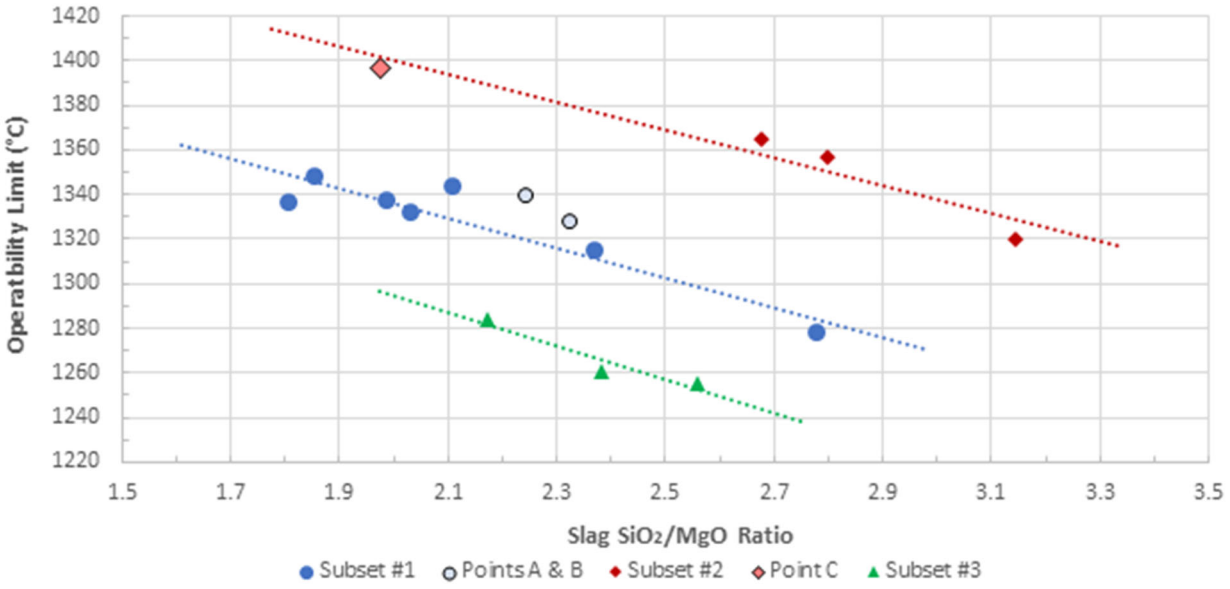

FIG 7 – Operability limit correlation with Slag SiO_2/MgO ratio, %CaO and matte %Fe.

TABLE 3

Data subset operating conditions.

Data subset	Slag wt% CaO	Slag Fe/SiO_2	Matte wt%Fe
Subset #1	Mid (5–8 wt%)	Mid (0.8–1.1)	Mid (8–13 wt%)
Points A & B	Mid (6–7 wt%)	Low (0.5–0.6)	Low (5 wt%)
Subset #2	Low (1 wt%)	Low (0.5)	Mid (9–13 wt%)
Point C	Low (2 wt%)	Mid (0.9)	Mid (8 wt%)
Subset #3	Mid (5–7 wt%)	Mid (0.8–1.0)	High (25–28 wt%)

Slag SiO_2/MgO ratio

Operability limits were strongly influenced by the slag SiO_2/MgO ratio, evidenced by the consistent slope of data sets in Figure 7. Modelling in FactSage™ confirmed the strong effect of SiO_2/MgO ratio on the slag liquidus temperature and hence, solids fraction in slag but also suggested minimal impact of slag SiO_2/MgO ratio on the liquid slag viscosity (Figure 8).

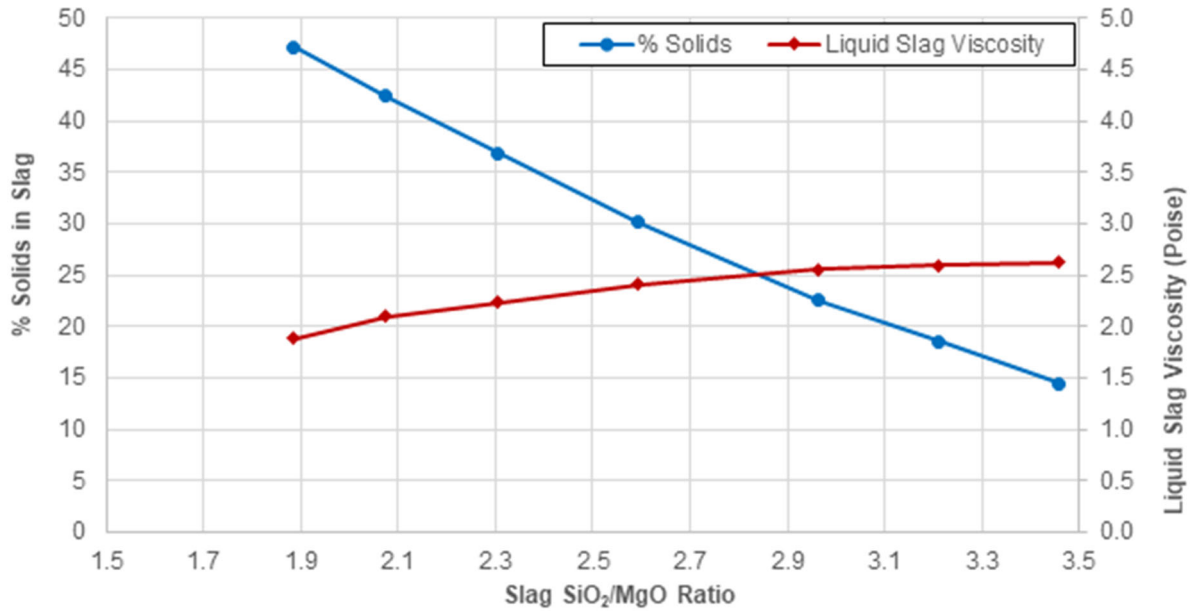

FIG 8 – Slag% solids and viscosity correlation with SiO_2/MgO ratio (calculated with FactSage™ at 1320°C, 5 wt per cent CaO and 15 wt per cent Fe in matte).

Slag% CaO

Decreasing slag wt per cent CaO necessitated operation at higher temperatures across the range of slag compositions examined in the test work. This finding is supported by results from Factsage™ modelling, which indicated not only an increased solids content at low wt per cent CaO, particularly at low SiO_2/MgO ratio (Figure 9) but also a significant increase in liquid slag viscosity (Figure 10). Consequently, it was reasoned that operability limits for data Subset #2 and Point C, were dictated by both the slag solids concentration and liquid slag viscosity.

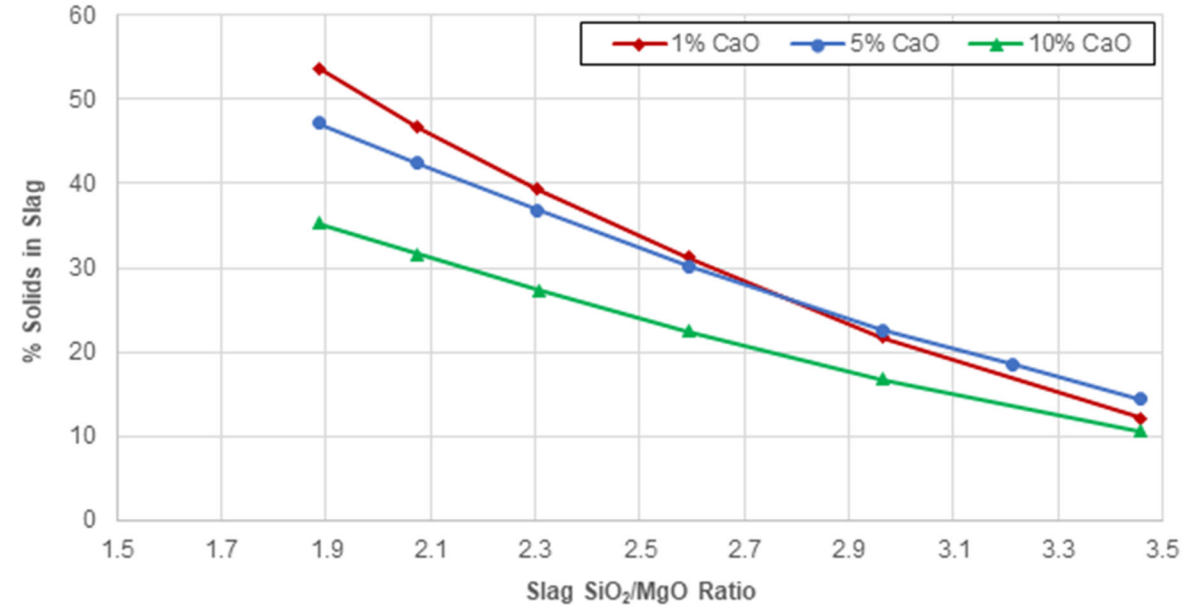

FIG 9 – Slag% solids correlation with SiO_2/MgO ratio at variable wt per cent CaO (calculated with FactSage™ at 1320°C and 15 wt per cent Fe in matte).

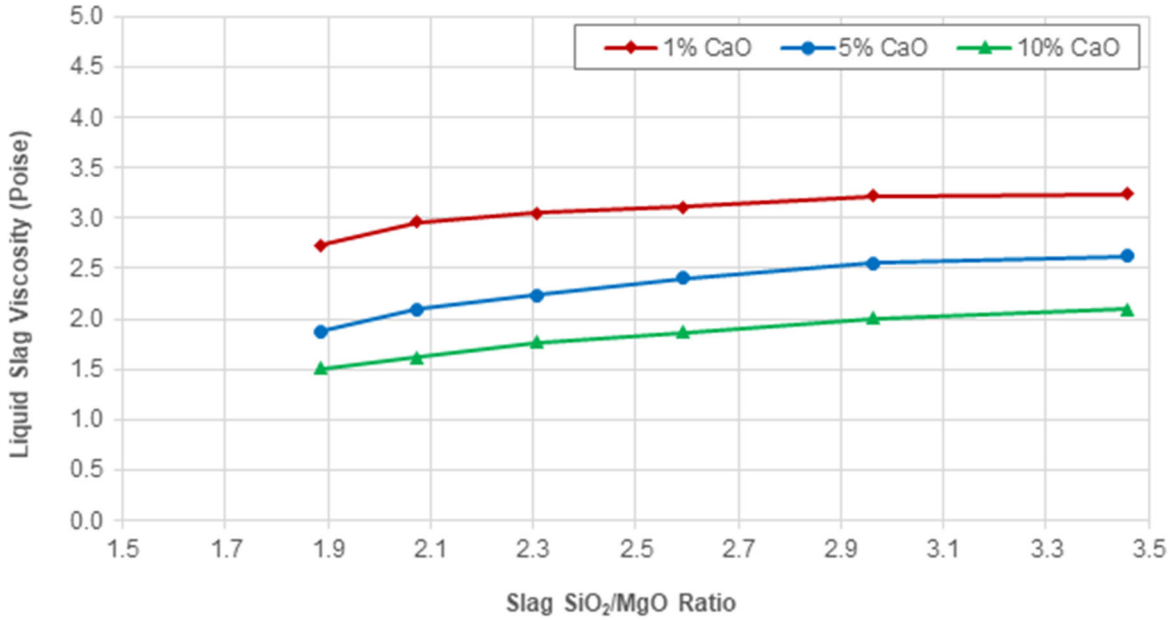

FIG 10 – Slag viscosity correlation with SiO_2/MgO ratio at variable wt per cent CaO (calculated with FactSage™ at 1320°C and 15 wt per cent Fe in matte).

Matte%Fe

Increasing wt per cent Fe in matte (ie decreasing matte grade) enabled operation at lower temperatures across the range of matte grades examined in the test work. Modelling in FactSage™ indicated a significantly higher slag solids content with decreasing wt per cent Fe in matte, particularly at high SiO_2/MgO ratio (Figure 11), due to displacement of MgO by NiO within the olivine structure and consequently, an increasing quantity of MgO reporting to the liquid slag phase. FactSage™ modelling also suggested minimal effect of matte grade on the liquid slag viscosity (Figure 12), operability limits for data Subset #3, were almost entirely dictated by the slag solids content.

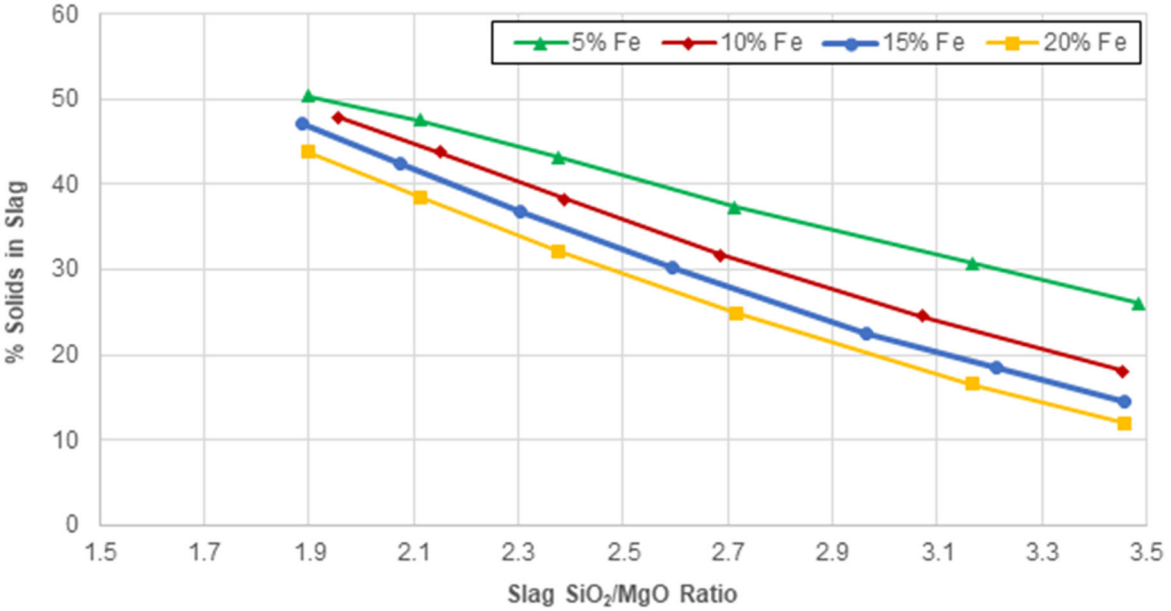

FIG 11 – Slag% solids correlation with SiO_2/MgO ratio at variable wt per cent Fe in matte (calculated with FactSage™ at 1320°C, Fe/SiO_2 = 0.8 and 5 wt per cent CaO in slag).

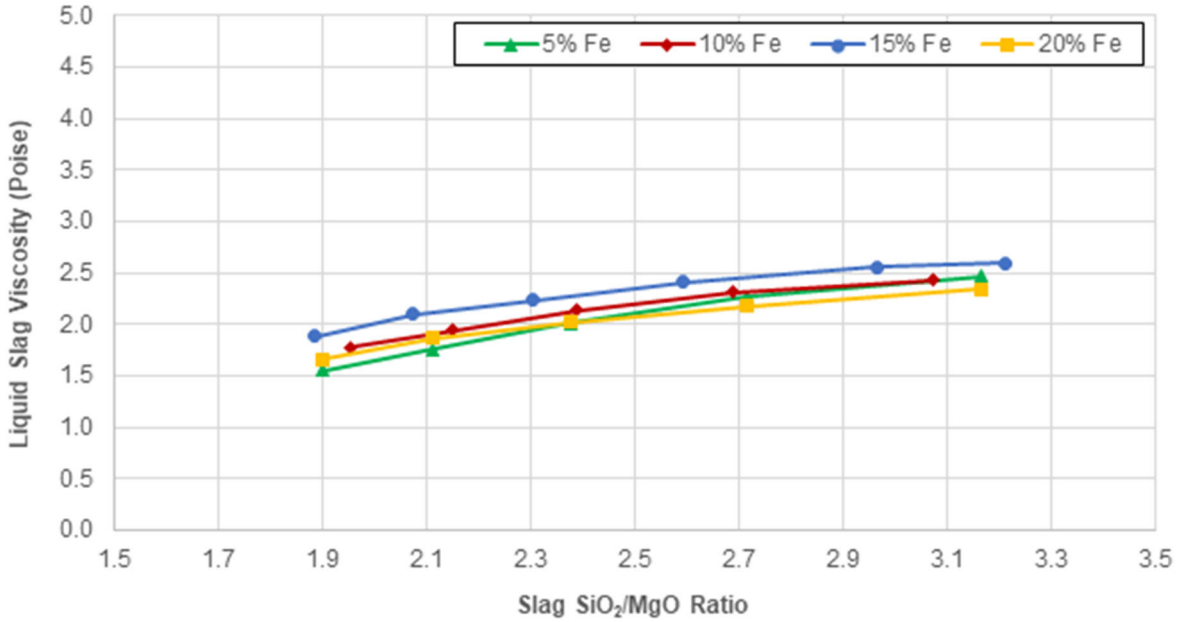

FIG 12 – Slag viscosity correlation with SiO_2/MgO ratio at variable wt per cent Fe in matte (calculated with FactSage™ at 1320°C, Fe/SiO_2 = 0.8 and 5 wt per cent CaO in slag).

Slag Fe/SiO_2 ratio

Variability in slag Fe/SiO_2 ratio was found to have minimal impact on identified operability limits across the range of slag compositions examined in the test work. Whilst limits at low Fe/SiO_2 ratio were typically higher, this was rationalised by variability in matte grade (Points A and B) and wt per cent CaO (Point C). Modelling in FactSage™ indicated limited influence of Fe/SiO_2 ratio on the slag solids concentration, except at elevated Fe/SiO_2 ratios (Figure 13). Of greater significance, however, is the significant increase in liquid slag viscosity predicted at low Fe/SiO_2 ratio (Figure 14), which is likely to have impacted findings from the test work.

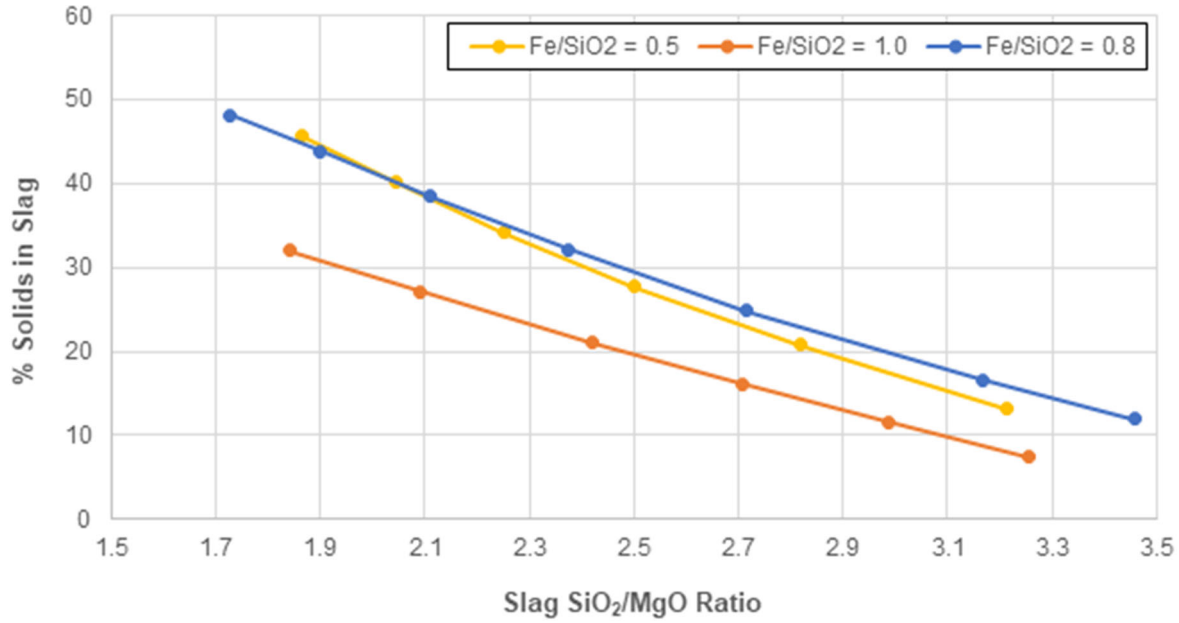

FIG 1 – Slag% solids correlation with SiO_2/MgO ratio at variable Fe/SiO_2 ratio (calculated with FactSage™ at 1320°C, 20 wt per cent Fe in matte and 5 wt per cent CaO in slag).

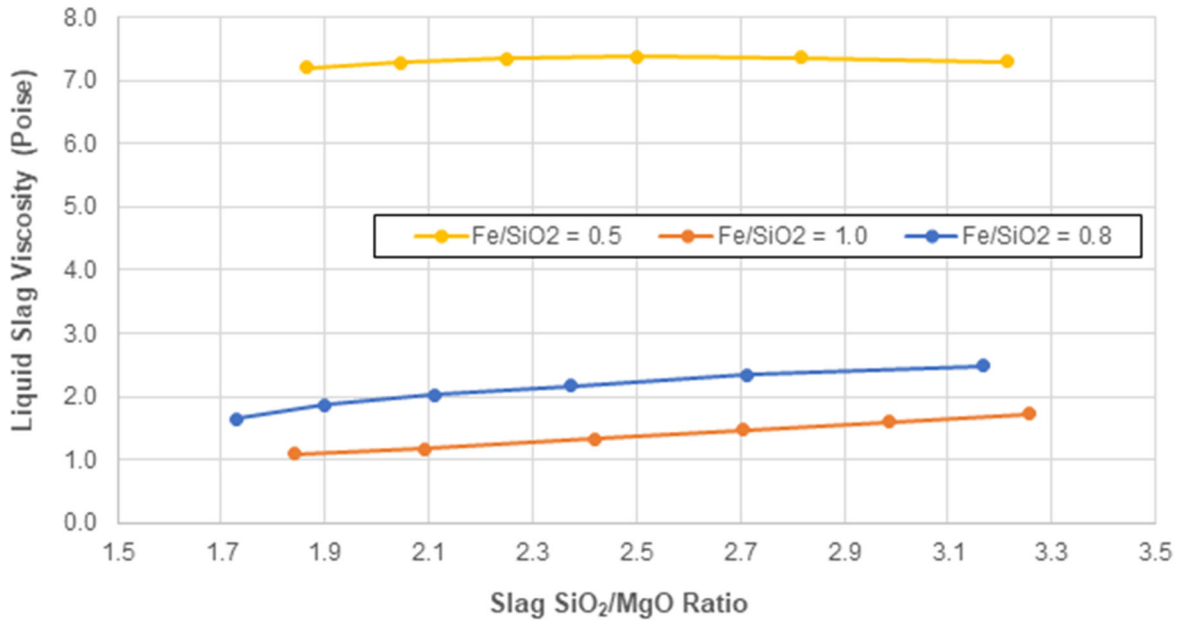

FIG 14 – Slag viscosity correlation with SiO_2/MgO ratio at variable Fe/SiO_2 ratio (calculated with FactSage™ at 1320°C, 20 wt per cent Fe in matte and 5 wt per cent CaO in slag).

Slag EPMA analysis

Quenched slag samples taken throughout the test work were analysed by the UQ to visually determine the solids concentration in slag at the operability limit(s) identified in each trial. Slag samples were for the most part, characterised by a visual solids content in slag of 15–30 per cent. FactSage™ was also used to determine the theoretical slag solids content for each operability limit, which suggested a much higher solids fraction than observed via EPMA (Figure 15). The reasons for discrepancies between these two data sets were not clear and as this was not a primary objective of the test work, this was not investigated further.

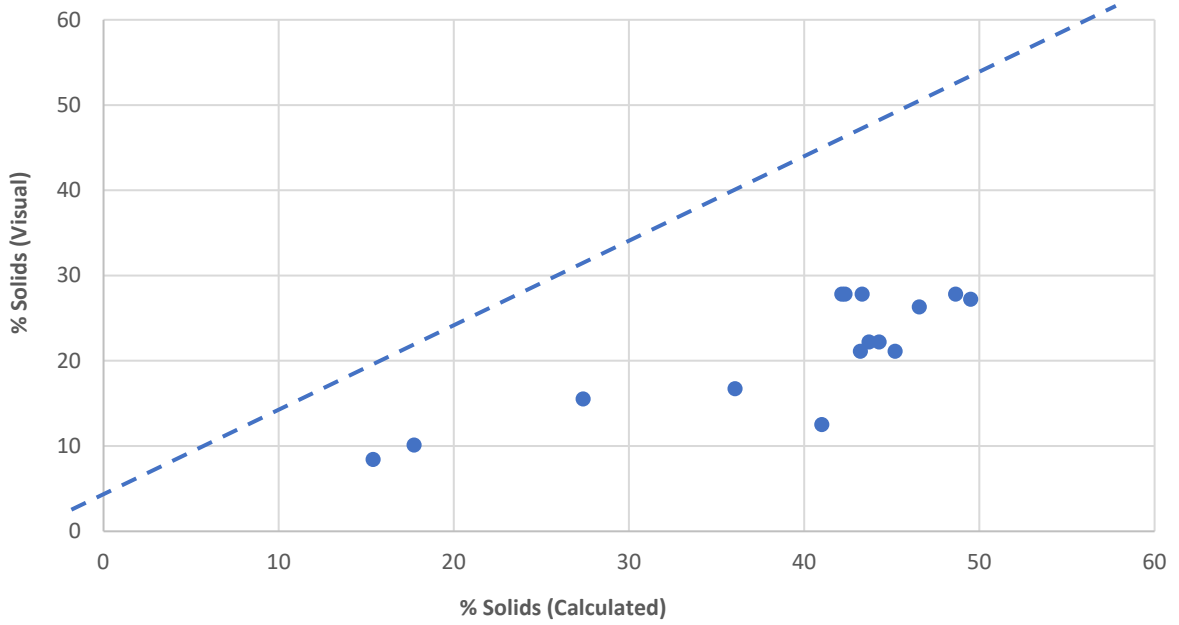

FIG 15 – Correlation in slag solids content.

Operability limit definition

Operability limits were for the most part, characterised by a slag solids content of 40–50 per cent and liquid slag viscosity of 1–3 Poise (as determined with FactSage™), with the exception of data Subset #2 (low per cent CaO and Fe/SiO_2 ratio) which was had only 15–30 per cent solids and

viscosity of 6–7 Poise. These results indicated the relative contribution of solids content and liquid slag viscosity in defining the operability limit for a particular set of conditions, varied with slag composition. Figure 16 presents the relationship between per cent solids and liquid slag viscosity (determined with FactSage™) for operability limits identified in the test work. A suggested range of conditions, for which stable operation could be achieved is also illustrated by the shaded region in the figure, noting that further test work would be required to expand the understanding of permissible operating conditions, particularly at low Fe/SiO_2 ratio.

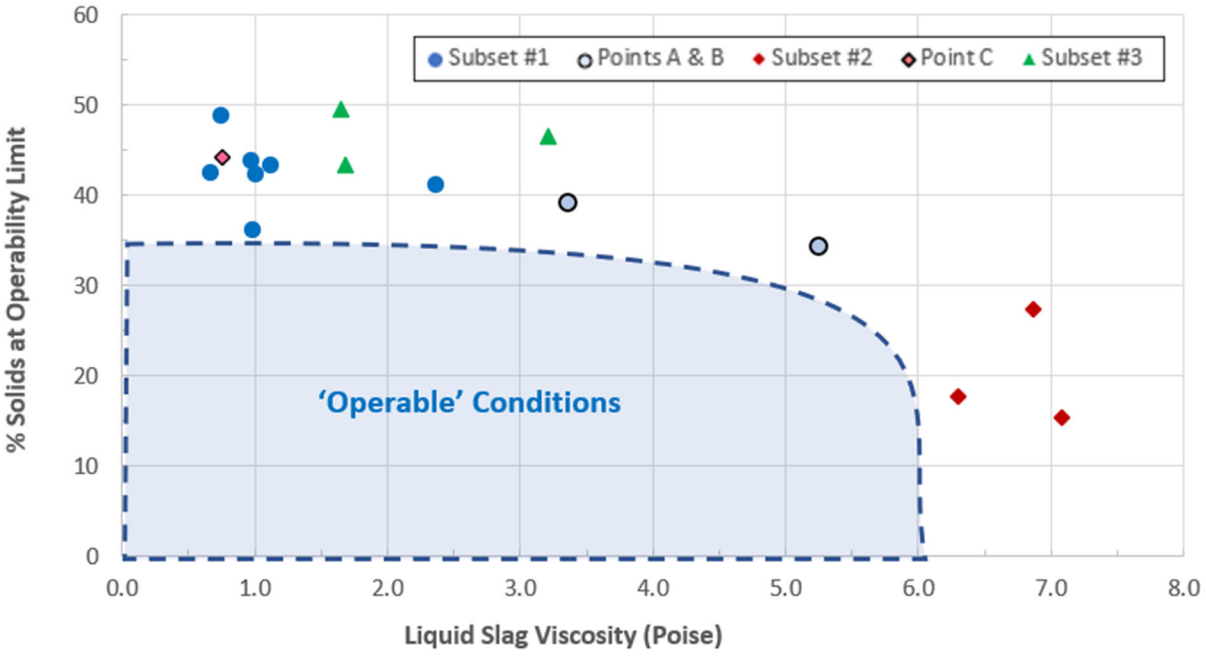

FIG 16 – Operability limit variation with per cent solids and liquid slag viscosity.

COMMERCIAL SCALE OPERATIONS

Results from the test work indicated the Ausmelt TSL nickel smelting process can operate with 30–40 per cent solids in slag (determined with FactSage™) across a wide range of conditions and particularly at low matte grades (> 20 wt per cent Fe). This is supported by data from commercial-scale, Ausmelt TSL nickel smelters operated by JJNI (Si *et al*, 2017) and JNMC (January 2021, personal communication), for which FactSage™ predicts a slag solids content in the range from 25–35 per cent.

The ability to operate with a significant solids content in slag, provides enormous operational and economic benefits. In addition to a reduction in process oxygen and fuel consumptions by roughly 10 per cent and 20 per cent respectively, refractory wear rates are greatly reduced at lower temperatures, ensuring an extended furnace campaign life and thus reduced expenditure on refractory lining demolition and installation activities. The possibility of operating well below the slag liquidus also provides enhanced flexibility to handle short and long-term variability in feed material compositions and easily recover from periods of bath temperature instability.

Operability limits in the test work manifested primarily as difficulties tapping molten slag and to a lesser extent, accretion build-up around the furnace roof ports and offtake. Owing to the design and sizing of the pilot-scale furnace employed in the trials, these issues were somewhat exaggerated, meaning operation at lower temperatures may be possible on a commercial scale. The combination of an intensely-cooled copper taphole block and small taphole openings, resulted in material freezing without regular 'working' of the taphole to keep slag flowing. These issues are readily mitigated on a commercial scale with appropriate furnace design (large taphole openings, short taphole length and multiple tapholes). For reference, JNMC utilise three slag tapholes with openings of 80 mm (January 2021, personal communication), with one or more tapholes in use more or less continuously (Figure 17). Similarly, the Ausmelt TSL converter operated by Anglo Platinum in South Africa, utilises slag taphole inserts with an opening size of 75 mm (Hoosen, Schione and Ramblyana, 2018).



FIG 17 – Commercial scale taphole configuration.

To a lesser extent, accretion build-up around the furnace roof ports and offtake also dictated operability limits observed in the trials. This is a persistent issue in the pilot-scale furnace due to both the relatively small freeboard height and significant air-ingress. On a commercial scale these issues are addressed with appropriate furnace design (sufficient freeboard height, tight sealing of ports and provision for freeboard burners to deliver localised heat input for melting of accretions).

CONCLUSIONS

Test work conducted in Metso's pilot test work facility in Dandenong, Australia confirmed the possibility of treating high high-MgO, nickel sulfide concentrates using Ausmelt TSL technology. The test work examined behaviour of the SiO_2-FeO-MgO-CaO-NiO slag system across a wide range of conditions with the goal of determining the lowest bath temperature at which stable process and equipment operation could be maintained. Slag SiO_2/MgO ratio, wt per cent CaO and matte grade found to have the greatest impacts on identified operability limits.

Contrary to initial thinking, results from the test work indicated operability limits were not solely determined by the slag solids content, with the liquid slag viscosity also playing a role, particularly at low wt per cent CaO and Fe/SiO_2 ratio.

The test work highlighted inherent flexibility of the Ausmelt TSL process to operate across a large slag compositional range and recover from process disturbances an interruption to feed introduction. Results from the trials indicated the Ausmelt process is capable of operating with a high concentration of suspended solids in slag, without negative impacts to slag fluidity. The test work also demonstrated the possibility for Ausmelt TSL technology to process concentrates with an Fe/MgO ratio as low as 1.4, which has important implications to the commercial-scale processing of high-MgO content feeds.

REFERENCES

Aspola, L, Matusewicz, R, Haavanlammi, K and Hughes, S, 2012. Outotec Smelting Solutions for the PGM Industry, in *Proceedings Platinum 2012*, pp 235–250 (The Southern African Institute of Mining and Metallurgy).

Hoosen, A, Schione, M and Ramblyana, I, 2018. Improvements to the Anglo Converting Process (ACP) Tap-Block Management, in *Proceedings from Furnace Tapping 2018*, pp 49–56 (The Southern African Institute of Mining and Metallurgy).

Hundermark, R, Mncwango, S, de Villiers, L and Nelson, L, 2011. The smelting operations of Anglo American's Platinum Business: An Update, in *Proceedings Southern African Pyrometallurgy 2011*, pp 295–307 (The Southern African Institute of Mining and Metallurgy).

Si, J, Zhao, Y, Wang, C and Geng, J, 2017. A Brief Analysis of the Method of Reducing the Nickel Content of Slag in Nickel Smelting Production, *China Nonferrous Metallurgy*, August 2017, (4):36–39.

Wood, J, Hoang, J and Hughes, S, 2017. Energy Efficiency of the Outotec® Ausmelt Process for Primary Copper Smelting, *JOM*, 69(6):1013–1020.

Wood, J and Hughes, S, 2016. Future Development Opportunities for the Outotec® Ausmelt Process, in *Proceedings 9th International Copper Conference 2016*, pp 361–372 (The Mining and Materials Processing Institute of Japan).

Zhou, M, Wan, A, Li, G, Baldock, R and Li, H, 2010. Industrial Operation of JAE Nickel Smelting Technology at Jinchuan Nickel Smelter, in *Supplemental Proceedings: Volume 1: Materials Processing and Properties 2010*, pp 525–534 (The Minerals, Metals and Materials Society).

A fundamental investigation on welding flux tunability geared towards high heat input submerged arc welding for shipbuilding applications

DOI: 10.62053/YFBH5605

H Yuan[1], H Tian[2], Y Zhang[3], Z Wang[4] and C Wang[5]

1. PhD Candidate, School of Metallurgy, Northeastern University, Shenyang 110819, China. Email: yuanhangneu@foxmail.com
2. PhD Candidate, School of Metallurgy, Northeastern University, Shenyang 110819, China. Email: tianhuiyu@omgmail.cn
3. Postdoctoral Researcher, School of Metallurgy, Northeastern University, Shenyang 110819, China. Email: yanyun_zhang@foxmail.com
4. Associate Professor, School of Metallurgy, Northeastern University, Shenyang 110819, China. Email: wangzhanjun@smm.neu.edu.cn
5. Professor, FASM, School of Metallurgy, Northeastern University, Shenyang 110819, China. Email: wangc@smm.neu.edu.cn

ABSTRACT

Submerged arc welding (SAW) is one of the significant metal-joining processes for manufacturing marine vessels, steel pipes, and offshore structures with high deposition rate and engineering reliability. Welding flux serves several essential functions, including atmospheric shielding, arc stabilisation, bead morphology control and weld metal (WM) refinement. Therefore, from a thermodynamic point of view, the focus for flux design and WM compositional/microstructural modification has been placed to elucidating the transfer pathways and mechanisms of major alloying elements, such as Si, Mn, Ti and O during welding. To this end, a thermodynamic model has been established to predict alloying element contents in the WM. Such functions are enabled by the physicochemical properties of the fluxes, which are inherently rooted in the nature of the fluxes. A unique yet systematical investigation, including physicochemical property changes and structural evolution behaviours, has been conducted over the wide range of fluxes applied to actual welding of EH36 shipbuilding steels. Combined with spectroscopic methods, structural behaviours of network formers such as SiO_2, Al_2O_3 and TiO_2 and network modifiers such as MgO, MnO and CaO have been illustrated. Viscosity and ionic conductivity have been found to be positively associated with the degree of polymerisation.

INTRODUCTION

High heat input submerged arc welding (SAW) technology, known for high deposition efficiency and excellent weld metal formability, has found widespread applications in various engineering fields (Yuan *et al*, 2023). However, high heat input could produce coarse yet brittle microstructural constituents in the weld metal (WM), thus deteriorating mechanical properties of the entire weldment (Wu *et al*, 2023). During SAW, various redox reactions and heat transfer events could occur in the arc cavity, in which fluxes could play significant roles in forming atmospheric shielding, refining WM and preventing heat loss (Wang and Zhang, 2021). Such needed functions are enabled by appropriate flux thermophysical properties, such as viscosity and thermal conductivity (Zhang *et al*, 2022a). It is well known that thermophysical properties are structure dependent and largely dictated by the extent of chemical and topological disorder in the molten state (Wang *et al*, 2023a). Therefore, a clear yet comprehensive understanding of flux structures is crucial to optimised design and enhanced welding performance. However, the current flux design mainly relies on empirical methods, lacking a comprehensive and systematic exploration of the flux structure and physicochemical properties. This deficiency leads to an ambiguous evolution of the flux structure-physicochemical properties.

Furthermore, fluxes should improve their metallurgical properties aside from satisfying the welding process. The WM mechanical properties under high heat input welding can be improved by fine-tuning the flux composition to precisely optimise the metallurgical properties. Specifically, the flux composition contributes significantly to the WM chemistry through chemical reactions occurring in the welding process (Zhang *et al*, 2022b). For example, Zhang, Leng and Wang (2019) designed TiO_2-containing basic-fluoride-type fluxes, enabling the transfer of Ti, Mn and Si to the WM. They

emphasised that optimal mechanical properties were achieved with the addition of 6 wt per cent TiO_2 in the flux. Therefore, addressing the roles of fluxes in regulating WM composition becomes urgent, as they are directly linked to the element transfer behaviours between the flux and WM.

This study aims to concentrate on the microstructure and physicochemical properties of flux modification. This work will gain an in-depth understanding of the flux characteristics and help to determine the guidelines for flux design in high heat input welding.

EXPERIMENTAL

All the experimental samples for the present welding fluxes were prepared from the reagent-grade powders of SiO_2, Al_2O_3, TiO_2, MnO, MgO and CaO. The samples were thoroughly mixed and placed inside a pure molybdenum crucible, and were then pre-melted in the high-temperature region of the resistance furnace at 1550°C under a pure argon atmosphere (>99.999 per cent, 0.3 L/min). After being held at that temperature for 1 hr, the molten slags were quenched in cold water rapidly and then dried at 200°C for 4 hrs to remove any moisture. The as-quenched samples were crushed and ground into powders of less than 200 mesh. Viscosity measurements were carried out using the rotating cylinder method with Brookfield viscometer, where one molybdenum crucible filled with 150 g flux sample was placed in an electric resistance furnace.

Structural information was identified through spectroscopic analyses using Raman spectroscopy and X-ray photoelectron spectroscopy (XPS). Raman was carried out by a laser confocal Raman spectrometer (LabRam HR800, Horiba, United States) with a 1-mW semiconductor laser using a 532 nm excitation wavelength. The spectra were recorded with a 1 cm^{-1} resolution ranging from 400 to 1600 cm^{-1}. At least ten spectra were acquired for each sample to increase the reliability of the measures. XPS analysis was performed using an imaging photoelectron spectrometer (Thermo Scientific K-Alpha, United States) at room temperature with a monochromatic Al-Kα X-ray source with a pass energy of 50 eV. The spectra were calibrated by taking the C 1s peak as the reference binding energy at 284.8 eV.

Double-wire SAW was performed on the base metal of EH36 shipbuilding steel. Welding parameters (electrode forward: DC-850 A/32 V, electrode backward: AC-625 A/36 V) were kept constant with the travel speed at 500 mm/min.

RESULTS AND DISCUSSIONS

Transfer behaviours of Si, Mn, Ti and O

The element transfer between slag and WM is quantified by a Δ value and refers to the difference between analytical composition and nominal composition of the WM (Zhang, Wang and Coetsee, 2021). The Δ value indicates the contribution of flux to the WM composition. A positive Δ value implies that a specific element has been transferred from flux (slag) to WM. A negative Δ value means that a given element has been lost from WM to slag. For a specific element, a zero Δ value implies that an apparent equilibrium condition has been reached between the slag and WM (Zhang, J *et al*, 2020).

In the droplet zone of the SAW, where droplet forms at the electrode tip and travels through the arc, most oxides are susceptible to decompose and thus increase the O level of the droplet by increasing the local pO_2 via Equations 1 and 2 under the presence of the arc. In this period, O level of the droplet increases, and negligible amount of alloy transfer, such as Si and Mn, may occur.

$$(MnO) = Mn(g) + 1/2O_2(g) \quad (1)$$

$$(SiO_2) = SiO(g) + 1/2O_2(g) \quad (2)$$

Subsequently, the droplet is diluted by the weld pool and the transfer of Mn and O at slag-metal interface would be governed by Equation 3.

$$(MnO) = [Mn] + [O] \quad (3)$$

Table 1 summarises the Δ values of the WMs. As can be seen from Table 1, the ‘neutral point’ of Mn for WMs, where equilibrium is built between slag and WM apparently, lies at between

10~20 wt per cent MnO. For Flux with MnO addition of 0 and 10 wt per cent, the WMs lose 0.318 and 0.162 wt per cent Mn to the slags, respectively; for the MnO-rich fluxes, the WMs gain up to 0.588 wt per cent Mn from the slags. All WMs gain Si from the slags with an average value of about 0.187 wt per cent. The transfer of Si appears to be independent of MnO content in the fluxes.

TABLE 1

Changes of chemical compositions of WMs (wt%).

CaF_2-40%SiO_2-MnO				CaO-40%SiO_2-MnO				25%CaF_2-SiO_2-CaO-TiO_2		
MnO	**ΔSi**	**ΔMn**	**ΔO**	**MnO**	**ΔSi**	**ΔMn**	**ΔO**	**TiO_2**	**ΔTi**	**ΔO**
0	0.212	-0.318	0.015	10	0.081	0.218	0.058	0	-0.002	0.018
10	0.193	-0.162	0.033	20	0.071	0.244	0.061	5	0.002	0.021
20	0.164	0.125	0.038	30	0.082	0.278	0.069	10	0.005	0.023
30	0.16	0.092	0.045	40	0.118	0.344	0.084	15	0.007	0.025
40	0.163	0.318	0.058	50	0.167	0.327	0.092	20	0.01	0.027
50	0.216	0.437	0.085	60	0.16	0.377	0.085			
60	0.201	0.588	0.08							

Flux plays a major role in O uptake of the WM in SAW (Zhang *et al*, 2023). MnO and SiO_2 are reported as primary sources of O in SAW. It is observed from Table 1 that there is a significant increase in ΔO values from 150 to 850 ppm as MnO content increases from 0 to 60 wt per cent. In the droplet zone, O is transferred to the droplet via the increase of pO_2 in Equations 1 and 2 as mentioned previously. It is deduced from Equation 1 that pO_2 would increase with higher MnO content in the fluxes for a given amount of SiO_2. In the weld pool zone, the transfer of O to the WM increases with MnO addition as Equation 3 is promoted to the right side.

Although the transfer mechanism of O from CaO to WM remains ambiguous, it is accepted that CaO is one of the most stable oxides with a lower O potential than MnO. The amount of O contributed from the flux, *viz* ΔO value, increases from 576 to 920 ppm at higher MnO content. It is seen that the ΔSi value generally increases with higher MnO additions in the flux. The addition of MnO tends to increase the activity of SiO_2, which, in turn, promotes the transfer of Si from flux to the weld metal. Only a slight improvement of measured ΔMn value from 0.218 to 0.377 wt per cent is observed, although the MnO addition level dramatically increases from 10 to 60 wt per cent. This can be attributed to the fact that the evaporation of Mn from the weld pool tends to occur at the plasma-metal interface, reducing the magnitude of ΔMn value.

Gas–slag–metal model

Results above have quantified the element transfer behaviours. Therefore, to precisely predict the essential element contents, a gas–slag–metal equilibrium model is established, based on the assumption that the the O level is controlled by pO_2 (derived from the decomposition of the oxide in flux) in the arc plasma. Figure 1 shows the predicted contents by gas–slag–metal equilibrium calculations for Si, Mn and O. It can be seen that this model offers excellent prediction accuracy for O content, and can differentiate the O content of the weld metals produced by fluxes with varying formulas but same basicity index. Furthermore, when the gas–slag–metal equilibrium model is applied, the prediction error for Si and Mn contents is significantly reduced as compared to the slag–metal equilibrium model. Thermodynamic calculation data indicates that the consideration of gas formation, which essentially controls the predicted flux O potential and oxide activity, is necessary to improve the overall prediction accuracy.

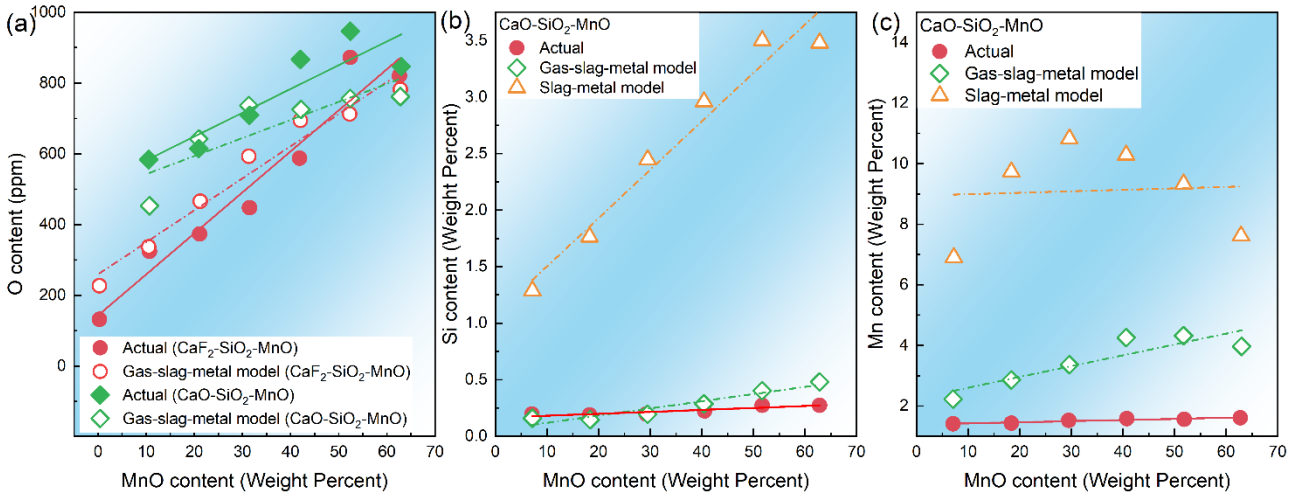

FIG 1 – Predicted contents by gas–slag–metal equilibrium calculations for: (a) O, (b) Si and (c) Mn content as a function of MnO level in fluxes.

Transfer pathway of oxygen

It is revealed that O transfer behaviour could likely be a dynamic process involving O gain and loss. A practical challenge is that the dynamic process is covered under molten flux, which is difficult to observe and quantify directly. O transfer processes are related to O transfer pathways that can be deciphered by WM O gain and loss. However, controversies remain regarding the transfer pathway for O, which dims the understanding of the O transfer mechanism. Hence, further investigations are called upon to account for the transfer pathway of O in pertinent welding fluxes.

At the slag–metal reaction interface, the transfer of O is largely enabled simultaneously with the transfer of other alloying elements via Equations 4 and 5 in CaF_2-SiO_2-CaO-(0~20 wt per cent)TiO_2 system. Table 2 shows the WM O gain by slag–metal reactions. O contributions from SiO_2 and TiO_2 are denoted as $\Delta O_{Si}O_2$ and $\Delta O_{Ti}O_2$, respectively. It is seen that positive $\Delta O_{Si}O_2$ and $\Delta O_{Ti}O_2$ values increase with higher TiO_2 content in the flux, indicating O transfer from the flux to the WM. WM O gain is favoured with enhanced TiO_2 content, which will increase the activities of SiO_2 and TiO_2. What stands out is that, for any given TiO_2 content, $\Delta O_{Si}O_2$ value is over ten times that of $\Delta O_{Ti}O_2$, which could be attributed to the fact that the O potential of SiO_2 is reportedly higher than that of TiO_2 during the welding process, as manifested by the high WM O levels for multi-component acidic fluxes with high SiO_2 contents. Moreover, Table 2 also shows actual changes of the O content in the WM. Total O gain of the WM through slag–metal reactions increases from 0.267 to 0.389 wt per cent. However, actual WM ΔO ranges from 0.018 to 0.027 wt per cent, suggesting that there is O loss in the WM after WM gains O by slag–metal reactions.

$$(TiO_2) = [Ti] + 2[O] \quad (4)$$

$$(SiO_2) = [Si] + 2[O] \quad (5)$$

TABLE 2

Weld metal ΔO content as a function of TiO_2 content in the flux (wt%).

TiO_2(%)	ΔO	Gain O			Loss O		
		ΔSiO₂	ΔTiO₂	gas	C	Mn	Fe
0	0.018	0.269	0	0.003	-0.008	-0.029	-0.217
5	0.021	0.272	0.004	0.018	-0.01	-0.033	-0.23
10	0.023	0.288	0.007	0.036	-0.014	-0.04	-0.254
15	0.025	0.313	0.012	0.045	-0.014	-0.054	-0.277
20	0.027	0.338	0.017	0.053	-0.018	-0.057	-0.306

O loss incurred by Fe, Mn and C is denoted as ΔOF_e, ΔO_{Mn} and ΔO_C. It is demonstrated that ΔOF_e, ΔO_{Mn} and ΔO_C are always negative, and their absolute values increase with higher TiO_2 content, indicating O loss from the WM to the slag. O loss by oxidation of Fe from the WM increases from 0.23 to 0.31 wt per cent, which is significantly larger than those of ΔO_{Mn} and ΔO_C, suggesting that deoxidation of the WM is mainly attributed to oxidation of Fe. In addition, the WM O content reduced by deoxidation is 0.268 to 0.389 wt per cent with TiO_2 increase from 0 to 20 wt per cent, which is greater than that of the O gain (0.267 to 0.355 wt per cent) by slag–metal reactions, indicating another pathway for the WM to gain O is through gas–metal reactions. It is concluded that gas–metal reactions mainly occur in the 'droplet zone', the region where droplets form at the electrode tip and travel through the arc cavity. Wt conservation calculations of WM can be used to calculate O gain (ΔO_{gas}) through gas–metal reactions, which can be calculated by Equation 6. ΔO_{gas} content picks up from 0.017 to 0.062 wt per cent as TiO_2 content in the flux increases from 0 to 20 wt per cent.

$$\Delta O_{WM} = (\Delta O_{SiO_2} + \Delta O_{TiO_2} + \Delta O_{gas}) - (\Delta OF_eO + \Delta O_{Mn}O + \Delta OCO) \quad (6)$$

WM O gain is primarily driven by gas–slag–metal reactions, while O loss is largely enabled by slag–metal reactions. The total O gain and loss increase from 0.286 to 0.416 and 0.268 to 0.389 wt per cent, respectively and WM O gain is greater than its loss. This result indicates a net O gain (Total O gain minus total O loss, 0.018 to 0.027 wt per cent) in the WM, resulting in increased WM O content compared to the BM or electrode. Moreover, ΔO_{SiO_2} contributes above 80 per cent to the total O gain, indicating that SiO_2 in the flux is the main O source for the WM. Fe deoxidation is the largest contributor to the WM O loss, demonstrated by ΔOF_e, which accounts for more than 80 per cent of the total O loss.

It can be concluded that oxides dissociate under the high temperature of the arc plasma, and O generated by TiO_2 and SiO_2 dissolves into the electrode droplets and WM. O generated by TiO_2 and SiO_2 dissolves into the electrode droplets and WM by gas–metal reactions, which accounts for 5.91 to 14.68 per cent of the total O gain. In addition, O also transfers from the molten flux into the WM through Equations 4 and 5, and SiO_2 in the flux is the most significant contributor to the O gain for the WM, accounting for more than 80 per cent of the total O gain. The solubility of O in WM decreases after the molten welding pool cools down from higher temperature to the solidification temperature. Therefore, Fe, Mn and C will react with dissolved O, and then the deoxidation products will transfer into the slags. Oxidation of Fe is the main way for O loss from the WM, which has been demonstrated by ΔOF_e accounts for more than 80 per cent of the total O loss.

Structure and physicochemical properties

The optical basicity (Λ) is a measure of the electron donor properties of different ions (Mills, Yuan and Jones, 2011; Mills *et al*, 2012). It was also used as a theoretical measure of the depolymerisation of the melt. In terms of experiment methods, XPS analysis possesses a unique function by showcasing features of various oxygen species, including O^- (non-bridging oxygen), O^0 (bridging oxygen) and O^{2-} (free oxygen), which are closely related to the degree of polymerisation of the flux structure (Wang *et al*, 2023b; Zhang, Y *et al*, 2020). Therefore, the non-bridging oxygen distributions as a function of optical basicity for varied flux systems are shown in Figure 2a. It can be seen that the fraction of non-bridging oxygen increases with an increase in optical basicity for all the fluxes, which is consistent with earlier study (Yang, Wang and Sohn, 2022).

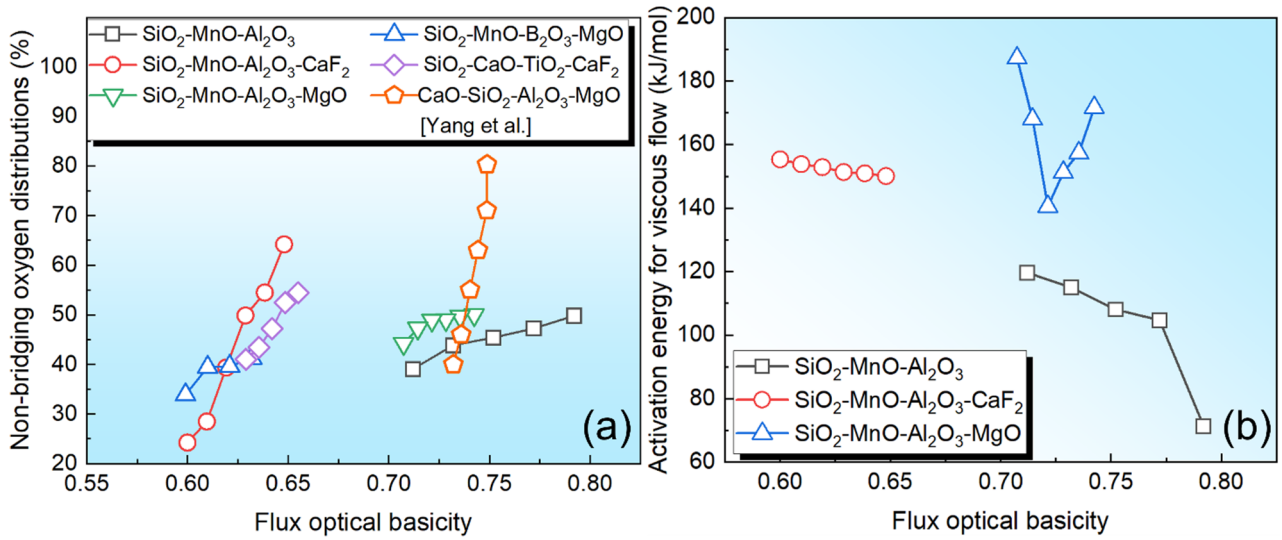

FIG 2 – Relationship between flux optical basicity and: (a) non-bridging oxygen, and (b) activation energy for viscous flow.

The activation energy (E_a) represents the frictional resistance within the structural units of the liquid flux that needs to be overcome during shearing (Wang *et al*, 2022). For Newtonian fluids, E_a can be obtained from the Arrhenius equation, as shown in Equation 7:

$$\text{Ln}\eta = \text{ln}\eta_0 + (E_a)/R \cdot 1/T \quad (7)$$

where:

η	is the viscosity (Pa s)
η_0	is a pre-exponential factor (Pa s)
E_a	is the activation energy for viscous flow (J/mol)
T	is the absolute temperature (K)
R	is the ideal gas constant (8.314 J mol^{-1} K^{-1})

The calculated E_a values with different Al_2O_3 contents are shown in Figure 2b. As can be seen, E_a gradually decreases as the optical basicity increases. However, for the SiO_2-MnO-Al_2O_3-CaF_2 system, E_a decreases from 171.68 to 140.53 kJ mol^{-1} as the Al_2O_3 content increases from 0 to 15 wt per cent and then E_a shows a significant increase from 168.05 to 187.26 kJ mol^{-1} with further addition of Al_2O_3, which correlates well with the 'V'-shaped variation trend of the viscosity.

CONCLUSIONS

In summary, the transfer pathways and mechanisms of major alloying elements, such as Si, Mn, Ti and O during welding have been elucidated. A thermodynamic model has been established to predict alloying element contents in the WM. Combined with spectroscopic methods, the flux optical basicity has been found to be positively associated with the degree of polymerisation. Moreover, the activation energy for viscous flow gradually decreases as the optical basicity increases.

ACKNOWLEDGEMENTS

The authors sincerely thank the National Natural Science Foundation of China (Grant Nos. U20A20277 and 52350610266) and National Key Research and Development Program of China (Grant No. 2022YFE0123300).

REFERENCES

Mills, K C, Yuan, L and Jones, R T, 2011. Estimating the physical properties of slags, *Journal of the Southern African Institute of Mining and Metallurgy,* 111:649–658.

Mills, K C, Yuan, L, Li, Z, Zhang, G H and Chou, K C, 2012. A review of the factors affecting the thermophysical properties of silicate slags, *High Temperature Materials and Processes,* 31(4–5):301–321.

Wang, C and Zhang, J, 2021. Fine-tuning weld metal compositions via flux optimization in submerged arc welding: An overview, *Acta Metallurgica Sinica,* 57(9):1126–1140.

Wang, Z, Li, Z, Zhong, M, Li, Z and Wang, C, 2023a. Elucidating the effect of Al_2O_3/SiO_2 mass ratio upon SiO_2-MnO-CaF_2-Al_2O_3-based welding fluxes: Structural analysis and thermodynamic evaluation, *Journal of Non-Crystalline Solids,* 601:122071.

Wang, Z, Shen, B, Zhong, M, Li, Z and Wang, C, 2023b. A structure-oriented elucidation for viscous flow of SiO_2-MnO-Al_2O_3 fused submerged arc welding fluxes, *Journal of Non-Crystalline Solids,* 612:122360.

Wang, Z, Zhang, J, Zhong, M and Wang, C, 2022. Insight into the viscosity–structure relationship of MnO–SiO_2–MgO–Al_2O_3 fused submerged arc welding flux, *Metallurgical and Materials Transactions B,* 53:1364–1370.

Wu, Y, Yuan, X, Kaldre, I, Zhong, M, Wang, Z and Wang, C, 2023. TiO_2-Assisted microstructural variations in the weld metal of EH36 shipbuilding steel subject to high heat input submerged arc welding, *Metallurgical and Materials Transactions B,* 54(1):50–55.

Yang, J, Wang, Z and Sohn, I, 2022. Topological understanding of thermal conductivity in synthetic slag melts for energy recovery: An experimental and molecular dynamic simulation study, *Acta Materialia,* 234:118014.

Yuan, H, Wang, Z, Zhang, Y and Wang, C, 2023. Roles of MnO and MgO on structural and thermophysical properties of SiO_2-MnO-MgO-B_2O_3 welding fluxes: A molecular dynamics study, *Journal of Molecular Liquids,* 386:122501.

Zhang, J, Coetsee, T, Dong, H and Wang, C, 2020. Element transfer behaviors of fused CaF_2-SiO_2-MnO fluxes under high heat input submerged arc welding, *Metallurgical and Materials Transactions B,* 51(3):885–890.

Zhang, J, Leng, J and Wang, C, 2019. Tuning weld metal mechanical responses via welding flux optimization of TiO_2 content: application into EH36 shipbuilding steel, *Metallurgical and Materials Transactions B,* 50(5):2083–2087.

Zhang, J, Wang, C and Coetsee, T, 2021. Thermodynamic evaluation of element transfer behaviors for fused CaO-SiO_2-MnO fluxes subjected to high heat input submerged arc welding, *Metallurgical and Materials Transactions B,* 52:1937–1944.

Zhang, Y, Coetsee, T, Yang, H, Zhao, T and Wang, C, 2020. Structural roles of TiO_2 in CaF_2-SiO_2-CaO-TiO_2 submerged arc welding fluxes, *Metallurgical and Materials Transactions B,* 51(5):1947–1952.

Zhang, Y, Liu, H, Coetsee, T, Wang, Z and Wang, C, 2023. Identifying oxygen transfer pathways during high heat input submerged arc welding: a case study into CaF_2-SiO_2-CaO-TiO_2 fluxes, *Metallurgical and Materials Transactions B,* 54(6):2875–2880.

Zhang, Y, Wang, Z, Zhang, J, Li, Z, Basu, S and Wang, C, 2022a. Probing viscosity and structural variations in CaF_2–SiO_2–MnO welding fluxes, *Metallurgical and Materials Transactions B,* 53(5):2814–2823.

Zhang, Y, Zhang, J, Liu, H, Wang, Z and Wang, C, 2022b. Addressing weld metal compositional variations in EH36 shipbuilding steel processed by CaF_2-SiO_2-CaO-TiO_2 fluxes, *Metallurgical and Materials Transactions B,* 53:1329–1334.

Electrodeposition and electrochemical behaviour of molybdenum ions in $ZnCl_2$-NaCl-KCl molten salt

DOI: 10.62053/UFKL1666
H Zhang[1], S Li[1], Z Lv[1] and J Song[2]

1. Zhongyuan Critical Metals Laboratory, Zhengzhou University, Zhengzhou, Henan 450001, China; School of Material Science and Engineering, Zhengzhou University, Zhengzhou, Henan 450001, China.
2. Zhongyuan Critical Metals Laboratory, Zhengzhou University, Zhengzhou, Henan 450001, China; School of Material Science and Engineering, Zhengzhou University, Zhengzhou, Henan 450001, China. Email: jianxun.song@zzu.edu.cn

ABSTRACT

In this paper, a method for extracting and refining metallic molybdenum using low-temperature $ZnCl_2$-NaCl-KCl molten salt was proposed. The electrochemical behaviour of molybdenum ions in $ZnCl_2$-NaCl-KCl molten salt was investigated in detail, and pure metallic molybdenum was collected on the cathode. The reduction and diffusion processes of Mo(V) ions in $ZnCl_2$-NaCl-KCl molten salt were determined through a series of electrochemical methods. The diffusion coefficients and nucleation modes of Mo(V) ions were also studied, and electrolysis was conducted for a prolonged period at a constant current density. The results indicated that the electrode reduction of Mo(V) ions in $ZnCl_2$-NaCl-KCl molten salt proceeds through a three-step reaction: Mo(V) → Mo(IV) → Mo(III) → Mo at 250°C.

The Mo(V) → Mo(IV) reaction was reversible and diffusion-controlled, with a Mo(V) diffusion coefficient of 6.02×10^{-6} cm^2 s^{-1}. Additionally, the nucleation mode of Mo(V) ions was instantaneous nucleation. The products electro-deposited were confirmed of metallic molybdenum with a particle size of less than 1 μm.

INTRODUCTION

Molybdenum is a metal with the high melting point, high hardness, good thermal and electrical conductivity and strong corrosion resistance (Huang *et al*, 2016; Lv *et al*, 2021a, 2021b; Zhang *et al*, 2023), and is widely used in the fields of iron and steel, metallurgy, medical treatment, semiconductors and other fields (Luo *et al*, 2019; Kuroda *et al*, 2020). Among the various extraction and refining technologies for molybdenum metal, the electrolysis method has shown great potential for development and application with its high efficiency and environmentally friendly characteristics. In the process of electrolytic extraction and refining, the electrolyte composition has an important influence on the electrolysis process due to its different physical and chemical properties. Therefore, the choice of electrolyte composition is extremely important issue for the extraction and purification of molybdenum metal. Depending on the type of electrolyte used in the electrolysis extraction and refining of molybdenum metal, it can be divided into ionic liquid electrolytes and molten salt electrolytes.

Ionic liquid electrolyte is a special liquid substance mainly composed of a large number of cations and anions. Researchers attempted to successfully deposit high-purity and dense molybdenum metal using ionic liquids with high concentrations of acetic acid (Morley *et al*, 2012), ammonium acetate solution (Kuznetsov *et al*, 2018), and 1-butyl-3-methylimidazolium tetrafluoroborate ($BMIMBF_4$) (Tian *et al*, 2023) as the electrolyte. However, although the ionic liquid electrolyte has the advantages of fine-tuning and low-temperature electrolysis in the preparation of metallic molybdenum, its efficiency is low, with most of the current being used to electrolyse water and produce hydrogen, resulting in a high oxygen content in the product and a slow electrolysis rate.

Compared with ionic liquid electrolytes, molten salt electrolyte electrolysis has the advantages of high current efficiency, fast electrolysis rate and high product purity. High purity molybdenum metal was successfully prepared by adding K_3MoCl_6 to the molten salts of KCl-NaCl and LiCl-KCl, respectively, and electrolysing them at 900°C in an inert atmosphere (Senderoff and Brenner, 1954). After that, molybdenum metal with higher purity was successfully prepared from the molten salt system of NaF-KF-MoF_6 (Senderoff and Mellors, 1967) at 600°C. In addition to molybdenum halide

as solute in molten salt for molten salt electrolysis, researchers have also tried to use molybdenum oxide (Kou *et al*, 2023; Malyshev *et al*, 2018; Kushkhov and Adamokova, 2007) and metal molybdates (Kōyama, Hashimoto and Terawaki, 1987) as solutes, which can also successfully prepare molybdenum metal, but the oxygen content in the product will inevitably be higher. Therefore, the extraction and refining of molybdenum metal using molten salt electrolyte, although the current efficiency is high and the electrolysis speed is fast, the temperature required for electrolysis is usually above 450°C, and the energy consumption is high and the requirement of equipment is high. To address this problem, Nakajima, Nohira and Hagiwara (2006) investigated a new low-temperature molten salt system, ie $ZnCl_2$-NaCl-KCl system. $MoCl_3$ was added to the $ZnCl_2$-NaCl-KCl system at 250°C, and molybdenum metal was successfully obtained by electrodepositing on the cathode. The advantage of this molten salt system is that it can realise the electrodeposition of metallic molybdenum at a lower temperature, which will reduce the energy consumption and the volatilisation loss of molybdenum chloride. Carrying on electrodepositing in such melt, the current efficiency is much higher than that of ionic liquids, which is a more ideal electrolyte.

However, the results of the present study only demonstrate the feasibility of extracting metal molybdenum from the $ZnCl_2$-NaCl-KCl molten salt electrolyte. There are few studies on the electrochemical behaviour of Mo(V) in low-temperature molten salts, and no uniform conclusions have been drawn. In addition, the molybdenum metal has a complex dissolved valence state during the refining and extraction process. Therefore, it is of great significance to study the electrochemical behaviour of high-valent molybdenum ions in the $ZnCl_2$-NaCl-KCl (Moon *et al*, 2022). In summary, $ZnCl_2$-NaCl-KCl (3:1:1) was chosen as the electrolyte in this study, and thermodynamic calculations and various electrochemical tests were performed to probe deeply into the reduction and diffusion processes of Mo(V) ions. The diffusion coefficient and nucleation mode of molybdenum ions were investigated, and electrodeposition experiments were carried out at a constant current, and molybdenum metal was successfully obtained at the cathode.

EXPERIMENTAL

In this study, a total of 100 g of $ZnCl_2$-NaCl-KCl salt mixture was used as the electrolyte with a molar ratio of 3:1:1. The specific compositions were $ZnCl_2$ (99 per cent purity), NaCl (99.8 per cent purity), and KCl (99.8 per cent purity), which were purchased from McLean Biochemicals Ltd. The salt mixtures were first kept at a constant temperature of 200°C for 4 hrs to remove residual moisture, followed by a temperature increase to 250°C and maintained for 4 hrs to ensure that the molten salt mixtures were fully melted and well mixed. This was followed by a 12 hr pre-electrolysis treatment, followed by electrochemical tests and deposition experiments. Molybdenum ions were added to the molten salt as $MoCl_5$ (99.9 per cent purity, purchased from Macklin Biochemicals Ltd).

The whole experiment was carried out under argon atmosphere. A three-electrode system was used during the electrochemical tests. In this system, a tungsten wire (1 mm diameter, 99.99 per cent purity) was used as the working electrode (WE), while another tungsten wire was used as the reference electrode (RE) and a graphite rod (10 mm diameter, 99.99 per cent purity) was used as the counter electrode (CE). When constant current electrolysis was performed, a two-electrode system was used, in which molybdenum sheets (50 mm in length, 10 mm in width, and 1 mm in thickness) were used as cathode and anode, respectively, in different electrolysis steps. The electrochemical experiments were recorded by Nova 2.1 software (by Metrohm Autolab) controlled by AutoLab (PGSTAT 302N) and transient electrochemical techniques were used to study the electrochemical behaviour of Mo(V) in $ZnCl_2$-NaCl-KCl molten salt. The experiments were carried out at a current density of 0.06 A cm^{-2} in a constant current electrolysis test and the cathodic products were collected. In order to investigate the microstructure and morphology of the cathode products, scanning electron microscopy (SEM, including TESCAN MIRA LMS and ZEISS Sigma 300), as well as energy spectrometry (EDS), were used for the analysis.

RESULTS AND DISCUSSION

Redox behaviour of molybdenum ions in molten salt

The decomposition reactions corresponding to NaCl, KCl, $ZnCl_2$, and $MoCl_x$ ($x \leq 5$) were shown in Equations 1–4. Through thermodynamic calculations and the study of Nakajima, Nohira and

Hagiwara (2006), it was found that the decomposition potential of $ZnCl_2$ is the smallest when compared to NaCl and KCl under 250°C. Therefore, for extraction and refining of molybdenum metal by using this molten salt, the MoCl*x* ($x \leq 5$) decomposition potential must be lower than the $ZnCl_2$ decomposition potential. The Gibbs free energy changes for the Reactions 3 and 4 at 250°C were calculated using HSC Chemistry 6.0, from which the decomposition potentials of molybdenum chloride at different valence states as well as the theoretical electrochemical window of the molten salt electrolyte were determined by Equation 5.

$$2NaCl(s) = 2Na(l) + Cl_2(g) \quad (1)$$

$$2KCl(s) = 2K(l) + Cl_2(g) \quad (2)$$

$$ZnCl_2 = Zn + Cl_2(g) \quad (3)$$

$$2MoCl_x = 2MoCl_y + (x- y)Cl_2(g) \quad (4)$$

$$\Delta G = -nEF \quad (5)$$

Where ΔG represents the change in Gibbs free energy (kJ mol^{-1}); the relationship between x and y is $0 \leq y < x \leq 5$; n is the number of electrons transferred by the reaction (mol); E refers to the reduction potential (V) of the above chloride and sulfide, and F is the Faraday constant (C mol^{-1}).

The common valence states of molybdenum chloride were more complex (including 5, 4, 3, 2 and 0 valence states) and the calculated decomposition voltages were shown in Figure 1a. The electrolyte selection criteria for the electrolysis of molten salts was satisfied because the decomposition voltage of $MoCl_x$ (maximum -1.13 V) was lower than that at molten NaCl-KCl (-1.74 V) at 750°C. In addition, the reduction order of each valence state of each molybdenum ion in Figure 1a provided theoretical support for the subsequent molybdenum ion reduction process.

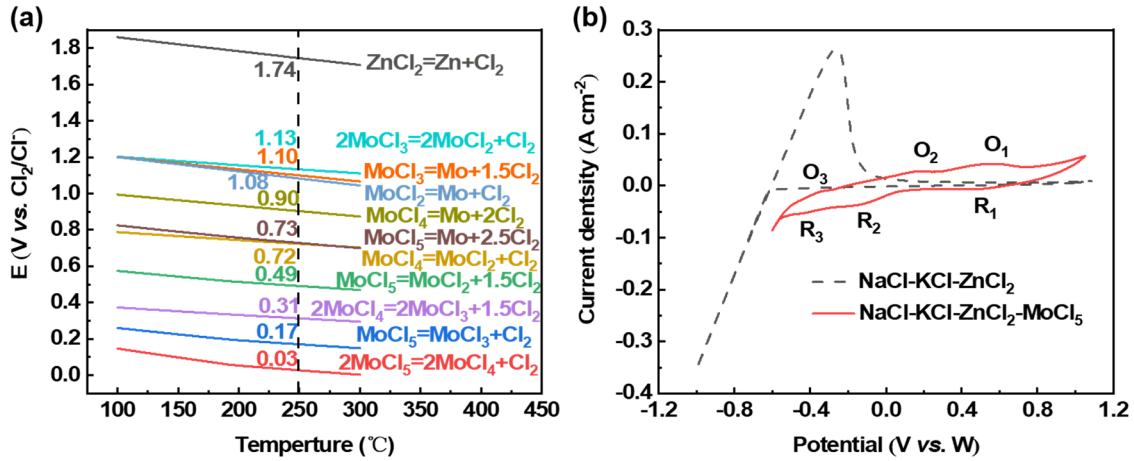

FIG 1 – (a) Molybdenum chloride and zinc chloride theoretical decomposition voltage as a function of temperature (all thermodynamic data from HSC 6.0 in activity (α = 1)); (b) Cyclic voltammograms before and after the addition of $MoCl_5$ in the molten $ZnCl_2$-NaCl-KCl salt; scan rate: 0.25 V s^{-1}

The results of the cyclic voltammetry (CV) tests, conducted before the addition of $MoCl_5$, were shown as the grey line in Figure 1b. The reduction of Zinc ions began near -0.6 V versus W, and there were no significant current density peaks observed between 1.1 V and -0.6 V, suggesting that no other reduction reactions occurred in this voltage range. Therefore, it was determined that the electrolyte system was suitable for performing electrochemical tests. After the addition of $MoCl_5$, the voltammetric curve appeared as the red line in Figure 1b. Three pairs of distinct current density peaks (R_1/O_1, R_2/O_2, and R_3/O_3) were observed, indicating that molybdenum ions were involved in redox reactions. Furthermore, all these reduction reactions of molybdenum ions occurred before the precipitation of Zinc ions, demonstrating that the selection of the $ZnCl_2$-NaCl-KCl-$MoCl_5$ system was feasible for the extraction and refining of molybdenum metal.

The cyclic voltammograms obtained after the addition of $MoCl_5$ were further analysed through Figure 2a, where it can be seen that the reduction peaks R_1, R_2, and R_3 occurred at reduction

potentials of 0.52 V, -0.08 V, and -0.42 V (versus W), respectively. Based on these observations, it can be inferred that the reduction of molybdenum ions occurred in three distinct steps. Subsequently, the electrochemical behaviour of Mo(V) was further investigated using the more precise square wave voltammetry (SWV) technique. The results obtained from this analysis are presented in Figure 2b, where three distinct electrode reduction reactions R_1, R_2, and R_3 can be observed at potentials of 0.53 V, -0.05 V, and -0.45 V (versus W), respectively. These findings suggest that the conversion of Mo(V) to metal in the $ZnCl_2$-NaCl-KCl molten salt involves three reduction processes, which is consistent with the results obtained from the previously conducted cyclic voltammetry tests.

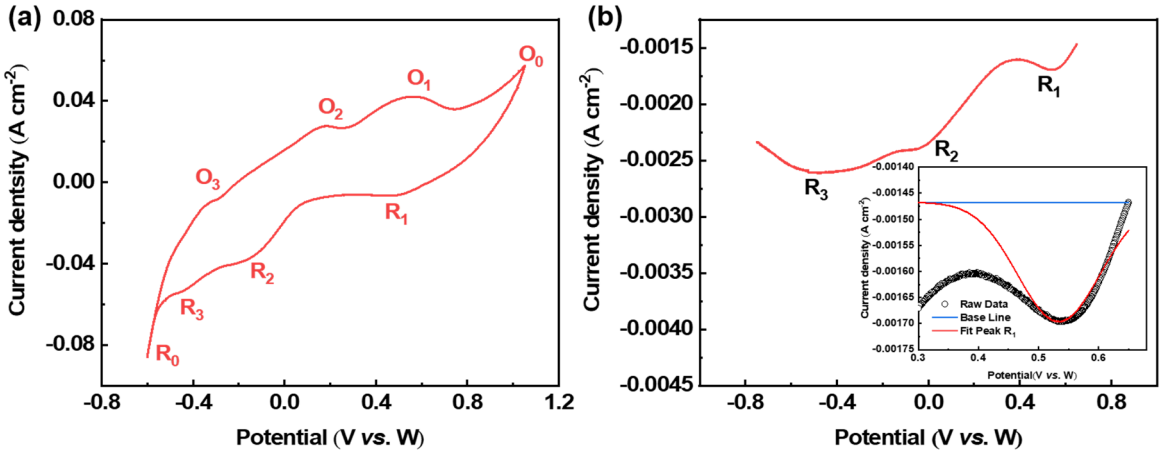

FIG 2 – Electrochemical test plots after addition of $MoCl_5$ to $ZnCl_2$-NaCl-KCl molten salt: (a) cyclic voltammetry; scan rate: 0.25 V s^{-1}; (b) square-wave voltammetry; scan frequency: 25 Hz; inset: Gaussian fit to R_1 peaks.

In addition, the peak potentials of R_1, R_2, and R_3 did not change with increasing scan rate or scan frequency in Figure 3a and Figure 4a, which indicates that R_1, R_2, and R_3 are reversible reactions. Where the number of transferred electrons corresponding to the reduction peak R_1 can be calculated by Equation 6 (Krause and Ramaley, 1969; O'Dea, Osteryoung and Osteryoung, 1981; Aoki *et al*, 1986):

$$W_{1/2}=3.52\frac{RT}{nF} \tag{6}$$

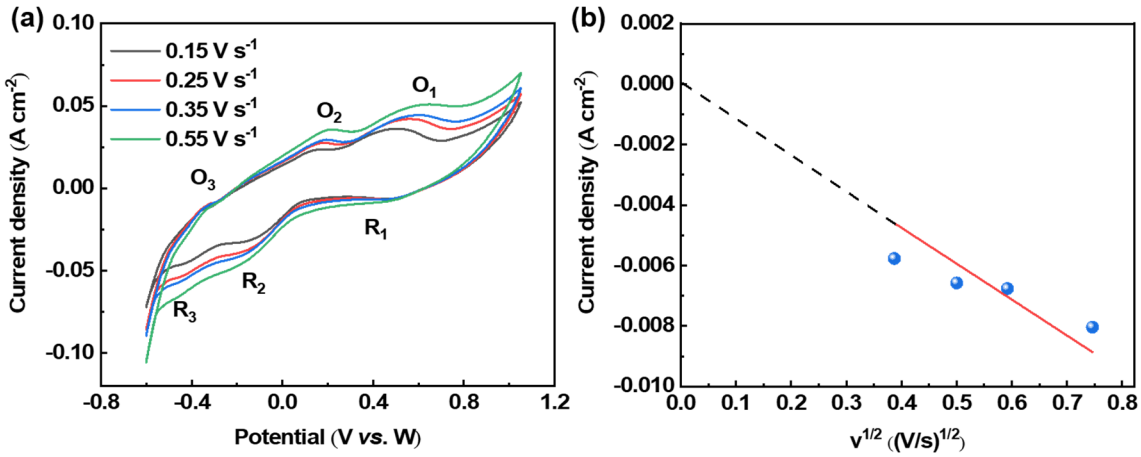

FIG 3 – (a) Cyclic voltammograms of $MoCl_5$ in molten $ZnCl_2$-NaCl-KCl on a tungsten wire electrode at different scan rates; (b) The relationship between the current density and the square root of scan rate.

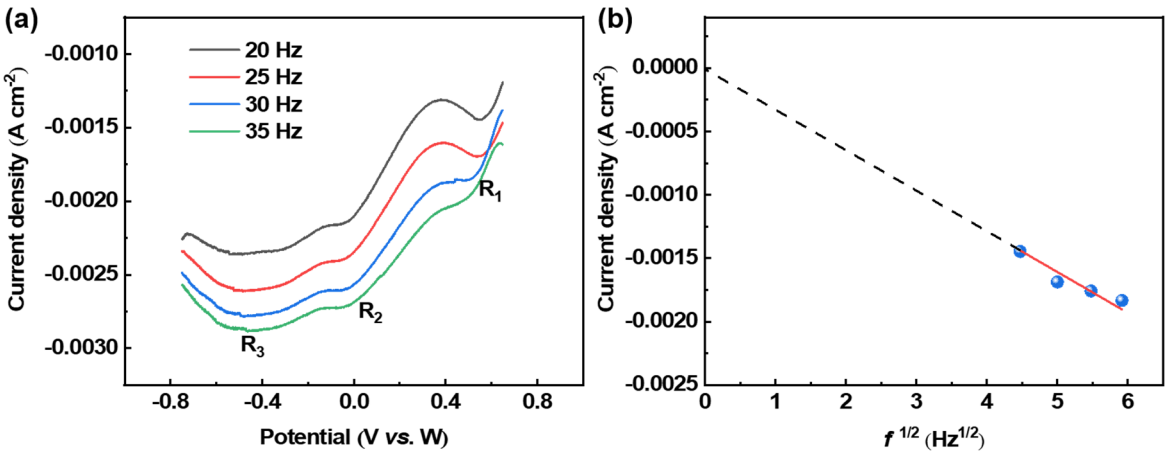

FIG 4 – (a) Square wave voltammetry of $MoCl_5$ in molten $ZnCl_2$-NaCl-KCl on a tungsten wire electrode at different frequencies; (b) The relationship between the current density and the square root of frequency.

A Gaussian fit was applied to R_1 in the square-wave voltammogram, and the fitted curve is presented in the inset of Figure 2b. The half-wave width of R_1 was determined to be 0.16. The number of electrons transferred corresponding to R_1 was calculated to be approximately 0.99, which was close to 1, indicating that the reduction step represented by the R_1 peak was Mo(V) → Mo(IV). Subsequently, Mo(IV) was reduced to metallic molybdenum through two further steps, R_2 and R_3. The reduction reaction of the Mo(IV) ion can be referenced to our previous determination in NaCl-KCl (Zhang *et al*, 2024): Mo(IV) → Mo(III) → Mo. Therefore, it is inferred that R_2 and R_3 correspond to the reduction steps of Mo(IV) → Mo(III) and Mo(III) → Mo, respectively. In conclusion, the reduction process of Mo(V) in the $ZnCl_2$-NaCl-KCl molten salt was Mo(V) → Mo(IV) → Mo(III) → Mo. This was consistent with the order of the Mo(V) reduction potential calculated thermodynamically in Figure 1a.

Diffusion coefficient of molybdenum ions in molten salt

To further investigate the kinetics of the electrode process of molybdenum ions in $ZnCl_2$-NaCl-KCl molten salt, cyclic voltammetry experiments were conducted at various scan rates within the scan interval of 0.9 V to -0.7 V (versus W). The resulting cyclic voltammetry curves were presented in Figure 3a, and the correlation between the potential of the reduction peak R_1 and the logarithm of the scan rate was depicted in Figure 3b. The peak potential of R_1 hardly varied with increasing scan rate and tended to level off with a value of 0.53 V (versus W), which indicated that the R_1 reduction was reversible (Yuan *et al*, 2021). The relationship between the maximal current density of reaction R_1 and the square root of the scan rate was subsequently investigated. As demonstrated in Figure 3b, the peak current density of the reduction reaction R_1 was linear with the square root of the scan rate, indicating that the electrode reduction reaction R_1 was controlled by diffusion.

The diffusion coefficient of Mo(V) ions in molten $ZnCl_2$-NaCl-KCl was determined by Equation 7 (Liu *et al*, 2019).

When the reactants and products were both soluble:

$$I_p = 0.4463 \frac{(nF)^{3/2} A D^{1/2} C_0 v^{1/2}}{(RT)^{1/2}} \quad (7)$$

When the product was insoluble, Equation 8 could be used to determine the diffusion coefficient:

$$I_p = 0.6102 \frac{(nF)^{3/2} A D^{1/2} C_0 v^{1/2}}{(RT)^{1/2}} \quad (8)$$

Where *Ip* is the peak current (A), *v* is the scan rate (V s^{-1}), and C_0 is the bulk concentration of the reducible ion (mol cm^{-3}). The concentration C_0 was determined to be 2.24 × 10^{-5} mol cm^{-3}. *A* is the surface area of the W working electrode (cm^2), and *D* is the diffusion coefficient of Mo(V) (cm^2 s^{-1}).

Mo(V) ions were calculated to have a diffusion coefficient of 6.02 × 10^{-6} cm^2 s^{-1} in molten $ZnCl_2$-NaCl-KCl at 250°C.

To further confirm the findings above, we conducted square wave voltammetry at various frequencies. The test results are displayed in Figure 4a. The responsive R_1, R_2 and R_3 potentials barely changed as the applied frequency increased. The linear fitting results were given in Figure 4b, which related the peak current density linearly to the square root of frequency. This was consistent with the finding made by cyclic voltammetry and leads to the conclusion that the electrode reduction reaction R_1 was a reversible diffusion reaction. The diffusion coefficient was calculated by Equations 9 and 10 (Song *et al*, 2016).

$$I_p = nFAC_0 \frac{1-\Gamma}{1+\Gamma}\left(\frac{Df}{\pi}\right)^{1/2} \tag{9}$$

$$\Gamma = \exp\left(\frac{nF\Delta E}{2RT}\right) \tag{10}$$

Where ΔE is the amplitude of SWV (0.02 V), and f indicates the frequency. The diffusion coefficient of Mo(V) in molten $ZnCl_2$-NaCl-KCl at 250°C was calculated to be 5.61 × 10^{-6} cm^2 s^{-1}. This was about on the same scale as what was discovered during cyclic voltammetry testing.

Nucleation mode of molybdenum ions

In this paper, the $MoCl_5$ nucleation mode was further investigated by using the time-current method, as shown in Figure 5a. Its time-current curve is shown in Figure 5a. The applied potential was set to -0.55 V versus W. The current decreased rapidly and stabilised with time, which was attributed to the fact that molybdenum would be deposited on the electrode at this potential, resulting in a decrease in the molybdenum ion concentration in the vicinity of the electrode, which led to a rapid decrease in the current because molybdenum ions in the molten salt were unable to diffuse to the surface of the electrode in time to replenish it. However, as the reaction proceeds, the diffusion rate of molybdenum ions on the cathode surface and the deposition rate of molybdenum gradually reached a dynamic equilibrium, which led to the gradual stabilisation of the current. This also showed that the reduction of Mo(V) ions was controlled by diffusion.

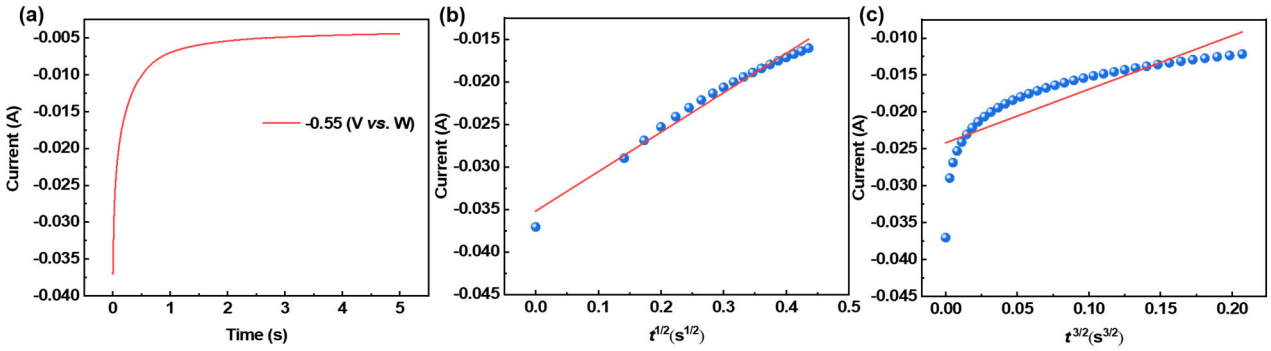

FIG 5 – (a) Timing current curve of $MoCl_5$ in $ZnCl_2$-NaCl-KCl molten salt; applied potential: -0.55 V versus W; (b) The relationship between the current and the square root of time; (c) The relationship between the current and the square root to the third power of time.

The nucleation mode of molybdenum ions can also be determined by the relationship between time and current in the chronoamperometry method. The nucleation modes are generally categorised into two: progressive nucleation and transient nucleation (Khelladi *et al*, 2009; Tylka, Willit and Williamson, 2017):

For instantaneous nucleation:

$$I(t) = \frac{zFN_0\pi(2DC)^{3/2}M^{1/2}}{\rho^{1/2}} t^{1/2} \tag{11}$$

For progressive nucleation:

$$I(t) = \frac{2zFK_nN_0\pi(2DC)^{3/2}M^{1/2}}{3\rho^{1/2}} t^{3/2} \tag{12}$$

where I (t) is the polarisation current at time t; t is the polarisation time (s); Z is the ion valence state; N_0 is the initial nucleation number; M is the atomic weight of the deposit (g mol^{-1}); K_n is the nucleation constant; and ρ is the density of the deposit (g cm^{-3}).

The current versus square root of time was shown in Figure 5b and 5c. The relationship between the current and the square root of time in Figure 5b remained linear after fitting, whereas the relationship between the current and the third power of the square root of time in Figure 5c had a poor correlation after fitting. Thus, molybdenum ions nucleated in a transient mode.

The diffusion coefficients and nucleation modes of Mo ions in different molten salt systems are shown in Table 1, and there are differences in the results in the molten salt system. This phenomenon may be due to different ionic species in the molten salt electrolyte, different experimental temperatures and the use of electrodes.

TABLE 1

Diffusion coefficients and nucleation modes of Mo ions obtained in different molten salt systems.

Molten salt	T (°C)	Diffusion coefficient (cm^2 s^{-1})		*n*	Nucleation mode	Reference
		CV	SWV			
NaCl-KCl-$MoCl_5$	750	1.22 × 10^{-4}	1.67 × 10^{-4}	2	progressive	Zhang *et al* (2024)
$ZnCl_2$-NaCl-KCl-$MoCl_5$	250	6.02 × 10^{-6}	5.61 × 10^{-6}	1	instantaneous	This work

Electrodeposition of molybdenum

After a series of electrochemical tests, in this paper, constant current electrolysis was carried out in molten $ZnCl_2$-NaCl-KCl-$MoCl_5$ (1.0 wt per cent) at 250°C in a two-electrode system. The current density was set at 0.06 A cm^{-2} and the electrolysis time was 20 hrs. Molybdenum sheets were used as cathode and anode, respectively. During the electrolysing of molybdenum metal, the anode molybdenum metal was oxidised and dissolved as molybdenum ions, which diffused to the cathode and were reduced to metal. The voltage change during the constant electrolysis process was recorded as shown in Figure 6a, and it can be found that the voltage was maintained near 1.65 V with little change during the electrolysis process, indicating that the electro-refining process was stable. After 20 hrs of electrolysis, a black deposit was collected at the cathode as shown in the inset in Figure 6a. The product was ultrasonically cleaned and vacuum-dried. The electrolysis product was analysed and detected using SEM and EDS, as shown in Figure 6b, the cathode product after electrolysis was metallic molybdenum and showed an irregular granular shape with particle size less than 1 μm, and this shape may be due to the transient nucleation of molybdenum ions in the electrochemical deposition process.

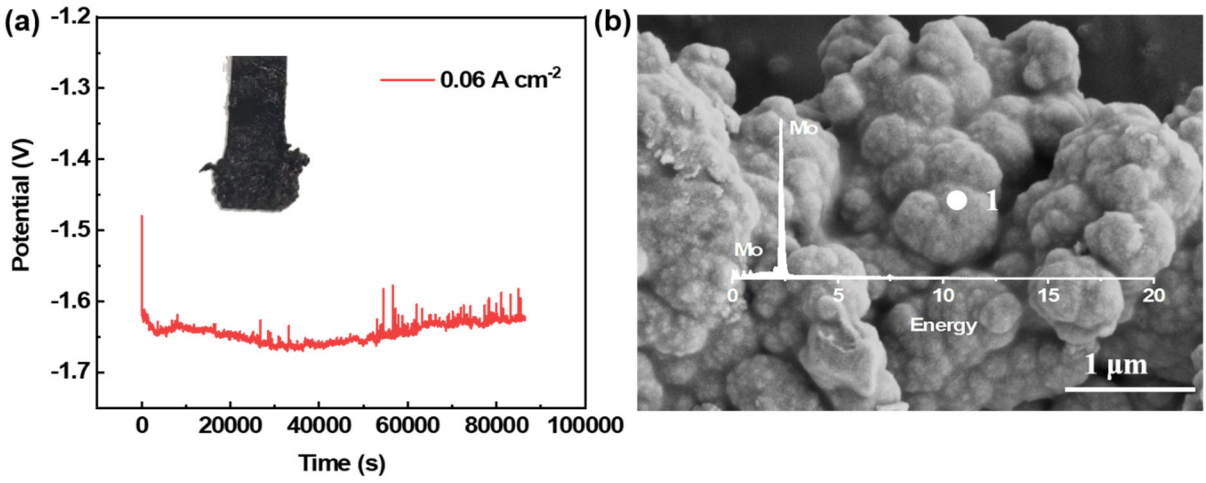

FIG 6 – (a) Time voltage curve at constant current density; inset: Cathode after 20 hr electrolysis; (b) SEM image of cathode product and the results of EDS analysis at point 1.

CONCLUSIONS

In this paper, the electrochemical behaviour of Mo(V) ions in molten $ZnCl_2$-NaCl-KCl at 250°C was investigated in detail. In the three-electrode system, thermodynamic calculations and a series of electrochemical tests were conducted to determine that Mo(V) in $ZnCl_2$-NaCl-KCl molten salt was reduced to molybdenum metal in three steps, namely, Mo(V) → Mo(IV) → Mo(III) → Mo, and the electrode reduction process was a diffusion-controlled reversible reaction.

The diffusion coefficients of Mo(V) were calculated to be 6.02×10^{-6} cm^2 s^{-1} and 5.61×10^{-6} cm^2 s^{-1}, respectively. Subsequently, the nucleation of Mo(V) ions in $ZnCl_2$-NaCl-KCl molten salts was determined to be a transient nucleation process through the use of the constant current method. Finally, electrolytic refining was performed for a prolonged duration at a current density of 0.06 A cm^{-2}, and the electrolytic process remained stable, resulting in the collection of metallic molybdenum at the cathode with a particle size of less than 1 μm. It indicates that $ZnCl_2$-NaCl-KCl holds potential as an electrolyte molten salt for the electrolytic extraction and refining of molybdenum metal.

ACKNOWLEDGEMENT

The authors thank the National Key Research and Development Program of China (Grant No. 2021YFC2901600). The work was also supported by project of Zhongyuan Critical Metals Laboratory (No. GJJSGFJQ202302), Youth Science and technology innovation of Henan Province (No. 23HASTIT009), Henan Province Youth Talent Support Program (2022).

REFERENCES

Aoki, K, Tokuda, K, Matsuda, H and Osteryoung, J G, 1986. Reversible square-wave voltammograms independence of electrode geometry, *Journal of Electroanalytical Chemistry and Interfacial Electrochemistry,* 207(1–2):25–39. https://doi.org/10.1016/0022-0728(86)87060-7

Huang, Z, Liu, J H, Deng, X G, Zhang, H J, Lu, L L, Hou, Z and Zhang, S W, 2016. Low temperature molten salt preparation of molybdenum nanoparticles, *International Journal of Refractory Metals and Hard Materials,* 54:315–321. https://doi.org/10.1016/j.ijrmhm.2015.08.01

Khelladi, M R, Mentar, L, Azizi, A, Sahari, A and Kahoul, A, 2009. Electrochemical nucleation and growth of copper deposition onto FTO and n-Si(100) electrodes, *Materials Chemistry and Physics,* 115(1):385–390. https://doi.org/10.1016/j.matchemphys.2008.12.017

Kou, Q, Jin, W L, Ge, C T, Pang, J, Zhang J, Haarberg, G M, Xiao, S J and Wang, P, 2023. Preparation of molybdenum coatings by molten salt electrodeposition in Na_3AlF_6-NaF-Al_2O_3-MoO_3 system, *Coatings,* 13(7):1266. https://doi.org/10.3390/coatings13071266

Kōyama, K, Hashimoto, Y and Terawaki, K, 1987. Smooth electrodeposits of molybdenum from KF-$Li_2B_4O_7$-Li_2MoO_4 fused salt melts, *Journal of the Less Common Metals,* 132(1):57–67. https://doi.org/10.1016/0022-5088(87)90174-3

Krause, M S and Ramaley, L, 1969. Analytical application of square wave voltammetry, *Analytical Chemistry,* 41(11):1365–1369. https://doi.org/10.1021/ac60280a008

Kuroda, P A B, Lourenço, M L, Correa, D R N and Grandini, C R, 2020. Thermomechanical treatments influence on the phase composition, microstructure and selected mechanical properties of Ti–20Zr–Mo alloys system for biomedical applications, *Journal of Alloys and Compounds*, 812:152108. https://doi.org/10.1016/j.jallcom.2019.152108

Kushkhov, K B and Adamokova, M N, 2007. Electrodeposition of tungsten and molybdenum metals and their carbides from low-temperature halide-oxide melts, *Russian Journal of Electrochemistry (Translation of Elektrokhimiya)*, 43(9):997–1006. https://doi.org/10.1134/s1023193507090030

Kuznetsov, V V, Volkov, M A, Zhirukhin, D A and Filatova, E A, 2018. Electroreduction of Mo(VI) compounds in ammonium-acetate solutions, *Russian Journal of Electrochemistry (Translation of Elektrokhimiya)*, 54(11):1006–1011. https://doi.org/10.1134/s1023193518130256

Liu, S Y, Wang, L J, Chou, K C and Kumar, R V, 2019. Electrolytic preparation and characterization of VCr alloys in molten salt from vanadium slag, *Journal of Alloys and Compounds*, 803:875–881. https://doi.org/10.1016/j.jallcom.2019.06.366

Luo, L M, Zhou, Y F, Zhang, Y X, Zan, X, Liu, J Q, Zhu, X Y and Wu, Y C, 2019. Current status and development trend of toughening technology of molybdenum-based materials, *Chinese Journal of Nonferrous Metals*, 29(3):525–537. https://doi.org/10.19476/j.ysxb.1004.0609.2019.03.12

Lv, C, Jiao, H D, Li, S L, Che, Y S, Li, S X, Liu, C, He, J L and Song, J X, 2021a. Liquid zinc assisted electro-extraction of molybdenum, *Separation and Purification Technology*, 279:119651. https://doi.org/10.1016/j.seppur.2021.119651

Lv, C, Li, S L, Che, Y S, Chen, H T, Shu, Y C, He, J L and Song, J X, 2021b. Study on the molybdenum electro-extraction from MoS_2 in the molten salt, *Separation and Purification Technology*, 258:118048. https://doi.org/10.1016/j.seppur.2020.118048

Malyshev, V, Gab, A, Shakhnin, D, Donath, C, Neacsu, E I, Popescu, A M and Constantin, V, 2018. Influence of electrolysis parameters on mo and w coatings electrodeposited from tungstate, molybdate and tungstate-molybdate melts, *Revista de Chimie*, 69(9):2411–2415. https://doi.org/10.37358/rc.18.9.6544

Moon, J, Myhre, K, Andrews, H and McFarlane, J, 2022. Potential of electrolytic processes for recovery of molybdenum from molten salts for ^{99}Mo production, *Progress in Nuclear Energy*, 152:104369. https://doi.org/10.1016/j.pnucene.2022.104369

Morley, T J, Penner, L, Schaffer, P, Ruth, T J, Bénard, F and Asselin, E, 2012. The deposition of smooth metallic molybdenum from aqueous electrolytes containing molybdate ions, *Electrochemistry Communications*, 15(1):78–80. https://doi.org/10.1016/j.elecom.2011.11.026

Nakajima, H, Nohira, T and Hagiwara, R, 2006. Electrodeposition of metallic molybdenum films in $ZnCl_2$–NaCl–KCl–$MoCl_3$ systems at 250°C, *Electrochimica Acta*, 51(18):3776–3780. https://doi.org/10.1016/j.electacta.2005.10.041

O'Dea, J J, Osteryoung, J and Osteryoung, R A, 1981. Theory of square wave voltammetry for kinetic systems, *Analytical Chemistry*, 53(4):695–701. https://doi.org/10.1021/ac00227a028

Senderoff, S and Brenner, A, 1954. The electrolytic preparation of molybdenum from fused salts: I, Electrolytic studies, *Journal of the Electrochemical Society*, 101(1):16–17. https://doi.org/10.1149/1.2781198

Senderoff, S and Mellors, G, 1967. Electrodeposition of coherent deposits of refractory metals: V, Mechanism for the deposition of molybdenum from a chloride melt, *Journal of the Electrochemical Society*, 114(6):556. https://doi.org/https://10.1149/1.2426648

Song, Y, Jiao, S Q, Hu, L W and Guo, Z C, 2016. The cathodic behavior of Ti(III) ion in a NaCl-2CsCl melt, *Metallurgical and Materials Transactions B*: *Process Metallurgy and Materials Processing Science*, 47(1):804–810. https://doi.org/10.1007/s11663-015-0521-9

Tian, H X, Gang, Q J, Ying, Y, Xin, L, Jun, L T and Li J, 2023. Approaches to electrodeposit molybdenum from ionic liquid, *Rare Metals*, 42(7):2439–2446. https://doi.org/10.1007/s12598-018-1040-z

Tylka, M M, Willit, J L and Williamson, M A, 2017. Electrochemical nucleation and growth of uranium and plutonium from molten salts, *Journal of the Electrochemical Society*, 164(8):H5327–H5335. https://doi.org/10.1149/2.0471708jes

Yuan, R, Lv, C, Wan, H L, Li, S L, Che, Y S, Shu, Y C, He, J L and Song, J X, 2021. Electrochemical behavior of vanadium ions in molten LiCl-KCl, *Journal of Electroanalytical Chemistry*, 891:115259. https://doi.org/10.1016/j.jelechem.2021.115259

Zhang, H K, Li, S L, Lv, Z P, Fan, Y and Song, J X, 2023. The role of zinc sulfide in the electrochemical extraction of molybdenum, *Separation and Purification Technology*, 311:123290. https://doi.org/10.1016/j.seppur.2023.123290

Zhang, H K, Lv, Z P, Li, S L, He, J L, Fan, Y and Song, J X, 2024. Electrochemical behavior and cathodic nucleation mechanism of molybdenum ions in NaCl-KCl, *Separation and Purification Technology*, 329:125121. https://doi.org/10.1016/j.seppur.2023.125121

Development of solid waste-based flux and its application in out-of-furnace dephosphorisation of low-silicon hot metal

DOI: 10.62053/DSNX3459

Z Zhao[1] and Y Zhang[2]

1. Phd Student, University of Science and Technology Beijing, Haidian District, Beijing 100083, China. Email: suc_zheng@163.com
2. Professor, University of Science and Technology Beijing, Haidian District, Beijing 100083, China. Email: ustbzly1108@163.com

ABSTRACT

The green production of the steelmaking process has urgent requirements for fluorine-free fluxes. In this article, a new solid waste-based slagging flux was applied in the external dephosphorisation test of low silicon hot metal to replace the traditional fluorite-lime dephosphorisation slag. The results showed that under laboratory conditions, the new flux was utilised for smelting low-silicon molten iron with a phosphorus content of 0.10~0.13 wt per cent, the temperature of the molten iron was 1350°C and the slag amount was controlled at 2 per cent. Within ten minutes of smelting, the dephosphorisation rate of the molten iron reached more than 50 per cent. When making slag with new flux, the slag melting time was about 40 seconds and the P_2O_5 content in the final slag was higher than 8 wt per cent. In the industrial test of a 150 t molten iron ladle, under the same molten iron conditions, an out-of-furnace dephosphorisation test was conducted in the Kambara Reactor (KR) process. The flux material consumption per ton of steel was 8~10 kg. Within 15 minutes of smelting, the dephosphorisation rate of the molten iron was about 30 per cent. During flux slag making, the slag melting time was about three minutes and the P_2O_5 content in the final slag was higher than 6 wt per cent. This new solid waste-based flux has significant cost advantages and out-of-furnace dephosphorisation effects and is expected to become the benchmark for a new generation of fluorine-free steelmaking fluxes.

INTRODUCTION

The pre-dephosphorisation process in molten iron significantly reduces converter slag emissions, offering notable advantages in smelting high-quality low-phosphorus steel. Additionally, it can lower the production costs of converter steelmaking, enhance production efficiency and allow for a modest relaxation of phosphorus content in blast furnace ores, demonstrating important practical significance (Gao *et al*, 2013; Li *et al*, 2014; Wu *et al*, 2020; Bai *et al*, 2020).

The lower temperature and higher phosphorus activity coefficient in the pre-treatment phase of molten iron are thermodynamically favourable for phosphorus removal, particularly in low-silicon conditions. However, insufficient heat and challenges in slag formation constrain the kinetic conditions for phosphorus removal (Li, Zhang and Guo, 2017; Gupta *et al*, 2023). Low-silicon molten iron can achieve desulfurisation through the KR process while also facilitating off-furnace phosphorus removal. However, off-furnace phosphorus removal processes typically employ fluorine or sodium-containing fluxes, resulting in multiple temperature drops, challenging operational procedures and causing environmental pollution. Few enterprises in China adopt this process (Kitamura *et al*, 2002; Zhou *et al*, 2017), highlighting the crucial importance of developing fluorine-free, low-melting-point fluxes.

Calcium ferrite, an excellent fluorine-free flux, possesses a low melting point and has the ability to quickly form a primary dephosphorisation slag with high oxidation and high alkalinity. Wright *et al* (2001) and Sukenaga *et al*, (2010) found the viscosity of the 19 wt per cent CaO–81 wt per cent FeO_X slag system to be 0.065 Pa·s, significantly lower than the 2.4 Pa·s of the $CaO\text{-}SiO_2\text{-}MgO\text{-}Al_2O_3$ slag system. A slag system with good fluidity can promote the transfer of phosphorus into the molten slag. Jeon, Jung and Sasaki (2010) and Paananen *et al* (2010) had investigated the formation mechanism of calcium ferrite. They had discovered that the reaction rate of Fe_3O_4 and CaO to form $Ca_2Fe_2O_5$ is faster than the reaction of Fe_2O_3 and CaO and that the higher the oxygen partial pressure, the slower the formation rate. This research has provided valuable insights into the formation of calcium ferrite and its influencing factors. Sayama *et al* (2002) and Lee and Barr (2002)

examined the mechanism and effect of calcium ferrite flux on lime melting. When the surface layer of lime had been coated with iron oxide, compared with the uncoated sample, more low-melting point calcium ferrite phases had been formed, which had reduced the mechanical properties of the lime and had been more easily dissolved and absorbed in steelmaking slag. Sato, Nakashima and Mori (2001) conducted high-carbon hot metal dephosphorisation experiments using three calcium ferrite fluxes: $CaO{\cdot}Fe_2O_3$(CF), $2CaO{\cdot}Fe_2O_3$(C2F), and $3CaO{\cdot}Fe_2O_3$(C3F). Results had indicated that C2F and C3F, with a higher CaO concentration in the flux, had higher dephosphorisation rates, while the decarburisation reaction had been inhibited. However, due to the higher melting points of C2F and C3F, their dephosphorisation rates had been slower than that of CF. Mi *et al* (1999) investigated the dephosphorisation behaviour of mechanically synthesised calcium ferrite under molten iron conditions of 1300°C. When 20 per cent of the $CaFe_2O_4$ content had replaced part of the CaF_2 and Fe_2O_3, it had resulted in an increase in the alkalinity of the slag and an improvement in its oxidation property. This had led to a dephosphorisation rate of 88.6 per cent, which had been higher than the 79.3 per cent dephosphorisation rate achieved when only adding CaF_2 flux slag. Wu *et al* (2022) conducted industrial experimental research on the dephosphorisation of hot metal using calcium ferrite synthesised from iron oxide scale and lime. Results had demonstrated that calcium ferrite had reduced the slag-making melting temperature in the early stage of the converter and had increased the slag discharge amount in the double-slag process. When slagging had been performed with calcium ferrite, the average dephosphorisation rate of hot metal had been 88.06 per cent and the average melting temperature had been 1137°C. These values had been superior to the 77.7 per cent dephosphorisation rate and 1296°C slag melting temperature that had been observed when slagging with fluorite. The aforementioned research findings suggest that calcium ferrite-based slag may emerge as the optimal flux to replace fluorite, yielding favourable outcomes in dephosphorisation and slagging. Indeed, the majority of calcium ferrite slag products are manufactured using iron concentrate powder as a primary ingredient. The high temperatures required for processing contribute to substantial costs. These factors can pose significant challenges to the large-scale application of these products.

Based on a new low-melting-point solid waste-based slagging flux, this study proposed a process concept for implementing outside-furnace dephosphorisation of low-silicon hot metal using the Kambara Reactor (KR) process. Dephosphorisation tests were carried out under laboratory conditions and 150 t-level industrial test conditions, and the key factors affecting the dephosphorisation effect were clarified, such as flux melting time, flux addition amount, phosphorus distribution and phosphorus content in the final slag. This further verified the huge advantages of the new flux in reducing production costs and improving the dephosphorisation effect of molten iron, thereby providing an important basis for industrial application.

DEVELOPMENT OF SOLID WASTE-BASED FLUXES – MINERAL COMPOSITION AND MELTING PROPERTIES

Among many pre-melted fluxes, calcium ferrite was an important slagging material due to its low melting point and its content of calcium oxide and iron oxide. In foreign countries, it was widely used in the hot metal dephosphorisation process, but there were few application research reports in China. The then-current standard YBT-4266-2011 showed the physical and chemical indicators of pre-melted calcium ferrite CF-55 for metallurgical use in Table 1. This study used an industrial solid waste (bayer red mud) produced by the aluminium industry to prepare a new type of flux. The specific preparation method referred to the authorised international invention patent (Zhang *et al*, 2023) that our team had obtained. Its composition was shown in Table 1. According to the $CaO\text{-}Fe_2O_3$ binary phase diagram (Figure 1a), the melting point of calcium ferrite ($CaO{\cdot}Fe_2O_3$) was about 1216°C. According to the $CaO\text{-}Fe_2O_3\text{-}Al_2O_3$ ternary phase diagram (Figure 1b), since Al^{3+} and Fe^{3+} had similar electrical properties, they were easily replaced by Al^{3+}.The melting point of composite calcium ferrite, $Ca(Al, Fe)_2O_4$, was about 1142°C.

TABLE 1

Physical and chemical indicators of pre-melted calcium ferrite and composition of solid waste-based flux (wt%).

Item	Fe_2O_3	CaO	SiO_2	MgO	Al_2O_3	TiO_2	Na_2O	P	S	density
CF-55	55~60	30~35	0~4	0~6	-	-	-	0.10	0.10	3.2 g/cm^3
SW-Flux	50.74	29.46	2.45	0.51	10.29	3.46	1.38	0.12	0.08	3.5 g/cm^3

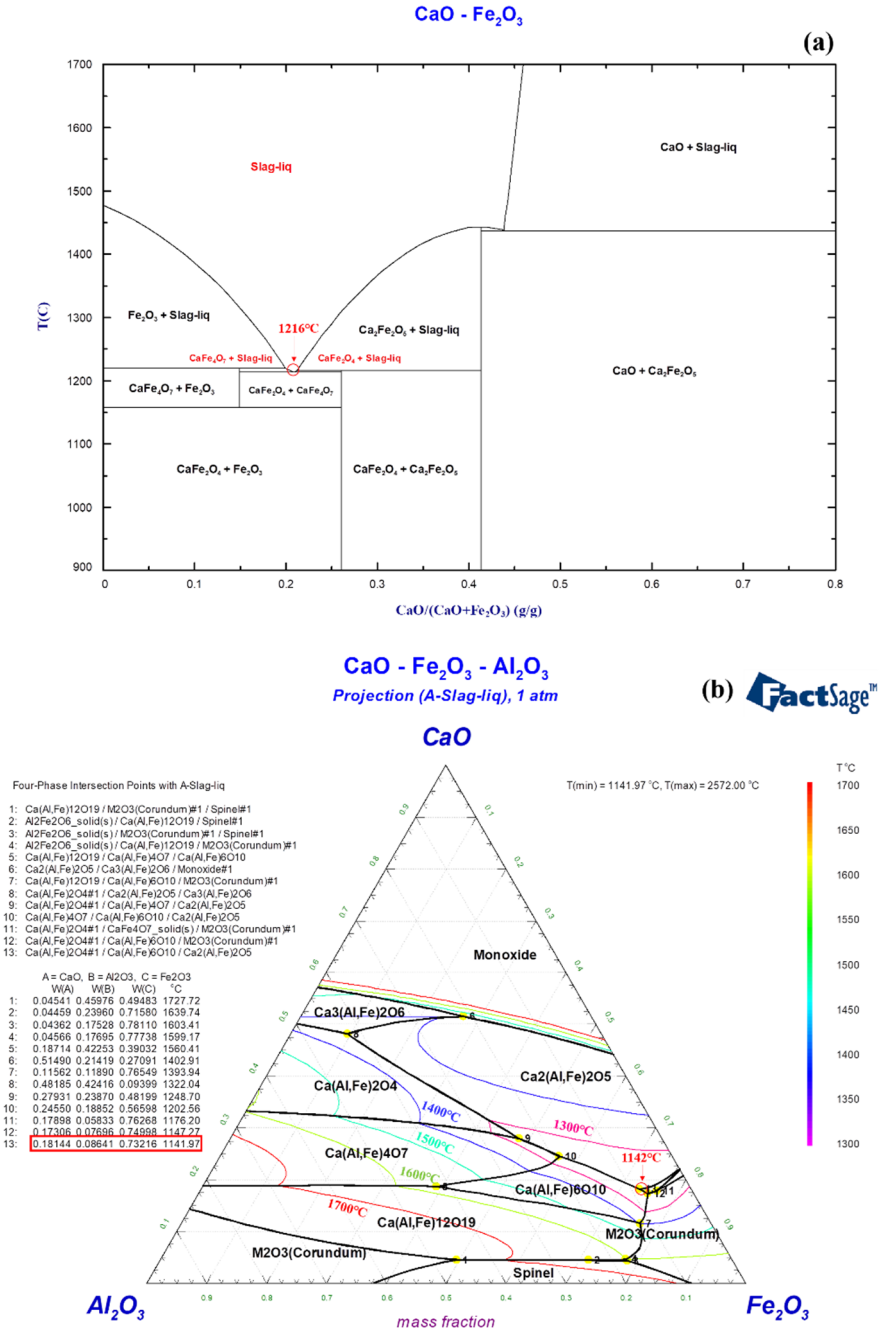

FIG 1 – (a) Preparation principle of flux: CaO-Fe_2O_3; and (b) CaO-Fe_2O_3-Al_2O_3 phase diagrams.

The two fluxes CF-55 and SW-Flux were prepared under laboratory conditions, as shown in Figure 2a. The main phases of CF-55 were $CaFe_2O_4$ and $Ca_2Fe_2O_5$, which were low melting point phases. The main phases in SW-Flux flux were $CaFe_2O_4$, $Ca_2Fe_2O_5$ and $Ca_2(Fe,Al)_2O_5$. It could be seen from the above components and phase characteristics that CF-55 flux had a lower melting point, was oxidising and could increase alkalinity. Industrially, calcium ferrite was usually obtained by pre-melting and cooling iron ore powder with lime and the preparation cost was high. In addition

to the calcium ferrite mineral phase, SW-Flux flux also had a calcium aluminoferrite mineral phase, which had a lower melting point, high oxidation and high alkalinity. This made SW-Flux flux possess the characteristics of calcium ferrite and could significantly reduce the preparation cost.

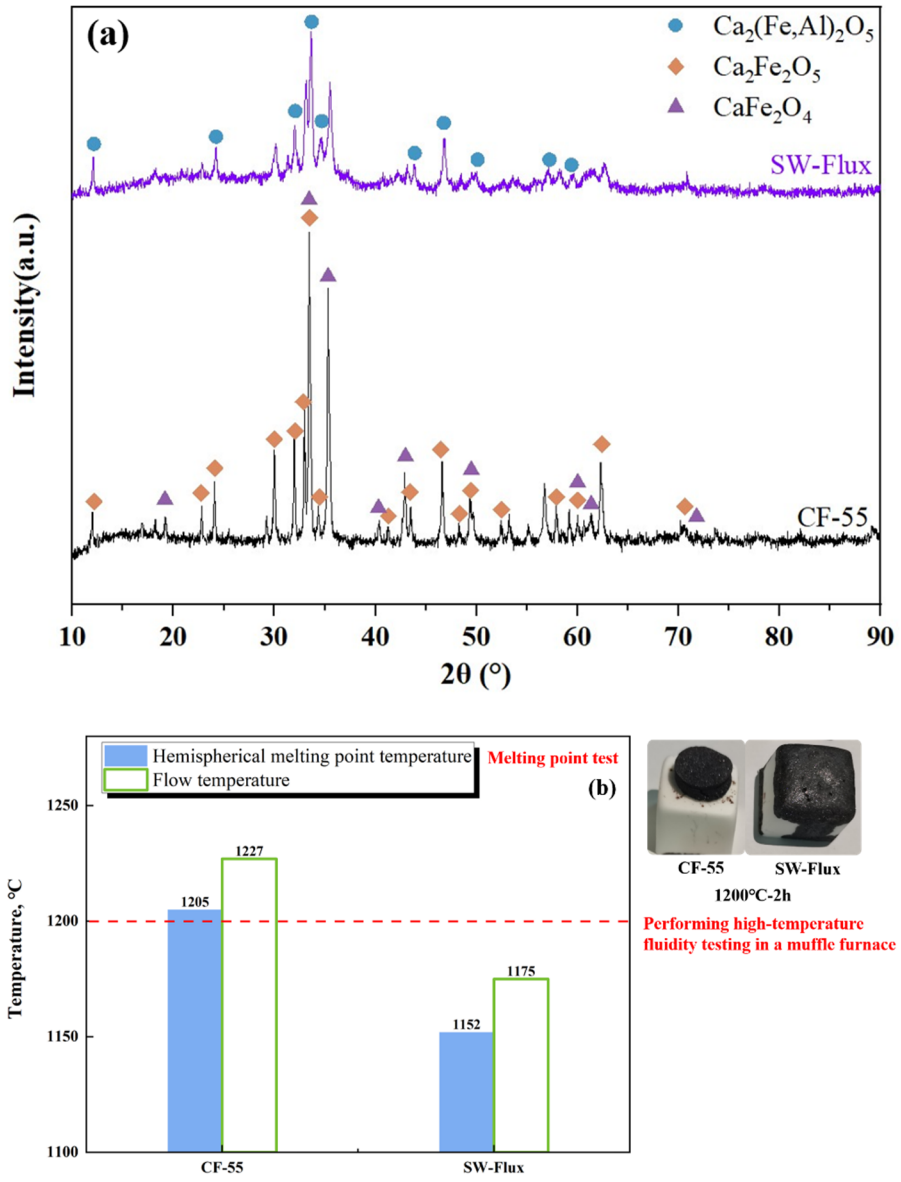

FIG 2 – (a) The XRD pattern; (b) and melting properties of flux.

As depicted in Figure 2b, the melting point test result of the flux indicates that the SW-Flux flux possesses a lower hemispheric softening point temperature and flow temperature, which are 1152°C and 1175°C respectively. These temperatures are much lower than 1300°C, sufficient to meet the temperature requirements of the desiliconisation and dephosphorisation process of molten iron (1300~1400°C), ensuring quick slag formation. The flux was placed on the refractory material and its high-temperature fluidity was tested in a muffle furnace. After being maintained at the same temperature of 1200°C for two hours, CF-55 exhibited significant shrinkage, a slight slump, and a sintered appearance. SW-Flux melted into a fluid state.

APPLICATION OF SOLID WASTE-BASED FLUX IN DEPHOSPHORISATION OF LOW SILICON MOLTEN IRON

According to the above research, the newly developed flux derived from solid waste exhibits a low melting point, high alkalinity and elevated oxidation levels. In Japanese steel companies, industrial calcium ferrite flux has been utilised as a slagging material in the production of low-phosphorus or ultra-low-phosphorus steel. The new flux studied in this study was used as a dephosphorisation

agent in the laboratory stage and in 150 t-level KR industrial tests, providing a basis for its application.

Equipment and methods

The laboratory dephosphorisation test was conducted in a vertical high-temperature $MoSi_2$ furnace, as shown in Figure 3. During the entire experiment, argon gas (99.9 per cent purity) was introduced from the top of the shaft furnace to prevent oxidation of the molten iron and maintain a relatively stable oxygen partial pressure and atmosphere. The pig iron used in the test was prepared from industrial pure iron (Fe 99.9 wt per cent), phosphorus iron (P 21.5 wt per cent) and sulfur iron (S 32.5 wt per cent). The composition is shown in Table 2.

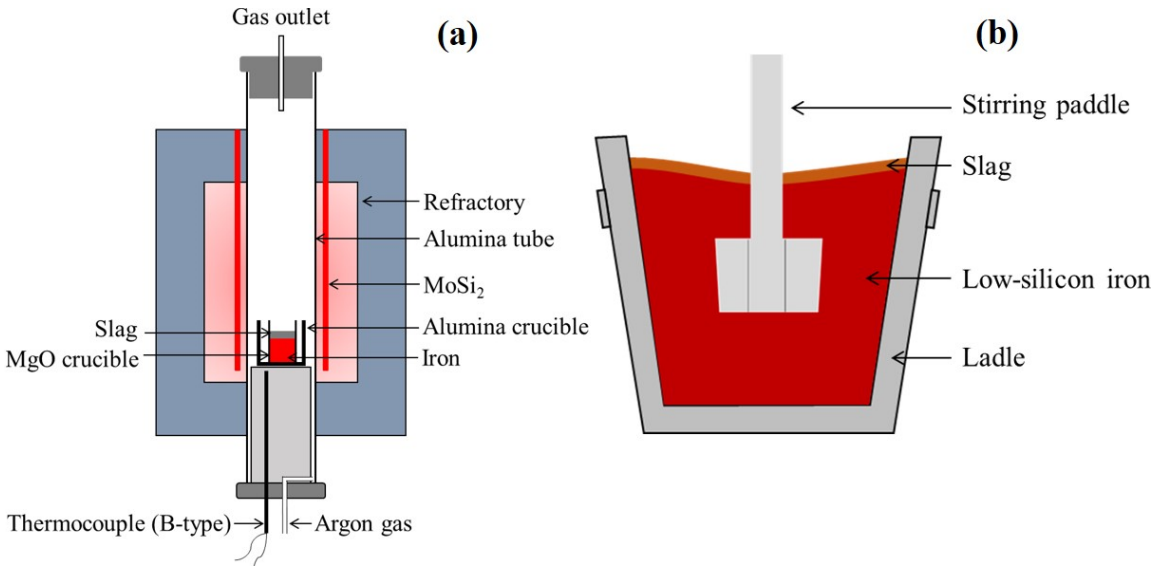

FIG 3 – (a) Laboratory; and (b) 150 t KR industrial test equipment.

TABLE 2

Semi-steel composition (wt%).

C	P	S	Si	Mn
3.8~4.0	0.10~0.13	0.04~0.06	0.01~0.10	0.01~0.05

First, the raw materials were put into a MgO crucible (D45 × H110 mm) and heated from room temperature to 300°C at a rate of 25°C/min, and then heated to 1350°C at a rate of 8°C/min. After the sample was kept at 1350°C for 20 minutes, dephosphorisation slag with a weight of 2 per cent of the molten iron was added to the surface of about 600 g of molten iron. In the test, refractory Al_2O_3 rods were used for stirring. After the slag gold reacted for a certain period of time, a high-purity quartz tube was used to take a molten iron sample. After the test, the crucible containing the quenched sample was put into the oven to completely dry the water and the slag and pig iron blocks were physically separated for further analysis. The experimental plan is shown in Table 3.

TABLE 3

Experimental programme (wt%).

No. 1	(Si)	(P)	Slag ratio	Stirring
1	0.01	0.11	2%	Without
2	0.01	0.13	2%	Yes
3	0.10	0.13	2%	Yes

The industrial test of dephosphorisation outside the furnace was conducted in the KR process. The capacity of the molten iron ladle is 150 t, the loading amount of low silicon molten iron is 142 t, the size of the molten iron ladle is H5200 × Φ3300 mm, the stirring paddle size of the KR process is H820 mm × L1100 mm, the rotation speed can be adjusted in the range of 10~90 rev/min and the stirring depth is fixed at 0.5 m. The molten iron composition was similar to the above and the temperature was 1260–1360°C. The specific experimental method involved opening the molten iron ladle to the desulfurisation position to perform desulfurisation operations first, and then removing the slag and taking samples after desulfurisation was completed. At the beginning of the dephosphorisation process outside the furnace, 15 per cent to 20 per cent dephosphorisation flux was added. 30 per cent to 40 per cent dephosphorisation flux was added while lowering the stirring paddle. After stirring started, the remaining dephosphorisation flux was added in batches for a total of two minutes. A low speed of 30~50 rev/min was used initially and then switched to a high speed of 70~90 rev/min. The duration of the mixing process was about 15 minutes. After the dephosphorisation process outside the furnace was completed, slag samples and metal samples were taken respectively, and the dephosphorisation slag was then removed and entered into the converter smelting process.

Analysis and testing

The sample analysis of laboratory tests and industrial tests is conducted using the same testing methods and instruments. The slag is ground to a size of less than 200 mesh for composition testing. Weigh out 0.1 g of scraps from the pig iron block and use 3 mL HCl and 1 mL HNO_3 in a Teflon test tube to completely digest it in a 45°C water bath. Examination was conducted by inductively coupled plasma mass spectrometry to determine the content of (P). The slag sample was ground to a size of less than 80 μm and the slag composition was analysed using X-ray fluorescence spectroscopy.

Experimental results and analysis

As depicted in Figures 4a and 4c, under laboratory conditions, a new flux was used to smelt low-silicon molten iron with a (P) content of 0.10~0.13 wt per cent. No. 1–No. 3 respectively simulated the pretreatment dephosphorisation of the flux in the molten iron ladle, the dephosphorisation of the flux outside the furnace during the KR stirring process and the KR stirring dephosphorisation under low silicon conditions. The (Si) content of No. 1 was extremely low. Without stirring, the slagging time was 40 seconds and the dephosphorisation rate was 57.3 per cent. No. 2 was under the same conditions as No. 1 molten iron (Si), but the stirring process was added. The slagging time of No. 2 was about 32 seconds and the dephosphorisation rate was 52.3 per cent. Stirring could shorten the slag removal time, but the dephosphorisation rate decreased slightly. The main reason is that there was a certain slag layer at the contact end of the Al_2O_3 refractory material during stirring, which reduced the amount of slag participating in the reaction and reduced the dephosphorisation effect. The (Si) of No. 3 was 0.10 wt per cent, the slagging time was about 29 seconds and the dephosphorisation rate was 28.5 per cent. When there was a small amount of (Si) in the molten iron, there was competition between (Si) removal and (P) removal. (Si) removal consumed the oxidant in the flux. At the same time, the amount of slag was too small, which had a more significant impact on dephosphorisation. It was worth noting that the C-O reaction was inhibited at this temperature and the main source of oxidant consumption was desiliconisation and dephosphorisation.

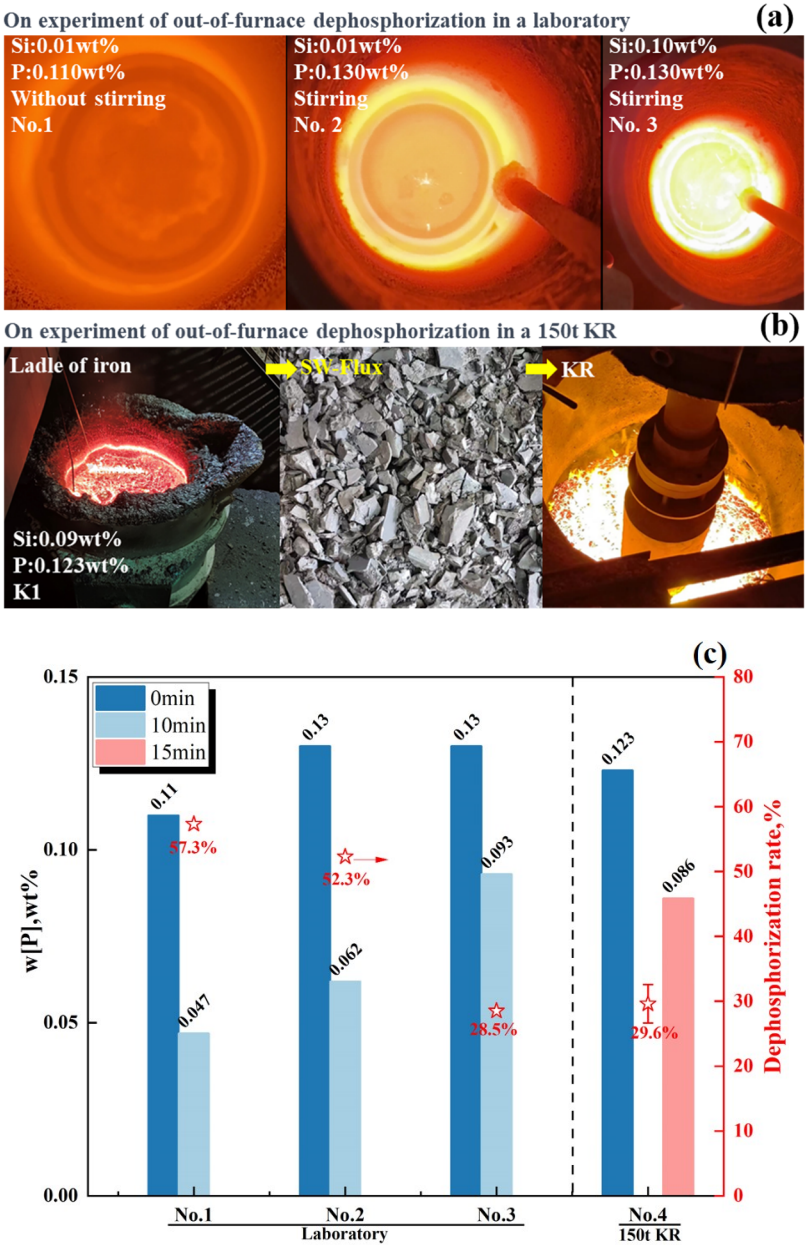

FIG 4 – (a) Simulation of out-of-furnace dephosphorisation in the laboratory; (b) on experiment of out-of-furnace dephosphorisation in a 150t KR; and (c) w(P) content and dephosphorisation rate in the experiments.

As depicted in Figures 4b and 4c, an out-of-furnace dephosphorisation experiment was conducted in a 150 t KR using solid waste-based flux as the slagging material. The test was performed for a total of five heats. When smelting low-silicon molten iron with (P) content of 0.10~0.13 wt per cent and (Si) content of 0.08~0.10 wt per cent, the average flux slagging material consumption was 10 kg/t iron and the average dephosphorisation rate of the molten iron was 29.6 per cent. The flux was added to KR and stirred. The material would completely melt in about 3 minutes and 40 seconds. The chemical composition of the slag at the end of the laboratory and 150 t KR out-of-furnace dephosphorisation industrial trials is depicted in Table 4.

TABLE 4

Final slag composition (wt%).

No.	SiO_2	CaO	MgO	Al_2O_3	Fe_2O_3	TiO_2	MnO	P_2O_5
1	2.92	32.60	2.92	12.40	25.10	3.28	-	8.26
4	16.71	36.22	1.54	8.69	27.67	4.03	4.52	6.73

As can be seen from Table 4, under extremely low silicon conditions, Group No. 1 could still maintain a high final slag alkalinity (CaO per cent/SiO_2 per cent) = 11.2 and the (P_2O_5) content in the slag was 8.26 per cent. In contrast, under low silicon molten iron conditions, Group No. 4 had a smaller amount of slag. The silicon oxide, which oxidised into the slag, reduced the final slag alkalinity to (CaO per cent/SiO_2 per cent) = 2.17 and the (P_2O_5) content in the slag was 6.73 per cent.

Analysis of economic benefits

Firstly, the application of the flux in steelmaking introduces very few harmful impurity elements (P, S), eliminating the need to consider the additional cost of removing these newly introduced impurities. Secondly, red mud, a solid waste product of the aluminium industry, serves as a highly useful and low-cost feedstock for steel production. Therefore, the new pre-melting fluxes can offer significant advantages over the use of commercial calcium ferrate and CaF_2, as demonstrated in Table 5 (Ban-Ya *et al*, 1989; Wu *et al*, 2022).

TABLE 5

Advantages of new pre-melted fluxes.

BOF smelting process	Hot metal pretreatment process	Hot metal pretreatment process	Effect of process improvement
CaF_2, cost USD205/t	Commercial calcium ferrate, cost USD310/t	Solid waste-based calcium ferrate, cost USD211/t	Reduction of raw material cost
Slag forming time is about 5~6 min	Slag forming time is about 5~6 min	Slag forming time is about 3~4 min	Reduction of smelting time
2~5 kg/t iron	40 kg/t iron, dephosphorisation rate >80%	20 kg/t iron, dephosphorisation rate is 50~60%	Better dephosphorisation
Iron-free raw materials	Recycling of high-priced iron-containing raw materials	Recycling of low-priced iron-containing raw materials	Increased revenue
Need to control hot metal (P) stabilisation	Able to cope with fluctuations in hot metal (P)	Able to cope with fluctuations in hot metal (P)	Appropriately relax the requirements for hot metal (P)

In terms of process, by adopting a KR-like dephosphorisation method outside the furnace, SW-Flux can replace CF-55. Currently, the price of CF-55 is USD310/t, while the cost of SW-Flux is estimated to be USD211/t. Given the addition of 20 kg/t iron, the dephosphorisation rate of iron can be between 50 per cent and 60 per cent and the cost can be reduced by USD1.98/t. Assuming that the dephosphorisation process is adopted in the BOF furnace, the SW-Flux can be used as a substitute for CaF_2, serving as a non-fluorine steelmaking flux. At present, the price of fluorite is USD205/t and the cost is about USD0.62/t for the addition of 3 kg/t iron. For the same dephosphorisation effect, the cost of pre-melting flux is about USD1.27/t for the addition of 6 kg/t iron and the cost of dephosphorisation of molten iron only increases by USD0.65/t. Therefore, this study suggests that the utilisation of this melt is more beneficial in terms of dephosphorisation efficiency and cost and it is entirely viable to substitute fluorite and costly commercial calcium ferrate.

In practical application, using the full amount of calcium ferrate as a flux for out-of-furnace dephosphorisation is suitable for the smelting of high-quality steel grades with ultra-low phosphorus steel. It can also replace fluorite in BOF smelting to reduce the environmental threat of fluorine-containing melts.

CONCLUSIONS

- The flux was prepared from industrial solid waste and primarily consisted of $CaFe_2O_4$, $Ca_2Fe_2O_5$ and $Ca_2(Fe,Al)_2O_5$. These mineral phases were referred to as complex calcium ferrite phases. These phases exhibited low melting points, high oxidising properties and high alkalinity.
- This flux was utilised as a dephosphorisation slagging material. Under laboratory conditions, the phosphorus content of the smelted low-silicon molten iron was 0.10~0.13 wt per cent. The temperature of the molten iron reached 1350°C and the slag amount was controlled at 2 per cent. Within ten minutes of smelting, the dephosphorisation rate of the molten iron exceeded 50 per cent. When making slag with new flux, the slag melting time approximated 40 seconds and the P_2O_5 content in the final slag exceeded 8 wt per cent.
- An industrial test of 150 t hot metal ladle was conducted. Under the same hot metal conditions, an out-of-furnace dephosphorisation test was performed in the KR process. The flux material consumption for per ton of steel was 8~10 kg. Within 15 minutes of smelting, the dephosphorisation rate of the hot metal approximated 30 per cent. During flux slag making, the slag melting time approximates 3 minutes and 40 seconds and the P_2O_5 content in the final slag exceeds 6 wt per cent.
- In the development of steelmaking technology, this new solid waste-based flux possesses significant cost advantages and out-of-furnace dephosphorisation effects. It is anticipated to represent a new generation of fluorine-free steelmaking flux and possesses extremely high promotion and application value.

ACKNOWLEDGEMENTS

This work was supported by the National Key R&D Program of China (2019YFC1905701), the National Natural Science Foundation of China (U1960201).

REFERENCES

Bai, X, Sun, Y, Luo, L and Zhao C, 2020. Effect of direct charging of hot recycled slag on hot metal pretreatment dephosphorization in a dephosphorization furnace, *Journal of Iron and Steel Research International*, 27:148–159. https://doi.org/10.1007/s42243-019-00296-w.

Ban-Ya, S, Hino, M, Nagabayashi, R and Terayama, O, 1989. Dephosphorization and Desulphurization of Hot Metal with CaO-Al_2O_3-FexOyFlux, *Tetsu-to-Hagané*, 75(1):66–73. https://doi.org/10.2355/tetsutohagane1955.75.1_66.

Gao, X, Matsuura, H, Miyata, M and Tsukihashi, F, 2013. Phase Equilibrium for the CaO–SiO_2–FeO–5mass%P_2O_5–5mass%Al_2O_3 System for Dephosphorization of Hot Metal Pretreatment, *ISIJ International*, 53(8):1381–1385. https://doi.org/10.2355/isijinternational.53.1381.

Gupta, P, Kumar, S, Babu, J H, Mali, G S and Roy, T K, 2023. Production of low phosphorous steel from low silicon high phosphorous hot metal in BOF, *Ironmaking and Steelmaking*, 50:1014–1021. https://doi.org/10.1080/03019233.2023.2173877.

Jeon, J-W, Jung, S-M and Sasaki, Y, 2010. Formation of Calcium Ferrites under Controlled Oxygen Potentials at 1273 K, *ISIJ International*, 50:1064–1070. https://doi.org/10.2355/isijinternational.50.1064.

Kitamura, S-Y, Yonezawa, K, Ogawa, Y and Sasaki, N, 2002. Improvement of reaction efficiency in hot metal dephosphorization, *Ironmaking and Steelmaking*, 29:121–124. https://doi.org/10.1179/030192302225004070.

Lee, M S and Barr, P V, 2002. Production and properties of burnt lime coated with dicalcium ferrite, *Ironmaking and Steelmaking*, 29(2):96–100. https://doi.org/10.1179/030192302225001983.

Li, F, Zhang, Y and Guo, Z, 2017. Pilot-Scale Test of Dephosphorization in Steelmaking Using Red Mud-Based Flux, JOM, 69:1624–1631. https://doi.org/10.1007/s11837-017-2449-9.

Li, J, Wang, S-J, Xia, Y-J and Kong, H, 2014. Study on dephosphorization of hot metal pretreatment with Al_2O_3 to replace CaF2 in slag, *Ironmaking and Steelmaking*, 42(1):70–73. https://doi.org/10.1179/1743281214y.0000000213.

Mi, G, Murakami, Y, Shindo, D, Saito, F, Shimme, K and Masuda, S, 1999. Mechanochemical Synthesis of Calcium Ferrite by a Planetary Mill and Its Dephosphorization Characteristic from Molten Iron, *Shigen-to-Sozai: Journal of the Mining and Materials Processing Institute of Japan*, 115(9):683–687. https://doi.org/10.2473/shigentosozai.115.683.

Paananen, T, Heikkinen, E, Kokkonen, T and Kinnunen, K, 2010. Preparation of mono-, di- and hemicalcium ferrite phases via melt for reduction kinetics investigations, *Steel Research International*, 80(6):402–407. https://doi.org/10.2374/sri09sp016.

Sato, T, Nakashima, K and Mori, K, 2001. Dephosphorization rate of high carbon iron melts by CaO-based slags, *Tetsu-to-Hagané*, 87:643–649. https://doi.org/10.2355/tetsutohagane1955.87.10_643.

Sayama, H, Tanaka, S, Ito, M and Machinaga, O, 2002. Calcination process of limestone coated with iron oxide and aluminum oxide, *J Soc Inorg Mat*, 9:218–223.

Sukenaga, S, Gonda, Y, Yoshimura, S, Saito, N and Nakashima, K, 2010. Viscosity Measurement of Calcium Ferrite Based Slags during Structural Relaxation Process, *ISIJ International*, 50(2):195–199. https://doi.org/10.2355/isijinternational.50.195.

Wright, S, Zhang, L, Sun, S and Jahanshahi, S, 2001. Viscosities of calcium ferrite slags and calcium alumino-silicate slags containing spinel particles, *Journal of Non-Crystalline Solids*, 282(1):15–23. https://doi.org/10.1016/S0022-3093(01)00324-6.

Wu, W, Yang, Q, Gao, Q and Zeng, J, 2020. Effects of calcium ferrite slag on dephosphorization of hot metal during pretreatment in the BOF converter, *Journal of Materials Research and Technology*, 9(3):2754–2761. https://doi.org/10.1016/j.jmrt.2020.01.009.

Wu, W, Zhao, B, Zhao, B and Meng, H-D, 2022. Hot metal dephosphorization process using calcium ferrite slag without fluorite, *Ironmaking and Steelmaking*, 49(7):661–668. https://doi.org/10.1080/03019233.2022.2037040.

Zhang, Y, Zhao, Z, Zhang, W, Yu, K and Zhang, Y, 2023. Red Mud-Based Composite Calcium Ferrite and Preparation Method and use Thereof, United States Patent US11773025B2.

Zhou, J, Bi, X, Yue, R and Yang, F, 2017. Phosphorus Distribution Ratio between Multi Phase CaO–FeOt–SiO_2–P_2O_5 (6%–13%) Slags with MP Near Hot Metal Temperature and C-saturated Molten Iron at 1573 K, *ISIJ International*, 57(4):706–712. https://doi.org/10.2355/isijinternational.isijint-2016-592.

Analysis on composition and physico-chemical property change of PbO-bearing slag in Pb smelting

DOI: 10.62053/YQJS8628

J X Zhao[1], Y R Cui[2], G Cao[2], G H Wang[2], B Li[2], M M Ren[2], Z M Wang[3] and H P Gui[3]

1. School of Metallurgical Engineering, Xian University of Architecture and Technology, Xian, Shaanxi 710055, China. Email: zhaojunxue1962@126.com
2. School of Metallurgical Engineering, Xian University of Architecture and Technology, Xian, Shaanxi 710055, China.
3. Hanzhong Zinc Co. LTD, Hanzhong, Shaanxi 724200, China.

ABSTRACT

Pyro-metallurgy is still the main process for lead production and a lot of lead direct smelting processes have been developed in recent years. All the processes will experience two steps in common. The first is the oxidisation of PbS to PbO and then reduction from PbO to Pb, furthermore, from ZnO to Zn. So, the composition of melts, especially the slag composition at reduction step change continuously. Up to now, there are few systematic results on the slag physical-chemical properties with its composition change. In this work, the typical lead direct smelting processes were analysed from theoretical and practical standpoints. The full-period slag composition and slag melting point change were compared. Especially, to the PbO and ZnO reduction steps, based on the full-period slag composition change, the slag properties were predicted. Based on dust composition and test results, the mechanism of Pb compound evaporation and its effect on practice and measurement of high PbO bearing slag physical-chemical property is discussed. It is suggested that to restrain the evaporation in practice and to obtain more accurate measurement results of physicochemical properties of smelting slag are the key problem not only to set high efficiency, energy saving process, but also to environmental pollution control.

INTRODUCTION

Up to now, pyro-metallurgy is still the main route for lead production. At earlier stage, sintering and blast furnace was used with galena concentrate as raw material. Since the 1970s a lot of direct reduction processes have been developed, such as QSL (Queneau and Siegmund, 1996), SKS (Zhang, 2013), Kivcet process (Slobodkin, Sannikov and Grinin, 2013), Ausmelt/ISAsmelt (Wang, Zhou and Feng, 2004), Kaldo, bottom blowing/side submerged blowing and so on (Li, Yang and Cheng, 2011; Cui, Li and He, 2013; Chen, Yang and Bin, 2014a; Chen, Hao and Yang, 2015). At the beginning, blast furnace is widely used to reduce the higher PbO-content slag from upstream smelter, such as SKS process, Ausmelt/ISA smelter (Queneau and Siegmund, 1996; Zhang, 2013; Wang, Zhou and Feng, 2004; Wang and Chen, 2016), and then it is being gradually replaced by other oxygen-enriched blowing smelters.

In all these processes, two steps are experienced, that is oxidation first and then reduction. In the oxidising smelting step, Pb sulfide concentrate is oxidised and melted. Some molten lead is formed and slag with high-PbO concentration produced concurrently. In the reduction step, slag with high-PbO concentration is reduced with coal, semicoke or natural gas as reductant (Chen, Yang and Liu, 2014b; Li, Zhan and Fan, 2017; Zhang, Li and Zhan, 2018; Yang, Cui and Hao, 2020), such as Kivcet/flash smelting process (Jiang, Li and Guo, 2018). To recover the Zn in the reduction slag, further reduction is necessary sometimes. To keep the process working at high temperature, oxygen enriched blowing is widely adopted.

In recent years, the triple-furnace system of molten high-lead slag direct reduction smelting applied in the metallurgical industry in China (Slobodkin, Sannikov and Grinin, 2013; Wang and Chen, 2016). Bottom blowing furnace or side submerged blowing furnace is used as oxidising smelter or reduction furnace respectively (Li, Yang and Cheng, 2011; Chen, Yang and Liu, 2014b; Li, Zhan and Fan, 2017; Zhang, Li and Zhan, 2018). In addition, fuming furnace is used for further reduction and ie ZnO recovery (Li, Zhan and Fan, 2017; Zhang, Li and Zhan, 2018). In these processes, the slag with high PbO, ZnO bearing slag or melt is involved.

Generally, the oxidising step is a continuous process, PbS concentrate is added with oxygen blowing, and PbO (with some molten Pb) formed until it accumulated up to tapped. The reduction step is a batch process, reducing reaction with C or natural gas as reductant to the slag formed until the high-PbO bearing slag changes to the low-PbO bearing slag (contains about 2.5 per cent Pb) and molten Pb forms at the same time, and then high-ZnO bearing slag changes to the low-ZnO bearing slag. So, the composition of melts, especially the slag composition at reduction step will changes continuously. Up to now, there are few reports on the slag physical-chemical properties with its composition change systematically (Huang, Zhang and Cheng, 2021; Cui, Guo and Chen, 2016; Jak and Hayes, 2002). In this paper, we will try to draw up the relationship between slag composition and physico-chemical property change in whole process.

BASIC REACTION AND TYPICAL SLAG FORMING AND COMPOSITION CHANGE

Basic reaction

To take the typical direct reduction process as example (as shown in Figure 1), the process can be divided into three steps, ie oxidisation smelting, PbO reduction and further reduction for Zn recovery.

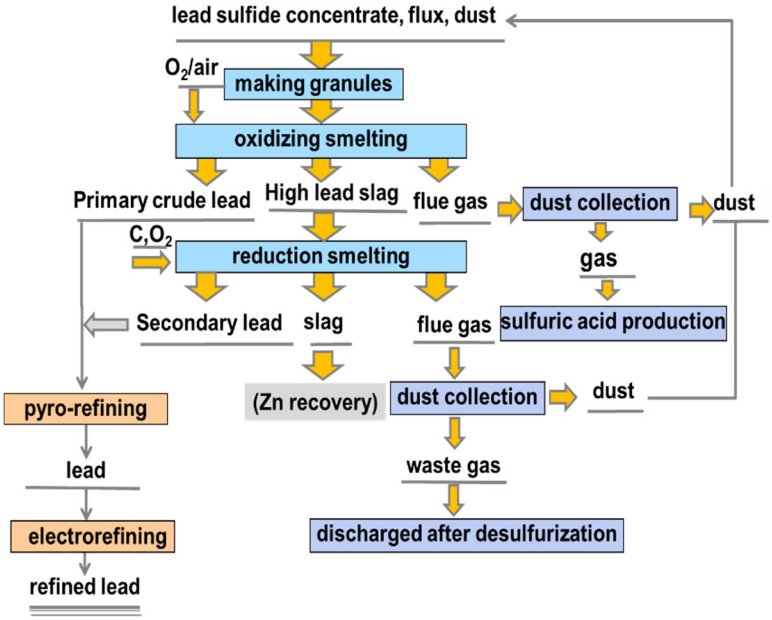

FIG 1 – Typical direct reduction process.

Oxidising smelting

The sulfide concentrates (oxides or lead sulfate can be used as regulator for heat balance), flux (limestone and quartz), coal or semicoke, and recycled dust are prepared in a suitable proportion, and mixed. Then, the mixture is added into oxidising smelter, ie side submerged or bottom blowing smelter. Oxygen enriched air is blown into the smelter to oxidise the sulfide concentrate and fuel, if needed, to generate heat to keep the molten bath at high temperature and quick reaction.

The main reaction in this step is showing as following Equations 1–3, high-PbO slag and some crude lead is formed as a result in this step. The FeS and ZnS is changed into oxides, and turn into slag with other gangue. So the main slag system is PbO-ZnO-FeO-CaO-SiO_2. There is less fuel added because the reactions are exothermal. To prevent PbS evaporation, the temperature should be kept at a relatively lower level. The predominance diagram of Pb-Zn-S-O system is displayed in Figure 2 (Yang, Cui and Hao, 2020) district I.

$$PbS + O_2 = Pb + SO_2 \quad (1)$$

$$PbS + O_2 = PbO + SO_2 \quad (2)$$

$$PbS + PbO = Pb + SO_2 \quad (3)$$

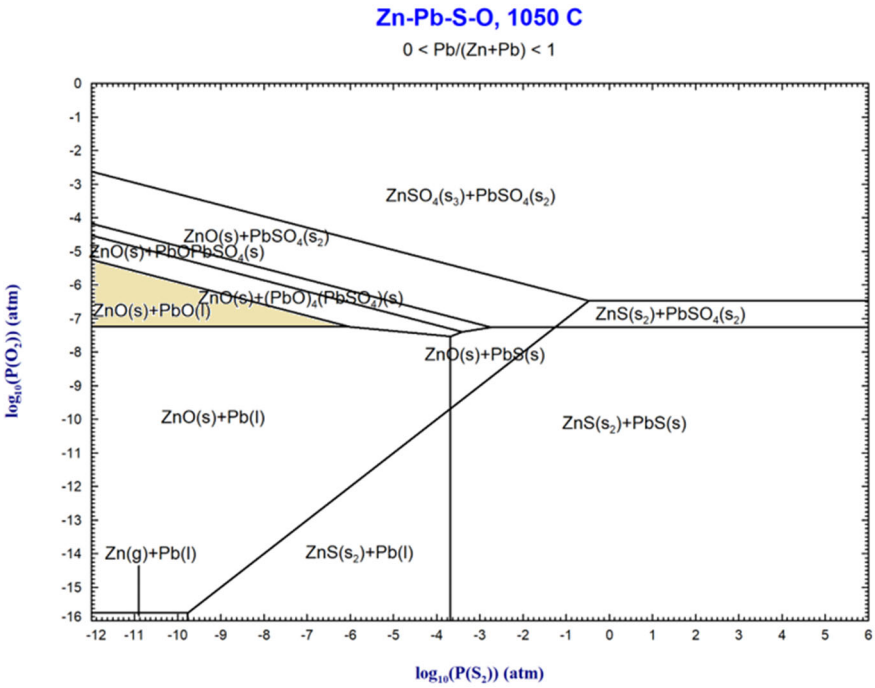

FIG 2 – Predominance diagram of Pb-Zn-S-O system, 1050°C.

The atmosphere is controlled between the Pb(l) and +PbO(l) regions to ensure that ZnO in slag is not reduced, some crude lead and high lead bearing slag is formed. In practice, a relatively high oxidation smelting temperature (1000~1050°C) is selected, the PO_2 is controlled between 10^{-5} ~ 10^{-6} atm, and $P_SO_2 \leq 10^{-4}$ atm.

PbO reduction

High-PbO slag is added into the reduction smelter, ie side-submerged or bottom blowing furnace with proportional flux and fuel. Oxygen enriched air is blown in as well. The main reaction in this step is as Equations 4–5.

$$PbO+C = Pb+CO \quad (4)$$

$$PbO+CO = Pb+CO_2 \quad (5)$$

The temperature and atmosphere are controlled to prevent ZnO reduction. So crude lead and slag with higher ZnO content is formed in this step, as shown in Figure 2 district II. The reactions are endothermic. Coal or semicoke or natural gas as fuel and reductant have to be added.

Because FeO and CaO can replace PbO from silicate and promote activity of PbO, increasing FeO/SiO_2 and CaO/SiO_2 is in favour of PbO reduction.

Further reduction for Zn recovery

ZnO bearing slag is reduced in fuming furnace to recover Zn in general. The reaction is as Equation 6.

$$ZnO + C = Zn_{(g)} + CO \quad (6)$$

Zinc is reduced and evaporates, as shown in Figure 2 district III. Then Zn is reoxidised to ZnO and collected for further use. increasing FeO/SiO_2 and CaO/SiO_2 is in favour of ZnO reduction.

Above reactions are common to all direct reduction processes.

Parameters in practice

The smelting temperature is usually selected at 1000–1350°C according to the slag properties. The melting temperature should be 80–150°C higher (superheat) than the liquidus temperature (complete fusion temperature).

According to relevant results that the slag liquidus temperature decreases with the Pb content or w(FeO)/w(SiO_2) increase, and ZnO content decrease. It is determined that *w*(FeO)/*w*(SiO_2) = 1.0–2.0, *w*(CaO)/*w*(SiO_2) = 0.4–0.8. In practical application, the relevant parameters can be adjusted properly.

Oxidising stage

Generally, the composition of mixed ore prepared for smelting is at about Pb 45–60 per cent, S 15–17 per cent, Zn 6–7 per cent, Cu < 0.7 per cent. At the same time, appropriate amount of the flux limestone (CaO > 40 per cent), silica sand (SiO_2 > 85 per cent), coal (C > 73 per cent) is added.

The slag composition in this stage is with a high PbO content and relatively lower ZnO content. When Pb content is above 40 per cent, the slag physico-chemical properties is mainly determined by Pb content.

Some slag composition and smelting temperature in practice is given in Table 1 (Li and Jia, 2010).

TABLE 1

Typical slag composition and smelting temperature.

No.	Pb,%	Zn,%	*w*(FeO)/*w*(SiO_2)	*w*(CaO)/*w*(SiO_2)	Smelting temp °C
1	42	7–8	1.0	0.33–0.49	1040–1090
2	39.57	9.95	0.93	0.64	1100–1150
3	53.47	6.40	1.46	0.65	980
4	45.02	4.81	1.19	0.48	866
5	49.59	4.42	1.62	0.44	807

Different plants may have different operation parameters. In an oxygen-enriched bottom blowing smelting plant, w(FeO)/w(SiO_2) = 1.3–1.6 (target: 1.5), w(CaO)/w(SiO_2) = 0.4–0.7 (target: 0.5) in oxidising step. The bath temperature is 1000–1100°C. The crude lead output is 40–60 per cent. Fume rate is 11–16 per cent. Pb content in high-PbO slag is 40–48 per cent (Li and Jia, 2010).

The typical raw materials, slag composition and dust composition to a triple-furnace system, ie side oxygen-enriched submerged blowing + side oxygen-enriched submerged blowing+ fume furnace, is listed in Table 2 (Chen, 2021).

TABLE 2

The raw materials, slag composition and dust composition in side oxygen-enriched blowing.

Stage	Materials	Composition, %							Fluxes/fuel
		Pb	Zn	Cu	Fe	CaO	SiO_2	S	
Oxidising step	Mixed ore	55.0	4.7	0.80	8.25	0.35	3.8	17.0	Lime stone and silica sand Coal
	Dust	49.0	4.7	0.12	0.83	0.04	0.38	7.17	
	High-PbO slag	42.11	6.54	0.45	11.66	7.42	10.60	0.19	
Reduction step	Dust	50.78	5.28	0.05	1.88	1.20	1.71	0.10	Small amount of limestone coal
	slag with higher Zn	2.38	12.35	0.41	22.15	18.99	21.10	0.07	
Further reduction	Final slag	0.42	1.46	0.47	26.40	24.63	24.40	0.06	Coal
	Dust	10.94	60.0	0.06	2.99	25.71	2.86	0.12	

It can be seen that the sulfide in mixed ore changes to oxides and part of Pb compound is reduced. As a result, slag with the remaining PbO is formed. The Pb content in slag is about 42 per cent.

The dust rate is about 15 per cent (to take mixed ore as reference) in this step. Dust with higher PbO content and much lower FeO, SiO_2 and CaO content than mixed ore and slag is obtained. That means there is selective evaporation of Pb compound is the main reason, rather than mechanical carrying of exit gas.

With higher PbO content, the slag can be kept in melt state well in this stage.

PbO and ZnO reduction stage

As shown in Table 2, In the PbO reduction step, the Pb content in slag decreases gradually from about 42 per cent to < 2 per cent, and Zn content in the slag increases accordingly. The smelting temperature is at about 1200–1250°C.

The dust rate is about 13 per cent (to take high-Pb slag as reference) in PbO reduction step. As in oxidising step. The dust with higher PbO content and much lower FeO, SiO_2 and CaO content than mixed ore and slag is obtained. It can also be concluded that selective evaporation of Pb and its compounds takes place rather than mechanical carrying of exit gas.

In the further reduction step, the ZnO content in the slag gradually decreased from 12.35 per cent to 1.5 per cent, and Pb content decreased further to 0.42 per cent. The smelting temperature is at about 1300–1400°C.

Higher temperature can promote the reduction anyway.

Apart from the high lead slag, there is no detailed results on slag composition and property change for reference up to now.

ANALYSIS ON PHYSICO-CHEMICAL PROPERTIES OF SLAG IN WHOLE PROCESS

Basic research results

As listed in Table 2, the high-PbO slag is formed at oxidising step. And then the PbO is reduced gradually in reduction step. Finally, the ZnO and rest PbO is further reduced.

Slag physico-chemical properties is the key reference for smelting process. Up to now, there is fewer results on slag physico-chemical properties of lead direct smelting.

Some works are focused on final slag, ie FeO-CaO-SiO_2 system when PbO and ZnO is completely reduced (Zhang and Dai, 2020). Jak and Hayes (2002; 2003a; 2003b) researched the phase equilibrium of PbO-CaO, PbO-CaO-SiO_2, and PbO-ZnO-SiO_2 system. Yang, Dou and Zhang (2019) studied the high-lead slag with Zn content of 15–32 per cent. It is found that the decrease of ZnO/PbO and FeO/SiO_2 leads to the drop of viscosity (Yang, Dou and Zhang, 2019). Cui, Li and He (2013) and Cui, Guo and Chen (2016) investigated phase diagram and melting characteristic of PbO-ZnO-FeO-CaO-SiO_2 system using FactSage™ ver 7.1 (by CRCT-ThermFact Inc.& GTT-Technologies). It is pointed out that the melting temperature reduces with FeO/SiO_2 increase (1.2–2.0) when the PbO content in slag is more than 10 per cent, in accordance with Perez-Labra, Romero-Serrano and Hernandez-Ramirez (2012) results.

Huang, Zhang and Cheng (2021) measured the melting temperature and viscosity of PbO-ZnO-FeO-CaO-SiO_2 slag with high-Pb content (about Pb 40 per cent), Fe/SiO_2 (0.9–1.3), CaO/SiO_2 (0.4–0.8) and ZnO content (5–11 per cent), and obtained a similar measurement result of physico-chemical properties as Cui, Li and He (2013). It is suggested that the appropriate Fe/SiO_2 is 1.0–1.1 and CaO/SiO_2 0.6 and ZnO content <7 per cent in oxygen-enriched smelting process. The main results are as Figure 3. This is relatively comprehensive and can reflect the research state of high Pb-bearing slag. Anyway, the slag property in whole reduction process is in lacking up to now.

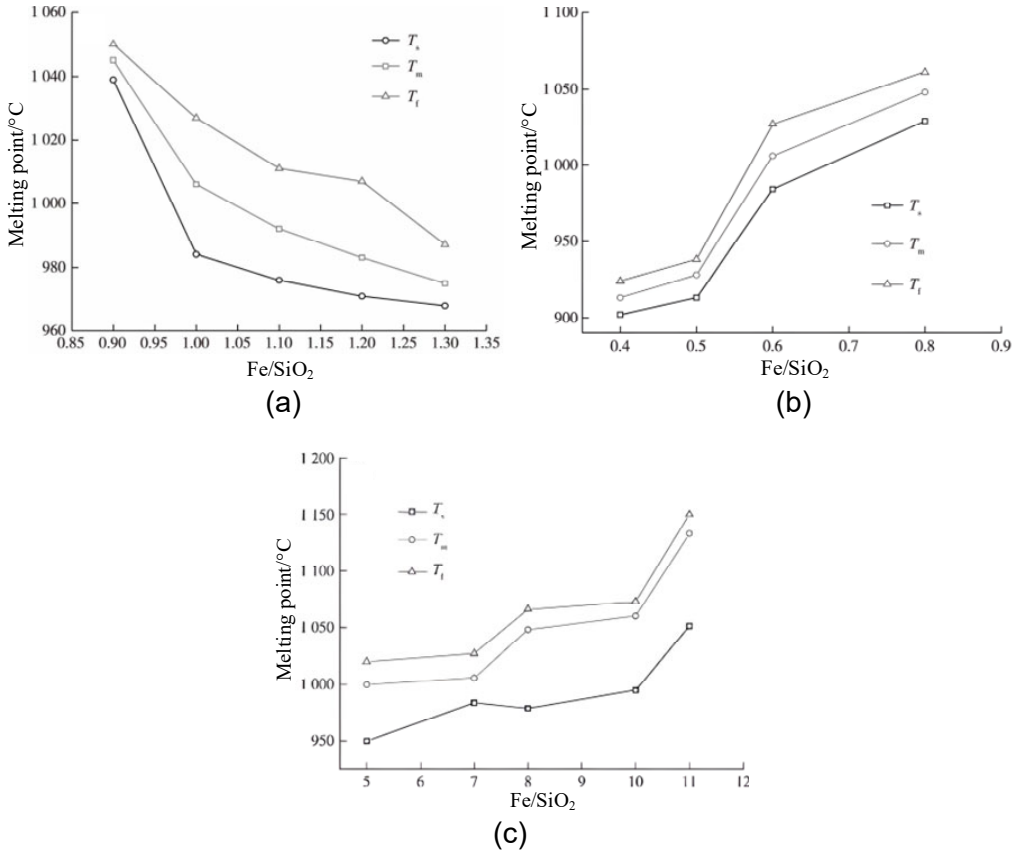

FIG 3 – Effects of Fe/SiO_2, CaO/SiO_2 and ZnO on melting point respectively. (a) (CaO/SiO_2 = 0.6, Pb per cent = 38, ZnO = 7 per cent); (b) (Fe/SiO_2 = 1.0, Pb per cent = 38, ZnO = 7 per cent); (c) (Fe/SiO_2 = 1.0, Pb per cent = 38, CaO/SiO_2 = 0.6).

Theoretical analysis on slag properties in whole reduction process

To demonstrate the slag property with the composition change, an iso-liquidus temperature curve based on PbO-FeO-CaO-SiO_2-ZnO system and relevant composition is drawn as Figure 4. The point A and B is the beginning and end of PbO reduction step respectively. The point B and C is the beginning and end of ZnO reduction step respectively. In PbO reduction process (as shown in line A to B), FeO/SiO_2 = 1.4, CaO/SiO_2 = 0.7, ZnO/FeO = 0.54, only PbO content decreases. As the result, FeO+CaO+SiO_2+ZnO content increase proportionally. As a result, the ZnO content can reach about 20 per cent in mass. In ZnO reduction process (as shown in line BC), FeO/SiO_2 = 1.4, CaO/SiO_2 = 0.7, PbO = 0.54, only ZnO content decreases and FeO+CaO+SiO_2 increase proportionally. It can be seen that the whole reduction process is in a composition range with lower melting point (1100–1250°C).

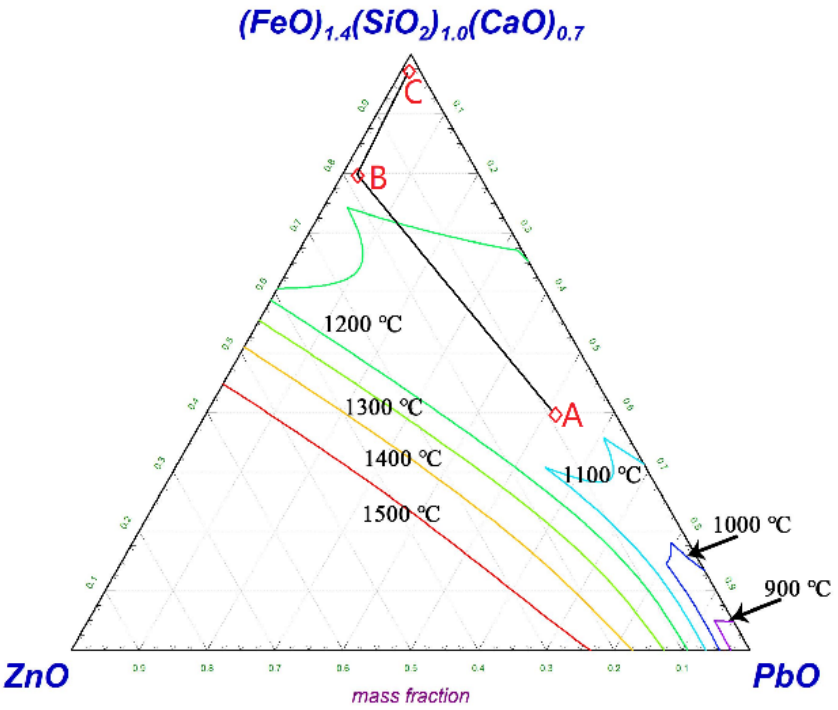

FIG 4 – Calculated PbO-FeO-CaO-SiO_2-ZnO liquid phase diagram with liquidus isotherms.

For further analysis, the liquidus melting point was calculated with FactSage™ and shown in Figure 5.

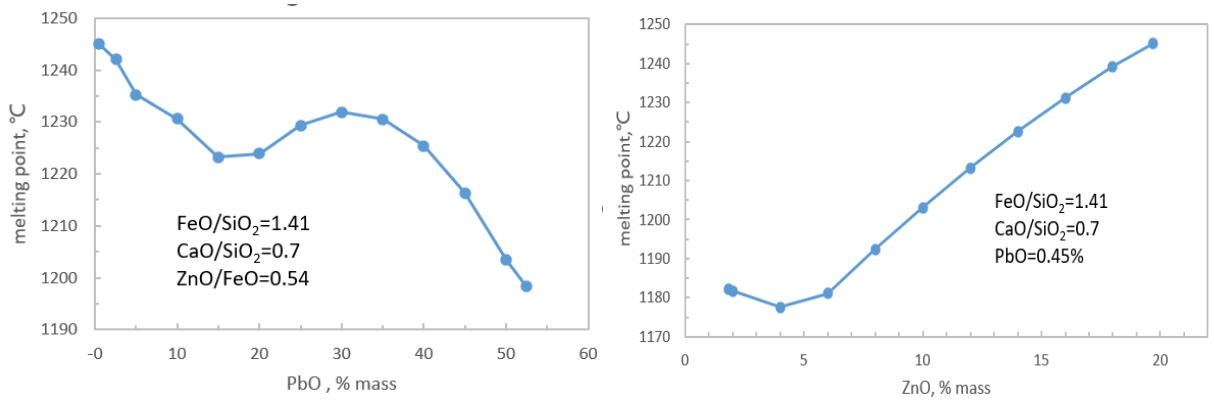

FIG 5 – Relation among melting point with PbO and ZnO content in slag.

It can be seen that with the PbO reduction, the slag melting point will increase gradually from 1198°C to 1245°C. And then to further reduction of ZnO, the slag melting point will decrease gradually from 1245°C to 1182°C with the ZnO content decrease. The smelting temperature should be at 1300–1350°C. The slag melting point will experience increase until the end of PbO reduction and then decrease with the PbO reduction. This is in accordance with relevant practical results. The smelting temperature and slag composition should be adjusted properly according to these changes.

The results of some relevant slag property measurement

Based on high PbO slag reduction process, the properties of some slag samples with different composition were measured. The results is listed in Table 3. It can be seen that with the PbO reduction, the ZnO and other components in the slag increased. The melting point increased accordingly. When PbO is reduced from 53.86 per cent to 2.69, the melting point increased from 841°C to 1296°C. Higher than that of theoretical calculation with FactSage™.

TABLE 3

Some properties measurement results of slag samples with different composition.

Slag No.	Composition, %					Liquidus, °C	Viscosity, Pa.s		
	PbO	ZnO	FeO	CaO	SiO_2		1180°C	1230°C	1280°C
1	53.86	6.0	21.04	5.46	13.64	841	0.05		
2	43.09	6.0	26.69	6.92	17.3	1158	0.31	0.1	0.05
3	32.32	8.0	31.29	8.11	20.28				
4	21.54	10.0	35.89	9.3	23.26	1285	0.62	0.12	0.11
5	10.77	13.0	39.96	10.36	25.9				
6	2.69	13.0	44.2	11.46	28.65	1296	0.38	0.11	0.098

THE EVAPORATION OF SLAG COMPONENTS AND ITS EFFECT

Evaporation and its effect in practice

In the whole process, Pb, PbO, PbS, Zn, ZnO and even relevant sulfate appear. It is well known that PbS, PbO, Pb and Zn are volatile material at high temperature (Osada, Osada and Kokado, 2004; Nakada, Mihara and Kawaguchi, 2008; Guo, Cui and Zhao, 2016).

In practice, the evaporation information can be found in collected dust as listed in Table 2.

In oxidising step, the dust composition is obviously different from either raw material concentrate or high-Pb slag. Low Fe and SiO_2 concentrations reflect that the dust is neither concentrate mechanical carrying nor high-Pb slag splashing. To take the Fe or SiO_2 content as a reference, the concentrate mechanical carrying is about one tenth, a small part. A higher sulfur content reflects that PbS evaporates in main. It is imagined that the PbS evaporates first and then some oxidised to PbO.

In reduction step, there is more Pb and low Fe, Si, and Ca in dust than in slag. This reflects that the dust is not high-Pb slag splashing, but evaporation in main. The main volatiles should be PbO and Pb.

The dust and fume rate are about 13–15 per cent of the charge in relevant steps. This exposed that the importance of evaporation to slag composition and properties, as well as the process control in mass and heat balance.

In another point, dust is circulated in the smelting processes. The Pb in dust per unit of bullion lead is about 0.31 t/t Pb to oxygen-enriched bottom blowing process (Zhong, 2014). This can not only lead to the low efficiency of smelting process, but also potential risk of Pb emission and pollution. How to reduce the amount of recycling dust should be studied.

Zn is more easily to evaporate in further reduction step. That is good for Zn recovery. But the Pb compound evaporation is not good for Pb recovery and should be limited.

Evaporation and its effect to property measurement

In the physicochemical property measurement, these volatiles will evaporate continuously in heating or high temperature keeping process, so to the production process. The higher, the temperature is, or the longer the keeping time is, the great the loss of volatile from the slag is. That means the slag composition will be changed continuously. As a result, the measured slag physicochemical properties will change (Guo, Cui and Zhao, 2016; Cui, Wang and Zhao, 2018; Wang, Cui and Yang, 2020). It is referred as uncertainty of slag property for brief. Some weight loss results with TG-DSC on lead bearing slag is listed in Table 4. To consider the weight loss at 410°C–736°C is the crystal water and decomposition of compound, it can be seen that the weight loss is very evident at temperature 736°C–1450°C. This part of weight loss represents the evaporation effect. From the results in Table 4, almost all of the PbO in the slag can exit from the slag at 1450°C. With the increase of FeO/SiO_2 and CaO/SiO_2, the weight loss increases.

TABLE 4

The weight loss of slag sample with PbO at high temperature (Guo, Cui and Zhao, 2016).

Slag type	Composition		Weight loss 410°C–736°C	Weight loss 736°C–1450°C
	FeO/SiO_2, CaO/SiO_2	PbO		
Slag with low PbO content	1.54, 0.4	2.69%	12.88%	3.95%
	1.8, 0.6	2.69%	13.3%	4.66%
Slag with medium PbO content	1.54, 0.4	21.54%	9.34%	21.62%
	1.8, 0.6	20%	9.69%	24.4%
Slag with high PbO content	1.54, 0.4	43.09%	7.92%	38.69%
	1.8, 0.6	40%	8.09%	43.3%

So either to physico-chemical property measurement or production process, the evaporation of PbS, PbO, Pb and Zn should be given more attention. Relevant work should be push forward further. The evaporation can lead the results of melting point higher than it should be.

It is suggested to use premelted Pb-bearing slag in physicochemical property measurement to prevent evaporation effect. But anyway, the way should be evaluated seriously. No credible results are reported in detail. Zhao *et al* (2023) suggested a method to measure the physicochemical properties in traditional way, and modify the in-time composition based on evaporation to the measured property data. This is a promising method worthy of detected.

CONCLUSION

- Sulfide concentrates direct reduction processes are the main trend for crude Pb production, bottom blowing/side submerged blowing based processes is well developed. Two steps (oxidising and reduction) or three steps (oxidising, reduction and further reduction for Zn recovery) is common in these processes. That is reasonable and practical, but there are less basic research results for reference on direct reduction processes. The practical processes are controlled mainly by experience.
- The slag composition at reduction step will changes continuously. The slag melting point will increase first until the end of PbO reduction and then decrease with the ZnO reduction. The variation range is about 50–60. Proper slag composition selection of $(FeO)/(SiO_2)$ at 1.0–2.0, $(CaO)/(SiO_2)$ at 0.4–0.8 and ZnO < 7 per cent–8 per cent can guarantee smelting process go on wheels.
- Evaporation in practical oxidising step and PbO reduction step is mainly PbS and PbO respectively. These consist of the main composition in the dust. Mechanical carrying of exit gas is only a small part unless the dust recycled is carried out in a mass.
- PbO in slag evaporates evidently and can causes physical-chemical property measurement uncertainty to high PbO-containing slag. Relevant fundamental research should be pushed forward to give references for Pb-smelting parameters control and process optimisation.
- How to restrain the evaporation and to obtain more accurate measurement results of physicochemical properties of smelting slag are the key not only to set high efficiency, energy saving process, but also to environmental pollution control.

ACKNOWLEDGEMENTS

The work is supported by NSFC (No.51674185) and relevant enterprises.

REFERENCE

Chen, L, 2021. Molecular dynamics simulation on composition regulation of PbO-FeOx-CaO-SiO_2-ZnO system for the high-lead slag, Master's thesis, Xi'an University of architecture and technology, Xi'an.

Chen, L, Hao, Z and Yang, T, 2015. A Comparison Study of the Oxygen-Rich Side Blow Furnace and the Oxygen-Rich Bottom Blow Furnace for Liquid High Lead Slag Reduction, *JOM,* 67(5):1123–1129.

Chen, L, Wang, Z H and Chen, W, 2018. Thermodynamic simulation on elements distribution of lead concentrate oxidative smelting in oxygen-rich bottom-blow smelting process*, Nonferrous Metals (Extractive Metallurgy)*, (09):1–6.

Chen, L, Yang, T Z and Bin, S, 2014a. An Efficient Reactor for High-Lead Slag Reduction Process: Oxygen-Rich Side Blow Furnace, *JOM,* 66(9):1664–1669.

Chen, L, Yang, T Z and Liu, W F, 2014b. Distribution of valuable metals in liquid high lead slag during reduction process, *The Chinese Journal of Nonferrous Metals*, 24(04):1056–1062.

Cui, Y R, Guo, Z L and Chen, A L, 2016. Phase equilibria of PbO-FeO_x-CaO-SiO_2-ZnO high-lead slag system for direct reduction process, *Chinese Journal of Rare Metals*, 40(09):928–933.

Cui, Y R, Li, K M and He, J S, 2013. Melting point of molten high-lead slag in direct reduction process, *Chinese Journal of Rare Metals*, 37(03):473–478.

Cui, Y R, Wang, G H and Zhao, J X, 2018. Volatilization Kinetics of PbO-FeO_x-CaO-SiO_2-ZnO Lead-bearing Slag, *The Chinese Journal of Process Engineering*, 18(02):393–398.

Guo, Z L, Cui, Y R and Zhao, J X, 2016. Deviation prediction on physicochemical properties of high-lead slag, *Journal of Liaoning University of Science and Technology*, 39(1):47–51.

Huang, H, Zhang, J L and Cheng, Y Q, 2021. Study on Melting Temperature and Viscosity of PbO-FeO-CaO-SiO_2-ZnO System, *Nonferrous Metals (Extractive Metallurgy)*, (5):11–16.

Jak, E and Hayes, P C, 2002. Experimental liquidus in the PbO-ZnO-Fe_2O_3-(CaO+SiO_2) system in air, with CaO/SiO_2 = 0.35 and PbO/(CaO+SiO_2) = 3.2, *Metallurgical and Materials Transactions B,* 33B(5):851–863.

Jak, E and Hayes, P C, 2003a. The effect of the CaO/SiO_2 ratio on the phase equilibria in the ZnO-Fe_2O_3-(PbO+CaO+SiO_2) system in air: CaO/SiO_2 = 0.1, PbO/(CaO+SiO_2) = 6.2 and CaO/SiO_2 = 0.6, PbO/(CaO+SiO_2) = 4.3, *Metallurgical and Materials Transactions B,* 34B(4):369–382.

Jak, E and Hayes, P C, 2003b. Experimental Study of Phase Equilibria in the PbO-ZnO-Fe_2O_3 -(CaO-SiO_2) System in Air for the Lead and Zinc Blast Furnace Sinters (CaO/SiO_2)Weight Ratio of 0.933 and PbO/(CaO+SiO_2) Ratios of 2.0 and 3.2), *Metallurgical and Materials Transactions B,* 34B(8):383–397.

Jiang, J X, Li, X R and Guo, H J, 2018. Kivcet lead smelting process practice, *World Nonferrous Metal*, (18):7–9.

Li, W F and Jia, Z H, 2010. Lead sulphide concentrate smelting with bottom or top oxygen-enriched blowing, 12 p (Central South-University Press: Changsha).

Li, W F, Yang, A G and Cheng, H C, 2011. Technology Study on Direct Reduction of Lead-Rich Slag, *Nonferrous Metals (Extractive Metallurgy)*, (4):10–13.

Li, W F, Zhan, J and Fan, Y Q, 2017. Research and Industrial Application of a Process for Direct Reduction of Molten High-Lead Smelting Slag, *JOM,* 69(4):784–789.

Nakada, H, Mihara, N and Kawaguchi, Y, 2008. Volatilization behavior of lead from molten slag under conditions simulating municipal solid waste melting, *Journal of Material Cycles and Waste Management*, 10(1):19–23.

Osada, S, Osada, M and Kokado, M, 2004. Thermodynamic Study of the Behavior of Elements with Low Boiling Points in the Melting Process, *Journal of the Japan Society of Waste Management Experts*, 15(5):353–362.

Perez-Labra, M, Romero-Serrano, A and Hernandez-Ramirez, A, 2012. Effect of CaO/SiO_2 and Fe/sio_2 ratios on phase equilibria in PbO-ZnO-CaO-SiO_2-Fe_2O_3 system in air, *Transactions of Nonferrous Metals Society of China*, 22(3):665–674.

Queneau, P E and Siegmund, A, 1996. Industrial-scale lead making with the QSL continuous oxygen converter, *JOM,* 48(48):38–44.

Slobodkin, L, Sannikov, Y and Grinin, Y, 2013. The Kivcet Treatment of Polymetallic Feeds In book: *Lead-Zinc 2000,* pp 687–692 (John Wiley and Sons, Inc: New York).

Wang, C Y and Chen, Y Q, 2016. The lead and zinc metallurgy technology situation and development trend of China: lead metallurgy, *Nonferrous Metals Science and Engineering*, 7(6):1–7.

Wang, G H, Cui, Y R and Yang, Z, 2020. Volatilization characteristics of high-lead slag and its influence on measurement of physicochemical properties at high temperature, *Journal of Mining and Metallurgy – Section B – Metallurgy*, 56(1):59–68.

Wang, J K, Zhou, T X and Feng, G L, 2004. ISA-YMG Smelting Process for Lead Bullion, *Chinese Engineering Science*, (4):61–66.

Yang, K O, Dou, Z H and Zhang, T A, 2019. Viscosities in PbO-ZnO-Fe_xO-SiO_2–CaO system for lead and zinc smelting slags, *Metallurgical Research and Technology*, 116(6):606.

Yang, Z, Cui, Y R and Hao, Y, 2020. Optimization on bottom blowing-side blowing lead smelting for utilizing of lead-silver leaching residues, *The Chinese Journal of Process Engineering*, 20(11):1304–1312.

Zhang, L R, 2013. *Modern Lead Metallurgy*, pp 180–186 (Central South University Press: Changsha).

Zhang, Z T and Dai, X, 2020. Effect of Fe/SiO_2 and CaO/SiO_2 mass ratios on metal recovery rate and metal content in slag in oxygen-enriched direct smelting of jamesonite concentrate, *Transactions of Nonferrous Metals Society of China*, 30(2):501–508.

Zhang, Z T, Li, W F and Zhan, J, 2018. The Effect of Coal Ratio on the High-lead Slag Reduction Process, *Journal of Mining and Metallurgy Section B – Metallurgy*, 54B(2):179–184.

Zhao, J X, Wang, Z and Wang, G H, 2023. A method on evaluating the effect of evaporation of component in slag, Chinese Patent 2021114176146.

Zhong, Q D, 2014. Pb element flow in typical Pb smelting process, Master thesis, Chinese Academy of Environmental Sciences, Beijing.

Slag volume effects on direct-reduced iron (DRI)-based electric furnace steelmaking

DOI: 10.62053/SWVV2474
Q Zhuo[1], P C Pistorius[2] and M N Al-Harbi[3]

1. PhD candidate, Carnegie Mellon University, Pittsburgh PA 15213, USA. Email: qzhuo@andrew.cmu.edu
2. POSCO Professor, Carnegie Mellon University, Pittsburgh PA 15213, USA. Email: pistorius@cmu.edu
3. Research Fellow, Hadeed, Jubail 31961, Saudi Arabia. Email: harbimn@hadeed.sabic.com

ABSTRACT

A likely increasingly important pathway for future low-carbon ironmaking and steelmaking is the combination of gas-based direct reduction with electric furnace steelmaking (DRI-EAF route), or with electric smelting (DRI-ESF route). In the DRI-EAF route, the gangue that is present in the iron ore is fluxed and removed as slag in the melting (steelmaking) step. This is in contrast with integrated steelmaking, in which the gangue is removed as part of blast furnace ironmaking. For DRI-EAF steelmaking, the amount and composition of slag depend on the iron ore composition, flux additions and iron yield. Slag volume and composition affect phosphorus removal, foaming behaviour and the process energy requirements. In this work, heat data from a year of DRI-EAF production was analysed to test whether the expected relationship between slag volume and electricity consumption for EAF steelmaking was observed. The data include slag analyses (one sample per shift), and heat-level information on all inputs, final steel temperature and dissolved oxygen concentration, electricity consumption, tapped steel mass and tap-to-tap time. In analysing the data, the slag volume was estimated from the assayed slag CaO concentration and CaO inputs to the EAF. The expected effect of slag volume on steelmaking energy consumption was calculated with a mass and energy balance, considering the heat of mixing of the slag. The calculated energy requirement of slag formation is in line with previous estimates reported in the literature.

INTRODUCTION

Gas-based direct reduction is expected to become an increasingly important ironmaking route, since it could utilise green hydrogen to produce iron from ore with low or zero carbon dioxide emissions. The direct-reduced iron (DRI) product retains the impurities (mainly gangue oxides and phosphorus) that are present in the ore feed; these impurities need to be removed as slag during subsequent melting or electric arc furnace (EAF) steelmaking. Currently, relatively high-grade pellets (total iron concentration > 67 per cent) are mainly used to produce DRI to serve as EAF feed (Kim and Sohn, 2022); in comparison, blast furnace pellets typically contain 63–65 per cent Fe (Poveromo, 1999). As the globally consumed tonnage of pellets for DRI increases, the availability of high-grade pellets is expected to become a constraint for DRI-EAF production (Barrington, 2022).

DRI that is produced from lower-grade pellets can be used in EAF steelmaking, but with disadvantages due to the increased slag volume (mass of slag relative to steel mass): the disadvantages include the increased energy consumption (to heat and melt the slag), lower iron yield (more iron lost to the slag), the production of more by-product and lower production rate (because of the higher electricity requirement). Already in 1980 effects of increased DRI used in EAF steelmaking were noted – in particular, the increased electricity consumption related to slag formation (Kishida *et al*, 1980). In addition, the release of acidic gangue from DRI during the initial part of the heat, before lime and doloma fluxes have dissolved, tends to cause the formation of acidic slag, leading to attack on the refractory lining of the furnace (Song, Zhao and Pistorius, 2020). If lime additions are insufficient to maintain a high slag basicity when melting DRI with acidic gangue, poorer dephosphorisation results (Heo and Park, 2018).

In this work, data from an operating plant that utilises a high proportion of DRI in EAF steelmaking was used to test whether the expected effects of slag volume on electricity consumption, iron yield and power-on time are observed. Details of the plant operation and data are summarised in the next section, followed by analysis of the data and comparison with the theoretically expected trends.

PLANT DETAILS

The plant uses a mixture of scrap and cold DRI as metallic feed, with lime and doloma as fluxes. Natural gas is used in oxyfuel burners and additional oxygen is injected. The DRI contains around 2 per cent carbon (by mass); additional carbon is fed through the top of the furnace and also injected. Data from one year of production was analysed. Slag analyses were recorded approximately three times per day, resulting in data for around 800 heats (after removing missing analyses). Out of these, 'pour back' – return of steel from secondary metallurgy to the EAF – occurred during 16 heats.

DRI compositions were available for the year of production, but were not related to specific heats in the analysis presented here. The variability in the gangue content of the DRI was taken to be the main cause of changes in slag volume. The DRI analysis reported the mass percentages of carbon, metallic iron and oxidic iron (taken to be FeO); the balance of the DRI was assumed to be gangue. The distributions of DRI compositions for the year of production are given in Figure 1. The median DRI composition was 2.2 per cent carbon, 90.3 per cent total iron, 83.2 per cent metallic iron and 5.3 per cent gangue (calculated value).

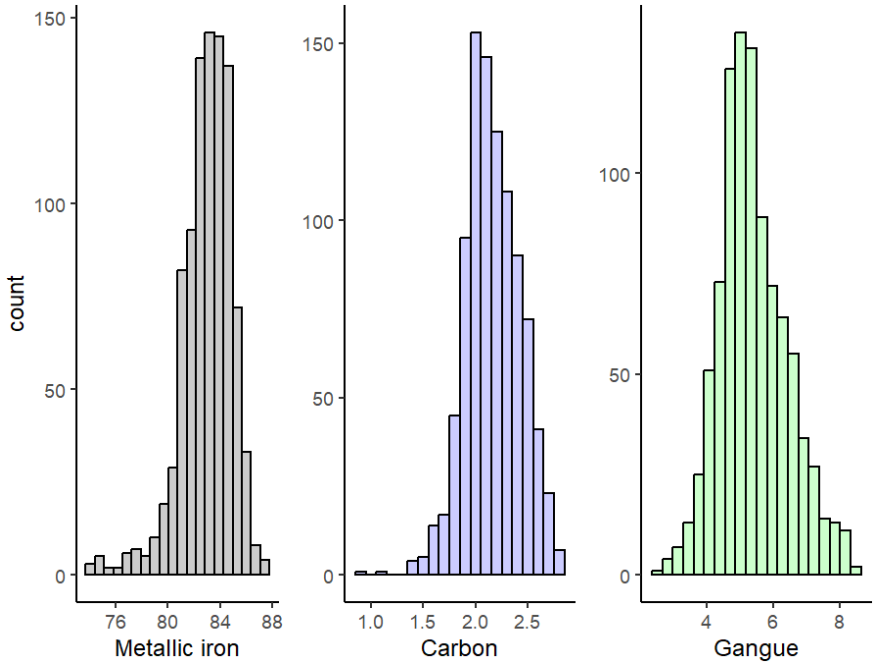

FIG 1 – Distribution of direct-reduced iron (DRI) compositions (mass percentages).

The main metallic input is DRI (Figure 2), with the scrap input accounting for about 40 per cent of the tap mass on average.

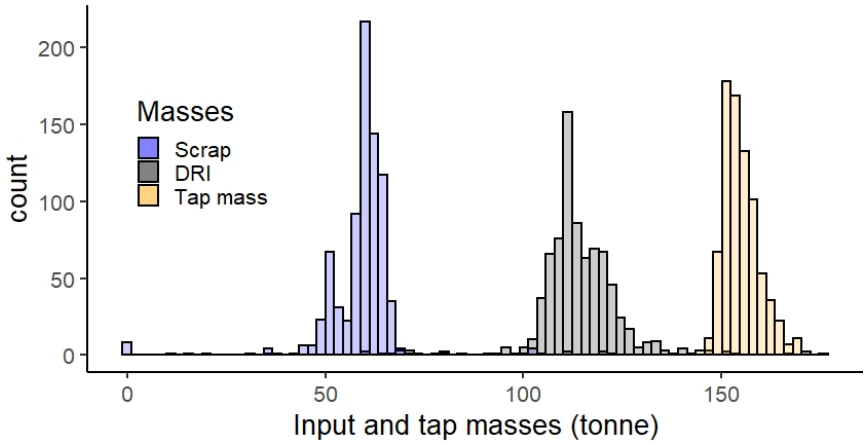

FIG 2 – Steel input and tap masses.

The power-on time was around 50 minutes (Figure 3), with a wider range of tap-to-tap times. The power during arcing was near the median value of 95 MW for all the heats (Figure 4). The slag volume was estimated from the (%CaO) in the slag and additions of lime and doloma (the average slag composition is given in Table 1, and the distribution FeO and MgO concentrations, and slag basicity, in Figure 5). In this calculation, it was assumed that the only sources of CaO were the fluxing additions and that the lime was pure CaO and the doloma pure stoichiometric CaO.MgO. The calculated slag volume varied significantly between heats (Figure 4), allowing evaluation of the effects of slag volume from the recorded data. The Fe yield (also shown in Figure 4) was estimated from the tap mass of steel (approximated as 100 per cent Fe), the scrap mass (also taken to be 100 per cent Fe) and the DRI input (using the median total Fe in DRI of 90.3 per cent). In some cases the calculated iron yield was greater than 100 per cent, likely reflecting variations in the amount of steel retained in the furnace between taps, as a hot heel. Similar values for the Fe yield were found using the analysed iron concentration in the slag, the calculated slag volume and the tap mass of steel: both approaches gave median Fe yields of 95.3 per cent.

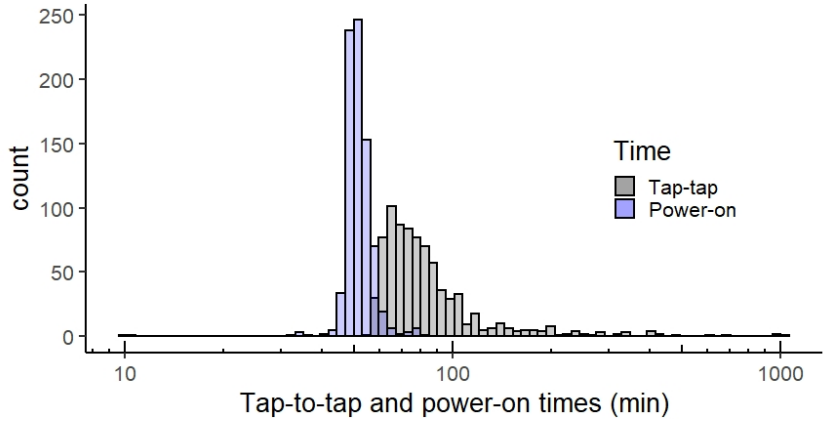

FIG 3 – Distribution of tap-to-tap and power-on times.

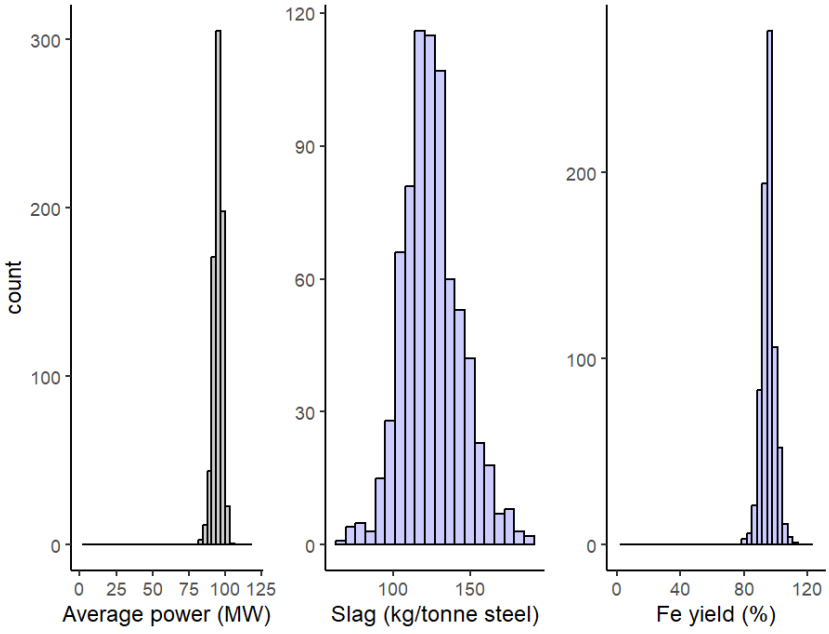

FIG 4 – Furnace power during arc heating, with the calculated slag volume and Fe yield.

TABLE 1

Average slag composition (mass percentages).

%CaO	%SiO_2	%MgO	%Al_2O_3	%MnO	%'FeO'	B3*
24.0	14.2	5.99	4.93	2.39	42.9	1.33

*B3 = (%CaO) / (%SiO_2 + %Al_2O_3).

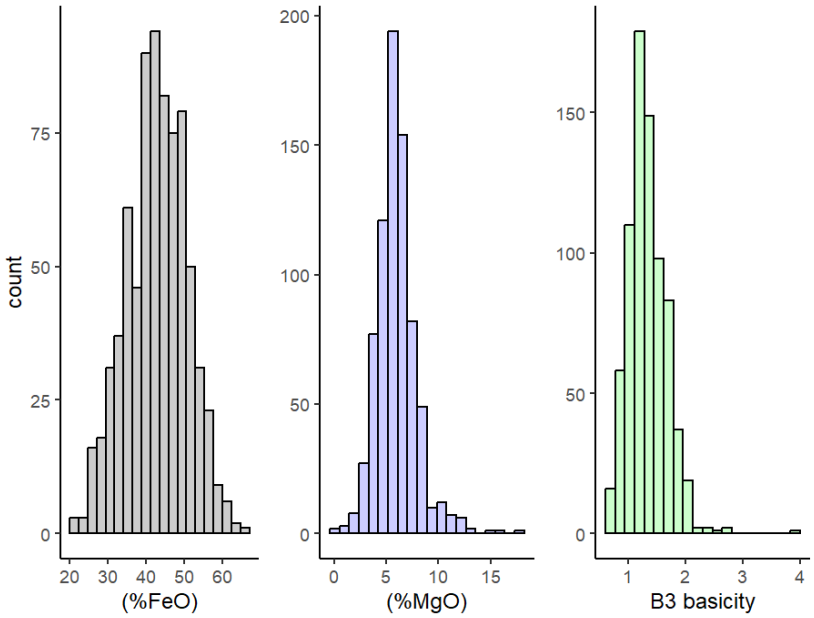

FIG 5 – Slag composition parameters: iron content, percentage MgO and B3 = (%CaO) / (%SiO_2 + %Al_2O_3).

The reported concentration of iron in the slag likely includes a contribution of entrained metallic iron. One mechanism for iron entrainment is incomplete settling: the DRI is top-fed into the furnace, requiring the iron to travel through the slag layer before reaching the metal bath. However, because information on the metallic iron concentration in the slag was not available, in these calculations all the iron in the slag was taken to be oxidic.

FITTED AND EXPECTED TRENDS

Correlations of electricity consumption, power-on time and iron yield are shown in Figure 6. Before fitting these trends (and plotting the data) outliers were removed using the approach of Iglewicz and Hoaglin (National Institute of Standards and Technology, 2020) to account for measurement and reporting errors; the total number of heats removed as outliers was 51 out of a total of 808. In Figure 6, the lines are separate linear fits to each of these correlations, with the slopes of the lines reported in Table 2. While the R^2 values of the correlations are low, the small P values do indicate significance and the fitted slopes are close to the theoretically expected values, as discussed below.

The expected slopes were calculated as follows: The effect of slag volume on energy consumption was estimated from the estimated average oxide composition of DRI. In the absence of detailed DRI analyses, it was assumed that the relative masses of SiO_2, Al_2O_3 and MnO in the DRI were the same as in the slag (that is, it was assumed that the main source of these species in the slag was the DRI). The ratio of FeO to gangue (SiO_2, Al_2O_3 and MnO) in the DRI was found from the DRI analyses. The required additions of CaO and CaO.MgO were calculated from the analysed MgO/CaO ratio in the slag and the B3 basicity value. The resulting mass balance (for 1 kg additional slag mass) is summarised in Figure 7. As this figure indicates, the composition of the additional slag that is estimated using this approach is similar to the average slag composition of Table 1.

For the energy balance, the input species were taken to be the simple compounds listed in Figure 7. To calculate the enthalpy of the slag, the heat of mixing of the liquid slag (relative to pure oxides) was based on a slag thermodynamics model (Björkvall, Sichen and Seetharaman, 2001). Based on this energy balance, the heat transfer required to melt and heat 1 kg of slag to 1600°C was estimated as 0.55 kWh/kg. This is close to the value of 0.53 kWh/kg mentioned in the classic study of the effects of DRI on EAF steelmaking (Rigaud, Marquis and Dancy, 1976). In comparison, the fitted slope was 0.78 kWh/kg.

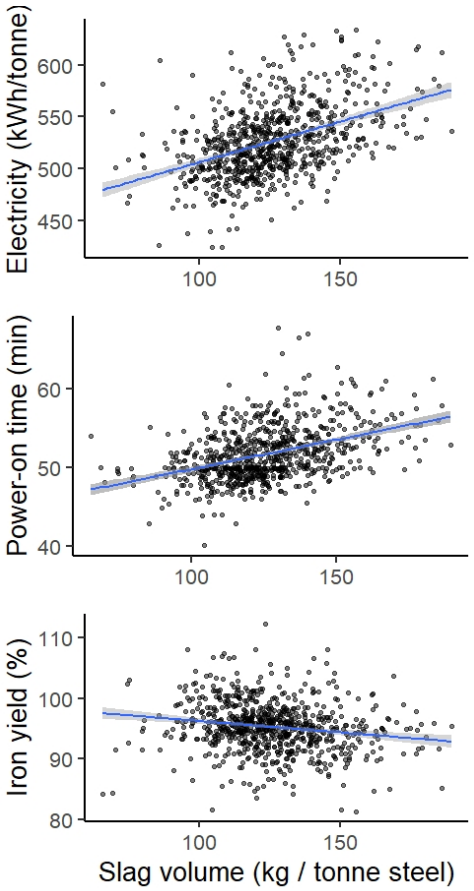

FIG 6 – Observed correlations between the slag volume, electricity consumption, power-on time and Fe yield. The lines show fitted linear relationships, with 95 per cent confidence intervals around these lines.

TABLE 2

Fitted and expected effects of changes in slag volume on electricity consumption, power-on time and Fe yield.

Output variable	Units	Theor coeff	Fitted coeff	Std error	Units of coefficient	R^2	*P* value
Electricity	kWh/tonne	0.55	0.78	0.06	kWh / kg slag	0.19	$<2 \times 10^{-16}$
Power-on time	min	0.076	0.075	0.006	min / (kg slag / tonne steel)	0.17	$<2 \times 10^{-16}$
Fe yield	%	-0.031	-0.038	0.008	% / (kg slag / tonne steel)	0.03	1.2×10^{-6}

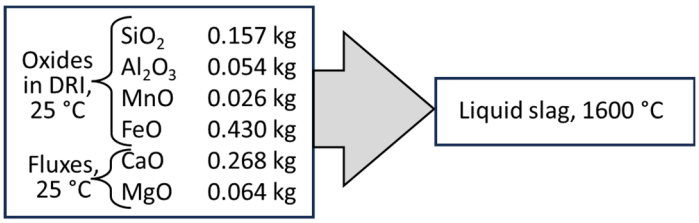

FIG 7 – Schematic of the inputs to the mass and energy balance used to estimate the effect of slag volume on electric arc furnace (EAF) energy consumption.

The expected effect of slag volume on the power-on time was calculated by using the observed relationship between the slag volume and electricity consumption (0.78 kWh/kg slag), together with the median power during arcing (95 MW); this gave an expected increase of 0.076 mins for every 1 kg/tonne increase in slag volume. The observed slope was nearly the same, at 0.075 min/(kg/tonne) (Table 2).

The effect of slag volume on iron yield was estimated by assuming that the slag composition would remain unchanged with increases in slag volume (Figure 4 does show that the relative variation in slag volume is much greater than the variation in the iron concentration in the slag). The yield is then given by the steel tap mass, divided by the sum of the tap mass and the mass of iron in the slag:

$$\text{Yield} = (100\%) / [1 + (W_{slag}/WFe^{tap})(\%Fe)_{slag}/100]$$

where:

W_{slag} is the slag mass

WFe^{tap} is the tap mass of steel

$(\%Fe)_{slag}$ is the iron concentration in the slag

This dependence was well approximated by a linear relationship between yield and slag volume, for values of the slag volume from 90 kg/tonne to 160 kg/tonne. The slope of this expected relationship is -0.031 per cent/(kg/tonne), which is similar to the fitted slope of -0.038 per cent/(kg/tonne) listed in Table 2.

The low R^2 value of the fitted correlation between slag volume and electricity consumption reflects the reality that several other process conditions strongly influence energy consumption. A previously fitted correlation for the electricity consumption includes tap-to-tap time, tapping temperature and injection of oxygen and natural gas, together with variables related slag volume (DRI and flux additions) (Kleimt *et al*, 2005). A similar approach was tested here, using the process variables listed in Table 3. These variables differed from those used by Kleimt *et al* in that the effects of DRI and flux additions were captured with the single variable of slag volume and carbon input was added as a variable. The carbon input was the sum of top-added carbon, injected carbon and the carbon in the DRI (calculated from the DRI mass and its average carbon concentration of 2.16 per cent).

TABLE 3

Process variables considered in multiple linear correlation for electricity consumption, with the observed ranges of the variables in the plant data.

Variable	Units	Min	Lower quartile	Upper quartile	Max
Slag	kg/tonne	65.6	113	137	189
Natural gas	Nm³/tonne	0	0.94	1.36	2.65
Carbon	kg/tonne	12.2	23.8	28.7	39.8
Oxygen	Nm³/tonne	13.7	19.7	22.5	27.3
Tap temp.	°C	1578	1620	1648	1714
Tap-to-tap	minutes	54.5	66.4	89.6	430
Pour-back*	tonne/tonne	0	0	0	0.32

*Only 16 heats out of 757 had non-zero pour-back amounts.

The coefficients from the multiple linear regression are reported in Table 4. The theoretical coefficients were calculated from mass and energy balances, with inputs and outputs as summarised in Table 5. The results of these calculations are summarised in Table 4 as the 'Theoretical coefficients'. The expected effect of pour-back is equal to the enthalpy of liquid iron at 1600°C, which is 377 kWh/tonne, similar to the previously used value of 385 kWh/tonne (Rigaud, Marquis and Dancy, 1976).

Table 4 shows that the fitted effects of slag volume, natural gas injection and carbon addition are similar to the theoretically calculated effects. Burning natural gas with oxygen decreases the electricity requirement: the natural gas burners are effective at melting scrap early in the heat. Carbon addition **increases** the electricity requirement, because the added carbon tends to reduce FeO from the slag; the reduction reaction (C + FeO → CO + Fe) is endothermic. The fitted effect of tap temperature is weaker than expected, but with a relatively large *P* value. The fitted benefit of pour-back is not as strong as expected, but this is based on a small number of heats.

Oxygen injection would be expected to decrease the electricity consumption because oxidation of iron is strongly exothermic; this is the basis for the theoretical coefficient of -5.4 kWh per Nm^3 of oxygen, as listed in Table 4. However, the fitted trend is that increased oxygen injection correlates with **higher** electricity consumption. A likely mechanism is that increased oxygen injection would increase the iron oxide concentration in the slag. An increased iron oxide concentration lowers the slag foaming index (Jung and Fruehan, 2000); poorer slag foaming can lead to increased heat loss to the furnace side walls, resulting in increased electricity consumption despite the exothermicity of iron oxidation.

TABLE 4

Theoretically calculated effects of process variables on electricity consumption (in kWh/tonne), with the coefficients from multiple linear correlation.

Variable	Theor coeff	Fitted coeff	Std error	*P* value
Slag	0.55	0.31	0.06	1.7×10^{-8}
Natural gas	-8.1	-7.9	2.7	0.0038
Carbon	3.3	3.0	0.26	$<2 \times 10^{-16}$
Oxygen	-5.4	4.6	0.49	$<2 \times 10^{-16}$
Tap temp.	0.23	0.08	0.04	0.056
Tap-to-tap	–	0.24	0.02	$<2 \times 10^{-16}$
Pour-back	-377	-169	44	0.00012

R^2 = 0.47; Residuals: 1st quartile -16.7 kWh/tonne; 3rd quartile 16.1 kWh/tonne.

TABLE 5

Summary of inputs and outputs used to estimate the effects of process variations on energy consumption.

Case	Inputs, with temperature	Outputs, with temperature
Natural gas combustion	CH_4 and stoichiometric O_2 (25°C)	CO_2, H_2O (1200°C)
Oxygen lancing	Fe (1600°C), stoich. O_2 (25°C)	FeO (1600°C)
Carbon injection	FeO (1600°C), stoich. C (25°C)	Fe (1600°C), CO (1200°C)
Melting DRI gangue	See Figure 7 for inputs (25°C)	Molten slag (1600°C)

The fitted and actual electricity consumption for all the heats is compared in Figure 8. The background shading in the figure shows the distribution of the data points. Most of the values cluster close to the median electricity consumption of 522 kWh/tonne. As noted in Table 4, half the fitted values of electricity consumption lie within 17 kWh/tonne of the actual values.

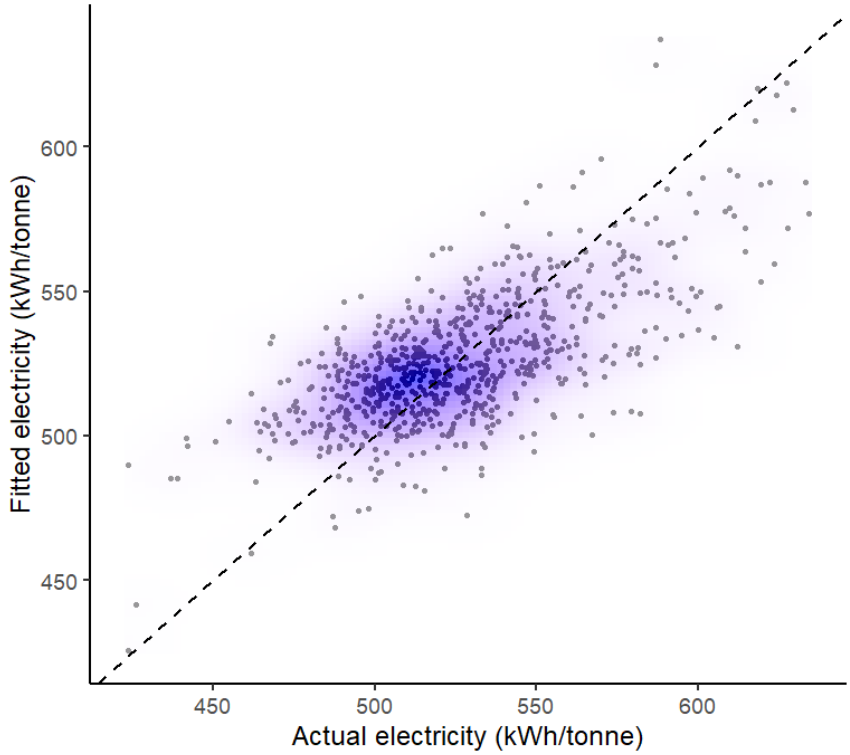

FIG 8 – Comparison of actual electricity consumption per heat and the consumption calculated with the coefficients from the multiple linear regression. The broken line shows the 1:1 relationship and the shading indicates the density of the distribution of points.

CONCLUSIONS

Analysis of a year's production data of an EAF plant that uses a large proportion of DRI confirmed the expected effects of the increased slag volume that would result from a higher input of gangue in DRI: Higher electricity consumption per tonne of steel, longer power-on times and decreased iron yield. The effects of process variables on process heating requirements – from multiple linear regression – generally agree with the quantitative relationships derived from simple mass and energy balances. A notable exception is oxygen usage: For the conditions considered here, increased oxygen injection was associated with higher electricity consumption, possibly because of a negative effect on slag foaming.

ACKNOWLEDGEMENTS

Support of this project by the industrial members of the Center for Iron and Steelmaking Research is gratefully acknowledged.

REFERENCES

Barrington, C, 2022. OBMs and Carbon Neutral Steelmaking, Paper 3 Future DRI Production and Iron Ore Supply [online], International Iron Metallics Association. Available from: <https://www.metallics.org/assets/files/Public-Area/Decarbonisation/Paper3_DRIProduction.pdf>

Björkvall, J, Sichen, D and Seetharaman, S, 2001. Thermodynamic model calculations in multicomponent liquid silicate systems, *Ironmaking and Steelmaking*, 28(3):250–257. https://doi.org/10.1179/030192301678118

Heo, J H and Park, J H, 2018. Effect of Direct Reduced Iron (DRI) on Dephosphorization of Molten Steel by Electric Arc Furnace Slag, *Metallurgical and Materials Transactions B*, 49(6):3381–3389. https://doi.org/10.1007/s11663-018-1406-5

Jung, S-M and Fruehan, R J, 2000. Foaming Characteristics of BOF Slags, *ISIJ International*, 40(4):348–355. https://doi.org/10.2355/isijinternational.40.348

Kim, W and Sohn, I, 2022. Critical challenges facing low carbon steelmaking technology using hydrogen direct reduced iron, *Joule*, 6(10):2228–2232. https://doi.org/10.1016/j.joule.2022.08.010

Kishida, T, Fukumoto, Y, Mogi, K and Kitazawa, T, 1980. The Result of Melting Direct Reduced Iron by UHP Arc Furnace, *Steel Times*, 208(2):137–143.

Kleimt, B, Köhle, S, Kühn, R and Zisser, S, 2005. Application of models for electrical energy consumption to improve EAF operation and dynamic control, 8th European Electric Steelmaking Conference, Birmingham.

National Institute of Standards and Technology, 2020. *NIST/SEMATECH e-Handbook of Statistical Methods (NIST Handbook 151).* https://doi.org/10.18434/M32189

Poveromo, J J, 1999. Iron ores, *The Making, Shaping and Treating of Steel*, *Ironmaking Volume* (ed: D H Wakelin), AISI Steel Foundation.

Rigaud, M, Marquis, H A and Dancy, T E, 1976. Electric arc furnace steelmaking with prereduced pellets, *Ironmaking and Steelmaking*, 3(6):366–372.

Song, S, Zhao, J and Pistorius, P C, 2020. MgO Refractory Attack by Transient Non-saturated EAF Slag, *Metallurgical and Materials Transactions B*, 51(3):891–897. https://doi.org/10.1007/s11663-020-01788-x

Research on –
New energy and metal production technologies

An attempt towards ferrochromium production using molten oxide electrolysis

DOI: 10.62053/NJRR1937

J Biswas[1], L Klemettinen[2], D Sukhomlinov[3], W Malan[4] and D Lindberg[5]

1. Assistant Professor, IIT Bombay, Powai, Mumbai, Maharashtra 400076, India. Email: biswasj@iitb.ac.in
2. Staff Scientist, Aalto University, Espoo, 00076 Aalto, Finland. Email: lassi.klemettinen@aalto.fi
3. Post-doctoral researcher, Aalto University, Espoo, 00076 Aalto, Finland. Email: dmitry.sukhomlinov@aalto.fi
4. Post-doctoral researcher, Aalto University, Espoo, 00076 Aalto, Finland. Email: willem.malan@aalto.fi
5. Associate Professor, Aalto University, Espoo, 00076 Aalto, Finland. Email: daniel.k.lindberg@aalto.fi

ABSTRACT

In order to mitigate the effects of climate change, our society must be able to drastically reduce its CO_2 emissions. As the metallurgical industry is a considerable contributor to these emissions, new greener technologies must be invented and developed. One option could be the direct production of metals from oxides using renewable electricity.

The aim of this study was to investigate the possibility of using high-temperature molten oxide electrolysis (MOE) for iron and ferrochrome production. FactSage™, ver 8.2 (by Thermfact Ltd and GTT-Technologies) was utilised for estimating a feasible equilibrium electrolyte composition, and the experiments were conducted at 1550–1580°C in conical alumina crucibles with iridium wire as the cathode and platinum wire as the anode. The sources of iron and chromium were either pure FeO powder or industrial chromite pellets. Voltage was applied to the electrolysis cell for 6 hrs and the resulting current was measured, along with oxygen concentration in the off-gas line.

The electrolyte comprised of SiO_2, Al_2O_3, MgO and CaO. First, the effect of FeO concentration on iron reduction efficiency was investigated using only pure oxide powders as starting materials. The results indicated that 10 wt per cent FeO mixed with the electrolyte resulted in more efficient iron reduction compared to 20 wt per cent. In further experiments, industrial chromite pellets were ground and mixed with the CaO-free electrolyte. Iron and chromium reduction efficiencies were higher when approximately 19 wt per cent of the total sample mass consisted of pellets compared to increasing the pellet amount to 37 wt per cent. Generally, the chromium solubility in the liquid electrolyte was relatively low, and most of the chromium was confined to the spinel solid solution, from where its dissolution to the liquid electrolyte was very slow, resulting in slow reduction kinetics. For larger scale applications, economically more viable electrode materials should be investigated.

INTRODUCTION

The global challenge to mitigate the greenhouse gas emission has impacted steel industry, which accounts for 7 to 9 per cent of global greenhouse gas emissions (Kim *et al*, 2022). The traditional iron production process involves coke for iron ore reduction, resulting in a carbon footprint of 1.6–2 tons of CO_2 per ton of crude steel (Somers, 2021). Currently, the EU aims to decrease the greenhouse gas emissions by 80–95 per cent by 2050 compared to the level in 1990 (European Commission, 2011), which will also require a technological breakthrough in the steel industry. In order to address this challenge, extensive research is ongoing globally for example regarding hydrogen steelmaking (Patisson and Mirgaux, 2020), carbon capture and storage (Raza *et al*, 2019) and molten oxide electrolysis (Allanore, 2015). Molten oxide electrolysis (MOE) is a process where metals can be produced directly by electrolysis of oxidic ores or concentrates (Allanore, 2015). In recent years, this technology has drawn the attention of several steelmakers as a possible clean metals production route. The main challenges in iron ore electrolysis can be summarised as: 1) the operating temperature should be above the melting temperature of iron (1538°C); 2) most metals that could be used as anodes do not survive under the corrosive and oxidising conditions at the

anode; 3) the multivalent state of iron causes loss of current due to electronic conduction in the melt (Allanore, Yin and Sadoway, 2013).

In recent years, there has been some progress about anode materials and more information has been obtained regarding the electrochemical nature of iron ions in oxide melts (Zhou *et al*, 2017a). Initially, Kim *et al* (2011) proposed iridium as an anode material, but only for acidic melts. Later, Allanore, Yin and Sadoway (2013) proposed a chromium-based alloy for anode, which exhibited limited consumption during iron extraction and oxygen evolution due to formation of an electronically conductive solid solution of chromium and aluminium oxide. Wiencke *et al* (2018) studied production of iron from acidic melt by electrolysis, utilising platinum as anode and an alloy of platinum and 30 per cent rhodium as cathode. In another work, Zhou *et al* (2017a) produced Fe and Fe-Ni alloys from CaO-MgO-SiO_2-Al_2O_3-Fe_2O_3 and CaO-MgO-SiO_2-Al_2O_3-Fe_2O_3-NiO melts using a graphite anode and molybdenum cathode. Jiao *et al* (2018) produced Ti-Fe alloys via MOE from CaO-Al_2O_3-MgO-TiO_2 melt using liquid iron as cathode and graphite as anode. Liu, Zhang and Chou (2015) have also demonstrated iron production from CaO-Al_2O_3-SiO_2-Fe_2O_3 melt via electrolysis using molybdenum cathode and graphite anode. Although some progress has been made, the technology is still facing several other challenges, such as low current efficiency and lack of inexpensive, inert anode materials. The use of graphite as an anode is feasible, but as the oxygen formed at the anode reacts with carbon, some direct CO_2 emissions will be produced. More research is required to mature this technology for industrial iron production without any direct CO_2 emissions.

In this study, a set-up for molten oxide electrolysis experiments was established and experiments were conducted with synthetic MgO-SiO_2-Al_2O_3-CaO-FeO mixtures to produce molten iron by electrolysis. Some experiments were also conducted with industrial chromite pellets, with an objective to test the feasibility of producing ferrochrome alloy via molten oxide electrolysis in laboratory scale.

EXPERIMENTAL

Materials

The raw materials for the study were synthetic oxide powders and industrial chromite pellets supplied by Outokumpu (Finland), as presented in Tables 1 and 2. For each experiment, a total of approximately 16 g of the oxide mixture was prepared by grinding the oxides at different mass ratios using mortar and pestle, followed by pressing the mixtures into pellets. The starting compositions for all four experiments presented in this work are shown in Table 3.

TABLE 1

Materials used in the experiments.

Material	Supplier	Purity	Notes
Al_2O_3	Sigma Aldrich	> 99%	
SiO_2	Sigma Aldrich	99%	
MgO	Sigma Aldrich	> 99%	
CaO	Sigma Aldrich	99.9%	
FeO	Sigma Aldrich	99.7%	
Chromite pellets	Outokumpu, Finland	See Table 2	From Kemi mine, diameter approximately 10 mm
Pt (anode and wiring)	Johnson-Matthey Noble Metals	> 99.9%	Diameter 0.5 mm (anode) and 0.25 mm (wires)
Ir (cathode)	Johnson-Matthey Noble Metals	> 99.9%	Diameter 0.5 mm
Al_2O_3 (crucible)	Kyocera	> 99.5%	Conical, max diameter 29 mm, height 38 mm
Al_2O_3 (tubes)	Kyocera	> 99.5%	OD 8 mm (supporting rod), OD 1 mm (electrode and wiring protection)
Al_2O_3 cement (two-component)	Morgan Advanced Materials Haldenwanger GmbH		Used for building the supporting rod and attaching electrodes

TABLE 2

Composition of chromite pellets.

	SiO_2	Al_2O_3	MgO	Fe_2O_3	FeO	Cr_2O_3	MnO	TiO_2	CaO
wt%	3.3	13.8	11.2	23.8	2.9	43.8	0.20	0.50	0.6

TABLE 3

Starting compositions for the experiments, in wt%.

Oxide melt code	Al_2O_3	SiO_2	MgO	FeO	Fe_2O_3	Cr_2O_3	CaO	MnO	TiO_2
A	20.0	48.0	12.0	10.0			10.0		
B	17.5	42.0	10.5	20.0			10.0		
C	18.5	31.8	23.8	1.0	8.5	15.7	0.2	0.07	0.18
D	19.9	39.7	27.3	0.5	4.3	7.9	0.1	0.04	0.09

Apparatus

A vertical laboratory furnace (Nabertherm RHTV 120-150/18, equipped with molybdenum disilicide heating elements) with 38 mm inner diameter alumina work tube was used for the experiments. The furnace gas outlet was connected to an oxygen sensor (Rapidox 2100ZF) for the measurement of the oxygen concentration using Rapidox software, ver 7.0.85 (by Cambridge Sensotec). The furnace was also connected to a potentiostat-galvanostat (VersaSTAT 4, Princeton Applied Research) for the application of potential and VersaStudio software, version 2.62.2 (by Ametek Scientific Instruments) was used for recording the data. The electrolysis cell consisted of a conical alumina crucible of 29 mm max diameter and 38 mm outer height, and the final design used an iridium wire cathode of 0.5 mm diameter and a platinum wire anode of 0.5 mm diameter. Trials were conducted using thinner electrode wires, which resulted in the wires breaking during the experiments. Similar problems were also encountered when iridium was tested as the anode.

The electrodes were immersed from the top of the crucible and secured with alumina cement at approximately diametric opposite locations (Figure 1). The cathode wire was placed at the bottom of the electrolysis cell, and the vertical part was covered by a thin alumina tube. The anode was placed on the other side of the cell, approximately 12 mm above the bottom of the cell. At the beginning of each experiment, the distance from the tip of the cathode to the tip of the anode was approximately 12 mm. To hold the electrolysis cell, a bigger cylindrical crucible (35 mm outer diameter and 50 mm height) was connected to a hollow supporting rod. The anode and cathode wires from the cell were welded to the electrical wires (0.25 mm diameter platinum) and passed through the supporting rod to the outside of the furnace and connected to the potentiostat. One of the electrical wires within the supporting rod was covered by a thin alumina rod, to avoid any possibility of a short circuit.

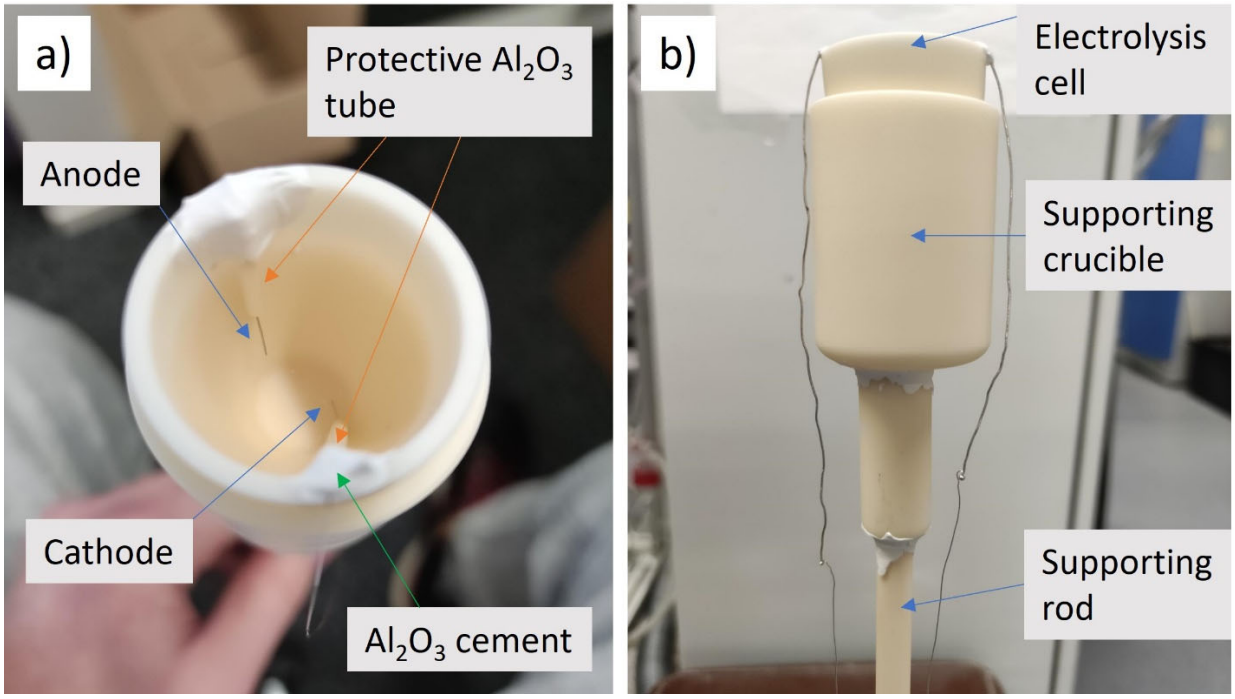

FIG 1 – (a) Electrolysis cell from the top, showing the cathode and anode, (b) Electrolysis cell inside the supporting crucible, attached to the supporting rod.

Procedure

For the experiments, the electrolysis cell with the oxide mixture was first lifted to the middle of the furnace at room temperature using the support rod, after which the furnace was sealed. The furnace was heated to the target temperature at 4°C/min under continuous flow of argon with 120 mL/min flow rate. The oxygen measurement was started approximately 30 mins after starting to heat the furnace, and the measurement interval was 10 secs. At the target temperature, the experiments were conducted in potentiostatic mode of the potentiostat-galvanostat, ie a constant potential was applied to the cell for a certain period of time and the resulting electrical current data was recorded every 5 secs. After the completion of the experiment, the furnace was cooled to room temperature under argon atmosphere, after which the cell was removed from the furnace, the sample was collected and broken using a hammer, and the weight of the formed metal alloy droplet at the cathode was recorded.

Characterisation

The preliminary elemental compositions of the metal alloys, slags and spinels were analysed using a scanning electron microscope (SEM, Mira3, Tescan, Czech Republic) equipped with an energy dispersive spectrometer (UltraDry Silicon Drift EDS, Thermo Fisher Scientific, USA). The final chemical compositions of all three phases were characterised using EPMA (SX100, Cameca SAS, France) with 20 kV acceleration voltage and 40 nA beam current. Depending on the phase, either focused, 5 µm or 20 µm defocused beam diameters were employed. The used standards as well as X-ray lines analysed and peak and background dwell times have been presented in Table 4. The elements Mn and Ti were present only in trace quantities and originated from the industrial chromite pellets.

TABLE 4

EPMA parameters – analysed elements, X-ray lines, peak and background dwell times and standard materials utilised.

Element	O	Si	Al	Cr	Mg	Ir	Pt	Ca	Mn	Fe	Ti
Line	Kα	Kα	Kα	Kα	Kα	Lα	Lα	Kα	Kα	Kα	Kα
Peak dwell time (s)	20	20	20	30	20	20	30	20	20	20	20
Total background dwell time	20	20	20	30	20	20	30	20	20	20	20
Standard material	Al_2O_3	Quartz	Al_2O_3	Chromite	Diopside	Ir metal	Pt metal	Diopside	Rhodonite	Hematite	Rutile

RESULTS AND DISCUSSION

Electrolysis for iron production

The first electrolysis experiment for iron oxide reduction was performed in potentiostatic mode with 10 per cent CaO, 12 per cent MgO, 48 per cent SiO_2, 20 per cent Al_2O_3, 10 per cent FeO (melt A) at 1540°C. The phase diagrams for the melt, in two oxygen partial pressures at 1550°C, are presented in Figure 2. In a molten oxide electrolysis cell, oxygen pressure at the anode increases due to oxygen evolution reaction. The slag composition for this experiment was selected in the fully liquid region as marked in Figure 2. When the oxygen partial pressure increases during electrolysis, the slag should still remain fully liquid throughout the electrolysis cell, according to Figure 2b.

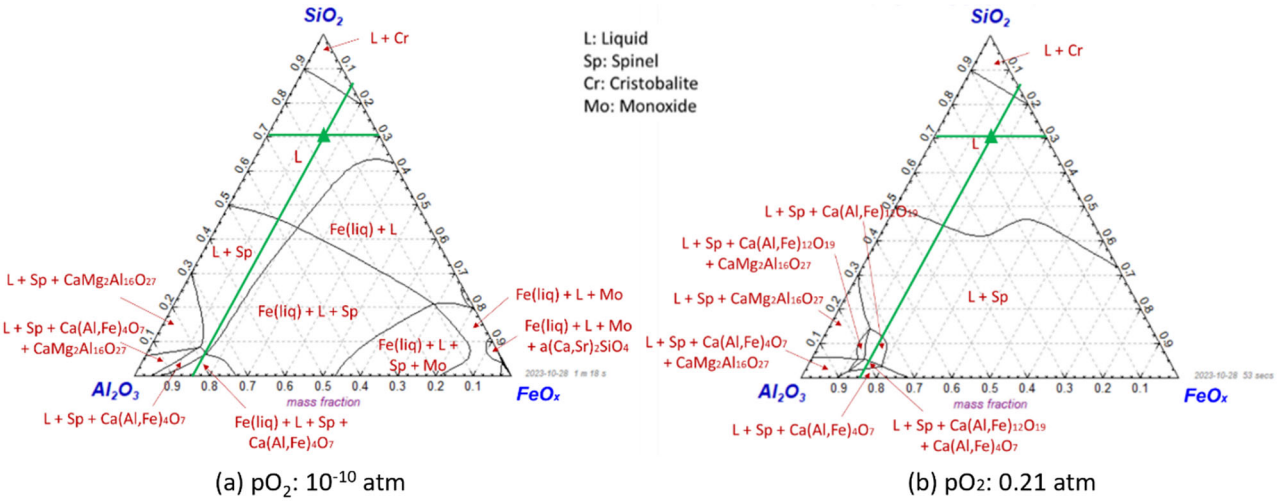

(a) pO_2: 10^{-10} atm (b) pO_2: 0.21 atm

FIG 2 – SiO_2-Al_2O_3-FeO_x ternary phase diagrams at 1550°C with fixed CaO and MgO concentrations (10 wt per cent each) at oxygen partial pressure of 10^{-10} and 0.21 atm in (a) and (b), respectively. The green triangle represents the starting composition in the first experiment (melt A). The lower oxygen partial pressure represents the area around the cathode and the higher represents the area around the anode.

A potential of 3V was applied to the oxide melt for 6 hrs. The resulting electrical current and the oxygen concentration in the off-gas line as a function of time have been presented in Figure 3. For the experiments where only iron oxide reduction occurred, 3V potential was chosen in order to imitate the experimental conditions chosen by Wiencke *et al* (2018).

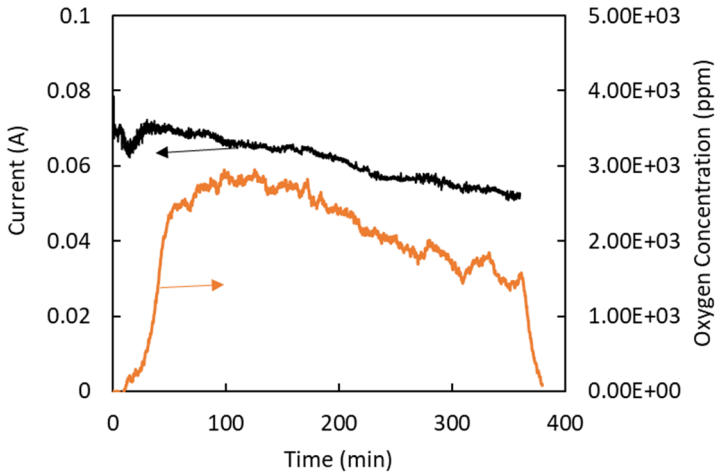

FIG 3 – Current in the electrolysis cell (black line) and oxygen concentration (orange line) as a function of time for electrolysis of 10 per cent CaO, 12 per cent MgO, 48 per cent SiO_2, 10 per cent Al_2O_3, 10 per cent FeO melt at 1540°C with 3V potential.

Initially, the current through the cell was approximately 80 mA and it decreased with the progression of reduction, reaching a value of slightly over 50 mA at the end of the 6 hr experiment. Previous studies on electrical properties of FeO-CaO, FeO-SiO_2, CaO-SiO_2 and CaO-FeO-SiO_2 slags/melts have revealed that cations (such as Ca^{2+} or Fe^{2+} ions) are the exclusive ionic charge carriers in these melts and contribute significantly to the ionic conductivity (Barati and Coley, 2006a, 2006b). Other ions, such as $(SiO_4)^{4-}$ and $(FeO_4)^{5-}$ are relatively immobile due to their large tetrahedral structures, hence their contribution to ionic conductivity can be ignored. Therefore, for CaO-MgO-SiO_2-Al_2O_3-FeO melt, it can be assumed that ionic conduction happens through only Ca^{2+}, Fe^{2+} and Mg^{2+} ions. As the electrolysis time increases, the concentration of Fe^{2+} ions decreases in the melt due to reduction into metallic iron, which in turn decreases the ionic conductivity of the melt. This is in agreement with observations from electrolysis in aqueous medium (Yuan and Haarberg, 2009; King and Botte, 2011), and is the reason for the slow decrease in the measured current value with time in Figure 3. The corresponding oxygen concentration could be seen to increase to as high as approximately 2750 ppm during the electrolysis. It could also be noted that there exist few small peaks, indicating fluctuations and sudden rises in the oxygen concentration. Generally, these oxide melts are viscous, which may cause difficulties in releasing the generated oxygen bubbles from the anode. There is a possibility of a fraction of the anode surface area being blocked by oxygen bubbles, which would decrease the available surface area for further anodic reactions. The sudden release of these bubbles from anode possibly results in sudden rises in oxygen concentrations (small peaks at different times). This phenomenon at the anode has also been reported by Zhou *et al* (2017b).

After 6 hrs of electrolysis for this melt, a metal droplet weighing 0.14 g was recovered at the cathode and the composition of this metal alloy droplet was 79.1 wt per cent Fe and 20.4 wt per cent Ir according to EPMA analysis. An SEM image of the metal droplet is shown in Figure 4b. Even though a significant amount of Ir dissolved in the metal alloy droplet, the cathode retained roughly its original shape after several hours of electrolysis. An image of the electrolyte, showing spinel formation at the crucible-electrolyte interface and within the electrolyte, is shown in Figure 4a.

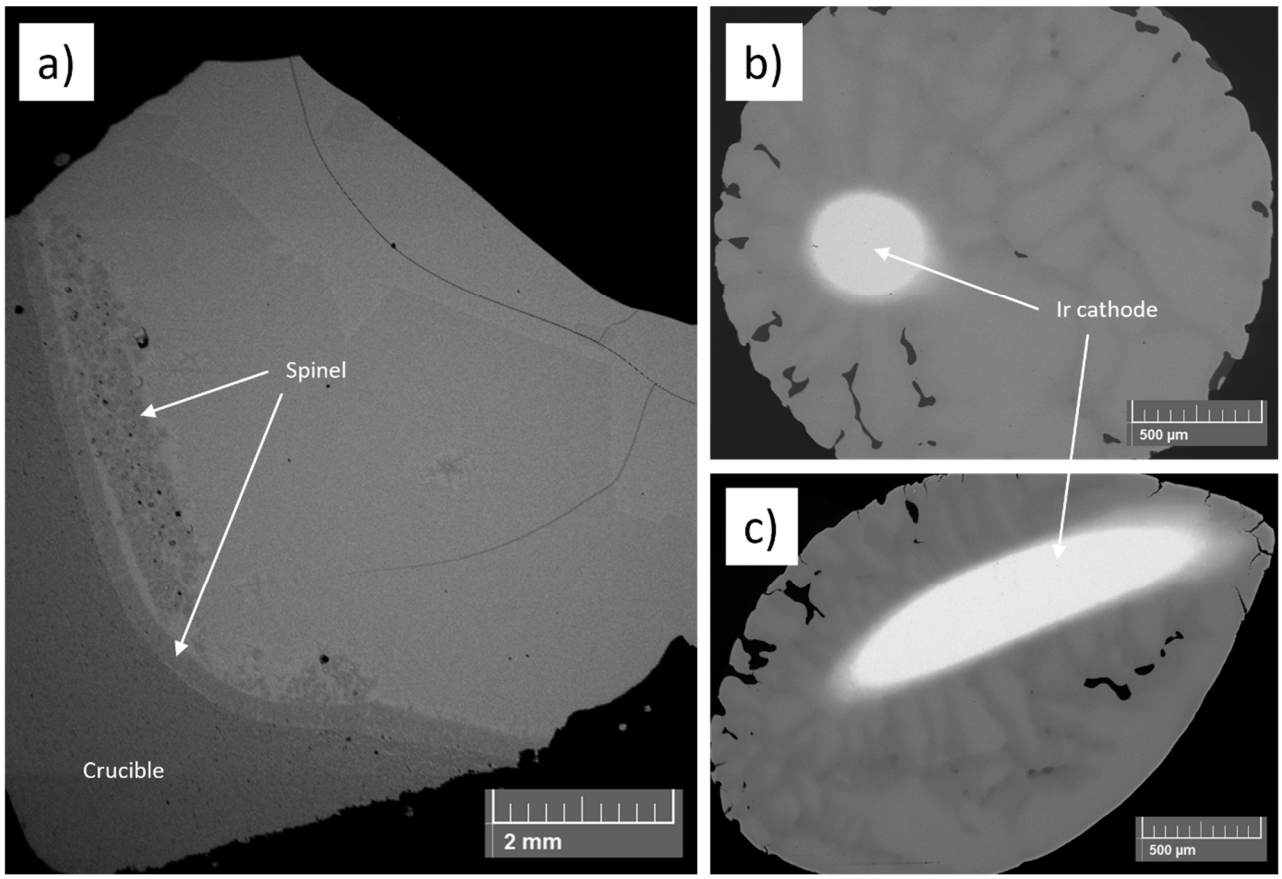

FIG 4 – (a) Microstructure of the electrolyte (slag) after FeO reduction with 10 wt per cent FeO and 10 wt per cent CaO (melt A); (b) metal alloy droplet formed during the experiment with 10 wt per cent FeO and 10 wt per cent CaO; (c) metal alloy formed during the experiment with 20 wt per cent FeO and 10 wt per cent CaO (melt B). 3V potential was applied in all cases.

The cathodic efficiency was calculated according to Equation (1) from the iron recovered at the cathode and the total transferred charge from the cathode, assuming all charge transfer was due to the cathodic reaction of iron oxide reduction.

$$Cathodic\ efficiency = \frac{Fe_{recovered}}{Fe_{current}} * 100\% \quad (1)$$

Where $Fe_{recovered}$ is the total moles of iron recovered from the cell and $Fe_{current}$ is the moles of Fe generation expected based on the cell current, assuming all charge is involved in iron reduction.

The results from the current study were compared with the results obtained by Wiencke *et al* (2018). They performed electrolysis by applying 3V potential for 6 hrs on 15 per cent FeO, 17 per cent Al_2O_3, 56.1 per cent SiO_2, 11.9 per cent MgO melt at 1550°C. Interestingly, the current in their electrolysis cell seemed to increase from 70 mA to around 80 mA, whereas in our case, the current decreased with time. Wiencke *et al* obtained a cathodic efficiency of 36 per cent, which is quite comparable with the value of 27.6 per cent obtained in the current study.

To gain a better understanding of the iron reduction process with MOE, another experiment was conducted using a higher FeO starting concentration (20 wt per cent, melt B). The iron oxide concentrations of 10 and 20 wt per cent in this work were chosen based on the work of Sadoway (1995). A potential of 3 V was applied for 6 hrs, and the formed metal alloy droplet is shown in Figure 4c. Interestingly, the cell current almost doubles (from 70 mA to 118 mA) by doubling the Fe-ion concentration in the melt, as presented in Figure 5. The cathodic efficiencies for the experiments with 10 and 20 wt per cent FeO were calculated according to Equation (1). Table 5 presents the viscosities from Factsage™, cathodic efficiencies, as well as ionic and electronic conductivities for both melts. The ionic conductivities were calculated from Nernst Einstein Equation (Barati and Coley, 2006b), where cations Ca^{2+}, Fe^{2+} and Mg^{2+} were assumed to be the exclusive ionic charge carriers. For this calculation, the diffusivities of Ca^{2+} and Fe^{2+} were adopted from the values reported by Barati

and Coley (2006b) and modified according to the respective slag viscosities. As the data for Mg^{2+} diffusivity was not available, it was assumed to be the same as Ca^{2+}. The electronic conductivities of the melts were calculated based on the diffusion assisted charge transfer model developed by Barati and Coley (2006b). Both ionic and electronic conductivities in the melt increase with total Fe-ion concentration increase. This illustrates the reason for higher cell current with higher FeO concentration. Although the cell current rises with increasing FeO concentration, the cathodic efficiency decreases and the Fe recovery from melt also decreases, indicating very poor performance with the melt containing more iron oxide. According to Table 5, the ionic conductivity increases by 33 per cent with increasing total FeO concentration from 10 per cent to 20 per cent, while at the same time the electronic conductivity increases by 470 per cent. The higher electronic conductivity increases cell current losses, and this possibly results in lower cathodic efficiency and decreased Fe recovery from electrolysis of higher iron oxide melt. On the other hand, FeO being a network breaker, viscosity decreases with increasing iron oxide concentration, which should ease the escape of O_2 bubbles from the melt. It should also be noted that the electrolysis cell broke towards the end of the experiment with 20 wt per cent FeO (current decrease after 300 min in Figure 5), resulting in some of the electrolyte leaking to the support crucible. This also has some contribution to the poor reduction performance. The breakage was most likely due to significant alumina dissolution from the crucible (electrolysis cell) because the starting composition of the electrolyte was relatively far from the liquid-spinel saturation boundary shown in the phase diagrams of Figure 2.

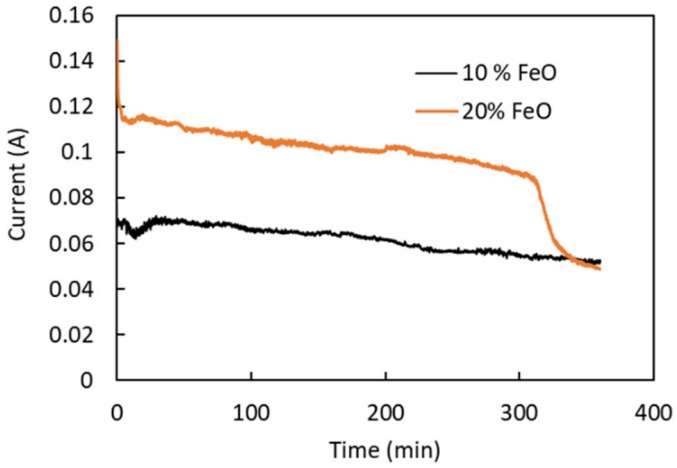

FIG 5 – Cell current profile for electrolysis of CaO-SiO_2-Al_2O_3-MgO-FeO melts with two different concentrations of FeO at 1540°C.

TABLE 5

Comparison of CaO-SiO_2-Al_2O_3-MgO-FeO melt electrolysis performance at 1540°C with 3V potential by varying the FeO concentration.

Oxide melt code	Electrolyte FeO (wt%)	Viscosity (poise)	Cathodic efficiency (%)	Electronic conductivity (S/m)	Ionic conductivity (S/m)	Fe recovery (%)
A	10	9.30	27.6	0.03	18.62	9.15
B	20	3.36	13.1	0.17	24.86	3.43

The overall Fe recovery percentage was calculated based on Equation (2):

$$Fe\ Recovery\ (\%) = \frac{Fe_{recovered}}{Fe_{total}} * 100\% \quad (2)$$

where Fe_{total} is the total moles of Fe in the oxide melt at the beginning of the experiment. The iron recovery was approximately 9.2 per cent with 10 wt per cent FeO in the starting mixture and

decreased to 3.4 per cent when FeO concentration was increased to 20 wt per cent. These values are very low compared to the traditional ironmaking processes.

Electrolysis for ferrochrome production

The feasibility of MOE for ferrochrome production was also investigated with two experiments. The electrolyte consisted of Al_2O_3-SiO_2-MgO mixed with chromite pellets (Table 2) at different mass ratios. Two phase diagrams for the pellet-containing system are presented in Figure 6 at 1550°C for $pO_2 = 10^{-10}$ and 0.21 atm. The green triangle represents the starting composition for the experiment with melt C (Table 3). The single-phase liquid region almost disappears when the oxygen pressure increases from 10^{-10} atm to 0.21 atm, indicating that with any melt composition, there will always be spinels present near the anode, ie high oxygen partial pressure region. In this case, when using chromite pellets in the starting mixture, the composition will always be in the liquid-spinel region. This means that the melt viscosity will increase, but the alumina crucible dissolution will decrease, increasing the lifetime of the electrolysis cell.

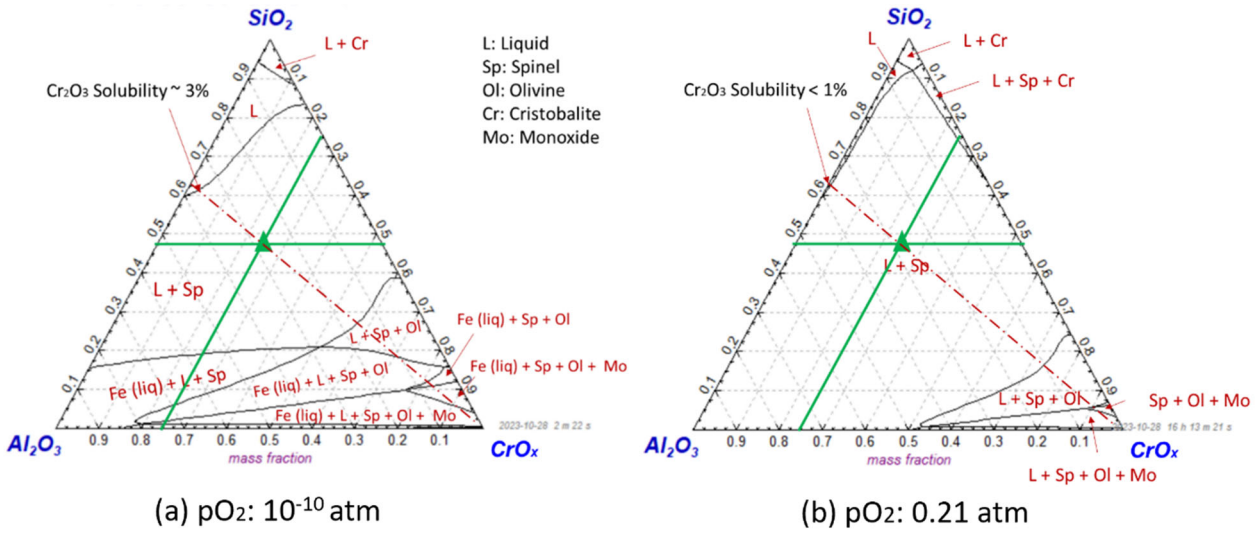

FIG 6 – SiO_2-Al_2O_3-CrO_x ternary phase diagrams at 1550°C with MgO, Fe_2O_3 and CaO concentrations fixed at 23.8 wt per cent, 9.71 wt per cent and 0.21 wt per cent, respectively, for oxygen partial pressures of 10^{-10} and 0.21 atm.

The first experiment with chromite pellets was performed at approximately 1580°C with 5.8 g of pellets, resulting in 8.5 wt per cent Fe_2O_3, 1.0 wt per cent FeO and 15.7 wt per cent Cr_2O_3 in the melt (oxide melt C in Table 3). As the reduction potential of chromium is higher than that of iron, a higher cell potential was selected for this case. A potential of 6V was applied for 6 hrs, and a metal droplet of approximately 0.45 g (64.5 wt per cent Fe, 2.4 wt per cent Cr and 32.6 wt per cent Ir according to EPMA analyses) was reduced at the cathode. The cell current profile as well as the oxygen concentration profile are presented in Figure 7, and the formed metal alloy droplet is shown in Figure 8b. The cell current slowly increases during the first 100 mins, after which it remains stable for about 150 mins and then it decreases. The oxygen evolution profile shows almost similar trend, but with few additional peaks. Interestingly, the cell current for electrolysis of synthetic iron oxide, as presented in Figures 3 and 5, was observed to decrease continuously as a function of time. In the synthetic iron oxide case, all the conducting ions (Ca^{2+}, Mg^{2+}, Fe^{2+}) were more or less uniformly distributed in the liquid oxide, where the concentration of Fe^{2+} ions decreased due to reduction, and this resulted in decreasing ionic conductivity with increasing electrolysis time. In contrast to that, for the oxide system with pellets, a large amount of the conducting ions are expected to be bound inside the solid spinel phase (Figure 6 and Figure 8a). These ions (Cr^{3+}, $Fe^{3+,2+}$, Mg^{2+}) slowly dissolve to the liquid electrolyte, maintaining its composition almost the same during the electrolysis process. Therefore, the conductivity variation over time should be lower in this case, resulting in a relatively stable cell current. The peaks in oxygen profile could be due to sudden escape of O_2 bubble clusters from the anode. However, these peaks are more prominent during chromite pellet reduction compared to synthetic FeO reduction. Oxygen evolution in molten oxides is likely controlled by the

oxygen-containing reactant transport (Allanore, 2013), and some explanations may be found from spatiotemporal differences in transport properties of the melts during the electrolysis process.

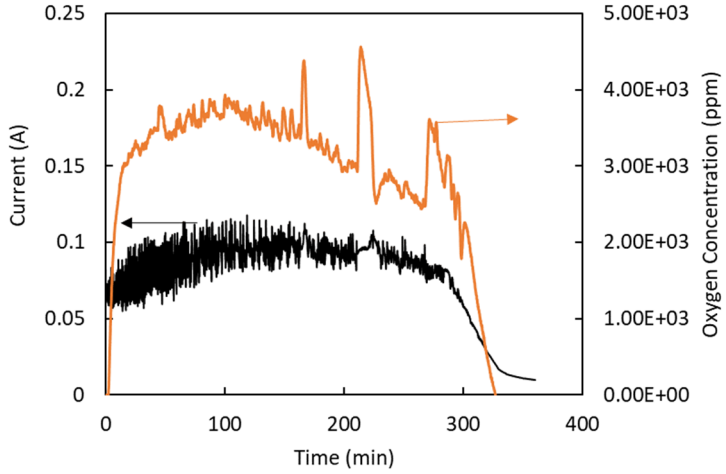

FIG 7 – Cell current (black line) and oxygen concentration (orange line) as a function of time for electrolysis of oxide melt C at 1580°C with 6V cell potential.

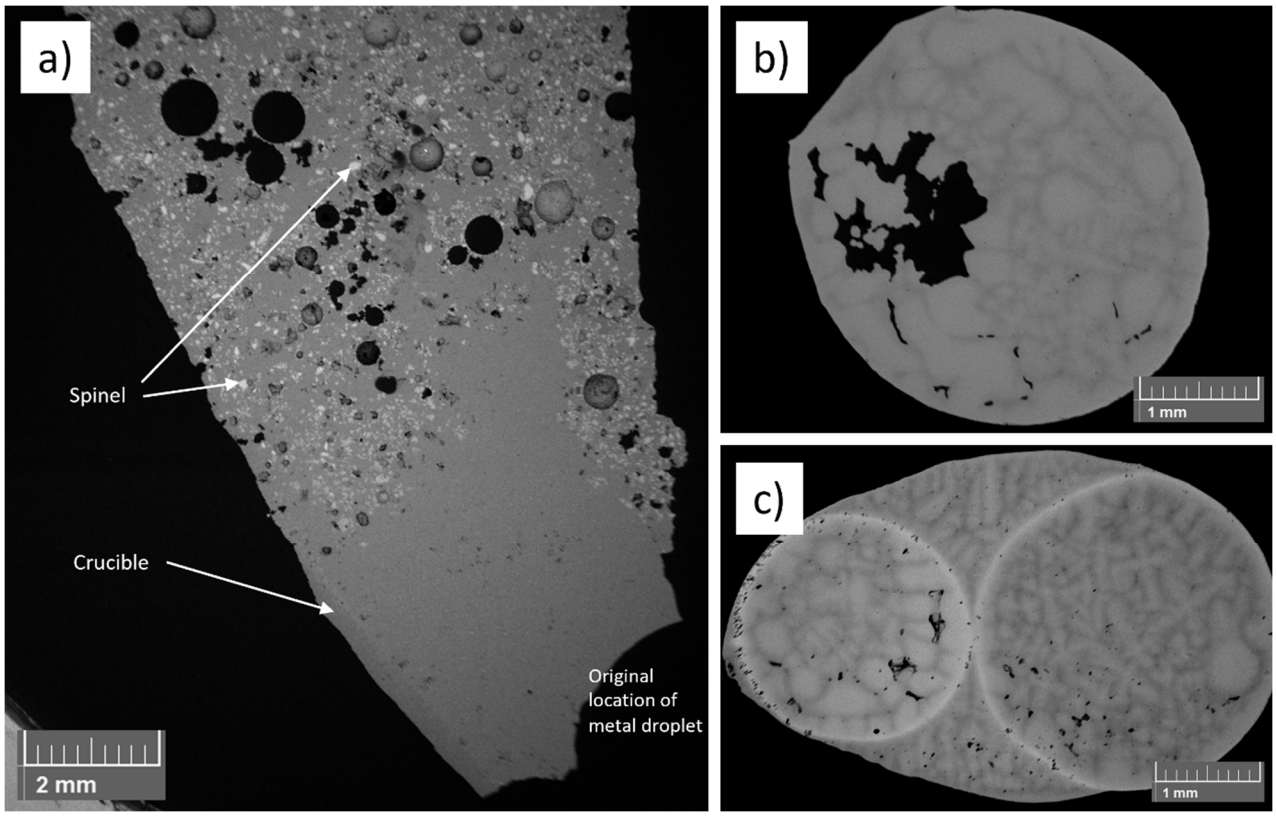

FIG 8 – a) Microstructure of the electrolyte (slag) after iron and chromium reduction from chromite pellets with melt D; b) metal alloy droplet formed during reduction with melt C; c) alloy formed during reduction with melt D. 6V potential was applied in all cases.

The recoveries of Fe and Cr, according to Equation (2), were calculated to be 26.4 per cent and 0.6 per cent, respectively. Although the iron recovery is higher with chromite pellets compared to synthetic FeO reduction, the Cr recovery seems to be very low. The main challenge for chromium reduction is the low solubility of chromium oxide in the liquid electrolyte at the experimental temperature. The chromium reduction seems to be a three-step process: 1) chromium oxide dissolution from the spinel to the liquid phase; 2) transport of chromium ions in the liquid phase to the cathode; and 3) reduction of chromium ions at the cathode. Furthermore, chromium is a multivalent ion, therefore its reduction occurs firstly from 3+ to 2+, followed by reduction into metallic

Cr at the cathode. It is unclear which stage is the rate limiting in this case, but the complexity of chromium reduction process is evident.

The second electrolysis experiment containing chromite pellets was conducted by decreasing the pellet mass (melt D). SEM images of the electrolyte and formed metal alloy are shown in Figure 8a and 8c, respectively. Cell current profile comparison for melts C and D is presented in Figure 9 and the starting composition comparison is shown in Table 3. Interestingly, the cell current is much lower for the higher iron and chromium oxide containing melt compared to the melt with lower concentration of these oxides. The recovery of iron and chromium could also be observed to increase with decreasing pellet mass, as shown in Table 6. When decreasing the pellet mass, the starting composition is closer to the liquid phase boundary shown in Figure 6, indicating a lower fraction of spinel and lower total viscosity, which increases the mobility of the conducting ions and could explain the higher cell current as well as higher Fe and Cr recoveries.

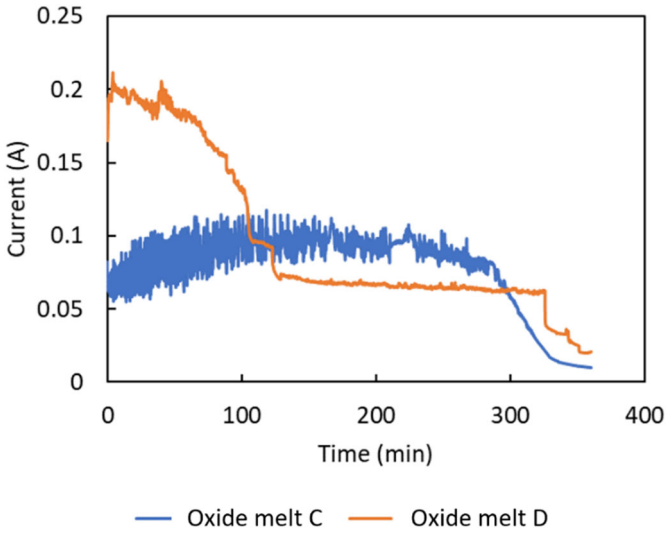

FIG 9 – Cell current profiles for electrolysis of $CaO\text{-}SiO_2\text{-}Al_2O_3\text{-}MgO\text{-}Fe_2O_3\text{-}Cr_2O_3$ melts with different masses of ferrochrome pellets at 1580°C.

TABLE 6

Electrolysis performance comparisons of ferrochrome containing oxide systems C and D at 1580°C with 6V cell potential.

Oxide system code	Mass of pellets / total sample mass (g)	Viscosity (Poise)	Fe recovery (%)	Cr recovery (%)
C	5.8 / 16	Higher	26.4	0.62
D	3.0 / 16	Lower	30.9	1.77

According to Sadoway (1995), the MOE technology could be capable of producing ferrochromium (80 per cent Fe – 20 per cent Cr) with less energy than the existing processes, and naturally with considerably less process carbon. However, based on the results of the current study, a huge amount of work is required before ferrochromium production using MOE can be considered feasible and attractive.

CONCLUSIONS

In this study, the performance of molten oxide electrolysis for the reduction of iron oxide and chromite pellets was investigated. For $CaO\text{-}SiO_2\text{-}Al_2O_3\text{-}MgO\text{-}FeO$ melt, the iron recovery was less than 10 per cent and it decreased with increasing concentration of FeO from 10 to 20 wt per cent in the starting mixture. When adding industrial chromite pellets to the melt without CaO, the iron recovery improved significantly compared to synthetic iron oxide reduction. Decreasing the pellet mass from

5.8 g to 3 g (total mass approximately 16 g) resulted in a slight increase in iron recovery while chromium recovery almost tripled, however, it still remained below 2 per cent.

Provided that green electricity is available, molten oxide electrolysis is a clean metal production technology and could be a potential route for larger iron production in the future. However, extensive research is required to make the process efficient enough for production of chromium-containing alloys, and in general to make the process industrially attractive.

ACKNOWLEDGEMENTS

This study is part of the Business Finland-funded TOCANEM Project (Grant number 2118452). During the work, the Academy of Finland's RawMatTERS Finland Infrastructure (RAMI) based at Aalto University, GTK, and VTT in Espoo was utilised.

REFERENCES

Allanore, A, 2013. Electrochemical engineering of anodic oxygen evolution in molten oxides, *Electrochimica Acta*, 110:587–592.

Allanore, A, 2015. Features and Challenges of Molten Oxide Electrolytes for Metal Extraction, *Journal of The Electrochemical Society*, 162(1):E13–E22.

Allanore, A, Yin, L and Sadoway, D, 2013. A new anode material for oxygen evolution in molten oxide electrolysis, *Nature*, 497:353–356.

Barati, M and Coley, K S, 2006a. Electrical and Electronic Conductivity of CaO-SiO_2-FeO_x Slags at Various Oxygen Potentials: Part I, Experimental Results, *Metallurgical & Materials Transactions B*, 37B:41–49.

Barati, M and Coley, K S, 2006b. Electrical and Electronic Conductivity of CaO-SiO_2-FeO_x Slags at Various Oxygen Potentials: Part II, Mechanism and a Model of Electronic Conduction, *Metallurgical & Materials Transactions B*, 37B:51–60.

European Commission, 2011. A Roadmap for Moving to a Competitive Low Carbon Economy in 2050. Available from: <https://eur-lex.europa.eu/LexUriServ/LexUriServ.do?uri=COM:2011:0112:FIN:en:PDF> [Accessed: 11 January 2024].

Jiao, H, Tian, D, Tu, J and Jiao, S, 2018. Production of Ti-Fe alloys via molten oxide electrolysis at a liquid iron cathode, *RSC Advances*, 8:17575–17581.

Kim, H, Paramore, J, Allanore, A and Sadoway, D R, 2011. Electrolysis of Molten Iron Oxide with an Iridium Anode: The Role of Electrolyte Basicity, *Journal of The Electrochemical Society*, 158(10):E101–E105.

Kim, J, Sovacool, B K, Bazilian, M, Griffiths, S, Lee, J, Yang, M and Lee, J, 2022. Decarbonizing the iron and steel industry: A systematic review of sociotechnical systems, technological innovations, and policy options, *Energy Research & Social Science*, 89:102565.

King, R L and Botte, G G, 2011. Hydrogen production via urea electrolysis using a gel electrolyte, *Journal of Power Sources*, 196(5):2773–2778.

Liu, J-H, Zhang, G-H and Chou, K-C, 2015. Electrolysis of Molten FeO_x-Containing CaO-Al_2O_3-SiO_2 Slags under Constant Current Field, *Journal of the Electrochemical Society*, 162(12):E314–E318.

Patisson, F and Mirgaux, O, 2020. Hydrogen Ironmaking: How It Works, *Metals*, 10:922.

Raza, A, Gholami, R, Rezaee, R, Rasouli, V and Rabiei, M, 2019. Significant aspects of carbon capture and storage – A review, *Petroleum*, 5(4):335–340.

Sadoway, D R, 1995. New opportunities for metals extraction and waste treatment by electrochemical processing in molten salts, *Journal of Materials Research*, 10:487–492.

Somers, J, 2021. Technologies to decarbonise the EU steel industry, EUR 30982 EN, Publications Office of the European Union, Luxembourg, JRC127468. https://doi.org/10.2760/069150

Wiencke, J, Lavelaine, H, Panteix, P J, Petitjean, C and Rapin, C, 2018. Electrolysis of iron in a molten oxide electrolyte, *Journal of Applied Electrochemistry*, 48:115–126.

Yuan, B and Haarberg, G M, 2009. Electrowinning of Iron in Aqueous Alkaline Solution Using Rotating Disk Electrode, *Rev Met Paris*, 106(10):455–459.

Zhou, Z, Jiao, H, Tu, J, Zhu, J and Jiao, S, 2017a. Direct Production of Fe and Fe-Ni Alloy via Molten Oxides Electrolysis, *Journal of The Electrochemical Society*, 164(6):E113–E116.

Zhou, Z, Wang, S, Jiao, H and Jiao, S, 2017b. The Feasibility of Electrolytic Preparation of Fe-Ni-Cr Alloy in Molten Oxides System, *Journal of The Electrochemical Society*, 164(14):D964–D968.

Ferroalloy extraction from a Zimbabwean chrome ore using a closed DC furnace

DOI: 10.62053/PWNQ7247

S Dandi[1], M J Masamvu[2], S M Masuka[3], S Bright[4] and E K Chiwandika[5]

1. BSc student, University of Zimbabwe, Harare 263, Zimbabwe. Email: dandisimbarashe1@gmail.com
2. Lecturer, University of Zimbabwe, Harare 263, Zimbabwe. Email: malbeniajomasamvu@gmail.com
3. Lecturer, University of Zimbabwe, Harare 263, Zimbabwe. Email: shebarmasuka@gmail.com
4. Lecturer, University of Zimbabwe, Harare 263, Zimbabwe. Email: sharrydonbright@gmail.com
5. Lecturer, Harare Institute of Technology and module Lecturer, University of Zimbabwe, Harare 263, Zimbabwe. Email: chiwandikae@gmail.com

ABSTRACT

The depletion of high-grade hard and lumpy chrome ores has forced Zimbabwean ferrochrome producers to resort to low-grade friable ores that have an average of 28 per cent fines against a set limit of 12 per cent. Submerged open arc furnaces currently in use are associated with eruptions within the furnace because of the high amounts of fines, high energy consumption, as well as high SO_2 and CO_2 emissions. Traditionally employed agglomeration methods such as pelletising and the use of coke in the furnace have been discarded because of the pressure to lower operational costs and to achieve higher profit margins. This research aims to develop a method to incorporate low-grade friable ore fines and unprocessed coal into production while lowering CO_2 and SO_2 emissions through a closed direct current (DC) arc furnace. The closed DC arc furnace could incorporate the friable ores and coal while maintaining above 90 per cent reduction rates. Preliminary findings also show that energy consumption could be reduced by up to 35 per cent by incorporating a pre-heating and pre-reduction system using the flue gases from the furnace. In the proposed circuit, the cost of production per ton of ferrochrome might be potentially lowered by an average of 30 per cent.

INTRODUCTION

Global ferrochrome production has been steadily increasing over the past few decades, primarily due to the growing demand for ferrochrome by-products. This trend is expected to continue as industrial and usage demands for ferrochrome continue to rise (Fortune Business Insights, 2023) due to the rise in demand for stainless steel (du Preez *et al*, 2023). In Zimbabwe, ferrochrome production is mainly from four smelters (Chitambira, Miso-Mbele and Gumbie, 2011) where the most common method used for ferrochrome production is the submerged arc furnace (SAF) that uses an electric current to increase temperature enhancing the reduction reactions of chromite (Yu *et al*, 2023).

The depletion of high-grade lumpy ores has resulted in the utilisation of fine ores in open alternative current (AC) furnaces causing frequent eruptions and high energy consumption, approximately 3.8 to 4.0 MWh/MT FeCr (Chitambira, Miso-Mbele and Gumbie, 2011). Agglomeration techniques have proved to be expensive for Zimbabwean ferrochrome producers and as such, there is a need to find new ways to smelt chromite fines to produce ferrochrome using methods that are cost-effective and environmentally friendly. A possible alternative to an open AC furnace is the closed direct current (DC) furnace (Sager *et al*, 2010), which will incorporate pre-treatment techniques and utilise low-grade fine ores.

The conventional smelting of ferrochrome is done in electric reduction furnaces with electrodes submerged in the burden materials, ore-bearing material, a carbonaceous reductant, and fluxes. For high efficiencies, the gas flow should be uniform, and channelling of the CO produced during the reactions should not be avoided. This is achieved by the use of hard lumpy ores that are not friable to avoid excessive degradation and generation of fines in the furnace. The depletion of hard lumpy ores and the increased mechanisation in mining operations has resulted in considerable utilisation of fine ore material of much smaller grain sizes that require agglomeration (Alison, 2019), and the use of friable ores that generate fines (Goel, 1997).

Agglomeration of chromite fines and friable material currently utilises a combination of sintering and briquetting methods (Xiaohai *et al*, 2019; Alison, 2019). This improves the smelting efficiency while simultaneously reducing the power consumption of the furnace. Electrical energy consumption typically ranges from 3.0 to 3.5 MWh/MT alloy for sintered or briquette feed, compared to 3.8 to 4.0 MWh/MT alloy for raw fines (Chitambira, Miso-Mbele and Gumbie, 2011).

The DC arc furnace was developed as a way of allowing for the direct smelting of fine chromite that emanated from highly friable ores without the need for costly agglomeration techniques (Jone and Erwee, 2016). Non-coking coal can also be used as the carbonaceous reductant and theoretically, the smelter power input is independent of the burden composition since the resistance is manipulated by the arc length, making it a low-cost technology for ferrochrome production (Grant *et al*, 2010). The DC arc uses a single solid carbon electrode as the cathode and is normally open or semi-submerged. Burden materials can be charged directly into the furnace or through a hollow electrode.

Innovations in smelting technology, such as the Premus process have been developed that can decrease electrical energy consumption during smelting by partly reducing pelletised chromite ores in a rotary kiln using energy obtained from combustion of pulverised coal and hot gases generated from the closed submerged arc furnace (Naiker, 2007; Chima, 2012). Pre-reduction and pre-heating techniques that have been employed enhanced the quality and the grade of the ferrochrome product, by increasing the chromium recovery and the chromium-to-iron ratio and decreasing the carbon and silicon contents. Pre-reduction of pelletised chromite ore was the best option with the lowest specific energy consumption using the submerged arc furnace (Neizel *et al*, 2013). Generally, higher temperatures (+1000°C) longer times (+60 mins), finer particles (-10 mm), and higher reductant ratios are favourable for achieving higher degrees of pre-reduction (Jian, Yang and Deqing, 2014).

In this study, a novel structure of the DC arc furnace is being investigated for ferrochrome production in an attempt to utilise fine chromite ore while maintaining low power consumption. In addition, this new structure is expected to process low-grade fine ore material and friable ores while avoiding agglomeration of the fine ore through sintering and briquetting techniques which are expensive and economically non-viable for local smelters. It is also the aim of this study to investigate the effect of pre-heating and pre-reduction techniques on the recovery of metal using off-gas.

EXPERIMENTAL

Materials

The chromite ore fines used in this study were low-grade (A), high-grade (B) and middle-grade (C). which were obtained from Shurugwi, Mutorashanga, and Ngezi chrome fields. The grades of the ores are classified according to the percentage of Cr_2O_3 as shown in Table 1. The coal was obtained from Zambezi Gas Company in Hwange, and the quartz from Kwekwe.

TABLE 1

Chemical composition of different chromite ore grades.

Sample ID	% Cr_2O_3	% FeO	Cr/Fe	% SiO_2	% MgO	% Al_2O_3	% CaO	% TiO_2	% P	% Others
Low-grade fines (A)	25.13	18.71	1.19	17.29	24.45	5.23	1.38	0.17	0.0011	7.64
High-grade Fines(B)	40.23	17.7	2.18	7.46	15.03	10.41	0.43	0.33	0.001	8.41
Middle grade fines (C)	32.71	16.63	1.89	11.73	20.42	7.40	1.24	0.2	0.0013	9.67

Sample preparations and experimental procedures

Ten samples of 1 kg each were randomly taken from stockpiles of fine ores using an ore sample cutter of 3 m height to obtain a good representation of ore. To determine the particle size distribution of the ores, the samples were first dried using drying ovens at 110°C for 20 hrs and then sieved with different sieve sizes to obtain a representative particle size distribution shown in Figure 1.

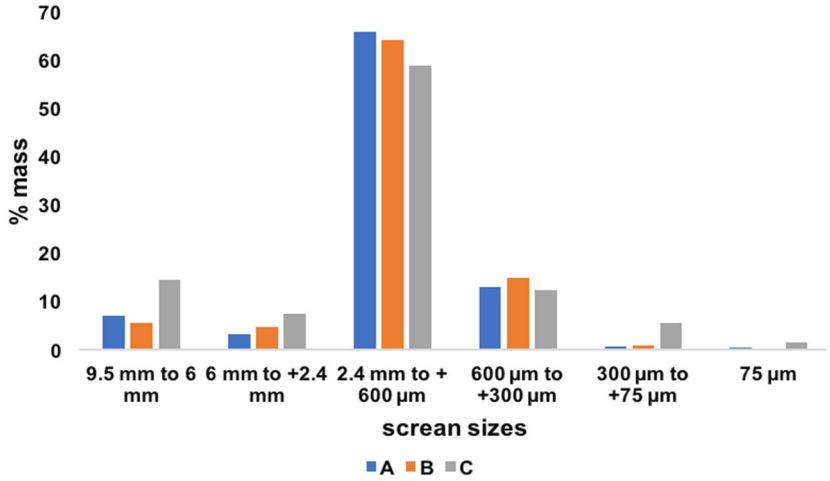

FIG 1 – Particle size distribution of the chromite ore sample.

An average of 65.8 per cent of particles fall within the size range of 2.4 mm to +600 µm. This indicates that the chromite ore samples are primarily composed of fine-sized particles. A noticeable 4 per cent of those with sizes of 75 µm and below, indicate that the sample contains a relatively small proportion of ultra-fine particles. The sample also includes a notable proportion of large particles above 6 mm, constituting 18 per cent of the samples.

To obtain a homogeneous feed of less than 2 mm, the chromite ores were first crushed using a laboratory jaw crusher, then pulverised then assayed for the average chrome head grade using a wet chemical analysis and an Inductively Coupled Plasma - Optical Emission Spectroscopy (ICP-OES). The chemical composition of the chromite ore is shown in Table 1. Quartz, used for basicity adjustment, was crushed using a laboratory jaw crusher from 40–50 mm to below 2 mm and then dried using an oven, followed by pulverisation and chemical analysis. The coal fines were sieved and screened to 90 per cent fines in the range of 1 mm to 2 mm. Results from the characterisations of the coal and quartz are shown in Tables 2 and 3 respectively.

TABLE 2

Coal proximate analysis.

Material (wt%)	Volatile combusted matter	Ash	Fixed carbon	S	P	Moisture (%)
ZG Coal	22.05	9.92	66.8086	1.01	0.0014	0.21

TABLE 3

Quartz characterisation.

Material (wt%)	SiO_2	FeO
Quartz	99.37	0.63

The proximate analysis for the coal fines was done according to the Indian Standard IS:1350 (Part-I)-1984. The samples were blended according to the desired mass proportions of different chromite ores as shown in Table 4 and the chemical composition of the blends is shown in Table 5.

TABLE 4

The mass blend proportions of the chromite ores.

Sample ID	Blend 1 (%)	Blend 2 (%)	Blend 3 (%)	Blend 4 (%)	Blend 5 (%)	Blend 6 (%)
A	100	80	70	60	40	0
B	0	10	15	30	50	100
C	0	10	10	10	10	0

TABLE 5

Chemical composition of the different blends.

Sample ID	% Cr_2O_3	% FeO	Cr/Fe	% SiO_2	% MgO	% Al_2O_3	% CaO	% TiO_2
Blend 1	25.13	17.91	1.79	11.70	19.32	8.13	0.85	0.25
Blend 2	27.03	18.71	1.79	12.01	19.85	7.92	0.90	0.24
Blend 3	28.33	19.46	1.84	11.83	19.90	7.97	0.89	0.22
Blend 4	30.73	20.96	1.95	11.46	20.01	8.07	0.88	0.23
Blend 5	33.73	23.21	1.89	11.65	19.95	8.02	0.89	0.23
Blend 6	40.23	17.7	2.18	7.46	15.03	10.41	0.43	8.41

A mixture of 100 g of chromite and quartz (flux material for separation between gangue and ferrochrome), in proportions shown in Table 6, firstly underwent pre-treatment in a muffle furnace using carbon monoxide from gas cylinders. The temperature within the muffle furnace was deliberately altered in order to observe and analyse the production of metallic chromium and iron (pre-reduction). Then subsequently for smelting in a laboratory-scale closed DC furnace made from the magnisite refacrory paste, coal as reducing agent was added into the mixture. The amount of coal used in every reaction was based on stoichiometry. The operational voltage was established at 500 volts, while a current of 60 amperes was utilised. The power supply employed for this operation was a robust DC welding machine designed for heavy-duty applications. The power-conducting media within the furnace consisted of gauging rods, with 80 per cent graphite content. The furnace was sealed with a lid which was made from the same material, which has two holes where the electrodes are introduced (Shotanov *et al*, 2023).

TABLE 6

The amount of raw material used in each blend.

Sample ID	Chromite (g)	Coal (g)	Quartz (g)
Blend 1	100	18.608	54.831
Blend 2	100	19.8	53.67
Blend 3	100	20.695	54.45
Blend 4	100	22.39	53.23
Blend 5	100	24.655	54.17
Blend 6	100	25.547	53.987

Each sample was smelted for 30 secs after carrying out preliminary experiments on reaction time, taking into consideration the size of the sample and the crucible used as shown in Figure 2, as

elucidated by Asish, Somnath and Sarada (2020) and Pankaj *et al* (2024). The products were discharged from the top of the furnace and allowed to cool down with natural air. Once cooled, the alloy and slag were analysed using an ICP-OES technique and wet chemical analysis. Figure 3 illustrates the experimental stages.

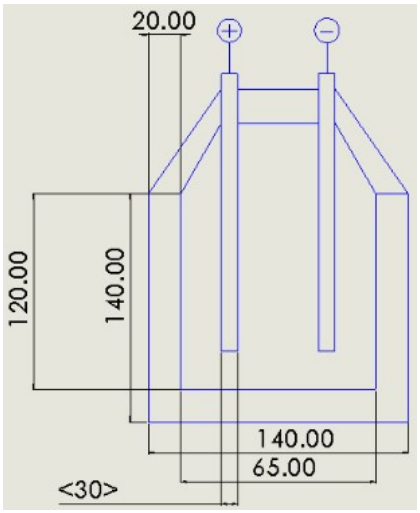

FIG 2 – Technical drawing of the furnace used for experiments (dimensions in mm).

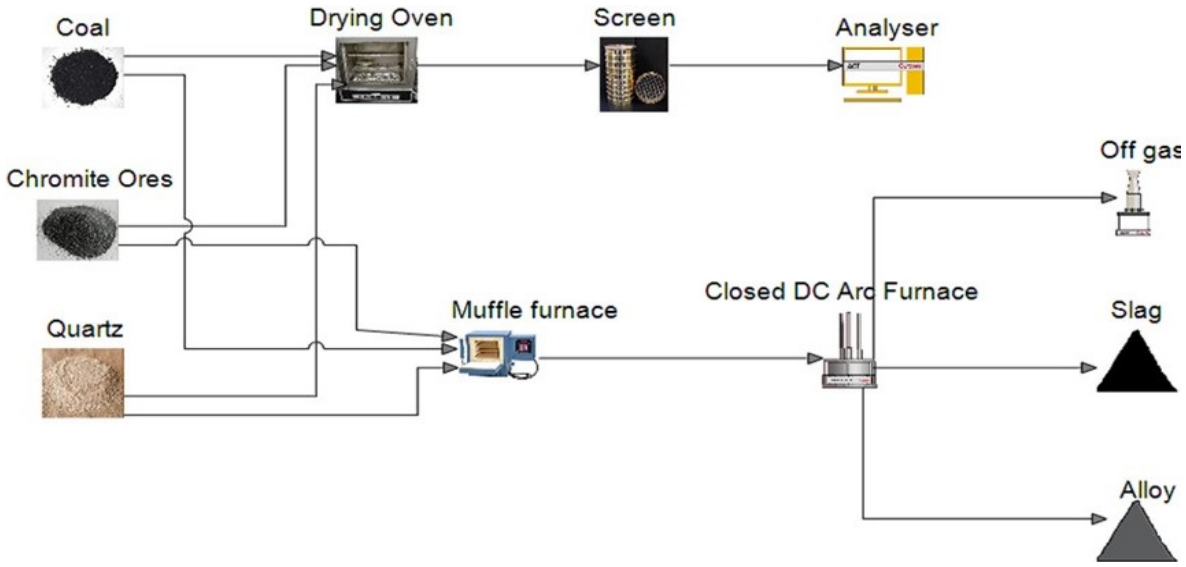

FIG 3 – Schematic presentation of ferrochrome production using DC arc furnace.

RESULTS AND DISCUSSION

Effect of chrome grade on metal recovery

This was done to investigate the effect of chromite grade on the metal recovery. The chromite grade was achieved by varying the different proportions of the chromite ores, as shown in Table 4. The results from the six blends are shown in Figure 4 showing the tapping stage recovery (TSR) based on the changes in blends. Equation 1 shows how the TSR is determined.

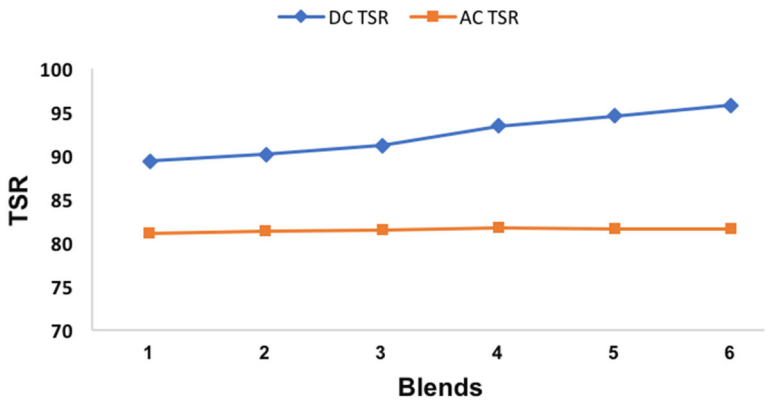

FIG 4 – Trends in tapping stage recovery based on the changes in Cr_2O_3 and the Cr/Fe ratio.

$$TSR = \frac{Amount\ of\ Cr\ in\ the\ alloy}{Amount\ of\ Cr\ in\ the\ ore} \times 100 \quad (1)$$

It can be observed from Figure 4 that there is an increase in the TSR for the DC arc from about 89 per cent to approximately 96 per cent on the sixth blend, which can be attributed to the increase in both Cr_2O_3 content and the Cr/Fe ratio from blend 1 to blend 6. The results obtained from the AC furnace serve as a reference point for comparison purposes, indicating the high energy conversion efficiency of the closed DC arc furnace. This implies that a significant portion of the input energy is effectively utilised in the DC furnace, resulting in improved recovery rates during the tapping stage. The chemical composition of the tapped alloy is shown in Table 7.

TABLE 7

Alloy chemical composition.

Sample ID	Cr (%)	Fe (%)	Cr/Fe	Si (%)	Mn (%)	P (%)	Ni (%)	Co (%)	Ti (%)	V (%)	C (%)
Blend 1	59.75	28.97	2.06	1.00	0.28	0.03	0.33	0.06	0.30	0.20	7.79
Blend 2	61.45	32.27	1.90	1.76	0.20	0.02	0.37	0.06	0.12	0.21	7.52
Blend 3	62.54	33.04	1.89	1.33	0.18	0.02	0.39	0.06	0.08	0.21	7.46
Blend 4	62.86	32.96	1.91	1.29	0.18	0.02	0.39	0.06	0.08	0.21	7.35
Blend 5	64.98	33.70	1.92	1.23	0.17	0.02	0.41	0.07	0.08	0.21	7.09
Blend 6	67.56	33.90	1.99	1.30	0.17	0.02	0.41	0.07	0.08	0.20	7.15

Generally, the percentage of Cr and Fe in the alloy increases as the Cr_2O_3 and FeO grades in the blends increase. There is a noticeable increase in the percentage of Cr and Fe in the alloy from 59.75 per cent to 62.54 per cent and 28 per cent to 33 per cent for blend 1 to blend 3 respectively, but between blend 3 and 4, there is a slight increase due to smaller difference between Cr_2O_3, FeO and the Cr/Fe ratio in these blends. From blend 4 to blend 6, there is a significant increase in Cr and Fe in the alloy because of an increase in Cr/Fe. The amount of Si and C was almost constant due to a constant reductant mass used across all blends. The amount of Cr that reported to slag is shown in Figures 4 and 5.

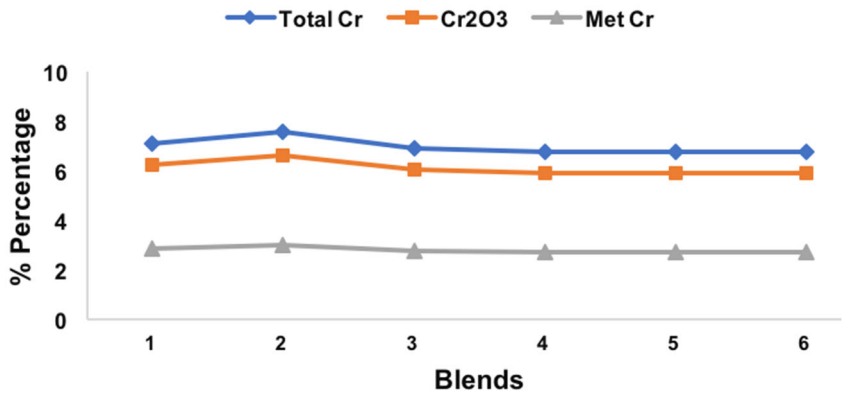

FIG 5 – Slag analysis.

Figure 5 shows the slag analysis from the closed DC arc furnaces, indicating the total Cr, unreduced Cr_2O_3, and metallic Cr in the slag. The total Cr content in the slag is uniformly low at around 8 per cent across all the blends, with Cr_2O_3 content less than 7 per cent. This indicates the high reduction efficiency of the closed DC arc furnace. A minimum metallic Cr content remains in the slag at around 3 per cent across all blends, which is a positive indication of effective separation by the flux.

Effect of basicity on separation efficiency

The MgO/SiO_2 and MgO/Al_2O_3 ratios of the blends are shown in Figure 6 and these ratios might affect slag fluidity.

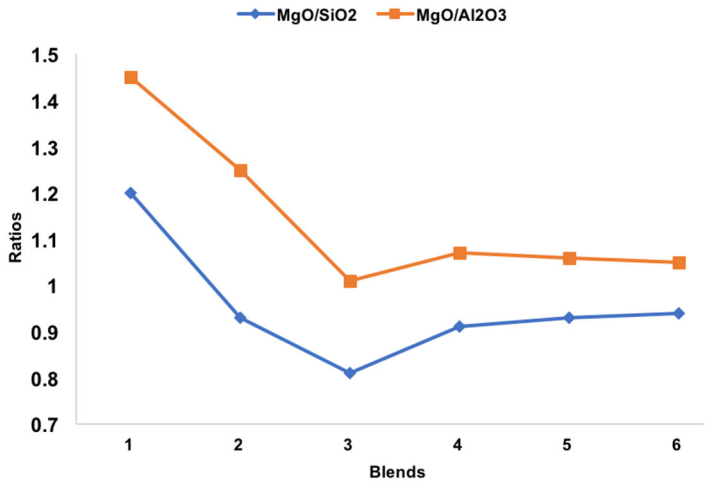

FIG 6 – Slag analysis on separation efficiency.

The MgO/SiO_2 ratio shows a decreasing trend from blend 1 to 3, suggesting a decrease in separation efficiency due to an increase in SiO_2 relative to MgO since there was a corresponding increase of the Cr reporting to slag in blend 2, as shown in Figure 5. This was also supported by the slow increase in tapping stage recovery between Blend 1 and 3 shown in Figure 6 followed by a rapid increase in recovery afterwards. This shift in ratio from blend 1 to 3 might have increased the melting point of slag which results in a specific energy consumption (SEC) increase and an increase in viscosity of the slag decreasing the separation efficiency between the slag and alloy. On the other hand, the MgO/Al_2O_3 ratio remains relatively constant, indicating stable separation efficiency and consistent proportions of these compounds across the samples. This implies that the difference in melting points during slag chemistry due to the difference in MgO, Al_2O_3 and SiO_2 affects the separation efficiency.

Specific energy required

The different trends of SEC with and without pre-treatment techniques is shown in Figure 7. These were calculated from Equation 2 (How to determine the specific energy required).

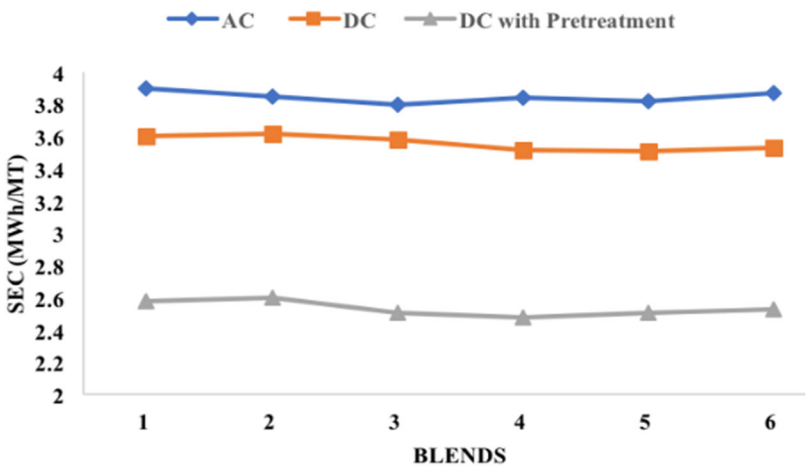

FIG 7 – SEC comparison of with and without pre-treatment methods.

$$\text{SEC} = \frac{\text{Amount of Electrical energy used}}{\text{amount of alloy produced}} \quad (2)$$

Figure 7 compares the SEC in MWh/MT of alloy between AC furnaces, DC furnaces, and DC with pre-treatment. AC furnaces consistently show low SEC, averaging 3.9 MWh/MT due to the inherent characteristics of AC furnaces. DC furnaces exhibit better SEC than AC furnaces due to higher operating temperatures, minimum heat losses and more efficient energy transfer. DC furnaces with pre-heating and pre-reduction have much better SEC, with an average SEC of 2.5 MWh/MT. This suggests that pre-heating and pre-reduction significantly improve the performance of DC arc furnaces, by reducing the energy required for smelting. However, the SEC remains constant throughout the samples, indicating that the efficiency of DC furnaces is not significantly affected by the grade of chromite fines. There was a general increase in SEC from blend 1 to 2 in the DC with a pre-heating curve that corresponded to an increase in the MgO/SiO_2 that resulted in a slight increase in Cr reporting to slag, shown in Figure 6. Blend 4 was then considered the optimal blend based on both recovery and SEC. This blend was used in the subsequent experiments.

SEC and tapping stage recovery

This smelting experiment was performed to check on the tapping stage recovery using blend 4 and pre-calculated SEC. Figure 8 shows the effects of SEC on the taping stage recovery.

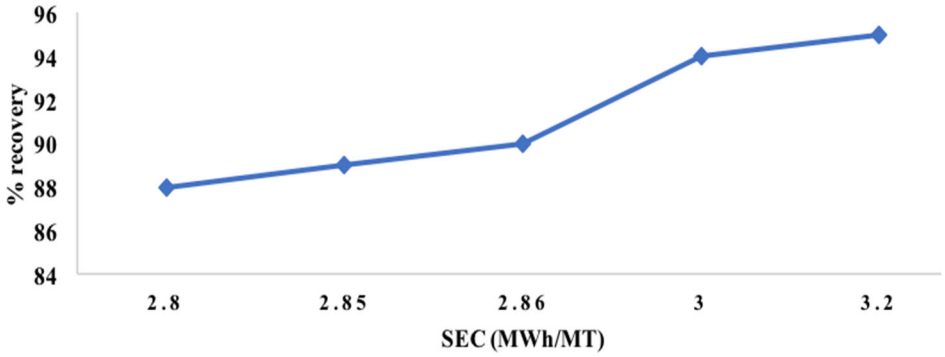

FIG 8 – The effects of Specific energy consumption on Recovery.

There is a clear correlation between SEC and percentage recovery in the given data. As the SEC increases from 2.8 MWh/MT to 3.2 MWh/MT, there is a noticeable increase in the percentage recovery from 88 per cent to 95 per cent. The most significant increase in recovery occurs between the SEC levels of 2.86 MWh/MT and 3 MWh/MT, where the recovery surges from 88 per cent to 94 per cent. Although there is only a slight increase in recovery from 3 MWh/MT to 3.2 MWh/MT, it is still evident that better SEC leads to higher recovery rates. However, for optimum operation, the range of 3 MWh/MT to 3.2 MWh/MT appears to be more viable. Within this range, the cost of SEC remains relatively lower, while achieving a high recovery rate of 94 per cent.

Effect of arc length on TSR

Figure 9 shows the recovery of Cr in ferrochrome at different arc lengths during the tapping stage in smelting using a closed DC arc furnace.

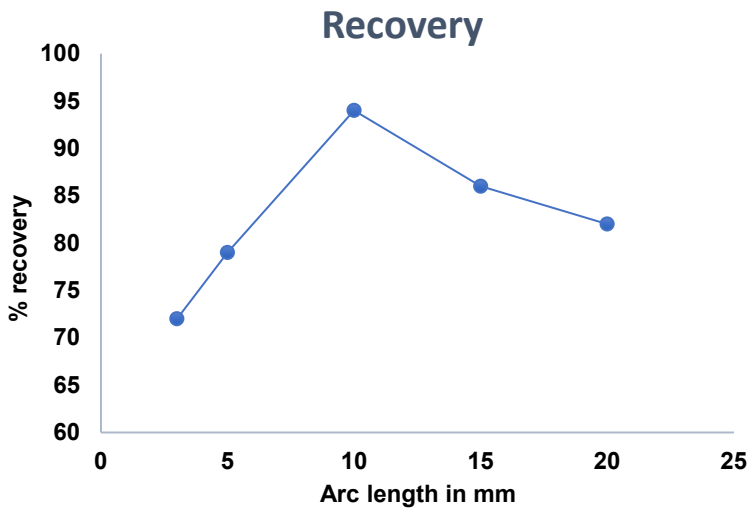

FIG 9 – Effects of arc length on the tapping stage recovery.

The recovery increases with an increase in arc length up to 10 mm, after which it starts to decline as the arc length continues to increase. This suggests that 10 mm is an optimal arc length for maximum recovery of Cr in ferrochrome of 94 per cent, this could be due to the optimal balance between heat generation and heat loss at this arc length, which facilitates the reduction of Cr_2O_3 to Cr. A decline in recovery for arc length beyond 10 mm, is due to excessive heat loss at larger arc lengths, which reduces the efficiency of the smelting process.

Effect of pre-heating and pre-reduction

Figure 10 shows the % Cr and Fe reduced after pre-treatment of the sample at different temperatures using CO as a reducing agent in blend 4. During the pre-heating and pre-reduction process, the temperature of the chromite ore fines raised to approximately 450°C, when pretreated with CO at a temperature of 700°C which is the estimated temperature of the off-gas leaving the furnace. The difference in temperature between the off-gas and the ore is due to the partial energy lost during the transfer of CO to ore and the energy used to raise the temperature of the ores. This therefore limits the overall reduction efficiency. At 400°C, only 10 per cent of FeO was reduced of Fe and an insignificant amount of Cr_2O_3 was reduced.

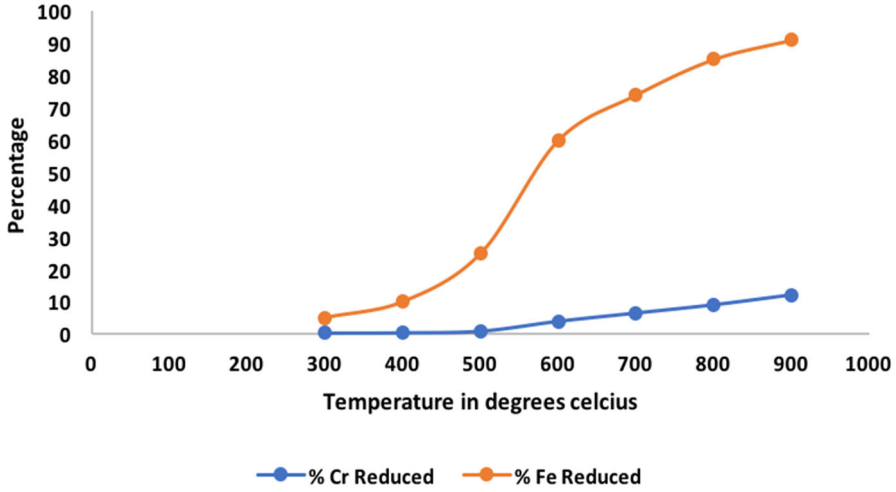

FIG 10 – Pre-reduction percentages of Cr and Fe using CO.

There is minimal reduction in both Cr and Fe at low temperatures less than 300°C as indicated in Figure 10. Above 400°C, Fe shows a significant increase in metallic percentage of Cr and Fe as temperature increases, reaching close to 100 per cent reduction at 1000°C. The reduction of FeO to Fe is highly temperature-dependent and becomes more efficient at higher temperatures. In contrast, Cr reduction is relatively steady and minimal across the entire temperature range. The reduction of Cr_2O_3 to Cr is less efficient than that of FeO to Fe under the same conditions as can easily be seen by the thermodynamic data for Equations 3 and 5 (Lee, 1999).

$$\mathrm{FeO}(s) + \mathrm{CO}(s) = \mathrm{Fe}(s) + \mathrm{CO_2}(g) \quad (3)$$

$$\Delta G° = 11000 - 156.9T \text{ J/mol (T = 298–973 K)} \quad (4)$$

$$\mathrm{Cr_2O_3}(s) + 3\mathrm{CO}(s) = 2\mathrm{Cr}(s) + 3\mathrm{CO_2}(g) \quad (5)$$

$$\Delta G° = 279400 - 452.7T \text{ J/mol (T = 298–973 K)} \quad (6)$$

ENERGY REQUIREMENTS FOR FERROCHROME SMELTING

The probable reactions that may occur during the smelting of chromite fines with pre-heating and pre-reduction effects were predicted using basic thermodynamics, taking into account the chemical composition of the blends. It should be emphasised that the thermodynamic analysis was conducted to provide theoretical insight on the energy requirement despite the use of natural chromite ore with varying chemical interactions.

In order to determine the energy required in Figure 10 to elevate the temperature of each compound from the reference temperature to the pre-heating temperature using the off-gas from the furnace, the specific heat capacities of each compound within the chromite ore were employed. Shomate constant data obtained from the thermodynamics database (Chase, 1998) as depicted in Table 8, which shows the specific heat capacity (Cp) and total enthaplies ($H-H_{298}$). The masses of the compounds were ascertained by computing the proportions of each compound based on the percentage composition of the 0.1 kg sample utilised.

The Cp (J/mol.K) data from Table 8, was converted to Cp (Kwh/Kg.K). The specific energy in Table 9 was calculated using Equation 7 and calculated Cp (Kwh/Kg.K). The total energy consumption for pre-heating the chromite ore to 700 K was found to be 0.012386 kWh. This value represents the cumulative energy needed to heat all the components in the ore to the desired pre-heating temperature.

TABLE 8

Specific heat capacity and total enthalpy from shamote data (Chase, 1998).

Compound	Temp (K)	Cp (J/mol.K)	$H-H_{298}$
Preheating			
FeO	700	56.11	-
Cr_2O_3		122.7	-
SiO_2		68.77	-
CaO		51.54	-
Al_2O_3		116.5	-
MgO		148.69	-
Pre-reduction			
FeO	700	56.11	21.42
CO		7.45	2.87
CO_2		49.57	17.75
Fe		34.48	12.08
Smelting zone			
FeO	2000	-	104.5
Cr_2O_3		-	216.9
SiO_2		-	111.5
Cr		-	61.06
Fe		-	68.85
Si		-	46.28
CO		-	13.56
CaO		58.48	-
Al_2O_3		136.6	-
MgO		55.70	-

TABLE 9

Energy required for pre-heating to 700 K.

Compounds	Mass (Kg)	$Cp*10^{-5}$ (kWh/Kg.K)	Energy (kWh)
FeO	0.011558	21.61	0.0010166
Cr_2O_3	0.033812	22.42	0.0030853
SiO_2	0.0115	31.83	0.0014898
MgO	0.01737	48.321	0.003416
Al_2O_3	0.01186	31.73	0.0015316
CaO	0.0139	32.64	0.001847
		Total energy	**0.012386**

$$Q = mc_p\Delta T \quad (7)$$

To determine the energy required for pre-reduction using the off-gas from the furnace and the smelting process inside the furnace, the total enthalpies of each component within the chromite ore were employed. These enthalpies were obtained from Shomate constant data as presented in Table 8 (Chase, 1998).

Equations 8, 9 and 10 were used in the evaluation of the values obtained in Tables 10 and 11 (Toulouevski and Zinurov, 2009). The energy/mol was calculated using enthalpies data from Table 8 and Equation 8. Reaction for the pre-reduction stage shown in Equation 11 and its associated energy consumption are shown in Table 10. The mass of Fe is based on the percentage of metallic iron produced in the pre-reduction graph. By combining the specific energy requirement and the mass of Fe reduced, an estimation of the energy consumption for Fe reduction during pre-reduction can be obtained. This energy consumption value is typically expressed in kWh and quantifies the amount of electrical energy needed to facilitate the reduction reaction.

$$\text{Energy per mol} = \text{total enthalpies of the final products} - \text{total enthalpies of the reactants} \quad (8)$$

$$\text{Specific energy required(SER)} = \text{Energy per mol} \times \text{molecular mass of the species} \quad (9)$$

$$\text{Energy used} = \text{SER} \times \text{mass of the species} \quad (10)$$

TABLE 10

Energy used in the pre-reduction.

Product species	Mass of product species (Kg)	Energy/mol (kWh/mol)	SER (kWh/kg)	Energy (kWh)	
				Alloy	Off-gas
Fe	0.001631	0.001539	0.0275	0.000044825	
CO_2	0.00128	0.001539	0.03498		0.000044825

TABLE 11

Reactions and Energyrequired in the smelting phase.

Reduction reactions	Product species	Product species Mass (kg)	Energy/mol (kWh/mol)	SER (kWh/kg)	Energy (KWh)	
					Alloy	Off-gas
$Cr_2O_3 + 3C \Rightarrow 2Cr + 3CO$	Cr	0.01997	-0.0446	0.7964	0.0159	
	CO	0.015	-0.0446	1.014		0.0159
$FeO + C \Rightarrow Fe + CO$	Fe	0.013885	-0.01598	0.2854	0.00396	
	CO	0.0069	-0.01598	0.5707		0.00396
$SiO_2 + 2C \Rightarrow Si + 2CO$	Si	0.00114	-0.0303	1.0809	0.00123	
	CO	0.00113	-0.0303	1.0802		0.00123
				Total energy	**0.02109**	

$$FeO + CO \Rightarrow Fe + CO_2 \quad (11)$$

The energy/mol required for smelting are shown in Table 11, were calculated using enthalpies data from Table 8 and Equation 8.

From Tables 11 and 12, the amount of energy required for ferrochrome production is 0.05226 kWh. However, after subtracting the pre-heating and pre-reduction energies, the overall energy required for smelting becomes 0.03983 KWh. Based on the nature of the experiments, which were performed on a small scale, considering this factor, the approximate amount of energy converted to smelting is 52 per cent of the total energy supplied. Thus, the total energy required for smelting is:

$$\frac{0.03983}{0.52} = 0.07659\ kWh$$

TABLE 12

Amount of Energy used in raising temperature of materials which reported to slag.

Compounds	Mass (Kg)	$Cp*10^{-5}$ (kWh/Kg.K)	Energy (kWh)
CaO	0.00089	40.61	0.0006059
Al_2O_3	0.00807	37.2	0.005295
MgO	0.0201	38.7	0.01317
SiO_2	0.054	36.11	0.03319
		Total	**0.05226**

The amount of ferrochrome alloy produced in the reaction amounted to 0.03051 kg. The SEC was therefore evaluated to be 2.51 MWh/MT using Equation 1.

CONCLUSIONS

The results shown in this study provide a baseline for the viability of the transition from the traditionally used AC furnace to the closed DC arc furnace with pre-treatment stages. This confirms that fine chromite ores can be processed using a closed DC arc furnace without going through agglomeration techniques.

The DC arc furnace proved to be efficient regardless of the quantity of fines in the blend but rather recovery was determined by the grade of the ore. Comparison between the DC and AC furnace TSR indicated high energy conversion efficiency of the closed DC arc furnace because the input energy is effectively utilised in the DC furnace, resulting in improved recovery rates during the tapping stage.

SEC was significantly lowered by 35.8 per cent from 3.9 MWh/MT to 2.5 MWh/MT when pre-treatment techniques were employed. Also, the implementation of coal as the reductant and use of low-grade fines chromite ore aid in lowering the overall cost of production by an average of 30 per cent. This significant difference is important because it shows the potential of the closed DC arc furnace to achieve the goal of lowering energy consumption in ferrochrome production.

ACKNOWLEDGEMENTS

This research was funded by the Zimbabwe Mining and Smelting Company (ZIMASCO).

REFERENCES

Alison, C, 2019. Sintering: A Step Between Mining Iron Ore and Steelmaking [online]. Available from: <https://www.thermofisher.com/blog/mining/sintering-a-step-between-mining-iron-ore-and-steelmaking/> [Accessed: 5 January 2024].

Asish, K D, Somnath, K and Sarada, P, 2020. Processing of Low-Grade Chromite Ore for Ferroalloy Production: A Case Study from Ghutrigaon, Odisha, India, *Transactions of the Indian Institute of Metals*, 73:2309–2320.

Chase, M, 1998. NIST-JANAF Thermochemical Tables [online]. Available from: <https://webbook.nist.gov/cgi/cbook.cgi?ID=C1345251&Mask=2> [Accessed: 16 April 2024].

Chima, U, 2012. Innovative Systems Design and Engineering, *Technology Innovations in the Smelting of Chromite Ore*, 3(12):48–54.

du Preez, S P, van Kaam, T P M, Ringdalen, E, Tangstad, M, Morita, K, Bessarabov, D and van Zyl, P, 2023. An overview of currently applied ferrochrome production processed and their waste management practices, *Minerals*, 13(06):809.

Fortune Business Insights, 2023. Ferrochrome Market Size, Share and COVID-19 Impact Analysis, By Product Type (High Carbon, Low Carbon and Others), By Application (Stainless Steel, Specialty Steel and Others) and Regional Forecast, 2023–2030. *Specialty and Fine Chemicals*.

Goel, R P, 1997. Smelting technologies for ferrochromium production - Recent trends, in *Ferro Alloy Industries in the Liberalised Economy* (eds: A K, Vaish, D S, Singh, N, Goswami and P, Ramachandrarao), pp 37–50 (National Metallurgical Laboratory: Jamshedpur).

Grant, D, Stadle, R, Schreiter, T and Sager, D, 2010. Low cost ferroalloy extraction in DC-arc furnace at Middleburg Ferrochrome, *Journal Of the Southern African Institute of Mining and Metallurgy*, 110:717–724.

Chitambira, B, Miso-Mbele, D and Gumbie, M, 2011. Ferrochrome Smelting in Zimbabwe [online]. Available from: <https://www.saimm.co.za/download/saimmbranches/zimbabwe/FERROCHROME%20SMELTING%20IN%20ZIMBABWE.pdf> [Accessed: 22 December 2023].

Jian, P, Yang, C and Deqing, Z, 2014. Solid State Reduction of Preoxidized Chromite-iron Ore Pellets by Coal, 55(4):727–735.

Jone, R T and Erwee, M W, 2016. Simulation of ferro-alloy smelting in DC arc furnaces using Pyrosim and FactSage, *CALPHAD: Computer coupling of phase diagrams and thermochemistry*, 55:20–25.

Lee, H-G, 1999. *Chemical Thermodynamics for Metals and Materials*, 1st ed (Imperial College Press: London).

Naiker, O, 2007. Development and advantages of Xsrata's Premus process [online]. Available from: <https://www.yumpu.com/en/document/read/22811900/the-development-and-advantages-of-xstratas-premus-pyrocoza> [Accessed: 09 January 2024].

Neizel, B W, Beukes, J P, van Zyl, P G and Dawson, N F, 2013. Why is CaCO3 not used as an additive in the pelletised chromite pre-reduction process?, *Minerals Engineering*, 45:115–120.

Pankaj, K, Sunil, K T, Nilamadhaba, S and Gajanan, U, K, 2024. Valorization From Waste: Combined Reduction of Chromite Ore Processing Tailing and Sub-Grade Manganese Ore to Produce 200 Series Stainless Steel Scrap, *Mining, Metallurgy and Exploration*, 41:297–309.

Sager, D, Grant, D, Stadler, R and Schreiter, T, 2010. Low cost ferroalloy extraction in DC-arc furnace at Middleburg Ferrochrome, *The Journal of The Southern African Institute of Mining and Metallurgy ,* 110:720–724.

Shotanov, A, Nurgali, N Z, Roshchin, A V, Panfilov, V P, Baysanov, S O, Almagambetov, M S and Dossekenov, M S, 2023. Smelting of High-Carbon Ferrochrome from Prereduced Chromite Raw Materials of the Donskoy Ore Mining and Processing Plant, *Metallurgist*, 66:1619–1624.

Toulouevski, Y and Zinurov, I, 2009. *Innovation in Electric Arc Furnaces*, 1st edition (Springer Scientific).

Xiaohai, F, Wong, G, Gan, M K H and Chen, X, 2019. Sintering Characteristic and Consolidation Behaviour of Chromite Fines, in *Proceedings of the 10th International Symposium on high temperature Metallurgical Processing*, pp 257–267.

Yu, Y, Li, B, Liu, Z, Qi, F, Liu, C, Rong, W and Kuang, S, 2023. Analysis of Electrical Energy Consumption in a Novel Direct Current Submerged Arc Furnace for Ferrochrome Production, *Metallurgical and Materials Transactions B*, 54:2370–2382.

Production of molybdenum disilicide using a silicon-containing molten bath via the hot dipping method

DOI: 10.62053/LGHS3844

J Gamutan[1], H Fukaya[2] and T Miki[3]

1. Lecturer, Curtin University, Kalgoorlie WA 6430. Email: jonah.gamutan@curtin.edu.au
2. Assistant Professor, Tohoku University, Sendai 980–8579, Japan. Email: hiroshi.fukaya.c8@tohoku.ac.jp
3. Professor, Tohoku University, Sendai 980–8579, Japan. Email: miki@argon.material.tohoku.ac.jp

ABSTRACT

Molybdenum disilicide ($MoSi_2$) is a promising material for thermal applications due to its excellent heat and oxidation resistance. It can operate at temperatures of up to 1800°C as furnace heating elements and protect refractory metals such as molybdenum from rapidly reacting with air to form volatile molybdenum oxides at elevated temperature. In this work, the feasibility of forming $MoSi_2$ on a molybdenum substrate by hot dipping in a silicon-saturated molten metal bath was investigated. This method is simple, predictable and can be used to coat large components and complex parts.

It was found that tetragonal $MoSi_2$ can be successfully synthesised on the surface of the substrate after dipping for 15 mins at 1000°C using molten tin (Sn), bismuth (Bi) and copper (Cu) baths. The growth of the $MoSi_2$ layer was fast within the first 15 mins and then gradually slowed down with time. After dipping for 60 mins at 1000°C, the thickness of the $MoSi_2$ layer were measured as 441.5, 19.5 and 13.1 μm for the copper, tin, and bismuth baths, respectively. The $MoSi_2$ coating synthesised in this study provided oxidation resistance at 1150°C by forming a protective SiO_2 layer on the surface. The SiO_2 layer prevented the sample from rapidly oxidising by inhibiting direct contact between the molybdenum substrate and oxygen in the atmosphere.

Compared to conventional methods, the proposed hot dipping method produces a $MoSi_2$ layer more rapidly and at much lower operating temperatures. This makes it a more attractive option for coating large and complex components, with the potential to enable the use of $MoSi_2$ in a wider range of applications.

INTRODUCTION

High-temperature applications in oxidising environments, including power generation, metal processing and aerospace industries, require materials with exceptional resistance against heat and oxidation. Molybdenum disilicide ($MoSi_2$) is a candidate material for these purposes due to its low density (6.31 g/cm^3), high melting point (2030°C), excellent oxidation resistance, satisfactory electrical and thermal conductivities, chemical inertness and relatively low coefficient of thermal expansion (Shah, 1992; Vasudévan and Petrovic, 1992; Jeng and Lavernia, 1994). However, despite these outstanding physical and chemical properties, limitations associated with conventional manufacturing methods for $MoSi_2$ components and $MoSi_2$-coatings restrict its application to simple shapes and small components.

Molybdenum and its alloys, on the other hand, are considered the next-generation materials to replace nickel super alloys (Kamata *et al*, 2018). However, the poor heat and oxidation resistance of molybdenum seriously limits its applications. At elevated temperatures, molybdenum readily reacts with oxygen in air to form volatile molybdenum oxide species, such as MoO_3 and MoO_2, leading to material loss and failure (Brewer and Lamoreaux, 1980).

To address the limitations of both $MoSi_2$ and molybdenum alloys, surface modification of molybdenum alloys to produce an oxidation resistant $MoSi_2$ layer on the surface emerges as a promising solution. The $MoSi_2$ is expected to provide a uniform protective layer that prevents direct contact between molybdenum and oxygen, significantly enhancing material performance. Among various siliconising techniques such as the halide-activated pack cementation (Ito *et al*, 2003; Sakidja *et al*, 2005; Majumdar, 2012; Sun *et al*, 2016), slurry sintering (Suzuki, Ishikawa and Ono, 2000; Cai *et al*, 2017; Li *et al*, 2018), spark plasma sintering (Reisel *et al*, 2001; Nomura *et al*, 2003;

Zhu *et al*, 2019; Sun, Li and Zhang, 2019) and chemical vapor deposition (Cox and Brown, 1964; Rice and Sarma, 1981; Govindarajan *et al*, 1995; Yoon *et al*, 2002), the hot dipping method emerges as the most practical way to produce $MoSi_2$ due to its short treatment time, simple and straightforward procedure, and applicability to large and complex shapes (Gamutan and Miki, 2022).

Table 1 shows the various molten bath compositions used to siliconise molybdenum and its alloys using the hot dipping method. Zhang *et al* (2021) used pure molten silicon at elevated temperatures (1480°C to 1560°C) to create a multi-layered surface of Si, $MoSi_2$, Mo_5Si_3 and Mo_3Si. Meanwhile, Christian and Narita (1998) employed molten In-Si bath under vacuum at 1000–1200°C to achieve an $MoSi_2$ layer with a thin Mo_5Si_3 interlayer. Due to its lower melting temperature, silicon-containing molten aluminium baths were also used at dipping temperatures of 700°C to 1000°C to form $Mo(Si,Al)_2$ layers (Sharifitabar, Oukati Sadeq and Shafiee Afarani, 2021; Nanko *et al*, 2001; Yanagihara, Maruyama and Nagata, 1994). However, the use of these molten metal baths is limited due to the high dipping temperatures required and the cost of silicon and aluminium. Additionally, In-Si melts involve the use of indium, a very rare and highly volatile element. Therefore, for practical applications, a readily available, inexpensive and low-melting silicon-containing bath is desired.

TABLE 1

Molten bath composition and the growth rate of different hot dipping methods to siliconise molybdenum and its alloys.

Molten bath composition	Temperature (°C)	Growth rate (μm/h)	References
Si bath	1480–1560	120	Fu *et al* (2024); Zhang *et al* (2021, 2022)
In–Si bath	1000, 1200	2.8, 7.2	Christian and Narita (1998)
Al–12%Si bath	950	33.3	Sharifitabar, Oukati Sadeq and Shafiee Afarani (2021)
Al–26%Si bath	700	0.9	Nanko *et al* (2001)
Al–50%Si bath	1000	35.0	Yanagihara, Maruyama and Nagata (1994)

This work explores the feasibility of using molten tin (Sn), bismuth (Bi) and copper (Cu) baths with silicon to form oxidation resistant $MoSi_2$ layers on pure molybdenum substrates. Commonly used in food packaging and soldering applications, molten tin and bismuth baths are excellent candidates due to their low melting points ($T_{m,Sn}$ = 232°C and $T_{m,Bi}$ = 271°C) and relatively low cost and abundance. Moreover, according to the Sn-Si (Olesinski and Abbaschian, 1984) and Bi-Si (Olesinski and Abbaschian, 1985) binary phase diagrams, the solubilities of silicon in tin and bismuth are almost negligible, suggesting that when molybdenum is immersed into silicon-containing molten tin or bismuth bath, molybdenum should readily react with silicon to form $MoSi_2$. While copper has a relatively high melting point ($T_{m,Cu}$ = 1085°C), its thermodynamic relationship with silicon (Okamoto, 2012) and molybdenum (Subramanian and Laughlin, 1990) is similar to that of tin and bismuth, making it another potential candidate for this application.

The key aspect of this work involves investigating the composition, growth, and oxidation resistance of the $MoSi_2$ layers formed on pure molybdenum substrates using silicon-containing tin, bismuth, and copper baths. This technique has the potential to overcome the challenges of existing siliconising methods and develop more efficient and cost-effective $MoSi_2$ coatings.

EXPERIMENTAL METHOD

Sample preparation and hot dipping

Figure 1 shows a schematic diagram of the experimental set-up employed in this work. Molybdenum sheets (99.95 per cent Mo) cut into 1 × 10 × 50 mm plates were used as the substrates for hot dipping in silicon-containing tin (98.8 per cent Sn – 1.2 per cent Si), bismuth (98.0 per cent Bi –

2.0 per cent Si) and copper (73.5 per cent Cu – 26.5 per cent Si) baths. The bath compositions were selected such that it fell within the two-phase region of the Sn-Si, Bi-Si and Cu-Si systems, where the thermodynamic activity of silicon remains close to unity.

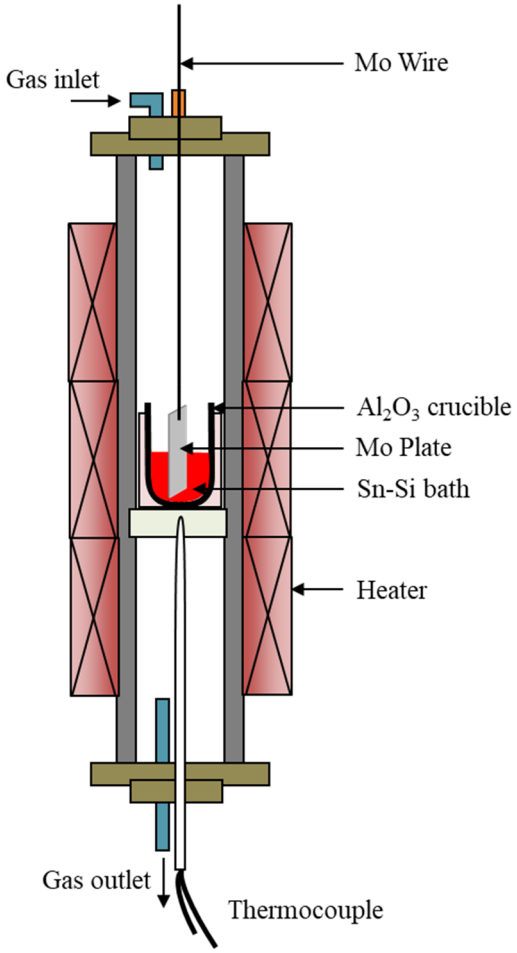

FIG 1 – Schematic diagram of the experimental set-up.

Prior to dipping, the Mo-plates were polished with silicon carbide paper and ultrasonically cleaned in ethanol. Then, the samples were positioned in the top-most portion of the furnace using a molybdenum wire (ø 2 mm). The same wire was used to push the samples down into the bath once the target temperature of 1000°C was achieved and stabilised. Immersion times were varied at 15, 30 and 60 mins while the atmosphere was kept inert in argon (400 mL/min). After dipping, the Mo-substrates were pulled back to the top-most portion of the furnace and allowed to cool down to room temperature.

Characterisation of samples

To characterise phase composition of the hot dipped samples, X-ray diffraction (XRD) technique with Cu-Kα radiation at a 5° min^{-1} scanning speed from 20° to 80° was employed. The raw XRD data were then analysed and indexed using Rigaku PDXL software. Meanwhile, Scanning Electron Microscopy with Energy Dispersive Spectrometry (SEM-EDS) was used to investigate the morphology and composition of the sample cross-sections. Samples for SEM-EDS were prepared by mounting in a resin, polishing using silicon carbide paper and a final ultrasonic cleaning step in ethanol.

Finally, to assess the oxidation resistance of the formed $MoSi_2$-layer, isothermal oxidation tests of fully coated and uncoated samples at 1150°C for 2 hrs in air were conducted. Prior to testing, sample edges were protected with a SiO_2 ceramic paste. The change in weight of the samples before and after the oxidation tests were also measured to estimate the extent of oxidation reactions.

RESULTS AND DISCUSSION

Phase composition and growth

Sn-Si bath (98.8 per cent Sn – 1.2 per cent Si)

The XRD patterns of the bulk Mo-substrate samples before and after siliconising in a molten Sn-Si bath for 15 and 60 mins at 1000°C are shown in Figure 2. While the peaks of molybdenum remain, the formation of new $MoSi_2$ peaks with a strong preferred orientation on the (103) crystal face was observed after dipping for 15 and 60 mins. It was found that with longer immersion times, the intensity of $MoSi_2$ relative to molybdenum increased. These results suggest the successful formation and growth of the formed $MoSi_2$ layer on the surface of the Mo-substrate by hot dipping at 1000°C in a silicon-containing tin bath. Peaks of tin were also detected in samples after hot dipping, suggesting incomplete removal of the residual material during cleaning, or penetration of the $MoSi_2$ layer by molten tin (Gamutan and Miki, 2022).

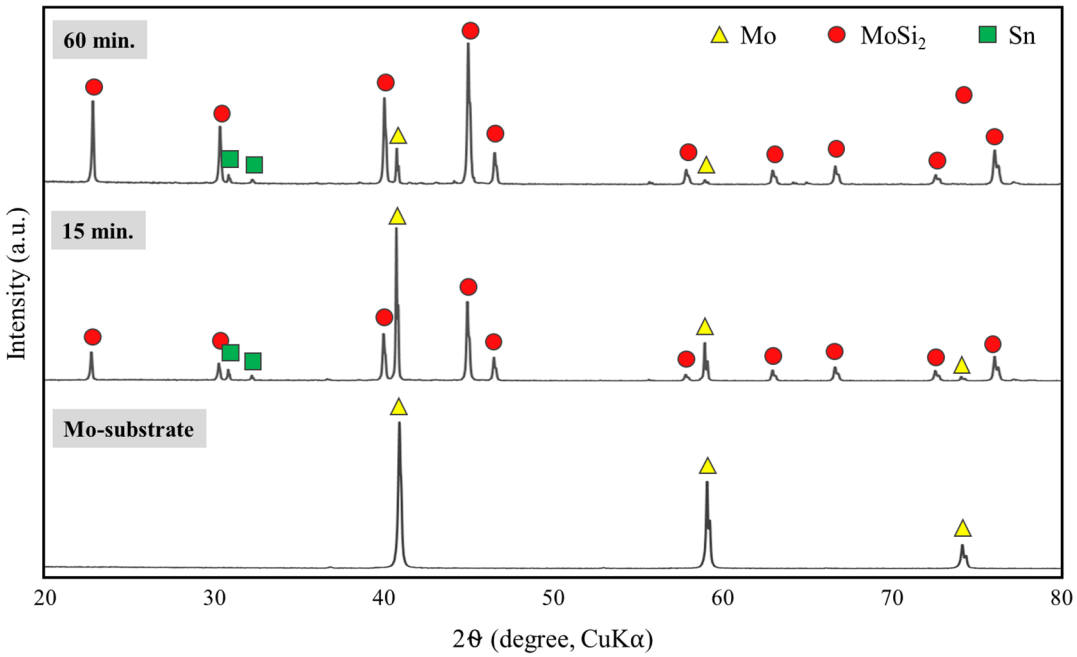

FIG 2 – XRD patterns of the bulk Mo-substrate before after hot dipping in a Sn-Si bath for 15 and 60 mins at 1000°C.

SEM micrograph and EDS investigation of the sample cross-sections after dipping for 15 and 60 mins are shown in Figure 3. The black-coloured area in the micrographs corresponds to the carbon resin used to mount the samples, while the grey-coloured area corresponds to the sample cross-section. EDS mapping of the sample cross-section suggests the formation of a dense layer containing molybdenum and silicon approximately 10–20 µm thick on the surface of the Mo-substrate. Point analysis indicate that the Mo:Si atomic ratio of the formed layer is approximately 1:2, confirming the formation of $MoSi_2$. EDS results also reveal about 0.5 per cent Sn in the formed $MoSi_2$ layer, confirming that appearance of the peaks of tin observed via XRD was due to the uptake of molten tin by the $MoSi_2$ layer.

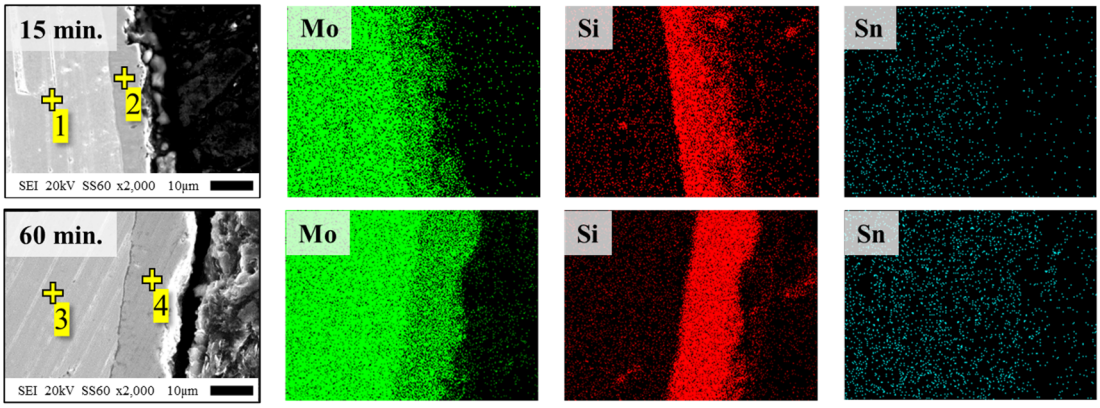

Dipping Time	Point	Mo	Si	Sn	Remarks
15 minutes	1	99.45	0.35	0.20	Mo-substrate
	2	64.55	34.86	0.59	$MoSi_2$
60 minutes	3	99.73	0.27	-	Mo-substrate
	4	64.49	35.08	0.44	$MoSi_2$

(mass %)

FIG 3 – Cross-section micrographs and EDS analysis of the siliconised molybdenum samples after hot dipping in Sn-Si bath at 1000°C for 15 and 60 mins.

Bi-Si bath (98.0 per cent Bi – 2.0 per cent Si)

Figure 4 shows the XRD patterns of the samples before and after dipping in a silicon-containing molten bismuth bath at 1000°C for 15 and 60 mins. While the peaks of molybdenum remain, new peaks of Mo_5Si_3 and $MoSi_2$ were observed after hot dipping for 15 and 60 mins. As dipping time increased, the intensities of Mo_5Si_3 and $MoSi_2$ peaks relative to the molybdenum peak increased, confirming the successful formation and growth of Mo_5Si_3 and $MoSi_2$ layers on the molybdenum surface through hot dipping at 1000°C in a molten Bi-Si bath.

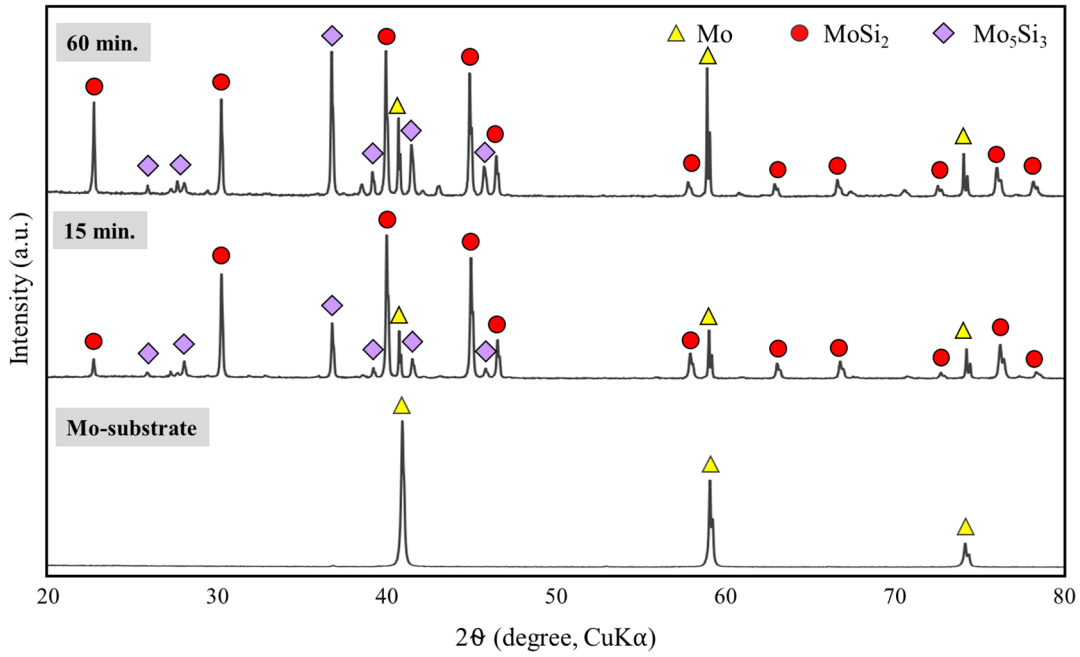

FIG 4 – XRD patterns of the bulk Mo-substrate before after hot dipping in a Bi-Si bath for 15 and 60 mins at 1000°C.

Figure 5 shows the cross-section micrographs and EDS analysis results of the siliconised molybdenum samples after hot dipping in Bi-Si bath at 1000°C for 15 and 60 mins. Similar with the results when using a Sn-Si bath, SEM-EDS results suggest the formation of about 12 µm thick layer, which contains both molybdenum and silicon, on the surface of the Mo-substrate. Point analysis of the layer reveals a Mo:Si atomic ratio of 1:2, confirming the formation of $MoSi_2$. However, the presence of other silicide compounds of molybdenum, such as Mo_5Si_3 which were determined via XRD, was not detected using SEM-EDS. In contrast, the presence of 0.39 per cent and 3.52 per cent Bi in the formed $MoSi_2$ layer was measured using EDS point analysis, but peaks of bismuth were not detected via XRD analysis.

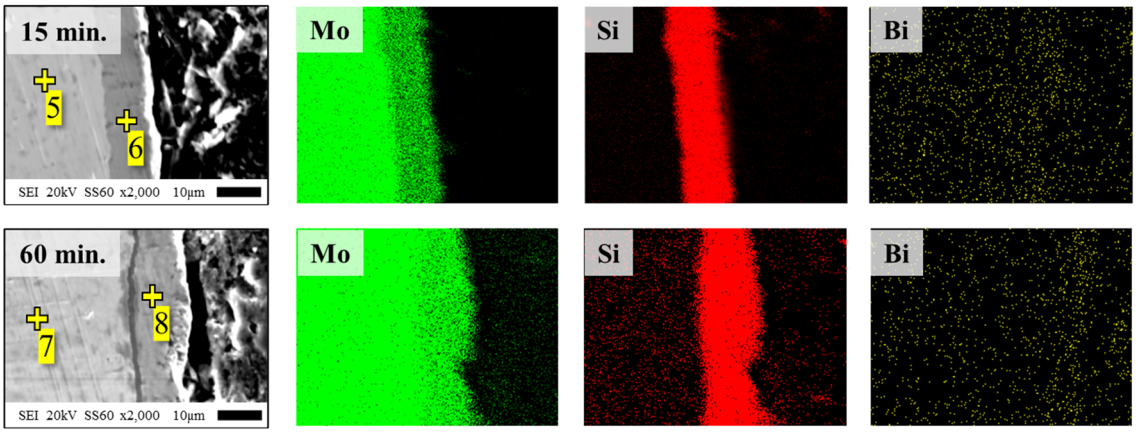

Dipping Time	Point	Mo	Si	Bi	Remarks
15 minutes	5	99.84	0.16	-	Mo-substrate
	6	64.30	35.31	0.39	$MoSi_2$
60 minutes	7	99.68	0.14	0.18	Mo-substrate
	8	62.50	33.98	3.52	$MoSi_2$

(mass %)

FIG 5 – Cross-section micrographs and EDS analysis of the siliconised molybdenum samples after hot dipping in Bi-Si bath at 1000°C for 15 and 60 mins.

Cu-Si bath (73.5 per cent Cu – 26.5 per cent Si)

Due to the irregularity in shape and the difficulty in obtaining good measurement results, only the XRD patterns of the sample immersed in molten Cu-Si bath for 15 mins at 1000°C were obtained in this work, as shown in Figure 6. After dipping for 15 mins, formation of the characteristic peaks of $MoSi_2$ were found, while the formation of new Cu_3Si peaks were also observed. However, continuous dipping for 60 mins resulted in the formation of thick, dendrite-like protrusions along the sample edges, impeding true and representative sampling for XRD analysis without breaking off or damaging the surface.

Figure 7 shows the cross-section micrographs and EDS analysis results of the samples after dipping for 15 and 60 mins. These results confirm the formation of $MoSi_2$ on the surface of the Mo-substrate and a new layer composed primarily of copper and silicon. Point analysis of this layer revealed a Cu:Si atomic ratio of approximately 3, confirming the formation of Cu_3Si, which was also identified via XRD analysis. The Cu_3Si layer was found primarily located on the outermost surface of the sample, but it also appeared in between the Mo-substrate and formed $MoSi_2$ layers, particularly in the sample immersed for 60 mins.

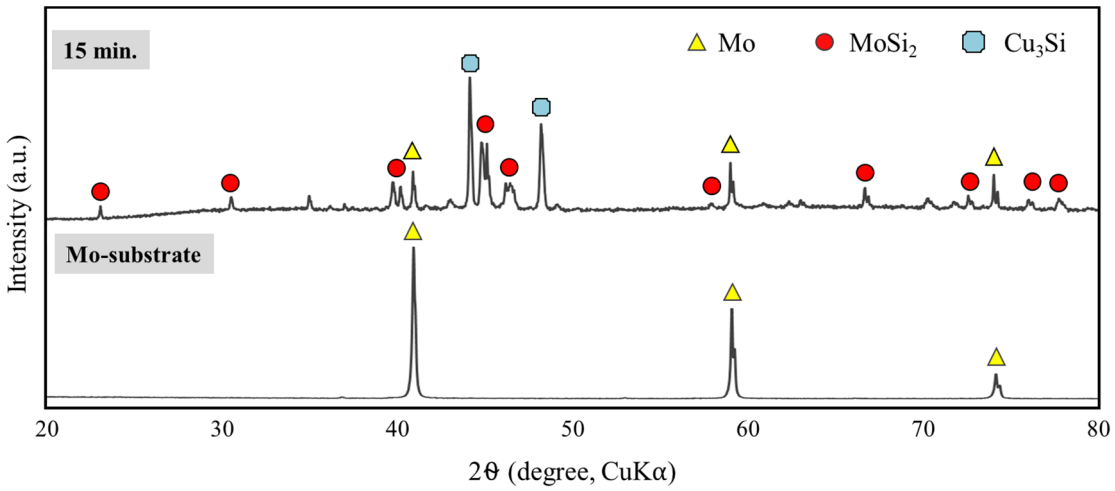

FIG 6 – XRD patterns of the bulk Mo-substrate before after hot dipping in a Cu-Si bath for 15 mins at 1000°C.

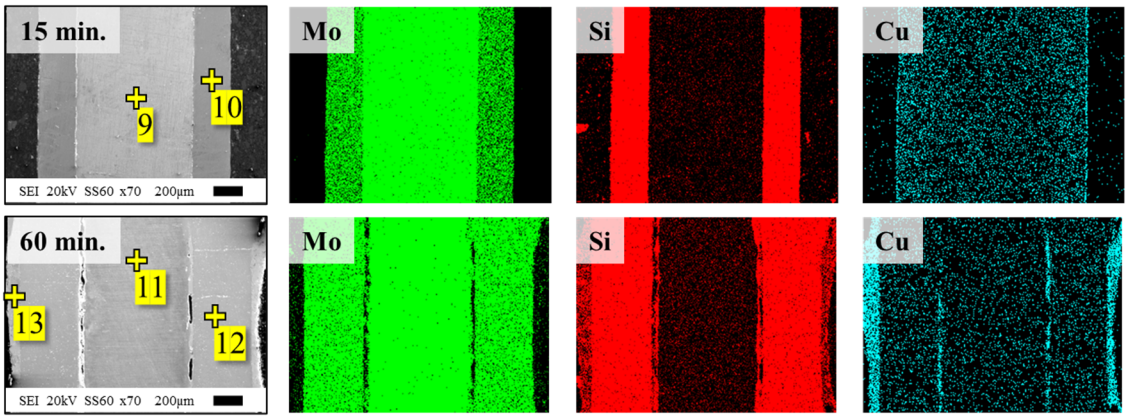

Dipping Time	Point	Mo	Si	Cu	Remarks
15 minutes	9	99.42	0.57	0.02	Mo-substrate
	10	60.28	34.47	5.25	$MoSi_2$
60 minutes	11	99.40	0.28	0.32	Mo-substrate
	12	61.15	34.74	4.11	$MoSi_2$
	13	0.25	12.78	86.97	Cu_3Si

(mass %)

FIG 7 – Cross-section micrographs and EDS analysis of the siliconised molybdenum samples after hot dipping in Cu-Si bath at 1000°C for 15 and 60 mins.

The formation of other molybdenum silicide compounds was not detected using either XRD or SEM-EDS analysis, but the presence of about 4–5 per cent Cu in the formed $MoSi_2$ layer was identified using EDS point analysis. While we cannot draw definitive conclusions without XRD data for longer dipping times, the extremely rapid growth of the $MoSi_2$ layer when using molten Cu-Si bath and the substantial concentration of copper within the layer suggest that penetration of copper caused significant expansion of the $MoSi_2$ lattice, facilitating the faster diffusion of silicon towards the unreacted Mo-substrate (Gamutan and Miki, 2022).

The thickness of the formed $MoSi_2$ layers after dipping for 15 and 60 mins, measured at 268 µm and 441 µm, respectively, showed a tenfold increase in growth rate when using molten Cu-Si bath compared to samples immersed in molten Sn-Si and Bi-Si baths.

Mechanism and kinetics of $MoSi_2$ formation

The above-mentioned findings indicate that the formation of $MoSi_2$ at the surface of the Mo-substrate was possible by dipping molybdenum in various silicon-containing tin (98.8 per cent Sn – 1.2 per cent Si), bismuth (98.0 per cent Bi – 2.0 per cent Si) and copper (73.5 per cent Cu – 26.5 per cent Si) baths. The concentration of silicon in these baths were designed such that the thermodynamic activity of silicon in this melt was close to unity and molybdenum reacts with silicon in the bath according to the following equation:

$$Mo(s) + 2\underline{Si} = MoSi_2(s) \quad (1)$$

Meanwhile, the formation of intermediate compounds of molybdenum and silicon, such as Mo_5Si_3, also suggest the occurrence of following equation:

$$5Mo(s) + 3\underline{Si} = Mo_5Si_3(s) \quad (2)$$

The measured thickness of the $MoSi_2$ layer formed by hot dipping in various silicon-containing molten baths is shown in Figure 8a. The thickness was an average of six measurements made at different positions in the sample. It was found that the $MoSi_2$ layers grew with dipping time and growth was fastest when using molten Cu-Si bath, followed by molten Sn-Si and Bi-Si baths.

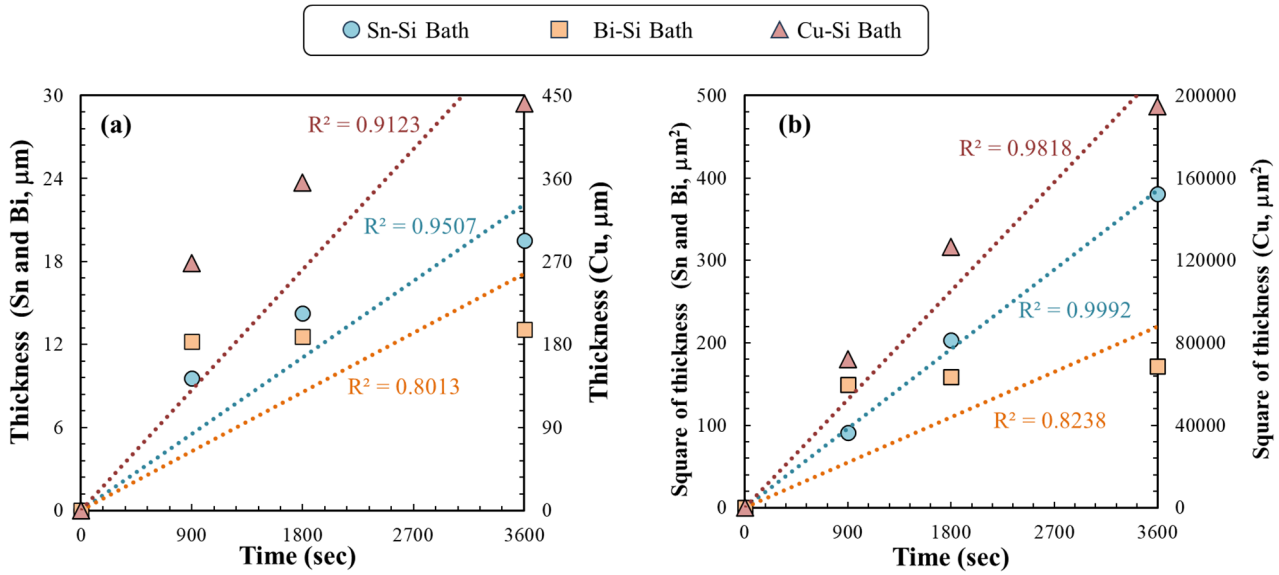

FIG 8 – Growth of $MoSi_2$ layer thickness as a function of time according to: (a) reaction-controlled growth mechanism, and (b) diffusion-controlled growth mechanism.

To determine whether the growth of the $MoSi_2$ layer was controlled either by the reaction at the Mo-substrate interface or by diffusion through the formed $MoSi_2$ product layer, variation in thickness versus time was plotted as follows. For a reaction-controlled growth, it is known that $MoSi_2$ layer thickness should increase linearly with time according to the following equation:

$$y = kt \quad (3)$$

where y is the $MoSi_2$ layer thickness (µm) at a certain dipping time t (sec). For a diffusion-controlled growth, the thickness should increase parabolically with time according to the following equation:

$$y^2 = kt \quad (4)$$

Plotting the measured $MoSi_2$ layer thickness from this study revealed through linear regression that R^2 values were closer to unity for the parabolic growth rate model, as shown in Figure 8b. This suggests that siliconisation of the Mo-substrate via the hot dipping method was primarily a diffusion-controlled process. This is particularly true for samples immersed in molten Sn-Si and Cu-Si bath, with very high R^2 values of 0.9992 and 0.9818, respectively. Consequently, promoting diffusion of silicon through the formed $MoSi_2$ layer could potentially improve growth, which aligns with the findings above, particularly in the case of silicon-containing copper bath.

However, attempts to apply both reaction and diffusion-controlled growth models to samples dipped in a molten Bi-Si bath did not achieve very strong linear relationships. In fact, the thickness of the formed $MoSi_2$ layer barely increased. These results imply that another factor influenced the growth kinetics of the $MoSi_2$ layer. Based on our observations, the formation and presence of the intermediate phase, Mo_5Si_3, might be the rate-limiting step. Further investigation is required to solidify this conclusion.

To summarise, the mechanism of growth of the $MoSi_2$ layer on the surface of Mo-substrate can be schematically described as shown in Figure 9. When pure molybdenum is dipped into the silicon-containing bath, silicon initially diffuses through the molten bath, as shown in Figure 9a, until it comes into contact with the molybdenum surface. Due to the elevated temperature conditions employed in the hot dipping experiment, diffusion of silicon through the molten bath is assumed to be fast enough such that its influence on the kinetics of growth could be neglected.

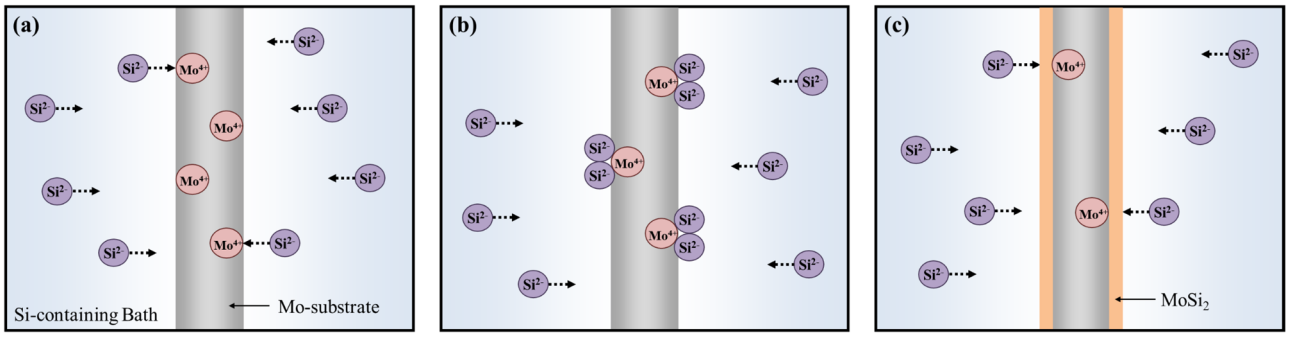

FIG 9 – Proposed mechanism of $MoSi_2$ formation via the hot dipping method.

Next, once the silicon, with thermodynamic activity close to unity, comes into contact with molybdenum, both elements react together according to Equation 1 to produce $MoSi_2$ as shown in Figure 9b. Potentially, Equation 2 also occurs to form Mo_5Si_3, particularly when using molten Bi-Si bath, due to low silicon concentrations within the interface. Eventually, the $MoSi_2$ layer grows and thickens, forming a product layer, which substantially slows down the rate at which silicon reaches the unreacted molybdenum surface, as shown in Figure 9c.

Oxidation resistance behaviour

Fully coated samples produced via hot dipping in molten Sn-Si bath at 1000°C for 60 mins were subjected to oxidation test carried out at 1150°C for 2 hrs in air. While the bare uncoated molybdenum sample was completely oxidised and lost in the form of gaseous molybdenum oxides, the fully coated samples suffered a mass loss of about 4 per cent only. These results suggest that formation of a $MoSi_2$ layer on the surface of molybdenum imparts oxidation resistance at elevated temperatures, a promising solution to address the challenges to both $MoSi_2$ and molybdenum alloys.

Figure 10 shows the cross-section micrograph and EDS analysis results of the siliconised molybdenum samples after the oxidation test. As evident from the micrograph, the density of the $MoSi_2$ layer did not change significantly and the oxidised surface consisted of three layers – an outer SiO_2 layer followed by the $MoSi_2$ layer and a thin intermediate layer on top of the Mo-substrate. Area analysis of this intermediate layer showed a Mo:Si atomic ratio of about 5:3, indicating that the main phase composition of this layer is Mo_5Si_3. Line scan also supports the formation of these three layers, revealing a clear change in molybdenum and silicon concentrations. To determine the exact oxidation resistance mechanism of the $MoSi_2$ layer, further tests with higher temperatures, longer holding times and enhanced sensitivity is necessary.

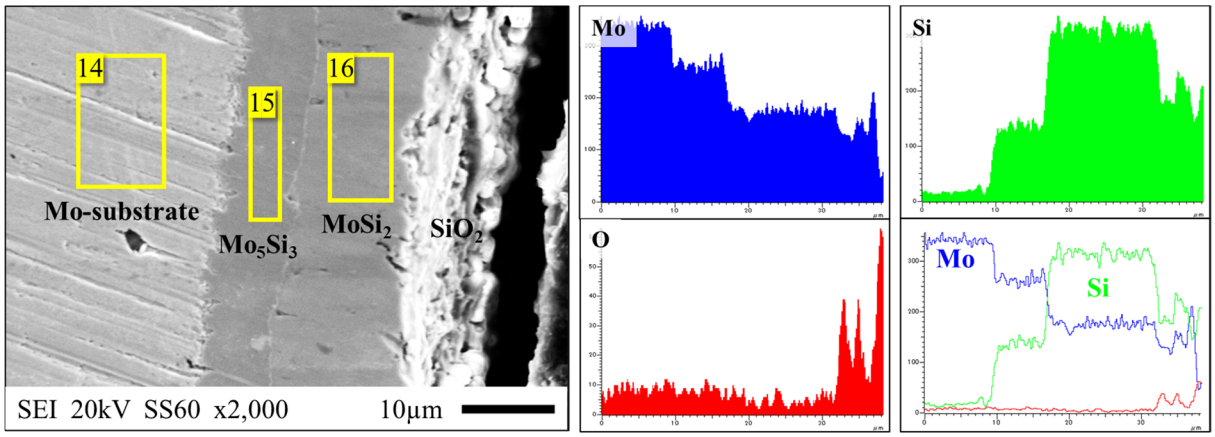

Area Analysis	Si	Mo	Sn	Remarks
14	-	99.78	0.22	Mo-substrate
15	14.30	85.69	0.01	Mo_5Si_3
16	35.41	64.59	-	$MoSi_2$

(mass %)

FIG 10 – Cross-section micrograph and EDS analysis of the siliconised molybdenum samples after the oxidation test at 1150°C for 2 hrs in air.

CONCLUSIONS

The present work demonstrates the feasibility of a novel hot dipping method to produce a protective $MoSi_2$ layers on pure Mo-substrate using silicon-containing tin (98.8 per cent Sn – 1.2 per cent Si), bismuth (98.0 per cent Bi – 2.0 per cent Si) and copper (73.5 per cent Cu – 26.5 per cent Si) baths. This simple and straightforward method enabled the formation of a dense $MoSi_2$ layer after hot dipping at 1000°C for 15–60 mins with thickness of about 10–20 µm, 12 µm and 268–441 µm, respectively. The silicon-containing molten copper bath allowed $MoSi_2$ to be synthesised most rapidly, followed by tin and bismuth.

Siliconisation of the Mo-substrate using Sn-Si and Cu-Si baths was found to be mainly a diffusion-controlled process. Meanwhile, other factors, such as the formation of an intermediate Mo_5Si_3 layer, were found to be potentially rate-limiting when using a Bi-Si bath. Finally, oxidation test of the fully coated samples confirms the potential of $MoSi_2$ to protect molybdenum and its alloys from rapid oxidation loss at elevated temperatures.

REFERENCES

Brewer, L and Lamoreaux, R H, 1980. The Mo-O system, *Bulletin of Alloy Phase Diagrams*, 1:85–89.

Cai, Z, Liu, S, Xiao, L, Fang, Z, Li, W and Zhang, B, 2017. Oxidation behavior and microstructural evolution of a slurry sintered Si-Mo coating on Mo alloy at 1650°C, *Surface and Coatings Technology*, 324:182–189.

Christian, F and Narita, T, 1998. Siliconizing of molybdenum metal in indium-silicon melts, *Materials Transaction JIM*, 39:658–662.

Cox, A R and Brown, R, 1964. Protection of molybdenum from oxidation by molybdenum dilicide based coatings, *Journal of the Less-Common Metals*, 6:51–69.

Fu, T, Zhang, Y, Chen, L, Shen, F and Zhu, J, 2024. Micromorphology evolution, growth mechanism and oxidation behaviour of the silicon-rich MoSi2 coating at 1200°C in air, *Journal of Materials Research and Technology*, 29:491–503.

Gamutan, J and Miki, T, 2022. Surface modification of a Mo-substrate to form an oxidation-resistant MoSi2 layer using a Si-saturated tin bath, *Surface and Coatings Technology*, 448:128938.

Govindarajan, S, Mishra, B, Olson, D L, Moore, J J and Disam, J, 1995. Synthesis of molybdenum disilicide on molybdenum substrates, *Surface and Coatings Technology*, 76–77:7–13.

Ito, K, Murakami, T, Adachi, K and Yamaguchi, M, 2003. Oxidation behavior of Mo-9Si-18B alloy pack-cemented in a Si-base pack mixture, *Intermetallics*, 11:763–772.

Jeng, Y L and Lavernia, E J, 1994. Review: Processing of molybdenum disilicide, *Journal of Materials Science*, 29:2557–2571.

Kamata, S H, Kanekon, D, Lu, Y, Sekido, N, Maruyama, K, Eggeler, G and Yoshimi, K, 2018. Ultrahigh-temperature tensile creep of TiC-reinforced Mo-Si-B based alloy, *Scientific Reports*, 8:10487.

Li, W, Fan, J, Fan, Y, Xiao, L and Cheng, H, 2018. MoSi2/(Mo,Ti)Si2 dual-phase composite coating for oxidation protection of molybdenum alloy, *Journal of Alloys and Compounds*, 740:711–718.

Majumdar, S, 2012. Formation of MoSi2 and Al doped MoSi2 coatings on molybdenum base TZM (Mo-0.5Ti-0.1Zr-0.02C) alloy, *Surface and Coatings Technology*, 206:3393–3398.

Nanko, M, Kitahara, A, Ogura, T, Kamata, H and Maruyama, T, 2001. Formation of Mo(Si,Al)2 layer on Mo dipped in Al melt saturated with Si and the effects of transition metals added in the melt, *Intermetallics*, 9:637–646.

Nomura, N, Suzuki, T, Yoshimi, K and Hanada, S, 2003. Microstructure and oxidation resistance of a plasma sprayed Mo-Si-B multiphase alloy coating, *Intermetallics*, 11:735–742.

Okamoto, H, 2012. Cu-Si (Copper-Silicon), *J Phase Equilibria and Diffusion*, 33:415–416.

Olesinski, R W and Abbaschian, G J, 1984. The Si-Sn (silicon-tin) system, *Bulletin of Alloy Phase Diagrams*, 5:273–276.

Olesinski, R W and Abbaschian, G J, 1985. The Si-Bi (silicon-bismuth) system, *Bulletin of Alloy Phase Diagrams*, 6:359–361.

Reisel, G, Wielafe, B, Steinhäuser, S, Morgenthal, I and Scholl, R, 2001. High temperature oxidation behavior of HVOF-sprayed unreinforced and reinforced molybdenum disilicide powders, *Surface and Coatings Technology*, 146–147:19–26.

Rice, M J and Sarma, K R, 1981. Interaction of CVD silicon with molybdenum substrates, *Journal of the Electrochemical Society*, 128:1368–1373.

Sakidja, R, Park, J S, Hamann, J and Perepezko, J H, 2005. Synthesis of oxidation resistant silicide coatings on Mo-Si-B alloys, *Scripta Materialia*, 53:723–728.

Shah, D M, 1992. MoSi2 and other silicides as high temperature structural materials, in *Proceedings of the 7th International Symposium on Superalloys* (eds: S D Antolovich, R W Stusrud, R A MacKay, D L Anton, T Khan, R D Kissinger and D L Klarstrom), pp 409–422 (The Minerals, Metals and Materials Society).

Sharifitabar, M, Oukati Sadeq, F and Shafiee Afarani, M, 2021. Synthesis and kinetic study of Mo(Si,Al)2 coatings on the surface of molybdenum through hot dipping into a commercial Al-12wt.%Si alloy melt, *Surface and Interfaces*, 24:101044.

Subramanian, P R and Laughlin, D E, 1990. The Cu-Mo (copper-molybdenum) system, *Bulletin of Alloy Phase Diagrams*, 11:169–172.

Sun, J, Fu, Q G, Guo, L P, Liu, Y, Huo, C X and Li, H J, 2016. Effect of filler on the oxidation protective ability of MoSi2 coating for Mo substrate by halide activated pack cementation, *Materials and Design*, 92:602–609.

Sun, J, Li, T and Zhang, G P, 2019. Effect of thermodynamically metastable components on mechanical and oxidation properties of the thermal-sprayed MoSi2 based composite coating, *Corrosion Science*, 155:146–154.

Suzuki, R, Ishikawa, M and Ono, K, 2000. MoSi2 coating on molybdenum using molten salt, *Journal of Alloys and Compounds*, 306:285–291.

Vasudévan, A K and Petrovic, J J, 1992. A comparative overview of molybdenum disilicide composites, *Mat, Sci and Eng*, A155:1–17.

Yanagihara, K, Maruyama, T and Nagata, K, 1994. Dip-coating of Mo(Si,Al)2 on Mo with an Al-Si melt, *Tetsu-to-Hagane*, 80:178–182.

Yoon, J K, Byun, J Y, Kim, H G, Kim, J S and Choi, C L, 2002. Growth kinetics of three Mo-silicide layers formed by chemical vapor deposition of Si on Mo substrate, *Surface and Coatings Technology*, 155:85–95.

Zhang, Y, Cui, K, Fu, T, Wang, J, Shen, F, Zhang, X and Yu, L, 2021. Formation of MoSi2 and Si/MoSi2 coatings on TZM (Mo-0.5Ti-0.1Zr-0.02C) alloy by hot dip silicon-plating method, *Ceramics International*, 47:23053–23065.

Zhang, Y, Fu, T, Yu, L, Shen, F, Wang, J and Cui, K, 2022. Improving oxidation resistance of TZM alloy by deposited Si-MoSi2 composite coating with high silicon concentration, *Ceramics International*, 48:20895–20904.

Zhu, L, Zhu, Y, Ren, Z, Zhang, P, Qiao, J and Feng, P, 2019. Microstructure, properties and oxidation behavior of MoSi2-MoB-ZrO2 coating for Mo substrate using spark plasma sintering, *Surface and Coatings Technology*, 375:773–781.

Reduction and melting behaviours of carbon – iron oxide composite using iron carbides and free carbon obtained by vapour deposition

DOI: 10.62053/WEWM2079

R Higashi[1], D Maruoka[2], Y Iwami[3] and T Murakami[4]

1. Graduate Student, Graduate School of Environmental Studies, Tohoku University, Sendai 980-8579, Japan. Email: ryota.higashi.r3@dc.tohoku.ac.jp
2. Assistant Professor, Graduate School of Environmental Studies, Tohoku University, Sendai 980-8579, Japan. Email: daisuke.maruoka.e6@tohoku.ac.jp
3. Senior Researcher, JFE Steel Corporation, Fukuyama 721-8510, Japan. Email: yu-iwami@jfe-steel.co.jp
4. Professor, Graduate School of Environmental Studies, Tohoku University, Sendai 980-8579, Japan. Email: taichi@material.tohoku.ac.jp

ABSTRACT

The ironmaking industry consumes a large amount of fossil fuel derived carbon as heat source, reducing agent of iron ores and carburising agent of reduced iron. Although the demand for drastic decrease of carbon dioxide emission, carbon is an essential element for smelting process of molten iron. The carbon recycling ironmaking process by circulating CO has been already proposed to achieve carbon neutrality. However, the production of molten hot metal is not considered in this process because sufficient amount of carbon does not dissolve in reduced iron by CO. Therefore, our group has suggested a new carbon recycling ironmaking process which can produce hot metal. In this process, free carbon and iron carbides produced by carbon deposition reaction using metallic iron as a catalyst are used. It is known that only Fe_3C is obtained as iron carbide by using CO gas, however, Fe_5C_2 is also produced by adding H_2 gas. The composite agglomerated with these carbonaceous materials and fine iron ore (Deposited Carbon-Iron oxide Composite: DCIC) is reduced and melted in a furnace. It is reported that Fe_3C in DCIC accelerates the reduction reaction and melting of the composite. In this study, the effects of iron carbides and free carbon on the melting behaviour of DCIC are investigated.

Fe_3C, Fe_5C_2 and free carbon were produced by vapour deposition using porous iron whiskers and CO-CO_2-H_2 gas. These were agglomerated with hematite reagent at a certain ratio to prepare DCIC samples with and without Fe_5C_2. The samples were heated up to 1300°C in inert atmosphere. The DCIC containing Fe_5C_2 completely melted and iron nuggets were obtained after the experiment. This behaviour was not observed in the composite without Fe_5C_2. This indicates that using Fe_5C_2 is more preferable than Fe_3C for molten iron production using DCIC.

INTRODUCTION

The blast furnace ironmaking process has been adopted as the main process at integrated steel mills because of its high efficiency. However, it needs a large amount of fossil fuel derived carbon for its heat source, reducing agent of iron ores and carburising agent of reduced iron. Thus, it is essential to develop a new process to achieve carbon-neutral steelmaking. Currently, research and development for the commercialisation of hydrogen reduction ironmaking with shaft furnace have been conducted around the world. However, ironmaking processes based on Direct Reduced Iron (DRI) production such as MIDREX® process, are largely limited by the grade of the iron ore. This is because the gangue in the DRI obstructs the conduction of heat to the metallic iron. Another matter is the increase in the amount of molten slag in the melting process of DRI with Electric Arc Furnace (EAF). To improve this problem, it is effective to produce hot metal separated from molten slag before the refining process. Nonetheless, carbon must be added to reduced iron for the production of the hot metal. Therefore, attempts using biomass char as a carburising agent have been made to produce hot metal carbon-neutrally (Robinson *et al*, 2022; Norgate *et al*, 2012). Practical application, however, is difficult in countries with large crude steel production such as China and Japan. This is because of difficulty to supply the required amount of carbon with biomass. As long as the amount of available biomass char is limited, the application of Carbon Capture and Utilization (CCU) is inevitable to achieve carbon neutrality in ironmaking process.

Examples of CCU application in steel mills include iACRES (Kato, 2010) and carbon recycling blast furnace (Kawashiri, Nouchi and Kashihara, 2022). iACRES is designed to recycle CO reformed by high-temperature electrolysis of CO_2 and the reverse water gas shift reaction as shown in Equation 1 and Equation 2, respectively. CH_4 produced by the methanation reaction described as Equation 3, on the other hand, is reused in the carbon recycling blast furnace. In both cases, the carbon cycle is achieved by reforming and reusing the CO_2 recovered from the exhaust gas, but its scope is limited to the reduction process. To extend the scope to oxidation refining, a carburising agent for hot metal production should be reused.

$$2CO_2 = 2CO + O_2 \quad (1)$$

$$CO_2 + H = CO + H_2O \quad (2)$$

$$CO_2 + 4H_2 \rightarrow CH_4 + 2H_2O \quad (3)$$

There are mainly two routes for carburisation of iron. One is direct carburisation by solid carbon and another is indirect one by CO gas. The reaction equations are described as Equation 4 and Equations 5–6, respectively.

$$Fe(s) + C(s) = Fe(s) + \underline{C} \quad (4)$$

$$CO(g) = C^* + O^* \quad (5)$$

$$CO(g) + O^* = CO_2(g) \quad (6)$$

$$C^* = \underline{C} \quad (7)$$

(*) and (_) mean the atom absorbing on and dissolving in Fe, respectively. Murakami and Nagata (2003) compared the melting rate of metallic iron plate by direct carburisation with a graphite piece and gas carburisation with CO at 1250°C and reported that the melting proceeded more than 1000 times faster with direct contact carburisation than with gas carburisation. This is because the mass transfer of carbon to molten iron at the boundary between the carburising agent and solid iron is the rate-limiting factor for iron melting. Indirect carburisation, which requires the desorption process of gas molecules, supplies carbon to molten iron slower than direct one. Therefore, considering hot metal production in carbon recycling ironmaking, it is desirable to reform the CO_2 in the exhaust gas to solid carbon. However, the solid carbon is recovered in a fine powder state, which causes handling problems.

Therefore, the authors propose the following new ironmaking process named Carbon Recycling Ironmaking Process (CRIP) using Deposited Carbon-Iron Ore composite (DCIC) (CRIP-D), which extends the scope of carbon recycling to steel production without fossil fuel derived carbon. Hydrogen and energy are added to the gas generated from iron ore reduction process and hot metal refining process. The gas is reformed to CO-rich gas through reverse water gas shift reaction catalysed by porous iron. Regarding the production of the porous iron, it has been reported that metallic iron whiskers were produced by reducing carbon-iron ore composite prepared using charcoal (Murakami *et al*, 2017b). Due to intertwining the fibrous structure, the porous iron showed about 95 per cent of porosity. This porous iron is also used as a substrate for carbon deposition reaction using reformed CO-rich gas. The carbon in the gas, therefore, can be recovered as not only free carbon but also iron carbide. Furthermore, the reaction rate can be improved by increasing the catalytically active area, and the handling of carbon powder can be more easily by incorporating the deposited carbon into the pores. Nishihiro *et al* (2019) conducted carbon deposition reaction catalysed by metallic iron particles. They reported that a larger amount of carbon was deposited by using CO-H_2 mixed gas than pure CO gas. Sawai, Iguchi and Hayashi (1999a; 1999b) also reported that cementite (Fe_3C) was produced by using CO-CO_2 mixed gas for carbonising metallic iron particles, while not only cementite but also Hägg iron carbide (Fe_5C_2) were produced by using CO-CO_2-H_2 mixed gas. Regarding the utilisation of iron carbides, Sato *et al* (2011) conducted melting experiment under elevated temperature using tablets made of metallic iron powder with cementite or graphite powder. The melting rate of the tablet with cementite was higher than that with graphite. This indicates iron carbides are suitable for a carburising agent. Murakami *et al* (2017a) also conducted elevated temperature test on the carbon-iron ore composite using coal and graphite. The reduction and carburisation reactions were reported to be accelerated by dividing the function of carbonaceous materials as reducing and carburising agents. Thus, DCIC with high reactivity may be

prepared by using the free carbon and iron carbides recovered in the proposed process as reducing and carburising agents, respectively. Hot metal can be produced with DCIC in rotary hearth furnaces and shaft furnaces (Hasanbeigi, Arens and Price, 2014). By replacing some of the raw materials in the blast furnace with DCIC, it is expected to reduce CO_2 emissions while using the facilities in the proven integrated steelmaking technology (Yokoyama *et al*, 2014). The gas after the carbon deposition reaction is introduced in to hot metal production process as a reducing agent and heat source since the gas contains certain amount of CO and H_2. Carbon recycling is achieved by reforming the gases emitted in the reducing, hot metal production and refining process.

In this study, the porous iron whiskers with high porosity are focused on, as a substrate for carbon deposition reaction. Furthermore, the reduction and melting behaviours of carbon-iron oxide composite prepared using recovered deposited carbon are investigated to examine the fundamental possibility of CRIP-D.

EXPERIMENTAL

Sample preparation

Hematite reagent (1 μm size, purity 99.9 per cent) and biomass char (53–150 μm size) were well mixed to have the molar ratio of fixed carbon in the char to oxygen in the hematite, C/O ratio, was 0.75. The biomass char contained 95.2 mass per cent of the fixed carbon. The porous iron was prepared by carbothermal reduction of the mixture in the crucible with 26 mm diameter at 1000°C in an inert atmosphere. The reduced iron showed high porosity of 94.6 per cent due to its fibrous structure. The sample for carbon deposition experiment was prepared by cutting the porous iron with 5 mm in thick and was set in an experiment apparatus shown in Figure 1. The sample holder has meshed bottom woven by Pt wire with 0.5 mm in diameter. The wire was coated with ceramic to avoid the carbon deposition reaction on the wire. The sample holder was prepared by sandwiching the porous iron sample between the ring with preheater zone and another mullite ring. The gap between the sample side and the ring was filled with inorganic adhesive. In addition, the surface of the adhesive was coated with ceramic wool to protect the reaction tube. Curing of the inorganic adhesive and pre-reduction were conducted in Ar-10 per centH_2 atmosphere at 250°C and 800°C, respectively. The carbon deposition reaction proceeded for 120 mins in two conditions. One is used pure CO at 800°C. The other is used CO-CO_2-H_2 gas mixture at 600°C. The gas flow rate was set as 500 mL/min. After the carbon deposition reaction, the samples were pulverised. The Sample labelled ‘a’ is obtained from the carbon deposition experiment using CO gas. Whereas, the sample obtained using the gas mixture had grey and black layers, which were separated into two samples.

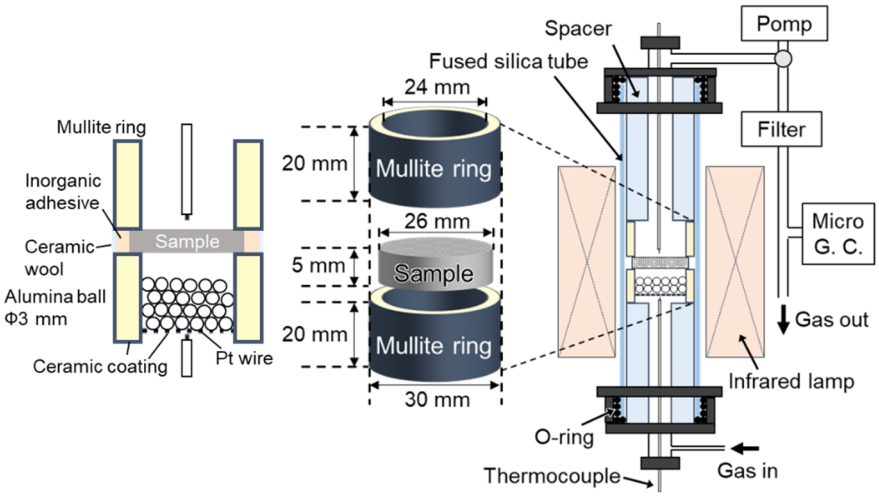

FIG 1 – Schematic diagram of an apparatus for carbon deposition using an image furnace.

Each layer was also pulverised separately into Samples b and c. Figure 2 shows XRD profiles obtained for each deposited carbon sample using a sealed X-ray tube with a Fe anode (tube voltage 40 kV, tube current 30 mA) as an X-ray source. Some noises appeared in Sample c. Fe_3C is the

only iron carbide phase in Sample a. Fe_5C_2, on the other hand, exists in Samples b and c. A broad graphite peak is observed in Sample c, suggesting free carbon deposition. The carbon contents analysed by infrared absorption method after combustion are 14.3 per cent, 6.62 per cent and 48.5 per cent in Samples a, b and c, respectively.

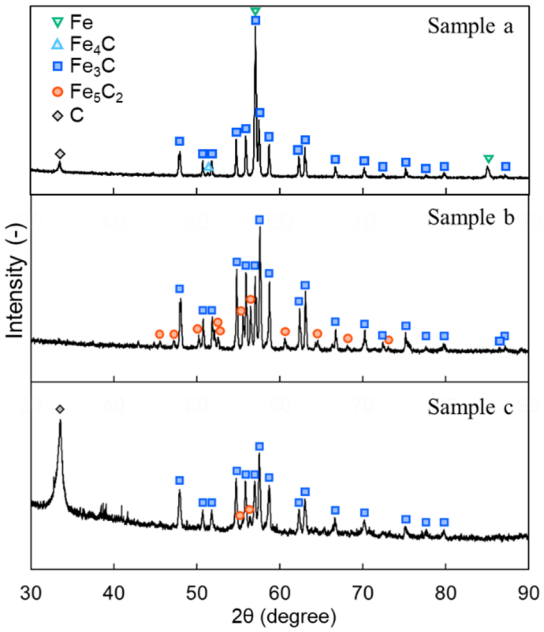

FIG 2 – XRD profiles of samples with deposited carbon obtained by using CO gas and CO-CO_2-H_2 gas mixture.

In situ XRD Measurement

Decomposition behaviour of different types of iron carbides was investigated *in situ* using XRD at elevated temperatures. X-ray enters the chamber through a window made of beryllium. The chamber can be sealed, allowing control of the internal atmosphere. Sample b was filled in a black quartz glass sample holder and heated by an infrared heating equipment attached to the chamber. The sample temperature was monitored using a thermocouple with a sheath inserted into the sample holder. The sample temperature elevated by 10°C/min to 700°C under N_2 atmosphere. The gas flow rate was set as 200 mL/min. XRD measurement were repeatedly conducted in the range of 2θ = 55°~58°.

Reduction experiment using deposited carbon-iron oxide composite

The deposited carbon-iron oxide composite was prepared by press-shaping of the mixture of the hematite reagent (1 μm size, purity 99.9 per cent) and deposited carbon samples sieved under 106 μm into a cylindrical composite. Fe_2O_3-θ was the composite sample using Sample 'a' so that C/O ratio was 1.0. The C/Fe ratio of Fe_2O_3-θ was 0.52. Fe_2O_3-χ was also prepared by mixing Samples b and c with hematite so that C/O = 1.0 and C/Fe = 0.52. The composite sample was set in the experimental apparatus as shown in Figure 3. After evacuating air in the chamber, Ar-5 per centN_2 gas was introduced at the rate of 500 mL/min under atmospheric pressure. Then, the sample was heated up to 1300°C at a heating rate of 10°C/min using an infrared image furnace and cooled down by turning off the power. The temperature at 1 mm upper the surface of the sample was monitored using an R-type thermocouple. The concentrations of CO, CO_2 and N_2 of the outlet gas were measured during the experiment at 90 sec intervals by a gas chromatography. N_2 gas was used as a tracer to estimate the amount of gas generated from the sample. Reduction degree (RD) of the sample was calculated by Equation 8 using the amounts of generated gas.

$$RD = \frac{M_{CO}+2M_{CO_2}}{M_{\text{total O}}} \quad (8)$$

M_{CO} and M_{CO_2} are the molar amounts of CO and CO_2 gases detected by the gas chromatography, respectively. $M_{\text{total O}}$ is the molar amount of monatomic oxygen in the Fe_2O_3 reagent.

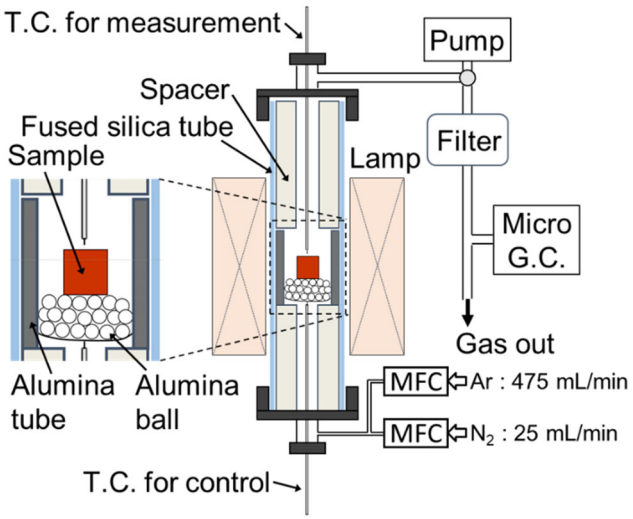

FIG 3 – Schematic diagram of an experimental apparatus for reduction experiment.

RESULTS AND DISCUSSION

In situ XRD measurement

Figure 4 shows changes in XRD profiles obtained for Sample b with temperature. The peaks of Fe_3C, Fe_5C_2 and Fe are detected at room temperature before heating up. However, the peaks of Fe_5C_2 are decreasing from 620°C and disappeared at 660°C. The peaks of Fe_3C, on the other hand, remains after heating up to 700°C. This indicates that the two different iron carbides obtained by carbon deposition reaction are expected to show different reactivity as a reducing and carburising agent. Fe_5C_2 is more easily decomposed than Fe_3C.

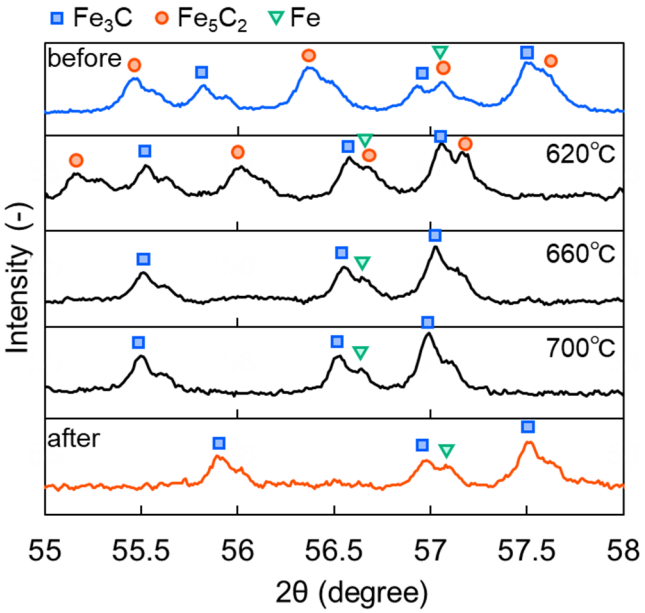

FIG 4 – XRD profiles of sample b heated up to 700°C and at room temperature before and after heating.

Reduction experiment using deposited carbon-iron oxide composite

The appearance of Fe_2O_3-θ and Fe_2O_3-χ after the reduction experiment are shown in Figure 5. Each sample shows metallic luster. Fe_2O_3-θ keeps cylindrical shape, while Fe_2O_3-χ becomes an iron nugget. This indicates the reactivity of iron carbide affects the melting behaviour of carbon-iron oxide composite.



FIG 5 – Appearances of Fe_2O_3-θ and Fe_2O_3-χ after reduction heated up to 1300°C.

Figure 6 shows the changes in the partial pressure ratio of CO to $CO+CO_2$ gas (CO gas ratio) generated from the composite, and the reduction degree of iron oxide with temperature, drawn on the Fe-O phase diagram. The equilibrium line of the Boudouard reaction ($C + CO_2 = 2CO$) is represented as dashed line in the diagram. The CO gas ratio obtained for Fe_2O_3-θ starts to be increase along with the equilibrium line of the Boudouard reaction. Then, the ratio reaches the Fe_3O_4/FeO equilibrium at 650°C and FeO/Fe equilibrium at 800°C. The ratio obtained for Fe_2O_3-χ, on the other hand, starts to increase above the equilibrium line of Boudouard reaction at 620°C, which corresponds to the decomposition of Fe_5C_2. This suggests the possibility of improving the reducibility of the carbon-iron oxide composite since the carbon generated by the decomposition of Fe_5C_2 is easily gasified. The ratio then directly reaches the FeO/Fe equilibrium at 720°C. The reduction degrees are drastically increased soon after the gas ratio moves to Fe-single phase region in both composites. The metallic iron has a catalytic effect for gasification of carbon and accelerates the reduction reaction of iron oxides (Higashi *et al*, 2023). Therefore, almost all of the iron oxides in the composites are reduced to metallic iron by heating up to 1300°C.

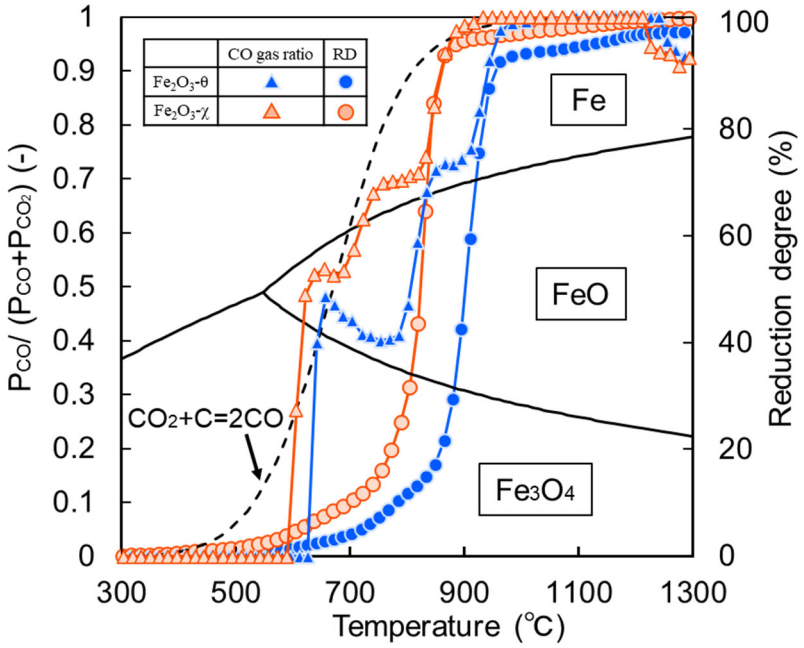

FIG 6 – Changes with temperature in the ratio of CO to $CO+CO_2$ for the Fe_2O_3-θ and Fe_2O_3-χ and in the reduction degree, plotted on the phase diagram of the Fe-O system.

CONCLUSIONS

In this study, the porous iron whiskers with high porosity were focused on, as a substrate for carbon deposition reaction. Furthermore, the reduction and melting behaviours of carbon-iron oxide composite prepared using recovered deposited carbon were investigated. The following results were obtained.

- Fe_3C is obtained as iron carbides by using CO gas for carburising the porous iron. Fe_5C_2 is also produced by using CO-CO_2-H_2 gas mixture.
- Fe_5C_2 is more easily decomposed than Fe_3C.
- Carbon-Iron oxide composite containing not only Fe_3C but also Fe_5C_2 shows rapid reduction reaction at lower temperature and complete melting of metallic iron at 1300°C.

ACKNOWLEDGEMENT

This work was supported by JSPS Grant-in-Aid for JSPS Fellows Grant Number 22KJ0282, Steel Foundation for Environmental Protection Technology and JFE 21st Century Foundation.

REFERENCES

Hasanbeigi, A, Arens, M and Price, L, 2014. Alternative emerging ironmaking technologies for energy-efficiency and carbon dioxide emissions reduction: A technical review, *Renew Sust Energ Rev*, 33:645–658.

Higashi, R, Maruoka, D, Kasai, E and Murakami, T, 2023. Low Temperature Reduction Mechanism of Carbon-Iron Ore Composite Using Woody Biomass, *ISIJ Int*, 63(12):1972–1978.

Kato, Y, 2010. Carbon Recycling for Reduction of Carbon Dioxide Emission from Iron-making Process, *ISIJ Int*, 50(1):181–185.

Kawashiri, Y, Nouchi, T and Kashihara, Y, 2022. Reduction of CO_2 Emissions from Blast Furnace with Carbon Recycling Methane, *JFE TECHNICAL REPORT*, 28:9–15.

Murakami, T and Nagata, K, 2003. New ironmaking process from the viewpoint of carburisation and iron melting at low temperature, *Extr Metall Rev*, 24:253–267.

Murakami, T, Ohno, M, Suzuki, K, Owaki, K and Kasai, E, 2017a. Acceleration of Carburisation and Melting of Reduced Iron in Iron Ore–Carbon Composite Using Different Types of Carbonaceous Materials, *ISIJ Int*, 57(11):1928–1936.

Murakami, T, Takahashi, T, Fuji, S, Maruoka, D and Kasai, E, 2017b. Development of Manufacturing Principle of Porous Iron by Carbothermic Reduction of Composite of Hematite and Biomass Char, *Material Transactions*, 58(12):1742–1748.

Nishihiro, K, Maeda, T, Ohno, K and Kunitomo, K, 2019. Effect of Concentration on Carbon Deposition Reaction by CO-H_2 Gas Mixture at 773 K to 973 K, *ISIJ Int*, 59(4):634–642.

Norgate, T, Haque, N, Somerville, M and Jahanshahi, S, 2012. Biomass as a Source of Renewable Carbon for Iron and Steelmaking, *ISIJ Int*, 52(8):1472–1481.

Robinson, R, Brabie, L, Pettersson, M, Amovic, M and Ljunggren, R, 2022. An Empirical Comparative Study of Renewable Biochar and Fossil Carbon as Carburiser in Steelmaking, *ISIJ Int*, 62(12):2522–2528.

Sato, K, Noguchi, T, Miki, T, Sasaki, Y and Hino, M, 2011. Effect of Fe_3C on Carburisation and Smelting Behavior of Reduced Iron in Blast Furnace, *ISIJ Int*, 51(8):1269–1273.

Sawai, S, Iguchi, Y and Hayashi, S, 1999a. Carbidization Rate of Reduced Iron with CO-CO_2 Gas Mixture (in Japanese), *Tetsu-to-Hagané*, 85(1):6–13.

Sawai, S, Iguchi, Y and Hayashi, S, 1999b. Carbidization Rate of Reduced Iron Ore in H_2-CO-CO_2 Gas Mixture (in Japanese), *Tetsu-to-Hagané*, 85(1):20–26.

Yokoyama, H, Higuchi, K, Ito, T and Oshio, A, 2014. Decrease in the Carbon Consumption of a Commercial Blast Furnace by Using Carbon Composite Iron Ore (in Japanese), *Tetsu-to-Hagané*, 100(5):601–609.

Electrolytic reduction of metal sulfides/oxides in molten salts for sustainable metal production

DOI: 10.62053/UNYJ2040
X Hu[1], L Sundqvist Ökvist[2] and J Björkvall[3]

1. Senior Researcher, SWERIM AB, Luleå 974 37, Sweden. Email: xianfeng.hu@swerim.se
2. Associate Professor, Luleå University of Technology, Luleå 971 87, Sweden. Email: lena.sundqvist-oqvist@ltu.se
3. Senior Researcher, SWERIM AB, Luleå 974 37. Email: johan.bjorkvall@swerim.se

ABSTRACT

The metal production industry is a significant contributor to global CO_2 emissions due to the use of fossil fuels such as coal and coke. To mitigate these emissions and meet climate goals, innovative and sustainable technologies are required. Molten salt electrolysis is a promising technology that directly produces metals from their precursor sulfides or oxides using electricity. When combined with renewable electricity and an inert anode, the electrolysis process can be carbon neutral.

This paper presents the results of two pilot-scale studies on the electrolytic reduction of metal oxides and sulfides in molten salts. The first study focuses on the electrolytic reduction of chalcopyrite in molten NaCl-KCl salt. The results demonstrate that *in situ* separation of copper, iron, and sulfur is possible, enabling the extraction of all valuable elements without CO_2 emissions. Furthermore, the findings underscore the capability to eliminate impurities like zinc, antimony, arsenic, and mercury from the electrolysis product. The second study investigates the electrolytic reduction of pure/synthetic chemicals of wüstite, hematite, and magnetite, as well as a magnetite-type iron ore in molten NaOH salt. The findings reveal a stepwise reduction of iron oxides from high valence to low valence, ultimately leading to the production of metallic iron electrolytically. Notably, this study underscores the challenges associated with the selection of an economically viable and durable inert anode material for efficient oxygen generation.

These results indicate that molten salt electrolysis provides a sustainable and green route for base metal production. The use of this technology has the potential to significantly reduce CO_2 emissions in the metal production industry, contributing to achieving climate goals.

INTRODUCTION

The base metal production industry is a major emitter of CO_2 due to its heavy reliance on fossil fuels for reduction and heating processes. For instance, steelmaking in blast furnaces and basic oxygen furnaces emits 1800 kg of CO_2 per metric tonne of steel produced (Suopajärvi *et al*, 2018). Achieving carbon neutrality in this industry requires transitioning to renewable energy sources or agents for metal extraction from compounds, typically sulfides and oxides. Promising candidates for renewable energy sources or agents include bio-based materials like biocarbon, green hydrogen, and renewable electricity. While bio-based materials show potential to replace fossil fuels in metallurgical processes, their supply is limited (Pei *et al*, 2020). Hydrogen, produced via water electrolysis using renewable electricity, serves as a green energy and reducing agent for metal oxide reduction. However, its application is limited by thermodynamic constraints, particularly in reducing metal sulfides and oxides like chromium oxide (Davies *et al*, 2022), manganese oxide (Safarian, 2022), and silicon oxide (Itaka *et al*, 2015). Moreover, the two-step process of hydrogen production and subsequent metal oxide reduction lowers process efficiency. Electrons derived from renewable electricity are potent reducing agents suitable for electrolysis processes to convert metal compounds to metals. Two notable examples of electrolysis approaches are molten salt electrolysis (FFC process (Chen and Fray, 2020; Mohandas and Fray, 2004)) and molten oxide electrolysis (MOE process (Allanore, Ortiz and Sadoway, 2011; Allanore, Yin and Sadoway, 2013; Sadoway, 2017)). The FFC process involves controlled liberation of oxygen or sulfur ions from metal oxides or sulfides within a molten salt electrolyte, primarily chloride salt, positioned at the cathode. This process yields sponge-like metal at the cathode while generating oxygen or sulfur at an inert anode (Cox and Fray, 2008; Tan *et al*, 2016). Operating at lower temperatures compared to conventional methods, the FFC process reduces energy consumption. The MOE process dissolves iron ore in a molten oxide

electrolyte, leading to electrolytic reduction of iron ions and continuous liquid metal production with an inert anode and renewable electricity, thereby avoiding CO_2 emissions. Despite the environmental benefits, challenges remain in both processes, particularly in finding durable and economically viable anode materials (Allanore, Yin and Sadoway, 2013).

This study investigates the electrolytic reduction of chalcopyrite and iron oxides in molten NaCl-KCl and NaOH salts in a pilot-scale electrolysis reactor to further explore the potential of molten salt electrolysis for sustainable metal production.

METHODOLOGY

Materials and their preparation

Materials and preparation for electrolytic reduction of chalcopyrite/pyrite

Two samples, designated as Concentrate A and Concentrate B, were chosen for the electrolysis trials:

- Concentrate A, a chalcopyrite material, is composed of 33.9 per cent iron (Fe), 31.2 per cent copper (Cu), and 18.5 per cent sulfur (S).
- In contrast, Concentrate B, a pyrite material, contains 50.6 per cent Fe, 0.75 per cent Cu, and 22.7 per cent S.

These materials were subjected to thorough analysis utilising X-ray Fluorescence (XRF) for elemental composition, LECO combustion for carbon and sulfur content, and X-ray Diffraction (XRD) for mineralogical characterisation. The analyses confirmed that Concentrate A is primarily chalcopyrite (CuFeS2), with a Fe to Cu ratio of approximately 1.1:1. Meanwhile, Concentrate B is predominantly composed of pyrite (FeS2), with a substantially higher Fe to Cu ratio of 67.5:1 and a marked presence of impurities such as antimony (Sb) and arsenic (As).

To prepare these concentrates for the electrolysis experiments, they were processed into briquettes. This involved first sieving the concentrates to ensure 90 per cent of the particles were finer than 250 μm (D_{90} = 250 μm). Following sieving, the concentrates were mixed with 2 per cent bentonite and 2 per cent water to form a mixture. This mixture was then compacted under a pressure of 200 kN for 5 mins, resulting in briquettes measuring 40 mm in diameter and 6 mm in thickness (Φ40×6 mm). The final step involved drying and sintering the briquettes in an oven set at 150°C for about 40 hrs. Once completed, the briquettes were stored in plastic bags, ready for subsequent use in electrolysis processes.

Materials and preparation for electrolytic reduction of iron oxides

Wüstite, hematite, magnetite, and iron ore concentrate served as the primary materials in this study. Wüstite was synthesised through the thorough blending of chemical-grade iron powder and magnetite powder in a precise stoichiometric ratio. This mixture was then subjected to a heat treatment process in a vertical furnace at 900°C for 24 hrs, under a continuous flow of argon gas. The successful formation of wüstite was subsequently verified through XRD analysis. Both hematite and magnetite used in the experiments were of high purity, classified as pure chemicals. The iron ore concentrate (total iron content 64.6 per cent), characterised as a magnetite-type ore with a particle size where 80 per cent of the material is below 82 μm (D_{80} = 82 μm), was procured from a local iron ore producer. For the electrolysis experiments, the iron oxides underwent a process to form briquettes, employing a methodology akin to that previously described. This process ensures the creation of briquettes from the iron oxide materials to facilitate their use in the electrolysis experiments.

Experimental set-up and procedure

Figure 1 shows the experimental set-up for the electrolytic reduction of chalcopyrite and pyrite. A steel crucible (inner diameter 230 mm and height 508 mm) with lid was placed in a pit furnace and then the crucible was filled with ca. 25 kg mixture of chemical pure NaCl (purity > 98 per cent) and KCl (purity > 99.8 per cent) of equal mole. The salt in the crucible was heated to a desired

temperature (around 680–870°C) into a molten salt at a heating rate of 10°C/min. Two electrodes (namely, anode and cathode) were placed in the molten salt. The anode is a graphite block connected on copper conductor; the cathode is a molybdenum net, which is used to hold the as-prepared briquettes. The net was made by folding molybdenum mesh into a bag hold either two or four briquettes. The net was connected to a stainless steel plate and then to a copper conductor. This is to avoid the damage of the molybdenum net and copper conductor, which could otherwise easily get oxidised at the molten slag/gas interface by oxygen and the generated sulfurous gas.

During the electrolysis the chamber above the molten salt was purged by N_2 or Ar gas in order to protect the electrodes from oxidation and expel the generated sulfurous gas. For electrolytic reduction of iron oxides, a similar experimental set-up, as it is shown in Figure 1, was applied. In this case, the steel crucible was filled with ca. 25 kg NaOH (purity > 99.8 per cent) and the operation temperature was set to be ca. 500°C.



FIG 1 – Experimental set-up for molten salt electrolysis at SWERIM.

In all the electrolysis trials, constant voltage electrolysis was conducted. Each electrolysis trial began with a short series, during which the voltage was increased from 0 to 2.5 V for chalcopyrite electrolysis in molten NaCl-KCl salt or 1.7 V for iron oxides in molten NaOH salt. The electrolysis process was terminated after several hours. After each experiment, the molybdenum net with sample was detached from the cathode. Figure 2 shows the appearances of the obtained sample. The sample with the net was placed in distilled water. Then the glass was put in an ultrasonic water bath to make the salt in the sample dissolved in the water. Thereafter, the sample for the chalcopyrite/pyrite trials was able to be separated into two sub-samples. These samples were carefully washed with distilled water and filtrated several times to get rid of the salt. The sample from the iron oxide trials only has one single sample for each experiment. The resulting samples were then filtered out and dried in an oven at a temperature of 105°C for over 12 hrs to remove any remaining water. Selected samples were analysed by XRD, XRF and scanning electron microscope (SEM) methods.



FIG 2 – Appearance of the cathode sample after electrolysis.

RESULTS AND DISCUSSION

Electrolytic reduction of chalcopyrite/pyrite

Sulfur content in the sample or subsample is an important index to evaluate the extent of electrolytic reduction. A lower sulfur content in the sample indicates a higher degree of electrolytic reduction. After electrolysis, the sulfur contents in the samples were analysis by LECO analysis. It is seen that the samples had quite low S contents (as low as 0.01 per cent) compared to that in the original samples (18.5 per cent S in the chalcopyrite sample and 22.7 per cent S in the pyrite sample). This indicates an almost complete reduction of chalcopyrite/pyrite in the electrolysis trials.

Figure 3 shows an example of the obtained two sample fractions from one electrolysis trial using chalcopyrite. It is seen that the one sample fraction had reddish colour, while another sample fraction had dark green colour. The difference in colours in the two sample fractions is attributed to the difference in chemical compositions that later confirmed by chemical analysis. The reddish fraction is referred to as Cu-rich fraction and the dark green fraction as Fe-rich fraction. The chemical analysis results show that the Cu-rich fractions contain 43.1 per cent Cu and 40.1 per cent Fe, while the Fe-rich fractions contain 4.9 per cent Cu and 55.3 per cent Fe. The high amount of Fe in the Cu-rich fraction is attribute to the fact that during scratching the coagulated materials from the Mo net, some iron particles were also taken down. Further, it should be noted that the collected Cu-rich fraction is far below the balanced amount according to the amount of the charged materials during electrolysis. This is due to that some copper particles were lost in the molten salt. These results clearly indicate that during electrolytic reduction of chalcopyrite, the *in situ* separation of copper, iron and sulfur is possible.

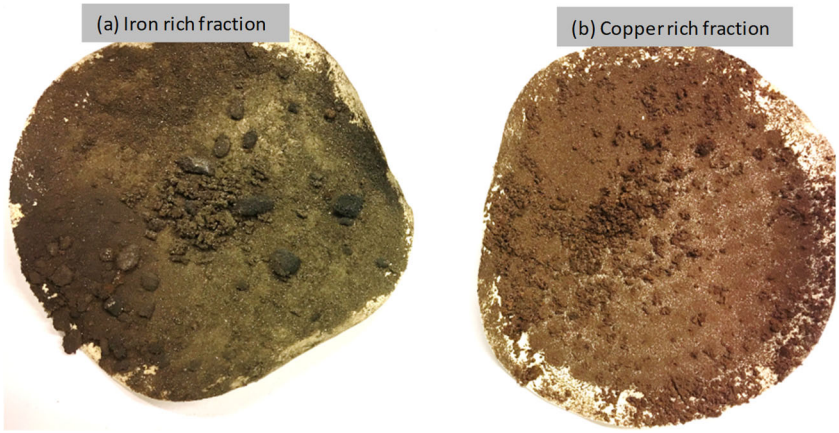

FIG 3 – Appearances of the obtained samples of iron-rich and copper-rich fractions from one electrolysis trials using chalcopyrite.

After electrolytic reduction of pyrite, it was found that the materials coagulated on the Mo were found quite less and not be able to be collected. Therefore, this electrolysis sample was taken a whole and analysed by XRD and XRF methods. By combining the LECO analysis result for the same sample, it can conclude that iron and copper were completely reduced after the electrolysis of pyrite, the leading phase in the obtained product is iron. The SEM analysis of the reduced pyrite sample shows that the reduced iron particles have a cubic shape in the scale of several to several tens of microns.

It is known that in the used pyrite sample it contains several trace elements, the concentrations of which are in noticeable level. To evaluate how these trace elements behave during the electrolysis, the removal efficiency of these trace elements was calculated, by combining the chemical compositions of the original pyrite and the reduced products. It is seen that elements Zn, Sb, As and Hg can be removed; elements Pd and Cd can be partially removed after electrolysis.

Electrolytic reduction of iron oxides

During electrolytic reduction of wüstite, it is found that wüstite was reduced to iron in a single step. However, for the electrolytic reduction of hematite, magnetite, and magnetite ore, co-existence of FeO, Fe_2O_3, and Fe_3O_4 were found in the incompletely reduced samples. This indicates a stepwise

reduction of iron oxides from high valence to low valence, ultimately leading to the production of metallic iron electrolytically. It should be noted, during electrolytic reduction of iron oxides, graphite was used as the anode. This has led to the generation of CO/CO_2. The future research focus will be investigating the use of inert anode to reach the carbon neutrality of the process. Scaling up the process to a scale comparable to the conventional ironmaking process can be quite challenging; however, the process may still find its use to produce high-quality iron product or product other metal products that cannot be produced in a conventional or sustainable way.

CONCLUSIONS

A pilot-scale molten salt electrolysis reactor was established at SWERIM to study the molten salt electrolysis of sulfur ore, chalcopyrite and pyrite, and various iron oxides, including wüstite, hematite, magnetite, and magnetite-type iron ore. The results from electrolytic reduction of chalcopyrite/pyrite demonstrate that *in situ* separation of copper, iron, and sulfur is possible, enabling the extraction of all valuable elements without CO_2 emissions. Furthermore, the findings underscore the capability to eliminate impurities like zinc, antimony, arsenic, and mercury from the electrolysis product. The results from electrolytic reduction of iron oxides/ore demonstrate the stepwise reduction of iron oxides from high valence to low valence, ultimately leading to the production of metallic iron.

ACKNOWLEDGEMENTS

The work on electrolytic reduction of chalcopyrite/pyrite was funded by Hugo Carlsson foundation via the Swedish Iron producers' Association (Jernkontoret). The work on electrolytic reduction iron oxides/ore is funded by the Swedish Energy Agency (Energimyndigheten). Centre for Advanced Mining and Metallurgy, is acknowledged for supporting the work for preparing this manuscript.

REFERENCES

Allanore, A, Ortiz, L A and Sadoway, D R, 2011. Molten Oxide Electrolysis for Iron Production: Identification of Key Process Parameters for Large scale Development, *TMS Annual Meeting*, pp 121–129.

Allanore, A, Yin, L and Sadoway, D R, 2013. A new anode material for oxygen evolution in molten oxide electrolysis, *Nature*, 4977449:353–356. https://doi.org/10.1038/nature12134

Chen, G Z and Fray, D J, 2020. Invention and fundamentals of the FFC Cambridge Process, *Extractive Metallurgy of Titanium: Conventional and Recent Advances in Extraction and Production of Titanium Metal*, chpt 11, pp 227–286. https://doi.org/10.1016/B978-0-12-817200-1.00011-9

Cox, A and Fray, D J, 2008. Electrolytic formation of iron from haematite in molten sodium hydroxide, *Ironmaking and Steelmaking*, 35(8):561–566. https://doi.org/10.1179/174328108X293444

Davies, J, Paktunc, D, Ramos-Hernandez, J J, Tangstad, M, Ringdalen, E, Beukes, J P, Bessarabov, D G and Du Preez, S P, 2022. The Use of Hydrogen as a Potential Reductant in the Chromite Smelting Industry, *Minerals*, 12(5). https://doi.org/10.3390/min12050534

Itaka, K, Ogasawara, T, Boucetta, A, Benioub, R, Sumiya, M, Hashimoto, T, Koinuma, H and Furuya, Y, 2015. Direct carbothermic silica reduction from purified silica to solar-grade silicon, *Journal of Physics: Conference Series*, 596(1). https://doi.org/10.1088/1742-6596/596/1/012015

Mohandas, K S and Fray, D J, 2004. FFC Cambridge process and removal of oxygen from metal-oxygen systems by molten salt electrolysis: An overview, *Transactions of the Indian Institute of Metals*, 57(6):579–592.

Pei, M, Petäjäniemi, M, Regnell, A and Wijk, O, 2020. Toward a Fossil Free Future with HYBRIT : Development of Iron and Steelmaking Technology in Sweden and Finland, *Metals*, 10(7):972. https://doi.org/10.3390/met10070972

Sadoway, D R, 2017. Towards Carbon-free steelmaking by molten oxide electrolysis, Presentation. http://web.mit.edu/course/3/3.a30/www/refs/present_env_brf_sadoway.pdf

Safarian, J, 2022. A sustainable process to produce manganese and its alloys through hydrogen and aluminothermic reduction, *Processes*, 10(1). https://doi.org/10.3390/pr10010027

Suopajärvi, H, Umeki, K, Mousa, E, Hedayati, A, Romar, H, Kemppainen, A, Wang, C, Phounglamcheik, A, Tuomikoski, S, Norberg, N, Andefors, A, Öhman, M, Lassi, U and Fabritius, T, 2018. Use of biomass in integrated steelmaking – Status quo, future needs and comparison to other low-CO_2 steel production technologies, *Applied Energy*, 213(January):384–407. https://doi.org/10.1016/j.apenergy.2018.01.060

Tan, M, He, R, Yuan, Y, Wang, Z and Jin, X, 2016. Electrochemical sulfur removal from chalcopyrite in molten NaCl-KCl, *Electrochimica Acta*, 213:148–154. https://doi.org/10.1016/j.electacta.2016.07.088

Aluminothermic production of silicon using different raw materials

DOI: 10.62053/KZGL1297

K Jakovljevic[1], N Simkhada[2], M Zhu[3], M Wallin[4] and G Tranell[5]

1. Researcher, Norwegian University of Science and Technology, Trondheim 7034, Norway. Email: katarina.jakovljevic@ntnu.no
2. Research Engineer, Norwegian University of Science and Technology, Trondheim 7034, Norway. Email: nishan.simkhada@ntnu.no
3. Postdoctoral Researcher, Norwegian University of Science and Technology, Trondheim 7034, Norway. Email: mengyi.zhu@ntnu.no
4. Researcher, Norwegian University of Science and Technology, Trondheim 7034, Norway. Email: maria.wallin@ntnu.no
5. Professor, Norwegian University of Science and Technology, Trondheim 7034, Norway. Email: gabriella.tranell@ntnu.no

ABSTRACT

Silicon is a vital element in many products today, such as electronic components, solar devices, high-quality alloys, and many others. The growing global demand highlights the need for the development of sustainable production methods to meet this demand as an alternative to the current carbothermic reduction, submerged arc furnace (SAF) based process. An alternative to this is the aluminothermic reduction of quartz in a CaO-SiO_2 slag, which not only reduces direct carbon dioxide emissions but also promotes the utilisation of secondary raw materials such as quartz fines, aluminium dross and scrap as well as secondary alumina (SA) from dross recycling.

In the current study, the effects of SA and CaF_2 additions to slag on the resulting metal composition and metal yield were explored. Results were compared with thermodynamic simulations using FactSage™ 8.1.

Experimental results show that, in agreement with thermodynamic simulations, the silicon content of the alloy is increased, while the Ca is decreased for starting slags where CaO-SiO_2 is partly replaced by CaF_2. Similarly, the addition of SA to the initial slag results in an alloy with a higher silicon content.

INTRODUCTION

Silicon is the second most abundant element in the Earth's crust and one of the most important elements in high-tech applications. Traditionally, metallurgical-grade silicon (MG-Si), typically containing 96–99 per cent Si, is produced by reducing silicon dioxide (SiO_2) with carbon in a submerged arc furnace (SAF) (Schei, Tuset and Tveit, 1998). In this process, a mixture of quartz (crystalline SiO_2) and carbon (coke, coal, charcoal, and/or wood chips) is heated to produce silicon. The energy is supplied through electrodes, and it takes 10–13 MWh to produce one tonne of silicon. Using carbon materials as reductants leads to emissions primarily of carbon dioxide (approximately 5 t CO_2 per tonne of silicon produced), NO_x, SO_x, methane, polycyclic aromatic hydrocarbons (PAH) etc (Kero, Grådahl and Tranell, 2017). In addition to the high greenhouse gas (GHG) emissions and high energy demands, the requirements for the quartz used in the process need to be met. Aside from purity, there are strict requirements for size since particles that are too small reduce gas permeability in the furnace, increasing the likelihood of blow-outs due to gas build-up, which means that sand of high purity cannot be used in the traditional production process (Schei, Tuset and Tveit, 1998).

Aluminium, having a stronger affinity for oxygen than silicon, may hence be utilised as a reducing agent for the production of silicon, and this process can be considered a viable alternative to the carbothermic process. The SisAl process, based on the aluminothermic reduction of silica in slag, aims to produce silicon in a more environmentally beneficial way (Tranell, Safarian and Wallin, 2020). This is achieved by eliminating the need for primary carbon reductants and lumpy quartz raw materials and using residues from the silicon and aluminium industries instead. No carbon use means no direct emission of CO_2 and other gaseous pollutants.

In the SisAl process, SiO_2 can be used in the form of fines to produce slag, which means that less costly quartz sand can also be used as a SiO_2 source. By introducing an aluminium source (end-of-

life scrap, dross) for the reduction of SiO_2 in CaO-SiO_2 slag, silicon alloy and Al_2O_3-CaO slag are produced according to the following equation:

$$SiO_{2(in\ SiO_2-CaO\ slag)} + \frac{4}{3}Al_{(liq)} \rightarrow Si_{(liq)} + \frac{2}{3}Al_2O_{3(in\ Al_2O_3-CaO\ slag)}\ \Delta H_{1550°C} = -174.8\ \frac{kJ}{mol}$$

The generated slag is isolated from the metal, and the CaO and Al_2O_3 may be separated through a hydrometallurgical technique. CaO can be reintroduced back into the SisAl process, while the Al_2O_3 can be sent to primary aluminium production. Due to lower operating temperatures and an exothermic reduction reaction, the SisAl process consumes less energy compared to the carbothermic reduction in SAF.

A diverse range of waste by-products is generated in the aluminium sector. Dross is a byproduct created during the handling of liquid alloy and is a mixture of Al alloy and oxides as well as some amount of carbides, nitrides etc) and is formed as the melt oxidises. The quantity of waste material produced during the process of aluminium production is influenced by factors such as the quality and type of raw materials, operation conditions, the operator's skill, the kind of furnace utilised, and the dimensions, types, and techniques of alloying (Lazzaro, Eltrudis and Pranovi, 1994; Yoshimura *et al*, 2008). Approximately 15–25 kg of dross is produced for every tonne of molten aluminium (Liu and Chou, 2013).

The primary objective of the present study was to investigate the impact of various input materials on the overall process, with a particular emphasis on the final products. This study includes an examination of the suitability of aluminium by-products, such as dross and secondary alumina from treated dross obtained from Befesa Alumino, Spain, as reductants and additions in the process of aluminothermic production of silicon in terms of alloy composition. Recovery of materials in dross at Befesa is made through two cycles; in the first, the aluminium contained in the dross is recovered in a salt-based rotary furnace process, producing aluminium alloys, and in the second, recycling of salt slags, the waste that was traditionally discarded in landfills is recovered, transforming them into secondary raw materials, applicable in different industrial sectors. The recovered high-alumina fraction, in the following called secondary alumina (SA), contains some amount of residual fluorine, as discussed below.

The addition of CaF_2 to silicate slags typically decreases the viscosity and lowers the melting temperature (Park, Min and Song, 2002). As such, it was of interest to investigate the effect of limited fluorine additions on the SisAl process and its product compositions.

EXPERIMENTAL PROCEDURE

Overview of experimental procedure

The study on the impact of different input materials and process parameters on the overall process of aluminothermic production of silicon is organised into two subsections, as shown in the flow chart (Figure 1).

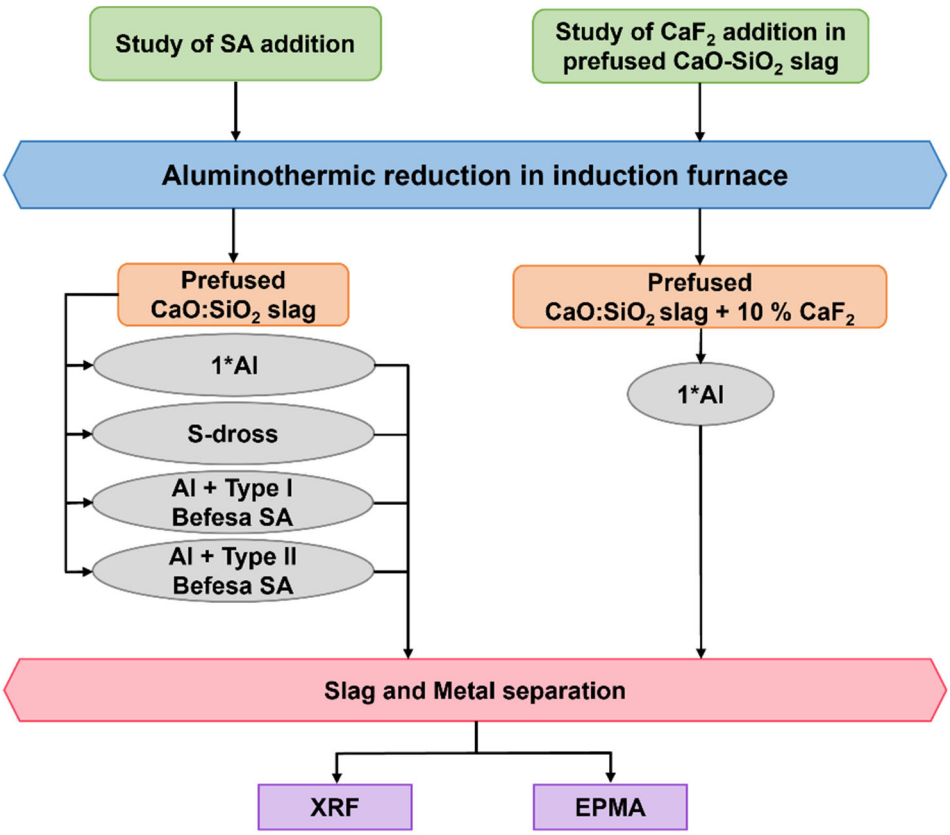

FIG 1 – The flow chart representing an overview of the experimental procedure.

Materials

The pre-fused slag utilised in this study as a SiO_2 source had a $CaO:SiO_2$ ratio of 1.018. A fine fraction of dross (denoted S-dross), with particle size ≤5 mm, which contains 30 per cent Al and 70 per cent Al_2O_3, and pure aluminium (~99 per cent pure) was acquired. Two different SA samples were used along with pure aluminium as a reductant in the study of SA addition. The chemical composition of the materials used is presented in Table 1.

TABLE 1

Composition of materials used in the present study.

Species	Material composition (%)		
	Prefused $CaO-SiO_2$ slag	Befesa Type I SA	Befesa Type II SA
CaO	49.9	2.76	3.56
MgO	0.42	7.69	6.14
SiO_2	49.00	4.97	10.57
Al_2O_3*	0.43	75.20	67.07
Fe_2O_3	0.15	2.14	2.39
K_2O	0.03	0.90	1.14
SO_3	0.03	~	~
Cl	~	0.82	0.59
CuO	~	0.65	0.82
F	~	0.85	2.40
MnO	~	0.34	0.35
Na_2O	~	1.18	2.48
NiO	~	0.04	0.05
P_2O_5	~	0.09	0.10
TiO_2	~	0.95	0.76
ZnO	~	0.25	0.35
S	~	0.07	0.11
Cr_2O_3	~	~	~
ZrO_2	~	~	~
SrO	~	~	~
BaO	~	~	~
Co_3O_4	~	~	~

* The values for Befesa Type I SA and Befesa Type II SA include both Al_2O_3 and metallic aluminium converted to oxide. The metallic aluminium content is estimated to be between 2.6 and 5.3 per cent, based on Befesa analysis.

Apparatus and procedure

The aluminothermic reduction tests in this work were carried out in an Induction Furnace (75 kW, 3000 Hz). Each set of experiments utilised three small-sized resin crucibles, which were placed within a single large crucible and then inserted into the furnace. The inner sides and the base of the crucible were wrapped with graphite paper to prevent input from interacting with the graphite and to facilitate the effortless removal of the final product from the crucible. A C-type thermocouple was used to measure the temperature. The pre-fused slag (with CaF_2 in the second set of experiments) and reductant mixture were kept in crucibles, heated to a selected temperature, and held for a specific time. Throughout the experiment, argon gas was continuously purged to maintain an inert environment inside the system.

The experimental matrix of the present study is shown in Table 2. Prior to the experiment, dross, SA, and pre-fused $CaO-SiO_2$ slag were dried to remove all the moisture content. Pure aluminium was used along with Befesa SA in relative weights to mimic the same $Al:Al_2O_3$ ratio as that in the S-dross.

TABLE 2

Experimental matrix of the present study.

Study	Type	Expt no	SiO_2/slag source		Reductant/addition			Process parameters	
			Prefused $CaO:SiO_2$ slag (g)	CaF_2 (g)	Pure Al (g)	S-dross (g)	SA (g)	Temp (°C)	Holding time (min)
Study of SA addition	Pure Al	1	141.9	-	41.58	-	-	1650	30
		2	141.6	-	41.49	-	-	1650	30
	S-dross	1	100.03	-	-	87.7	-	1700	60
		2	100.03	-	-	87.7	-	1700	60
		3	100.02	-	-	87.7	-	1700	60
	Al + Befesa Type I SA	1	100.03	-	26.46	-	82.08	1650	60
		2	100.05	-	26.66	-	82.00	1650	60
		3	100.03	-	26.40	-	82.05	1650	60
	Al + Befesa Type II SA	1	100.02	-	26.60	-	92.03	1650	60
		2	100.17	-	26.65	-	92.15	1650	60
		3	100.02	-	26.58	-	92.05	1650	60
Study of CaF_2 addition in prefused $CaO-SiO_2$ slag	Effect of CaF_2	1	90	10	25.98	-	-	1650	60

Characterisation

Electron probe microanalyzer (EPMA)

Metal samples were investigated using a JXA-8500F Field Emission Electron Probe Microanalyzer (EPMA). Backscattered electrons were used for sample imaging to visually represent different phases in the metal sample. EPMA's focus was on determining the elemental distribution and composition of silicon metal produced. Wavelength dispersive X-ray spectrometer (WDS) helped in performing elemental analysis of the different phases, while energy-dispersive X-ray spectrometer (EDS) was used over a particular area to determine an estimate of the element distribution of the different main elements.

X-ray fluorescence (XRF)

Samples from the Study of CaF_2 addition in prefused slag were also analysed using the X-ray fluorescence (XRF) technique at Degerfors Laboratorium AB in Bruksparken, Sweden. The slag and alloy samples were analysed using Thermo Fischer Scientific's ARL 9900 Series XRF device. The samples obtained from tests using pure Al and S-dross were analysed at RWTH, IME-Process Metallurgy and Metal Recycling, Aachen, Germany, using the RFA Omnian 37/S via combustion method. Similarly, the Department of Geoscience and Petroleum (IGP) at NTNU in Trondheim, Norway, conducted an analysis of the samples obtained from trials using Befesa Type I and Type II SA.

Theoretical calculations- FactSage™

Thermodynamic simulations were performed using the software FactSage™, version 8.1 (by Thermfact Ltd. and GTT-Technologies) with databases FToxid and FTlite (see https://www.crct.polymtl.ca/fact/documentation/FSData.htm).

RESULTS AND DISCUSSION

Results from SA addition experiments

This section gives details regarding the observations derived from experiments conducted using different Al sources. These observations encompass the resulting product's physical characteristics, the alloy's yield, and its composition.

Physical structure

This section presents the variations in the physical structure and appearance of aluminothermic reduction products obtained using different reductants.

It was observed that the structure of almost all the samples upon dissection exhibited a consistent pattern: a hemispherical Si alloy located at the uppermost part, with a slag layer positioned beneath the silicon metal (Figure 2). However, in some products, the silicon alloy was not observed at the top. In those products, the silicon metal was slightly below the top portion, entirely encircled by slag in every direction. When pure aluminium was employed as a reducing agent, the resulting product consisted entirely of a silicon alloy at the uppermost section and a slag at the bottom (Figure 2a). In the experiment where S-dross was used as a reductant, tiny drops of silicon alloy were seen above the topmost silicon part, as depicted in Figure 2b. The slag obtained was greenish brown in colour, which deviated slightly from the slags produced in experiments involving alternative reductants. XRF analysis of the slag revealed that the amount of Si in the slag from the trial with S-dross is relatively lower than that using pure Al and Befesa SA, which can be the reason for such appearance of slag. When SA, both Type I and Type II were utilised as a reductant, the topmost part was not entirely covered with silicon alloy. Observations revealed the presence of circular silicon alloys encased by slag. In one sample from the trial involving Al+Type II SA as a reductant, the silicon alloy was found to be positioned slightly below the top layer (Figure 2d). XRF analysis of SA identified several other impurities like Cl, CuO, F, Fe_2O_3, K_2O, and MgO. These impurities might have hindered the rapid reduction reaction at 1650°C and the non-uniform deposition of the reduced Si alloy.

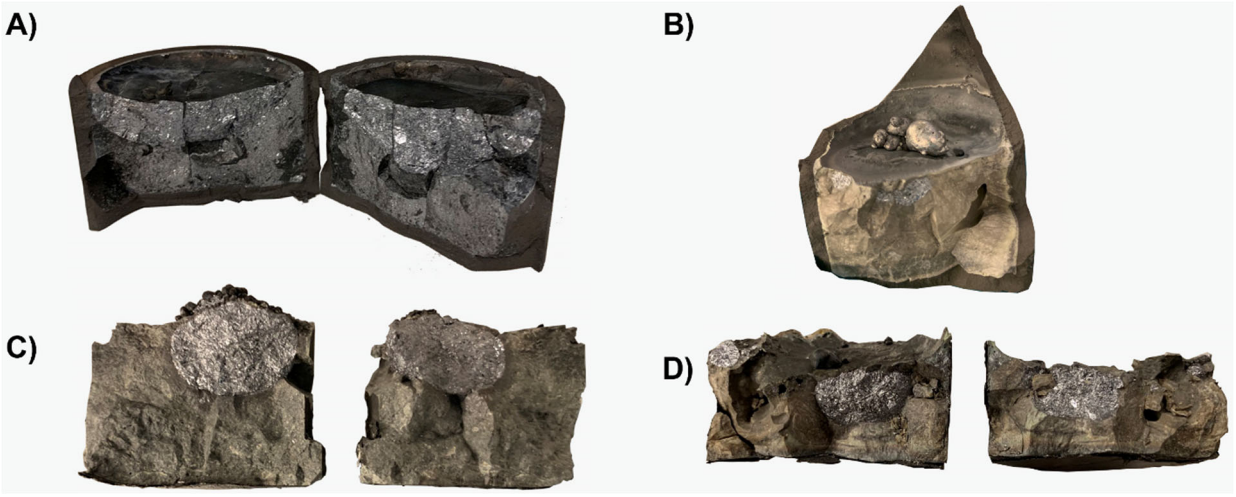

FIG 2 – Different structures of products obtained from aluminothermic reduction with the use of: (a) pure Al, (b) S-dross, (c) Al +Type I SA, and (d) Al +Type II SA.

Metal yield and mass loss

The loss in mass was calculated from the difference between the total input feed and output. The amount of silicon alloy yielded/added Al unit from each crucible, where different reductants were

used, was measured. The percentage mass loss and the average amount (from three parallels) of Si per unit Al reductant produced using different reductants are shown in Figure 3.

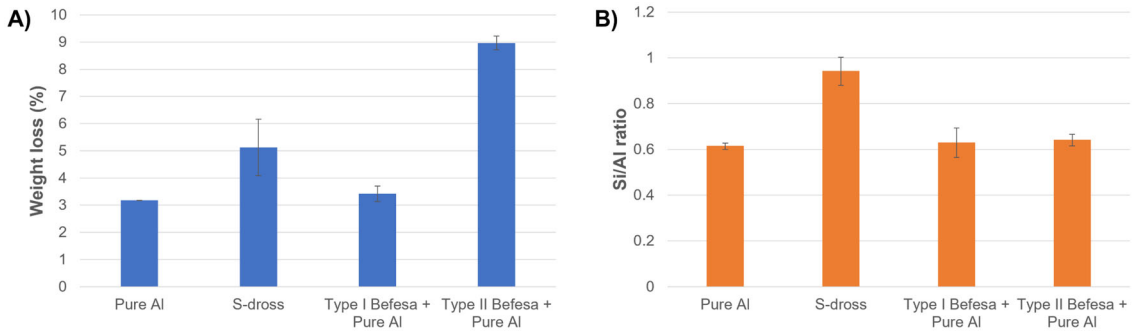

FIG 3 – (a) Mass loss, and (b) Si/Al ratio in experiments using different reductants. The values shown for reductant are the average of three trials conducted, except for pure Al, where values represent the average of two trials.

The Si/Al ratio, when the reductant used was S-dross, was higher than that yield obtained in all other experiments, while the trials using SA gave a comparatively similar but slightly higher metal output than the experiments using pure Al. Many small silicon droplets were present in different locations of the slag, making it difficult to collect the entire silicon alloy produced and consequently leading to comparatively high metal loss.

The weight loss could be attributed to a combination of SiO production/losses and the presence of halides and as such, since SA samples contain more volatiles (alkali, F etc), evaporation is expected to be higher for these materials, leading to a considerably higher loss in weight when SA was utilised.

Chemical composition

Figure 4 displays the predicted chemical composition of metal and slag by FactSage™ and the EDS results for metal and XRF results for slag as mean values of three areas measured in each of the three crucibles, in which different reductants were used.

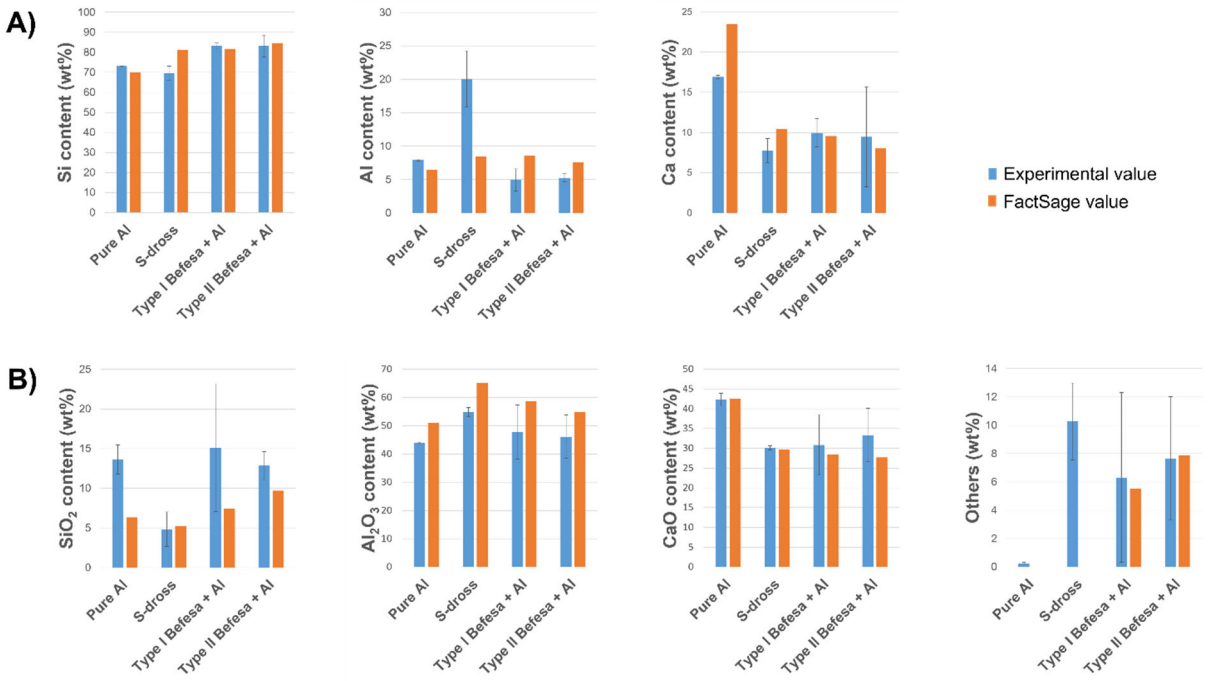

FIG 4 – The chemical composition of (a) metal and (b) slag obtained from experiments utilising different reductants, compared with the chemical composition based on FactSage™ simulations. The given experimental values represent the average of three trials for each experiment, except for the one with pure aluminium as a reductant, where values represent the average of two trials.

The composition of metal samples from each crucible was analysed with EDS. The samples produced in experiments employing pure aluminium had a higher Ca content and lower or similar Al content than other samples, which mostly aligned with the observed pattern in the FactSage™ simulation. The reverse result was obtained from experiments where S-dross was used, ie the content of Al was higher, and the content of Ca was lower. Since the metallic Al accounts for 2.6–5.3 per cent of SA, it has no significant impact on the graph. While the concentration trend for the produced metal in each experiment aligns with the simulation pattern, the most significant deviation in concentration is observed for S-dross, ie Si content is lower while Al content is much higher than predicted. This occurrence may be attributed to the composition of S-dross. The metallic Al content in S-dross was found by dissolving it in a NaCl-KCl-CaF_2 salt melt at 800°C, a method with certain inaccuracy. Those values are taken for Al content for FactSage™ calculation, which may, due to the heterogenous nature of dross, have affected the variation between experimental and predicted values. By using the two types of SA as additions to metallic Al, a metal with a higher Si content and a lower Al and Ca content was obtained compared to the metal obtained using pure Al.

An XRF analysis of SiO_2, Al_2O_3, and CaO content in the slag was conducted to examine the composition of the slag formed in experiments utilising different reductants. The remaining slag contained various impurities such as Cl, Mg, P, K, Fe, etc. No significant differences were seen while comparing the SiO_2, Al_2O_3, and CaO content in these samples from trials with different reductants. However, the composition of SiO_2 in slag samples from experiments using S-dross as a reductant was somewhat lower than the SiO_2 content present in other samples. As in the case of metal samples, the concentration trend aligns well with the FactSage™ simulation, with a slight deviation in concentration values compared to the predicted ones.

BSE images

EPMA analysis of metal was conducted to provide backscatter electron imaging of the phases present. A significant difference in phase composition was not observed, as most of the EPMA results for metal showed similar phases (Figure 5a–5d). Regardless of the type of reductant used, three distinct phases were consistently seen in all metal samples: Si, Si_2Al_2Ca, and Si_2Ca. Agreeing with the higher Si content measured by XRF, the presence of the Si phase was more prominently observed in BSE images of metal samples from trials with SA Type I and Type II. In the metal samples obtained from experiments using S-dross as a reductant, traces of $Si_{13}AlMnFe_4$ were observed, resulting from impurities in the dross.

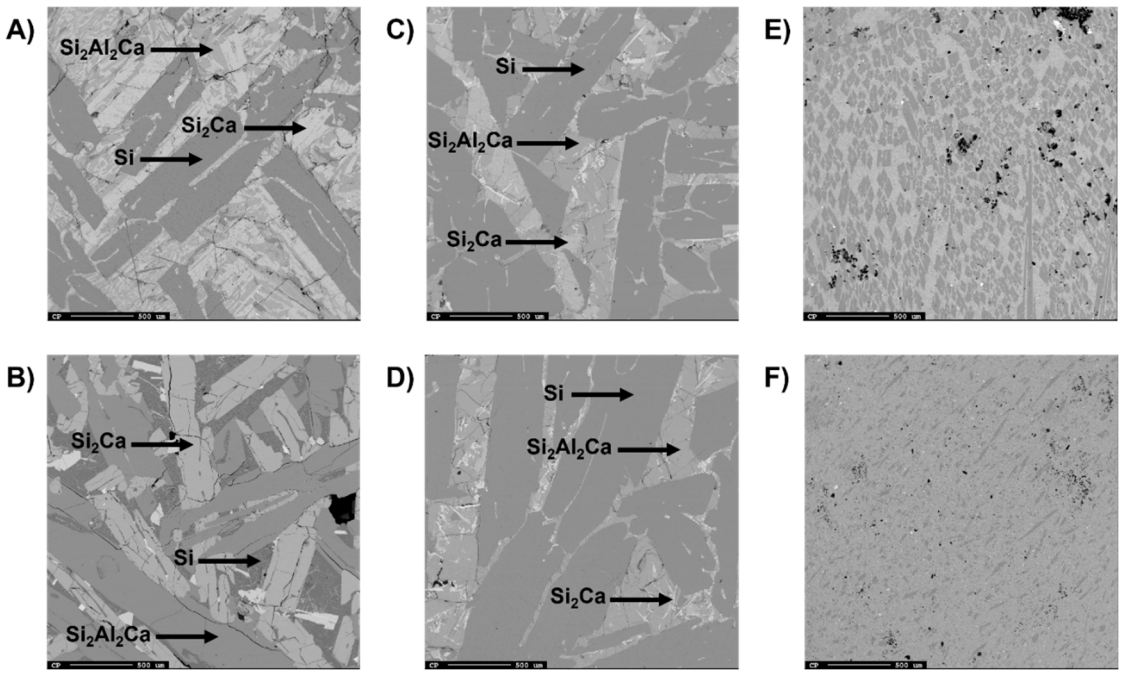

FIG 5 – BSE-image of: (a) metal from Pure Al experiment, (b) metal from S-dross experiment, (c) metal from Type I SA + Pure Al experiment, (d) metal from Type II SA + Pure Al experiment, (e) slag from Type I SA + Pure Al experiment, and (f) slag from Type II SA + Pure Al experiment.

The BSE images of the slags obtained from experiments using two different reductants, Type I SA and Type II SA, revealed the presence of two distinct phases (Figure 5e and 5f). One phase, characterised by a darker appearance, mainly consisted of Al_2O_3-CaO, with Al_2O_3 being the predominant component, while the second phase, appearing lighter in colour, was primarily composed of CaO-Al_2O_3, with CaO being the dominant constituent. Small concentrations of SiO_2 (lighter) were rarely seen on BSE images of slag samples from trials with Type II SA, as EDS analysis revealed the composition of SiO_2 to be much lower compared to slag from experiments with Type I SA.

Results from experiments using CaF2

The results of an aluminothermic reduction experiment in which a set concentration of CaF_2 was added to the slag included observations of its physical structure, the metal yield determination, and the chemical composition of the alloy and slag produced. A comparison was also made between an aluminothermic reduction experiment using CaF_2 in slag and an experiment without using CaF_2. Furthermore, this study's findings encompass comparing the composition of metal produced and simulated composition using FactSage™ software.

The product obtained from the experiment using CaF_2 in pre-fused slag with stoichiometric aluminium as a reductant exhibits a similar structure to a product from the experiment without CaF_2 (Figure 2a). A rigidly structured product contains hemispherical-shaped silicon alloy at the top and heavily dense bluish-grey slag at the bottom, as shown in Figure 6.



FIG 6 – Physical structure of the product obtained from the experiment using CaF_2 in prefused slag and pure aluminium as a reductant.

A loss in mass and amount of Si per unit Al reductant, compared with the experiment without using CaF_2, are shown in Figure 7a. Compared with experiments with stoichiometric Al and rec slag without CaF_2, weight loss has been significantly lower in experiments using CaF_2. Weight loss might be caused by some formation/losses of SiO. However, calculating total SiO loss accurately by FactSage™ is not trivial and will be the focus of future studies. Si yield from the product is similar for both cases, as a stoichiometric reductant in the same amount was used in both.

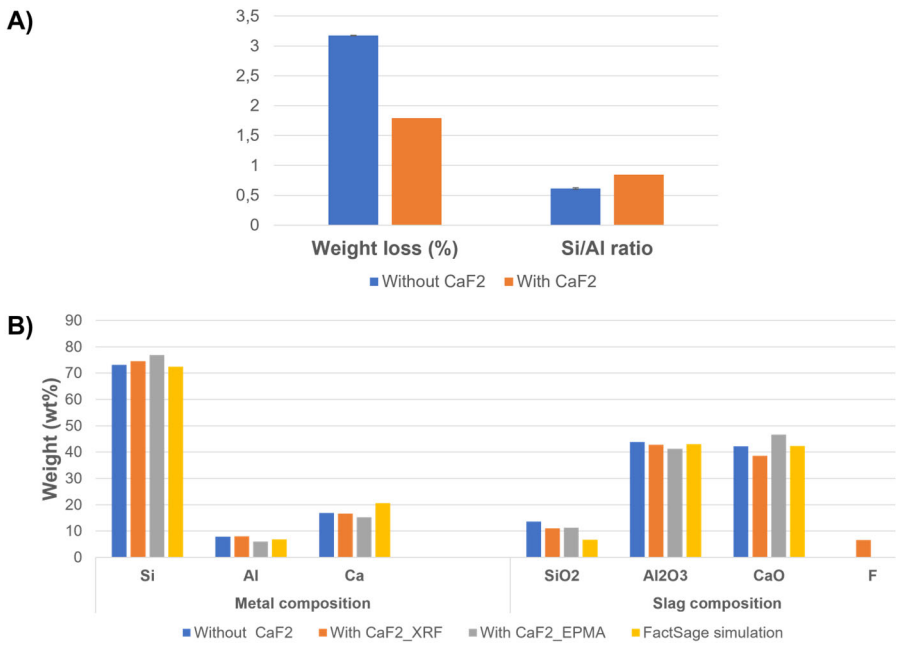

FIG 7 – (a) Mass loss and metal yield, and (b) chemical composition of metal and slag obtained from the experiment using CaF_2 in prefused slag compared to FactSage™ simulation values, and the metal and slag composition obtained from the experiment without CaF_2.

The slag and metal obtained from this experiment were subjected to both XRF and EPMA analysis, and results were compared with the experiment without using CaF_2 and also with FactSage™ simulation values, as shown in Figure 7b. When compared to the experiments without CaF_2, minor differences in metal and slag composition were seen, ie a slight increase in Si content, while the Al and Ca content in metal decreased in the experiment where CaF_2 was used. In the case of slag, the results are similar to experiments without CaF_2; however, SiO_2 and Al_2O_3 contents were slightly lower. When comparing XRF and EPMA results, the only difference was a slightly lower concentration of CaO in slag in the XRF analysis results. The XRF analysis of the slag obtained from this experiment indicates the presence of 6.63 wt per cent of F.

The experimental results closely resemble the predictions made by the FactSage™ simulation but with a slightly elevated Si concentration and reduced Al and Ca content in the metal. The same is the case with the content of SiO_2 in the slag, but the opposite is true in the case of CaO, where the FactSage™ simulation predicted a lower value than the one obtained by the EPMA analysis.

Backscattered image obtained from EPMA for metal sample obtained in this experiment is shown in Figure 8.

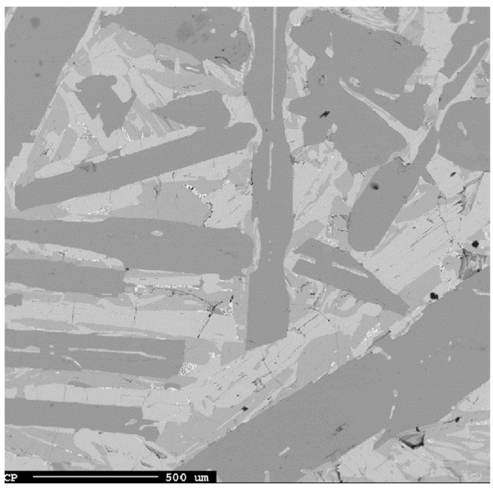

FIG 8 – BSE image of metal obtained from an aluminothermic reduction experiment in which CaF_2 was added to the silicate slags.

Three dominant phases have been identified in metal, similar to what we observed in the metal produced in experiments without CaF_2. The portion of dark-coloured Si is relatively equal in both cases, which is expected considering the similar Si content observed in XRF analysis results. Si_2Ca and Si_2Al_2Ca phases have been abundant, whereas only a few minor phases of impurities such as Fe, Mn, and Mg have been detected.

CONCLUSIONS

The primary aim of this study was to assess the feasibility of producing Si via an aluminothermic reduction process, focusing on achieving a high yield and minimising the calcium content. This study focused on investigating the impact of several factors on the aluminothermic reduction process, including the usage of different aluminium by-products as reductants/additions and the influence of calcium fluoride.

Using SA combined with pure aluminium as a reductant resulted in a slightly higher purity of Si alloy than using other reductants. When pure aluminium was used as a reductant, the alloy produced had a higher concentration of Ca. When S-dross was added as a reductant, the situation was reversed, but the Al concentration was elevated. The dross contains a significant amount of Al_2O_3, so its use resulted in an increase in the concentration of Al_2O_3 in the slag.

Results from the study of CaF_2 addition also showed constructive results in obtaining pure Si. A small mass loss and high metal yield were observed from the experiment using pre-fused slag with 10 per cent CaF_2. Si content in metal has been increased with the use of CaF_2. At the same time, Al and Ca content has been reduced, which is a favourable outcome.

ACKNOWLEDGEMENTS

This work was funded by the EU H2020 through the research project ‘SisAl Pilot’ (Grant No 869268).

REFERENCES

Kero, I, Grådahl, S and Tranell, G, 2017. Airborne Emissions from Si/FeSi Production, *JOM*, 69(2):365–380.

Lazzaro, G, Eltrudis, M and Pranovi, F, 1994. Recycling of aluminium dross in electrolytic pots, *Resources, Conservation and Recycling*, 10(1):153–159.

Liu, N W and Chou, M S, 2013. Reduction of secondary aluminum dross by a waste pickling liquor containing ferrous chloride, *Sustainable Environment Research*, 23(1):61–67.

Park, J H, Min, D J and Song, H S, 2002. The effect of CaF_2 on the viscosities and structures of $CaO\text{-}SiO_2(\text{-}MgO)\text{-}CaF_2$ slags, *Metallurgical and Materials Transactions B*, 33(5):723–729.

Schei, A, Tuset, J K and Tveit, H, 1998. *Production of High Silicon Alloys* (Tapir: Trondheim).

Tranell, G, Safarian, J and Wallin, M, 2020. SisAl - A New Process for Production of Silicon, in *Silicon for the Chemical and Solar Industry XV*, pp 129–139 (The Norwegian University of Science and Technology: Trondheim).

Yoshimura, H N, Abreu, A P, Molisani, A L, de Camargo, A C, Portela, J C S and Narita, N E, 2008. Evaluation of aluminum dross waste as raw material for refractories, *Ceramics International*, 34(3):581–591.

Manufacturing of FeSiB high-temperature phase change material by silicothermic reduction

DOI: 10.62053/VPUJ4722

J Jiao[1], M Wallin[2], W Polkowski[3] and M Tangstad[4]

1. Postdoc Researcher, Norwegian University of Science and Technology, Department of Materials Science and Engineering, 7491 Trondheim, Norway. Email: jian.m.jiao@ntnu.no
2. Researcher, Norwegian University of Science and Technology, Department of Materials Science and Engineering, 7491 Trondheim, Norway. Email: maria.wallin@ntnu.no
3. Researcher, Norwegian University of Science and Technology, Department of Materials Science and Engineering, 7491 Trondheim, Norway. Email: polkowski.wojciech@ntnu.no
4. Professor, Norwegian University of Science and Technology, Department of Materials Science and Engineering, 7491 Trondheim, Norway. Email: merete.tangstad@ntnu.no

ABSTRACT

Fe-26Si-9B (wt per cent) alloy has been identified as a potential high-temperature phase change material (PCM) due to its attractive properties, such as its high latent heat of fusion and low volumetric change during solid/liquid transition. For the successful utilisation of this alloy into thermal energy storage (TES) systems, the development of a cost-effective production method is essential. Presently, the Fe-26Si-9B alloy is produced by mixing FeSi alloys with either pure boron element or FeB alloys. However, the use of pure boron is financially prohibitive, and the carbothermic reduction results in high greenhouse gas emissions and high energy consumption in the production of FeB alloys. In this regard, our study proposes a silicothermic reduction method to produce Fe-26Si-9B PCM by using FeSi alloys and B_2O_3-based oxides. Accordingly, the influence of various parameters on the production process was investigated, including operating temperature, holding time, B_2O_3 content in the added oxides, and initial Slag/Metal (S/M) ratio. Based on the experimental results, the optimal parameters for producing FeSiB alloys with over 9 wt per cent boron were determined. Consequently, it was documented that the FeSi alloys and the added oxides enriched with 50–65 wt per cent B_2O_3 should be subjected to temperatures ranging from 1550–1650°C, maintain an initial S/M ratio exceeding 1, and ensure a holding duration beyond 1 hr. Moreover, the energy consumption of this process was estimated to be ~1.86 MWh/t metal and the mass loss was lower than 7 per cent. Therefore, silicothermic reduction offers a sustainable approach for producing FeSiB alloys with a boron content above 9 wt per cent.

INTRODUCTION

Renewable energy sources, such as solar and wind, play an important role in achieving climate neutrality (EASE, 2023). However, a mismatch between energy supply and energy demand is the main challenge in their applications. By addressing this problem, thermal energy storage (TES) techniques have been developed, in which using of phase change materials (PCMs) has emerged as a particularly promising solution (IEA, 2019). Recently, Fe-26Si-9B (wt per cent) eutectic alloy stood out due to its moderate melting temperature, high energy storage capacity, low volumetric change, and high thermal conductivity (Grorud, 2018; Sellevoll, 2018, 2019; Sindland, 2018; Jiao *et al*, 2019a, 2019b; Jiao, 2020; Jiao, Safarian and Tangstad, 2022). However, the traditional methods of producing this alloy are based either on mixing pure iron (Fe), silicon (Si), and boron (B) elements, or on mixing ferroboron (FeB) and ferrosilicon (FeSi) alloys (Jiao *et al*, 2023). The former approach is financially prohibited, particularly due to the cost of pure boron. The latter suffers from its high greenhouse gas emissions and a high energy consumption.

To tackle these challenges, a new route is proposed for manufacturing Fe-26Si-9B PCM from raw and waste materials in the Thermobat project funded by the European Commission. The strategy is to produce this alloy by using a metallothermic reduction, for which silicon is selected as the reducing agent. The primary reaction between silicon and B_2O_3 is exothermic, and thus, this method has a low energy consumption. The process starts with mixing FeSi and B_2O_3-based oxides at high temperatures followed by a production of molten mixture of FeSiB alloys and SiO_2-based slags. Additionally, the chemical composition of FeSiB alloys can be adjusted at its molten state before tapping. Besides, the raw materials are abundant and cheap and can be obtained from iron and FeSi

scraps, silicon kerf-loss waste and discarded FeSi and silicon fines. Thus, this process is expected to produce FeSiB alloys with a low cost.

The present study focused on optimising the production process of FeSiB alloys. Firstly, the experimental process is established theoretically through thermodynamic analyses. Then, we explore the effect of process parameters on the boron content in the resulting FeSiB alloys. The investigated process variables include holding time, B_2O_3 content in the added oxides, initial Slag/Metal (S/M) ratio, and operating temperature.

MATERIALS AND METHODS

In the production of FeSiB alloys, Fe-75Si and iron alloys, CaO, B_2O_3, and colemanite powders ($CaO{\cdot}2B_2O_3{\cdot}5H_2O$) were used in the experiments. Fe-75Si alloy was sourced from Finnfjord AS, Norway, and the chemical composition of iron and silicon was analysed to be 25.78 wt per cent and 74.22 wt per cent using Inductively Coupled Plasma Sector Field Mass Spectrometry (ICP-SFMS), respectively. Iron metal (99.99 wt per cent) and CaO powder (99.95 wt per cent) came from Alfa Aesar. B_2O_3 powder (98 wt per cent) obtained from Thermo Scientific, and commercial colemanite powder (particle size <75 μm) was provided by Eti Maden company (ETi Maden, 2015). It is important to note that prior to use colemanite, it must undergo calcination to eliminate its crystal water. This involved maintaining the colemanite powders in a muffle furnace at 600°C for 180 min. The content of B_2O_3 was analysed to be ~55 wt per cent in the calcinated colemanite using the ICP-SFMS technique.

The experiments were conducted in a resistance furnace under an argon (99.999 per cent Ar) atmosphere. 7 to 24 g of B_2O_3-based oxides and 5 to 15 g of FeSi alloys were placed in the BN-coated SiC crucibles. The thin BN spray coating was applied to prevent the oxides creeping from the crucible due to its good wetting behaviour with SiC. Notably, the B_2O_3-based oxides were either pre-produced by mixing pure B_2O_3 and CaO powders or taken directly from the calcinated colemanite. The added oxides were placed at the bottom of crucible, and the Fe-41Si master alloy pieces were layered at the top of these oxides, where the Fe-41Si master alloy was produced by mixing Fe-75Si and iron metals in an induction furnace. This arrangement aimed to enhance mass transfer during the process, as after melting, the molten alloys would settle at the crucible's bottom, and the molten slags would ascend due to their density differentials. Subsequently, the holding temperature was set in the range of 1500–1650°C, maintaining this for a duration of 5 to 180 min. The purpose was to find the optimal parameters to produce FeSiB alloy having the boron content above 9 wt per cent. After experiments, the chemical composition of the produced alloys was analysed using ICP-SFMS. Furthermore, thermodynamic analyses were conducted by FactSage™ 8.1, using databases such as FactPS, FTlite, FToxide, and Melts database within the viscosity module. The energy consumption associated with the process was estimated using the Heat and Material Balance module of HSC Chemistry 9 software.

RESULTS AND DISCUSSION

Silicothermic reduction process design

The Fe-26Si-9B eutectic alloy was initially designed by FactSage 7.2 using the FTlite database (Jiao *et al*, 2019a). However, the experimental results have revealed that the actual eutectic alloy's composition was near but not precisely at the eutectic point (Jiao, 2020). The Fe-29Si-10B alloy was further regarded as the eutectic alloy based on the phase distribution in the observed eutectic structures (Jiao, 2020). Then, when a new version of FactSage 8.1 was applied in the thermodynamic analyses, the composition of this eutectic FeSiB alloy was changed to Fe-24Si-11B. This led to the assumption that the eutectic point for this system was in a range of 61–65 wt per cent iron, 24–29 wt per cent silicon, and 9–11 wt per cent boron. For this research, the silicothermic reduction process was designed based on the FactSage 8.1 using the FTlite and FToxide databases. The chemical reactions were expressed as:

$$CaO = (CaO) \quad (1)$$

$$B_2O_3 = (B_2O_3) \quad (2)$$

$$Fe = \underline{Fe} \quad (3)$$

$$Si = \underline{Si} \quad (4)$$

$$\underline{3Si} + 2(B_2O_3) = 3(SiO_2) + 4\underline{B} \quad (5)$$

Here, the parentheses indicate that the oxides are in a molten state, and the underline denotes that the metal elements are in their molten state.

Figure 1 shows the calculated iso-boron lines of FeSiB alloys within the CaO-SiO_2-B_2O_3 liquidus region at 1500°C, fixing a constant Fe content at 65 wt per cent. It is observed that an increase in the boron content in FeSiB alloys is directly proportional to the increased content of B_2O_3 in the equilibrium slags. Here, the 11 per cent boron line shows the composition of the equilibrium CaO-SiO_2-B_2O_3 slags corresponding to the production of Fe-24Si-11B alloy. So, to produce an FeSiB alloy with a boron content over 11 per cent, the added CaO-SiO_2-B_2O_3 oxides should ideally be situated within the light green area in the diagram, where the B_2O_3 content exceeds 25 wt per cent in the equilibrium CaO-SiO_2-B_2O_3 slags.

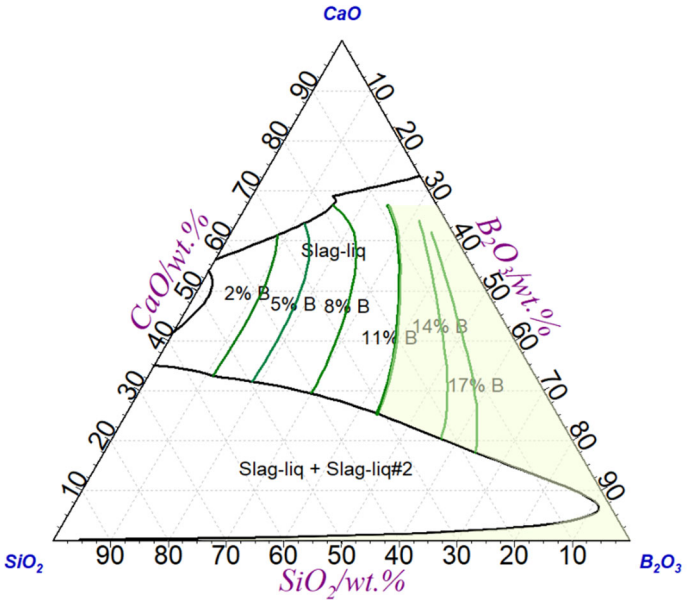

FIG 1 – CaO-SiO_2-B_2O_3 phase diagram at 1500°C, showing iso-boron lines (in green) for Fe-Si-B alloys (65 wt per cent iron) with their equilibrium slags. The light green region indicates the compositional range of the added oxides to produce the Fe-24Si-11B alloys (FTlite + FToxide databases).

Figure 2 presents the predicted effects of B_2O_3 content in the added oxides on both the mass of CaO-B_2O_3 oxides added and the viscosity of the equilibrium CaO-SiO_2-B_2O_3 slags. In the production of 1 ton Fe-24Si-11B alloy, it is found that an increase of B_2O_3 content and consequently a decrease in the CaO content, less slag will be produced and hence it leads to a decrease of the requested mass of CaO-B_2O_3 oxides. Conversely, the viscosity of the equilibrium slags increases with higher B_2O_3 content in the added CaO-B_2O_3 oxides. In the production process, the goal is to use as little of the added CaO-B_2O_3 oxides as possible while keeping the slags fluid enough. However, it's hard to achieve both low mass of the CaO-B_2O_3 oxides added and its low viscosity at the same time. According to Figure 2, a critical intersection point of these parameters is ~55 wt per cent B_2O_3. Hence, the added CaO-B_2O_3 oxides containing the B_2O_3 in the range of 50–65 wt per cent are investigated in the experiments. Ideally, this B_2O_3 composition range corresponds to an input mass for the added oxides between 1.6–2.7 t and a viscosity range for the equilibrium slags of 1–1.8 poise in the production of 1 ton Fe-24Si-11B alloy.

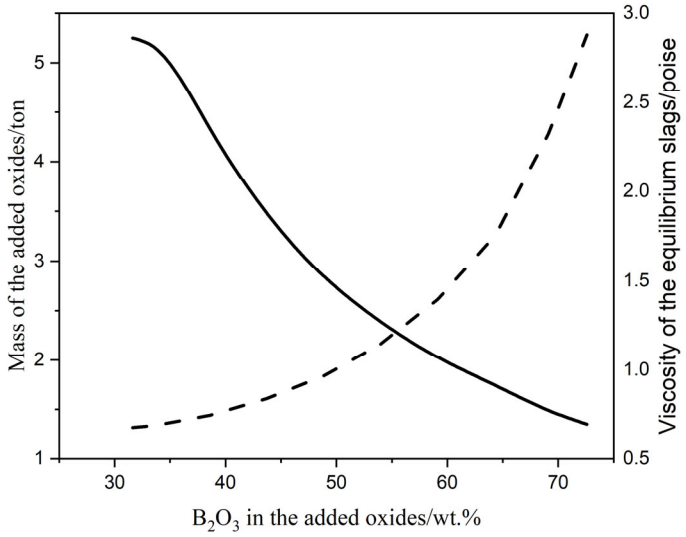

FIG 2 – The solid line shows the relationship between the content of B_2O_3 in CaO-B_2O_3 added oxides and the mass for producing 1 ton Fe-24Si-11B alloy at 1500°C, and the dashed line shows its corresponding viscosity of the equilibrium CaO-SiO_2-B_2O_3 slags (Melts, FTlite, and FToxide databases).

Effect of holding time

Figure 3 shows the influence of holding time on the boron content in the produced FeSiB alloys, where the Fe-41Si master alloy and CaO-65B_2O_3 oxides were subjected to 1650°C for the holding time ranging from 5 to 120 min with the fixed initial S/M ratio of 1.6. It is observed that the boron content increased with the increase in holding time, tending the towards to the equilibrium concentration of 10.3 wt per cent, as shown in the dashed line. It reveals a rapid initiation of the S/M reaction within the initial 5 min, achieving a boron content ranging from 2.6 to 5 wt per cent. Then, a more gradual increase was observed over time. The system was close to its equilibrium state after 60 min holding time, where the boron content was increased to ~9 wt per cent. Interestingly, the boron content was higher than the predicted equilibrium content after 120 min holding time, which was impossible. This deviation might be caused by the inaccuracy in the FactSage database. These results show that a holding time of 60 min is necessary to achieve a boron content over 9 wt per cent in the FeSiB alloys.

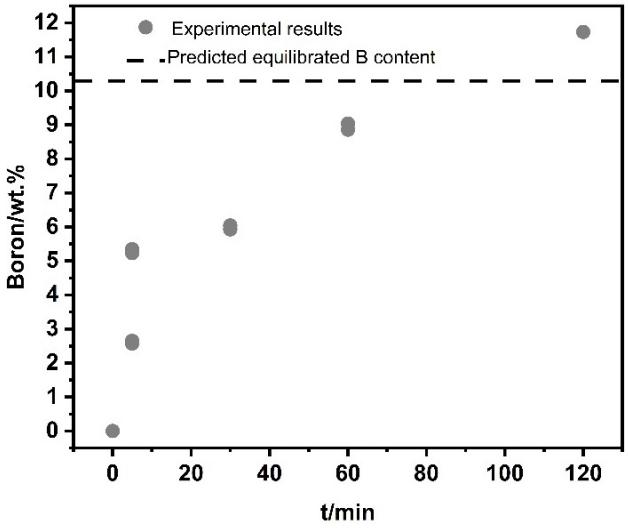

FIG 3 – The effect of holding time on boron content in the produced FeSiB alloys. Fe-41Si and CaO-65B_2O_3 oxides is reacted at 1650 ºC with the initial S/M ratio of 1.6. The dashed line represents the predicted equilibrium B content (FTlite, and FToxide databases).

Effect of B_2O_3 content in the added oxides

Figure 4 presents a comparison of the experimental results and thermodynamic predictions regarding the impact of B_2O_3 content in the added oxides on the boron content in the produced FeSiB alloys. In the experiments, Fe-41Si master alloys reacted with a range of B_2O_3-based oxides at an initial S/M ratio of 1.6 during 60 min holding time at 1650°C. It is noted that 55 wt per cent B_2O_3 based oxides were used directly from the calcinated colemanite, whereas 50 wt per cent and 65 wt per cent B_2O_3 based oxides were synthesized by blending pure CaO and B_2O_3 powders. It is seen from the modelling results that the boron content increased slightly in the produced FeSiB alloys with a higher B_2O_3 content in the added oxides. Experimental results showed that the boron content in the alloys had a good agreement with the thermodynamic predictions by using 50 wt per cent and 55 wt per cent B_2O_3 based oxides. Conversely, when employing 65 wt per cent B_2O_3 based oxides, the analysed boron content was lower than the predicted equilibrium boron content. indicating that the reaction did not reach equilibrium within a 60 min holding time. It implicates that the mass transfer was likely the limiting step in this process. Therefore, an increase in the B_2O_3 content in the added oxides from 50 wt per cent to 65 wt per cent, a longer holding time is expected to achieve equilibrium.

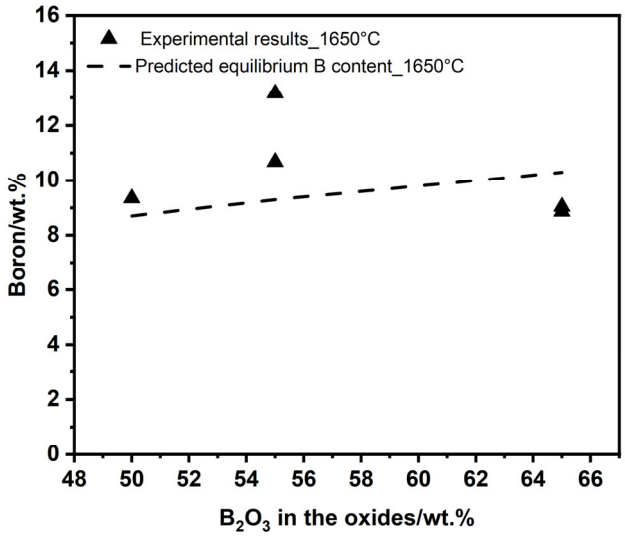

FIG 4 – The effect of B_2O_3 content in the added oxides on boron content in the produced FeSiB alloys. The points represent the experimental results, and the dotted line represents the predicted results based on FactSage 8.1 using FToxide and FTlite databases. The calcinated colemanite was used as the 55 wt per cent B_2O_3 based oxides.

Effect of the initial S/M ratio

Figure 5 shows the relationship between the initial S/M ratio and boron content in the produced FeSiB alloys. These experiments involved a reaction of Fe-41Si master alloys with the calcined colemanite (~55 wt per cent) at different initial S/M ratios, maintaining the reaction for 60 min at 1650°C. The analysed boron content in the produced alloys was summarised in the figure, accompanied by the predicted equilibrium boron content represented by the dashed line. There was a clear trend indicating that the boron content increased with an increasing initial S/M ratio, as a higher initial S/M ratio would give a higher B_2O_3 for a given boron content, and hence the driving force would be higher. Significantly, the boron content was higher than 9 wt per cent in the FeSiB alloys when the initial S/M ratio was over 1. In the comparison of the experimental results and the predicted equilibrium boron content, it is found that the experimental results were close to or higher than that from the thermodynamic modelling, as mentioned before, this deviation might be caused by an inaccurate FactSage database. According to the experimental results, to achieve a boron content higher than 9 wt per cent in our target FeSiB alloys, the initial S/M ratio should be greater than 1.

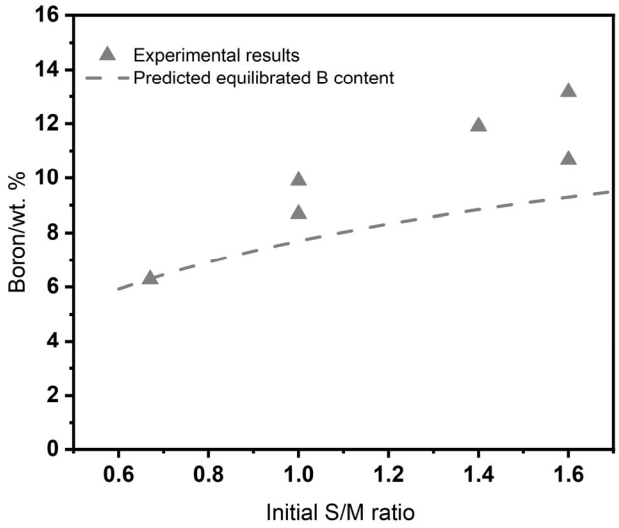

FIG 5 – The effect of initial Slag/Metal (S/M) ratio on boron content in the produced FeSiB alloys. The points represent the experimental results, and the dash line represents the predicted result by FactSage 8.1 using FToxide and FTlite databases.

Effect of operating temperature

Figure 6 shows the impact of operating temperature on the boron content in the produced FeSiB alloys. These alloys were produced by reacting Fe-41Si master alloys with the calcined colemanite at the initial S/M ratio of 1 and 1.6, within a 60 min holding time at temperatures range of 1500–1650°C. The figure summarised the experimental results, with the dashed lines indicating the predicted equilibrium boron content for these initial S/M ratios. The experimental data reveals that an increase in temperature at a constant initial S/M ratio led to a higher boron content. In contrast, the predicted equilibrium boron content decreases with increasing temperature, indicating that equilibrium was not achieved at lower temperatures (1550°C and 1500°C) within 60 min holding time. It is noted that a lower temperature was preferable for the silicothermic reduction process. However, a lower temperature also resulted in a higher viscosity of the molten slag, which impeded mass transfer during the process. Thus, at a holding time of 60 min, mass transfer became the limiting factor.

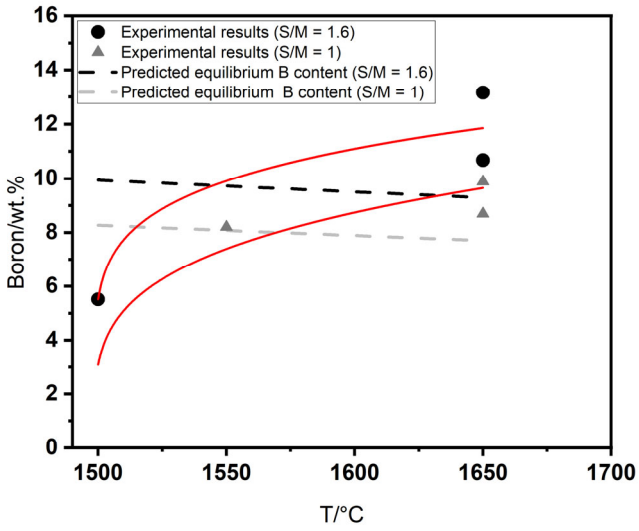

FIG 6 – The effect of temperature on boron content in the produced FeSiB alloys. The points represent the experimental results, and the dash lines represent the predicted results based on FactSage 8.1 using FToxide and FTlite databases.

The two red lines in the figure shows the trend of B content with increasing temperature at initial S/M ratios of 1 and 1.6, respectively. These two lines were drawn based on the experimental data. It was

observed that a higher initial S/M ratio resulted in a higher boron content at a given temperature and holding time, due to a stronger driving force in the slag/metal systems with a higher initial S/M ratio. Consequently, the system with a higher S/M ratio was likely to reach equilibrium in a shorter holding time at a constant temperature. Therefore, for a 60 min holding time and an initial S/M ratio greater than 1, the optimal operating temperature is approximately 1650°C for the calcinated colemanite. To achieve equilibrium at temperatures below 1650°C, a longer holding time would be necessary.

Mass loss

Figure 7 presents a plot of mass loss as a function of holding time under various temperatures, in the production of FeSiB alloys using B_2O_3-based oxides. The measurement of mass loss was conducted by comparing the total weight of raw materials before and after conducting the experiments. It reveals that the mass loss was below 7 per cent. In the experiments using CaO-65B_2O_3 at 1500°C, the mass loss increased proportionally with holding time, from 0.4 per cent after 5 min to 3.5 per cent after 180 min. Additionally, when examining the impact of temperature on mass loss with a constant holding time of 60 min using the CaO-65B_2O_3, an increase in temperature led to an increase in mass loss, from 0.1 per cent at 1400°C to 4.1 per cent at 1650°C. In contrast, when it came to the calcinated colemanite, the behaviour was less predictable. It varied in the range of 2–7 per cent after 60 min holding time at 1650°C. A review of the data indicates that the use of calcinated colemanite led to a higher mass loss compared to CaO-65B_2O_3 master oxides. Figure 8 shows the partial pressure of potential species in the CaO-SiO_2-B_2O_3 system across a temperature range of 1200–1700°C. This suggests that the mass loss was primarily due to the evaporation of B_2O_3 in the system. Given these findings, it is suggested to compensate for this loss by adding an additional B_2O_3 to the oxides charged in the FeSiB alloy production process.

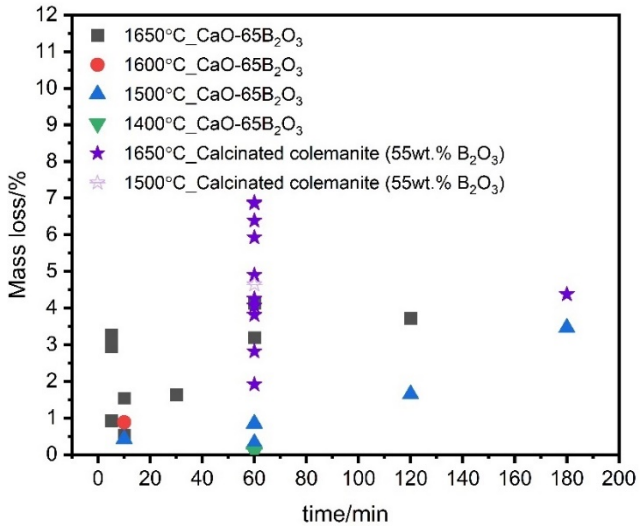

FIG 7 – Mass loss versus holding time in the silicothermic reduction process.

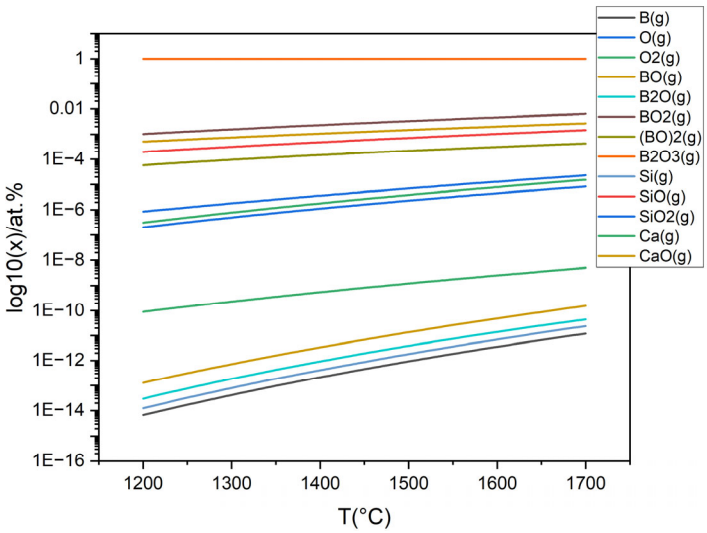

FIG 8 – The partial pressure of possible species in the CaO-SiO_2-B_2O_3 system at a standard atmosphere. It was calculated by FactSage 8.1 using FactPS database.

Energy balance

In the production of 1 ton Fe-24Si-11B alloy, the estimated theoretical energy consumption was 1860 kWh/t metal. This estimation was calculated based on a mass balance achieved at 1650°C under thermodynamic equilibrium. The relevant stoichiometry equation is as follows:

$$1.7t(35CaO-65B_2O_3)+1.1t(59Fe-41Si)=1.8t(33CaO-24SiO_2-43B_2O_3)+1t(65Fe-24Si-11B) \quad (6)$$

Further analysis of the electrical energy consumption was carried out by using HSC Chemistry software (version 9). This analysis was based on the principle of enthalpy conservation, as shown in the equation:

$$\text{enthalpy in input materials + electrical energy = enthalpy in output products} \quad (7)$$

Subsequently, the energy flow involved in the production of 1 ton Fe-24Si-11B alloy was illustrated in the Sankey diagram, as it is presented in Figure 9. It is observed that the energy from the input metal was slightly higher than the energy from the output metal, attributed to the exothermic reaction between silicon an B_2O_3. The electrical energy (1860 kWh/t of metal) was directly transformed to the heat in the output metal and slag. Given these observations, the challenge was to develop an efficient method to reuse the heat in the products. This is crucial for improving energy efficiency and sustainability of the proposed production process.

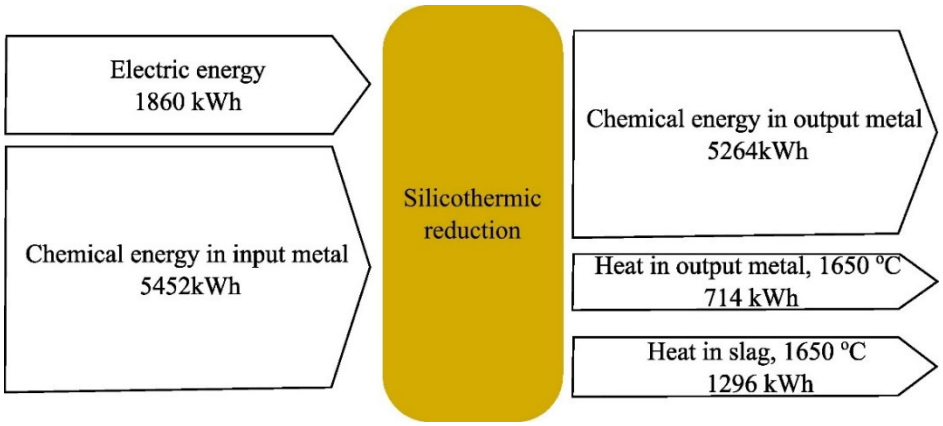

FIG 9 – Sankey diagram, illustrating the energy flow for the production of 1 ton Fe-24Si-11B alloy. Fe-41Si and CaO-65B_2O_3 oxides reacted at 1650ºC with an initial S/M ratio of 1.6. Thermal loss was not included.

CONCLUSIONS

This research aimed to develop a method to produce FeSiB alloys, targeting a composition of 61–65 wt per cent iron, 24–29 wt per cent silicon, and 9–11 wt per cent boron. This method was based on the silicothermic reduction between silicon and B_2O_3. In this regard, the experiments were conducted in a resistance furnace under an argon atmosphere. The parameters in the influence of the boron production in the alloys were investigated. According to the experimental results, the optimal procedure involved reacting an Fe-41Si master alloy with oxides containing over 50 wt per cent B_2O_3 by maintaining an initial Slag/Metal (S/M) ratio of 1–1.6. The mixture was then subjected to the temperatures above 1550°C for a duration over 60 min. The mass loss was observed to be below 7 per cent, and the energy consumption was estimated to be ~1860 kWh/t metal. These findings provided a basis to develop reliable and efficient method for producing the targeted FeSiB alloys with the boron content above 9 wt per cent.

ACKNOWLEDGEMENTS

The THERMOBAT project received funds from European Commission under grant agreement 10105754. The sole responsibility for the content of this publication lies with the authors. It does not necessarily reflect the opinion of the European Union. Neither the REA nor the European Commission is responsible for any use that may be made of the information contained therein.

REFERENCES

ETi Maden, 2015. Product Specification – Ground Colemanite. Available from: <https://www.etimaden.gov.tr/storage/uploads/2018/01/16-2017-Ground-Colemanite-75-Micron.pdf> [Accessed: 18 April 2023].

European Association for Storage of Energy (EASE), 2023. Thermal Energy Storage. Available from: <https://ease-storage.eu/publication/thermal-energy-storage/>

Grorud, B, 2018. Interaction of Eutectic Fe-Si-B Alloy with Graphite Crucibles, Master thesis, Norwegian University of Science and Technology.

International Energy Agency (IEA), 2019. World Energy Outlook 2019. Available from: <https://www.iea.org/reports/world-energy-outlook-2019>

Jiao, J M, 2020. Si-based phase change materials in thermal energy storage systems, PhD thesis, Norwegian University of Science and Technology (NTNU).

Jiao, J Safarian, J and Tangstad, M, 2022. The Use of Fe-26Si-9B Alloy as Phase Change Material in Si3N4 Container, *Crystals*, 12(3):376. https://doi.org/10.3390/cryst12030376

Jiao, J, Grorud, B, Safarian, J and Tangstad, M, 2019b. Wettability of molten Fe-Si-B alloy on graphite, Al2O3, and h-BN substrates, in *Proceedings of the Liquid Metal Processing and Casting Conference 2019,* pp 425–433.

Jiao, J, Grorud, B, Sindland, C, Safarian, J, Tang, K, Sellevoll, K and Tangstad, M, 2019a. The use of eutectic Fe-Si-B alloy as a phase change material in thermal energy storage systems, *Materials*, 12(14). https://doi.org/10.3390/ma12142312

Jiao, J, Jayakumari, S, Wallin, M and Tangstad, M, 2023. Graphite crucible interaction with Fe–Si–B phase change material in pilot-scale experiments, *High Temperature Materials and Processes*, 42(1):20220288. https://doi.org/10.1515/htmp-2022-0288

Sellevoll, K, 2018. Interactions of Eutectic Fe-Si-B Alloy with Graphite Crucibles, Specialization project report, Norwegian University of Science and Technology (NTNU).

Sellevoll, K, 2019. Interactions of FeSi Alloys with Graphite Crucibles, Master thesis, Norwegian University of Science and Technology (NTNU).

Sindland, C, 2018. Production of Eutectic Si-Fe-B and Si-Cr-B alloy and their Interaction with Graphite Crucibles, Summer job report, Trondheim: Norwegian University of Science and Technology (NTNU). https://doi.org/10.1093/jicru/os9.1.report16

Physical properties optimisation of the Zimbabwean limonite ore-carbon composite pellets as a sustainable feed for pig iron production

DOI: 10.62053/PDZR2358

S M Masuka[1], D Simbi[2], S Maritsa[3] and E K Chiwandika[4]

1. Lecturer, University of Zimbabwe, Harare 263, Zimbabwe. Email: shebarmasuka@gmail.com
2. BTech student, Harare Institute of Technology, Harare 263, Zimbabwe. Email: h200741h@hit.ac.zw
3. Lecture, Harare Institute of Technology, Harare 263, Zimbabwe. Email: steven.maritsa@gmail.com
4. Lecturer, Harare Institute of Technology, Harare 263, Zimbabwe. Email: chiwandikae@gmail.com

ABSTRACT

The steel industry is facing challenges on a global scale that include depletion of resources, huge energy consumption, and the emission of CO_2. The demand for iron products is increasing due to the increased infrastructural development. Zimbabwe produced cast iron from scrap metals. However, there is currently a shortage of scrap, and yet Zimbabwe is rich in limonite ores that are currently being underutilised. The possibility of using limonite ore as a sustainable feed for pig iron production was investigated by preparing some limonite ore carbon composite pellets. The results showed that the addition of coal to the limonite ore and calcium carbonate mix to form the composite pellets resulted in a decrease in the drop number as well as the dry compressive strength of the composite pellets. This research aims to improve the physical properties of the green pellets by the careful addition of hydroxyethyl cellulose as a binder that was found to improve the physical properties of the green pellet. This is important for materials handling during the production process of the composite pellets. Results showed that the drop number was substantially improved by the addition of 0.4 wt per cent hydroxyethyl cellulose while the dry compression strength improved from 2.5 kg/pellet to around 23 kg/pellet irrespective of the amount of binder added. The binder improved the physical strength of the iron-carbon composite pellets enough to allow for large-scale production of the pellets that can be an alternative and sustainable feed for cast iron production. However more results on the indurated compression strength and other properties such as the reduction degradation index, swelling index, and the reducibility test are required.

INTRODUCTION

The huge demand for equipment and infrastructure for clean energy technologies as a result of the need to achieve net zero emissions by 2050 has resulted in massive demand for iron and steel products since these play a pivotal role in the development of such infrastructure (International Energy Agency, 2023). Global steel consumption is expected to continue rising to meet this demand and yet the high-grade iron ores have depleted, forcing players in the industry to utilise lower-grade iron ores. The mineralogy of these underutilised ores is often very complex and requires innovative processing techniques that can yield low-impurity molten metal from these low-grade iron ores resources (Liang *et al*, 2023).

Zimbabwe has low-grade limonite ores that are not being utilised in the Ripple Creek Deposits, located in the Midlands Province of central Zimbabwe which are estimated to be 111 million tonnes (Mt). Of these iron ores, 59 per cent meet the blast furnace requirements and the remainder are soft limonite ores that generate fines during mining and processing. Sintering of these limonite ores results in a product of poor quality because of more pores in the sinter due to the high water of crystallisation content and the high loss on ignition of the same affects the sinter strength, making sinter made from these ores unsuitable for blast furnace feed. The production of high-quality sinter from this resource would require a high coke rate and subsequently high carbon dioxide emissions (Clout and Manuel, 2015). Hence investigations on the utilisation of this resource through the production of some limonite ore-carbon composite pellets are being done by Chisahwira *et al* (2023).

The preparation of limonite–carbon composite pellets will increase reduction efficiency by improving reactivity and lower carbon dioxide emissions thus contributing towards Zimbabwe's aim to reduce

emissions by 40 per cent per capita by 2030. However, the physical strength of the green pellets was found to decrease with increasing coal addition (Chisahwira *et al*, 2023) which is detrimental to the productivity during mass production of the pellets hence the need to investigate ways to improve the strength by the addition of an organic binder, hydroxyethyl cellulose.

The use of binders in the agglomeration of fine iron ores through pelletisation has always been a major step in the utilisation of lower-grade iron ores. Bentonite has in the past been the most commonly used binder because it controls moisture and adds to the physical strength of the pellets but the major disadvantage is the high content of acid constituents, namely, silica and alumina which are approximately 65 per cent and 20 per cent respectively (Devashayam, 2018). In addition, bentonite has been associated with availability challenges and high costs. Binders that can produce the same quality of iron ore pellets in terms of pellet strength, at sustainable prices while also avoiding the addition of more impurities would be ideal for use in the limonite ore-carbon composite pellets.

The most extensively researched group of binders are organic binders since they are free of silica and have exhibited good binding properties and wet strength (Eisele and Kawatra, 2003). However, they have lacked in terms of fired pellet strength because of their low burning temperature. At high firing temperatures, organic binders that burn with no residue cannot provide the necessary bonding strength to iron oxide grains (Sivrikaya and Arol, 2014). On the other hand, this elimination during firing can be viewed as an advantage because this ensures that there are no impurities in the iron ore pellets, which has not been the case with inorganic binder (Guanzhou *et al*, 2002). As such, research and development on the use of organic binders in iron ore pelletisation has continued through the years.

A review of organic binders in a report by Halt and Kawatra (2014) stated that a range of organic materials from synthetic chemicals such as acrylamides and naturally occurring materials such as starch and cellulose and their derivatives have been explored as binders in the agglomeration of iron ore. Some binders that were successful at laboratory scale production failed at pilot scale production and underlying reasons are often difficult to determine. However, the general overview is that purely organic binders enhance the green-ball formation, and the green-ball quality increases with the binder's ability to thicken and the ability to form an adhesive film after drying.

In an investigation by Ngara *et al* (2023), where organic binders were used as alternatives to bentonite in the pelletisation of low-grade iron ore, and known industrial standards used for references, it was determined that organic binders could be used as effective alternatives in iron ore pelletisation. The organic binders, corn starch, sodium lignosulfonate, and carboxymethyl cellulose produced pellets whose drop indices were comparable to bentonite and could be used in synthesizing green pellets. However, indurated pellets produced from lignosulfonate and carboxymethyl were weaker than those with bentonite even though they surpassed the minimum industrial standards (Ngara *et al*, 2023). As such, these organic binders were deemed viable alternatives to bentonite in low-grade iron ore pelletisation.

Research by Guanzhou *et al* (2002) on the functions and molecular structure of organic binders based on molecular design and interface science indicated that structurally good binders should have sufficient polar groups and hydrophilic groups. Functionally, a good binder should improve the wettability of the iron ore particles, have great adhesive force to the iron ore, as well as good cohesive strength and thermal stability. According to this study, the structure of an organic binder for iron ore should have a polar group, a hydrophilic group, an organic chain skeleton, and a degree of polymerisation. The binder used in this study, (hydroxyethyl cellulose) based on the findings by Guanzhou *et al* (2002) could potentially be used as a binder for limonite-carbon composite pellets because of its relatively higher molecular weight, which is reported to increase mechanical strength. The presence of the hydroxyl and ethyl groups, which act as the hydrophilic and polar parts of the polymer, respectively, is also expected to aid in the effective bonding of the iron ore and carbon particles and offer significant mechanical strength to the composite pellets. It is expected that the binder will increase the physical strength of the iron-carbon composite pellets enough to allow for large-scale production of the pellets as an alternative and sustainable feed for cast iron production. It should be noted that limonite-carbon composite pellets have been previously produced with the indurated compression strength greater than 250 kg/pellet, but the green physical properties were

not sufficient enough for mass production in our previous research (Chisahwira *et al*, 2023). Hence this research only focused on the improvement of the green pellet physical properties.

EXPERIMENTAL

Materials

Limonite ore obtained from Kwekwe, in the Midlands province of central Zimbabwe, and coal fines obtained from waste dumps at Hwange Colliery Company (HCC) were used in this study. The chemical composition of the limonite and limestone is shown in Table 1 while proximate analysis for the coal fines was done according to the Indian Standard IS:1350 (Part I) (Bureau of Indian Standards, 1984) (Table 2).

TABLE 1

Chemical composition of the Zimbabwean Limonite ores and limestone.

Analyte	T-Fe	SiO_2	CaO	Al_2O_3	MgO	Mn	S	P	LOI
Zimbabwean limonite ore	52.51	8.78	1.32	1.30	0.59	2.1	0.005	0.04	11.87
Limestone	1.32	7.10	45.70	1.19	4.22	0.31	0.17	0.01	39.96

TABLE 2

Coal proximate analysis.

Fixed carbon	Volatile matter	Ash content	Moisture content
64.28	24.12	10.40	1.20

The major phases in the iron ore were determined using X-ray diffraction at a scanning speed of 0.5 with increments of 0.02 at a 2θ range of 10–80° and were determined to be hematite, goethite and silica as shown in Figure 1.

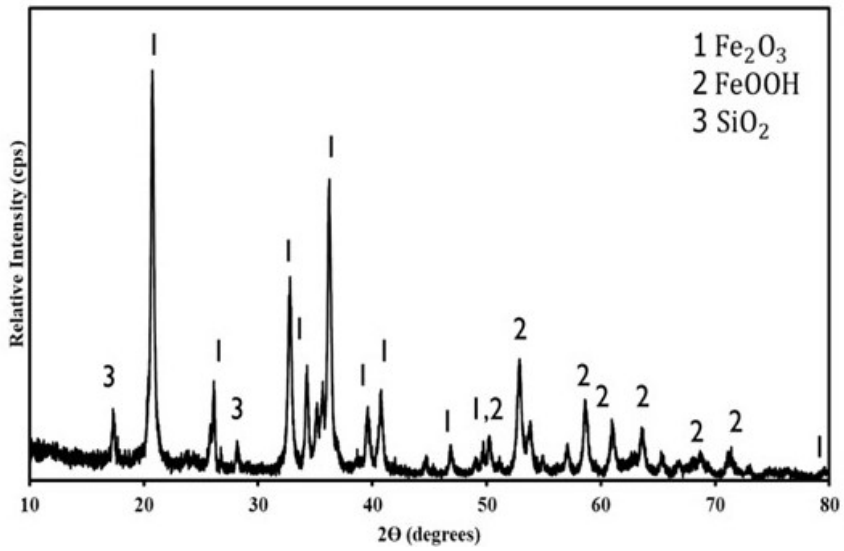

FIG 1 – Phase identification of limonite ore.

Preparation of raw materials

Moisture was removed from limestone and limonite by oven drying at 383 K for 24 hrs. Size reduction for the ore, limestone, and coal was done to achieve 80 per cent passing 75 µm using a pulveriser. The samples were sieved on a 75 micron sieve and the oversize material was re-pulverised until the target size of less than 75 µm was achieved to ensure uniform mixing of the raw materials for efficient

pelletising. The limestone and coal optimised sample was then mixed with 0.1–1 wt per cent hydroxyethyl cellulose as the binder with the representative molecular structure shown in Figure 2.

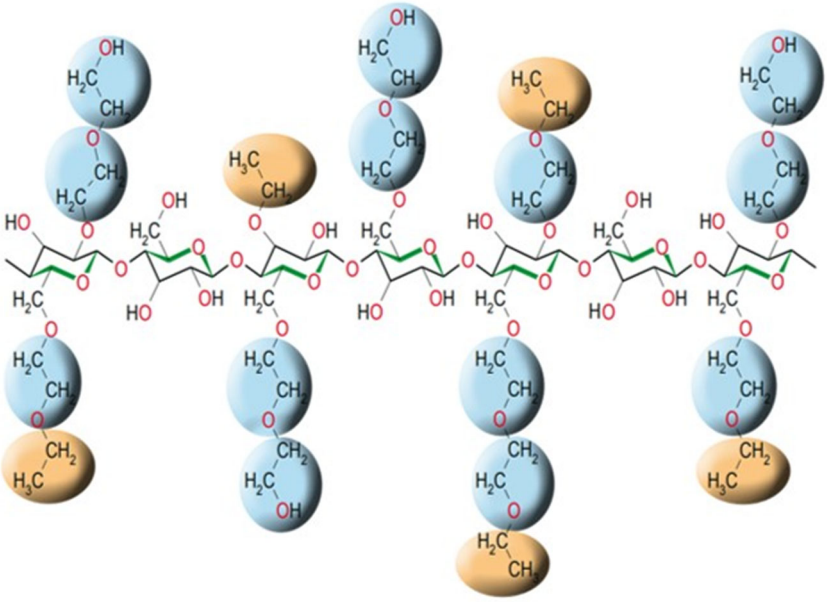

FIG 2 – Representative molecular structure of the hydroxyethyl cellulose used as the binder.

After homogenisation, a pelletising disc of 610 mm diameter, rotating at 28 rev/min and inclined at 40° was then used to make green pellets. The necessary amount of water was added to the rolling pellet feed for green pellet formation which were removed when an average target size of between 12–16 mm was attained. Drop tests were performed on the pellets by dropping randomly selected ten pellets from each batch on a steel plate at a height of 45 cm. The number of drops that were required to break an individual pellet was noted as the drop number. The average of the ten pellets was then considered as the drop number of that batch.

$$Drop\ number_{batch} = \frac{\sum drop\ number\ of\ each\ pellet}{10}$$

Dry compressive strength was done using the Electronic Universal Testing Machine (ADW-50S) on 20 pellets. The average maximum load a pellet was able to crack was recorded as compressive strength in units of kg/pellet.

RESULTS AND DISCUSSION

Effect of hydroxyethyl cellulose on the drop index and the dry compressive strength

Hydroxyethyl cellulose was added as a binder and the effects on the drop index of the composite pellets are shown in Figure 3. Drop tests are essential to ensure that the pellets have enough strength to minimise fractures and breakages during green pellet handling (Geerdes, 2009).

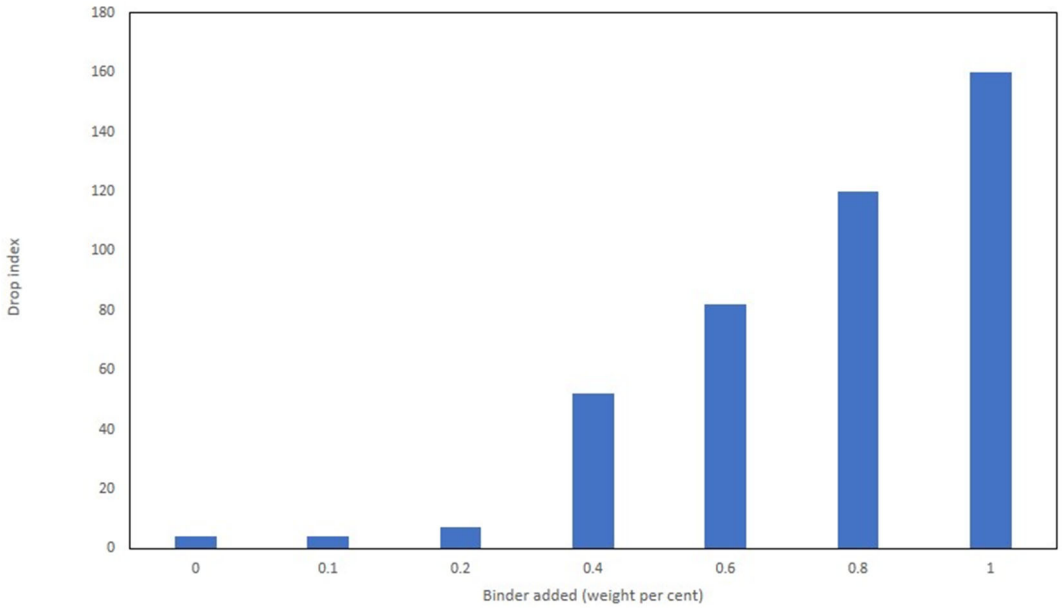

FIG 3 – Drop index with increasing binder.

The addition of a small amount of hydroxyethyl cellulose binder of up to 0.2 wt per cent showed little improvement in the drop index. The drop index was largely improved from 0.4 wt per cent addition onwards. This was largely due to the capillary forces that are imparted on the material through the action of the binder (Halt and Kawatra, 2014) the hydrophilic groups on the organic groups allow for the binder to be effectively dispersed and form strong capillary forces that result in an operative binding effect (Kawatra and Claremboux, 2022). Since the industrial required drop index is above 4 (Sivrikaya and Ali, 2012), the proposed recommended addition level of this binder was 0.4 wt per cent otherwise any addition above this will result in an unnecessary cost of production.

A minimum dry pellet strength is necessary so that pellets can withstand a load of pellet layers or pressure from gases flowing through the charge on traveling grates (Sivrikaya and Arol, 2014). Figure 4 shows the effect of binder addition on the dry compressive strength of the composite pellets.

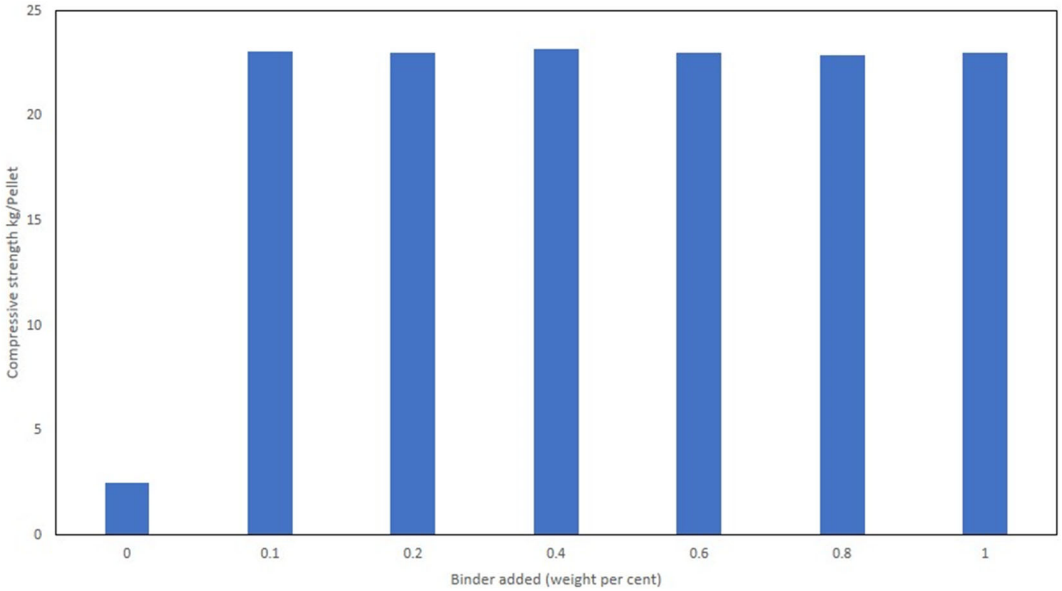

FIG 4 – Dry compressive strength with an increasing binder.

The addition of the binder improved the dry compressive strength from 2.5 kg/pellet to around 23 kg/pellet irrespective of the amount of binder added. This can again be attributed to the chemical structure of the organic binder where the hydrophilic groups aid in the dispersion of the binder into the binding medium resulting in a good binding effect (Ngara *et al*, 2023). Investigations show that

hydroxyl groups are good hydrophilic groups and their presence in hydroxyethyl cellulose may be attributed to the increase in the physical strength of the pellets (Guanzhou *et al*, 2002).

This improvement in the strength of the green pellet is a desirable characteristic during material handling in mass production of the pellets. The dry compressive strength of the pellets was well above the industrial requirement of at least 2.2 kg/pellet (Sivrikaya and Ali, 2012). The recommended hydroxyethyl cellulose addition level was determined to be 0.4 wt per cent basing on both the drop number and the dry compression strength. However more investigation into the indurated compression strength is needed to fully understand the behaviour of the produced pellets.

CONCLUSIONS

The organic binder used in this study, hydroxyethyl cellulose, increased the physical strength of the green pellets as indicated by the results of the drop index and the dry compressive strength. The drop index increases significantly from 0.4 wt per cent to 52 which was then recommended as the optimum amount of binder addition. Any further increase in the amount of binder was deemed to be an unnecessary cost on the production of the pellets since the drop index value at 0.4 wt per cent was above the industrial minimum requirement. The dry compressive strength of the composite pellets upon the addition of the organic binder increased, ranging above 20 kg/pellet for all values of binder from 0.1–1 wt per cent. It can be concluded that the optimum amount of hydroxyethyl cellulose binder for the palletisation of Zimbabwean limonite-ore carbon composite pellets is 0.4 wt per cent. However more results on the indurated compression strength and other properties like the reduction degradation index, swelling index, and the reducibility test are required to fully understand the behaviour of the produced pellets.

REFERENCES

Bureau of Indian Standards, 1984. IS:1350-1 (1984): Methods of Test for Coal and Coke, Part I: Proximate Analysis [PCD 7: Solid Mineral Fuels] [online]. Available from: <https://law.resource.org/pub/in/bis/S11/is.1350.1.1984.pdf>

Chisahwira, T, Masuka, S M, Maritsa, S and Chwandika, E K, 2023. The use of Zimbabwean limonite-coal composite pellet as a sustainable feed for pig iron production, in *Proceedings of Iron Ore 2023 Conference*, p 391 (The Australasian Institute of Mining and Metallurgy: Melbourne).

Clout, J M F and Manuel, J R, 2015. Mineralogical, Chemical and physical characteristics of iron ore, in *Iron Ore: Mineralogy, Processing and Environmental Sustainability* (ed: L Liming), pp 45–84 (Woodhead Publishing).

Devashayam, S, 2018. A novel iron ore pelletization for increased strength under ambient conditions, *Sustainable Materials and Technologies*, 17:1–27.

Eisele, T C and Kawatra, S K, 2003. A review of binders in iron ore pelletization, *Mineral Processing and Extractive Metallurgy Review*, 24:1–90.

Geerdes, M, 2009. The Ore Burden: Sinter, Pellets, Lump Ore, in *Morden Blast Furnace Iron Making: An Introduction*, pp 31–35 (IOS Press: Amsterdam).

Guanzhou, Q, Tao, J, Hongxu, L and Dianzou, W, 2002. Functions and molecular structure of organic binders for iron ore pelletization, *Colloids and Surfaces A: Physicochemical Engineering Aspects*, 224:11–22.

Halt, J A and Kawatra, S, 2014. Review of organic binders for iron ore concentrate agglomeration, *Minerals and Metallurgical Properties*, 24(1):73–94.

International Energy Agency (IEA), 2023. Energy Technology Perspectives 2023, IEA. Available from: <https://www.iea.org/reports/energy-technology-perspectives-2023>

Kawatra, S K and Claremboux, V, 2022. Iron ore pelletisation: part, I, fundamentals, *Mineral Processing and Extractive Metallurgy Review*, 43(4):1–16.

Liang, Z, Peng, X, Haung, Z, Li, J, Yi, L, Houng, B and Chen, C, 2023. The innovative methodology for comprehensive utilization of refractory low-grade iron ores, *Powder Technology*, 418(15):118283.

Ngara, T, Mavengere, S, Bright, S and Mapamba, L, 2023. Investigating the effectiveness of organic binders as an alternative to bentonite in the pelletization of low-grade iron ore, *Physicochemical Problems of Mineral Processing*, 59(6):1–12.

Sivrikaya, O and Ali, I, 2012. The bonding/strengthening mechanism of colemanite added organic binders in iron ore pelletization, *International Journal of Minerals Processing*, pp 90–100.

Sivrikaya, O and Arol, A, 2014. Alternative binders to bentonite for iron ore pelletizing, Part I: Effects on physical and mechanical properties, *Holos*, 3:94–103. https://doi.org/10.15628/holos.2014.1758

State-of-the-art of electroslag refining and challenges in the control of ingot cleanness

DOI: 10.62053/ODTY2070

L Medovar[1], G Stovpchenko[2] and G Jianjun[3]

1. Foreign Chief Scientist, Tianjin Heavy Industries Research and Development Co, Ltd, Tianjin 300457, China; EO Paton Electric Welding Institute of NASU, Kyiv 03150, Ukraine. Email: medovar@ukr.net; medovar@cfhi.com
2. Foreign Chief Scientist, Tianjin Heavy Industries Research and Development Co, Ltd, Tianjin 300457, China; EO Paton Electric Welding Institute of NASU, Kyiv 03150, Ukraine. Email: anna_stovpchenko@ukr.net; stovpchenko@cfhi.com
3. Head of Steelmaking Department, Tianjin Heavy Industries Research and Development Co, Ltd, Tianjin 300457, China. Email: guojj@cfhi.com

ABSTRACT

Electroslag remelting (ESR) today and into the future, will still be the main process for producing high-quality ingots by suppressing segregation, not just refining chemical composition from impurities. This paper analyses state-of-the-art electroslag refining with a focus on ESR with consumable electrodes, and recent technology with liquid metal supply (ESR LM) in view of their refining abilities and development trends, taking into consideration that the size of the ingots required by industry continues to grow, and the composition of new materials sophisticates to withstand increasingly higher mechanical and temperature loads . The yield of suitable metal in large ingots produced by conventional casting is low due to problems of element segregation by height and cross-section. For example, conventional ingots for nuclear powerplant rotors today reach nearly 700 t in weight. Attempts to directly replace such giant ingots with big-diameter ESR ingots weighing approximately 400 t were also unsuccessful because of growing segregation. Modern ESR equipment and technologies produce 200–250 t of ingots of satisfactory quality, reaching 2.5 m in diameter, implementing the change of consumable electrodes during remelting to increase ingot length. Another way to mitigate segregation is to enlarge the smaller diameter ESR ingot by a 500–800 mm coaxial layer to the desirable diameter by ESR in the current-supplying mould (CSM). Modelling and experiments prove that refining from impurities and non-metallic inclusions at ESR most effectively occurs at the slag bath and liquid metal pool interface because the ESR LM has provided the same desulfurisation. ESR's special refining capabilities in CSM come from the much longer time of LM residence shown at titanium purification from hard-melting nitride inclusions that are unremovable in vacuum arc remelting (VAR) and electron beam melting (EBM). Implementation of ESR technologies in CSM, especially with LM supply, is prospective to produce heavy enlarged and hollow forging ingots with prevented development of segregation due to dividing cross-section and reducing overheat of solidifying metal.

INTRODUCTION

Electroslag remelting (ESR) is currently the leading process for producing high-alloyed steels and alloy ingots used in critical industries. This position is due to its unique ability to refine both the chemical composition through slag treatment and the structure of the ingot by suppressing segregation, achieved through the constant renewal of the liquid metal bath of small depth.

Since Medovar and Paton made the first ingot in 1952 (Paton, Medovar and Latash, 1958; Medovar and Boyko, 1991), areas of application of electroslag remelting were widened and partially changed due to rethinking its role and importance. The development of ladle refining, and later the widespread use of additional degassing at vacuum treatment of steel, have led to a widespread reduction in the application of ESR furnaces for nearly two decades at the end of the last century.

The primary objectives now are to improve ESR metal's homogeneity and cleanness for producing sophisticated steel and alloy grades, reduce production costs and increase the competitiveness of the ESR. Today's trends include increasing the ESR ingot weight, improving automation and efficiency of equipment and recent interest in new specified slag systems intended for certain steel and alloy grades. Improvements in ESR technology and new innovative technical solutions for ESR

equipment are crucial for product competitiveness, given that the demand for high-quality steels and alloys is expected to continue to rise in the coming years.

Heavy mechanical engineering has significantly progressed in recent years. Specifically, there has been an impressive intensification in the power of certain machines, industrial vessels, and aggregates. This expansion in the power of a single unit has been accompanied by an equally impressive rise in the size of their components and parts and the temperature and pressure in production processes where these machines are in use.

One of the biggest consumers of heavy metal parts is the power sector. Renewables (wind and photovoltaic power) become major electric power supply sources worldwide, but their output fluctuates daylong, destabilising the power system. That means that fossil fuel energy now and nuclear energy in the future are necessary to compensate power systems to deal with fluctuations in renewable output and customer demand. As a result, the manufacturing of big-size steel ingots and forgings from them will grow. The same tendency is in nuclear energy, the petrochemical industry, metallurgy, etc. For example, advanced ultra-supercritical steam turbine rotors operating at temperatures exceeding 700°C and pressure surpassing 30 MPa require clean steels and alloys with dense, stable, homogenous structures.

What makes ESR unique is its ability to combine remelting and gradual solidification of a continuously renewed liquid metal pool in a single process. This results in the formation of ingots that are much more chemically homogeneous and have a surface ready to be deformed due to a thin slag skin. Naturally, the constant complication requirements to products evoke new ESR technologies and equipment, which have undergone several advancements to keep up with the industry's ever-increasing demands. Therefore, the article aims to analyse the state-of-the-art electroslag remelting and identify trends for further development and improvement of technologies and equipment.

A SHORT LOOK AT THE HISTORY OF ELECTROSLAG REMELTING TECHNOLOGIES AND EQUIPMENT DEVELOPMENT

The priority in the ESR invention in its modern state (Figure 1a) with the use of alternating current of industrial frequency belongs to Borys Medovar (1916–2000) and Borys Paton (1918–2021). To eliminate misunderstandings that sometimes arise, we emphasise that in the 'Kellogg process', invented a decade earlier in the USA by H Hopkins, direct current was used as it was mistakenly assumed that the current flow through the slag was in the form of a soft arc (Hopkins, 1940) and the purpose of direct current usage was to minimise arc instability.

The first pilot furnace for melting 500 kg round ingots (type R-909) was built in 1956–1957 under Borys Medovar's leadership (Figure 1b).

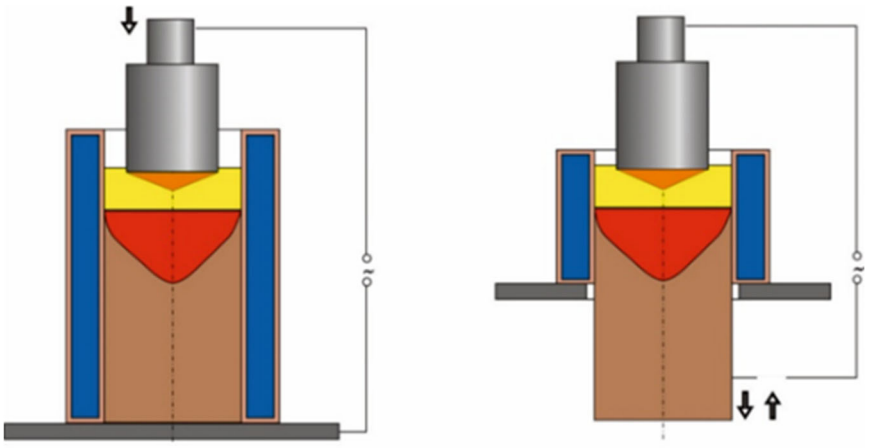

(a)

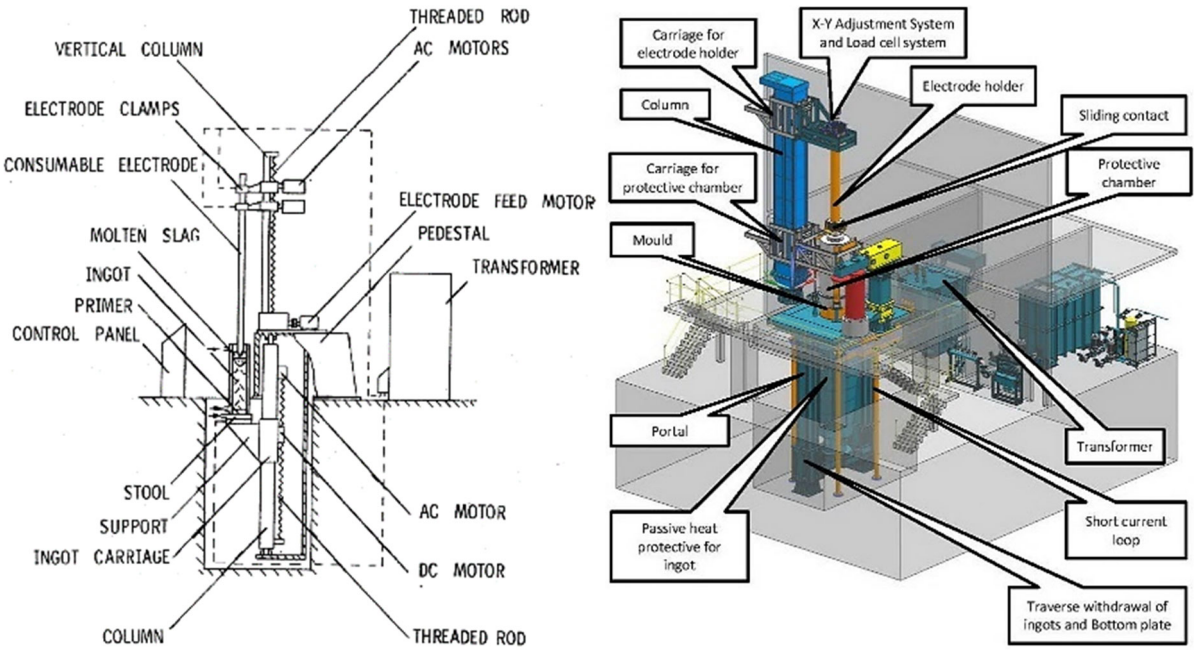

FIG 1 – The most common diagrams (a) of ESR remelting in a stationary mould (left) and short collar mould (right), the layout of the first furnace R-909 (b) of modern ESR process, and today's ESR plant structure (c).

The world's first electroslag furnace was put into industrial operation in 1958 at the Dniprospetsstal electrometallurgical plant in Zaporizhzhia, Ukraine. During the 70 years of electroslag remelting, engineers from many countries have invented, worked out, tested, or commercialised in the industry several drastic improvements of the original ESR of the consumable electrode and new types of related technologies.

Among them, the most widespread ESR technologies have become:

- Inert Gas Electroslag Remelting (IESR) – single phase one consumable electrode remelting at atmospheric pressure in a closed chamber filled with protective inert gas (argon) is today's benchmark process. Change of the consumable electrodes is used to reduce the height of the furnace (Holzgruber and Holzgruber, 2001; Jarczyk and Franz, 2012; Arh, Podgornik and Burja, 2016).
- Pressure Electroslag Remelting (PESR) – single phase one consumable electrode remelting in a closed chamber filled with nitrogen for melting steels with an excess nitrogen content (Stein and Menzel, 2014; Ritzenhoff *et al*, 2013).
- Three-phase ESR, using three parallel electrodes connected to a three-phase line or six electrodes arranged as three bifilar pairs, is still in use in China (Liu *et al*, 2021) for stainless and other steel remelting. Despite difficulties in providing reliable protection atmosphere and uneven melting of electrodes in bifilar pairs, it is a very good decision due to even electrical load.

The following options of ESR with a consumable electrode in the copper water-cooled mould are less general but have a certain potential in areas of their use:

- Electroslag Remelting Under Vacuum (VAC-ESR or VSR-Vacuum Electroslag Remelting) is designed for deep degassing during remelting of superalloys and titanium alloys, the efficiency of which was not high enough due to the barrier effect of the slag layer or gas evacuation and because of evaporation of slag components (Radwitz, Scholz and Friedrich, 2013).
- Arc Slag Remelting (ASR) is an energy-saving process of obtaining high-nitrogen steels and titanium and its alloys by remelting a consumable electrode due to an electric arc between it and the surface of the liquid slag bath (Medovar, 1997; Paton *et al*, 2004).

The recent technologies using the short collar current-supplying (synonym – current conductive) mould (Figure 2a) are still of interest:

- Electroslag Rapid Remelting Process (ESRR) for high-productive manufacturing of high-alloyed steels and superalloys by remelting a single large-diameter electrode (3–10 times larger than the ingot) in a T-shaped mould connected with a power source to increase process productivity (Alghisi, Milano and Pazienza, 2005; Karimi-Sibaki *et al*, 2018).
- Electroslag Remelting with Two Circuits (ESR TC) for gradual formation of the homogenous ingot from segregation-prone steels and superalloys (Medovar *et al*, 2005) due to breaking the rigid dependence between the speed of electrode melting and ingot formation to control of heat input and temperature of slag and metal baths to form shallow liquid metal bath, which is difficult to achieve in a standard ESR (Figure 2b).

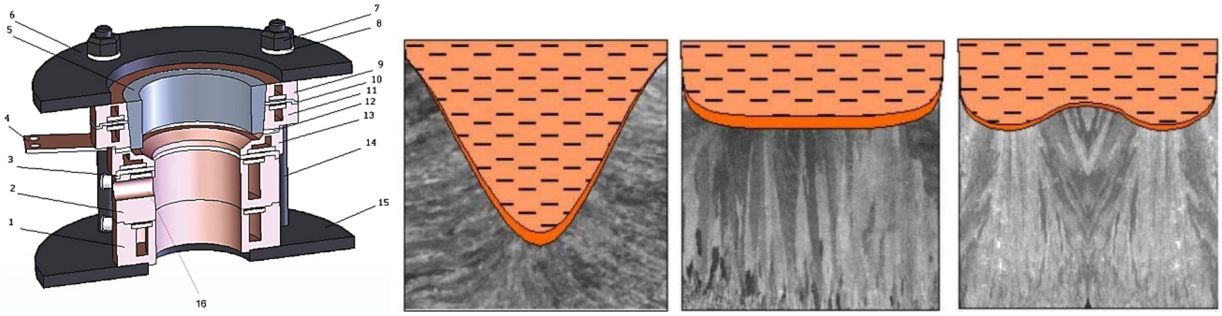

(a) (b)

FIG 2 – Current supplying mold structure: (a) 1, 2 – forming section; 3, 8, 10, 12 – electric insulation; 7 – nut; 4 – current supplying bus; 5 – protective graphite ring; 6 – upper flange; 9, 11 – current supplying section; 13 – dividing section; 14 – stud; 15 – lower flange; 16 – metal level sensor); and liquid metal pool shape; (b) at different ESR methods: from left to right – standard ESR, ESR TC, ESR LM (Medovar, *et al*, 2005).

Extra opportunities are provided by electroslag processes using a current-supplying mould (Medovar, Stovpchenko and Petrenko, 2016; Paton *et al*, 2007; Medovar *et al*, 2018) without consumable electrodes:

- Electroslag Surfacing by and recycling of discrete materials (fines, powder, shavings etc) in a current supplying mould for the production or renewal of a working layer of rolling mill rolls, rotors of electric motors, stamps of high-speed and tool steels, tungsten carbides etc (Kuskov *et al*, 2018).
- Electroslag Refining using Liquid Metal (ESR LM) and Electroslag Surfacing by Liquid Metal – ESS LM (Figure 2b) for the production of highly homogeneous ingots of solid cross-section, hollow ingots and composites with coaxial or horizontal arrangement of layers from steels and alloys prone to segregation ((Medovar *et al*, 2018; Medovar *et al*, 2020).

This article compares the two most different technologies—classical ESR with consumable electrodes and ESR LM—to better understand and highlight their abilities to refine a metal's chemical composition and structure.

ELECTROSLAG TECHNOLOGIES' ABILITY TO REFINE THE CHEMICAL COMPOSITION OF METALS

Along with the term 'electroslag remelting', another name for this technology in English-language sources is 'electroslag refining'. The latter retained the context associated with one of the first purposes of the process – remelting ingots or rolled products rejected due to the high content of impurities, primarily sulfur and non-metallic inclusions (NMI). ESR technologies are limited in refining agent addition during the process, first, because of the lack of ability to control resulting changes in both slag and metal phases.

Refining from impurities and NMI during ESR is ensured by the use of fluoride and fluoride-oxide slags (system of CaF_2–Al_2O_3–CaO–(SiO_2, MgO)), which were initially selected from the experience of electro-slag welding. Pure calcium fluoride was the first slag for the ESR to maximise the refining effect from oxide, sulfide and nitrides. CaF_2 is still used today for remelting the most critical alloys (including titanium alloys) despite its high price, low conductivity (which makes an inversely proportional effect on energy consumption at ESR) and some technological limitations.

From the point of view of refining, the main impurity and alloying elements involved in the electroslag remelting of steels and nickel-based alloys can be divided into four main groups (Table 1).

TABLE 1

Elements classification on their behaviour in the ESR slag-metal system concerning Fe- and Ni-based alloys.

Process components	Elements present in metal, absent in initial slag and able to react with slag	Elements present in both phases, and able to transfer from one to another via exchange and redox reactions	Elements present in slag, absent in metal due to extra low solubility and acting in slag-metal reactions	Trace elements present in steel, absent in slag and do not react with slag
Consumable electrode	Fe, Mn, C, Cr, Ti, Mo, V, W, B	O, N, S, H, Al, Si		P, Ni, Cu, Sn, Pb, Zn, Sb
Slag: CaF_2–Al_2O_3–CaO–(SiO_2, MgO)		S^{2-}, O^{2-}, N^{4-}, $3Al^{3+}$, Si^{4+}	F-, Ca^{2+}, Mg^{2+}, Na^{+}, K^{+}	
Reactions (compounds are coming into slag or forms NMI)	$X[Me]+Y\{O^{2-}\} = \{Me_xO_y\}$ $[Me] + \{S2^{-}\} = \{3MeS\}$ $\{Me_xO_y\}+\{O^{2-}\}=Me_xO_{y+1}\}$ $[Me] + \{N2^{-}\} = \{MeN\}$			No
Ingot	Fe↓, Mn↓,C↓, B↓, Cr↓, Ti↓, V↓, Mo↔, W↔,	S↓↓, N↔ O↑↓, Al↑↓, Si↑↓- Depending on concentrations	NMI of CaS, CaO, MgO, MgS and their complexes with other oxides and nitrides	P, Ni, Cu, Sn, Pb, Zn, Sb etc: all ↔
In process slag	FeO↑↑, MnO↑↑, MnS↑ ↑, B_2O_3↑, BN↑, Cr_2O_3↑, TiO_2↑, TiN, V_2O_5↑, MoO_3↔, WO_3 ↔	CaS↑↑ Al_2O_3↑↑↓, SiO_2↑↑↓↓, MgS↑, MgO↑ Depending on concentrations		No

1. Elements that are contained in the metal and are absent in the initial slag but can react with its components, which can pass from the metal to the slag and *vice versa* as a result of displacement or redox reactions, mainly forming oxides, sulfides, nitrides, or carbides. These are manganese, iron, carbon, chromium, vanadium, molybdenum, and other alloying elements, the oxidation of which violates the specified chemical composition, structure and steel properties. The same situation applies to titanium and boron, in which oxide addition in slag is made to prevent their enhanced oxidation, trying to shift the equilibrium in favour of metal.
2. Elements are contained in the slag and participate in slag-metal reactions but are not in the metal due to their vanishingly low solubility. These are fluorine, calcium, magnesium, alkali and alkaline earth metals. The oxides of the last group of elements ensure the removal of sulfur and change the composition of the initial non-metallic oxide-type inclusions from a consumable electrode.
3. Elements are present in both phases, which can transfer from one phase to another via an exchange in redox reactions. These are, first of all, sulfur, oxygen and nitrogen, the removal

of which from the metal composition is one of the tasks of the process, the realisation degree of which depends on their initial concentration (at high initial content in the metal the refining occurs and *vice versa*). In addition to impurities, aluminium and silicon play a substantial role in the refining processes, competing in redox reactions involving oxygen being an active steel deoxidiser and, simultaneously, are contained as oxides in the initial ESR slag in significant quantities.

4. Trace elements are present in the steel in low concentrations and are not existent in and interact with an initial slag. These are phosphorus, nickel, copper, lead, tin and others. Accordingly, metal refining from these elements in the ESR process using slag is practically impossible.

The following refining actions occur at the remelting with slags of CaF_2–Al_2O_3–CaO–(SiO_2, MgO) system that is typical for steels and nickel-base alloys:

- chemical interactions between the slag and metal (redox reactions, ie sulfides, oxides, nitrides formations/removal), which happen at all interfaces between slag and metal (Figure 3) and NMI removal to slag accompanied by change in their chemical composition and new inclusions formation occurring by:
  - NMI interaction with slag on all interfaces resulting in their composition change or complex particle formation.
  - Elements from NMI dissolve in a metal (thermal dissolution with no contact with slag) and re-precipitate at a temperature reducing while cooling and solidification form new particles in the metal, ie saturated by liquates near the growing solidification front (Burja *et al*, 2018; Persson *et al*, 2020).

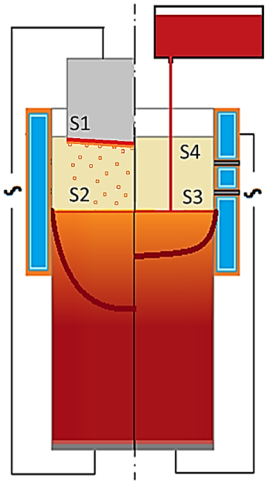

FIG 3 – The slag-metal interaction surfaces S1–S4 (description in text) at the ESR with a consumable electrode, left part, and ESR with liquid metal, right part (Stovpchenko *et al,* 2020).

The efficiency of NMI removal from metal depends on their properties (size, density, solid or liquid states and their surface tension with metal and slag) and the shapes and intensity of macro- and microflows in a metal pool. Depending on the combination of these factors, the non-metallic inclusions can be either assimilated by the slag surface, captured by the solidification front or still be circulating until the metal's last portions solidify.

Many years of ESR refining practice have proven a drastic reduction in the size and number of NMI and their type and composition changes. Endogenous particles of oxides, nitrides, sulfides and oxysulfides mostly represent NMI in ESR metals. However, exogenous inclusions from the lining of the steel-teeming ladle or tundish still occur (often, they differ by a high magnesium or silicon content depending on the lining type and casting powder). The size of inclusions found in laboratory-scale trials is usually between 1–5 μm but more commonly ≤2 μm. However, larger inclusions are often present in industrial-size ingots, especially when larger sample areas are analysed (Persson *et al*, 2021). The high thermal inertia of ESR and steady remelting conditions make it possible to organise

microalloying the metal from slag. Still, control of results is post-melted, which is impossible to correct. The most used recently is boron-bearing additions to slag to keep stable boron content in the ESR ingot.

THE CONTRIBUTION OF SLAG-METAL INTERACTION SURFACES IN REFINING AT ELECTROSLAG TECHNOLOGIES

The issue about the main place of metal refining at electroslag remelting was disputable for years. To answer the question of the contribution of different interaction surfaces, we made two ingots using two different technologies in comparable conditions. In our comparative experiments, we use the same T-shape current supplying mould (Figure 1a) and produce two ingots from the same chemistry metal by standard ESR and by electroslag refining by liquid metal pouring (ESR LM). The same current supplying mould (180 mm in diameter), steel grade St45 and ANF29 slag (layer height of 200 mm) were used at the ESR and ESR LM to ensure comparable conditions. Process productivity was 120–160 kg/h (speed of ingot withdrawal – 15–17 mm/min). A comparison of the interaction surfaces was made for a 160 kg/h feed rate, which is typical for the stationary stage. The size and number of drops were measured and counted on a 160 mm electrode after its tip was rapidly frozen. The specific power consumption at ESR averaged 1350 kWh/ton of ingot (due to the necessity to melt a solid electrode), while at ESR LM – 900 kWh/ton at the same productivity level (Stovpchenko *et al*, 2020).

We compared cross-sections of contact surfaces and measured sulfur content before and after both technologies. In the standard ESR process, slag-metal interaction occurs on three contact surfaces (Figure 3).

The first surface (S1) belongs to the liquid metal film at the tip of the melting consumable electrode contacting with slag. The second area (S2) is the surface of the drops of liquid metal rain inside a slag layer. The third area (S3) is the interface between the liquid slag bath and metal pool – the same for both ESR processes with and without electrodes. The S4 is the analogue of S2, which refers to the square area of a liquid metal stream in the ESR LM process that works without consumable electrodes. A formal comparison of the values of slag-metal contact surfaces of a standard ESR with a consumable electrode and an ESR LM without an electrode supply was performed.

According to the characteristic filling ratio, the molten metal film surface (S1) on the electrode tip is 0.5 to 0.7 of the ingot surface (Figure 4a).

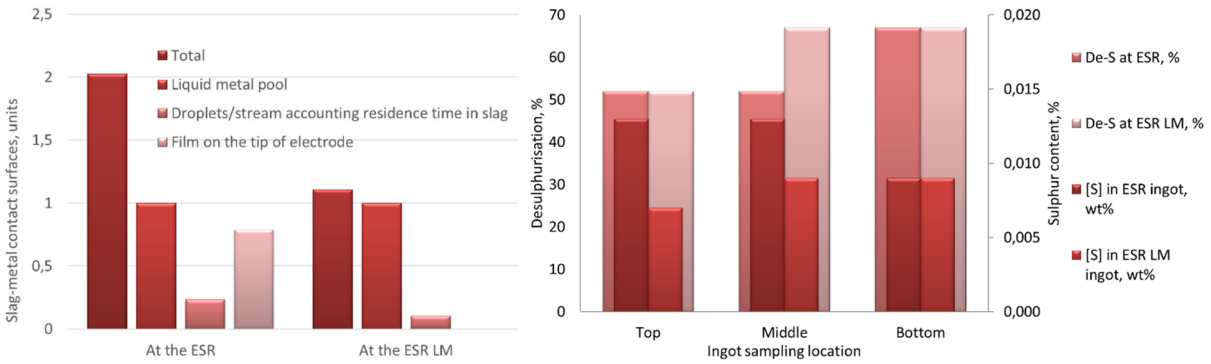

FIG 4 – Geometrically defined values of slag-metal contact surfaces (a) and the sulfur content and degree of desulfurisation (b) in ESR and ESR LM ingots at comparable conditions (Stovpchenko *et al,* 2020).

In our direct experiment, the total interface of the metal and slag phases in ESR was twice as large as that in ESR LM. Specifically, it was 2.03 in ESR and 1.12 in ESR LM. The main difference was due to the electrode surface, which was 0.79 in our experiment (due to the T-shape mould used).

The size of drops is directly related to the diameter of an electrode and can range from 1 to 10 mm found by direct experiments (Campbell, 1970) and numerical simulations (Kharicha, Ludwig and Wu, 2011; Wang *et al*, 2016; Dong *et al*, 2016; Liu *et al*, 2021). The largest drops have an equivalent

diameter of 10 to 15 mm and the smallest drops measure 1 to 4 mm. Due to the small size and short residence time in the slag of the drops, the part of their surface constitutes 0.23 of the liquid metal pool. During the ESR LM process, the liquid metal stream (S4) has permanent contact with the slag bath and can be broken into smaller drops. For the sake of simplicity, we can ignore the drop formation and express the interaction surface as a cylinder having a stream diameter (up to 20 mm – 0.11 of the surface of the metal bath) and a length that matches the mass of the metal at the same productivity as a standard ESR process.

Direct comparison of sulfur content before and after ESR and ESR LM (Figure 4b) shows the same value of desulfurisation (Stovpchenko *et al*, 2020), proving that the contact surface between a slag bath and metal pool is the most effective interface in refining (first of all from sulfide and oxysulfide non-metallic inclusions).

It is worth highlighting that despite the absence of film at the tip of the electrode and another type of metal transfer through the slag (a stream instead of drops), the refining ability of the ESR-LM is the same. The reason is that, due to the lower density of non-metallic inclusions, they move towards the slag under the influence of the Archimedes force, and, in addition, the value of surface tension at a flat interface between slag and metal bath is less than at near-spherical shape surface for metal droplets in slag. In the film at the tip of the electrodes, the conditions for NMI removal are even worse because the Archimedes force counteracts their movement to the slag bath (Figure 5).

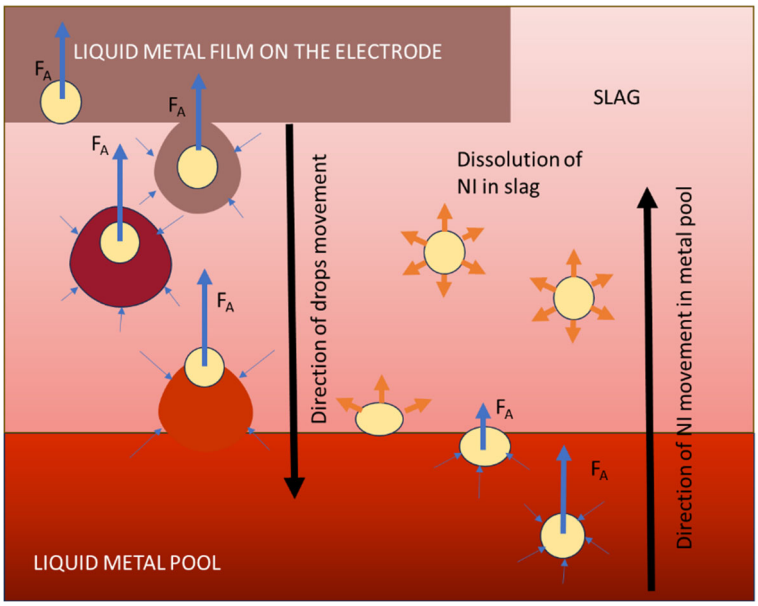

FIG 5 – Simplified scheme illustrating NMI (light spheres) movement on the different slag-metal contact at standard ESR: F_A is Archimede force, thin arrows show elements exchange between metal drops and slags.

The physical reason is that non-metallic inclusions move towards the slag under the influence of hydrostatic lift force (Archimedes' force – F_A) due to their lower density in comparison with liquid metal (three times and more difference). In addition, the value of surface tension at a flat interface between the slag bath and metal pool is less than at droplets having a near-spherical surface in slag. In a film at the tip of electrodes, the action of Archimedes' force on non-metallic inclusions is directed opposite to the location of the slag bath. In the liquid drops, the inner friction forces make them turbulent inside, make more difficult for NMI to be assimilated by slag. For these reasons, the main refining action of NMI removal much more easily occurs on the contact surface of the slag and metal baths and not in a film on the tip of the electrode.

Performed simulation of liquid metal drops' movement in the slag also shows that already during the passage of metal drops having size 2–10 mm through a 200 mm layer of slag, they heat up to the temperature of the slag (modelling parameters and more detailed results are available in (Stovpchenko *et al*, 2020). Large droplets move faster than small ones due to their internal flows and turbulence, making Stokes' law-based predictions inaccurate. Classical ESR has smaller droplets

that move more slowly and heat up more than the ESR LM being compared. Turbulent flows (inside bigger liquid drops (from 6 to 10 mm) deformed their shape from sphere to flatter spheroid and also can cause their splitting into smaller parts, increasing the contact surface between metal and slag (Krivtsun *et al*, 2021).

The extrapolation of the established features of the movement of solid and liquid drops explains the better removal of liquid-state non-metallic inclusions. At smaller sizes, the difference in movement speeds between solid and liquid particles tends to be zero due to smaller inner friction in liquids, but the separation of liquid inclusions from steel proceeds similarly. In contrast, the assimilation of liquid inclusions in slag goes much easier without diffusion restrictions. Moreover, at a residence of liquid metal drops in oxygen-bearing ionic slag with free O^{2-} anion, oxidation of active elements from a liquid metal and other reactions between it and slag components are unavoidable and forming non-metallic inclusions can be removed from the liquid metal pool mainly.

Slag temperature also affects refining ability at the ESR because of its increasing enhanced dissolution of previously formed NMI and their assimilation due to lower viscosity and rate of chemical reactions between slag and metal, resulting in new NMI formation in the liquid metal drops and pool. The temperature of the slag bath at ESR with a consumable electrode is typically estimated to be 100–250 K higher than the liquidus temperature of the steel or alloy and of metal droplets overheat – 90–100°C (Klyuev and Volkov, 1984). The conventional ESR process uses the resistive type of heating that requires high overheating of slag to ensure contact melting of an electrode immersed in a slag, but ESR LM is devoid of this shortcoming. Due to an induction heated furnace, the liquid metal overheating is minimised to keep metal liquid during the short period (seconds) to be poured into the current supplying mould.

A decrease in the temperature of the slag bath is also favourable due to reducing the evaporation of volatile fluorides, which, along with exchange reactions, causes changes in the chemical composition and properties of the slag. No less important is the slag bath temperature for ESR ingot formation. It is the most important factor defining ESR process productivity, flow conditions and depth of the liquid metal pool and creating a high gradient of temperature is crucial for the solidification pattern and structure of the formed ingot.

Comparing the standard ESR and ESR LM allows asserting that the physicochemical conditions of refining in the ESR LM are more favourable due to the less slag-metal contact at the droplet stage and the consumable electrode absence with liquid metal film on it. At these contact surfaces in the standard ESR, conditions for non-metallic inclusion removal are less convenient and high temperatures can cause oxidation of elements from the metal composition. There is no need for electrode melting, resulting in reduced slag heating and no overheat of metal that comes with preset temperature from induction heated furnace (temperature 70–95° less than for drops at ESR), allowing the forming of a shallower liquid metal bath that is favourable for the solidification control of ingots from segregation-prone grades of steels and alloys, where ESR LM technology can be prospective. Moreover, no need to melt the electrodes reduces electricity consumption on the value of heat required for the solid-liquid phase transition.

Despite the attractiveness of ESR with the liquid metal, it has a specific niche. The standard ESR with consumable electrodes in protective gas is often the perfect decision, especially when strict gas protection is critical and stationary mould is preferable. The current supplying mould works with ingot withdrawing, which requires a more precise operation; thus, it is worth using the ESR with consumable electrodes when a very low melting rate and flat liquid metal pool are needed to reduce segregation or for hollow ingot manufacturing.

Summarising, all ESR technologies stand apart from the steelmaking primary and secondary refining methods: it is refining by high-temperature slag only; other possible refining actions are not effective because of no direct contact of gas phase or alloying additives with liquid metal, causing difficulties with vacuum treatment and alloying (microalloying) organisation and control. Despite the much higher temperature of the ESR process than any treatment in traditional steelmaking, single melts go hours and decent hours to receive a very dense dendrite structure with minimal segregation due to good conditions in water-cooled copper mould with the gradual renewal of liquid metal pool for metal solidification control and ingot structure refining.

Specific case – ESR of titanium as a way to dissolve titanium nitrides

It is often overlooked that the first ESR plant was constructed to manufacture titanium ingots. Being the first to attempt this was difficult and led to dangerous accidents, which prevented commercialisation for many years. High reactivity of titanium at liquidus temperatures, severe limitations on flux compositions and only alkaline-earth and lanthanide-series fluorides are suitable for titanium ESR (Paton *et al*, 1999).

Nevertheless, the research made worldwide on lab and pilot scales. The produced commercial batches of titanium and titanium alloys prove that it can compete with other remelting technologies (such as vacuum arc remelting (VAR) and electron beam cold hearth melting (EBCHM)) for titanium manufacturing in terms of ingot quality and product efficiency and even have an advantage – titanium refining from nitride inclusions, which was shown experimentally at titanium sponge remelting using ESR TC technology in the current supplying mould. The problem with hard-alpha phase defects is that the melting temperatures of these nitrogen-rich inclusions are much higher than the melting temperature of titanium itself. As a result, the time for dissolution of large inclusions coming from titanium sponge is longer than the time of their hovering in melting bath at VAR or EBCHM – standard now processes for titanium remelting.

ESR with active slags containing metallic calcium helps to accelerate the dissolution process (Figure 6), which value observed at level $2 \cdot 10^{-4}$ m/s (Paton *et al*, 1999) that is much faster than at VAR – $2.2 \cdot 10^{-6}$ m/s (Bewlay and Gigliotti, 1997) and EBM – 4.2×10^{-5} to 4.9×10^{-5} m/s (Xu *et al*, 2022).



FIG 6 – The appearance of frozen after ESR tips of the consumable electrode with the films of nitrogen-rich phase-light spots (Paton *et al,* 1999).

The successful experiments proved a perspective to include electroslag remelting of sponge as a consumable electrode or lump pieces for refining titanium from large-size nitride inclusions to achieve its uniform distribution in ingot volume before the final VAR. The ability to refine titanium from nitride inclusions gives opportunities for cost-effective commercial ingot production using ESR.

The results allow us to conclude that the slag layer at ESR works like refining media and heat buffer, helping to provide enough time for inclusions to remove being assimilated by the slag bath or to be dissolved fully or partially to be reborn in smaller sizes and even distribution. That is why ESR refines titanium from hard-to-melt titanium nitrides and white spot defects are not characteristic of the ESR ingots.

ESR TECHNOLOGIES' ABILITY IN SOLIDIFICATION CONTROL FOR INGOT STRUCTURE REFINING

The industry has three primary technologies for receiving huge forge ingots – conventional casting, casting with electroslag hot topping and electroslag remelting. It is well known that the bigger an ingot diameter is, the longer its solidification takes, resulting in an elevated degree of macro-segregation. The final portions of solidifying metal in conventionally cast ingot hold the highest concentration of elements displaced by the solidification front, shrinkage and porosity. These parts are concentrated near the centre and top of the ingot. Therefore, huge forging ingots are designed with extra-hot top parts meant to be removed. Sometimes, the whole length of the central part is removed through trepanning. Naturally, this results in a low yield from ingot to ready forging, making sense for hollow ingot manufacturing. For ordinary people, it is difficult to imagine that for manufacturing backup roll or turbine rotors for nuclear powerplants weighing 250–260 t, the cast

forging ingots of 700 t are in use (Figure 7). At heavy hollow vessels and reactors (for nuclear and petrochemical industry) manufacturing by forging from huge cast solid ingots, the metal yield to ready part also does not exceed 25–35 per cent (Medovar *et al*, 2023).

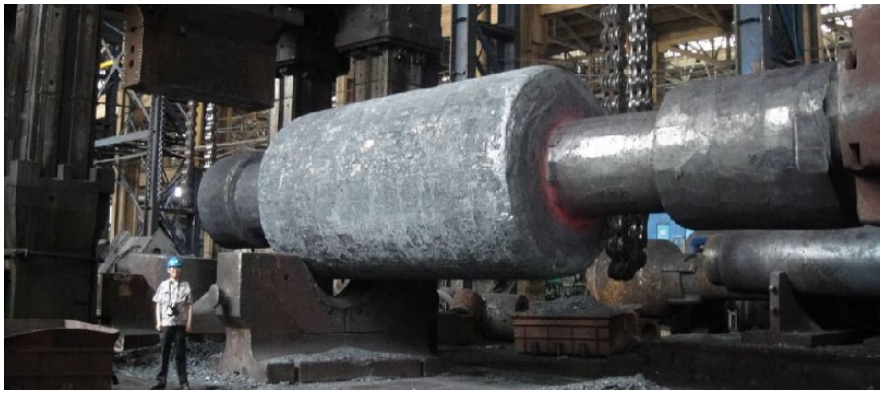

FIG 7 – Low-pressure rotor forging 408 t in weight maximal diameter 3650 mm forged from 715 t conventional casted ingot of 30Cr2Ni4MoV (Courtesy of China First Heavy Industries).

Electroslag hot topping eliminates shrinkage, and increases yield but only partially weakens segregation as it does not change the residual melt composition saturated by impurities. Chemical composition purifying helps but does not fully resolve this problem. Even at very low concentrations of segregation-prone impurities, inner defects can arise like well visible A-segregation in 20 t slab ingot (1680 × 780 mm) of 09Mn2SiV grade with sulfur content 0.004 per cent (Figure 8).

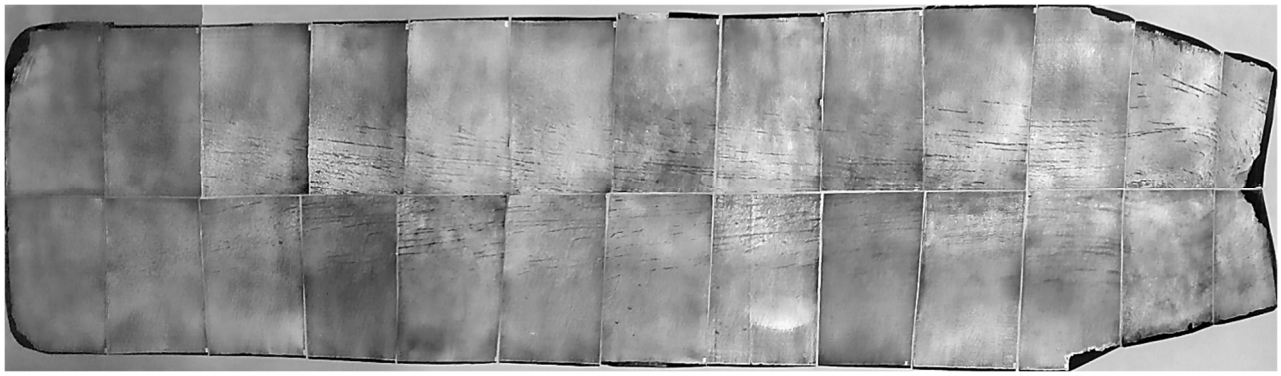

FIG 8 – Macrostructure of 20 t conventional cast slab ingot 780 mm side from 09Mn2SiV steel with sulfur content 0.004 per cent and heavy A segregation in the central part (hot etching in 50 per cent vol HCl).

The lines of A segregation form when solidification front stop – the point of columnar-to-equiaxed growth transition (CET) – a place where the heat sink is reduced, melt mixing flows low and impurities accumulate – so the non-metallic inclusions and excessive phases have enough time to grow and agglomerate. The mitigation of segregation is crucial in producing sound huge forging ingots, especially for sophisticated grades containing many alloying elements of varying physical properties and chemical activities in their composition.

The ESR rate of ingot formation is much lower than that of traditional metallurgy methods of pouring liquid metal into ingots or continuously cast billets. ESR deliberately significantly reduces the melting process productivity for the sake of solidification control for the high quality of an ingot, minimising the volume of the liquid metal pool, which helps prevent the segregation-caused redistribution of elements and formation of shrinkage defect.

The charge for the ESR is ingots or even forged or rolled billets after ladle treatment and vacuum degassing, which are pre-final products for most metallurgical applications. Naturally, the ESR with consumable electrodes is quite costly. However, the quality and yield of ESR ingot are significantly higher (85–95 per cent) because the volume of metal that solidifies in one time is smaller, its composition is constantly renewed and heat removal in a copper water-cooled mould is better than

in an iron mould. Therefore, the efficiency rule is easy: the bigger the ingot size and alloy grade price, the more effective the use of ESR. The sulfur print of the ESR ingot of the same cross-section we planned to put aside, but it occurs white because for such a cross-section, due to progressive renewal of liquid metal, the pool provides a 100 per cent dendrite structure with a density close to the theoretical value.

Today, the ESR heavy forging ingots reach 250 t in weight and 2.6 m in diameter (Kubin *et al*, 2013; Bettoni *et al*, 2014). Nevertheless, the attempts to directly replace giant cast ingots with ESR-made ingots weighing approximately 400 t were unsuccessful because of growing segregation at increasing the ingot diameter to 3.5 m and, accordingly, the volume of simultaneously solidifying metal and depth of liquid metal pool.

The bigger the diameter of the ESR ingot, the deeper the liquid metal bath became and the solidification conditions tend to approach those in a conventional ingot. The zone of equiaxed crystal appears and as a result, segregation defects worsen.

The practice has shown that the ultimate diameter (mass) of the electroslag ingot, which retains quality advantages over the usual one (cast in iron mould), is different for steels and alloys of various degrees of alloying. Thus, for carbon and low-alloy steels, this ultimate diameter of ESR ingot is 2000–2600 mm (up to 250 t), for high-alloy steels (stamping, corrosion-resistant, and high-speed steels) and alloys (including some superalloys) it is significantly less – near 1000 mm (usually it is to 20 t), and for grade Inconel 718, the critical diameter is just 500 mm (2.5–3 t). The last limitation is well known due to Professor Alec Mitchel's calculation of Local Solidification Time (LST) showing that the critical point could be reached at an ESR ingot size of 1050 mm in diameter (Figure 9).

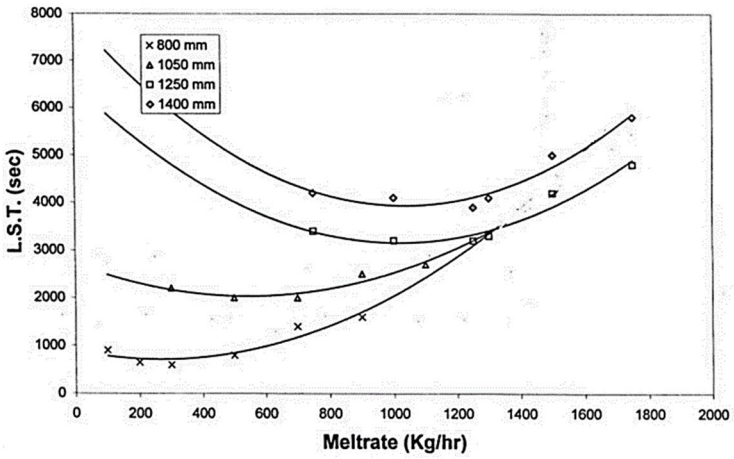

FIG 9 – LST versus ESR melt rate for different diameter ingots (Persson *et al*, 2021).

Detailed investigation (Persson *et al*, 2021) of NMI in ESR and PESR Remelted Martensitic Stainless Steel commercial ingots shows that as the ingot diameter increases and dendrite growth approaches the centre, the growth of inclusion number and size is near linear. Still, when the centre of the ingot solidifies in equiaxial mode, the increase in inclusion number and size is much higher. For the martensitic stainless steel grade 0.4Cr13MnSiV, the transition from dendritic to equiaxial solidification mode happens in the 800 to 1050 mm diameter ingot. It is also well-known that consumable electrode quality is critical for ESR ingot cleanness and casting is the critical procedure causing NMI entraining, mostly reoxidation products (Campbell, 2023).

The reason is that at traditional ESR with one consumable electrode, the ingot is formed under direct dependence of the melting speed on the electric power (which cannot be less than a certain value to provide a smooth surface). The central supply and peripheral removal of heat lead to the formation of a deep metal bath of a conical shape, which solidification can be accompanied by segregation whose manifestation is the bigger, the larger the cross-section. Therefore, the problem of producing high-quality, huge-size ingots must be resolved using approaches other than increasing diameter.

There are three ways to resolve this task with increasing ingot weight at keeping or increasing ingot diameter:

1. Increase the ESR ingot length.
2. Maximally reduce ESR technology productivity as was shown at ESR TC technology (Medovar *et al*, 2005; 2018) to keep shallow liquid metal bath and at ESR LM with an additional reduction of an overheat of slag and metal (Medovar *et al*, 2018; 2020).
3. Reduce the cross-section of solidifying metal by using an inner cooler – hollow ingot manufacturing or enlargement of smaller diameter and weight ingot into larger one. It is obvious that the reduction of a cross-section of an ingot diminishes the volume of simultaneously solidifying metal and weakens segregation (Medovar *et al*, 2011, 2023; Medovar, Stovpchenko and Petrenko, 2016).

Colleagues from INTECO (personal communication, 2023) decided to use the first approach: to keep the already reached diameter of the ingot with satisfying quality and to increase its length and weight to 300 t for a confidential customer in China. This equipment and technology implement the change of consumable electrodes during remelting, ie in fact, there is a kind of liquid phase welding of individual parts of a large ingot into a single whole and an increase in the mass of the ingot is achieved through increased length. Such giant production takes weeks and its handling is not easy.

We suppose the realisation of the last listed approach using technology with the current mould supply and producing huge weight ingots with central coolers as it is realised in hollow or enlarged ingots. Much smaller consumable electrodes (ESR TC technique) with less inherited segregation or liquid metal supply can be used for such ingot manufacturing. In the last case, we avoid the stage of consumable electrode casting/forging (rolling), where large-size NMI can be captured from the casting mixture or formed in the central part of the ingot when equiaxed dendrite growth occurs.

In traditional ESR, a depth of liquid metal bath approximates an ingot radius or more. However, at hollow or enlarged (by surfacing) ingots formation by ESR LM in current supplying mould, the liquid metal bath can be drastically reduced and reshaped, as shown in Figure 1 and proved by macrostructures in Figure 10a, 10b. The electroslag enlargement technology divides the cross-section of an electroslag ingot into coaxial layers, which are formed sequentially. Even better conditions to form the sound low-segregation ingot of heavy weight with fewer cross-sections of simultaneously solidifying metal are in ESR hollow ingot for large pipes and shell manufacturing.

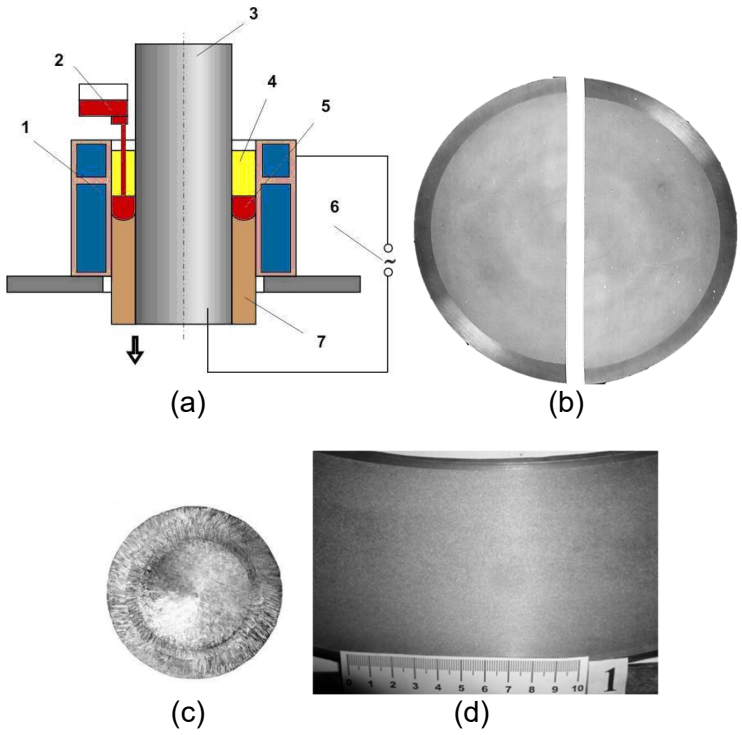

FIG 10 – ESR enlargement/surfacing/hollow ingot manufacturing principle: (a) 1 – current supplying mould; 2 – pouring furnace; 3 – ingot to enlarge/billet for surfacing/water-cooled inner mould; 4 – slag bath; 5 – liquid metal pool; 6 – power source; 7 – ready product; (b) cross-section

of 740 mm HSS surfaced rolled mill roll; (c) lab-scale enlarged ingot 70/110 mm; (d) hollow ingot wall; were produced by ESR/ESS LM (Medovar *et al,* 2018).

The enlargement, in principle, is the same method as electroslag surfacing by liquid metal (ESS LM-Figure 10a), successfully developed for surfacing a working layer of rolling mill rolls at NKMZ (Ukraine). The fusion zone is of high quality (Figure 10b), even when dissimilar steels in the central ingot and the deposited layer are connected.

Central ingot can be done by ESR or other methods providing the required quality. When the central ESR ingot is settled upside down, the parquet-like arrangement of its dendrites to dendrites of deposited layers increases metal properties.

Having an inner cooler inside the enlarged ingot solidification occurs at much better conditions than a solid one with the same diameter: sizes of carbides and the distance between axes of secondary dendrites in each layer, including the central ingot, are sufficiently less according to both modelling and experimental results (Medovar *et al*, 2009). Due to the two-stage process, the enlargement of ingots by surfacing is *a priori* more expensive than conventional ESR or ESR LM, so it is advisable to use this method for expensive alloys prone to segregation. We believe the enlargement method will find its place primarily for large-diameter forging ingots from superalloys. Since today, the maximum diameter of such ingots has been less than 1050 mm because of freckle formation. The deposition of a 500–800 mm thick layer around the central ingot with a critical diameter of 1050 mm makes it possible to obtain an ESR ingot of a size desirable for forging rotors or large rolling rolls. The appropriate equipment and slags were designed and tested to ensure the reliable connection of similar or different composition layers in composite ingots into a single whole and also hollow ingot manufacturing (Medovar *et al*, 2018; Stovpchenko *et al*, 2018), making possible start wide implementation of the ESR/ESS LM technologies.

Employing ESR technology with current supplying mould and, especially, using liquid metal, including for electro slag enlargement and hollow ingots, to produce large-diameter forging ingots with prevented development of segregation due to dividing cross-section and reducing metal overheat is prospective.

CONCLUSION

The concept of metal cleanness in ESR ingots is considered in terms of refining the metal from sulfur and non-metallic inclusions in combination with solidification control.

Analysis of trends in engineering further development and comparison of modern ESR technological varieties show prospects of electroslag technologies, including techniques with a liquid metal to achieve high-quality ingots and final products, including forgings for power engineering.

It has been demonstrated through modelling and experiments that metal melt refining from sulfides and oxysulfides most effectively goes in the contact surface between the slag bath and liquid metal pool.

The experimental studies conclusively prove that ESR has the potential to purify titanium from nitride inclusions (hard alpha phase) having high melting temperature, which are otherwise impossible to remove using other remelting methods for producing ingots from titanium and titanium alloys.

The potential of employing ESR technology with liquid metal, including electroslag enlargement, to produce large-diameter forging ingots with prevented development of segregation due to dividing cross-section and reducing slag and metal overheating is substantiated.

REFERENCES

Alghisi, D, Milano, M and Pazienza, L, 2005. From ESR to continuous CC-ESRR process: development in remelting technology towards better products and productivity, *La Metallurgia Italiana*, 1:21–32.

Arh, B, Podgornik, B and Burja, J, 2016. Electroslag remelting: A process overview, *Materiali in Tehnologije*, 50(6):971–979. https://doi.org/10.17222/mit.2016.108

Bettoni, P, Biebricher, U, Franz, H, Lissignoli, A, Paderni, A and Scholz, H, 2014. Large ESR forging ingots and their quality in production, *La Metallurgia Italiana*, 10:13–21.

Bewlay, B P and Gigliotti, M F X, 1997. Dissolution rate measurements of TiN in Ti-6242, *Acta Materialia*, 45(1):357–370. https://doi.org/10.1016/s1359-6454(96)00098-5

Burja, J, Tehovnik, F, Godec, M, Medved, J, Podgornik, B and Barbič, R, 2018. Effect of electroslag remelting on the non-metallic inclusions in H11 tool steel, *Journal of Mining and Metallurgy, Section B, Metallurgy*, 54(1):51–57. https://doi.org/10.2298/jmmb160623053b

Campbell, J, 1970. Fluid flow and droplet formation in the electroslag remelting process, *JOM*, 22(7):23–35. https://doi.org/10.1007/bf03355649

Campbell, J, 2023. A Future for Vacuum Arc Remelting and Electroslag Remelting: A Critical Perspective, *Metals*, 13(10):1634. https://doi.org/10.3390/met13101634

Dong, Y-W, Jiang, Z-H, Fan, J-X, Cao, Y-L, Hou, D and Cao, H-B, 2016. Comprehensive mathematical model for simulating electroslag remelting, *Metall Mater Trans B*, 47:1475–1488. https://doi.org/10.1007/s11663-015-0546-0

Holzgruber, W and Holzgruber, H, 2001. Development trends in electroslag remelting, *Medovar Memorial Symposium 2001*, pp 71–77.

Hopkins, R K, 1940. Production of High quality metal in a water cooled mould, US Patent No. US2191479.

Jarczyk, G and Franz, K, 2012. Vacuum melting equipment and technologies for advanced materials, *Archives of Materials Science and Engineering*, 56(2):82–88.

Karimi-Sibaki, E, Kharicha, A, Wu, M, Ludwig, A, Bohacek, J, Holzgruber, H, Ofner, B, Scheriau, A and Kubin, M, 2018. A multiphysics model of the electroslag rapid remelting (ESRR) process, *Applied Thermal Engineering*, 130:1062–1069. https://doi.org/10.1016/j.applthermaleng.2017.11.100

Kharicha, A, Ludwig, A and Wu, M, 2011. 3D Simulation of the Melting during an Electro-Slag Remelting Process, in *EPD Congress 2011* (eds: S N Monteiro, D E Verhulst, P N Anyalebechi and J A Pomykala), pp 770–778 (John Wiley & Sons, Inc.: Hoboken). https://doi.org/10.1002/9781118495285.ch84

Klyuev, M, and Volkov, S, 1984. Electroslag remelting, Moscow, *Metallurgiya* [in Russian], 208 p.

Krivtsun, I V, Sidorets, V M, Sybir, A V, Stovpchenko, G P, Polyshko, G O and Medovar, L B, 2021. Effect of deformation of molten metal drops on their movement and heating in a slag layer at ESR, *Sovremennaâ Èlektrometallurgiâ*, 2021(1):9–16. https://doi.org/10.37434/sem2021.01.01

Kubin, M, Scheriau, A, Knabl, M, Holzgruber, H and Kawakami, H, 2013. Operational Experience of Large Sized ESR Plants and Attainable Quality of ESR Ingots with a Diameter of up to 2600mm, in *Proceedings of the 2013 International Symposium on Liquid Metal Processing & Casting*, pp 57–64. https://doi.org/10.1007/978-3-319-48102-9_8

Kuskov, Y M, Soloviov, V G, Osechkov, P P and Osin, V V, 2018. Electroslag surfacing of billet end faces with application of consumable and nonconsumable electrodes, *The Paton Welding Journal*, 2018(2):38–41. https://doi.org/10.15407/tpwj2018.02.08

Liu, Z-L, Medovar, L, Stovpchenko, G, Petrenko, V, Sybir, A and Volchenkov, Y, 2021. Phenomena at three-phase electroslag remelting, *China Foundry*, 18(6):557–564. https://doi.org/10.1007/s41230-021-0125-8

Maknenko, V, Medovar, L, Saenko, V and Korolyova, T, 2009. Modeling of the ESR ingot enlargement, *International Symposium on Liquid Metal Processing and Casting (LMPC-2009)*, pp 287–294.

Medovar, B I and Boyko, G A (eds), 1991. *Electroslag Technology* (Springer eBooks). https://doi.org/10.1007/978-1-4612-3018-2

Medovar, B I, 1997. Arc-Slag remelting of steel and alloys (Cambridge International Science Publication). https://ci.nii.ac.jp/ncid/BA27851308

Medovar, L B, Petrenko, V L, Tsykoulenko, A K, Saenko, V Y and Fedorovsky, B B, 2005. ESR with two power sources and process control, *International Symposium on Liquid Metal Processing and Casting (LMPC-2005),* pp 131–135.

Medovar, L B, Polishko, G, Petrenko, V and Stovpchenko, G, 2020. Modern electroslag technologies of electrode remelting and processing of liquid metal (review), *Theory and Practice of Metallurgy*, 125:17–25. https://doi.org/10.34185/tpm.2.2020.03

Medovar, L B, Stovpchenko, A P, Saenko, V Ya, Noshchenko, G V, Fedorovskii, B B, Petrenko, V L, Lantsman, I A and Zhuravel, V M, 2011. Concept of a universal ESR furnace for the production of large ingots, *Russian Metallurgy (Metally)*, 2011(12):1118–1123. https://doi.org/10.1134/s003602951112010x

Medovar, L, Polishko, G, Stovpchenko, G, Kostin, V, Tunik, A and Sybir, A, 2018. Electroslag refining with liquid metal for composite rotor manufacturing, *Archives of Materials Science and Engineering*, 2(91):49–55. https://doi.org/10.5604/01.3001.0012.5489

Medovar, L, Stovpchenko, G and Petrenko, V, 2016. Current Supplying Mould (CSM®) — Possibilities and Restrictions, *Medovar Memorial Symposium, MMS-100*, pp 180–182.

Medovar, L, Stovpchenko, G, Sybir, A, Gao, J, Ren, L and Kolomiets, D, 2023. Electroslag hollow ingots for nuclear and petrochemical pressure vessels and pipes, *Metals*, 13(7):1290. https://doi.org/10.3390/met13071290

Paton, B E, Medovar, B I and Latash, Y V, 1958. The Electroslag Melting of Steels and Alloys in Water Cooled Copper Moulds, *Automaticheskaya Svarka*, 11:5–15.

Paton, B E, Medovar, B I, Benz, M G, Nafziger, R H and Medovar, L B, 1999. ESR for titanium: yesterday, today, tomorrow, *Titanium-9, Science and Technology 1999,* 3:1385–1398.

Paton, B E, Medovar, L B and Saenko, V Y, 2007. ESS LM as a Way for Heavy Ingots Manufacturing, *International Symposium on Liquid Metal Processing and Casting (LMPC-2007)* pp 23–28.

Paton, B E, Saenko, V Ya, Pomarin, Yu M, Medovar, L B, Grigorenko, G M, Fedorovskii, B B, Petrenko, V L and Chernets, A V, 2004. Arc slag remelting for high strength steel and various alloys, *Journal of Materials Science*, 39(24):7269–7274. https://doi.org/10.1023/b:jmsc.0000048741.47509.b3

Persson, E S, Karasev, A, Mitchell, A and Jönsson, P G, 2020. Origin of the inclusions in Production-Scale electrodes, ESR ingots and PESR ingots in a martensitic stainless steel, *Metals*, 10(12):1620. https://doi.org/10.3390/met10121620

Persson, E S, Brorson, S, Mitchell, A and Jönsson, P G, 2021. Impact of solidification on inclusion morphology in ESR and PESR remelted martensitic stainless steel ingots, *Metals*, 11(3):408. https://doi.org/10.3390/met11030408

Radwitz, S, Scholz, H and Friedrich, B, 2013. Investigation of Slag Compositions and Pressure Ranges Suitable for Electroslag Remelting under Vacuum Conditions, in *Proceedings of the 2013 International Symposium on Liquid Metal Processing & Casting*, pp 87–93. https://doi.org/10.1007/978-3-319-48102-9_12

Ritzenhoff, R, Medovar, L, Petrenko, V and Stovpchenko, G, 2013. Comparison of ARC Slag Remelting vs, P-ESR Melting for High Nitrogen Steels, in *Proceedings of the 2013 International Symposium on Liquid Metal Processing & Casting*, pp 159–162. https://link.springer.com/chapter/10.1007/978-3-319-48102-9_24

Stein, G and Menzel, J, 2014. High pressure electroslag remelting – a new technology of steel refining, *International Journal of Materials and Product Technology*, 10(3–6):478–488. https://doi.org/10.1504/IJMPT.1995.036470

Stovpchenko, G P, Sybir, A V, Polishko, G O, Medovar, L B and Gusiev, Ya V, 2020. Mass Transfer in Electroslag Processes with Consumable Electrode and Liquid Metal, *Uspehi Fiziki Metallov*, 21(4):481–498. https://doi.org/10.15407/ufm.21.04.481

Stovpchenko, G, Medovar, L, Polishko, G, Goncharov, I and Lisova, L, 2018. Self-disintegrating slag for electroslag remelting of hollow ingot, *Ironmaking and Steelmaking*, 46(8):782–788. https://doi.org/10.1080/03019233.2018.1428418

Wang, H, Zhong, Y, Li, Q, Fang, Y, Ren, W, Lei, Z and Ren, Z, 2016. Visualisation study on the droplet evolution behaviours in electroslag remelting process by superimposing a transverse static magnetic field, *ISIJ International*, 56(2):255–263. https://doi.org/10.2355/isijinternational.isijint-2015-581

Xu, J, Ou, J, Lane, C D, Cockcroft, S L, Maijer, D M, Akhtar, A and Marciano, Y, 2022. Dissolution of Ti–N inclusions in liquid titanium during electron beam melting, *Journal of Materials Research and Technology,* 17:1522–1539. https://doi.org/10.1016/j.jmrt.2022.01.096

Hydrogen plasma in extractive metallurgy application

DOI: 10.62053/VZPF5242

B Satritama[1], D Fellicia[2], M I Pownceby[3], S Palanisamy[4], A Ang[5], G A Brooks[6] and M A Rhamdhani[7]

1. PhD Student, Swinburne University of Technology, Melbourne Vic 3122. Email: bsatritama@swin.edu.au
2. PhD Student, Swinburne University of Technology, Melbourne Vic 3122. Email: dfellicia@swin.edu.au
3. Senior Principal Research Scientist, CSIRO Mineral Resources, Clayton Vic 3168. Email: mark.pownceby@csiro.au
4. Director of Manufacturing Futures Research Platform, Swinburne University of Technology, Melbourne Vic 3122. Email: spalanisamy@swin.edu.au
5. Co-Director of Space Technology and Industry Institute, Swinburne University of Technology, Melbourne Vic 3122. Email: aang@swin.edu.au
6. Professor, Swinburne University of Technology, Melbourne Vic 3122. Email: gbrooks@swin.edu.au
7. Professor, Swinburne University of Technology, Melbourne Vic 3122. Email: arhamdhani@swin.edu.au

ABSTRACT

Metal production have long been using carbon sources as both reducing agents and energy sources. Consequently, the global extractive metal sector contributes significantly to greenhouse gas emissions, accounting for approximately 9.5 per cent. Hydrogen gas offers as a promising eco-friendly alternative to carbon in metallurgical processes, serving as both a reductant and energy supplier with a by-product being only water vapour. However, the implementation of molecular hydrogen faces certain challenges related to the thermodynamics and kinetics of metal oxide reduction. In addressing these challenges, researchers have explored the application of hydrogen plasma, generated by subjecting molecular hydrogen to high energy to produce atomic, ionic and excited hydrogen species. Hydrogen plasma offers thermodynamic and kinetic advantages over molecular hydrogen and carbon-based reductants, exhibiting lower standard Gibbs free energy of reaction and activation energy. Therefore, hydrogen plasma can produce metal in fewer steps, process any oxide feed and feed size and even be used to refine metals. Despite these advantages, challenges exist in utilising hydrogen plasma in extractive metallurgy, including electricity costs, potential reverse reactions and industrial-scale implementation. This study provides a mini review of prior research on hydrogen plasma for metal oxides reduction, particularly iron oxide, as well as state-of-the-art techniques for its use in extractive metallurgy applications by mentioning several reactor types. Future prospects and scale-up possibilities of the hydrogen plasma in extractive metallurgy will also be presented.

INTRODUCTION

The field of extractive metallurgy continues to grow, driven by the growing demand for metals in human needs. Traditionally, carbon-based reductants and energy sources have been heavily relied upon due to their affordability and abundance. However, this reliance contributes to climate change, with carbon dioxide (CO_2) emissions accounting for a significant 9.5 per cent of global greenhouse gas emissions (Carvalho, 2023). Recently, there is a rising interest in hydrogen as a sustainable alternative for various sectors, including extractive metallurgy, as it holds the potential to eliminate scope 1 CO_2 emissions. Unlike traditional methods, using hydrogen in metal production results in the production of water vapour as a byproduct. Despite its promise, hydrogen faces challenges as a weaker reductant compared to carbon at higher temperatures based on thermodynamics. One alternative to address this challenge is the utilisation of hydrogen plasma, a higher state of hydrogen gas. Hydrogen plasma is achieved by subjecting molecular hydrogen to high energy until it transforms into excited (H_2^*), atomic (H), and/or ionised (H^+) hydrogen. The main advantages of hydrogen plasma include its ability to enhance the feasibility of metal oxide reduction and its reaction rates. Its high thermal conductivity facilitates efficient heat transfer, while low viscosity enables rapid mass transfer (Sahu, 2014). This mini review paper systematically compiles and reviews recent and

current studies on the application of hydrogen plasma in the context of extractive metallurgy. The aim is to provide information that supports future scale-up efforts. A more comprehensive and complete review on the topic is presented by the authors elsewhere (Satritama *et al*, 2024).

OVERVIEW OF HYDROGEN PLASMA

To generate a plasma state in a specified reactor, energy in the form of DC or AC electricity and/or electrodeless microwave electromagnetic must be applied to the gas. When an electric arc forms between two electrodes or an electromagnetic field is present in the gas, the gas becomes electrically conductive, leading to excitation, dissociation and eventual ionisation. Hydrogen fully dissociating into H atoms at 5000°C and complete ionisation occurring at 25 000°C under atmospheric pressure (Satritama *et al*, 2024). Lowering the pressure significantly decreases the required temperatures for both dissociation and ionisation. Plasma is broadly categorised as thermal or non-thermal, also known as non-equilibrium or cold plasma. Thermal plasma is characterised by uniform temperature among all plasma particles (electrons, ions and neutral atoms), while non-thermal plasma exhibits a temperature differences, with heavy particles (T_i and T_n denoting ions and neutral species temperature) significantly lower than free electrons (T_e). This temperature difference arises from low particle collisions at low pressure conditions, typically lower than 1 atm (Inui *et al*, 2010). There are a few plasma reactors used for metallurgical application which include batch, continuous feeding and in-flight reactors (Figure 1). The difference between continuous feeding and in-flight reactors is that in-flight reactors combine continuous feed and plasma gas into a single stream.

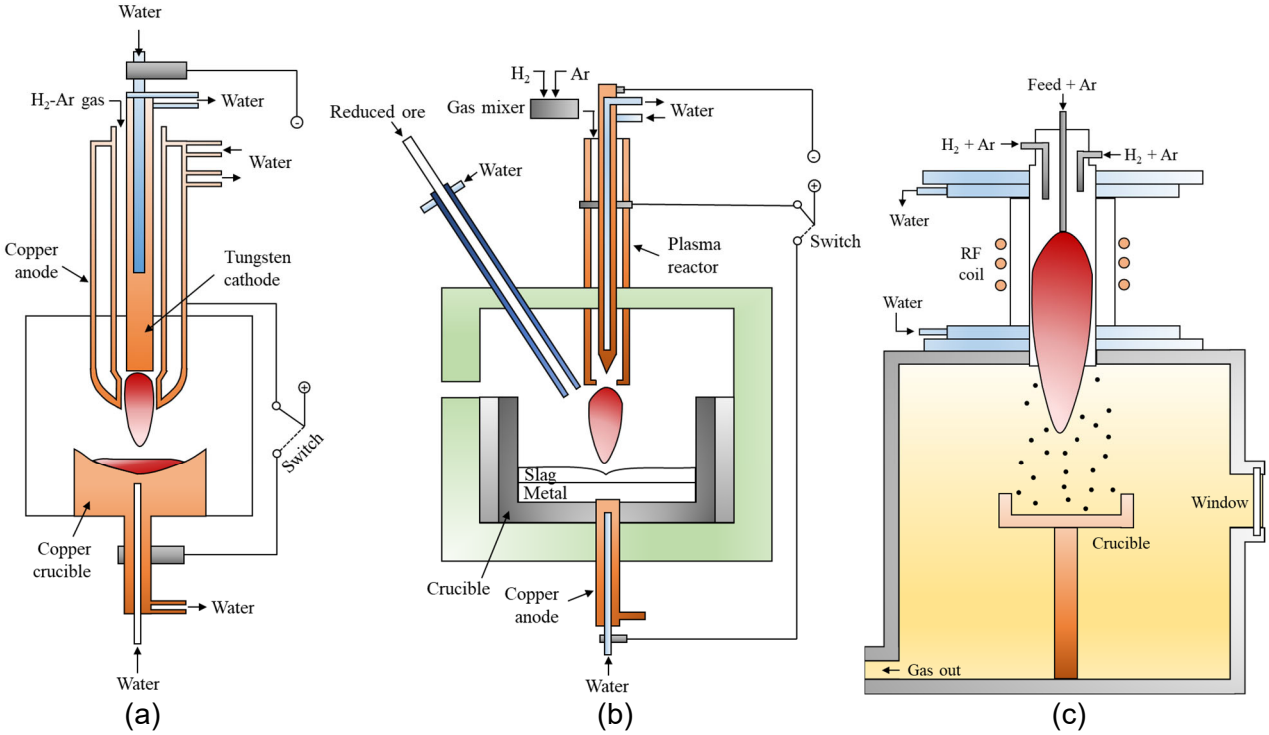

FIG 1 – Type of plasma reactors, including: (a) batch DC non-transferred and transferred plasma, (b) continuous DC non-transferred and transferred plasma, (c) in-flight microwave plasma. Adapted from (Yvon *et al*, 2003; De Sousa *et al*, 2016; Rains and Kadlec, 1970) by (Satritama *et al*, 2024).

HYDROGEN PLASMA FOR EXTRACTIVE METALLURGY

Thermodynamics and kinetics of hydrogen plasma in extractive metallurgy

Hydrogen plasma demonstrates the ability to reduce a broad spectrum of metal oxides, overcoming limitations observed with molecular hydrogen. Thermodynamic calculations reveal that the use of molecular hydrogen for most metal oxide reductions tends to yield positive Gibbs free energy, hinders spontaneous reaction. In contrast, hydrogen plasma addresses this challenge due to its

enhanced energy profile. An Ellingham diagram (Figure 2) was generated using FactSage 8.2 database, illustrating the Gibbs free energy of metal oxide formation (from its elemental state with 1 mol of O_2) alongside reductants like carbon, hydrogen gas and hydrogen plasma at a total pressure of 1 atm. It is evident that carbon can serve as a reductant for most metal oxides at high temperatures, while hydrogen gas can reduce specific metal oxides at all temperatures and others at higher temperatures. In contrast, the application of hydrogen plasma in the form of atomic H and/or H^+ significantly broadens the range of reducible oxides, offering the additional advantage of lower temperatures favouring the reduction process.

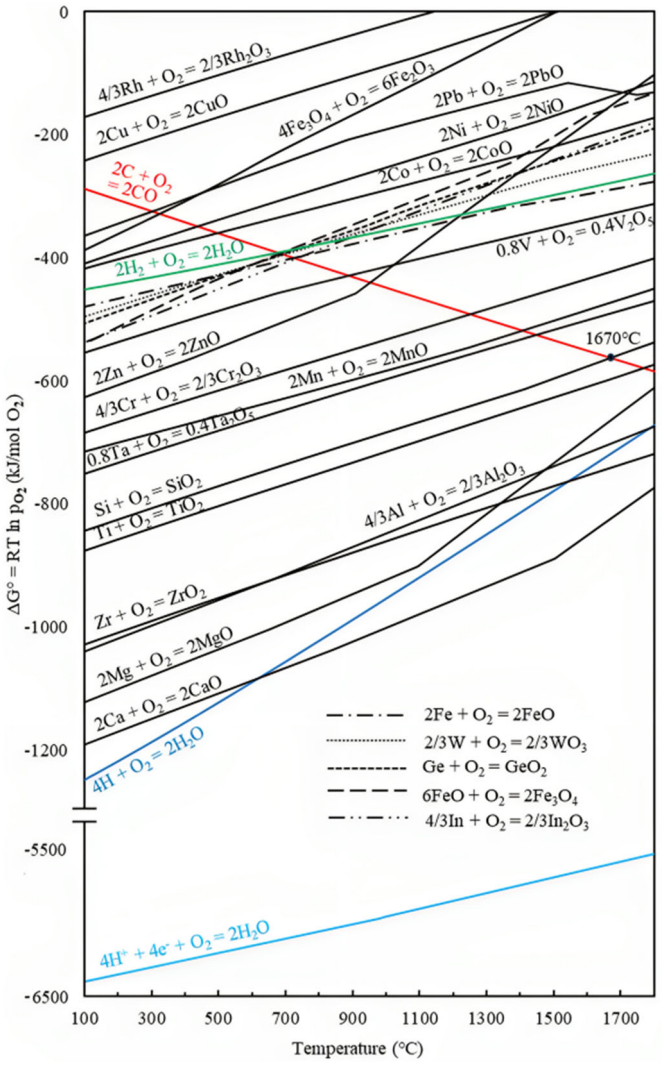

FIG 2 – Ellingham diagram of metal oxides stability in a function of temperature (Satritama *et al*, 2024).

In addition to meeting the Gibbs free energy criteria, the reactants must surpass the activation energy for a chemical reaction to take place. Activation energy (E_a) represents the minimum energy required for a reaction to proceed. The reduction of metal oxide to metal using molecular hydrogen may face challenges due to a high activation energy ($E_{a,1}$). Hydrogen plasma, in atomic ($E_{a,2}$) and excited atomic hydrogen forms ($E_{a,3}$), can significantly decrease the activation energy of the process, with the order $E_{a,1} > E_{a,2} > E_{a,3}$ (Sabat *et al*, 2013). There is limited research on the kinetics of metal oxide reduction using hydrogen plasma. Cobalt oxide reduction involves multiple steps, with the activation energy from Co_3O_4 to CoO (26.2 kJ/mol) higher than from CoO to Co (13.3 kJ/mol) metal (Sabat *et al*, 2015). Two kinetic studies on Cu_2O reduction to Cu metal indicate that the activation energy is nearly four times lower at lower temperatures (300–400°C) (Ramos *et al*, 2021), that is 19.06 kJ/mol, compared to higher temperatures (470–900°C) (Sabat, Paramguru and Mishra, 2016), that is 75.64 kJ/mol. These results align with hydrogen plasma's preference for lower temperatures as a reductant. A similar trend is observed in the study of Fe_2O_3 reduction to Fe metal by Rajput *et al*

(2013, 2014) with the activation energy four times lower at lower temperatures (300–800°C), that is 5.069 kJ/mol, compared to higher temperature (690–1150°C), that is 20.54 kJ/mol. Gonoring *et al* (2022) reported a significantly higher activation energy for Fe_2O_3 reduction (68.5 kJ/mol), attributed to the lower frequency parameter of microwave plasma (3.4 kHz) compared to Rajput *et al* (2013) (2.45 GHz), resulting in lower energy during the induction process by the microwave plasma and incomplete dissociation and/or ionisation of hydrogen gas.

This mini review briefly discusses the utilisation of hydrogen plasma for metal oxides reduction, where a more comprehensive discussion of its broader application in extractive metallurgy, which include for reduction, metals refining and wastes processing, is presented in other work (Satritama *et al*, 2024).

Reduction of metal oxides using hydrogen plasma

The reduction of metal oxides using hydrogen plasma is categorised into heterogeneous reactions, involving the interaction between hydrogen plasma and solid/liquid metal oxides and homogeneous reactions. Certain metals, such as aluminium and chromium, are efficiently produced through homogeneous reactions. This process involves vapourising the metal oxide, breaking the metal-oxygen bond, utilising hydrogen plasma to bind with the oxygen and depositing the pure metal vapour in a cooler zone. Referred to as dissociative reduction, this method requires a water-cooled reactor wall and a quench probe that can optionally inject quench gas (Rains, 1968). General reaction mechanism is given in the Figure 3 by distilling from several experimentation results (Sabat *et al*, 2015; Sabat, Paramguru and Mishra, 2018; Sabat, 2019; Zarl *et al*, 2022).

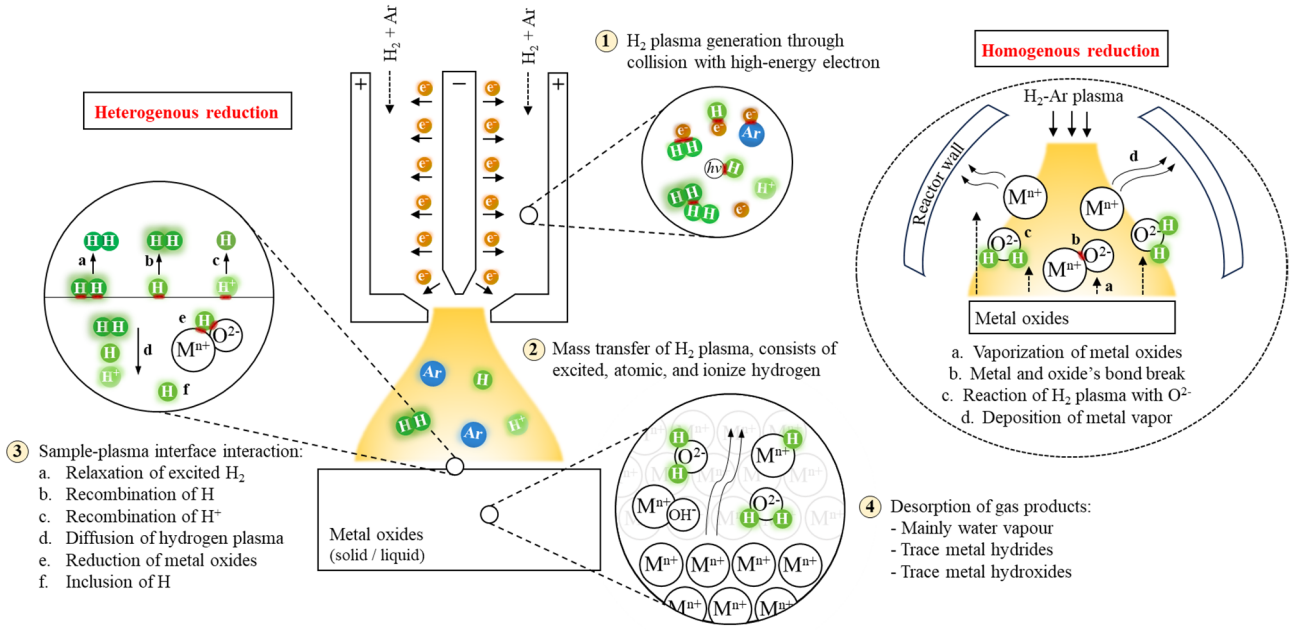

FIG 3 – General reaction mechanism of metal oxides reduction with hydrogen plasma (Satritama *et al*, 2024).

In the heterogeneous process, the initial step involves generating plasma by injecting gas between electrodes with different potentials, illustrated in the schematic mechanism using DC plasma. Microwave energy can also serve as a source to produce hydrogen plasma, as discussed earlier. H_2 plasma is formed through collisions with high-energy electrons sputtering from the cathode to the anode. These collisions elevate hydrogen to an excited state, leading to dissociation and ionisation. Additionally, collisions with photons (*hv*) can occur, further enhancing the hydrogen state. Photons are generated when high-energy electrons collide with hydrogen gas, reducing their state and releasing photons. Heat transfer between gas molecules allows higher-state hydrogen to transfer energy to lower-state hydrogen, improving the equilibrium of hydrogen plasma. The hydrogen plasma then flows through a constricted anode into the sample. In many instances, argon is injected alongside hydrogen to broaden the radial distribution of plasma within the sample, as hydrogen's high specific heat results in a more constricted plasma arc.

The reduction process initiates from the upper interface of the solid/liquid-gas layer in the sample and gradually proceeds downward as more interfaces of metal oxides undergo reduction. The interaction between hydrogen plasma and the metal oxides interface is complex. Some hydrogen plasmas undergo relaxation and recombination at the interface, experiencing sudden temperature changes upon contact with the sample surface. These processes induce local heating on the sample's surface, enabling the energy to surpass the activation energy required for oxide reduction. Other types of hydrogen plasma can bind oxygen at the interface and diffuse further into the sample to reduce additional oxide. This process requires intensive control, as several studies have noted that reduction with hydrogen plasma may result in the inclusion of trace amounts of hydrogen inside the sample. A higher entrapment of hydrogen may lead to hydrogen embrittlement (Sabat, Paramguru and Mishra, 2018).

Certain metals are efficiently produced through homogeneous reactions with hydrogen plasma in the vapour state (Huczko and Meubus, 1988; Kitamura, Shibata and Takeda, 1993). A study by Kitamura, Shibata and Takeda (1993) revealed that hydrogen plasma can evaporate metal oxides much faster than argon plasma. Using hydrogen plasma, Fe_2O_3, Cr_2O_3, TiO_2 and Al_2O_3 can be evaporated in 1.4, 1.8, 2 and 5.9 ms, respectively. Once metal oxides evaporate, the bonds between metal and oxide breakdown, allowing hydrogen plasma to bind free oxygen. The resulting metal vapour can then be deposited in the cooler part of the reactor. Rains (1968) employed an additional quench probe inserted into the bottom of the vertical reactor, alongside its water-cooled reactor casing. This water-cooled quench probe injects cooled gas to enhance metal vapour deposition.

Iron oxide reduction

Several studies have examined the effectiveness of different hydrogen plasma methods in reducing iron ore (Fe_2O_3) to metallic iron, positioning hydrogen plasma as a leading technology for oxide reduction compared to other metals. Microwave non-thermal plasma with H_2 has been particularly investigated, demonstrating rapid reduction of bulk Fe_2O_3. Bergh (1965) observed colour changes indicative of iron oxide reduction with atomic H at a relatively low temperature of 40°C, significantly lower than the 310°C required for molecular hydrogen. Rajput *et al* (2014, 2013) achieved over 95 per cent reduction within two hours using low power (500–1500 W), attributing this efficiency to the lower activation energy of hydrogen plasma compared to molecular hydrogen. Microwave power density (MWPD) emerges as a critical factor in microwave plasma reduction, influenced by reaction temperature and pressure, reflecting the efficiency of microwave energy absorption by plasma. Study from Sabat, Paramguru and Mishra (2017) estimated an MWPD of 4–9 W/cm³ in their process, translating to a mere 1–2 per cent conversion of molecular hydrogen into atomic H based on Hassouni, Grotjohn and Gicquel (1999) findings.

Extensive research on DC thermal plasma reduction with hydrogen plasma, commonly known as Hydrogen Plasma Smelting Reduction (HSPR), has been conducted at Montanuniversität Leoben as part of the SuSteel project, a collaboration between Montanuniversität Leoben and Voestalpine aimed at scaling up the process to a pilot scale (Seftejani *et al*, 2020). Zarl *et al* (2022) developed a promising six-step batch and continuous plasma reduction process using H_2 for potential industrial-scale applications. The process includes argon purging, pre-melting (electrode contact with a steel pin), pre-reduction to complete melting with $Ar+H_2$, reduction and sample charging, post-reduction until H_2 content in the off-gas reached 40 per cent and Ar/N_2 flushing. Filho *et al* (2022) examined a hybrid approach, combining molecular hydrogen direct reduction with hydrogen plasma. This method resulted in complete conversion in just 15 minutes for the plasma step, as opposed to 40–70 minutes for direct reduction alone.

Increased microwave power and temperature generally result in higher rates and degrees of reduction (Gilles and Clump, 1970; Rajput *et al*, 2013; Filho *et al*, 2022; Gonoring *et al*, 2022). However, accurately measuring temperature during hydrogen plasma reduction poses a challenge due to uneven heat distribution within the reactor. Kumar *et al* (2023) proposed an innovative method involving the placement of reflective aluminium foil beneath the sample and analysing the emitted light to estimate temperature based on black-body radiation principles. Beyond assessing reaction rate and degree, optimising hydrogen utilisation is critical for efficient reduction. Although higher hydrogen concentrations and flow rates enhance reduction rates, they typically lead to decreased utilisation (Behera *et al*, 2018; Plaul, Krieger and Bäck, 2005). Seftejani *et al* (2020) observed an

initial peak in hydrogen utilisation (60 per cent), followed by a gradual decline to near zero by the conclusion of the reduction process.

Other oxides reduction

The initial endeavour to reduce alumina using hydrogen plasma dates to 1970, conducted by Rains and Kadlec (1970). They achieved a dissociative reduction, separating aluminium from oxygen through evaporation and the reaction of oxygen with hydrogen plasma. Subsequent studies have expanded on this work. Lyubochko *et al* (2000) achieved a higher conversion of 50–60 per cent in a batch system with higher power input, surpassing Rains and Kadlec, who achieved a 30 per cent alumina conversion with an in-flight system. Rains and Kadlec successfully produced aluminium with a quench system and lower power input, while Kitamura, Shibata and Takeda (1993) encountered challenges in producing Al due to reoxidation into alumina. This underscores the significance of an effective quenching system in homogeneous reduction.

Reduction of chromium oxide can occur through both heterogeneous and homogeneous reactions. Although prior studies reported incomplete reduction or the need for optimised parameters, homogeneous reactions generally exhibit higher efficiency. Huczko and Meubus (1988) found that vapour-phase reduction is more efficient than solid-vapor reduction, showing increased efficiency (up to 47 per cent) with higher H_2 flow rates. Their calculations indicated that the diffusivity of Cr in H_2-Ar plasma is higher than that of Cr_2O_3, with the value increasing with temperature. This suggests that Cr can more easily diffuse in the gas system, facilitating its deposition. Kitamura, Shibata and Takeda (1993) stressed the importance of exceeding 2000 K for Cr vapourisation and subsequent quenching to form solid Cr. Dalaker and Hovig (2023) achieved a heterogeneous reaction, obtaining a metallic phase with 90 per cent Cr, primarily due to the low reaction time (only six mins, with 12 cycles of 30 s each), vacuum conditions and relatively low current (30–100 A), preventing Cr oxide from vapourising. They proposed a potential mechanism of Cr oxide reduction as Cr_2O_3 to CrO to Cr.

Although copper oxides can be reduced using molecular hydrogen, research has been conducted on their reduction with hydrogen plasma. The typical reduction steps for Cu oxides involve $CuO \rightarrow Cu_4O_3 \rightarrow Cu_2O \rightarrow Cu$ (Sabat, Paramguru and Mishra, 2016). Ramos *et al* (2021) observed that the reduction step from Cu_2O is directly to Cu, without the presence of metastable phases. However, Sabat, Paramguru and Mishra (2017) suggested a different reaction sequence, stating that the steps are $CuO \rightarrow Cu_2O \rightarrow Cu$ when iron oxide is added to the process (Sabat, Paramguru and Mishra, 2017). The reported activation energy for Cu_2O reduction is 75.64 kJ/mol (Sabat, Paramguru and Mishra, 2016), while Ramos *et al* reported an activation energy of 19.06 kJ/mol for Cu_2O reduction. Furthermore, Ramos *et al* found that the activation energy for H_2 plasma reduction was almost four times lower than that for molecular H_2 reduction (73.79 kJ/mol compared to 19.06 kJ/mol). Atomic hydrogen seems to be more efficient for reduction compared to molecular hydrogen, as observed by Bergh (1965). They noted that the reduction temperature for Cu_2O and CuO ranges from 225–450°C and 100–225°C, with a colour change occurring at 265°C and 140°C, respectively. In contrast, the colour changes with H occurred at 25°C, consistent with findings by Fleisch and Mains (1982).

Same case applies to nickel oxide as it can be reduced using molecular hydrogen, but some researchers also tried to reduce it with hydrogen plasma. Bergh (1965) observed a reduction in NiO occurring at a notably lower temperature (62°C) when exposed to atomic hydrogen, in contrast to molecular hydrogen (250°C). Sabat (2021) achieved complete reduction of pure NiO within five mins, employing a power input of 750 W. The reduction exceeded 100 per cent due to excess lattice oxygen in non-stoichiometric NiO. They calculated the specific enthalpy for NiO reduction as 32.8 kWh/kg, with the potential for reduction to 7.37 kWh/kg Ni when considering a 60 per cent reactor power efficiency and simultaneous multi-pellet reduction. Despite these intriguing results, justifying the additional energy consumption of converting hydrogen to plasma for CuO and NiO reduction requires stronger arguments as these oxides are easily reduced with molecular hydrogen.

Most research on SiO_2 reduction with hydrogen plasma primarily results in the formation of SiC (Salinger, 1972; Hollabaugh *et al*, 1983; Meyer *et al*, 1987; Asakami, Hokazono and Kato, 1988; Pirzada, 1990; Kong, Huang and Pfender, 1986), SiO (Kong, Huang and Pfender, 1986), or Si_3N_4 (Lee, Eguchi and Yoshida, 1990; Allaire and Dallaire, 1991) with the production of silicon metal

proving challenging due to the complex behaviour of SiO_2 reduction. Only two studies, conducted by Watanabe *et al* (1999) and De Sousa *et al* (2016), have successfully produced silicon metal from silicon oxide samples. Watanabe *et al* utilised a mixture of silica and alumina with argon and hydrogen plasma in a 4 kW DC non-transferred thermal plasma, discovering that argon plasma could generate silicon, while hydrogen was crucial for alumina reduction. Silicon with 98.3–99 per cent purity was formed within a 15-minute treatment. De Sousa *et al* investigated the deoxidation of silicon kerf, a byproduct generated during wafer slicing in solar panel manufacturing, using in-flight DC non-transferred plasma. They found that the reaction time between hydrogen plasma and the silicon kerf sample was crucial. The deoxidation rate increased with an increasing nozzle diameter at low hydrogen content due to the resulting lower gas velocity. The oxygen wt per cent in silicon kerf decreased from 17.3–23.4 per cent to 5.4–8.7 per cent and the deoxidation rate increased with an increasing nozzle diameter with low hydrogen content (<5 L/m).

FUTURE PROSPECTS AND SCALE UP POSSIBILITY

While there is considerable research on metal oxide reduction with hydrogen plasma, its application to reduce complex ores, is still in the early stages of exploration. However, building on successful studies of pure metal oxides reduction with hydrogen plasma, there is potential to produce various metals from complex oxide ores by carefully controlling the process parameters. Future investigations should also consider exploring the use of hydrogen plasma for rare earth metal production to support advanced applications, as these metals often necessitate high temperatures or strong reductants for extraction. Implementation of in-flight plasma process holds promise for future applications. This method offers higher reaction times, leading to increased reduction degrees and enhanced hydrogen utilisation, facilitated by the extensive surface area of the sample. Additionally, this approach appears economically viable for industrial-scale implementation, given its higher productivity compared to batch processing. When considering a larger-scale application, a thorough techno-economic assessment is crucial by evaluating cost-effectiveness, energy efficiency and practical challenges associated with implementing hydrogen plasma technology. Furthermore, interdisciplinary collaboration between metallurgists and plasma physicists is essential to address existing knowledge gaps and facilitate the successful scale-up of hydrogen plasma technology in extractive metallurgy.

CONCLUSIONS

Hydrogen plasma is emerging as a viable option for low-carbon extractive metallurgy, addressing the limitations associated with molecular hydrogen as a weaker reductant, particularly at elevated temperatures. Typically, hydrogen plasma is generated by subjecting molecular hydrogen to high energy, resulting in vibrationally and rotationally excited, atomic hydrogen and/or ionised hydrogen. This combination of species finds diverse applications in extractive metallurgy, particularly in the reduction of various metal oxides. While existing research predominantly focuses on the reduction of iron ore or iron oxides, numerous studies have explored the efficacy of hydrogen plasma in reducing oxides such as Al_2O_3, Co_3O_4, Cr_2O_3, CuO, NiO, SiO_2 and others, revealing promising results and showcasing its superiority over molecular hydrogen. Hydrogen plasma demonstrates effective reduction even for more stable oxides like Al_2O_3, TiO_2 and SiO_2. Less stable oxides such as NiO and CuO are more efficiently and sustainably reduced using molecular hydrogen, as it proves sufficient for less stable oxides. The added cost of electricity required to generate plasma does not justify the benefits in terms of reaction time, based on current research findings. Despite the manifold advantages, hydrogen plasma utilisation in extractive metallurgy poses several challenges, which ongoing studies are actively addressing and must be further optimised in the future.

ACKNOWLEDGEMENTS

This work was conducted as part of the PhD study of Bima Satritama and Dian Mughni Fellicia. Bima Satritama is co-funded by Swinburne University of Technology (SUT), Victorian Hydrogen Hub (VH2) and Commonwealth Scientific and Industrial Research Organisation (CSIRO). Dian Mughni Fellicia is co-funded by SUT and CSIRO.

REFERENCES

Allaire, F and Dallaire, S, 1991. Synthesis and characterization of silicon nitride powders produced in a dc thermal plasma reactor, *Journal of Materials Science,* 26:6736–6740.

Asakami, O, Hokazono, S and Kato, A, 1988. Preparation of SiC Powders from SiO_2 Powders by RF-Plasma Technique, *Journal of the Ceramic Society of Japan,* 96:1203–1205.

Behera, P R, Bhoi, B, Paramguru, R K, Mukherjee, P S and Mishra, B K, 2018. Hydrogen Plasma Smelting Reduction of Fe_2O_3. *Metallurgical and Materials Transactions, B,* 50:262–270.

Bergh, A A, 1965. Atomic hydrogen as a reducing agent, *The Bell System Technical Journal,* 44:261–271.

Carvalho, D, 2023, 25 August. Beyond electricity: is hydrogen the key to greener smelting and refining? [online], Wood Mackenzie. Available from: <https://www.woodmac.com/news/opinion/beyond-electricity-is-hydrogen-the-key-to-greener-smelting-and-refining/> [Accessed 10 December 2023].

Dalaker, H and Hovig, E W, 2023. *Hydrogen Plasma-Based Reduction of Metal Oxides, Advances in Pyrometallurgy*, pp 85–94 (Springer).

De Sousa, M, Vardelle, A, Mariaux, G, Vardelle, M, Michon, U and Beudin, V, 2016. Use of a thermal plasma process to recycle silicon kerf loss to solar-grade silicon feedstock, *Separation and Purification Technology,* 161:187–192.

Filho, I R, Springer, H, Ma, Y, Mahajan, A, Da Silva, C C, Kulse, M and Raabe, D, 2022. Green steel at its crossroads: Hybrid hydrogen-based reduction of iron ores, *Journal of Cleaner Production,* 340:130805.

Fleisch, T H and Mains, G J, 1982. Reduction of copper oxides by UV radiation and atomic hydrogen studied by XPS, *Applications of Surface Science,* 10:51–62.

Gilles, H L and Clump, C W, 1970. Reduction of iron ore with hydrogen in a direct current plasma jet, *Industrial and Engineering Chemistry Process Design and Development*, 9(2):194–207. https://doi.org/10.1021/i260034a007.

Gonoring, T B, Franco, A R, Vieira, E A and Nascimento, R C, 2022. Kinetic analysis of the reduction of hematite fines by cold hydrogen plasma, *Journal of Materials Research and Technology,* 20:2173–2187.

Hassouni, K, Grotjohn, T A and Gicquel, A, 1999. Self-consistent microwave field and plasma discharge simulations for a moderate pressure hydrogen discharge reactor, *Journal of Applied Physics,* 86:134–151.

Hollabaugh, C M, Hull, D E, Newkirk, L R and Petrovic, J J, 1983. RF-plasma system for the production of ultrafine, ultrapure silicon carbide powder, *Journal of Materials Science,* 18:3190–3194.

Huczko, A and Meubus, P, 1988. Vapor phase reduction of chromic oxide in an Ar-H2 Rf Plasma, *Metallurgical and Materials Transactions, B,* 19:927–933.

Inui, H, Takeda, K, Kondo, H, Ishikawa, K, Sekine, M, Kano, H, Yoshida, N and Hori, M, 2010. Measurement of hydrogen radical density and its impact on reduction of copper oxide in atmospheric-pressure remote plasma using H2 and Ar mixture gases, *Applied Physics Express,* 3:126101. https://doi.org/10.1143/apex.3.126101.

Kitamura, T, Shibata, K and Takeda, K, 1993. In-flight reduction of Fe_2O_3, Cr_2O_3, TiO_2 and Al_2O_3 by Ar-H2 and Ar-CH4 plasma, *ISIJ International,* 33:1150–1158.

Kong, P, Huang, T T and Pfender, E, 1986. Synthesis of ultrafine silicon carbide powders in thermal arc plasmas, *IEEE Transactions on Plasma Science,* 14:357–369.

Kumar, S, Xiong, Z, Held, J, Bruggeman, P and Kortshagen, U R, 2023. Rapid carbon-free iron ore reduction using an atmospheric pressure hydrogen microwave plasma, *Chemical Engineering Journal,* 472.

Lee, H J, Eguchi, K and Yoshida, T, 1990. Preparation of ultrafine silicon nitride and silicon nitride and silicon carbide mixed powders in a hybrid plasma, *Journal of the American Ceramic Society,* 73:3356–3362.

Lyubochko, V A, Malikov, V V, Parfenov, O G and Belousova, N V, 2000. Reduction of aluminum oxide in a nonequilibrium hydrogen plasma, *Journal of Engineering Physics and Thermophysics,* 73:568–572. https://doi.org/10.1007/BF02681800.

Meyer, T N, Becker, A J, Edd, J F, Smith, F N and Liu, J, 1987. Plasma synthesis of ceramic powders, *ISPC-8 Tokyo,* pp 2006–2011. Available from: <https://plas.ep2.rub.de/ispcdocs/ispc8/content/8/08-2006.pdf>

Pirzada, S A, 1990. Silicon carbide synthesis and modeling in a non-transferred arc thermal plasma reactor, PhD thesis, University of Idaho.

Plaul, J F, Krieger, W and Bäck, E, 2005. Reduction of Fine Ores in Argon-Hydrogen Plasma, *Steel Research International,* 76:548–554.

Rains, R K and Kadlec, R H, 1970. The reduction of Al_2O_3 to aluminum in a plasma, *Metallurgical Transactions,* 1:1501–1506. https://doi.org/10.1007/BF02641992.

Rains, R K, 1968. Reduction of aluminum-oxide to aluminum in radio frequency generated plasmas, thesis, Chemical Engineering, University of Michigan. https://dx.doi.org/10.7302/15672.

Rajput, P, Bhoi, B, Sahoo, S, Paramguru, R K and Mishra, B K, 2013. Preliminary investigation into direct reduction of iron in low temperature hydrogen plasma, *Ironmaking and Steelmaking,* 40:61–68.

Rajput, P, Sabat, K C, Paramguru, R K, Bhoi, B and Mishra, B K, 2014. Direct reduction of iron in low temperature hydrogen plasma, *Ironmaking and Steelmaking,* 41:721–731.

Ramos, S V, Cisquini, P, Nascimento Jr, R C, Franco Jr, A R and Vieira, E A, 2021. Morphological changes and kinetic assessment of Cu2O powder reduction by non-thermal hydrogen plasma, *Journal of Materials Research and Technology,* 11:328–341.

Sabat, K C, 2019. Formation of CuCo alloy from their oxide mixtures through reduction by low-temperature hydrogen plasma, *Plasma Chemistry and Plasma Processing,* 39:1071–1086.

Sabat, K C, 2021. Production of nickel by cold hydrogen plasma, *Plasma Chemistry and Plasma Processing,* 41:1329–1345.

Sabat, K C, Paramguru, R K and Mishra, B K, 2016. Reduction of copper oxide by low-temperature hydrogen plasma, *Plasma Chemistry and Plasma Processing,* 36:1111–1124.

Sabat, K C, Paramguru, R K and Mishra, B K, 2017. Reduction of oxide mixtures of (Fe_2O_3 + CuO) and (Fe_2O_3 + Co3O4) by low-temperature hydrogen plasma, *Plasma Chemistry and Plasma Processing,* 37:979–995.

Sabat, K C, Paramguru, R K and Mishra, B K, 2018. Formation of copper–nickel alloy from their oxide mixtures through reduction by low-temperature hydrogen plasma, *Plasma Chemistry and Plasma Processing,* 38:621–635.

Sabat, K C, Paramguru, R K, Pradhan, S and Mishra, B K, 2015. Reduction of cobalt oxide (Co3O4) by low temperature hydrogen plasma, *Plasma Chemistry and Plasma Processing,* 35:387–399.

Sabat, K C, Rajput, P, Paramguru, R K, Bhoi, B and Mishra, B K, 2013. Reduction of oxide minerals by hydrogen plasma: an overview, *Plasma Chemistry and Plasma Processing,* 34:1–23.

Sahu, M, 2014. An Investigation on Treatment of Bauxite through Hydrogen Plasma, thesis, Masters of Technology, National Institute of Technology.

Salinger, R M, 1972. Preparation of silicon carbide from methylchlorosilanes in a plasma torch, *Industrial and Engineering Chemistry Product Research and Development,* 11:230–231.

Satritama, B, Cooper, C, Fellicia, D, Pownceby, M I, Palanisamy, S, Ang, A, Mukhlis, R Z, Pye, J, Rahbari, A, Brooks, G A and Rhamdhani, M A, 2024. Hydrogen plasma for low-carbon extractive metallurgy: oxides reduction, metals refining and wastes processing, submitted to *Journal of Sustainable Metallurgy*.

Seftejani, M, Schenk, J, Spreitzer, D and Zarl, M, 2020. Slag formation during reduction of iron oxide using hydrogen plasma smelting reduction, *Materials (Basel),* 13.

Watanabe, T, Soyama, M, Kanzawa, A, Takeuchi, A and Koike, M, 1999. Reduction and separation of silica-alumina mixture with argon–hydrogen thermal plasmas, *Thin Solid Films,* 345(1):161–166.

Yvon, A, Fourmond, E, Ndzogha, C, Delannoy, Y and Trassy, C, 2003. Inductive plasma process for refining of solar grade silicon silicon, in *Proceedings of EPM 2003, Fourth International Conference on Electromagnetic Processing of Materials*, HAL Open Science, pp 125–130. https://hal.science/hal-00551473.

Zarl, M A, Ernst, D, Cejka, J and Schenk, J, 2022. A new methodological approach to the characterization of optimal charging rates at the hydrogen plasma smelting reduction process part 1: method, *Materials,* 15:4767.

Challenges facing non-ferrous metal production

DOI: 10.62053/VTJD2567

P Taskinen[1] and D Lindberg[2]

1. Professor Emeritus, Aalto University, Espoo FI-00076, Finland. Email: pekka.taskinen@aalto.fi
2. Professor, Aalto University, Espoo FI-00076, Finland. Email: daniel.k.lindberg@aalto.fi

ABSTRACT

The increase in metals demand in the electrifying globe means significant growth in the smelting of copper, nickel, zinc, and lead, produced from primary sulfide sources or using sulfide mattes as the intermediates of the process chains. This means that leaner and complex mineral deposits will be evaluated as ores and are in the future traded in the commodity market for smelting and refining to pure metals.

An important issue in the trend is the technology metals, like antimony, tellurium, and gallium, which exist as trace elements in sulfide ores and form no ores of their own. Their recovery becomes important in the coming decades as will be the case with growing slag amounts without use in other industries. The key is to produce environmentally acceptable slags in the smelting operations. It sets new boundary conditions to the treatment of flue dusts. This means that all material streams of smelting and refining must be re-evaluated for the deportments of the main and minority metals.

In copper smelting, the recoveries of precious metals are today important for the feasibility of the custom smelters but due to low prices of many minority metals they are discarded in slag landfills. It is one of the emerging issues also in the secondary copper smelting today and once the demand grows, the same question will be faced also in the mining-beneficiation-smelting-refining chain of the primary production of nickel, zinc, and lead. The distributions of many technology metals in the copper and nickel smelting have been recently studied using methods where the chemically bound trace elements in the slag and its phases at the smelting conditions have been studied. Thus, the key data about options for process modifications and additional processing steps are piling up.

Short processing routes in the metals smelting and refining are attractive due to their simplicity. At the same time, complexity of many raw materials challenges the fluxing at high oxygen partial pressures in low silica slags with high metal concentrations. The compromise between high primary recovery and safe operation is a demanding task in conditions where slag foaming outside the processing window is evident.

The increase in the demand of pure nickel is challenging the raw material basis where low-grade sulfide ores are soon smelted along with nickel laterites to matte. It is a demanding task at high MgO concentrations. The low solubility of MgO in iron silicate slags requires new fluxing strategies and new smelting end points for the operation at reasonable temperatures; the direct nickel matte smelting in one-matte mode may be an option.

INTRODUCTION

The increase in metals' demand anticipated in the electrifying world means growth in the smelting of, for example copper, nickel, and lead which primarily are produced from primary sulfide minerals or using sulfide mattes as the intermediate product. This means that leaner and more complex mineral deposits will be evaluated and classified as ores and are traded in the commodity market for smelting and refining. Whether this is possible, the key is in the development of agile smelting and refining technologies. The question also is, who will have 'patient money' to carry out and commit to the long-term basic and applied research, aiming at CO_2-lean and environmentally lean technologies. Another side of the coin is the common need of less special knowledge and skills to operate the plants and to do that in a safe way. In that, for example novel online measurements, like direct oxygen partial pressure from the smelting vessels, robotics, and AI, will play vital roles.

A simple calculation of global demand of refined copper indicates that 3 per cent annual growth ends up from the present about 25 Mt pa (International Copper Study Group, 2023) to 50 Mt pa in 2050. This means a significant increase in the mine production, due to the long end-of-lifetime for copper products. In terms of smelter capacity, it means one to two new large scale greenfield smelters each

year in 2025 and two to three in 2050. This requirement of ‘new metal’ is stricter for copper than in, say alloy steels, where substituting alloys can be developed, whereas most copper use and essentially all future growth is in high-purity metal to be used for heat and in particular for electricity transfer purposes. This means that 99.99 per cent pure A-grade cathode must be able to be produced also using the low-grade and complex raw materials. At the same time, the discard slag production is at least doubled which lowers the primary yield and increases the production costs, when the slag recycling will be the preferred option instead of landfilling. The same is valid with nickel and zinc as well as to some degree with lead.

Running large scale smelting and refining operations today includes reliable life cycle management of the equipment and forecasting the maintenance needs several months, even more than half a year beforehand, due to the availability and long delivery times of many critical spares. Such vulnerable areas in the non-ferrous smelting and refining are the refractory bricks, cooling jackets, and many electric and electronic components.

The recovery of all trace elements in copper, nickel, zinc, and lead smelting is a future challenge which requires re-thinking of the process chains for optimising the recoveries and allowing the circular economy also in the small so-called technology metals. They today deport and deplete in slags without hope of recovery. On the other hand, the global distributions of many toxic elements in copper, nickel and lead smelting are very uneven (Risopatron, 2018) which emphasises the need of using available technological advancements for limiting mercury, arsenic and lead emissions also in the current facilities when increasing the production.

The regulation in industrialised countries today is hostile to metal making. That discourages the activities to develop the present technologies and makes long-term commitment of the industry less attractive. This again has a major impact in the technology development and innovations which lead to new and more green metal making processes in a field where major technology improvements need decades to mature. The development is evident when looking at the distribution of fundamental and engineering publications by country over the last two to three decades.

THE IMPURITY PROBLEM

In the non-ferrous metallurgy, most trace elements in the primary and secondary raw materials are either technology metals or harmful elements. The former must be recovered, and latter eliminated for environmental reasons. The fundamental knowledge in finding the optimal end points, eg for the processing of matte, converting, and refining steps, includes the elements’ equilibrium distributions between matte, slag and gas, and the thermodynamic properties of their species in the phases. Thus, the individual conditions for the maximum deportments of the impurity elements in the various side streams can be evaluated. Such accurate and reliable fundamental data also allows digitalisation of the processing operations.

In the non-ferrous industry, with exception of aluminium production, the use of hydrogen and fossil-free metals in terms of Scope 1, 2 and 3 greenhouse gas emissions (US EPA, 2023) will not be as demanding as in the ferrous and especially in ferroalloys industries. There is no fundamental restriction from thermodynamic point of view even if the degrees of utilisation of hydrogen in some processing steps, like slag cleaning, may be realised on a relatively low level.

The smelter flow sheets of today include closed flue dust circulation which forces all volatile elements into the two existing outlets of the smelter, namely the crude metal/matte and the slag, see Figure 1. Independently from the slag cleaning technology used, the closed operation mode leads to high trace element concentrations in the metal product and the discard slag when/if they are not removed from the material streams.

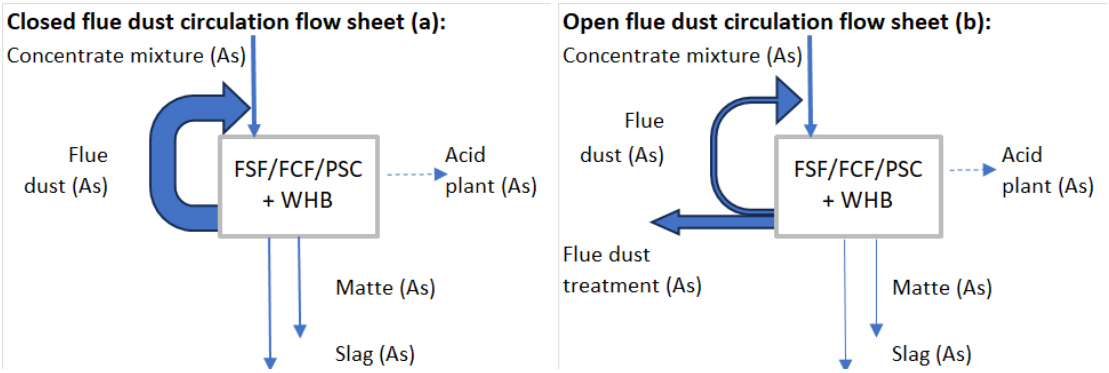

FIG 1 – Schematic flow sheets of the present closed-type flue dust treatments and an open circuit mode with the suspension smelting technology as an example (FSF – flash smelting furnace; FCF – flash converting; PSC – Peirce Smith converting; WHB – Waste heat boiler).

The utilisation of the opportunity of high particle temperature in the gas-concentrate suspension in the copper and nickel in the flash smelting processes and also the vigorous agitation in the bath smelting processes allow us to split several impurity elements from the main metal stream and redirect them into safe treatment instead of mixing them in the discard slag and crude metal. The key trace elements in the copper production by International Copper Study Group (ICSG) today and in near future are arsenic, lead and bismuth (Risopatron, 2018).

RECOVERY OF THE TRACE ELEMENTS

The sulfide ores are important sources of several minority metals some of which do not have ores of their own. Typical examples are selenium, tellurium, antimony, and bismuth. Their recoveries are part of the smelting and refining steps in cases there is economy behind the extraction. Today, a lot of these minor elements (often called technology metals) are lost in the earlier steps prior to smelting due to commercial reasons (Moats, Alagha and Awuah-Offei, 2021; Nassar *et al*, 2022), ie lack of demand and low price.

The deportment of minority components will be a more vital issue in the case where the trace elements from secondary resources will be recovered. The use of standard primary copper smelting circuits is out of question because many elements deport in the smelting and converting slags and cannot be recovered from there in the slag cleaning operations due to their thermodynamic properties and low concentrations (Lennartsson *et al,* 2018; Faraij *et al*, 2022). Thus, the focus of Waste Electrical or Electronic Equipment (WEEE) recycling has been so far on the recovery of the platinum metals (PM) and platinum group metals (PGM) values only. Therefore, the optimal routes for the primary and secondary raw feeds must be evaluated in future from this perspective (Alvear Flores, Risopatron and Pease, 2020).

Losses of trace elements in beneficiation-smelting-refining chain are evident and often intentional due to penalties involved in concentrate trading. Recent detailed analyses on some trace elements in the primary copper ores and their recovery in the current beneficiation-smelting-refining chains and technologies (Moats, Alagha and Awuah-Offei, 2021; Nassar *et al*, 2022) indicate that significant fractions are lost or actively suppressed in the gangue or slag streams. Thus, they are led to the tailings at mine site and slag landfills at smelters which seem to contain large quantities of them accumulated as reserves over the past decades.

An important issue in this context is the technology metals in copper, zinc, and nickel smelting, like, eg antimony, tellurium, molybdenum in copper extraction, and gallium in zinc and alumina processing, which exist as trace elements in many sulfide ores and form no ores of their own. Thus, their increased demand is essentially linked with the use and availability the primary sources of those metals. Many of them are on the critical metals/materials lists of the geographical areas, eg in EU and USA (European Commission, 2023; USGS, 2022). Their effective recovery may become important in the coming decades as will be the case with growing slag amounts without sustainable use in the other industries. The key is to produce environmentally acceptable slags and other by-products in the smelting operations which sets new boundary conditions to such things as the

treatment of flue dusts and its volatile elements as well as the hydrometallurgical iron residues (Salminen *et al*, 2020).

The recovery of many technology metals in copper and nickel smelting is problematic because they do not volatilise, and they oxidise in the matte smelting step or converter stage. In many cases they deport in the slag when the extraction process advances from reducing to oxidising. This is clearly seen when studying the equilibrium distributions as the function of the prevailing oxygen partial pressure. The thermodynamic parameter independent of the scale demonstrating the issue can be defined (Park, Takeda and Yazawa, 1984) as:

$$L^{s/}m(Me) = [wt\%Me]_{matte/metal}/(wt\%\ Me)_{slag}. \quad (1)$$

And it can be derived from the thermodynamic properties of the element in the phases in contact or from the assays of the phases in the industrial or laboratory conditions. Typically, they are measured in equilibrium conditions using chemical analyses made from the homogeneous part of the phase at process conditions. That was often neglected in the past, and bulk analyses were used instead of *in situ* phase analyses which leads to too small (apparent) distribution coefficient values if they deviate strongly (>1000) from unity (Klemettinen, Avarmaa and Taskinen, 2017). For this reason, the experiments where the phases were sampled from a large pool of slag and quenched the presence of inclusions is difficult to trace and separate from the 'clean' phase. Then also the chemical composition is only average and contains average values of the phase including the uncertainties of composition gradients (from volatile species) and inclusions (not belonging to the phase) (Jak *et al*, 2022). An important issue is that in such cases, volatilisation and inhomogeneities in the phases remain undetected.

A separate recovery step is needed for preventing the loss of trace elements to the discard slag or other residues. This may include re-thinking of the flue dust treatment, as discussed earlier, due to volatile nature of some trace elements. The situations for indium in black copper and copper matte smelting can be seen in Figure 2 and those of tin in Figure 3. The matte/metal-slag distribution coefficients are unbiased to the gas-melt equilibria and thus, the volatility of each element and its deportment in the flue dust must be studied as a separate case. For that purpose, typically mass distributions of elements obtained from the mass balance are used (Nakajima *et al*, 2009). Particularly problematic is the situation in cases like indium and tin in black copper smelting where the distribution coefficient in reducing conditions is strongly on the metal side and in oxidising conditions in a similar way on the slag side.

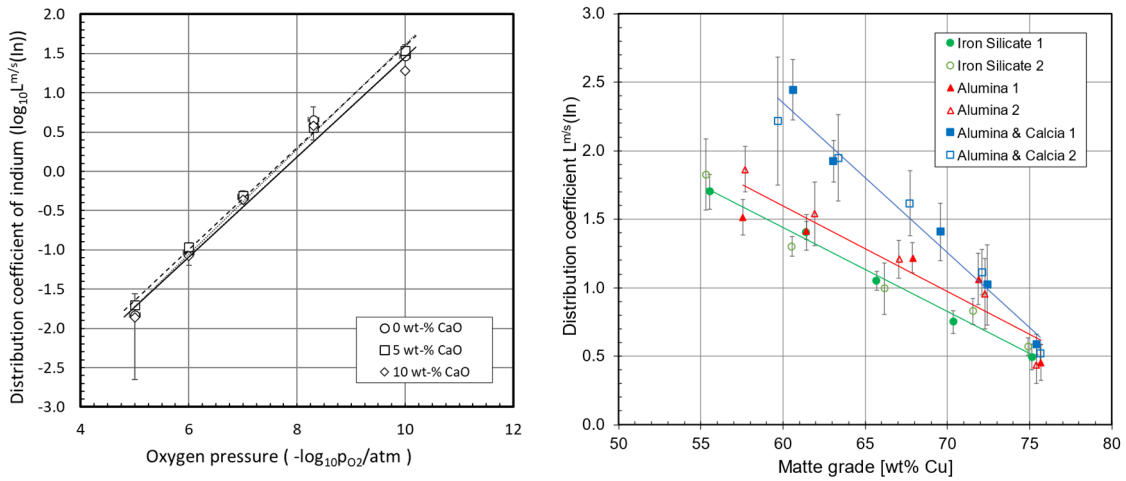

FIG 2 – The metal-slag equilibrium distribution coefficients of indium between copper/copper matte and slag as a function of the prevailing oxygen partial pressure at 1300°C (Sukhomlinov *et al*, 2020a; 2020b).

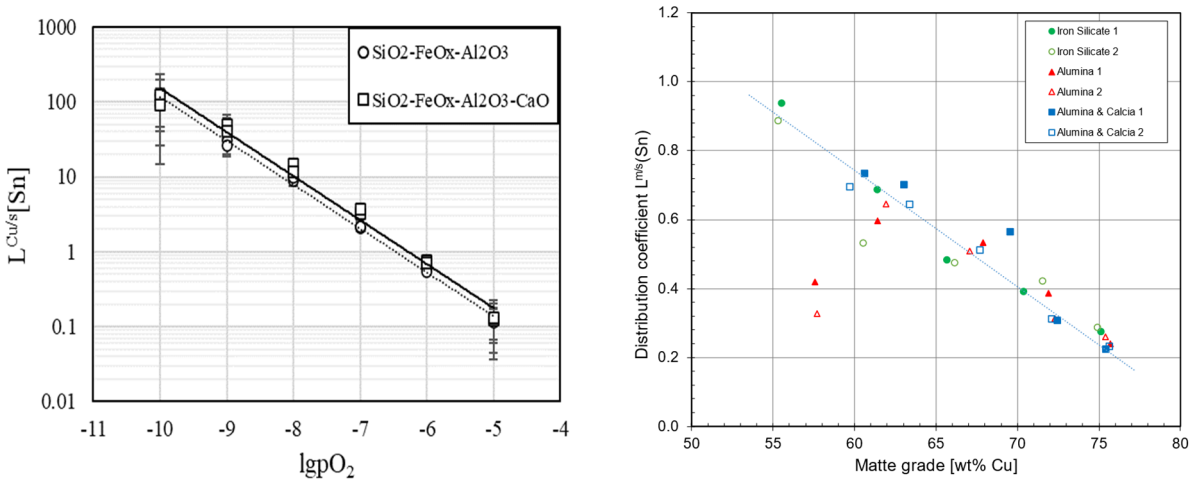

FIG 3 – The metal-slag distribution coefficients of tin between (a) copper (b) copper matte and slag as a function of the prevailing oxygen partial pressure at 1300°C (Avarmaa, Yliaho and Taskinen, 2018; Sukhomlinov *et al*, 2020b).

Figure 4 shows an example of copper matte smelting which is one important source of gold and palladium. All elements with a high distribution coefficient between matte/metal and slag suffer from the systematic technical problem of matte/metal entrainment in the slag. A simple mathematical exercise shows that when the distribution coefficient is $Lm^{/s}[M] > 1000$ the apparent values of the experimental results remain at around 10–100 if the separation of matte/metal droplets in the slag is ignored, ie assumed negligible without proof, or made unsuccessfully.

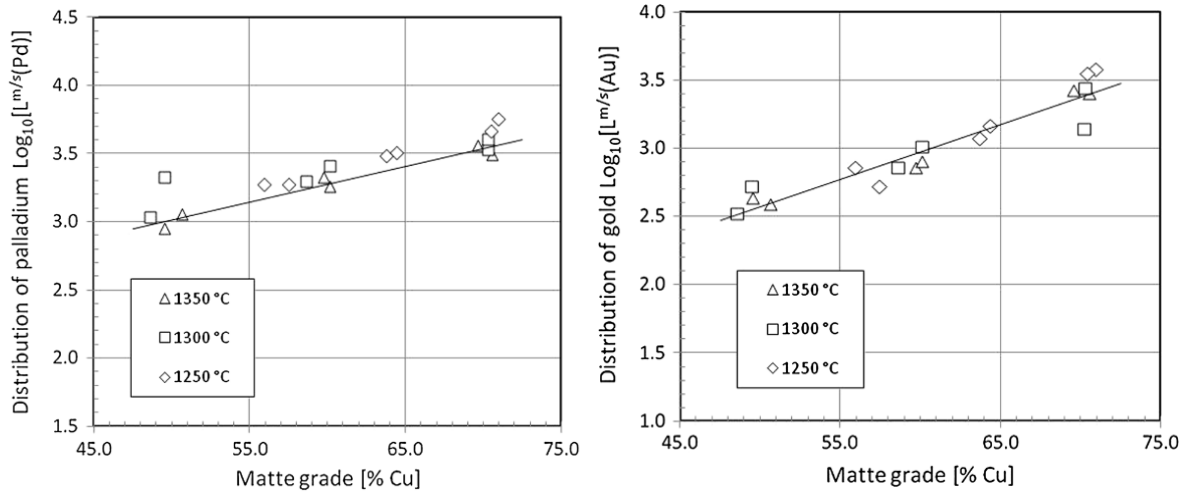

FIG 4 – The experimental distribution coefficients of (a) gold and (b) palladium between copper matte and iron silicate slag saturated with silica as a function of the matte grade (Avarmaa *et al*, 2015).

The high accuracy and significantly larger experimental equilibrium values of the distribution coefficients compared with the previous data (Baba and Yamaguchi, 2013) was justified by the spatial accuracy of the used LA-ICP-MS (laser ablation – inductively coupled plasma – mass spectrometry) technique which allowed selecting inclusion free phase areas of the slag for the analysis (Klemettinen, 2021). Also, the isotope fluxes as a function of time in the MS analyses (ie time resolved analysis (TRA) signals) provide information about the presence of micro/nano nuggets in the samples (Richter *et al*, 2004).

The behaviours of many technology metals in the primary and secondary copper and nickel smelting have been recently studied to facilitate their extraction. The used methods have enabled to locate where the chemically bound trace elements in the slag and its phases at the smelting conditions deport in the various processing steps. Thus, the key data for process modifications and additional

processing steps for separating them from the slag, matte and flue dust streams, is gradually piling up and soon allows the assessments of their thermodynamic properties.

IMPORTANCE OF THE SLAG CHEMISTRY AND FLUXING

The short processing routes in the metals smelting and refining are attractive due to their better recoveries and potentially, smaller capital expenditures. The key is to eliminate internal circulations within the smelter. A fundamental issue is limiting wider use of such processes, namely the shortage of low-iron or high-copper ores. Thus, only less than ten such smelters exist today. An option for increasing the use of such processing routes is a pre-concentration of standard sulfide concentrates and cleaning of complex bulk concentrates (Tuominen and Kojo, 2005; Tuominen, Anjala and Björklund, 2007; Awe, 2010; Fuentes, Vinals and Herreros, 2009). For such purposes, straightforward processing concepts are needed which eliminate most minority and trace metals and gangue from the copper minerals and at the same time, allow increasing the copper-to-iron ratio.

Another option may be the production of a bulk concentrate and to split that into two streams at mine site, one with a high Cu/Fe ratio and the other with most impurities and low copper for hydro-metallurgical processing which can handle the impurities in a comprehensive way (Risopatron, 2018). This strategy would allow deposition of the nasties in a concentrated form and avoid their spreading at low concentrations, eg in the slag landfills.

In the direct-to-blister copper smelting, the shorter process chain means the absence of the entire converter isle which allows more compact building and the movement of all molten materials in covered launders which eliminates scattered fugitive emissions at the smelter. An example of the streamlined lay-out is in Figure 5 which also indicates the lack of internal material circulations in the process and the option of selecting the slag cleaning technology based on the local needs.

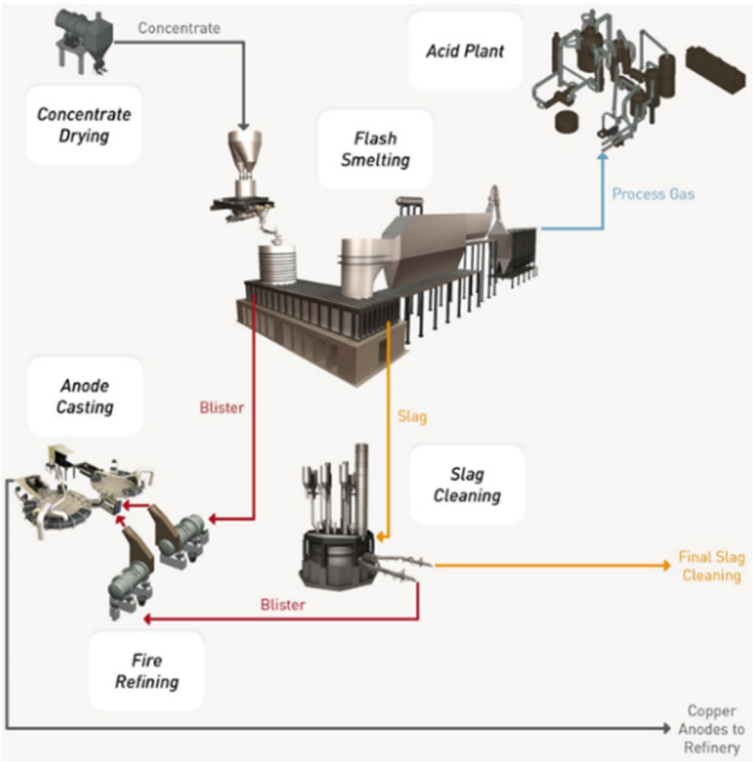

FIG 5 – A schematic of the direct-to-blister flash smelter: feed preparation, the furnace-waste heat boiler- electrostatic precipitator (ESP), and the auxiliary crude copper, off-gas, and slag treatments steps prior to the electrolytic refining to 4N copper cathodes; the material flows are also demonstrated (Outotec).

In the high-grade matte or direct blister production, major increase in the oxidation degree exposed to the charge brings challenges to the fluxing at the prevailing high oxygen partial pressures in low silica slags with high copper concentrations. The compromise between high primary recovery and

safe operation is a demanding task in the conditions where slag foaming outside the processing window is evident.

The complexity of sulfide concentrates in nickel smelting does not limit the use of the direct high-grade nickel matte smelting which allows in a flexible way the use of all possible nickel sulfide concentrates either as such or together with the electric furnace matte which fulfil the heat balance at reasonable oxygen enrichments.

Case studies – direct-to-blister copper smelting

The shortest way and smelter chain in sulfide smelting is the direct production of metal or its intermediate high-grade matte for refining in one smelting step. Such industrial examples are the direct-to-blister smelting of copper (Kojo and Huppe, 2011; Taskinen, 2011), direct-to-high-grade matte smelting of nickel (Mäkinen *et al*, 2005) and direct lead smelting by suspension technologies (Bryk, Malmström and Nyholm, 1966). In those technologies, the feed mixture with its gangue minerals goes through the heating and combustion steps in the reaction shaft of the smelting vessel. There in copper and lead smelting, the oxidation conditions have been adjusted for oxidising almost all sulfur and iron from the matte allowing production of low-sulfur metal. In the direct nickel matte smelting, the product is essentially iron-free sulfide matte. Thus, the fluxing in metal making conditions must take into consideration also the gangue components.

The forming slag is determined in such conditions, at much higher oxygen partial pressures than conventionally, by the end point of the crude metal in copper smelting and in nickel that of the high-grade matte smelting. To achieve this condition, the metal droplets generate a large volume of SO_2 in the reaction shaft and the forming slag must dissolve the iron oxides together with gangue and maintain exactly the correct degree of oxidation for the iron oxides present. An example of the challenges is given in Figure 6 where the high-silica sulfide concentrate will form silica-saturated slags without any fluxing ie it locates within the primary field of silica (the red circle). Note the steep saturation boundaries of silica (tridymite on the right) and pseudo wollastonite (on the left side) which indicate that the correct fluxing is the key for avoiding foaming.

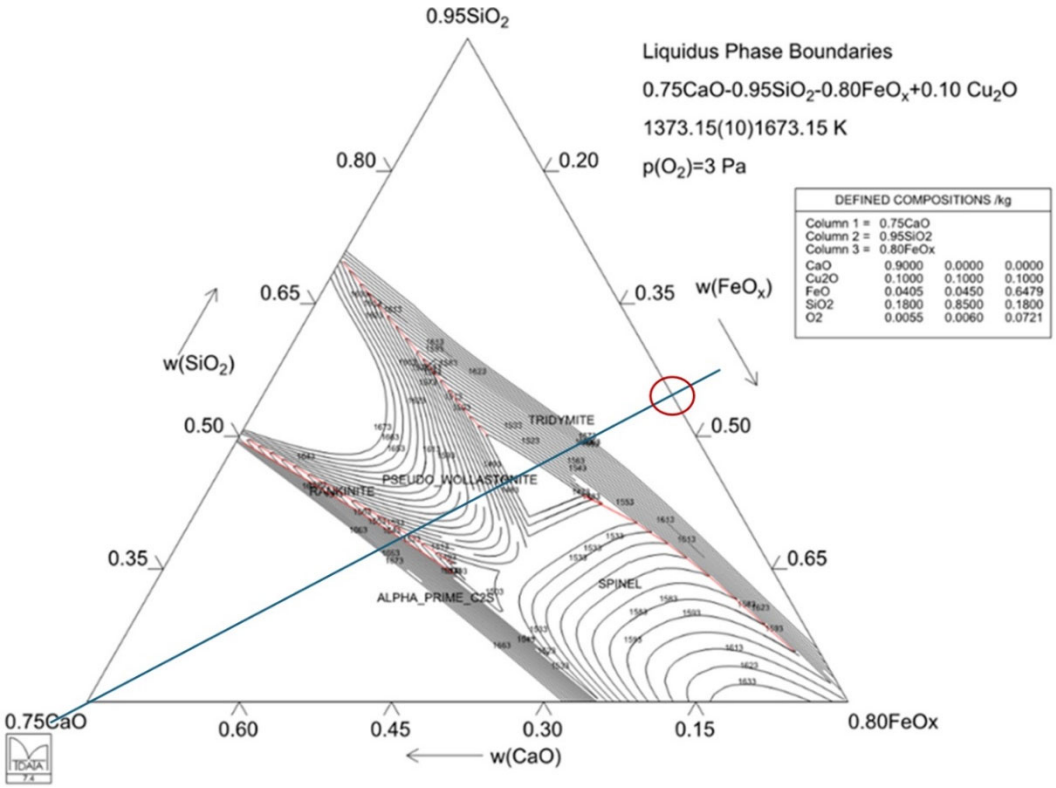

FIG 6 – Operation line of slag in a DtoB smelter when it is fluxed with lime depicted on an isothermal, quasiternary Gibbs triangle at constant oxygen partial pressure of 3×10^{-5} atm and 10 wt per cent Cu_2O; blue line shows fluxing as a function of CaO and the red circle is the unfluxed slag of the feed mixture (MTDATA).

The correct operation of the smelting may need some sort of preprocessing for the complex and low calorific value concentrates for removing selected harmful sulfide minerals and gangue components. This will stabilise the smelting step and remove slag fluidity problems when the composition of the feed mixture can be kept within narrow bounds in terms of its iron and sulfur concentrations.

Auxiliary fuel in sulfide smelting

Another issue is the smelting of low-calorific value sulfide concentrates which need additional fuel for the smelting for maintaining the process temperature. For effective recovery of minority components, the primary smelting step or matte making may end up at matte grades lower than the present 60–65 per cent Cu which additionally limits the heat generation in the smelting step. A fossil-free low-CO_2 alternative is the use of pyrite as fuel, but the downside is increased S/M ratio and the growing slag amount which requires improved copper recovery and lower residual copper in the discard slag.

Thermodynamic equilibrium calculations at fixed matte grade of 65 per cent Cu indicate that the slag amount is doubled at a pyrite addition of slightly less than 50 wt per cent of chalcopyrite content of the feed mixture (in case $CuFeS_2$ is the only copper carrier). The extra heat provided by pyrite is, however, significant as shown in Figure 7. An addition of about 42 wt per cent FeS_2 doubles the heat input in copper smelting in a case where high oxygen enrichment is used in the Flash Smelting Furnace (see the used constraints of Figure 7). No process gas preheating was assumed (Pesonen *et al*, 2022), all raw materials were at 25°C, and the products at 1300°C.

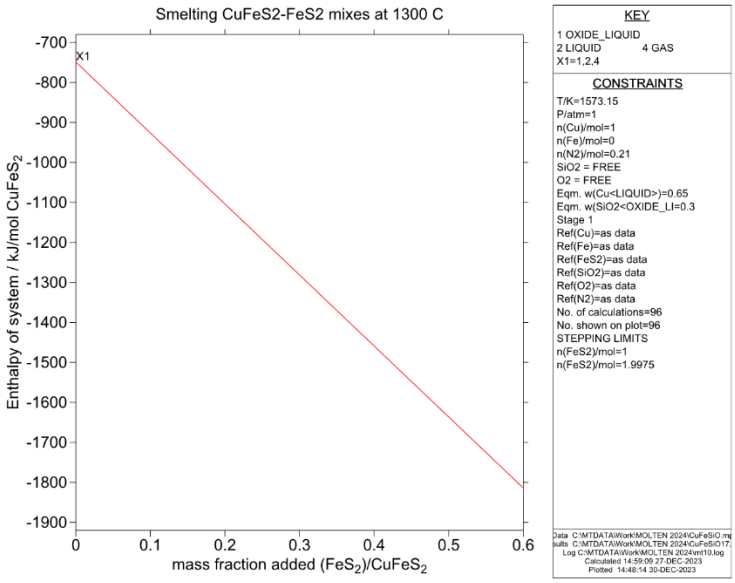

FIG 7 – Extra enthalpy generated by FeS_2 when added in a lean chalcopyrite concentrate, producing a fixed matte grade of 65 per cent Cu and fluxing the slag to 30 wt per cent (SiO_2); a simplified heat balance without considering the effects of gauge minerals on the slag chemistry (MTDATA 7.4 with MTOX database 8.2).

Thus, from the point of view of the CO_2 footprint, it is more sustainable to use pyrite as additional fuel than the present hydrocarbons or coal/coke.

SUMMARY AND CONCLUSIONS

If countries and geographic areas are truly worried about the criticality of metals and minerals, that should be not the interest of commercial actors only. In the copper making the environmental and fugitive emissions must be eliminated and the recovery of trace elements need significant technological advancements. The deficiency of nickel and cobalt output will be a clear challenge which needs totally new technologies for the extraction.

Radical improvements in technology have so far not emerged without thorough fundamental information about the physics, chemistry, and engineering behind the inventions. This fact requires

significant Research and Technology development (RTD) input from the mining and smelting community for decarbonising their operations and maximising the metal value yields to the thermodynamic limits.

The environmental awareness of the consumers is an important issue of today which supports transparency to the entire production chain of metals. Carbon free metals and sulfuric acid over the production chain are today's slogan but when that option is reality in many mining operations in remote areas is a question mark. It will be seen whether the consumers are willing to pay premium for environmentally friendly metals' options in the end use. That also means, to cover the cost of recycling the metals when the demand will be 2–5 per cent larger next year to the present and some investment goods have a life span on several decades instead of six months of the cell phones of today. Or is such an option viable that you're allowed to get a new cell phone, car battery, or PC only when you after payment return the old one to an authorised dealer for reuse or recycling?

In copper and nickel sulfide smelting, the recoveries of precious metals are today important for the feasibility of the custom smelters, but due to low prices of many minority metals they are discarded in slag landfills. It is one of emerging issues in the secondary copper smelting today. Once the demand of the trace elements 'technology elements' grows, the same question will be faced also in the mining-beneficiation-smelting-refining chains of the primary production of nickel, zinc, and lead. The distributions of many technology metals in the copper and nickel smelting have been recently studied using methods where the chemically bound trace elements in the slag and its phases at the smelting conditions have been studied. Thus, the key data about options for process optimisation, modifications, and additional processing steps are piling up.

An important issue in the process development is the needs of mode accurate fluxing control in the intensive processing technologies compared with the old processes. Then, the practical operation must more and more rely on on-line or off-line computational tools for maintaining the heat balance and the intended fluxing. For that purpose, digital tools and AI may bring added value.

ACKNOWLEDGEMENTS

The authors are indebted to several R&D programs funded by Tekes and Business Finland over the years 2013–2023 (eg ARVI, SIMP, SYMMET, TOCANEM) as well as Metso-Outotec and Boliden for their encouragement, industrial contribution, and financial support.

REFERENCES

Alvear Flores, G, Risopatron, C and Pease, J, 2020. Processing of complex materials in the copper industry: Challenges and opportunities ahead, *JOM*, 72(10):3447–3461.

Avarmaa, K, O'Brien, H, Johto, H and Taskinen, P, 2015. Equilibrium distribution of precious metals between slag and copper matte at 1250–1350°C, *J Sustain Metall*, 1(3):216–228.

Avarmaa, K, Yliaho, S and Taskinen, P, 2018. Recoveries of rare elements Ga, Ge, In and Sn from waste electric and electronic equipment through secondary copper smelting, *Waste Mngmnt*, 71:400–410.

Awe, S, 2010. Hydrometallurgical upgrading of a tetrahedrite rich copper concentrate, Lic Thesis, Tech Univ Luleå, Sweden, 106 p.

Baba, K and Yamaguchi, K, 2013. The solubility of platinum in the FeO_x-SiO_2 slag at 1573 K, *JMMIJ*, 129:208–212.

Bryk, P, Malmström, R and Nyholm, E, 1966. Flash smelting of lead concentrates, *JOM*, 18(12):1298–1302.

European Commission, 2023. European Critical Raw Materials Act 2023, Directorate-General for Internal Market, Industry, Entrepreneurship and SMEs. Available from: <https://single-market-economy.ec.europa.eu/publications/european-critical-raw-materials-act_en>

Faraij, F, Golmohammadzadeh, R and Pickles, C, 2022. Potential and current practices of recycling waste printed circuit boards: A review of the recent progress in pyrometallurgy, *J Environm Mngmnt*, 316:115242.

Fuentes, G, Vinals, J and Herreros, O, 2009. Hydrothermal purification and enrichment of Chilean copper concentrates, Part 2: The behavior of the bulk concentrates, *Hydrometall*, 95(1–2):113–120.

International Copper Study Group (ICSG), 2023. *World Copper Factbook 2023*. Available from: <https://icsg.org/copper-factbook/>

Jak, E, Shishin, D, Shevchenko, M and Hayes, P, 2022. Integrated experimental phase equilibria and thermodynamic modelling research and implementation in support of pyrometallurgical copper processing, in *Copper-Cobre 2022 The Igor Wilkomirsky Symposium of Pyrometallurgy*, pp 609–634.

Klemettinen, L, 2021. Behaviour of trace elements in copper smelting processes- LA-ICP-MS as a tool for sample characterisation, PhD thesis, Aalto University, 64 p.

Klemettinen, L, Avarmaa, K and Taskinen, P, 2017. Trace element distributions in black copper smelting, *World of Metallurgy-Erzmetall*, 70(5):257–264.

Kojo, I and Huppe, H, 2011. Sustainable copper production processes from mine to cathode copper: some process selection considerations, in *9th Int Conf on Clean Technologies for the Mining Industry*, 10 p.

Lennartsson, A, Engström, F, Samuelsson, C, Björkman, B and Pettersson, J, 2018. Large-scale WEEE recycling integrated in an ore-based Cu-extraction system, *J Sust Metall*, 4(2):222–234.

Mäkinen, T, Fagerlund, K, Anjala, Y and Rosenback, L, 2005. *Outokumpu's Technologies for Efficient and Environmentally Sound Nickel Production* in *COM 2005*, pp 71–80 (CIM-MetSoc: Montreal).

Moats, M, Alagha, L and Awuah-Offei, K, 2021. Towards resilient and sustainable supply of critical elements from the copper supply chain: A review, *J Clean Prod*, 307:127207.

Nakajima, K, Takeda, O, Miki, T and Nagasaka, T, 2009. Evaluation of methods of metal resource recyclability based on thermodynamic analysis, *Mater Trans*, 50(4):453–460.

Nassar, N, Kim, H, Frenzel, M, Moats, M and Hayes, S, 2022. Global tellurium supply potential from electrolytic copper refining, *Res Conserv Recycl,* 184:106434.

Park, M, Takeda, Y and Yazawa, A, 1984. Equilibrium relations between liquid copper, matte and calcium ferrite slag at 1523 K, *Trans JIM,* 25(10):710–715.

Pesonen, L, Johto, H, Jyrkönen, S and Lindgren, M, 2022. Expanded comparison of modern copper smelting technologies and related downstream processes, in *Proceedings of Copper-Cobre 2022 Symposium The Igor Wilkomirsky Symposium of Pyrometallurgy*, pp 165–181.

Richter, K, Campbell, A, Humayun, M and Hervig, R, 2004. Partitioning of Ru, Rh, Pd, Re, Ir and Au between Cr-bearing spinel, olivine, pyroxene and silicate minerals, *Geochim Cosmochim Acta*, 68(4):867–880.

Risopatron, C, 2018. Impurities in copper raw materials and regulatory advances in 2017, A global overview, in *Int Semin Impurities in Copper Raw Materials*, p 85 (International Copper Study Group: Portugal). Available from: <http://www.jogmec.go.jp/content/300358430.pdf>

Salminen, J, Nyberg, J, Imris, M and Heegard, B, 2020. Smelting jarosite and sulphur residue in a plasma reactor, in *9th Int Symp PbZn* (eds: A Siegmund, S Alam, J Grogan, U Kerney and E Shibata), pp 391–403.

Sukhomlinov, D, Avarmaa, K, Virtanen, O, Taskinen, P and Jokilaakso, A, 2020a. Slag-copper equilibria of selected trace elements in black-copper smelting, Part II, Trace element distributions, *Miner Process Extr Metall*, 41(3):171–177.

Sukhomlinov, D, Klemettinen, L, O'Brien, H, Taskinen, P and Jokilaakso, A, 2020b. Behavior of Ga, In, Sn and Te in copper matte smelting, *Metall Mater Trans B*, 50(6):2723–2732.

Taskinen, P, 2011. Direct-to-blister smelting of copper concentrates: the slag fluxing chemistry, *Miner Process Extr Metall*, 120(4):240–246.

Tuominen, J and Kojo, I, 2005. Blister flash smelting-Efficient a flexible low-cost continuous copper process, in *Converter and Fire Refining Practices* (eds: A Ross, T Warner and K Scholey), pp 271–282.

Tuominen, J, Anjala, Y and Björklund, P, 2007. Slag cleaning of Outokumpu direct-to-blister flash smelting slags, in *Copper-Cobre 2007 International Conference*, pp 339–350 (MetSoc: Montreal).

United States Geological Survey (USGS), 2022. US Geological Survey releases 2022 list of critical minerals (media release). Available from: <https://www.usgs.gov/news/national-news-release/us-geological-survey-releases-2022-list-critical-minerals>

US EPA, 2023. Scope 3 Inventory Guidance. Available from: <https://www.epa.gov/climateleadership/scope-3-inventory-guidance>

The extraction of white phosphorus in molten salt

DOI: 10.62053/LTCW2444

X Yang[1]

1. Principle Investigator, Westlake University, Hangzhou, China.
   Email: yangxiao@westlake.edu.cn

ABSTRACT

White phosphorus (P_4) is a critical element in industry, but its current production from phosphate rock using the carbothermal reduction method raises significant environmental and health concerns. This pressing issue necessitates the development of new technologies that facilitate the sustainable production of P_4. In response, my team is actively developing an innovative, coke-free approach for white phosphorus production. This method involves the dissolution of phosphate rock in molten $CaCl_2$, followed by the extraction of P_4 through electrochemistry at relatively low temperatures. Moreover, this approach has the potential to utilise phosphate-bearing solid wastes as raw materials, further enhancing its environmental benefits. By employing this cutting-edge technique, we aim to revolutionise the phosphorus chemical industry towards greener and more sustainable practices. This paper provides evidence of the feasibility and effectiveness of our proposed approach.

INTRODUCTION

White phosphorus (P_4) is the starting material for various critical chemicals, such as phosphoric acids, chlorides, sulfides and phosphides. The global demand for P_4 has been steadily increasing in recent years. However, the P_4-manufacturing industry is facing significant challenges as the production process is highly energy-intensive and environmentally harmful. The supply of P_4 is susceptible to national trade policies, further complicating its availability in the market. Consequently, securing a stable supply of P_4 has become an urgent concern for many countries.

The industrial production of P_4 involves heating a mixture of phosphate rock [$Ca_5(PO_4)_3F$], sand (SiO_2) and coke (C) in an electric furnace at around 1500°C. This energy-intensive process, depicted in Figure 1a, consumes a substantial amount of electricity (13.5~15 MWh per ton of P_4) due to the highly endothermic nature of the carbon-driven reduction of phosphate. Ensuring product quality is challenging as the high temperatures make the process susceptible to impurity contamination, necessitating additional purification steps for high-purity product production. Furthermore, the emission of significant quantities of hazardous by-products poses severe environmental concerns.

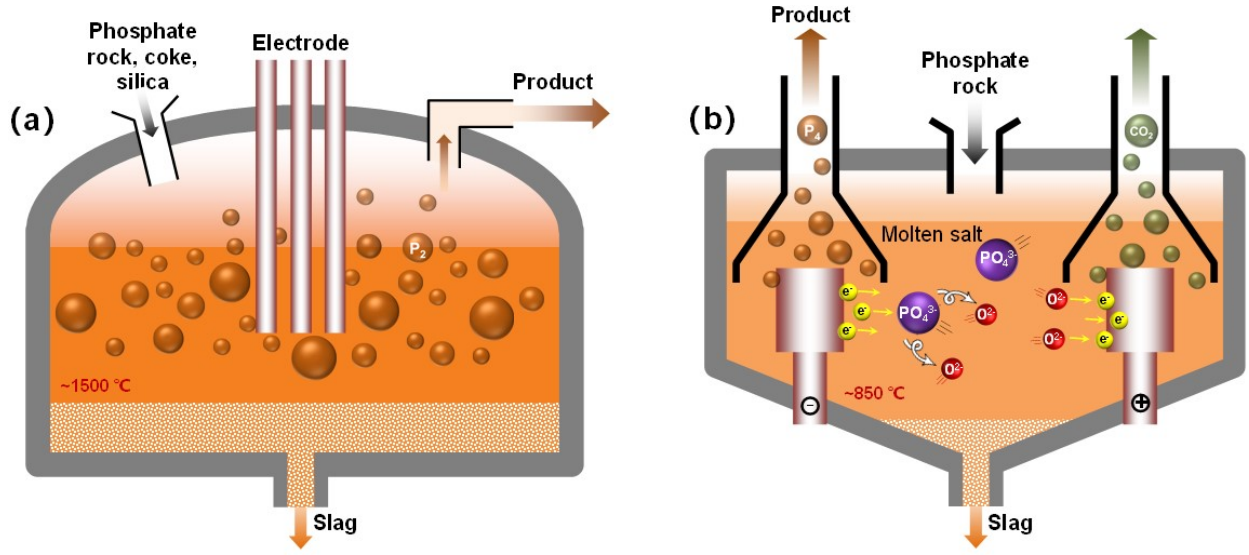

FIG 1 – Illustration of white phosphorus production processes: (a) the carbothermal reduction process; and (b) the electrochemical reduction process.

The advancement of P_4-manufacturing technology is crucial for sustainable development. In this study, we present a novel process for producing P_4 (Yang and Nohira, 2020; Liu, Ma and Yang, 2024), as illustrated in Figure 1b. This innovative process involves dissolving phosphate rock in molten $CaCl_2$, followed by the electrochemical extraction of P_4. Notably, this approach eliminates the need for coke and operates at a lower temperature of approximately 850°C. As a result, the electrochemical method is expected to offer substantial advantages over the traditional carbothermal process, particularly in terms of simplicity and cleanness. This paper demonstrates the feasibility and effectiveness of our proposed approach.

EXPERIMENT

Molten $CaCl_2$ was employed as the solvent and electrolyte. Pure $Ca_5(PO_4)_3F$ and natural phosphate rock (mined in Hubei, China) were added into molten $CaCl_2$ at 850°C, respectively. Figure 2a shows the set-up used to study the dissolution behaviour of $Ca_5(PO_4)_3F$ or natural phosphate rock in molten $CaCl_2$. The experiment was performed in a crucible furnace. The melts sampled at regular time intervals by dipping an Al_2O_3 rod into the melt bath were analysed by inductively coupled plasma – mass spectroscopy (ICP-MS) to reveal the concentration of soluble phosphorus.

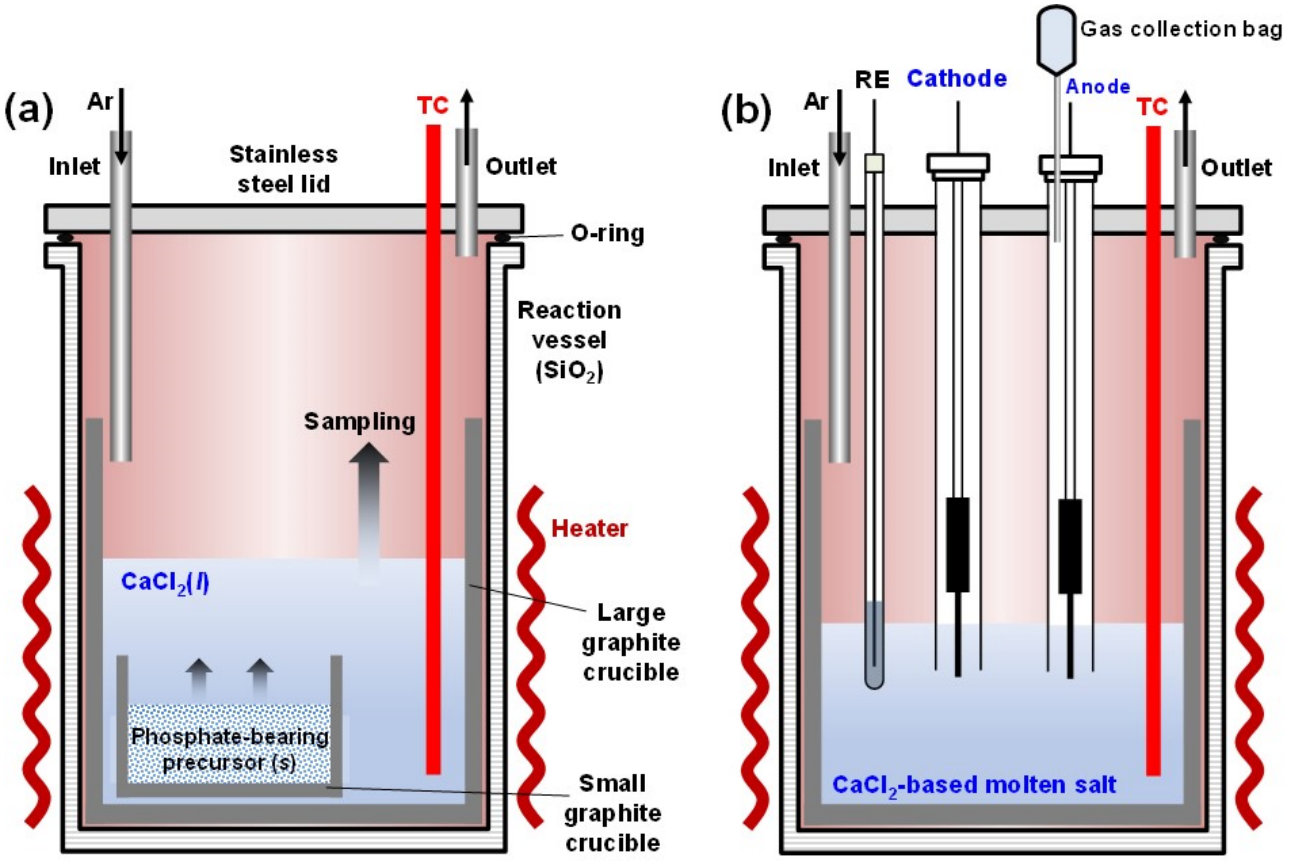

FIG 2 – Schematic diagram of experimental set-ups for (a) dissolution of $Ca_5(PO_4)_3F$ or phosphate rock in molten $CaCl_2$ and (b) electrochemical tests and P_4 extraction.

Electrochemical experiments were conducted in the melt after dissolving 20 g of phosphate rock in 300 g of molten $CaCl_2$ for 48 hr at 850°C. Cyclic voltammetry (CV) and electrolysis were conducted in a three-electrode manner. The reference electrode (RE) was an Ag^+/Ag electrode prepared by immersing an Ag wire in $CaCl_2$ containing 0.5 mol per cent AgCl in a SiO_2 tube. A graphite rod (diameter 5 mm) enclosed by a quartz tube was used as the cathode and anode, which were immersed in the melt to a depth of 25 mm. The cathodic product after dissolving in CS_2 was tested by 600 MHz Solution NMR Spectrometer. The anodic gas was analysed by Gas Chromatography.

RESULTS AND DISCUSSION

In Figure 3a, the dissolution profiles of P from excessive phosphate rock in 300 g of molten $CaCl_2$ at different temperatures are presented. The results indicate that the concentrations of P in the melt increase rapidly and reach a plateau in less than 10 mins, suggesting a fast and efficient dissolution process. The plateau values represent the solubility of P at each temperature, as they are lower than the theoretical concentration of P assuming complete dissolution of P in phosphate rock. The solubility of P is observed to increase with temperature. It should be noted that, in comparison to the dissolution of $Ca_5(PO_4)_3F$, the dissolution rate of P from phosphate rock is evidently higher, while the solubility is slightly lower. This difference can be attributed to the presence of impurities in the phosphate rock.

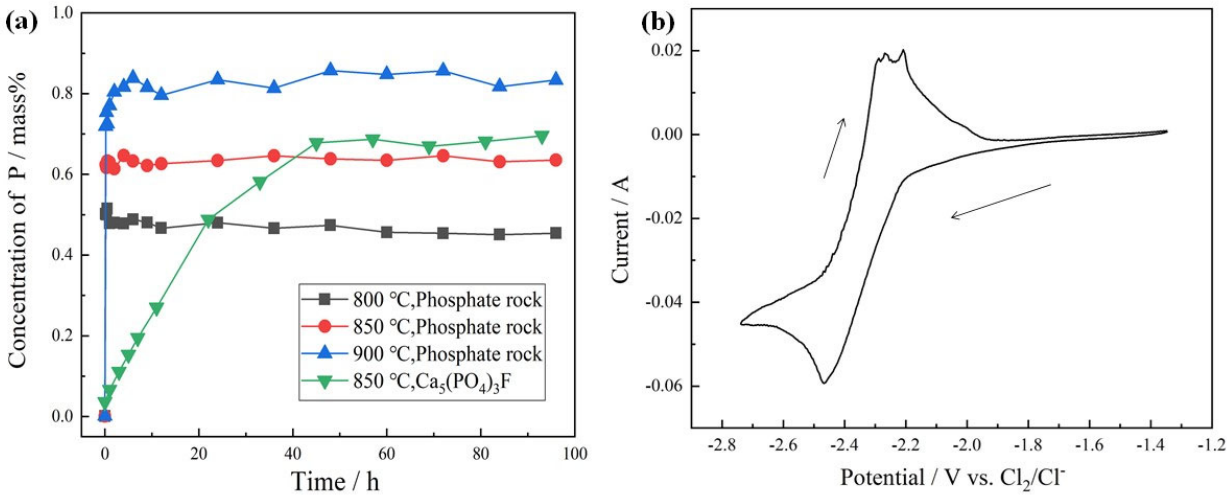

FIG 3 – (a) Dissolution profiles of P from phosphate rock and $Ca_5(PO_4)_3F$ in molten $CaCl_2$ at various temperatures. (b) Cyclic voltammograms at a graphite rod electrode (diameter 3 mm, immersion depth 1 mm) in 300 g of molten $CaCl_2$ after dissolving 20 g of phosphate rock for 48 hr at 850°C.

Figure 3b shows the cyclic voltammograms in the melt. Considering the electrical resistance of the melt, 70 per cent IR compensation was applied. Cathodic currents increase at potentials negative than –2.0 V (vs Cl_2/Cl^-), which is attributed to the electrochemical reduction of PO_4^{3-}. Subsequent investigations confirm that the product is P_4. A single cathodic peak can be clearly observed in most cases, suggesting that the electrochemical reduction of PO_4^{3-} can be approximated as a one-step (five-electron transfer) reduction process. The anodic peaks observed in the CV curves correspond to the oxidation of newly formed P_4 adhered on the cathode surface. The presence of multiple anodic peaks suggests that the oxidation process is more complex than the reduction process and may involve several intermediate products and electron transfer steps.

Following the cyclic voltammetry test, constant current electrolysis was conducted. Figure 4a shows the photographs of the upper section of the cathode after electrolysis at -0.1 A cm^{-2} for 10 hrs. Yellow substance condensed on the inner wall of the quartz tube was confirmed to be P_4 by ^{31}P NMR analysis. Chemical analysis indicates that the obtained P_4 product through molten salt electrolysis is of significantly higher purity compared to the industrial-grade commercial product produced by the carbothermal reduction process.

Figure 4b shows the chromatograms of the anodic gas collected at different moments during the electrolysis. Both CO and CO_2 were identified in the anodic gas and the quantitative analysis showed that CO_2 was the dominant one. These results suggest that the following electrode reactions occur during electrolysis:

$$\text{Cathode: } 4PO_4^{3-} + 20e^- \rightarrow 16O^{2-} + P_4(g) \quad (1)$$

$$\text{Anode: } C(s) + 2O^{2-} \rightarrow CO_2(g) + 4e^- \quad (2)$$

$$\text{Overall: } 4PO_4^{3-} + 5C(s) \rightarrow 6O^{2-} + 5CO_2(g) + P_4(g) \quad (3)$$

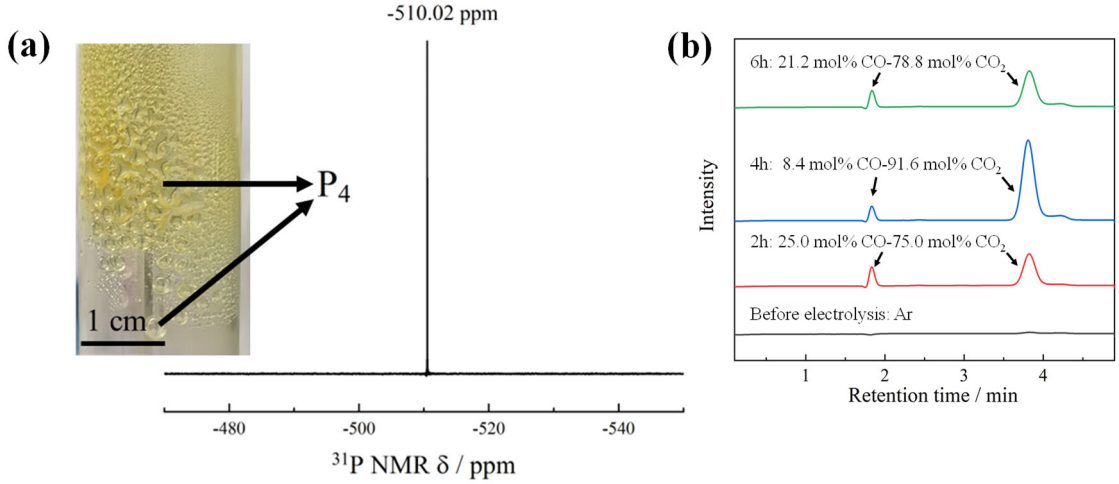

FIG 4 – (a) Photograph of the upper section of the quartz tube enclosing the cathode and ^{31}P NMR spectrum of the product after electrolysis at -0.1 A cm^{-2} for 10 hrs in the melt after dissolving 20 g of phosphate rock in 300 g of molten $CaCl_2$ for 24 hrs at 850°C. (b) Chromatograms of three anodic gas samples collected at different moments during the electrolysis and pure Ar.

CONCLUSIONS

This work demonstrates a more environmentally friendly and efficient approach for extracting white phosphorus from phosphate rock through molten salt electrolysis. In this process, phosphate rock dissolves in molten $CaCl_2$, allowing the soluble PO_4^{3-} to be electrochemically reduced. Notably, the operating temperature required for producing white phosphorus is only 850°C, which is significantly lower than that required in the conventional carbothermal reduction process. Additionally, white phosphorus produced through molten salt electrolysis exhibits a higher purity level compared to the industrial-grade commercial product obtained through carbothermal reduction. The electrochemical process also shows decreased electricity and carbon consumption. These findings underscore the potential of the electrochemical reduction process as a future method for extracting high-purity white phosphorus.

REFERENCES

Liu, G, Ma, Y and Yang, X, 2024. Cleaner extraction of white phosphorus from phosphate rock through molten salt electrolysis, *J Cleaner Prod,* 434(1):1403.

Yang, X and Nohira, T, 2020. A new concept for producing white phosphorus: electrolysis of dissolved phosphate in molten chloride, *ACS Sustain Chem Eng,* 8(36):13784–13792.

Research on –
Recycling and environment sustainability

The effect of FeO/SiO_2 ratio on the feasibility of utilising iron silicate slags as supplementary cementitious materials

DOI: 10.62053/GRUA2777

A Andersson[1], J Isaksson[2], L Brander[3], A Lennartsson[4], Å Roos[5] and F Engström[6]

1. Associate Senior Lecturer, Luleå University of Technology, Luleå 971 87, Sweden. Email: anton.andersson@ltu.se
2. Associate Senior Lecturer, Luleå University of Technology, Luleå 971 87, Sweden. Email: jenny.isaksson@ltu.se
3. Senior Scientist, Research Institutes of Sweden, Mölndal 431 53, Sweden. Email: linus.brander@ri.se
4. Senior Lecturer, Luleå University of Technology, Luleå 971 87, Sweden. Email: andreas.lennartsson@ltu.se
5. Product Manager, Boliden Smelters, Stockholm 101 20, Sweden. Email: ake.roos@boliden.com
6. Associate Professor, Luleå University of Technology, Luleå 971 87, Sweden. Email: fredrik.i.engstrom@ltu.se

ABSTRACT

Slags are the most voluminous solid by-products generated in pyrometallurgical operations, and, as such, finding an application for these oxidic materials is pertinent to maintaining resource efficiency. In particular, pyrometallurgical copper production is associated with high slag rates, typically ranging from 2.2 to 3.0 tons of slag per ton produced copper, which necessitates slag valourisation. A possible application for these iron silicate slags is as supplementary cementitious materials (SCMs), which effectively lowers the CO_2 emissions per ton of cementitious material. Although utilising iron silicate slags as SCMs has been studied in previous work, the scientific literature has limited data on the effect of composition on the inherent reactivity in cementitious systems. More specifically, no reports on the impact of FeO/SiO_2 ratio have been presented in previous publications. Therefore, the present study aimed to isolate this parameter in a synthetic FeO-SiO_2-Al_2O_3-CaO-MgO-Cr_2O_3 system. Since the amorphous content is a pertinent parameter for SCMs, a high-temperature confocal laser scanning microscope (HT-CLSM) was utilised to assess the crystallisation behaviour at continuous cooling conditions. Furthermore, high-temperature rheological experiments were conducted to measure the viscosities of the slags in relation to the crystallisation behaviour. The experiments showed that depolymerising the slag by increasing the FeO/SiO_2 ratio generated a less viscous slag, which showed higher tendencies for crystallisation. Furthermore, experiments assessing the inherent reactivity as an SCM showed that depolymerising the slag by increasing the FeO/SiO_2 ratio as the sole independent parameter generated an initially more reactive slag. However, replacing SiO_2 with FeO was found to negatively affect the reactivity as measured over seven days within the tested compositional range.

INTRODUCTION

The pyrometallurgical extraction of copper is associated with slag rates in the range of 2.2 to 3.0 tons of slag per ton produced copper (Shi, Meyer and Behnood, 2008; Gabasiane *et al*, 2021), and this necessitates slag valourisation to ensure a resource-efficient process. Multiple external applications are reported for the recycling of copper slags, eg sand blasting media, auxiliary to sand in cement, and various construction applications excluding cement (Al-Jabri *et al*, 2006; Shi, Meyer and Behnood, 2008; Murari, Siddique and Jain, 2015; Gabasiane *et al*, 2021; Kero Andertun *et al*, 2022). An attractive valourisation route for the slag is the utilisation as an supplementary cementitious material (SCM), which lowers the carbon dioxide emissions per ton cementitious material since the SCM requires neither calcination nor clinkering (Lothenbach, Scrivener and Hooton, 2011).

As summarised in a previous publication (Andersson *et al*, 2023a), several studies have been published addressing iron silicate copper slags in SCM applications, and the assessed compositions span wide ranges in the major components. For a specific slag composition, several parameters affect the reactivity of the slag as an SCM. These parameters include, eg the amorphous content, specific surface area, and thermal history (Skibsted and Snellings, 2019). Furthermore, in addition to generating specific surface area, the milling can be operated to cause amorphisation (Feng *et al*,

2019a) or activation by introducing surface defects (Romero Sarcos *et al*, 2021; Andersson *et al*, 2023a), both of which improve reactivity. The review of previously studied slag compositions showed that the slags were generated using different cooling processes, amounting to different amorphous contents, and, in addition, the slags were milled to different specific surface areas and evaluated for their performance as SCMs using different methodologies (Andersson *et al*, 2023a). Consequently, the previous data cannot be used across studies to evaluate the compositional aspect since essential parameters are not fixed between studies. Nevertheless, research on the isolated effects of CaO content (Feng *et al*, 2019b) and Al_2O_3 content (Zhang *et al*, 2023) on the performance of iron silicate slag in SCM applications have been performed. However, no study on the implications of changing the FeO/SiO_2 ratio has been published.

Assuming that the slag composition is fixed, two main parameters affect the appropriateness of using the slag as an SCM. Firstly, the cooling process, which correlates to the degree of crystallinity of the slag and possibly the polymerisation (Stebbins, 1988). Crystalline phases are generally considered inert in SCM applications (Snellings, 2013; Kucharczyk *et al*, 2018; Glosser *et al*, 2021), which means that the cooling rate must supersede crystallisation. Secondly, the subsequent milling of the solidified slag, which determines the specific surface area, as well as the possible amorphisation (Feng *et al*, 2019a), or activation from introducing surface defects (Romero Sarcos *et al*, 2021; Andersson *et al*, 2023a). Ramanathan, Tuen and Suraneni (2022) argued that the reactivity of SCMs is controlled by the surface area, extent of amorphous phases, and compositions of the amorphous phases. Consequently, to compare the effect of chemical composition, the slags require similar specific surface areas and amorphous contents.

Based on the above, the present study aimed to offer insight into the effect of FeO/SiO_2 ratio on the suitability of forming a reactive SCM. The aim was addressed using a synthetic FeO-SiO_2-CaO-Al_2O_3-MgO-Cr_2O_3 system and evaluating how the FeO/SiO_2 ratio influences the crystallisation behaviour under continuous cooling conditions and how this relates to the viscosity of the slag. Furthermore, the effect of the FeO/SiO_2 ratio on the inherent reactivity in the SCM application for slags cooled under repeatable conditions and milled to similar specific surface areas was assessed.

METHOD

Synthesis of samples

Two iron silicate slag samples in the FeO-SiO_2-CaO-Al_2O_3-MgO-Cr_2O_3 system were synthesised, and their intended compositions given in atomic percent (at%) are presented in Table 1. The methodology of synthesising and granulating the samples has been accounted for in detail in a previous publication (Andersson *et al*, 2023b), and, therefore, the present description offers a summary.

TABLE 1

Composition of the samples included in the study [at%].

Sample	FeO/SiO_2	FeO	SiO_2	CaO	Al_2O_3	MgO	Cr_2O_3
A	1.25	51.2	41.0	1.2	5.0	1.5	0.08
B	2.00	61.5	30.7	1.2	5.0	1.5	0.08

The compositions in Table 1 were mixed based on the reagent grade chemicals Fe, Fe_2O_3, SiO_2, $CaCO_3$, Al_2O_3, MgO, and Cr_2O_3. Each synthetic slag was melted in an iron crucible (>99.82 per cent Fe), which ensures that a partial pressure of oxygen relevant to iron silicate slags undergoing the zinc fuming process is attained (Andersson *et al*, 2023b). Figure 1 illustrates the graphite resistance-heated furnace employed in the experiments, and this set-up was operated under inert atmosphere achieved by introducing nitrogen (99.996 per cent N_2) and argon (99.999 per cent Ar) at flow rates of 12 L/min and 3 L/min, respectively. The temperature was ramped at a rate of 10 K/min to 100 K above the calculated liquidus temperature of each respective slag composition (disregarding the spinel phase in case of primary crystallisation, ie 100 K above the first crystal to co-precipitate). These calculations were performed using the Equilib module of FactSage™ ver 8.2 (by ThermFact

Inc. and GTT-Technologies) employing the GTOx database (Bale *et al*, 2016; Yazhenskikh *et al*, 2019). The idea of including Cr_2O_3 and subsequently not considering the primary crystallisation of the spinel was accounted for in the previous publication (Andersson *et al*, 2023b). Based on the calculations, slag A and B were synthesised at 1509 and 1517 K, respectively. After an isothermal section of two hrs at the respective temperature, the crucible was removed manually from the furnace, and the slag was granulated in water jets operating with cold tap water at a flow rate of 1.1 L/s. The methodology has been shown to produce synthetic iron silicate slags with relevant and repeatable results (Andersson *et al*, 2023b).

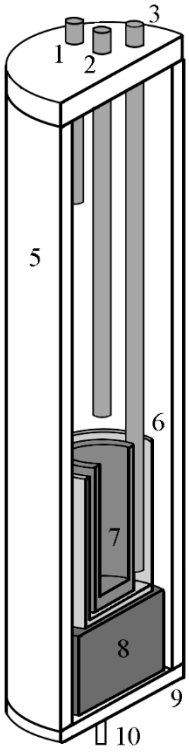

1. N_2 2 L/min
2. Ar 3 L/min
3. S-type thermocouple
4. Lid, not gas tight
5. Graphite working tube
6. Al_2O_3 crucible
   - Outer diameter 85 mm
   - Inner diameter 80 mm
   - Outer height 105 mm
   - Inner height 100 mm
7. Fe crucible
   - Outer diameter 60 mm
   - Inner diameter 50 mm
   - Outer height 100 mm
   - Inner height 90 mm
8. Graphite gas distributor
9. Bottom plate
10. N_2 10 L/min

FIG 1 – Schematic overview of the experimental set-up.

The synthesised slags were analysed for their chemical composition by an accredited laboratory using inductively coupled plasma mass spectrometry. The digestion of the samples prior to the analyses was achieved via microwave-assisted dissolution in a mixture of hydrochloric acid, nitric acid, and hydrofluoric acid after fusion with lithium metaborate.

Rietveld powder X-ray diffraction (XRD) with an internal standard was used to determine the amorphous content of the two slags. The internal standard calcite (99.5 per cent $CaCO_3$) was mixed to obtain 10 wt per cent in each sample. Mixing was made using a ring mill, and the subsequent scans were performed between 10 and 90 °2θ with copper K_α generated at 45 kV and 40 mA using a Malvern Panalytical Empyrean X-ray diffractometer (Malvern Panalytical, Malvern, UK). The refinement was performed using HighScore+ and the COD database (Gražulis *et al*, 2009).

Crystallisation and viscosity

A high-temperature confocal laser scanning microscope (HT-CLSM) (Yonekura VL2000DX-SVF17SP) was utilised to study the crystallisation behaviour of the two slags under continuous cooling experiments. The measurements were performed on sample sizes of 115 mg in molybdenum crucibles. The crucible choice was based on the alloying of platinum with iron experienced for iron silicate slags. Prior to the cooling cycle, the slags were allowed to homogenise at 1673 K for 300 secs. The primary crystallisation was determined for the cooling rates of 10, 25, 50, 100, 250, 500, and 1000 K/min.

In accordance with the evaluation of using different crucible and spindle materials for measuring the viscosity of iron silicate slags (Isaksson *et al*, 2023), the viscosity measurements in the present study were made using the rotating cylinder technique with a spindle and crucible made of molybdenum

(tzm molybdenum 364). Details related to the experimental set-up, eg manufacturer, placement of the thermocouple, gas atmosphere, calibration, and control of performance, have been accounted for in a previous publication (Isaksson *et al*, 2023).

The viscosity was measured at increments of 50 K during a cooling cycle from 1723 to 1423 K. Prior to each measurement at a new temperature, the slag was allowed to homogenise at a constant shear rate until stable values of the viscosity were achieved. The actual measurements were performed at shear rates of 1, 2, 4, 8, and 16 1/sec.

Inherent reactivity

The synthetic slags were milled iteratively to a similar specific surface area using a planetary ball mill operated at 600 revolutions per minute with 18 tungsten carbide balls of 10 mm in diameter in 45 mL tungsten carbide grinding bowls. The Brunauer, Emmet, and Teller (BET) specific surface area was measured after degassing at 573 K for 60 min.

The milled samples were subjected to the isothermal calorimetry-based rapid screening test for SCMs outlined by Snellings and Scrivener (2016), further developed and referred to as the rapid, relevant, and reliable (R^3) test by Avet *et al* (2016). This method was chosen based on the study presented by Li *et al* (2018), which demonstrated that the R^3 test results correlated strongly with the strength of mortars, independent of the type of SCM and with great repeatability between laboratories. Furthermore, this calorimetry-based testing method tests the inherent reactivity of the SCM without the influence of cement hydration (Hallet, De Belie and Pontikes, 2020; Sivakumar *et al*, 2021). Mixtures were prepared in accordance with Li *et al* (2018), and the heat flow was measured for seven days using a TAM Air isothermal calorimeter. A detailed description of the procedure employed at the current laboratory has been accounted for in a previous publication (Andersson *et al*, 2023c).

RESULTS AND DISCUSSION

Chemical and mineralogical composition

The analysed chemical compositions of the slags are presented in Figure 2a. For slag A, the FeO and SiO_2 contents were analysed to 53.3 and 38.2 at per cent, respectively. Analogously, for slag B, the FeO and SiO_2 contents were analysed to 61.7 and 30.4 at per cent, respectively. As no volatile components were included in the slags, deviations from the mixed composition should be solely attributed to the possible interaction with the crucible or to analytical errors. Stable oxides such as CaO, Al_2O_3, MgO, and SiO_2 are expected to interact less with the crucible, which is consistent with Figure 2a. More specifically, in comparison to the theoretical or mixed compositions, CaO, Al_2O_3, and MgO were within the experimental error reported by the accredited laboratory. The FeO/SiO_2 ratio of slag B was satisfactory, while slag A deviated from the mixed composition. Additional FeO might enter the slag from oxidation of the ferrous iron to ferric and the subsequent reduction of ferric iron to ferrous iron by the crucible, which could constitute the higher FeO/SiO_2 ratio. However, the experimental set-up was operated in an inert atmosphere, which should mitigate the proposed mechanism. Accounting for the reported error in the analysis, the quotient of slag A, determined to be 1.39, is within the experimental error of the theoretical ratio of 1.25. In conclusion, although the FeO/SiO_2 ratio of slag A was analysed to a higher quotient than aimed for, the attained chemical compositions successfully isolated the FeO/SiO_2 ratio as a parameter.

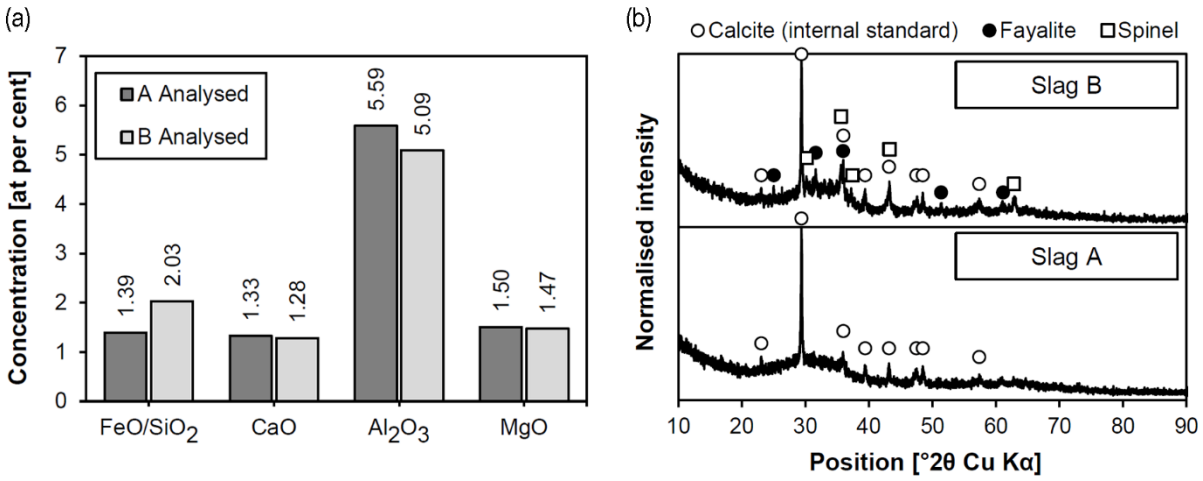

FIG 2 – (a) Chemical compositions in at% and quotient of at% for the FeO/SiO_2 ratio. (b) X-ray diffractograms of both slags including calcite as internal standard.

The mineralogical compositions of the samples are presented in Figure 2b. Slag A, having a lower FeO/SiO_2 ratio, was not analysed for any crystalline phases except the mixed internal standard. Therefore, an entirely amorphous slag was generated. On the other hand, slag B, with an FeO/SiO_2 ratio representing stoichiometric fayalite, was analysed for both fayalite and spinel. Based on the Rietveld refinement accounting for the internal standard, slag B was calculated to contain 90.1 wt per cent amorphous slag. Furthermore, spinel and fayalite were determined to constitute 3.3 and 6.6 wt per cent of the sample, respectively.

Crystallisation behaviour and measured viscosities

Based on the equilibrium-type cooling calculations, the liquidus temperatures of slag A and B were estimated to 1553 and 1610 K, respectively. Both slags experienced primary crystallisation of spinel with olivine, ie fayalite-forsterite solid solution, as the first crystal to co-precipitate. The co-precipitation was calculated to start at 1409 and 1417 K for slag A and B, respectively. Figure 3a presents the results of the HT-CLSM experiments. The dashed lines in the figure represent the continuous cooling temperature curves, and the plotted circles represent the crystallisation, ie the continuous cooling transformation curves. In comparison to the calculated temperature of primary crystallisation, the slowest cooling rate suggests lower temperatures than those predicted by the GTOx database.

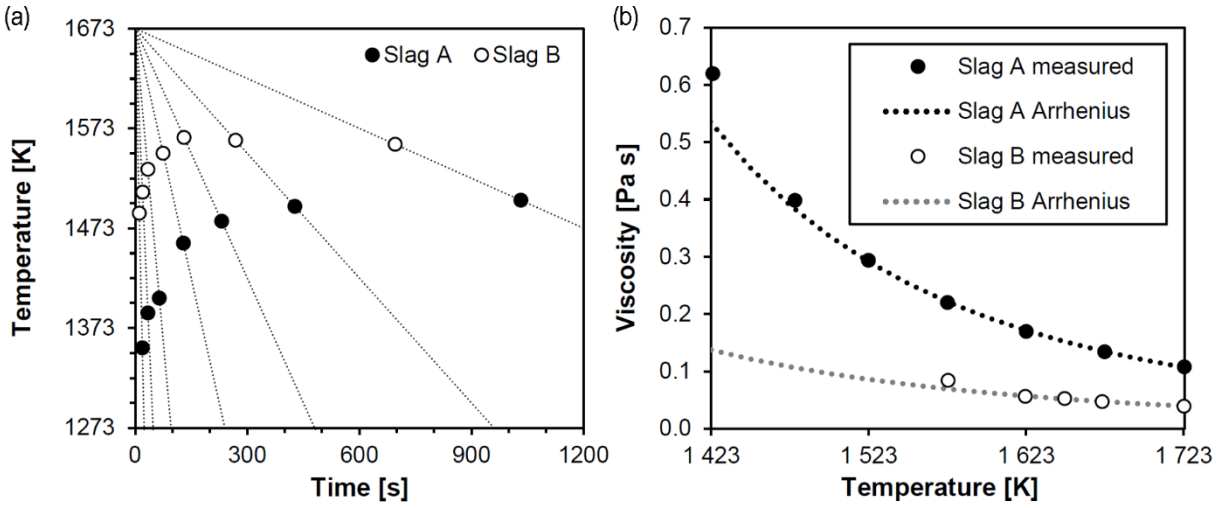

FIG 3 – (a) continuous cooling transformation diagram of the slags. (b) Measured viscosities of the slags.

The juxtaposition of the continuous cooling transformation curves of slag A and B in Figure 3a shows that the former slag is less prone to crystallisation. Both the absolute and relative temperature difference between the crystallisation at 10 K/min and 1000 K/min is more considerable for slag A in comparison to slag B, and, therefore, the granulation of slag A should more easily generate an entirely amorphous material. During the synthesis of the samples, the temperature of onset granulation for slag B (1517 K) was below the temperature of observed primary crystallisation, Figure 3a, which explains the presence of spinel in slag B, Figure 2b. However, in addition to spinel, fayalite was found in slag B, and this observation complies with the data related to the higher tendencies towards crystallisation.

Since low ion migration is related to energy barriers for crystallisation (Deng *et al*, 2022), the viscosities of slag A and B were measured to indirectly assess the differences in the degree of polymerisation and ion mobility. The average viscosity of 20 measurement points at a shear rate of 8 1/sec, at each temperature, is presented as circles in Figure 3b. For slag B, temperatures below 1573 K did not generate consistent values, which indicated that significant crystallisation had occurred. Therefore, the measurements in the cooling cycle were discontinued at 1523 K, and a supplementary measurement at 1648 K was included to incorporate an additional data point in the liquidus region. The viscosity data was used to calculate the activation energy of flow using an Arrhenius-type equation (Equation 1).

$$\eta = Aexp\left(\frac{E_a}{RT}\right) \quad (1)$$

where:

η	is the viscosity [Pa s]
A	is the pre-exponential factor [Pa s]
E_a	is the activation energy of flow [J/mol]
R	is the gas constant [J/mol K]
T	is the temperature [K]

Since Equation 1 is valid for a fully liquid slag, the calculations of the activation energy of flow were performed for the data points above the liquidus temperature. For slag A, the lowest temperature included in the calculations was 1523 K, which is consistent with the HT-CLSM data presented in Figure 3a. Analogously, for slag B, the calculations were performed with the four data points at 1623 K and above. This approach resulted in activation energies of 109.1 and 84.9 kJ/mol for slag A and B, respectively. Furthermore, the pre-exponential factors were calculated to 53 and 106 μPa s for slag A and B, respectively. The values represent what can be seen in Figure 3b, ie slag A has higher internal friction of flow. In addition, the activation energies highlight the structural changes with temperature, suggesting that lowering the temperature has higher implications on the structural changes of slag A compared to slag B. Finally, the plotted calculated viscosity for fully liquid slags using the parameters from Equation 1, labelled Arrhenius in Figure 3b, deviates from the measured viscosity in accordance with the crystallisation shown in Figure 3a.

The measured viscosities and the calculated activation energies of flow agree with the degree of polymerisation of the two slags, which can be compared using the ratio between non-bridging oxygen and tetragonally coordinated oxygen (NBO/T) calculated according to the method accounted for in the literature (Mills, 1995). More specifically, the NBO/T was calculated to be 1.92 and 2.91 for slag A and B, respectively, highlighting the network-breaking character of the ferrous oxide. Thus, the data support the observations from the crystallisation experiments and the mineralogical composition after the water granulation. A caveat can be introduced in accordance with the review on the viscosity of glass-forming systems (Zheng and Mauro, 2017), ie the viscosity-temperature relationship in the fully liquidus state does not necessarily represent the behaviour for a fully liquid supercooled melt. However, as SiO_2 behaves as a strong liquid with Arrhenius behaviour under supercooling while more depolymerised silicate melts are classified as fragile, the viscosity difference of slag A and B during supercooling might be enhanced. In conclusion, generating an entirely amorphous slag during granulation is comparatively more feasible for slag A than for slag B, which is positive for an intended application as an SCM.

Reactivity as a supplementary cementitious material

A previous study on SCMs have shown that the reactivity measured using the R^3 isothermal calorimetry-based experiment correlates to dissolved aluminium and silicon in cement pore solution conditions (Ramanathan *et al*, 2021). This is consistent with the formation of calcium-silicate-hydrate gel and calcium-aluminium-silicate-hydrate gel, as well as the alumina ferric oxide tri-substituted and mono-substituted phases upon the SCMs consumption of portlandite (Hallet, De Belie and Pontikes, 2020; Sivakumar *et al*, 2021). In the present study, the iterative milling generated samples with BET specific surface areas of 1.04 and 1.11 m^2/g for slag A and B, respectively. Therefore, the differences in the reactivities measured in the R^3 test, presented in Figure 4, can be attributed to the chemical and mineralogical characteristics of the slags, translating to the dissolution of silicon and aluminium from the slags to the cementitious system.

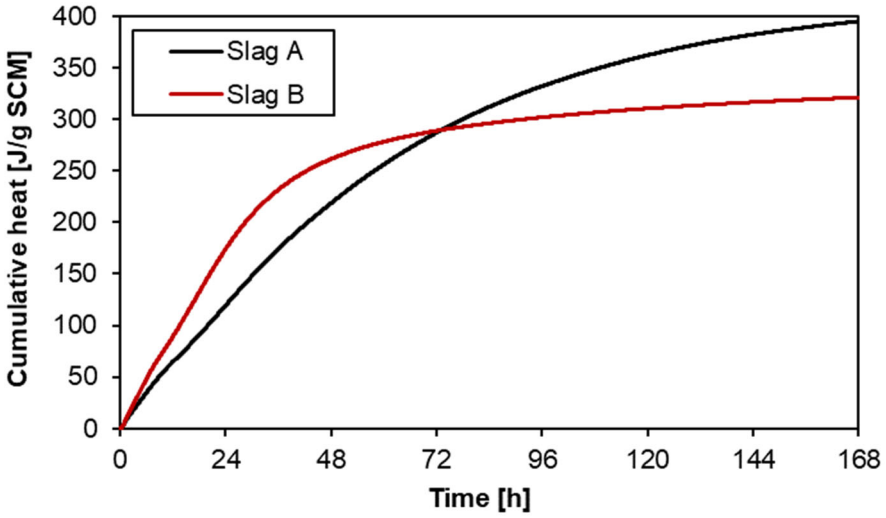

FIG 4 – Cumulative heat from the R^3 isothermal calorimetry experiment.

By depolymerising the slag via the replacement of silica with ferrous oxide, the contribution of silicon per mass unit of dissolved slag is less. Therefore, according to the data presented in Figure 4, slag B has an initially higher dissolution rate, which is consistent with previous studies showing that more depolymerised SCMs have higher dissolution rates in cement pore solution conditions (Snellings, 2013; Schöler *et al*, 2017).

Despite having an initially higher reaction rate, slag B is less reactive, as seen over the whole experimental period. This observation is still valid if the crystalline content of 9.9 wt per cent is considered inert, ie if the reactivity in Figure 4 is normalised for the amorphous part of slag B. Dissolving iron into the solution at alkaline pH and redox potentials relevant for cement pore solution conditions has been indicated to be less favourable (Andersson *et al*, 2023c), which might facilitate the generation of diffusion barriers upon dissolution of the slag. Such a diffusion barrier would be more pronounced for a higher FeO/SiO_2 ratio. Furthermore, depolymerising the slag by replacing silica with ferrous iron oxide lowers the total potential silicon available for the cementitious system. Consequently, the progressively lower heat flow of slag B, generating the intersection observed at 74 hrs in Figure 4, can be attributed to either mechanism or a combination of both.

CONCLUSIONS

In the present study, two synthetic slags within the $FeO\text{-}SiO_2\text{-}CaO\text{-}Al_2O_3\text{-}MgO\text{-}Cr_2O_3$ system were studied to isolate the effect of the changed FeO/SiO_2 ratio on the feasibility of utilising the slags as SCMs. Based on the experimental work, the following was concluded:

- By increasing the FeO/SiO_2 ratio from 1.39 to 2.03 (at%/at%), the viscosity was lowered at comparable temperatures above the liquidus of both slags owing to the network-breaking characteristics of FeO.

- Continuous cooling transformation experiments showed that the slag with higher FeO/SiO_2 ratio had higher inclination towards crystallisation, which corresponds to the mobility within the melt.
- Although the more depolymerised slag had higher initial reactivity as an SCM, the seven-day reactivity was lower, which in combination with the tendency to crystallise suggest that the lower FeO/SiO_2 ratio of the present study is more attractive for slag valourisation as an SCM.

ACKNOWLEDGEMENTS

The present study was financed by Boliden AB and conducted within the Centre for Advanced Mining and Metallurgy (CAMM) at Luleå University of Technology. The assistance of Britt-Louise Holmqvist and Jakob Kero Andertun is gratefully acknowledged.

REFERENCES

Al-Jabri, K S, Taha, R A, Al-Hashmi, A and Al-Harthy, A S, 2006. Effect of copper slag and cement by-pass dust addition on mechanical properties of concrete, *Construction and Building Materials*, 20:322–331.

Andersson, A, Brander, L, Lennartsson, A, Roos, Å and Engström, F, 2023a. Ground Granulated Iron Silicate Slag as Supplementary Cementitious Material: Effect of Prolonged Grinding and Granulation Temperature, *Journal of Cleaner Materials*, 10:100209.

Andersson, A, Brander, L, Lennartsson, A, Roos, Å and Engström, F, 2023b. A method for synthesizing iron silicate slags to evaluate their performance as supplementary cementitious materials, *Applied Sciences*, 13(14):8357.

Andersson, A, Isaksson, J, Lennartsson, A and Engström, F, 2023c. Insights into the valorization of electric arc furnace slags as supplementary cementitious materials, *Journal of Sustainable Metallurgy*, pp 1–14.

Avet, F, Snellings, R, Diaz, A A, Haha, M B and Scrivener, K, 2016. Development of a New Rapid, Relevant and Reliable (R^3) Test Method to Evaluate the Pozzolanic Reactivity of Calcined Kaolinitic Clays, *Cement and Concrete Research*, 85:1–11.

Bale, C W, Bélisle, E, Chartrand, P, Decterov, S A, Eriksson, G, Gheribi, A E, Hack, K, Jung, I-H, Kang, Y-B, Melançon, J, Pelton, A D, Petersen, S, Robelin, C, Sangster, J, Spencer, P and Van Ende, M-A, 2016. Reprint of: FactSage Thermochemical Software and Databases, 2010–2016, *CALPHAD*, 55:1–19.

Deng, L, Yao, B, Lu, W, Zhang, M, Li, H, Chen, H, Zhao, M, Du, Y, Zhang, M, Ma, Y and Wang, W, 2022. Effect of SiO_2/Al_2O_3 ratio on the crystallization and heavy metal immobilization of glass ceramics derived from stainless steel slag, *Journal of Non-Crystalline Solids*, 593:121770.

Feng, Y, Kero, J, Yang, Q, Chen, Q, Engström, F, Samuelsson, C and Qi, C, 2019a. Mechanical Activation of Granulated Copper Slag and Its Influence on Hydration Heat and Compressive Strength of Blended Cement, *Materials*, 12:772.

Feng, Y, Yang, Q, Chen, Q, Kero, J, Andersson, A, Ahmed, H, Engström, F and Samuelsson, C, 2019b. Characterization and evaluation of the pozzolanic activity of granulated copper slag modified with CaO, *Journal of Cleaner Production*, 232:1112–1120.

Gabasiane, T S, Danha, G, Mamvura, T A, Mashifana, T and Dzinomwa, G, 2021. Environmental and Socioeconomic Impact of Copper Slag—A Review, *Crystals,* 11:1–16.

Glosser, D, Suraneni, P, Burkan Isgor, O and Jason Weiss, W, 2021. Using glass content to determine the reactivity of fly ash for thermodynamic calculations, *Cement and Concrete Composites*, 115:103849.

Gražulis, S, Chateigner, D, Downs, R T, Yokochi, A F T, Quirós, M, Lutterotti, L, Manakova, E, Butkus, J, Moeck, P and Le Bail, A, 2009. Crystallography Open Database - an Open-Access Collection of Crystal Structures, *Journal of Applied Crystallography*, 42:726–729.

Hallet, V, De Belie, N and Pontikes, Y, 2020. The impact of slag fineness on the reactivity of blended cements with high-volume non-ferrous metallurgy slag, *Construction and Building Materials*, 257:119400.

Isaksson, J, Andersson, A, Lennartsson, A and Samuelsson, C, 2023. Interactions of Crucible Materials With an FeO_x–SiO_2–Al_2O_3 Melt and Their Influence on Viscosity Measurements, *Metallurgical and Materials Transactions B,* 54B:3526–3541.

Kero Andertun, J, Samuelsson, C, Peltola, P and Engström, F, 2022. Characterisation and leaching behaviour of granulated iron silicate slag constituents, *Canadian Metallurgical Quarterly*, 61:14–23.

Kucharczyk, S, Sitarz, M, Zajac, M and Deja, J, 2018. The effect of CaO/SiO_2 molar ratio of CaO-Al_2O_3-SiO_2 glasses on their structure and reactivity in alkali activated system, *Spectrochimica Acta Part A*: *Molecular and Biomolecular Spectroscopy,* 194:163–171.

Li, X, Snellings, R, Antoni, M, Alderete, N M, Haha, M B, Bishnoi, S, Cizer, Ö, Cyr, M, De Weerdt, K, Dhandapani, Y, Duchesne, J, Haufe, J, Hooton, D, Juenger, M, Kamali-Bernard, S, Kramar, S, Marroccoli, M, Joseph, A M,

Parashar, A, Patapy, C, Provis, J L, Sabio, S, Santhanam, M, Steger, L, Sui, T, Relesca, A, Vollpracht, A, Vargas, F, Walkley, B, Winnefeld, F, Ye, G, Zajac, M, Zhang, S and Scrivener, K L, 2018. Reactivity Tests for Supplementary Cementitious Materials: RILEM TC, 267-TRM Phase 1, *Materials and Structures*, 51:151.

Lothenbach, B, Scrivener, K and Hooton, R D, 2011. Supplementary cementitious materials, *Cement and Concrete Research*, 41:1244–1256.

Mills, K C, 1995. Structure of liquid slags, in *Slag Atlas* (ed: D Springorum), pp 1–8 (Verlag Stahleisen GmbH: Düsseldorf).

Murari, K, Siddique, R and Jain, K K, 2015. Use of waste copper slag, a sustainable material, *Journal of Material Cycles and Waste Management*, 17:13–26.

Ramanathan, S, Perumal, P, Illikainen, M and Suraneni, P, 2021. Mechanically activated mine tailings for use as supplementary cementitious materials, *RILEM Technical Letters*, 6:61–69.

Ramanathan, S, Tuen, M and Suraneni, P, 2022. Influence of supplementary cementitious material and filler fineness on their reactivity in model systems and cementitious pastes, *Materials and Structures*, 55(5):136.

Romero Sarcos, N, Hart, D, Bornhöft, H, Ehrenberg, A and Deubener, J, 2021. Rejuvenation of granulated blast furnace slag (GBS) glass by ball milling, *Journal of Non-Crystalline Solids*, 556:120557.

Schöler, A, Winnefeld, F, Haha, M B and Lothenbach, B, 2017. The effect of glass composition on the reactivity of synthetic glasses, *Journal of the American Ceramic Society*, 100(6):2553–2567.

Shi, C, Meyer, C and Behnood, A, 2008. Utilization of copper slag in cement and concrete, *Resources, Conservation and Recycling,* 52:1115–1120.

Sivakumar, P P, Matthys, S, De Belie, N and Gruyaert, E, 2021. Reactivity assessment of modified ferro silicate slag by R^3 method, *Applied Sciences*, 11(1):366.

Skibsted, J and Snellings, R, 2019. Reactivity of supplementary cementitious materials (SCMs) in cement blends, *Cement and Concrete Research*, 124:105799.

Snellings, R and Scrivener, K L, 2016. Rapid Screening Tests for Supplementary Cementitious Materials: Past and Future, *Materials and Structures*, 49:3265–3279.

Snellings, R, 2013. Solution-controlled dissolution of supplementary cementitious material glasses at pH 13: the effect of solution composition on glass dissolution rates, *Journal of the American Ceramic Society*, 96(8):2467–2475.

Stebbins, J F, 1988. Effects of temperature and composition on silicate glass structure and dynamics: Si-29 NMR results, *Journal of Non-Crystalline Solids*, 106:359–369.

Yazhenskikh, E, Jantzen, T, Hack, K and Müller, M, 2019. A New Multipurpose Thermodynamic Database for Oxide Systems, *Rasplawy,* 2:116–124.

Zhang, Q, Deng, D, Feng, Y, Wang, D, Liu, B and Chen, Q, 2023. Effect of Al_2O_3 on the Structural Properties of Water-Quenched Copper Slag Related to Pozzolanic Activity, *Minerals*, 13(2):174.

Zheng, Q and Mauro, J C, 2017. Viscosity of glass-forming systems, *Journal of the American Ceramic Society*, 100(1):6–25.

Pyrometallurgical treatment of nickel smelting slag with biochar

DOI: 10.62053/CFLQ6633

D Attah-Kyei[1], D Sukhomlinov[2], M Tiljander[3], L Klemettinen[2], P Taskinen[2], A Jokilaakso[2] and D Lindberg[2]

1. Department of Chemical and Metallurgical Engineering, School of Chemical Engineering, Aalto University, Kemistintie 1, FI-00076 Aalto, Finland. Email: desmond.attah-kyei@aalto.fi
2. Department of Chemical and Metallurgical Engineering, School of Chemical Engineering, Aalto University, Kemistintie 1, FI-00076 Aalto, Finland.
3. Geological Survey of Finland, Vuorimiehentie 2, 02150 Espoo, Finland.

ABSTRACT

In this study, the use of carbon neutral biochars as reducing agents in the pyrometallurgical treatment of nickel slag was investigated at 1400°C in order to recover valuable elements such as copper and nickel from the slag. A large amount of slag is generated during the nickel matte smelting. Nickel slag contains valuable elements such as copper, nickel and cobalt, which can be recovered. Disposal of this slag results in loss of resources and may cause pollution of the environment. It is important to retrieve these metals for environmental and economic reasons.

In this study, the slag was reacted with non-fossil reducing agents (biochar) which were produced from hydrolysis lignin and black pellet biomass pyrolyzed at 600 and 1200°C and with metallurgical coke for comparison. The reduction experiments were done at 1400°C for 15, 30 and 60 mins under inert gas atmosphere. The samples were quickly quenched and analysed with Electron Probe X-ray Microanalysis (EPMA). The results showed that the use of biochar resulted in faster reaction kinetics in the reduction process compared to coke. The fast reaction kinetics is attributed to the relatively high content of volatiles in this biochar, leading to gas formation and thus mixing of the sample material. Moreover, thermodynamic modelling was also performed using FactSage™ to simulate equilibria with different amounts of biochar. The metal to slag distribution coefficient calculated from the results of thermodynamic modelling were consistent with experimental results. In addition, thermodynamic calculations confirmed that nickel is reduced rapidly and it deports to the metal alloy phase. As the reduction progresses or extra reductant is available for reactions, more iron is deported to the metal phase. The calculations also revealed that Zn vaporises into the gas phase.

INTRODUCTION

Nickel is an important non-ferrous metal which is widely used in machinery, architecture, steelmaking, military and other fields due to its physical and chemical properties. During the pyrometallurgical production of nickel, about 6–16 tons of nickel smelting slag is generated per ton of nickel produced (Sun *et al*, 2021; Zhang *et al*, 2020). The slag usually contains some valuable elements such as copper, cobalt and nickel and these valuable metals can exist in the form of sulfides, oxides, or dissolved elements. It is important to effectively extract valuable elements from nickel slag to ensure environmental sustainability and efficient resource utilisation since negligent disposal of this waste stream results in environmental pollution and loss of valuable elements (Zhang *et al*, 2020).

Dańczak *et al* (2021) employed anodic graphite of spent batteries as reductant in nickel slag reduction at 1350°C. They reported that metal alloy, matte, and slag phases were formed after reduction, and concluded that the metal/matte to slag distribution coefficient increases with an increase in the amount of spent battery. Avarmaa *et al* (2020), on the other hand, studied the reduction of nickel slag at 1400°C with biochar and battery scrap mixture to recover valuable metals and compared the results to the reduction with coke. They reported that biochar enhanced reaction kinetics compared to coke and the presence of battery scrap greatly increased the distribution coefficients of valuable metals.

While nickel slag cleaning aims to recover valuable metals such as nickel, cobalt, and copper as much as possible in the metal alloy phase, it is important to minimise the iron content as it is very difficult to separate during downstream processes. Since some of the metals have similar reduction

properties as iron, some losses of valuable metals are unavoidable in the slag cleaning (Jones *et al*, 2002).

The metallurgical industry consumes great amounts of fossil fuels such as coke, which is mainly used as fuel and reducing agent resulting in large emissions of carbon dioxide and other greenhouse gases. In recent times, the use of non-fossil reductants in metal production have gained more attention (Cholico-González *et al*, 2021; Guo *et al*, 2017). One such option of non-fossil reductant is biocoke or biochar obtained from pyrolyzed biomass. Since biomass absorbs CO_2 from the atmosphere during their growth, they release the absorbed CO_2 in the reduction process, thus creating a closed loop carbon cycle (Adrados *et al*, 2016; Suopajärvi, Pongrácz and Fabritius, 2013). Several research groups have investigated the use of biomass or biochar as reductant in metal production (Avarmaa *et al*, 2020; Demey *et al*, 2021; Wiklund *et al*, 2017).

Adrados *et al* (2016) compared biocokes pyrolyzed from olive and eucalyptus trees with commercial reducing agents (metallurgical coke, petroleum coke and anthracite). They reported that based on proximate and ultimate analysis, olive, and eucalyptus biocokes (bioreducers) have better quality than the usual reducing agents, since the bioreducers have lower ash and sulfur contents. Moreover, the bioreductants used have much higher specific surface area and porosity than that of the commercial reductants, making them much more reactive. In their study on the effectiveness of using biomass-based reducing agent in blast furnace, Koskela *et al* (2019) concluded that the utilisation of biomass as raw material in blast furnace ironmaking can have an enormous contribution to the mitigation of CO_2 emissions in steelmaking. Moreover, Mousa *et al* (2016) reported that the use of biomass as a source of energy and reducing agents provides a promising alternative solution for green steel production.

The aim of this study was to ascertain the potential and effectiveness of using biochar as reducing agent to recover valuable metals like Co, Ni and Cu from nickel smelting slag as well as to understand the effects of reaction time.

EXPERIMENTAL

Materials

Industrial (ground) nickel smelting slag provided by Boliden Harjavalta Oy (Harjavalta, Finland) was used experiments. The slag used was XRF (X-ray fluorescence) as well as *magnetite content analyses (Satmagan) for the slag were conducted at Boliden Harjavalta Oy, see Table 1.

TABLE 1

Composition of Ni slag by XRF and it's *magnetite content.

Fe	Ni	Cu	Co	Cr	Zn	S	SiO_2	MgO	Al_2O_3	CaO	*Fe_3O_4
37	3.62	0.77	0.42	0.08	0.08	0.11	33.7	7.6	2.1	1.74	22

Four different kinds of reductants were tested in the experiments, ie black pellets pyrolyzed at 600°C (B600) and 1200°C (B1200) and hydrolysis lignin pyrolyzed at 600°C (L600) and 1200°C (L1200). The ultimate and proximate analysis (shown in Table 2) of these reductants were done with Elemental Analyzer Flash 2000. Ash analysis of lignin and black pellet was conducted using inductively coupled plasma-optical emission spectroscopy (ICP-OES) and is shown in Table 3.

Table 2 shows that a biomass pyrolyzed at a higher temperature has higher fixed carbon and lower volatile matter contents. In addition, the ash content of black pellet is much higher than that of lignin. The ash analysis revealed that black pellets contain relatively high concentrations of Ca, K and Si. Most of the elements in the ash deport to the slag phase during reduction reactions. It can be seen in Table 2 that lignin has higher fixed carbon content compared to black pellet. The analysis reveals that biochar pyrolyzed at higher temperature contain higher carbon and lower hydrogen and nitrogen composition (Table 2). When biochar is employed as fuel or reducing agent in some metallurgical industries, low ash contents and high volatile matter may be advantageous (Wiklund *et al*, 2017).

TABLE 2

Ultimate and Proximate analyses of biochar.

	Properties	B600	B1200	L600	L1200
Ultimate analysis	C	76.62	81.21	87.90	96.73
	H	1.56	0.00	1.73	0.07
	O	7.33	5.73	8.50	2.15
	N	0.47	0.12	0.97	0.13
	S	0.00	0.00	0.00	0.00
Proximate analysis	Volatile matter	10.82	3.57	6.39	1.31
	Fixed Carbon	76.16	83.19	91.62	97.54
	Ash content	12.32	12.83	1.29	0.92

TABLE 3

Ash analysis of biochar used for the reduction study.

Element		Ca	Mg	Na	K	P	S	Fe	Al	Si	Mn	Ba
Lignin	mg/kg	290	51.0	<10	130	74	1100	810	14	<10	41	4.8
Black Pellet	mg/kg	13900	960	210	2600	560	-	680	680	7400	400	200

The stoichiometric amount of carbon required for reduction was calculated based on the composition of nickel slag after converting the metal concentrations to oxides, as shown in Equations (1) to (5). The stoichiometric mass of carbon to be used was calculated using Equations (6) to (11). The amount of reductant needed was calculated from the amount of carbon required.

$$2Cu + 0.5O_2 = Cu_2O \quad (1)$$

$$Zn + 0.5O_2 = ZnO \quad (2)$$

$$Ni + 0.5O_2 = NiO \quad (3)$$

$$Co + 0.5O_2 = CoO \quad (4)$$

$$2Cr + 1.5O_2 = Cr_2O_3 \quad (5)$$

$$Fe_3O_4 + C = 3FeO + CO \quad (6)$$

$$Cu_2O + C = 2Cu + CO \quad (7)$$

$$ZnO + C = Zn + CO \quad (8)$$

$$NiO + C = Ni + CO \quad (9)$$

$$CoO + C = Co + CO \quad (10)$$

$$Cr_2O_3 + 3C = 2Cr + 3CO \quad (11)$$

Method

The vertical-tube furnace (Figure 1) used was Lenton LTF 16/450 (Lenton Furnaces and Ovens, Hope Valley, UK) The furnace temperature was set to 1400°C. The furnace was purged with argon gas (99.999 vol per cent purity, Wiokoski Oy, Finland) with a flow rate of 300 mL/min, controlled by a rotameter (Kytölä Instruments, Jyväskylä, Finland ±5 per cent full scale) during the experiments. The cone-shaped silica glass Heraeus HSQ®300 crucibles (fused quartz with purity of >99.998 wt per cent by Finnish Special Glass Oy, Espoo, Finland), with a diameter of 25 mm and height of 15 mm were employed for nickel slag containment.

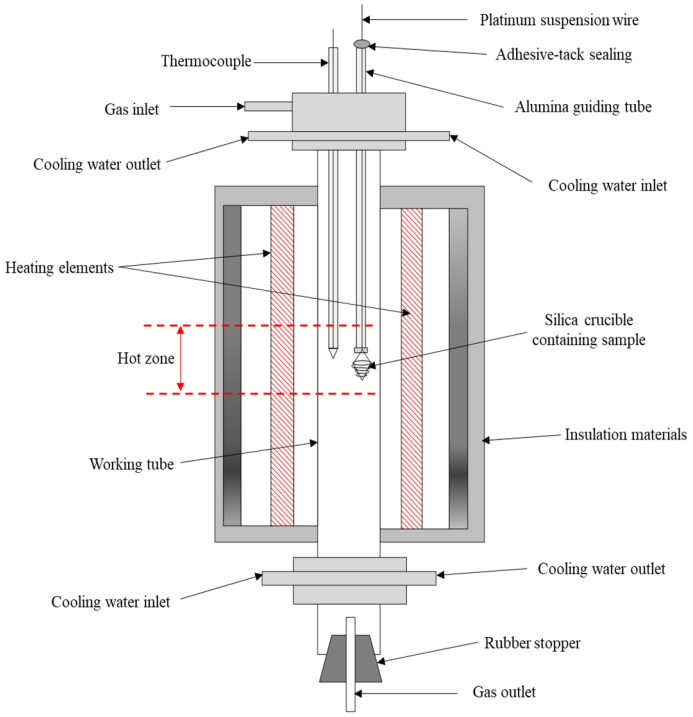

FIG 1 – Schematic of the vertical furnace used for nickel slag reduction experiments.

The drop-quench technique which have been employed by Avarmaa *et al* (2020) was used in this study. One gram of the slag was mixed with the calculated amount of biochar, pelletised and placed in a crucible. The crucible was placed in a basket and attached to platinum wire hanging from inside of the furnace and subsequently lifted to the lower end of the furnace of the furnace before sealing the work tube with a rubber plug. 300 mL/min argon gas was used to purge the furnace to create an inert atmosphere. After about 15 min, the sample was lifted to the hot zone where the reduction reactions took place. After reaching the desired reaction time, the sample was dropped into ice water by pulling the platinum wire, which caused the sample-basket assembly to detach and fall. Reduction experiments were carried out at 1400°C for 15, 30 and 60 mins for each of the reductants.

Characterisation of Sample

The samples were dried and cast in epoxy resin and after curing, they were cut in half and again mounted in epoxy resin and cured. The samples were then polished and carbon coated for scanning electron microscopy (SEM) and electron probe microanalysis (EPMA). Mira 3 Scanning Electron Microscope (Tescan, Brno, Czech Republic) equipped with an UltraDry Silicon Drift Energy Dispersive X-ray Spectrometer (EDS) was used to perform preliminary elemental analyses and microstructural imaging. The compositions of the metal and slag phases were measured using EPMA with an SX100 (Cameca SAS, Gennevilliers, France) microprobe equipped with five wavelength dispersive spectrometers (WDS).

RESULTS AND DISCUSSION

Reduction experiments

At the hot zone of the furnace (1400°C), the sample melts. Metal oxides (MeO) present in the slag react with the carbon in biochar producing metal (Me) as shown in Equation (12). Carbon monoxide produced may also take part in the reduction of metal oxides (see Equation (13)). As time progresses, more carbon and carbon monoxide react leading to a decrease in concentration of metals in the slag. The metal species produced from reduction of metal oxides as well as the mechanically droplets entrapped grow and form a metal alloy:

$$MeO(l) + C(s) = Me(l) + CO(g) \quad (12)$$

$$MeO(l) + CO(g) = Me(l) + CO_2(g) \quad (13)$$

Figure 2 shows the SEM micrographs of sample polished sections prepared from nickel slag reduction with biochar at 15, 30 and 60 mins. It can be observed that a metal alloy droplet was obtained with every contacting time, which suggests that the contact between the slags and reductants was good and the reactions proceeded rapidly. The round shaped bright regions seen in the images are the metal alloy droplets and the grey regions are the slag areas (see Figure 2). The samples from reduction were rapidly quenched (<3 sec) and the slag phase was generally homogenous.

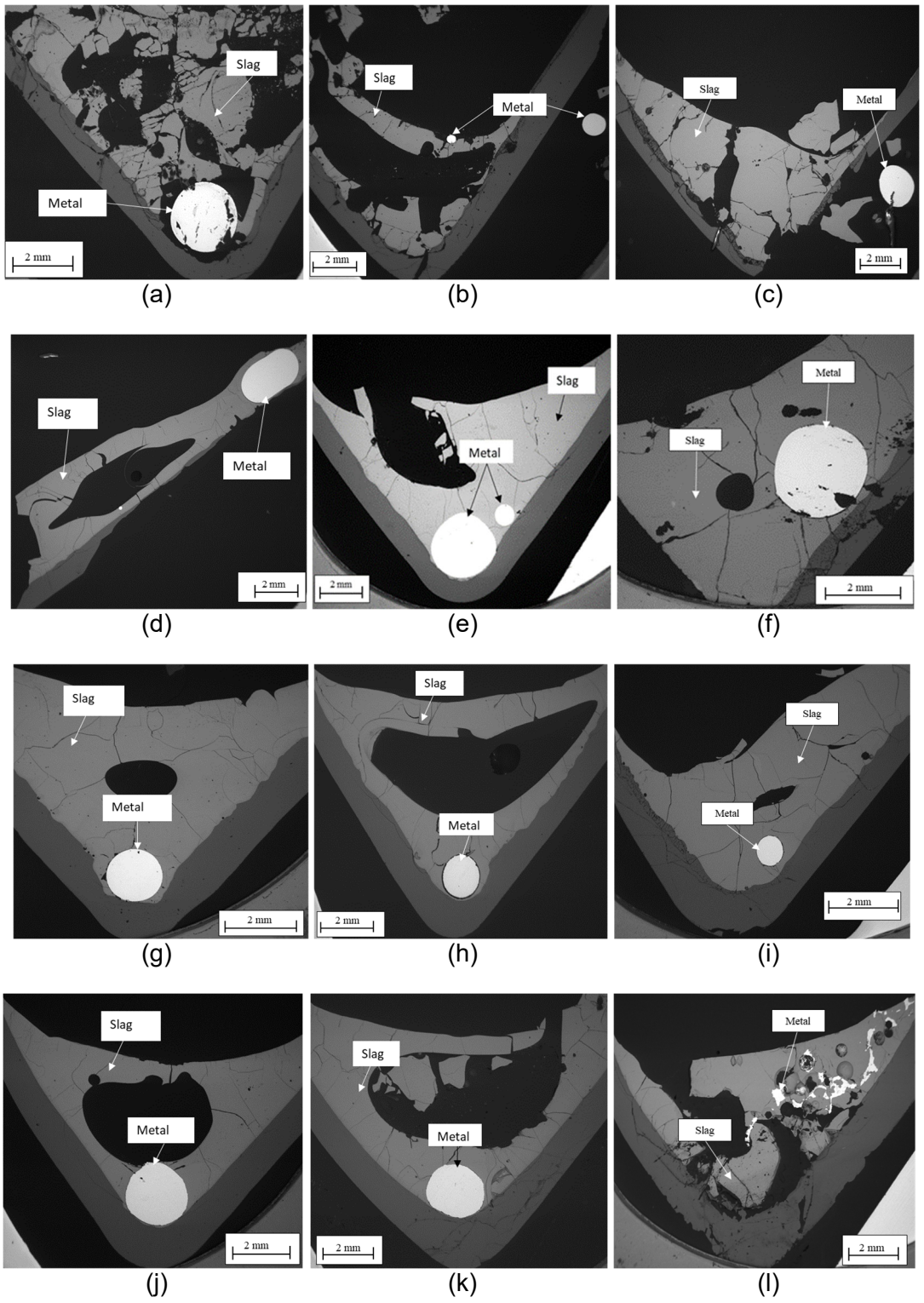

FIG 2 – SEM micrographs of sample polished sections of nickel slag reduction with: (a) L1200 for 15 mins, (b) L1200 for 30 mins, (c) L1200 for 60 mins (d) L600 for 15 mins, (e) L600 for 30 mins,

(f) L600 for 60 mins, (g) B1200 for 15 mins, (h) B1200 for 30 mins, (i) B1200 for 60 mins, (j) B600 for 15 mins, (k) B600 for 30 mins, and (l) B600 for 60 mins.

Since some of the slags were brittle because of rapid quenching, the metal droplets as well as slag pieces were sometimes detached from the rest of the sample while cutting. The dark regions (epoxy) found within the slag are attributed either to this or to gas formation within the melt.

The formed metal generally settled at the bottom of the crucible although some smaller droplets were found in various locations inside the crucibles. Avarmaa *et al* (2020) observed similar microstructures and attributed the presence of the smaller droplets found at the edges of the crucibles to the surface and interfacial tensions between the phases of the system. In some of the reduction tests, two metal droplets were found (a bigger one and a smaller one: see Figure 2b, 30 mins). It is believed that the bigger droplet (>1 mm diameter) is the first metal that was formed and the smaller one(s) is(are) later generated. Analysis of the smaller metal droplets revealed that the nickel, cobalt and copper concentrations were higher but iron concentration was lower compared to the bigger droplet.

Nickel slag reduction was also conducted with metallurgical coke (Figure 3) to compare with the results from slag reduction with biochar. It was observed that biochar is a more reactive reducing agent compared to metallurgical coke. A large metal alloy droplet (~2 mm diameter) was formed (Figure 2) when the different biochars were used, but such large alloy droplets were not found in the samples reduced with coke.

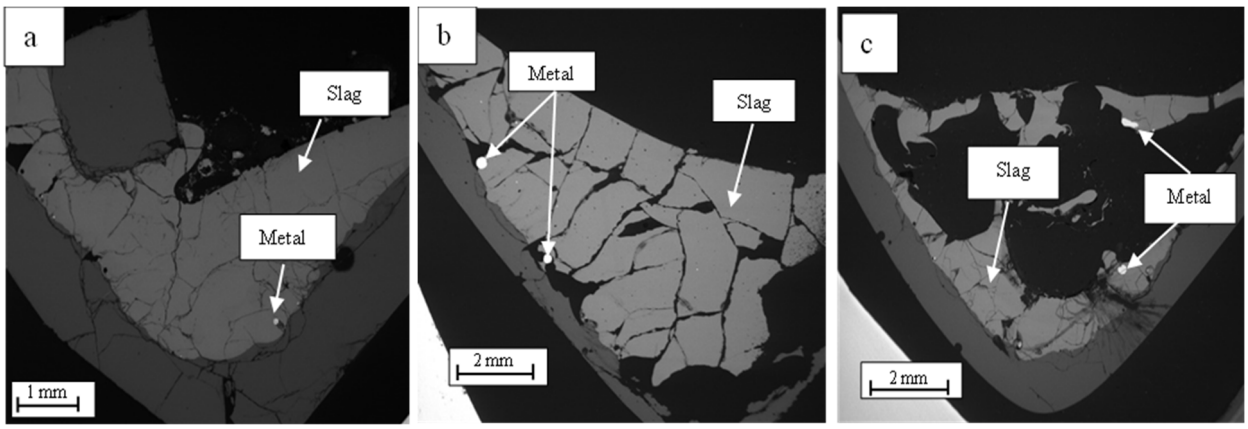

FIG 3 – SEM micrographs of sample polished sections of nickel slag with coke for (a) 15, (b) 30, and (c) 60 mins.

Figure 4 shows the concentrations of nickel, cobalt, copper and iron in the slag before (0 mins) and after reduction (15, 30 and 60 mins). This gives an indication of the amount of elements that have reduced to the metal phase or have been volatilised. The concentrations of nickel, cobalt and copper in the slag decrease as reduction time increases for all the biochar types. Within the first 15 mins of the reduction, nickel concentration within the slag reduced from 3.62 to 1.06 wt per cent when metallurgical coke was employed. Higher metal removal was achieved when biochar was used, yielding nickel percentages in slag below 0.5 wt per cent. Biochars pyrolyzed at 600°C (L600 and B600) showed higher reduction potentials than biochars pyrolyzed at 1200°C. When B600 and L600 were employed as reducing agents, the nickel concentration in the slag after 15 mins was 0.06 and 0.07 wt per cent, respectively, while those for B1200 and L1200 were 0.48 and 0.24 wt per cent, respectively. While biochars pyrolyzed at 1200°C have higher carbon contents, the higher volatile matter concentrations in L600 and B600 may be indirectly responsible for their higher reactivity, ie showed faster reduction kinetics.

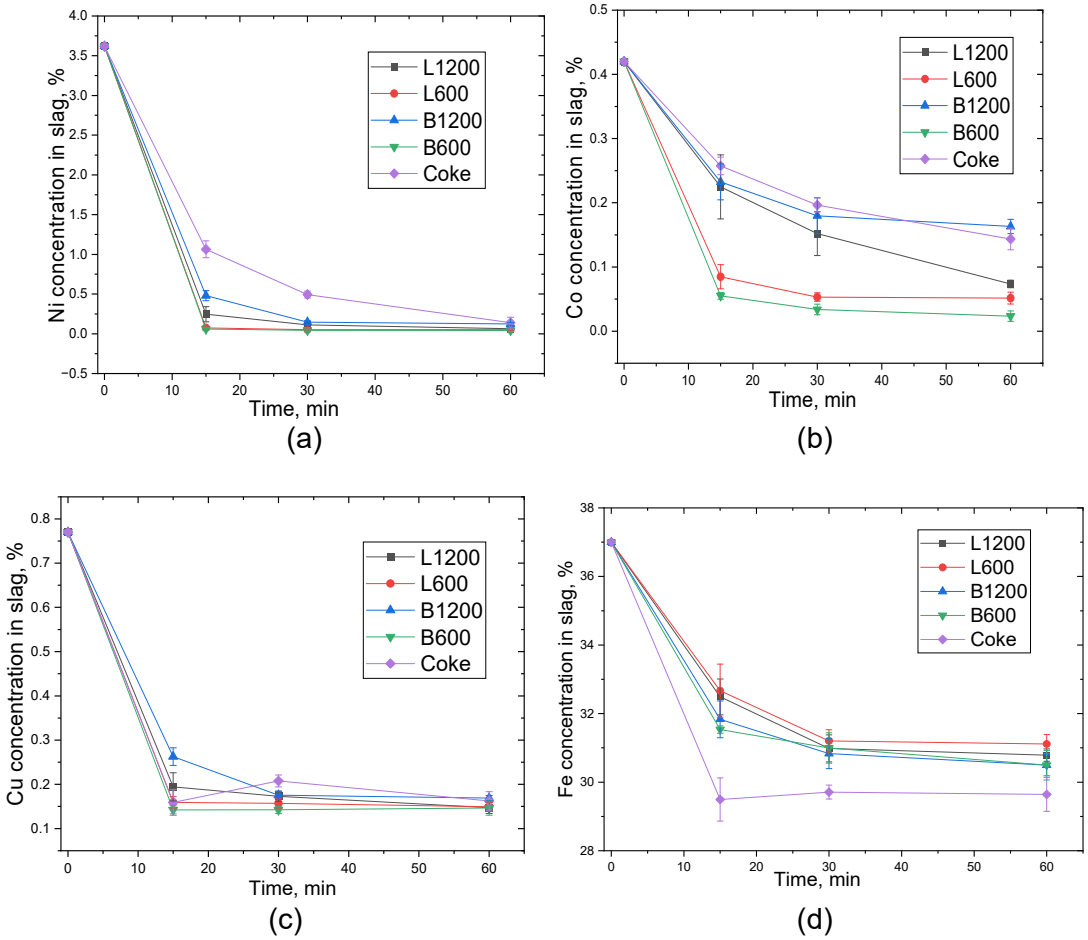

FIG 4 – Concentrations of (a) nickel, (b) cobalt, (c) copper, and (d) iron in slag as a function of time during nickel slag reduction with L1200, L600, B1200 and B600 biochar and metallurgical coke.

It is commonly stated that in slag cleaning processes (at 1300–1400°C) and eg in titania smelting, volatiles are not contributing the reduction processes. This means that they are not considered when calculating the stoichiometric amounts of reductant needed in the process. However, the volatile matter upon moving to the gas phase increases the surface area for sufficient slag and reductant reaction (Lotfian *et al*, 2017). Moreover, compared to the coke and biochar pyrolyzed at 1200°C, more CO_2 is produced by biochar pyrolyzed at 600°C which quickly reacts with solid carbon as shown in Equation 14 (Boudouard reaction). Also, the generated CO take part in the reduction. Since reduction with solid carbon is slower compared to CO, the higher CO present during biochar reduction increases its effectiveness as reductant compared to coke (Lahijani *et al*, 2015):

$$CO_2(g) + C(s) = 2CO(g) \quad (14)$$

After 60 mins reduction, the final concentrations of nickel in the slags were very close to each other with all reductants studied. Similar patterns regarding reduction kinetics of different reductants were observed for cobalt and copper as well, with the difference that the final concentration of cobalt in slag after 60 mins was more than double with coke and B1200 compared to L600 and B600 reductants. Regarding iron concentration in slag, all the biochars behaved similarly, however, the use of coke resulted in the lowest iron concentrations.

Biochar reactivity has been compared to that of coke. The reactivity of biochar was calculated from the ratio of volatile matter to fixed carbon (VM/FC) (Cui *et al*, 2023). Biochar with a high VM/FC ratio is more active and more advantageous in biofuel and chemical applications. It can be observed in Table 4 that the biochars are more reactive than metallurgical coke with B600 have reactivity close to 15 time that of coke.

TABLE 4

Reactivity of reductant calculated from volatile matter and fixed carbon.

Reductant	B600	B1200	L600	L1200	Coke
Reactivity (VM/FC)	0.1420	0.0428	0.0697	0.01343	0.0097

Distribution coefficients of the elements

The distribution coefficient is a parameter that is used to estimate the progress of the reduction reaction. It gives an indication of the behaviour of the various elements in the reduction study. In this work, the distribution coefficient between metal alloy and slag is used, and thus, a higher distribution coefficient indicates higher deportment to the alloy. The distribution coefficient of an element, Me, was calculated using Equation (15) (Avarmaa *et al*, 2020):

$$L^{m}/_{s} = \frac{wt\%\ Me\ in\ metal}{wt\%\ Me\ in\ slag} \tag{15}$$

where *m* represents the metal phase and *s* the slag phase.

The uncertainty (*ΔL*) of the distribution coefficient was calculated using the relation in Equation (16):

$$\Delta L^{m}/_{s} = \left\{\left[\frac{\Delta Me}{wt\%\ Me\ in\ metal}\right] + \left(\frac{\Delta Me}{wt\%\ Me\ in\ slag}\right)\right\} \times L^{m}/_{s} \tag{16}$$

where *ΔMe* is the standard deviation of element Me calculated from the EPMA results.

Figure 6 shows the distribution coefficient of nickel, cobalt, copper and iron between metal alloy and slag at 1400°C as a function of time. The results from this work have been compared to other studies where battery scrap (Dańczak *et al*, 2021) and mixture of battery scrap and biochar (Avarmaa *et al*, 2020) were used as reductants for nickel slag reduction.

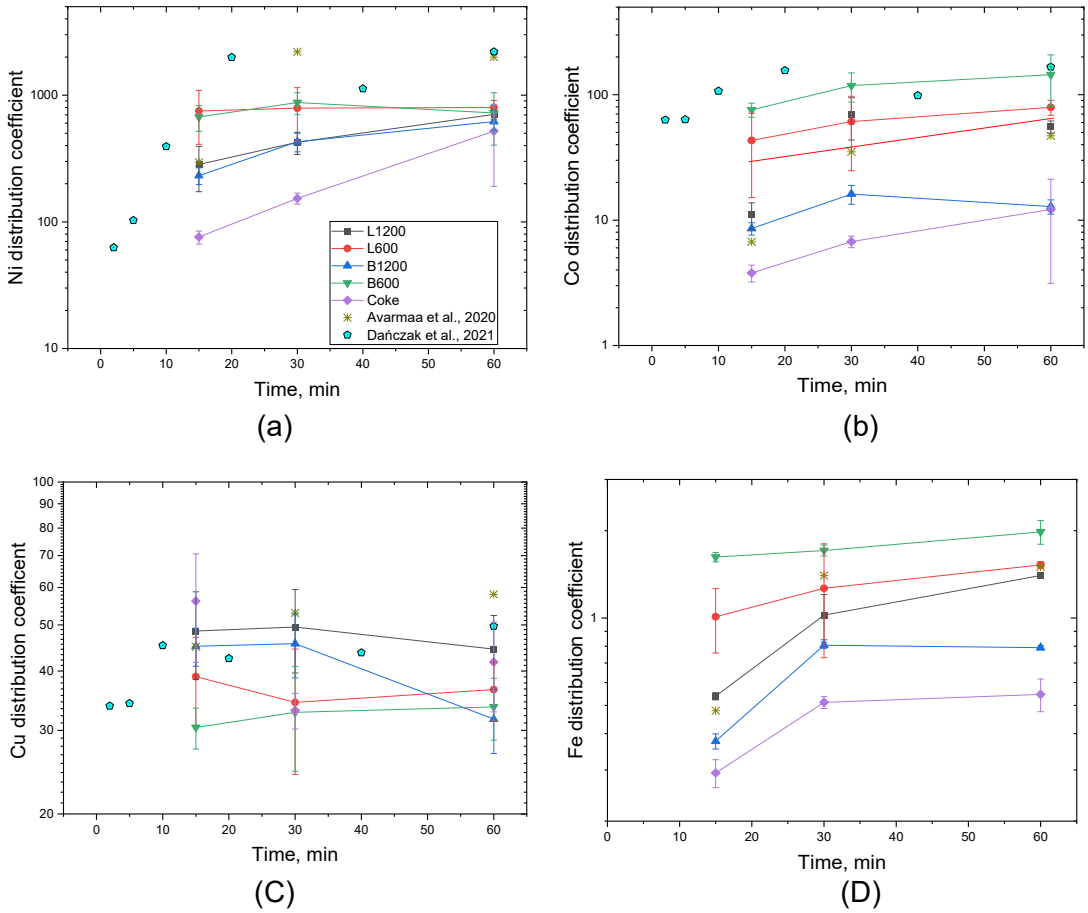

FIG 6 – Metal alloy to slag distribution coefficient of (a) Ni, (b) Co, (c) Cu and (d) Fe as time progresses at 1400°C. Note the difference in the y-axis scale.

Generally, the distribution coefficients of all the metals using the various reductants increase with time. It can be inferred that the reduction proceeds quickly, and the metal oxides are efficiently reduced to the alloy already after 15 mins reduction time since distribution coefficient values increase only slightly afterward. The use of B600 resulted in the highest distribution coefficients for nickel, cobalt and iron, closely followed by L600 biochar. The distribution coefficients of nickel, cobalt, and iron had the lowest values with coke reduction, although these values have the highest increase as a function of time. This is attributed to the slower reaction kinetics of coke compared to the different biochars. The distribution coefficient values for Ni and Cu are similar for coke and the biochars after 60 mins of reduction. It can be inferred from Figure 6 that in terms of the distribution coefficient values, the reductants can be ranked according to effectiveness or reactivity as B600 > L600 > L1200 > B1200 > Coke. This corresponds to reactivity of biochar that has been calculated.

Thermodynamic modelling

FactSage™ thermodynamic software package, version 8.0 was used in this study to investigate the effect of addition of biochar on the composition of metal and slag from nickel slag reduction. The composition of nickel slag, based on XRF analysis, as well as the ultimate and ash analyses of biochar were used as inputs in the software. The databases used for the calculations were custom collected based on the databases FactPS (pure substances), FToxid (optimised for oxide systems) and FSCopp (optimised for copper-containing solid and liquid alloys). The phases selected for the calculations were the spinel (solid solution phase with stoichiometry AB_2O_4, A, B = divalent and trivalent metals), slag (liquid oxide silicate phase), monoxide phase (solid solution), FCC, BCC, HCP-A3 (three solid multicomponent alloys; Face-Centred Cubic, Body-Centred Cubic, Hexagonal Close-Packed) and liquid metal. Ideal gas and pure solids were also selected before the calculations were done at 1400°C.

Effect of addition of biochar

One gram of nickel slag was reacted with different masses of biochar. The phases formed during reduction, as predicted by FactSage™, plotted as a function of addition of biochar are shown in Figure 7. It is observed that as the reduction progresses, the mass of slag decreases while the masses of metal and gas increase until about 0.15 g of biochar addition. After this point the masses of metal as well as the gas and slag remain constant. About 0.45 g of metal is formed with >0.15 g of biochar addition. Moreover, the thermodynamic simulation reveals that relatively more gas is produced when L600 and B600 are employed as reductants compared to their respective biochars pyrolyzed at 1200°C.

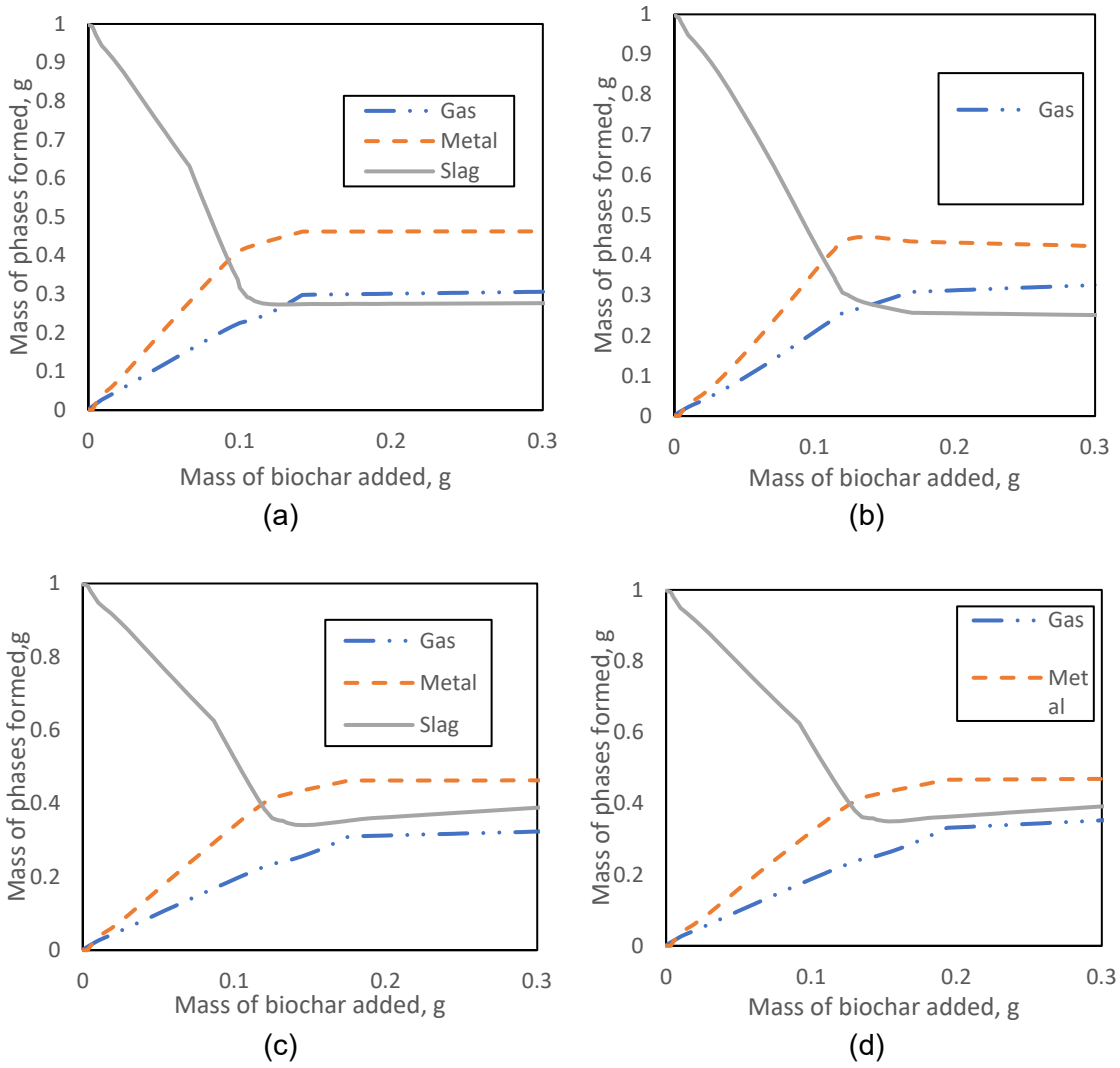

FIG 7 – Formation of gas, metal and slag phases during nickel slag reduction with varying addition of (a) L1200 (b) L600, (c) B1200, and (d) B600 biochar to 1 g of nickel slag at 1400°C as predicted by FactSage™.

The mass percentages of selected metals (Zn, Cu, Ni, Co and Fe) that were present in the gas, metal and slag phases have been shown in Figure 8. The results from reduction of Ni slag with B600 have been selected for plotting since the calculated results were remarkably similar with all investigated biochars. When 0.01 g of biochar is added to 1.0 g of nickel slag, at equilibrium, 80 wt per cent of the metal formed is nickel. This percentage continually decreases when higher amounts of biochars are added. Although the mass of nickel formed does not decrease with biochar addition, more iron is reduced, which consequently decreases the relative nickel concentration in the metal phase. In addition, the relative concentrations of copper and cobalt in the metal alloy increase to their highest values, 11 per cent and 4 per cent respectively, with less than 0.03 g biochar addition, after which they begin to decrease. The mass content and mass balance were not determined in the experimental section of this work, as it was not possible to separately collect all the phases from the quenched samples.

Nickel and copper have the highest concentrations of 80 per cent and 10 per cent, respectively, when 0.01 g of biochar is reacted with 1 g slag. The concentration of iron in the metal phase is the lowest at this addition. Since the formation of solid iron is undesired in industrial operation, it is important to recover other valuable metals like nickel and copper with low iron concentration.

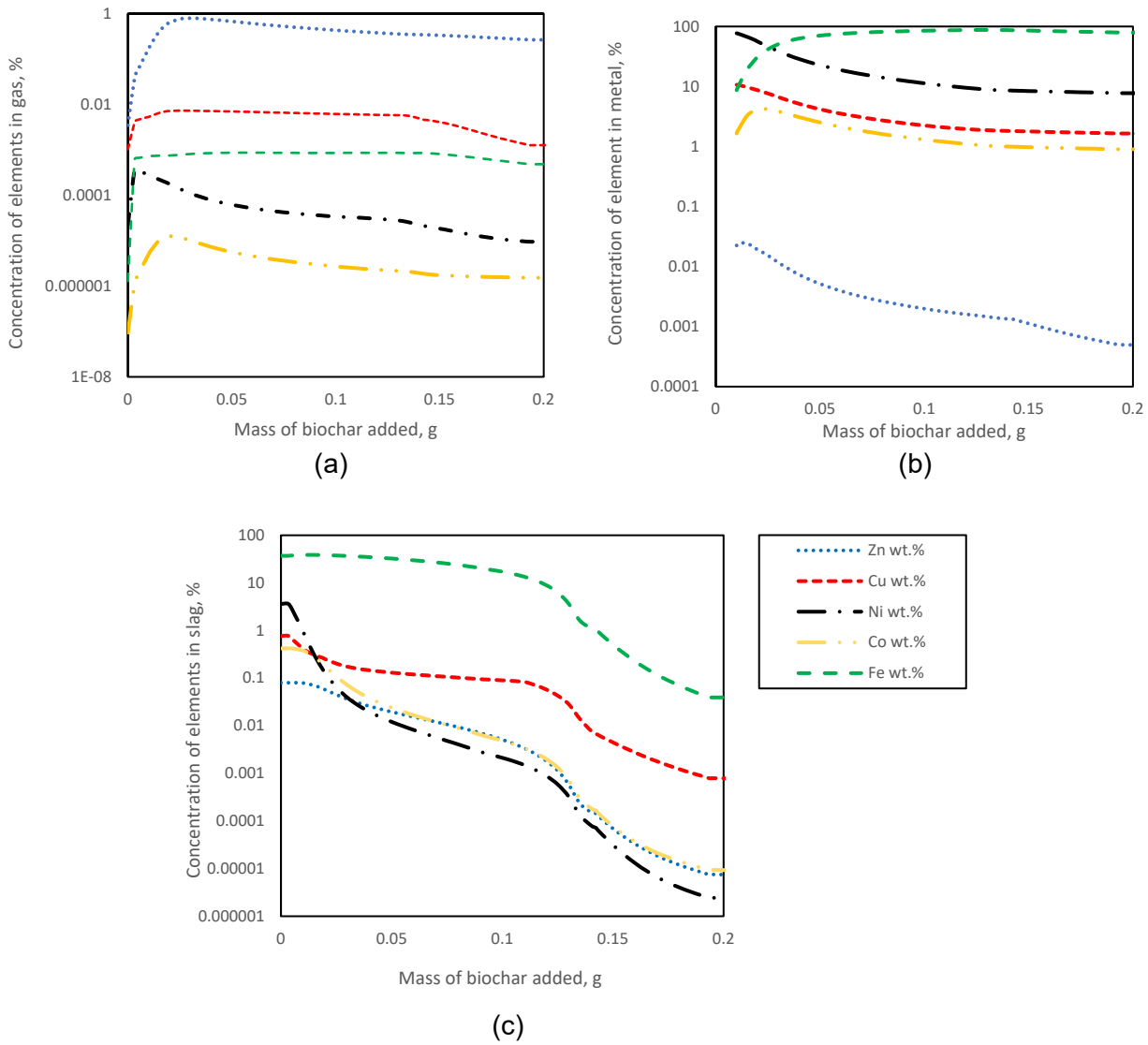

FIG 8 – Concentrations of copper, nickel, cobalt, zinc, and iron in (a) gas, (b) metal and (c) slag phase during nickel slag reduction with varying addition of B600 biochar to 1 g of nickel slag as predicted by FactSage™.

In the slag, nickel concentration plummets to about 0.1 wt per cent when 0.02 g of biochar is added to a gram of slag, and it continuously decreases until the nickel oxide in slag is almost completely reduced and Ni deported to the metal phase. Cobalt followed a similar trend as nickel in the slag. However, efficient copper oxide reduction from the slag requires a higher amount of reductant compared to nickel and cobalt. According to the calculations, approximately 0.15 g of biochar (to 1 g of slag) is enough to reduce all the iron oxides from the slag to metallic iron. As can be seen from Figure 8 a, zinc evaporates into the gas phase.

SUMMARY AND CONCLUSIONS

In this study, the use of carbon neutral biochars as reducing agents in the pyrometallurgical treatment of nickel slag was investigated at 1400°C to recover valuable elements such as copper and nickel from the slag. Black pellet and lignin, each pyrolyzed at 600 and 1200°C, were employed as reductants and the recoveries of nickel, copper and cobalt were investigated and compared to the results when using fossil coke as the reductant. The biochars pyrolyzed at 1200°C had higher fixed carbon and lower volatile matter contents compared to those pyrolyzed at 600°C. While this may be preferred in industrial applications, the cost of energy required for pyrolyzing at higher temperatures might deter the use of biomass pyrolyzed at higher temperatures. B600 appeared to be the most efficient biochar, although it has lower carbon content compared to the other chars. The fast reaction

kinetics is thought to be attributed to the relatively high content of volatiles in this biochar, leading to gas formation and thus mixing of the sample material. During the slag cleaning, biochars showed higher reactivity and faster reduction kinetics compared to coke. This, again, may be attributed to high concentration of volatile matter present. Although it is stated that at high temperatures (1300–1400°C) volatile matter do not contribute to the reduction process, it is possible that the volatiles create pores upon moving into the gas phase, increasing thus the surface area for reaction. In addition, CO_2 generated reacts with carbon (Boudouard reaction) resulting in more CO produced which takes part in the reduction reaction. Higher distribution coefficients between metal alloy and slag were obtained for Ni, Co and Fe using any biochar, compared to using coke.

Thermodynamic modelling was performed with FactSage™ and the distribution coefficients calculated were compared to the experimental results, which were consistent with the thermodynamic modelling. In addition, thermodynamic calculations confirmed that nickel is reduced rapidly, and it deports to the metal alloy phase when enough ferric oxide has been removed from the slag. As the reduction progresses or extra reductant is available for reactions, more iron is deported to the metal phase. The calculations also revealed that Zn vaporises into the gas phase.

ACKNOWLEDGEMENTS

This study received financial support from Aalto University, School of Chemical Engineering TOCANEM Project (Business Finland grant 2118452), BOLIDEN Harjavalta Oy for providing the nickel slag; University of Oulu for preparing and providing the biochars. The utilisation of the Academy of Finland's RawMatTERS Finland Infrastructure (RAMI) based at Aalto University, GTK and VTT in Espoo is appreciated.

REFERENCES

Adrados, A, De Marco, I, López-Urionabarrenechea, A, Solar, J, Caballero, B M and Gastelu, N, 2016. Biomass pyrolysis solids as reducing agents: Comparison with commercial reducing agents, *Materials*, 9(1). https://doi.org/10.3390/ma9010003

Avarmaa, K, Järvenpää, M, Klemettinen, L, Marjakoski, M, Taskinen, P, Lindberg, D and Jokilaakso, A, 2020. Battery scrap and biochar utilization for improved metal recoveries in nickel slag cleaning conditions, *Batteries*, 6(4):1–21. https://doi.org/10.3390/batteries6040058

Cholico-González, D, Lara, N O, Miranda, M A S, Estrella, R M, García, R E and Patiño, C A L, 2021. Efficient metallization of magnetite concentrate by reduction with agave bagasse as a source of reducing agents, *International Journal of Minerals, Metallurgy and Materials*, 28(4):603–611. https://doi.org/10.1007/s12613-020-2079-z

Cui, D, Zheng, X, Zou, J, Yu, S, Kong, X, Cai, J and Zhang, X, 2023. Physicochemical Characterization and Chemical Reactivity of Biochar from Pyrolysis of Dried Distiller's Grains with Solubles (DDGs), *Combustion Science and Technology*. https://doi.org/10.1080/00102202.2023.2204521

Dańczak, A, Ruismäki, R, Rinne, T, Klemettinen, L, O'Brien, H, Taskinen, P, Jokilaakso, A and Serna-guerrero, R, 2021. Worth from waste: Utilizing a graphite-rich fraction from spent lithium-ion batteries as alternative reductant in nickel slag cleaning, *Minerals*, 11(7). https://doi.org/10.3390/min11070784

Demey, H, Rodriguez-Alonso, E, Lacombe, E, Grateau, M, Jaricot, N, Chatroux, A, Thiery, S, Marchand, M and Melkior, T, 2021. Upscaling severe torrefaction of agricultural residues to produce sustainable reducing agents for non-ferrous metallurgy, *Metals*, 11(12). https://doi.org/10.3390/met11121905

Guo, D, Li, Y, Cui, B, Chen, Z, Luo, S, Xiao, B, Zhu, H and Hu, M, 2017. Direct reduction of iron ore/biomass composite pellets using simulated biomass-derived syngas: Experimental analysis and kinetic modelling, *Chemical Engineering Journal*, 327:822–830. https://doi.org/10.1016/j.cej.2017.06.118

Jones, R T, Denton, G M, Reynolds, Q G, Parker, J A L and Van Tonder, G J J, 2002. Recovery of cobalt from slag in a DC arc furnace at Chambishi, Zambia, *Journal The South African Institute of Mining and Metallurgy*, 102(1):5–9.

Koskela, A, Suopajärvi, H, Mattila, O, Uusitalo, J and Fabritius, T, 2019. Lignin from bioethanol production as a part of a raw material blend of a metallurgical coke, *Energies*, 12(8). https://doi.org/10.3390/en12081533

Lahijani, P, Zainal, Z A, Mohammadi, M and Mohamed, A R, 2015. Conversion of the greenhouse gas CO_2 to the fuel gas CO via the Boudouard reaction: A review, *Renewable and Sustainable Energy Reviews*, 41:615–632. https://doi.org/10.1016/j.rser.2014.08.034

Lotfian, S, Ahmed, H, El-Geassy, A H A and Samuelsson, C, 2017. Alternative Reducing Agents in Metallurgical Processes: Gasification of Shredder Residue Material, *Journal of Sustainable Metallurgy*, 3(2):336–349. https://doi.org/10.1007/s40831-016-0096-y

Mousa, E, Wang, C, Riesbeck, J and Larsson, M, 2016. Biomass applications in iron and steel industry: An overview of challenges and opportunities, *Renewable and Sustainable Energy Reviews*, 65:1247–1266. https://doi.org/10.1016/j.rser.2016.07.061

Sun, W, Li, X, Liu, R, Zhai, Q and Li, J, 2021. Recovery of valuable metals from nickel smelting slag based on reduction and sulfurization modification, *Minerals*, 11(9):1–14. https://doi.org/10.3390/min11091022

Suopajärvi, H, Pongrácz, E and Fabritius, T, 2013. The potential of using biomass-based reducing agents in the blast furnace: A review of thermochemical conversion technologies and assessments related to sustainability, *Renewable and Sustainable Energy Reviews*, 25:511–528. https://doi.org/10.1016/j.rser.2013.05.005

Wiklund, C M, Helle, M, Kohl, T, Järvinen, M and Saxén, H, 2017. Feasibility study of woody-biomass use in a steel plant through process integration, *Journal of Cleaner Production,* (142):4127–4141. https://doi.org/10.1016/j.jclepro.2016.09.210

Zhang, G, Wang, N, Chen, M and Cheng, Y, 2020. Recycling nickel slag by aluminum dross: Iron-extraction and secondary slag stabilization, *ISIJ International*, 60(3):602–609. https://doi.org/10.2355/isijinternational.ISIJINT-2019-173

An investigative study on the interfacial behaviour of waste graphite resource with liquid iron

DOI: 10.62053/GBJN2330

S Biswal[1], S Udayakumar[2], F Pahlevani[3], N Sarmadi[4] and V Sahajwalla[5]

1. Researcher, Centre for Sustainable Materials Research and Technology (SMaRT@UNSW), UNSW Sydney, Sydney NSW 2052. Email: s.biswal@unsw.edu.au
2. Research Assistant, Centre for Sustainable Materials Research and Technology (SMaRT@UNSW), UNSW Sydney, Sydney NSW 2052. Email: s.udayakumar@unsw.edu.au
3. Associate Professor, Centre for Sustainable Materials Research and Technology (SMaRT@UNSW), UNSW Sydney, Sydney NSW 2052. Email: f.pahlevani@unsw.edu.au
4. Research Assistant, Centre for Sustainable Materials Research and Technology (SMaRT@UNSW), UNSW Sydney, Sydney NSW 2052. Email: n.sarmadi@unsw.edu.au
5. Professor, Centre for Sustainable Materials Research and Technology (SMaRT@UNSW), UNSW Sydney, Sydney NSW 2052. Email: veena@unsw.edu.au

ABSTRACT

Recent times have witnessed a notable momentum in the interest surrounding technology dedicated to harnessing waste as valuable resources, prompted by the mounting challenges posed by waste accumulation and the swift depletion of natural resources. The carbon dissolution process within a molten iron bath stands as a pivotal reaction within the metal processing sector. The current study explores the utilisation of waste graphite electrodes (WGE) (obtained after being utilised in an electric arc furnace) as a secondary resource of carbon for dissolution into liquid iron. Experimental investigations were carried out at 1550°C using the sessile drop approach. High purity iron powder was used and the carbonaceous substrates were prepared from the ground WGE. The carbon pickup was determined using a suitable carbon analyser. Furthermore, an examination of the interfacial area between the molten iron and the WGE substrate was conducted beneath the metallic droplet, which effectively represents the iron/carbon interface. This interfacial analysis was carried out on two different samples obtained after a varying period of heat treatments at 1550°C. The interface layer was investigated using scanning electron microscopy (SEM) in conjunction with energy-dispersive X-ray spectroscopy (EDS).

INTRODUCTION

Steel production is vital for global infrastructure, industry and job creation, with applications ranging from construction to transportation. The industry is responding to sustainability concerns by embracing cleaner technologies, such as furnaces powered by renewable energy and adopting circular economy principles through increased recycling. Governments are implementing regulations, certifications like ResponsibleSteel™ (2018) are promoting responsible practices, and there is a growing emphasis on supply chain transparency. While the economic importance of steel is undeniable, efforts to balance it with environmental and social considerations are underway to ensure a more sustainable future (Muslemani *et al*, 2021; Ben Ellis, 2020). Global steel production in the year 2022 stands at approximately 1885 Mt (World Steel Association, 2023).

The transition to steel production through electric arc furnace (EAF) is gradually gaining momentum. Sponge iron (also known as direct reduced iron) can be used in conjunction with scrap steel in EAFs. This dual-feed approach allows for a flexible raw material mix, optimising the use of both recycled and virgin materials based on availability and market conditions. Moreover, the steel industry has been witnessing investments in EAF technology, with some companies expanding their EAF capacities. This suggests a positive outlook for the role of EAFs in future steel production. It's been predicted that the EAF steel production will increase to around 50 per cent by the year 2050 (Wood Mackenzie, 2023).

Carbon is a crucial element in steel production, influencing its strength, hardness and overall performance. To enhance sustainability, the steel industry is exploring innovative ways to utilise waste resources. By incorporating recycled steel, not only does it reduce the demand for virgin raw materials, but it also minimises the environmental impact associated with traditional production

processes. Similarly, efforts to optimise the carbon content in steel while embracing circular economy principles play a vital role in mitigating the environmental footprint of the industry. Carbon in the form of coke/coal is used as a fuel source, reducing agent and carburiser at various steps in steelmaking production (Ahmed, 2018). Incorporating secondary carbon resources into the steelmaking process helps reduce the overall carbon footprint. The use of recycled materials, such as carbon-containing waste, requires less energy compared to the extraction and processing of virgin raw materials. Incorporating secondary carbon resources, especially recycled materials, can lead to cost savings for steel producers. This flexibility also enhances resilience in the face of market fluctuations and supply chain disruptions.

Waste graphite electrodes from EAFs in steelmaking is one such notable byproduct with potential for recycling and environmental sustainability. Graphite electrodes are essential components in EAFs, conducting the electrical charge needed for melting scrap steel. The usage of graphite electrodes in electric furnaces is commonly regarded as the third most significant cost factor in the production of molten steel, following scrap steel and electrical energy (Xuran New Materials Limited, 2024). Consumption typically falls within the range of 1.8–9.9 kg per ton of crude steel (Babich and Senk, 2013). Once these electrodes reach the end of their usable life, they are considered a waste. However, with appropriate treatment and processing, the carbon content in these electrodes can be recovered and reused, contributing to the circular economy within the steel industry.

The incorporation of carbon into a molten iron bath is a crucial reaction. Numerous investigations have concentrated on examining the principles of carbon dissolution by utilising graphite, coke and coal as carburising materials. The current research work investigates the dissolution of carbon present in the waste graphite electrode (WGE) through the sessile drop technique.

MATERIALS AND EXPERIMENTAL METHODS

The WGE was obtained from a steel manufacturing facility in New South Wales, Australia. The as-received WGE was first pulverised to a powder (100–150 μm) using a ring mill. The powdered sample was then subjected to CHNS analysis (Carbon (C), Hydrogen (H), Nitrogen (N), and Sulphur (S); Vario MACRO CUBE) as shown in Table 1.

TABLE 1

CHNS analysis (Carbon (C), Hydrogen (H), Nitrogen (N), and Sulphur (S)) of waste graphite electrodes (WGE) sample.

Sample	C(%)	H(%)	N(%)	S(%)
WGE	97.2	0.83	0.01	0.34

Sessile drop approach was used to investigate the interaction between WGE and molten iron. The WGE sample weighing 1 gram (each substrate) was transferred into cylindrical steel die set. The set of WGE sample and the die were subjected to a pressure of 200 bar for 5 mins at room temperature using a hydraulic press equipment. The prepared tabular substrate of WGE sample was placed on a bed of alumina powder. Approximately 0.25 g of high purity iron powder (Sigma Aldrich, ≥ 99.8 per cent) was placed on the top of the substrate. The assembly was then put inside a horizontal tube furnace which was continuously purged with an argon flow of one litre/min. Initially, it was held in the cold zone of the furnace for 10 mins to avoid any kind of thermal shock, after which it was pushed to the hot zone at a temperature of 1550°C for different durations of time. Carburised metallic droplets were obtained and further cleaned with ethanol to remove any superficially attached carbonaceous particles. The percentage of carbon pickup in the metallic droplets was measured using LECO carbon analyser. Some metallic droplets were selected for cross-section study using a Scanning Electron Microscope (Hitachi S3400N) coupled with an Energy Dispersive Spectroscopy (SEM-EDS). Metallic droplets obtained at the end of 1 and 15 mins along with the WGE substrate were cold mounted using epoxy resin in a cylindrical mold and then subjected to a vacuum environment for removal of air bubbles. After that, it was cured for 15 hrs followed by cutting with a diamond blade on a Minitom equipment to obtain the cross-sections. The cross-sectioned samples were polished to 1 micron (using diamond suspension) and then placed on suitable SEM stubs. The operating conditions used for the imaging are 15 kV accelerating voltage and a probe current of 50.

RESULTS AND DISCUSSIONS

Figure 1 represents the percentages of carbon pick-up from WGE into molten iron as a function of time.

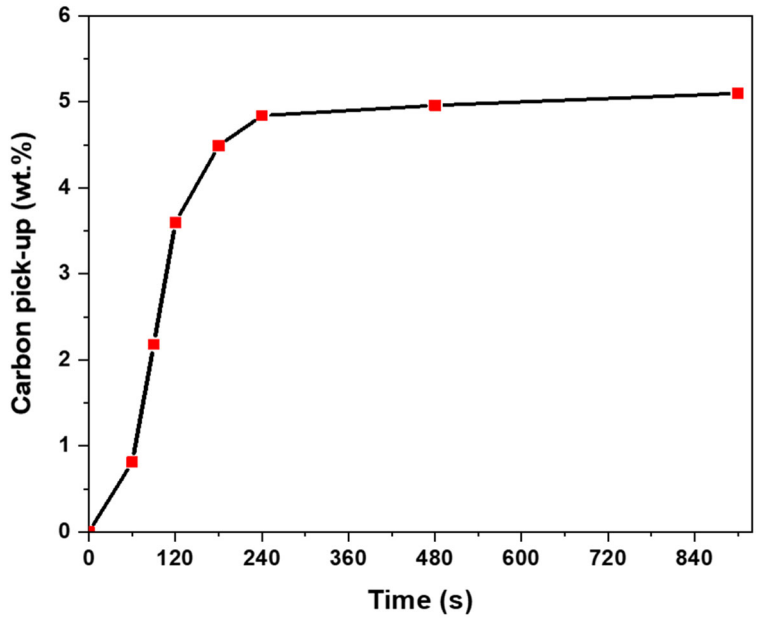

FIG 1 – Carbon pick-up from waste graphite electrodes (WGE) as a function of time at 1550°C.

As observed from Figure 1, there was a steep increase in carbon pick-up within the first 3 mins with a slight increase at a time period of 4 mins followed by a very slow pick-up phase till 15 mins.

The general rate constant for carbon dissolution (K) was determined through the application of the following equations (Mansuri *et al*, 2013, 2018):

$$\frac{dCt}{dt} = \frac{Ak}{V}\, x\, (C_s - C_t)$$

$$\ln \frac{C_s - C_t}{C_s - C_o} = -K\, x\, t$$

In these equations, C_s and C_t denote the saturation solubility and carbon concentration (wt per cent) in liquid iron at time t respectively. The first-order rate constant is represented by k ($m \cdot s^{-1}$) and A and V correspond to the interfacial area of contact and the volume of the liquid iron bath, respectively. C_o is the initial carbon concentration in the liquid metal (wt per cent) and since 99.98 per cent pure iron powder was utilised, the value of C_o is assumed as zero. The overall carbon dissolution rate constant, $K = (Ak/V)$, was determined from the negative slope of the natural logarithm of $(C_s - C_t)/(C_s - C_o)$ versus time plot. It was assumed that there was negligible change in the contact area during this brief initial contact period.

The saturation carbon limit for a particular melt composition can be calculated using the below equation (Wu, Wiblen and Sahajwalla, 2000):

$$C_s\ (\text{wt\%}) = 1.3 + 0.00257T - 0.31Si - 0.33P - 0.45S + 0.28Mn$$

As high purity iron powder was used, the saturation carbon limit was calculated to be 5.28 wt per cent. Figure 2 represents the plot of natural logarithm of $(C_s - C_t)/(C_s - C_o)$ versus time for the duration of first 3 mins.

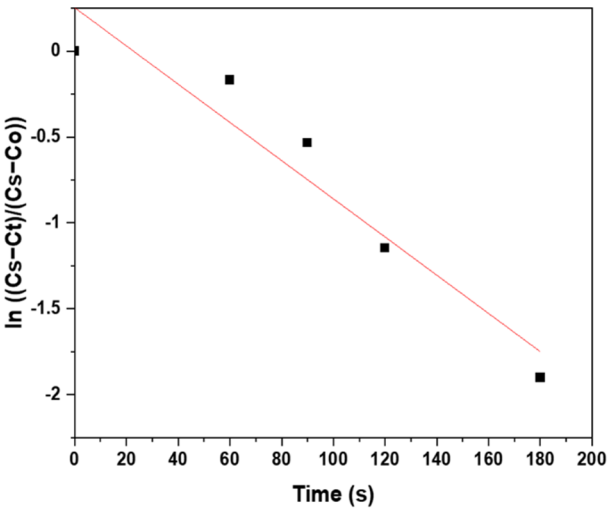

FIG 2 – The plot of ln $(C_s-C_t)/(C_s-C_o)$ versus time for waste graphite electrodes (WGE) for the duration of initial 3 mins.

The apparent rate constant K was obtained from the slope of Figure 2 and was found to be 11.1 × 10^{-3} s^{-1}. The following rate constants mentioned in Table 2 have been reported from literature using the sessile drop approach and various other carbonaceous materials.

TABLE 2

Apparent rate constants calculated using sessile drop approach with various carbonaceous materials.

Sample material	Apparent rate constant, K × 10^{-3} s^{-1}	References
Coke	0.003	Kongkarat *et al* (2012)
Coal char-1	0.1	McCarthy (2005)
Coal char-4	0.3	
Natural graphite	10.68	Wu, Wiblen and Sahajwalla (2000)

It could be observed from Table 2 that the apparent rate constant of WGE is similar to that of natural graphite. Cham *et al* (2004) observed an augmented dissolution of carbon, corresponding to an elevated crystalline order of coke. Studies (Cham *et al*, 2004; Wu and Sahajwalla, 2000) have also underscored an interconnected relationship between structural ordering and the rate of carbon dissolution, indicating that carbonaceous materials with greater Lc (crystallite size) values generally manifest a heightened carbon dissolution rate. In the case of graphitic carbonaceous materials, the dissociation of carbon atoms occurs at a swifter pace owing to the arrangement of carbon atoms in two-dimensional arrays, as opposed to coke and char (Mansuri *et al*, 2013). Consequently, a higher Lc value is conducive to facilitating the dissociation of carbon atoms. This specific occurrence can be characterised as the separation of carbon and the subsequent breakdown of the carbonaceous structure. The extent to which C (carbon) dissolves in molten iron is not determined by the mass transfer of C but rather by C's ability to dissociate from the carbonaceous matrix. The carbonaceous matrix structure influences the dissociation of carbon atoms, leading to the notable difference in the carbon dissolution limits, with graphite exhibiting a considerably higher limit than others. Reports indicate that the crucial step governing the rate of carbon dissolution from graphite is the diffusion of C from the liquid boundary layer at the interface into the bulk melt (Sun *et al*, 2021; Jang *et al*, 2012).

The following reactions highlight the phenomenon of carbon dissolution into molten iron mass (Wu and Sahajwalla, 2000):

$$C\ (crystal) = C\ (interface)$$

$$C\ (interface) = C\ (bulk\ metal\ Fe)$$

The examination of the interface of the iron-carbon alloy situated between molten iron and the char substrate on the underside of the iron droplet was conducted through SEM/EDS analysis. Figure 3 presents SEM images integrated with EDS for the interfacial layer on the iron side. The pivotal role of ash in the carbon dissolution reaction has been thoroughly elucidated by numerous researchers. Various studies have shown the impact of ash impurities on carbon dissolution, highlighting that the ash present in diverse carbonaceous materials can distinctly shape the composition of the liquid iron during the reaction (Mansuri *et al*, 2018). The results of the SEM/EDS analysis unequivocally establish the total absence of an ash layer at the interface connecting molten iron and the char substrate. The EDS spectra exhibited solely carbon and iron peaks, with no detection of any other elements or phases at the interfacial layer. This comprehensive analysis provides robust evidence supporting the exclusive presence of carbon and iron within the examined interface, underscoring the elemental composition and purity of the interface. It is also interesting to observe that 15 min-SEM image show the random distribution of carbon-based specks and laths along the interface compared to that of 1 min-SEM image. It is evident that with longer duration of exposure, the carbon particles penetrated into the iron mass and this mass transfer across the interface would have occurred till the maximum saturation. This investigation conclusively validates the potential utilisation of discarded graphite electrodes as a viable supplementary carbon source in the production of Iron-Carbon alloys as a carburiser.

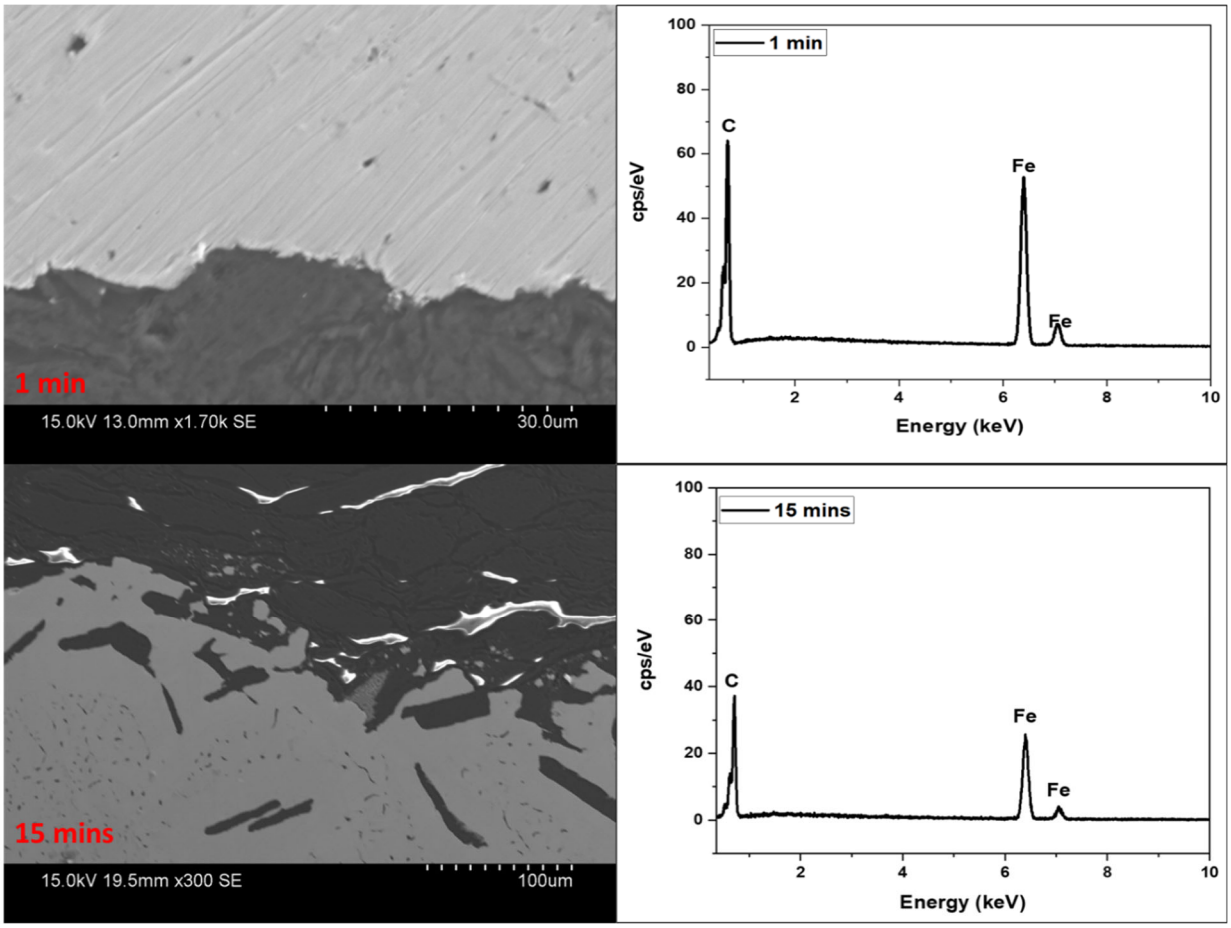

FIG 3 – Scanning electron microscopy (SEM) images coupled with energy-dispersive X-ray spectroscopy (EDS) of metal/carbon interface of waste graphite electrodes (WGE) substrate and iron.

CONCLUSIONS

The elevated rate of carbon dissolution into molten iron was evidently observed when utilising waste graphite electrode as a carbon source, resulting in a significant 5.1 wt per cent of carbon pick-up. Notably, the carbon dissolution rate achieved with graphite electrode surpassed that of various other carbonaceous materials, including metallurgical coke and coal chars and was similar to that of natural graphite. This heightened efficiency can be attributed to the substantial carbon content and

low ash content characteristic of waste graphite electrode. This indicates the potential reuse of waste graphite electrodes, even after going through numerous cycles of operation in the EAF. The study underscores the sustainable and effective utilisation of waste graphite electrodes, emphasising their transformation into a higher carbon iron-carbon alloy as a carburiser. This approach not only establishes waste graphite electrodes as a valuable resource but also aligns with environmentally conscious practices, contributing to the advancement of sustainable metallurgical processes.

ACKNOWLEDGEMENTS

This research was cooperated under the Australian Research Council's Research Hub for microrecycling of battery and consumer wastes (grant no. IH190100009). The authors acknowledge the staff at Mark Wainwright Analytical Centre at the University of New South Wales for their help and technical support.

REFERENCES

Ahmed, H, 2018. New Trends in the Application of Carbon-Bearing Materials in Blast Furnace Iron-Making, *Minerals*, 8:561. https://doi.org/10.3390/min8120561

Babich, A and Senk, D, 2013. Chapter 12 – Coal use in iron and steel metallurgy, in *The Coal Handbook: Towards Cleaner Production* (ed: D Osborne), (Woodhead Publishing).

Ellis, B and Bao, W, 2020. Pathways to decarbonisation episode two: steelmaking technology [online], BHP Insights. Available from: <https://www.bhp.com/news/bhp-insights/2020/11/pathways-to-decarbonisation-episode-two-steelmaking-technology>

Cham, S, Sahajwalla, V, Sakurovs, R, Sun, H and Dubikova, M, 2004. Factors Influencing Carbon Dissolution from Cokes into Liquid Iron, *ISIJ International,* 44:1835–1841.

Jang, D, Kim, Y, Shin, M and Lee, J, 2012. Kinetics of Carbon Dissolution of Coke in Molten Iron, *Metallurgical and Materials Transactions B,* 43:1308–1314.

Kongkarat, S, Khanna, R, Koshy, P, Paul, Kane, O and Sahajwalla, V, 2012. Recycling Waste Polymers in EAF Steelmaking: Influence of Polymer Composition on Carbon/Slag Interactions, *ISIJ International,* 52:385–393.

Mansuri, I A, Khanna, R, Rajarao, R and Sahajwalla, V, 2013. Recycling Waste CDs as a Carbon Resource: Dissolution of Carbon into Molten Iron at 1550°C, *ISIJ International,* 53:2259–2265.

Mansuri, I, Farzana, R, Rajarao, R and Sahajwalla, V, 2018. Carbon Dissolution Using Waste Biomass–A Sustainable Approach for Iron-Carbon Alloy Production, *Metals,* 8:290.

McCarthy, F, 2005. Interfacial Phenomena and Dissolution of Carbon from Chars into Liquid Iron During Pulverised Coal Injection in a Blast Furnace, PhD thesis, University of New South Wales.

Muslemani, H, Liang, X, Kaesehage, K, Ascui, F and Wilson, J, 2021. Opportunities and challenges for decarbonizing steel production by creating markets for 'green steel' products, *Journal of Cleaner Production,* 315:128127.

ResponsibleSteel™, 2018. What we do [online]. Available from: <https://www.responsiblesteel.org/what-we-do> [Accessed: 17 Jan 2024].

Sun, M, Pang, K, Zhang, J, Li, K and Li, H, 2021. In Situ Monitoring and Dissolution Limit of Carbon Dissolution in Hot Metal, *Steel Research International*, 92:2100111. https://doi.org/10.1002/srin.202100111

Wood Mackenzie, 2023. Steel decarbonisation to redefine supply chains by 2050 [online]. Available from: <https://www.woodmac.com/press-releases/steel-decarbonisation-to-redefine-supply-chains-by-2050> [Accessed: 19 Jan 2024].

World Steel Association, 2023. World Steel in Figures 2023 [online]. Available from: <https://worldsteel.org/steel-topics/statistics/world-steel-in-figures-2023/> [Accessed: 17 Jan 2024].

Wu, C and Sahajwalla, V, 2000. Dissolution rates of coals and graphite in Fe-C-S melts in direct ironmaking: Dependence of carbon dissolution rate on carbon structure, *Metallurgical and Materials Transactions B,* 31:215–216.

Wu, C, Wiblen, R and Sahajwalla, V, 2000. Influence of ash on mass transfer and interfacial reaction between natural graphite and liquid iron, *Metallurgical and Materials Transactions B,* 31:1099–1104.

Xuran New Materials Limited, 2024. Graphite Electrode Overview [online]. Available from: <https://www.graptek.com/products/graphite-electrode.html> [Accessed: 19 Jan 2024].

Distribution of impurity elements in oxygen-enriched top-blowing nickel smelting with Fe extraction-oriented slag adjustment

DOI: 10.62053/KVUF6383
G Cao[1], J Zhao[2], J Wang[1], S Yue[1], B Li[1], J Zheng[3], Y Cui[1] and H Zong[3]

1. School of Metallurgical Engineering, Xi'an University of Architecture and Technology, Xi'an, Shaanxi 710055, China.
2. School of Metallurgical Engineering, Xi'an University of Architecture and Technology, Xi'an, Shaanxi 710055, China. Email: zhaojunxue1962@126.com
3. Jinchuan Nonferrous Metal Group Corporation, Jinchang, Gansu 737100, China.

ABSTRACT

The iron (Fe) concentration in nickel slag is high, making its recovery and utilisation a hot and challenging topic. In the nickel smelting process, using CaO instead of SiO_2 to adjust slag's composition, and then directly reducing Fe from the output of molten slag is a more feasible method in practice for Fe recovery in nickel slag. The adjustment of slag's composition in the nickel smelting process will have an impact on the distribution of impurity elements such as Pb, Zn, and As. In this paper, the slag adjustment of nickel smelting process was carried out with the oxygen-enriched top-blowing system. The distribution of impurity elements in the smelting products with each composition slag was conducted by using thermodynamic software. Experimental verification was performed with rich oxygen top-blowing, and the distribution characteristics of impurity elements in the smelting products were characterised to explore the differences in mineral phases of impurity elements with each smelting conditions, elucidating the distribution patterns of Pb, Zn, and As in each phase. The results indicate that after slag adjustment, impurity elements are more easily to volatilisation and removal into the gas, reducing their total concentration in slag and matte. In the slag, the existence form of Pb, Zn is changed from silicate to ferrate, and As is changed from arsenate to low-valent arsenic oxide. It is easier to decompose the impurity-containing mineral phase and remove the impurity elements in the subsequent iron extraction process.

INTRODUCTION

In the nickel pyrometallurgical process, approximately 6~16 tons of slag are generated per ton of nickel produced (Marenych and Kostryzhev, 2020; Wu *et al*, 2018; Xia *et al*, 2018). To the smelting with sulfide concentrate, the slag contains a small amount of valuable metal elements such as Ni, Cu, Co, as well as a significant amount of Fe, with Fe typically constituting around 40 per cent of the nickel slag (Guo *et al*, 2018b; Li *et al*, 2020a; Park *et al*, 2011; Sun *et al*, 2021; Wu *et al*, 2020; Zhang *et al*, 2020a). The output of the same kind of slag can be estimated at 5 000 000 tons per annum (tpa) in China (Zhang *et al*, 2020b). The iron in the nickel slag is taken as potential resource, but up to now remains unextracted and unused. Currently, nickel slag is primarily disposed of through stacking and landfill. With the long-term effects of chemical weathering and physical erosion, impurity elements in unprotected nickel slag may can be released into the surrounding environment, posing a potential threat to human health (Dimitrijevic *et al*, 2009; Dosmukhamedov and Kaplan, 2016; Guo *et al*, 2018a; Kobayashi and Hirano, 2016; Yang *et al*, 2017; Zhong, Li and Tan, 2017).

The recovery of Fe from nickel slag has consistently been a focus of research. Methods such as high-temperature oxidation and reduction smelting have been attempted. In the process of high-temperature oxidation of nickel slag, CaO is introduced as a flux and the slag oxidised. Fe in the slag ultimately transform into iron oxides, and then selected with–magnetic separation. This process is relatively long and difficult to put into use for extracting Fe from nickel smelting slag (Gyurov *et al*, 2014; Shen *et al*, 2018). Most of research introduced the method of molten reduction for Fe extraction from nickel slag (Li *et al*, 2013, 2020b; Long *et al*, 2016; Zhang *et al*, 2015). During the reduction process, a significant amount of CaO has to be added to displace FeO in olivine, which leads to a substantial consumption of CaO and reducing agent (Wang *et al*, 2014; 2015; Yu *et al*, 2021). as a results, a large consumption of energy is necessary and a lot of slag in Fe extraction is produced. This makes the Fe extraction process unfeasible. Currently, most research on Fe extraction from nickel slag remains in the experimental stage, and due to cost constraints, it cannot

be implemented in industrial production (Li *et al*, 2021; Wang *et al*, 2020, 2021). Some industrial practice failed.

In the traditional nickel concentrates smelting process, SiO_2 is utilised as a slag-making agent for the separation of Fe and other gangue from the matte formed. The reaction formula is depicted in Equation 1. The iron silicate is generated during the nickel smelting stage, and it is stable and very difficult to be reduced, leading to difficulties in Fe extraction from the slag. In all of the works mentioned above, this kind of slag was used as raw material for Fe extraction and deduced the process problems. Our team suggested that adjustments were to use CaO as flux instead of SiO_2 in traditional process. The slag forming reaction is changed, as indicated in Equation 2. Without affecting the concentration of Fe and other valuable elements in the slag of nickel smelting, the new slag composition suitable for Fe extraction can be obtained through slag adjustment (Zhao *et al*, 2018; Cao *et al*, 2023; Wang *et al*, 2023).

$$2FeS + SiO_2 + 2O_2\,(g) = Fe_2SiO_4 + SO_2\,(g) \quad (1)$$

$$2FeS + 7/2O_2\,(g) + CaO = CaFe_2O_4 + 2SO_2\,(g) \quad (2)$$

Because of the presence of impurity elements such as Pb, Zn, and variety of nickel concentrates sources, the control of impurity elements in products is a key problem for high attention. Impurity elements in the nickel smelting process can distribute in nickel matte, slag, dust and gas. The distribution of impurity elements depends on factors such as smelting process, temperature, reaction intensity, oxygen potential, slag and matte composition and so on. During the smelting stage of nickel matte, increasing carbon concentration and Fe/SiO_2 ratio can reduce the As concentration in the charge, enhancing the stability of As in the matte and slag. As the grade of nickel matte increases, Pb and Zn are more likely to transfer from the matte to the slag (Wang *et al*, 2017; Yang *et al*, 2017). In this paper, the slag adjustment is carried out with CaO instead of SiO_2 as flux in oxygen-enriched top-blowing nickel smelting process. There must be some changes in the transforming of impurity elements in the slag during smelting. The distribution of impurity elements in nickel smelting was studied to provide a theoretical basis for subsequent parameter control and pollution control in the smelting process.

EXPERIMENTAL METHODOLOGIES

Based on the oxygen-enriched top-blowing smelting and the idea of slag adjustment for Fe extraction, theoretical calculations on the distribution of Pb, Zn, and As after reactions were conducted using FactSage™ ver 7.1 (by CRCT-ThermFact Inc.& GTT-Technologies). Smelting experiments were conducted with the slag samples which chemical composition for matte production was chosen in previous work as adjustment for Fe extraction. The concentration of impurity elements in the produced slag and matte after the reactions were analysed through chemical analysis. The forms of impurity elements in the slag and matte samples were investigated by using X-ray photoelectron spectroscopy (XPS) and scanning electron microscopy with energy-dispersive X-ray spectroscopy (SEM-EDS).

Experimental materials

The materials used in the experiment were based on the traditional nickel smelting furnace slag with top-blowing (as shown in Table 1). Analytically pure reagents are used for adjustment, including CaO, SiO_2. The relevant materials were crushed to a size below 0.045 mm and subsequently dried at 473 K for 3 hrs before use.

TABLE 1

Composition of nickel concentrates and slag (per cent).

Element	Ni	Cu	Fe	Co	S	CaO	MgO	SiO_2	Pb	Zn	As
Nickel concentrates	3.44	3.54	22.69	0.16	19.48	1.12	6.25	16.54	0.053	0.169	0.039
Top blowing slag	1.26	1.62	28.9	0.14	3.03	3.33	10.99	29.11	0.019	0.181	0.011
Nickel matte	8.60	14.53	25.07	0.46	26.33	0.14	0.10	0.91	-	-	-

Theoretical calculation

Using the Reaction module in Factsage 7.1, the simulations were conducted under oxygen-enriched top-blowing smelting conditions, introducing different flux agent additions for matte smelting. The analysis on the distribution of Pb, Zn, and As among products after the reactions was carried out. The theoretical calculation set the reaction temperature at 1400°C (the actual temperature of Nickel smelting). The slag composition from traditional smelting was taken as the reference for comparison. The selected range for variations in slag composition for slag adjustment was defined as follows: CaO/SiO_2 ratio from 0.4 to 1.2, Fe/SiO_2 ratio from 0.6 to 1.4, MgO concentration from 7 per cent to 15 per cent. In investigating the effect of CaO/SiO_2 ratio, only the concentration of CaO and SiO_2 in the slag is altered, while keeping their total mass constant. For examining the impact of the Fe/SiO_2 ratio, the total mass of Fe and SiO_2 is maintained unchanged. When studying the effect of MgO concentration on the distribution of impurity elements, as the MgO concentration increases, the mass of the remaining substances is proportionally reduced, ensuring the total mass of the slag remains constant. In the calculations, the mass ratio of slag to nickel matte is set to 2:1. This approach ensures that the mass of nickel matte remains constant under different conditions.

Test apparatus and procedures

Slag and balance system

Smelting experiments were carried out with the slag samples which chemical composition for matte production was chosen in previous as shown in Table 2. In the traditional oxygen-enriched top-blowing smelting process of nickel sulfide ore, 8 per cent silicon dioxide is added as a flux. The traditional nickel smelting slag is shown in 1#. During the slag adjustment process, the silicon dioxide concentration in the slag is reduced by adding other oxides, followed by additional calcium to adjust slag's composition. 3# is a scheme that no SiO_2 added but 10 per cent CaO added as flux in smelting process, as a result, SiO_2 changed from 36.11 per cent to 27.56 per cent and CaO from 4.13 per cent to 13.85 per cent. 2# represents an intermediate state between 1# and 3#, where the SiO_2 concentration is adjusted from 36.11 per cent to 30.5 per cent, and CaO from 4.13 per cent to 10.91 per cent. To replace SiO_2 with CaO in the reaction process, SiO_2 concentration in the slag is diluted by adding CaO, MgO and FeO. 4# involves adding more CaO than 3# to alter the form of Fe in the produced nickel slag and minimise CaO addition in next step of Fe extraction, resulting a composition change of SiO_2 from 36.11 per cent to 25.56 per cent, and CaO from 4.13 per cent to 20.11 per cent. With the increase in CaO concentration, the hemispherical temperature gradually decreases and can meet the requirement of nickel smelting well.

TABLE 2

The initial slag composition used in the experiments.

Slag type	FeO/%	CaO/%	MgO/%	SiO_2/%	CaO/SiO_2	Fe/SiO_2
1#	46.12	4.13	13.63	36.11	0.11	0.99
2#	45.22	10.91	13.36	30.50	0.36	1.15
3#	45.21	13.85	13.36	27.56	0.50	1.27
4#	41.92	20.11	12.39	25.56	0.79	1.27

Test procedure and equipment

based on the conditions outlined in Table 2. After mixing nickel slag with nickel matte in 2:1 ratio, the materials were introduced into a well-type of electric furnace (as illustrated in Figure 1). The heating rate during the matte smelting process was controlled at 5°C/min to 1400°C. Ar is introduced at a flow rate of 100 mL/min. After maintaining the temperature at 1400° for 6 hrs, the crucible is removed from the furnace and quickly cooled. Subsequently to the smelting reaction, samples were separately collected from the slag and matte for analysis.

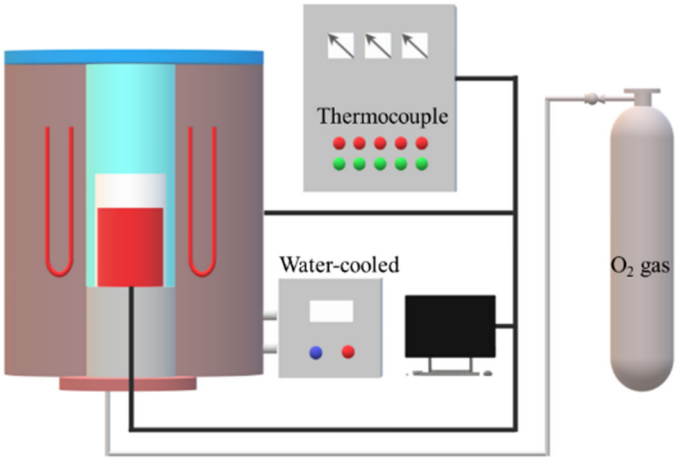

FIG 1 – Schematic diagram of the smelting and matte-making process.

Sample analysis and characterisation

The concentration of Pb, Zn, and As in the samples before and after the reaction were determined using inductively coupled plasma atomic emission spectroscopy (ICP-AES). The form of impurity elements in the resulting slag was analysed using XPS. The samples were crushed to a particle size of 200 mesh. XPS (Thermo Scientific K-Alpha) was employed to investigate changes in the valence states of each element, with orbital and binding energy ranges specified in Table 3. After embedding the post-reaction bulk slag and matte samples in resin molds, surface polishing and gold sputtering treatment were applied. Subsequently, SEM-EDS (JSM-7001F, GeminiSEM500) was carried out to analyse the microstructure and mineral phase composition of the post-reaction slag and matte.

TABLE 3

XPS detection orbits and binding energy ranges.

Elements	Orbitals	Binding energy range (eV)
Pb	Pb4f	130~150
Zn	Zn2p	1010~1060
As	As3d	40~50

RESULTS AND DISCUSSION

Theoretical analysis of the distribution of impurity elements with the composition of slag changes

Thermodynamic calculations of the nickel smelting process were performed using Factsage 7.1 to explore the influence of each factor on the distribution of impurity elements at 1400°C.

Distribution of Pb

The primary reactions involving Pb are illustrated in Equations 3 and 4. The Main form of Pb in the nickel concentrates is sulfide. In the process of matte smelting from nickel concentrates, Part of lead sulfide in the nickel slag is oxidised into lead oxide and forms slag. In the molten smelting process, with a low oxygen partial pressure, typically around 10^{-7} atm, part of lead oxide reacts with iron sulfide to generate lead sulfide into matte and ferrous oxide into slag. Because of the relatively low boiling point of PbS (1114°C), part of Pb directly vaporises into the flue gas during the smelting process and is finally collected as dust.

$$2PbS + 3O_2\,(g) = 2PbO + 2SO_2\,(g) \quad (3)$$

$$PbO + FeS = PbS + FeO \quad (4)$$

The impact of changes in the CaO/SiO_2 ratio on the distribution of Pb in each phase is depicted in Figure 2a. With an increase in the CaO/SiO_2 ratio, the distribution of Pb shows an upward trend in the gas and slag and a downward trend in the matte. During the process of increasing the CaO/SiO_2 ratio from 0.4 to 1.2, the distribution of Pb in the matte decreases from 26.3 per cent to 22.7 per cent. With an increase in the CaO concentration in the slag, the activity coefficient of PbO in slag increases. As a result, most of Pb exists in the form of oxides, making it more prone to entering the slag. The effect of changes in the Fe/SiO_2 ratio on the distribution of Pb in each phase is illustrated in Figure 2b. With an increase in the Fe/SiO_2 ratio, the distribution of Pb shows an initial increase followed by a decrease in the gas, increase in the matte, and decrease in the slag. During the process of increasing the Fe/SiO_2 ratio from 0.6 to 1.4, the distribution of Pb in the slag decreases from 15.6 per cent to 7.4 per cent. The distribution of Pb in the matte increases from 20.6 per cent to 25.6 per cent, and the distribution of Pb in the gas increases from 63.8 per cent to 67.1 per cent. The impact of changes in the MgO concentration on the distribution of Pb in each phase is shown in Figure 2c. With an increase in the MgO concentration, the distribution of Pb increases in the gas, decreases in the matte, and increases in the slag.

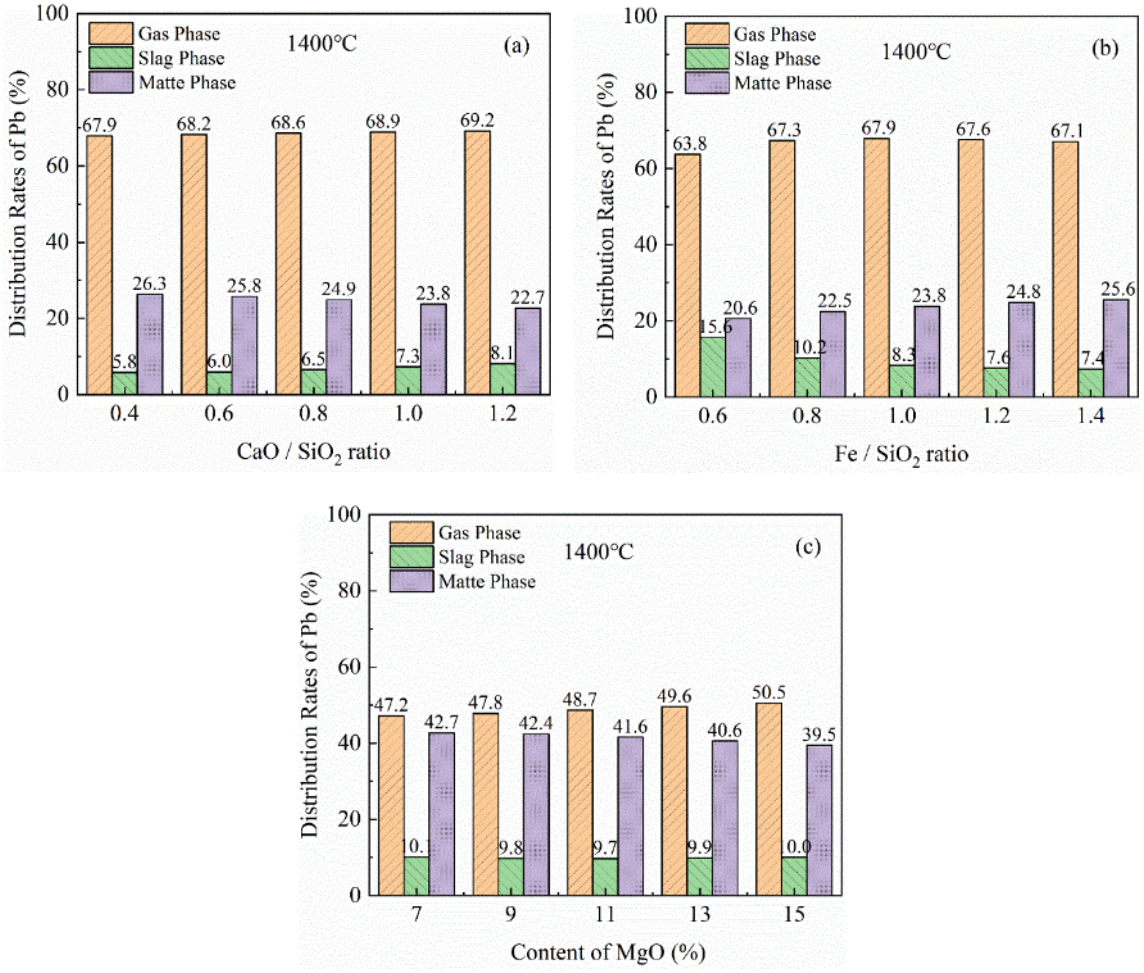

FIG 2 – The influence of slag composition changes on the distribution ratio of Pb in each phase: (a) CaO/SiO_2 ratio; (b) Fe/SiO_2 ratio; (c) MgO).

Distribution of Zn

The main form of Zn in the nickel concentrates is ZnS. The main reactions involving Zn in the smelting process are represented by Equations 5–8. A substantial portion of ZnS is oxidised by iron oxides to ZnO and then combines with silica to form zinc silicate. Part of ZnS undergoes carbon reduction, and this portion of Zn volatilises into gas. The remaining portion of Zn, in sulfide form, turns into the matte along with nickel and copper.

$$ZnS + 9Fe_2O_3 = ZnO + 6Fe_3O_4 + SO_2\ (g) \quad (5)$$

$$ZnS + 3Fe_3O_4 = ZnO + 9FeO + SO_2\ (g) \quad (6)$$

$$2ZnO + SiO_2 = Zn_2SiO_4 \quad (7)$$

$$ZnS + 2C = 2Zn\ (g) + 2CO\ (g) + S\ (g) \quad (8)$$

At 1400°C, the impact of changes in the CaO/SiO_2 ratio on the distribution of Zn in each phase is illustrated in Figure 3a. With an increase in the CaO/SiO_2 ratio, the distribution of Zn exhibits an upward trend in the gas and slag and a downward trend in the matte. During the process of increasing the CaO/SiO_2 ratio from 0.4 to 1.2, the distribution of Zn in the matte decreases from 29.2 per cent to 24.0 per cent. The increase in the CaO/SiO_2 ratio is conducive to more FeO being displaced from silicate by CaO, the activity coefficient of ZnO in slag decreases. The influence of changes in the Fe/SiO_2 ratio on the distribution of Zn in each phase is shown in Figure 3b. With an increase in the Fe/SiO_2 ratio, the distribution of Zn shows an increasing trend in the gas and matte and a decreasing trend in the slag. Changes in the MgO concentration and their impact on the distribution of Zn in each phase are depicted in Figure 3c. With an increase in the MgO concentration, the distribution of Zn increases in the gas and decreases in the slag and matte.

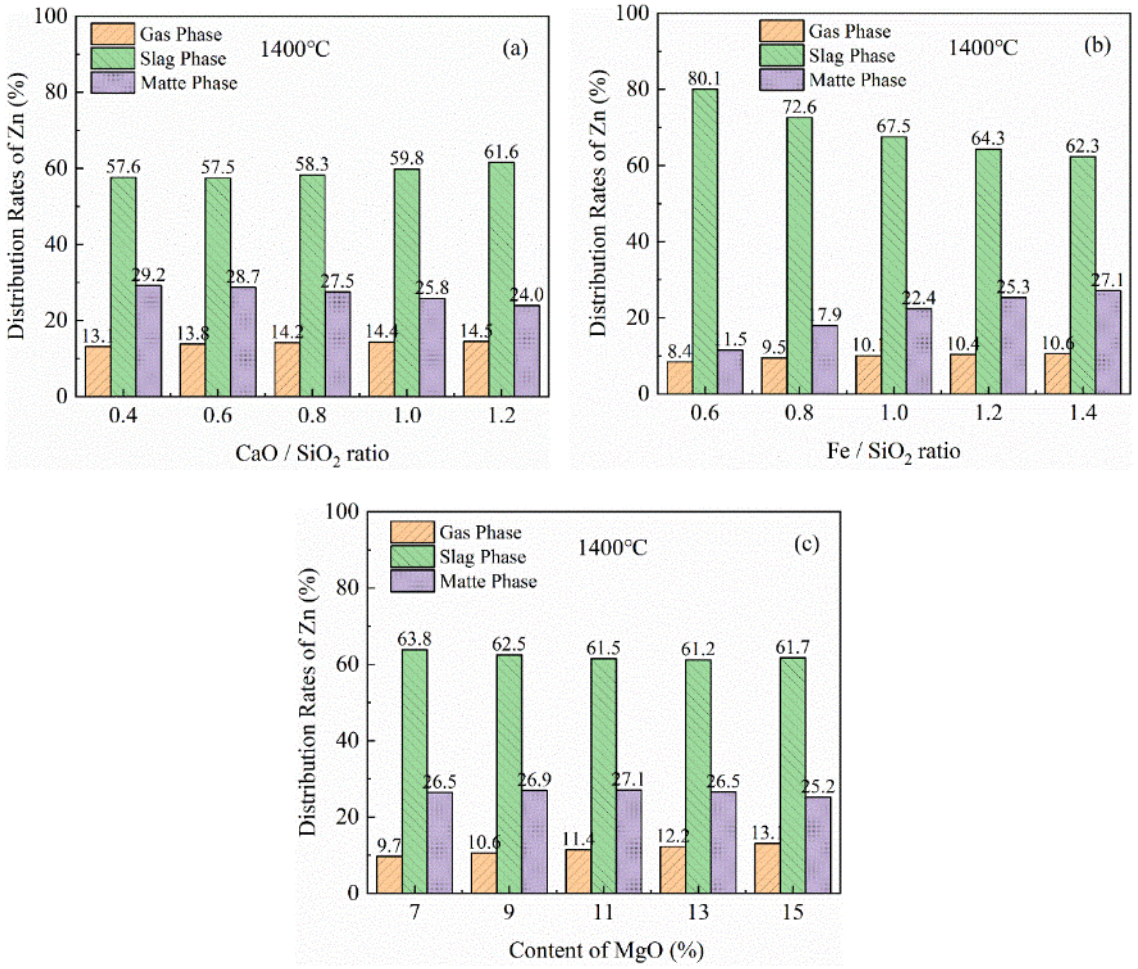

FIG 3 – The influence of changes slag composition on the distribution ratio of Zn in each phase (a) CaO/SiO_2 ratio; (b) Fe/SiO_2 ratio; (c): MgO.

Distribution of As

In the nickel concentrates, As primarily exists in the form of As_2S_3 or FeAsS. During the smelting process, arsenic sulfides undergo thermal decomposition to elemental As and then is oxidised. Most of the As oxides evaporates into the gas (Chen and Jahanshahi, 2010; Chen, Zhang and Jahanshahi, 2010; Swinbourne and Kho, 2012), while some arsenic oxides are embedded in the silicate matrix. The main reactions are illustrated in Equations 9–11.

$$4As + 3O_2\ (g) = 2As_2O_3\ (g) \quad (9)$$

$$2As_2S_3 + 9O_2\,(g) = 2As_2O_3 + 6SO_2\,(g) \quad (10)$$

$$As_2O_3 + 2Fe_2O_3 = As_2O_5 + 4FeO \quad (11)$$

At 1400°C, the influence of the CaO/SiO_2 ratio changes on the distribution of As in each phase is illustrated in Figure 4a. With an increase in the CaO/SiO_2 ratio, the distribution of As shows an upward trend in the slag and a downward trend in the gas and matte. During the process of increasing the CaO/SiO_2 ratio from 0.4 to 1.2, the distribution of As in the matte decreases from 1.0 per cent to 0.9 per cent. The distribution of As in the gas decreases from 60.2 per cent to 53.7 per cent, and the distribution of As in the slag decreases from 38.7 per cent to 45.4 per cent. Increase of CaO in slag will reduce the activity coefficient of As_2O_3 and As_2O_5, hence increase As capacity in slag. The volatilisation of arsenic oxides has been reduced. The impact of changes in the Fe/SiO_2 ratio on the distribution of As in each phase is shown in Figure 4b. With an increase in the Fe/SiO_2 ratio, the distribution of As exhibits an initial increase followed by a decrease in the gas, a decrease in the matte, and an initial decrease followed by an increase in the slag. Changes in the MgO concentration and their impact on the distribution of As in each phase are depicted in Figure 4c. With each temperature condition, with an increase in the MgO concentration, the distribution of As shows an upward trend in the matte and slag and a downward trend in the gas.

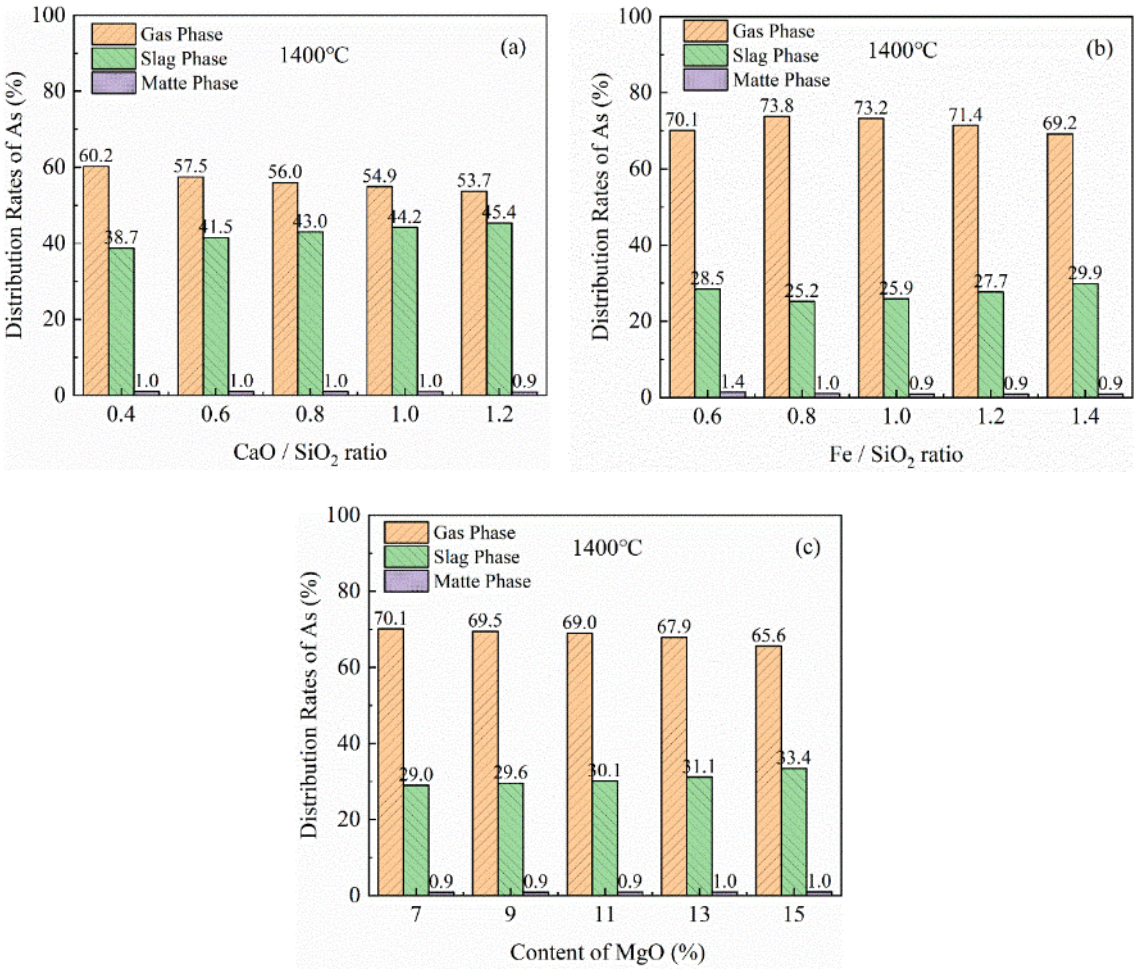

FIG 4 – The influence of slag composition changes on the distribution ratio of As in each phase (a) CaO/SiO_2 ratio; (b) Fe/SiO_2 ratio; (c) MgO.

Test results on the migration trends of impurity elements

The concentration of Pb, Zn, and As in each phase from tests is shown in Figure 5. The impurity element concentration in nickel slag and nickel matte was determined by chemical analysis, while the impurity element concentration in the gas was calculated using the formula:

$$g_x=(a\times S_{x1}+b\times M_{x1}-c\times S_{x2}-d\times M_{x2})/(S_{x1}+M_{x1}-S_{x2}-M_{x2}),\% \quad (12)$$

where:

g_x the proportion of impurity elements in the gas, per cent

a the proportion of impurity elements in the nickel slag before reaction, per cent

b the proportion of impurity elements in the nickel matte before reaction, per cent

c the proportion of impurity elements in the nickel slag after reaction, per cent

d the proportion of impurity elements in the nickel matte after reaction, per cent

S_{x1} the mass of nickel slag before reaction, g

M_{x1} the mass of nickel matte before reaction, g

S_{x2} the mass of nickel slag after reaction, g

M_{x2} the mass of nickel matte after reaction

From Figure 5a, it can be observed that with an increase in alkalinity, the concentration of Pb in nickel slag and nickel matte shows a decreasing trend, while in the flue gas, it exhibits an increasing trend. In comparison to the traditional process (scheme 1#), the Pb concentration in nickel matte in the scheme 4# decreases from 0.105 per cent to 0.093 per cent, the Pb concentration in the slag decreases from 0.017 per cent to 0.009 per cent, and the Pb concentration in the flue gas increases from 0.113 per cent to 0.197 per cent. Figure 5b presents the distribution rate of Pb in each phase. It can be observed that with the traditional process, 19 per cent Pb, 59 per cent Pb and 21 per cent Pb distribute in slag, matte and gas, respectively. In contrast to the Pb distribution with the traditional process (scheme 1#), in the scheme 4#, 10 per cent Pb, 53 per cent Pb, 37 per cent Pb distribute in slag, matte and gas, respectively. The change in the Pb distribution may be attributed to the decrease in melting temperature resulting from the addition of CaO during slag adjustment, providing higher superheat for matte smelting, thereby enhancing the fluidity of reactant and facilitating the easier release of volatile substances in gas form.

Figure 5c displays the proportion of Zn in each phase. With an increase in alkalinity, the concentration of Zn in nickel slag shows a decreasing trend, while in nickel matte and flue gas, it exhibits an increasing trend. In comparison to the traditional process (scheme 1#), the Zn concentration in the slag in the scheme 4# decreases from 0.097 per cent to 0.062 per cent, the Zn concentration in nickel matte increases from 0.172 per cent to 0.177 per cent, and the Zn concentration in the flue gas increases from 0.592 per cent to 0.787 per cent. Figure 5d illustrates the distribution rate of Zn in each phase. With the traditional process, 18 per cent Zn, 52 per cent Zn and 30 per cent Zn distribute in slag, matte and gas, respectively. In contrast to the Zn distribution with the traditional process (scheme 1#), in the scheme 4#, 22 per cent Zn, 31 per cent Zn, 47 per cent Zn distribute in slag, matte and gas respectively. with CaO addition for slag adjustment, more Zn volatilises into the gas, and this phenomenon is similar with the distribution trend of Pb.

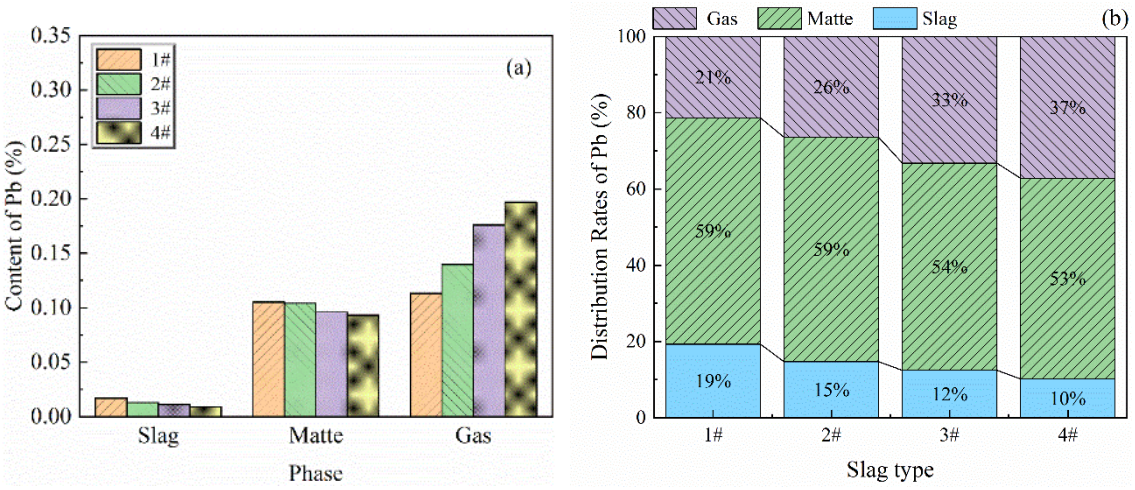

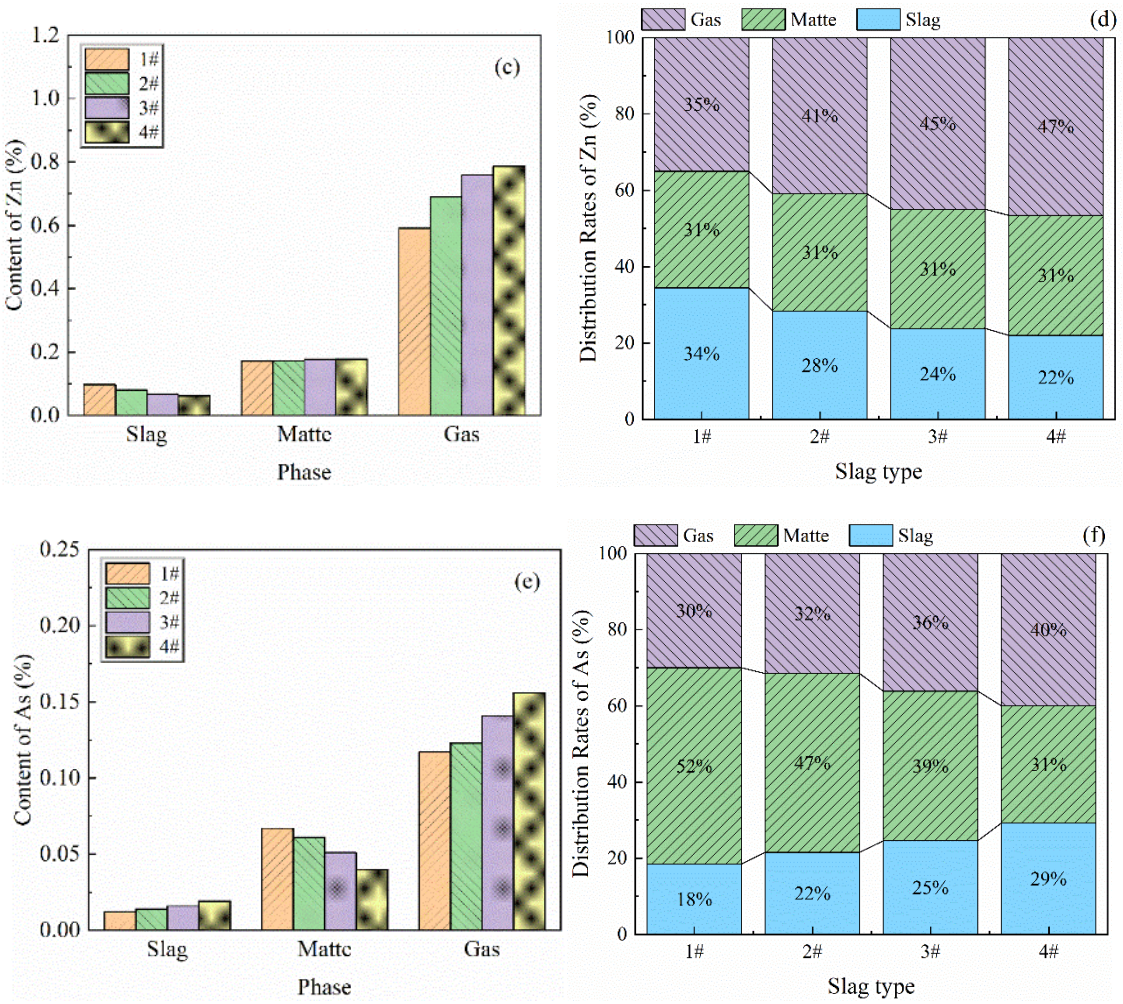

FIG 5 – The distribution of impurity elements in each phase after smelting and refining: (a) Proportion of Pb in each phase; (b): Distribution rate of Pb; (c) Proportion of Zn in each phase; (d) Distribution rate of Zn; (e) Proportion of As in each phase; (f) Distribution rate of As.

Figure 5e depicts the proportion of As in each phase. With an increase in alkalinity, the concentration of As in nickel slag shows a decreasing trend, while in nickel matte and flue gas, it exhibits an increasing trend. In comparison to the traditional process (scheme 1#), the As concentration in nickel matte in the scheme 4# decreases from 0.067 per cent to 0.04 per cent, the As concentration in the slag increases from 0.012 per cent to 0.019 per cent, and the As concentration in the flue gas increases from 0.117 per cent to 0.156 per cent. Figure 5f illustrates the distribution rate of As in each phase. It can be seen that to the traditional process, 72 per cent As, 6 per cent As and 21 per cent As distribute in slag, matte and gas respectively. In contrast to the As distribution in the traditional process (scheme 1#), in the scheme 4#, 29 per cent As, 31 per cent As and 40 per cent As distribute in the slag, matt and gas respectively. with CaO addition for slag adjustment, As volatilises more from the slag into the gas.

The theoretical calculation results of impurity element distribution indicate that with an increase in alkalinity, the Pb concentration decreases in the matte and an increase in gas. This is consistent with the experimental results. Contrary to the experimental results, the Pb concentration in the slag increases, attributed to the elevated alkalinity enhancing the oxidative atmosphere in the reaction. This enhanced the migration of lead sulfides from the matte to the slag. In the theoretical calculation, process reaches to equilibrium state, the amount of Pb transformed from the matte to the slag exceeds the volatile concentration in the slag, resulting in an increase in Pb concentration in the slag with the increasing alkalinity.

The Zn concentration in the slag and gas gradually increases with the rise in alkalinity. While in the matte, the Zn concentration gradually decreases. This trend aligns with the variations observed in Pb concentration and the results of theoretical calculations. In the traditional smelting process, the

Zn concentration in the slag gradually decreases with the increase in alkalinity, contrasting with the theoretical calculation results. The reasons for the difference are similar to those explained for the changes in Pb concentration.

With the increase in alkalinity, As concentration in the slag and matte exhibits an increasing and decreasing trend respectively, consistent with the experimental results. In the gas, As concentration shows a decreasing trend, which is not in accordance with the experimental results. The discrepancy lies in the theoretical calculation where the reaction is in a state of complete equilibrium; most of the As has entered the gas during in a state of complete equilibrium. In the experimental process, Calcium ions (Ca^{2+}) have a higher affinity for arsenide ions (As^{3-}) than oxide ions (O^{2-}). With the alkalinity increases, there is a reduction in the emitted concentration of arsenic oxide in the furnace gas. The reaction is controlled by kinetic conditions, leading to an increase in As concentration in the gas.

The morphology analysis of impurity elements in nickel slag

Utilising SEM-EDS analysis to examine the mineralogical embedding characteristics of impurity elements, the results are presented in Figure 6. The major phases in the nickel slag with the traditional process (scheme 1#) are illustrated in Figure 6a. The matrix composition of the produced nickel slag mainly consists of olivine, with brighter regions representing magnetite phases composed of Fe and O, which constitute the primary phases in the slag. The bright portions precipitated in the nickel matte are primarily composed of copper sulfide, while the matrix consists mainly of nickel sulfide. The line scan results reveal that, after smelting, Pb and Zn are mainly present in the nickel matte in the form of sulfides. Pb and Zn in the slag exhibit a relatively uniform distribution. As is primarily present in the slag in the form of arsenic oxides. The baseline of As in the slag fits better with the baselines of Fe and Si, indicating that As in the slag is mainly enveloped by iron silicate. From Figure 6b–6d, it can be observed that crystals precipitated in the slag after slag adjustment are iron oxides, while a significant amount of iron sulfate mineral phases appear in the matrix. This suggests that slag adjustment promotes the transformation of iron silicate to iron sulfate. Comparing the morphology of slag and matte produced with different slag condition, it is evident that with increasing alkalinity during the reaction process, there are partially entrapped nickel mattes in the slag. This phenomenon might be related to differences in density, viscosity, and interfacial tension between sulfides and slag. As primarily exists in the slag in the form of arsenic oxides, entangled and embedded with olivine, rather than combined with iron sulfate.

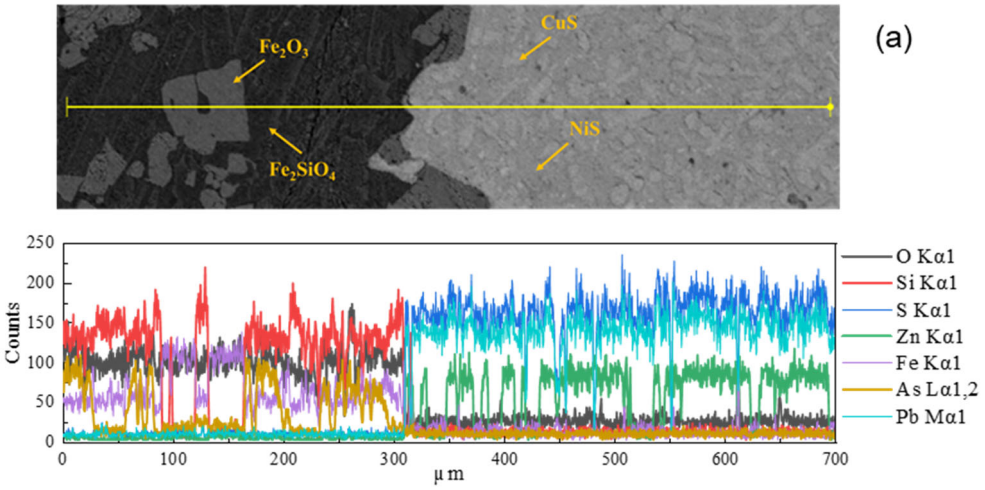

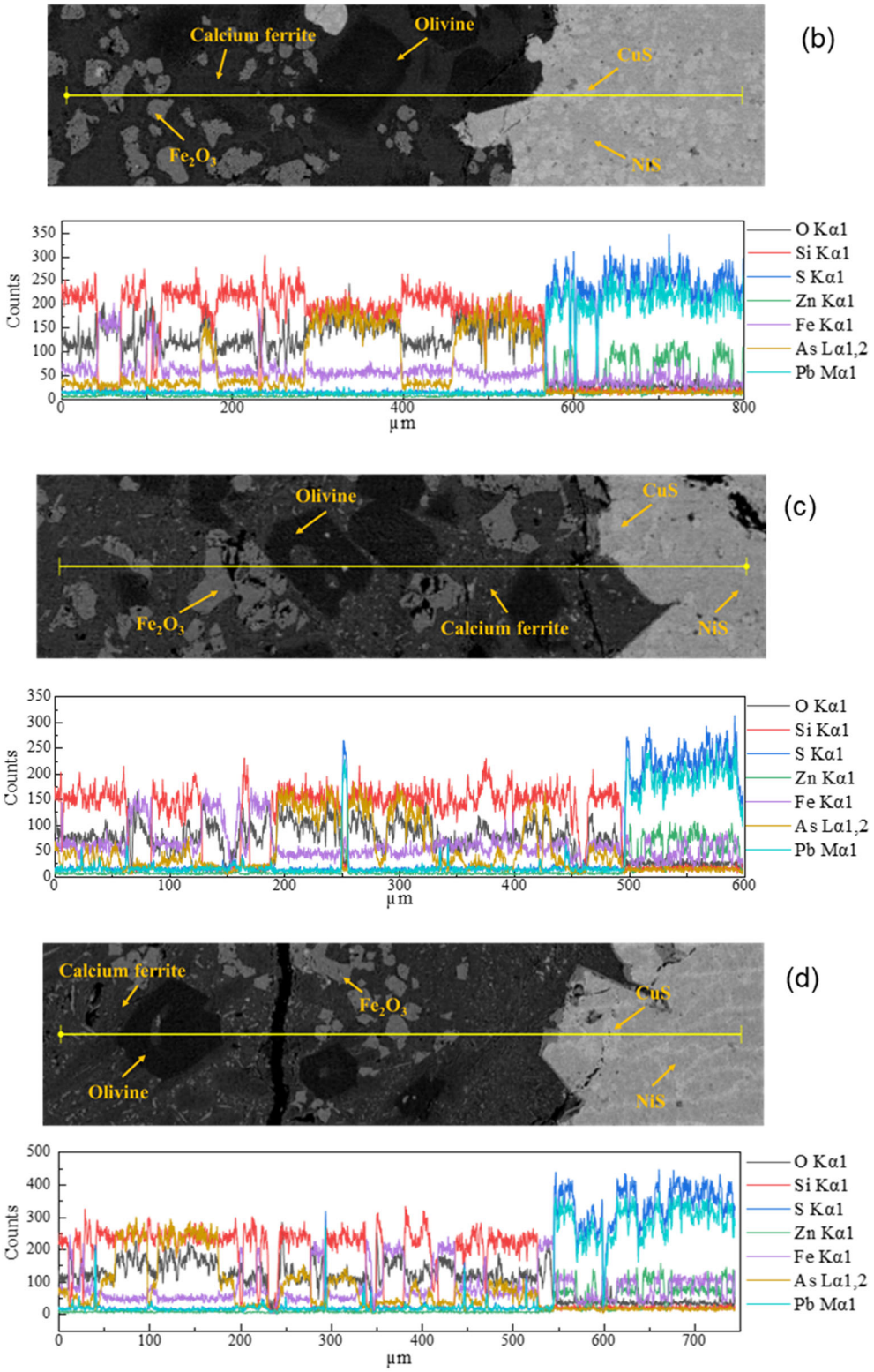

FIG 6 – The microstructure and surface scanning spectrum results near the slag-matte interface: (a) scheme 1#; (b) scheme 2#; (c) scheme 3#; (d) scheme 4#.

The chemical valence analysis of impurity elements in nickel slag

The chemical valence of Pb in nickel slag with different slag condition are depicted in Figure 7, typically represented as Pb, PbO, PbO_2, $PbSO_4$. The binding energy difference between Pb4f 7/2 and Pb4f 5/2 is 4.87 eV. The peak position indicating metallic Pb in the main peak of Pb4f 7/2 is approximately between 136~137 eV. The binding forms of Pb oxide in nickel slag may exhibit two peak positions, one in the range of 137~138 eV and the other around 138.5 eV. There is a gap in the binding energy of Pb oxide in each mineral phase, with the binding energy peaks of Pb, Pb-O

(Pb/Fe/O), and Pb-O (Pb/Si/O) increasing sequentially. The primary forms of Pb in nickel slag include metallic lead, lead silicate, and lead sulfate. With the traditional process, a semi-quantitative analysis of Pb in the nickel slag produced indicates that the metallic Pb concentration is 45 per cent, lead sulfate concentration is 20 per cent, and lead silicate concentration is 35 per cent. Through adjusting slag's composition, introducing CaO as a flux during the nickel matte smelting stage, the overall form of metallic Pb in the slag tends to decrease. During the smelting process, adjusting slag's composition enhance the stability of Pb compounds in the slag, and reducing the risk of Pb release, while the concentration of lead iron sulfate gradually increases. When the slag has higher alkalinity, CaO more easily combines with silicate ions, displacing Fe and resulting in lower lead silicate concentration and higher lead iron sulfate concentration in the slag.

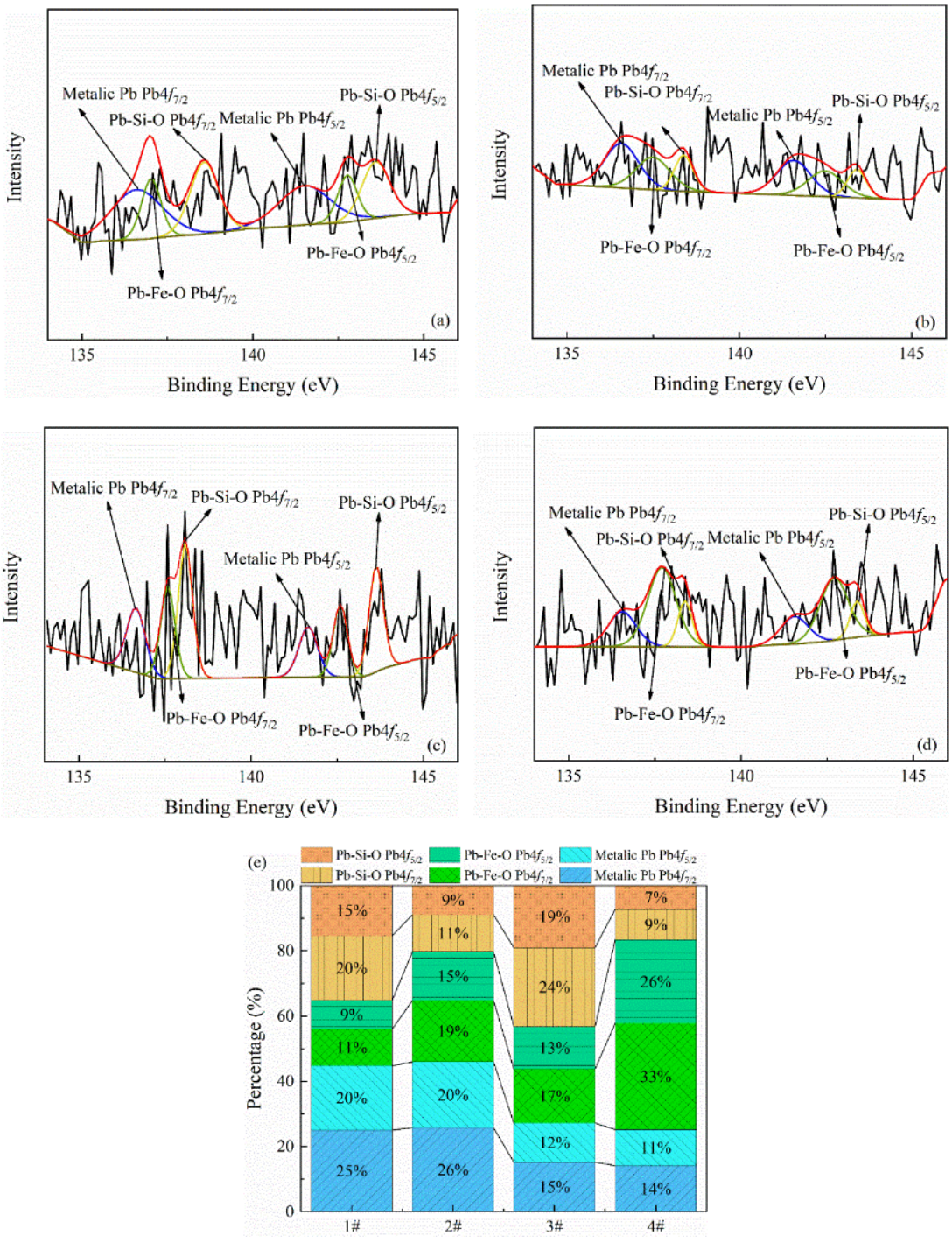

FIG 7 – The chemical forms of Pb in nickel slag with each composition: (a) scheme 1#; (b) scheme 2#; (c) scheme 3#; (d) scheme 4#; (e) Intensity ratio of each valence state of Pb.

The chemical forms of Zn in nickel slag with each condition are illustrated in Figure 8. The XPS analysis for Zn is similar to Pb, and zinc oxide exhibits two peak positions in each mineral phase. The binding energy of the Zn2p 3/2 fitting peak for zinc oxide (Zn/Fe/O) is roughly between 1021 and 1021.9 eV. Peaks above 1022 eV in the Zn2p 3/2 fitting are considered indicative of zinc oxide (Zn/Si/O). The fitting peak position for Zn sulfide is close to that of metallic Zn, with a binding energy difference of 23 eV between Zn2p 3/2 and Zn2p 1/2. XPS analysis of the main forms of Zn in nickel slag produced during nickel smelting with each scenario reveals that Zn in nickel slag is mainly present in the forms of zinc silicate and zinc iron sulfate. Zinc iron sulfate is typically found or associated with Fe-containing silicate mineral phases, and its peak position is lower compared to zinc silicate. Using CaO instead of SiO_2, there is an increasing trend in the proportion of zinc iron sulfate in the slag, while the proportion of zinc silicate decreases. With high alkalinity, the increased combination of sulfate ions with calcium ions may be influenced by the dissolution and loss of metal sulfides in the slag.

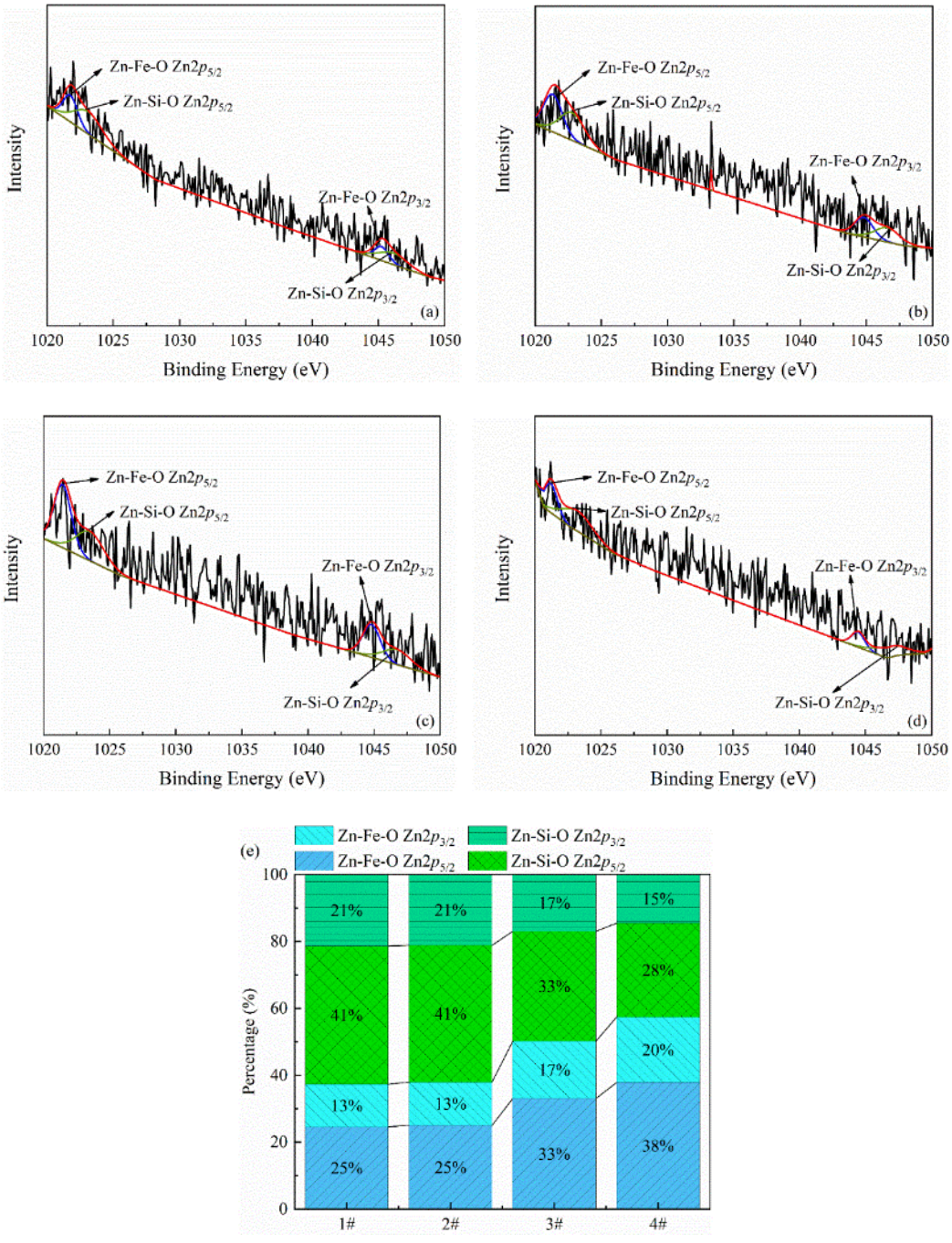

FIG 8 – The chemical forms of Zn in nickel slag with each composition: (a) scheme 1#; (b) scheme 2#; (c) scheme 3#; (d) scheme 4#; (e) Intensity ratio of each valence state of Zn.

The chemical forms of As typically include metallic As, arsenic sulfides, As^{3+} (As_2O_3), and As^{5+} (As_2O_5). In this research, As3d was employed investigate the chemical states of As in nickel slag. The As3d orbital comprises As3d 5/2 and As3d 3/2 double peaks (with a set binding energy difference of 0.7±0.1 eV), where the As (III) peak in As3d is generally 1 eV lower than As (V). Analysis of the chemical forms of As in nickel slag with each scenario, as shown in Figure 9, reveals that blue represents metallic As or arsenic sulfides, green represents As(III) oxide, and yellow represents As(V)-O oxide. In the traditional process, As in nickel slag mainly exists in the form of As(V)-O arsenate, with small amounts of trivalent arsenic oxide and metallic or sulfide arsenic. In scheme 2#, scheme 3#, and scheme 4#, As exists mainly in the form of trivalent arsenic oxide. When using CaO instead of SiO_2 as a flux in the nickel smelting process, it is observed that the overall presence of sulfide arsenic or metallic As in the slag tends to decrease, while the proportion of As_2O_3 in nickel slag shows an increasing trend. Compared to arsenates, As_2O_3 is more easily removed in the subsequent Fe reduction process.

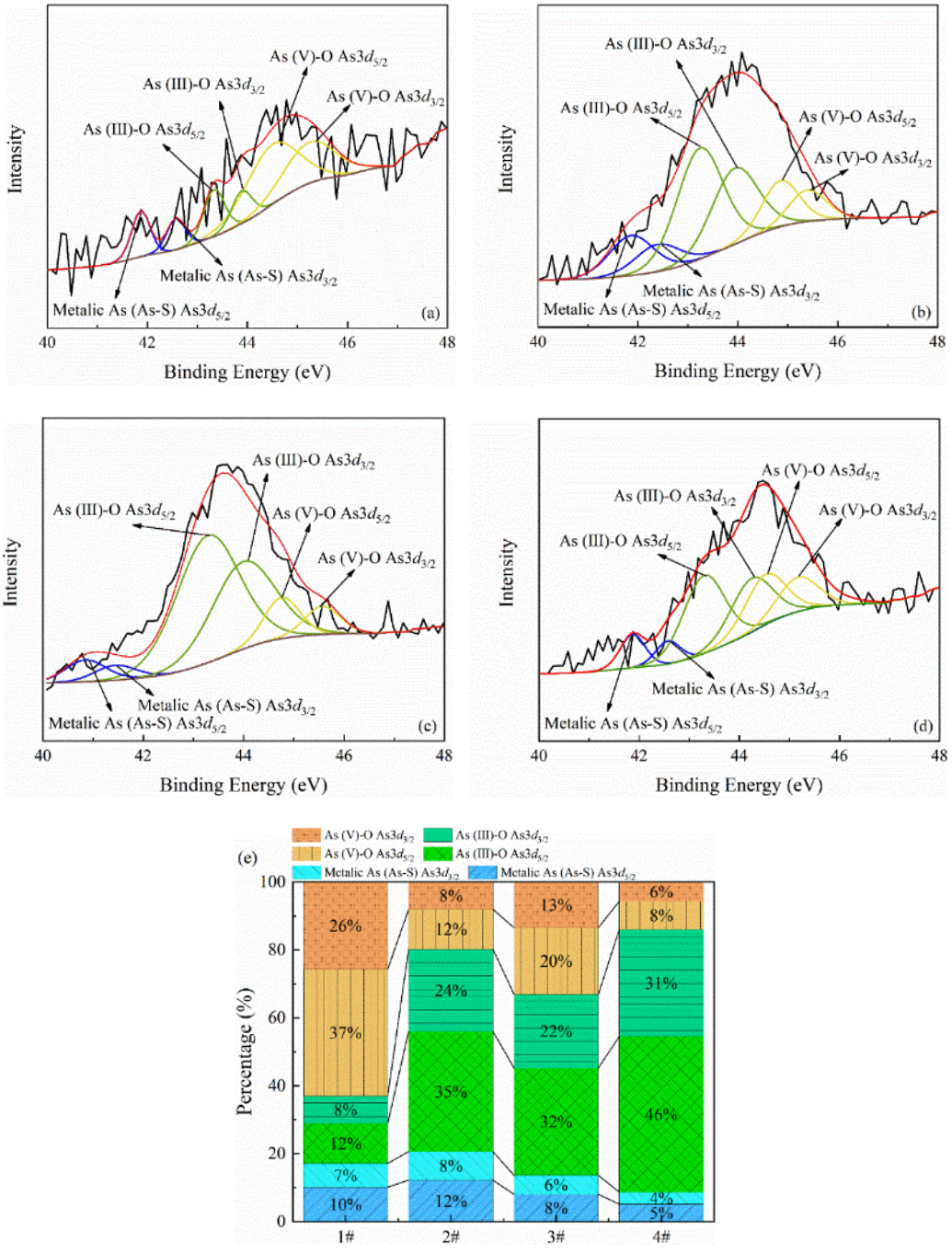

FIG 9 – The chemical forms of As in nickel slag with each composition: (a) scheme 1#; (b) scheme 2#; (c) scheme 3#; (d) scheme 4#; (e) Intensity ratio of each valence state of As.

CONCLUSIONS

Based on the oxygen-enriched top-blowing process, the distribution patterns of Pb, Zn, and As were explored in nickel sulfide concentrates smelting with different slag. The main conclusions are as follows:

- In theoretical equilibrium state, Pb has the highest concentration in the gas, followed by the matte, with the lowest concentration in the slag. As also has the highest concentration in the gas, followed by the slag, with the lowest concentration in the matte. Zn has the highest concentration in the slag, followed by the matte, with the lowest concentration in the gas. The increase in the calcium-to-silicon ratio results in an increase of impurity element concentration in the slag.
- To traditional operating conditions, 79 per cent of Pb, 34 per cent of Zn, and 72 per cent of As enter the slag. 6 per cent of Pb, 31 per cent of Zn, and 6 per cent of As enter the matte. 14 per cent of Pb, 35 per cent of Zn, and 21 per cent of As enter the gas, respectively. The deviation between test results and theoretical calculations is attributed to the difference between equilibrium state and the nonequilibrium state in experimental process.
- With increasing CaO, the proportion of Pb entering gas increases, and the proportion entering slag, matte decreases, respectively. The proportion of Zn entering the slag decreases, the proportion entering the matte remains unchanged, and the proportion entering gas increases. The proportion of As entering matte decreases, the proportion entering slag, gas increases, respectively. Adjusting slag's composition is advantageous for the volatilisation and enrichment of impurity elements in the gas and slag.
- With slag composition adjustment with CaO addition, the chemical forms of Pb in the slag produced during the nickel smelting process transform from metallic lead and lead silicate to lead iron sulfate; the chemical form of Zn changes from zinc silicate to iron zinc sulfate; the form of As transforms from arsenic sulfide and arsenate to As_2O_3. Iron sulfate and As_2O_3 are more easily reduced compared to silicate and arsenate, making it easier to remove impurity elements in the next iron extraction process.
- With slag composition adjustment with CaO addition, Impurity elements tend to be entrained into the gas, reduces the impact of impurity elements on product performance during subsequent matte refining and iron extraction from nickel slag process.

ACKNOWLEDGEMENTS

This research was financially supported by the National Natural Science Foundation of China (No. 51674185).

REFERENCES

Cao, G, Zhao, J X, Wang, G J, Zheng, J H, Zong, H X, Li, B and Cui, Y R, 2023. The research status and development analysis of iron resource recovery from nickel smelting slag, *Nonferrous Metals Science and Engineering*, 9 p. Available from: <http://kns.cnki.net/kcms/detail/36.1311.TF.20230920.1642.002.html> [Accessed: 11 September 2023].

Chen, C and Jahanshahi, S, 2010. Thermodynamics of Arsenic in FeOx-CaO-SiO2 Slags, *Metallurgical and Materials Transactions B*, 41:1166–1174.

Chen, C, Zhang, L and Jahanshahi, S, 2010. Thermodynamic Modeling of Arsenic in Copper Smelting Processes, *Metallurgical and Materials Transactions B*, 41:1175–1185.

Dimitrijevic, M, Kostov, A, Tasic, V and Milosevic, N, 2009. Influence of pyrometallurgical copper production on the environment, *Journal of Hazardous Materials*, 164(2–3):892–899.

Dosmukhamedov, N K and Kaplan, V, 2016. Efficient Removal of Arsenic and Antimony During Blast Furnace Smelting of Lead-Containing Materials, *JOM*, 69:381–387.

Guo, Z, Pan, J, Zhu, D and Zhang, F, 2018a. Green and efficient utilization of waste ferric-oxide desulfurizer to clean waste copper slag by the smelting reduction-sulfurizing process, *Journal of Cleaner Production*, 199:891–899.

Guo, Z, Zhu, D, Pan, J and Zhang, F, 2018b. Innovative methodology for comprehensive and harmless utilization of waste copper slag via selective reduction-magnetic separation process, *Journal of Cleaner Production*, 187:910–922.

Gyurov, S, Rabadjieva, D, Kovacheva, D and Kostova, Y, 2014. Kinetics of copper slag oxidation under nonisothermal conditions, *Journal of Thermal Analysis and Calorimetry*, 116(2):945–953.

Kobayashi, Y and Hirano, S, 2016. Distribution and Excretion of Arsenic Metabolites after Oral Administration of Seafood-Related Organoarsenicals in Rats, *Metals*, 6(10).

Li, K Q, Ping, S, Wang, H Y and Ni, W, 2013. Recovery of iron from copper slag by deep reduction and magnetic beneficiation, *Int J Min Met Mater*, 20(11):1035–1041.

Li, X M, Yang, H B, Ruan, J B, Li, Y, Wen, Z Y and Xing, X D, 2020a. Effect of mechanical activation on enhancement of carbothermal reduction of nickel slag, *Journal of Iron and Steel Research International*, 27(11):1311–1321.

Li, X, Li, Y, Xing, X, Wang, Y, Wen, Z and Yang, H, 2021. Effect Of Particle Sizes Of Slag On Reduction Characteristics Of Nickel Slag-Coal Composite Briquette, *Archives of Metallurgy and Materials*, 66(1):127–134.

Li, X, Zhang, X, Zang, X and Xing, X, 2020b. Structure and Phase Changes of Nickel Slag in Oxidation Treatment, *Minerals*, 10(4).

Long, H, Chun, T, Di, Z, Wang, P, Meng, Q and Li, J, 2016. Preparation of Metallic Iron Powder from Pyrite Cinder by Carbothermic Reduction and Magnetic Separation, *Metals-Basel*, 6(4).

Marenych, O and Kostryzhev, A, 2020. Strengthening Mechanisms in Nickel-Copper Alloys: A Review, *Metals-Basel,* 10(10).

Park, J G, Eom, H S, Huh, W W, Lee, Y S, Min, D J and Sohn, I, 2011. A Study in the Thermodynamic Behavior of Nickel in the MgO-SiO2-FeO Slag System, *Steel Research International,* 82(4):415–421.

Shen, Y, Huang, Z, Zhang, Y, Zhong, J, Zhang, W, Yang, Y, Chen, M and Du, X, 2018. Transfer Behavior of Fe Element in Nickel Slag during Molten Oxidation and Magnetic Separation Processes, *Materials Transactions*, 59(10):1659–1664.

Sun, W, Li, X, Liu, R, Zhai, Q and Li, J, 2021. Recovery of Valuable Metals from Nickel Smelting Slag Based on Reduction and Sulfurization Modification, *Minerals*, 11(9).

Swinbourne, D and Kho, T S, 2012. Computational Thermodynamics Modeling of Minor Element Distributions During Copper Flash Converting, *Metallurgical and Materials Transactions B*, 43:823–829.

Wang, G J, Zhao, J X, Cao, G, Zheng, J H, Li, B, Mang, Y F, Cui, Y R and Zong, H X, 2023. Study of nickel smelting slag melting temperature regulation based on slag transfer and iron lifting, *The Chinese Journal of Nonferrous Metals*, 17 p. Available from: <http://kns.cnki.net/kcms/detail/43.1238.TG.20230906.1517.002.html> [Accessed: 7 September 2023].

Wang, G, Cui, Y, Li, X, Yang, S, Zhao, J, Tang, H and Li, X, 2020. Molecular Dynamics Simulation on Microstructure and Physicochemical Properties of FexO-SiO2-CaO-MgO-'NiO' Slag in Nickel Matte Smelting under Modulating CaO Concentration, *Minerals*, 10(2).

Wang, G, Cui, Y, Yang, J, Li, X, Yang, S, Zhao, J and Tang, H, 2021. Fe/SiO2 Ratio on the Properties, Microstructure and Fe-Containing Phases of Nickel Matte Smelting Slag, *Metallurgical and Materials Transactions B-Process Metallurgy and Materials Processing Science*, 52(3):1463–1471.

Wang, Q, Guo, X, Tian, Q, Chen, M and Zhao, B, 2017. Reaction Mechanism and Distribution Behavior of Arsenic in the Bottom Blowing Copper Smelting Process, *Metals-Basel*, 7(8):302.

Wang, S, Ni, W, Li, K, Wang, C and Wang, J, 2014. Effect of basicity on recovering iron, nickel and copper by deep reduction process of nickel slag pellets, *Transactions of Materials and Heat Treatment*, 35(9):23–28.

Wang, S, Ni, W, Li, K, Wang, C and Wang, J, 2015. Effect of carbide slag as additive on recovering iron by deep reduction process of nickel slag, *Transactions of Materials and Heat Treatment*, 36(12):7–12.

Wu, Q, Chen, Q, Huang, Z, Gu, B, Zhu, H and Tian, L, 2020. Preparation and characterization of porous ceramics from nickel smelting slag and metakaolin, *Ceramics International*, 46(4):4581–4586.

Wu, Q, Wu, Y, Tong, W and Ma, H, 2018. Utilization of nickel slag as raw material in the production of Portland cement for road construction, *Construction and Building Materials*, 193:426–434.

Xia, B D, Li, R F, Zhao, X Y, Dang, Q L, Zhang, D P and Tan, W B, 2018. Constraints and opportunities for the recycling of growing ferronickel slag in China, *Resources Conservation and Recycling*, 139:15–16.

Yang, W, Tian, S, Wu, J, Chai, L and Liao, Q, 2017. Distribution and Behavior of Arsenic During the Reducing-Matting Smelting Process, *JOM,* 69:1077–1083.

Yu, J, Qin, Y, Gao, P, Sun, Y and Ma, S, 2021. The Growth Characteristics and Kinetics of Metallic Iron in Coal-Based Reduction of Jinchuan Ferronickel Slag, *Minerals*, 11(8).

Zhang, G, Wang, N, Chen, M and Cheng, Y, 2020a. Recycling Nickel Slag by Aluminum Dross: Iron-extraction and Secondary Slag Stabilization, *ISIJ International*, 60(3):602–609.

Zhang, J, Qi, Y H, Yan, D L and Xu, H C, 2015. A New Technology for Copper Slag Reduction to Get Molten Iron and Copper Matte, *Journal of Iron and Steel Research International*, 22(5):396–401.

Zhang, T T, Zhi, S W, Guo, L J, Wu, Z L and Han, J N, 2020b. Research Progress of Resource Utilization of Copper-Nickel Smelting Slag, *Gold Science and Technology*, 28(05):637–645.

Zhao, J, Zhao, Z, Cui, Y, Shi, R, Tang, W, Li, X and Shang, N, 2018. New Slag for Nickel Matte Smelting Process and Subsequent Fe Extraction, *Metallurgical and Materials Transactions B-Process Metallurgy and Materials Processing Science*, 49(1):304–310.

Zhong, D P, Li, L and Tan, C, 2017. Separation of Arsenic from the Antimony-Bearing Dust through Selective Oxidation Using CuO, *Metallurgical and Materials Transactions B*, 48:1308–1314.

Lessons learned from attempts at minimising CO_2 emissions in process metallurgy – pyrolysed secondary raw materials, bio-coke, and hydrogen as alternative reducing agents

DOI: 10.62053/ZKQG2762

F Diaz[1], M Sommerfeld[2], G Hovestadt[2], D Latacz[2] and B Friedrich[2]

1. Group Leader Automation and Digital Transformation for Process Metallurgy; Institute of Process Metallurgy and Metal Recycling IME, RWTH Aachen University, 52056 Aachen, Germany. Email: fdiaz@ime-aachen.de
2. Institute of Process Metallurgy and Metal Recycling IME, RWTH Aachen University, 52056 Aachen, Germany.

ABSTRACT

The metallurgical sector significantly contributes to the global carbon footprint and encounters the challenge of developing more sustainable production methods. This study introduces novel approaches aimed at reducing CO_2 emissions within the industrial sector, some of which have been developed up to the demonstration scale.

In two case studies, urban waste from the agricultural sector (corn, olives, coconut etc) and waste electrical or electronic equipment (WEEE) recycling residues (shredder light fractions (SLF)) were subjected to thermal treatment. The resulting materials were then used as substitutes for conventional fossil-based reducing agents in both the copper and ferroalloy industries. Furthermore, hydrogen was employed at different scales to assess its efficacy as a reducing agent for recovering metal oxides from fayalitic copper slags.

Our findings reveal promising prospects and defined specific challenges for the integration of these alternative reducing agents in the industry. The synergistic use of pyrolysed SLF, bio-coke, and hydrogen presents a viable pathway to significantly diminish CO_2 emissions while simultaneously improving the sustainability of the metallurgical sector.

INTRODUCTION

The metallurgical industry produced approximately 1.9 billion tonnes (Bt) of steel, 69 Mio tonnes of aluminium and 22 Mio tonnes of copper in 2022 (US Geological Survey, 2023), contributing to roughly 5.2 per cent of the total anthropogenic CO_2 emissions together with other industries like cement and chemicals. In comparison to other industrial sectors, the metallurgical industry accounts for approximately 30 per cent of these emissions, closely competing with the cement industry (Malischek, Baylin-Stern and McCulloch, 2019).

Greenhouse gas emissions are a significant concern due to the climate crisis, especially within the metallurgical industry. The primary source of CO_2 emissions is iron production, specifically in blast furnaces, which employ carbothermal reduction, resulting in substantial direct CO_2 emissions. Furthermore, processes like pelletising, coking, sintering, and steelmaking also contribute to direct CO_2 emissions (Cavaliere, 2016). In addition to the direct CO_2 emissions generated during carbothermal reduction processes for metal production, there are other, less-discussed sources of CO_2 emissions that are also relevant. These include the production of metallurgical slags and the subsequent handling of such metallurgical waste materials, often involving high temperatures that require fuels or energy and carbothermal reduction, which requires reducing agents. This is especially significant, given that for instance in the copper sector, flash smelters can yield up to 3 t of slag per tonne of copper (Gorai, Jana and Premchand, 2003; Zhang, Zhang and Zheng, 2022), containing 1 per cent to 5 per cent copper by weight, equivalent to up to 10 per cent of the copper in the input material (Gorai, Jana and Premchand, 2003; Gonzalez *et al*, 2005; Roy, Datta and Rehani, 2015), thus post-handling of such a slag is ultimately required.

The European Union has already established significant targets and signed the ‘Green Deal’, aiming to achieve a net CO_2-free economy by 2050 (European Commission, 2021). This initiative creates a compelling demand for innovative process solutions within the ferrous and non-ferrous industry for the metal production and the handling of metallurgical slags.

In the context of circular economy and sustainable practices, there is extensive research underway to identify viable alternatives to fossil reducing agents. These alternatives can be broadly classified into two categories: alternative solid reducing agents sourced from ‘waste’ materials and alternative reducing gases. Figure 1 illustrates these alternative reducing materials in relation to their role in metallurgical applications. This, in the context of decarbonisation of the metallurgical sector.

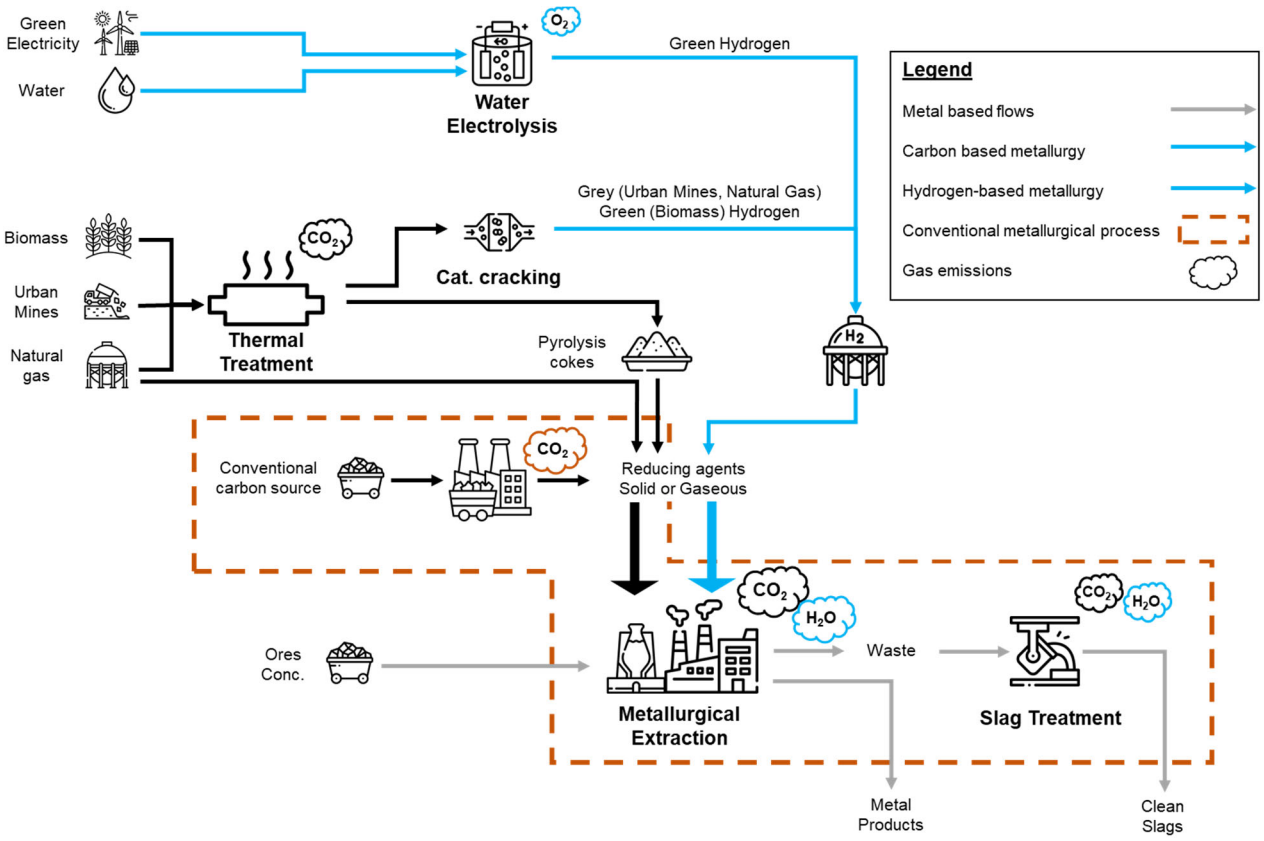

FIG 1 – Decarbonisation alternatives for the metallurgical industry.

Alternative solid reducing agents are produced through the thermal treatment or cracking of organic materials using methods such as pyrolysis, torrefaction, or hydrothermal carbonisation (Alamgir Ahmad *et al*, 2023). These processes entail elevated temperatures and in the case of pyrolysis, the absence of oxygen. During such a process, polymers or organic structures are broken down into smaller intermediate substances, including oil, gas, and solid (Alamgir Ahmad *et al*, 2023; Diaz, Latacz and Friedrich, 2023). The solid product of the cracking process can be referred to as ‘Bio-coke’ when derived from agricultural waste or ‘Pyrolysed secondary raw material’ if sourced in the context of urban mines, from complex organic anthropogenic materials such as plastics, textiles, or electronic scrap.

In the case of alternative reducing gases, hydrogen has emerged as a primary focus in recent years. However, to be sustainable, the method of hydrogen production also plays a crucial role. For example, hydrogen can be generated through energy-intensive electrolysis, wherein water molecules are split into hydrogen and oxygen. To produce 1 t of hydrogen direct reduced iron, approximately 50–54 kg (545 Nm^3) of hydrogen is needed, requiring between 2.5 to 3.5 MWh of energy for the water electrolysis (Vogl, Åhman and Nilsson, 2018; Patisson and Mirgaux, 2020). To put this in perspective, it is equivalent to the energy consumption of an individual in Germany over a span of two years. Therefore, it is imperative that hydrogen used for metallurgical applications is produced from renewable sources. In this case, this reducing gas can refer as ‘green’ hydrogen.

In addition to electrolysis, hydrogen can also be produced through the thermal treatment or cracking of organic material-rich substances such as biomass and materials from urban mines. These processes are used to generate bio-coke or to pyrolyse secondary raw materials. During such treatments, hydrogen is often produced alongside with carbon dioxide and other reducing gases like carbon monoxide, methane, and various hydrocarbons (Diaz, Latacz and Friedrich, 2023). This

mixture, depending on its composition, is commonly referred to as ‘syngas’. While syngas and natural gas share some similar characteristics, they are distinct in composition. Syngas, often derived from sources like coal or biomass, and natural gas can undergo different processing methods to produce hydrogen. When natural gas is catalytically cracked down to produce hydrogen, and the CO_2 byproduct is not captured, the hydrogen produced is typically referred to as ‘grey hydrogen’. In contrast, hydrogen produced from biomass can be considered ‘green hydrogen’, especially when the biomass is sourced sustainably and the energy used in the process is from renewable sources (AlHumaidan *et al*, 2023).

This article aims to offer insights into the lessons learned, key characteristics, advantages, and the identification of essential comparative criteria in the utilisation of bio-coke, pyrolysed secondary raw materials, and hydrogen. These are considered as alternative resources to traditional fossil-based reducing agents in metallurgical applications.

CASE STUDY – PYROLYSED SECONDARY RAW MATERIALS AS REDUCING AGENT

The shredder light fraction (SLF) is a byproduct of the mechanical treatment of waste electrical and electronic equipment (WEEE), constituting approximately 4.2 per cent of the output materials and containing high concentrations of primary metals like copper, tin, lead, zinc, silver, and gold (Ueberschaar, 2017). The presence of valuable resources in SLF, coupled with rising disposal costs, drives pre-processing companies to seek more efficient approaches for its management. However, direct incorporation into conventional metallurgical processes introduces complexities. These include handling halogens from flame retardants, managing diverse composition, and addressing intricate morphology for charging into the smelters (Diaz, Latacz and Friedrich, 2023).

In this study, SLF was obtained from a local German electronic scrap processing company, consisting of fine particles including dust, rubble, biological fragments, fibres, and plastic sheets. It has relatively low metal content, mainly fine copper wires and electronic components. SLF is carbon-rich (40.6 per cent), with notable oxygen (17 per cent), nitrogen (5.73 per cent), and hydrogen (0.48 per cent). It also contains metals like copper (1 per cent), aluminium (3.34 per cent), silicon (7.51 per cent), and trace elements, resulting in a low lower heating value (LHV) of approximately 18.8 $MJ*kg^{-1}$ (Diaz, 2020). During pyrolysis, SLF transforms into pyrolysis gas (P.Gas), pyrolysis oil and water (P.Oil), and a solid product (PSLF) with metals, oxides, and pyrolysis coke, experiencing a mass loss of about 40 per cent (Diaz, Latacz and Friedrich, 2023).

PSLF can be described as a concentrated version of metals found in SLF, characterised by a black powder containing pyrolytic carbon and oxides. It is highly brittle and contains notable elements, including oxygen (24 per cent), silicon (14.29 per cent), aluminium (6.14 per cent), and copper (3.3 per cent), at higher concentrations than SLF. Additionally, it includes trace amounts of various other elements, including precious metals (PMs). The LHV registered for PSLF was approximately 7 $MJ \cdot kg^{-1}$. Further details about the research methods, SLF and PSLF characterisation, and the pyrolysis process applied to SLF from WEEE can be found in Diaz, Latacz and Friedrich (2023).

This case study explores an innovative recycling process for printed circuit boards (PCBs), utilising pyrolysis shredder light fraction (PSLF) as an alternative reducing agent to recover copper from oxidised slag. Figure 2 illustrates this process, which is aligned with the principles of a circular economy, converting waste streams–SLF and PCBs–into valuable resources, such as copper and energy.

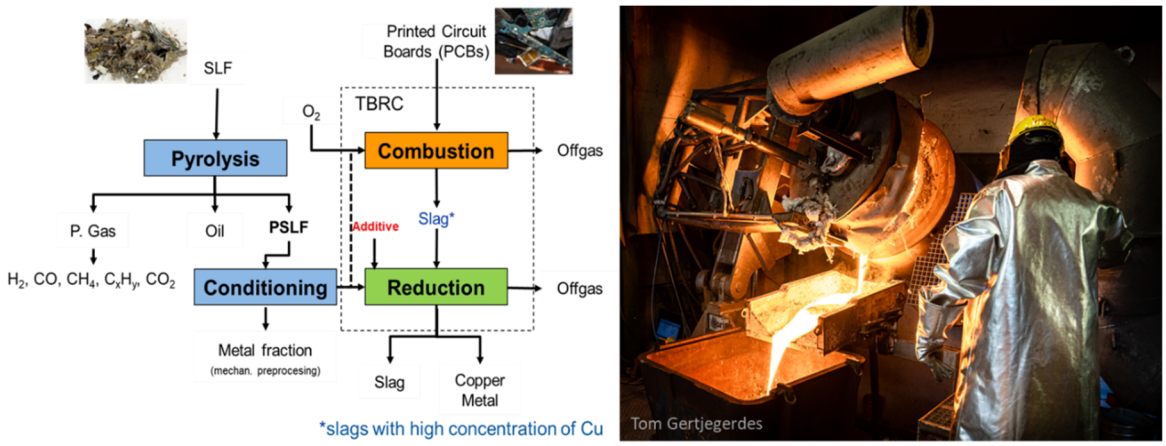

FIG 2 – Sustainable PCB recycling process using PSLF as a reducing agent (Diaz, 2020).

The recycling process commences with two primary inputs: SLF and PCBs. PCBs undergo an autothermal smelting, a combustion in the presence of oxygen that leverages the organic materials within the PCBs as an energy source. This results in the formation of copper-rich slag due to the oxidation of metallic components at high temperatures.

Simultaneously, SLF is processed through pyrolysis, yielding pyrolysis gas, oil, and PSLF. This carbon-rich PSLF, potentially conditioned to remove undesired metals, is then introduced into the smelter as a reducing agent. During the reduction stage, PSLF facilitates the chemical reduction of copper oxide in the slag, producing elemental copper.

The process yields three main outputs: off gas, which is managed to meet environmental standards; residual slag, which may contain non-metallic elements; and the recovered copper metal, now ready for subsequent refining and product development. By leveraging waste-derived materials for metal recovery, this process offers a more sustainable and cost-effective alternative to conventional recycling methods. The main advantage of this approach is that neither for smelting nor for the slag reduction are fossil fuels required.

Experimental work and main results

The experimental work involved the use of a demo scale top blown rotary converter (TBRC) for upscaling. The TBRC located at IME Institute of the RWTH Aachen University in Germany, is a cylindrical reactor with a 240 L volume, capable of processing up to 100 L of molten material. It utilises an Oxyfuel burner that uses natural gas and pure oxygen for heating, providing the advantage of adjustable lambda (λ 0.7–1.3) to control the atmosphere inside the reactor during experiments. The TBRC can rotate at speeds ranging from 0 to 10 rev/min and tilt at angles from 0 to 110°, making it versatile for various applications. It is lined with Cr-magnesite (MgCr) material, suitable for copper-based materials and corrosion-resistant up to 1600°C.

The TBRC includes an off gas cleaning system with two main pathways: hygiene gas and process gas. The system has a maximum suction capacity of 10 000 Nm^3/h and utilises fabric filters and electrostatic filters for dust collection. The off gases are transported to a scrubber with a pH of 10 for removal of halogens and heavy metals like As, Cd, Pb, among others, before being released into the environment.

In the trial, 120 kg of Cu-slag was charged into the preheated TBRC at around 800°C. The furnace was heated to 1350°C using the Oxyfuel burner, and the TBRC was set to rotate at 2 rev/min. The reduction experiment occurred in two phases: manual charging and injection of the PSLF. Copper concentration in the slag was monitored throughout the trial.

The stoichiometric amount of carbon needed to reduce copper oxide in the slag was calculated, resulting in the manual charging of PSLF in three periods: 72.5 per cent, 100 per cent, and 145 per cent of the required amount. Rotation speed was increased to 8 rev/min during manual charging to enhance turbulence. After manual charging, the injection of PSLF took place using the

same molten slag. The idea was to evaluate the effect of injection and obtain some insights on the kinetics using PSLF as reducing agent.

During the injection phase, the TBRC was placed vertically, rotation speed initially set to 2 rev/min, and PSLF injected at a speed of ~2.75 kg/min using nitrogen as the carrier gas. The first injection period involved injecting 50 per cent of the required PSLF, and subsequent injection periods varied the quantity. After each injection, a gas flushing period occurred. The second injection set-up used a lower λ value to enhance reduction conditions and included an extra stirring period. More details about the experimental set-up can be found in (Diaz, 2020).

The results indicated that manual charging led to poor copper reduction efficiency (7.1 per cent) due to inadequate turbulence and surface burning. On the other hand, injection trials achieved up to 48 per cent efficiency during the first injection period. By optimising PSLF dosification and extending stirring periods, the efficiency increased to 82 per cent, using PSLF equivalent to 93 per cent of the required amount. Besides the outstanding performance, further PSLF charging was hindered by technical problems and clogging of the injector device caused by very small Cu-wires present in PSLF.

Figure 3 illustrated the relationship between Cu reduction efficiency and C:CuO ratio in the system based on the art of charging in the TBRC, showing that process efficiency with manual charging was nearly cero under the tested conditions. Injection technology and submerged gas stirring were identified as crucial factors for improving the utilisation of pyrolysed materials as reducing agents for Cu-slags.

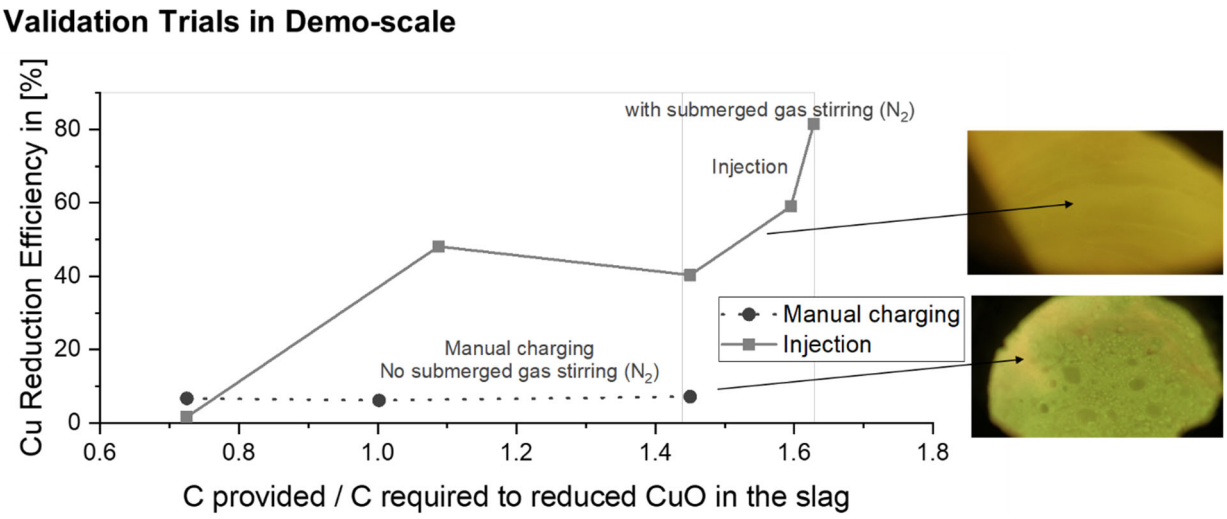

FIG 3 – Cu reduction efficiency versus C:CuO ratio in the system according to the art of charging in the TBRC (Diaz, 2020).

Similar experiments were conducted for other accompanying elements, including Ag, Pb, Zn, Ni, Sn, and Sb. Manual charging resulted in poor reduction efficiencies for these elements, but injection and submerged gas stirring significantly improved their reduction efficiencies. For example, Sb reached 100 per cent reduction, Sn achieved 63 per cent, Ag 100 per cent, Pb 75 per cent, Zn 53 per cent, and Ni 17 per cent.

Thermochemical simulations (FactSage™) identified four key reduction stages when using PSLF as a reducing agent for copper-rich slags: initial copper reduction, metallothermic reduction involving less noble metals, a copper co-reduction phase with metals like Ni, Sn, and Pb, and eventual iron reduction. The limited copper reduction efficiency did not result from chemical limitations but rather from challenges related to melt handling. Future improvements may involve adapting the injector to handle small wires in PSLF or enhancing mechanical conditioning of PSLF to remove some undesired metals.

In the slag system, the addition of PSLF would increase viscosity due to its SiO_2 content, primarily present in glassy structures from WEEE. A suggested slag design included the addition of CaO and

Na_2O to improve viscosity and reduce liquidus temperature. A more detailed publication on the slag design considering PSLF as reducing agent for copper slags is currently under review.

CASE STUDY – BIO-COKE AS REDUCING AGENT

The production of metals, including ignoble ones like chromium, manganese, and silicon, has long relied on submerged arc furnaces, with fossil carbon serving as the primary reducing agent. However, this conventional practice contributes significantly to direct CO_2 emissions, urging the exploration of more sustainable alternatives. Bio-based carbon or Bio-coke has emerged as a promising candidate to replace fossil carbon in metallurgical processes.

Bio-coke, in contrast to traditional metallurgical coke, exhibits distinct proximate analysis characteristics. It is characterised by a lower fixed carbon content and a higher volatile matter content, making it more responsive to temperature changes during high-temperature processes. Additionally, bio-coke boasts a lower ash content and a higher moisture content, which impacts its combustion and reactivity properties (Sommerfeld and Friedrich, 2021).

Accompanying elements in bio-coke also diverge from metallurgical coke, with higher alkaline, chlorine, and phosphorus content, while sulfur content remains notably lower. Furthermore, the ash produced by bio-coke is characterised by increased acidity (Sommerfeld and Friedrich, 2021).

Bio-coke's physical properties further differentiate it, featuring a lower density, higher CO_2 reactivity, and somewhat inferior mechanical stability. More details on general characteristics of bio-coke can be found in the review (Sommerfeld and Friedrich, 2021).

Bio-coke, derived from sources such as coconut, corn, olive, and bamboo, is an emerging carbonaceous material that has been rigorously evaluated in comparison to conventional coke. This exploration has opened doors to its potential applications in metallurgy, particularly in the production of environmentally sustainable ferroalloys (Sommerfeld and Friedrich, 2021).

In the area of metallurgy, bio-coke exhibits promise in several key processes. As it is shown in Figure 4, Its versatility allows for applications in pre-reduction, agglomeration, and direct smelting, each demanding specific attribute such as fixed carbon content, mechanical stability, purity, reactivity, and electrical conductivity. By meeting these varied requirements, bio-coke has the potential to drive the development of greener and more eco-friendly ferroalloy production methods, contributing to the reduction of carbon emissions and the promotion of sustainable practices in the metallurgical industry (Sommerfeld and Friedrich, 2021).

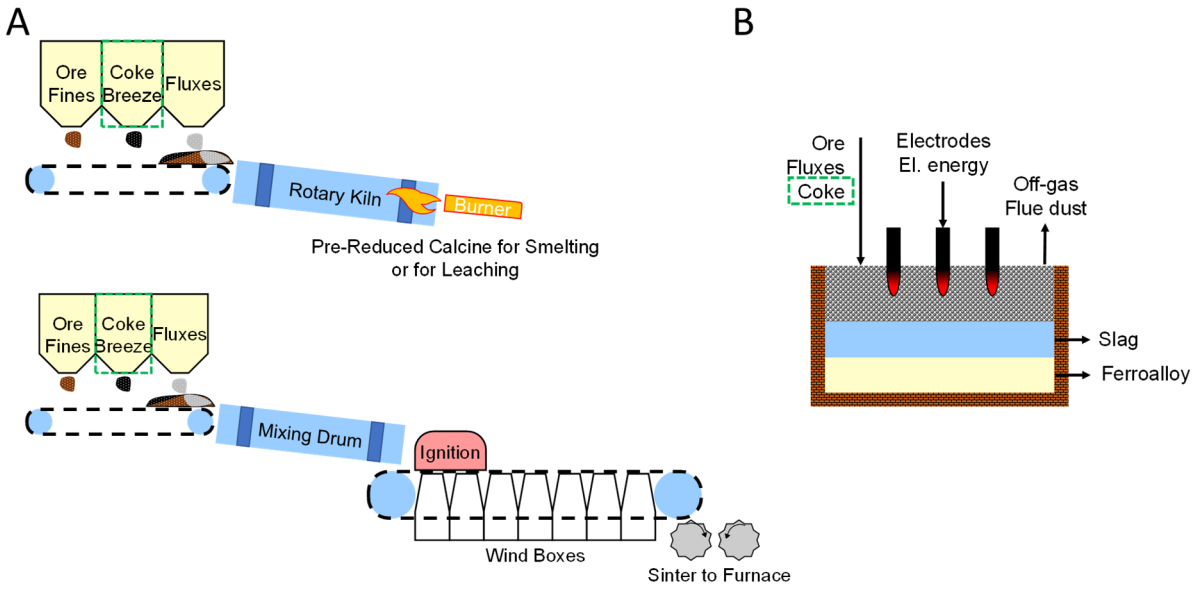

FIG 4 – (a) Prereduction and agglomeration using bio-coke in solid state, (b) bio-carbon for ferroalloy production via submerged electric arc furnaces.

Experimental work and main results

Experiences gathered in this case study are focused on two primary aspects. In the first stage, the study explores the pre-reduction of iron ore containing chromium in solid state. In the second stage, it involves a comparison of melting operations using pre-reduced ore and co-smelting with bio-coal (biomass).

During the initial phase, laboratory-scale experiments were conducted to investigate the pre-reduction process using bio-coke as an alternative reducing agent. A resistance heating furnace was employed for these trials, with each starting with an initial sample mass of 35 g. Different combinations of ore and reductants were explored at varying ratios. Mass loss measurements following each trial assessed chemical reactions, and individual heating of ore and reductants helped isolate their respective mass losses. Samples were charged in 99.7 per cent pure alumina crucibles (50 mm diameter, 75 mm height) and continuously flushed with 5 Nl/min of argon to prevent oxidation. The 16 litre volume furnace chamber accommodated a maximum of six crucibles, ensuring uniform sample temperature. The experiments varied the maximum temperature and duration at that temperature, with a 3.5 hr heating process and uncontrolled cooling. Results are illustrated in Figure 5.

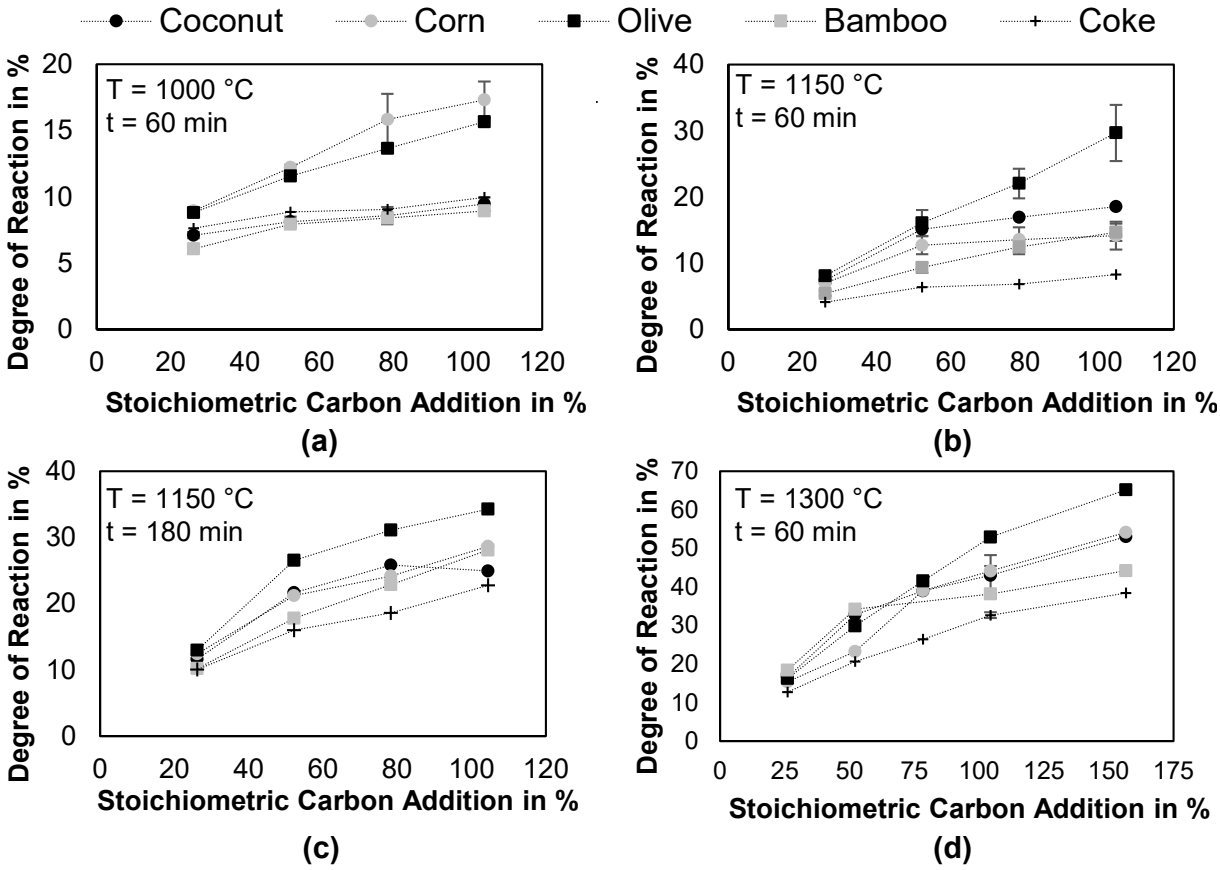

FIG 5 – Degree of reaction dependent on the carbon addition for various reducing agents and temperatures; (a) T = 1000°C, t = 60 min; (b) T = 1150°C, t = 60 min; (c) T = 1150°C, t = 180 min; (d) T = 1300°C, t = 60 min (Sommerfeld and Friedrich, 2022).

Figure 5 provides a comprehensive comparison of various carbonaceous materials as reducing agents for chromite pre-reduction, categorised by operational temperatures. The degree of reaction on the graph represents the portion of carbon involved in reducing the chromite ore.

At the lower temperature of 1000°C, bio-carbons like corn exhibit a moderate degree of reaction after 60 mins, reaching up to 17.4 per cent. Olive, another bio-carbon, demonstrates similar modest reactivity at this temperature. Coke, Coconut and Bamboo performed poorly at this temperature with less than 10 per cent degree of reaction.

Elevating the temperature to 1150°C significantly alters the reaction landscape. Within a 60 min window, all materials, particularly Olive and Coconut, show increased degrees of reaction. Coke as reference stands out with the lowest degree of reaction, indicating low reactivity within this intermediate temperature range and conditions.

Prolonging the duration at 1150°C to 180 mins incrementally raises the degree of reaction for all materials. Although olive's performance improves slightly, it suggests a potential plateau in reactivity at this temperature. Coke improved the degree of reaction, indicating a poor kinetic performance compared to bio-coke at these conditions.

The most striking results are observed at the upper threshold of 1300°C. Here, bio-carbons, while still exhibiting increased reactivity for all materials, are surpassed by Olive, reaching around 60 per cent of the degree of reaction. Coke performs the worst, reaching only 30 per cent of the degree of reaction.

In the second stage of the investigation, various reducing agents were employed for ferrochrome production, involving pre-reduction for different durations and operations without pre-reduction. Notably, both coke and bio-coal (biomass) yielded comparable chromium output during the smelting process. However, the use of bio-coal led to phosphorus content in green ferrochrome exceeding ASTM and DIN standards, whereas lignite coke met these standards. Sulfur content remained consistent regardless of the chosen reducing agent.

Thermochemical simulations were conducted to assess relative energy demand and off-gas production. The base-case scenario involved the use of unreduced material with coke. The results indicated an increase in specific energy demand when bio-based carbon was employed. Nevertheless, pre-reduction effectively mitigated the heightened energy demand associated with bio-based carbon, resulting in reduced energy requirements for the smelting process, thanks to enhanced pre-reduction. A similar trend was observed for off-gas production, with bio-based carbon contributing to increased emissions, but pre-reduction successfully mitigated this effect. It is important to note that the details of this work are currently under review.

CASE STUDY – HYDROGEN AS REDUCING AGENT FOR COPPER SLAGS

The central objective is to produce copper-steel with inherent antibacterial properties using hydrogen as the reducing agent. The primary focus is on efficiently reducing valuable metal oxides, particularly copper, while minimising the formation of undesirable by-products. Environmental and economic sustainability considerations are essential in this study, encompassing evaluations of energy consumption, emissions, and the feasibility of scaling up the process for potential industrial applications.

Research into copper reduction from slags to produce Copper containing steel alloys has primarily utilised carbon carriers like coal and natural gas. Busolic *et al* (2011) demonstrated a two-stage reduction process, achieving significant copper recovery (up to 51 per cent) from slags initially containing copper oxide and copper sulfide. Gonzalez *et al* (2005) employed carbothermal reduction, resulting in a ferrous metal phase with high purity. Sarfo *et al* (2017) and Zhang *et al* (2018) explored carbothermal and natural gas reduction processes, respectively, obtaining varying copper content in the final slag. Blenau, Stelter and Charitos (2021) investigated graphite injection for improved kinetics, yielding copper-rich metal alloys. These studies underscore the potential for selective copper reduction within iron recovery processes.

Hydrogen-based reduction processes show promise in extracting valuable metals from slags. Qu *et al* (2020) investigated synthesis gas rich in hydrogen (70 per cent) with copper-sulfur slag, resulting in the formation of a significant copper-rich matte phase. Zhang, Zhang and Zheng (2022) reduced low-grade copper slag using hydrogen in the solid-state, achieving a metal phase with 10.4 wt per cent copper. These studies introduce hydrogen treatment as a viable option for processing low copper slags, offering good insights for the current research.

In Figure 6, the process concept is introduced, aiming to utilise hydrogen as a reducing agent for treating slags generated during sulfur burning. The objective is to eliminate remaining sulfur from the slag and reduce copper oxide to produce a copper-containing steel product (Hovestadt and Friedrich, 2022).

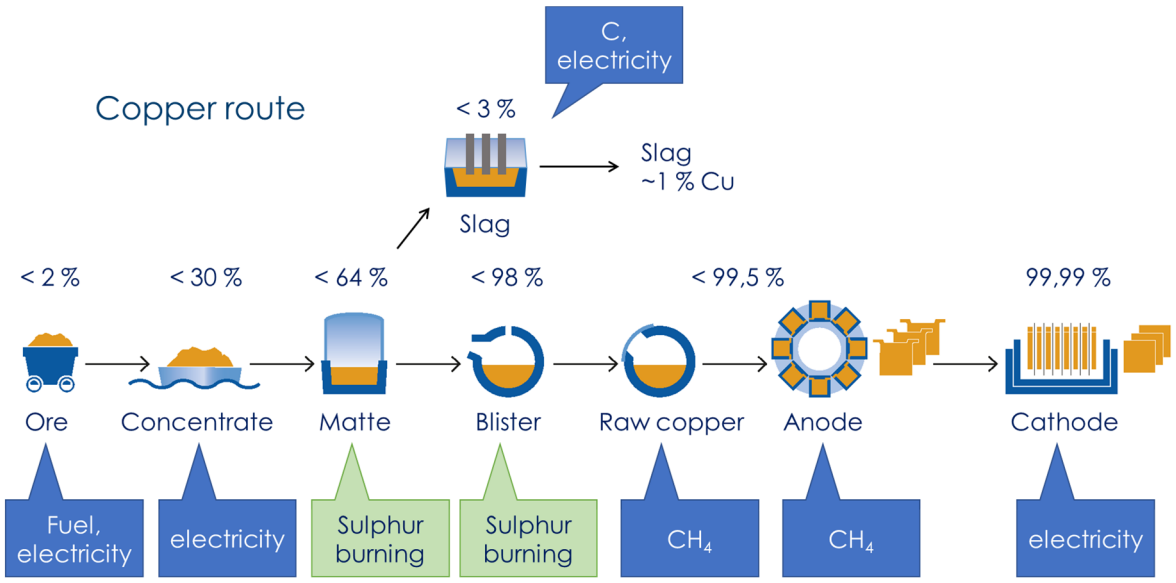

FIG 6 – Hydrogen based-reduction process for Cu-slag cleaning (Hovestadt and Friedrich, 2022).

The project, funded by the European Union under the name HARARE, aims to explore the potential of hydrogen-based reduction processes. It focuses on two residue streams from the metallurgical industry, with the goal of advancing the technology readiness level (TRL) from laboratory scale to potentially extract important technology metals in the future. This project is a collaborative effort led by Sintef AS, involving six European universities and research institutes, along with the assistance of four companies.

In the context of this project, one of the research directions is the reduction of primary copper slags, which is the subject of this report. The objective is to scale up the process from handling 1 kg to up to 3 t of slag melt. The approach involves a two-step reduction process. In the first step, the focus is on achieving a copper-rich metal phase, followed by a second step to obtain a copper-poor iron phase and valuable metal-free slag. The primary emphasis is placed on the selectivity of the first reduction stage.

In their 2022 study, Hovestadt and Friedrich, highlight the importance of safety during the injection of molten materials, emphasizing the need to monitor several precautions and parameters. This includes maintaining a temperature above a 1000°C for direct ignition. The protocol also involves post-combusting hydrogen before initiating the cooling process in a quenching box. Another key safety measure is to avoid cold mixtures containing less than 4 vol per cent hydrogen. Lastly, it is essential to prevent the formation of explosive mixtures outside the melt at temperatures exceeding 560°C.

Experimental work and main results

In this study, the experimental set-ups range from lab-scale to demo-scale. The conditions for both set-ups are presented as follows. However, the main focus of this report is on the demo-scale experiments.

The lab-scale (Figure 7a) equipment includes a resistant heated furnace, refractory lining, ceramic lance, and has a temperature capability of 1300°C. It can process up to 1.5 kg of input material with a volume flow of 2 L/min of hydrogen-reducing gas, equivalent to 4.66 mins per melt volume.

On the other hand, demo-scale (Figure 7b) operations handle 400 to 500 kg of slag, using an oxyfuel burner for heating and injecting 30 Nm^3/h of gas, with hydrogen concentrations ranging from 50 to 100 vol per cent. A ceramic shielded steel lance is employed in this larger-scale set-up. The melting unit dimensions and off-gas cleaning system details of the demo-scale plant remain consistent with those presented in the section titled ‘Case study – pyrolysed secondary raw materials as a reducing agent’.

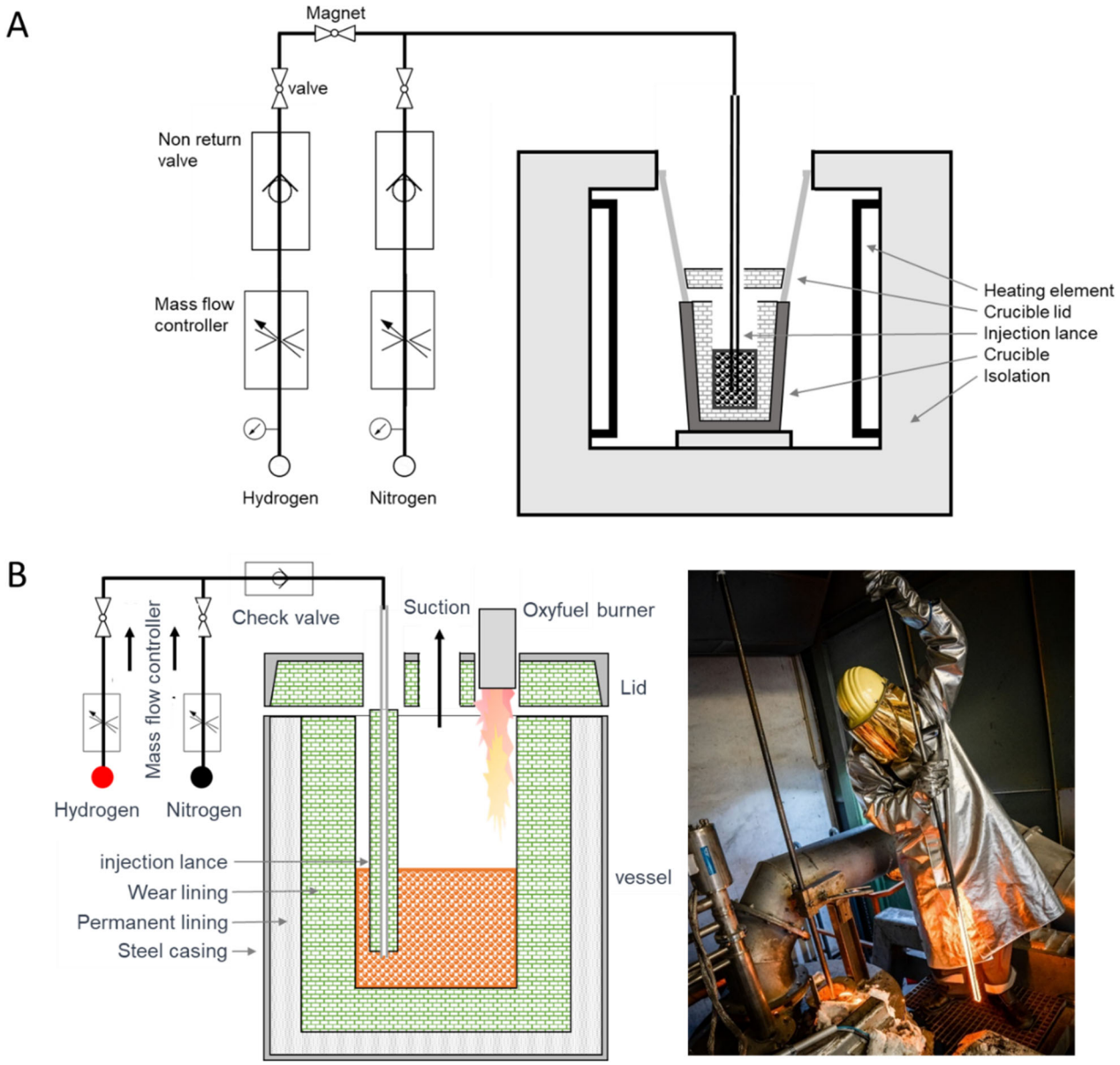

FIG 7 – (a) lab-scale set-up; (b) demo-scale set-up, for H_2 reduction of Cu-slags.

Figure 8 depicts the trends in metal concentration during a two-stage hydrogen reduction process. The results in the left figure indicate a decrease in copper and lead concentrations, both diminishing as the hydrogen volume increases. Copper begins at nearly 1 per cent by weight and falls sharply in the initial stage, then stabilises in the second, suggesting that most copper reduction occurs after 90 L of H_2 per kg of slag. Lead follows a similar pattern, starting below 0.5 per cent by weight and decreasing to almost negligible levels, which implies a significant impact of hydrogen in reducing lead content during these stages.

Regarding zinc, its concentration starts above 4 per cent by weight and exhibits fluctuations with a slight increase as the hydrogen volume rises per cent, likely due to the reduction of other metals, but then decreases to below 1 per cent. However, the second stage shows a clear downward trend in zinc concentration as the hydrogen volume increases. Iron, on the other hand, displays a contrasting behaviour; its concentration increases more steadily in the first stage and even more so in the second, indicating that iron is more reactive to the process as the hydrogen volume rises and copper reduction takes place. Overall, the process demonstrates the differential reactivity of metals during hydrogen reduction, with increasing iron concentrations in the slag, while copper, zinc, and lead are reduced, reflecting their distinct affinities and reaction kinetics with hydrogen.

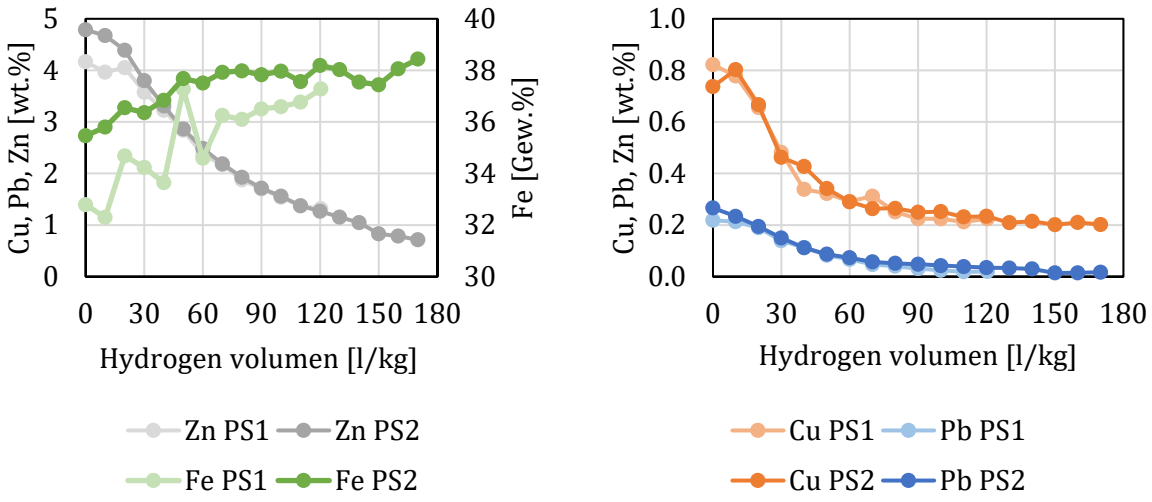

FIG 8 – Composition trends of pilot experiments based on the amount of hydrogen (1300°C, 90 vol H2, 30 Nm^3/h and 1350°C, 100 vol H2, 36 Nm^3/h).

Table 1 indicates the overall efficiencies and end concentrations of metals in the two-stage hydrogen reduction process. As it can be seen, for copper (Cu), the recovery efficiency in the first stage is 74 per cent, with a final concentration of 0.22 wt per cent. The efficiency slightly increases to 75 per cent in the second stage, with the final concentration remaining at 0.22 wt per cent. This suggests a stable end concentration of copper across both stages.

TABLE 1

Metal recovery efficiencies and final concentrations in a two-stage hydrogen reduction process.

Element	Yield PS1 in% (Process Stage 1)	Final Content PS1 in wt%	Yield PS2 in% (Process Stage 2)	Final Content PS2 in wt%
Cu	74	0.22	75	0.22
Zn	70	1.32	86	0.72
Pb	91	0.02	94	0.02

Zinc (Zn) shows a recovery efficiency of 70 per cent in PS1 with a final concentration of 1.32 wt per cent. There's a notable increase in efficiency to 86 per cent in PS2, accompanied by a decrease in final concentration to 0.72 wt per cent. This indicates a more effective reduction of zinc in the second stage, leading to a lower residue concentration.

Lead (Pb) has a high recovery efficiency of 91 per cent in the first stage, with a very low final concentration of 0.02 wt per cent. In the second stage, the efficiency slightly improves to 94 per cent, maintaining the final concentration at 0.02 wt per cent. The consistently low final content of lead suggests a highly effective reduction process across both stages.

The data reflect the varying responsiveness of different metals to the hydrogen reduction process. The process is especially effective for lead, moderately so for zinc, with the highest reduction occurring in the second stage, and least effective for copper, which maintains a consistent concentration post-reduction after the first stage.

Table 2 provides a comprehensive comparative overview of three alternative reducing agents evaluated in this study: pyrolysed secondary raw materials (Pyrolysed SLF), Bio-coke, and Hydrogen. It highlights their source materials, production processes, carbon footprints, energy efficiency, and metal recovery efficiencies. Pyrolysed SLF is derived from WEEE recycling by-products, Bio-coke from agricultural waste, and Hydrogen typically from water through electrolysis or steam reforming. The table assesses each agent's carbon footprint, energy efficiency, metal recovery efficiency, final metal purity, and process compatibility, revealing distinct advantages for

each. The sustainability potential, reached TLR (Technology Readiness Level), economic viability, and technical challenges are discussed, along with their environmental impact in terms of reducing landfill waste, CO_2 emissions, and fossil fuel dependence.

TABLE 2

Comparative of tested alternative reducing agents.

Comparative factors	Pyrolysed secondary raw materials (Pyrolysed SLF)	Bio-coke	Hydrogen
Source material	WEEE recycling by-products	Agricultural waste (corn, olives etc)	Water (via electrolysis/steam reforming)
Production process	Pyrolysis	Pyrolysis, torrefaction, or hydrothermal carbonisation (from biomass)	Electrolysis/Steam Reforming
Carbon footprint	Low to moderate (depends on the process and energy source for pyrolysis)	Low (considering biomass growth absorbs CO_2)	Low to zero (if produced using renewable energy or biomass)
Energy efficiency	Variable (dependent on pyrolysis efficiency, organic and metal content)	High (bio-coke can have high energy content)	High (especially at high temperatures)
Metal recovery efficiency	High for copper and other primary metals	Moderate to high (depending on the metal)	High for iron, variable for others (for Cu < 1 wt per cent)
Final metal purity	High (after metal recovery process)	Variable (affected by ash and other biomass constituents)	High (pure H2 can reduce metals without contaminating)
Process compatibility	Compatible with smelting processes	Suitable for use in furnaces during smelting and potentially in direct reduced iron (DRI) processes	Suitable for both smelting and DRI processes
Sustainability potential	High (turns waste into resource)	High (renewable and carbon-neutral potential)	High (if produced from renewable sources)
Technology readiness level (TLR)	Up to demonstration scale (TLR 5)	Laboratory (TLR 3-4)	Up to demonstration scale (TLR 5)
Economic viability	Moderate (influenced by the value of recovered metals)	Moderate to high (cost-effective if sourced from waste biomass)	High (long-term savings from potential carbon credits and lower emissions)
Technical challenges	Handling halogens, diverse composition, intricate morphology	Lower fixed carbon content, higher volatile matter content, ash composition, high phosphorus content	Infrastructure for hydrogen production and handling
Environmental impact	Reduction in landfill waste, possible emission control challenges	Reduction in direct CO_2 emissions, beneficial use of agricultural waste	Significant potential to reduce CO_2 emissions and fossil fuel dependence

CONCLUSIONS

In conclusion, the search for an optimal approach to minimise CO_2 emissions in the metal production sector underscores the necessity for diverse solutions. As evolving requirements for steel and copper slag metallurgy necessitate alternative carbon sources by 2050, bio-coke and pyrolysed materials from the urban mine sector could play a crucial role. These materials align with the industry's shift towards sustainability, offering pathways to reduce the carbon footprint of the metallurgical industry. However, relying solely on bio-coke for metal production poses technical and logistical challenges, primarily due to limited biomass availability in the required quality, for instance low phosphorous content, in contrast to substantial carbon demand. An integrated approach that combines multiple strategies and materials is required to address this limitation. In this dynamic landscape, the pursuit of sustainable practices remains a primary goal in the metallurgical industry's journey towards a greener and more environmentally friendly future. Transitioning towards sustainable energy resources such as pyrolysed secondary raw materials, bio-coke, and hydrogen presents a promising pathway towards reducing environmental impact and enhancing energy efficiency. Given their varying technological readiness levels and environmental benefits, it is crucial to prioritise further research and development, particularly in advancing production processes and improving economic viability. Fundamental analysis on the exergy distribution of the studied systems through their incorporation in the metal production chain, scaling up technologies to improve the purity of recovered metals in pyrolysis, and enhancing the energy content of bio-coke and pyrolysis gas are key areas that could significantly impact their market readiness and adoption. Moreover, investment in infrastructure to support widespread hydrogen production and utilisation will be essential. Embracing these technologies not only supports waste reduction and resource recovery but also aligns with global efforts to mitigate climate change and foster a sustainable future. Policymakers and industry leaders should consider these factors in their strategic planning to ensure a balanced and effective transition to greener energy alternatives.

ACKNOWLEDGEMENTS

The authors would like to express their gratitude to their technical staff for their support in this publication. This investigation was partially funded by the European Union's Horizon 2020 research and innovation program, under grant agreement number 958307. The work also received support from the collaborative project RessourcenKolleg.NRW, funded by the Ministry of Science of North Rhine-Westphalia.

REFERENCES

Alamgir Ahmad, K, Ahmad, E, Al Mesfer, M K and Nigam, K D, 2023. Bio-coal and bio-coke production from agro residues, *Chemical Engineering Journal*, 473:145340. https://doi.org/10.1016/j.cej.2023.145340

AlHumaidan, F S, Absi Halabi, M, Rana, M S and Vinoba, M, 2023. Blue hydrogen: Current status and future technologies, *Energy Conversion & Management*, 283:116840. https://doi.org/10.1016/j.enconman.2023.116840

Blenau, L, Stelter, M and Charitos, A, 2021. Carbothermic Reduction of Fayalitic Slag with Graphite – Understanding Reaction Kinetics for Pig Iron Production*, Slag Valorisation Symposium 7*, pp 63–67 (Leuven).

Busolic, D, Parada, F, Parra, R, Sanchez, M, Palacios, J and Hino, M, 2011. Recovery of iron from copper flash smelting slags, *Mineral Process Extractive Metall*, 120(1):32–36. https://doi.org/10.1179/037195510X12772935654945

Cavaliere, P, 2016. *Ironmaking and Steelmaking Processes* (Springer International Publishing: Cham).

Diaz, F, 2020. Process concept based on pyrolysis for integration of Shredder light fractions (SLF) in the Recycling of Waste Electrical and Electronic Equipment (WEEE), PhD thesis, RWTH Aachen University, IME publication series, 162 p.

Diaz, F, Latacz, D and Friedrich, B, 2023. Enabling the recycling of metals from the shredder light fraction derived from waste of electrical and electronic equipment via continuous pyrolysis process, *Waste Management (New York, NY)*, 172:335–346. https://doi.org/10.1016/j.wasman.2023.11.001

European Commission, 2021. 'Fit for 55': delivering the EU's 2030 Climate Target on the way to climate neutrality, COM(2021) 550 final, European Economic and Social Committee. Available from: <https://www.eesc.europa.eu/en/our-work/opinions-information-reports/opinions/fit-55-delivering-eus-2030-climate-target-way-climate-neutrality>

Gonzalez, C, Parra, R, Klenovcanova, A, Imris, I and Sanchez, M, 2005. Reduction of Chilean copper slags: a case of waste management project, *Scandinavian Journal of Metallurgy*, 34(2):143–149. https://doi.org/10.1111/j.1600-0692.2005.00740.x

Gorai, B, Jana, R K and Premchand, 2003. Characteristics and utilisation of copper slag—a review, *Resources, Conservation and Recycling*, 39(4):299–313. https://doi.org/10.1016/S0921-3449(02)00171-4

Hovestadt, G and Friedrich, B, 2022. Hydrogen reduction of entrapped metal oxides from fayalitic copper slags, *Conference Copper 2022,* Santiago de Chile, November.

Patisson, F and Mirgaux, O, 2020. Hydrogen Ironmaking: How It Works, *Metals*, 10(7):922. https://doi.org/10.3390/met10070922

Qu, G, Wei, Y, Li, B, Wang, H, Yang, Y and McLean, A, 2020. Distribution of copper and iron components with hydrogen reduction of copper slag, *Journal of Alloys and Compounds*, 824:153910. https://doi.org/10.1016/j.jallcom.2020.153910

Malischek, R, Baylin-Stern, A and McCulloch, S, 2019. Transforming Industry Through CCUS, International Energy Agency. Available from: <https://www.iea.org/reports/transforming-industry-through-ccus>

Roy, S, Datta, A and Rehani, S, 2015. Flotation of copper sulphide from copper smelter slag using multiple collectors and their mixtures, *International Journal of Mineral Processing*, 143:43–49. https://doi.org/10.1016/j.minpro.2015.08.008

Sarfo, P, Das, A, Wyss, G and Young, C, 2017. Recovery of metal values from copper slag and reuse of residual secondary slag, *Waste Management (New York, NY)*, 70:272–281. https://doi.org/10.1016/j.wasman.2017.09.024

Sommerfeld, M and Friedrich, B, 2021. Replacing Fossil Carbon in the Production of Ferroalloys with a Focus on Bio-Based Carbon: A Review, *Minerals*, 11(11):1286. https://doi.org/10.3390/min11111286

Sommerfeld, M and Friedrich, B, 2022. Toward Green Ferroalloys: Replacement of Fossil Reductants in the Pre-reduction Process of Chromite by Bio-Based Alternatives, in *REWAS 2022: Developing Tomorrow's Technical Cycles* (Eds: A Lazou, K Daehn, C Fleuriault, M Gökelma, E Olivetti and C Meskers), vol I, pp 607–619 (Springer International Publishing: Cham).

US Geological Survey 2023. Mineral commodity summaries 2023. Reston, VA, Mineral Commodity Summaries 2023. https://doi.org/10.3133/mcs2023

Ueberschaar, M, 2017. Assessing recycling strategies for critical raw materials in waste electrical and electronic equipment, Dissertation Paper, flieger Verlag.

Vogl, V, Åhman, M and Nilsson, L J, 2018. Assessment of hydrogen direct reduction for fossil-free steelmaking, *Journal of Cleaner Production*, 203:736–745. https://doi.org/10.1016/j.jclepro.2018.08.279

Zhang, B, Zhang, T, Niu, L, Liu, N, Dou, Z and Li, Z, 2018. Moderate Dilution of Copper Slag by Natural Gas, *JOM,* 70(1):47–52. https://doi.org/10.1007/s11837-017-2670-6

Zhang, B, Zhang, T and Zheng, C, 2022. Reduction Kinetics of Copper Slag by H2, *Minerals*, 12(5):548. https://doi.org/10.3390/min12050548

A short review – hydrogen reduction of copper-containing resources

DOI: 10.62053/WHJG1173

D M Fellicia[1], M I Pownceby[2], S Palanisamy[3], R Z Mukhlis[4] and M A Rhamdhani[5]

1. PhD Student, Swinburne University of Technology, Melbourne Vic 3122. Email: dfellicia@swin.edu.au
2. Senior Principal Research Scientist, CSIRO Mineral Resources, Melbourne Vic 3169. Email: mark.pownceby@csiro.au
3. Director of Manufacturing Futures Research Platform, Swinburne University of Technology, Melbourne Vic 3122. Email: spalanisamy@swin.edu.au
4. Lecturer, Swinburne University of Technology, Melbourne Vic 3122. Email: rmukhlis@swin.edu.au
5. Director Fluid and Process Dynamics, Swinburne University of Technology, Melbourne Vic 3122. Email: arhamdhani@swin.edu.au

ABSTRACT

The trend of global copper production has prospectively increased over time. Based on typical mined ore grades, 1 t of copper ore generates approximately 6–10 kg of copper, which requires much energy, usually in the form of metallurgical coke. Copper production using carbon as a fuel and reductant contributes up to 0.3 per cent to global greenhouse gas (GHG) emissions. As a result, research into decarbonisation processes applicable to reducing low-grade copper sulfide ores, copper oxides, electronic wastes and other alternative complex Cu-rich materials has increased. Alternative fuels for reducing carbon-rich emissions in pyrometallurgical copper processing include methane, ammonia, biomass, solar and wind power, but in recent times increased focus has been on hydrogen as a potential fuel and reducing agent for materials such as oxidised copper scrap, Cu_2O/CuO and Cu-rich slags/e-wastes. From a thermodynamic perspective, hydrogen exhibits a significantly more negative standard Gibbs free energy ($\Delta G°$) than copper oxide making it a suitable reductant and the exothermic thermal effect from reaction between hydrogen and Cu_2O/CuO may be used to control process parameters. These characteristics renders hydrogen an ideal gas for reducing copper oxides and copper-containing slags/e-wastes. This review article assesses previous research on utilising hydrogen for producing and refining copper from primary and secondary feed materials.

INTRODUCTION

Worldwide copper production increased marginally from 24.99 Mt in 2022 to 25.34 Mt in 2023 and is predicted to rise to 26.17 Mt in 2024 (International Copper Study Group (ICSG), 2023). The global copper demand is predicted to rise by 350 per cent in 2050 (Elshkaki *et al*, 2016). Currently, there are two significant sources of copper able to meet the demand. Natural ores containing primary copper-bearing minerals such as chalcopyrite ($CuFeS_2$) and chalcocite (Cu_2S), as well as less abundant alteration minerals including Cu-rich sulfates, hydroxy-silicates, oxides and carbonates. Secondary resources, including scrap copper, copper alloys and copper-containing resources, such as slag (Schlesinger *et al*, 2021). The carbon emissions generated by the process heat requirement and the Cu reduction, and ultimately how hydrogen can potentially be incorporated, will depend on the copper resource input used and the process route selected to manufacture the copper.

In conventional primary copper production, for example through a flash smelting route as shown in Figure 1, the copper concentrate is oxidised in a flash furnace to form matte. The matte is further oxidised in a converter to produce blister copper with 99 wt per cent purity, while the slag from smelting is processed in a slag cleaning furnace. The heat for the smelting and converting are supplied mainly by the oxidation reactions themselves. The blister copper is further refined in an anode furnace before going into electrolytic refining. Figure 1 also shows opportunities for decarbonising the process by using hydrogen in specific unit processes. For example, hydrogen can be used as a reducing agent or for generating process heat and can potentially be introduced in the slag cleaning furnace and anode furnace (Schlesinger *et al*, 2021; Roeben *et al*, 2021).

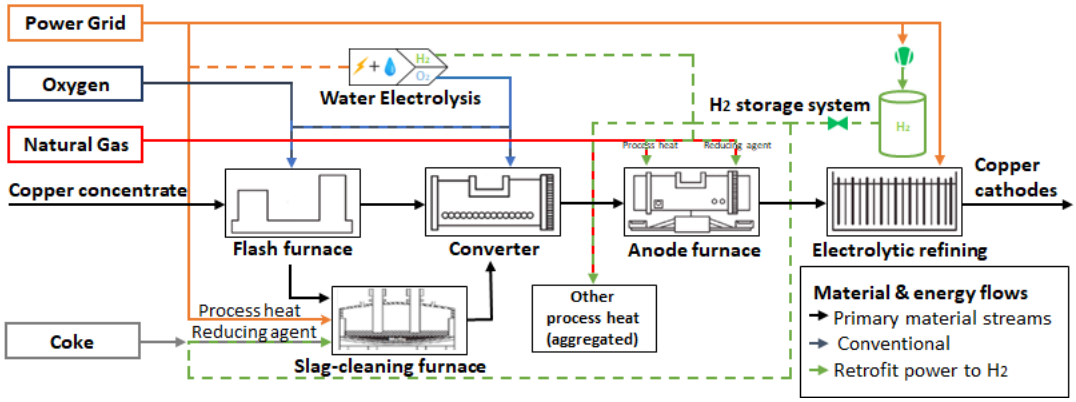

FIG 1 – Flow sheet of primary copper production process, showing possible decarbonisation/hydrogenation approaches (Roeben *et al*, 2021).

For secondary copper resources, such as black copper smelting, the material is either reduced then oxidised (or *vice versa* depending on the input composition and type), before being electro-refined. Figure 2 shows a generic process flow sheet showing where hydrogen can be potentially implemented as a reductant and fuel for heat requirement (eg in a reduction stage). Mairizal *et al* (2023) evaluated the prospects for hydrogen incorporation through a preliminary thermodynamic analysis and found that 82.17 per cent Cu can be obtained in the reduction stage while 94 per cent Cu purity can be achieved from the oxidation stage. In the reduction stage scenario, 59 kg H_2O off-gas is generated with zero CO_2 emissions. In an alternative scenario using copper slag as a feed, a printed circuit board (PCB) as the reductant and H_2 gas as the heat supply, producing 46.6 kg H_2O off-gas and 33.7 kg CO_2 formed.

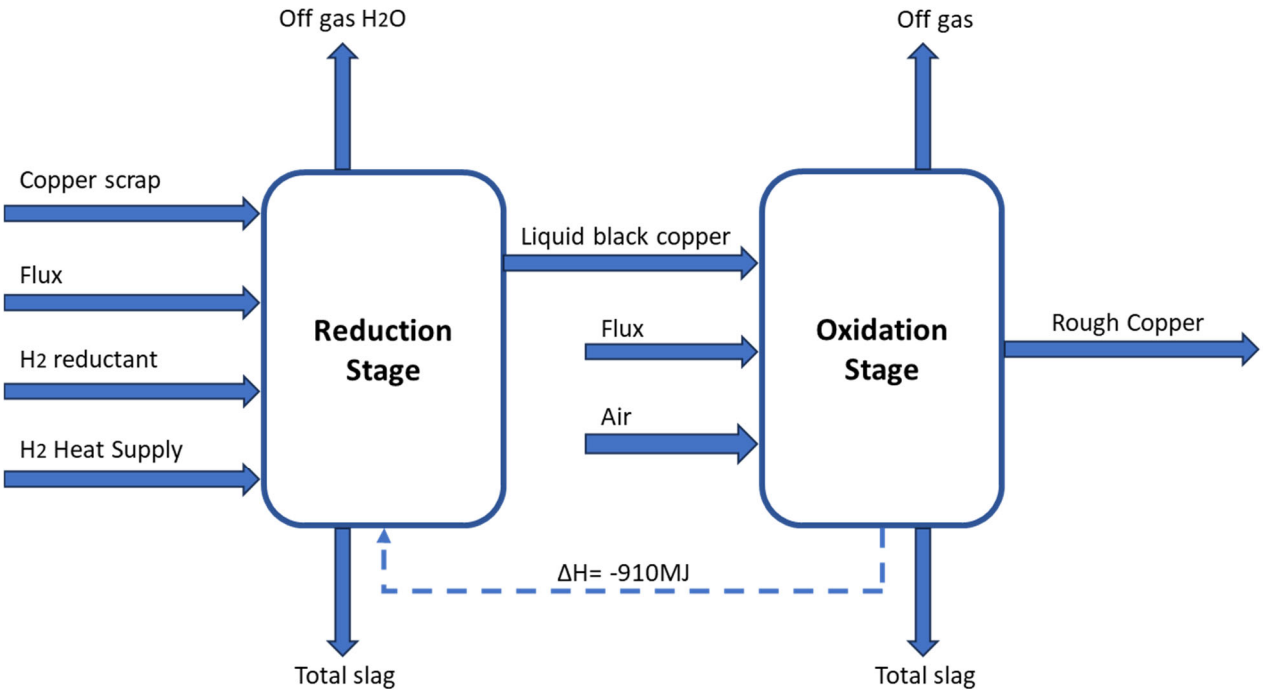

FIG 2 – Process flow sheet for secondary Cu sources using hydrogen as both fuel and reductant (Mairizal *et al*, 2023).

Although some work has commenced, there is a need for a fundamental understanding of the detailed hydrogen reduction mechanism for the different copper sources to optimise its implementation in future processes. This article reviews the use of hydrogen as a reductant for copper-containing materials. The paper starts with a thermodynamic analysis, showing the feasibility of using hydrogen for the critical reactions involved in Cu reduction in the relevant processes. The paper continues with a review and discussion of previous studies that focus on the hydrogen

reduction of chalcopyrite, chalcocite, Cu_2O/CuO, and complex copper-containing secondary resources, both in the solid and liquid states. Most of these works were carried out only at a laboratory scale. Nevertheless, they provide the baseline for future industrial applications.

THERMODYNAMICS OF HYDROGEN REDUCTION OF COPPER-CONTAINING RESOURCES

From a thermodynamic perspective, hydrogen reduction reactions have significantly lower standard Gibbs free energies (ΔG°) compared to copper oxidation reactions, as shown in Figure 3. Hence, hydrogen makes an excellent reducing agent for reducing copper-containing ores and slag/e-wastes. Figure 3 also illustrates reaction equilibria for the traditionally used carbon and for plasma hydrogen (H and H^+) which are potentially other hydrogen reducing sources. Equations 1 and 2 show the reactions involved for the reduction of a metal oxide to its lower oxide and/or metal state by molecular hydrogen (Rukini *et al*, 2023):

$$MO_x + H_2(g) \rightarrow MO_{x-1} + H_2O(g) \qquad \Delta G = \Delta G° + RT \ln (pH_2O/pH_2) \qquad (1)$$

$$MO_x + xH_2(g) \rightarrow M + xH_2O(g) \qquad \Delta G = \Delta G° + xRT \ln (pH_2O/pH_2) \qquad (2)$$

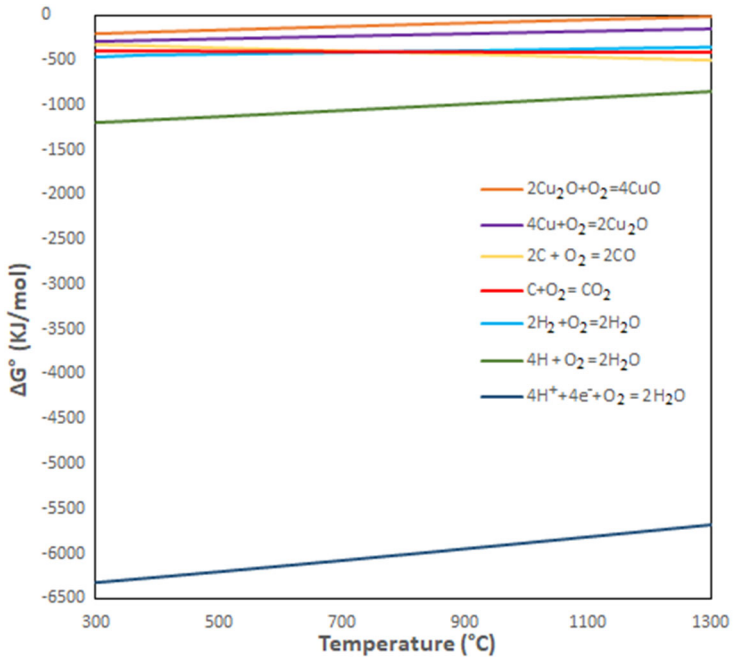

FIG 3 – Ellingham diagram of Cu reduction reactions and including reactions involving carbon, molecular and plasma hydrogen.

In the case of copper oxides, the reactions and associated free energies for the reduction of Cu_2O and CuO at 250°C are shown in Equations 3 and 4 (Gargul, Małecki and Włodarczyk, 2013):

$$Cu_2O(s) + H_2(g) \rightarrow 2Cu(s) + H_2O(g) \qquad \Delta G° = -87.1727 \text{ kJ} \qquad (3)$$

$$CuO(s) + H_2(g) \rightarrow Cu(s) + H_2O(g) \qquad \Delta G° = -110.8195 \text{ kJ} \qquad (4)$$

The ΔG° of the reduction reaction for CuO is lower compared to that of Cu_2O, which indicates greater thermodynamic feasibility for the reaction at the same temperature. Kinetically the observed activation energy for reduction of CuO is 14.5 kcal/mol, meanwhile Cu_2O is 27.4 kcal/mol (Kim *et al*, 2003).

Chalcopyrite and chalcocite are the most common ores used for the primary production of copper. As discussed in the previous section, there is possibility for hydrogen reduction of these primary sulfide sources. However, analysis indicates that direct hydrogen reduction of metal sulfides has unfavourable thermodynamics. The equilibrium constant for Equation 5 at 800°C ranges from 2×10^{-3} to 6×10^{-3} for Cu, Ni, Co and Fe sulfides. Shifting the equilibria to the right can boost metal yield by removing hydrogen sulfide (H_2S) immediately after the reaction. This can be achieved by adding a flux with a strong H_2S affinity to the sulfide compound (Equation 6). CaO is a flux that

favours the reduction of chalcopyrite by hydrogen at 800°C and this can be achieved through additions of different amounts of CaO as shown in Equation 7–10 (Habashi, Dugdale and Nagamori, 1974; Habashi and Yostos, 1977):

$$MS + H_2 \leftrightarrow M + H_2S \quad (5)$$

$$MS + H_2 + CaO \rightarrow M + CaS + H_2O \quad (6)$$

$$2CuFeS_2(s) + H_2(g) + CaO(s) \rightarrow Cu_2S.2FeS(s) + CaS(s) + H_2O(g) \quad \Delta G° = -90.0245\ kJ \quad (7)$$

$$2CuFeS_2(s) + 3H_2(g) + 3CaO(s) \rightarrow Cu_2S(s) + 2Fe(s) + 3CaS(s) + 3H_2O(g) \quad \Delta G° = -94.5911\ kJ \quad (8)$$

$$2CuFeS_2(s) + 4H_2(g) + 4CaO(s) \rightarrow 2Cu(s) + 2Fe(s) + 4CaS(s) + 4H_2O(g) \quad \Delta G° = -91.7521\ kJ \quad (9)$$

$$2CuFeS_2(s) + H_2(g) + 6CaO(s) \rightarrow 2Cu(s) + 2CaO.Fe_2O_3(s) + 4CaS(s) + H_2O(g) \quad \Delta G° = -71.0521\ kJ \quad (10)$$

PREVIOUS STUDIES ON SOLID STATE REDUCTION OF COPPER OXIDES

The kinetics of CuO/Cu_2O reduction in H_2/CO gas mixtures have mainly been studied on submicron-sized powder mixes (Rodriguez *et al*, 2003; Kim *et al*, 2003; Jelić, Tomić-Tucaković and Mentus, 2011; Yao *et al*, 2018), pressed powder pellets (Sabat, Paramguru and Mishra, 2016) and nanoaggregates such nanoparticles, nanowires, rods etc (Pike *et al*, 2006; Shrestha, Sorensen and Klabunde, 2010). In micro- and nano-scaled assemblies, the building blocks (eg particles, rods, platelets) and their aggregates have broad size and shape distributions, resulting in very different surface morphologies, defect structures and $CuO:Cu_2O$ phase fractions (Jelić, Tomić-Tucaković and Mentus, 2011). Different properties and characteristics of the Cu_2O/CuO powders resulted in contradictive findings regarding the duration of incubation, reaction rates and phase changes during the reduction. There was however, four main findings. Full transformation reduction $CuO \rightarrow Cu_4O_3 \rightarrow Cu_2O \rightarrow Cu$ was observed in the reduction of CuO by hydrogen plasma (Sabat, Paramguru and Mishra, 2016). Meanwhile according to (Rodriguez *et al*, 2003; Kim *et al*, 2003; Tyagi, 2018) $CuO \rightarrow Cu$ directly reduced without any intermediate phase of Cu_2O or Cu_4O_3. Sequential reduction of $CuO \rightarrow Cu_2O \rightarrow Cu$ was also reported by some workers (Li, Mayer and Tu, 1992; Pike *et al*, 2006; Unutulmazsoy *et al*, 2022). Reduction occurring as a single step of $Cu_2O \rightarrow Cu$ was studied by (Tilliander, Aune and Seetharaman, 2006). A summary of previous studies in solid state reduction of Cu_2O and CuO is presented in Table 1. All these studies were carried out at laboratory scale and the main findings are discussed below for each oxide.

Cu_2O

In secondary sources such as copper slag, the copper oxide form mainly is Cu_2O. Most Cu_2O reduction research has focused on catalysts and has been carried out only at a lab-scale. Reduction of Cu_2O with hydrogen is an autocatalytic process (Hamada, Kudo and Tojo, 1992). Recent investigations on Cu_2O reduction have focused on the kinetics and the mechanism of reduction. *In situ* time-resolved X-ray diffraction (XRD) involving reducing Cu_2O thin films to metallic copper was studied by Unutulmazsoy *et al* (2022). High-resolution scanning electron microscopy of the products showed the presence of nano porous copper formation after reduction. Copper film grain size, strain and peak area were all found to be important parameters in real-time reduction kinetics data. Much slower than oxidation, reduction at 300°C was found to take 680s to 1800s to convert Cu_2O to Cu. A single-phase Cu_2O film produced by thermal oxidation of a 300 nm Cu film at 275°C was reduced at 300°C to measure Cu_2O to Cu transformation rates. H_2 exposure causes grain boundaries and porosity at the Cu_2O film surface to behave as short-circuit diffusion routes, trapping hydrogen. Hydrogen diffusion along intergranular areas might cause compressive stress, reminiscent of how atoms diffuse along grain boundaries during the growth of films (Chason *et al*, 2002; Floro *et al*, 2001). Another study of the kinetics of reduction Cu_2O by hydrogen gas using thermogravimetric analysis (TGA) at temperatures 300–400°C was conducted by Tilliander, Aune and Seetharaman (2006). This study discovered that the stability of the oxide and the existence of other elements, such as nickel (Ni) or nickel oxide (NiO), did not influence the reduction process. The pace of reduction may be controlled by adjusting the hydrogen flow.

TABLE 1

Summary of previous works on solid state reduction of Cu_2O and CuO using hydrogen.

Author	System and parameters	Key results
Xu *et al* (2022)	Cu_2O powder - H2, thin film Cu_2O T = 27 - 377°C, 30 min - 23.4 hr pO_2: 5.0×10^{-7}Torr, H_2 pressure: 1.54 - 1.64Torr	• Activation energy for Cu_2O “29”/Cu (111) reduction by H_2 was 23 kcal/mol, “29” stands for row structure of Cu_2O, meanwhile (111) stands for orientation of the crystal structure. • Cu_2O-“29”Cu and solid Cu were present on the surface before fully turning into Cu (111).
Unutulmazsoy *et al* (2022)	Cu_2O film - 5%H_2/Ar Cu films: 50, 150 and 300 nm T = 300°C, 30 min	• Reduction of Cu_2O to Cu was identified in 50 nm thick CuO films with an average grain size of 20 nm. • Single-phase Cu_2O and CuO films may be converted to porous Cu, whose size and shape depend on the original Cu-oxide phase’s grain size and thickness.
Tyagi (2018)	CuO powder-H_2 pO_2: 76Torr CuO_{red} T = 160°C - 252°C, 40 min CuO_{red} 0.67 T = 160°C and 200°C, 100 min	• Activation energy of $CuO_{0.67}$ reduction was 10.2 ± 0.7 kcal/mol while CuO was 14.2 kcal/mol. • $CuO_{0.67}$ demonstrated a reduced density and faster reduction rate compared to CuO. • The reduction of $CuO_{0.67}$ occurs at 200°C and ranges from 2% to 85%. In the case of CuO, the reduction ranges from 0.75% to 90% at 150°C.
Tilliander, Aune and Seetharaman (2006)	Cu_2O/NiO/Ni powder-H_2/Ar T = 300 - 400°C, 42 min Heating Rates: 6, 9, 12, 15, 18 K/min Hydrogen flow rate: 0.6 L/min, Mass: 15 mg	• Diffusion through the bed affected the decrease rate using different sample masses. • Presence of Ni/NiO did not affect the reduction kinetics. • Activation energy: isothermal Cu_2O: 92±5 kJ/mol, while non-isothermal Cu_2O: 111±5 kJ/mol.
Jelić, Tomić-Tucaković and Mentus (2011)	CuO powder - H_2 25% H_2 - 99.995% Ar 80 mL/min T = 300 - 450°C Heating rate: 2.5 - 30°C/min	• Both synthesised CuO and commercial CuO with purity >99% were reduced to Cu metal after a 19.7% loss of mass. • No intermediate copper oxidation was found. • Reduced copper particle size was temperature dependent and significantly increased due to sintering at 300–400°C.
Yamukyan, Manukyan and Kharatyan (2009)	CuO powder - H_2 Hydrogen pressure: 0.01 MPa - 2.5 MPa Sample density: 0.42 - 0.57 Combustion temperature: 400 - 600°C Heating rate: 5 - 10 K/s	• Self-propagating diffusion regime can reduce CuO by H_2. • H_2 internal pressure range spans from 0.01 - 2.5 MPa, establishing a surface combustion regime. • The combustion temperature and velocity exhibited constancy at a constant H_2 pressure of 0.075 MPa while operating within a defined density range of 0.42 to 0.57 MPa.
Kim *et al* (2004)	CuO powder - 5% H_2/95%He T = 150 - 300°C	• CuO reduced to Cu at H_2 flow 15 mL/min while forming intermediate phase Cu_2O at hydrogen flow <1 mL/min. • H_2 flow rate did not influence intermediate phase presence.
Kim *et al* (2003)	CuO powder - 5% H_2/95%He T = 150 to 300°C, flow rate gas 5 - 15 mL/min H_2 2.5×10^{-6} m^3/s, 150 - 400 min	• Pressure and temperature increase linearly with microwave power and hydrogen flow rate. • Best result for reduction efficiency is 94.5%. • Activation energy of CuO reduction is 14.5 kcal/mol, while Cu_2O is 27.4 kcal/mol.
Rodriguez *et al* (2003)	CuO powder - 5% H_2/95%He, Gas flow rate 1 - 20 mL/min, 200 - 400°C, pH_2 10^{-4} to 5Torr	• Activation energy 27.4 kcal/mol. • Cu^{1+} was not a stable intermediate in reducing CuO, resulting in a straight CuO to Cu transition.

CuO

The exothermic reaction between CuO and H_2 to produce metallic Cu and H_2O gas may be divided into induction, autocatalytic and decreasing rate processes. The properties of the initial oxide influence the reduction rates in each step (Tyagi, 2018). Single phase CuO film reduction by 5 per centH_2/Ar at 300°C was evaluated and the phase transformations involving CuO → CuO + Cu_2O → CuO + Cu_2O + Cu → Cu_2O + Cu → Cu was observed by *in situ* XRD (Unutulmazsoy *et al*, 2022). Three phases, Cu, Cu_2O and CuO, coexist together during the reduction after an incubation

time of 1300 sec and with average grain size 30 nm within a 300 nm thick Cu film. Contrary to this, for a 50 nm CuO film with average grain size 20 nm, the formation of Cu metal occurs only after the CuO is completely reduced to Cu_2O (Unutulmazsoy *et al*, 2022). As oxygen vacancies continue to form on the CuO surface, Cu^+ and Cu^0 coexist. Oxygen vacancies move to the subsurface and create a partly reduced CuO superlattice structure, allowing the Cu_2O phase to nucleate (Sun *et al*, 2021; Hao *et al*, 2016; Maimaiti, Nolan and Elliott, 2014). The reduction time for CuO → Cu_2O can be reduced by increasing temperature and increasing the partial pressure of hydrogen (Rodriguez *et al*, 2003; Kim *et al*, 2003). CuO reduction occurs under two circumstances. First, Cu aggregates form around oxide defects on the surface or bulk in a nonuniform reduction. The reduction mainly occurs at the Cu-CuO surface. Second, most CuO loses oxygen in stages until it becomes metallic copper. Further studies found that when exposed to a steady hydrogen supply with flow rates more than 15 mL/min at temperatures over 200°C, CuO underwent straight reduction to Cu without forming intermediate suboxides (Kim *et al*, 2003, 2004; Rodriguez *et al*, 2003).

PREVIOUS STUDIES ON LIQUID STATE REDUCTION OF CU-CONTAINING MATERIALS

Slag

Each ton of copper produced produces 2–3 t of primary copper slag with contains up to 1 per cent copper by weight (Hovestadt and Friedrich, 2023; ICSG, 2023; Gilsbach, 2020) In 2021, copper production generated 57.2 Mt of slag (Jin and Lihua, 2022). From an industrial point of view, the recovered copper content in the slag both from primary smelting and e-waste recycling can produce 350 kt/a copper with 70 per cent recovery rate (Hovestadt and Friedrich, 2023).

A study of primary fayalitic slag reduction using hydrogen was conducted to examine what happened when different flow rates and hydrogen concentrations were added to two slags containing 1 per cent and 2 per cent Cu by weight. Experimental work was conducted at 1300°C with a variation in hydrogen concentration of 15–100 per cent and with a flow rate of around 1–2 L/min. Copper concentration in slag was lowest at 0.3 wt per cent. Turbulence increased the response rate by 40 per cent, suggesting liquid transport was the rate-limiting step (Hovestadt and Friedrich, 2023). Furthermore, the presence of hydrogen gas in slag facilitates the evaporation of zinc and lead. Hydrogen produces equal Zn and Pb levels throughout a broad range of reduction gas concentrations. Thus, increasing hydrogen concentration might significantly reduce the processing time. Zinc concentrations declined linearly over a threshold and decreasingly below 1 wt per cent. Fumigation promoted slag zinc oxide diffusion (Hovestadt and Friedrich, 2023). From thermodynamic point of view, Cu, Zn and Pb oxides were easily reduced, but reducing sulfides was more challenging. The optimal conditions for reducing copper slag were 1450°C, 1.2 alkalinity and 0.225 reducing agent ratio. The newly developed procedure recovered 95.49 per cent copper and iron from slag, as well as 83.54 per cent Pb and 98.30 per cent Zn (Zhang, Zhang and Zheng, 2022). Table 2 represents previous studies of liquid state reduction of copper-containing resources using hydrogen.

Preliminary industrial studies/trials

Current initiatives in Cu metal production by industry seek to use hydrogen to decarbonise copper manufacture. For example, the main Hamburg Cu smelter operated by Aurubis AG, which features two anode furnaces with a capacity of 270 t/batch, has been supplied by hydrogen from September to December 2021. Before this, natural gas treated unwrought copper, emitting much CO_2. Using hydrogen (H_2) as a reducing agent is expected to reduce the Hamburg plant's CO_2 emissions by at least 5000 t/a. Tests using two new anode furnaces showed that the furnaces functioned more effectively and used 30 per cent less natural gas, saving roughly 1.2 t of CO_2 per annum and decarbonised Aurubis output before enough hydrogen was available. Replacing anode furnaces improves metal extraction from metal concentrates and recycling, in addition to climate advantages (Aurubis AG, 2023; Edens and Steindor, 2023).

TABLE 2

Summary of previous works on liquid state reduction of copper containing resources using hydrogen.

Author	System and parameters	Key results
Mairizal *et al* (2023)	Modelling study, 1200°C - 1400°C pO_2 ranged between 10^{-7} and 10^{-9} atm	• 73% reducing CO_2 emissions using hydrogen as a heat source. • PCBs significantly reduces carbon dioxide (CO_2) emissions from 183.7 kg/h to 123.14 kg/h.
Hovestadt and Friedrich (2023)	Modelling and experimental study Primary slag and Slag mix (≤2%Cu) T = 1300°C, t > 150 min H_2: 15% - 100% and 1 - 2 L/min	• Simulations showed after 0.5 L hydrogen addition, Cu_2O% reduced to 0.54 wt%. • Copper content decreased below the predicted limit of 0.49 wt% across all concentrations. • Lowest slag copper content was 0.31 wt% Cu.
Edens and Steindor (2023)	Industrial trial of 275 t Cu Initial O_2 0.9 - 1.2%, 60 - 97%H_2/N_2, H_2 flow rate 1400 - 2000 m^3/h, 150 - 190 min	• Hydrogen decreases O_2 oxygen content with 90% effectiveness. • Low gas H_2 efficiency is produced by unstable operation, such as blockage and leakages, which reduces valid measurements. Uninterrupted operation is predicted to be more efficient.
Hovestadt and Friedrich (2023)	1500 g secondary copper smelter slag T = 1300°C, H_2 flow 0.5 - 2 L/min H_2 25 - 100% H_2 90 L	• Increased hydrogen injection volumes improve fuming and accelerate the reduction process. • Fuming process of H_2 did not follow a clear pattern with different concentrations (25, 50, 75% H_2), but the quantity and turbulence of H_2 (0.5, 1.0, 1.5/L/min H_2) did affect fuming and reduction.
Zhang, Zhang and Zheng (2022)	Experimental Cu slag pellet with 10%H_2 - Ar H_2 flow 4 L/min, pH_2 40% T = 1500°C, 4 hrs, CaO addition	• Activation energy of H_2 copper slag reduction 29.107–36.082 kJ/mol. • Increasing the reducing gas flow rate improves the reduction ratio but after 4 L/min that the reduction process is controlled by internal diffusion, interface chemical reaction control and mixed control.
Huaiwei *et al* (2021)	Experimental work of copper slag T = 1100°C, t < 1350 sec CO/H_2 Ratios (0 - 6/0 - 4)	• Fastest response rates were seen when the entering gas was hydrogen gas for 300 sec. • Primary cause of the loss of valuable components in the copper slags was the high magnetite content. Activation Energy = 58.8 kJ/mol.
Fasshauer *et al* (2000)	Industrial trial of 145 t Cu Initial O_2 0.9%, 53 - 81%H_2/Ar, gas flow 200 - 350 m^3/h, T = 1250°C	• Optimal hydrogen volume percentage in the H_2/N_2 combination was 60–72% by volume. • Preferable pressure of the reducing gas introduced into the melt at 8 to 12 bar.
Iwamura *et al* (1991)	40 kg molten copper with O_2 10 ppm H_2 5 - 50%/Ar, T = 1200°C, 10 min	• Increasing volume H_2 > 50% reduce reaction efficiency. • Produced pure Cu with O_2 < 3 ppm by weight.
Fukunaka *et al* (1991)	5 mm Cu droplets with H_2/Ar, T = 1697°C Initial O_2 0.036 - 1.9 wt%, pH_2 4 kPa Gas flow rate 2×10^{-4} m^3/s	• Deoxidation dropped droplet weight by a few percent and raised temperature in 30 sec during vaporisation. Deoxidation rises with hydrogen partial pressure and gas flow rate (mixed rates control). • Copper droplets deoxidise faster at high oxygen levels and slower at low oxygen levels.

CONCLUSIONS

Recent investigations have shown significant advances regarding hydrogen's potential in reducing primary and secondary copper resources. The laboratory-scale investigations explicitly focused on the reduction kinetics and reaction mechanisms. More detailed investigations in a simple system (CuO and Cu_2O) and a complex system (copper slag and copper-containing resources) at higher temperatures must be caried out to better understand interaction between phases during the reduction. Variations in the composition of the reductant gas mixture, temperature and reduction time need to be further investigated since these parameters will vary the kinetic driving force. The influence of the H_2/H_2O ratio also needs to be determined to examine its effect on the kinetics and microstructures of the reduction process. Laboratory studies and industrial research indicate that hydrogen reduction can be applied to primary and secondary copper resources, contributing to

industrial decarbonisation efforts. However, more research is needed to understand better the parameters impacting hydrogen reduction treatment.

ACKNOWLEDGEMENTS

This article was part of Dian Mughni Fellicia's PhD work, co-funded by Swinburne University of Technology and CSIRO.

REFERENCES

Aurubis AG, 2023. H_2-Ready: Aurubis Investing in Hydrogen-Capable Anode Furnaces in the Hamburg Plant [press release], Aurubis AG. Available from:<https://www.aurubis.com/en/media/press-releases/press-releases-2023/h2-ready-aurubis-investing-in-hydrogen-capable-anode-furnaces-in-the-hamburg-plant> [Accessed: 1 December 2023].

Chason, E, Sheldon, B W, Freund, L B, Floro, J A and Hearne, S, J, 2002. Origin of Compressive Residual Stress in Polycrystalline Thin Films, *Physical Review Letters*, 88:156103. https://doi.org/10.1103/PhysRevLett.88.156103

Edens, T and Steindor, J, 2023. Using Hydrogen as a Reductant in Fire Refining at Aurubis Hamburg's 'Down-town' Smelter, in *Proceedings of the 61st Conference of Metallurgists (COM 2022)*, pp 211–228 (Springer: Cham). https://doi.org/10.1007/978-3-031-17425-4_31

Elshkaki, A, Graedel, T E, Ciacci, L and Reck, B, 2016. Copper demand, supply and associated energy use to 2050, *Global Environmental Change*, 39:305–315. https://doi.org/10.1016/j.gloenvcha.2016.06.006

Fasshauer, K, Steffner, F, Dauterstedt, H-J, Albrech, M and Wernicke, E, 2000. Process for Poling Copper with Hydrogen and Nitrogen, Germany Patent Application 99119000.0.

Floro, J A, Hearne, S J, Hunter, J A, Kotula, P, Chason, E, Seel, S C and Thompson, C V, 2001. The dynamic competition between stress generation and relaxation mechanisms during coalescence of Volmer–Weber thin films, *J Appl Phys*, 89(9):4886–4897. https://doi.org/10.1063/1.1352563

Fukunaka, Y, Tamura, K, Taguchi, N and Asaki, Z, 1991. Deoxidation Rate of Copper Droplet Levitated in Ar-H_2 Gas Stream, *Metallurgical Transactions B*, 22(5):631–639. https://doi.org/10.1007/BF02679018

Gargul, K, Małecki, S and Włodarczyk, M, 2013. Reducing agents in fire refining of copper — analysis of the reduction process and its costs, *Journal: Rudy i Metale Nieżelazne*, 58(12):843–849.

Gilsbach, L, 2020. Copper – Sustainability Information [online], Bundesanstalt für Geowissenschaften und Rohstoffe. Available from: <https://www.bgr.bund.de/EN/Gemeinsames/Produkte/Downloads/Informationen_Nachhaltigkeit/kupfer_en.pdf?__blob=publicationFile&v=4> [Accessed: 01 February 2024].

Habashi, F and Yostos, B I, 1977. Copper from chalcopyrite by direct reduction, *JOM*, 29:11–16. https://doi.org/10.1007/BF03354324

Habashi, F, Dugdale, R and Nagamori, M, 1974. The Recovery of Copper, Iron and Sulfur from Chalcopyrite Concentrate by Reduction (published in German), *Metall (Berlin),* 28(11):1051–1054.

Hamada, S, Kudo, Y and Tojo, T, 1992. Preparation and Reduction Kinetics of Uniform Particles from Copper(I) Oxides with Hydrogen, *Colloids And Surfaces*, 67(6):45–51. https://doi.org/10.1016/0166-6622(92)80284-9

Hao, G, Zhang, R, Li, J, Wang, B and Zhao, Q, 2016. Insight into the Effect of Surface Structure on H_2 Adsorption and Activation Over Different Cuo (1 1 1) Surfaces: A First-Principal Study, *Computation Materials Science*, 122(9):191–200. https://doi.org/10.1016/j.commatsci.2016.05.023

Hovestadt, G and Friedrich, B, 2023. Fuming process of zinc rich slags by hydrogen injection [presentation], 8th Slag Valorization Symposium, 11 p. https://doi.org/10.13140/RG.2.2.29850.72643

Huaiwei, Z, Bao, L, Chen, Y, Xuan, W and Yuan, Y, 2021. Efficiency improvements of the CO-H2 mixed gas utilization related to the molten copper slag reducing modification, *Process Safety and Environmental Protection*, 146:292–299. https://doi.org/10.1016/j.psep.2020.09.011

International Copper Study Group (ICSG), 2023, 28 April. ICSG Copper Market Forecast 2023/2024 [online]. Available from: <https://icsg.org/download/2023-04-28-press-release-icsg-copper-market-forecast-2023-2024/> [Accessed: 15 January 2024].

Iwamura, T, Koya, T, Sukekawa, I, Hagiwara, H, Asao, H, Shigematsu, T and Sato, H, 1991. Method For Manufacturing Oxygen-Free Copper. US Patent US5037471A.

Jelić, D, Tomić-Tucaković, B and Mentus, S, 2011. A Kinetic Study of Copper (Ii) Oxide Powder Reduction with Hydrogen, Based on Thermogravimetry, *Thermochimica Acta*, 521:211–217, https://doi.org/10.1016/j.tca.2011.04.026

Jin, Q and Lihua, C, 2022. A Review of the Influence of Copper Slag on the Properties of Cement-Based Materials, *Materials,* 15(23):8594. https://doi.org/10.3390/ma15238594

Kim, J Y, Rodriguez, J A, Hanson, J C, Frenkel, A I and Lee, P L, 2003. Reduction of CuO and Cu2O with H2: H embedding and kinetic effects in the formation of suboxides, *Journal of the American Chemical Society*, 125(35):10684–10692. https://doi.org/10.1021/ja0301673

Kim, J, Hanson, J, Frenkel, A, Lee, P and Rodriguez, J, 2004. Reaction of CuO with Hydrogen Studied by Using Synchrotronbased X-Ray Diffraction, *Journal of Physics: Condensed Matter*, 16(33). https://doi.org/10.1088/0953-8984/16/33/008

Li, J, Mayer, J W and Tu, K N, 1992. Nucleation and growth of Cu2O in the reduction of CuO thin films, *Physical Review, B: Condensed Matter*, 45(10):5683–5686. https://doi.org/10.1103/physrevb.45.5683

Maimaiti, Y, Nolan, M and Elliott, S, 2014. Reduction mechanisms of the CuO(111) surface through surface oxygen vacancy formation and hydrogen adsorption, *Physical Chemistry Chemical Physics*, 16(7):3036–3046. https://doi.org/10.1039/C3CP53991A

Mairizal, A Q, Sembada, A Y, Tse, K M, Haque, N and Rhamdhani, M A, 2023. Assessment of Mass and Energy Balance of Waste Printed Circuit Board Recycling through Hydrogen Reduction in Black Copper Smelting Process, *Processes*, 11(5):1506. https://doi.org/10.3390/pr11051506

Pike, J, Chan, S-W, Wang, X and Hanson, J, 2006. Formation of Stable Cu2O from Reduction of CuO Nanoparticles, *Appl Catal A*, 303(2):273–277. https://doi.org/10.1016/j.apcata.2006.02.008

Rodriguez, J A, Kim, J Y, Hanson, J C, Pérez, M and Frenkel, A I, 2003. Reduction of CuO in H2: In Situ Time-Resolved XRD Studies, *Catalysis Letters*, 85:247–254. https://doi.org/10.1023/A:1022110200942

Roeben, F, Schöne, N, Bau, U, Reuter, M, Dahmen, M and Bardow, A, 2021. Decarbonizing Copper Production by Power-to-Hydrogen: A Techno-Economic Analysis, *Journal of Cleaner Production*, 306:127191. https://doi.org/10.1016/j.jclepro.2021.127191

Rukini, A, Rhamdhani, M A, Brooks, G and Bulck, A, 2023. Lead Recovery from PbO Using Hydrogen as a Reducing Agent, *Metallurgical and Materials Transactions B*, 54:996–1016. https://doi.org/10.1007/s11663-023-02745-0

Sabat, K, Paramguru, R and Mishra, B, 2016. Reduction of Copper Oxide by Low-Temperature Hydrogen Plasma, *Plasma Chemistry and Plasma Processing*, 36:1111–1124. https://doi.org/10.1007/s11090-016-9710-9

Schlesinger, M E, Sole, K C, Davenport, W G and Flores, G R F A, 2021. *Extractive Metallurgy of Copper*, 6th edition, pp 1–30 (Elsevier: Amsterdam).

Shrestha, K M, Sorensen, C M and Klabunde, K J, 2010. Synthesis of CuO Nanorods, Reduction of CuO into Cu Nanorods and Diffuse Reflectance Measurements of CuO and Cu Nanomaterials in the Near Infrared Region, *J Phys Chem*, 114:14368–14376.

Sun, X, Wu, D, Zhu, W, Chen, X, Sharma, R, Yang, J C and Zhou, G, 2021. Atomic Origin of the Autocatalytic Reduction of Monoclinic CuO in a Hydrogen Atmosphere, *The Journal of Physical Chemistry Letters*, 12:9547–9556.

Tilliander, U, Aune, R and Seetharaman, S, 2006. Kinetics studies of hydrogen reduction of Cu2O, *Zeitschrift fuer Metallkunde/Materials Research and Advanced Techniques*, 97:72–78. https://doi.org/10.1515/ijmr-2006-0011

Tyagi, D, 2018. Kinetics of Reduction of Copper Oxide, *International Journal for Research in Applied Science and Engineering Technology*, 6:3928–3932. https://doi.org/10.22214/ijraset.2018.4645

Unutulmazsoy, Y, Cancellieri, C, Lin, L and Jeurgens, L P H, 2022. Reduction of Thermally Grown Single-Phase CuO and Cu_2O Thin Films by In-Situ Time-Resolved XRD, *Applied Surface Science*, 588:152896. https://doi.org/10.1016/j.apsusc.2022.152896

Xu, F, An, W, Baber, A E, Grinter, D C, Senanayake, S D, White, M G, Liu, P and Stacchiola, D J, 2022. Enhanced Oxide Reduction by Hydrogen at Cuprous Oxide–Copper Interfaces near Ascending Step Edges, *Journal of Physical Chemistry: C*, 126(4):18645–18651. https://doi.org/10.1021/acs.jpcc.2c03719

Yamukyan, M, Manukyan, K and Kharatyan, S. 2009. Copper oxide reduction by hydrogen under the self-propagation reaction mode, *Journal of Alloys and Compounds*, 473:546–549. https://doi.org/10.1016/j.jallcom.2008.06.031

Yao, T, Matsuda, T, Sano, T, Morikawa, C, Ohbuchi, A, Yashiro, H and Hirose, A, 2018. In Situ Study of Reduction Process of CuO Paste and its Effect on Bondability of Cu-to-Cu Joints, *J Electron Mater*, 47:2193–2197.

Zhang, B, Zhang, T and Zheng, C, 2022. Reduction Kinetics of Copper Slag by H2, *Minerals*, 12(5):548. https://doi.org/10.3390/min12050548

Smelting of different hydrogen-reduced bauxite residue-calcite pellets for iron and alumina recovery

DOI: 10.62053/NHUU7429
M K Kar[1] and J Safarian[2]

1. PhD Researcher, Department of Materials Science and Engineering, NTNU, 7041 Trondheim, Norway. Email: manish.k.kar@ntnu.no
2. Professor, Department of Materials Science and Engineering, NTNU, 7041 Trondheim, Norway. Email: jafar.safarian@ntnu.no

ABSTRACT

Bauxite residue is one of the most important by-products from the alumina industry with no commercial use till now. The utilisation of bauxite residue through pelletising with different lime additions, hydrogen reduction, and smelting has been studied in this work. Three different types of green pellets were made with varying calcite-to-bauxite residue ratio and subsequently sintered at elevated temperatures. The sintered pellets were isothermally reduced at 1000°C under hydrogen gas followed by smelting of the reduced pellets in argon at 1500°C. Smelting of the reduced pellets leads to the recovery of metallic iron and the formation of a leachable calcium aluminate slag. X-ray diffraction (XRD) and scanning electron microscope (SEM) were used to characterise the phases and microstructural analysis. The iron produced in the smelting process has a high purity, above 99.5 wt per cent. While the iron content of the slags is quite low, and the slags shows variations of krotite ($CaAl_2O_4$), gehlenite ($Ca_2Al_2SiO_7$), and perovskite ($CaTiO_3$) phases based on the variation of calcite addition. It was found that the more calcite addition in pelletising yields higher percentage of krotite phase as compared to lower calcite-containing pellets. Employing quantitative XRD analysis, the krotite phase fraction was found approximately 85 wt per cent for higher calcite-added pellet, and around 74 wt per cent for lower calcite-added pellet. FactSage™, ver 8.1 (Thermfact and GGT-Technologies) thermodynamic software was used to evaluate the obtained experimental data, they both revealed that the components of the bauxite residue are mostly distributed into the calcium aluminate slag phase.

INTRODUCTION

As society undergoes continuous modernisation, there is a concurrent rise in the demand for iron metal. However, the quality of traditional iron ore has seen a decline over time. Consequently, iron manufacturers are compelled to explore alternative secondary resources to meet the escalating demand. One such secondary source is bauxite residue, which boasts iron oxide content ranging from 40 to 60 wt per cent (Kar, Önal and Borra, 2023; Kar *et al*, 2023). Certainly, during the Bayer process, which is employed in the production of alumina from bauxite ore, red mud byproduct is generated. This red mud consists of undigested oxides and other impurities that remain after the extraction of alumina from the bauxite ore. It is a residue with a distinctive reddish colour due to the presence of iron oxide of Fe_2O_3. Managing and finding environmentally sustainable solutions for the disposal of red mud is a significant challenge in the alumina refining industry (Evans, Nordheim and Tsesmelis, 2016; Lazou *et al*, 2020; Cardenia, Balomenos and Panias, 2019). It is generated in from of slurry and the dewatered form of red mud is known as bauxite residue (Kar and Safarian, 2023). On average, approximately 1.2 tons of bauxite residue is generated per ton of alumina produced. The annual generation of bauxite residue is above 150 million tons which was reported in the year of 2019 (Archambo and Kawatra, 2020). This generated bauxite residue quantity is influenced by various factors, including the processing parameters of the Bayer process and the origin of the bauxite ore. Globally, there is a stockpile of around 4.5 billion tons of bauxite residue (Kar, Önal and Borra, 2023). Numerous utilisation methods and strategies are under exploration to effectively manage and find potential applications for bauxite residue. These applications encompass the production of building materials, decorative tiles, and door filler materials. Additionally, bauxite residue is being investigated for its potential to extract valuable metal elements. Beyond industrial applications, it is being employed for environmental treatment and ecological restoration purposes. This includes its use in water purification, flue gas purification, soil improvement, bauxite residue reclamation, and preparation for environmental restoration materials. The multifaceted potential of

bauxite residue utilisation highlights ongoing efforts to transform this byproduct into valuable resources across various domains (Chao *et al*, 2022). Among these, all the utilisation technology, various metal recovery from the bauxite residue will be the most economical. Many works are focusing on iron and alumina recovery from the bauxite residue through the carbothermic route (Ekstrøm *et al*, 2021; Lazou *et al*, 2020).

In earlier studies, iron oxides were reduced to metallic iron utilising carbon as a reductant. However, due to growing concerns about environmental greenhouse gas emissions, using carbon as a reductant has raised issues as it produces greenhouse gases during the reduction process. A more sustainable alternative to carbon is hydrogen, which serves as a reductant for iron oxide, leading to the production of water vapor as a byproduct, in contrast to the carbon monoxide (CO) and carbon dioxide (CO_2) gases generated in carbothermic reduction.

The primary emphasis of this study lies in the examination of phase formation dynamics during the smelting process involving various bauxite residue calcite mixtures that have undergone hydrogen reduction. The investigation encompasses not only the separation of iron from the slag but also delves into the specific types of calcium aluminate phases ($CaAl_2O_4$, krotite) that manifest during the melting of the slag.

MATERIALS AND METHODS

The overall experimental processes of the research work have been presented in the Figure 1. Three different types of bauxite residue calcite pellets have been made and these are named as 1, 2 and 3. The $CaO:Al_2O_3$ (BR) mole ratio was varied 0.85, 1 and 1.15 to examine effect of CaO addition on the formation of calcium aluminate,calcium silicate and calcium titanate phase during hydrogen reduction, and in the slag produced via a further smelting process.

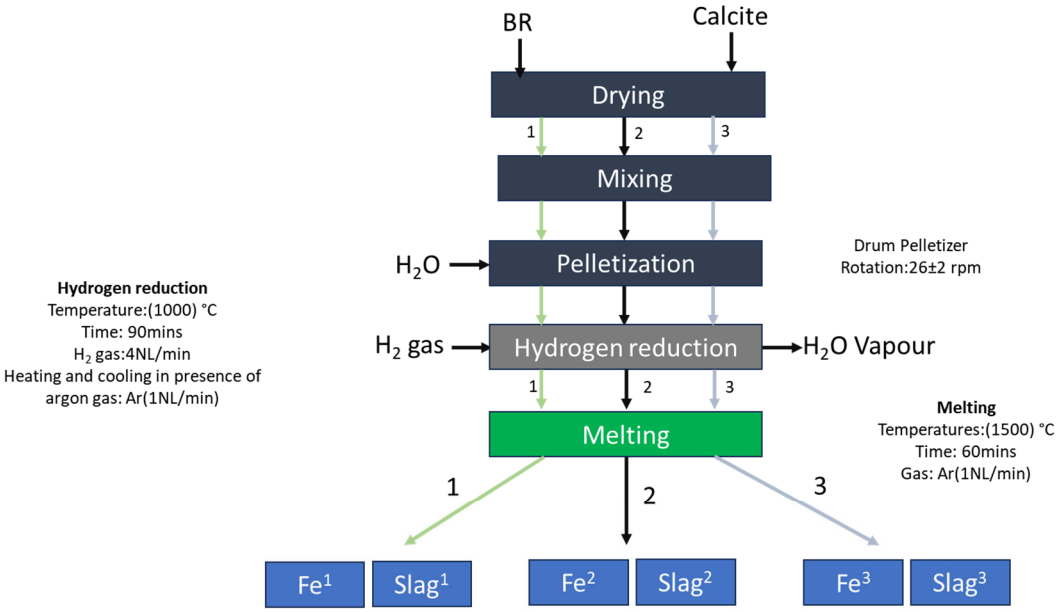

1. Pellet compostion($C_{0.85}A$)
2. Pellet compostion(C_1A)
3. Pellet compostion($C_{1.15}A$)

FIG 1 – Overall flow sheet of the experimental work.

Hydrogen reduction

Three distinct varieties of bauxite residue calcite were produced by employing a drum pelletiser, each characterised by different percentages of calcite. Following the pelletisation process, these pellets underwent sintering at 1150°C for 120 mins to enhance their strength. The sintered pellets were subjected to hydrogen reduction in a TG (Thermogravimetric) furnace. The procedure involved heating the sintered pellets in the presence of argon with a flow rate of 1 Nl/min. Once the target

temperature of 1000°C was achieved, the gas flow was switched to hydrogen at a flow rate of 4 Nl/min for 90 mins. Upon completion of the reduction cycle, the reduced pellets were cooled to room temperature in an argon atmosphere. The heating, reduction,and cooling cycle was similar for all types of pellets. The XRD of the three different composition-reduced pellets are shown in Figure 2.

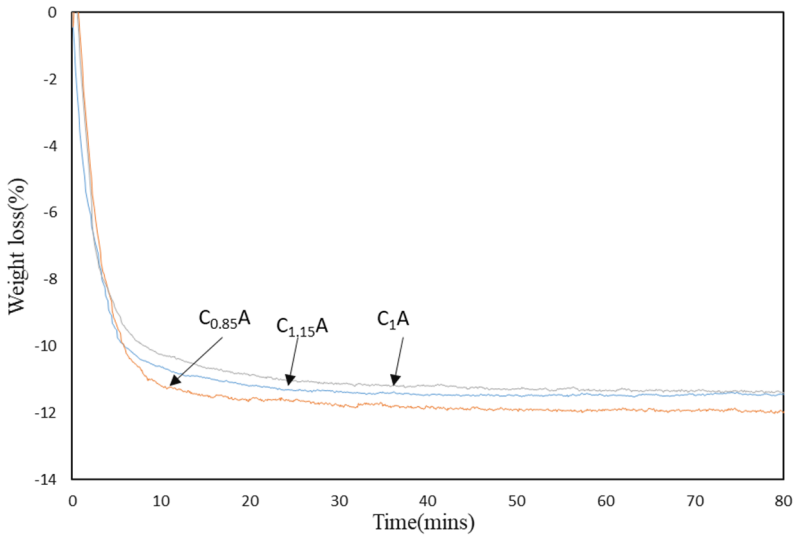

FIG 2 – Weight loss versus Time for different composition bauxite residue calcite pellets (1000°C, 4 Nl/min H_2 flow rate).

Smelting reduced pellets

Following the reduction process of various bauxite residue calcite pellets, smelting was conducted in a vertical tube furnace at 1500°C for 60 mins, maintaining an argon atmosphere. The primary objective of utilising argon during the smelting process was to prevent the oxidation of metallic iron. The complete furnace description and working principle are described here (Rasouli *et al*, 2022). An Alumina crucible was used to hold the samples.

Characterisation

The phase analysis of slag was conducted through X-ray diffraction (XRD) using CuKα radiation (wavelength λ=1.54 Å) on a Bruker AXS GmbH instrument in Karlsruhe, Germany. The diffractometer scanned within the 15° to 75° 2θ range with a 0.03° step size. Qualitative phase analysis of the raw data employed DIFFRAC.EVA software with the PDF-4+ database (2014, ICDD, Philadelphia, Pennsylvania, USA). Standard samples for XRD were prepared by milling materials in a WC vibratory disk mill (RS 200, RETSCH GmbH, Haan, Germany) for 45 secs at 800 revolutions per minute (rev/min).

Quantitative analysis of phases, including krotite, gehlenite, and perovskite, utilised topas software based on the Rietveld method. To enhance quantitative analysis accuracy, specific parameters in the topas software, such as Zero error, LP (Lorentz–polarization) factor, sample displacement, and background, were adjusted. Microstructural analysis of the slags was conducted using a scanning electron microscope (SEM) (Zeiss Ultra FESEM) equipped with an XFlash® 4010 Detector from the Bruker Corporation for Energy-Dispersive X-Ray Spectroscopy (EDS). Energy dispersive spectroscopy (EDS) was employed to assess the elemental composition in various regions of the slags.

RESULTS AND DISCUSSION

Weight loss during hydrogen reduction

Figure 2 illustrates the weight loss over time for various compositions of bauxite residue calcite sintered pellets. It is evident from the figure that the weight loss is more pronounced for the $C_{0.85}A$ sintered pellets compared to the other two compositions. This higher weight loss can be attributed to the relatively higher fraction of iron oxide within the same mass of sintered pellets. On the other

hand, the $C_{1.15}A$ pellets exhibit a higher initial rate of reduction, primarily due to their increased porosity. The elevated porosity of the $C_{1.15}A$ pellets stems from the higher percentage of $CaCO_3$ present, which undergoes decomposition during sintering, resulting in increased porosity. Theoretically, the weight loss should be greater for C_1A pellets compared to $C_{1.15}A$ pellets. However, the figure shows that the difference in weight loss between the two compositions is almost negligible.

Phase analysis of the reduced pellets and obtained slags

As depicted in Figure 3, the primary phases present in the reduced pellets include iron, mayenite, perovskite, larnite, gehlenite, and lime. These phases exhibit a consistent pattern across all the different compositions of bauxite residue-calcite reduced pellets, with variations in intensity observed among the different pellets.

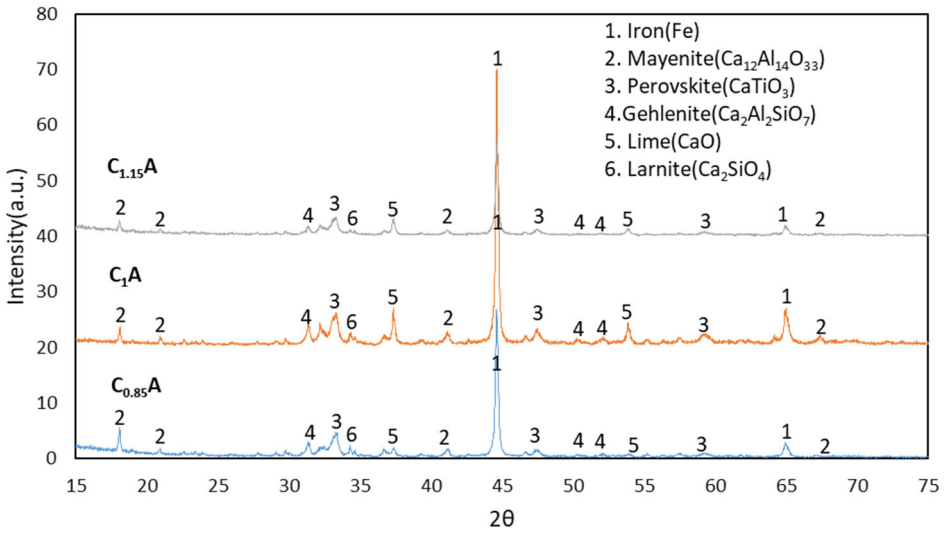

FIG 3 – Phase analysis of different reduced pellets.

Figure 4 illustrates the phases formed in the slags obtained in the smelting of hydrogen-reduced bauxite residue-calcite pellets. Three primary phases, namely krotite ($CaAl_2O_4$), gehlenite ($Ca_2Al_2SiO_7$), and perovskite ($CaTiO_3$), were identified in all smelted slag samples. Krotite emerged as the predominant phase in all the analysed slag samples. From the quantitative XRD analysis, Krotite was high for the higher calcite-added pellets and lower for lower calcite pellets as shown in Table 1.

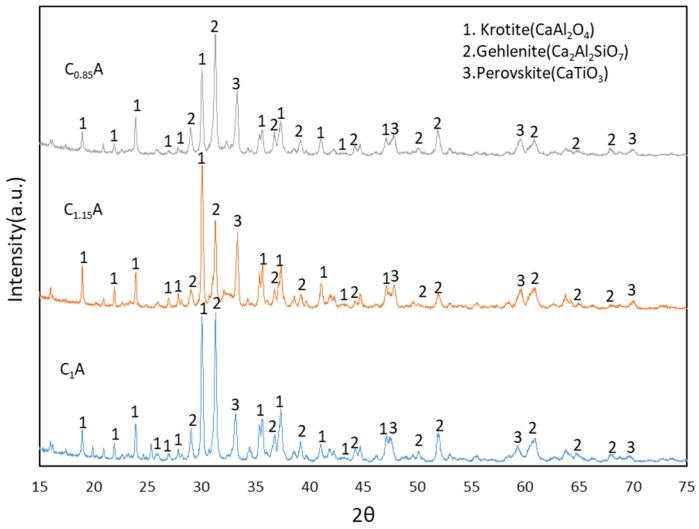

FIG 4 – Phase analysis of different slags (C_1A, $C_{1.15}A$ and $C_{0.85}A$).

TABLE 1

Quantitative XRD analysis of the calcium aluminate phases in slags.

	$C_{0.85}A$	C_1A	$C_{1.15}A$
Gehlenite	17.94	15.41	8.38
Perovskite	10.53	9.89	5.67
Krotite	71.53	74.70	85.95

Microstructure

Figure 5 presents the elemental mapping of slag C_1A. As depicted in the figure, there is a significant overlap of calcium, aluminium, and oxygen in most areas, indicating the presence of krotite. This observation aligns with XRD data, where krotite constitutes a major fraction. In certain regions, the overlap of calcium, aluminium, silicon, and oxygen suggests the potential presence of the gehlenite phase. Additionally, the overlap of calcium, titanium, and oxygen is indicative of the perovskite phase. The presence of iron particles in the slag phase is notable, possibly resulting from incomplete iron separation due to the higher viscosity of the slag. The higher alumina fraction in the slag contributes to increased viscosity.

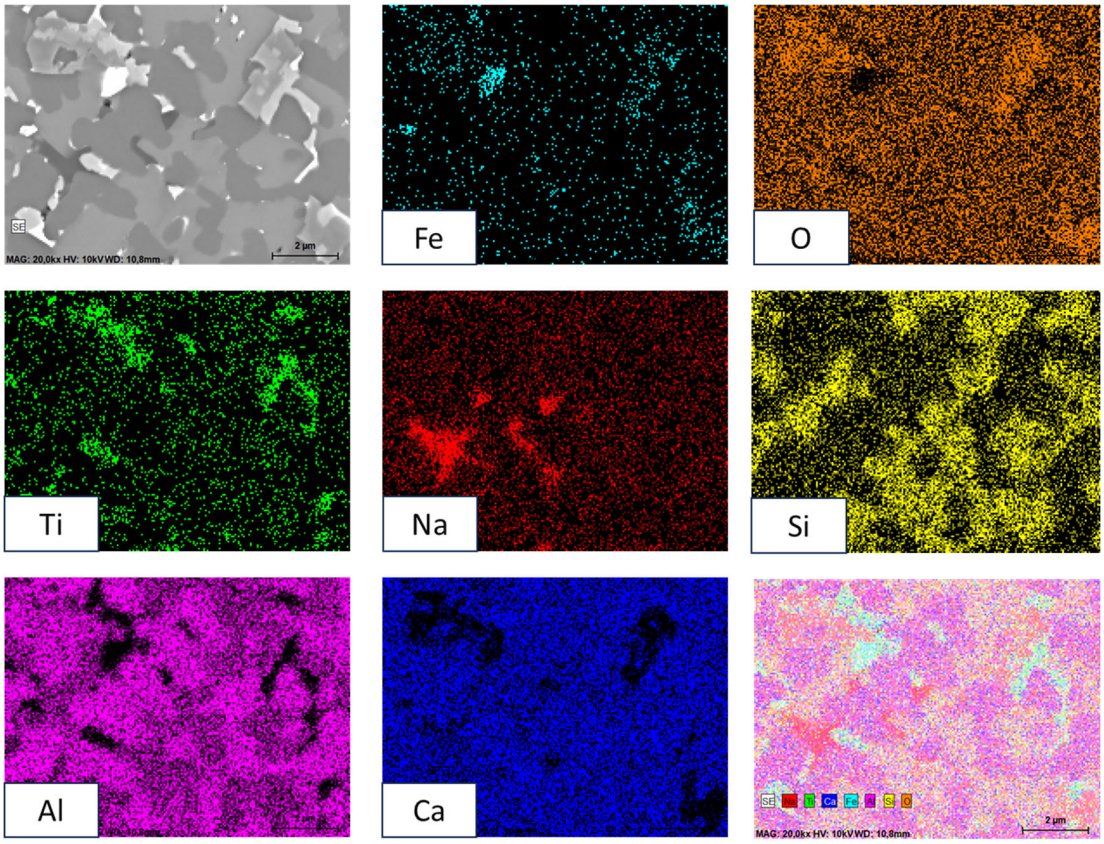

FIG 5 – Elemental mapping of slag C_1A.

Figure 6 displays the elemental analysis of the C_1A slag and metals. On the left side of the figure, the bright areas represent pure iron. On the right side, three distinct phases are observed. The light grey phase consists predominantly of calcium, titanium, and oxygen, with a minor fraction of aluminium. This phase is likely the perovskite phase. The dark phase is composed of calcium, aluminium, and oxygen, with the addition of sodium, indicative of the krotite phase with some sodium present in the lattice. The light dark phase contains calcium, aluminium, oxygen, and silicon, representing the gehlenite phase.

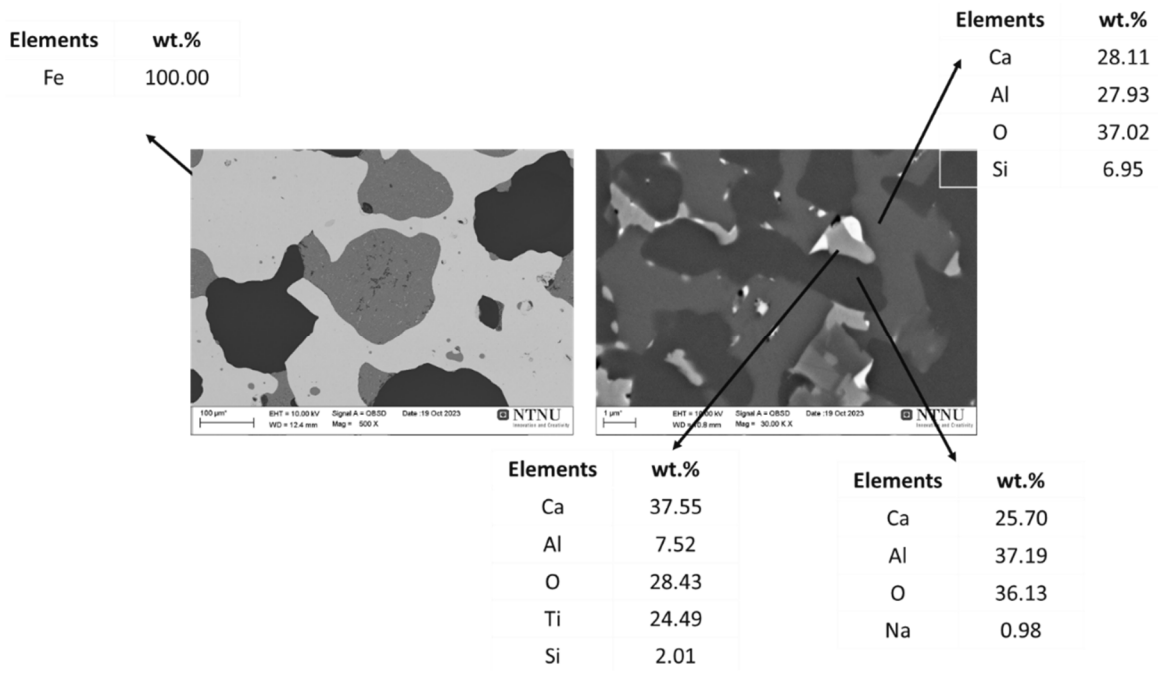

FIG 6 – Elemental analysis of different phases of slag C_1A.

The elemental mapping of $C_{0.85}A$ and $C_{1.15}A$ are similar (Figures 7 and 8 respectively). However, it has difference in the amount of phases such as krotite, gehlenite, and perovskite, which is shown in the Table 1.

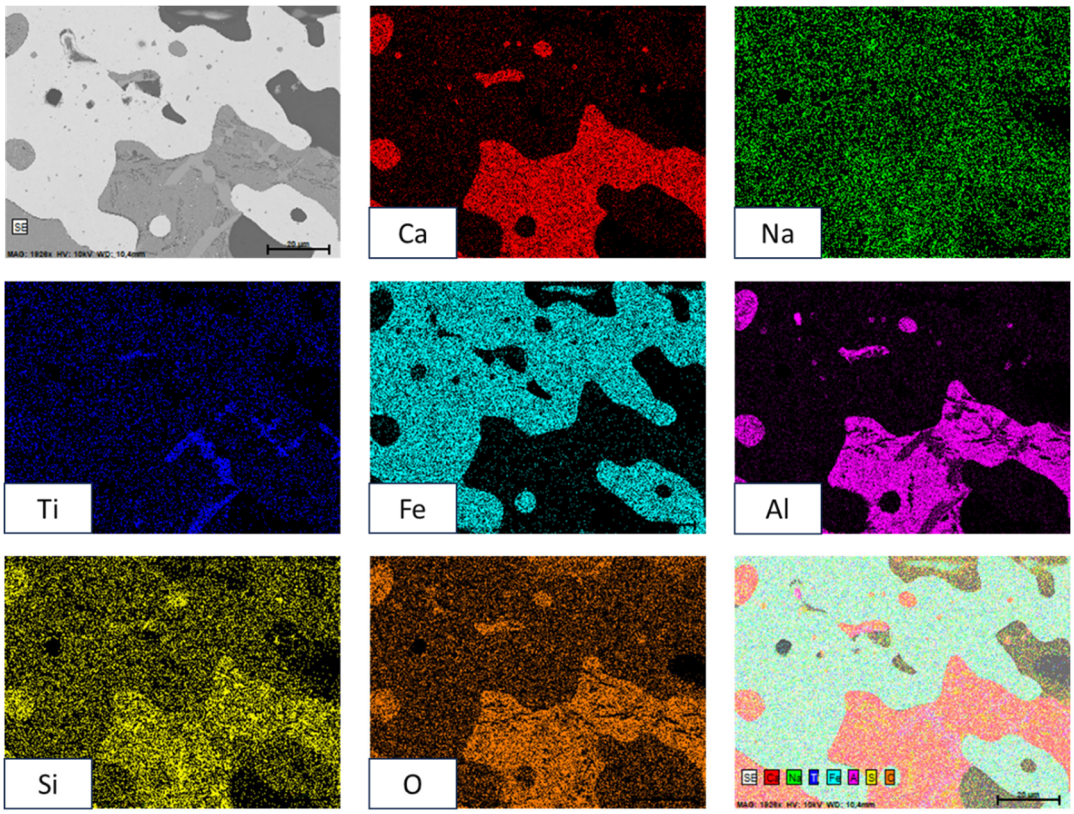

FIG 7 – Elemental mapping of slag $C_{0.85}A$.

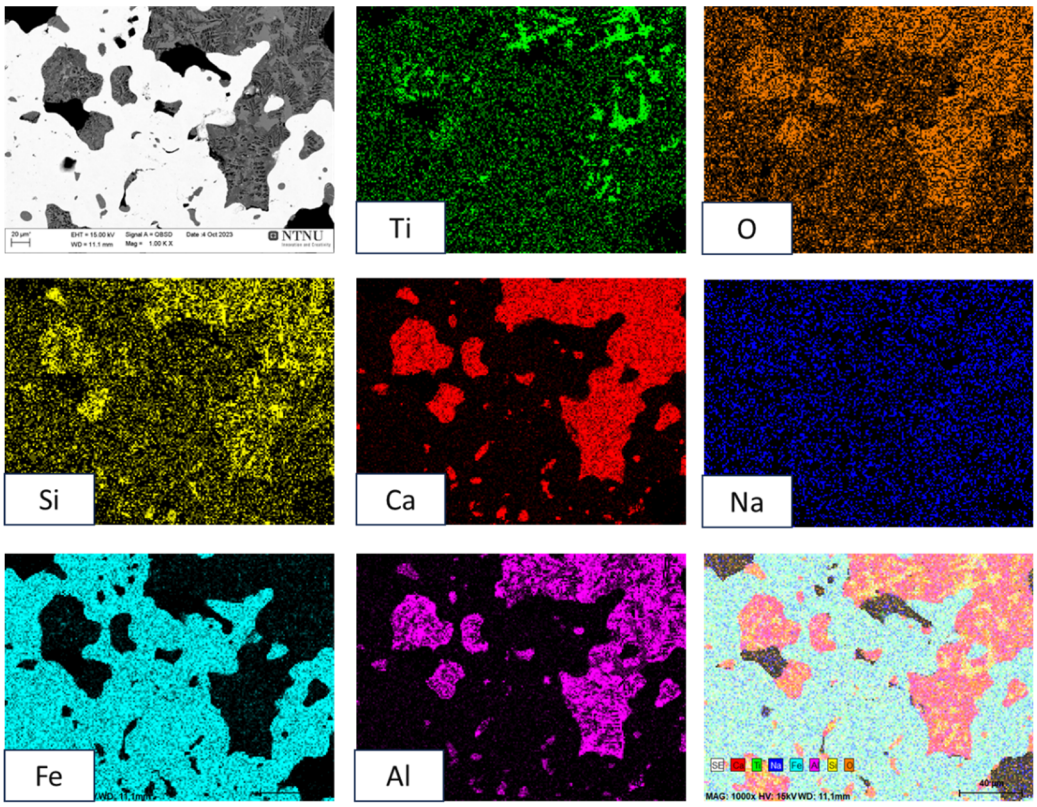

FIG 8 – Elemental mapping of slag $C_{1.15}A$.

The elemental analysis of $C_{0.85}A$ slag of different phases is shown in Figure 9. As shown in the figure white area are the metallic iron with little impurity of calcium, which is likely come from the surroundings signals as the elemental analysis area is smaller. Similar to the previous elemental analysis of C_1A, the light white area is the calcium titanate, and the dark area is the calcium aluminate. As shown in the right image of Figure 9, the shrunk areas are the calcium silicate.

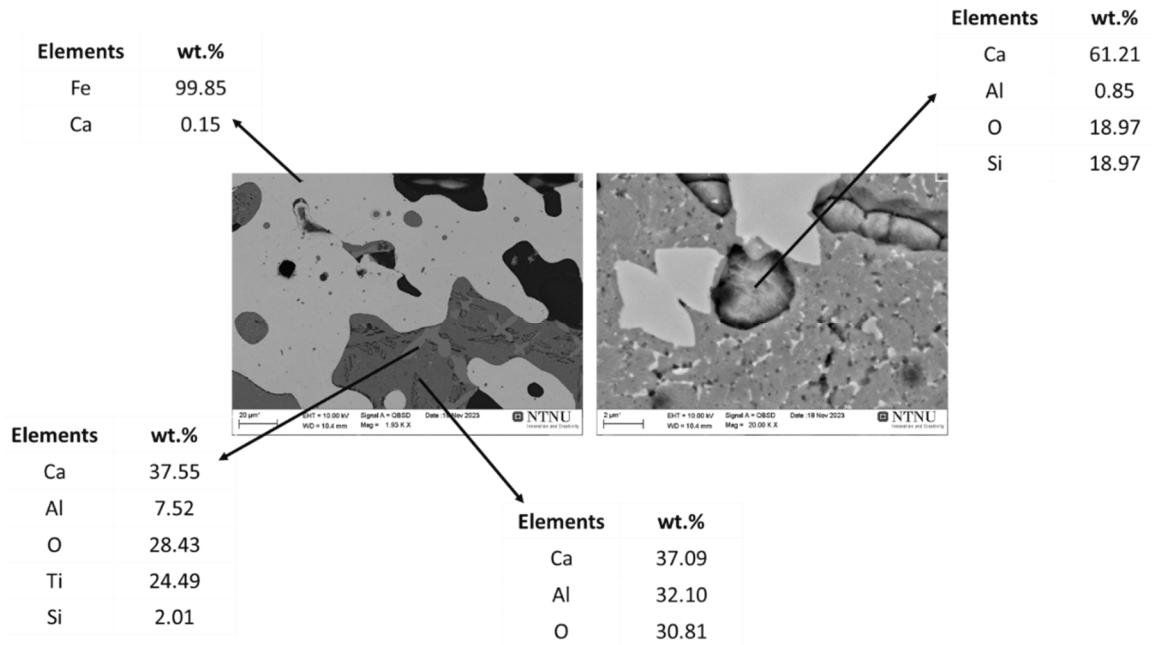

FIG 9 – Elemental analysis of different phases of slag $C_{0.85}A$.

Similar to Figure 9, the shrunk areas correspond to calcium silicate with a minor fraction of aluminium. The observed shrunk areas may be attributed to the higher volume shrinkage of calcium

silicate compared to other phases, such as calcium alumino silicate, calcium titanate, and calcium aluminate. The elemental analysis of smelted slag of $C_{1.15}A$ is presented in Figure 10.

Elements	wt.%
Ca	39.98
Al	9.51
O	28.96
Ti	21.56

Elements	wt.%
Fe	100

Elements	wt.%
Ca	55.86
Al	1.32
O	28.97
Si	13.85

Elements	wt.%
Ca	37.69
Al	28.40
O	33.91

FIG 10 – Elemental analysis of smelted slag of different phases $C_{1.15}A$.

Phase formation

During the slags solidification after the smelting of the reduced pellets of different bauxite residue-calcite pellets, three major phases formed in the slag are krotite, perovskite, and gehlenite. The phases formed are as follows:

$$CaO + Al_2O_3 \rightarrow CaAl_2O_4 \quad (1)$$

$$2CaO + Al_2O_3 + SiO_2 \rightarrow Ca_2Al_2SiO_7 \quad (2)$$

$$CaO + TiO_2 \rightarrow CaTiO_3 \quad (3)$$

Thermodynamic calculations of slag phases were performed using FactSage™ 8.1 with the FT oxide database. The calculation considered four major oxides from actual measurements in experimental work, namely CaO, Al_2O_3, SiO_2, and TiO_2. Notably, sodium oxide (Na_2O) was excluded from these calculations due to observed sodium losses during hydrogen reduction. The thermodynamic calculations were conducted at a temperature of 1500°C and a pressure of 1 atm, mirroring the experimental conditions.

The Scheil-Gulliver cooling model was selected for thermodynamic calculations, chosen for its faster cooling rate. Figure 11 illustrates that the major phases identified in the calculation include $CaAl_2O_4$, $Ca_3Al_2O_6$, Ca_2SiO_4, and $Ca_3Ti_2O_7$. However, in the experimental analysis, the calcium aluminate phase was observed in krotite form, calcium alumino silicate manifested in gehlenite, and calcium titanate appeared in perovskite form. The observed variation in phases between experimental and thermodynamic calculations may be attributed to the faster cooling rate of the slag and the interactions between high-temperature slag with the crucible.

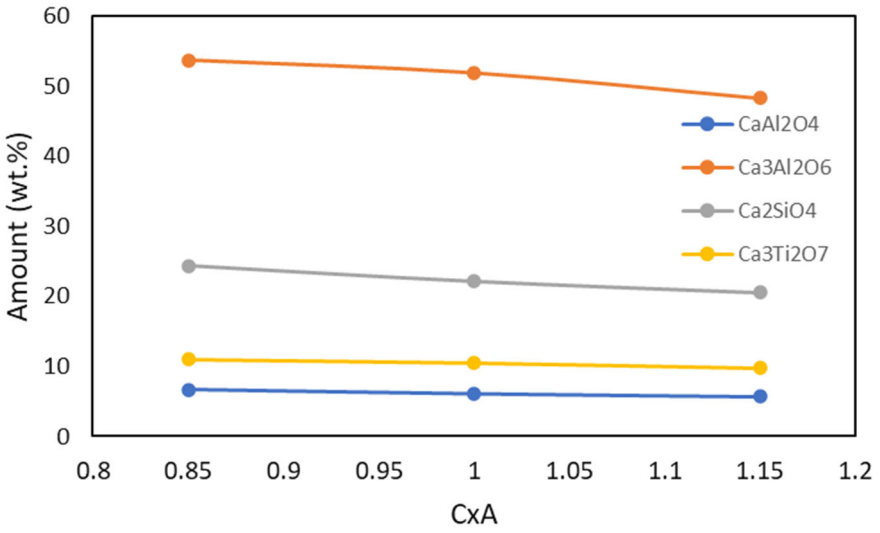

FIG 11 – Phase fraction of different phases calculated by using FactSage™ 8.1.

Gehlenite phase was not found in the thermodynamics calculation may be due to the dissociation of gehlenite to calcium silicate and alumina. The reaction equation is as follows:

$$Ca_2Al_2SiO_7 \rightarrow 2CaO.SiO_2 + Al_2O_3 \quad (4)$$

CONCLUSION

The following conclusions from the hydrogen reduction and smelting of different mixtures of bauxite residue and calcite:

- Metallic iron and mayenite dominate as the major phases in the reduced pellets. The phases formed in the reduced pellets from different bauxite residue calcite compositions exhibit similarities with variations in phase fraction.
- Following the smelting of distinct reduced pellets, the primary phases observed in the resulting slag include krotite, gehlenite, and perovskite.
- The leachable calcium aluminate phase, identified as krotite, is present in higher quantities in the pellets with higher calcite content, as revealed by quantitative phase analysis of the slag.
- Thermodynamic calculations indicate that the major phases anticipated in the slag are $CaAl_2O_4$, $Ca_3Al_2O_6$, Ca_2SiO_4, and $Ca_3Ti_2O_7$. Discrepancies between experimental and thermodynamic results may be attributed to the faster cooling rate and interactions during the melting process, including those with the alumina crucible, which could introduce variations in the outcomes.
- The iron purity achieved during the smelting of the reduced pellets exceeds 99.0 wt per cent.

ACKNOWLEDGEMENTS

This study was performed and financially supported by The European Union's Horizon 2020 research and innovation program under grant number of 958307 (HARARE project).

REFERENCES

Archambo, M and Kawatra, S K, 2020. Red mud: Fundamentals and new avenues for utilization, *Mineral processing and extractive metallurgy review*, 24 p.

Cardenia, C, Balomenos, E and Panias, D, 2019. Iron recovery from bauxite residue through reductive roasting and wet magnetic separation, *Journal of Sustainable Metallurgy*, 5(1):9–19.

Chao, X, Zhang, T, Lv, G, Chen, Y, Li, X and Yang, X, 2022. Comprehensive application technology of bauxite residue treatment in the ecological environment: a review, *Bulletin of Environmental Contamination and Toxicology*, 6 p.

Ekstrøm, K E, *et al,* 2021. Recovery of iron and aluminum from bauxite residue by Carbothermic reduction and slag leaching, *Journal of Sustainable Metallurgy*, 7(3):1314–1326.

Evans, K, Nordheim, E and Tsesmelis, K, 2016. Bauxite residue management, *Light metals 2012*, pp 63–66.

Kar, M K and Safarian, J, 2023. Characteristics of Bauxite Residue–Limestone Pellets as Feedstock for Fe and Al_2O_3 Recovery, *Processes*, 11(1):137.

Kar, M K, *et al* 2023. Properties of self-hardened CaO-added bauxite residue pellets and their behavior in hydrogen reduction followed by leaching and magnetic separation for iron and alumina recovery, *International Journal of Hydrogen Energy*.

Kar, M K, Önal, M A R and Borra, C R, 2023. Alumina recovery from bauxite residue: A concise review, *Resources, Conservation and Recycling*, 198:107158.

Lazou, A, *et al,* 2020. High temperature smelting reduction of bauxite residue and a $CaCO_3$-rich bauxite for aluminate slag production and pig iron recovery, in *Proceedings of the 3rd International Bauxite Residue Valorisation and Best Practices Conference, Virtual*, pp 77–83.

Rasouli, A, *et al,* 2022. Magnesiothermic Reduction of Natural Quartz, *Metallurgical and Materials Transactions B,* 53(4):2132–2142.

Effect of mill-scale and calcined dolomite on high Al_2O_3 sinter and its reduction behaviour

DOI: 10.62053/OWYV6941

S J Kim[1], L Tomas da Rocha[2], S W Kim[3] and S Jung[4]

1. PhD student, Graduate Institute of Ferrous and Eco Materials Technology, Pohang University of Science and Technology, Pohang, North Gyeongsang Province, 37673, South Korea. Email: sjkim96@postech.ac.kr
2. Post-doctorate Researcher, Graduate Institute of Ferrous and Eco Materials Technology, Pohang University of Science and Technology, Pohang, North Gyeongsang Province, 37673, South Korea. Email: leonardoroc@postech.ac.kr
3. Senior Researcher, Ironmaking and FINEX Research Group, Process and Engineering Research Labs., POSCO, Pohang, North Gyeongsang Province, 37763, South Korea. Email: sungwankim@posco.com
4. Professor, Graduate Institute of Ferrous and Eco Materials Technology, Pohang University of Science and Technology, Pohang, North Gyeongsang Province, 37673, South Korea. Email: smjung@postech.ac.kr

ABSTRACT

Al_2O_3 has been regarded as a harmful gangue component in iron ore, especially causing reduction degradation in industrial sintering of iron ore. The current study aimed to utilise low-grade iron ore containing high Al_2O_3 content in sintering process. In order to counteract the adverse effect of Al_2O_3 on reduction behaviour of iron ore sinter, mill-scale and calcined dolomite were chosen as FeO- and MgO-bearing materials. Firstly, mill-scale was added to high Al_2O_3 sinter and addition was optimised as 10 wt per cent, then calcined dolomite was added further. Magnetite and magnesio-ferrite were identified as the major phases in iron ore sinter when adding mill-scale and calcined dolomite. As the dosage of calcined dolomite increased beyond 4 wt per cent of in sinter mix, unreacted MgO particles were observed, which is ascribed to the limitation of MgO dissolution into magnetite matrix. Both mill-scale and calcined dolomite were effective in improving compressive load and Reduction Disintegration Index (RDI) of iron ore sinter although its reduction degree was highly decreased. The addition of both FeO and MgO-bearing materials to high Al_2O_3 sinter has a potential to improve the sinter quality, also contribute to the recycling of industrial by-product. However, the amount should be optimised in views of phase development and deterioration of reducibility.

INTRODUCTION

The price of raw materials being used in steel industry is gradually increasing in recent years (Chai *et al*, 2019; Wang *et al*, 2020). Since several countries with limited mineral resource are largely depending on the import iron ores, ironmaking companies are attempting to substitute low-grade iron ores in their industrial process for high-grade iron ores. This urgent agenda is connected to the numerous studies (Yamaoka *et al*, 1974; Pimenta and Sechadri, 2002; Yang, 2005; Xue *et al*, 2020) in ironmaking research field to clarify the influence of gangue component on characteristics of iron ore sinter in sintering process where low-grade iron ores might be utilised.

Al_2O_3 has been known to be a representative of harmful gangue components affecting iron ore sinter. Several researchers (Yamaoka *et al*, 1974; Xiao *et al*, 2017) reported that Al_2O_3 increased the formation temperature of primary melt during the sintering process. Okazaki *et al* (2003) reported that Al_2O_3 inhibits the penetration of melt with high viscosity and suppresses assimilation between nuclei and adhering fines. This strongly affected the irregular pore distribution and further deteriorated the sinter strength, (Pimenta and Sechadri, 2002; Loo and Leung, 2003) which is inferior to the bed permeability of blast furnace (Umadevi *et al*, 2014). Degradation of sinter matrix is also one of the critical problems when Al atom was entrapped in lattice of hematite and magnetite phase and resulted in rapid propagation of cracks (Sinha and Ramna, 2009).

For counteracting the adverse effect of Al_2O_3 on iron ore sinter, several researchers (Yadav *et al*, 2002; Higuchi *et al*, 2004; Umadevi *et al*, 2012; Umadevi, Mahapatra and Prabhu, 2013) considered the small addition of FeO and MgO. They found that increased FeO is directly connected to the

magnetite (Fe_3O_4). Sinter volume was decreased during the reduction of hematite to magnetite, which caused the microstructure of sinter dense (Biswas, 1981). This phenomenon is closely related to the improvement the overall sinter strength as shown by increase of Reduction Disintegration Index (Umadevi *et al*, 2012). Reduction behaviour of MgO in sintering process is similar to that of FeO because ionic radii of both cations are close. Panigrahy, Verstraeten and Dilewijns (1984) explained that MgO favours the formation of magnetite (Fe_3O_4) and Mg^{2+} ions replaced part of Fe^{2+} ions to stabilise the spinel structure. It implies that replacement of Fe^{2+} ions with Mg^{2+} ions can ensure the increase in excess Fe^{2+} content, which might contribute to the improvement of melting behaviour of iron ore sinter (Iwanaga, 1982; Ono-Nakazato, Sugahara and Usui, 2002; Lee *et al*, 2004; Chuang, Hwang and Liu, 2009).

In this study, combined addition of FeO- and MgO-bearing materials to sinter mix with high Al_2O_3 ore was investigated on the basis of reduction behaviour during sintering process. Mill-scale and calcined dolomite were selected to be the source of FeO and MgO, respectively. Mill-scale is FeO-based waste produced during hot-rolling and it is regarded as reusable by-product in both ironmaking and steelmaking process. Dolomite contains both CaO and MgO so melting behaviour control as well as fluxing effect can be expected through addition to high Al_2O_3 sinter. Calcination of dolomite was conducted to exclude the endothermic reaction on reduction process. Mineralogical analyses by X-ray diffraction (XRD) and Scanned electron microscopy (SEM-EDS) were employed to figure out how the combined addition of mill-scale and calcined dolomite interact and affect to the sinter microstructure. Physical properties of sinters were measured by Compression test and Reduction Disintegration Index (RDI) test to assess final sinter quality.

Materials preparation

All raw materials used in the study were supplied by POSCO, an industrial steelmaking company (Table 1). To produce standard sinter mix being used in general ironmaking industrial factory, two kinds of iron ores were prepared: Ore A and Ore B. Ore A is Goethite, FeO(OH)-based ore with high SiO_2 content and Loss on ignition (LOI). Ore B is high-grade hematite-based iron ore, containing low gangue content. Unlike these two iron ores, Ore C, which is typical pisolitic ore, was used as an Al_2O_3 source because it has been classified as a high-Al_2O_3 ore in several ironmaking companies. Dolomite was calcined at 1000°C before experiment.

TABLE 1

Chemical composition of raw materials (wt%).

Raw materials	T.Fe	M.Fe	FeO	Al_2O_3	CaO	SiO_2	MgO	MnO	P_2O_5	LOI
Ore A	57.00	0.07	0.17	1.59	0.06	5.39	0.08	0.02	0.08	10.38
Ore B	65.20	0.07	0.46	1.25	0.07	1.52	0.05	0.22	0.15	3.20
Ore C	57.10	0.06	0.20	3.14	0.04	5.35	0.05	0.03	0.14	8.59
Mill-scale	72.60	2.50	60.40	0.31	0.70	1.00	0.06	0.52	0.05	0.70
Calcined dolomite	-	-	-	-	56.19	-	38.78	-	-	2.53

To make uniform mixture, all samples were crushed under 50 μm and dried in oven for 24 hours. Ore A and Ore B were mixed with the mass ratio of 80 to 20 (Reference 1), which is simple blending of iron ores being typically utilised in actual ironmaking process. Reference 2 was prepared by mixing Ore A, Ore B and Ore C with the mass ratio of 48:12:40. Reference 2 has 2.31 wt per cent Al_2O_3 so that it is possible to compare it Reference 1 (1.76 wt per cent Al_2O_3) in terms of the adverse effect of Al_2O_3. Basicity, defined in this study as CaO/SiO_2, of two mixtures was adjusted to be 1.85 by adding a reagent-grade of CaO (purity 98 per cent) while mill-scale and calcined dolomite were added without considering basicity (Table 2). The sinter mixes were homogenised using a Turbula mixer for three hours and pressed into disk shape for 20 MP by a hydraulic work press machine.

TABLE 2

Calculated chemical composition of sinter mix with addition of mill-scale and calcined dolomite (wt%).

Sample	T.Fe	M.Fe	FeO	Al_2O_3	CaO	SiO_2	MgO	MnO	P_2O_5	CaO/SiO_2
Ref 1	53.97	0.07	0.21	1.40	7.87	4.26	0.07	0.06	0.09	1.85
Ref 2	52.71	0.06	0.19	2.28	8.56	4.63	0.05	0.04	0.11	1.85
Mill5	53.66	0.17	3.06	2.19	8.18	4.45	0.05	0.06	0.11	1.85
Mill10	54.52	0.28	5.67	2.10	7.84	4.30	0.06	0.08	0.11	1.85
Mill15	55.30	0.38	8.05	2.02	7.53	4.15	0.06	0.10	0.10	1.85
Mill10-Dol2	53.54	0.28	5.57	2.06	8.64	4.22	0.70	0.08	0.10	2.05
Mill10-Dol4	52.61	0.27	5.47	2.02	9.41	4.15	1.33	0.08	0.10	2.27
Mill10-Dol6	51.70	0.27	5.37	1.99	10.16	4.07	1.93	0.08	0.10	2.50

Sintering process

A disk-shaped sinter mix was sintered in a vertical tube furnace. That is, it was sintered while heating for seven mins in a furnace at 1280°C by preliminary experiment to optimise the fraction of SFCA phase. SFCA is abbreviation of Silico-Ferrite of Calcium and Aluminium, which is bonding phase in iron ore sinter as complex form of Calcium ferrite ($CaO{\cdot}Fe_2O_3$). This phase is known as desirable for high reducibility and sinter strength of iron ore sinter (Nicol *et al*, 2018). After heating, the sinter was cooled down inside the furnace for 30 mins. Heating was conducted in an atmosphere consisting of CO, CO_2 and Ar with the ratio of 2:23:75 to maximise the formation of bonding phases according to Hsieh and Whiteman (1989).

Materials characterisation

All sinters were crushed to 500 μm and analysed by X-ray diffraction (XRD) using wavelength of 1.63Å (Cu-Kα) in the scanning range of 20 to 80°. Then, the sinter was mounted by cold resin and polished up to 1 μm grain size to employ Scanning electron microscopy (SEM). Elemental Dispersive (EDS) X-ray spectrometry was carried out to evaluate the elemental composition of each phase detected by XRD.

To assess the reduction behaviour of sinter, Compression Test and Reduction Disintegration Index (RDI) Test were performed. Compression Test was executed by Instron M5548 machine to characterise the superficial strength of sinter, measuring the maximum compressive load after gradual compression (Zhang *et al*, 2015). RDI Test was performed based on the international standard (ISO 4696-2:2015) Ten disk-shaped sinters were heated at 550°C for 30 mins in an atmosphere of 30 vol per cent CO and 70 vol per cent N_2 in a gold image furnace. After heating, the sinters were rotated inside Turbula Mixer at 60 rev/min for 15 mins. $RDI_{-2.8}$ was evaluated based on the weight of sinters retained on the 2.8 mm sieve. Reduction degree was calculated to describe the reducibility of a sinter based on ISO 7215:2015 where the sinter was heated at 900°C for three hours in an atmosphere 30 vol per cent CO and 70 vol per cent N_2 gas atmospheres in a gold image furnace.

RESULTS

Effect of adding mill-scale to sinter mix containing high Al_2O_3 ore on sinter quality

Mill-scale was added to Reference 2 up to 15 wt per cent to evaluate the effect of FeO-bearing materials on sinter mix containing high Al_2O_3. Three phases were mainly identified by X-ray diffraction (Figure 1): hematite (Fe_2O_3), magnetite (Fe_3O_4) and SFCA ($Ca_{2.3}Mg_{0.8}Al_{1.5}Fe_{8.3}Si_{1.1}O_{20}$). Existence of high Al_2O_3 ore in the sinter did not show a meaningful difference in case XRD patterns

of Reference 1 and Reference 2 were compared. As two sinters showed similar XRD patterns, iron ore sinter manufactured by blending high Al_2O_3 ore in this study is under acceptable range in a view of phase development. This is connected to the previous study that low Al_2O_3 content in the sinter showed positive effect on SFCA formation (Scarlett *et al*, 2004; Webster *et al*, 2012), rather than contribution to the formation of slag phase. Hematite was dominant among the phases of all the sinters while magnetite was drastically increased as 10 wt per cent of mill-scale was added to Reference 2 (Mill10), eventually exceeding the hematite at 15 wt per cent addition (Mill15). Although hematite and magnetite shared the same peak at 33~34° and 62.5~63.5° in the scanning range, the portion of magnetite in the peak intensity is dominant in Mill15. In addition, the fraction of SFCA was barely changed up to Mill10, but it was decreased at Mill15. FeO in mill-scale is helpful to form bonding phases combined with Ca, Si and Al, but excess Fe^{2+} prevents the formation of SFCA because reducing atmosphere is induced during sintering process (Wang *et al*, 2016). At reducing atmosphere, FeO dissolves into Fe_2O_3 to form magnetite. From reason that phase composition with sufficient SFCA and hematite phase is maintained, mill-scale addition can be optimised as 10 wt per cent into high Al_2O_3 sinter.

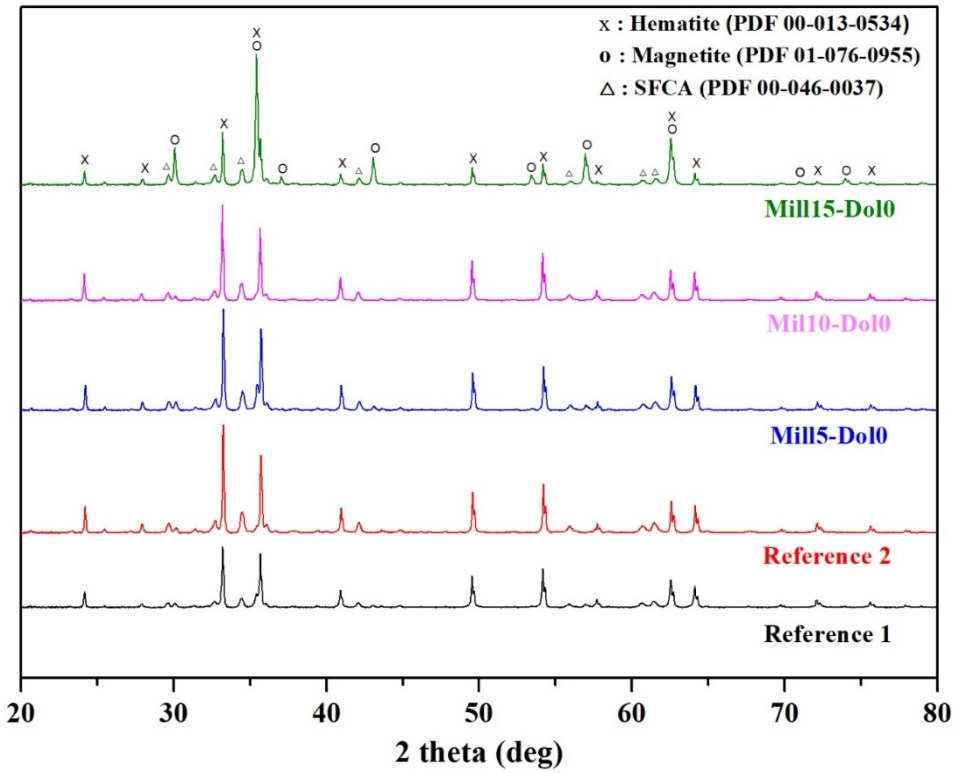

FIG 1 – Phase identification of the sinters to which mill-scale was added by X-ray diffraction.

Figure 2 is the backscattered electron images of the sinters with increasing added amount of mill-scale and EDS results of the selected points at Figure 2 is shown in Table 3. White grains composed of hematite occupied the sinter matrix (Point 1, 3, 5, 7) and grey SFCA were partly observed as the acicular form (Point 4, 6, 8) or columnar form (Point 2, 6, 10). When 5 wt per cent and 10 wt per cent of mill-scale was added, sinters maintained their microstructure and the ratio of hematite and SFCA was consistent from Reference 2. Meanwhile, the fraction of Fe was largely increased at Point 9 in Mill15, indicating that magnetite possessed more area than hematite. Acicular and columnar texture were decomposed as more Fe was diffused into magnetite matrix and the boundaries between magnetite and SFCA were observed to be blurred. It is clearly indicated at Point 10, which portion of Fe in SFCA phase was notably increased compared to that at Point 6 and Point 8. It is not recommended for overall sinter quality, since the irregular morphology of SFCA is detrimental for reducibility and cold strength of iron ore sinter (Ying, Jiang and Xu, 2006; Takayama, Murao and Kimura, 2018).

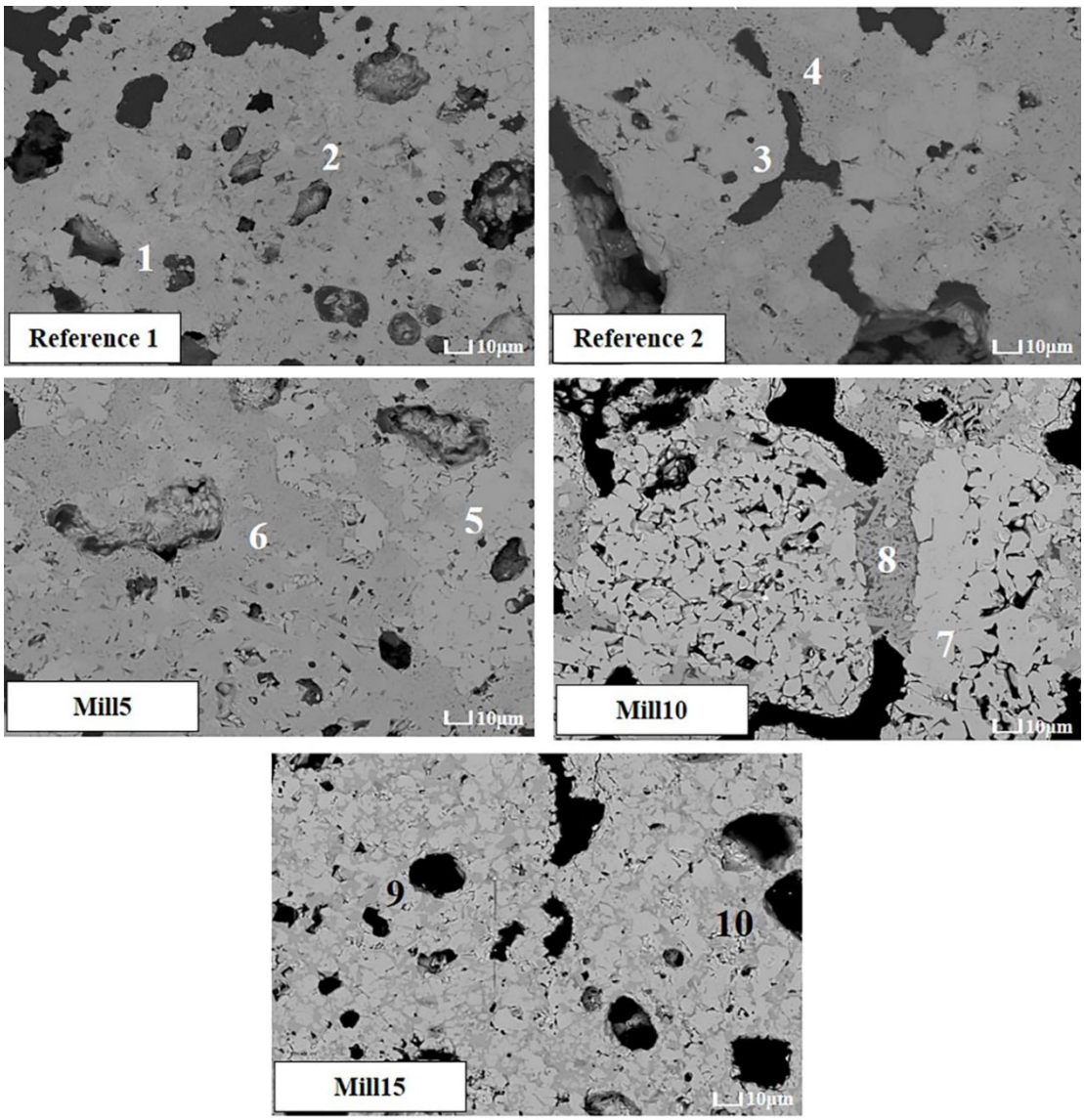

FIG 2 – Morphological features of the sinters to which mill-scale was added.

TABLE 3

Elemental distribution of selected points in the sinters to which mill-scale was added (at%).

Sinters	Pts	Elemental composition						Identified phases
		Fe	Ca	Si	Al	Mg	O	
Reference 1	1	37.15	0.14	0.13	0.49	-	62.09	Fe_2O_3
	2	33.81	4.10	2.69	1.87	-	57.53	SFCA
Reference 2	3	37.93	0.16	0.05	0.55	-	61.23	Fe_2O_3
	4	26.17	7.95	3.29	2.42	-	59.86	SFCA
Mill5	5	34.93	2.29	0.91	0.48	-	61.39	Fe_2O_3
	6	29.74	8.45	3.45	3.15	-	55.26	SFCA
Mill10	7	36.89	0.51	0.31	1.43	-	60.85	Fe_2O_3
	8	31.34	7.75	3.29	2.35	-	55.29	SFCA
Mill15	9	42.28	0.05	0.12	0.38	-	57.16	Fe_3O_4
	10	23.79	8.34	5.26	3.71	-	58.91	SFCA

Figure 3a depicts the reduction behaviour of the sinters as mill-scale was added to the sinter mix. Reduction degree was slightly decreased as high Al_2O_3 ore was blended, which is affected by Al_2O_3 content (Umadevi *et al*, 2009; Sinha *et al*, 2017). In case mill-scale was added to sinters, reduction degree was firstly increased at Mill5, but decreased then. Even it showed lower reducibility than that of Reference 2. It is obvious that FeO acted as a strong factor affecting the decrease in the reduction degree of sinters by increasing portion of magnetite in the sinter. These can be also applied into the change in compressive load and $RDI_{-2.8}$ of the sinters as shown in Figure 3b. For Reference 2, compressive load was decreased while $RDI_{-2.8}$ was increased compared to those of Reference 1. Both trends showed clear improvement after adding mill-scale. Several researchers have already reported that magnetite has a potential to prevent the low-temperature degradation (Umadevi *et al*, 2012; An, 2022), so adding mill-scale into high Al_2O_3 sinter can be the solution of reduction degradation.

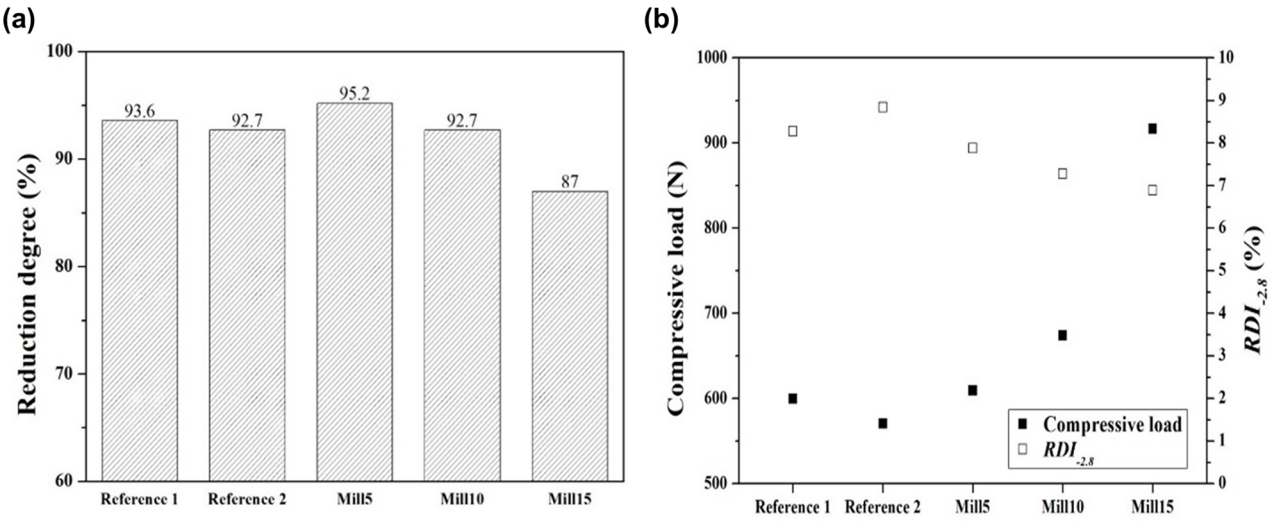

FIG 3 – (a) Change in reduction degree of the sinters to which mill-scale was added; (b) Change in strength and disintegration behaviour of the sinters to which mill-scale was added.

Combined effect of adding mill-scale and calcined dolomite to sinter mix containing high Al_2O_3 ore on sinter quality

Based on the obtained results in the previous section, calcined dolomite was added to the sinter mix (Mill10) up to 6 wt per cent. As shown in Figure 4, three major phases were identified as similar to the case in Figure 2, however, magnesio-ferrite ($MgO{\cdot}Fe_2O_3$) was mainly observed instead of magnetite at identical peaks. It is required to be considered that several Mg^{2+} ions diffused into magnetite and replaced the Fe^{2+} sites since the cations of Mg^{2+} and Fe^{2+} have the similar ionic radius (Panigrahy, Verstraeten and Dilewijns, 1984). In addition, the fraction of SFCA was maintained at Mill10-Dol2, but it was gradually decreased as more than 4 wt per cent of calcined dolomite was added (Mill10-Dol4). Magnesio-ferrite was increased and became dominant at Mill10-Dol6. The portion of magnesio-ferrite was largest among all other sinters in this study although the total amount of FeO and MgO was lower than that in Mill15. That is, the effect of adding calcined dolomite on the stabilisation of this magnesio-spinel structure was more remarkable than that of adding mill-scale.

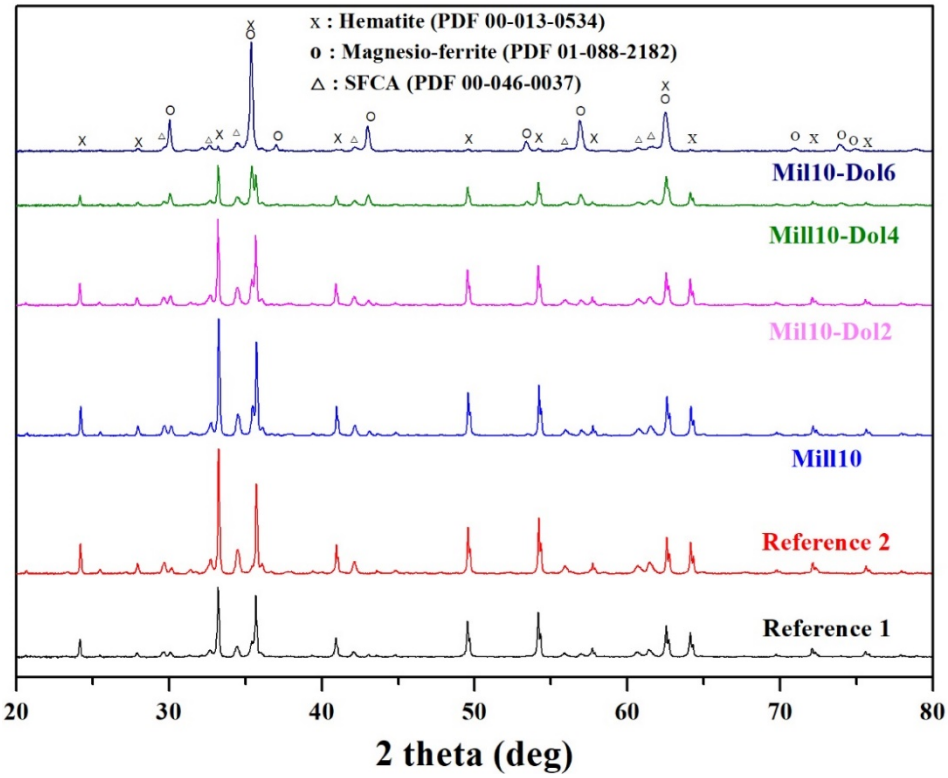

FIG 4 – Phase identification of the sinters to which mill-scale and calcined dolomite were added by X-ray diffraction.

Figure 5 shows the backscattered electron images of the sinters when mill-scale and calcined dolomite were added. Mg was found to be distributed in Fe-enriched regions of all the sinters containing calcined dolomite. EDS results of the selected points at Figure 5 is shown in Table 4. Mill10-Dol2 showed similar morphology to that of the sinter not containing dolomite (Mill10), but residual MgO in hematite matrix was concentrated at Mill10-Dol4 and Mill10-Dol6, which was indicated at Point 8. Residual MgO was surrounded by magnesio-ferrite (Point 9) and calcium silicate (Point 10) while other regions without MgO segregation showed typical microstructure consisting of magnesio-ferrite (Point 5) and SFCA (Point 7). Higuchi, Tanaka and Sato (2007) found similar phenomenon that rim structure consisting of magnetite solid solution was formed by the interaction between MgO and hematite or calcium ferrite, which is similar to the morphology of Mill10-Dol6 in Figure 5. Also, Al_2O_3 preferred to be absorbed into SFCA (Point 2, 4, 7) except Point 10. As addition of calcined dolomite was expanded, more Al_2O_3 became remained in Calcium silicate and caused the increase of slag phase.

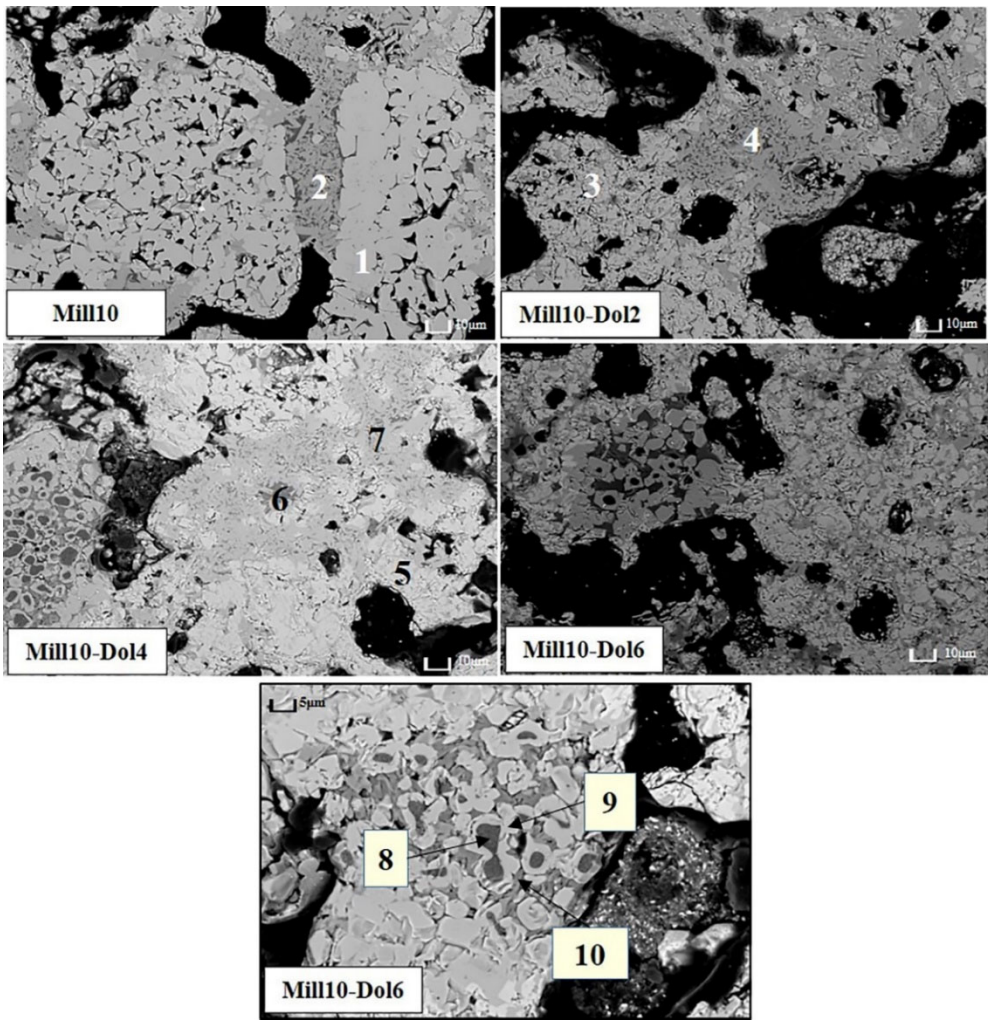

FIG 5 – Morphological features of the sinters to which mill-scale and calcined dolomite were added.

TABLE 4

Elemental distribution of selected points in the sinters to which mill-scale and calcined dolomite were added (at%).

Sinters	Pts	Elemental composition						Identified phases
		Fe	Ca	Si	Al	Mg	O	
Mill10	1	36.89	0.51	0.31	1.43	-	60.85	Fe_2O_3
	2	31.34	7.75	3.29	2.35	-	55.29	SFCA
Mill10-Dol2	3	37.88	1.32	0.25	0.89	0.94	58.72	Fe_2O_3
	4	23.71	7.77	4.63	2.47	0.25	61.16	SFCA
Mill10-Dol4	5	26.13	0.81	0.19	1.37	12.28	59.21	Fe_2O_3, $MgO·Fe_2O_3$
	6	1.47	21.31	14.88	0.50	0.12	61.73	$2CaO·SiO_2$, $CaO·SiO_2$
	7	25.81	7.43	3.50	2.93	0.54	59.80	SFCA
Mill10-Dol6	8	4.47	0.25	0.19	0.08	44.13	50.88	MgO
	9	28.08	0.72	0.21	2.27	12.09	56.63	$MgO·Fe_2O_3$
	10	3.95	14.84	12.32	3.09	4.03	61.77	$CaO·SiO_2$

Figure 6 show relationship between portion of magnetite and sinter strength of sinters when calcined dolomite was added together with mill-scale. There was no significant difference in reduction degree when calcined dolomite was added 2 wt per cent into Mill10, but it was declined from 4 wt per cent addition. Reduction degree in Mill10-Dol6 was calculated as 69.6 per cent, which is not suitable in industrial sintering process (Umadevi *et al*, 2014). Both compressive load and $RDI_{-2.8}$ were worsened compared to those of Mill10, but it changed to be improved along the calcined dolomite addition. Calcined dolomite seems to be acted as same as mill-scale to improve sinter strength and reduction degradation of high Al_2O_3 sinter, but further explanation is required to determine the individual role of calcined dolomite separated from that of mill-scale.

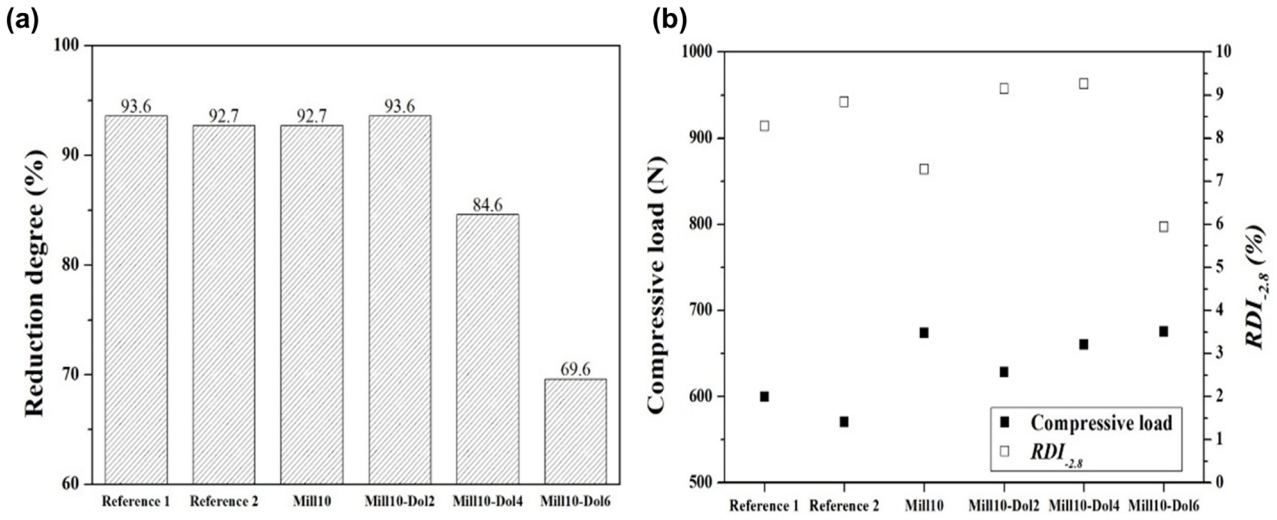

FIG 6 – (a) Change in reduction degree of the sinters to which mill-scale and/or calcined dolomite were added; (b) Change in strength and disintegration behaviour of the sinters to which mill-scale and/or calcined dolomite were added.

DISCUSSION

To clarify the mechanism of phase development of high Al_2O_3 sinter when mill-scale and calcined dolomite was added, the elemental distribution of Mill10-Dol6 was specified by EDS mapping as shown in Figure 7. The clusters consisting of Mg were surrounded by reddish part comprising Mg and Fe. MgO remained unreacted rather than forming magnesio-ferrite in the sintering process in case the large amount of calcined dolomite was added. It is clear that there is certain limitation in the dissolution of MgO into magnetite matrix. Or the relict MgO with high sintering temperature will block the further assimilation of bonding phases, further act as harmful to overall sinter qualities such as reducibility and toughness (Han *et al*, 2019; Shi *et al*, 2020). In case of Ca and Si, they were locally concentrated around MgO segregation and formed slag phase indicated by blue part. Excessive CaO supplied by calcined dolomite did not react with Fe to form Calcium Ferrite or SFCA. Instead, calcium silicate was formed in microstructure, so this slag phase would affect to the poor reducibility of high Al_2O_3 sinter.

Physical properties of high Al_2O_3 sinter with addition of mill-scale and calcined dolomite also can be explained based on phase development after iron ore sintering. Al was found to be homogeneously distributed in whole microstructure, respectively. It is desirable in terms of reduction degradation, since Al was reported to be entrapped in hematite matrix during reduction of hematite to magnetite (Sinha and Ramna, 2009; Umadevi *et al*, 2009) to induce lattice distortion. Since Al_2O_3 exists in between the lattices of hematite and magnetite and leads rapid crack propagation (Sinha and Ramna, 2009), even distribution of Al in microstructure has an advantage on relaxing this crack propagation by forming dense matrix (Umadevi *et al*, 2012). It is similar to the result of Zhu *et al* (2020), who found the decreased crack density of iron ore sinter to which MgO content was increased. MgO generally decreases the porosity of sinter (Umadevi *et al*, 2014) by stabilising the spinel structure of magnetite so called magnesio-spinel (Panigrahy, Verstraeten and Dilewijns, 1984). Magnesio-spinel phase changes the magnetite matrix dense to resist against external pressure, further contributes to the improvement of compressive strength of iron ore sinter. This effect is dominant in this study,

showing the increase of compressive load of iron ore sinter when calcined dolomite was utilised. However, MgO segregation should be considered in detail when controlling the addition of MgO-bearing material into high Al_2O_3 sinter. The portion of the phases where Al_2O_3 can diffuse would be decreased if the portion of MgO clusters is expanded. It implies the acceleration of reduction degradation caused by diffusion of Al into hematite-magnetite matrix. Thus, addition of calcined dolomite in high Al_2O_3 sinter in this study is recommended to be under 4 wt per cent to avoid MgO segregation shown in Figure 7.

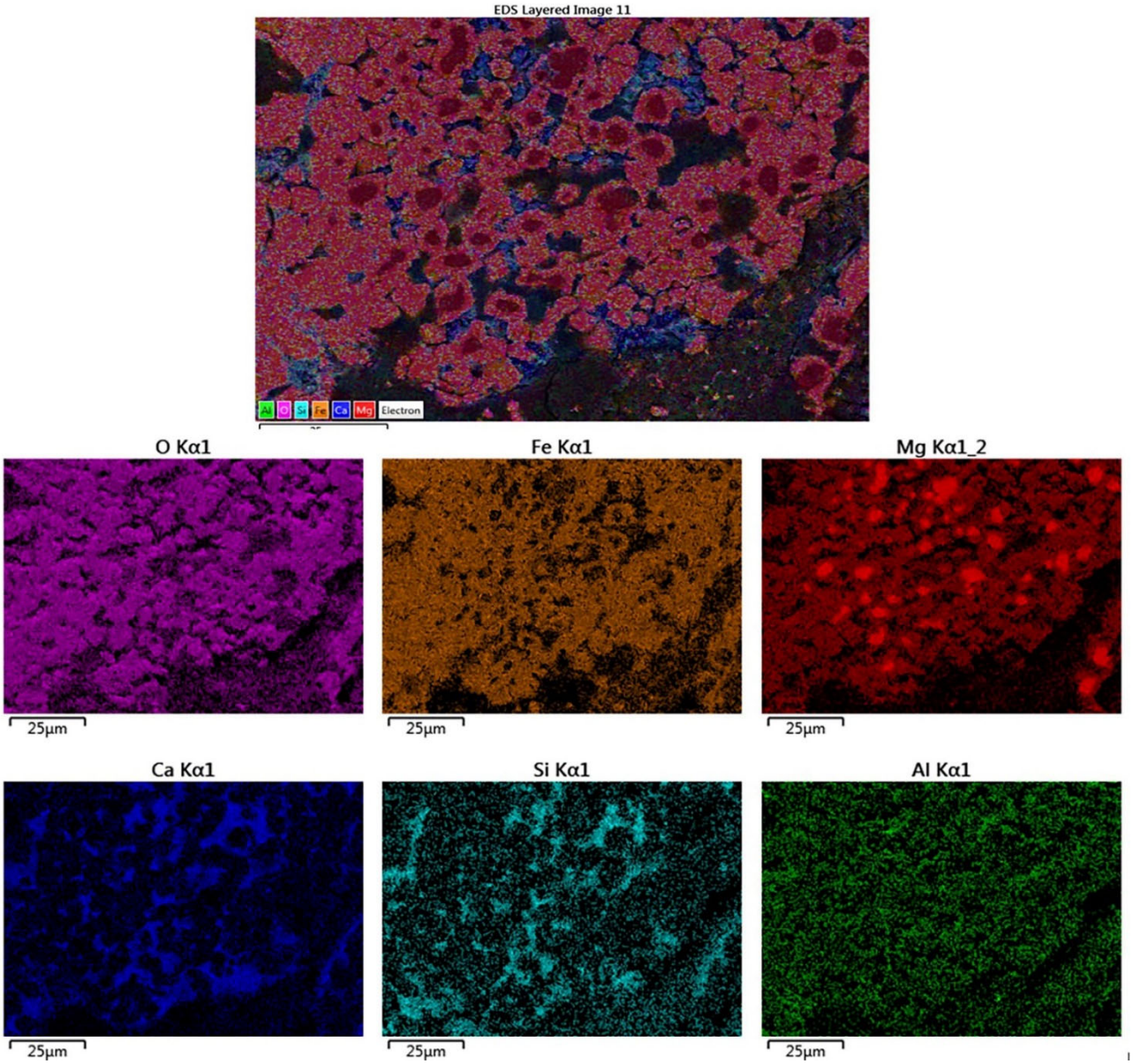

FIG 7 – Elemental distribution of selected area in the sinter to which 10 wt per cent of mill-scale and 6 wt per cent of calcined dolomite were added (Mill10-Dol6) by EDS mapping.

CONCLUSIONS

To clarify the combined effect of adding mill-scale and calcined dolomite to sinter mix containing high Al_2O_3 ore on sinter quality, the reduction behaviour of iron ore sinters was investigated. From the findings, the following conclusions were obtained:

- Magnetite became a dominant phase in the sinter with increasing mill-scale up to 15 wt per cent of mill-scale to sinter mix while magnesio-ferrite was formed instead of magnetite when calcined dolomite was added to sinter mix along with mill-scale. MgO stabilised the magnetite phase, so that magnesio-ferrite in iron ore sinter was remarkably increased while SFCA phase was decreased, respectively.

- Several MgO clusters were observed as a residue with adding more than 4 wt per cent of calcined dolomite to sinter mix. Due to the limitation in the dissolution of MgO into magnetite matrix, MgO remained unreacted in the sintering process, resulting in the suppression of bonding phases including calcium ferrite. In addition, CaO supplied by calcined dolomite formed Calcium silicate as slag phase rather than forming Calcium ferrite or SFCA.
- $RDI_{-2.8}$ and compressive load of the iron ore sinters were improved while their reduction degrees were decreased when adding mill-scale and calcined dolomite. Calcined dolomite can play a same role as mill-scale to stabilise the magnesio-spinel for improving sinter strength and reduction degradation. It has a strong advantage of utilisation of both FeO and MgO-bearing materials for counteracting the adverse effect of Al_2O_3 in high Al_2O_3 sinter, also decreasing FeO amount in final manufactured sinter. However, the total content of additives should be restricted under certain amount to avoid MgO segregation and maintain the overall sinter qualities.

ACKNOWLEDGEMENTS

The authors would like to thank Mr Sang Yeol Lee for help with preparation of experimental procedures.

REFERENCES

An, H, Shen, F, Jiang, X, Zhou, Y, Zheng, H and Gao, Q, 2022. Effects of Fine MgO-Bearing Flux on the Strength of Sinter before and after Low-Temperature Reduction, *ACS Omega*, 7:8686–8696.

Biswas, A, 1981. *Principles of Blast Furnace Ironmaking: Theory and Practice*, pp 105 (Cootha Publishing House: Brisbane).

Chai, Y, Yu, W, Zhang, J, An, S, Peng, J and Wang, Y, 2019. Influencing mechanism of Al_2O_3 on sintered liquid phase of iron ore fines based on thermal and kinetic analysis, *Ironmaking and Steelmaking*, 46:424–430.

Chuang, H, Hwang, W and Liu, S, 2009. Effect of Basicity and FeO Content on the Softening and Melting Temperatures of the CaO-SiO_2-MgO-Al_2O_3 Slag System, *Mater Trans*, 50:1448–1456.

Han, H, Shen, F, Jiang, X, Bi, C, Zheng, H and Gao, Q, 2019. Fundamental mechanism of effects of MgO on sinter strength, *J Iron Steel Res Int*, 26:1171–1177.

Higuchi, K, Naito, M, Nakano, M and Takamoto, Y, 2004. Optimization of Chemical Composition and Microstructure of Iron Ore Sinter for Low-temperature Drip of Molten Iron with High Permeability, *ISIJ Int*, 44:2057–2066.

Higuchi, K, Tanaka, T and Sato, T, 2007. Reaction Behaviour of Dolomite Accompanied with Formation of Magnetite Solid Solution in Iron Ore Sintering Process, *ISIJ Int*, 47:669–678.

Hsieh, L and Whiteman, J, 1989. Sintering Conditions for Simulating the Formation of Mineral Phases in Industrial Iron Ore Sinter, *ISIJ Int*, 29:24–32.

International Organization for Standardization (ISO), 2015a. ISO 4696-2:2015 – Iron ores for blast furnace feedstocks – Determination of low-temperature reduction-disintegration indices by static method – Part 2: Reduction with CO and N2, September 2015.

International Organization for Standardization (ISO), 2015b. ISO 7215:2015 – Iron ores for blast furnace feedstocks – Determination of the reducibility by the final degree of reduction index, August 2015.

Iwanaga, Y, 1982. Fundamental Study on the Softening Properties of Sinter by Measuring the Apparent Softening Viscosity, *Tetsu-to-Hagane*, 68:2223–2230.

Lee, Y, Min, D, Jung, S and Yi, S, 2004. Influence of Basicity and FeO Content on Viscosity of Blast Furnace Type Slags Containing FeO, *ISIJ Int*, 44:1283–1290.

Loo, C and Leung, W, 2003. Factors Influencing the Bonding Phase Structure of Iron Ore Sinters, *ISIJ Int*, 43:1393–1402.

Nicol, S, Chen, J, Pownceby, M and Webster, N, 2018. A review of the Chemistry, Structure and Formation Conditions of Silico-Ferrite of Calcium and Aluminum ('SFCA') Phase, *ISIJ Int*, 58:2157–2172.

Okazaki, J, Higuchi, K, Hosotani, Y and Shinagawa, K, 2003. Influence of Iron Ore Characteristics on Penetrating Behaviour of Melt into Ore Layer, *ISIJ Int*, 43:1384–1392.

Ono-Nakazato, H, Sugahara, C and Usui, T, 2002. Effect of Slag Components on Reducibility and Melt Formation of Iron Ore Sinter, *ISIJ Int*, 42:558–560.

Panigrahy, S, Verstraeten, P and Dilewijns, J, 1984. Influence of MgO Addition on Mineralogy of Iron Ore Sinter, *Metal Trans B*, 15:23–32.

Pimenta, H and Sechadri, V, 2002. Characterisation of structure of iron ore sinter and its behaviour during reduction at low temperatures, *Ironmaking and Steelmaking*, 29:169–174.

Scarlett, N, Pownceby, M, Madsen, I and Christensen, A, 2004. Reaction Sequences in the Formation of Silico-Ferrite of Calcium and Aluminum in Iron Ore Sinter, *Metal Mater Trans B*, 35:929–936.

Shi, B, Zhu, D, Pan, J, Liu, X and Li, S, 2020. Combined effect of MgO and basicity varied by different dolomite and burnt lime addition on sintering performance of magnetite concentrates, *Ironmaking and Steelmaking*, 47:567–573.

Sinha, M and Ramna, R, 2009. Effect of Variation of Alumina on the Microhardness of Iron Ore Sinter Phases, *ISIJ Int*, 49:719–721.

Sinha, M, Nistala, S, Chandra, S, Mankhand, T and Ghose, A, 2017. Correlating mechanism properties of sinter phases with their chemistry and its effect on sinter quality, *Ironmaking and Steelmaking*, 44:100–107.

Takayama, T, Murao, R and Kimura, M, 2018. Quantitative Analysis of Mineral Phases in Iron-ore Sinter by the Rietveld Method of X-ray Diffraction Patterns, *ISIJ Int*, 58:1069–1078.

Umadevi, T, Brahmacharyulu, A, Karthik, P, Mahapatra, P, Prabhu, M and Ranjan, M, 2012. Recycling of steel plant mill scale via iron ore sintering plant, *Ironmaking and Steelmaking*, 39:222–227.

Umadevi, T, Brahmacharyulu, A, Sah, R, Mahapatra, P and Prabhu, M, 2014. Optimisation of MgO addition in low and high silica iron ore sinter to improve sinter reducibility at JSW Steel Limited, *Ironmaking and Steelmaking*, 41:270–278.

Umadevi, T, Mahapatra, P and Prabhu, M, 2013. Influence of MgO addition on microstructure and properties of low and high silica iron ore sinter, *Miner Proc Extr Metall*, 122:238–248.

Umadevi, T, Nelson, K, Mahapatra, P, Prabhu, M and Ranjan, M, 2009. Influence of magnesia on iron ore sinter properties and productivity, *Ironmaking and Steelmaking*, 36:515–520.

Wang, Z, Maeda, T, Ohno, K and Kunitomo, K, 2020. Effect of Magnetite on Mineral Phase Formation in Sintering Process, *ISIJ Int*, 60:233–237.

Wang, Z, Pinson, D, Chewm, S, Monaghan, B, Pownceby, M, Webster, N, Rogers, H and Zhang, G, 2016. Effect of Addition of Mill Scale on Sintering of Iron Ores, *Metal Mater Trans B*, 47:2848–2860.

Webster, N, Pownceby, M, Madsen, I and Kimpton, J, 2012. Silico-ferrite of Calcium and Aluminum (SFCA) Iron Ore Sinter Bonding Phases: New Insight into Their Formation During Heating and Cooling, *Metal Mater Trans B*, 43:1344–1357.

Xue, Y, Pan, J, Zhu, D, Guo, Z, Yang, C, Lu, L and Tian, H, 2020. Improving High-Alumina Iron Ores Processing via the Investigation of the Influence of Alumina Concentration and Type on High-Temperature Characteristics, *Minerals*, 10:1–26.

Xiao, Z, Chen, L, Yang, Y, Li, X and Barati, M, 2017. Effect of Coarse-grain and Low-grade Iron Ores on Sinter Properties, *ISIJ Int*, 57:795–804.

Yadav, U, Pandey, B, Das, B and Jena, D, 2002. Influence of magnesia on sintering characteristics of iron ore, *Ironmaking and Steelmaking*, 29:91–95.

Yamaoka, Y, Nagaoka, S, Yamada, Y and Ando, R, 1974. Effect of Gibbsite on Sintering Property and Sinter Quality, *Transaction ISIJ*, 14:185–194.

Yang, L, 2005. Sintering Fundamentals of Magnetite Alone and Blended with Hematite and Hematite/Goethite Ores, *ISIJ Int*, 45:469–476.

Ying, Z, Jiang, M and Xu, L, 2006. Effect of Mineral Composition and Microstructure on Crack Resistance of Sintered Ore, *Journal of Iron and Steel Research, International*, 13:9–12.

Zhang, G, Wu, S, Que, Z, Hou, C and Jiang, Y, 2015. Influencing factor of sinter body strength and its effects on iron ore sintering indexes, *Int J Min Metal Mat*, 22:553–561.

Zhu, D, Xue, Y, Pan, J, Yang, C, Guo, Z, Tian, H, Wang, D and Shi, Y, 2020. An investigation into alumina occurrence impact on SFCA formation and sinter matrix strength, *J Mater Res Tech*, 9:10223–10234.

Slag-metal interfacial reactions in pyrometallurgical processing of industrial wastes for recovery of valuable metals

DOI: 10.62053/XMOA4398

H J Kim[1], R R Kim[2], H S Park[3] and J H Park[4]

1. Student, Department of Materials Science and Chemical Engineering, Hanyang University, Ansan 15588, South Korea. Email: kimhyunju1158@naver.com
2. Student, Department of Materials Science and Chemical Engineering, Hanyang University, Ansan 15588, South Korea. Email: krr0432@naver.com
3. Senior Researcher, Korea Institute of Geoscience and Mineral Resources (KIGAM), Daejeon 34132, South Korea. Email: hyunsik.park@kigam.re.kr
4. Professor, Department of Materials Science and Chemical Engineering, Hanyang University, Ansan 15588, South Korea. Email: basicity@hanyang.ac.kr

ABSTRACT

This study focuses on the recovery of valuable metals, specifically silver (Ag) and palladium (Pd), from copper-containing sludge (with copper content less than 20 per cent) generated during PCB processing and from spent petrochemical catalysts used in vapour decomposition during oil refining processes. The present results indicate that an increase in the mixing ratio of alumina-based spent catalyst leads to a decrease in the recovery rate of Ag and Pd. The recovery rates for Ag and Pd range from 84 per cent to 96 per cent and 80 per cent to 98 per cent, respectively. This trend is attributed to the increased emulsification of copper droplets containing Ag and Pd in the slag. The emulsification is caused by the decrease in the settling velocity of the copper droplets due to the increased viscosity of the slag as well as by the decrease in the slag-metal interfacial tension due to an increase in sulfur content at higher mixing ratio of spent catalyst.

INTRODUCTION

Wasted printed circuit boards (WPCBs) are components of electronic waste that contain high concentrations of precious metals, such as gold (Au) and silver (Ag), exceeding average ore concentrations by 20 to 30 times (Ebin and Isik, 2016). Similarly, in the petrochemical industry, catalysts rich in precious metals like platinum group metals (PGMs) such as Pt, Pd and Rh exhibit concentrations approximately five times higher than those found in natural resources (Ghalehkhondabi, Fazlali and Daneshpour, 2021). The rise in industrial waste has a negative impact on the environment, but it also presents opportunities for extracting valuable metals and raw materials.

Several studies have been conducted on the recovery of metals from industrial wastes. Kim *et al* (2004) developed smelting processes that extract precious metals, such as Au, Pd and Pt, through mixing PCBs and auto catalysts. Up to 90 per cent of Au, Pd and Pt in the raw materials were concentrated in a Cu-Sn alloy phase. Kwon, Han and Jeong (2005) and Shin *et al* (2008) conducted similar experiments and reported that for the efficient recovery of valuable metals, it is advantageous to use fluxes that can lower the melting point and viscosity of the slag.

Therefore, in the present study, we aim to determine the optimal slag conditions for the recovery of valuable metals through the CaO-Al_2O_3 based slag system, which is generated when the spent petrochemical catalyst and copper sludge were employed as raw materials. Several factors (eg basicity, viscosity and interfacial tension) influencing the recovery efficiency of valuable metals were discussed.

EXPERIMENTAL PROCEDURE

The compositions of the raw materials for valuable metal extraction, ie copper sludge and spent petrochemical catalysts, were analysed using an X-ray diffraction (XRD), Inductively Coupled Plasma – Atomic Emission Spectroscopy (ICP-AES) (ACROS, Spectro) and combustion analyser (CS800, ELTRA). The results are presented in Table 1.

TABLE 1

Composition of copper sludge and spent petrochemical catalysts (wt%).

	Al_2O_3	$CaCO_3$	Cu_2O	Fe_2O_3	SnO_2	P_2O_5	SiO_2	MgO	C	S	Ag	Pd
Copper sludge	0.7	29.9	24.7	22.3	6.7	3.5	2.6	1.7	5.6	2.4	0.01	-
Spent catalyst	99.7	-	-	-	-	-	-	-	-	-	-	0.3

When blending the Al_2O_3-based spent catalyst and copper sludge, the mixing ratio of the spent catalyst was varied from 10 per cent to 30 per cent. Here, the mixing condition aims to limit the Al_2O_3 content not more than 30 wt per cent to prevent an abrupt increase in melting point of the slag. Three experiments were carried out using a high frequency induction furnace (Figure 1). A mixture of 100 g raw materials (copper sludge and spent petrochemical catalyst) and 60 g copper powder (to form collecting melt pool) were loaded in a fused magnesia crucible with a graphite heater for efficient heating. The furnace was filled with purified Ar gas controlled by a mass flow controller at a flow rate 500 mL/min. After the equilibration for 60 min at 1773 K, the samples were cooled under an Ar gas atmosphere.

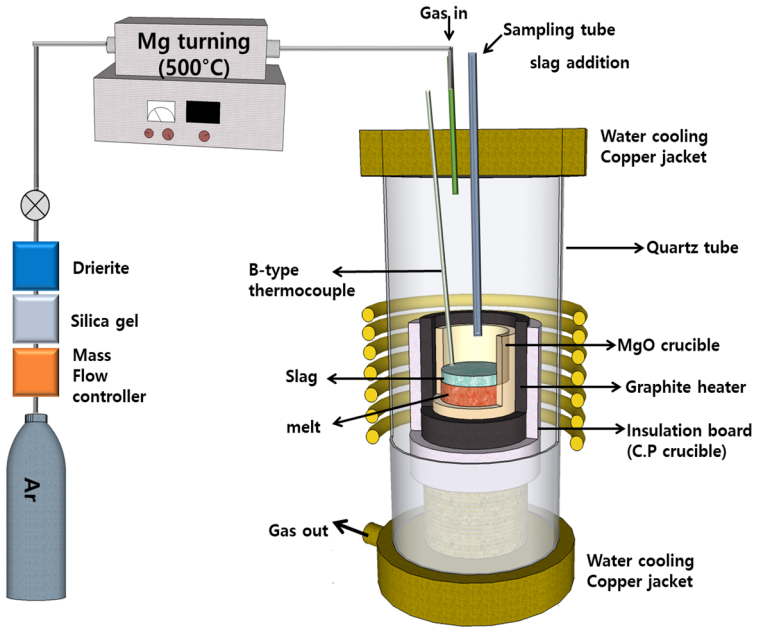

FIG 1 – Schematic diagram of the experimental apparatus.

RESULTS AND DISCUSSION

After experiments, the slag and metal were carefully separated from the crucible. the interface between the metal and slag was clearly defined and allowed a complete separation.

The slag was ground to a fine powder for chemical analysis. The equilibrium composition of the slag was analysed by ICP-AES (OPTIMA 8300; PerkinElmer, Waltham, MA) and combustion analyser (TC-300, LECO). The results of all experiments are represented in Figure 2. Metal droplets and oxides in the slag were observed by using Field Emission – Scanning Electron Microscope (FE-SEM) and Energy Dispersive X-ray Spectroscopy (EDS) (Nova Nano SEM 450, FEI).

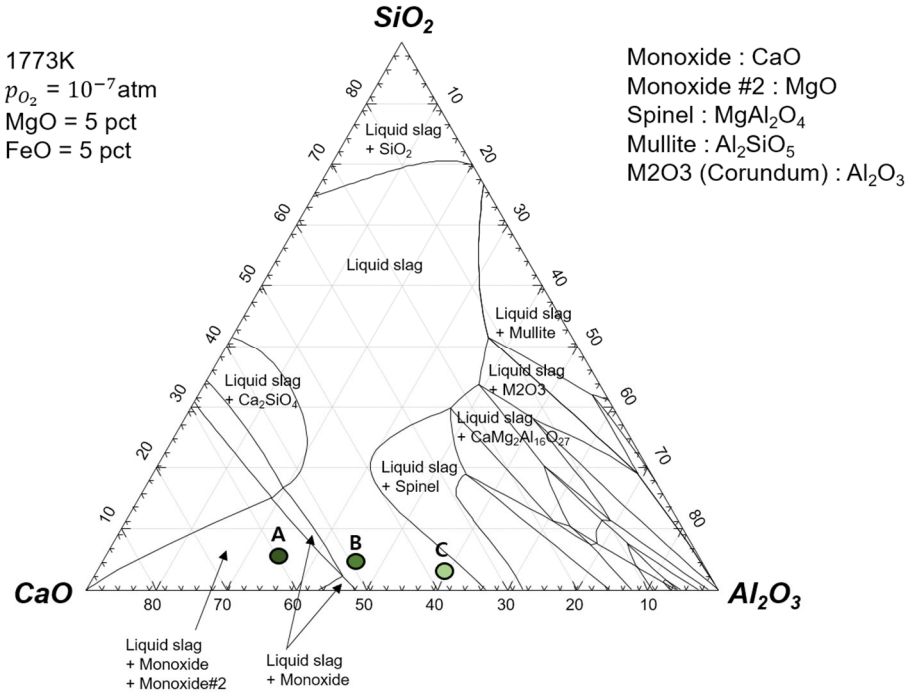

FIG 2 – The 1773 K isotherm in the CaO-SiO_2-Al_2O_3 slag system (wt per cent) (A, B and C represent the final slag compositions with spent catalyst ratios of 10 per cent, 20 per cent and 30 per cent).

As shown in Table 2, the vertical section of metal ingots obtained from the experiments with 20 per cent and 30 per cent spent catalyst, both Cu-rich (yellow) and Fe-rich (grey) phases are present, while the only Cu-rich ingot is produced from the 10 per cent catalyst experiment. However, Ag and Pd have a high solubility in copper phase, representing that they exist in the Cu-rich phase. The recovery rate was calculated using the following formula (Lee *et al*, 2010).

$$\text{Recovery rate of M}(=\text{Ag, Pd})\ (\%) = \frac{Recovered\ amount\ of\ M\ in\ metal\ ingot\ (g)}{Total\ content\ of\ M\ in\ raw\ materials\ (g)} \times 100 \quad (1)$$

TABLE 2

Morphology of metal and slag separated after smelting experiments.

	10% spent catalyst	20% spent catalyst	30% spent catalyst
Metal ingot			
Cross-section of ingot			
Slag			

As the alumina content increases, which indicates an increase in the spent catalyst mixing ratio, the rate of recovery of Ag and Pd significantly decreases, as shown in Figure 3a. Figure 3b and 3c illustrate the presence of copper droplets confined to the slag formed during 30 per cent spent catalyst experiment, indicating the incomplete metal separation. Therefore, physical entrainment of copper droplets is the primary cause of copper loss as well as lower recovery rate of Ag and Pd.

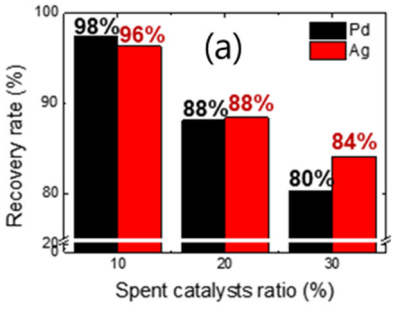

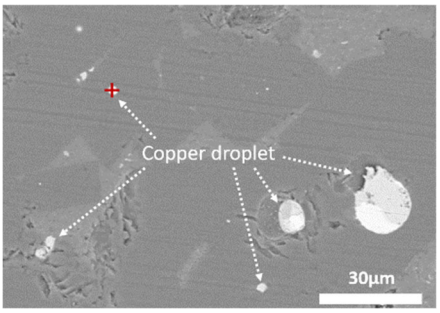

Element	At. No.	Mass [%]	Mass Norm. [%]	Atom [%]
Al	13	2.35	2.75	6.94
Ca	20	0.91	1.06	1.80
Fe	26	0.71	0.83	1.01
Pd	46	4.90	5.74	3.67
Sn	50	15.75	18.46	10.57
Cu	29	60.46	70.88	75.84
Ag	47	0.23	0.27	0.17
		85.31	**100.00**	**100.00**

(a) (b) (c)

FIG 3 – (a) Recovery rate of valuable metals as a function of spent catalysts ratio, (b) SEM image and (c) EDS result of copper droplets confined to the slag (30 per cent catalyst experiment).

In the present study, the terminal velocity of copper droplets in the slag was calculated. It was assumed that copper droplets in the slag were spherical in shape. The force balance among gravity, buoyancy and frictional forces on particles was taken into account. Assuming a Stokes regime due to no intentional stirring in the slag, the terminal velocity of metal droplet can be described by Equation 2 (Poirier and Geiger, 1994).

$$v_t = \frac{2}{9}\frac{r^2(\rho_m - \rho_s)g}{\eta} \text{ (m/s)} \quad (2)$$

From Figure 4, a decrease in the C/A ratio of the slag increases the viscosity, which reduces the settling velocity of copper droplets in the slag. As a result, the recovery rate of Ag and Pd decreases. Therefore, it is crucial to precisely control the settling velocity of copper droplets to maximise the recovery of valuable metals.

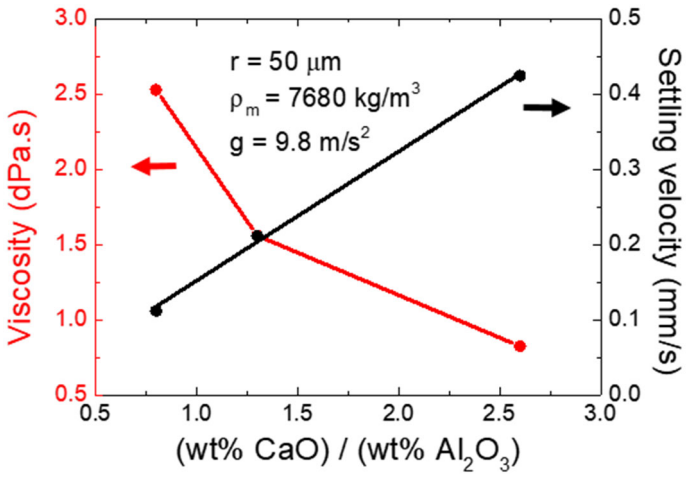

FIG 4 – Relationship between viscosity and settling velocity as a function of the CaO/Al_2O_3 ratio.

CONCLUSIONS

Loss of valuable metals due to physical entrainment means that copper droplets were not settled down completely but rather dispersed in the slag layer during smelting process. To quantitatively evaluate the physicochemical behaviour of slag-metal interfacial phenomena, the interfacial tension of the slag-metal system and settling velocity of copper droplets was estimated. As the interfacial tension and settling velocity decrease with higher mixing ratio of spent catalyst, the higher the probability of copper droplets in the slag, resulting in a decrease of the recovery rate of valuable metals.

REFERENCES

Ebin, B and Isik, M I, 2016. Pyrometallurgical processes for the recovery of metals from WEEE, *WEEE recycling*, pp 107–137.

Ghalehkhondabi, V, Fazlali, A and Daneshpour, F, 2021. Electrochemical extraction of palladium from spent heterogeneous catalysts of a petrochemical unit using the leaching and flat plate graphite electrodes, *Separation and Purification Technology*, 258:117527.

Kim, B S, Lee, J C, Seo, S P, Park, Y K and Sohn, H Y, 2004. A process for extracting precious metals from spent printed circuit boards and automobile catalysts, *JOM*, 56:55–58.

Kwon, E H, Han, J W and Jeong, J K, 2005. Melting of PCB scrap for the Extraction of Metallic Components, *Korean Journal of Materials Research*, 15(1):31–36.

Lee, B D, Jung, H J, Baek, U H, Hong, S H, Han, J W, Yoo, B D and Lee, J C, 2010. Recovery of Valuable Metals Using Pyrometallurgical Treatment, *Journal of the Korean Society of Mineral and Energy Resources Engineers*, 47(5):628–646.

Poirier, D R and Geiger, G H, 1994. Transport phenomena in materials processing, *The Minerals, Metals and Materials Society*, 5(2.1).

Shin, D Y, Lee, S D, Jeong, H B, You, B D, Han, J W and Jung, J K, 2008. Pyro-metallurgical Treatment of used OA Parts for the Recovery of Valuable Metals, *Resources Recycling*, 17(2):46–54.

Towards integration of pyro- and hydrometallurgical unit operations for efficient recovery of battery metals from waste lithium-ion batteries

DOI: 10.62053/EURL8600

L Klemettinen[1], J Biswas[2], A Klemettinen[3], J Zhang[4], H O'Brien[5], J Partinen[6] and A Jokilaakso[7]

1. Staff Scientist, Aalto University, Department of Chemical and Metallurgical Engineering, 00076 Aalto, Finland. Email: lassi.klemettinen@aalto.fi
2. Assistant Professor, IIT Bombay, Powai, Mumbai, Maharashtra 400076, India. Email: biswasj@iitb.ac.in
3. University Teacher, Aalto University, Department of Chemical and Metallurgical Engineering, 00076 Aalto, Finland. Email: anna.klemettinen@aalto.fi
4. Associate Professor, Wuhan University of Science and Technology- The State Key Laboratory of Refractories and Metallurgy, Wuhan 430081, Hubei, PR China. Email: zhangjuhua@wust.edu.cn
5. Senior Researcher, Geological Survey of Finland, 02150 Espoo, Finland. Email: hugh.obrien@gtk.fi
6. Doctoral Researcher, Aalto University, Department of Chemical and Metallurgical Engineering, 00076 Aalto, Finland. Email: jere.partinen@aalto.fi
7. Associate Professor, Aalto University, Department of Chemical and Metallurgical Engineering, 00076 Aalto, Finland. Email: ari.jokilaakso@aalto.fi

ABSTRACT

Waste lithium-ion batteries (LIBs) are important secondary sources of many valuable materials, including Critical Raw Materials (CRMs) defined by the European Union (EU): lithium, cobalt, manganese, and graphite. Additionally, LIBs typically contain nickel and copper, which are classified as Strategic Raw Materials for EU since 2023. In recent years, great effort has been made to develop efficient recycling processes for waste LIBs. Pyrometallurgical processes have been essential in industrial production of metals for many decades. These technologies are relatively mature, with high adaptability for different raw materials. Pyrometallurgical treatment in LIB recycling typically involves the use of smelting processes, in which waste batteries are heated above their melting points and metals are separated through a reduction reaction in the liquid phase. Through this recycling route, cobalt, copper, and nickel can be efficiently recovered in the form of a metal alloy, whereas lithium and manganese are lost in the slag phase.

The goal of this work was to increase the recoveries of valuable battery metals through a combination of hydro- and pyrometallurgical unit operations. First, industrial Li-ion battery scrap underwent a selective sulfation roasting stage, where the aim was to transform $LiCoO_2$ and Mn-oxides into Li, Co and Mn sulfates. After roasting, the battery scrap was leached in distilled water with a solid to liquid ratio of 100 g/L at 60°C and recovered 95 per cent of Li, 61 per cent of Mn and 35 per cent of Co. After leaching, the solid leach residue was mixed with industrial Ni-slag and biochar, followed by reduction at 1350°C in argon atmosphere. The high-temperature smelting experiments were conducted as a function of time (5–60 mins) to investigate the reduction behaviour of battery metals. The results show that Co and Ni from the slag and leach residue can be efficiently recovered in the slag cleaning stage.

INTRODUCTION

Lithium-ion batteries (LIBs) have become extremely important for portable electronics, green energy technologies, electric vehicles, and energy storage systems. Consequently, research related to batteries has drastically increased over last decade (Li *et al*, 2018). Researchers from all over the world are focusing on improving the design of new batteries, developing new battery materials, as well as developing new routes for the recovery valuables from end-of-life LIBs. Waste lithium-ion batteries are important secondary sources of many valuable materials, including Critical Raw Materials (CRMs) defined by the European Union (EU): lithium, cobalt, manganese, and graphite. Additionally, LIBs typically contain nickel and copper, which are classified as Strategic Raw Materials for EU since 2023 (Grohol and Veeh, 2023).

Current developments in the LIB recycling have been described in recently reviewed papers (Makuza *et al*, 2021; Baum *et al*, 2022; Brückner, Frank and Elwert, 2020). Typical recycling processes consist of discharging and mechanical separation followed by pyrometallurgical and/or hydrometallurgical treatment (Neumann *et al*, 2022). To make the battery recycling processes economically more attractive, they can be integrated with already existing primary metal production processes. In our previous studies (Ruismäki *et al*, 2020a; Dańczak *et al*, 2021; Rinne *et al*, 2022), we have investigated the possibility of integrating different battery scrap flotation fractions with pyrometallurgical slag cleaning processes. The slag used in this study came from an industrial nickel flash smelting furnace. It was iron-silicate slag with some magnesia (MgO) and nickel oxide, as well as minor concentrations of Co and Cu (Crundwell *et al*, 2011). As spent lithium-ion batteries typically contain a high concentration of Co and some Ni and Cu, it was proved earlier (Ruismäki *et al*, 2020b) that it is beneficial to mix a battery scrap fraction rich in Co with nickel slag in order to increase the recovery of Co during the slag cleaning process. In the laboratory-scale Ni-slag cleaning process, Ni, Co and Cu from both waste batteries as well as industrial Ni-slag were recovered in metal alloy and matte phases (Ruismäki *et al*, 2020a, 2020b; Dańczak *et al*, 2021). Graphite from waste LIBs was found to be an effective reductant for metal oxides and the reduction reactions appeared to be very fast. No additional reductant was needed in the investigated smelting process. However, lithium and manganese were lost in the slag, therefore the need for an additional pre-treatment stage before the smelting process was identified in order to maximise the valuable metal recoveries. It is not economically viable to recover Li and Mn from huge volumes of base metal smelting slags, which means that their recovery must occur before the smelting process.

The aim of this research was to combine pyro- and hydrometallurgical unit operations for efficient recovery of battery metals Co, Ni, Cu, Li and Mn from Li-ion battery scrap. First, industrial Li-ion battery scrap underwent a sulfation roasting step, where the aim was to transform Li- and Co-containing oxides into Li and Co sulfates. As the formed sulfates were expected to be water soluble, the next step was leaching in water. Water leaching was also selected as it excludes the use of hazardous chemicals and leaching conditions. After water leaching, the solid leaching residue was mixed with industrial nickel slag and smelted in reducing conditions in order to recover Ni, Cu and the remaining Co. Biochar was used as a reductant in the smelting stage, and the experiments were conducted at 1350°C for different times (5–60 mins) to investigate the reduction behaviour of the metals of interest as a function of time. The data provided in this study will be useful for integrating Li-ion battery recycling with already existing industrial-scale unit processes.

EXPERIMENTAL

Sulfation roasting

The main raw material for this study was LCO-rich lithium-ion battery scrap, supplied by AkkuSer Oy (Finland), where the samples were pretreated with a dry technology – two stages of crushing followed by magnetic and mechanical separation (Pudas, Erkkilä and Viljamaa, 2015). A size fraction of <125 µm was separated from the industrial scrap by sieving and employed for the current study. The chemical composition of the battery scrap fraction used in the experiments is presented in Table 1.

TABLE 1

Li-ion battery scrap composition before sulfation roasting.

Element	Al	Co	Cu	Fe	K	Li	Mg	Mn	Na	Ni	P	C	Rest
wt%	1.64	26.45	2.72	0.61	0.05	3.87	0.09	1.67	0.06	2.74	0.45	33	26.65

For each experiment, a batch of 4 g battery scrap was placed in a silica boat in the cold zone of a horizontal tube furnace (Lenton, UK) with a hot zone temperature of 850°C, after which the furnace was sealed and Ar gas flow (500 mL/min) was started. An ejector was used for creating an under-pressure inside the furnace. After approximately 5 mins, the sample was pushed to the hot zone in three stages, keeping a 2 min pause between the stages to avoid crucible cracking, followed by changing the gas mixture to 10 per cent SO_2 – 10 per cent O_2 – Ar gas when the sample reached

the hot zone. These conditions were selected based on our previous investigation with LCO-rich black mass (Biswas *et al*, 2023). According to the thermodynamic stability diagram (Biswas *et al*, 2023), it was expected that all lithium and cobalt transform into sulfates, whereas other metals should remain as oxides. After 60 mins of sulfation roasting, the samples were taken out of the furnace following the same three-stage procedure as previously. In total, four roasting experiments were conducted with the same parameters. The roasted battery scrap was analysed using X-ray diffraction technique (XRD, X'Pert Pro MPD, PANanalytical, Netherlands) with a scan rate of 2°/min for 10° to 90° angles using Cu-K_α radiation and HighScore Plus software (version 4.8, PANanalytical).

Water leaching

The sulfation roasted samples were mixed together and a 10 g batch was leached in distilled water for 60 mins with a solid to liquid ratio of 100 g/L at 60°C and with magnetic stirring at 300 rev/min. After leaching, the residue was filtered and the concentrations of metals were analysed by atomic absorption spectroscopy (AAS, Thermo Scientific iCE 3000, USA) after digesting a part of the residue in concentrated aqua-regia (HCl (37 per cent, Merck) and HNO_3 (65 per cent, Merck Supelco) at 3:1 molar ratio). AAS was used for the leaching solution analysis as well. The solid residue was also analysed using the X-ray diffraction technique described in the previous section.

Smelting

The smelting experiments were conducted under simulated conditions of an industrial Ni-slag smelting process. Industrial Ni-slag (Table 2) was used in the experiments. The main reductant in the experiments was biochar prepared from black pellets by pyrolysing at 600°C, obtained from University of Oulu (Finland), containing 76.6 wt per cent carbon. The biochar was supplied as pellets, but it was ground in a mortar into fine powder before the experiments in order to increase the reactive surface area. Detailed analysis of the biochar has been presented previously (Attah-Kyei *et al*, 2023).

TABLE 2

Chemical compositions of the Ni-slag and concentrate used in the experiments.

Slag, concentrations in wt%													
Fe_3O_4	**Fe**	**Si**	**Ni**	**Mg**	**Ca**	**Al**	**Cu**	**Co**	**Na**	**K**	**Ti**	**S**	**Mn**
20	35.42	10.61	3.41	3.16	0.91	0.84	0.69	0.43	0.35	0.32	0.21	0.16	0.03
Concentrate, concentrations in wt%													
2	29.32	9.25	8.06	2.79	1.05		1.85	0.31				24.41	

Two series of experiments were conducted. In series A, 90 wt per cent of Ni-slag was mixed with 10 wt per cent leaching residue. In series B, 5 wt per cent of the slag was replaced with industrial sulfidic Ni-concentrate (Table 2). The stoichiometric amount of carbon required for complete reduction of NiO to Ni, CuO to Cu, CoO to Co and magnetite (20 wt per cent in slag) to FeO was calculated, assuming the reaction gas to be CO, and 1.25 times the stoichiometric amount was used in both series. For both series, enough reagents for five experiments were weighed and thoroughly mixed in an agate mortar. After mixing, 1.0 g of the mixture was used in each experiment. The weight ratios in the final mixtures were 85.97/9.55/4.48 for slag/leaching residue/biochar in series A and 81.30/9.56/4.78/4.36 for slag/residue/concentrate/biochar in series B, respectively. The small difference in the amount of biochar is due to the concentrate used in series B, which was already sulfidic and therefore did not require reductant.

The experiments were conducted in a vertical tube furnace (Lenton, UK). 1.0 grams of starting mixture was placed in a conical silica crucible and attached to Kanthal A-wire hanging from inside the furnace. The sample was first lifted to the cold zone of the furnace, followed by closing the furnace work tube with a rubber plug. Next the furnace was flushed with Argon (300 mL/min) for 15 mins before lifting the sample to the hot zone at 1350°C and keeping there for 5, 10, 30 or 60 mins. After the set time, the sample was rapidly quenched to ice-water mixture without breaking the inert atmosphere. Before characterisation, the samples were mounted in epoxy, cut in a half by

a diamond cutting wheel, mounted in smaller epoxy moulds, ground, and polished with traditional wet metallographic methods. After polishing, the sample surfaces were coated with carbon for microstructural and compositional characterisation.

The sample microstructures and elemental compositions of phases were characterised using a scanning electron microscope (SEM; Mira 3, Tescan, Czech Republic) coupled with an energy dispersive spectrometer (EDS; Thermo Fisher Scientific, USA). The beam current was approximately 10 nA and the acceleration voltage was 15 kV. The elemental analyses were conducted using standards supplied by Astimex, as shown in Table 3.

TABLE 3

EDS standards as well as LA-ICP-MS detection limits (ppmw = parts-per-million by weight).

Element	EDS standard	LA-ICP-MS isotope and detection limit (ppmw)
O	Diopside	
Mg	Magnesium	
Al	Aluminium	
Si	Quartz	
S	Marcasite	
Ca	Fluorite	
Fe	Hematite	
Co	Cobalt	^{59}Co: 0.02
Ni	Nickel	^{60}Ni: 0.21
Cu	Copper	^{65}Cu: 0.04
Mn		^{55}Mn: 0.09
Li		^{7}Li: 0.04

Trace and minor element concentrations in the slags were below reliable detection with EDS, therefore the slags were analysed using laser ablation-inductively coupled plasma-mass spectrometry (LA-ICP-MS). The laser spot size was set to 40 µm with 50 µm preablation and the laser energy was 40.1 per cent of 5 mJ. The fluence, ie energy delivered per unit area, was 1.25 J/cm^2 on the sample surface. The laser was operated at 10 Hz frequency and 40 sec of ablation data was collected from each spot. NIST610 glass (Jochum *et al*, 2011) was used as an external standard, ^{29}Si (from EDS) as the internal standard. NIST612, USGS BHVO-2G and BCR-2G glasses (Jochum *et al*, 2005) were analysed as unknowns. The obtained time-resolved analysis signals were treated with Glitter software (Van Achterberg *et al*, 2001), and the detection limits are shown in Table 3.

RESULTS AND DISCUSSION

Sulfation roasting and water leaching

The XRD pattern of the LCO-rich black mass in Figure 1 suggests that there are two main phases, $LiCoO_2$ and graphite, which originate from the cathode and anode, respectively. The elemental analysis of the black mass in Table 4 also shows 26.6 wt per cent of Co and 3.87 wt per cent Li along with small concentrations of Ni, Mn and Cu, confirming this as LCO-rich black mass. At the first stage of this study, the LIB black mass samples were roasted using 10 per cent SO_2 – 10 per cent O_2 – Ar gas flow at 850°C for 60 mins. The XRD pattern of the sulfation roasted powder in Figure 1 confirms the formation of Li and Co sulfates, while a fraction of Co could be observed to remain as oxide. $LiCoO_2$ peaks were not observed in the roasted powder sample, indicating a high degree of sulfation

(and partial transformation into CoO as observed in the XRD graph). The carbon peak also disappeared after sulfation roasting, suggesting full combustion of carbon. At this temperature, it is also expected that the binders, plastics and organic electrolytes are removed during the roasting process.

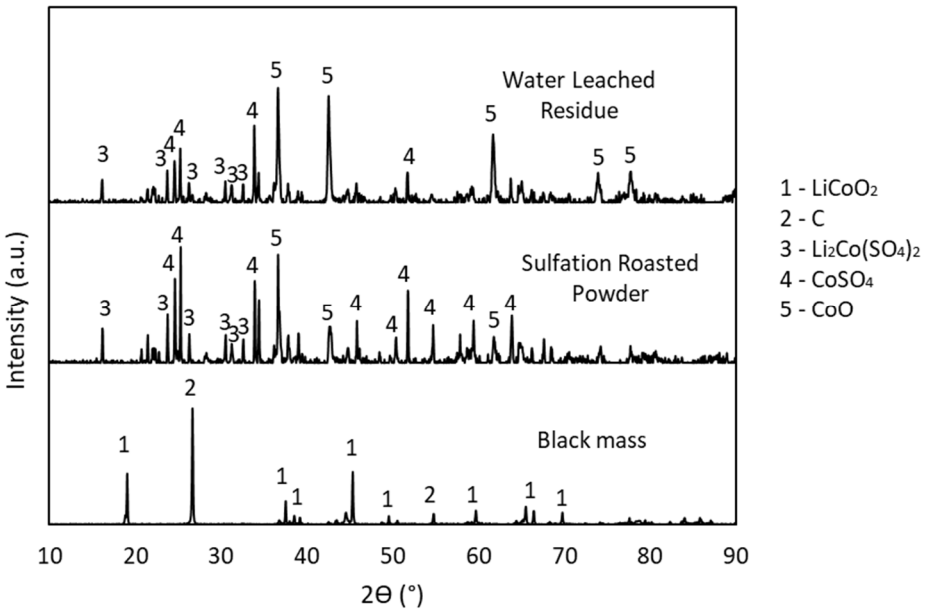

FIG 1 – XRD patterns of black mass, sulfation roasted powder and leach residue after water leaching.

TABLE 4

Elemental composition of black mass and leach residue. The chemical analysis is based on sample digestion in concentrated aqua-regia, followed by atomic absorption spectroscopy.

Element	Co	Ni	Mn	Cu	Fe	Li	Others
black mass, wt%	26.45	2.74	1.67	2.72	0.61	3.87	61.94
leach residue, wt%	43.00	6.10	1.40	6.00	0.20	0.20	43.1

After roasting, the samples were leached with distilled water, where the water-soluble metal sulfates were expected to dissolve, leaving metal oxides in the residue phase. The elemental composition of the leach residue, obtained from the water leaching process, is presented in Table 4. The residue consisted of approximately 43 wt per cent Co, 6 wt per cent Ni, 6 wt per cent Cu and low concentrations of Fe, Li and Mn. The XRD pattern of the water leached residue in Figure 1 shows several strong peaks of CoO along with few peaks of $Li_2Co(SO_4)_2$ and $CoSO_4$. This indicates that majority of Li and a fraction of Co were extracted during the water leaching stage. A longer period of water leaching could have been beneficial for the extraction of remaining sulfates. The composition of the residue shows that it contains valuable metals in high concentrations, and it will be a very good raw material for Ni-slag cleaning furnace, where an alloy containing mostly Ni and Co (as well as Fe) is formed.

The extraction yields of different metals after leaching, presented in Table 5, were calculated based on metal concentrations in water-leached solution and residue digested solution obtained from AAS analyses. Equation 1 was used in the calculations:

$$\%\ Extraction = \frac{m_1}{m_{1+}m_2} \cdot 100\% \quad (1)$$

where:

m_1 is the total mass of the specific metal dissolved in water during leaching

m_2 is the total mass of the specific metal remaining in the residue

TABLE 5

Recoveries of metallic elements after sulfation roasting and water leaching.

Element	Co	Ni	Mn	Cu	Fe	Li
Solution after leaching, mg	1130	28	103	12	<1	198
Leach residue, mg	2051.1	291.0	66.8	286.2	9.5	9.5
% Extraction	35.5	8.8	60.7	4.0	<9.5	95.4

Based on the results, approximately 95 per cent of Li, 61 per cent of Mn and 36 per cent of Co were extracted from the black mass in the water leaching stage. According to the thermodynamic stability diagram (Biswas *et al*, 2023), Mn should remain as oxide in the selected roasting conditions, but based on the obtained results, more than half of the Mn-containing oxides were actually transformed to sulfates, as indicated by the 61 per cent extraction efficiency. The surprisingly high Mn extraction during water leaching is beneficial because Mn deports to the slag and cannot be recovered in Ni-slag cleaning stage.

In this research, the focus was mostly on the recovery of metals from the leach residue through Ni-slag cleaning process. The precipitation and purification of metal compounds from the leaching solution was not investigated.

Smelting

The leaching residue was mixed with industrial nickel slag and subjected to a laboratory-scale Ni-slag cleaning process, as described in the Experimental section. SEM images of sample microstructures after smelting in reducing conditions are presented in Figure 2. A typical microstructure consists of the silica crucible (dark grey), glassy slag (medium grey) and matte/metal alloy phase (white). The matte phase had a round shape and was typically found near the bottom of the crucible. In samples without Ni-concentrate (series A, Figure 2a–2b), the matte phase seemed much smaller than in the samples with Ni-concentrate (series B, Figure 2c–2d). Additionally, in the samples without Ni-concentrate, a metal alloy phase was found mostly on the top of the slag layer, which is in line with previous studies on integrating battery scrap recycling with Ni-slag cleaning process (Ruismäki *et al*, 2020a; Dańczak *et al*, 2021).

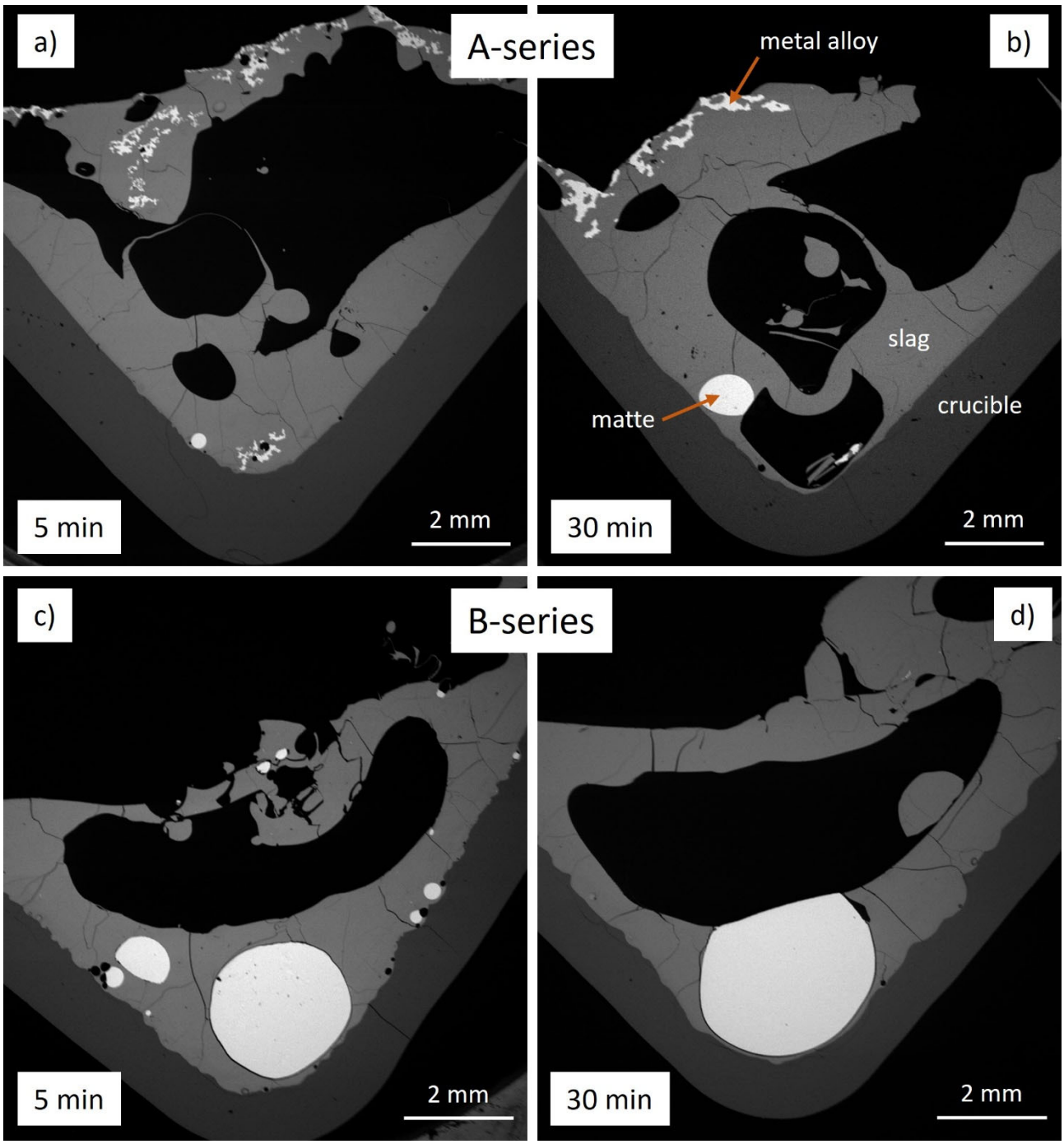

FIG 2 – Microstructures of samples after different reduction times. (a) and (b) are from series A, while (c) and (d) are from series B.

Besides the largest matte phase area close to the bottom of the crucible, some smaller round matte droplets were also found in other places of the samples. In both series, the smaller matte droplets increasingly coalesced with the largest droplet as the reduction time was increased.

A higher magnification SEM-BSE image of a typical microstructure of the matte phase is shown in Figure 3a, and a typical microstructure of the Fe-rich metal alloy present on top of the slag in the samples without Ni-concentrate is shown in Figure 3b. Within the whole matte phase, three different phase areas were distinguished, as marked in Figure 3a: area (1) was metallic Ni-Fe-Co alloy, area (2) was Cu-Ni-Fe sulfide and area (3) was Fe-Ni-Co sulfide. The metal alloy shown in Figure 3b consisted mainly of Fe-Co-Ni alloy, with minor sulfide areas segregated at the grain boundaries.

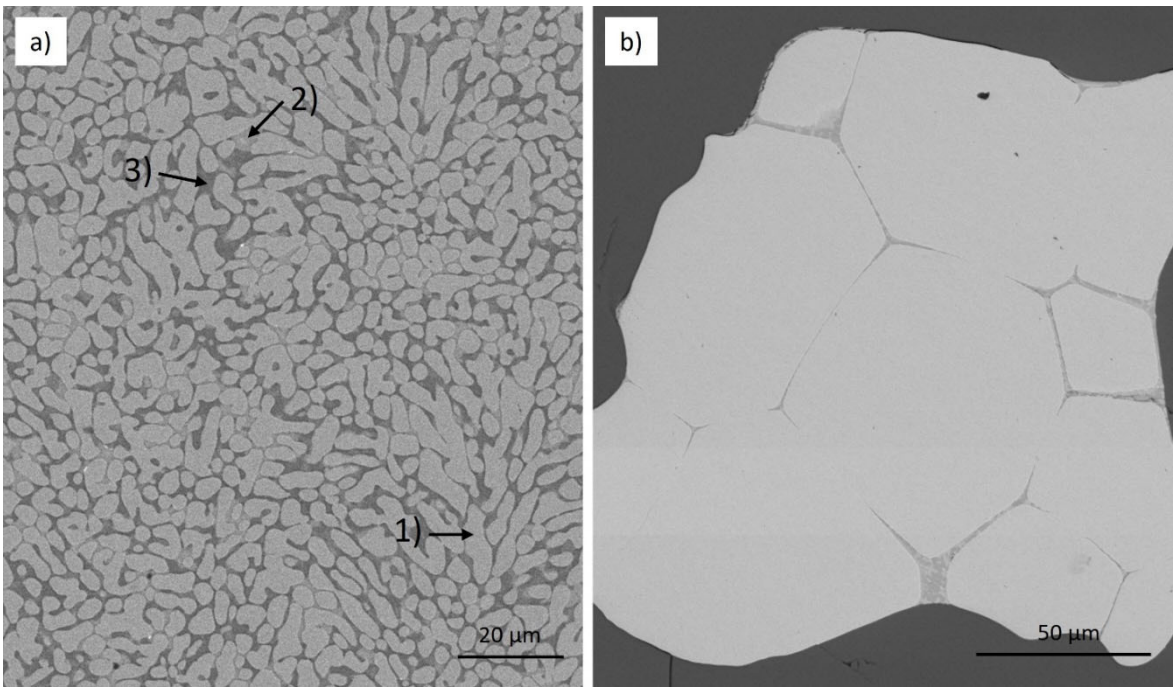

FIG 3 – Microstructure of: (a) matte, showing three separate phase areas; (b) Fe-rich metal phase formed on top of the slag in series A. Both images are from the sample reduced for 10 mins.

Chemical composition of the slag phase

The concentrations of Fe and SiO_2 in the slags are presented in Figure 4, left side. In both experimental series, Fe concentration decreased as the reduction time increased, and at the same time the concentration of SiO_2 increased. An increase in SiO_2 concentration in the slag was caused by iron reduction as well as dissolution of the silica crucible during smelting. The presence of Ni-concentrate in the samples resulted in faster rates of SiO_2 concentration increase and Fe decrease compared to the series without concentrate. The concentrations of MgO, Al_2O_3 and CaO in the slags are shown in Figure 4, right side. There are no significant differences between the two series, and the concentrations remain relatively stable after 10 mins of reduction.

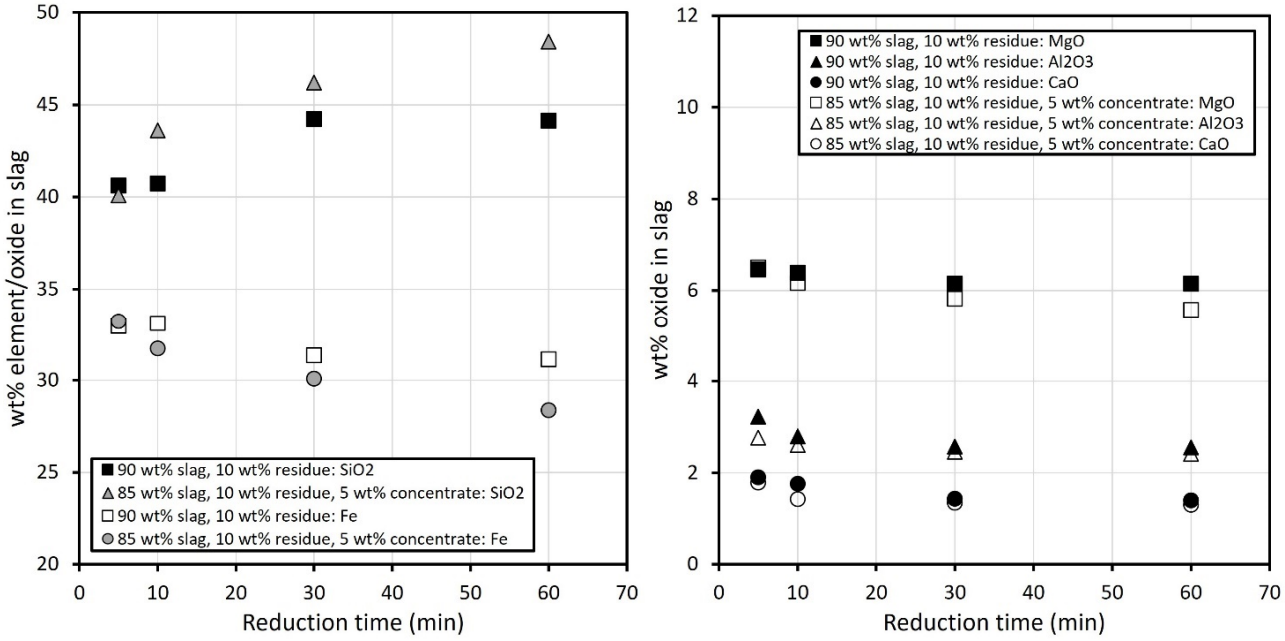

FIG 4 – Concentrations of SiO_2 and Fe (left side) as well as MgO, Al_2O_3 and CaO (right side) in slags after 5–60 min reduction time.

The concentrations of Co, Ni, Cu, Mn and Li in the slag phase are shown in Figure 5. The concentrations of Mn and Li remained relatively constant after 10 mins. This indicates that the slag volume increase that would have been caused by crucible dissolution, resulting in diluted concentrations of stable oxides such as Li_2O and MnO, was quite effectively compensated by iron reduction from the slag.

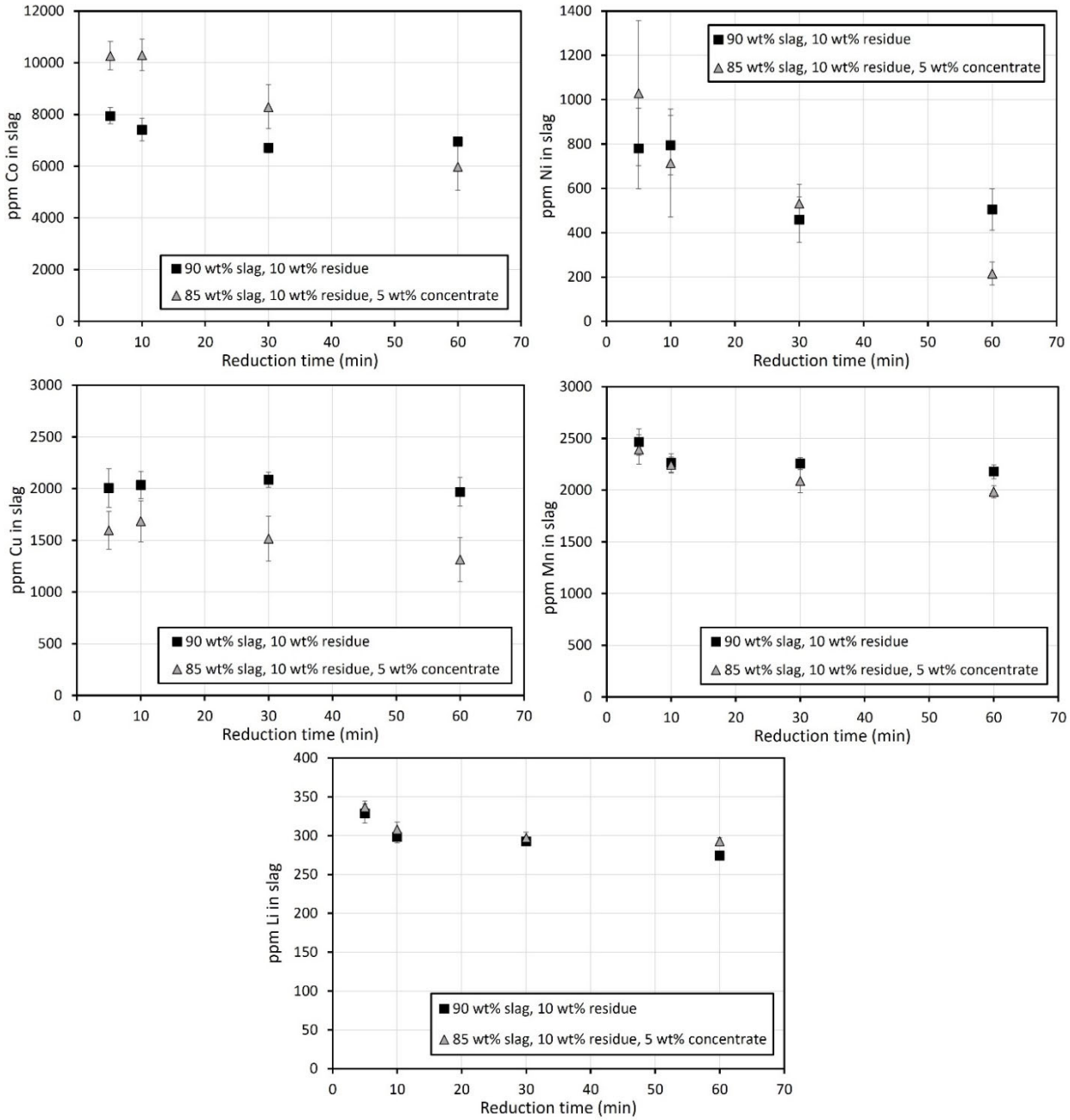

FIG 5 – Concentrations of Co, Ni, Cu, Sn, Pb and Li in slag phase as a function of reduction time at 1350°C.

The concentrations of Co and Ni decreased significantly as the reduction time increased, especially in series B with Ni-concentrate. The concentration decreases in series A stopped after 30 mins of reduction, whereas in series B the decrease continued until 60 mins. At 60 mins, the concentrations of Ni and Co were lower in series B compared to series A. The concentration of Cu in the slag remained surprisingly constant during the entire reduction time range in series A (without Ni-concentrate). In series B (with Ni-concentrate), a decrease in Cu-concentration was observed as the reduction time increased. Mn and Li originated mostly from the leaching residue, and as the residue amount did not change between the experimental series, neither did their concentrations in the slag significantly.

Chemical composition of the matte and metal phases

As presented in Figure 3a, the matte consisted of three different phase areas. The average composition of the matte was calculated according to the method presented by Rinne *et al* (2022). First, the composition of each phase area was analysed using SEM-EDS. Then, several SEM-images were taken from the matte phase of each sample, followed by phase area quantification using ImageJ software and calculation of average composition.

The average concentrations of Fe, Ni, Co, Cu and S in matte after ImageJ calculations are shown in Figure 6. In the series without concentrate, after 10 min reduction, the Ni concentration began to decrease and Fe as well as Co concentrations increased as the reduction time increased. It should be highlighted that even though Ni concentration seems to decrease, it does not mean that the amount of reduced Ni decreased but rather the ratio between Ni and Fe changed as the reduction of iron oxides progressed and the total mass of matte phase increased. The concentrations of Cu and S remained constant after 30 mins of reduction. The elements in the series with concentrate (Figure 6, right side) behaved differently: at all reduction times, the concentration of cobalt was higher than that of nickel, and the iron concentration did not show an increasing trend as a function of reduction time.

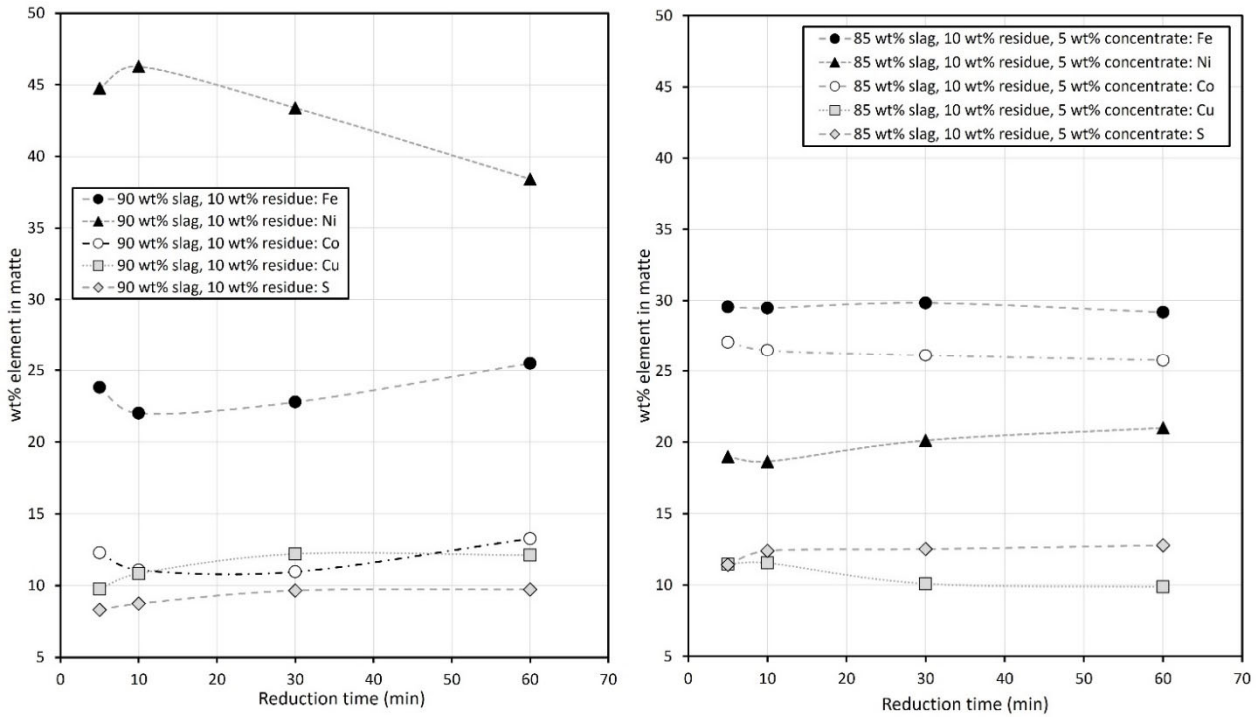

FIG 6 – Concentrations of Fe, Ni, Co, Cu and S in matte as a function of reduction time. Series A on the left side, series B on the right.

The concentrations of iron, nickel, cobalt and copper in the metal phase formed on top of the sample (see Figures 2a–2b and 3b) in series A, without Ni-concentrate, are presented in Figure 7. This phase is rich in iron and cobalt, which explains the lower iron and cobalt concentrations in the matte phase of this series compared to the series with concentrate, where no metal phase was formed on the sample surface. The elemental concentrations in the metal phase were calculated only based on the concentrations in the metallic grains, excluding the small sulfide areas visible in Figure 3b. It should be noted that the formation of such a metal alloy on top of the slag is not desirable from industrial perspective, because it cannot be tapped out of the slag cleaning furnace due to not settling below the slag layer.

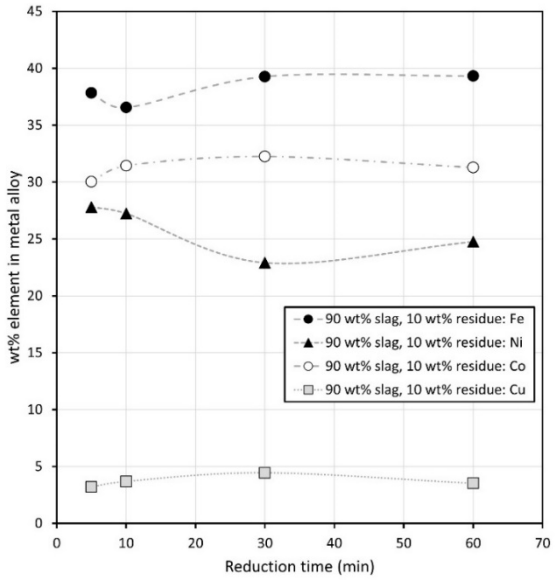

FIG 7 – Concentrations of Fe, Ni, Co and Cu in metal phase of series A.

Distribution coefficients of Co, Ni and Cu between matte and slag

Matte-slag distribution coefficients of Co, Ni and Cu are presented in Figure 8 and were calculated based on Equation 2:

$$L^{m/s}Me = [Me\ wt\%]/(Me\ wt\%) \quad (2)$$

where:

Me	represents the metal of interest
$Lm^{/s}$	is the distribution coefficient of *Me* between matte and slag
[*Me wt%*]	is the concentration of *Me* in matte
(*Me wt%*)	is the concentration of *Me* in slag

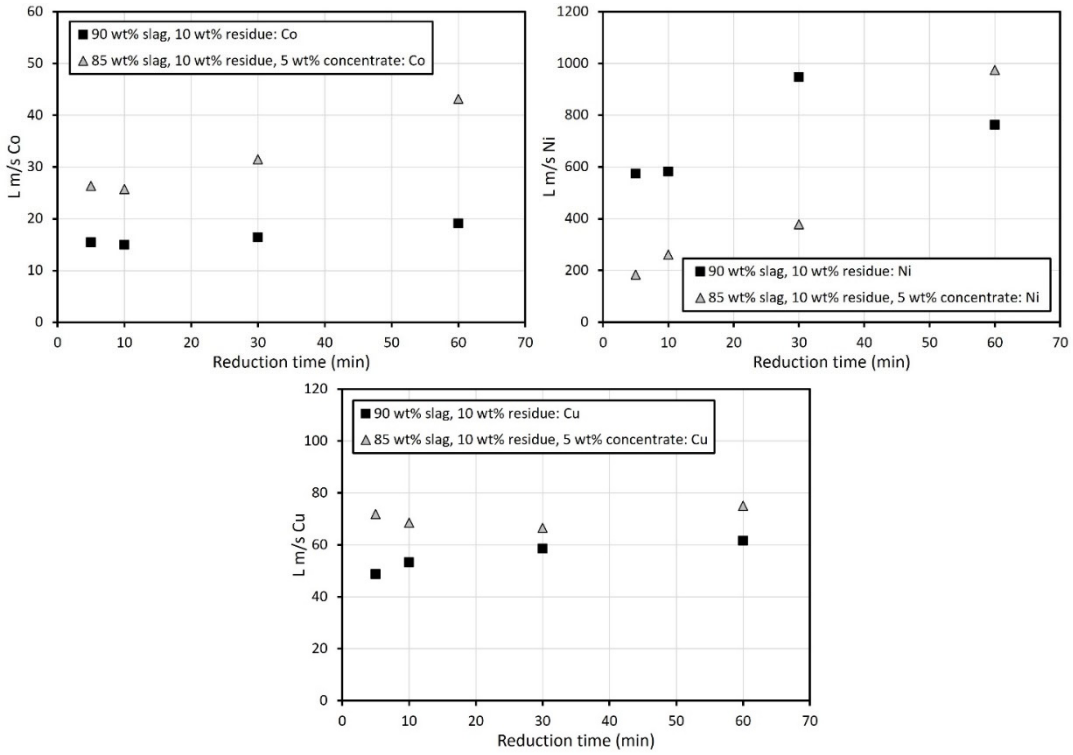

FIG 8 – Matte-slag distribution coefficients of Co, Ni and Cu as a function of reduction time.

The distribution coefficient values of Co and Ni increased significantly as the reduction time increased. The recovery of Co in the matte was significantly increased with concentrate addition (series B) compared to series A, as the distribution coefficient value after 60 mins was approximately 43 compared to 19, respectively. For Ni, the values were systematically higher in the series without concentrate, except for the longest reduction time. In general, the recovery of Ni in matte was approximately 20 times higher compared to Co. The distribution coefficient values for Cu were between 50 and 75, and they did not increase significantly as a function of reduction time. The differences between the two series were relatively small.

The results for Co fit very well with the values obtained previously by Dańczak *et al* (2021) using graphite from battery scrap as a reductant in Ni-slag cleaning. They also reported approximately doubled $L_m^{/s}$ Co values when adding Ni-concentrate, compared to without concentrate. Their $L_m^{/s}$ Ni values after 60 mins were approximately 600, which are slightly on the lower side compared to this work. For Cu, Dańczak *et al* reported higher values than obtained in this study, however the trends as a function of time were the same.

Attah-Kyei *et al* (2023) compared the reduction efficiencies of four different biochars with metallurgical coke in Ni-slag cleaning at 1400°C. The biochar employed in our work was the one which they concluded was the most effective reductant. The distribution coefficient values reported by Attah-Kyei *et al*, for Ni after 60 mins were similar as obtained in this study, for Cu they were somewhat lower and for Co they were two to three times higher. A major difference in their work compared to the current study was that only a metal alloy phase was formed and settled at the bottom of the crucible instead of matte phase. Because of this, a direct comparison of distribution coefficient values is not possible.

CONCLUSIONS

Waste lithium-ion batteries are complex mixtures of chemical elements and their compounds. In order to recover as much valuable metals as possible, smart combinations of mechanical and thermal pretreatment steps as well as pyro- and hydrometallurgical processing are needed. This study is based on the concept that battery recycling could be integrated with already existing technologies for primary metals production.

In this study, the mechanically pretreated battery scrap was subjected to sulfation roasting, where lithium and cobalt should transform into water-soluble sulfates according to thermodynamic stability diagrams. Analysis of the roasted battery scrap confirmed the presence of lithium in form of sulfates, whereas cobalt was in form of both sulfate and oxide. The roasted batteries were then used as feed in water leaching, where 95 per cent of Li and 36 per cent of Co were extracted. The low extraction yield of Co is in line with the XRD results, which showed that Co was only partially transformed to sulfate during the roasting step. The extraction yield of Mn reached 61 per cent, which was contradictory to the initial predictions based on the thermodynamic stability of Mn-compounds in the roasting conditions.

The high recovery rate of Li and the relatively good recovery of Mn indicate that the removal of these metals from the battery scrap before further high-temperature treatment is possible, and with further optimisation of the roasting conditions, improved Mn recovery rates are expected. Apart from the roasting parameter optimisation, a second round of water leaching would most likely increase the recoveries of Li, Mn and possibly Co. The low recovery of cobalt in water leaching is actually not an issue, as it is further recovered in smelting process unlike Li and Mn. In our study, the water leaching residue was mixed with industrial Ni-slag and subjected to a laboratory-scale Ni-slag cleaning process conducted at 1350°C, using biochar as a reductant. In the smelting process, the valuable metals Co, Ni and Cu heavily deported to the matte and metal alloy phases formed during reduction. The addition of Ni-concentrate to the smelting mixture had two clear benefits; it increased the deportment of valuables to matte and eliminated the formation of the iron-rich metal alloy on top of the slag. The biochar used in this work, obtained by pyrolysing black pellets at 600°C, was an effective reductant for metal oxides from both battery scrap and industrial Ni-slag.

During sulfation roasting at 850°C in oxygen-containing gas atmosphere, graphite from the battery scrap reacted with oxygen, forming CO_2 emissions and resulting in the loss of graphite, which is also classified as a CRM. From the elemental recovery perspective, it could make sense to separate as

much of the graphite as possible before the roasting process, using for example froth flotation. However, this would add another processing stage to the recycling process already containing several stages, leading to negative impacts on exergy efficiency for example. In the future, holistic studies should be conducted regarding the process investigated here as well as other possible processes in terms of economic viability, circularity, life-cycle assessment as well as exergy efficiency and exentropy analysis (Vierunketo *et al*, 2023).

ACKNOWLEDGEMENTS

This research work has been supported by the Business Finland BatCircle 2.0 project (Grant number 43830/31/2020), and the Academy of Finland's RawMatTERS Finland Infrastructure (RAMI) based at Aalto University, GTK and VTT.

REFERENCES

Attah-Kyei, D, Sukhomlinov, D, Tiljander, M, Klemettinen, L, Taskinen, P, Jokilaakso, A and Lindberg, D, 2023. A Crucial Step Towards Carbon Neutrality in Pyrometallurgical Reduction of Nickel Slag, *Journal of Sustainable Metallurgy,* 9:1759–1776.

Baum, Z J, Bird, R E, Yu, X and Ma, J, 2022. Lithium-Ion Battery Recycling–Overview of Techniques and Trends, *ACS Energy Letters,* 7(2):712–719.

Biswas, J, Ulmala, S, Wan, X, Partinen, J, Lundström, M and Jokilaakso, A, 2023. Selective Sulfation Roasting for Cobalt and Lithium Extraction from Industrial LCO-Rich Spent Black Mass, *Metals,* 13(2):358.

Brückner, L, Frank, J and Elwert, T, 2020. Industrial Recycling of Lithium-Ion Batteries – A Critical Review of Metallurgical Process Routes, *Metals*, 10(8):1107.

Crundwell, F K, Moats, M S, Ramachandran, V, Robinson, T G and Davenport, W G, 2011. Chapter 18: Flash Smelting of nickel sulfide concentrates, in *Extractive Metallurgy of Nickel, Cobalt and Platinum-Group Metals*, pp 215–232 (Elsevier: Oxford).

Dańczak, A, Ruismäki, R, Rinne, T, Klemettinen, L, O'Brien, H, Taskinen, P, Jokilaakso, A and Serna-Guerrero, R, 2021. Worth from Waste: Utilizing a Graphite-Rich Fraction from Spent Lithium-Ion Batteries as Alternative Reductant in Nickel Slag Cleaning, *Minerals,* 11:784.

Grohol, M and Veeh, C, 2023. Study on the critical raw materials for the E U, 2023: final report, European Commission, Directorate-General for Internal Market, Industry, Entrepreneurship and SMEs (Publications Office of the European Union). Available from: <https://data.europa.eu/doi/10.2873/725585>

Jochum, K P, Weiss, U, Stoll, B, Kuzmin, D, Yang, Q, Raczek, I, Jacob, D E, Stracke, A, Birbaum, K, Frick, D A, Günther, D and Enzweiler, J, 2011. Determination of Reference Values for NIST SRM 610–617 Glasses Following ISO Guidelines, *Geostandards and Geoanalytical Research,* 35:397–429.

Jochum, K P, Willbold, M, Raczek, I, Stoll, B and Herwig, K, 2005. Chemical Characterisation of the USGS Reference Glasses GSA-1G, GSC-1G, GSD-1G, GSE-1G, BCR-2G, BHVO-2G and BIR-1G Using EPMA, ID-TIMS, ID-ICP-MS and LA-ICP-MS, *Geostandards and Geoanalytical Research,* 29:285–302.

Li, M, Lu, J, Chen, Z and Amine, K, 2018. 30 Years of Lithium-Ion Batteries, *Advanced Materials,* 30(33):1800561.

Makuza, B, Tian, Q, Guo, X, Chattopadhyay, K and Yu, D, 2021. Pyrometallurgical options for recycling spent lithium-ion batteries: A comprehensive review, *Journal of Power Sources,* 491:229622.

Neumann, J, Petranikova, M, Meeus, M, Gamarra, J D, Younesi, R, Winter, M and Nowak, S, 2022. Recycling of Lithium-Ion Batteries—Current State of the Art, Circular Economy and Next Generation Recycling, *Advanced Energy Materials*, 12:2102917.

Pudas, J, Erkkilä, A and Viljamaa, J, 2015. Battery Recycling Method, US patent US8979006B2.

Rinne, T, Klemettinen, A, Klemettinen, L, Ruismäki, R, O'Brien, H, Jokilaakso, A and Serna-Guerrero, R, 2022. Recovering Value from End-of-Life Batteries by Integrating Froth Flotation and Pyrometallurgical Copper-Slag Cleaning, *Metals*, 12:15.

Ruismäki, R, Dańczak, A, Klemettinen, L, Taskinen, P, Lindberg, D and Jokilaakso, A, 2020b. Integrated battery scrap recycling and nickel slag cleaning with methane reduction, *Minerals,* 10:435.

Ruismäki, R, Rinne, T, Dańczak, A, Taskinen, P, Serna-Guerrero, R and Jokilaakso, A, 2020a. Integrating flotation and pyrometallurgy for recovering graphite and valuable metals from battery scrap, *Metals,* 10(5):680.

Van Achterberg, E, Ryan, C G, Jackson, S E and Griffin, W L, 2001. Data reduction software for LA-ICP-MS: Appendix, in *Laser ablation-ICP-Mass Spectrometry in the Earth Sciences: Principles and Applications; Short Course Series* (ed: P J Sylvester), Mineralogical Association of Canada, pp 239–243.

Vierunketo, M, Klemettinen, A, Reuter, M A, Santasalo-Aarnio, A and Serna-Guerrero, R, 2023. A multi-dimensional indicator for material and energy circularity: Proof-of-concept of exentropy in Li-ion battery recycling, *iScience*, 26(11):108237.

Physicochemical properties of steelmaking slags for the mitigation of CO_2 emissions in steel sector

DOI: 10.62053/JXUN4592

M J Lee[1], J H Heo[2] and J H Park[3]

1. Student, Department of Materials Science and Chemical Engineering, Hanyang University, Ansan 15588, Korea.
2. Senior Researcher, Korea Institute of Geoscience and Mineral Resources (KIGAM), Daejeon 34132, South Korea.
3. Professor, Department of Materials Science and Chemical Engineering, Hanyang University, Ansan 15588, Korea. Email: basicity@hanyang.ac.kr

ABSTRACT

In this paper, the challenging points regarding the high temperature physical chemistry of slags to achieve the improved and stable electric arc furnace (EAF) or electric smelting furnace (ESF) technology on the way to green steel will be reviewed, and the recent experimental and modelling research will be discussed. For example, the initial melting phenomena of hot briquetted iron (HBI) and the slag formation behaviour was observed using a high-frequency induction furnace. Main component of gangue oxides in HBI was SiO_2, Al_2O_3, and CaO in conjunction with unreduced iron oxide. To increase the dephosphorisation efficiency, the distribution ratio of phosphorus between metal and slag was calculated using FactSage™ software, version 8.2 (CRCT ThermFact, Inc., Montreal, Canada) and was compared to the measured results. The optimisation of slag chemistry is required not only for maximum dephosphorisation efficiency with good slag foamability but also for minimum slag volume with less refractory corrosion in EAF process. The slag chemistry is also one of key parameters affecting the operation efficiency in ESF in view of FeO reduction behaviour, viscosity, sulfide capacity, etc.

INTRODUCTION

It is well known that global CO_2 emission from iron and steel sector is *ca*. 7 per cent, which is approximately 1/3 of industrial energy use. Hence, many steel companies are trying to develop the electric arc furnace (EAF) and/or electric smelting furnace (ESF) steelmaking processes instead of blast furnace (BF) and basic oxygen furnace (BOF) integrated routes by employing high amounts of direct-reduced iron (DRI) and/or hot briquetted iron (HBI) to mitigate CO_2 emissions. The DRI/HBI as substitutes for virgin scrap in EAF has been used because DRI/HBI does not have tramp elements. Unfortunately, however, commercially available DRI contains the relatively high levels of phosphorus and gangue oxides, which adversely affects not only the steel properties but also the operation efficiency. Alternatively, integrated steel mills have focused on the ESF process by keeping conventional BOF to produce high-end quality products. The H_2-reduced DRI or HBI are able to be charged in ESF in conjunction with fluxes and carbon sources, producing hot metal and BF type slag. The high-grade iron ores (Fe>68 per cent) are economically used in EAF, whereas low-grade iron ores (Fe<65 per cent) are targeted to be used in ESF (Wimmer, Rosner and Voraberger, 2023).

CHEMISTRY OF DIRECT-REDUCED IRON (DRI)

The composition distributions of gangue oxides including unreduced iron oxide in commercially produced DRI are shown in the CaO-SiO_2-FeO ternary phase diagram (Figure 1). Here, the oxide composition was normalised to ternary system by excluding metallic iron (M.Fe). So, the chemical compositions of oxide phases widely vary, ie 5 to 25 per cent CaO, 10 to 30 per cent SiO_2, and 60 to 80 per cent FeO with minor amounts of MgO and Al_2O_3. By adding fluxing materials such as lime and dolomite, the EAF refining slag can be formed and be working in dephosphorisation reaction after melt-down of the charged raw materials such as DRI, HBI and scrap.

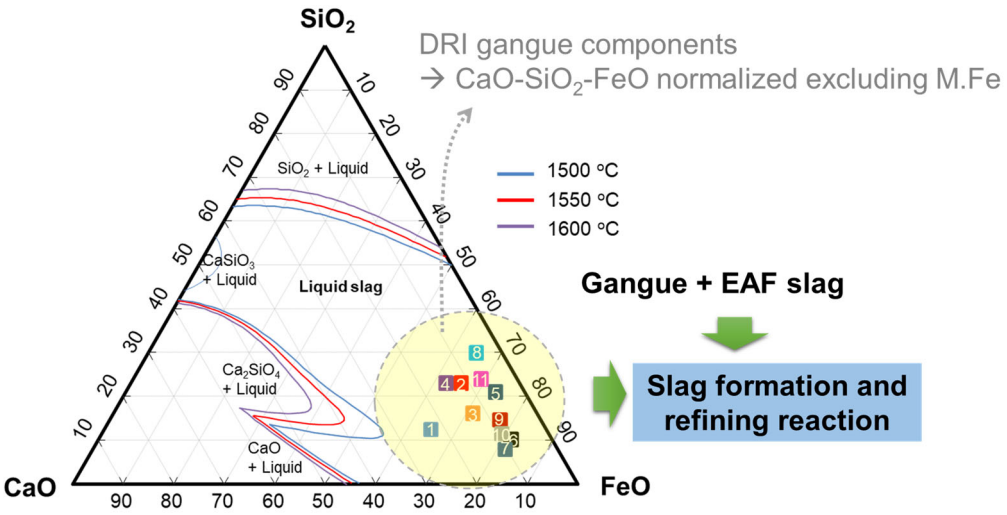

FIG 1 – Compositions of gangue oxides normalised into the CaO-SiO_2-FeO ternary phase diagram.

SLAG FORMATION DURING MELTING HOT BRIQUETTED IRON (HBI)

The reaction phenomena for the state of initial melting of HBI during heating are shown in Figure 2. Before melting, HBI samples were cut into small pieces and polished to characterise the gangue oxides and carbon distributions in HBI. A high-frequency induction furnace was used to observe the melting behaviour and the slag-metal reactions. A 400 g HBI was charged in a fused magnesia crucible. The experimental temperature was increased by 10°C/min rate and hold at 1550°C. Partially melted iron briquette, FeO-SiO_2 (fayalite) based slag and CO gas evolutions were observed during initial melting. Here, CO gas originated from carbothermic reaction between FeO and carbon in HBI as given in Equation 1.

$$FeO(s) + C(s) = Fe(l) + CO(g) \quad (1)$$

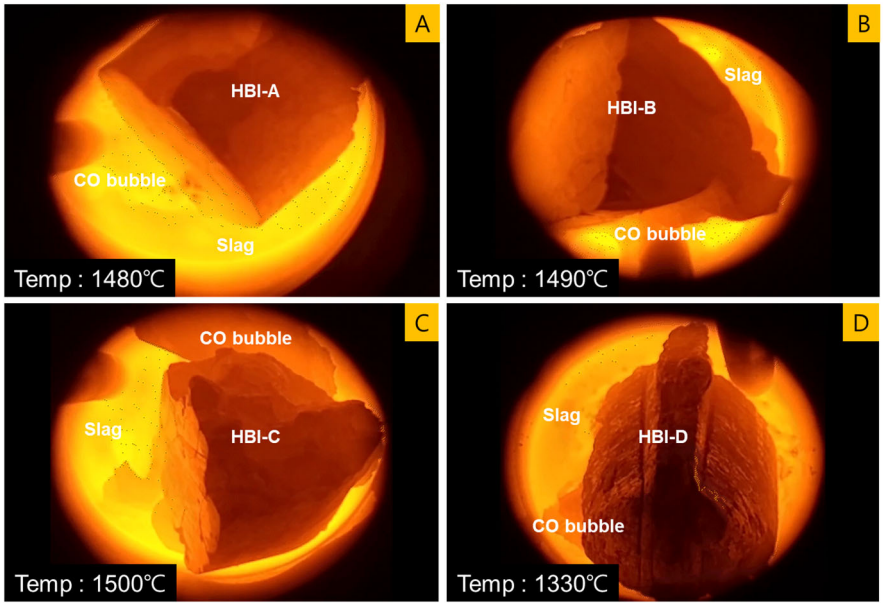

FIG 2 – Snapshot for initial melting of HBI with carbon content of (a) 1.3, (b) 1.0, (c) 1.4 and (d) 2.1 wt per cent.

In Figure 2, it is interesting that the melting initiation temperature decreases from about 1490(±10)°C to 1330(±10)°C by increasing the carbon content in HBI from about 1.2(±0.2) to 2.1(±0.1) wt per cent. It was reported that 1 wt per cent carbon in DRI or HBI can potentially contribute to an increase of productivity (+0.8 to 1.5 per cent) and iron yield (*ca*. +1 per cent) as well as to a decrease of

electrode consumption (-0.1 to 1.5 kg/t) and electric power (-15 to 25 kWh/t) in EAF operations (Sunyal, 2015; Hornby, 2021). Also, thin slag layer on the surface of molten steel was produced by the melting of gangue oxides in HBI and the absolute quantity of slag produced by gangue oxides in HBI increased with increasing HBI content. After melting, slag foaming was induced by CO gas evolution from the reaction between FeO in the molten slag with carbon in the molten steel. At this point, the changes in composition and amount of slag are strongly dependent on HBI content. Therefore, it is vital to evaluate the behaviour of phosphorus in molten steel and slag according to HBI mixing ratio during specific reaction stages, such as melting and slag–metal reaction, to thermodynamically understand the dephosphorisation reaction.

EFFECT OF DRI ON PHOSPHATE CAPACITY OF EAF SLAG

Phosphate capacity as a measure of the ability of a slag to absorb phosphorus can be defined as a function of temperature, basicity, and the stability of phosphate ion in the slag as follows (Wagner, 1975).

$$\frac{1}{2}\mathrm{P_2(g)} + \frac{3}{2}(\mathrm{O^{2-}}) + \frac{5}{4}\mathrm{O_2(g)} = (\mathrm{PO_4^{3-}}) \tag{2}$$

$$C_{\mathrm{PO_4^{3-}}} = \frac{K_{[2]} \cdot a_{\mathrm{O^{2-}}}^{3/2}}{f_{\mathrm{PO_4^{3-}}}} = \frac{(\%\mathrm{PO_4^{3-}})}{p_{\mathrm{P_2}}^{1/2} \cdot p_{\mathrm{O_2}}^{4/5}} \tag{3}$$

where $K_{[2]}$ is the equilibrium constant of Equation 2, $a_{\mathrm{O^{2-}}}$ is the activity of free $\mathrm{O^{2-}}$ ion, $f_{\mathrm{PO_4^{3-}}}$ is the activity coefficient of phosphate ion in slag, and p_i is the partial pressure of the gaseous component i. Slag composition is expected to change with DRI content because gangue oxides in DRI dissolve into the slag. In particular, because SiO_2 content in DRI as a gangue oxide is relatively high (~5 wt per cent), slag basicity, which is the driving force of dephosphorisation reaction based on Equation 2, will decrease. Thus, it is vital to confirm the relationship between modified basicity index, eg $\log\{(X_{\mathrm{BO(=CaO+Na_2O+BaO+MnO)}}/X_{\mathrm{AO(=SiO_2+B_2O_3)}}\}$ and phosphate capacity, $\log C_{\mathrm{PO_4^{3-}}}$, as shown in Figure 3a (Heo and Park, 2018). Phosphate capacity, $\log C_{\mathrm{PO_4^{3-}}}$ clearly decreased with decreasing basicity and with increasing DRI content, indicating that a higher content of DRI unambiguously reduced dephosphorisation efficiency by contributing SiO_2.

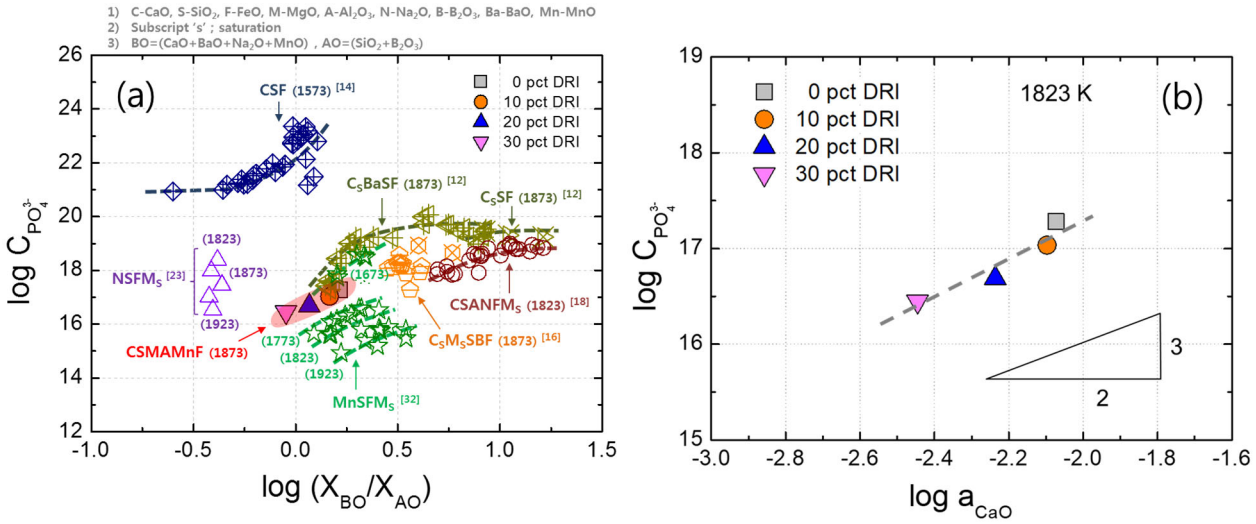

FIG 3 – Phosphate capacity, $\log C_{\mathrm{PO_4^{3-}}}$ as a function of (a) modified basicity index, $\log(X_{\mathrm{BO}}/X_{\mathrm{AO}})$ for the FeO-bearing slags and (b) $\log a_{\mathrm{CaO}}$ for the CaO-SiO_2-FeO-MgO-Al_2O_2-MnO slag.

Activity of CaO decreases and that of SiO_2 increases with increasing DRI content. CaO is known to behave as a representative basic component by contributing free oxygen ions (O^{2-}) in the slag as outlined in the following reaction (Sano, 1997).

$$(\mathrm{CaO}) = (\mathrm{Ca^{2+}}) + (\mathrm{O^{2-}}) \tag{4}$$

$$a_{O^{2-}} = \frac{K_{[4]} \cdot a_{CaO}}{a_{Ca^{2+}}} \quad (5)$$

By combining Equations 3 and 5, the correlation between CaO activity and phosphate capacity can be deduced as follows:

$$\log C_{PO_4^{3-}} = \frac{3}{2}\log a_{CaO} - \frac{3}{2}\log a_{Ca^{2+}} - \log f_{PO_4^{3-}} + \text{Const.} \quad (6)$$

Based on Equation 6, the phosphate capacity and activity of CaO are expected to exhibit a linear relationship with a slope of 1.5 on a logarithmic scale assuming that the composition dependencies of $a_{Ca^{2+}}$ and $f_{PO_4^{3-}}$ are not critical at a given temperature. Here, the activity of CaO was calculated from FactSage™ (ver 8.2) software with FTOXID and FACTPS databases. Figure 3b shows the linear relationship between phosphate capacity and the activity of CaO obtained using least square regression (Heo and Park, 2018). Hence, the activity of CaO can be used as a useful index representing the basicity of slag based on the linear relationship between phosphate capacity and the activity of CaO. It is noteworthy that the phosphate capacity of slag is strongly affected by the activities of CaO and SiO_2 in the slag.

CONTROL OF PHASE EQUILIBRIA FOR GOOD FOAMABILITY OF EAF SLAG

Slag foaming is strongly affected by the slag viscosity, which is dependent on the MgO content as well as basicity. The (Mg,Fe)O monoxide (magnesiowüstite, MW) and Ca_2SiO_4 (dicalcium silicate, C_2S) compounds suspended slags are frequently occurred in commercial EAF plant operation due to the heterogeneous slag composition, temperature fluctuations, and impurities in the fluxing agents. The solid+liquid multiphase slag affects the foamability and dephosphorisation efficiency. For slag composition beyond the MW saturation limit, it is expected that slag viscosity is relatively higher than fully liquid slag due to precipitation of solid compounds according to Einstein-Roscoe equation (Roscoe, 1952; Heo and Park, 2021). A higher viscosity increases the foaming index (Σ), which is equal to the retention or traveling time of gas in the slag, which can be used as a quantitative index of foam stability (Ito and Fruehan, 1989). Hence, it is required to evaluate the effect of basicity on the foaming index. In the present study, the empirical equation of the foaming index of a multicomponent slag system was suggested by considering the thermophysical properties of slags as follows:

$$\Sigma = k\frac{\eta}{\sqrt{\rho \cdot \sigma}} \quad (7)$$

where k, η, ρ, and σ are a constant, viscosity [Pa·s], density [kg/m^{-3}], and surface tension [N/m], respectively. The constant k was assigned a value of 999 due to the value obtained from a similar slag composition by Kim, Min and Park (2001) The viscosity can be obtained by FactSage™ software. Here, the effect of solid precipitation on slag viscosity is considered by using the Einstein-Roscoe equation. In addition, the density and surface tension are estimated using the polynomial expression by considering pure components, which are functions of temperature. Temperature dependencies of surface tension and density of slag components are available elsewhere (Heo and Park, 2019).

The foaming index of the FeO-bearing slags are compared in Figure 4 including data from Ito and Fruehan (1989) and Jiang and Fruehan (1991) (Heo and Park, 2021). The foaming index of the CaO-SiO_2-FeO-Al_2O_3-MgO-MnO system EAF slag and data from Ito and Fruehan (1989) and Jiang and Fruehan (1991) generally decreases with increasing basicity up to C/S=1.0–1.2, depending on the slag composition, and it rebounds with increasing basicity, which is in excess of the liquidus composition. This behaviour is strongly affected by the slag viscosity based on Equation 7. For slag basicity, C/S<1.2, the viscosity decreases with increasing basicity but beyond 1.2, the viscosity that apparently increases with increasing basicity is affected by the precipitation of solid compounds, contributing to increase the foam stability.

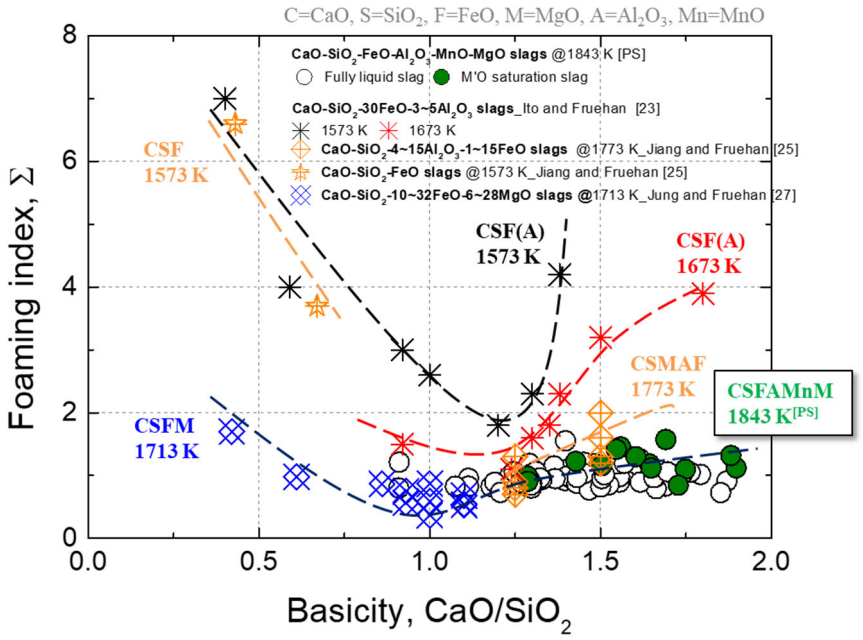

FIG 4 – Effect of CaO/SiO_2 ratio of slag and temperature on the foaming index (Σ) of FeO-bearing EAF slags.

CONCLUSIONS

The active use of H_2-reduced DRI and/or HBI has been widely increasing to mitigate the CO_2 emissions in steel sector. The contents of unreduced FeO (ie metallisation degree) as well as gangue oxides such as SiO_2, Al_2O_3 etc are significant factor affecting the electric furnace operations efficiency including FeO reduction, carburisation, melting rate of DRI/HBI, dephosphorisation, slag foaming, refractory corrosion etc. These phenomena are expected to be quite different from conventional experiences using NG-reduced DRI/HBI in conjunction with virgin scrap. Consequently, the physicochemical properties of molten slags and fluxes should be further investigated by combining the experimental methodologies and computational modelling.

REFERENCES

Heo, J H and Park, J H, 2018. Effect of direct reduced iron (DRI) on dephosphorization of molten steel by electric arc furnace slag, *Metall Mater Trans B*, 49B:3381–3389.

Heo, J H and Park, J H, 2019. Assessment of physicochemical properties of electrical arc furnace slag and their effects on foamability, *Metall Mater Trans B*, 50B:2959–2968.

Heo, J H and Park, J H, 2021. Effect of slag composition on dephosphorization and foamability in the electric arc furnace steelmaking process: Improvement of plant operation, *Metall Mater Trans B*, 52B:3613–3623.

Hornby, S, 2021. Hydrogen based DRI EAF steelmaking – Fact or fiction?, Proceeding of AISTech2021, Nashville, TN.

Ito, K and Fruehan, R J, 1989. Study on the foaming of CaO-SiO2-FeO slags, *Metall Trans B*, 20B:509–521.

Jiang, R and Fruehan, R J, 1991. Slag foaming in bath smelting, *Metall Trans B*, 22B:481–489.

Kim, H S, Min, D J and Park, J H, 2001. Foaming behavior of CaO-SiO2-FeO-MgOsatd-X (X=Al2O3, MnO, P2O5 and CaF2) slags at high temperatures, *ISIJ Int*, 41:317–324.

Roscoe, R, 1952. The viscosity of suspensions of rigid spheres, *Br J Appl Phys*, 3:267–269.

Sano, N, 1997. *Advanced Physical Chemistry for Process Metallurgy* (Academic Press: New York).

Sunyal, S, 2015. The value of DRI – Using the product for optimum steelmaking, Direct from Midrex, 1Q 2015.

Wagner, C, 1975. The concept of the basicity of slags, *Metall Trans B*, 6B:405–409.

Wimmer, G, Rosner, J and Voraberger, B, 2023. Smelter for processing of low grade DRI, Proceedings of 6th ESTAD, 2023, Düsseldorf, Germany.

Understanding zinc-containing species in basic oxygen steelmaking dust

DOI: 10.62053/RJFR5683

R J Longbottom[1], *D J Pinson*[2,5], *S J Chew*[3,5] *and B J Monaghan*[4,5]

1. Research Fellow, Faculty of Engineering and Information Science, University of Wollongong, Wollongong NSW 2522. Email: rayl@uow.edu.au
2. Senior Technology and Development Engineer, BlueScope Coke and Ironmaking Technology, Port Kembla NSW 2505. Email: david.pinson@bluescopesteel.com
3. Principal Technology and Development Engineer, BlueScope Coke and Ironmaking Technology, Port Kembla NSW 2505. Email: sheng.chew@bluescopesteel.com
4. Professor, Faculty of Engineering and Information Science, University of Wollongong, Wollongong NSW 2522, Email: monaghan@uow.edu.au
5. ARC Research Hub for Australian Steel Innovation, Wollongong NSW 2522.

ABSTRACT

Recycling steel plant by-products is a critical issue for achieving both environmental and economic sustainability of integrated steel plants. A key steel plant by-product stream is dust from basic oxygen steelmaking (BOS), which can be recycled back to the BOS vessel as iron units and to aid slag formation. The major limitations for its recycling are zinc and the uncertainty in zinc speciation of the dust. This uncertainty affects the amount of dust recycled and how it interacts with the slag during processing. BOS dust in stockpiles can undergo self-sintering reactions that oxidise the iron-bearing components. As this occurs, zinc (or oxide) may combine with iron oxides to form a zinc-iron spinel solid solution phase. Knowing which zinc-bearing species are present in the BOS dust is a key aspect in understanding and developing an efficient recycling process for the dust.

To overcome difficulties associated with phase identification in the BOS dust (both fresh and self-sintered), particularly the magnetite-zinc ferrite spinel solid solution using X-ray diffraction (XRD) / scanning electron microscopy (SEM) / energy dispersive spectroscopy (EDS), high end characterisation tools, transmission electron microscopy (TEM) and Mössbauer spectroscopy, were also used. Such an approach allowed improved phase identification of key zinc- and iron-bearing phases that were not previously resolvable.

The zinc in fresh BOS dust was mostly present as extremely fine separate particles of zinc oxide, attached to the iron particles. These extremely fine particles were <10 nm in size. Additionally, a small amount of zinc ferrite was also identified within the sample (most likely contained within a magnetite-zinc ferrite spinel solid solution).

However, the zinc in the self-sintered BOS dust, was found to be present entirely in a magnetite-zinc ferrite spinel solid solution. While this spinel phase had been previously identified by XRD, it was not clear that it contained zinc. The Mössbauer results provided definitive evidence of zinc within the spinel phase.

INTRODUCTION

On-plant recycling of steel plant by-products will help achieve the environmental and economic sustainability of integrated steel plants, reducing emissions by replacing raw materials and recovering the valuable components within the by-products (Nyirenda, 1991; Ahmed *et al,* 2015). One key by-product in an integrated steel plant is dust from the basic oxygen steelmaking (BOS) process. When oxygen is blown at supersonic velocity to decarburise steel, significant amounts of dust are generated. This dust is made up of very fine particles of steel and slag droplets, as well as flux fines. When the dust is recycled back to the BOS, these slag droplets and flux fines have value and aid slag formation (Longbottom *et al,* 2019a, 2019b).

Unfortunately, there are limitations on the recycling of BOS dust, primarily Zn and the uncertainty in Zn speciation of the dust (Stewart and Barron, 2020; Longbottom *et al,* 2020). Which Zn-bearing phases are present in the BOS dust strongly affects how the BOS dust interacts with the slag during processing. As such, the uncertainty in the Zn speciation in the dust affects the amount that can be

recycled to the BOS. Hence, it is important to understand what Zn-bearing phases are present in the BOS dust, whether as metallic Zn, ZnO or in a complex zinc ferrite-magnetite ($ZnFe_2O_4$-Fe_3O_4) spinel solid solution.

Zn in the BOS dust results from the high temperatures (>>1600°C) in the BOS process causing volatilisation of Zn (and other tramp elements) to the gas phase (Nedar, 1996). As the gas phase is cooled in the extraction process, the volatilised Zn can condense as separate particles or onto existing dust particles.

BOS dust is often removed from the off-gas using a wet scrubbing process, resulting in a slurry that is usually dewatered to produce a low moisture filter cake that is stockpiled for future recycling. When stored in stockpiles prior to recycling, BlueScope BOS dust has been found to self-sinter (Longbottom *et al*, 2019a, 2019b, 2020). Using TGA-DSC (thermogravimetric analysis – differential scanning calorimeter) and *in situ* X-ray diffraction (XRD) techniques, the self-sintered dust has been shown to have undergone exothermic oxidation reactions in the stockpiles (Longbottom *et al,* 2019a, 2019b, 2020). As part of these oxidation reactions, ZnO reacted with iron oxides to form the $ZnFe_2O_4$-Fe_3O_4 spinel solid solution. The formation of the $ZnFe_2O_4$ side of the solid solution is shown in Equation (1).

$$ZnO_{(s)} + Fe_2O_{3(s)} = ZnFe_2O_{4(s)} \quad (1)$$

However, these studies also highlighted a number of issues in the characterisation of the Zn bearing phases. Using scanning electron microscopy (SEM) with energy dispersive spectroscopy (EDS) showed that the BOS dust consisted of very fine iron/iron oxide particles (~200–500 nm) (Longbottom *et al,* 2019a, 2019b). However, it was found that due to the fine particle size, it was difficult to fully resolve the smaller particles and it was not possible to fully resolve the Zn-containing phase/particles by EDS. Similar microstructures containing these very fine particles have been reported in other BOS dust samples (Jabłońska *et al*, 2021; Stewart *et al*, 2022; Wang *et al*, 2021; Hleis *et al*, 2013) and Electric Arc Furnace (EAF) dust samples (Suetens *et al*, 2015; Sofilić *et al*, 2004; Lin *et al*, 2017).

There were also issues with the use of XRD to characterise these samples. It is well known that Fe_3O_4 and $ZnFe_2O_4$ have very similar lattice spacings, resulting in very similar XRD patterns (Stewart and Barron, 2020). In addition, Fe_3O_4 and $ZnFe_2O_4$ form a solid solution, which again is difficult to identify and quantify using XRD. For these reasons, in previous studies a single 'spinel' phase was used to encompass any Fe_3O_4 and $ZnFe_2O_4$ or solid solution (Longbottom *et al,* 2020). Often, these issues can be overcome by substituting a longer wavelength X-ray source, which may also help overcome issues with iron fluorescence with a Cu-Kα source. However, peak broadening from the fine particle size of the BOS dust likely masks any peak shift with composition even with a longer wavelength X-rays.

The aim of the study was to overcome these difficulties in identifying the Zn-bearing phases by characterising the BOS dust using high resolution transmission electron microscopy (TEM) and Mössbauer spectroscopy. TEM microscopy was used to help with the resolving of the very fine particles in the BOS dust samples. Mössbauer spectroscopy was used to help overcome the limitations in XRD in differentiating between Fe_3O_4, $ZnFe_2O_4$ and their solid solution. In this study BOS dust in two conditions was studied, fresh dust collected immediately after the dewatering process, as well as self-sintered dust collected from the stockpiles at BlueScope's Port Kembla steelworks.

EXPERIMENTAL

TEM and Mössbauer spectroscopy were used to characterise BOS dust samples. Fresh and self-sintered samples were both characterised. The fresh dust sample was collected immediately after dewatering, while the self-sintered dust was collected from the stockpiles at BlueScope's Port Kembla steelworks. The composition of the two samples, measured by XRF, is given as simple oxides in Table 1. The speciation of iron (and other phases) is not given by XRF and was initially characterised by XRD phase analysis (see Figure 1) using Cu-kα (λ = 0.154 nm) radiation. It may be seen that iron was mainly present as wüstite and metallic Fe in the fresh BOS dust sample, with a minor amount of 'magnetite'. In the self-sintered sample, iron was mainly present as 'magnetite' with

a small amount of hematite. Iron speciation and oxidation state was further investigated as part of this study using Mössbauer spectroscopy.

TABLE 1

XRF analyses of the BOS dust samples. The compositions are given in mass%.

Sample	MgO	Al_2O_3	SiO_2	P_2O_5	SO_3	K_2O	CaO	TiO_2	MnO	Fe_2O_3	ZnO
Fresh	1.8	trace	1.4	trace	trace	trace	3.2	trace	trace	78.2	13.8
Self-sintered	1.5	trace	4.4	trace	trace	trace	3.9	trace	trace	79.8	8.0

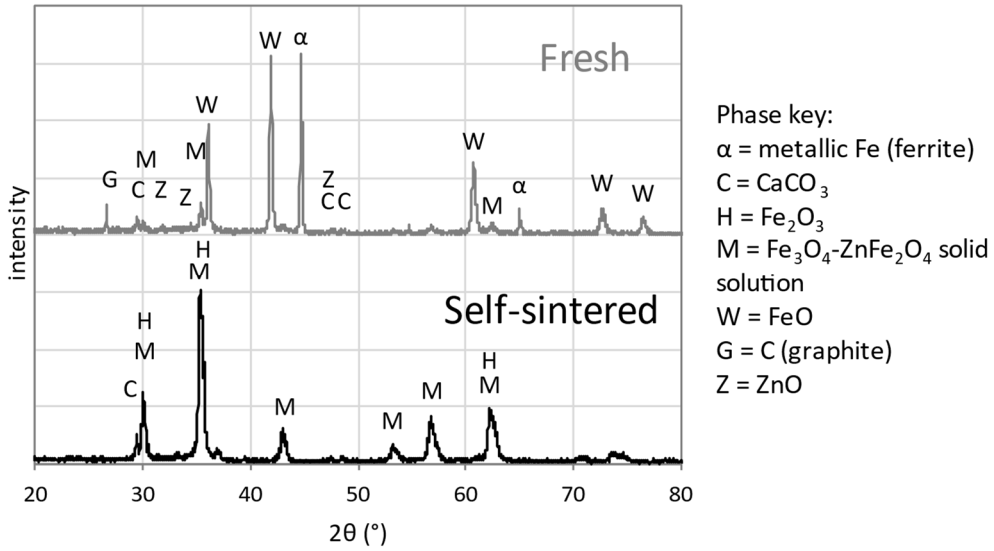

FIG 1 – XRD phase analysis of the BOS dust samples. XRD carried out using Cu-kα radiation (λ = 0.154 nm) at 1 KW power.

TEM characterisation

TEM characterisation was carried out using an aberration corrected JEOL ARM200F equipped with an 80 mm^2 JEOL Centurio SDD EDS detector. The TEM was equipped with bright field and secondary electron scanning TEM detectors. Each detector measures different characteristics of the samples:

- **Bright field:** image from transmitted beam, related to sample thickness and density.
- **Secondary electron:** equivalent to SEM images, information about surface of particles.

Sample preparation of the fresh BOS dust for TEM was carried out by suspending the sample in ethanol, with the resulting suspension then held for 5 mins in an ultrasonic cleaner to break up clumps. This suspension was then diluted further with more ethanol, which was then drawn into a transfer pipette. Two drops of the suspension were then placed onto a lacy carbon grid.

A ~20 g sample of the self-sintered BOS dust sample for the TEM was ground in a ring grinder for 30 sec to a fine particle size so that the particles would be electron transparent. This powder was then prepared for TEM in a similar manner to that for the fresh BOS dust.

Mössbauer characterisation

^{57}Fe Mössbauer spectra were obtained at room temperature using the standard transmission mode. A ^{57}Co isotope on a Rh foil (^{57}CoRh) was used as the γ-ray source. The velocity scale was calibrated using a 6 μm thick α-Fe foil, and all isomer shifts are quoted relative to the α-Fe calibration at source velocity (V) values of 4 and 12 mm/s. The calibration gave a Doppler velocity amplitude of 11.4885 mm/s for the nominal V = 12 mm/s setting and 3.8942 mm/s for the nominal V = 4 mm/s setting.

The collected spectra were fitted using the NORMOS™ software (by Wissenschaftliche Elektronik GMBH) to allow identification of the phases. The sum of expected spectra from different phases were fitted to the measured values. Quantification of the fits to the Mössbauer spectra was conducted without standards. As such, caution should be used when considering the absolute values.

RESULTS

To gain a better understanding of the Zn-bearing phases in BOS dust, fresh and self-sintered samples were characterised by TEM and Mössbauer spectroscopy. As both techniques use small samples (especially in the case of TEM), concerns about sample representation mean that the results (especially with quantification) should be taken as indicative rather than absolute.

Fresh BOS dust

Bright field and secondary electron images of the fresh BOS dust sample are shown in Figure 2. EDS elemental mapping (Figure 3) was used to identify the elements present within the sample, and high magnification images of the lattice fringes (Figure 4) within the sample were used to measure lattice spacing and to aid identification of phases.

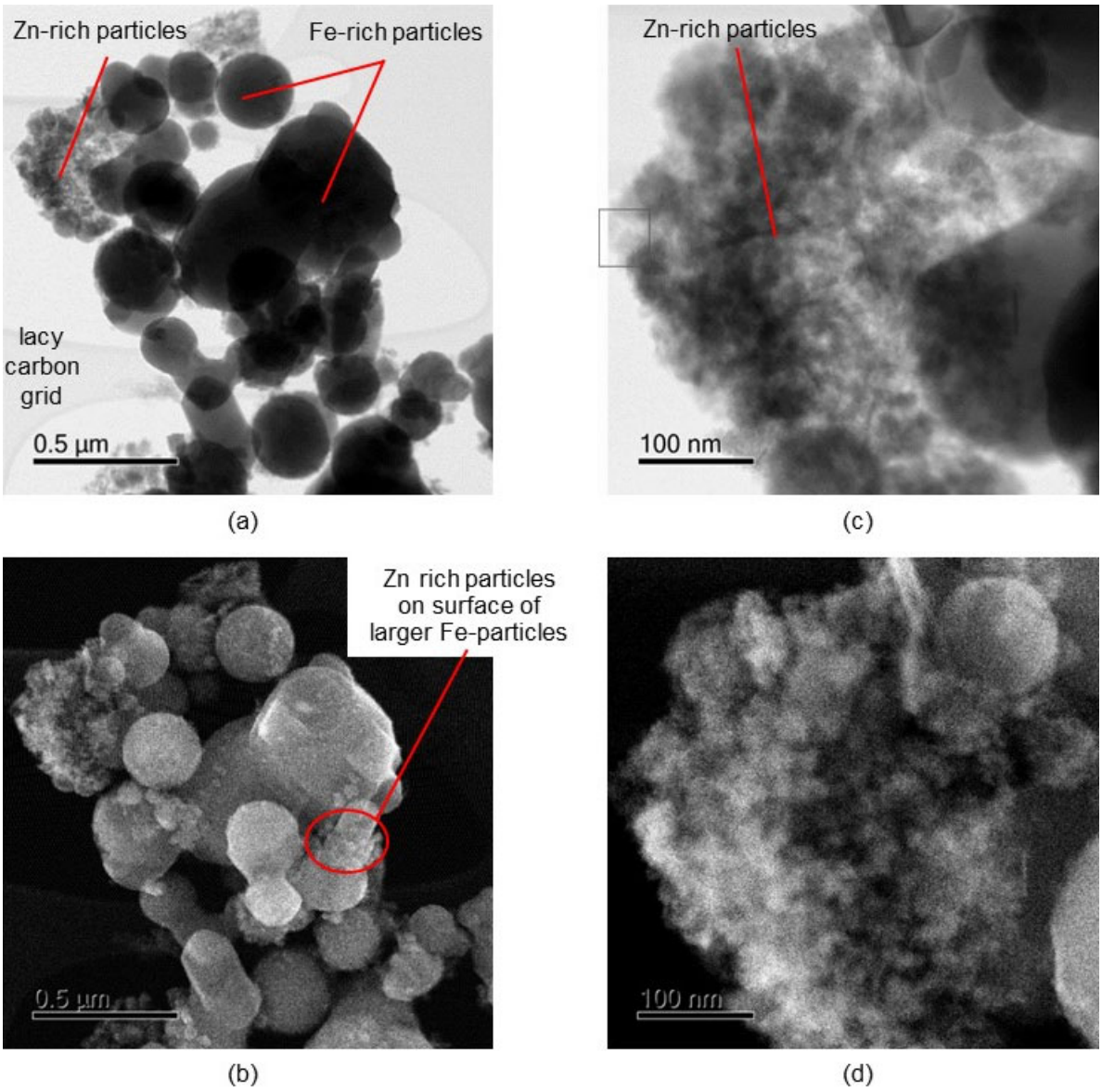

FIG 2 – TEM micrographs of fresh BOS dust. Lower magnification images: (a) bright field; and (b) secondary electron. Higher magnification images: (c) bright field; and (d) secondary electron.

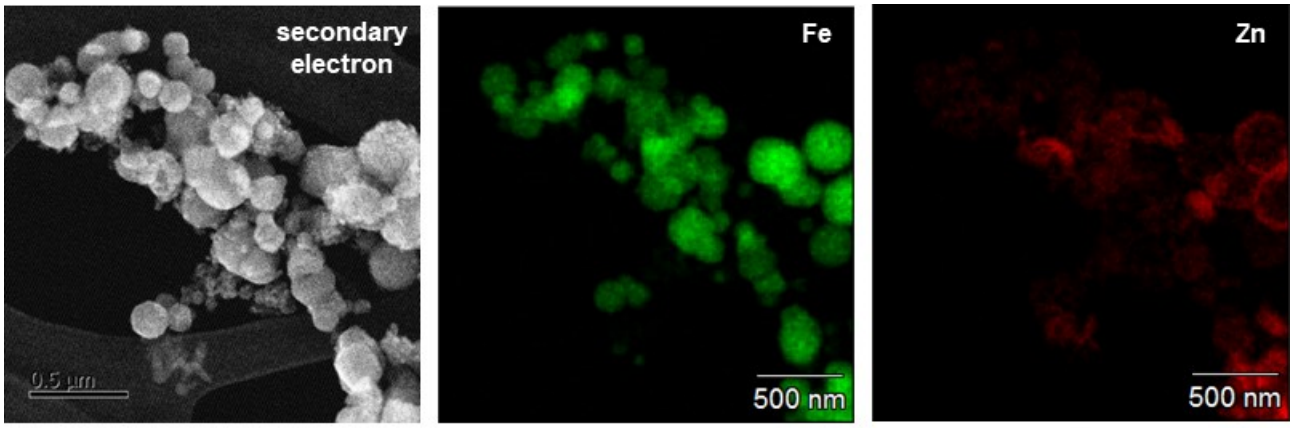

FIG 3 – TEM EDS elemental mapping of a fresh BOS dust sample. (a) Secondary electron image; (b) Fe elemental map; and (c) Zn elemental map.

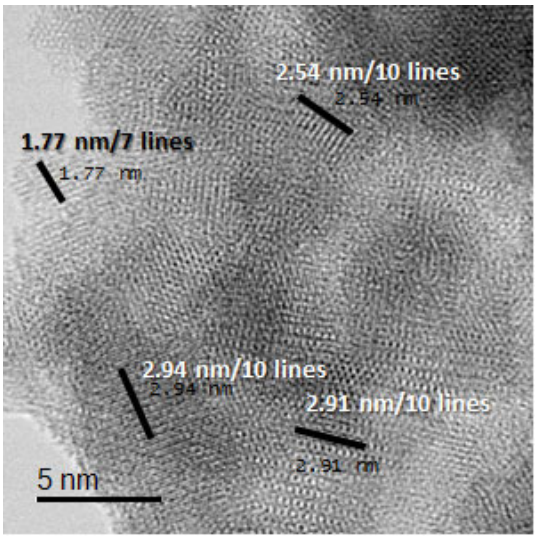

FIG 4 – High magnification bright field TEM image of fresh BOS dust (for the region shown by the rectangle in Figure 2b) showing lattice fringes.

Clumps of particles were observed attached to the carbon grid. Iron was found to be present predominantly as an oxide, but with some metallic particles. The Fe-rich particles were small, with a typical particle size being in the range 200–500 nm. This matches well with the previously reported SEM results (Longbottom *et al,* 2019b).

Zn was mostly found present as extremely fine separate particles, attached to the iron particles. As these particles were extremely small and clustered together, it is difficult to be definitive about the particle size, even from the high magnification TEM images (Figures 2 and 3). Many of the particles appear to be <10 nm in size. These Zn-rich particles were typically much smaller than the Fe-rich particles to which they were attached. In some cases (see Figure 3), the very small Zn-rich particles were found as a layer around metallic Fe particles. However, this behaviour was uncommon, even within the small number of clumps examined, where Zn-rich particles were more often found as clumps of Zn-rich particles attached to both metallic and oxide particles.

Examining the lattice fringes in Figure 4, crystallographic spacing (d-spacing) between the lattice planes was measured (Table 2). Comparing the measured values with the reported values for metallic Zn and ZnO (also given in Table 2), it appears that there is a strong match for hexagonal ZnO, with the measured and published d-spacings matching well. It is possible that there is a limited amount of metallic Zn in the material, with a reasonable match for the (002) reflection for metallic Zn.

TABLE 2

Measured d-spacings from lattice fringes (Figure 4) and Published d-spacings for metallic Zn and ZnO (Downs and Hall-Wallace, 2003; Gražulis *et al*, 2009, 2012, 2015; Merkys *et al*, 2016, 2023; Quirós *et al*, 2018; Vaitkus, Merkys and Gražulis, 2021; Vaitkus *et al*, 2023).

Average measured d-spacing (nm)	Metallic Zn (hexagonal)		ZnO (hexagonal)	
	reflection plane lattice indices	d-spacing (nm)	reflection plane lattice indices	d-spacing (nm)
0.293	(002)	0.247	(100)	0.290
0.253	(100)	0.231	(002)	0.261
–	(101)	0.169	(101)	0.254

Mössbauer spectroscopy results of fresh BOS dust, along with the fitted spectra for metallic iron, wüstite and $ZnFe_2O_4$ are shown in Figure 5. The spectrum of the BOS dust was fitted reasonably well with a non-magnetite, quadrupole-split doublet (likely corresponding to wüstite) between 0–2 mm/s and a magnetite sextet (likely corresponding to metallic iron) spreading out to larger velocity scale values. A third unrestricted non-magnetic phase likely corresponded to $ZnFe_2O_4$. This analysis only considered the iron bearing phases, as only Fe nuclei are detected by Mössbauer spectroscopy using a ^{57}CoRh γ-ray source.

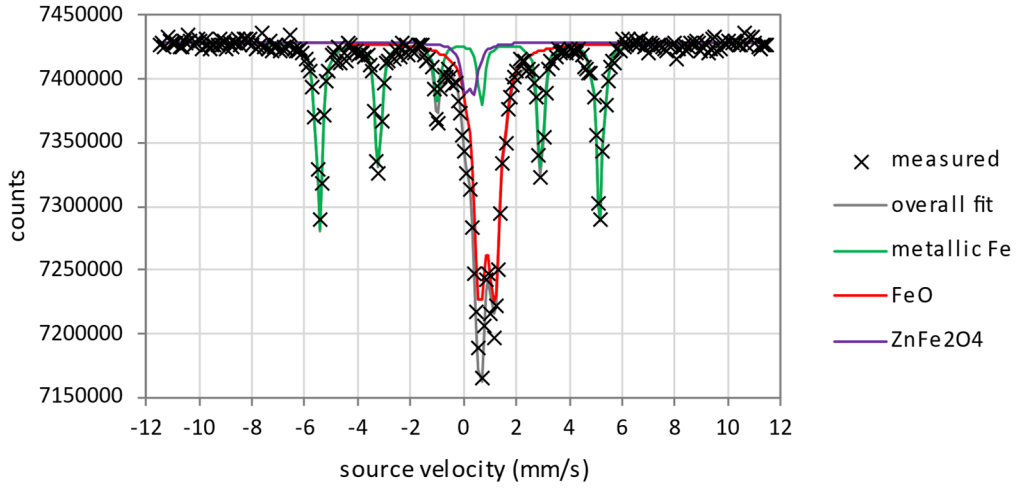

FIG 5 – Mössbauer spectra of fresh BOS dust showing the fitted spectra for metallic Fe, FeO and $ZnFe_2O_4$.

Self-sintered BOS dust

TEM images of a self-sintered BOS dust sample are shown in Figure 6, while EDS elemental maps are shown in Figures 7. Clumps of particles were found attached to the carbon grid (Figure 6). The particles in these clumps were of varying sizes, with relatively few larger particles (>1 μm), with more particles being in the 100–500 nm range. It should be noted that these samples were ground to ensure electron transparency, therefore both the clumps and particle size distributions are artefacts of sample preparation. While there were some very fine particles (<50 nm) attached to the clumps, they appeared quite different to those seen in the fresh BOS dust (Figure 2). At high magnifications (Figure 6) these particles appeared to be strongly crystalline. EDS mapping (Figure 7) showed that most of the particles appear uniform in their Fe and Zn levels, indicating that the particles are likely a Fe_3O_4-$ZnFe_2O_4$ spinel solution.

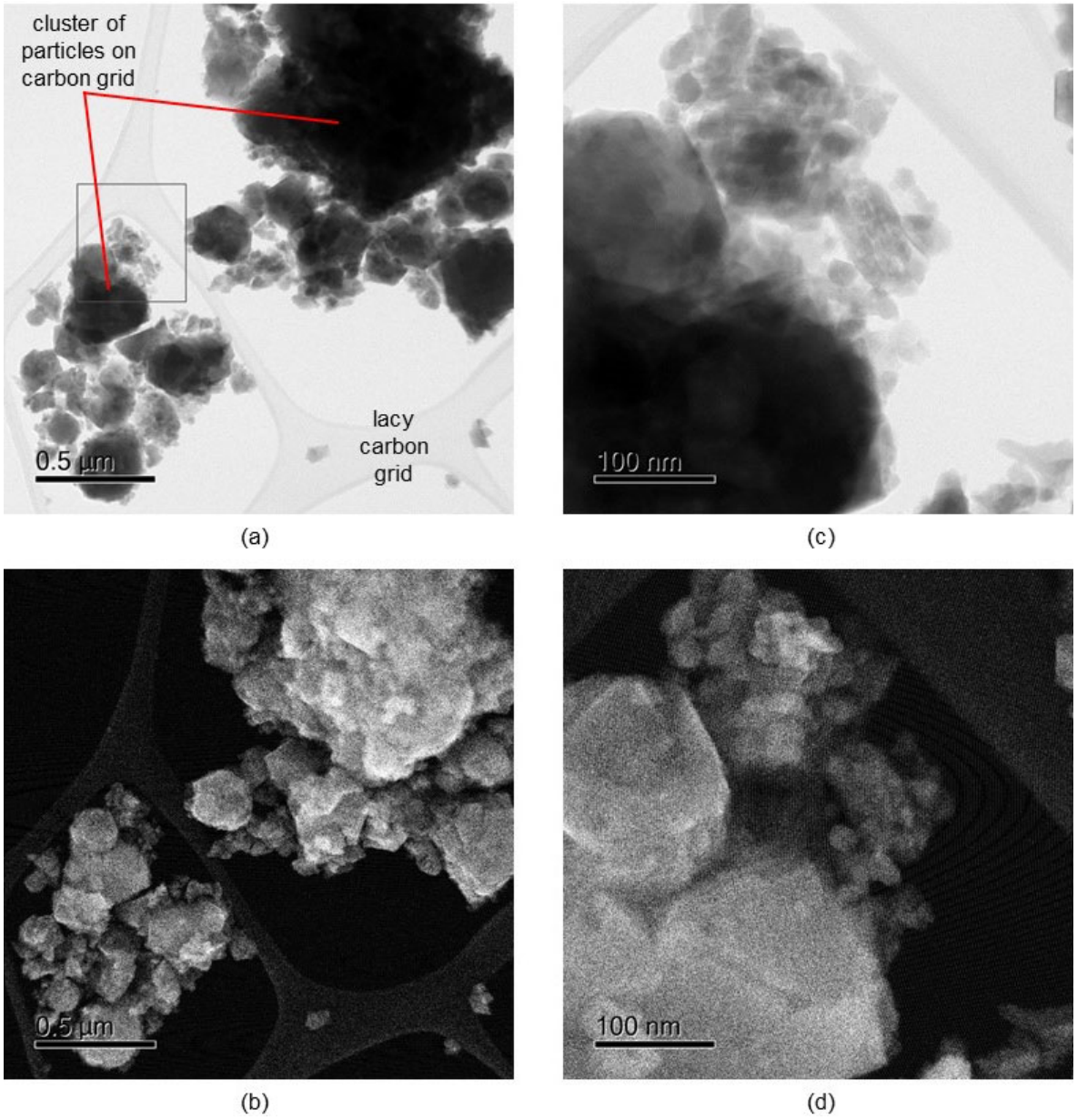

FIG 6 – TEM micrographs of self-sintered BOS dust. Lower magnification images: (a) bright field; and (b) secondary electron. Higher magnification images: (c) bright field; and (d) secondary electron.

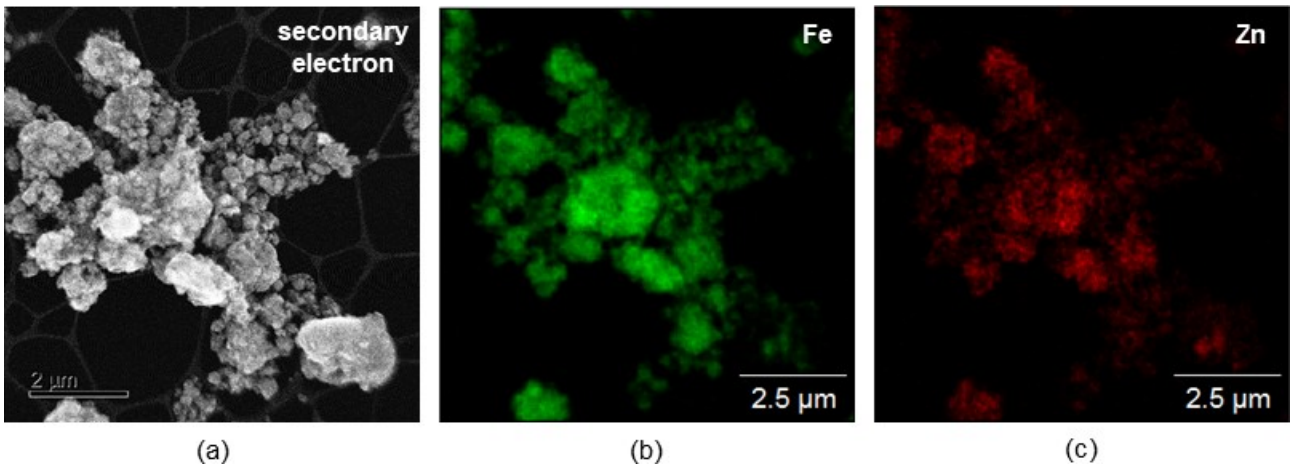

FIG 7 – TEM EDS elemental mapping of a self-sintered BOS dust sample. (a) Secondary electron image; (b) Fe elemental map; and (c) Zn elemental map.

The Mössbauer spectrum for the self-sintered BOS dust is given in Figure 8. This spectrum consisted of a broad magnetic sextet and a non-magnetic doublet. The broad magnetic sextets likely correspond to hematite (major proportion), magnetite (minor proportion) and a third iron oxide component that is likely to be Zn-substituted magnetite (ie the Fe_3O_4-rich end of the Fe_3O_4-$ZnFe_2O_4$ solid solution) or possibly hydrated iron oxides (such as goethite or feroxyhyte, both FeO(OH)). The non-magnetic doublet closely matches $ZnFe_2O_4$. The phases present indicate that the self-sintered dust is oxidised in comparison to the fresh sample, consistent with previously reported work (Longbottom *et al,* 2019a, 2019b, 2020). The broadness of the troughs in the sextet may indicate that these phases may have been heavily substituted (most likely with Zn, which would be consistent with the presence of the Fe_3O_4-$ZnFe_2O_4$ solid solution) or were poorly crystalline (Cadogan, November 2020, personal communication).

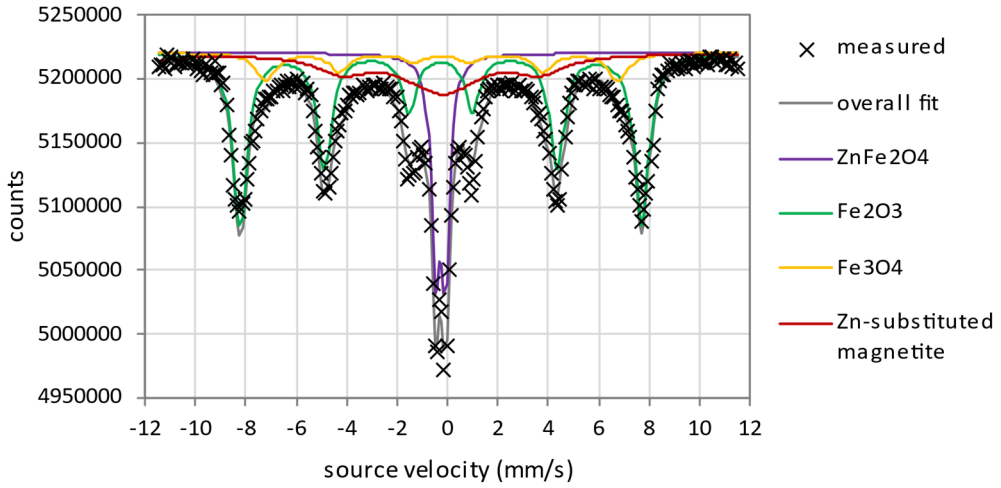

FIG 8 – Mössbauer spectra of self-sintered BOS dust showing the fitted spectra for $ZnFe_2O_4$, Fe_2O_3, Fe_3O_4 and Zn-substituted magnetite.

DISCUSSION

Steel plant by-products such as these BOS dust samples are not commonly examined using these techniques, often considered to be too 'dirty' (eg containing possible volatile components) to be characterised under high vacuum. However, by extensive characterisation of these materials using more routine techniques, such as XRD, X-ray fluorescence (XRF), optical microscopy and SEM, these concerns can be allayed.

It should be noted that there are some limitations to the techniques used. The main issue with both the TEM and Mössbauer characterisation was with the small sample size and whether or not the sample is representative of the bulk material. For this study, there was already a comprehensive characterisation of the bulk material (Longbottom *et al,* 2019a, 2019b, 2020). With this being the case, sample representation was less of an issue. The emphasis of this study was on addressing specific issues with the pre-existing analysis around the Zn-bearing phases. The very fine particulate nature of the fresh BOS dust was identified by SEM (Longbottom *et al,* 2029b), but it was not possible to fully resolve the sample with respect to particle size.

This indicated a higher resolution technique, such as TEM was required. The detailed existing characterisation and understanding of the BOS dust samples, using XRD, SEM-EDS and XRF, allowed the use of TEM and Mössbauer spectroscopy in this study without having to characterise many samples.

Mössbauer spectroscopy used in this study was only able to characterise iron bearing phases due to the γ-ray source (^{57}Co) used. This means that the presence of ZnO could not be tested using this technique. While Zn is Mössbauer active, it is not commonly analysed in this way. $ZnFe_2O_4$ could be identified through its iron component.

The results also indicate that Mössbauer spectroscopy has general applicability in characterisation of metallurgical samples. While Mössbauer spectroscopy is not routinely used in slags, it would be

a useful tool, aiding identification of Fe-bearing phases, or using the appropriate radiation source, phases containing any Mössbauer active elements.

Further, slags are almost always characterised at room temperature, often by XRF and/or XRD. The ability of Mössbauer spectroscopy to identify components and associations in less crystalline or amorphous phases, such as glass in quenched slags, offers opportunities to improve the characterisation of these phases within slags, not possible using XRD. When used in conjunction with other techniques (XRD, XRF, SEM-EDS or Wavelength Dispersive Spectrometry (WDS)), Mössbauer spectroscopy will allow a fuller understanding of the slag and the phases that it contains.

The focus of this characterisation of the BOS dust was to better identify the Zn-bearing phases and their form or morphology. There were a few possible Zn-bearing phases in the BOS dust that were examined. These included metallic Zn, ZnO and $ZnFe_2O_4$. The TEM and Mössbauer characterisation given here, in conjunction with existing XRD, XRF and SEM-EDS characterisation (Longbottom *et al,* 2019a, 2019b), have allowed identification of whether these Zn-bearing phases were present in the BOS dust samples.

Zn

There was little evidence of metallic Zn in either the fresh or self-sintered BOS dust samples. In the fresh BOS dust samples, there is a possibility that the d-spacing measured from the lattice fringes (Table 2) may match that for metallic Zn. However, this measured d-spacing was a better match for ZnO, especially when considered with the other measured d-spacing values (Table 2). Hence, it is unlikely that metallic Zn was present in either the fresh or self-sintered BOS dust samples.

ZnO

The fresh BOS dust samples most likely contained ZnO, as very fine particles surrounding the slightly larger Fe-rich particles, as shown in Figure 2.

One of the motivations for this study was due to a discrepancy between the amount of Zn in the fresh BOS dust (identified through XRF, Table 1) and the amount of Zn that would be contained in the phases identified through XRD, as shown in Figure 1 and in Longbottom *et al* (2020). The results from the TEM characterisation (Figure 2) give a plausible cause for this discrepancy. While a small amount of ZnO was detected by XRD (Figure 1), the TEM results showed that the ZnO particles were extremely small. Hence, it is likely that at least some of these fine particles will lead to poor diffraction patterns, and as such are likely to report to the amorphous/non-bulk crystalline fraction and unlikely to be identified as ZnO by XRD. This may also be reflected in the low intensities of the ZnO peaks for the fresh BOS dust sample in Figure 1, which may be expected to be higher with 13.8 per cent ZnO in the sample. These very low intensities of the ZnO peaks also made estimation of the particle size from the diffraction pattern difficult.

It is unclear whether these fine ZnO particles had formed by oxidation of metallic Zn particles that had condensed during cooling of the gas, or by oxidation of Zn vapour in the gas phase. What effect these different formation mechanisms would have on the particle size and morphology of the ZnO particles is also unclear.

There was little evidence of ZnO in the self-sintered BOS dust sample.

$ZnFe_2O_4$

In the fresh BOS dust samples, the Mössbauer spectroscopy indicated the presence of $ZnFe_2O_4$. This is consistent with the presence of a spinel phase in the XRD of the fresh BOS dust samples (Figure 1). While it was not possible to determine through XRD whether the spinel was Fe_3O_4, $ZnFe_2O_4$ or a solution of the two, the Mössbauer spectroscopy showed that there was some $ZnFe_2O_4$ in the fresh BOS dust sample, while not detecting Fe_3O_4.

In the self-sintered BOS dust sample, the major Zn-bearing phase was $ZnFe_2O_4$, most likely contained within a Fe_3O_4-$ZnFe_2O_4$ solid solution. Previous characterisation by XRD indicated the presence of spinel with lattice spacing close to that of both Fe_3O_4 and $ZnFe_2O_4$ (Figure 1). This is supported by the TEM characterisation of the sample, which indicated that the sample was largely a single phase (Figure 7). The Mössbauer spectroscopy of the self-sintered sample directly identified

$ZnFe_2O_4$, while also reporting the presence of magnetite with some substitution of Fe with Zn. While the Mössbauer shows the presence of both Fe_3O_4 and $ZnFe_2O_4$, the technique measures iron nuclei, with the response depending on the surrounding atoms in the crystal lattice (Sharma, Klingelhofer and Nishida, 2013). Due to this, a single phase solid solution may be reported as two separate phases. While this seems a drawback with the Mössbauer spectroscopy, it offers a positive identification of the presence of Zn within the spinel phase. Previously this could only be speculated on from the XRD data, due to the similar lattice parameters of Fe_3O_4 and $ZnFe_2O_4$. Thus, it is most likely that the sample contains a Fe_3O_4-$ZnFe_2O_4$ solid solution with differing levels of Zn, consistent with the results from the XRD and TEM characterisation.

The improved understanding of the Zn-bearing phases within the BOS dust will allow better predictions of how it will behave during recycling. Since the Zn in the BOS dust was found to be oxidised, a reductant would be required to volatilise the Zn if extraction or separation of Zn from the dust is necessary. For recycling into the BOS vessel, the Zn-bearing phases in the fresh and self-sintered BOS dust are different, affecting how each would interact with slag. ZnO (high ZnO activity, very small particle size) in the fresh dust will interact differently with the BOS slag than the Fe_3O_4-$ZnFe_2O_4$ solid solution (lower ZnO activity) found in the self-sintered dust.

Comparison with reported steel plant by-products

Other studies have characterised BOS dust samples from steel plants around the world. The current BOS dust samples contain high Zn levels in comparison to other reported compositions for BOS dust (Kelebek, Yörük and David, 2004; Steer *et al*, 2014; Vereš, Šepelák and Hredzák, 2015; Gargul, Jarosz and Małecki, 2016; Jabłońska *et al*, 2021; Stewart *et al,* 2022). Typically, the phases found in the BOS dust samples were a close match to those in the fresh BOS dust sample, with metallic iron, wüstite and smaller amounts of magnetite and/or hematite. The Zn-bearing phases reported in other BOS samples are summarised in Table 3.

TABLE 3

Reported Zn-bearing phases in BOS dust.

Study	Technique(s)	Majority phases	Reported Zn-bearing phases
Kelebek, Yörük and David (2004)	XRD, SEM	FeO, Fe_2O_3	$ZnFe_2O_4$ identified by XRD, not differentiated from Fe_3O_4
Steer *et al* (2014)	XRD, wet sizing	not reported	ZnO
Vereš, Šepelák and Hredzák (2015)	XRD, Mössbauer	metallic Fe, FeO, Fe_3O_4, Fe_2O_3	ZnO, $ZnFe_2O_4$
Gargul, Jarosz and Małecki (2016)	XRD	metallic Fe, FeO, Fe_3O_4	ZnO
Jabłońska *et al* (2021)	XRD	Fe_3O_4, ZnO, $ZnFe_2O_4$	ZnO, $ZnFe_2O_4$ identified by XRD, differentiated from Fe_3O_4 using Rietveld fitting
Stewart *et al* (2022)	Mössbauer, XRD, SEM, XRF, digestion + Atomic absorption spectroscopy (AAS)	metallic Fe, FeO, Fe_3O_4, Fe_2O_3	Small amount of Zn in solution in Fe_3O_4 No $ZnFe_2O_4$ identified

Several studies on BOS dust have used different techniques to identify the presence of $ZnFe_2O_4$ (Table 3). In general, $ZnFe_2O_4$ was identified, although often identified by XRD, which may result in difficulties in differentiation between $ZnFe_2O_4$ and Fe_3O_4 (Stewart and Barron, 2020).

Some studies used Mössbauer spectroscopy to attempt to identify $ZnFe_2O_4$, with some studies reporting $ZnFe_2O_4$ and others not (Vereš, Šepelák and Hredzák, 2015; Stewart and Barron, 2020). The variability between samples was speculated to be related to the specific dust extraction-gas

cleaning systems and dust storage for each plant, with samples that contain more oxidised samples having more $ZnFe_2O_4$. These findings correspond well with the phases in the fresh and self-sintered BOS dust samples in the current study, with the more oxidised self-sintered sample containing more $ZnFe_2O_4$ than the fresh sample.

Electric Arc Furnace (EAF) dust often contains more Zn than BOS dust (Suetens *et al*, 2015; Sofilić *et al*, 2004), due to the higher proportion of scrap in the feed. As such, it is useful to consider EAF dust in comparison to the Zn-rich BOS dust samples from the current study. These Zn-rich EAF dust samples were found to contain both ZnO and $ZnFe_2O_4$. Again, these samples compare well with the BOS dust samples in the current study.

CONCLUSIONS

Characterisation of fresh and self-sintered BOS dust by TEM and Mossbauer spectroscopy was carried out to give a better understanding of the Zn-bearing phases within the samples, to improve the understanding of how the BOS dust will behave during recycling.

In the fresh BOS dust sample, TEM showed that Zn was mostly present as extremely fine separate particles of ZnO, attached to the iron particles. These extremely fine particles were <10 nm in size. While most of the Zn was contained within these extremely small particles, Mössbauer spectroscopy identified a small amount of $ZnFe_2O_4$ within the sample (most likely contained within a Fe_3O_4-$ZnFe_2O_4$ spinel solid solution).

The self-sintered BOS dust sample was significantly different. The Zn-bearing phase in this sample was a Fe_3O_4-$ZnFe_2O_4$ solid solution. While this phase had previously been identified by XRD, Mössbauer spectroscopy gave positive identification of Zn within the spinel phase.

The ability to positively identify the phases in complex samples such as these BOS dust indicate that these techniques should have further application in the characterisation of slag, or other metallurgical by-product materials.

ACKNOWLEDGEMENTS

The authors acknowledge use of the facilities and the assistance of David Wexler and David Mitchell at the UOW Electron Microscopy Centre. This research used equipment funded by the Australian Research Council (ARC) Linkage, Infrastructure, Equipment and Facilities (LIEF) grant LE120100104 located at the UOW Electron Microscopy Centre. The authors thank Sean Cadogan (UNSW Canberra) for the Mössbauer analysis measurements and interpretation of results. Funding support from the Australian Research Council Industrial Transformation Research Hubs Scheme (Projects IH130100017; IH200100005) and BlueScope is gratefully acknowledged.

REFERENCES

Ahmed, H M, Persson, A, Ökvist, L S and Björkman, B, 2015. Reduction behaviour of self-reducing blends of in-plant fines in inert atmosphere, *ISIJ International*, 55(10):2082–2089.

Downs, R T and Hall-Wallace, M, 2003. The American Mineralogist Crystal Structure Database, *American Mineralogist*, 88:247–250.

Gargul, K, Jarosz, P and Małecki, S, 2016. Alkaline Leaching of Low Zinc Content Iron-Bearing Sludges, *Arch Metall Mater,* 61(1):43–50.

Gražulis, S, Chateigner, D, Downs, R T, Yokochi, A T, Quiros, M, Lutterotti, L, Manakova, E, Butkus, J, Moeck, P and Le Bail, A, 2009. Crystallography Open Database – an open-access collection of crystal structures, *Journal of Applied Crystallography*, 42:726–729. https://doi.org/10.1107/S0021889809016690

Gražulis, S, Daškevič, A, Merkys, A, Chateigner, D, Lutterotti, L, Quirós, M, Serebryanaya, N R, Moeck, P, Downs, R T and LeBail, A, 2012. Crystallography Open Database (COD): an open-access collection of crystal structures and platform for world-wide collaboration, *Nucleic Acids Research*, 40:D420–D427. https://doi.org/10.1093/nar/gkr900

Gražulis, S, Merkys, A, Vaitkus, A and Okulič-Kazarinas, M, 2015. Computing stoichiometric molecular composition from crystal structures, *Journal of Applied Crystallography*, 48(1):85–91. https://doi.org/10.1107/S1600576714025904

Hleis, D, Fernández-Olmo, I, Ledoux, F, Kfoury, A, Courcot, L, Desmonts, T and Courcot, D, 2013. Chemical profile identification of fugitive and confined particle emissions from an integrated iron and steelmaking plant, *J of Hazardous Materials*, (250–251):246–255.

Jabłońska, M, Rackwał, M, Wawer, M, Kądziołka-Gaweł, M, Teper, E, Krzykawski, T and Smołka-Danielowska, D, 2021. Mineralogical and Chemical Specificity of Dusts Originating from Iron and Non-Ferrous Metallurgy in the Light of Their Magnetic Susceptibility, *Minerals*, 1(2):216.

Kelebek, S, Yörük, S and David, B, 2004. Characterization of basic oxygen furnace dust and zinc removal by acid leaching, *Minerals Engineering*, 17:285–291.

Lin, X, Peng, Z, Yan, J, Li, Z, Hwang, J-Y, Zhang, Y, Li, G and Jiang, T, 2017. Pyrometallurgical recycling of electric arc furnace dust, *J Cleaner Production*, 149:1079–1100.

Longbottom, R J, Monaghan, B J, Pinson, D J and Chew, S J, 2019b. Understanding the Self-Sintering Process of BOS Filter Cake for Improving Its Recyclability, *J Sustainable Metallurgy*, 5:429–441.

Longbottom, R J, Monaghan, B J, Pinson, D J, Webster, N A S and Chew, S J, 2020. *In situ* Phase Analysis during Self-sintering of BOS Filter Cake for Improved Recycling, *ISIJ International*, 60(11):2436–2445.

Longbottom, R J, Monaghan, B J, Zhang, G, Pinson, D J and Chew, S J, 2019a. Self-sintering of BOS Filter Cake for Improved Recyclability, *ISIJ International*, 59(3):432–441.

Merkys, A, Vaitkus, A, Butkus, J, Okulič-Kazarinas, M, Kairys, V and Gražulis, S, 2016. COD::CIF::Parser: an error-correcting CIF parser for the Perl language, *Journal of Applied Crystallography*, 49(1):292–301. https://doi.org/10.1107/S1600576715022396

Merkys, A, Vaitkus, A, Grybauskas, A, Konovalovas, A, Quirós, M and Gražulis, S, 2023. Graph isomorphism-based algorithm for cross-checking chemical and crystallographic descriptions, *Journal of Cheminformatics*, 15. https://doi.org/10.1186/s13321-023-00692-1

Nyirenda, R L, 1991. The processing of steelmaking flue-dust: A review, *Minerals Engineering*, 4(7–11):1003–1025.

Quirós, M, Gražulis, S, Girdzijauskaitė, S, Merkys, A and Vaitkus, A, 2018. Using SMILES strings for the description of chemical connectivity in the Crystallography Open Database, *Journal of Cheminformatics*, 10. https://doi.org/10.1186/s13321-018-0279-6

Sharma, V K, Klingelhofer, G and Nishida, T, 2013. Mössbauer Spectroscopy: Applications in Chemistry, Biology and Nanotechnology, Part V Iron Oxides, pp 349–532 (John Wiley and Sons).

Steer, J, Grainger, C, Griffiths, A, Griffiths, M, Heinrich, T and Hopkins, A, 2014. Characterisation of BOS steelmaking dust and techniques for reducing zinc contamination, *Ironmaking and Steelmaking,* 41(1):61–66.

Stewart, D J C and Barron, A R, 2020. Pyrometallurgical removal of zinc from basic oxygen steelmaking dust – A review of best available technology, *Resources*, *Conservation and Recycling*, 157:104746.

Stewart, D J C, Scrimshire, A, Thomson, D, Bingham, P A and Barron, A R, 2022. The chemical suitability for recycling of zinc contaminated steelmaking by-product dusts: The case of the UK steel plant, *Resources*, *Conservation and Recycling Advances*, 14:200073.

Suetens, T, Guo, M, Van Acker, K and Blanpain, B, 2015. Formation of the $ZnFe_2O_4$ phase in an electric arc furnace off-gas treatment system, *J of Hazardous Materials*, (287):180–187.

Vaitkus, A, Merkys, A and Gražulis, S, 2021. Validation of the Crystallography Open Database using the Crystallographic Information Framework, *Journal of Applied Crystallography*, 54(2):661–672. https://doi.org/10.1107/S1600576720016532

Vaitkus, A, Merkys, A, Sander, T, Quirós, M, Thiessen, P A, Bolton, E E and Gražulis, S, 2023. A workflow for deriving chemical entities from crystallographic data and its application to the Crystallography Open Database, *Journal of Cheminformatics*, 15. https://doi.org/10.1186/s13321-023-00780-2

Vereš, J, Šepelák, V and Hredzák, S, 2015. Chemical, mineralogical and morphological characterisation of basic oxygen furnace dust, *Mineral Processing and Extractive Metallurgy*, *Transactions of the Institutions of Mining and Metallurgy*: *Section C,* 124(1):1–8.

Wang, J, Zhang, Y, Cui, K, Fu, T, Gao, J, Hussain, S and AlGarni, T S, 2021. Pyrometallurgical recovery of zinc and valuable metals from electric arc furnace dust – A review, *J Cleaner Production*, 298:126788.

Nedar, L, 1996. Dust formation in a BOF converter, *Steel Research*, 67(8):320–327.

Sofilić, T, Rastovčan-Mioč, A, Cerjan-Stefanović, Š, Novosel-Radović, V and Jenko, M, 2004. Characterization of steel mill electric-arc furnace dust, *J of Hazardous Materials*, (B109):59–70.

Effect of oxygen on the interfacial phenomena and metal recovery rate in recycling process

DOI: 10.62053/JGTC1866
J Park[1], Y-B Kang[2] and J H Park[3]

1. Student, POSTECH, Pohang 37673, South Korea; and formerly Hanyang University, Ansan, South Korea, 15588. Email: jhpark7273@potsech.ac.kr
2. Professor, POSTECH, Pohang 37673, South Korea. Email: ybkang@potsech.ac.kr
3. Professor, Hanyang University, Ansan 15588, South Korea. Email: basicity@hanyang.ac.kr

ABSTRACT

In order to understand the effect of oxygen injection into the molten metal on the valuable metals (VM) recovery and interfacial phenomena, several high-temperature experiments were conducted using a high-frequency induction furnace with a quartz tube as the reaction chamber at 1673 K. Copper-based waste printed circuit board (PCB) that contains some impurities was selected as the end-of-life resource. CaO-SiO_2 based pre-fused slag and oxygen gas were used in present works. The composition change and microstructure of the samples were analysed.

As oxygen was injected into the system, impurities were rapidly removed. After the removal of impurities, continuously injected oxygen lowered interfacial tension between liquid slag and liquid metal. Lowered interfacial tension induced Cu loss into the slag.

INTRODUCTION

Sustainable development and recycling process

Recently, numerous research have been continued for sustainable development. The metal-based scrap recycling process is a representative method. Electronic wastes (E-waste) are usually used as the raw materials in such recycling processes.

In order to recover valuable metals (VM) in E-waste, a batch-type arc furnace is often used (Hagelüken, 2006). Figure 1 shows a comprehensive sequence for a Cu-based scrap recycling process. In the converting stage, oxygen is blown to melt to remove oxidative impurities. Because converting and tapping stage are dynamic, significant amounts of droplets are entrapped in slag phase. In order to recover metal droplets from the slag, additional process such as ‘slag cleaning’ should be adopted.

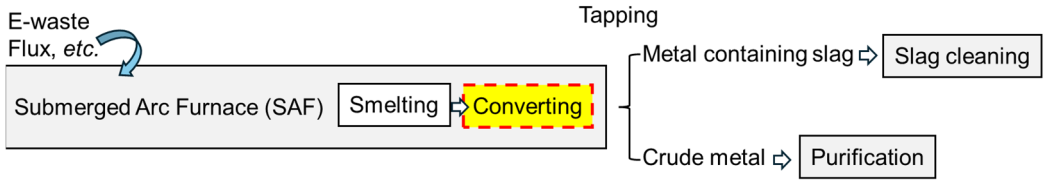

FIG 1 – Recycling process for valuable metals-contained materials (E-waste).

The chemical effect of oxygen blowing

Oxygen can influence on surface tension of the liquid metal. Previous researchers concluded that high oxygen potential reduces the surface tension of liquid metal, and its quantitative description is available (Belton, 1976). However, reports about the effect of oxygen on the quantity of metal loss in molten slag are rare.

The physical effect of oxygen blowing

There have been several research regarding the droplet formation mechanism at the metal/slag interface (Han and Holappa, 2003). It was revealed that the metal droplets were formed by rising bubbles.

Present study focuses on coupled effects of oxygen blowing on Cu loss in order to understand metal loss mechanisms in recycling process.

EXPERIMENTAL PROCEDURE

Furnace information

A high-frequency induction furnace was employed. Metal samples collected from PCB were initially put in a fused magnesia crucible (60 (OD) × 50 (ID) × 120 (H), mm), which was located in a graphite susceptor (80 (OD) × 65 (ID) × 120 (H), mm) for heating of samples. The graphite susceptor was surrounded by a commercial purity alumina board for insulation. A quartz tube (120 (OD) × 114 (ID) × 400 (H), mm) was used as the reaction chamber.

Preparation of the crude metal and the synthetic slag samples

Pre-molten printed circuit board (PCB) was used in the present experiments. Slag samples was using reagent grade powders. Especially, CaO was prepared by calcinating $CaCO_3$ in a muffle furnace at 1273 K for 24 hrs. The mixed powder and was molten at 1873 K for 30 mins in graphite crucible. Collected slag was crushed and calcinated at 1273 K in a muffle furnace for 48 hrs to remove trace C. Information of each sample were also listed in Tables 1 and 2, respectively.

TABLE 1

Mass and chemical composition of the crude metal.

Series ID	Mass (g)	Cu (wt%)	Fe (wt%)	Si (wt%)	O (wt%)
No Slag (B) – 500	500	86.9	12.6	0.3	0.001
CASM (B) – 500	500	88.6	10.9	0.3	0.002
CASM (B) – 300	300	84.7	14.3	0.8	0.001
CSM (B) – 300	300	91.4	8.1	0.4	0.001
CSM (T) – 300	300	86.9	12.5	0.4	0.002

TABLE 2

Mass and chemical composition of the synthetic slag.

Series ID	Mass (g)	CaO (wt%)	Al_2O_3 (wt%)	SiO_2 (wt%)	MgO (wt%)
No Slag (B) – 500	-	-	-	-	-
CASM (B) – 500	130	34.6	19.2	34.6	11.5
CASM (B) – 300	80	34.6	19.2	34.6	11.5
CSM (B) – 300	80	41.2	-	41.2	17.6
CSM (T) – 300	80	41.2	-	41.2	17.6

Procedure for the metal-slag reaction

The reaction was carried out at 1673 K. Temperature of the induction furnace was controlled within ±2 K using a proportional integral differential controller connected to a B-type thermocouple.

When the temperature reached 1673 K and stabilised, molten metal was sampled using a quartz tube and then quenched in ice water. This moment was set to t = 0. The synthetic slag was added to the metal, then oxygen gas (99.99 per cent purity) was blown in metal (bottom blowing, (B), 1 mm above from the crucible bottom) using an alumina lance (10 (OD) × 5 (ID) × 350 (H), mm). In ‘CSM (T) – 300’, oxygen was injected into surface of the slag. Each sample was sampled periodically using a quartz tube and iron rod, respectively. All of samples were dried using an oven at 323 K for 24 hrs.

Analysis

Metal samples were analysed by combustion method for the O content (TC-300, LECO), by inductively-coupled plasma spectroscopy (ICP-AES, SPECTRO ARCOS). Fe^{2+} content in the slag samples was analysed by titration technique, and Fe^{3+} content was estimated as (%T. Fe)-(% Fe^{2+}) (KS-E-3016). Morphology of the samples was observed using a Field-Emission Scanning Electron Microscope (FE-SEM, S-4800, HITACHI) imaging and Energy-Dispersive X-ray Spectroscopy (EDS, Nova Nano SEM 450, FEI).

RESULTS AND DISCUSSION

Impurity removal and oxygen accumulation

Figure 2 shows the composition evolution of the metal: normalised contents of Si and Fe during oxygen blowing. At the early stage, Si and Fe in the metal rapidly disappeared: the oxygen reacted with Si and Fe by Reaction (1) and (2) (Sigworth and Elliott, 1974). This stage is designated as 'impurity removal regime'. Si was removed faster than Fe, because of the higher affinity of O to Si than to Fe.

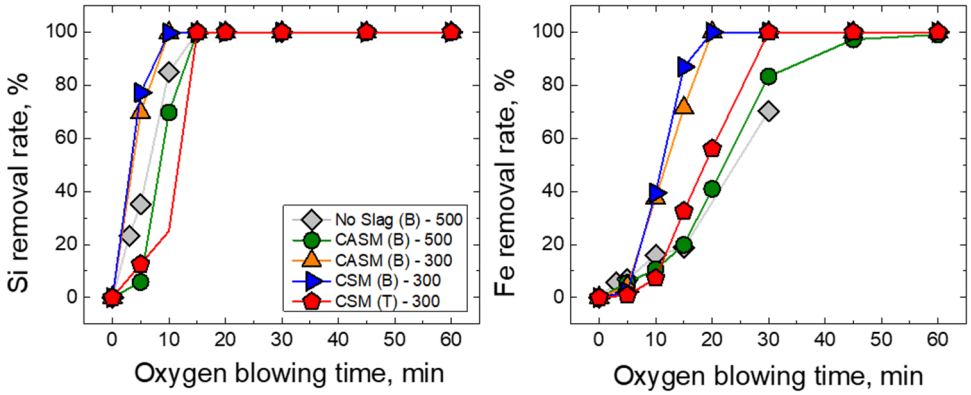

FIG 2 – Si and Fe contents change during the oxygen blowing.

$$Si_{Cu} + O_{2(g)} = (SiO_2);\ \Delta G° = -884{,}100 + 232.1\ T\ (J\ mol^{-1}) \quad (1)$$

$$Fe_{Cu} + O_{2(g)} = (FeO);\ \Delta G° = -295{,}000 + 92.5\ T\ (J\ mol^{-1}) \quad (2)$$

Figure 3 shows the composition evolution of the slag. Except for 'No slag (B)', all the other cases show an increase in the ratio: oxidising the slag. In particular, 'CSM(T)' shows a considerably higher ratio than the other cases. It has been known that the top blowing can increase the oxygen potential of slag, thereby stabilising Fe_2O_3 relative to FeO. Sano, Lü and Riboud (1997) suggested that stabilising Fe_2O_3 or Fe_3O_4 would increase the melting point and viscosity of slag. Therefore, in case of recycling process which uses Fe-containing sources, top blowing is not recommended.

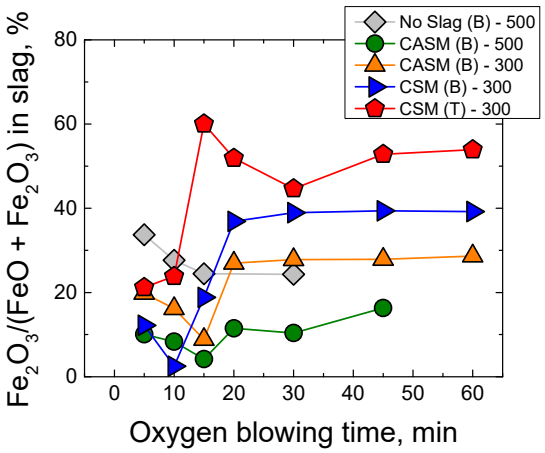

FIG 3 – Fe_2O_3 change in the slag during the oxygen blowing.

As shown in Figure 4, (%T. Cu) increased abruptly during the oxygen blowing. 'No Slag (B) – 500' and 'CASM (B) – 500' were excluded because of lack of related data. The moment of the abrupt increase in (%T. Cu) is more or less close to the moment of termination of the impurity removal (see Figure 2). Therefore, a hypothesis can be developed that excessive oxygen blowing can lead the Cu loss. This moment is considered as a transition from the 'impurity removal regime' to the 'over-blown regime'.

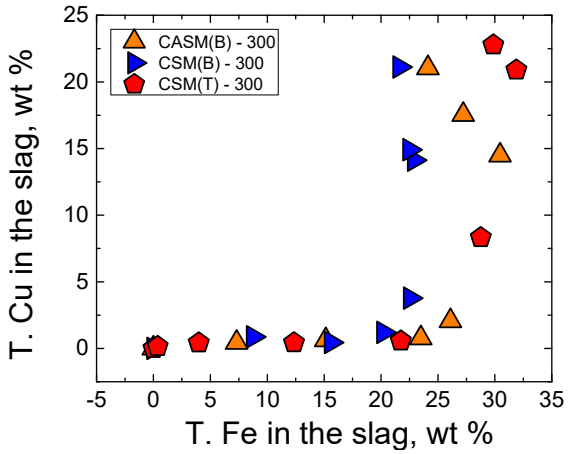

FIG 4 – Changes of (%T. Fe) and (%T. Cu) contents in the slag. Sudden increase of (%T. Cu) is an indicator of the transition point between the impurity removal regime and the over-blown regime.

Surface tension and interfacial tension change

In order to evaluate the physical effect and the chemical effect of oxygen injection, the blowing number (N_B) was evaluated (Subagyo *et al,* 2003) as expressed as Equation 3.

$$N_B = \frac{\rho_g v_g^2}{2\sqrt{g\sigma_M \rho_M}} \quad (3)$$

where ρ_g (kg m^{-3}), v_g (m s^{-1}), σ_M (mN m^{-1}), ρ_M (kg m^{-3}), and g (m s^{-2}) are the density and the velocity of the oxygen gas, the surface tension and the density of liquid Cu, and the gravitational acceleration respectively. Authors concluded that when N_B is over 1, physical turbulence by any gas blowing occurs. As a result, N_B was approximately ~10^{-4}. Therefore, physical effect of oxygen blowing is negligible.

Figure 5 shows the quenched final sample after the experiment of 'CSM (B) – 300'. In all the cases, the two phases stuck close together. It can be assumed that interfacial state is far from other experiment where oxygen is not used.

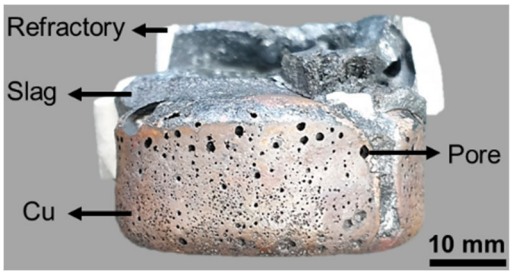

FIG 5 – Snapshot of slag/metal samples after experiment.

Researchers have investigated the effect of oxygen potential on the surface tension of liquid Cu (alloy). Following Belton (1976), σ_M (mN m^{-1}) can be calculated using Equations 4 and 5:

$$\sigma_M = \sigma_M^\circ - RT\Gamma_{sat.}^\circ \cdot \ln(1 + K_O \cdot a_O) \quad (4)$$

$$\Gamma_{sat.}^\circ = -\frac{1}{RT}\left(\frac{\delta\sigma_M}{\delta \ln a_O}\right)_{constant} \quad (5)$$

where σ°_{M} (mN m^{-1}), KO, aO, and $\Gamma^{\circ}_{sat.}$ are the surface tension of pure liquid Cu, the absorption coefficient, the activity of O in the liquid Cu alloy and the surface tension absorption at the saturation, respectively. KO was reported to be 40 at 1673 K (Morita and Kasama, 1980). $\Gamma^{\circ}_{sat.}$ was reported by others (Monma and Suto, 1961). Surface tension of liquid Cu was calculated using Equations 4 and 5. Surface tension of the slag, σ_S, (mN m^{-1}) was roughly estimated as shown in Equation 6:

$$\sigma_S = \sum X_i \sigma^{\circ}_{i,\,pure} \tag{6}$$

where $\sigma^{\circ}_{i,\,pure}$ (mN m^{-1}) and X_i are the surface tension and the mole fraction of the pure oxide component i in the slag. Related data are summarised in Mills and Keene's report (1987). Change in σ_S does not appear to be significant compared to the change of σ_M. The interfacial tension, $\sigma_{M/S}$ (mN m^{-1}) was calculated using the equation as shown in Equation 7 (Girifalco and Good, 1957):

$$\sigma_{M/S} = \sigma_M + \sigma_S - 2\phi\sqrt{\sigma_M \sigma_S} \tag{7}$$

$$\text{where: } \phi = 0.5 + 0.3X\text{FeO} \tag{8}$$

Figure 6 shows relationship between calculated $\sigma_{M/S}$ and (%T. Cu) in the slag. In impurity removal regime, calculation of surface tension of liquid Cu using Belton's equation is not valid. Therefore, points where impurities were not removed completely were excluded.

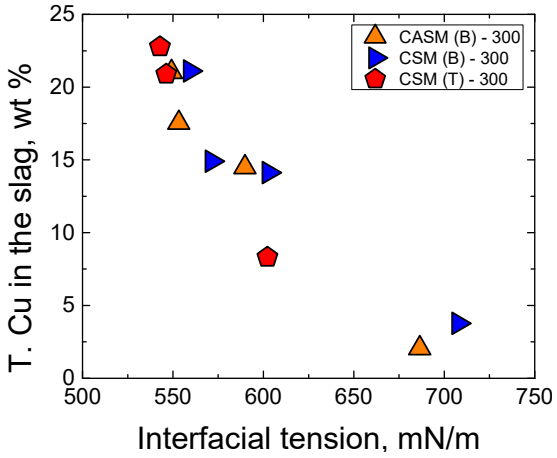

FIG 6 – Relationship between $\sigma_{M/S}$ and Cu loss into slag phase.

After impurity removal, continuously supplied oxygen was then lowered the surface tension of the liquid Cu, thereby lowering the interfacial tension between the liquid Cu and the liquid slag. This was a major reason leading the Cu loss (Park, Lee and Park, 2021).

CONCLUSIONS

The role of the oxygen blowing on the impurity removal and the Cu metal loss was concerned. Entire reaction can be divided with two regimes: the impurity removal regime and the over-blown regime. Key findings of the present study are:

- At the early stage of reaction, oxygen could be used to remove impurities in molten crude Cu metal. Composition of the slag did not show noticeably impact on the impurity removal tendency.
- After the impurity removal, continuously injected oxygen in the liquid Cu lowered surface tension. It was a major reason to lower the interfacial tension between the liquid Cu and the liquid slag. The lower interfacial tension was thought to be a main reason of the Cu metal loss.

REFERENCES

Belton, G R, 1976. Langmuir adsorption, the Gibbs adsorption isotherm and interfacial kinetics in liquid metal systems, *Metallurgical Transactions, A, Physical Metallurgy and Materials Science*, 7(1):35–42. https://doi.org/10.1007/bf02652817

Girifalco, L A and Good, R J, 1957. A theory for the estimation of surface and interfacial energies, Derivation and application to interfacial tension, *The Journal of Physical Chemistry*, 61(7):904–909. https://doi.org/10.1021/j150553a013

Hagelüken, C, 2006. Recycling of Electronic Scrap at Umicore's Integrated Metals Smelter and Refinery, *World of Metallurgy – ERZMETALL,* 59:152–161. Available from: <https://www.researchgate.net/publication/240629115_Recycling_of_Electronic_Scrap_at_Umicores_Integrated_Metals_Smelter_and_Refinery>

Han, Z and Holappa, L, 2003. Mechanisms of Iron Entrainment into Slag due to Rising Gas Bubbles, *ISIJ International*, 43(3):292–297. https://doi.org/10.2355/isijinternational.43.292

Mills, K C and Keene, B J, 1987. Physical properties of BOS slags, *International Materials Reviews*, 32(1):1–120. https://doi.org/10.1179/095066087790150296

Monma, K and Sutô, H, 1961. Effects of dissolved sulphur, oxygen, selenium and tellurium on the surface tension of liquid copper, *Materials Transactions*, 2(3):148–152. https://doi.org/10.2320/matertrans1960.2.148

Morita, Z and Kasama, A, 1980. Effect of slight amount of dissolved oxygen on the surface tension of liquid copper, *Trans Jpn Inst Met*, 21:522–530. https://doi.org/10.2320/matertrans1960.21.522

Park, J, Lee, J and Park, J H, 2021. Effect of oxygen blowing on copper droplet formation and emulsification phenomena in the converting process, *Journal of Sustainable Metallurgy*, 7(3):831–847. https://doi.org/10.1007/s40831-021-00421-8

Sano, N, Lü, W and Riboud, P V, 1997. *Advanced Physical Chemistry for process metallurgy*, Available from: <https://ci.nii.ac.jp/ncid/BA31247737>

Sigworth, G K and Elliott, J F, 1974. The thermodynamics of dilute liquid copper alloys, *Canadian Metallurgical Quarterly*, 13(3):455–461. https://doi.org/10.1179/cmq.1974.13.3.455

Subagyo, S and Brooks, G A, 2003. Generation of Droplets in Slag-Metal Emulsions through Top Gas Blowing, *ISIJ International*, 43(7):983–989. https://doi.org/10.2355/isijinternational.43.983

Measuring circular economy through life cycle assessment – challenges and recommendations based on a study on recycling of Al dross, bottom ash and shavings

DOI: 10.62053/IOXD6464

E Pastor-Vallés[1], A Vallejo-Olivares[2], G Tranell[3] and J B Pettersen[4]

1. PhD Candidate, Industrial Ecology Programme, NTNU, Trondheim 7034, Norway. Email: elisa.p.valles@ntnu.no
2. PhD Candidate, Department of Materials Science, NTNU, Trondheim 7034, Norway. Email: alicia.vallejo.olivares@gmail.com
3. Professor, Department of Materials Science, NTNU, Trondheim 7034, Norway. Email: gabriella.tranell@ntnu.no
4. Associate Professor, Industrial Ecology Programme, NTNU, Trondheim 7034, Norway. Email: johan.berg.pettersen@ntnu.no

ABSTRACT

Metals are essential for the sustainability transition and decarbonisation of society. Yet, it will be paramount to produce them sustainably and minimise the affiliated resource and energy use and the associated emissions. In the circular economy, the metallurgical industry should recycle existing material stocks, and improve its utilisation of wastes, residues and side streams. This increases the complexity of processes, as they become both (often multi-fraction) waste treatment as well as material production processes and brings complexity to the assessment of environmental benefits.

Assessing the environmental impact of technological developments frequently is supported by life cycle assessment (LCA). While the method is well documented, its implementation involves several methodological choices that deserve reasoning and analysis, such as how to define the product when former wastes are turned into new products, the selection of impact methodology when converting emissions to environmental indicators, the definition of system boundaries and co-product allocation and the interpretation of sensitivity and uncertainty in final outcomes.

In this exploratory study, we investigate how the variation of LCA set-up affects the environmental burden of the system. We consider a metallurgical process where a mix of hard-to-recycle aluminium-containing streams is used to produce aluminium cast alloys in a rotary furnace. Re-melting with salt-fluxes allows recovering metals from partly oxidised/contaminated streams, such as dross, bottom ash and industrial shavings, but at the expense of generating significant amounts of salt-slag/salt-cake hazardous waste. The study considers different system alternatives such as landfilling the salt-slag residues versus valourising them into salts, aluminium concentrates, ammonium sulfate and non-metallic-compounds to be used by the metallurgical, construction or chemical industries. Practical recommendations are outlined to facilitate the implementation of LCA in assessing the potential benefits of the circular economy in the metallurgical sector.

INTRODUCTION

Metals are critical for meeting the needs of our society, and we rely on them in multiple applications eg in the energy, transportation, packaging, construction and communications industries. Applied ubiquitously across different sectors, some inherent sustainability implications are associated with their large lifespans and potential for recycling (Norgate and Rankin, 2002), in addition to being critical enablers of some relevant technologies for decarbonisation, such as renewable energy generation, batteries or electronics (World Energy Outlook, 2021).

Facing an unprecedented climate crisis, the demand for major metals might increase up to six-fold over this century as the global population and living standards rise (Watari, Nansai and Nakajima, 2021). Despite the economic and environmental benefits of metal production, sustaining the future provision of metals while considering the ecosystems' limited assimilation and provision capacity remains challenging. The production of metals alone entails resource use (2.8 billion tonnes (Bt) of metal produced each year) (based on information from US Geological Survey, 2023), energy-intensive processes (7–8 per cent of the global energy consumption) (UN Environment Programme, 2017) and emissions of pollutants (among others, approximately 10 per cent of global green house

gas emissions) (UN Environment and International Resource Panel, 2019). Some impacts derived from the extraction and processing of these metals are, for instance, climate change, biodiversity loss and particulate matter health impacts (UN Environment and International Resource Panel, 2020).

With increasing environmental pressures to reduce the consumption of resources and generation of emissions in the production of metals, life cycle assessment (LCA) has emerged as a method that quantifies the potential environmental burdens of a product system, identifying hotspots (or the parts of the system where environmental impacts are more significant) and possibilities for improvement. However, even though this method is well documented, its application involves several methodological choices that could significantly influence the results. Reasoning and consideration of these can be critical, especially when dealing with circular economy systems, in which material stocks are recycled and the utilisation of wastes, residues and side streams improved. The complexity of these systems lies in that they become both (often multi-fraction) waste treatment as well as material production processes.

Although LCA is a standard methodology to evaluate the impact through the life cycle of metallurgical systems, there is a lack of specific guidelines for the metallurgical industry that test the influence of methodological choices when implementing circular economy concepts. A study by PE International (2014) and Santero and Hendry (2016) highlights some methodological choices that affect the results of a metallurgical LCA, such as system boundaries, allocation and impact categories. However, their influence has not been tested quantitatively in a case study. In addition, the present article expands on other relevant methodological choices.

Case study

The original model for this study is found in Vallejo Olivares *et al* (2024). The system analysed considers the recycling of hard-to-recycle (partly oxidised or contaminated) aluminium-containing flows via a rotary furnace. This process allows, through re-melting with salt-fluxes and the rotational movement of the furnace, to separate the metal from the non-metallic contaminants (eg oxide layer, carbonaceous residues) and promote its coalescence, while also protecting the molten metal from oxidation during the high-temperature process (Milani and Timelli, 2023).

Even though from an environmental and economic perspective recycling aluminium is considered to be more sustainable than producing it anew (Olivieri, Romani and Neri, 2006; Damgaard, Larsen and Christensen, 2009), the use of salts has a significant downside in the generation of salt slag residues (a mix of salts, non-metallic compounds (NMCs) and entrapped metallic droplets), that are classified as hazardous waste (Environmental Protection Agency, 2002) and pose risks for landfilling (Office of Research and Development, 2015). Another option is to valourise these slags by crushing and dissolving them in water, obtaining both salts and aluminium concentrates that can be fed back into the rotary furnace, as well as ammonium sulfate and NMCs that the chemical and construction industries can benefit from. Various salt-slag recovery treatments are described in the non-ferrous industry's Best Available Techniques (BAT) reference document (Joint Research Centre, 2017).

The LCA methodology is applied to test the influence of relevant methodological choices in the environmental impact for this case study and draw practical recommendations for the use of LCA for the evaluation of metallurgical and circular economy systems for the industry.

LCA methodology

Life cycle assessment is described by the international standards ISO 14040 and ISO 14044 as 'the compilation and evaluation of the inputs, outputs and the potential environmental impacts of a product system throughout its life cycle' (International Standard Organization, 2006a, 2006b).

The evaluation of environmental impacts through LCA is carried out in four iterative steps (Figure 1):

1. *Goal and scope* definition, where the methodological choices of the LCA are defined.
2. *Inventory analysis*, or the calculation of all inputs (resources) and outputs (emissions) that pose a burden in the environment.

3. *Impact assessment*, or the quantification of the environmental impact associated to the flows calculated during the *inventory analysis*.
4. *Interpretation*, in which the outcomes of the previous phases are evaluated in accordance to the *goal and scope*.

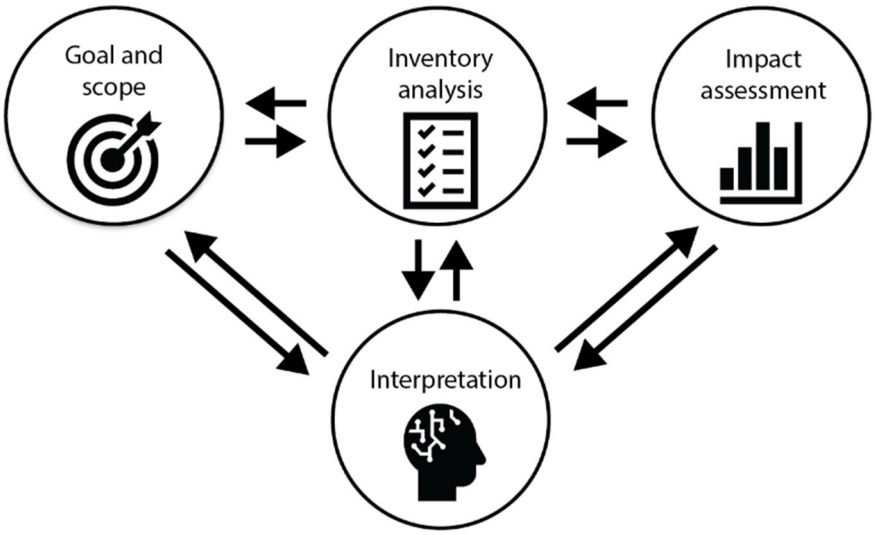

FIG 1 – Phases of an life cycle assessment (LCA).

While methodological choices affect the entire study of an LCA, they are broadly decided during the *goal and scope* phase. However, as LCA is an iterative process, it allows for feedback loops between the different stages and correcting for these when necessary. That could be, for instance, if better information is available or if the application of the study has changed.

The areas identified in the LCA methodology that significantly affect the assessment results are system boundaries; functional unit and allocation procedures; database, impact categories and impact method; and temporal, geographical and data quality considerations. These are thoroughly discussed and evaluated in the next sections.

EVALUATION OF METHODOLOGICAL CHOICES

System boundaries

ISO 14040 states that:

> *The system boundary determines which unit processes shall be included within the LCA (…) The deletion of life cycle stages, processes, inputs or outputs is only permitted if it does not significantly change the overall conclusions of the study* (International Standard Organization, 2006a).

The term ‘cradle-to-grave’ involves considering a product’s life cycle. However, the metallurgical industry produces many ‘cradle-to-gate’ studies, ie from the extraction of raw materials to the semi-finished product, excluding its further transport, use and disposal, as these are often uncertain (PE International, 2014). For example, an aluminium sheet can be used in multiple applications (eg in construction, packaging or transport), over which the producer has no control. In contrast, when assessing finished products, such as home appliances, the LCA studies usually take a cradle-to-grave approach.

Since this case study evaluates the production of a semi-finished product (aluminium ingots), a cradle-to-gate approach is preferred. Two different scenarios are considered, as shown in Figure 2:

Scenario 1: Salt slag residue is landfilled.

Scenario 2: Salt slag is processed into recycled salts recirculated in the process and NMCs and ammonium sulfates, which the cementitious and chemical industries can use further.

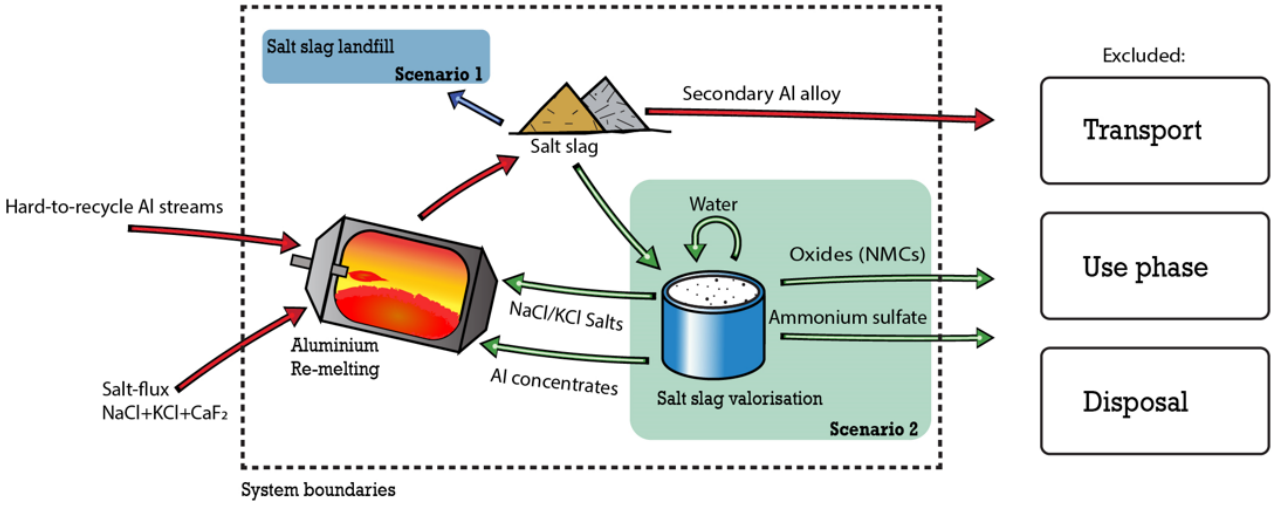

FIG 2 – The system boundaries for this study consider raw material extraction and production but exclude the use and final disposal of products. Modified from Vallejo Olivares *et al* (2024).

The inventory, or inputs and outputs translated to environmental impacts during the LCA, differs depending on the scenario and system boundaries considered and is displayed in Table 1. Note that the quantity of inputs needed when the system boundaries include the recycling of salts (Scenario 2) is generally higher. However, more by-products are also obtained by this process.

Regarding the last negative flow of hard-to-recycle aluminium, it implies that the evaluated process treats 1 tonne of material mix, which would otherwise be considered waste and end up handled by waste management systems. This is based on the assumption that the characteristics of the scrap mix (oxidation, contamination, low aluminium content) make it unsuitable for utilisation by other recycling processes. If treating scrap streams with a higher content of aluminium (eg used beverage containers), this flow should instead be replaced by an input of aluminium secondary material, partly decreasing the benefit of recycling aluminium through the current process. This is because the inherent value of the waste fraction makes it suitable for other recycling processes. There is also a third option, which involves the input of burden-free aluminium, leading to neither positive nor negative impacts. This is called the cut-off approach, in which only the impacts directly caused by a product are considered; in this case, the impacts caused by the collection and treatment of the scrap. The influence of these assumptions is studied later in the section 'Temporal, geographical and data quality considerations'.

To compare the environmental performance of Scenario 1 and 2, the environmental burdens must be distributed among the different co-products through allocation procedures. This will be discussed in the next section, together with the functional unit.

TABLE 1

Life cycle inventory for treating 1 tonne of aluminium-containing waste streams.

Input/output	Unit	Scenario 1: Salt slag landfill	Scenario 2: Salt slag valourisation
Products			
Secondary cast aluminium product	tonne	0.70	0.72
By-product: oxides (NMCs)	tonne	-	0.35
By-product: ammonium sulfate	tonne	-	0.033
Inputs			
Sodium chloride	tonne	0.098	0.01
Potassium chloride	tonne	0.042	0.0046
Calcium fluoride	tonne	0.0028	0.0029
Sulfuric acid	kg	-	10.22
Lime	kg	0.71	0.74
Liquid oxygen	kg	83.84	86.73
Nitrogen	kg	-	0.40
Water	m^3	0.5	1.07
Electricity	kWh	63.88	116
Heat from natural gas	kWh	670.72	917
Diesel	kg	1.04	1.41
Emissions and solid waste			
Carbon dioxide	tonne	0.170	0.233
Sulfur dioxide	tonne	0.21	0.21
Nitrogen oxides	kg	0.10	0.14
Particulates	kg	0.015	0.016
Hydrochloric acid	kg	0.019	0.020
Hydrogen fluoride	kg	0.004	0.004
Heavy metals	kg	0.0006	0.0007
Methane	kg	-	0.028
Dust	tonne	0.02	0.02
Sludge to landfill	tonne	0.53	-

NMC – non-metallic compounds.

Functional unit and allocation procedures

The functional unit (FU) is the reference flow to which all other inputs and outputs are scaled to.

It expresses the function of the system. For example, in a system where the production of a metal is assessed, it can relate to the mass of the product. In multi-output systems, however, selecting one functional unit is not straightforward. In our case study, the main product is the aluminium cast alloy; however, the treatment of the residue fraction is another function provided by this system.

In addition, the studied system produces other by-products: ammonium sulfates and NMCs. The inputs and outputs must be allocated among these co-products, to attribute the corresponding impact to each of them. Allocation is carried out in the following order of preference (International Standard Organization, 2006a):

1. Whenever possible, allocation should be avoided by subdividing the input and output data to each of the co-products, or by expanding the product system (system expansion approach). When two functions are provided in the same system, this last approach is equivalent to crediting the system with the impacts avoided by the alternative production of the secondary function, in the most likely way of producing it (Hauschild, Rosenbaum and Olsen, 2018).
2. Mass allocation – allocating on a physical basis.
3. Economic allocation – allocating on a monetary basis.

The influence of selecting different functional units and allocation methods is tested in this study.

Functional unit

Regarding the functional unit, the results for the global warming impact when considering two functional units: one tonne of hard to recycle mixed scrap to treatment and one tonne of aluminium produced, are displayed in Figure 3. These functional units are tested for the two different scenarios of landfilling the salts (Scenario 1) versus recycling them (Scenario 2).

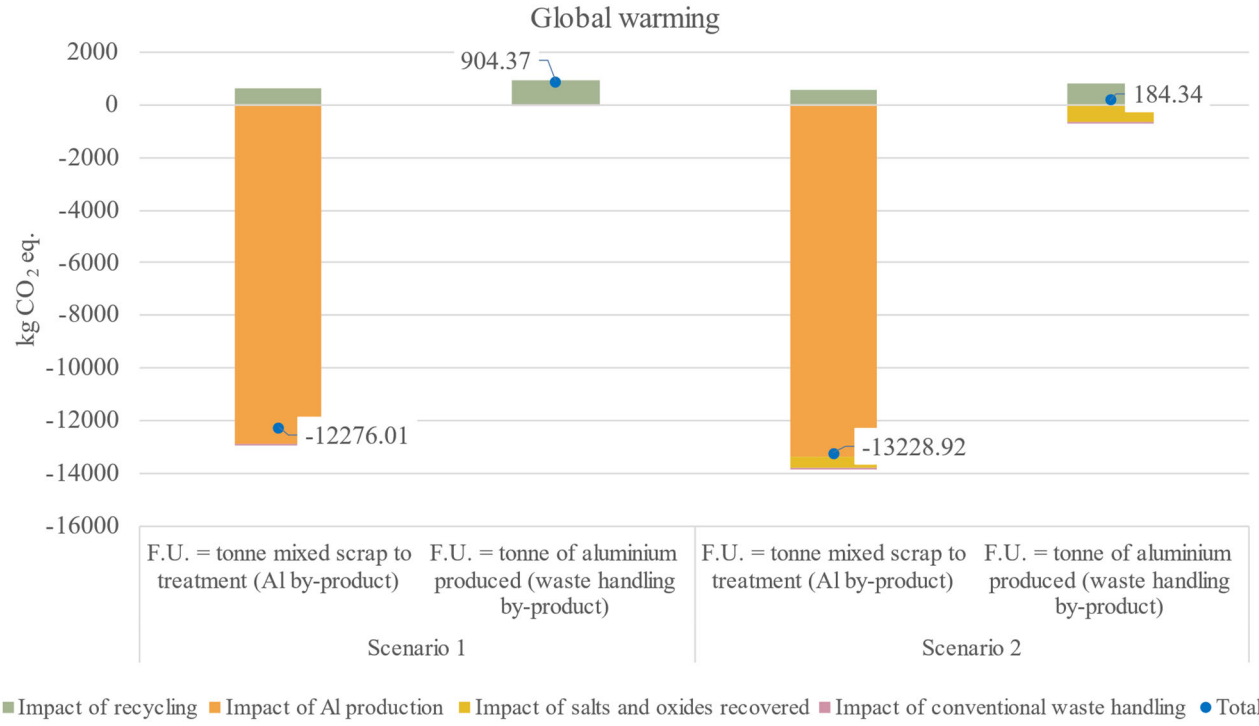

FIG 3 – Global warming impact (evaluated through ReCiPe 2016 Midpoint (H)).

In both scenarios it is observed that, when the FU refers to the treatment of scrap, the impact is negative, meaning an avoided impact on the environment or benefit. Following the system expansion approach, the impacts avoided are more significant than the impacts produced because the impact of the conventional means of producing aluminium (orange bar) outweighs the impact of recycling itself (green bar). Similarly, the impact of producing one tonne of aluminium is still credited with the avoided waste handling (pink bar). However, this is almost inappreciable compared to the impact of producing aluminium. When LCAs are used for comparative assertions, as is the case, the selection of the functional unit must be equivalent for all systems studied. The first FU could be used to compare different waste handling processes for the same waste mix, and the second FU could be used to compare different processes that produce a tonne of cast aluminium.

In addition, and regardless of the functional unit considered, the comparison between Scenario 1 and 2 always results in a higher benefit for the second one: the recovery of salts and oxides contributes to the negative (avoided) impact of the second scenario, being also the process yields higher, with more aluminium produced and lowering the impact per functional unit.

Another important consideration in metallurgical systems when dealing with the functional unit is that, in many cases, we cannot compare the same material of two different qualities. For instance, we cannot develop an LCA comparing high-purity alumina extracted from bauxite through the Bayer process to the lower-purity alumina in the NMC fraction recovered from the salt-slag valourisation because their functions differ. It is also relevant to note that in many applications, mass is not a suitable unit for comparison, especially when comparing two different materials with the same functionality: in the example of producing beverage packaging, the functional unit could be set to eg a container holding half a litre of fluid. If we assess two options, aluminium and glass containers, the mass required to perform this function is not equivalent. In addition, we need to take into account that the lifetime of these containers is not equal; if, for instance, there was a return scheme in place to collect glass containers and refill them again, the same container could be used more than once, which would certainly decrease its impact over its life cycle.

When insufficient data is available, system expansion is not possible and allocation is applied to multi-functional systems. In the next section, allocation methods are discussed.

Allocation method

As explained before, system expansion, such as in Figure 3, is prioritised by the ISO when sufficient data is available.

Whenever system expansion is not possible, the LCA practitioner can apply either mass or economic allocation, where the last is recommended for eg precious metals (PE International, 2014; Santero and Hendry, 2016). The reason behind this is that, in the case of precious metals, these are the ones driving demand and not the other co-products, and it could be unfair to credit the impact on a mass basis, given that, frequently, the less valuable co-products are found in a larger proportion.

In Table 2, it can be observed how the impact of the aluminium produced decreases when by-products are considered. The aluminium cast alloy has the lowest impact when applying mass allocation. Since it is also considered more valuable in the market, this material increases its carbon footprint with economic allocation. When a material is driving demand, one could argue economic allocation is preferable to mass allocation, especially if the difference in mass is substantial.

TABLE 2

Results for three different allocation methods (Scenario 2 – evaluated through ReCiPe 2016 Midpoint (H), for global warming impact).

Product	Mass output (per tonne mixed scrap to treatment)	Unit price	100% allocation to aluminium	Mass allocation	Economic allocation
FU	-	-	Aluminium cast alloy, 1 t	Production of 1 t (per product)	Production of 1 t (per product)
Aluminium cast alloy	0.72 t	$1150	813 kg CO_2 eq per tonne aluminium	533 kg CO_2 eq	696 kg CO_2 eq
Oxides (NMCs)	0.35 t	$375	0	533 kg CO_2 eq	227 kg CO_2 eq
Ammonium sulfate	0.033 t	$300	0	533 kg CO_2 eq	182 kg CO_2 eq

In addition to differences in the allocation method, the results of an LCA will depend on the impact categories and impact methods considered. These are treated in the next section.

Impact categories and impact methods

Previously we have been describing the different methodological choices using global warming and the ReCiPe method (2016) as an example. However, LCA is a methodology intended to study more than one environmental impact, to avoid burden shifting between impact categories, such as eg acidification or human toxicity potentials.

Impact methods are defined as the specific methodologies to convert inventory data into environmental impacts, with different spatial coverage (eg European, global…). Impact methods also look at a wide range of environmental impacts. ReCiPe, the impact method considered in this study, involves the assessment of 13 impact categories (midpoints), which are aggregated in three areas of protection (AoPs) or end points: human health, ecosystems and resources (Huijbregts *et al*, 2017). In the white paper of PE International (2014), later published by Santero and Hendry (2016), some categories such as global warming potential, acidification potential, eutrophication potential, smog potential and ozone depletion potential are recommended to be assessed by metallurgical industry, while others such as resource depletion, toxicity, land use change and water scarcity are considered still too uncertain for the decision-making processes. However, standards and guidelines, the interest of the stakeholders, or the specific case study might broaden the consideration of impact categories.

Another way of considering impact categories is by starting the analysis with areas of protection, and then deciding which environmental impacts to include based on the impacts that have a higher effect on these. An example for the human health impact is shown in Figure 4.

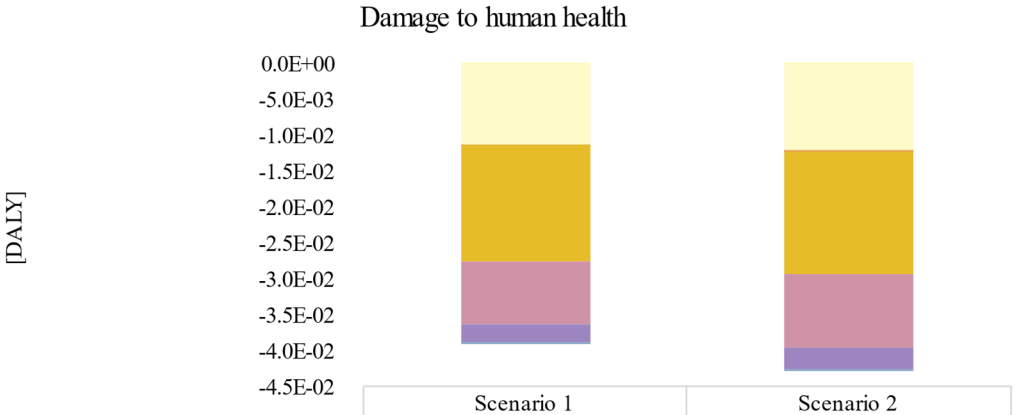

	Scenario 1	Scenario 2
Water consumption, Human health	-6.52E-05	-7.27E-05
Human non-carcinogenic toxicity	-2.58E-03	-2.98E-03
Human carcinogenic toxicity	-8.68E-03	-1.04E-02
Fine particulate matter formation	-1.62E-02	-1.70E-02
Ozone formation, Human health	-2.89E-05	-3.10E-05
Ionizing radiation	-1.80E-06	-1.94E-06
Stratospheric ozone depletion	-1.64E-06	-1.80E-06
Global warming, Human health	-1.14E-02	-1.23E-02

FIG 4 – End point analysis and midpoint contribution, in ReCiPe 2016 (H). Example for human health end point, FU = tonne mixed scrap to treatment.

It is observed that the categories of global warming, fine particulate matter and human carcinogenic toxicity significantly impact human health. Therefore, this is a relevant manner of selecting impact categories for the study. While end points give an overview of the impacts, the decision-maker might prefer midpoints as they are easier to communicate because these show more primary effects. It is important to emphasise that the selection of impact categories should be justified to avoid falling into greenwashing practices by just showing some impact categories that are beneficial to a process or product, especially in comparative assertions.

When midpoint categories have been selected, an in-depth analysis, also called contribution analysis, is developed in Figure 5.

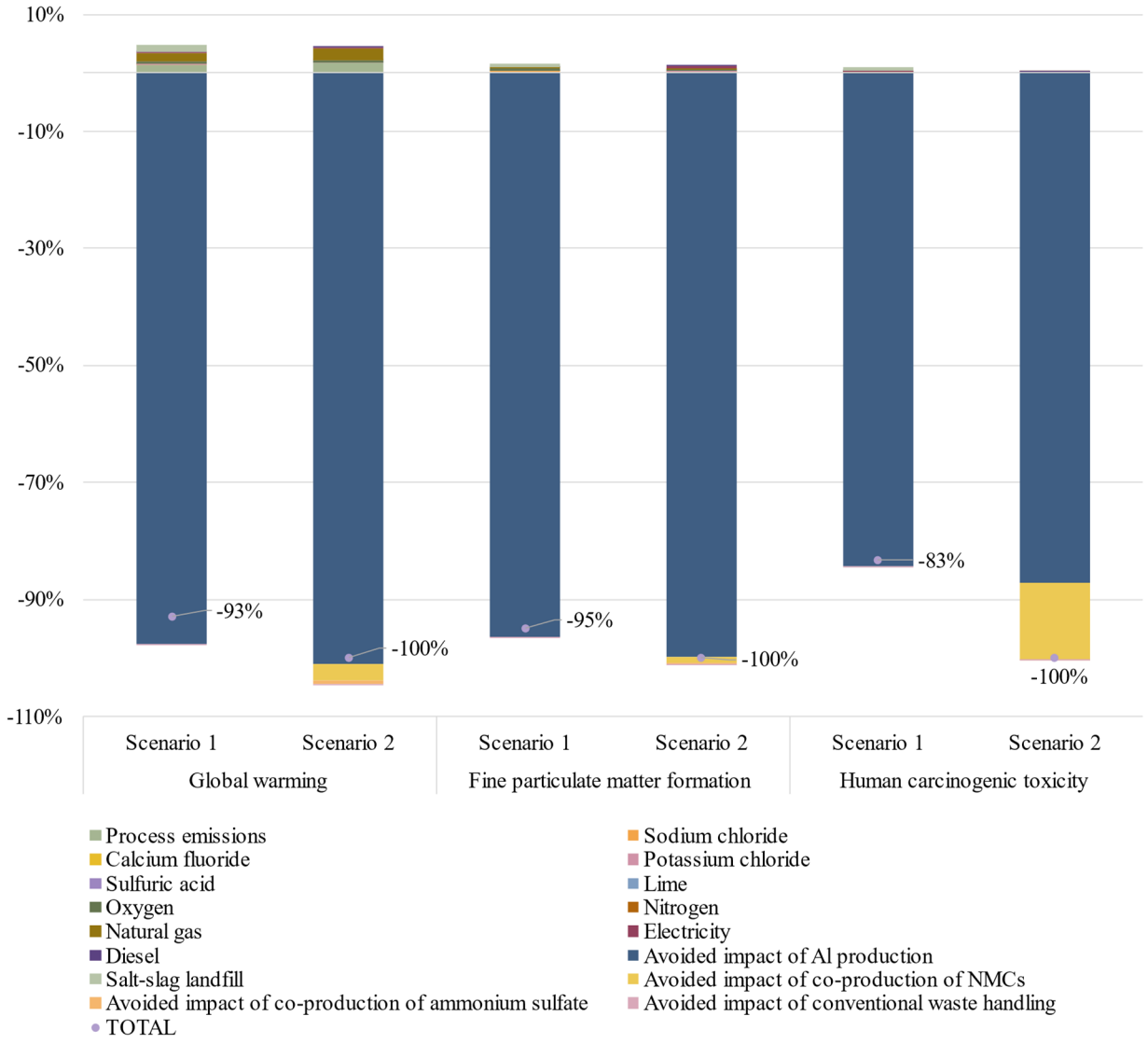

FIG 5 – Contribution analysis (ReCiPe 2016 Midpoint (H)), FU = tonne mixed scrap to treatment. Results are analysed further in Vallejo Olivares *et al* (2024).

Temporal, geographical and data quality considerations

In Figure 5, the avoided impacts of aluminium production stand out in all impact categories studied. Therefore, to truly understand what is driving the environmental impact, the conventional production of aluminium (cast alloy) should be analysed more closely. The initial LCA of this system (Vallejo Olivares *et al*, 2024) considered aluminium from the global market and this flow was chosen in the ecoinvent 3.6 database. Running an analysis of this process in SimaPro, electricity, specifically from China, makes up for more than 44 per cent of this material's global warming environmental impact, evidencing its reliance on the electricity mix of the country of origin. Considering China accounts for almost 90 per cent of coal thermal power, shifting towards producing low-carbon energy sources remains one of the most significant opportunities for reducing its carbon footprint (Saevarsdottir, Magnusson and Kvande, 2021).

In this regard, the geographical scope is highly relevant to determine the impact of the process. As mentioned in the previous example, the electricity source is a dominant parameter in the environmental impact of this and other production systems. Other important parameters could be related to eg the supply chain. In addition, the vulnerability of the ecosystem varies for each location; for instance, regarding water consumption, water scarcity in each territory will affect how sensitive each area is to water use. Spatial-explicit LCA, or regionalised LCA, is a growing field that, over the

last decade, has assessed regional impact categories such as air pollution, particulate matter, or land use (Mutel *et al*, 2019).

Temporal data is also relevant in that, for instance, the average electricity mix changes and is predicted to become greener in the future (International Energy Agency, 2023). With a less carbon-intensive electricity mix, the global warming potential from processes that are dependent on energy will also decrease. Investments, the alternative use of waste materials, market considerations, and the vulnerability of the ecosystems, all might be subject to changes in the future. These are studied in different ramifications of LCA (prospective, consequential, dynamic LCAs…), which are not inside the scope of this paper but hold a significant influence in the environmental assessments of metal production and could be analysed further in future research.

Last but not least, data quality should be evaluated regarding eg the age of the data, adequacy of the process, or representativeness. Uncertainty and sensitivity analysis are crucial for assessing the effects of data quality on the LCA results. For instance, as discussed during the 'System boundaries', the input of secondary aluminium could be considered of different qualities, both a material to waste management and an input of secondary aluminium to the process, considering the system expansion approach. Sensitivity to the type of aluminium input is tested in Figure 6.

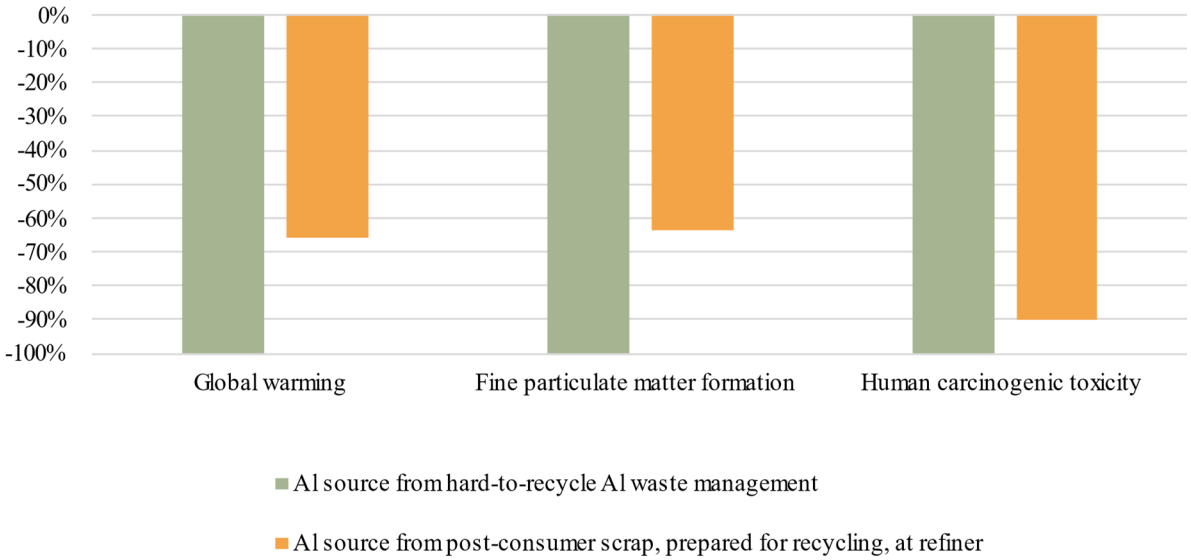

FIG 6 – Effect of different aluminium input considerations (evaluated through ReCiPe 2016 Midpoint (H)).

Even though all impact categories studied still benefited from the recycling of the waste stream, the advantage was smaller when considering an input of post-consumer Al scrap than when considering a flow of hard-to-recycle aluminium-containing streams to waste management. When considering post-consumer Al scrap, it is assumed that this flow is taken from other processes in the technosphere, and the impact of taking out this material from circulation is then added to the process under study because of the system expansion approach. When considering a waste material that is hard to recycle and assumed not currently being used by other processes, then the benefit is higher given that there is no alternative use of this material, highlighting the importance of choosing the correct data and assumptions when developing an LCA assessment of any waste flow.

CONCLUSIONS

The main conclusions and recommendations of this article are summarised in Table 3:

TABLE 3

Relevant methodological choices recommendations summary.

System boundaries	• Depends on the object of study:
	  o Product oriented → usually cradle-to-grave.
	  o Material oriented → usually cradle-to-gate.
	• Possible to use scenario analysis to assess different configurations of the processes included in the system boundaries.

Functional unit	• Depends on the function of the system:
	  o Single-function, eg mass of product.
	  o Multifunction: FU accounting for material(s) produced or waste management. A key point is to always take the same functional unit for comparative assertions.
	  o Always comparing materials that are able to provide the same function and that often means they present similar quality.
	  o Lifetime can be relevant in the comparison among products.

Allocation procedures	• Allocation can be done by:
	  o System expansion: prioritised, when enough data.
	  o Mass allocation: generally all other metals, or when the objective is assessing co-products separately.
	  o Economic allocation: mainly for precious metals, or if a material is driving demand.

Impact categories and impact method	• Various impact methods, depending on eg spatial coverage.
	• Selection of impact categories:
	  o Low uncertainty.
	  o Standards and guidelines.
	  o Interest of stakeholders.
	  o Effect on AoPs.

Temporal, geographical and data quality considerations	• Geographical scope: changes regarding electricity source and supply chain dominant parameters and vulnerability of ecosystems.
	• Temporal data: influenced by future-dependant process impacts, market conditions and ecosystems changes.
	• Other data quality considerations:
	  o Age of data.
	  o Adequacy to the process.
	  o Representativeness.

ACKNOWLEDGEMENTS

The authors would like to gratefully acknowledge the European Research Council for funding the project SisAl (Grant Agreement #869268) and the Norwegian Research Council for funding the project Alpakka—Circular Aluminium Packaging in Norway (NFR Project #296276).

REFERENCES

Damgaard, A, Larsen, A W and Christensen, T H, 2009. Recycling of metals: accounting of greenhouse gases and global warming contributions, *Waste Manag Res*, 27:773–780. https://doi.org/10.1177/0734242X09346838

Environmental Protection Agency, Ireland, 2002. European Waste Catalogue and Hazardous Waste List [online]. Environmental Protection Agency, Ireland. Available from: <https://www.lehaneenvironmental.com/wp-content/uploads/2016/08/EWC_HWL.pdf>

Hauschild, M Z, Rosenbaum, R K and Olsen, S I (eds), 2018. *Life Cycle Assessment: Theory and Practice* (Springer International Publishing: Cham). https://doi.org/10.1007/978-3-319-56475-3

Huijbregts, M A J, Steinmann, Z J N, Elshout, P M F, Stam, G, Verones, F, Vieira, M, Zijp, M, Hollander, A and van Zelm, R, 2017. ReCiPe2016: a harmonised life cycle impact assessment method at midpoint and endpoint level, *Int J Life Cycle Assess*, 22:138–147. https://doi.org/10.1007/s11367-016-1246-y

International Energy Agency, 2021. The Role of Critical Minerals in Clean Energy Transitions [online], World Energy Outlook report. Available from: <https://www.iea.org/reports/the-role-of-critical-minerals-in-clean-energy-transitions>

International Energy Agency, 2023. Renewables [online]. International Energy Agency (IEA). Available from: <https://www.iea.org/energy-system/renewables> [Accessed: 19 January 2024].

International Standard Organization, 2006a. ISO 14040:2006 – Environmental management – Life cycle assessment – Principles and framework.

International Standard Organization, 2006b. ISO 14044:2006 – Environmental management – Life cycle assessment – Requirements and guidelines.

Joint Research Centre, 2017. Best available techniques (BAT) reference document for the non-ferrous metals industries: Industrial Emissions Directive 2010/75/EU (integrated pollution prevention and control). Publications Office of the European Union, LU.

Milani, V and Timelli, G, 2023. Solid Salt Fluxes for Molten Aluminum Processing – A Review, *Metals*, 13:832. https://doi.org/10.3390/met13050832

Mutel, C, Liao, X, Patouillard, L, Bare, J, Fantke, P, Frischknecht, R, Hauschild, M, Jolliet, O, Maia de Souza, D, Laurent, A, Pfister, S and Verones, F, 2019. Overview and recommendations for regionalized life cycle impact assessment, *The International Journal of Life Cycle Assessment*, 24:856–865. https://doi.org/10.1007/s11367-018-1539-4

Norgate, T and Rankin, W, 2002. The Role of Metals in Sustainable Development, Green Processing 2002 – in Proceedings of the International Conference on the Sustainable Processing of Minerals.

Office of Research and Development, 2015. Secondary Aluminum Processing Waste: Salt Cake Characterization and Reactivity [online]. Available from: <https://cfpub.epa.gov/si/si_public_record_report.cfm?Lab=NRMRL&dirEntryId=311174> [Accessed: 19 January 2024].

Olivieri, G, Romani, A and Neri, P, 2006. Environmental and economic analysis of aluminium recycling through life cycle assessment, *International Journal of Sustainable Development and World Ecology*, 13:269–276. https://doi.org/10.1080/13504500609469678

PE International, 2014. Harmonization of LCA methodologies for metals – a white paper providing guidance for conducting LCAs for metals and metal products. Available from: <https://international-aluminium.org/wp-content/uploads/2021/06/Harmonization-of-LCA-Methodologies-for-Metals.pdf>

Saevarsdottir, G, Magnusson, T and Kvande, H, 2021. Reducing the Carbon Footprint: Primary Production of Aluminum and Silicon with Changing Energy Systems, *Journal of Sustainable Metallurgy*, 7:848–857. https://doi.org/10.1007/s40831-021-00429-0

Santero, N and Hendry, J, 2016. Harmonization of LCA methodologies for the metal and mining industry, *Int J Life Cycle Assess*, 21:1543–1553. https://doi.org/10.1007/s11367-015-1022-4

UN Environment and International Resource Panel, 2019. Global Resources Outlook: Natural Resources for the Future we Want. Available from: <https://wedocs.unep.org/handle/20.500.11822/27517>

UN Environment and International Resource Panel, 2020. Resource Efficiency and Climate Change: Material Efficiency Strategies for a Low-Carbon Future. Available from: <https://wedocs.unep.org/handle/20.500.11822/34351>

UN Environment Programme, 2017. Environmental Risks and Challenges of Anthropogenic Metals Flows and Cycles. Available from: <https://www.unep.org/resources/report/environmental-risks-and-challenges-anthropogenic-metals-flows-and-cycles>

US Geological Survey, 2023. Mineral commodity summaries [online]. Available from: <https://pubs.usgs.gov/publication/mcs2023> [Accessed: 7 December 2023].

Vallejo Olivares, A, Pastor-Vallés, E, Pettersen, J B and Tranell, G, 2024. LCA of recycling aluminium incineration bottom ash, dross and shavings in a rotary furnace and environmental benefits of salt-slag valorisation, *Waste Management*, 182:11–20. https://doi.org/10.1016/j.wasman.2024.04.023

Watari, T, Nansai, K and Nakajima, K, 2021. Major metals demand, supply and environmental impacts to 2100: A critical review, *Resources, Conservation and Recycling*, 164:105107. https://doi.org/10.1016/j.resconrec.2020.105107

A thermodynamic and sustainability assessment of PCB recycling through the secondary Cu smelting process

DOI: 10.62053/ETCM6782

P Tikare[1], M Mohanasundaram[2], R Kumar[3] and A Kamaraj[4]

1. MTech student, Indian Institute of Technology Hyderabad, Sangareddy Telangana 502285, India. Email: praveentikare@alumni.iith.ac.in
2. Principal Scientist, CSIR National Metallurgical Laboratory, Jamshedpur Jharkhand 831007, India. Email: madan@nmlindia.org
3. Scientist E, Centre for Materials for Electronics Technology, Hyderabad Telangana 500057, India. Email: rajesh@cmet.gov.in
4. Assistant Professor, Department of Materials Science and Metallurgical Engineering, Greenko School of Sustainability, Indian Institute of Technology Hyderabad, Sangareddy Telangana 502285, India. Email: ashokk@msme.iith.ac.in

ABSTRACT

This study presents a comprehensive thermodynamic optimisation and sustainability analysis of the secondary copper smelting process for Waste Printed Circuit Board (WPCB) recycling. The study investigates various scenarios with different proportions of WPCB in the input stream, ranging from 0 per cent to 100 per cent. Through thermodynamic modelling using FactSage™ version 8.1, the optimisation process is conducted in three stages. The results of the thermodynamic modelling indicate that the best-case scenario for WPCB recycling is achieved with a 40 per cent proportion of WPCB in the input stream. This case exhibits a maximum copper recovery of 99.93 per cent while minimising the formation of other waste. In addition to the thermodynamic analyses, environmental factors such as the carbon emission index and resource utilisation efficiency are studied. The 40 per cent WPCB recycling case exhibits a resource utilisation efficiency of 93.055 per cent and a carbon emission rate of 0.133. The present investigation highlights the significant benefits of a 40 per cent WPCB recycling scenario through a secondary copper smelting process in terms of base metal recovery and energy efficiency, thus emphasising its potential for sustainable PCB waste management and resource utilisation.

INTRODUCTION

Pyrometallurgical processes utilise elevated temperatures to extract metals from various sources. These processes encompass a range of techniques such as dressing, incineration, furnace-based smelting, sintering, melting and high-temperature reactions in a gaseous phase. The primary objective is to recover common metals and precious metals from different wastes (Wu *et al*, 1993). During smelting, e-waste is introduced into a high-temperature furnace, often integrated with a base metal production process such as copper, lead, or zinc smelting. In this process, the base metal acts as a medium for collecting valuable metals such as gold, silver, platinum and palladium (Ghodrat *et al*, 2017). Over the past few decades, pyrometallurgical methods have been extensively employed to recover metals from diverse waste materials.

Processes like smelting in furnaces, incineration, combustion and pyrolysis are commonly used to recycle electronic waste (e-waste). Numerous studies have documented substantial metal retrieval achieved through pyrometallurgical methods; however, the prominent drawbacks of these processes include their high cost, substantial energy requirements and the emission of hazardous fumes into the environment (Chauhan *et al*, 2018). It should also be noted that advanced smelters and refineries have proven effective in extracting valuable metals while also isolating hazardous substances. During the pyrometallurgical process, waste electrical and electronic equipment (WEEE) is subjected to high temperatures and combined with fluxes such as copper slag or various salts (eg NaOH) to facilitate the formation of slag. The resulting molten WEEE containing valuable metals is then brought into contact with a molten metal pool, where the valuable metals dissolve and accumulate. This molten metal pool acts as a collector metal (Syed, 2012).

Printed circuit boards (PCBs) play a critical role in electronic and electrical equipment (EEE) and form the backbone of modern electronic and electrical infrastructure (Liu *et al*, 2016). The PCBs are

made up of glass fibre-reinforced epoxy and various metallic materials, including valuable metals (Choubey *et al*, 2015; Bai *et al*, 2016). WPCB represents a significant reserve of recyclable resources (Holgersson *et al*, 2018), with the concentration of metals, especially precious metals, exceeding that of primary minerals, highlighting the economic advantages of recyclability (Cucchiella *et al*, 2016). Moreover, the WPCBs recycling positions them as valuable urban mineral resources (He and Duan, 2017), underscoring their significance in the context of sustainable resource management.

PCBs are crucial components in electronic products, but their recycling presents challenges. PCBs contain precious metals and hazardous elements, requiring proper management to minimise environmental and health risks. These boards consist of materials like phenolic / cellulose paper or epoxy, woven glass fibre and various metals such as copper, tin and lead (Ning *et al*, 2018) Valuable precious metals like gold, nickel, platinum, palladium and silver can be recovered from WPCBs, making them economically attractive for recycling (Lu and Xu, 2016). However, it is essential to recognise that certain chemical elements in circuit boards, such as bromine, antimony, cadmium and lead, exceed their natural crust composition, posing potential environmental and health risks. (Chauhan *et al*, 2018). Aier, Prabhakaran and Kannadasan (2013) utilised NaOH salt during the melting of waste PCB from mobile phones and computers to increase the recovery of copper. Hagelüken (2006) reported that loss of copper during the recycling process will make up for 7 to 42 per cent value loss. ISASMELT process for reductive smelting of e-waste has been extensively studied to understand the major challenges such as control of slag composition, temperature, fume formation due to Zn, Pb and Sn (Stuart *et al*, 2023). Therefore, efficient recycling processes towards maximising the base metal recovery as well as minimising the environmental impact are essential for sustainable e-waste practices. In the present study, thermodynamic simulations are adopted to identify the optimum condition for recycling WPCB towards maximum base metal recovery and minimum environmental impact.

METHODOLOGY

FactSage™ simulation

The present study investigates the material flow while processing copper scrap and WPCBs in the black copper smelting process. The chemical thermodynamic modelling and process flow sheet simulations were employed to generate data for calculations. The thermodynamic calculations were conducted using the FactSage™ thermochemical package (version 8.1), allowing for accurate process modelling. Thermodynamic modelling and calculations offer a comprehensive approach to understanding the behaviour of copper scrap and WPCBs during the black copper smelting process. Varying e-waste and copper scrap proportions (varied from 0 to 100) were utilised as input parameters to simulate the black copper smelting process. Other input material streams are Coal, FCS Slag, enriched air and flux. The proportion of flux used in the simulation is maintained constant, as described in the previous work (Ghodrat *et al*, 2017) for 12 tonnes of charge materials. The detailed composition of various input streams considered in thermodynamic modelling can be found in the annexure (Ghodrat *et al*, 2017). The composition of black copper formed in the different cases is presented in the annexure. It should be noted that there are no solid phases observed in both the output streams (molten black copper and slag) under optimised conditions. By examining different scenarios, the research aimed to gain insights into the material flow during different percentages of e-waste recycling through the secondary Cu smelting process. The results obtained from this study contribute to the knowledge base surrounding the recycling and recovery of valuable metals from electronic waste. The study also informs potential process improvements for sustainable and efficient resource utilisation. Different proportions of the input stream are presented in Table 1.

TABLE 1

List of basic input streams considered for FactSage™ simulation (Ghodrat *et al*, 2017).

WPCB recycling (%)	WPCB (tonne)	Copper scrap (tonne)	FCS slag (tonne)
0	0	12	0.42
10	1.2	10.8	0.42
20	2.4	9.6	0.42
30	3.6	8.4	0.42
40	4.8	7.2	0.42
50	6	6	0.42
60	7.2	4.8	0.42
70	8.4	3.6	0.42
80	9.6	2.4	0.42
90	10.8	1.2	0.42
100	12	0	0.42

Thermodynamic optimisation

A fixed input quantity of 12 tonnes comprising various proportions of e-waste and copper scrap, as detailed in Table 2, was used as input to determine the optimised process parameters. The thermodynamic optimisation has been done stage-wise, as listed:

Stage 1: Identification of coal-air ratio for maximum Cu recovery and minimum residual solid carbon in the product stream.

Stage 2: Identification of optimised process temperature based on maximum liquid slag formation.

Stage 3: Identification of the optimum amount of flux (lime) addition to enhance liquid slag formation and suppress solid slag formation.

In the first stage of thermodynamic optimisation, the coal-air ratio was systematically varied, keeping all other input streams constant. It should be noted that the WPCB in the input stream also contains carbon as a part of plastics. Consequently, the optimal amount of coal addition must be determined for maximum recovery of base metal copper while minimising the formation of solid carbon residue in the output stream.

In the second stage, the process temperature was optimised to enhance the formation of a maximum quantity of liquid slag to facilitate the efficient separation of molten metal and slag. In this stage, the temperature was varied within a specified range, and the temperature at which the weight percentage of liquid slag reached its peak was identified as the optimal temperature.

In the third stage, the optimal amount of flux (lime), was determined to promote the formation of liquid slag in the output stream. The objective was to eliminate the formation of solid slag in the output stream and maximise the quantity of liquid slag, thereby facilitating the separation of metal and solid slag. Lime addition for each case was carefully selected to have minimum slag viscosity, further aiding the separation process.

The distribution coefficient of the element is a measure that compares the amount of element present in black copper (metal phase) to the combined amount of metal found in slag, exhaust gas and metal dust (waste streams). It provides valuable insights into the distribution of valuable metal between these useful products and waste streams.

$$\text{Distribution coefficient} = \frac{\text{weight of element i in black Cu (kg)}}{\text{weight of element i in slag+dust+gas (kg)}} \quad (1)$$

Metal recovery of element ‘i’ is defined as a measure that compares the amount of element ‘i’ present in black copper (metal phase) to the amount of element ‘i’ found in input streams.

$$\text{Metal recovery} = \frac{\text{weight of element i in black Cu (Kg)}}{\text{weight of element i in input streams (Kg)}} \quad (2)$$

Sustainability assessment

The environmental implications associated with current smelting systems have become increasingly important due to stricter emission targets and escalating energy costs. The present study’s primary focus was to examine three indicators from environmental responsibility and sustainability perspectives.

The resource utilisation efficiency is determined by the ratio of the mass of metal/alloy produced and recycled resources to the total input mass, as defined by the following equation:

$$£ = \frac{(M_p + M_r)}{M_{inp}} \times 100 \quad (3)$$

where:

M_p (Kg) is the mass of the alloy

M_r (Kg) is recycled mass used

M_{inp} (Kg) total input stream mass

The carbon dioxide emission ratio is quantified as the quantity of carbon dioxide (Kg) emitted per metric ton of alloy produced, as defined by the following equation:

$$\mu = \frac{M_{CO_2}}{M_{alloy}} \quad (4)$$

where:

M_{CO_2}(Kg) is the mass of CO_2 and CO emitted

M_{alloy} (Kg) is the mass of alloy generated

The above two parameters are obtained from the FactSage™ simulation results.

RESULTS AND DISCUSSION

Thermodynamic analysis of the secondary Cu smelting process

In the first stage, thermodynamic optimisation has been done to identify an optimised coal air ratio (CAR) for maximum base metal (copper) recovery and minimum solid carbon residue formation in the output streams. Figure 1 shows the variation of the optimised coal-air ratio for the maximum recovery of base metal and minimum formation of solid carbon residue in the output streams with the WPCB per cent in the input stream. CAR variation with WPCB shows that the coal-air ratio value decreases as the percentage of WPCB increases in the input stream. It depicts the requirement for less amount of coal while increasing the WPCB in the Cu smelter for processing. This is attributed to the presence of carbon in the WPCB. The maximum value is 0.875, which is for 0 per cent e-waste because there will be no plastics. The minimum value is 0.1375, which is for 100 per cent WPCB because it will have the highest number of plastics.

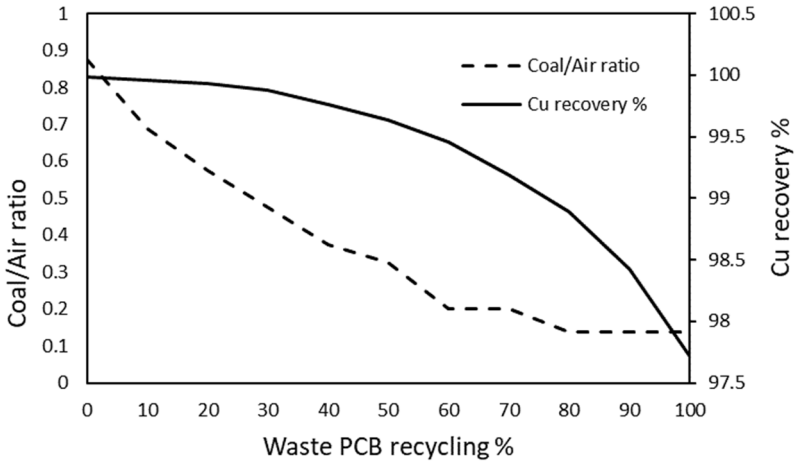

FIG 1 – Variation of optimised CAR for different WPCB recycling per cent.

In the second stage of thermodynamic optimisation, the optimum process temperature towards the formation of maximum liquid slag along with maximum base metal recovery has been identified. The optimised process temperature was determined considering the CAR in the simulation optimised in the previous step. The temperature in the simulation studies has been varied from 1100 to 1600°C to identify the optimum process temperature.

In the final stage, an additional parameter ie flux (lime) addition, was introduced to facilitate liquid slag and minimise solid slag formation. Optimisation of flux addition has been performed to identify the process window for complete liquid slag formation with less viscosity. Introducing lime into the input stream, the intention is to promote the formation of a complete liquid slag with less viscosity. This can significantly improve the overall process performance in terms of refining as well as slag-metal separation. Reducing slag viscosity can facilitate better mass transport, enhancing metal recovery and process efficiency. The simulation experiments have been performed for the optimised CAR and process temperature conditions. Based on the optimisation results, the composition of the slag was identified for each case and is presented in Table 2, along with the optimised process temperature and viscosity of the slag. Slag viscosity has been estimated using the viscosity module of FactSage™ 8.1.

TABLE 2

Optimum CAR, process temperature, slag composition, and viscosity of slag for WPCB recycling in secondary Cu smelter.

WPCB Recycling	CAR	Temperature	Al_2O_3	SiO_2	CaO	MgO	FeO	Viscosity
(%)	-	(°C)	(wt%)					(PaS)
0	0.875	1350	4.73	61.65	27.58	0	5.21	7.723
10	0.687	1550	26.36	34	36.90	1.96	0.008	0.502
20	0.575	1600	40.72	24.48	32.69	1.59	0.001	0.483
30	0.455	1550	38.74	26.53	32.48	1.96	0.001	0.705
40	0.375	1400	19.91	36.45	40.55	2.96	0.008	0.91
50	0.325	1400	21.24	37.09	38.752	2.84	0.008	1.133
60	0.2	1450	24.17	36.40	36.681	2.69	0.005	0.996
70	0.2	1450	23.64	36.30	37.23	2.76	0.005	0.926
80	0.137	1450	22.39	35.69	38.963	2.915	0.004	0.877
90	0.137	1450	23.835	36.647	36.749	2.745	0.004	0.984
100	0.137	1450	23.51	36.548	37.125	2.784	0.003	0.937

Figure 2 illustrates the variation of copper recovery in the final optimised case as a function of the WPCB recycling percentage. The results indicate a marginal decrease in Cu recovery with an increase in the amount of WPCB in the input stream. The maximum recovery of 99.99 per cent, is observed for the 0 per cent WPCB recycling case, indicating optimal conditions for copper recovery in the absence of WPCB. The initial decrease in the Cu recovery is due to more Cu metal dust formation at higher process temperatures (say 1550 to 1600°C). When considering the input stream containing WPCB, the maximum copper recovery achieved is 99.93 per cent for the 40 per cent WPCB recycling case. Conversely, the minimum recovery of 99.7 per cent is recorded for the 100 per cent waste recycling case. The content of Cu in the base metal decreases with the WPCB amount in the input stream. Further, the amount of Cu reported to the dust portion increases with WPCB recycling. This may be due to the influence of other elements that join base metals, such as Fe, Sn and Si, decreasing the activity coefficient of Cu. Considering all these, the 40 per cent WPCB recycling case emerges as the most favourable scenario for achieving maximum copper recovery while recycling WPCB through the secondary copper smelting process.

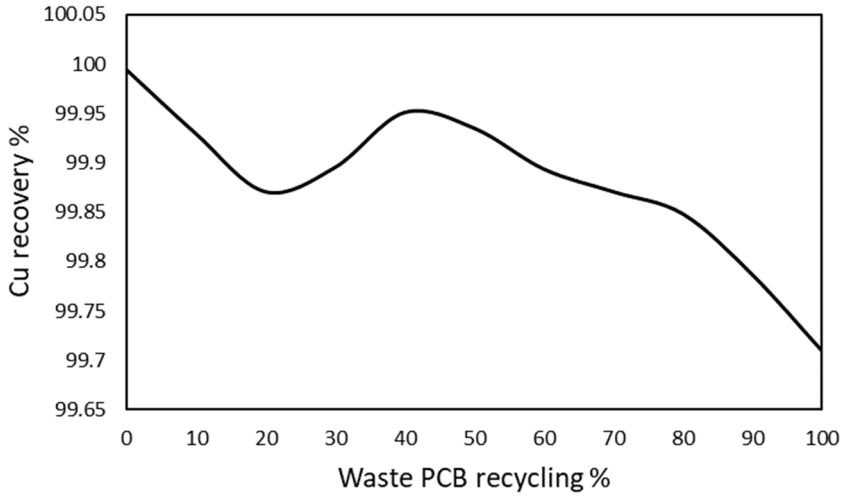

FIG 2 – Recovery of Cu during WPCB recycling through secondary Cu smelting under optimised condition.

The present work aims to recover the maximum precious metals in black copper along with other base metals such as Fe, Si, Sn etc. The discussion pertaining to the formation of fume due to high vapor pressure elements present in the scrap and e-waste in relation with the slag formation will be reported as a part of the future work.

Sustainability analysis

The findings of the environmental analysis are presented and discussed in the following sections. Figure 3a depicts the relationship between resource utilisation efficiency and WPCB recycling percentage. The findings demonstrate a clear trend: resource utilisation efficiency initially rises with increasing WPCB in the input stream till 30 per cent WPCB recycling case. Subsequently, it declines at 40 per cent, gradually increasing till 100 per cent WPCB recycling scenario. Notably, the minimum resource utilisation efficiency is observed when there is no recycling of WPCB (0 per cent recycling case), as it utilises the least amount of recycled mass in the input stream. Conversely, the maximum resource utilisation efficiency occurs at the 100 per cent WPCB recycling case, which utilises the most recycled mass available.

Figure 3b illustrates the relationship between the carbon emission ratio and WPCB recycling percentage. A similar trend has been observed in resource utilisation efficiency. The lowest carbon emission rate is observed when no WPCB is in the input stream. When comparing the cases with WPCB in the input stream, the minimum carbon emission rate occurs at the 40 per cent WPCB recycling case, while the maximum is observed at the 100 per cent WPCB recycling case. This indicates that adopting a recycling rate of 40 per cent WPCB through the secondary Cu smelting process significantly improves the overall environmental and economic sustainability of the process.

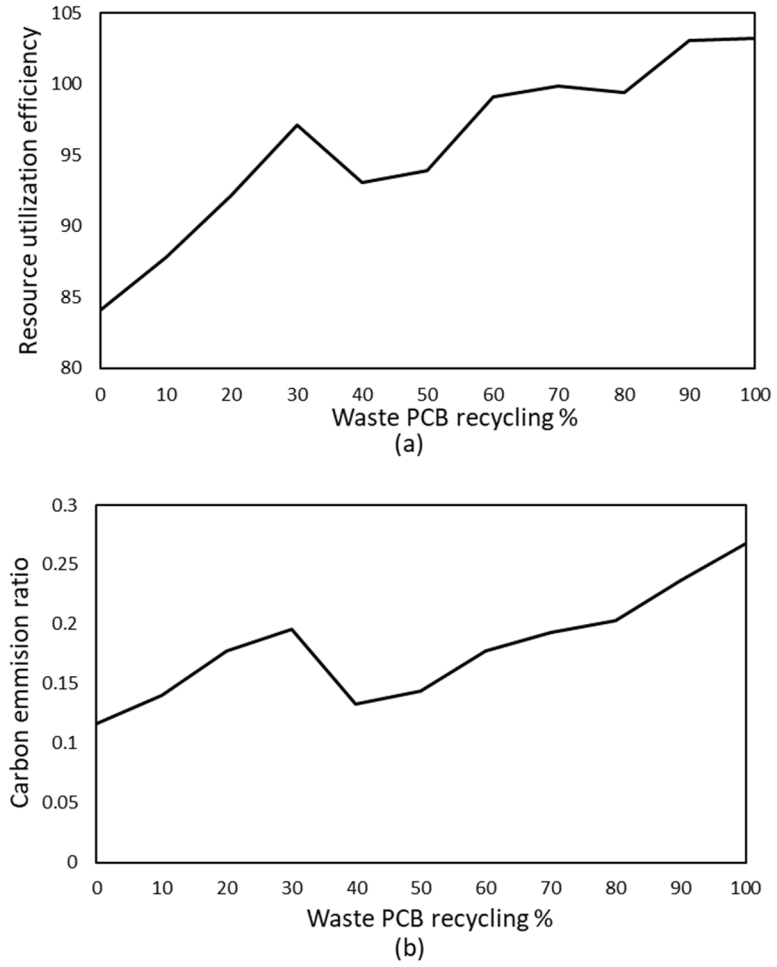

FIG 3 – Sustainability assessment of WPCB recycling through secondary Cu smelting route: (a) resource utilisation efficiency, (b) CO_2 emission rate.

CONCLUSIONS

The salient features of the present investigation are as follows:

- The coal-air ratio decreases with an increase in the WPCB in the input stream. This is attributed to the energy demand required for the process being met from the carbon present in WPCB as plastics.
- The minimum process temperature required to form the maximum amount of liquid slag has been identified for different WPCB recycling rates for the optimised CAR. The optimised process temperature varies from 1350 to 1600°C with extra flux (ie lime) addition to form 100 per cent liquid slag for efficient molten metal-slag separation. However operating at such a high temperature will impact the furnace design and metal and slag containment.
- The 40 per cent WPCB recycling through the secondary copper smelting process under the optimised condition emerges as the efficient scenario for achieving maximum base metal recovery, ie copper.
- It is observed that the resource utilisation efficiency increases with an increase in the WPCB content in the input stream of the process. However, the carbon emission ratio is observed to be minimum (0.133) for 40 per cent of waste PCB recycling cases.
- Adopting a recycling rate of 40 per cent WPCB through the secondary Cu smelting process significantly improves the overall environmental and economic sustainability of the process.

ACKNOWLEDGEMENTS

The authors would like to thank the Director of the Indian Institute of Technology Hyderabad and the Centre for Materials for Electronics Technology (C-MET) Hyderabad for their permission to publish this work. The author acknowledges financial support from the IIT Hyderabad, India, under grant SG/IITH/F282/2022–23/SG-120.

REFERENCES

Aier, A, Prabhakaran, D and Kannadasan, T, 2013. Recovery of Noble Metals from Electronic Waste by Pyrometallurgy Process, *International Journal of Scientific Research,* 2(12):209–212.

Bai, J, Gu, W, Dai, J, Zhang, C, Yuan, W, Deng, M, Luo, X and Wang, J, 2016. The Catalytic Role of Nitrogen-Doped Carbon Nanotubes in Bioleaching Copper from Waste Printed Circuit Boards, *Polish Journal of Environmental Studies*, 25(3):951–957.

Chauhan, G, Jadhao, P R, Pant, K K and Nigam, K D P, 2018. Novel technologies and conventional processes for recovery of metals from waste electrical and electronic equipment: challenges and opportunities – a review, *Journal of Environmental Chemical Engineering*, 6(1):1288–1304.

Choubey, P K, Panda, R, Jha, M K, Lee, J C and Pathak, D D, 2015. Recovery of copper and recycling of acid from the leach liquor of discarded Printed Circuit Boards (PCBs), *Separation and Purification Technology*, 156:269–275.

Cucchiella, F, D'Adamo, I, Rosa, P and Terzi, S, 2016. Automotive printed circuit boards recycling: an economic analysis, *Journal of Cleaner Production*, 121:130–141.

Ghodrat, M, Rhamdhani, M A, Brooks, G, Rashidi, M and Samali, B, 2017. A thermodynamic-based life cycle assessment of precious metal recycling out of waste printed circuit board through secondary copper smelting, *Environmental Development*, 24:36–49.

Hagelüken, C, 2006. Improving metal returns and eco-efficiency in electronics recycling, *IEEE International Symposium on Electronics and the Environment*, San Francisco.

He, J and Duan, C, 2017. Recovery of metallic concentrations from waste printed circuit boards via reverse floatation, *Waste Management*, 60:618–628.

Holgersson, S, Steenari, B M, Björkman, M and Cullbrand, K, 2018. Analysis of the metal content of small-size Waste Electric and Electronic Equipment (WEEE) printed circuit boards – part 1: Internet routers, mobile phones and smartphones, *Resources, Conservation and Recycling*, 133:300–308.

Liu, J, Xu, H, Zhang, L and Liu, C T, 2020. Economic and environmental feasibility of hydrometallurgical process for recycling waste mobile phones, *Waste Management*, 111:41–50.

Lu, Y and Xu, Z, 2016. Precious metals recovery from waste printed circuit boards: A review for current status and perspective, *Resources, Conservation and Recycling*, 113:28–39.

Ning, C, Lin, C S K, Hui, D C W and McKay, G, 2018. Waste printed circuit board (PCB) recycling techniques, *Chemistry and Chemical Technologies in Waste Valorization*, pp 21–56.

Stuart, N, Benjamin, H, Oscar, M and Stuart, N, 2023. Extraction and Recovery of critical metals from electronic waste using ISASMELT Technology, *Processes*, 11(4):1012.

Syed, S, 2012. Recovery of gold from secondary sources — A review, *Hydrometallurgy*, 115:30–51.

Wu, P, Eriksson, G, Pelton, A D and Blander, M, 1993. Prediction of the thermodynamic properties and phase diagrams of silicate systems–evaluation of the FeO-MgO-SiO_2 system, *ISIJ International*, 33(1):26–35.

ANNEXURE

The composition of input streams used in the simulation is given below.

Cu scrap

Cu	Cu_2O	SnO_2	PbO	ZnO	NiO
(wt%)					
70	7	5	8	5	5

E-waste

E-waste	Element or compound	wt%
Metal	Cu	18.36
	Pb	5.50
	Fe	7.98
	Zn	3.67
	Au	0.091
	Ag	0.18
	Al	4.59
	Sn	3.67
	Ni	1.83
Oxide	Al_2O_3	5.50
	SiO_2	22.03
Plastics	C_2H_3Cl	1.10
	C_2H_4	2.19
	CH_3NO_2	0.66
	$C_7H_8O_2$	1.53
	$C_{12}H_6Cl_4$	0.66
	$C_{12}H_8Br_2$	2.63
	$C_{15}H_{16}O_2$	13.16
	H_2O	4.59

Metallurgical coke

C	H_2O	S	Al_2O_3	FeO
90	5	0.8	2	2.2

FCS slag

FeO	CaO	SiO_2
45	17	38

FCS slag

O_2	N_2
54	46

Lime

CaO	MgO	SiO_2
84.32	6.48	9.18

The composition of black copper produced.

Waste PCB recycling (%)	Black copper (wt%)											
	Ag	Al	Au	Cu	Fe	Mg	Ni	Pb	Si	Sn	Zn	Ag
0	0.00	0.00	0.00	81.85	1.23	0.00	4.22	6.87	0.00	4.23	1.60	0.00
10	0.02	0.06	0.01	82.46	2.38	0.00	4.36	4.63	1.02	4.58	0.47	0.02
20	0.04	0.38	0.02	80.86	3.54	0.00	4.40	3.04	2.60	4.87	0.24	0.04
30	0.07	0.35	0.04	78.43	4.83	0.00	4.40	2.99	3.49	5.15	0.23	0.07
40	0.10	0.02	0.05	76.20	6.34	0.00	4.44	5.94	0.64	5.51	0.75	0.10
50	0.14	0.02	0.07	74.05	8.17	0.00	4.52	5.46	0.97	5.97	0.63	0.14
60	0.18	0.06	0.09	71.59	10.38	0.00	4.62	3.64	2.56	6.54	0.33	0.18
70	0.23	0.06	0.12	68.33	13.04	0.00	4.72	3.08	2.91	7.20	0.28	0.23
80	0.29	0.07	0.15	64.31	16.37	0.00	4.86	2.57	3.09	8.04	0.24	0.29
90	0.36	0.06	0.20	58.68	20.47	0.00	4.99	1.79	4.23	9.02	0.18	0.36
100	0.43	0.06	0.25	51.49	25.89	0.00	5.17	1.19	5.00	10.33	0.13	0.43

Melting behaviour investigation of municipal solid waste incineration fly ash samples from different incineration technologies for metal recovery – an integrated experimental and thermodynamic modelling approach

DOI: 10.62053/SQTV9191

E Soylu[1] and G Tranell[2]

1. PhD candidate, Norwegian University of Science and Technology, 7004.
   Email: ece.soylu@ntnu.no
2. Professor, Norwegian University of Science and Technology, 7004.
   Email: gabriella.tranell@ntnu.no

ABSTRACT

Municipal solid waste incineration fly ash (MSWI FA) is an important waste product that holds considerable potential for valourisation. In addition to major phases such as $CaSO_4$, $CaCO_3$, NaCl, KCl, and silicates, these ashes contain significant amounts of valuable elements like copper (Cu), zinc (Zn), lead (Pb), and others, where the specific composition depends on the source of the waste and the incineration process used. This study aims to investigate the melting behaviour of municipal MSWI FA samples from various incineration technologies, including rotary kiln, grate furnace, and circular fluidised bed, as a background for pyro/hydrometallurgical metal extraction. The experimental study was designed to research the effect of salt composition on the melting temperature and phase formations of different ash types, as well as metal migration between phases, using a sessile drop furnace. As a complimentary approach to the experimental study, thermodynamic modelling (FactSage™ ver 8.3, by Thermfact/CRCT and GTT-Technologies) was used to predict the phase formations of different fly ashes using Scheil-Gulliver cooling of molten ash. The observed melting point of the samples varied between 1000–1400°C depending on the ash type, without any trend of salt composition effect on the melting point. Upon solidification, there were three distinct phases observed in the samples: a metallic phase, a crystalline, non-metallic phase with inhomogeneous shape pattern, and an amorphous matrix phase. The findings indicate that the predominant component in the matrix phase was Ca-O-Si, implying the formation of calcium silicate slag. Elemental mapping showed metallic droplets consisting of primarily Fe-P phases, while the crystalline non-metallic phase is concentrated in Ca and S. The furnace atmosphere (Ar versus CO) had no significant impact on the phase formations. Thermodynamic modelling results were in good agreement with the experimental study, except for P-rich metallic phases, showing the formation of non-metallic and complex silicate slag phase formations.

INTRODUCTION

Municipal solid waste incineration fly ash (MSWI FA) is a by-product of the incineration process, which involves the combustion of waste at high temperatures reducing its volume by 85–90 per cent, mass by 60–90 per cent, and organic matter by up to 100 per cent (Zhang *et al*, 2021). Globally, the share of incineration in waste management practices is 11 per cent, where bottom ash and fly ash residue from MSWI account for approximately 30 wt per cent and 1–5 wt per cent of the input waste weight, respectively (Kaza *et al,* 2018; Tian *et al,* 2021). Different technologies such as grate, rotary kiln, and fluidised bed are used for incineration practices. In Europe, approximately 90 per cent of MSW treatment installations are grates, where the share of fluidised beds and rotary kiln are 5 per cent and 2 per cent, respectively (Neuwahl *et al*, 2019). The operation temperature of incinerators varies depending on the feed material and incineration plant, which results in high versatility in the ash composition (Nedkvitne *et al*, 2021). FA contains considerable number of high-value metals such as Zn, Cu, Ni, Co etc along with silicates and varying calcium bearing compounds with a potential of being used in different industries such as construction and glass ceramics (Zhao *et al*, 2021; Fan *et al*, 2022). A study where the chemical composition of approximately 900 different FA samples were analysed showed that 1 kg of fly ash contains 10 g of Zn and 1.2 g of Cu, on average (Nedkvitne *et al*, 2021). Even though the variations are high, and composition of FA depends on many factors such as location, season, incineration technology used etc, FA holds a great potential for recovery of critical metals competing with the ore grades in the concentration of critical metals (Nedkvitne *et al*, 2021; Nedkvitne, Eriksen and Omtvedt, 2023). The current best

available technologies (BATs) for utilisation of FA are: 1) stabilisation of heavy metals in FA, 2) utilisation of FA as construction material after stabilisation, and 3) resource recovery in the means of metal and salt extraction via thermal/hydrometallurgical processes (Jadhav and Hocheng, 2012; Becidan, 2018; Wang *et al*, 2021).

There are various studies on the melting characteristics of FA. One study investigated the effect of the chemical composition on metal separation efficiency during melting (Okada and Tomikawa, 2013). It was observed that decreasing the Cl to Na and K molar ratio in the ash reduced Fe and Cu volatilisation, enhancing metal separation. The studies that investigated the impact of atmosphere on the volatility of metals revealed that volatility of metals was also affected by the amount of liquid slag formed and the temperature. It was concluded that under oxidising conditions and elevated temperatures, elements like As, Bi, Sb, Sn, and Zn tended to be mainly concentrated in condensed phases, whereas, under reducing conditions and high temperatures, these elements were predominantly released into the gas phase, however, Cu and Pb volatility was suppressed under reducing conditions (Lane *et al*, 2020a, 2020b). Another study suggested a reverse trend for Zn, reducing atmosphere hindering vaporisation of Pb, Zn, Cu, Cr, Co, and Ni due to increased liquid slag formation (Jiao *et al*, 2022). Other study that investigated the melting characteristic of FA concluded that ash composition was the main parameter affected the melting temperature, whereas atmosphere had minimal impact by a slight shift to higher temperature in oxidising atmosphere. Also, addition of CaO increased the melting point by the formation of new compounds (Li *et al*, 2007). In one study, it was found that all crystalline structures transformed into molten slag at temperatures exceeding 1300°C (Gao *et al*, 2021).

Metal extraction from FA via hydrometallurgical methods, has been extensively investigated in the literature (Karlfeldt Fedje *et al*, 2010; Huang *et al*, 2011; Tang and Steenari 2016; Jadhav and Hocheng, 2012; Wen *et al*, 2020; Wang *et al*, 2021). In terms of metal extraction via pyrometallurgical processes, the main approach has been thermal separation of heavy metal (HM) compounds by taking the advantage of the high volatility of chlorides (Nowak *et al*, 2012; Yu *et al*, 2016; Wang *et al*, 2021). Experimental findings indicated that both Pb and Zn possess considerable volatility, with approximately 80 per cent volatilisation achieved at 900°C even without the addition of chlorination agents (Kurashima *et al*, 2019). Another pyrometallurgical method investigated for metal extraction from FA is molten salt treatment, in which molten salt served as a metal extraction and separation medium, and requiring relatively low-temperature (600–800°C) processes (Xie *et al*, 2020). Commonly used reagents include chloride-based salts such as sodium chloride (NaCl) and potassium chloride (KCl), as well as eutectic salt mixtures (eg NaCl-$CaCl_2$).

Even though there are considerable number of technologies available for ash valourisation, the complexity, compositional variations, and relatively low metal concentrations are the biggest limitations for techno-economically robust solutions. This study aims at giving insights into the melting behaviour of different ash types with the prospect of utilising thermal treatment for metal recovery as a part of more holistic FA recovery process. The main focus of the study was on investigating the metallic, non-metallic, and amorphous phase formations upon melting as a basis for potential exploitation of leachability of different crystal structures in varying mediums.

MATERIALS AND METHODS

The fly ash samples investigated in this study were obtained from different incineration plants located in various countries and using different incineration technologies, such as grate furnace (denoted as GF), rotary kiln (denoted as R), and circular fluidised bed (denoted as C). Both raw and salt-washed fly ash samples are used for the experiments, with ‘W’ denoting the washed samples. The samples were melted without any prior compacting or pelletising steps. The particle size of the raw and washed samples ranges between 37.66–139.52 μm and 30.41–83.38 μm, respectively. The chemical composition of the samples is presented in Table 1. It was determined via X-ray diffraction that the major compounds in fly ash samples were salts (such as KCl, NaCl, and $NaSO_4$), Ca-compounds (including CaO, $CaCO_3$, and $CaSO_4$), and complex alumina silicates.

TABLE 1

ICP-MS results of ash samples (reduced table containing only major and critical elements).

	wt%									
Elements	**R**	**GF1**	**GF2**	**GF3**	**C**	**RW**	**GF1W**	**GF2W**	**GF3W**	**CW**
Al	1.80	2.10	2.10	3.60	1.20	3.50	7.70	4.20	4.70	10.00
Ba	1.60	0.11	0.07	0.28	0.19	3.30	0.13	0.10	0.33	0.21
Ca	3.30	30.00	28.00	21.00	23.00	6.60	23.00	29.00	24.00	22.00
Cl	8.00	9.90	12.00	3.80	3.80	0.36	0.31	0.36	0.15	0.38
Cu	0.27	0.06	0.05	0.08	0.47	0.49	0.07	0.09	0.08	0.57
Fe	2.80	1.20	0.92	2.10	1.90	6.00	2.40	1.80	2.50	2.60
K	5.20	2.20	2.10	4.30	0.91	2.50	0.56	0.34	0.66	0.45
Mg	0.58	0.78	0.70	0.15	1.50	1.20	1.50	1.50	2.00	2.00
Mn	0.15	0.05	0.05	0.10	0.10	0.30	0.08	0.11	0.16	0.13
Mo	0.10	0.00	0.00	0.00	0.02	0.19	0.00	0.00	0.00	0.00
Na	19.00	2.70	3.40	5.20	1.90	7.20	0.64	0.58	0.79	0.93
Ni	0.10	0.00	0.01	0.01	0.01	0.21	0.01	0.02	0.01	0.02
P	5.90	0.55	0.44	0.75	0.35	11.00	0.71	0.78	0.88	0.47
Pb	0.35	0.21	0.18	0.31	0.20	0.44	0.12	0.20	0.20	0.21
S	8.40	3.60	4.50	11.00	1.60	1.00	2.40	4.00	8.00	1.80
Si	3.60	5.70	3.70	6.60	9.30	6.60	11.00	7.50	8.40	12.00
Ti	1.10	0.54	0.49	1.30	0.24	2.20	1.00	1.00	1.60	1.70
Zn	2.30	0.82	0.82	1.90	0.45	4.50	1.30	1.50	2.30	0.60

In the experimental set-up, a sessile drop furnace was employed to investigate the melting behaviour of fly ash samples. The furnace is composed of a stainless-steel chamber with two windows, featuring a graphite heating element and radiation shield, a pyrometer, and a control C-type thermocouple. Additionally, the furnace is equipped with a high-speed digital CCD camera (Microtron MC 1310, Microtron GmbH, Unterschleissheim, Germany) at 50 frames per sec, allowing real-time observation of the samples during heating (Bao *et al*, 2021; Bublik *et al*, 2021; Canaguier and Tangstad, 2021). To determine the melting point, the ash samples were heated under argon (Ar, 99.9999 per cent purity) atmosphere until the onset of melting was observed in the camera. Before starting the experiments, a calibration experiment with pure iron (Fe) was done to ensure accurate temperature reading. To investigate the salt composition effect on melting temperature, one set of ash samples was washed with water to remove salts and one set of samples are used without any treatment. Based on the melting temperature observations in these experiments, a second part of experiments was conducted at T_m+100°C with a holding time of 1 hr, and under both Ar and carbon monoxide (CO, 99.9993 per cent purity) gas atmospheres. Only washed samples were used in the subsequent experiments. The focus of the second set of experiments was to observe the phase disintegrations and metal migration after melting, and to investigate the effect of a reducing atmosphere (when CO is used) on the system. All experiments were conducted with a consistent gas flow of 0.1 L/min. Alumina was used as the substrate for the experiments, and the sample amount varied between 80–100 mg. The characterisation of ash melts was done using Scanning Electron Microscopy-Energy Dispersive Spectroscopy (SEM-EDS) and Electron Probe Micro-Analysis (EPMA), and samples were epoxy-cast twice to get cross-sectional imaging.

The thermodynamic modelling study was conducted using FactSage™ 8.3 software (Thermfact/CRCT, Montreal; GTT-Technologies, Aachen), where the Gibbs free energy minimisation is applied. The phase formation upon solidification was modelled in the Equilibrium module selecting FactPS and FTOxide databases (FactSage™). To simplify the system, the chemical composition of ash samples was registered as the main sulfate or carbonate compounds, depending on the sample composition, where the quantitative data was obtained by Rietveld analysis of X-ray diffraction (XRD) scanning, and for metal oxides deriving from elemental composition data provided in Table 1.

RESULTS AND DISCUSSION

Effect of salt composition on the melting temperature

The melting temperatures of the raw and salt washed MSWI FA samples were determined based on the visual observations with a high-speed digital camera during heating. The images are shown in Figure 1, where the first clear images were taken when the temperature reached 900°C. A complete wetting at the melting point was observed for all samples, except sample R. During the heating of sample GF3, gasification of some amount of sample was recorded when the temperature reached close to the melting point, and the evaporation accelerated with further increase in the temperature. On the other hand, sample GF3W did not show any excess gasification, however, bubbling on the melt surface was observable to some extent. This suggests the evaporation of chlorine compounds in the unwashed samples, whereas the removal of most chlorine salts after washing limits the gasification in the washed sample. The results show that the melting temperature of the fly ash samples varies between 1000–1400°C, depending on the ash type and the effect of decreased salt content (Table 2). Salt washing did not have the same effect for all ash types, the melting temperature of samples R and C decreases, whereas the melting point of samples GF1 and GF3 remains constant after salt removal. An increase in melting temperature was observed only in sample GF2. These results were higher than the reported melting temperatures of FA in the literature. According to the previous search results, the melting temperature of MSWI FA varied depending on the specific conditions and composition of the sample. One study found that the melting process of fly ash consisted of three main transitions: dehydration (100–200°C), polymorphic transition (480–670°C), and fusion (1101–1244°C) (Li *et al*, 2007). Another study reported that the ash fusion temperatures of MSWI FA ranged from 1167°C to 1211°C (Gao *et al*, 2021).

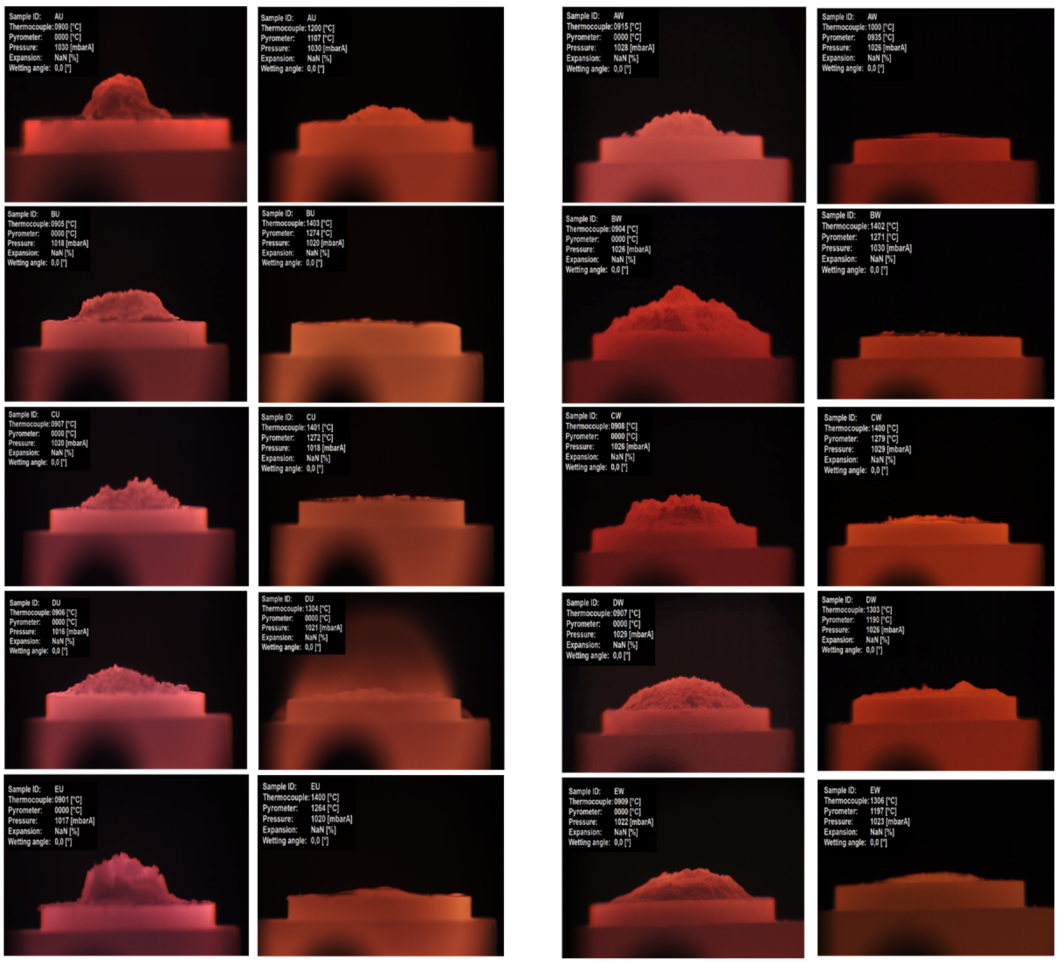

FIG 1 – Images captured during the heating of fly ash samples (Registered sample IDs in the furnace and their corresponding sample denotations: AU=R, AW=RW, BU=GF1, BW=GF1W, CU=GF2, CW=GF2W, DU=GF3, DW=GF3W, EU=C, and EW=CW).

TABLE 2

Approximate melting temperatures of raw and washed ash samples.

Sample	Temp (°C)	Sample	Temp (°C)
R	1200	RW	1000
GF1	1400	GF1W	1400
GF2	1200	GF2W	1400
GF3	1300	GF3W	1300
C	1400	CW	1300

Effect of chemical composition and atmosphere on phase formations and metal migration

To investigate the effect of composition on solidification, three representative samples were chosen based on their major compounds: RW (Na_2SO_4-rich), GF1W ($CaCO_3$-rich), and GF3W ($CaSO_4$-rich). The SEM-EDS results of the melted and solidified ash samples under Ar and CO atmospheres are shown in Figures 2 and 3, respectively. The results suggest that there are three distinct phases upon solidification: a metallic phase, a crystalline, non-metallic phase with inhomogeneous shape pattern, and an amorphous matrix phase. The EDS data points show that metallic droplets mainly contain Fe and phosphorous (P), with some extent of silicon (Si), and other elements such as molybdenum (Mo), nickel (Ni), aluminium (Al), titanium (Ti) and manganese (Mn) found in the metallic phase depending on the initial sample composition. In some samples (Figures 2b and 3a), Cu is found in

Fe-containing metallic phases, suggesting coalescence upon reduction. In Figure 2b, the Cu concentration is high (67.54 per cent) with no P detected in the phase. EDS data points of non-metallic phases reveals that the phase is mainly composed of calcium (Ca) and sulfur (S), suggesting the formation of a CaS phase. It is also observed that non-metallic phases contain some amount of Si, O, Mn, and Al (Figures 2c and 3a–3c), suggesting migration of these elements into the CaS phase. The formation of CaS can be attributed to the reduction of $CaSO_4$ during melting, which also suggests that some extent of reductive conditions provided in the system also under Ar atmosphere that led to formation of CaS, eg in sample GF3W. The sources of reductant, possibly carbon (C), can be the graphite furnace wall in the sessile drop furnace and the elemental C present in the initial composition of the ash. The analysis of carbon is not available for the samples used in this study; however, it is known that most ash samples might contain significant amount of C (5–20 wt per cent) coming from flue gas cleaning operations where activated carbon is added (Geng *et al*, 2020). In sample RW, S is not found in the Ca-rich non-metallic phase, as opposed to the detected amount of O which is high along with some amount of P, suggesting the formation of $Ca_5(PO_4)$ phase. The results suggest the formation of amorphous Ca-rich $CaO\text{-}SiO_2\text{-}Al_2O_3$ slag phase as the matrix in the samples where $CaCO_3$ and $CaSO_4$ are the major compounds. In sample RW, however, Ca is not detected in the matrix phase and the results suggest that it is composed of complex $SiO_2\text{-}Al_2O_3\text{-}K_2O\text{-}P_2O5\text{-}Na_2O$ slag. In terms of the effect of atmosphere on phase formations, there is no substantial difference between phases that could be linked to furnace atmosphere.

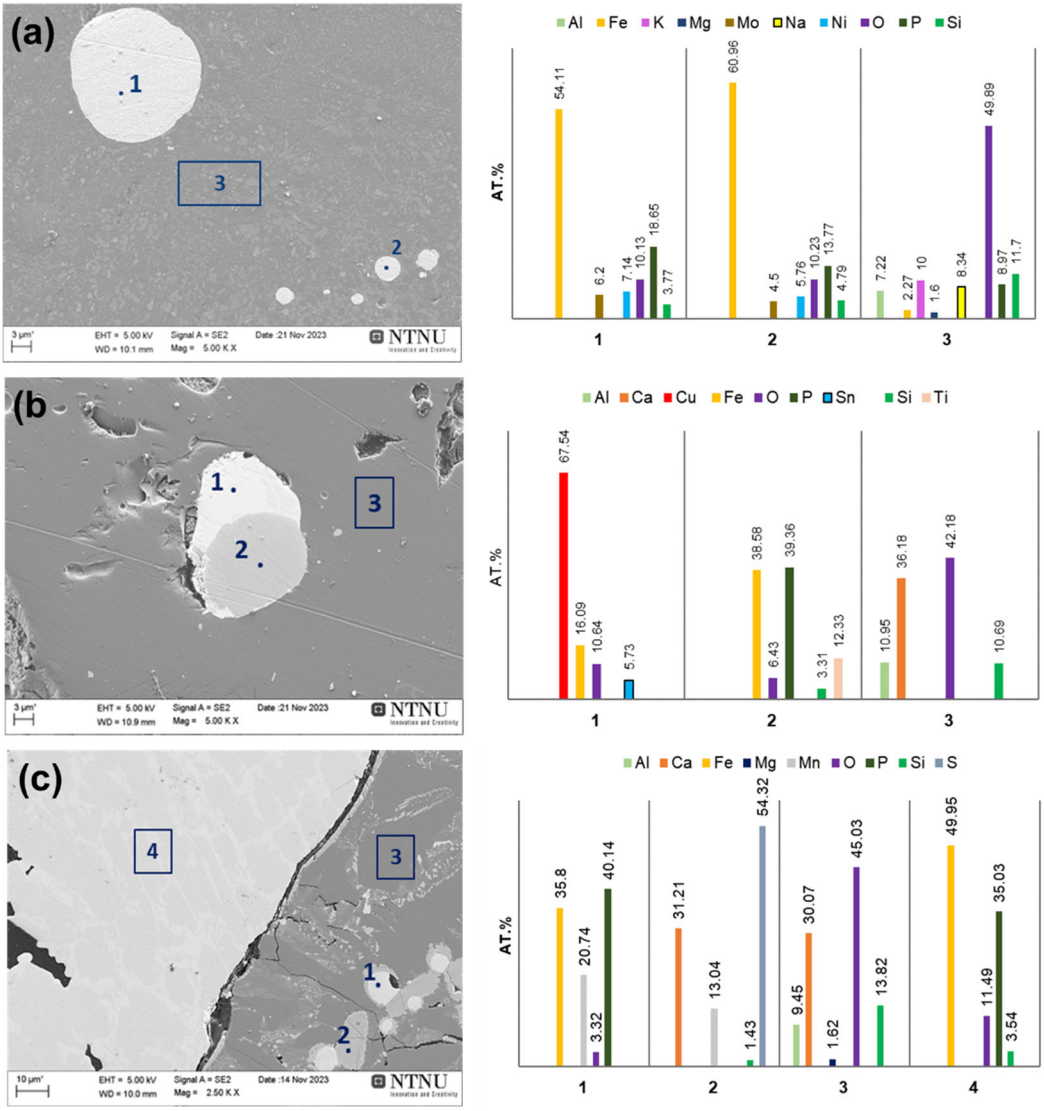

FIG 2 – SEM-EDS results of ash melts under AR atmosphere: (a) RW, (b) GF1W, and (c) GF3W.

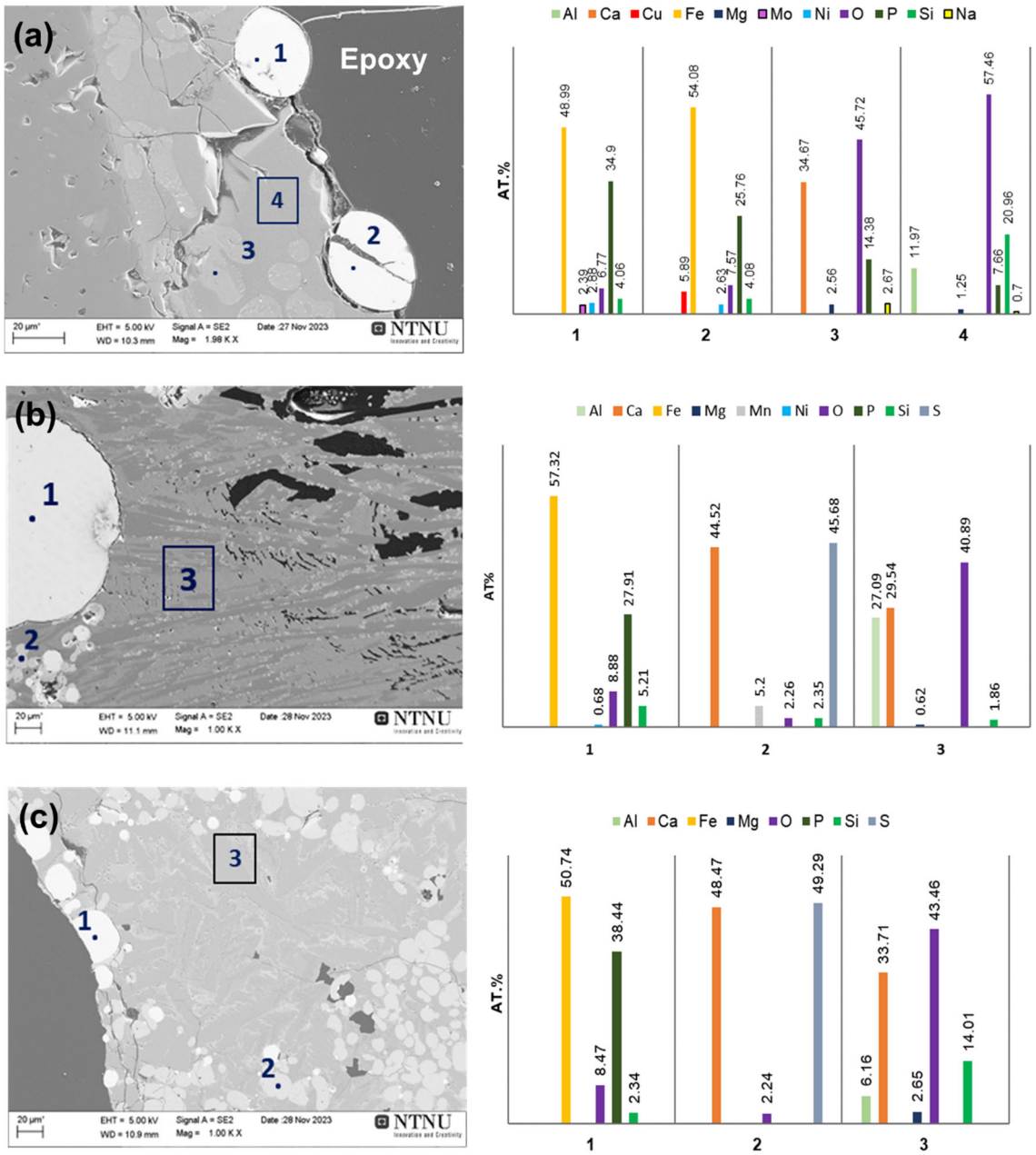

FIG 3 – SEM-EDS results of ash melts under CO atmosphere: (a) RW, (b) GF1W, and (c) GF3W.

Elemental mapping in EPMA correlates well with the EDS data, except for O, where EPMA imaging does not show any O in the Fe-P phase regions as opposed to EDS spectra (Figure 4), as would be expected. It is also observed that metallic droplets composed of two phases, suggesting solidification into different Fe-rich phases, eg Fe_3P and Fe_2P, upon solidification (Okamoto, 1990). The images showed some amount of Cu and Zn in the metallic phase, which indicates reduction followed by coalescence. Differently from EDS results, Zn and Cu are found throughout the sample, concentrating in the metallic phase. The elemental map confirms the formation of non-metallic CaS and Ca-P phases having some amount of Na along with O. The oxygen concentration in the Ca-phase (Figure 4a) is less than P and Ca, which differs from EDS data. Figure 4b suggests regions in the matrix phase where Al_2O_3 and SiO_2 concentrated.

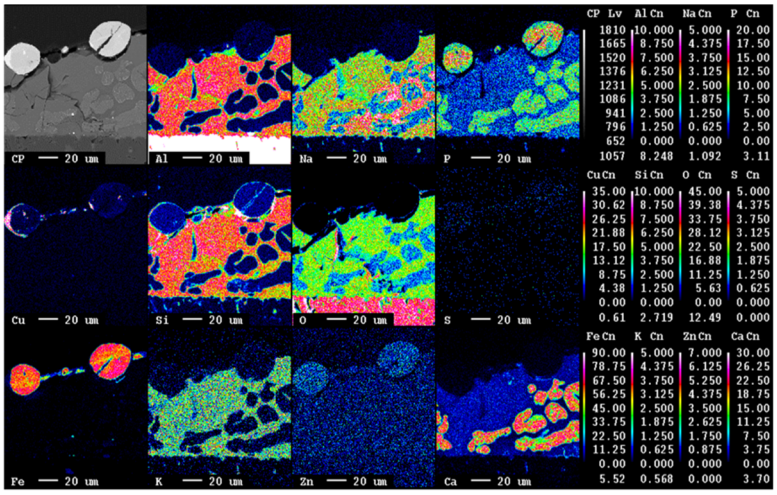

(a)

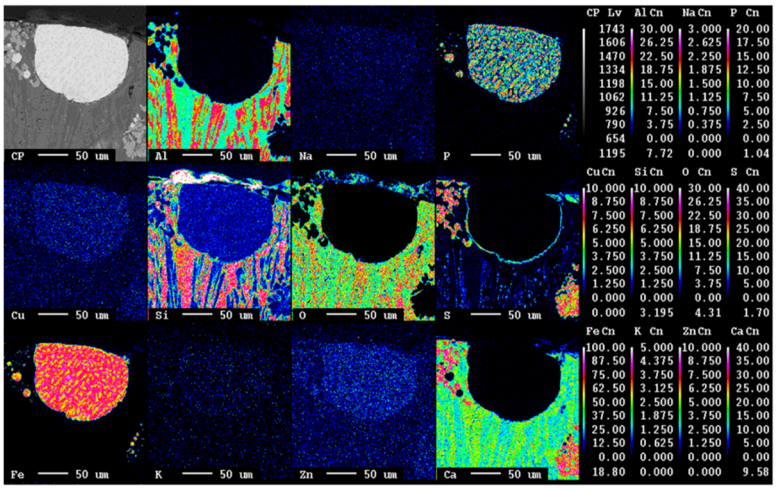

(b)

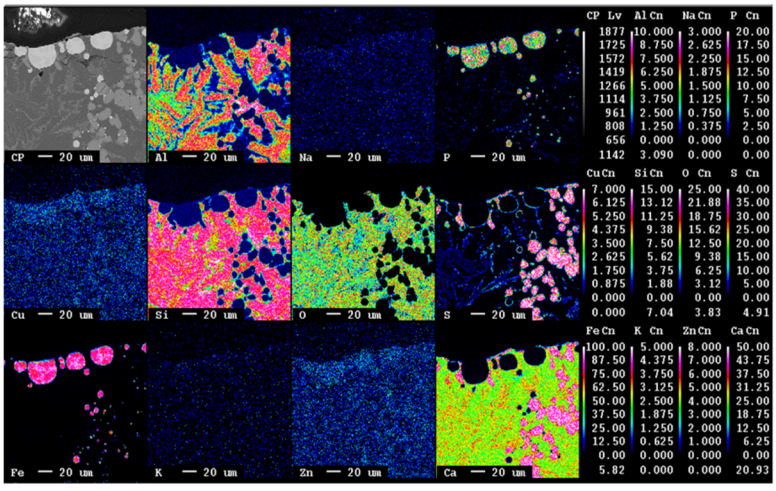

(c)

FIG 4 – EPMA results of selected ash samples melted under CO: (a) RW, (b) GF1W, and (c) GF3W.

FactSage™ modelling

In Figure 5, the calculations of equilibrium phases during heating and cooling of the representative samples under CO atmosphere are shown. Taking into account the composition of the ash systems, initial compositions were used as input to the calculations as shown in Table 3. The melting temperature is interpreted as the temperature where liquid slag formation starts in the heating graphs. The calculated melting temperature of RW and GFW1 is 700°C, and the melting temperature of GF3W is 900°C. These calculated temperatures are lower than the experimental temperature since the melting temperature indicates complete melting of the samples in the experimental observations, whereas, thermodynamic modelling shows the melting initiation temperatures. In the experimental study, high-temperature recording is only possible after 900°C, thus, melting initiation temperatures cannot be observed for low temperatures. The registered complete melting temperatures correspond the temperatures where liquid slag formation has reached its peak, which corresponds to 1100°C for RW, and 1400°C for GF1W and GF3W. In terms of the effect of the dominant compounds on the melting temperatures, it is concluded that high concentration of Na_2SO_4 decreases the melting point, whereas high amounts of Ca-bearing compounds have the opposite effect. The phase formation upon solidification of different ash types was calculated by cooling the liquid slag from 1600°C, using the Scheil-Gulliver functionality in FactSage™. The temperatures for complete solidification were found as 537°C, 642°C, and 546°C for RW, GF1W, and GF3W, respectively. The systems that include $CaSO_4$ shows CaS formation upon cooling, whereas, the calculations suggest the formation of $Na_2Ca_2P_2O_7$ and $Na_2CaP_2O_8$ compounds in RW. In regards to metallic phases, the thermodynamic calculations suggest the presence of FeS and ZnS compounds, starting to form later in the solidification stage. The modelling results on metallic phase formation does not correlate with the experimental observations, where results indicate the solidification of Fe-P compounds. This can be attributed to the well-known limitations in the FactSage™ databases for P containing compounds. The modelling results show the formation of complex silicates ($K_2MgSi_3O_8$, $CaMgSi_2O_6$, $Ca_2FeSi_2O_7$, $Ca_2Al_2SiO_7$, $Ca_7P_2SiO_2O_{16}$ etc) showing a good correlation with the experimental matrix phase observations. The system that has $CaSO_4$ as the major compound shows silicate containing oxide solid solutions (FToxid-BRED, FToxid-bC2SA, and FToxid-Mel_A) along with $Ca_7P_2Si_2O_{16(s)}$ phase:

- [FToxid-Bred] Bredigite OXIDE solution: $Ca_3(Ca,Mg)_4Mg(SiO_4)_4$ – a solid solution originating from $Ca_7Mg(SiO_4)_4$ by substitution of some Ca by Mg.
- [FToxid-bC2SA] OXIDE solution alpha-prime $(Ca,Sr,Ba)_2SiO_4$: Ca_2SiO_4 – Sr_2SiO_4 – Ba_2SiO_4 solution + (Mg_2SiO_4, Fe_2SiO_4, Mn_2SiO_4, Pb_2SiO_4, Zn_2SiO_4, $Ca_3B_2O_6$ in dilute amounts). End-members in pure compound database FToxidBase.cdb: Ca_2SiO_4(S2), Sr_2SiO_4(S2) and Ba_2SiO_4(S1).
- [FToxid-Mel_A] OXIDE solution-melilite: Mineralogical names: Akermanite ($Ca_2MgSi_2O_7$), Iron-akermanite ($Ca_2FeSi_2O_7$), Gehlenite ($Ca_2Al_2SiO_7$), Iron-gehlenite ($Ca_2Fe_2SiO_7$), Hardystonite ($Ca_2ZnSi_2O_7$). End-members in pure compound database FToxidBase.cdb: $Ca_2MgSi_2O_7$, $Ca_2FeSi_2O_7$, $Ca_2Al_2SiO_7$, $Ca_2ZnSi_2O_7$, $Pb_2ZnSi_2O_7$.

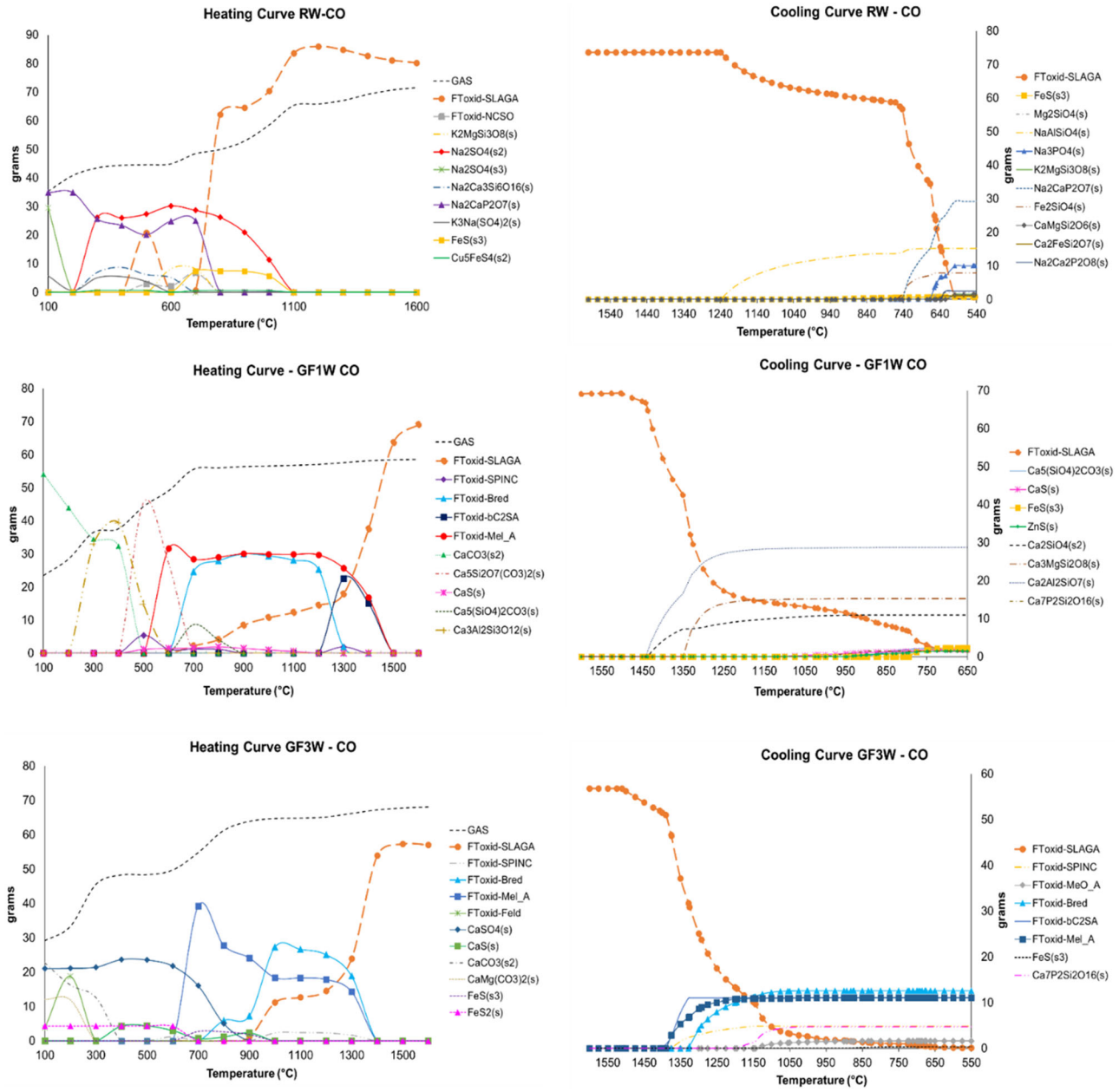

FIG 5 – FactSage™ 8.3 calculations.

TABLE 3

Compositional data used for FactSage™ 8.3 calculations.

RW (wt%)		GF1W (wt%)		GF3W (wt%)	
Na_2SO_4	38.91	$CaCO_3$	55.06	$CaCO_3$	2.09
Al_2O_3	6.17	$CaSO_4$	9.23	$CaSO_4$	64.13
Fe_2O_3	8.00	Al_2O_3	11.13	Al_2O_3	7.49
MgO	1.86	Fe_2O_3	2.62	Fe_2O_3	3.01
MnO	0.18	MgO	1.90	MgO	2.80
SiO_2	13.18	SiO_2	18.00	SiO_2	15.15
P_2O_5	23.52	P_2O_5	1.24	P_2O_5	1.70
K_2O	2.81	K_2O	0.52	K_2O	0.67

CONCLUSION

In conclusion, the findings of this study reveal that, not surprisingly, the most significant effect that has an impact on melting temperature and phase formation upon solidification is the composition of the ash samples. The experimentally observed melting points of the raw and salt-washed samples ranged from 1000–1400°C, showing differences before and after salt-washing, however, without exhibiting a discernible trend. Both experimental findings and thermodynamic modelling indicate that an elevated concentration of Na_2SO_4 lowers the melting point, while the presence of Ca-bearing compounds has the opposite effect. The findings indicate that during the solidification process, three separate phases form: a metallic phase, a non-metallic phase with a crystalline structure and an uneven shape pattern, and a phase characterised by an amorphous matrix. The EDS data show that metallic droplets mainly contain Fe and P, whereas non-metallic phase is mainly composed of Ca-S, suggesting the formation of CaS under reducing conditions. In some samples, low concentration of other metals such as Cu, Ni, Mo etc were detected in the metallic phase, indicating a co-reduction followed by coalescence mechanism. Also, in the CaS phase, the migration of some elements such as Si, O, Mn, and Al into the non-metallic phase is observed. The results indicate the formation of an amorphous Ca-rich CaO-SiO_2-Al_2O_3 slag phase as the predominant matrix in samples characterised by the presence of $CaCO_3$ and $CaSO_4$ as major compounds. Conversely, in sample RW, the absence of Ca in the matrix phase suggests a composition comprising a complex SiO_2-Al_2O_3-K_2O-P_2O_5-Na_2O slag. Regarding the influence of atmospheric conditions on phase formation, no discernible distinctions were observed between phases that could be attributed to variations in the furnace atmosphere. The modelling results were in good correlation showing the formation of complex silicates ($K_2MgSi_3O_8$, $CaMgSi_2O_6$, $Ca_2FeSi_2O_7$, $Ca_2Al_2SiO_7$, $Ca_7P_2SiO_2O_{16}$ etc) as the major components in the solidified system.

REFERENCES

Bao, S, Tangstad, M, Tang, K, Kristian, E, Syvertsen, M, Onsøien, M, Kudyba, A and Bublik, S, 2021. Investigation of Two Immiscible Liquids Wetting at Elevated Temperature: Interaction Between Liquid FeMn Alloy and Liquid Slag, *Metallurgical and Materials Transactions B*: *Process Metallurgy and Materials Processing Science,* 52(5):2847–2858.

Becidan, M, 2018. Fly ash treatment technologies: An overview of commercial and upcoming technologies for Norway and Scandinavia, report for NOAH AS, SINTEF Energi AS.

Bublik, S, Bao, S, Tangstad, M and Einarsrud, K E, 2021. Interfacial Behaviour in Ferroalloys: The Influence of Sulfur in FeMn and SiMn Systems, *Metallurgical and Materials Transactions B*: *Process Metallurgy and Materials Processing Science,* 52(6):3624–3645.

Canaguier, V and Tangstad, M, 2021. In situ observation of the carbothermic reduction and foaming of slags in silicomanganese production, *Processes,* 9(11).

Fan, C, Wang, B, Ai, H and Liu, Z, 2022. A comparative study on characteristics and leaching toxicity of fluidized bed and grate furnace MSWI fly ash, *Journal of Environmental Management,* 305.

Gao, J, Wang, T, Zhao, J, Hu, X and Dong, C, 2021. An experimental study on the melting solidification of municipal solid waste incineration fly ash, *Sustainability (Switzerland,* 13(2):1–10.

Geng, C, Liu, J, Wu, S, Jia, Y, Du, B and Yu, S, 2020. Novel method for comprehensive utilization of MSWI fly ash through co-reduction with red mud to prepare crude alloy and cleaned slag, *Journal of Hazardous Materials*, 384.

Huang, K, Inoue, K, Harada, H, Kawakita, H and Ohto, K, 2011. Leaching of heavy metals by citric acid from fly ash generated in municipal waste incineration plants, *Journal of Material Cycles and Waste Management*, 13(2):118–126.

Jadhav, U U and Hocheng, H, 2012. A review of recovery of metals from industrial waste, *Journal of Achievements in Materials and Manufacturing Engineering*, 54(2):154–167.

Jiao, F, Ma, X, Liu, T, Wu, C, Hanxu, L and Dong, Z, 2022. Effect of Atmospheres on Transformation of Heavy Metals during Thermal Treatment of MSWI Fly Ash: By Thermodynamic Equilibrium Calculation 2018, *Molecules*, 27(2):738–754.

Karlfeldt Fedje, K, Ekberg, C, Skarnemark, G and Steenari, B M, 2010. Removal of hazardous metals from MSW fly ash-An evaluation of ash leaching methods, *Journal of Hazardous Materials*, 173(1–3):310–317.

Kaza, S, Yao, L, Bhada-Tata, P and Woerden, F, Van, 2018. *What a Waste 2.0: A Global Snapshot of Solid Waste Management to 2050,* Urban Development Series. https://doi.org/10.1596/978-1-4648-1329-0

Kurashima, K, Matsuda, K, Kumagai, S, Kameda, T, Saito, Y and Yoshioka, T, 2019. A combined kinetic and thermodynamic approach for interpreting the complex interactions during chloride volatilization of heavy metals in municipal solid waste fly ash, *Waste Management*, 87:204–217.

Lane, D J, Jokiniemi, J, Heimonen, M, Peräniemi, S, Kinnunen, N M, Koponen, H, Lähde, A, Karhunen, T, Nivajärvi, T, Shurpali, N and Sippula, O, 2020a. Thermal treatment of municipal solid waste incineration fly ash: Impact of gas atmosphere on the volatility of major, minor and trace elements, *Waste Management*, 114:1–16.

Lane, D J, Hartikainen, A, Sippula, O, Lähde, A, Mesceriakovas, A, Peräniemi, S and Jokiniemi, J, 2020b. Thermal separation of zinc and other valuable elements from municipal solid waste incineration fly ash, *Journal of Cleaner Production*, 253.

Li, R, Wang, L, Yang, T and Raninger, B, 2007. Investigation of MSWI fly ash melting characteristic by DSC-DTA, *Waste Management*, 27(10):1383–1392.

Nedkvitne, E N, Borgan, Ø, Eriksen, D Ø and Rui, H, 2021. Variation in chemical composition of MSWI fly ash and dry scrubber residues, *Waste Management*, 126:623–631.

Nedkvitne, E N, Eriksen, D Ø and Omtvedt, J P, 2023. Grade and Tonnage Comparison of Anthropogenic Raw Materials and Ores for Cu, Zn and Pb Recovery, *Resources*, 12(3). https://doi.org/10.3390/resources12030033.

Neuwahl, F, Cusano, G, Benavides, J G, Holbrook, S and Roudier, S, 2019. Best Available Techniques (BAT) Reference Document for Waste Incineration, report, Industrial Emissions Directive 2010/75/EU (Integrated Pollution Prevention and Control), Joint Research Centre (European Commission) Science for Policy Report.

Nowak, B, Frías Rocha, S, Aschenbrenner, P, Rechberger, H and Winter, F, 2012. Heavy metal removal from MSW fly ash by means of chlorination and thermal treatment: Influence of the chloride type, *Chemical Engineering Journal*, 179:178–185.

Okada, T and Tomikawa, H, 2013. Effects of chemical composition of fly ash on efficiency of metal separation in ash-melting of municipal solid waste, *Waste Management*, 33(3):605–614.

Okamoto, B, 1990. The Fe-P (Iron-Phosphorus) System, *Bulletin of Alloy Phase Diagrams*, 11:404–4012.

Tang, J and Steenari, B M, 2016. Leaching optimization of municipal solid waste incineration ash for resource recovery: A case study of Cu, Zn, Pb and Cd, *Waste Management*, 48:315–322.

Tian, X, Rao, F, Li, C, Ge, W, Lara, N O, Song, S and Xia, L, 2021. Solidification of municipal solid waste incineration fly ash and immobilization of heavy metals using waste glass in alkaline activation system, *Chemosphere*, 283.

Wang, H, Zhu, F, Liu, X, Han, M and Zhang, R, 2021. A mini-review of heavy metal recycling technologies for municipal solid waste incineration fly ash, In *Waste Management and Research,* 39(9):1135–1148.

Wen, T, Zhao, Y, Zhang, T, Xiong, B, Hu, H, Zhang, Q and Song, S, 2020. Selective recovery of heavy metals from wastewater by mechanically activated calcium carbonate: Inspiration from nature, *Chemosphere*, 246.

Xie, K*,* Hu, H, Xu, S, Chen, T, Haung, Y, Yang, Y, Yan, F and Yao, H, 2020. Fate of heavy metals during molten salts thermal treatment of municipal solid waste incineration fly ashes, *Waste Management*, 103:334–341.

Yu, J, Sun, L, Ma, C, Qiao, Y, Xiang, J, Hu, S and Yao, H, 2016. Mechanism on heavy metals vaporization from municipal solid waste fly ash by MgCl2·6H2O, *Waste Management*, 49:124–130.

Zhang, Y, Wang, L, Chen, L, Ma, B, Zhang, Y, Ni, W and Tsang, D C W, 2021. Treatment of municipal solid waste incineration fly ash: State-of-the-art technologies and future perspectives, *Journal of Hazardous Materials*, 411.

Zhao, S Z, Zhang, X Y, Liu, B, Zhang, J J, Shen, H L and Zhang, S G, 2021. Preparation of glass–ceramics from high-chlorine MSWI fly ash by one-step process, *Rare Metals*, 40(11):3316–3328.

Conversion of hard-to-use wastes to new raw materials for low-energy glass/mineral-wool manufacturing

DOI: 10.62053/TDAA6553

Z Yan[1], T Htet[2], S Zhang[3] and Z Li[4]

1. Research fellow, Advanced Steel Research Centre WMG, University of Warwick, Coventry CV4 7AL, UK. Email: zhiming.yan@warwick.ac.uk
2. Process Engineer, BUSS Chem Tech., Pratteln CH-4133, Switzerland. Email: theint.htet@buss-ct.com
3. PhD student, College of Materials Science and Engineering, Chongqing University, Chongqing 400044, PR China. Email: xiaoshuo32188@126.com
4. Professor, Advanced Steel Research Centre WMG, University of Warwick, Coventry CV4 7AL, UK. Email: z.li.19@warwick.ac.uk

ABSTRACT

During the pyrometallurgical processes, a substantial quantity of high-temperature ironmaking and steelmaking slags, generated at temperatures ranging from 1400 to 1600°C, is wasted, as the heat contained in these slags is released into the environment during the tapping process without effective utilisation. On the other hand, a significant amount of energy is required to reheat the cold materials for the manufacturing of glass and mineral-wool, often necessitating the addition of high-silica materials to facilitate the production process. In this study, an innovative approach is presented to harness the heat present in molten metallurgical slags to directly produce new raw materials for glass and mineral-wool manufacturing while simultaneously reducing energy consumption and mitigating CO_2 emissions. The theoretical amount of waste glass that can be effectively added in the process has been estimated via thermodynamic calculation. Experimental assessments were conducted to examine the impact of high-silica waste materials on the dissolution, melting and fluidity. Potential recipes for glass and mineral-wool manufacturing were suggested and an assessment of the energy savings, and reduction in CO_2 emissions with manufacturing of glass and mineral-wool using this innovative approach were included. It was determined that the processes could lead to a reduction of over 26 kg of CO_2 emissions per 100 kg of new material used, primarily due to the utilisation of heat from slag and the accelerated smelting process.

INTRODUCTION

The glass and mineral-wool industries are energy intensive foundation sectors, facing significant challenges in reducing energy consumption and CO_2 emissions (Dewick and Miozzo, 2002; Kiss, Manchón and Neij, 2013; Springer and Hasanbeigi, 2017). A significant amount of energy is consumed in raw material preparation and melting, and a great portion of CO_2 emissions is released from carbonate decomposition of raw materials (Deng *et al*, 2023; Schmitz *et al*, 2011). The glass and mineral-wool traditionally produced from cold raw materials, incurs high energy consumption, with heating accounting for over 70 per cent of the total energy use. Now low cost, environmentally friendly, energy-saving and increased-recycling are major driving forces for new raw materials. The glass industry endeavours to maximise the recycled glass content, but a significant amount (100 kTs per annum in the UK) of poor-quality recycled glass is unsuitable to be used in glass furnace due to issues such as contamination and particle size being too fine, in addition to large number of other wastes such as glass fibre (Iacovidou *et al*, 2018). Metallurgical slags such as blast furnace (BF) slag and basic oxygen furnace (BOF) slag offer significant environmental benefits over mined raw materials, such as a higher melting rate and provide a carbonate-free source of calcium (Pan *et al*, 2016).

Molten slag, a high-temperature by-product of the metallurgical industry, holds substantial potential as a valuable resource for the glass and mineral-wool industries. The current focus is largely on investigating BF slag (Oge *et al*, 2019; Piatak, 2018; Piatak, Parsons and Seal, 2015). However, the widespread use of BF slag as a cement raw material has a high utilisation rate. Meanwhile, the considerable volume of steelmaking slag generated by the BOF process and electric arc furnace (EAF) process remains underutilised. This is attributed, in part, to its low acidity (SiO_2/CaO), leading to high melting temperature and strong crystallisation performance that are unfavourable for glass

and mineral-wool production. Additionally, the presence of FeO (~25 wt per cent) further hampers product quality. The acidity of metallurgical slag is usually lower than 1.0, while the acidity of mineral-wool is required to be more than 1.2 and even higher for glass (Zhao, Zhang and Cang, 2019). Then high-silica raw materials are needed to adjust the composition of the metallurgical slags and high-silica wastes, such as the waste glass become a potentially available resource.

This research aims to use the waste energy during molten slag tapping to convert various hard-to-use wastes into high value, new raw materials for glass or mineral-wool manufacturing. In this work, the energy utilisation and the effective use of waste glass in new materials generation were calculated. Thermodynamic calculations and experiments were carried out to assess the impact of waste glass on molten mixture properties. Modified mixtures were suggested to meet glass and mineral-wool manufacturing requirements. The study also evaluated energy savings and CO_2 emission reductions achieved through this innovative approach.

EXPERIMENTAL

Materials preparation

The BF slag, BOF slag and low-quality waste glass were sourced from industrial partners. The mineral phases of BOF slag and amorphous phase of BF slag and waste glass were confirmed by X-ray diffraction (XRD) as showed in Figure 1. The chemical composition of slags and glass were analysed by X-ray fluorescence (XRF) as presented in Table 1. The BOF slag exhibits a high content of FeO and a low acidity, contributing to the facile crystallisation of steel slag. The XRD pattern of the BOF slag appears intricate, revealing numerous overlapping peaks indicative of the diverse minerals present in the sample. Iron oxides are prevalent and beyond the presence of FeO, the XRD pattern suggests the likely existence of brownmillerite ($Ca_2(FeAl)_2O_5$) and magnesioferrite ($MgFe_2O_4$).

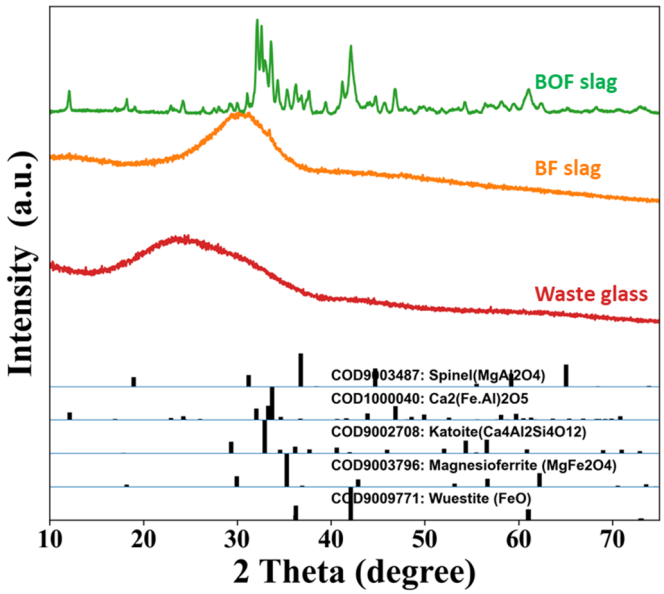

FIG 1 – XRD results of raw materials.

TABLE 1

Composition of BOF slag and waste glass, wt per cent.

wt%	CaO	SiO_2	MgO	Al_2O_3	SO_3	P_2O_5	K_2O	TiO_2	MnO	FeO	Na_2O	Acidity
BF slag	41.10	37.01	7.85	11.24	0.91	/	0.58	0.64	0.37	0.35	/	0.90
BOF slag	40.78	16.28	5.57	4.66	0.32	1.68	/	0.64	2.07	27.55	/	0.40
Waste glass	11.25	72.00	1.15	1.50	0.25	/	0.50	/	/	0.05	13.30	6.40

Thermodynamic calculation

The thermodynamic calculation was conducted by FactSage™ ver 8.2 (by Thermfact and GTT-Technologies) using FactPS and FToxid databases. This includes determining the effect of waste glass addition on the temperature and composition of mixture, the equilibrium phases during slag cooling, the melting behaviour and viscosity of raw materials. When calculating the theoretical addition of waste glass into molten slag during tapping, a key consideration is maintaining the slag-glass mixture in a liquid state. The calculations assumed a BF slag tapping temperature of 1480°C and BOF slag tapping temperature of 1550°C. The oxygen potential keeps at 0.21. Adiabatic calculations were also employed to get the temperature after mixing. The viscosity module was used to calculate the viscosity of the slags and molten mixture at liquid stage, with the aim of evaluating the effect of adding waste glass on the fluidity of the mixture.

Waste glass dissolution

The experiments of dissolving waste glass into BF slag were carried out in a high-temperature laser scanning confocal microscope at 1400°C and 1450°C in Argon, the schematic diagram for device and the temperature program are shown in Figure 2. The dissolution times were 0 sec, 10 sec, 30 sec and 60 sec. The heating and cooling rates were set as quickly as possible at 200°C/min and 300°C/min, respectively. About 100 mg of slag was first melted and then cooled down. A glass particle around 5 mg was placed on the top of the slag and reheated to the target temperature for a certain time. The cooled samples were analysed using a scanning electron microscope (SEM, Zeiss, Sigma) equipped with energy dispersive X-ray spectroscopy (EDS, Oxford, Ultim Extreme).

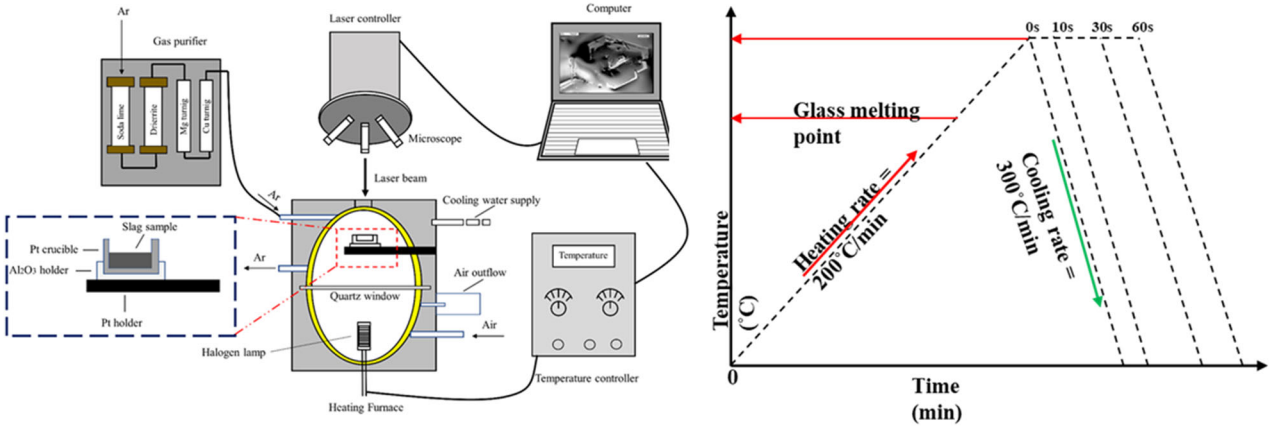

FIG 2 – Waste glass dissolution in BF slag via high-temperature laser scanning confocal microscope.

Melting temperature measurement

Based on the composition range of mineral-wool in the literature, a potential recipe was proposed. A high-temperature vacuum furnace was utilised to determine the melting temperature (T_h) using the Leitz microscope test method. Further information on the equipment and test procedure is available in a previously published paper (He *et al*, 2023). A cylindrical sample (3 mm in diameter and 3 mm in height) was prepared. During this heating phase, the shape of a compressed cylinder of slag powder was continuously monitored every second with a high-resolution optical camera when the chamber temperature over 1100°C. The heating rate was maintained at 6°C/min. The melting temperature is defined as the point at which the height of sample is reduced to half of its original size. Additionally, the fluidity temperature (T_f) is determined as the temperature at which the height of sample is reduced to one-quarter of its initial height.

Mineral-wool preparation

Utilising the proposed recipe, mineral-wool was manufactured through a centrifugal process. The details of the centrifugal apparatus were described in previous paper (He *et al*, 2023, 2020). For the process, a crucible containing 200 g of mixture was heated to approximately 1550°C in the induction furnace and maintained at this temperature for about 30 mins. It was then brought up to a

predetermined speed via the rotational drive system. The molten slag was gradually poured from the crucible onto the rotating cup, where it was transformed into wool fibres by centrifugal force. The mineral-wool obtained was observed using a digital optical microscope (OM, Keyence VHX7000).

RESULTS

Thermodynamic calculation

The basic melting characteristics and fluidity of the raw materials can be obtained via thermodynamic calculation, as shown in Figure 3. The liquidus temperature of BF slag is approximately 1375°C. After cooling, the predominant phase formed is Mellite. When the temperature drops to 25°C below the liquidus, the solid phase content exceeds 50 per cent. This indicates a significant increase in the solid fraction at relatively small deviations from the liquidus temperature, reflecting the sensitivity of BF slag composition to temperature changes. The melting point of BOF slag is over 1600°C. Owing to its high basicity and FeO content, the spinel phase is precipitate first. Then there is an extensive precipitation of Dicalcium Silicate (C_2S) due to the high basicity. As the temperature falls, there is a rapid reduction in the quantity of the liquid phase, highlighting the sensitivity of BOF slag to temperature changes as well. The glass starts to soften and transition into a semi-molten state at temperatures above 500°C, with its liquidus temperature being approximately 1150°C. At this stage, the wollastonite phase is the first to precipitate. The viscosity of BF slag in its liquid phase is less than 0.6 Pas, demonstrating relatively low resistance to flow. In contrast, BOF slag exhibits a lowe viscosity even solid phases presents, below 2.0 Pas using the Einstein equation (Yue *et al*, 2018), indicating excellent fluidity. This fluidity is directly influenced by the slag basicity: higher basicity enhances fluidity. This is due to alkaline oxides like CaO, MgO, and FeO disrupting the [SiO_4] network structure in molten slag, which consequently reduces the degree of polymerisation of slag (Yan, Reddy and Lv, 2019; Yan *et al*, 2016). As a result, slag with higher basicity presents lower viscosity in its liquid phase. Conversely, glass, with its significantly high SiO_2 content, exhibits a much higher viscosity.

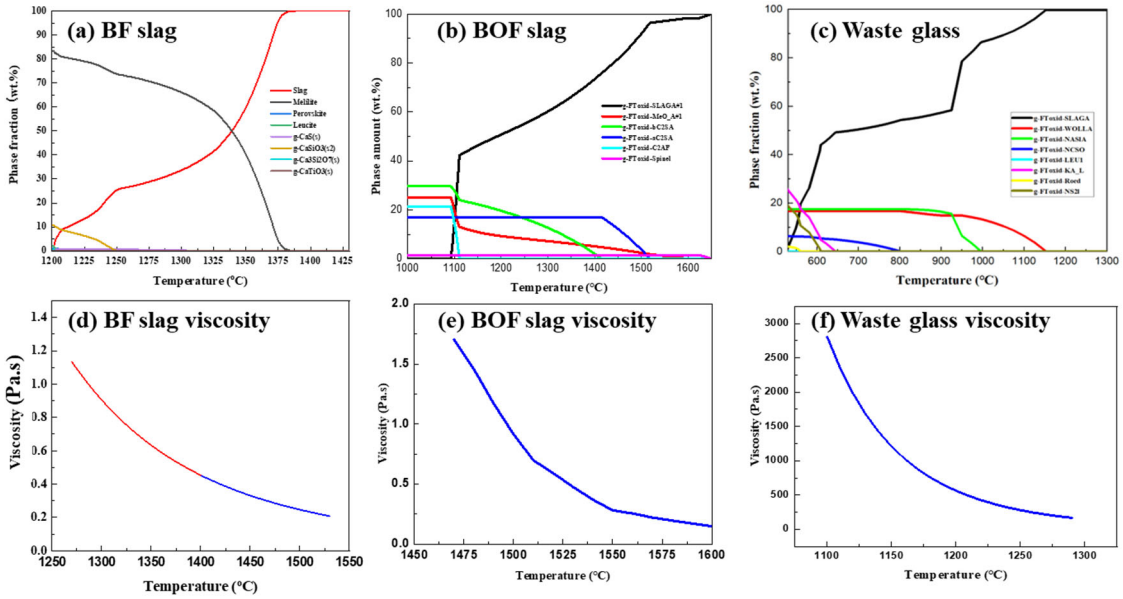

FIG 3 – The equilibrium phases during cooling of raw materials: (a) BF slag, (b) BOF slag, (c) Waste glass, and the viscosity of raw materials obtained via FactSage™: (d) BF slag, (e) BOF slag, (f) Waste glass.

Through adiabatic calculations, the impact of waste glass addition on the temperature of BF slag during tapping was assessed and the melting temperature of these mixtures was also determined. The findings are presented in Figure 4. It should be noted that waste glass can introduce a certain amount of carbon, as it may contain organic oil or plastic. The oxidation of this carbon contributes additional heat. The addition of waste glass results in a gradual decrease in the temperature when waste glass containing 0 per cent carbon and more than 9.4 kg of waste glass led to a temperature

less than the liquids (Figure 4a). Conversely, adding more than 50 kg of waste glass with 5 per cent carbon into slag content keeps the mixture in a liquid state (Figure 4b). As shown in Figure 4c, when the temperature is reduced to 1350°C, the viscosity of the mixture with 30 per cent added glass remains below 2 Pa·s, maintaining a good fluidity. For BOF slag, due to the oxidation of FeO and 0 per cent carbon, the slag temperature under adiabatic conditions will exceed 2000°C, as shown in Figure 5. The temperature of the mixture is still higher than the melting temperature when the amount of waste glass added exceeds 50 kg. It is worth noting that heat loss is not considered here. Since the BOF slag possesses a higher basicity compared to the BF slag, its viscosity is more favourable when the same quantity of waste glass is added. Consequently, maintaining fluidity is less challenging with BOF slag.

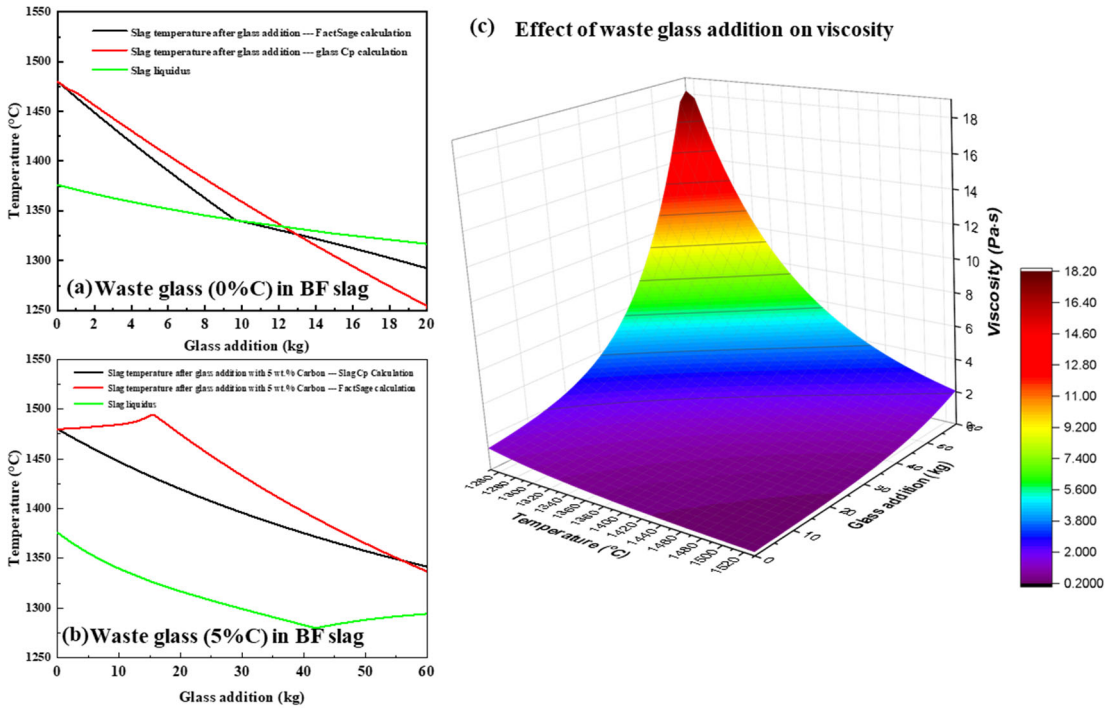

FIG 4 – The theoretical addition of waste glass with different carbon content into BF slag during tapping: (a) 0 per cent Carbon, (b) 5 per cent carbon, and the effect of temperature and waste glass addition on the viscosity.

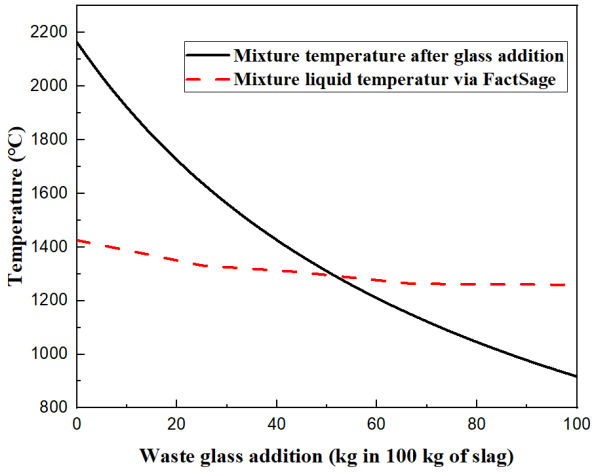

FIG 5 – The theoretical addition of waste glass with 0 per cent carbon into BOF slag during tapping.

Dissolution of waste glass in molten slag

Figure 6 displays the SEM-EDS results illustrating the cross-section microstructure of waste glass dissolution in BF slag at 1400°C and 1450°C for 60 sec. The top surface layer of the slag is identified

as glass, characterised by a high concentration of sodium and silicon, as revealed by EDS analysis in Figure 6a. At a temperature of 1400°C, the glass has completely melted, and the liquid glass layer begins to dissolve, but the dissolution is not complete. Remarkably, when the temperature is increased to 1450°C, the glass layer in the BF slag can be completely dissolved in less than 60 sec. Since no apparent stratification is evident and the distribution of sodium is uniform throughout, it indicates a homogenous composition in the slag layer. Due to the high SiO_2 content in waste glass, a lower SiO_2 concentration in the slag leads to a stronger driving force for dissolution, accelerating the dissolution rate. Additionally, SiO_2 dissolution is faster at higher temperatures and lower viscosities. Consequently, at same temperature, waste glass dissolves faster in BOF slag compared to BF slag. The melting and dissolution processes are further enhanced by stirring during the addition of waste glass.

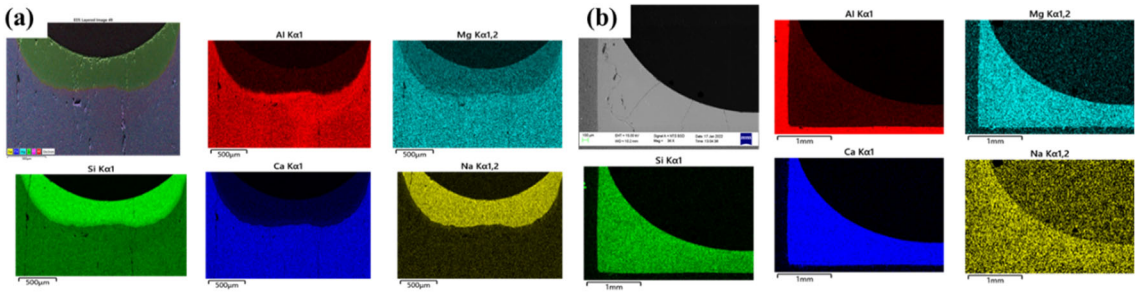

FIG 6 – Dissolution of waste glass in BF slag at different temperature for 60 sec: (a) 1400°C, and (b) 1450°C.

DISCUSSION

Integrating hard-to-use waste glass into the metallurgical slag during the tapping process promises to achieve the multiple purposes of waste utilisation, energy saving and waste heat recovery, as schematically illustrated in Figure 7. This process utilises the sensible heat of metallurgical slag and the heat of reaction from the oxidation of iron and organics, mixing hard-to-use high-silica waste with molten slag to form new raw materials suitable for glass manufacturing or mineral-wool production. The application of the new material after mixing is determined based on the compositional requirements of glass and mineral-wool. According to thermodynamic calculations of melting performance, fluidity, and solubility experiment results, for BF slag, if there is 5 per cent carbon in the waste glass, the addition of waste glass is about 30 per cent which still meets the requirements for slag transportation and tapping. For BOF slag, the addition of waste glass can exceed 50 per cent due to the high tapping temperature, high basicity and high FeO content. Depending on the composition of the new material and the final composition of the expected products, glass or mineral wool is prepared by adding other raw materials. Generally speaking, the new material obtained by BF is suitable for glass manufacturing, while the new material obtained by BOF is suitable for mineral wool. Two common approaches to utilising these materials will be explored below.



FIG 7 – Conversion of wastes to new raw materials for glass and mineral-wool manufacturing.

Based on a typical container glass composition (Shelby, 2020), a potential formula has been proposed as shown in Table 2. This recipe allows for the use of only 20 per cent new raw materials in the manufacturing of container glass. As a result, about 30 per cent of waste glass and 15 per cent BF slag are used in this glass production. By incorporating this new material, there is a notable reduction in lime consumption, which consequently leads to a decrease in CO_2 emissions. The new raw material contains sulfur which is a powerful refining agent and benefits glass manufacturing (Hujova and Vernerova, 2017). Additionally, the new material serves as a replacement for nepheline syenite and feldspar, which are the primary sources of alumina in traditional glassmaking. This substitution not only utilises waste materials but also maintains the necessary chemical composition for high-quality glass production.

TABLE 2

A potential recipe for soda-lime-silica (container glass) using new material, wt per cent.

	Ratio	CaO	SiO_2	MgO	Al_2O_3	SO_3	K_2O	TiO_2	MnO	Fe_2O_3	Na_2O
New material 1: 50 kg waste glass in 100 kg BF slag	20	32.12	47.58	5.84	8.31	0.71	0.56	0.45	0.26	0.28	4.00
SiO_2 sand	46	0.28	98.2	0.03	0.28	0.07	0.01	0	0	0	0.03
Soda ash	16	0	0	0	0	0	0	0	0	0	58.49
Waste glass (good quality)	23	11.25	72	1.15	1.5	0.25	0.5	0	0	0.05	13.3
Lime	2	92.01	1.51	0	0.93	0	0	0	0	0.11	0.00
Proposed glass composition		10.67	70.78	1.30	1.96	0.22	0.22	0.08	0.05	0.06	14.04
Typical container glass composition		10–12	70–73	0.5–2	0–2	0–0.5	0–1	0–0.1	/	0–1	12–15

Referring to the composition ranges of mineral-wool documented in the literature (Yliniemi *et al*, 2021), a potential recipe was proposed, as shown in Table 3. This formulation permits the incorporation of approximately 60 per cent new raw materials. Consequently, in producing this specific type of mineral-wool, around 20 per cent of the raw materials are derived from waste glass and another 40 per cent from BOF slag. In the laboratory experiments, analytically pure reagents (SiO_2, Al_2O_3 and MgO) were used for replacing silica sand, bauxite and dolime. These were mixed with BOF slag and waste glass to create a mixture with a similar composition to the recipe. Then this mixture was used for both the measurement of the melting temperature and the preparation of mineral-wool and the results are presented in Figure 8. The Lab-made mixture shows a melting temperature at approximately 1160°C and its fluidity temperature is around 1225°C. The diameter of fibres is a crucial determinant of the properties of mineral-wool products, affecting characteristics such as chemical stability and sound absorption (He *et al*, 2023; Liu *et al*, 2013). The mineral-wool produced has fibres measuring approximately 10–20 μm in diameter, which are over twice as thick as those found in commercial rock wool products. A high-speed, four-roller centrifuge will be utilised to produce wool fibres and will be investigated in future work.

TABLE 3

A potential recipe for mineral-wool using new material, wt per cent.

	Ratio	CaO	SiO_2	MgO	Al_2O_3	K_2O	TiO_2	MnO	Fe_2O_3	Na_2O
New material 2: 50 kg waste glass in 100 kg BOF slag	60	25.8	45.45	3.2	3.48	0.25	0.33	1.06	14.57	4.66
SiO_2 sand	15	0.28	98.2	0.03	0.28	0.01	0	0	0	0.03
Bauxite	15	0	18.68	0	56.29	0	2.33	0	1.29	0
Dolime	10	54.75	3.55	40.1	0.33	0.08	0.05	0.03	0.38	0.02
Proposed material composition		21.00	45.16	5.93	10.61	0.16	0.55	0.64	8.97	2.80
Mineral-wool composition from literature		10–25	41–53	6–16	6–14	0–2	0–3.5	0–1.1	0–13	0–6

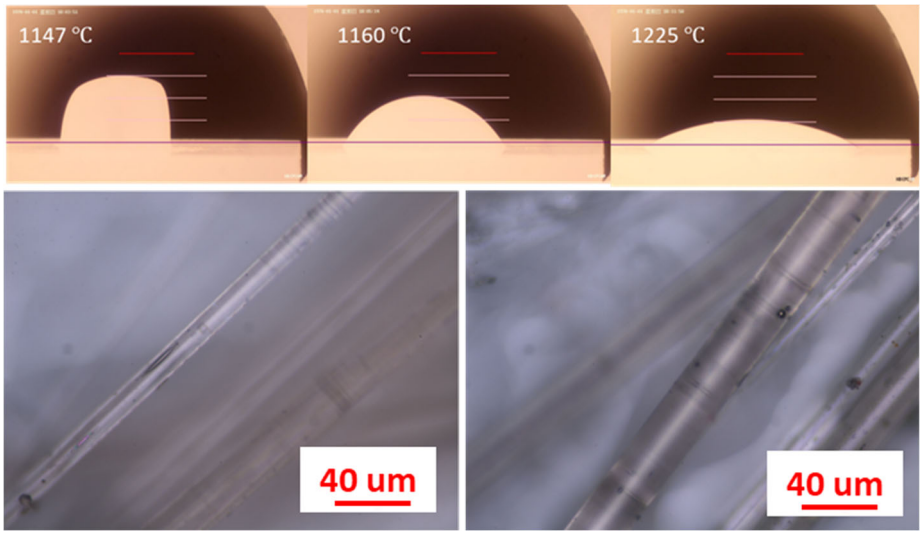

FIG 8 – Height changes of Lab sample (a), and the morphology of obtained mineral-wool (b).

When the raw materials are used directly in their molten state for production, it can significantly enhance the melting rates, reduce the batch-free times and decrease the bubble content in the final product. In this case, the heat from slag could be recovered directly. By directly using the sensible heat and exothermic reactions of slag, there is a potential energy saving of 0.16 GJ per 100 kg of new material with 1350°C used. This translates to a reduction in standard coal consumption by 7 kg and cuts carbon dioxide emissions by 26 kg. When considering the energy used for melting natural raw materials, the reduction in CO_2 emissions is further amplified by replacing natural raw material with these new raw materials. This approach not only contributes to lowering greenhouse gas emissions but also promotes the recycling of waste glass, aligning with sustainable waste management practices and environmental conservation efforts.

CONCLUSIONS

- This study introduces an innovative approach for recovering the heat from high-temperature ironmaking and steelmaking slags, which are typically discarded and release heat into the environment during the tapping process. This heat is instead utilised to recycle hard-to-use waste glass in producing raw materials directly for glass and mineral-wool manufacturing.
- Thermodynamic assessments indicate that for BF slag with 5 per cent carbon in waste glass, up to 30 per cent waste glass can be added without affecting transport and tapping requirements. For BOF slag, over 30 per cent waste glass even with 0 per cent carbon content addition is feasible owing to its higher tapping temperature, basicity and FeO content.

- New recipes for container glass and mineral-wool have been suggested, based on the typical products composition ranges. Utilising the sensible heat and reaction heat of slag could reduce coal consumption by 7 kg and CO_2 emissions by 26 kg for every 100 kg of the new material.

ACKNOWLEDGEMENTS

The authors wish to acknowledge the Transforming Foundation Industries Network+ (EPSRC grant EP/V026402/1) for funding this work.

REFERENCES

Deng, W, Backhouse, D J, Kazi, F K, Janani, R, Holcroft, C, Magallanes, M, Marshall, M, Jackson, C M and Bingham, P A, 2023. Alternative raw material research for decarbonization of UK glass manufacture, *International Journal of Applied Glass Science*, 14(3):341–365.

Dewick, P and Miozzo, M, 2002. Sustainable technologies and the innovation–regulation paradox, *Futures*, 34(9–10):823–840.

He, W-C, Luo, M-S, Deng, Y, Qin, Y-L, Zhang, S, Lv, X-W, Zhao, Y, Jiang, C-Z and Pang, Z-D, 2023. Preparation of high acidity coefficient slag wool fiber with blast furnace slag and modifying agents, *J Iron Steel Res Int*, 30(7):1440–1450.

He, W-C, Lv, X-W, Yan, Z-M and Fan, G-Q, 2020. Ferrosilicon alloy granules prepared through centrifugal granulation process, *J Iron Steel Res Int*, 27(11):1–12.

Hujova, M and Vernerova, M, 2017. Influence of fining agents on glass melting: a review, part 1, *Ceramics-Silikaty*, 61(2):119–126.

Iacovidou, E, Hahladakis, J, Deans, I, Velis, C and Purnell, P, 2018. Technical properties of biomass and solid recovered fuel (SRF) co-fired with coal: Impact on multi-dimensional resource recovery value, *Waste Management*, 73:535–545.

Kiss, B, Manchón, C G and Neij, L, 2013. The role of policy instruments in supporting the development of mineral-wool insulation in Germany, Sweden and the United Kingdom, *J Clean Prod*, 48:187–199.

Liu, J, Jiang, M, Wang, Y, Wu, G and Wu, Z, 2013. Tensile behaviors of ECR-glass and high strength glass fibers after NaOH treatment, *Ceramics International*, 39(8):9173–9178.

Oge, M, Ozkan, D, Celik, M B, Gok, M S and Karaoglanli, A C, 2019. An overview of utilization of blast furnace and steelmaking slag in various applications, *Materials Today: Proceedings*, 11:516–525.

Pan, S-Y, Adhikari, R, Chen, Y-H, Li, P and Chiang, P-C, 2016. Integrated and innovative steel slag utilization for iron reclamation, green material production and CO_2 fixation via accelerated carbonation, *J Clean Prod*, 137:617–631.

Piatak, N M, 2018. Environmental characteristics and utilization potential of metallurgical slag, in *Environmental Geochemistry*, pp 487–519 (Elsevier).

Piatak, N M, Parsons, M B and Seal, R R, 2015. Characteristics and environmental aspects of slag: A review, *Applied Geochemistry*, 57:236–266.

Schmitz, A, Kamiński, J, Scalet, B M and Soria, A, 2011. Energy consumption and CO_2 emissions of the European glass industry, *Energy Policy*, 39(1):142–155.

Shelby, J E, 2020. *Introduction to Glass Science and Technology* (Royal Society of Chemistry).

Springer, C and Hasanbeigi, A, 2017. Emerging energy efficiency and carbon dioxide emissions-reduction technologies for the glass industry, Energy Analysis and Environmental Impacts Division, Lawrence Berkeley National Laboratory: Berkeley, CA, USA.

Yan, Z, Lv, X, Liang, D, Zhang, J and Bai, C, 2016. Transition of Blast Furnace Slag from Silicates-Based to Aluminates-Based: Viscosity, *Metall and Materi Trans B*, 48(2):1092–1099.

Yan, Z, Reddy, R G and Lv, X, 2019. Structure Based Viscosity Model for Aluminosilicate Slag, *ISIJ International*, 59(6):1018–1026.

Yliniemi, J, Ramaswamy, R, Luukkonen, T, Laitinen, O, de Sousa, Á N, Huuhtanen, M and Illikainen, M, 2021. Characterization of mineral-wool waste chemical composition, organic resin content and fiber dimensions: Aspects for valorization, *Waste Management*, 131:323–330.

Yue, H, He, Z, Jiang, T, Duan, P and Xue, X, 2018. Rheological evolution of Ti-bearing slag with different volume fractions of TiN, *Metall Materi Trans B*, 49(4):2118–2127.

Zhao, G, Zhang, L and Cang, D, 2019. Fundamental and industrial investigation on preparation of high acidity coefficient steel slag derived slag wool, *Journal of the Ceramic Society of Japan*, 127(3):180–185.

Research on –
Refractory-melt interactions

Radical involved reaction and weak magnetic effect between alumina refractory and high alumina slags

DOI: 10.62053/ZNNJ3222

A Huang[1], S H Li[2] and H Z Gu[3]

1. Professor, the State Key Laboratory of Refractories and Metallurgy, Wuhan 430081, China. Email: huangao@wust.edu.cn
2. Doctor, the State Key Laboratory of Refractories and Metallurgy, Wuhan 430081, China. Email: lishenghao@wust.edu.cn
3. Professor, the State Key Laboratory of Refractories and Metallurgy, Wuhan 430081, China. Email: guhuazhi@wust.edu.cn

ABSTRACT

High aluminium steel is a promising advanced steel known for its exception properties and holds significant economic and strategic importance. However, the CaO-Al_2O_3-SiO_2 based slag with high alumina content reacts vigorously with alumina refractories during the smelting process at high temperature, seriously affecting the safe and efficient production of furnaces and resulting in the formation of Al_2O_3-MgO non-metallic inclusions within the molten steel. This is a bottleneck problem for high-quality steel refining, and the key reaction path during the corrosion remains unclear. The dissolution reaction mechanism of alumina refractories in high alumina CaO-Al_2O_3-SiO_2 slags under a weak static magnetic field was investigated in this work, using high temperature laser confocal microscopy and *in situ* radiation spectroscopy techniques. The results indicate that the interaction between the high alumina slags and the alumina refractories is governed by free radical reactions. The dissolution of alumina forms AlO and AlO_2 radicals. The reaction rate increases with the C/S ratio of the slag due to its low polymerisation. The reaction between non-bridging oxygen and AlO_2 free radicals accelerates the generation of AlO and $O_2^{\cdot-}$ radicals. The reaction layer composed of calcium aluminate is formed through the recombination of AlO, $Ca^{\cdot+}$ and $O_2^{\cdot-}$ radicals. The weak static magnetic field induces the Zeeman splitting of free radical pairs and intersystem crossing occurs, promoting the formation of triplet free radical pairs through the hyper-fine coupling effect. The reaction can be significantly inhibited as the triplet free radical pair does not meet Pauli's incompatibility principle. This discovery perfects the structure theory of molten slags with radicals and provides supplement to the design of the highly slag-resistant refractories, and provides the theoretical basis for the development of external field protection technologies for high-quality steel refining.

INTRODUCTION

High aluminium steel, distinguished by its remarkable strength, plasticity, high strain hardening, and energy absorption capacity, shows broad prospects in applications in national defence, military industries and transportation sectors (Zuazo *et al*, 2014; Zhang *et al*, 2015). The use of CaO-Al_2O_3-SiO_2 and CaO-Al_2O_3 slags are widely used for high aluminium steel refining (He *et al*, 2020; Zhang and Wang, 2002; Zhao *et al*, 2021; Tang *et al*, 2017; Wang, D *et al*, 2012; Wang, W *et al*, 2019), and the high alumina steel can cause the formation of high alumina content slag, which can cause continuous and periodic corrosion patterns at the reaction interface of the slag and the corundum refractory, resulting in rapid dissolution and damage to the refractory (Zou *et al*, 2020a). The periodicity of corrosion patterns is unrelated to the spatiotemporal evolution, but its geometric parameters was highly correlated with the C/S ratio and the dissolution rate of aluminium (Li *et al*, 2021). Free radicals were discovered in the CaO-Al_2O_3-SiO_2 based slag, and the recombination of AlO_4 and SiO_4 tetrahedra in the slag of higher C/S ratio is one of the causes for the formation of radicals. $O_2^{\cdot-}$ and $Ca^{\cdot+}$ radicals involved in the interface reaction between the corundum refractory and the slag, the Turing pattern corrosion at the interface of alumina ceramic is caused by an increase in $O_2^{\cdot-}$ radical content in the slag (Li *et al*, 2023; Peng *et al*, 2023a, 2023b). This not only affects the safe and efficient operation of furnaces (Dong *et al*, 2022; Jiang *et al*, 2022), but also leads to the formation of non-metallic inclusions in the steel, which is one of the key bottlenecks restricting the development of high-quality steel smelting (Wang, Song and Xue, 2023; Liu *et al*, 2023; Zhou *et al*, 2015; Tsuda *et al*, 1992).

With the development of modern metallurgical technology, electric field and magnetic field have been widely used in metallurgical processes such as electroslag remelting, electromagnetic induction melting, electromagnetic stirring and electromagnetic continuous casting. The physical parameters of slag and the service life of refractories can be affected by external high-intensity electric and magnetic fields. The alternating magnetic field promotes the interface reaction between slag and refractories, accelerating the corrosion and penetration of slag on the refractories (Aneziris *et al*, 2013; Ren *et al*, 2019, 2021), whereas the static magnetic field has the effect of enhancing the corrosion degree of slag on refractory (Huang *et al*, 2018).

An 8.5 mT static magnetic field can induce an 'electromagnetic damping effect' on the slag, leading to a reduction in wettability between the slag and the refractory (Zou *et al*, 2020b). However, the physical effects of the magnetic field, such as electromagnetic damping and polarisation of the reactive group, can only be fully utilised when the magnetic flux density and frequency are high enough to improve the slag resistance of the refractory (Bian *et al*, 2018). Different from the electric field, high intensity magnetic field or alternating magnetic field, it was also found that the weak static magnetic field with a millitesla magnetic flux density has the potential to improve the slag resistance of refractories. The weak static magnetic field of 5 to 10 Gs can influence the chemical reactions between slag and alumina-based refractories, and delaying the occurrence of interface Turing pattern corrosion (Li *et al*, 2022, 2023). Weak static magnetic field has the potential to inhibit the chemical reactions between slag and alumina refractories, offering possibilities for enhancing the slag resistance of the refractory.

However, the interaction between alumina refractories and high alumina slag is rather complex. The lack of information during corrosion at high temperatures limits the exploration of reaction mechanisms (Zhang *et al*, 2021; Ponomar *et al*, 2022). In this work, the dissolution reaction mechanism of alumina refractory in high alumina CaO-Al_2O_3-SiO_2 slags under a weak static magnetic field was clarified, and the key reaction path and magnetic field inhibition mechanism were revealed based on high temperature laser confocal microscopy and *in situ* radiation spectroscopy techniques.

EXPERIMENTAL

Al_2O_3 powder (analytical purity, $Al_2O_3 \geq 99$ wt per cent, Shanghai Macklin Biochemical Co., Ltd), CaO powder (analytical purity, CaO ≥ 98 wt per cent, Shanghai Macklin Biochemical Co., Ltd), and SiO_2 powder (analytical purity, $SiO_2 \geq 98$ wt per cent, Sinopharm Chemical Reagent Co., Ltd) were weighed according to the mass ratios presented in Table 1. The powder were mixed via ball milling at a speed of 60 rev/min for 30 mins. Afterward, the mixed power were pre-melted in a high-frequency induction furnace (Supersonic Frequency Induction Heating Equipment, Hubei Changjiang Precision Manufacturing Technology Co., Ltd). The molten slag was then poured onto a copper plate floating above circulating water to prevent the molten slag from segregating and crystallising. Subsequently, the glassy molten was ground in an agate mortar. The alumina balls (Al_2O_3: 95 wt per cent, SiO_2: 4.5 wt per cent, CaO: 0.5 wt per cent, $\rho = 3.8$ g/cm^3) with a diameter of 1.20 ± 0.05 mm and a mass of 3.45 ± 0.05 mg were selected as alumina refractories.

TABLE 1

Composition of the pre-melted powders (wt%).

No.	CaO	Al_2O_3	SiO_2	C/S ratio
S1	52.00	35.00	13.00	4
S2	54.17	35.00	10.82	5
S3	55.71	35.00	9.29	6

A small amount, 0.2 g, of pre-melted slag was compresses into a platinum crucible measured 8 mm in diameter and 4 mm in height. The crucible was placed on the high temperature laser confocal microscope (HT-CSLM, VL2000DX-SVF18SP, Mikura Seisakusho Co., Ltd., Japan) and heated to 1600°C in an argon atmosphere (the heating ratio referred to Li *et al*, 2022). After soaking at 1600°C for 180 sec, the alumina ball was fed into the slag by using the high-temperature anti-oxidation

feeding system (GC-500901, Mikura Seisakusho Co., Ltd.). A pair of magnets as shown in Figure 1, applied a static magnetic field throughout the experiment and it could be adjusted by changing the number of magnets. The flux density of static magnetic in the reaction region was calibrated using a Tesla meter (Changsha Tianheng Measurement and Control Technology Co., Ltd.). The magnetic flux density for each sample is shown in Table 2.

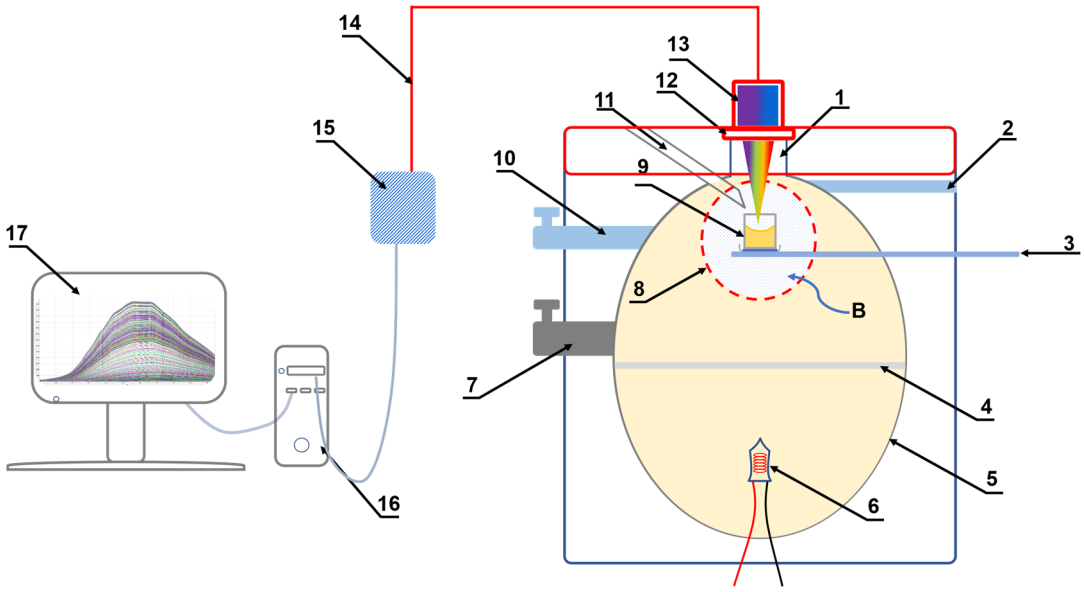

1-Quartz window; 2-Gas outlet valve; 3-Thermocouple with platinum stent; 4-Quartz spacer; 5-Furnace chamber; 6-Halogen lamp
7-Vacuum valve; 8-NdFeB magnet; 9-Pt crucible; 10-Intake valve; 11-oxidation protection feeder; 12-Filter group; 13-Cosine corrector
14- Fibre-optical; 15-Spectrograph; 16-Computing system; 17-Signal output system

FIG 1 – Schematic diagram of the device.

TABLE 2

Magnetic flux density produced in the experimental area.

No.	Magnetic flux density/Gs	
S1	0	15
S2	0	10
S3	0	10

The *in situ* radiation spectroscopic system is composed of a spectrograph (Avenir GmbH, Germany) and a filter group. The radiation passing through the filter group, and the transmitted through a cosine corrector (Avenir GmbH, Germany) and finally analysed by the spectrograph, as shown in Figure 1. The radiation spectrum and the morphology of alumina refractory in dissolution process were recorded by the device.

The quenched samples were longitudinally cut, and polished and gold-plated using vacuum ion sputtering, the microstructure and composition at the interface between slag and alumina balls were analysed by scanning electron microscope (SEM, JSM-6610, JEOL, Tokyo, Japan) and energy dispersive X-Ray spectroscopy (EDX, QUANTAX, Bruker, Berlin, Germany). The synthetic slag was ground into micropowder (0.074 mm), and the superoxide radicals were analysed using electron paramagnetic resonance spectrometer (EPR, A300, Bruker, Saarbrücken, Germany) with DMPO capture agent in a non-light environment.

The average dissolution rate of alumina balls is determined by (Huo *et al*, 2022):

$$\bar{v} = \frac{\Delta W}{\bar{A} \cdot t} \tag{1}$$

$$\bar{A} = \pi D^2 \tag{2}$$

where:

ΔW is the mass change of the alumina ball, g

$\overline{A}$ is the average superficial area of the alumina ball, cm^2

D is the diameter of the alumina ball, cm

t is the dissolution time, sec.

RESULTS AND DISCUSSION

Weak magnetic field effect on the dissolution of alumina balls

The rapid dissolution of alumina balls in the high alumina content slag, refer to Figure 2, and the dissolution rate increased with the increasing C/S ratio of the slag, as shown in Figure 3. However, the dissolution can be significantly inhibited by the external weak static magnetic field, and the dissolution rates of alumina balls in slag S1~S3 experienced a decrease of approximately 20.3 per cent, 27.5 per cent and 35.0 per cent, respectively.

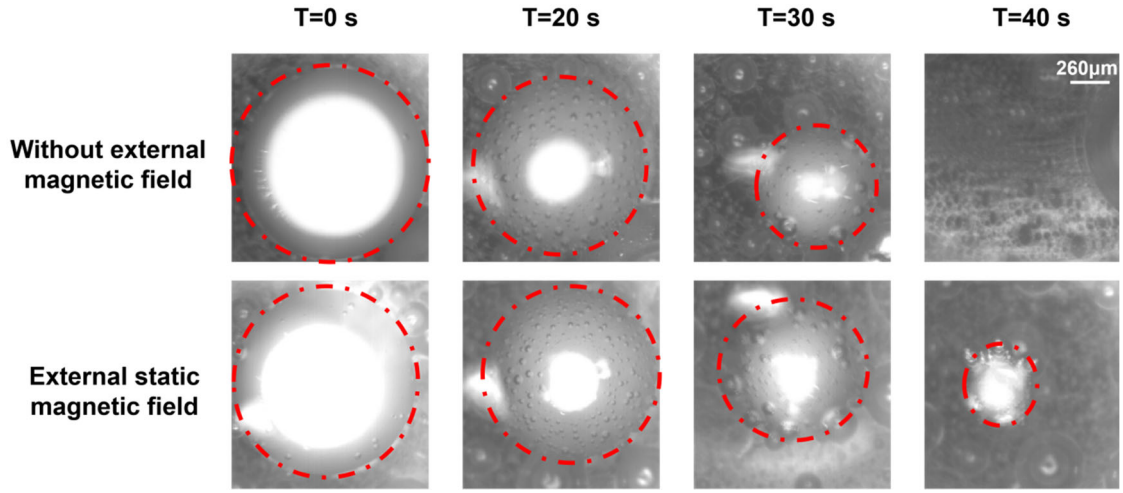

FIG 2 – The recorded picture of the dissolution process of alumina balls in slag at 1600°C.

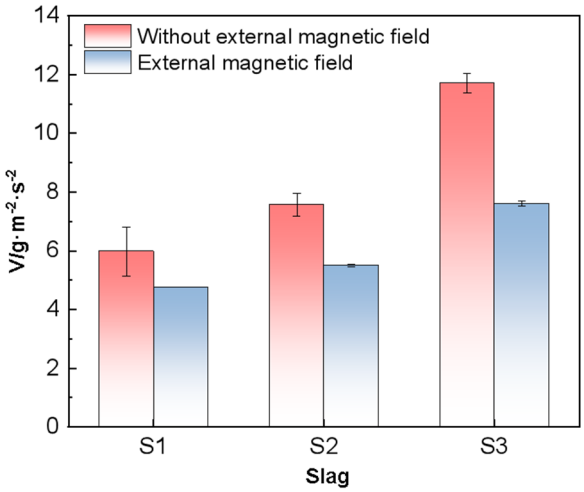

FIG 3 – Dissolution rate of alumina balls in slags.

As an illustration, S3 slag was utilised to investigate, the microstructure of the reaction interface between the alumina balls and the slags during the dissolution was analysed, as shown in Figure 4. A reaction layer composed of calcium aluminate with a thickness of 76.32 μm was observed at the reaction interface as shown in Figure 4 and Table 3, when an external weak static magnetic field was applied the thickness of the layer was reduced to 41.25 μm.

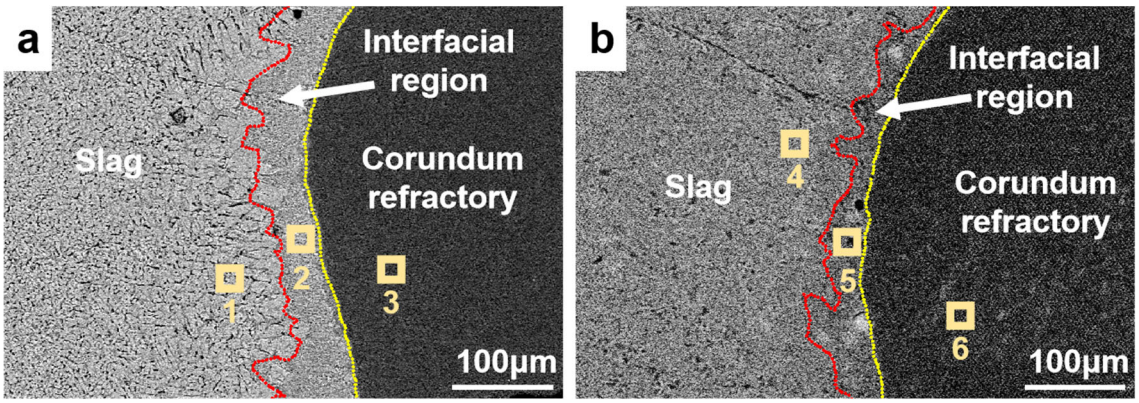

FIG 4 – Microstructure of the reaction interface between the alumina ball and melts at 1600°C in 20 sec, (a) without static magnetic field, (b) with weak static magnetic field.

TABLE 3

Energy dispersive spectroscopy (EDS) analysis results (at %).

Area	Ca	Al	Si	O
Area 1	-	45.76	-	54.24
Area 2	23.35	18.11	2.43	56.12
Area 3	25.87	16.54	2.19	55.40
Area 4	-	45.50	-	54.50
Area 5	24.07	19.29	2.62	54.02
Area 6	28.07	13.38	1.73	56.82

Radical reaction mechanism in the dissolution of alumina balls

The concentration of superoxide radicals in the slags increased with the increasing C/S ratio, as shown by the stronger signals in Figure 5a. Additionally, the concentration of superoxide radicals in the slags gradually increased with the dissolution of alumina balls, as shown in Figure 5b.

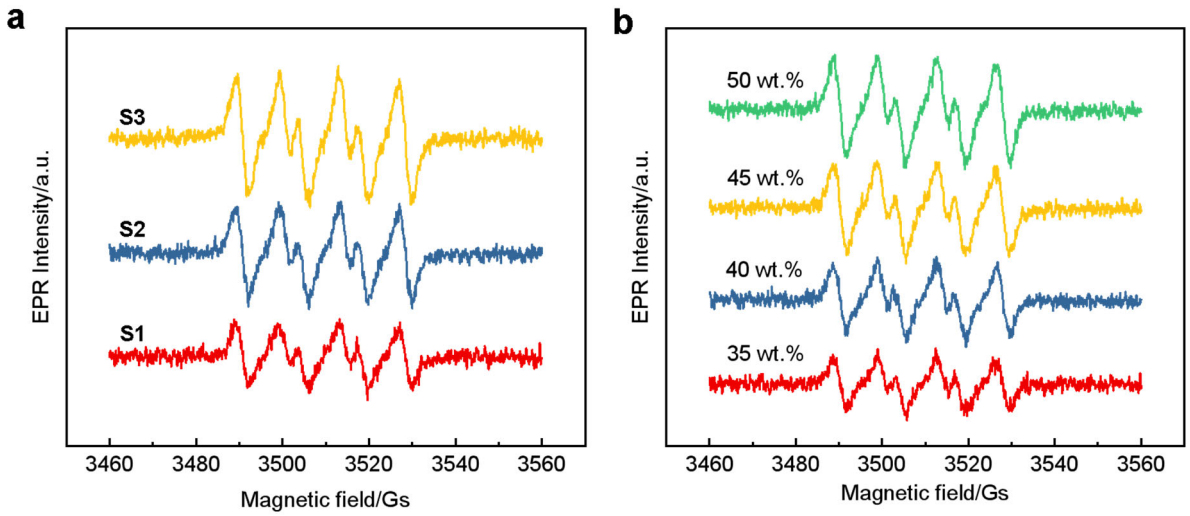

FIG 5 – (a) EPR spectra of S1~S3 slag; (b) EPR spectra of S3 slag with the increase of alumina concentration.

Comparing the radiation spectra before and during the reaction at 1600°C, a signal at 484.21 nm was detected (as shown in Figure 6a), indicating the formation of AlO radical (Varenne *et al*, 2000; Starik *et al*, 2014). The signal intensity gradually increased with the increase in the C/S ratio,

indicating a higher formation of AlO radical. The application of an external static magnetic field inhibited the generation of AlO radical as shown in Figure 6b.

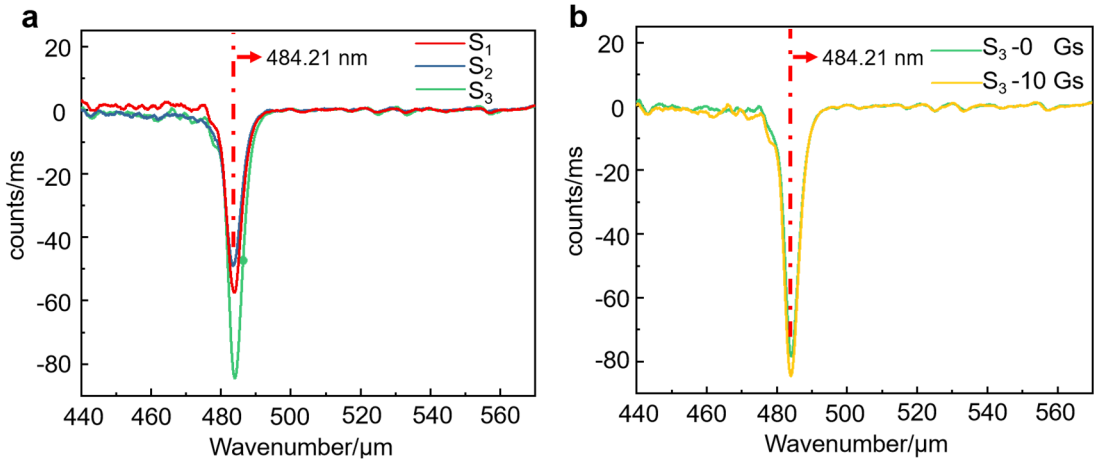

FIG 6 – *In situ* radiation spectrum during the alumina dissolution, (a) in S1~S3 slags, (b) in S3 slag with and without external static magnetic field.

The reaction path between the alumina refractory and the slag is as Equations 3 and 4. The AlO and AlO_2 radicals can be generated by the homolysis of Al_2O_3 in molten slag, the non-bridging oxygen can be attacked by AlO_2 radicals, which accelerates the dissolution of alumina refractory and generates $O_2^{\cdot-}$:

$$Al_2O_3 \rightarrow AlO + AlO_2 \quad (3)$$

$$AlO_2 + O^- \rightarrow AlO + O_2^{\cdot-} \quad (4)$$

Non-bridging oxygen (O^-) in slag plays a crucial role. In slags characterised by a higher (C/S) ratio, a greater concentration of non-bridging oxygen, as indicated by Li *et al* (2023), facilitates Equation 4 and resulting in the rapid dissolution of alumina refractory.

According to our previous investigations (Li *et al*, 2021, 2022, 2023; Peng *et al*, 2023a, 2023b) have indicated that $O_2^{\cdot-}$ and $Ca^{\cdot+}$ are formed spontaneously through the uniform decomposition of CaO_2 in the $CaO\text{-}Al_2O_3\text{-}SiO_2$ slag. The reaction layer composed of calcium aluminate can be formed through the recombination of AlO, $Ca^{\cdot+}$ and $O_2^{\cdot-}$ radicals at the reaction interface as shown in Equation 5 and Figure 7.

$$2AlO + Ca^{\cdot+} + O_2^{\cdot-} \rightarrow CaAl_2O_4 \quad (5)$$

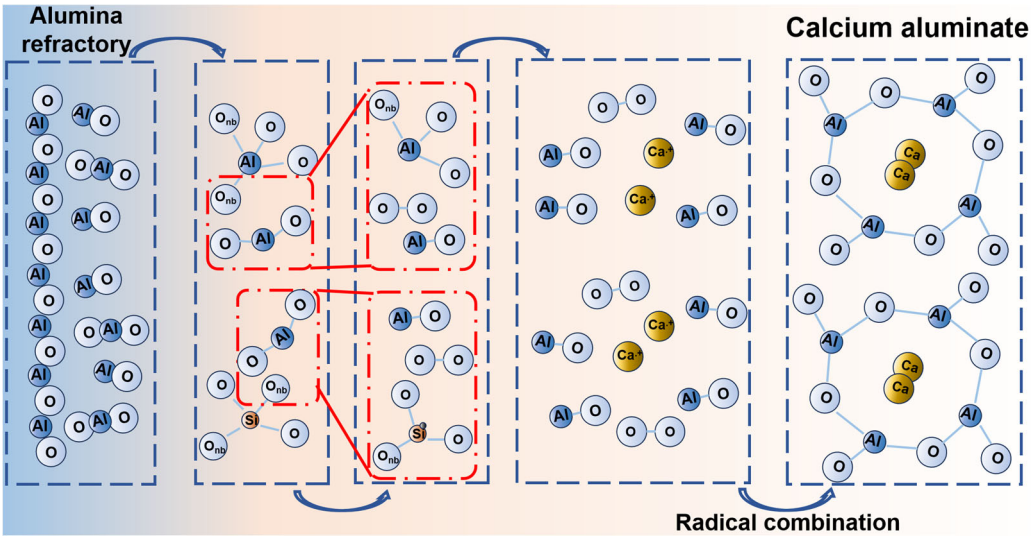

FIG 7 – Possible radical reaction mechanism at the interface between the alumina refractory and the molten slags.

The energy formula for singlet and triplet state free radical pairs with the external static magnetic field is given by (Zimmt, Doubleday and Turro, 1985):

$$E(S) = \left\langle S, \chi_N \middle| H_{ex} + H_{mag} \middle| S, \chi_N \right\rangle = J \tag{6}$$

$$E(T_n) = \left\langle T_n, \chi_N \middle| H_{ex} + H_{mag} \middle| T_n, \chi_N \right\rangle = -J + ng\mu_B B + \frac{n}{2}\left(\sum_i^j a_i m_i + \sum_k^l a_k m_k\right) \tag{7}$$

where:

a_i is the hyperfine coupling constant of the i atom

m_i is the spin quantum number of the i nucleus

According to Equations 6 and 7, it is clear that the Zeeman splitting (represented by g$\mu B \cdot B$) of free radical pairs induced by the static magnetic field is the main factor affecting the energy of free radicals in the singlet and triplet states. When an external magnetic field with the appropriate flux density is applied and the Zeeman splitting energy matches the energy difference of the free radical pairs, the intersystem crossing occurs under the hyperfine coupling effect as shown in Figure 8. The transformation of free radical pairs from singlet to triplet states (Sarpoolaky, Zhang and Lee, 2003; Hayashi, 2004) results in a reduction of the bonding probability of free radicals, thereby inhibiting chemical reactions of Equations 4 and 5, and decreasing the interfacial reaction and the dissolution rate of alumina balls in the slags.

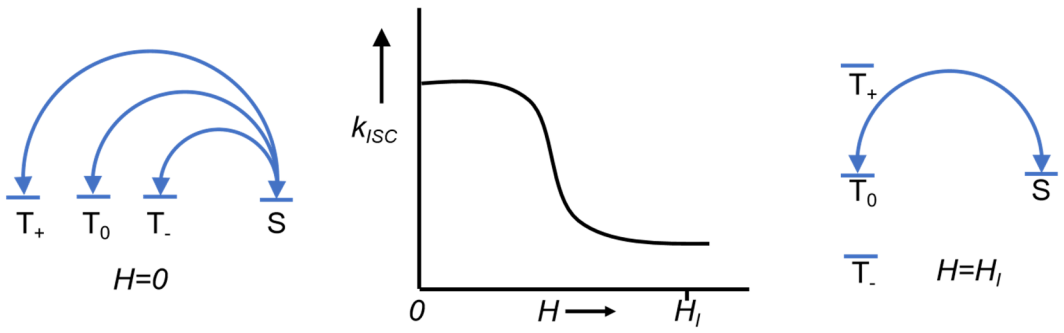

FIG 8 – Effect of magnetic field on the radical intersystem crossing (Hayashi, 2004).

CONCLUSIONS

The dissolution mechanisation of the alumina refractory in high alumina content slag was clarified based on high temperature laser confocal microscopy combined with *in situ* radiation spectroscopy techniques. The radical reaction path and the effect of weak static magnetic field during the dissolution of alumina refractory was revealed. The main conclusions are as follows.

- Alumina refractory involved in the intense interfacial radical reaction with high alumina content slag, resulting in the rapid dissolution of refractory and the formation of a calcium aluminate reaction layer on the refractory/slag interface. Free radical splays a crucial role in the process, however when a static magnetic field is applied, the reaction rate decreases significantly and the thickness of the calcium aluminate reaction layer. Taking S3 slag as an example, the dissolution rate of the alumina ball decreased by 35.0 per cent, and the thickness of the interface reaction layer decreased by 46.0 per cent with external the static magnetic field.
- The reaction path between alumina refractory and the slag was revealed. Free radicals including AlO, AlO_2, and $O_2^{\cdot -}$ were generated during the dissolution of alumina refractory at 1600°C. The reaction layer composed of calcium aluminate is formed through the recombination of AlO, $Ca^{\cdot +}$ and $O_2^{\cdot -}$ radicals at the reaction interface. For the slag with a higher C/S ratio, the non-bridging oxygen was attacked by AlO_2 radicals, thereby accelerating the dissolution rate of alumina refractory.

- The weak static magnetic field induces the Zeeman splitting of free radical pairs and enhances the hyperfine coupling, resulting in intersystem crossing from singlet to triplet states. The radical reactions are inhibited as the triplet free radical pair does not meet Pauli's incompatibility principle. This reduces the interfacial reaction rate between alumina refractories and slags. This work perfects the structure theory of molten slags with radicals and supports the development of external field protection techniques for carbon-free/low-carbon refractories, which is significant for the safe and efficient production of high-quality steel.

ACKNOWLEDGEMENTS

This work was financially supported by the National Natural Science Foundation of China (52272022), Key Program of Natural Science Foundation of Hubei Province (2021CFA071).

REFERENCES

Aneziris, C G, Schroeder, C, Emmel, M, Schmidt, G, Heller, H P and Berek, H, 2013. In situ observation of collision between exogenous and endogenous inclusions on steel melts for active steel filtration, *Metallurgical and Materials Transactions B*, 44:954–968.

Bian, Y, Ding, W, Hu, L, Ma, Z, Cheng, L, Zhang, R, Zhu, X, Tang, X, Dai, J, Bai, J, Sun, Y and Sheng, Z, 2018. Acceleration of Kirkendall effect processes in silicon nanospheres using magnetic fields, *Cryst Eng Comm*, 20(6):710–715.

Dong, J, Gu, H, Huang, A and Xue, Z, 2022. Corrosion behavior of high alumina and low silicon CaO-Al_2O_3 slags on corundum/calcium hexaaluminate based castables, *Journal of Iron and Steel Research,* 34(8):825–833.

Hayashi, H, 2004. *Introduction to dynamic spin chemistry: magnetic field effects on chemical and biochemical reactions*, pp 130–163 (World Scientific Publishing Company: Singapore).

He, S, Chen, Y, Pan, W, Wang, Q, Zhang, X and Wang, Q, 2020. Study on composition control for melting and flowing properties of CaO-Al_2O_3 based mold fluxes with low reactivity, *Journal of Iron and Steel Research*, 32(9):771–778.

Huang, A, Lian, P, Fu, L, Gu, H and Zou, Y, 2018. Modeling and experiment of slag corrosion on the lightweight alumina refractory with static magnetic field facing green metallurgy, *Journal of Mining and Metallurgy, Section B*: Metallurgy, 54(2):143–151.

Huo, Y, Gu, H, Huang, A, Ma, B, Chen, L, Li, G and Li, Y, 2022. Characterization and mechanism of dissolution behavior of Al_2O_3/MgO oxides in molten slags, *Journal of Iron and Steel Research International*, 29(11):1711–1722.

Jiang, X, Huang, A, Gu, H, Fu, L and Xue, Z, 2022. Effect of Al_2O_3 content in CaO-Al_2O_3-SiO_2 slag on corrosion resistance of alumina magnesia castable, *Journal of Iron and Steel Research*, 34(9):991–998.

Li, S, Huang, A, Gu, H, Zeng, F, Zou, Y and Fu, L, 2021. Visual measurement and characterisation of quasi-volcanic corrosion at alumina ceramic-oxides melt-air interface, *Journal of the European Ceramic Society*, 41(16):400–410.

Li, S, Huang, A, Gu, H, Wang, R, Zou, Y and Fu, L, 2022. Corrosion resistance and anti-reaction mechanism of Al_2O_3-based refractory ceramic under weak static magnetic field, *Journal of the American Ceramic Society*, 105(4):2869–2877.

Li, S, Huang, A, Jiang, T, Gu, H, Zeng, F, Wang, X and Zhang, S, 2023. Revealing of rich living radicals in oxide melts via weak magnetic effect on alumina dissolution reaction, *Journal of Molecular Liquids*, 375:121391.

Liu, D, Xue, Z and Song, S, 2023. Effect of cooling rate on non-metallic inclusion formation and precipitation and micro-segregation of Mn and Al in Fe-23Mn-10Al-0.7 C steel, *Journal of Materials Research and Technology*, 24:4967–4979.

Peng, Y, Huang, A, Li, S, Chen, X and Gu, H, 2023b. Radical reaction-induced Turing pattern corrosion of alumina refractory ceramics with CaO-Al_2O_3-SiO_2-MgO slags, *Journal of the European Ceramic Society*, 43(1):166–172.

Peng, Y, Li, S, Huang, A, Gu, H, Zou, Y and Fu, L, 2023a. Effect of slag basicity on turing pattern corrosion of alumina refractory ceramics in the presence of free radicals, *Journal of the American Ceramic Society*, 106(10):6211–6220.

Ponomar, V, Adesanya, E, Ohenoja, K and Illikainen, M, 2022. High-temperature performance of slag-based Fe-rich alkali-activated materials, *Cement and Concrete Research*, 161:106960.

Ren, X, Ma, B, Li, S, Li, H, Liu, G, Zhao, S, Yang, W, Qian, F and Yu, J, 2019. Slag corrosion characteristics of MgO-based refractories under vacuum electromagnetic field, *Journal of the Australian Ceramic Society*, 55:913–920.

Ren, X, Ma, B, Li, S, Li, H, Liu, G, Yang, W, Qian, F, Zhao, S and Yu, J, 2021. Comparison study of slag corrosion resistance of MgO-$MgAl_2O_4$, MgO-CaO and MgO-C refractories under electromagnetic field, *Journal of Iron and Steel Research International*, 28:38–45.

Sarpoolaky, H, Zhang, S and Lee, W, 2003. Corrosion of high alumina and near stoichiometric spinels in iron containing silicate slags, *Journal of European Ceramic Society*, 23(2):293–300.

Starik, A M, Kuleshov, P S, Sharipov, A S and Titova, N S, 2014. Kinetics of ignition and combustion in the Al–CH_4–O_2 system, *Energy & Fuels*, 28(10):6579–6588.

Tang, H, Wu, G, Wang, Y, Li, J, Lan, P and Zhang, J, 2017. Comparative evaluation investigation of slag corrosion on Al_2O_3 and MgO-Al_2O_3 refractories via experiments and thermodynamic simulations, *Ceramics International*, 43(18):16502–16511.

Tsuda, M, Yamaguchi, H, Kaneko, K, Moritani, T and Shinme, K, 1992. Production of ultra super purity ferritic stainless steel by the powder top blowing method under reduced pressure (VOD-PB), *Electric Furnace Conference Proceedings*, 50:259–262.

Varenne, O, Fournier, P G, Fournier, J, Bellaoui, B, Faké, A I, Rostas, J and Taïeb, G, 2000. Internal population distribution of the B state of AlO formed by fast ion beam bombardment or laser ablation of an Al_2O_3(Al) surface, *Nuclear Instruments and Methods in Physics Research Section B: Beam Interactions with Materials and Atoms*, 171(3):259–276.

Wang, D, Li, X, Wang, H, Mi, Y, Jiang, M and Zhang, Y, 2012. Dissolution rate and mechanism of solid MgO particles in synthetic ladle slags, *Journal of Non-Crystalline Solids*, 358(9):1196–1201.

Wang, J, Song, S and Xue, Z, 2023. Transient evolution of non-metallic inclusions in molten high aluminum and high manganese steel contacting with slag and crucible: experimental investigation and FactSage macros modeling, *Journal of Materials Research and Technology*, 25:2841–2853.

Wang, W, Xue, L, Zhang, T, Zhou, L, Chen, J and Pan, Z, 2019. Thermodynamic corrosion behavior of Al_2O_3, ZrO_2 and MgO refractories in contact with high basicity refining slag, *Ceramics International*, 45(16):20664–20673.

Zhang, D and Wang, H, 2002. Corrosion behavior of refining slags with different basicities to corundum-spinel castable, *Naihuo Cailiao*, 36(4):215–217.

Zhang, J, Wang, C, Jiao, K, Zhang, J, Liu, Z, Ma, H, Fan, X and Guo, Z, 2021. Effect of BaO and MnO on high-temperature properties and structure of blast furnace slag, *Journal of Non-Crystalline Solids*, 571:121066.

Zhang, M, Chen, W, Cheng, Z, Shao, J, Jia, X and Pang, W, 2015. Influence of Physical Property of Silicon Steel Slag with High Alumina on Ladle Slag Buildup, *Bulletin of the Chinese Ceramic Society*, 34(4):1160–1164.

Zhao, X, Zhang, R, Jia, J, Qi, J and Min, Y, 2021. Effect of basicity on the microstructure of molten slag of CaO-SiO_2-Al_2O_3 system, *Journal of Materials and Metallurgy*, 20(3):179–184.

Zhou, M, Yang, S, Jiang, T and Xue, X, 2015. Influence of MgO in form of magnesite on properties and mineralogy of high chromium, vanadium, titanium magnetite sinters, *Ironmaking & Steelmaking*, 42(4):320–320.

Zimmt, M B, Doubleday, J C and Turro, N J, 1985. Magnetic field effect on the intersystem crossing rate constants of biradicals measured by nanosecond transient UV absorption, *Journal of the American Chemical Society*, 107(23):6726–6727.

Zou, Y, Huang, A and Gu, H, 2020a. Novel phenomenon of quasi-volcanic corrosion on the alumina refractory-slag-air interface, *Journal of the American Ceramic Society*, 103(11):6639–6649.

Zou, Y, Huang, A, Wang, R, Fu, L, Gu, H and Li, G, 2020b. Slag corrosion-resistance mechanism of lightweight magnesia-based refractories under a static magnetic field, *Corrosion Science*, 167:108517.

Zuazo, I, Hallstedt, B, Lindahl, B, Selleby, M, Soler, M, Etienne, A, Perlade, A, Hasenpouth, D, Massardier-Jourdan, V, Cazottes, S and Kleber, X, 2014. Low-density steels: complex metallurgy for automotive applications, *JOM*, 66(9):1747–1758.

On the stability of CaS in liquid steel containing alumina or spinel inclusions

DOI: 10.62053/BSCR2842

S Kumar[1], N N Viswanathan[2] and D Kumar[3]

1. PhD Research Scholar, IIT Bombay, Mumbai, Maharashtra 400076, India. Email: sandeep_kumar@iitb.ac.in
2. Sajjan Jindal Steel Chair Professor, IIT Bombay, Mumbai, Maharashtra 400076, India. Email: vichu@iitb.ac.in
3. Assistant Professor, IIT Bombay, Mumbai, Maharashtra 400076, India. Email: deepook@iitb.ac.in

ABSTRACT

In secondary steelmaking, calcium treatment is practised to modify the solid alumina or spinel inclusions into liquid or partially liquid calcium aluminates. It has been seen that the dissolved calcium reacts with sulfur or oxygen present in the steel to form CaS or CaO type of transient inclusions. Post-calcium treatment these transient inclusions further react with pre-existing alumina or spinel inclusions and modify them. In addition, direct modification of pre-existing inclusions is also reported in the literature.

In the present study, laboratory-scale induction furnace-based experiments are carried out to melt electrolytic iron in an alumina crucible followed by deoxidation with aluminium. The CaS-based composite material, prepared in-house, is added after the aluminium deoxidation to study the stability of CaS at the steelmaking temperature. Multiple steel samples were also taken to track the dissociation of CaS by means of sulfur pick-up in steel. Additionally, inclusion analysis of these steel samples was also performed to track changes in the chemical composition of inclusions in response to CaS addition. It has been seen that the CaS dissociates leading to a gradual pick-up of sulfur in steel. The scanning electron microscope – energy dispersive X-ray spectroscopy (SEM-EDS) analysis reveals that the alumina crucible and floated alumina inclusions are modified into calcium aluminates and the extent of modification depends on the contact time of CaS with the two sources of alumina mentioned earlier. However, the modification of alumina inclusions in the bulk steel did not occur during these experiments.

INTRODUCTION

As the demand for clean steel steadily increases, particularly within the automotive and defence sectors, global steelmakers are not only paying importance to control impurity levels but are also placing a significant emphasis on controlling non-metallic inclusions in the steel. The early works of Hilty and Farrel (1975a, 1975b) on the effect of calcium in aluminium-killed steel for the inclusion modification opened new horizons for controlling non-metallic inclusions in steel. As a result, calcium treatment is a well-established process nowadays at the secondary steelmaking process stage to convert deleterious solid non-metallic inclusions into liquid or partially liquid non-metallic inclusions to enhance castability and improve the mechanical properties of the steel. In aluminium-killed steel, two major types of inclusions are alumina and spinel inclusions. This study primarily focuses on alumina inclusions which can be modified into liquid calcium aluminates with calcium treatment. Verma *et al* (2011a) reported the sequence of reactions after calcium additions as Equations 1–4.

$$\mathrm{Ca(s)} \rightarrow \mathrm{Ca(l)} \rightarrow \mathrm{Ca(g)} \rightarrow [\mathrm{Ca}] \quad (1)$$

$$[\mathrm{Ca}] + [\mathrm{O}] \rightarrow \mathrm{CaO} \quad (2)$$

$$[\mathrm{Ca}] + [\mathrm{S}] \rightarrow \mathrm{CaS} \quad (3)$$

$$[\mathrm{Ca}] + \left(\mathrm{x} + \tfrac{1}{3}\right)\mathrm{Al_2O_3} \rightarrow \mathrm{CaO.xAl_2O_3} + \tfrac{2}{3}[\mathrm{Al}] \quad (4)$$

It can be seen from the reactions that the added calcium first melts, vapourises and then dissolves in the liquid steel. Dissolved calcium reacts with dissolved oxygen and sulfur if present in the liquid steel and forms CaO/CaS type of inclusions. The extent of formation of CaS or CaO type of inclusions depends on the dissolved sulfur or dissolved oxygen in the liquid steel. Further, the dissolved calcium

reacts with the pre-existing alumina inclusions and converts them into liquid calcium aluminates. The expected alumina modification route was reported by Faulring, Farrel and Hilty (1980) as $Al_2O_3 \rightarrow CA_6 \rightarrow CA_2 \rightarrow CA_x$ (C: CaO, A: Al_2O_3). This route is reported in almost all the literature for the modification of alumina into calcium aluminates. It should be noted here that the activity of alumina in the calcium aluminates decreases with an increase in CaO content in the inclusion. The above mechanism of modification is often referred to as direct modification of inclusion.

Turkdogan (1988) observed the formation of a CaS layer around the calcium aluminate in high sulfur steels and concluded that the CaS layer hinders the extent of modification of alumina inclusions. (Lu, Irons and Lu, 1994; Higuchi *et al*, 1996; Ye, Jönsson and Lund, 1996; Ren, Zhang and Li, 2014) also reported an increase in CaS or CaO content immediately following calcium treatment, followed by a subsequent decrease, suggesting the formation of CaS/CaO as transitional products. They also suggested that the high sulfur and oxygen can enhance the calcium absorption rate. Verma *et al* (2011b) reported that apart from being CaS or CaO a transient phase they also play a critical role in alumina inclusion modification. They observed that in high sulfur steels, these transient CaS inclusions tend to nucleate on alumina inclusions and destabilise the alumina inclusions and later modify them by the reaction as shown by Equation 5. This modification can be referred to as indirect modification of alumina inclusion and the schematic is shown in Figure 1:

$$3CaS + Al_2O_3 \rightarrow 3(CaO) + 2[Al] + 3[S] \quad 5$$

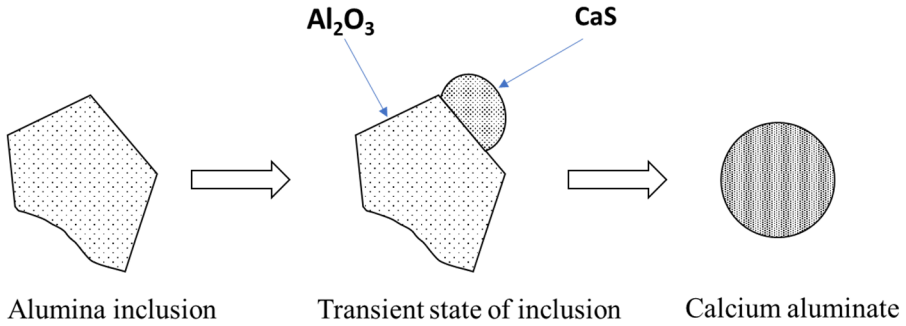

FIG 1 – Schematic of indirect modification of alumina inclusion showing CaS evolution as a transient phase Verma *et al* (2011b).

It should be noted here that the above reaction involves three condensed phases, two solid and one liquid steel phase. It is expected that the reaction will occur via the liquid steel phase. The reaction mechanism can be:

- CaS dissociates into calcium and sulfur.
- Calcium transfer to alumina inclusion through liquid steel and sulfur rejection in liquid steel.
- Alumina inclusion modification to liquid calcium aluminates.

As previously mentioned, the CaS is a transient inclusion. This work focuses on examining the stability of CaS in liquid steel containing alumina inclusions. Thermodynamic calculations were also conducted to explore the conditions determining the stability or dissociation of CaS. The Fe-CaS-based composite material was prepared in-house and its stability was investigated through various experiments involving different durations of experimentation.

EXPERIMENTAL PROCEDURE

The Fe-CaS-based composite material was prepared by melting pure calcium and iron sulfide in an induction furnace under an argon atmosphere (Kumar and Kumar, 2022). The density of the composite material was measured using a helium pycnometer. Microstructural characterisation and elemental composition of the composite lump were carried out using scanning electron microscopy equipped with energy-dispersive X-ray spectroscopy (SEM-EDS, Make and Model: Jeol JSM IT800).

The schematic of the experimental set-up and sampling apparatus is shown in Figure 2. Two sets of high-temperature experiments (No. 1 and No. 2) were performed in the induction furnace by varying the experimentation time. In both experiments, about 800 g of electrolytic iron flakes (containing

dissolved oxygen of about 300 ppm and dissolved sulfur of 30 ppm) were kept in the alumina crucible (OD: 57 mm, Height: 87 mm and capacity: 170 mL). The alumina crucible with electrolytic iron was then placed inside the induction furnace chamber. The chamber was evacuated with a rotary vacuum pump followed by continuous backfilling with pure argon (purity: 99.99 per cent) at 1–3/L/min to prevent reoxidation of the liquid steel. The sample was then heated to 1600°C and held at that temperature for homogenisation. Based on the preliminary experiments, a holding time of 15 min was chosen to ensure homogenisation (uniform temperature and composition of bath).

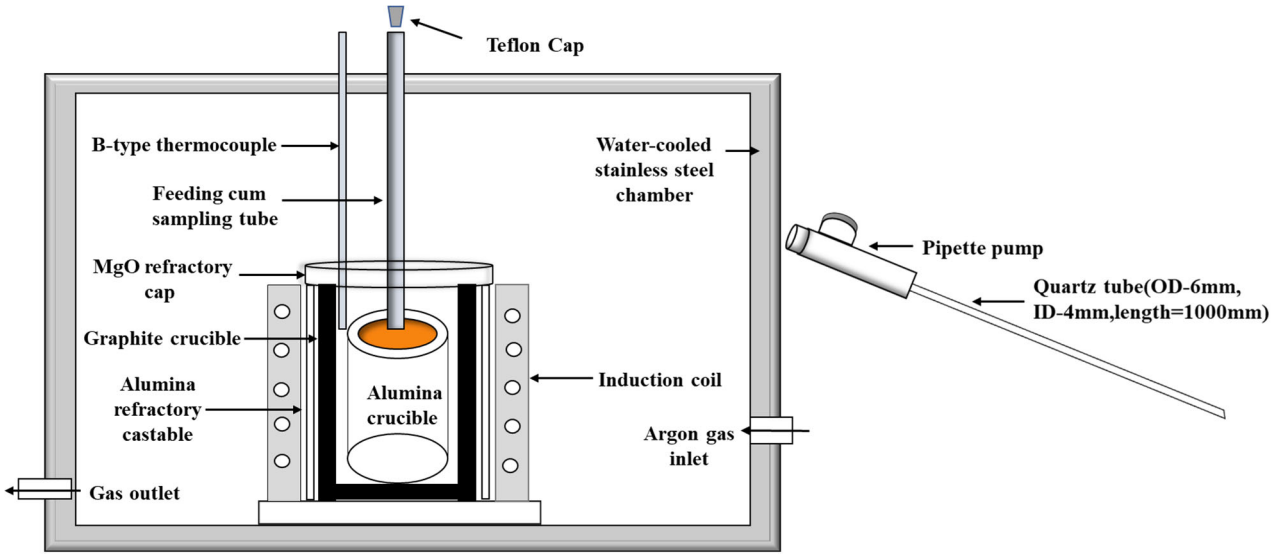

FIG 2 – Schematic of the Induction furnace and sampling apparatus.

After homogenisation, 0.1 wt per cent of pure aluminium chunks (purity >99 per cent) were added through a feeding cum sampling tube to deoxidise the steel melt. The time of Al addition was taken as a reference time and is denoted as t=0. Experimentation time for experiment 1 was 15 min, whereas 60 min for experiment 2. The addition sequence and the sampling timelines for both experiments are shown in Figure 3. After the deoxidation of the steel melt, a pre-determined amount of the Fe-CaS-based composite material powder wrapped in a mild steel foil was dropped into the liquid steel through the feeding tube. Samples from the bulk steel melt were taken at various time intervals by inserting the fused quartz tube (OD: 6 mm, ID: 4 mm and length: 1000 mm) followed by water quenching of the quartz tube containing the steel sample. The sampling cum feeding tube, which was sealed with a Teflon cap during the entire heating cycle to ensure an air-tight chamber; was opened for a very short duration for additions and sampling.

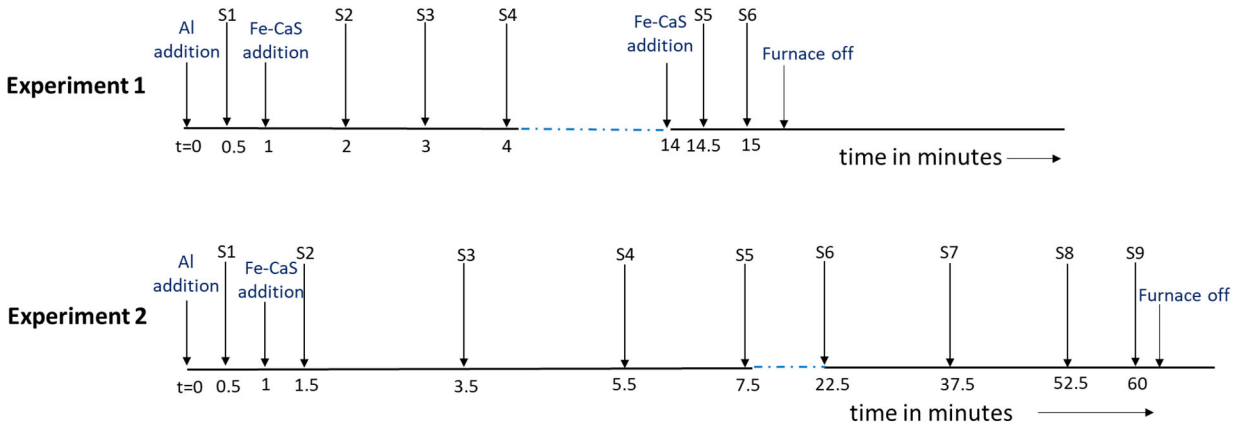

FIG 3 – Sampling timelines and additions for experiments 1 and 2.

The added amount of electrolytic iron, pure aluminium and composite material for both experiments are shown in Table 1.

TABLE 1

Raw material and additions for experiments 1 and 2.

Experiment #	Electrolytic iron (grams)	Aluminium (grams)	Fe-CaS composite (grams)
1	800	0.8	1.44
2	800	0.8	0.72

The bulk steel cylindrical samples aspirated using the quartz tube were then cut into smaller sections approximately 6–12 mm in size. These sections were hot-mounted in the longitudinal direction and subsequently grinded using SiC emery papers of grit sizes of 200, 400, 600, 800, 1000, 1200, 1500 and 2000 respectively. Following this, the samples were mirror polished using 3-micron and 1-micron diamond paste and washed with ethanol. It should be noted that the CaS particles are fairly hydrophilic, so water was not used during the final polishing. Microstructural investigation of these samples was carried out using SEM-EDS for the analysis of inclusion morphology (two-dimensional) and composition. Additionally, the top surface of the solidified steel ingot obtained from experiments no. 1 and 2 was also analysed using SEM-EDS, as floated alumina inclusion is expected at the top portion of the solidified ingot.

Furthermore, the alumina crucible used in both experiments was broken and the inner surface of the alumina crucible, which had been in contact with the solidified steel ingot, was analysed using SEM-EDS. The sulfur content of samples collected at different time intervals (experiment 2) was measured using a LECO CS744 carbon sulfur analyser at a third-party laboratory.

RESULTS AND DISCUSSION

The microstructural features of the composite material are illustrated in Figure 4. Notably, pure CaS microparticles and pure iron particles are embedded within the Fe-CaS network. The sizes of the CaS microparticle vary from 10–100 microns. The average size of CaS particles was determined through ImageJ™ software, ver 1.54g, revealing an average particle size of 50 microns. It should be noted the composite material produced was highly brittle and, thus, difficult to polish. Therefore, the composite material lump was mechanically grinded for SEM analysis, as evidenced by a few scratch marks in the electron image.

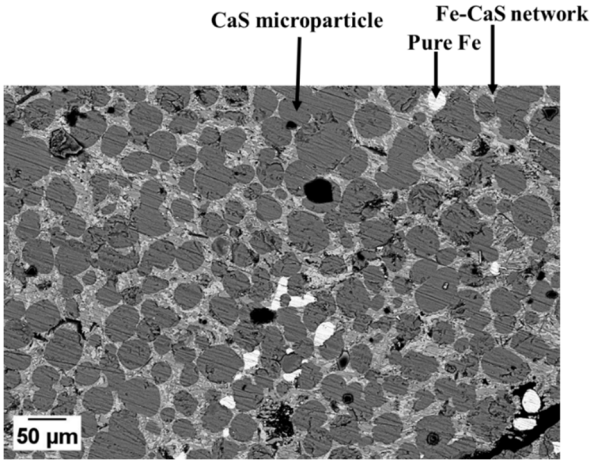

FIG 4 – Microstructure of the Fe-CaS composite material.

The composite material has an average density of 3.95 g/cc, nearly half that of liquid steel, as determined through a helium pycnometer.

In both experiments, the Fe-CaS-based composite material was added one minute after the aluminium deoxidation. The duration of experiment 1 and experiment 2 were 15 mins and 60 mins, respectively. The SEM-EDS analysis of bulk steel samples, obtained through a quartz tube at different time intervals for both experiments to track changes in inclusions composition is shown in

Figure 5. The EDS spectra reveal the irregular morphology and unmodified alumina inclusions within the specified time frame. The CaS particles are expected to have a very short residence time in the liquid steel due to density differences and shallow melt depths of 30–40 mm. It should also be noted here that the CaS particles were not observed in any bulk steel samples during SEM-EDS analysis. The sampling methodology (aspirated through quartz tube) to track changes in inclusion composition has been widely reported in the literature.

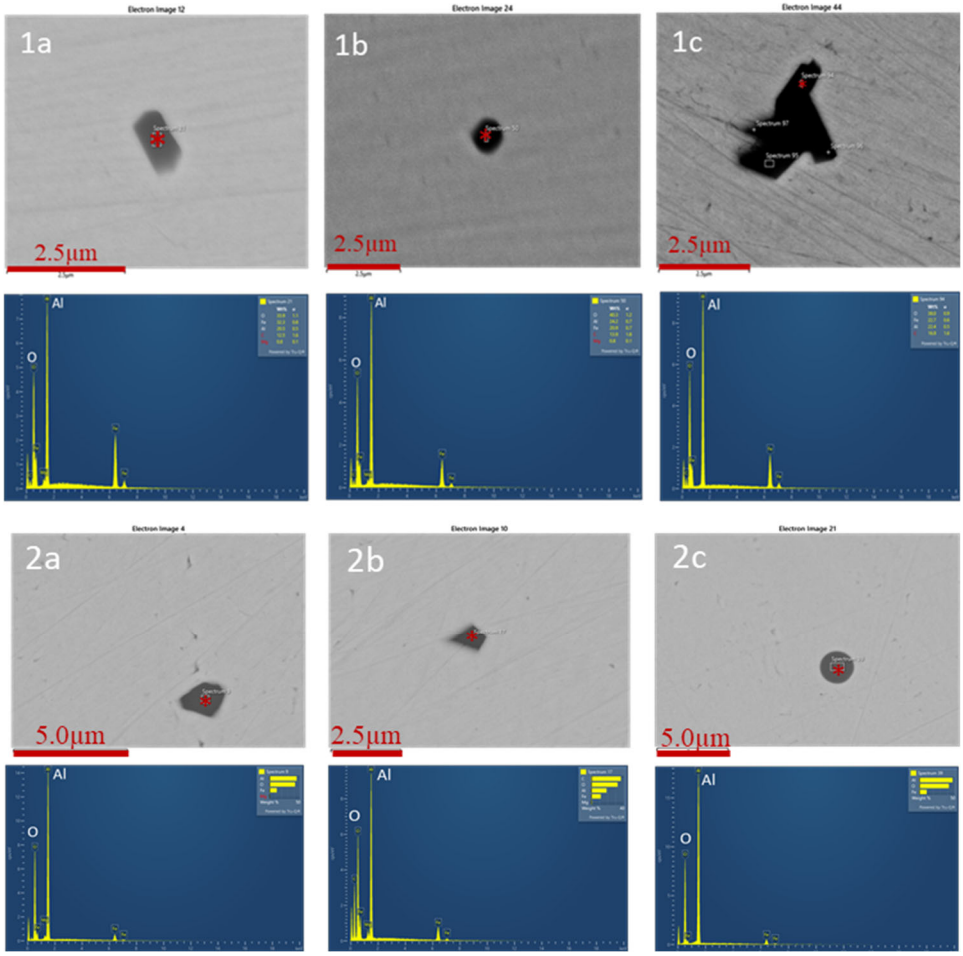

FIG 5 – SEM-EDS spectra of bulk steel samples for experiments 1: (a) 1 min; (b) 2 min; (c) 14 mins; and experiment 2: (a) 0.5 min; (b) 2.5 min; (c) 21.5 mins after composite material addition.

To investigate the dissociation of CaS in the liquid steel the alumina crucible was carefully observed for both experiments. The microstructure and SEM-EDS spectra of the inner surface of the alumina crucible after 15 minutes and 60 minutes of contact time with liquid steel treated by the composite material are shown in Figure 6.

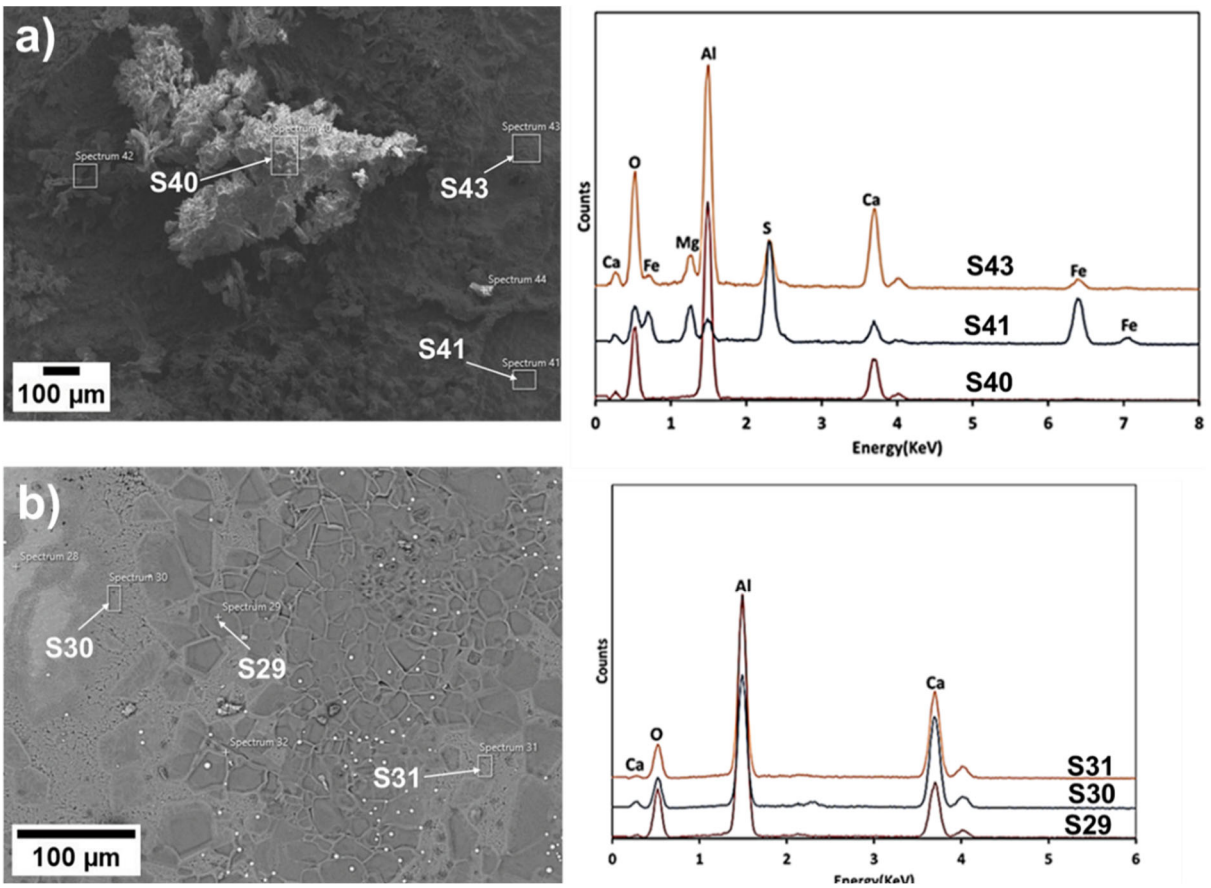

FIG 6 – SEM-EDS analysis of the crucible in contact with the solidified ingot for: (a) experiment 1: contact time – 15 mins; (b) experiment 2: contact time – 60 mins.

Location S40 in Figure 6a clearly shows the presence of a significant amount of CaO and no sulfur. The nearby regions S41 and S42 show a mixture of calcium aluminate and calcium sulfide. However, in experiment no. 2 where the experimentation time was 60 mins (see Figure 6b). A thin layer of liquid calcium aluminates across the crucible's inner surface can be seen. The modification of alumina into calcium aluminates is visible at all locations in Figure 6b. Also, the absence of sulfur peaks at all locations indicates that sulfur must have dissolved in liquid steel. These results indicate that the reaction between CaS and alumina is kinetically driven; that is, the CaS particles in the composite material for experiment no. 1 had insufficient time for complete dissociation and complete modification of alumina, whereas the CaS particles had sufficient time to dissociate and modify alumina crucible for experiment no. 2. To further confirm these findings: (a) the inclusion analysis of the top portion of the solidified ingot, and (b) sulfur pick up in the bulk steel sample at different time intervals for experiment no. 2 have been investigated.

The top surface of the solidified ingot has also been examined to observe the CaS particle flotation and their interaction with floated alumina inclusions. It should be noted here that the top surface also contains floated alumina inclusions after aluminium deoxidation. Upon investigating the solidified steel ingot, the SEM-EDS analysis for experiment no. 1, shown in Figure 7a, reveals partial modification of floated alumina inclusions. The locations S18 and S21 in the SEM micrograph show the floated unmodified alumina inclusions and locations S19 and S20 show the modified alumina inclusions. The SEM-EDS analysis for experiment no. 2 is shown in Figure 7b, which shows that the floated alumina inclusions are modified to calcium aluminates and CaS particles were not observed on the top of the solidified ingot.

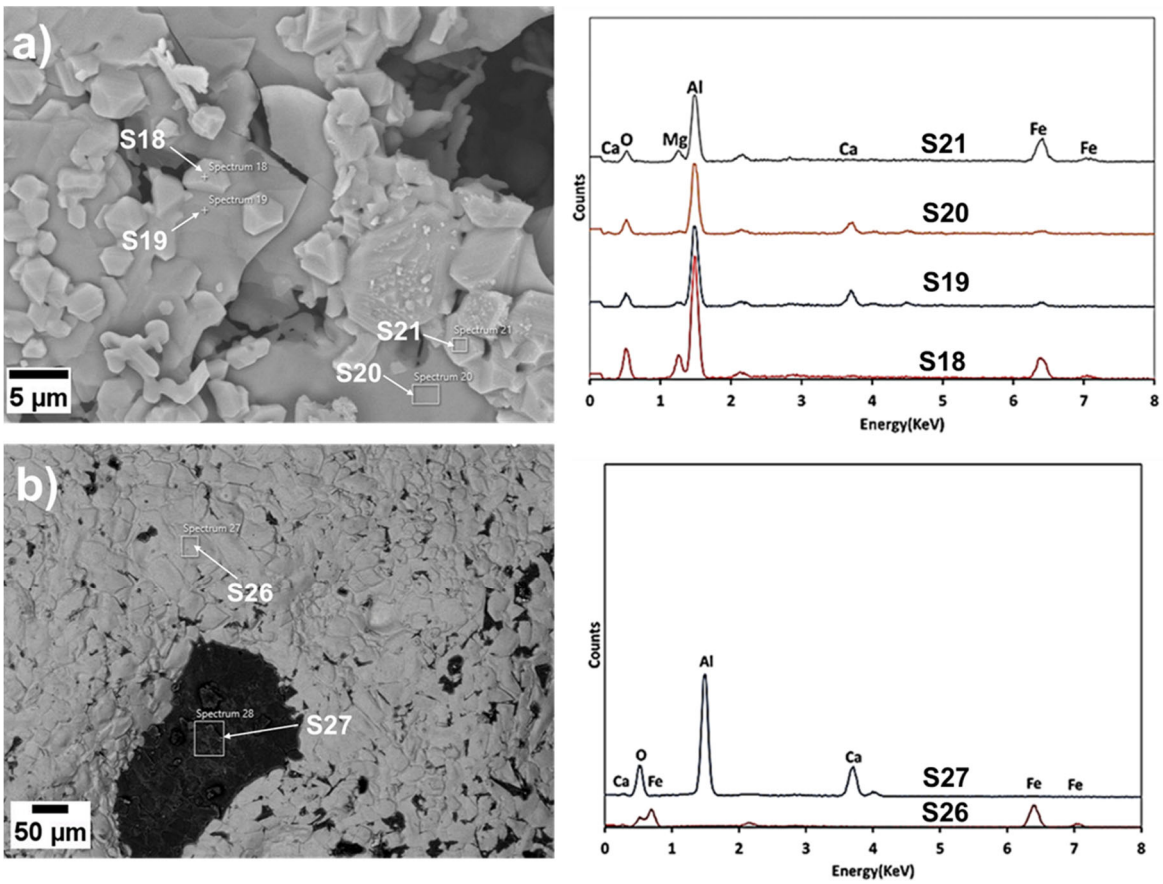

FIG 7 – SEM-EDS analysis of the solidified ingot top: (a) experiment 1; (b) experiment 2.

Furthermore, the steel samples for experiment no. 2 were collected at different time intervals to track the sulfur pick-up in the liquid steel, as shown in Figure 8. The rate of sulfur pick-up is very large at early times, followed by a steady increase in the sulfur concentration. It is evident that the CaS-based composite material undergoes dissociation, facilitating the transfer of calcium to liquid steel for the modification of oxide inclusions and rejecting the sulfur into the liquid steel.

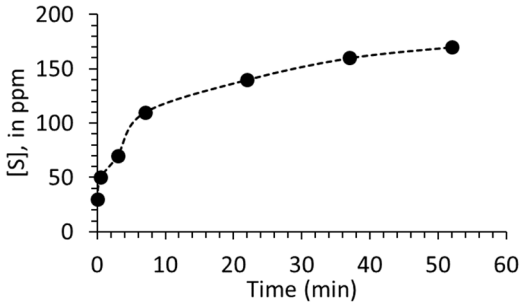

FIG 8 – Sulfur analysis of steel samples at different time intervals for experiment 2.

The thermodynamic stability of CaS in liquid steel was evaluated using the FactSage™ 8.1 thermodynamic software Bale *et al* (2016). The calculations were performed using FactSage™ 8.1 (Equilib module, Databases: FactPS, FactOxid and FTMisc) at 1600°C temperature and 1 atm pressure. The activity of CaS was set to 1 for these calculations. The saturation line representing the equilibrium concentration for S content and total oxygen at which CaS activity is one is shown in Figure 9. The concentration (sulfur, oxygen) region above this line represents CaS is stable, whereas, CaS will dissociate below this saturation line. Both the stability region and dissociation region are depicted in Figure 9.

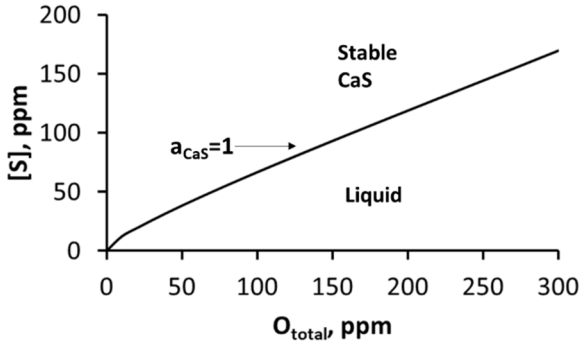

FIG 9 – CaS stability diagram at 1600°C using FactSage™ 8.1.

It can be seen from Figure 9 that a high total oxygen content favours CaS dissociation. The total oxygen in the present system comes from the steel (Fe-Al-Ca-O-S) and the Al_2O_3 crucible interface is expected to have a high oxygen content. Consequently, CaS dissociation is feasible for a wide range of sulfur content, which reasonably aligns with the experimental results. As observed in the experiments, the dissociation of CaS into liquid steel, followed by the transfer of calcium to inclusions and sulfur to melt, depends not on dissolved oxygen but rather on the total oxygen content.

SUMMARY AND CONCLUSIONS:

In the current study, laboratory experiments and thermodynamic calculations were performed to investigate the CaS stability in the liquid steel containing alumina inclusions. Experiments were conducted by adding Fe-CaS-based composite material and the following conclusions can be obtained.

- As expected, since the CaS-Al_2O_3 interaction involves three condensed phases, two solid phases and a liquid steel phase the transfer of chemical species occurs via liquid phase.
- The dissociation of CaS, subsequent calcium transfer to alumina inclusions, and sulfur transfer to the melt are influenced by the total oxygen content from both dissolved oxygen in the melt and oxygen present in the inclusions.
- The CaS dissociation is a kinetic-driven process. The dissociation and subsequent chemical species transfer can depend on the mass transfer coefficients of the species in the liquid steel.

ACKNOWLEDGEMENTS

We would like to acknowledge the financial support of the following funding agencies:

- Industrial Research and Consultancy (IRCC), Centre of Excellence in Steel Technology (CoEST) and Department of Metallurgical Engineering and Materials Science, IIT Bombay.
- Science and Engineering Research Board (SERB), Grant number SRG/2020/001495
- Prime Minister's Research Fellowship contingency grant (PMRF, Ministry of Education) Govt. of India.

REFERENCES

Bale, C W, Belisle, E, Chartrand, P, Decterov, S A, Eriksson, G, Gheribi, A E, Hack, K, Jung, I H, Kang, Y B, Melancon, J, Pelton, A D, Petersen, S, Robelin, C, Sangster, J, Spencer, P and Van Ende, M A, 2016. FactSage thermochemical software and databases, 2010–2016, *CALPHAD,* 54:35–53.

Kumar, D and Kumar, S, 2023. A composite for refining of steel and method for preparation thereof, Indian patent application: 202221076794.

Faulring, G M, Farrel, J W and Hilty, D C, 1980. Steel flow through nozzles influence of calcium, *Iron Steelmaker*, 7(2):14–20.

Higuchi, Y, Numata, M, Fukagawa, S and Shinme, K, 1996. Inclusion Modification by Calcium Treatment, *ISIJ International*, 36:S151–S154.

Hilty, D C and Farrel, J W, 1975a. Modification of inclusions by calcium – Part, I, *Iron Steelmaker*, 2(5):17–22.

Hilty, D C and Farrel, J W, 1975b. Modification of inclusions by calcium – Part II, *Iron Steelmaker*, 2(6):20–27.

Lu, D, Irons, G and Lu, W, 1994. Kinetics and mechanism of calcium dissolution and modification of oxide and sulphide inclusion in steel, *Ironmaking and Steelmaking*, 21(5):362–371.

Ren, Y, Zhang, L and Li, S, 2014. Transient evolution of inclusions during calcium modification in line pipe steels, *ISIJ International*, 54(12):2772–2779.

Turkdogan, E T, 1988. *Proceedings of 1st International Calcium Treatment Symposium*, pp 3–13 (The Institute of Metals, London).

Verma, N, Pistorius, P C, Fruehan, R J, Potter, M, Lind, M and Story, S, 2011a. Transient inclusion evolution during modification of alumina inclusions by calcium in liquid steel: Part I background experimental techniques and analysis methods, *Metallurgical and Materials Transactions B*: *Process Metallurgy and Materials Processing Science*, 42(4):711–719.

Verma, N, Pistorius, P C, Fruehan, R J, Potter, M, Lind, M and Story, S R, 2011b. Transient Inclusion Evolution During Modification of Alumina Inclusions by Calcium in Liquid Steel: Part II, Results and Discussion, *Metallurgical and Materials Transactions B*, 42(4):720–729.

Ye, G, Jönsson, P and Lund, T, 1996. Thermodynamics and kinetics of the modification of Al_2O_3 inclusions, *ISIJ International*, 36.

Corrosion behaviour of ferrite and aluminate refractories in cryolite-aluminium melts

DOI: 10.62053/WIXM4726

R Z Mukhlis[1] and M A Rhamdhani[2]

1. Lecturer, Fluid and Process Dynamics (FPD) Research Group, Swinburne University of Technology, Hawthorn Vic 3122. Email: rmukhlis@swin.edu.au
2. Professor, Fluid and Process Dynamics (FPD) Research Group, Swinburne University of Technology, Hawthorn Vic 3122. Email: arhamdhani@swin.edu.au

ABSTRACT

Removing the ledge formation in the Hall-Heroult cell during the electrolysis process may significantly reduce the energy requirement of the aluminium production process. In the absence of the ledge, however, the sidewall-material types become heavily restricted since the cryolite is very corrosive at the electrolysis temperatures. This paper study the corrosion behaviour of sintered nickel ferrite, nickel aluminate, and magnesium aluminate refractories (as possible candidates for sidewall material) in molten aluminium and cryolite melts with various alumina content at 980°C. Immersion tests of refractories with various porosity were conducted to assess the suitability of the refractories in the corrosive environment of the electrolysis cells. Microstructural change of the refractory after immersion were analysed using secondary scanning electron microscopy (SEM). Sampling of the melts were taken at 0, 10 min, 30 min, and each hour up to 6 hrs, and subsequently analysed by Inductively Coupled Plasma (ICP) spectroscopy. Based on the projected concentration of the refractories constituents in the melts, it was predicted that the corrosion rate of $NiFe_2O_4$, $NiAl_2O_4$ and $MgAl_2O_4$ in cryolite with 11 wt per cent Al_2O_3 were 461 × 10^3, 1.03 × 10^3, and 798 × 10^3 cm/a, respectively. Much lower corrosion rate of 2.3 cm/a for $NiFe_2O_4$, 2.6 cm/a for $NiAl_2O_4$ and 0.3 cm/a for $MgAl_2O_4$ were predicted if the refractories in contact with aluminium melts. Erosion played an important role in the corrosion as the concentration of the refractory constituents in the melts were beyond its solubility limit. It is therefore crucial to increase the densities of the refractory and improve its wetting characteristics.

INTRODUCTION

Aluminium is produced commercially from alumina through the Hall-Heroult process at around 965°C where the overall chemical reaction produces metallic aluminium and carbon dioxide, as follows:

$$2Al_2O_{3(s)} + 3C_{(s)} = 4Al_{(l)} + 3CO_{2(g)} \quad (1)$$

There are two major issues suffered by the process: high cost and great environmental impact. The high cost is the consequence of its high capital cost and its eminent energy requirement. The total specific energy requirement, W_{el} (kWh/kg), of the Hall-Heroult process can be determined through the following relationship by estimating the cell voltage (Thonstad *et al*, 2001):

$$W_{el} = \frac{UF|V_e|}{3600M_{Al}x_{Al}v_{Al}} = 2.98\frac{U}{M_{Al}} \quad (2)$$

where:

- U is the cell voltage
- F is Faraday constant
- $M_{(Al)}$ is the molar weight of Al
- $x_{(Al)}$ is the corresponding current efficiency fraction
- $|V_e|$ and $v_{(Al)}$ are the stoichiometric numbers of electrons and of product of cathodic reaction, respectively

By considering Reaction 1 and Equation 2, the theoretical energy required to produce 1 kg aluminium at 1000°C and 100 per cent current efficiency is 5.06 kWh. In practice, the energy consumed to produce 1 kg aluminium is ranging from 12 to 15 kWh (Schwarz, 2008; Kvande and Haupin, 2001; Haraldsson and Johansson, 2020). This energy includes the thermodynamic energy needed by the

reaction, and additional energy that is required to heat the reactant from room temperature to the operational temperature and to maintain at that temperature. The necessity to have high heat loss through the side of the cell container to form protective frozen ledge is also significantly contributing to the high energy consumption.

The significant environmental impact of the Hall-Heroult process has a strong correlation with its high energy demand, particularly if the source of electricity is coming from fossil fuel. Moreover, the fact that the Hall-Heroult process uses consumable carbon anode and the main reaction of the process produce carbon dioxide gas, induce its effect on global warming even more escalated.

It has been considered since long that the breakthrough technology of inert anode, the anode that theoretically will not be consumed during electrolysis, may revolutionise the Hall-Heroult process (Kvande and Drabloss, 2014). Not only can it alter the aluminium electrolytic process from carbon dioxide generating reaction to oxygen producing reaction (Reaction 3); the implementation of inert anode will eliminate all cost associated with the consumable carbon anode. The capital cost itself has been indicated to be reduced by one-quarter to one-third of the capital cost of the carbon anode potline (Thonstad *et al*, 2001).

$$2Al_2O_{3(dis)} = 4Al_{(l)} + 3O_{2(g)} \quad (3)$$

The implementation of inert anode to the Hall-Heroult process will also increase its environmental friendliness by eliminating the production of CO, perfluorocarbon gases ie CF_4 and C_2F_6, fluoride and dust emissions during anode change, and the elimination of carbon butts (Kvande and Drabloss, 2014). The inert anode technology, however, needs to be underpinned with the significant advancement in materials technology and the heat flow control (Mukhlis, Rhamdhani and Brooks, 2010).

It is important to be noted that due to the absence of carbon-oxygen reaction that provide energy, the use of inert anode will increase the theoretical energy consumption to 6.54 kWh per kg aluminium production. Lower heat loss, is therefore, required in the cell that used inert anode to be able to have the same amount of energy requirement as the conventional cell.

In the case that heat loss needs to be lowered, the protective frozen ledge will be difficult to be maintained and the sidewall materials will be exposed directly to the very corrosive environments of cryolite bath, the highly reducing molten aluminium zone, as well as the oxidative upper part of the cell due to the existence of air and oxygen at high temperatures. Consequently, the life of the sidewall materials will be significantly reduced. It is obvious that the implementation of inert anode in the cell calls for new ledge-free sidewall materials.

In general, the required properties of the ledge-free sidewalls are very much the same as the required properties of inert anodes except for its electrical conductivity, where in contrast with inert anode, sidewall materials should have low electrical conductivity (Mukhlis, 2015; Yan *et al*, 2011). Spinel based materials, particularly nickel ferrite ($NiFe_2O_4$), have been proposed as inert anode and ledge free sidewall material for aluminium smelter, mainly due to its low solubility and high corrosion resistance against cryolite and high oxidation resistance (Yan, Pownceby and Brooks, 2007; Mukhlis, Rhamdhani and Brooks, 2010; Longbottom, Nightingale and Monaghan, 2014). While these properties make the spinel suit to be applied in both gas zone and cryolite zone, this is not the case for the application in the aluminium zone. It has been predicted thermodynamically that in equilibrium, liquid aluminium will be contaminated by 29.1 mol per cent Ni and 7.8 mol per cent Fe when 10 mol of aluminium is in contact with 1 mol $NiFe_2O_4$ at 965°C. $NiFe_2O_4$ should therefore be combined with other material that have high resistance against molten aluminium if it is to be used as ledge-free sidewall material.

The current paper study the corrosion behaviour of $NiFe_2O_4$, $NiAl_2O_4$ (nickel aluminate), and $MgAl_2O_4$ (magnesium aluminate) in both aluminium and cryolite melts. $NiAl_2O_4$, and $MgAl_2O_4$ were chosen as both are aluminium contained materials, which hypothetically suit to be applied in aluminium zone, low electrical conductivity as well as having similar crystal structure as $NiFe_2O_4$ for the joining compatibility.

MATERIALS AND METHOD

In the present work, the $NiFe_2O_4$, $NiAl_2O_4$, $MgAl_2O_4$ powders were made from its oxide precursors where the details can be found elsewhere (Mukhlis *et al*, 2011). About 15g of each powder were compacted uniaxially in metal dies at 91 MPa into rectangular bar shape samples, and subsequently sintered under air at 1450°C for 6 hrs for corrosion test. The sintered $NiFe_2O_4$, $NiAl_2O_4$, and $MgAl_2O_4$ sample contained porosity of 12.0 per cent, 42.0 per cent, and 22.4 per cent, respectively, determined by ASTM C20-00 standard (ASTM, 2000). Higher density $NiAl_2O_4$ (25.5 per cent) porosity and $MgAl_2O_4$ (11.7 per cent porosity) were also tested for comparison.

All surfaces of the sintered bars were grounded up to 800 grits to homogenise the surface roughness and to eliminate the part that may have reacted with the crucible during sintering. Following that, one end of the sintered bar was assembled into a stainless-steel holder that jointed to a stainless-steel rod connected to an overhead electronic stirrer (Figure 1). The assembly were covered with alumina tube to ensure that during experiments, no steel surface is directly exposed to molten bath or molten aluminium and to the atmosphere inside the reactor.

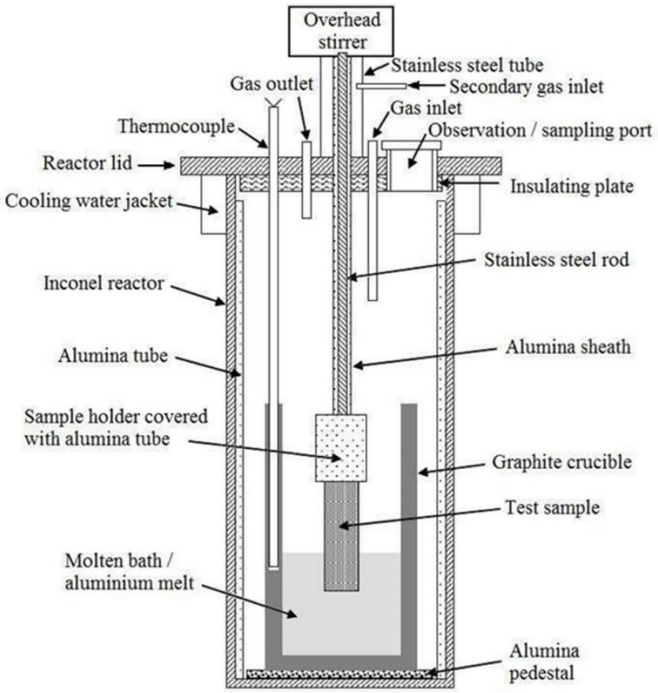

FIG 1 – Schematic diagrams of the stirred finger test apparatus.

The finger test-type apparatus was used to study the corrosion behaviour of the spinel (Figure 1). A pit furnace was used to melt the electrolyte and aluminium. The molten bath or aluminium melt was hold by a graphite crucible with a dimension of 45 mm inner diameter, 65 mm outer diameter and 175 mm high. Type-K thermocouple that was inserted into the hole drilled in the crucible was used to measure the melt temperature. The gastight closure of the reactor enabled the control of the atmosphere.

To study the corrosion behaviour of the spinel materials against Hall-Héroult cell environment, the spinel bar samples were immersed (15 mm deep) in a molten aluminium or in cryolite-based melt with a low cryolite ratio of 2.3 (which is equal to 11 wt per cent excess of AlF_3) contained 6 to 11 wt per cent alumina addition. The corrosion tests were conducted for 6 hrs at a rotation speed of 25 rev/min under flowing argon atmosphere of 0.1 L/min. All experiments were carried out at 980 ± 2°C. During the experiment, samples of cryolite-based bath were taken through the observation port by rapid freezing onto a high purity copper rod which was quickly immersed into the bath, while the aluminium sampling was made using a quartz tube. The sampling was made at 0 min (just before the immersion), 10 min, 30 min, 1 hr, then every hour up to 6 hrs. The solidified bath/aluminium samples were then used for elemental analysis using Inductively Coupled Plasma (ICP) spectrometry.

RESULTS AND DISCUSSIONS

Corrosion test of $MgAl_2O_4$ in cryolite

Figure 2 shows the photographs of $MgAl_2O_4$ sample with 22.4 per cent porosity that were taken before and after corrosion testing in cryolite-based melt with 2.3 CR contained 11 wt per cent alumina at 980°C. No sample left after corrosion testing despite only 15 mm of the sample (out of 34.3 mm length of unsealed sample) immersed in the cryolite. It indicates that the reaction between the melt and the sample took place beyond the surface of the sample that had direct contact with the melt.

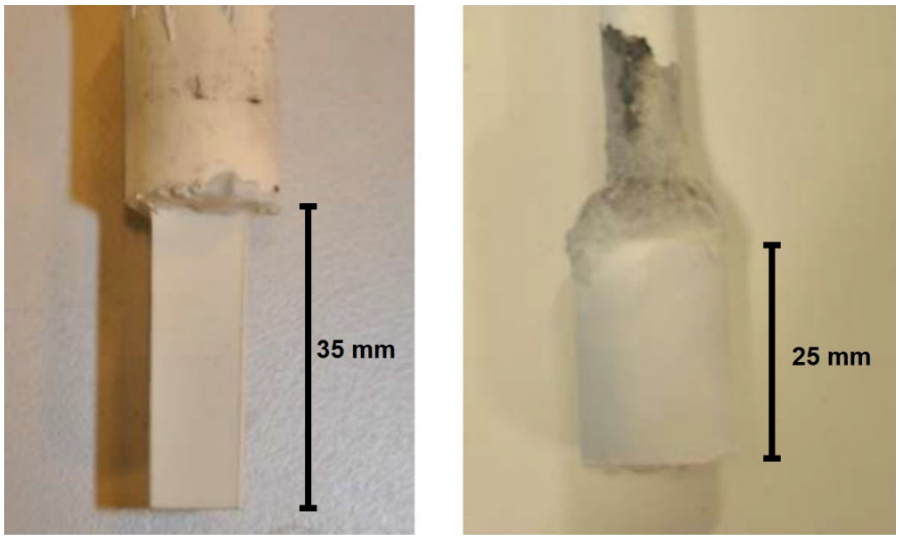

FIG 2 – Sample of $MgAl_2O_4$ with 22.4 per cent porosity: (left) initial sample (b) after corrosion testing.

A liquid in contact with porous substrate may penetrate and progress through the pores of the substrate due to capillarity when the contact angle between the liquid and the substrate is less than 90°. In a separate study conducted by the authors (Mukhlis *et al*, 2014), it was found that the measured apparent contact angle of electrolyte with 0 wt per cent, 6 wt per cent, and 11 wt per cent alumina content on $MgAl_2O_4$ substrate was 19.4°, 12.2°, and 9.3°, respectively.

The photographs of the $MgAl_2O_4$ sample with apparent porosity of 11.75 per cent are shown in Figure 3. Despite there was still some sample left after testing, the denser sample exhibited similar behaviour with the less-dense sample (shown in Figure 2), in which the corrosion proceeded beyond the sample surface that had direct contact with the melt. From 39.7 mm length of the original unsealed sample, only about 10 mm of it remained solid after testing (indicated by ‘S’ in Figure 3). The rest of the sample were either fully corroded or corroded on its inner part, leaving a hollow structure.

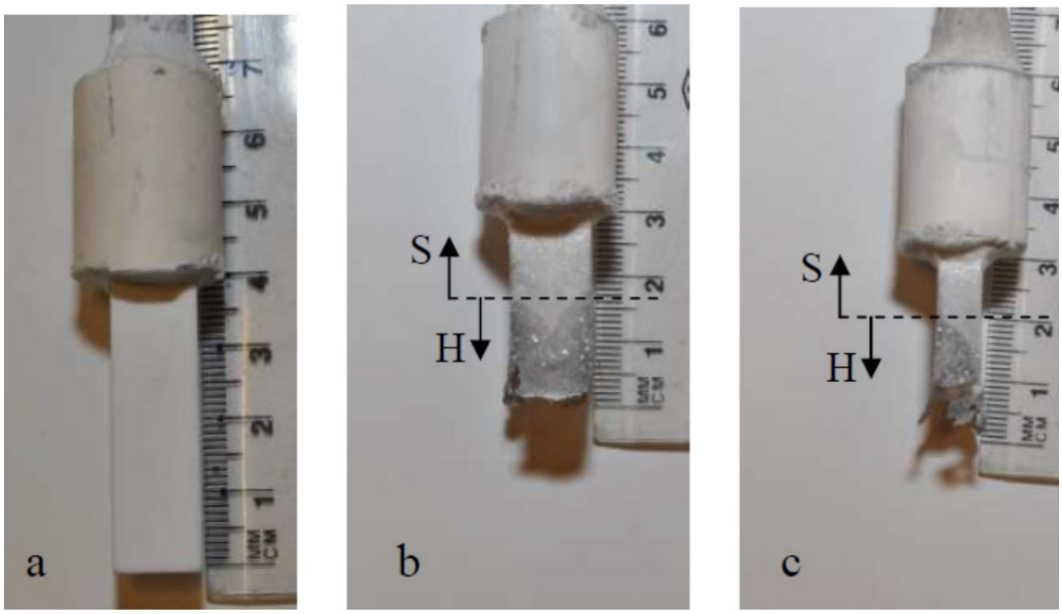

FIG 3 – Photograph of $MgAl_2O_4$ sample with apparent porosity of 11.74 per cent reacted with cryolite-based melt (CR = 2.3) contained 11 wt per cent alumina at 980°C: (a) before corrosion testing; (b) after testing (front view); (c) side view. S and H denote solid and hollow, respectively.

The amount of magnesium dissolved in the cryolite-based melt originated from the $MgAl_2O_4$ samples over time as per ICP-AES analysis are plotted in Figure 4.

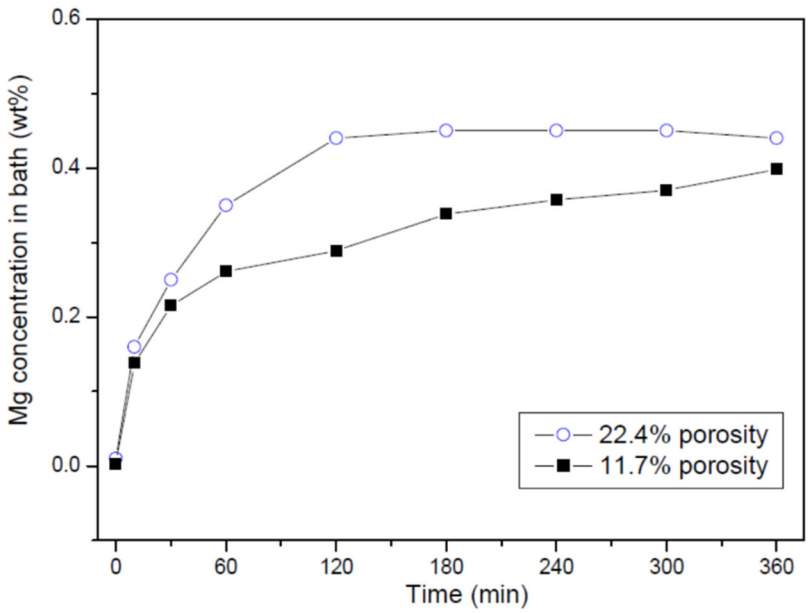

FIG 4 – Elemental analysis of the dissolved magnesium originated from $MgAl_2O_4$ with different porosity level in the cryolite-based melt.

It can be clearly seen from the curves plotted in Figure 4 that the amount of magnesium in the melts rose rapidly at the first 10 mins in which the gradient of both curves nearly the same. The concentration of magnesium in the melt increased with time at a reduced rate. As the corrosion proceeds, the surface area of the spinel sample that had direct contact with the melt decreased gradually, which may explain the less steep gradient of the curves over the time. In the case of the experiment with the sample with 22.4 per cent porosity, the increase in the magnesium concentration in the melt ceased at a relatively stable value of 0.44 to 0.45 wt per cent after 120 mins.

Based on the dimension of the unsealed part of the 22.4 per cent porosity sample, it theoretically contains 0.946 g of magnesium since the magnesium concentration in stoichiometric $MgAl_2O_4$

sample is 17.08 wt per cent. If the entire unsealed sample is dissolved into 200 g of the cryolite-based melt, the concentration of the magnesium in the melt is expected to be 0.46 wt per cent, which is very close to the steady state value shown in Figure 4. Through the similar dimensional calculation as above, and by also considering the hollow part of the sample, the expected concentration of magnesium in the melt originated from the 11.75 per cent porosity sample is 0.36 wt per cent, which is also close to the maximum concentration of magnesium from the sample shown in Figure 4.

From these calculations, it is concluded that 0.46 wt per cent is not the solubility limit of the $MgAl_2O_4$ in the cryolite-based electrolyte melt with 2.3 CR contained 11 wt per cent alumina. It merely indicated that all available samples have been corroded and all magnesium from the sample has been dissolved as supported by Figure 3. It is expected that if there is still available sample of $MgAl_2O_4$ in contact with the melt, the amount of magnesium in the melt will still increase over time until it reached the solubility limit. As for comparison, the solubility limit of MgO in pure cryolite and in cryolite that contain 5 wt per cent alumina at 1010°C was found to be 11.65 wt per cent and 10.6 wt per cent, respectively (Grjotheim *et al*, 1982).

Corrosion test on the $MgAl_2O_4$ sample with apparent porosity of 22.4 per cent immersed in cryolite-based melt with 2.3 CR contained 6 wt per cent alumina was conducted to study the effect of alumina concentration in the melt to the corrosion behaviour of $MgAl_2O_4$. The concentration of magnesium in the bath over time as per ICP-AES analysis is plotted in Figure 5.

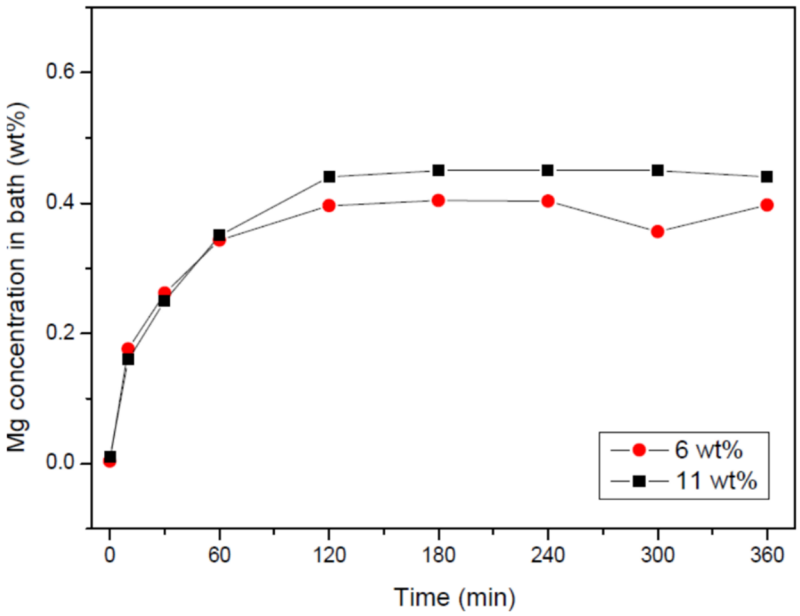

FIG 5 – Elemental analysis of the dissolved magnesium originated from $MgAl_2O_4$ in cryolite-based melts contains different alumina concentration.

As shown in Figure 5, the amount of magnesium in the cryolite-based melt that contain 6 wt per cent alumina increased sharply for the first 30 mins and further increased with a reduced rate up to 60 mins. Up to this period, the gradient of the curve is nearly the same as that for the melt that contain 11 wt per cent alumina. The magnesium concentration in the melt that contain 6 wt per cent alumina reached a plateau at 0.4 wt per cent within 120 mins. Again, this steady value did not indicate the solubility limit, rather indicate that all available $MgAl_2O_4$ sample has been corroded by the melt and all the magnesium has been dissolved into the melt. It should be noted that the Mg concentration at 300 min was slightly lower than expected, however, this most likely due to the variation from the measurement eg slightly smaller sample hence lower amount of available Mg. While overall trend is quite clear, further test at 300 min immersion is planned to validate the results.

All the above results showing a significant corrosion attack of the melt against magnesium aluminate. These results agree with the thermodynamic study that suggest $MgAl_2O_4$ is not suitable to be applied as ledge free sidewall in contact with the cryolite-based electrolyte.

The typical microstructures of the corroded $MgAl_2O_4$ sample are shown in Figure 6, which is associated with Figure 3.

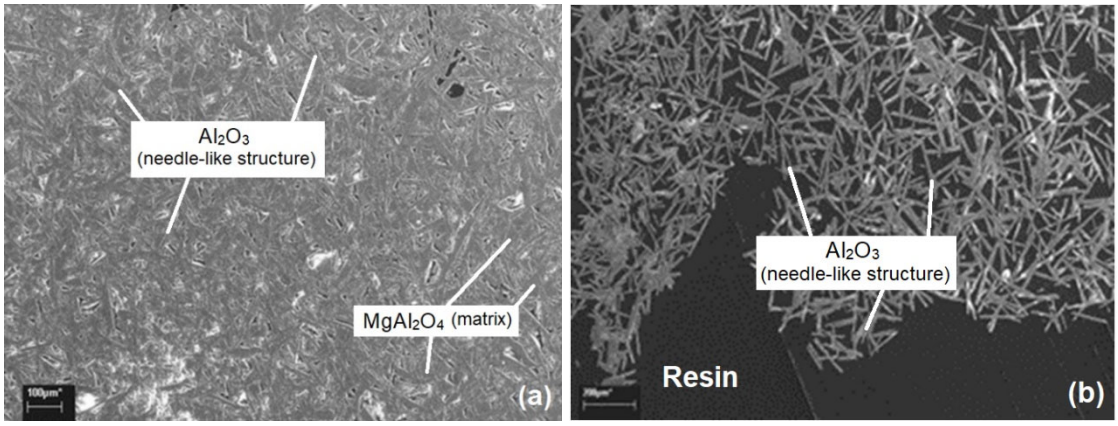

FIG 6 – Microstructure of the $MgAl_2O$ sample that was shown in Figure 3: (a) top section of the solid part; (b) bottom section of the hollow part.

As shown in Figure 6, the microstructures of both solid part and hollow part of the sample contained needle like structures that less than 5 μm width. The only significant difference is that for solid part (Figure 6a), most of the space in-between the needle like structure was filled with solid structures. The energy dispersive X-ray spectroscopy (EDS) point-analysis suggested that the needle-like structure was Al_2O_3, while the solid structures were solidified electrolyte melts. The presence of the solidified cryolite-based melt – in the top section of the solid part of $MgAl_2O_4$ sample – support the previous hypothesis, which suggested that the melt penetrate into $MgAl_2O_4$ beyond the surface that had direct contact with the melt.

In order to investigate whether there are still un-corroded $MgAl_2O_4$ left in the sample, elemental mapping on the top section of solid part of the sample (refer to Figure 3) has been conducted and the result is shown in Figure 7.

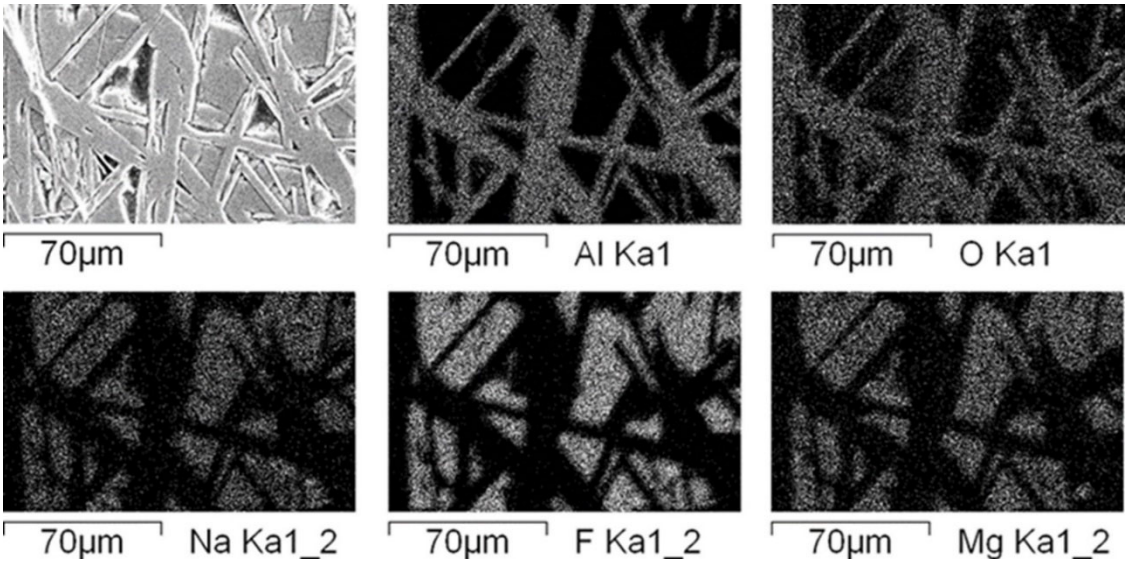

FIG 7 – Elemental mapping on the top section of solid part of $MgAl_2O_4$ sample that shown in Figure 3.

Elemental mapping revealed that there were significant compositional changes on the sample after corrosion testing. Most of the aluminium and oxygen were exist in the needle-like structures. On the other hand, most of magnesium was exist in the solid structure surrounded the needle-like structure. Only insignificant trace of magnesium was detected in the needle-like structure. This indicated that no $MgAl_2O_4$ left in the magnesium aluminate sample after 6 hr immersion in the cryolite-based electrolyte. The concentration of magnesium in the stoichiometric $MgAl_2O_4$ is 17.08 per cent.

Consequently, for a phase to be qualified to be suggested as $MgAl_2O_4$, the trace of magnesium should be substantial at the place where the trace of both aluminium and oxygen are also significant.

Since most of the magnesium were detected on the area where the sodium and fluorine were substantial, it is argued that the magnesium from $MgAl_2O_4$ was dissolved into the cryolite-based melt. It is also reasonable to conclude that the corrosion mechanism of $MgAl_2O_4$ by cryolite-based melt involve reactions that produce Al_2O_3. One of the plausible reactions is the reaction in Equation 4:

$$MgAl_2O_4 + {}^{2}/_{3}\,Na_3AlF_6 = MgF_2 + 2NaF + {}^{4}/_{3}\,Al_2O_3 \quad (4)$$

This however needs to be studied further.

Corrosion test of $NiAl_2O_4$ in cryolite

Figure 8 shows the pictures of $NiAl_2O_4$ sample before and after corrosion testing in the 2.3 CR cryolite containing 6 wt per cent Al_2O_3. The $NiAl_2O_4$ samples showed similar behaviour with the $MgAl_2O_4$ samples discussed earlier, in which the part that had direct contact with cryolite – about 15 mm – disintegrated from the sample and went into the melt.

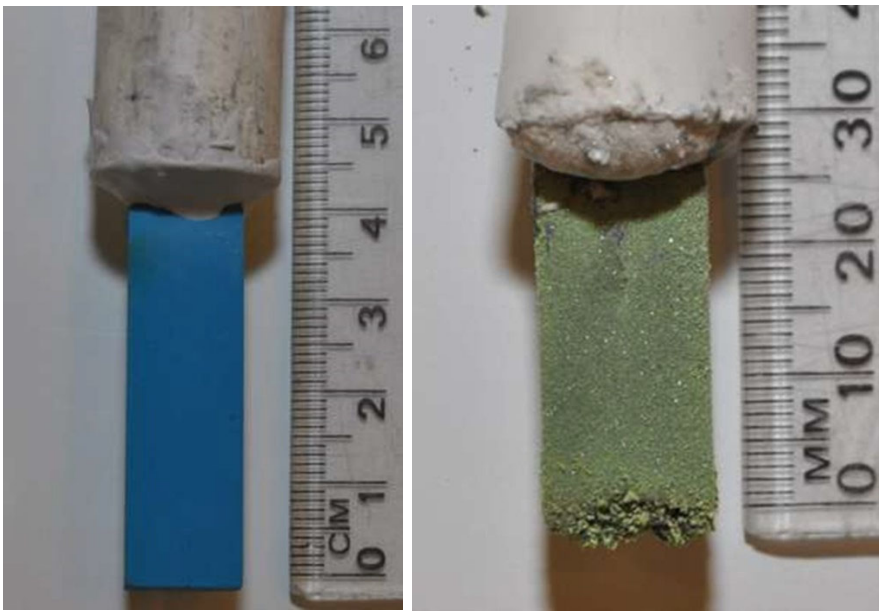

FIG 8 – Typical $NiAl_2O_4$ samples before (left) and after corrosion test (right). The part of the sample that had direct contact with cryolite goes into the melt.

If one considering only the thermodynamics stability of the nickel aluminate in cyolite melts, the effect of the melts to the sample as shown in Figure 8 was rather unexpected. The Gibbs free energy of the reaction between $NiAl_2O_4$ with cryolite at 980°C is positive (Bale *et al*, 2022). Moreover, predominance area diagram of the nickel solid phase at 980°C shown that $NiAl_2O_4$ was predicted to be a stable phase in the alumina-saturated melts. The $NiAl_2O_4$ samples were therefore expected not to be severely corroded, particularly by the alumina-saturated cryolite melts.

The concentration of nickel from $NiAl_2O_4$ in the cryolite melt over the sampling time is plotted in Figure 9. In general, the amount of nickel in the melts increased as the time increase. The total amount of nickel in the melt containing 6 wt per cent was higher than the nickel in alumina-saturated melt. The rate of the increase in the nickel content was also higher for the melt containing 6 wt per cent alumina.

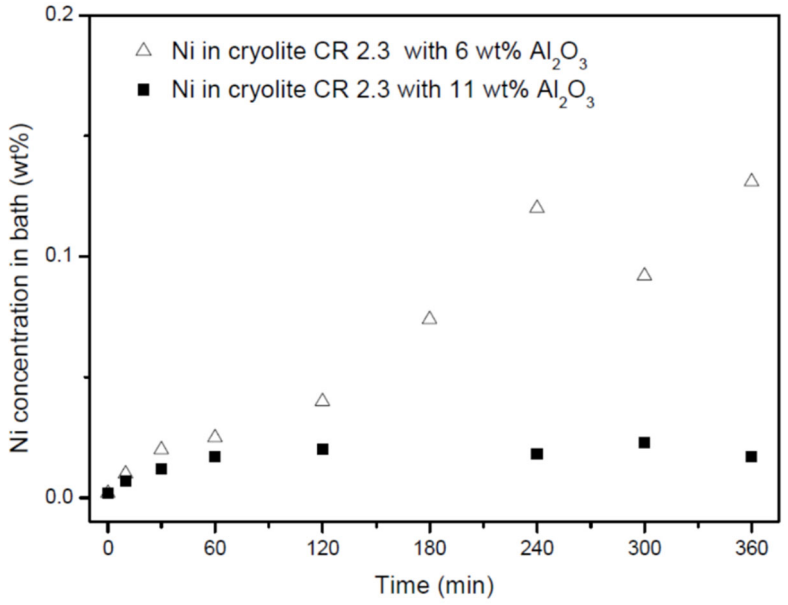

FIG 9 – Concentration of nickel originated from $NiAl_2O_4$ in cryolite-based melts contains different alumina concentration.

According to the previous research conducted by Lorentsen (2000), the saturation concentration, ie solubility limit, of nickel from $NiAl_2O_4$ in cryolite containing 6 wt per cent and 11 wt per cent alumina is 3.8×10^{-2} and 0.86×10^{-2} wt per cent, respectively. Surprisingly, after 6 hrs of experiment, the nickel contents in the melts were much beyond the solubility limit. The concentration of nickel in the melt containing 6 wt per cent and 11 wt per cent alumina was found to be 0.13 and 0.02 wt per cent. Owing to this, it was argued that the corrosion of $NiAl_2O_4$ by cryolite-based melts in current study was not only due to the dissolution of spinel constituents into the melts, but also due to the erosion on the spinel by the melts. The concentrations of nickel in the melt found in current study were suggested as the summation of the dissolved nickel in the melt and the nickel aluminate particles inside the melts due to erosion. By considering the integrity and the density of $NiAl_2O_4$ that were very low, it was reasonable to expect the high erosion level on the sample.

The microstructure of the $NiAl_2O_4$ sample after corrosion testing is shown in Figure 10. The microstructure shown in Figure 10a is associated with the top section of the solid part of the sample closer to sample holder, while Figure 10b is associated with the bottom section of the sample near to the immersed section (refer to Figure 8).

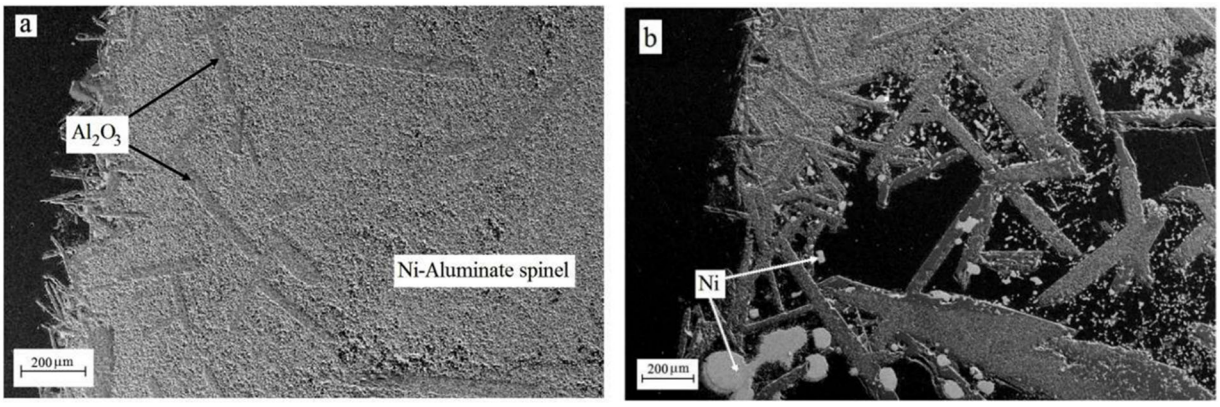

FIG 10 – Microstructure of $NiAl_2O_4$ sample after corrosion testing: (a) section of the sample closer to sample holder; (b) section of the sample near to the immersed section.

Both sections of the corrosion-tested $NiAl_2O_4$ sample in Figure 10 contained needle like-structures which are surrounded by the solid structures. Interestingly, in addition to these microstructures, there was some roundish white microstructure found in the section of the sample near to the immersed

section (Figure 10b). EDS point-analysis suggested that the needle like structure was Al_2O_3. The solid structure was suggested as nickel aluminate as it contains Ni, Al and O; while the roundish white microstructure was suggested as metal since nickel was the only element detected in the spot. To further study the microstructure, EDS elemental mapping had been conducted on the zoomed part of the middle section and the bottom section as shown in Figures 11 and 12, respectively.

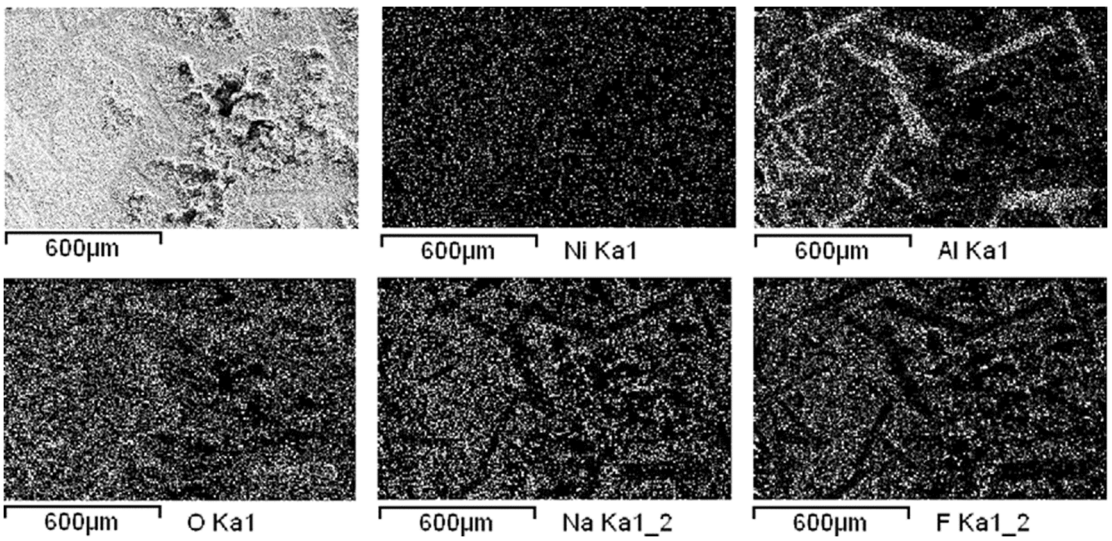

FIG 11 – EDS elemental mapping on the middle section of the corrosion-tested $NiAl_2O_4$ sample.

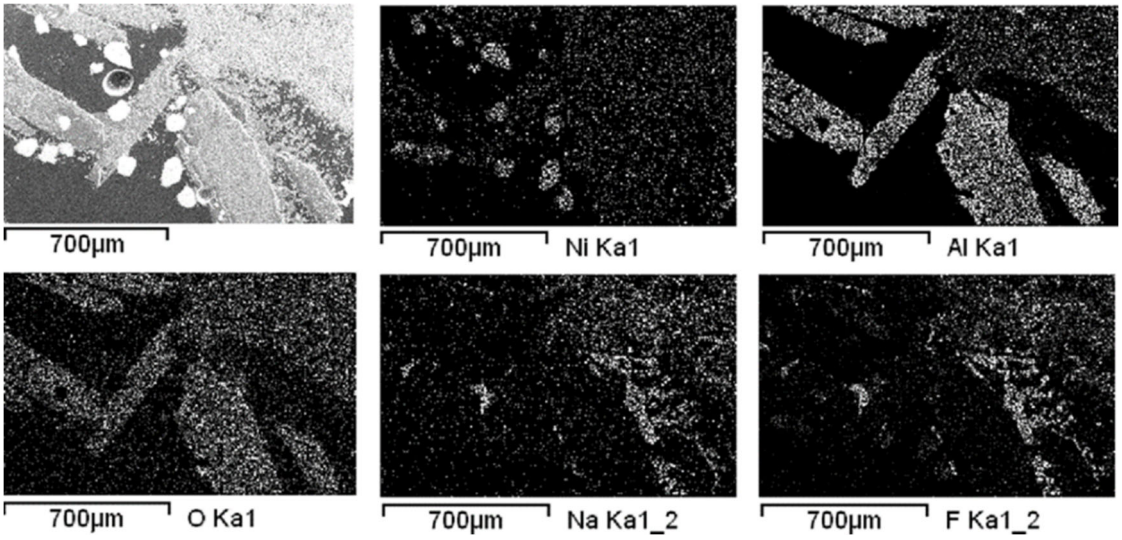

FIG 12 – EDS elemental mapping on the section of the corrosion-tested $NiAl_2O_4$ sample close to the immersed section.

The EDS elemental mapping results confirmed that there were sodium and fluorine elements exist in the solid structure that surrounded the Al_2O_3. This suggests that the cryolite penetrated into the $NiAl_2O_4$ sample beyond the section where the sample had direct contact with the molten bath. However, unlike the $MgAl_2O_4$ where there was no magnesium aluminate left in the sample after corrosion tested, there were still nickel aluminate left in the $NiAl_2O_4$ sample. This support the hypothesis that suggests the corrosion of the $NiAl_2O_4$ sample was not only due to dissolution of the spinel constituent by the melt, but also due to erosion.

Since there were significant amount of Al_2O_3 found in the corrosion-tested $NiAl_2O_4$ sample, the reaction in Equation 5 seems plausible.

$$NiAl_2O_4 + {}^{2}/_{3}\, Na_3AlF_6 = NiF_2 + 2NaF + {}^{4}/_{3}\, Al_2O_3 \quad (5)$$

The presence of metallic nickel in the bottom section of the sample suggested that NiF_2 dissociated into Ni. The explanation on how the nickel was formed need further study.

Corrosion test of $NiFe_2O_4$ in cryolite

The pictures of $NiFe_2O_4$ sample before and after corrosion testing are shown in Figure 13. The typical sample before test is shown in Figure 13a, while the appearance of the sample after 6 hrs immersion in the cryolite-based melts with CR 2.3 containing 6 wt per cent alumina and 11 wt per cent alumina is shown in Figure 13b and Figure 13c, respectively.

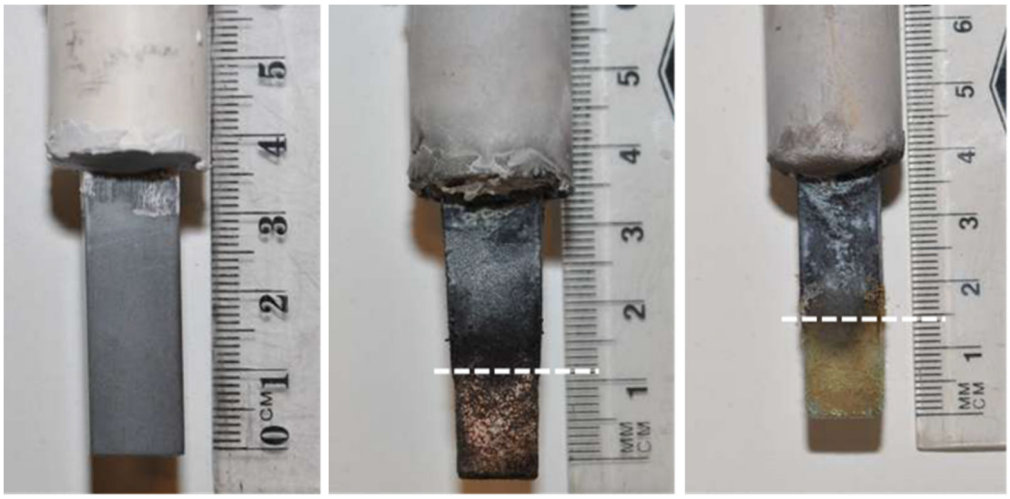

(a) (b) (c)

FIG 13 – $NiFe_2O_4$ sample for corrosion test in cryolite-based melts: (a) Typical sample before test; (b) after immersion in melt containing 6 wt per cent alumina; (c) after immersion in melt containing 11 wt per cent alumina. The white lines in (b) and (c) indicate the depth of immersion.

On the contrary to the cases of $MgAl_2O_4$ and $NiAl_2O_4$ samples, most of the immersed sections of the $NiFe_2O_4$ samples were still retained. There were indeed noticeable discolorations on the immersed sections. However, the dimension of the section immersed in the melts containing 6 wt per cent alumina ie length, width and thickness was slightly reduced, while the dimension of the section immersed in the melts containing 11 wt per cent alumina showed no change. This indicated that in cryolite-based melts, particularly in the alumina-saturated melt, $NiFe_2O_4$ exhibited the lowest corrosion compared to $MgAl_2O_4$ and $NiAl_2O_4$.

The change in the concentration of nickel ferrite constituents in the melt over time is plotted in Figure 14. In general, the concentration of the constituent increased as the time increase.

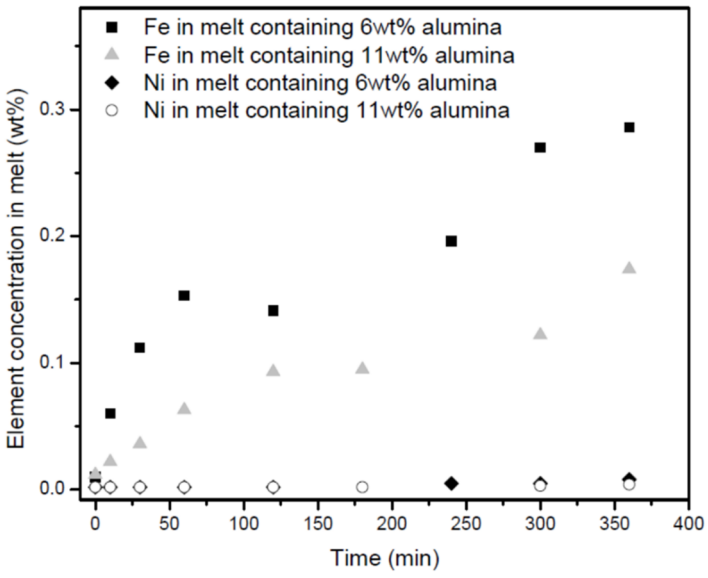

FIG 14 – Concentration of nickel ferrite constituents in cryolite-based melts as a function of time at 980°C.

It can be seen clearly in Figure 14 that the change in the iron concentration was considerably more rapid than the change in the nickel concentration. In both melts containing 6 wt per cent and 11 wt per cent alumina, the final iron concentration after 6 hrs test was also significantly higher than nickel and it did not reflect the stoichiometric ratio of iron to nickel in nickel ferrite. These results indicate preferential dissolution of iron in the melts, which agreed with other' studies (Yan, Pownceby and Brooks, 2007; Olsen and Thonstad, 1999a, 1999b). Compared to the melt containing 6 wt per cent alumina, the total concentration of $NiFe_2O_4$ constituents in the alumina-saturated melt was lower. The rate at which the concentration of the constituent changed over the time was also lower in the alumina-saturated melt. This indicates that the corrosion resistant of nickel ferrite increased as the alumina concentration in the melt increase.

The typical microstructure of nickel ferrite sample after 6 hrs corrosion test and its associated EDS elemental mapping are shown in Figure 15.

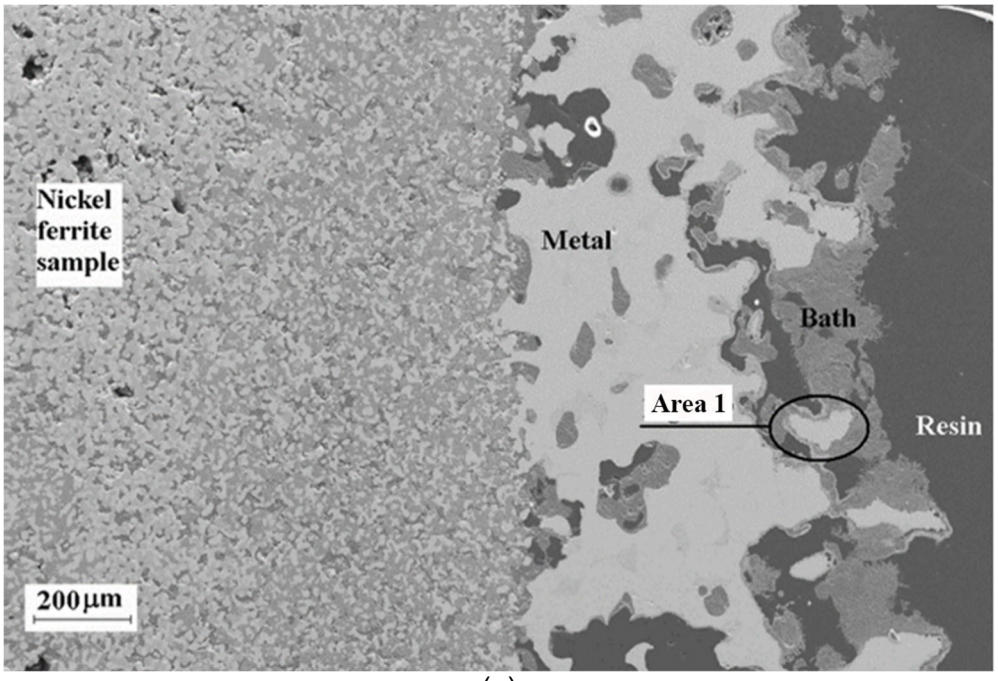

(a)

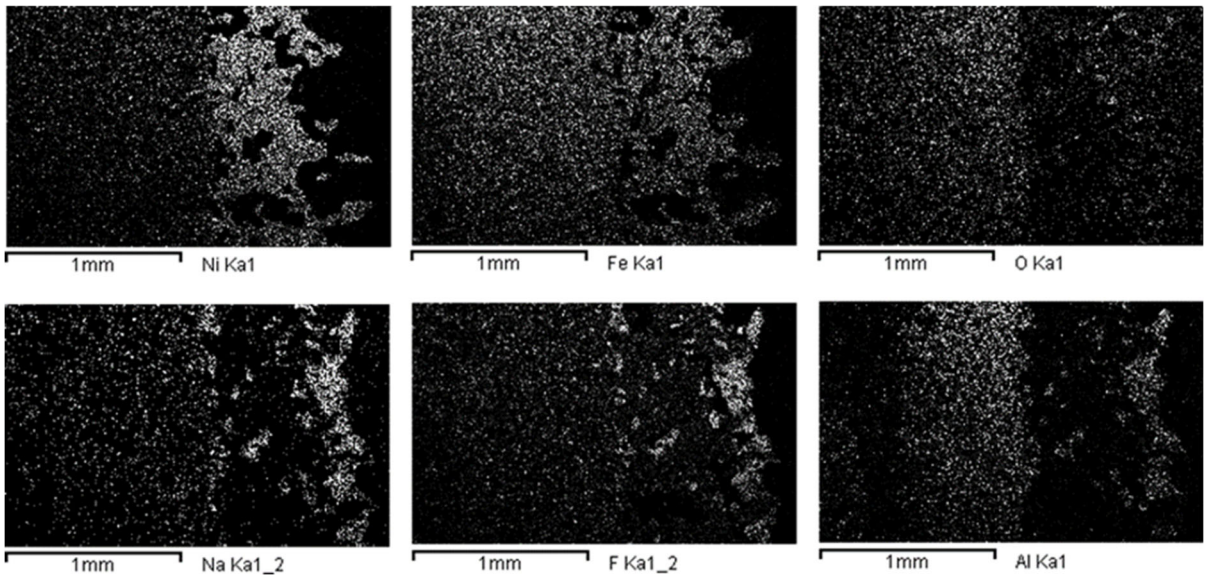

(b)

FIG 15 – (a) Typical microstructure of nickel ferrite sample near the sample-bath interface after 6 hrs corrosion testing in non-saturated cyolite based-melt; (b) EDS elemental mapping confirming the presence of Fe-Ni metallic phase at the sample-bath interface.

Figure 15 shows that there were significant composition changes occurring near the sample-bath interface where Ni-Fe metallic phase was formed. The presence of sodium, fluoride and aluminium in the bulk nickel ferrite sample indicated that the bath penetrated into the sample. A higher magnification of the area designated as 'Area 1' in Figure 15a revealed that there were several different microstructures surrounding the Ni-Fe metallic phases as shown in Figure 16.

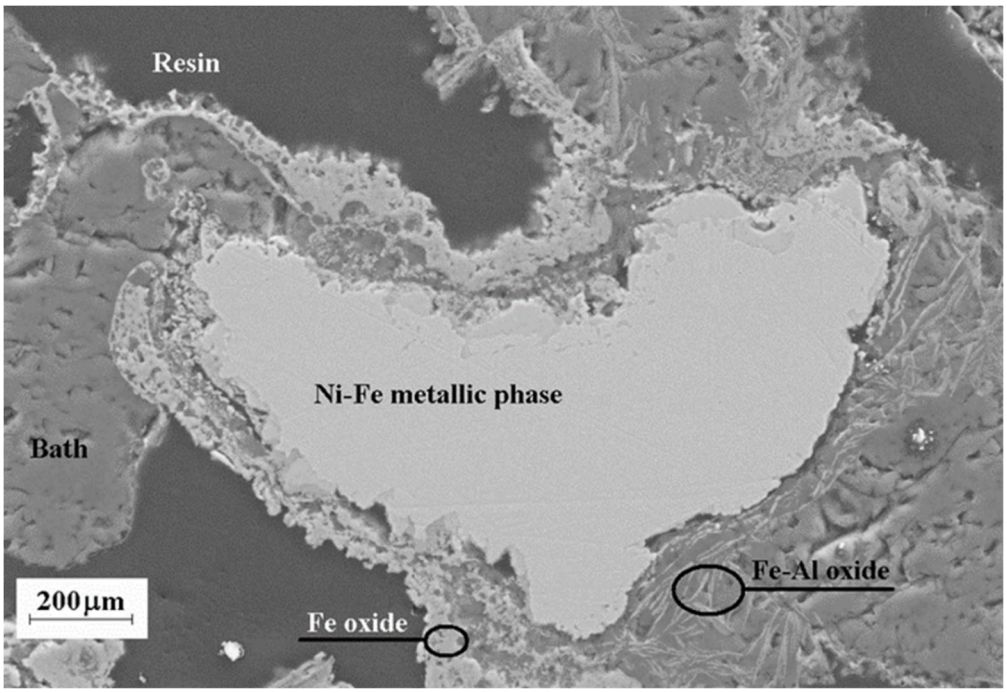

FIG 16 – Higher magnification of the area designated as 'Area 1' in Figure 15a. The phases were suggested by EDS point analysis and elemental mapping.

Dissolution of spinel constituents into cryolite-based melt

The kinetics and the dissolution rate of ferrite and aluminate spinels into cryolite-based melts have been studied elsewhere by the author (Mukhlis, 2015). Plot of $(V/A)(\ln[(c_{sat}-c_0)/(c_{sat}-c)])$ against time time (t) were used to determine the mass transfer coefficient rate (k value) of the process. Here:

V	is the volume of electrolyte in m^3
A	is the surface area of spinel sample that have direct contact with melt in m^2
c_{sat}	is the initial amount of spinel constituent in the melt plus the maximum amount of the spinel constituent that can enter the melt from the sample in wt per cent
$c(t)$	is the time dependent concentration of species in the electrolyte in wt per cent
c_0	is the initial concentration of spinel constituent in melt
k	is the mass transfer coefficient of species from spinel to electrolyte in m/s

The same approach, ie plot of $(V/A)(\ln[(c_{sat}-c_0)/(c_{sat}-c)])$ against time (t), using the data shown in Figure 14, was applied in the current study to determine the k value which then used to calculate the corrosion rate. The projected annual corrosion rate for each spinel samples is tabulated in Table 1.

TABLE 1

Projected corrosion rate of spinels against cryolite-based melt with CR 2.3 at 980°C.

Sample	Constituent	Alumina concentration in melt	Projected corrosion rate (cm/a)
$MgAl_2O_4$	Mg	6 wt%	644×10^3
		11 wt%	798×10^3
$NiAl_2O_4$	Ni	6 wt%	4.7×10^3
		11 wt%	1.03×10^3
$NiFe_2O_4$	Ni + Fe	6 wt%	947×10^3
		11 wt%	461×10^3

Projected corrosion rate was calculated based on the assumption that 1 year is equal to 365 days. The value for $NiFe_2O_4$ is the combination of values for Ni + Fe. As seen in Table 1, the projected corrosion rates for all spinel in cryolite-based electrolyte were very high.

Corrosion of $NiFe_2O_4$, $NiAl_2O_4$, $MgAl_2O_4$ in molten aluminium

The results of the finger test experiments of spinels in molten aluminium at 980°C through ICP analysis are shown in Figure 17. The concentration of spinel constituents – ie magnesium, nickel, and iron – in aluminium were plotted against the sampling time. The non-zero concentration of the constituents at t = 0 represented the impurity levels of the aluminium used in current study before the immersion of the spinel sample, which agreed with the specification from the manufacturer.

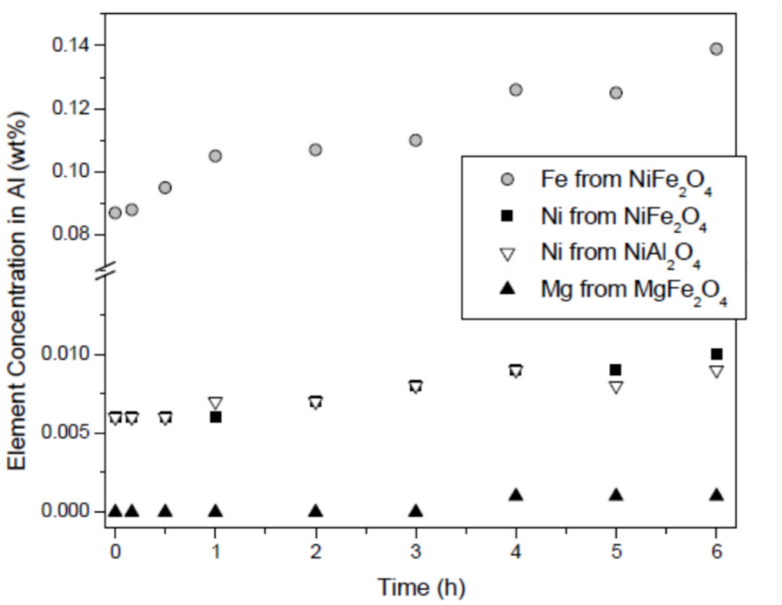

FIG 17 – Element concentrations in molten aluminium from spinel sample.

One can see from Figure 17 that in general, the concentrations of the spinel constituents in aluminium increased with increasing time up to 6 hrs. In agreement with the thermodynamics analysis, $MgAl_2O_4$ sample showed the lowest level of contamination to the aluminium at the end of the 6 hr experiments. The amount of nickel contaminations from $NiAl_2O_4$ and $NiFe_2O_4$ were at the same order of magnitude. The highest contamination in aluminium determined by current study was iron that came from nickel ferrite sample, which reached 0.14 wt per cent after 6 hrs immersion; that was two orders of magnitude higher than the magnesium contamination originated from magnesium aluminate.

Similar to the evaluation on the Spinel-Cryolite system, the rate constant of the corrosion of the spinel due to dissolution of its constituents into molten aluminium (ie mass transfer coefficient) was

evaluated from the experimental data points plotted in the coordinates of $(V/A)(\ln[(c_{sat}-c_0)/(c_{sat}-c)])$ against time (t).

In contrast with the spinel-cryolite system, there were no visible changes of dimension on the spinel sample after 6 hr corrosion test in molten aluminium. Therefore, the confidence level of the corrosion rate value of the spinel-aluminium system is higher than that of spinel-cryolite system. The c_{sat} for Mg, Ni and Fe used in current study were 100, 38.2, and 15.5 wt per cent, respectively, which was determined from the associated Mg-Al, Ni-Al, and Fe-Al phase diagrams constructed using Swinburne University of Technology licensed FactSage™ 6.4. FactSage™ is an integrated database computing systems in chemical thermodynamics developed by Thermfact and GTT-Technologies.

Through the identical approach as the calculation for spinel-cryolite melt system, the projected values of the maximum corrosion rate of spinel due to dissolution of its constituent into molten aluminium were calculated to be 0.3, 2.6, and 78.4 cm/a for $MgAl_2O_4$, $NiAl_2O_4$, and $NiFe_2O_4$, respectively. It should be noted that the corrosion rate for $NiFe_2O_4$ is the summation of the dissolution rate of nickel and iron (refer to Table 2).

TABLE 2

Mass transfer coefficient and projected maximum corrosion rate of spinels constituents against molten aluminium.

Sample	Constituent	Element concentration in Al after 6 hr test	Highest possible mass transfer coefficient	Projected maximum corrosion rate
$MgAl_2O_4$	Mg	0.1×10^{-2} wt%	10.0×10^{-11} m/s	0.3 cm/a
$NiAl_2O_4$	Ni	0.9×10^{-2} wt%	8.25×10^{-10} m/s	2.6 cm/a
$NiFe_2O_4$	Ni	1.0×10^{-2} wt%	7.26×10^{-10} m/s	2.3 cm/a
	Fe	13.9×10^{-2} wt%	2.41×10^{-8} m/s	76.1 cm/a

Based on the data tabulated in Table 2, one can conclude that in the molten aluminium environment, $MgAl_2O_4$ showed the best performance as it had the lowest corrosion rate as well as the lowest contamination to the molten aluminium. The data also revealed that $NiFe_2O_4$ will not be suitable to be applied in direct contact with molten aluminium as it will promote substantial contamination to the metal. The projected corrosion rate of $NiFe_2O_4$ was also significantly high, about 50 times higher than the acceptable corrosion rate of the materials applied in the Hall-Héroult cell, which is supposed to be not higher than 1 to 1.5 cm/a (Xiao *et al*, 1996; Oye and Welch, 1998; Galasiu, Galasiu and Thonstad, 2007).

CONCLUSIONS

The observation on the spinel samples after corrosion testing indicate that $NiFe_2O_4$ has the best corrosion resistance against acidic cryolite-based melt (CR 2.3) compared to the other spinels. After 6 hrs immersion in the melt at 980°C, there were insignificant changes in the dimension of $NiFe_2O_4$ sample from its initial dimension. In contrast, the $MgAl_2O_4$ and $NiAl_2O_4$ samples were corroded heavily. All part of the samples that immersed in the melt disintegrated from the sample bulk and entered the melt. In the case of corrosion test against aluminium, all spinel samples (ie magnesium aluminate, nickel aluminate, and nickel ferrite) showed no dimensional changes macroscopically.

The projected corrosion rates, assuming linear behaviour, of the spinels against the bath were higher than the acceptable corrosion rate of materials applied in the aluminium smelter application. The projected corrosion rates of the spinels against molten aluminium, on the other hand was acceptable except for $NiFe_2O_4$. It was found that the corrosion rate for magnesium aluminate, nickel aluminate, and nickel ferrite against molten aluminium were 0.3, 2.6, and 78.4 cm/a. This result is in agreement with the thermodynamic analysis that suggests $MgAl_2O_4$ is the most stable spinel in aluminium environment compared to the other two spinels.

The nickel in the cryolite-based melt that originated from $NiAl_2O_4$ sample were found to be higher than the solubility limit of the respective element in the given bath composition. This indicate that the corrosion of the spinel not only due to dissolution of the spinel constituent into the bath, but also enhanced with the erosion of the sample. This was supported with the observation on the $NiAl_2O_4$ sample after corrosion test, where all part of the sample immersed in the bath (about 15 mm) was disintegrated from the sample bulk.

The presence of sodium and fluorine in the top part of the samples that far from the immersed section indicate that the cryolite-based melt had a good wettability against spinels; particularly $MgAl_2O_4$ and $NiAl_2O_4$. When the melt wetted the sample, it can readily penetrate into the sample through the sample pores.

The increase of the spinel constituent in the bath over the time for the denser spinel sample was found to be slower than that of high porosity sample. It is then recommended to use a much denser spinel for the aluminium smelter application. The use of denser spinel will reduce the erosion-induced corrosion and the penetration of the bath into the spinel. This however will hinder its industrial application since it will increase the cost and add more complexities to the industry.

Microstructural study on the corroded spinel sample suggested that $MgAl_2O_4$ spinel was unstable in the cryolite-based melt environment as there were no spinel left in the sample even at the section that far from the immersed part of the sample. All magnesium dissolved into the bath, leaving only aluminium oxide in the sample. $NiAl_2O_4$ and $NiFe_2O_4$ appeared to have better resistance to the reaction against cryolite-based melt (kinetically), particularly against alumina-saturated melt, as there were still plenty of spinel left in the sample after 6 hrs immersion. The $NiAl_2O_4$ samples however were susceptible to erosion.

ACKNOWLEDGEMENTS

The first author acknowledges Swinburne University of Technology and Commonwealth Scientific and Industrial Research Organisation (CSIRO) for providing scholarship to conduct the study. The co-supervision of Prof. Geoffrey Brooks, Dr. Kathie McGregor, and Dr. Xiao Yong Yan in the study are also acknowledged.

REFERENCES

ASTM, 2000. ASTM C20-00 Standard test method for apparent porosity, water absorption, apparent specific gravity and bulk density, *ASTM International,* (15).

Bale, C W, Chartrand, P, Degterov, S A, Eriksson, G, Hack, K, Ben Mahfoud, R, Melancon, J, Pelton, A D and Petersen, S, 2002. FactSage thermochemical software and databases, *CALPHAD*, 26(2):189–228.

Galasiu, I, Galasiu, R and Thonstad, J, 2007. *Inert anodes for aluminium electrolysis,* Dusseldorf: Aluminium-Verlag.

Grjotheim, K, Krohn, C, Malinovsky, M, Matiasovsky, K and Thonstad, J, 1982. *Aluminium Electrolysis - Fundamentals of the Hall-Héroult Process,* 2nd edition, Dusseldorf: Aluminium-Verlag.

Haraldsson, J and Johansson, M T, 2020. Effects on primary energy use, greenhouse gas emissions and related costs from improving energy end-use efficiency in the electrolysis in primary aluminium production, *Energy Efficiency*, 13(7):1299–1314.

Kvande, H and Drablos, P A, 2014. The Aluminum Smelting Process and Innovative Alternative Technologies, *Journal of Occupational and Environmental Medicine,* 56:S23–S32.

Kvande, H and Haupin, W, 2001. Inert anodes for Al smelters: Energy balances and environmental impact, *JOM*, 53(5):29–33.

Longbottom, R J, Nightingale, S A and Monaghan, B J, 2014. Thermodynamic considerations of the corrosion of nickel ferrite refractory by Na3AlF6-AlF3-CaF2-Al_2O_3 bath, *Mineral Processing and Extractive Metallurgy, Trans Inst Min Metall C*, 123(2):93–103.

Lorentsen, O A, 2000. Behaviour of nickel, iron and copper by application of inert anodes in aluminium production, Doctoral Thesis, Trondheim: Department of Electrochemistry, Norwegian University of Science and Technology.

Mukhlis, R Z, 2015. Analysis of Spinel Materials for Aluminium Smelter Applications, Doctoral dissertation, Swinburne University of Technology Melbourne, Australia.

Mukhlis, R Z, Rhamdhani, M A, Brooks, G A and Yan, X Y, 2011. Fabrication of spinel composites for sidewall of Al smelter application, In *European Metallurgical Conference* 2011, pp 865–880.

Mukhlis, R Z, Rhamdhani, M A, Brooks, G and McGregor, K, 2014. Wetting characteristics of cryolite-based melts on spinels substrate, *Light Metals 2014,* pp 609–614.

Mukhlis, R, Rhamdhani, M and Brooks, G, 2010. Sidewall materials for the Hall-Heroult process, *Light Metals*, pp 883–888.

Olsen, E and Thonstad, J, 1999a. Nickel ferrite as inert anodes in aluminium electrolysis: Part I Material fabrication and preliminary testing, *Journal of Applied Electrochemistry*, 29(3):293–300.

Olsen, E and Thonstad, J, 1999b. Nickel ferrite as inert anodes in aluminium electrolysis: Part II material performance and long-term testing, *Journal of Applied Electrochemistry*, 29(3):301–311.

Øye, H A and Welch, B J, 1998. Cathode performance: The influence of design, operations, and operating conditions, *JOM,* 50(2):18–23.

Schwarz, H G, 2008. Technology diffusion in metal industries: driving forces and barriers in the German aluminium smelting sector, *Journal of Cleaner Production,* 16(1):S37–S49.

Thonstad, J, Fellner, P, Haarberg, G M, Hives, J, Kvande, H and Sterten, A, 2001. Aluminum electrolysis, *Fundamentals of the Hall-Heroult Process,* 3rd edition, Dusseldorf: Aluminum-Verlag.

Xiao, H, Hovland, R, Rolseth, S and Thonstad, J, 1996. Studies on the corrosion and the behavior of inert anodes in aluminum electrolysis, *Metallurgical and Materials Transactions B*, 27(2):185–193.

Yan, X Y, Mukhlis, R Z, Rhamdhani, M A and Brooks, G A, 2011. Aluminate spinels as sidewall linings for aluminum smelters, *Light Metals 2011*, pp 1085–1090.

Yan, X Y, Pownceby, M I and Brooks, G, 2007. Corrosion behavior of nickel ferrite-based ceramics for aluminum electrolysis cells, *Light Metals 2007*, pp 909–913.

The interaction between slag and MgO refractory at conditions relevant to nickel laterite ore smelting

DOI: 10.62053/GRTD1797

Y H Putra[1], Z Zulhan[2], A D Pradana[3], D R Pradana[4] and T Hidayat[5]

1. Junior Business Analyst, PT Bukit Asam, Tanjung Enim, South Sumatera 31716, Indonesia. Email: yudhithp.13@gmail.com; Previously: Researcher, Metallurgical Engineering Research Group, Faculty of Mining and Petroleum Engineering, Bandung Institute of Technology, Bandung, West Java 40132, Indonesia.
2. Professor, Metallurgical Engineering Research Group, Faculty of Mining and Petroleum Engineering, Bandung Institute of Technology, Bandung, West Java 40132, Indonesia. Email: zulfiadi.zulhan@itb.ac.id
3. Business Development Manager, PT Gunbuster Nickel Industry, Jakarta 12190, Indonesia. Email: gika@bharuna.com
4. Operation Supervisor, PT Gunbuster Nickel Industry, Jakarta 12190, Indonesia. Email: dimas@efi.co.id
5. Lecturer, Metallurgical Engineering Research Group, Faculty of Mining and Petroleum Engineering, Bandung Institute of Technology, Bandung, West Java 40132, Indonesia. Email: t.hidayat@itb.ac.id

ABSTRACT

The high temperature processing of nickel laterite ore is currently dominated by the Rotary Kiln-Electric Furnace (RKEF) technology. The ratio of SiO_2/MgO (S/M) in the ore is one of the critical parameters that determines the success of the RKEF process. Incompatible S/M ratios in the ore can cause aggressive chemical interaction between the slag and MgO refractory. The slag-refractory interaction at conditions relevant to nickel laterite ore smelting was investigated in the present study. Synthetic mixtures representing the slag compositions of nickel laterite ore smelting were prepared by mixing MgO, SiO_2, Al_2O_3, CaO, Fe_2O_3, and Fe and heating the mixtures in steel containers at 1300°C under an argon atmosphere for 3 hrs. Pure MgO crucible were used as containment material in the melting process of the mixtures to represent the MgO refractory. The kinetics of the slag-refractory reaction were investigated using samples with selected initial S/M ratios of 2.0 and 3.0 (wt/wt) (with constant CaO = 3 wt per cent, Al_2O_3 = 5 wt per cent, FeO = 10 wt per cent) by performing melting at 1500°C in MgO crucibles for 5, 30, and 120 mins under an argon atmosphere. The effect of the S/M ratio in slag on the slag-refractory interaction was also investigated by performing melting of mixtures with different initial S/M ratios of 1.75, 2.0, 2.5, and 3.0 (wt/wt) in MgO crucibles at 1500°C for 120 mins under an argon atmosphere. After the melting process, each sample was quenched in water, mounted in resin, ground, polished, and coated. The interaction between the slags and MgO refractory was then evaluated by analysing the polished samples using a scanning electron microscope equipped with an energy dispersive spectroscopy (SEM-EDS). Thermodynamic simulations using FactSage™ 8.0 thermochemical software were performed based on the experimental slag compositions, refractory, and conditions to support the evaluation process. The results show that a higher S/M ratio in slag leads to a higher tendency for the refractory component to dissolve into the slag. A higher S/M ratio in slag also leads to an increasing extent of solid-state diffusion of iron oxide into the remaining refractory grains. The dissolution of MgO into the slag is rapid; the MgO concentration in the final slag increased by 2.4 wt per cent and 5.7 wt per cent at initial S/M ratios of 2.0 and 3.0 wt/wt, respectively, within 5 and 30 mins of the melting process.

INTRODUCTION

The Rotary Kiln – Electric Furnace (RKEF) technology is commonly employed for the production of ferronickel (FeNi) or nickel pig iron (NPI), with nickel and iron contents ranging from 10–30 per cent and 70–90 per cent respectively (Crundwell *et al*, 2011). The simplified flow sheet of RKEF process is provided in Figure 1. The RKEF process involves three primary stages in processing nickel ore. The initial stage entails drying the ore in a rotary dryer at 250°C, which serves to decrease the water content from 30 per cent to 20 per cent. Subsequently, the ore undergoes calcination in a rotary kiln

at temperatures between 750–900°C, during which remaining water content is removed and the nickel oxide and iron oxide are partially reduced by the reductant. The resulting calcine, which is the product from the rotary kiln, is then smelted in an electric furnace at temperatures ranging from 1450–1550°C in order to form and separate the metal product from the slag. In a few RKEF plants, an additional purification step may be carried out using a ladle furnace to reduce impurity content in the final product.

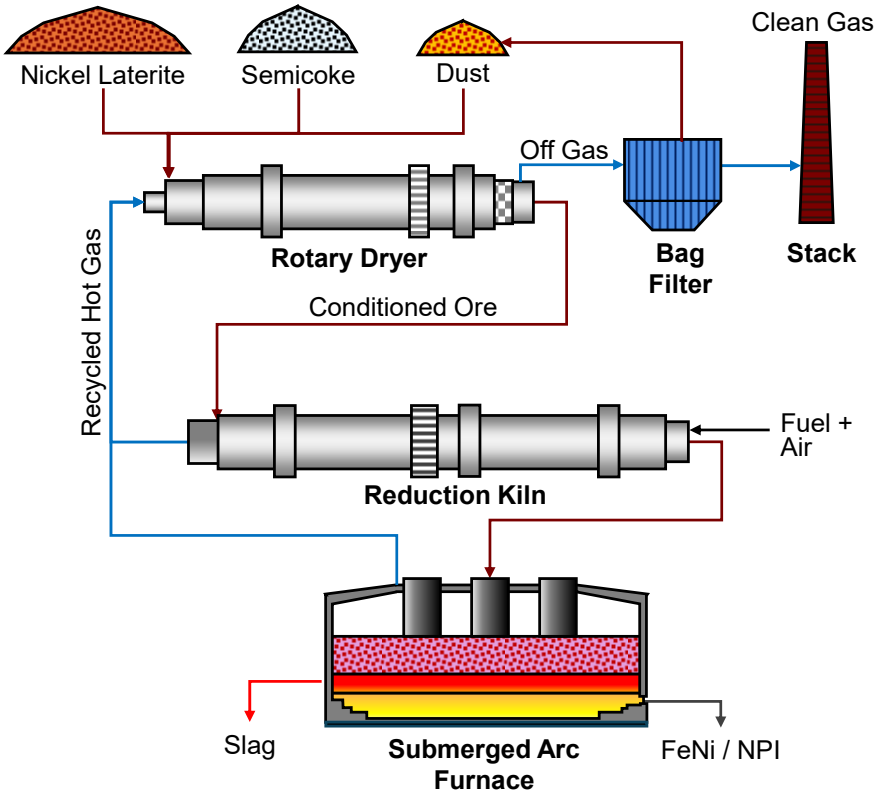

FIG 1 – Simplified flow sheet of RKEF process.

The electric furnace is a widely employed smelting technology in various metal industries. It operates on the principle of resistance heating, where the burden materials such as calcine, slag, and molten metal are heated through the application of electric current (Degel *et al*, 2007). To withstand the high temperatures and harsh conditions within the furnace, refractory materials are used for lining purposes. In the nickel industry, magnesia (MgO) refractory is utilised as a lining for the electric furnace. This choice is due to the high melting point of magnesia, its favourable mechanical properties at elevated temperatures, and its resistance to adverse environments. However, there are a few disadvantages of using MgO refractory, such as it has a very high conductivity, which can result in significant heat loss during the smelting process (Ruh and McDowell, 1962) and it has a relatively high thermal expansion compared to other types of refractories (Gangler, 1950).

The malfunction of refractory material not only leads to a loss of productivity but also poses risks to the surrounding environment (Zhang and Lee, 2013). Consequently, the investigation of the interaction between slag and refractories has garnered significant attention from researchers (Huang, Xue and Wang, 2017; Sagadin *et al*, 2016, 2017, 2018a, 2018b, 2021; Wagner *et al*, 2017) within the nickel industry. Generally, refractory damage can be attributed to three primary factors: chemical attack, thermal pressure, and mechanical pressure. Among these, chemical attack predominantly occurs as a result of the chemical interaction between the refractory and slag. In a number of electric furnaces, water-cooling components are incorporated into the lining structure to absorb heat. This facilitates the formation of a thin freeze lining, which serves to protect the refractories from corrosion caused by the slag (Kotzé, 2002). While in some of electric furnaces, the water-cooling components are not available, hence the furnace integrity relies heavily on the chemical interaction between slag and refractory material. This study aims to investigate the slag and refractory interaction under conditions relevant to ferronickel or NPI smelting as a function of

initial SiO_2/MgO ratio in slag and melting time. Synthetic slag was used to replicate the industrial slag and a dense pure MgO crucible was used to simulate the actual refractory material. The use of a dense MgO crucible eliminates the effects of physical infiltration of slag due to the heterogeneity and porosity commonly found in the refractory material, thus focusing the investigation mainly on the chemical attack of slag on the refractory material.

EXPERIMENTAL

Preparation and characterisation of synthetic slag

The synthetic slag used in this experiment was produced by mixing high purity reagents, including MgO, SiO_2, Al_2O_3, CaO, Fe_2O_3, and Fe. These reagents were then blended with specific compositions to achieve constant FeO, Al_2O_3, and CaO contents of 10 per cent, 5 per cent, and 3 per cent, respectively, in the slag. The chosen compositions were based on typical slag compositions in one of the ferronickel or NPI plants. As for the SiO_2 and MgO, their compositions were adjusted so that the final SiO_2/MgO or S/M ratios were set around 1.75, 2.0, 2.5, and 3.0. The reagents were mixed and homogenised using a mortar for 10 mins. The resulting mixtures were then placed in cylindrical stainless steel 304 crucibles with dimension of 20 mm in diameter and 60 mm in height. The crucibles were then positioned on an alumina boat to enable heating using a horizontal tube furnace. The synthetic slags were heated in the horizontal tube furnace at a temperature of 1300°C, aimed at pre-reacting the oxides within the synthetic slags before melting them with the MgO crucible. The synthetic slags obtained from the heating in the horizontal tube furnace were then homogenised again using a mortar for 10 mins. The compositions of the synthetic slags with different S/M ratios were checked using scanning electron microscope with energy dispersive spectroscopy (SEM-EDS). The results of the SEM-EDS semi-quantitative analysis for all samples are presented in Table 1.

TABLE 1

Semi-quantitative EDS-measured composition of synthetic slag.

Target S/M	Composition (wt%)					
	SiO_2	MgO	FeO	Al_2O_3	CaO	S/M
1.75	51.9	31.1	8.9	5.4	2.6	1.67
2.0	56.2	27.2	8.6	4.8	2.9	2.07
2.5	60.4	24.2	8.6	4.4	2.4	2.50
3	62.4	21.0	10.1	4.0	2.5	2.97

Melting in vertical tube furnace

There are several experimental methods commonly used to study the slag-refractory interaction, including (Zhang and Lee, 2004):

1. Button or sensible drop test.
2. Dipping, immersion, or finger test.
3. Crucible, cavity, cup, or brick.
4. Induction furnace test.
5. Rotating finger test.
6. Rotating slag test

The interaction between slag and refractory in this study was conducted using the cup test technique. This technique is easier to implement and ensures that the entire slag interacts with the refractory compared to other techniques, such as the finger test. However, this technique also has limitations, such as the inability to study the corrosion effects of fluid movement and the tendency of slag samples to become saturated due to the significantly smaller proportion of slag compared to the

refractory. In industrial settings, the proportion of slag should be much larger than that of the refractory. The synthetic slag was weighed at 1.3 g and then placed into the MgO crucible. The MgO crucible with dimension of 16 mm in diameter and 20 mm in height was used. The fusion of synthetic slag with the MgO refractory was carried out using a vertical tube furnace. The sample was suspended using molybdenum wire and held within the hot zone of the furnace under argon atmosphere at 1500°C for 5, 30, and 120 mins. After melting, the samples were rapidly quenched in water.

Product preparation and examination

The quenched samples were dried and embedded in resin to prevent them from breaking during the sample preparation process. The samples were then cut in half at their midsection using a ceramic cutter, remounted in resin, and polished using an automated polishing device. The polished samples obtained from the experiments were examined using an optical microscope (Jiangxi Phoenix L2030A Trinocular Microscope) and semi-quantitatively analysed using scanning electron microscope with energy dispersive spectroscopy (SEM-EDS, JEOL NeoScope JCM-7000). The semi-quantitative SEM-EDS analysis was conducted at the refractory-slag interface at 12 different locations distributed approximately 0.5 mm towards the refractory and 0.5 mm towards the slag, as shown in Figure 2. Various reference materials were used to validate the accuracy of the compositional analysis by the EDS detector. The reference materials used in the present measurement were Basaltic glass (NMNH 113498-1) and Springwater Olivine (USNM 2566) of the Smithsonian Microbeam Standards obtained from the Smithsonian National Museum of Natural History, USA. It was observed that the compositions measured by EDS were within a deviation of less than 1.4 per cent by weight compared to those reported in the reference certificates.

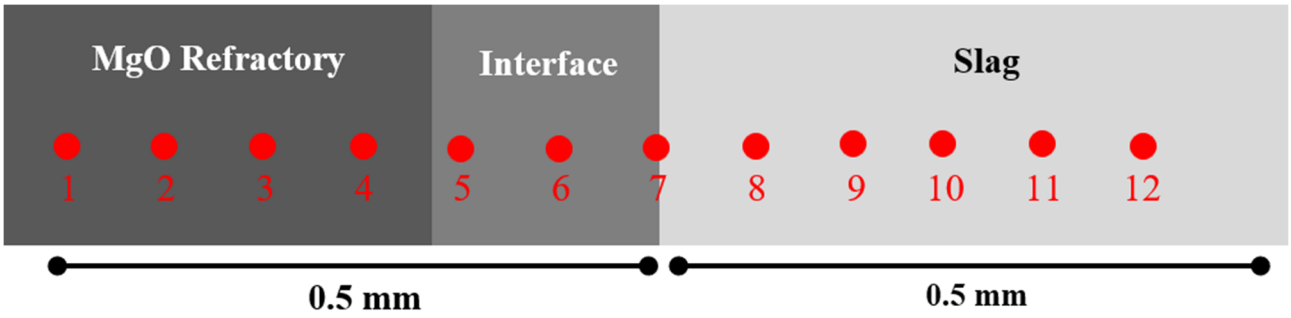

FIG 2 – Illustration of semi-quantitative analysis of composition along refractory and slag interface.

RESULTS AND DISCUSSION

The reaction kinetics of MgO dissolution from MgO refractory into slag

The kinetics of MgO dissolution from the refractory into the slag were investigated at a temperature of 1500°C using synthetic slags with initial SiO_2/MgO (S/M) ratios of 2.00 and 3.00, with melting times varied between 5, 30, and 120 mins. An example of secondary electron image from kinetic experiments using a mixture with an initial S/M ratio of 3.00 reacted at 1500°C can be seen in Figure 3. After melting for 5 mins, the sample shows both slag and several solid particles (see Figure 3a). The solid particles appear to be part of oxides from the initial synthetic slag mixture, which are in the process of dissolving into the liquid slag phase. A fully liquid slag is observed after melting for 30 mins (see Figure 3b). After 120 mins of melting, slag along with olivine is observed (see Figure 3c). It is worth noting that the surface of the MgO refractory appears relatively smooth after melting for 5 and 30 mins compared to after 120 mins of melting. The relatively smooth MgO surface indicates the ongoing dissolution process of solid MgO into the liquid slag.

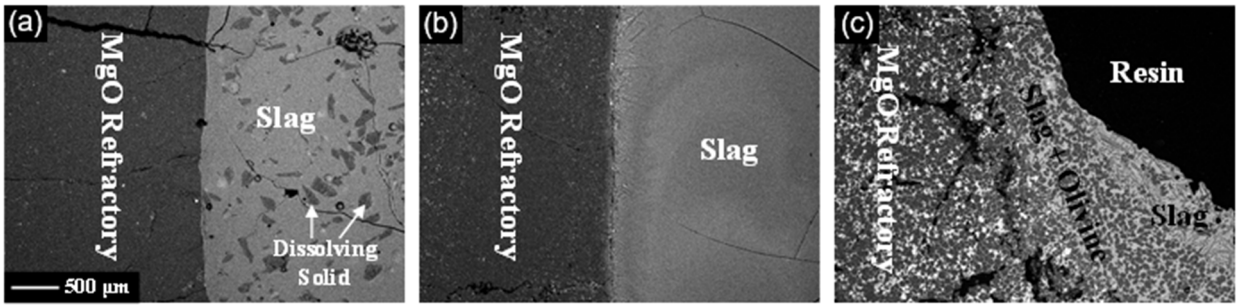

FIG 3 – Examples of secondary electron images from samples melted at 1500°C with an initial SiO_2/MgO ratio in slag of 3.00 for melting times of: (a) 5 mins; (b) 30 mins; and (c) 120 mins.

The semi-quantitative EDS measured compositions of the samples along refractory and slag interface from kinetic experiments using samples with initial S/M ratios of 2.00 and 3.00 are provided in Tables 2 and 3, respectively. The compositions of the dominant components, ie MgO, SiO_2, and FeO, are plotted in Figures 4 and 5. The dissolution of MgO appears to be rapid so that after the reaction continued from 5 mins to 30 mins, the MgO concentration in slag increased significantly, approaching the MgO concentration from melting for 120 mins. On the other hand, SiO_2 concentration in slag continuously decreases due to dilution by the dissolving MgO. There appears to be no clear trend regarding FeO concentration in slag with melting time. In the case of the MgO refractory composition, it appears to remain unchanged in most of experiments, except for the experiment using a sample with an initial S/M ratio in slag of 3.00 and a melting time of 120 mins, which showed a significant increase in FeO concentration within the refractory.

TABLE 2

Semi-quantitative EDS measured composition along refractory-slag interface from samples melted at 1500°C with an initial SiO_2/MgO ratio in slag of 2.00 for melting times between 5 and 120 mins.

Sample		Position											
		1	2	3	4	5	6	7	8	9	10	11	12
t = 5 min	MgO	98.6	98.9	98.2	99.0	98.7	98.6	87.8	30.6	30.3	24.7	24.8	26.9
	SiO_2	0.7	0.6	0.4	0.3	0.3	0.5	0.7	53.5	51.7	56.1	56.3	55.3
	Al_2O_3	0.3	0.3	0.4	0.3	0.5	0.4	2.3	2.7	5.1	5.2	5.6	5.3
	CaO	0.2	0.1	0.7	0.2	0.1	0.1	0.3	1.5	2.5	2.6	2.7	2.6
	FeO	0.2	0.2	0.5	0.1	0.4	0.4	8.9	11.7	10.4	11.4	10.7	10.0
t = 30 min	MgO	98.9	99.0	98.7	98.4	97.9	95.7	82.9	45.3	37.3	30.6	31.8	29.3
	SiO_2	0.4	0.3	0.3	0.7	0.6	0.8	1.1	45.7	48.4	51.0	50.4	52.3
	Al_2O_3	0.5	0.5	0.5	0.4	0.4	0.6	0.3	0.9	3.6	5.2	4.9	5.1
	CaO	0.1	0.0	0.1	0.2	0.1	0.2	0.2	0.4	1.6	2.7	2.1	2.6
	FeO	0.2	0.2	0.5	0.3	1.1	2.7	15.5	7.7	9.1	10.5	10.8	10.8
t = 120 min	MgO	98.6	98.1	98.1	96.4	95.5	92.3	54.3	37.8	34.0	32.4	32.3	31.4
	SiO_2	0.3	0.3	0.3	0.8	0.3	0.5	42.0	50.7	49.1	48.4	49.5	52.0
	Al_2O_3	0.4	0.3	0.5	0.6	0.7	1.1	1.5	3.3	5.5	6.5	6.0	4.5
	CaO	0.0	0.1	0.0	0.0	0.0	0.1	0.1	1.3	2.5	3.4	3.1	3.2
	FeO	0.6	1.2	1.1	2.2	3.4	6.0	2.1	6.9	8.9	9.4	9.1	8.9
		REFRACTORY						OLIVINE	SLAG				

TABLE 3

Semi-quantitative EDS measured composition along refractory-slag interface from samples melted at 1500°C with an initial SiO_2/MgO ratio in slag of 3.00 for melting times between 5 and 120 mins.

Sample		Position											
		1	2	3	4	5	6	7	8	9	10	11	12
t = 5 min	MgO	98.8	97.6	98.8	98.6	97.6	96.4	85.9	26.5	26.7	26.5	26.0	24.2
	SiO_2	0.6	1.0	0.6	0.6	1.2	1.2	1.7	58.1	59.4	59.8	60.5	59.5
	Al_2O_3	0.5	0.7	0.4	0.6	0.6	0.5	0.8	4.0	3.5	3.8	4.0	4.2
	CaO	0.2	0.3	0.1	0.1	0.2	0.3	1.9	2.8	2.4	2.3	2.4	2.9
	FeO	0.0	0.3	0.2	0.1	0.5	1.6	9.8	8.6	8.0	7.7	7.1	9.2
t = 30 min	MgO	98.5	98.8	98.1	97.9	97.2	94.3	67.6	39.1	30.7	27.4	31.0	29.9
	SiO_2	0.1	0.3	0.8	0.5	0.5	1.2	6.0	50.2	54.8	56.9	54.6	55.7
	Al_2O_3	0.5	0.6	0.6	0.6	0.6	0.6	2.2	1.5	3.4	3.9	4.0	4.2
	CaO	0.0	0.1	0.1	0.1	0.1	0.2	0.2	0.7	2.0	2.4	2.0	2.2
	FeO	0.8	0.3	0.4	0.9	1.6	3.7	24.1	8.5	9.2	9.4	8.4	8.0
t = 120 min	MgO	84.1	84.8	84.7	79.3	65.4	68.6	46.0	41.1	40.1	31.2	30.9	28.9
	SiO_2	3.7	1.0	1.3	1.4	6.5	2.2	32.6	46.0	46.6	50.2	51.4	52.5
	Al_2O_3	3.0	1.0	0.6	1.1	1.6	1.4	4.9	4.2	4.1	6.5	5.1	5.9
	CaO	0.9	0.6	0.5	0.8	3.5	0.8	2.5	2.1	1.8	3.3	2.4	2.6
	FeO	8.4	12.6	13.0	17.4	23.1	27.0	14.0	6.6	7.4	8.8	10.3	10.3
		REFRACTORY						OLIVINE	SLAG				

The bulk compositions of liquid slag (the compositions of liquid slag at the furthest position from the refractory, ie at point 12) from the kinetic experiments using samples with initial S/M ratios in slag of 2.00 and 3.00 are provided in Figure 6a and 6b, respectively. The increasing MgO and decreasing SiO_2 in the slag can be seen clearly in both figures. Both of these lead to an increasing S/M ratio in the final liquid slag with increasing melting time, as shown in Figure 6c. The dissolution of MgO is rapid, so as the reaction proceeds from 5 mins to 30 mins, the MgO concentration in the slag increases significantly by 2.4 wt per cent and 5.7 wt per cent for initial S/M ratios of 2.0 and 3.0 wt/wt, respectively. However, when the reaction proceeds from 30 mins to 120 mins, the dissolution of MgO is less rapid and approaches completion. The slowdown in the dissolution of MgO is possibly due to the reduced driving force for the MgO dissolution as the liquid approaches MgO saturation condition, which later can lead to the formation of olivine precipitates on the MgO surface.

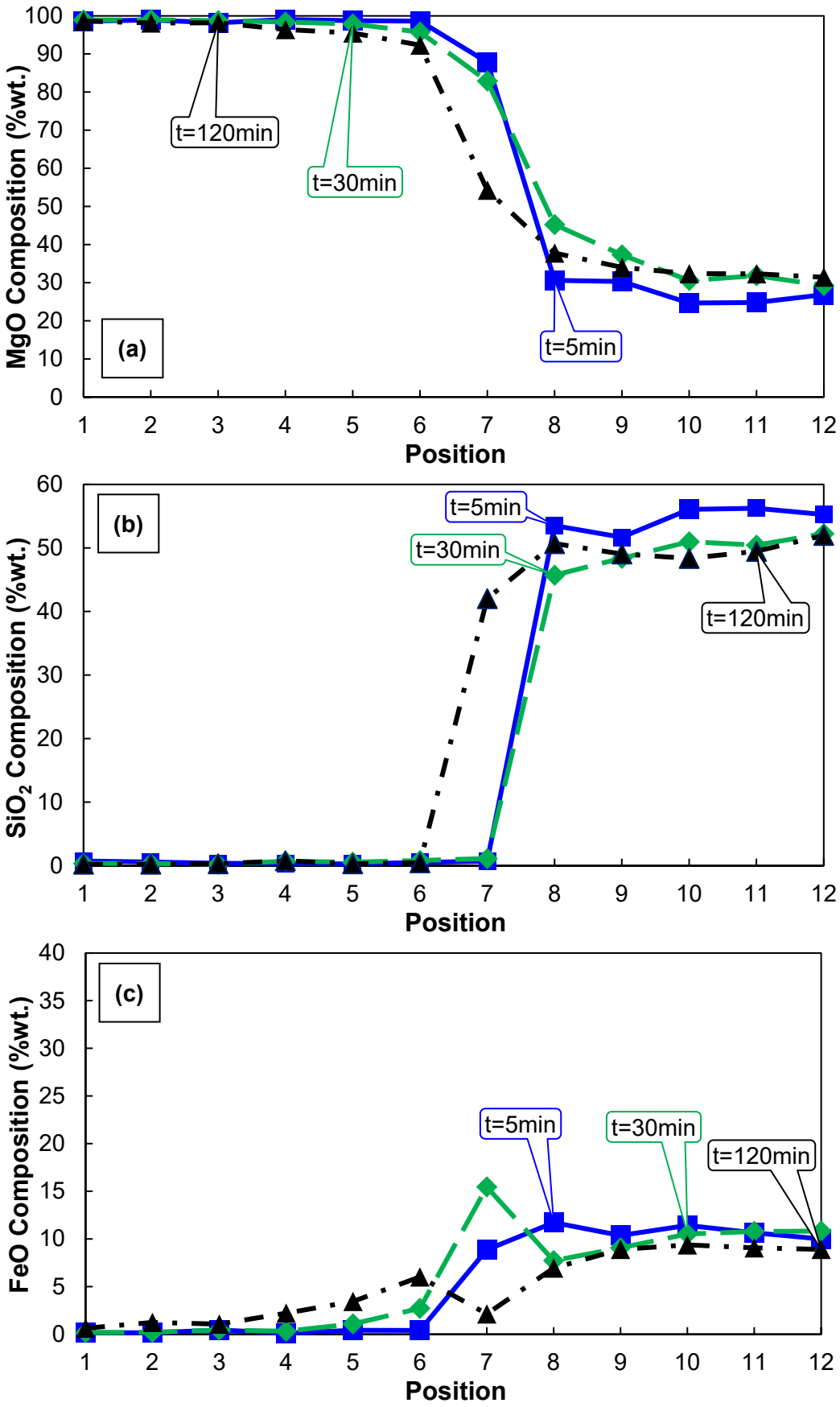

FIG 4 – Semi-quantitative compositional analysis along refractory-slag interface from samples melted at 1500°C with an initial SiO_2/MgO in slag ratio of 2.00 for melting time between 5 and 120 mins: (a) MgO composition; (b) SiO_2 composition; and (c) FeO composition.

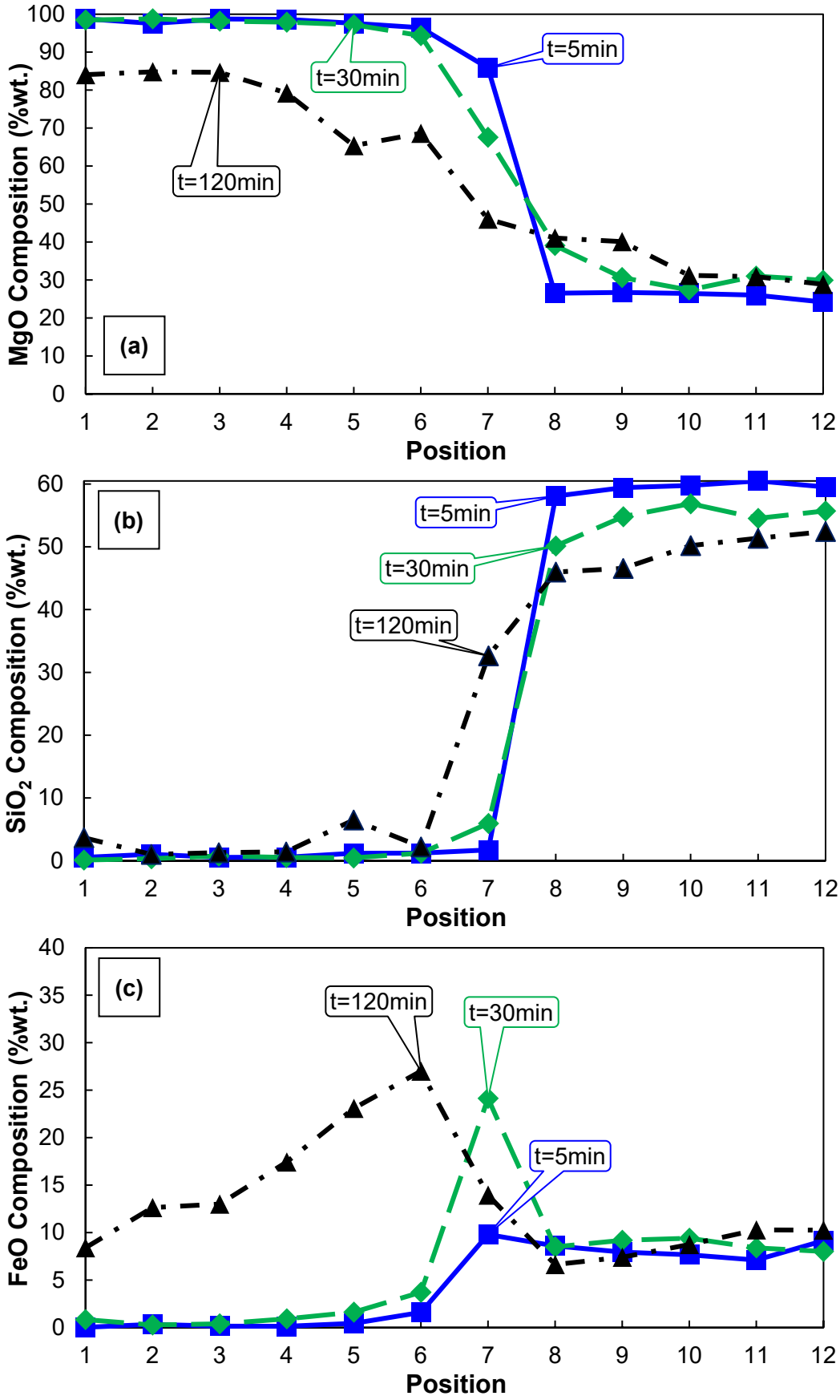

FIG 5 – Semi-quantitative compositional analysis along refractory-slag interface from samples melted at 1500°C with an initial SiO_2/MgO ratio in slag of 3.00 for melting time between 5 and 120 mins: (a) MgO composition; (b) SiO_2 composition; and (c) FeO composition.

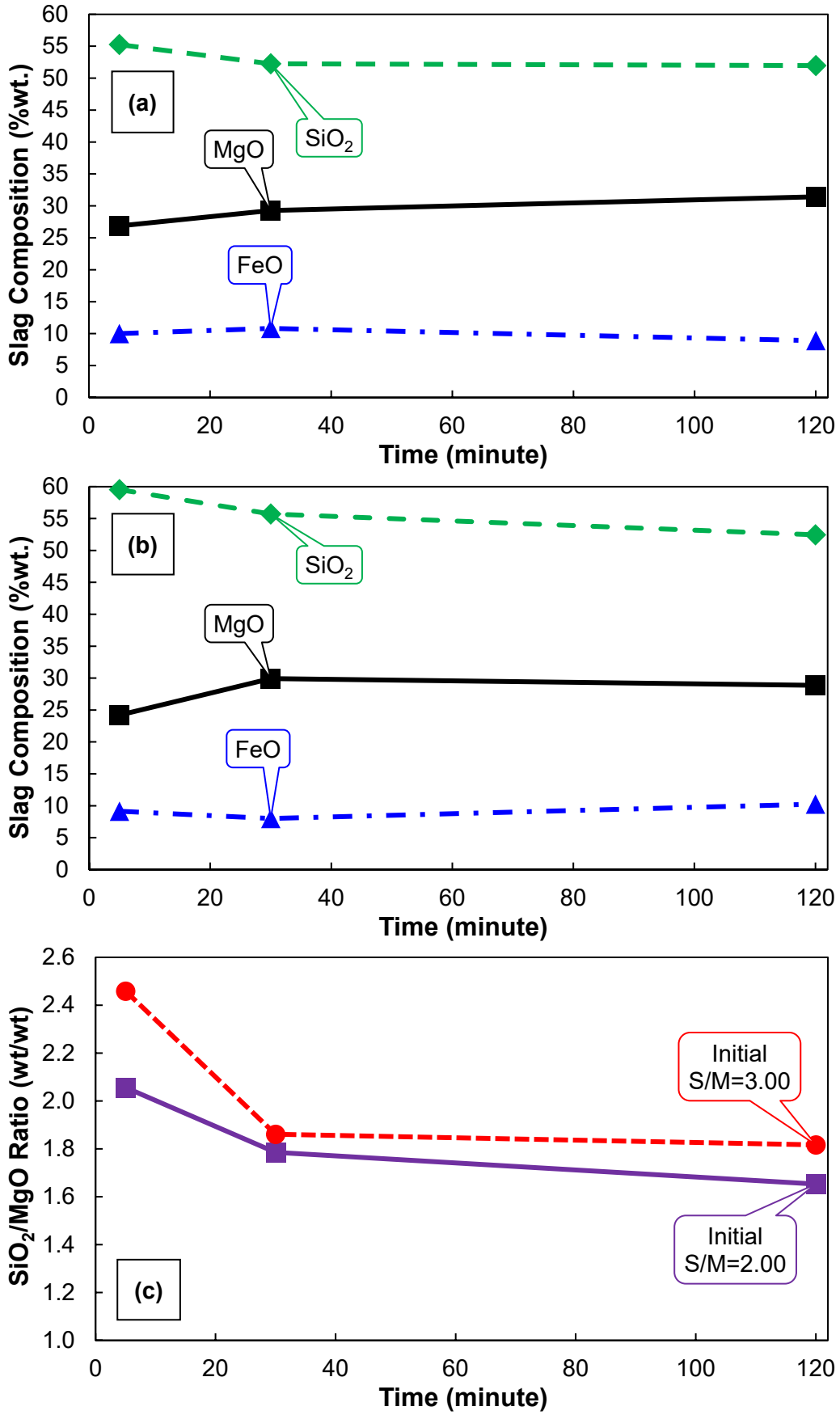

FIG 6 – Bulk composition of liquid slag from semi-quantitative compositional analysis of samples melted at 1500°C for melting time between 5 and 120 mins: (a) Sample having initial SiO_2/MgO ratio in slag of 2.00; (b) Sample having initial SiO_2/MgO ratio in slag of 3.00; and (c) SiO_2/MgO ratio in the final slag.

The pseudo-ternary diagram MgO-FeO-SiO_2, at constant CaO content of 3 wt per cent and Al_2O_3 content of 5 wt per cent, relevant to the slag system in the present study, is shown in Figure 7. The diagram was calculated using FactSage™ 8.0 (Bale *et al*, 2011) with the liquid Fe activity set to 0.9, corresponding to the activity of iron in the NPI metal. The initial slag compositions for samples with initial S/M ratios in slag of 2.00 and 3.00 are plotted in the figure. Additionally, the slag compositions from samples melted at 1500°C with initial S/M ratios in slag of 2.00 and 3.00 for melting times of 5 mins, 30 mins, and 120 mins are also included in the figure. Contacting the mixtures with MgO refractory at 1500°C results in the movement of the liquid slag composition toward the MgO corner of the ternary diagram. Theoretically the movement of the liquid slag should conclude at the liquidus of olivine for 1500°C, where the liquid slag is saturated by MgO and olivine solid is formed. However, the measured liquid slag composition extends beyond the 1500°C liquidus. This discrepancy may arise due to several reasons, including inaccurate liquids prediction by FactSage™ due to an unoptimised database, inaccuracy in temperature set-up during melting experiments, inclusion of olivine solid in the measurement of liquid slag composition, or chemical segregation of the liquid slag during cooling which results in the measured slag composition not accurately representing its actual composition at high temperature.

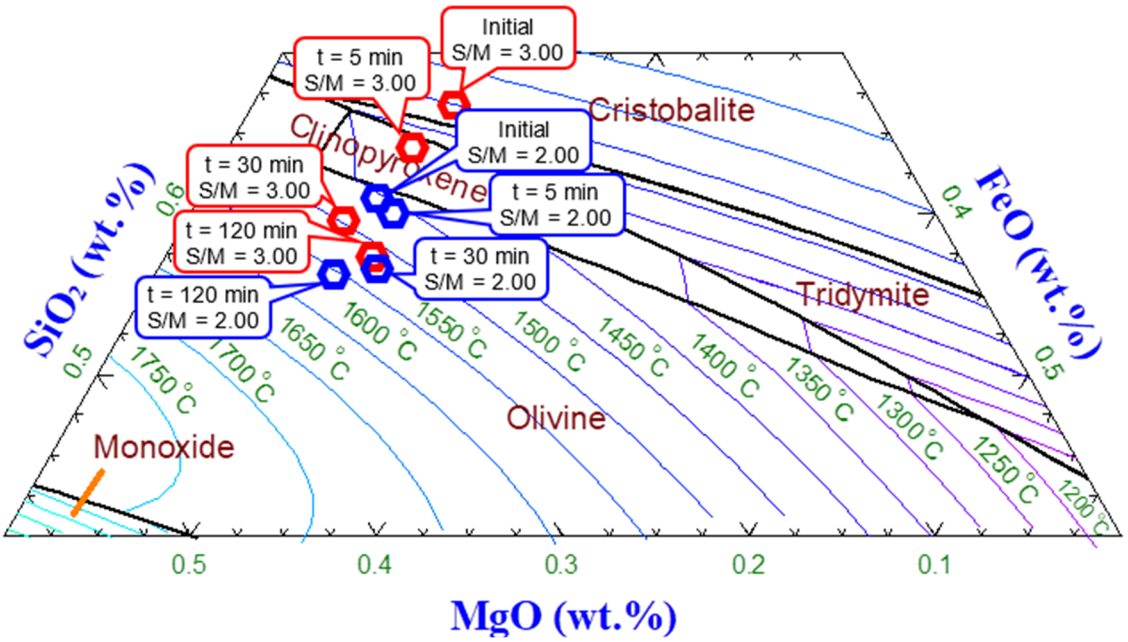

FIG 7 – FactSage™ calculated pseudo-ternary diagram of MgO-FeO-SiO_2 at CaO = 3 wt per cent and Al_2O_3 = 5 wt per cent in equilibrium with liquid Fe (αFe_e = 0.9).

The effect of SiO_2/MgO ratio in the initial slag on the interaction between slag and MgO refractory

The effect of initial slag composition on the interaction between slag and MgO refractory was investigated by conducting melting of samples with initial SiO_2/MgO (S/M) ratios in slag of 1.75, 2.00, 2.50, and 3.00 at 1500°C. A melting time of 120 mins was selected to ensure that the interaction between slag and refractory approaches completion, as demonstrated by the melting time variation experiments. Moreover, the 120 mins melting time was chosen since it closely resembles the residence time of melts in the electric furnace in the industrial practice. The secondary electron image and elemental mapping of the melted samples with various initial S/M ratios in slag at 1500°C are provided in Figure 8.

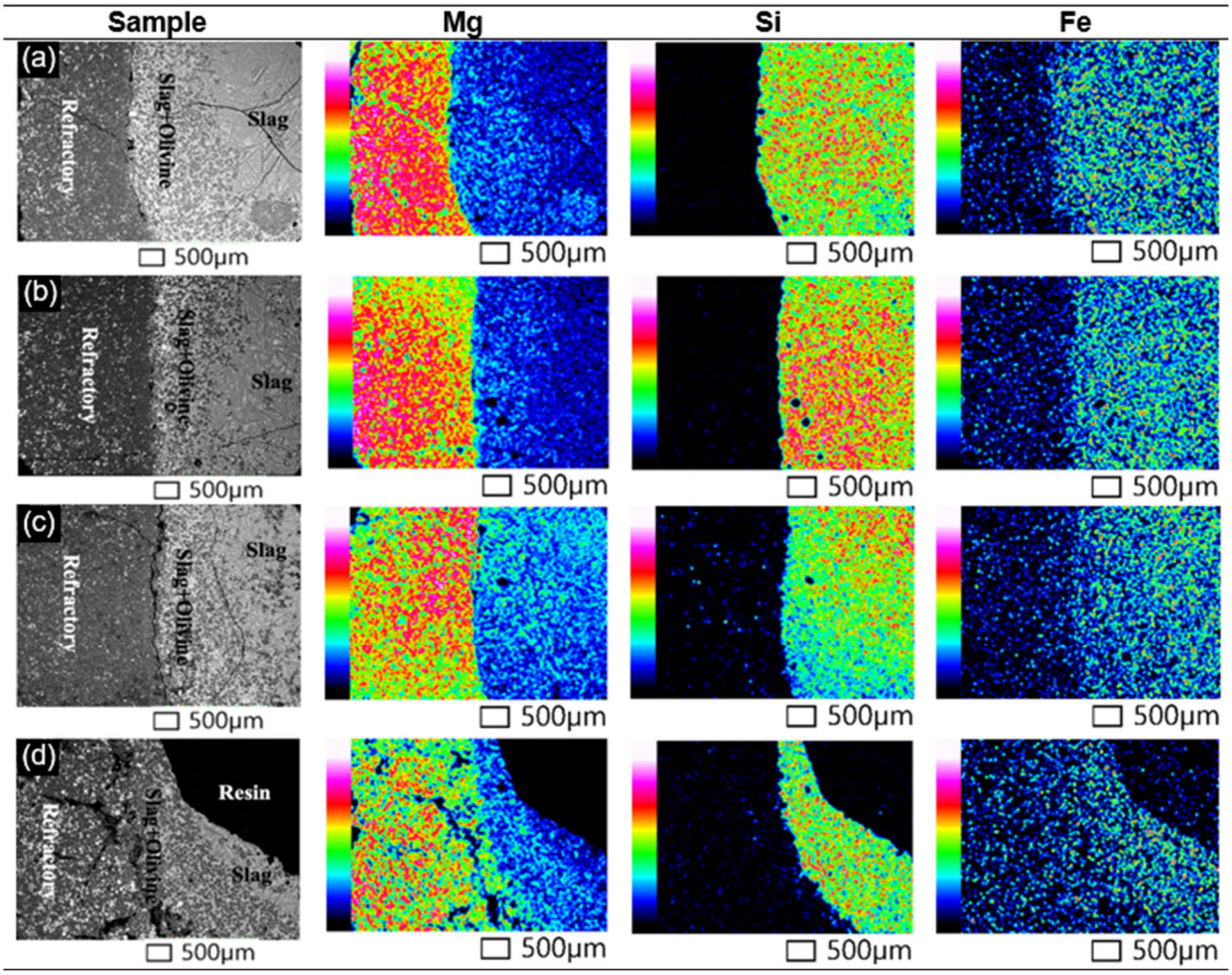

FIG 8 – Secondary electron image and elemental mapping from samples melted at 1500°C for melting time of 120 mins with initial SiO_2/MgO ratios in slag of: (a) 1.75; (b) 2.00; (c) 2.50; and (d) 3.00.

All samples exhibit areas of slag, slag-olivine mixture, and dense MgO. The sample with an initial S/M ratio of 3.00 shows a smaller slag area (see Figure 8d) due to a more extensive reaction between the slag and the MgO refractory. The results of the mapping analysis of Mg and Fe elements in the samples indicate that as the S/M ratio of the slag increases, the interaction between slag and the refractory material becomes more significant. This is evident through the decreasing intensity of Mg and increasing Fe intensity in the crucible. The penetration of FeO into the MgO crucible appears to be more pronounced than that of SiO_2. This phenomenon may be attributed to the ability of FeO to diffuse through and combine with the MgO monoxide solid solution.

The semi-quantitative EDS measured composition of the samples along the refractory and slag interface is provided in Table 4, with the compositions of the dominant components, MgO, SiO_2, and FeO, plotted in Figure 9. The experimental results indicate that the MgO concentration in most of the slags increases after the melting experiments, indicating the dissolution of MgO from the refractory into the slag (see Figure 9a). Conversely, the SiO_2 concentration in the slags decreases after the melting experiments due to dilution by dissolved MgO (see Figure 9b). There is no significant penetration of the MgO solid by the SiO_2. However, the most significant penetration of the MgO solid was by FeO, as clearly observed in the sample with an initial S/M ratio in slag of 3.00, resulting in FeO concentrations in the MgO refractory ranging from 8.4 to 27 wt per cent (see Figure 9c).

TABLE 4

Semi-quantitative EDS measured composition along refractory-slag interface from samples melted at 1500°C for melting time of 120 mins with initial SiO_2/MgO ratios in slag between 1.75 and 3.00.

Sample		Position											
		1	2	3	4	5	6	7	8	9	10	11	12
Initial S/M = 1.75	MgO	98.5	98.4	98.3	97.3	96.0	93.0	90.2	45.1	41.7	37.9	41.5	38.3
	SiO_2	0.2	0.4	0.1	0.2	0.2	0.3	0.6	45.2	47.8	47.2	46.8	46.3
	Al_2O_3	0.5	0.5	0.7	0.5	0.7	1.0	1.9	2.9	3.4	4.2	4.3	3.8
	CaO	0.1	0.1	0.0	0.1	0.1	0.1	0.2	0.9	1.6	2.0	0.9	4.3
	FeO	0.7	0.7	1.0	1.9	3.1	5.6	7.1	5.9	5.5	8.6	6.5	7.4
Initial S/M = 2.00	MgO	98.6	98.1	98.1	96.4	95.5	92.3	54.3	37.8	34.0	32.4	32.3	31.4
	SiO_2	0.3	0.3	0.3	0.8	0.3	0.5	42.0	50.7	49.1	48.4	49.5	52.0
	Al_2O_3	0.4	0.3	0.5	0.6	0.7	1.1	1.5	3.3	5.5	6.5	6.0	4.5
	CaO	0.0	0.1	0.0	0.0	0.0	0.1	0.1	1.3	2.5	3.4	3.1	3.2
	FeO	0.6	1.2	1.1	2.2	3.4	6.0	2.1	6.9	8.9	9.4	9.1	8.9
Initial S/M = 2.50	MgO	98.1	96.2	95.2	93.1	93.7	92.3	49.1	40.5	37.3	27.4	29.8	31.6
	SiO_2	0.4	0.4	0.7	1.0	0.1	0.3	31.3	46.2	49.6	50.0	51.6	53.8
	Al_2O_3	0.5	0.6	0.6	1.0	1.0	1.3	2.7	4.3	4.1	8.5	5.8	4.3
	CaO	0.1	0.4	0.1	0.7	0.0	0.1	2.4	1.9	1.5	3.6	3.0	2.3
	FeO	1.0	2.4	3.4	4.3	5.2	6.0	14.5	7.1	7.5	10.5	9.8	8.1
Initial S/M = 3.00	MgO	84.1	84.8	84.7	79.3	65.4	68.6	46.0	41.1	40.1	31.2	30.9	28.9
	SiO_2	3.7	1.0	1.3	1.4	6.5	2.2	32.6	46.0	46.6	50.2	51.4	52.5
	Al_2O_3	3.0	1.0	0.6	1.1	1.6	1.4	4.9	4.2	4.1	6.5	5.1	5.9
	CaO	0.9	0.6	0.5	0.8	3.5	0.8	2.5	2.1	1.8	3.3	2.4	2.6
	FeO	8.4	12.6	13.0	17.4	23.1	27.0	14.0	6.6	7.4	8.8	10.3	10.3
		REFRACTORY						OLIVINE		SLAG			

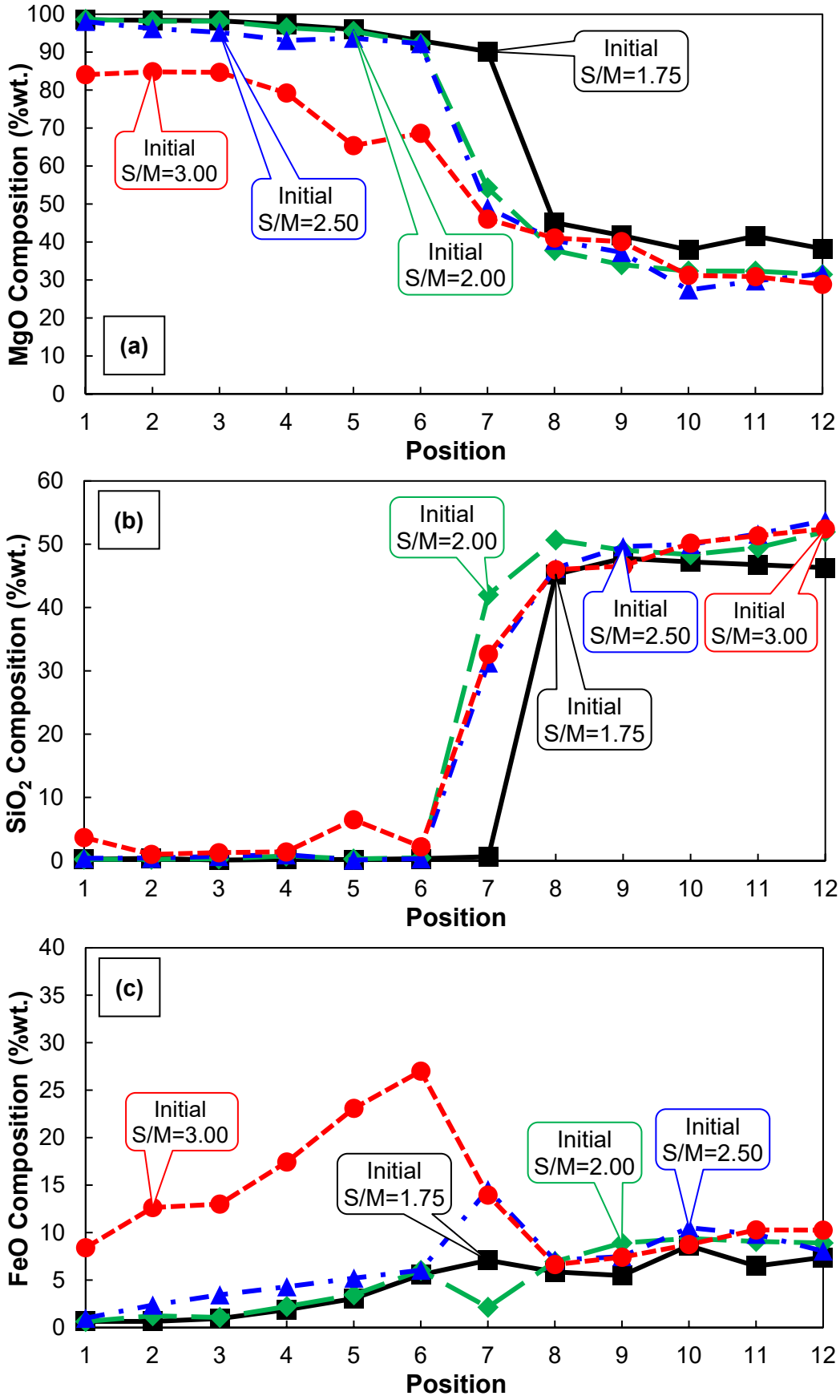

FIG 9 – Semi-quantitative compositional analysis along refractory-slag interface from samples melted at 1500°C for 120 mins with initial SiO_2/MgO ratios in slag between 1.75 and 3.00: (a) MgO composition; (b) SiO_2 composition; and (c) FeO composition.

The corrosion mechanism of MgO refractory by slag

The phases and their compositions resulting from the interaction between MgO refractory and slag at 1500°C are predicted using FactSage™, as shown in Figure 10. The trends demonstrated by FactSage™ predictions can serve as a guide for understanding the refractory-slag interaction. In the case of sample with an initial SiO_2/MgO (S/M) ratio in slag of 2.00, the slag is entirely liquid and can accommodate MgO up to 29.4 wt per cent. Further addition of MgO leads to the formation of olivine; olivine forms when the ratio of MgO to slag is 4:96. A higher ratio of MgO to slag above 30:70 leads to the stabilisation of monoxide together with traces of olivine. For sample with an initial S/M ratio in slag of 3.00, the slag is fully liquid and becomes saturated with olivine at a ratio of MgO to slag of 10:90. As the ratio of MgO to slag reaches above 33:67, the slag dissipates and is replaced by monoxide with traces of olivine. In general, the phases predicted by FactSage™ are consistent with those observed in actual experiments.

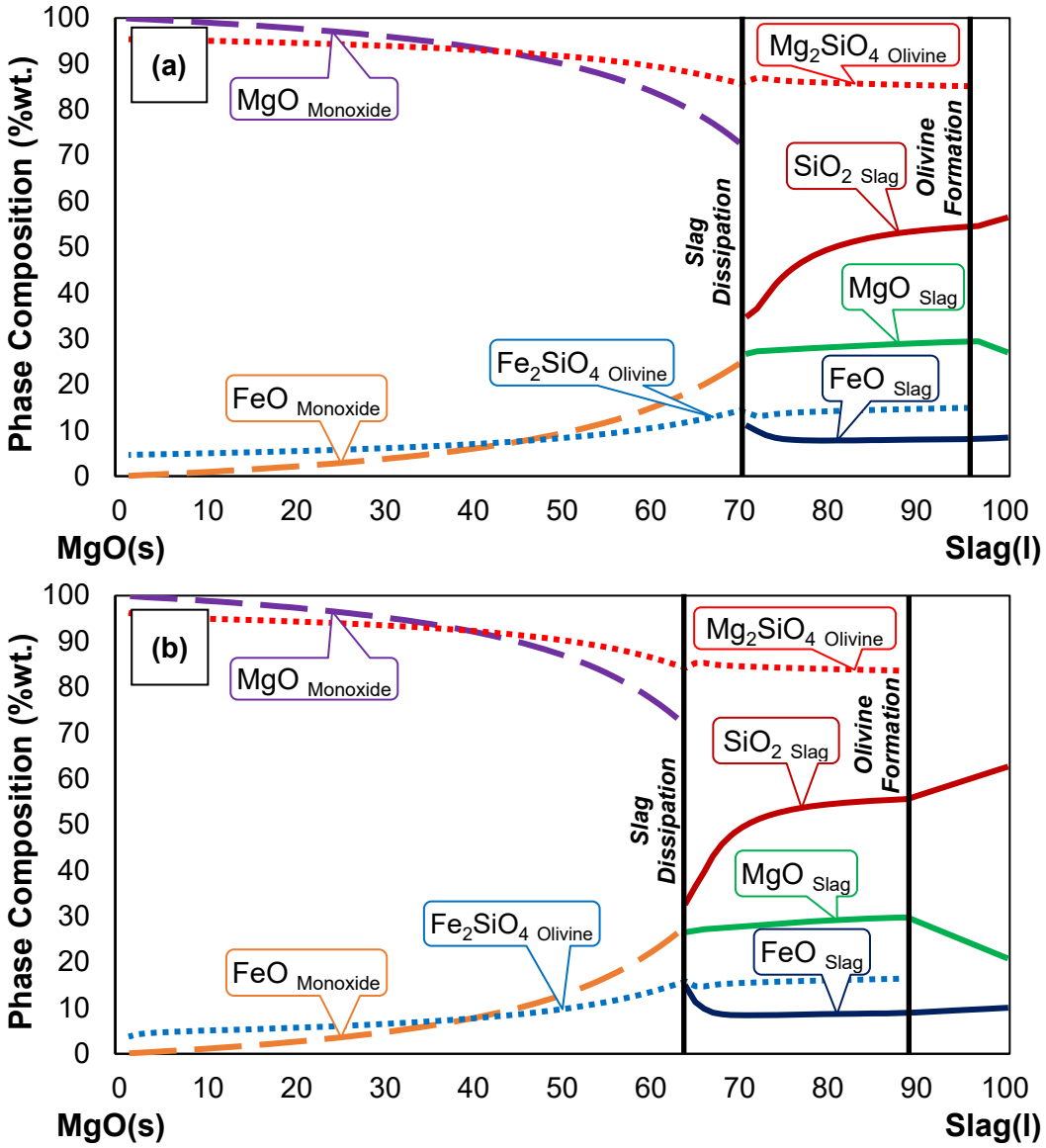

FIG 10 – FactSage™ calculated phase composition from interaction between MgO refractory with slag at 1500°C with initial SiO_2/MgO ratio in slag: (a) 2.00; and (b) 3.00.

The sub-processes involved in refractory corrosion are depicted in Figure 11. Mass transfer of slag components such as FeO and SiO_2 (step-1) to the refractory-slag interface, and MgO (step-6) from the interface can occur due to the concentration gradient between bulk slag and the interface. Contact between FeO from the slag and MgO solid can lead to the incorporation of FeO into the MgO solid solution (step-2); later, this can result in solid-state diffusion of FeO within the MgO

refractory (step-3). On the other hand, contact between SiO_2 from the slag and MgO solid (step-4) can lead to the dissolution of MgO into the slag (step-5). Continuous dissolution of MgO into the slag can lead to the saturation of the slag by MgO, which leads to the formation of olivine (step-5b) on the surface of the MgO solid or the formation of olivine crystals within the slag (step-7). The olivine layer protects the MgO refractory from direct contact with SiO_2 but does not hinder the transfer of FeO and MgO via solid-state diffusion through the olivine layer (step-3b and 3c).

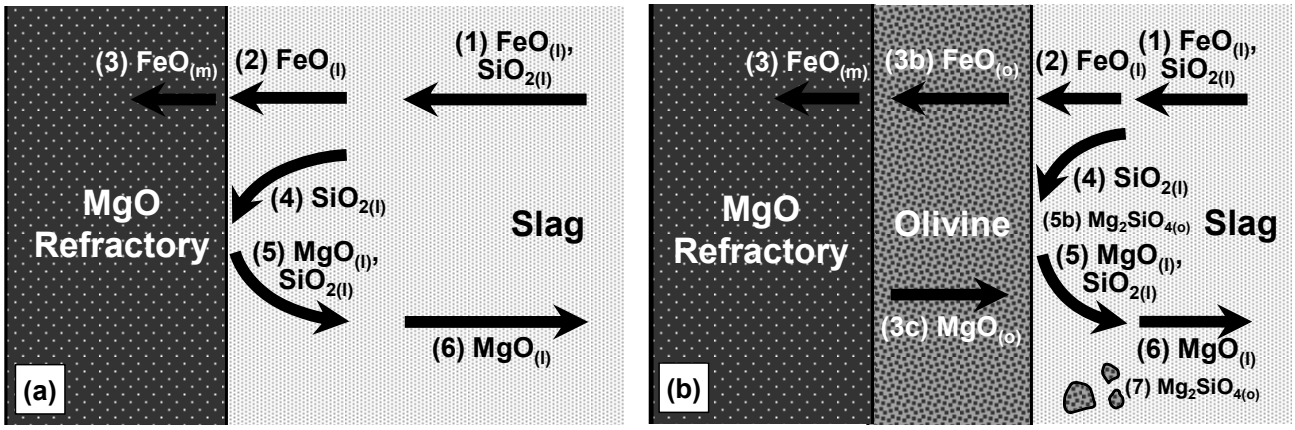

FIG 11 – Mechanism of refractory-slag interaction: (a) without olivine layer; and (b) with olivine layer.

All of the sub-processes in Figure 11 take place simultaneously, and the overall refractory corrosion rate will be controlled by the slowest sub-process. The formation of the olivine layer is expected to minimise the rate of refractory corrosion since it eliminates direct contact/reaction between MgO solid and slag, creating a barrier between the two phases that can only be penetrated by slag components through relatively slow solid-state diffusion. Consequently, the composition of slag in FeNi or NPI smelting must be carefully controlled to aim for the formation of a stable, dense phase that can protect the surface of the MgO refractory and minimise the refractory and slag interaction.

CONCLUSIONS

The interaction between slag and refractory has been examined under conditions relevant to nickel laterite ore smelting. Industrial slag was replicated using synthetic slag, while the actual refractory material was replicated using a dense, pure MgO crucible. The kinetics of the slag-refractory reaction were investigated by conducting experiments at 1500°C for 5, 30, and 120 mins using samples with selected initial S/M ratios in slag of 2.0 and 3.0 (wt/wt) at constant CaO = 3 wt per cent, Al_2O_3 = 5 wt per cent, FeO = 10 wt per cent. The dissolution of MgO into the slag occurs at a rapid rate that within 5 to 30 mins of melting the MgO concentration in slag increases by 2.4 wt per cent and 5.7 wt per cent for initial S/M ratios of 2.0 and 3.0 wt/wt, respectively. The dissolution of MgO is less rapid between 30 and 120 mins, possibly due to a lesser driving force for MgO dissolution as the liquid approaches MgO saturation condition. The slag-refractory interaction was also studied at 1500°C for 120 mins using initial mixtures with different initial SiO_2/MgO (S/M) ratios in slag of 1.75, 2.0, 2.5, and 3.0 (wt/wt). All samples from the 120 mines melting experiments exhibit areas of slag, slag-olivine mixture, and dense MgO. It was found that as the initial S/M ratio of the slag increases, the interaction between the slag and the refractory material becomes more significant, as observed from the increasing dissolution of MgO from the refractory into the slag. A higher S/M ratio in slag also results in a greater extent of solid-state diffusion of FeO into the remaining MgO grains. It is anticipated that the presence of an olivine layer can reduce the rate of corrosion on the refractory material. Therefore, it is crucial to carefully control the slag composition in FeNi or NPI smelting to ensure the formation of a stable and dense protective layer on the surface of the refractory brick.

ACKNOWLEDGEMENTS

The authors would like to acknowledge the support from PT Gunbuster Nickel Industry for providing the Scanning Electron Microscope-Energy Dispersive X-ray Spectroscopy (JCM-7000 NeoScopeTM. JEOL. Tokyo. Japan) used for the analysis of the samples in this work. The authors

would also like to acknowledge the support from the Department of Mineral Sciences of the Smithsonian Institution for providing Basaltic Glass and Springwater Olivine reference materials.

REFERENCES

Crundwell, F, Moats, M, Ramachandran, V, Robinson, T and Davenport, W, 2011. *Extractive Metallurgy of Nickel, Cobalt and Platinum Group Metals* (Elsevier: Amsterdam).

Degel, R, Kempken, J, Kunze, J and König, R, 2007. Design of a modern large capacity FeNi smelting plant, in *INFACON XI*, pp 605–620 (The Indian Ferro Alloy Producers' Association).

Gangler, J J, 1950. Some physical properties of eight refractory oxides and carbides, *Journal of the American Ceramic Society*, 33:367–374.

Huang, S, Xue, J and Wang, Z, 2017. Effect of FeO content in laterite nickel slag on the corrosion behaviour of refractory materials, in *8th International Symposium on High-Temperature Metallurgical Processing*, pp 679–688 (The Minerals, Metals and Materials Society).

Kotzé, I J, 2002. Pilot plant production of ferronickel from nickel oxide ores and dusts in a DC arc furnace, *Minerals Engineering*, 15:1017–1022.

Ruh, E and McDowell, J S, 1962. Thermal conductivity of refractory brick, *The American Ceramic Society*, 45:189–195.

Sagadin, C, Luidold, S, Wagner, C and Wenzl, C, 2016. Melting behaviour of ferronickel slags, *JOM,* 68:3022–3028.

Sagadin, C, Luidold, S, Wenzl, C and Wagner, C, 2017. Evaluation of high temperature refractory corrosion by liquid Al_2O_3–Fe_2O_3–MgO–SiO_2, in *8th International Symposium on High-Temperature Metallurgical Processing*, pp 161–168 (The Minerals, Metals and Materials Society).

Sagadin, C, Luidold, S, Wagner, C and Spanring, A, 2018a. High temperature phase formation at the slag/refractory interphase at ferronickel production, in *Extraction 2018,* pp 137–147 (The Minerals, Metals and Materials Society).

Sagadin, C, Luidold, S, Wagner, C, Spanring, A and Kremmer, T, 2018b. Phase reactions between refractory and high-acidic synthetic CaO-ferronickel slag, *JOM,* 70:34–40.

Sagadin, C, Luidold, S, Wagner, C, Pichler, C, Kreuzer, D, Spanring, A, Antrekowitsch, H, Clarke, A and Clarke, K, 2021. Thermodynamic refractory corrosion model for ferronickel manufacturing, *Metallurgical and Materials Transactions B,* 52:1052–1060.

Wagner, C, Wenzl, C, Gregurek, D, Kreuzer, D, Luidold, S and Schnideritsch, H, 2017. Thermodynamic and experimental investigations of high-temperature refractory corrosion by molten slags, *Metallurgical and Materials Transactions B,* 48:119–131.

Zhang, S and Lee, W E, 2013. Use of phase diagrams in studies of refractories corrosion, *International Materials Reviews*, 45:41–58.

Zhang, S and Lee, W E, 2004. Direct and indirect slag corrosion of oxide and oxide-c refractories, in *VII International Conference on Molten Slags Fluxes and Salts*, pp 309–319 (The South African Institute of Mining and Metallurgy).

AUTHOR INDEX

Abadias Llamas, A 599
Abdeyazdan, H 279
Akhtar, M 287
Akouch, A 663
Al-Harbi, M N 1337
Alvear Flores, G R F 611
Anand, R A 201
Andersson, A 81, 1471
Ang, A 1445
Aoki, H 159
Arkhipin, A S 743
Atmuri, R 705
Attah-Kyei, D 1481
Avarmaa, K 301, 495
Aya, K 17
Baben, M 771
Bai, C 181
Bang, J 313
Barati, M 471
Barrett, N 625
Basu, S 57, 1149
Beckstein, F 517
Bellemans, I 27, 149, 715
Bessada, C 165
Bhaskara Venkata Rao, M 1235
Bielefeldt, W 1087
Biswal, S 1495
Biswas, J 1349, 1571
Biswas, K 1177
Björkvall, J 1395
Boeykens, P-J 27
Borowski, N 663
Borra, C R 101
Brander, L 1471
Brooks, G 301, 495, 569, 965, 1445
Burrows, A 477
Büyükuslu, Ö K 771
Cai, D 1267
Canaguier, V 219
Canizarès, A 165
Cao, G 1325, 1501
Cao, W 73
Cha, W-Y 971
Chatterjee, S 635
Chen, C 433
Chen, J 301, 321, 647, 1029
Chevreux, P 211
Chew, S J 807, 1591
Chinosengwa, S B 1361
Chintinne, M 839
Chiwandika, E K 1135, 1361, 1423
Cho, J W 1007
Cho, Y-M 971
Choe, W O 335
Choi, B 831
Chowdhury, R 781
Chu, R 651
Chung, Y 831
Copland, E 625
Coveney, J 1281
Creedy, S 1281
Cui, Y 1325, 1501
Dandi, S 1361
De Staercke, T 141
Degel, R 663
Deng, T 585
Deng, X 651
Diao, J 353
Diaz, F 1519
Dong, J W 1061
Dong, X F 795, 807
Duchateau, M 211

Duffy, A R 569
Dymov, I M 1187
Eisenbart, B 569
Emami, A 821
Engström, F 1471
Eom, C-H 871
Evans, G 781
Fabritius, T 73
Fadhlurrahman, D 3
Fellicia, D 1445, 1533
Ferreira, R 807
Forzatti, R 847
Friedrich, B 1519
Fukaya, H 1375
Gamutan, J 1375
Gandhre, P 39
Gardin, P 807
Gerald II, R E 117
Gezgin, S 517
Goso, X C 343
Goto, Y 653
Gowravaram, S L A 57
Graf, D 279
Grimsey, D 847, 1281
Grogan, J 279
Gruber, N 979
Gu, H Z 1655
Gu, W F 353
Gui, H P 1325
Gyakwaa, F 73, 81
Hackl, G 839
Haimi, T 997
Hamuyuni, J 997
Hariswijaya, D 361
Hasegawa, M 375, 505
Hayashi, M 389
Hayes, P 3, 321, 1029
Hecker, E 663
Heo, J H 1585
Hidayat, T 1693
Higashi, R 1387
Hogg, B 477, 647
Honeyands, T 625, 781
Hou, P 181
Hovestadt, G 1519
Htet, T 1643
Hu, M 181
Hu, X 1395
Huang, A 1655
Huang, J 117
Huss, J 401, 581
Huttula, M 73
Hyun, S H 1007
Inoue, R 133, 1013
Isaksson, J 81, 1471
Ishfaq, M 413
Ishmurzin, A 839
Iwama, T 133, 1013
Iwami, Y 1387
Jain, M 251
Jak, E 27, 279, 287, 321, 447, 531, 559, 647, 901, 931, 1029
Jakovljevic, K 1401
Jayakumari, S 219
Jayasekara, A 807
Jeon, Y D 871
Jiang, Z 181, 1061
Jianjun, G 1429
Jiao, J 1413
Jokilaakso, A 1481, 1571
Jun, Y J 423, 427
Jung, D Y 427
Jung, I H 313, 335, 857
Jung, S 1553
Kado, N 1013
Kamaraj, A 1235, 1621
Kan, T 433
Kandalam, A 599

Kang, S C 427
Kang, Y 91, 427, 487, 915, 971, 1603
Kar, M K 1543
Karimi-Sibaki, E 239
Karosiya, S 251
Kawanishi, S 653
Khadhraoui, S 663
Kharicha, A 239, 839
Khartcyzov, G 447
Kim, E 231
Kim, H 459, 671, 685, 1565
Kim, J K 261
Kim, K S 871
Kim, M 231
Kim, R R 1565
Kim, S J 1553
Kim, S W 1553
Kim, W-Y 487
King, G 73
Kirmse, C 663
Klaffenbach, E 1231
Klemettinen, A 1571
Klemettinen, L 1349, 1481, 1571
Kojola, N 401
Kon, T 675
Kondratiev, A 725, 743
Krupnov, L V 1187
Kumar, D 251, 1169, 1665
Kumar, N 857
Kumar, P 1077
Kumar, R 1621
Kumar, S 251, 1665
Laidens, B 1087
Latacz, D 1519
Lee, H 91, 831
Lee, J 231, 459
Lee, M J 427, 1117, 1585
Lee, S 1109
Lennartsson, A 81, 1471
Li, B 1325, 1501
Li, S 1305, 1655
Li, X 651
Li, Y M 1061
Li, Z 267, 1123, 1643
Liang, W 705
Lichtinger, A 517
Lindberg, D 1349, 1455, 1481
Lindgren, M 997
Ling, X 471
Lisova, L 949
Liu, Y 705
Longbottom, R J 1591
Lu, L 165
Ludwig, A 839
Lv, Z 1305
Ma, X 735
Mahboob Basha, S 1235
Malakhov, P V 1187
Malan, W 1349
Maritsa, S 1135, 1423
Martinsson, J 581
Maruoka, D 1387
Masamvu, M J 1361
Maslov, A 715
Masuka, S M 1135, 1361, 1423
Medovar, L 949, 1429
Mendoza, O J 477
Michelic, S K 239, 1195
Midhun, P M 1149
Miki, T 1375
Mita, Y 133
Mitra, S 625, 781
Mohanasundaram, M 1621
Moiseev, A E 725
Monaghan, B J 781, 795, 807, 1591
Montenegro, V 1231
Moosavi-Khoonsari, E 471
Morita, K 159

Mu, W 1169, 1259
Muhmood, L 39
Mukhlis, R Z 1533, 1675
Müller, A 1231
Müller, M 517
Murakami, T 1387
Nahian, M K 895
Nakashima, K 17
Nakayama, A 159
Natsui, S 653
Nekhoroshev, E 901, 931, 1029
Nell, J 343
Ni, H W 1259
Nicol, S 477, 647
Nigam, A 1177
Nikolic, S 477, 647
Nogami, H 653
O'Brien, H 1571
O'Dea, D 625
O'Malley, R J 117
Ohno, K 675
Ostrovski, O 1267
Pahlevani, F 1495
Pakhomov, R A 1187
Palai, P 101
Palanisamy, S 1445, 1533
Panda, S K 635
Pande, M M 201, 251, 413
Park, G H 423
Park, H S 1565
Park, J 231, 261, 423, 427, 459, 1117, 1169, 1565, 1585, 1603, 1603
Park, K S 261
Park, S J 427
Park, Y-J 487, 915
Partinen, J 1571
Pastor-Vallés, E 1609
Petersen, J 343
Petersen, S 771
Petrus, H T B M 495
Pettersen, J B 1609
Pihlasalo, J 997
Pinson, D 807, 1591
Pistorius, P C 1249, 1337
Polkowski, W 1413
Pownceby, M I 1445, 1533
Pradana, A D 1693
Pradana, D R 1693
Prasad, R 705
Preisser, N 1195
Putera, A 301, 495
Putra, Y H 1693
Qi, J 517
Qin, H 353
Qin, S 1123
Ranjan, M 101
Rapp, D 517
Reddy, R G 189, 895, 923, 1205
Ren, M M 1325
Reuter, M 663
Rhamdhani, M A 301, 495, 569, 1445, 1533, 1675
Rich, A 847, 1281
Rimal, V 1217
Ringdalen, E 219
Rodrigues, C M G 839
Roos, Å 1471
Safarian, J 361, 759, 1077, 1543
Sahajwalla, V 1495
Sahoo, P P 101
Saito, K 375, 505
Saito, N 17
Samuelsson, C 81
Sander, T 117
Sarkar, R 1177
Sarmadi, N 1495
Sartor, G 847
Sasaki, Y 353

Satritama, B 1445
Scheunis, L 27
Schickbichler, M 239
Schmidt, A 1231
Scimone, D 781
Sergeev, D 517
Serp, S 211
Sert, D 807
Seveno, D 715
Sharma, A 251
Shaw, M G 569
Shen, C 1169
Shevchenko, M 27, 279, 287, 447, 531, 559, 901, 931, 1029
Shibata, H 1259
Shim, S-C 91
Shin, H 91
Shishin, D 531, 559, 901, 931, 1029
Shrotri, V 39
Shu, Q 73, 81, 585
Shukla, A K 569
Simbi, D 1423
Simkhada, N 1401
Sineva, S 559
Singh, H 73
Singh, S P 569
Smith, J D 117
Sohn, I 1109
Sommerfeld, M 1519
Song, B 585
Song, J 1305
Soumya Varanasi, S 1235
Souza, D 1087
Soylu, E 1631
Specht, A 1231
Sripushpa, K 1235
Starykh, R 27
Stepanenko, D 949
Stovpchenko, G 949, 1429
Su, P 1249
Su, Y 261
Suh, I-K 231
Sukenaga, S 1259
Sukhomlinov, D 1349, 1481
Sumita, T 17
Sun, M J 671, 685
Sundqvist Ökvist, L 1395
Susa, M 389
Suzuki, M 107
Takahashi, A 389
Takahashi, J 653
Tang, F 771
Tang, K 165, 735
Tang, X 165
Tang, Y 821
Tangstad, M 691, 1217, 1413
Taskinen, P 1455, 1481
Tekle, H 117
Tesfaye, F 997
Tian, H 1297
Tian, J L 1061
Tikare, P 1621
Tiljander, M 1481
Togobitskaya, D 949
Tomas da Rocha, L 1553
Tranell, G 691, 735, 1401, 1609, 1631
Uchisawa, Y 389
Udayakumar, S 1495
Ueda, S 133, 353, 1013
Vallejo-Olivares, A 1609
Vallo, K 997
Van den Bulck, A 27, 141, 149
van der Sluijs, S 821
van Ende, M 635, 821, 857
Van Rompaey, T 141
Verbeken, K 27, 149, 715
Vergote, O 149
Vickerfält, A 401, 581

Viswanathan, N N 201, 251, 1665
Voller, N 839
Wallin, M 1401, 1413
Wan, S 165
Wang, C 1297
Wang, D 585
Wang, G H 1325
Wang, J 1501
Wang, Q 1169, 1267
Wang, S 73
Wang, Y 1259
Wang, Z 1297, 1325
Watanabe, T 389
Webler, B A 1249
Wen, J 181
White, M 847
Williams, M A 1123
Wilson, P 1123
Wingate, E 705
Winkler, S 1231
Wood, J 1281
Wu, M 839
Xuan, C 1169
Yahya, A 923
Yamada, S 159
Yan, B 585
Yan, Z 267, 1123, 1643
Yang, M 267
Yang, X 1123, 1465
Yoon, C M 871
You, J 165, 735
Yu, H F 353
Yu, W 181
Yuan, H 1297
Yue, S 1501
Yusuf, T 663
Zhang, B 117
Zhang, C 1267
Zhang, F 165
Zhang, H 1259, 1305
Zhang, J 1267, 1571
Zhang, Q 165
Zhang, S 1643
Zhang, T 1123
Zhang, Y 1297, 1315
Zhang, Z 189
Zhao, J 1325, 1501
Zhao, Z 1315
Zheng, J 1501
Zhomin, G M 743
Zhu, M 735, 759, 1401
Zhuo, Q 1337
Zietsman, J H 877
Zong, H 1501
Zschiesche, C 599
Zulhan, Z 1693
Zulli, P 795, 807
Zummar, S 141